THERMODYNAMICS AND KINETICS OF HYDROPHOBIC ORGANIC COMPOUND SORPTION IN NATURAL SORBENTS AND QUANTIFICATION OF BLACK CARBON BY ELECTRON MICROSCOPY

by

Dave T. F. Kuo

M.A.Sc., Chemical Engineering and Applied Chemistry, University of Toronto, 2002
B.A.Sc., Chemical Engineering and Applied Chemistry, University of Toronto, 2001

Submitted to the Department of Civil and Environmental Engineering
In Partial Fulfillment of the Requirements for the Degree of

Doctor of Philosophy
in the field of Civil and Environmental Engineering

at the

MASSACHUSETTS INSTITUTE OF TECHNOLOGY

June 2010

© 2010 Massachusetts Institute of Technology. All rights reserved.

MASSACHUSETTS INSTITUTE OF TECHNOLOGY
JUL 15 2010
LIBRARIES

ARCHIVES
Vol. 1

Signature of Author _____
Department of Civil and Environmental Engineering
April 7, 2010

Certified by _____
Philip M. Gschwend
Professor of Civil and Environmental Engineering
Thesis Supervisor

Accepted by _____
Daniele Veneziano
Chairman, Departmental Committee for Graduate Studies

Thermodynamics and Kinetics of Hydrophobic Organic Compound Sorption in Natural Sorbents and Quantification of Black Carbon by Electron Microscopy

By
Dave T. F. Kuo

Submitted to the Department of Civil and Environmental Engineering
April 7, 2010 in Partial Fulfillment
of the Requirements for the Degree of
Doctor of Philosophy in the field of Civil and Environmental Engineering

Abstract

The sorption behaviors of hydrophobic organic compounds (HOCs) in sediments were investigated using pyrene. Native pyrene desorbed slowly, taking from weeks to months to equilibrate. The end-point data suggested that, at nanogram-pyrene-per-liter porewater levels, sorption was much stronger than conventionally expected. The non-linearity of the isotherm may indicate physical occlusion of native sorbate and/or sorption onto micropore surfaces of char/charcoal. Between 30–70% of the native pyrene may be occluded. Conceptual pictures for both hypotheses were presented with supportive evidence from experiments and literature. Analysis of experimental and literature data suggested $\log K_{OC}$ (organic-carbon normalized partition coefficient) and $\log K_{BC}$ (black-carbon normalized partition coefficient) values were fairly constant across different geosorbents (around 4.5–5.7 and 5.6–6.3, respectively), while the non-linearity exponent varied substantially. This may explain the orders of magnitude scatter in $\log K_{OC}$'s and $\log K_{BC}$'s reported in recent reviews.

An *a priori* non-linear numerical model based on Intra-particle Porewater Diffusion (IPD) was constructed and successfully predicted the desorption kinetics of native pyrene. Fitted kinetic parameters correlated with system and sorbate/sorbent properties. This suggested the empirical approach can be replaced by the *a priori* model and the diverse HOC desorption rates in the literature can be reconciled if relevant physicochemical properties are known.

The regional fate of pyrene in Boston Harbor was evaluated with a box model using derived kinetic and equilibrium properties. Realistic predictions can be obtained when assuming pseudo steady state conditions, but not equilibrium partitioning, for the bed sediment and the water column. Furthermore, model results and literature evidence suggested that sediment resuspension may be a significant mobilization mechanism for sedimentary HOCs in estuaries and harbors.

A new BC quantification method based on energy dispersive X-ray spectroscopy (EDX) was developed. The method identified/quantified Organic Carbon (OC) or Black Carbon (BC) by analyzing the elemental ratios of C, N, and O of the sample. Agreeable OC/BC estimates on a variety of carbonaceous materials were obtained using the method. The good analytical potential of the method warranted further exploration and methodological refinement.

This study has great implications for the sequestration and bioavailability of HOCs in the environment.

Thesis Supervisor: Philip M. Gschwend
Title: Professor of Civil and Environmental Engineering

Acknowledgments

I would like to thank: my advisor Prof. Phil Gschwend for allowing me to work on this project, especially with the rare opportunity to learn and use analytical electron microscopy, and I am very grateful for his support and guidance through the years; Prof. Robert Chen, at University of Massachusetts Boston, for letting me to access the LIF system, without which much of this work would be difficult; Prof. Charles Harvey and Prof. John Vandersande for overseeing my research progress as my thesis committee members, and giving me much advice and insights regarding modeling and electron microscopy.

I am grateful to Dr. Anthony Garrett-Reed, Dr. Yong Zhang, and Patrick Boisvert of the electron microscopy facility at the Center for Materials Science, MIT, for providing training and assistance in using HB603 VG-STEM, JEOL 200CX, JEOL 2010FEG, FEI/Philips XL30 FEG ESEM, ion miller and microtome. In particular, Dr. Yong Zhang has helped me tremendously with JEOL 2010FEG.

I am greatly indebted to: John MacFarlane, who has taught me all the analytical techniques for organic chemistry as well as lab instrumentation, and has given me much encouragement throughout the years; Dr. Steven Rudnick, who has helped me with the maintenance on the LIF system.

The many 'supergroup' meetings have been very beneficial for my own intellectual and personal growth. These were the occasions where I learned the secrets in asking good questions and making good presentations. For that, I thank Prof. Harry Hemond, Sarah-Jane White, Amy Mueller, Matthew Orosz, Schuyler Senft-Grupp, Charu Varadharajan, Rebecca Neumann, Hanan Karam, Xanat Flores-Cervantes, Loretta Fernandez, Desiree Plata, Dave Griffith, Elizabeth Finn, Alexandra Tcaciuc.

I'll also miss the greater Parsons community very much: Sheila Frankel, Vicky Murphy, Sheila Anderson, Jim Long; Mack Durham, Gift Piyatida, Marcos, Kathryn Kauffman, and many other folks.

I want to share the completion of this work with my family – My father and my stepmother have been very supportive throughout the years; my grandmother, almost 90 years old, who has, on several occasion, inquired about the exact nature of my research; my mother and grandfather, who have not lived to see what I have been doing, but have helped me with many good memories. I am also very grateful to the continual encouragement and support from a few friends from across the Pacific: Sara, Wei-mei, Carrie and Jing-wu.

Thermodynamics and Kinetics of Hydrophobic Organic Compound Sorption in Natural Sorbents and Quantification of Black Carbon by Electron Microscopy

Volume I

Text

TABLE OF CONTENT

VOLUME I (TEXT)

Chapter 1: General Introduction 15
Chapter 2: Desorption of Native Pyrene at Minute- to Month-Timescales by Time-Gated Fluorescence Spectroscopy 33
Chapter 3: Equilibration of HOC Partitioning in Sediment-Water System 51
Chapter 4: Enhanced Pyrene Sorption at Environmentally Relevant Concentrations 73
Chapter 5: Pyrene Sorption Isotherm 101
Chapter 6: Thermodynamics of Absorption and Adsorption 125
Chapter 7: Desorption Kinetics of Native Sedimentary Pyrene – Mechanistic Modeling & Prediction 147
Chapter 8: Intraparticle Porewater Diffusion Model: General Application and Particular Scenarios 193
Chapter 9: Regional Modeling of Pyrene in Harbors & Estuaries 219
Chapter 10: Quantification of Organic Carbons & Black Carbons by EDX and STEM-EDX 245
Chapter 11: Conclusion 287

VOLUME II (FIGURES AND TABLES)

FIGURES

Chapter 1 301
Chapter 2 313
Chapter 3 325
Chapter 4 341
Chapter 5 368
Chapter 6 388
Chapter 7 393
Chapter 8 427
Chapter 9 454
Chapter 10 475

Chapter 11 533

TABLES

Chapter 1 536
Chapter 2 543
Chapter 3 549
Chapter 4 555
Chapter 5 562
Chapter 6 576
Chapter 7 584
Chapter 8 601
Chapter 9 606
Chapter 10 613

VOLUME III (APPENDICES AND REFERENCE)

APPENDICES

Chapter 2 624
Chapter 3 628
Chapter 4 650
Chapter 5 668
Chapter 6 766
Chapter 7 790
Chapter 8 902
Chapter 9 928
Chapter 10 966
Appendix A: EDX (Spot) Spectra 1000
Appendix B: STEM-EDX Elemental Maps 1036
Appendix C: STEM-EDX Mapping Scripts 1094
Appendix D: Isotherm Regression Scripts 1106
Appendix E: Desorption Kinetics Scripts 1112
Appendix F: Quantification of Black Carbons by EELS and STEM-EELS 1168
Appendix G: EELS Mapping Scripts 1192
Reference 1198

TECHNICAL INDEX

Black carbon: BC quantification methods (literature) - **Ch.1 §4.4, Fig 1-14**; BC content in sediment samples - **Tab 3-1 & 4-2**; See also under Carbonaceous materials.

Box model (regional): Bed-water pyrene profiles - **Fig 9-9 & 9-10**; Boston Harbor map - **Fig 9-4, App 9-10**; Characteristic timescales of processes in Boston Harbor - **Ch.9 §2.1, Tab 9-1**; Equilibrium partitioning model (EqP) - **Ch.9 §2.2, 3.2 & 3.3, Fig 9-2, 9-5 to 9-8, Tab 9-4 & 9-5**; Model condition summary - **Tab 9-2 & 9-3**; Model limitations - **Ch.9 §3.7**; PAH distribution in sediment size fractions (literature & this study) - **Fig 9-17**; Processes contributing to sediment-bed porewater flushing - **Fig 9-19**; Pyrene inventory in Boston Harbor - **Fig 9-4**; Steady state model (3-rate) - **Ch.9 §2.3, 2.3.2, 3.4, Fig 9-11**; Steady state model (3-rate) - **Ch.9 §2.3, 2.3.3, 3.5, Fig 9-12 to 9-16, & 9-18**.

Carbonaceous materials: BC quantification methods (literature) - **Ch.1 §4.4, Fig 1-14**; BC/EC continuum (literature) - **Ch.1 §4.3, Fig 1-10 to 1-13**; BC/EC production & sources - **Ch.1 §4.2**; Densities of various materials - **App 10-10**; Elemental atomic ratios of various carbonaceous materials - **Fig 10-30, Tab 10-9**; OC contents in typical soils and sediments - **App 7-22**; Pore distribution in soot, charcoal & activated carbon - **Tab 4-4**; Soft vs Hard Carbon - **Tab 1-6**; Structures of lignin, soot & coal - **Fig 10-31 to 10-33**; Surface areas of various condensed carbonaceous materials - **Tab 4-3**.

Electron Microscopy (EM: EDX & EELS): BC quantification by point-EDX elemental ratio - **Ch.10 §3.3, Fig 10-8, 10-11 to 10-13, 10-17 & 10-18, Tab 10-4, App A**; BC quantification by STEM-EDX mapping - **Ch.10 §3.4, Fig 10-20 to 10-29, Tab 10-6 to 10-8, App B**; Data processing - **Ch.10 §2.4, App C (for EDX) & App F (for EELS)**; EELS - **App F, App G**; Hydrocarbon contamination - **Fig 10-9**; Soot TEM images - **Fig 10-5 & 10-7**; Specimen preparation - **Ch.10 §2.2**; Specimen summary – **Ch.10 §2.1, Tab 10-4, 10-6 to 10-8**.

Enhanced sorption at ng/L levels: At different temperatures - **Fig 4-3**; Comparison with current OC-BC models - **Fig 4-10**; Core-derived pyrene 'sorption isotherm' - **Fig 4-8**; Enhanced sorption at ng/L levels, pyrene - **Fig 4-2, 4-3, 4-7**; High-affinity micropore surface adsorption - **Ch.4 §3.4.3, Fig 4-14**; Occlusion mechanisms - **Ch.4 §3.4.2, Fig 4-11 & 4-12**; Testing occlusion hypothesis - **Ch.4 §3.5**.

Enthalpies & entropies (*sorption, adsorption, absorption*) (Ch.6): ΔH & ΔS for PAH phase changes (dissolution, fusion, sublimation, vaporization) - **Tab 6-5**; $\Delta H_{d,app}$ for pyrene (this study) - **Tab 6-2**; $\Delta H_{d,app}$ for HOCs (literature) - **Tab 6-3**; $\Delta S_{d,app}$ for pyrene (this study) - **Tab 6-4**; Mole fraction of adsorbate - **Ch.6 §2.1.4.1**; Non-idealities of adsorption onto geosorbents - **Fig 6-1**; Summary of ΔG and K^x for overall sorption, absorption, and adsorption - **Tab 6-1**; Summary of ΔH and ΔS for pyrene sorption, adsorption, and absorption - **Tab 6-6**.

Equilibrium, sorption: Criteria for equilibrium model - **Tab 1-5**; Equilibration time (general HOCs) - **Ch.3 §3.2, Fig 3-13, Tab 3-2, & 3-4, App 3-6**; Equilibration time ($\tau_{95\%}$, linear sorption) - **Fig 3-13**; Factors influencing equilibration - **Tab 3-3**; General guideline for sufficient equilibration - **Ch.3 §3.2.3**; Pyrene equilibration time (this study) - **Ch.3 §3.1, Fig 3-3 to 3-12, App 3-3 & 3-5**.

Experimental setup & conditions: Adsorption equilibrium experiment - **Ch.3 §2.2.1, Tab 3-1**; Conditions (sorbent & system properties) - **Tab 3-1**; Desorption kinetic experiments - **Ch.2 §2.3, Ch.3 §2.2.2 & 2.2.3, Tab 3-1**; PE-sediment-water desorption experiment - **Ch.4 §2.2, Tab 4-5**.

High-affinity micropore surface adsorption: Adsorption at various pore surface (summary) - **Fig 4-14**; Estimated adsorption capacity in char/charcoal - **App 4-4**.

HOCs: PAH adverse effects - **Ch.1 §2.1, Tab 1-4**; Dissolved PAH and pyrene concentrations in natural waters - **Tab 4-1** ; Sedimentary ΣPAHs concentration - **Fig 1-4, Tab 1-1**; Sedimentary quality guidelines - **Tab 1-2**.

Isotherm: Form, composite - **Ch.5 §2.2, Tab 5-1**; Form, singular - **Ch.5 §2.1**; Native vs equilibrium pyrene - **Fig 5-2 & 5-3, App 5-1 & 5-2**; Rationale for composite forms - **Ch.5 §3.1.2, Fig 5-2 & 5-3**; Regression codes (Matlab) - **App D**; Regression by composite form - **Ch.5 §3.1.2, Fig 5-4 & 5-5, Tab 5-2, App 5**; Regression by singular form - **Ch.5 §3.1.1, Fig 4-4 & 4-5**; Regressed parameters - **Tab 5-2 & 5-3**.

Kinetic model (Ch.7 & 8): *A priori* predictions - **Ch.7 §4.3.1, Fig 7-15 to 7-20** ; BC in aggregates - **Ch.7 §3.1.1, Fig 7-1**; Best-fit modeling - **Ch.7 §4.3.2, Fig 7-21 & 7-22**; Boundary layer δ - **Ch.8 §2.1, Fig 8-1**; Char-silt dual domain - **Ch.8 §2.2, Fig 8-2 & 8-3, 8-17 to 8-24, App E**; Concentration profile within aggregate over time - **Fig 8-6, 8-18, 8-19**; Desorption activation energy, pyrene - **App 7-25**; Empirical kinetic regression codes (Matlab) - **App E**; Empirical vs mechanistic predictions - **Ch.7 §4.4, Fig 7-23 to 7-25,** ; Half-lives of pyrene desorption (this study) - **Tab 7-9**; Infinite bath (linear K_d) - **Fig 8-7**; Infinite bath (non-linear) - **Fig 8-8 to 8-12, 8-22 to 8-25, App E**; Intraparticular Porewater Diffusion Model (Concept) - **Ch.7 §3.3, Fig 7-3**; Intraparticular Porewater Diffusion Model (Finite difference scheme) - **Ch.7 §3.6, Fig 7-8 & 7-9, App E**; Intraparticular Porewater Diffusion Model (Mathematics) - **Ch.7 §3.5**; Modeled isotherms - **Ch.7 §3.7, Tab 7-2**; Modeling conditions (summary) - **Tab 7-3**; Regression of desorption kinetic data - **Ch.7 §3.8, Tab 7-11 & 7-12, App 7-19 & 7-21**; Regression of desorption kinetic data (literature) - **Tab 7-13**; Sensitivity analysis (summary) - **Tab 7-4 & 7-5, App 7-2 to 7-9**; Transport within aggregates (survey & discussion) - **Ch.7 §3.2 & 3.2, Fig 7-4 to 7-7, Tab 7-6**; Validation (Finite bath, homogeneous) - **Ch.7 §4.2, Fig 7-10 to 7-14, Tab 7-10**; Validation (Infinite bath) - **Ch.8 §3.1, Fig 8-4, Tab 8-1**; Validation (Char-Silt, dual-domain) - **Ch.8 §3.2, Fig 8-5 & 8-6**.

LIF (Ch.2): Calibration (pyrene) - **Fig 3-1**; Experimental setup & procedure - **§2.2 & 2.3**; Inner-filtering correction - **§3.1.1 ,Tab 2-4**; Instrumentation - **§2.2, Fig 2-1**; Method validation - **§3.1, Fig 2-3 to 2-6, Fig 2-8, Tab 2-5**; Pyrene fluorescence emission spectrum **Fig 2-2, Tab 2-1**; Signal Processing - **§2.2.3, App 2-2**; Uncertainties & error analysis - **Ch.2 §2.2.2, Ch.3 §2.4, Tab 3-1**.

Non-linearity, sorption: dependence of n_{Fr} on adsorption site occupancy - **Ch.5 §3.2.2.3 & 3.2.2.4, Fig 5-7**. See also under Isotherm and Enhanced sorption at ng/L levels.

Occlusion: fraction occluded estimation - **Ch.4 §3.4.2.5, Ch.5 §3.1.2.6, Fig 4-13, Tab 5-4 (summary)**;

Partition coefficients & n: n in various 'soft' carbonaceous materials - **Tab 5-10**; n_{BC} from various HOC sorption studies - **Tab 5-8**; K_{BC} & n_{BC} (literature) - **Tab 5-7**; K_{OC} and K_{BC} of selected PAHs (for modeling) - **Tab 8-2, App 8-1**; K_{OC} and K_{BC} summary (this study) - **Ch.5 §3.2.1, Tab 5-6, Tab 5-9**; K_{TOC} of various carbonaceous sorbents (literature) - **Tab 5-5**; Summary of K_{OC} & K_{BC} range for pyrene (survey & this study) - **Ch.5 §3.2.2.1, Tab 5-9**; Regionalized Freundlich regression of pyrene sorption isotherm - **Fig 5- 6, App 5-12**; "Universal" pyrene K_{OC} and K_{BC} - **App 7-16, Tab 7-3**; Variation in $\log K_{OW,PAHs}$ - **App 5-10**.

PE-sediment-water desorption experiment: agreement with adsorption experiment - **Fig 4-19**; discussion - **Ch.4 §3.5, Fig 4-15 to 4-20**; estimated equilibration time - **Tab 4-5, App 4-5**; setup & condition - **Ch.4 §2.2, Tab 4-5**.

Pyrene adsorption: Isotherm - **Fig 4-3, 4-6, 4-7, 4-10**; See also under Isotherm and Enhanced sorption at ng/L levels.

Pyrene desorption: Kinetic curve - **Fig 2-9 to 2-11**; Summary of concentrations after desorption - **Tab 2-6**.

Suspended solids: Experimental R_{sw}'s - **Tab 3-1**; Modeling R_{sw}'s - **Tab 7-3 & 8-3**; Suspended solid concentrations in selected water bodies - **Tab 2-7**.

Chapter 1. General Introduction

Table of Content for Chapter 1

1. General Introduction 17

1.1. Cost of Modern Life: More Pollution and Newer Pollutants 17

2. Organic Pollution in Sediments 18

2.1. PAHs & Other HOCs 18

2.2. Two Fundamental Questions for HOCs in the Environment 18

2.2.1. Distribution of HOCs in Environmental Phases/Media 19

2.2.1.1. Absorption into OC (Linear) 19

2.2.1.2. Adsorption onto BC (Non-Linear) 19

2.2.2. Bioavailability of Sedimentary HOCs to Living Organisms 20

2.2.2.1. Bioavailability Assuming Equilibrium Partitioning 20

3. Complexity and Challenges 21

3.1. Why Understanding/Predicting the Fate of HOCs is so Difficult? 21

3.2. The Entangled Factors Influencing HOCs in the Environment 23

3.2.1. Example (I): what causes "Sorption Hysteresis" 23

3.2.2. Example (II): the Dimension of Time 23

4. Characterization of Organic Matter 24

4.1. Dichotomous Divisions of Environmental Organic Matter 24

4.2. Black/Elemental Carbon: Overview 24

4.3. BC/EC: Meta Definition and Physicochemical Continuums 25

4.3.1. Meta-BC/EC 25

4.3.2. Continuums of Meta-BC/EC 25

4.4. Quantification of Environmental BC 26

4.4.1. Variety of BC Quantification Methods 26

4.4.2. No 'Best' Method for Quantifying BC 26

4.4.3. Thermal Oxidation Method (CTO-375°C-24h) for HOC Studies 26

4.4.4. Quantification of BC by Electron Microscopy: a Novel Approach 27

4.4.5. Concluding Statements 27

5. Desorption of HOCs from Geosorbents 28

5.1. Disequilibrium of HOCs in Surficial Sediment 28

5.2. Mobilization of Sedimentary HOCs via Resuspension 28

5.3. Slow Response of Porewater to Influx of Particulate PAHs 28
5.4. Numerical Simulations on the Release of bound-HOCs 28
6. Thesis Objectives 29

1. General Introduction

1.1. Cost of Modern Life: More Pollution and Newer Pollutants

It is no mere coincidence that the most populated/urbanized (Figure 1-1) and wealthiest regions (Figure 1-2) of the Earth should conglomerate along great rivers, estuaries, deltas, and harbors (Figure 1-3). Accessibility to harbors, ports, rivers, and lakes has been a critical geographical factor for the growth and development of cities and civilizations, as it promotes trade, communication, and agriculture.

The extent of aquatic pollution certainly worsened with the advent of industrialization in two ways. Certain 'pollutants', such as polycyclic aromatic hydrocarbons (PAHs), are naturally produced (e.g. PAHs from biomass burning) and are thus present in the environment even in the absence of anthropogenic activities. Industrial activities greatly increased the levels of these organic compounds in natural environment, as evidenced by observations in sediment core studies (Ohta et al. 1983; Yamashita et al. 2000; Donahue et al. 2006; Elmquist et al. 2007). The ability to synthesize, manufacture and applied new chemical compounds in large scale also leads to the exposure of the aquatic systems (and the related ecological systems) to xenobiotic pollutants (that which is 'foreign' to the environment).

Although not all xenobiotics are harmful to the environment, there are some widely applied ones that have been infamous for their persistence and/or toxicity: for example, polychlorinated biphenyls (PCBs), *p,p'*-dichlorodiphenyl trichloroethane (DDT), trichloroethene (TCE), and trinitrotoluene (TNT). The environmental/health impacts of these compounds, as well as those of PAHs, have been the focus of many scientific studies and remediation efforts. Despite the many hard lessons 'taught'/'offered' by these pollutants, it is questionable that humans would/could stop producing another compound whose harm/hazard is not known until many years after its wide spread application when the harm becomes manifested in the least expected fashion (e.g. the impact of DDT on egg shell thickness)[1]. This claim is supported by a plethora of recent lawsuits associated with various xenobiotic pollutants (Table 1-3).

[1] This claim reflects the author's various personal skepticisms: (i) that the ability of Free Market economy to avert harm in the distant future is greatly hampered by the inability to quantify future risk and by the desire for immediate profits, for the 'future' is less quantifiable than the 'immediate', (ii) that most people, 'layman' and 'experts' alike, find a 'solution' with innovative technological basis to be persuasive, (iii) that the individuals tend to lack the critical spirit to question whether the mainstream lifestyle is necessary and suitable for their own happiness, (iv) the current way of measuring economic 'well being' encourages consumerism, which always drives up for newer and 'better' products.

2. Organic Pollution in Sediments

2.1. PAHs & Other HOCs

Sediment is an important compartment of the aquatic ecosystems because it embodies a great biodiversity of microflora, benthic animals and fish communities (Levinton, 2001; Wetzel, 2001). Approximately 10% of the sediment in U.S. surface waters is contaminated with pollutants and poses potential threats to human health and the environment (U.S. EPA, 1998). Roughly 10% of coastal embayments has been found to be toxic to the survival of amphipods (N.O.A.A., 1998). It is also estimated that about 20% of National Priorities List (NPL) sites contain contaminated sediments, and 75% of these sites require costly dredging or excavation[2].

The major contaminants of concern are heavy metals and hydrophobic organic compounds (HOCs). HOCs such as PCBs and PAHs are well-documented for their toxicity, persistence, and bioaccumulation tendency. They are known mutagens and/or carcinogens (Brookes et al. 1979; Neff, 1979; Grimmer, 1983; White, 1986). The adverse effects of HOCs on benthic organisms are also well documented. Some of these impacts are listed in Table 1-4.

PAHs can be released via petroleum usage, produced in the combustion of fossil fuels/biomass and/or industrial operation (e.g. smelting). Their presence is, therefore, indicative of the level of environmental stress imposed by industrial activities and/or urbanization. Furthermore, sediment core studies showed that other persistent HOCs often coexist with PAHs (Yamashita et al. 2000; Ikenaka et al. 2005). Hence, sedimentary PAH level is a good indicator of the extent of organic pollution on harbor or estuarine sediments.

Using sedimentary PAH level as an overall indicator of organic pollution, many water bodies located in/nearby highly industrialized and urbanized regions appear to be impacted by HOC pollution (Figure 1-4; Table 1-1). Many of the listed sites in Table 1-1 contain PAHs at levels exceeding the guideline values recommended by government agencies and/or toxicologists (Table 1-2).

2.2. Two Fundamental Questions for HOCs in the Environment

The survey on sedimentary PAHs clearly suggested that HOC pollution can be significant in many estuarine or river systems. These HOC-contaminated urban/coastal sediments directly affect the well-being of benthic organisms (Table 1-4), and can serve as pollution sources to the overlying water during resuspension events (Ko et al. 1995; Achman et al. 1996; Latimer et al. 1999; Mitra et al. 1999; van Geen et al. 1999; Schneider et al., 2002) even when other pollution sources are terminated (Larsson 1985; Salomons et al. 1987; Burgess et al. 1992). Remedial action for these sites often involves dredging or excavation of the sediment bed — an expensive and time-

[2] *http://www.epa.gov/superfund/resources/sediment/index.htm*

consuming operation. A good understanding of fate of sediment-associated HOCs will help making the appropriate regulatory/engineering decision (e.g., comparing half-life with the estuary flushing half-life). Establishing regulatory standards or permissible levels for sediment-HOCs also requires the knowledge of HOC-bioavailability to benthic organisms (U.S. EPA, 2003; Nat. Acad. Sci., 2003).

Two questions are of scientific, regulatory, and engineering interest: (i) how would HOC be distributed in different phases/media in the environment, and (ii) what would be the actual toxicity of the sedimentary HOC to living organisms?

2.2.1. Distribution of HOCs in Environmental Phases/Media

The knowledge of HOC distribution in different environmental compartments (e.g. water, air, soil/sediment) allows us to assess the fate of the compound.

2.2.1.1. Absorption into OC (Linear)

The distribution of HOCs among different environmental phases/media depends on how strongly they are sorbed to the sedimentary phase. It is generally accepted that the organic components in soil/sediment are responsible for the binding of HOCs (Chiou et al. 1979; Karickhoff et al. 1979; Pignatello and Xing, 1996; Luthy et al. 1997; Allen-King et al. 2002). The equilibrium distribution (or partitioning) of HOCs in solid-water systems was conceptualized as the ***ab***sorption of HOCs into the Organic Carbon phase (OC) in soil or sediment. According to this 'Classical' view, the OC-phase behaves as an energetically uniform 'solvent' in its uptake and association with HOCs. This physicochemical picture was consistent with the linear uptake of various HOCs from aqueous/dissolved phase by natural organic matter (NOM) (Chiou et al., 1979; Karickhoff et al., 1979; Means et al., 1980). This Classical model gave rise to a linear isotherm – a thermodynamic function describing the equilibrium concentrations ratio of the HOC in the two partitioning compartments. In the case of the Classical model, the isotherm takes the following form:

$$K_d \equiv \frac{S_i}{C_{iw}} = f_{OC} K_{OC}$$

Eqn. 1 - 1

where C_{iw} is the aqueous phase concentration of sorbate i ($\mu g_i/L_w$),

f_{OC} is mass fraction of organic carbon in the solid phase (g_{OC}/g_{solids}),

K_d is the solid-to-water partitioning coefficient/constant for sorbate i (L_w/kg_{solids}),

K_{OC} is the OC-normalized partition coefficient for sorbate i (L_w/kg_{OC}),

S_i is the solid phase concentration of sorbate i ($\mu g_i/kg_{solids}$).

2.2.1.2. Adsorption onto BC (Non-Linear)

Non-linear equilibrium partitioning of HOCs between natural solids and aqueous phase, with the isotherm function modeled by the Freundlich or the Langmuir form, was later

revealed (Miller et al. 1986; Farrell et al. 1994; Huang et al. 1997b). Studies demonstrated that the ubiquitous presence of a recalcitrant and structurally rigid carbon phase in natural solids (i.e. soils/sediments) (Gustafsson et al. 1997; Cornelissen et al. 2005b). This recalcitrant carbonaceous phase, hereafter referred as Black Carbon (BC), exerts a much stronger sorption affinity for HOCs than OC (Gustafsson et al. 1997; Accardi-Dey and Gschwend 2002, 2003). HOCs are associated to BC via ***ad***sorption to the structurally condensed carbon surface (e.g. aromatic, graphitic). The non-linear isotherms observed for BC (Huang et al 1997b; Accardi-Dey and Gschwend 2002) may be interpreted as a consequence of the surface having a distribution of binding energies (Adamson et al. 1997). The revised isotherm now assumes a dual-domain form (Accardi-Dey and Gschwend 2002):

$$K_d \equiv \frac{S_i}{C_{iw}} = f_{OC} K_{OC} + f_{BC} K_{BC} C_{iw}^{(n_{BC}-1)}$$

Eqn. 1 - 2

where f_{BC} is mass fraction of black carbon in the solid phase (g_{BC}/g_{solids}),

K_{BC} is the BC-normalized partitioning coefficient/constant for sorbate i $(\mu g_i/kg_{BC})(L_w/\mu g_i)^{nBC}$,

n_{BC} is the Freundlich exponent (dimensionless).

Although typically a small fraction of the total organic carbon (TOC) of the sample (Cornelissen et al. 2005b), BC exhibits great affinity for HOCs. BC is ~100 times more effective than OC in sorbing HOCs from aqueous phase (Gustafsson et al. 1997; Kleineidam et al. 1999; Karapanagioti et al. 2000; Bucheli et al. 2000; Accardi-Dey and Gschwend 2002). This has also been supported by other studies showing the apolar HOCs sorbed to natural solids are predominantly associated with BC. This has been demonstrated for PAHs and PCBs (Ghosh et al. 2000, 2003; Adams 2003; Hong et al. 2003), diuron (Yang et al. 2003), polychlorinated dibenzo-*p*-dioxins (PCDDs) and polychlorinated dibenzofurans (PCDFs) (Barring et al., 2002; Lohmann et al., 2005).

2.2.2. Bioavailability of Sedimentary HOCs to Living Organisms

The toxicological effect of a contaminated sediment is a function of (i) the intrinsic toxicity of the compound, (ii) the availability of the compound to living organisms, (iii) the exposure time (e.g. single vs chronic exposure), and (iv) the physicochemical properties of the organism of concern (e.g. body weight, lipid/protein content). The intrinsic toxicity and the dependence on dosage and exposure time can be understood/quantified through toxicological experiments; what is more difficult is to determine the bioavailability of the sediment-bound HOCs – how much of it is truly available to the living organisms of concern.

2.2.2.1. Bioavailability Assuming Equilibrium Partitioning

One way to assess sediment-associated HOC bioavailability is by assuming equilibrium partitioning (EqP) of HOCs among the sediment, interstitial water, and benthic organism compartments. This implies (1) that all three compartments have identical HOC activity,

and (2) that HOC concentrations of the other two compartments can be inferred/predicted from a known concentration in the third compartment. One application of EqP theory is the equilibrium partitioning sediment benchmarks (ESBs) established by EPA for the protection of benthic organisms from PAHs (U.S. EPA, 2003).

A common measure of the bioavailability of solid-associated HOCs is the *biota-sediment (or biota-soil) accumulation factors* (BSAFs), which is the ratio of HOC concentration in the lipid phase to that in the organic carbon phase of the solid (Schwarzenbach et al., 2003):

$$\mathrm{BSAF} \equiv \frac{S_{i,lipid}}{S_{i,OC}} = K_{i,lipid-OC}$$

Eqn. 1 - 3

where $K_{i,lipid-OC}$ is the lipid-to-OC partition coefficient for the sorbate i (kg_{OC}/kg_{lipid}),

$S_{i,lipid}$ is concentration of i in the lipid phase of the organism ($\mu g_i/kg_{lipid}$),

$S_{i,OC}$ is concentration of i in the OC phase of the sediment ($\mu g_i/kg_{OC}$).

BSAF data and literature studies strongly suggest that the assumption of equilibrium partitioning is often inappropriate for persistent HOCs in sediment-water-biota systems. If EqP applies, the measured BSAF should match the lipid-organic carbon partition constant, K_{lip-oc}, or $BSAF/K_{lip-oc}$ should be equal to 1. This is not the case as shown in Figure 1-5. The same trend has been observed in other studies (Krauss et al., 2000; Matschenko et al., 2002; Kraaij et al., 2002a; Jager et al., 2003). With $BSAF/K_{i,lip-oc/om} < 1$, HOC-activity is higher in sediment/soil than in the biota. This means that HOCs are often still desorbing from the contaminated sediment. The hypothesis of sedimentary/soil-HOC bioavailability being controlled by their desorption kinetics is also supported by a number of independent studies on the uptake/degradation of HOCs by various organisms (White et al. 1996; Guerin et al. 1997; Cornelissen et al. 1998; Lamoureux et al. 1999; Kraaij et al. 2002a;; Guthrie-Nichols et al., 2003; Shor et al., 2003).

3. Complexity and Challenges

3.1. Why Understanding/Predicting the Fate of HOCs is so Difficult?

However, in reality, both the distributions and bioavailabilities of HOCs in polluted soils/sediments are rather difficult to assess. On the question of distribution, the recent reviews by Hawthorne et al. (2006, 2007) concluded that the partition coefficients K_{OC}'s and K_{BC}'s are widely distributed (3–4 orders of magnitude) for PAHs. In another review by Arp et al. (2009), the level of uncertainty in predicting dissolved phase HOC concentration is reduced to 30 times, and concluded that "...*the only way to accurately*

obtain accurate porewater concentrations is to measure them directly, and not infer them from sediment concentrations." (Arp et al. 2009). Since the release kinetics of the sorbed HOCs largely controls their bioavailability (section 2.2.2.1), the question of bioavailability can be solved if we can predict/understand the rate of desorption. Birdwell et al. (2007) reviewed much of the available HOC desorption kinetic data. They attempted to relate the rate constant of desorption, k_{des}, to the chemical properties of the sorbate but were unsuccessful. The failure in the predicting K_{OC}/K_{BC} or k_{des} is very disheartening considering that the chemistry of HOCs in natural geosorbents has been studied for over three decades, with tens of thousands of publications produced (nearly 20000 articles just for PAHs studies; Figure 1-6)

Why is understanding or predicting the behavior/impact of HOCs in natural environment so difficult? The difficulty is partly due to the variability of physicochemical properties in natural systems. To describe and simplify a complex system into a few properties is conceptually and analytically challenging, as will be shown in the discussion on OC and BC quantification.

The second challenge is that the behavior of real geosorbents with field aging of HOCs is different from that of samples manipulated or prepared under laboratory conditions. This has been demonstrated in many studies showing that the native sedimentary/soil HOCs and the spiked sedimentary/soil HOCs have different bioavailabilities (Kraaij et al., 2001; van Hoff et al., 2001; Tabak et al. 2003) and chemical extractabilities (Macleod et al. 2000; Northcott et al. 2001a; Kraaij et al. 2002b; Tabak et al. 2003).

The behavioral difference between native and spiked HOCs and the variability in natural geosorbents implies that we need to understand the chemistry of sorbed HOCs by studying HOCs sorption on field soil/sediment samples (not synthetic sorbents) with widely ranging physicochemical properties. Yet, taking PAHs as an example, despite the large number of publications over the past decades (Figure 1-6), only a very small fraction of them is suitable for constructing meta-level correlative models for kinetic (see Chapter 7 section 1.1.4) or equilibrium behaviors (e.g. linear free energy relationships).

Why are most studies not suitable for the construction of meta-level correlative models? This is because the necessary 'criteria' (Table 1-5) have often been only partly met. For instance, in their ambitious review on HOCs desorption rate constants (k_{des}), Birdwell et al. (2007) could not advance their analysis by correlating the observed rate beyond sorbate properties (e.g. aqueous solubility, K_{OW}, K_{OC}, free aqueous phase diffusivity) because key system properties such as sorbent particle size and solids-to-water ratio are often neglected or are only ambiguously mentioned (e.g. only the total range of R_{sw} was reported, lacking specificity to individual rates). These parameters, which are doubtlessly key to any kinetic questions in closed systems, have been neglected partly because they are not needed for empirical description of the kinetic data (Table 7-11; also section 1.1.4, Chapter 7). For this reason, it is not surprising that Birdwell et al. could not establish any meta-level model where k_{des} can be inferred from the chemical properties of HOCs and the system factors (e.g. R_{sw}, sorbent particle size).

We will broadly outline the overall complexity in describing the behavior of HOCs in natural environment, and then discuss the topic of BC or organic phase characterization

in the next major section. The latter discussion not only serves to illustrate the complexity in HOCs chemistry, but also provides important background and motivations for this work.

3.2. The Entangled Factors Influencing HOCs in the Environment

A great number of factors affect the distribution or bioavailability of HOCs in the environment, as illustrated in Figure 1-7. Even without considering the dimension of transport/mobility, there are many important parameters that affect the sorption chemistry of HOCs. For instance, the chemical/physical nature of the sorbate itself can interact with the physical properties of BC, resulting in different degree of sorption non-linearity (e.g. the Freundlich n_{BC} for activated carbon is often less than the n_{BC} observed for sedimentary BC; see Table 5-7 and 5-8). The domain BC type may in turn depend on the type of solid-phase (e.g. soot in sediment vs char in forest soil). If transport processes and/or kinetics are brought in, the overall picture of dependence becomes even more complicated. Now we have to consider the timescales of competing processes in addition to the kinetics of adsorption/desorption occurring at the μm intra-aggregate spatial scale.

But the cartoon in Figure 1-7 is only a rough sketch on the complexity of the HOC problem. The actual interconnectedness between various factors is far more complicated. We will use "sorption hysteresis" and the dimension of time as examples.

3.2.1. Example (I): what causes "Sorption Hysteresis"

A widely reported phenomenon in sorption literature is that of "sorption hysteresis", which refers to the situation where adsorption and desorption produce different distribution ratios (i.e. S_i/C_{iw}). Hysteresis is often observed because of inadequate equilibration time for adsorption, and in this case it may be regarded as a kind of 'artifact'. However, true hysteresis may also occur when the sorbent phase undergoes structural alteration (e.g. diagenesis) or when the internal pore structure experiences swelling and contraction, which results in the entrapment of sorbed HOCs. Hence, there is the interplay between time (both short term and long term), sorbent type and physical properties, and the physicochemical nature of the sorbate (Figure 1-8).

3.2.2. Example (II): the Dimension of Time

The dimension of time also illustrates the interconnected nature of different factors affecting the fate of HOCs in natural systems (Figure 1-9). The cartoon shows how time affects the interpretation of sorption data (as kinetic or as equilibrium), how adsorption/desorption is competing with other 'physical' processes such as porewater flushing or aerosol deposition, and how it may alter sorbent properties via compaction.

4. Characterization of Organic Matter

The earlier discussion on non-linear isotherms (section 2.2.1.2) has briefly described the nature of black carbon (BC). In view of BC's key role in controlling the uptake of HOCs into the geosorbents, we shall examine BC and the categorization of organic phase in greater detail, with focus on what may be limiting our ability to understand/predict HOCs behavior in the environment.

4.1. Dichotomous Divisions of Environmental Organic Matter

According to major reviews (Horvath 1993; Penner et al. 1996; Luthy et al. 1997; Haywood et al. 2000; Hedges et al. 2000; Allen-King et al. 2002; Cornelissen et al. 2005b; Nienow et al. 2006), environmental organic matter – the totality of organic carbon species[3] in atmosphere, hydrosphere, pedosphere, subsurface, natural or anthropogenic in origin – may be divided into two major categories which exhibit qualitatively distinct physicochemical properties and behaviors. The 'soft' carbon is structurally loose and flexible, and, as a result, relatively degradable and behaviorally similar to that of organic solvents. Examples of soft carbon are lipids, proteins, and humic substances, and they are typically considered as OC in environmental chemistry literature (Schwarzenbach et al. 2003)

In comparison to the 'soft' carbon, the 'hard' carbon is structurally condensed and rigid, and hence impenetrable to other chemical species and strongly resistant to biochemical changes except at extraordinary conditions (i.e. high temperatures or pressures). Examples of hard carbon are coal, graphite, diamond, C-rich combustion byproducts (soot, charcoal), and industrial carbonaceous products (activated carbon, carbon blacks). These materials, with the exception of diamond, are currently considered as BC in HOCs sorption literature (Cornelissen et al. 2005b).

Rather than being definitive, the categorical divisions of soft and hard carbons serve as behavioral and physicochemical ideals for a continuum of carbonaceous matter. The multi-dimensional qualitative contrasts between soft and hard carbons (Table 1-6) make the 'hard'-'soft' distinction suitable for understanding phenomena in atmospheric physics and chemistry, biogeochemistry, soil science, and environmental chemistry.

4.2. Black/Elemental Carbon: Overview

Black Carbon (BC) or Elemental Carbon (EC) refers to carbon-rich phases or particles with physical and chemical properties (e.g. high aromaticity, low in O, N, H) that render them good absorbers of light/heat (Horvath 1993; Haywood et al. 2000), good sorbents for non-polar or hydrophobic organic compounds (Luthy et al. 1997; Allen-King et al. 2002; Cornelissen et al. 2005b), and good indicators for the record of past natural or anthropogenic events (Hedges et al. 2000). These carbonaceous particles/phases are produced from the incomplete combustion of fuels or biomass (Goldberg 1985),

[3] Excluding inorganic gases such as CO_2, CH_4, low-C volatile gases, and mineral carbonates.

diagenesis/weathering (Buseck et al. 1985; Masiello and Druffel, 2001; Dickens et al., 2004; Glaser et al. 2008), and other human activities such incense burning (Wang et al. 2007), meat cooking, rubber tire erosion (Hildemann et al., 1991; Schultz 1994), and industrial operations (Breedveld et al. 2007). As a result of its diverse production modes, BC/EC is ubiquitously present in air, soil (Skjemstad et al., 1996, 2002; Czimczik et al. 2007), sediments (estuarine, riverine, oceanic) (Gustafsson et al., 1997; Mitra et al., 1999; Masiello et al., 2001), and aquifer materials (Kleineidam et al., 1999).

4.3. BC/EC: Meta Definition and Physicochemical Continuums

4.3.1. Meta-BC/EC

The division of total organic carbon into 'soft' carbon (or OC) and 'hard' carbon (or BC) may be conceptually convenient for brainstorming hypotheses and for understanding various physicochemical phenomena qualitatively, such a division falls short of (i) representing the continuum in structure and properties of environmental organic matter, and (ii) relating structural properties of the continuum to phenomenal effect in a quantitatively rigorous manner. For instance, most 'hard' carbon is good absorber of light, but diamond is not; most 'soft' carbon takes up HOCs via absorption, but it is unclear if sorption to lignin or peat proceed by absorption or adsorption; aged humic substances and immature coal categorically lie in the grey zone between soft and hard carbons.

It is important to note that the continuum of BC/EC means differently in different fields of study. In atmospheric physics, BC/EC is a spectrum of carbonaceous components that exhibit exceptional heat/light absorption capacity; in environmental chemistry, it is a continuum of sorbents that binds HOCs very strongly via surface adsorption; in biogeochemistry and soil science, it is the subset of carbonaceous materials that show high resistance to biological and chemical transformation.

4.3.2. Continuums of Meta-BC/EC

Several categorical schemes have been proposed in major reviews to the organization of different carbonaceous matter as meta-BC/EC (Figure 1-10 to 1-13). These proposed continuums attempt to highlight the different aspects of carbonaceous materials in the context of a particular set of scientific questions. For instance, the biogeochemical continuum (Figure 1-10) values material source, biochemical resistance, and long-range transport very highly, and this reflects the biogeochemists' interest in flux or cycle questions. Such characterization, however, is not suitable for determining the distribution/bioavailability of soil/sediment HOCs, where properties such as elemental composition, surface area, and morphological features are of greater importance (Figure 1-11, 1-12). And for atmospheric questions (such as the absorption of solar irradiation), optical absorptivity and thermochemical resistivity become properties of great significance. The variety in the continuums of meta-BC/EC demonstrates the difficulty in defining a "universal" BC/EC applicable to different research disciplines. Some level of ambiguity appears to be unavoidable even when considering BC/OC (and similarly for OC) as a concept.

4.4. Quantification of Environmental BC

Just as there are different continuums of meta-BC/EC, the operational or analytical definition of BC is also non-unique. There are two main difficulties in refining the analytical identity of BC: (i) which property should be analyzed (e.g. thermal resistance? oxidation resistance? light absorbance? size? morphology?), and (ii) how should the BC-phase be separated or distinguished from the background matrix.

4.4.1. Variety of BC Quantification Methods

BC is currently being quantified by a variety of methods: (i) wet chemical oxidation (Kralovec et al., 2002; Simpson et al. 2004a,b), (ii) thermal oxidation (Kuhlbusch 1995; Gustafsson et al. 1997; Linuma et al. 2007), (iii) thermogravimetry and calorimetry (Lopez-Capel et al. 2005), (iv) UV photooxidation (Skjemstad et al. 1996; Schmidt et al. 2002), (v) acidification and oxidation (i.e. BPCA) (Glaser et al. 1998; Brodowski et al. 2005), (vi) thermal/optical transmittance and reflectance (Chow et al. 1993; Huang et al. 2006), (vii) chemical IR-spectroscopy (Smith et al. 1973, 1975), (viii) photoacoustic spectrometry (Petzold et al. 1996; Arnott et al. 1999; Zielinska et al. 2004), (ix) laser-induced incandescence (Moteki et al. 2007), (x) time-of-flight mass spectroscopy (Ferge et al. 2006), (xi) microscopic counting/inspection (Clark et al. 1988b; Cheng et al. 2008; Turner et al. 2008). This great variety of methods reflects the different conceptual pictures held in different disciplines.

4.4.2. No 'Best' Method for Quantifying BC

A number of comparative studies on different BC quantification methods have been carried out, but the evaluation for the 'best' method has been inconclusive due to the strength and weakness of individual methods (Hitzenberger et al. 1999; Schmidt et al., 2001; Currie et al., 2002; Hammes et al. 2007; Reisinger et al .2008). Furthermore, variation in operation conditions exists even within an individual method. For instance, the thermal oxidation method contains several variants in temperature, air-composition, and oxidation duration (Cachier et al. 1989a,b,c; Gustafsson et al. 1997; Kuhlbusch 1995; Petzold et al. 1995, 1997; Linuma et al. 2007).

4.4.3. Thermal Oxidation Method (CTO-375°C-24h) for HOC Studies

For the study of HOC sorption, the thermal oxidation method (CTO-375°C for 24 h) has been one of the most widely applied BC quantification methods (e.g. Gustafsson et al. 1997; Bucheli et al. 2000; Accardi-Dey and Gschwend 2002; Cornelissen et al. 2004a,b; Nguyen et al. 2004a,b; Lohmann et al. 2005; Ran et al. 2007a,b; Flores-Cervantes et al. 2009). In this method, the sample is first ground and spread out, acidified to remove carbonate, and then subjected to oxidation at 375°C for 24hrs in air (Gustafsson et al., 1997b; Accardi-Dey and Gschwend 2002; Flores-Cervantes et al. 2009). The combusted carbon fraction is regarded as OC and the residual fraction represents BC.

The CTO-375°C-24h method involves minimal transfer and chemical additions, and thus substantially reduces the likelihood of contamination in compare with other methods. However, there is concern for charring of OC as positive artifact to BC (Birch 1998; Gelinas et al. 2001), but a radiocarbon study suggested that thermal oxidized BC should be free of charring residues (Reddy et al. 2002). Middelburg et al. (1999) commented

that the thermal approach should be more accurate than wet chemical oxidation, and Lavanchy et al. (1999a,b) found the method yielded comparable results with those from using other methods such as optical detection and off-gas detection. Furthermore, the thermal oxidation method typically gives a very low BC-to-OC ratio, implying only the highly resistant fraction of organic matter is measured (Currie et al. 2002).

What may be the major limitation of the CTO-BC method is its tendency to underestimate BC content in soil/sediment. In the intercomparison study by Hammes et al. (2007), the CTO method was found to under-quantify both grass char and wood char substantially. It is also unable to detect coal, which exhibits comparable sorption affinity for HOCs (Cornelissen et al. 2005a). Nguyen et al. (2004a) and Accardi-Dey (2003) also reported cases where wood-char and soot were partially burnt off.

4.4.4. Quantification of BC by Electron Microscopy: a Novel Approach

As early as in the late 70s and early 80s, soot and char particles have been imaged using scanning electron microscopy (SEM) (Griffin et al. 1979, 1981; Cope et al. 1980; Medalia et al. 1982; Kralovec et al., 2002) and extensively characterized for their physical (surface area, shape, porosity), elemental (C-H-N analysis) and spectroscopic (^{13}C NMR) properties (Rockne et al. 2000; Fernandes et al. 2003). However, these studies have examined either BC extracted from natural solids (Schmidt et al., 2002; Kralovec et al., 2002) or soot and char particles (Rockne et al., 2000; Fernandes et al., 2003), but not BC as exists in sediment/soil aggregates.

Considering the limitations and uncertainties in the conventional BC quantification methods and the need for intra-aggregate spatial distribution of BC, it is desirable to observe and quantify BC in natural solids without stripping or removal of the surrounding matrix. The recent electron microscopic (EM) studies on BC-related materials (Stoffyn-Egli et al. 1997; Ghosh et al. 2000; Schmidt et al. 2002; Brodowski et al. 2005) suggested that it may be possible to obtain quantitative mapping of BC using scanning electron microscopy (SEM), energy dispersive X-ray spectroscopy (EDX), and electron energy-loss spectroscopy (EELS). The successful application of electron microscopic analysis to map out natural organic matter in sediments (Furukawa 2000) and cells (Watteau et al. 1996) is particularly encouraging for a potential, new EM-based BC quantification method.

4.4.5. Concluding Statements

One of the major problems in understanding the fate of HOCs in the environment has been the uncertainty in the quantification of BC (and/or OC) due to methodological limitations. Since individual method biases against different types of BC to different extents, BC-associated uncertainty/error may partly explain the widely scattered K_{BC}'s and K_{OC}'s. Currently, there is no consensus on which analytical method being the best for BC (Hammes et al. 2007); however, a combination of BC-methods may better characterize the organic phase in soil/sediment. For instance, one may use the thermal oxidation to quantify soot-BC, and use chemical oxidation to measure char or coal (see Figure 1-14). The successful application of electron microscopy analyses on environmental and biological samples may promise a novel and independent way of assessing BC as well as its distribution within soil/sediment aggregates.

5. Desorption of HOCs from Geosorbents

Results from recent studies (Adams 2003; Accardi-Dey and Gschwend 2003) suggested that native HOCs have not equilibrated between sediment and water. These observations suggested that the behavior of HOCs in natural environment may be controlled by the kinetics of desorption rather than equilibrium. Earlier, the importance of desorption kinetics on HOC bioavailability has been discussed (section 2.2.2). Here, field observations that also suggested the importance of desorption kinetics in dictating the fate of HOCs will be briefly reviewed.

5.1. Disequilibrium of HOCs in Surficial Sediment

In a sediment core study, McGroddy et al. (1995) reported that the porewater PAH concentrations were lower than the equilibrium predictions using the linear, Classical-OC isotherm (section 2.2.1.1) by at least one order of magnitude. A follow-up analysis taking BC into account did bring the predicted pore water PAHs concentrations closer to the observed, but a discrepancy by a factor of about 3 to 4 still remained within the surficial bed layer (Accardi-Dey and Gschwend 2003).

5.2. Mobilization of Sedimentary HOCs via Resuspension

The field observations in Adams (2003) suggested that sedimentary PAHs/PCBs may be released via resuspension events in the Hudson River Estuary. The dissolved pyrene concentration in the water column was found to be higher in April, following the spring snowmelt. The observed levels could not be explained by estuarine dilution process. However, this was not observed in the fall. This suggested that the April observation may be caused by the release of pyrene from resuspended sediment as triggered by shearing influx of spring water.

5.3. Slow Response of Porewater to Influx of Particulate PAHs

Maruya et al. (1996) found that sediment-porewater distribution quotients (i.e. S_i/C_{iw}) for PAHs in the wet season (high surface runoff) were about one order of magnitude higher than those measured in the dry period. They attributed the higher distribution quotients to the presence of sooty particles carried in the surface runoff. Furthermore, they found the wet season porewater PAH concentrations to be relatively constant despite the variation in the sediment phase. This highly suggested that the fresh influx of relatively PAH-rich particles from runoff have not equilibrated with the sediment porewater.

5.4. Numerical Simulations on the Release of bound-HOCs

Cheng et al. (1995) modeled desorption of HOCs during resuspension events using a linear-OC model and concluded that equilibrium assumption was not valid for parameters of typical natural systems. Another simulation study (Wiberg et al. 2002b)

also suggested that resuspension of HOC-loaded sediment could be an important mobilization pathway of sorbed HOCs.

6. Thesis Objectives

Using pyrene (a 4-ring PAH) as a model HOC, this thesis aimed at advancing the understanding of the fate of HOCs in sediment-water systems. The following are the objectives of this thesis:

(i) To examine the release kinetics of sedimentary pyrene in conditions typical to harbors and estuaries and other water bodies (Chapter 2 & 7),
(ii) To investigate the equilibrium partitioning behavior of PAHs to sediment and water at environmentally realistic concentration levels (Chapter 3 – 6),
(iii) To construct an *a priori* numerical model which describes and predicts the release kinetics of sorbed HOCs in natural environment (Chapter 7 & 8),
(iv) To construct a preliminary evaluation on the relative importance of sediment resuspension as a mobilization pathway of sedimentary HOCs (Chapter 9), and
(v) To developing a novel BC quantification method based on electron microscopic analyses (Chapter 10).

The conclusion of this thesis as well as a list of future work can be found in Chapter 11.

Chapter 2. Desorption of Native Pyrene at Minute- to Month-Timescales by Time-Gated Fluorescence Spectroscopy[1]

CHAPTER ABSTRACT

We investigated desorption of native pyrene from field-aged sediments using time-gated, laser-induced fluorescence (LIF) spectroscopy. LIF is superior to conventional analytical methods for measuring quickly changing dissolved pyrene analysis as it allows observations at minute-scale resolution, has a low detection limit (~1 ng/L), and minimizes sample loss and/or disturbance as it requires no system subsampling and chemical analysis. The efficacy of LIF was demonstrated in studies of pyrene desorption from Boston Harbor sediment segregated into different size-fractions (38-75, 75-106, 180-250 μm diameter) and used in varying solid-to-water ratios (20, 70, 280 mg_{solids}/L). The effects of particle size and solid loading on desorption were consistent with diffusion physics. At suspension conditions between 20-280 mg_{solids}/L, we observed desorption continuing towards an apparent plateau level over the course of weeks to months. This implies that the characteristic desorption-time of pyrene from fine sediments, and by inference other sediment-bound hydrophobic organic compounds (HOCs) of similar hydrophobicity, exceeds the typical characteristic-times for pore water flushing and resuspension events. Consequently, assuming local sorption equilibrium in modeling efforts would be inappropriate.

[1] A reduced version of this chapter was published (Kuo et al. 2007).

Table of Content for Chapter 2

1. Chapter Introduction, Scope, and Objective 35

1.1. Introduction 35

1.2. Objectives 36

2. Materials and Methods 36

2.1. Sediment 36

2.2. Laser-Induced Fluorescence (LIF) System 37

2.2.1. Description and Operational Principle of LIF 37

2.2.2. Start-Up, Signal-to-Noise Ratios, Measurement Uncertainties and Drift 37

2.2.3. Processing of Fluorescence Signals 37

2.3. Desorption Experiment 38

2.4. Sediment and Dissolved Pyrene Measurements by GC-MS 39

3. Results & Discussion 39

3.1. Validation of LIF Measurements 39

3.1.1. Inner-Filter Effect Correction for Conical Illumination Volume 39

3.1.2. Early-time LIF Measurements 41

3.1.3. Measurements by LIF and GC-MS 41

3.2. Experimental Results 42

3.2.1. Sediment and Dissolved Pyrene Measurements 42

3.2.2. Reproducibility of Desorption Kinetics 42

3.2.3. Desorption Kinetics Trends 42

3.3. Discussion 43

3.3.1. Analytical Advantages of LIF 44

3.3.2. Very Slow Desorption vs Equilibrium 44

3.3.3. Limitations 45

3.3.4. Implications and Significance 45

4. Conclusion 46

1. Chapter Introduction, Scope, and Objective

1.1. Introduction

The chemical behaviors of persistent hydrophobic organic compounds (HOCs) associated with sediments are of great legal, regulatory, and engineering interest (Ehler et al. 2003). Ideally, regulatory or remediation benchmarks for natural solid-associated HOCs can be set with the knowledge of a particular HOC's mobility and bioavailability in the system of interest. Hazards from persistent, solid-associated HOCs based on total solid-phase HOC concentrations (Alexander 2000) or assuming solid-water equilibrations (Kraaij et al. 2002a, Lohmann et al. 2004) are commonly overestimated due to HOC sequestration from aging (Luthy et al. 1997) and the slow kinetics of desorption from organic matrices (Pignatello et al. 1996). Recent studies strongly suggest that desorption processes control rates of biodegradation and assimilation for persistent HOCs that associate with natural solids (Cornelissen et al. 1998b; Lamoureux et al. 1999; Ghosh et al. 2003; Huesemann et al. 2003; Jager et al. 2003; Ahn et al. 2005b; Gomez-Lahoz et al. 2005; Cornelissen et al. 2006). Clearly, knowledge of both sorption equilibria and dynamics are essential for accurate risk assessments of persistent HOCs.

HOC desorption kinetics have been examined previously using field or synthetic sorbents spiked with HOCs (e.g., Gomez-Lahoz et al. 2005, Schlebaum et al. 1999; Young et al. 1999; Johnson et al. 2001b; Northcott et al. 2001a; Kukkonen et al. 2003) or field sorbents with natively associated HOCs (e.g., Cornelissen et al. 1998b; Rockne et al. 2002). The spiking approach offers greater control and freedom in variable manipulation, thus potentially allowing clear insights into particular mechanistic aspects of desorption. However, studies have demonstrated that persistent HOCs desorb more slowly and become less extractable with longer aging (Northcott et al. 2001a; Kan et al. 1994; Huang et al. 1998a; Gong et al. 1998a; Braida et al. 2003). Furthermore, for spiking studies, complications with desorption kinetics may arise when the sorbents are insufficiently prewetted (Nguyen et al. 2005), when they are exposed to high HOC concentrations (Lu et al. 2002), or when adsorption equilibrium has not been established (Huang et al. 1998a). Hence, it appears that the mobility and bioavailability of HOCs cannot be fully understood from spiking studies alone.

However, several analytical challenges need to be resolved when investigating desorption of native HOCs. Ideally, it is desirable to have fine temporal resolution and minimal system disturbance. Unfortunately, working with contaminated sorbents collected from the field, the solid phase HOC loading range is restricted. This often implies dissolved concentrations as low as ng/L levels, thus requiring relatively large volumes of aqueous samples for analysis. One approach to circumvent this problem is to study desorption at relatively high solids concentrations, but the tradeoff is losing the kinetic features of the initial desorption period (Accardi-Dey and Gschwend 2002) where the desorption rate and extent are most significant (Cornelissen et al. 1998b; Rockne et al. 2002). Conventional extraction and instrumental analyses (e.g., GCMS) inhibit use of frequent samplings at early times and limit the total number of observations. A

secondary hydrophobic matrix (such as Tenax beads or SPME) (Cornelissen et al. 1998b; Gomez-Lahoz et al. 2005; Kukkonen et al. 2003; Rockne et al. 2002; Conder et al. 2003; Mayer et al. 2000b) may be introduced to probe the changing dissolved HOC concentration. This approach, however, complicates the interpretations since the uptake kinetics of HOCs onto/into the probing matrix may limit observation frequency, and the driving force for desorption is influenced by the adsorption kinetics of the desorbed HOCs onto the probing matrix.

Time-resolved laser-induced fluorescence (LIF) spectroscopy may overcome the aforementioned constraints for study of native polycyclic aromatic hydrocarbons (PAHs), a well-known class of HOCs that include suspected carcinogens (Ramesh et al. 2004) and teratogens (Miller et al. 2004). Fiber optics and laser excitation allow organic compounds to be detected and distinguished based on their characteristic fluorescence lifetimes (Inman et al. 1990; Niessner et al. 1991). LIF is particularly suitable for detecting dissolved PAHs among background organic matter because many PAHs have fluorescence lifetimes that are much longer than those of natural organic compounds (e.g., humic substances; Inman et al. 1990; Chen et al. 1997). LIF is capable of *in situ* and on-line detection of PAHs at ng/L levels (Niessner et al. 1991) without loss of sample volume/mass. Its proficiency for measuring PAHs in field settings has already been demonstrated in recent studies on groundwater (Baumann et al. 2000), seawater (Inman et al. 1990; Chen et al. 1997; Rudnick et al. 1998), and submerged sediments (Grundl et al. 2003).

1.2. Objectives

The objectives of this study were to (a) demonstrate the efficacy of time-gated laser-induced fluorescence spectroscopy for studying the desorption kinetics of native, geosorbent-associated HOCs, and (b) use LIF to investigate the desorption kinetics of field-aged/native HOCs from fine-sized natural sediments (i.e., ~10 to ~300 μm) at realistic suspended-solids concentrations (i.e., ~10 to ~300 mg_{solids}/L) under laboratory-controlled conditions. Pyrene, a four-ring PAH, was chosen as the target HOC due to its long fluorescence lifetime (Lakowicz 2006) and its ubiquitous occurrence as an organic pollutant. This report describes our efforts to validate the LIF method, and interpret the observed desorption behavior of pyrene as a representative HOC.

2. Materials and Methods

2.1. Sediment

Surficial sediment was collected from the Moon Head area (42°18.10'N, 71°00.00'W) in Quincy Bay, Boston, in December, 1999. Pure water was obtained from an Aries system (ion-exchange (18 mΩ), activated carbon filter, UV oxidation, and a 0.22 μm filter). Wet sieving was done using standard sieves yielding size fractions of 38-75 μm, 75-106 μm, and 180-250 μm. The sieved sediments were allowed to settle in amber

glass jars resulting in ~60% solids by weight. All subsequent desorption experiments and chemical analyses were performed on these processed sediments (stored at 4°C in dark).

2.2. Laser-Induced Fluorescence (LIF) System

2.2.1. Description and Operational Principle of LIF

A complete description of the LIF system is available in the original publications (Rudnick 1998; Rudnick et al. 1998). Briefly, the operation of the system is as follows. Photon pulses at 337 nm (optimal excitation for pyrene) were used. Before each pulse travels through the probe and excites the chromophores, it triggers a time-gating mechanism. The time-gating mechanism imposes a time-window on the detection of emitted photons, allowing only those emitted 128 to 256 ns after the pulse-excitation to be counted. This mechanism captures most of the emissions from dissolved pyrene, which has a fluorescence lifetime of 120-130 ns (Inman et al. 1990; Lakowicz 2006; Kotzick 1996), and filters out the short-lived fluorescence signals due to other chromophores. A schematic of the instrument is shown in Figure 2-1. More details on the system are included in Appendix 2-1.

2.2.2. Start-Up, Signal-to-Noise Ratios, Measurement Uncertainties and Drift

For this use, the LIF system was warmed up for at >40 min to stabilize the laser pulse strength, and this stability was verified by monitoring the water Raman peak. Each LIF pyrene measurement involved the accumulated emission photon counts of 100 excitations, while each LIF Raman measurement (no delay) was the accumulated emission counts for 50 pulses. Measurement and data transmission were completed in approximately 1 min. The detection limit was about 1-2 ng pyrene/L in water (signal:noise=2.0±0.2 and 4.1±0.4 at 0.8 ng_{pyr}/L and 3 ng_{pyr}/L, respectively). Measurement uncertainty varied with pyrene concentration. Typical uncertainties (1 s.d.) were ±10-15% for 1-5 ng pyrene/L and ±5-10% for higher concentrations. Dissolved pyrene concentrations were determined from the fluorescence at 387 nm (see Appendix 2-2 for details of fluorescence signal processing.) Measurement sessions began with the calibration standards, followed by the blank, the test solutions and controls, and finally two calibration standards. The standards were chosen such that they bracketed test solution pyrene levels. Calibration standards were analyzed immediately before and after sets of observations, and dissolved pyrene level was inferred from the two calibrations with time-weighting assuming linear drift (≤10%).

2.2.3. Processing of Fluorescence Signals

Dissolved pyrene concentrations were determined from the peak height of fluorescence signals at characteristic emission wavelengths. High frequency noise (Figure 2-2) was eliminated by re-expressing via Fourier series (Matlab) using frequency truncation suited maintaining the linearity of the calibration curve (0-60 ng pyr/L, r^2>0.99) as well as pyrene's characteristic emission peaks. Peak height was determined from a baseline established by the averaged intensity over the 340-360 μm range. Because the relative intensities of the other characteristic peaks changed somewhat with the dissolved

concentration (Table 2-1), pyrene's 387 nm peak was used to infer dissolved pyrene concentrations.

2.3. Desorption Experiment

Desorption of native pyrene was studied at specific solid-to-water ratios (R_{sw}). Prior to each desorption experiment, a fraction of sieved sediment was homogenized, weighed, and dried overnight at 60°C to determine the dry solid content. Suspensions were prepared in 1-L narrow-mouthed amber glass bottles (Qorpak) using aliquots of the wet sediment to give approximately 20, 70, and 280 mg_{solids}/L_w suspensions. Prior to use, the bottles were pre-combusted at 450°C overnight, rinsed with water, and air-dried. Each experiment involved three vessels: one for the test (sediment suspension), one for the blank (clean water), and one for the control (typically with 12 ng/L dissolved pyrene but no sediment). The test vessels contained 960 mL of water and and sodium azide (1 mM; Fluka Chemika) to inhibit microbial activity (Schlebaum et al. 1999; Young et al. 1999). A set of pyrene standards (0.75, 3, 6, 12, 30, 60 ng_{pyr}/L) was also prepared in water from certified methanol-based pyrene stock solution (1000 μg pyrene/mL methanol, EPA-1157, Ultrascientific). All standard and control solutions had 1 mM sodium azide and were prepared on a monthly basis. In addition, a separate control (30 ng pyrene/L) was placed among the test solutions over the 8 mo period to assess any losses (≤3% observed).

Desorption experiments were carried out at constant temperature using a 25±1°C water bath (Thermomix 1419, B. Braun). The blank, control, test, and standard solutions were all equilibrated in the bath for at least 24 hr before experiments started. Sediment suspensions were continuously stirred for 3 to 4 weeks (Pyrex-coated, stir bar at about 500±100 rpm), and then turned end-to-end by hand 10 times once every 5 to 7 days. In test solutions, initial dissolved pyrene was measured (to ensure 0 ng/L pyrene background prior to suspension formation), and subsequently weighed sediment was added (within 30 sec). Dissolved pyrene measurements were made every minute for the first 2 h, and then less frequently over time. During each measurement, the LIF probe was immersed in the solution at 10 to 12 cm above the vessel bottom. Each reported data point was the time-averaged pyrene fluorescence response of 5 (first 2-hr data) to 7 (later data) consecutive LIF measurements (i.e., 500 to 700 pulse excitations). In between test solutions, the probe was rinsed with methanol (99.8%, J. T. Baker), then water, and finally wiped dried with a lint-free tissue.

Two types of interference were identified and addressed. First, substantial interference arose when the LIF probe was placed too close to the vessel bottom. A minimum distance of 4 cm was required to avoid interference (Table 2-2), and a distance of 10-12 cm was used for all LIF measurements reported here. Second, the magnetic stir bar also produced a minor interference. This problem did not occur in the typical measurements (i.e., after the first 2 hr) when stirring was stopped. Artifact signals were avoided in the initial 2-hr measurements by applying stirring intermittently every 10 to 15 min and keeping the stir bar aside during measurements. The LIF system responded linearly to dissolved pyrene level in the 0-60 ng/L range, with an averaged response

factor of about 200 counts/($ng_{pyr}L^{-1}$) and a typical r^2 of >0.99. No monotonic relationship was found between LIF response factor and time with the Kendall Ranking test (Kendall τ=0.018, s=0.079, n=75, at significance levels of 5% and 10%; Table 2-3), indicating the response of LIF was stable throughout the 8-month period.

2.4. Sediment and Dissolved Pyrene Measurements by GC-MS

The dissolved and the solid-associated pyrene concentrations of the sediment suspensions were also measured by gas chromatography-mass spectrometry (GC-MS) at the end of the experiment. The suspensions were allowed to settle for 14 days. After LIF measurements, two replicate supernatant aliquots were removed, extracted 5× with dichloromethane, and transferred into hexane. Settled sediments were extracted with 50 mL of dichloromethane-methanol (9:1 v/v ratio) within the experimental vessels. The extracts were analyzed on a JEOL GCmate gas chromatograph-mass spectrometer as reported previously (Accardi-Dey and Gschwend 2002; Adams 2003). Deuterated pyrene (d_{10}-pyr) and p-terphenyl (d_{14}-p-terp) were used as recovery and injection standards, respectively.

3. Results & Discussion

3.1. Validation of LIF Measurements

Fluorescence measurement of dissolved pyrene in sediment suspensions may be subject to the following non-ideal effects: (i) scattering of excitation/emission radiation by suspended particles, (ii) absorption of excitation/emission radiation by organic chromophores (inner-filter effects), (iii) background fluorescence from non-pyrene fluorophores, and (iv) fluorescence from solid-associated pyrene. It has been previously shown that (iii) is negligible (Rudnick et al. 1998). LIF measurements during resuspension and after settling for 7 to 14 days showed that measurements were not statistically different with the two treatments for the aggregated data (linear regression: $y = 1.03(\pm0.05)x + 0.11(\pm0.48)$ or r^2=0.92 for a y=x fit; see Figure 2-3) and for each of the three size fractions and three solids-to-water ratios (Figure 2-4). Raman corrections did not improve the correspondence (mean resuspended-to-settled measurement ratios were 1.12(±0.10) and 0.96(±0.08) for Raman corrected and uncorrected cases, respectively, see Figure 2-5). These results suggested that suspended sediment particles would not give rise to statistically significant signal artifact in the investigated size fractions and R_{sw}s.

3.1.1. Inner-Filter Effect Correction for Conical Illumination Volume

To assess the impact of inner filter effects, the absorptions of excitation (λ_{exc}=337nm) and emission (λ_{exc}=387nm) wavelengths in our suspensions were determined using a Beckman DU600 spectrophotometer. The illumination geometry of the LIF system differs from the common cuvette-type configurations (Parker 1968), so we adapted the approach of Srinivas and Mutharasan (1987) to evaluate our inner-filter effects:

$$\frac{F_{in\ fil}}{F_{no\ fil}} = \left(\int_0^L 10^{-(\alpha_{exc}+\alpha_{ems})x} G(x)dx\right) / \left(\int_0^L 10^{-(\varepsilon_{exc}+\varepsilon_{ems})C_{pyr}\,x} G(x)dx\right)$$

Eqn. 2 - 1

where α_{exc} and α_{ems} are the attenuation coefficients (abs.cm^{-1}) of the suspensions measured at λ =337nm and 387nm at relevant solid-to-water ratios,

ε_{exc} and ε_{ems} are the extinction coefficients (abs.cm^{-1}Lμg$_{pyr}^{-1}$) of dissolved pyrene λ =337nm and 387nm,

C_{pyr} is the dissolved pyrene concentration (μg_{pyr}/L),

$G(x)$ is the geometric factor for illumination volume variation as a function of illumination distance,

L is the maximum illumination pathlength (~4 cm; see Table 2-2).

The integrals were solved by numerically integrating Eqn. 2 - 1 with $G(x)$ approximated as the ratio of the reception area at the probe-tip to the total area of spherical emission from distance x:

$$G(x) \cong \frac{\text{Area of reception}_{x=0}}{\text{Area of illum. sphere}_x} = \frac{\pi r_o^{\,2}}{4\pi x^2}$$

Eqn. 2 - 2

where r_o is the radius of the probe-tip reception area,

x is the illumination distance between an emitting dissolved pyrene molecule and the probe-tip.

Inner-filtering resulted in a <1-3% reduction in pyrene fluorescence for the settled solutions, and <1-8% reduction for the resuspended solutions (Table 2-4). Because the inner-filter effects were comparable to the instrumental uncertainty (5-15%), the reported data have not been corrected for this.

We also tested the assumption of no fluorescence emission from solid-associated pyrene. The measured fluorescence from pyrene, F, can be expressed as a contributed sum from the dissolved pyrene, F_W, and the solid-associated pyrene, F_S:

$$F = F_W + F_S = P(C + \phi_S S R_{SW})$$

Eqn. 2 - 3

where C is the dissolved pyrene concentration ($\mu g_{pyr}/L_{water}$),

ϕ_s is the fluorescence efficiency of solid-associated pyrene relative to dissolved pyrene, ranging from 0 (perfect fluorescence quenching) to 1 (no quenching upon binding),

P is the response factor (intensity unit/$\mu g_{pyr} L_{water}^{-1}$) for dissolved phase pyrene,

$P\phi_s$ is the response factor (intensity unit/$\mu g_{pyr} L_{water}^{-1}$) for solid-bound pyrene,

R_{sw} is the solids-to-water ratio (kg_{solids}/L_{water})

S is the solid-associated concentration ($\mu g_{pyr}/kg_{solids}$).

It should be noted that ϕ_s is not the same as fluorescence quantum yield of the bound pyrene. F can be normalized to F_o, the fluorescence of dissolved pyrene in the absence of any quenchers (Backhus et al. 1990):

$$\frac{F}{F_o} = \frac{1 + \phi_S R_{SW} (S/C)}{1 + R_{SW} (S/C)}$$

Eqn. 2 - 4

And Eqn. 2 - 4 can also be re-arranged to:

$$\frac{F}{F_o} = (1 - \phi_S) f_w + \phi_S$$

Eqn. 2 - 5

with $f_w=1/(1+R_{sw}S/C)$, the fraction of dissolved pyrene. Regression of F/F_o vs f_w (best fit to $F/F_o = (1-\phi_s)f_{pyr,w} + \phi_s$ gave $\phi_s=0.002$ and $r^2=0.92$; see Figure 2-6) gave $\phi_s<1\%$, suggesting fluorescence due to solid-associated pyrene was insignificant.

3.1.2. Early-time LIF Measurements

The observed desorption trend may be unreliable due to the choice of temporal resolution or instrument drift. We found the temporal trend of dissolved pyrene observed at the 1-min resolution was consistent with those from the 5-, 10-, or 20-min averaged profiles (see Figure 2-7). With proper warm-up, instrument drift was <5% during a 3-hr period. Further, when the early-time dissolved pyrene profiles were compared to corresponding observations for dissolved standards, the pyrene standards changed much less over time (Figure 2-7; Table 2-3). Our findings on pyrene desorption were thus not affected by either factor.

3.1.3. Measurements by LIF and GC-MS

To assess the reliability of our use of LIF, all suspensions at the end of the desorption experiment were examined for pyrene using both LIF and supernatant solvent extraction followed by GC-MS (see Figure 2-8). The data from the two methods were consistent ($[Pyr]_{LIF} = 1.06(\pm0.14)[Pyr]_{GC\text{-}MS} - 0.95(\pm1.53)$, $R^2=0.85$). A student t-test also showed

that the average ratio $[Pyr]_{GC\text{-}MS}/[Pyr]_{LIF}$ was not statistically different from 1 at 1-10% significance levels (see Table 2-5). The match between LIF and GC-MS also supports our assumption that significant fluorescence was not contributed by non-pyrene fluorophores.

3.2. Experimental Results

3.2.1. Sediment and Dissolved Pyrene Measurements

In general, our sediment and dissolved pyrene measurements corresponded well with previous studies. Pyrene has been reported at about 10 $\mu g_{pyr}/g_{solids}$ (Shiaris et al. 1986; Lohmann et al. 2005) for sediments at locations in close proximity to our site (Table 2-6). Other PAHs in our sediment (data not shown) were also approximately 2-5 times less than those previously reported (Shiaris et al. 1986; Lohmann et al. 2005). Interestingly, the solid-phase pyrene concentration was greatest in the largest particle size class, and lowest in the smallest (Table 2-6). A similar trend was observed by Rockne et al. (2002), while Kukkonen et al. (2003) reported HOCs to be primarily associated with the extremely-fine-to-colloidal fraction (<20μm) in lake sediments. As for the dissolved pyrene levels, we observed 5-15 ng_{pyr}/L at the end of desorption experiments, similar to the levels reported for Boston Harbor seawater ranges of 5-20 ng_{pyr}/L for parts of the harbor with sediment-pyrene concentrations of about 1-10 $\mu g_{pyr}/g$ (Rudnick 1998; Rudnick et al. 1998; Shiaris et al. 1986; Lohmann et al. 2005).

3.2.2. Reproducibility of Desorption Kinetics

Reproducibility of the LIF desorption method was investigated using the smallest size fraction, 38-75 um (Figure 2-9). Fitting the time courses using a 1st-order equation of the form, $C_{obs}(t)=C_{long\ time}(1-e^{-kt})$ (k as *fitting* parameter), the estimated plateau values were 4±1 (or ±25%) ng/L and 11 (or ±30%) ng/L for the 20 mg_{solids}/L and the 270-290 mg_{solids}/L cases, respectively. The relative variabilities were similar in the two cases, although the absolute variability was more prominent at high R_{sw} (Figure 2-9). Subsample-to-subsample heterogeneity may have caused the observed variability.

3.2.3. Desorption Kinetics Trends

The general features observed in pyrene desorption profiles (Figure 2-10) were similar to those reported previously (Cornelissen et al. 1998b; Gomez-Lahoz et al. 2005; Schlebaum et al. 1999; Young et al. 1999; Johnson et al. 2001b; Kukkonen et al. 2003; Rockne et al. 2002; Gong et al. 1998a). Pyrene desorbed rapidly initially, with dissolved concentrations reaching 50% or more of the final levels by the 100th hr. After the initial phase, the release curve slowed considerably. The times at which the dissolved pyrene concentration reached ~90% of the plateau levels were approximately 200-800 hr, 700-1500 hr, and 2000-3200 hr for 38-75μm, 75-106μm, and 180-250μm size-fractions, respectively, where the first value in each range was for the highest R_{sw} and the second value was for the lowest R_{sw} (values for middle R_{sw}'s not listed). Such rapid-releases and plateaus in concentrations have been also observed in many other HOC desorption studies (Cornelissen et al. 1998b; Gomez-Lahoz et al. 2005; Schlebaum et al. 1999; Young et al. 1999; Johnson et al. 2001b; Kukkonen et al. 2003; Rockne et al. 2002; Gong et al. 1998a).

Various factors influence HOC desorption kinetics (Johnson et al. 2001b; Wu et al. 1988; Ball et al. 1991; Werth et al. 1997). Although the exact mathematical formulations differ, the effects of such factors are qualitatively always similar. For example, in one model, assuming a linear isotherm (Wu et al. 1988), the desorption rate coefficient, k^* (s^{-1}), and the fraction retained in geosorbent as a function of time, S_t/S_o, depend on these four parameters according to the following expressions:

$$k^* \propto \frac{D_{eff}}{r^2}$$

Eqn. 2 - 6

$$S_t = (S_o - S_\infty)\exp[-k^*(K_d R_{SW} + 1)t] + S_\infty$$

Eqn. 2 - 7

where D_{eff} is the effective diffusivity of the sorbate (m^2/s),

K_d is system partition coefficient (L_{water}/ kg_{solids}),

r is the particle radius (m),

R_{sw} is the solids-to-water ratio (kg_{solids}/L_{water}),

S_o, S_t, and S_∞ are the solid-phase pyrene concentrations at initial time, time t, and infinite time, respectively ($\mu g_{pyr}/kg_{solids}$).

Of course, the expression will change if one has a case with a non-linear K_d , but the qualitative dependence of desorption rate on particle size and system R_{sw} remains the same. The trends we found were generally consistent with such expectations (Figure 2-10a; Figure 2-11). At any given solid loading, one would expect the dissolved pyrene plateau to be established faster when pyrene is desorbing from smaller particles. For example, at a constant solid loading of 70 mg/L, the 38-75 μm size fraction reached the plateau phase after about 1000 hours, whereas for the 180-250 μm size fraction, the plateau was not established until after 3000 hours.

3.3. Discussion

To our knowledge, this is the first report on desorption behavior of natively associated HOCs from sediments at suspended-solids concentrations and particle sizes representative of water columns that are typical of estuary/harbor/tributary water column conditions. The concentration and particle sizes of suspended-solids in these natural systems typically range from <20-<500 mg_{solids}/L and 30-90 μm (see Table 2-7), respectively. These ranges were well covered in this study (20-270 mg_{solids}/L, 38-250 μm). Our use of field-aged sediments also circumvented the potential problem of spiked HOCs desorbing differently from field-aged HOCs (Northcott et al. 2001a; Kan et al. 1994; Huang et al. 1998a; Gong et al. 1998a; Braida et al. 2003*).*

This is also the first documentation at minute-resolved early desorption, where the extent and the rate of desorption are most dramatic. For typical sediments, approximately 50-90% of the desorbed PAHs entered the dissolved phase in less than 1 day (Cornelissen et al. 1998b; Gomez-Lahoz et al. 2005; Schlebaum et al. 1999; Young et al. 1999; Johnson et al. 2001b; Kukkonen et al. 2003; Rockne et al. 2002; Gong et al. 1998a). This fast kinetics is often empirically modeled using a 'rapidly' desorbing rate constant (k_{rap}). However, due to the time-demanding nature of conventional analytical techniques, often only a few data points are available for characterizing this initial desorption phase. Uncertainties in desorption k_{rap} values as high as 75% have been reported and were attributed to insufficient observation points during the initial desorption phase (Cornelissen et al. 1998b).

3.3.1. Analytical Advantages of LIF

LIF is superior to conventional analytical methods for our sorption investigation purposes. First, LIF allowed minute-resolved measurements. Second, analyte loss/contamination and sample change were unlikely with LIF because of minimal sample handling and few transfer steps. Moreover, LIF was more precise than the extraction-GC-MS scheme (see Figure 2-8). Capturing desorption kinetics of native PAHs/HOCs often requires a compromise between release speeds and measurable concentrations. The dissolved PAHs/HOCs concentrations can be increased with higher solids-to-water ratios at the price of shortening the equilibration time, thus making the kinetically significant phase less observable. A common solution is to introduce a secondary hydrophobic phase as a passive sampling medium to take up most of the desorbed HOCs (Cornelissen et al. 1998b; Gomez-Lahoz et al. 2005; Schlebaum et al. 1999; Young et al. 1999; Johnson et al. 2001b; Kukkonen et al. 2003; Rockne et al. 2002). This, however, convolutes the kinetics of pyrene desorption and the kinetics of pyrene uptake by the passive sampler sink.

3.3.2. Very Slow Desorption vs Equilibrium

It was uncertain if sorption equilibria were achieved by the end of our 3-8 month-long desorption experiments (see note a in Table 2-6; Figure 2-11), despite apparent concentration plateaus in dissolved pyrene (Figure 2-10a). We noted that, at the end of desorption experiments, the empirical ratio of the pyrene concentration in the solid phase to that in the dissolved phase, Q_d, was generally higher than the estimated equilibrium concentration ratio based on an OC+BC sorption model, K_d (Figure 2-12a; Accardi-Dey and Gschwend 2002; Adams 2003; Lohmann et al. 2005; Bucheli et al. 2000). Sensitivity analyses showed that uncertainties in our measured C_{pyr} and S_{pyr} (±20% variations) could not account for the discrepancy. If slow desorption was still occurring, the Q_d values should depend on R_{sw} and particle size. One would expect that the deviation from equilibrium should increase with smaller R_{sw} or with larger particle size (see Eqn. 2 - 7). Both effects were seen in our results (Figure 2-12b). This suggested that desorption was still proceeding after 3-8 months.

However, it is also possible that K_d values may have been underestimated due to use of inaccurate K_{bc} values. Accardi-Dey and Gschwend (2002) found a $\log K_{bc}$ of 6.25±0.14 using unsieved Boston Harbor sediment and pyrene-spiked water. With polyethylene-sediment equilibration experiments to follow native pyrene, Lohmann et al. (2005) found

a logK_{bc} of 6.4±0.26 for Boston Harbor and New York Harbor sediments. In contrast, Adams (2003) conducted a pyrene desorption kinetic experiment on sieved sediments from Lower Hudson Estuary (NY) at conditions similar to ours (diameter = 38-88 um, R_{sw}~300 mg_{solids}/L). Although the desorption period in Adams' study was only 10 d, if these results represented equilibrium, then a logK_{bc} of 6.8±0.4 was estimated. If this logK_{bc} value is used, then most of the Q_d's, observed in our study after a 3- to 8-month period match the expected K_ds (Figure 2-12a).

The discrepancies in reported K_{bc}s for similar sediments may be due to sieving. Sieving may leach competing sorbates present in the natural solids and thereby increase the K_{bc} for a particular case This is consistent with the lower logK_{bc} observed by Accardi-Dey and Gschwend and Lohmann et al. (Accardi-Dey and Gschwend 2002; Adams 2003; Lohmann et al. 2005), where unsieved sediments were used. Sieving may also fractionate the mix of BC solids present and pyrene may exhibit different affinities (per unit sorbent mass) for various BC materials such as fossil-fuel derived soots and biomass burning chars. We are currently testing these hypotheses and by characterizing the BC in our sediments with electron microscopy.

In summary, our analysis suggested that either desorption was still proceeding after the 3-8 months or that we did not accurately estimate K_d values. Regardless of whether the plateau represented sorption equilibrium or not, it took from weeks to months for the three size fractions to reach that apparent plateau.

3.3.3. Limitations

Our approach certainly has some limitations. First, time-gated LIF is not suitable for HOCs with short fluorescence lifetimes. Second, stirring to keep the particles in suspension may lead to the degradation of the sediment aggregates over time. An experiment on the large size fraction (180-250 um) showed that ~50% of the particles were reduced to <180 um during a 3-d continuous stirring. This partially explained why the kinetic dependence on particle size was less distinctive despite a 4-times difference in size (see Figure 2-11). This experimental artifact, however, would not change the qualitative observation of long equilibration times because desorption would have proceeded even more slowly had the aggregates remained intact. Finally, LIF is susceptible to non-ideal effects such as light scattering, inner-filter effects, and wall effects; and these must be accounted for in any experimental design.

3.3.4. Implications and Significance

One problem of great practical importance has involved quantifying the fates and effects of solid-associated HOCs for real world sites of interest. The dissolved concentration of an HOC is often used to evaluate an HOC's bioavailability (Cornelissen et al. 1998b; Lamoureux et al. 1999; Ghosh et al. 2003; Huesemann et al. 2003; Jager et al. 2003; Ahn et al. 2005b; Gomez-Lahoz et al. 2005; Cornelissen et al. 2006); but to use this approach for sediment beds, one must assume sorptive equilibration, a criterion that is never checked in the field. In Boston Harbor cores (McGroddy et al. 1995), it has been shown that the surficial bed sediments and the porewater are not in equilibrium, even when adsorption onto BC has been considered (Accardi-Dey and Gschwend 2003).

The major physical processes controlling sediment-water contact times can be relatively fast at some sites in comparison with the week to month equilibration times observed in this study. This suggests that both the rate of release and the distribution of HOCs in different phases in harbor/estuary systems are kinetically determined, and use of a sorption equilibrium model may be quite inaccurate for HOCs.

4. Conclusion

We have successfully demonstrated a new way of studying desorption kinetics of natively bound sedimentary pyrene using time-gated laser-induced fluorescence (LIF) spectroscopy. It has been well documented that soil/sediment bound HOCs become mobilized very rapidly in the early time of desorption process, and that this rapid release fraction is closely connected with and/or representative of the bioavailability of the HOCs. With the minute-scale observations made possible by the LIF system, we can now advance our kinetic understanding on the release of HOCs in the early desorptive period.

Furthermore, LIF is superior to conventional analytical methods in that it can detect pyrene at levels as low as 1 ng/L with minimal sample loss and/or disturbance. In recent years, an alternative method – which uses secondary solid-phase organic/plastic media as sampling device for kinetic observations – has been widely adopted in the study of HOCs desorption kinetics. The secondary-medium method has at least one potential problem, that its presence in the system can interfere or make ambiguous the desorption dynamics of the HOCs in question. In this respect, LIF is a fairly 'neutral' and non-interfering method.

The most significant analytical limitation of time-gated LIF is certainly that it is only suitable for HOCs with relatively long fluorescence lifetimes (when compared to the background fluorescence signals from dissolved or solid organic matter). A less serious problem of LIF is that fluorescence methodology is susceptible to the non-ideal effects of light scattering, inner-filter effects, and wall effects. However, these can be properly accounted or corrected for.

The efficacy of LIF was demonstrated in the tracking the desorption dynamics of pyrene from Boston Harbor sediment. The observed dynamics with respect to both particle size and solid-to-water ratio were consistent with diffusion physics. Toward the end of the 4–8 month long experiments, desorption of pyrene appeared to have reached a plateau level. It was unclear if sorption equilibrium was established at the end of the experiment. There were evidence supporting either the claim of very slow desorption or the claim of equilibrium for the end-point observations.

Regardless of the interpretation of the desorption end-point, the data suggested that the characteristic desorption-time of pyrene from fine sediments, and by inference other sediment-bound hydrophobic organic compounds (HOCs) of similar hydrophobicity, very likely exceeds the typical characteristic-times for pore water flushing and

resuspension events. Consequently, assuming local sorption equilibrium in modeling efforts would be inappropriate.

Chapter 3. Equilibration of HOC Partitioning in Sediment-Water System

CHAPTER ABSTRACT

Sorption equilibrium may serve as a baseline for assessing the fate of hydrophobic organic compounds in geosorbent-water systems. Recent reviews, however, suggested that the partitioning of Hydrophobic Organic Compounds (HOCs) in soil/sediment-water systems is highly variable. Furthermore, sorption equilibrium is also critical in understanding phenomena such as sequestration, irreversible sorption, and the release kinetics of solid-associated HOCs. The sorption equilibrium of HOCs was re-examined using pyrene as a surrogate organic pollutant.

Analyses suggested that monthly timescales were required for the three experiments (Short-Term Desorption Experiment, Long-Term Desorption Experiment, and Long-Term Adsorption Equilibrium Experiment) to reach equilibrium. The observation of monthly or longer equilibration times for the three experiments suggested that many previous HOC sorption studies may not have reported truly equilibrium observations. From this study and the experimental conditions of previous sorption studies, it appeared that a monthly or longer equilibration time was necessary for PAH sorption experiments with typical sorbent and system properties.

A general guideline for estimating/assessing equilibration time was proposed to assist the interpretation of HOC sorption data and the planning of sorption experiments. The actual required incubation time is dependent on an array of physical and chemical factors that affect uptake or release kinetics of PAHs. It is recommended that equilibrium should be checked using on-going kinetic data and *a priori* modeling of sorbate uptake or release.

The need to study HOC sorption with longer incubation time has profound implications on the interpretation of existing sorption literature as well as how sorption of HOCs in natural geosorbents may be understood. It appears that irreversible sorption might be less frequent than past studies have claimed/suggested.

Table of Content for Chapter 3

1. Chapter Introduction, Scope, and Objective 54

1.1. Introduction 54

1.1.1. Assessing the Fate of Pollutants in Complex Natural Systems 54

1.1.2. Chemical Equilibrium as an Evaluative Baseline 54

1.2. Motivations 55

1.2.1. Variability in Prediction of HOCs Partitioning onto Natural Sorbents 55

1.2.2. Persistence of non-volatile HOCs in the Soil/Sediment Environment 56

1.2.2.1. Persistence or Sequestration of HOCs 56

1.2.2.2. Extractability/Lability of Sorbed HOCs 56

1.2.2.3. Irreversible Sorption 57

1.2.3. Sorption Equilibrium as Foundation for Kinetic Phenomena 57

1.2.4. Extrapolative Prediction of HOCs Sorption in Natural Systems 58

1.3. Objective 58

2. Methodology 59

2.1. Materials 59

2.1.1. Sediment 59

2.2. Experiments 59

2.2.1. Long Term Extended-Range Pyrene Adsorption Equilibrium Experiment 59

2.2.2. Short-Term Desorption Experiment 60

2.2.3. Long-Term Desorption Equilibrium Experiment 60

2.3. Methods/Analyses 60

2.3.1. Measurement of Dissolved Pyrene 60

2.3.2. Solid-to-Water Pyrene Distribution Coefficients (Q_d, K_d) 61

2.3.3. Pyrene Mass Conservation 62

2.3.4. Sediment/Suspension Extract Analysis by GC-MS 62

2.3.5. Sedimentary Organic Carbon & Black Carbon Measurement 62

2.4. Instrumental Uncertainties & Error Analysis 62

2.4.1. Analytical Uncertainties 62

2.4.2. Pyrene Conservation for Sorption Equilibrium Experiment 63

2.4.3. Q_d Uncertainty in Extended-Range Sorption Equilibrium Experiment 63

3. Results & Discussion 63

3.1. Equilibration of Pyrene Sorption Experiments 63

3.1.1. Determining Equilibrium: By Slope or by Matching $C_{pyr}(t)$ Measurements 63

3.1.2. Equilibration of Short-Term Desorption Experiment 64

3.1.3. Equilibration of Long-Term Desorption Equilibrium Experiment 64
3.1.4. Equilibration of Long Term Extended-Range Pyrene Adsorption Equilibrium Experiment 65
3.2. Equilibration of Generic HOCs Sorption Experiments 65
3.2.1. Typical Sorption Experiment Insufficiently Equilibrated 65
3.2.2. Equilibration Time as Suggested by Past Sorption Studies 66
3.2.2.1. Equilibration Time for Low-TOC Systems 66
3.2.2.2. Equilibration Time for BC-Dominated Systems 66
3.2.3. General Guideline for Sufficient Equilibration 67
3.2.3.1. Extrapolating Equilibration Time from Early Kinetic Observations 67
3.2.3.2. Comparing Concentrations at Two Distant Times 67
3.2.3.3. A priori Estimate of Equilibration Time 67
3.3. Implications of Long Equilibration for HOCs Phase-Partitioning 68
4. Conclusion 69

1. Chapter Introduction, Scope, and Objective

1.1. Introduction

1.1.1. Assessing the Fate of Pollutants in Complex Natural Systems

The assessment of the fate of organic pollutants in natural environment or their impact on biological communities is often complicated by the multitude of processes (degradations, adsorption, absorption, volatilization, advection, diffusion, etc), and phases (sediment, water, air, various boundary layers and sub-compartments) involved. Furthermore, there are physical factors such as geometry of the compartments (e.g. size and shape of estuaries), hydro/aero-dynamics in the system, or distribution uniformity of phases/biomass/pollutants. Although all these factors collectively contribute to the fate of organic pollutants in natural systems, often only a few of them are the dominating factors in a given system.

The great improvement in computational power in recent years potentially allows the modeling of all physical and chemical processes relevant to the fate of organic pollutants at high spatial/temporal resolutions and attentive to high levels of theoretical details But to take every case by such approach is not only inefficient but also difficult – for such models often require large number of observation points of the system as initial and/or boundary conditions. Moreover, many such 'realistic models' are only selectively realistic – they are often comprehensive only in a particular aspect (e.g. hydrodynamic or chemical) of the system. To the limited knowledge of the author, the literature of environmental fate and transport has yet seen a truly robust computational package where physicochemical theories developed from different disciplines are assembled at adequate and yet comparable depth. Thus, to resort to a particular computationally intensive model implies making implicit assumptions regarding the relative importance of the chemistry, the hydrodynamics, the sedimentary transport, or the biology of the studied system.

From the regulatory and engineering points of view, it is useful to establish a basecase/baseline scenario for any investigated system. Such basecase scenario serves as a reference state for the natural state (or an engineered state) of the system. With respect to the fate of pollutants in environmental systems, the questions are now the following:

1. How should the basecase be formulated in a given system?
2. Is it possible to have a unified approach to all environmental systems, with all the variability in geochemical, physical, and pollutant characteristics be explained?
3. What is the set of minimal properties to quantify such a basecase?

1.1.2. Chemical Equilibrium as an Evaluative Baseline

System chemical equilibrium – or chemical equilibria among all compartments/phases in the system of interest – may provide a general evaluative baseline common for various questions. By considering chemical equilibrium as the basecase scenario, one eliminates the complexity arises from interphasal transports and temporal variability.

The basecase scenario is now a function of basic physicochemical properties: those of the pollutants and the constituent phases/compartments. This implies that a universal and *a priori* "sea-level" of the chemical behavior of pollutants can be established from a minimal set of system information/properties, and thus allowing different systems to be compared from a common origin.

More specifically, for low volatility persistent organic compounds (e.g. Polycyclic Aromatic Hydrocarbons (PAHs); Polychlorinated Biphenyls (PCBs)) in water bodies, the solid-water chemical partitioning is the key determinant of the system equilibrium baseline. It is believed that organic phases (e.g. protein, lipid, aged/weathered plant tissues) in natural geosorbents hold up most of the solid-bound organic compounds. The partitioning of organic compounds in various organic phases-water systems thus holds the key to understanding the basecase scenario for fate or bioavailability questions. The continuing interest and effort in understanding the equilibrium partitioning of HOCs in different solid-water systems and the various attempts to characterize the geosorbent organic phases over the last 30 years (e.g. Chiou et al. 1979; Karickhoff et al. 1979; Means et al. 1980) are the manifestation of such belief.

1.2. Motivations

1.2.1. Variability in Prediction of HOCs Partitioning onto Natural Sorbents

Despite the great number of studies on HOC sorption equilibrium, substantial variability and uncertainty still hinder our ability to predict accurately (i.e. within a factor of 2) the equilibrium partitioning of HOCs in natural solid-water systems. Organic carbon (OC) and black carbon (BC), which are both ubiquitously present in natural geosorbents, have been identified to be the dominant phases controlling the extent of HOCs uptake in solid phase (Cornelissen et al. 2005b).

However, the recent reviews by Hawthorne et al. (2006, 2007) strongly suggested that we do not have universally valid quantitative partitioning models for OC or BC yet. They examined the solid-to-water partitioning of PAHs in 100+ sediment samples from sites where the PAHs have undergone decades of field aging. They found that both K_{OC} and K_{BC} for a particular PAH varied over 3-4 orders of magnitude (Hawthorne et al. 2007). Variation in K_{OC} for PCDD/Fs as high as 2 log units has also been reported (Kim et al. 2004). A more recent review by Arp et al. (2009) on the sediment-porewater partitioning of PAHs/Cl-PAHs concluded with a very pessimistic tone. First, they concluded that the most currently accurate models (coal-tar free energy relationship and the Raoult's Law models) – which have no place for quantitative OC or BC – can predict phase distribution only within a factor of 30. Second, they concluded that due to compositional diversity and structural complexity of natural geosorbents, accurate phase distribution behavior can only be measured on a site-by-site basis.

The reviews by Hawthorne et al. and Arp et al. seem to suggest that the *a priori* predictive approach for HOCs sorption in natural systems is doomed to be unattainable. It should be emphasized, however, that their findings neither logically imply that the classical OC and/or BC conceptualization of HOC sorption is faulty, nor sufficiently prove the ultimate failure of the *a priori* approach. The flaws in the current predictive

models could mean (i) that the simple OC-BC binary model fails to capture the mechanistic complexity of sorption phenomena occurring in natural systems, (ii) that our definitions of OC and/or BC, which are both operational in nature, requires re-examination and refinement, and/or (iii) that the sorption equilibrium experiments upon which the predictive models are constructed/derived may be partly faulty.

1.2.2. Persistence of non-volatile HOCs in the Soil/Sediment Environment

1.2.2.1. Persistence or Sequestration of HOCs

A question of great interest is what causes the persistence of certain HOCs in natural environments. The persistence of various HOCs in the soil/sediment environment long after they were being emitted or produced is well documented (Singh et al. 1995; Kraaij et al. 2002; Moermond et al. 2007; Yang et al. 2008). While their resilience to natural transformations (e.g. oxidation, biodegradation) can be explained by their highly stable chemical structures, their persistence in the solid-phase environments is somewhat perplexing – why and how did these residual HOCs remain in soil/sediment, withstanding decades of leaching or flushing?

The apparent resistance of field-aged HOCs to long-term volatilization, dissolution, or biodegradation, hereafter referred to as **Sequestration**, is rather unexpected from the thermodynamic observations gathered from standard sorption studies using soils/sediments as model natural sorbents. The disagreement between the observed persistence and the expected dissipation implies the existence of significant knowledge gap in phase-partitioning thermodynamics and/or the transport/transfer kinetics.

1.2.2.2. Extractability/Lability of Sorbed HOCs

A related theme of the persistence of solid-bound HOCs is their extractability over time of exposure in soil/sediment. It has been observed that the chemically extractable fraction of soil/sediment-bound HOCs always decreases with increasing incubation/exposure time (or 'aging'). This has been demonstrated by a number of moderate- to long-term studies (6 mo. or longer) on various infamous organic pollutants and xenobiotic toxins: 3-5 rings PAHs (Northcott et al. 2001a, b), DDT and its derivatives (Singh et al. 1995), explosives such as TNT (Hundal et al. 1997; Robertson et al. 2005) and RDX (Singh et al. 1998), polychlorinated dibenzo-*p*-dioxins/dibenzofurans (PCDD/Fs) (Adriaens et al. 1995), polychlorinated biphenyls (PCBs) (Moermond et al. 2007), and various herbicides (Barriuso et al. 1997; Johnson et al. 1999; Schnitzler et al. 2007).

How can a fraction of the sorbed HOCs become inaccessible even to extraction by organic solvent? Why does the extractability decrease with longer incubation time? For example, up to 30-40% of the "sorbed" TNT could be irreversibly bound with the soil humic substances in the form of chemical linkage to existing humic chains (Hundal et al. 1997).

For other HOCs where such 'humification' is less likely, the unextractable fraction possibly signifies the fraction that is reversibly bound but with its release rate limited by mass transfer through soil/sediment organic matter (Gilchrist et al. 1993; Adriaens et al. 1995; Northcott et al. 2001a). This interpretation of the unextractable HOCs is further

supported by the fact that the desorption kinetics of a fraction of the natively-bound/field-aged HOCs (for instance, PAHs, PCBs, PCDD/Fs) is generally very slow (Cornelissen et al. 1998a; ten Hulscher et al. 1999; Kuo et al. 2007; Sormunen et al. 2008).

1.2.2.3. Irreversible Sorption

An alternative explanation for the sequestration of HOCs in soils/sediments is that the sorbent matrices undergo structural changes which allow a fraction of the sorbed HOCs to be entrapped and thus made inaccessible to phase partitioning. Such scenarios would lead to an *apparent solid-water distribution coefficient*, $\mathcal{K}_d$ (=total solid-phase concentration/dissolved phase concentration), that varies over time (presumably increases over time as more sorbed HOCs become inaccessible), as the sorbent matrix undergo structural alteration/rearrangment. Studies have reported/claimed that a significant discrepancy between $\mathcal{K}_d$ derived from adsorption vs desorption experiments, and that the desorption-derived $\mathcal{K}_d$ is always higher. This discrepancy in $\mathcal{K}_d$, also known as **Sorption Irreversibility** or **Sorption Hysteresis** (Fu et al. 1994; Huang et al. 1997a; Hatzinger et al. 2004), has been reported/claimed for PCBs (DiToro et al. 1982; Hunter et al. 1996), PAHs (Fu et al. 1994; Huang et al. 1997a; Ran et al. 2003a), TNT & RDX (Sheremata et al. 1999; Hatzinger et al. 2004), and herbicides such as atrazine (Laird et al. 1994; DeSutter et al. 2003; Krutz et al. 2003) and others (Graham et al. 1992; Carton et al. 1997; Morrica et al. 2000).

Although irreversible sorption of HOCs in natural soils/sediments has often been claimed, its mechanism has rarely been elucidated. To the author's limited knowledge, the only mechanistic study on irreversible sorption with convincing evidence has been conducted using high surface-area pure charcoal as sorbent (Braida et al. 2003). How irreversible sorption may proceed in natural matrices has yet to be demonstrated. Even if sorption of HOCs in natural soils/sediments indeed takes place irreversibly, is it still possible to predict phase distribution behavior of HOCs in natural systems?

1.2.3. Sorption Equilibrium as Foundation for Kinetic Phenomena

The equilibrium partitioning behavior of HOCs also forms an important foundation for quantitative analysis or prediction of kinetic-dependent phenomena: it dictates how the transport of HOC may be slowed down (or retarded) in the presence of sorptive solids. In estuarine systems, for instance, HOCs may undergo inter-phase transports when (i) contaminated sedimentary aggregates are resuspended into water column by tidal waves, (ii) porewater of the surficial bed is flushed out and replenished, (iii) aerosols loaded with high concentrations of HOCs are deposited and undergone settling, or (iv) algae, benthic biota, or fishes take in (or exude) organic-rich particulates. While the activities of HOCs are transient on the systemic scale, on a local and microscopic scale, chemical equilibrium should exist at the interface. Thus the overall dynamics will depend upon both the nature of the interfacial/interphasal equilibrium and how the effect of the interfacial equilibrium is felt on the systemic scale (see, for instance, the kinetics of desorption in Chapter 7).

1.2.4. Extrapolative Prediction of HOCs Sorption in Natural Systems

A significant gap exists between the HOC levels in the field and the HOC levels examined in laboratory studies. For instance, earlier sorption studies on PAHs (Chiou et al. 1979; Karickhoff et al. 1979; Means et al. 1980; Chin et al. 1992; Kan et al. 1994; Huang et al. 1997b; Chiou et al. 1998; Xia et al. 1999; Johnson et al. 2001a; Accardi-Dey and Gschwend 2002; Kleineidam et al. 2002) were often restricted to the μg/L range due to limitations of analytical capacities. The field-observed PAHs levels, however, are often in the ng/L levels, in both the sediment porewater phase (McGroddy et al. 1996; Lohmann et al. 2005) and the water column (Bouloubassi et al. 1991; Law et al. 1997; Rudnick et al. 1998; Adams et al. 2007). Bridging the gap between laboratory-studies and field observations may provide partial answer to the phenomenon of sequestration.

It is often assumed that isotherms derived from laboratory sorption studies (often in the μg/L range) can be extrapolated for predicting dissolved phase PAHs in the field (often in the ng/L range). This assumption, which is implicit in the construction of generic equilibrium partitioning models such as linear free-energy relationships (Nguyen et al. 2005) has remained unexamined. It is thus imperative to validate the extrapolative approach, which is currently held unquestioned. The phenomenon of sequestration may be partially explained as an artifact arisen from extrapolation. The advancement in both instrumentation (e.g. time-gated laser-fluorescence spectroscopy; Rudnick et al. 1998) and various pre-concentration methods (e.g. polymeric devices as concentration medium for hydrophobic analytes; Cornelissen et al. 2004b; ter Laak et al. 2006) now allows the ng/L range sorption behavior to be explored.

1.3. Objective

The above discussion suggests that it is necessary to re-examine HOCs partitioning in solid-water systems more thoroughly. The current physicochemical characterization of the geosorbent organic phases, or even the physicochemical picture of how sorption takes place in natural geosorbents, may require revision. This chapter and the following (Chapter 4 & 5) will re-examine equilibrium partitioning using pyrene as model sorbate and sediment-water as representative environmental system.

The main objective of this chapter is to follow up on a question from previous chapter: were the end observations of the desorption experiment documented in Chapter 2 at equilibrium[1]?

[1] See Chapter 2, section 3.3.2.

2. Methodology

2.1. Materials

2.1.1. Sediment

Sediment was collected from the Moon Head area (42°18.10'N, 71°00.00'W) in North Quincy Bay, Boston, in December, 1999. It was wet-sieved with water[2] to give a size fraction with particle diameter less than 425 μm (hereafter referred as NQB/BH#6 <425 μm) and a solid content of about 40% by weight. This size fraction was used for the Long Term Extended-Range Pyrene Adsorption Equilibrium Experiment (section 2.2). A second size fraction (dia.: 38-75 μm) (hereafter referred as NQB/BH6 38-75 μm), which contained about 45% solids by weight, was used for the Long-Term Desorption Equilibrium Experiment (section 2.2.3). Both sieved sediment fractions were stored in amber glass jars at 5°C.

2.2. Experiments

2.2.1. Long Term Extended-Range Pyrene Adsorption Equilibrium Experiment

A series of sorption equilibrium experiments on pyrene was performed in a suspension consisted of the sieved sediment (dia. <425 μm) and aqueous pyrene solutions at different temperatures. Pyrene and the sieved sediment were selected as model HOC and model natural geosorbent, respectively. Aqueous pyrene solutions were prepared from stock solution (1000 μg pyrene/mL methanol, EPA-1157, Ultrascientific) in clean water (see Aries system above) to give initial pyrene concentrations of 50, 500, 5000, and 25000 ng/L. A series of sediment suspensions were prepared in these pyrene solutions with solids-to-water ratio (R_{sw}) ranging from ~20 to ~600 mg_{solids}/L. The exact solid content of the sieved sediment was determined prior to experiment by drying (60°C). Each suspension contained an appropriate mass of sediment in 120 mL of pyrene solution (ranging from 50 to 25000 ng_{pyr}/L). These suspensions were kept in 125-mL narrow-mouthed amber glass bottles (soap-washed, dried, pre-combusted overnight at 450°C, aluminum sealed) to minimize photodegradation and volatilization. The equilibrium experiment was carried out at four temperatures: 6°C (refrigeration unit, Puffer Hubbard), 15°C (bath-circulator unit, Forma Scientific), 22°C (laboratory ambient temperature), and 37°C (water bath, Thermomix 1419, B. Braun). At each temperature, 24 suspensions (6 for each initial pyrene concentration) were prepared. In order to minimize biodegradation, all solutions and suspensions contained 10 mM sodium azide (Fluka Chemika). A total equilibration time of ~10 months was allowed. All suspensions were hand-tumbled (10 times end-to-end) daily for the first 5 months, and then once every few days for the later months. Controls (pyrene solution without sediment) were prepared to monitor pyrene loss due to non-sorption processes. They showed a pyrene loss of <10% over the 10-month period. An independent check on a separate series of pyrene standards also showed a loss of ~10% over a 14-month period.

---

[2] An Aries system consisted of an ion exchange unit, an activated carbon filter, a UV oxidation unit, and a 0.22 μm filter.

2.2.2. Short-Term Desorption Experiment

This was the native pyrene desorption experiment on three size fractions of the NQB/BH#6 sediment as described in Chapter 2. Briefly, sediment suspensions (NQB#6; dia.: 38-75, 75-106, 180-250 μm) were prepared in initially pyrene-free water to allow solid-bound pyrene to release over time. Although the release kinetics of solid-associated pyrene had been the main interest, all suspensions were allowed to equilibrate for a total time period of ~4-8 months. Please refer to Chapter 2 (or Kuo et al. 2007) for details on experimental conditions and physicochemical properties of the sediment fractions.

2.2.3. Long-Term Desorption Equilibrium Experiment

This experiment was conducted to evaluate whether equilibrium was established in the later observations of the Short-Term Desorption Experiment. To ensure partitioning equilibrium, we (i) used only the 38-75 μm NQB#6 sediment, which was the smallest size fraction in the Short-Term experiment, (ii) subjected the fraction to the presence or absence of mechanical grinding, and (iii) extended the equilibration time period to 12 months. A portion of the original sediment fraction (dia.: 38-75 μm) was hand-ground with mortar and pestle (agate, dia.~4-5 cm) for 15 min. The solid contents of both ground and unground fractions were determined (dried at 60°C and weighed). Suspensions of sediment were then prepared in 125 or 250 mL narrow-mouthed amber glass bottles (soap-washed, dried, pre-combusted overnight at 450°C, aluminum sealed) with solids-to-water ratio (R_{sw}'s) at approximately 1000, 2000, and 4000 mg_{solids}/L_{water}. The suspensions, with either ground or unground sediment, were continuously tumbled (at ~20 rpm) for the first month, and then hand-tumbled daily for the next 3-4 months and once a few days for the remaining time. Measurements of dissolved pyrene were taken at various times, and the suspensions were also allowed to settle for at least 3-5 days in advance. The pre-measurement settling ensured a clear supernatant zone for TG-LIF analysis. The last measurements were taken 12 months after the beginning of the experiment.

2.3. Methods/Analyses

2.3.1. Measurement of Dissolved Pyrene

Dissolved pyrene concentrations were measured by synchronous fluorescence spectroscopy (Syn-F) and time-gated laser-induced fluorescence spectroscopy (TG-LIF) depending on the concentration range. The two analytical methods were chosen for their capability to filter out interferences from non-pyrene sources. The Syn-F, with a detection limit of ~0.5 $\mu g_{pyr}/L$, was used for measuring the μg/L-level of dissolved pyrene (i.e., suspensions with initial pyrene concentrations of 5000 or 25000 ng/L). The ng/L range measurements (i.e., suspensions with initial pyrene concentrations of 50 or 500 ng/L) were taken using TG-LIF. The sensitivity of TG-LIF has decayed considerably and its detection limit was only about 10 ng_{pyr}/L at the time of the sorption experiment. To ensure measurement consistency, the pyrene calibration standards used in Syn-F and TG-LIF were all prepared from the same original stock solution.

Synchronous Fluorescence Spectroscopy (Syn-F). In Syn-F, the fluorescence emissions from an excited solution are captured at a delta wavelength ($\Delta\lambda$). Undesirable interferences can be minimized by selecting an optimal $\Delta\lambda$ for a given analyte. The Syn-F system used (Luminescence Spectrometer LS50B, Perkin Elmer) was set to the following scan conditions for the measurement of dissolved pyrene: start-scan wavelength = 300 nm, end-scan wavelength = 350 nm, $\Delta\lambda$ = 50 nm, excitation slit = 5.0 nm, emission slit = 8.0 nm, and scan speed = 150 nm/min. The Syn-F system was very stable and only required calibration once a day of measurement (~3-4 hr). Dissolved pyrene concentrations were inferred from the peak heights of emitted spectra at 371 nm and 384 nm. The instrument response was linear over the studied concentration range (0-25 $\mu g_{pyr}/L$) (Appendix 3-1).

Time-Gated Laser-Induced Fluorescence Spectroscopy (TG-LIF). In TG-LIF (Rudnick et al. 1998; Kuo et al. 2007; Hawthorne et al. 2008), laser pulse-induced fluorescence emissions are subjected to time-filtering, and only signals emitted within specified time window (on the order of ns) are registered. It is particularly suitable for analysis of fluorophores with long fluorescence decay-lifetimes (e.g. pyrene, decay-lifetime ~120 ns) because most of the background fluorescent responses are short-lived (of order 10 ns). The system configuration and measurement procedure were identical to those described previously (Kuo et al. 2007; see also Chapter 2). For detailed description of the system, please refer to the original publications (Rudnick et al. 1998) Briefly, photon pulses at 337 nm are generated to excite dissolved pyrene in sample. Each individual pulse triggers the time-gating mechanism, which allows only the fluorescence emitted 128-256 ns after the pulse-excitation to be counted. For pyrene quantification, the peak height at ~387 nm of the collected spectrum was used. The instrument response was linear over the studied concentration range (0-500 ng_{pyr}/L) (Figure 3-1).

2.3.2. Solid-to-Water Pyrene Distribution Coefficients (Q_d, K_d)

Solid-to-water pyrene distribution coefficients (Q_d), defined as the ratio of solid-bound pyrene (S_{pyr}) to pyrene in aqueous phase (C_{pyr}) at a particular time Eqn. 3 - 1, were determined by mass balance on pyrene before and after the sorption experiment Eqn. 3 - 2.

$$Q_d = \frac{S_{pyr}(t)}{C_{pyr}(t)}; Q_{d,t\to\infty} = K_d$$

Eqn. 3 - 1

$$S_{pyr,o} M_{solids} + C_{pyr,o} V_{water} = S_{pyr,t} M_{solids} + C_{pyr,t} V_{water}$$

Eqn. 3 - 2

where M_{solids} and V_{water} denote the mass of solids [kg] and the volume solution [L] in a bottle, respectively; the subscript 'o' and 't' denote the initial state and the state at time t, respectively. Since the initial pyrene masses in all bottles were known, the solid phase pyrene concentration at time t, $S_{pyr,t}$, can be determined if $C_{pyr,t}$ was known from Syn-F or TG-LIF measurements.

2.3.3. Pyrene Mass Conservation

Since the solid-to-water pyrene distribution coefficients (Q_d) were estimated under the supposition of pyrene conservation, mass balance check was performed on eight selected samples representative of different sorption conditions (e.g., temperature, R_{sw}'s, initial pyrene concentration) after 10 months of equilibration. The end-of-sorption pyrene concentrations (both solid and aqueous phase) were determined with Syn-F or TG-LIF in combination of gas chromatography-mass spectrometry. Briefly, the selected samples were allowed to settle for a week, after which 100-110 mL of supernatant was transferred to clean bottles. Pyrene contents in the transferred supernatants were determined by either Syn-F or TG-LIF. The remaining 10-20 mL of suspensions were quantitatively extracted, transferred, and pre-concentrated in hexane. These extracts were analyzed with GC-MS.

2.3.4. Sediment/Suspension Extract Analysis by GC-MS

Pyrene contents of the original sediment and the suspensions/slurries (i.e., section 2.3.3) were analyzed by gas chromatography-mass spectrometry (GC-MS). Sediment/slurry samples were extracted with dichloromethane-methanol mixture (9:1 v_{DCM}/v_{MeOH} ratio; 5 x 25 mL mixture) in amber glass vials, concentrated (evaporation, N_2-drying), and quantitatively transferred into hexane. For the original sediment fractions (i.e., dia. <425 μm and 38-75 μm), three replicates were extracted/processed and analyzed. As for the end-of-sorption suspensions, there was no replicate for any specific sorption conditions. The concentrated extracts were then analyzed on a HP-JEOL GC-MS system (HP-6890 GC system, Hewlett Packard; JMS-GCmate, JEOL) as described previously (Accardi-Dey and Gschwend 2002; Adams 2003). Deuterated pyrene (d_{10}-pyr) and p-terphenyl (d_{14}-p-terp) were used as recovery and injection standards, respectively. The % recovery of d_{10}-pyr ranged from about 95-110% for the original sedimentary extracts, and from about 85-100% for the suspensions selected for mass balance check.

2.3.5. Sedimentary Organic Carbon & Black Carbon Measurement

Organic carbon (OC) and black carbon (BC) contents of the samples were measured by elemental analysis after proper thermal oxidation procedures (Accardi-Dey and Gschwend 2002). Sediment sample was first dried overnight at 60°C. Then, a known, appropriate mass (~2-6 mg) of the sample was spread out on an unfolded silver capsule (8×5 mm, Elemental Microanalysis). The sample was then acidified (H_2SO_3, 6.3%, Fischer Scientific) to remove inorganic carbonates and re-dried at 60°C. Some of these capsule-samples were analyzed for total organic carbon (TOC) by CHN elemental analyzer (Vario EL-III; Elementar); others were subjected to thermal oxidation at 375°C in air for 24 hr, which were then analyzed for BC content also with elemental analyzer. The OC content was determined as TOC less BC.

2.4. Instrumental Uncertainties & Error Analysis

2.4.1. Analytical Uncertainties

The uncertainties associated with measurements from Syn-F, TG-LIF, and GC-MS were at acceptably low levels. Syn-F had the best precision, with a <2% uncertainty in all

measurements. TG-LIF gave more varied results, typically with uncertainty level ranging from 5 to 15%. Higher levels of uncertainty were present in samples with concentration of the order 10 ng_{pyr}/L, and the precision improved to <10% for samples above ~100 ng_{pyr}/L. GC-MS measurements had the highest uncertainties. The uncertainties in solid-phase pyrene concentrations associated with the original sediment fractions were 8 and 20%, for the 38-75 μm and the <425 μm fractions, respectively. The errors in other PAHs were also <20% in general. Small experiments on measurement order and time-lag revealed that both short-term and long-term instrumental drifting was insignificant (<5%) and that same level of inter-replicate variability was consistently observed (Appendix 3-1). This implied that the observed uncertainties in the replicates were most likely coming from (i) sample-to-sample heterogeneity and, (ii) inconsistency during the extraction/pre-concentration steps.

2.4.2. Pyrene Conservation for Sorption Equilibrium Experiment

Generally, the mass balance check on the end-of-sorption suspensions (section 2.3.3) suggested that pyrene was not conserved over the 10-month period. A conservation plot showed that, on average, about 20% of the initial pyrene was lost (Figure 3-2). The 1-to-1 line was within the reach of 1σ for six data points. Two of the eight observations, however, deviated substantially from the regressed line: one as the final total pyrene significantly less than the initial, one as the opposite (Figure 3-2). Since GC-MS showed satisfactory % recovery on both extracts (~85 to 90%), it was unlikely that the discrepancies were due to mishandling during the extraction/pre-concentration steps. The final equilibrium data points were corrected for pyrene loss (Appendix 3-2).

2.4.3. Q_d Uncertainty in Extended-Range Sorption Equilibrium Experiment

The uncertainty in Q_d ($=S_{pyr,t}/C_{pyr,t}$) – uncertainty propagated based on 1 σ's – was around 15-20% on average (depending on what mass correction scheme was applied). Scattering on Q_d uncertainties was observed, with some as low as ~5% and some as high as ~60% (Appendix 3-1). Uncertainty in $S_{pyr,t}$ (uncertainty propagated based on 1 σ's) was the dominant source of error in Q_d, and the variability of the error was rooted in the estimation of $S_{pyr,t}$ from mass balance. The estimation, the summary, and the distribution diagram of Q_d errors are included for reference (Appendix 3-1).

3. Results & Discussion

3.1. Equilibration of Pyrene Sorption Experiments

Any discussion on partitioning/sorption experiments from a thermodynamic perspective would be inappropriate without the assurance that the studied system has indeed reached chemical equilibrium (i.e. K_d rather than $Q_d(t)$; see Eqn. 3 - 1).

3.1.1. Determining Equilibrium: By Slope or by Matching $C_{pyr}(t)$ Measurements

Sorption (adsorption/desorption) equilibrium can be recognized when no system or component properties are varying with time. This can be confirmed by checking (i) the rate of change of sorbate concentration (i.e., a zero $\Delta C_{pyr}/\Delta t$) over a significant time

period, or (ii) the correspondence/matching between C_{pyr}'s observed at two different but well-separated times. Although the rate-of-change approach will give the most convincing evidence for establishment of chemical equilibrium, it requires frequent concentration observations over time. The correspondence approach, on the other hand, relies only on observations made at two particular times, and is therefore not as comprehensive as the rate-of-change approach. In either case, the choice on the length of time-period/time-frame of analysis is crucial – for the analyst can always define a small enough time-period of analysis to conclude that sorption equilibrium has been established.

3.1.2. Equilibration of Short-Term Desorption Experiment

By the end of a 4-month period, chemical equilibrium was established in most of the sedimentary suspensions in the Short-Term Desorption Experiment. Since more frequent observations were available for these suspensions, equilibration was assessed by considering whether $\Delta C_{pyr}/\Delta t$ was statistically different from zero (Figure 3-3). T-test statistics (at α=0.10) were computed from the $\Delta C_{pyr}/\Delta t$'s and their estimated errors to test the hypothesis that dissolved pyrene was not changing with time (i.e. $\Delta C_{pyr}/\Delta t$=0). For observations of C_{pyr}'s made within the 1800^{th}-3500^{th} hour time-frame, the $\Delta C_{pyr}/\Delta t$'s of the suspensions of 38-75 and 75-106 μm fractions were statistically indistinguishable from zero (or, $|t_{test}/t_{\alpha/2}| < 1$, the shaded region in Figure 3-4), suggesting chemical equilibrium had been established. The same figure, however, showed that, within the 1800^{th}-3500^{th} hour time-frame, dissolved pyrene was still increasing significantly in the 180-250 μm suspensions.

It can be showed that at least two months of equilibration were necessary even for suspensions with the smaller size fractions. At the time-frame of ~1000^{th}-3500^{th} hour, some of the lower R_{sw} suspensions on the 38-75 μm size fraction began to exhibited a significantly positive $\Delta C_{pyr}/\Delta t$ (Figure 3-5). By extending the time-frame to ~200^{th}-3500^{th} hour, almost all suspensions showed a significant positive rate of change of C_{pyr} (Figure 3-6). This, therefore, indicates that, at the studied solids-to-water ratios, even a 1000-hour incubation (with continuous tumbling/mixing) may be insufficient to establish sorption equilibrium. Indeed, analysis showed that ~1800 and ~3500 incubation hours were required for the 38-75 and the 180-250 μm suspensions, respectively, to reach pyrene equilibrium between the sedimentary and the aqueous phases (Figure 3-7, 3-8).

3.1.3. Equilibration of Long-Term Desorption Equilibrium Experiment

The suspensions in the Long-Term Desorption Equilibrium Experiment reached equilibrium after 250 d of incubation. With less frequent observations on dissolved pyrene (Figure 3-9; Appendix 3-5), the $C_{pyr}(t)$-matching approach (section 3.1.1) (Figure 3-10) was taken to check if equilibrium had been established. In all suspensions the dissolved pyrene levels observed after 250 d were statistically not differentiable from those at 400 d. As for the exceptional case in Figure 3-10 (UnG-2000), the mismatch between the 250 d and 400 d readings was likely due to daily variation in TG-LIF performance, which had been occasionally observed (e.g. dark arrows in Figure 3-3 & 3-9). Such variation has been reported previously (Kuo et al. 2007) and may occur within a 5-hr time period. In view of the fact that sorption equilibrium has been

established in batches with lower solid content, the exceptional case may be disregarded. The claim of equilibrium was further supported by the fact that a ~300 d (~7200 hr) incubation time was much longer than those observed for the same size fraction but at lower R_{sw}'s (see section 3.1.2).

3.1.4. Equilibration of Long Term Extended-Range Pyrene Adsorption Equilibrium Experiment

In this experiment, partitioning equilibrium of pyrene was generally established within 5 months. Due to the lack of frequent C_{pyr} measurements over the 10-12 months period, the correspondence approach (section 3.1.1) was used to verify whether equilibrium was established at all four temperatures (6, 15, 22, 37°C) (Figure 3-11). The 1-to-1 plots for 15, 22, and 37°C experiments showed excellent correspondence between the dissolved pyrene concentrations after 5 months with those after 10 months. For the 6°C experiment, dissolved pyrene measured after 5 months were significantly higher than those measured after 10 months (Figure 3-12). This suggested that the pyrene uptake was still proceeding. A good measurement correspondence for the 6°C set, however, was observed between the 10-month and the 12-month data (Figure 3-13). For the 37°C experiment, the poor correspondence in the lower range (C_{pyr} < 0.5 μg/L) was due to poor temperature control during sample transport and LIF measurement.

3.2. Equilibration of Generic HOCs Sorption Experiments

3.2.1. Typical Sorption Experiment Insufficiently Equilibrated

The equilibration analyses on all three experiments (sections 3.1.2, 3.1.3, and 3.1.4) suggested that many previous studies on HOCs sorption equilibrium may not have made truly equilibrium observations. A brief survey of incubation times used in different pyrene/phenanthrene phase distribution equilibrium studies is presented in Table 3-2. All cited studies had claimed chemical equilibrium for their reported observations, but rarely did a study, such as that of Huang et al. (1998a) or Bucheli et al. (2000), actually presented kinetic data to support the claim. Sorption equilibrium was often simply assumed or claimed (e.g. Karickhoff 1979; Means et al. 1980; Chiou et al. 1998; Kleineidam et al. 2002; Wang et al. 2007); in others 'apparent equilibrium' was declared (e.g. Huang et al. 1998b; Ran et al. 2002; Wang et al. 2005; Ran et al. 2007) – here 'apparent equilibrium' may refer to insignificant rate of change in sorbate level which was arbitrarily defined/adopted (e.g. '... *apparent equilibrium here means that a decrease in solute concentration was less than 3% by keeping the tubes shaking one additional day after 5 days of mixing.*', Wang et al. 2005). There were also cases where an earlier study demonstrated the need for very long equilibration time (90-180+ d for various sediment, soil, and shale samples) (Huang et al. 1998a) and then had the finding disregarded in later studies (14-21 d equilibration period was declared 'sufficient' in Huang et al. 1998b, Xiao et al. 2004). Finally, there were cases where the time-course of adsorption was provided and hinted that the sorbate uptake might be still proceeding at very slow rate (Kan et al. 1994; Piatt et al. 1996; Accardi-Dey and Gschwend 2002; Pignatello et al. 2006; see selected adsorption time-course from literature in Appendix 3-6).

3.2.2. Equilibration Time as Suggested by Past Sorption Studies

The rate of equilibration or the rate of organic sorbate uptake (or release) by the sorbent is generally dictated by: (i) system variables, (ii) sorbent morphology and structure, (iii) characteristics and quantities of various organic carbon phases, and (iv) sorbate characteristics (Table 3-3). Some of these factors, such as R_{sw} and particle size, are well understood (e.g. Wu et al. 1986, 1988) and have often been exploited to speed up partition equilibrium. For instance, various studies have looked at HOCs sorption at very high R_{sw} (~100000 mg_{solids}/L) to reduce equilibration time (Karickhoff 1979; Means et al. 1980; Kan et al. 1994; Piatt et al. 1996; Huang et al. 1997b).

Even without analyzing all the relevant equilibration factors listed in Table 3-3, previous sorption studies still provided evidence that sorption experiments often require longer than expected equilibration times. It should be noted that these equilibration times from past studies only served to illustrate/emphasize the need to equilibrate for longer times – they were by no means 'correct' or applicable to all sorption experiments.

3.2.2.1. Equilibration Time for Low-TOC Systems

It seems that at least a 1-month incubation time is required for – though it may not guarantee – phase distribution equilibrium of phenanthrene or pyrene in sorbent-water systems where the sorbent total organic carbon content is relatively low. The data from Johnson et al. (2001a) suggested that ~21 d of equilibration were needed for phenanthrene partitioning in peat/soil-water systems. Likewise, Huang et al. (1998a) showed that systems with low f_{TOC} sediment/soil samples (i.e. f_{TOC} ~<0.02) may reached equilibrium after 30-42 d. The pyrene adsorption time-course in Accardi-Dey and Gschwend (2002) for untreated sediment system also suggested that a minimal 1-month equilibration would be necessary. Here, the author found that native pyrene was still desorbing after 2-3 weeks (Figure 3-6) even for the smallest size fraction (dia.:38-75 μm) under continuous stirring of sediment suspensions.

3.2.2.2. Equilibration Time for BC-Dominated Systems

In some cases, however, the equilibration time for HOC sorption may be much longer. Qualitatively, the rate of partitioning (i.e. time for the system to reach a certain M_τ/M_∞ for adsorption (or a certain $(M_o-M_\tau)/(M_o-M_\infty)$ in the case of desorption)) increases with higher sorbent loading (higher R_{sw}) or when the sorbent exerts less affinity for the sorbate (lower K_d; the sorbate experiences less 'retardation' as it diffuses in/out of the sorbent). Here, two cases where extension in incubation time is necessary are examined:

(A) Sorbents rich in organic carbon or condensed carbon phases (i.e. soot, char, charcoal, activated carbon, kerogen, shale, coal). The high OC or BC content often restricts the amount of sorbent to be added, for excessive addition may lead to undetectable sorbate levels at equilibrium. This means that a lower R_{sw} is needed, and hence a longer equilibration time. In addition, the presence of 'hard' condensed carbon phases, which exhibit much stronger sorption affinity for organic sorbates (~1-2 order of magnitude stronger than 'soft' organic carbons), slows down equilibration rate considerably by enhancing retardation on sorbate

diffusion. Thus high OC/BC sorbents impose a two-fold disadvantage for quick equilibration. The supporting observations were provided in Table 3-4.

(B) Organic matter/coating stripped condensed carbon phases. Condensed carbon phases that have been subjected to removal of organic matter tend to exhibit a stronger affinity for HOCs. This was supported by the following evidence: (i) combusted (i.e. CTO-375°C) sediment exhibited a slower pyrene uptake kinetics than untreated sediment (Accardi-Dey and Gschwend 2002, Figure 2); (ii) sediment where native organic sorbates thermally volatilized/'stripped' (at ~100°C) had a higher sorptive capacity by about two times than the untreated sample (Cornelissen et al. 2004b); (iii) char unexposed to organic macromolecules (e.g. humic/fulvic acids) sorbed phenanthrene much stronger than char with organic coating (Pignatello et al. 2006).

3.2.3. General Guideline for Sufficient Equilibration

What then is the proper equilibration/incubation time length for sorption studies of HOCs in geosorbent-water systems? For sorbents with properties that greatly extend equilibration time, when should the system be considered as at equilibrium? As the system approaches equilibrium, the rate of sorbate uptake (or release) decreases with the diminishing thermodynamic drive (i.e. diminishing concentration gradient). One may argue that true state of equilibrium may never be established within finite time – a modified version of Zeno's Achilles and the Tortoise – and hence a practical state of equilibrium must be adopted. And even an arbitrary 5% or 10% deviance from the true equilibrium is acceptable (e.g. Wang et al. 2005), if the equilibrium endpoint is unknown, how would one ascertain the supposed practical equilibrium has been reached?

3.2.3.1. Extrapolating Equilibration Time from Early Kinetic Observations

A multiple-check approach may be the best way to ensure sufficient equilibration time. First, one can estimate the true equilibrium state based on the early kinetic measurements. This requires sufficient numbers of kinetic observations so that extrapolation at infinite time can be made with confidence. Measurements can then be compared against those estimated for true equilibrium.

3.2.3.2. Comparing Concentrations at Two Distant Times

Second, one should check that sorbate concentrations at two distant time points are statistically indifferentiable. The progress towards equilibrium varies with logarithmic time (Figure 4 in Wu et al. 1988, or Figure 19.18 in Schwarzenbach et al. 2003). Hence, the time points at which the comparison be made should be well separated, ideally, in order of magnitude of difference. At the very least, subsequent measurements should be taken at times double or more of those preceding (e.g. Huang et al. 1998a; Xia et al. 1999; Bucheli et al. 2000; Abu et al. 2006; this study).

3.2.3.3. A priori Estimate of Equilibration Time

Third, one may also compare the actual equilibration time with that expected from *a priori* kinetic model. For instance, if one assumes the practical equilibrium to be 5% within the true equilibrium (i.e. $|K_{d,Eqm,true}-Q_{d,Eqm}(t_{95\%})|/K_{d,Eqm,true} \leq 0.05$), one can model the time required to reach the practical equilibrium for a given solid-water system. The *a priori* model would require knowledge on system properties (e.g. R_{sw}, particle size)

and sorbent/sorbate properties (e.g. OC/BC contents, isotherm). As an example, the dimensionless equilibration time, $\tau_{95\%}$, as a function of K_dR_{sw}'s assuming the Classical, OC-only sorption model is presented in Figure 3-13. If BC is also present, one would need to simulate the kinetics using a non-linear mechanistic model (e.g. the Intra-particle Porewater Diffusion model in Chapter 7 & 8).

It is important to note that the mentioned checks all have their only limitations. For instance, the empirical extrapolation (section 3.2.3.1) relies strongly on the available observations as well as the empirical model chosen; the two-point approach (section 3.2.3.2) may show that concentrations at two distant times are similar, but it does not reveal where and what the equilibrium state may be; the *a priori* estimate of equilibration time (section 3.2.3.3) assumes the knowledge of isotherm and sorbent/sorbate properties. To ensure sorption equilibrium of HOCs with water and natural geosorbents is not a simple, straightforward matter.

3.3. Implications of Long Equilibration for HOCs Phase-Partitioning

Three important implications of long equilibration time for HOCs sorption are highlighted here. First, long equilibration time for HOCs sorption implied that the accuracy of the many reported 'equilibrium' properties, such as solids-water distribution coefficient (K_d), Gibb's free energy of sorption (ΔG_d), and enthalpy of sorption (ΔH_d), for strongly hydrophobic HOCs may be highly questionable due to insufficient equilibration time.

Second, for a given sorbent, its equilibration time is likely to be non-uniform across a wide sorbate concentration range. Studies showed that condensed carbons, both isolated from geosorbents (Cornelissen et al. 2004b; Ran et al. 2007b) or formed without substantial prior exposure to organic matter (Pignatello et al 2006) tend to have a more non-linear isotherm than those of the bulk geosorbents or the OC-dominated phases. The resulting systematic trend is that isotherms of different carbonaceous phases usually converge at the higher dissolved sorbate range but diverge as sorbate concentration decreases (Figure 3-14). Since equilibration rate decreases with increasing sorbent-sorbate affinity (section 3.2.2.2), longer equilibration time is required at low sorbate concentration (roughly extended by a factor of $K_{d,low\text{-}Ciw}/K_{d,hi\text{-}Ciw}$), assuming all other system properties such as R_{sw} or particle size remain the same.

Third, as a result of insufficient equilibration time, many studies may not have produced strongly conclusive observations for the existence of irreversible sorption. Adsorption-desorption cycle experiments are typically conducted with relatively short adsorption times (<30 d) and even shorter desorption times (Kan et al. 1994; Huang et al. 1997a; Ran et al. 2003a). Although these studies maintained that true sorption hysteresis[3] had been observed, the discrepancy between the adsorption and desorption distribution ratios (i.e. $Q_{d,i\text{-}ads}(t)=(C_i/S_i)_{ads}$ or $Q_{d,i\text{-}des}(t)=(C_i/S_i)_{des}$) they reported are also explainable by insufficient equilibration. Huang et al. (1997a) and Ran et al. (2003a) may be two of the many studies that presented some of the most convincing arguments for irreversible

[3] 'True' hysteresis in the sense that the observed hysteresis is not due to experimental artifact or kinetics. See Pignatello et al. (1996).

sorption of HOCs in natural geosorbents. In these studies, the desorption-associated distribution coefficients for phenanthrene ($\log Q_{d,phen}$'s) were consistently higher than those associated with adsorption, though by no more than 0.2 $\log_{10}$ unit. The incubation times they used for adsorption/desorption (<21 d) were clearly insufficient to establish equilibrium in kerogen-dominated systems (see Table 3-4). The equilibration times in Table 3-4 are, however, compiled based on a tolerance of 0.1 $\log_{10}$ unit in Q_d for change over time. This means that the 0.2 $\log_{10}$ unit difference between the adsorption and the desorption $\log Q_{d,phen}$'s is also within the sum of errors accrued through non-equilibrium in both the adsorption and the desorption steps. This implied that insufficient equilibration, in addition to irreversible sorption, can also explain the observations in Huang et al. (1997a) and Ran et al. (2003a).

4. Conclusion

Various analyses on the observations suggested that the three experiments had reached equilibrium at their end-points. In the Short-Term Desorption Experiment, (desorption) equilibrium appeared to have established in sediment suspensions with the smaller size fractions after 2.5 months (dia. 38–75, 75–106 μm; Figure 3-4). The Long-Term Desorption Equilibrium Experiment reached equilibrium after 250 d. This was probably a rather conservative estimate as much higher solid-to-water ratios were used. In the Long-Term Extended-Range Adsorption Equilibrium Experiment, chemical equilibrium seemed to have established after 5 months' time at all temperatures (Figure 3-11) except at 6°C which took longer time.

The observation of monthly or longer equilibration times for the three experiments suggested that many previous HOC sorption studies may not have reported truly equilibrium observations (section 3.2.1). After reviewing the experimental conditions and the concentration-time profiles from a large number of sorption studies, it appeared that a monthly or longer equilibration time was necessary for PAH sorption experiments (with typical sorbent and system properties). The actual required incubation time is dependent on an array of physical and chemical factors that affect uptake or release kinetics of PAHs.

To assist planning of future HOC sorption experiments, a general guideline for estimating/assessing equilibration time was proposed. It is recommended that equilibrium should be checked using on-going kinetic data and *a priori* modeling of sorbate uptake or release.

The need to study HOC sorption with longer incubation time has profound implications on the interpretation of existing sorption literature as well as how sorption of HOCs in natural geosorbents may be understood. It appears that irreversible sorption might be less frequent than past studies have claimed/suggested.

Chapter 4. Enhanced Pyrene Sorption at Environmentally Relevant Concentrations

CHAPTER ABSTRACT

This chapter examined the partitioning of pyrene in sediment-water system at environmentally realistic concentration levels. Desorption of native sedimentary pyrene yielded ng/L-level concentrations. The implied sorption coefficients greatly exceeded those predicted using previously reported organic/black carbon-based estimates.

In order to confirm that these desorption data reflected sorptive equilibrium, 12-month-long desorption (with ground sediment and at elevated solid-concentrations) and adsorption experiments were conducted on sediment with natively associated pyrene. The results from both experiments suggested that the isotherm became highly nonlinear as the dissolved concentration decreased. The observed concentration-dependency could not be explained using common experimental errors or artifacts. It appeared that either a fraction of the native sorbate was physically occluded and therefore not involved in the partitioning reaction, and/or that native sorbate may be sorbed to very high-affinity micropore-surface of bio-char/charcoal. Potential mechanisms and preliminary evidence for both hypotheses were discussed. A polyethylene(PE)-sediment desorption experiment was further conducted to test the physical occlusion hypothesis. However, the experiment did not produced results that would lead to the rejection or acceptance of the physical occlusion hypothesis.

The observed concentration dependency has very important implications for the bioavailability and sequestration of soil/sediment-bound organic contaminants, and the sorption of hydrophobic organic compounds to natural geosorbents. The results may also partly explain the widely scattered K_{OC}/K_{BC}'s reported in recent reviews.

Table of Content for Chapter 4

1. Chapter Introduction, Scope, and Objective 76

1.1. Introduction & Motivation 76

1.2. Objective 76

2. Methodology 76

2.1. Materials and Experiments 76

2.2. Sediment-PE-Water Desorption Experiment 76

3. Results & Discussion 78

3.1. Equilibration of Pyrene Sorption Experiments 78

3.2. Short-Term & Long-Term Desorption Experiments 78

3.2.1. Effect of Grinding on Sorption Equilibrium of Pyrene 78

3.2.2. Lower-Range Partitioning Not Predictable by Current OC-BC Model 78

3.3. Long-Term Adsorption Equilibrium Experiment 79

3.3.1. Concave-Up Sorption Isotherm 79

3.3.2. Typical PAH Sorption Isotherm: Freundlich or Langmuir 80

3.3.3. Concave-Up Isotherm: Real or Artifact? 80

3.3.3.1. Observational Chemical Consistency 80

3.3.3.2. Shape Consistency at Different Temperatures 81

3.3.3.3. Linear Instrumental Response and Analytical Consistency 81

3.3.3.4. Observational Coherence with Sediment Cores 81

3.3.3.5. Unlikely Presence of Substantial Measurement Errors 82

3.4. Strong Sorption Affinity at Lower Concentration: Sources and Questions 83

3.4.1. Strong Affinity at Lower Sorbate Concentrations. 83

3.4.2. Hypothesis 1: Physical Occlusion of Sorbate. 83

3.4.2.1. Irreversible Sorption as Experimental Artifacts 84

3.4.2.2. Occlusion Mechanisms: (I) Structural Swelling & Contraction 84

3.4.2.3. Occlusion Mechanisms: (II) Thermally Induced Aggregate-Densification 84

3.4.2.4. Occlusion Mechanisms: (III) Encasement via Mineral Precipitation 85

3.4.2.5. Fraction Pyrene Occluded (Estimated via Visual Inspection) 86

3.4.3. Hypothesis 2: High-Affinity Micropore Sorption 87

3.4.3.1. Support for Micropore Sorption: (I) Comparable Adsorption Capacity 88

3.4.3.2. Support for Micropore Sorption: (II) Comparable Freundlich Parameters 88

3.4.3.3. Support for Micropore Sorption: (III) Reasonable E_A of Desorption 88

3.4.4. Hypothesis 3: Mixed Scenario of Occlusion and Micropore Sorption 89

3.4.5. Concluding Remarks on Physical Occlusion and High-Affinity Adsorption 89
3.4.5.1. Reversible Equilibrium State, Irreversible Phase-Transfer Kinetics 89
3.4.5.2. Physical Occlusion Reduces Enthalpic/Entropic Changes 89
3.4.5.3. Sorbate Loading and Sorbent Structural Changes 90
3.5. Testing the Physical Occlusion Hypothesis 90
3.5.1. Expected Profiles for PE-Extractable Pyrene 90
3.5.2. Results on Occlusion Hypothesis 90
3.5.3. Argument for Disequilibrium after 50 d 91
3.5.4. Argument for Equilibrium after 50 d 91
3.5.5. Considerations Based on Equilibration Rate 92
3.5.5.1. Basic Assumptions on $K_{d,pyr}$ and Diffusion in PE-phase 92
3.5.5.2. Kinetic Analysis I: First-Order Approximation 92
3.5.5.3. Kinetic Analysis II: Radial Diffusion with Constant D_{eff} Approximation 94
3.5.6. Concluding PE-Sediment Experiment 95
3.6. Implications 95
3.6.1. Sequestration of HOCs 95
3.6.2. Bioavailability of HOCs 95
3.6.3. Predicting Partitioning of HOCs 95
4. Conclusion 96

1. Chapter Introduction, Scope, and Objective

1.1. Introduction & Motivation

The various needs to understand sorption equilibrium of HOCs in natural systems containing geosorbents (soil, sediment) and water have been discussed in Chapter 3 (section 1.1–1.2). In Chapter 2, a substantial discrepancy was reported between the final observations in the desorption experiment and the equilibrium end points predicted from the OC-BC model. The equilibrium analysis in Chapter 3 strongly suggested that the observation-prediction discrepancy was not caused by slow kinetics.

It is hypothesized that the partitioning of pyrene between sediment and water at field conditions may be different from that predicted from earlier sorption studies (Chapter 2, section 3.3.2; see also Figure 2-12). Due to analytical limitations, earlier studies often investigated pyrene (or other HOCs) sorption in the $\mu g_{pyr}/L_w$ range (Chiou et al. 1979; Karickhoff et al. 1979; Means et al. 1980; Chin et al. 1992; Kan et al. 1994; Huang et al. 1997b; Chiou et al. 1998; Xia et al. 1999; Johnson et al. 2001a; Accardi-Dey and Gschwend 2002; Kleineidam et al. 2002); however, the field dissolved pyrene (and total PAHs as well) concentrations are often in the ng_{pyr}/L_w range (Table 4-1a, b). It is currently assumed that isotherms valid for μg/L range can be applied to predict partitioning of HOCs at field conditions (ng/L range).

1.2. Objective

The objective of this chapter is to examine whether or not HOCs would exhibit the same partitioning behavior in the ng/L range as in the μg/L range. This will be done by examining the pyrene equilibrium sorption coefficients (K_d) in a sediment containing native pyrene.

2. Methodology

2.1. Materials and Experiments

Three experiments had been conducted: (i) the Short-Term Desorption Experiment, (ii) the Long-Term Desorption Experiment, and (iii) the Long-Term Adsorption Equilibrium Experiment (Table 4-2). The materials and experimental setup as well as the analytical methods for these experiments have been documented in Chapter 3.

2.2. Sediment-PE-Water Desorption Experiment

An experiment was also conducted after the results from the three ads/desorption experiments were analyzed. The objective of this experiment was to test the physical occlusion hypothesis (section 3.4.2) by exposing the sediment with native pyrene to

varying the degree of desorptive drive. The occlusion hypothesis would be rejected if substantial fraction (i.e. >20% as estimated in section 3.2.1) of native pyrene could desorb from the sediment matrix into PE strips.

The experimental setup was similar to that of the two desorption experiments except that strips of PAHs-free polyethylene (PE) were also present in the sediment suspensions. The setup was briefly as follows. Commercial PE (25.4 μm thick "Plastic Dropcloth", Trimaco US) was pre-cleaned (2× soaking in dichloromethane, 2× soaking in ethanol, and 2× soaking in clean water, with each soaking lasting 24 hr) and kept in clean water until use. PE strips were handled with tweezers and cut with scissors, both pre-rinsed with dichloromethane and air-dried. Boston Harbor sediment (NQB <425 μm) was used to prepare sediment-suspensions in 115 mL of initially pyrene-free clean water (with 10 mM sodium azide) as in earlier experiments (see **Error! Reference source not found.**, **Error! Reference source not found.**). Strips of pre-cleaned PE (dimension 3 × {5-30} cm) were cut and added into the sediment suspensions.

Two groups of sediment-PE suspensions were prepared. In the first group, sediment concentration was held constant at around 300 mg_{solids}/L_{water} while the PE content was allowed to vary from 100 to 3000 mg_{PE}/L_{water}. This group served to show if the extractable pyrene fraction would reach some limiting threshold as the desorptive drive was raised (higher PE content). In the second group, PE content was held constant at 300 mg_{PE}/L_{water} while sediment-to-water ratio varied from 100 to 1000 $mg_{solids}/_{water}$. The second group allowed us to know to what extent the sediment-PE partitioning of pyrene would be kinetically controlled. The range selected was constrained by the availability of sediment sample and the concern that excessive addition of PE would result in poor water-PE contact (i.e. strips folding up with most surfaces not in contact with water).

The sediment-PE suspensions were tumbled continuously for 50+ days. The PE strips initially floated on the suspension due to their hydrophobic nature; however, they eventually became submerged in the suspension with good surface contact with the water. This was made possible by the continuous tumbling and the surfactant action of the dissolved/particulate organic matter helping the PE strips to stay submerged. At the end of 50 d, the PE strips were retrieved. Particles adhered to the PE surface were rinsed off with water. The strips were then gently dried by tissue (Kimwipe) and immediately stored in combusted (450°C) amber vials, where they were extracted with dichloromethane (4 sequential extractions, each last a day, occasionally hand-shaken.), concentrated via N_2 blow-down, transferred to hexane with a volume of about <50-100 uL, and analyzed with GC-MS with proper recovery standard (deuterated pyrene, d_{10}-pyr; added onto dried, retrieved PE strips) and injection standard (p-terphenyl, d_{14}-p-terp; added prior to analysis).

3. Results & Discussion

3.1. Equilibration of Pyrene Sorption Experiments

The equilibration of the three experiments (Table 4-2; Short-Term Desorption experiment, the Long-Term Desorption experiment, and the Extended-Range Adsorption experiment) has been discussed in Chapter 3 (section 3.1; Figure 3-4, 3-10, 3-11).

3.2. Short-Term & Long-Term Desorption Experiments

3.2.1. Effect of Grinding on Sorption Equilibrium of Pyrene

In general, the grinding treatment produced no statistically discernible effect on the equilibrium distribution coefficient (K_d) of pyrene at all three solids-to-water ratios (Figure 3-16b, c). Ground samples seemed to show higher dissolved pyrene levels than the unground (Figure 3-16a). However, batch suspensions with ground samples generally had higher solids-to-water ratio than the unground ones by approximately 10% (Appendix 4-1), and so the difference in C_{pyr} may not reflect the effect of grinding treatment on sorption equilibrium. The plots of $K_{d,pyr}$, either by mass balance (measured C_{pyr} then calculated S_{pyr}; Figure 3-16b) or by measurement (measured both C_{pyr} and S_{pyr}; Figure 3-16c) showed that grinding did not change $K_{d,pyr}$ of the sediment within statistical errors. This result reinforced the conclusion that equilibrium was established for the unground samples after 12 months. It also suggested that the interior of the sediment particles/aggregates seemed to exhibit identical chemical affinity for the sorbate.

The mean $K_{d,pyr}$'s of ground samples, however, were often slightly lower than those of the unground (although not statistically significant; e.g. Figure 3-16c). Considering that grinding potentially 'opens up' the interior of sediment particles/aggregates, one may hypothesize that (i) a fraction of the natively present pyrene remained inaccessible to phase-partitioning reaction, and (ii) the ground suspensions gave the true partitioning coefficient for pyrene. With these assumptions, one can estimate the amount of pyrene physically occluded based on the results from the unground sediment. Such exercise suggested that about 20–30% of natively bound pyrene may be 'locked up' in the unground sediment samples (Appendix 4-2). Note that this 'locked up' estimate was comparable with the analytical uncertainty for solid-phase pyrene concentration (Chapter 3, section 2.1.10).

3.2.2. Lower-Range Partitioning Not Predictable by Current OC-BC Model

Experimental evidence suggested that previously reported isotherms could not predict pyrene partitioning in the ng_{pyr}/L_w range. The Long-Term Desorption Experiment and the Short-Term Desorption Experiment produced consistent $K_{d,pyr}$'s in the ng_{pyr}/L_w range (Figure 4-2a). The observed ng/L-range $K_{d,pyr}$'s were significantly higher than the predictions from the Classical OC sorption model or from isotherms involving both OC and BC (Bucheli et al. 2000; Accardi-Dey and Gschwend 2002) (Figure 4-2b).

The results from the Short-Term and Long-Term Desorption experiments have very significant implications regarding the desorption kinetic experiments studied earlier (Kuo et al. 2007). The newer experimental results have provided very strong evidence for (de)sorption equilibrium for most of the suspensions in the previous study – the end-point phase distribution ratio of pyrene, $Q_{d,pyr}(=S_{pyr}/C_{pyr})$, was indeed the equilibrium solid-to-water distribution coefficient $K_{d,pyr}(=S_{pyr,eqm}/C_{pyr,eqm})$. The substantial discrepancies between the experimentally observed $Q_{d,pyr}$'s$(=S_{pyr}/C_{pyr})$ and the $K_{d,pyr}$'s predicted from various isotherms (Figure 4-2b) may not be explained by on-going desorption, as evidence greatly supported for sorption equilibrium in the observations (Figure 3-4 for the Short-Term Desorption data; Figure 4-1 for the Long-Term Desorption data). Thus the "very-slowly desorption" hypothesis suggested in Chapter 2 (Chapter 2, section 3.3.2) may be rejected. It also means that partitioning of pyrene at the ng_{pyr}/L_w range requires a new isotherm. This theme will be further supported by the observations from the Long-Term Adsorption Equilibrium Experiment.

3.3. Long-Term Adsorption Equilibrium Experiment

A sorption isotherm describes how a sorbate is distributed between two phases at chemical equilibrium. It represents the set of possible thermodynamic states at given temperature and pressure, with the freedom to specify the chemical activity of the sorbate in one of the phases. This section will discuss the sorption isotherm of pyrene in sediment-water system. It will begin with a general description of the observed isotherm (section 3.3.1), followed by the validation of its representation and comparison with isotherms of similar systems reported previously (section 3.3.2). The main discussion will be on the observed shape/form of the isotherm – whether the observed shape is likely to be true or not.

3.3.1. Concave-Up Sorption Isotherm

The pyrene sorption isotherms (i.e., $S_{pyr,Eqm}$-vs-$C_{pyr,Eqm}$) showed the expected monotonic trend (i.e. $f(x_2)\geq f(x_1)$ for $x_2>x_1$) of the dissolved pyrene level increasing with the solid-bound pyrene concentration (Figure 4-3). This has been observed at all four temperatures and within the entire examined concentration range (Figure 4-3). The monotonic trend was consistent with the sorption of organic compounds observed in both solid-water (Karickhoff 1981; Huang et al. 1997b; Xia et al. 1999) and solid-air systems (Storey et al.1992; Lohmann et al. 2000).

However, the sediment-water pyrene sorption isotherm generally exhibited a concave-up curvature in log-log space. Such isotherm shape is rather unusual, and, to the author's knowledge, has not been reported in previous PAHs sorption literature for systems involving aqueous phase and natural geosorbents (Huang et al. 1997; Accardi-Dey and Gschwend 2002).

Insufficient equilibration time was an unlikely cause for the concave-up curvature. Analyses in Chapter 3 (section 3.1.4; also Figure 3-11 and Figure 3-12) have shown that sorption equilibrium was established at the end of the adsorption experiment. Data from the desorption kinetic experiments (Chapter 3 section 3.1.2) suggested that equilibrium can be reached with a 4-month incubation, much shorter than the incubation

time of the adsorption experiment (Table 4-1). For this reason, it is very unlikely for the isotherm to move to a linear-form with longer incubation time. The consistency of the isotherm at its upper range with the previous work (Accardi-Dey and Gschwend 2003) also suggested that the partition of pyrene between sediment and water should be non-linear.

3.3.2. Typical PAH Sorption Isotherm: Freundlich or Langmuir

The Freundlich and the Langmuir models have been the most widely applied isotherm models in PAHs sorption literature. Although more complex, composite isotherm forms (e.g. composite forms of linear, Freundlich, Langmuir, Polanyi-Dubinin-Manes) had been endorsed/advocated on the basis of mechanistic superiority and/or physicochemical consistency (Huang et al. 1997b; Manes 1998; Allen-King et al. 2002), the observed equilibrium distribution was often still mathematically well described by either simple Freundlich or simple Langmuir models. The simple Freundlich model usually describes isotherm well for geosorbents containing from small to relatively large amount of OCs or BCs such as typical soils, sediments, aquifer materials, dissolved organic carbon/matter, kerogens, humic substances, peats, and extracted natural organic matter (e.g. cuticle, humin) (Huang et al. 1997; Chefetz et al. 2000; Karapanagioti et al. 2000; Accardi-Dey and Gschwend 2002; Kleineidam et al. 2002; Ran et al. 2003; Xiao et al. 2004; Lohmann et al. 2005; Sander et al. 2006; Ran et al. 2007).

On the other hand, sorption isotherms tend to approach saturation when the sorbents are highly condensed carbonaceous materials, with surface area of the order 100 m^2/gC or more, such as activated carbon, charcoal, or coke. In these cases, a single Langmuir model would often be descriptively sufficient (Walters et al. 1984; Kleineidam et al. 2002). Here, however, regression analysis revealed that both simple Freundlich or Langmuir models were inappropriate for the equilibrium distribution of pyrene, for both models introduced substantial systematic biases in the prediction of $K_{d,pyr}$ despite the reasonably good fits (see Figure 4-4 & 4-5).

3.3.3. Concave-Up Isotherm: Real or Artifact?

The disagreement in isotherm shape between this study and most of the previous PAHs/HOCs sorption studies in similar solid-water systems needs to be addressed. First, was the concave-up feature real? Second, if it is real, why the isotherm may have such a shape? Third, how can the isotherm be described (mathematically)?

The observed isotherm curvature was concluded to be real on the following pieces of evidence: (i) observational consistency with earlier studies, (ii) shape consistency at all studied temperatures, (iii) linear instrumental responses and inter-methodological consistency, (iv) observational coherence with studies on sediment cores (beneath bioturbation layer), and (v) unlikely presence of substantial measurement errors.

3.3.3.1. Observational Chemical Consistency

The higher concentration range observations from this study were thermodynamically consistent with those reported by an earlier study on similar sediments from the Boston Harbor (Table 3-1) (Accardi-Dey and Gschwend 2002). Among all previous equilibrium partitioning studies, the OC-BC partitioning model by Accardi-Dey and Gschwend

(2002) was most applicable to the results here. Accardi-Dey and Gschwend looked at the partitioning of pyrene on sediment (site #5) closely located to NQB#6 (see map in Appendix 9-10), and similarly sized (dia. <425 μm). They formulated a predictive partitioning model based upon sorbent characteristics (e.g. OC, BC contents) and equilibrium observations (for $C_{pyr,Eqm}$: ~0.5 to 20 μg/L) at 22°C. The isotherm constructed from NQB#6 sediment (this study) and that from South Dorchester Bay sediment (Accardi-Dey and Gschwend 2002) had comparable n and TOC-normalized K_{Fr} in the range $C_{pyr,Eqm}$ of 0.5-20 μg_{pyr}/L (Figure 4-6 and caption therein).

While the dual-domain OC-BC model gave good prediction for the higher range observations, the model tended to underestimate the solid phase pyrene levels at $C_{pyr,Eqm}$ < 0.1 μg_{pyr}/L (Figure 3-18). The underestimations by the OC-BC model could not be explained by uncertainties in parameters such as f_{OC}, f_{BC}, n_{BC}, or K_{BC} (Figure 4-7). The higher than expected partitioning at lower concentration was also reported in an earlier desorption study (~0.03 μg_{pyr}/L range; Adams 2003) and polyethylene-sediment tumbling study (~0.03-0.5 μg_{pyr}/L range; Lohmann et al. 2005). This means that the observations in this study also qualitatively agree with those in literature.

3.3.3.2. Shape Consistency at Different Temperatures

The concave-up curvature was observed at all four temperatures, suggesting that the observed shape was systematic rather than accidental (Figure 4-3 & 4-6). If the curvature was an artifact caused by preferential volatilization and/or biodegradation of pyrene, one would expect a stronger curvature at warmer temperatures, where volatilization and biological activities are facilitated and favored, and a weaker curvature at colder temperatures, where such losses are much reduced. The adsorption equilibrium observations at different temperatures, however, did not support this hypothesis.

3.3.3.3. Linear Instrumental Response and Analytical Consistency

Systematic error due to the use of different analytical methods (LIF and Syn-F) was unlikely. The isotherm may be viewed as the combination of a linear, high-concentration region, and a curving, lower concentration region. These two regions corresponded, roughly, to the analytical ranges of the Syn-F (high concentration) and the LIF (low concentration) systems. However, since the calibration standards for both instruments were prepared from the same source stock solution, and that both instruments exhibited linear responses within the analytical range of concern (Figure 3-1), systematic error due to instrumental difference may be eliminated. Instrumental bias associated with LIF was also unlikely because it has been verified with GC-MS in two independent occasions (Rudnick et al. 1998; Kuo et al. 2007).

3.3.3.4. Observational Coherence with Sediment Cores

Pyrene phase distribution studies on coastal sediment cores by independent researchers also qualitatively support the experimental observations in this study at the lower range ($C_{pyr,Eqm}$ <0.5 μg_{pyr}/L). Phase distribution in sedimentary cores may provide support by showing: (i) that similar $K_{d,pyr}$'s (or OC/BC normalized partition coefficients) are observed in the ng_{pyr}/L_w range, and/or (ii) that the solid-phase concentration remains relatively constant in the ng_{pyr}/L_w range. If partitioning equilibrium between different

phases can be claimed for bulk sediments at different depths beneath the surficial bioturbation layer (typically 10-15 cm), then an 'isotherm' may be constructed from the solid-phase, S_{pyr}'s, and pore-water free pyrene concentrations, $C_{pyr,pw}$, observed at these depths. Here, such 'isotherms' are reconstructed from three sediment core studies (McGroddy 1993; Mitra et al. 1999; King et al. 2007) where both solid phase and pore-water phase (excluding colloidal OC) pyrene levels were measured. The 'isotherms' reconstructed from five harbor/estuarine sediment cores are shown in Figure 4-8.

The S_{pyr}'s (or $S_{pyr,BC}$'s) observed in this study agree with those derived from the coastal sediment cores within 1 order of magnitude in the ng_{pyr}/L_w range (Figure 4-8). This implies that $K_{d,pyr}$'s from this study and the cores are also distributed within 1 order of magnitude. It is reasonable to expect scattering in S_{pyr}'s as the cores, collected from different harbors/estuaries, had aged in different environments (e.g. different initial HOCs loadings, different diagenetic 'force'). Considering that a 3–4 orders of magnitudes of scattering have been reported for K_{OC} and K_{BC} (Hawthorne et al. 2006, 2007), one may consider the sorption data and the core data in Figure 4-8 to be in good agreement with each other.

It is also noticeable in the reconstructed 'isotherms' that S_{pyr}'s tend to be constant in the ng_{pyr}/L_w range. This was true for the Peddocks Island and the Mersey 2 cores in the 0.01 to 0.1 ng_{pyr}/L_w range and for the Newark Bay core at ~0.1 ng_{pyr}/L_w (Figure 4-8). This constancy of S_{pyr}'s was similar to that shown in Figure 4-3 & 4-7 (also at around or less than 0.1 ng_{pyr}/L_w). This observational coherence with phase distribution in sediment cores strongly suggested that the concave-up isotherm shape, though unprecedented in previous adsorption equilibrium studies (Walters et al. 1984; Huang et al. 1997; Accardi-Dey and Gschwend 2002; Kleineidam et al. 2002; Sander et al. 2006; Ran et al. 2007) could be, nonetheless, real.

3.3.3.5. Unlikely Presence of Substantial Measurement Errors

Another way to examine the reliability of the observed isotherm shape is to presume a hypothetical 'true' isotherm, then assess the level of 'errors' that have to be present for the observed data to conform to the supposed isotherm, and to ask whether the estimated levels of errors are likely. Previous works (Huang et al. 1997; Accardi-Dey and Gschwend 2002; Sander et al. 2006; Ran et al. 2007) showed that PAHs (or HOCs) sorption equilibrium in most sediment-water systems can often be empirically well described by a single Freundlich model. Suppose that (i) the isotherm derived from the extended range adsorption experiment ought to have conformed to a Freundlich form, but (ii) systematic errors from unknown sources distorted our observations and gave it a concave-up structure, and (iii) the experimental data were at least partially true either in the lower or the higher concentration range. The supposed systematic errors can be estimated by comparing the observed dissolved pyrene concentration, $C_{pyr,obs}$, with the hypothetical dissolved pyrene concentration, $C_{pyr,hypo}$, as a single Freundlich isotherm would have required. Such hypothetical exercises revealed that the supposed, 'true' $C_{pyr,hypo}$ would have to be ~2 to 10 times higher than the observed $C_{pyr,Eqm}$ (Figure 4-9). Considering (a) the analytical competency and uncertainties of the Syn-F and the LIF systems, (b) the linear instrumental response over the entire studied concentration

range, (c) the calibration routine preceding all measurements, (d) the satisfactory balance of total pyrene before and after the experiments, and (e) the precaution of preparing multiple sets of calibration solutions from different stock solutions and cross-checked each with the others, the author concludes that a 2-10 times 'error' in observed dissolved pyrene concentrations to be very unlikely.

3.4. Strong Sorption Affinity at Lower Concentration: Sources and Questions

The author has argued that the isotherm curvature – a concave-up shape – can be considered as real based on various evidence. The next question is why the isotherm should assume such a shape.

3.4.1. Strong Affinity at Lower Sorbate Concentrations.

The extended range adsorption isotherm of pyrene in sediment-water system exhibited a remarkable trend: the affinity of the sedimentary phase for the sorbate, as measured by K_d, increased more significantly than that predicted by the OC-BC model or the classical absorptive-OC model (Figure 4-10). Regression analysis on the arbitrarily subdivided adsorption isotherm with a single Freundlich form revealed that the enhancement of K_d was primarily expressed in the variation of the Freundlich exponent, n, rather than the coefficient K_{Fr} (Figure 4-10). This feature was also consistently present in the isotherms obtained at other temperatures (not shown). This raised questions about the nature and cause of such enhancement in adsorption affinity for pyrene. Two physicochemical scenarios will be discussed and evaluated.

3.4.2. Hypothesis 1: Physical Occlusion of Sorbate.

The first explanation was that the enhancement of K_d, as illustrated in (Figure 3-21), was illusory in nature due to the presence of physically occluded pyrene in the sedimentary phase. Physically occluded (ad)sorbate, here defined as the confinement of sorbate in solid phase through various mechanisms, would not be able to participate in phase transfer reactions. The idea of physical occlusion was related to the phenomenon of irreversible sorbate-transfer behavior through adsorption-desorption cycle(s).

Irreversible sorption means that multiple solid-phase HOC concentrations exist for a given dissolved phase concentration. Earlier studies have, for instance, reported the irreversible sorption of PAHs with various quantitative indices for the irreversibility (Kan et al. 1994, 1998; Huang et al. 1997; Braida et al. 2003; references therein). For an adsorption-then-desorption cycle, these studies consistently reported higher solid-phase PAH concentrations at the desorption end-points than those at the adsorption end-points. When one considers the combined adsorption and desorption profiles (i.e. S_{HOC}-C_{HOC}, where $S_{HOC} = S_{HOC,ads}$ or $S_{HOC,des}$, whichever is higher) reported in these studies, one would find that such 'joined' S-C profiles often showed the concave-up curvature similarly observed in this study. Since the sediment examined here contained natively present pyrene, the observed K_d may be interpreted as the composite partitioning of the native solid-bound sorbate desorbing *and* the amended aqueous phase sorbate

adsorbing. Thus the apparently enhanced $K_{d,pyr}$ observed here would be consistent with the physical occlusion hypothesis.

3.4.2.1. Irreversible Sorption as Experimental Artifacts

Various causes of irreversible sorption have been identified in literature. These causes include experimental 'artifacts' such as sorbate degradation and insufficient equilibration (Pignatello et al. 1993; Kan et al. 1994), and physicochemical phenomena such as chemisorption (Kan et al. 1994), and prolonged diffusion of deeply bound sorbate (Pignatello et al. 1993; Luthy et al. 1997). This is also discussed in details in the third implication under section 3.3 in Chapter 3.

3.4.2.2. Occlusion Mechanisms: (I) Structural Swelling & Contraction

Physical occlusion by pore swelling in highly porous carbonaceous sorbent has been convincingly demonstrated by Braida et al. (2003). Using benzene as a model adsorbate and a highly porous charcoal (400 $m^2_{surface\ area}/g_{solids}$) as a model sorbent, Braida et al. showed that sorbed-benzene could be entrapped as the charcoal micropores underwent adsorbate-induced structural deformation (pore swelling & collapse) through an adsorption-desorption cycle. The support for structural swelling and contraction was the dependence of sorbent pore volume with sorbate dosage: that sorbent pore volume increases with the amount of sorbate added (Figure 10 in Braida et al.).

The swell-&-collapse occlusion mechanism by Braida et al. may not be applicable to natural soils and sediments where the highly porous carbonaceous phases (e.g. charcoal, char) are absent or negligible. Natural sediments are primarily made up of mineral phases and often contain little OC (f_{OC}~<0.05-0.10 g_{OC}/g_{solids}) or BC (or condensed, 'hard' carbons) (f_{BC}~10% of f_{OC}). Except where BC deposition is dominated by industrially produced activated charcoal/carbon, typical natural sedimentary BC should comprise primarily of fuel-derived soot, biomass-derived char/charcoal, or kerogen. Freshly derived diesel soots are typically less porous and have smaller surface area (~50-90 m^2/g) than 'activated' types of charcoals/carbons (~500-2000 m^2/g). As for biomass-derived chars/charcoals, their surface areas are generally comparable or even less than those of soots (~2-50 m^2/g) (Table 4-3). This implies the sedimentary condensed carbon phase should be relatively diminished in micropores and that the swell-&-collapse mechanism may not dominate.

3.4.2.3. Occlusion Mechanisms: (II) Thermally Induced Aggregate-Densification

A recent work by Blake et al. (2007) points to a thermally induced occlusion mechanism for organic sorbates and organic matter (Figure 3-25). Blake et al. observed that fire can consolidate component grains in soil aggregates by reducing intra-aggregate pore space with two key evidential supports. First, they found that, on average, burned soil aggregates settled almost 3 times faster than the unburn aggregates. Second, they observed that that the porosity of burnt soil aggregates decreased dramatically from >90% in large aggregates (dia. ~1000 μm) down to ~10-20% in finer aggregates (dia. ~100 μm). These two observations imply that the arrangement of the component mineral grains can further 'close up' after the interstitial water is evaporated and the attached organic matter partially volatilized or combusted.

Another study by Ketterings et al. (2000) showed that burning could affect soil mineralogy by transforming existing minerals into finer grains of other types. The production of finer grains potential allow better packing within the aggregates to reduce total pore volume. Ketterings et al. also speculated the possibility of glassy protective mineral structure forming in the soil during heat treatment. The findings of both studies suggest that residual organic matter (and sorbates) may be protected in the pore space enclosed within the densified aggregates after a burning event. Any organic sorbates/contaminants associated with the residual organic matter can be, therefore, effectively sealed off from phase exchange reactions.

The idea of fire-induced occlusion of organic matter (and hence organic sorbates) is also consistent with the observation that soil horizon that had experienced more fire events tend to have a greater total organic C storage in the long-term (Johnson and Curtis 2001) and the report that substantial soil organic matter can survive high intensity crown fire (Litton et al. 2003) and that residual C in burnt soil is significantly more resistant to mineralization in months to years after the burn (Fernandez et al. 1999). It should be reminded that the cited evidence on residual-C from burnt soils may also be interpreted as the existence of biochemically recalcitrant carbon forms (i.e. graphitic carbon) rather than physically inaccessible ones (i.e. occluded).

Occluded organic sorbates in sediments can be related to thermal densification of terrestrial aggregates. It is known that soil organic matter improves the stability of soil aggregates against aeolian or fluvial erosion by promoting the water repellency of the aggregate surface via hydrophobic coating (Certini et al. 2005). Fire has been shown to reduce the soil aggregates hydrophobicity (or water repellency), making the aggregates more wettable by water (Mataix-Solera et al. 2004) and more susceptible to fluvial erosion and transport (Kim et al. 2003; Doerr et al. 2006; Blake et al. 2007).

3.4.2.4. Occlusion Mechanisms: (III) Encasement via Mineral Precipitation

HOCs may also become physically occluded as the organic matter becomes encased in mineral phase via the dissolution and precipitation of mineral oxides (Figure 4-12). Organic carbon has been observed in natural iron oxides (Yapp et al. 1986) and aquifer sand (Holmen et al. 1996). About 0.2–2wt % of organic carbon encased in goethites (Yapp et al. 1986), and this is comparable with typical soil/sediment f_{OC} (Cornelissen et al. 2005b). The work by Holmen et al. (1997) also provided indirect kinetic and thermodynamic evidence for the encasement of a fraction of the organic matter within the mineral matrix. Native HOCs will be occluded if they are sorbed to the organic matter encased in mineral matrix.

Natural mineral phases can undergo dissolution and precipitation reactions (Stumm et al. 1996) and the organic matter can become entrapped in the dissolution-precipitation process. Mineral phases can undergo dissolution when exposed to water with low metal contents or when the pH is lowered (Stumm et al. 1996). Bacterial promoted dissolution/mineralization of iron oxide has also been reported (Ferris et al. 1989). The dissolved metal ions are mobile and can be relocated to different surfaces of the aggregates. There, they can be re-oxidized, forming nm-scale precipitates (Swartz et al. 1997). However, is there evidence that organic matter is present on mineral surfaces –

especially those associated with small pores where it can be easily encased via dissolution-precipitation of mineral oxides?

Studies have shown that mineral grain micropores can contain organic matter/coating. Mayer (1994) surveyed a number of coastal sediments and showed the abundance of sedimentary organic matter was positively correlated with the grain mineral surface area. Surface area analysis on sedimentary particles/aggregates revealed that about 60-90% of the surface area was associated with pores of diameter <10nm. Furthermore, Hayase et al. (1983) showed that surficial sedimentary humic substances have a lower surface tension (~30-45 dynes/cm^2 at 25°C) than water (72 dynes/cm^2 at 25°C) and thus sedimentary organic matter could 'wet' the grain surface better. The OM coating the mineral phase is in micron-scale, with thickness ranging from 10-100 μm (Holmen et al. 1997). Curry et al. (2007) used transmission electron microscopy and silver-staining technique to visualize the association of organic matter with marine sedimentary mineral grains. They demonstrated that some of the sedimentary or fecal-pellet associated OM resides in mesopores (<50 nm) formed between neighboring mineral grains. Zimmerman et al. (2004a, 2004b) also provided evidence that organic matter preferentially adsorb onto/into the mineral pores

3.4.2.5. Fraction Pyrene Occluded (Estimated via Visual Inspection)

The fraction of occluded native sedimentary pyrene may be estimated supposing that (i) physical occlusion was the principal cause for the apparent enhancement in $K_{d,pyr}$ (Figure 4-10), and (ii) the equilibrium distributions of the total non-occluded pyrene should conform to a single Freundlich model. Based on these assumptions, the 'correct' fraction pyrene occluded should correspond to the case where the data points appear linear on a log-log plot of accessible solid-phase pyrene concentration (total solid-phase pyrene less the occluded solid-phase pyrene) versus dissolved pyrene concentration (Figure 4-13). Such exercise suggested that about 80–90% (by visual inspection) of the natively bound pyrene has to be inaccessible to partitioning reaction.

Other evidence supports the occlusion hypothesis. The solid-phase pyrene concentrations in the ng_{pyr}/L_w range were about 'constant' around 5000 $\mu g_{pyr}/kg_{solids}$ at 6, 15, and 22°C (Figure 4-3). This showed that the solid-phase pyrene concentration had not changed much from the initial concentration of 5200 $\mu g_{pyr}/kg_{solids}$ (Table 4-2). Analysis on the equilibrium observations at other temperatures also gave a similar estimate of ~90% occlusion. The results from the Short-Term Desorption experiment (Table 4-2) also show consistency with the idea of occlusion. In the Short-Term Desorption Experiments (Table 4-2) where all pyrene was initially bound to the sediment, the end-point dissolved phase pyrene accounted for about 1-20% of the total native sedimentary pyrene. This implied that ~80+% of the native pyrene remained in the sedimentary phase. This is consistent with (but not necessarily supportive of) the fraction occlusion estimated from above. At the very least, the Short-Term Desorption and the Long-Term Adsorption Equilibrium results are not in conflict with each other.

It should be noted that the second assumption – isotherm assumes a Freundlich form – does not have to be true. As reported in literature, isotherms with composite domains (e.g. dual or triple sorption terms) will appear to be slightly curved in a log-S vs log-C

space (e.g. Huang et al. 1997b; Accardi-Dey and Gschwend 2002). The fraction pyrene occluded can also be estimated through a more rigorous regression scheme. This will be presented and discussed in Chapter 5.

Why is sorbate occlusion not examined more commonly in previous HOC sorption studies? This may be because the past studies have not examined sorption equilibrium on geosorbents and their native HOCs. Earlier sorption studies often involved addition/'spiking' of high HOCs dosages without long incubation time. This means that the adsorbed HOCs did not have enough time to become occluded (e.g. occlusion via mineral dissolution-precipitation). Furthermore, native HOCs may be formed/occluded during with the formation of the geosorbents (e.g. via combustion processes).

3.4.3. Hypothesis 2: High-Affinity Micropore Sorption

The observed enhancement $K_{d,pyr}$ at ng_{pyr}/L_w range (Figure 4-10) may be thermodynamically authentic. Under this hypothesis, all sorbed pyrene in the lower concentration range is assumed to be accessible for phase transfer, and hence an increasing $K_{d,pyr}$ reflects a real increase in the sorbent's affinity for pyrene. The failure of the OC-BC model at the lower $C_{pyr,eqm}$ range implied that BC, operationally defined by the thermal oxidation method ('CTO-375°C-24hr'), may not explain the enhancement of $K_{d,pyr}$. While the 'CTO-375°C-24hr' method generally captured the presence of soots, it systematically missed other BC/condensed carbonaceous phases such as biomass-derived char/charcoal (Nguyen et al. 2004; Elmquist et al. 2006; Hammes et al. 2007), kerogen, or coal (Hammes et al. 2007). Hence the prevailing OC-BC sorption model may not fully account for HOC sorption contributed by non-soot BC. Suppose that the soot-BC surface is predominantly aromatic/graphitic, adsorption of pyrene onto soot surface is then chemically similar to pyrene molecules condensing onto a solid of itself. This means that the unknown BC phase must exhibit an even greater affinity for pyrene than the soot-BC. One such possible BC phase is the surface of the micropores (pore dia. < 2 nm) in char/charcoal.

The author hypothesizes that the enhanced affinity for pyrene is caused by adsorbing onto char/charcoal micropore (dia.: <2 nm) surface while the relatively weaker affinity exhibited by soot-BC was due to the weaker mesopore (dia.: 2-50 nm) adsorption. The association of mesoporous adsorption with soot-BC and microporous adsorption with char-BC was supported by the pore distribution for soot and char/charcoal (Table 4-4): (i) soot-BC contains primarily mesopores and macropores (dia.: >50 nm) (~90% pore surface area/volume in mesopores/macropores, Table 4-4) whereas (ii) the pore structure of biomass-derived char/charcoal (total surface area ≤ 100 m^2/g_{solids}) and the industrially prepared activated char/charcoal (total surface area ~500-2000 m^2/g_{solids}) is generally dominated by micropores (dia.: <2 nm) (≥90% by pore surface area/volume).

Adsorption onto the micropore surface is expected to be stronger due to the fact that the adsorbate is exposed to (i) the molecular attraction from the adsorbing surface and (ii) the long-range attraction from the surrounding micropore wall (Figure 4-14). The maximum dimension of pyrene (~1 nm; Appendix 4-3) is comparable to the upper limit of micropores (<2 nm), and hence an adsorbing pyrene will certainly 'feel' the additional pore-wall interaction once it enters a micropore. This 'wall-effect' declines when pyrene

is adsorbing to the surface of a wider pore (e.g. mesopore, dia.: 2-50 nm) and becomes completely absent when pyrene is adsorbing onto non-pore surface (Figure 4-14). Empirically, enhanced adsorption of amino acids and proteins onto mineral pore-surface has been observed when the adsorbate dimension is roughly a half of the pore width (Zimmerman et al. 2004). Theoretically, the 'wall-effect' cartoon is qualitatively consistent with the energetic implication of Polanyi's pore-adsorption formulation (Polanyi 1920; Manes 1998).

3.4.3.1. Support for Micropore Sorption: (I) Comparable Adsorption Capacity

Two preliminary analyses supported the hypothesis that the observed enhanced adsorption affinity was due to char/charcoal micropores. First, one may estimate an area-based capacity for the char/charcoal micropores in NQB#6, and compare it with that derived from literature. With appropriate assumptions and uncertainties regarding the type of char/charcoal and its pore distribution, the amount of char present in the sediment, and the amount of adsorbed pyrene associated with the sedimentary char/charcoal phase (Appendix 4-4), it is estimated that ~4000-5000 ug_{pyr}/kg_{solids} may be attributed to adsorption on bio-char. This gave an estimated $S^{A}_{biochar,micro,pyr}$ of ~100-240 $ug_{pyr}/m^2_{micropore}$ for the potentially present bio-char in NQB#6 sediment. This was comparable with the micropore-adsorption capacity of pyrene of a commercial activated carbon (70-90 $ug_{pyr}/m^2_{micropore}$) in a previous study (Walters et al. 1984).

3.4.3.2. Support for Micropore Sorption: (II) Comparable Freundlich Parameters

Second, the extent of adsorption enhancement observed here was semi-quantitatively consistent with that reported in similar adsorption studies. PAH adsorption on char/charcoal/activated carbon generally has a Freundlich exponent, n_{Fr}, ranging from ~0.4-0.65 (Walters et al. 1984; Nguyen et al. 2007; Sun et al. 2008). Taking $C_{pyr,Eqm} \approx 0.5\ ug_{pyr}/L_w$ roughly as the boundary between the meso/macropore-dominated (i.e. predictable by a OC-BC_{soot} model) and the micropore-dominated (char-BC; where OC-BC_{soot} prediction failed) adsorption regimes (Figure 4-10), we observed n_{Fr} ranged from ~0.15-0.5, which was comparable with the value range reported.

The lower value of 0.15 observed here was most likely due to the fact that our sediment sample was field-aged whereas the chars/charcoals in quoted studies were freshly prepared. Field-aging enables some micropores to be filled with natural organic matter (Mayer 1994), and hence increases the heterogeneity of adsorption site energies. In all the surveyed studies, the char/charcoal samples have not been field-aged (Walters et al. 1984; Nguyen et al. 2007; Sun et al. 2008), not to mention that some of the studies may be short of equilibration time (e.g. Walters et al. 1984, Sun et al. 2008). Furthermore, the NOM-loaded micropores would exert an affinity (NOM+'wall-effect') for the adsorbate at even greater levels than the pores without NOM-filling (only 'wall-effect'). A lower n_{Fr} is consistent with the presence of secondary attraction due to NOM-coating/filling (i.e. higher $K_{d,pyr}$ at a given $C_{pyr,eqm}$) and/or an increasingly heterogeneous adsorption energy distribution (Adamson et al. 1997).

3.4.3.3. Support for Micropore Sorption: (III) Reasonable E_A of Desorption

A third piece of support for micropore sorption was that reasonable/feasible estimates of desorption activation energies ($E_{A,des,app}$) was obtained from the desorption kinetic data. Since the hypothesis suggests strong sorption of pyrene (or other HOCs) onto

char/charcoal micropore surfaces, pyrene sorbed onto these surfaces should desorb very slowly. If the apparent activation energy of desorption associated with the micropore surfaces is of unrealistic magnitude, one may reject the micropore sorption hypothesis.

Since the desorption kinetics of native pyrene was examined only at room temperature, $E_{A,des,app}$ has to be estimated from an assumed pre-exponential constant (i.e. "A" in $k=Aexp(-E_{A,des,app}/RT)$). Assuming (i) an elapsed desorption time of 8 mo (or 5760 h) as the "very slowly" desorbing period, (ii) an average value of $A \sim 0.001\ s^{-1}$ (!![1]) (Kim et al. 2004), and (iii) the fitted kinetic parameters for the desorption experiment (i.e. Appendix 7-21(III)), $E_{A,des,app}$ for native pyrene was estimated to be around 30 kJ/mol. Increasing the incubation time did not change $E_{A,des,app}$ substantially (e.g. for t_{des}=5 yr, $E_{A,des,app} \sim <$ 35 kJ/mol). This is certainly less than the 60–70 kJ/mol reported in literature (Cornelissen et al. 1997b) and implies that the micropore sorption hypothesis is energetically consistent with the desorption kinetic observations. The estimation of $E_{A,des,app}$ can be found in Appendix 7-25.

3.4.4. Hypothesis 3: Mixed Scenario of Occlusion and Micropore Sorption

Physical occlusion and high-affinity micropore adsorption may both contribute significantly towards the enhanced sorption in the lower concentration range (Figure 4-7 & 4-10). In this case, the next set of questions will be: (I) Under what circumstances does each mechanism become important? (II) How can one quantitatively separate the two adsorbed fractions? (III) What suite of analytical procedures may be designed to quickly characterize the fraction occluded from the fraction strongly adsorbed on microporous surface?

3.4.5. Concluding Remarks on Physical Occlusion and High-Affinity Adsorption

The differences between the hypotheses of physical occlusion and high-affinity micropore adsorption are important and must be emphasized. These differences may also be considered as 'implications' of the two sorption pictures.

3.4.5.1. Reversible Equilibrium State, Irreversible Phase-Transfer Kinetics

First, the micropore adsorption hypothesis implies that sorption equilibrium (adsorbing or desorbing) should be reversible. However, reversibility in equilibrium state does not always implies reversibility in the kinetics of transfer, for it is possible to imagine scenarios where the sorbate adsorb quickly but desorb at a slow speed. This would be the case, for instance, when HOCs may adsorb quickly to the high-energy pore surface in a freshly emitted/released aggregates, and then desorb through the organic matter that has deposited into the micropores during the aging of the aggregates. Hence the observation of a slower desorbing profile is not a sufficient proof of irreversible sorption.

3.4.5.2. Physical Occlusion Reduces Enthalpic/Entropic Changes

Second, micropore adsorption implies all sorbed sorbates are accessible to phase transfer reaction, and hence any change in K_d reflects genuine change in the energetics

[1] Note that the "A" taken corresponded to the desorption of phenol from activated carbon into acetone, N,N-dimethylformamide, and methanol. Thus the $E_{A,des,app}$ should be taken as a very crude estimate of the real activation energy.

of adsorption. In contrast, physical occlusion means that the observed S/C is only an 'apparent' distribution coefficient (or $\mathfrak{K}_d=S_{Tot,Eqm}/C_{Eqm}$). The true, thermodynamically meaningful K_d ($=S_{accessible,Eqm}/C_{Eqm}$) should be numerically less than $\mathfrak{K}_d$. While the fraction occluded may have temperature dependence (for instance, higher temperature opens up some of the enclosed pocket, making the adsorbates therein accessible to phase-transfer and responsible to thermochemical gradient), the physically inaccessible fraction will always reduce the sensitivity of the apparent K_d to temperature effect. This would mean that the enthalpic (or entropic) change in a system where physical occlusion is significant tends to lesser in magnitude when compared with that in a system with fully accessible sorbates or surface.

3.4.5.3. Sorbate Loading and Sorbent Structural Changes

Third, the micropore adsorption picture presupposes no changes in the physicochemical and structural properties of the sorbent surface between adsorption and desorption. In contrary, structural changes in the sorbent (e.g. pore structure and accessibility) are allowed in the physical occlusion picture (e.g., change in char pore structure as in Braida et al. 2003). This is to say that, in the physical occlusion picture, the true K_d would reflect changes in both the sorbate activity and the sorbent structure.

3.5. Testing the Physical Occlusion Hypothesis

Since physical occlusion of native pyrene may explain the observed concave-up isotherm (section 3.4.2; Figure 4-3 & 4-7), a desorption experiment using PE-strip as the sorbing phase was conducted. Since the occluded fraction would be extracted by organic solvent (i.e. via swelling of the solid matrix, making occluded sorbate accessible for partitioning), PE-strips were used to serve as a non-swelling reservoir that had high affinity for pyrene. This section will present and discuss the results from this experiment.

3.5.1. Expected Profiles for PE-Extractable Pyrene

Ideally, the sediment-PE experiment would give results which either support or reject the physical occlusion hypothesis. To show that physical occlusion is the case, one needs to demonstrate that the PE-extractable fraction has an upper-limit (i.e. $f_{critical}$ as in Figure 4-15) beyond which no further desorption of native sedimentary pyrene will be possible at excessive amount of PE. One may further anticipate that a distribution of sorption energy/binding force exists within the extractable fraction such that the differential energetic cost increases with desorptive force (i.e. higher amount of PE) (curve (b) in Figure 4-15). On the contrary, we can confidently reject the occlusion hypothesis should we observe that the fraction extractable exceeds the estimated upper-limit (curve "non-occluded" in Figure 4-15). Thus, the key lies in the determination/estimation of the critical fraction of native pyrene extractable ($f_{critical}$).

3.5.2. Results on Occlusion Hypothesis

The experiment produced inconclusive results regarding the physical occlusion hypothesis. Less than 3 % of the natively associated pyrene has been taken up by the PE after 50 d. Taking the more extreme estimate for $f_{critical}$ (partition-accessible fraction) to be 10-20% (or 80-90% occluded; see section 3.4.2.5), this means that the 3 % uptake by PE was consistent, but not necessarily supportive, with the idea of physical

occlusion. This was due to the fact that the fraction extracted had not reached the plateau regime as discussed (i.e. $f_{critical}$ in Figure 4-15). The amount of pyrene extracted by PE was still increasing at the highest PE:BC mass ratio at 1900 g_{PE}/g_{BC}.

3.5.3. Argument for Disequilibrium after 50 d

It also appeared unclear whether equilibrium was established in the PE-sediment-water system after 50 d. There was some evidence for disequilibrium. First, there seemed to be allowance for further uptake of pyrene by PE. Although the amount of pyrene extracted in all cases varied narrowly between ~2 to 4 ng (Figure 4-16), the pyrene concentration in the PE, $C_{pyr,PE}$, varied for more than 10 times (Figure 4-17). This translated into widely ranged $S_{pyr}/C_{pyr,PE}$ ratios which were all present, however, at a more or less constant S_{pyr}. This suggested that chemical disequilibrium might exist at least in some of the PE-sediment suspensions.

Second, a quick comparison of $Q_{d,pyr}$ from the PE-sediment experiment against the earlier observed $K_{d,pyr}$ also suggested partition disequilibrium. If we may use the $K_{d,pyr}$ from the Long-Term Extended Range Adsorption Equilibrium experiment as reference, we would expect the highest $K_{d,pyr}$ to be ~2×10^5 L/kg at ng/L levels of pyrene (i.e. Figure 4-10; section 3.4.1). Although PE was the dominant uptake phase, we can estimate an equivalent $Q_{d,pyr}$ (or $Q_{eqvl\text{-}d,pyr}$) for the PE-sediment experiment by converting mass of PE into equivalent volume of water:

$$Q_{eqvl-d,pyr} = \frac{S_{pyr}}{C_{pyr,eqvl.wat}} \cong \frac{S_{pyr}}{C_{pyr,PE}/K_{pyr,PEW}}$$

Eqn. 4 - 1

where $C_{pyr,eqvl.wat}$ is the equivalent dissolved pyrene concentration ($\mu g_{pyr}/L_{eqvl.wat}$), $C_{pyr,PE}$ is the PE phase pyrene concentration ($\mu g_{pyr}/kg_{PE}$), and $K_{pyr,PEW}$ is the the PE-to-water partitioning coefficient for pyrene (L_{wat}/Kg_{PE}). Taking $\log K_{pyr,PEW}$ to be 4.7±0.1 (Fernandez et al. 2009), this means that 1 g_{PE} is chemically equivalent to about 5 L of water for the partitioning of pyrene. The computed equivalent $Q_{d,pyr}$ from the PE-sediment suspensions was found to be 10-100 times higher than the reference $K_{d,pyr}$ of 2×10^5 L/kg (Figure 4-18).

It is important to note the assumption here: one expects that adsorption of pyrene onto/into PE may still be proceeding. However, as the next section will demonstrate, this expectation of on-going adsorption may not be true.

3.5.4. Argument for Equilibrium after 50 d

The main piece of evidence supporting equilibrium after 50 d was the coherence of the PE-sediment data with the trend exhibited in the earlier adsorption equilibrium experiment. The idea of equivalent $Q_{d,pyr}$ (or equivalent $C_{pyr,w}$; see Eqn. 4 - 1) allows results from the PE-sediment experiment to be compared with the full set of adsorption equilibrium experiment discussed earlier (section 3.4.1; Figure 4-10).

The $Q_{eqvl\text{-}d,pyr}$–$C_{pyr,eqvl.wat}$ data pairs obtained from the PE-sediment experiment almost fall within the regressed prediction of the adsorption equilibrium data (Figure 4-19a),

suggesting that the two groups of observations, though located in different ranges, may be unified by the same trend (i.e. coherent). It may be argued that the coherence was simply an artifact of variable manipulation: that one correlates a function g(x,y,z) with itself (x). Here, however, $Q_{eqvl\text{-}d,pyr} = S_{pyr}{}^{*}K_{pyr,PEW}/C_{pyr,PE}$, where both S_{pyr} and $K_{pyr,PEW}$ are both much larger than $C_{pyr,PE}$, so any uncertainty in $C_{pyr,PE}$ or S_{pyr} would be magnified rather than diminished. A similar trend is also observed when plotting S_{pyr} against $C_{pyr,w}$ or $C_{pyr,eqvl.wat}$ (Figure 4-19c)

The coherence of the PE-sediment experiment with the adsorption equilibrium experiment suggested that the PE-sediment suspensions might be, in fact, at or close to equilibrium (e.g. within a factor of 2) after 50 d.

3.5.5. Considerations Based on Equilibration Rate

Equilibrium or disequilibrium can also be examined from kinetic considerations. Two kinetic analyses were performed. However, the question of disequilibrium remained unresolved due to assumptions unavoidable in both approaches. The two approaches will be discussed in the following paragraphs.

3.5.5.1. Basic Assumptions on $K_{d,pyr}$ and Diffusion in PE-phase

As a starting point, two major assumptions were made. First, $K_{d,pyr}$ is assumed to vary insignificantly while native sedimentary pyrene absorb/adsorb into/onto PE. This assumption reduces mathematical complexity due to non-linear isotherm.

Second, PE was converted to a water-equivalent phase assuming that transport within PE was not rate-limiting. This assumption allows a simple two-phase kinetic analysis and that an equivalent system solid-to-water ratio be computed. The equivalent solid-to-water ratio, $R_{s\text{-}eqvl.wat}$, is a measure of the effective mass-to-volume ratio of the desorbing phase (sediment) to the uptake phase (water+PE) by converting PE to equivalent volume of water:

$$R_{s-eqvl.wat} = \frac{Mass_{solid}}{Volume_{eqvl.wat}} = \frac{Mass_{solid}}{Volume_{wat} + Mass_{PE} K_{pyr,PEW}}$$

Eqn. 4 - 2

$R_{s\text{-}eqvl.wat}$ is, therefore, a sorbate-dependent property (i.e. a function of $K_{HOC,PEW}$). Taking $\log K_{pyr,PEW}$ to be 4.7±0.1 (Fernandez et al. 2009), this means that 1 g_{PE} is chemically equivalent to about 5 L of water for the partitioning of pyrene. The $R_{s\text{-}eqvl.wat}$'s of the studied PE-sedimentary suspensions are shown in Figure 4-20.

3.5.5.2. Kinetic Analysis I: First-Order Approximation

In the first approach, it is assumed that all adsorption onto (or desorption from) binding sites can be sufficiently described by a first-order kinetic model. An identical effective rate constant is thus applicable to adsorption (or desorption) reaction on all sorption sites. This is to say that adsorption/desorption occurring deep within a sedimentary aggregate is assumed to be immediately 'visible' the uptaking phase and so bears no kinetic penalty. This implied that:

$$\frac{dS}{dt} = \sum_{i=1}^{n} k_{-i}C - \sum_{j=1}^{m} k_j S \cong k_{-1}C - k_1 S$$

Eqn. 4 - 3

$$\frac{dC}{dt} = \sum_{j=1}^{m} k'_j S - \sum_{i=1}^{n} k'_i C \cong k'_{-2}S - k'_2 C$$

Eqn. 4 - 4

where k_x (or k_x') is rate constant for site with x^{th} binding energy,

C is the dissolved phase sorbate concentration,

S is the total solid phase sorbate concentration.

Following Eqn. 4 - 3 and Eqn. 4 - 4, partition coefficient K_d is simply:

$$K_d = \left(\frac{S}{C}\right)_{\frac{dS}{dt} \text{ or } \frac{dC}{dt}=0} = \frac{k_{-1}}{k_1} = \frac{k'_2}{k'_{-2}}$$

Eqn. 4 - 5

With conservation of sorbate, it can be shown that:

$$\frac{C_t}{C_\infty} = 1 - \exp\{-k(K_d R_{sw} + 1)t\}$$

Eqn. 4 - 6

where C_t and C_∞ are the dissolved phase sorbate concentrations at time t and infinite time (i.e. equilibrium),

R_{sw} is the solid-to-water ratio (kg_{solids}/L_w).

The time for the system to approach 95% of equilibrium, $t_{95\%\text{-Eqm}}$, can be evaluated as:

$$t_{95\%-Eqm} = \frac{\ln 20}{k(K_d R_{sw} + 1)}$$

Eqn. 4 - 7

With the 'intrinsic' rate constant, k, estimated from the Short-Term Desorption Experiment, $t_{95\%\text{-Eqm}}$ was estimated for all PE-sediment suspensions (see Appendix 4-5 for details). The $t_{95\%\text{-Eqm}}$'s estimated under the 1st order approximation model ranged from <1 to ~5000+ d (Table 3-7). The widely varying $t_{95\%\text{-Eqm}}$'s was mostly due to the uncertainty in estimating the 'intrinsic' rate constant k (Appendix 4-5).

3.5.5.3. Kinetic Analysis II: Radial Diffusion with Constant D_{eff} Approximation

The second approach is more realistic in that it does not assume equal accessibility of sorbate in the solid phase. Here, retardation of diffusion within particle/aggregate is reflected in the kinetic expression, although the effective diffusivity, D_{eff}, is assumed to be constant. The constant D_{eff} idea is consistent with the first general assumption (section 3.5.5.1) since $D_{eff} \propto 1/K_d$. Under the 1-D radial diffusion model, the local intra-particle sorbate concentration, S'(r,t), can be expressed as:

$$\frac{\partial S'}{\partial t} = \frac{1}{r^2}\left[\frac{\partial}{\partial r}\left(D_{eff}\frac{\partial S'}{\partial r}\right)\right] = D_{eff}\left[\frac{\partial^2 S'}{\partial r^2} + \frac{2}{r}\frac{\partial S'}{\partial r}\right]$$

Eqn. 4 - 8

The analytical solution for Eqn. 4 - 8 is provided by Crank (1979) to be:

$$\frac{M_o - M_t}{M_o - M_\infty} = 1 - \sum_{n=1}^{\infty} \frac{6\beta(\beta+1)\exp\{-D_{eff}q_n^2 t/r^2\}}{9 + 9\beta + q_n^2\beta^2}$$

Eqn. 4 - 9

$$\tan q_n = \frac{3q_n}{3 + \beta q_n^2}; \{\text{for } q_n > 0\}$$

Eqn. 4 - 10

$$\beta = \frac{1}{K_d R_{sw}}$$

Eqn. 4 - 11 (see also Chapter 7 section 4.1)

where the effective diffusivity, D_{eff}, is defined as such (Wu et al. 1988):

$$D_{eff} = \frac{D_{iw}\theta^2}{(1-\theta)\rho_s K_d + \theta}$$

Eqn. 4 - 12

Here, $t_{95\%\text{-}Eqm}$ is the time at which $(M_o\text{-}M_t)/(M_o\text{-}M_\infty) = 0.95$.

The radial diffusion model generally gave smaller estimates for $t_{95\%\text{-}Eqm}$, which ranged from <1 to 2000 d (Table 4-5). According to this model, a 50-d equilibration time was rather sufficient for some of the PE-sediment suspensions (e.g., No. 17-22). Here, the equilibration time depends strongly on the size of the particle/aggregate. For the remaining suspensions, a mixed state most probably existed at the end of 50 d: the finer fraction would be very likely at equilibrium while pyrene desorption might still take place for the larger aggregates/particles (e.g. 100-200 μm). A further analysis considering desorption in different size fractions was prevented by the absence of particle size distribution information for individual suspensions.

3.5.6. Concluding PE-Sediment Experiment

The PE-sediment experiment did not produced results that would lead to the rejection of the physical occlusion hypothesis. It appeared that the suspension should be sequentially extracted by clean PE for multiple times before one could estimate how much of the natively present pyrene was extractable in an aqueous environment.

It should be emphasized that if occlusion was indeed responsible for the low extraction of native sediment pyrene by PE, then the use of organic solvent clearly alter the sorbent structure substantially such that all sites where the native sorbates are held and blocked can be opened up and made accessible. The same is also true for the micropore surface sorption hypothesis (i.e. sorbate held on char/charcoal micropores).

3.6. Implications

The partitioning observations presented in this chapter have significant implications on the fate of persistent organic compounds in the environment and how HOC contaminated soils/sediments may be regulated or remediated. It was shown that the equilibrium phase distribution of pyrene at environmentally relevant levels (ng/L range) could not be predicted with isotherm derived from a higher concentration range (e.g. μg/L). This suggested that HOCs sorption isotherm derived from analytically convenient ranges (~1 ug_{pyr}/L or higher) may be unsuitable for predicting the equilibrium phase distributions of HOCs at typically realistic sub-ppb levels.

3.6.1. Sequestration of HOCs

Sequestration of HOCs has been traditionally attributed to extremely slow desorption (Luthy et al. 1997) and/or change in sorbent structural properties that gives rise to true hysteresis (Braida et al. 2003). However, the persistence of organic pollutants being 'surprising' may be partly due to our ill-formed expectation of their equilibrium distributions. Analogous to the relatively dominance of soot-BC over OC in the binding of HOCs, sequestration may be better understood by the existence of a third sorption phase with sorption affinity for HOCs greatly surpassing those of soot-BC, for instance.

3.6.2. Bioavailability of HOCs

The observations from this study raised a fundamental question for assessing the bioavailability of soil/sediment-bound HOCs – do we even have the appropriate basis for formulating reasonable phase distribution expectation of the sorbates? HOCs bioavailability can be assessed by assuming equilibrium phase partitioning or by considering the release kinetics (Ehlers et al. 2003; Stokes et al. 2006). This study suggests that our understanding on phase partitioning of native HOCs at ng/L range may be inadequate. Therefore, to have meaningful assessments of HOCs bioavailability, either with the equilibrium or the kinetic approach, we must first obtain accurate sorption isotherms covering environmentally relevant concentration range.

3.6.3. Predicting Partitioning of HOCs

The strong dependence of partition coefficient, K_d, on sorbate concentration provides new clues to the scattering of K_{BC} or K_{TOC} reported in literature. The recent review by Hawthorne et al. gave a very bleak prospect for predicting equilibrium phase partitioning

of HOCs. They showed that the K_{BC}'s of field-aged PAHs varied greatly by 2-3 order of magnitude without forming any significant correlation with key sedimentary physicochemical properties. Their analyses, however, proceeded on the assumption that the Freundlich exponent for the BC term was constant around 0.7. Given their porewater PAHs, which typically ranged from ~1 ng_{PAHi}/L_w to ~≥100 $\mu g_{PAHi}/L_w$, the assumption of constant Freundlich exponent may have been inappropriate, as the results in this chapter have demonstrated. The author thus holds a more optimistic opinion that an *a priori* predictive model, with reasonable accuracy and precision, for equilibrium partitioning of HOCs in natural sorbent-water systems may still be possible, if the key sorbate/sorbent physicochemical properties are known.

4. Conclusion

This chapter examined the partitioning of pyrene in sediment-water system at environmentally realistic concentration levels (i.e. ng_{pyr}/L_w). It was hypothesized that the partitioning of pyrene between sediment and water at field conditions may not be predicted from isotherms derived at a higher concentration range (i.e. $\mu g_{pyr}/L_w$). This was examined using the equilibrium observations from the three ad/desorption experiments discussed in Chapter 3 (see Table 4-1).

In the Long-Term Desorption Experiment, the dissolved pyrene level in ground suspensions seemed to be slightly (~10–20%) higher than the suspensions without grinding treatment. This might be interpreted as a portion of the native pyrene (~20–30%) being inaccessible to phase exchange. The Short-Term Desorption and the Long-Term Desorption Experiments showed good agreement in $K_{d,pyr}$s in the ng_{pyr}/L_w range. Furthermore, current isotherms (based on OC or OC/BC contents) systematically underpredicted the observed $K_{d,pyr}$s (Figure 4-2).

Results from the Long-Term Adsorption Equilibrium Experiment showed that the partitioning behavior of pyrene in the ng_{pyr}/L_w range was different from that in the $\mu g_{pyr}/L_w$ range. The isotherm exhibited an unusual 'concave-up' curvature in the $logS_{pyr}$-$logC_{pyr}$ space – the solid-phase pyrene concentration became relatively constant in the ng_{pyr}/L_w range (section 3.3.1). The isotherm shape was concluded to be real on the account of five pieces of reasoning/evidence: (i) observational consistency in the $\mu g_{pyr}/L$ range with a preceding study (section 3.3.3.1), (ii) consistency on shape at different temperatures (section 3.3.3.2), (iii) analytical consistency and linearity in instrumental response over the examined concentration range (section 3.3.3.3), (iv) observational agreement with partitioning data derived from coastal sediment cores (section 3.3.3.4), and (v) unlikely presence of substantial measurement errors (section 3.3.3.5).

Equilibrium data from all three experiments all suggested that the current isotherms (OC or OC/BC based) may not be extended to the ng_{pyr}/L level observations (section 3.2.2). The concave-up isotherm curvature suggested that pyrene (or native pyrene) may be very strongly bound in the low ng_{pyr}/L concentration region. Two hypotheses were proposed to explain this: (I) Physical Occlusion of Sorbate – that the higher affinity was

due to the fact that a fraction of the natively present pyrene was physically entrapped within the mineral matrix, and was thus inaccessible to partitioning reaction (section 3.4.2), and (II) Adsorption to High-Energy Micropore Surface – the increasing K_d reflected the disclosure of increasingly high energy sites which were associated with high surface area carbonaceous materials such as charcoal/char (section 3.4.3). Potential mechanisms and preliminary evidence for both hypotheses were discussed.

The implications of the Physical Occlusion and the Micropore Adsorption hypotheses were also highlighted: (i) that irreversible sorption kinetics would not prove that the existence of irreversible sorption endpoints (section 3.4.5.1), (ii) that physical occlusion would 'blur out' the thermodynamic signatures of sorption (section 3.4.5.2), and (iii) that physical occlusion also implies structural changes (e.g. pore structure and accessibility) in the sorbent, which would be reflected in the apparent $\mathfrak{K}_d$ of the system (section 3.4.5.3).

A polyethylene(PE)-sediment desorption experiment was conducted to test the physical occlusion hypothesis. The idea was to use PE strips as a highly-sorptive reservoir to extract as much of the natively bound pyrene as possible without swelling the sedimentary matrix. The physical occlusion hypothesis would be rejected if the natively bound pyrene could be extracted beyond the estimated occluded fraction (section 3.5.1). Unfortunately, the experiment did not produced results that would lead to the rejection of the physical occlusion hypothesis. Further analyses – by equilibrium arguments (section 3.5.3 & 3.5.4) or by kinetic considerations (section 3.5.5.2 & 3.5.5.3) – have not provided sufficient evidence for the rejection or the acceptance of the hypothesis. The occlusion hypothesis should be further tested with a sequential PE-sediment experiment.

The results in this chapter have important implications for the bioavailability and sequestration of soil/sediment-bound organic contaminants, and the sorption of hydrophobic organic compounds to black carbon. The observed concentration dependency may partly explain the widely scattered K_{OC}/K_{BC}'s reported in recent reviews.

Chapter 5. Pyrene Sorption Isotherm

CHAPTER ABSTRACT

Pyrene partitioning data obtained in previous chapters were successfully regressed by a number of composite isotherm models. These composite models contained descriptive terms representing the contribution due to (i) absorption into organic carbon (OC), (ii) adsorption onto soot or char black carbon (BC), and (iii) physical occlusion of sorbate in the background matrix. The regression-derived $\log K_{OC}$'s (4.7–5.6) and $\log K_{BC}$'s (6.0–6.3) generally agreed with those reported in literature. From the two occlusion-based models, it was estimated that 30–70 % of the native pyrene could be occluded in the sediment phase.

A brief survey showed that $\log K_{OC}$'s and $\log K_{BC}$'s of pyrene for different carbonaceous materials were generally well constrained to within 1 log unit. This implied that there may be 'universal' K_{OC} or K_{BC} for the sorption of HOCs in various natural sorbents, in contrary to the conclusions made in recent reviews. It was hypothesized that isotherm becomes more non-linearity (i.e. decreasing n_{Fr} or n_{BC}) when the heterogeneous binding sites are less occupied. This was supported by the correlation between n_{Fr} and the relative occupancy of the binding sites based on the past sorption studies involving different sorbents.

The constancy in $\log K_{OC}$ and $\log K_{BC}$ for pyrene suggested that the dependence of n_{Fr} or n_{BC} is the key in predicting the equilibrium partitioning of HOCs accurately. This might partially explain the orders of magnitude scattering in $\log K_{OC}$'s or $\log K_{BC}$'s presented in the review by Hawthorne et al. (2006, 2007) and the unsuccessful application of OC/BC models for partitioning prediction in Arp et al. (2009).

Table of Content for Chapter 5

1. Chapter Introduction, Scope, and Objective 104

1.1. Introduction 104

1.2. Objectives 104

2. Methodology 104

2.1. Isotherm Form 104

2.1.1. Singular Form 104

2.1.2. Composite Isotherm Form 106

2.2. Isotherm Fitting 106

2.2.1. Data Regression 106

2.2.2. Parameter Uncertainties, Goodness of Fit & Regression Errors 106

2.2.3. Criteria for Acceptable Regression 107

3. Results and Discussion 107

3.1. Isotherm of Pyrene Partitioning in Sediment-Water System 107

3.1.1. Regression by Singular Isotherm Forms 107

3.1.2. Regression by Composite Isotherm Forms 108

3.1.2.1. Preliminary Observations 108

3.1.2.2. Basis for Constructing Composite Isotherm 108

3.1.2.3. Evidence for Two-Domain Division of Sorption Isotherm 109

3.1.2.4. Composite Isotherm Forms 109

3.1.2.5. Isotherm Parameters (Composite Forms) 111

3.1.2.6. Implications for Occlusion and Micropore Adsorption 112

3.2. Interpreting Isotherm Parameters: Physicochemical Meanings 113

3.2.1. K_{OC}, K_{BC}, and n_{BC} Derived from Isotherm Parameters 113

3.2.1.1. Estimating K_{OC}, K_{BC} and n_{BC} from Isotherm Parameters 113

3.2.1.2. $K_{OC,pyr}$ 114

3.2.1.3. $K_{BC,pyr}$ 115

3.2.1.4. $n_{BC,pyr}$ 115

3.2.2. n_{BC} as the Key of Determining Sorption of HOCs 116

3.2.2.1. Universal $\log K_{OC}$ and $\log K_{BC}$ for HOC Sorption 116

3.2.2.2. n_{BC} (or n_{Fr}) as the Source of Variation in K_d's 116

3.2.2.3. Occupancy of Adsorption Sites 117

3.2.2.4. Dependence of n_{BC} or n_{Fr} on Occupancy of Adsorption Sites 118

3.2.3. Langmuir-Freundlich/Two-Freundlich Models 119

3.2.3.1. The Char-Soot Sorption Picture 119

3.2.3.2. The OC-BC Sorption Picture: an Alternative View.....119
3.2.4. Concluding Physicochemical Interpretation of Isotherm Parameters.....120
4. Conclusion 121

1. Chapter Introduction, Scope, and Objective

1.1. Introduction

Summarizing/presenting HOC partition behavior with a mathematical form is desirable for several reasons. Condensing partition data into a single expression is the first step in constructing a universal sorption model (Chiou et al. 1979; Accardi-Dey and Gschwend 2002; Nguyen et al. 2005; Arp et al. 2009). A succinct representation of partitioning behavior is also needed in modeling the dynamics of adsorption/desorption (e.g. Wu et al. 1986, 1988; Cheng et al. 1995; Werth et al. 1997). Furthermore, mechanistic insights (e.g. absorption vs adsorption and their thermodynamic properties) on HOC sorption may also be gained from its isotherm – if the isotherm is of a physically meaningful form.

1.2. Objectives

In the previous chapters, it has been shown that the isotherm of pyrene exhibited an unusual concave-up shape in the ng_{pyr}/L_w range (Figure 4-3 & 4-7). Various evidence suggested that the isotherm was real (Chapter 4, section 3.3.3). The next question is how the isotherm should be mathematically represented.

There are several objectives in this chapter. The first objective is to mathematically describe/summarize the pyrene sorption isotherm(s) obtained in Chapter 4. This would involve data regression using various isotherm forms. Next, the regressed isotherm parameters will be examined. This would be done along with a brief review on pyrene partitioning coefficients reported in literature. Finally, the author would like to use pyrene sorption to address the larger question of uncertainty in predicting the partitioning of HOCs between water and natural sorbents (Chapter 3, section 1.2.1).

2. Methodology

2.1. Isotherm Form

Different isotherm forms (both singular and composite forms) were used to describe the pyrene sorption data. These forms will be briefly described in the following sections.

2.1.1. Singular Form

Equilibrium partitioning observations can be summarized using purely empirical forms. Since the raw data show a concave-up shape in log-S vs log-C space, one may consider regression using a quadratic function (Eqn. 5 - 1) or a hyperbolic function (Eqn. 5 - 2):

$$\textbf{Quadratic:} \quad \ln S_{pyr,Eqm} = a\left(\ln C_{pyr,Eqm}\right)^2 + b\left(\ln C_{pyr,Eqm}\right) + d$$

Eqn. 5 - 1

$$\textbf{Hyperbolic Sine:} \quad \ln S_{pyr,Eqm} = B\sinh\left[A\left(\ln C_{pyr,Eqm}\right) + D\right]$$

Eqn. 5 - 2

where: a, b, d are the empirical coefficients for the quadratic form,

A, B, D are the empirical coefficients for the hyperbolic form,

$C_{pyr,Eqm}$ is the dissolved phase concentration at equilibrium ($\mu g_{pyr}/L_w$),

$S_{pyr,Eqm}$ is the solid phase concentration at equilibrium ($\mu g_{pyr}/kg_{solids}$).

While these mathematical forms may fit equilibrium data well, they are not mechanistically meaningful models. It is more often to describe sorption equilibrium using the Linear form (Eqn. 5 - 3), the Freundlich form (Eqn. 5 - 4) or the Langmuir form (Eqn. 5 - 5) (Chapter 4, section 3.3.2):

$$\textbf{Linear:} \quad S_{pyr,Eqm} = K_{Lnr} C_{pyr,Eqm}$$

Eqn. 5 - 3

$$\textbf{Freundlich:} \quad S_{pyr,Eqm} = K_{Fr} C_{pyr,Eqm}^{\,n_{Fr}}$$

Eqn. 5 - 4

$$\textbf{Langmuir:} \quad S_{pyr,Eqm} = \frac{S_{Lgmr,Max} C_{pyr,Eqm}}{C_{Lgmr,½} + C_{pyr,Eqm}}$$

Eqn. 5 - 5

where: K_{Fr} is the Freundlich coefficient $[(\mu g_{pyr}/kg_{solids})/(\mu g_{pyr}/L_{water})^{nFr}]$,

K_{Lnr} is the Linear form coefficient (L_w/kg_{solids}),

n_{Fr} is the Freundlich exponent (dimensionless),

$S_{Lgmr,Max}$ is the maximum sorbed pyrene concentration in the high-affinity domain (i.e. $C_{pyr,Eqm} >> C_{Lgmr,½}$, $S_{pyr,Eqm,Lgmr} \rightarrow S_{Lgmr,Max}$) ($\mu g_{pyr}/kg_{solids}$),

$C_{Lgmr,½}$ is the half-point dissolved pyrene concentration (i.e. $C_{pyr,Eqm} \rightarrow C_{Lgmr,½}$, $S_{pyr,Eqm,Lgmr} \approx 0.5 S_{Lgmr,Max}$) ($\mu g_{pyr}/L_w$).

The Linear form describes *absorptive* type of partitioning, with the implication that the sorbate absorption/'dissolution' energy is homogeneous through the absorbing phase. The Langmuir form describes the monolayer adsorption of sorbate onto surface sites with uniform binding energy. The Freundlich form represents adsorption onto surface sites with a heterogeneous energy distribution and thus may be considered as an extension of the Langmuir form. Thus a good fit to the Freundlich form may indicate multiple Langmuir-type sites all acting in parallel.

A recent study (Filipe et al. 2009) reported the partitioning of pesticides to soil organic matter using the Brunauer-Emmett-Teller (BET) form. The BET isotherm (Brunauer et al. 1938), which describes multilayer adsorption and may be derived from the Langmuir form (Adamson et al. 1997), is as follows (Hinz 2001; Filipe et al. 2009).

$$\textbf{BET:} \quad S_{pyr,Eqm} = \frac{K_1 C_{pyr,Eqm}}{(1 - K_2 C_{pyr,Eqm})(1 + K_3 C_{pyr,Eqm})}$$

Eqn. 5 - 6

where: K_1, K_2, and K_3 are the empirical coefficients of the BET form.

2.1.2. Composite Isotherm Form

Composite isotherm forms have been used to describe equilibrium partitioning of HOCs in solid-water (Huang et al. 1997b; Kan et al. 1998; Bucheli et al. 2000; Accardi-Dey and Gschwend 2002). A generic composite isotherm is simply a sum of two or more of the singular forms listed above (Eqn. 5 - 1 to Eqn. 5 - 6). The actual forms examined are listed in Table 5-1 and will be discussed also in section 2.1.2.

2.2. Isotherm Fitting

2.2.1. Data Regression

Sorption equilibrium data were fit to different isotherm forms using linear regression function (Excel) or non-linear regression routines (Matlab scripts; documented as Appendix D). Linear regression was used when fitting the data to singular forms (i.e. Linear, Freundlich, or Langmuir forms). Data regression to the composite forms (e.g. Linear–Freundlich) or non-linear forms (e.g. Hyperbolic Sine) were mostly performed in Matlab. The Two-Freundlich and the Langmuir-Freundlich models were first regressed with Matlab. However, because the optimization results were sensitive to the initial guess values (Appendix 5-7), a manually optimized Excel procedure (Appendix 5-8) was used to give optimized range of values for the model parameters (see also section 3.1.2.5).

2.2.2. Parameter Uncertainties, Goodness of Fit & Regression Errors

The errors/uncertainties in fit isotherm parameters were also estimated. Errors in the linearly regressed parameters were estimated using the built-in commercial in Excel (Data Analysis Tool – Regression module). Uncertainties of the non-linearly regressed parameters were determined by the confidence interval of the parameters corresponding to $\pm 1\sigma$ (see Matlab scripts in Appendix D).

The goodness of fit was measured by either r^2 (linear regression) or χ_υ^2 (non-linear regression). A perfect fit should give $r^2=1$ or $\chi_\upsilon^2=1$. r^2 was computed by the built-in function in Excel. χ_υ^2, the reduced chi-square, was computed from the following expressions (Bevington et al. 1992):

$$\chi^2 \equiv \sum \left(\frac{1}{\sigma_i^2} [y_{pred,i} - y_{obs,i}]^2 \right)$$

$$\chi_\nu^2 = \frac{\chi^2}{\nu}$$

$$\nu = N - m$$

Eqn. 5 - 7

where: σ_i^2 is the variance associated with the i^{th} observation,

N is the number of data points fit,

m is the number of regression parameters in the model,

υ is the degrees of freedom,

$y_{pred,i}$ is the model prediction for the i^{th} data point,

$y_{obs,i}$ is the i^{th} observation,

χ^2 is the chi-square of the regression,

χ_υ^2 is the reduced chi-square of the regression.

Mean squares of errors were also computed for non-linear regressions using built-in Matlab function (see scripts in Appendix D).

2.2.3. Criteria for Acceptable Regression

The regression of sorption data by a particular isotherm model was examined on a number of criteria. A model was accepted when: (i) there was no systematic error associated with the prediction (i.e. residual plots), (ii) all regressed parameters assumed physically sensible values (i.e. K_{OC}, K_{BC} must be positive), (iii) no indication of redundancy in parameters (e.g. a model with an explicit linear term, and yet the regressed n_{Fr} was found to be 1), (iv) the prediction had a tight confidence interval, and (v) the relative errors of the regressed parameters were not significant (e.g. 1 σ >> parameter).

3. Results and Discussion

3.1. Isotherm of Pyrene Partitioning in Sediment-Water System

3.1.1. Regression by Singular Isotherm Forms

Sorption data could not be fit well by most of the singular isotherm forms. Significant systematic errors were observed when the data were regressed with the singular Langmuir, Freundlich, BET, Linear, and Hyperbolic Sine forms (Figure 4-5, 5-1). The

only exception was the quadratic form, which fit S_{pyr} and C_{pyr} well in a log-log space (r^2>0.95; see Figure 4-4).

Despite the good fit of the data, the quadratic isotherm form had several limitations. First, the quadratic form suggested the existence of a partitioning minimum along $C_{pyr,Eqm}$. This appeared to be a physicochemically impossible scenario. Such case has not been observed or classified in literature (Brunauer et al. 1940; Adamson et al. 1997). Second, the quadratic form may not be applied in cases where substantial extrapolation is necessary. Third, the quadratic form did not reveal any physicochemical understanding of pyrene partitioning.

It is, therefore, necessary to re-examine the sorption data with some physicochemical understanding or hypothesis, and to describe the data with a mathematical form based on such framework. The sorption data were also regressed by composite models that were combinations of the Linear, the Freundlich, and the Langmuir forms.

3.1.2. Regression by Composite Isotherm Forms

3.1.2.1. Preliminary Observations

Some observations on the isotherm (Figure 4-3) may help justifying the choices on composite form. First, the isotherm may be divided into two regions, one corresponding to the low-concentration range ($C_{pyr,Eqm}$ ~< 0.1 $\mu g_{pyr}/L_w$), the other covering the $\mu g_{pyr}/L_w$ range. These two regions appeared to have different slopes, implying a change in the dependence of sorption affinity with respect to $C_{pyr,Eqm}$.

Second, the high-concentration range data (C_{pyrEqm} ~> 1 $\mu g_{pyr}/L_w$) can be sufficiently described by a singular Freundlich model. Indeed, the upper range of the isotherm (i.e. $C_{pyr,Eqm}$: ~0.5 to 20 $\mu g_{pyr}/L_w$) was consistent with that reported previously (Figure 4-7).

Third, the solid-phase concentration appeared to be constant around ~5000 $\mu g_{pyr}/kg_{solids}$ at different temperatures (Figure 4-3). This was very close to the initial/native pyrene concentration on the sediment (5200±1040 $\mu g_{pyr}/kg_{solids}$).

3.1.2.2. Basis for Constructing Composite Isotherm

The fore-mentioned observations may be used to formulate a basis for selecting the appropriate composite form for pyrene sorption isotherm:

(i) the sorption sites can be divided into two domains, one with high-affinity and the other with low-affinity for pyrene,
(ii) that natively present pyrene is primarily bound in the high-affinity domain,
(iii) that amended pyrene is primarily sorbed onto the low-affinity domain,
(iv) that the overall isotherm is dictated by the relative dominance of the sorption in the two domains, and
(v) that the two domains have independent and distinct thermodynamical signatures for pyrene partitioning

3.1.2.3. Evidence for Two-Domain Division of Sorption Isotherm

The division of the isotherm into 'native' (or high-affinity domain; $C_{pyr,Eqm}$ ~< 0.1 $\mu g_{pyr}/L_w$) and 'amended' (or low-affinity domain, $C_{pyr,Eqm}$ ~> 1 $\mu g_{pyr}/L_w$) domains requires some justifications. The first piece of support was that the relative abundance of native pyrene followed the isotherm closely. Since the sorption experiment was conducted on sediment with native sorbate, one can estimate the relative presence of native pyrene in the system according to the following ratio:

$$MR_{pyr,s,native/eqm} = \frac{S_{pyr,native}}{S_{pyr,Eqm,T}} = \frac{S_{pyr,o}}{S_{pyr,Eqm,T}}$$

Eqn. 5 - 8

where: $MR_{pyr,s,native/eqm}$ is the ratio native pyrene to sorbed pyrene at equilibrium,

$S_{pyr,native}$ is the native pyrene concentration ($\mu g_{pyr}/kg_{solids}$),

$S_{pyr,o}$ is the initial sedimentary pyrene concentration ($\mu g_{pyr}/kg_{solids}$),

$S_{pyr,Eqm,T}$ is the total sedimentary pyrene concentration at equilibrium, including both native and amended pyrene ($\mu g_{pyr}/kg_{solids}$).

It appeared that the shape of the isotherm conformed well to $MR_{pyr,s,native/eqm}$ (Figure 5-2; Appendix 5-1). The similarity in the $S_{pyr,Eqm}$-vs-$MR_{pyr,s,native/eqm}$ and the isotherm hinted that the isotherm curvature may be described with the relative abundance of natively bound pyrene.

The second piece of evidence for the two domain idea was that the experimental observations seemed to be organized in two distinct groups in a $K_{d,pyr}$-$MR_{pyr,s,native/eqm}$ space (Figure 5-3a, b). The observed and the hypothetical cases were both shown in Figure 5-3a. The hypothetical case assumed that the sorption isotherm contained only a singular Freundlich term, with the associated parameters derived from actual data in the high-concentration range (i.e. $C_{pyr,Eqm}$ ~>1 $\mu g_{pyr}/L_w$). The 'data points' in the hypothetical case were calculated using observed $C_{pyr,Eqm}$ and solids-to-water ratio as independent variables. The figure showed clearly that the actual observations did not form a smoothly continuous curve as the hypothetical isotherm (singular Freundlich) would have predicted (Figure 5-3a). An expanded view in the $K_{d,pyr}$-$MR_{pyr,s,native/eqm}$ space showed that the observed data points formed two regions with very distinctive slopes (Figure 5-3b). This two-zone feature was also observed at higher temperatures (Appendix 5-2).

3.1.2.4. Composite Isotherm Forms

A total of nine composite isotherm forms were considered to fit the pyrene sorption data (Table 5-1). Some of these forms would be important for later discussions and they would be briefly described.

The $\mu g_{pyr}/L_w$ range (or 'low-affinity' domain) partitioning of pyrene seemed to be best fitted by the Freundlich model as it was shown earlier (e.g. Figure 4-7, 4-9). The BET

form has not been used because it has one more degree of regressional freedom. For the ng_{pyr}/L_w range (or 'high-affinity' domain) – where native pyrene dominated sorption – both the Freundlich and the Langmuir forms were used. In this case, the success of one model over another will have mechanistic implications (see section 3.1.1). These reasons lead to the Two-Freundlich (Eqn. 5 - 9) and the Langmuir-Freundlich (Eqn. 5 - 10) forms for isotherm regression:

$$\mathbf{Two-Fr:} \quad S = K_{Fr,H} C^{n_H} + K_{Fr,L} C^{n_L}$$

Eqn. 5 - 9

where: S is the equilibrium solid-phase pyrene concentration ($\mu g_{pyr}/kg_{solids}$),

C is the equilibrium dissolved phase pyrene concentration ($\mu g_{pyr}/L_w$),

$K_{Fr,H}$ and $K_{Fr,L}$ are the Freundlich coefficients in the high-affinity domain and the low-affinity domain, respectively, $[(\mu g_{pyr}/kg_{solids})/(\mu g_{pyr}/L_w)^n$, with n = n_L or $n_H]$,

n_H and n_L are the Freundlich exponents in the high-affinity domain and the low-affinity domain, respectively.

$$\mathbf{Lgmr-Fr:} \quad S = K_{Fr} C^n + \frac{S_{Max} C}{C_{½} + C}$$

Eqn. 5 - 10

where: K_{Fr} is the Freundlich coefficient for pyrene sorption in the low-affinity domain $(\mu g_{pyr}/kg_{solids})(L_w/\mu g_{pyr})^n$,

n is the Freundlich exponent for pyrene sorption in the low-affinity domain,

S_{Max} is the maximum sorbed pyrene concentration in the high-affinity domain (i.e. $C >> C_{½}$, $S \rightarrow S_{Max}$) ($\mu g_{pyr}/kg_{solids}$),

$C_{½}$ is the half-point dissolved pyrene concentration (i.e. $C \rightarrow C_{½}$, $S \approx 0.5S_{Max}$) ($\mu g_{pyr}/L_w$).

As reference, the Linear-Freundlich form (Eqn. 5 - 11) previously used for describing pyrene sorption data (Accardi-Dey and Gschwend 2002) was also considered:

$$\mathbf{Lnr-Fr:} \quad S = K_{Lnr} C + K_{Fr} C^n$$

Eqn. 5 - 11

The isotherm models described by Eqn. 5 - 9 & Eqn. 5 - 10 may be considered as representative of the case of high-affinity micropore adsorption (Chapter 4, section 3.4.3). The Linear-Freundlich form (Eqn. 5 - 11) assumed no difference between soot and char/charcoal in their adsorptive uptake of pyrene – the regression would simply re-evaluate the isotherm parameters.

The case of physical occlusion (Chapter 4, section 3.4.2) can be built upon the above isotherm models with the addition of an occlusion term S_{occlu} (Eqn. 5 - 12 & Eqn. 5 - 13):

$$\textbf{Occlusion} - \textbf{Lnr} - \textbf{Fr}: \quad S = S_{occlu} + K_{Lnr} C + K_{Fr} C^n$$

Eqn. 5 - 12

where: S is the equilibrium solid-phase pyrene concentration ($\mu g_{pyr}/kg_{solids}$),

S_{occlu} is concentration of pyrene occluded in the sorbent ($\mu g_{pyr}/kg_{solids}$),

C is the equilibrium dissolved phase pyrene concentration ($\mu g_{pyr}/L_w$),

K_{Fr} is the Freundlich coefficient ($\mu g_{pyr}/kg_{solids}$)($L_w/\mu g_{pyr}$)^n,

n is the Freundlich exponent for pyrene sorption.

$$\textbf{Occlusion} - \textbf{Fix}: \quad S = S_{occlu} + f_{OC} K_{OC} C + f_{BC} K_{BC} C^n$$

Eqn. 5 - 13

where: f_{OC} and f_{BC} are the OC and BC contents measured by CTO-375°C-24h method (g_{OC}/g_{solids} or g_{BC}/g_{solids}),

K_{OC} is the OC-normalized partitioning coefficient (L_w/kg_{OC}); it is fixed to be $10^{4.7}$ according to earlier studies (Karickhoff 1981; Schwarzenbach et al. 2003),

K_{BC} is the BC-normalized partitioning coefficient ($\mu g_{pyr}/kg_{solids}$)($L_w/\mu g_{pyr}$)^n; it is fixed to be $10^{6.25}$ according to Accardi-Dey and Gschwend (2002),

n is the Freundlich exponent.

The two occlusion isotherm models were the same except that Eqn. 5 - 12 did not assume known K_{OC} or K_{BC} while Eqn. 5 - 13 did.

It should be noted that the two-domain division does not mean that the isotherms will have two terms, but rather that the isotherm is, overall, dominated by two of the terms. In many cases (e.g. Eqn. 5 - 12, Eqn. 5 - 13; see also Table 5-1) the absorptive linear term (i.e. $K_{Lnr}C$) was the 'minor' term'; it was included to make a more complete mechanistic picture of sorption.

3.1.2.5. Isotherm Parameters (Composite Forms)

All composite isotherm models provided satisfactory fit of the sorption data (Figure 5-4). The regression results (i.e. isotherm parameters) for the sorption data at 22°C are summarized in Table 5-2. Complete regression details of the different isotherm models are documented in Appendices 5-3 to 5-6. The regression by the 'Occlusion-Lnr-Fr' model (4-parameter) is described in Appendix 5-6. The regression results at other temperatures are available in Table 5-3.

The more complex 5 to 6-parameter models (e.g. 'Lnr-Lgmr-Fr', 'Three-Fr' in Table 5-2) appeared to be over-parameterized, as suggested by presence of artifacts in both the fit lines and the optimized coefficients (i.e., huge magnitudes and/or negative values in K, n, S_{Max}, or $C_{½}$). The 5 to 6-parameter models were thus rejected and excluded in further analysis/discussion (noted in Table 5-2). The 'Lnr-Fr(soot)-Fr(char)' model, which explicitly considered char contribution, was also rejected for similar reasons (see Table 5-2).

The non-linearly regressed parameters for the Two Freundlich and the Langmuir-Freundlich forms should be looked upon with discretion. The non-linearity of either forms have lead to non-ideal regression results – there existed multiple sets of regressed parameters for both forms (Appendix 5-7) with some of the optimized parameters being non-sensible (e.g. $K_{Fr} < 0$, which implies negative sorbate concentration; $n_{Fr} < 0$, which implies the most thermodynamically favorable sites being sorbed/filled later than the less favorable sites). Furthermore, the parameters for the high-affinity domain (low $C_{pyr,Eqm}$ range) were often highly uncertain (i.e. 1 σ >> n_{Fr} or K_{Fr}). Both forms might be fit (optimized) with multiple sets of parameters without affecting the goodness of fit significantly (Appendix 5-7).

In view of the fore-mentioned problem of 'ambiguous fit', regression by the Two-Freundlich and the Langmuir-Freundlich models was applied manually (see Appendix 5-8 for details and figures) so that various constrains (e.g. uncertainties in parameters, overall goodness of fit, uncertainties in observations, sensible regressed parameters) can be all considered. The modeled isotherms fit through the observations very well (Figure 5-5; see also Appendix 5-9). As a result of regression ambiguity, a range of values, rather than a single value, were presented for each model parameter (Table 5-3b, c).

3.1.2.6. Implications for Occlusion and Micropore Adsorption

Regression analysis by the two Occlusion models ('Occlusion-Fix' and 'Occlusion-Lnr-Fr' in Table 5-2) provided new estimates for fractions of native pyrene occluded. The 'Occlusion-Lnr-Fr' model estimated that about 30% of the native sedimentary pyrene was occluded. This was consistent with the results from the grinding experiment. The estimated fraction occluded increased to about 60–80% if the K_{OC} and K_{BC} were constrained to current literature values ($K_{OC}=10^{4.7}$; $K_{BC}=10^{6.25}$; see Table 5-1) or if a single non-linear isotherm was extrapolated from higher concentrations and the divergence assessed at lower concentrations (i.e. "visual inspection"). A summary of all the estimates on fraction occluded is provided in Table 5-4.

It should also be noted that the rejection of the explicit char models (i.e. 'Lnr-Fr(soot)-Fr(char)' in Table 5-1, 5-2) does not imply the rejection of the micropore adsorption hypothesis (Chapter 4, section 3.4.3). The micropore or char adsorption hypothesis may still be true as the sorption data were also fit well with non-occlusion models (e.g. the Two-Freundlich and the Langmuir-Freundlich models; Table 5-2, 5-3).

3.2. Interpreting Isotherm Parameters: Physicochemical Meanings

The regressed parameters summarized in Table 5-2 have certain physicochemical implications for the sorption of pyrene. Although a good fit by an isotherm model does not pinpoint and/or confirm the mechanistic nature of sorption, it can suggest certain mechanistic possibilities regarding the phenomenon itself and the nature of natural geosorbents. The isotherm parameters reported in last section will be examined here for their physicochemical significance.

3.2.1. K_{OC}, K_{BC}, and n_{BC} Derived from Isotherm Parameters

3.2.1.1. Estimating K_{OC}, K_{BC} and n_{BC} from Isotherm Parameters

The Linear+Freundlich form (Eqn. 5 - 11) is comparable to the earlier proposed OC-BC model (Accardi-Dey and Gschwend 2002) where the linear OC-term describes *absorption* of sorbate *into* OC ('soft' organic carbon) and the Freundlich term describes *adsorption onto* BC:

$$S = f_{OC} K_{OC} C + f_{BC} K_{BC} C^{n_{BC}}$$

Eqn. 5 - 14

It is thus logical to compare the analogous terms of the Linear-Freundlich regression to those from the OC-BC model. This analogy can be extended to the two Occlusion-based models ('Occlusion-Fix' and 'Occlusion-Lnr-Fr' models; Table 5-1, 5-2). The partitioning coefficients, K_{OC} and K_{BC}, can thus be computed as:

$$K_{OC} = \frac{K_{Lnr}}{f_{OC}}$$

$$K_{BC} = \frac{K_{Fr}}{f_{BC}}$$

Eqn. 5 - 15

where: f_{OC}(=0.0296) and f_{BC}=(0.0049) were the OC and BC contents measured by CTO-375°C-24h method (g_{OC}/g_{solids} or g_{BC}/g_{solids}),

K_{OC} is the OC-normalized partitioning coefficient (L_w/kg_{OC}),

K_{BC} is the BC-normalized partitioning coefficient ($\mu g_{pyr}/kg_{solids})(L_w/\mu g_{pyr})^n$.

It is less clear how the K_{Lnr}-K_{OC} (or K_{Fr}-K_{BC}) analogy can be extended to the Two-Freundlich and the Langmuir-Freundlich models. For the purpose of this discussion, the high-concentration range (or 'amended' domain; C_{pyr} ~> 1 $\mu g_{pyr}/L_w$) term was assumed to reflect contribution due to OC-absorption (i.e. 'K_{OC}'=K_{Fr}/f_{OC}); the low-concentration range (or 'native' domain; C_{pyr} ~< 0.1 $\mu g_{pyr}/L_w$) was assumed to be associated with adsorption onto BC. The physicochemical meanings of these two models can be interpreted in different ways, and they will be examined in section 3.2.3.

3.2.1.2. $K_{OC,pyr}$

The $logK_{OC,pyr}$'s derived from the different isotherm models ranged from 5.1–5.6 (Table 5-6). The only exception was the 'Occlusion-Fix' model which assumed a $K_{OC,pyr}$ of $10^{4.7}$ for pyrene sorption (Table 5-6). This means that the derived $K_{OC,pyr}$'s generally exceed the current adopted value of 4.7-4.8 as suggested by linear free-energy relationships (LFER) (Karickhoff 1981; Schwarzenbach et al. 2003). The LFER-estimated $logK_{OC,pyr}$ is fairly consistent with the $logK_{OC,pyr}$'s derived from various synthetic polymers/plastics such as polyethylene and poly(dimethylsiloxane) (Table 5-5) while the $logK_{OC,pyr}$'s estimated from this study are closer to the values reported for sorption with natural organic matter such as the various humic substances (Table 5-5).

Although experimental uncertainties may not be neglected (e.g. variation in $logK_{OW,PAHs}$ ~ <0.05-0.20 Appendix 5-10), the variation of $logK_{OC,pyr}$'s with different carbonaceous phases (Table 5-5) suggests certain real, systematic features of HOC sorption in natural organic matter: (i) that different types of natural organic phases have distinctive characteristic sorption energies, and (II) that a distribution of *absorption energy* exists within a particular natural organic phase. These two features may explain the significant difference between the $logK_{OC,pyr}$'s estimated from this study and the supposed $logK_{OC,pyr}$ for general NOM.

Different organic phases exhibit significantly different $logK_{OC,pyr}$ (Table 5-5): cellulose being the weakest medium for pyrene uptake ($logK_{OC,pyr}$<3), followed by fulvic acids ($logK_{OC,pyr}$~4), dissolved and colloidal OM ($logK_{OC,pyr}$~4.5 to 4.8), synthetic polymers ($logK_{OC,pyr}$~4.7 to 5.0), and with various humic acids humic substances being the most favorable sorbent/binding-phase for pyrene ($logK_{OC,pyr}$~4.7 to 5.6). Previous studies on 'soft', non-condensed organic carbon have shown that K_{OC} varied with the physicochemical features of the carbon phase: K_{OC} tends to increase with (i) lower polarity (i.e. hydroxyl/carbonyl functionality) (Chiou et al. 1986), (ii) higher molecular mass (Chin et al. 1997), (iv) system pH (Schlautman et al. 1993; Pan et al. 2007), and (iii) higher aromatic-to-alkyl carbon content (Peminova et al. 1999). The extent of branching (Chiou et al. 1986) and cross-linking (Niederer et al. 2007) also affect affinity for organic sorbates, but their influences are less well understood.

The distribution of absorption energy within the 'soft', non-condensed carbon can be partially justified by the variation in K_{OC} of natural OC/OM (Table 5-5) and by experimental observations. Using commercial humic acid as a surrogate for NOM, Pan et al. (2007) showed that the partitioning coefficients for both phenanthrene and pyrene increased slightly with lower sorbate concentration. The distribution of binding energy within the humic acid was sufficient to cause a 'deviation' in $logK_{OC}$ from as small as 0.05 to as large as 0.25 units, even within the μg/L range (i.e. $C_{pyr,Eqm}$ ~ 1 to 100 μg/L), and this enhancement in K_{OC} can be expected to be even more substantial at the ng/L level. The question for natural geosorbent-water systems, however, is whether this energy distribution would have been made less detectable in the presence of other sorbates or even macromolecules. A second argument is the fact that NOM is a molecularly and structurally complex and diverse phase (Kelleher et al. 2006; Lam et al. 2007), structurally similar to a composite of 'pure' organic phases with different structural features (i.e., cellulose, synthetic polymers, etc). Such a composite phase is

bound to have a variation in absorption energy if its constituents exhibit different binding affinities for HOCs as shown in Table 5-5. A third piece of evidence was provided by the $\log K_{OC,pyr}$ reported for a common reference phase but by different methods. Taking Aldrich humic acid as an example, the solubility enhancement method (which considers $\log K_{OC}$ at the saturation of the solute/sorbate; Chiou et al. 1986; Danielsen et al. 1995), gave a $\log K_{OC,pyr}$ of ~5.2 (Chin et al. 1997), which is lower than that measured by fluorescence quenching or solid-phase extraction (Table 5-5)[1].

3.2.1.3. $K_{BC,pyr}$

The $\log K_{BC,pyr}$'s derived from the different isotherm models ranged from 6.0–6.3 (Table 5-6). The derived $\log K_{BC,pyr}$ estimated in this study also agreed well with an earlier isotherm study by Accardi-Dey and Gschwend (2002) on two Boston Harbor sediments ($\log K_{BC,pyr}$ ~6.24-6.28), a single-point partitioning study by Lohmann et al. (2005) on two harbor sediments (Boston Harbor sediment: $\log K_{BC,pyr}$ ~6.3-6.4; New York Harbor sediment: $\log K_{BC,pyr}$ ~5.9-6.8), and another single-point partitioning study by Jonker et al. (2002) on seven BC materials ($\log K_{BC,pyr}$ ~5.7-6.8).

There is also a general agreement with earlier pyrene partitioning studies where BC had not been quantified. Taking the typical f_{BC} of sediment/soil to be of ~10-20% of the total OC content (e.g. f_{BC}:f_{OC} ratios in Table 4-1; also the review of Cornelissen et al. 2005b), $\log K_{BC,pyr}$ in earlier sorption studies can be estimated. Such exercise estimated that $\log K_{BC,pyr}$ ranged from (i) 5.6-6.1 for freshwater sediments derived isotherms, (ii) 5.8-6.2 for marine sediments derived isotherms, (iii) 6.0-6.3 for soil derived isotherms, (iv) 6.4-6.7 for marine particulate organic matters, and (v) 6.5-7.0 for char/charcoal derived isotherms (Table 5-7). Although the difference in $\log K_{BC,pyr}$ between different sorbent categories remains to be resolved, one may conclude that $\log K_{BC}$ appears to be much more constrained (for pyrene, $\log K_{BC}$ is approximately 6.5±0.5) when compared with the 3-4 order variation reported by Hawthorne et al. (2007).

3.2.1.4. $n_{BC,pyr}$

The n_{BC} derived from this study varied greatly between different isotherm models (n_{BC} = 0.15–0.80; Table 5-6). The n_{BC}'s (or n_{Fr}'s) observed here were generally low compared to the values reported in all past literature on PAHs sorption (Table 5-7). Typical n_{Fr} values ranged from ~0.6-1.0. Some studies reported n_{Fr} as low as ~0.4 and these mostly involved high fractions of condensed carbons (i.e. BC, char, etc) ('synthetic carbons' in Table 5-7). An n_{Fr} of 0.4 was obtained from the regression on the South Dorchester Bay data provided by Accardi-Dey and Gschwend (2002) (Appendix 5-11). Another study on Boston Harbor sediment by Lohmann et al. (2005) showed that n_{BC} could be highly 'ambiguous' while $\log K_{BC}$ remained relatively 'constant': they reported that nFr could vary from 0.4–1.0 for a logKBC of 6.3–6.4. This is also consistent with the regression results in this study (Table 5-6). The higher-end n_{BC} observed (i.e. from

[1] Noted that the complexation-flocculation derived $\log K_{OC,pyr}$ might be biased (i.e. less effective for binding pyrene) due to charge-induced structural alterations in the humic acid, and that a greater error should be allowed for the solid-phase extraction measured value as the method requires also the fiber-water partitioning coefficient as well.

the 'Occlusion-Fix' model, n_{BC}=0.62–0.8) agreed well with that from the previous studies (Accardi-Dey and Gschwend 2002).

Very low values of n_{Fr} have been reported for other aromatic sorbates on Carbon-phase-Water systems (Table 5-8) in particular where high surface area condensed carbonaceous materials (e.g. activated carbon, char/charcoal) were studied. For instance, studies independently conducted showed that n_{Fr} ranged from about 0.1–0.5 for toluene and benzene when adsorbing to activated carbon (Cotoruelo et al. 2007; Shih et al. 2009).

3.2.2. n_{BC} as the Key of Determining Sorption of HOCs

Recent views (Hawthorne et al. 2006, 2007; Arp et al. 2009) suggested that K_{OC} and K_{BC} may be too variable to be useful for predicting partitioning of HOCs in real soil/sediment samples. Here, the author holds the opposite view that sorption of HOCs in geosorbents can be satisfactory predicted by an OC-BC model. Furthermore, the author hypothesizes/speculates that the apparent scattering of $logK_{OC}$'s and $logK_{BC}$'s is due to the highly variable n_{BC}. This section will present evidence and support for this hypothesis.

3.2.2.1. Universal $logK_{OC}$ and $logK_{BC}$ for HOC Sorption

The previous sections suggested that K_{OC}'s and K_{BC}'s may be much less variable than those observed in the recent reviews (Hawthorne et al. 2006, 2007; Arp et al. 2009). The $logK_{OC}$'s and $logK_{BC}$'s for pyrene are generally well-constrained regardless of difference in sorbents, isotherm non-linearity and forms (Table 5-9). Taking $logK_{BC}$ as example, the $logK_{BC}$ estimated from the Two-Freundlich form ($logK_{BC}$ ~ 6.0–6.3) was similar to those estimated from the Lnr-Freundlich model ($logK_{BC}$ ~ 6.3±0.1; section 3.2.1.3) or those reported in previous studies on sediment-water systems ($logK_{BC}$ ~ 5.8–6.3; Table 5-7).

The remarkable agreement among the $logK_{OC}$'s and $logK_{BC}$'s derived from different sorption studies for different sorbents suggested an important implication. There seems to be a universal range for $logK_{OC}$ or $logK_{BC}$ of natural geosorbents (soil/sediment). This range is relatively well constrained to about 0.5–1 in $logK_{BC/OC}$ (Table 5-9). If a universal $logK_{BC}$ or $logK_{OC}$ does exist, then the ability to make good estimate of $n_{Fr,BC}$ is the key in predicting HOCs sorption to natural sorbents. An accurate model for n_{Fr}'s can potentially lead to much better sorption predictions than those suggested in the reviews of Hawthorne et al. (2007) and Arp et al. (2009).

3.2.2.2. n_{BC} (or n_{Fr}) as the Source of Variation in K_d's

Evidence from this study also suggested that n_{Fr} (or n_{BC}) is highly variable and may be the major source of variation in predicting K_d's of organic compounds. The pyrene sorption equilibrium data were fit well with the quadratic isotherm form (section 3.1.1). The quadratic form may be re-expressed to a form similar to the Freundlich model (Eqn. 5 - 16)

$$\textbf{Quadratic:} \quad \ln S = a(\ln C)^2 + b(\ln C) + d$$

$$S = K_{Quad}\, C^{(a\ln C + b)} = K_{Fr}\, C^{n}$$

Eqn. 5 - 16

The Freundlich exponent (n, n_{BC} or n_{Fr}) can be considered as an overall measure of the heterogeneity of the partition energy. The above equation suggested that a varying n was the mathematical cause of the concave-up shape of the isotherm in log-log space (e.g. Figure 4-7, 5-1). Furthermore, n exhibited a dependence on the dissolved phase concentration (i.e. C). This was also demonstrated when the sorption isotherm were arbitrarily sub-divided into zones each regressed with the Freundlich form (Figure 5-6; Appendix 5-12). If one assumes n (or n_{BC}, n_{Fr}) to be constant over dissolved pyrene concentration range, then one would conclude K_{BC} (and similarly K_{OC}, if one stays with the Classical-OC sorption picture; e.g. Hawthorne et al. 2006) to be highly variable. And this was the very assumption that Hawthorne et al. (2007) made in their analysis of $\log K_{BC}$'s of different HOCs.

3.2.2.3. Occupancy of Adsorption Sites

The Freundlich exponent (n_{BC} or n_{Fr}) can be considered as an overall measure of the heterogeneity of the partition energy. The author hypothesizes that lower values of n_{Fr} are usually observed (i) when the dissolved sorbate concentration is generally low (as in this study) or (ii) when the binding sites are relatively abundant (as in studies with high surface area activated carbon; see Table 5-8). The heterogeneity of sorbate-sorbent interaction can be better manifested when the sorbate is relatively rare and the sorbent/binding sites are mostly 'unoccupied'. This suggests that the relative state of site occupancy should reveal the energetic heterogeneity of the sorbent, which is measured by n_{Fr}. Quantitatively, the state of occupancy by the sorbate may be approximated from the fraction of adsorption sites occupied (Ω_i):

$$\Omega_i = \frac{N_{=i}}{N_{=} + N_{=}i + N_{=HOC}}$$

Eqn. 5 - 17

where Ω_i is the maximum fraction of surface site occupied by sorbate i over all possible binding site accessible to i,

$N_{=}$, $N_{=i}$, $N_{=HOC}$ are the number of sites accessible to i that are unoccupied, sorbed with i, and sorbed with other HOCs, respectively.

Due to the lack of information of $N_{=}$, $N_{=i}$, and $N_{=HOC}$ and sorbent surface information (pore volume distribution, surface area, etc), the following approximation of Ω_i would be more practical for typical HOCs sorption studies on environmental sorbents:

$$\Phi_i \left(= \frac{S_{i,Max,surf}}{f_{surf.org.}} \right) \cong \frac{S_{i,Max,BC}}{f_{BC}} = \frac{S_{i,Max}}{f_{BC}}$$

Eqn. 5 - 18

where $f_{surf.org.}$ is the mass fraction of surficial organic phase capable of binding i ($kg_{surf.org.}/kg_{solids}$),

f_{BC} is the mass fraction of 'hard' condensed carbons (kg_{BC}/kg_{solids}),

Φ_i is the mass or mole of sorbate i per mass of surficial organic phase capable of binding i (unit: $\mu g_i/kg_{BC}$),

$S_{i,Max}$ is the maximum concentration of sorbed i at equilibrium ($\mu g_i/kg_{solids}$),

$S_{i,Max,surf}$ and $S_{i,Max,BC}$ are the maximum concentrations of i adsorbed onto surficial sites and BC/BC-like sites at equilibrium, respectively ($\mu g_i/kg_{surf.org.}$ or $\mu g_i/kg_{BC}$)

It is important to note that the use of Φ_i assumes: (i) BC and BC-like phases are responsible for most of the adsorption (i.e. $K_{d,BC} >> K_{d,OC}$), (ii) mass of BC/BC-like phases is proportional to their adsorptive area (i.e. BC/BC-like phases adsorb onto the background mineral matrix; not all of their surfaces are freely accessible to the sorbate), and (iii) different types of BC have comparable surface area and pore volume distribution. It should be emphasized that Φ_i is still a crude measure of binding site occupancy – a better measure should also account for the range of occupancy (i.e. $S_{i,Lo,surf}/f_{surf.org}$) and exclude the contribution from OC phase (which may be non-linear by itself) (Table 5-10).

3.2.2.4. Dependence of n_{BC} or n_{Fr} on Occupancy of Adsorption Sites

A coarse correlation seems to exist between n_{Fr} and $\log(S_{i,Max}/f_{BC})$ as shown in Figure 5-7a. Data from most of the isotherm studies involving natural geosorbents (e.g. marine/freshwater sediments, soils, marine particulate organic matter) have fallen into the shaded-region. The coherence in n_{Fr}'s in Figure 5-7a is remarkable consider that data are taken from ~10 independently conducted studies and that these sorbents are mostly geosorbents from the environment, naturally exposed and field-aged.

Data disagreement between the activated carbon/char from the natural geosorbents can be attributed to the violation of assumptions (ii) and (iii) in using $\Phi_i = S_{i,Max}/f_{BC}$ and the fact that these synthetic carbons have not been aged/exposed to natural organic matters/biopolymers and competing sorbates. A greater agreement between the synthetic carbonaceous sorbents and the natural geosorbents can be obtained the surface area difference is corrected for (Figure 5-7b).

The correlation exhibited between n_{Fr} and $\log(S_{i,Max}/f_{BC})$ is also consistent with the ideas that (i) the energetically most favorable adsorption/binding sites are taken first, (ii) the very favorable sites, which roughly associates with only the condensed carbons, are limited, and (iii) the strongly binding sites become 'unnoticeable' (i.e. increasing isotherm linearity) when an overwhelming amount of sorbates become bound at more moderately ranged energies. The last point is illustrated with a simulated isotherm (Figure 5-8) with site distribution function that results in Freundlich-like isotherm form according to Adamson et al. (1997). The simulated isotherms at various n_θ (about the same as n_{Fr}) are shown in Figure 5-8a; the strongly binding sites being quickly filled up is illustrated in Figure 5-8b; the dominance of particular range of energy sites over total adsorption is shown in Figure 5-8c.

The trend in n_{Fr} suggested in Figure 5-7a is also consistent with earlier studies. In studying the sorption of phenanthrene (3-ring PAH) onto different types of coal, Cornelissen et al. (2005a) reported that all sorption isotherms were non-linear, and that the linearity decreased with %C in the coal. Re-interpreting their observations with Φ_i (Figure 5-7c) $n_{Fr,phen,coal}$ also exhibited a monotonic trend similar to that shown in Figure 5-7a or 5-7b. n_{Fr} has also been reported to increase with O/C or (O+N)/C ratio for sorption onto shale/kerogen (Huang et al. 1997a) and several soils/sediments (Wang et al. 2005). The increase in (O+N)/C ratio may be considered as an indirect measure of a lower BC content. The reported n_{Fr}-(O+N)/C trend is thus qualitatively consistent with Figure 5-7a for n_{Fr} approaches linearity with decreasing f_{BC} (i.e. greater $\log(S_{i,Max}/f_{BC})$). Ran et al. (2007b) also reported a similar trend with non-hydrolyzable carbon (NHC) where n_{Fr} decreased with increasing aromatic C% (i.e. increasing f_{BC}, decreasing $\log(S_{i,Max}/f_{BC})$).

3.2.3. Langmuir-Freundlich/Two-Freundlich Models

The parameters associated with the Two-Freundlich and the Langmuir-Freundlich models can be interpreted in two conceptual frameworks: (i) char-BC and soot-BC as the dominant sorptive phases, and (ii) OC and BC as the dominant sorptive phases. These two sorption pictures will be discussed below.

3.2.3.1. The Char-Soot Sorption Picture

In this picture, it was assumed that the high-concentration region (C_{pyr} ~≥ 1 $\mu g_{pyr}/L_w$) represented adsorption onto soot-BC and the low-concentration region (C_{pyr} ~< 0.1 $\mu g_{pyr}/L_w$) reflective the sorptive contribution by the char-BC. The corresponding n_{BC} for the soot-BC and the char-BC domains would be 0.65–0.85 and 0.15–0.20, respectively (see the 'Two-Fr' and 'Lgmr-Fr' cases in Table 5-2). While the soot-n_{BC} would be comparable with that reported earlier (n_{BC}=0.62–1; see Table 5-6), the char-n_{BC} value appeared to be on the lower end of the range observed in activated carbon studies (Table 5-8). In this picture, $\log K_{BC,soot}$ was estimated to be about 6.0–6.3.

3.2.3.2. The OC-BC Sorption Picture: an Alternative View

In this picture, the high-concentration region would be associated with absorption into OC and the lower region linked to adsorption onto BC. This picture, thus, suggested that absorption of HOCs into OC can be non-linear if the sorbate concentration becomes relative low.

A number of sorption studies have reported non-linear sorption of PAHs to non-BC carbon with similar range for n_{Fr} as in this study. Peat or peat-extracted humic fractions have exhibited non-linear uptake of phenanthrene ($n_{Fr,OC,phen}$ ~ 0.7–0.9; Huang et al. 1997a; Weber et al. 2002; Kang et al. 2005; Wen et al. 2007) and pyrene ($n_{Fr,OC,pyr}$ ~ 0.65–0.95; Chefetz et al. 2000; Pan et al. 2007) at $\mu g_{PAH}/L_w$ levels. Similarly, non-linear sorption of pyrene by biopolymers (lignin, chitin, cellulose) ($n_{Fr,OC,pyr}$ ~ 0.6–0.95; Chefetz et al. 2000; Wang et al. 2007) has also been reported at $\mu g_{PAH}/L_w$ levels. It should be noted, however, that the presence of other competing sorbates at substantial levels can increase the linearity of the sorption isotherm. This has been shown for the sorption of PAHs (Xia et al. 2000; Weber et al. 2002; Pan et al. 2007) and a number of pesticides (Xing et al. 1996b) in 'soft' organic materials. Although the organic materials examined

in the literature (e.g. peat-extracted humic substances; isolated or extracted biopolymers) may not fully represent the true sedimentary/soil NOM, the regressed $n_{Fr,pyr}$ and $logK_{OC,pyr}$ were, nonetheless, consistent with those reported in literature (Table 5-10).

A key question still remains to be answered: how strongly does the natively present competing sorbates affect the sorption linearity of a targeted sorbate? Most of the previous works on competitive sorption have examined competition at concentrations of sorbate/co-sorbates (i.e. 10 μg/L to mg/L+ levels) much higher than the typical levels observed in soil/sediment samples (Xing et al. 1996b; White et al. 1999; Xia et al. 2000; Weber et al. 2002; Sander et al. 2007) where HOC sequestration is of concern. It is possible that the absorption of non-polar HOCs at environmental typical/realistic levels to OC phase may be somewhat non-linear.

An alternative mechanistic picture can be drawn from the regression results of the two isotherm models (Figure 5-9). In this picture, sorption of HOCs is non-linear in both the low-affinity (*ab*sorption into OC) and the high-affinity (*ad*sorption onto BC) domains. Non-linearity arises from the structural heterogeneity within the domains. For *ab*sorption, sorption heterogeneity is caused by the organization of structurally diverse parts of the OC-constituent macromolecules. This organization leads to a distribution of solvation energies for the sorbate (Figure 5-9e). For *ad*sorption, sorption heterogeneity is attributed to both compositional and geometrical variations on the sorbent surface. While a flat, graphitic surface (Figure 5-9a) may be available, the presence of microporous structure (Figure 5-9b), the presence of other surface functional groups (Figure 5-9c), and the association of NOM/OC onto the surface (Figure 5-9d) can give rise to heterogeneity in binding energies.

3.2.4. Concluding Physicochemical Interpretation of Isotherm Parameters

Although the n_{BC} derived from this study did form a coherent picture with other studies (i.e. Figure 5-7a, b) and that extremely non-linear systems have been documented in other sorbate-sorbent systems (Table 5-8), the author is somewhat uneasy with certain 'conflicting interpretations' between the low n_{Fr} here and the observations from previous studies. The overall concern is that the unresolved conflicts may be indicative of an incomplete sorption picture, misinterpretation of experimental data, or even a poor set of observations. These 'conflicting interpretations' are documented in Appendix 5-13.

Despite the question in interpreting n_{Fr} (Appendix 5-13) or the different physicochemical implications of the isotherm models (sections 3.2.1.1, 3.2.3.1, 3.2.3.2), the author argues that there is a clear, systematic picture on how NOM affects absorption or adsorption of HOCs (Figure 5-10). Structural heterogeneity (i.e. different functional groups and branching) of the NOM or the BC surface can lead to a distribution of sorption energy (Figure 5-10, Case (II) and (III); see also past studies quoted in section 3.2.3.2). Earlier (Chapter 4, section 3.4.3; Figure 4-14), the author also argued that NOM may enhance adsorption affinity of the condensed carbon surface. The association of NOM with condensed graphitic phase may also increase the absorptive affinity of the NOM phase by virtue of the long-range interaction exerted by the graphitic surface. The graphitic surface can offer additional attraction for sorbates bound in the

volume of OC within the vicinity of the condensed carbon surface (Figure 5-10, Case (IV)). In all these cases, enhancement in sorption affinity due to NOM-condensed carbon association or interaction will be translated into a higher non-linearity in the isotherm.

Unfortunately, many factors affect n_{BC} (or n_{OC}), which is a measure of the distribution of sorption energies in the sorbent. Here, four possible determining factors on n's were highlighted (details in Appendix 5-13): (i) relative availability of binding sites, (ii) sorbate and sorbent characteristics, (iii) competitive sorption and association of OC, and (iv) pre-treatment of sorbent. More work needs to be done before a quantitative picture for the distribution of sorption energy can be constructed.

4. Conclusion

The pyrene sorption equilibrium data derived in Chapter 4 were regressed with various isotherm models. Evidence suggested that the sorption data may be divided into two domains, implying that composite (or multi-term) isotherm model was needed. A number of the composite isotherm models could provide good fit of the data (Table 5-2). K_{OC}, K_{BC} and n_{BC} of pyrene were derived from the modeled parameters (Table 5-6).

The regression-derived K_{OC}'s and K_{BC}'s generally agreed with those reported in literature (Table 5-5 & 5-7). $\log K_{OC}$ of pyrene was estimated to range from 5.1–5.6 from all models except one ('Occlusion-Fix'; Table 5-1 & 5-2) where KOC was assumed to be $10^{4.7}$. $\log K_{BC}$ of pyrene was estimated to range from 6.0–6.3. A brief survey showed that $\log K_{OC}$'s and $\log K_{BC}$'s of pyrene for different carbonaceous materials were generally well constrained to within 1 log unit. This implied that there may be 'universal' K_{OC} or K_{BC} for the sorption of HOCs in various natural sorbents, in contrary to the conclusions made in recent reviews.

The apparent scattering of K_d (or K_{OC}, K_{BC}) observed in past literature and the recent reviews was hypothesized to be caused by variation in isotherm non-linearity (i.e. n_{Fr} or n_{BC}). Regression analysis on sub-divided isotherm zones showed that K_{Fr} was relatively constant while n_{Fr} decreased with dissolved phase concentration (Figure 5-6).

It was hypothesized that the increase in isotherm non-linearity (i.e. decreasing n_{Fr} or n_{BC}) was due to the heterogeneous binding sites being relatively more available to the adsorbate. The correlation between n_{Fr} from other pyrene sorption studies and the relative occupancy of the binding sites showed that the isotherm quickly approached linearity as the high-energy sites become taken (Figure 5-7a). The same trend was also observed for the adsorption of pyrene onto activated carbon (Figure 5-7b), coal (Figure 5-7c), or even the absorption into OC (section 3.2.2.4).

Although certain conflicting implications of n_{BC} still need to be resolved (section 3.2.4; Appendix 5-13), the constancy in both $\log K_{OC}$ and $\log K_{BC}$ suggested that the dependence of the non-linearity index is the key in predicting the equilibrium partitioning of HOCs accurately. This might partially explain the lack of unity in $\log K_{OC}$'s or $\log K_{BC}$'s

presented in the review by Hawthorne et al. (2006, 2007) and the unsuccessful application of OC/BC models for partitioning prediction in Arp et al. (2009).

Chapter 6. Thermodynamics of Absorption and Adsorption

CHAPTER ABSTRACT

In order to predict the sorption equilibrium of PAHs in soil/sediment-water systems at realistic temperature range, to advance our understanding on the energetics of PAH absorption/adsorption and how they may be related to organic carbon (OC) and black carbon (BC), the thermodynamics of pyrene (as a model HOC) partitioning in sediment-water was examined. The thermodynamic expressions for adsorption and absorption were reconsidered to account for the presence of background non-sorbate organic matter in natural sorbents. Enthalpic (ΔH) and entropic (ΔS) expressions were formulated following the thermodynamic convention for phase transition reactions (i.e. mole fraction based distribution coefficients, K^x's).

The overall enthalpy of pyrene sorption, estimated to be –10 to –30(±10) kJ/mol agreed well with previous reported values. The enthalpy of *ab*sorption was comparable with the $-\Delta H$ for the dissolution of pure solid pyrene in water ($-\Delta H_{diss,pyr}$ = –35 kJ/mol). The enthalpy of *ad*sorption, found to be around –10 to –20(±3) kJ/mol, appeared to be generally weaker than the enthalpy of *ab*sorption.

Thermodynamic analysis suggested that the system generally gained entropy (freedom in molecular motion and/or arrangement) via sorption. The entropy of *ab*sorption, estimated to be around 40–60(±30) J/mol.K, was similar to those for the dissolution of pure solid or sub-cooled liquid pyrene in water. The entropy of *ad*sorption was very sensitive to the mechanistic approximations made, and significantly different estimates of adsorption entropy were obtained. A modified entropic expression for adsorption which allows a fraction of organic co-adsorbate displaced by the adsorbing pyrene to stay associated with the sorbent phase has been proposed. It seemed that entropic change was the dominating term in determining the energetics of HOCs adsorption.

This study provided a new thermodynamic framework for analyzing HOC sorption onto/into natural geosorbents where the sorption sites may be initially occupied by competing co-sorbates or organic matter.

Table of Content for Chapter 6

1. Chapter Introduction, Scope, and Objective 127

1.1. Introduction 127

1.1.1. Limitations of Current Theories for HOCs Sorption 127

1.1.2. Relating the Thermodynamics of Sorption to Phase Transition Reactions 128

1.2. Objectives 128

2. Theory 128

2.1.1. Enthalpy, Entropy, Free Energy, and Equilibrium Constant of Sorption 129

2.1.2. Convention for the Thermodynamics of Phase Change Reactions 129

2.1.3. Thermodynamics of Absorption into Organic Phase 131

2.1.4. Thermodynamics of Adsorption into Organic Phase 132

2.1.4.1. Defining 'Mole Fraction' of Adsorbate i 132

2.1.4.2. 'Absorption'-Like Formulation 133

2.1.4.3. Adsorption onto H_2O-Bound Sites 134

2.1.4.4. Adsorption onto Organic Macromolecule-Bound Sites 135

2.1.4.5. Adsorption onto Heterogeneous Sites with Multiple Co-adsorbates 136

2.1.5. Thermodynamics of Overall Sorption (Absorption+Adsorption) 138

2.1.6. Concluding Thermodynamics of Sorption 139

3. Results & Discussion 140

3.1. Enthalpy, Entropy, and Free Energy for Pyrene Sorption 140

3.1.1. Enthalpy of Pyrene Sorption 140

3.1.1.1. Apparent/Overall Enthalpy of Sorption ($\Delta H_{d,app}$) 140

3.1.1.2. Enthalpy of Absorption ($\Delta H_{d,abs}$) 141

3.1.1.3. Enthalpy of Adsorption ($\Delta H_{d,ads}$) 141

3.1.2. Entropy of Pyrene Sorption 142

4. Conclusion 142

1. Chapter Introduction, Scope, and Objective

1.1. Introduction

Enthalpy (ΔH_d) and entropy (ΔS_d) of sorption are useful in the following respects: (i) they are important thermodynamic properties for the partitioning of HOCs; (ii) they are indicative of the nature of the partition process, and may thus provide insights on the process at the mechanistic and the molecular levels; (iii) the enthalpy of sorption allows distribution coefficients of sorbate to be estimated at relevant environmental temperatures, which are not necessarily the same as room temperature; (iv) they may serve as further evidence of experimental consistency with previous works.

1.1.1. Limitations of Current Theories for HOCs Sorption

A number of previous studies have characterized thermodynamic properties of sorption such as the apparent enthalpy of sorption or the free energy of sorption (Kile et al. 1989; Young et al. 1995; Piatt et al. 1996; Gustafsson et al. 1997b; Tremblay et al. 2005; Ran et al. 2007a). While the enthalpy of sorption may be estimated by simply regressing $\ln K_d$ against the inverse of temperature, the entropy or the free energy of sorption depends on how the partitioning constant is defined. Although the thermodynamic foundation of sorption has been laid down in earlier works (Chiou et al. 1979; Karickhoff 1981; Chiou et al. 1983; Spurlock et al. 1984; Young et al. 1995; Gustafsson et al. 1997b), these earlier formulations are insufficient in several ways. The pioneering works by Karickhoff (1981) and Chiou et al. (1983) focused mainly on the linear absorption of HOCs. Later, Spurlock et al. (1984) extended the thermodynamic foundation to cases where non-linear absorption was observed.

Gustafsson et al. (1997b) appeared to present the first thermochemical analysis on adsorption. Their main objective was to provide *a priori* estimates of the adsorption capacity of BC for various PAHs from the thermodynamics of phase change reactions, so the enthalpic and entropic properties of the adsorbates (PAHs) were estimated rather than measured. A number of simplifying implicit assumptions on the nature of adsorption were also made. For instance, (i) adsorption was taken to be 'absorption-like' –that the ad/desorption of co-adsorbates do not contribute significantly for the equilibrium, or (ii) only sooty/graphitic surface and water exist, though it is known that soot carbon contain up to almost 40% of OC (Bucheli et al. 2000). They found good agreement (within 1 unit in $\log K_{BC}$) between the estimates and the measured uptake capacities reported in two activated carbon studies (Dobbs et al. 1980; Walters et al. 1984) (here partially included in Appendix 6-1). It should be pointed out, however, that the referenced adsorption data mostly likely did not represent true equilibrium: adsorption time was only 1–3 d in Walters et al. (1984), and only a bare 2 h in the work by Dobbs et al. (1980). While the short equilibration time may be sufficient for polar organic adsorbates, it is clearly inadequate for the sorption of multi-ringed PAHs onto AC (Chapter 3, section 3.2.1; also Table 3-4; Dobbs et al. also admitted disequilibrium for their data). All these implied that the estimates by Gustafsson et al. were likely to be on the lower end of BC/AC's true adsorption capacities.

1.1.2. Relating the Thermodynamics of Sorption to Phase Transition Reactions

$\Delta G_{d,app}$ and $\Delta S_{d,app}$ can be characterized according to the practical, conventional concentration-based K_d, but this prevents the comparison between the ΔG and ΔS of sorption with the ΔG's and ΔS's for phase change/transition (e.g. vaporization, sublimation, fusion, dissolution). Such comparison will provide valuable insights on the nature of sorption in the context of other phase change reactions.

The overall (or apparent) enthalpy of sorption, $\Delta H_{d,app}$, can be determined regardless of the definitions of K_d; the overall free energy of sorption ($\Delta G_{d,app}$) and the overall entropy of sorption ($\Delta S_{d,app}$), however, depend on (i) what reference energy state is selected, and (ii) how K_d is defined. Thus it is necessary to re-formulate another K for sorption such that the new K – which is linked to the operational, concentration-based K_d – would provide ΔG_d and ΔS_d that can be compared with those of phase change reactions. Currently, equilibrium partitioning coefficients (or phase distribution coefficients) are typically in concentration units (e.g. $K_{d,HOC}$ in $(\mu g_{HOC}/kg_{solids})(L_w/\mu g_{HOC})$). Since sorption of HOCs to geosorbents can be broken down into absorption and adsorption, it is of also interest to consider the thermodynamics of these two modes of sorption, and see how they are incorporated in the practical, concentration-based K_d.

1.2. Objectives

In view of the limitations in the early thermodynamic models, the need to compare experimental K_d with the thermodynamics of phase change, and the need to understand the energetic contributions of absorption and adsorption, the author would like to reconsider the energetics of sorption from the most basic principles.

This chapter has two main objectives: to re-examine how the thermodynamics of sorption may be formulated, and to estimate the thermodynamic properties of HOC sorption in geosorbent-water systems using pyrene as a model organic sorbate.

2. Theory

The thermodynamic expressions of HOC sorption in geosorbent-water systems will be developed in this section. The general approach will be to progress from the simplest case/system, where many simplifications and assumptions are made, to the more complicated but realistic ones. If this section appears to be rather formalistic, the reader may wish to proceed directly to section 2.1.6 for a brief summary of the derivations (Table 6-1) and the special case where partial dissociation of competing co-adsorbate is allowed (Appendix 6-6). The physicochemical complexity of natural geosorbents greatly complicates the thermodynamics of sorption to the extent that approximations are necessary for evaluating ΔG_d or ΔS_d. Thus various approximations or simplifications will also be considered.

2.1.1. Enthalpy, Entropy, Free Energy, and Equilibrium Constant of Sorption

At constant temperature and pressure, the enthalpy (ΔH_d) and entropy (ΔS_d) of sorption are related to the distribution/partition coefficient (K_d) and the Gibbs free energy of sorption (ΔG_d) as follows:

$$-RTlnK_d = \Delta G_d = \Delta H_d - T\Delta S_d$$

Eqn. 6 - 1

where T is the system temperature (°K) and R is the gas constant (8.314 $Jmol^{-1}K^{-1}$).

ΔH_d, which can be understood as the change in the binding force of the sorbate by its surrounding, and ΔS_d, which can be understood as the change in freedom of molecular motion (Schwarzenbach et al. 2003), can be determined from the lnK_d-1/T plot:

$$lnK_d = \frac{-\Delta H_d}{RT} + \frac{\Delta S_d}{R}$$

Eqn. 6 - 2

For sorption of HOCs, the thermodynamic relationship is more complicated as K_d is a sum of both *ab*sorption and *ad*sorption reactions:

$$K_d = K_{d,abs} + K_{d,ads}$$

Eqn. 6 - 3

An overall or apparent enthalpy of sorption (both adsorption and absorption), $\Delta H_{d,app}$, can be determined from the slope according to Eqn. 6 - 2 regardless of the definition of K_d. This $\Delta H_{d,app}$ can be directly compared with ΔH's of other reactions (e.g. condensation of sorbate into its pure phase). To obtain an overall entropy of sorption ($\Delta S_{d,app}$) that can be compared with other reactions, we need to convert K_d (or ΔG_d) such that the thermodynamic reference point is identical between sorption and other reactions. This requires a further examination on K_d.

2.1.2. Convention for the Thermodynamics of Phase Change Reactions

The thermodynamics of phase change reactions (e.g. vaporization, fusion, dissolution, etc) is often considered on a mole fraction based definition of K (equilibrium partitioning constant) and with pure liquid state as the reference state for the chemical of interest (Schwarzenbach et al. 2003).

Briefly, for a simple, generic phase change reaction where a chemical i undergoes phase change from phase-A to phase-B, the chemical potentials (u) of the 'product' and the 'reactant' sides can be expressed as:

$$\textbf{Reaction:} \qquad i_{(A)} \leftrightarrow i_{(B)}$$

$$u_{prod} = u_{iB} \equiv u^*_{iL} + RTln(x_{iB}) + RTln(\gamma_{iB})$$

$$u_{reactant} = u_{iA} \equiv u^*_{iL} + RTln(x_{iA}) + RTln(\gamma_{iA})$$

Eqn. 6 - 4

where u_{iA}, u_{iB}, and u^*_{iL} are the chemical potentials of i in phase A, B, and the pure liquid state of i, respectively (J/mol),

x_{iA} and x_{iB} are the mole fractions of i in phase A and B, respectively (mol_i/mol_A),

γ_{iA} and γ_{iB} are the activity coefficients of i in phase A and B, respectively (dimensionless),

R and T are the gas constant ($R=8.314\ Jmol^{-1}K^{-1}$) and temperature (^oK).

The x_{iA} (or x_{iB}) term describes the contribution of dilution to the chemical potential. The γ_{iB} (or γ_{iB}) term describes the contribution due to non-ideality in the interaction between i and the bulk phase environment *with respect to* the reference state (Schwarzenbach et al. 2003). That is to say, with pure liquid of i as the reference state, the activity coefficient of i in pure liquid of itself (γ_{iL}) is, by definition, 1.

When chemical equilibrium is established for the generic reaction, $u_{prod} = u_{reactant}$, or:

$$RTln(x_{iB}) + RTln(\gamma_{iB}) = RTln(x_{iA}) + RTln(\gamma_{iA})$$

Eqn. 6 - 5

For phase change reaction, the free energy of reaction, ΔG^x_{rxn}, is often defined as the difference in the γ_{iphase} terms, and is related to the mole-fraction based equilibrium constant as follows:

$$\Delta G^x_{rxn} = RTln\left(\frac{\gamma_{iB}}{\gamma_{iA}}\right) = -RTln\left(\frac{x_{iB}}{x_{iA}}\right) = -RTlnK^x_{rxn}$$

$$K^x_{rxn} \equiv \frac{x_{iB}}{x_{iA}}$$

Eqn. 6 - 6

where ΔG^x_{rxn} is the free energy of the generic phase change reaction such that equilibrium constant is in the mole fraction basis (J/mol),

K^x_{rxn} is the mole fraction based equilibrium constant for the reaction.

In the subsequent sub-sections, the same definition of ΔG^x_{rxn} and K^x_{rxn} will be extended to absorption, adsorption, and overall sorption. Furthermore, attempts will be made to relate the mole fraction based K^x_{rxn} to the practical, concentration-based K_d's (e.g. L_w/kg_{solids} or $(\mu g/kg_{solids})(L_w/\mu g)^n$).

2.1.3. Thermodynamics of Absorption into Organic Phase

For absorption of HOC into a soft, organic phase (e.g. lipid, protein, non-condensed carbon materials, etc), the free energy of absorption ΔG^{x}_{abs} can be defined in manner similar to Eqn. 6 - 4 to Eqn. 6 - 6:

$$\textbf{Absorption:} \qquad i_{(w)} \leftrightarrow i_{(org)}$$

$$u_{prod} = u_{iorg} \equiv u^{*}_{iL} + RTln(x_{iorg}) + RTln(\gamma_{iorg})$$

$$u_{reactant} = u_{iw} \equiv u^{*}_{iL} + RTln(x_{iw}) + RTln(\gamma_{iw})$$

$$\Delta G^{x}_{abs} = RTln\left(\frac{\gamma_{iorg}}{\gamma_{iw}}\right) = -RTln\left(\frac{x_{iorg}}{x_{iw}}\right) = -RTlnK^{x}_{abs}$$

$$K^{x}_{abs} \equiv \frac{x_{iorg}}{x_{iw}}$$

Eqn. 6 - 7

where $u_{i\,org}$, u_{iw}, and $u^{*}_{i\,L}$ are the chemical potentials of i in absorbed phase (organic material), in the aqueous/dissolved phase, and its pure liquid, respectively (J/mol),

x_{iorg} and x_{iw} are the mole fractions of i in the absorbed phase (organic material) and the aqueous/dissolved phase, respectively (mol_i/mol_{phase}),

γ_{iorg} and γ_{iw} are the activity coefficients of i in the absorbed phase (organic material) and the aqueous/dissolved phase, respectively (dimensionless),

ΔG^{x}_{abs} is the free energy of i absorbed into the organic phase (the mole fraction basis) (J/mol),

K^{x}_{abs} is the mole fraction based equilibrium constant for absorption.

The practical concentration based $K_{d,abs}$ (L_w/kg_{solids}) is thus related to K^{x}_{abs} as:

$$K_{d,abs} = \frac{S_{i,abs}}{C_{iw}}$$

$$\left(\frac{S_{i,abs}}{C_{iw}}\right)\frac{MW_{org}/f_{org}}{\bar{V}_{w}} = K^{x}_{abs} = \frac{x_{iorg}}{x_{iw}}$$

Eqn. 6 - 8

where f_{org} is the mass fraction of organic phase in the solids (kg_{org}/kg_{solids}),

MW_{org} is the molar mass of the organic phase (kg_{org}/mol_{org}),

C_{iw} is the aqueous/dissolved phase concentration of i (mol_i/L_w or $\mu g_i/L_w$),

$S_{i,abs}$ is the solid phase concentration of absorbed i (mol_i/kg_{solids} or $\mu g_i/kg_{solids}$),

$\bar{V}_w$ is the molar volume of water, and is equal 0.018 L_w/mol_w.

In an ideal case a chemically uniform organic phase, MW_{org} is well defined. However, for environmental organic phase, an average MW_{org} will have to be used. Perminova et al. (1999) reported a molar mass of about 5000–20000 g/mol for a wide range of terrestrially derived 'soft' organic matter. Assuming the molar mass of typical 'soft' organic matter to be approximately of the same as those of terrestrial DOM (!!!), a geometric mean MW_{org} would be about 10 kg_{org}/mol_{org}.

2.1.4. Thermodynamics of Adsorption into Organic Phase

Adsorption of HOC onto natural geosorbents is more complex to describe than absorption of HOC. Here, the thermodynamics of adsorption will be developed from the simplest formulation progressively toward the more realistic formulations of ΔG^x_{ads} and K^x_{ads}.

2.1.4.1. Defining 'Mole Fraction' of Adsorbate i

Before proceeding further, one should consider what the 'mole fraction' of adsorbed i ($x_{i\exists}$) means. By definition of mole fraction, $x_{i\exists}$ should means moles of adsorbed i over the total moles of adsorbed species (both i and non-i). However, complications soon arise (Figure 6-1) when the non-i adsorbates are of different size than i. For instance, a non-i molecule (e.g. fatty acids) may take up multiple binding spots for i, or vice versa for very small adsorbates (e.g. multiple H_2O occupying 1 binding site for pyrene). Thus, $x_{i\exists}$ may vary substantially even when the amount of surface-bound i is fixed. Furthermore, it is quite possible that the co-adsorbates may be partially adsorbed (Figure 6-1). These 'non-idealities' make it very difficult to quantify/estimate $x_{i\exists}$, for not only must one know how much i is bound but also how many mole of different co-adsorbates are also bound at the surface. To the author's knowledge, none of the mentioned issues with $x_{i\exists}$ have been treated in standard reference text such as that by Adamson and Gast (1997).

To circumvent the practical difficulty in quantifying the moles of bound non-i co-adsorbates, the author approximates $x_{i\exists}$ with the surface coverage by i, Θ_i, which is defined as:

$$x_{i\exists} \cong \Theta_i \equiv \frac{\#\text{ moles of surface sites } \mathbf{actually} \text{ bound with } i}{\#\text{ moles of total surface sites } \mathbf{potentially} \text{ bound with } i}$$

Eqn. 6 - 9

This approximation gives several advantages: (i) Θ_i (hence $x_{i\exists}$) is independent of the adsorption states of other co-adsorbates, (ii) Θ_i can be related to solid-phase concentration of i (S_i, $\mu g_i/kg_{solids}$) very easily, if the potential binding capacity of the surface is known or can be estimated, (iii) following from (i), it allows the thermodynamic expression for the adsorption of i to be separated from the adsorption/desorption

reactions of other co-sorbates. The approximation also implies the $x_{i\exists} = 1$ when all potential sites for i have been occupied by i.

It must be noted that the approximation of $x_{i\exists}$ with Θ_i somewhat violates the principle of typical chemical reactions, where molecules are the basis of chemical changes. In reality, however, probably a mixed definition with both elements of Θ_i and the strict mole-fraction definition of adsorbed i over total adsorbed molecules is more appropriate. This task is, however, well beyond the scope of this study and the capability of the author.

2.1.4.2. 'Absorption'-Like Formulation

The simplest case is to formulate adsorption analogous to absorption. The assumptions of this formulation are: (i) homogeneous binding energy for all surface sites, (ii) ideal adsorption where no molecular interaction takes place between sites in close vicinities, (iii) the surface sites are either free of adsorbate or bound to it, and (iv) only one chemical, the adsorbate i, is present in the system. The free energy of adsorption, $\Delta G^x_{ads\text{-}ss}$, is therefore:

$$\textbf{Adsorption (simple, single} - \textbf{i)}: \qquad i_{(w)} \leftrightarrow i_{(\exists)}$$

$$u_{prod} = u_{i\exists} \equiv u^*_{iL} + RTln(x_{i\exists}) + RTln(\gamma_{i\exists})$$

$$u_{reactant} = u_{iw} \equiv u^*_{iL} + RTln(x_{iw}) + RTln(\gamma_{iw})$$

$$\Delta G^x_{ads-ss} = RTln\left(\frac{\gamma_{i\exists}}{\gamma_{iw}}\right) = -RTln\left(\frac{x_{i\exists}}{x_{iw}}\right) = -RTlnK^x_{ads-ss}$$

$$K^x_{ads-ss} \equiv \frac{x_{i\exists}}{x_{iw}} = \frac{\Theta_i}{x_{iw}}$$

Eqn. 6 - 10

where $\exists$ signifies the adsorbed/surface-bound state,

Θ_I is the surface coverage of i as defined in Eqn. 6 - 9.

The practical concentration based $K_{d,ads}$ (L_w/kg_{solids}) is thus related to $K^x_{ads\text{-}ss}$ as:

$$\frac{K_{d,ads}}{\kappa_{i,ads}\bar{V}_w/MW_i} = \frac{S_{i,ads}/\kappa_{i,ads}}{C_{iw}\bar{V}_w/MW_i} = \frac{\Theta_i}{x_{iw}} = K^x_{ads-ss}$$

Eqn. 6 - 11

where MW_i is the molar mass of i ($\mu g_i/mol_i$),

C_{iw} is the aqueous/dissolved phase concentration of i ($\mu g_i/L_w$),

$\kappa_{i,ads}$ is the adsorption capacity for i ($\mu g_i/kg_{solids}$)

$S_{i,ads}$ is the solid phase concentration of surface-bound i ($\mu g_i/kg_{solids}$),

$\bar{V}_w$ is the molar volume of water, and is equal 0.018 L_w/mol_w.

It is clear that the adsorption capacity is related to the surface coverage of i as:

$$\Theta_i \equiv \frac{\#\text{ sites } \mathbf{actually} \text{ bound with } i}{\#\text{ total sites } \mathbf{potentially} \text{ bound with } i} = \frac{\text{mass adsorbed } i}{\text{max. mass of adsorbed } i} = \frac{S_{i,ads}}{\kappa_{i,ads}}$$

Eqn. 6 - 12

2.1.4.3. Adsorption onto H_2O-Bound Sites

In this case, it is assumed that: (i) homogeneous binding energy for all surface sites, (ii) ideal adsorption where no molecular interaction takes place between sites in close vicinities, (iii) the surface sites are either bound with water molecule or the adsorbate i. The free energy of adsorption, $\Delta G^x_{ads\text{-}sH2O}$, is therefore:

$$\textbf{Adsorption (simple, } \mathbf{H_2O - i}\textbf{):} \qquad i_{(w)} + H_2O_{(\exists)} \leftrightarrow i_{(\exists)} + H_2O_{(w)}$$

$$u_{prod} = u_{i\exists} + u_{H2Ow}$$

$$u_{i\exists} \equiv u^*_{iL} + RTln(x_{i\exists}) + RTln(\gamma_{i\exists})$$

$$u_{H2Ow} \equiv u^*_{H2OL} + RTln(x_{H2Ow}) + RTln(\gamma_{H2Ow})$$

$$u_{reactant} = u_{iw} + u_{H2O\exists}$$

$$u_{iw} \equiv u^*_{iL} + RTln(x_{iw}) + RTln(\gamma_{iw})$$

$$u_{H2O\exists} \equiv u^*_{H2OL} + RTln(x_{H2O\exists}) + RTln(\gamma_{H2O\exists})$$

$$\Delta G^x_{ads-sH2O} = RTln\left(\frac{\gamma_{i\exists}\gamma_{H2Ow}}{\gamma_{iw}\gamma_{H2O\exists}}\right) = -RTln\left(\frac{x_{i\exists}x_{H2Ow}}{x_{iw}x_{H2O\exists}}\right) = -RTlnK^x_{ads-sH2O}$$

$$K^x_{ads-sH2O} \equiv \frac{x_{i\exists}x_{H2Ow}}{x_{iw}x_{H2O\exists}} = \frac{\Theta_i}{x_{iw}(1-\Theta_i)}$$

Eqn. 6 - 13

where $u_{i\exists}$, u_{iw}, and u^*_{iL} are the chemical potentials of i in adsorbed phase, dissolved phase, and the pure liquid state of itself, respectively (J/mol),

$u_{H2O\exists}$, u_{H2Ow}, and u^*_{H2OL} are the chemical potentials of H_2O in adsorbed phase, dissolved phase, and the pure liquid state of itself, respectively (J/mol),

$x_{i\exists}$ and x_{iw} are the mole fractions of i in the adsorbed phase and the aqueous/dissolved phase, respectively (mol_i/mol_{phase}),

$x_{H2O\exists}$ and x_{H2Ow} ($x_{H2Ow} \cong 1$ for typical environmental solutions) are the mole fractions of H_2O in the adsorbed phase and the aqueous/dissolved phase, respectively (mol_i/mol_{phase}),

$\gamma_{i\exists}$ and γ_{iw} are the activity coefficients of i in the adsorbed phase and the aqueous/dissolved phase, respectively (dimensionless),

$\gamma_{H2O\exists}$ and γ_{H2Ow} ($\gamma_{H2Ow}\equiv 1$ by definition of reference state) are the activity coefficients of H_2O in the adsorbed phase and the aqueous/dissolved phase, respectively (dimensionless).

The practical concentration based $K_{d,ads}$ (L_w/kg_{solids}) is thus related to $K^x_{ads\text{-}sH2O}$ as:

$$\frac{K_{d,ads}}{\kappa_{i,ads}\,\bar{V}_w/MW_i}\times\frac{1}{\left(1-\frac{S_{i,ads}}{\kappa_{i,ads}}\right)}=\frac{S_{i,ads}/\kappa_{i,ads}}{C_{iw}\,\bar{V}_w}\times\frac{1}{(1-\Theta_i)}=\frac{\Theta_i}{x_{iw}(1-\Theta_i)}=K^{x}{}_{ads-sH2O}$$

Eqn. 6 - 14

where MW_i is the molar mass of i ($\mu g_i/mol_i$),

C_{iw} is the aqueous/dissolved phase concentration of i ($\mu g_i/L_w$),

$\kappa_{i,ads}$ is the adsorption capacity for i ($\mu g_i/kg_{solids}$)

$S_{i,ads}$ is the solid phase concentration of surface-bound i ($\mu g_i/kg_{solids}$),

$\bar{V}_w$ is the molar volume of water, and is equal 0.018 L_w/mol_w.

2.1.4.4. Adsorption onto Organic Macromolecule-Bound Sites

In real environmental geosorbents such as soils and sediments, the surface sites are often bound, initially, not with H_2O but with various HOCs (e.g. other PAHs, alkanes, etc) and large organic macromolecules (e.g. proteins, lipids, other biopolymers). Here, the case where the sorption sites are initially bound with large organic molecules shall be considered.

It is assumed that: (i) homogeneous binding energy for all surface sites, (ii) ideal adsorption where no molecular interaction takes place between sites in close vicinities[1] (!), (iii) sites initially bound HOCs are much less than sites bound with large organic macromolecules, (iv) the surface sites are either bound with some 'average' large organic macromolecules or the adsorbate i. With the expression analogous to those shown in Eqn. 6 - 14, the free energy of adsorption, $\Delta G^x_{ads\text{-}sorg}$, is:

$$\textbf{Adsorption (simple, org}-\textbf{i)}: \qquad i_{(w)}+\mathrm{org}_{(\exists)}\leftrightarrow i_{(\exists)}+\mathrm{org}_{(w)}$$

$$u_{prod}=u_{i\exists}+u_{orgw}=u_{reactant}=u_{iw}+u_{org\exists}$$

$$u_{i\exists}\equiv u^*{}_{iL}+RT\ln(x_{i\exists})+RT\ln(\gamma_{i\exists});\qquad u_{orgw}\equiv u^*{}_{orgL}+RT\ln(x_{orgw})+RT\ln(\gamma_{orgw})$$

$$u_{orgw}\equiv u^*{}_{orgL}+RT\ln(x_{orgw})+RT\ln(\gamma_{orgw});\qquad u_{iw}\equiv u^*{}_{iL}+RT\ln(x_{iw})+RT\ln(\gamma_{iw})$$

[1] This assumption, of course, is already inconsistent with the picture that the site binding energy can be altered when the adsorbate is to be 'sandwiched' between the surface and the macromolecule (see Figure 3-43 & 3-44).

$$\Delta G^{x}_{ads-sorg} = RTln\left(\frac{\gamma_{i\exists}\gamma_{orgw}}{\gamma_{iw}\gamma_{org\exists}}\right) = -RTln\left(\frac{x_{i\exists}x_{orgw}}{x_{iw}x_{org\exists}}\right) = -RTlnK^{x}_{ads-sorg}$$

$$K^{x}_{ads-sorg} \equiv \frac{x_{i\exists}x_{orgw}}{x_{iw}x_{org\exists}} = \frac{x_{orgw}\,\Theta_i}{x_{iw}(1-\Theta_i)}$$

Eqn. 6 - 15

where $u_{org\exists}$, u_{orgw}, and u^{*}_{orgL} are the chemical potentials of the 'average' organic macromolecule in adsorbed phase, dissolved phase, and the pure liquid state of itself, respectively (J/mol),

$x_{org\exists}$ and x_{orgw} are the mole fractions of the 'average' organic macromolecule in the adsorbed phase and the aqueous/dissolved phase, respectively (mol_i/mol_{phase}),

$\gamma_{org\exists}$ and γ_{orgw} are the activity coefficients of the 'average' organic macromolecule in the adsorbed phase and the aqueous/dissolved phase, respectively (dimensionless).

The practical concentration based $K_{d,ads}$ (L_w/kg_{solids}) is thus related to $K^{x}_{ads-sorg}$ as:

$$\frac{K_{d,ads}}{\kappa_{i,ads}\bar{V}_w/MW_i} \times \frac{C_{orgw}\,\bar{V}_w/MW_{org}}{\left(1-\frac{S_{i,ads}}{\kappa_{i,ads}}\right)} = \frac{S_{i,ads}/\kappa_{i,ads}}{C_{iw}\bar{V}_w/MW_i} \times \frac{x_{orgw}}{(1-\Theta_i)} = \frac{x_{orgw}\,\Theta_i}{x_{iw}(1-\Theta_i)} = K^{x}_{ads-sorg}$$

Eqn. 6 - 16

where MW_i and MW_{org} are the molar masses of i and the 'average' large macromolecule, respectively (μg/mol),

C_{iw} and C_{orgw} are the aqueous/dissolved phase concentrations of i and the 'average' macromolecule, respectively ($\mu g/L_w$),

$\kappa_{i,ads}$ is the adsorption capacity for i ($\mu g_i/kg_{solids}$)

$S_{i,ads}$ is the solid phase concentration of surface-bound i ($\mu g_i/kg_{solids}$),

$\bar{V}_w$ is the molar volume of water, and is equal 0.018 L_w/mol_w.

2.1.4.5. Adsorption onto Heterogeneous Sites with Multiple Co-adsorbates

The three thermodynamic formulations presented so far ('ads-ss', 'ads-sH2O', 'ads-sorg') are derived from a number of 'ideal' conditions which are hardly present in the adsorption of HOCs onto environmental geosorbents. Even in 'lab-bench' studies where the sorbent is initially free of sorbate (e.g. self-prepared activated carbon, charcoal), the homogeneous surface-binding energy assumption is clearly inappropriate (i.e. n_{Fr} or $n_{BC} < 1$; Table 5-7 & 5-8).

The author will consider here the scenario most resembling adsorption onto realistic geosorbents which are preloaded with organic matter and HOCs. For the adsorption of i onto a site $\exists_m$ with energy m which is adsorbed with n^{th} organic non- i adsorbate a_n:

$$\textbf{Adsorption (complex):} \qquad i_{(w)} + a_{n(\exists m)} \leftrightarrow i_{(\exists m)} + a_{n(w)}; \quad K^{x}_{an\exists m} = \frac{x_{i\exists m} x_{anw}}{x_{iw} x_{an\exists m}}$$

Eqn. 6 - 17

A total of M×N expressions analogous to Eqn. 6 - 17 can be written for adsorption of i onto a_n (n=1..N) pre-adsorbed sites with energies $\exists_m$ (m=1..M). An overall $\Delta G^{x}_{ads\text{-}cplx}$ and $K^{x}_{ads\text{-}cplx}$ for the MxN adsorption reactions can be shown to be:

$$\Delta G^{x}_{ads-cplx} = \sum_{m=1}^{M}\sum_{n=1}^{N} \Delta G^{x}_{ads}(@a_n\exists_m) = \sum_{m=1}^{M}\sum_{n=1}^{N} RT\ln\left(\frac{\gamma_{i\exists m}\gamma_{anw}}{\gamma_{iw}\gamma_{an\exists m}}\right) = - \sum_{m=1}^{M}\sum_{n=1}^{N} RT\ln\left(\frac{x_{i\exists m}x_{anw}}{x_{iw}x_{an\exists m}}\right)$$

Eqn. 6 - 18

$$K^{x}_{ads-cplx} = \prod_{n,m=1}^{N\times M} K^{x}_{an\exists m} = \prod_{n,m=1}^{N\times M} \frac{x_{i\exists m}x_{anw}}{x_{iw}x_{an\exists m}} = \frac{\prod_{1}^{M} x^{N}_{i\exists m} \prod_{1}^{N} x^{M}_{anw}}{x^{NxM}_{iw} \prod_{1,1}^{N,M} x_{an\exists m}}$$

Eqn. 6 - 19

$$\Theta_i = \sum_{m=1}^{M} \Theta_{i\exists m}; \quad \text{where } x_{i\exists m} \cong \Theta_{i\exists m}, \text{and } \sum_{m=1}^{M} x_{i\exists m} + \sum_{m=1}^{M}\sum_{n=1}^{N} x_{an\exists m} = 1$$

Eqn. 6 - 20

The derivation showed that it is very difficult to relate the observed $K_{d,ads}$ (L_w/kg_{solids}) to the $K^{x}_{ads\text{-}cplx}$, which gives a more realistic description of the adsorption of i onto sediment/soil. Thus, one can still estimate ΔG_{ads} or ΔS_{ads} for adsorption of HOC, though these values may not be directly comparable to the ΔG's or ΔS's of phase change reactions.

The author will conclude the section on adsorption thermodynamics by considering other non-idealities that are beyond the complex formulation presented in last sub-section. The current model assumes monolayer adsorption on the surface, which may not be true for sorbents with high proportion of micropores such as char or activated carbon. Although adsorption of HOCs on most sediment is likely to be within the monolayer capacity (Appendix 6-2), it is still possible for some of the sorbate to be bound in multiple layers. This implies that the total number of potential sites may be changing with the extent of adsorption. And if the multi-layer adsorbates are chemically identical, it is more proper to regard those molecules as pure solid of itself. In this case,

adsorption would be overlapping with 'condensation' reaction (i.e. 'condensation' of dissolved i onto surface of amorphous i). It seems improper to count the later condensing adsorbate as caused/'responsible' by the sorbent surface, for the 'adsorbed' i may be separated into truly surface-bound i and that belongs to pure solid or liquid of i (Figure 6-1c). In this case, what really happens is the combination of adsorption and 'precipitation' (dissolved i forming pure solid phase of itself) and/or 'condensation' (dissolved i forming pure liquid phase of itself):

$$\textbf{Adsorption:} \quad i_{(w)} + \mathrm{org}_{(\exists)} \leftrightarrow i_{(\exists)} + \mathrm{org}_{(w)}; \quad \mathrm{K}^{x}{}_{\mathrm{ads,org}} = \frac{x_{i\exists} x_{orgw}}{x_{iw} x_{org\exists}}$$

$$\textbf{'precipitation'}: \quad i_{(w)} \leftrightarrow i_{(s)}; \quad \mathrm{K}^{x}{}_{\mathrm{solidif.}} = \frac{x_{is}}{x_{iw}}$$

$$\textbf{'condensation'}: \quad i_{(w)} \leftrightarrow i_{(L)}; \quad \mathrm{K}^{x}{}_{\mathrm{solidif.}} = \frac{x_{iL}}{x_{iw}}$$

Eqn. 6 - 21

Another kind of non-ideality is that the displaced co-adsorbate may still 'adhere' onto the surface rather than being solvated in the bulk aqueous phase (Figure 6-1d). This means that a displaced co-adsorbate may not be desorbed (hence may not appear in the dissolved co-adsorbate mole-fraction x_{orgw}), and that the site binding-energy changes during the displacement:

$$\textbf{Adsorption:} \quad i_{(w)} + \mathrm{org}_{(\exists)} \leftrightarrow i_{(\exists+org)}; \quad \mathrm{K}^{x}{}_{\mathrm{ads},\exists+org} = \frac{x_{i\exists+org}}{x_{iw} x_{org\exists}}$$

Eqn. 6 - 22

2.1.5. Thermodynamics of Overall Sorption (Absorption+Adsorption)

It may be desirable to evaluate the overall thermodynamics of HOCs sorption to soils/sediments. Although such evaluation may not yield ΔG or ΔS suitable for comparing with the phase change reactions, it does provide a qualitative picture of the energy of sorption and some insights into the nature of sorption.

To characterize an overall ΔG or ΔS for sorption of HOC is to evaluate the thermodynamic properties without distinguishing between adsorption and absorption. As an approximation, we may formulate the expressions for $\Delta G^{x}_{d,app}$ similar to that for absorption (section 2.1.3; Eqn. 6 - 8):

$$\textbf{Overall Sorption:} \quad i_{(w)} \leftrightarrow i_{("d")}$$

$$\Delta \mathrm{G}^{x}{}_{\mathrm{d,app}} = \mathrm{RTln}\left(\frac{\gamma_{i"d"}}{\gamma_{iw}}\right) = -\mathrm{RTln}\left(\frac{x_{i"d"}}{x_{iw}}\right) = -\mathrm{RTlnK}^{x}{}_{\mathrm{d,app}}$$

$$\mathrm{K}^{x}{}_{\mathrm{d,app}} \equiv \frac{x_{i"d"}}{x_{iw}}$$

Eqn. 6 - 23

where $x_{i"d"}$ and x_{iw} are the mole fractions of i in the overall solid phase "d" and the aqueous/dissolved phase, respectively (mol_i/mol_{phase}),

$\gamma_{i"d"}$ and γ_{iw} are the activity coefficients of i in the overall solid phase "d" and the aqueous/dissolved phase, respectively (dimensionless),

$\Delta G^x_{d,app}$ is the apparent/approximate overall free energy of sorption of i to the sorbent (the mole fraction basis) (J/mol),

$K^x_{d,app}$ is the mole fraction based equilibrium constant for the overall sorption.

The practical concentration based K_d (L_w/kg_{solids}) can be related to $K^x_{d,app}$ through an overall sorption capacity, κ_{id}:

$$K_d = \frac{S_i}{C_{iw}}$$

$$\frac{K_d}{\kappa_{id}\bar{V}_w/MW_i} = \frac{S_{i,ads}/\kappa_{id}}{C_{iw}\bar{V}_w/MW_i} = K^x{}_{d,app} = \frac{x_{i"d"}}{x_{iw}}$$

Eqn. 6 - 24

where MW_i is the molar masses of the sorbate i ($\mu g_i/mol_i$),

C_{iw} is the aqueous/dissolved phase concentrations of i ($\mu g_i/L_w$),

κ_{id} is overall sorption capacity (absorption+adsorption) of the sorbent for i ($\mu g_i/kg_{solids}$),

S_i is the total solid phase concentration of sorbed i ($\mu g_i/kg_{solids}$),

$\bar{V}_w$ is the molar volume of water, and is equal 0.018 L_w/mol_w.

2.1.6. Concluding Thermodynamics of Sorption

The theoretical ground of characterizing the energetics of sorption (i.e. $\Delta G^x_{d,app}$, $K^x_{d,app}$) has been considered in a way where we may compare the thermodynamics of sorption with those of phase change reactions. Various degrees of complexity have been investigated, from the simplest approximations to those which are more realistic. In most of these scenarios, the sorption (adsorption/absorption/overall sorption) equilibrium coefficients K^x's (mole-fraction based) can be related to the practical K_d commonly used in HOCs sorption literature. A summary of the thermodynamic expressions for the examined cases is available in Table 6-1.

It should be emphasized that significant assumptions are often implicitly made when computing the thermodynamic properties of HOC sorption. For instance, the frequently reported non-linear isotherms for PAH sorption on highly condensed carbons (e.g. soot,

char, activated carbon, coal) indicates that heterogeneity in surface binding energy. Also, the surface of natural soils/sediments is often pre-loaded with other competing co-sorbates or natural organic phases (e.g. lipid, proteins and other biopolymers.

Furthermore, as Table 6-1 shows, properties such as the fraction of organic phase (f_{org}), molar mass of "average" organic macromolecule (MW_{org}), adsorption capacity ($\kappa_{i,ads}$), or overall sorption capacity (κ_{id}) all need to be estimated. Consequently, greater extent of 'disagreement' should be allowed when comparing the ΔG^x or ΔS^x of HOC sorption to those of phase change reactions. The qualitative implications of ΔG^x or ΔS^x, however, should be true.

3. Results & Discussion

3.1. Enthalpy, Entropy, and Free Energy for Pyrene Sorption

The energetics of sorption of pyrene to NQB/BH#6 sediment will be examined here. This section will begin by evaluating the overall enthalpy (ΔH) of pyrene sorption, and those of *ab*sorption and *ad*sorption ($\Delta H_{d,abs}$ or $\Delta H_{d,ads}$). With ΔH of specific cases determined, the entropy (ΔS) and free energy (ΔG) of pyrene sorption can be estimated according to the thermodynamic expressions derived in the previous section (i.e. Table 6-1). These properties will then be compared against those reported in literature and those of pyrene's phase change reactions.

3.1.1. Enthalpy of Pyrene Sorption

3.1.1.1. Apparent/Overall Enthalpy of Sorption ($\Delta H_{d,app}$)

Three approaches were taken to estimate the apparent or overall enthalpy of pyrene sorption ($\Delta H_{d,app}$): (i) by using the raw observations without imposition of any interpretative model, (ii) by using a purely descriptive fit of isotherm, and (iii) by using the regressed isotherms generated from the Two-Domain models described previously (i.e. Linear+Freundlich, Two-Freundlich, Langmuir-Freundlich regression).

It may be difficult to study the change of $\Delta H_{d,app}$ as a function of dissolved sorbate concentration. $\Delta H_{d,app}$ derived from raw observations revealed no clear trend with respect to dissolved pyrene concentration (C_{pyr}) (Table 6-2). The $\Delta H_{d,app}$–C_{pyr} plot showed that the trend exhibited by $\Delta H_{d,app}$ was highly sensitive to the form of isotherm used for regression (Figure 6-2). Despite the fact that all four isotherm forms were able to describe the sorption data quite well, they gave incompatible trends. For instance, the quadratic form (purely descriptive) and the Linear+Freundlich form both showed a decreasing ($-\Delta H_{d,app}$) in the lower C_{pyr}, while the Two-Freundlich and the Langmuir-Freundlich showed an opposite trend; also, the Linear+Freundlich curve showed greater disagreement with the other three forms at high C_{pyr} (Figure 6-2). With this disagreement and the high uncertainty in mind, it is perhaps more appropriate to comment on the range of ΔH_d or ΔS_d observed.

The apparent enthalpy for pyrene sorption was negative over the investigated concentration range (Table 6-2). The $\Delta H_{d,app}$ for pyrene was about –10 to –30 kJ/mol_{pyr} regardless of the method taken, consistent with reported in previous studies for soils and sediments (Table 6-3). The enthalpies of PAH sorption reported by Ran et al.(2007a) have not been included in the table. Their enthalpies were obtained at high pressure (100 bar) with the soil/sediment exposed to organic solvent(s), and hence not applicable at all to PAH-partitioning in natural systems. Note also that the values in Table 6-2 were geometric means of the enthalpies estimated at the lower and upper ends of a given C_{pyr} range.

3.1.1.2. Enthalpy of Absorption ($\Delta H_{d,abs}$)

To investigate the enthalpy of absorption ($\Delta H_{d,abs}$) for pyrene, we need to quantitatively separate the contribution of absorption from adsorption. This means that both the raw data approach and the purely descriptive approach (quadratic form) could not be used. For the three remaining isotherm forms (i.e. Linear+Freundlich, Two-Freundlich, Langmuir-Freundlich), it was assumed that the lower-affinity term represented the absorption domain, and the higher-affinity term the adsorption domain. It was also assumed that the organic matter in the sediment had an average molar mass of 10 kg/mol_{org} (section 2.1.3) and f_{OC} was a good measure of its abundance. With these assumptions, $\Delta H_{d,abs}$ for pyrene was estimated by regressing $\ln K_{d,abs}$ (where $K_{d,abs} = S_{pyr\text{-}absorbed}/C_{pyr,w}$) against 1/T.

The $\Delta H_{d,abs}$ for pyrene absorption into natural OC was estimated from the three isotherms, and it ranged from about –26 to –35 (± 9 to 13) kJ/mol. All three isotherms showed close agreement in both the value of $\Delta H_{d,abs}$. They also showed a similar trend in $\Delta H_{d,abs}$ being invariant respect to C_{pyr} (Figure 6-3). This invariance of $\Delta H_{d,abs}$ to dissolved absorbate concentration was consistent with the physicochemical picture of absorption – that the heat of absorption should remain constant for dilute concentration of the absorbate. The suspensions contained, on average, about 20–600 mg_{solids}/L_w (Table 4-1), which translated into about 600–18000 $\mu g_{OC}/L$. At C_{pyr}=20 $\mu g_{pyr}/L_w$ (the maximum dissolved pyrene concentration studied), the *ab*sorbed-pyrene-to-OC mass ratio was less than 1 wt %. Thus pyrene absorbed into the OC-phase may be regarded as a 'dilute' solute solvated by OC. The $\Delta H_{d,abs}$ for pyrene may also be extended to higher concentration levels – for at C_{pyr}=140 $\mu g_{pyr}/L_w$ (pyrene solubility at 20°C), the *ab*sorbed-pyrene-to-OC mass ratio would increase to, at most, 3 %.

3.1.1.3. Enthalpy of Adsorption ($\Delta H_{d,ads}$)

In a similar manner for enthalpy of absorption, one may assess enthalpy of adsorption ($\Delta H_{d,ads}$) for pyrene through the two-domain isotherms. It was assumed that the higher-affinity term represented the adsorption domain, and that the f_{BC} was a good measure of the organic phase responsible for adsorption.

The enthalpy of adsorption required a greater analysis as the $\Delta H_{d,ads}$–C_{pyr} plot showed disagreement between the three isotherms (Figure 6-4). The $\Delta H_{d,ads}$ derived from the Linear+Freundlich became increasingly negative with greater C_{pyr}. The Langmuir-Freundlich and the Two-Freundlich forms, on the other hand, gave an opposite trend, showing a diminishing enthalpic advantage for adsorption with higher C_{pyr}. Furthermore,

at higher C_{pyr} end, the Langmuir-Freundlich derived $\Delta H_{d,ads}$ seemed to have reached a limiting value, wherein the Two-Freundlich derived $\Delta H_{d,ads}$ continued to move toward zero. How should these differences be judged and resolved?

The $\Delta H_{d,ads}$'s obtained at the lower concentration range (< 1 $\mu g_{pyr}/L_w$) were more likely to be true for the reason that adsorption of pyrene was, as indicated by the isotherm parameters, dominant at the lower C_{pyr} range. There would be less error by analyzing adsorption enthalpy only in the adsorption-dominant range – for the error in separating absorption from adsorption becomes relatively less important. For sorption at 22°C, absorption and adsorption became about equally important at C_{pyr} ~ 1 $\mu g_{pyr}/L_w$. Pyrene adsorbed-to-pyrene absorbed increased to ~2 and ~5 as C_{pyr} decreased to 0.5 and 0.2 $\mu g_{pyr}/L_w$, respectively. Taking $C_{pyr} \approx$ 0.2–0.5 $\mu g_{pyr}/L_w$ as the upper limit of the adsorption-dominant region, it was estimated that $\Delta H_{d,ads}$ for pyrene ranged from about –10 to –20 kJ/mol with uncertainties[2] of about ±2-4 kJ/mol. Note that the $\Delta H_{d,ads}$ shown in Figure 6-4 was calculated based on converting $K_{d,ads}$ to the mole-fraction based $K^x_{d,app\text{-}ss}$. There was a small difference (~0.5 kJ/mol) between $\Delta H_{d,ads\text{-}ss}$ and $\Delta H_{d,ads\text{-}sH2O/sOrg}$, which have the $1\text{-}\Theta_i$ ($\Theta_i = 1\text{-}S_{i,ads}/\kappa_{i,ads}$) factor incorporated (Table 6-1). $\Delta H_{d,ads\text{-}sH2O}$– and $\Delta H_{d,ads\text{-}sOrg}$–$C_{pyr}$ plots can be found in Appendix 6-3.

3.1.2. Entropy of Pyrene Sorption

Analyses suggested that a gain in entropy is associated with the sorption of pyrene to sediment particles from aqueous phase. The entropy of absorption was found to be around 40–60 (±30) J/mol.K, which was comparable to the entropic change of pure pyrene dissolution (Table 6-5). The entropy of adsorption was less certain because of its dependence on the assumptions regarding the sorbate and the surface. A detail discussion on the derivation/estimation of pyrene sorption entropies is available in Appendix 6-6.

4. Conclusion

Sorption data at different temperatures allow enthalpic and entropic change of sorption to be observed. Considering the limitations of current thermodynamic theories for sorption (section 1.1.1) and the need to relate the energetics of sorption to those of other phase transition reactions (section 1.1.2), the thermodynamics of sorption was re-examined. Following the thermodynamic convention for phase transition reactions (section 2.1.2), mole-fraction based distribution coefficients (K^x's) and the corresponding expressions of concentration-based K_d's into K^x's were developed for absorption (section 2.1.3), adsorption (section 2.1.4), and the overall sorption (section 2.1.5). For adsorption in particular, different scenarios with varying degree of simplifications were examined (Table 6-1).

The enthalpies and entropies of overall sorption, absorption, and adsorption for pyrene to sediment were estimated (Table 6-6) according to the developed thermodynamic

[2] as derived from the more 'precise' Langmuir-Freundlich and Two-Freundlich $\Delta H_{d,ads}$'s.

expressions (Table 6-1). The estimated apparent/overall enthalpy of sorption agreed well with previously reported values (Table 6-3). In general, heat was released ($\Delta H < 0$) as pyrene became sorbed to the sedimentary phase. The enthalpy of absorption was comparable with $-\Delta H$ for the dissolution of pure solid pyrene in water. The enthalpic change associated with adsorption appeared to be generally weaker than ΔH for absorption (Table 6-6).

The system generally experienced a gain in entropy (freedom in molecular motion and/or arrangement) in sorption. The entropy of absorption was similar to those for the dissolution of pure solid or sub-cooled liquid pyrene in water (Table 6-6). The entropy of adsorption was very sensitive to the mechanistic approximations made, and significantly different estimates of adsorption entropy were obtained (Table 6-6). A modified adsorption model allowing a fraction of organic co-adsorbate displaced by the adsorbing pyrene to stay associated with the sorbent phase was proposed (Appendix 6-6). The true entropy of adsorption should be bound within the estimates of the simpler models, but more in the direction of greater entropies gain. It seemed that entropic change was the dominating term in determining the energetics of HOCs adsorption.

Chapter 7. Desorption Kinetics of Native Sedimentary Pyrene – Mechanistic Modeling & Prediction

CHAPTER ABSTRACT

A finite-difference numerical model for non-linear HOCs desorption kinetics based on the Intra-particle Porewater Diffusion (IPD) mechanistic picture was successfully constructed. The model can handle variability in aggregate geometry and spatial distributions of OC, BC, porosity, tortuosity, and initial sorbate concentration.

The developed model was applied to the pyrene kinetic data obtained from the closed-system desorption experiment (Chapter 2). Four pyrene sorption isotherms were used for the simulation: the Classical-OC, the Old-OC-BC, the New-OC-BC, and the Occlusion-OC-BC isotherms. Simulation results indicated that the *a priori* Occlusion-OC-BC model gave the best prediction for kinetics observed in all fifteen suspensions. The *a priori* New-OC-BC model could predict the dissolved pyrene concentration in about half of the suspensions; the Classical-OC and the Old-OC-BC models failed to capture the observed data.

Despite the success of the model in predicting experimental observations, a number of inadequacies were identified and discussed. First, significant disparities in desorption half-times were observed between the simulation and the data. This was attributed to the non-idealities of aggregation/disaggregation dynamics and non-spherical aggregate geometry. Second, sensitivity analysis showed that the kinetic character (e.g. desorption halftime) of actual desorption data was generally harder to predict. Third , the success of the *a priori* Occlusion-OC-BC model should not be considered as evidence that physical occlusion of pyrene (and other HOCs) in sediment was true and significant – for equally 'accurate' concentration profiles can be obtained using other isotherms with best-fitted n_{BC}'s.

The good model-observation agreement on pyrene suggested that *a priori* prediction of sedimentary HOC desorption kinetics may be possible. The *a priori* IDP model should be further tested with more desorption observations. This may also help in correlating the empirically fitted kinetic parameters with the physicochemical properties of sorbate/sorbent. The assumptions underlying the IDP mechanistic picture and the conditions under which the IDP model would be valid were also thoroughly examined and elucidated.

Table of Content for Chapter 7

1. Chapter Introduction, Scope, and Objective 151

1.1. Introduction 151

1.1.1. Kinetics Control Bioavailability of Soil/Sediment HOCs 151

1.1.2. Kinetics for Determining Sorption Equilibrium 151

1.1.3. Release Kinetics Controls Fate of HOCs 152

1.1.3.1. Disequilibrium of HOCs in Surficial Sediment 152

1.1.3.2. Mobilization of Sedimentary HOCs via Resuspension 152

1.1.3.3. Slow Response of Porewater to Influx of Particulate PAHs 152

1.1.3.4. Numerical Simulations on the Release of bound-HOCs 152

1.1.4. Low Applicability of Past HOCs Kinetic Studies 153

1.1.4.1. Empirically Fitted Rates not Universally Applicable 153

1.1.4.2. Spiking vs Field-Aged HOCs 153

1.1.4.3. Use of Secondary Sorption Media 153

1.1.5. Mechanistic Kinetic Models 154

1.1.5.1. Non-Linear Partitioning 154

1.1.5.2. Mechanistic Framework with Parameter Fitting 154

1.2. Objectives 154

2. Methodology: Experimental 155

2.1. Materials and Methods 155

2.1.1. Sediment 155

2.1.2. Short-Term Desorption Experiment 155

2.1.3. Measurement of Dissolved Pyrene 155

2.1.4. Sedimentary Pyrene Concentration, Organic Carbon, and Black Carbon Measurement 156

3. Methodology: Modeling 156

3.1. Conceptual Picture of Sorption Dynamics 156

3.1.1. Black Carbon and Natural Aggregates: A Brief Survey on Size 156

3.1.1.1. Size of Natural Aggregates 156

3.1.1.2. Size of Black Carbon (I): μm-scale 156

3.1.1.3. Size of Black Carbon (II): nm-scale 157

3.1.2. Idealized Distribution of BC in Natural Aggregates 158

3.1.2.1. Homogeneously Distributed nm-BC, Heterogeneously Distributed μm-BC.. 158

3.1.2.2. Limitations of the Idealized Distribution Pictures 158

3.2. Intra-Sorbent Diffusion: a Brief Survey of Transport Models 159

3.3. Intra-particle Pore Diffusion Model 159
3.3.1. Local Sorbate Partitioning Equilibrium 159
3.3.2. Diffusion through Intra-aggregate Pore-Fluid Phase 161
3.3.3. Radial Diffusion, Initial Sorbate Distribution, Aggregation Dynamics 161
3.3.3.1. Radial Diffusion (1-D Diffusion) 161
3.3.3.2. Radially Distributed (Uniform-Shell) Sorbate Concentration 162
3.3.3.3. Neglect Aggregation Dynamics 162
3.3.4. Retardation by Phase-Distribution/Partitioning 162
3.4. Dominance of Transport Pathways 162
3.4.1. $D_{eff,pw}$, $D_{eff,OM}$, & $D_{eff,surf}$ 162
3.4.2. Diffusion through OM vs Diffusion through pore-water. 164
3.4.3. Surface Diffusion vs Diffusion through pore-water 165
3.4.4. Summary on Intra-Sorbent Transport Pathways 166
3.5. Mathematics of Intra-Particle Porewater Diffusion Model 167
3.5.1. Diffusion with Non-linear Partitioning Function ($K_d(C_{iw})$) 167
3.5.1.1. Intermediate-shells (Spherical) 167
3.5.1.2. Core-Shell (Spherical) 168
3.5.1.3. Aggregate-Volume Averaged Quantity (Spherical) 169
3.5.1.4. Outermost/Edge-Shell (Spherical) 169
3.5.1.5. Dimensionless Form (Generic Aggregate Geometry) 170
3.6. Finite Difference Implementation of Nonlinear Diffusion Model 171
3.6.1. Homogeneous Aggregate (Uniformly Distributed nm-BC) 171
3.6.1.1. Intermediate-shells (2^{nd} to m-1^{th} grids) 171
3.6.1.2. Core-shell (1^{st} grid) 172
3.6.1.3. Aggregate-Volume Averaged Quantity (Spherical) 172
3.6.1.4. Outermost-shell (m^{th} grid) 173
3.6.2. Stability Criterion for the Explicit Scheme 174
3.6.3. Solving the Root of Nonlinear Equation 175
3.7. Isotherms for Modeling 175
3.8. Regression of Kinetic Observations by Empirical Models 175
4. Results & Discussion 176
4.1. Analytical Solution of Radial Desorption 176
4.2. Validation of Desorption Kinetics Numerical Code 177
4.2.1. Validation (I): Convergence on K_dR_{sw}'s 178
4.2.2. Validation (II): Convergence on Forms of K_d 178

4.2.3. Validation (III): Convergence on Discretization (Grid Numbers) 178
4.2.4. Validation (IV): Convergence on Time Steps 178
4.2.5. Validation (V): Aggregate Shapes 178
4.3. Modeling of Pyrene Desorption Profiles (BH#6 Fractions) 178
4.3.1. *A priori* Modeling of Desorption Dynamics 179
4.3.1.1. Modeling Parameters 179
4.3.1.2. A priori Model Results vs Observations: End-Point C_{pyr} 179
4.3.1.3. Sensitivity Analysis for End-Point C_{pyr} 180
4.3.1.4. A priori Model Results vs Observations: Kinetics 180
4.3.1.5. Sensitivity Analysis for Kinetics 181
4.3.2. Modeling of Desorption Kinetics with Best Fitted Isotherms 181
4.3.3. Conclusion on *a priori* and Best-Fit Kinetic Modeling 182
4.4. Correlating Empirical Kinetic Regression with *a priori* Properties 183
4.4.1. Limitations of Empirical Kinetic Expressions 183
4.4.2. Empirical Desorption Rate: Comparison with Literature 184
4.4.3. Desorption Physics Buried in Empirical Kinetics 184
4.4.3.1. F_{rapid}/F_{slow} vs R_{sw} 184
4.4.3.2. F_{rapid}/F_{slow} vs OC/BC-Associated Pyrene 185
4.4.3.3. k_{rapid}/k_{slow} vs a priori Time Constant Estimate (κ) 185
4.4.3.4. Interdependence in Regressed Parameters 186
4.4.4. Concluding Remarks on Empirical Regression of Desorption Kinetics 186
4.4.4.1. Empirical Models as Pure Descriptor of HOCs Desorption Kinetics 186
4.4.4.2. Bridging Empirical Rates with Physicochemical Model 187
4.4.4.3. Recommended Practice for Future HOCs Kinetic Studies 187
5. Conclusion 187
5.1. Summary 187
5.2. Implications 189

1. Chapter Introduction, Scope, and Objective

1.1. Introduction

There are many reasons why we should care about the kinetics of HOCs uptake (or release) by (or from) geosorbents. Some of these reasons are highlighted below.

1.1.1. Kinetics Control Bioavailability of Soil/Sediment HOCs

One way to assess sediment-associated HOC bioavailability is by assuming equilibrium partitioning (EqP) of HOCs among the sediment, interstitial water, and benthic organism compartments. This implies (1) that all three compartments have identical HOC activity, and (2) that HOC concentrations of the other two compartments can be inferred/predicted from a known concentration in the third compartment. One application of EqP theory is the equilibrium partitioning sediment benchmarks (ESBs) recently established by EPA for the protection of benthic organisms from PAHs (U.S. EPA 2003).

However, the application of the EqP assumption to the sediment-water-biota system is often invalid for the interpretation of HOCs bioavailability (Pignatello et al. 1996; Luthy et al. 1997; Alexander 2000). A number of independent studies have suggested that the bioavailability or the biodegradability of HOCs is generally controlled by desorption kinetics from natural solids. Lamoureux and Brownawell (1999) and Kraaij et al (2002) found that the bioavailability of HOCs to benthic deposit-feeders was controlled by their desorption kinetics from sediments. Similarly, desorption kinetics also controls microbial degradation of PAHs in sediment, soils and synthetic sorbents (Guerin et al. 1997; Guthrie-Nichols et al. 2003; Shor et al. 2003; Lu et al. 2006). Biodegradability of HOCs also appears to decline with increasing desorption-resistant fraction (White et al. 1996; Cornelissen et al. 1998b), and this fraction has been shown to increase with aging/incubation time of the HOCs (Schwartz et al. 1999; Northcott et al. 2001a, b).

It should be noted that even in surficial sediment bed – where high solid-to-water ratios greatly favor partitioning equilibria of HOCs – bioavailability is still likely to be dictated by kinetics rather than equilibrium partitioning due to the presence of other transformation processes (biodegradation, diffusion out of bed, etc) and the lack of sufficient mixing (ter Laak et al. 2007).

1.1.2. Kinetics for Determining Sorption Equilibrium

Adsorption/desorption kinetics of HOCs can serve as an alternative tool for checking whether equilibrium has been established in HOCs sorption experiment. As discussed in Chapter 3, for many past sorption studies, it was unclear if the reported sorption coefficients (i.e. $Q_d=S_i/C_{iw}$) represented equilibrium or non-equilibrium observations. Furthermore, literature studies have suggested a strong dependence of the equilibration time on sorbent and sorbate properties. If we understand the uptake/release kinetics of HOCs in typical soil/sediment, then we can expect how much equilibration time is needed, and use that as a secondary criterion for sorption equilibrium.

1.1.3. Release Kinetics Controls Fate of HOCs

Results from field studies suggested that partition equilibrium may not exist in sediment-water systems. These observations suggested that the behavior of HOCs in natural environments may be controlled by the kinetics of desorption. Some of these observations will be briefly reviewed.

1.1.3.1. Disequilibrium of HOCs in Surficial Sediment

In a sediment core study, McGroddy et al. (1995) reported that the porewater PAH concentrations were lower than the equilibrium predictions using the linear, Classical-OC isotherm (i.e. $K_d=f_{OC}K_{OC}$) by at least one order of magnitude. A follow-up study was conducted (Accardi-Dey and Gschwend 2003) to incorporate the sorption effect of BC into account. The inclusion of BC did bring the predicted pore water PAHs concentrations closer to the observed, but a discrepancy by a factor of about 3 to 4 still remained for measurements from the surficial sediment bed layer (~10 cm) (Accardi-Dey and Gschwend 2003).

1.1.3.2. Mobilization of Sedimentary HOCs via Resuspension

Sediment-bound HOCs can be released into the bulk water column via resuspension of bed solids. The relative importance of desorption via sediment resuspension to that from diffusion out of the surficial-bed porewater is not clear. Kalnejais et al. (2007) recently suggested that resuspension, rather than diffusion from pore fluids, can be a major release pathway of particulate metals.

The field observations in Adams (2003) suggested that sedimentary PAHs may be released via resuspension events in the Hudson River Estuary. The dissolved pyrene concentration in the water column was found to be higher in April, following the spring snowmelt. The observed levels could not be explained by estuarine dilution process (i.e. from the salinity-distance curve). Such phenomenon was, however, not observed in the fall. This suggested that the April observation may be caused by the release of pyrene from resuspended sediment as triggered by shearing influx of spring water.

1.1.3.3. Slow Response of Porewater to Influx of Particulate PAHs

Maruya et al. (1996) found that sediment-porewater distribution quotients (i.e. S_i/C_{iw}) for PAHs in the wet season (high surface runoff) were about one order of magnitude higher than those measured in the dry period. They attributed the higher distribution quotients to the presence of sooty particles carried in the surface runoff. Furthermore, they found the wet season porewater PAH concentrations to be relatively constant despite the variation in the sediment compartment. This suggested that the fresh influx of relatively PAH-rich particles from runoff has not equilibrated with the sediment porewater.

1.1.3.4. Numerical Simulations on the Release of bound-HOCs

Cheng et al. (1995) modeled desorption of HOCs during resuspension events using a linear-OC model and concluded that equilibrium assumption was not valid for parameters of typical natural systems.

Concerning about the fate of sedimentary DDE on the Palos Verdes shelf, Wiberg et al. (2002b) suggested that as much as 25–50% of the surficial DDE could have been released via resuspension events. While the question of bioavailability of HOCs in the

sedimentary bed has been the focus of most kinetic studies, their potential release via resuspension events has not received much attention in general.

1.1.4. Low Applicability of Past HOCs Kinetic Studies

Although much effort has been devoted to the understanding of HOCs desorption kinetics from soil/sediment, very few studies have documented rate observations in a way applicable to broader circumstances. Some of the issues will be briefly mentioned here.

1.1.4.1. Empirically Fitted Rates not Universally Applicable

Most studies have reported kinetic results in empirical rate constants (Table 7-14b). In many of these studies, system parameters (e.g. R_{sw}) and sorbent characteristics (e.g. size) have not been documented (e.g. Cornelissen et al. 1998b; Ghosh et al. 2001; Johnson et al. 2001b; Rockne et al. 2002; van den Heuvel et al. 2003; Kukkonen et al. 2003; van Noort et al. 2003; Gomez-Lahoz et al. 2005). This means that the reported kinetic information may not be applicable to scenarios with different system or sorbent properties. For instance, kinetic data obtained from studies using high solid-loadings (to mimic sediment-bed like conditions) may not be used for evaluating the release of HOCs via resuspension. Other limitations of the rate-fitting approach will be further discussed (sections 4.4.1, 4.4.3.4).

1.1.4.2. Spiking vs Field-Aged HOCs

Studies have shown that spiked and field-aged HOCs exhibited different desorption kinetics. Thus kinetic data obtained from spiked geosorbents may not be 'usable' for evaluating the release of native HOCs in contaminated soil/sediment. The extractability of PAHs generally decreased with increasing solid-chemical contact time, molecular weight, and non-polarity for both soils (Macleod et al. 2000; Northcott et al. 2001a) and sediments (Gong et al. 1998a; Kraaij et al. 2002b). The dependence of kinetics on sorbate-sorbent contact time is also shown indirectly by the relationship among HOC incubation time, their bioavailability, and their extractability. A great number of studies have also demonstrated that the following all decline with increasing aging/incubation time: the extent of HOC bioaccumulation (Kraaij et al. 2001; van Hoff et al. 2001), biodegradation (Conrad et al. 2002; Guthrie-Nichols et al. 2003; Tabak et al. 2003), mineralization, earthworm uptake, and extractability (Hatzinger et al. 1995; White et al. 1999, Nam et al. 2003).

1.1.4.3. Use of Secondary Sorption Media

In order to increase the signal sensitivity, many desorption kinetic experiments (Table 7-14a, b) have used a secondary sorption medium which has comparable sorption affinity as that of OC (e.g. Pignatello 1990; White et al. 1999). The purpose of this secondary medium, which is typically polymeric in nature (e.g. polyethylene or Tenax) is to take up and concentrate most of the desorbed HOC. The secondary medium also serves the purpose of maintaining the system near the infinite bath condition. While the use of secondary sorption media can increase analytical sensitivity and simplify the extraction procedure, its presence also introduces artifacts – the observed kinetics now consists of the desorption of HOCs from the suspension as well as the uptake of dissolved HOCs

into/onto the secondary medium. Consequently, the kinetic data are hard to interpret unless the kinetic effect of the secondary medium can be separated.

1.1.5. Mechanistic Kinetic Models

A number of past studies (Table 7-14a) have modeled HOC uptake or release kinetics using mechanistic models where the model parameters are related to the physicochemical properties of both the sorbent and the sorbate. The description of some of these models can be found in section 3.2. However, these past studies have a number of limitations. Some of these have been mentioned earlier (e.g. spiked samples, secondary sorption media); others will be briefly discussed here.

1.1.5.1. Non-Linear Partitioning

The earlier kinetic studies often examined adsorption or desorption kinetics assuming a linear sorption isotherm (e.g. Carroll et al. 1994; Stapleton et al. 1994; Gong et al. 1998a; Ghosh et al. 2001). Although non-linear isotherm has been incorporated into the diffusion model in the later studies (e.g. Karapanagioti et al. 2001; Shor et al. 2003b), their mathematical formulations of the effective diffusivity, D_{eff}, was inconsistent with the non-linearity of the isotherm (see Appendix 7-23). This has led to incorrect solution (e.g. in Shor et al. 2003b, an 'analytical' solution, equation (5) therein, was presented for non-linear diffusion problem) or simulation (e.g. Karapanagioti et al. 2001). In the case where D_{eff} was correctly defined, however, the study was on adsorption rather desorption of native HOCs (e.g. Rugner et al. 1999; Table 7-14a).

1.1.5.2. Mechanistic Framework with Parameter Fitting

Although past kinetic studies have used mechanistic models (e.g. polymer or intraparticle diffusion models), the modeling of kinetic data often required parameter fitting (Table 7-14a). Thus the modeled curves were not really 'predictions' of the kinetic observations – they were 'tuned' after-the-fact to the data. For instance, effective diffusivity (D_a/α^2) has often been used a fitting parameter (Karapanagioti et al. 2000, 2001; Ghosh et al. 2001); other tuning parameters include tortuosity factor (Rugner et al. 1999; Shor et al. 2003), sphere-equivalent diameter (Carroll et al. 1994), fast diffusing fraction (Shor et al. 2003), and mass transfer coefficients across different media boundary (Gong et al. 1998b). The only study which has not used any model parameters for 'tuning' or 'calibration' was that by Stapleton et al. (1994).

1.2. Objectives

There are two main objectives in this chapter: (i) to develop a finite-difference numerical model which works with non-linear sorption isotherm, and (ii) to see how well the numerical model can predict experimental kinetic observations (data from Chapter 2).

This chapter will begin by considering how BC may affect the physical picture of desorption at the aggregate or particle level (section 3.1). Then, we will briefly review three mechanistic pictures for intra-sorbent transport of HOCs (section 3.2). We will examine the idea and assumptions behind the Intra-particle Porewater Diffusion (IPD) (section 3.3) – upon which the numerical code will be constructed. A brief comment/analysis will be made on when and where IPD may be the dominant transport

mechanism (section 3.4). Finally, we will cover the mathematical foundation of the numerical model (section 3.5) as well as its implementation (section 3.6).

After the numerical model is validated (section 4.1, 4.2), we will examine how well the model can fit or predict the kinetic observations of pyrene desorption (section 4.3). The modeling part will consist of: (i) *a priori* simulation based on known/measured physicochemical properties, (ii) simulation of desorption based on best fitted n_{BC}, and (iii) sensitivity analysis on the model to parameter uncertainty. This chapter will end with an attempt to relate empirically fitted kinetic parameters to the a priori properties of the sorbate and/or the sorbent (section 4.4).

2. Methodology: Experimental

2.1. Materials and Methods

2.1.1. Sediment

Sediment from Boston Harbor (BH#6/NQB; Table 4-1) was used for the pyrene desorption kinetic experiment. The location of the sediment, the time of collection, the storage procedure, and the wet-sieving procedure have been described in Chapter 2. Three nominal size fractions were obtained and used: dia. 38-75 μm, 75-106 μm, and 180-250 μm. All sieved sediment fractions were stored in amber glass jars at 5°C.

2.1.2. Short-Term Desorption Experiment

This was the native pyrene desorption experiment on three size fractions of the NQB/BH#6 sediment as described in Chapter 2. Briefly, sediment suspensions (dia.: 38-75, 75-106, 180-250 μm) were prepared in initially pyrene-free water to allow solid-bound pyrene to release over time. For each size fraction, three different solid loadings were chosen, with the solid-to-water ratio (R_{sw}) ranging from ~20 to ~270 mg_{solids}/L_w). For the smallest size fraction (dia.: 38-75 μm), triplicates of suspensions were studied for statistical purpose. A summary of the physicochemical properties of the individual suspensions is provided in Table 7-1. Please refer to Chapter 2 (or Kuo et al. 2007) for details on experimental conditions and physicochemical properties of the sediment fractions.

2.1.3. Measurement of Dissolved Pyrene

Dissolved pyrene concentrations were measured by time-gated laser-induced fluorescence spectroscopy (TG-LIF). In TG-LIF (Rudnick et al. 1998; Kuo et al. 2007; Hawthorne et al. 2008), laser pulse-induced fluorescence emissions were subjected to time-filtering, and only signals emitted within specified time window (on the order of ns) are registered. The system configuration, the measurement procedure, and the calibration for dissolved pyrene have been described in detail in Chapter 2 or Kuo et al. (2007).

2.1.4. Sedimentary Pyrene Concentration, Organic Carbon, and Black Carbon Measurement

The native sedimentary pyrene concentration ($S_{pyr,native}$) was measured by organic solvent extraction followed by gas chromatography-mass spectrometry (GC-MS) (Accardi-Dey and Gschwend 2002; Chapter 2 & 3). The organic carbon (OC) and black carbon (BC) contents were measured by elemental analysis after chemical-thermal oxidation treatment (Gustafsson et al. 1997; Accardi-Dey and Gschwend 2002; Flores-Cervantes 2008; Chapter 3).

3. Methodology: Modeling

Since the modeling of desorption dynamics of HOCs is a key objective of this chapter, the modeling component also requires some discussion. The following paragraphs will cover: (i) the conceptual picture behind the model, (ii) the mathematical formulation of the model, and (iii) the numerical implementation of the model. The author will begin by envisioning how black carbon may be present in natural soil or sedimentary aggregates/particles.

3.1. Conceptual Picture of Sorption Dynamics

3.1.1. Black Carbon and Natural Aggregates: A Brief Survey on Size

Black carbon in natural aggregates may be conceptually treated as homogeneously distributed within the aggregates or as a heterogeneous phase distinct from the background mineral/OC components of the aggregates. To determine the intra-aggregate distribution of BC, it is necessary to consider the sizes of the different types of BC, and compare them to the size of natural aggregates and the constituent grains.

3.1.1.1. Size of Natural Aggregates

The size of natural aggregates typically falls within the μm to mm size range. This has been observed for soil aggregates (Weakly et al. 1967; Wagner et al. 1994; Fredlund et al. 2000; Selley 2000) and sedimentary aggregates (McDowell et al. 1977; Kranck 1991). Electron micrographs of natural aggregates from previous literature suggested that the constituent grains of natural aggregates are generally around 0.5–1+ μm in size (McDowell et al. 1977; Bennett et al. 1981; Bennett et al. 1991; Chiou et al. 1991; Pamukcu et al. 1991). This was also observed in the current study (Appendix 7-18).

3.1.1.2. Size of Black Carbon (I): μm-scale

With respect to particle size, Black carbon may be broadly divided into μm-scale and nm-scale categories. The μm-scale category includes particles such as char/charcoal particles, coal particles, and typical commercial activated carbon. Char/charcoal, incompletely combusted plant residue and coal in natural environments are often within the micron range (1–100μm) (Cope et al. 1980; Medalia et al. 1982; Karls et al. 1998). It should be noted that the large BC particulates are not restricted to the μm range –

coal and coke with size in the mm-scale or even cm-scale have been observed in sedimentary core (Goldberg et al. 1977).

3.1.1.3. Size of Black Carbon (II): nm-scale

The nm-scale BC consists of primarily soot particles and/or clusters produced from combustion of fuel or biomass. Typical soot particles from diesel engines (i.e. *primary soot particle* or individual soot sphere) have diameter around 10–40 nm (Medalia et al. 1982; Palotas et al. 1996; Chen et al. 2005; Mathis et al. 2005; Lapuerta et al. 2007; Miller et al. 2007; also from this study, see Chapter 10). Although the size of soot particles varies with combustion condition and engine characteristics, the mean diameter of freshly produced diesel soot particles is relatively stable. Freshly released diesel soot particles are generally around 20–25 nm in diameter despite the variation in engine/combustion parameters such as air/fuel ratio, engine speed, exhaust gas recirculation, fuel injection pressure, and flame temperature (Mathis et al. 2005; Lapuerta et al. 2007). Soot particles, however, tend to form clusters. Particle analysis suggested that fresh soot clusters typically do not exceed 1 μm in size (Figure 1a in Chen et al. 2005; Figure 2c in Mathis et al. 2005).

Biomass-originated soot is, however, more variable in size as both the fuel quality (i.e. biomass composition, moisture) and the combustion conditions are much more variable both spatially and temporally. Bright-field TEM images of biomass fire smoke samples showed that primary soot particles were about 20–50 nm in diameter (Posfai et al. 2003; Semeniuk et al. 2007). However, some images did show a frequent presence of larger soot-like spheres (~80–90 nm) (e.g. Figure 1 in Posfai et al. 2003). These particles did not seem to resemble amorphous 'organic particles' or 'tar-balls' (a term used by Posfai et al. 2003) in shape or structure. The agglomeration of biomass-soot results in soot clusters with similar size as the diesel soot clusters (Posfai et al. 2003; Semeniuk et al. 2007). While nm-scale BC particles from freshly emitted diesel exhaust may exist in larger clusters, TEM evidence suggests that the tendency to self-agglomerate declines in the presence of other particles such as sulfate aerosols (Posfai et al. 1999) or μm-scale organic particles (Semeniuk et al. 2007).

While most soot morphological studies have shown that soots are mostly nm-scale particles, it may not be proper to equate soot with the nm-scale BC category. For instance, clusters of sub-micrometer soots (each sphere about 200 nm in diameter) have been observed from the combustion of coal (Jonker et al. 2002; Chen et al. 2005). In this case, the soot cluster (~2 μm) belongs more to the μm-scale BC category than the nm-scale one. Larger particles, such the amorphous but relatively impure 'organic particles' and the highly carbonaceous 'tar balls', also exist in biomass-smoke sample. At this point, it is not clear if these entities have similar HOCs sorption capacities as BC. These particles are usually around 200 nm in diameter (Posfai et al. 2003; Alexander et al. 2008) and no greater than 400 nm.

3.1.2. Idealized Distribution of BC in Natural Aggregates

3.1.2.1. Homogeneously Distributed nm-BC, Heterogeneously Distributed μm-BC

With the brief survey on the typical size of natural aggregates and BC particles, we can now construct a conceptual picture for the intra-aggregate distribution of BC. In this picture (Figure 7-1), the nm-scale BC particles are considered to be homogeneously distributed in natural aggregates while the μm-scale char/charcoal/coal particles, when present, are to be treated as a distinct phase in the aggregates. This conceptual framework is built upon two quantitative justifications: the relative size of BC particles and their relative numbers in typical natural aggregates.

The relative size of BC particles favors mathematically treating nm-scale BC homogeneously within the aggregate. The nm-scale BC particles/clusters are generally smaller than the primary aggregate grains while the μm-scale BC particles are often larger than the constituent grains. If one takes the primary grain size (~1μm) as the dimension of an intra-aggregate elementary volume, then the nm-scale BC particles/clusters are certainly within the elementary dimension. The μm-scale BC particles, on the other hand, form a distinct phase within typical natural aggregates as their size often exceeds those of the primary grains. Thus we have to use a larger elementary dimension to ensure compositional homogeneity throughout the aggregate. If the μm-scale BC is the dominant form in soil/sediment, a two-comparment model (i.e. char/charcoal and sooty-silt) would be more appropriate

The relative abundance of BC particles/clusters to the primary grains also justifies spatial homogeneity for the nm-scale BC and spatial heterogeneity for the μm-scale BC. For a 200-μm soil/sediment aggregate with typical BC content, there would be about 10^7–10^9 diesel soot particles (or about 10^5–10^7 soot clusters) within the aggregate, which approximately consists of 10^3–10^6 primary grains (Figure 7-2; see also Appendix 7-10). If all BC present is in the form of μm-scale particles, the same BC content would give only about <1–7 particles per aggregate (Appendix 7-10(iii), radius = 100 μm; also Figure 7-2). These estimates, together with the analysis on relative particle size, clearly demonstrated that the need for different intra-aggregate pictures for nm-scale and μm-scale BC.

3.1.2.2. Limitations of the Idealized Distribution Pictures

It should be noted that spatial homogeneity does not always associate with nm-BC (e.g. soot) and heterogeneity with μm-BC (e.g. char). For instance, char-BC may be assumed to be homogeneously distributed within mm-scale natural aggregates (Figure 7-2) or when the soil/sediment contains a very high BC content.

The homogeneous distribution case also implicitly assumes that all the constituent grains within an aggregate are potentially subjected to disaggregation. This is generally valid for freshly formed natural aggregates which undergo dynamic break-up and agglomeration (Eisma 1986; van Leussen 1993; McAnally et al. 2001). Such assumption, however, may be less appropriate for aged or buried aggregates where some of the intra-aggregate components are physically occluded (see Chapter 5).

3.2. Intra-Sorbent Diffusion: a Brief Survey of Transport Models

It is generally accepted that the release or uptake rate of organic sorbate in natural soils or sediments is controlled by the partitioning affinity of the sorbate in the solid-phase. The diffusion rate of a sorbate within the solid-phase is slowed down (or *retarded*) in proportion to its partitioning affinity toward the solid-phase. It is also affected by the internal physical structure of the solid (i.e. pore structure, open/closed pore volume, flow path and width, etc.). For hydrophobic organic compounds (HOCs), the retardation of transport within the aggregate is mainly partition-limited, as HOCs generally exhibit high solid-to-water distribution coefficients (K_d's).

Although researchers have long recognized the important role of phase partitioning on determining the release (or uptake) of HOCs from (or into) soils or sediments, there is no mechanistic agreement on how HOCs diffuse within natural geosorbents. Several mechanistic models have been proposed, but *how* and *where within geosorbent* is diffusion limited remains the focus of contention between different models. The *Intra-Organic Matter Diffusion Model* conceptualizes HOCs diffusing through the organic matrix within the aggregate as the rate determining step and is retarded (as compared with that in free aqueous phase) by the partitioning affinity of the organic matrix for HOCs (Brusseau et al. 1989, 1991). The *Intra-Particle Pore Diffusion Model* envisions the diffusion of HOCs through the intra-particle (intra-aggregate) pore water as the transport-rate limiting step, with the retardation controlled by the partition of HOC between the pore water and the hydrophobic coating along the pore walls (Wu et al. 1986, 1988; Ball et al. 1991). In the *Dual-Mode Sorption Model*, HOCs diffuse through the solid matrix with partitioning into soil organic matter (SOM) ("soft" or "rubbery") and irreversible entrapment in 'holes' ("hard" or "glassy") analogous to those in glassy polymers (Xing et al. 1997; Zhao et al., 2001). This model leads to a two-compartment ("rapid" and "slow" fractions) treatment of kinetic data (Cornelissen et al., 1997a,b; Ghosh et al., 2001). Other studies have also tried to reconcile experimental data with mechanistic picture (Gong et al. 1998a, b; Young and Ball, 1999). Although only the *intra-particle pore diffusion* model will be applied in this study, it is important to note that other kinetic models have also been applied with some success.

3.3. Intra-particle Pore Diffusion Model

The Intra-Particle Pore Diffusion Model can be conceptually divided into a number of components or assumptions (Figure 7-3):

3.3.1. Local Sorbate Partitioning Equilibrium

In this model, it is assumed that solid-water partitioning equilibrium of the sorbate exists at the local scale within natural aggregates. This assumption is a core concept for the intra-particle model. Although the intra-particle kinetic model has been successfully applied in the past (e.g. Wu et al. 1986; Ball et al. 1991), the studied chemicals did not exhibit partitioning affinity to OC/BC as strong as those of PAHs or PCBs. Hence, it is necessary to re-examine the validity of the local partitioning equilibrium assumption

before proceeding any further. The author will attempt to provide a justification for the assumption using timescale analysis on the relevant transfer processes (Figure 7-4).

The *local partitioning equilibrium* assumption can be justified if the timescale of the organic sorbate *desorbing from* the solid-bound BC/OC (i.e. "1" in Figure 7-4) is significantly shorter than the timescale of the pore (retarded) diffusion process ("2"+"3" in Figure 7-4). The timescale of pore diffusion (with or without retardation) can be easily determined if the diffusion length scale is known. Measuring the surface desorption rate, however, can be experimentally challenging, and the author has not found any relevant literature. Instead of conducting an elaborate experiment, one may assess if the local equilibrium assumption is consistent with the actual observed desorption rate. This is the approach that the author will take.

Let us consider the timescale of intra-pore diffusion at the local scale. Local scale is here taken to be roughly as one or more of the following length scales: (i) discretization scale (grid size) of the numerical model (~≥0.5 μm; Table 7-3), (ii) primary/constituent grain size (~≥1 μm; section 3.1.1.1), or (iii) elementary, intra-aggregate volume that satisfies the homogeneous picture of nm-scale BC (≤0.5 μm; section 3.1.1.3). Suppose that the local cell[1] has a length scale of about 1 μm, the characteristic time for local pore-diffusion, $t_{\text{local pore-diffusion}}$, will be:

$$t_{\text{local pore-diffusion}} = \frac{(x_{\text{local}})^2}{D_i}$$

Eqn. 7 - 1

where D_i is the local diffusion coefficient of organic sorbate *i* in aqueous phase (with or without retardation) (m^2/s),

x_{local} is the characteristic length scale of the local intra-aggregate cell (m),

For D_i, one may use the free-water diffusion coefficient (D_{iw}) or the effective diffusivity (D_{eff}) which takes into account retardation arisen from sorption to BC/OC adjacent to the pore flow-path ("3" in Figure 7-4). For pyrene, D_{iw} at 25°C is about 7.6×10^{-10} m^2/s (by the correlation in Hayduk et al. 1974; also in Schwarzenbach et al. 2003). Since D_{eff}, varies roughly inversely with $K_{d,pyr}(t)$, it was evaluated at the initial and the end of the desorption experiment. The initial and the end K_d were about 20000–80000 L_w/kg_{solids} and 100000–720000 L_w/kg_{solids}, respectively (Appendix 7-11). The t_{local} pore-diffusion was estimated to be about 0.03–0.14 hr and 0.2–1.4 hr at the beginning and end of the desorption kinetic experiment (Appendix 7-11).

The observed characteristic desorption timescale, $t_{des,obs}$, can be estimated as the inverse of the desorption rate constant, k_{des}, as derived from the kinetic data The $t_{des,obs}$ at the beginning of the experiment was estimated to be about 0.2–80 hr, while that at the end was around 1200+ hr (Appendix 7-11). Using rate constants reported from two

[1] An imaginary "cell" or volume within which partitioning equilibrium of HOCs can be claimed.

independent kinetic studies also yielded $t_{des,obs}$ in the same order (initial $t_{des,obs}$ = 0.5 hr (Enell et al. 2005); end $t_{des,obs}$ = 300 – 400 hr (Cornelissen et al. 1997b)).

The above timescale analysis showed that the local equilibrium assumption (i.e. hourly timescale) was consistent with the timescale of the desorption experiment (i.e. monthly timescale). Since $t_{des,obs} > t_{local\ pore\text{-}diffusion}$ at both the early and the end times, one may conclude that the pore-diffusion at the local scale (i.e. ~1 μm) is not the rate limiting. However, this would not be true if a longer x_{local} is used (e.g. 10 or 100 μm Appendix 7-11). It should be noted that the timescale analysis has not ruled out the possibility of surface diffusion (i.e. "1" in Figure 7-4) as the rate determining step, that is, $t_{local\ pore\text{-}diffusion} < t_{surface\ diffusion} < t_{des,obs}$. If this was the case, the timescale of surface diffusion may exceed $t_{local\ pore\ diffusion}$ (with retardation) by no more than a factor of 10 (i.e. ratio of initial $t_{des,obs}$ to $t_{local\ pore\ diffusion}$).

3.3.2. Diffusion through Intra-aggregate Pore-Fluid Phase

The second major assumption is that sorbate transport within aggregates is primarily dominated by diffusion via intra-aggregate pore structure. This is to claim that both 3-D diffusion through intra-aggregate organic matter (OM) and 2-D diffusion on the sorbent surface (2-D) are minor diffusion pathways at the local scale (Figure 7-5). The total apparent diffusion coefficient, $D_{tot,app}$, within the aggregate is the sum of (i) the effective diffusivity through intra-aggregate pore-water, $D_{eff,pw}$, (ii) the effective diffusivity through the intra-aggregate organic matter, $D_{eff,OM}$, and (iii) the effective diffusivity through the intra-aggregate surface, $D_{eff,surf}$:

$$D_{tot,app} = D_{eff,pw} + D_{eff,OM} + D_{eff,surf}$$

Eqn. 7 - 2

where $D_{tot,app}$, $D_{eff,pw}$, $D_{eff,OM}$, $D_{eff,surf}$ are the diffusion coefficients in the dimension of aggregate length (irrespective of porewater, OM/OC, BC, or mineral phase) (m^2_{agg}/s).

The intra-particle porewater diffusion model, therefore, assumed that $D_{eff,pw} >> D_{eff,OM}$ and $D_{eff,surf}$; this assumption, however, is not always valid (see section 3.4).

3.3.3. Radial Diffusion, Initial Sorbate Distribution, Aggregation Dynamics

3.3.3.1. Radial Diffusion (1-D Diffusion)

The third assumption is that most of the intra-sorbent diffusion proceeds in one axial/spatial direction (for idealized spherical aggregate, the radial direction). This assumption is not fundamental to the Intra-particle Pore-Diffusion Model; however, it would simplify the governing equation and reduce the computational demand substantially. This simplification is valid for negligible concentration gradient in other directions (e.g. angular or rotational axes in spherical coordinates.). Thus the radial diffusion also implies that (i) large μm-scale BC has to be located at the center of the aggregate, and (ii) the initial intra-sorbent HOC distribution does not lead to angular/rotational flux.

3.3.3.2. Radially Distributed (Uniform-Shell) Sorbate Concentration

The second case leads to the assumption that the initial sorbate concentration must be consistent within each intra-aggregate shell, or that sorbate concentration only vary in one dimension. The kinetic simulations in this study will assume uniform distribution of initial sorbent-pyrene concentration along the radial axis.

3.3.3.3. Neglect Aggregation Dynamics

The Intra-aggregate Pore-Diffusion Model also neglects aggregation dynamics of particles. Aggregates are not stable entities and they undergo disaggregation and conglomeration in natural waters (Eisma 1986; van Leussen 1993; McAnally et al. 2001) as well as in synthetic environment (Farley et al. 1986; Gregory 1989). Aggregation dynamics certainly affects the uptake/release kinetics of HOCs by changing their intra-aggregate distribution. Although aggregation dynamics can be combined with the physics of intra-aggregate diffusion (e.g. adding a statistical component describing change in HOC distribution due to grain-reorganization at different time), re-organizing of primary grains will introduce angular or rotational concentration gradient within aggregates. Therefore, aggregation dynamics is neglected for consistency with the radial (or uni-axial) diffusion and the radial sorbate concentration assumptions.

3.3.4. Retardation by Phase-Distribution/Partitioning

A fundamental assumption in the Intra-aggregate Pore-Diffusion Model is that pore-water diffusion rate is reduced according to the sorption potential of the sorbate into/onto the sorbent (e.g. Eqn. 7 - 3, Eqn. 7 - 4). It is important to note that diffusion is partitioning-controlled only when equilibrium is established at the solid-porewater interface. This has been discussed in details earlier (section 3.3.1).

3.4. Dominance of Transport Pathways

Porewater diffusion does not always dominate over surface diffusion or intra-OM diffusion. This section aims to discuss when and where intra-sorbent transport of organic sorbates may be controlled by pathways rather than retarded pore-water diffusion (Figure 7-7).

3.4.1. $D_{eff,pw}$, $D_{eff,OM}$, & $D_{eff,surf}$

The three effective diffusion coefficients (derivations shown in Appendix 7-12) are related to the physicochemical properties of the sorbate (diffusant) and the aggregate in the following manner:

Diffusion via Porewater:
$$D_{eff,pw} = \frac{\emptyset_{pw} F_{pw} D_{iw}}{K'_d \rho_s \emptyset_s + \emptyset_{pw} + K'_{OM} \emptyset_{OM}}$$

Diffusion through OM:
$$D_{eff,OM} = \frac{\emptyset_{OM} F_{OM} D_{iOM}}{K'_{d-OM} \rho_s \emptyset_s + \frac{1}{K'_{OM}} \emptyset_{pw} + \emptyset_{OM}}$$

Diffusion on Surface:

$$D_{eff,surf} = \frac{\rho_s \emptyset_s F_s D_{is}}{\rho_s \emptyset_s + \frac{1}{K'_d}\emptyset_{pw} + \frac{1}{K'_{d-OM}}\emptyset_{OM}}$$

Eqn. 7 - 3

where $D_{tot,app}$, $D_{eff,pw}$, $D_{eff,OM}$, $D_{eff,surf}$ are the diffusion coefficients in the dimension of aggregate length (irrespective of porewater, OM/OC, BC, or mineral phase) (m^2_{agg}/s).

D_{iw}, D_{iOM}, D_{is} are the diffusivities of the sorbate in free water, OM, and on the sorbent (mineral+BC) surface, respectively (m^2/s),

F_{pw}, F_{OM}, F_s are the tortuosity function for pore-water diffusion, OM-diffusion, and surface diffusion, respectively,

K'_d is the solid (mineral+BC) to water partitioning coefficient of the sorbate (L_{pw}/kg_{solids}),

$K'_{d\text{-}OM}$ is the solid (mineral+BC) to OM partitioning coefficient of the sorbate (L_{OM}/kg_{solids}),

K'_{OM} is the OM to water partitioning coefficient of the sorbate (L_{pw}/L_{OM}),

ϕ_{pw}, ϕ_{OM}, ϕ_s are the volume fractions of pore-water, OM, and solid (mineral+BC) phase, respectively (L_{pw}/L_{agg}, L_{OM}/L_{agg}, L_{solids}/L_{agg}),

ρ_s is the solid phase density (kg_{solids}/L_{solids}).

Pore-water diffusion should be the dominant/principal intra-aggregate diffusion pathway for organic sorbates in surficial or unconsolidated sediments. The first reason is that the poor connectivity of the intra-aggregate OM phase and solid phase would favor diffusion through pore-water. Surficial sedimentary aggregates are typically highly porous (i.e. $\phi_{pw} >> \phi_{OM}$ or ϕ_s). According to the study by Migniot (1968; as referred in Nichols et al. 1985) freshly deposited sedimentary aggregates form highly porous fluid-mud or surficial bed ($\phi_{pw} \sim \geq 0.88$). The surficial bed (top 10 cm) porosity is typically around 0.75–0.85 (McGroddy 1993; Lavoie et al. 1996; Ravens et al. 1997). The porosity of marine aggregates/particles is typically around 0.5–0.75 (Bennett et al. 1989; Chiou et al. 1991; Lavoie et al. 1996; Curry et al. 2007). If the aggregate volume is dominated by water, the OM or solid-phase may not be well-connected – micrographs of marine particles fabric showed that the mineral grains are often relatively 'isolated' and surrounded by void (Bennett et al. 1989; Chiou et al. 1991). This means that OM/surface-diffusion would take a very tortuous path (F_{OM} or $F_s << F_{pw}$) or may have to diffuse through porewater at some points along its pathway (Figure 7-6 (i) & (iii)). Hence the sorbate can diffuse fastest through porewater.

3.4.2. Diffusion through OM vs Diffusion through pore-water.

In order to evaluate whether OM-diffusion or pore-water diffusion dominates in natural aggregates, one has to consider $D_{eff,pw}$ and $D_{eff,OM}$. The two diffusivity expression can be further simplified if we disregard the porosity terms in the denominator:

$$D_{eff,pw} \approx \frac{\emptyset_{pw} F_{pw} D_{iw}}{K'_d \rho_s \emptyset_s + K'_{OM} \emptyset_{OM}} \approx \frac{\emptyset_{pw} F_{pw} D_{iw}}{K'_d \rho_s \emptyset_s}$$

$$D_{eff,OM} \approx \frac{\emptyset_{OM} F_{OM} D_{iOM}}{K'_{d-OM} \rho_s \emptyset_s}$$

Eqn. 7 - 4

Consider a 'neutral' case where porosity (ϕ) and tortuosity/constrictivity factor (F) for pore-water and OM are comparable, $D_{eff,OM}/D_{eff,pw}$ is approximately:

$$\frac{D_{eff,OM}}{D_{eff,pw}} \approx \frac{\emptyset_{OM} F_{OM} D_{iOM} K'_d}{\emptyset_{pw} F_{pw} D_{iw} K'_{d-OM}}$$

$$\left(\frac{D_{eff,OM}}{D_{eff,pw}}\right)_{\emptyset,F-neutral} = \frac{D_{iOM} K'_d}{D_{iw} K'_{d-OM}} = \frac{D_{iOM} S'/C'}{D_{iw} S'/\omega'} = \frac{D_{iOM} K'_{OM}}{D_{iw}}$$

Eqn. 7 - 5

where C' is the local pore-water sorbate *i* concentration ($\mu g_i/L_{pw}$),

S' is the local solid-phase sorbate *i* concentration ($\mu g_i/kg_{solids}$),

ω' is the local OM-phase (non-BC) sorbate *i* concentration ($\mu g_i/L_{OM}$).

HOCs generally diffuse faster through porewater phase than through OM. A brief survey on diffusion coefficients (Table 7-7) demonstrates that the diffusivities of PAHs in organic phase are at least 3–4 orders of magnitude lower than the D_{iw}'s. The diffusivities in three particular organic phases are particularly noteworthy: biofilm, biofilm+HA, and creosote NAPL (Table 7-7). In the absence of diffusion observation in soil/sediment OM, biofilm may be regarded as a type of 'natural' OM. $D_{ibiofilm}$ ($2–3\times10^{-14}$ m^2/s; Wicke et al. 2008) is about 4 orders lower than the respective D_{iw}'s (Table 7-7b). Wicke et al. showed that the diffusivity through a biofilm-soil humic acid composite phase decreased in roughly the same proportion as the fraction of soil HA added. This suggested that real soil (and perhaps sedimentary as well) OM may be even more resistant to HOCs diffusion. The creosote NAPL case may ($D_{icreosote-NAPL}$ ~8 orders of magnitude smaller than D_{iw}), on the other hand, represent an 'anthropogenic' scenario where man-made organic substances dominate the total soil/sediment OM. From the biofilm and the NAPL observations, we may therefore expect D_{iw} to exceed D_{iOM} by 4–8 orders of magnitude.

We may also assume that the OM-water partitioning coefficient, K'_{OM} (L_{OM}/L_{pw}), is simply K_{OC}. For pyrene ($K_{OC} \approx 10^5$ L_{OC}/L_w) $D_{eff,OM}/D_{eff,pw}$ ranges approximately from 10^{-3} to 10

(assuming neutral ϕ's and F's). However, typical surficial soil/sediment OM is generally small ($f_{OM} \approx 2f_{OC}$ ~<0.05–0.10; Appendix 7-22). Supposing that the density of natural OM ranges between 0.9–1.3 kg_{OM}/L_{OM} (i.e. ~ρ_{lipid} to $\rho_{polymer}$), for a typical soil (bulk density ρ_b ~1.2–1.4 kg_{mass}/L_{bulk}; e.g. Saini 1966) or sediment (estuaries & harbor: ρ_b ~1.05–1.25 kg_{mass}/L_{bulk}; Migniot 1968; Nichols et al. 1985; Li et al. 1991; riverine: ρ_b ~1.2–1.4 kg_{mass}/L_{bulk}; Li et al. 1991). The void fractions (L_{void}/L_{bulk}) in typical soil and sediment aggregates/particles are about 0.4–0.55 and 0.74–0.9, respectively (Appendix 7-13). And this translates into a volume fraction of OM of ≤25% of the total void+OM volume (Appendix 7-13). It is important to note that at low volume fraction, OM may not exist as a continuous phase – there may be 'islands' and 'pockets' of OM amidst continuous porewater phase and large mineral grains (Figure 7-6, case (iii)). Thus the intra-aggregate connectivity of the OM-phase in typical sediment is generally poorer than that of the intra-aggregate pore-water[2]. Thus for typical soil/sediment, $D_{eff,pw} > D_{eff,OM}$.

3.4.3. Surface Diffusion vs Diffusion through pore-water.

This section would evaluate the relative significance of surface diffusion for sorbate transport in typical natural aggregates (unconsolidated soil, sediment). We, likewise, simplify the effective surface diffusivity expression further:

$$D_{eff,surf} \approx \frac{\rho_s \emptyset_s F_s D_{is}}{\rho_s \emptyset_s} = F_s D_{is}$$

$$D_{eff,pw} \approx \frac{\emptyset_{pw} F_{pw} D_{iw}}{K'_d \rho_s \emptyset_s}$$

Eqn. 7 - 6

Unlike D_{iOM} and D_{iw}, it is more difficult to measure D_{is} of natural geosorbents directly. In reality, $D_{eff,surf}$ is often reported as a fitted parameter in a intra-sorbent transport kinetic model which contains a surface diffusion term (e.g. Weber et al. 1988; Stapleton et al. 1994; Ahn et al. 2005; Valderrama et al. 2008). The *a priori* pyrene $D_{eff,pw}$'s as derived from the K_d's (OC+BC) found in this study was about 10^{-16}–10^{-14} m^2/s (for K_d corresponding from 10^6 down to 10^4 L_w/kg_{solids}). A quick comparison of $D_{eff,pw}$ with the literature pyrene $D_{eff,surf}$ (10^{-17}–10^{-13} m^2/s; Table 7-8) may suggest that surface diffusion is at least comparable with pore-water diffusion.

However, the author would argue that for HOCs uptake or release in typical soil/sediment, surface diffusion may be operationally neglected. This is based on the following reasoning: (i) inherited ambiguity in $D_{eff,surf}$, (ii) likely poor connectivity of surface, (iii) $D_{eff,surf}$ (or D_{is}) is not yet predictable like D_{iOM} or D_{iw}.

In HOCs literature, $D_{eff,surf}$ is often derived from fitting uptake/release observations to kinetic model, its magnitude is, therefore, somewhat ambiguous and uncertain. Re-examining Table 7-8, one can see that the reported $D_{eff,surf}$ for pyrene on activated carbon differed by a factor of 100 between the value reported by Valderrama et al.

[2] For unsaturated soil, gaseous diffusion via void (analogous to pore-water) should be the dominant intra-sorbent transport mechanism. For water-saturated soil, pore-water diffusion should dominate.

(2008) and that by Ahn et al. (2005). The disparity might be partly due to the use of different activated carbon samples; however, it seems more likely that the discrepancy was in fact an artifact of model fitting, as different kinetic models have been used[3]. Furthermore, it is also surprising that pyrene $D_{eff,surf}$ on activated carbon (highly carbonaceous and condensed) and that on a Great Lake offshore sediment (very low BC) should be within the same order of magnitude (Table 7-8). Both problems suggested that the reported $D_{eff,surf}$'s are somewhat operational and lack of overall consistency.

Second, non-OM surface (i.e. BC) where surface diffusion of PAHs would proceed is likely to be poorly connected. Let us suppose that, for pyrene, $D_{eff,surf}$ on activated carbon and $D_{eff,pw}$ on soil/sediment are both comparable (see before). The diffusive surface (i.e. BC-like surface) on activated carbon is extensive and well-connected; this is not the case, however, in typical soil or sediment, for f_{BC} is no more than 10% of f_{OC} (Cornelissen et al. 2005b), and f_{OC} ~≤ 10% of total mass (Appendix 7-22). The much poorer connectivity of diffusive-active surface implies that purely surface diffusion should play a rather diminished in compared to pore-water diffusion.

Third, given that $D_{eff,surf}$ is typically derived from model fitting and not yet predictable, in case where $D_{eff,surf}$ and $D_{eff,pw}$ are of comparable magnitude, the former simply serves as another 'adjustment factor' in the kinetic model. Although surface diffusion as a phenomenon has been carefully delineated from pore-diffusion many decades ago (Komiyama et al. 1974a, b; Suzuki et al. 1982; Itaya et al. 1987), the effort on simple sorbate-sorbent systems is still on-going (e.g. Miyabe et al. 1997, 2001). Consider the structural complexity and the OC/BC compositional variety in natural aggregates, *a priori* estimation of $D_{eff,surf}$ still appears distant from the current state of knowledge.

3.4.4. Summary on Intra-Sorbent Transport Pathways

Scenarios of HOCs transport in porous media may be classified into two categories: (i) *Dynamic Sorbent* – where sorbent particles undergo physical displacement/transport in the presence of hydrodynamic (or aerodynamic) force field, and (ii) *Static Sorbent* – where sorbent is physical stable. The former transport problems include HOCs uptake/release by aerosols, resuspended sediment, or runoff/eroded soil. The surrounding turbulence ensures a thin diffusive-film around the particles/aggregates, and hence the overall rate is dominated by intra-sorbent transport. The Static Sorbent category includes uptake/release of HOCs in aquifer or non-surficial soil/sediment bed. Here, intra-aggregate and inter-aggregate transports may be important, depending on the porous structure within the aggregates and that of the bed, and whether the bed is exposed to a percolating flow field (i.e. advective transport).

For Dynamic Sorbent, pore-water (or pore-air) diffusion should dominate in sorbent with low organic matter (OM) content (Figure 7-7 (iv)). This would be true for the typical porous or unconsolidated soil or sediment. Diffusion through intra-aggregate OM

[3] Valderrama et al. used an intraparticle model with pore-water diffusion and surface diffusion terms; Ahn et al. used a branched pore-diffusion model, which consists of a linear-driving force formulation (empirical) for microporous diffusion, and a surface diffusion for macroporous diffusion (see Peel et al. 1981).

becomes increasingly important for sorbent with high f_{OC} (section 3.4.2). For geosorbents such as peat or muck (f_{OC} ~ 50%; Chiou et al. 1990; Huang et al. 1997b), OM-diffusion should be the principal intra-sorbent pathway for sorbate transport (Figure 7-7 (ii)). Surface diffusion becomes important when the sorbent surface exerts a very strong affinity for the sorbate (i.e. very high K_d) such that the adsorbed state is energetically much preferred, and when such surface are well connected within the aggregate (Figure 7-7 (i) & (iii)). Hence surface diffusion should be the dominant intra-sorbent pathway for HOCs on sorbents with very high BC content (e.g. activated carbon) and/or high pore-surface to pore-void ratio (e.g. highly compressed carbonaceous matter).

The same diffusion analysis applies at the intra-aggregate level for Static Sorbent cases. However, it may be necessary to integrate the aggregate-scale uptake/release rate with the transport processes occurring at larger spatial scale (e.g. dispersion, advection, bioturbation, etc) (for sediment system, see Berner 1980, Boudreau 1997; for aquifer system, see Hundsdorfer et al. 2003; also the review by Haggerty et al. 1995).

3.5. Mathematics of Intra-Particle Porewater Diffusion Model

In this section, the governing equations for nonlinear porewater diffusion will be briefly described. The governing equations for an idealized spherical aggregate will be presented according to the location in the aggregate (intermediate shell, core, and edge of aggregate; section 3.5.1.1 to 3.5.1.4) (Figure 7-8). The dimensionless forms of the equations will be presented in section 3.5.1.5.

3.5.1. Diffusion with Non-linear Partitioning Function ($K_d(C_{iw})$)

3.5.1.1. Intermediate-shells (Spherical)

Considering the case where intra-sorbent transport of HOC is dominated by pore-water diffusion, the generic radial diffusion equation for intra-aggregate pore-water dissolved concentration of sorbate in the intermediate shells (Figure 7-8) is:

$$\frac{\partial C'}{\partial t} = F_{Tor}\frac{1}{r^2}\left[\frac{\partial}{\partial r}\left(r^2 D_{iw}\frac{\partial C'}{\partial r}\right)\right]$$

Eqn. 7 - 7

where C' is the local pore-water sorbate i concentration ($\mu g_i/L_{pw}$),

D_{iw} is the free aqueous diffusivity of i (m^2/s),

F_{Tor} is the tortuosity factor accounting for longer diffusive path ($F_{Tor} \leq 1$; dimensionless),

r is the radial dimension (i.e. with respect to the aggregate) (m),

t is time (s).

The above expression is based on the assumptions that: (i) intra-aggregate diffusion is the system rate limiting step for sorbate uptake or release, (ii) the absence of intra-aggregate advective or dispersive transport, (iii) the absence of angular and rotational diffusion, and (iv) negligible diffusive contribution from OM and surface diffusion (Appendix 7-12). With assumption (iv), a local, aggregate-volume based concentration, q', can be formulated:

$$q' \equiv \frac{\text{mass or mol } i}{\text{volume of aggregate}} = S'\rho_s(1-\emptyset) + C'\emptyset = [K_d\rho_s(1-\emptyset)+\emptyset]C'$$

Eqn. 7 - 8

where ϕ is the intra-aggregate porosity (or volume fraction of porewater phase) (L_{pw}/L_{agg}),

K_d = S'/C' = solid-water partition coefficient of the sorbate (L_w/kg_{solids}),

ρ_s is the average or effective solid-phase density for all solids (mineral, BC, OC) (kg_{solids}/L_s),

q' is the aggregate-volume based concentration of i ($\mu g_i/L_{agg}$).

Without surface diffusion or OM-diffusion, the rate of change in q' is related to the rate of change of C' by the porosity:

$$\frac{\partial q'}{\partial t} = \emptyset\frac{\partial C'}{\partial t} = \emptyset F_{Tor}\frac{1}{r^2}\left[\frac{\partial}{\partial r}\left(r^2 D_{iw}\frac{\partial C'}{\partial r}\right)\right]$$

Eqn. 7 - 9

Upon substitution of C' according to Eqn. 7 - 8, we get:

$$\frac{\partial q'}{\partial t} = \emptyset F_{Tor}\frac{1}{r^2}\left[\frac{\partial}{\partial r}\left(r^2 D_{iw}\frac{\partial[\frac{q'}{K_d\rho_s(1-\emptyset)+\emptyset}]}{\partial r}\right)\right]$$

Eqn. 7 - 10

However, since K_d is a function of C', and C' a function of radius, the factor $[K_d\rho_s(1-\phi)+\phi]$ cannot be taken out of the inner derivative.

3.5.1.2. Core-Shell (Spherical)

In order to implement finite difference scheme, the governing equation of the innermost core-shell (Figure 7-8) of the aggregate needs to be reformulated. It can be shown (see Appendix 7-14) that the rate of change in the core-shell C' is:

$$\left(\frac{\partial C'}{\partial t}\right)_{core} = F_{Tor}\frac{3D_{iw}}{r}\frac{\partial C'}{\partial r}$$

Eqn. 7 - 11

Hence the rate of change in q' of the innermost core is:

$$\left(\frac{\partial q'}{\partial t}\right)_{core} = \emptyset\left(\frac{\partial C'}{\partial t}\right)_{core} = \emptyset F_{Tor}\frac{3D_{iw}}{r}\frac{\partial C'}{\partial r}$$

Eqn. 7 - 12

3.5.1.3. Aggregate-Volume Averaged Quantity (Spherical)

It will be useful to calculate an overall aggregate quantity for various properties (e.g. overall sorbate concentration, Q). For some general aggregate property, j, which is a function of the intra-aggregate radial position, r, the overall or aggregate-volume averaged quantity, J, is simply:

$$J = \frac{\int_{\forall} j d\forall}{\forall_{agg}} = \frac{\int_0^{R_{agg}} j 4\pi r^2 dr}{4\pi {R_{agg}}^3/3} = \frac{3\int_0^{R_{agg}} j r^2 dr}{{R_{agg}}^3}$$

Eqn. 7 - 13

where R_{agg} is the aggregate radius (m),

$\forall_{agg}$ is the aggregate volume (m^3).

3.5.1.4. Outermost/Edge-Shell (Spherical)

There are two ways to determine C' at the outermost region of an aggregate: (i) by boundary film diffusion or (ii) by equating the edge-shell C' with the bulk phase dissolved concentration (C_{bulk}). In the boundary film method, the change in the edge-shell C' is controlled by the incoming flux of sorbate from the inner-shells and the outgoing flux through an aggregate boundary film/layer, δ (m). Mathematically, we have (Appendix 7-14):

$$\left(\frac{\partial C'}{\partial t}\right)_{edge} = -\frac{3D_{iw}}{R}\left[F_{Tor}\left.\frac{\partial C'}{\partial r}\right|_{R-} + \left(\frac{C_{bulk} - C'}{\delta}\right)\right]$$

Eqn. 7 - 14

where C_{bulk} is the bulk aqueous concentration of sorbate ($\mu g_i/L_w$).

Note that (a) the tortuosity factor does not apply to the boundary film diffusion, and (b) the porewater concentration gradient is discontinuous at the edge-shell[4], and $(\partial C'/\partial r)|_{R-}$ refers to the differential slope from within the aggregate.

In the second approach, C' at the edge is assumed to be in equilibrium with C_{bulk} (i.e. $C'_{edge} = C_{bulk}$), and C'_{edge} is determined from mass balance. This method is, therefore,

[4] The concentration gradient is discontinuous because of the presence of retardation within the aggregate but the absence of it in the ambient phase. The dissolved phase concentration is, of course, continuous.

only applicable to a closed system. An implicit assumption is that the boundary film δ is very thin such that $C'_{edge} \rightarrow C_{bulk}$. It is as if the native sorbate is desorbing into the combined pool of the bulk phase + the edge shell (Appendix 7-14):

$$\frac{d}{dt}\left(\frac{\int_{\forall_{core}+\forall_{intrm.}} q' d\forall}{\forall_{core}+\forall_{intrm.}}\right) = -R_{bulk\ aq./agg}\frac{dC_{bulk}}{dt} - \frac{d}{dt}\left(\frac{\int_{\forall_{edge}} q'_{edge}\, d\forall}{\forall_{edge}}\right)$$

$$q'_{edge} = S'_{edge}\,\rho_s(1-\emptyset) + C'_{edge}\,\emptyset = [K_d\rho_s(1-\emptyset)+\emptyset]C_{bulk}$$

Eqn. 7 - 15

where $\forall_{one\ agg.}$ is the volume for one aggregate (m^3),

$\forall_{bulk\ aq.\ one\ agg.}$ is the volume of bulk aqueous phase for one aggregate (m^3),

$\forall_{core}$, $\forall_{intrm.}$, and $\forall_{edge}$ are the aggregate volumes of core, intermediate, and the edge shells, respectively (m^3),

$R_{bulk\ aq./agg}$ is the ratio of bulk aqueous phase volume to aggregate volume.

The boundary film method is applied when analyzing kinetics in an open system. For closed systems such as the desorption experiments in this study, one may choose either method. The author has adopted the mass-balance approach. The mass balance approach does not require any estimation of δ. Furthermore, the error from assuming $C'_{edge}=C_{bulk}$ can be reduced by increasing radial discretization of the aggregate.

3.5.1.5. Dimensionless Form (Generic Aggregate Geometry)

In order to simulate release kinetics in other aggregate geometries (spherical, cylindrical, planar, and any shapes intermediate), we need to re-formulate the governing equations in dimensionless form. The diffusion equations for the intermediate shells and the core shell in dimensionless spatial-temporal form are (see Appendix 7-14):

$$\textbf{Intermediate Shells:}\quad \frac{\partial q'}{\partial \tau} = \emptyset F_{Tor}\frac{1}{x^{\gamma-1}}\left[\frac{\partial}{\partial x}\left(x^{\gamma-1}\frac{\partial C'}{\partial x}\right)\right]$$

$$\textbf{Core Shell:}\quad \left(\frac{\partial q'}{\partial \tau}\right)_{core} = \emptyset F_{Tor}\frac{\gamma}{x}\frac{\partial C'}{\partial x}$$

$$\textbf{Edge Shell:}\quad \frac{d}{dt}\left(\frac{\int_{\forall_{core}+\forall_{intrm.}} q' d\forall}{\forall_{core}+\forall_{intrm.}}\right) = -R_{bulk\ aq./agg}\frac{dC_{bulk}}{dt} - \frac{d}{dt}\left(\frac{\int_{\forall_{edge}} q'_{edge}\, d\forall}{\forall_{edge}}\right)$$

$$\textbf{Aggregate – Volumed Averaged Property:}\quad J = \gamma\int_0^1 j x^{\gamma-1} dx$$

$$\gamma = \textbf{Shape Factor} = \begin{cases} 1\ (\text{planar coordinate}) \\ 2\ (\text{cylindrical coordinate}) \\ 3\ (\text{spherical coordinate}) \end{cases}$$

Eqn. 7 - 16

where the dimensionless time, τ, and the dimensionless length-scale, x, are:

$$x = \frac{r}{R}; \qquad dx = \frac{dr}{R}$$

$$\tau = \frac{tD_{iw}}{R^2}; \qquad d\tau = \frac{D_{iw}\,dt}{R^2}$$

Eqn. 7 - 17

Note that the dimensionless time is defined in terms of D_{iw} rather than D_{eff} as in Wu et al. (1988) due to nonlinear K_d.

3.6. Finite Difference Implementation of Nonlinear Diffusion Model

This section will provide a brief description of implementing an explicit finite difference scheme (Smith 1985; Strikwerda 1989) on the nonlinear version of the Intra-particle Porewater Diffusion Model. We will first consider the case where the intra-aggregate BC and OC can be considered as homogeneously distributed within an aggregate (single-phase) (section 3.6.1). The stability criterion for the model will be considered (section 3.6.2), and the solution of non-linear equation briefly discussed (section 3.6.3). The more complex case of a char embedded within an aggregate (i.e. char-in-aggregate dual phase) will be discussed in Chapter 8. The Matlab modeling scripts can be found in Appendix E (Script E-3 to E-5).

3.6.1. Homogeneous Aggregate (Uniformly Distributed nm-BC)

The aggregate is discretized into m number of grids (Figure 7-9) where the intermediate shells (2^{nd} to m-1^{th} shells) are of thickness Δx and the core and the edge shells $\Delta x/2$[5].

3.6.1.1. Intermediate-shells (2^{nd} to m-1^{th} grids)

Following an explicit scheme, the porewater diffusion in the intermediate shells at the i^{th} intermediate shell (Figure 7-9 (i)) is simply:

$$\textbf{Gov. Eqn:} \quad \frac{\partial C'}{\partial \tau} = F_{Tor}\,\frac{1}{x^{\gamma-1}}\left[\frac{\partial}{\partial x}\left(x^{\gamma-1}\,\frac{\partial C'}{\partial x}\right)\right]$$

[5] The core/edge shell thickness is $\Delta x/2$ because of the discretization scheme. See Figure 7-9.

$$\textbf{Finite Diff.:}\quad \frac{{C'_i}^{n+1} - {C'_i}^{n}}{\Delta\tau} = \frac{F_{Tor}}{{x_i}^{\gamma-1}\Delta x}\left[\left(\frac{{C'_{i+1}}^{n} - {C'_i}^{n}}{\Delta x}\right){x_{i+0.5}}^{\gamma-1} - \left(\frac{{C'_i}^{n} - {C'_{i-1}}^{n}}{\Delta x}\right){x_{i-0.5}}^{\gamma-1}\right]$$

Eqn. 7 - 18

where n denotes the variable at n^{th} dimensionless timestep (i.e. 'current' state),

n+1 denotes the variable at the $n+1^{th}$ timestep (i.e. 'next' state).

Further simplification allows C' at the next timestep to be evaluated by variables of the current state:

$${C'_i}^{n+1} = \varepsilon_i {x_{i+0.5}}^{\gamma-1}{C'_{i+1}}^{n} + \varepsilon_i {x_{i-0.5}}^{\gamma-1}{C'_{i-1}}^{n} + (1 - \varepsilon_i {x_{i+0.5}}^{\gamma-1} - \varepsilon_i {x_{i-0.5}}^{\gamma-1}){C'_i}^{n}$$

$$\text{where:}\quad \boldsymbol{\varepsilon_i} = \frac{\Delta\tau F_{Tor}}{(\Delta x)^2 {x_i}^{\gamma-1}}$$

Eqn. 7 - 19

3.6.1.2. Core-shell (1st grid)

The finite difference (explicit) diffusion equation for the core-shell (i.e., the first grid) (Figure 7-9 (ii)) is:

$$\textbf{Gov. Eqn:}\quad \left(\frac{\partial C'}{\partial\tau}\right)_{core} = F_{Tor}\frac{\gamma}{x}\frac{\partial C'}{\partial x}$$

$$\textbf{Finite Diff.:}\quad \frac{{C'_1}^{n+1} - {C'_1}^{n}}{\Delta\tau} = \frac{F_{Tor}\gamma}{x_{1.5}}\left(\frac{{C'_2}^{n} - {C'_1}^{n}}{\Delta x}\right)$$

Eqn. 7 - 20

Or, more succinctly as:

$${C'_1}^{n+1} = (1-\epsilon){C'_1}^{n} + \epsilon {C'_2}^{n}$$

$$\text{where:}\quad \boldsymbol{\epsilon} = \frac{\Delta\tau F_{Tor}\gamma}{x_{1.5}\Delta x}$$

Eqn. 7 - 21

3.6.1.3. Aggregate-Volume Averaged Quantity (Spherical)

Integration of properties (i.e. f(x)) over aggregate volume is done using Simpson's 1/3 rule. Simpson's 1/3 rule states that:

$$\int_a^b f(x)dx \cong \frac{\Delta x}{3}\left(f(x_1) + 4f(x_2) + 2f(x_3) + 4f(x_4) + \cdots 4f(x_{m-1}) + f(x_m)\right); \qquad x_1 = a, x_m = b$$

Applying the integration scheme to calculate aggregate-volume averaged property J from the local property $j(x_i)=j_i$, we get:

$$J = \gamma \int_0^1 j x^{\gamma-1} dx$$

$$J \cong \frac{\gamma \Delta x}{3} \sum_{i=1}^{m} \mathcal{S}_i j_i {x_i}^{\gamma-1}$$

Eqn. 7 - 22

where $\mathcal{S}_i$ is the i^{th} coefficient (i.e. 1, 4, 2, 4, ..., 4, 1). The property j can be C', S', q' or even sorbent properties such as ϕ, f_{OC} and f_{BC}.

3.6.1.4. Outermost-shell (m^{th} grid)

For the outermost shell (Figure 7-9 (iii)) C'_m is determined following the mass balance approach. The sorbate mass balance in the system at timesteps n and n+1 is simply:

$$\forall_{\text{bulk aq.}} {C^{n+1}}_{\text{bulk}} + \forall_{\text{total agg.}} Q^{n+1} = \forall_{\text{bulk aq.}} {C^n}_{\text{bulk}} + \forall_{\text{total agg.}} Q^n$$

$$Q^n \cong \frac{\gamma \Delta x}{3} \sum_{i=1}^{m} \mathcal{S}_i {q'_i}^n {x_i}^{\gamma-1}$$

$$Q^{n+1} \cong \frac{\gamma \Delta x}{3} \left[\left(\sum_{i=1}^{m-1} \mathcal{S}_i {q'_i}^{n+1} {x_i}^{\gamma-1} \right) + \mathcal{S}_m {q'_m}^{n+1} {x_m}^{\gamma-1} \right]$$

Eqn. 7 - 23

Note that ${C^n}_{bulk}$ and Q^n are known quantities from current timestep; ${q'_i}^{n+1}$ (for i=1 to m-1) can be estimated with the core shell or intermediate shell difference equations. Therefore, the only unknowns are ${q'_m}^{n+1}$ and ${C^{n+1}}_{bulk}$. However, assuming that $C'_m = C_{bulk}$, and knowing that $q'_m = S'_m \rho_s (1-\phi) + C'_m \phi$, ${C'_m}^{n+1}$ (or ${C^{n+1}}_{bulk}$) can be solved. It can be shown (Appendix 7-15) that ${C'_m}^{n+1} = {C^{n+1}}_{bulk}$ is the positive root of the following non-linear equation:

$$\mathcal{A}_{1st} {C'_m}^{n+1} + \mathcal{A}_{nBC} \left({C'_m}^{n+1} \right)^{nBC} = \left({C^n}_{bulk} + \frac{\forall_{\text{total agg.}} Q^n}{\forall_{\text{bulk aq.}}} - \mathcal{B} \right)$$

Eqn. 7 - 24

where the three constants are:

$$\mathcal{A}_{1st} = \left\{ 1 + \frac{\forall_{\text{total agg.}}}{\forall_{\text{bulk aq.}}} \left(\frac{\gamma \Delta x}{3} \mathcal{S}_m {x_m}^{\gamma-1} \right) \left[f_{OC,m} K_{OC} \rho_s (1 - \emptyset_m) + \emptyset_m \right] \right\}$$

$$\mathcal{A}_{nBC} = \left\{ \frac{\forall_{total\ agg.}}{\forall_{bulk\ aq.}} \left(\frac{\gamma \Delta x}{3} \mathcal{S}_m x_m{}^{\gamma-1} \right) \left[f_{BC,m} K_{BC} \rho_s (1 - \emptyset_m) \right] \right\}$$

$$\mathcal{B} = \left\{ \frac{\forall_{total\ agg.}}{\forall_{bulk\ aq.}} \frac{\gamma \Delta x}{3} \left(\sum_{i=1}^{m-1} \mathcal{S}_i q'_i{}^{n+1} x_i{}^{\gamma-1} \right) \right\}$$

Note that for flexibility, the model also allows 'radial' variation of f_{OC}, f_{BC}, and ϕ.

3.6.2. Stability Criterion for the Explicit Scheme

The use of explicit finite difference scheme can lead to unstable modeling results when improper values of the time increment ($\Delta\tau$) or the differential length (Δx) are selected. For purely advective problems, an explicit finite-difference model would yield numerical stable results if it satisfies the Courant number, which is a measure of the ratio of advective displacement ($u\Delta t$) compared to model characteristic length (L), is less than some threshold value $N_{Co,limit}$ (which varies with the nature of the problem):

$$Co = \frac{u\Delta t}{L} = \frac{\text{"advective displacement"}}{\text{characteristic length}} < N_{Co,limit}$$

Eqn. 7 - 25

Similarly, for advective-diffusive problems, there is a 'stability' criterion which prevents numerical oscillations (Mattheij et al. 2005) due to improper choice of differential timestep and spatial resolution. Here, the stability criterion is described by the Peclet number, which is a measure of the ratio of advective 'diffusivity' to molecular diffusivity:

$$Pe = \frac{Lu}{D} = \frac{\text{"advective diffusivity"}}{\text{molecular diffusivty}} < N_{Pe,limit}$$

Eqn. 7 - 26

In general, both $N_{Co,limit}$ and $N_{Pe,limit}$ are roughly around unity (Smith 1985; Strikwerda 1989; Mattheij et al. 2005). Thus, the two stability criteria can be conceptually summarized as that oscillatory concentration-dynamics will appear if the solute is 'over-transported' as a result of a Δt too large. Based on this principle, one may devise a stability criterion for explicit intraparticle porewater diffusion as:

$$\Delta\tau_{eff} \equiv \frac{D_{eff}\Delta t}{R_{agg}{}^2} = \frac{\text{"incremental timescale"}}{\text{"effective diffusive timescale"}} \sim < 1$$

Eqn. 7 - 27

Note that the above stability criterion is also consistent with the Co and the Pe criteria as $\Delta\tau_{eff}$=Co/Pe. Due to the non-linear nature of the isotherm, $\Delta\tau=D_{iw}\Delta t/R_{agg}{}^2$ rather than $\Delta\tau_{eff}$, has to be used as the incremental timestep. This means that:

$$\Delta\tau_{eff} = \frac{D_{eff}\Delta t}{R_{agg}{}^2} = \frac{1}{K_d(C')}\frac{D_{iw}\Delta t}{R_{agg}{}^2} = \frac{\Delta\tau}{K_d(C')} \sim < 1$$

Or, that the stable numerical solution can be obtained when:

$$\Delta\tau \equiv \left(\frac{D_{iw}\Delta t}{R_{agg}{}^2}\right) \sim < K_d(C')$$

Eqn. 7 - 28

With Eqn. 7 - 28, computational time can be greatly reduced.

3.6.3. Solving the Root of Nonlinear Equation

The root, **y**, of non-linear equation in the form $ay + by^n = c$ (where a, b, c are constants; n is real number) is solved by Newton's method – an iterative procedure where the slope of an initial guess is used to produce an improved guess until a convergence criterion is met. The code for the Matlab routine is documented in Appendix E (Script E-2).

3.7. Isotherms for Modeling

The Intra-particle Pore Diffusion model was applied with several pyrene sorption isotherms (Table 7-2). The isotherms used were: (i) the classical OC model (Karickhoff 1981; Schwarzenbach et al. 2003), (ii) an OC-BC isotherm reported previously (the 'Old OC-BC' isotherm; Accardi-Dey and Gschwend 2002), (iii) a new OC-BC isotherm derived in Chapter 5 (the 'New OC-BC' or the 'Lnr-Fr' isotherm as in Table 5-6), and (iv) an OC-BC model that included an occlusion term (the 'Occlusion-OC-BC' or the 'Occlusion-Lnr-Fr' isotherm as in Table 5-6).

In this study, the Occlusion-OC-BC isotherm (which supposed 30±10% occlusion) was chosen for modeling because the fraction occluded was 'optimized' using sorption data from all four different temperatures (6, 15, 22, and 37°C; see Appendix 5-6). The model can be easily updated with different fraction occluded and/or $\log K_{OC}$'s or $\log K_{BC}$'s. The script for desorption modeling with occlusion can be found in Appendix E (Script E-3, E-5).

3.8. Regression of Kinetic Observations by Empirical Models

The pyrene desorption kinetic data were also regressed using various non-linear empirical models (e.g. exponential forms, polynomial forms, statistical distributed models; see Table 7-11 and Appendix 7-21). Regression was performed in Matlab and the associated scripts can be found in Appendix E (Script E-6). The regressed parameters from the Exponential model (Constrained, Two-Compartment model; Table 7-11, Appendix 7-21) will be analyzed and discussed for the question of correlating empirical kinetic parameters to sorbent/sorbate properties (see section 4.4). Regressed

parameters from other models will not be discussed here, but they are available in Appendix 7-21.

4. Results & Discussion

4.1. Analytical Solution of Radial Desorption

The analytical solution for the 1-D radial desorption problem is needed for validating the numerical model. The following scenario was used to validate the numerical mode: radial desorption of a sorbate from aggregates/particles (assumed to be spherical) into a limited volume of water where no dissolved/aqueous sorbate is initially present.

The analytical solution for this closed-system problem according to Crank (1979) is:

$$\frac{M_o - M_t}{M_o - M_\infty} = 1 - \sum_{n=1}^{\infty} \frac{6\lambda(\lambda+1)\exp\{-D_{eff} q_n^2 t/r^2\}}{9 + 9\lambda + q_n^2\lambda^2}$$

$$\tan q_n = \frac{3q_n}{3 + \lambda q_n^2}; \{\text{for } q_n > 0\}$$

$$\lambda = \frac{1}{K_d R_{sw}}$$

Eqn. 7 - 29

where: $(M_o\text{-}M_t)/(M_o\text{-}M_\infty)$ is a ratio that describes the mass of sorbate desorbed at time t $(M_o\text{-}M_t)$, normalized to the total mass of sorbate desorbed at equilibrium $(M_o\text{-}M_\infty)$,

D_{eff} is the effective diffusivity of the sorbate in the aggregate/particle phase,

q_n is the n^{th} positive, non-zero roots to the tangent equation, and

λ is a dimensionless factor which describes the magnitude of partitioning and solid content,

K_d is the solid-to-water partitioning coefficient for the sorbate (L_w/kg_{solids}),

R_{sw} is the solid-to-water ratio (a measure of solids concentration in the system) (kg_{solids}/L_w)

For reference, the parameter, λ, is related to the fraction of sorbed sorbate at equilibrium:

$$f_{is,Eqm} = \frac{M_\infty}{M_o} = \frac{1}{1 + {}^{1}/_{K_d R_{sw}}} = \frac{1}{1+\lambda}$$

Eqn. 7 - 30

where M_0 and M_∞ are the initial and equilibrium sorbate concentrations in the solid phase.

Note that Eqn. 7 - 30 and the definition of λ here are consistent with equation (6.37) in Crank's text (p. 96)[6].

The effective diffusivity, D_{eff}, is defined as such (Wu et al. 1988):

$$D_{eff} = \frac{D_{iw}\theta^2}{(1-\theta)\rho_s K_d + \theta}$$

Eqn. 7 - 31

The analytical solutions at various system K_dR_{sw}'s are plotted in Figure 7-10. The figure shows the fraction desorbed (normalized with fraction desorbed at infinite time) at a given τ. The curves show the correct trend that the rate of desorption increases with higher K_dR_{sw} (or lower f_{iw}). The actual Matlab code can be found in Appendix E, Script E-1. The code for calculating the analytical solution was checked separately. Briefly, the form of the solution (i.e. the infinite series as in Eqn. 7 - 29) was altered slightly to conform to the solution for *adsorption* (Crank 1979). The resulting adsorption profile agreed well with those shown in Crank (1979) and Wu et al. (1988) (Table 7-10a).

4.2. Validation of Desorption Kinetics Numerical Code

The numerical code for simulation of HOCs desorption kinetics required validation. The analytical solutions for desorption problems with constant partitioning coefficient (K_d) are well known for plate, cylindrical, and spherical geometries (Crank 1979). According to standard texts on applied partial differential equations (Hildebrand 1962; Weinberger 1965; Carrier et al. 1976; Farlow 1993; Mei 1995), there appears to be no analytical solutions when the dependence of K_d on dissolved sorbate concentration assumes the Freundlich form (i.e. $K_d = K_{Fr}C_{iw}^n$). Thus, the numerical code could only be validated for cases where K_d's are constant.

The non-linear desorption simulation routine was validated by the convergence of the simulated pyrene profile (kinetic) with that from the analytical solution. Convergence was checked for: (i) different K_dR_{sw}'s, (ii) forms of K_d, (iii) degree of discretization (number of grids), and (iv) increment in time step (Figure 7-11). In most cases, partitioning of pyrene was assumed to be due to OC-phase only. However, since the numerical model contained codes that handle the non-linear term (i.e. the Freundlich term due to adsorption onto BC), this also required validation. This was done by examining the "forms" of K_d by considering three scenarios: pure-OC contributed K_d, OC-BC composite K_d, and pure-BC contributed K_d.

[6] Equation (6.37) describes the fraction of sorbate in dissolved phase at equilibrium $f_{iw,eqm}$. "M_∞" in Crank's text refers to dissolved phase sorbate mass at equilibrium (i.e $C_\infty V_{aq}$). Analogous to Eqn. 7 - 30, it can be shown that λ (or "α" in Crank's text) = $1/(K_dR_{sw})$.

4.2.1. Validation (I): Convergence on K_dR_{sw}'s

The numerical model showed convergence on the pyrene-time profile with the analytical solution at all four examined K_dR_{sw}'s (Figure 7-12). Since discretization is necessary in the modeling of pyrene (as well as other HOCs) desorption, the prediction/simulation at 'early' times generally contains more error than those predicted at later times. Thus the later time predictions should be used for convergence check. With this in mind, it was clear that the simulated pyrene-time profiles matched the analytical solutions very well (Figure 7-12).

4.2.2. Validation (II): Convergence on Forms of K_d

Good convergence was observed between the modeled pyrene-time profiles and the analytical solutions for all three forms of K_d (pure-OC, equal OC/BC, pure-BC). The convergence of purely-OC K_d has been shown in Figure 7-12. The convergence with analytical solution for mixed OC/BC (i.e. $K_d = K_{OC}f_{OC} + K_{BC}f_{BC} = 2K_{OC}f_{OC} = 2K_{BC}f_{BC}$) and the purely-BC cases is shown in Figure 7-13.

4.2.3. Validation (III): Convergence on Discretization (Grid Numbers)

The numerical model also produced consistent desorption profiles at different degree of discretization (Figure 7-12, 7-13). The model discretizes an aggregate (or a 'particle') into distinctive cells (e.g. spherical shells for spherical aggregate, cylindrical shells for cylindrical aggregate, etc). The local equilibrium assumption is good when the cell is relatively small but may not hold when the cell becomes larger. Hence a rough discretization (very few grids or cells) unavoidably leads to greater error in the early time. Therefore, the deviation of the model prediction from the analytical solution is expected to increases with (i) decreasing number of grids, and (ii) increasing K_dR_{sw}. Both of these have been observed (Figure 7-12a-d).

4.2.4. Validation (IV): Convergence on Time Steps

The model prediction also converged with the analytical solution at different increment in time step (Figure 7-14). The pyrene profiles generated from all increments ($\Delta\tau$ = 1, 4, 16, 32, 64) were all consistent with each other and with the analytical solution. Note that increment in time step was dimensionless, and was defined as $\Delta\tau(D_{iw}) = D_{iw}\Delta t/(\Delta x)^2$, where D_{iw} is the aqueous diffusivity of pyrene rather than the effective diffusivity of pyrene D_{eff}. This change is necessary as $D_{eff}(t)$ varies with $K_d(C_{iw}(t))$.

4.2.5. Validation (V): Aggregate Shapes

Since the model can allow non-spherical aggregate geometries (i.e. varying the Shape Factor (υ) in the code), it was also necessary to validate the model at different geometries. Model profiles were generated for cylindrical and planar aggregates, each with two different retardation scenarios. The modeled predictions agreed very well with those shown in the classical work by Crank (1979) (Table 7-10b,c).

4.3. Modeling of Pyrene Desorption Profiles (BH#6 Fractions)

In this section, the observed pyrene desorption profiles observed in Chapter 2 (BH#6 sediment, fractionalized into three nominal size groups: dia. = 38-75 μm, 75-106 μm,

and 180-250 μm) will be modeled using the Intraparticular Porewater Radial Diffusion model.

4.3.1. *A priori* Modeling of Desorption Dynamics

The observed data will be first modeled *without* any parameter fitting/manipulation. Four different pyrene sorption isotherms have been examined for the *a priori* modeling: (i) the classical OC-isotherm, (ii) the OC-BC isotherm reported in a preceding sorption study (Accardi-Dey and Gschwend 2002), and (iii) the OC-BC isotherm concluded from the sorption experiments in Chapter 5, and (iv) the occlusion-OC-BC isotherm, also obtained from Chapter 5. A summary of the isotherm forms and parameters is provided in Table 7-2 and the summary of modeling conditions in Table 7-3. Please refer to section 3.7 for more details.

4.3.1.1. Modeling Parameters

Most of the modeling parameters were derived from direct measurement (e.g. R_{sw}, $S_{pyr,init}$, f_{OC}, f_{BC}), separation procedure (e.g. radius from wet-sieving), or statistical analysis (e.g. $\log K_{OC}$, $\log K_{BC}$, n_{BC}, $S_{pyr,occluded}$). The only parameters with assumed values were the solid density ρ_s and the intra-aggregate porosity ϕ. ρ_s was assumed to be 2.5 kg_{solids}/L_w. This is a reasonable value for soils and sediments with typical f_{OC} (Appendix 7-13). For ϕ, a value of 0.13 was used as fitted in a previous, independent study (Wu et al. 1986, 1988). This value does not represent the typical intra-aggregate porosity of sediment (see section 3.3.2), but rather as an fitted parameter (Wu et al. 1988; Stapleton et al. 1994) for all non-idealities in the aggregate physicochemical properties or other system-level non-idealities (e.g. aggregation dynamics, film-layer diffusion, etc).

4.3.1.2. A priori Model Results vs Observations: End-Point C_{pyr}

In general, simulations that used the Occlusion-OC-BC isotherm (which assumed 30% of native pyrene was occluded) gave the end-time C_{pyr}'s that matched experimental observations. The simulated dissolved phase concentration profiles, $C_{pyr}(t)$, and the actual observations (solid diamonds) for four selected suspensions are shown in Figure 7-15. In order to assess the end-point accuracy of the four models, the simulated end-point results were compared against the observed (Figure 7-16). The model using Occlusion-OC-BC isotherm accurately predicted the final C_{pyr}'s from all 15 suspensions within the errors of the isotherm parameters. The next best isotherm was the New OC-BC model (Table 7-2), which accurately predicted ~50% of the observed end-point C_{pyr}'s. The predictions from the Old OC-BC model (Table 7-2) were about 5 times higher than the observed C_{pyr}. The least accurate model of all was the Classical OC-only model, which overestimated C_{pyr} by 10–100 times.

Another model assessment is to consider whether model predicted C_{pyr}'s exhibit any systematic trend with respect to system parameters such as solid-to-water ratio (R_{sw}) or the nominal aggregate/particle size. Let us first consider the dependence of predicted C_{pyr}'s on R_{sw} (Figure 7-17). In the figure, model predicted end-point C_{pyr}'s (normalized with respect to the actual observed values) did not appear to exhibit systematic dependence on R_{sw} for all isotherm models except the Classical-OC model. Likewise, when examining the relationship between the predicted end-point C_{pyr}'s and the particle

size (Figure 7-18), we see no significant dependence on nominal diameter in all isotherm models except, again, the Classical-OC model.

The inter-model comparison (Figure 7-16) clearly demonstrated the need to include BC for the evaluation of PAH distributions in soil/sediment-water systems. However, the R_{sw} and aggregate size analyses (Figure 7-17, 7-18) revealed a very significant weakness of the Classical-OC model – its inaccuracy will be greater in systems with higher solid loadings or larger aggregates. The implication of this variable inaccuracy is particularly significant if the availability of surface soil/sediment HOCs is assessed using the Classical-OC model.

4.3.1.3. Sensitivity Analysis for End-Point C_{pyr}

The basecase predictions derived from the New-OC-BC isotherm (which assumes no occlusion of native pyrene; Table 7-2) only matched ~50% of the observation. A comprehensive sensitivity analysis on six key parameters was conducted for the New-OC-BC isotherm prediction (Table 7-4). The analysis showed that the end-point prediction was most sensitive to n_{BC}; however, even uncertainty in n_{BC} could only account for ~80% of the observed end-point C_{pyr}'s, Uncertainty in other parameters could not explain the disparity between prediction and observation, and that variation in f_{OC} or $\log K_{OC}$ produce no discernible effects on the model prediction (Table 7-4). The results from the sensitivity analysis thus seemed to favor the idea of physical occlusion of native HOCs (i.e. pyrene) in natural geosorbents. It is also clear that the variation in OC-related parameters (f_{OC}, $\log K_{OC}$) has little consequence on the overall sorption capacity of natural soil/sediment.

4.3.1.4. A priori Model Results vs Observations: Kinetics

The kinetic profile generated from the Occlusion-BC-OC isotherm (Table 7-2) also matched the experimental $C_{pyr}(t)$ reasonably well (Figure 7-19; Appendix 7-20). In most of the test suspensions, the observed $C_{pyr}(t)$ was within the uncertainty (i.e. n_{BC}) of the isotherm for all time points. The performance of the model was quite good considering that the modeled curve involved no parametric manipulation/fitting.

Despite the apparent good match between the modeled and the observed concentration profiles, several systematic trends indicative of non-ideal conditions can be observed. First, for suspensions with the smallest sediment size fraction (dia.:38–75 μm), the modeled curve tended to underestimate the actual observations in the early times (~10 h) (Figure 7-19a). This tendency appeared to diminish with nominal particle/aggregate size (compare Figure 7-19b,c) and with an increase in R_{sw}. This may suggest the importance of aggregation dynamics in the early desorption times. One likely hypothesis is that particles disaggregate immediately as the suspension is formed. The breaking-up of particles led to greater contact surface area, greater desorptive flux, and hence a higher-than-expected $C_{pyr}(t)$. Aggregates undergo structural re-organization via breakup and re-formation in both natural waters (Sheldon et al. 1973; Eisma 1986; van Leussen 1993) and laboratory conditions (Farley et al. 1986; Wu et al. 1986). The proposed hypothesis is consistent with the observed dependence on nominal particle size (i.e. diminishing overestimating with larger particles) and the fact that aggregates

generally breakup more at low solid-concentrations and less so (or even conglomerate) at higher R_{sw}'s (Farley et al. 1986).

Second, the actual desorption appeared to be often slower than the modeled profile around the 10^{th}–100^{th} h (Figure 7-20; Appendix 7-1). The observed trend was not a simulation artifact, as the degree of discretization did not affect $C_{pyr}(t)$ in the 10^{th}–100^{th} h time range (Figure 7-12, 7-13). A possible hypothesis is that the actual aggregates may be non-spherical. Desorption rate of native sorbate decreases as the aggregate geometry varies from spherical (3-D diffusion) toward planar (1-D only) configuration. This may partly explain the observed trend in the 10^{th}–100^{th} period (Table 7-5; Appendix 7-9). Aggregate studies suggested that typical sedimentary aggregates are not spherical, and may have an aspect ratio (defined as the length along the long axis over the length along the short axis) ranging from 1.5 to 3 or 4 (Pike et al. 1996).

Although most of the kinetic observations were predicted within the uncertainty in n_{BC}, the kinetic half-times were poorly predicted (Table 7-9). The table compares the End-Point desorption half-time ($t_{1/2,EndPoint}$) – defined as $C_{pyr,w}(t_{1/2,EndPoint})=0.5C_{pyr,w}(t_{EndPoint})$ – as predicted by the model and as obtained from the raw data (by direct read-off and by empirical fitting of raw observations.). The model-predicted $t_{1/2,EndPoint}$ were generally about 10 times shorter than the half-times from raw data, primarily because of two 'non-idealities' (i.e. faster initial release and slower mid-point desorption) discussed in the two preceding paragraphs. It is unclear what level of uncertainty may be allowed for the modeled kinetic half-times.

4.3.1.5. Sensitivity Analysis for Kinetics

It is more challenging to predict kinetics (e.g. $t_{1/2}$) accurately as the additional factors of aggregate size, geometry, and intra-aggregate porosity/tortuosity affect kinetics significantly (Table 7-5). Furthermore, the size distribution, geometry distribution and intra-aggregate porosity information are often not as well quantified than the partitioning-related parameters (e.g. K_{OC}, f_{OC}, K_{BC}, f_{BC}, etc) in a given system.

The sensitivity analysis (Table 7-5) also revealed an expected trend: if a change in isotherm parameters increases the equilibrium dissolved phase concentration ($C_{pyr,Eqm}$), then the desorption equilibrium half-time ($t_{1/2,Eqm}$; $C_{pyr,w}(t_{1/2,Eqm})=0.5C_{pyr,w,Eqm}$) in a closed system also tends to increase.

4.3.2. Modeling of Desorption Kinetics with Best Fitted Isotherms

Despite the success of the *a priori* Occlusion-OC-BC isotherm in predicting kinetic observations of aqueous pyrene levels, it may be desirable to consider if some other isotherms can also do as well or even better than the Occlusion model. One may still consider the option with no occlusion, and compare the results from the 'best-fit' no-occlusion models with those from the a priori Occlusion model.

The pyrene desorption data can be modeled with universal $\log K_{OC}$ and $\log K_{BC}$ instead of the isotherm specific to the BH#6/NQB sediment. The surveys on K_{OC} and K_{BC} in the earlier chapters (See Table 5-5 for K_{OC}, Table 5-7 for K_{BC}; summary of both literature survey and experimental K's in Table 5-9) have shown that $\log K_{OC}$ and $\log K_{BC}$ are relatively constant for a sorbate across different sorbents. The $\log K_{OC}$ and $\log K_{BC}$ for

the New-OC-BC were estimated to be 5.25 and 6.25, respectively; the $\log K_{OC}$ and $\log K_{BC}$ for sedimentary Universal-OC-BC (averaged from literature values; see Appendix 7-16) were estimated to be 4.75 and 5.95, respectively.

In another case, the pyrene desorption kinetic data were modeled with best fit constant partition coefficients (i.e. linear isotherm). Experiment-specific linear partition coefficients (K_{TOC}) were estimated from the end-point observations of the individual experiments and the total OC+BC contents (Appendix 7-24). These K_{TOC}'s were then input into the IDP model assuming linear isotherm (i.e. $n_{TOC}=1$). The 'Forced Linear' $\log K_{TOC}$'s of the individual experiments are summarized in Appendix 7-24.

Since n_{BC} (i.e. the New-OC-BC and the Universal-OC-BC logK's) or K_{TOC} (i.e. 'Forced Linear' case) were the fitting parameters, good agreement would be 'guaranteed' between the observed and the modeled end-point $C_{pyr,w}$'s. Thus one needs to examine the consistency of the fitted n_{BC} or K_{TOC} among the different suspensions as well as the predicted kinetic features in general.

In general, the observed end-point $C_{pyr,w}$'s could be fitted by a consistent range of n_{BC}. The best-fit n_{BC} for the New-OC-BC isotherm was about 0.3–0.4; the best-fit n_{BC} for the Universal-OC-BC was lower at around 0.15–0.2 (Appendix 7-17). The best fit n_{BC} appeared to be consistent across the size of the sediment aggregates. For the kinetic feature of the desorption file, the two best-fit models and the *a priori* Occlusion model all gave very similar predictions (Figure 7-21). Given the analytical uncertainty of the actual observations, none of the three models may be considered superior than the others.

The modeled curves with constant, best-fit K_{TOC} ($n_{TOC}=1$) matched the observations reasonably well at low R_{sw}'s (Figure 7-22a) but not at high R_{sw} (Figure 7-22b). The Forced Linear model (constant K_{TOC}, $n_{TOC}=1$) often overestimated $C_{pyr,w}$'s in the early phase of desorption (Figure 7-22b). Note that the K_{TOC} predictions matched the end-point data perfectly because K_{TOC}'s were computed from the end-point data assuming equilibrium (Appendix 7-24); however, all end-point $C_{pyr,w}$ observations were within the uncertainty in n_{BC} of the Occlusion model in all suspensions (Figure 7-16; see also Appendix 7-1).

The reader should also note that the best-fit $\log K_{TOC}$ generally decreased with increasing R_{sw} (the table in Appendix 7-24) and it ranged from 6.3– 7.3. The one log unit uncertainty in K_{TOC} for a *single sample* was very high, considered the similar level of scattering in literature $\log K_{OC}$'s (Table 5-9). The high uncertainties in best fit K_{TOC}'s and the fact that $\log K_{TOC}$'s greatly exceeded the typical $\log K_{OC}$ or $\log K_{BC}$'s (Table 5-9) suggested that the Forced Linear approach was inappropriate.

4.3.3. Conclusion on *a priori* and Best-Fit Kinetic Modeling

If a kinetic model may be considered as 'sufficient' as long as the actual observations are within bound of the model uncertainties (e.g. n_{BC} in the isotherm), then a greater level of uncertainty should be allowed for the kinetic half-time. The *a priori* Intraparticle Porewater Diffusion model (with Occlusion-OC-BC isotherm) was clearly 'sufficient' – for it captures the actual observations successfully in all fifteen suspensions. Since the

problems of *faster initial release* and *slower mid-point desorption* (section 4.3.1.4) are likely to be caused by physical/hydrodynamic factors, their effects should be universally observed in sediment from different estuaries/harbors. It is likely that the model prediction can be further improved if empirical results from aggregation dynamic studies are incorporated and typical sediment dimensional properties better refined.

The comparisons between the two best-fit models and the *a priori* model suggested the isotherm parameters could be varied without affecting both the endpoint $C_{pyr,w}$ and the desorption half-times. The determination of isotherm parameters at the ng_{pyr}/L_w can be statistically challenging – for instance, a flat isotherm easily gives rise to non-unique 'best-fitted' n_{BC}, K_{OC}, K_{BC}. Furthermore, the two best-fit cases (New-OC-BC, Universal-OC-BC) did not assume occlusion of the sorbed pyrene. Therefore, it is important not to consider the success of the *a priori* Occlusion model (as shown in section 4.3.1) as strong evidence for the hypothesis of native pyrene being physically occluded in the sediment sample.

4.4. Correlating Empirical Kinetic Regression with *a priori* Properties

In order to compare the observed kinetics with those reported in literature, it was necessary to describe the kinetic data using empirical forms. Furthermore, since the majority of kinetic studies have described the desorption kinetics of HOCs with empirical forms (see review by Birdwell et al. 2007), it is of great interest to understand how the parameters of these empirical kinetic expressions may be related to certain *a priori* physicochemical sorbent/sorbate properties.

4.4.1. Limitations of Empirical Kinetic Expressions

A great variety of empirical forms for desorption kinetics are available for choice (Table 7-11), and the conceptual origins behind them have been discussed (Wells et al. 2004, 2005). Despite the varying forms of these different empirical expressions and their different origins, they share two common limitations: (i) the regressed parameters would change with the duration of observations, and (ii) the expressions fail to converge with the equilibrium state prescribed by the chemistry of the sorption.

The first limitation implies that these expressions are purely descriptive, and that their applicability does not extend beyond the regressed duration. For instance, in the cases of the Orthogonal-Polynomial form and the Elovich Model (Table 7-11), the residual solid phase concentration will become negative at infinite time for any sets of positive regressed parameters. Likewise, the simple, Discrete-Compartmental models allow bound-sorbate to be completely depleted at very large times. These models may be applicable to scenarios where sorbed HOCs are released into a clean, infinite aqueous phase, but they are often used in cases of desorbing into limited aqueous volumes (Cornelissen et al. 1997b; van den Heuvel et al. 2003).

The second limitation refers to the model failure when a final, equilibrium concentration can be expected. To compensate for this limitation, some of the empirical models have been modified such that the dissolved phase concentration converges at large times to an equilibrium value (i.e. 'S_X-$S_{Eqm|End}R_{sw}$' in Table 7-11). This amendment for

convergence could not be done for the polynomial models (Table 7-11) due to their mathematical nature.

Although a large number of desorption kinetic studies have been performed, a recent review (Birdwell et al. 2007) suggested that desorption/release rates (or rate constants) for even the most frequently studied PAHs and PCBs span across 6–7 orders of magnitude. Multiple causes are, no doubt, behind this substantial divergence in release rate; however, the use of non-converging empirical regression is, in the author's opinion, also likely to be one of the contributing causes.

4.4.2. Empirical Desorption Rate: Comparison with Literature

Empirically regressed desorption rates from the BH#6/NQB suspensions were generally different from those reported in literature. In view of the popularity of the Discrete-Compartmental models in recent studies (references within Table 7-13), desorption data have been fitted to both the Two- and the Three-Compartment model (Table 7-11). The regressed rate constants in both models are summarized in Table 7-12. Only the Two-Compartmental rate constants for the 38–75 μm suspensions were somewhat comparable to those reported in literature: k_{slow} and k_{rapid} for BH#6/NQB data were about 0.5–16 h^{-1} and 60–800×10^{-6} h^{-1}, respectively; k_{slow} and k_{rapid}'s from previous studies ranges from 0.1–1.6 h^{-1} and 10–2000×10^{-6} h^{-1}, respectively (Table 7-13). With the larger size fractions, the fitted rate constants were generally orders of magnitude lower than the literature values (Table 7-12). This may be partly explicable by the fact that the faster rates (or higher k's) are usually associated with kinetics studies where spiked geosorbents have been used (Table 7-13). This re-emphasizes the importance of aging on the mobility of the bound HOCs, and the necessary differentiation between laboratory processed and field-aged samples.

Substantial discrepancy in the rapidly (F_{rapid}) and slowly (F_{slow}) desorbing fractions also existed between this study and the literature. F_{rapid} from literature ranges from 10–95 %, with most studies reporting around 30–50 % (Table 7-13); here, we saw F_{rapid} smaller than 10% for all suspensions (Table 7-12). A similar difference can also be seen for the F_{slow} (or $F_{v.slow}$).

The widely scattering $k_{v.slow}$'s in the Three-Compartment model (varying 5 to 8 orders of magnitudes) were probably indicative of the model being excessive in fitting parameters. For this reason, the forth-coming discussion and analysis would focus only on the regressed rates with the Two-Compartment model.

4.4.3. Desorption Physics Buried in Empirical Kinetics

A preliminary examination on the regressed parameters (with Constrained Two-Compartmental model) on the BH#6/NQB desorption data reveals the fact that these parameters are highly related to both the physics of desorption and the physicochemical properties of the suspensions.

4.4.3.1. F_{rapid}/F_{slow} vs R_{sw}

Both the rapidly and the slowly desorbing pyrene fractions (empirically fitted) varied strongly with the system R_{sw}. F_{rapid}'s was found to decrease with increasing R_{sw} (F_{rapid} ~5–7% at 22 mg_{solids}/L_w, but it decreased to ~1 % at 270 mg_{solids}/L_w) (Appendix 7-19).

For the slowly desorbing fraction, a very distinct trend can be observed if we consider the actual slow-fraction desorbed (i.e. $[S_{slow,o}-S_{Eqm|End}]/S_o$): the slow-fraction desorbed decreased from ~20–35 % at 22 mg_{solids}/L_w to ~2–5 % at the maximum R_{sw} of 270 mg_{solids}/L_w (Appendix 7-19).

Both trends were consistent with the expectation that greater fraction of pyrene would desorb at lower R_{sw}: as the total amount of pyrene in the system increase, less of it is required to desorb before reaching equilibrium.

4.4.3.2. F_{rapid}/F_{slow} vs OC/BC-Associated Pyrene

It can be shown that the rapidly and the slowly desorbing fractions closely relate to the total amount of pyrene associated with the OC and the BC phases. Supposing an isotherm for the native sedimentary pyrene (i.e. Occlusion-OC-BC or New-OC-BC isotherms), the portion of pyrene associated with OC and BC phases (i.e. $S_{pyr,OC}$ and $S_{pyr,BC}$) can be estimated. The total system pyrene associated with OC or BC is then simply $S_{pyr,OC}R_{sw}$ or $S_{pyr,BC}R_{sw}$. Let us suppose that the rapidly desorbing fraction correspond mostly to the release of OC-bound pyrene (i.e. smaller K_d or retardation), and the slowly desorbing fraction to that of the BC-associated pyrene (i.e. larger K_d or retardation), then one should expect F_{rapid} (or F_{slow}) to decrease as the system OC (or BC) associated pyrene increases. This was shown to be the case (Figure 7-23).

4.4.3.3. k_{rapid}/k_{slow} vs a priori Time Constant Estimate (κ)

Similarly, the empirically fitted rate constants, k_{rapid} (or k_{slow}), may be related to physicochemical properties of both the sorbent and the sorbate. Following the earlier assumption (i.e. OC ~ 'rapid' desorption, BC ~ 'slow' desorption), one can make a crude estimate on the release rate of OC- and BC-bound pyrene. From an assumed isotherm, one can estimate the $K_{d,pyr}$ for a closed suspension system. This $K_{d,pyr}$ is the sum of the sorptive contributions by the sedimentary OC and BC phases (i.e. $K_{d,pyr}=K_{d,OC}+K_{d,BC}$). One can construct an estimator, κ (with unit $time^{-1}$), that describes the desorption rate constant. Supposing an intra-particle porewater diffusion model with corresponding retardation by $K_{d,BC}$ (or $K_{d,OC}$) one possible κ_{BC} (or κ_{OC}) may be:

$$\kappa_{BC} = \frac{D_{eff,BC}\,(R_{sw}/R_{sw,ref})}{R^2}$$

$$D_{eff,BC} \cong \frac{D_{iw}}{K_{d,BC}\,R_{sw}}$$

Eqn. 7 - 32

where $D_{eff,BC}$ is the effective diffusivity associated with sorption onto BC (m^2/s),

D_{iw} is free aqueous phase diffusion coefficient for the sorbate i (m^2/s),

$K_{d,BC}$ is the BC-contributed sorption coefficient for the sorbate (L_w/kg_{solids}),

κ_{BC} is the time-dimensional number for desorption rate (s^{-1}),

R is the aggregate radius (m),

R_{sw} is the system solid-to-water ratio (mg_{solids}/L_w),

$R_{sw,ref}$ is a unit-normalizing factor and has a value of 1 mg_{solids}/L_w.

Note that κ_{BC} (or κ_{OC}) is NOT an estimate of desorption rate constant. It is, rather, *a relative measure of rate constant* one may expect base on the *a priori* sorbate/sorbent physicochemical properties. The formulation of κ is consistent with the qualitative expectation that: (i) a faster diffusing sorbate will desorb faster ($D_{eff,BC} \uparrow$, $\kappa_{BC} \uparrow$), (ii) a system with greater solid-loadings will desorb faster ($R_{sw} \uparrow$, $\kappa_{BC} \uparrow$), and (iii) a faster release rate for smaller particles/aggregates ($R \downarrow$, $\kappa_{BC} \uparrow$).

Both k_{rapid} and k_{slow} (from Constrained Two-Compartment regression; Appendix 7-21) seemed to increase with increasing κ_{OC} and κ_{BC} (Figure 7-24), with the trend being more obvious for k_{slow}-κ_{BC}. The greater ambiguity in the k_{rapid}-κ_{OC} plot may be explained by the fact that the early desorption data were, in general, less well fitted by the compartmental models. The key point is that k_{rapid}'s and k_{slow}'s appear to be related to physicochemical properties of the sorbent and the sorbate.

4.4.3.4. Interdependence in Regressed Parameters

The regressed parameters also appeared to correlate with each other in a way consistent with the physics of mass transfer. Both k_{rapid} and k_{slow} appeared to decrease with increasing $S_{pyr,rapid}$ and $S_{pyr,slow}$ (Figure 7-25). This interdependence is significant in several ways. First, the meanings of the fitted parameters are vague – since they are not independent of each other, how many independent descriptors do we actually have? Second, the interdependence implies that the fitted parameters will co-vary together, so the rapidly or slowly desorbing fractions (F_{rapid}, F_{slow}) will often change with time (i.e. F's and k's vary with the duration of all kinetic observations).

4.4.4. Concluding Remarks on Empirical Regression of Desorption Kinetics

The limiting nature of empirical kinetic models raises the following questions: (i) To what extent may these empirical kinetic models be useful? (ii) With regard to the reported desorption rates by the past studies, are there ways that one can extract physicochemical properties from the empirically fitted parameters? (iii) How should we conduct kinetic studies in the future?

4.4.4.1. Empirical Models as Pure Descriptor of HOCs Desorption Kinetics

Empirical kinetic models are useful as descriptor or summary of the kinetic observations, but one can obtain a misleading picture for the kinetic behavior of bound HOCs if the regressed parameters are taken as 'absolute' rate indicators. The widely scattering rate constants reported for PAHs and PCBs could not be brought to give a unified picture on the release rate of HOCs (Birdwell et al. 2007). Most past studies on HOCs desorption kinetics have used non-converging equations for fitting (e.g. Karickhoff et al. 1985; Cornelissen et al. 1998b; Ghosh et al. 2001; Johnson et al. 2001b; Rockne et al. 2002; van den Heuvel et al. 2003; Kukkonen et al. 2003; van Noort et al. 2003; Gomez-Lahoz et al. 2005; also see references within Birdwell et al. 2007); one would encounter mathematical artifacts when extending these regressed kinetic parameters to longer time frame (section 4.4.1). The interdependence between the regression parameters

themselves (Figure 7-25; section 4.4.3.4) also reinforces the fact that the 'rapid' or 'slow' fractions/rates do not have absolute meanings.

For these reasons, the author has some reservation against using rapidly/slowly desorbing fractions to examine HOCs sorption capacity on geosorbents (e.g. van den Heuvel et al. 2005; 2006) or to understand HOCs bioavailability (Cornelissen et al. 1998b). To be fair, the empirically regressed fractions may be good quantifiers for *short-term* HOCs bioavailability; in this case, it is an approach as valid as the other bioavailability assessment methods such as Tenax extraction (ten Hulscher et al. 2003; Moermond et al. 2007), n-hexane extraction (Schwartz et al. 1999; Tao et al. 2006), solvent-saponification extraction (Northcott et al. 2001a), or alcohol-extraction (Kelsey et al. 1997). However, these measurements cannot represent the total HOCs bioavailable in soil/sediment, or how they may behave in the long-term.

4.4.4.2. Bridging Empirical Rates with Physicochemical Model

An original plan has been to construct a way to correlate empirically regressed parameters (e.g. k_{rapid}, k_{slow}) to physicochemical properties (e.g. isotherm, sorbate diffusivity, aggregate size, R_{sw} etc). While a strong correlation was seen between F_{rapid} /F_{slow} and the *a priori* properties (section 4.4.3.2), the fitted rate constants were more scattered with respect to the *a priori* time constants (κ) (section 4.4.3.3). This objective, therefore, is yet to be fulfilled with further efforts.

If there were a way to bridge the empirical rates with the physicochemical properties, one can potentially access all past kinetic observations and back-extract useful sorbent properties and the sorption affinity for some sorbates. One may even construct an engineering function describing the desorption rate of some 'typical' organic sorbates in soils/sediments-water system – analogous to the engineering functions encountered in Heat Transfer or Mass Transfer in standard engineering texts.

4.4.4.3. Recommended Practice for Future HOCs Kinetic Studies

Since the empirical kinetic equations are relatively simple and descriptive, and they have widely used in kinetic studies, they may be used for archiving experimental results. In conjunction with empirical fitting, however, the physicochemical properties of the sorbent, the sorbate, and the overall system should be carefully documented along. The author cannot help entertaining such a thought: had the system properties been meticulously recorded in past studies, Birdwell et al. could have found a stronger correlation between the empirical kinetic parameters and the physicochemical properties of the system in their review on the desorption kinetics of PAHs/PCBs.

5. Conclusion

5.1. Summary

This chapter examined how the kinetics of pyrene desorption (Chapter 2) can be modeled. In view of the presence of black carbon in the sample and the non-linear nature of the pyrene sorption isotherm, the modeling of intra-sorbent transport has been

re-examined. Three competing modes of intra-sorbent transport were identified: diffusion through interstitial pore-water, diffusion through organic matter, and diffusion on the actively sorbing intra-sorbent surface. After considering the relevant intra-sorbent studies, the diffusivity data of pyrene in various media, and the physical properties of typical soil/sediment particles/aggregates, the diffusion thorough the intra-particle porewater should be the dominant diffusion mechanism in typical soil/sediment. To complete the larger picture of intra-sorbent diffusion, the cases where the other intra-sorbent pathways may dominate were also highlighted.

Next, the mathematics of Intra-particle Porewater Diffusion was re-developed for non-linear isotherm. With non-linear isotherm, the concept of effective diffusivity no longer mathematically applies as the partition coefficient, K_d, is now a function of local pore-water phase concentration (C'_{pyr}) and spatial position within the aggregate.

The numerical code, written in spatially and temporally dimensionless form, was constructed to handle (i) variability in aggregate geometry, (ii) potential spatial distribution of OC, BC, porosity, and tortuosity. The code was validated against the analytical solution on the convergence of (i) varying K_dR_{sw}, (ii) forms of K_d, (iii) discretization size, (iv) time-step variation, and (v) particle geometry. Convergence with analytical solution and/or earlier numerical solution was observed in all cases.

The developed code was applied to the pyrene kinetic data on four pyrene sorption isotherms: the Classical-OC, the Old-OC-BC, the New-OC-BC, and the Occlusion-OC-BC isotherms. Simulation results indicated that the *a priori* Occlusion-OC-BC model gave the best prediction for kinetics observed in all fifteen suspensions. The *a priori* New-OC-BC model could predict the dissolved pyrene concentration in about half of the suspensions; the Classical-OC and the Old-OC-BC models simply missed the observed data.

This simulation exercise strongly demonstrated the proficiency of the Intra-particle Porewater Diffusion Model in predicting/modeling desorption kinetics of native sedimentary pyrene. Several points should, however, be emphasized.

First, it may be premature to conclude from the success of *a priori* Occlusion-OC-BC model that physical occlusion of HOCs was significant, because equally 'accurate' concentration profiles can be generated from the New-OC-BC or the Universal-OC-BC models with best-fitted n_{BC}. The author believes that this can be better resolved with more kinetic experiments over HOCs with different hydrophobicities and sizes.

Second, although experimental dissolved pyrene observations could all be predicted within the uncertainty of the Occlusion-OC-BC isotherm, substantial discrepancy in the desorption half-time existed between the model expectation and the actual value. This has been attributed to two 'non-idealities' in the model: that the aggregation/disaggregation dynamics of particles was neglected, and that actual sedimentary aggregates probably have an elliptical rather than a spherical geometry. Although the idea of aggregation dynamic could not be tested, the elliptical aggregate proposition was consistent with the sensitivity of the dissolved pyrene-time profile to aggregate shape-factor. The fact that more factors can alter the rate of intra-particle

diffusion implies the kinetic character of the actual desorption curve is generally more variable and harder to predict. However, the author believes that *a priori* prediction can be further improved when model-correction for aggregation/disaggregation physics is introduced.

5.2. Implications

This work has significant implications for understanding the kinetic behavior of naturally aged HOCs in natural soils and sediments. It showed that one can predict the release of sorbed HOCs *if* their isotherms are known. Sorption equilibrium knowledge is, therefore, also crucial for kinetic questions.

The analysis on the kinetic-fitting approach demonstrated the deficiencies of the empirical models (e.g. not converging to equilibrium at infinite time, case-specific parameters not applicable to other scenarios; section 4.4.1). The fair correlation between the empirical kinetic parameters and the sorbent+sorbate physicochemical properties (section 4.4.3) suggested that the fit parameters can be understood by the physics of desorption. Consequently, the scattering of desorption rate constants reported in recent review (i.e. Birdwell et al. 2007) does not imply our inability to predict the release rate; rather, it reflects the unfortunate fact that physicochemical properties crucial for kinetics have been left out in many previous studies.

Chapter 8. Intraparticle Porewater Diffusion Model: General Application and Particular Scenarios

CHAPTER ABSTRACT

Two models describing the desorption/diffusion of hydrophobic organic compounds (HOCs) in Infinite-Bath environment and that in Char-Silt dual-domain heterogeneous aggregates have been developed. The Infinite-Bath model incorporates the diffusive transport of sorbate across the mass-transfer boundary layer film (δ), which varies with the hydrodynamic turbulence in the solid-water system. The Char-in-Silt model allows desorption from heterogeneous aggregates to be simulated/modeled. To the author's knowledge, this has not yet been reported in the modeling literature in environmental chemistry/engineering. A great level of parametric flexibility (e.g., aggregate shape; variable spatial porosity, tortuosity factor, f_{OC}, f_{BC}, δ, char size) has been allowed in both models.

The dependence of intraparticle diffusion on the following parameters has been examined via simulation: aggregate configurations (i.e. silt, char-in-silt, char only), system nature (closed-system vs infinite-bath), HOC hydrophobicity (e.g. K_{OC} or K_{OW}), isotherm non-linearity (n_{BC}), and other physicochemical parameters. From this modeling exercise, a number of important points can be made regarding the release kinetics of HOC desorption from natural geosorbents. First, the phenomenon of HOC 'sequestration' may be explained by their slow release kinetics as a result of highly non-linear sorption isotherm. Second, isotherm non-linearity is relatively insignificant for the kinetic modeling of low hydrophobicity HOCs, but very critical for assessing accurately the dynamics of high hydrophobicity HOCs. This has been demonstrated using selected PAHs. Third, in closed systems, the fraction HOCs that can be desorbed (f_{des}) often increases with the desorption halftime ($\tau_{iw,1/2}$). This relationship is variable for non-linear, BC sorption but not for the linear, Classical-OC sorption view. The non-linear f_{des}-$\tau_{iw,1/2}$ profiles may explain why the most dramatic attenuation of the bound-HOCs concentrations is often observed in sites that are recently contaminated or where the contaminant concentrations have been relatively high.

In the Char-Silt model, the Char-to-Aggregate size ratio (R_c/R_{agg}) and the solid-to-water ratio (R_{sw}) appear to be the key parameters in determining the desorption profiles in Char-in-Silt configurations. Comparative simulations in Infinite-Bath mode showed that char-core or char-particles should not be simplified as 'purely-OC' phase. In this respect, further methodological work may be necessary for identifying the presence of char in natural soils/sediments. However, the kinetics of desorption may be reasonably estimated without knowing exactly the BC-purity of the char-domain.

Table of Content for Chapter 8

1. Chapter Introduction, Scope, and Objective 196

1.1. Introduction 196

1.2. Objectives 196

2. Methodology: Modeling 197

2.1. Infinite Bath Systems (Explicit, Finite Difference Scheme) 197

2.1.1. Diffusional Flux through Boundary Layer Film δ 197

2.1.2. Edge-Shell Concentration C'_m: Linear Interpolation 199

2.2. Char-in-Silt Case (Explicit, Finite Difference Scheme) 199

2.2.1. Char-Domain 199

2.2.1.1. Aggregate-Volume Averaged Quantity 199

2.2.1.2. Spatial Discretization (Δx_c) 200

2.2.2. Silt-Domain 200

2.2.2.1. Aggregate-Volume Averaged Quantity 200

2.2.2.2. Spatial Discretization (Δx_s) 201

2.2.3. Char-Silt Interfacial Diffusion 202

2.2.4. Edge Shell of Aggregate or Silt-Domain 203

3. Results & Discussion 204

3.1. Validation of Infinite-Bath Diffusion Model 204

3.1.1. Validation (I): Varying 'R_{sw}' 204

3.1.2. Validation (II): Congruence with Analytical Solutions 204

3.2. Validation of Char-in-Silt Diffusion Model 205

3.3. Infinite-Bath Diffusion 206

3.3.1. Effect on Desorption Rate: (I) Boundary Layer Film Thickness (δ) 206

3.3.1.1. With Linear K_d 206

3.3.1.2. With Nonlinear K_d 206

3.3.2. Effect on Desorption Rate: (II) Bulk-Aqueous Phase Concentration (C_{bulk}) 207

3.3.3. Implication for Persistence of HOCs 207

3.4. Infinite-Bath Diffusion – Selected PAHs 208

3.4.1. Assumptions and Approach 208

3.4.2. Effect on Desorption Rate: (III) Sorbate Hydrophobicity 209

3.4.3. Effect on Desorption Rate: (IV) Solid-Phase Sorbate Concentration 209

3.5. Closed-System Diffusion 209

3.5.1. Assumptions and Approach 210

3.5.2. Effect on Desorption Rate: (I) Solids-to-Water Ratio (R_{sw}) 210
3.5.3. On Interpreting the Rate in Closed-System: f_{des} vs $\tau_{iw,1/2}$ 210
3.6. Char-in-Silt (Closed-System) 211
3.6.1. Preliminary Notes 211
3.6.1.1. Assumptions and Approach 211
3.6.1.2. Concept (I): Initial Porewater Concentration ($C_{agg,pw,o}$) 211
3.6.1.3. Concept (II): Char-to-Aggregate Size Ratio (R_c/R_{agg}) 211
3.6.1.4. OC and Soot-BC in the Silt Domain 212
3.6.2. Effect on Desorption Rate: (I) Char-to-Aggregate Size Ratio (R_c/R_{agg}) 212
3.6.3. Effect on Desorption Rate: (II) R_{sw} 212
3.6.4. Effect on Desorption Rate: (III) Char Domain Porosity/Tortuosity 213
3.7. Char-in-Silt (Infinite-Bath) 213
3.7.1. Effect on Desorption Rate (I): R_c/R_{agg} Size Ratio 213
3.7.2. Effect on Desorption Rate (II): $C_{agg,pw,o}$ 213
3.7.3. Comparison with Other Configurations: Concluding Char-in-Silt Model 213
4. Conclusion 214

1. Chapter Introduction, Scope, and Objective

1.1. Introduction

In Chapter 7, it has been shown that experimental desorption kinetics can be predicted by a non-linear Intraparticle Porewater Diffusion Model (IPDM) – with *a priori* isotherm or with best-fitted isotherm. This suggests that the release of HOCs in real environmental solid-water systems (e.g. estuaries, rivers, lakes) may be predicted *a priori* if the sorption isotherms for the HOCs are accurate.

The non-linearity of HOC sorption isotherms, however, greatly complicates the interpretation and use of the model – we can no longer condense and generalize the kinetics of all possible systems into a single dimensionless plot. Furthermore, the dependence of partition coefficient (K_d) on dissolved phase concentration (C_{iw}) also means that K_d varies both spatially and temporally within the particle/aggregate. This interesting dynamics needs to be further explored.

Although the non-linear IPDM presented in Chapter 7 can be applied to Infinite Bath cases (i.e., by setting R_{sw} to 0), it neglects the diffusive transport of sorbate across the aggregate boundary layer film. The presence of boundary layer films around solids suspended in fluids (Levich 1962; Deen 1998; Probstein 2003) introduces additional mass transfer resistance to adsorption or desorption. However, the boundary layer effect on diffusion has been often neglected in HOC kinetics/modeling studies (Wu et al. 1988; Ball et al. 1991; Rugner et al. 1999; Karapanagioti et al. 2001; Ghosh et al. 2001; Shor et al. 2003b).

In addition, there is currently no diffusion model to describe the uptake or release of HOCs from μm-scale BC in soil or sediment (e.g. char or coal in soil/sediment; see Figure 7-1). Ghosh et al. (2001) used a 'rind' model to describe the diffusion of PAHs in coal particles. Although the model allowed a radially-distributed initial PAH loadings, it assumed a homogeneous porous matrix, and hence the rind model may not be extended to char/coal-containing aggregates. Other surveyed kinetic studies have always assumed homogeneous aggregates. In view of the ubiquitous presence μm-scale BC in soils (), it is of great interest to model the desorption kinetics of HOCs from aggregates with char/coal embedded within.

1.2. Objectives

The objectives of this chapter are as follows. First, the numerical setting and implementation of two new diffusion models will be developed: (i) Infinite-Bath Diffusion with mass transfer across boundary layer film, and (ii) Char-in-Silt (heterogeneous) Diffusion model. These models will be validated by various simulation tests and by comparing against the available analytical solutions (section 3.1, 3.2).

Next, the simulation results from the Infinite-Bath model will be examined. The sensitivity of the model to key parameters will be briefly examined (section 3.3). After

that, the model will be applied to four selected PAHs to illustrate some potential implications for modeling the release kinetics of typical HOCs (section 3.4).

We will return briefly to the diffusion model for Closed System (homogeneous), with focus on the importance of sorbate hydrophobicity and R_{sw}, and the relationship between desorption timescale and fraction sorbate desorbed (section 3.5).

After that, the nature of the Char-in-Silt model in both Closed Systems (section 3.6) and Infinite-Bath settings (section 3.7) will be examined.

Due to isotherm non-linearity, the author could not generate a generically applicable dimensionless desorption plots as those shown in Crank (1979). Instead of presenting or documenting all possible cases for a wide range of HOCs in an exhaustive manner, the author has aimed at highlighting some of the key features in modeling non-linear intra-sorbent diffusion of HOCs. Efforts have been made to use realistic values for model parameters which are representative of typical sediment/soil reported in HOCs literature.

2. Methodology: Modeling

The conceptual assumptions and basic mathematical equations for the Intraparticle Porewater Diffusion Model (IPDM) have been covered in detail in the previous chapter. Here, the implementation of the model to the Infinite Bath case and the Char-in-Silt case will be discussed. Sample scripts for the different models are documented in Appendix E (Script E-7 to E-9).

2.1. Infinite Bath Systems (Explicit, Finite Difference Scheme)

2.1.1. Diffusional Flux through Boundary Layer Film δ

The finite difference equations for the Infinite Bath case are practically the same as those for the closed system with the exception at the Edge-Shell (see Chapter 7, secion 3.5.1.4). The governing mathematical equation for the Edge-Shell of a spherical aggregate (Eqn. 7-14) is:

$$\left(\frac{\partial C'}{\partial t}\right)_{edge} = -\frac{3D_{iw}}{R}\left[F_{Tor}\left.\frac{\partial C'}{\partial r}\right|_{R-} + \left(\frac{C_{bulk} - C'}{\delta}\right)\right]$$

Eqn. 8 - 1

where C' is the local pore-water sorbate *i* concentration ($\mu g_i/L_{pw}$),

C_{bulk} is the local pore-water sorbate *i* concentration ($\mu g_i/L_w$),

D_{iw} is the free aqueous diffusivity of *i* (m^2/s),

δ is the mass transfer boundary layer film surrounding the aggregate (m),

F_{Tor} is the tortuosity factor accounting for longer diffusive path ($F_{Tor} \leq 1$; dimensionless),

r is the radial position (i.e. with respect to the aggregate) (m),

R is the aggregate radius (m),

t is time (s).

In dimensionless form, the equation becomes:

$$\left(\frac{\partial q'}{\partial \tau}\right)_{edge} = \gamma\left\{-\emptyset F_{Tor}\left.\frac{\partial C'}{\partial x}\right|_{R-} + \frac{(C_{bulk} - C')}{\delta/R}\right\}$$

Eqn. 8 - 2

where q' is the local aggregate-volume based concentration of *i* concentration ($\mu g_i/L_{agg}$),

γ is the Shape Factor (=3 for spherical, 2 for cylindrical, 1 for planar),

δ is the mass transfer boundary layer film surrounding the aggregate (m),

F_{Tor} is the tortuosity factor accounting for longer diffusive path ($F_{Tor} \leq 1$; dimensionless),

ϕ is the intra-aggregate porosity (L_{pw}/L_{agg}),

x is the dimensionless spatial variable (x = r/R),

τ (= τ_{iw}) is the dimensionless time variable ($\tau = D_{iw}t/R^2$).

Note that the dimensionless time, τ (or τ_{iw}), is NOT defined by the effective diffusivity, D_{eff}.

In an explicit, finite difference scheme, the above equation becomes:

$$\frac{{C'_m}^{n+1} - {C'_m}^{n}}{\Delta\tau_{iw}} = \gamma\left[-F_{Tor}\left(\frac{{C'_m}^{n} - {C'_{m-1}}^{n}}{\Delta x}\right) + \left(\frac{{C_{bulk}}^{n} - {C'_m}^{n}}{\delta/R}\right)\right]$$

Eqn. 8 - 3

Where C_{bulk}^{n} is the bulk aqueous phase concentration of the sorbate (*can be constant or a user-specified function of time*),

δ/R is the dimensionless mass transfer boundary layer film thickness,

n denotes the variable at n^{th} dimensionless timestep (i.e. 'current' state),

n+1 denotes the variable at the $n+1^{th}$ timestep (i.e. 'next' state),

m denotes the Edge-Shell grid.

2.1.2. Edge-Shell Concentration C'_m: Linear Interpolation

However, the numerical code using Eqn. 8 - 3 is unstable: (i) it requires very small $\Delta\tau_{iw}$ (e.g. ~0.01) even for linear K_d, (ii) negative, imaginary, or oscillatory C'_m is easily produced. This instability is most likely caused by the fact that (a) the Edge-Shell is relatively small compared to the boundary layer film, and (b) that the diffusion across δ/R is faster than intra-aggregate diffusion.

To resolve this issue, $C'_m{}^{n+1}$, was computed via linearly interpolating between $C'_{m-1}{}^{n}$ and $C_{bulk}{}^{n}$. The choice of linear interpolation (rather than, say, polynomial) is justified on the basis that δ should be of the order of R, while $\Delta x << R$, hence the real concentration profile between C'_{m-1} and C_{bulk} is practically a straight line (Figure 8-1). This leads to:

$$C'_m{}^{n+1} = \Delta x\left(\frac{C_{bulk}{}^{n} - C'_{m-1}{}^{n}}{\Delta x + \delta/R}\right) + C'_{m-1}{}^{n}$$

Eqn. 8 - 4

The code with Eqn. 8 - 4 is very stable, and $\Delta\tau_{iw}$ as large as 500 (compared with 0.01) can be used.

Another difference in the code, as compared to the closed system case, would be the desorption progress. The progress of desorption may be defined by the ratio of the sorbate mass desorbed at time t over the sorbate mass that will be desorbed after infinite time. Here, the mass desorbed after infinite time is simply the initial sorbate mass less the mass as restricted by the bulk phase sorbate concentration.

2.2. Char-in-Silt Case (Explicit, Finite Difference Scheme)

There are two main challenges in modeling the heterogeneous Char-embedded-in-Silt scenario (Figure 8-2): (i) how should diffusion be modeled at the Char-Silt interface, given that different discretization (numbers of grids) scheme may be needed for the two phases, and (ii) how would the change in phase geometry affect the governing equations, and hence the finite difference equations. The modeling of such a scenario, to the author's knowledge, has not been reported in environmental literature. In the spirit to invite scrutiny, comment, and suggestions for further improvement, the formulation of this model will be done in great detail. It should be noted that this model assumes radial (or uni-axial, in the cases of other geometries) diffusion.

2.2.1. Char-Domain

2.2.1.1. Aggregate-Volume Averaged Quantity

With geometry analogous to the single-domain aggregate, the overall char-domain volume averaged quantity of a particular property (e.g. porewater sorbate concentration), J_c, for the char domain (here assumed spherical) is simply a volume integral of the local property, j(r):

$$J_c = \frac{\int_{\forall} j d\forall}{\forall_{char}} = \frac{\int_0^{R_c} j 4\pi r^2 dr}{4\pi {R_c}^3/3} = \frac{3\int_0^{R_c} j r^2 dr}{{R_c}^3}$$

Eqn. 8 - 5

where j is some local property,

J_c is the overall char-domain volume-averaged property,

R_c is the radius of char (m),

$\forall_{char}$ is the aggregate volume for char-domain (include solid-char +void in char) (m^3).

In dimensionless form, this translates into:

$$J_c = \gamma \int_0^1 j {x_c}^{\gamma-1} dx_c$$

Eqn. 8 - 6

where γ is the Shape Factor (=3 for spherical, 2 for cylindrical, 1 for planar)

x_c is the dimensionless spatial variable in the char-domain.

Note that x_c is defined as r/R_c, where R_c is the char radius.

2.2.1.2. Spatial Discretization (Δx_c)

The spatial discretization in the char-domain depends on the char radius and the number of grids, m_c. It can be shown that Δx_c (dimensionless distance between two adjacent grid points) is:

$$\Delta x_c = \frac{\Delta r_c}{R_c} = \frac{1}{R_c}\frac{R_c}{(m_c - 1)} = \frac{1}{(m_c - 1)}$$

Eqn. 8 - 7

The distance of the i^{th} grid in the char domain from the aggregate core is simply:

$$x_{c,i} = \frac{r_i}{R_c} = (i - 1)\Delta x_c$$

Eqn. 8 - 8

2.2.2. Silt-Domain

2.2.2.1. Aggregate-Volume Averaged Quantity

The overall silt-domain volume averaged property requires some consideration. For a spherical aggregate, J_s is:

$$J_s = \frac{\int_{\forall} j d\forall}{\forall_{silt}} = \frac{\int_{R_c}^{R_{agg}} j 4\pi r^2 dr}{\forall_{agg} - \forall_{char}} = \frac{\int_{R_c}^{R_{agg}} j 4\pi r^2 dr}{\frac{4}{3}\pi {R_{agg}}^3 \left[1 - \left(\frac{R_c}{R_{agg}}\right)^3\right]} = \frac{3\int_{R_c}^{R_{agg}} j r^2 dr}{{R_{agg}}^3 \left[1 - \left(\frac{R_c}{R_{agg}}\right)^3\right]}$$

Eqn. 8 - 9

Where R_{agg} is the radius of the overall aggregate (m),

$\forall_{silt}$ and $\forall_{agg}$ are the volumes for silt-domain and the overall aggregate, respectively (m^3).

In dimensionless form, J_s is:

$$J_s = \frac{\gamma \int_{x_{s,B}}^{1} j {x_s}^{\gamma-1} dx_s}{(1 - {x_{s,B}}^{\gamma})}$$

Eqn. 8 - 10

where γ is the Shape Factor (=3 for spherical, 2 for cylindrical, 1 for planar)

x_s is the dimensionless spatial variable in the silt-domain.

Note that the x_s is defined differently from x_c, and that $x_{s,B}$ is the dimensionless distance from the aggregate-core to the char-silt boundary:

$$\textbf{Definition of } \mathbf{x_s}\textbf{:} \qquad x_s = \frac{r}{R_{agg}}; \qquad dx_s = \frac{r}{R_{agg}}$$

$$\textbf{at Char} - \textbf{Silt Boundary:} \qquad x_{s,B} = \frac{R_c}{R_{agg}}; \qquad x_{c,B} = \frac{R_c}{R_c} = 1$$

Eqn. 8 - 11

2.2.2.2. Spatial Discretization (Δx_s)

Analogous to the char-domain, with the silt domain sub-divided into m_s numbers of grids, Δx_s (dimensionless distance between two adjacent grid points) is:

$$\Delta x_s = \frac{\Delta r_s}{R_{agg}} = \frac{1}{R_{agg}} \frac{(R_{agg} - R_c)}{(m_s - 1)} = \frac{(1 - x_{s,B})}{(m_s - 1)}$$

Eqn. 8 - 12

The distance of the i^{th} grid in the silt domain <u>from the aggregate core</u> is simply:

$$x_{s,i} = \frac{r_i}{R_{agg}} = \frac{R_c}{R_{agg}} + (i - 1)\Delta x_s = x_{s,B} + (i - 1)\Delta x_s$$

Eqn. 8 - 13

2.2.3. Char-Silt Interfacial Diffusion

An 'imaginary' or 'shadow' grid approach was used for quantifying the char-silt interfacial diffusional flux. The idea is to create an imaginary grid point that has the same discretization distance (i.e. Δx) beyond the interface in the other domain, and use porewater concentration in that grid point to estimate the flux at the edge, as if the edge-grid is one of the intermediate shells. A cartoon of the 'imaginary' approach is shown in (Figure 8-3). A number of criteria/clarifications should be noted:

(i) $C'_{c,mc}$ represents the local dissolved/porewater phase concentration at the edge of the char in volume from ($R_c - \Delta r_c/2$) to R_c. (i.e. only half as wide as the normal shells). Other variables ($q'_{c,mc}$, $S'_{c,mc}$, and the same corresponding variables for the silt domain) have the same meaning.

(ii) Since diffusion takes place in dissolved phase (porewater), C' (local porewater concentration) must be continuous. That is: $C'_{c,mc}$ (edge grid in char domain) = $C'_{s,1}$ (first grid in silt domain).

(iii) But q' and S' can be discontinuous at the interface, since the char and the silt domains are likely to have different sorption coefficients (i.e. K_d). The two different (q')s or (S')s 'co-exists' at the interface.

(iv) With (ii) and assuming local equilibrium applies, q' and S' in the first shell in the silt-domain can be computed as $C'_{s,1} = C'_{c,mc}$.

Let us calculate the interfacial diffusional flux from the char-domain, supposing a shadow grid with spacing Δx_c exists in the silt domain next to the interfacial grid, (i.e. the m_c^{th} grid). Applying the governing equation for intermediate shells, we get:

$$\left(\frac{\partial q'}{\partial \tau}\right)_{cs} = \left\{\frac{\phi}{x^{\gamma-1}}\left[\frac{\partial}{\partial x}\left(F_{Tor}\, x^{\gamma-1}\frac{\partial C'}{\partial x}\right)\right]\right\}_{cs}$$

Eqn. 8 - 14

The subscript, **cs**, denotes that all variables are in the neighborhood of the char-silt interface. The 2nd order derivative essentially represents the difference of diffusional flux between the char-side and the silt-side. Thus, in finite difference form, the derivative term utilize properties from both the silt and the char domains:

$$\frac{{q'_{c,mc}}^{n+1} - {q'_{c,mc}}^{n}}{\Delta \tau_{iw}} = \frac{\phi_{cs}}{{x_{c,mc}}^{\gamma-1}\Delta x_c}[\mathbf{A} - \mathbf{B}]$$

$$\textbf{Silt} - \textbf{side Contribution:} \quad \mathbf{A} = \left(\frac{{C'_{c,mc+1}}^{n} - {C'_{c,mc}}^{n}}{\Delta x}\right){x_{c,mc+0.5}}^{\gamma-1} F_{Tor,S,mc+0.5}$$

$$\textbf{Char} - \textbf{side Contribution:} \quad \mathbf{B} = \left(\frac{{C'_{c,mc}}^{n} - {C'_{c,mc-1}}^{n}}{\Delta x}\right){x_{c,mc-0.5}}^{\gamma-1} F_{Tor,C,mc-0.5}$$

Eqn. 8 - 15

where γ is the Shape Factor (=3 for spherical, 2 for cylindrical, 1 for planar)

subscripts: 'c' for char, 's' for silt, 'mc' for edge grid of char,

superscripts: n for current timestep, n+1 for next timestep,

ϕ_{cs} is composite porosity at the interface and is approximated as $0.5(\phi_{c,mc}+\phi_{s,1})$.

Note that the finite difference equation for $\left(\frac{\partial C'}{\partial \tau}\right)_{cs}$ would be the same EXCEPT without the composite interfacial porosity ϕ_{cs}.

The imaginary/shadow grid porewater concentration can be fitted by a low-order polynomial. It should be noted that with the shadow grid, the outflux (or influx) from the interface into the silt can be so large that it produces unstable solution (e.g. oscillatory or negative concentrations). This has been observed for the boundary layer transfer problem (section 2.1.2). Second, in the case of char-silt interfacial diffusion, linear interpolation may not be appropriate as the concentration profiles in both domains are not likely to be linear.

2.2.4. Edge Shell of Aggregate or Silt-Domain

For closed system, the Edge Shell of the aggregate, $C'_{s,ms}{}^{n+1}$, was calculated by conservation of mass:

$$(Q_{char}\,\forall_{char} + Q_{silt}\,\forall_{silt} + C_{bulk}\,\forall_{bulk})^{n+1} = (Q_{char}\,\forall_{char} + Q_{silt}\,\forall_{silt} + C_{bulk}\,\forall_{bulk})^{n}$$

Eqn. 8 - 16

where Q's are the domain-averaged sorbate concentrations ($\mu g_i/L_{agg}$),

$\forall$'s are the volumes for the domains.

superscripts: n for current timestep, n+1 for next timestep.

All quantities at current time (n) are available, and most of the quantities at the next timestep can be calculated. The only two unknowns are Q_{silt} and C_{bulk} at n+1th timestep.

With Simpson's one-third rule, $Q_{silt}{}^{n+1}$ is simply

$$\int_a^b f(x)dx \cong \frac{\Delta x}{3}\left(f(x_1) + 4f(x_2) + 2f(x_3) + 4f(x_4) + \cdots 4f(x_{m-1}) + f(x_m)\right); \qquad x_1 = a, x_m = b$$

Eqn. 8 - 17

where $\mathcal{S}_i$ is the ith coefficient (i.e. 1, 4, 2, 4, ..., 4, 1).

$$\mathbf{Q_{silt}}^{\mathbf{n+1}} = \frac{\gamma \int_{x_{s,B}}^{1} j x_s{}^{\gamma-1} dx_s}{(1 - x_{s,B}{}^{\gamma})} = \frac{\gamma \Delta x_s}{3(1 - x_{s,B}{}^{\gamma})}\left[\left(\sum_{i=1}^{ms-1} \mathcal{S}_i q'_{s,i}{}^{n+1} x_{s,i}{}^{\gamma-1}\right) + \mathcal{S}_{ms} q'_{s,ms}{}^{n+1} x_{s,ms}{}^{\gamma-1}\right]$$

Eqn. 8 - 18

Assuming the silt-edge concentration is identical with the bulk phase concentration ($C'_{s,ms}=C_{bulk}$), it can be shown that:

$$\mathcal{A}_{1st}\,{C'_m}^{n+1} + \mathcal{A}_{nBC}\left({C'_m}^{n+1}\right)^{nBC} = \mathcal{B}$$

Eqn. 8 - 19

where the constants are:

$$\mathcal{A}_{1st} = \left\{\forall_{bulk\ aq.} + \frac{\forall_{silt}\,\gamma\Delta x_s}{3(1-x_{s,B}{}^{\gamma})}\left(\sum_{i=1}^{ms-1}\mathcal{S}_i\,{q'_{s,i}}^{n+1}\,x_{s,i}{}^{\gamma-1}\right)\left[f_{OC,s,ms}\,K_{OC}\,\rho_s\left(1-\emptyset_{s,ms}\right)+\emptyset_{s,ms}\right]\right\}$$

$$\mathcal{A}_{nBC} = \left\{\frac{\forall_{silt}\,\gamma\Delta x_s}{3(1-x_{s,B}{}^{\gamma})}\mathcal{S}_{ms}\,x_{s,ms}{}^{\gamma-1}\left[f_{BC,s,ms}\,K_{BC}\,\rho_s\left(1-\emptyset_{s,ms}\right)\right]\right\}$$

$$\mathcal{B} = \left({Q_{char}}^{n}\forall_{char} + {Q_{silt}}^{n}\forall_{silt} + {C_{bulk}}^{n}\forall_{bulk} - {Q_{char}}^{n+1} - \mathcal{C}\right)$$

$$\mathcal{C} = \left\{\frac{\forall_{silt}\,\gamma\Delta x_s}{3(1-x_{s,B}{}^{\gamma})}\left(\sum_{i=1}^{ms-1}\mathcal{S}_i\,{q'_{s,i}}^{n+1}\,x_{s,i}{}^{\gamma-1}\right)\right\}$$

Eqn. 8 - 20

3. Results & Discussion

3.1. Validation of Infinite-Bath Diffusion Model

Since the Infinite-Bath model was modified from the closed-system code, it was not validated as extensively as the parent code. Two validation tests were conducted: (i) that of varying 'R_{sw}', and (ii) that of varying aggregate geometry. The modeled output was compared against the analytical curves presented in Crank (1979).

3.1.1. Validation (I): Varying 'R_{sw}'

If the code for Infinite-Bath diffusion is correct, then it should produce identical profile for different 'R_{sw}' inputs. The code was run with 'R_{sw}' varying from 20–20000 mg_{solids}/L_w, and the resulting dimensionless profiles were all identical (Figure 8-4). Other parameters for the test are shown on the figure.

3.1.2. Validation (II): Congruence with Analytical Solutions

At the limit where the boundary layer film is completely absent (i.e. $\delta/R = 0$), the correct Infinite-Bath model should reproduce the desorption profiles from analytical solutions. To check this, the model was run at $\delta/R=0$ at three geometries ($\gamma=1$ to 3). For all three geometries, the model outputs were consistent with the analytical values (Table 8-1).

3.2. Validation of Char-in-Silt Diffusion Model

Since the Char-in-Silt model required greater modification on the code and involved making assumptions regarding the interfacial transfer, one would like to test the model at conditions such that potential error may be the most substantial. The model was validated against the analytical solution for: (i) varying K_dR_{sw}, and (ii) varying the relative radius ratio of the char-domain in the aggregate. In the validation runs, both domains were set to have the same properties (e.g. initial sorbate concentration, porosity, f_{OC}, K_{OC}, etc).

The model outputs generally agree well with the analytical solutions except for the later phase of desorption (~ 70–90% of completion) (Figure 8-5). The model appeared to predict a slower desorption rate at later time. The reason for the delay has not yet been identified; however, it could be associated with the interfacial diffusion. The indirect evidence for this can be observed in the desorption curves at K_dR_{sw}=0.1 (Figure 8-5). Two model outputs were shown where the one with a smaller char domain (R_c/R_{agg}=0.20) appeared to be much closer to the analytical curve. It the 'shadow grid' approach (section 2.2.3) tends to underestimate desorption rate across the char-silt boundary, then the delay should increase with greater interfacial area. This is consistent with the model outputs for K_dR_{sw}=0.1.

A good match in overall desorption progress with the analytical solution, however, is not a sufficient proof of the model's validity. The spatial-temporal local porewater concentration within the char-silt aggregate, $C'(x,\tau_{iw})$, exhibits a discontinuity in concentration gradient at the interface (Figure 8-6). This is not expected if both the char and the silt domains had identical physicochemical properties (e.g. constant K_d, $S_{pyr,o}$, porosity, etc) in the validation protocol. Despite that the R_c/R_{agg}=0.20 case matched well with the analytical solution (Figure 8-5), its $C'(x,\tau_{iw})$ actually exhibited a more abrupt discontinuity at the interface than the R_c/R_{agg}=0.50 case (Figure 8-6).

To what extent should the Char-in-Silt numerical code be trusted? The validation results in Figure 8-5 suggest that the model should be fairly accurate when (i) K_dR_{sw} is high, and (ii) the char domain is relatively small in the aggregate. Suppose that a typical char particle is ~10 μm in its longest dimension, the relative char radius (R_c/R_{agg}) would be ≤0.2 if it is embedded in an aggregate with size of 50 μm or greater. The error should not be significant for aggregates larger than 50 μm. And even for relatively large char-to-aggregate radius (R_c/R_{agg}), the model prediction is likely to be robust for determining desorption halftimes (i.e. time at which $(M_o-M_t)/(M_o-M_\infty)$=0.5). Although the model produces the numerical artifact at the char-silt interface (Figure 8-6), this issue should be much less important for real aggregates embedded with char. The reason is that the sorption coefficient (K_d) of real char/charcoal is of orders of magnitude higher than that of typical silt, for the former is high in both OC/BC contents. We would, therefore, expect concentration gradient discontinuity similar to those shown in Figure 8-6 to be present for real char-silt particles. This is to say that the numerical artifact may be less relevant for real aggregates.

3.3. Infinite-Bath Diffusion

With the Infinite-Bath numerical model validated, desorption of HOCs (with non-linear sorption isotherm) under infinite-bath conditions can be examined. In this section, we will look into how HOC desorption rates vary with the mass-transfer boundary layer film thickness (δ) and the bulk aqueous phase concentration (C_{bulk}). The detail simulation parameters are listed in Table 8-3

3.3.1. Effect on Desorption Rate: (I) Boundary Layer Film Thickness (δ)

The effect of mass transfer boundary layer is often neglected in the modeling of HOC transfer between geosorbents and aqueous phase. The classical analytical solutions for diffusion problems by Crank (1979), for instance, do not account for boundary layer effect. This may be understandable for two reasons. First, the boundary layer thickness enters the problem as an additional independent variable. Second, the determination of boundary layer film thickness is by itself non-trivial for the film thickness is a function of the system hydrodynamic properties and sorbent/particle characteristics (Levich 1962; Deen 1998; Probstein 2003).

Here, it is assumed that the boundary layer film thickness, δ, can be determined with proper knowledge of the hydrodynamic condition in a given solid-water system. For the purpose of simulating mass-transfer across the film, we assume that the maximum δ to be comparable to the characteristic size of the aggregate – that is, $\delta/R=1$ (R is the aggregate radius).

3.3.1.1. With Linear K_d

The diffusion rate generally decreases with thicker boundary layer film (Figure 8-7). Taking the no-film scenario (i.e. Crank's solution) as reference, desorption can slow down by as much as about 10 times (for $\delta/R=1$). While a film thickness of $\delta/R=1$ may be inappropriate for solids in high turbulence system (e.g. entrainment in riverine flow, resuspension), it may be realistic for the aggregates in sediment beds. This additional 'retardation' due to boundary layer film should be noted when evaluating the diffusive flux of HOCs out of solids present in low turbulence systems.

3.3.1.2. With Nonlinear K_d

The diffusion/desorption rate decreases dramatically with increasingly non-linear isotherm. Simulation was conducted on the four isotherms discussed earlier (Chapter 7, Table 7-2) at some typical OC/BC contents (here assumed $f_{OC}=0.02$ and $f_{BC}=0.002$[1]) and sedimentary pyrene concentration (assumed $S_{pyr,o}=1000\ \mu g_{pyr}/kg_{solids}$). The simulation results show that desorption rate varies substantially with different isotherms (Figure 8-8). For instance, the desorption half-time, $t_{1/2}$, for the Classical-OC model is about 4 d; that for the Old-OC-BC or the Occlusion models is about 2–10 mo; and the $t_{1/2}$ for the New-OC-BC is as long as 6 yr (Figure 8-8; $\delta/R=1$). Similar effect of non-linearity on desorption half-time is also observed at constant $\log K_{OC}$ and $\log K_{BC}$ but with a varying n_{BC} (Figure 8-9). Considering the fact that (i) $\log K_{OC}$'s and $\log K_{BC}$'s are fairly

[1] This was based on the typical sedimentary f_{TOC} (Appendix 7-22) and the report that sedimentary BC is approximately 10% of sedimentary TOC (Cornelissen et al. 2005b).

constant across the different isotherms (Table 7-2), and (ii) the partitioning coefficient, K_d, is a strong function of n_{BC}, it is clear that n_{BC} – or isotherm non-linearity – plays a key role in determining the diffusion/desorption rate of HOCs.

3.3.2. Effect on Desorption Rate: (II) Bulk-Aqueous Phase Concentration (C_{bulk})

For systems with non-linear isotherms, the rate of desorption is also sensitive to the bulk aqueous phase sorbate concentration, C_{bulk}. For $n_{BC}<1$, the presence of small amount of sorbate in the bulk aqueous phase generally shortens the desorption time-length of bound sorbate (Figure 8-10). In the figure, the cases where $C_{bulk}=0.01\ \mu g_{pyr}/L_w$ appear to have a slightly shorter desorption half-time than those with $C_{bulk}=0$. Note that the linear case (labeled as 'Classical-OC', $n_{BC}=1$) does not respond to different C_{bulk}. This is because K_d of the linear case remains constant throughout the time course of desorption.

Although C_{bulk} affects the progress of desorption, its effect is comparatively small. First, smaller reduction in desorption time is observed for slightly non-linear cases – even at $n_{BC}=0.62$ (i.e. the 'Old-OC-BC' case in Figure 8-10), the curves for $C_{bulk}=0$ and 0.01 $\mu g_{pyr}/L_w$ are very close to each other until towards the completion of desorption. The differences only become more distinct with the Occlusion and the New-OC-BC model ($n_{BC}=0.42$ and 0.25, respectively; Figure 8-10, lower graph). Second, the effect of C_{bulk} is much less pronounced at the early phase of desorption (i.e. sorbate desorbed at t/sorbate desorbed at t_∞) than near completion (both graphs in Figure 8-10). Based on these two observations, one may estimate/approximate the rate of desorption in the early phase with that from a 'similar' C_{bulk}.

3.3.3. Implication for Persistence of HOCs

The strong dependence of desorption/diffusion rate with isotherm non-linearity may partly explain the persistent presence of HOCs in sediment-water systems. With the Classical-OC isotherm, one would form an 'incorrect' expectation that soil/sediment bound HOCs should be half gone after a few days upon intensive flushing (e.g. tidal flushing, riverine wash-out, rain/surface runoff). Isotherm non-linearity, however, slows down the release rate of the sorbate significantly – the desorption half-time is still on the yearly timescale even with continual exposure to clean water. If we further consider the fact that natural sedimentary particles are typically non-spherical (Pike et al. 1996), the actual desorption rate would be even slower (e.g. Figure 8-7; also see Crank 1979).

With improper assumptions regarding isotherm linearity, we would *incorrectly* anticipate organic pollutants to be long gone when, by nature of their non-linear sorption to geosorbents, they actually desorb very slowly. In such cases, therefore, it is not proper to describe the bound organic sorbates as 'sequestered' (which means long residence time and chemical/biological inaccessibility due to physical occlusion or other 'unknown' causes), but rather as a very slowly accessible pool. This is not a mere issue of terminology – sequestration suggests that the bound sorbate does not have the potential *at all* to be bioavailable or chemically accessible.

The regional fate of HOCs with highly non-linear sorption is also less predictable in environments similar to the Infinite-Bath scenario (e.g. sedimentary PAHs in harbor

well-flushed by oceanic water). With monthly to yearly long desorption half-time comparable to the timescale of sedimentation, these HOCs may be 'buried' before they become released into the water column or relocated/washed to a different location. However, the loosely formed surficial bed layer may be vulnerable to the shear of storms. The 'buried' HOCs can be mobilized via desorption during and immediately after storm episodes. That is to say, episodic weather events may impose a huge forcing on the fate of HOCs on top of their 'normal', day-to-day interactions with the harbor/estuarine/riverine environment.

3.4. Infinite-Bath Diffusion – Selected PAHs

The Infinite-Bath diffusion model can now be extended to a wider range of HOCs. For illustration, the following four PAHs were selected for modeling: naphthalene, phenanthrene, pyrene, and benzo(a)pyrene. They were selected for (i) their varying degree of hydrophobicity (i.e. $\log K_{OW}$), (ii) their molecular structures (e.g. number of rings; all planar), (iii) their potential/confirmed toxicity, and (iv) availability of their sorption data in literature (i.e. $\log K_{OC}$ and $\log K_{BC}$).

3.4.1. Assumptions and Approach

A number of assumptions were made for the modeling of the PAH desorption. First, it was assumed that the $\log K_{BC}$ of an individual remained constant, and that the distribution of $\log K_{BC}$ reported in literature was mostly due to the variation in n_{BC}. Earlier, the author has argued both $\log K_{OC}$ and $\log K_{BC}$ for pyrene appears to be relatively well constrained (distribution of values within 1 log unit; see Chapter 5, Table 5-9), and that the observed range of n_{BC} is mostly likely due to the relative ratio of BC sorptive area/sites to sorbate concentration (Chapter 5, section 3.2.2.3 and Figure 5-7). $\text{Log}K_{BC}$'s of the PAHs were estimated (as average of the reported range) based on both reported values from past sorption studies. The average, observed $\log K_{BC}$'s were then checked against the linear-free energy relationship (LFER) derived $\log K_{BC}$'s proposed in Schwarzenbach et al. (2003) and Lohmann et al. (2005). $\text{Log}K_{OC}$'s of the four PAHs were estimated using the correlation suggested in Schwarzenbach et al. (2003). A summary of $\log K_{OC}$'s, $\log K_{BC}$'s and free water diffusivities for the four PAHs is provided in Table 8-2. The reported literature and LFER $\log K_{BC}$'s are summarized in Appendix 8-1.

Second, it was assumed that (i) n_{BC} could vary from the linear case (n_{BC}=1) to the highly non-linear scenarios (n_{BC}=0.2), (ii) the initial sorbate concentration ranged from 'low' to 'high' ($S_{PAH,o}$ = 200, 1000, 5000 $\mu g_{PAH}/kg_{solids}$), (iii) the geosorbent contains 'typical' amounts of OC and BC (here assumed f_{OC}=0.02 and f_{BC}=0.002), and (iv) the dimensionless boundary layer film could vary from δ/R = 0–1. This simulation exercise only examined a 'moderately large' aggregate (R=100 μm). Other simulation parameters are summarized in Table 8-3.

Note that the 'linear' case (n_{BC}=1) corresponded to the Classical-OC model. That is, $\log K_{BC}=\log K_{OC}$=4.7 and f_{OC}=0.022 (f_{BC}=0). The linear Classical case served as reference for comparison. All simulated desorption curves for the four PAHs can be found in Appendix 8-2.

3.4.2. Effect on Desorption Rate: (III) Sorbate Hydrophobicity

Desorption rate generally decreases with increasing hydrophobicity, as expected from knowing how intra-particle diffusion is retarded by the diffusate to the sorbent surface/domain (Figure 8-11). The figure also demonstrates different PAHs desorb/diffuse at rates that differ by orders of magnitude. For instance, the time of complete desorption for naphthalene occurred at around $\tau_{iw}=10^3$; that for phenanthrene was around 10^4; and τ_{iw} ranged from about 10^4–10^5 for pyrene and benzo(a)pyrene (Figure 8-11).

It is also clear, from Figure 8-11, that the sensitivity of kinetics to isotherm non-linearity increases significantly with sorbate hydrophobicity. For naphthalene, the simulated curves at $n_{BC}=0.2$–0.8 were all very close to each other. On the other hand, those for pyrene or benzo(a)pyrene spread out very widely with respect to time (τ_{iw}). The desorption half-time for pyrene was about 3 orders of magnitude apart between $n_{BC}=0.2$–0.8, whereas that for benzo(a)pyrene was about 8 orders of magnitude apart for the same n_{BC} range.

The insensitive nature of Infinite-Bath diffusion to n_{BC} at low K_{OW} organic sorbates has a practical implication. If the Intra-particle Porewater Diffusion model is indeed a correct conceptualization of HOCs desorption in real geosorbents, then it appears that the diffusional behavior of low hydrophobicity HOCs (e.g. naphthalene) can be modeled simply assuming a linear isotherm. That is, the knowledge of n_{BC} becomes irrelevant for the purpose of modeling the uptake/release kinetics. In contrast, to understand the kinetics of high hydrophobicity HOCs, and subsequently their bioavailability in the environment, an accurate knowledge of n_{BC} is necessarily and critical.

3.4.3. Effect on Desorption Rate: (IV) Solid-Phase Sorbate Concentration

As non-linear isotherms imply the dependence of partition coefficient on sorbate concentration, one can expect that the rate of desorption/diffusion will have some dependency on the initial solid-phase sorbate concentration ($S_{PAH,o}$). This is indeed the case for high hydrophobicity PAHs, as shown in the upper graph of Figure 8-12 (for pyrene). Desorption half-time varies by 1 order of magnitude for the range of $S_{pyr,o}$ from 200 – 5000 $\mu g_{pyr}/kg_{solids}$ ($n_{BC=0.6}$) Such dependency was completely absent in the the linear, Classical case ($n_{BC}=1$).

A similar insensitivity of kinetics to $S_{PAH,o}$ was also observed for naphthalene (lower graph of Figure 8-12). The plot again demonstrated that the sorption of low hydrophobicity HOCs may be treated as linear for practical estimation of their uptake/release kinetics.

3.5. Closed-System Diffusion

Non-linear diffusion in closed systems is of interest not only for understanding release kinetics of HOCs in batch experiments but also for desorption in realistic environments. In the last section, it has been shown that episodic storm events may promote release of bound HOCs by disturbing/mobilizing the surficial sedimentary layer. In such cases, the local volume of water column near the disturbed bed may behave more like a closed

system. Here, only the diffusion/desorption of naphthalene and pyrene have been examined as representative of low and high hydrophobicity HOCs, respectively.

3.5.1. Assumptions and Approach

Similar assumptions regarding $\log K_{BC}$, $\log K_{OC}$ and n_{BC} were made as for the Infinite-Bath case (section 3.4.1). The values of $\log K_{OC}$'s, $\log K_{BC}$'s and free water diffusivities are listed in Table 8-2. The simulation parameters are summarized in Table 8-3. Due to the fact that closed-system with highly non-linear sorption isotherm reaches equilibrium very quickly (e.g. n_{BC}=0.2), a very high degree of discretization would be need to compensate the edge-grid error (see Chapter 7, section 4.2.3). Furthermore, solving highly non-linear equations require greater numbers of numerical iterations. For these two reasons, the lowest n_{BC} simulated was 0.4 rather than 0.2. Also for the reason of edge-grid contributed error, the early time portion of the concentration-time curves for high R_{sw}'s should not be taken as accurate as that at later times.

Note again that the 'linear' case (n_{BC}=1) corresponded to the Classical-OC model ($\log K_{BC}=\log K_{OC}$=4.7 and f_{OC}=0.022, f_{BC}=0). The simulated desorption curves for naphthalene and pyrene are available in Appendix 8-3.

3.5.2. Effect on Desorption Rate: (I) Solids-to-Water Ratio (R_{sw})

For high hydrophobicity HOCs, the rate of desorption is highly affected by both R_{sw} and isotherm linearity (Figure 8-13). The figure shows the simulation at three R_{sw}'s for linear case (n_{BC}=1) and non-linear case (n_{BC}=0.4). The spreading of the mass desorbed-time curves was much more significant in the non-linear case. Also note that the initial solid-phase concentration ($S_{pyr,o}$) has a weak but noticeable effect of the locations of the curves as well.

In the case of naphthalene, the desorption curves appear to be utterly insensitively to variation in R_{sw}'s for both linear and non-linear isotherms (Figure 8-14). The collapse of all curves into one region can be easily appreciated when we consider the fact that retardation for naphthalene at R_{sw}=1000 mg_{solids}/L_w range is rather insignificant. At $C_{naph,w} \leq 50$ $\mu g_{naph}/L_w$, $K_{d,naph}$ (at f_{OC}=0.02, f_{BC}=0.002) would be no more than 1000 L/kg; taking the highest R_{sw} tested (2000 $mg_{solids}/L_w = 2\times10^{-3}$ kg_{solids}/L_w), this would means the tested scenarios are close to the Infinite-Bath limit. Hence all the desorption curves for naphthalene are in close vicinity to each other. A similar case is observed for pyrene at 2000 mg_{solids}/L_w (Figure 8-15).

3.5.3. On Interpreting the Rate in Closed-System: f_{des} vs $\tau_{iw,1/2}$

It should be noted that in Closed-System diffusion, a shorter desorption half-time often correlates with a smaller fraction of desorbed sorbate. If the question of interest is a purely kinetic one – with no concern on the fraction of HOCs remaining in the solid-phase – then the mass desorbed-time curve can be used as is. If, however, both how much can be desorbed and the rate of desorption are of concern, then one should reconsider the issue of desorption speed. This would be the case, for instance, when analyzing the bioavailability of soil/sediment bound HOCs.

It turns out that the fraction of sorbate that can be desorbed (f_{des}) – defined as $(M_{pyr,o}-M_{pyr,\infty})/M_{pyr,o}$ – increases with the desorption halftime, $\tau_{iw,1/2}$ (Figure 8-16). The figure

suggested that it may not be possible to locate a simple 'optimal' point between fraction desorbed and the rate. The trend in fraction desorbed-$\tau_{iw,1/2}$ across the three initial solid-phase concentrations ($S_{pyr,o}$) also demonstrates why we would see the most dramatic attenuation of the sorbed-HOCs in sites with very high initial solid-phase HOC concentrations (e.g. after oil/organic waste spillage, or the application of dynamite or pesticide in soil, etc). For instance, at $S_{pyr,o}$=5000 $\mu g_{pyr}/kg_{solids}$, about 40% (i.e. ½ of 80%) of the bound pyrene can be desorbed after a τ_{iw} of ~10000; while at $S_{pyr,o}$=1000 $\mu g_{pyr}/kg_{solids}$, the same fraction of removal requires a much longer desorption time (Figure 8-16). Note that in the case of the linear, Classical-OC isotherm (n_{BC}=1), the sorbate would not experience a diminished release over time.

3.6. Char-in-Silt (Closed-System)

3.6.1. Preliminary Notes

3.6.1.1. Assumptions and Approach

Similar assumptions regarding $logK_{BC}$, $logK_{OC}$ and n_{BC} were made as for the Infinite-Bath case (section 3.4.1). The values of $logK_{OC}$'s, $logK_{BC}$'s and free water diffusivities are listed in Table 8-2. The simulation parameters are summarized in Table 8-3. The char-domain was assumed to be purely BC in composition (f_{BC}=1). This assumption was made for illustrating any special features, at their maximal extent, in the desorption curve of the Char-in-Silt configuration. Due to the high computational cost, n_{BC} was set at 0.6 rather than the lower values of 0.2 or 0.4. Only the non-linear isotherm was examined.

3.6.1.2. Concept (I): Initial Porewater Concentration ($C_{agg,pw,o}$)

Since there are two domains of different sorptive capacities in the Char-in-Silt configuration, it is more convenient to discuss the sorbent-phase concentration using the Aggregate Porewater Concentration. In all the subsequent numerical results, it was assumed that sorption equilibrium was completely established within the aggregate between both char and silt domains. This means that the Initial Aggregate Porewater Concentration, $C_{agg,pw,o}$, in both domains is set to be equal.

3.6.1.3. Concept (II): Char-to-Aggregate Size Ratio (R_c/R_{agg})

The desorption profiles in Char-in-Silt scenarios would vary with the relative size of the char domain. In the subsequent sections, the relative size of the char domain will be described with the Char-to-Aggregate Radius/Size Ratio, which is defined as:

$$\text{Char} - \text{to} - \text{Aggregate Ratio} = \frac{R_c}{R_{agg}} = \frac{\text{radius of char domain}}{\text{radius of entire aggregate}} \leq 1$$

Eqn. 8 - 21

This definition also conforms well with other dimensionless spatial quantities (e.g. x=r/R, δ/R, etc).

3.6.1.4. OC and Soot-BC in the Silt Domain

The silt domain can have OC and BC contents that are different from that of the char domain. The model assumed that BC in the silt domain existed as soot particles/clusters homogeneously distributed throughout the domain. The OC and BC contents in the char and the silt domains are summarized in Table 8-3b.

3.6.2. Effect on Desorption Rate: (I) Char-to-Aggregate Size Ratio (R_c/R_{agg})

It is much harder to summarize the features in the desorption profiles for the Char-in-Silt cases (Figure 8-17). In the cases where the Char-to-Aggregate ratio is small (R_{agg}=50, 100 μm), two phases seemed to exist in the desorption curve. The 'intermediate plateau' (highlighted region in Figure 8-17) was, however, absent in when the char-domain is relatively large (R_{agg}=25 μm); instead, the curve seemed to have a prolonged early desorption phase. As a result of this prolonged/delayed desorption, the case with the highest Char-to-Aggregate size ratio had the longest desorption halftime ($\tau_{iw,1/2}$ = 9.4×10^5), followed by the 50-μm-radius aggregate ($\tau_{iw,1/2}$ = 4.2×10^5) and the 100-μm-radius aggregate ($\tau_{iw,1/2}$ = 3.7×10^4).

One can get a clearer picture of desorption dynamics by examining the profiles of local porewater sorbate concentration, $C'_{pyr}(x,\tau)$, as a function of both time and space (Figure 8-18). The small arrows on the figure indicated where the Char-Silt interface was located on the dimensionless spatial scale. In all three R_c/R_{agg}'s, the char-domain porewater concentration remained unchanged from the initial value until around $\tau_{iw}=2\times10^5$, where the concentration front (sharpest slope) coincided with the location of the Char-Silt interface. The aggregate with relatively larger char-core also desorbs less, as the equilibrium/end-point C'_{pyr} tends to increases with R_c/R_{agg} ratio. Note that in all cases, the char radius was assumed to be 10 μm (Table 8-3b).

The local partition/sorption affinity in the char and the silt domains can be observed in a $K'_{d,pyr}$-x profile (Figure 8-19). The char domain, assumed to be purely BC in composition, exerted a much higher sorption affinity for pyrene than the silt domain. $K'_{d,pyr}$ in both domains changed with the progression of desorption, with the most significant change occurring near the edge of the aggregate (x=1) at an early time ($\tau_{iw}=10^3$).

3.6.3. Effect on Desorption Rate: (II) R_{sw}

A higher R_{sw} affects the desorption of HOCs from char-embedded silt in two ways: it shortens the desorption halftime and it blurs out the features peculiar to the Char-in-Silt configuration. At two R_c/R_{agg} size ratios (Figure 8-20), it can be seen that desorption speeds up with higher R_{sw}. It can also be observed that at R_{sw}=2000 mg_{solids}/L_w, the desorption curve loses the transitory feature (i.e. around $\tau_{iw}=10^4$–10^5 in Figure 8-20) visible at lower R_{sw}'s. This may be explained by the fact that at high R_{sw}, the minute amount of pyrene desorbing from the silt domain is sufficient to bring the system to sorption equilibrium without having the char domain feels the presence of a strong concentration gradient.

This means that if char particles are indeed present in real environment, they may not be 'perceivable' unless they are exposed to a huge desorptive driving force (i.e. low R_{sw},

high f_{des}) for long period of time. In contrast, the presence of sooty BC, even in minute amount (f_{BC}~10%f_{OC}) can be observed by the non-linearity of BC adsorption, by the variability of desorption halflife, or by their effect on fraction desorbed (f_{des}).

3.6.4. Effect on Desorption Rate: (III) Char Domain Porosity/Tortuosity

While the intra-aggregate porosity of typical surficial sedimentary particles (or aggregates, flocs) may be similar, the porosity of char particles can vary very substantially, depending on their combustion history and condition. It is therefore necessary to evaluate how porosity/tortuosity may affect the release of bound HOCs in char-embedded aggregates.

As expected, desorption proceeds faster at high porosity (e.g. ϕ_{char}=0.9 in Figure 8-21) than at the 'silt' porosity (ϕ_{char}=0.15). Char-domain porosity also blurs out the feature specific to char in a way similar to R_{sw}. However, the importance of char-porosity diminished with the R_c/R_{agg} size ratio. For instance, in a 100-μm-radius aggregate, the desorption curves almost coincide with each other even when ϕ_{char} varies substantially. On comparing Figure 8-21 (char-porosity effect) with Figure 8-20 (R_{sw} effect), char-porosity may be considered as a kinetic parameter of secondary importance.

3.7. Char-in-Silt (Infinite-Bath)

3.7.1. Effect on Desorption Rate (I): R_c/R_{agg} Size Ratio

The desorption halftime generally decreases with smaller R_c/R_{agg} size ratio (Figure 8-22). For the particular simulation condition Figure 8-22, $\tau_{iw,1/2}$ for the 100-μm radius case was around 10^5; the halftimes for the 50-μm and the 25-μm were about 10^6 and 3×10^6, respectively. From the simulation results, one can expect an order of magnitude uncertainty in desorption rate as contributed by the relative size of the char-domain.

3.7.2. Effect on Desorption Rate (II): $C_{agg,pw,o}$

For HOCs with non-linear sorption, the retardation of intra-sorbent diffusion is highly dependent on the local dissolved phase HOC concentration, and hence one may expect the initial aggregate porewater HOC concentration, $C_{agg,pw,o}$, to affect the rate of diffusion somewhat significantly. It turned out that $C_{agg,pw,o}$ plays only a secondary role in determining the rate of desorption (Figure 8-23). The figure showed that the desorption timescale shift by no more than 0.5 log unit for a 25-times variation in $C_{agg,pyr,o}$ (at n_{BC}=0.6) In the Infinite-Bath scenario, the retardation of diffusion is controlled more by the bulk phase concentration rather than the initial aggregate porewater concentration. In fact, one may argue that the ordering of the desorption curves in Figure 8-23 can be conceptually explained by the increasing driving force for desorption (i.e. $C_{agg,pw,o}$–$C_{bulk,constant}$).

3.7.3. Comparison with Other Configurations: Concluding Char-in-Silt Model

The author will conclude the discussion on the Char-in-Silt model by comparing it with other aggregate configurations. Consider the chemical nature of the char domain: how would the desorption curve change with different char-domain composition? Some representative numerical results are shown in Figure 8-24. The simulation results

suggested that, even with half of the domain replaced as OC rather than BC, the char-domain can still exert a similar degree of retardation on the diffusion of pyrene as the purely BC case (i.e. the curve with $f_{BC,char}=1$). On the other hand, in aggregates with purely OC core (i.e. $f_{OC,char}=1$), pyrene would desorb much faster than from ones with purely BC core.

Two implications may be drawn from these observations. First, we have to differentiate BC from OC for assessing the kinetics of HOCs release/uptake accurately. Treating char-BC as 'OC' would distort our expectation of the kinetics of the diffusate. In view of the ubiquitous production of char in the environment (e.g. forest fire → soil → erosion → river/lake/estuary, etc), if we care about the fate of bound-HOCs in the presence of char, we would need a robust analytical method for identifying its presence in environmental samples. From the results presented in one recent inter-laboratory comparison study on BC quantification method (Hammes et al. 2007), it is unclear whether μm-BC (e.g. char) can be methodologically distinguished from nm-BC (e.g. soot). It appears to the author that a combination of analytical-BC methods with additional size distribution analysis may be necessary.

The second implication from Figure 8-24 is the 'purity' of the char-domain may be relatively less important for kinetic questions on the fate of the bound HOCs. As long as the presence of a char-core is identified and its size known, the kinetics of desorption can be reasonably predicted.

We will end this discussion by comparing the release dynamics of HOCs from a Char-in-Silt aggregate with that from a homogenous sooty-silt aggregate, and that from a single, char-only particle. Simulations at typical silt/char dimensions showed that the presence of char makes a significant difference in the rate of HOCs diffusion (Figure 8-25). This, again, pointed to a need to identify the presence of char particles in environmental samples.

4. Conclusion

In this chapter, the Intraparticle Porewater Diffusion model has been applied to the modeling of HOC desorption dynamics in Infinite-Bath environment and from the heterogeneous Char-embedded-Silt aggregates. In the Infinite-Bath model, the diffusive delay due to boundary-layer transport has been incorporated. It allows the user to link up the hydrodynamic properties (e.g. turbulence) in a solid-water system with the mass transfer of HOCs. In the Char-in-Silt model, the user can simulate the diffusive transport of HOCs within aggregate with compositional (e.g. BC or OC content) heterogeneity. To the author's knowledge, this has not yet been reported in the modeling literature in environmental chemistry/engineering. The heterogeneous model is by no means limited to char – it can be extended to other general dual-domain diffusive problems. A great level of parametric flexibility (e.g., variable aggregate shape; variable spatial porosity, tortuosity factor, f_{OC}, f_{BC}, etc) has been allowed in both models. The model codes are documented in Appendix E (Script E-7 to E-9).

The influence of different aggregate configurations (i.e. silt, char-in-silt, char only), system nature (closed-system vs infinite-bath), HOC hydrophobicity (e.g. organic sorbates of different K_{OC} or K_{OW}), isotherm non-linearity (n_{BC}), and many other physicochemical parameters on intraparticle diffusion kinetics have been explored. Although the effort was not exhaustive, a number of important points can be made regarding the modeling of HOCs desorption from soil/sediment. They are the following:

(i) Isotherm non-linearity can affect the release dynamics of HOCs very significantly. The claim of observing sequestration (or thermodynamically 'unexpected' persistence) of HOCs in natural soils/sediments may be partly explained by the negligence of non-linear effects (section 3.3.3).

(ii) For diffusate of low hydrophobicity (i.e. small $\log K_{OW}$, $\log K_{OC}$), its desorption dynamics appears to be insensitive to isotherm non-linearity, initial solid-phase loadings, or the distinction between OC and BC. This means that the release kinetics of low hydrophobicity HOCs may be conveniently evaluated in the Classical-OC framework (e.g. from the dimensionless plots in Wu et al. 1988). In PAHs, naphthalene is a representative for a low hydrophobicity sorbate (section 3.4.2, 3.4.3).

(iii) For diffusate of high hydrophobicity, the timescale of desorption is highly dependent on isotherm linearity. Taking the diffusion in Infinite-Bath as an example, desorption halftimes can vary up to 3 and 8 orders of magnitude of pyrene and benzo(a)pyrene, respectively (section 3.4.2). An accurate knowledge of isotherm non-linearity and initial sorbate concentration (which affects the partition coefficient, K_d, and hence the extent of retardation) is, therefore, critical for the kinetic evaluation of high hydrophobicity HOCs.

(iv) In closed-system diffusion, the fraction of sorbate that can be desorbed, $f_{des}=(M_{pyr,o}-M_{pyr,\infty})/M_{pyr,o}$, increases with the desorption halftime, $\tau_{iw,1/2}$, without exhibiting any optimal or maximal point (Figure 8-16). Isotherm non-linearity makes it harder to desorb the same fraction at lower residual HOCs concentration. This may partly explain why the most dramatic attenuation of the bound-HOCs concentrations is often observed in sites with high initial solid-phase concentrations (e.g. after oil/organic waste spillage or the application of dynamite/pesticide in soil) (section 3.5.3).

(v) In Char-in-Silt diffusion, the kinetics of desorption depends strongly on the relative size ratio of the char domain to the entire aggregate (i.e. R_c/R_{agg} size ratio) and the solids-to-water ratio of the system (R_{sw}) (section 3.6.2, 3.6.3).

(vi) Simulation results in Infinite-Bath diffusion suggested that, for kinetic questions, it is critical to not to treat char as a core of OC. In this respect, further methodological work may be necessary for identifying the presence of char in natural soils/sediments. What is more 'fortunate' is that we may reasonably estimate the kinetics of desorption without knowing the purity of the char-domain (i.e. what much of char is purely BC, how much OC?) (section 3.7.3).

Chapter 9. Regional Modeling of Pyrene in Harbors & Estuaries

CHAPTER ABSTRACT

The applicability of a simple box model to harbors and estuaries with persistent HOCs was examined, using pyrene as a model HOC and Boston Harbor as a model water body. The model results showed that the assumption of equilibrium partitioning between the harbor water and the surficial bed is inappropriate and would give rise to unrealistic predictions on dissolved and sediment-phase pyrene concentrations.

However, realistic predictions can be obtained when assuming the harbor was at pseudo steady-state amidst the different pyrene transformation and transport processes. Results from the steady-state model also suggested that mobilization from resuspended sediment is important in Boston Harbor. The potential significance of resuspension in mobilizing sedimentary HOCs in other estuaries and harbors was raised. A preliminary review of field observations and experimental evidence from other studies also found support for the idea of resuspension-mediated HOCs release.

This chapter showed that a simple steady-state box model can be a useful and cost-effective tool for assessing the 'background' state(s) of persistent HOCs (such as pyrene) in estuaries, harbors, and lakes. The model results also suggested the potential importance of resuspension-mediated HOC mobilization – a process that has been inadequately documented in field studies and the dynamics of which is currently poorly understood. With the knowledge that sediment resuspension, due to both natural causes and/or anthropogenic activities, is common in many highly urbanized or industrialized estuaries/harbors and coastal zones, it is necessary to further our understanding on how sediment resuspension may contribute to the release of bed-associated HOCs.

Table of Content for Chapter 9

1. Chapter Introduction, Scope, and Objective 222

1.1. Introduction 222

1.1.1. Mobilization of Bound-HOCs from Sediment 222

1.1.1.1. Sediment Dredging Induced Suspension 222

1.1.1.2. Natural Forces Induced Suspension 222

1.1.1.3. Navigation Induced Suspension 223

1.1.2. How Significance is Sediment Resuspension on the Fate of HOCs? 223

1.1.3. Box Modeling 223

1.2. Objectives 224

2. Methodology of Analysis: Approach and Assumptions 225

2.1. Characteristic Times of Various Processes in Boston Harbor 225

2.2. Equilibrium Partitioning Approach 225

2.2.1. Surficial-Bed Layer & Water Column at Sorption Equilibrium 226

2.2.1.1. Solving Pyrene Concentration in Water Column ($C_{pyr,WC}$) 226

2.2.1.2. Solving Depletion Half-time for Sediment-Bed Pyrene ($t_{bed,1/2}$) 227

2.2.2. Total Suspended Solids (TSS) & Water Column at Sorption Equilibrium 228

2.2.2.1. Solving Pyrene Concentration in Water Column ($C_{pyr,WC}$) 228

2.2.2.2. Solving Depletion Half-time for Sediment-Bed Pyrene ($t_{bed,1/2}$) 229

2.3. Steady State Approach 230

2.3.1. General Assumptions 230

2.3.2. Steady State Model: Three-Rate Model 231

2.3.2.1. TSS Desorption 231

2.3.2.2. Porewater Flushing 232

2.3.2.3. Water Column Flushing 233

2.3.3. Steady State Model: Seven-Rate Model 233

2.3.3.1. Atmospheric Deposition of Pyrene 234

2.3.3.2. Biodegradation of Pyrene 234

2.3.3.3. Freshwater Inflow of Pyrene 234

2.3.3.4. Photolysis of Pyrene 235

2.4. Sensitivity Analysis 235

3. Results & Discussion 235

3.1. Field Observed $C_{pyr,WC}$ and $S_{pyr,bed}$ in Boston Harbor 235

3.2. Bed-Water Column EqP Model 236

3.3. Total Suspended Solids (TSS)-Water Column EqP Model 236
3.4. Three-Rate Steady State Model 237
3.4.1. Importance of Desorption from Suspended Solids 237
3.5. Seven-Rate Steady State Model 238
3.5.1. Atmospheric and Riverine Input of Pyrene 238
3.5.2. Predicting Seasonal Variation of $C_{pyr,WC}$ 239
3.6. Secondary Supports for TSS-Desorption as Key Pathway of HOCs 239
3.6.1. Observations on Pollutants and Sediment Resuspension 239
3.6.2. Observations on Distribution of PAHs in Sediment Particles 239
3.7. Model Limitations 240
3.7.1. Depth-Averaging of Properties 240
3.7.2. Disregard Dynamics of Resuspension 240
3.7.3. Spatial Heterogeneity, First Order Processes, and Temperature Dependence 241
3.7.4. Simplifications of the Dynamics of Sink/Source Processes 241
4. Conclusion 242

1. Chapter Introduction, Scope, and Objective

1.1. Introduction

1.1.1. Mobilization of Bound-HOCs from Sediment

Sediment-bound HOCs can become mobilized when the sediment bed is disturbed. The bed can be disturbed by dredging operations (Jing et al. 1996; Hossain et al. 2004; National Research Council 2007; Bridges et al. 2008), by natural forces such as tidal exchange and/or storm events (Schubel 1968; Eisma 1993; Senus et al. 2004), by shearing due to vessel navigation (Ravens 1997), or via bioturbation (Berner 1980).

1.1.1.1. Sediment Dredging Induced Suspension

The environmental impact of sediment dredging has been of an issue of regulatory, engineering, and scientific concern. Sediment dredging is not only restricted to clean-up operations at contaminant sites (National Research Council 2007; OSPAR Commission 2008), but also for maintaining the clearance for navigation channel (Jing et al. 1996; Hossain et al. 2004; Bridges et al. 2008) and the harvesting of fishes and clams (Pranovi et al. 1994). However, bed dredging not only can disrupt the benthic ecological system (Pagliai et al. 1985; de Grave et al. 1999; Sanchez-Moyano et al .2004), but may also lead to the mobilization of sediment-bound HOCs from the inactive bed layer (Ehlers et al. 2003; Eggleton et al. 2004; National Research Council 2007; Bridges et al. 2008). With respect to the latter problem, effort has been devoted to minimizing the effect of bed disturbance by testing different dredging buckets (Welp et al. 2001). The study by Howdeshell et al. (1994), for instance, highlighted the possibility of inter-lake transport of sedimentary HOC via particle resuspension. In Boston Harbor, dredging operations may increase the solid concentration in water column up to 80–200 mg_{solids}/L_w (Welp et al. 2001), about 4 to 10 times the normal level (Chapter 2, Table 2-7).

1.1.1.2. Natural Forces Induced Suspension

Sediment resuspension can also be caused by tidal exchange and storm events. Tidal induced resuspension of sediment has been widely observed in harbors/estuaries (Eisma 1993; Jing et al. 1996; Yuan et al. 2008). The total suspended solids (TSS) concentration has been shown to vary with the current velocity in the tidal zone of estuaries/harbors (Schubel 1968; Yuan et al. 2008). The less frequent high wind/swell events also promote sediment resuspension (Jing et al. 1996). High-energy storm events can increase the harbor/estuarine suspended solids concentration by as high as 10 times of the normal TSS level, pushing the TSS concentration from the ~O(10) mg_{solids}/L_w into the O(100) mg_{solids}/L_w range (Ravens 1997; Senus et al. 2004). Howdeshell et al. (1994) showed that HOC-loaded sediments from Lake Erie (average depth at ~19m; Howdeshell et al. 1994) could be transported into Lake Ontario via episodic wind-induced resuspension events. In should be noted that, water bodies (rivers, estuaries) may also have a very high background TSS concentration levels into the 1000s mg_{solids}/L_w range (Eisma 1993).

1.1.1.3. Navigation Induced Suspension

Sediment can also be resuspended by navigational activities. Smart et al. (1985) reported boat traffic has contributed a 5–20% increase in suspended solids in zone with water depth ~5–10 m in the Upper Mississippi River. Sediment resuspension induced by ferry traffic at similar water depths in Tallinn Bay, Estonia was also reported (Erm et al. 2008). In Boston Harbor, Ravens (1997) reported the maximum bottom stress produced by boats to be 0.17 Pa, exceeding the critical stress for bed-erosion/suspension (τ_c=0.085 Pa). Although these studies have not provided the quantitative importance of navigation-induced resuspension, surface traffic can certainly disturb the surficial bed layer in addition to natural causes or large scale operation such as dredging or harvesting.

1.1.2. How Significance is Sediment Resuspension on the Fate of HOCs?

From the viewpoint of organic pollutant management in surface waters (e.g. rivers, estuaries, harbors, lakes, etc), four questions related to the chemical fate of PAHs (or other HOCs) are of particular interest. First, how fast is desorption, as a PAHs-release process, compared with other PAHs input/removal or transformation processes? Second, can we assess the release (or uptake) of PAHs from suspended sediment particles with an equilibrium model, or do we have to consider the kinetics? Third, if desorption kinetics may not be neglected, can we get a good estimate of dissolved phase PAHs concentrations from known sediment physicochemical properties? Finally, how significant is desorption from suspended sediments as a release pathway of PAHs into the aqueous phase, among other paths, such as release through bed pore-water flushing or release from freshly deposited particles?

Despite knowledge on sediment resuspension in harbors/estuaries, very few studies have examined the role resuspension plays in the fate/transport of HOCs. The mobilization of sedimentary heavy metals has been often documented and better understood. For instance, the release of sediment-bound copper, lead, silver via resuspension was recently demonstrated using sediment samples from Boston Harbor (Kalnejais et al. 2007). In another study, *in situ* vertical profiles of heavy metals and suspended solid loadings clearly demonstrated the importance of resuspension in the mobilization of the bound heavy metals (Robert et al. 2004).

The analogous studies on sediment-bound HOCs, however, have been relatively few. Lab-bench experiments have been conducted in the context of understanding uptake/release kinetics of HOCs in suspension-like systems (Gong et al. 1998; Brion et al. 2005). There has also been efforts to model the release of HOCs from suspended solids using Intra-particle Porewater Diffusion model (Wiberg et al. 2002b). It has been suggested that the flushing of sediment-bed porewater, assisted by bioturbation, could be the major pathway for the release of sedimentary HOCs into water bodies (Thibodeaux et al. 2001, 2003). The same group has reported a short-term HOC release model considering sediment resuspension (Birdwell et al. 2007b).

1.1.3. Box Modeling

The box model approach may be one of the most cost-efficient ways to obtain a preliminary assessment of the status of HOCs in surface water systems. The box

model approach reduces the complexity of an environmental system into homogeneous compartments that represent different compartments (Mackay 2001). Despite the simplicity of the box model, it has been applied to a variety of systems (Baker et al. 1990; Gevao et al. 2000; McLachlan et al. 2002; Erickson et al. 2005; Greenfield et al. 2005).

Typically, a box model is used for estimating the flux of HOCs in/out of a compartment (Figure 9-1(i)). For example, it was used to assess the flux of HOCs across water-air boundary (Baker et al. 1990), soil-air boundary (McLachlan et al. 2002), sediment-water boundary (Erickson et al. 2005), their net degradation rate (Greenfield et al. 2005) or mass fluxes in/out of a lake (Gevao et al. 2000).

Here, the author will attempt to use the box model to identify the average chemical state of HOCs within a water body (Figure 9-1(ii)), with the key transformation and transport fluxes being 'known'. And while doing so, we may estimate the significance of sediment resuspension as a potential HOC-mobilization pathway.

1.2. Objectives

The main objective of this chapter was to apply the simple box model for assessing the distribution/content of HOCs in the dissolved phase and solid phase in a water body with open exchanges with other compartments. This would be done using pyrene as a model HOC and Boston Harbor as a model system. The distribution and measurement of pyrene (and other PAHs) in Boston Harbor are relatively well studied and documented to the extent that we may have an 'answer' against which the model results can be compared/evaluated.

This chapter will begin with a brief overview on the characteristic times of different transformation and transport processes in Boston Harbor (section 3.1). From there, the author will examine whether partition equilibrium of pyrene, the simplest physicochemical model possible, may be applicable to the harbor (section 3.2, 3.3). Next, we shall consider a pseudo steady-state model where transformations and transport of pyrene are described by simple first-order expressions (section 3.4, 3.5). The results from the steady-state model will be discussed with implications for the role of sediment resuspension in mobilizing sedimentary pyrene (or HOC). Other secondary observations relevant to the mobilization-through-resuspension thesis will also be discussed (section 3.6). This chapter will end with a summary of the important limitations of the box model approach (section 3.7).

2. Methodology of Analysis: Approach and Assumptions

2.1. Characteristic Times of Various Processes in Boston Harbor

Knowledge on the characteristic timescales of different processes allows us to identify the major transformation/transport processes that control the chemical behavior of HOCs in river/harbor/estuarine/lake systems. The estimated characteristic timescales of processes in Boston Harbor are summarized in Table 9-1.

All of the listed processes have comparable characteristic timescales except indirect photolysis of pyrene, which occurs at rate about 10 times slower than other processes. The fastest processes in Boston Harbor are hydrodynamic processes such as tidal-induced sediment resuspension (t~0.25d) (Ravens et al. 1997) harbor water column flushing ($t_{wc,flush}$~3-10d) (Stolzenbach et al. 1998), and bed-porewater flushing assisted via bioturbation ($t_{bed,pw,flush}$~5-20d) (McGroddy et al. 1995).

Although the timescales of photolytic degradation and microbial degradation of pyrene are comparable to those of the hydrodynamic or desorption processes, they are very sensitive to light intensity, dissolved oxygen level, water depth, temperature as well as seasonal variation, so they are of secondary importance in general.

The timescale of desorption (or desorption half-lives) may be more variable than the range shown in Table 9-1, which was derived from the pyrene desorption experiment discussed earlier (Chapter 2 & 7). It is more variable because the rate of desorption is dependent on a number of factors (e.g. R_{sw}, particle/aggregate size, OC/BC contents, etc).

Another complexity for characteristic desorption timescale is due to the fact that desorption half-life represents the mean time for half desorption set against a specific timeframe/end-point (e.g., 15 d, 30 d, 90 d; see section 2.3.2.1), and so does not represent the true, instantaneous desorption rate, which is fastest in the beginning and declines rapidly with time (e.g. Cornelissen et al., 1998; Ghosh et al. 2001; Johnson et al. 2001; Rockne et al. 2002; Kukkonen et al. 2003; van Noort et al. 2003; Gomez-Lahoz et al. 2005). $t_{1/2,des}$ is thus time-biased and decreases with shorter reference period (i.e., faster average desorption rate as reference time-point is advanced). It is, therefore, arguable that the effective halftimes within 1-3d (i.e., $t_{1/2,des,1\text{-}3d}$) may be comparable or even shorter than those of sediment resuspension or water column flushing, and hence the validity of the equilibrium model.

2.2. Equilibrium Partitioning Approach

Equilibrium partitioning is the simplest model for estimating the dissolved and the solid phase HOC concentrations in water bodies. To predict HOC concentrations by the equilibrium model is to imply the assumption that the rates of desorption and re-adsorption are much faster than the rates of other release or removal processes in a water body.

In a natural water body, the equilibrium approach may be applied in two ways: (i) the water column and the surficial sediment layer are at sorption equilibrium and (ii) the water column and the suspended sediment particles/aggregates are at sorption equilibrium.

2.2.1. Surficial-Bed Layer & Water Column at Sorption Equilibrium

This model assumes that the partitioning/sorption equilibrium (for the HOCs in question) is established between the surficial sediment-bed layer, of thickness L_B, and the overlaying water column, with water-depth L_W. A cartoon of the system is shown in Figure 9-2(i). Here, it is assumed that all transformation/transport processes for HOCs – except that of desorption and adsorption from/to the sedimentary bed – are kinetically insignificant (i.e. slow relative to sorptive exchange) so that the surficial bed and the water column can be simplified to a closed system.

2.2.1.1. Solving Pyrene Concentration in Water Column ($C_{pyr,WC}$)

The surficial sedimentary bed layer is assumed to be 'well-mixed' by virtue of both physical forces and/or bioturbation. Note that such an assumption may be unrealistic for HOCs of high partition coefficient (Lick 2006). Mathematically, the total mass of sorption-active solids is then:

$$M_{surf.bed-solids} = (A_{\perp} L_B)(1 - \phi_{surf.bed})\rho_s$$

Eqn. 9 - 1

where $A_{\perp}$ is the unit bed-water contact area (m^2) (assumed to be 1 m^2 for convenience),

L_B is the surficial sedimentary bed thickness or depth (m),

$M_{surf,bed-solids}$ is the total bed solids available for the partitioning of HOCs (kg_{solids}),

$\phi_{surf.bed}$ is the surficial bed porosity (m^3_{pw}/m^3_{bed}),

ρ_s is the sedimentary solid density (kg_{solids}/m^3_{solids}).

For modeling purposes, $\phi_{surf.bed}$ and ρ_s will be assumed to be 0.8 m^3_{pw}/m^3_{bed} and 2500 kg_{solids}/m^3_{solids}. The values chosen for both parameters are realistic and consistent with literature reported values.

At equilibrium, the system bed and dissolved phase pyrene concentrations has to converge on the partition/sorption coefficient, $K_{d,pyr}$, satisfying the constraint from mass balance and from sorption isotherm:

$$K_{d,pyr} = \left(\frac{S_{bed,pyr,Eqm}}{C_{WC,pyr,Eqm}}\right)_{mass\ balance} = \left(\frac{S_{bed,pyr,Eqm}}{C_{WC,pyr,Eqm}}\right)_{isotherm}$$

Eqn. 9 - 2

where $C_{WC,pyr,Eqm}$ is the equilibrium water column dissolved pyrene concentration ($\mu g_{pyr}/L_w$),

$S_{bed,pyr,Eqm}$ is the equilibrium sedimentary bed solid-phase pyrene concentration ($\mu g_{pyr}/kg_{solids}$),

$K_{d,pyr}$ is the solid-to-water partition coefficient for pyrene (L_w/kg_{solids}).

2.2.1.2. Solving Depletion Half-time for Sediment-Bed Pyrene ($t_{bed,1/2}$)

A correct model has to predict $C_{pyr,WC}$ that agrees with field observations and give correct prediction on the lifetime of pyrene bound to the surficial sediment bed. One way to evaluate this lifetime is by estimating the depletion half-time for the bed-associated pyrene, $t_{bed,1/2}$. By the assumption of pyrene partitioning equilibrium between the sediment-bed and the water column the following should hold true for all time, including at $t_{bed,1/2}$:

$$S_{bed,pyr}\left(t_{bed,1/2}\right) = K_{d,pyr,1/2} C_{pyr,WC}\left(t_{bed,1/2}\right)$$

Eqn. 9 - 3

With the assumption that the surficial bed pyrene content controls $C_{pyr,WC}$, we may (i) neglect other input functions of pyrene and (ii) consider that the water body is constantly replenished by clean, pyrene-free oceanic water (or 'WC-flushing'). With these two assumptions, $C_{pyr,WC}(t)$ would be a simple exponential decay function:

$$\frac{dM_{pyr,sys}}{dt} = \frac{d\left(S_{pyr,B} M_B + C_{pyr,WC} V_{WC}\right)}{dt} = \dot{In} - \dot{Out} = -k_{WC-flush} C_{pyr,WC} V_{WC}$$

$$\frac{d\left[\left(K_{d,pyr} R_{sw,bed-WC} + 1\right) C_{pyr,WC}\right]}{dt} = -k_{WC-flush} C_{pyr,WC} V_{WC}$$

Eqn. 9 - 4

where $k_{WC\text{-}flush}$ is the region-averaged water column flushing rate constant for the water body in question (d^{-1}),

$K_{d,pyr}$ is the sorption coefficient for pyrene (L_w/kg_{solids}),

$R_{sw,bed\text{-}WC}$ is the solid to water ratio for the bed-WC system (kg_{solids}/L_w),

t is the time elapsed from initial state (d).

Note that the above differential equation is non-linear as $K_{d,pyr}$ is a function of $C_{pyr,WC}$. But by integrating it numerically, the following exponential decay function may serve as an approximate solution:

$$\frac{C_{pyr,WC}(t)}{C_{pyr,WC,o}} \approx \exp\left[\frac{-k_{WC-flush}\, t}{\left(K_{d,pyr} R_{sw,bed-WC} + 1\right)}\right], \quad \text{for some mean } K_{d,pyr}$$

Eqn. 9 - 5

Hence, the depletion half-time for bed-pyrene is simply:

$$t_{bed,1/2} = \frac{(K_{d,pyr} R_{sw,bed-WC} + 1)}{k_{WC-flush}} \ln\left[\frac{C_{pyr,WC,o}}{C_{pyr,WC}(t_{bed,1/2})}\right]$$

Eqn. 9 - 6

The basecase model parameters are summarized in Table 9-2(A).

2.2.2. Total Suspended Solids (TSS) & Water Column at Sorption Equilibrium

In this model (Figure 9-2(ii)), it is assumed that pyrene-bound to total suspended solids (TSS) controls the dissolved phase pyrene concentration in the water column. This means that we are assuming the contribution from sediment-bed porewater is insignificant, compared with that desorbing from the solids resuspended from the bed. This model is, therefore, contrary to the view of porewater flushing being the controlling process of the release of sedimentary HOCs (Thibodeaux et al. 2001; 2003).

It is also assumed that (i) resuspended solids all settle out in any single event, (ii) resuspended solids are not substantially removed from the regional water body by inflowing oceanic current. Both assumptions ensure that there are long-term, pseudo-steady states on TSS concentrations in the water column.

2.2.2.1. Solving Pyrene Concentration in Water Column ($C_{pyr,WC}$)

Assuming the resuspended sedimentary particles/aggregates to be at sorption equilibrium with the water column, the dissolved pyrene concentration in the water column, $C_{pyr,WC}$, can be estimated in manner similar to that presented earlier (section 2.2.1.1):

$$M_{TSS} = R_{SW,TSS}(A_{\perp} L_{WC})$$

$$K_{d,pyr} = \left(\frac{S_{TSS,pyr,Eqm}}{C_{WC,pyr,Eqm}}\right)_{mass\ balance} = \left(\frac{S_{TSS,pyr,Eqm}}{C_{WC,pyr,Eqm}}\right)_{iso\,therm}$$

Eqn. 9 - 7

where $A_{\perp}$ is the unit bed-water contact area (m^2) (assumed to be 1 m^2 for convenience),

$C_{WC,pyr,Eqm}$ is the equilibrium water column dissolved pyrene concentration ($\mu g_{pyr}/L_w$), L_{WC} is the average depth of the water column (m),

$K_{d,pyr}$ is the solid-to-water partition coefficient for pyrene (L_w/kg_{solids}),

M_{TSS} is the mass of total suspended/resuspended solids available for the partitioning of HOCs (kg_{solids}),

$R_{SW,TSS}$ is the solid-to-water ratio of TSS to water column (kg_{solids}/L_{WC}),

$S_{TSS,pyr,Eqm}$ is the equilibrium TSS solid-phase pyrene concentration ($\mu g_{pyr}/kg_{solids}$).

2.2.2.2. *Solving Depletion Half-time for Sediment-Bed Pyrene ($t_{bed,1/2}$)*

The depletion half-time for the bed-associated pyrene, $t_{bed,1/2}$, can be estimated by assuming that any settled TSS will be well-mixed with the remaining mass in the surficial bed layer.

The change in the total bed pyrene mass upon <u>one</u> resuspension event is simply $\Delta S^{n+1}{}_B M_B$:

$$\Delta S^{n+1}{}_B M_B = -\left(S^n{}_B - S^n{}_{Eqm}\right) M_{TSS}$$

Eqn. 9 - 8

where M_B is the total mass of solids in the surficial sediment-bed (kg_{solids}),

M_{TSS} is the mass of total suspended/resuspended solids (kg_{solids}),

$\Delta S^{n+1}{}_B$ is change in bed pyrene concentration resulting from the n^{th} resuspension events such that $S^{n+1}{}_B = S^n{}_B + \Delta S^{n+1}{}_B$ ($\mu g_{pyr}/kg_{solids}$),

$S^n{}_B$ is bed pyrene concentration after n^{th} resuspension events ($\mu g_{pyr}/kg_{solids}$),

$S^n{}_{Eqm}$ is TSS pyrene concentration after n^{th} resuspension events ($\mu g_{pyr}/kg_{solids}$) (note: $S^n{}_{Eqm}$ is at sorption equilibrium with $C_{pyr,WC}$).

We can express the change in bed pyrene content as a fractional change, $\Delta f^{n+1}{}_B$, by normalizing both sides by $S^n{}_B M_B$, we get:

$$\Delta f^{n+1}{}_B = \frac{\Delta S^{n+1}{}_B M_B}{S^n{}_B M_B} = \frac{-\left(S^n{}_B - S^n{}_{Eqm}\right) M_{TSS}}{S^n{}_B M_B} = -\left(1 - \frac{S^n{}_{Eqm}}{S^n{}_B}\right)\frac{M_{TSS}}{M_B}$$

or:

$$\Delta f^{n+1}{}_B = -(1 - f^n{}_{retain})\frac{M_{TSS}}{M_B}$$

Eqn. 9 - 9

where $\Delta f^{n+1}{}_B$ is fractional change in bed pyrene content resulting from the n^{th} resuspension events (dimensionless),

$f^n{}_{retain}$ (= $S^n{}_{Eqm}/S^n{}_B$) is the fraction of pyrene retained on the TSS after equilibrating in the water column (dimensionless).

The ratio of $S^n{}_{Eqm}/S^n{}_B$ (or f_{retain}) is simply the <u>fraction of pyrene retained</u> in the solid-phase after the TSS equilibrated with the water column per resuspension. It can be shown that for the bed to lose half of the pyrene (i.e. $\Delta f_B = -0.5$), f_{retain} is approximately

constant (Appendix 9-9). With this assumption, we can solve for the number of resuspension events, $m_{1/2}$, needed for a bed to deplete its pyrene content by half:

$$\Delta f^{m_{1/2}}{}_B = -0.5 \approx \left[-(1 - f_{retain}) \frac{M_{TSS}}{M_B}\right] m_{1/2}, \qquad \text{for } m_{1/2} \in \mathbb{I}^+$$

Eqn. 9 - 10

The depletion half-time for the bed, $t_{bed,1/2}$, is simply the time between two resuspension events multiply by the number of resuspension events:

$$t_{bed,1/2} = t_{one\ resusp} . m_{1/2} = t_{one\ resusp} . \frac{0.5}{(1 - f_{retain})} \frac{M_B}{M_{TSS}}$$

Eqn. 9 - 11

The basecase model parameters are summarized in Table 9-2(A).

2.3. Steady State Approach

We may extend beyond the equilibrium partitioning model by considering a steady state model where the dissolved phase pyrene concentration of the water column is determined by the balance between different competing physical or chemical processes in the water body.

2.3.1. General Assumptions

There are two major assumptions under the steady state model. First, it is assumed that pseudo steady states exist for pyrene in both the sediment and the water column. This means that there exists some 'typical' $C_{pyr,WC}$ or $S_{bed,pyr}$ within the seasonal timescale (for instance, over tidal-induced re-suspension timescale). The estimated steady-state $C_{pyr,WC}$ may be valid for a few years, but not for decadic timescales. This assumption may be justified on the observation that the dissolved phase concentrations of HOCs in water column are typically comparable on a day–to–day basis, but not between, say, winter and summer periods.

Second, it is assumed that there is no distribution of physicochemical properties in the vertical dimension. This assumption should be viewed in the time-frame demanded by the first assumption rather than, say, within the duration of a tidal cycle. With this assumption, we may disregard the vertical dynamics and distributions of TSS and $C_{pyr,WC}$ as a function of both time and vertical dimension. The (depth-averaged) dissolved phase concentration in the water column, $C_{pyr,WC}$, is therefore:

$$\frac{d(V_{WC} C_{pyr,WC})}{dt} = \sum r_{release} - \sum r_{removal} \approx 0$$

Eqn. 9 - 12

where $r_{release}$ and $r_{removal}$ are the terms describing the release rate or removal rate of pyrene due to various transformation or transportation processes ($\mu g_{pyr}/d$).

2.3.2. Steady State Model: Three-Rate Model

To consider the simplest scenario, we shall consider only three processes: (i) desorption of pyrene from suspended sediments ($r_{TSS,des}$), (ii) flushing of pyrene from surficial sediment bed porewater ($r_{pw,f}$), and (iii) removal of dissolved pyrene by flushing of water column ($r_{wc,f}$) (Figure 9-3(i)). Rewriting the rate expression, we get:

$$\textbf{Three} - \textbf{Rate S. S. Model:} \quad \frac{d(V_{WC}\, C_{pyr,WC})}{dt} \approx r_{TSS,des} + r_{pw,f} - r_{WC,f} = 0$$

$$\textbf{TSS Desorption:} \quad r_{TSS,des} = k_{TSS,des}\, S_{TSS,pyr}\, R_{sw,WC}\, V_{WC}$$

$$\textbf{Porewater Flushing:} \quad r_{pw,f} = k_{pw,f} C_{pyr,pw}\, V_{bed}\, \phi_{bed}$$

$$\textbf{Water Column Flushing:} \quad r_{WC,f} = k_{WC,f} C_{pyr,WC}\, V_{WC}$$

Eqn. 9 - 13

where $C_{pyr,pw}$ and $C_{pyr,WC}$ are the dissolved phase pyrene concentrations in the sediment porewater and water column, respectively ($\mu g_{pyr}/L_w$),

$k_{TSS,des}$, $k_{pw,f}$ and $k_{WC,f}$ are the rate constants for desorption from TSS, porewater-flushing, and water column-flushing, respectively (d^{-1}),

ϕ_{bed} is the surficial bed porosity (L_{pw}/L_{bed}),

$R_{sw,WC}$ is solid-to-water ratio for TSS and water column (kg_{solids}/L_w),

$S_{TSS,pyr}$ is solid-phase pyrene concentration of TSS ($\mu g_{pyr}/kg_{solids}$),

V_{WC} and V_{bed} are the volumes of water column and surficial sedimentary bed, respectively (L_{WC} and L_{bed}).

With $C_{pyr,WC}$ being the only unknown in the equation, it can be easily solved.

The basecase model parameters are summarized in Table 9-2(B).

2.3.2.1. TSS Desorption

In principle, it is most exact to compare process timescale using an overall process rate constant, k. However, there are two major difficulties. First, description of HOCs desorption kinetics often involves the empirical n-compartments exponential models ($n \geq 2$, # fitting parameters=2n-1; see Chapter 7), the reported multiple rate constants and relative phase distribution make direct comparison very difficult and unintuitive. Second, the time-dependent nature of HOC desorption rates also require setting

arbitrary reference point for comparison (e.g. comparing desorption rates at after 1 week vs after 1 month).

Upon these two considerations, the author decided to quantify desorption timescale using desorption halftime ($t_{1/2,des}$) – defined as time at which desorption has proceeded halfway to that of a pre-selected endpoint or a reference time (t_{frame}). This definition is illustrated in Figure 9-21. Thus $t_{1/2,des}$ could be calculated from fitted rate constants (e.g. k_{slow}'s and k_{rapid}'s from a Two-Compartment Model; Appendix 7-21) and compartment fractions (e.g. rapidly desorbing fraction, f_{rapid}; see Appendix 7-21(III)), or read off directly from desorption curves. For the purpose of modeling $C_{pyr,WC}$, desorption half-lives were first estimated from the experimental observations discussed earlier (Chapter 2 & 7); the rate constant for desorption, $k_{TSS,des}$, was then calculated (assuming a first order decay function) as $k_{TSS,des}=\ln 2/t_{1/2,des}$. Because the early observations from desorption experiments were not well fitted by the empirical compartmental equation (e.g. see Figure 9-21b), $t_{1/2,des}$ was estimated using both the fitted parameters and via visual inspection of the raw data. The fitted parameters and the estimated $t_{1/2,des}$'s at different timeframe/end-point were documented in detail in Appendix 9-6.

Since $t_{1/2,des}$ decreases with a shorter desorption timeframe/end-point (t_{frame}) (Figure 9-21b), it is necessary to know what t_{frame} should be used. However, it appeared unclear to the author where the end-point should be set. In real harbor/estuarine systems, the HOC-loaded aggregates could have entered the system as 'fresh' (thus in the rapidly desorbing phase) or could have been desorbing for weeks or months already (thus in the slowly desorbing phase). Instead of selecting and justifying a particular t_{frame}, $t_{1/2,des}$ was considered to be 'variable' and evaluated at t_{frame}=7.5, 15, 30, and 90 d. The resulting $t_{1/2,des}$'s, averaged across different R_{sw}'s and particle sizes, were 0.9, 1.5, 2.2, and 3.9 d, at t_{frame} of 7.5, 15, 30, and 90 d, respectively (Appendix 9-6, table B). These halftimes appeared to be comparable with those derived from other PAH desorption studies (Appendix 9-6, table C).

A justification is necessary for averaging the effects of particle size, solids-to-water ratio, and initial solid-phase pyrene loading to obtain estimates of $t_{1/2,des}$. The distinction of particle sizes and R_{sw}'s may be neglected here as the resulting uncertainty level in $t_{1/2,des}$ (0.9-3.9d) was comparable to those in water column and porewater flushing halftimes (Table 9-1) in both magnitude and order of difference between the extreme values. Furthermore, since the factors influencing the timescales of other processes were neglected, the same level of 'ignorance' or 'uncertainty' should be also extended to desorption from suspended sediment for consistency.

2.3.2.2. Porewater Flushing

The porewater flushing timescale for Boston Harbor sediment was reported to range from ~5–20 d (McGroddy et al. 1995). In the box model, local variations in bed porosity, abundance of benthic life/coverage, and the efficiency of hydrodynamic pumping were all neglected. The basecase sediment-bed porewater flushing timescale was assumed to be 10 d (geometric mean of 5–20 d).

The contribution of pyrene by porewater flushing also requires an estimate on the porewater pyrene concentration, $C_{pyr,pw}$. In order to estimate $C_{pyr,pw}$, we need to know (i)

how the sediment-bed pyrene concentration ($S_{bed,pyr}$) may vary within the surficial layer, and (i.e. $S_{bed,pyr}$ as a function of depth, z) (ii) how $C_{pyr,pw}$ and $S_{bed,pyr}$ are related.

The core study by McGroddy (1993) provided information on the variation of $S_{bed,pyr}$ in bed depth. In the study, three sediment cores from Boston Harbor were collected and analyzed for PAHs as a function of bed depth. All three cores showed an increasing $S_{bed,PAH}$ with depth within the surficial layer (or 'well-mixed' layer), and this is demonstrated in Figure 9-10 for $S_{bed,pyr}(z)$. From Figure 9-10, we may expect that $S_{bed,pyr}$ generally varies with depth, even within the surficial layer (~10 to 15 cm). For this study, the basecase surficial bed profile ratio, defined as $S_{bed,pyr}(z=0)/S_{bed,pyr}(z=L_B)$, was assumed to be 0.6. With this ratio, an 'average' $S_{bed,pyr}(z)$ can be constructed.

The study by McGroddy (1993) also suggested that sorption disequilibrium generally exists between the porewater phase and the solid-phase in the surficial layer, as shown in Figure 9-9. The surficial $C_{pyr,pw}(z)$-$S_{bed,pyr}(z)$ data from three cores appeared to be sufficiently well-correlated and summarized by an empirical relationship (Figure 9-9), from which a non-equilibrium $C_{pyr,pw}(z)$ may be estimated.

The average surficial bed $C_{pyr,pw}$ was estimated by taking the average of the non-equilibrium $C_{pyr,pw}$ at the surface (z=0) and the equilibrium $C_{pyr,pw}$ at the depth immediately beneath the surficial layer ($z=L_B+$). Since we envision the surficial bed layer, but not the deeper layers, being subjected to physical mixing (e.g. bioturbation by benthic organisms or shearing caused by current), this picture is consistent with the assumption that sorption equilibrium may be established at $z=L_B+$, where both the solid-phase and the porewater phase are 'undisturbed'.

2.3.2.3. Water Column Flushing

The turnover time for water in Boston Harbor was reported to be about 3–10 d (Stolzenbach et al. 1998). By assuming the entire Boston Harbor as a 'box', we neglected the spatial heterogeneity of water residence time. The basecase water column flushing timescale was assumed to be 5.5 d (geometric mean of 3–10 d).

2.3.3. Steady State Model: Seven-Rate Model

In this model, additional sources/sinks of dissolved pyrene would be considered as well as the seasonal factor. In addition to desorption from TSS, bed porewater flushing and harbor flushing, we would account for biodegradation, photodegradation, riverine input, and atmospheric deposition (Figure 9-3(ii)). Mathematically, the steady state expression becomes a sum of seven rates ($r_{process}$'s, in unit $\mu g_{pyr}/d$)

Seven – Rate S. S. Model:

$$\frac{d(V_{WC}\,C_{pyr,WC})}{dt} \approx r_{TSS,des} + r_{pw,f} + r_{fresh} + r_{atm,dep} - r_{WC,f} - r_{biodeg,} - r_{h\nu} = 0$$

Biodegradation: $r_{biodeg.} = k_{biodeg.} C_{pyr,WC} V_{WC}$

(Direct) Photolysis: $r_{h\nu} = k_{h\nu} C_{pyr,WC} V_{WC}$

Freshwater Input: $r_{fresh} = m_{pyr,fresh}$

Atmospheric Deposition: $r_{atm,dep} = \dot{m}_{pyr,atm-dep}$

Eqn. 9 - 14

where $k_{biodeg.}$ and $k_{h\upsilon}$ are the rate constants for first order biodegradation and photolysis of pyrene, respectively (d^{-1}),

$\dot{m}_{pyr,atm-dep}$ and $\dot{m}_{pyr,fresh}$ are the atmospheric deposition and freshwater/riverine input of pyrene ($\mu g_{pyr}/d$).

The estimation of the rates or rate constants of the various transformation/transport processes will be discussed in the following sub-sections. The basecase model parameters are summarized in Table 9-2(B).

2.3.3.1. Atmospheric Deposition of Pyrene

The atmospheric depositional rates of pyrene for Boston Harbor were estimated from the study by Golomb et al (1997). In the study, they investigated the seasonal wet and dry deposition of PAHs at two stations in the vicinity of Boston Harbor. These two locations are, in this study, taken as representative of the high depositional rate from the urbanized area and the low depositional rate from the more rural-like region. For the purpose of this study, we estimated the mean seasonal depositional rate of pyrene (geometric mean of the urban and the rural rate) for both the summer and the winter cases (Table 9-2(B)). The details of the estimation are shown in Appendix 9-4.

Some assumptions implicit in this approach should be noted and explained. First, for simplicity, it is assumed that all deposited atmospheric pyrene becomes dissolved in the harbor water (which is not true). Consider that ~75% of deposited pyrene enters the harbor water body via dry deposition (Appendix 9-4), this implies that at least 75% of the deposited pyrene is bound to aerosols/particulate matter. In reality, the solid-bound pyrene would also need to desorb from the aerosols/particles. The fact that these aerosols/particles enter the harbor in 'dry' state probably implies that their associated pyrene follows a different desorption kinetics as the hydrophobic components in the aerosols/particles need to be 'wetted' first (Nguyen et al. 2004b). Second, it is assumed that the deposited particles are negligible in comparison with the native TSS, and that they remain 'suspended' in the water column. We thus also neglect the settling and coagulation dynamics of deposited PAH-enriched aerosol particles.

2.3.3.2. Biodegradation of Pyrene

The biodegradation rate of pyrene was estimated from the study by Shiaris (1989) where field Boston Harbor sediments (at three sites, of varying initial PAH loadings) were used (Table 9-1, 9-2). The estimation is described in detail in Appendix 9-3.

2.3.3.3. Freshwater Inflow of Pyrene

The freshwater pyrene input into Boston Harbor has been estimated to be ~100 kg_{pyr}/yr (Alber et al. 1994). Assuming the entire Boston Harbor area to be about 100 km^2 (Figure 9-4), the average freshwater input was estimated to be about 2.8 $\mu g_{pyr}/d$ (per m^2 harbor area).

2.3.3.4. Photolysis of Pyrene

Both direct and indirect photolysis rates of pyrene have been estimated for both the summer and the winter cases. The half-life of pyrene direct photolysis ($t_{1/2,pyr,dir\text{-}photolysis}$) was estimated to be about 0.7–23 d and 3–91 d for summer and winter scenarios, respectively. On the other hand, indirect photolysis was only about one hundredth as fast as direct photolysis, and was thus neglected from the calculation.

The average photolysis rate of pyrene was estimated by taking the geometric mean of the upper and lower estimates at different water depths. The mean photolysis half-life correlates linearly with the water depth (Figure 9-20; Appendix 9-5). The slope from the figure was used for the calculation of the steady state $C_{pyr,WC}$.

2.4. Sensitivity Analysis

Sensitivity analysis was performed to compensate for the fact that many model parameters, in both the EqP and the steady-state approaches, have been estimated, and the fact that both approaches involve substantial simplifications regarding spatial variations of harbor properties. These will be discussed along the basecase results of the different regional model.

3. Results & Discussion

3.1. Field Observed $C_{pyr,WC}$ and $S_{pyr,bed}$ in Boston Harbor

This section will provide a brief summary of pyrene inventory in Boston Harbor hitherto reported. A map of the regionalized Boston Harbor and the respective pyrene concentrations is provided in Figure 9-4. Extensive field measurements conducted via multiple sampling cruises showed that typical dissolved pyrene levels ranged from 5-20 ng_{pyr}/L with maxima around 120-140 ng_{pyr}/L_w. The lower end of observed $C_{pyr,WC}$'s were consistent with (i) the levels observed in the desorption kinetic and desorption equilibrium observations made in this study (e.g. Chapter 2 & 7), (ii) those reported by other independent studies (Lohmann et al. 2005; Adams et al. 2007), and (iii) the documented sediment-bed porewater levels (McGroddy 1993). As expected, the observed $C_{pyr,WC}$ varied with both location and season (Rudnick 1998).

In the most contaminated sediment sites in Boston Harbor, sedimentary pyrene ranged from ~5000-50000 $\mu g_{pyr}/kg_{solids}$ (Shiaris et al. 1986). This together with the measurements by Rudnick et al. (1998) suggested that dissolved pyrene levels to be only around 100 ng_{pyr}/L_w even at sedimentary loading as high as $>10^4$ $\mu g_{pyr}/kg_{solids}$.

The sedimentary pyrene level may also be relatively stable over yearly timescales. The independent studies of Shiaris et al. (1986) and Lohmann et al. (2005) reported 10400 $\mu g_{pyr}/kg_{solids}$ and 11000 $\mu g_{pyr}/kg_{solids}$, respectively, for two closely located sites (site #14 in Shiaris et al. 1986). The unpublished sedimentary pyrene data by Ewald (2000) also supported the claim that sedimentary pyrene concentration may be relatively stable over

long term (Appendix 9-10). This suggested that a certain degree of persistence of the sedimentary pyrene may be expected.

3.2. Bed-Water Column EqP Model

The bed-WC EqP model tends to overestimate $C_{pyr,WC}$'s at high $S_{pyr,bed}$ values, as shown in Figure 9-5. The four curves on the figure represent the predictions given by the two isotherms (Old-OC-BC, Occlusion) on two OC-BC conditions (generic and BH#6/NQB). The dark gray lenses represent the field-observed ranges of $C_{pyr,WC}$ and $S_{pyr,bed}$ as reported in literature (Shiaris et al. 1986; Rudnick 1998; Rudnick et al. 1998; Ewald 2000; Wang et al. 2001). The field observation of $C_{pyr,WC}$ was conducted with time-gated LIF by Rudnick (1998), and it had a detection limit of ~5 ng_{pyr}/L_w at the time of the study. The lightly-shaded area located at $S_{pyr,bed} < 500$ $\mu g_{pyr}/kg_{solids}$ represents roughly where lower $C_{pyr,WC}$ may be present in reality but not observable by LIF then. A 'perfect match' occurs when the predicted $C_{pyr,WC}$ falls onto both the dark gray lenses and the lightly-shaded region.

It can be seen that the predictions using the Old-OC-BC isotherms overestimate $C_{pyr,WC}$ substantially at $S_{pyr,bed} > 1000$ $\mu g_{pyr}/kg_{solids}$, while those with the Occlusion isotherm appear to predict slightly better, but not beyond $S_{pyr,bed} > 10000$ $\mu g_{pyr}/kg_{solids}$. A sensitivity analysis on the model with BH#6/NQB condition and the Occlusion isotherm showed that variation in most parameters would not help lowering the predicted $C_{pyr,WC}$ (Table 9-4)

The projected bed-pyrene depletion profiles also suggested that the model with Old-OC-BC would overestimate the depletion rate of the bed-bound pyrene (Figure 9-6, upper plot). On the other hand, the bed-WC EqP model with the Occlusion isotherm seemed to give a more realistic bed-pyrene profile – it could explain why residual concentrations around 100–500 $\mu g_{pyr}/kg_{solids}$ can exist over a long time period. Such levels of residual pyrene has been observed in various harbors/estuaries (McGroddy 1993; Rudnick 1998; Mitra et al. 1999; King et al. 2007).

From the prediction of $C_{pyr,WC}$, the sensitivity analysis and the projected bed depletion time profile, the bed-water column EqP model was concluded to be inadequate for predicting realistic dissolved and solid-phase pyrene levels in Boston Harbor.

3.3. Total Suspended Solids (TSS)-Water Column EqP Model

The suspended solids-water column EqP model gave more realistic $C_{pyr,WC}$ predictions (Figure 9-7). $C_{pyr,WC}$ predicted from all four variations of the model agreed well with the field observation up to about 10^4 $\mu g_{pyr}/kg_{solids}$. Pyrene loadings on Boston Harbor sediments were mostly around 500–5000 $\mu g_{pyr}/kg_{solids}$, except in the highly polluted Inner Harbor zone (from Chelsea River/Charles River exits to Fort Point Channel; Shiaris et al. 1986; Wang et al. 2001) where $S_{pyr,bed}$ has been reported to be around ~5000–50000 $\mu g_{pyr}/kg_{solids}$. The estimated $C_{pyr,WC}$'s were somewhat consistent with the field measured dissolved pyrene levels.

However, does the suspension-water column equilibrium model give realistic $S_{pyr,bed}(t)$? The projected bed-pyrene profiles showed that the sedimentary pyrene concentration would decline from 10000 $\mu g_{pyr}/kg_{solids}$ down to ~500 $\mu g_{pyr}/kg_{solids}$ in less than 5 years (Figure 9-8). The rapid depletion of bed-pyrene is in conflict with the persistence of sediment PAHs loadings reported in previous studies (section 3.1). Sensitivity analysis for the most 'accurate' model (BH#6/NQB condition with Occlusion isotherm) also suggested that the TSS-WC EqP model systematically overestimates at higher $S_{pyr,bed}$ ranges. For instance, at $S_{pyr,bed}$=50000 $\mu g_{pyr}/kg_{solids}$, the model often predicts $C_{pyr,WC}$ to be at least 3 times higher (Table 9-5). Analyses thus seemed to suggest that the EqP model was unable to give realistic predictions of C_{pyr} or S_{pyr} in Boston Harbor.

Although one may use, as a preliminary assessment, the models with the Occlusion isotherm (e.g. Figure 9-7) to get a rough estimate of $C_{pyr,WC}$ for the slightly to moderately PAH-contaminated sediment sites (i.e. $S_{pyr,bed} \sim< 10^4$ $\mu g_{pyr}/kg_{solids}$), it should be emphasized that the state of partition equilibrium does not often prevail in reality. For instance, the observations in McGroddy (1993) show that sorption equilibrium may not exist between the porewater and the bed solids even within the surficial bed layer (approx. 0–10 cm of the bed) (Figure 9-9).

3.4. Three-Rate Steady State Model

In order to evaluate the importance of suspended solids desorption as a source of dissolved pyrene, the steady state model was run with and without desorption. The desorption-absent results may be considered as a 'control' scenario.

3.4.1. Importance of Desorption from Suspended Solids

The steady state predictions suggested that field measurements of dissolved pyrene in Boston Harbor were more accurately predicted when pyrene desorption from suspended solids was considered (Figure 9-11). The dark lenses in the figure represented field observed ranges of $C_{pyr,WC}$ and $S_{pyr,bed}$ (e.g. Shiaris et al. 1986; Rudnick 1998; Ewald 2000; Wang et al. 2001; Lohmann et al. 2004), whereas the slightly shaded area signified where realistic $C_{pyr,WC}$ may exist but below the detection limit of LIF (Rudnick 1998). A prediction that falls on either area may be considered as 'good' or 'satisfactory'. Field sediment $S_{pyr,bed}$ (200-67000 $\mu g_{pyr}/kg_{solids}$) spanned much wider than S_{pyr} observed in this study (1000-5000 $\mu g_{pyr}/kg_{solids}$). Since $t_{1/2,des}$'s were estimated from the desorption experiments, they might be less suitably applied to the unstudied ranges, which were signified by dashed-lines in Figure 9-11.

The figure (Figure 9-11) showed that porewater flushing alone (curve (v)) gave poor prediction on $C_{pyr,wc,avg}$ for the curve barely overlapped the field-observation area. Even with the extreme cases (curve (vi-viii)) that favor pyrene release via bed-porewater flushing, porewater flushing alone underestimated dissolved pyrene levels significantly in the lower $S_{pyr,bed}$ range (200-10000 $\mu g_{pyr}/kg_{solids}$), which accounted for 80% of the sediment pyrene measurements observed (Shiaris et al. 1986; Ewald 2000). Sensitivity analyses to uncertainties in other less influential parameters also leads to the same conclusion that $C_{pyr,wc,avg}$ predicted from porewater flushing alone was generally 10-100

times lower than the observed values at $S_{pyr,bed}$ < 10000 $\mu g_{pyr}/kg_{solids}$ (Appendix 9-7). Most of the field $S_{pyr,bed}$ and $C_{pyr,wc}$ observations, however, could be reasonably predicted when suspended sediment desorption was included (curve (i-iv)). The $C_{pyr,wc}$ observed at $S_{pyr,bed}$<1000 $\mu g_{pyr}/kg_{solids}$ also fell within the sensitivity range of sediment-suspension desorption to parameters such as water column R_{sw} (Appendix 9-8).

3.5. Seven-Rate Steady State Model

The importance of desorption from suspended solids was also demonstrated with the inclusion of other sources/sinks of dissolved pyrene (Figure 9-12). Predictions of $C_{pyr,WC}$ at different desorption half-times ($t_{1/2,des}$) are shown in Figure 9-13 for both the summer and the winter cases. Despite the variation in TSS-desorption half-life, the prediction agreed reasonably well with reported field-observations (Figure 9-13). These results suggested that the dissolved phase pyrene in the harbor water may be predicted, with reasonably accuracy, when desorption from suspended solids is considered.

3.5.1. Atmospheric and Riverine Input of Pyrene

Atmospheric deposition and freshwater input were important potential sources of dissolved pyrene for Boston Harbor. The predicted $C_{pyr,WC}$'s at low $S_{pyr,bed}$ were substantially raised when atmospheric deposition and riverine input were accounted for (compare the 'simple' case with either the 'Summer' or the 'Winter' prediction; Figure 9-12). This raised the question: can these two fluxes overwhelm the importance of desorption from suspended particles?

The depositional study by Golomb et al. (1997) suggested that the total depositional pyrene flux into Boston Harbor to be between 20-130 $ng_{pyr}/m^2.d$ in summer and 70-440 $ng_{pyr}/m^2.d$ in winter (Appendix 9-4). Atmospheric depositional flux was much lower than suspension-solids desorptive flux, which ranged from ~400-85000 $ng_{pyr}/m^2.d$ (for $S_{pyr,bed}$ ~200-10000 $\mu g_{pyr}/kg_{solids}$). Desorptive flux and atmospheric depositional flux became comparable only at the low bed load of <200 $\mu g_{pyr}/kg_{solids}$ and slow desorption (e.g. $t_{1/2,des}$ = 3.9 d). Furthermore, since deposited pyrene and PAHs are predominantly associated with solids, the actual release flux of pyrene from deposited atmospheric particles, which also involved desorption, will be much less than $440ng_{pyr}/m^2.d$, and thus relatively negligible to desorption flux (section 2.3.3.1).

Freshwater outflows from the Mystic, the Charles, the Chelsea, and the Neponset River contributed dissolved pyrene into the harbor at ~$100kg_{pyr}$/yr (Alber et al. 1994). This is equivalent to an average riverine pyrene flux of ~3000 $ng_{pyr}/m^2.d$, assuming an averaged harbor area of 100 km^2 (section 2.3.3.3; Stolzenbach et al. 1998). Assuming that the Inner Harbor (area~10 km^2; Figure 9-4) received most of the riverine pyrene, riverine input, now at ~30000 $ng_{pyr}/m^2.d$, would be comparable to that of desorption (~10000-85000 $ng_{pyr}/m^2.d$ for $S_{pyr,bed}$ of 5000-10000ug_{pyr}/kg_{solids}). Thus the riverine pyrene flux may sufficiently explain the observed dissolved pyrene level in the Inner Harbor or even that in the Northwest Harbor. However, riverine source cannot account for the observed dissolved pyrene levels in the Central Harbor and the Southeast Harbor (Figure 9-4). Furthermore, it can be argued that 'dissolved pyrene' in freshwater outflows would be partially released from resuspension of PAHs-rich riverine sediment.

Hence it may be concluded that riverine input may not replace the importance of suspended solid desorption as a source of dissolved pyrene.

3.5.2. Predicting Seasonal Variation of $C_{pyr,WC}$

The dissolved phase pyrene levels in Boston Harbor exhibited seasonal variation, with the highest concentration typically observed in wintertime (Figure 9-14). Taking the June and December observations of $C_{pyr,WC}$ as representative of the summer and the winter case, the steady-state model can be better evaluated for its ability to predict realistic $C_{pyr,WC}$ levels. The seven-rate model gave predictions that agreed with field observations in both the summer and winter scenarios (Figure 9-15). One can also estimate the relative contribution of different processes in the release of dissolved pyrene into the harbor water (Figure 9-16).

3.6. Secondary Supports for TSS-Desorption as Key Pathway of HOCs

The steady-state model results in this chapter suggested that desorption from suspended particles may be an important pathway for releasing sedimentary-HOCs in harbors and estuaries. A number of other independent observations also seem to support the idea that resuspension of sediment particles may control the dissolved HOCs level in estuarine systems. They will be briefly discussed in this section.

3.6.1. Observations on Pollutants and Sediment Resuspension

Baker et al. (1991) observed upward fluxes of PAHs and PCBs from lake sediment bed. Furthermore, they reported the HOC loadings on resuspended particles to be 10–100 times than those on the freshly settling particles. Their observations would be consistent with the idea of mobilization through resuspension. Ravens et al. (1998) observed that the sediment-Pb and sediment-PCB concentrations in Quincy Bay were negatively correlated to the annual excess skin stress. This means that sediment pollutant loadings decrease with increasing average suspended-solids concentration (i.e., higher excess skin stress). Zhou et al. (1996) also reported that the dissolved atrazine and lindane levels in the Humber Estuary to be positively correlated with the total suspended-solids concentrations. Adams (2003) reported that a higher than expected level of dissolved pyrene in the tidal influx zone in the lower Hudson Estuary during April. This was, however, not observed in October. The April observation was attributed to resuspension release caused by the increased river outflow due to spring snowmelt.

3.6.2. Observations on Distribution of PAHs in Sediment Particles

Distributions of native PAHs in different sediment particle size fractions also support similar claims. Previous studies have shown that native sediment-PAH concentrations generally decline as particle size increases (Wang et al. 2001; Kukkonen et al. 2003; this study) (Figure 9-17). The observed trend is consistent with the fact that smaller particles are more easily resuspended and stay longer in the water column once resuspended.

An opposite trend in sediment-PAHs and size was reported by Ghosh et al. (2000). However, they have observed that coal/wood derived particles or phases were

responsible for sorbing ~60% of total PAHs in Milwaukee Harbor sediments. The author believes that the smaller particles would have lower activities of PAHs (i.e. normalized with respect to coal/wood-water partitioning) for the Milwaukee Harbor sediments as well. However, since PAHs-size distribution for the coal/wood phases was not reported in Ghosh et al., this 'hypothesis' could not be tested. The observation reported by Ghosh et al. did illustrate the importance to consider the BC/BC-like phase (i.e., coal, char, soot, kerogen) in addition to the 'soft' organic carbon when interpreting the equilibrium or kinetic fate of HOCs in both solid or dissolved phases.

3.7. Model Limitations

The limitations of pseudo steady-state (i.e. within a season) single compartment model should be re-emphasized. This section will briefly discuss the key limitations of the (pseudo) steady-state box model.

3.7.1. Depth-Averaging of Properties

Vertical profiles of dissolved pyrene, suspended-solids, and horizontal velocity are neglected by allowing depth averaging. While the overall harbor suspended-solid concentrations are generally low (1–50 mg_{solids}/L_w; Table 2-7 in Chapter 2), a previous *in situ* study by Ravens et al. (Ravens 1997; Ravens et al. 1998) showed that peak near-bottom solids concentration in Boston Harbor to be around 100 mg_{solids}/L at non-storm conditions, or much higher at boat-wave dominant or storm conditions. This implies that dissolved HOCs levels would be the highest near the bed regardless of whether desorption or porewater flushing being the dominant HOC-release pathway. Consequently, vertical transport, predominantly via eddy diffusion, may have to be considered. Vertical eddy diffusivities in a ~20 m deep lake (Imboden et al. 1978) and at sea surficial-layers (Pritchard et al. 1966) were found to be approximately 0.1-10cm^2/s and 1-10cm^2/s, at summer and winter, respectively. Depth averaging with respect to dissolved HOCs levels may be appropriate for winter conditions, where vertical mixing timescales would be about 0.3-3d (assuming 5m average depth for Boston Harbor), but it is much less appropriate for summer conditions, where vertical mixing is ~10 times slower due to thermal stratification. Last but not least, variation in horizontal velocity along water-depth (Dyer et al. 1986) implies the upper layers of the water column would be flushed faster than the near-bottom layers.

3.7.2. Disregard Dynamics of Resuspension

The simple steady-state model also disregards the dynamics/kinetics of resuspension, which would in turn affect the dynamics of HOC desorption from the suspended solids. In estuaries where resuspension is significant, the concentration of suspended solids can vary dramatically. For instance, the local R_{sw} at a particular water depth may vary by as high as a factor of 10 with each resuspension cycle (about 6 hours) (Schubel 1968). The rate of desorption depends strongly on the local R_{sw}, which is now a function of time; and even if we may use a 'constant' desorption rate constant (e.g., $k_{TSS,des}= \ln(2)/t_{1/2,des}$), the rate of desorption is by itself proportional to the local R_{sw} (i.e. the first order approximation in Eqn. 9 - 13).

Related to resuspension is the issue of differential settling of different particle/aggregate size. In reality, fine-sized particles are suspended more frequently than the big, heavy ones. The box steady-state model does not have the physics which produce a size-differentiated distribution of PAHs in the sedimentary phase, as shown in Figure 9-17.

3.7.3. Spatial Heterogeneity, First Order Processes, and Temperature Dependence

The simple box model disregards large-scale spatial heterogeneity in estuarine/harbor system. Using Boston Harbor as an example, it would be more realistic to apply the model to one of the sub-region (e.g. the Inner Harbor or the Central Harbor) within which the hydrodynamic and/or chemical properties are more consistent.

The assumption of first order processes may be appropriate for photolysis or biodegradation of HOCs, but it is a simplification for desorption. Wu and Gschwend (1988) have shown even in systems with linear sorption isotherms, the first order approach may, at the best, only approximate the true kinetics of adsorption/desorption. This approximation certainly becomes even less appropriate with sorption onto BC being non-linear (see Chapter 7).

A better model requires additional information on the temperature dependence of specific processes. For instance, the author found it difficult to evaluate the winter case due to a lack of rate information for some of the processes. The modeled winter scenario presented earlier (section 3.5.2) assumed constant TSS-desorption half-lives as in the summer case. We may get a better estimate of the winter desorption half-lives by applying the 10°C-double-up rule-of-thumb so that $t_{1/2,des,winter}$ ranges from 3.6–15.6 d (assuming a 20°C difference between summer and winter). The new desorption half-lives now produce a different modeled picture for the harbor (Figure 9-18) with the estimated $C_{pyr,WC}$ being on the lower end of field observations. While desorption rate may be 'corrected' this way, the winter riverine influx requires actual 'measurement' or independent estimate. And since porewater flushing is, in reality, a lumped term for a variety of physical, chemical and biological processes (Figure 9-19), it is also hard to be 'corrected' for a change in system temperature.

3.7.4. Simplifications of the Dynamics of Sink/Source Processes

A number of simplifications on the dynamics of transformation processes were made in this study. First, the estimated photochemical degradation rate has ignored the oxidative contribution from singlet oxygen (Schwarzenbach et al. 2003). Degradation of dissolved HOCs by singlet oxygen is an important indirect photolysis pathway in the winter scenario. Second, it was assumed that all sorbed pyrene degraded as fast as dissolved. This assumption was not valid given the desorption kinetic observations (i.e. Chapter 2) and the simulation studies (Chapter 7 & 8). However, this assumption allows the upper limit of biodegradation rate to be estimated – the real biodegradation rate can never exceed this estimate. The same rationale is also applied to the atmospheric pyrene source (i.e. assuming all deposited pyrene to be in dissolved form).

4. Conclusion

We have applied the simple box-model approach to the estimation of pyrene abundance in Boston Harbor. The box model greatly simplified the complexity of the real harbor by disregarding all spatial heterogeneity (in both vertical and horizontal directions), and thus may be considered as a rough assessment tool for harbor/estuarine systems. The characteristic times of major transformation and transport processes in Boston Harbor suggested that equilibrium partitioning (EqP) of pyrene could be valid.

Two pyrene EqP scenarios were examined: that of equilibrium between the surficial bed layer and the harbor water, and that between the suspended particles and the harbor water. Model results suggested that neither EqP scenario yielded satisfactory predictions of $C_{pyr,WC}$ and demonstrated the persistence of sedimentary phase pyrene content over decadic timescale, as documented by field studies. This conclusion agreed with the sorption disequilibrium between the porewater and the bed-solid phase observed in the surficial bed layer in Boston Harbor.

With the EqP model appeared to be inadequate for Boston Harbor, we then considered a pseudo steady-state model. The model assumed that the sources and sinks of dissolved pyrene in the harbor water balanced out each other, and that a pseudo steady-state $C_{pyr,WC}$ existed over a seasonal to yearly timescale. Two versions of the steady-state models were examined, and both appeared to give reasonable predictions of $C_{pyr,WC}$ over a wider range of sedimentary pyrene concentrations.

Results from the steady-state model suggested that mobilization from resuspended (desorption from suspended sediment) sediment is important in Boston Harbor and that it should be considered in modeling studies. In the absence of the desorption term, the steady-state model failed to produce harbor dissolved pyrene concentrations agreeable with field observations. The potential significance of resuspension in mobilizing sedimentary HOCs in other estuaries and harbors was raised. Relevant evidence from other studies consistent with the idea of resuspension mobilization were reviewed and discussed.

This chapter showed that a simple steady-state box model can be a useful and cost-effective tool for assessing the 'background' state(s) of persistent HOCs (such as pyrene) in estuaries, harbors, and lakes. The model results also suggested the potential importance of resuspension-mediated HOC mobilization – a process that has been inadequately documented in field studies and the dynamics of which is currently poorly understood. With the knowledge that sediment resuspension, due to both natural causes and/or anthropogenic activities, is common in many highly urbanized or industrialized estuaries/harbors and coastal zones, it is necessary to further our understanding on how sediment resuspension may contribute to the release of bed-associated HOCs.

Chapter 10. Quantification of Organic Carbons & Black Carbons by EDX and STEM-EDX

CHAPTER ABSTRACT

A new BC quantification method based on energy dispersive X-ray spectroscopy (EDX) has been developed for both point/spot analysis and sample areal analysis. The method used elemental ratios of C, O, and N to quantify the abundance of OC and BC in a sample. Fundamental assumptions and approximations involved were examined and justified as thoroughly as possible.

In the point/spot-EDX mode, elemental ratios were computed from peak area/height of O, N, and C. Applying the point/spot analysis method to a variety of carbonaceous materials yielded elemental ratios that were consistent with literature. The high levels of uncertainty observed were attributed to low signals, limitations from signal processing, and probable compositional variation on a nanometer scale.

In the areal mode, samples were analyzed with a scanning transmission electron microscope (STEM-EDX) to obtain maps of C, N, and O. A purely carbon pixel (without O or N) was defined as graphitic. With a simple 'noise' reduction scheme and an internal background correction procedure, graphitic areal coverage of carbonaceous samples was estimated from the elemental maps of C, N and O. The graphitic fractions estimated from STEM-EDX not only showed an internally consistent trend between the different standards and environmental samples but also agreed fairly well with the aromatic fractions of similar carbonaceous matter estimated from quantitative ^{13}C-NMR or EELS analysis.

The limitations of the method were discussed along with possible modifications and/or solutions for further improvement. The preliminary success of the EDX/STEM-EDX method warrants further exploration and methodological refinement.

Table of Content for Chapter 10

1. Introduction and Objectives 249

1.1. Introduction 249

1.1.1. The Need for a New Black Carbon Quantification Method 249

1.1.2. Electron Microscopy (EM) for BC Identification & Quantification 249

1.1.2.1. Analytical Electron Microscopy 249

1.1.2.2. Identification of BC/OC Phases by EM 249

1.2. Chapter Objectives 250

2. Methodology & Experimental 251

2.1. Materials and Samples 251

2.1.1. Samples for EDX analysis 251

2.1.2. Materials for Microscopy Specimen Preparation 251

2.2. EM Specimen Preparation 251

2.2.1. Sediment specimen (Soot Amended) 251

2.2.1.1. Soot Amendment 251

2.2.1.2. Embedding Sediment-Soot in Sulfur 252

2.2.1.3. Microtomy of Embedded Samples 252

2.2.2. Humic Acid & Nicotinamide Specimen 252

2.2.3. Graphite Specimen 252

2.2.4. Standard Materials Specimen 252

2.2.5. Ultramicrotomy 253

2.3. Electron Microscope 254

2.3.1. Electron Microscope Specifications 254

2.3.2. Beam Broadening and Spatial Resolution of X-ray Analysis 254

2.4. Data Processing and Analysis 254

3. Results & Discussion 255

3.1. TEM Imaging of Soot Particles in Native Sediment Aggregates 255

3.1.1. Visualization of Native Soots by Morphological Features 255

3.1.2. Visualization by TEM and Complementary Analyses 256

3.1.3. General Challenges in EM-Quantification as Shown by TEM Visualization 256

3.1.3.1. Sample Thickness & Mis-Quantification 256

3.1.3.2. Preservation of Aggregate Structure 257

3.1.3.3. Low BC Content and Interferences 257

3.1.4. Concluding Remarks on TEM Visualization of soot-BC 258

3.2. Preliminary Considerations on BC Identification by EDX 258

3.2.1. Elemental Ratios as Indicators of BC 258
3.2.2. Hydrocarbon Contamination on EDX C-Peak 258
3.2.3. Soot + Single Mineral Phase 259
3.2.4. Soot + Multiple Mineral Phases 259
3.3. Elemental Ratio Signatures of Various Carbonaceous Matter by EDX Spot Analysis 260
3.3.1. Theoretical Basis, Assumptions, and Empirical Validations 260
3.3.1.1. Thin-Film Assumption 261
3.3.1.2. Equivalency in Intensity Ratio and Compositional Ratio 263
3.3.1.3. Peak-Height Approximation 263
3.3.1.4. Concluding Remarks on Quantitative EDX Assumptions 264
3.3.2. Considerations on Elemental Ratio Definition of BC & Micron-Scale Heterogeneity in Environmental Carbonaceous Matter 264
3.3.2.1. Cutoff Elemental Ratios for Defining BC 264
3.3.2.2. Probe Resolution for Micron-Scale Compositional Variance 265
3.3.3. Empirical Elemental Ratio Signatures of Various Carbonaceous Matter (EDX Spot Analysis) 266
3.3.3.1. Spot-EDX Analysis: N/C Atomic Ratio 266
3.3.3.2. Spot-EDX Analysis: O/C Atomic Ratio 267
3.3.3.3. Observational Agreement with Literature 267
3.3.3.4. Miscellaneous Remarks on O/C Ratio in Spot-EDX 267
3.3.4. Comparing SEM-EDX and TEM-EDX for BC Quantification 268
3.3.5. Sources of Uncertainties in TEM-EDX Derived Elemental-C Signatures 269
3.3.5.1. Increased Hydrocarbon Contamination under High Voltage Beam 269
3.3.5.2. Element-Specific Sensitivity Issue 269
3.3.5.3. Probe-Scale Compositional Heterogeneity 269
3.3.5.4. Interferences from Inorganic-O 269
3.3.6. Cumulated Error in Elemental Ratio 269
3.4. Quantification of BC by Elemental Mapping of C, N, and O by STEM-EDX 271
3.4.1. Methodological Issues Specific to STEM-EDX 271
3.4.1.1. Peak-Height Intensity & Low Counts 271
3.4.1.2. 'Noise' Pixels 271
3.4.1.3. O/C as the Operational Cutoff Ratio for BC 271
3.4.1.4. Background Correction for Inorganic-O Signals 272
3.4.2. Preliminary Comparison of STEM-EDX Data Treatment Options 272
3.4.2.1. Pixel Consolidation and Image Fine Features 272

3.4.2.2. 'Noise' Pixels 272
3.4.2.3. Compositional Distortion from Pixel Consolidation 272
3.4.2.4. Correction of Background Film Oxygen Signal 273
3.4.3. Quantification of BC by Elemental Mapping in Various Samples 273
3.4.3.1. Should N and O Signals be Corrected? 274
3.4.3.2. Graphitic Content of Individual Samples 275
3.4.3.3. Qualitative Consistency in Graphitic/Total C Fractions 275
3.4.3.4. Accuracy of EDX Mapping Derived Graphitic Content 276
3.4.3.5. Total Areal Graphitic Coverage 277
3.4.3.6. Intra-aggregate/particle Spatial Features 277
3.5. Methodological Limitations of STEM-EDX for BC Quantification 277
3.5.1. Purely Carbon Presence Not a Sufficient Evidence as Graphitic 277
3.5.2. In-Microscope Contamination, Beam Damage, and Bonding Alteration 278
3.5.3. Difficulty in Assessing Absolute OC/BC Contents 279
3.5.4. Separating Inorganic Carbon and Inorganic Oxygen Signals 279
3.6. Future Work on BC Quantification via STEM EDX-Mapping 281
3.6.1. Evaluating and Improving Multiphase O-Correction Scheme 281
3.6.2. Addressing Hydrocarbon Contamination 281
3.6.3. Mapping Model Systems 282
4. Conclusion 282

1. Introduction and Objectives

1.1. Introduction

1.1.1. The Need for a New Black Carbon Quantification Method

The dominance of black carbon (BC) in determining the fate of hydrophobic organic pollutants across different environmental compartments has prompted for the development of accurate BC quantification procedure. Different quantification procedures, which all define BC operationally based on distinct criteria, have been developed for various application contexts and merits. In view of the substantial discrepancies reported between these operational methods in a recent comprehensive effort (Hammes et al., 2007) and the potential biases of the methods, there is a need to search for an alternative BC quantification procedure that is analytically rigorous and unbiased, and procedurally independent of all subjective elements. Furthermore, BC, whether it exists in the form of the submicron-scale soots or the micron-scale char fragments, is likely to dictate the release or uptake timescales of pollutants in natural geosorbents such as soils and sediments. There is, therefore, also a separate need to observe and quantify the various natively present BC entities at the microscopic, aggregate-level. Such information will help to formulate a realistic picture for adsorption/desorption phenomena occurring in the sub-aggregate world.

1.1.2. Electron Microscopy (EM) for BC Identification & Quantification

1.1.2.1. Analytical Electron Microscopy

New possibilities for the quantification of environmental BC have been opened up with the breakthroughs in the instrumentation (Liu 2005; Sigle 2005) and signal processing capabilities (Mayer et al. 1997) of electron microscopy (EM) in the past two decades. The contemporary EM is capable of optical imaging at nanometer/sub-nanometer resolution (Redlich et al.1999; Liu 2005). Transmission electron microscopy (TEM) coupled with energy-dispersive X-ray (EDX) spectroscopy, electron energy loss spectroscopy (EELS), energy-filtered imaging (EF), or near-edge X-ray adsorption fine structure (NEXAFS) spectroscopy have been applied in the fields of biology (Laquerriere et al. 2002), biochemistry (Lobinski et al. 2006), material science (Zern et al. 2002), geochemistry (Liang et al. 2006), and soil science (Solomon et al. 2005) for quantitative or compositional questions involving carbon , nitrogen, and oxygen.

1.1.2.2. Identification of BC/OC Phases by EM

Stoffyn-Egli et al. (1997) and Brodowski et al. (2005) brought the technique of electron microscopy a step closer to the quantification of BC. The two groups studied various BC and non-BC carbonaceous phases with scanning electron microscopy (SEM) coupled with EDX. With signals obtained from SEM-EDX, they were able to identify the compositional fingerprints and to observe morphological features of various carbonaceous matter. However, both studies focused on particles of the order of 100 μm in size and certain level of visual discretion on particle morphology (e.g. sphericity, surface texture, porosity, etc) was required in the identification process. This implied methodological gaps in both the identification of nano-scale soot particles and the

quantification of total BC in a given sample. It was also unclear if the elemental-ratio signatures of various phases reported by Stoffyn-Egli et al. and Brodowski et al. were the signatures averaged over local heterogeneity in the sub-micron to nano scale, or the signatures were indeed representative of the 'pure' phases.

The coupling of scanning transmission electron microscopy (STEM) with EDX and/or EELS seems to be a promising combination for the quantification of environmental BCs. The specimen is raster-scanned by the electron beam in STEM mode, allowing intra-aggregate/particle features of both physical and chemical nature to be revealed at nanometer scale (Swartz et al. 1997). The analytical STEM-EELS/EDX, therefore, offers an unprecedented opportunity for the simultaneous quantification of environmental BC and characterization of the hosting geosorbent particles at realistic BC-size dimensions in a most chemically rigorous manner (from local bond type and atomic abundance to micron-scale quantification) and yet least influenced by human factors or methodological variations as in the conventional methods (Hammes et al. 2007). This possibility has long existed for more than two decades but has never been thoroughly examined.

1.2. Chapter Objectives

The main objective of this chapter is to explore the rich potentials of using analytical electron microscopy (AEM), with special focus on STEM-EDX, for sub-micron scale quantitative analysis of BC. The investigation will begin with the attempt to observe soot-BC in a background of sedimentary matrix under low resolution TEM (<25000x) (section 3.1). The TEM attempt will highlight certain issues critical to general analytical EM methodologies. The focus will then proceed to spot-EDX analysis of selected carbonaceous matter (sections 3.2, 3.3). The exercise with spot-EDX is useful and necessary in two ways: (i) for laying down the background theory for quantitative EDX analysis, and (ii) for revealing the strength and weakness generally associated with EDX analysis. Then the possibility of quantifying BC using elemental maps produced from STEM-EDX will be examined (section 3.4). The limitations of the STEM-EDX method will be discussed in section 3.5. This chapter will end with a list of the next logical questions to be addressed for STEM-EDX quantification of BC in section 3.6.

2. Methodology & Experimental

2.1. Materials and Samples

2.1.1. Samples for EDX analysis

Samples examined by EDX/STEM-EDX included sediment, chemicals, and standards studied in the BC quantification ring trial (Hammes et al. 2007). Sediment sample was obtained from Boston Harbor (site #6, see Appendix 9-10; nominal diameter from wet sieving: 180-250 μm). Chemicals included humic acid (Aldrich, sodium salt, technical grade, batch #21520BB, H16752-100G), nicotinamide ($C_6H_6N_2O$) (Sigma, N3376-100G), and graphite powder (Aldrich, 100 mesh, >99.99%); standard materials/samples included diesel particulate matter (or soot) (NIST SRM 1650a), chestnut wood lignocellulosic char (BC Standard Material, University of Zurich, Switzerland), melanoidin (from glucose and urea in a mass ratio of 100g:10g; BC Standard Material from University of Zurich, Switzerland; for reference, see http://www.geo.unizh.ch/phys/bc/), and urban dust (NIST SRM 1649a).

2.1.2. Materials for Microscopy Specimen Preparation

For samples that require fixation and microtomy, elemental sulfur powder (J.T.Baker, sublimed) was used as the fixation medium. For hydrophobic particles such as soot and lignocellulosic char, suspensions were made in ethyl acetate (BDH). Clean water (Milli-Q, 18mΩ, with UV lamp for TOC-reduction) was used to prepare aqueous solutions of soluble chemicals. Two types of microscopy grids were used for holding specimens: lacey SiO film on 200 mesh Cu-grid and lacey-C film on 200 mesh Cu-grid (Lacey formvar substrate, carbon coated, Cat #10975; Ladd Research, USA). All specimens were held on lacey SiO with the exception of graphite, lignocellulosic char, melanoidin which were placed on lacey-C.

2.2. EM Specimen Preparation

2.2.1. Sediment specimen (Soot Amended)

The preparation of soot-amended sedimentary EM specimen consisted of three steps: (i) addition of soot onto sediment particles, (ii) Embedding soot-amended sediment particles in elemental sulfur, and (iii) microtomy of the specimen block.

2.2.1.1. Soot Amendment

A soot-suspension in ethyl acetate was prepared (~0.2 g or a small spatula of soot in ~15 ml ethyl acetate). About 1 to 3 ml of the soot-suspension was dispensed onto pre-dried sediment particles (overnight oven-dried at 75°C; ~0.5 g dry weight). The soot-sediment slurry was briefly mixed and subsequently dried under a study lamp (60 W). Aluminum foil was cut and folded to make moulds (~1/2×1/4×3/8 inch) that would hold and shape molten sulfur into a rectangular block. The exact dimension of the mould was not critical though it should shape a sample block that can be fitted into the microtome holder.

2.2.1.2. Embedding Sediment-Soot in Sulfur

A number of studies have embedded carbonaceous samples in elemental sulfur to circumvent the problem of background carbon signal due to resins (Furukawa 2000; Lehmann et al. 2005). During sample fixation, a separate vessel (also aluminum) was used for holding additional molten sulfur. Both the specimen mould and the excess vessel were fully filled with elemental sulfur powder and heated at 150°C. A concave pyrex glass (~4 cm diameter) was also heated along with the sulfur. Sulfur powder became molten within 15 min. The molten sulfur appeared as a transparent, reddish-orange, oily liquid. When ready, the concave pyrex glass was took out and used as a working platform for all subsequent fixation steps. The glass platform served two purposes: to allow more time for specimen fixation by keeping the sulfur molten, and to prevent quick cooling of sulfur which resulted in very brittle block. Soot-amended sediment particles were then transferred into the specimen mould, which was about half-full with liquid sulfur. The particles usually stayed at the sulfur-air interface. The half-filled mould was then allowed to cool on the bench until the content assumed a rubbery, non-crystalline texture. The mould was placed once again on the glass platform, filled up with liquid sulfur from the excess vessel, and allowed to cool gradually.

2.2.1.3. Microtomy of Embedded Samples

The sample block was then microtomed to give ultrathin specimens (<100 nm) (see section 2.2.5 for further details). The microtomed and Cu grid-mounted specimen was then coated with a thin Au/Pd conductive layer (~10-20 Å) to reduce charging effect in viewing.

2.2.2. Humic Acid & Nicotinamide Specimen

EM specimens of humic acid and nicotinamide were prepared directly from their aqueous solutions. First, a solution of the desired chemical species was prepared by dissolving approximately 0.5 g of solids in 20-50 ml of Milli-Q water. Then a small volume of the solution (~<50 ul) was dispensed onto a 200-mesh Cu grid with either lacey-SiO film or pure SiO film. Excess water on the EM specimen was removed first by gently contacting the grid on a piece of tissue (lint-free Kimwipe) and then by heating/drying under a study lamp (60 W). The dried specimen on Cu grid may or may not be further coated with Au/Pd (~10-20 Å). It was found that both humic acid and nicotinamide were relatively stable in electron beams when prepared this way.

2.2.3. Graphite Specimen

Graphite powder was embedded in S, microtomed, and loaded onto lacey-C film. No conductive coating was required for graphite. EDX spectra of graphite were obtained exclusively from graphite pieces placed over the holes in the lacey-C film.

2.2.4. Standard Materials Specimen

Suspensions of char, melanoidin, and urban dust were prepared in ethyl acetate with approximately <0.1-0.2 g of mass in 3-5 ml of ethyl acetate. Char and urban dust looked very fine and were used without grinding. Melanoidin required grinding because of the presence of light-brownish mm-scale particles amidst the finer, white powder. Small amount (~10 uL) of the suspensions was dispensed onto Cu grid with lacey-C or

SiO film. The specimens were stored away for later view after being dried under a study lamp (60 W).

2.2.5. Ultramicrotomy

Ultrathin sections (<100 nm) of specimens were cut from the sample-sulfur block using a diamond knife (45° knife, Diatome, USA) mounted on a microtome (MTX Ultra Microtome, RMC, USA). The microtomy procedure may be divided into the phases of block-trimming, block-blade alignment, cutting, and loading.

Block-Trimming. The cooled, raw sample-sulfur blocks were trimmed in two ways. First, it was trimmed in a tapering manner so that a sediment-enriched spot was to be located at the tip (~1×1 mm). This step facilitated uniform microtomy of sulfur block at thickness of <100 nm. Second, the two surfaces that would be in contact with the block-holder of the microtome were trimmed to as smooth and level as possible. This helped to maximize the contact area with the block-holder, generating a greater friction to hold the block in place during the cutting. Both steps were necessary and critical because the sulfur block was brittle compared with the more traditional resin blocks.

Block-Blade Alignment. The sample-sulfur block was then mounted firmly into the block-holder with the tapered end facing the diamond knife. Extreme care was taken not to over-tighten the holder screw and break the block. The bowl area of the diamond knife block was pre-rinsed with Milli-Q water. The diamond blade was wetted with Milli-Q water, and then cleaned with softwood. After mounting the knife block to its holder, the tapered tip of the sulfur block was adjusted to the same height as the diamond blade and aligned them as close as possible together. With the blade barely touching the tapered tip of the sample block, tightened up the screw to affix the diamond knife block in firm position. This should be done gradually and gently because the diamond knife block would move and might damage the sulfur tip.

Cutting. After the gap between the blade and the tapper tip was closed (by rolling the sample block forward at ~500 nm distance), set the target thickness down to ~200 nm. The sample blocks were manually rolled against the blade until thin sections of approximately same size were generated by every cycle of motion. The cutting was repeated at 100 nm, then at ~30 to 50 nm. The diamond knife block contained a bowl area for filling clean water. Sample debris floating on the clean water was removed very gently by touching the water surface with a Kimwipe. The wiping action usually offset the blade-to-tip distance slightly, so cutting at ~30-50 nm was repeated until thin sections were relatively uniform.

Loading. Cutting was repeated until the water surface (i.e. in the bowl of the diamond knife block) to be at least half filled with specimen thin sections. With a pair of tweezers, a Cu-grid was slided into the bowl from the cleaner half of the bowl, and then gently lifted up at the thin sections filled half. The action was repeated until a good amount of thin sections were loaded onto the Cu-grid. After excess water was removed by gentle contact with Kimwipe tissue, the specimen-loaded Cu-grid was stored until viewing.

2.3. Electron Microscope

2.3.1. Electron Microscope Specifications

Three electron microscopes were used for obtaining micrographs and performing microanalysis.

Low Resolution TEM. Low resolution TEM images on soot clusters and sedimentary phases were obtained with a JEOL 200CX which operated at 200 kV and had a point-to-point resolution of 0.24nm. Digital images were acquired with a 1.3 Mpix AMT digital camera (Advanced Microscopy Techniques, USA).

EDX Spot Analysis. For the work on EDX spot analysis and STEM-EDX elemental mapping, two microscopic systems were used. Most of the EDX/STEM-EDX work was done with the VG-EDX system, which consisted of a HB603 scanning transmission electron microscope (STEM) (VG Microscopes, East Grinstead, UK) and an energy dispersive X-ray spectrometer (EDX) (Link Analytical). HB603 was operated at an accelerated voltage of 250 kV and had a resolution of 0.30 nm point-to-point.

STEM-EDX. The EDX/STEM-EDX work on char and melanoidin was done with the JEOL-EDX analytical system, which consisted of a JEOL 2010FEG analytical TEM and an energy dispersive X-ray spectrometer (Oxford Instrument, UK). JEOL 2010FEG was operated at 200 kV and had an image resolution of 0.195 nm point-to-point. In both systems, INCA (Oxford Instrument, UK) was the software for acquisition and EDX microanalysis (point analysis and elemental mapping).

2.3.2. Beam Broadening and Spatial Resolution of X-ray Analysis

The EDX microanalysis can be performed with a spatial resolution of approximately 1 nm in ideally thin samples. In real samples, however, resolution is compromised by beam broadening or spreading even in ultrathin specimens (<100 nm) (Goldstein 1979; Jones et al. 1981; Scott et al. 1995). Beam broadening, or the widening of the beam illuminating area, is caused by electron scattering due to the atomic nuclei in the sample. Based on the classical treatment of nuclear scattering by Rutherford, Goldstein et al. (Goldstein 1979; Jones et al. 1981; Scott et al. 1995) derived an estimate for beam broadening, b, as:

$$b \equiv k\frac{Z}{E_o}\left(\frac{\rho}{A}\right)^{0.5} t^{1.5}$$

Eqn. 10 - 1

For a specimen with a thickness of 100 nm, the broadening b has been estimated (Appendix 10-9), and the real X-ray probe resolution would be about 2 to 5 nm.

2.4. Data Processing and Analysis

Raw EDX spectra and elemental X-ray counts matrices were exported from INCA. With the exception of peak Integration, which was performed by an INCA analyzer module,

all data processing and analysis and map generation were done in routines coded in Matlab (Appendix C). Simpler data organizing tasks were performed in Excel.

The theoretical basis for EDX spot analysis and quantitative elemental mapping will be discussed in sections 3.3 and 3.4. Detailed data treatment procedures, equations, sample calculations, and raw data can be found in Appendices 10-5 and 10-6 for spot analysis and quantitative mapping, respectively.

3. Results & Discussion

3.1. TEM Imaging of Soot Particles in Native Sediment Aggregates

The first objective was to see the presence of soot particles using simple low resolution (<25000x) TEM. There are several reasons for pursuing this as the first step. First, we wanted to confirm the presence of soots in natural samples before engaging in the more time-consuming and exhaustive mapping procedure. Second, knowing that soots exhibit characteristic physical features (i.e., of 10-50 nm order in diameter, tend to be present in clusters due to their hydrophobicity), we want to verify the presence of soot by inspecting the micro images. Although subjective and at best qualitatively, visual inspection serves as an alternative method to other elemental analyses. It can potentially provide an independent check on results from the more elaborate AEM analyses. Third, low resolution TEM images may also reveal other physical information about the background mineral matrix. Information such as size of intra-aggregate pores, typical constituent grain size, and arrangement of the mineral grains are important to the modeling of intra-aggregate diffusion.

3.1.1. Visualization of Native Soots by Morphological Features

Attempts to identify soot BC native in Boston Harbor sediment in TEM images were unsuccessful. Instead, soot-BC could only be morphologically recognized in samples where soot particles were deliberately added (e.g. Figure 10-7a). The following reasons may explain why visualization of native soot with TEM was difficult.

Low BC Content. First, the sample was rather low in BC content. According to the thermal oxidation method (i.e. CTO-375°C-24hr), BC was present in the sediment samples around 0.3-0.5 wt% (see Table 3-1) (on a 2-5 mg_{solids} sample mass basis). It is, therefore, necessary to examine a large number of sedimentary aggregates before one can be sure, by statistical basis, that soot BC may be present.

Morphological Changes by Aging. Second, soot BC may have lost its distinct shapes as it 'aged' in the sediment bed. Soot BC long deposited into the bed is likely to be coated by marine organic matter, considering that the non-BC organic matter content is usually 10 times that of BC (Cornelissen et al. 2005b; Table 3-1). Furthermore, it is known that (i) marine organic colloids self-assemble into large polymermic gels (Chin et al. 1998), (ii) natural marine organic matter and humic substances adsorb to mineral oxide surfaces (Tipping 1981; Cosovic et al. 1989; Gu et al. 1994, 1995), and (iii) the saline and high solid-loading estuarine environment favors formation of flocs from smaller

particles/aggregates (Eisma 1986; Gregory 1989). Field-aged soot BC are, therefore, may look very different from that of the freshly produced soot.

Visual Interferences by Non-BCs. Third, the recognition of soot spheres by light-dark contrast in TEM mode is hindered by the dominant presence of large and high density mineral grains or the lighter organic phases in natural sediments. In samples where the background matrix has been properly dispersed, soot spheres/clusters can be readily recognized in TEM images by virtue of their shape (spherical or grape-like cluster) or their darker appearance against the background film. Such is the case for the soots in aerosols, which can be identified without ambiguity (Mathis et al. 2005; Gwaze et la. 2006; Muller et al. 2006; Lapuerta et al. 2007; Semeniuk et al. 2007; Moldanova et al. 2009). In cases where matrix-dispersion is undesirable, identification of soot BC by visual means becomes more difficult. For instance, soot clusters encapsulated in respiratory epithelial cells, which are considerably more transparent than sedimentary mineral matter, become rather difficult to recognize (Figure 1c in Penn et al. 2005). The difficulties of visual recognition of soots are also illustrated in Figure 10-4: (i) dense mineral phases (labeled "A")) may 'shield' soot particles; (ii) amorphous phases (white arrows) can also interfere with the identification of soot-BC based on morphology.

3.1.2. Visualization by TEM and Complementary Analyses

Morphological features alone appear to be insufficient for identification of soot-BC and that complementary information must be gathered as well. Structural information such as crystallographic signatures/lattice spacing, obtained by X-ray diffraction (XRD), selected area electron diffraction (SAED), or high-resolution TEM images (HRTEM), can confirm the presence of soot-BC (Palotas et al. 1996; Rainey et al. 1996; Chen et al. 2000; Song et al. 2006; Daly et al. 2009). However, since these types of information cannot be obtained in an automated manner, applying these techniques for BC recognition/quantification will be very labor intensive.

Alternatively, elemental markers may also be used. Heavy metals such as Fe, V, and Ni are often found associated with soot produced from crude oil/petroleum combustion (Zoller et al. 1973; Okada et al. 1992; Ault et al. 2009; Moldanova et al. 2009). It must be noted, however, that elemental/metal markers are not definitive indication of the presence of soot-BC: Fe is ubiquitously present in sedimentary mineral phases; Ni and V can be emitted in fly ash from industrial smelters or mining operations (Hsieh et al. 2003). Both approaches have been attempted on sedimentary samples (without soot amendment) and were concluded to be unsuccessful.

3.1.3. General Challenges in EM-Quantification as Shown by TEM Visualization

Although the low-resolution TEM approach was unsuccessful, the exercise reveals several key challenges in quantifying BC which are intrinsic to analytical EM in general.

3.1.3.1. Sample Thickness & Mis-Quantification

Microscopic quantification implies the need for mapping or counting. Mapping analysis requires samples to be cut (or microtomed) to very thin sections (~50 nm or less, 30 nm to be 'ideal' as is comparable to the diameter of typical soot particles). Ultrathin samples are desirable for generating sharp carbon EELS or EDX signals and for the fact that typical soot particles are of ~30 nm in size. Thick samples (>100 nm) increase

both the likelihood of multiple scattering and the zero-loss energy background signal, resulting in poor signal-to-noise ratio for carbon peak. Extra-thin samples (~30 nm) are also needed to reduce the likelihood of over-counting soot particles which are typically of ~30 nm in size. This second point is illustrated in Figure 10-1.

3.1.3.2. Preservation of Aggregate Structure

A second challenge was the preservation of aggregate structure through the microtome procedure. Aggregates need to be fixed in a secondary medium before they can be microtomed. Multiple challenges make it hard to preserve the native aggregate structures.

Drying. Typical resins also require samples to be pre-dried. The thinning or removal of water layer around the constituent grains change the attraction between neighboring grains, and thus alters the overall intra-aggregate structure. The pre-drying issue may be overcome by using water soluble resin such as Nanoplast® which allows wet aggregates/colloids to be embedded as is (Frosch et al. 1989; Leppard 1993). However, it remains unclear to what extent the stretching/compression problem can be alleviated. Potential intra-aggregate distortion resulting from fixation may have to be accounted for when analyzing intra-aggregate micrographs.

Mechanical Shearing. Aggregate structure is also susceptible to the mechanical shearing produced during sample microtomy as the constituent grains are loosely held rather than strongly bonded. Figure 10-2 highlights some typical structural alterations resulting from microtomy. Figure 10-3 shows a micrograph that suggests possible dislocation of mineral grains. Some of these structural alterations can be reduced when cutting a thicker section. For example, the author has found that mechanical breakup is much less frequent when cutting at a thickness of ~200 nm, whereas at a thickness of ~30 nm breaking is almost unavoidable in the author's experience.

3.1.3.3. Low BC Content and Interferences

The third difficulty lies in the fact that native soot in sediment is relatively low in quantity and therefore hard to recognize by inspection. Assuming that typical sediment samples contain approximately 2 to 5 % total organic carbon (TOC) by mass and that black carbon (BC) constitutes about 9 % of the sedimentary TOC (Cornelissen et al. 2005), BC is on average only about 0.2 to 0.5 % of the total sediment mass. Although the possible interferences by non-soot phases such as organic carbon and mineral grains background have been discussed earlier (section 3.1.1), this point is worthwhile to be emphasized again. As an example, compare Figure 10-4g, which shows amended soot particles nearby mineral grains, to Figure 10-4a to f, which show aggregate regions that may or may not have any native soot particles.

The use of sulfur as the embedding medium also introduces additional artifacts by blurring out soot particles (Figure 10-5a and b) or producing soot-like structures (Figure 10-6a to c). Figure 10-7a and b illustrate how soot-like structures can be misleading without careful inspection and further complementary information about BC-suspect structures.

3.1.4. Concluding Remarks on TEM Visualization of soot-BC

The difficulties highlighted in the previous sections and the selected TEM micrographs suggest three conclusions: (i) that qualitative verification of the presence of native soot particles in sediment samples by inspection alone is very difficult, (ii) quantitative description of soot and other BC structures at microscopic levels requires advanced analytical techniques, and (iii) that different sample preparations may be needed for obtaining different piece of information (i.e., BC content, intra-aggregate structure) of a single sample.

3.2. Preliminary Considerations on BC Identification by EDX

3.2.1. Elemental Ratios as Indicators of BC

Quantitative mapping of soot and other BC entities by EM techniques requires an analytical definition that distinguishes BC from other organic carbons. One approach is to use characteristic elemental ratios to map out BC. BC is known to have relatively high C:N, C:O, and C:H molar ratios. For example, NIST 1650 diesel particulate matter and anthracite coal were reported to have C:N molar ratios of ~60 and ~80, respectively (Accardi-Dey, 2003). The advantage of using characteristic elemental ratios is that data processing and analysis is relatively simple – for maps of elemental ratios can be readily constructed from STEM-EDX data (Wroblewski et al., 1991). The C:H ratio cannot be used due to instrumental limitation on H, and so we are left with C:N and C:O ratios as potential indicators of BC.

3.2.2. Hydrocarbon Contamination on EDX C-Peak

A series of experiments was performed to examine the feasibility of using C:N ratio for BC quantification. Figure 10-8 shows the EDX spectra of nicotinamide ($C_6H_6N_2O$), a compound with a C:N ratio of 3:1. Under the bombardment of high energy electrons, the sample is likely to be changed during X-ray emission. The sample at the beam spot can be thinned down by the electron beam, or thickened up as a result of material build-up induced by the beam. The later artifact typically involves the ubiquitously present carbon species and is for that reason commonly referred to as 'hydrocarbon contamination' in electron microscopy literature (Loretto 1994; Egerton et al. 2004). The term refers to the polymerization of hydrocarbon molecules on the specimen surface by high energy electrons, resulting in the thickening of the irradiated area (Egerton et al. 2004). Here, hydrocarbon contamination can be most problematic as organic carbon in geosorbents may serve as sources of volatile molecules for local build-up. Figure 10-9 illustrates the problem of build-up at a sample-free spot on a lacey-C film as revealed by growing EELS C-peak over time.

A series of preliminary experiments was conducted to understand how hydrocarbon contamination may alter/affect signal sensitivity and produce C artifact. The first experiment evaluated the potential extent of carbon contamination in STEM-EDX analysis. Eight sites were randomly selected for EDX spectrum acquisition. C:N ratio was estimated by taking the peak counts at energies corresponding to C and N. The exposure time to irradiation was also examined, and the mean C:N ratios observed at the sites are shown in Figure 10-10. The global mean C:N ratio across the 8 random

sites was 3.9±0.3, which was significantly higher than the expected value of 3. The overestimation of C:N ratio seemed to be invariant with time. Accurate reading of the N peak, located between C and O on the EDX spectrum (Figure 10-8), also becomes increasingly difficult when both C and O peaks are dominant and this may have contributed to the higher C:N ratio. A third kind of error becomes significant when the whole microscopic view is subjected to EDX analysis. Figure 10-11a shows the EDX spectra on nicotinamide for a ~15x15 μm area at three different exposure times. For reasons unknown, the C peak seemed to acquire higher signal while N and O peaks were suppressed, and the resulting C:N ratios were much higher than those obtained from spot-EDX analysis or the stoichiometric ratio (Figure 10-11b). The last kind of error may be insignificant when performing EDX in the scanning mode. Nonetheless, it points out the need for prudence when selecting EDX operational parameters.

3.2.3. Soot + Single Mineral Phase

Under soot-amended specimen and appropriate EM conditions, it is possible to recognize the presence of soot, and thus potentially BC, in the presence of non-BC entities. Figures 10-12a to c illustrate such possibility. The micrograph in Figure 10-12a shows both sedimentary mineral grains and spiked soot clusters on a lacey-SiO film. Figure 10-12b shows the EDX spectra from an isolated mineral piece (spectrum #1), the background lacey-SiO film (spectrum #2), and some soot particles (spectrum #3). When the SiO background signal was removed from the soot spectrum, a distinct, carbon-only signal stood out (Figure 10-12c). When applying quantitative analysis to Si and C peaks in these three spectra, we found that the mineral piece in spectrum #1 corresponded to Si_2O_3 (O/Si = 1.49), while for spectra #2 and #3, O/Si was about 0.90-0.92, which suggested SiO as expected. Small presence of carbon was also noticeable in both SiO-film and mineral+SiO (Figure 10-12d), and this again demonstrates the presence of carbon buildup during viewing. This buildup was non-uniform across the field of vision (inset in Figure 10-12d), and thus its contribution may not be removed simply by subtraction.

We may conclude, from Figure 10-12, that (i) if the specimen is thin enough so that only BC is present against a SiO background, the oxygen signal due to SiO can be removed from the BC-EDX spectrum, and so C:O ratio may be used for detecting the presence of condensed-C phase, (ii) the critical C:N and C:O ratios may need to be raised to account for the fact that the C-signal due to buildup is difficult to remove, and (iii) (semi-)quantitative analysis of elemental peaks can be potentially useful for dissociating inorganic C, N, and O from the organic ones.

3.2.4. Soot + Multiple Mineral Phases

However, it can be hard to judge the presence of BC even from spot/point EDX spectra. Figures 10-13a to f show the micrographs and EDX spectra from a predominantly mineral-looking region. In the region (Figures 10-13a), a number of bright, angular structures (~50 nm in size) were peppered over a somewhat amorphous but still angular mass (300-500+ nm in size). EDX spectra indicated the presence of Cu and Fe (off scale, not shown), and smaller amounts of Al and K. Some of the sulfur used for specimen-fixation was also retained. The presence of residual sulfur could be avoided by subliming the thin-sectioned samples in vacuum (Lehmann et al. 2005).

Despite the absence of morphological evidence for soot clusters in this region (Figure 10-13a), EDX spectra from five locations all showed strong presence of C. In four of the five spectra (Figure 10-13b, d-f), the C signal was comparable or higher than the signals of Si, O, and all other metals. Elemental analysis on the peaks suggested that all 5 locations were relatively deprived in oxygen (O/Si = 0.46 to 0.76, O/Cu = 0.22 to 0.58) such that no hypothesis could be made regarding the stoichiometry of the minerals. One is prompted to wonder if these spots contain BC (or condensed-C phase) or OC. EDX signals and preliminary analysis suggested that a highly condensed carbon phase, without no nitrogen and very little oxygen was present in all 5 spots, while visual inspection of the micrograph suggested the opposite. The spectra should be corrected for absorption effect, but this is very difficult for area with multiple mineral phases of unknown thicknesses overlapping one another (Loretto 1994; Scott et al. 1995). Figure 10-14 shows the potential difficulty of O or N correction in the presence of multiple phases. The inconclusive nature of the C signals here highlights the challenging tasks of disentangling inorganic N and O signals from the total N and O signals in a region with mixed mineral phases, and estimating the C:N and C:O ratios.

3.3. Elemental Ratio Signatures of Various Carbonaceous Matter by EDX Spot Analysis

It is useful to acquire single-spot EDX observations on some typical environmental carbonaceous samples before proceeding to the full-field elemental mapping. Such exercise serves the purposes of establishing empirical elemental ratio boundaries for different types of carbonaceous matter and revealing other potential operational difficulties.

Two different approaches were used to quantify the relative abundance between two elements. The first approach relates the presence of an element by the peak height at its characteristic X-ray energy(ies). The second method quantifies the abundance of an element by the integrated area of its characteristic X-ray peak(s). It is more rigorous and accurate in theory (Zaluzec 1979). In the mapping mode (STEM-EDX), however, instead of saving the full spectrum at each pixel, only the peak heights were available. With the peak-height approach being the inevitable choice for elemental mapping, it was compared against more standard integral-area approach.

3.3.1. Theoretical Basis, Assumptions, and Empirical Validations

Quantitative analysis on EDX spectrum for determining the C:N and C:O elemental ratios involves a number of assumptions and approximations. These assumptions and approximations are elaborated and discussed in the following paragraphs.

In general, the number of X-rays generated at a specific energy is expressed as (Zaluzec 1979; Loretto 1994):

$$N_{y,e} = Q\omega n_{y,e} i$$

Eqn. 10 - 2

where: $N_{y,e}$ is the total number of X-rays generated from element y with energy e,

Q is the ionization cross-section area, ω is the fluorescence yield of X-ray for element y,

n_y is the number of y-atoms in the irradiated volume, and

i is the incident electron flux through the electron bombarded area.

The actual intensity or number of X-rays observed by the EDX detector, $I_{y,e}$, which is reduced due to incomplete collection of emitted X-rays and detector inefficiency, can be expressed as (Zaluzec 1979; Loretto 1994):

$$I_{y,e} = Q\omega n_{y,e} i \alpha_e \eta_e$$

Eqn. 10 - 3

where: α_e represents the fraction of X-rays at energy actually detected,

η_e denotes the element-specific efficiency of the EDX detector.

3.3.1.1. Thin-Film Assumption

The first assumption is that the sample is reasonably thin so that secondary processes such as absorption of emitted X-rays and fluorescence can be neglected (Goldstein 1979; Scott et al. 1995). Since the X-ray fluorescence yield for C, N, and O are less than 0.01 (Appendix 10-2, Table (c)), only absorption of X-ray is being considered:

$$I_{y,t} = I_{y,o} e^{-\frac{\mu}{\rho}\delta \csc \alpha}$$

Eqn. 10 - 4

where: $I_{y,o}$ is the initial intensity of the X-ray emitted by element y,

$I_{y,t}$ is the X-ray intensity after it travels through the sample/specimen with a thickness of t [cm],

μ/ρ [cm^2/g] is the mass absorption (Goldstein 1979; Scott et al. 1995) or mass attenuation coefficient (Hubbell et al. 1996; Chantler et al. 2005) which describes how strongly the specimen is absorbing the X-ray of element y,

δ, known as the mass thickness [g/cm^2], is defined as the product of the specimen density and the thickness t (i.e., $\delta \equiv \rho t$),

$\csc\alpha$ correcting for the extended pathlength due to the placement of X-ray detector at an angle of α (i.e., X-ray take off angle)

For a composite specimen, the overall specimen mass absorption may be approximated as the simple weighted sum of the X-ray absorbing ability of all contributing elements (Hubbell et al. 1996):

$$\left(\frac{\mu}{\rho}\right)_{Comp} = \sum_{i} w_i \left(\frac{\mu}{\rho}\right)_i$$

Eqn. 10 - 5

With w_i and $(\mu/\rho)_i$ as the weight fraction and the mass absorption coefficient, respectively, of element i in the specimen. It should be noted that this in itself is an approximation, for the X-ray absorbing ability depends on the nature of the bonding (Scott et al. 1995). Two criteria for the validity of thin-film approximation have been proposed for judging the validity of such approximation. Tixier et al. (Goldstein 1979) suggested a single-element based criterion in which:

$$\varepsilon \equiv \left(\frac{\mu}{\rho}\right)_{Comp} \delta \csc\alpha < \varepsilon_{Crit}$$

Eqn. 10 - 6

where: ε is the error estimated for no X-ray absorption in the sample,

ε_{Crit} is the allowed/acceptable level of error or uncertainty resulting from no X-ray absorption correction.

Alternatively, Goldstein (1979) provided an error criterion based on two elements:

$$\varepsilon \equiv \left[\left(\frac{\mu}{\rho}\right)^{y}_{Comp} - \left(\frac{\mu}{\rho}\right)^{z}_{Comp}\right]\frac{\delta}{2}\csc\alpha < \varepsilon_{Crit}$$

Eqn. 10 - 7

The rationale of the Goldstein et al. formulation may be understood as follows. Since two elements are involved in the case of quantitative ratio analysis (i.e., I_y/I_z), error from secondary processes such as absorption or fluorescence is relativized, the error should be significant only if the X-rays emitted by the two elements are absorbed differently. Therefore, it is the difference of the absorptivity that determines if the thin-film assumption is appropriate to the quantitative elemental ratio.

The estimated allowable specimen thickness values (Table 10-1; Appendix 10-1) were generally less than the actual thickness (~70 to 100+ nm), and they may seem to invalidate the thin-film assumption. However, several notes should be made over the thickness estimates. The accuracy of the maximum thin-film thickness depends strongly on the accuracy of the mass absorption or attenuation coefficients. Good accuracy in the attenuation coefficient is difficult with photon of energies less than 1 keV (Chantler et al. 2005). The uncertainty in C and N self-absorption coefficients (i.e., photon energy < 500 eV) was estimated to be about 50-100%, and 5-20% for O (Henke et al.1993). Therefore, it is reasonable to consider a less stringent ε_{Crit}. Of the two thin-film criteria, the Goldstein et al. criterion seems to be better suit for quantitative elemental ratio analysis. Considering other uncertainties such as background X-ray noise, local heterogeneity, beam-induced chemical changes and so on, a ε_{Crit} of 0.25 or even 0.5 may be reasonable. This suggests that a specimen with thickness <100 nm

would still fall within the thin-film approximation for most materials (SiO_2, $C_6H_{12}O_6$, and $C_{12}H_{26}$) (Table 10-1). In the presence of SiO_2, which serves as the representative mineral of quartz, the specimen needs to be thin (~80 to 160 nm) in order for the approximation to hold. It is thus imperative that the ultrathin sections of sediment samples with thickness no more 100 nm are produced, if one wants to by-pass the complex, iterative X-ray absorption-correction procedure as outlined in Scott et al. (1995).

3.3.1.2. Equivalency in Intensity Ratio and Compositional Ratio

The second assumption is that elemental ratio between C, N, and O can be approximated as the intensity ratio of the respective elemental X-rays, or:

$$\frac{I_{y,K}}{I_{z,K}} = \frac{i(Q\omega n\alpha\eta)_{y,K}}{i(Q\omega n\alpha\eta)_{z,K}} = \Phi_{yz}\Gamma_{yz}\frac{n_y}{n_z} \approx \frac{n_y}{n_z}$$

Eqn. 10 - 8

where the subscripts y and z stands for the comparing elements, K denotes the K-line X-rays of C, N and O, Φ is the ratio of $Q\omega$'s, and Γ is the ratio of $\alpha\eta$'s.

The equivalency approximation will hold when $\Phi\Gamma$ for the comparing elements is close to unity. It is reasonable to assume that Γ is close to unity for elements with very close atomic number because Γ accounts for instrumental properties. As for Φ, it was estimated for C-N and C-O from both theoretical models and empirical observations of Q_K and ω_K (Table 10-2). Before commenting on the Φ's, it should be noted that considerable uncertainty was introduced in the estimation of ionization cross-section, Q_K, for all three elements. This was primary due to the fact that most Q_K models were derived at e^- energy conditions that was relatively low (i.e., $E_{\text{incident electron}}/E_{\text{K-edge}} \leq 100$) when compared to the those of the contemporary electron microscope (i.e., $E_{\text{incident electron}}/E_{\text{K-edge}} \geq 500$ for C, N, and O), and thus the estimates in Table 10-2 required extrapolation. Extrapolation was also carried out when calculating the X-ray fluorescence yield, ω_K, beyond the designated atomic number range as ω_K models often exclude the light elements (C, N, and O). With this in mind, one may qualitatively conclude that both Φ_{CN} and Φ_{CO} should be close to unity. Even if one were to trust the accuracy of the Φ's and correct the elemental ratio, n_y/n_z, from the intensity ratio, $I_{y,K}/I_{z,K}$, the correction would be at most ~50% for both C/N and C/O atomic ratios. For models and calculation details please refer to Appendix 10-2.

3.3.1.3. Peak-Height Approximation

The third assumption, which concerns specifically the peak-height quantification approach, supposes that the observed intensity ratio between elements y and z, $I_{y,K}/I_{z,K}$, is equal to the peak height ratio of the two elements, $H_{y,K}/H_{z,K}$. With the continuous background (Bremsstrahlung) properly removed and that a characteristic EDX peak can be described by a Gaussian distribution, the intensity of the X-ray at a particular energy is simply the areal integral of the peak (Zaluzec 1979):

$$I_K = \int_{-\infty}^{\infty} He^{-\frac{x^2}{2\sigma^2}} dx = \sqrt{2\pi}\sigma H_K$$

Eqn. 10 - 9

where H_K is the peak height and σ is the standard deviation or energy spread of the peak. Taking a ratio of the intensity would result in the following expression:

$$\frac{I_{y,K}}{I_{z,K}} = \frac{\sigma_{y,K} H_{y,K}}{\sigma_{z,K} H_{z,K}}$$

Eqn. 10 - 10

Hence, in order to infer intensity ratio – which is now assumed to be equivalent to the atomic ratio, n_y/n_z – $\sigma_{y,K}$ and $\sigma_{z,K}$ have to be about the same. Because σ varies with the X-ray energy, two peaks with the same height do not necessarily imply same X-ray intensity (Zaluzec 1979). Plotting I_K vs H_K at varying intensities would allow σ's of C, N, and O to be determined (Table 10-3). The regression on the nitrogen σ (Figure 10-15d) was not as good as those of C, O, and Si (r^2~1; Figure 10-15a to c). The main cause of the uncertainty was the relatively low signal to background ratio at the nitrogen energy. However, taking the estimated $\sigma_{N,K}$ of 1.5 to be roughly accurate, $\sigma_{C,K}/\sigma_{N,K}$ would be about 1.1. In view of the much greater uncertainty in X-ray photon counting in STEM-EDX elemental mapping mode, a mere 10% error was inconsequential.

In the case of C and O, $\sigma_{C,K}/\sigma_{O,K}$ was found to be 0.97 – the intensity ratio and the height ratio being essentially identical. Since one may use Si X-ray intensity to correct for X-ray emitted by part of the inorganic oxygen (i.e., O in SiO film), $\sigma_{O,K}/\sigma_{Si,K}$ was also of interest, and was found to be ~0.82. The inorganic oxygen correction may also be done in a micrograph-by-micrograph case, and this would account for not only the error in $\sigma_{O,K}/\sigma_{Si,K}$ but also any local compositional heterogeneity of the background film.

3.3.1.4. Concluding Remarks on Quantitative EDX Assumptions

In this section, the major assumptions underlying the two methods, the integral-area and the peak-height approaches, for quantifying EDX elemental ratios between C, N, and O have been identified and discussed. It has been shown that inferring the atomic C/O and C/N ratios (i.e., n_y/n_z) from either the intensity ratios (i.e., $I_{y,K}/I_{z,K}$) or the peak-height ratios (i.e., $H_{y,K}/H_{z,K}$) would not introduce substantial error. And even if correction on intensity ratio or peak-height ratio is desirable, it can be performed.

3.3.2. Considerations on Elemental Ratio Definition of BC & Micron-Scale Heterogeneity in Environmental Carbonaceous Matter

3.3.2.1. Cutoff Elemental Ratios for Defining BC

Variety of Carbonaceous Matter. Although elemental ratio mapping by STEM-EDX is potentially ideal for quantifying BC, it does require a threshold C:N ratio for defining BC, and hence the method is not completely free from operational subjectivity. First, of the different types of BC, which one should be used to define the C:N cutoff ratio? The cutoff ratio would be ~<60 with NIST diesel particular matter (SRM 1650), but ~<80 for

anthracite coal, and infinitely higher if we choose pure graphite or graphene, which contain no N or O, as reference BC.

Compositional Variation. Second, within a particular class of carbonaceous matter, C:H, C:N, and C:O ratios vary considerably as well. The variation of the elemental ratios in different carbonaceous matter are shown in Figure 10-30a to c and Table 10-9. The variation seems to be independent of laboratories/research groups. For example, in the soot & diesel particulate matter category, the C:N ratio for NIST SRM 1650(a) was reported to be 54 (Fernandes et al., 2003) and 60 (Accardi-Dey, 2003). Taking this as the basis that the Fernandes et al. and the Accardi-Dey procedures as analytically equal, Fernandes et al. reported C:N ratio of 7 for urban dust (NIST SRM 1649) and 17 for domestic chimney soot. The broad intra-categorical variation for the condensed-C groups (e.g. char/charcoal, soot & DPM) makes it hard to pin-point, empirically, a particular ratio as the cutoff. Third, the intra-categorical variation causes the elemental ratios of the condensed-C group to overlap with those of the softer-C groups. Two examples can be shown in Figure 10-2b. Humic acid, grass & hay, and agricultural plants (Figure 10-2b) all have C:N between 10-100, which is well covered within the range of both the char/charcoal and the soot & DPM categories. The wood category (both unburned modern and old wood), which is not considered as BC in their sorption affinity for HOCs, actually has C:N ratio in the 100-1000 range, thus being one order of magnitude above those of kerogen and char/charcoal, both considered to be part of the condensed carbon geosorbent spectrum (Masiello 2004; Cornelissen et al. 2005).

It is, however, possible to counter-argue that the problem of requiring an arbitrary C:N cutoff and the problem of broad variation in the condensed-C categories both arise from the nature of bulk, elemental analysis. Figure 10-16 illustrates the limitation of bulk analysis. Bulk, elemental analysis disregards local variations and heterogeneities at sub-micron level and gives only sample-global mean elemental ratios. Thus using bulk analysis results as diagnostic signals for BC is bound to produce a smeared range of elemental ratios by quantitatively averaging different carbonaceous phases of a sample into one. The problem can be resolved if elemental analysis is performed at sub-micron level where the spatial resolution of the electron probe is sufficiently fine for recognizing the fundamental unit-structure of BC (i.e. one soot sphere). From the cartoons in Figure 10-31 and the wide consensus on the highly condensed structure as the defining feature of BC (Masiello 2004; Cornelissen et al. 2005), it is reasonable to suppose graphitic structure as the defining unit of BC.

3.3.2.2. Probe Resolution for Micron-Scale Compositional Variance

The next step is to establish the appropriate electron probe spatial resolution. The ideal resolution needs to be sufficiently fine to distinguish local variations in both elements (e.g., C, N, and O) and the bond types (e.g., C_{sp3}-C_{sp2}, C_{sp2}-C_{sp2}, or C_{ar}-C_{ar}). However, probe resolution imposes a practical constraint on the time-cost for mapping: the finer the probe, the smaller the mapped area, and the longer the total analysis time.

The probe resolution should not be so fine that it mistakes the aromatic components in soft carbon, such as lignin, as BC. This, in turn, requires the knowledge of the fundamental units of non-graphitic carbonaceous matter. The dimensions of these non-graphitic fundamental units thus set the maximum magnification possible without over-

counting aromatic-C. The fundamental units of non-graphitic carbons also give more accurate C:N and C:O ratios, for they are the basic, repeating units for a particular type of carbonaceous matter. For example, lignin (Figure 10-32) is formed from the polymerization of monolignols such as hydroxycinnamyl aldehydes and alcohols (Kim et al. 2000; Boerjan et al. 2003). These monomers typically consist of a substituted methoxy-phenol, with a short side chain (~3 carbon in length) containing aldehyde, alcohol, or ester functionality (Kim et al. 2000; Boerjan et al. 2003). Coal (Figure 10-33), on the other hand, is more variable in terms of its basic building structures. It is made up of polycyclic aromatic carbons (# rings ~<5), cyclic carbons, heterocyclic structures with N and S, and relative short alkyl chains (# C ~<10). Hence, coal may not be reduced to a repeatable structure with dimensions as small as those in cellulose or lignin.

The problem of ambiguous fundamental units for non-BC matter can be circumvented by using a larger probe area for analysis. If one takes the structural cartoons for lignin (Figure 10-32) and coal (Figure 10-33) as realistic and representative, with probe size of order similar to the cartoons, one can measure the realistic elemental ratios of these carbonaceous matter. The dimensions for both cartoons are less than 4 nm (i.e., if the maximum length/width is <4 nm when assuming both structures were flat, then the real structures, where bending and folding occur, will certainly be less than 4 nm in dimensions. See Appendix 10-3 for calculation). This implies that a probe with diameter of 4 nm should be sufficient for distinguishing purely graphitic structure from lignin or coal (e.g., frame a in Figure 10-16). But would the probe be too large for detecting soot-BC? Suppose a soot basic unit to be a sphere of radius 10 to 15 nm, it would have a projected area (i.e., πr^2) of 300 to 700 nm^2. With a probe of diameter 4 to 5 nm (or, 4-5 nm/pixel, a single soot sphere can be mapped out by about 10 to 40 pixels (see Appendix 10-4). So, in theory, even the potential heterogeneity in a given soot sphere (i.e., relatively oxidized surface vs reduced core) can be identified.

3.3.3. Empirical Elemental Ratio Signatures of Various Carbonaceous Matter (EDX Spot Analysis)

The first task was to investigate and see if the different types of carbonaceous matter have characteristic C/N and/or C/O ratio signatures. Although characteristic O/C ratios for selected carbonaceous matter have been obtained previously (Stoffyn-Egli et al. 1997) by SEM, it remains unclear that similar trend can be obtained using a TEM/EDX or STEM-EDX with very thin specimens. It is also unclear if C/N ratio may be useful for the identification and the quantification of BC. The elemental ratios between C and N or O determined using the peak-height and the integrated-area methods were summarized in Table 10-4 and presented in Figure 10-17. The ratios were reported as O/C and N/C due to the fact that in many cases very little or none of O or N was detected.

3.3.3.1. Spot-EDX Analysis: N/C Atomic Ratio

The O/C vs N/C plot (or van Krevelen plot) (Figure 10-17) showed that the examined carbonaceous matter may be divided into two groups; one (e.g., nicotinamide, humic acid, and melanoidin) had discernible and distinct N/C ratios while the other group seemed insensitive to N/C due to the complete absence of N signal. The main reason for the lack of sensitivity of N/C to types of carbon matter is that the N X-ray peak, being

sandwiched in between the C and the O peaks, is easily overwhelmed in samples that give both substantial C and O signals (e.g.: Figure 10-8). N/C ratio is therefore suitable only distinguishing samples with relatively high N content (e.g., nicotinamide) but not for differentiating the highly condensed carbons such as char, soot, and graphite.

3.3.3.2. Spot-EDX Analysis: O/C Atomic Ratio

The O/C ratio was found to be more responsive and revealing than N/C ratio of the different types of carbonaceous matter (Figure 10-18; Table 10-4). The trend observed in O/C as determined by both methods was consistent with the expected dominance of carbon in various samples. For examples, graphite, soot, and lignocellulosic char, all considered as highly condensed carbon matter (Masiello 2004), were found to have a very low O/C (~<0.15), while humic acid and nicotinamide, both considered as soft carbons, had O/C greater than 0.2.

3.3.3.3. Observational Agreement with Literature

It is also comforting to see the O/C results obtained here to be very consistent with those reported by Stoffyn-Egli et al. (1997) using analytical SEM and a completely different sample preparation procedure. Stoffyn-Egli et al. investigated the possibility of identifying black carbon particles by compositional ratio and morphological information obtained from analytical SEM (Stoffyn-Egli et al. 1997). A variety of carbonaceous matter, from non-BC sedimentary organic matter to particles from fuel and biomass combustion, were examined. They concluded that black carbon particles had a characteristic O/C ratio of <0.15 whereas the non-BC had higher O/C values, and that BC originating from biomass or fuel burning can be further differentiated within the O/C<0.15 range. They reported a mean O/C of 0.03±0.02 for oil/coal combustion derived BC; 0.05±0.01 for charcoal (considered as condensed carbon matter); 0.11±0.02 for softwood combustion derived BC; and 0.3 to 0.9 for a variety of non-BC such as lignin, cellulose, wood, and diatom (references within Stoffyn-Egli et al. 1997). Here, O/C for graphite and soot was observed to be ~0.02 to 0.03; lignocellulosic char, which may be considered as the same category as softwood burning-derived BC, had an O/C of ~0.05 to 0.08; and humic acid, which may be thought of as a combined form of lignin and cellulose, was found with O/C to be about 0.9 (all derived from the integrated-area method).

If one assumes the integrated-area method gives a more accurate O/C ratio, then the peak-height method seemed to have overestimated it by almost a factor of two (Figure 10-19). The problem of overestimating O/C was more severe with increasing O/C. Although the comparison suggests that the two methods are not equivalent, it also shows that if needed, elemental ratios determined from the peak-height method can be conveniently corrected. In the case of O/C, the correction can be done quite accurately (r^2 ~ 1 in Figure 10-19) across a wide spectrum of different natural carbonaceous matter. Alternatively, specifically for the object of BC quantification, one may argue that since O/C ratio of BC-like substances is so small (O/C <~0.10) that correction may not be necessary.

3.3.3.4. Miscellaneous Remarks on O/C Ratio in Spot-EDX

Several minor remarks are worth noting for the results in Table 10-4. First, the peak-height method gave an O/C ratio of ~1.5 for humic acid, inconsistent with that reported

from literature (O/C ~ 0.5–0.6 according to Table 10-9). This inconsistency with the stoichiometry (Table 10-9; Appendix 10-8) confirmed the fact that the peak-height method tends to overestimate the presence of O for the softer types of carbons such as humic substances. Second, the lower O/C ratio associated with the thinner char category suggested that the background lacey-C film had been contributing to the total C X-ray. Third, the O/C ratio associated with the SiO film re-emphasized the significance of hydrocarbon contamination. The average EDX spectrum of a supposedly carbon-clean SiO film would still have about 10 atomic % of C relative to O.

3.3.4. Comparing SEM-EDX and TEM-EDX for BC Quantification

Considering the high uncertainties in the results from this study, it may be worthwhile to compare TEM-EDX with analytical SEM. The method used by Stoffyn-Egli et al., which aimed to identify rather than quantify black carbon particles, may not be readily extended to quantitative BC analysis of environmental samples. First, they exclusively considered relatively large particles (diameter of 50 to 100+ μm) in their analysis, leaving the identification of the smaller-sized carbonaceous matter such as soot (BC) and colloidal organic matter (OC) in question. Second, the need for morphological information such as pore structure and shape requires (i) the isolation of BC particles from the others, and (ii) a case-by-case morphological judgment over the particles. This implies that aggregate structures have to be dispersed to the constituent particles before identification can be carried out, and in the case of the nm-scale soot spheres attached to μm-scale grains, they are most likely to be overlooked. It is also impractical to judge the morphological category of every single particle for BC quantitative purposes. Third, their method probed only the surficial composition of a particle, and thus may lead to error by missing BC (e.g., soot embedded in aggregates) or non-BC (e.g., partially burned wood/lignin) encrusted in the particle. Indeed, Brodowski et al. (2005) observed that O/C ratio increased from the interior to the surface of char particles.

However, it is difficult to conclude whether the analytical SEM or the TEM-EDX methodology is more suitable for BC quantification/recognition. In general, the SEM-EDX methodology has a simpler operating and sample preparation procedure, and seems to offer a better precision as suggested by previous studies (Stoffyn-Egli et al. 1997; Brodowski et al. 2005). On the other hand, TEM-EDX can reveal the intra-particular compositions and pore structure where as SEM-EDX can only probe the surficial makeup and infer inner pore structure from the surface pores (Sorensen et al. 2000). The higher vacuum power in TEM/STEM-EDX helps to minimize background organic volatiles, which contributes to hydrocarbon contamination, in the specimen chamber. However, TEM/STEM-EDX is also more prone to electron beam induced damage and hydrocarbon buildup. Electron beam in analytical SEM is typically relatively low in energy (~10 to 20 keV, at accelerated voltage of 10 to 20 kV), and thus greatly reduced the likelihood of irradiation-induced compositional alterations when compared to STEM-EDX (electron energy at ~200 to 250 keV). SEM does not require very thin specimen, sample preparation for SEM viewing is quite straightforward, by-passing all the worries with microtomy, conductive coating, or removal of volatile hydrocarbon (by lamp heating or ion milling). Stoffyn-Egli et al. estimate the uncertainty of their SEM procedure to be about 20% using a pure organic standard with a O/C ratio of 0.055 and reported a maximum error of ~67% for one of their BC samples, whereas

in this study the uncertainty of a given sample vary from 10% to 200% or more, especially when the O/C ratio is very close to zero.

3.3.5. Sources of Uncertainties in TEM-EDX Derived Elemental-C Signatures

What causes the high uncertainty in elemental ratios observed in this study? Are they artifacts resulting from the processing of the peak heights or areas, or are they "real", reflecting the true compositional variation in a given samples? The uncertainty ranged from about 10% to 200% for the O/C ratio and about 30% to 300% for the N/C ratio (Table 10-4).

3.3.5.1. Increased Hydrocarbon Contamination under High Voltage Beam

One source of error may be that hydrocarbon contamination was much more severe under a highly energetic electron beam (200-250 keV in this study; 10-20 keV in typical SEM settings). However, it is unclear if hydrocarbon contamination should raise the noise in a random or a systematic way (e.g. shifting O/C ratio of all samples toward a lower value) though this can be known by observing O and C deposition on an organic-free film (e.g., silicon nitride (Si_3N_4) film).

3.3.5.2. Element-Specific Sensitivity Issue

Second, a small signal peak can cause high error in elemental ratio. This may explain, for instance, (i) the higher uncertainty in N/C ratios than in O/C ratios, (ii) the N/C ratio of nicotinamide was more precise than those of melanoidin or humic acid, which had a much lower nitrogen content, and (iii) the poor precision associated with the O/C ratios of soot and graphite.

3.3.5.3. Probe-Scale Compositional Heterogeneity

However, signal-to-noise ratio may not explain the error in the O/C of humic acid where O and C were almost equally abundant. This leads to the third possibility, namely that the uncertainty in elemental ratios reflected the compositional heterogeneity in a given sample at the chosen probe-resolution. Compositional heterogeneity has been observed and reported for highly carbonaceous char phase (Brodowski et al. 2005).

3.3.5.4. Interferences from Inorganic-O

The fourth possibility is signal interference from O in inorganic mineral phases. While background oxygen from SiO film has been corrected for, there is currently no correction scheme for other inorganic oxygen.

3.3.6. Cumulated Error in Elemental Ratio

The cumulated error in elemental ratio estimated from spot-EDX spectra depends upon how the atomic/elemental ratio is assessed. In general, the estimated atomic ratio between two elements (y and z), n_y/n_z, is related to the X-ray intensity ratio, $I_{y,K}/I_{z,K}$, and the peak height ratio, $H_{y,K}/H_{z,K}$, as follows:

$$\frac{n_y}{n_z} = \frac{I_{y,K}/I_{z,K}}{\Phi_{yz}\Gamma_{yz}} = \frac{(\sigma_{y,K}/\sigma_{z,K})\,(H_{y,K}/H_{z,K})}{\Phi_{yz}\Gamma_{yz}}$$

Eqn. 10 - 11

where: σ represents the spread of the peak,

Φ_{yz} represents the relative X-ray fluorescence likelihood between the two elements, and

Γ_{yz} represents the relative instrumental efficiencies in detecting X-rays of the two elements (see 3.3.1.2 and 3.3.1.3).

The absolute error of the atomic ratio, $\Delta(n_y/n_z)$, can be estimated by evaluating the quantitative influence of the componential errors on the atomic ratio via partial derivatives. The absolute error when estimating from intensity ratio, $\Delta(n_y/n_z)|_{I\rightarrow n}$, (integrated-area approach) is:

$$\Delta\left(\frac{n_y}{n_z}\right)\Big|_{I\rightarrow n} = \frac{1}{\Phi_{yz}\Gamma_{yz}}\left[\Delta\left(\frac{I_{y,K}}{I_{z,K}}\right) + \frac{I_{y,K}}{I_{z,K}}\frac{\Delta\Phi_{yz}}{\Phi_{yz}}\right]$$

Eqn. 10 - 12

And the corresponding expression for peak-height derived error, $\Delta(n_y/n_z)|_{H\rightarrow n}$, is:

$$\Delta\left(\frac{n_y}{n_z}\right)\Big|_{H\rightarrow n} = \frac{1}{\Phi_{yz}\Gamma_{yz}}\left[\frac{H_{y,K}}{H_{z,K}}\Delta\left(\frac{\sigma_{y,K}}{\sigma_{z,K}}\right) + \frac{\sigma_{y,K}}{\sigma_{z,K}}\Delta\left(\frac{H_{y,K}}{H_{z,K}}\right) + \frac{H_{y,K}}{H_{z,K}}\frac{\sigma_{y,K}}{\sigma_{z,K}}\frac{\Delta\Phi_{yz}}{\Phi_{yz}}\right]$$

Eqn. 10 - 13

where $\Delta(.../...)$ or $\Delta()$ is the error of a particular variable.

If we evaluate the normalized error in atomic ratio, $\Delta(n_y/n_z)/(n_y/n_z)$, instead, the resulting error would simply be the sum of the normalized componential errors, that is:

$$\frac{\Delta(n_y/n_z)}{n_y/n_z}\Big|_{I\rightarrow n} = \frac{\Delta(I_{y,K}/I_{z,K})}{I_{y,K}/I_{z,K}} + \frac{\Delta\Phi_{yz}}{\Phi_{yz}}$$

Eqn. 10 - 14

$$\frac{\Delta(n_y/n_z)}{n_y/n_z}\Big|_{H\rightarrow n} = \frac{\Delta(\sigma_{y,K}/\sigma_{z,K})}{\sigma_{y,K}/\sigma_{z,K}} + \frac{\Delta(H_{y,K}/H_{z,K})}{H_{y,K}/H_{z,K}} + \frac{\Delta\Phi_{yz}}{\Phi_{yz}}$$

Eqn. 10 - 15

The normalized uncertainties in σ ratio and Φ were at maximum 0.10 and 0.50, respectively (see section 3.3.1.2 and 3.3.1.3). The normalized errors in intensity ratio and peak-height ratio, both after correction for background-O, ranged from about 10-150% and 10-200%, respectively (Table 10-4). Thus the maximum error would be about 70%-200% and 70%-250%, respectively, for integrated-area based and peak-height based estimates of O/C atomic ratio. It should be reminded that the error incurred from σ ratio and Φ can be eliminated if the instrumental performance for specific elemental combinations is calibrated with standards of known composition, and

that the error in area ratio or peak-height ratio may reflect local compositional heterogeneity rather than methodological noise.

3.4. Quantification of BC by Elemental Mapping of C, N, and O by STEM-EDX

The work on STEM-EDX quantification of BC was explorative in nature. Although some foundational aspects of elemental quantification has been discussed in the previous section, a number of new methodological issues unique to quantitative STEM-EDX elemental mapping have arisen, and they will be elaborated and discussed at length in the following sections.

3.4.1. Methodological Issues Specific to STEM-EDX

3.4.1.1. Peak-Height Intensity & Low Counts

First, in the scanning mode, instead of obtaining a continuous EDX spectrum as in the single-spot mode, only the number of X-ray counts of a particular element is reported for each pixel, leaving the peak-height ratio as the only feasible quantitative approach. The deviation of the peak-height approach from the more robust integrated-area approach can be adjusted by a correction factor as shown in Figure 10-19. Because the number of X-ray counts in individual pixels is much lower, the signal tailing problem of C and O on the N peak is not so significant.

3.4.1.2. 'Noise' Pixels

A new kind of signal artifact arises instead. The STEM-EDX mode produces 'noise' pixels of a particular element. These 'noise' pixels distort the quantitative analysis by over-claiming the presence of the particular element. This problem can be partially overcome in a number of ways. For instance, the significance of the 'noise' pixels can be reduced by consolidating signal counts of several pixels into one. Unfortunately, this runs at the expense of poorer spatial resolution and distorting the abundance of BC. A second way is to improve the signal-to-noise ratio by prolonging the mapping time. This, however, runs the risk of sample drifting and hydrocarbon contamination. A third way is to arbitrarily define a cutoff to filter out the 'noise' pixels before applying quantitative spatial analysis. A fourth way is to use the unoccupied film area to estimate the background frequency of 'noise' pixels, and then incorporate this information to obtain the actual coverage. However, this only work for elements which are not present in the background film (e.g., we can correct for the 'noise' pixels of C and N, but not O, in a SiO film).

3.4.1.3. O/C as the Operational Cutoff Ratio for BC

Second, operational cutoff is required for judging whether or not a pixel contains BC. Here, it is proposed that BC be defined as purely graphitic matter, and so any BC pixels should have both O/C and N/C being zero (or C/O and C/N approaching infinity). Operationally, however, the relative absence of N in both OC and condensed BC (see Table 10-4) may allow BC to be determined simply by the magnitude of O/C ratio.

3.4.1.4. Background Correction for Inorganic-O Signals

Third, it is necessary to exclude the sample-unoccupied area from the analysis for a number of reasons. In STEM-EDX mode, a background region needed to be defined for correcting O X-ray contribution from background SiO film and assessing the frequency of 'noise' pixel for N and C. Furthermore, since the ultimate objective is to quantify the abundance of BC by mass, the irrelevant area should be subtracted.

3.4.2. Preliminary Comparison of STEM-EDX Data Treatment Options

The objectives of this section are two-fold: (i) to illustrate a procedure for quantitative mapping of BC by showing a number of elemental ratio maps that explored various data treatment and correction options, and (ii) to recommend a suitable set of treatment parameters and options.

3.4.2.1. Pixel Consolidation and Image Fine Features

As mentioned previously, one way of alleviating the low signal-to-noise problem is to combine and analyze signals from multiple pixels as one cell. Consolidating multiple pixels into larger cells, however, runs the risk of smearing any fine features that are smaller than the defined cell, and thus may potentially overlook local compositional heterogeneity. Figure 10-20 shows the original dark field image (Figure 10-20a) of a soot-rich region in a soot-amended sediment sample, together with the same image undergoing various degrees of pixel consolidation (Figure 10-20b to e). Fine features were still reasonably retained at the 4-into-1 level (Figure 10-20c) but not beyond. This is also similarly demonstrated in Figure 10-21, which shows how background film region (non-occupied by sample) is recognized. The unoccupied pixels were determined by comparison image brightness data with a brightness cutoff that was manually optimized for individual image.

3.4.2.2. 'Noise' Pixels

The problem of 'noise' pixels typical to STEM-EDX operations is clearly shown in the contrast provided by Figure 10-22 and Figure 10-23. In Figure 10-22, X-rays recorded over the entire image field were subjected to elemental ratio calculation. One can observe the presence of C/N over the unoccupied area (see Figure 10-20 or 21 for the original image). Although these 'noise' C-N pixels in the SiO film region were relatively sparse, their presence can distort quantitative analysis of BC quite significantly by adding more pure-C pixels to the sample-occupied area. The two figures also show the difference between the cases without N-'noise' pixel removal (Figure 10-20a, 6-21a) and the cases with noise reduction (Figure 10-20b, 6-21b). The noise reduction scheme explored here was arbitrary and very simple: any pixel containing only a single N X-ray count was considered as an N 'noise' pixel, and was reassigned to have a zero N-count. The resulting difference was very subtle and hardly noticeable without careful inspection. It should be noted that the different reduction methods of 'noise' pixels have not been fully explored, partly due to the difficulty in dealing with the O 'noise' density, which is hard to assess because the background film contains O.

3.4.2.3. Compositional Distortion from Pixel Consolidation

Compositional maps of C/N and C/O atomic ratios (Figure 10-24 and 6-26) show that pixel consolidation can distort compositional information quite significantly, and that the

distortion is not necessarily monotonic with respect to pixel-to-cell ratio. At a consolidation ratio of 4-to-1 (4 pixels into 1 cell) (sub-figures (b)), the white spots coverage (C/O→∞) seemed to be comparable or even more with that without consolidation (sub-figures (a)). But as one moves to the higher consolidation ratios of 16-to-1 or 64-to-1, the coverage of purely C spots declined very dramatically (sub-figures (c) and (d)). Similar observations were also made on two other samples (Table 10-5; Appendix B). The graphitic fractions assessed by the two methods were within a factor of two between the basecase (1×1 into 1 cell) and the 2×2 into 1 cell case. Consistency was better maintained if one chooses the occupancy-based method with appropriate background O signal removal (~10% to 33% deviation between 1-to-1 and 4-to-1 scenarios). Manipulating pixel resolution thus seemed to be an inappropriate strategy for improving signal-to-noise ratio. The best measure, in the author's opinion, should be a combination of using longer acquisition time and applying a cutoff filter for noise. This has yet to be explored.

3.4.2.4. Correction of Background Film Oxygen Signal

In order to determine the C/O ratio, which can be indicative of the various types of carbonaceous matter (Stoffyn-Egli et al. 1997; Brodowski et al. 2005; this study) it is critical to remove any background C or O X-ray. Systematic background-C signals can be eliminated by using C-free films such as SiO or Si_3N_4. However, the C signals emitted from e^- beam-polymerized hydrocarbon are rather difficult to remove. This is because the hydrocarbon formation is a function of local composition, thickness, and microscope conditions, and is thus variable across a given sample (personal communication with Dr. A.J. Garrett-Reed). Systematic background-O signals can also be avoided if one chooses to work with Si_3N_4, which, however, is quite fragile and can be ripped off the grid easily. In the case where SiO is used, background-O can be corrected for, as is shown in Figure 10-25. The Si/O maps (Figure 10-27) showed that both non-occupied background area and the sample-occupied region had very similar Si/O atomic ratio (except the minor mineral phases) that the two were indistinguishable (Figure 10-27). The presence of soot was not visible in SiO maps at different levels of consolidations (Figure 10-28). This suggested that O-background signal can be correctly removed if (i) the background film Si/O ratio and (ii) the Si X-ray intensity over the occupied region are both known. Although the white spot coverage over the sooty region was clearly raised with the application of O-correction (Figure 10-25), it appeared to be overcorrecting at the two mineral regions in the lower part of the image (see Figure 10-20a or 21a for the original dark-field image, or the red zones in Figure 10-27). Thus, in a prudent spirit, it would be reasonable to suggest that the true BC coverage is bracketed by the two C/O maps: the C/O map without background-O correction (Figure 10-25a) provides a lower end estimate of areal BC coverage while the O-corrected map (Figure 10-25b) caps the upper end.

3.4.3. Quantification of BC by Elemental Mapping in Various Samples

This section discusses the application of the quantitative STEM-EDX BC mapping procedure on a number of samples containing both known 'standards' of carbonaceous matter as well as real sediment phases. Although the mapping procedure gave quantitative measures of dense-C phases, only a small number of sites on one type of samples have been mapped. The results presented here are, therefore, not statistically

representative of a particular type of carbonaceous matter, but only meaningful for that carbonaceous matter at the particular mapped sites.

It was beyond doubt that the occupancy-based method would give the most meaningful quantification because only sample-covered pixels were analyzed. However, as was discussed earlier, it was much less obvious how much signal correction should be applied, and which one gave the most accurate assessment of the areal graphitic content. Three different methods, all based on sample occupancy, were explored: (i) no correction for both O and N signals, (ii) background O signal was removed according to a background Si:O ratio, and (iii) N-'noise' pixels were removed in addition to background-O removal. The quantitative results from the three variant methods are summarized in Table 10-6.

Some explanatory notes should be made on the information and organization in Table 10-6 before proceeding further. Samples were grouped into seven categories. The first group, A to D, had known carbon content or were known standards of carbon matter, and thus represented a 'standard' group. The second group, E to G, contained sites that were from the sedimentary phases with the presence of graphitic phases being unknown. This second group thus represented a 'test' group.

Columns: $f_{C>0}$ denotes the fraction of pixels with C X-rays counted out of all sample-occupied pixels,

$f_{C/N=\infty}$ and $f_{C/O=\infty}$ denote the fraction of C pixels without any N or O. These were listed for showing how frequently N or O was co-observed with C,

$f_{C/N,C/O=\infty}$ represents the fraction of graphitic pixels (defined as purely-C with complete absence of O or N) out of all sample-occupied area.

The impact of background-O can be quantitatively observed by comparing, the fifth column, $f_{C/O=\infty}$ after O-correction, with the third column. Finally, the graphitic contents estimated from the three ways were summarized in column 5, 7, and 8 (i.e. in bold-italic, Table 10-6). The true fractional coverage of graphitic pixels in a given sample should lie within the range as defined by these values. Subsidiary information such as the background Si:O ratio and the sample-areal coverage were also listed.

3.4.3.1. Should N and O Signals be Corrected?

The first observation was that the absence or presence of background O-signal correction resulted in greatly differing graphitic content. The graphitic fractions (i.e., $f_{C/N,C/O=\infty}$) from the no-correction scheme can be as low as only one third of those after O-correction. In a SEM study on agricultural chars, Brodowski et al. (2005) also implemented a correction step for assessing the fraction of O that is bound to C:

$$O_C = O - (0.5\mathrm{Na} + \mathrm{Mg} + 1.5\mathrm{Al} + 2\mathrm{Si} + 0.5\mathrm{K} + \mathrm{Ca} + 1.176\mathrm{Fe} + 2.5\mathrm{P}) \text{ [all in atomic \%]}$$

Eqn. 10 - 16

The major assumptions underlying their correction expression are that both X-ray absorbance and fluorescence are insignificant and that all metals are bound up with O.

While the latter may be true for their samples, EDX spectra reported in this study often exhibited a relatively O-deprived content (see section 3.2.4). The problem of locally overcorrecting O-signal (see section 3.4.2.4), however, should make the O-corrected value as the upper limit of graphitic content in a sample.

The elimination of N 'noise' pixels, on the other hand, seemed to be unimportant, as the O-corrected graphitic fractions with and without N reduction differed only by 25% at the most (comparing column 6 and 7 in Table 10-6). This was hardly a surprise because pixels with N signals were much lower in number than those with O (i.e., $f_{C/N\infty}$, which represents the absence of N, approaches $f_{C>0}$ in almost all samples. The same is not true for $f_{C/O=\infty}$).

Two conclusions may be drawn. First, the correction of N 'noise' pixels may not be necessary as the step did not change the resulting fractional coverage significantly (<25% difference). Second, the O-signal coming from non-C sources appeared to be the major source of uncertainty in quantitative EDX analysis. Although the more rigorous correction equation such as that by Brodowski et al. may not be suitable, their approach does inspire an alternative empirical scheme. This will be discussed further in section 3.5.4.

3.4.3.2. Graphitic Content of Individual Samples

Graphitic contents of known standards seemed to be somewhat different from expectation (Table 10-7). For the soot samples, only about 50-60 % of the total C-containing pixels were quantified as graphitic. The graphitic fractions out of total sample-occupied area were also very low, especially for A2. Visual inspection of the unprocessed dark-field image of A2 (Figure 10-20a, 21a) would estimate over 70-80% of the occupied area as sooty whereas mapping estimated it to be ~20% only. The expectation from visual inspection was, of course, based on the assumption that all soot spheres are purely graphitic, which is not true (Muller et al. 2007). Similarly, at both of the char sites and the melanoidin sites (where the particles solely defined the sample-occupied area), only about half of the particles was considered as graphitic ($f_{graphitic,mean}$ ~ 0.4 to 0.55). In humic acid, about 10% of the total occupied area was considered as graphitic. All the unknown groups sites (E, F, G) have come from a soot-amended sedimentary samples, and a wide range of graphitic content was observed. For the apparently mineral sites (group E), both E1 and E3 had relatively low graphitic content ($f_{graphitic,mean}$<0.05), while E4 had a graphitic content similar to those of the humic acid sites. E2 was exceptional in its high graphitic content ($f_{graphitic,mean}$=0.19 and $f_{graphitic/Total\ C}$=0.79, both comparable to soot, char, or melanoidin), despite the fact that nothing char-like or soot-like seemed to be revealed by visual inspection. F1, which seemed to have soft-edged organic particles, and G1, a possible sedimentary aggregate, were again relatively low in graphitic content ($f_{graphitic,mean}$<0.05; $f_{graphitic/Total\ C}$~those of humic acids).

3.4.3.3. Qualitative Consistency in Graphitic/Total C Fractions

Does EDX elemental mapping give consistent results across samples with different graphitic content? Humic acids may serve as a model for generic organic matter in the environment. They possesses aromatic fraction from the alteration of source materials such as lignin, and its aromatic fraction is likely to be higher than that in the 'soft'

organic matter such as lipid, sugar, and protein. If we take the graphitic content of humic acids as a reference point (i.e., $f_{graphitic,mean}$~≤0.10 and $f_{graphitic/Total\ C}$~0.30) for typical non-BC organic matter, then E3, E4, F1 and G1 certainly fit well into the same category as humic acids. E5 seemed to be mostly mineral, but the carbon it possesses had graphitic content ($f_{graphitic/Total\ C}$=0.57) comparable to those of soot, char, and melanoidin.

One may rationalize the test group results in the following way: (i) E3, E4, F1 and G1 were sites unexposed to soot particles (although the sediment sample was amended with soot suspensions), and thus had graphitic signals resembling that of humic acid (or non-BC organic matter); (ii) E1 and E2 were exposed to very little and a lot of soot/char, respectively, and thus their graphitic/Total C fractions fell within that of soot/char/melanoidin. For the 'standard' groups, soot and char were essentially identical in graphitic quality (graphitic/Total C), while melanoidin seemed to have the most pure in graphitic content. If we were to neglect the oddity of the melanoidin graphitic purity, then the graphitic/Total C fractions of all samples/sites are qualitatively consistent.

3.4.3.4. Accuracy of EDX Mapping Derived Graphitic Content

How accurate is the graphitic/Total C fraction from EDX elemental mapping? In general, the graphitic/Total C fractions derived from STEM-EDX mapping seemed to be consistent, within a factor of 2, with the literature values (Table 10-8). The graphitic fraction estimated from this study was about 0.5-0.6. This is very close to the values of soot produced in diesel engine under regular operating condition 0.54-0.66 (Muller et al. 2007) (The 0.76 value corresponded to a condition tailored for high soot emission.). For char, Hammes et al. (2007) reported about 70% of C in wood & straw char being aromatic, and here about 40-50% of total C being aromatic. For melanoidin, STEM-EDX mapping gave an estimate of ~75% of all organic C to be graphitic, and this estimate seemed rather high in comparison to the literature value of 15-40% (Ikan et al. 1986a, b). For humic acids, STEM-EDX mapping estimated about 25-35% of total C being graphitic, and this is within the range reported in literature. It should be noted that the fraction of sp^2-C for humic acids may not be an accurate measure of truly aromatic-C because carbonyl-C and carboxyl-C, whose presence in humic acids are certainly significant, are also included (See also Appendix 10-7).

It is important to note that the literature reported values for aromatic fractions of different carbonaceous matter were mostly obtained using solid-state ^{13}C-NMR (Appendix 10-7). Quantitative solid-state ^{13}C-NMR, however, is known to exhibit systematic bias regarding aliphatic vs aromatic moieties in geochemical samples (Wilson et al. 1987, Vassallo et al. 1987; Skjemstad et al. 1999; Smernik et al. 2002a; Poirer et al. 2000; Gauthier et al. 2003). Although analytical procedures (Vassallo et al. 1987) or correction schemes (Faulon 1994; Mastral et al. 1997) may be applied to improve accuracy, quantitative characterization of natural geosorbents by ^{13}C-NMR should not be taken as the 'truth' – they should be judged on an individual basis along with other supporting observations or further experimental/theoretical verifications. Thus a disagreement between the STEM-EDX estimate and the reported literature value for

graphitic-C fraction should not be viewed as an indication that the STEM-EDX mapping approach is inferior to the 'standard' ^{13}C-NMR method.

3.4.3.5. Total Areal Graphitic Coverage

The interpretation of areal graphitic coverage (or $f_{graphitic,mean}$) is complicated by the fact that areal carbon coverage (or $f_{C>0}$) may not convey the true presence fully. In A2 (Figure 10-20a, 21a), visual inspection would suggest that the soot-covered region to be at least 60% of the sample-occupied area, but the $f_{C>0}$ measured is only half of that. In Figure 10-23, one can observe that, although the pixels outline the presence of soot, much of the area remains 'empty' of C signals. This raises an important point about elemental mapping: since not all C-containing pixels would be 'detected', only the relative abundance of graphitic pixels (i.e. $f_{graphitic/Total\ C}$) is quantitatively meaningful. This limiting aspect of EDX mapping is further discussed in section 3.5.3.

3.4.3.6. Intra-aggregate/particle Spatial Features

STEM-EDX elemental mapping is most suitable for observing spatial compositional or physical features within a particle or aggregate. The O/C map of char clearly revealed an O-rich interior and a purely-C surface of the particle (Figure 10-29a). The pattern was not an artifact, as the map before signal filtering or correction showed that O-signals were exclusively present only in the char area (Figure 10-29b). The observation here was opposite to that of Brodowski et al. (2005), and it was most likely due to methodological difference in char preparation. The char in this study was prepared from heating chestnut wood in pure N_2 (at 450°C, 5 h) (Hammes et al. 2006). Brodowski et al., on the other hand, prepared their char in enclosed furnace without deliberate O_2 removal. They also examined soil samples that were naturally exposed to air. Hence it was very likely that their char samples were more surface oxidized.

3.5. Methodological Limitations of STEM-EDX for BC Quantification

The power of STEM-EDX can be better appreciated with a clear understanding of its potentials and limitations. A number of limitations are present in the STEM-EDX methodology for BC quantifications. While some of the limitations can be overcome or alleviated with further procedural or analytical modifications, there are fundamental limitations and assumptions that cannot be easily resolved. The following paragraphs shall discuss these limitations in order of decreasing importance.

3.5.1. Purely Carbon Presence Not a Sufficient Evidence as Graphitic

The key fundamental limitation in quantifying BC with STEM-EDX is that one has to infer the presence of graphitic structure from purely elemental signals without any knowledge about the types of bonding involved. While pure graphite should have a purely-C signal in the EDX spectrum, the contrary is not necessarily true for any structures with a purely-C signal. Examples of non-graphitic samples that would be mistaken as BC with STEM-EDX are diamond, O/N-free polymers such as polyethylene, and aliphatic moieties in natural macromolecules. One may argue that the likelihood of diamond scattered in sedimentary phases to be fairly unlikely, but the presence of household polymeric wastes and petroleum leaks from marine vessels are not uncommon in coastal waters. Counting polymers and heavy alkanes erroneously as BC

is, therefore, a realistic problem for STEM-EDX. However, one should be reminded that similar assumption, though to different extent, is also implicit in a number of conventional BC quantification methods which use bulk elemental analysis. In those cases, the assumption being that the residual carbon measured by elemental analyzer after some harsh treatments (e.g., thermal oxidation, chemical oxidation, etc) only consists of graphitic carbon (or BC of whatever definition).

One way to reduce potential interference of non-graphitic carbons is to subject the samples to mild thermal pretreatment. Such procedure will reduce volatile species and heavy alkanes, but may be less effective against heavily cross-linked polymeric fragments.

3.5.2. In-Microscope Contamination, Beam Damage, and Bonding Alteration

Polymerization of volatile hydrocarbons and organic species, or "hydrocarbon contamination", is a well-known problem in EM literature (Hren 1979; Loretto 1994; Egerton et al. 2004) (see also sections 3.2.1 and 3.2.3). The extent of contamination is a complex function of various factors including, but not restricted to, local composition (Hren 1979), electron beam size (Hren 1979), electron dosage/current (Schamm et al. 2001), and specimen temperature (Egerton et al. 1976). It has been demonstrated that contamination can be quantified and kept track of in pure/near pure samples (Schamm et al. 2001). However, as a result of the variability in thickness and composition in environmental samples and drifting in instrumental performance, it is very difficult to predict/estimate the extent of contamination on a given viewed area for the thickness of the contamination build-up varies from region to region (private communication with Dr. Garratt-Reed, MIT Center for Materials Science and Engineering). It is less clear if carbon in the solid phase can be oxidized by volatile O-rich species, and if so, to what extent oxidation may take place.

Preventive measures such as lamp irradiation (regular lamp or UV) (Egerton et al. 2004) and focused ion-beam milling (private communication with Dr. Yong Zhang, MIT Center for Materials Science and Engineering) may be feasible pretreatment procedure for environmental carbonaceous phases, but schemes such as mild temperature heating (~300°C) (Egerton et al. 2004) or cryoshielding (cooling to reduce mobility of volatile species) (Hren 1979) are less ideal for organic carbon analysis as they introduce considerable extents of thermal stress to the specimen.

Mass loss due to irradiation has been a long known issue in analytical electron microscopy (Egerton et al. 1976; Hren 1979; Egerton et al. 2004). Recent EM studies on biological samples showed that C, N, and O all suffered mass loss due to electron irradiation, with oxygen more prone to irradiation loss than C and N, and hence distorting O/C and O/N ratios (Laquerriere et al. 2002; Zierold et al. 2005). Loss of oxygen was also reported in a study on colloidal lead isooctanoate (Wert et al. 1993). This preferential loss of oxygen atoms in analytical TEM/STEM creates the equivalent methodological weakness for BC quantification as charring does in bulk chemical analysis. In sedimentary samples, the possibility of metals acting as oxidation catalyst (Hren 1979) may not be ruled out.

3.5.3. Difficulty in Assessing Absolute OC/BC Contents

Elemental maps generated from STEM-EDX may not reflect fully all mass-occupied area (see section 3.4.3.5). One way to attempt absolute BC or OC quantification over viewed area is to increase EDX coverage with a longer acquisition time. But even prolonging acquisition time does not necessarily guarantee total capture of the entire occupied area. Alternatively, one way to estimate the absolute abundance of BC or OC is to reconstruct a total OC occupancy by utilizing EDX data of the higher Z elements. A feasible scheme of the total OC occupancy reconstruction may be the following:

$$\text{Total OC Areal \%} \approx \frac{A_C - A_{IC}}{A_{Sample\ ,STEM}} = \frac{A_{OC}}{A_C + A_{Non-C}}$$

Eqn. 10 - 17

where: $A_{Sample,STEM}$ is the total sample-occupied area as observed by STEM-EDX,

A_{OC} is the area (number of pixels) with organic carbons,

A_{IC} is the area (number of pixels) with inorganic carbons,

A_C is the STEM-recognized C-containing area, and the sum of A_{OC} and A_{IC},

A_{Non-C} is the STEM-recognized non-C area.

Once the total OC areal % is known, the total BC areal % can be determined with the graphitic/total C fraction, $f_{graphitic/Total\ C}$. If the mineral phases are known, total OC or BC contents in a mass/mass basis can also be estimated using density information of the different phases (Appendix 10-10)

This OC-occupancy reconstruction is built upon the key assumption that all beam-excited elements emit X-ray with equal likelihood, which is not true as we know the heavier elements have a more favorable X-ray fluorescence than the lighter (Loretto 1994; also see formulae for ω in Appendix 10-2). Thus the estimated OC or BC coverage/content should be less than what it really is.

3.5.4. Separating Inorganic Carbon and Inorganic Oxygen Signals

Since we define any pixels with C but no N and O as graphitic, the presence of inorganic carbon and oxygen, and to a much less extent inorganic nitrogen, can interfere with the interpretation of elemental maps. The issue of inorganic oxygen contributed from the background SiO film has been dealt with in section 3.4.2.4, but that of the mineral oxygen has so far been neglected. Brodowski et al. (2005) have suggested a more comprehensive O-correction scheme based on the abundance of potential O-binding elements such as Fe, Al, Si, etc (see section 3.4.3.1), but the issue of inorganic carbon remains unanswered. Disentangling inorganic C or O in a rigorous way becomes quite difficult when one considers the presence of inorganic carbonates in natural sediments. In this section, several options of reducing interference of inorganic C/O species will be discussed.

One simple solution is to remove inorganic carbonates prior to EM viewing via acidification (Gustafsson et al. 1997). However, inorganic carbonates entrapped within a sedimentary aggregate may not be acidified, and since we want to observe the aggregates in as much their native, intact state as possible, the option of exposing these entrapped carbonates via grinding is out of question. One may utilize the fact that inorganic carbonates should give an O/C atomic ratio of 3, which is statistically significantly higher than the ratios of typical carbonaceous matter (O/C ~< 1, see section 3.3.3), to distinguish their presence. As for non-carbonate mineral oxygen, the tendency to observe the mineral phases being more O-deprived (section 3.2.4) prompts for an empirical, rather than theoretical, correlation between metal abundance and oxygen. The empirical metal-oxygen correlation, which is to be computed on an image-by-image basis, also handles conveniently anoxic sedimentary samples where metals are not necessarily at their fully oxidized states.

A workable strategy may be to construct, on a map-by-map basis, the O-correlation coefficients for different O-binding species, and then use these coefficients to remove all the inorganic-O from the map. This empirical construction begins with the balance of total O X-rays, O_{Tot}, with the organic O (O_{Org}) and inorganic O (O_{Inorg}) ones:

$$O_{Tot} = O_{Org} + O_{Inorg}$$

Eqn. 10 - 18

For each pixel (at coordinates x,y), the total O signal may also be expressed as:

$$O_{Tot\,(x,y)} = O_{Residual\ (x,y)} + \sum_{all\ i} a_i M_{i(x,y)} = O_{Residual\ (x,y)} + a_{Si}\,Si_{(x,y)} + a_{Al}\,Al_{(x,y)} + \cdots$$

Eqn. 10 - 19

where: $O_{Residual(x,y)}$ is oxygen X-ray signal unaccounted by the association to inorganic phases in a given pixel located at (x,y),

$Si_{(x,y)}$ and $Al_{(x,y)}$ are X-ray counts at pixel at (x,y),

$M_{i(x,y)}$ is the X-ray count at a given pixel for a generic O-binding element (such as Fe, Ca, Mg, Si, etc),

a_{Si} and a_{Al} are the empirical O-binding correlation coefficients for Si and Al X-ray signals, and these coefficients are constant for all pixels on a given elemental X-ray map.

$O_{Residual(x,y)}$ is in essence the estimator for $O_{Org(x,y)}$, which will be used to compute O/C atomic ratio for the screening of BC. $O_{Residual(x,y)}$ will be known after the correlation coefficients, a_i's, are determined when correlations between O signals and M_i's signals are maximized. The maximization is subjected to the following constraints: (1) all a_i's must be positive real numbers; (2) none of the a_i's should imply a stoichiometric ratio of M_i to O_{Inorg} of exceeding that theoretically possible (e.g., for Al/O as in Al_2O_3 to be 1.5 at maximum); and (3) $O_{residual}$ should be ≥ 0 for all pixels in the sample-occupied region.

3.6. Future Work on BC Quantification via STEM EDX-Mapping

The following is a list of future steps that can be advanced:

3.6.1. Evaluating and Improving Multiphase O-Correction Scheme

Since the O/C atomic ratio is a better indicator for OC vs BC (section 3.4.1.3; Table 10-4), a better scheme for O-correction needs to be developed for STEM-EDX quantification of BC. The correction of inorganic-O signals need to be better explored, especially the O-atoms associated with the mineral phases. This should proceed by testing the proposed multi-phase O-correction scheme, outlined in 3.5.4, first on (i) model mixtures of known mineral phases (e.g. goethite, kaolinite and quartz), then on (ii) C-stripped sedimentary mineral matrices, and finally on (iii) sediment samples. Step (i) allows the scheme to be tested with the answers known.

Testing the O-correction scheme on C-stripped sediment (step (ii)) is necessary because the compositional heterogeneity and geometrical variation in real sediment (from small, nano-scale grains (e.g. Figure 10-13) to large, micron-scale pieces (e.g. Appendix B, TEM image of 20061013 Site#8)). The stripping of all C-phases is desirable for two main reasons. First, it allows a baseline of errors in O-correction to be be established without interferences from C-phases. This 'baseline of errors' is here envisioned as a map of the difference between observed O_{Tot} and estimated O_{Tot} Eqn. 10 - 19 in all pixels. Such map of baseline errors reveal the minimum level of errors we can have with the multiphase O-correction scheme. Second, it allows us to identify the major non-C elements present in the sample, and thus constrains the number of regression terms for the estimated O_{Tot} (i.e. Eqn. 10 - 19). Carbonaceous phases, including soot and char, can be stripped by thermal oxidation in air at elevated temperatures (i.e. >450°C).

The multiphase O-correction may be applied to the actual sediment sample. Ideally, the sediment specimen should be examined without pretreatment. However, a disaggregation pretreatment prior to sample fixation/encasement will be necessary if the problem of overlapping phases (section 3.2.4; Figure 10-14) leads to substantial error when correcting for signals from multiphase inorganic-O. Sedimentary aggregates can be disaggregated by rinsing with clean water and/or with the addition of deflocculant (Gregory 1989; van Leussen 1993).

3.6.2. Addressing Hydrocarbon Contamination

The ubiquitous nature of hydrocarbon contamination resulting from e^- beam radiation (section 3.2.2; see also Appendix B, the arrayed white dots on the TEM image of melanoidin #3) means that contamination contributes to the distortion of C/O or C/N atomic ratios, and hence the measurement of BC. Although observations of the extent of hydrocarbon contamination has been made on organic specimen (e.g. section 3.2.2; Figure 10-9, 6-10), the dependence of its variability and severity on different specimen matrix has not been examined in details.

There are two main objectives regarding hydrocarbon contamination: (I) to understand how hydrocarbon contamination varies in different model carbonaceous matter and over

different background matrix and (II) to develop a scheme which allows the effect of hydrocarbon deposition to be corrected for in real soil/sedimentary samples.

The first objective can be achieved by systematically examining the extent and the rate of hydrocarbon contamination first on individual model specimens (i.e. graphite, char, soot, humic substances, melanoidin, etc) in spirit similar to that reported earlier (Figure 10-9, 6-10). Such exercise is necessary for hydrocarbon contamination may be less problematic for certain type of carbonaceous matter (e.g. graphite) but more so for others (e.g. nicotinamide). The examination should also attempt to cover a range of specimen thickness and the absence/presence of mineral grains. It should be noted that a 'background' level of contamination – that on plain SiO film or purely mineral specimen – is also of value.

A correction scheme for hydrocarbon contamination may be developed by compilation of the results on individual model specimens. Ideally, by examining model specimen with varying O/C and N/C ratios, an empirical relationship between the *observed ratio* and the *stoichiometric ratio* can be established, and through such curve a better estimate of the atomic ratios can be made. The adjustment for hydrocarbon contamination can be further improved if 'internal standard' phases of varying C-content (e.g. minerals not native to the sample, and structures pre-coated with known carbonaceous matter via, for instance, chemical vapor deposition) can be added and probed along with the real soil/sediment matrix. The use of 'internal standard' phases allow instrumental instability of the EM or other local effects to be normalized, in a manner very much similar to the use of internal standards in analytical chemistry.

3.6.3. Mapping Model Systems

A final step in refining the STEM-EDX BC quantification methodology is to test it on model systems where both OCs and BCs, of known composition, exists. The pair of model OC and BC needs to have drastically different O/C (or N/C) ratio and different morphological appearance. A good test OC-BC pair will be nicotinamide and NIST soot, soot, being morphologically distinctive from the amorphous nicotinamide, can be visually quantified, providing an 'answer' to which the STEM-EDX derived estimate can be compared with. The complexity of the model OC-BC system is to be increased gradually to levels as close as the real soil/sediment matrix. For example, the next level system may consist of nicotinamide, char, and soot, and the system after that nicotinamide, char, soot, and goethite.

4. Conclusion

In view of the needs to quantify BC in an operationally impartial and analytically rigorous manner and to describe the intra-particle distribution of BC, the analytical possibility of using STEM-EDX mapping has been explored. This is a necessary step as the nanometer scale soot particles cannot be distinguished from the background mineral matrix by mere visual means (section 3.1). Furthermore, although EM techniques have been applied to environmental BC, they are currently applied only to micron-scale

carbonaceous matter (e.g. char), and only for semi-quantitative understanding or description.

We started out from the simplest case of viewing carbonaceous samples with a point/spot EDX spectroscopy. The preliminary but necessary observations on standard samples (section 3.2) allowed us to examine the fundamental assumptions and approximations involved in EDX or STEM-EDX analysis (section 3.3.1 and 3.3.2). From both theoretical estimation (section 3.3.1) and empirical observations on a series of standard carbon specimens (section 3.3.3), we concluded that O/C and N/C atomic ratios may be estimated using either integrated-areas or the peak heights in EDX spectra. The resulting errors from the assumptions were quantifiable and reasonable, and can be greatly reduced by calibrating the instrumental performance using C/N/O standards (section 3.3.6). The characteristic elemental ratios obtained using spot-EDX (TEM-EDX) analysis for a number of carbonaceous matter were consistent with the values reported by Stoffyn-Egli et al. (1997), though with a much greater uncertainties (section 3.3.3). The unusual high uncertainties were likely caused by low signals of a particular element and signal processing limitations, but they may also reflect authentic compositional variation on nanometer scale (section 3.3.5). The methodological limitations in SEM-EDX for comprehensive quantitative analysis (section 3.3.4) justified the exploration of STEM-EDX mapping as an alternative BC quantification scheme.

A number of issues specific to the STEM-EDX mode have been discussed (section 3.4.1 and 3.4.2). Two issues are in particular significant. First, the processing of mapped X-ray signals is complicated by the presence of 'noise'-pixels and the need to remove background oxygen signals. Second, it is necessary to assume that region with purely carbon but N or O signal represented the presence of graphitic structure, and this is not always true (section 3.5.1). A number of standard samples and environmental geosorbents were examined by STEM-EDX. The graphitic/total carbon areal fractions for the samples were estimated from the resulting maps of C, N, and O. The STEM-EDX derived graphitic fractions not only showed an internally consistent trend between the different standards and environmental samples (section 3.4.3.3) but also matched fairly well with the aromatic fractions of similar carbonaceous matter estimated from quantitative ^{13}C-NMR or EELS (section 3.4.3.4). The limitations of using STEM-EDX elemental mapping to quantify BC were briefly discussed with possible modifications or solutions to improve the method (section 3.5).

The work in this chapter has demonstrated the potential application of TEM-EDX and STEM-EDX to the quantification of BC. Despite the limitations of analytical EDX, the elemental mapping methodology by STEM-EDX is, in the author's opinion, a reasonably attractive alternative to the conventional BC quantification methods. The most prominent advantage of STEM-EDX over all current BC methods is that it is capable of disclosing both chemical and physical information at sub-micron to nanometer scale without any arbitrary operational definition for BC. In view of these strengths, the STEM-EDX methodology should be further explored. The logical future steps in refining the methodology have been outlined (3.6).

Chapter 11. Conclusion

Table of Content for Chapter 11

1. Summary of Findings and Accomplishments 288

1.1. On the Kinetic Behavior of Pyrene 288

1.2. On the Equilibrium Behavior of Pyrene 289

1.3. 7On Modeling Desorption Kinetics of Soil/Sediment HOCs 290

1.4. On Regional Analysis and the Importance of Resuspension 290

1.5. On OC/BC Quantification by Electron Microscopy (EM) 291

2. Future Work 291

2.1. More Kinetic and Equilibrium Observations Needed 291

2.2. Refining/Revising BC Quantification Strategy 292

2.3. Non-linearity of HOCs Sorption Isotherm 293

2.4. Physical Occlusion of HOCs: Bulk-Level 293

2.5. Physical Occlusion of HOCs: Microscopic-Level 293

2.6. Non-linear Intra-particle Porewater Diffusion Model 294

2.6.1. Desorption with Multiple-Size Fraction 294

2.6.2. Combining Diffusion and Resuspension Dynamics 294

2.7. Regional Fate of HOCs in Water Bodies 294

2.8. BC Quantification via Analytical Electron Microscopy 295

1. Summary of Findings and Accomplishments

This work attempted to advance our ability to characterize and predict the fate of HOCs in natural water bodies (e.g. harbor, estuary, lake, or river) where exchange/transport of HOCs between the sediment and the water column is possible. Using pyrene as a surrogate HOC, the author examined the kinetic and equilibrium behavior of HOC in solids-water systems at realistic sorbate concentration levels. A mechanistic numerical model was constructed and successfully applied to describe the kinetic observations of native pyrene desorbing from sediment suspension. The kinetic behavior and thermodynamic properties of pyrene were then applied to the modeling of its regional fate in a real water body (i.e. Boston Harbor). This modeling exercise provided a preliminary evaluation on the relative importance of sediment resuspension as a mobilization pathway of sedimentary HOCs. Finally, in view of the uncertainty and/or inadequacy of the current BC quantification methods, a novel analytical procedure based on electron microscopic analyses was developed.

1.1. On the Kinetic Behavior of Pyrene

It appeared that kinetics is the dominant factor in controlling the presence and/or mobilization of sorbed pyrene. The observations from the desorption kinetic experiment (Chapter 2) showed that the desorption half-times were often in the order of 20–400 h Chapter 7, Table 7-9) at realistic and typical suspension concentration levels (Table 2-7). Considering that the experiment was conducted in closed system and with an initially equilibrium sorbent (both features promoted a faster equilibration time), it can deduced that the field sediment – which is in open system, partially depleted with HOCs and with an internal concentration gradient – will exhibit an even slower desorption rate. This, along with the fact that BC greatly increases that the retardation factor for intra-sorbent transport, provides a good explanation as to why disequilibrium is observed even in the surficial sediment bed layer between the solid phase and the porewater phase.

Despite the fact that desorption kinetics of soil/sediment HOCs have been investigated many times in the past (e.g. as documented in the review of Birdwell et al. 2007), very few of the past studies have provided kinetic parameters and/or presented an assessment method that are applicable to generic conditions in the environment. The use of HOC-spiked/amended rather than field-aged geosorbents is doubtlessly a major obstacle in evaluating the hazard of HOC-contaminated geosorbents (e.g. bioavailability); however, the popularity of the empirical-fitting approach posed an even greater problem because it presents the kinetic phenomenon in a form isolated and disconnected from the physicochemical causes/factors (e.g. R_{sw}, size, f_{BC}, f_{BC}, etc). This work has demonstrated that kinetic parameters obtained from the empirical-fitting approach can be related to measurable properties of the sorbate and sorbent (Chapter 7, section 4.4). For instance, we showed that the so-called 'rapidly desorbing fraction' (F_{rapid}), which has been suggested to be indicative of the bioavailability of HOCs in a sample, actually correlates strongly to the system solids-to-water ratio (R_{sw}) (Chapter 7, section 4.4.3; Figure 7-23).

This work also demonstrated that the release kinetics of HOCs can be predicted *a priori* if the necessary sorbate/sorbent/system physicochemical properties are known and that an accurate sorption isotherm is available. This was demonstrated in the good agreement between observation and the *a priori* model prediction (Chapter 7, section 4.3.1; Figure 7-17, 7-20), with the isotherm (Occlusion-OC-BC) independently determined from sorption experiment (Chapter 5).

1.2. On the Equilibrium Behavior of Pyrene

Results from the desorption experiment suggested that pyrene may sorb much more strongly to the sediment phase than that predicted using a previously reported OC-BC isotherm (Chapter 2, section 3.3.2; Figure 2-12). Further sorption experiments were conducted (e.g. 12-month desorption equilibrium experiment, 12-month adsorption equilibrium experiment at different temperatures) and the same enhanced partitioning at ng_{pyr}/L-level was observed. The new pyrene sorption isotherm, which covered the ng_{pyr}/L to $\mu g_{pyr}/L$ concentration range, exhibited a trend unknown to sorption literature – the isotherm became increasingly non-linear as the dissolved phase concentration decreased. This observed trend was judged to be real for it could not be explained by measurement errors or propagated uncertainties. The experimental data at the ng/L-level agreed very well with the 'isotherm' constructed from data from multiple sediment cores at depths beneath the bioturbation/mixed surficial layer (i.e. partition equilibrium between porewater and sediment solids was highly probable). T

Two tentative hypotheses were proposed for the observed high affinity at the ng_{pyr}/L_w range: (i) that a fraction of the native sorbate is physically occluded from partitioning reaction, and/or (ii) that the native sorbate is sorbed to high-affinity micropore-surface of bio-char/charcoal (which is typically 'overlooked' by the thermal oxidation method for BC). Possible/feasible mechanistic pictures for both hypotheses were presented, supported by literature observations and preliminary evidence.

The derived pyrene sorption isotherm had very low n_{BC} value (n_{BC}=0.25 without occlusion; n_{BC}=0.42 if occlusion was allowed). A re-analysis of all available isotherm data from past studies suggested that K_{OC} and K_{BC} were generally quite constant while n_{BC} was highly variable. For pyrene, the average $\log K_{OC}$ and $\log K_{BC}$ were about 4.75 and 5.95, respectively, with variations contained within 1 log unit for different types of geosorbents. Since (i) isotherm non-linearity reflects the distribution of surface energies, (ii) that the high-affinity sites are to be first occupied, and (iii) that BC has variable energy sites at its surface, one would expect to see the isotherm becomes more non-linear (i.e. $n_{BC} \downarrow$) as the occupancy of BC surface sites (i.e. S_{pyr}/f_{BC}) decreases. A preliminary survey on reported pyrene-n_{BC} supported this idea.

The concentration dependency of sorption isotherm and the dependence of nBC on BC-surface occupancy may explain, partly, the widely scattered K_{OC}/K_{BC}'s reported in recent reviews (e.g. Hawthorne et al. 2006, 2007; Arp et al. 2009).

1.3. 7On Modeling Desorption Kinetics of Soil/Sediment HOCs

Three non-linear finite-difference numerical models have been developed: (i) diffusion in finite volume (used for predicting pyrene desorption kinetics), (ii) diffusion in infinite-bath with mass-transfer boundary layer film, and (iii) diffusion in dual-domain, char-in-silt configuration (finite volume and infinite bath conditions). The infinite-bath model attempted to incorporate the factor of hydrodynamic turbulence into the diffusion problem. This dual-domain model allows desorption from heterogeneous aggregates (e.g. a char fragment embedded inside a sooty aggregate) be simulated/modeled. To the author's knowledge, this has not yet been reported in the modeling literature in environmental chemistry/engineering. A great level of parametric flexibility (e.g., variable aggregate shape; variable spatial porosity, tortuosity factor, f_{OC}, f_{BC}, etc) has been allowed in all models.

Exploring numerical models under a variety of conditions and configurations revealed several important points regarding the fate of HOCs in the environment and the modeling of their release kinetics. First, the phenomenon of HOCs 'sequestration' (or thermodynamically 'unexpected' persistence) may be explained by their slow release kinetics due to highly non-linear sorption isotherm. Second, isotherm non-linearity is relatively insignificant for the modeling low hydrophobicity HOCs (e.g. naphthalene), but very critical for assessing accurately the release kinetics of high hydrophobicity HOCs (e.g. pyrene, bezno(a)pyrene). Third, in closed system, the fraction HOCs that can be desorbed (f_{des}) often increases with the desorption halftime ($\tau_{iw,1/2}$). This relationship is variable for non-linear, BC sorption but not for the linear, Classical-OC sorption view. The non-linear f_{des}-$\tau_{iw,1/2}$ profiles may explain why the most dramatic attenuation of the bound-HOCs concentrations is often observed in sites that are recently contaminated or where the contaminant concentrations have been relatively high. Fourth, comparative simulations in Infinite-Bath mode showed that char-core or char-particles should not be simplified as 'purely-OC' phase. In this respect, further methodological work may be necessary for identifying the presence of char in natural soils/sediments. However, the kinetics of desorption may be reasonably estimated without knowing exactly the BC-purity of the char-domain.

1.4. On Regional Analysis and the Importance of Resuspension

This work also demonstrated how kinetic and equilibrium properties of HOCs can be integrated and applied in analyzing their regional fate in natural water bodies using a simple box model. The regional model results suggested that the assumption of equilibrium partitioning (EqP) was not appropriate as it yield unrealistic predictions of dissolved pyrene concentration or depletion halftimes of pyrene in the surficial sediment layer. On the other hand, realistic predictions can be obtained when assuming the harbor was at pseudo steady-state amidst the different pyrene transformation and transport processes. We showed that a simple steady-state box model can be a useful and cost-effective tool for assessing the 'background' state(s) of persistent HOCs (such as pyrene) in estuaries, harbors, and lakes.

Results from the steady-state model also suggested that mobilization from resuspended sediment may be important in Boston Harbor, as its absence led to unrealistic predictions. The potential significance of resuspension in mobilizing sedimentary HOCs in other estuaries and harbors was raised. A preliminary review of field observations and experimental evidence from other studies also found support for the idea of resuspension-mediated HOCs mobilization.

1.5. On OC/BC Quantification by Electron Microscopy (EM)

In view of the limitations of conventional BC quantification method and the need to assess the biases of these methods, this work also developed a new BC quantification method based on energy dispersive X-ray spectroscopy (EDX). The EM-based method identified and quantified OC or BC in environmental samples by analyzing the elemental ratios of C, N, and O on either point/spot-EDX spectra or areal maps of elemental signals. Agreeable OC/BC estimates were obtained in the preliminary test of the method with a variety of carbonaceous materials. Despite the uncertainty in the OC/BC estimates and the limitations of the method, the EM-based method showed good potential for the characterization of geosorbents – not only can it provide estimates of OC/BC, but also how the organic phase is distribution in the sub-micron world.

2. Future Work

2.1. More Kinetic and Equilibrium Observations Needed

In order to understand and predict the distribution and/or bioavailability of HOCs in the environment, it is necessary to have a solid and yet broad set of observations, spanning across different types of geosorbents (OC and BC contents; soil, sediment, aerosol, aquifer) and different kinds of HOCs (hydrophobicity, dimension, etc). This set of observations will serve as the basis from which a universal HOCs fate model can be constructed.

At typical environmental concentration levels of HOCs, BC is most likely to be the dominant factor that controls the sorption and the kinetics of HOCs. However, most of the kinetic and sorption equilibrium studies (especially those prior to year ~2000) have not provided BC data in their reports. This means that we are lacking sufficient observations to construct a universal kinetic/equilibrium model. The lack of quality data is even more severe with desorption kinetics of HOCs, as most studies have summarized their kinetic findings with empirical parameters and yet not reporting relevant system properties such as R_{sw} or particle size (Chapter 1, section 3.1). Thus, the first future task should be to gather more quality observations, both kinetic and equilibrium, with real/natural geosorbents, and over realistic environmental conditions (for instance, not doing sorption study at dissolved phase concentrations close to aqueous solubility). This may sound very tedious and uncreative – but if we acknowledge the great compositional and structural varieties in natural geosorbents and the importance of studying HOCs as they are in the field (not amended/spiked), this is

the logical next step. And since we have not perfected our analytical method for BC (and perhaps also for O), sufficient quantity of the studied geosorbents should be saved for future analyses.

2.2. Refining/Revising BC Quantification Strategy

With BC and OC as the core factors controlling the partitioning and the transport of HOCs in the environment, it is of great importance and urgency to refine and/or revise our BC/OC quantification methods as soon as possible. Despite the operative efforts in comparing different BC methods (e.g. Currie et al., 2002; Hammes et al. 2007), it remains unclear what procedure can be taken when analyzing a natural geosorbent which may contain different types of BC (e.g. a forest soil sample which contains char residuals as well as sooty aggregates deposited from regions afar).

The author suggests the following steps to improve the current BC quantification strategy. First, we should re-examine and quantify the limitations of the conventional BC methods so as to understand the conditions under which each method is at its best or its worst. Taking wet chemical oxidation as an example, it is capable of quantifying char/charcoal substance but appears to be overestimating sedimentary BC (Figure 1-14; Hammes et al. 2007). A possible analytical question may be: under what circumstance would wet chemical oxidation 'burn away' char/charcoal, and under what circumstance would it produce reasonable estimate of sedimentary BC? A feasible experiment for the above question may be to observe f_{BC} as a function of oxidation parameters (e.g. duration, temperature, oxidants, etc) on natural and/or synthetic samples (e.g. sediment amended with known amount of fine-size graphite, which is, by definition, 'pure-BC').

Second, we need to have true BC standards which the different methods can be tested against. One of the limitations in the intercomparison studies published so far is the fact that different methods were tested on a selected set of carbonaceous samples the BC 'composition' of which were 'unknown'. For instance, the true BC content for wood char is not known. How can we have true BC standards with known 'purity'? The author suggests that graphite be used as pure BC (note: even soot contains non-aromatic organic component; see Bucheli et al. 2000). As for the large μm-scale char/charcoal components, the author suggested that the BC standard for them be prepared as usual but with a high-temperature pyrolysis as a final step. For instance, we may first burn a piece of ordinary wood at char-forming temperatures (e.g. ~<600°C), and then subject it to high-temperature pyrolysis (T~2000°C). Operation variables can be manipulated to graphitize the char-surface completely and produce char-like porous structure (e.g. to mimick high pore surface area). In this case, even though lignin residual may remain within the particle, all exposed surfaces have been graphitized, and the particle may be considered as 'pure BC' (in the sense that the whole mass should survive any treatment that aims to remove OC). We can also synthesize μm-scale char-like structure by heating soot/carbon black at high temperature (again, T~2000°C) to melt the individual spheres into an interconnected but somewhat porous pellets (Yue et al. 2006).

With the limitations of each method quantified and their performance on true, pure-BC standards known, we can integrate this information into a matrix for quantitative assessment and intercomparison of their strength and weakness. From this matrix, the author believes, a better BC quantification procedure (perhaps a 'cocktail' of methods) can emerge. As a parallel effort, we may also refine the EM-based method and use it as an alternative tool for assessment.

2.3. Non-linearity of HOCs Sorption Isotherm

This work suggested that for a given HOC, the K_{OC}'s and K_{BC}'s are relatively constant across different sorbents, and that what the key varying parameter is the isotherm non-linear factor (or the Freundlich exponent), n_{BC}. Furthermore, preliminary analysis supported the idea that n_{BC} (which is indicative of the distribution of surface sorption energies) tends to decrease (i.e. more non-linear) as the BC-surface becomes less occupied. If the idea of a variable n_{BC} is true, then solving the 'mystery' of n_{BC} would also resolve the alleged wide scattering of K_{OC}'s and K_{BC}'s reported in Hawthorne et al. (2006, 2007) and dismiss the pessimism expressed by Arp et al. (2009). A clearly picture of n_{BC} will emerge as we gather more isotherms for different sorbents.

2.4. Physical Occlusion of HOCs: Bulk-Level

Further work can be done to test the hypothesis of physical occlusion. Although the results from the preliminary PE-sediment-water suspension experiment (Chapter 5) appeared inconclusive, repeating the experiment further with periodic replenishment of fresh PE may yield results that support or reject the occlusion idea.

Alternatively, one may also test the proposed mechanisms of physical occlusion. Taking the proposed mechanism of compaction as an example, one can perform an experiment in which a spiked and well-aged (to ensure the spiked PAHs reached the micropore OC/OM) sediment sample undergoes different degree of compaction pressure and then subjected to sequential cleaning in water with reservoir of clean PE strips. If entrapment of PAHs within mineral pores is significant, then one would see a difference in water-extractable fractions of PAHs between compacted and untreated sediment samples.

2.5. Physical Occlusion of HOCs: Microscopic-Level

Microscopic imaging of the sorbate-sorbent association may provide the best supporting evidence for physical occlusion of organic sorbates in natural sorbents. The idea is to stain or 'tag' (i.e. using heavy metals) organic sorbate for the purpose of direct visualization, and observe the distribution and association of the sorbate within the soil/sediment aggregate matrix after some sorption treatments. For instance, one can incubate a pristine soil/sediment sample with the tagged sorbate and track the progress of adsorption visually over time – the microscopic concentration of the 'tag' (e.g. EDX peak intensity of the tagging metal) is indicative of the local abundance of the sorbate. If the geosorbent contains physically inaccessible organic matter, then one should

observe carbon-rich zones[1] (which are indicative of sorbent organic matter) that are free of the metal signal.

The above method may also be applied to test the specific occlusion mechanisms. For instance, one can test the mineral oxide dissolution-precipitation pathway using model mineral phase (e.g. amorphous goethite) and tagged organic sorbate. A possible experiment may be as follows. First, coat goethite with organic matter (e.g. lipid, protein) and allow organic sorbate to absorb into the organic matter. Allow the sorbate-loaded goethite to age after sorption equilibrium is established. At different aging time, a fraction of goethite is set aside for extractability measurement – using polyethylene (PE) strips to desorb as much of the sorbate as possible without inducing matrix swelling. The PE-strips can be solvent-extracted and analyzed for sorbate abundance; the PE-extracted goethite sample can be processed for electron microscopy imaging and analysis (e.g. EDX or EELS). This experiment not only tests whether physical occlusion can be caused by the dissolution-precipitation pathway, but also reveals the rate and extent to which occlusion of organic sorbate can take place.

The tagging approach can also be applied to the organic matter of geosorbents. Rather than testing whether organic sorbate may become occluded, one can examine whether there is organic matter can is physically occluded. This can be tested by incubating natural geosorbents to organic matter staining compounds, such as those used in previous studies (Verdin et al. 2005; Curry et al. 2007).

2.6. Non-linear Intra-particle Porewater Diffusion Model

2.6.1. Desorption with Multiple-Size Fraction

In order to better predict/model desorption of HOCs from real soils/sediments, the model should be expanded to allow flexibility in have multiple aggregate size fractions, each with individual initial physicochemical settings (e.g. S or $C_{agg,HOC,pw,o}$, radius, etc). This project has been started but not finished due to the complexity in modifying the core-iteration code (i.e. calculating the edge-shell concentration in the next time step).

2.6.2. Combining Diffusion and Resuspension Dynamics

A second project aims at incorporating the hydrodynamic forcing of resuspension into the modeling of HOCs desorption. The model would track the change in HOC concentration in different particle fractions according to their residence time in the water column upon periodic resuspension event. Some preliminary work has been done and is shown in Figure 11-1.

2.7. Regional Fate of HOCs in Water Bodies

Analogous to the possible work in the IPD numerical model, it would be a significant step forward if the physics of resuspension can be incorporated to the regional box model. The upgraded model will have vertical variation in resuspension concentration, and may also consider vertical mixing of both suspended matter and dissolved HOCs.

[1] Detected as carbon peak(s) by EDX or EELS.

We can incorporate the effect of average current into the estimation of vertical eddy diffusivities. The basic physics of resuspension and TSS profiles have been well established (Dyer et al. 1986), but it has been rarely coupled to the modeling of HOCs fate in the environment.

Further field work and/or literature survey on the nature of resuspended sediment (i.e. size, density, OC/BC content, sorbed HOCs concentrations) would also be helpful in clarifying the role of resuspension as a mobilization pathway for sedimentary HOCs.

The model can be further improved by considering sources of pyrene (or other HOCs) more thoroughly. For instance, the current model did not differentiate pyrene input from specific rivers and had neglected the inner-divisions of the Boston Harbor (i.e. the Inner, Northwest, Central, and Southeast zones; Figure 9-4). A better approach would be to model each inner-division as a homogeneous box with zone-specific sink/source rates (e.g. a higher harbor flushing rate for the Inner Harbor, which is located at the ends of the Charles River and the Mystic River).

2.8. BC Quantification via Analytical Electron Microscopy

The BC quantification method using energy dispersive X-ray spectroscopy (EDX) should be further explored and refined. A list of possible future work has been provided in Chapter 10 section 3.6.

In addition, the quantitative approaches (i.e. point/spot and areal analyses) taken in the EDX-method should be extended to electron energy loss spectroscopy (EELS) – a powerful analytical EM technique which allows different C-bond structures (i.e. the double-bond $C_{sp2}=C_{sp2}$ vs single-bond C_{sp3}-C_{sp3}) to be distinguished and quantified. Some preliminary work has been done for quantitative BC analysis using EELS. It is documented in Appendix F.

Thermodynamics and Kinetics of Hydrophobic Organic Compound Sorption in Natural Sorbents and Quantification of Black Carbon by Electron Microscopy

Volume II

Figures and Tables

TABLE OF CONTENT

VOLUME I (TEXT)

Chapter 1: General Introduction 15
Chapter 2: Desorption of Native Pyrene at Minute- to Month-Timescales by Time-Gated Fluorescence Spectroscopy 33
Chapter 3: Equilibration of HOC Partitioning in Sediment-Water System 51
Chapter 4: Enhanced Pyrene Sorption at Environmentally Relevant Concentrations 73
Chapter 5: Pyrene Sorption Isotherm 101
Chapter 6: Thermodynamics of Absorption and Adsorption 125
Chapter 7: Desorption Kinetics of Native Sedimentary Pyrene – Mechanistic Modeling & Prediction 147
Chapter 8: Intraparticle Porewater Diffusion Model: General Application and Particular Scenarios 193
Chapter 9: Regional Modeling of Pyrene in Harbors & Estuaries 219
Chapter 10: Quantification of Organic Carbons & Black Carbons by EDX and STEM-EDX 245
Chapter 11: Conclusion 287

VOLUME II (FIGURES AND TABLES)

FIGURES

Chapter 1 301
Chapter 2 313
Chapter 3 325
Chapter 4 341
Chapter 5 368
Chapter 6 388
Chapter 7 393
Chapter 8 427
Chapter 9 454
Chapter 10 475

Chapter 11 533

TABLES

Chapter 1 536
Chapter 2 543
Chapter 3 549
Chapter 4 555
Chapter 5 562
Chapter 6 576
Chapter 7 584
Chapter 8 601
Chapter 9 606
Chapter 10 613

VOLUME III (APPENDICES AND REFERENCE)

APPENDICES

Chapter 2 624
Chapter 3 628
Chapter 4 650
Chapter 5 668
Chapter 6 766
Chapter 7 790
Chapter 8 902
Chapter 9 928
Chapter 10 966
Appendix A: EDX (Spot) Spectra 1000
Appendix B: STEM-EDX Elemental Maps 1036
Appendix C: STEM-EDX Mapping Scripts 1094
Appendix D: Isotherm Regression Scripts 1106
Appendix E: Desorption Kinetics Scripts 1112
Appendix F: Quantification of Black Carbons by EELS and STEM-EELS 1168
Appendix G: EELS Mapping Scripts 1192
Reference 1198

Chapter 1: Figures

Figure 1 - 1. Urban centers of the World, 2009. 302
Figure 1 - 2. World GDP Density (1995)..... 303
Figure 1 - 3. Estuaries of the World..... 304
Figure 1 - 4. Total sedimentary PAHs (maximum range) (From Table 1-1)..... 305
Figure 1 - 5. Some observed BSAFs for PAHs and PCBs from literature..... 306
Figure 1 - 6. PAH publication number according to Science Direct. 306
Figure 1 - 7. The web of factors influencing the distribution and bioavailability of HOCs in the environment..... 307
Figure 1 - 8. Factors contributing to "sorption hysteresis"..... 308
Figure 1 - 9. The importance of the dimension of Time. 308
Figure 1 - 10. Continuum of meta-BC/EC: (I) Biogeochemical Scheme. 309
Figure 1 - 11. Continuum of meta-BC/EC: (II) Elemental/Compositional Scheme..... 310
Figure 1 - 12. Continuum of meta-BC/EC: (III) Sorption-Oriented Scheme. 310
Figure 1 - 13. Continuum of meta-BC/EC: (IV) Atmospheric Physics Scheme..... 311
Figure 1 - 14. Quantifications of BC in different geosorbents/materials..... 312

Figure 1 - 1. Urban centers of the World, 2009.

Map source: U.N. World Urbanization Prospects, the 2009 Revision (2010).

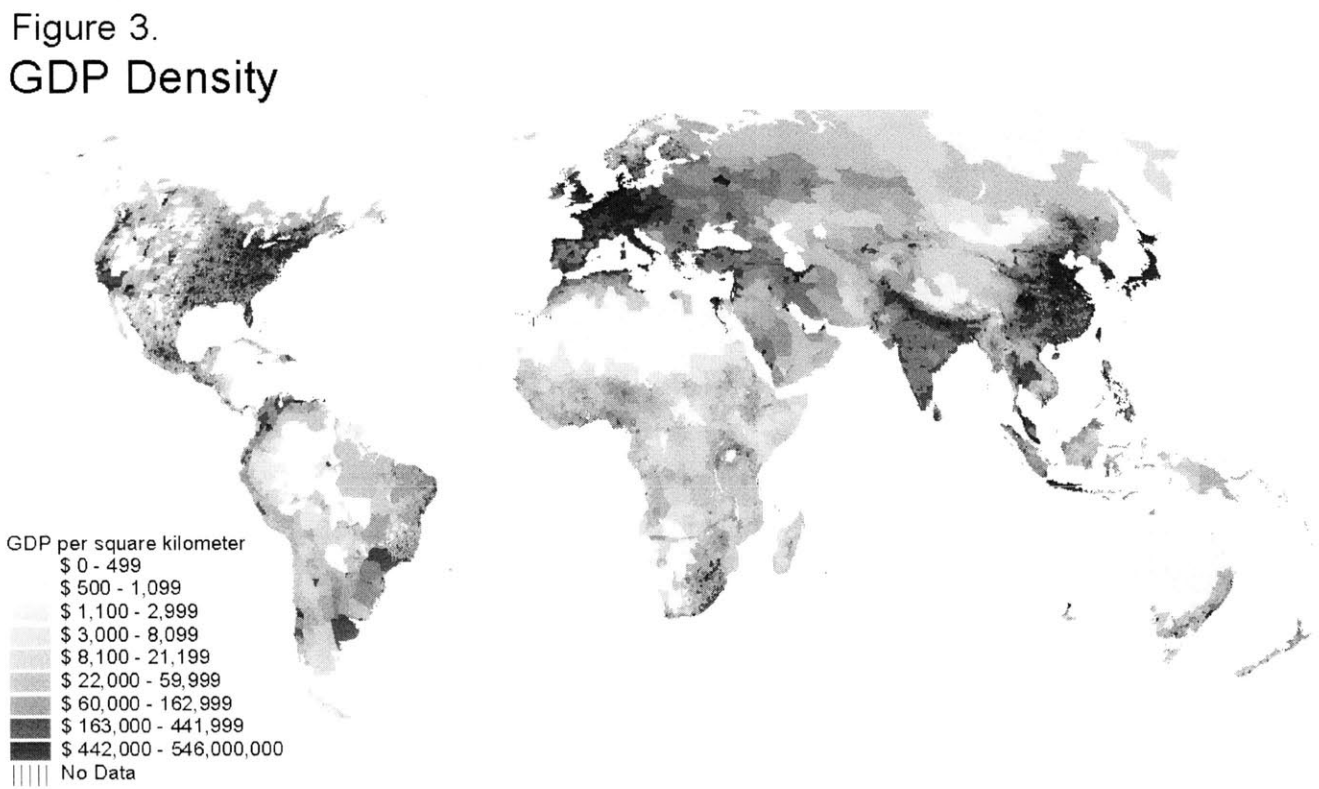

Figure 1 - 2. World GDP Density (1995).

From Gallup et al. (1999).

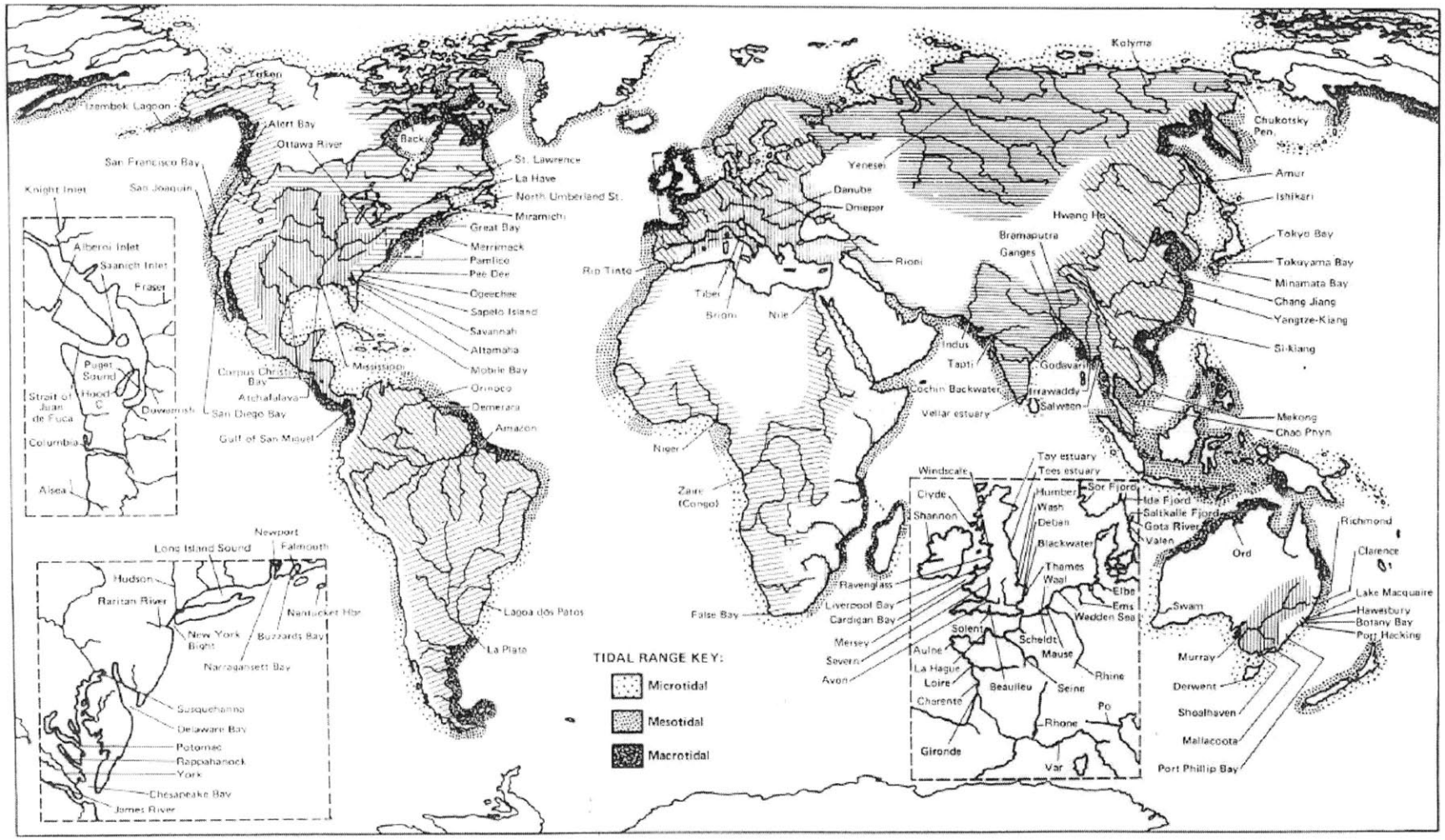

Figure 1 - 3. Estuaries of the World.

From Nichols et al. (1985).

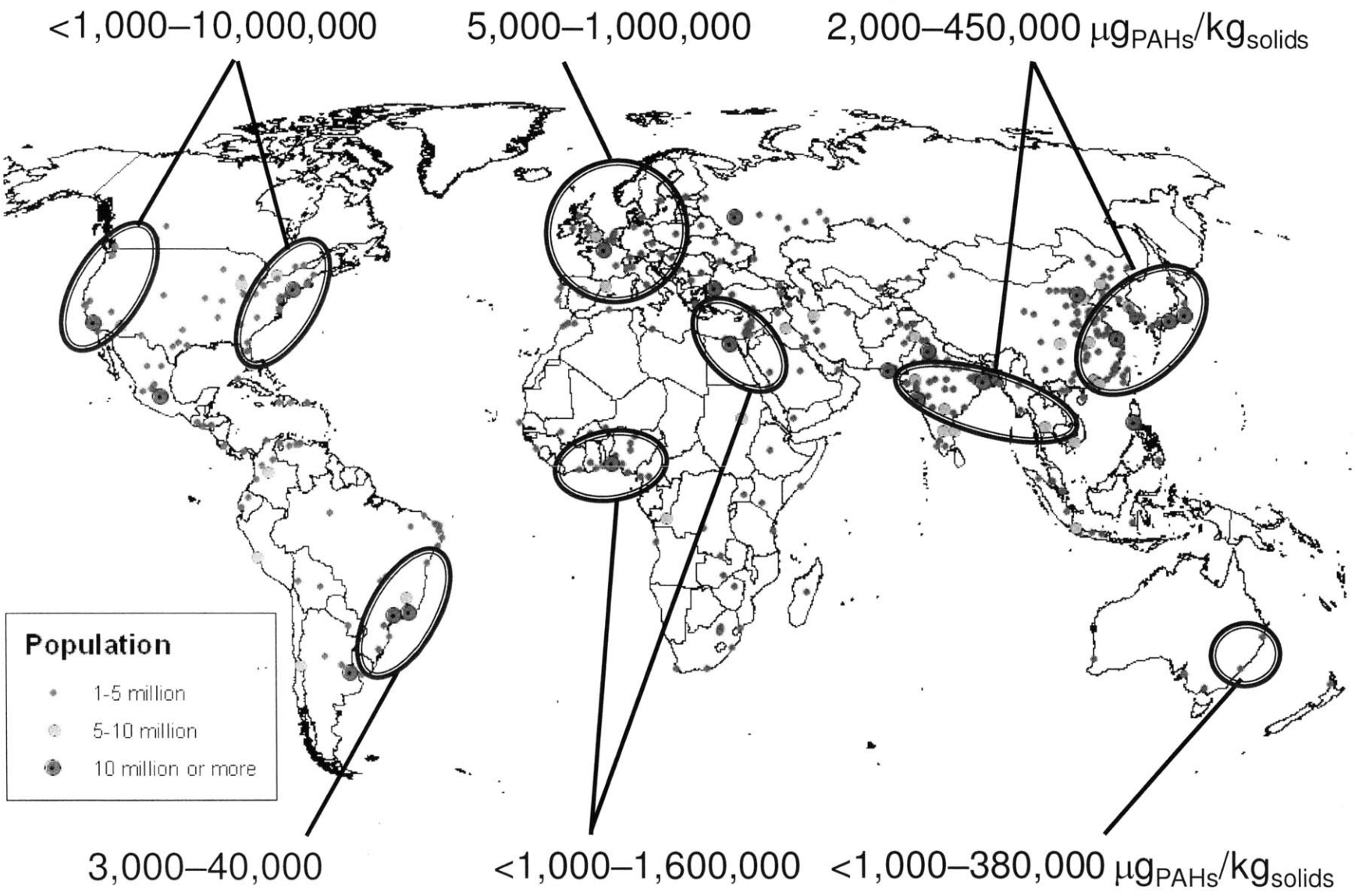

Figure 1 - 4. Total sedimentary PAHs (maximum range) (From Table 1-1)

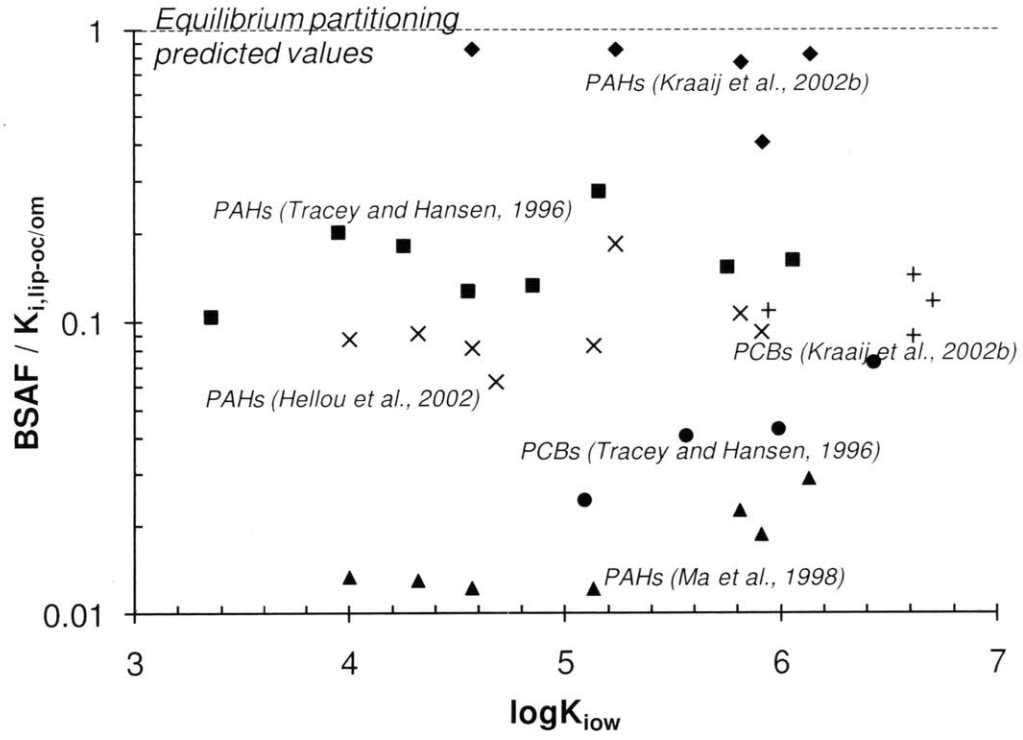

Figure 1 - 5. Some observed BSAFs for PAHs and PCBs from literature.

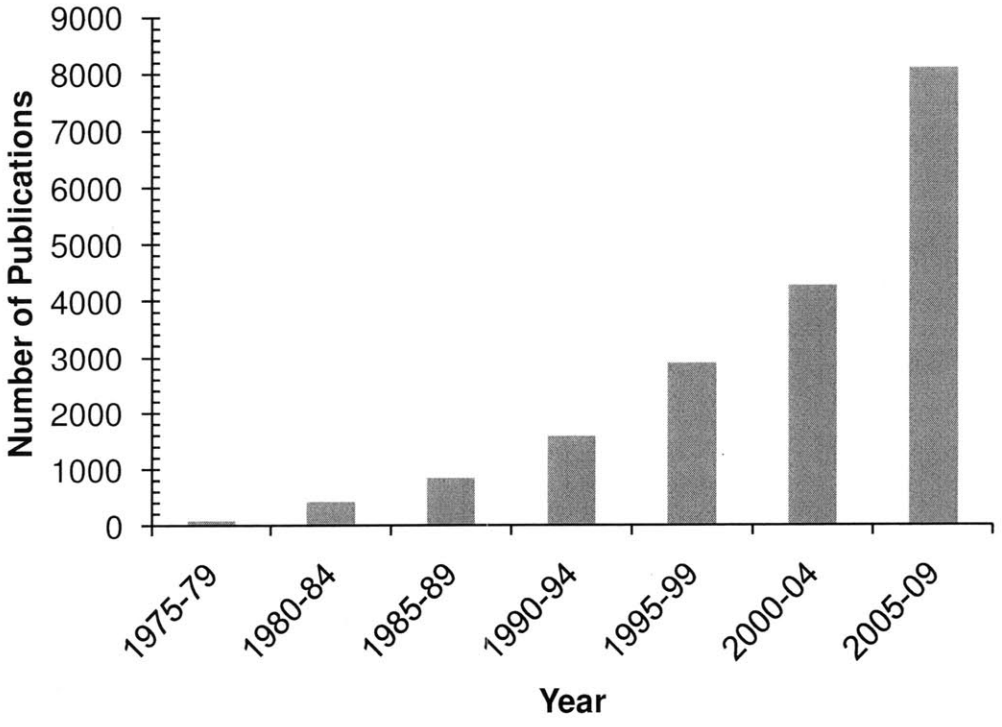

Figure 1 - 6. PAH publication number according to Science Direct.

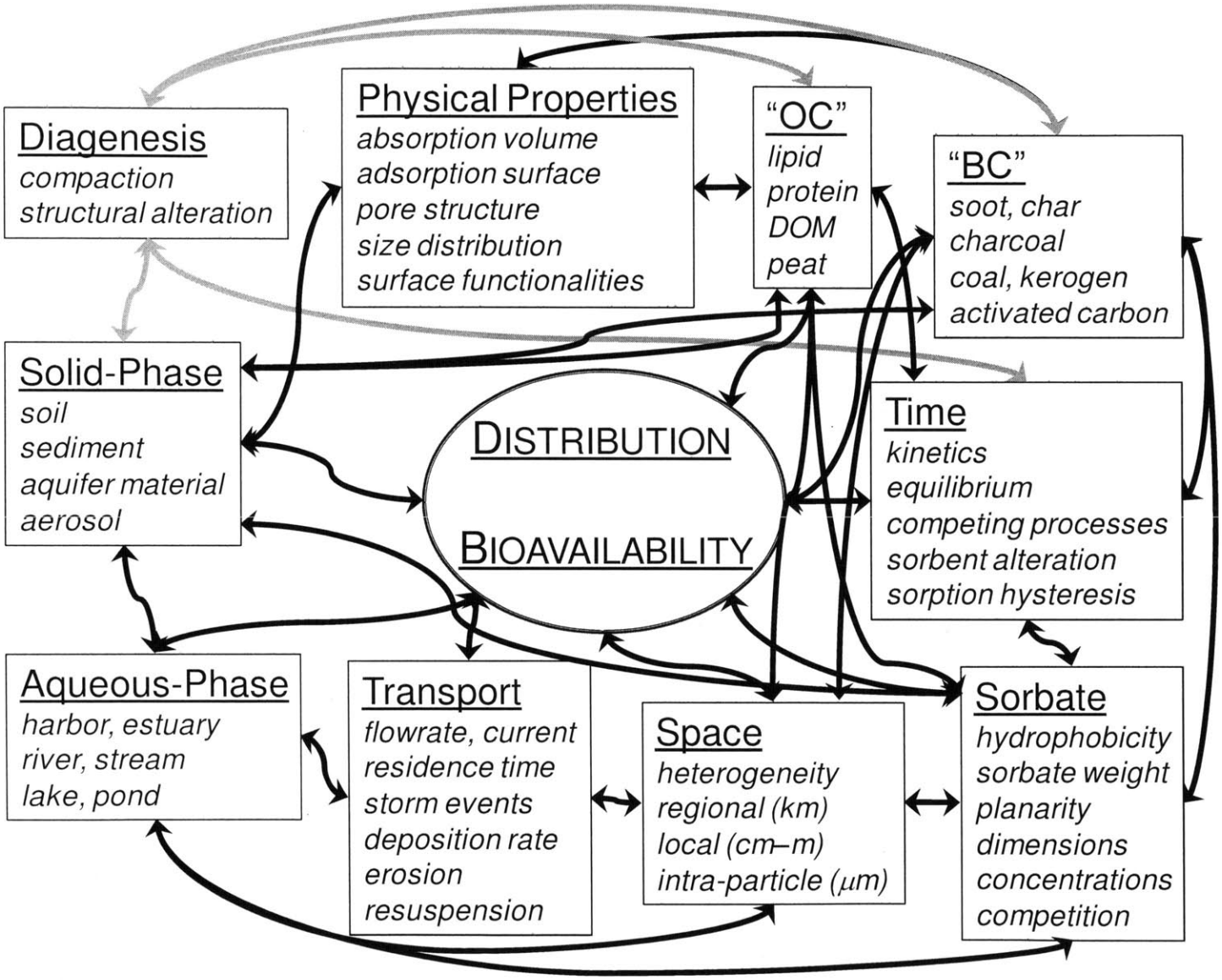

Figure 1 - 7. The web of factors influencing the distribution and bioavailability of HOCs in the environment.

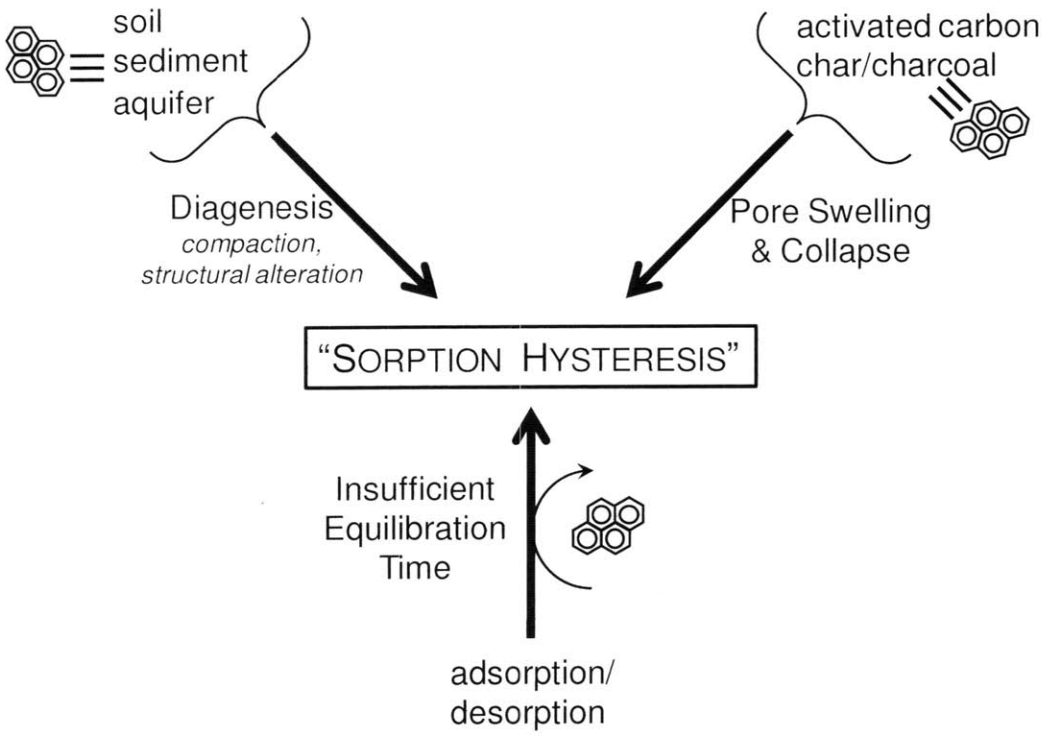

Figure 1 - 8. Factors contributing to "sorption hysteresis".

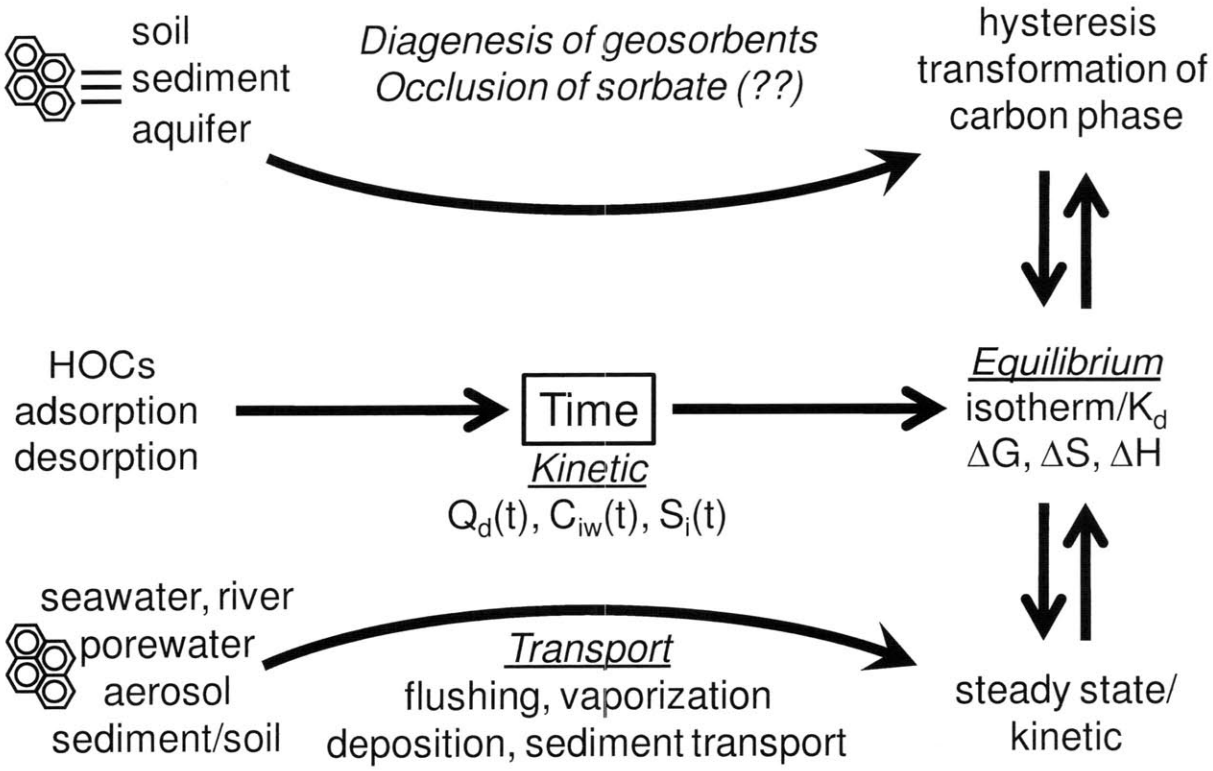

Figure 1 - 9. The importance of the dimension of Time.

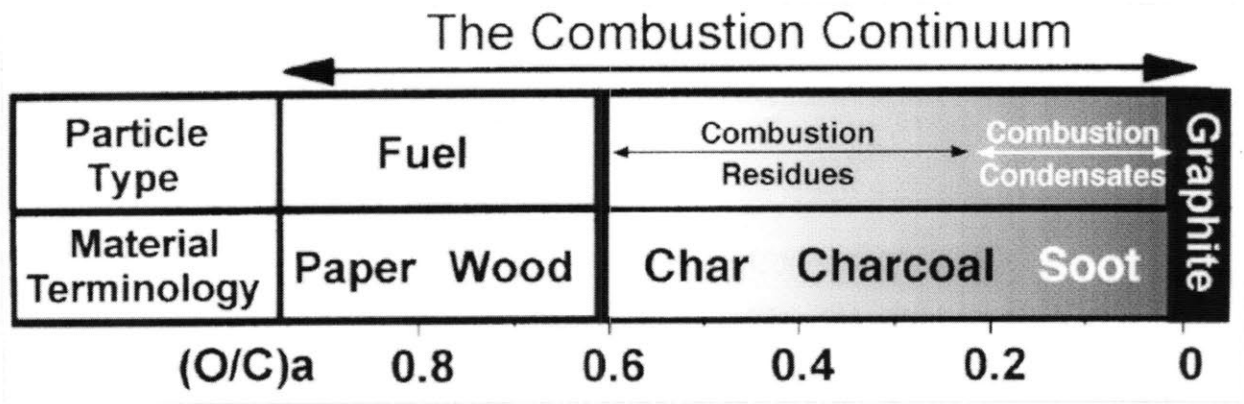

(a) From Hedges et al. (2000).

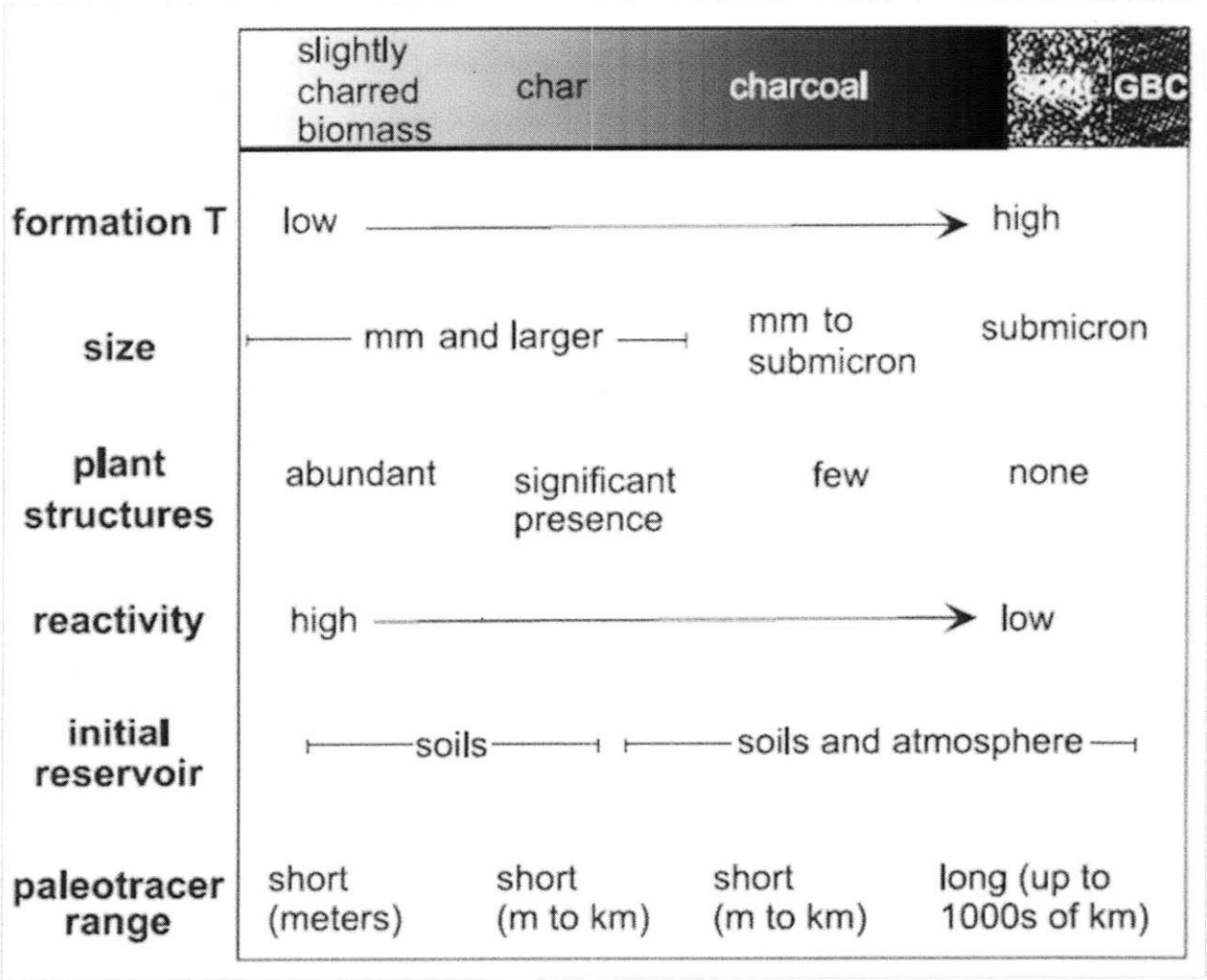

(b) From Masiello (2004)

Figure 1 - 10. Continuum of meta-BC/EC: (I) Biogeochemical Scheme.

This scheme focus on transport range, biochemical resistance, and material source.

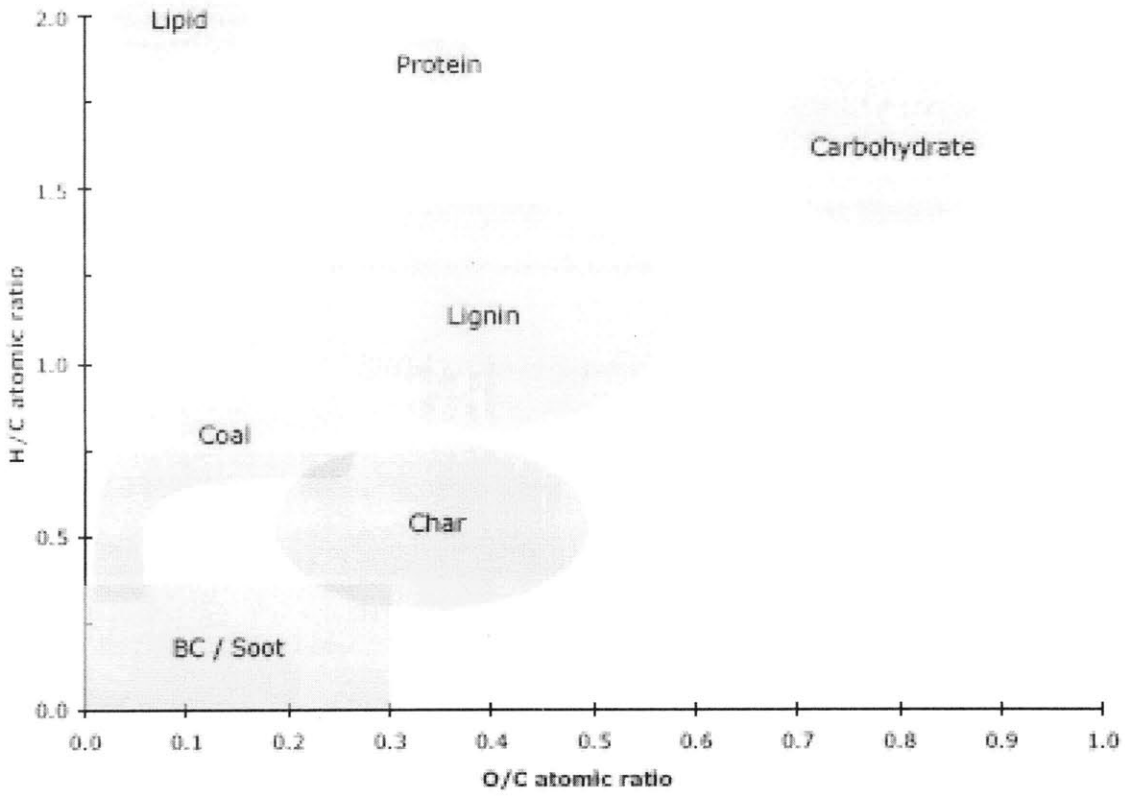

Figure 1 - 11. Continuum of meta-BC/EC: (II) Elemental/Compositional Scheme.

Here, different carbonaceous materials are mapped by their H/C and O/C elemental ratios (also known as the van Krevelen plot). Figure from Preston et al. 2006, after original diagram in Hammes et al. 2006.

BC	Formation	Material of Origin	Morphology	Special Features	Specific Surface Area
Soots Chars/charcoal Cenospheres Coke Lampblack Atmospheric tar balls					
Coal					
Kerogen					

Figure 1 - 12. Continuum of meta-BC/EC: (III) Sorption-Oriented Scheme.

Meta-BC/EC as organized by morphological features and surface/pore properties which are relevant to the characterization of kinetics and equilibrium of HOCs sorption in natural geosorbents. Simplified from Cornelissen et al. 2005b.

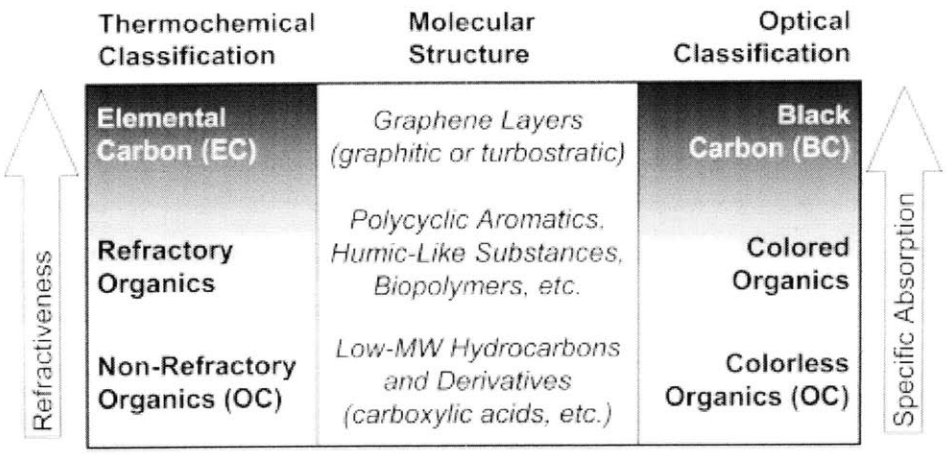

Figure 1 - 13. Continuum of meta-BC/EC: (IV) Atmospheric Physics Scheme.

This meta-BC/EC scheme highlights the association between molecular structures and their qualitative thermochemical and optical properties, which are of great interest to atmospheric physics and chemistry questions. Figure from Andreae et al. 2006 after Poschl 2003.

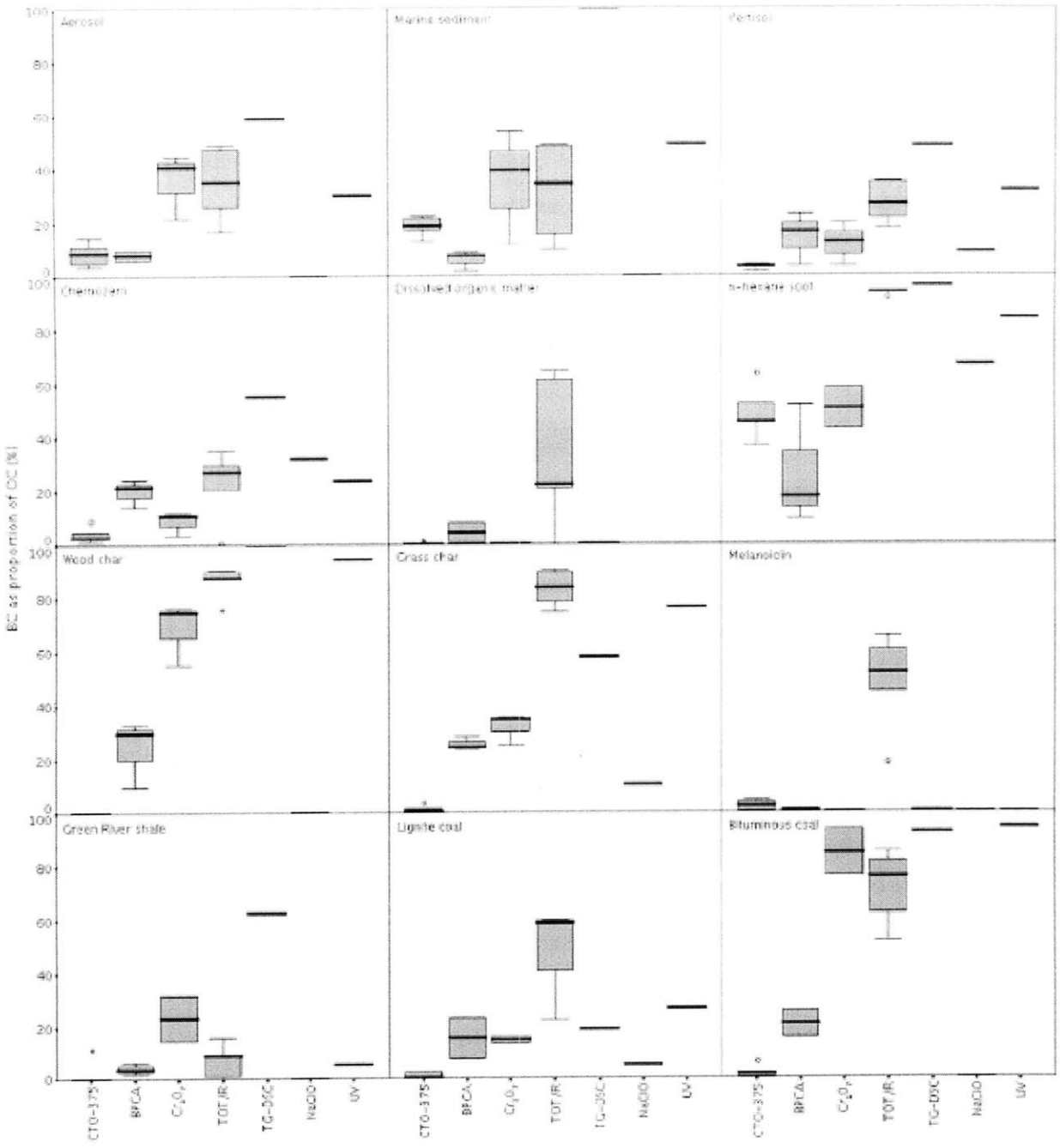

Figure 1 - 14. Quantifications of BC in different geosorbents/materials.

This meta-BC/EC scheme highlights the association between molecular structures and their qualitative thermochemical and optical properties, which are of great interest to atmospheric physics and chemistry questions. Figure from Hammes et al. 2007.

Chapter 2: Figures

Figure 2 - 1. Schematic of desorption experiment with laser induced fluorescence (LIF) system (adapted from Rudnick et al. 1998). 314
Figure 2 - 2. Pre-processed (thin line) and filtered (thick line) LIF fluorescence signals. 314
Figure 2 - 3. LIF measurements at resuspension and settled states (all data). 315
Figure 2 - 4. LIF measurement at resuspended vs seltted states for different size fractions 316
Figure 2 - 5. Correspondence of LIF Raman corrected and uncorrected resuspension measurements 317
Figure 2 - 6. Assessment of fluorescence from solid-associated pyrene. 318
Figure 2 - 7. LIF measurements at the early-time of pyrene desorption. 319
Figure 2 - 8. Supernatant dissolved pyrene as measured by LIF and GC-MS. 320
Figure 2 - 9. Reproducibility of native pyrene desorption time courses. 321
Figure 2 - 10. Desorption of native pyrene from Boston Harbor sediment. 322
Figure 2 - 11. Desorption of pyrene as a function of particle size fractions. 323
Figure 2 - 12. Equilibrium or Not – at the end of desorption experiment 324

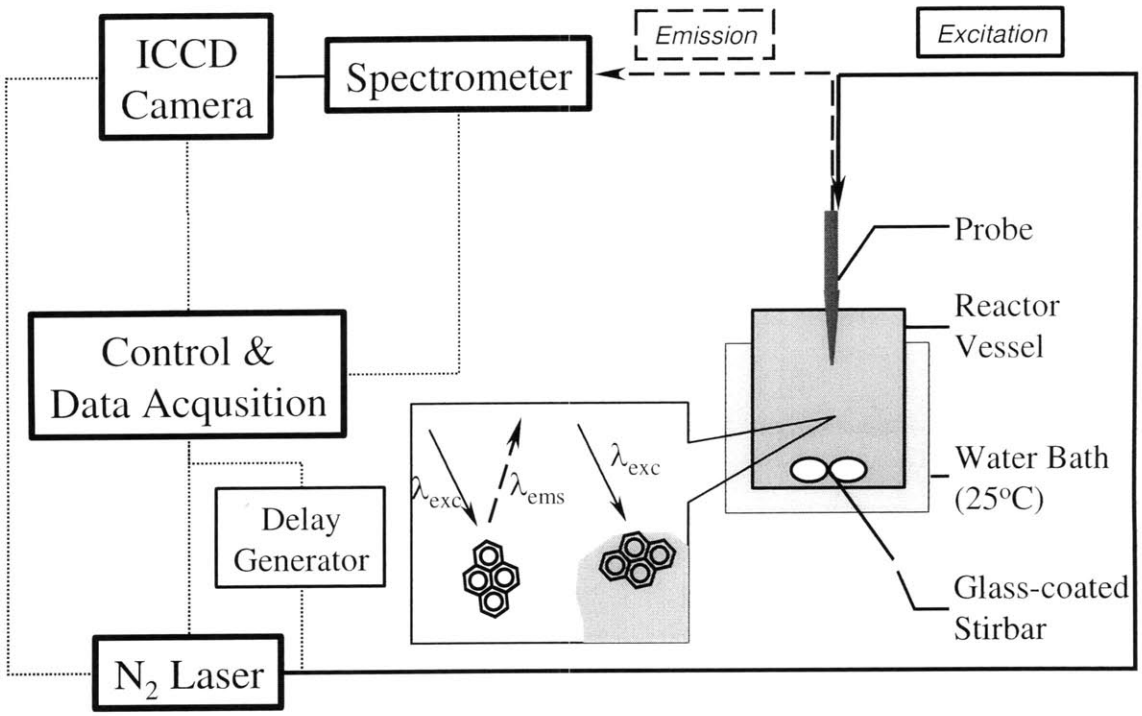

Figure 2 - 1. Schematic of desorption experiment with laser induced fluorescence (LIF) system (adapted from Rudnick et al. 1998).

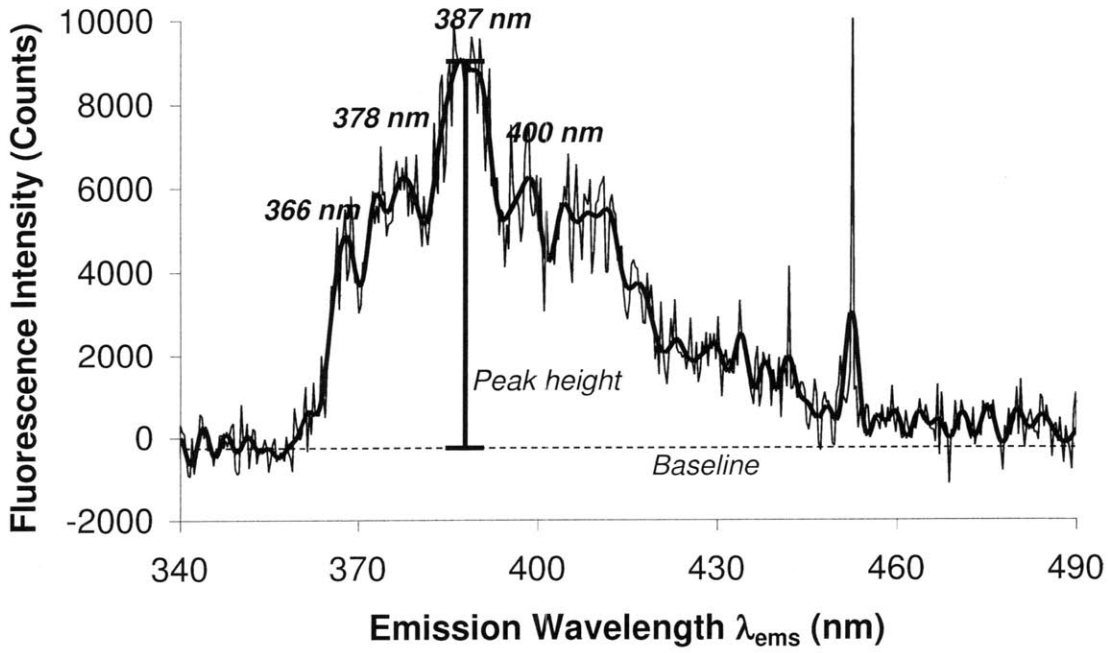

Figure 2 - 2. Pre-processed (thin line) and filtered (thick line) LIF fluorescence signals.

Wavelengths for the approximate locations of emission peaks characteristic to pyrene are noted.

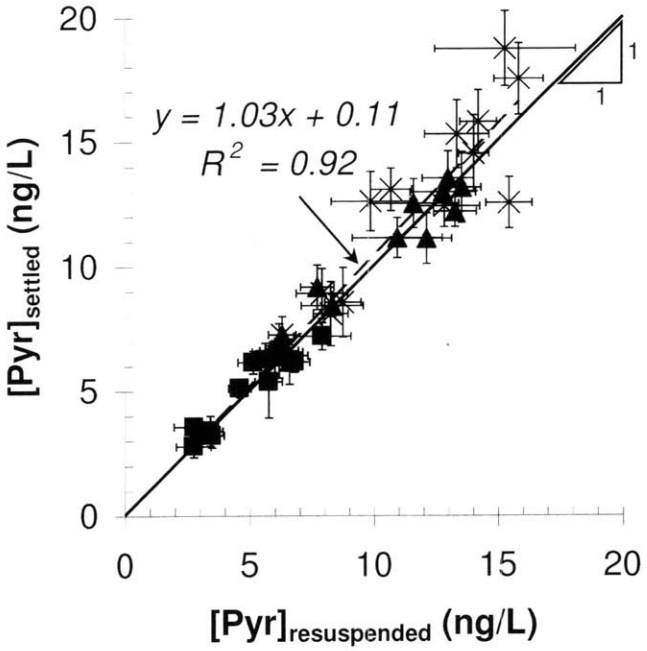

Figure 2 - 3. LIF measurements at resuspension and settled states (all data).

LIF measurement of pyrene when the sediment particles were settled vs. when they were suspended. Each point represents a measurement after 7-14 days of settling ($[Pyr]_{settled}$), followed by measurements immediately after resuspension ($[Pyr]_{resuspended}$). Three particle size fractions (not differentiated here) at three solid suspension concentration levels were used: 20 (■), 70-80 (▲), and 250-280 (×) mg solids/L. Solid line represents 1:1 match, dashed line represents the best linear fit. Errors are at ±1 standard deviation for 5 to 7 measurements.

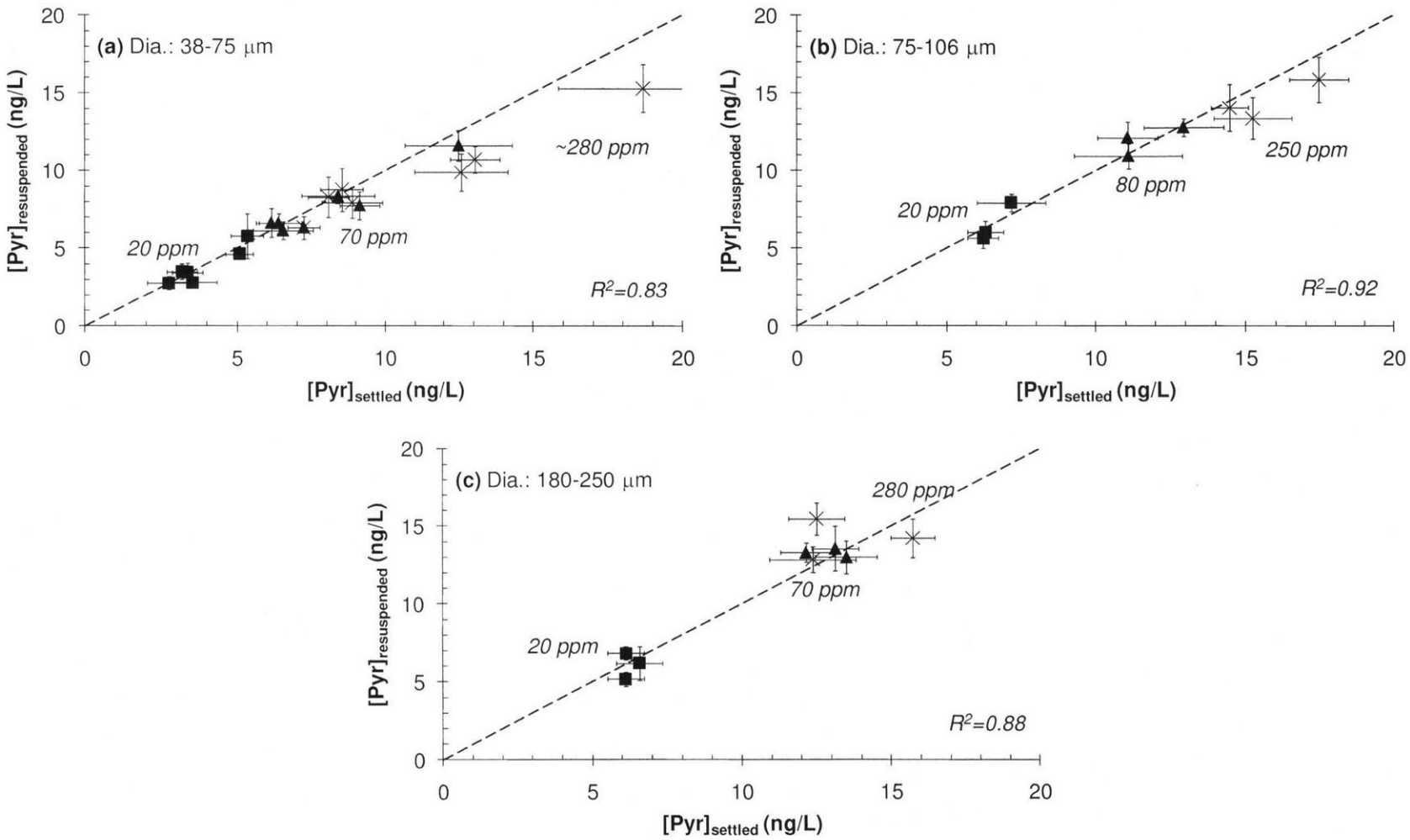

Figure 2 - 4. LIF measurement at resuspended vs seltted states for different size fractions.

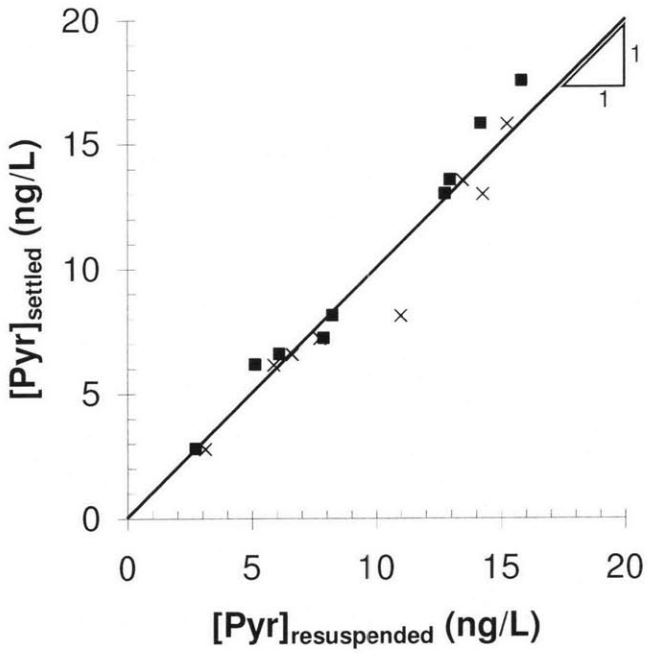

Figure 2 - 5. Correspondence of LIF Raman corrected and uncorrected resuspension measurements

Correspondence of LIF Raman corrected (■) and uncorrected (×) resuspension measurements ($[Pyr]_{resuspended}$) to LIF measurements of pyrene after 7-14 days of settling ($[Pyr]_{settled}$). The data were collected from all three particle size fractions at three solid suspension concentration levels (not differentiated here). Solid line represents 1:1 match.

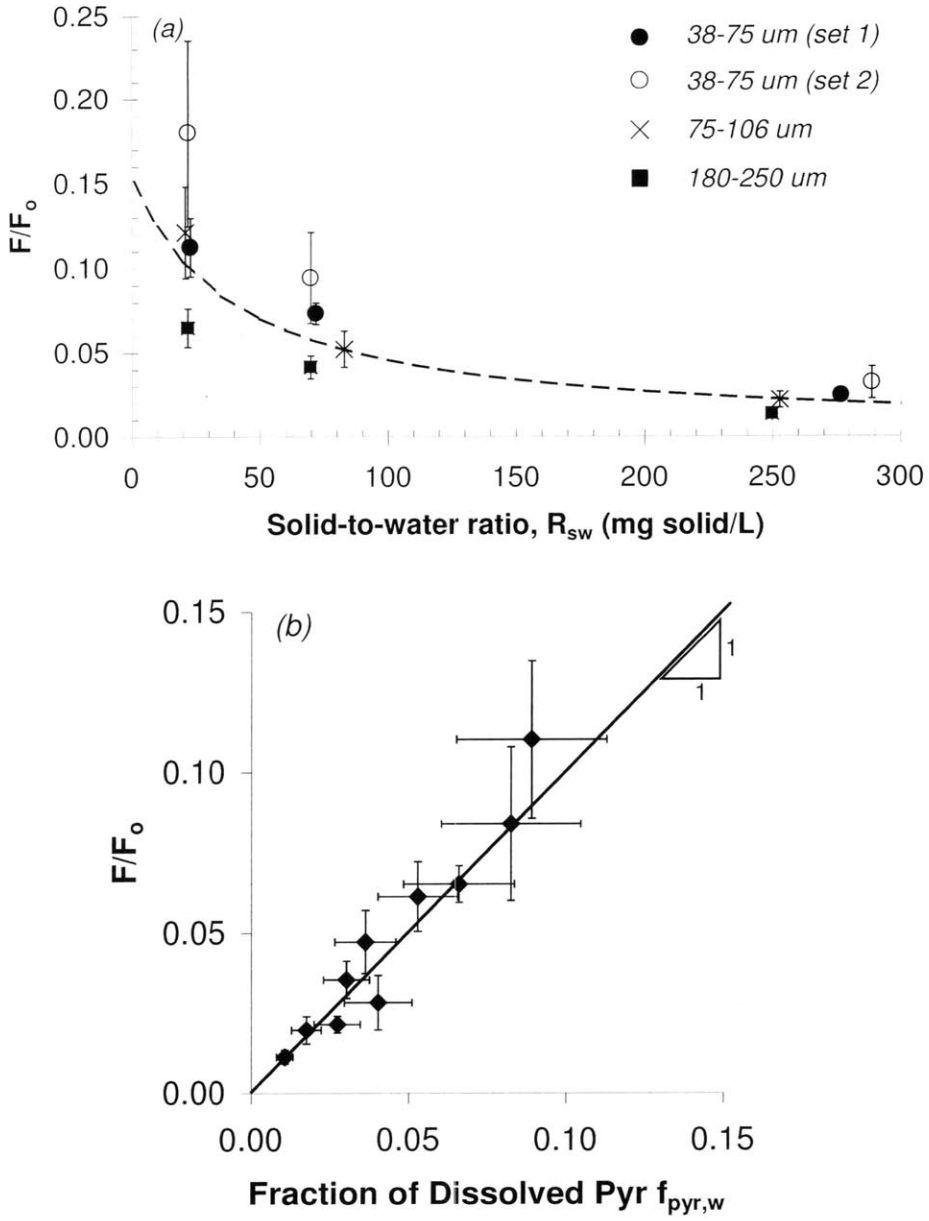

Figure 2 - 6. Assessment of fluorescence from solid-associated pyrene.

(a) Fraction of fluorescence-active pyrene as a function of total suspended solids concentrations. Y-axis shows the normalized fluorescent signal. Data points correspond to measurement at apparent equilibrium for all three sediment fractions: diam.=38-75 um (○●), dia.=75-106 um (×), and diam.=180-250 um (■). The dashed line represents the fit of $(F/F_o)^{-1}$ against R_{sw}, showing an asymptotic trend. (b) Estimation of fluorescence efficiency of solid-associated pyrene relative to dissolved pyrene, ϕ_s. The best fit of data to the equation $F/F_o = (1-\phi_s)f_{pyr,w} + \phi_s$ gave ϕ_s=0.002 and r^2=0.92. Fraction of dissolved pyrene, $f_{pyr,w}$, and normalized fluorescence, F/F_o, were determined from GC-MS measurement and LIF measurement, respectively, of supernatants at the end of the desorption experiment. Error bars represents ±1 standard deviation.

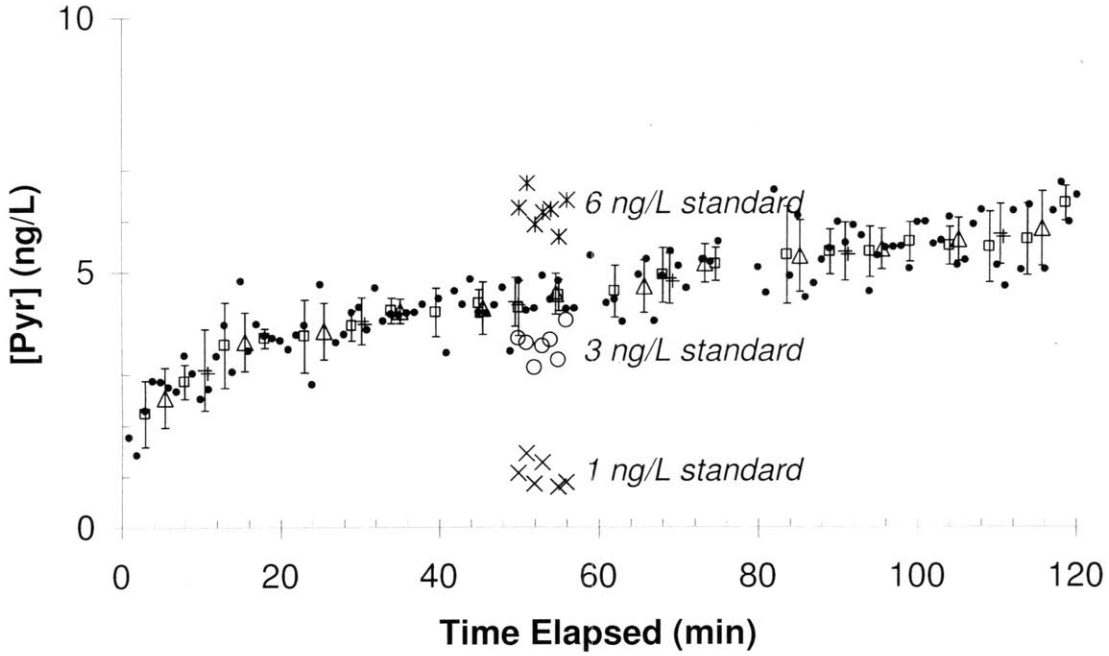

Figure 2 - 7. LIF measurements at the early-time of pyrene desorption.

Dissolved pyrene measured at 1-min (•), 5-min (□), 10-min (△), and 20-min (+) resolutions by LIF during first 2 hours of the desorption experiment for the 38-75 um size fraction at a R_{sw} of about 280 mg solids/L. Also shown are pyrene standard measurements at 1-min resolution (6-7 replicates). Error bars indicates ±1 standard deviation.

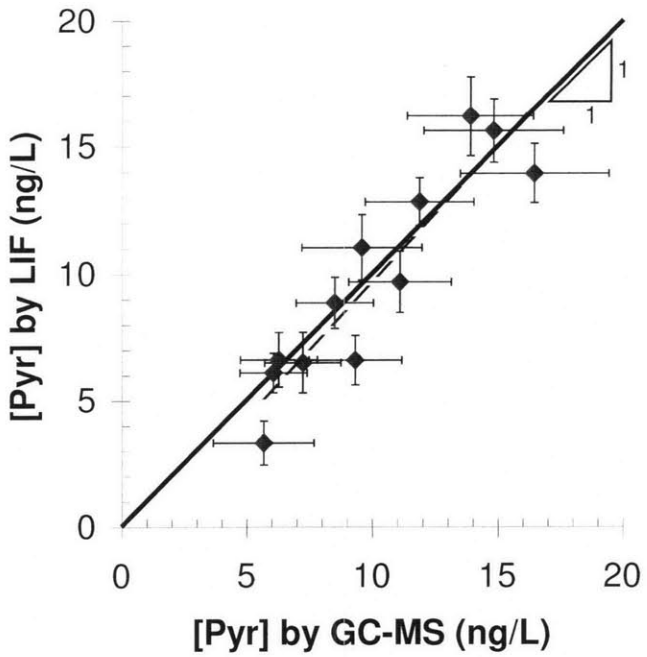

Figure 2 - 8. Supernatant dissolved pyrene as measured by LIF and GC-MS.

Supernatant pyrene concentration determined by LIF and GC-MS at the end of desorption experiment. Solid line shows 1:1 match; dashed line shows linear regression $y = 1.06(\pm 0.14)x - 0.95(\pm 1.53)$. Error bars designate ±1 standard deviation.

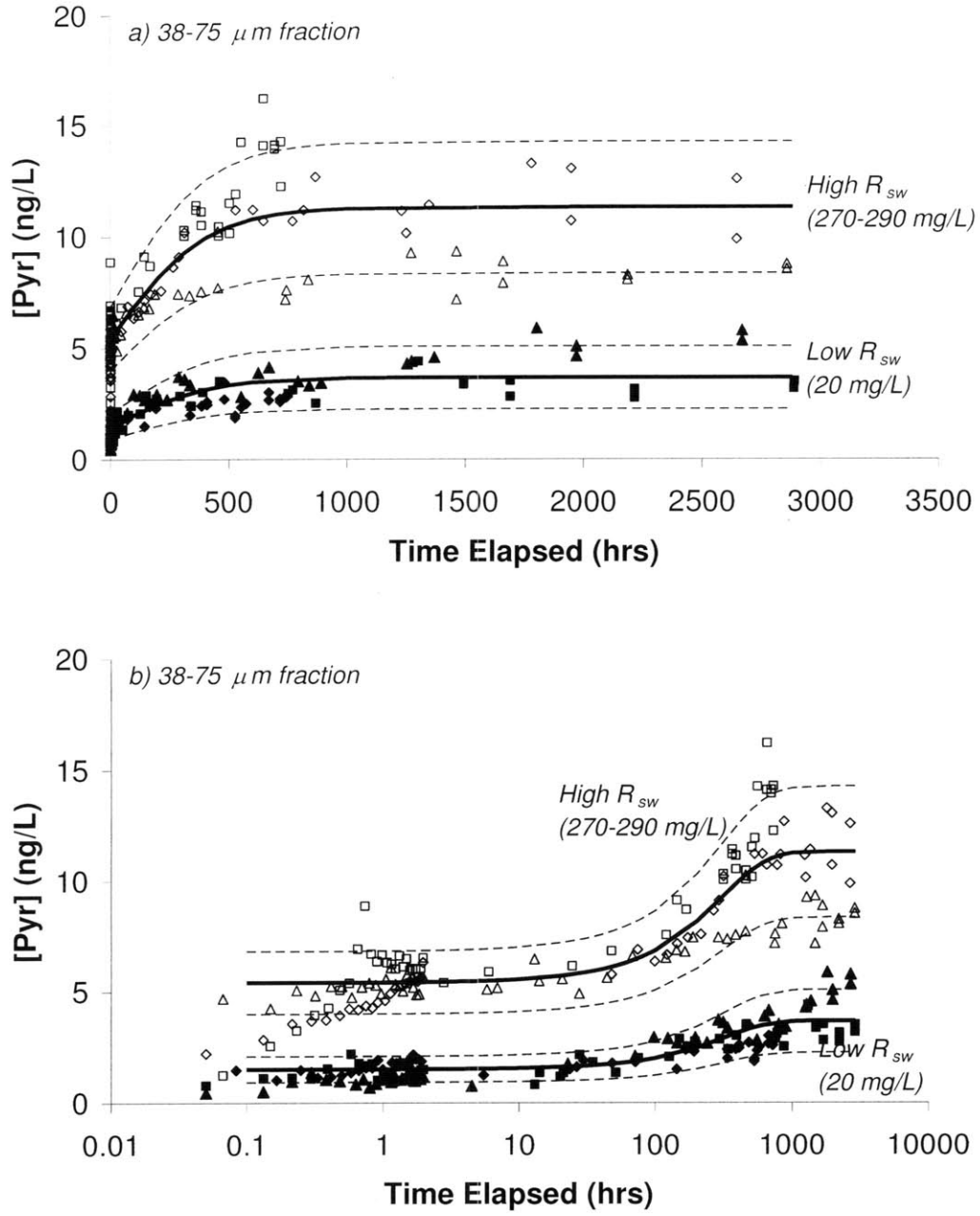

Figure 2 - 9. Reproducibility of native pyrene desorption time courses.

Three replicates of the desorption experiment are shown for high R_{sw} (270-290 mg/L; open symbols) and low R_{sw} (20 mg/L; closed symbols). The thick lines are the weighted fits of the replicates. The dash lines show the boundaries of ±1 standard deviation for the weighted fits. The replicates are shown in both normal time scale (a) and log time scale (b).

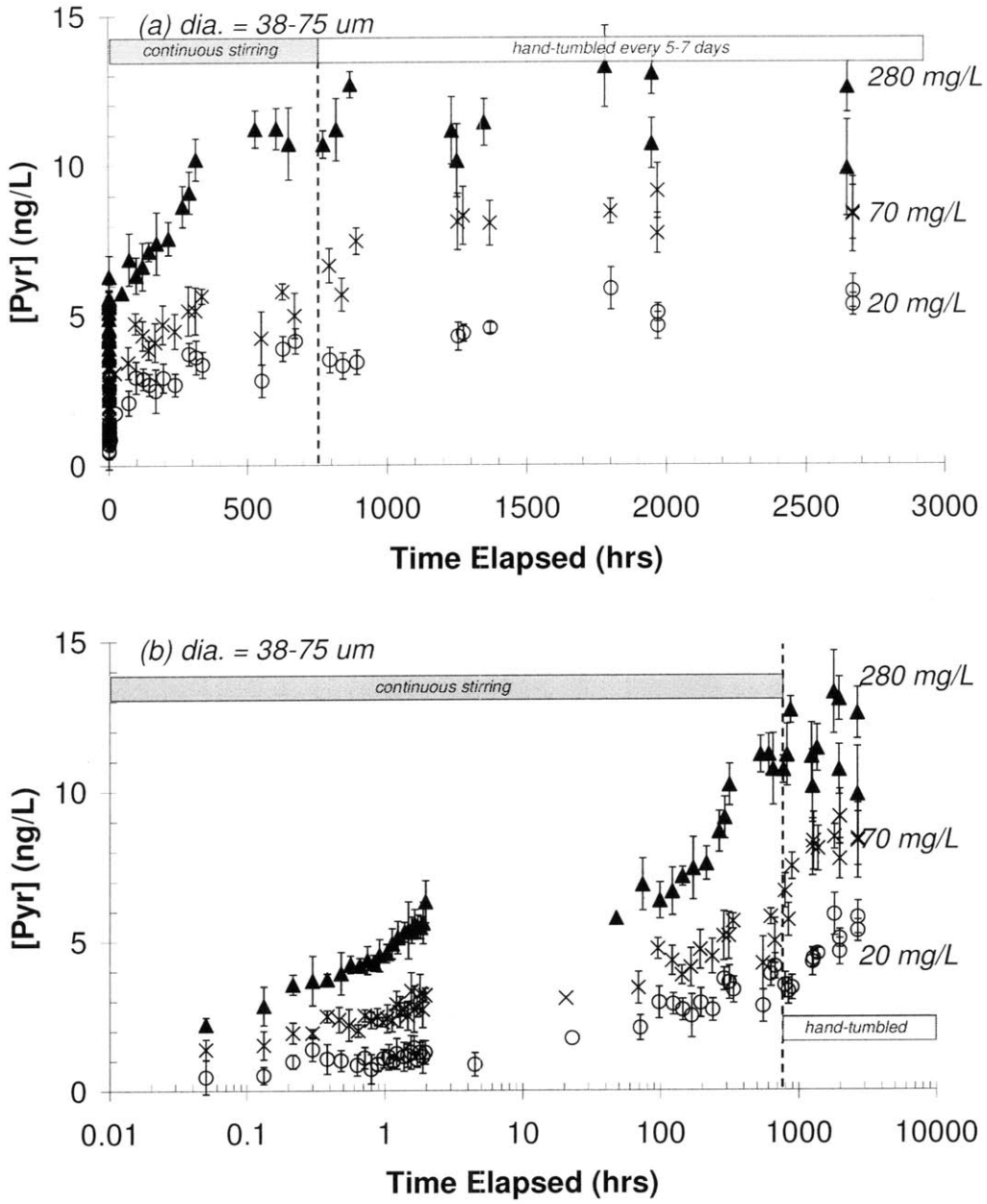

Figure 2 - 10. Desorption of native pyrene from Boston Harbor sediment.

Desorption of native pyrene as monitored by LIF for the size fraction of diam.=38-75 um at three solid-to-water ratios: R_{sw}=20 mg/L (O), 70 mg/L (×), and 280 mg/L (▲). The release profiles are shown in normal time scale (a) and log time scale (b). Continuous stirring was replaced with hand-tumbling (every 5-7 days) at ~720th hr (vertical dashed line).

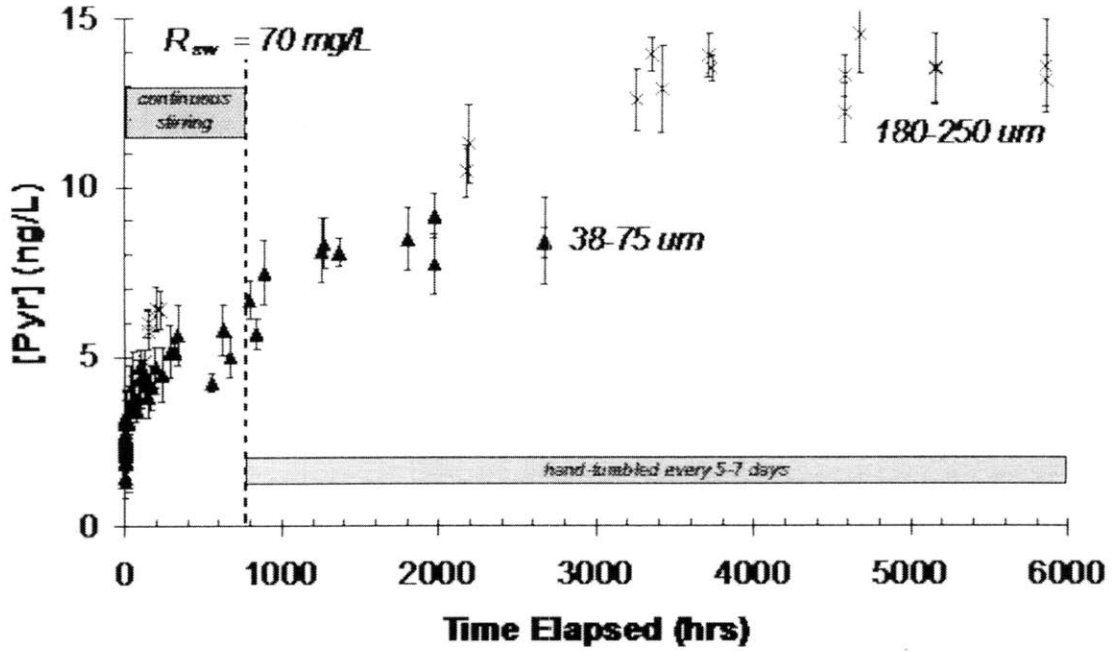

Figure 2 - 11. Desorption of pyrene as a function of particle size fractions.

Pyrene release as a function of particle size at a constant solid-to-water ratio of 70 mg solids/L water. Error bars give ±1 standard deviation. Continuous stirring was replaced with hand-tumbling (every 5-7 days) at ~720th hr (vertical dashed line)

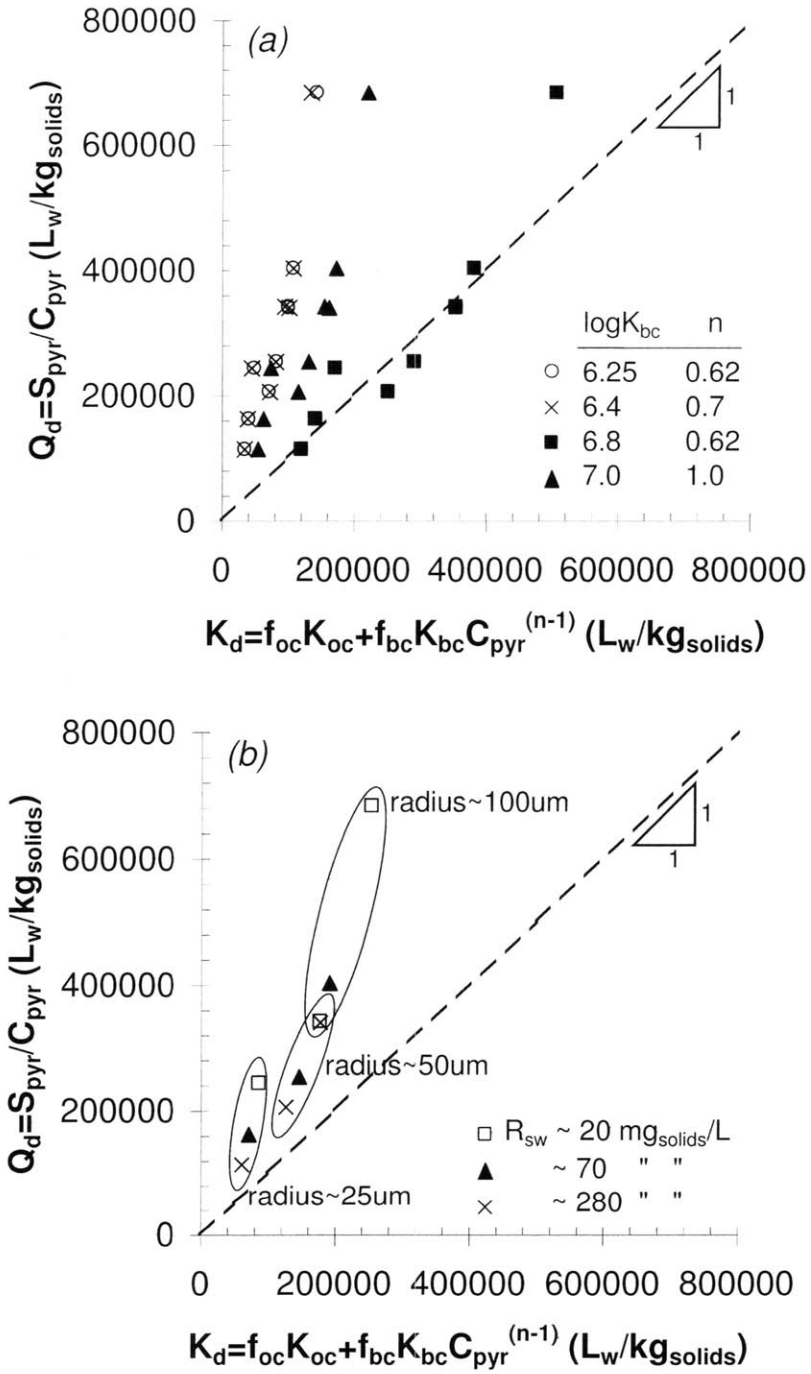

Figure 2 - 12. Equilibrium or Not – at the end of desorption experiment.

(a) Observed pyrene concentration ratio at the end of desorption experiment, Q_d, compared with equilibrium ratio, K_d, determined from OC-BC isotherm with different isotherm parameters: circles (Accardi-Dey and Gschwend 2002), crosses (Lohmann et al. 2005), squares (Adams 2003), triangles (Bucheli et al. 2000). In all cases, a log K_{oc} of 4.7 was used for pyrene. (b) Q_d vs K_d (with log K_{oc}=4.7, log K_{bc}=6.5, n=0.62) at different particle radius and solids-to-water ratios, R_{sw}'s.

Chapter 3: Figures

Figure 3 - 1. Calibration curves for Synchronous Fluorescence Spectroscopy and Time-Gated Laser-Induced Fluorescence Spectroscopy. 327
Figure 3 - 2. Conservation plot for pyrene for 10 months of sorption equilibration. ... 328
Figure 3 - 3. Dissolved pyrene profile over time and the test of sorption equilibrium. 329
Figure 3 - 4. Test of pyrene desorption equilibrium for Short-Term Desorption Experiment within the ~1800th-3500th hour time-frame..... 330
Figure 3 - 5. Test of pyrene desorption equilibrium for Short-Term Desorption Experiment within the ~1000th-3500th hour time-frame..... 331
Figure 3 - 6. Test of pyrene desorption equilibrium for Short-Term Desorption Experiment within the ~200th-3500th hour time-frame..... 332
Figure 3 - 7. Test of pyrene desorption equilibrium for the NQB/BH#6 38-75 μm fraction (set A) at 4 different time-frames. 333
Figure 3 - 8. Test of pyrene desorption equilibrium for the NQB/BH#6 180-250 μm fraction at 3 different time-frames..... 334
Figure 3 - 9. Pyrene equilibration time-course for Long-Term Desorption Equilibrium Experiment. 335
Figure 3 - 10. Verfication of equilibrium for the Long-Term Desorption Equilibrium Experiment. 336
Figure 3 - 11. Correspondence plot (1-to-1 plot) of dissolved pyrene levels for Long Term Extended-Range Equilibrium Experiment at 6, 15, 22, and 37°C..... 338
Figure 3 - 12. Dissolved pyrene levels after 5 and 10-month of equilibrium at 6°C (Long Term Extended-Range Equilibrium Experiment). 338
Figure 3 - 13. Equilibration time ($\tau_{95\%\text{-}Eqm}$) for adsorption/desorption with linear isotherm. 339
Figure 3 - 14. Generalized isotherms for different carbonaceous phases in a given geosorbent. 340

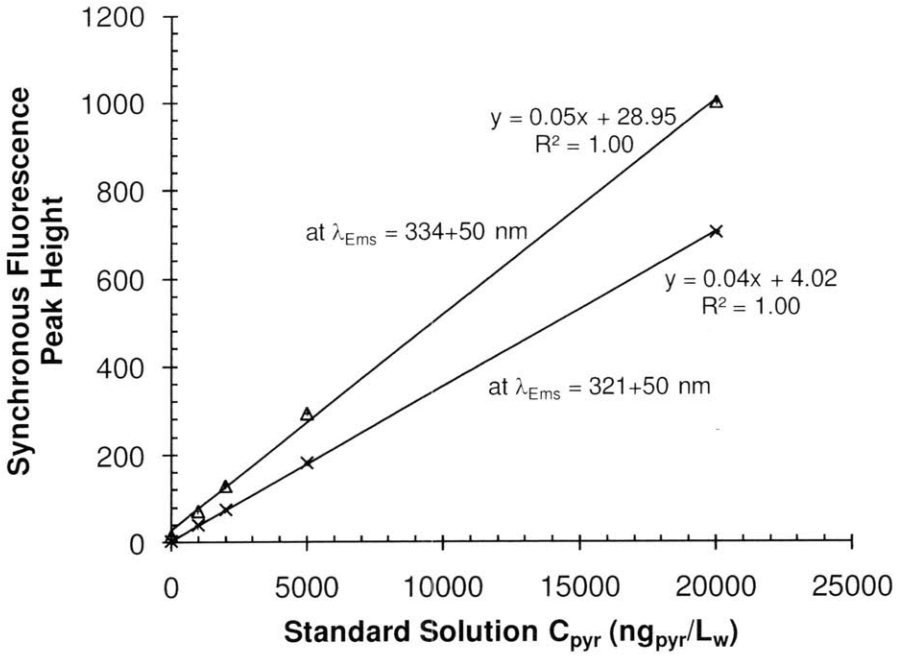

(a) Synchronous Fluorescence Spectroscopy

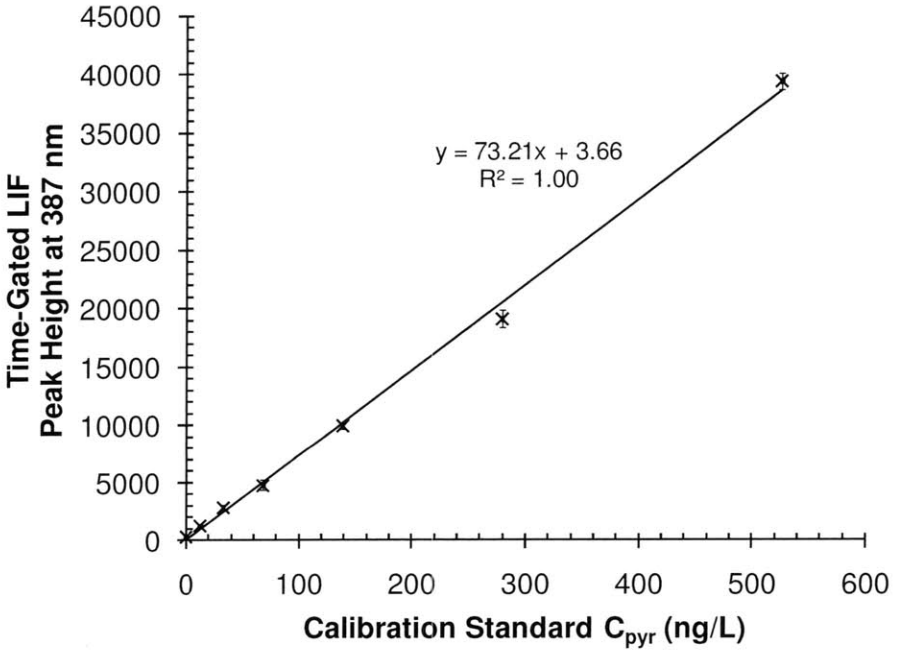

(b) Time-Gated Laser-Induced Fluorescence Spectroscopy

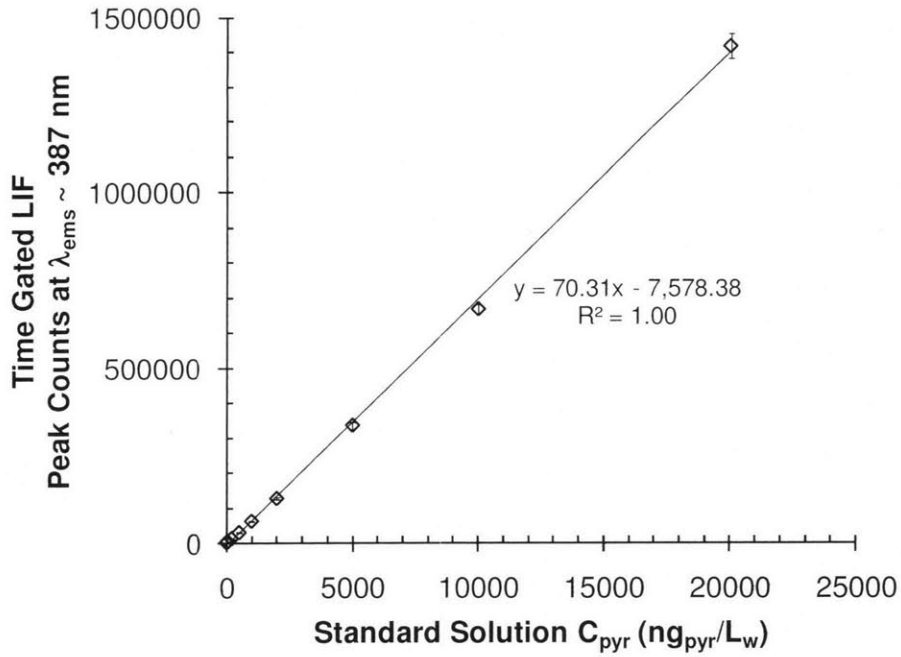

(c) Time-Gated Laser-Induced Fluorescence Spectroscopy (Extended range)

Figure 3 - 1. Calibration curves for Synchronous Fluorescence Spectroscopy and Time-Gated Laser-Induced Fluorescence Spectroscopy.

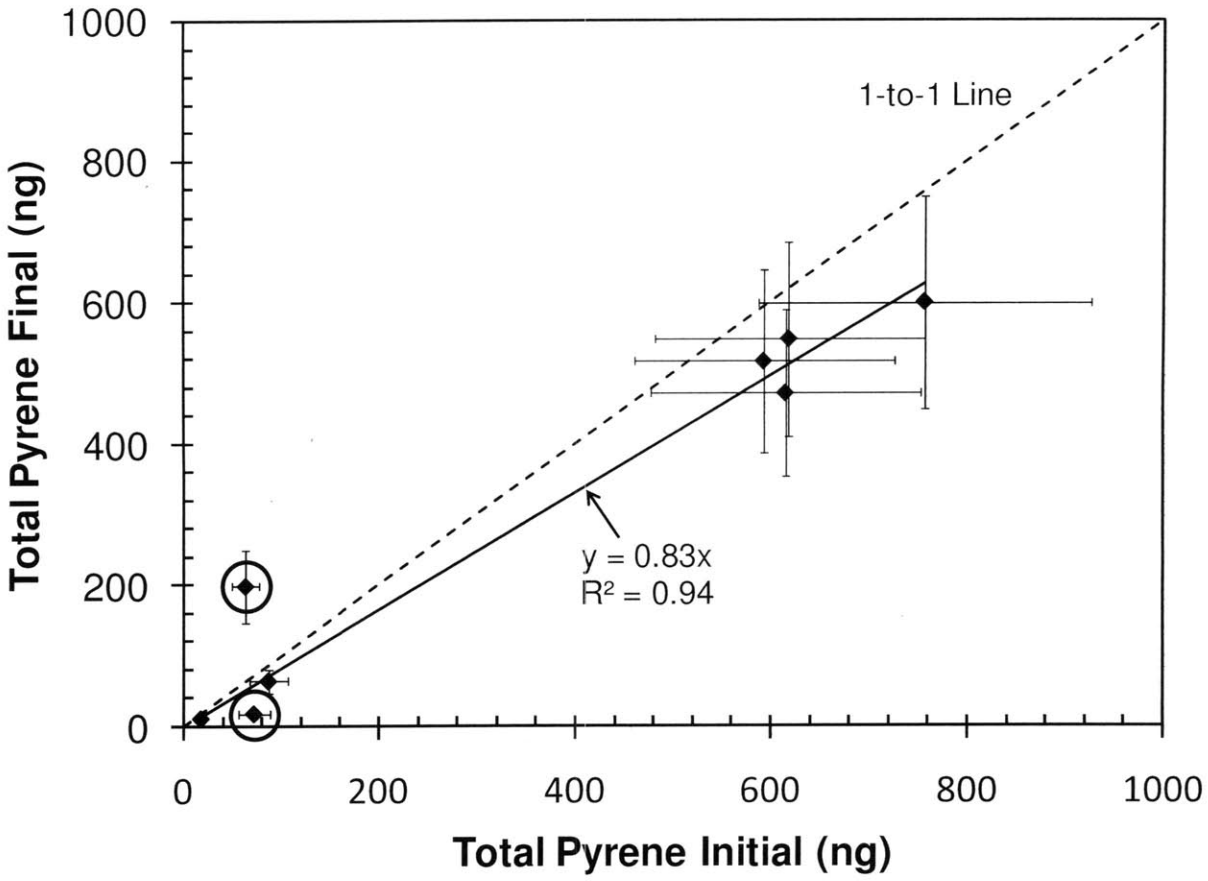

Figure 3 - 2. Conservation plot for pyrene for 10 months of sorption equilibration.

The axes show the pyrene at the beginning of the sorption equilibrium experiment (Total Pyrene Initial) and that at the end after ~10 months (Total Pyrene Final). The deviation of the regressed line ($y=0.83x$, $r^2=0.94$) from the 1-to-1 line suggested that pyrene is not conserved. The error bars give uncertainty in ±1 standard deviation. The circled observations had substantial discrepancies (± factor of 2 or more) between initial and final total pyrene.

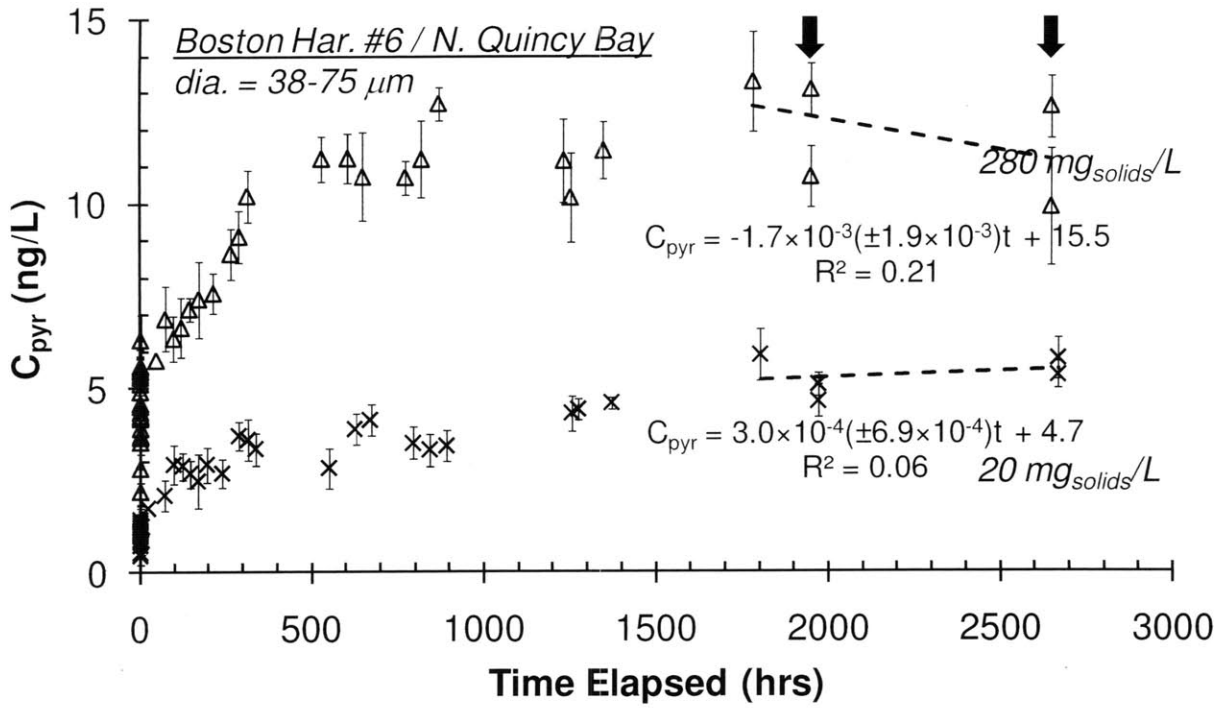

Figure 3 - 3. Dissolved pyrene profile over time and the test of sorption equilibrium.

Rate of change of dissolved pyrene near the end of desorption experiment for BH#6/NQB 38-75 μm size fraction within the time-frame of 1800^{th}-2700^{th} hour. Arrows highlight the instances of scattered measurement due to occasional instrumental instability. Dashed lines show the linear regression over the analyzed time-frame. Uncertainty in the regressed slope (i.e. $\Delta C_{pyr}/\Delta t$) is given in the parentheses (±1 standard error).

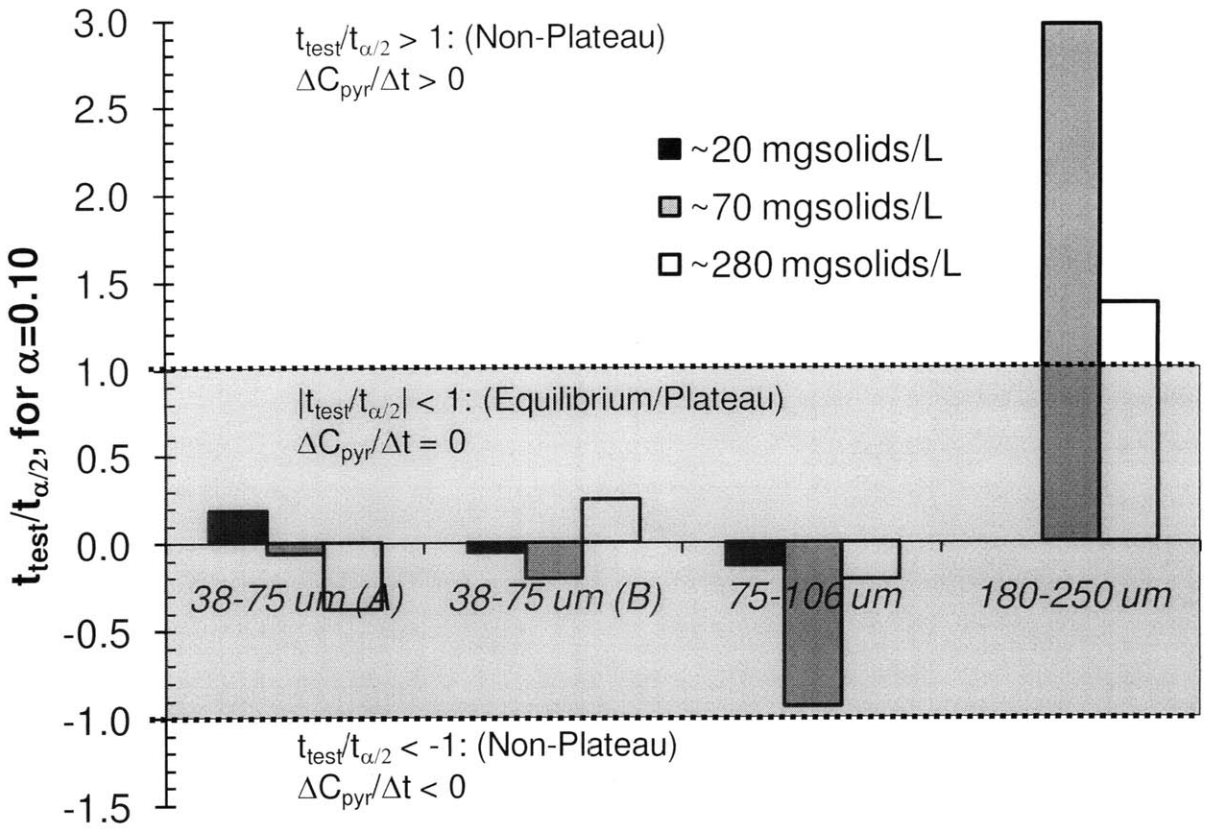

Figure 3 - 4. Test of pyrene desorption equilibrium for Short-Term Desorption Experiment within the ~1800th-3500th hour time-frame.

T-test statistics (normalized to $t_{\alpha/2}$, with α=0.10) for $\Delta C_{pyr}/\Delta t$ observed in the suspensions of BH#6/NQB sediment size fractions. Shaded zone denotes cases where $\Delta C_{pyr}/\Delta t$ is statistically zero (i.e. the hypothesis $\Delta C_{pyr}/\Delta t$=0 is accepted). For cases with $|t_{test}/t_{\alpha/2}|>1$, $\Delta C_{pyr}/\Delta t$ is significantly different from zero.

Note that no t-statistic was computed for the 180-250μm-20ppm suspension due to the lack of observations around the 1800th hour.

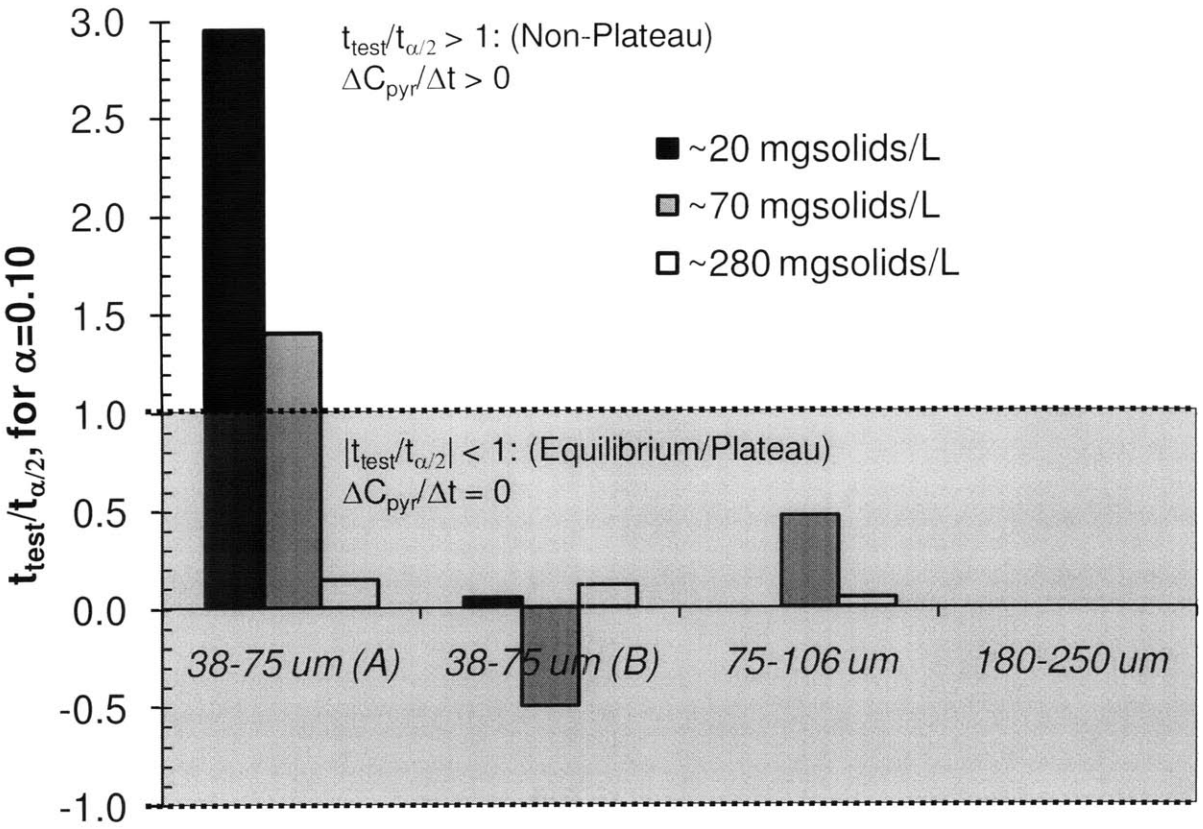

Figure 3 - 5. Test of pyrene desorption equilibrium for Short-Term Desorption Experiment within the ~1000th-3500th hour time-frame.

T-test statistics (normalized to $t_{\alpha/2}$, with α=0.10) for $\Delta C_{pyr}/\Delta t$ observed in the suspensions of BH#6/NQB sediment size fractions. Shaded zone denotes cases where $\Delta C_{pyr}/\Delta t$ is statistically zero (i.e. the hypothesis $\Delta C_{pyr}/\Delta t$=0 is accepted). For cases with $|t_{test}/t_{\alpha/2}|>1$, $\Delta C_{pyr}/\Delta t$ is significantly different from zero.

No t-statistic was computed for the 75-106μm-20ppm, and the 180-250μm suspensions due to the lack of observations around the 1000th hour.

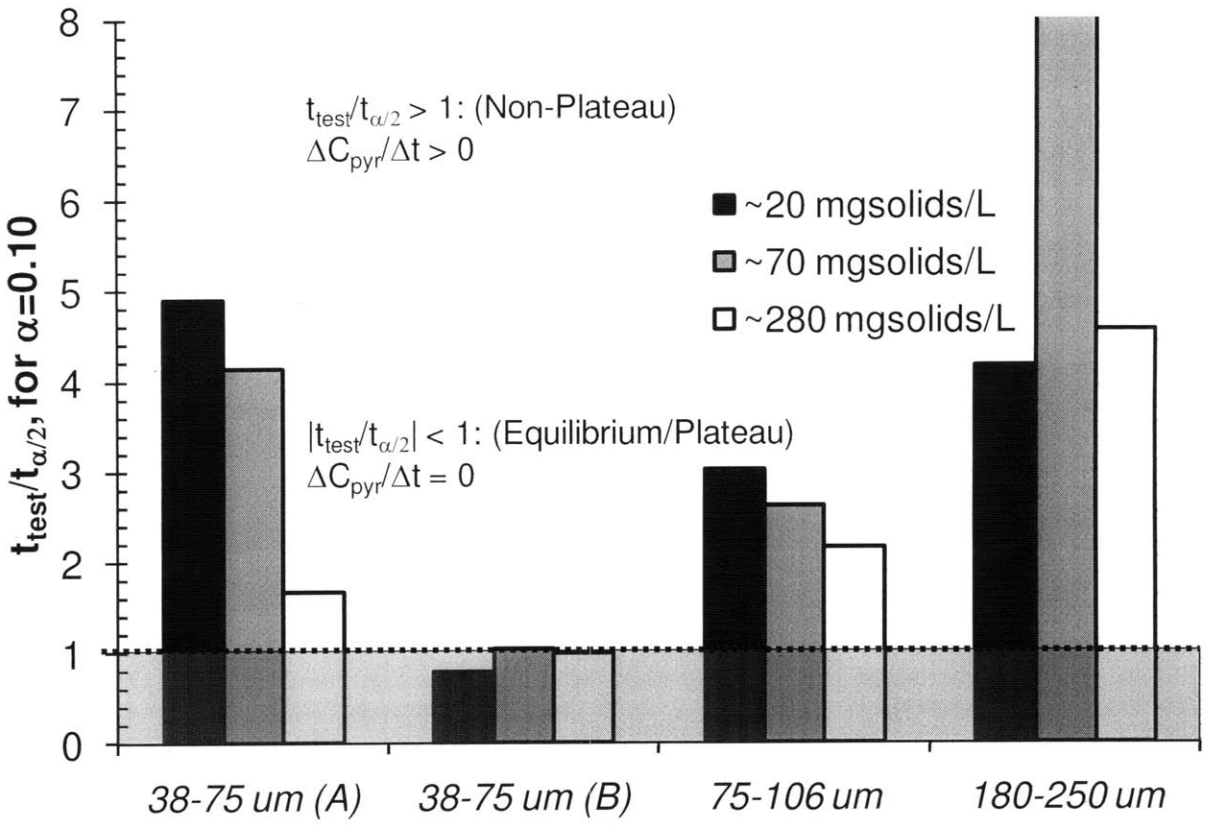

Figure 3 - 6. Test of pyrene desorption equilibrium for Short-Term Desorption Experiment within the ~200th-3500th hour time-frame.

T-test statistics (normalized to $t_{\alpha/2}$, with α=0.10) for $\Delta C_{pyr}/\Delta t$ observed in the suspensions of BH#6/NQB sediment size fractions. Shaded zone denotes cases where $\Delta C_{pyr}/\Delta t$ is statistically zero (i.e. the hypothesis $\Delta C_{pyr}/\Delta t$=0 is accepted). For cases with $|t_{test}/t_{\alpha/2}|>1$, $\Delta C_{pyr}/\Delta t$ is significantly different from zero.

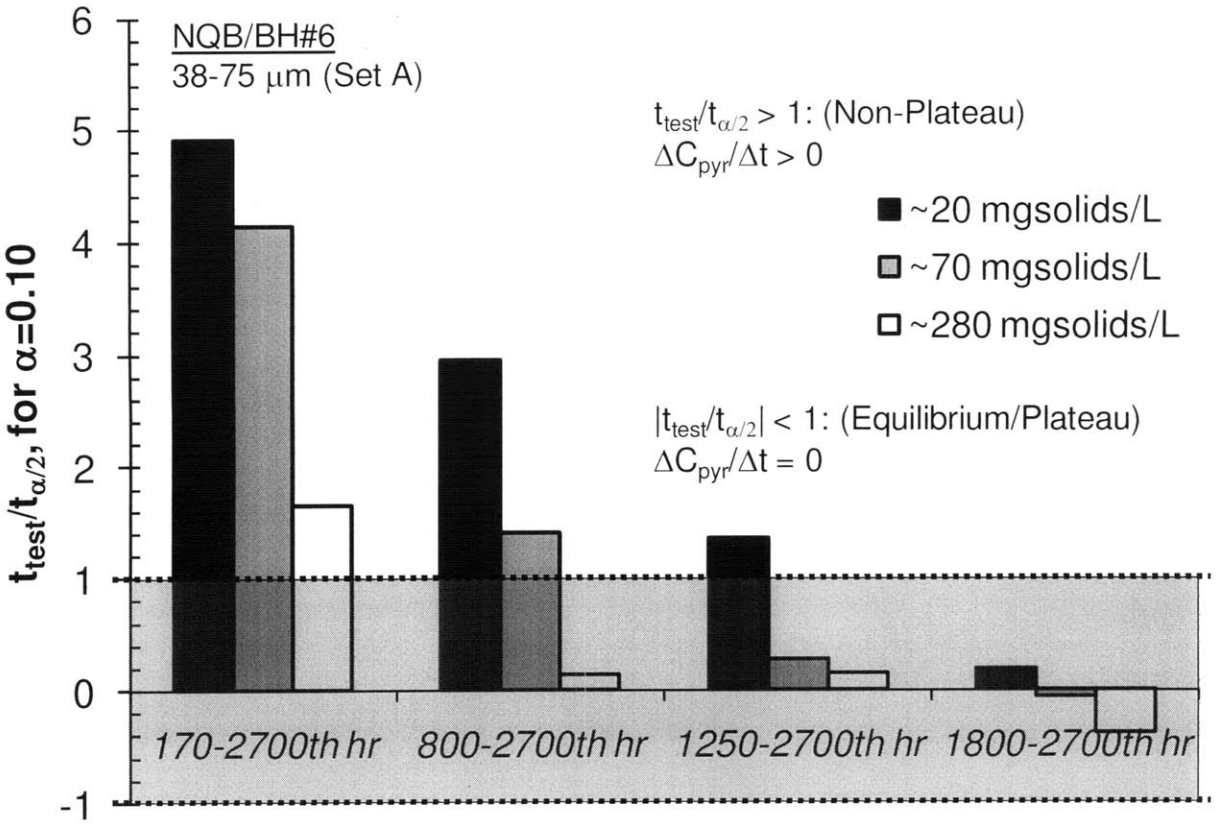

Figure 3 - 7. Test of pyrene desorption equilibrium for the NQB/BH#6 38-75 μm fraction (set A) at 4 different time-frames.

Dissolved pyrene concentrations observed within the specified time-frame were linearly regressed. T-test statistics (t_{test}) were computed from the regressed slope and its standard error. Shaded zone denotes cases where $\Delta C_{pyr}/\Delta t$ is statistically zero (i.e. the hypothesis $\Delta C_{pyr}/\Delta t=0$ is accepted). For cases with $|t_{test}/t_{\alpha/2}|>1$, $\Delta C_{pyr}/\Delta t$ is significantly different from zero.

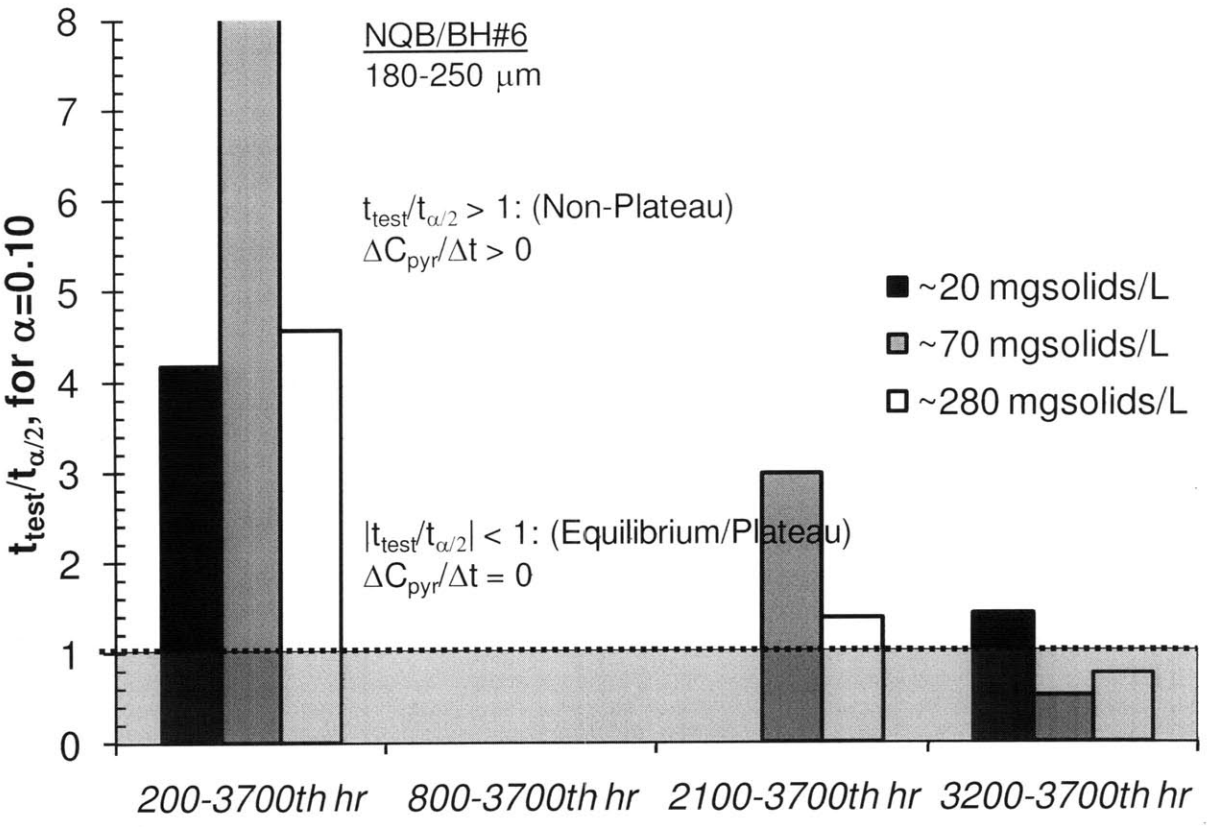

Figure 3 - 8. Test of pyrene desorption equilibrium for the NQB/BH#6 180-250 μm fraction at 3 different time-frames.

Dissolved pyrene concentrations observed within the specified time-frame were linearly regressed. T-test statistics (t_{test}) were computed from the regressed slope and its standard error. Shaded zone denotes cases where $\Delta C_{pyr}/\Delta t$ is statistically zero (i.e. the hypothesis $\Delta C_{pyr}/\Delta t=0$ is accepted). For cases with $|t_{test}/t_{\alpha/2}|>1$, $\Delta C_{pyr}/\Delta t$ is significantly different from zero. Note that observations were lacking to analyze the 800^{th}-3700^{th} hour time-frame.

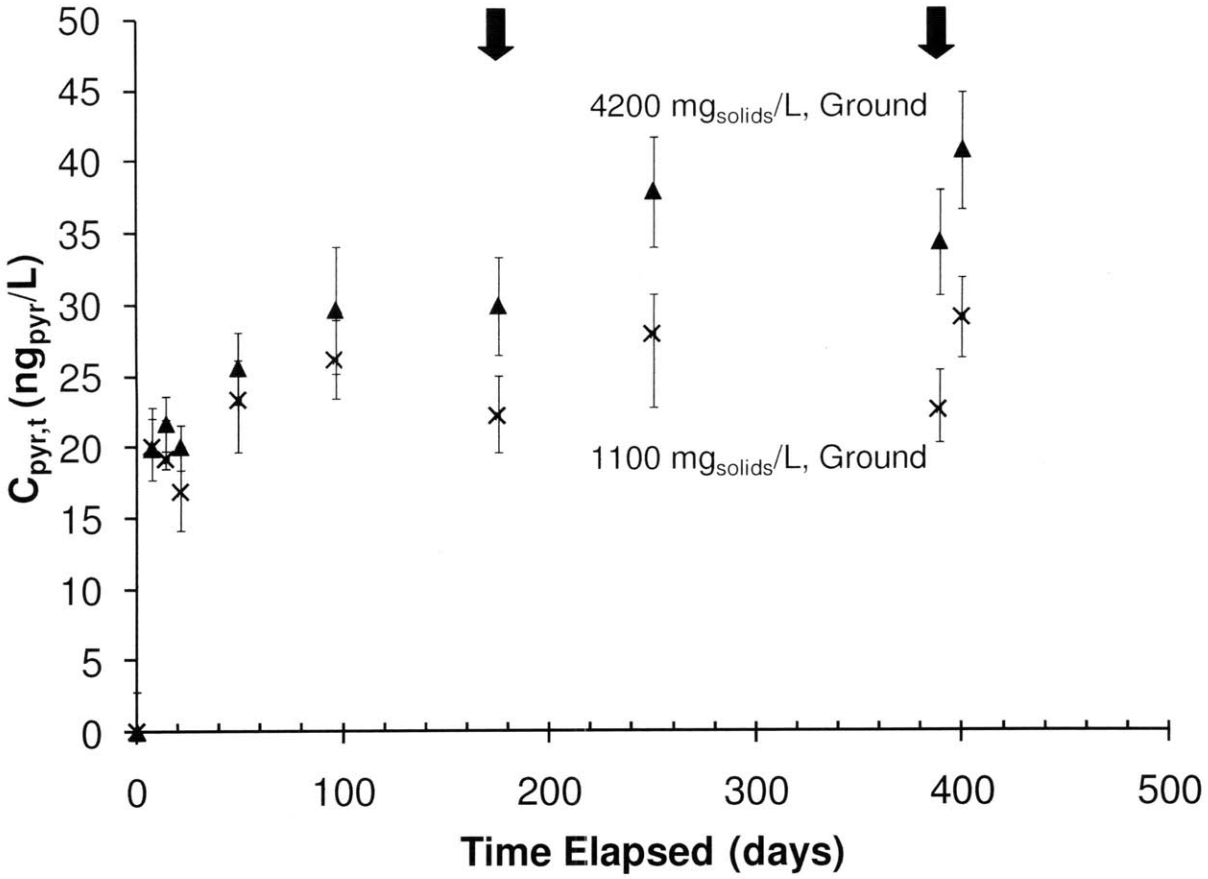

Figure 3 - 9. Pyrene equilibration time-course for Long-Term Desorption Equilibrium Experiment.

For clarity, only observations for two of the suspensions were shown. The dissolved pyrene time plots for the remaining suspensions can be found in Appendix 3-5. The error bars give uncertainty in ±1 standard deviation. Dark arrows highlight suspected observations taken when TG-LIF sensitivity was lower than usual.

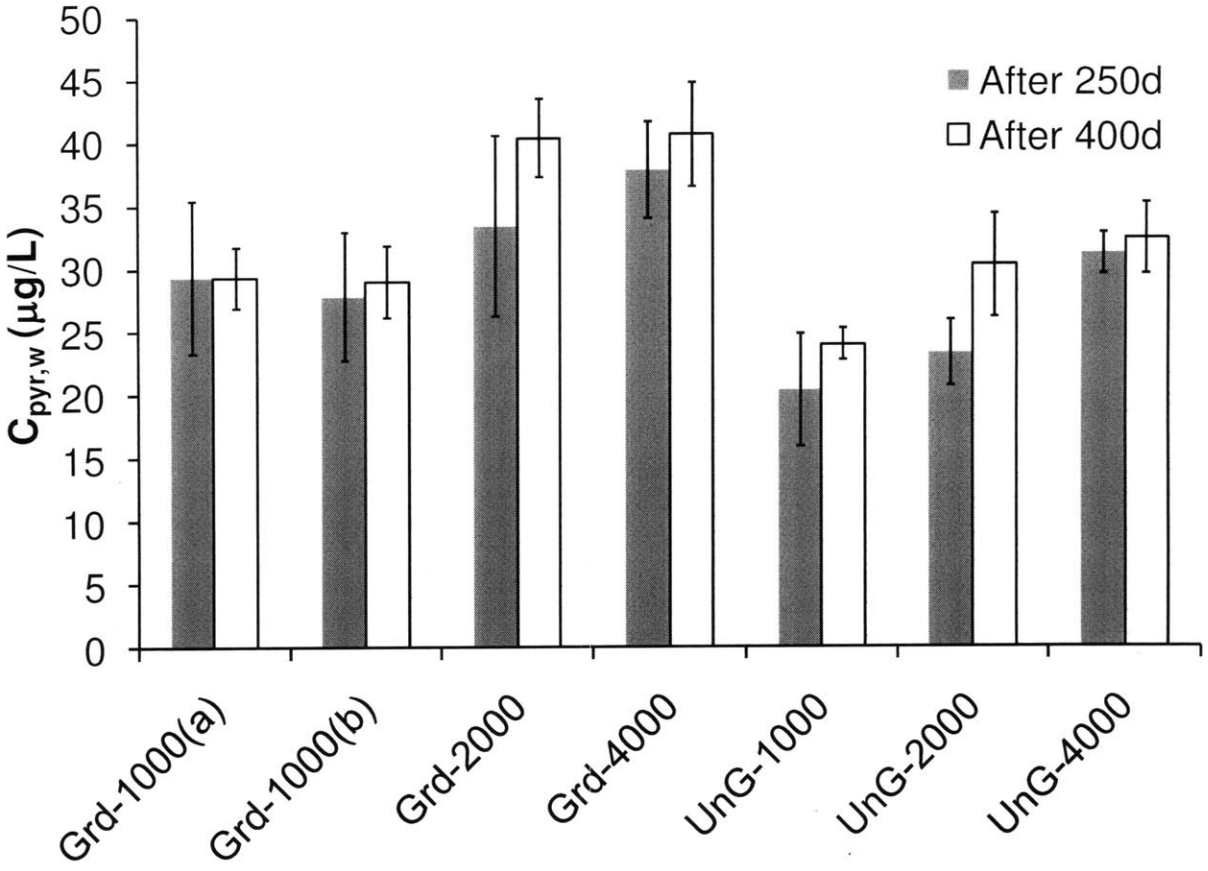

Figure 3 - 10. Verfication of equilibrium for the Long-Term Desorption Equilibrium Experiment.

The experiment consisted of 7 suspensions prepared from the NQB/BH#6 sediment (dia.: 38-75 µm size fraction). Dissolved pyrene measurements at 250d and 400d were not statistically different for both with and without grinding pre-treatment. 'Grd' and 'UnG' denoted suspensions with ground and unground sediments, and the following number refered to the approximate solid contents of the suspensions (mg_{solids}/L_{water}). Error bars denote $\pm 1\sigma$ of propagated uncertainties.

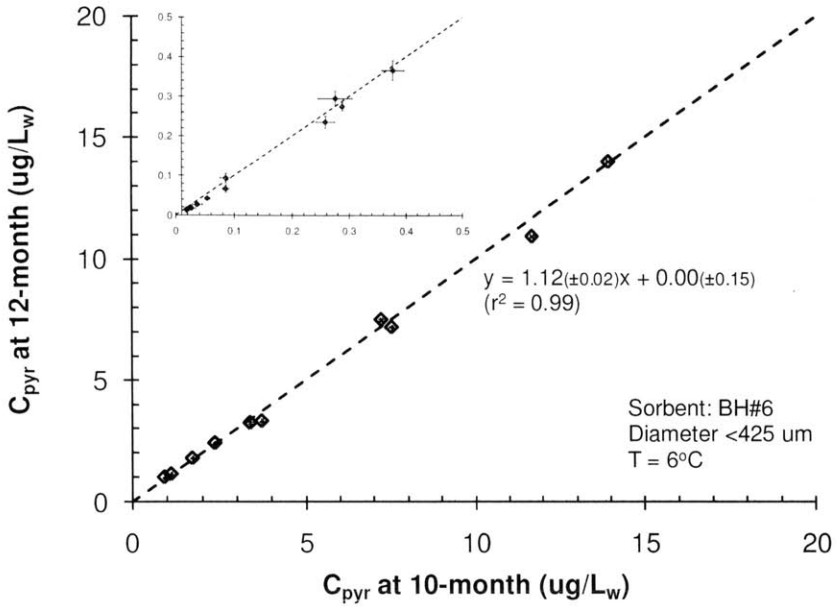
C_{pyr} at 12-month (ug/L_w)
C_{pyr} at 10-month (ug/L_w)
y = 1.12(±0.02)x + 0.00(±0.15)
(r^2 = 0.99)
Sorbent: BH#6
Diameter <425 um
T = 6°C

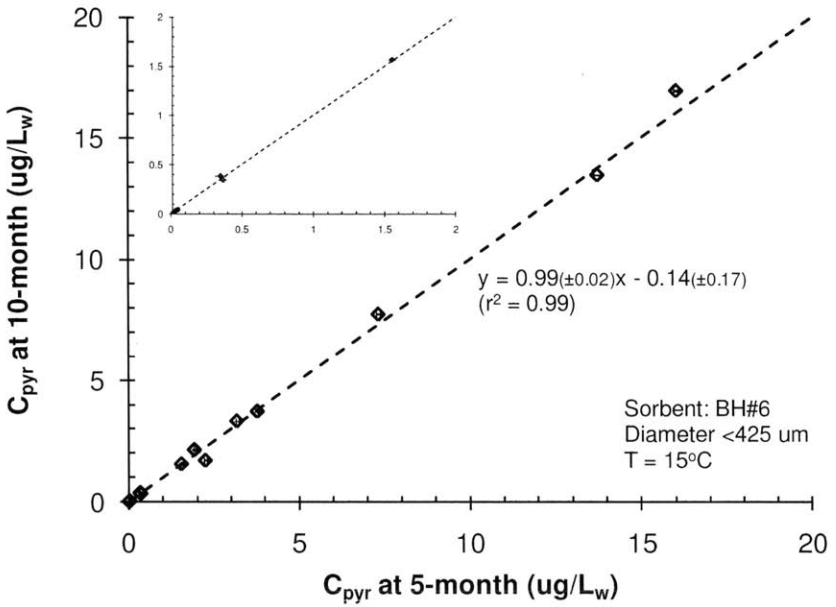
C_{pyr} at 10-month (ug/L_w)
C_{pyr} at 5-month (ug/L_w)
y = 0.99(±0.02)x - 0.14(±0.17)
(r^2 = 0.99)
Sorbent: BH#6
Diameter <425 um
T = 15°C

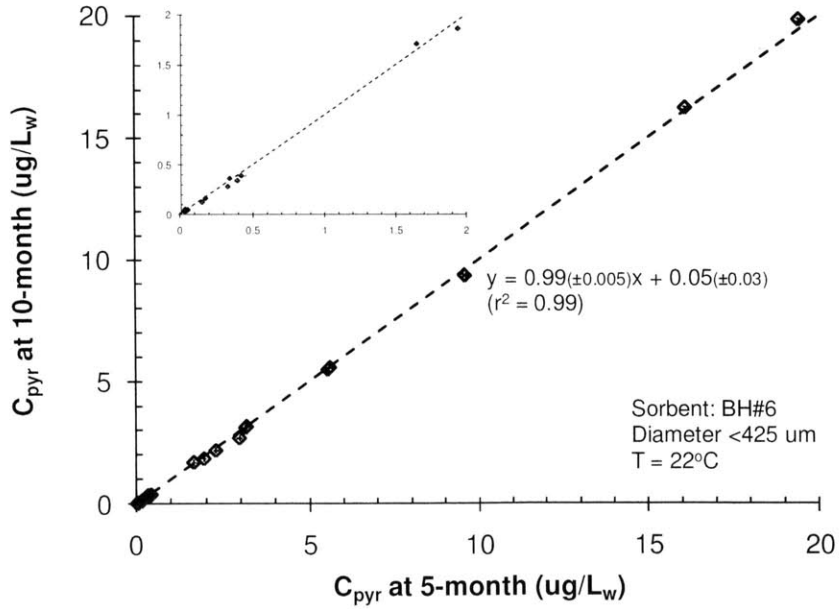
C_{pyr} at 10-month (ug/L_w)
C_{pyr} at 5-month (ug/L_w)
y = 0.99(±0.005)x + 0.05(±0.03)
(r^2 = 0.99)
Sorbent: BH#6
Diameter <425 um
T = 22°C

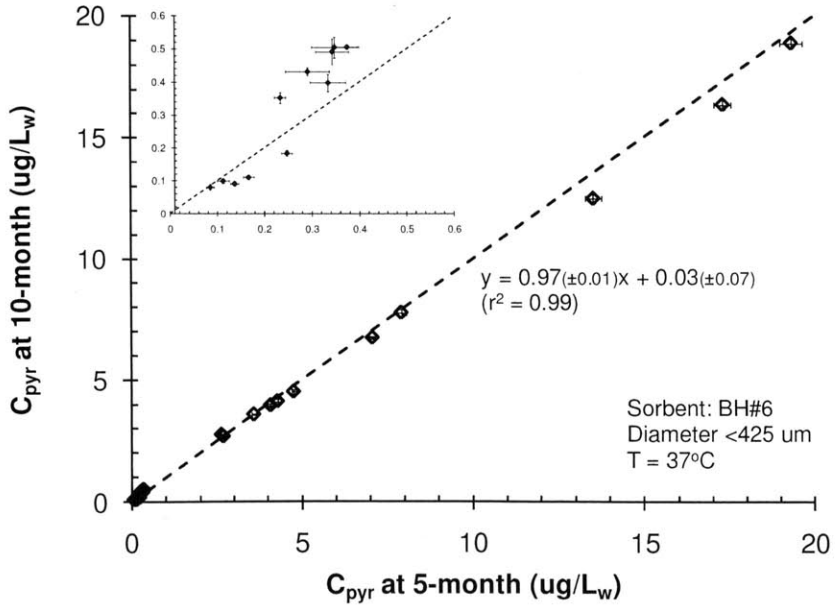
C_{pyr} at 10-month (ug/L_w)
C_{pyr} at 5-month (ug/L_w)
y = 0.97(±0.01)x + 0.03(±0.07)
(r^2 = 0.99)
Sorbent: BH#6
Diameter <425 um
T = 37°C

Figure 3 - 11. Correspondence plot (1-to-1 plot) of dissolved pyrene levels for Long Term Extended-Range Equilibrium Experiment at 6, 15, 22, and 37°C.

Suspensions prepared from BH#6/NQB sediment (dia.:<425 μm) and dissolved pyrene solution were allowed to equilibrate. Dissolved pyrene measured at two different times (5 months vs 10 or 12 months of equilibration) are plotted against each other. Insets show the correspondence between the earlier and the later measurements in the sub-μg/L range. Error bars denote ±1σ measurement uncertainties.

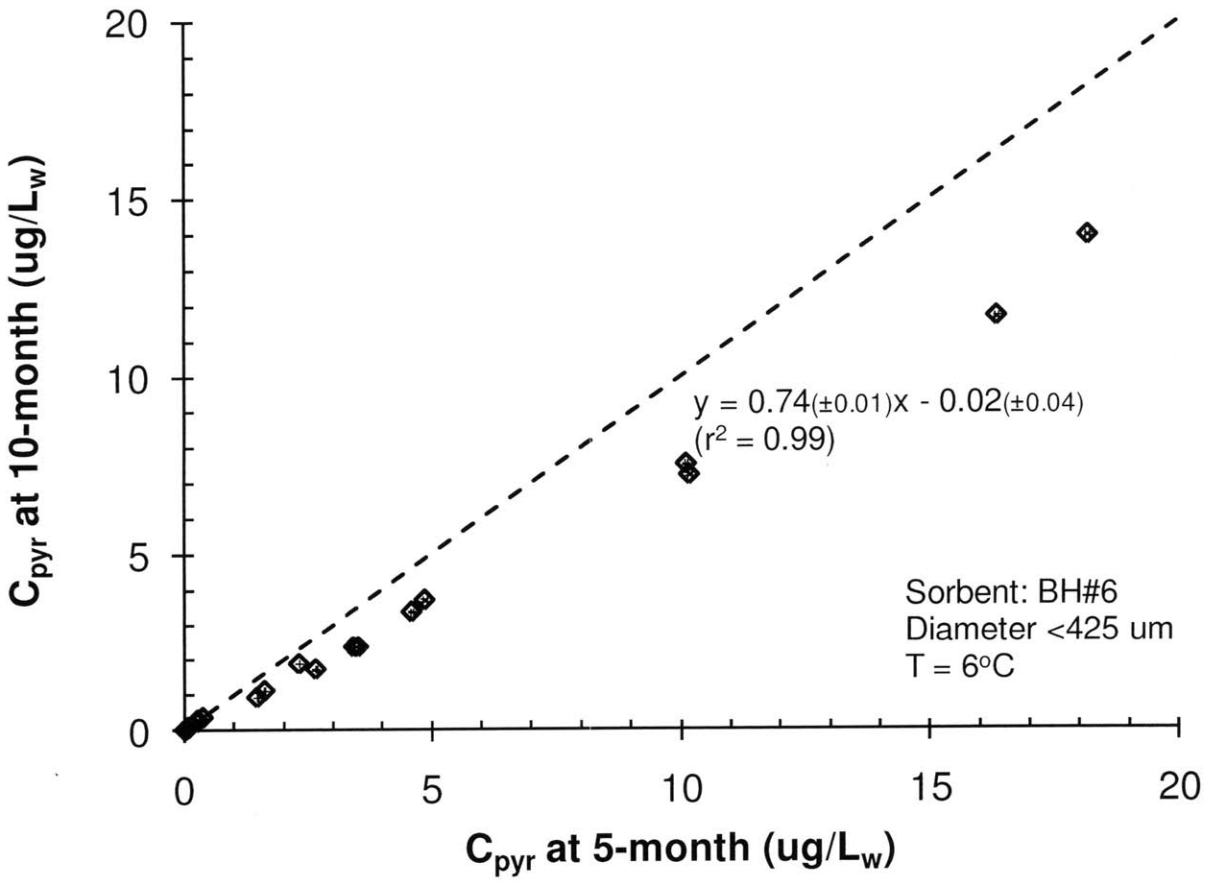

Figure 3 - 12. Dissolved pyrene levels after 5 and 10-month of equilibrium at 6°C (Long Term Extended-Range Equilibrium Experiment).

Suspensions contained BH#6/NQB sediment (dia.:<425 μm) and dissolved pyrene. Error bars denote ±1σ measurement uncertainties.

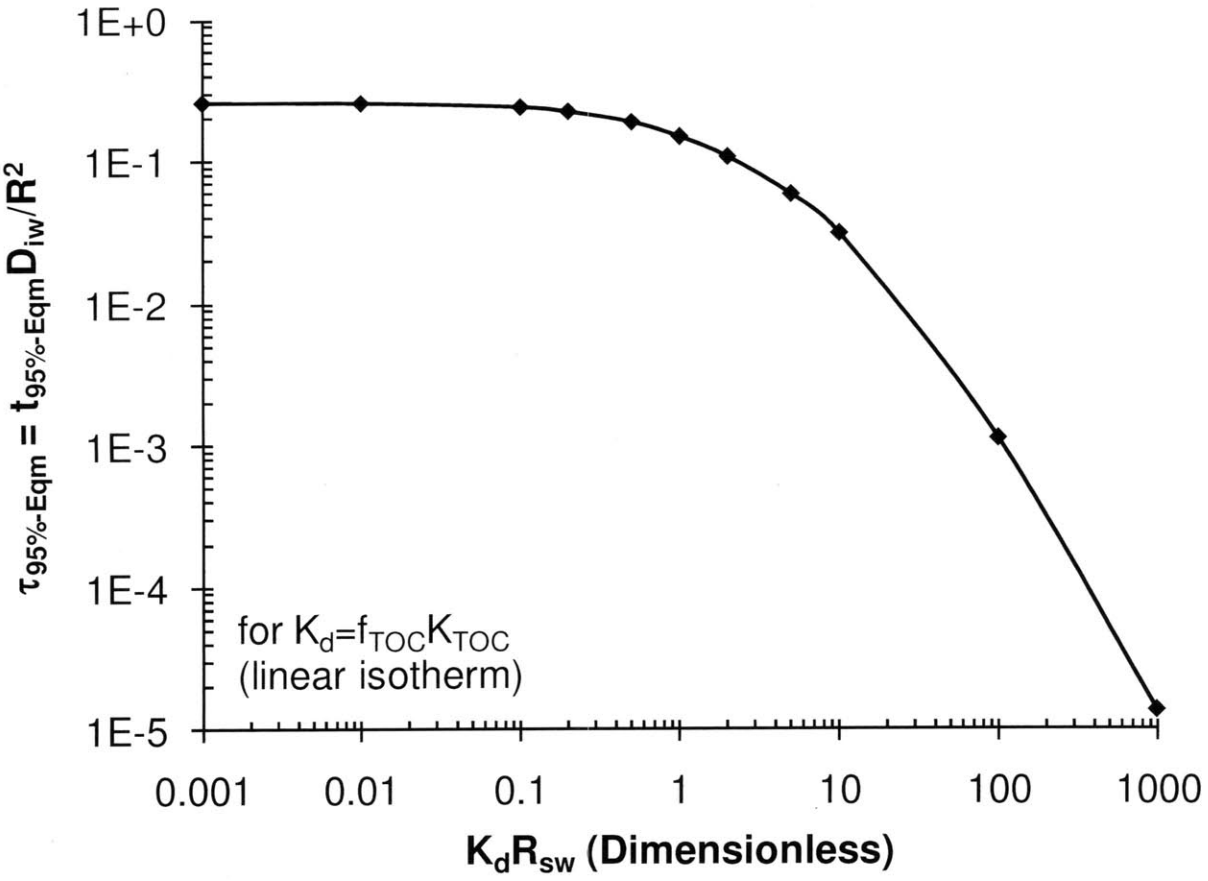

Figure 3 - 13. Equilibration time ($\tau_{95\%\text{-Eqm}}$) for adsorption/desorption with linear isotherm.

The curve was constructed from the analytical solution of adsorption kinetics in spherical coordinates (Crank 1979) at $\tau_{95\%\text{-Eqm}}$ such that $M_{\tau 95\%\text{-Eqm}}/M_{\infty} = 0.95$. Solid diamonds represent points where the analytical profiles have been plotted to obtain $\tau_{95\%\text{-Eqm}}$.

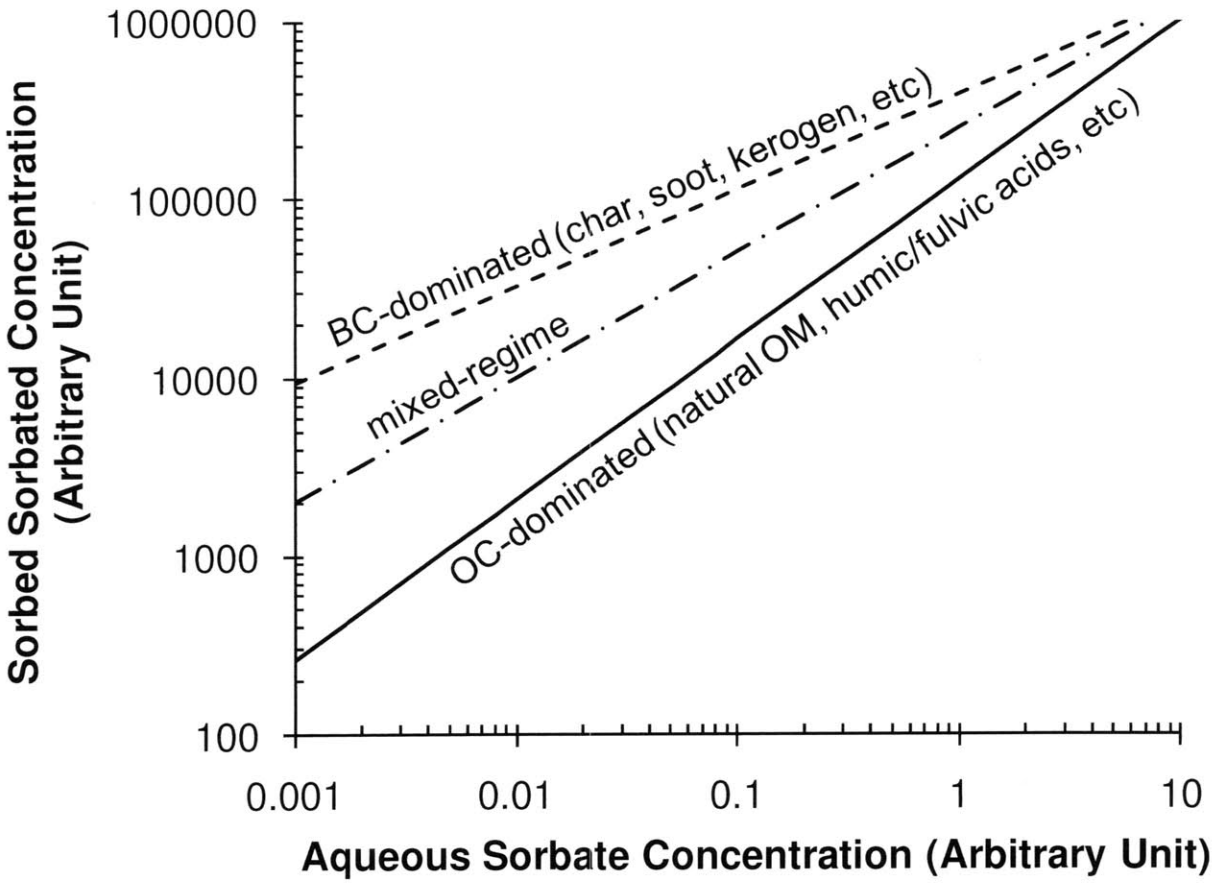

Figure 3 - 14. Generalized isotherms for different carbonaceous phases in a given geosorbent.

These are trends abstracted from the observations on phenanthrene sorption in soil/sediment-water systems by Cornelissen et al. (2004b), Pignatello et al. (2006), and Ran et al. (2007b).

Chapter 4: Figures

Figure 4 - 1. Effect of grinding on pyrene sorption (Long-Term Desorption Equilibrium Experiment)..... 343
Figure 4 - 2. $K_{d,pyr}$ (ng_{pyr}/L_w-range) from the two desorption experiments..... 345
Figure 4 - 3. Pyrene adsorption isotherm at 6, 15, 22, and 37°C..... 346
Figure 4 - 4. Regression of sorption data by Quadratic form and Freundlich form. ... 347
Figure 4 - 5. Residue plots for regressed vs observed LnQ_d (or LnK_d)..... 348
Figure 4 - 6. Comparing pyrene isotherm with a previous sorption study..... 349
Figure 4 - 7. Predictability of pyrene sorption capacity by OC-BC model..... 350
Figure 4 - 8. Pyrene sorption 'isotherms' constructed from coastal sediment cores.. 352
Figure 4 - 9. Hypothetical errors possible in pyrene sorption isotherm..... 353
Figure 4 - 10. Enhanced sorption affinity ($K_{d,pyr}$) as compared with OC-BC model and the classical linear-OC model..... 354
Figure 4 - 11. Physical occlusion by Thermally Induced Densification. 355
Figure 4 - 12. Physical occlusion by Encasement via Mineral Precipitation. 356
Figure 4 - 13. Estimates of fraction native pyrene inaccessible by visual inspection. 358
Figure 4 - 14. High-affinity sorption on mesopores and micropore surfaces..... 359
Figure 4 - 15. Theoretically expectations for the sediment-PE experiment..... 360
Figure 4 - 16. Pyrene extracted by polyethylene (PE) after 50 d of tumbling..... 361
Figure 4 - 17. Pyrene concentration in polyethylene (PE) after 50 d of tumbling..... 362
Figure 4 - 18. Equivalent $Q_{d,pyr}$ in PE-sediment suspensions after 50 d of tumbling.. 363
Figure 4 - 19. Coherence of PE-sediment experiment with Adsorption Experiment (K_d-C or S-C plots) 364
Figure 4 - 20. Equivalent R_{sw} vs PE content in the sediment-PE experiment..... 367

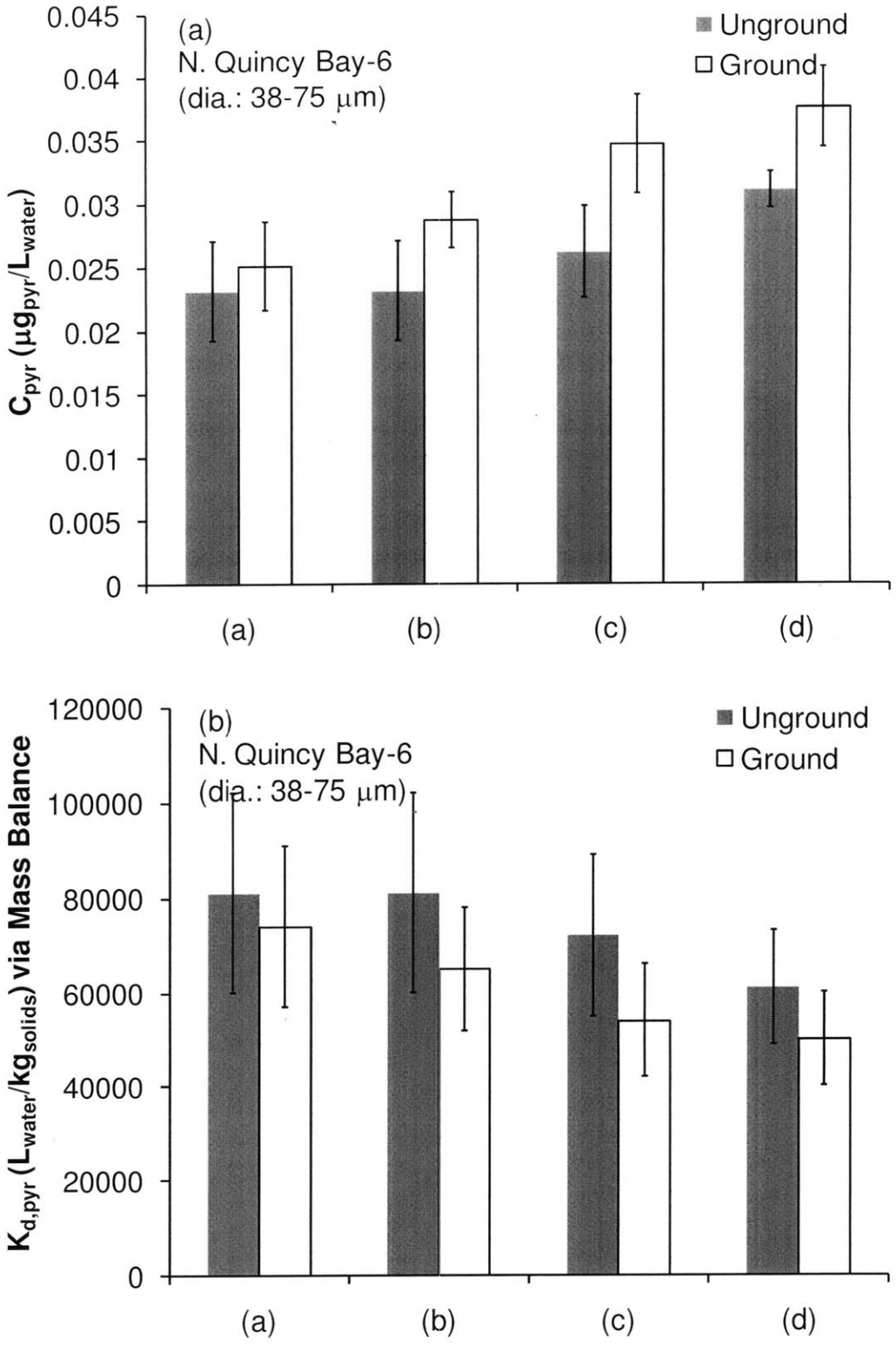
(a)
N. Quincy Bay-6
(dia.: 38-75 μm)
Unground
Ground
C_{pyr} ($\mu g_{pyr}/L_{water}$)
0.045
0.04
0.035
0.03
0.025
0.02
0.015
0.01
0.005
0
(a)
(b)
(c)
(d)
(b)
N. Quincy Bay-6
(dia.: 38-75 μm)
Unground
Ground
$K_{d,pyr}$ (L_{water}/kg_{solids}) via Mass Balance
120000
100000
80000
60000
40000
20000
0
(a)
(b)
(c)
(d)

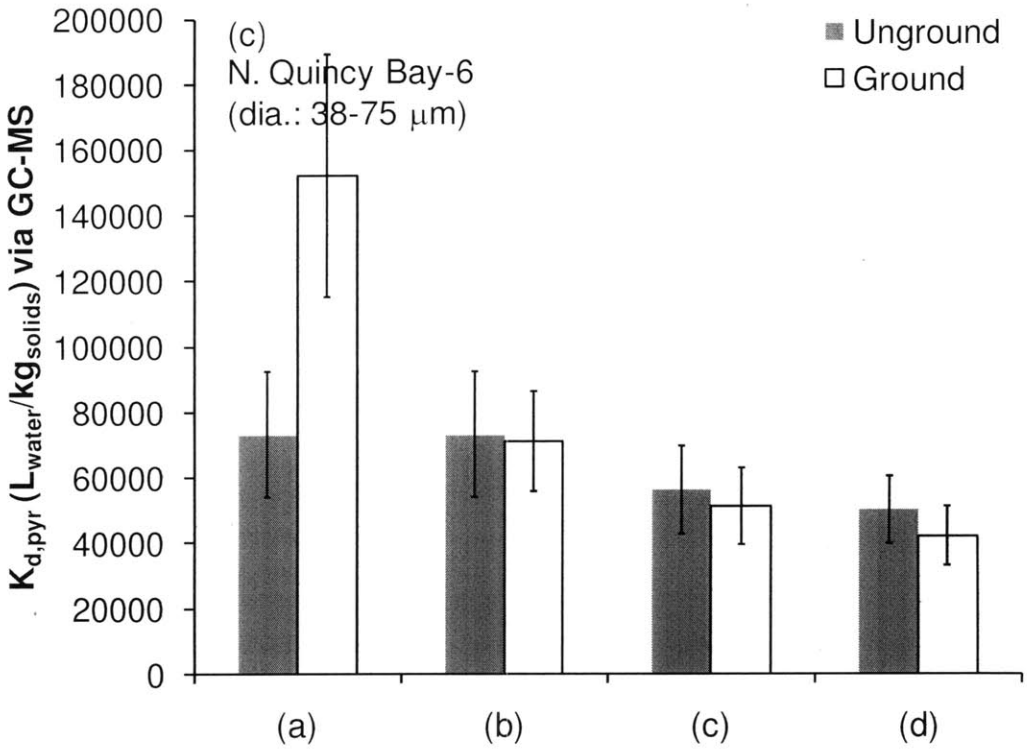

Figure 4 - 1. Effect of grinding on pyrene sorption (Long-Term Desorption Equilibrium Experiment).

(a) The dissolved pyrene concentrations of the untreated (dia. 38-75 μm) and the ground sediment (15-min wet-grinding) are compared at four cases after 400 d.

(b) Equilibrium distribution/partition coefficient of pyrene constructed from dissolved pyrene observations (after 400 d) at four comparable cases assuming that total mass of pyrene was conserved.

(c) Equilibrium distribution/partition coefficient of pyrene constructed from dissolved pyrene observations and sediment pyrene concentrations (measured by GC-MS) after 400 d at four comparable cases. The ground-a case was a likely outlier due to exceedingly high solid-phase pyrene concentration (i.e., error in extraction and/or GC-MS analysis).

The four cases (a-d) were batch suspensions with similar solids-to-water ratios at approximately 1000, 1000, 2000, and 4000 mg_{solids}/L, respectively, for cases a, b, c, and d. The exact values of C_{pyr}, $K_{d,pyr}$, and solids-to-water ratios for individual suspensions are summarized in Appendix 4-1. Error bar indicates ±1 σ of uncertainty.

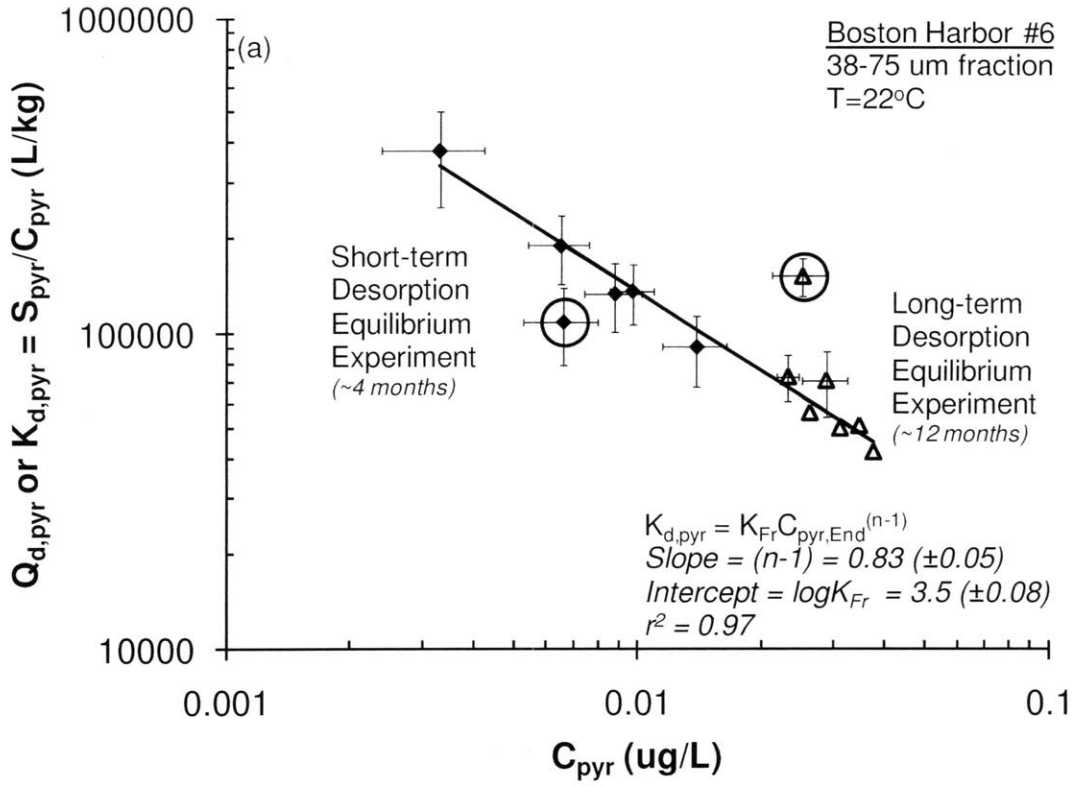
(a)
Boston Harbor #6
38-75 um fraction
T=22°C
Short-term
Desorption
Equilibrium
Experiment
(~4 months)
Long-term
Desorption
Equilibrium
Experiment
(~12 months)
$K_{d,pyr} = K_{Fr}C_{pyr,End}^{(n-1)}$
Slope = (n-1) = 0.83 (±0.05)
Intercept = $logK_{Fr}$ = 3.5 (±0.08)
r^2 = 0.97
1000000
100000
10000
0.001
0.01
0.1
$Q_{d,pyr}$ or $K_{d,pyr}$ = S_{pyr}/C_{pyr} (L/kg)
C_{pyr} (ug/L)

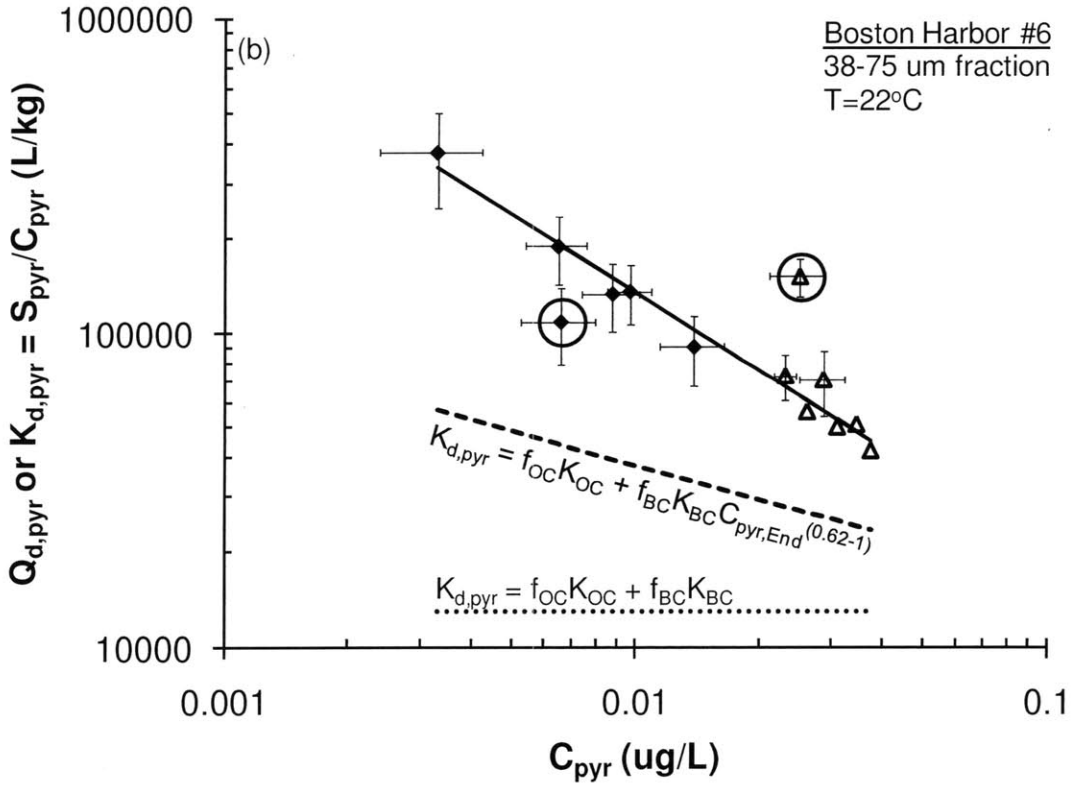
(b)
Boston Harbor #6
38-75 um fraction
T=22°C
$K_{d,pyr} = f_{OC}K_{OC} + f_{BC}K_{BC}C_{pyr,End}^{(0.62-1)}$
$K_{d,pyr} = f_{OC}K_{OC} + f_{BC}K_{BC}$
1000000
100000
10000
0.001
0.01
0.1
$Q_{d,pyr}$ or $K_{d,pyr}$ = S_{pyr}/C_{pyr} (L/kg)
C_{pyr} (ug/L)

Figure 4 - 2. $K_{d,pyr}$ (ng_{pyr}/L_w-range) from the two desorption experiments.

Figure 4-2 (a) shows that the $K_{d,pyr}$'s derived from the Short-Term (solid diamonds) and Long-Term (open triangles) Desorption observations form a consistent/unified trend with respect to dissolved phase concentration (C_{pyr}). The solid line shows the regression by a simple Freundlich form. The circled data points are possible outliers excluded from the regression analysis. Error bars denote $\pm 1\sigma$ of propagated uncertainties. Note that the data were obtained from suspensions prepared using the NQB#6 38–75 μm size fraction (Table 4-1).

Figure 4-2 (b) compares the $K_{d,pyr}$'s observed in this study with the expected K_d's estimated from two different OC-BC isotherms according to (i) Bucheli et al. (2000) (dotted line) and (ii) Accardi-Dey and Gschwend (2002) (dashed line). The expected K_d based on the Classical OC-only model was around 2000 L_w/kg_{solids} (off scale in the plot).

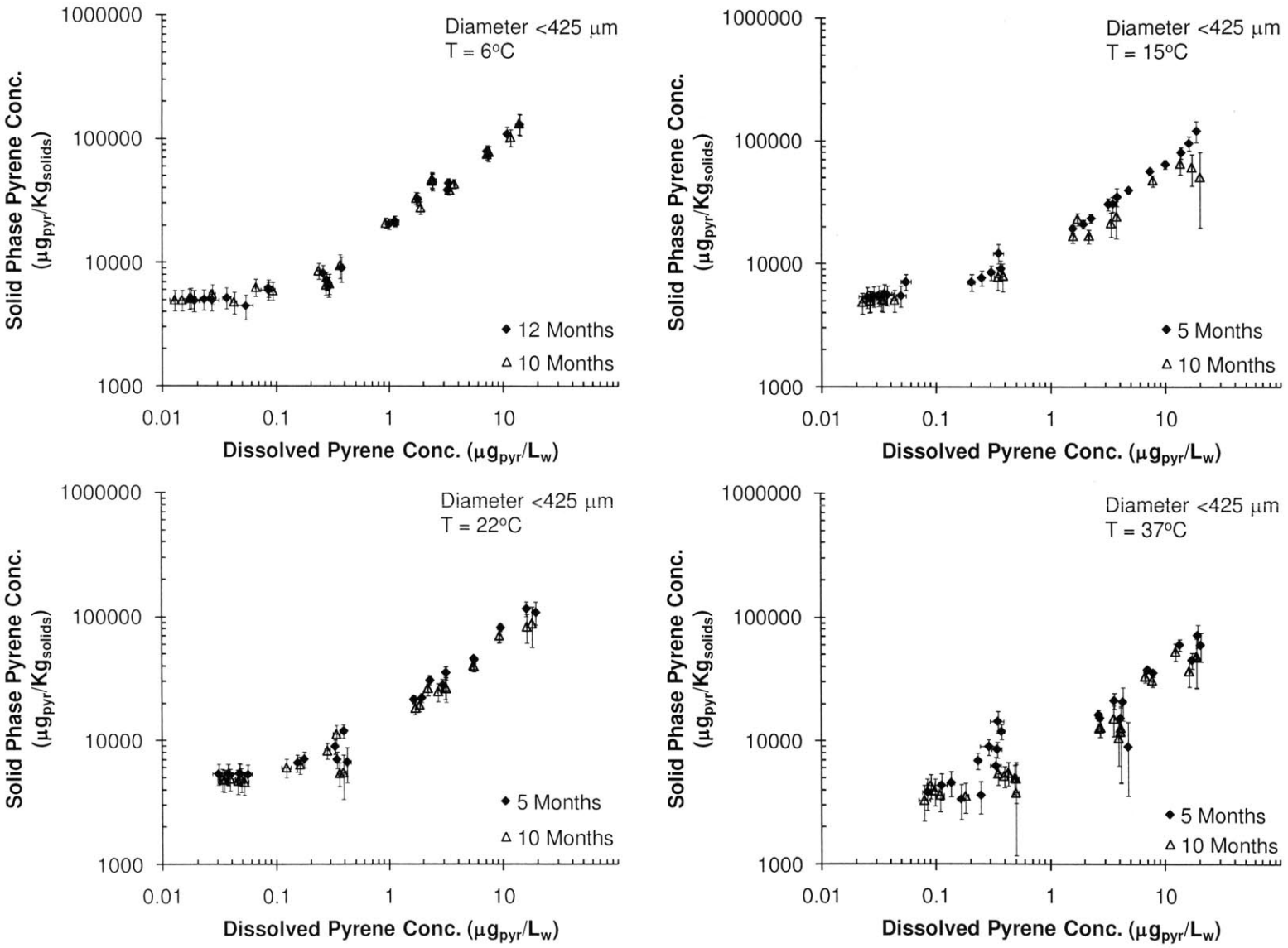

Figure 4 - 3. Pyrene adsorption isotherm at 6, 15, 22, and 37°C.

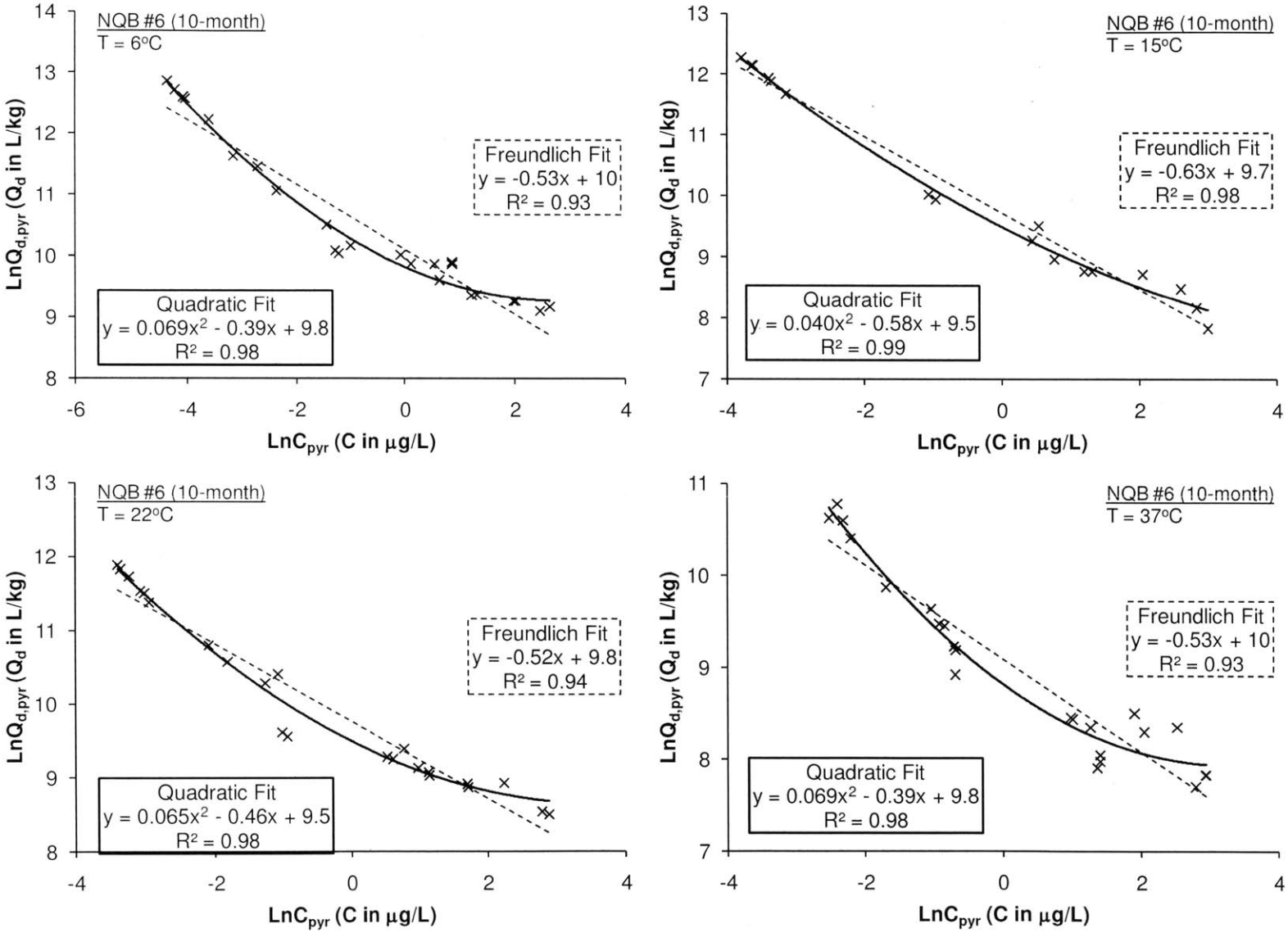

Figure 4 - 4. Regression of sorption data by Quadratic form and Freundlich form.

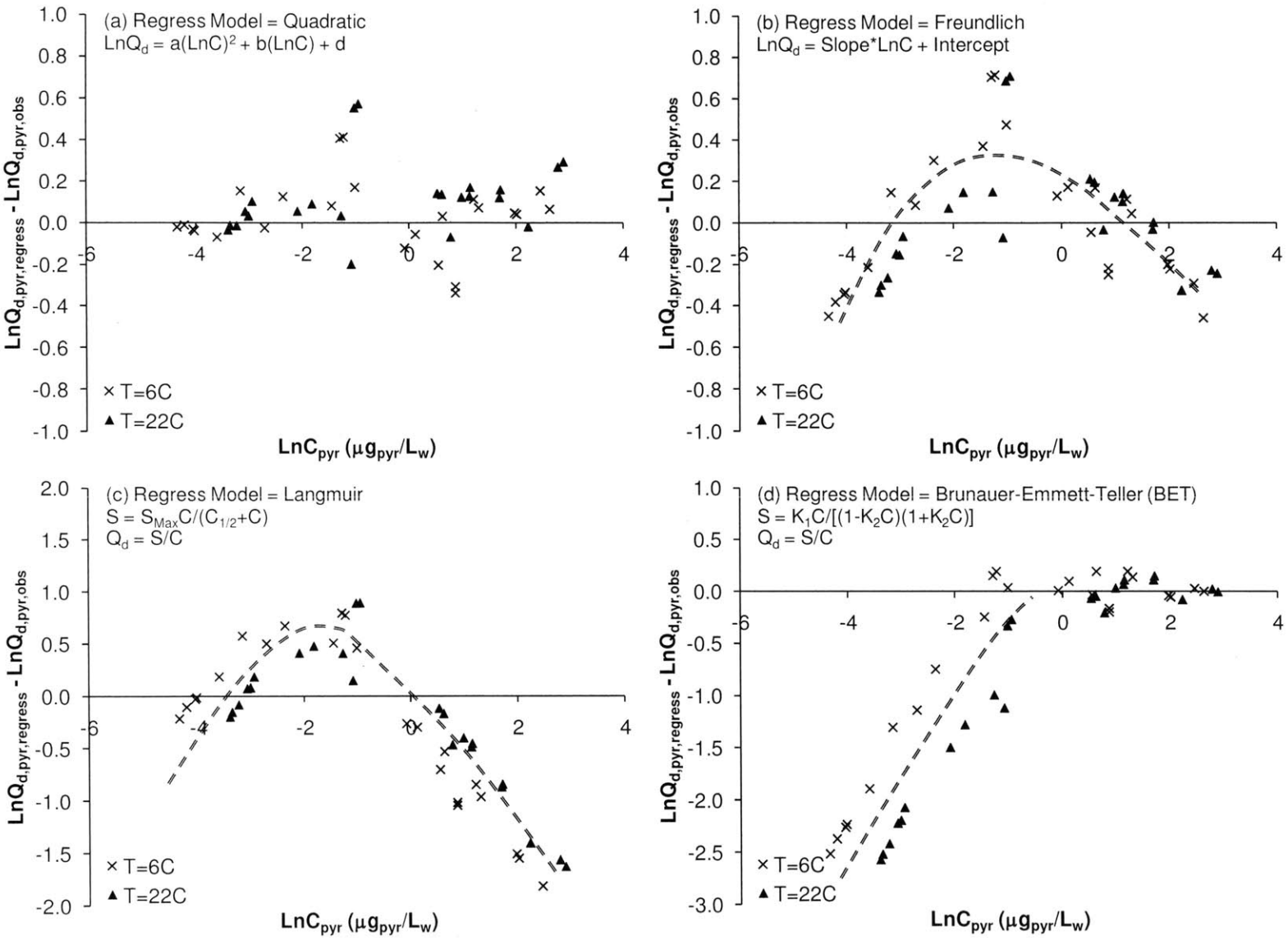

Figure 4 - 5. Residue plots for regressed vs observed LnQ_d (or LnK_d).

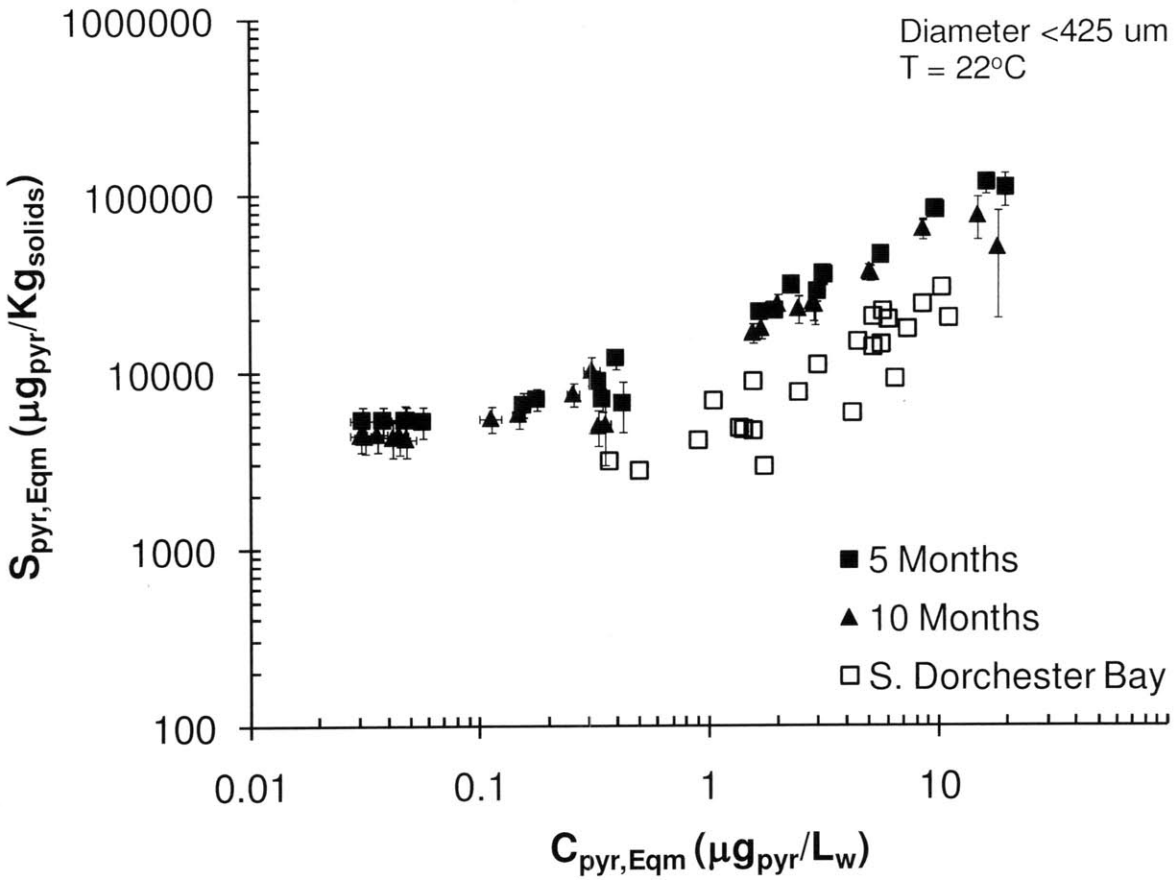

Figure 4 - 6. Comparing pyrene isotherm with a previous sorption study.

Adsorption equilibrium observations from this study (solid symbols; NQB site #6, dia.<425 μm) yielded coherent isotherm shape, slope, and parameters in the higher concentration range ($C_{pyr,Eqm}$ ~ 0.5-20 μg/L) with that reported by an earlier equilibrium study (Accardi-Dey and Gschwend 2002) on a different Boston Harbor sediment (open squares; SDB, dia.<425 μm).

The slopes (n_{Fr}) were 0.68±0.03|0.62±0.05 (5-month|10-month) and 0.68±0.08 for NQB#6 and SDB-derived isotherms, respectively. The total organic carbon normalized $\log K_{Fr,TOC}$'s [=$\log(K_{Fr}/f_{TOC})$] were 5.65±0.05|5.59±0.06 (5-month|10-month) and 5.49±0.05 for NQB#6 and SDB-derived isotherms, respectively.

The error bars give uncertainty in ±1 standard deviation.

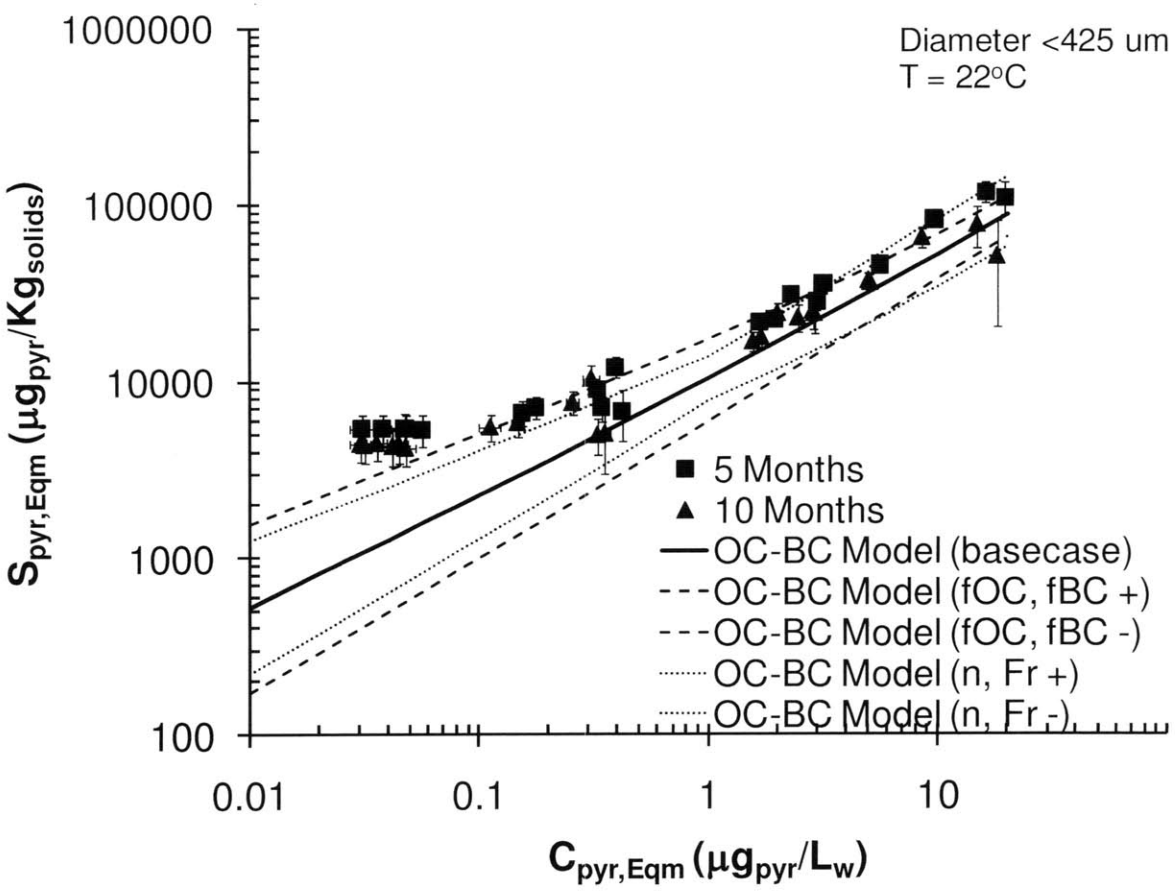

Figure 4 - 7. Predictability of pyrene sorption capacity by OC-BC model.

Predictability of pyrene sorption isotherm determined in this study by the OC-BC model developed previously (Accardi-Dey and Gschwend 2002) ($S = f_{OC}K_{OC}C + f_{BC}K_{BC}C^n$; $K_{OC} = 10^{4.7}$, $K_{BC} = 10^{6.25}$, $n = 0.62$).

The thick, solid line represented the basecase prediction ($f_{OC} = 0.0296$, $f_{BC} = 0.0049$). The dashed lines represented the sensitivity of the model prediction subjected to a 25% co-varying uncertainty in both f_{OC} and f_{BC} (dashed line) around the basecase values. The dotted lines represented a co-varying uncertainty of 1σ in both n_{BC} (± 0.12) and $\log K_{BC}$ (± 0.15).

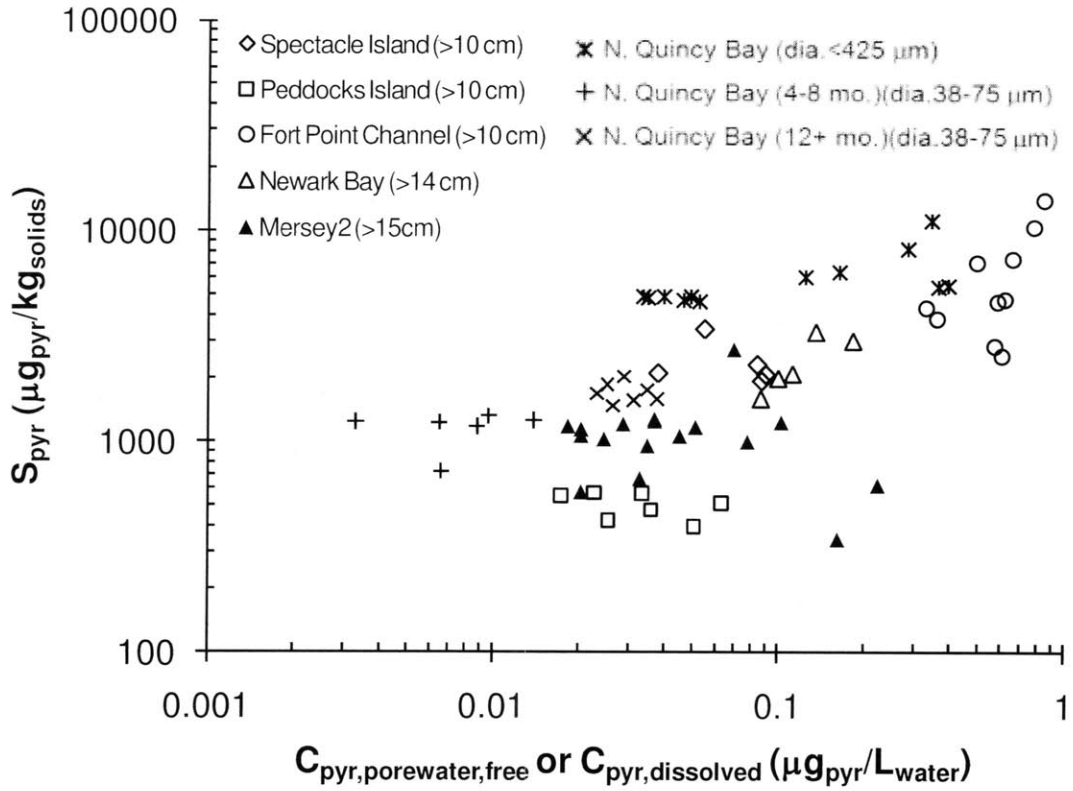
100000
10000
1000
100
0.001
0.01
0.1
1
◇ Spectacle Island (>10 cm)
□ Peddocks Island (>10 cm)
○ Fort Point Channel (>10 cm)
△ Newark Bay (>14 cm)
▲ Mersey2 (>15cm)
✱ N. Quincy Bay (dia.<425 μm)
+ N. Quincy Bay (4-8 mo.)(dia.38-75 μm)
× N. Quincy Bay (12+ mo.)(dia.38-75 μm)
S_{pyr} ($\mu g_{pyr}/kg_{solids}$)
$C_{pyr,porewater,free}$ or $C_{pyr,dissolved}$ ($\mu g_{pyr}/L_{water}$)

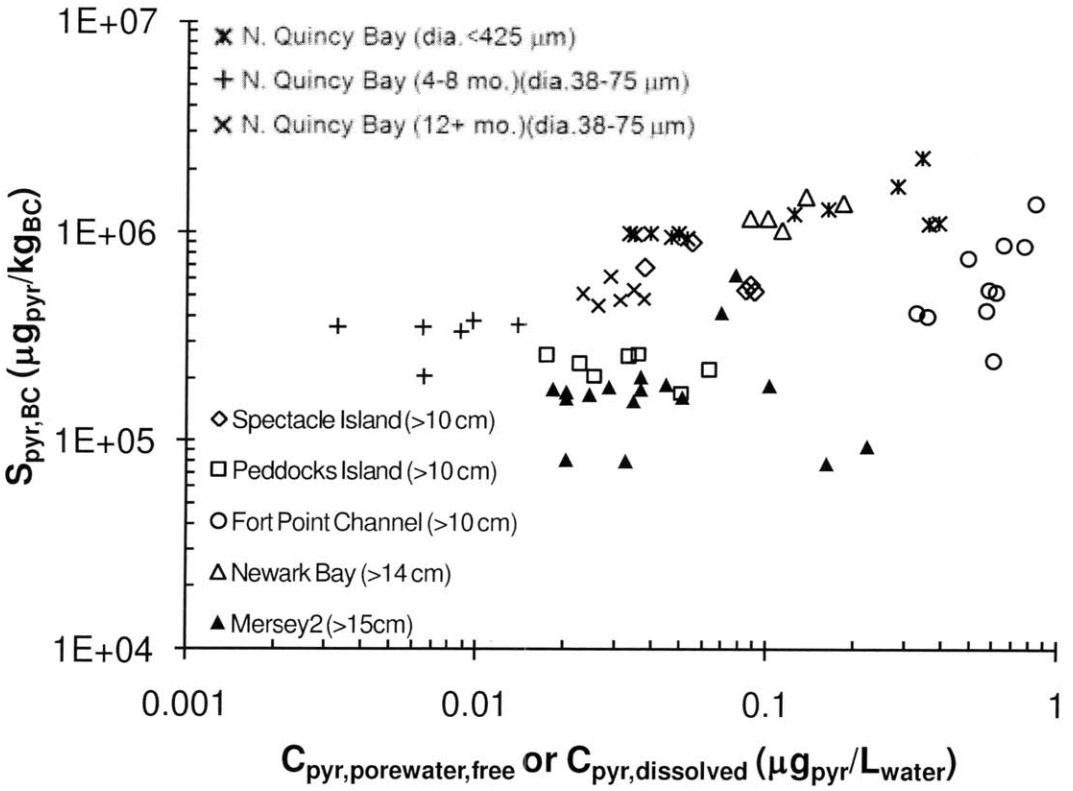
1E+07
1E+06
1E+05
1E+04
0.001
0.01
0.1
1
✱ N. Quincy Bay (dia.<425 μm)
+ N. Quincy Bay (4-8 mo.)(dia.38-75 μm)
× N. Quincy Bay (12+ mo.)(dia.38-75 μm)
◇ Spectacle Island (>10 cm)
□ Peddocks Island (>10 cm)
○ Fort Point Channel (>10 cm)
△ Newark Bay (>14 cm)
▲ Mersey2 (>15cm)
$S_{pyr,BC}$ ($\mu g_{pyr}/kg_{BC}$)
$C_{pyr,porewater,free}$ or $C_{pyr,dissolved}$ ($\mu g_{pyr}/L_{water}$)

Figure 4 - 8. Pyrene sorption 'isotherms' constructed from coastal sediment cores.

Observed solid-phase and porewater free pyrene concentrations (colloids-excluded) from studies on deep-sediment cores.

The Spectacle Island, Fort Point Channel, and Peddocks Island measurements were taken from McGroddy 1993, with BC content determined in Accardi-Dey and Gschwend 2003. The Newark Bay measurements were extracted from the figures in Mitra et al. 1999, and further assuming that BC to be ~10% of total organic carbons. The Mersey Estuary core measurements were extracted from figures in King et al. 2007. Uncertainties in measurements were either unavailable and/or omitted for clarity.

The data from this study are also plotted: (i) from the Long-Term Adsorption Equilibrium Experiment (*), (ii) from the Short-Term Desorption Experiment (+), and (iii) from the Long-Term Desorption Equilibrium Experiment (×). Conditions and details of these experiments can be found in Table 4-1.

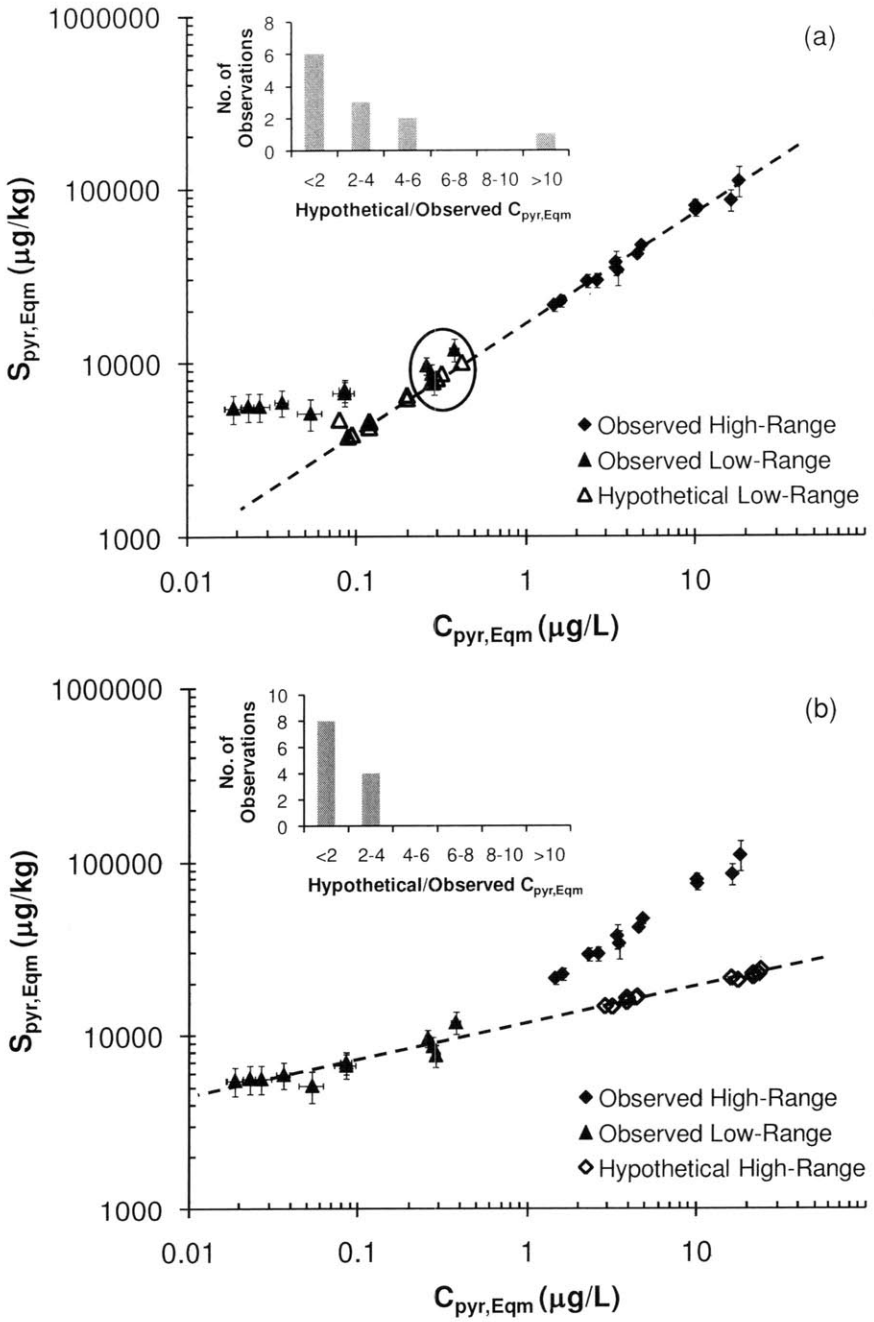

Figure 4 - 9. Hypothetical errors possible in pyrene sorption isotherm.

Hypothetical errors associated with (a) the low concentration range (<1 μg_{pyr}/L) and (b) the high concentration range (>1 μg_{pyr}/L) supposing the 'true' isotherm should assume a singular Freundlich model. Actual observations are represented by solid symbols. Open symbols are data points hypothetically adjusted and forced to conform to a singular Freundlich relationship. Inset shows the number of adjusted observations with the hypothetical/observed C_{pyr} ratio within different ranges. Error bars denote $\pm 1\sigma$ of measurement uncertainties.

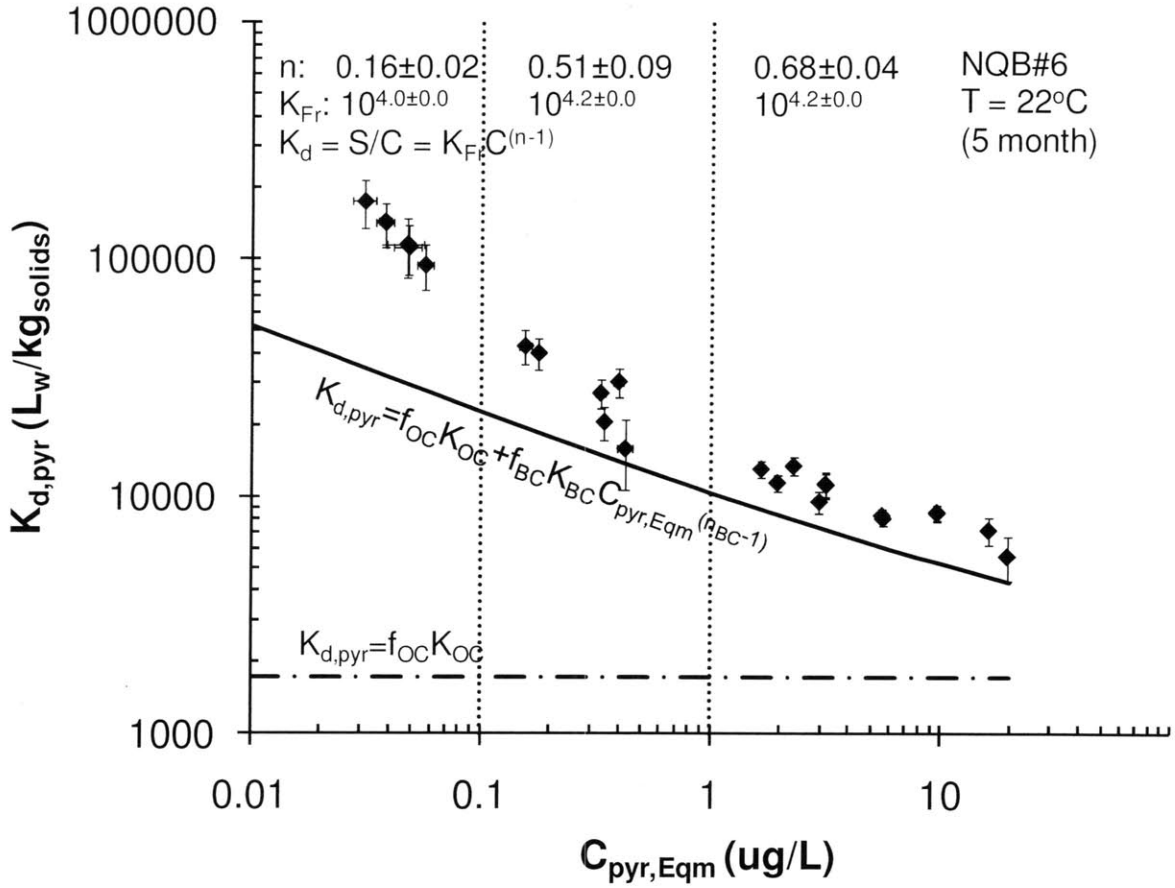

Figure 4 - 10. Enhanced sorption affinity ($K_{d,pyr}$) as compared with OC-BC model and the classical linear-OC model.

Experimental data (diamonds) from the Long-Term Adsorption Equilibrium Experiment showed that partitioning of pyrene to the solid-phase was enhanced at concentrations <1 ug_{pyr}/L when compared to the OC-BC model (solid line) or the classical OC model (dot-dashed line).

The two vertical dotted lines designated the boundaries of arbitrarily defined isotherm sub-regions. With each sub-region, phase distribution data were regressed by a simple Freundlich form. The regressed parameters for each sub-region are listed at the top of the figure.

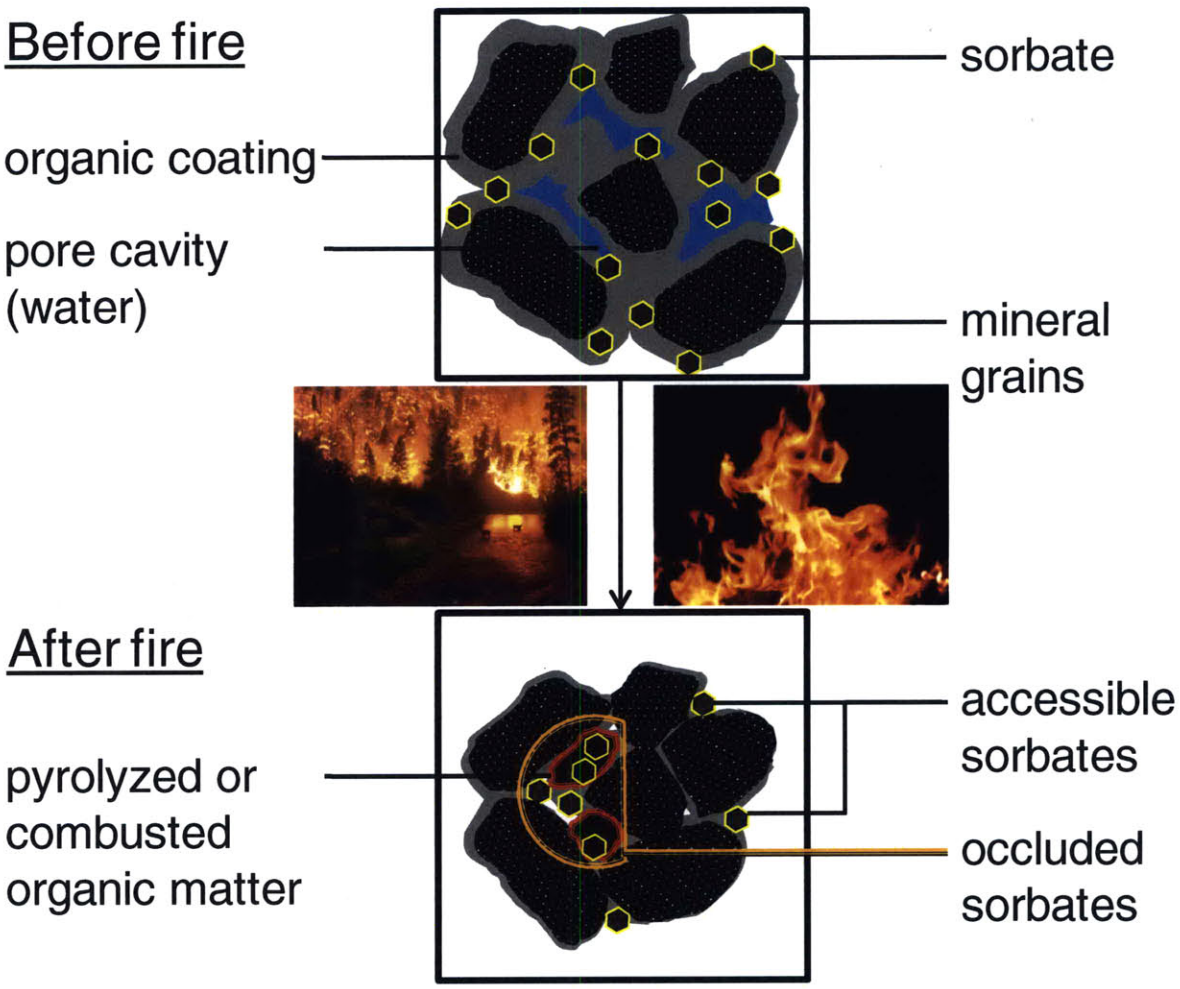

Figure 4 - 11. Physical occlusion by Thermally Induced Densification.

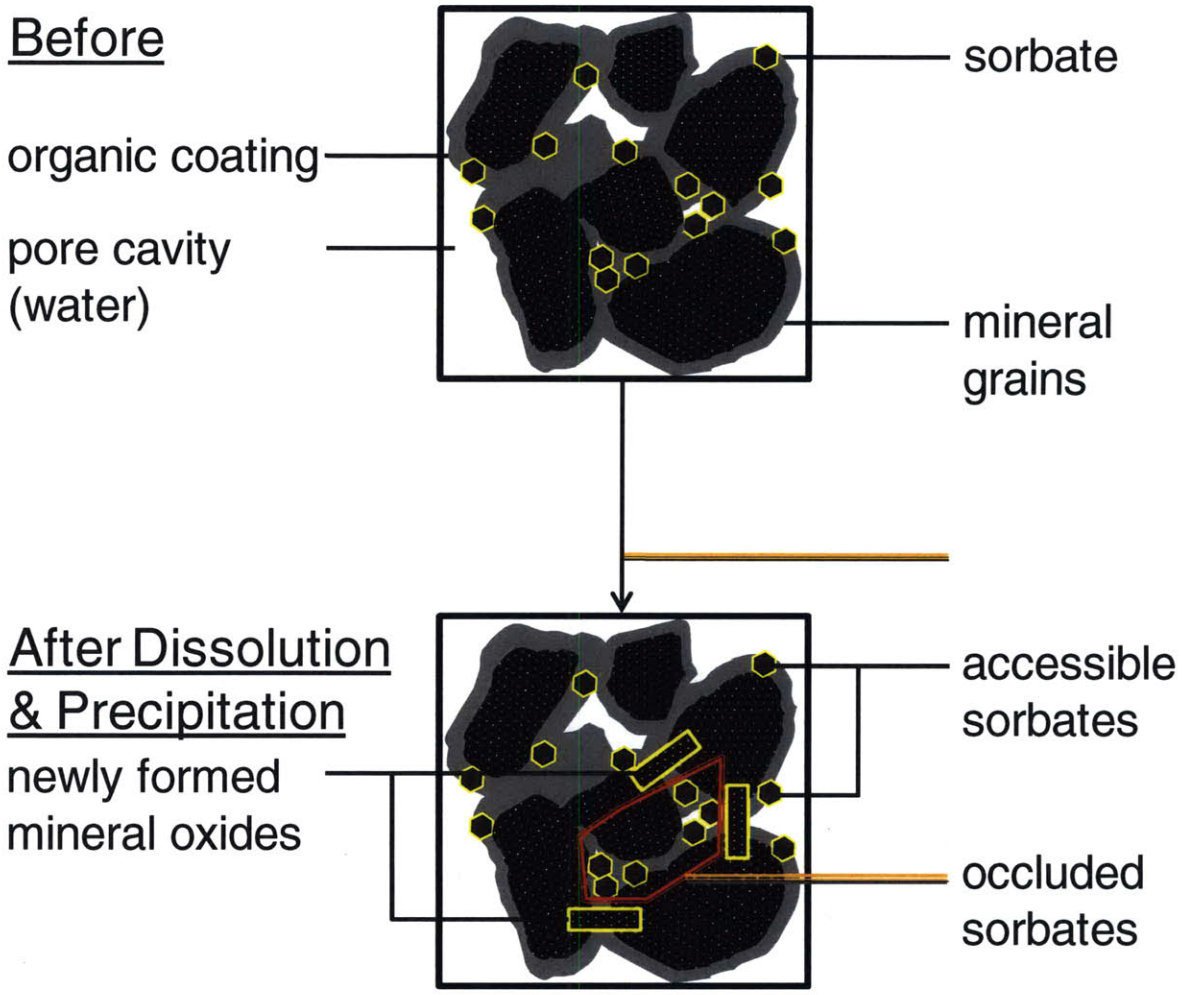

Figure 4 - 12. Physical occlusion by Encasement via Mineral Precipitation.

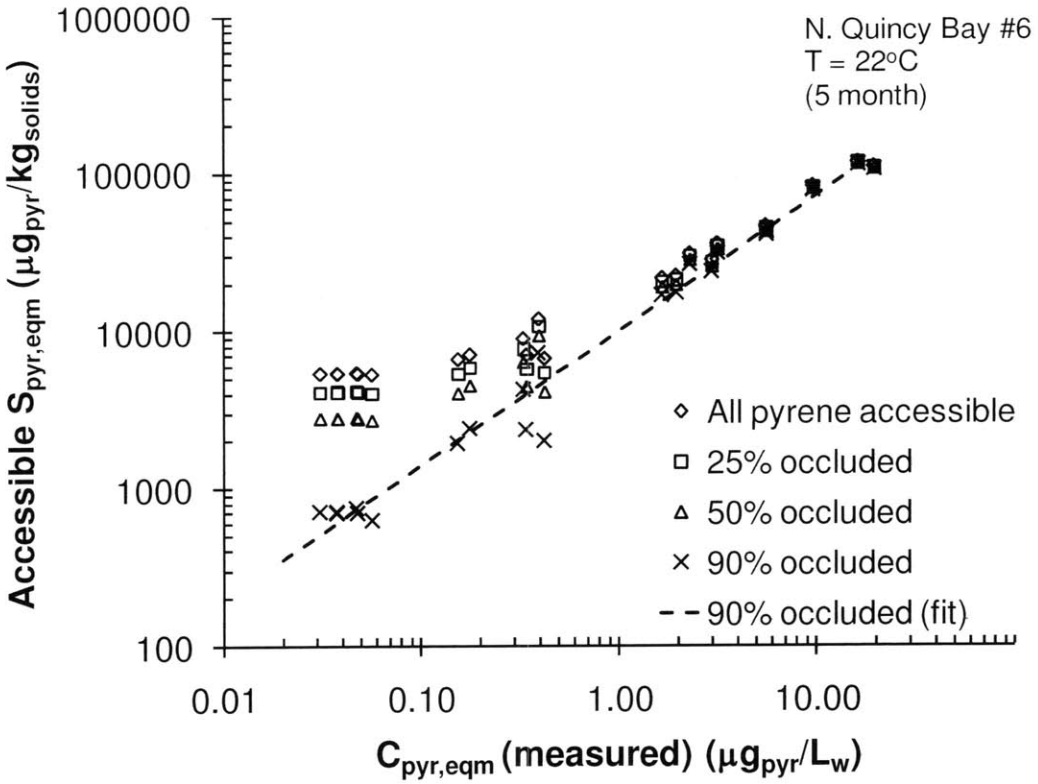
N. Quincy Bay #6
T = 22°C
(5 month)
All pyrene accessible
25% occluded
50% occluded
90% occluded
90% occluded (fit)
Accessible $S_{pyr,eqm}$ ($\mu g_{pyr}/kg_{solids}$)
$C_{pyr,eqm}$ (measured) ($\mu g_{pyr}/L_w$)
1000000
100000
10000
1000
100
0.01
0.10
1.00
10.00

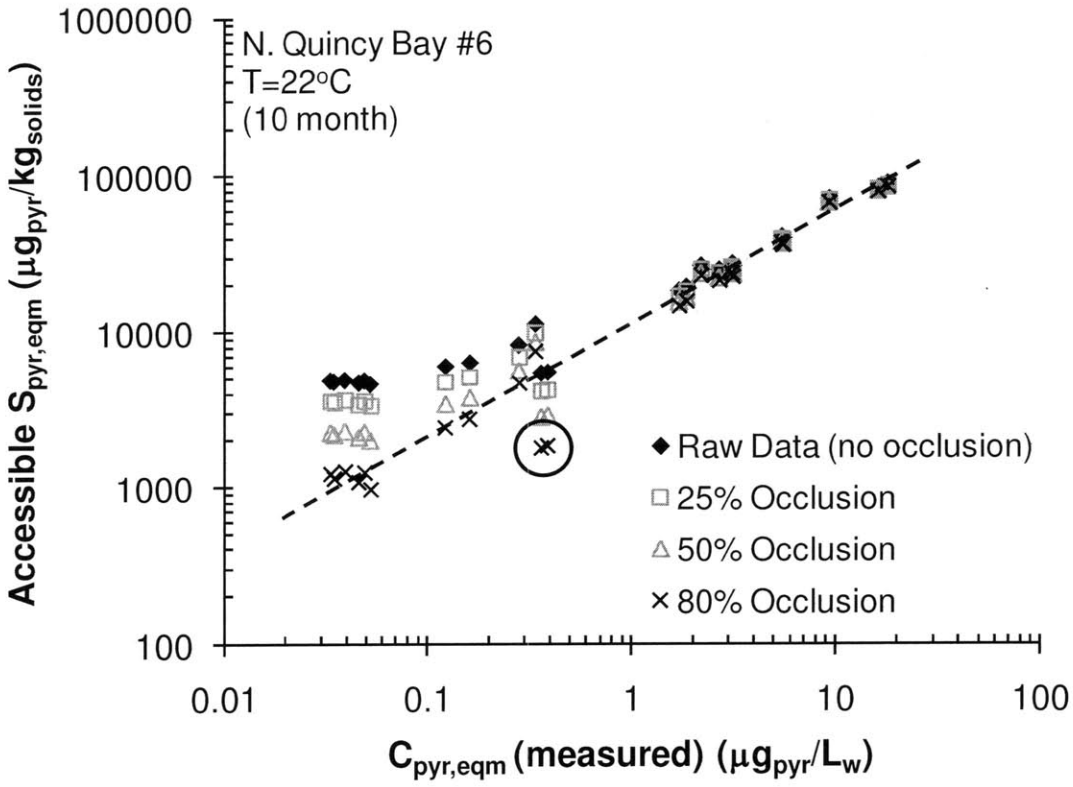
N. Quincy Bay #6
T=22°C
(10 month)
Raw Data (no occlusion)
25% Occlusion
50% Occlusion
80% Occlusion
Accessible $S_{pyr,eqm}$ ($\mu g_{pyr}/kg_{solids}$)
$C_{pyr,eqm}$ (measured) ($\mu g_{pyr}/L_w$)
1000000
100000
10000
1000
100
0.01
0.1
1
10
100

Figure 4 - 13. Estimates of fraction native pyrene inaccessible by visual inspection.

The figures show the partitioning of accessible pyrene in sediment-water system assuming varying degrees of physical occlusion.

A portion (25%-90%) of the native sedimentary pyrene ($S_{pyr,o}$~5200 $\mu g_{pyr}/kg_{solids}$) is assumed to be physically occluded. The fraction occluded pyrene is deducted from the total sedimentary pyrene to give the accessible solid-phase pyrene. The extent of occlusion produced little effect on the high $C_{pyr,eqm}$ range due to the overwhelming abundance of added/amended pyrene.

A satisfactory estimate is visually determined when the data assume a linear shape in the log-S vs log-C space (i.e. the dashed lines). Note that this estimation method assumes that a 'correct' isotherm must conform to a simple Freundlich form.

The circled points in the 10-month plot are not considered in the inspection for occluded fraction. Uncertainties have been omitted for visual clarity.

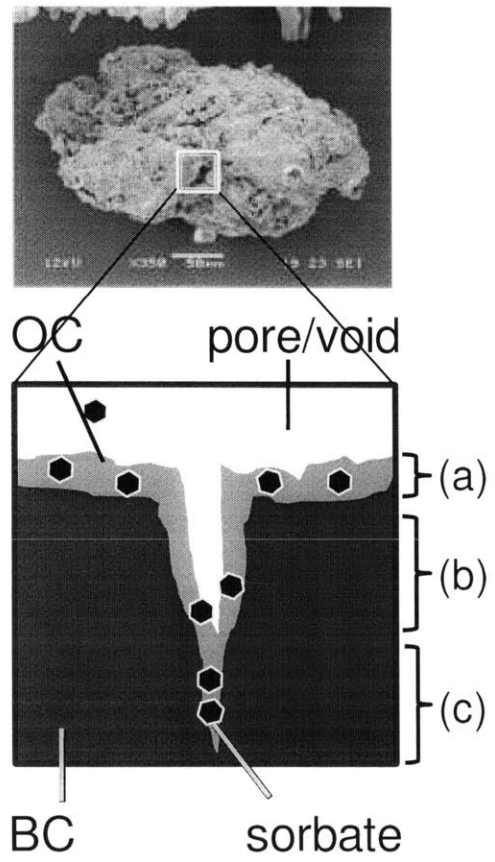

Adsorption Configuration	Description
(a)	**Macropore Adsorption** (dia.: >50 nm) Strong attraction from the adsorbing surface only.
(b)	**Mesopore Adsorption** weak 'wall-effect' (dia.: 2 – 50 nm) Strong attraction from the adsorbing surface and very weak attraction from the distant surface (upper).
(c)	**Micropore Adsorption** strong 'wall-effect' (dia.: <2 nm) Very strong attraction forces from both the adsorbing surface and the surrounding surfaces.

Figure 4 - 14. High-affinity sorption on mesopores and micropore surfaces.

Highly carbonaceous matter such as char/charcoal (SEM picture) often contain pores. The porous surface may be coated with non-rigid, humic-like or lipid-like organic matters. The sorbate experiences varying degrees of interactions, depending on whether long-range interaction from other surfaces is available (e.g., cases (a) to (c)). The SEM picture is taken from Biagini et al. 2008.

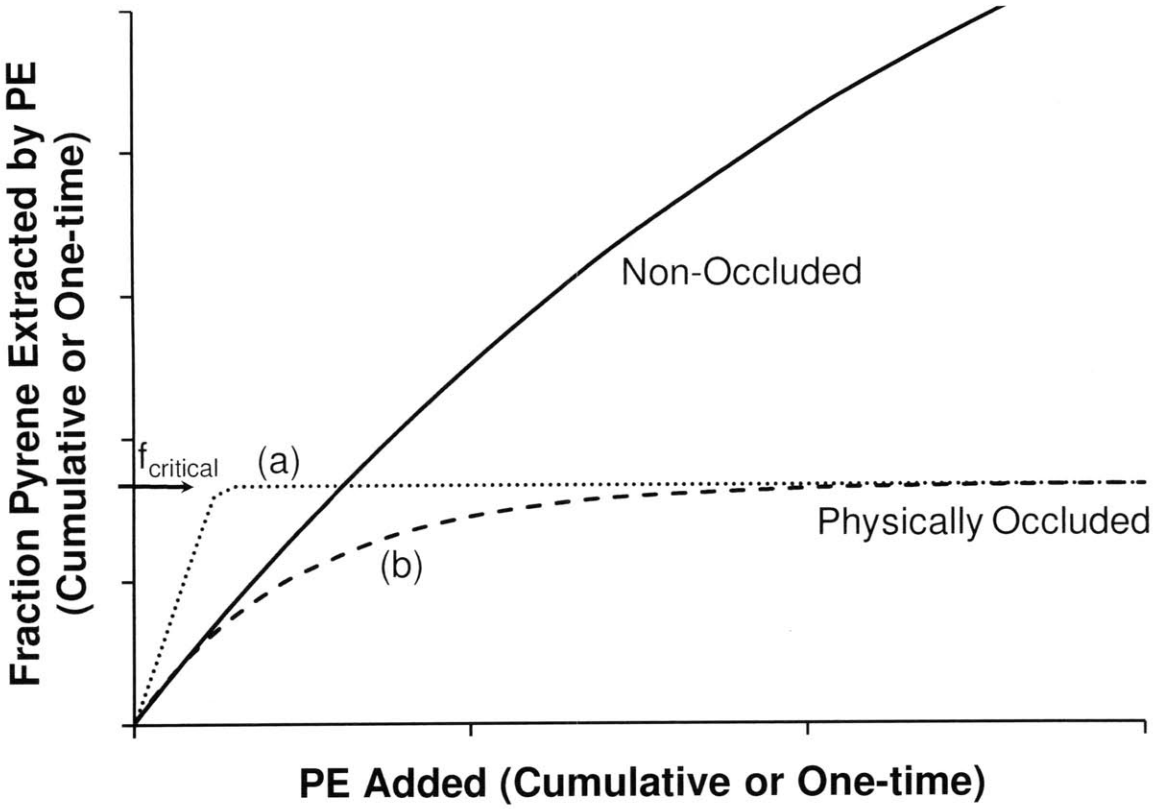

Figure 4 - 15. Theoretically expectations for the sediment-PE experiment.

This figure showed the theoretically expected profiles for PE-extractable pyrene (or other PAHs) fraction. The physical occlusion hypothesis is to be rejected ("Non-Occluded" solid line) when fraction pyrene extractable can be shown to exceed a critical value, $f_{critical}$.

Both (a) and (b) represent cases when physical occlusion of sorbed pyrene is truly significant. Case (a) is an idealized scenario where all extractable/accessible pyrene molecules are sorbed to the sedimentary phase with equal energy (hence a linear slope). Case (b) is a more realistic sorption picture where the PE-extractable pyrene becomes energetically more costly to desorb from the sedimentary matrix.

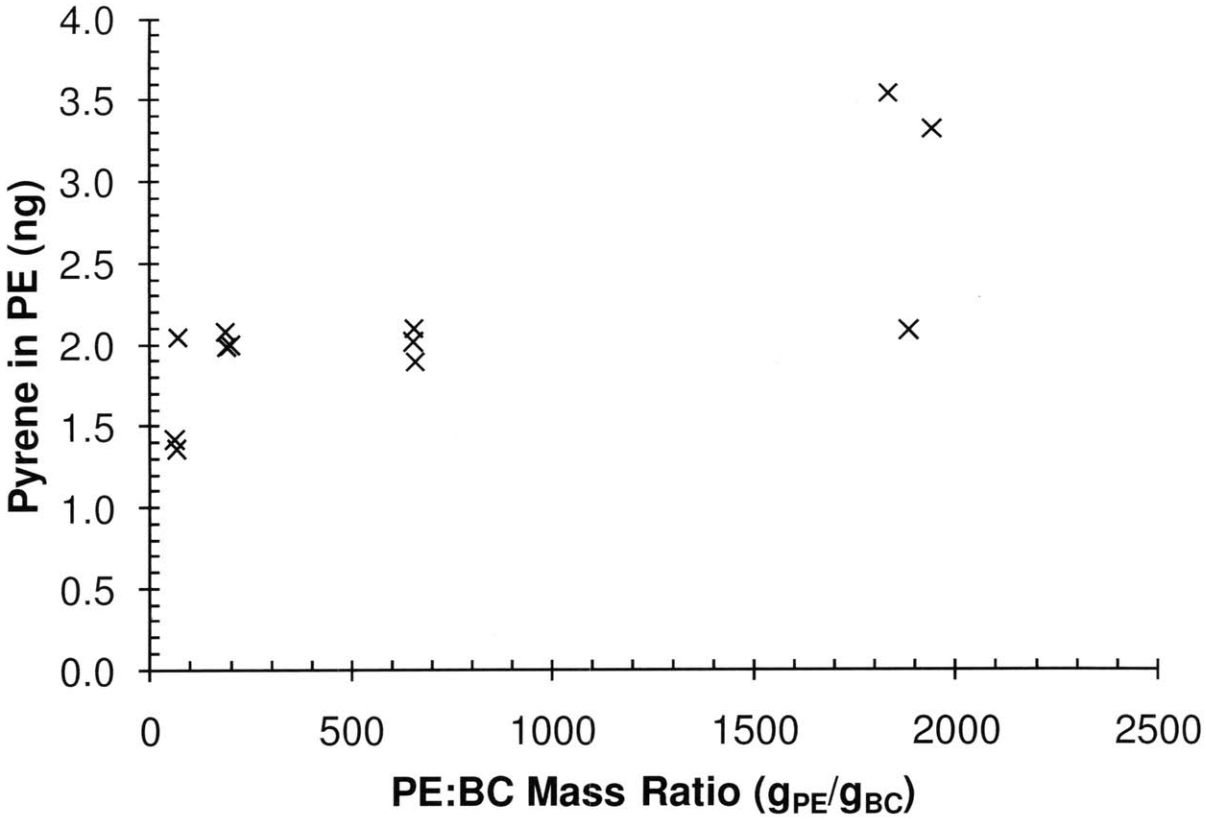

Figure 4 - 16. Pyrene extracted by polyethylene (PE) after 50 d of tumbling.

The amount of natively-bound pyrene absorbed into PE strips was plotted as a function of the PE-to-BC mass ratio. The PE:BC mass ratio is a measure of the relative chemical 'desire' for pyrene to reside in the PE phase vs the sedimentary BC phase. The higher the PE:BC mass ratio, the greater was the desorptive drive for pyrene to absorb into PE. The figure showed results from triplicates suspensions at mass ratios of 70, 190, 650, and 1900 g_{PE}/g_{BC}.

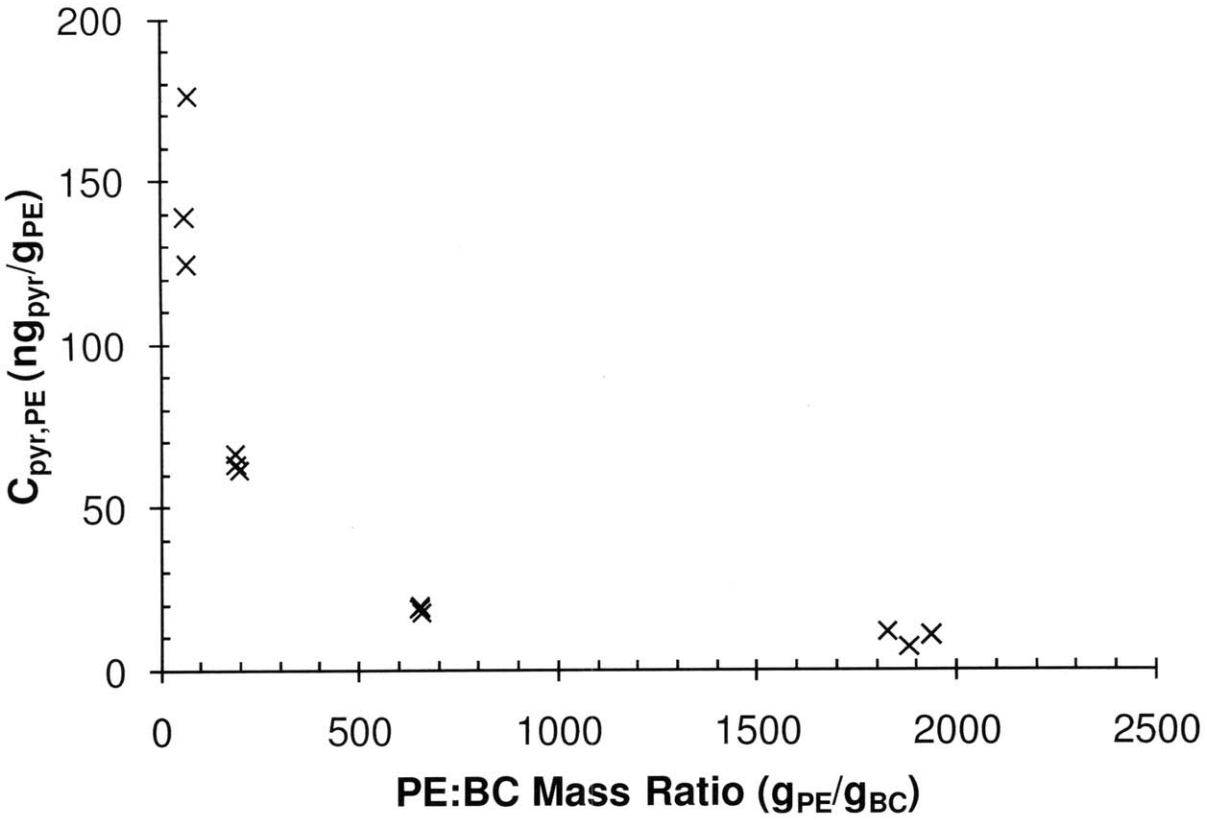

Figure 4 - 17. Pyrene concentration in polyethylene (PE) after 50 d of tumbling.

This figure tried to present the fact that PE-mass normalized pyrene level declined dramatically with higher PE content in the suspension.

The PE:BC mass ratio is a measure of the relative chemical 'desire' for pyrene to reside in the PE phase vs the sedimentary BC phase. The higher the PE:BC mass ratio, the greater was the desorptive drive for pyrene to absorb into PE. The figure showed results from triplicates suspensions at mass ratios of 70, 190, 650, and 1900 g_{PE}/g_{BC}.

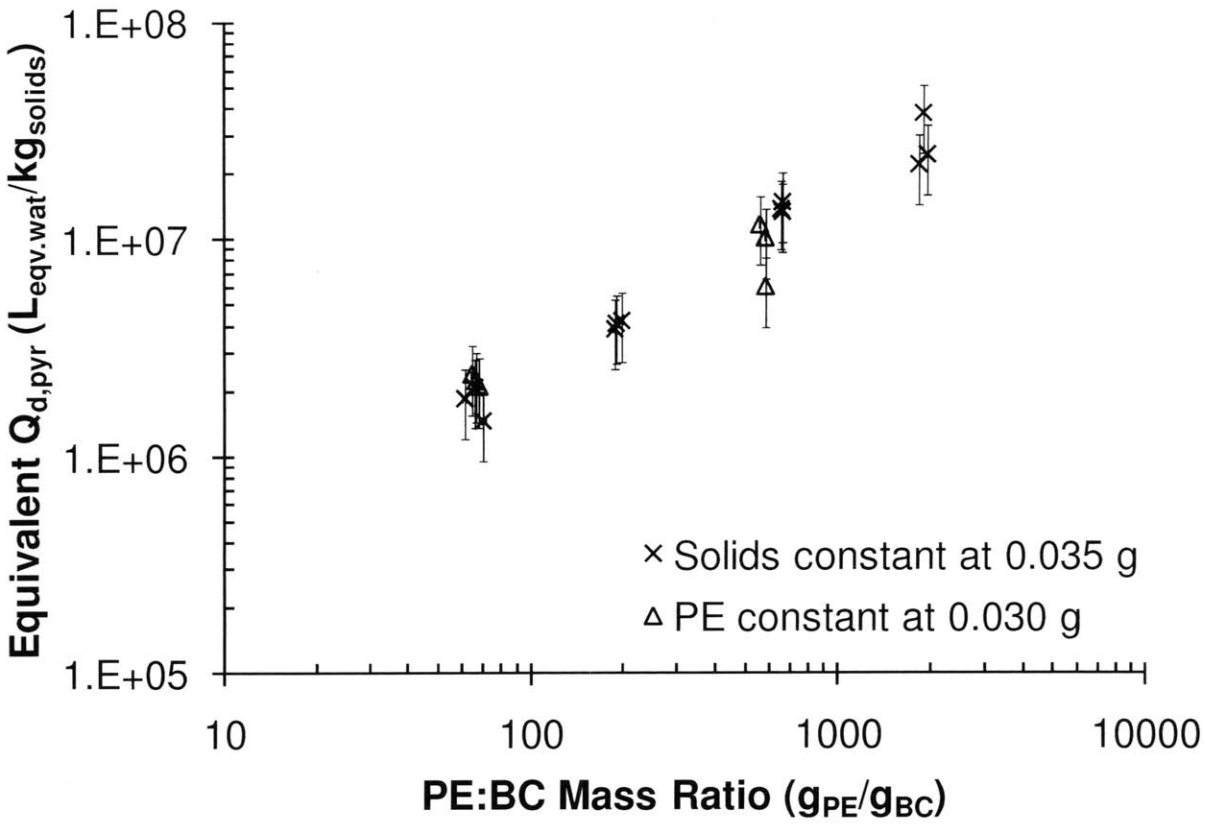

Figure 4 - 18. Equivalent $Q_{d,pyr}$ in PE-sediment suspensions after 50 d of tumbling.

Equivalent $Q_{d,pyr}$ ($=S_{pyr}{}^{*}K_{pyr,PEW}/C_{pyr,PE}$) was plotted against the PE-BC mass ratio for two groups of PE-sediment suspensions. In the first group (**X**), solid mass was kept constant at 0.035 g while PE mass was varied. In the second group (**O**), PE mass was kept constant at 0.030 g while the amount of solid present was varied. The figure showed results from triplicates suspensions at mass ratios of 70, 190, 650, and 1900 g_{PE}/g_{BC}.

The PE:BC mass ratio can be interpreted as a measure of the relative chemical 'desire' for pyrene to reside in the PE phase vs the sedimentary BC phase. The higher the PE:BC mass ratio, the greater was the desorptive drive for pyrene to absorb into PE.

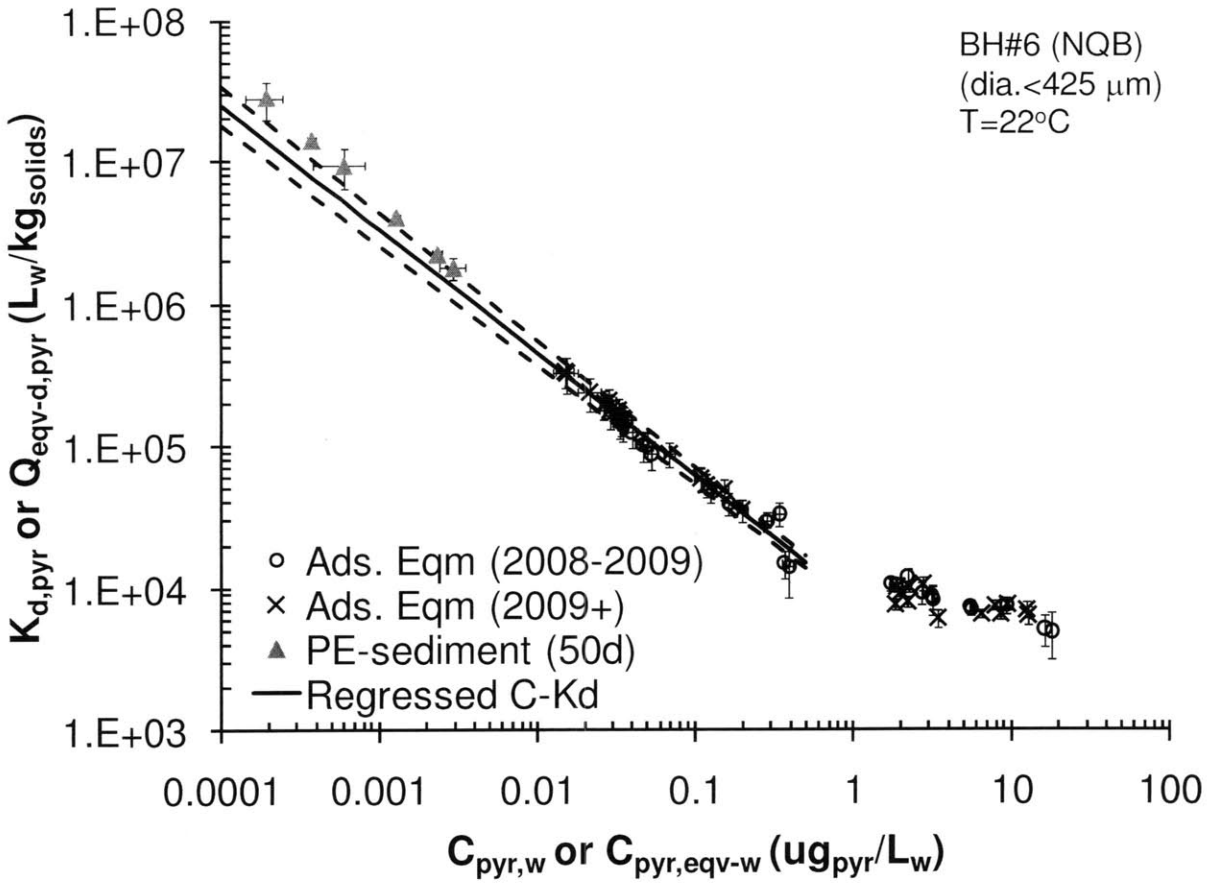

Figure 4 - 19. Coherence of PE-sediment experiment with Adsorption Experiment (K_d-C or S-C plots)

Figure 4 - 19a. Coherence of PE-sediment experiment with Long-Term Extended Range Adsorption Equilibrium Experiment.

PE-sediment experiment data (red triangle) are plotted along with data from the long-term extended range adsorption equilibrium experiment (**O**). The adsorption equilibrium experiment was also repeated later for 6+ mo. (**X**). The solid line is the regression (Freundlich) of the adsorption experiments data (both **O** and **X**) for $C_{pyr,w} < 1$ ug/L_w projected onto the equivalent dissolved phase range for the PE-sediment experiment data. Dashed-lines represent uncertainties of ±1 σ for the regression line. Error bars associated with the PE-sediment experiment data represented ±1 σ of propagated uncertainties for triplicates of suspensions.

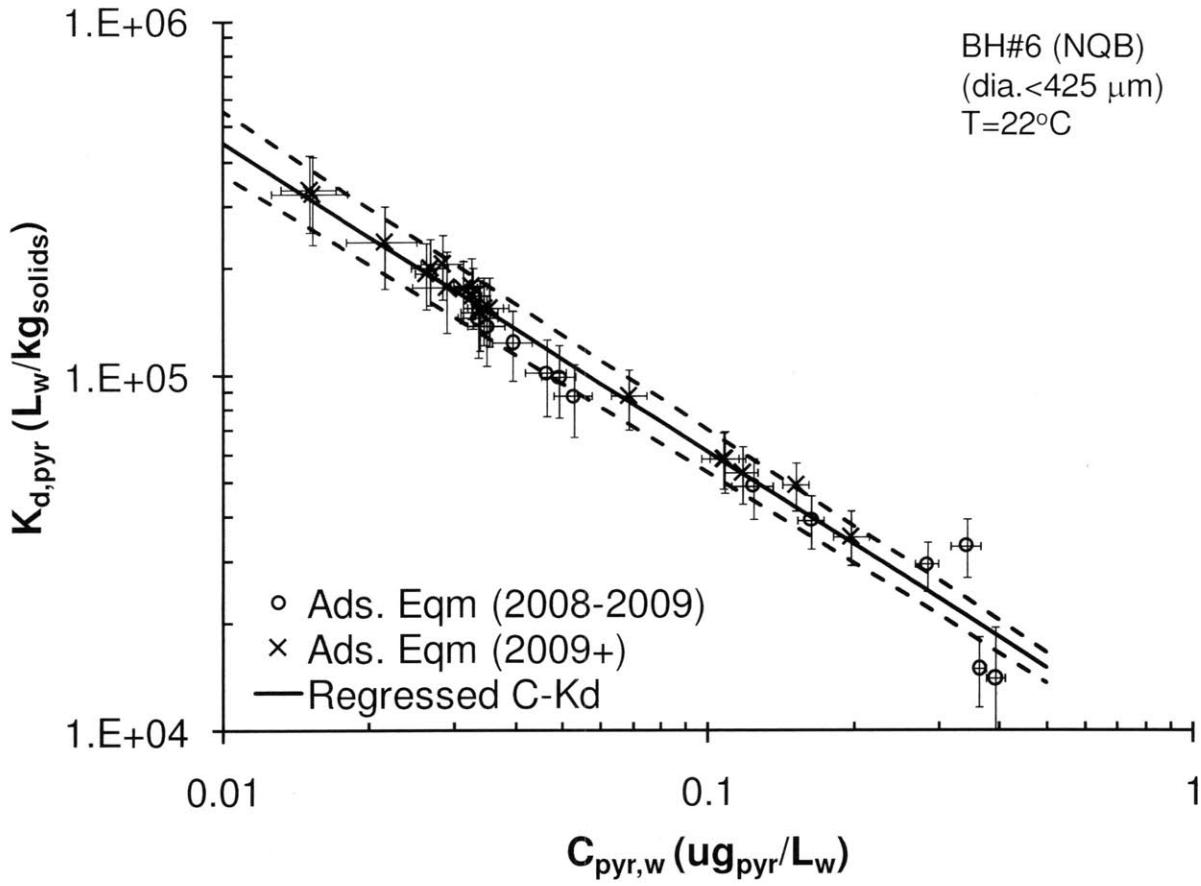

Figure 4 - 19b. Expanded view for (a) over the sub-ng_{pyr}/L_w range.

Data from the long-term extended range adsorption equilibrium experiment (1 yr) (**O**) and those from the repeated adsorption experiment (6+ mo) (**X**) were shown. The solid line is the regression (Freundlich) of the adsorption experiments data (both **O** and **X**). Dashed-lines represent uncertainties of ±1 σ for the regression line.

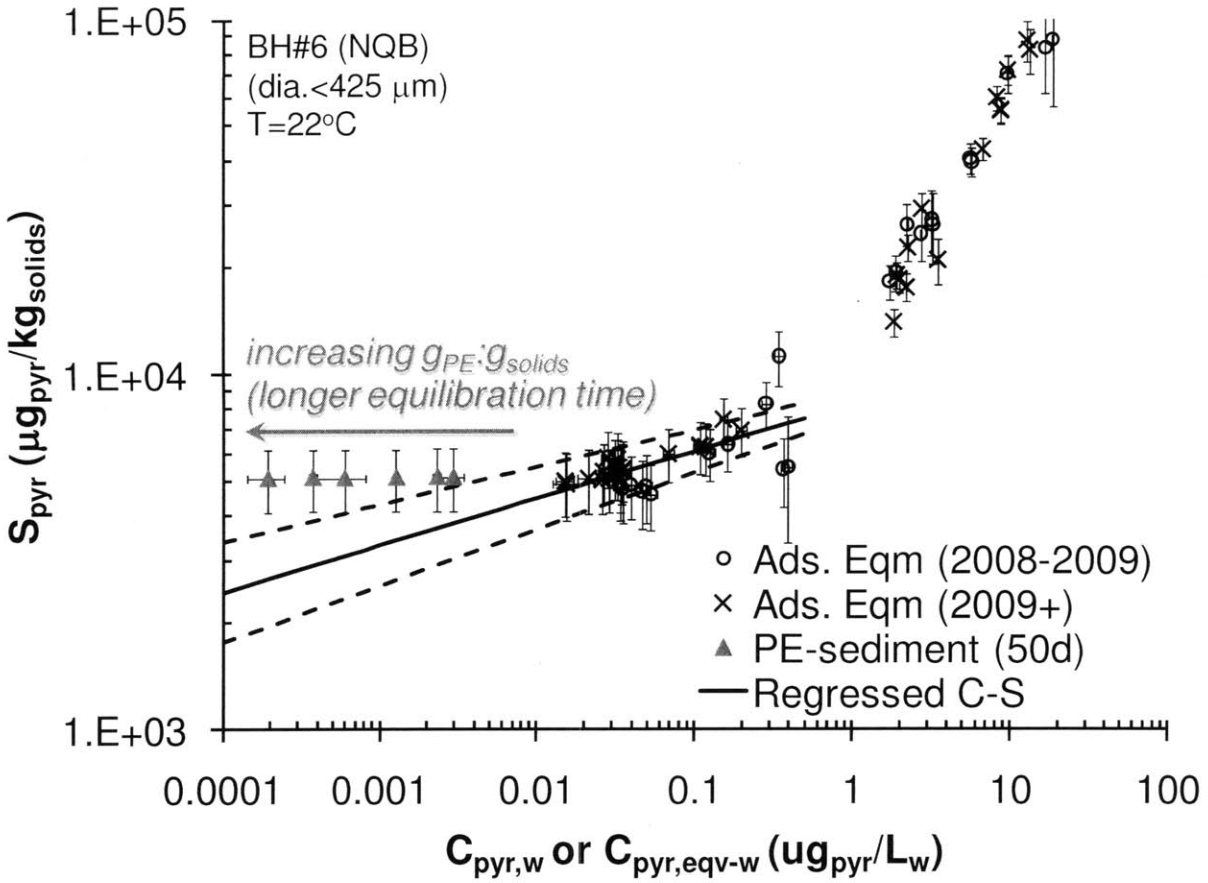

Figure 4-19c. Coherence of PE-sediment experiment with Long-Term Extended Range Adsorption Equilibrium Experiment.

PE-sediment experiment data (red triangle) are plotted along with data from the long-term extended range adsorption equilibrium experiment (**O**). The adsorption equilibrium experiment was also repeated later for 6+ mo. (**X**). The solid line is the regression (Freundlich) of the adsorption experiments data (both **O** and **X**) for $C_{pyr,w}$ < 1 ug/L_w projected onto the equivalent dissolved phase range for the PE-sediment experiment data.

Dashed-lines represent uncertainties of ±1 σ for the regression line. Error bars associated with the PE-sediment experiment data represented ±1 σ of propagated uncertainties for triplicates of suspensions.

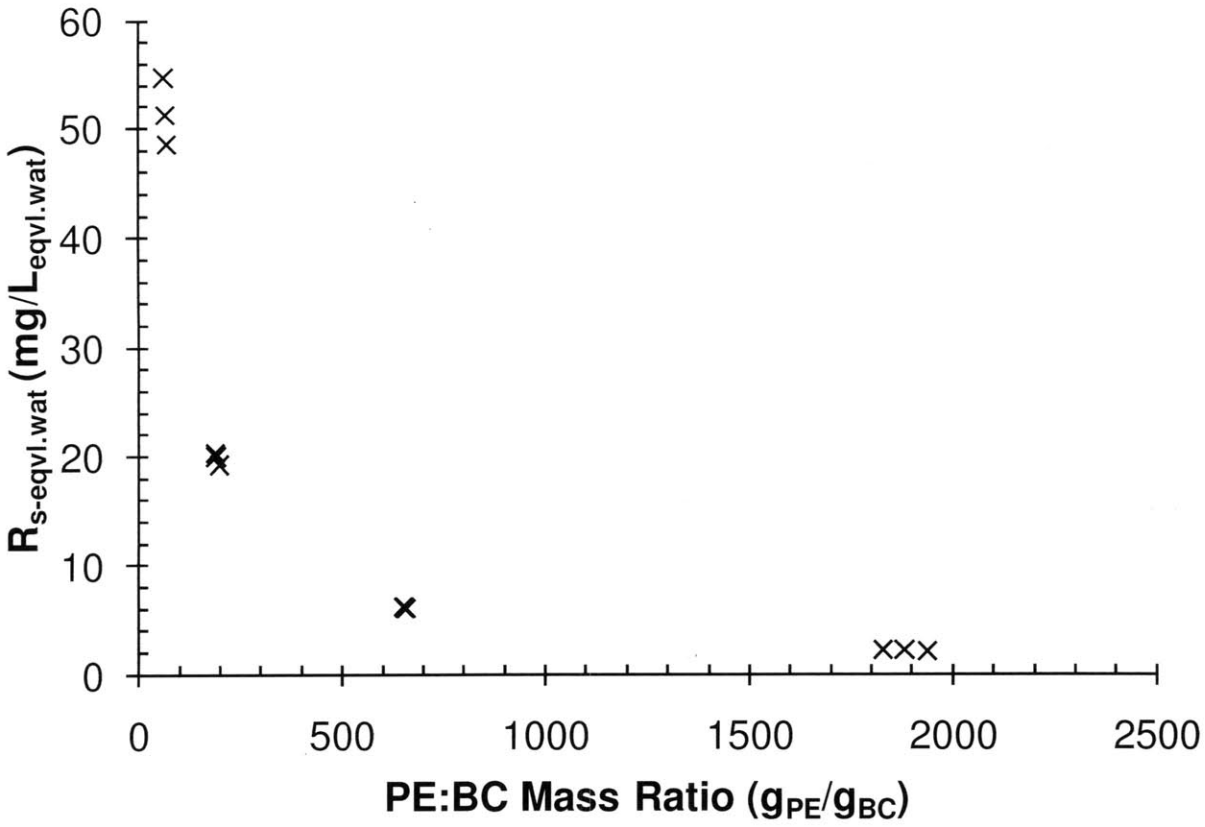

Figure 4 - 20. Equivalent R_{sw} vs PE content in the sediment-PE experiment.

This figure attempted to relate the kinetics of pyrene transfer from sediment phase to PE to the PE:BC mass ratio. The equilibration rate of a suspension increases with the solid-to-water ratio (R_{sw}) of the system. Hence, the equivalent R_{sw} (or $R_{s\text{-}eqvl.wat}$) can be interpreted, very crudely, as a measure of the relative 'chemical distance' between the system at time t and the system at equilibrium. $R_{s\text{-}eqvl.wat}$ was computed by converting the amount of PE present to sorption-equivalent volumes of water.

The PE:BC mass ratio is a measure of the relative chemical 'desire' for pyrene to reside in the PE phase vs the sedimentary BC phase. The higher the PE:BC mass ratio, the greater was the desorptive drive for pyrene to absorb into PE. The figure showed results from triplicates suspensions at mass ratios of 70, 190, 650, and 1900 g_{PE}/g_{BC}.

Chapter 5: Figures

Figure 5 - 1. Regression of pyrene sorption data by the Linear and the Sinh forms.. 369
Figure 5 - 2. Native/Equilibrium sorbed-pyrene ratio and sorption isotherm at 6°C.. 370
Figure 5 - 3. Native/Equilibrium sorbed-pyrene ratio and partition coefficient $K_{d,pyr}$.. 372
Figure 5 - 4. Non-linear regression of S_{pyr} and C_{pyr} by various composite isotherm forms. 377
Figure 5 - 5. Two-Domain regressions of S_{pyr} and C_{pyr}. 378
Figure 5 - 6. Regionalized Freundlich description of pyrene sorption at 22°C. 379
Figure 5 - 7. Dependence of Freundlich n_{Fr} on the occupancy of sorbing sites. 380
Figure 5 - 8. Simulated distribution of surface binding energy and isotherm nonlinearity. 385
Figure 5 - 9. Alternative mechanistic picture of HOC sorption. 386
Figure 5 - 10. Qualitative comparison of K_d's for uptake of HOCs in different sorbents. 387

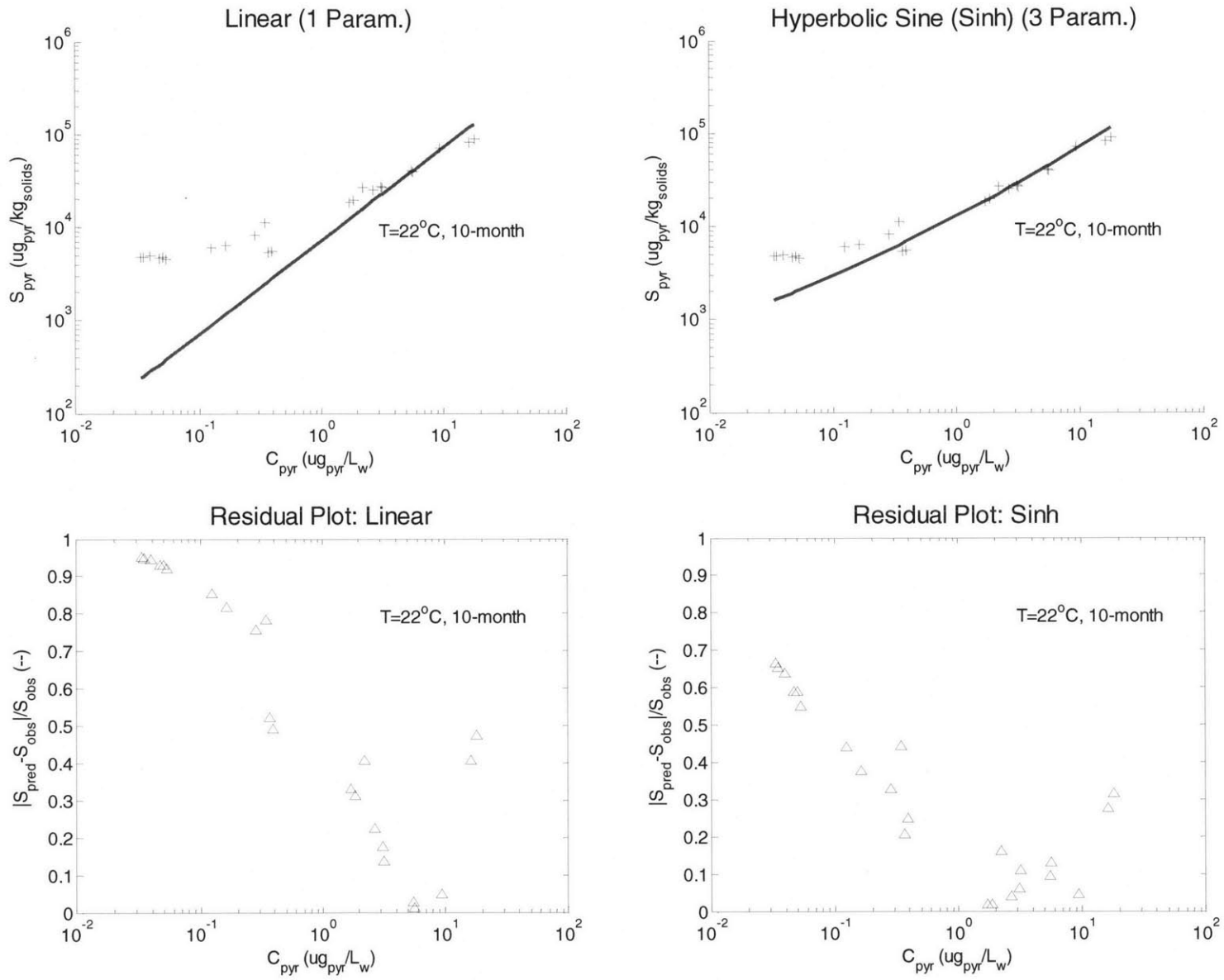

Figure 5 - 1. Regression of pyrene sorption data by the Linear and the Sinh forms.

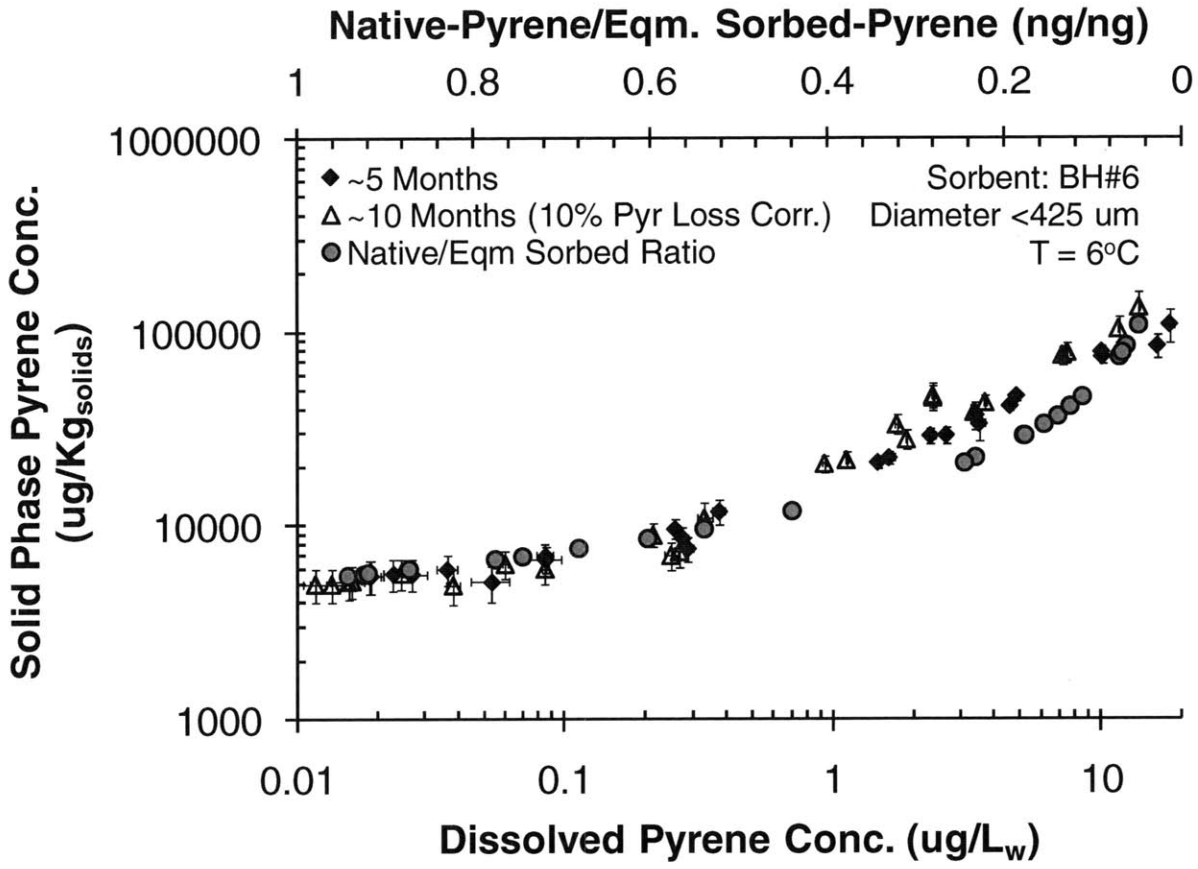

Figure 5 - 2. Native/Equilibrium sorbed-pyrene ratio and sorption isotherm at 6°C.

The figure showed that the shape of the isotherm was 'predictable' by the ratio of native pyrene to total sorbed pyrene (i.e. $MR_{pyr,s,native/eqm}$).

Error bars denoted ±1σ. The errors of the native/equilibrium ratio were omitted for clarity. Similar plots are other temperatures are available in Appendix 5-1.

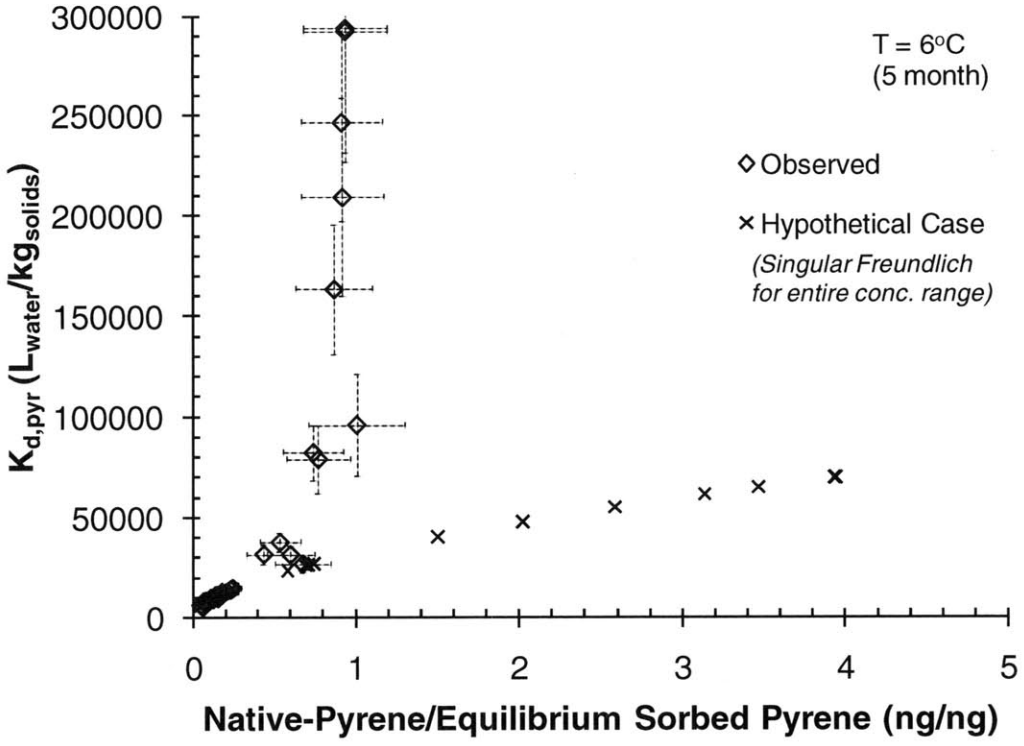

Figure 5 - 3a. $K_{d,pyr}$ vs $MR_{pyr,s,native/Eqm}$ (Observed vs Hypothetical Case)

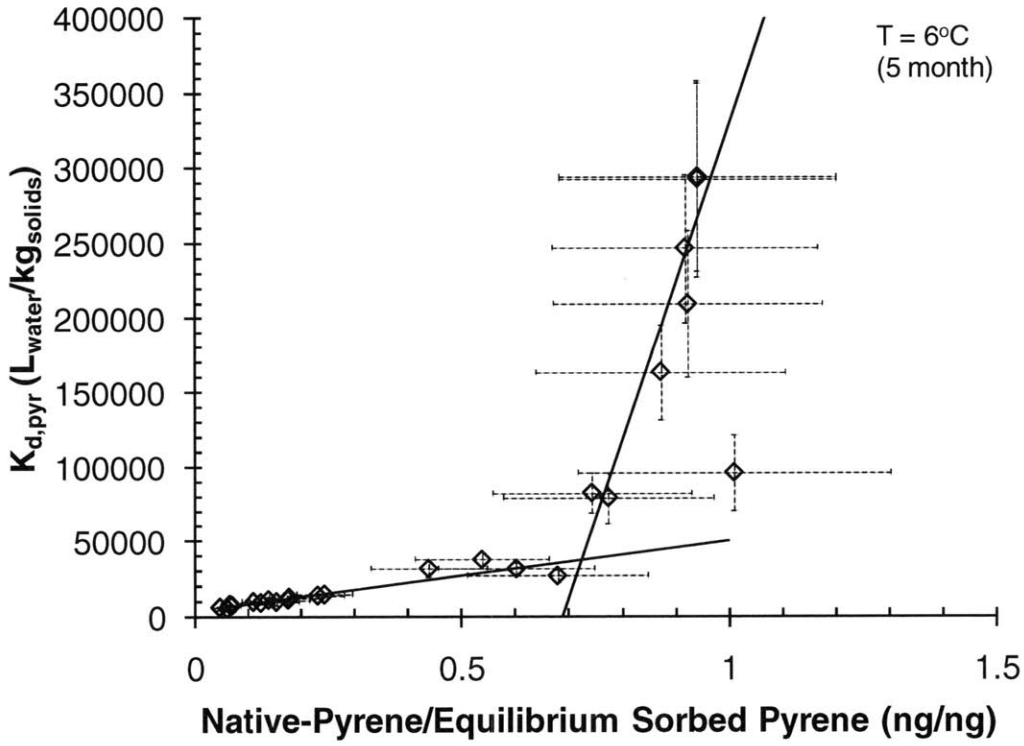

Figure 5 – 3b. $K_{d,pyr}$ vs $MR_{pyr,s,native/Eqm}$ (Expanded view of Observed Case)

Figure 5 - 3. Native/Equilibrium sorbed-pyrene ratio and partition coefficient $K_{d,pyr}$.

In both (a) and (b), pyrene partition coefficients in sediment-water system ($K_{d,pyr}$) were plotted against the ratio of native-pyrene to equilibrium sorbed pyrene (i.e. $MR_{pyr,s,native/Eqm} \equiv S_{pyr,o}/S_{pyr,Eqm}$; in unit ng/ng).

In (a), the observed $K_{d,pyr}$-$MR_{pyr,s,native/Eqm}$ plot was compared with that constructed from a hypothetical case. The hypothetical case assumed the sorption isotherm was fully characterized by a single Freundlich model. The model parameters K_{Fr} and n for the hypothetical scenario were obtained from the regression of the high-range concentration ($C_{pyr,Eqm}$ ~> 1 μg/L). The actual $C_{pyr,Eqm}$'s, $S_{pyr,o}$'s, and R_{sw}'s were used as input to the singular Freundlich model, which gave the hypothetical equilibrium solid-phase pyrene concentration ($S_{pyr,Eqm,Hypo}$) and hence allowed the hypothetical $K_{d,pyr}$ to be computed. Error bars showed ±1σ of the reported values. Similar plots for other temperatures can be found in Appendix 5-2.

In (b), only the observed data points were plotted. The solid lines were trends that the data points seemed to have suggested. Error bars represented ±1σ of the reported values. Similar plots with at other temperatures and the uncertainty of the estimated trend-line can be found in Appendix 5-2.

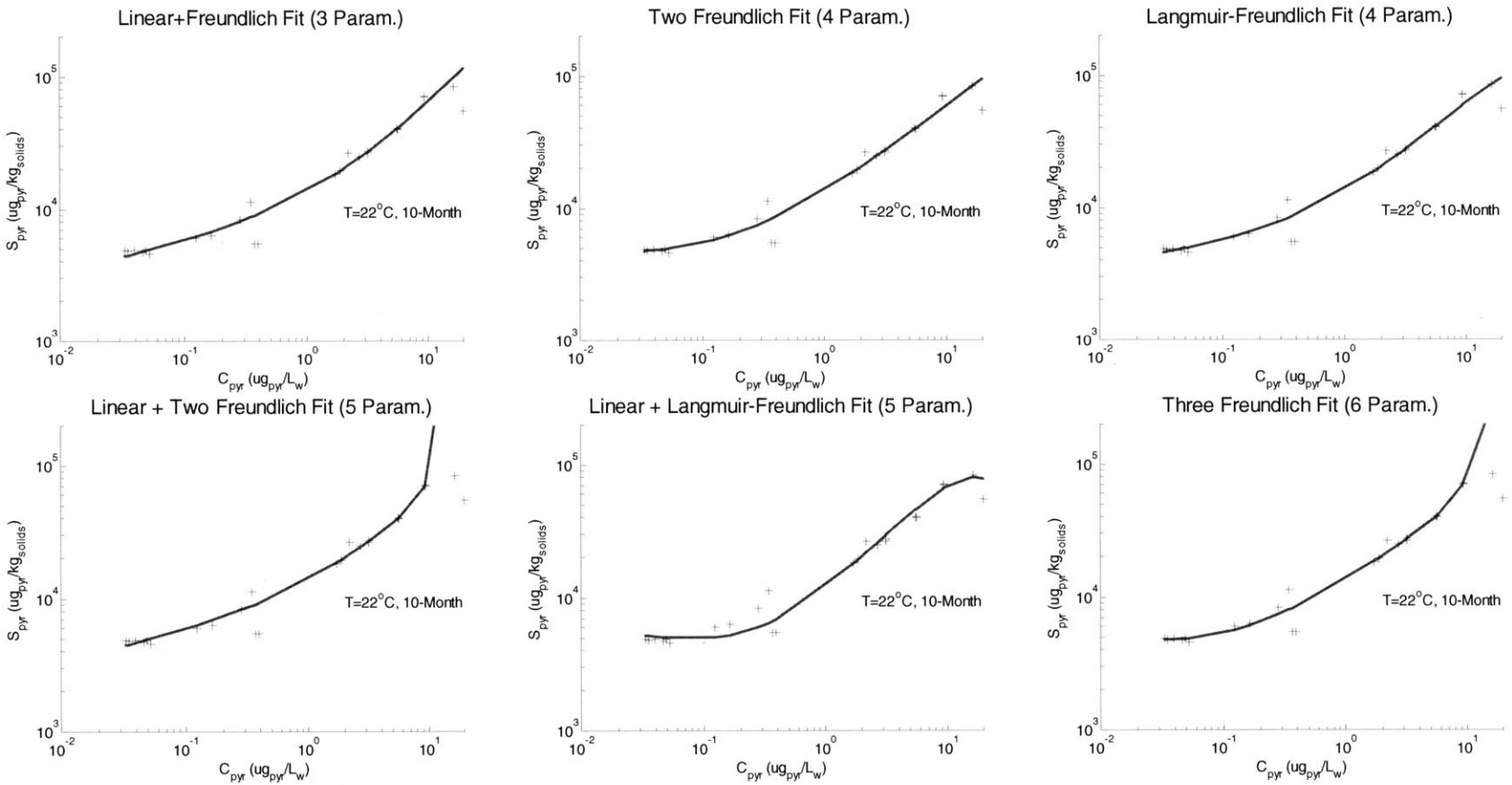

Figure 5 - 4a. Non-linear regression (Matlab): Composite forms with Linear, Freundlich, and Langmuir terms.

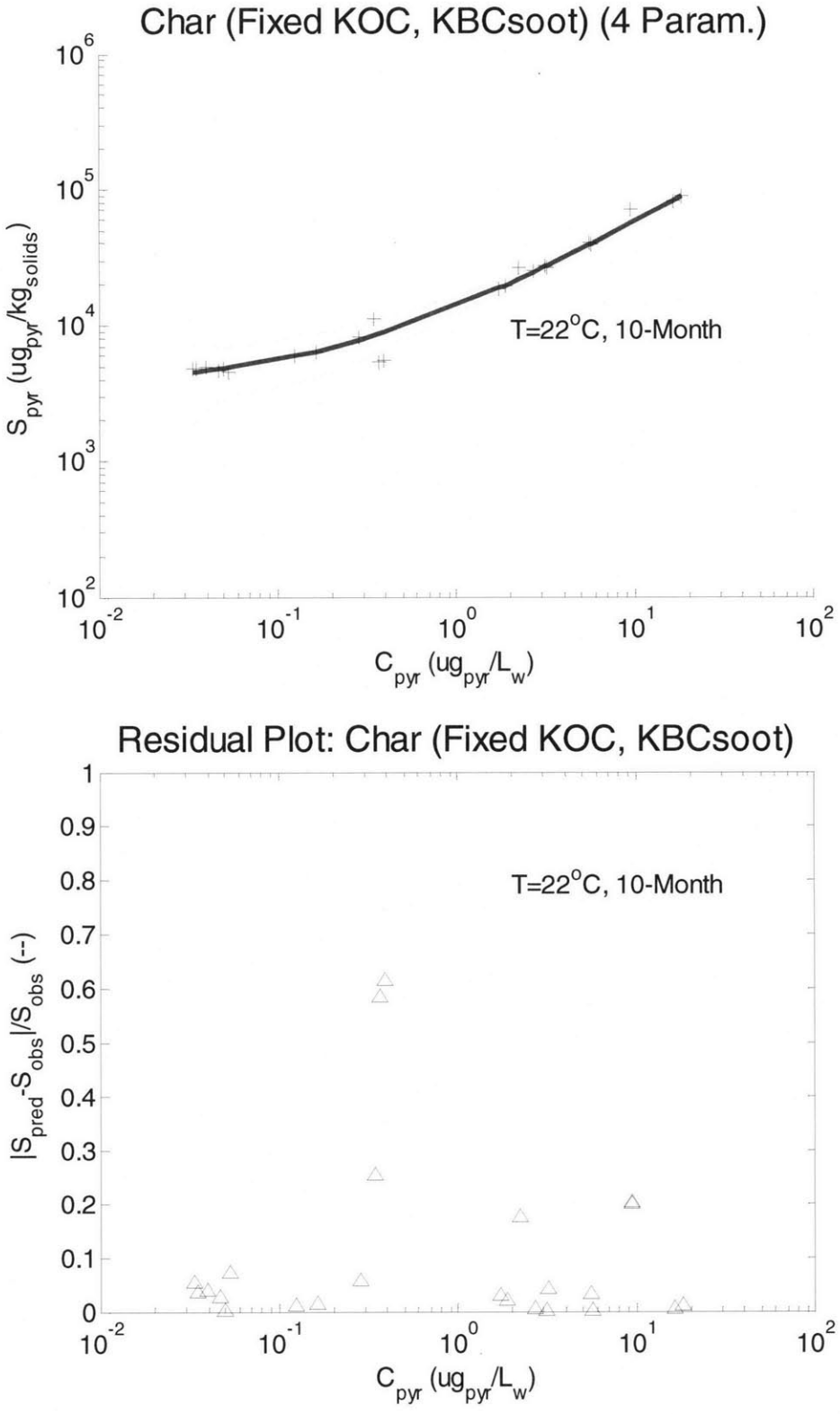

Figure 5 - 4b. Non-linear regression (Matlab): Explicit char-adsorption form.

Please refer to "Lnr-Fr(soot)-Fr(char)" model in Table 5-1 & 5-2 and Appendix 5-4.

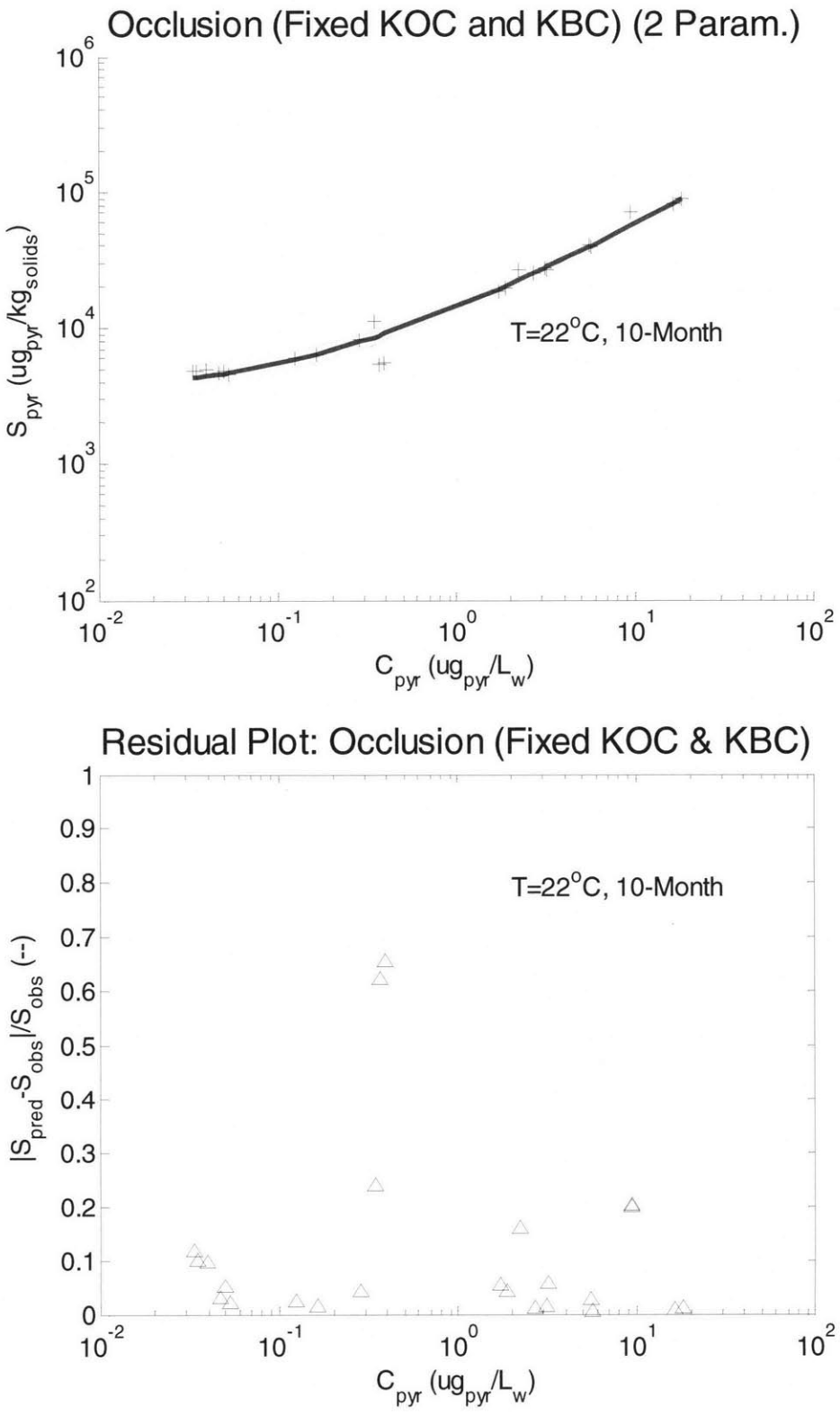

Figure 5 - 4c. Non-linear regression (Matlab): Occlusion (2-parameter).

Please refer to "Occlusion-Fix" model in Table 5-1 & 5-2 and Appendix 5-5.

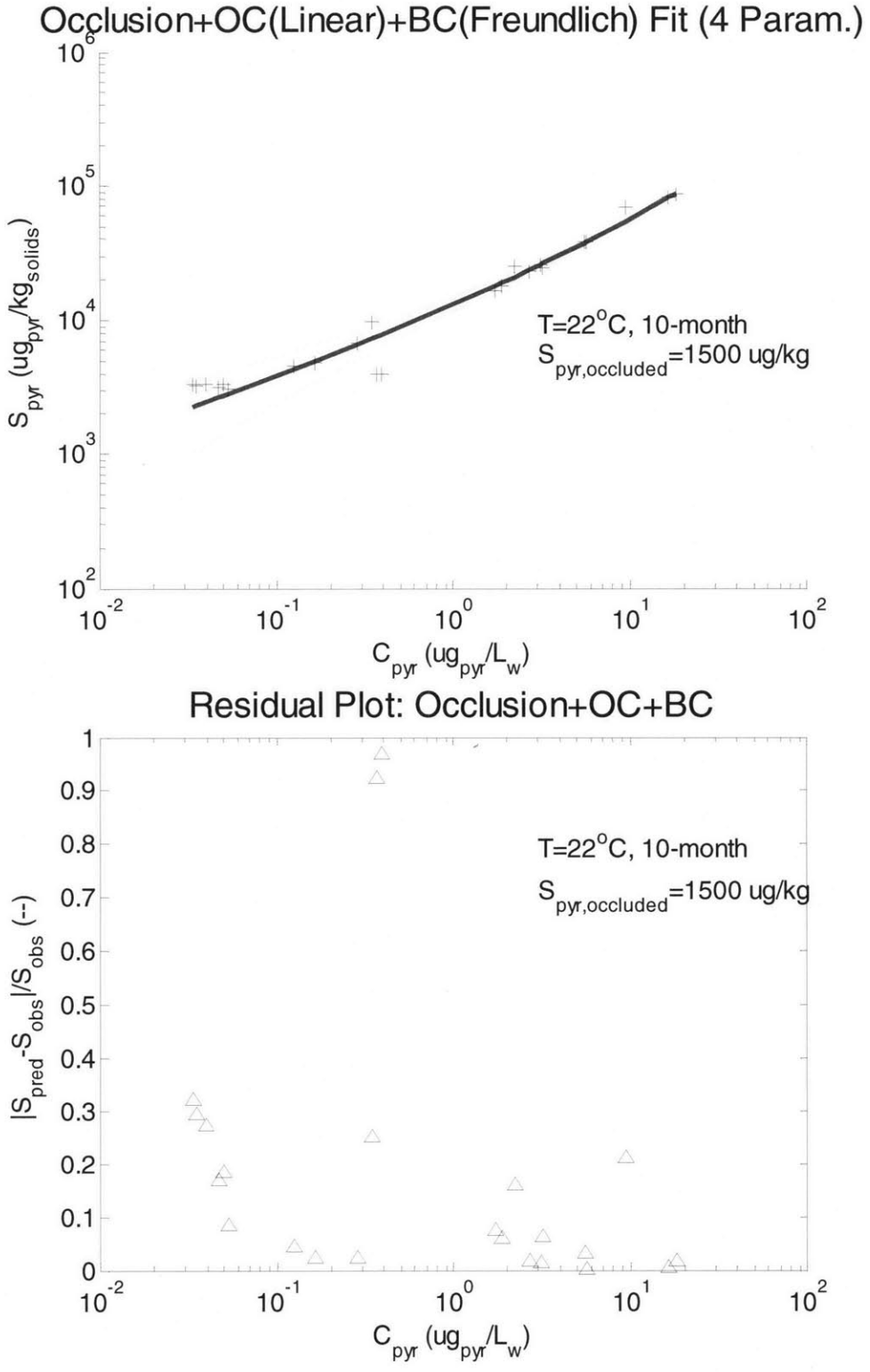

Figure 5 - 4d. Non-linear regression (Matlab): Occlusion (4-parameter).

Please refer to "Occlusion-Lnr-Fr" model in Table 5-1 & 5-2 and Appendix 5-6.

Figure 5 - 4. Non-linear regression of S_{pyr} and C_{pyr} by various composite isotherm forms.

Raw data (+) from the Long-Term Adsorption Equilibrium Experiment at 22°C (10-month) were plotted along with the prediction (solid line). Dashed lines indicate a $\pm 1\ \sigma$ uncertainty on the prediction. Regressed coefficients for individual isotherm models, regression curves, and the associated residue plots can be found in Appendix 5-3 to 5-6.

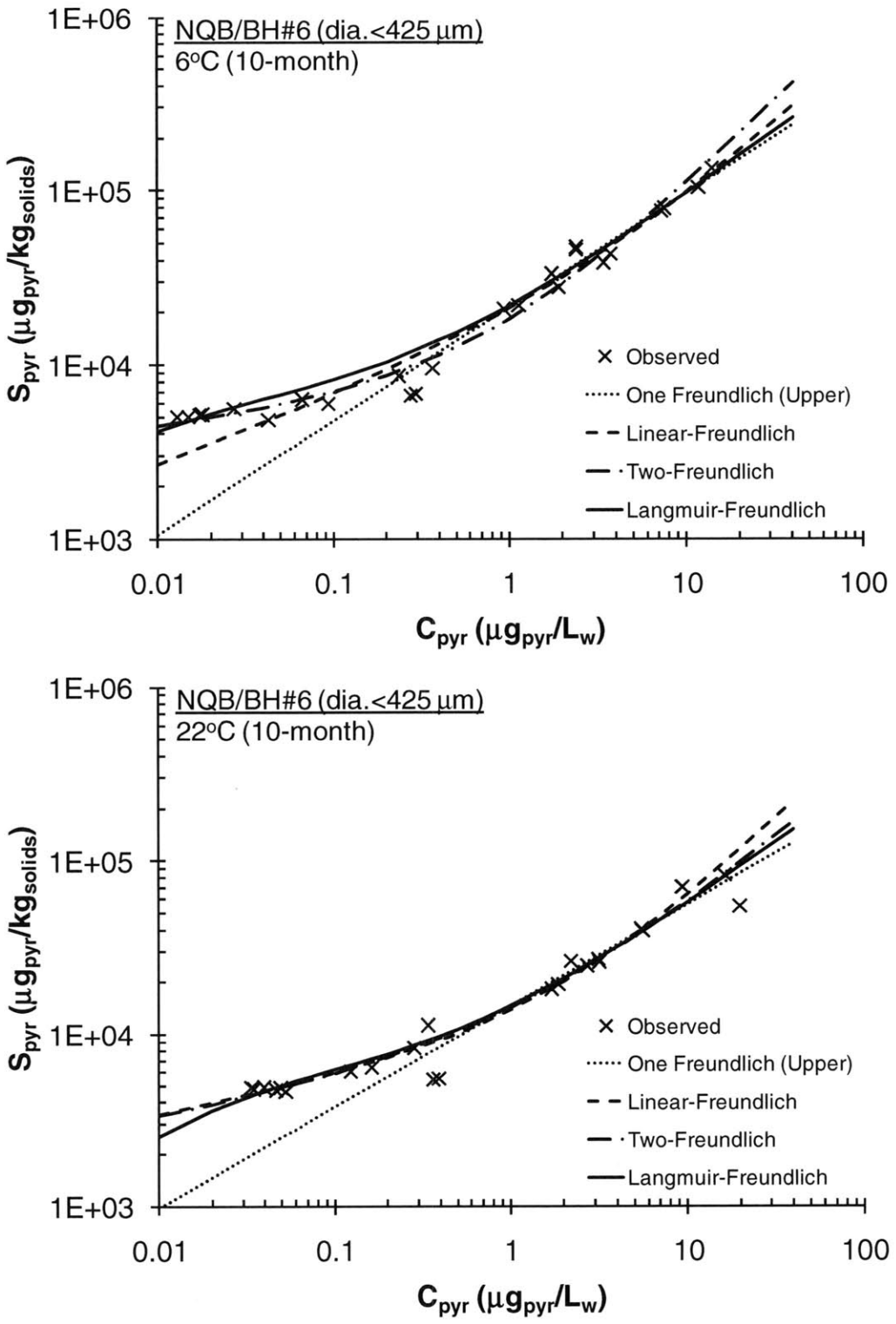

Figure 5 - 5. Two-Domain regressions of S_{pyr} and C_{pyr}.

See Appendix 5-9 for two-domain regression at other temperatures and times

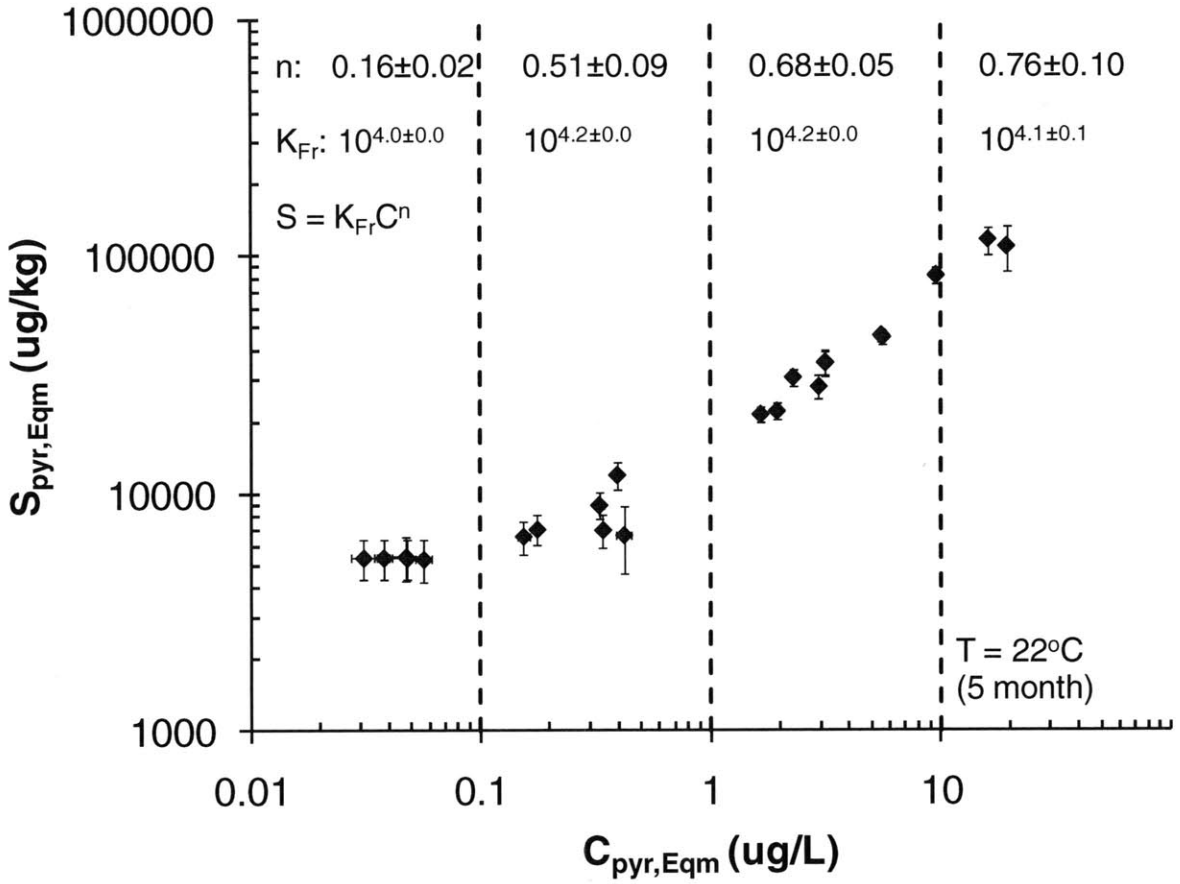

Figure 5 - 6. Regionalized Freundlich description of pyrene sorption at 22°C.

The isotherm was arbitrarily divided into concentration ranges. Observations within each range and those enclosing the range were then fitted to the Freundlich model. The regressed slope and intercept were n and $\log K_{Fr}$, respectively, of the regional isotherm. Error bars denote $\pm 1\sigma$. Regionalized description of sorption isotherm at all temperatures can be found in Appendix 5-12.

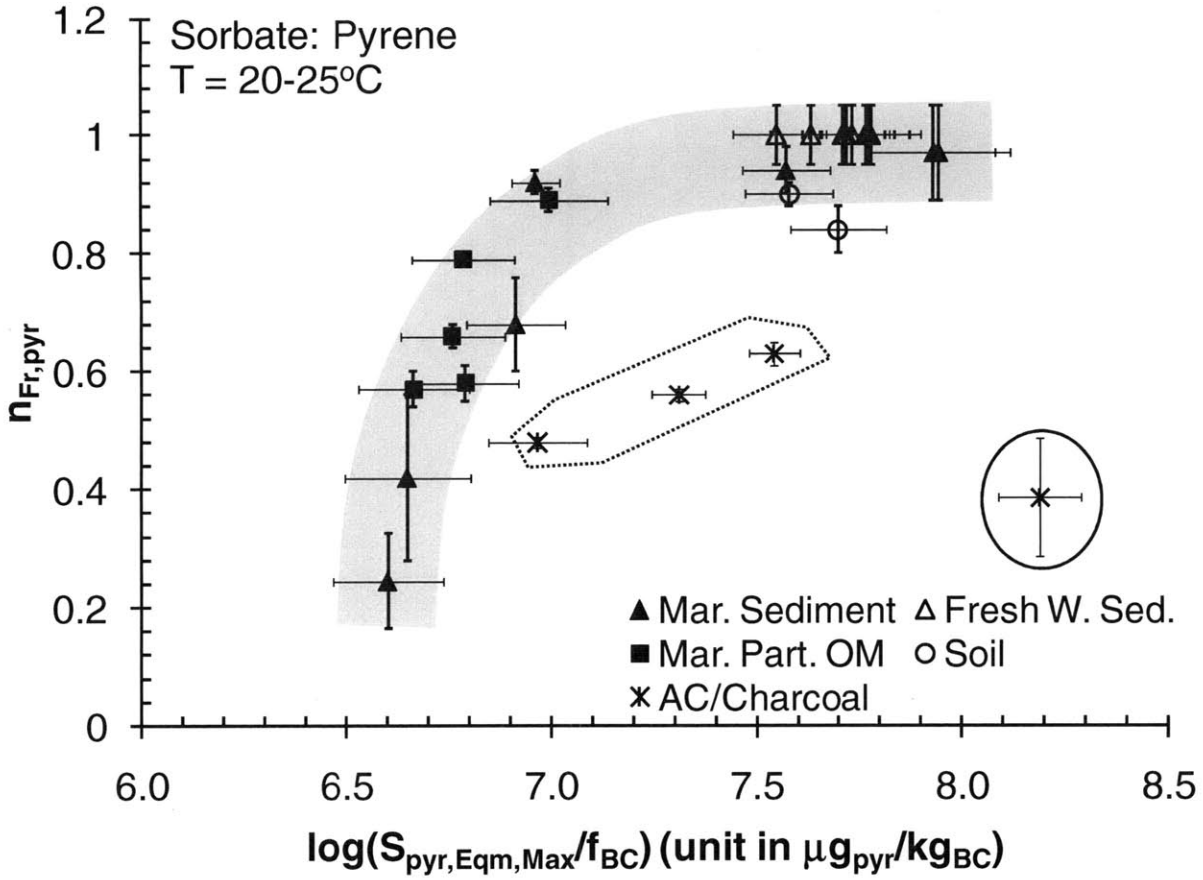

Figure 5 - 7. Dependence of Freundlich n_{Fr} on the occupancy of sorbing sites.

Figure 5 - 7a. n_{Fr} vs $\log(S_{pyr,Eqm,Max}/f_{BC})$.

The Freundlich exponent n_{Fr} is defined as in $S=K_{Lnr}+K_{Fr}C^{nFr}$ or $S=K_{Fr}C^{nFr}$. The occupancy of sorbing sites has been approximated as the maximum amount of pyrene sorbed at equilibrium per mass of BC present in the system ($S_{pyr,Eqm,Max}/f_{BC}$) in a particular isotherm study. Except the "AC(activated carbon)/charcoal" category, all other categories are natural geosorbents.

Data circled in dotted line involved saw-dust derived charcoal as sorbent (Sun et al. 2008). Data circled in solid line involved activated carbon as sorbent (Walters et al. 1984). The shaded region is a visual aid for highlighting the trend and it has no statistical significance. Error bars denote propagated uncertainty or statistical error in $\pm 1\ \sigma$.

Data points are derived from previous studies (Karickhoff et al. 1979; Walters et al. 1984; Chin et al. 1992; Chiou et al. 1998; Accardi-Dey and Gschwend 2002; ter Laak et al. 2006a; Sun et al. 2008; Flores-Cervantes et al. 2009; this study).

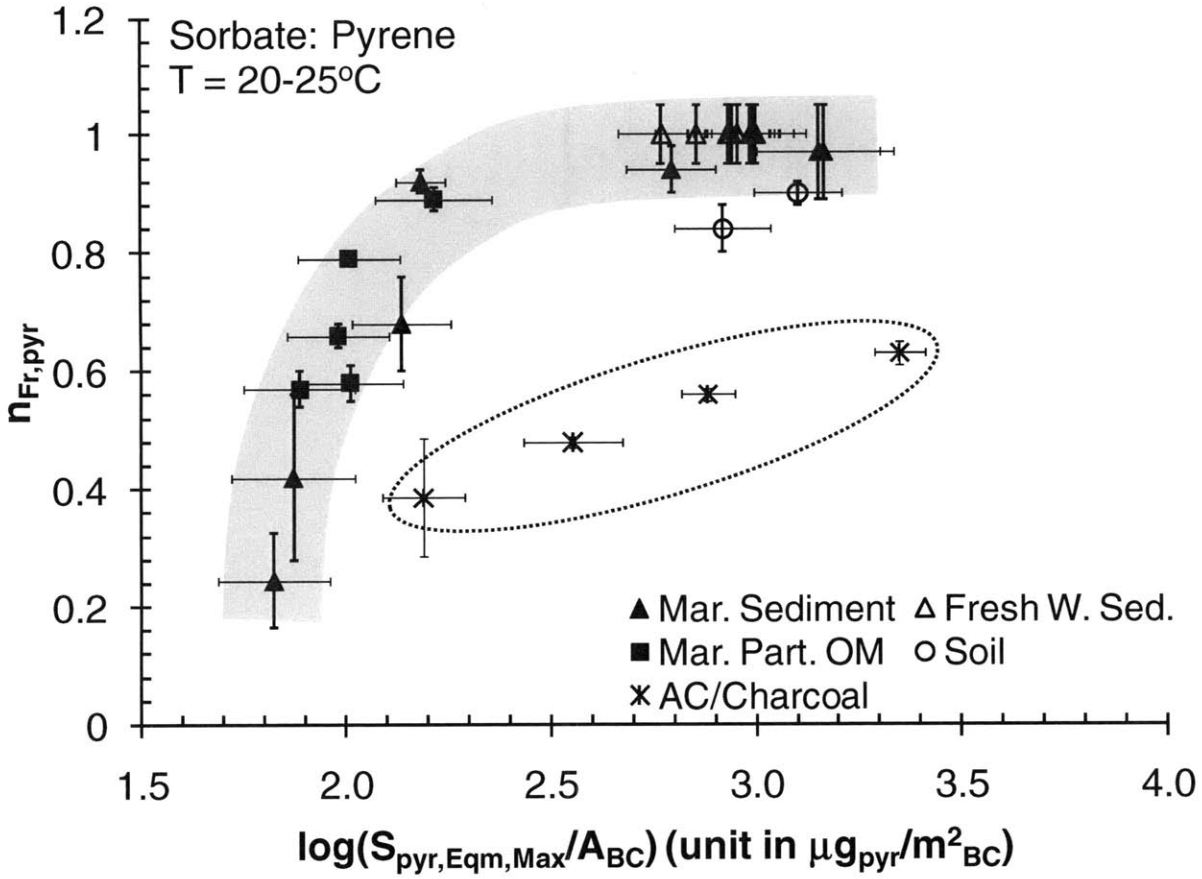

Figure 5 - 7b. n_{Fr} vs $\log(S_{pyr,Eqm,Max}/A_{BC})$.

The Freundlich exponent n_{Fr} is defined as in $S=K_{Lnr}+K_{Fr}C^{nFr}$ or $S=K_{Fr}C^{nFr}$. The occupancy of sorbing sites has been approximated as the maximum amount of pyrene sorbed at equilibrium per mass of BC present in the system ($S_{pyr,Eqm,Max}/f_{BC}$) in a particular isotherm study. Except the "AC(activated carbon)/charcoal" category (circled in dotted line), all other categories are natural geosorbents.

Regarding A_{BC}: (i) BC in natural geosorbents has been assumed to be primarily consisted of soot-BC (surface area ~50-60 m^2/g_{BC}). It was assumed that soot in natural geosorbent lost half of the surface area as they associated with the mineral matrix. So an ABC of 30 m^2/g_{BC} was used for all natural geosorbents; (ii) for activated carbons/charcoal, the surface areas reported in the original work were used.

The shaded region is a visual aid for highlighting the trend and it has no statistical significance. Error bars denote propagated uncertainty or statistical error in $\pm 1\ \sigma$.

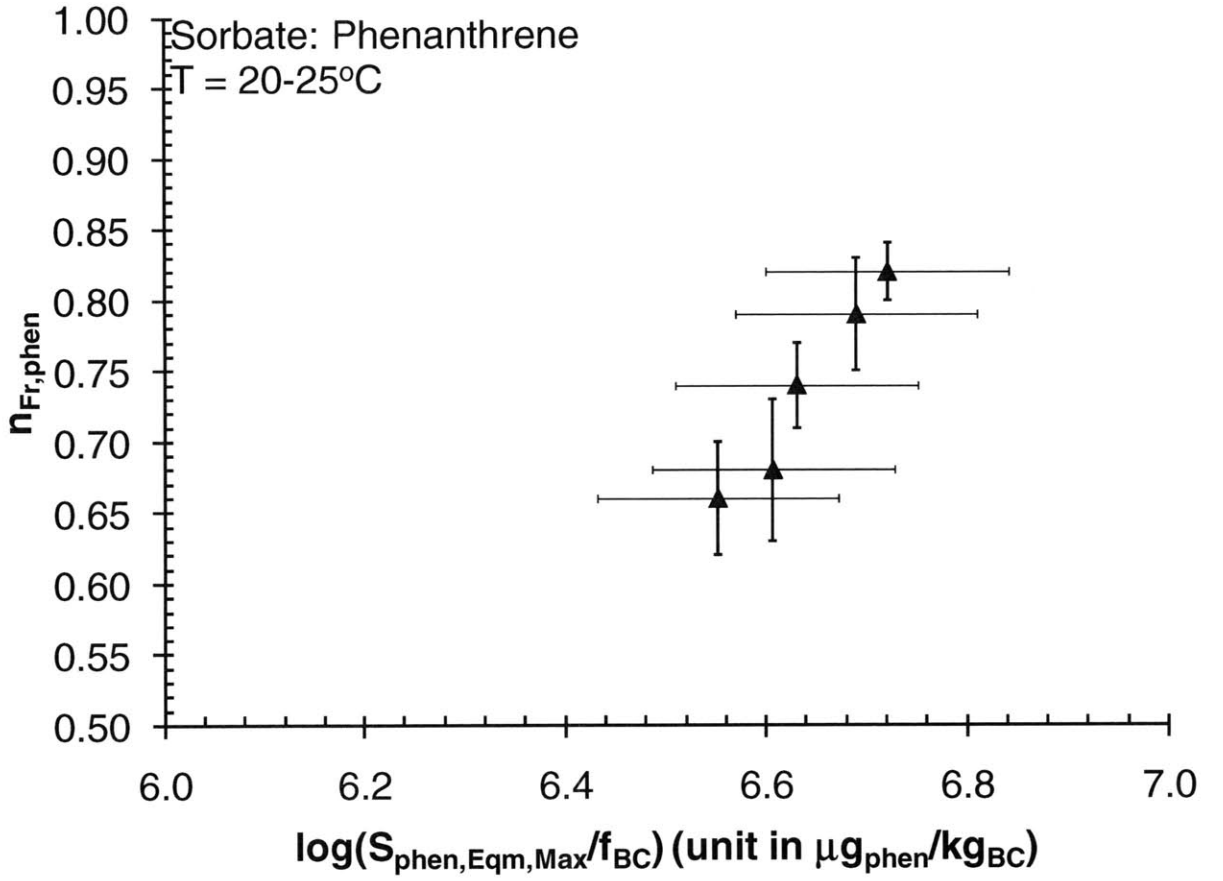

Figure 5 - 7c. n_{Fr} vs $\log(S_{phen,Eqm,Max}/f_{BC})$ for five coals (Data from Cornelissen et al. 2005a).

The Freundlich exponent n_{Fr} is defined as in $S=K_{Lnr}+K_{Fr}C^{nFr}$ or $S=K_{Fr}C^{nFr}$.

It was assumed that $f_{BC,Coal} = 0.5f_{TOC,Coal}$, with a 25% uncertainty in $f_{BC,Coal}$. The shaded region is a visual aid for highlighting the trend and it has no statistical significance. Error bars denote propagated uncertainty or statistical error in $\pm 1\ \sigma$.

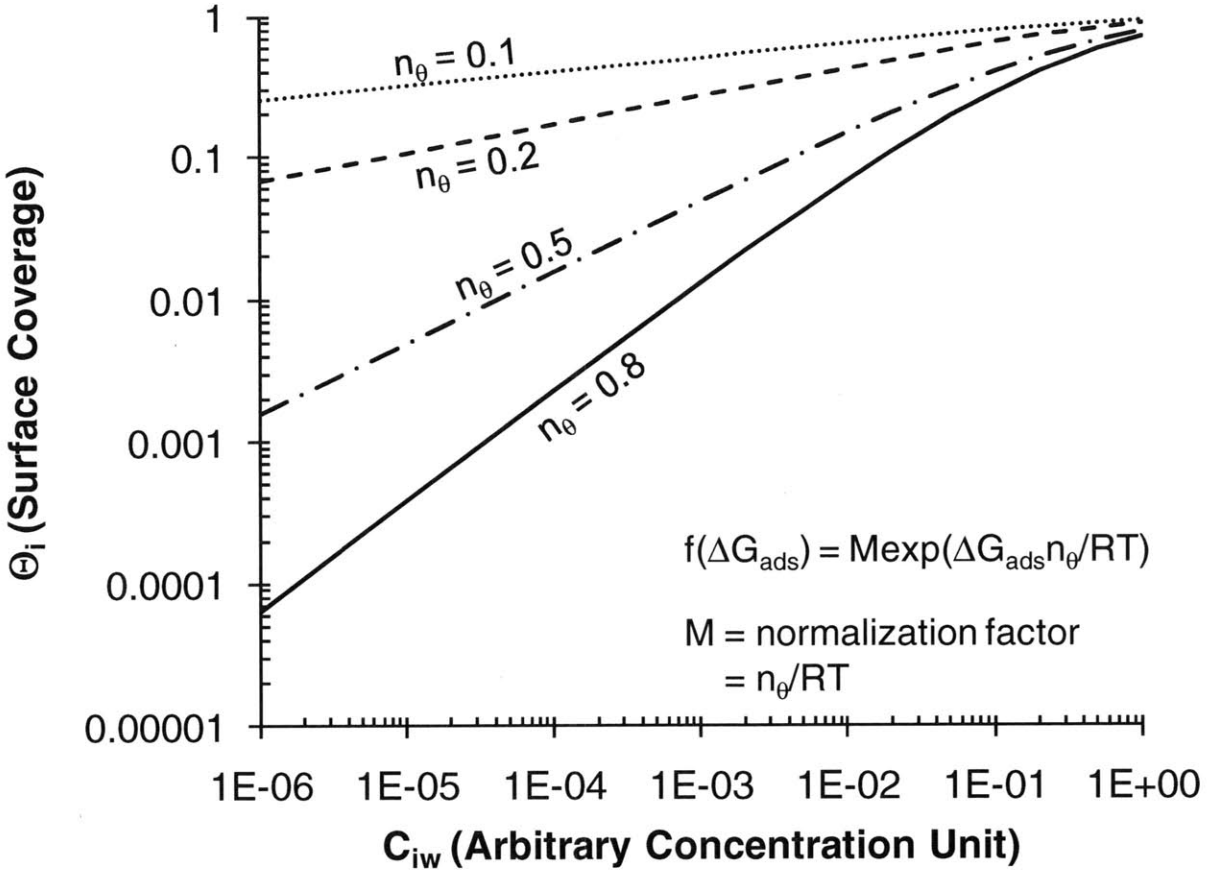

Figure 5 - 8a. Simulated sorption isotherms (exponential distribution of ΔG_{ads}).

Simulated sorption isotherms (at different n_θ) were constructed assuming (i) exponential distribution of ΔG_{ads} and (ii) monolayer adsorption according to modified version of the expressions shown in Adamson et al. (1997). The surface coverage is calculated as:

$$\Theta_i = \int g(K)\theta_i(K)dK = \int_{-\infty}^{0} f(\Delta G_{ads})\theta_i(\Delta G_{ads})d(\Delta G_{ads})$$

$$\theta_i(K) = \frac{KC_{iw}}{1 + KC_{iw}}; \qquad K = \exp(-\Delta G_{ads}/RT)$$

$$f(\Delta G_{ads}) = \frac{n_\theta}{RT}\exp(n_\theta \Delta G_{ads}/RT)$$

Where $f(\Delta G_{ads})$ is the probability density function for surface sites with adsorption energy ΔG_{ads} (ranging from $-\infty$ to 0), n_θ is a constant (≤ 1) on the distribution of ΔG_{ads}, θ_i is fraction coverage of i for all sites with a particular energy, and Θ_i is the total fraction coverage of i (i.e. all sites with all energies). It appeared that the constant n_θ is approximately equal to the Freundlich exponent n_{Fr}.

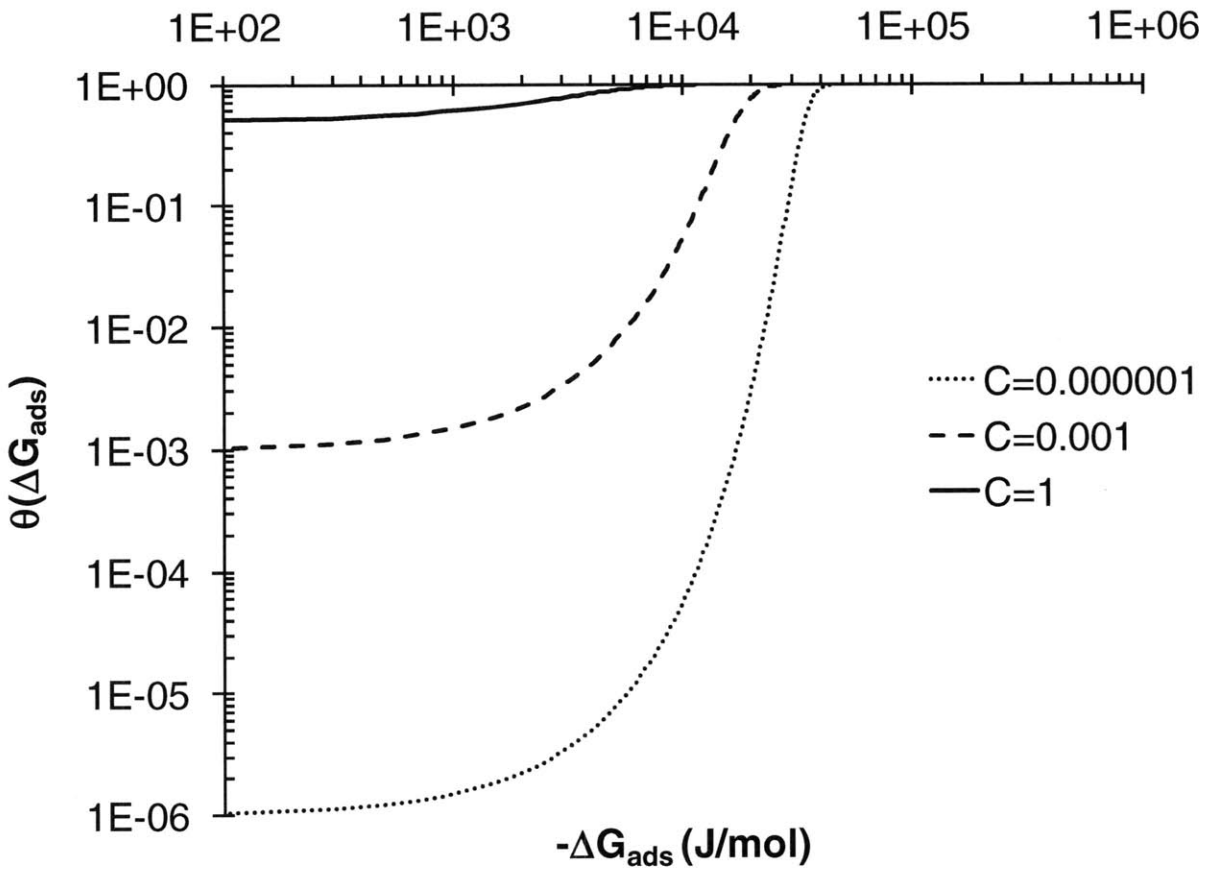

Figure 5 - 8b. Dependence of sites occupancy on dissolved adsorbate concentration.

This figure shows that the fraction coverage of high affinity sites (i.e.$-\Delta G_{ads}$ is large) are quickly filled up even at very low dissolved sorbate concentration levels (low C's). Thus, at relatively high C, it is the low affinity sites that dominate the overall/apparent ΔG_{ads}.

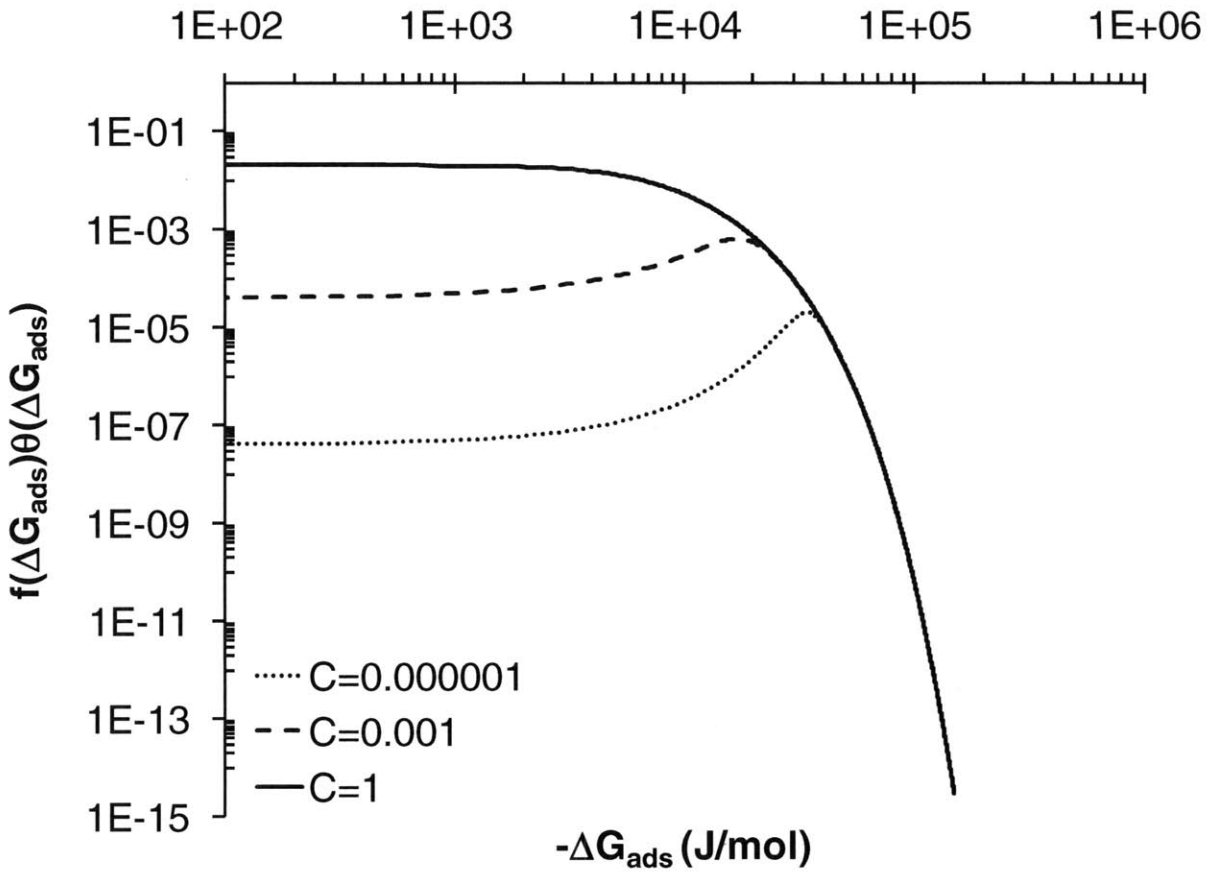

Figure 5 - 8c. Dependence of sites occupancy on dissolved adsorbate concentration with $n_\theta = 0.5$.

This figure shows the relative contribution to adsorption from the different energy sites. The contribution from sites with a particular energy (ΔG_{ads}^*) is the product of the site-specific fraction coverage and the frequency of the sites (i.e. $f(\Delta G_{ads}^*)\theta(\Delta G_{ads}^*)$.

The high affinity sites (high $-\Delta G_{ads}$) may only be dominant (i.e. peak of the curve) and 'observable' when the dissolved sorbate concentration is relatively low (e.g., $C = 10^{-6}$ or 10^{-3}).

Figure 5 - 8. Simulated distribution of surface binding energy and isotherm nonlinearity.

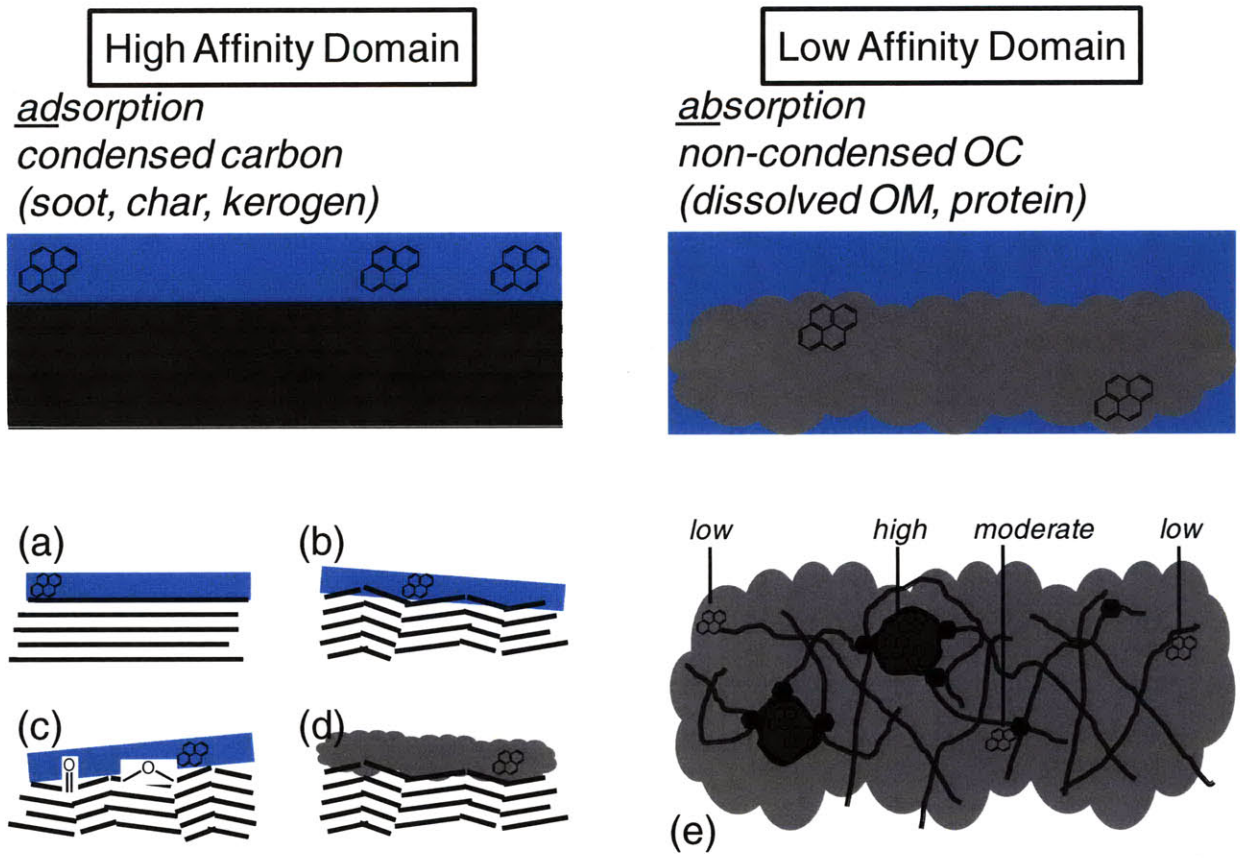

Figure 5 - 9. Alternative mechanistic picture of HOC sorption.

(a) *Ad*sorption onto homogeneous energy sites (e.g., flat, graphitic surface).

(b) *Ad*sorption onto graphitic surface with physical 'defects' (e.g., micropores or cracks).

(c) *Ad*sorption onto surface with other functional groups.

(d) *Ad*sorption onto graphitic surface coated with organic carbon.

(e) *Ab*sorption into structurally heterogeneous organic carbon.

Figure 5 - 10. Qualitative comparison of K_d's for uptake of HOCs in different sorbents.

Adsorption **(I)** Mineral Surface	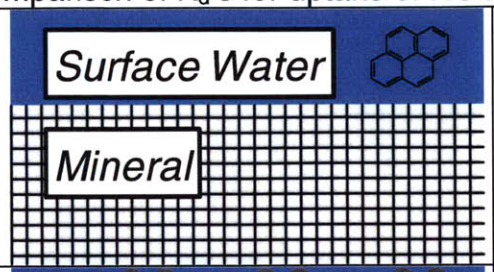		$K_{d,I}$ (weakest) < $K_{d,II}$ < $K_{d,III}$ < $K_{d,IV}$ (strongest)
Absorption **(II)** Bulk 'soft' organic matter (non-BC)	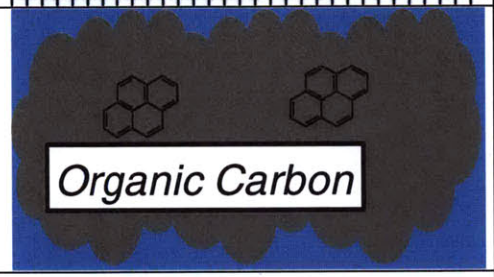	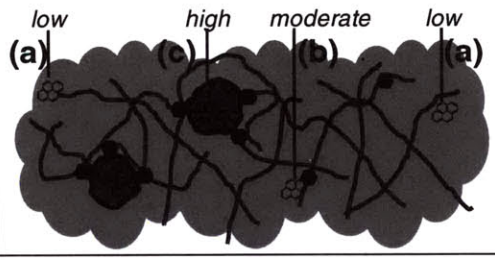	intra-OC structural heterogeneity $K_{d,IIa}$ < $K_{d,IIb}$ < $K_{d,IIc}$
Adsorption **(III)** Condensed carbon-water interface (e.g. soot/graphite/char-water)	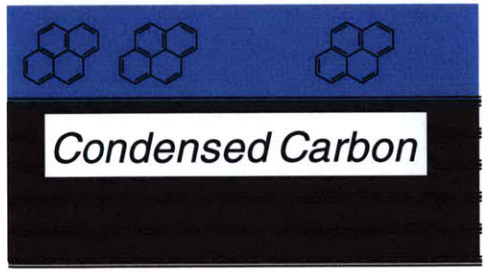	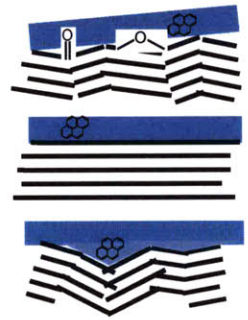	surface geometry, heterogeneity, and pore-surface (see also Figure 4-14) $K_{d,IIIa}$ < $K_{d,IIIb}$ < $K_{d,IIIc}$
Adsorption **(IV)** Condensed carbon-OC interface (e.g. soot/graphite/char-'soft' organic carbon)		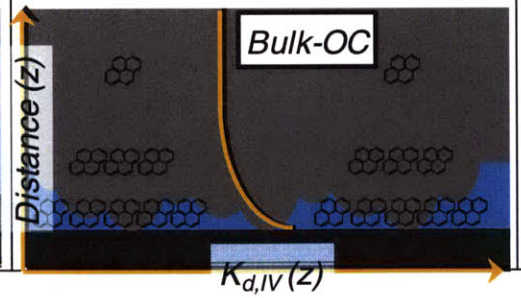	long-range effect from condensed carbon surface $K_{d,III}$ < $K_{d,IV}(0)$; K_d(large z) → $K_{d,II}$

Chapter 6: Figures

Figure 6 - 1. Some non-idealities in the adsorption of HOCs onto natural geosorbents. 389
Figure 6 - 2. Apparent/Overall enthalpy ($\Delta H_{d,app}$) of pyrene sorption vs C_{pyr}. 390
Figure 6 - 3. Absorption enthalpy ($\Delta H_{d,abs}$) of pyrene into sedimentary OC vs C_{pyr}. ...391
Figure 6 - 4. Adsorption enthalpy ($\Delta H_{d,ads}$) of pyrene into sedimentary OC vs C_{pyr}. ...392

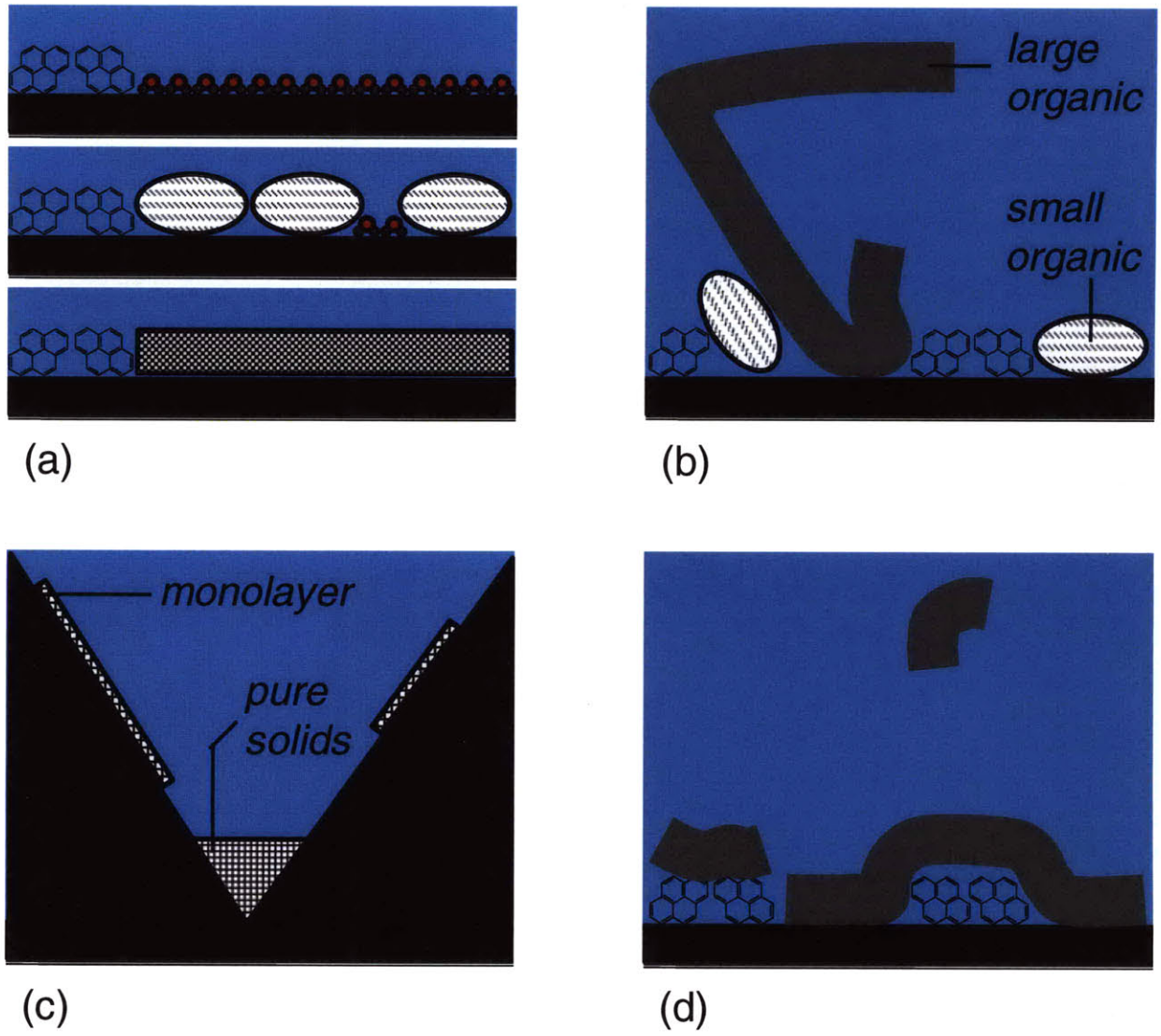

Figure 6 - 1. Some non-idealities in the adsorption of HOCs onto natural geosorbents.

Figure (a) shows how mole fraction of adsorbed pyrene varies with the adsorption of other species (H_2O, similar sized adsorbate, very large adsorbate) whereas the area covered by pyrene remains constant.

Figure (b) shows the case where a large organic 'adsorbate' is only partially bound to the surface.

Figure (c) suggests the possibility that adsorbate may form a locally pure (amorphous) solid of itself, while in other locations it only forms a monolayer association with the surface.

Figure (d) illustrates the case where the large organic fragment may not dissociate from the surface as it becomes displaced by the surface sites by the adsorbing pyrene molecules.

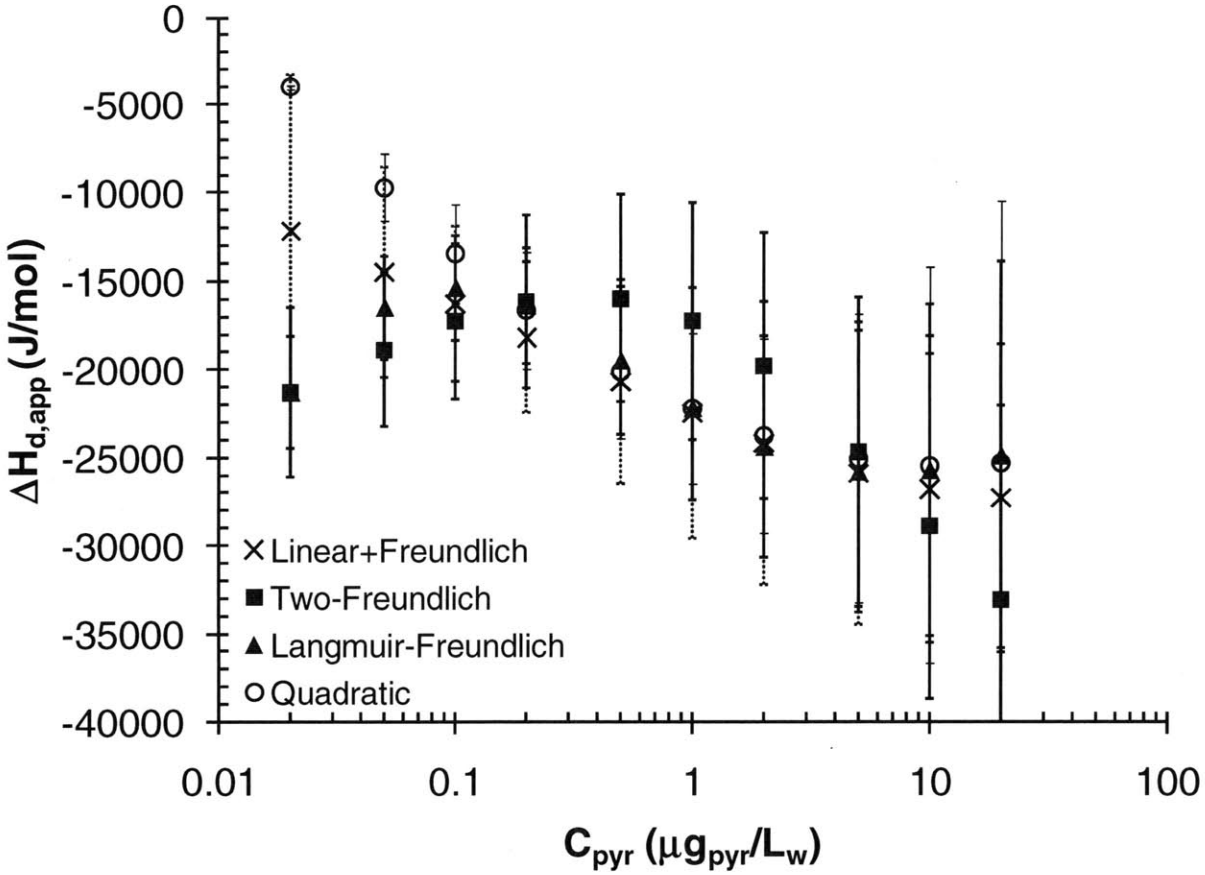

Figure 6 - 2. Apparent/Overall enthalpy ($\Delta H_{d,app}$) of pyrene sorption vs C_{pyr}.

The individual points are $\Delta H_{d,app}$'s at particular C_{pyr}'s evaluated by regression the $\ln K_{d,X}$(at C_{pyr}) vs 1/T, where the $K_{d,X}$'s were estimated from the listed isotherms regressed at 6, 15, 22, and 37°C. Consequently, the error bars represent the uncertainty ($\pm 1\sigma$) from the linear regressions of $\ln K_{d,X}$'s at particular C_{pyr}'s.

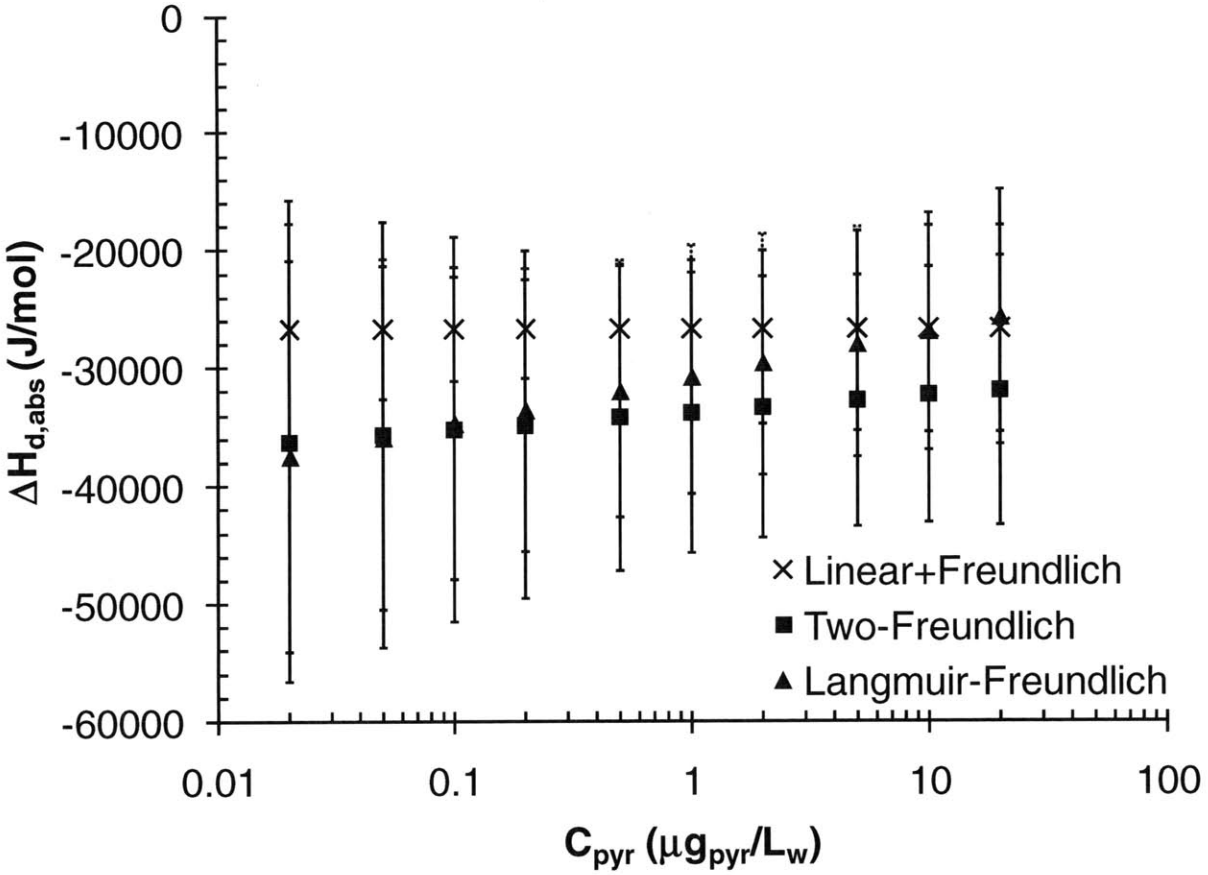

Figure 6 - 3. Absorption enthalpy ($\Delta H_{d,abs}$) of pyrene into sedimentary OC vs C_{pyr}.

The individual points are $\Delta H_{d,abs}$'s at particular C_{pyr}'s evaluated by regression the $\ln K_{d,abs,X}$(at C_{pyr}) vs 1/T, where the $K_{d,absX}$'s were estimated from the lower-affinity domain parameters regressed at 6, 15, 22, and 37°C. Consequently, the error bars represent the uncertainty ($\pm$ 1σ) from the linear regressions of $\ln K_{d,abs,X}$'s at particular C_{pyr}'s.

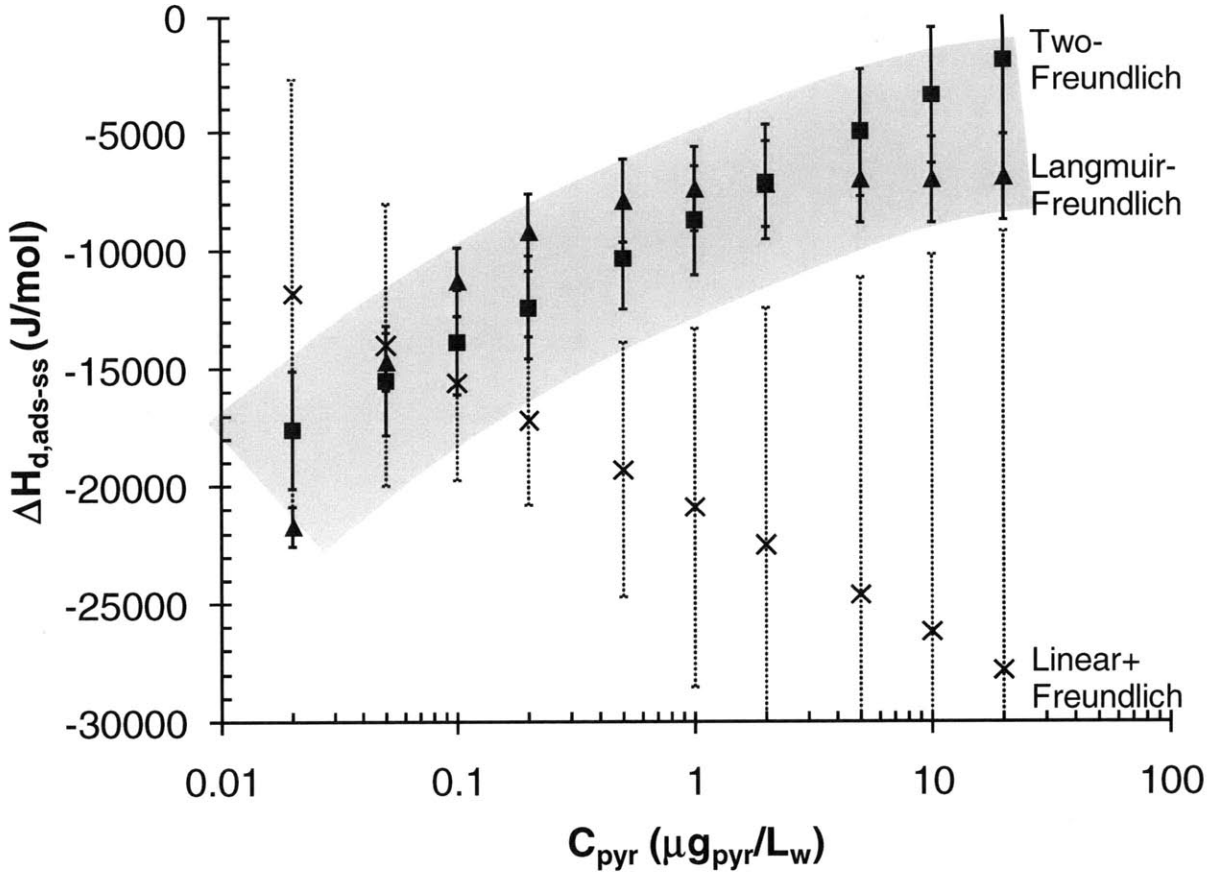

Figure 6 - 4. Adsorption enthalpy ($\Delta H_{d,ads}$) of pyrene into sedimentary OC vs C_{pyr}.

The individual points are $\Delta H_{d,ads}$'s at particular C_{pyr}'s evaluated by regression the $\ln K_{d,ads,X}$(at C_{pyr}) vs 1/T, where the $K_{d,adsX}$'s were estimated from the lower-affinity domain parameters regressed at 6, 15, 22, and 37°C. Consequently, the error bars represent the uncertainty (± 1σ) from the linear regressions of $\ln K_{d,ads,X}$'s at particular C_{pyr}'s.

Chapter 7: Figures

Figure 7 - 1. Idealized distribution of BC in natural soil/sedimentary aggregates.....394
Figure 7 - 2. Estimated numbers of Grains, nm-BC and μm-BC particles per in natural aggregates (f_{BC} = 0.002) 395
Figure 7 - 3. Intraparticular Pore Diffusion Model.....396
Figure 7 - 4. Transport of organic sorbates within natural aggregates. 397
Figure 7 - 5. Competing transport pathways of organic sorbates within aggregates..398
Figure 7 - 6. Connectivity of OM, solids, and porewater phase in natural aggregates. 399
Figure 7 - 7. Dominant HOCs diffusion mechanisms within selected sorbents. 400
Figure 7 - 8. Core, intermediate, and edge shells in an idealized aggregate. 401
Figure 7 - 9. Discretized aggregate, grid & label system, and shells (core, intermediate, edge).....402
Figure 7 - 10. Analytical Solution for Radial Diffusion Model ($\lambda = \beta = (K_d R_{sw})^{-1}$). 403
Figure 7 - 11. Validation of Numerical Model (non-linear 1-D Radial Retarded Diffusion) 404
Figure 7 - 12. Convergence of adsorbate-mass profiles (Pure OC) at four different $K_d R_{sw}$'s.....406
Figure 7 - 13. Convergence of adsorbate-mass profiles (Linear OC + Linear BC) at two different $K_d R_{sw}$'s. 407
Figure 7 - 14. Convergence of adsorbate-mass profiles at different time step increment $\Delta\tau(D_{iw})$ (at three $K_d R_{sw}$'s). 408
Figure 7 - 15. *A priori* predictions (four models) and the observed dissolved pyrene for selected suspensions.....409
Figure 7 - 16. *A priori* prediction of $C_{pyr,w,Eqm}$ for 15 BH#6/NQB suspensions from four isotherm models. 410
Figure 7 - 17. *A priori* predicted $C_{pyr,w,Eqm}$ vs solids-to-water ratio (R_{sw}). 412
Figure 7 - 18. *A priori* predicted $C_{pyr,w,Eqm}$ vs nominal diameter of sediment aggregates. 414
Figure 7 - 19. Selected C_{pyr}-Time profiles predicted by the Occlusion-OC-BC isotherm. 417
Figure 7 - 20. Model-Observation disparity in the 10^{th}–100^{th} h period.....419
Figure 7 - 21. Desorption dynamics by best-fit New-OC-BC, best-fit Universal-OC-BC, and *a priori* Occlusion-OC-BC models.....421
Figure 7 - 22. Desorption modeled by best-fit Forced Linear isotherm (K_{TOC}).....423
Figure 7 - 23. F_{rapid}, F_{slow} (empirical) vs total system OC-pyr, BC-pyr (*a priori*) 424
Figure 7 - 24. k_{rapid} & k_{slow} (empirical) vs κ_{OC} & κ_{BC} (*a priori*).....425
Figure 7 - 25. k_{rapid} & k_{slow} (empirical) vs $S_{pyr,rapid}$ & $S_{pyr,slow}$ (empirical).....426

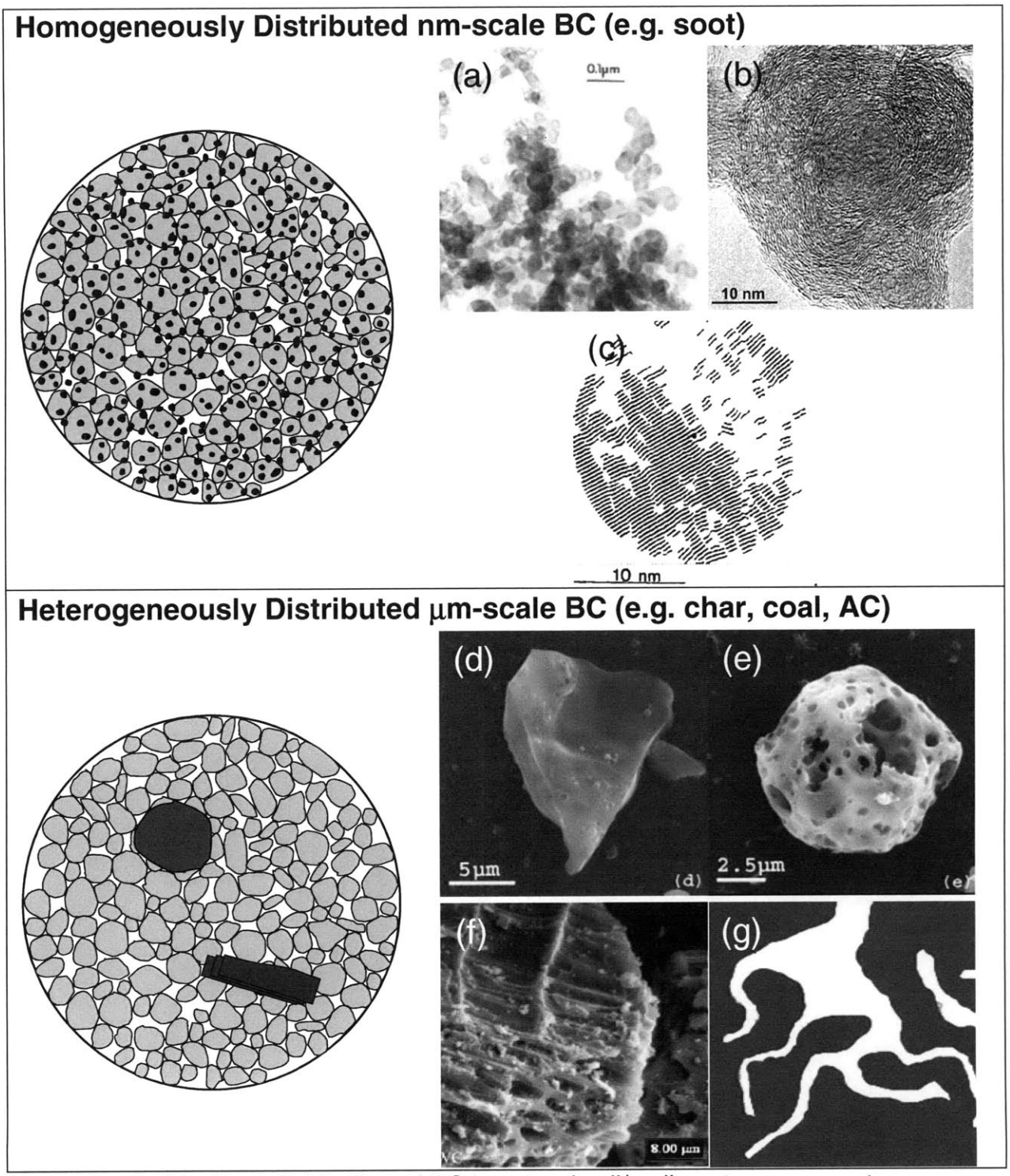

Figure 7 - 1. Idealized distribution of BC in natural soil/sedimentary aggregates.

Small figures show: (a) clusters of nm-soot from diesel engine exhaust (Murr et al. 2003); (b) & (c) the inter-planar structures typical for soot-BC (Rainey et al. 1997); (d) coal-originated char (Chen et al. 2005); (e) moderately porous char (Chen et al. 2005); (f) highly porous and large char (Fernandes et al. 2003); (g) a cartoon of the internal surfaces and pore structure of activate carbon particles.

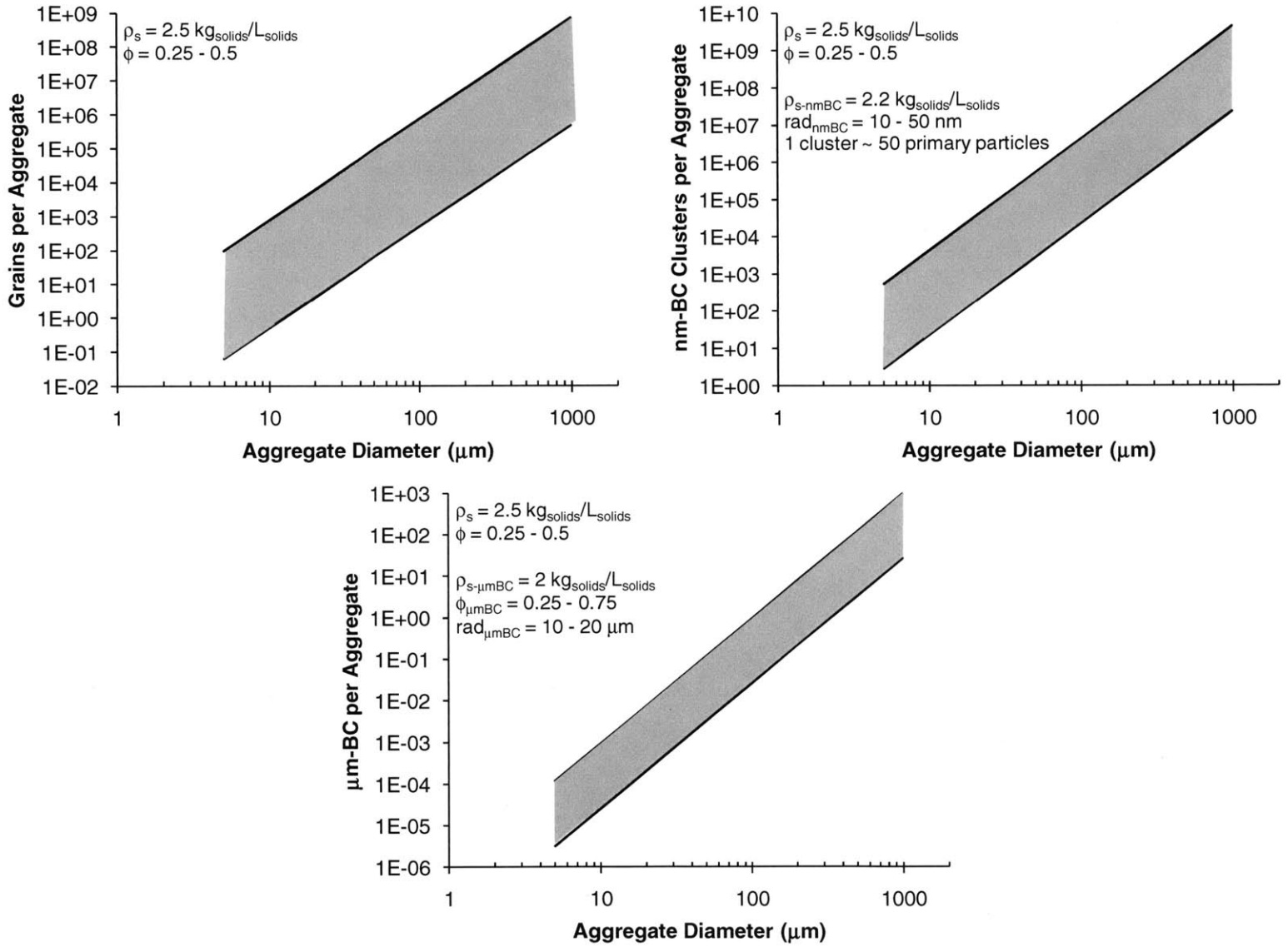

Figure 7 - 2. Estimated numbers of Grains, nm-BC and μm-BC particles per in natural aggregates (f_{BC} = 0.002)

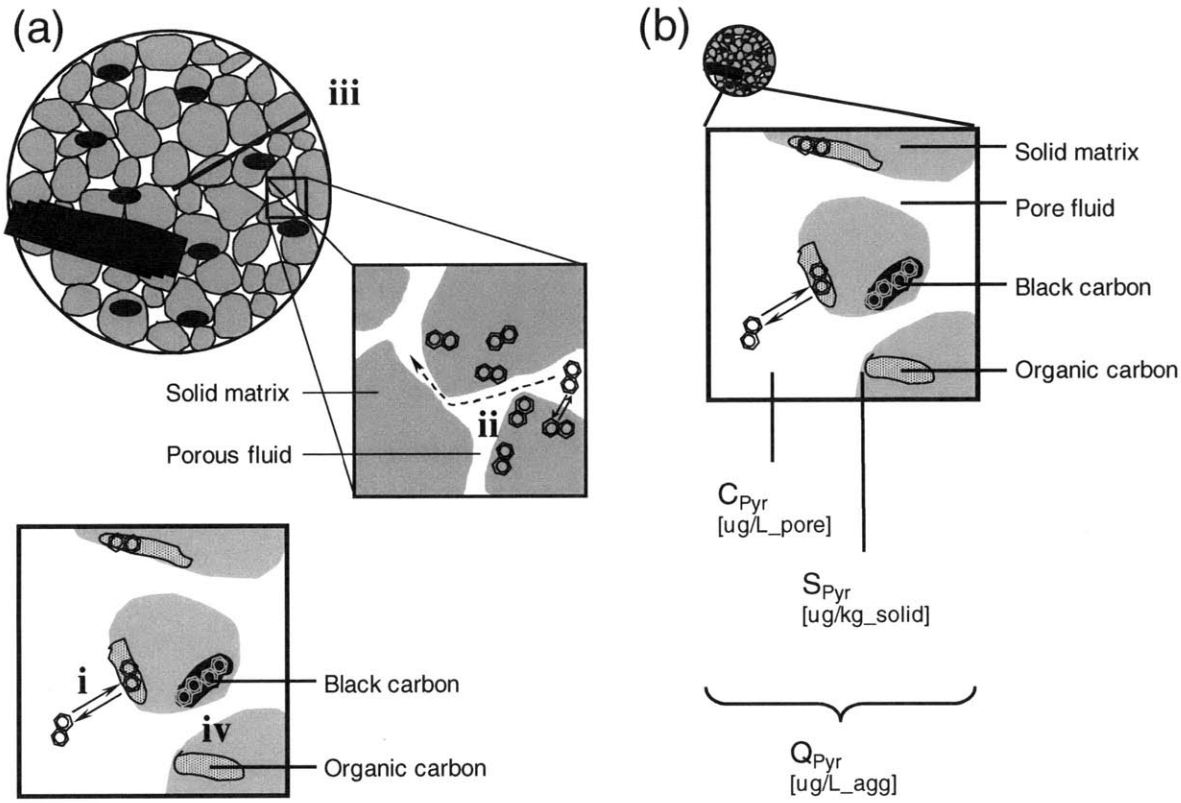

Figure 7 - 3. Intraparticular Pore Diffusion Model.

In (a), the major assumptions/components in the model were highlighted: (**i**) local partitioning equilibrium of sorbate between solid and fluid phases, (**ii**) dissolved organic sorbates migrate via diffusion in the fluid phase, (**iii**) diffusion of sorbates proceeds radially, assuming spherical aggregates, and (**iv**) diffusion of sorbates is slowed down (retarded) by the partitioning constant, $K_d(C'_{iw})$, which can be a function of the *local sorbate concentration in the fluid phase*.

In (b), the relevant absorbing (organic carbon) and adsorbing (black carbon) phases are shown with mineral phase as the bulk, sorption-inert (i.e. relative to OC/BC) matrix.

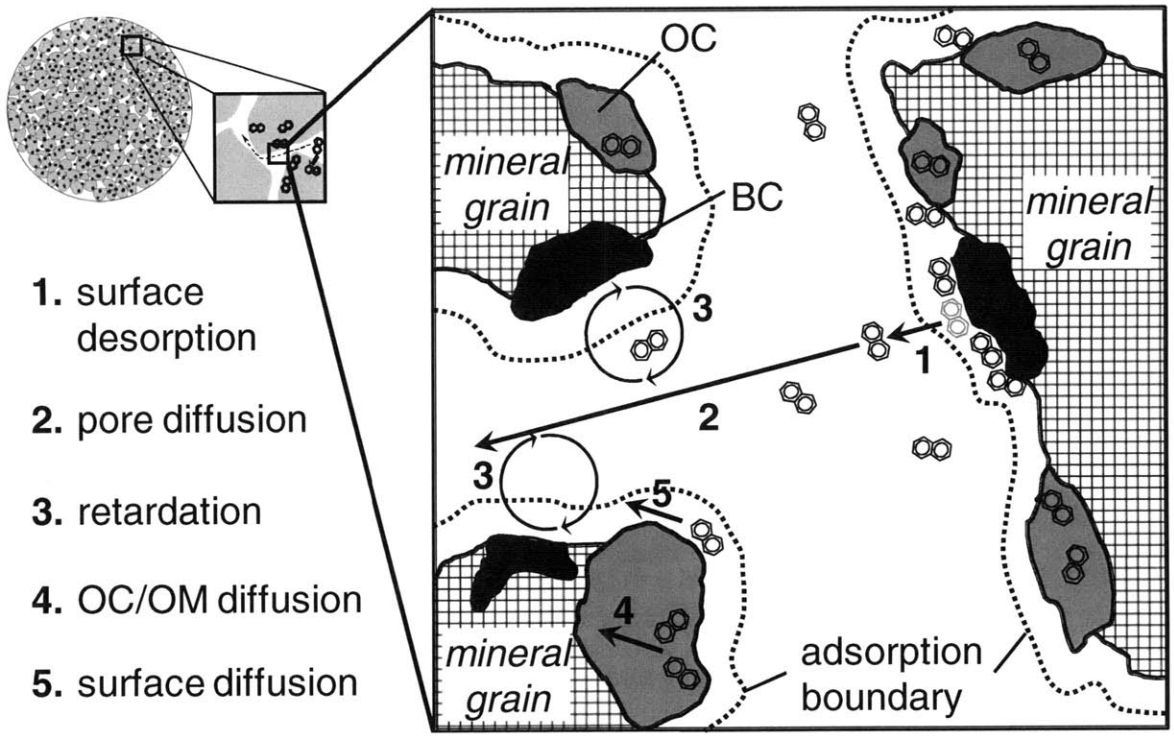

Figure 7 - 4. Transport of organic sorbates within natural aggregates.

In (a), the major assumptions/components in the model were highlighted: (**i**) local partitioning equilibrium of sorbate between solid and fluid phases,

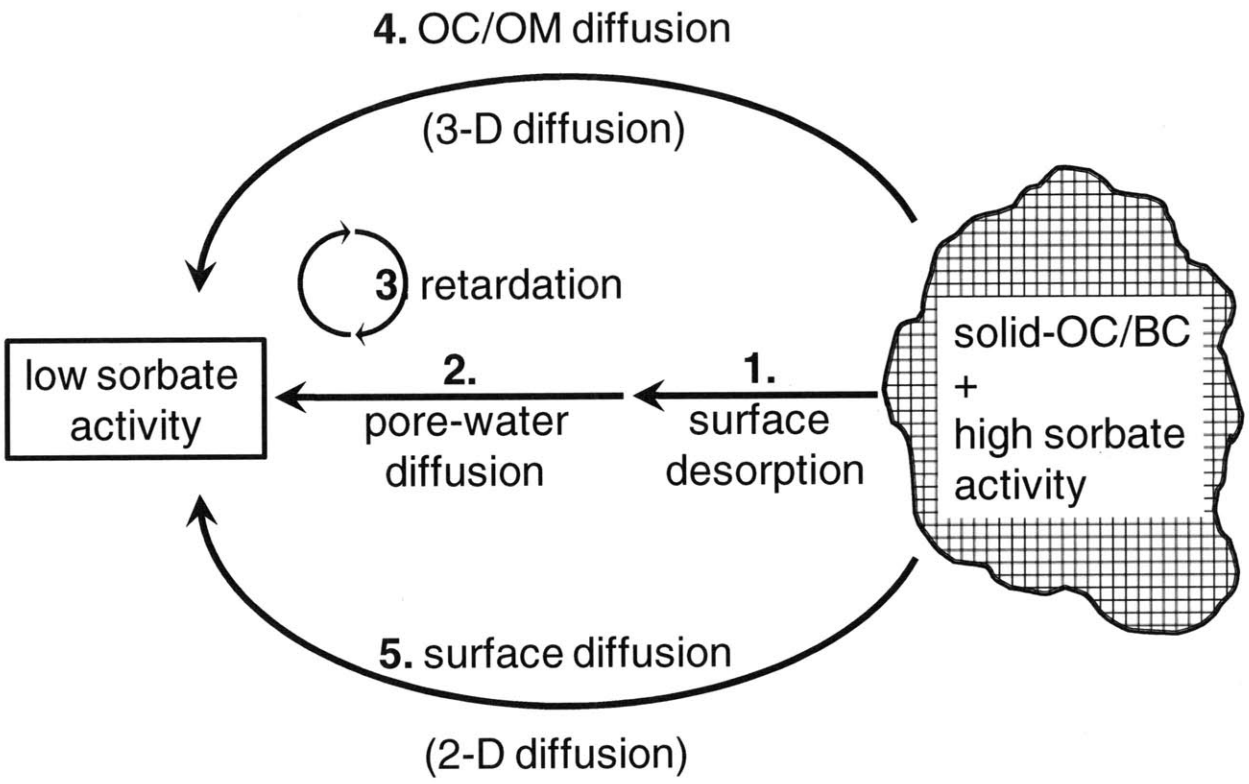

Figure 7 - 5. Competing transport pathways of organic sorbates within aggregates.

This is a conceptual diagram highlighting three competing pathways of sorbate transport at the local scale (~<1 μm) within natural aggregates. The sorbate migrates from region of high sorbate activity to that of low activity. This may occur by first desorbing from the solid phase into the pore water phase ("**1**"), and then proceeding by diffusion in pore-water ("**2**") with retardation ("**3**").

If extensive network of organic matter (OM) is present within the aggregate, the sorbate may also migrate by diffusing *through* the OM matrix ("**4**"). This would be a 3-D diffusion with the rate depending on the diffusivity of the sorbate in the OM matrix (approximately like polymeric structures).

If the solid-surface within the aggregate is well connected, the sorbate may also migrate by diffusing *on/along* the solid-surface ("**5**"). This would be a 2-D diffusion with an average diffusivity of the sorbate on the surface (possibly coated with OC/BC).

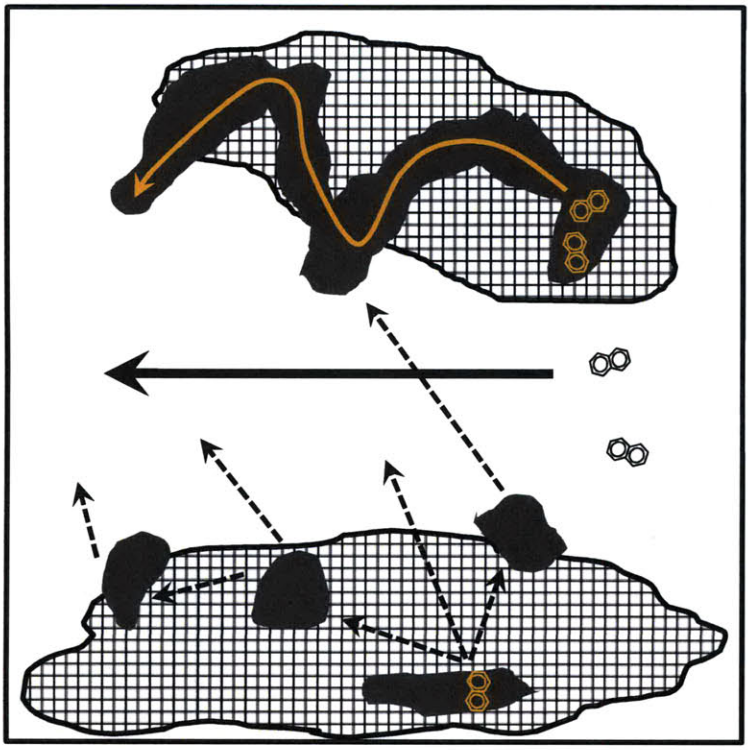

Figure 7 - 6. Connectivity of OM, solids, and porewater phase in natural aggregates.

The figure highlights three cases of how phase connectivity can affect diffusion. The chemical potential of the sorbate is such that the sorbate diffuses from right to left.

In (i), the organic phase (BC or OM) is connected but in a tortuous way, and this reduces the diffusion rate (through OM or on BC surface).

In (ii), sorbate molecules diffuse quickly through the relatively unobstructed porewater phase, which is the predominant non-mineral phase in this picture.

In (iii), the sorptive phase (BC or OM) exists in the form of isolated 'islands', thus the sorbate molecules have to desorb first into the pore-water phase, and then hop onto another island or diffuse via intra-aggregate porewater.

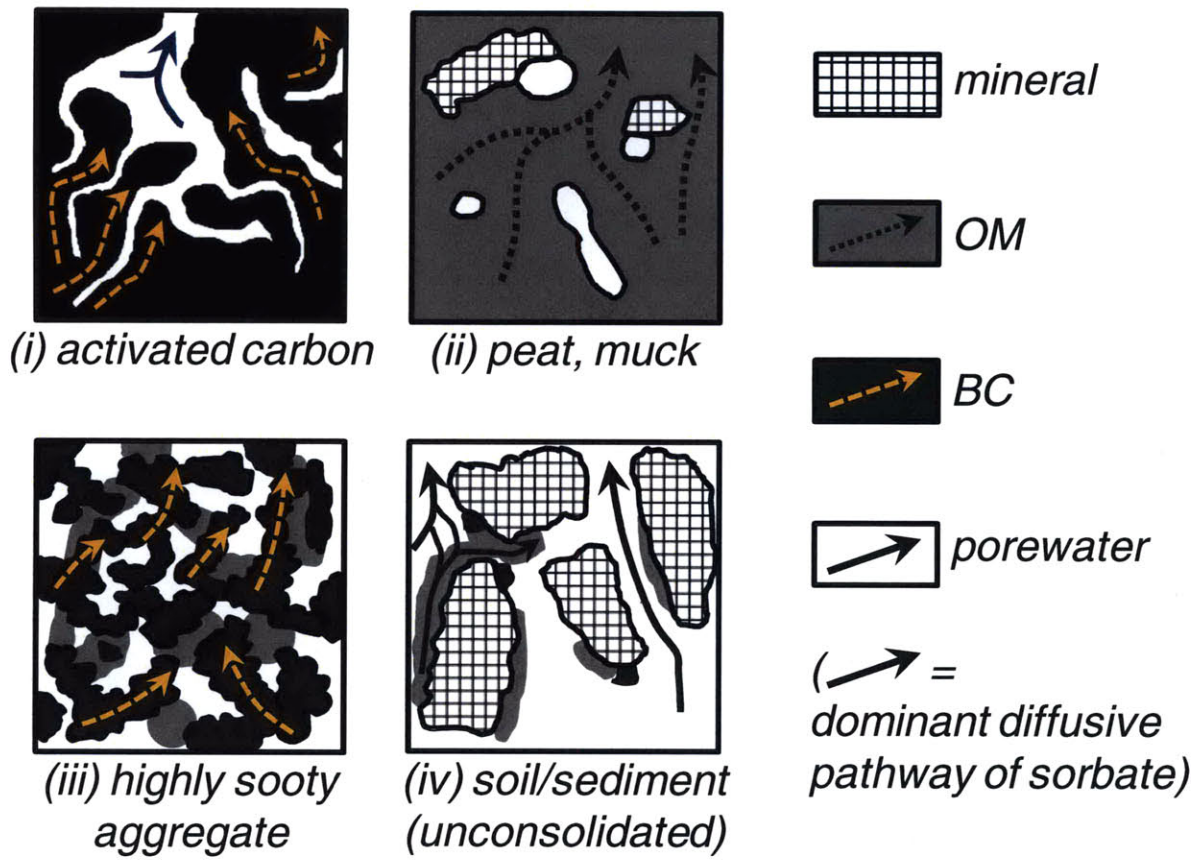

Figure 7 - 7. Dominant HOCs diffusion mechanisms within selected sorbents.

The figure highlights four cases where different intra-sorbent diffusion mechanism may be dominant for the transport of organic sorbates (HOCs) with natural aggregates. Note that in all cases, the sorbate is diffusing from right to left.

In (i), the well-connected and highly carbonaceous surface favors surface diffusion (dashed arrows) over porewater diffusion or diffusion through organic matter. In large pores where the surface to pore volume ratio is relatively low, intra-particle porewater diffusion may gain dominance (solid arrows).

In (ii), the highly OC-enriched peat/muck favors diffusion through organic matter. Intra-sorbent porewater phase (open vacuoles) is too disconnected to be effective.

In (iii), the highly soot aggregate (e.g. fresh exhaust gas particulate matter) contains highly connected soot-surface. Hence surface diffusion should dominate intra-aggregate kinetics.

In (iv), the unconsolidated soil/sediment aggregate contains large volume of porewater phase (or unsaturated pore volume, in the case of soil), which would favor porewater (or pore volume) diffusion.

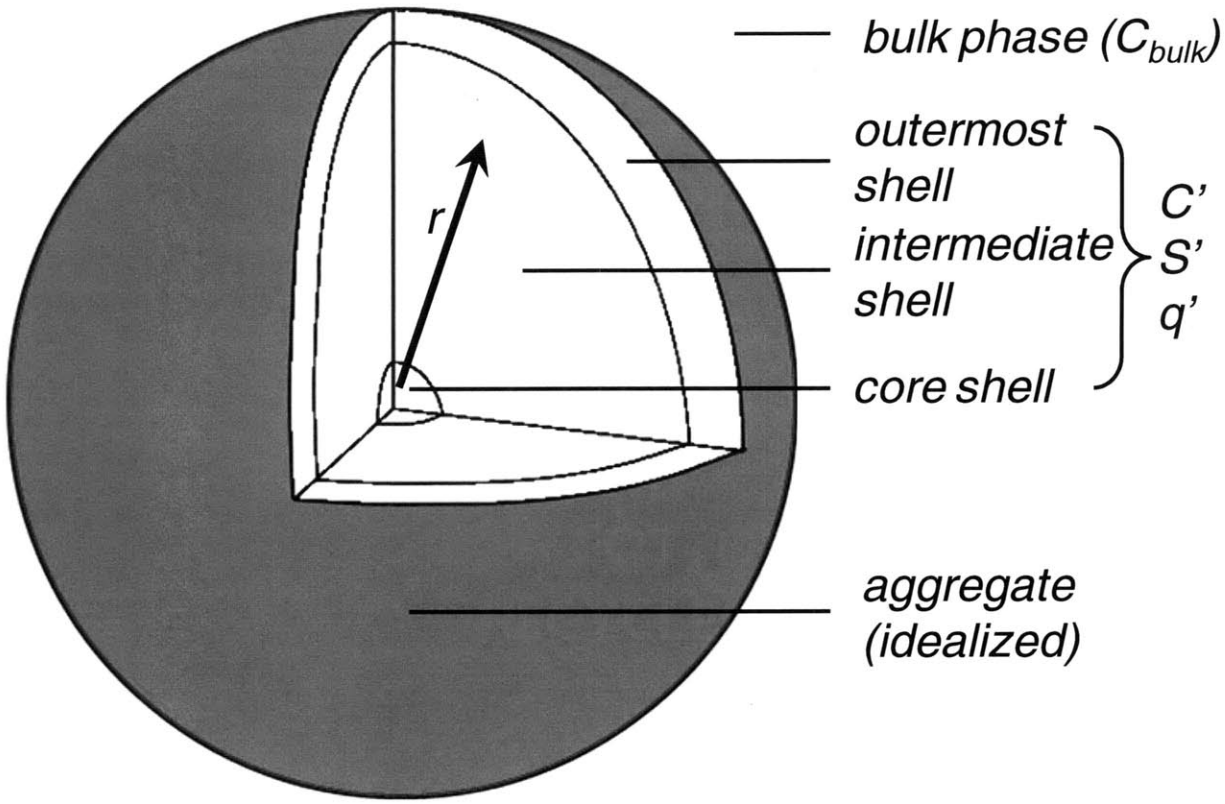

Figure 7 - 8. Core, intermediate, and edge shells in an idealized aggregate.

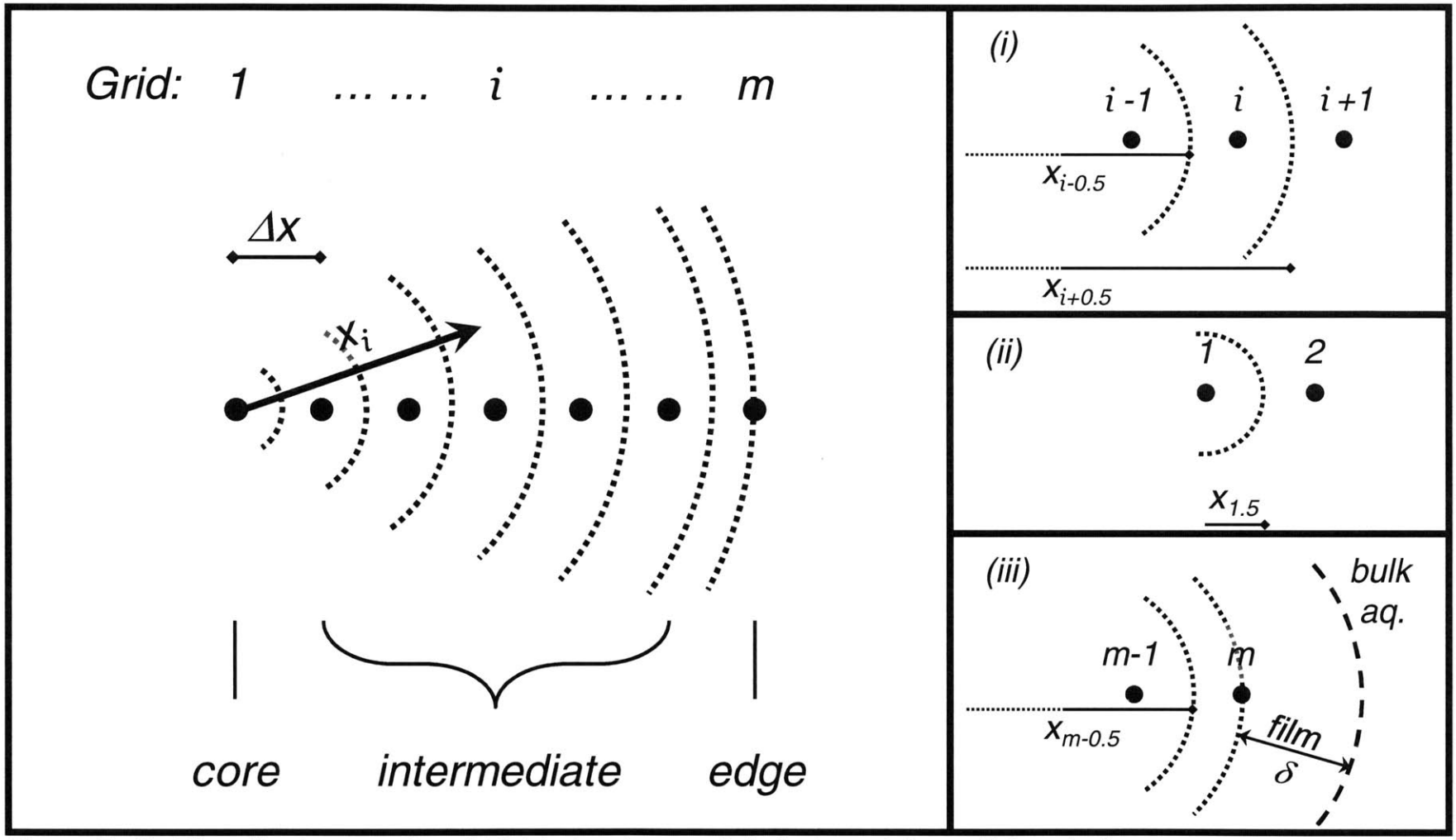

Figure 7 - 9. Discretized aggregate, grid & label system, and shells (core, intermediate, edge).

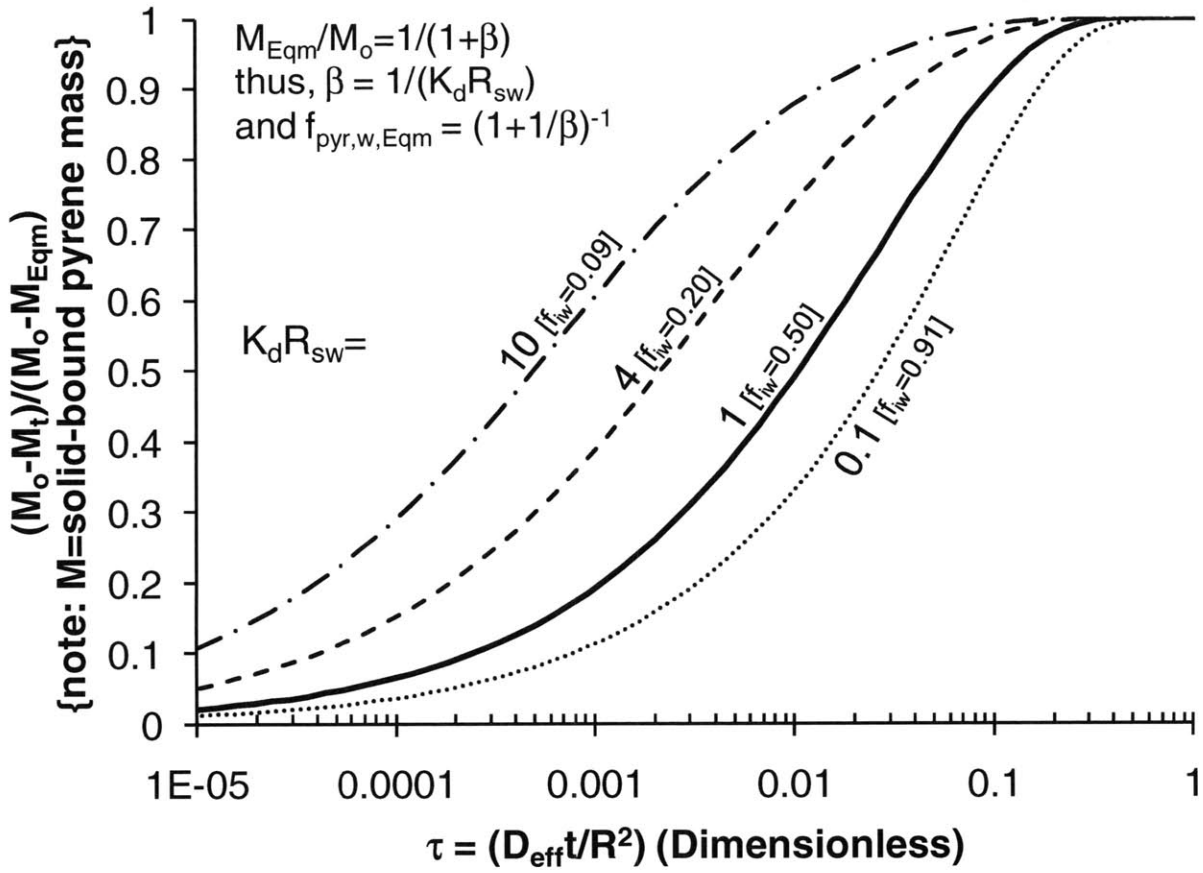

Figure 7 - 10. Analytical Solution for Radial Diffusion Model ($\lambda = \beta = (K_dR_{sw})^{-1}$).

This figure showed the dimensionless desorption kinetic profiles generated at four selected K_dR_{sw}'s with the $\lambda = \beta = 1/(K_dR_{sw})$. The profiles were generated with ~5000 q_n's. This choice of λ suggested that the rate of desorption should be the slowest in an infinite bath system.

The y-axis represented the normalized mass of desorbed sorbate; the x-axis stood for a dimensionless time τ.

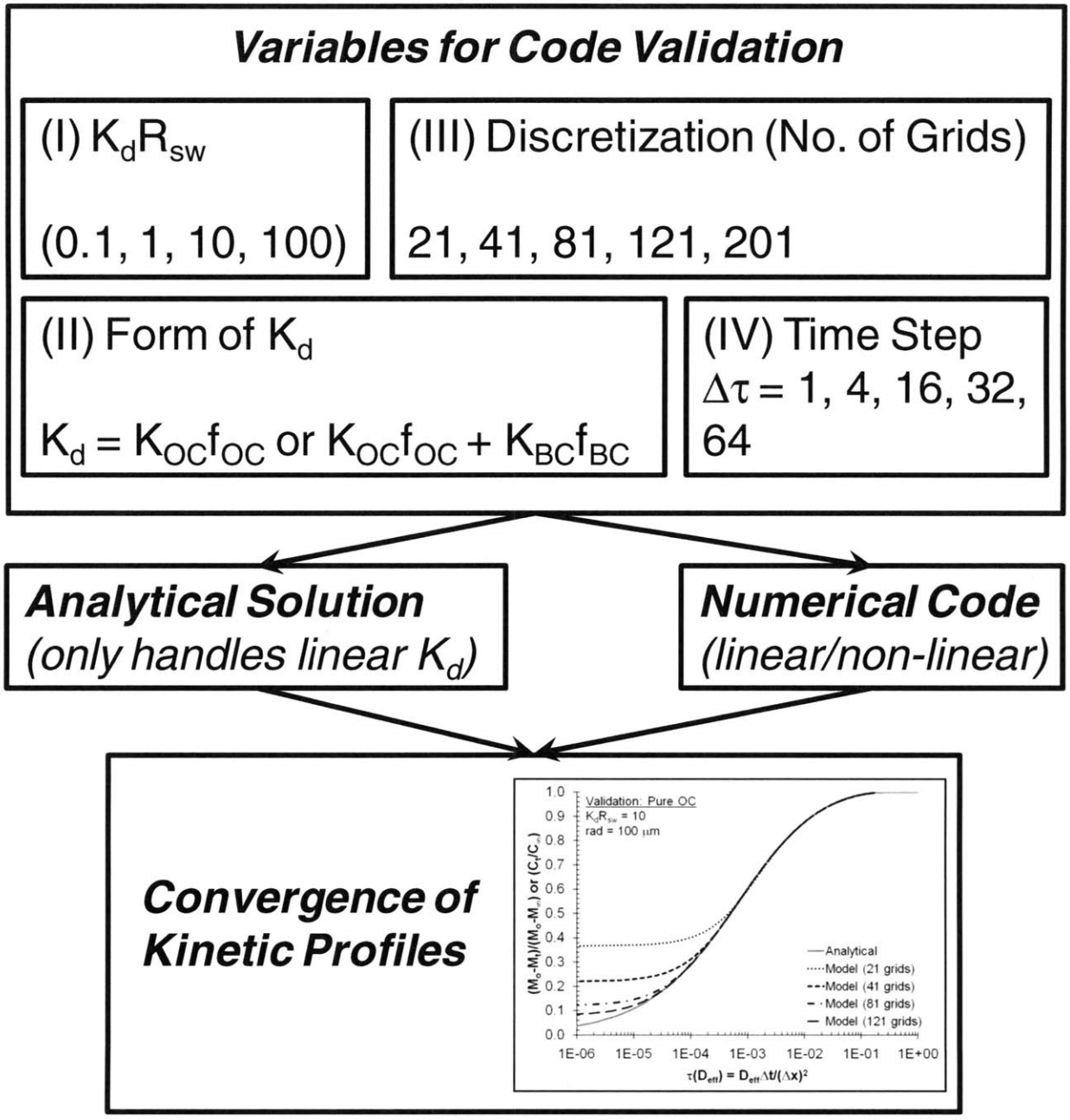

Figure 7 - 11. Validation of Numerical Model (non-linear 1-D Radial Retarded Diffusion)

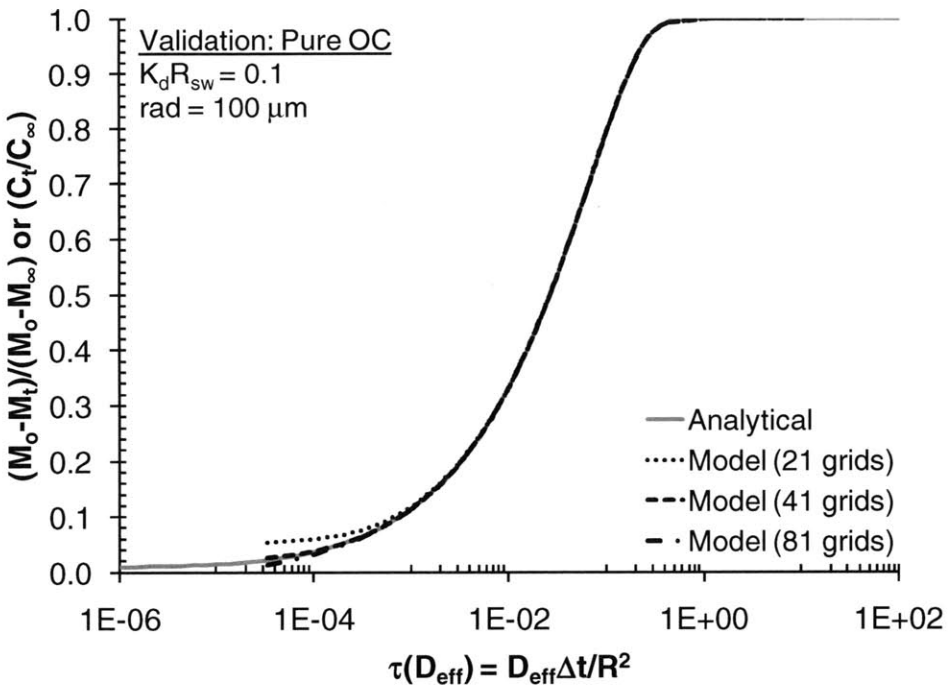
Validation: Pure OC
K_dR_{sw} = 0.1
rad = 100 μm
$(M_o-M_t)/(M_o-M_\infty)$ or (C_t/C_∞)
1.0
0.9
0.8
0.7
0.6
0.5
0.4
0.3
0.2
0.1
0.0
1E-06
1E-04
1E-02
1E+00
1E+02
$\tau(D_{eff}) = D_{eff}\Delta t/R^2$
Analytical
Model (21 grids)
Model (41 grids)
Model (81 grids)

(a)

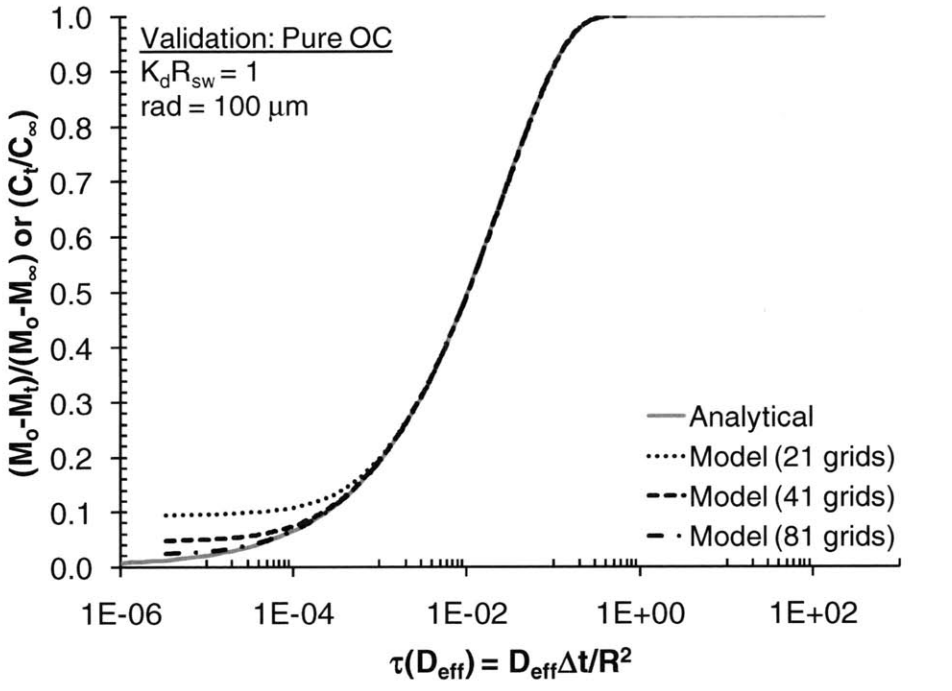
Validation: Pure OC
K_dR_{sw} = 1
rad = 100 μm
$(M_o-M_t)/(M_o-M_\infty)$ or (C_t/C_∞)
1.0
0.9
0.8
0.7
0.6
0.5
0.4
0.3
0.2
0.1
0.0
1E-06
1E-04
1E-02
1E+00
1E+02
$\tau(D_{eff}) = D_{eff}\Delta t/R^2$
Analytical
Model (21 grids)
Model (41 grids)
Model (81 grids)

(b)

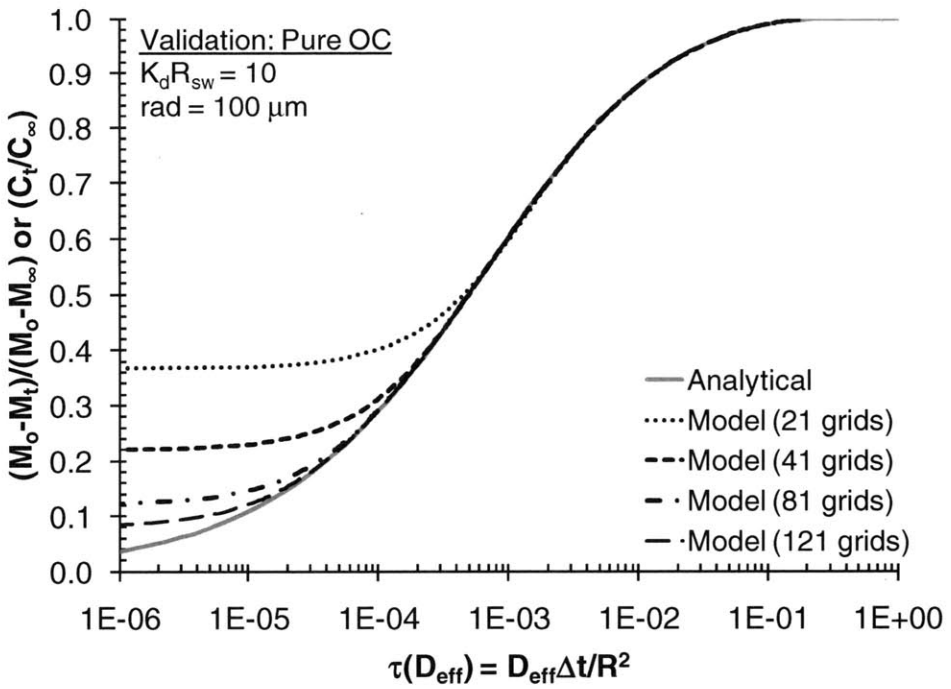

(c)

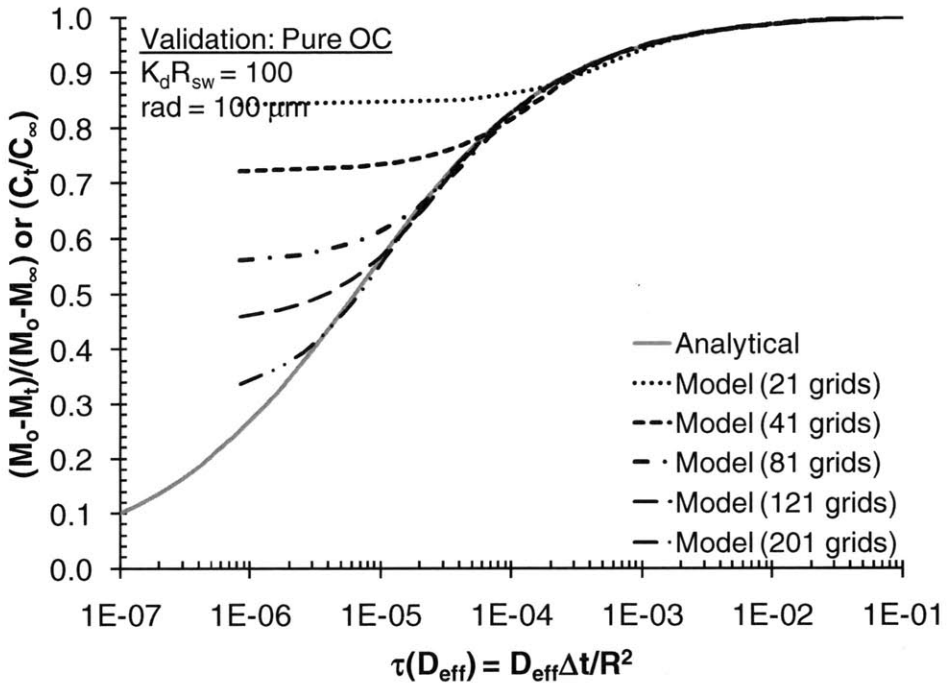

(d)

Figure 7 - 12. Convergence of adsorbate-mass profiles (Pure OC) at four different K_dR_{sw}'s.

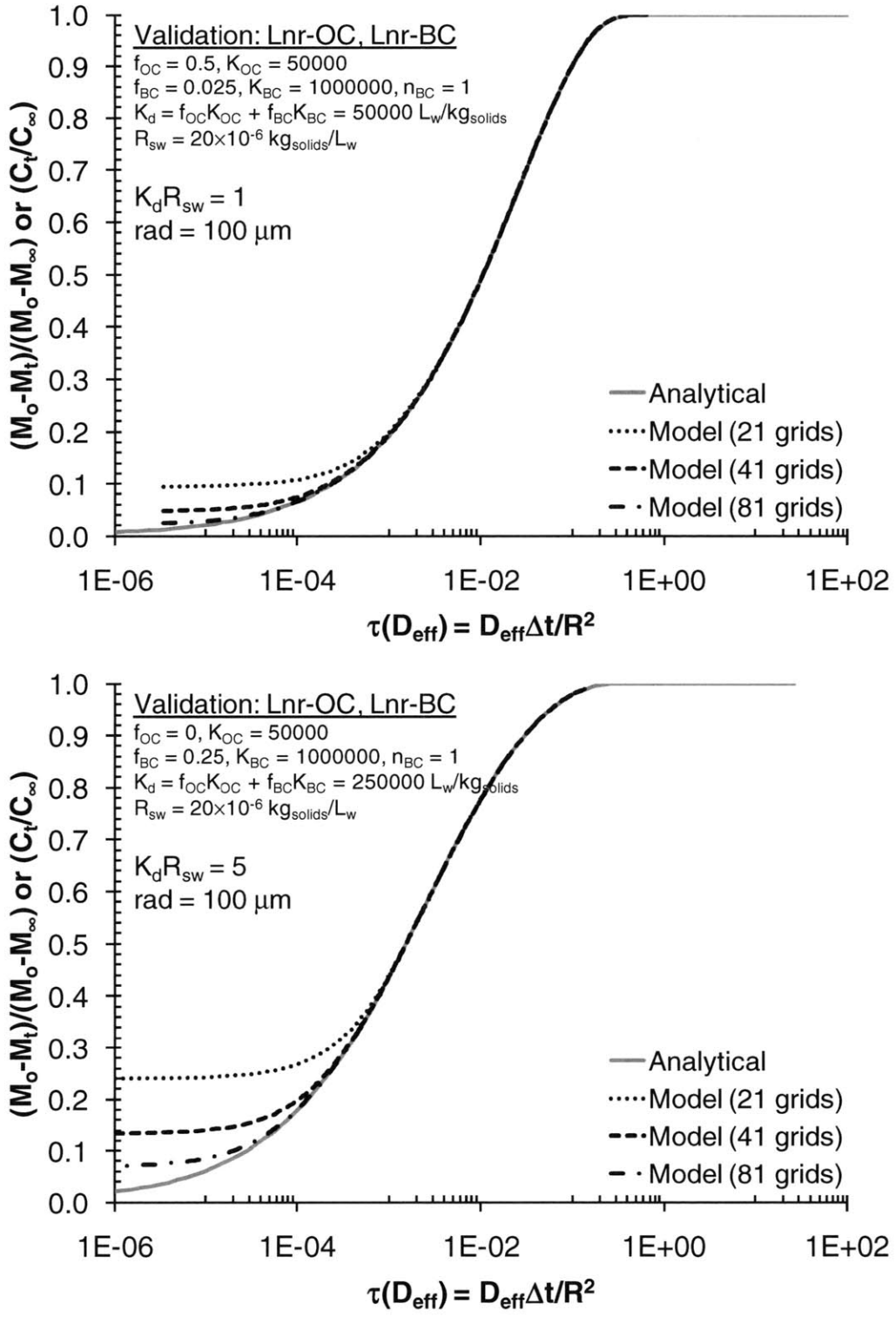

Figure 7 - 13. Convergence of adsorbate-mass profiles (Linear OC + Linear BC) at two different K_dR_{sw}'s.

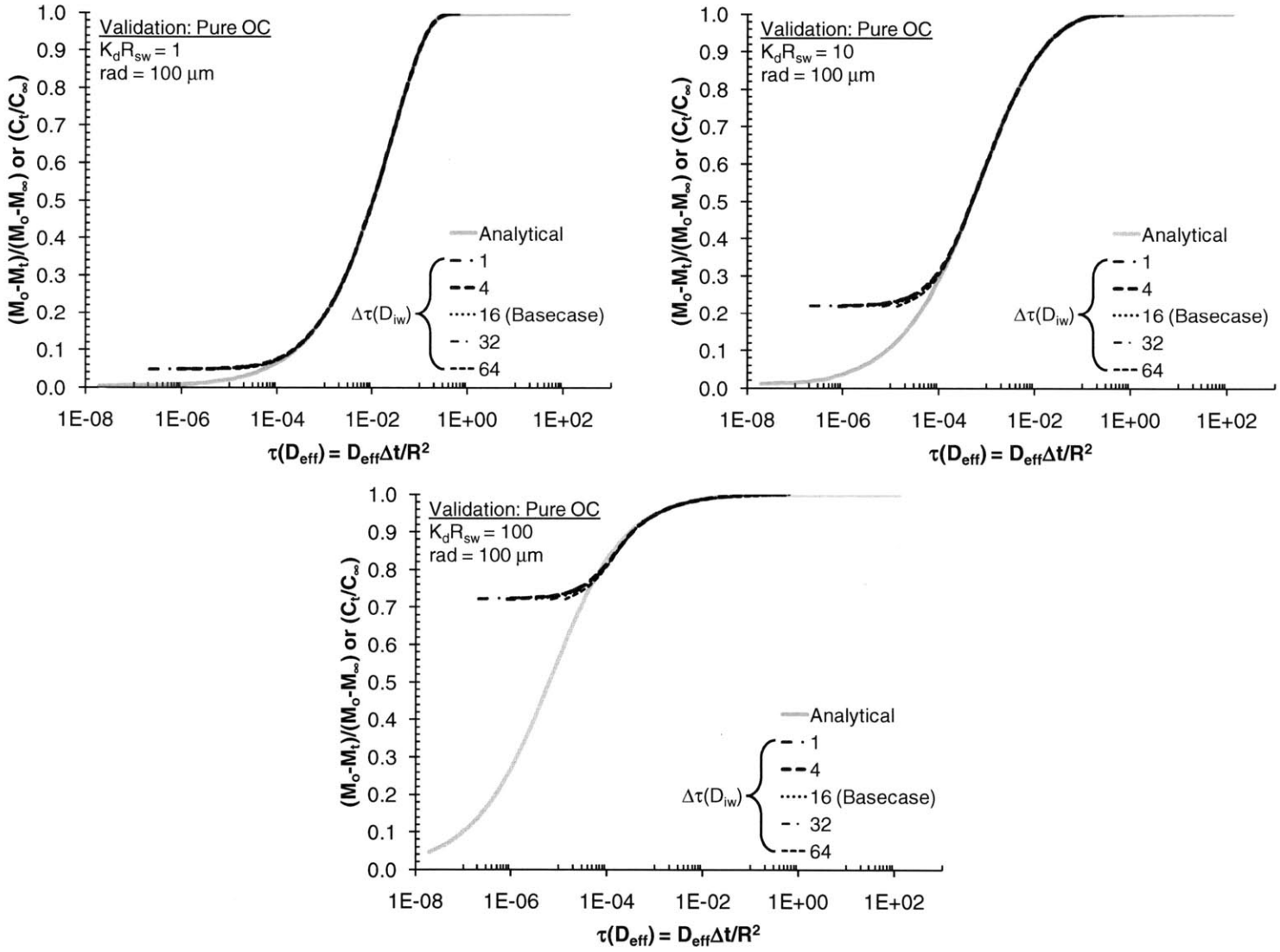

Figure 7 - 14. Convergence of adsorbate-mass profiles at different time step increment $\Delta\tau(D_{iw})$ (at three K_dR_{sw}'s).

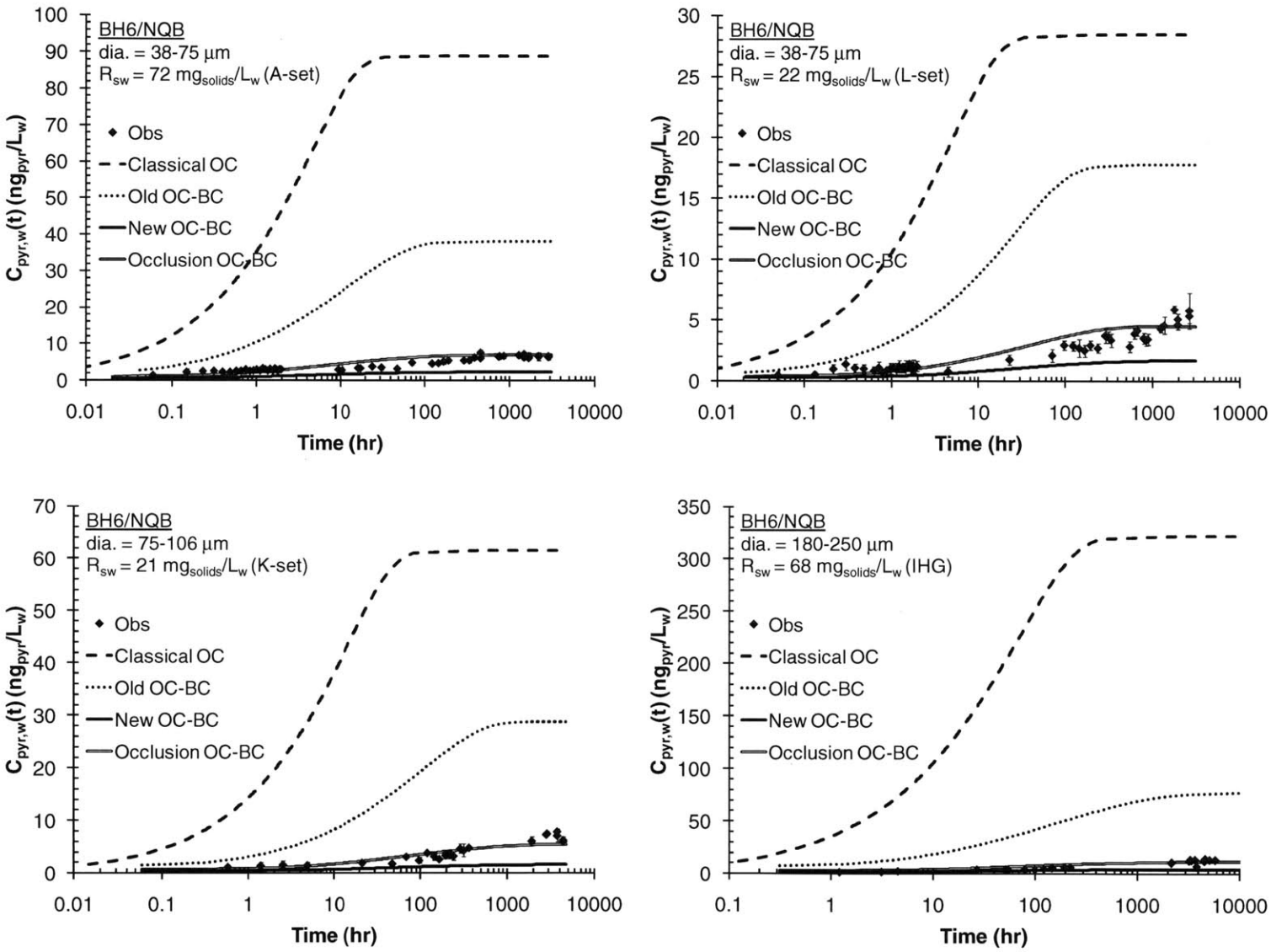

Figure 7 - 15. *A priori* predictions (four models) and the observed dissolved pyrene for selected suspensions.

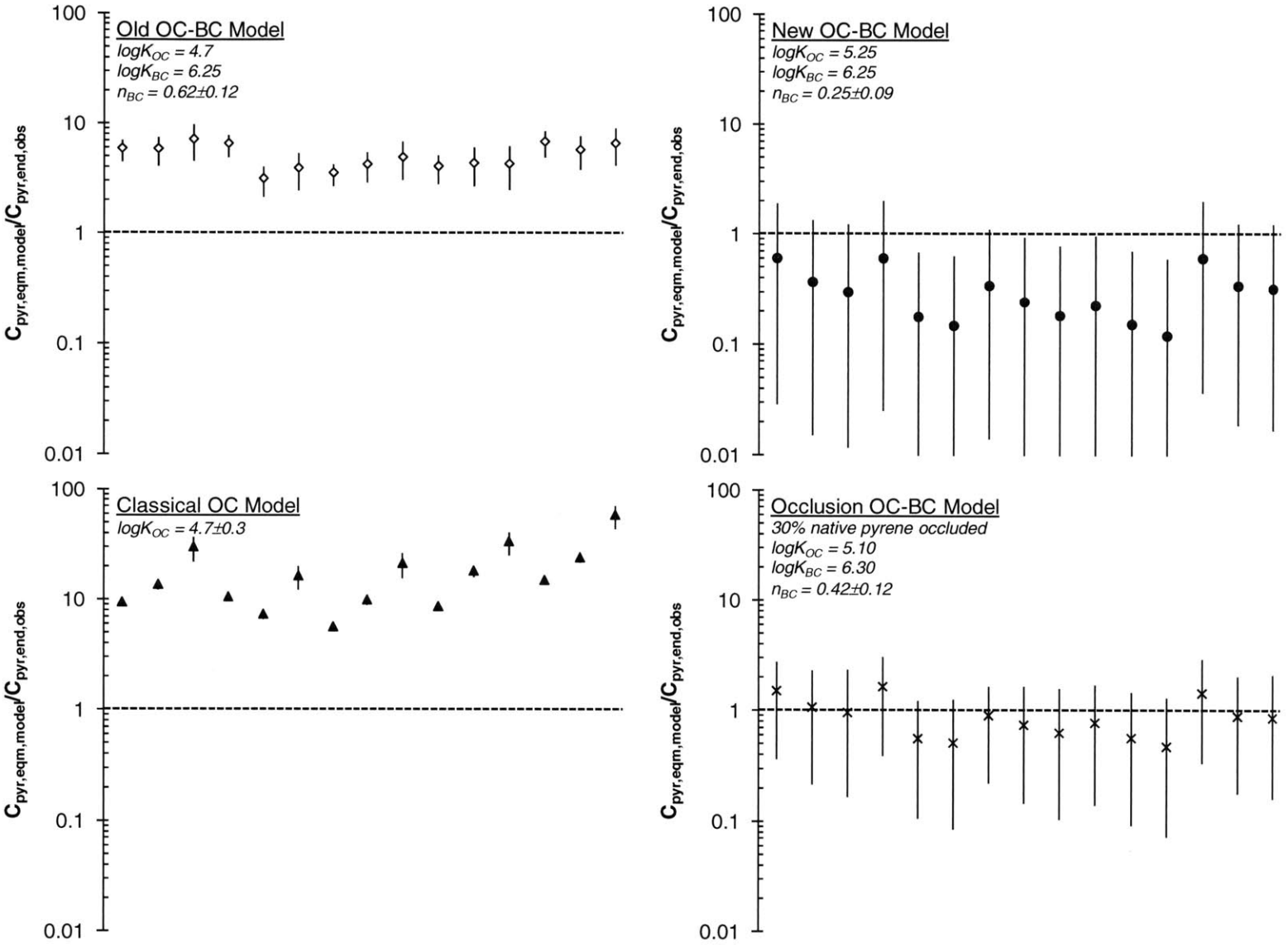

Figure 7 - 16. *A priori* prediction of $C_{pyr,w,Eqm}$ for 15 BH#6/NQB suspensions from four isotherm models.

The four figures show the *a priori* prediction of $C_{pyr,w,Eqm}$ by the four pyrene sorption isotherm models on the fifteen BH#6/NQB sediment suspensions. The predicted $C_{pyr,Eqm}$'s were normalized to the observed end-point $C_{pyr,w}$. The dashed line indicates unity in the C_{pyr} ratio, or a 1:1 correspondence between the prediction and the observation.

Error bars indicate uncertainties in $C_{pyr,w}$ ratio due to the modeled $C_{pyr,Eqm}$ (i.e. uncertainties associated with the isotherm parameters). In the case of OC-BC models, n_{BC} was chosen to be the key parameter contributing to prediction uncertainty, and the error bars reflect modeled uncertainties resulting from $\pm 1\ \sigma$ in n_{BC}. In the case of the Classical OC model, the error bars reflect modeled uncertainties due to uncertainty in $\log K_{OC}$ (assumed to be 0.3 unit; about half the range of literature $\log K_{OC}$'s for sedimentary pyrene. See Table 5-9, sedimentary $\log K_{OC}$: 4.5–5.0.)

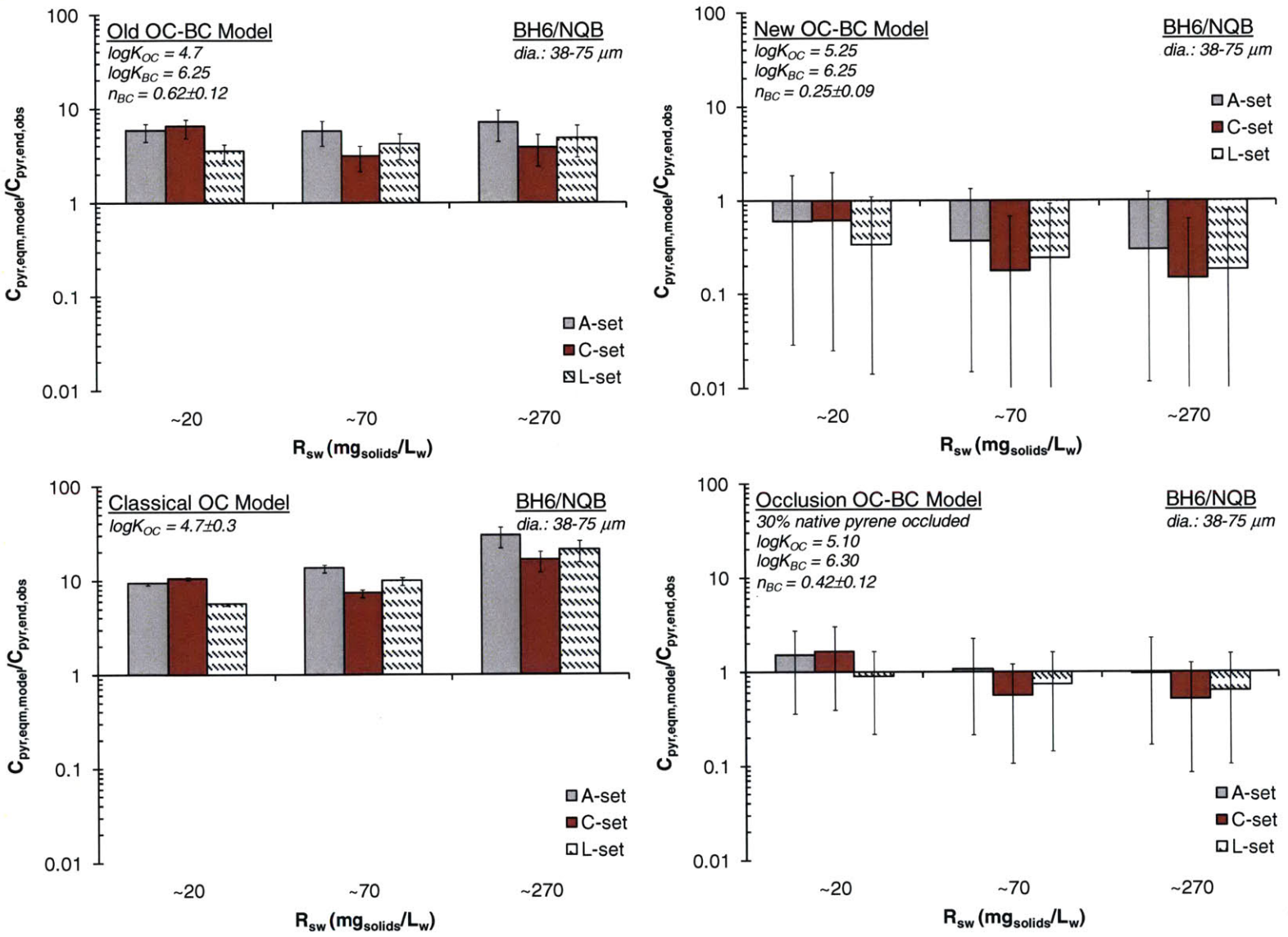

Figure 7 - 17. *A priori* predicted $C_{pyr,w,Eqm}$ vs solids-to-water ratio (R_{sw}).

The four figures show how the *a priori* prediction:observation ratio of $C_{pyr,w}$ varies with solids-to-water ratio (R_{sw}) for the suspensions with nominal dia. 38–75 μm.

Error bars indicate uncertainties in $C_{pyr,w}$ ratio due to the modeled $C_{pyr,Eqm}$ (i.e. uncertainties associated with the isotherm parameters). In the case of OC-BC models, n_{BC} was chosen to be the key parameter contributing to prediction uncertainty, and the error bars reflect modeled uncertainties resulting from ±1 σ in n_{BC}. In the case of the Classical OC model, the error bars reflect modeled uncertainties due to uncertainty in $\log K_{OC}$ (assumed to be 0.3 unit; about half the range of literature $\log K_{OC}$'s for pyrene. See Table 5-9, sedimentary $\log K_{OC}$: 4.5–5.0.)

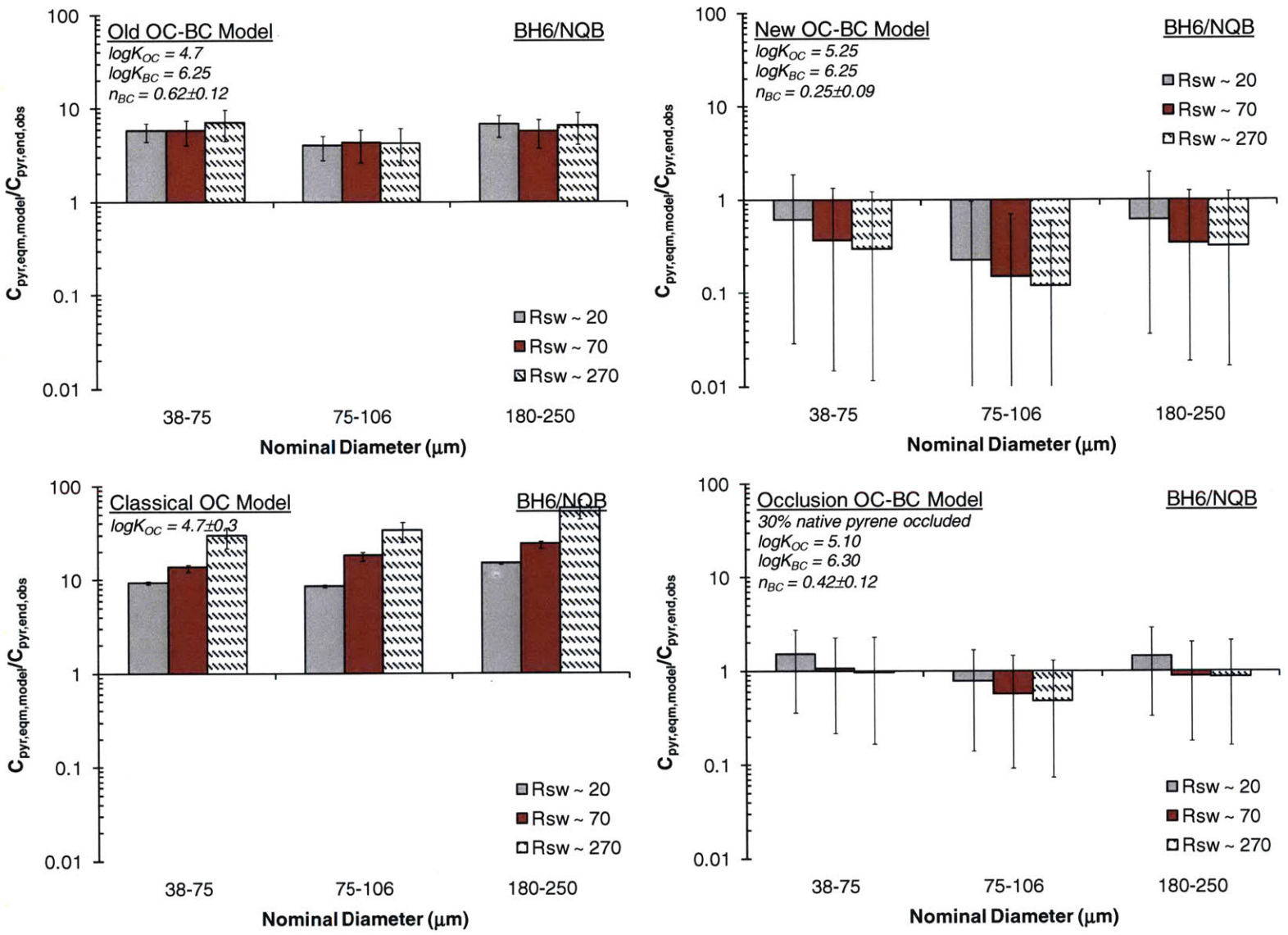

Figure 7 - 18. *A priori* predicted $C_{pyr,w,Eqm}$ vs nominal diameter of sediment aggregates.

The four figures show how the *a priori* prediction:observation ratio of $C_{pyr,w}$ does not varies significantly with the sediment aggregate nominal diameter.

Error bars indicate uncertainties in $C_{pyr,w}$ ratio due to the modeled $C_{pyr,Eqm}$ (i.e. uncertainties associated with the isotherm parameters). In the case of OC-BC models, n_{BC} was chosen to be the key parameter contributing to prediction uncertainty, and the error bars reflect modeled uncertainties resulting from $\pm 1\ \sigma$ in n_{BC}. In the case of the Classical OC model, the error bars reflect modeled uncertainties due to uncertainty in $\log K_{OC}$ (assumed to be 0.3 unit; about half the range of literature $\log K_{OC}$'s for pyrene. See Table 5-9, sedimentary $\log K_{OC}$: 4.5–5.0.)

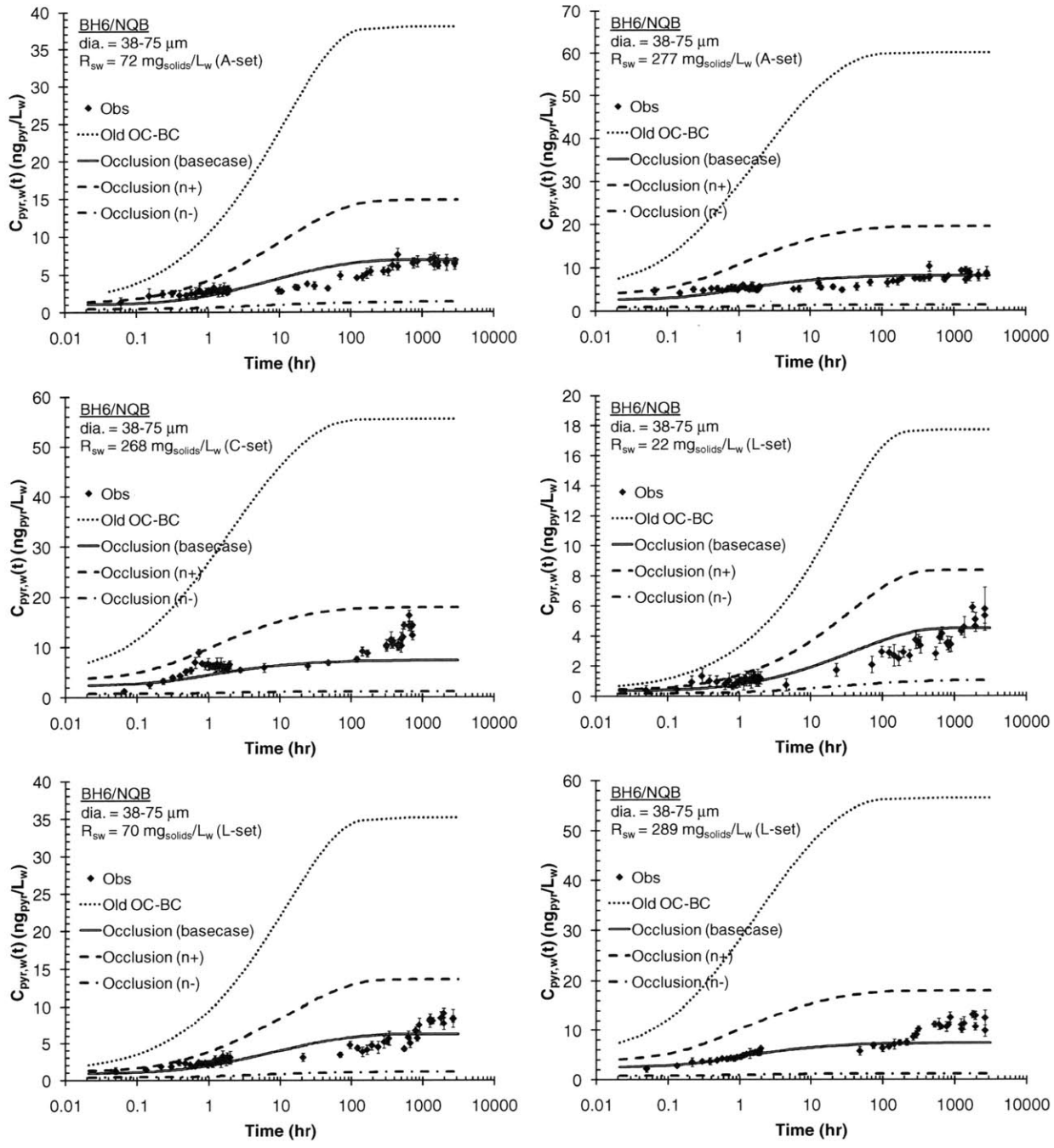

(a) 38–75 µm fraction suspensions (Set A, C, and L)

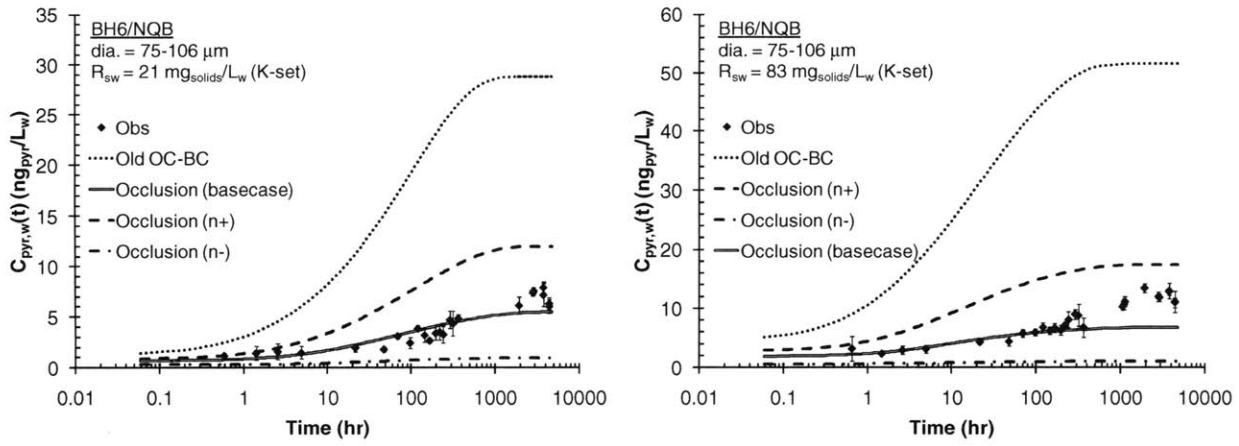

(b) 75–106 µm fraction suspensions (Set K)

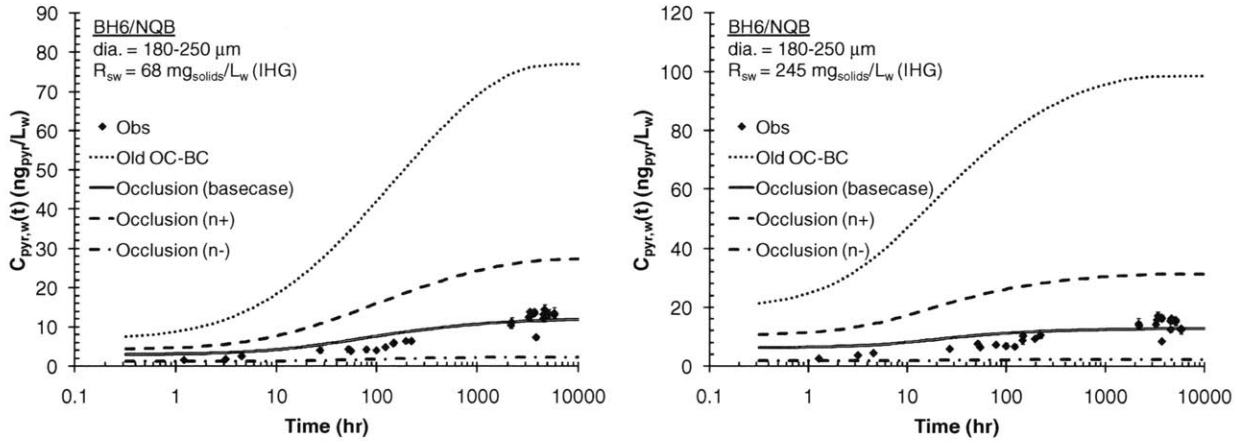

(c) 180–250 µm fraction suspensions (Set IHG)

Figure 7 - 19. Selected C_{pyr}-Time profiles predicted by the Occlusion-OC-BC isotherm.

A priori prediction based on the Occlusion-OC-BC isotherm ($logK_{OC}$=5.10±0.10, $logK_{BC}$=6.30±0.06, n_{BC}=0.42±0.12) for selected desorption experiments. In each figure, the basecase prediction (solid line) and its sensitivity to change in n_{BC} (by ±0.12) (dashed line & dashed-dotted line) were shown along with the experimental observations (solid diamonds). As a reference, the C_{pyr}-Time profiles predicted from the Old-OC-BC isotherm ($logK_{OC}$=4.7, $logK_{BC}$=6.25, n_{BC}=0.62) were also shown. The complete set of experimental observations and predicted desorption profiles can be found in Appendix 7-1.

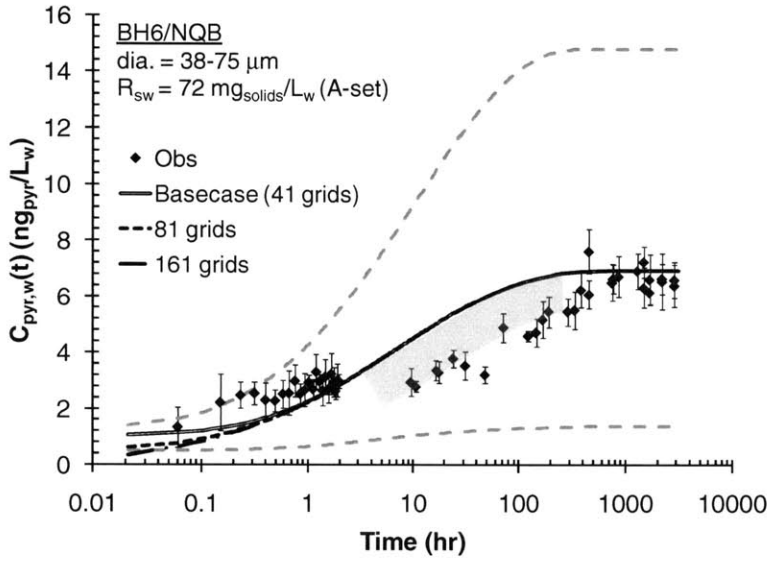
BH6/NQB
dia. = 38-75 µm
R_{sw} = 72 mg_{solids}/L_w (A-set)
Obs
Basecase (41 grids)
81 grids
161 grids
$C_{pyr,w}(t)$ (ng_{pyr}/L_w)
Time (hr)

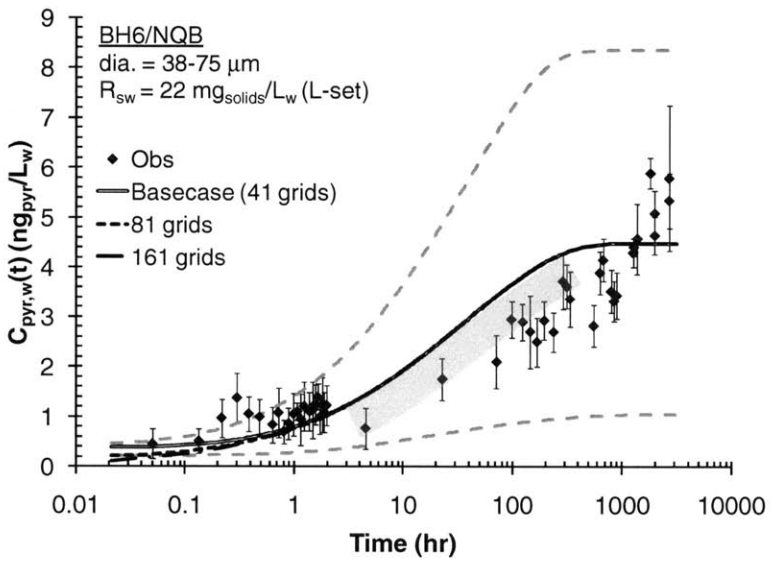
BH6/NQB
dia. = 38-75 µm
R_{sw} = 22 mg_{solids}/L_w (L-set)
Obs
Basecase (41 grids)
81 grids
161 grids
$C_{pyr,w}(t)$ (ng_{pyr}/L_w)
Time (hr)

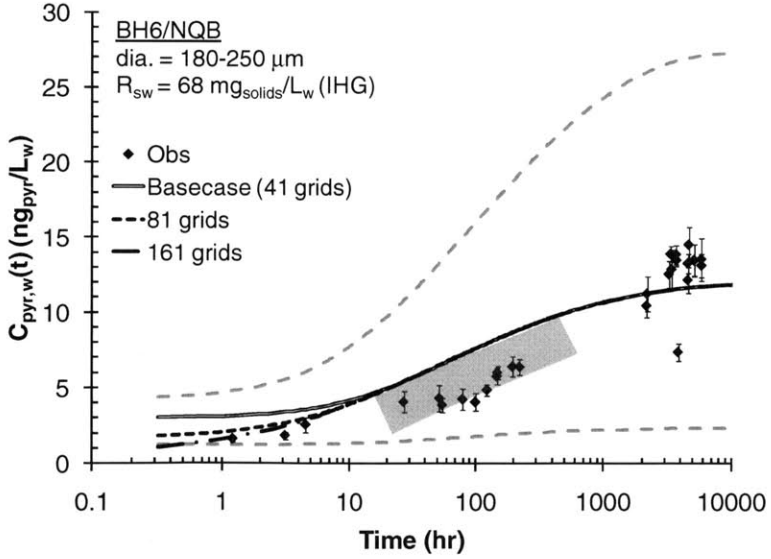
BH6/NQB
dia. = 180-250 µm
R_{sw} = 68 mg_{solids}/L_w (IHG)
Obs
Basecase (41 grids)
81 grids
161 grids
$C_{pyr,w}(t)$ (ng_{pyr}/L_w)
Time (hr)

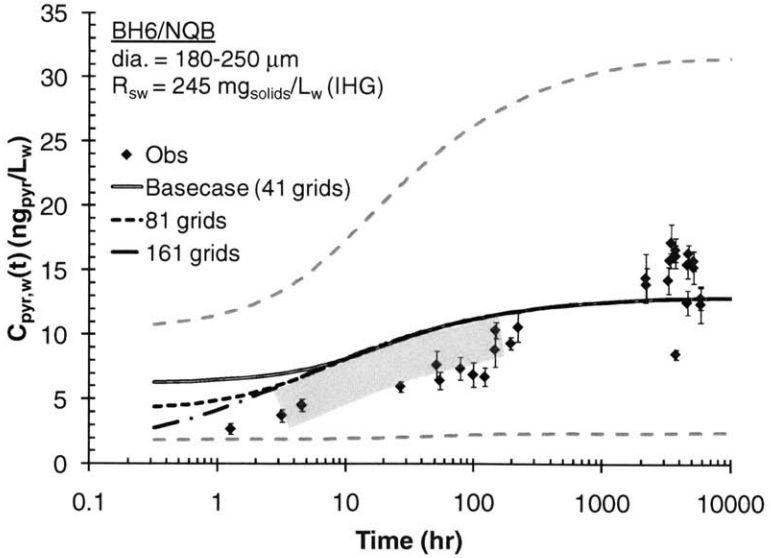
BH6/NQB
dia. = 180-250 µm
R_{sw} = 245 mg_{solids}/L_w (IHG)
Obs
Basecase (41 grids)
81 grids
161 grids
$C_{pyr,w}(t)$ (ng_{pyr}/L_w)
Time (hr)

Figure 7 - 20. Model-Observation disparity in the 10^{th}–100^{th} h period.

The figure showed that the discrepancy (shaded area) between the modeled results and the observations in the 10^{th}–100^{th} h period could not be accounted by modeling artifact such as the degree of discretization (i.e., from 41 grids to 161 grids). Grey dashed lines indicated the boundaries of prediction due to uncertainty in the n_{BC} of the isotherm. The basecase model assumed spherical aggregates with the Occlusion-OC-BC isotherm and a porosity of 0.13.

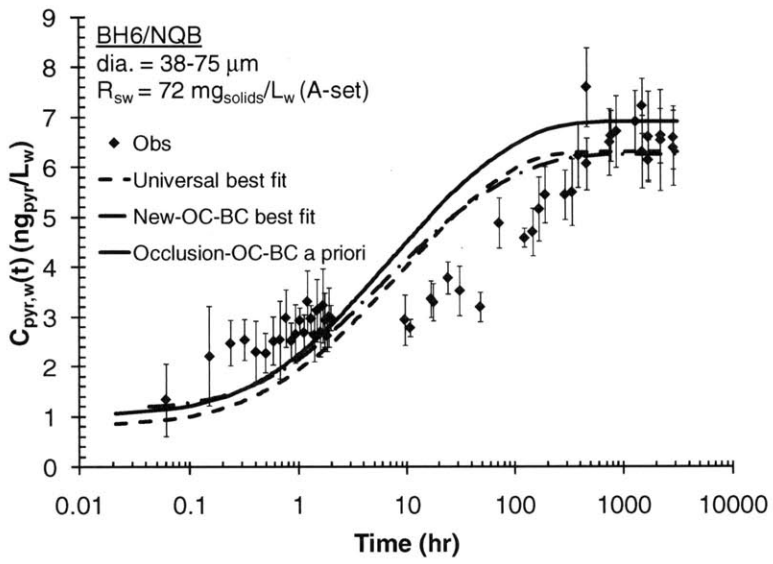
BH6/NQB
dia. = 38-75 µm
R_{sw} = 72 mg_{solids}/L_w (A-set)
Obs
Universal best fit
New-OC-BC best fit
Occlusion-OC-BC a priori
$C_{pyr,w}(t)$ (ng_{pyr}/L_w)
Time (hr)

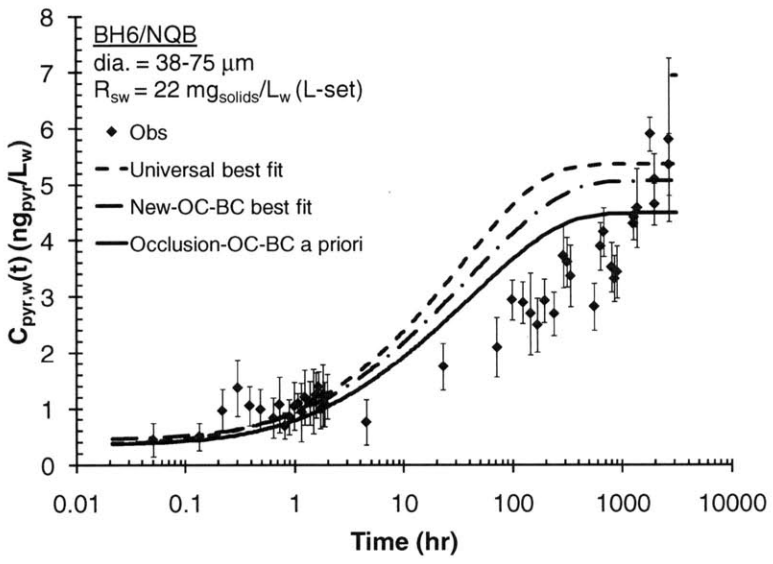
BH6/NQB
dia. = 38-75 µm
R_{sw} = 22 mg_{solids}/L_w (L-set)
Obs
Universal best fit
New-OC-BC best fit
Occlusion-OC-BC a priori
$C_{pyr,w}(t)$ (ng_{pyr}/L_w)
Time (hr)

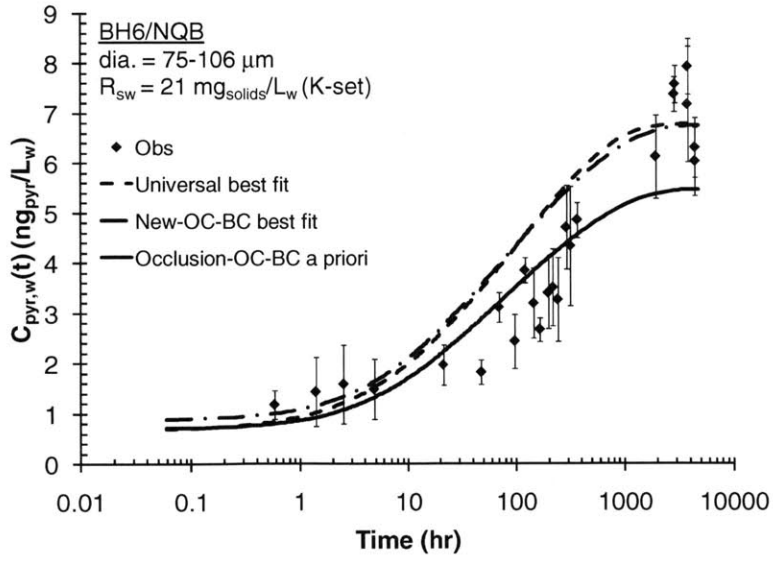
BH6/NQB
dia. = 75-106 µm
R_{sw} = 21 mg_{solids}/L_w (K-set)
Obs
Universal best fit
New-OC-BC best fit
Occlusion-OC-BC a priori
$C_{pyr,w}(t)$ (ng_{pyr}/L_w)
Time (hr)

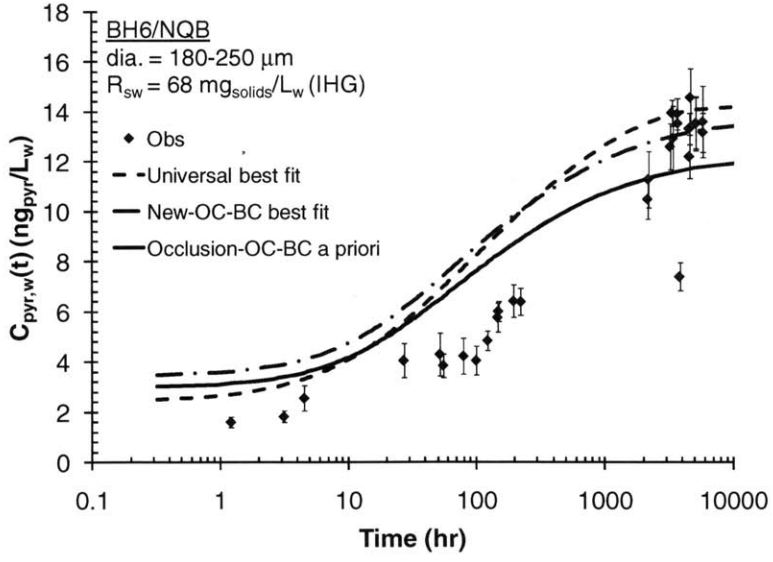
BH6/NQB
dia. = 180-250 µm
R_{sw} = 68 mg_{solids}/L_w (IHG)
Obs
Universal best fit
New-OC-BC best fit
Occlusion-OC-BC a priori
$C_{pyr,w}(t)$ (ng_{pyr}/L_w)
Time (hr)

Figure 7 - 21. Desorption dynamics by best-fit New-OC-BC, best-fit Universal-OC-BC, and *a priori* Occlusion-OC-BC models.

Simulations for kinetic observations at four selected suspensions by the three models were shown. The best-fit nBC was around 0.3–0.4 for the New-OC-BC model, and around 0.15–0.2 for the sedimentary Universal-OC-BC model. The *a priori* n_{BC} for the Occlusion-OC-BC based simulation was 0.42±0.12.

The figures were chosen on the ground that the predicted $C_{pyr,w}$'s by all three models were similar so that the kinetic profiles could be compared. Model predictions for other suspensions can be found in Appendix 7-17. The *a priori* Occlusion model may appear to be less accurate when compared with the two best-fit models; the actual observations were all within the uncertainty in n_{BC} of the Occlusion model (see Appendix 7-1).

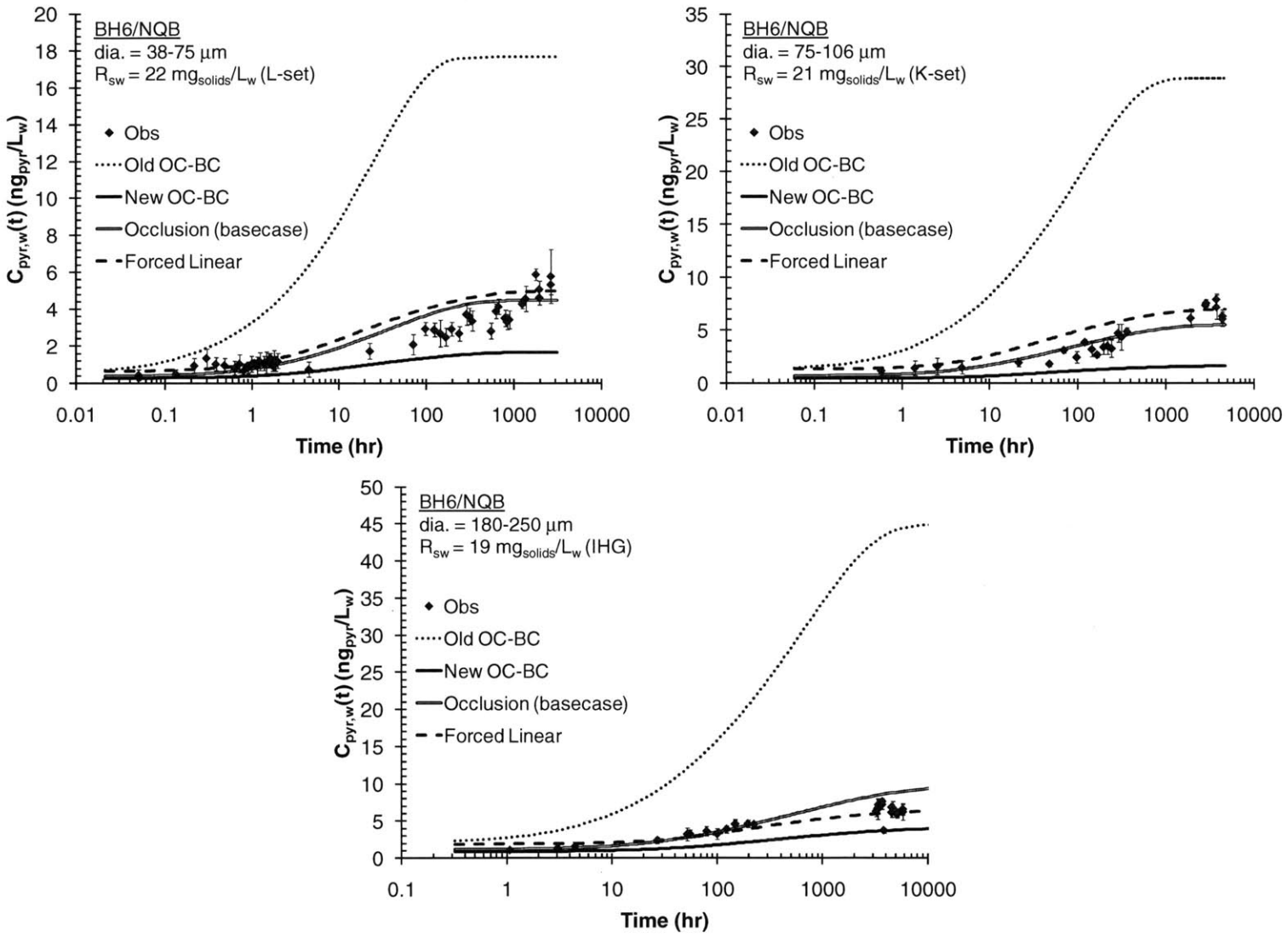

Figure 7 - 22a. Model results by best fit K_{TOC}'s ('Forced Linear') at low R_{sw}'s.

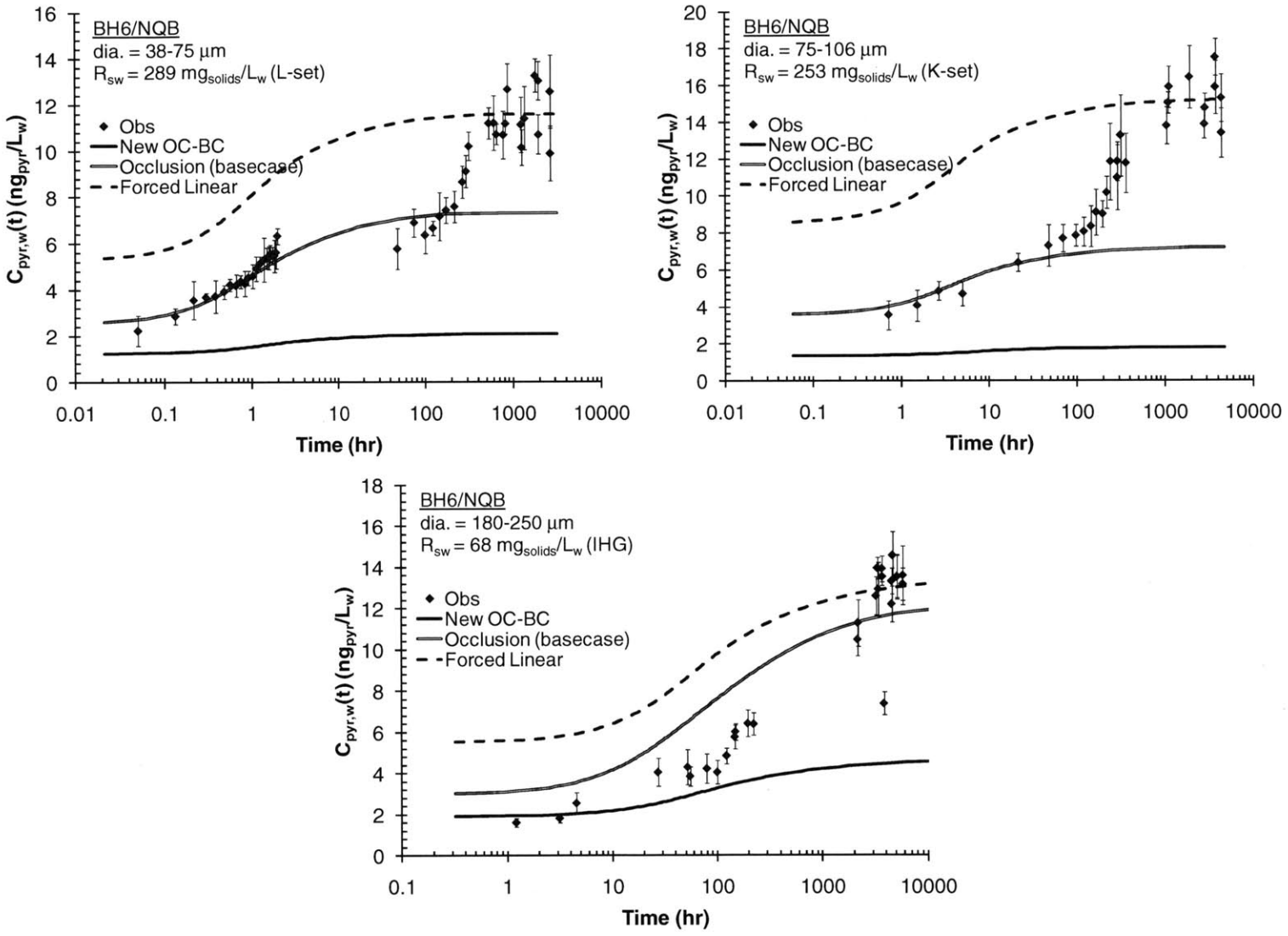

Figure 7 - 22b. Model results by best fit K_{TOC}'s ('Forced Linear') at low R_{sw}'s.

Figure 7 - 22. Desorption modeled by best-fit Forced Linear isotherm (K_{TOC})

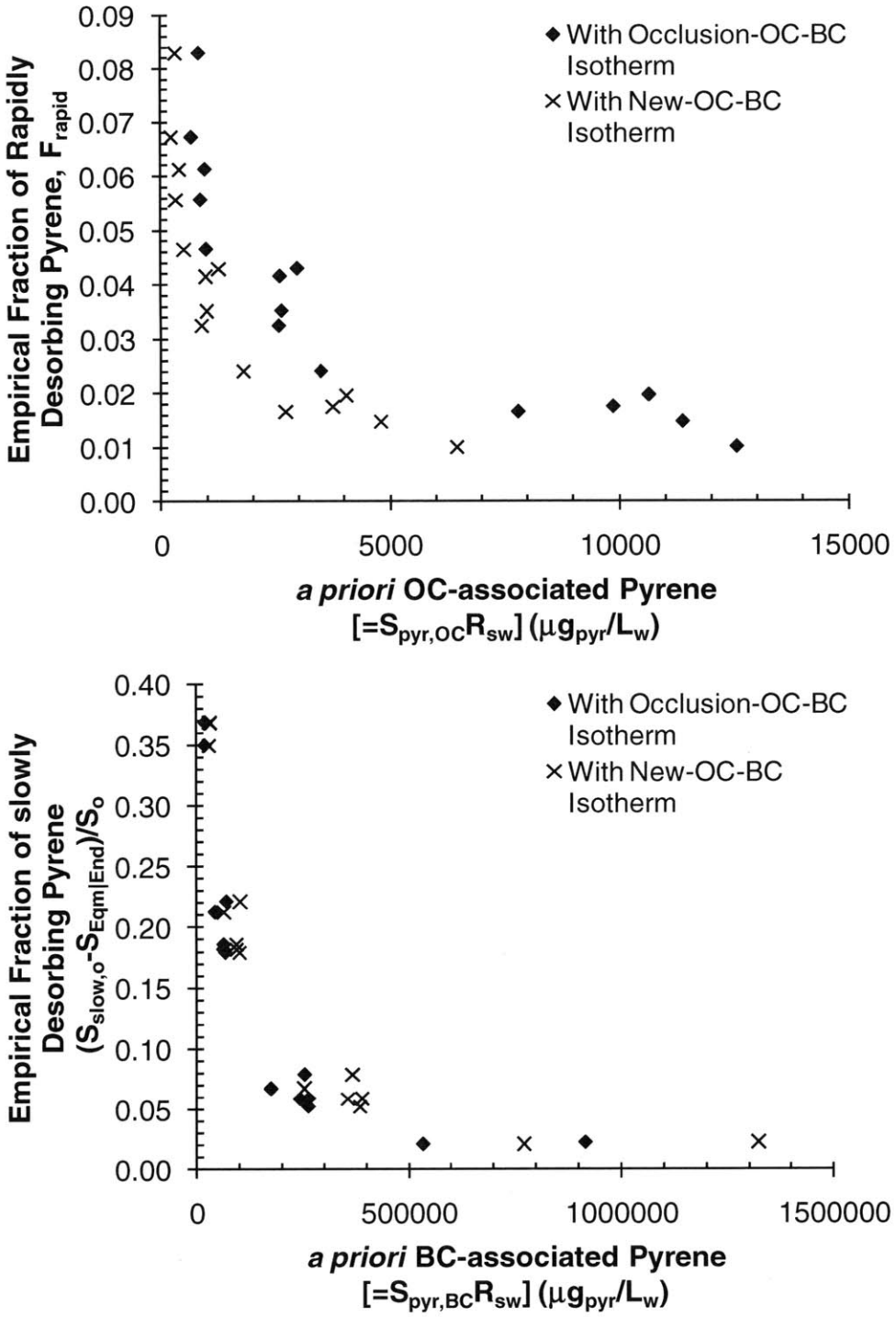

Figure 7 - 23. F_{rapid}, F_{slow} (empirical) vs total system OC-pyr, BC-pyr (*a priori*)

The total system OC/BC-bound pyrene ($S_{pyr,OC}R_{sw}$ or $S_{pyr,BC}R_{sw}$) was estimated from both the Occlusion-OC-BC and the New-OC-BC isotherms. For the slowly desorbing fraction, the ratio $(S_{slow,o}-S_{Eqm|End})/S_o$ is a better measure than F_{slow} for it represents the actual pyrene that will be desorbed at infinite time.

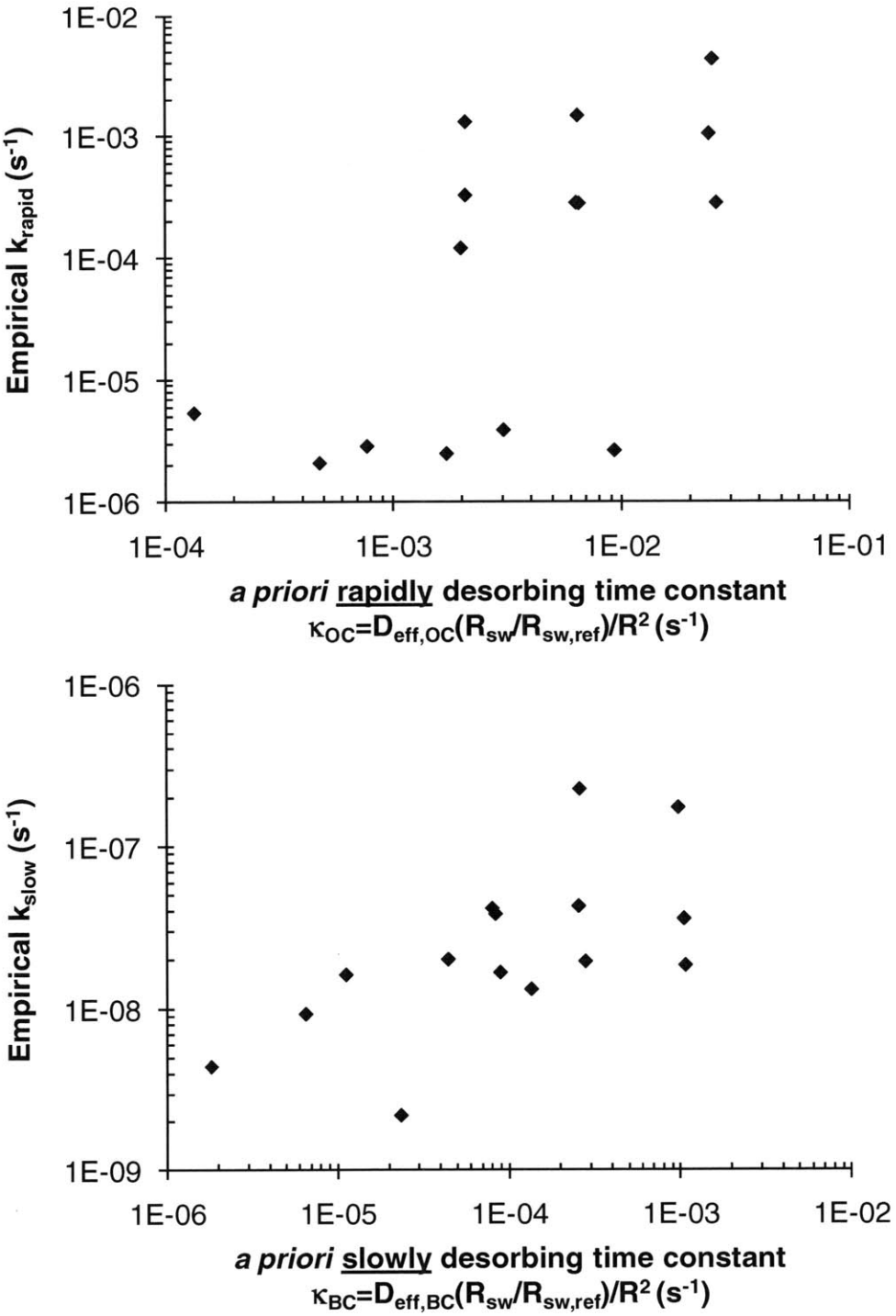

Figure 7 - 24. k_{rapid} & k_{slow} (empirical) vs κ_{OC} & κ_{BC} (*a priori*).

The rate constants, k's, were fitted by using the Constrained Two-Comparmental model. The *a priori* time constant estimates, κ's, were calculated based on the Occlusion-OC-BC isotherm; a similar trend was also observed with other isotherm. $R_{sw,ref}$ was be 1 mg_{solids}/L_w (for unit consistency).

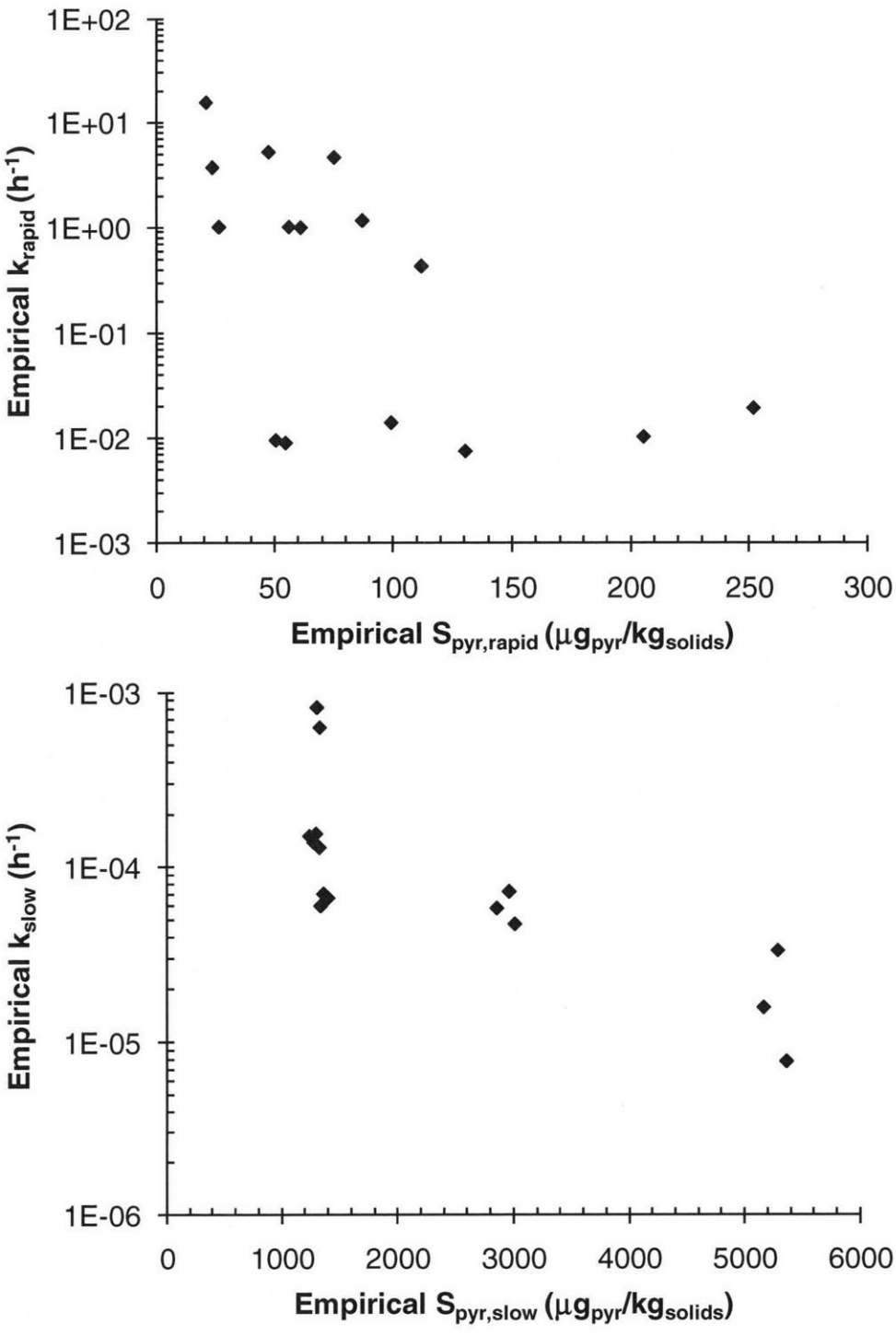

Figure 7 - 25. k_{rapid} & k_{slow} (empirical) vs $S_{pyr,rapid}$ & $S_{pyr,slow}$ (empirical).

Both the rate constants and the pyrene concentrations were fitted by using the Constrained Two-Comparmental model.

Chapter 8: Figures

Figure 8 - 1. Linear interpolation for Infinite-Bath Case with boundary layer film. 428
Figure 8 - 2. Char-Silt dual domains model (heterogeneous).....428
Figure 8 - 3. Char-Silt interfacial diffusional flux: the 'imaginary' grid approach.....429
Figure 8 - 4. Infinite-Bath model validation (I): varying 'R_{sw}'.....430
Figure 8 - 5. Char-in-Silt model validation.....431
Figure 8 - 6. Char-in-Silt model validation: C'(x,t) in two char/aggregate ratios. 432
Figure 8 - 7. Mass transfer profiles for Infinite-Bath diffusion at various Boundary Layer Thickness (δ/R).....435
Figure 8 - 8. Infinite-Bath diffusion for four non-linear isotherms involving OC and BC. 436
Figure 8 - 9. Infinite-Bath diffusion: effect of isotherm non-linearity (n_{BC}).....437
Figure 8 - 10. Infinite-Bath diffusion: effect of C_{bulk}.....438
Figure 8 - 11. Infinite-Bath diffusion for four PAHs at $S_{PAH,o}$=1000 $\mu g_{PAH}/kg_{solids}$ and δ/R=0.25. 439
Figure 8 - 12. Infinite-Bath diffusion for four PAHs: the diminished importance of n_{BC} for less hydrophobic compound. 440
Figure 8 - 13. Closed-System diffusion: the sensitivity to R_{sw} and n_{BC} for pyrene.....441
Figure 8 - 14. Closed-System diffusion: the sensitivity to R_{sw} and n_{BC} for naphthalene. 442
Figure 8 - 15. Closed-System diffusion: the insensitivity to R_{sw} and n_{BC} for pyrene. ..443
Figure 8 - 16. Closed-System diffusion: Fraction Desorbed ($M_{pyr,o}$-$M_{pyr,\infty}$)/$M_{pyr,o}$ vs Desorption Halftime ($\tau_{iw,1/2}$). 444
Figure 8 - 17. Char-in-Silt Closed-System diffusion: overall desorption-time profile. .445
Figure 8 - 18. Char-in-Silt Closed-System diffusion: $C'_{pyr}(x,\tau)$ corresponding to the three $R_{c/Ragg}$'s.....446
Figure 8 - 19. Char-in-Silt Closed-System: $K'_{d,pyr}(x,\tau)$. 447
Figure 8 - 20. Char-in-Silt Closed-System: effect of R_{sw}. 448
Figure 8 - 21. Char-in-Silt Closed-System: effect of char-domain porosity/tortuosity. 449
Figure 8 - 22. Char-in-Silt Infinite-Bath diffusion: effect of char-to-aggregate size ratio. 450
Figure 8 - 23. Char-in-Silt Infinite-Bath diffusion: effect of initial aggregate porewater concentration $C_{agg,pyr,o}$ (at n_{BC}=0.6) 451
Figure 8 - 24. Char-in-Silt Infinite-Bath diffusion: effect of char-domain 'composition'. 452
Figure 8 - 25. Infinite-Bath diffusion: Comparing three aggregate/particle configurations. 453

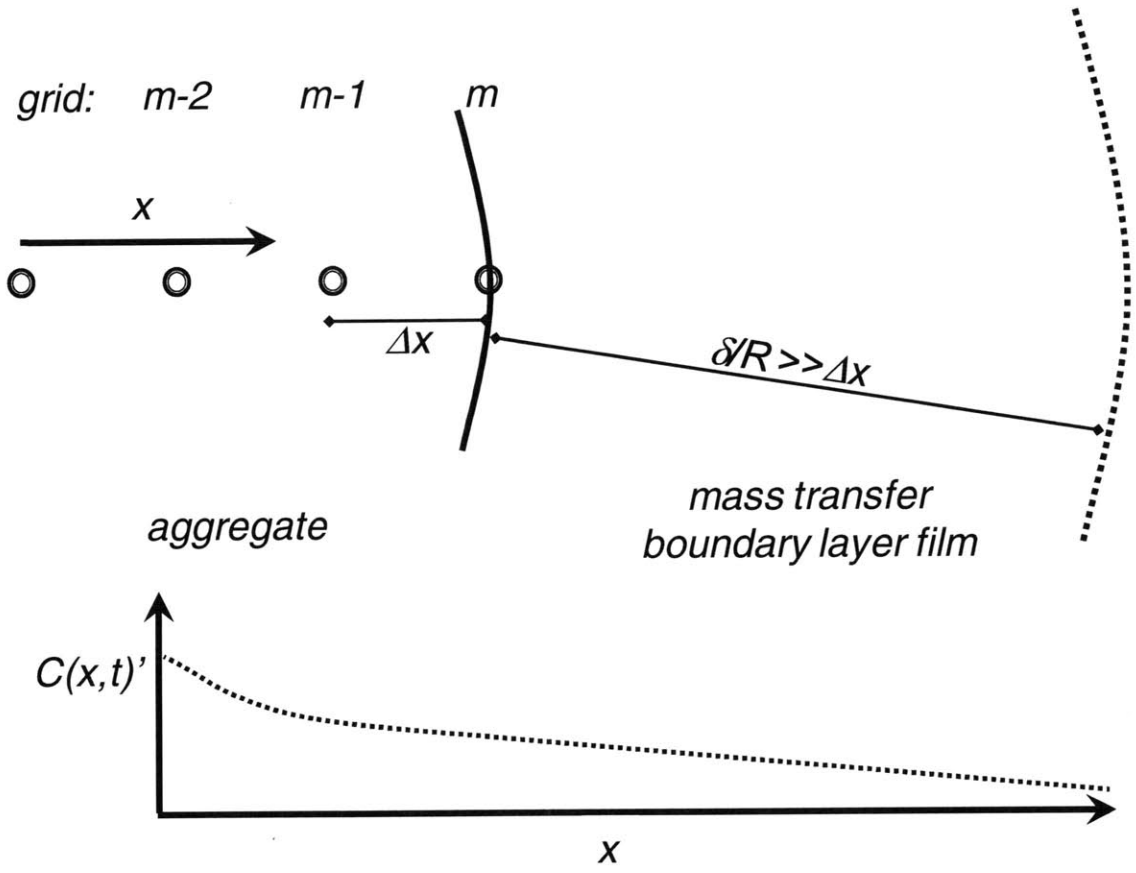

Figure 8 - 1. Linear interpolation for Infinite-Bath Case with boundary layer film.

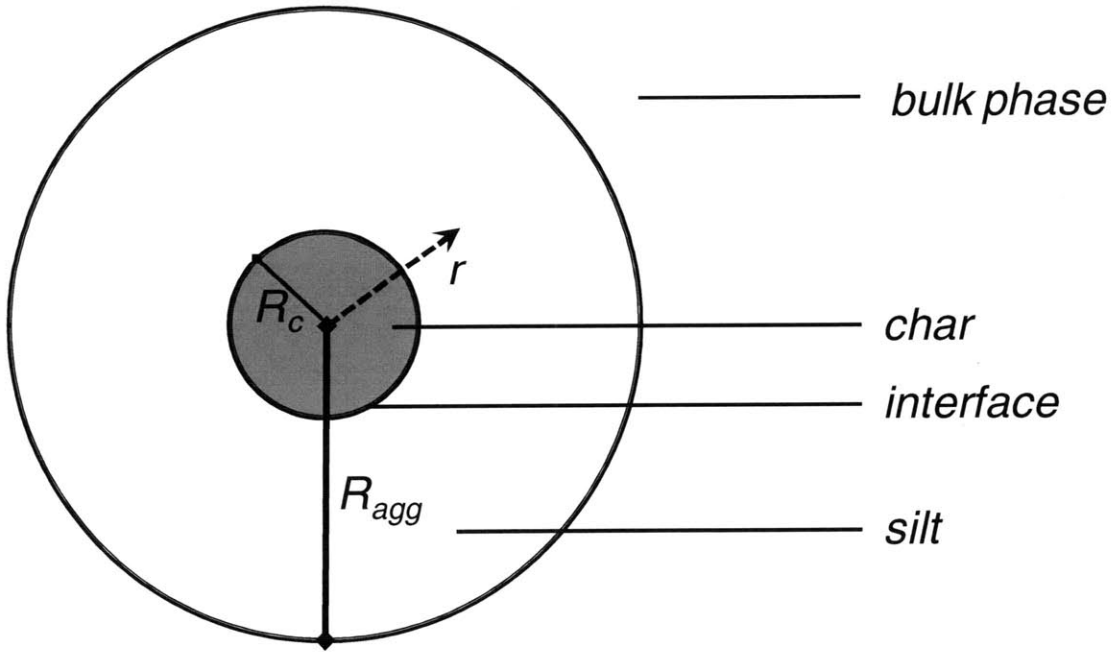

Figure 8 - 2. Char-Silt dual domains model (heterogeneous).

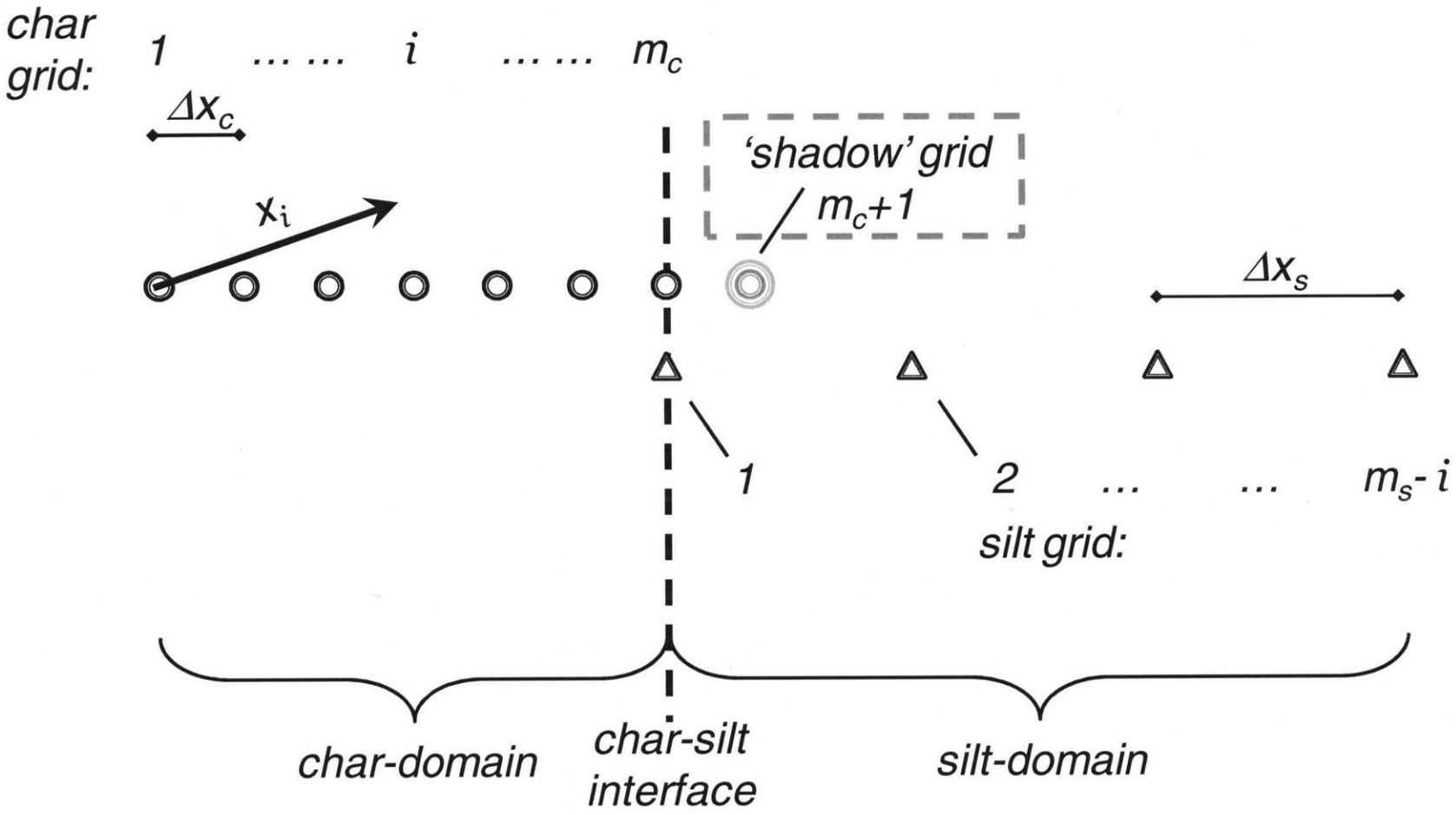

Figure 8 - 3. Char-Silt interfacial diffusional flux: the 'imaginary' grid approach.

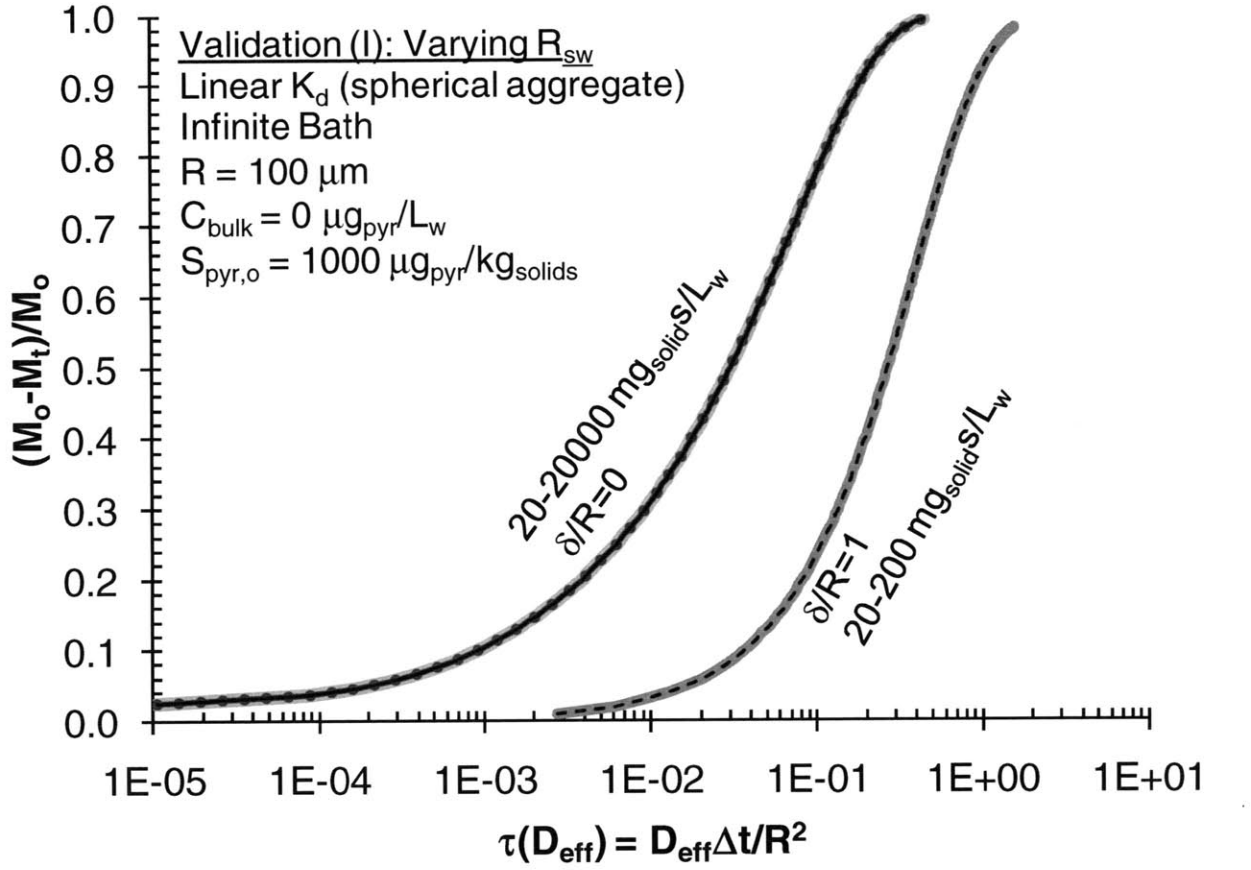

Figure 8 - 4. Infinite-Bath model validation (I): varying 'R_{sw}'.

The figure showed the simulation results for different R_{sw}'s at two different mass transfer boundary layer film thicknesses (δ/R).

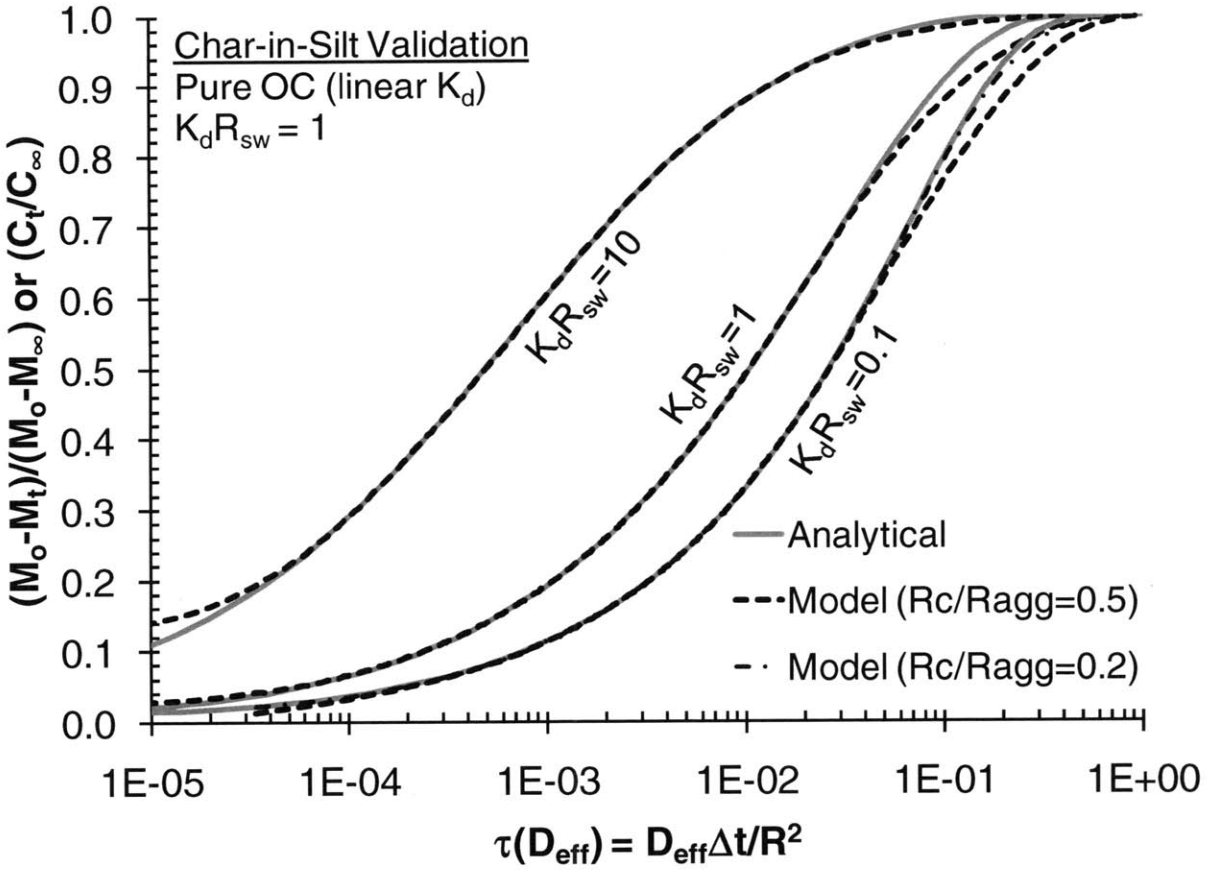

Figure 8 - 5. Char-in-Silt model validation.

Model outputs (black, dashed lines) were plotted with the analytical solutions (gray, solid lines) at three K_dR_{sw}'s. All model outputs were generated assuming that the radius of char domain to be half of that of the aggregate (black dashed line); for K_dR_{sw}=0.1, a model with char radius being 20% of the aggregate radius was also shown (black dashed-n-dotted line).

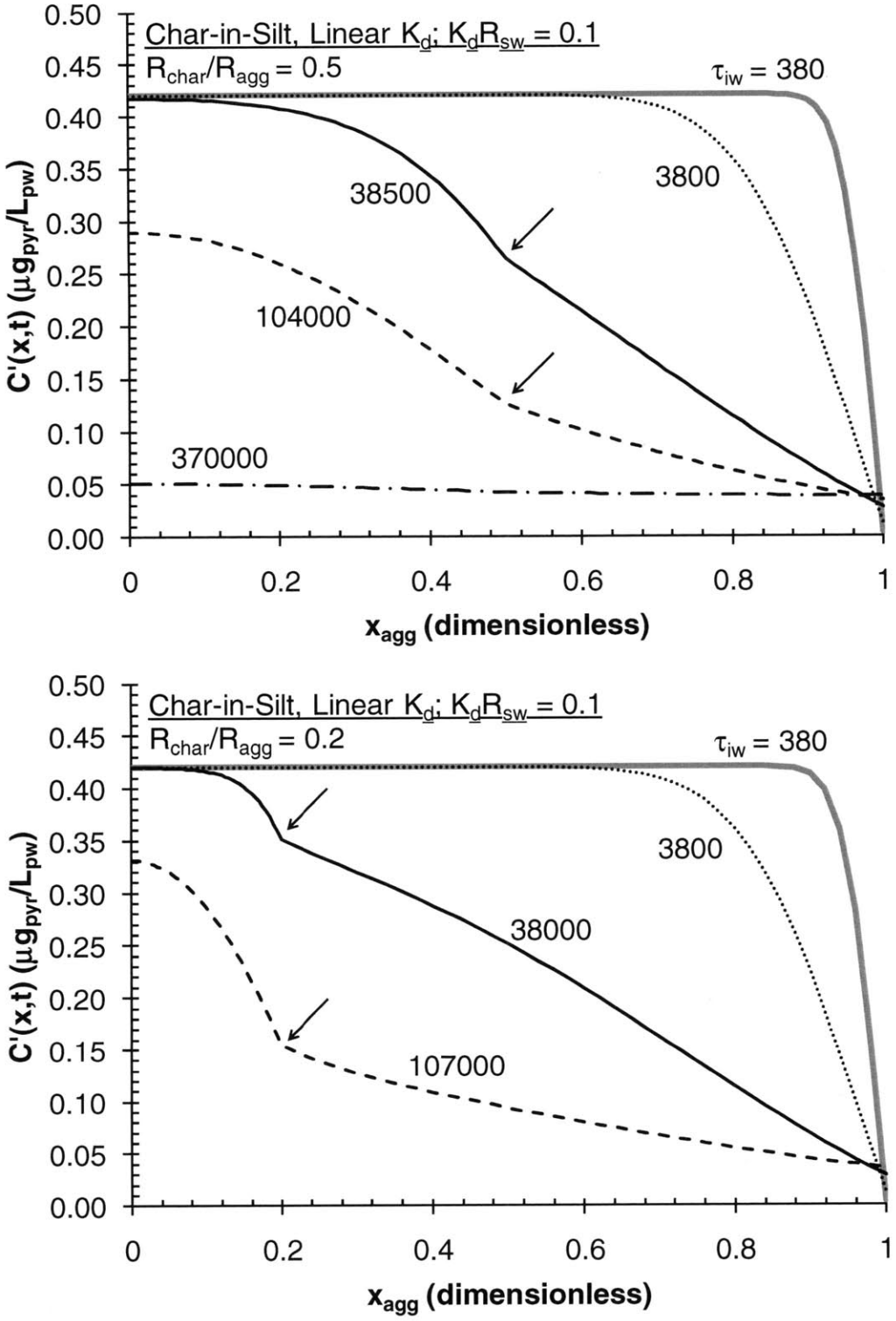

Figure 8 - 6. Char-in-Silt model validation: C'(x,t) in two char/aggregate ratios.

Arrows indicate char-silt interface and numerical artifacts. Both domains had identical and linear K_d, porosity, and initial sorbate concentration.

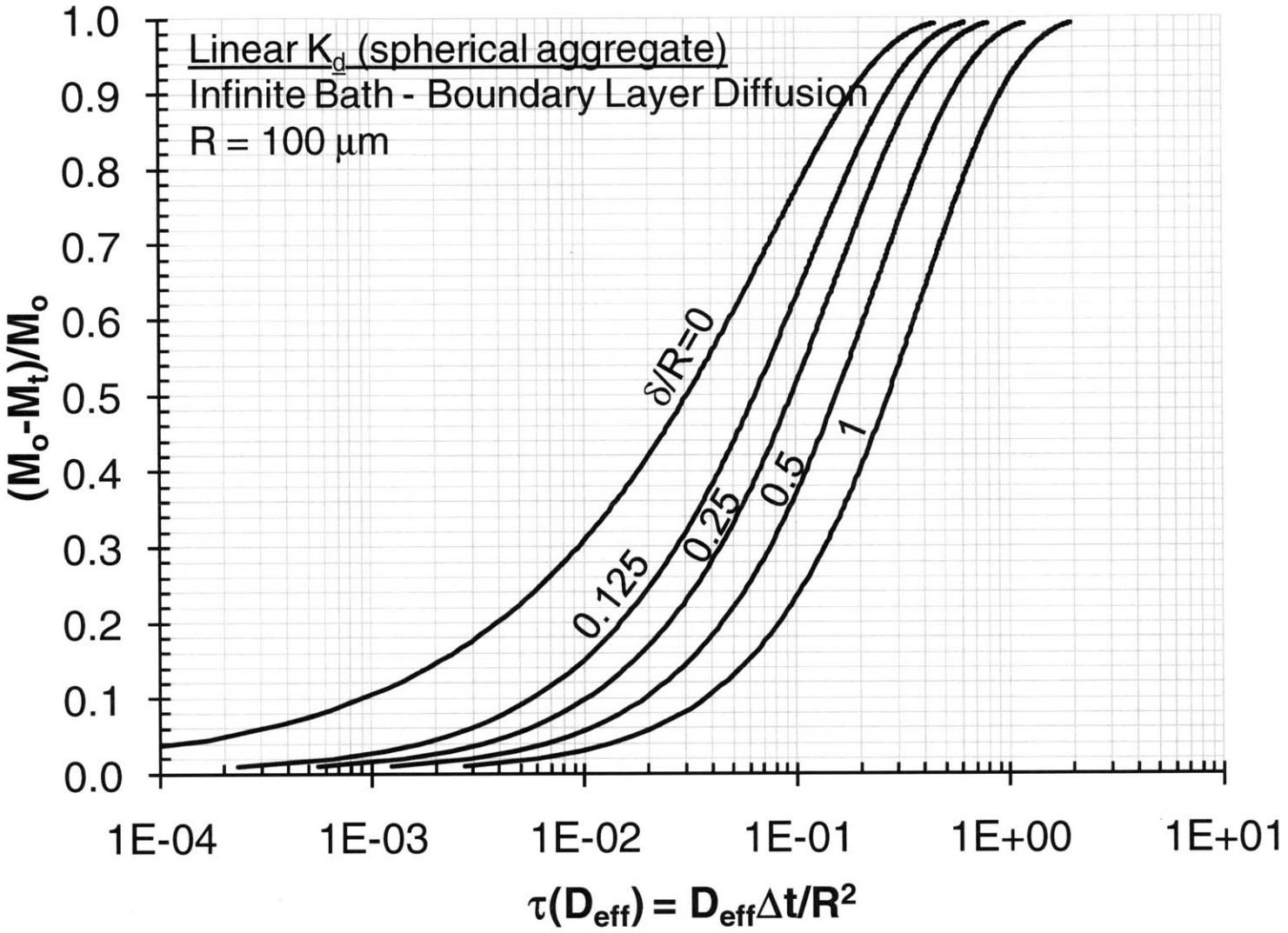

(a) Infinite-Bath Boundary Layer Diffusion with linear K_d for spherical geometry.

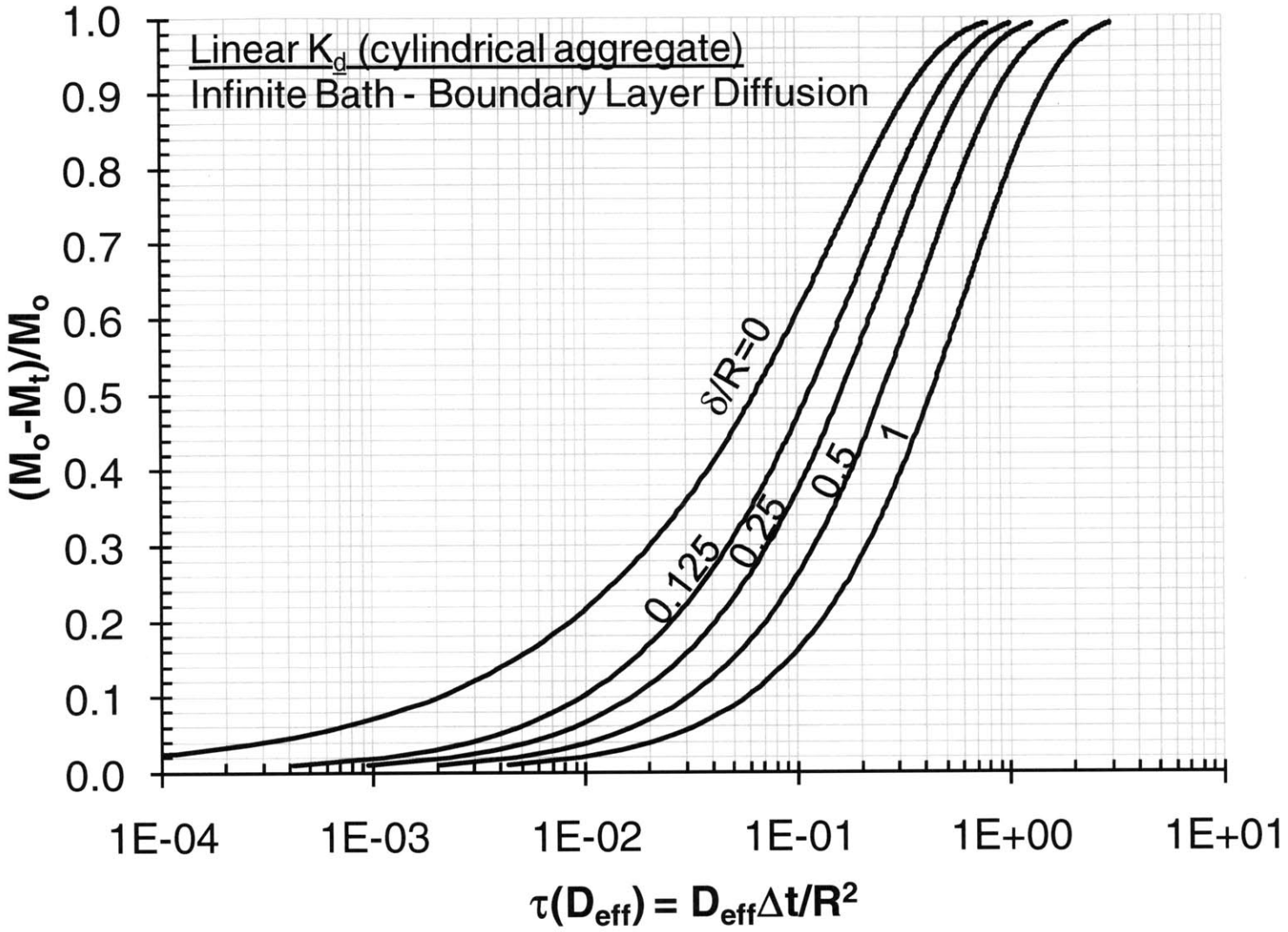

(b) Infinite-Bath Boundary Layer Diffusion with linear K_d for cylindrical geometry.

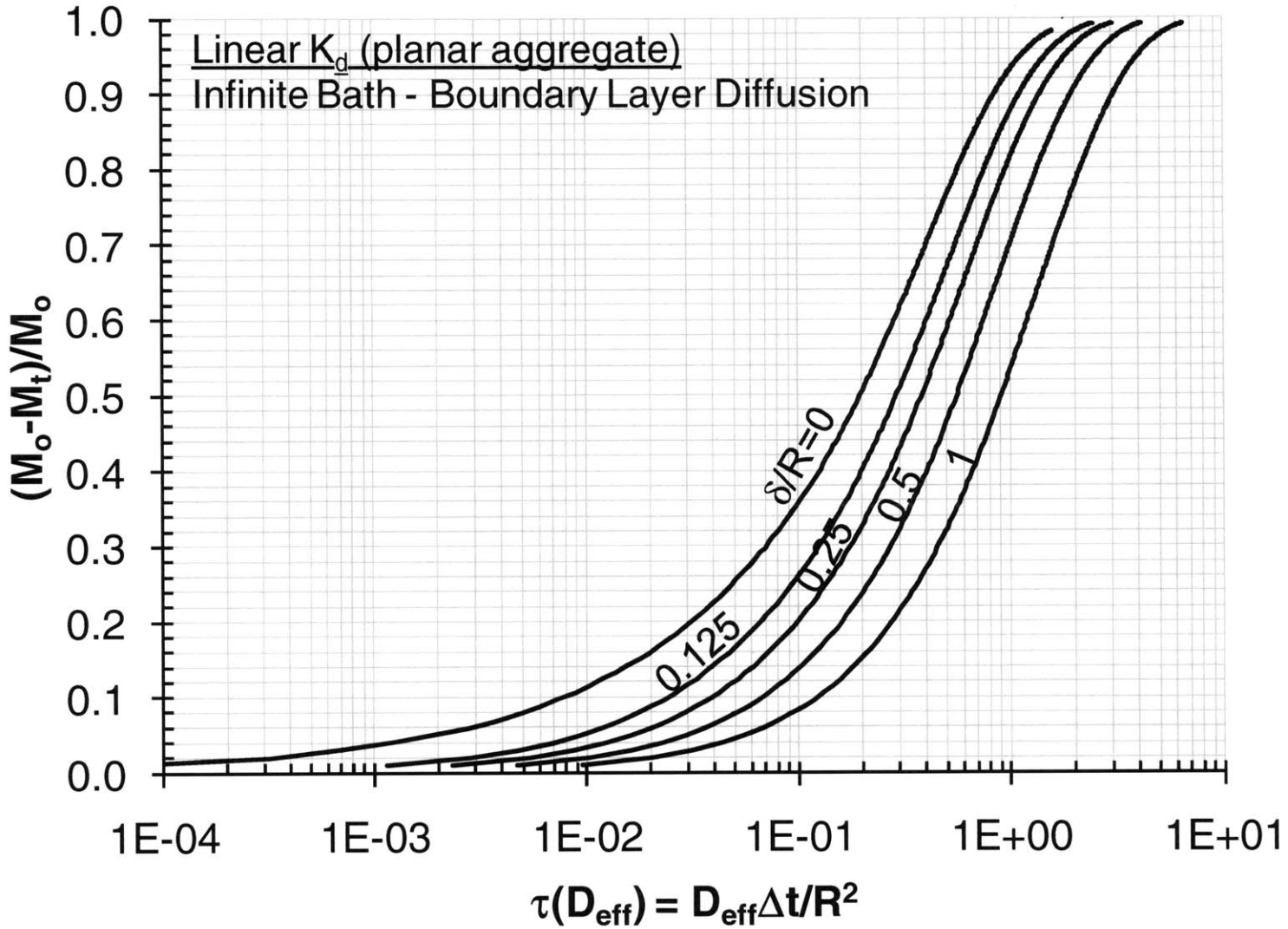

(c) Infinite-Bath Boundary Layer Diffusion with linear K_d for planar geometry.

Figure 8 - 7. Mass transfer profiles for Infinite-Bath diffusion at various Boundary Layer Thickness (δ/R).

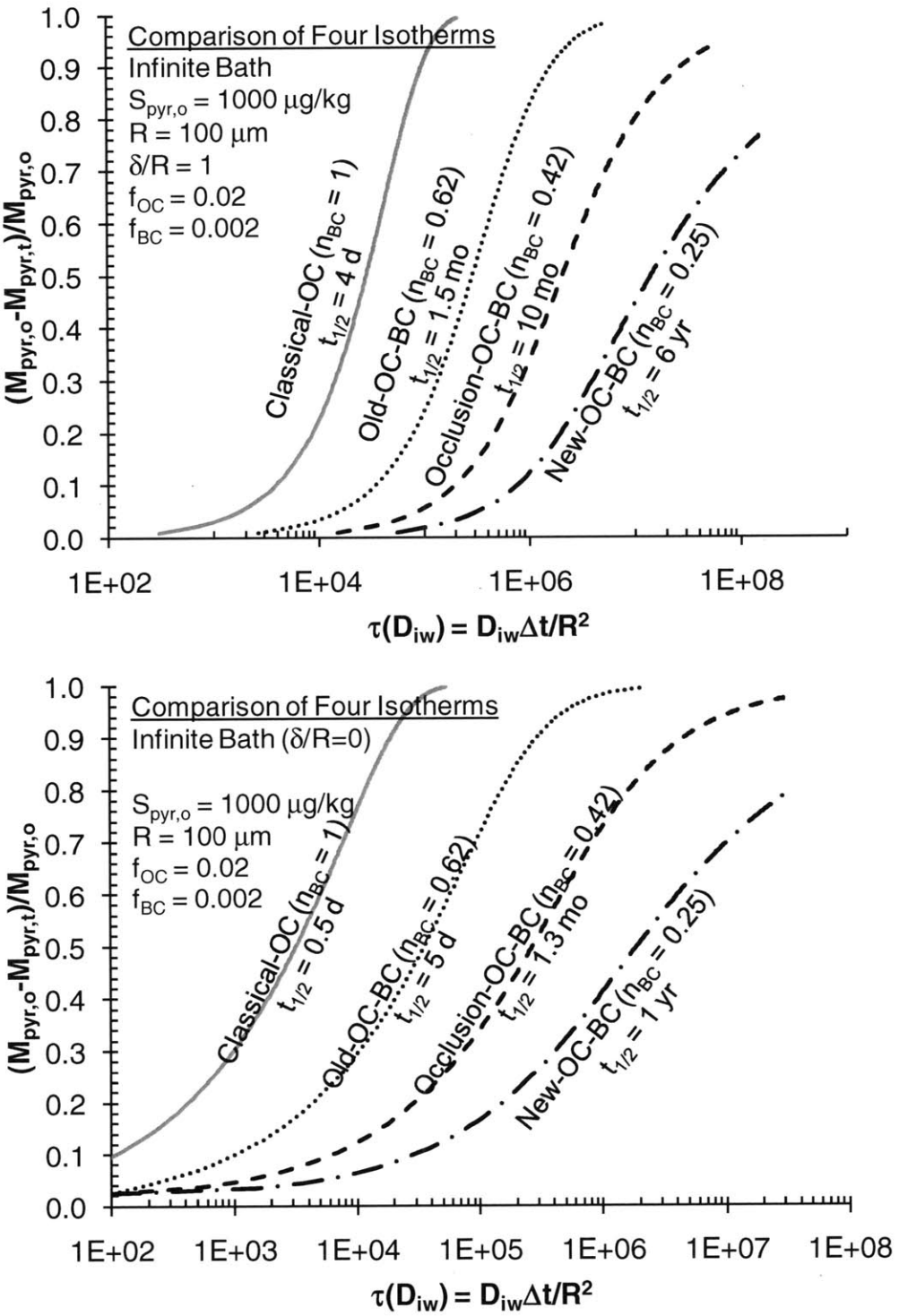

Figure 8 - 8. Infinite-Bath diffusion for four non-linear isotherms involving OC and BC.

The four isotherms are (i) Classical-OC ($\log K_{OC} = \log K_{BC} = 4.7$), (ii) Old-OC-BC ($\log K_{OC} = 4.7$; $\log K_{BC} = 6.25$; $n_{BC} = 0.62$), (iii) Occlusion-OC-BC ($\log K_{OC} = 5.1$; $\log K_{BC} = 6.3$; $n_{BC} = 0.42$; fraction occluded = 30%), (iv) New-OC-BC ($\log K_{OC} = 5.25$; $\log K_{BC} = 6.25$;; $n_{BC} = 0.25$). C_{bulk} was constant at 0 $\mu g_{pyr}/L_w$.

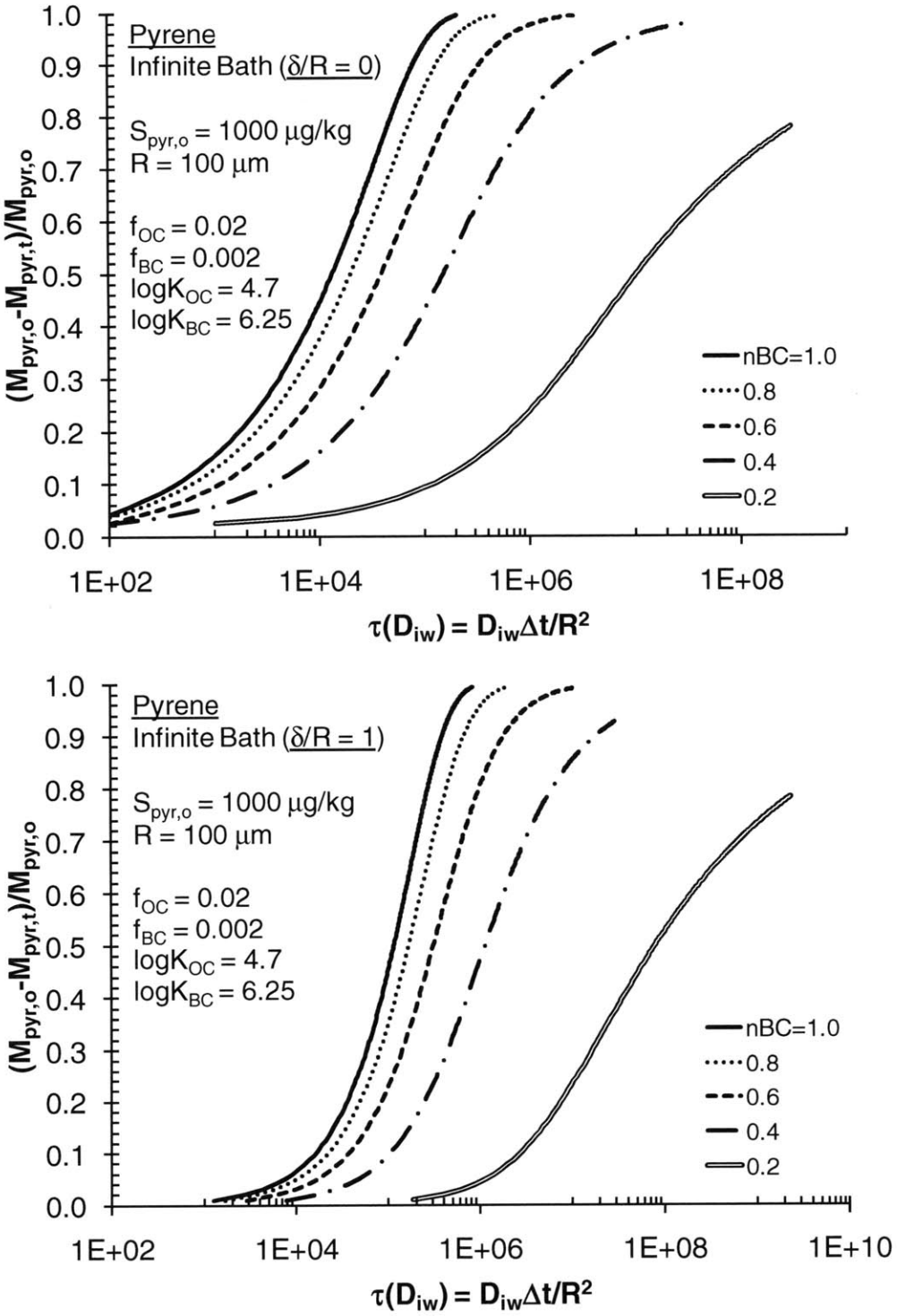

Figure 8 - 9. Infinite-Bath diffusion: effect of isotherm non-linearity (n_{BC}).

Based on $\log K_{OC}$=4.7 and $\log K_{BC}$=6.25.

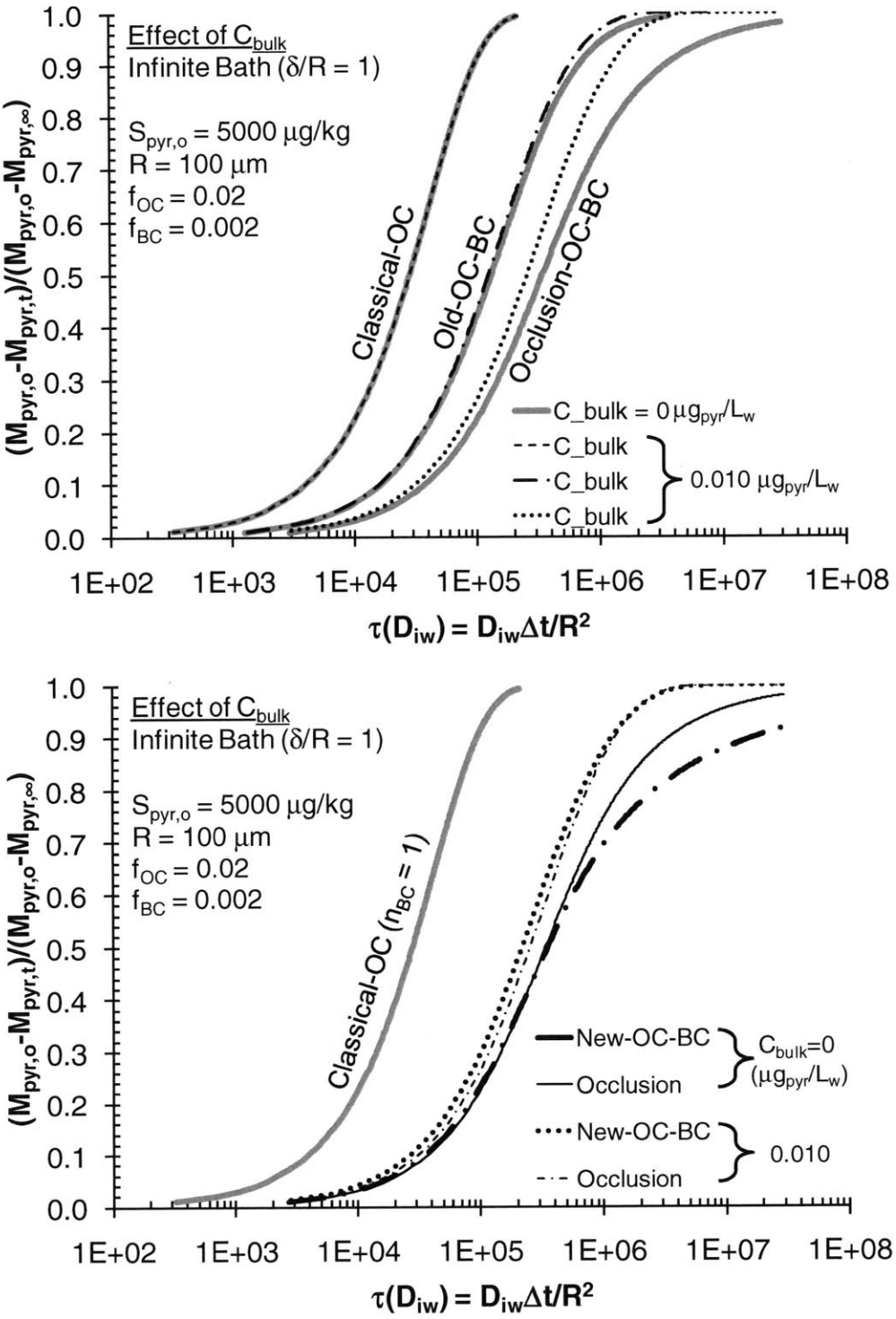

Figure 8 - 10. Infinite-Bath diffusion: effect of C_{bulk}.

The four isotherms are (i) Classical-OC ($logK_{OC}$ = $logK_{BC}$ = 4.7), (ii) Old-OC-BC ($logK_{OC}$ = 4.7; $logK_{BC}$ = 6.25; n_{BC} = 0.62), (iii) Occlusion-OC-BC ($logK_{OC}$ = 5.1; $logK_{BC}$ = 6.3; n_{BC} = 0.42; fraction occluded = 30%), (iv) New-OC-BC ($logK_{OC}$ = 5.25; $logK_{BC}$ = 6.25;; n_{BC} = 0.25).

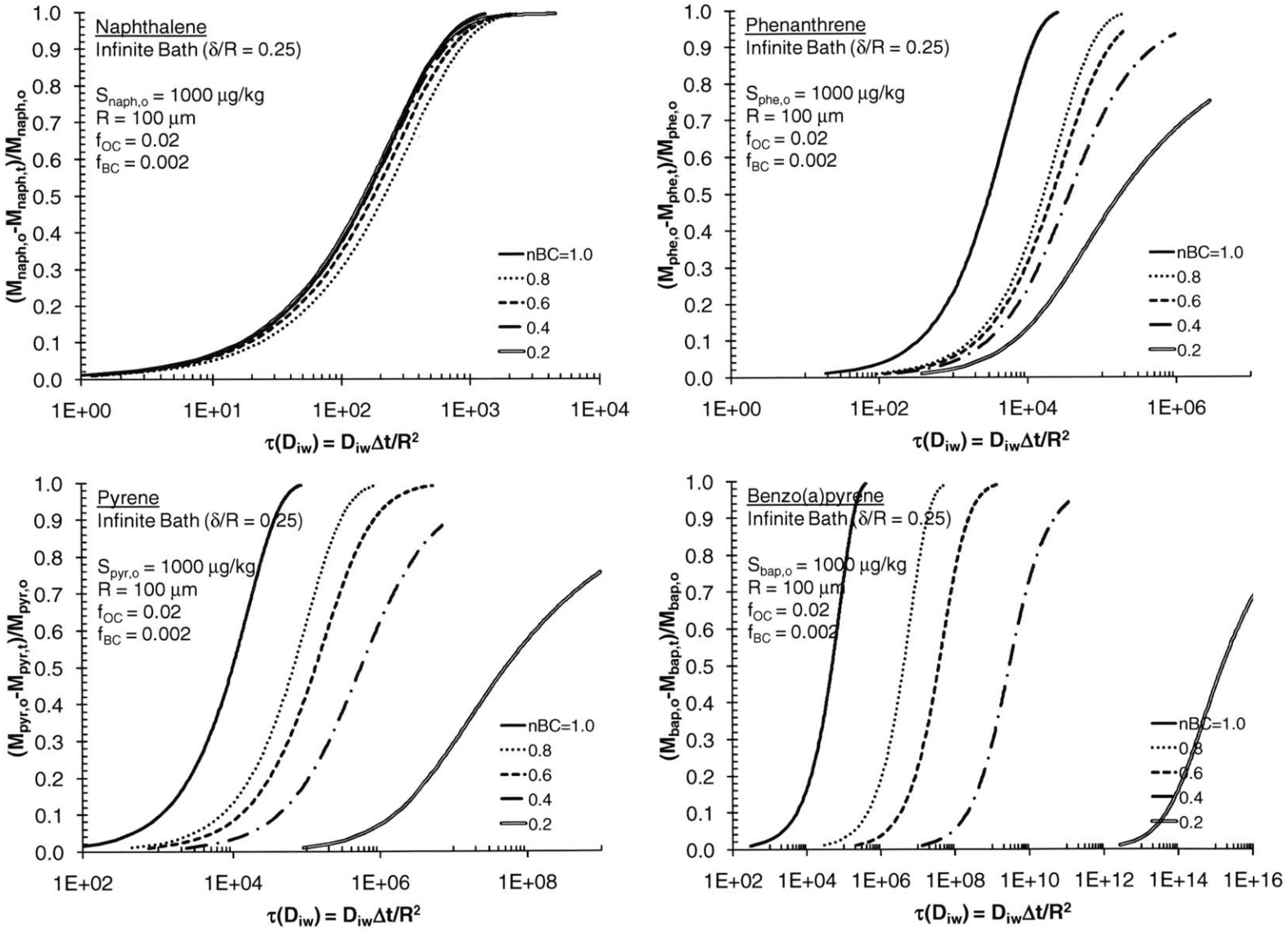

Figure 8 - 11. Infinite-Bath diffusion for four PAHs at $S_{PAH,o}$=1000 $\mu g_{PAH}/kg_{solids}$ and δ/R=0.25.

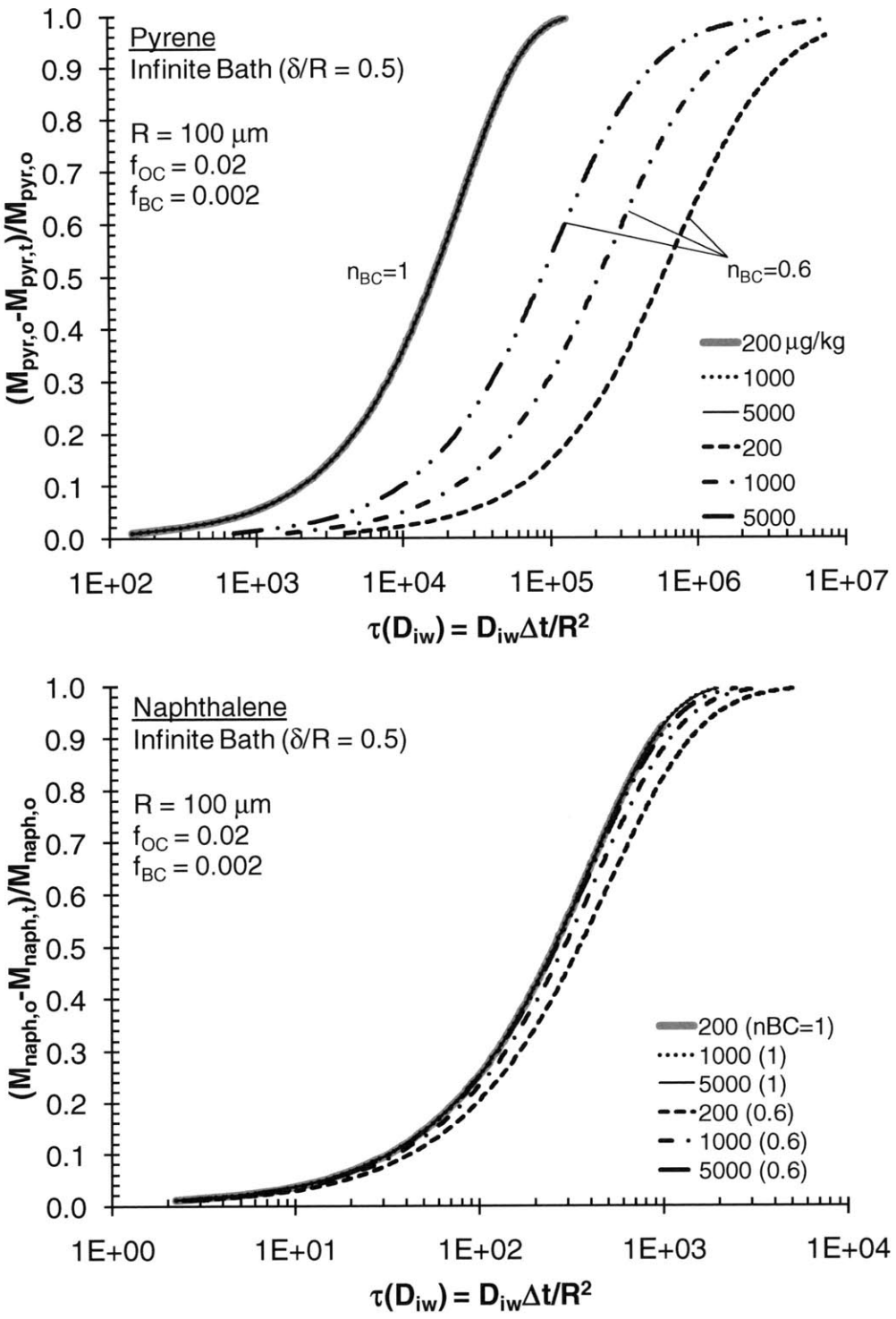

Figure 8 - 12. Infinite-Bath diffusion for four PAHs: the diminished importance of n_{BC} for less hydrophobic compound.

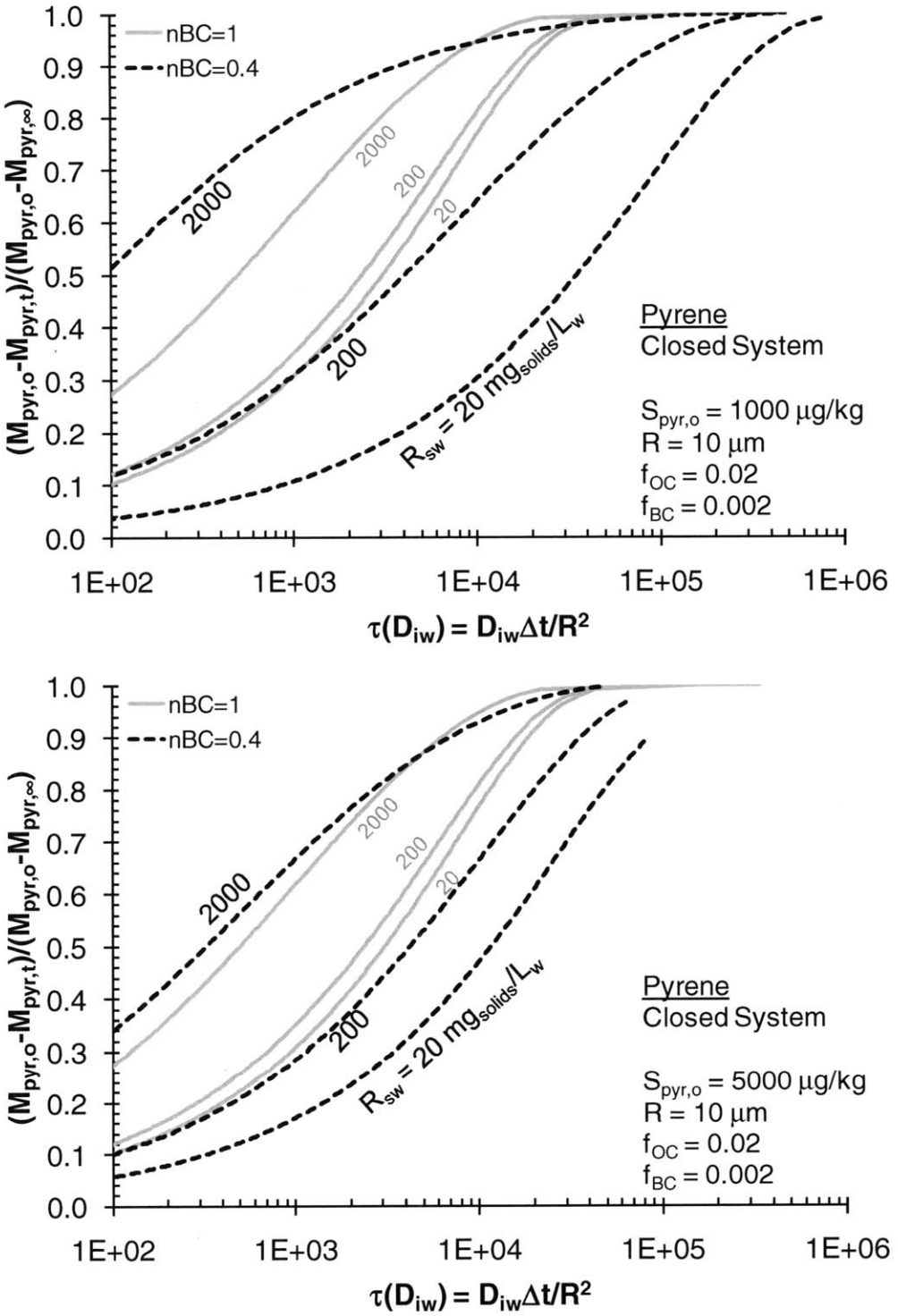

Figure 8 - 13. Closed-System diffusion: the sensitivity to R_{sw} and n_{BC} for pyrene.

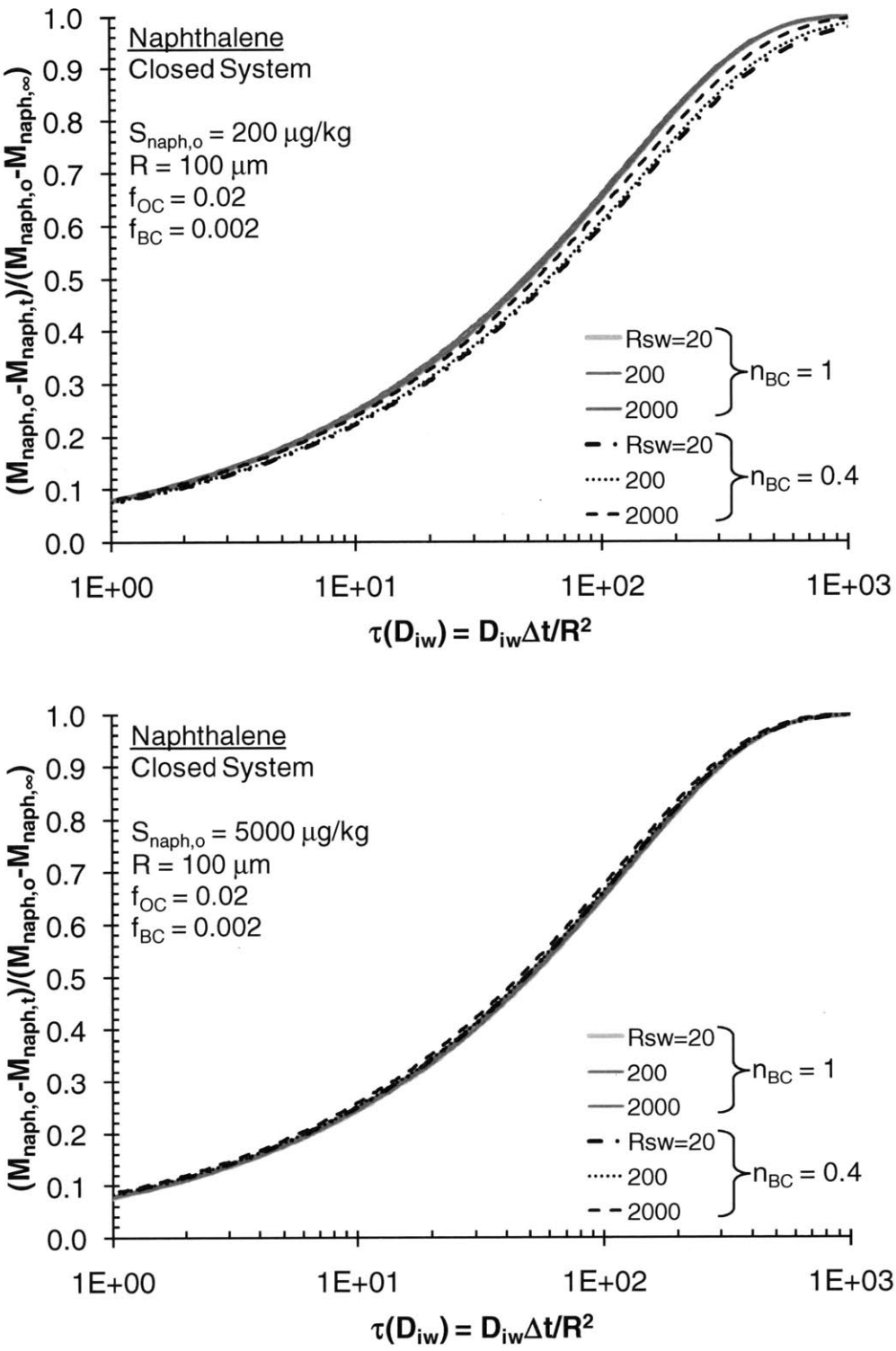

Figure 8 - 14. Closed-System diffusion: the sensitivity to R_{sw} and n_{BC} for naphthalene.

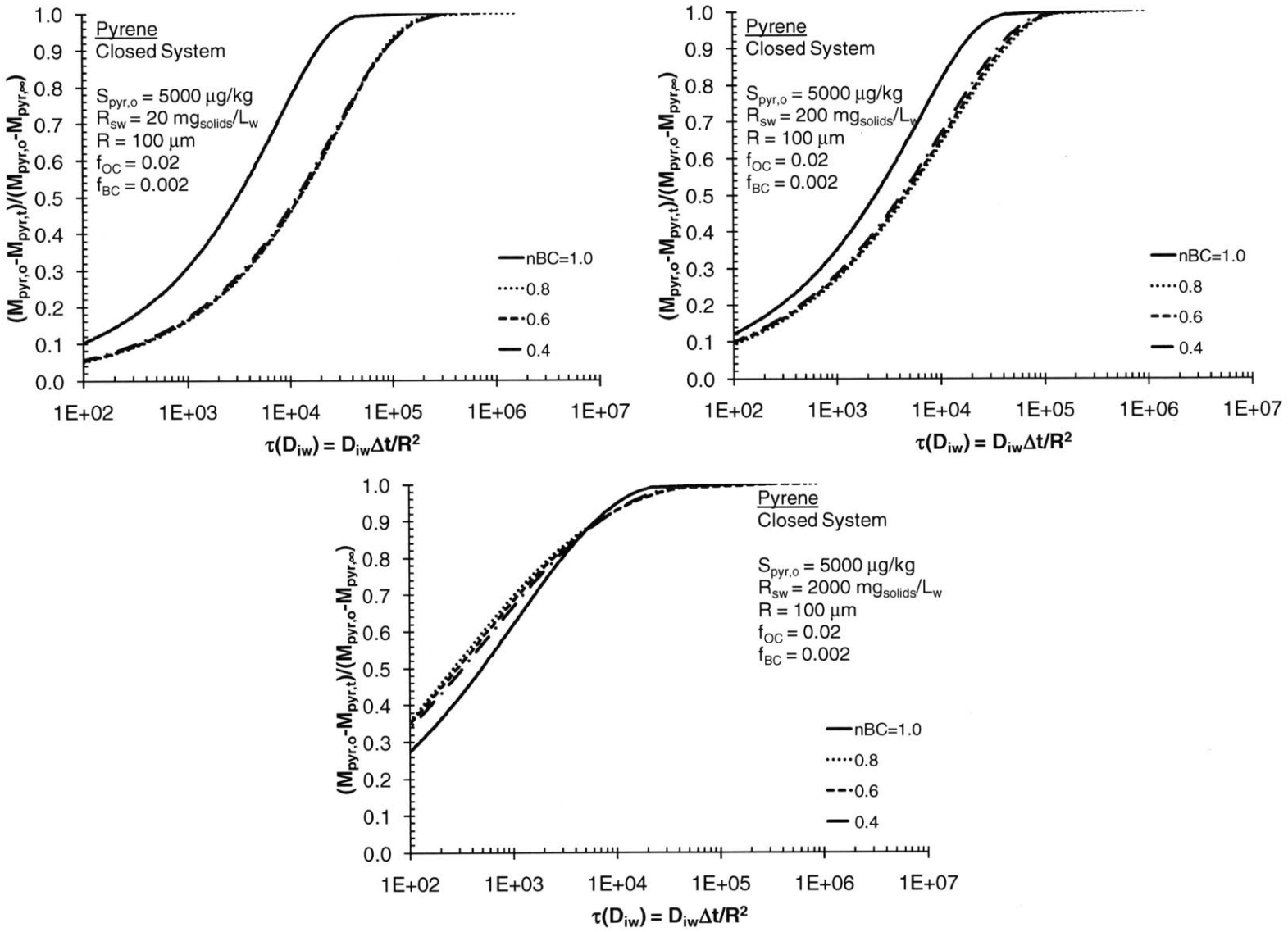

Figure 8 - 15. Closed-System diffusion: the insensitivity to R_{sw} and n_{BC} for pyrene.

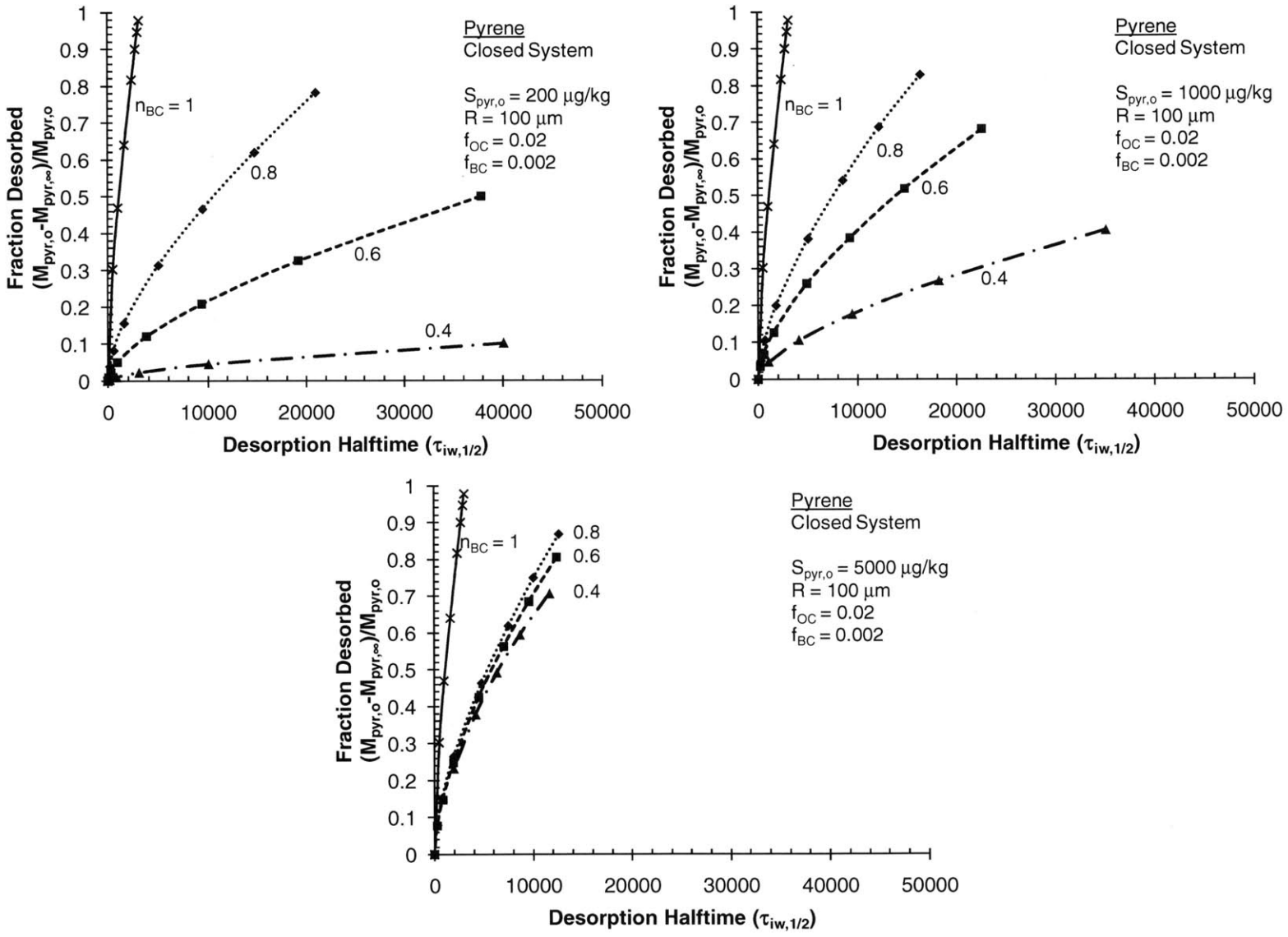

Figure 8 - 16. Closed-System diffusion: Fraction Desorbed $(M_{pyr,o}-M_{pyr,\infty})/M_{pyr,o}$ vs Desorption Halftime ($\tau_{iw,1/2}$).

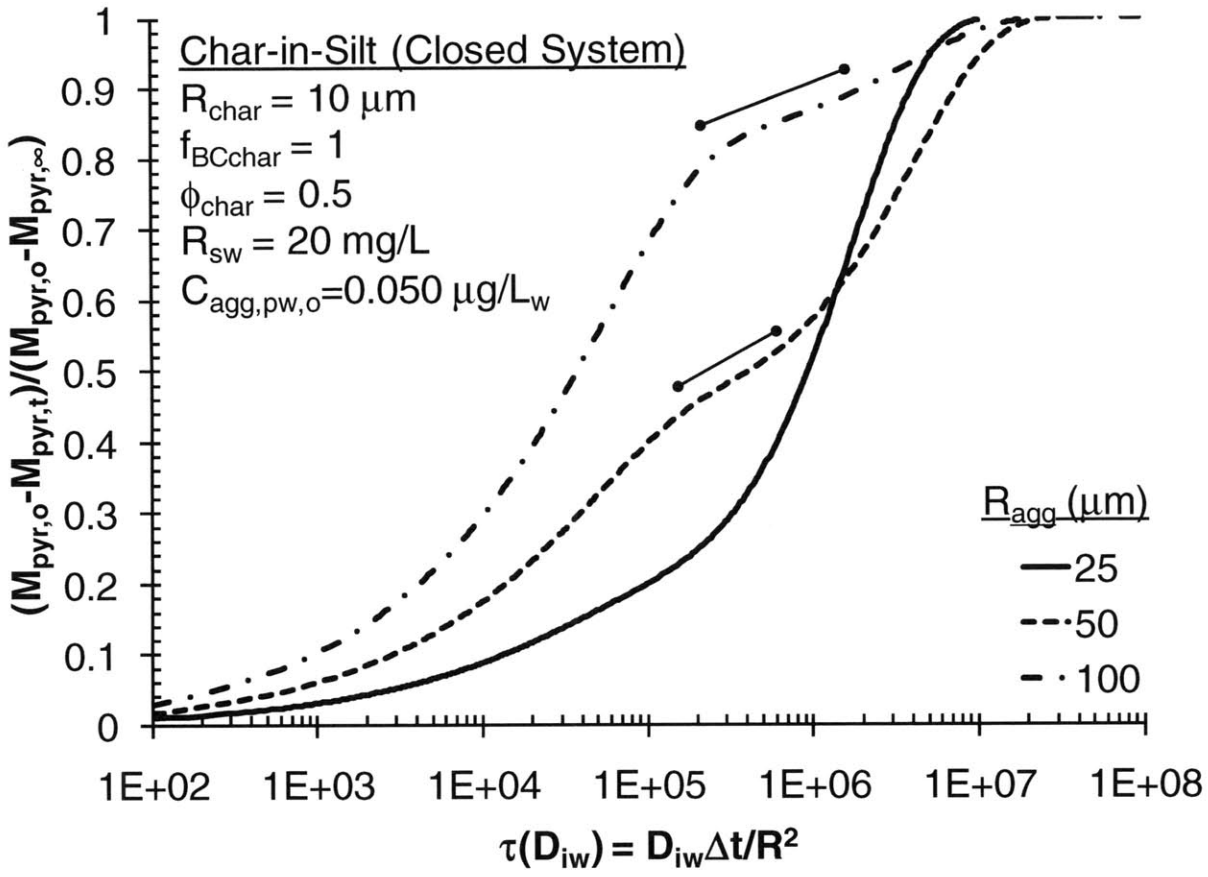

Figure 8 - 17. Char-in-Silt Closed-System diffusion: overall desorption-time profile.

The figure shows the normalized progress of desorption (fraction of sorbate desorbed: $(M_{pyr,o}-M_{pyr,t})/(M_{pyr,o}- M_{pyr,\infty})$) over dimensionless time at three different Char-to-Aggregate size ratio. The Char-to-Aggregate size ratio is defined as the radius of Char-domain over the radius of the entire aggregate (R_c/R_{agg}). The lines with rounded ends outlined where the 'intermediate plateau' is located on the curve.

Note that the radius of the Char-domain was kept constant at 10 μm. The initial aggregate porewater phase pyrene concentration, $C_{agg,pw,o}$, was set to be 0.05 $\mu g_{pyr}/L_w$.

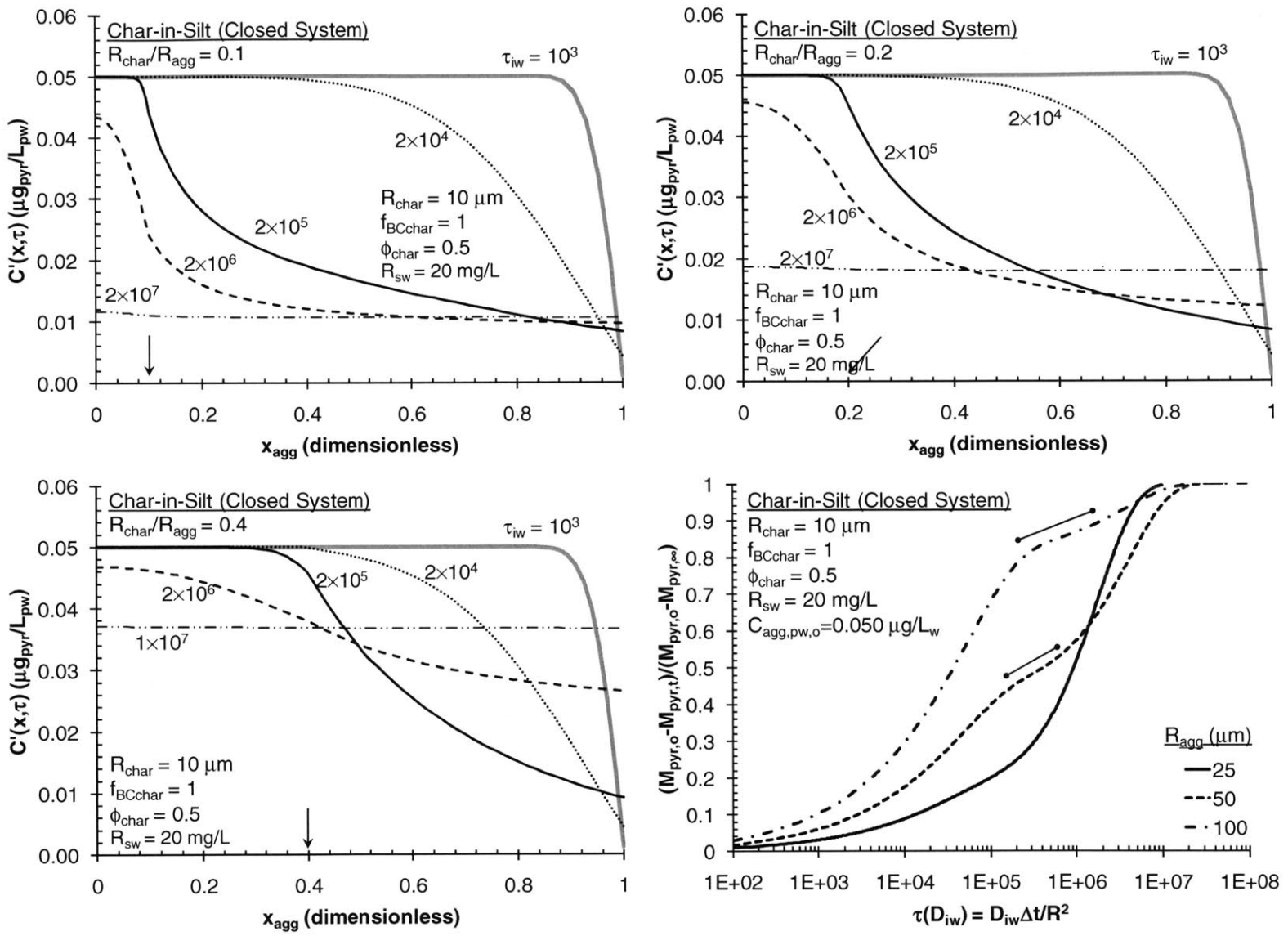

Figure 8 - 18. Char-in-Silt Closed-System diffusion: $C'_{pyr}(x,\tau)$ corresponding to the three $R_{c/Ragg}$'s.

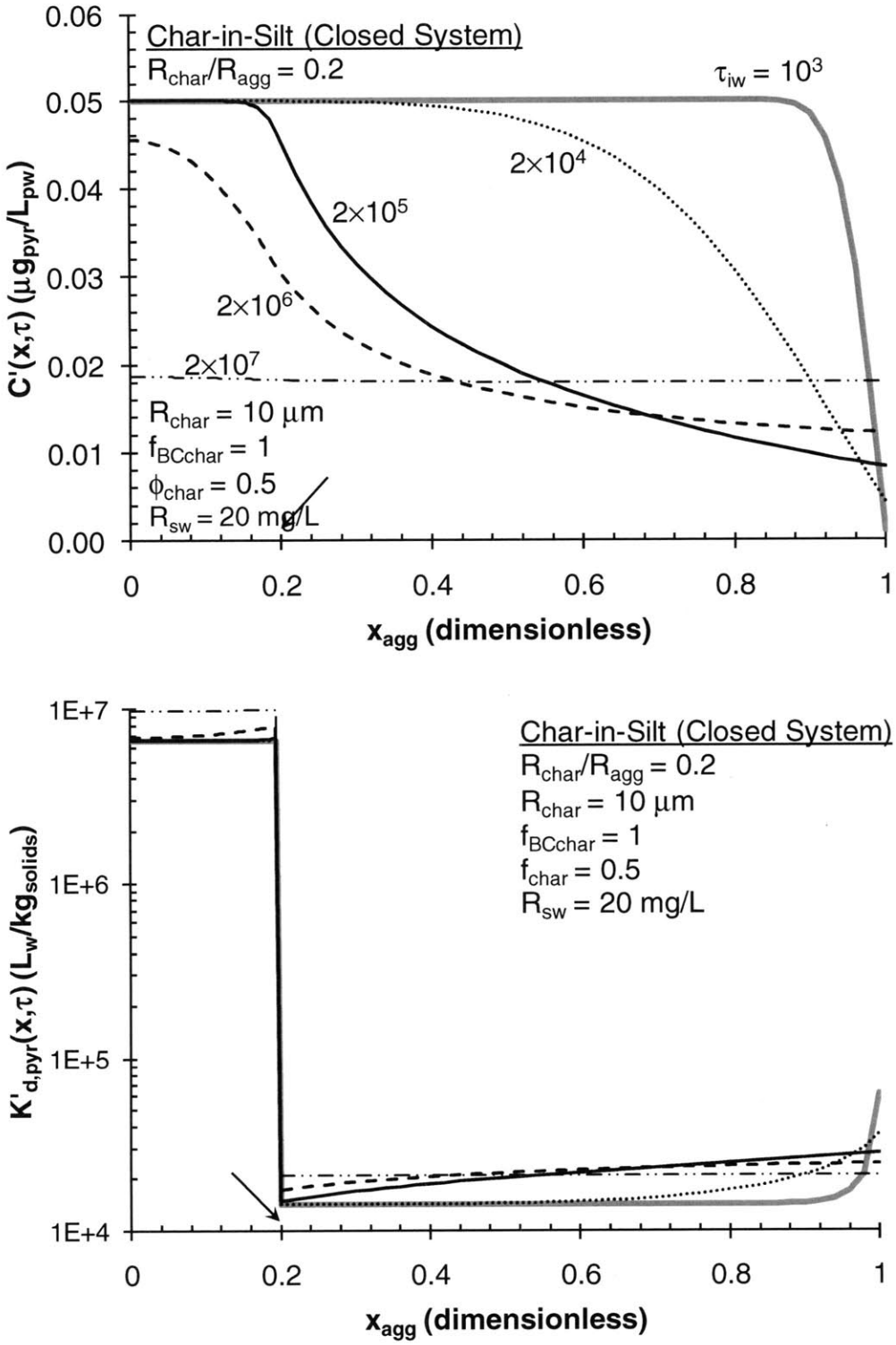

Figure 8 - 19. Char-in-Silt Closed-System: $K'_{d,pyr}(x,\tau)$.

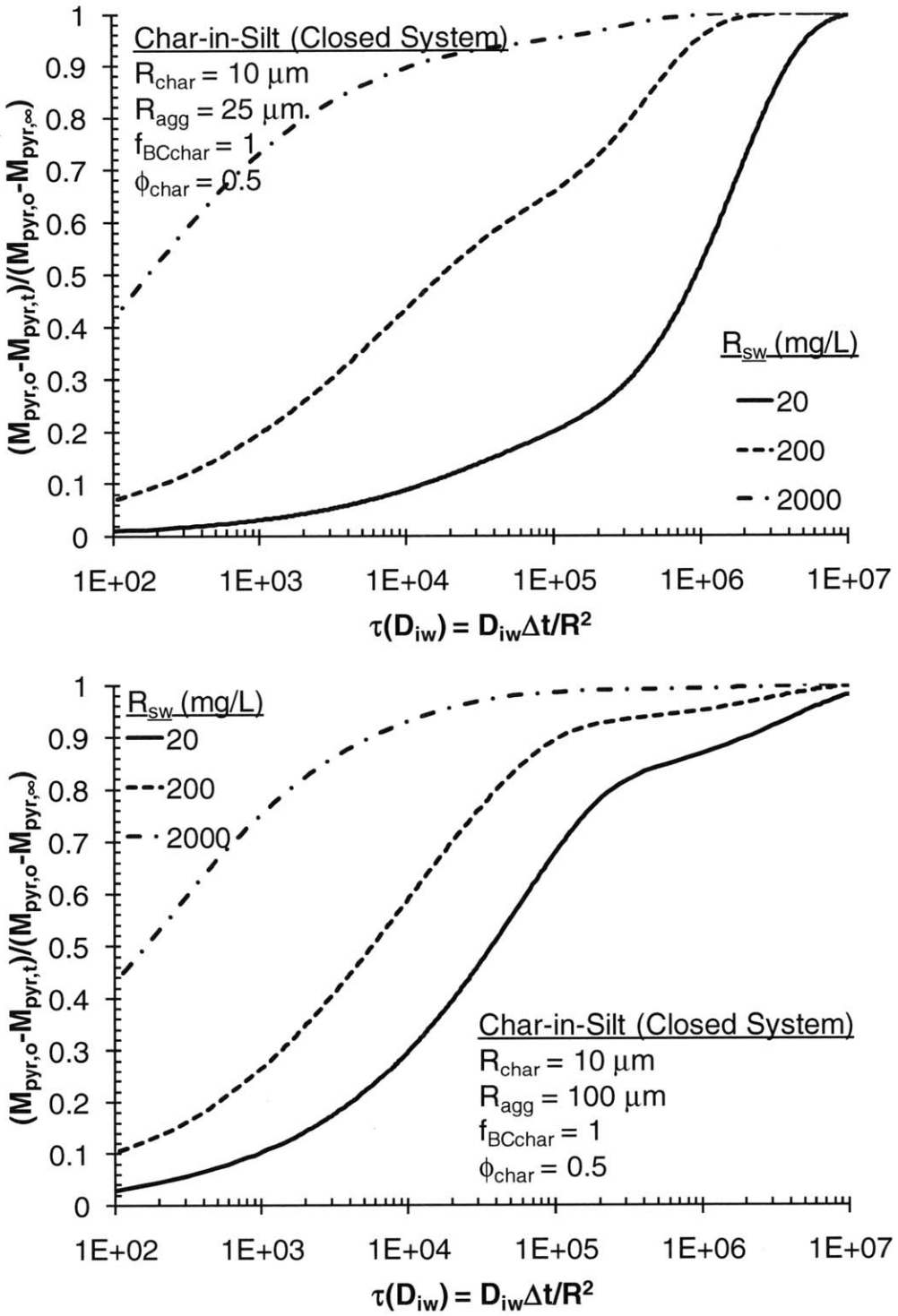

Figure 8 - 20. Char-in-Silt Closed-System: effect of R_{sw}.

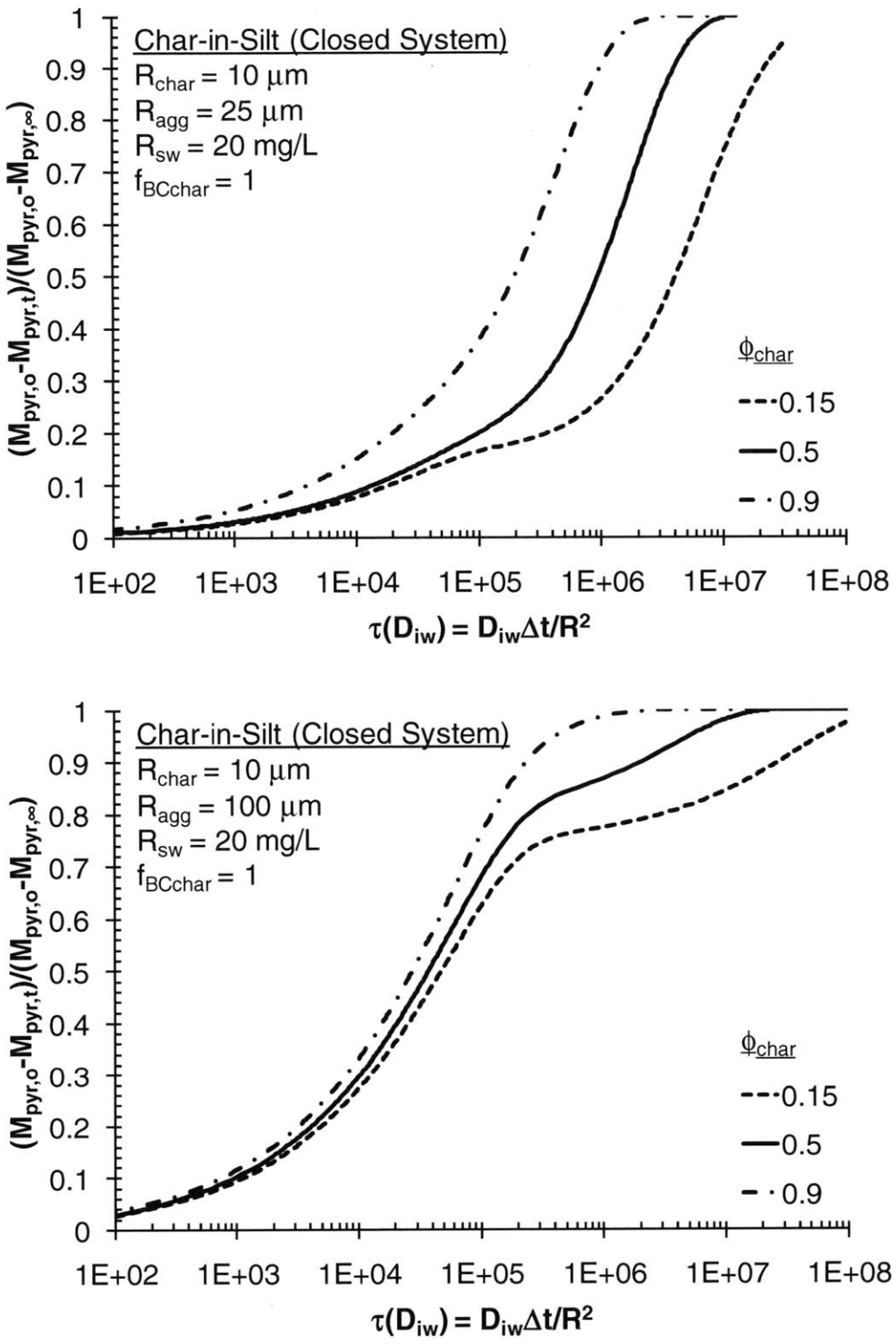

Figure 8 - 21. Char-in-Silt Closed-System: effect of char-domain porosity/tortuosity.

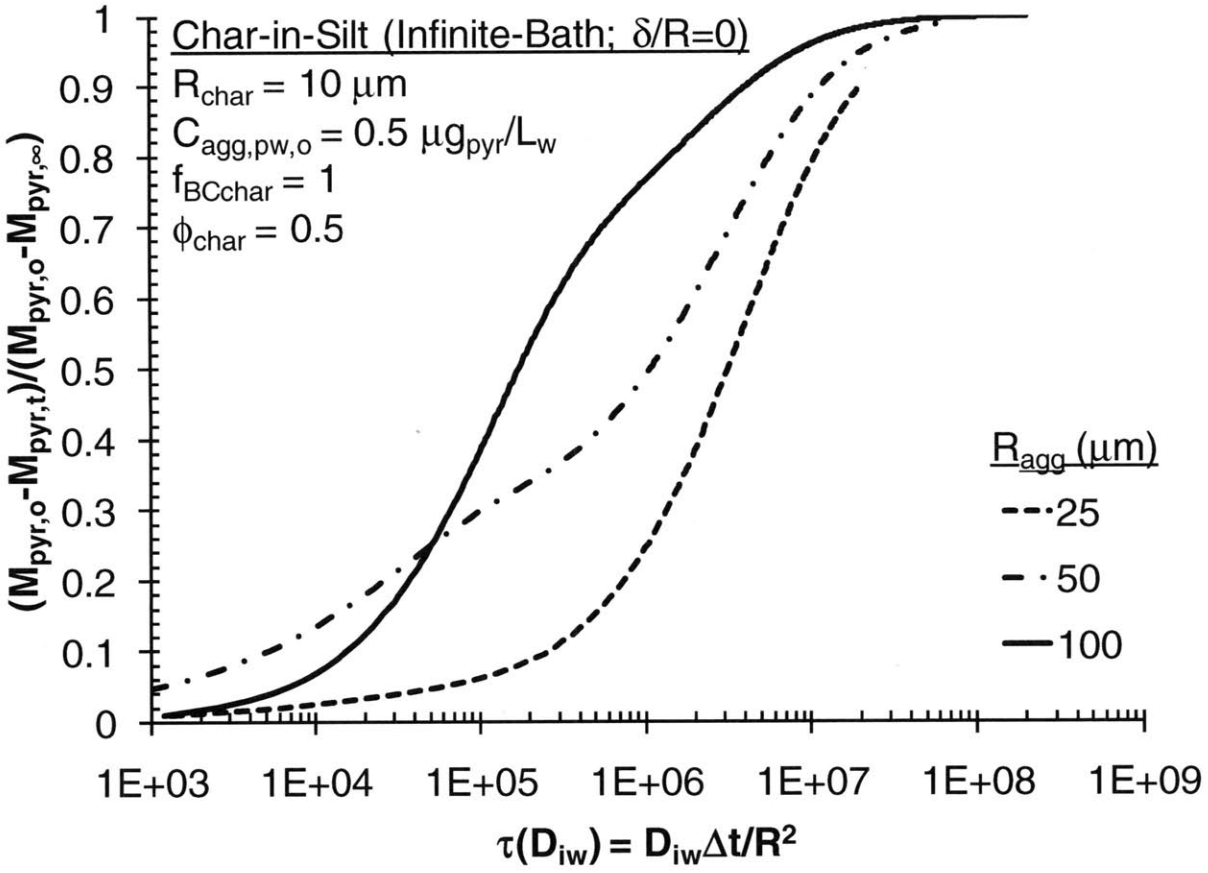

Figure 8 - 22. Char-in-Silt Infinite-Bath diffusion: effect of char-to-aggregate size ratio. Note that the bulk phase pyrene concentration was kept constant at zero.

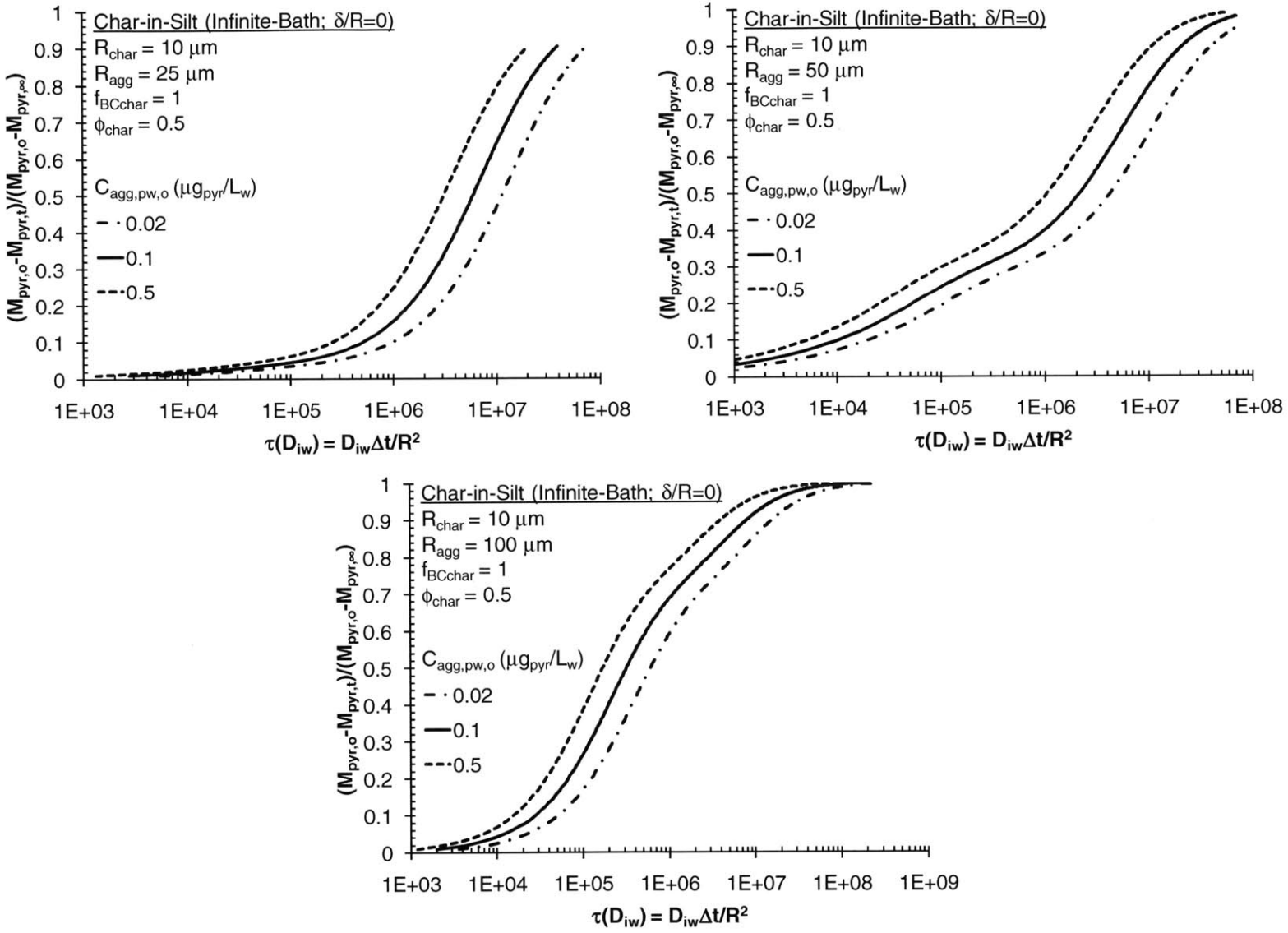

Figure 8 - 23. Char-in-Silt Infinite-Bath diffusion: effect of initial aggregate porewater concentration $C_{agg,pyr,o}$ (at n_{BC}=0.6)

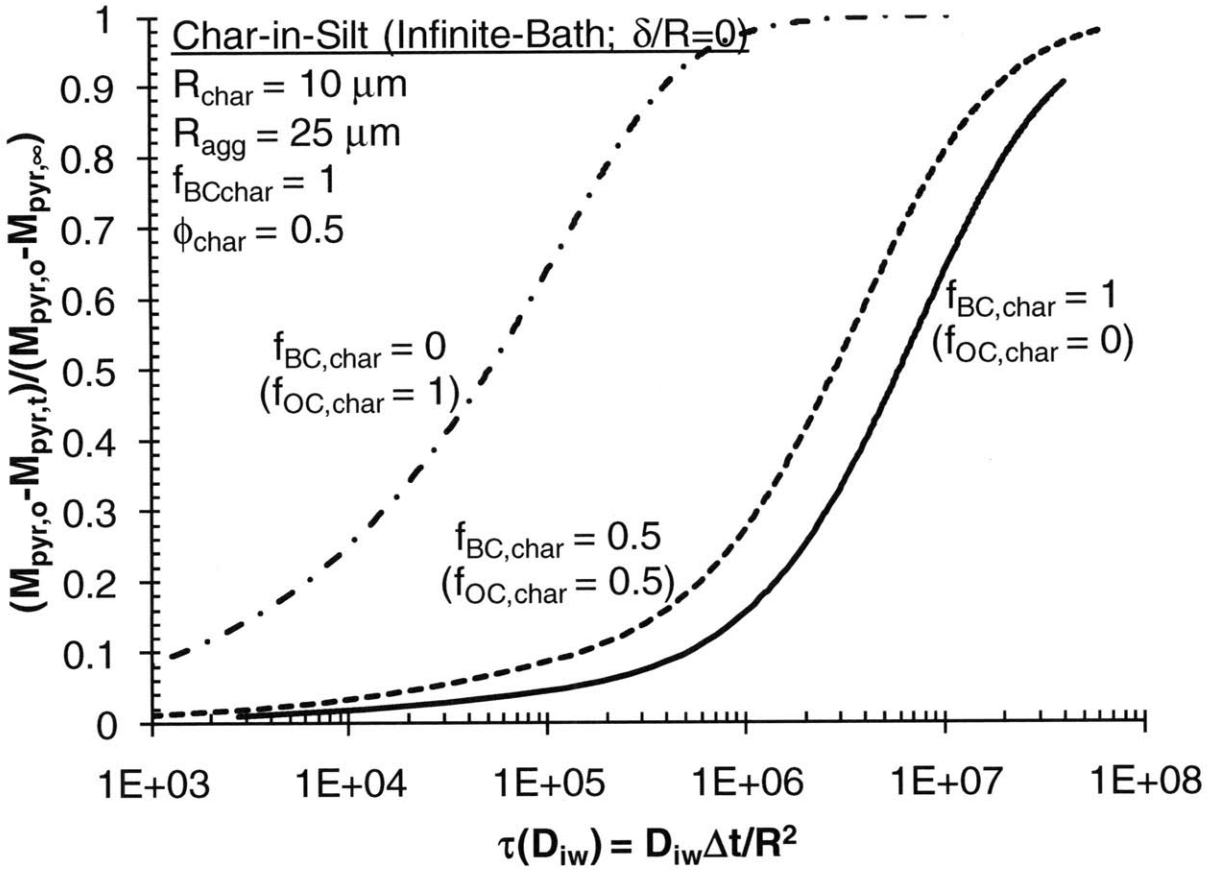

Figure 8 - 24. Char-in-Silt Infinite-Bath diffusion: effect of char-domain 'composition'.

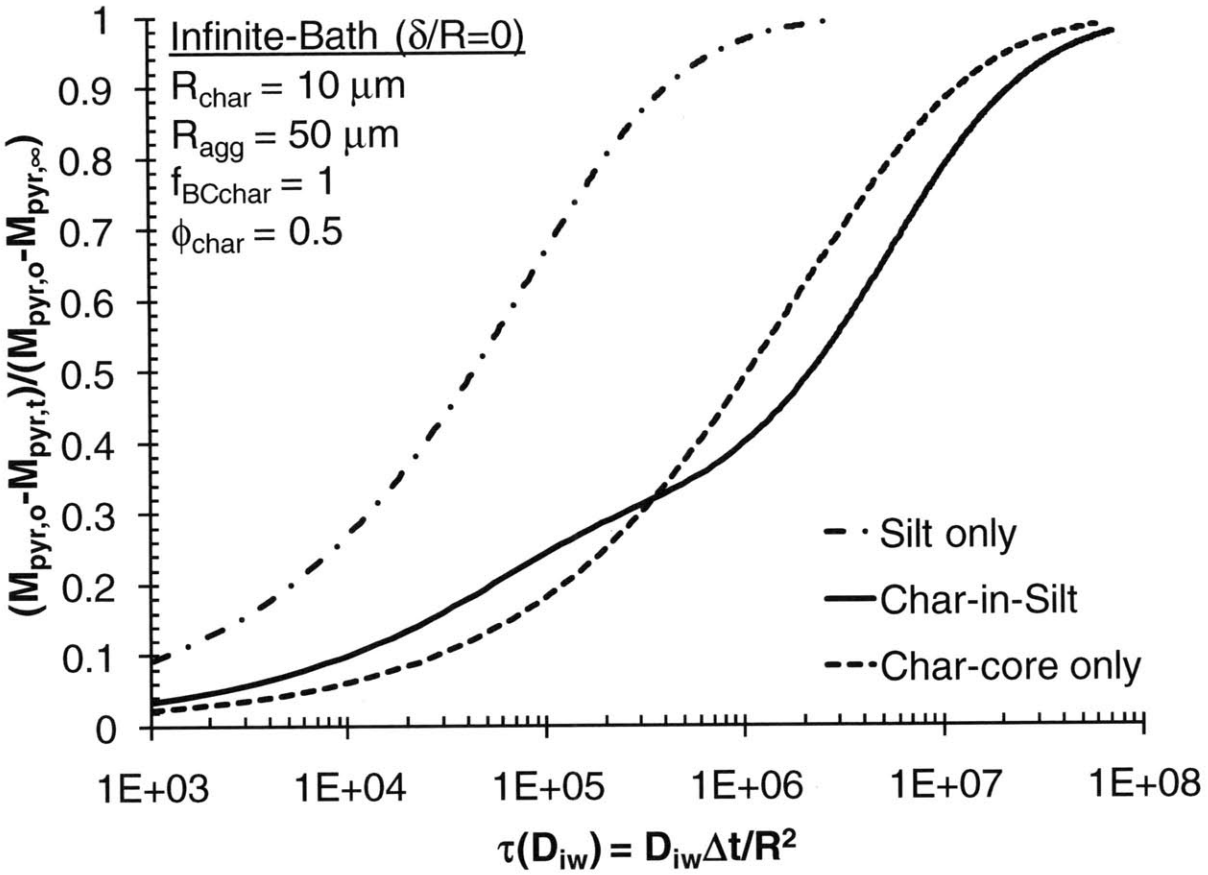

Figure 8 - 25. Infinite-Bath diffusion: Comparing three aggregate/particle configurations.

The physicochemical properties of the three configurations were as follow: (i) 'Silt only', radius = 50 μm, f_{OC}=0.02, f_{BC}=0.002; (ii) 'Char-in-Silt', char radius = 10 μm, aggregate radius = 50 μm, $f_{OC,silt}$=0.02, $f_{BC,silt}$=0.002, $f_{OC,char}$=0, $f_{BC,char}$=1; (iii) 'Char-core only', radius = 10 μm, f_{OC}=0, f_{BC}=1. The porosity of all silt-phase was set to be 0.15, while that for char-domain/core was set at 0.5.

Chapter 9: Figures

Figure 9 - 1. Box models and their 'questions'. 455
Figure 9 - 2. Cartoon of the equilibrium partitioning models (EqP)....455
Figure 9 - 3. Cartoon of the steady-state models ($\Sigma r_{sources} = \Sigma r_{sinks}$). 456
Figure 9 - 4. Pyrene inventory in regionalized Boston Harbor....457
Figure 9 - 5. Bed-Water Column EqP prediction of $C_{pyr,WC}$ (basecases). 458
Figure 9 - 6. Bed-WC EqP Model: projected depletion of sedimentary pyrene over time. 459
Figure 9 - 7. TSS-Water Column EqP prediction of $C_{pyr,WC}$ (basecases)....460
Figure 9 - 8. TSS-WC EqP Model: projected depletion of sedimentary pyrene over time. 461
Figure 9 - 9. Disequilibrium in surficial bed layer in three Boston Harbor cores. 462
Figure 9 - 10. Surficial bed pyrene concentration as a function of depth ($S_{bed,pyr}(z)$)..463
Figure 9 - 11. Steady-state model (3-rate) with and without desorption. 464
Figure 9 - 12. Steady-state model (7-rate) with and without desorption. 465
Figure 9 - 13. Steady-state model (7-rate): Predictions at different $t_{1/2,des}$. 466
Figure 9 - 14. Seasonal variation in $C_{pyr,WC}$ observed in Boston Harbor....467
Figure 9 - 15. Observed vs predicted $C_{pyr,WC}$ observed in Summer and Winter. 468
Figure 9 - 16. Relative contribution by different processes in the steady-state model (Summer case). 469
Figure 9 - 17. Distribution of PAHs on Different Sediment Size Fractions....470
Figure 9 - 18. The steady-state Winter scenario reassessed at $t_{1/2,des,winter}$ = 3.6–15.6 d ($4 \times t_{1/2,des,summer}$). 471
Figure 9 - 19. Various processes that contribute to sediment-bed porewater 'flushing'. 472
Figure 9 - 20. Mean direct photolysis halftime for pyrene as a function of water depth. 473
Figure 9 - 21. Determination of desorption halftime, $t_{1/2,des}$. 474

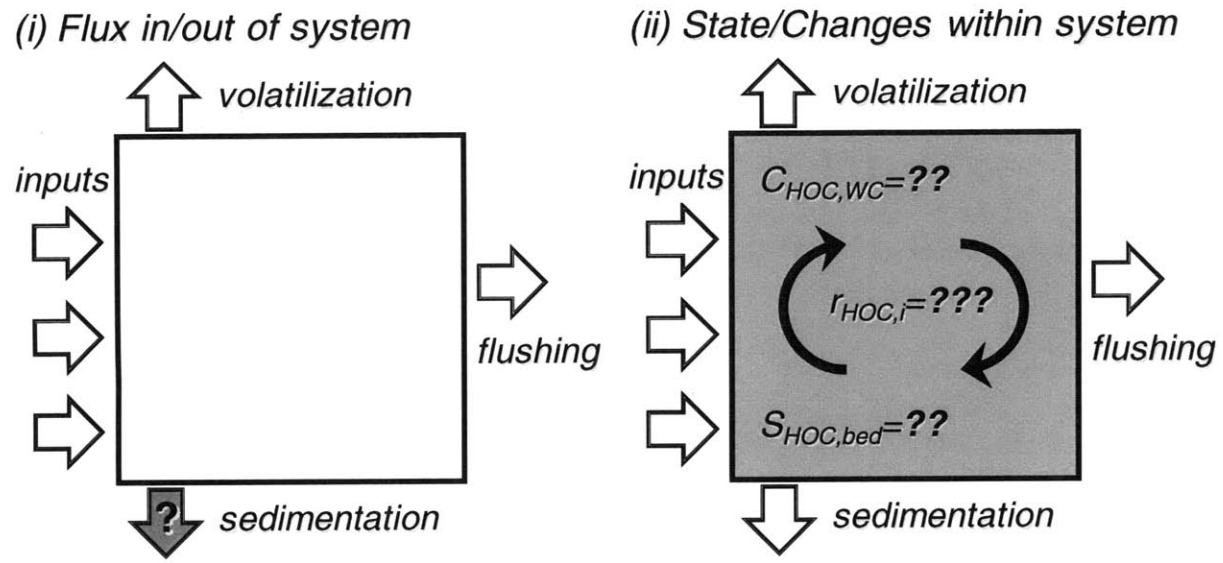

Figure 9 - 1. Box models and their 'questions'.

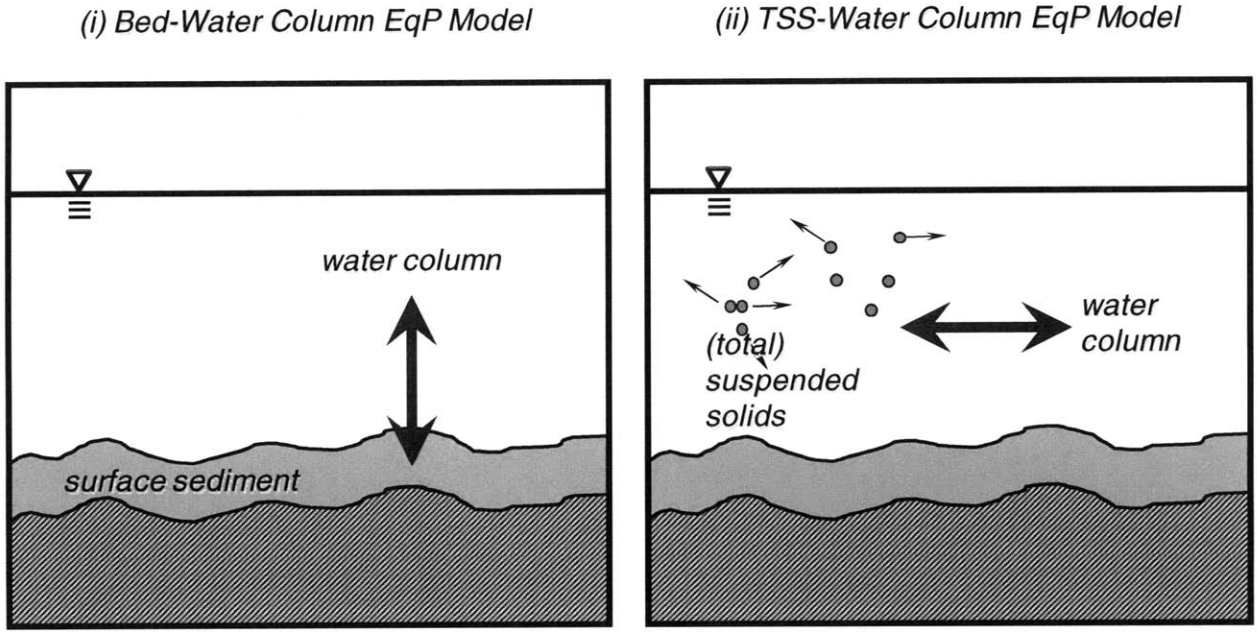

Figure 9 - 2. Cartoon of the equilibrium partitioning models (EqP).

In figure (i), the surface sediment bed layer is assumed to be at sorption/partition equilibrium with the overlaying water column. In figure (ii), it is the suspended sedimentary particles that are at equilibrium with the water column.

In both models all other sinks or sources of HOCs, spatial variation/heterogeneity, and hydrodynamical forcings are considered as negligible.

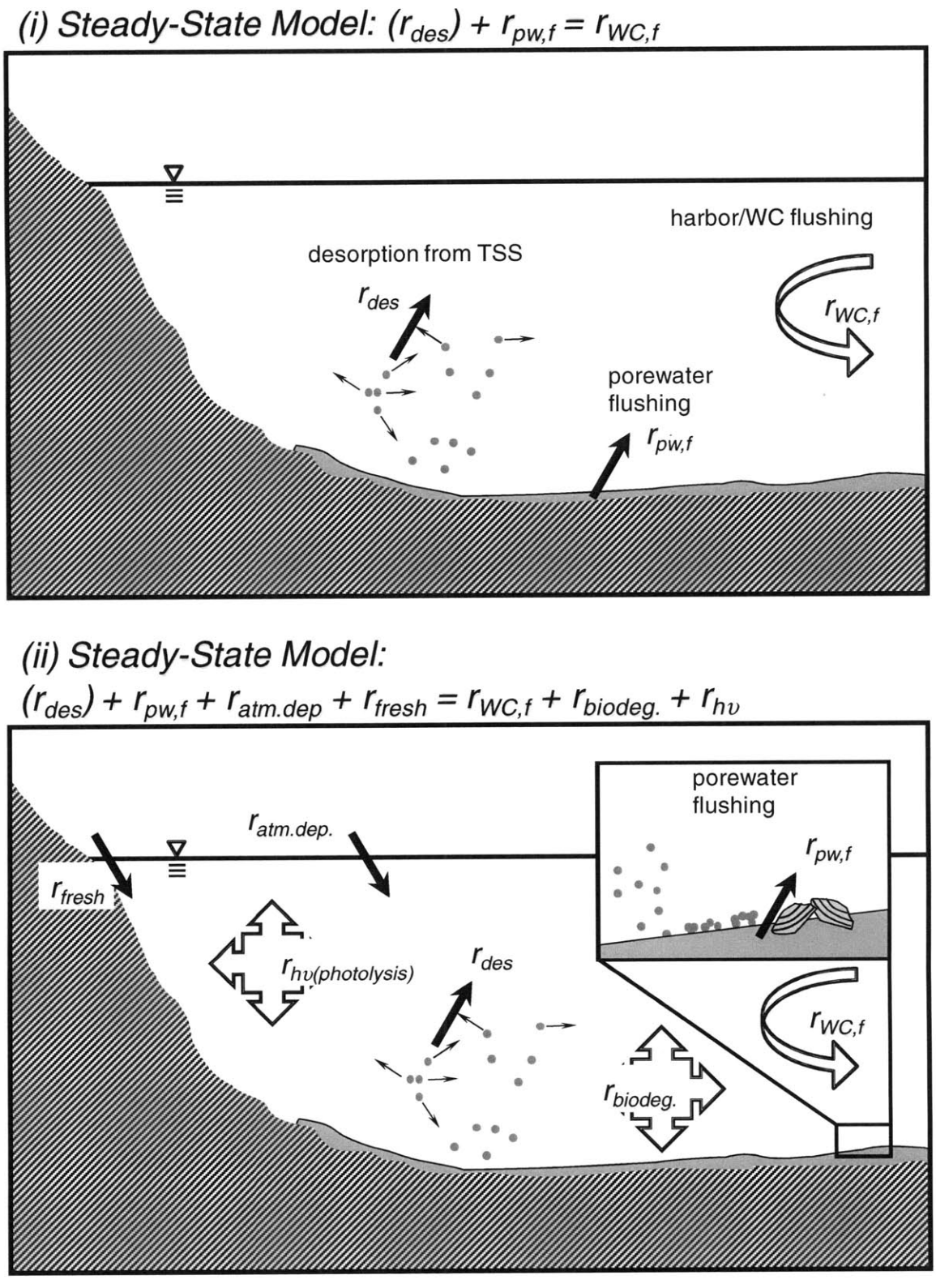

Figure 9 - 3. Cartoon of the steady-state models ($\Sigma r_{sources} = \Sigma r_{sinks}$).

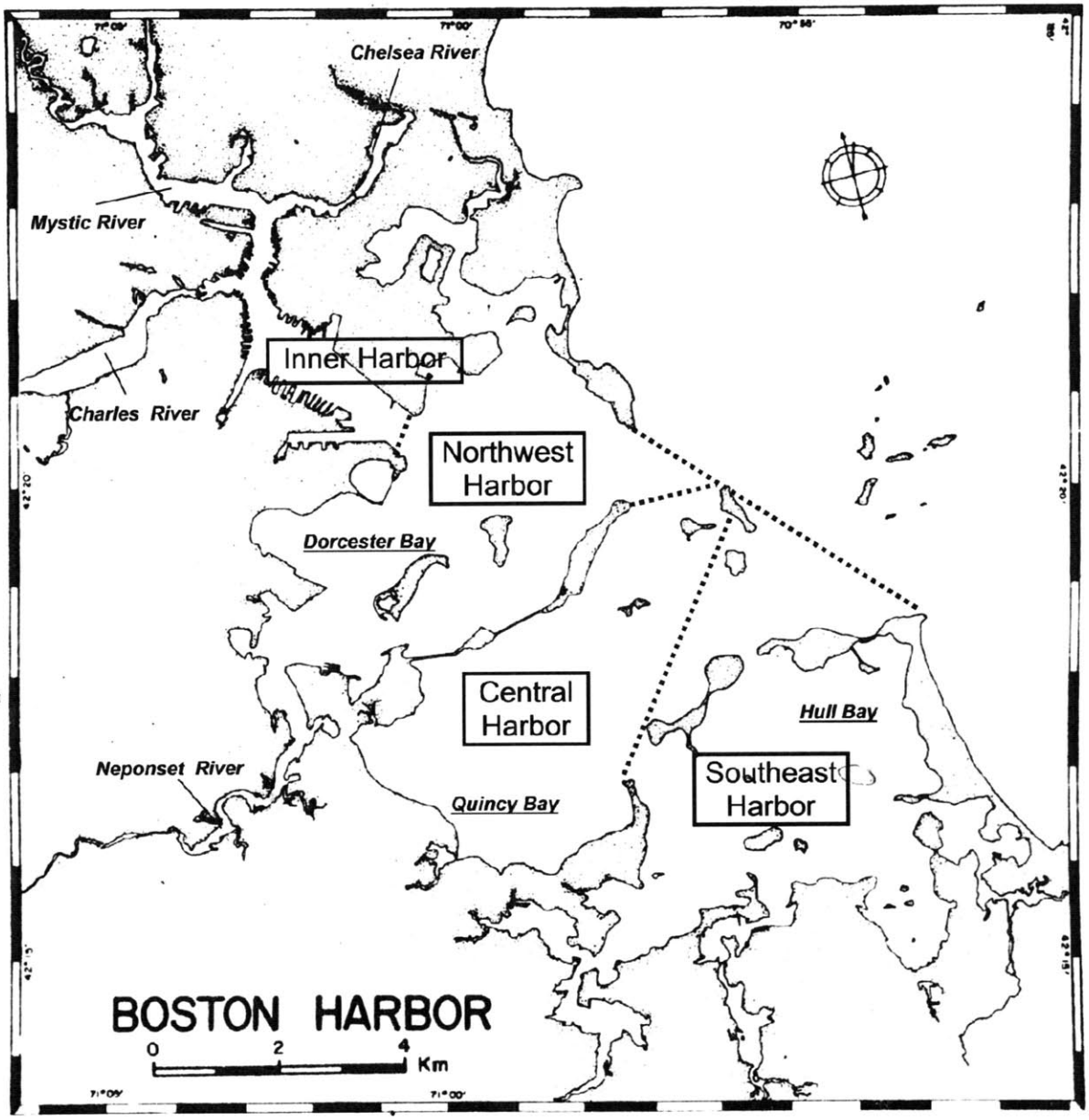

(Map adapted from Shiaris et al. 1986 and Stolzenbach et al. 1998)

Region	Area (km^2)[a]	$S_{pyr,bed}$ (ug_{pyr}/kg_{solids})[b]	$C_{pyr,wc}$ (ng_{pyr}/L)[c]
Inner	8	3000-70000 (n=5)	<10-140
Northwest	43	200-15000 (n=7)	<5-70
Central	38	600-10000 (n=2)	--
Southeast	19	200-2000 (n=5)	<5-15

a: From Stolzenbach et al.1998. b: From Shiaris et al. 1986. c: From Rudnick 1998.

Figure 9 - 4. Pyrene inventory in regionalized Boston Harbor.

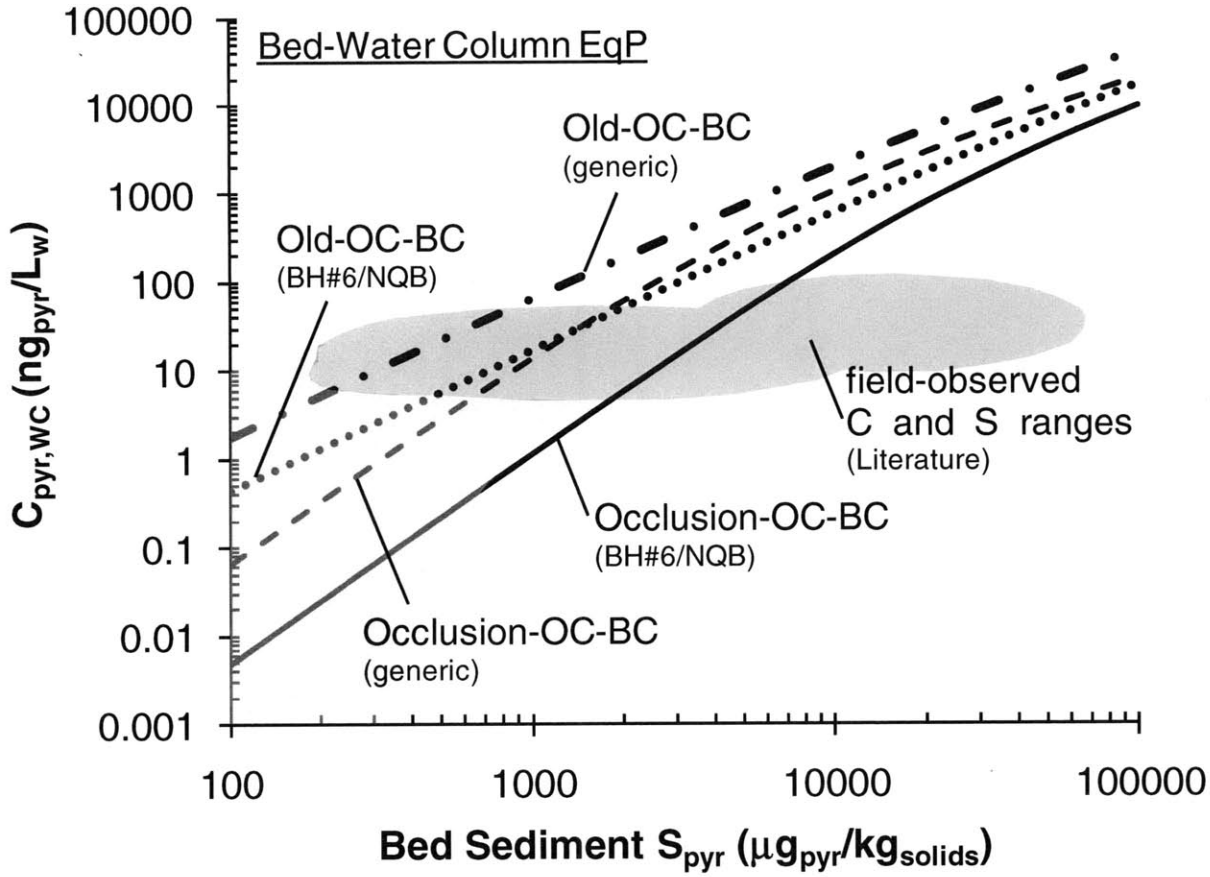

Figure 9 - 5. Bed-Water Column EqP prediction of $C_{pyr,WC}$ (basecases).

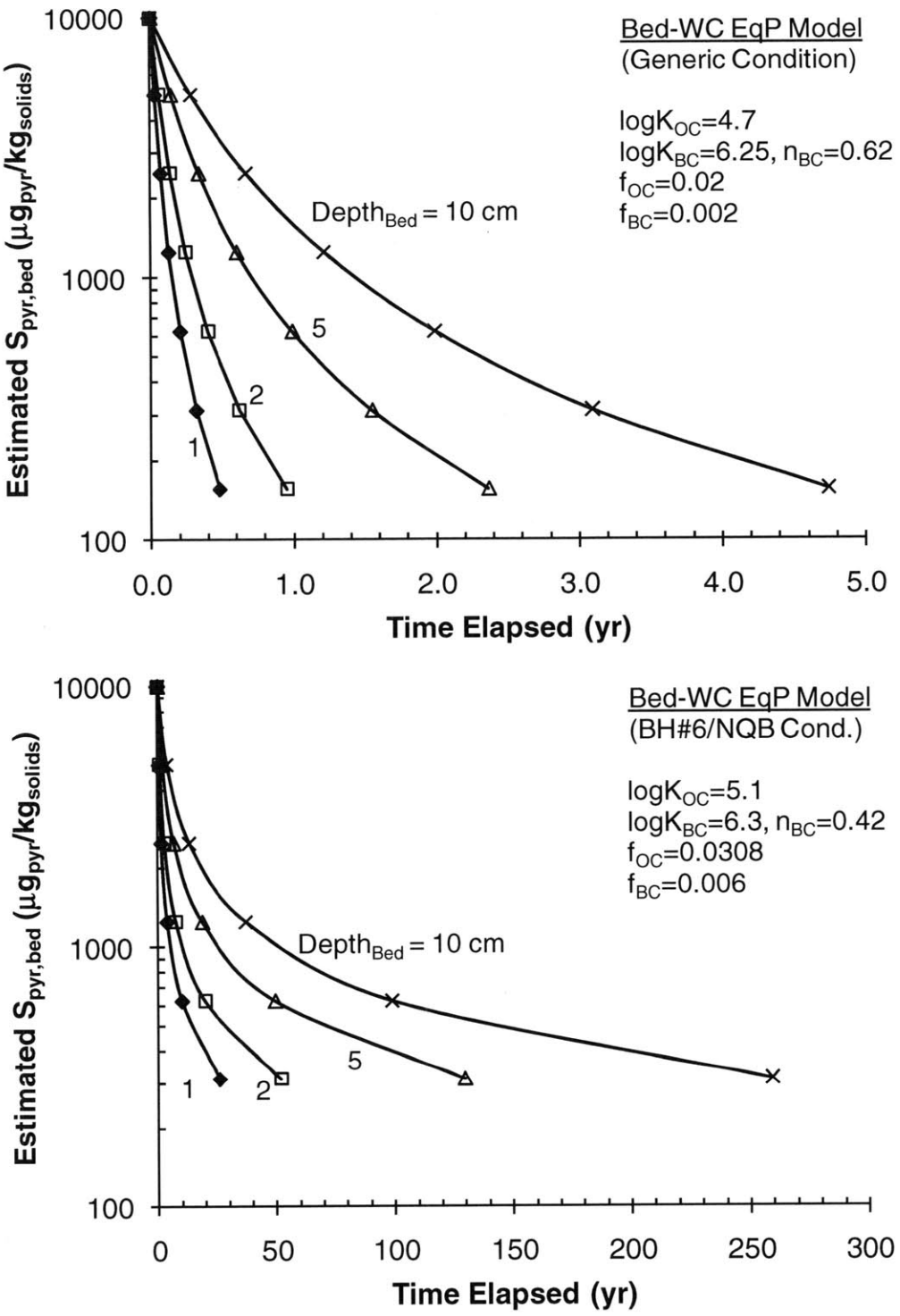

Figure 9 - 6. Bed-WC EqP Model: projected depletion of sedimentary pyrene over time.

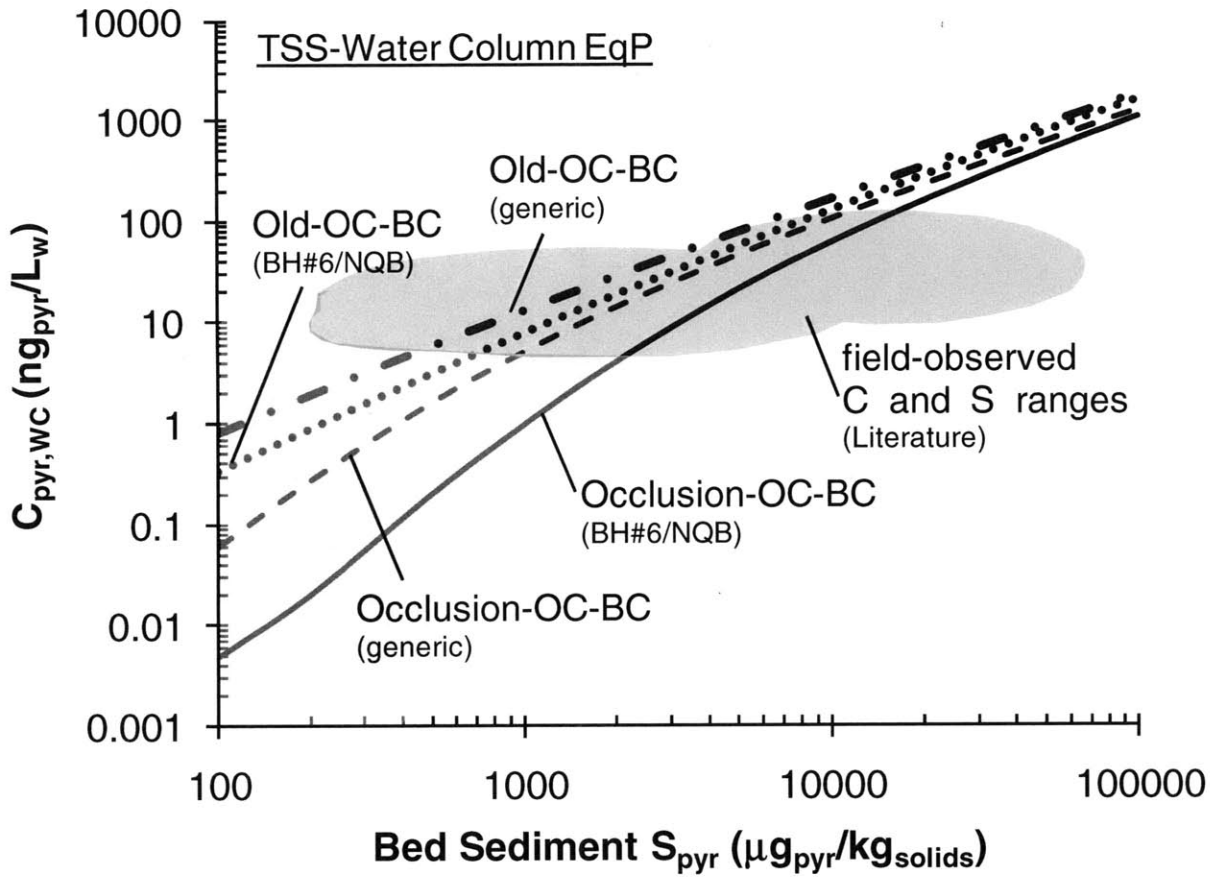

Figure 9 - 7. TSS-Water Column EqP prediction of $C_{pyr,WC}$ (basecases).

The parameters for the Old-OC-BC and the Occlusion isotherms are summarized in Table 9-2.

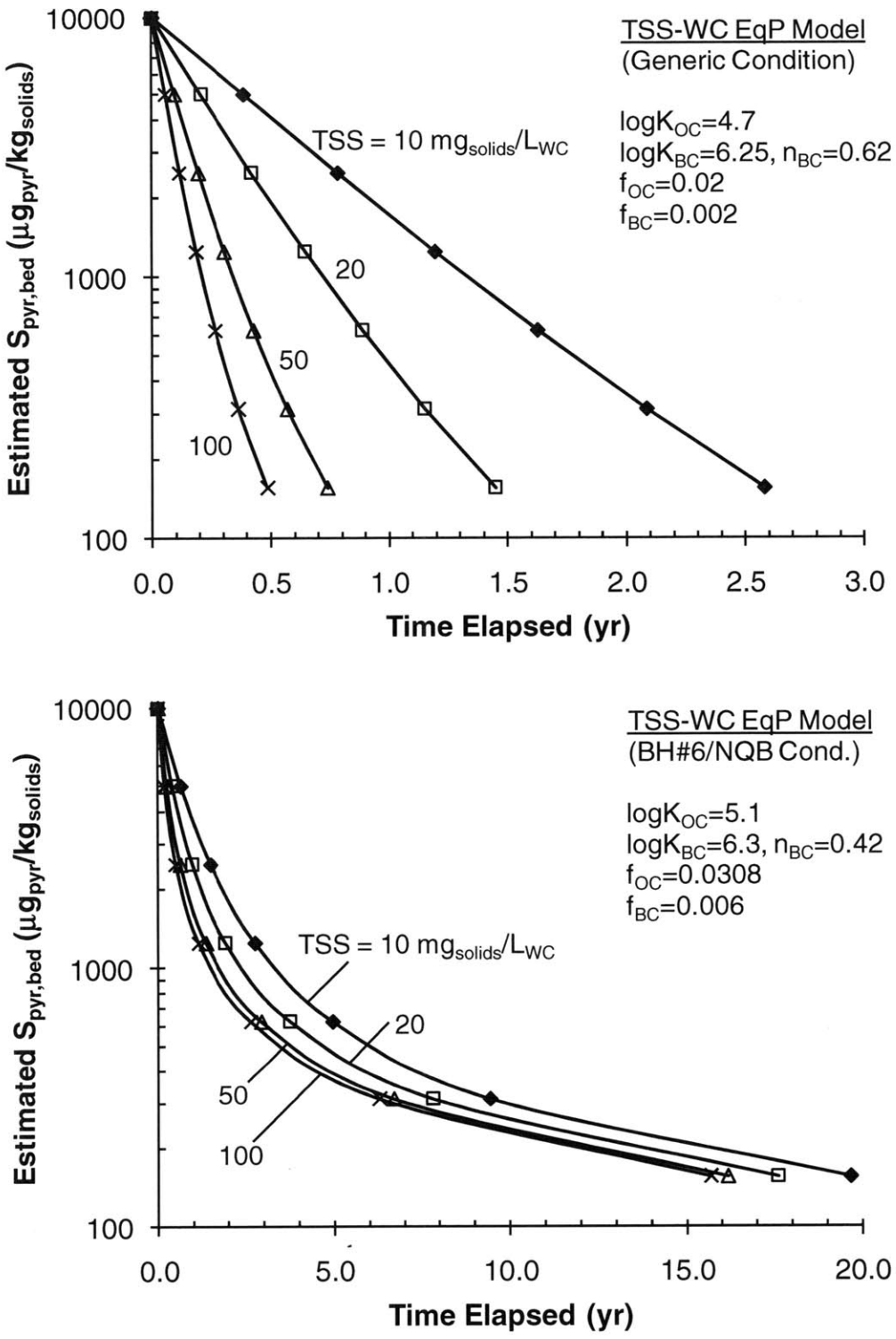

Figure 9 - 8. TSS-WC EqP Model: projected depletion of sedimentary pyrene over time.

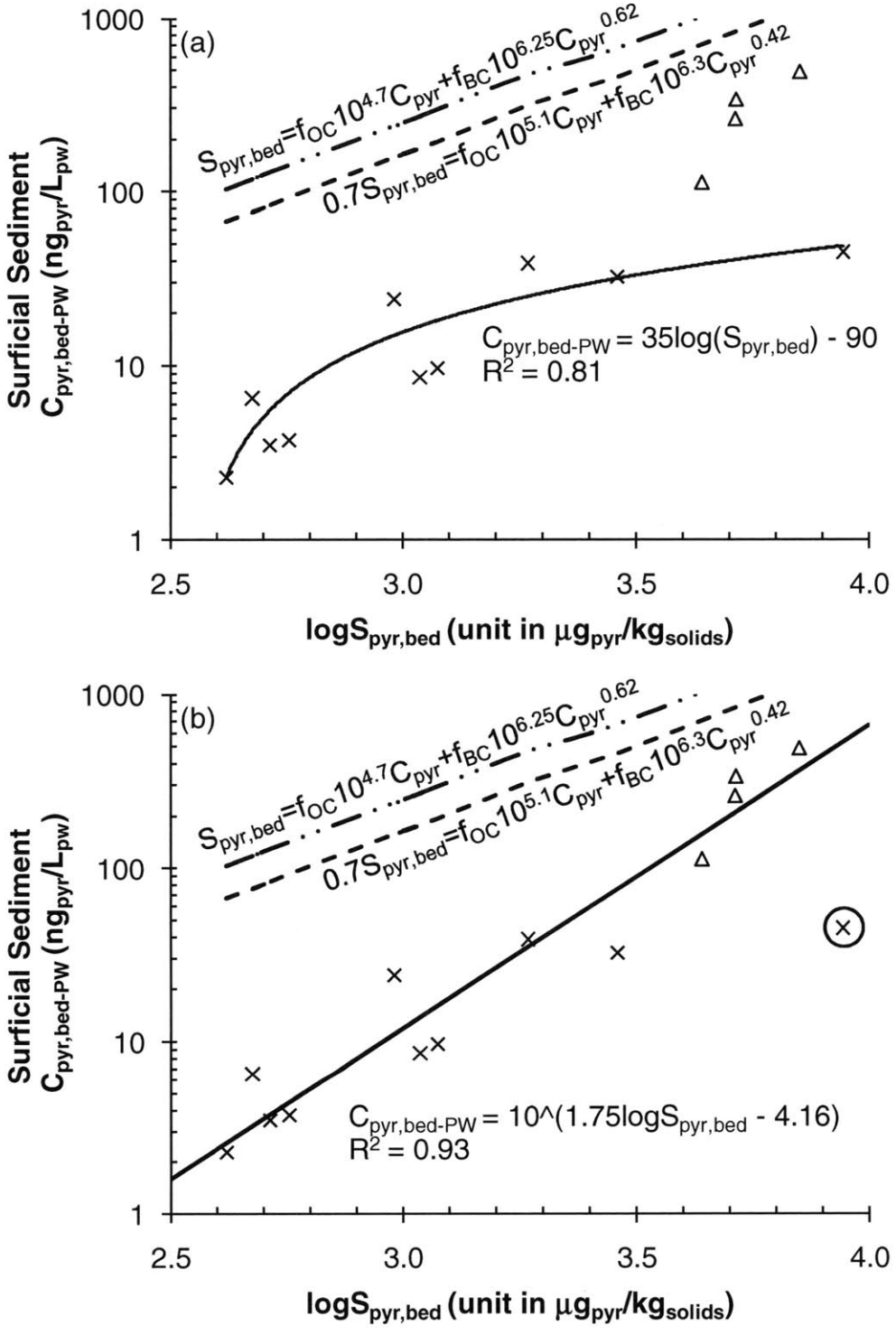

Figure 9 - 9. Disequilibrium in surficial bed layer in three Boston Harbor cores.

Surficial porewater and sedimentary pyrene data (z≤10 cm) from three cores reported in McGroddy 1993.

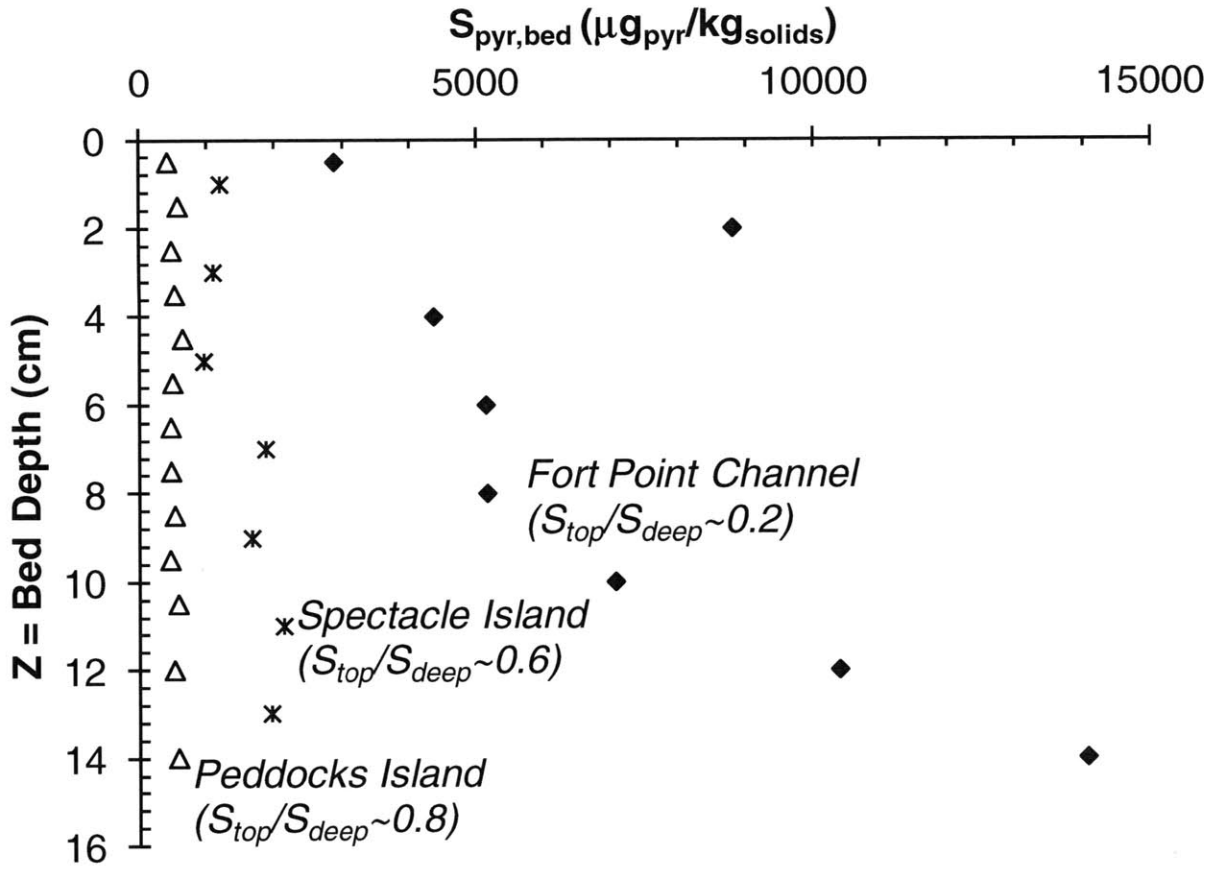

Figure 9 - 10. Surficial bed pyrene concentration as a function of depth ($S_{bed,pyr}(z)$).

The figure showed solid-phase pyrene concentration in the first 15 cm in three Boston Harbor sediment cores. The values in parentheses referred to the ratio of surficial S_{pyr} (i.e. $S_{bed,pyr}(Z=0)$) to 'deep'-layer S_{pyr} (i.e. $S_{bed,pyr}(Z=\sim 15$ cm)). Original concentration-depth data for pyrene were taken from McGroddy 1993.

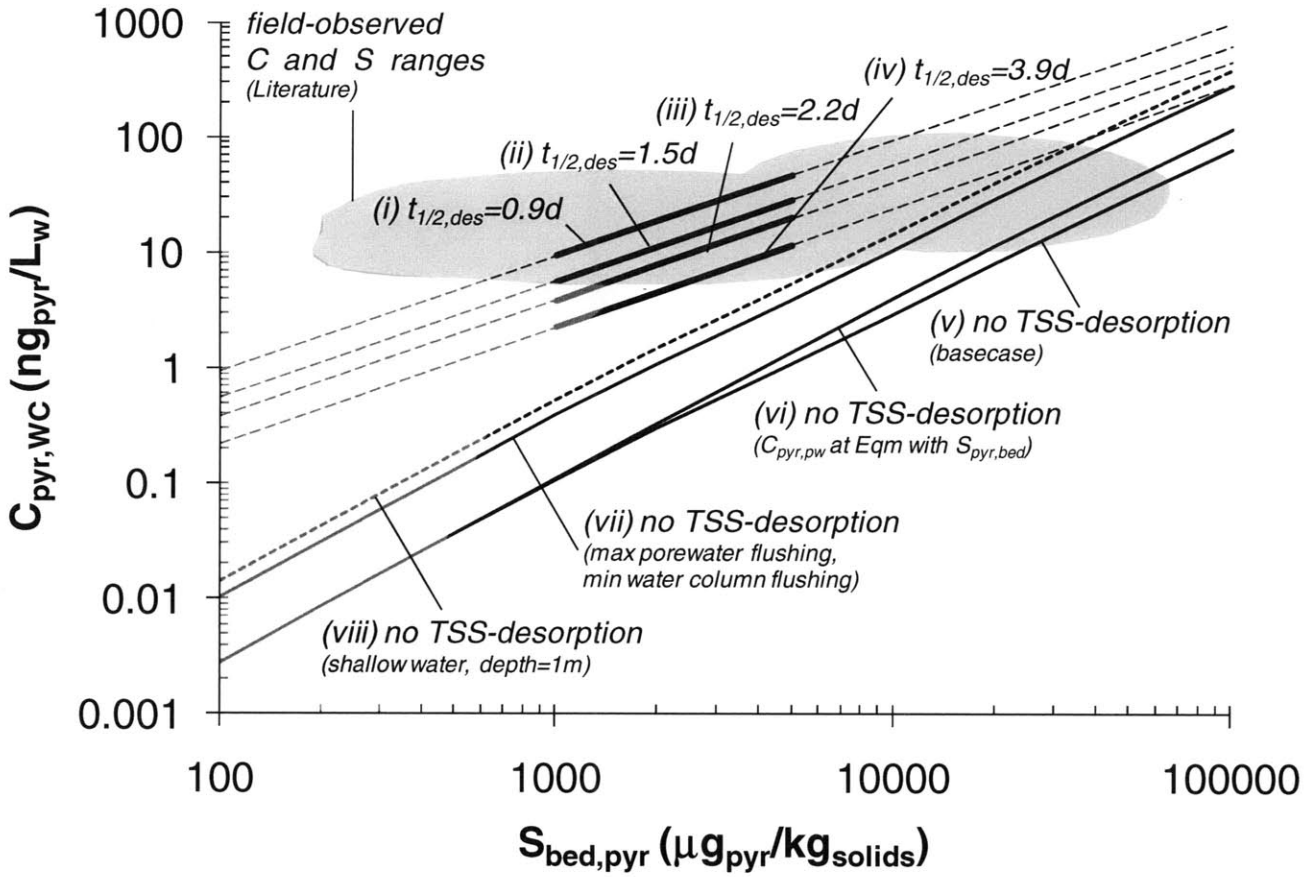

Figure 9 - 11. Steady-state model (3-rate) with and without desorption.

$C_{pyr,wc,avg}$'s were estimated as a function of surficial sediment bed loading, $S_{pyr,deep\text{-}bed}$, considering sediment bed porewater flushing and harbor flushing, with and without desorption from suspended sediment. Desorption-including case was examined at four desorption halftimes (i-iv); desorption-neglecting case was presented at basecase condition (v) and three extreme conditions where $C_{pyr,wc,avg}$'s were the highest possible (vi-viii). Because $t_{1/2,des}$'s were estimated from samples with S_{pyr} ranging from 1000-5000 ug_{pyr}/kg_{solids}, they were more realistic with the 1000-5000 ug_{pyr}/kg_{solids} range (bold line) than the unstudied ranges (dashed-line). Curve i to v were generated using basecase parameters.

The dark lenses represented field observed ranges of $C_{pyr,WC}$ and $S_{pyr,bed}$. The slightly shaded area signified where realistic $C_{pyr,WC}$ may exist but unobservable by LIF. A prediction that falls on either area may be considered as 'good' or 'satisfactory'.

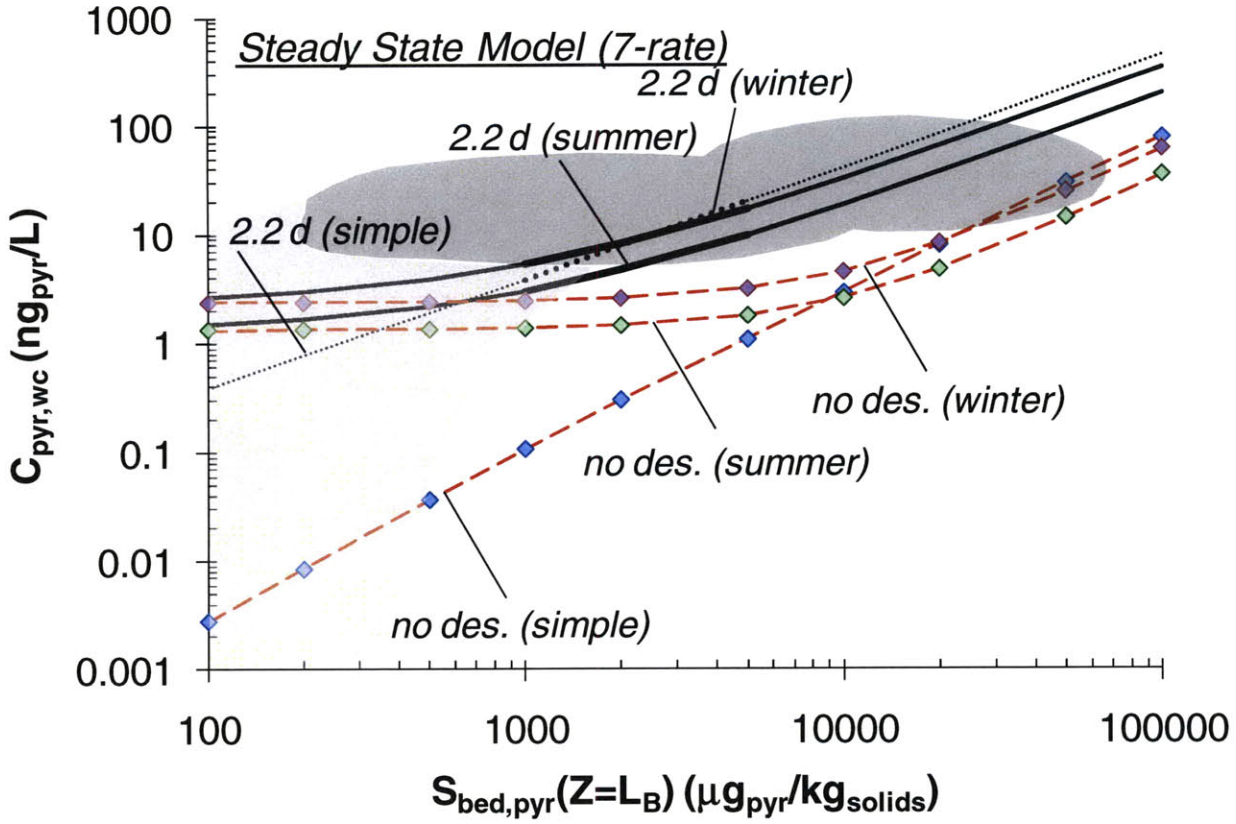

Figure 9 - 12. Steady-state model (7-rate) with and without desorption.

Desorption-including case was examined assuming a desorption half-life ($t_{1/2,des}$) of 2.2 d, at Summer and Winter conditions. Since $t_{1/2,des}$'s were estimated from samples with S_{pyr} ranging from 1000-5000 ug_{pyr}/kg_{solids}, they were more realistic with the 1000-5000 ug_{pyr}/kg_{solids} range (bold line) than the unstudied ranges (regular solid line). The 'simple' case (from the 3-rate model) was also plotted as a reference.

The dashed lines (with diamonds) represented the counterpart plots without desorption from suspended solids. The dark lenses represented field observed ranges of $C_{pyr,WC}$ and $S_{pyr,bed}$. The slightly shaded area signified where realistic $C_{pyr,WC}$ may exist but unobservable by LIF. A prediction that falls on either area may be considered as 'good' or 'satisfactory'.

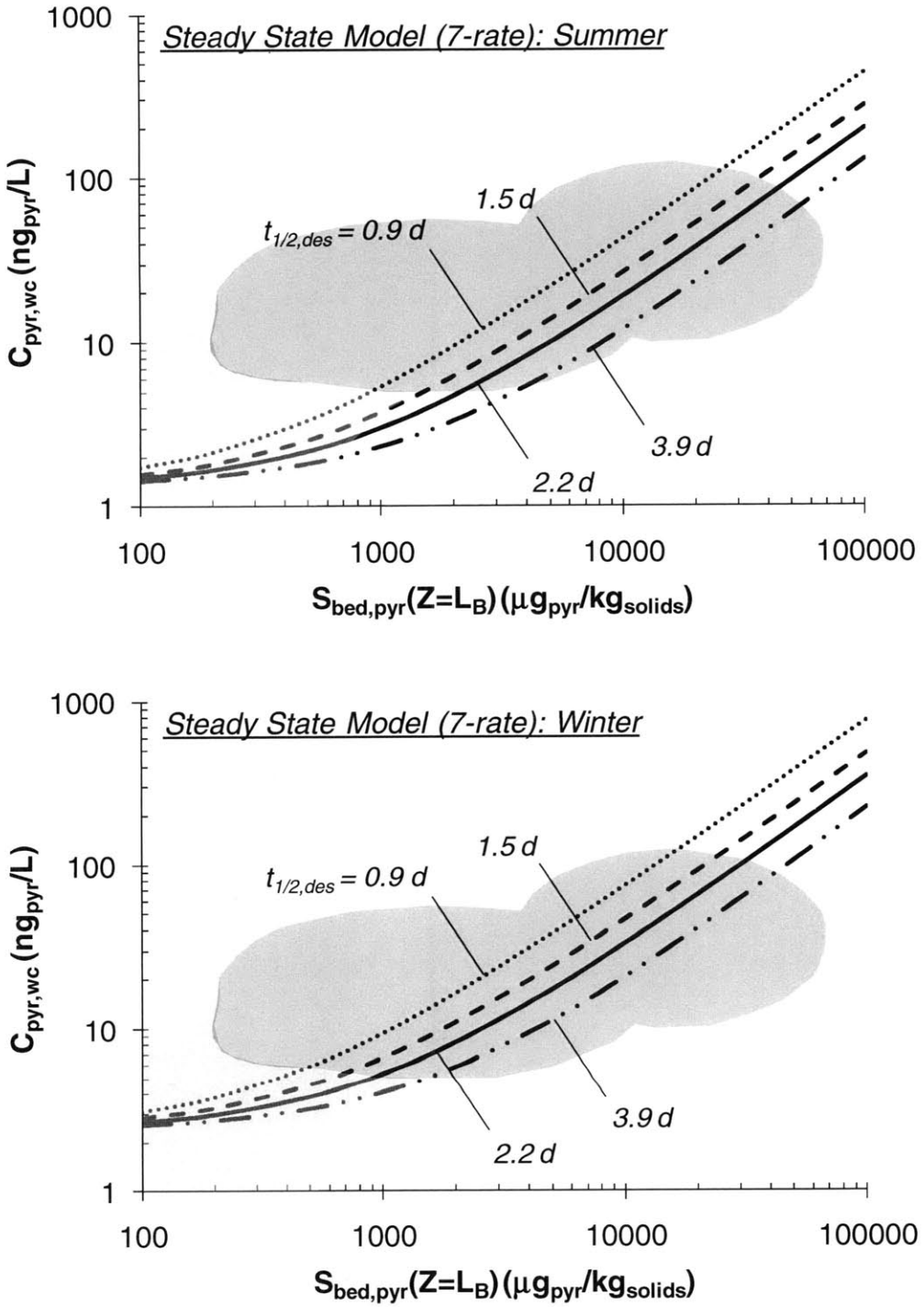

Figure 9 - 13. Steady-state model (7-rate): Predictions at different $t_{1/2,des}$.

The dark lenses represented field observed ranges of $C_{pyr,WC}$ and $S_{pyr,bed}$. The slightly shaded area signified where realistic $C_{pyr,WC}$ may exist but unobservable by LIF. A prediction that falls on either area may be considered as 'good' or 'satisfactory'.

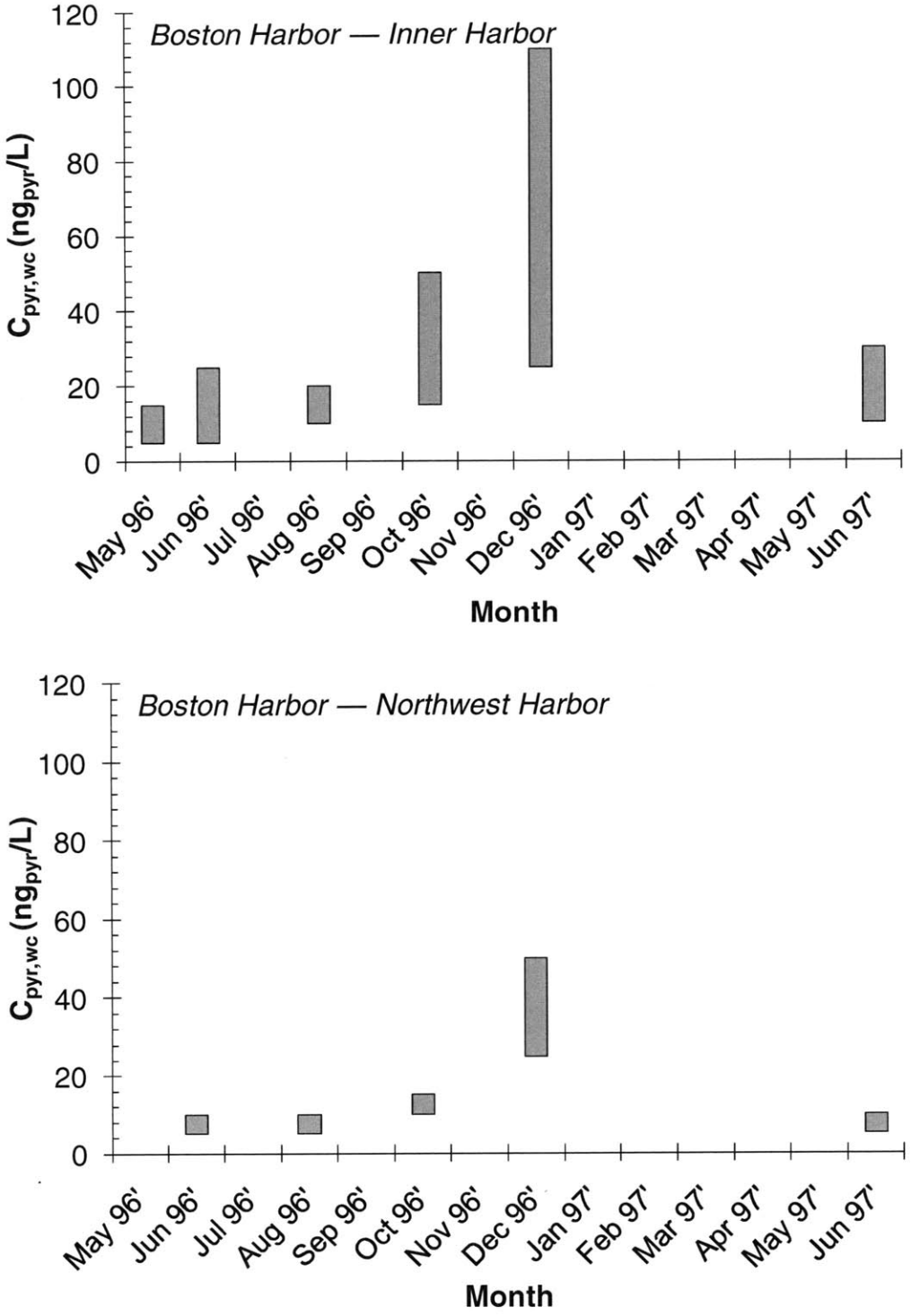

Figure 9 - 14. Seasonal variation in $C_{pyr,WC}$ observed in Boston Harbor. Data extracted from Rudnick (1998).

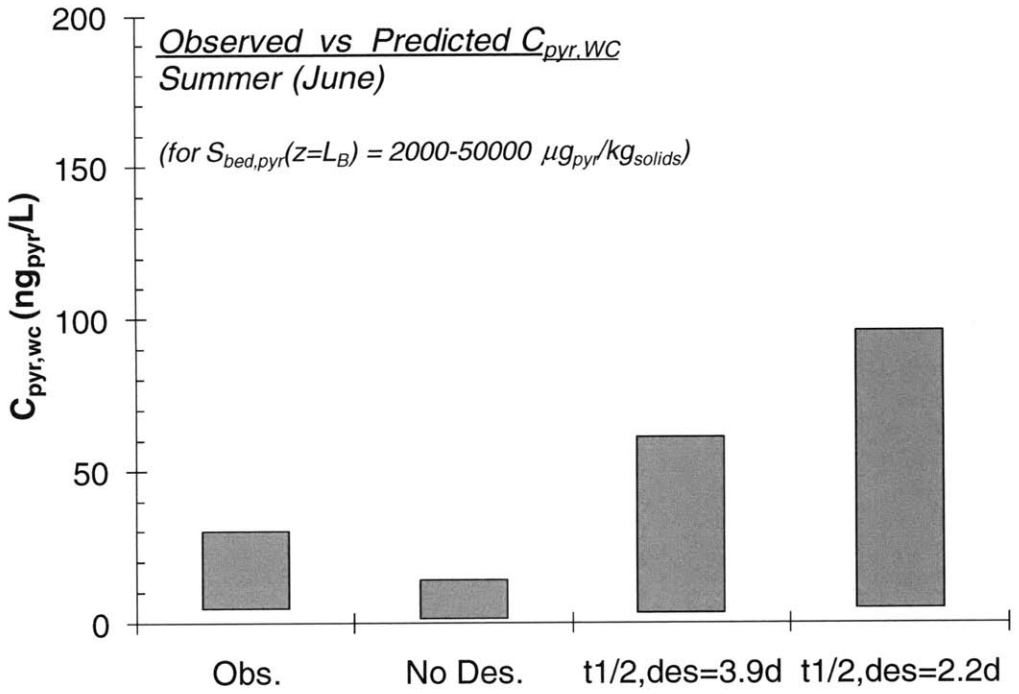

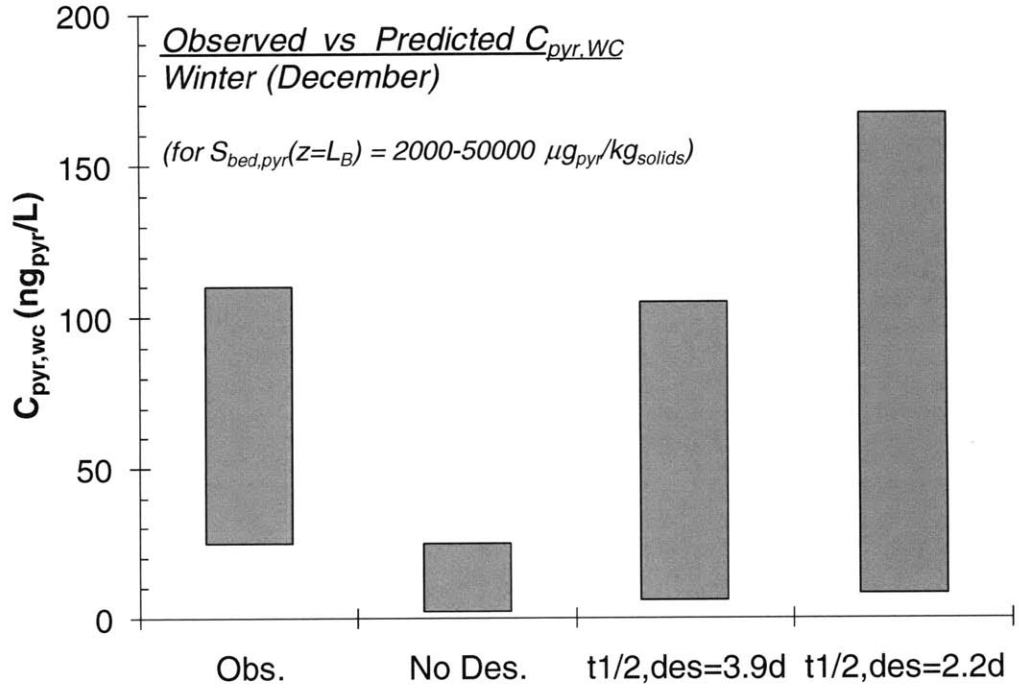

Figure 9 - 15. Observed vs predicted $C_{pyr,WC}$ observed in Summer and Winter.

The range of observed $C_{pyr,WC}$ was from the Inner Harbor and the Northwest Harbor. All predicted $C_{pyr,WC}$ was obtained from the seven-rate steady state model (with or without TSS desorption) for $S_{bed,pyr}$ ranging from 2000 – 50000 $\mu g_{pyr}/kg_{solids}$.

Steady-State Model (Summer):

$r_{des} + r_{pw,f} + r_{atm.dep} + r_{fresh} = r_{WC,f} + r_{biodeg.} + r_{h\upsilon}$

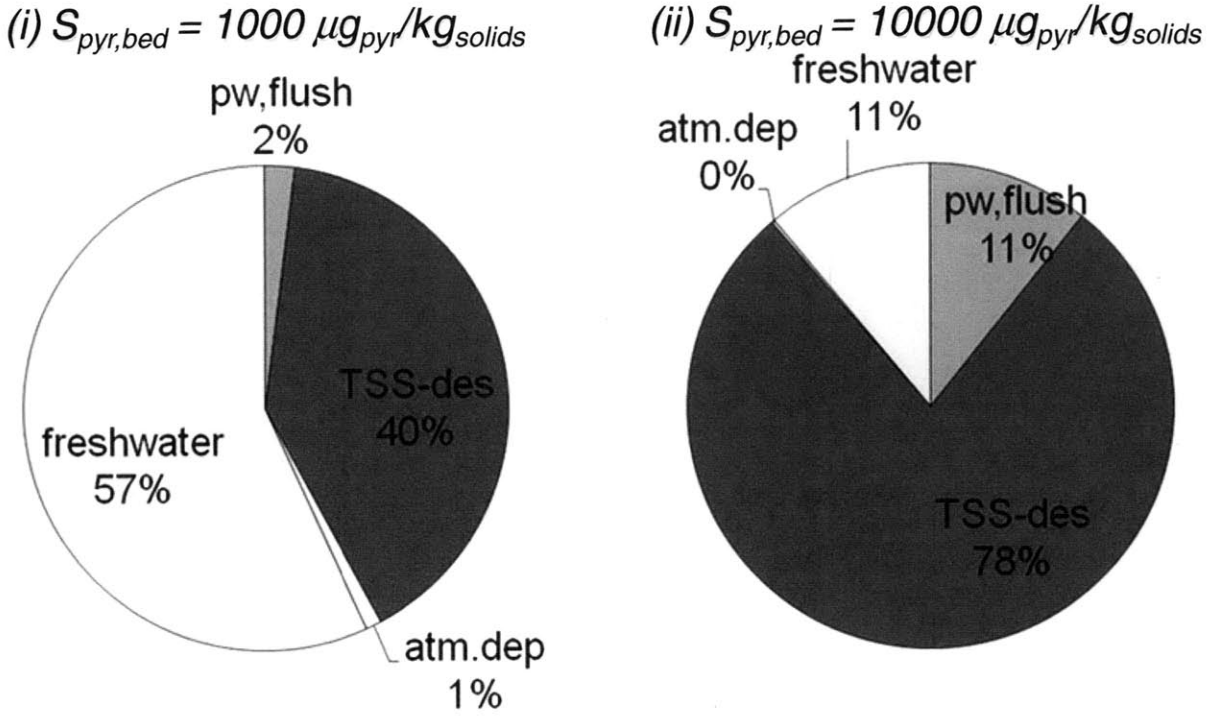

Figure 9 - 16. Relative contribution by different processes in the steady-state model (Summer case).

The pie charts showed the relative contribution of different processes as the source of dissolved pyrene in the steady state model (7-rate) for the Summer scenario with $t_{1/2,des}$ = 3.9 d (and all other parameters with basecase values).

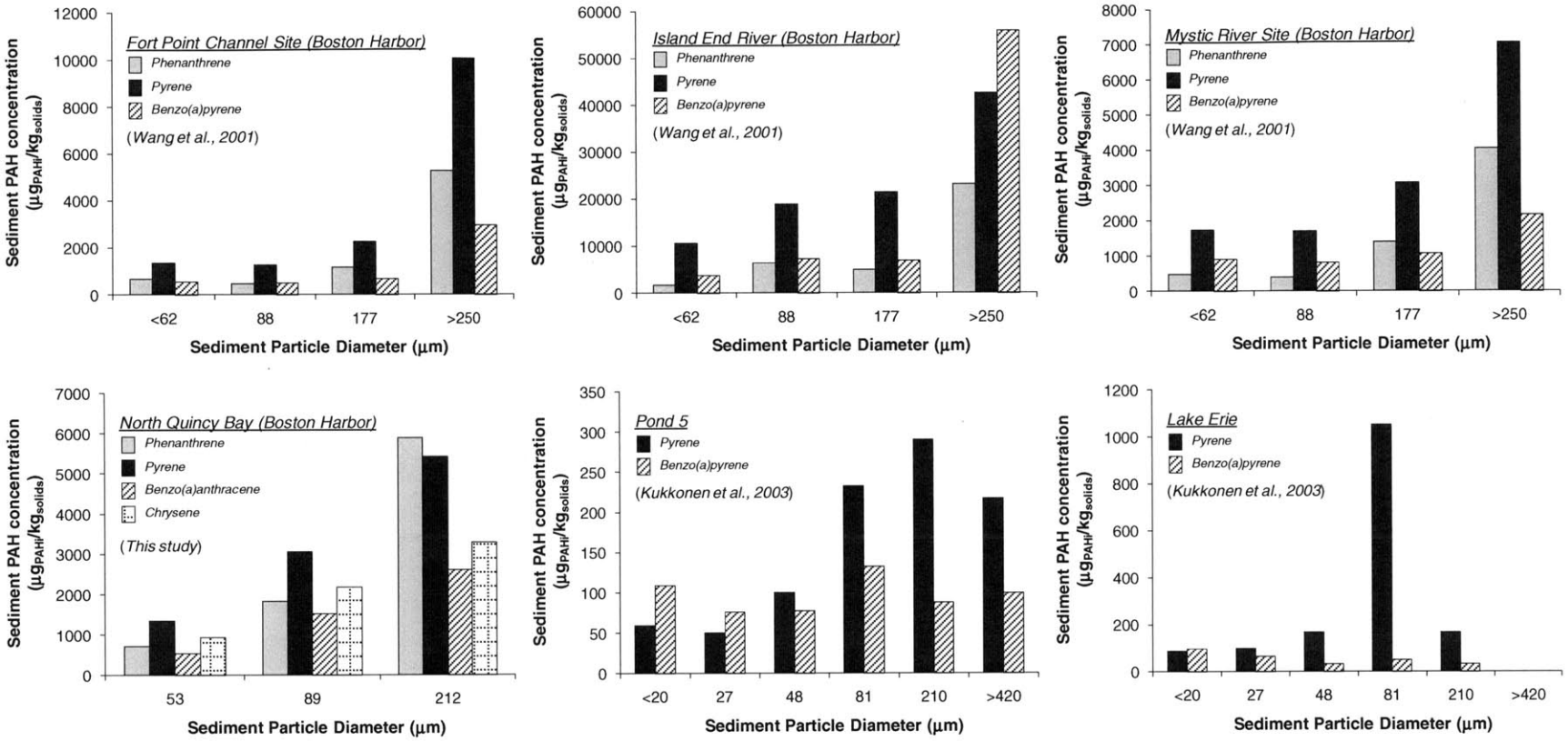

Figure 9 - 17. Distribution of PAHs on Different Sediment Size Fractions.

PAHs measurements of size-fractionated sediment samples from six sites in three water bodies were shown. Data were taken from Wang et al. 2001, Kukkonen et al. 2003 and from this study.

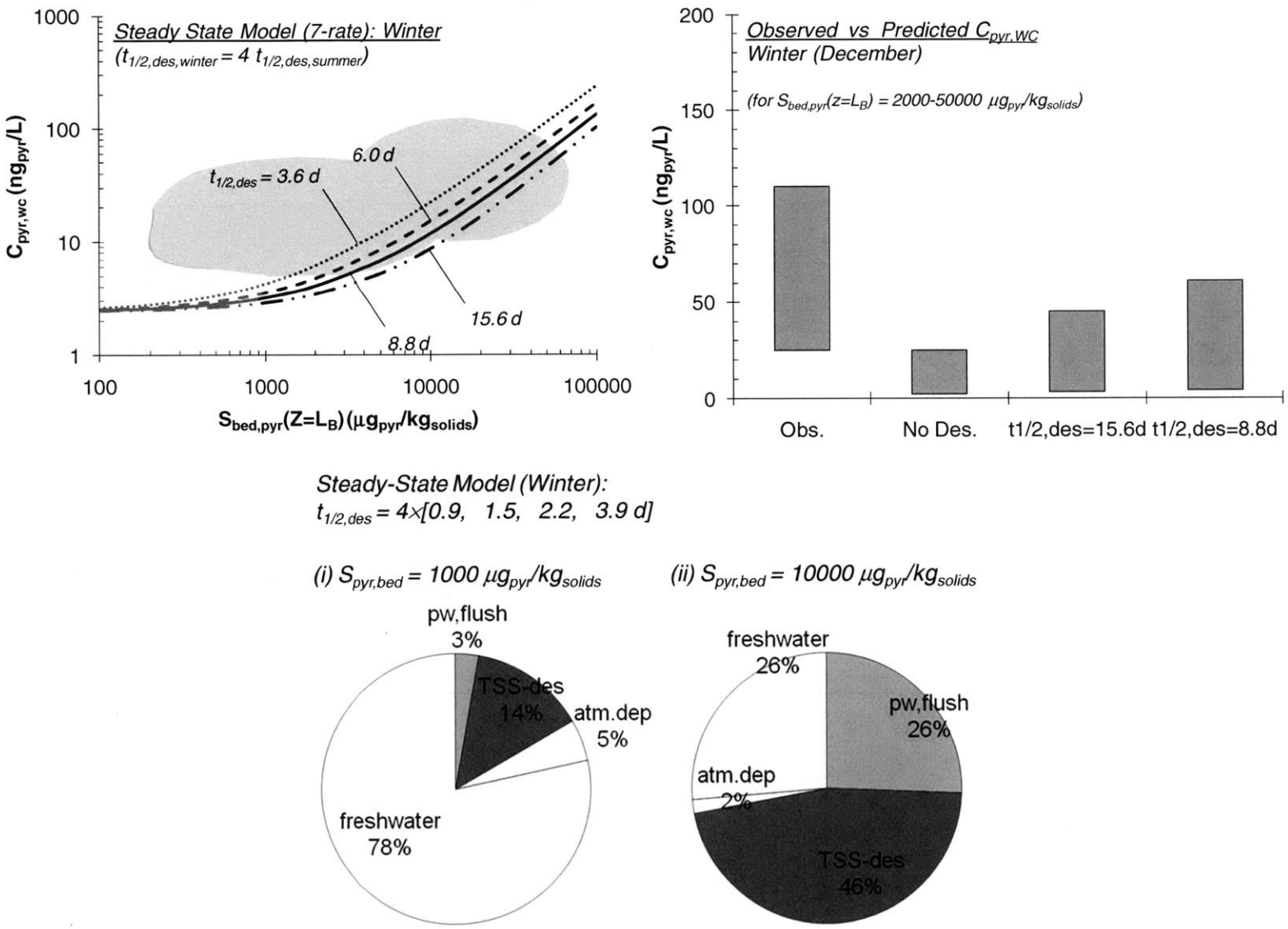

Figure 9 - 18. The steady-state Winter scenario reassessed at $t_{1/2,des,winter}$ = 3.6–15.6 d (4 x $t_{1/2,des,summer}$).

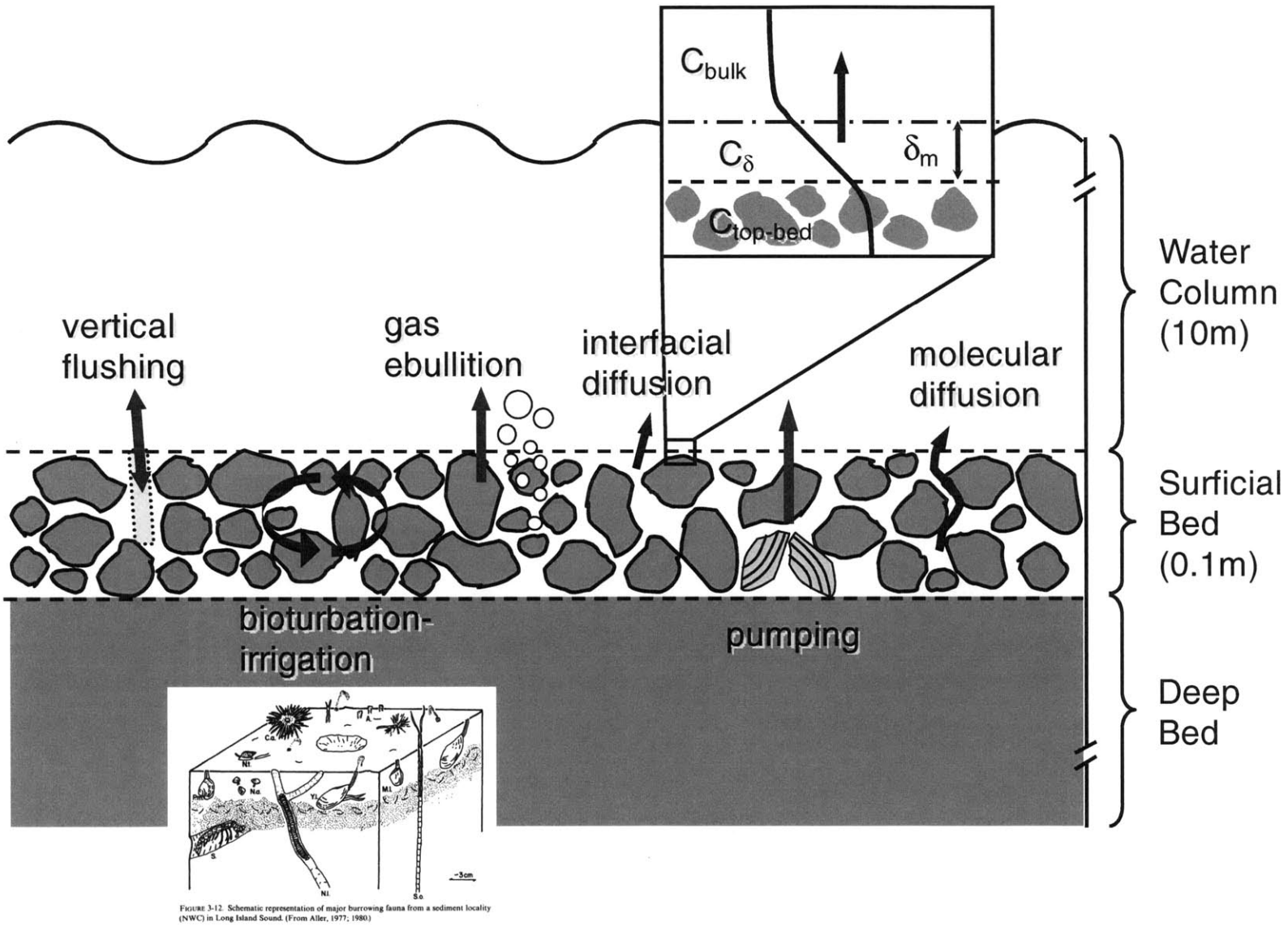

FIGURE 3-12. Schematic representation of major burrowing fauna from a sediment locality (NWC) in Long Island Sound. (From Aller, 1977; 1980.)

Figure 9 - 19. Various processes that contribute to sediment-bed porewater 'flushing'.

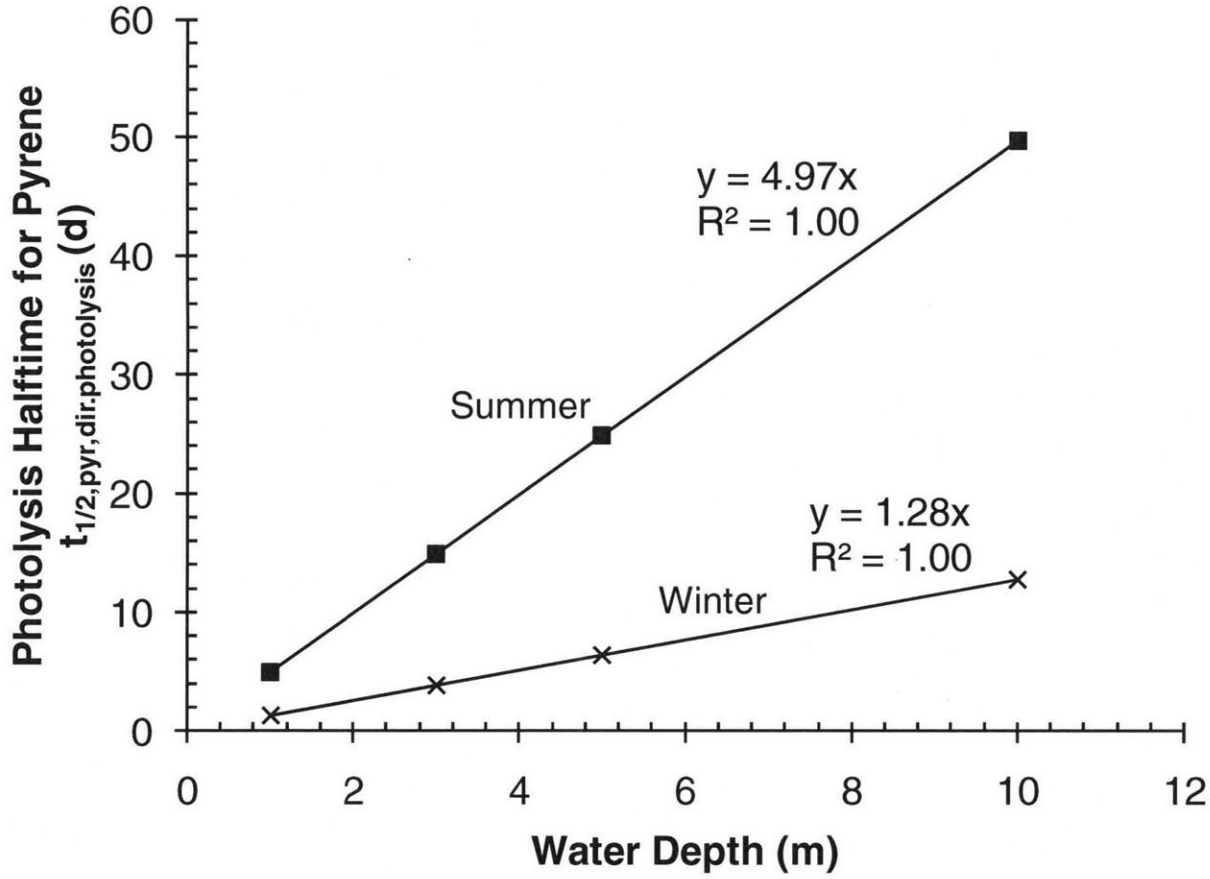

Figure 9 - 20. Mean direct photolysis halftime for pyrene as a function of water depth.

The data points were estimated geometric mean photolysis halftime assuming a [DOC] of 3–10 mg_{OC}/L_w. See Appendix 9-5 and 9-1 for more details.

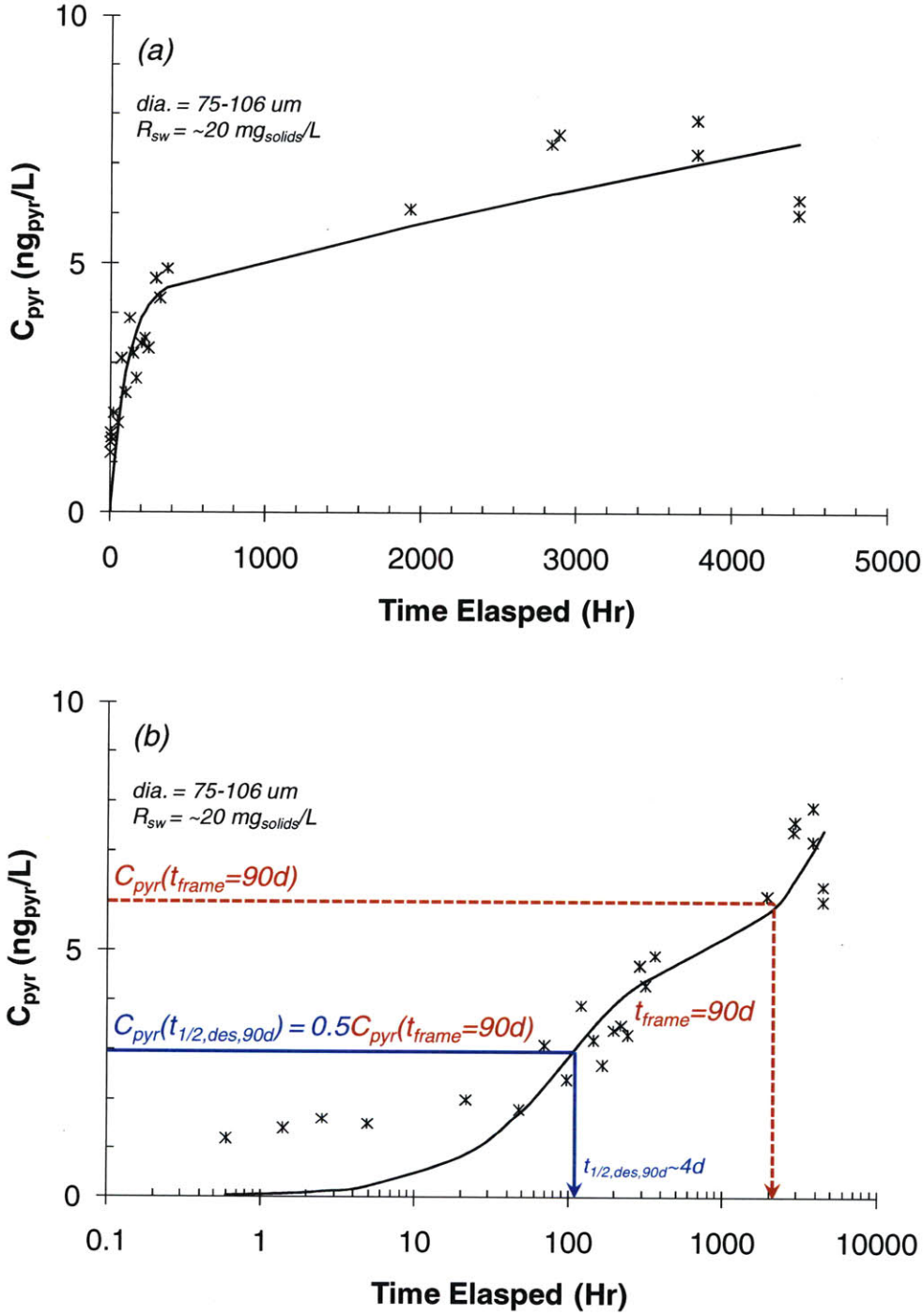

Figure 9 - 21. Determination of desorption halftime, $t_{1/2,des}$.

Figure (a) showed the experimental desorption observations fitted with a Constrained Two-Compartmental Exponential model (see Appendix 7-21). Figure (b) illustrated how the value of $t_{1/2,des}$ depends on the timeframe/'end-point' of desorption, signified by t_{frame}. $t_{1/2,des}$ is simply the time at which C_{pyr} is half of that at a specified timeframe/'end-point' (i.e. $C_{pyr}(t_{frame})$).

Chapter 10: Figures

Figure 10 - 1. Sample thickness & mis-quantification of soot volume. 476
Figure 10 - 2. Structural distortion of aggregates from microtomy of samples. 477
Figure 10 - 3. Possible rigging of sedimentary grains during microtomy. 478
Figure 10 - 4. TEM images of sedimentary grains (a-g) 479
Figure 10 - 5. Soot particles/clusters (a-b) 486
Figure 10 - 6. Sulfur artifacts (a-c). 488
Figure 10 - 7. Clusters of soot in soot-amended Boston Harbor sediments (a-b). 491
Figure 10 - 8. EDX spectra of nicotinamide ($C_6H_6N_2O$). 493
Figure 10 - 9. Build-up of amorphous carbon on EM thin samples. 494
Figure 10 - 10. Carbon build-up on nicotinamide ($C_6H_6N_2O$) from beam irradiation. 495
Figure 10 - 11. EDX spectra of nicotinamide (a-b). 496
Figure 10 - 12. TEM images and EDX spectra of soot amended sediments (a-d). 498
Figure 10 - 13. TEM image and EDX spectra of a mineral-dominant zone (a-f) 502
Figure 10 - 14. Correction of O signal in the presence of multiple oxygenated phases. 505
Figure 10 - 15. EDX elemental analysis: integrated area against peak height (a-d). 506
Figure 10 - 16. Heterogeneity of natural geosorbents and the limitation of bulk analyses 508
Figure 10 - 17. O/C vs N/C ratio of carbonaceous matters by point-EDX analysis. 509
Figure 10 - 18. O/C atomic ratios of selected carbonaceous matters by point-EDX analysis. 510
Figure 10 - 19. Discrepancy between peak-height and integrated-area derived O/C ratios. 511
Figure 10 - 20. Original TEM and pixel-consolidated images of a soot-rich region. 513
Figure 10 - 21. Occupancy filtered images of a soot-rich region. 515
Figure 10 - 22. C/N atomic ratio of a soot-rich region (without occupancy filtering). 516
Figure 10 - 23. C/N atomic ratio of a soot-rich region (occupancy filtered). 517
Figure 10 - 24. C/N atomic ratio of a soot-rich region at 4 different resolutions (occupancy-filtered). 519
Figure 10 - 25. C/O atomic ratio of a soot-rich region with and without O-correction (occupancy-filtered). 520
Figure 10 - 26. C/O atomic ratio of a soot-rich region at 4 different resolutions (occupancy-filtered, O-corrected). 522
Figure 10 - 27. Si/O atomic ratio of a soot-rich region with and without occupancy filtering. 523
Figure 10 - 28. Si/O atomic ratio of a soot-rich region at 4 different resolutions (occupancy-filtered). 525
Figure 10 - 29. C/O map of a char particle (a-b) 527
Figure 10 - 30. Elemental atomic ratios (C-H-N-O) of various carbonaceous matters. 527
Figure 10 - 31. Structure of hexane soot. 530
Figure 10 - 32. Structure of lignin. 531
Figure 10 - 33. Conceptual structure of bituminous coal. 532

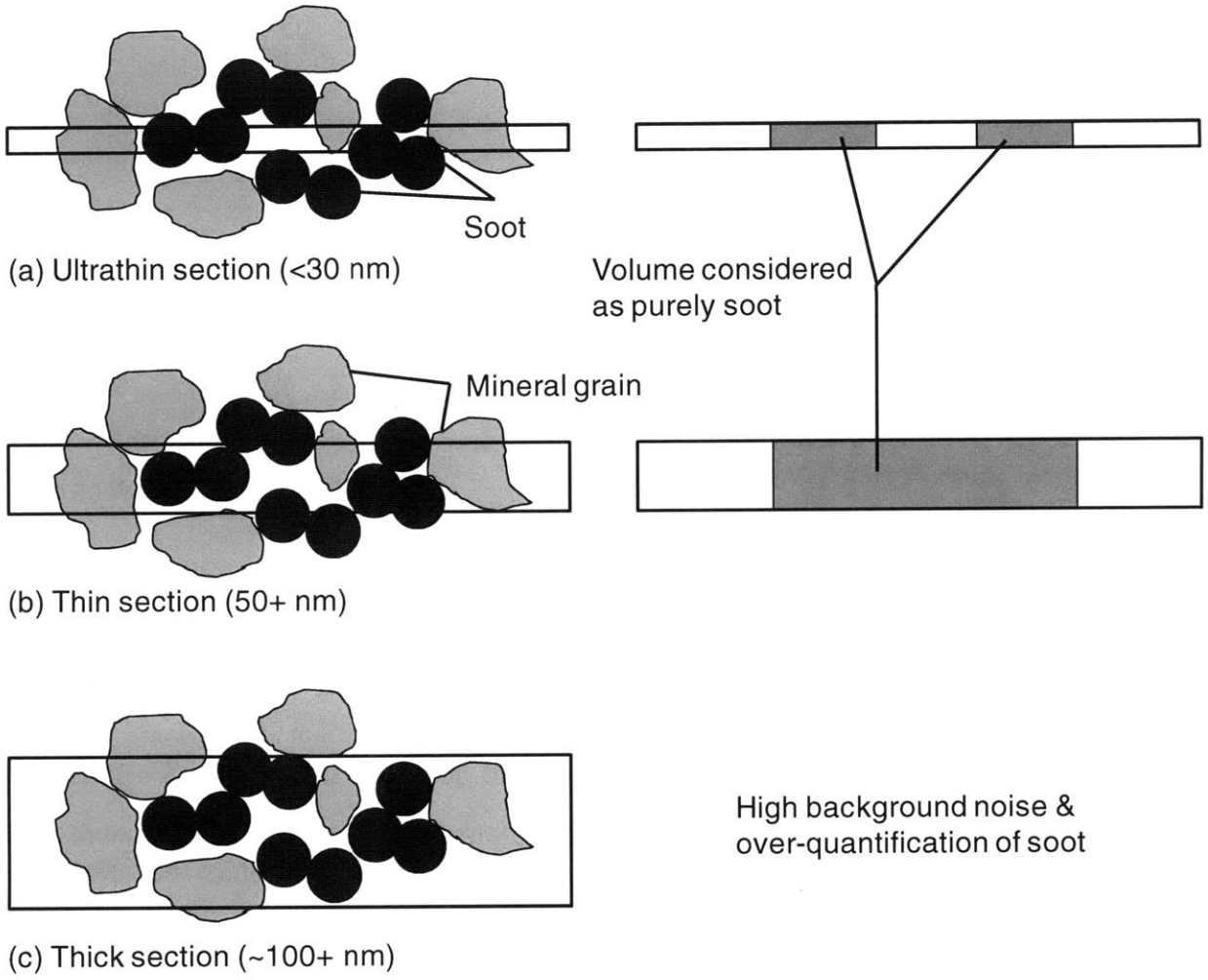

Figure 10 - 1. Sample thickness & mis-quantification of soot volume.

In (a), volume with soot is almost vertically full of soot, thus measuring soot-containing volume rather accurately. In (b), the soot-containing volume contains much non-soot space, and therefore overestimating the abundance of soot. In (c), the sample is so thick that high background noise and over-quantification, both being undesirable, occur. Figures are drawn roughly to scale.

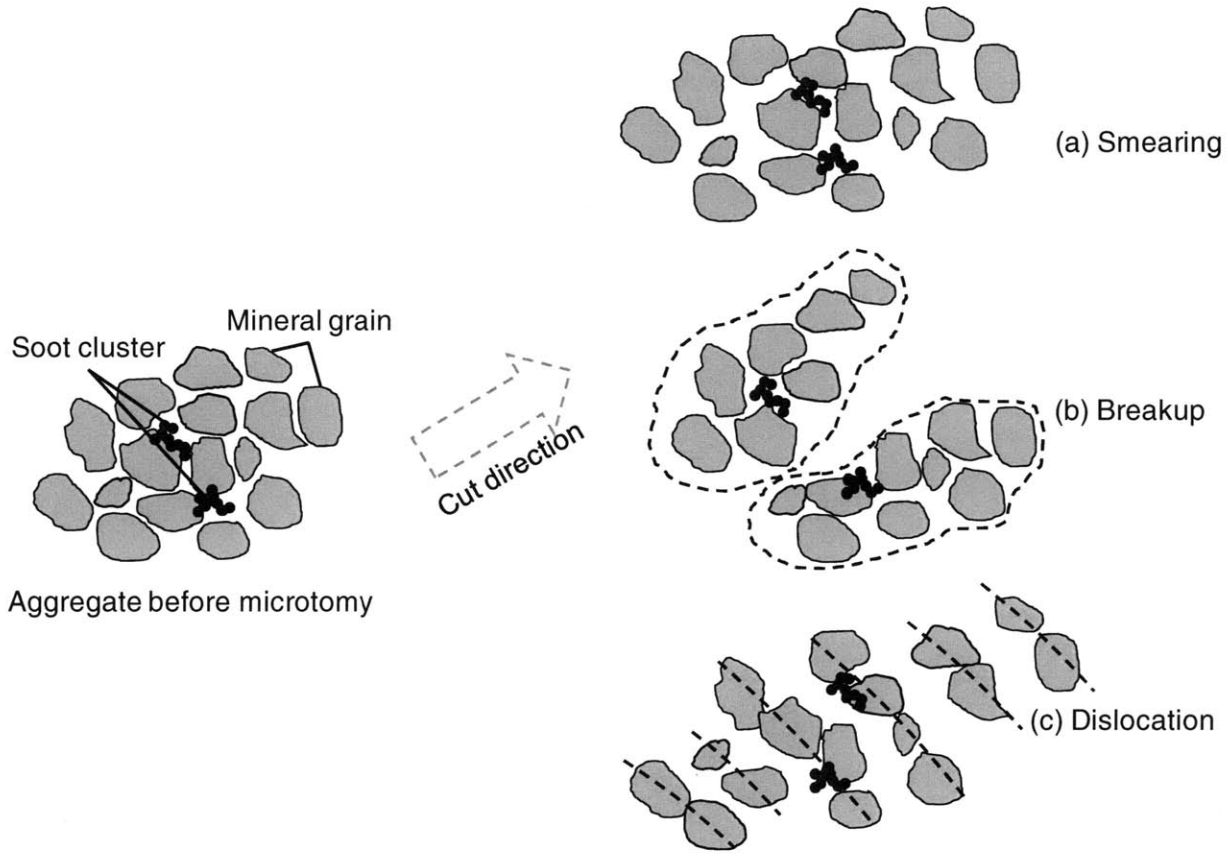

Figure 10 - 2. Structural distortion of aggregates from microtomy of samples.

Microtomy can produce sufficient mechanical shearing that distort the structural or morphological features of sedimentary aggregates. The dashed arrow indicates the cut direction. In (a), the constituent grains are smeared. In (b), the single aggregate is broken up into two groups. This can happen when the knife has local imperfection such as a nick. In (c), the aggregate is dislocated into strides.

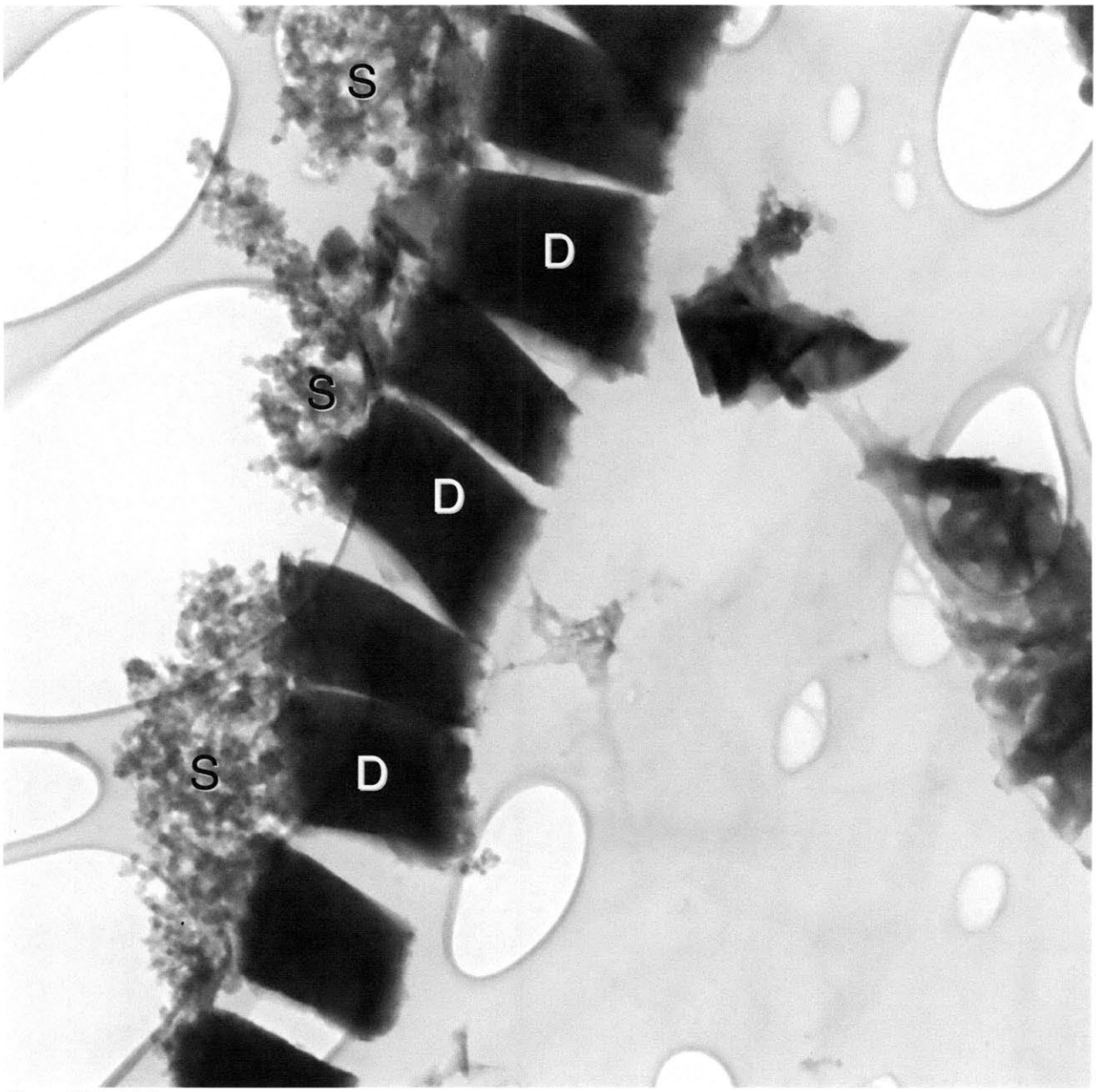

Figure 10 - 3. Possible rigging of sedimentary grains during microtomy.

The micrograph shows soot-amended Boston Harbor sediments on a lacey-carbon film. The dark, angular structures (white "D") (~500 nm) are mineral grains, and the tiny round spots (black "S") associated with the grains are soot particles.

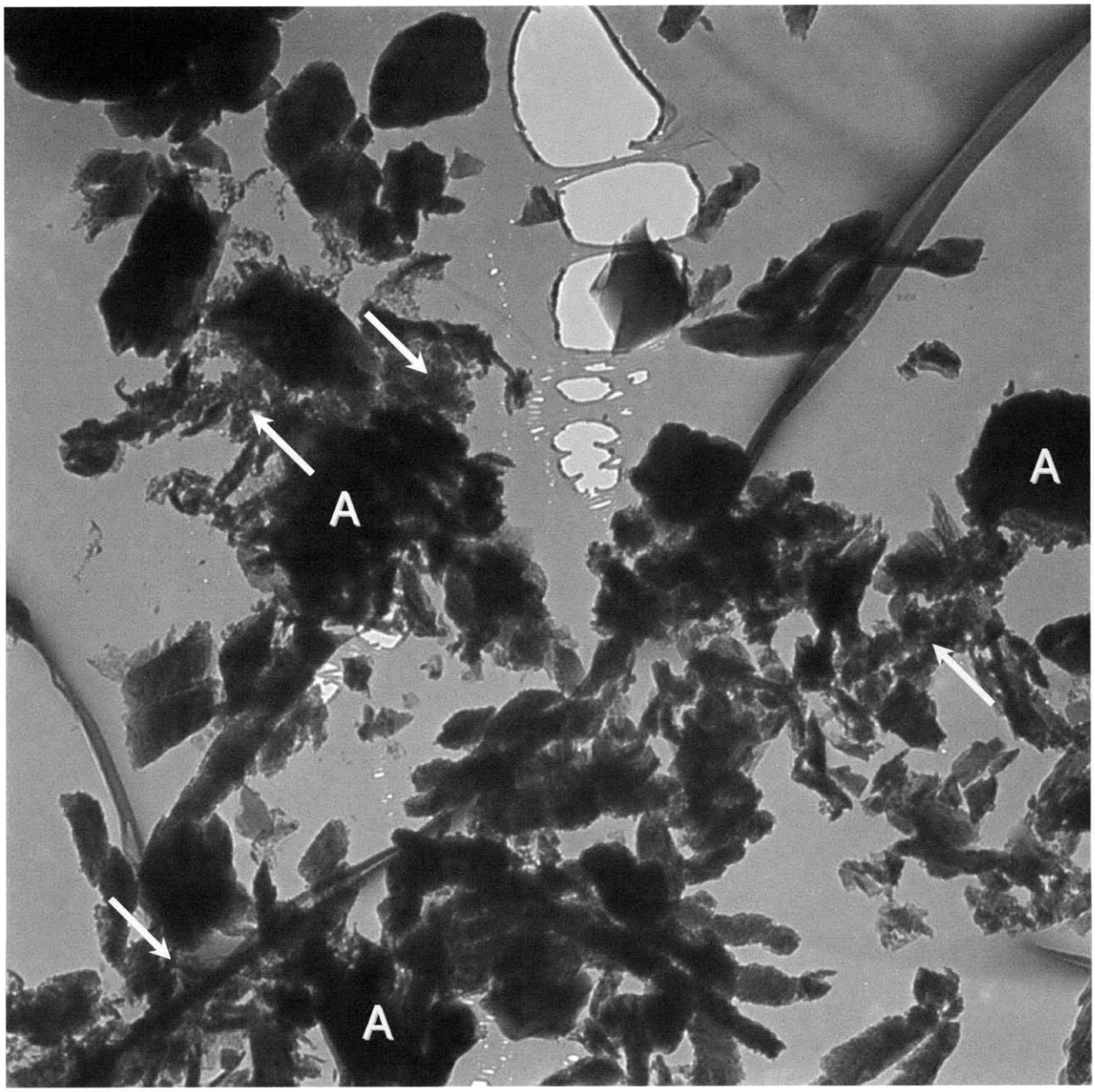

Figure 10 - 4. TEM images of sedimentary grains (a-g)

Figure 10 - 4. (a) Sedimentary grains (TEM image #1). Sample was embedded in elemental sulfur, microtomed by aiming a 70 nm thickness and subsequently mounted on a lacey SiO film on Cu grids. The following are labeled: mineral phases ("A"), soots ("S"), amorphous region which may/may not include soot (arrow).

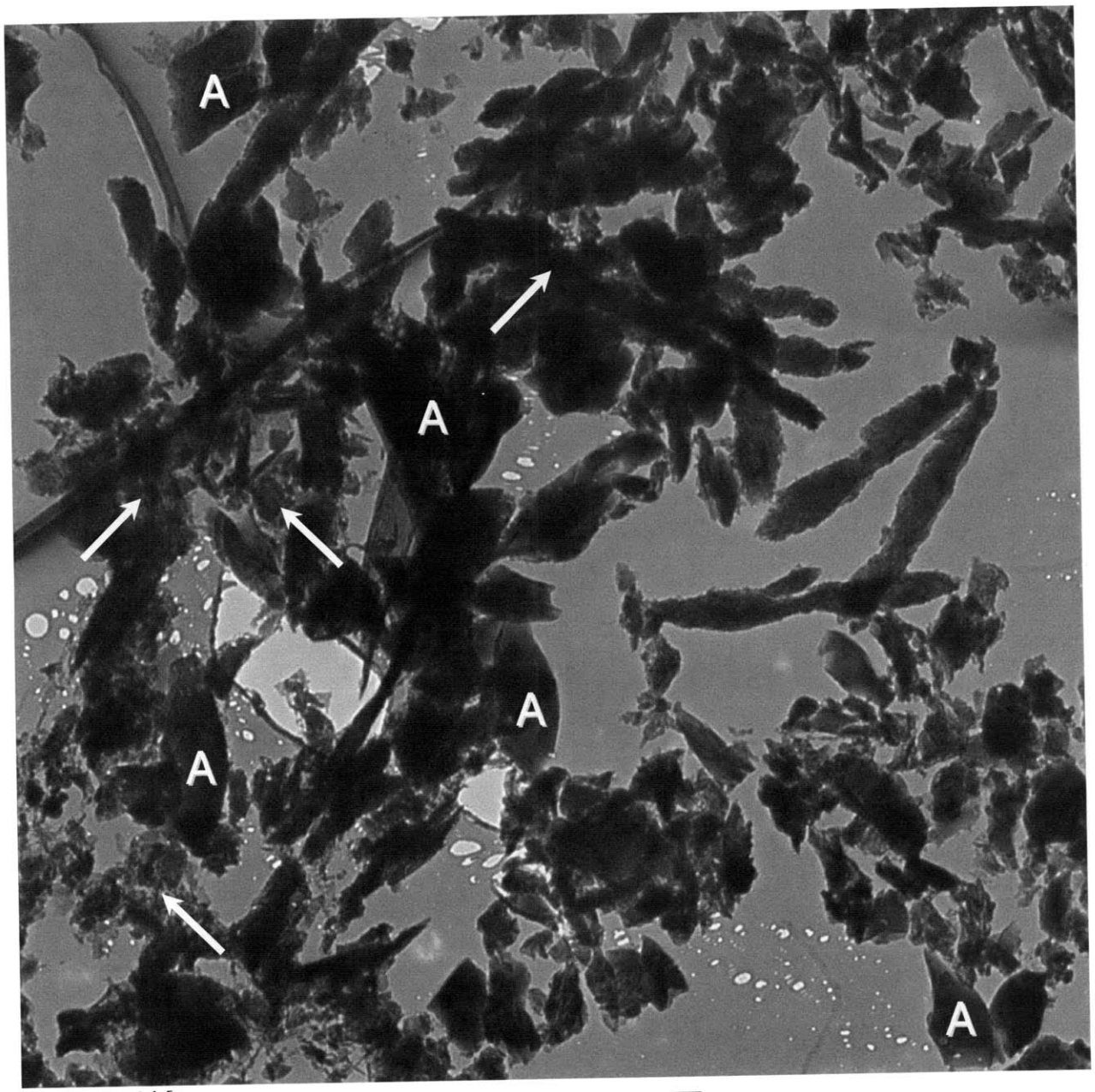

Figure 10 - 4. (b) Sedimentary grains (TEM image #2).

Sample was embedded in elemental sulfur, microtomed by aiming a 70 nm thickness and subsequently mounted on a lacey SiO film on Cu grids. See (a) for meanings of symbols.

Figure 10 - 4. (c) Sedimentary grains (TEM image #3).

Sample was embedded in elemental sulfur, microtomed by aiming a 70 nm thickness and subsequently mounted on a lacey SiO film on Cu grids. See (a) for meanings of symbols.

Figure 10 - 4. (d) Sedimentary grains (TEM image #4).

Sample was embedded in elemental sulfur, microtomed by aiming a 70 nm thickness and subsequently mounted on a lacey SiO film on Cu grids. See (a) for meanings of symbols.

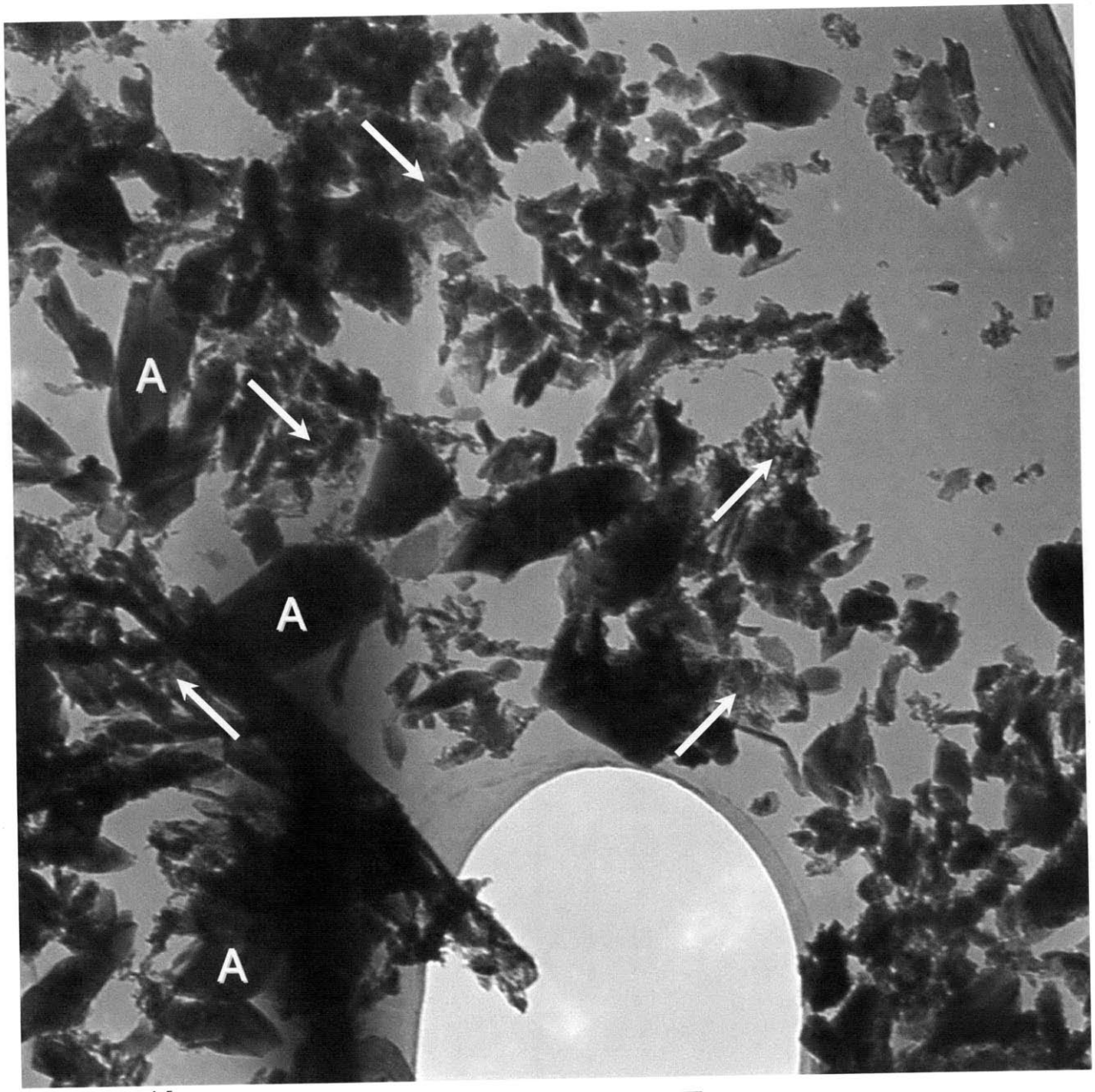

Figure 10 - 4. (e) Sedimentary grains (TEM image #5).

Sample was embedded in elemental sulfur, microtomed by aiming a 70 nm thickness and subsequently mounted on a lacey SiO film on Cu grids. See (a) for meanings of symbols.

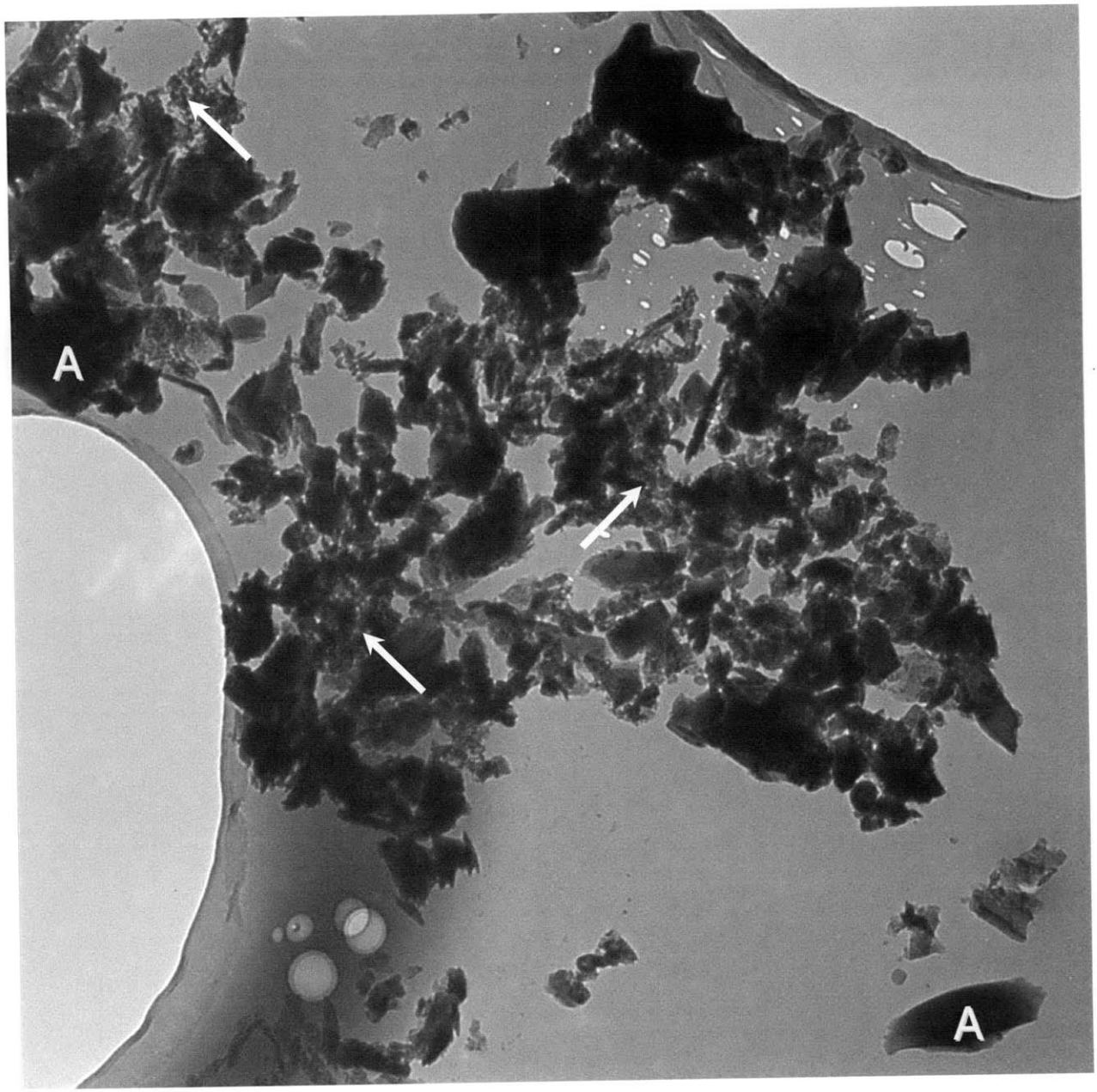

Figure 10 - 4. (f) Sedimentary grains (TEM image #6).

Sample was embedded in elemental sulfur, microtomed by aiming a 70 nm thickness and subsequently mounted on a lacey SiO film on Cu grids. See (a) for meanings of symbols.

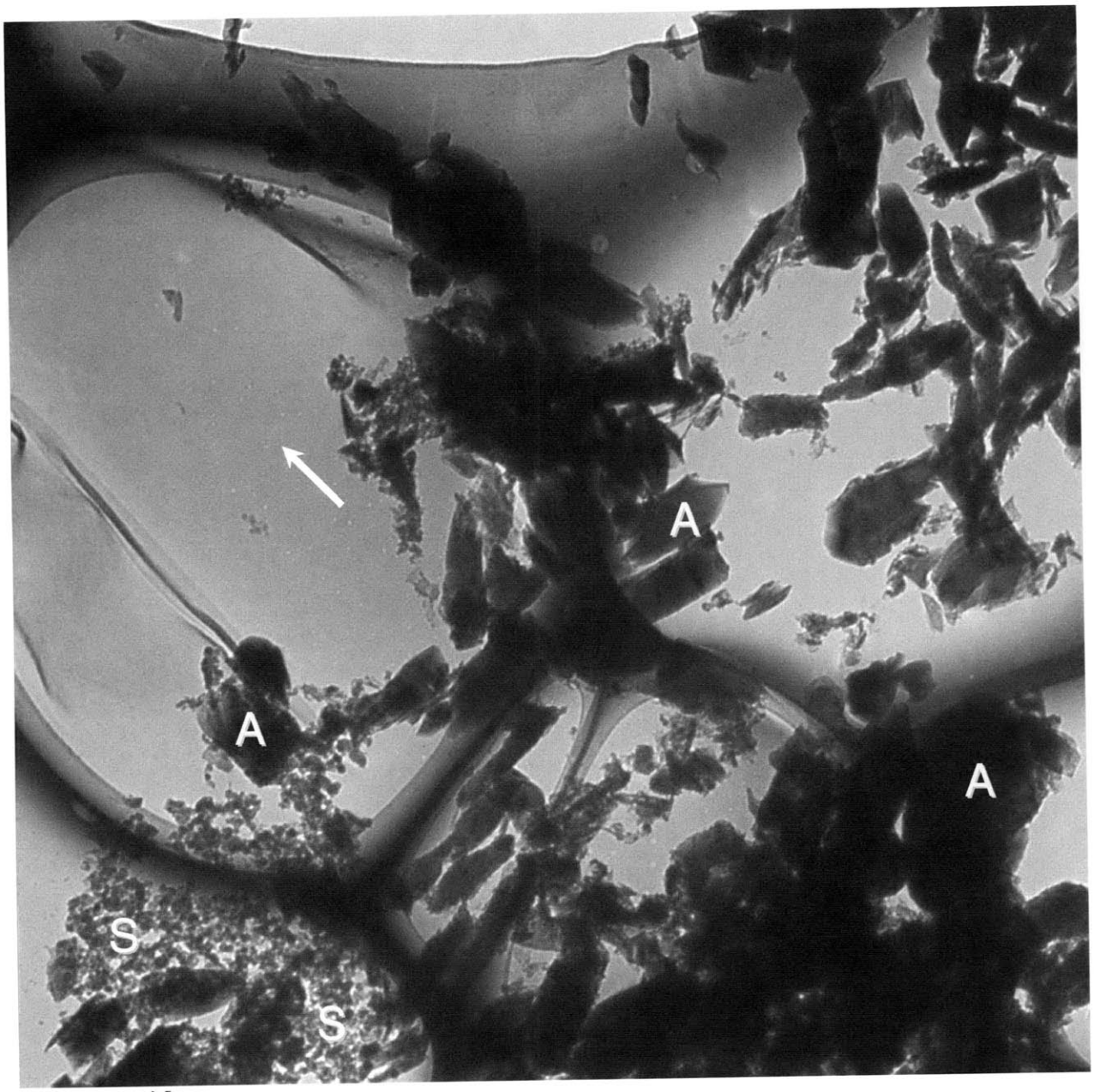

dkuo_046.tif
Bx93117_C1
All aggregates 2
Cal: 123.394pix/micron
14:52 10/03/06

500 nm
HV=200kV
Direct Mag: 2000x
Tilt:
AMT Camera System

Figure 10 - 4. (g) Sedimentary grains amended with soot particles.

A view of sedimentary grains amended with soot particles. The tiny spheres (white "S") at the lower left corner are soot particles. This figure serves as a reference for visual identification of native soot particles in Figure 10-4a to 6-4f, if there is any. Sample was embedded in elemental sulfur, microtomed by aiming a 70 nm thickness and subsequently mounted on a lacey SiO film on Cu grids. See (a) for meanings of symbols.

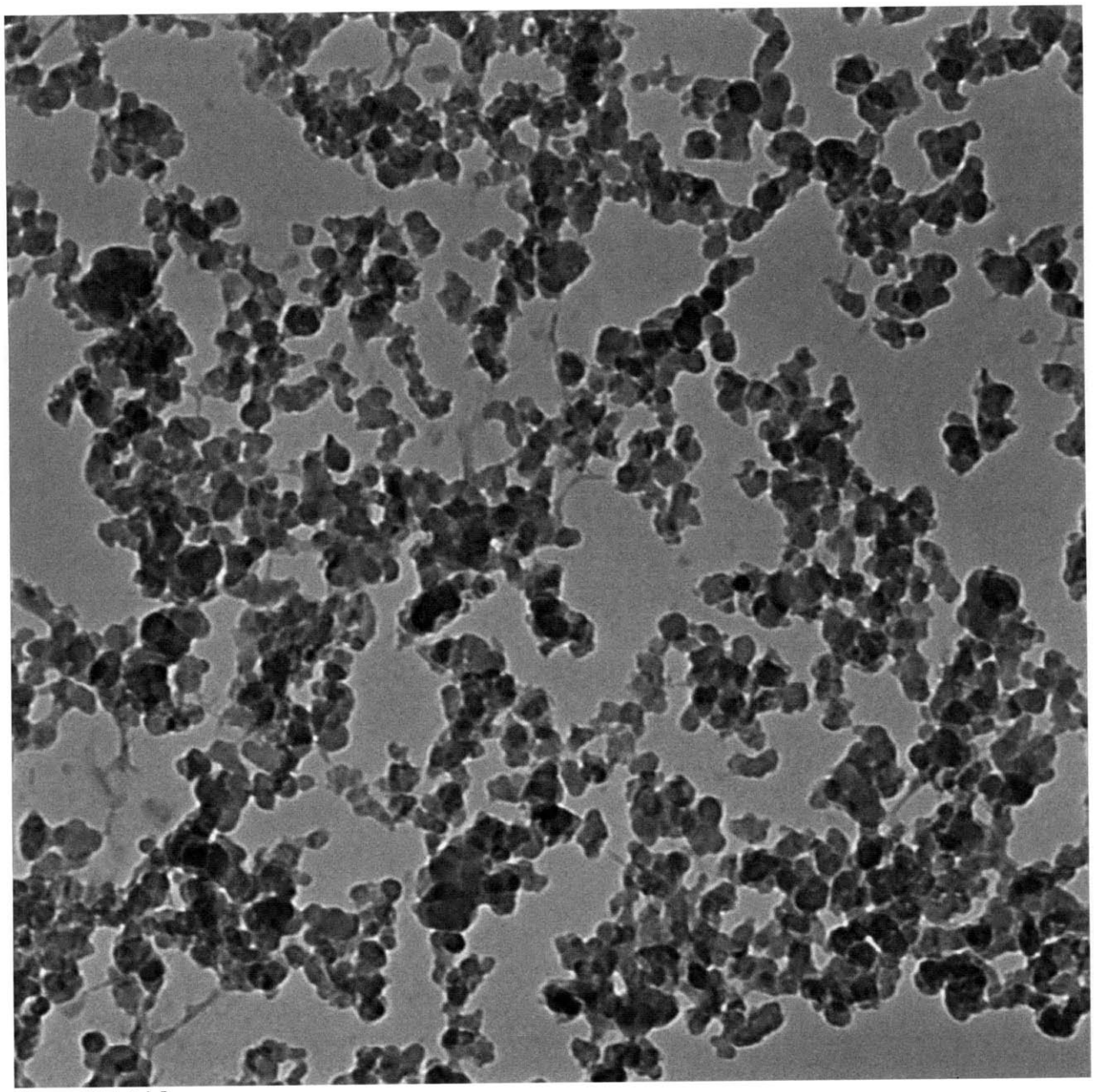

Figure 10 - 5. Soot particles/clusters (a-b)

Figure 10 - 5. (a) A view of soot particles blurred out by sulfur, the embedding medium.

Soot particles are 'glued' together to form larger, smooth-looking matters, which can be hard to distinguish in a background of dense mineral grains (see Figure 10-4a to 6-4g).

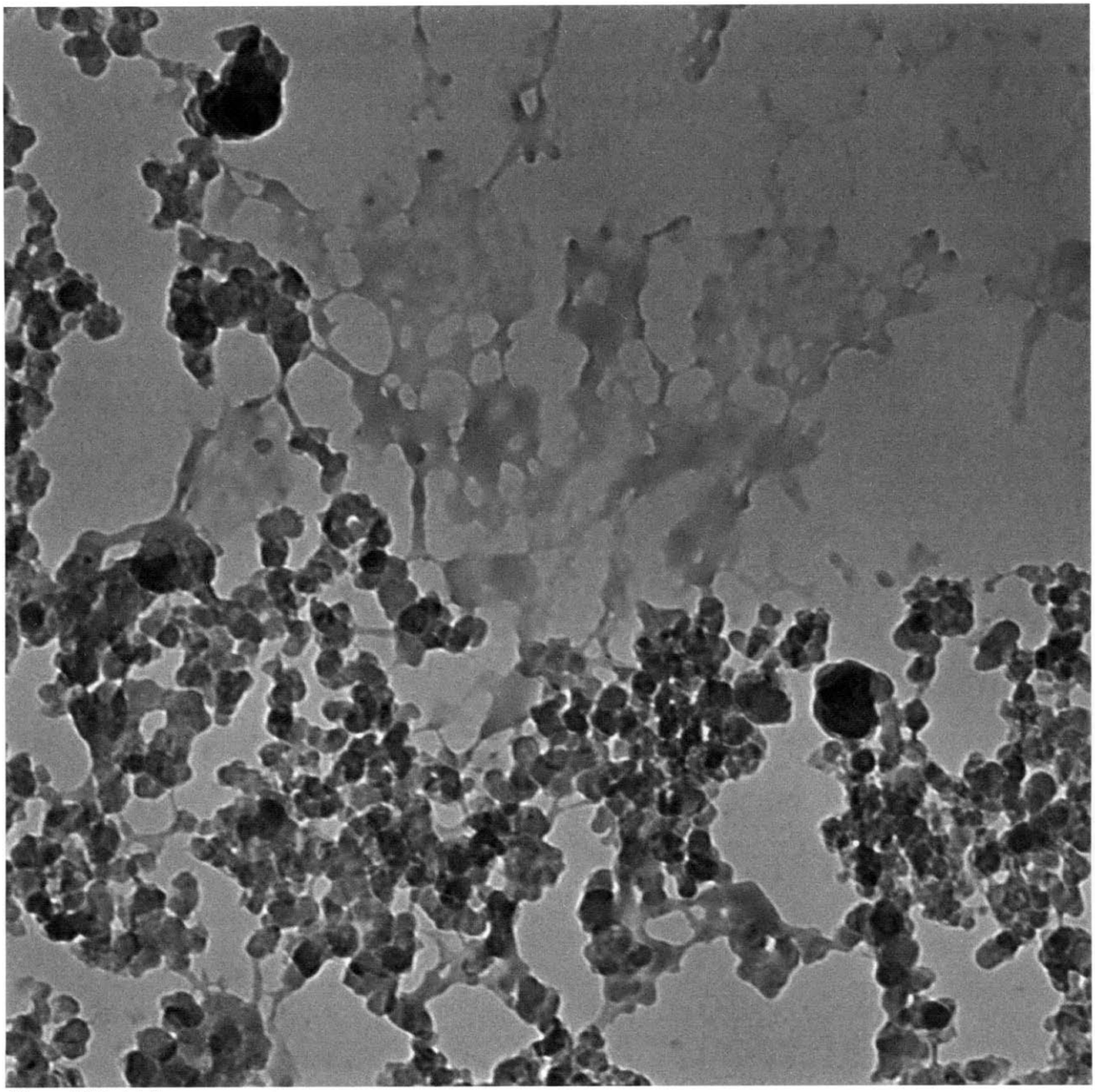

Figure 10 - 5. (b) A view of soot particles blurred out by sulfur, the embedding medium.

Here soot particles are 'glued' together to the extent that the characteristic grape cluster form is lost. The fainter stains in upper region of the micrograph are from sulfur. Compare soot particles here with those in Figure 10-4a to 6-4g.

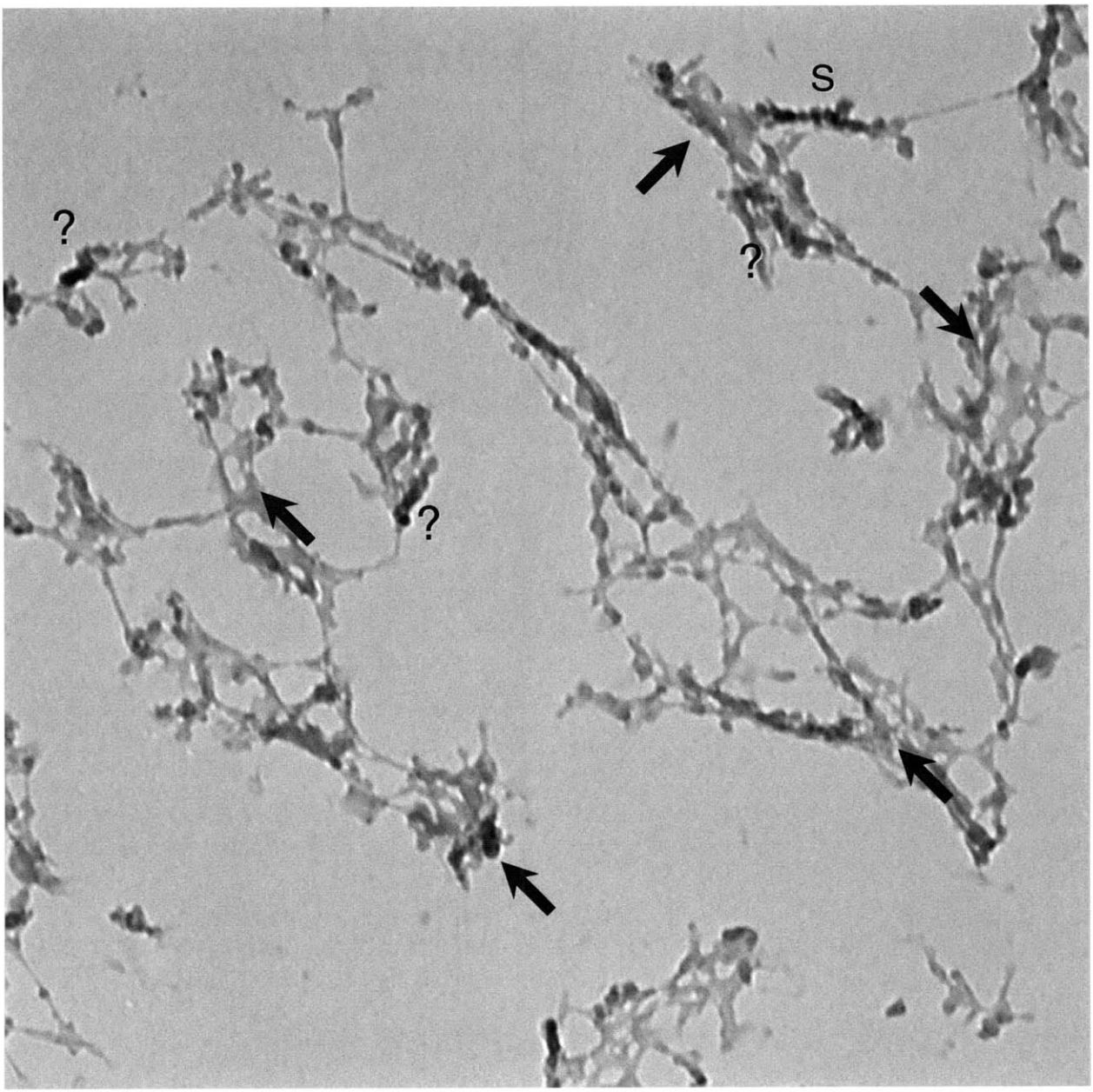

Figure 10 - 6. Sulfur artifacts (a-c).

Figure 10 - 6. (a) Sulfur artifact structures resembling soot particles.

A few soot particles may be present in the upper right corner ("S"), where darker, dense spheres are visible. The remaining watercolor-like stains are most likely to be pure sulfur (arrows). The doubtful structures are also indicated marked ("?").

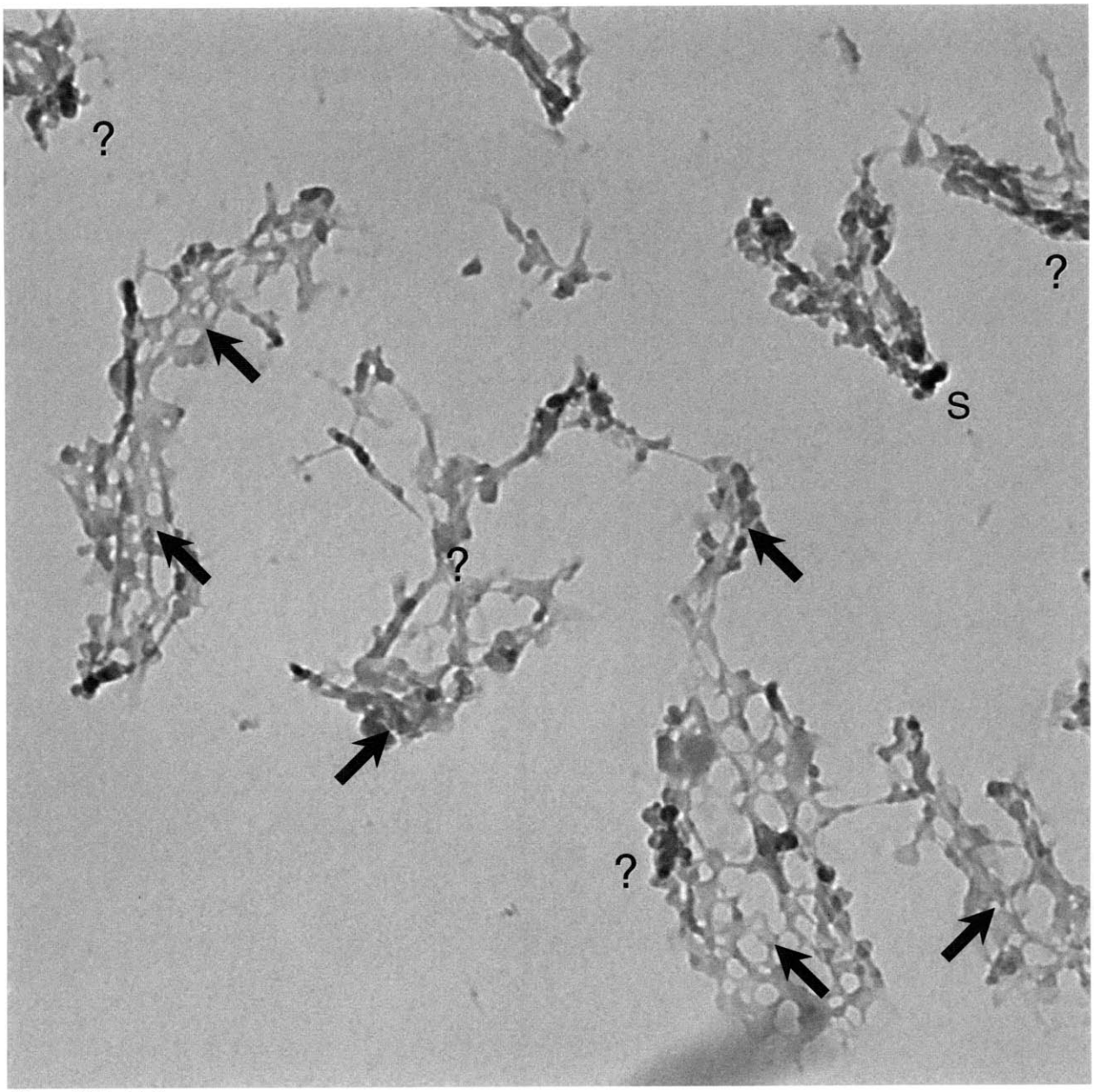

Figure 10 - 6. (b) Sulfur artifact structures resembling soot particles.

The darker, denser spheres may be soot particles, while the fainter stains are most likely to be pure sulfur. See (a) for meanings of symbols.

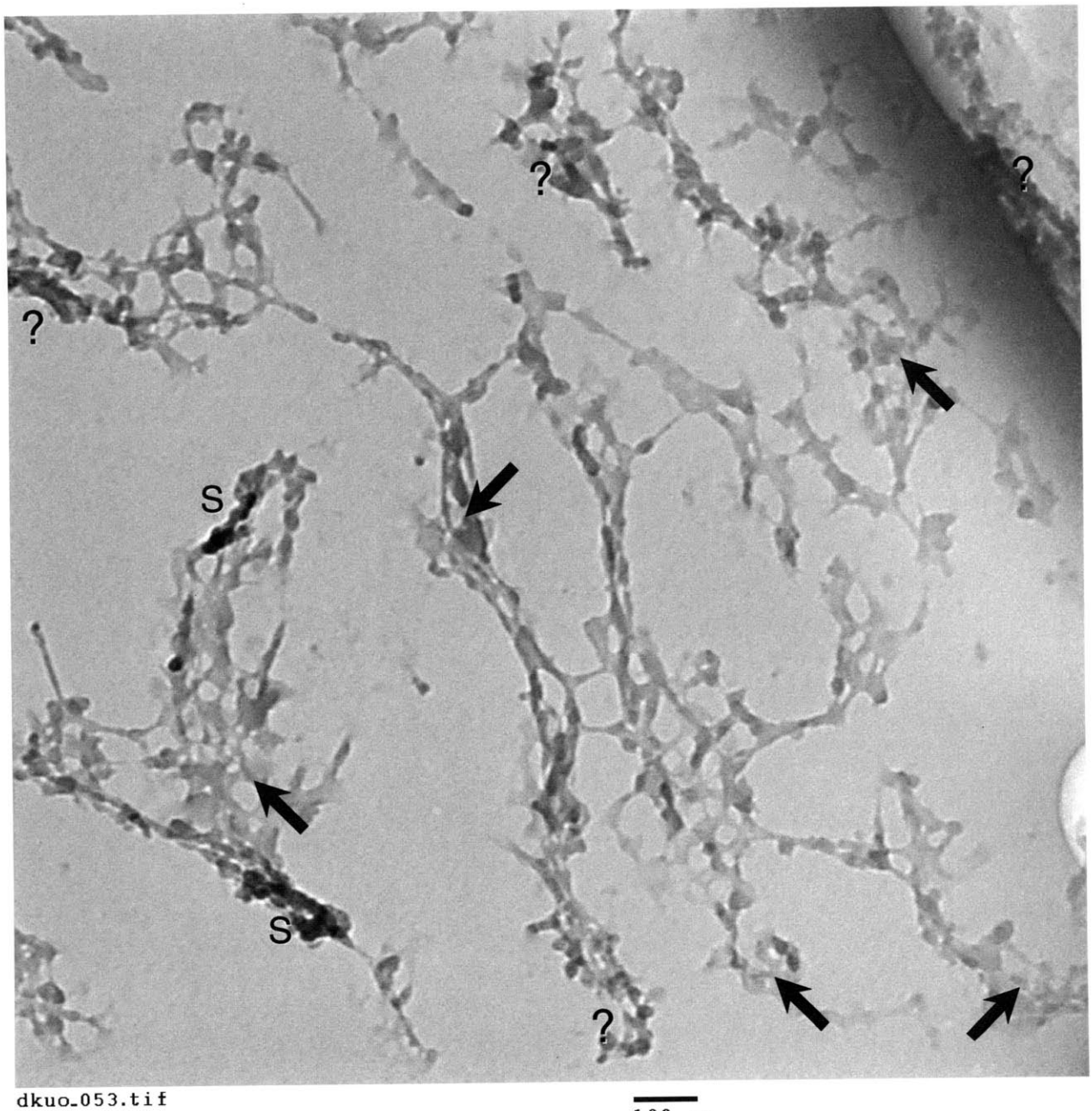

Figure 10 - 6. (c) Sulfur artifact structures resembling soot particles.

The darker, denser spheres may be soot particles, while the fainter stains are most likely to be pure sulfur. See (a) for meanings of symbols.

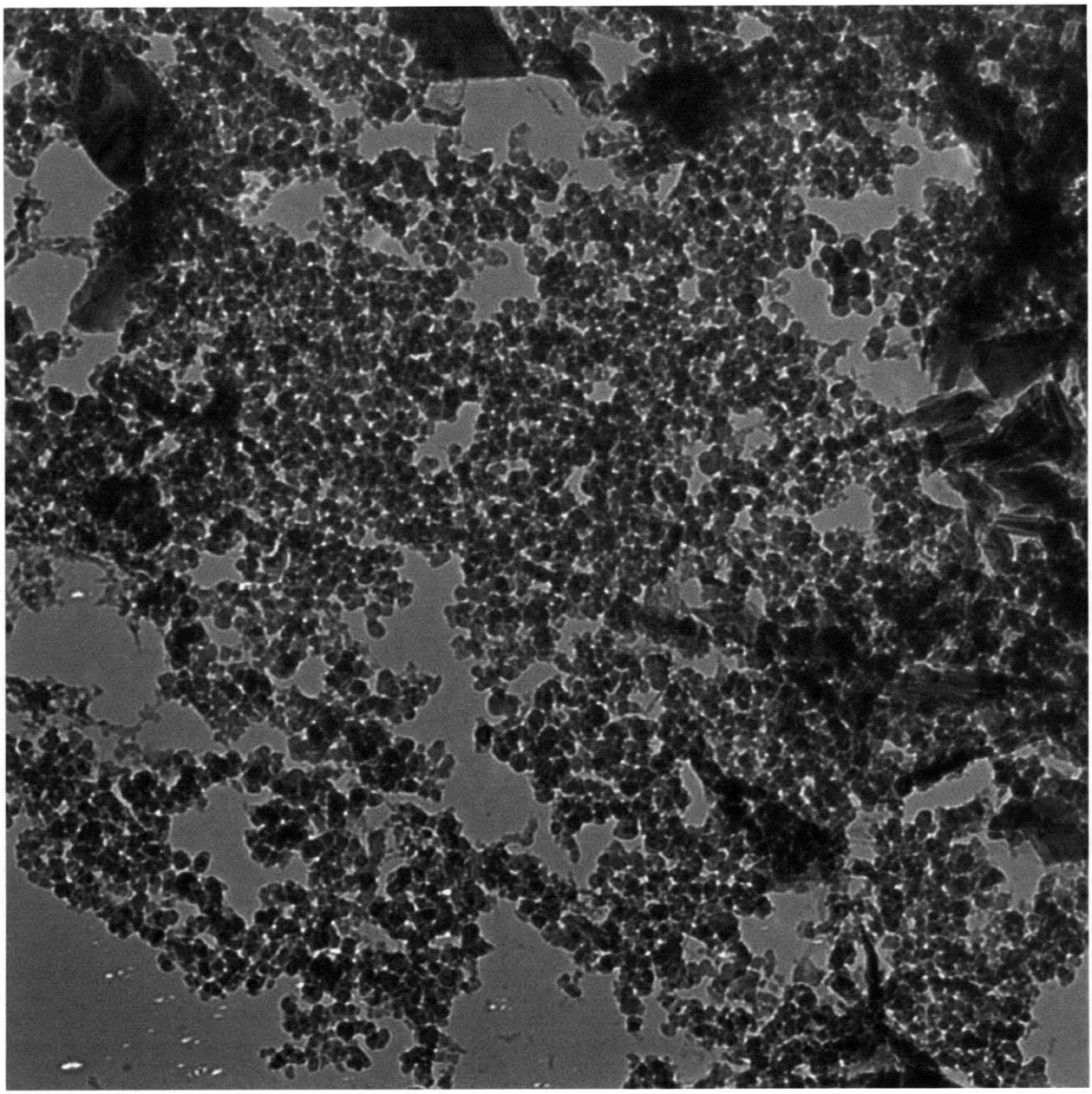

Figure 10 - 7. Clusters of soot in soot-amended Boston Harbor sediments (a-b).

Figure 10 - 7. (a) "Sea" of soot (#1). Sample was embedded in elemental sulfur, microtomed by aiming a 70 nm thickness and subsequently mounted on a lacey SiO film on Cu grids.

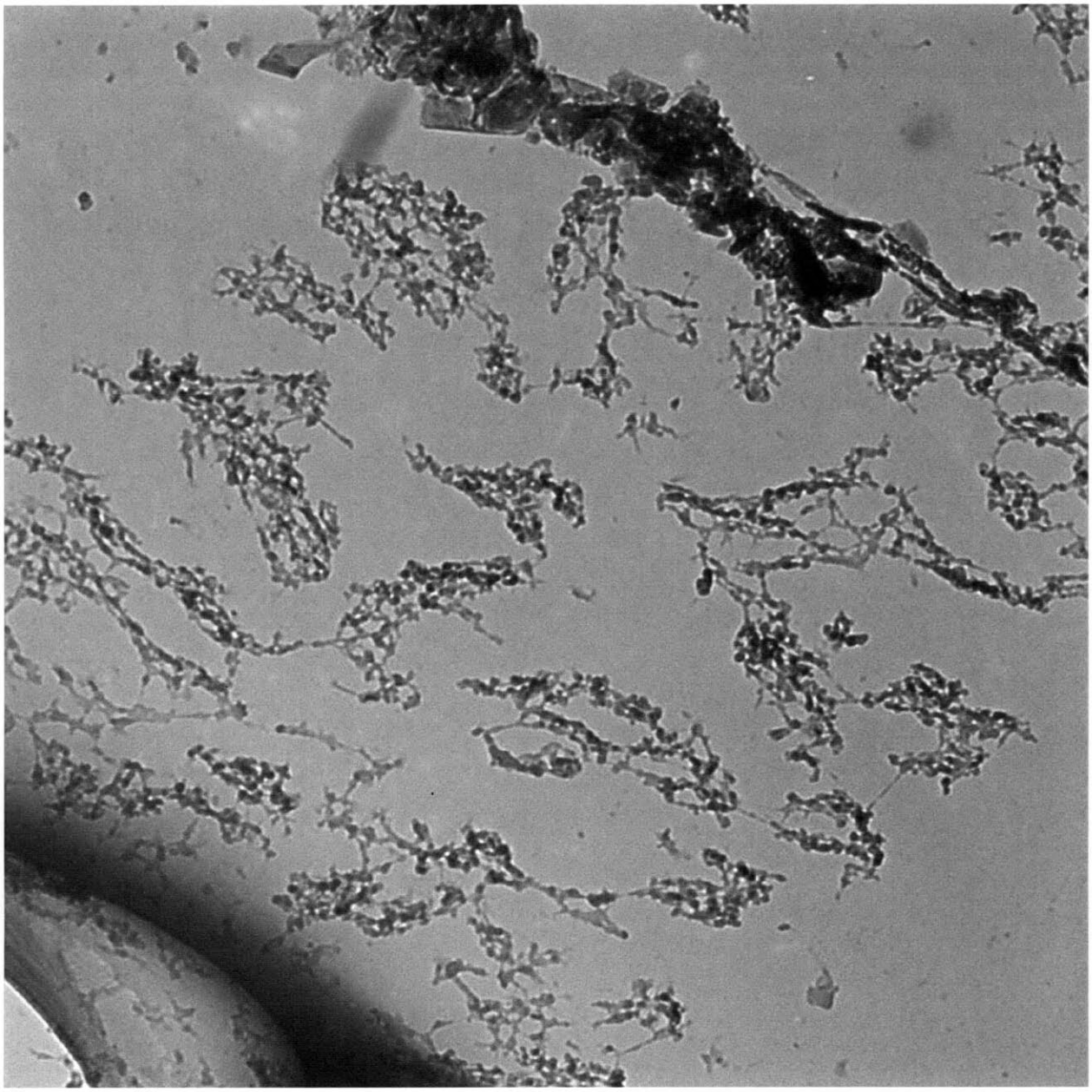

Figure 10 - 7. (b) A view of sulfur streaks that may contain some soot particles.

It is unclear how much of the streak structures contain soot particles. This micrograph is obtained from the same sample as in Figure 10-7b.

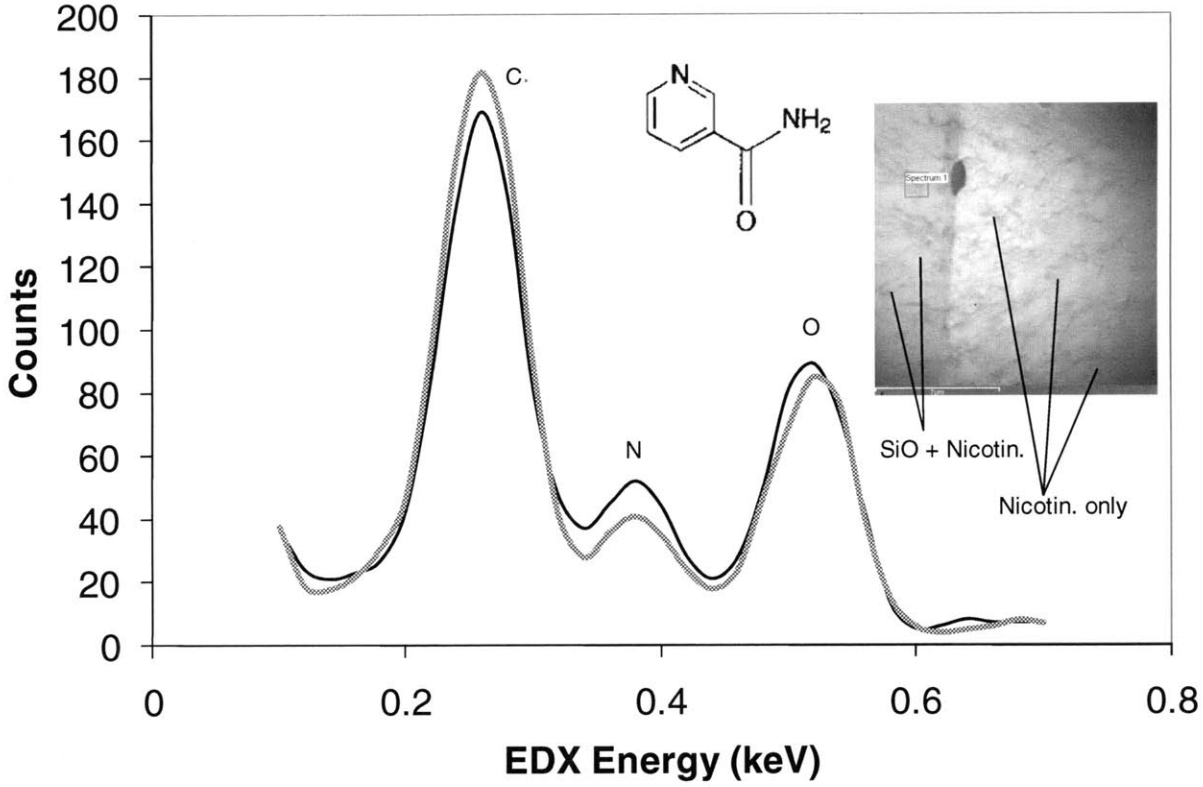

Figure 10 - 8. EDX spectra of nicotinamide ($C_6H_6N_2O$).

EDX spectra of nicotinamide ($C_6H_6N_2O$) on a SiO film on Cu grid. The sample was prepared by dispensing nicotinamide solution onto the SiO film.

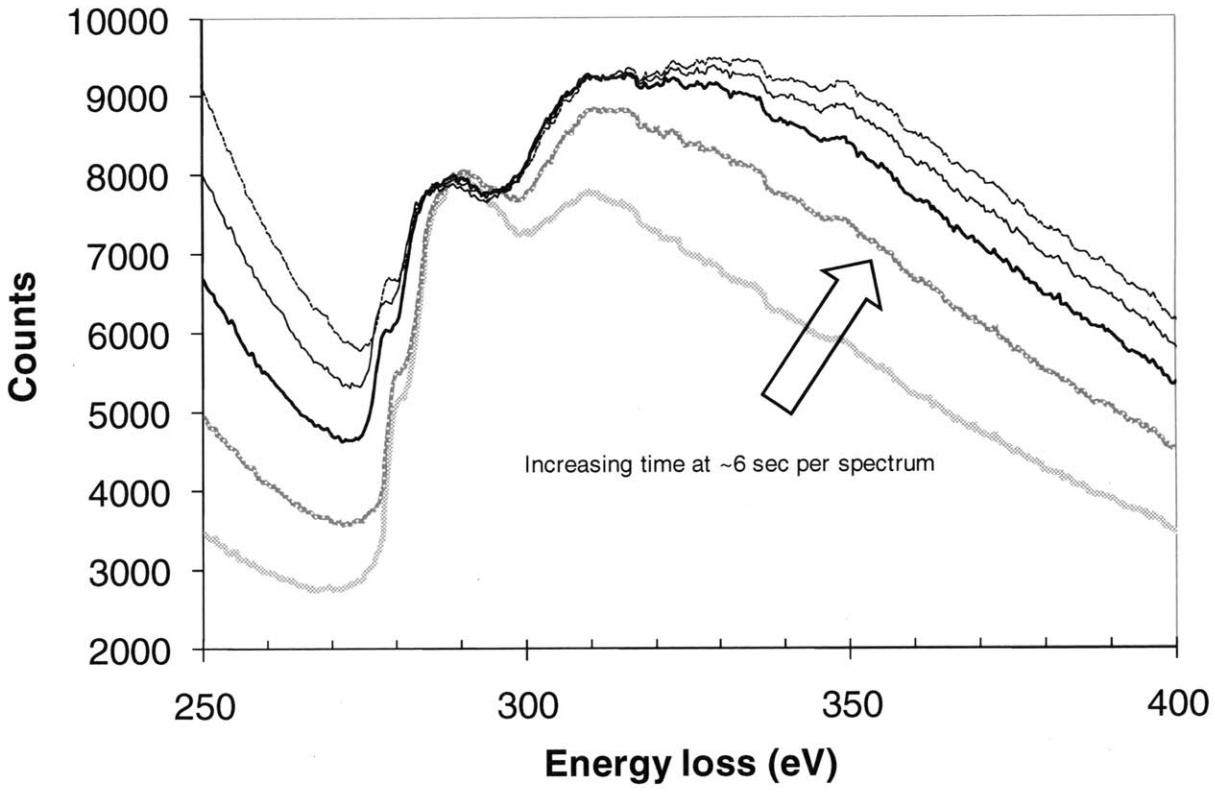

Figure 10 - 9. Build-up of amorphous carbon on EM thin samples.

EELS spectra showing the time evolution of matter building up at the electron beam irradiated point on lacey carbon film. The rising pre-C edge (~250 to 280 eV) and the broad structure after 300 eV together suggests the sampling spot was becoming thicker and thicker with time.

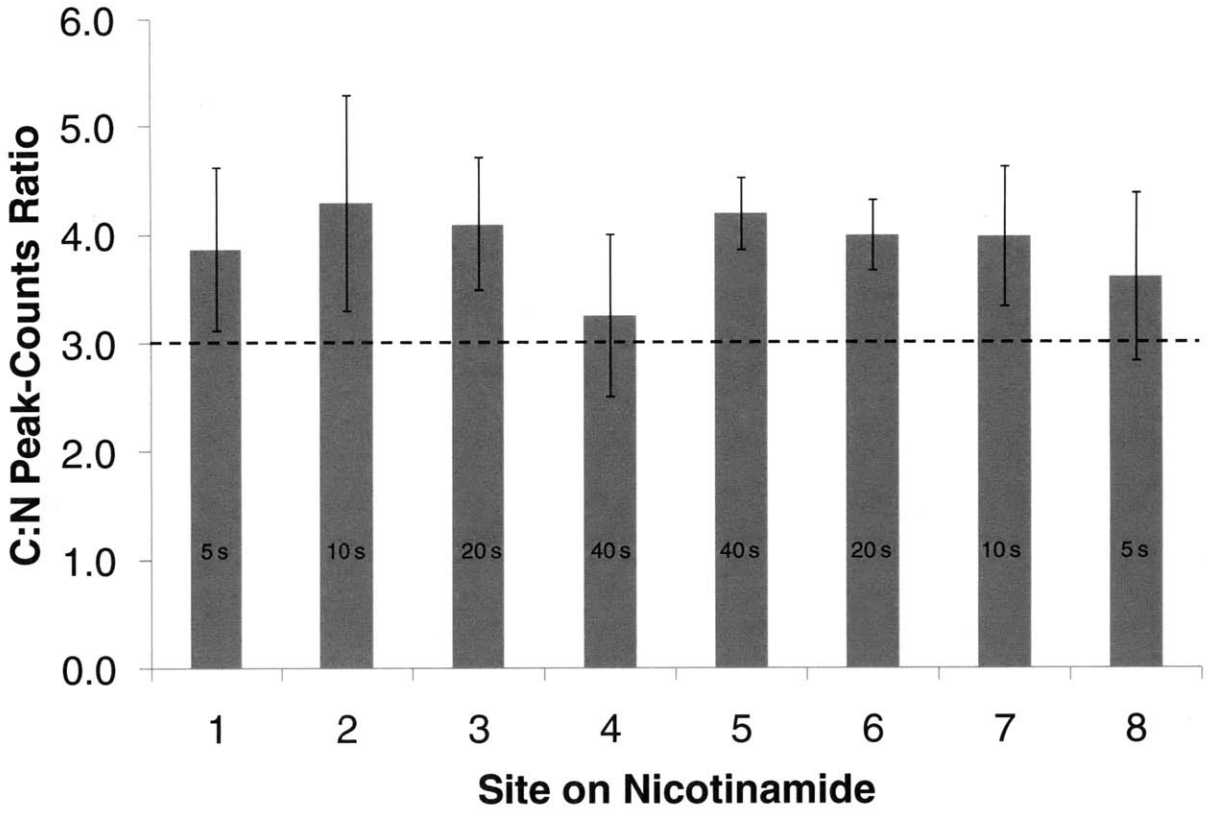

Figure 10 - 10. Carbon build-up on nicotinamide ($C_6H_6N_2O$) from beam irradiation.

The figure shows the extent of carbon build-up on nicotinamide ($C_6H_6N_2O$) as a result from beam irradiation. The bars show C:N ratios as determined from the EDX counts at C and N peaks at 8 locations at different electron beam exposure time (5, 10, 20, and 40 sec.) on the sample. The dashed line indicates the theoretical ratio of C:N for nicotinamide. Error bars measure 1 standard deviation from mean.

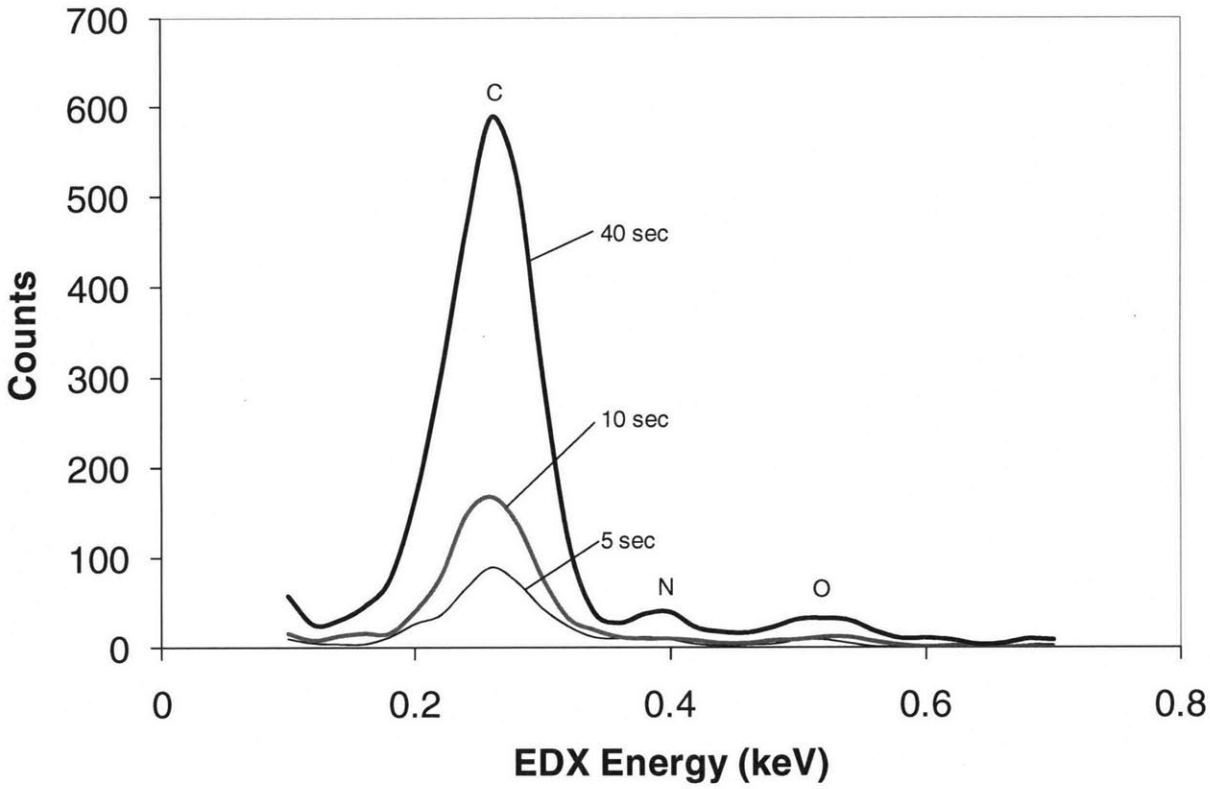

Figure 10 - 11. EDX spectra of nicotinamide (a-b).

Figure 10 - 11. (a) An area-averaged EDX spectra on nicotinamide.

The spectra was obtained over a ~15x15 um area at different exposure times. The N and O peaks seems to be suppressed when compared to Figure 10-8.

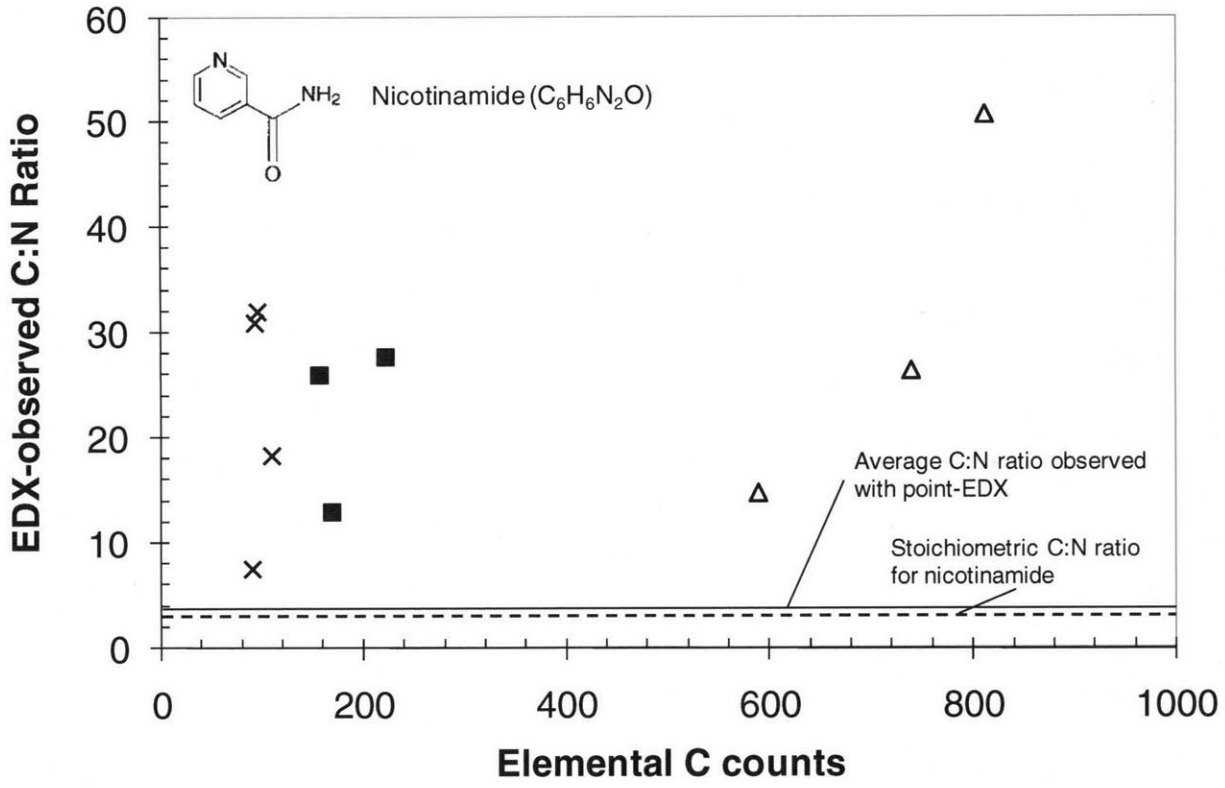

Figure 10 - 11. (b) C:N peak-ratios for nicotinamide as a function of total carbon counts. C:N peak-ratios obtained for different screening area on nicotinamide.

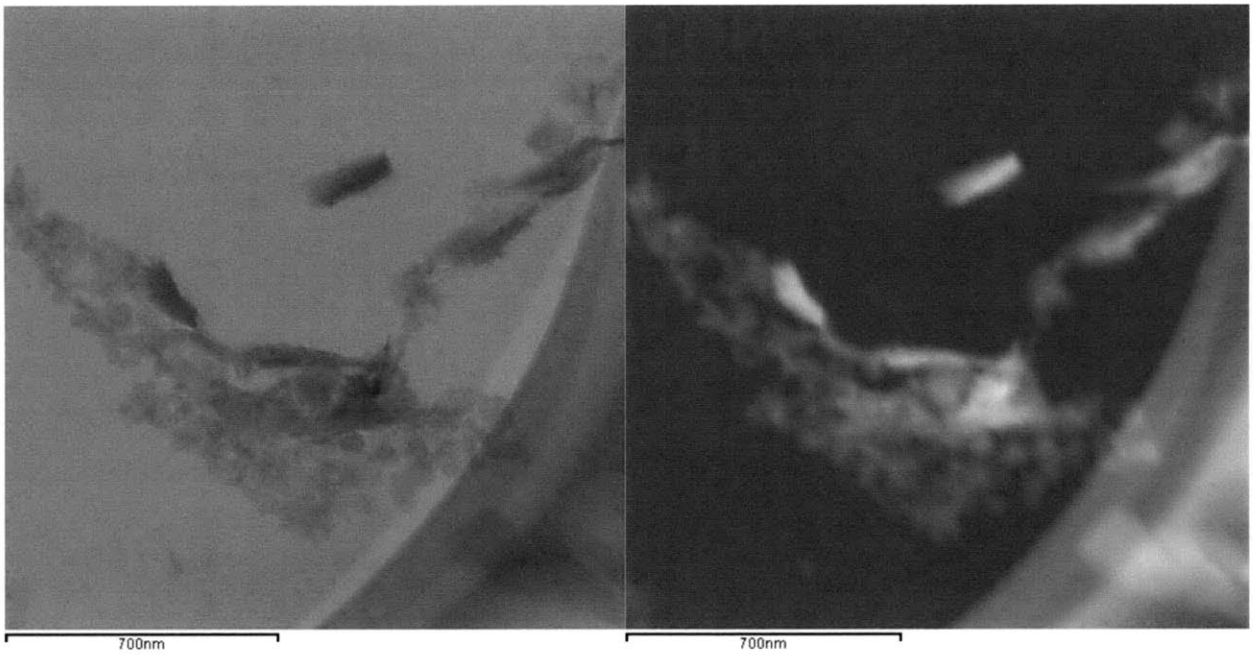

Figure 10 - 12. TEM images and EDX spectra of soot amended sediments (a-d).

Figure 10 - 12. (a) TEM images of NIST-soot.

TEM bright-field (left) and dark-field (right) images of NIST-soot (NIST SRM #1650 Diesel Particulate Matter) amended sediments on lacey-SiO film (20061010-Site#2). The angular, dense structures were sedimentary grains. The web/film looking structure in the lower right corner was part of the lacey-SiO film.

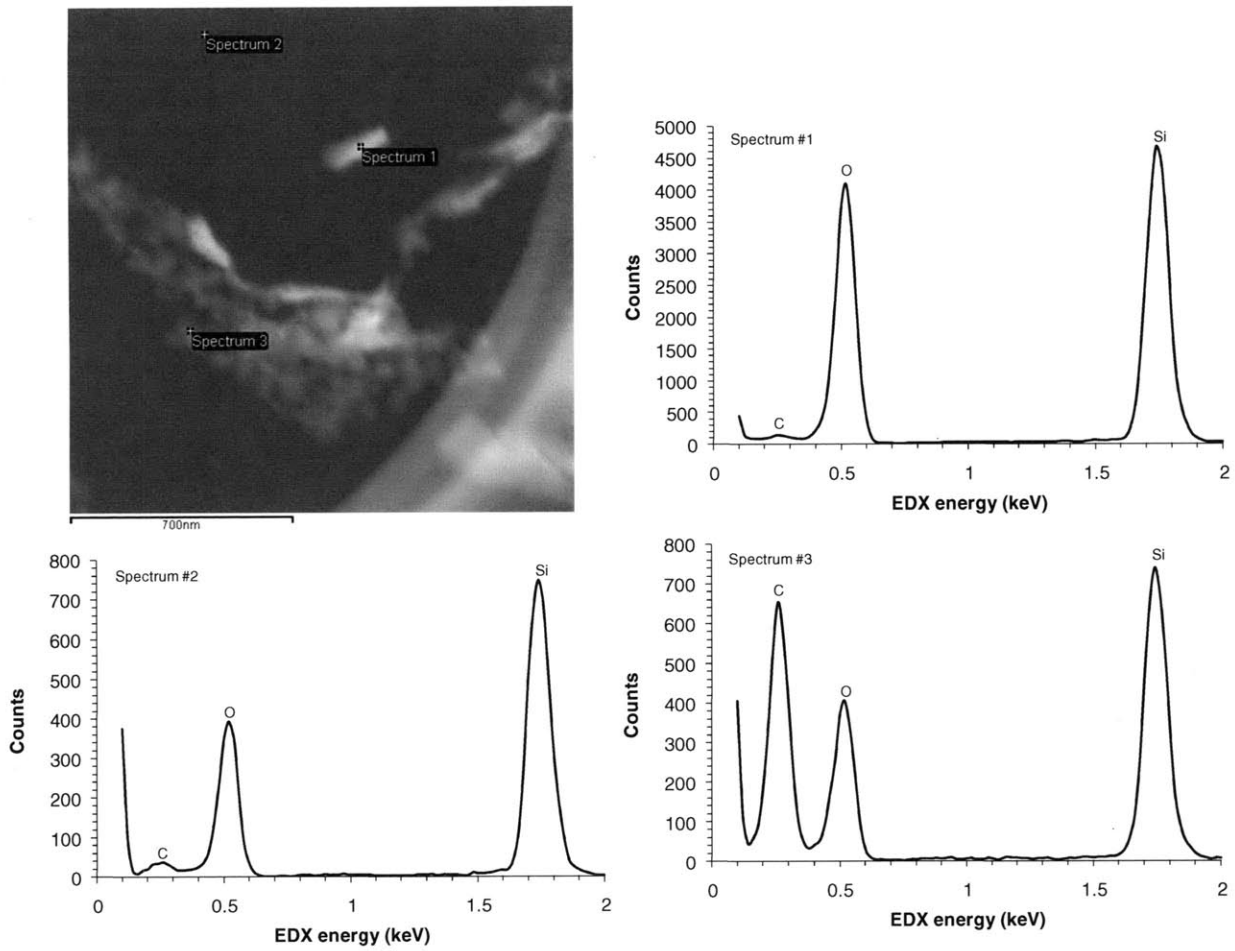

Figure 10 - 12. (b) EDX spectra of NIST-soot.

EDX spectra of NIST-soot (NIST SRM #1650 Diesel Particulate Matter) amended sediments on lacey-SiO film (20061010-Site#2). Spectrum #1 corresponds to an angular mineral grain (quartz). Spectrum #2 gives the background spectrum of the SiO film. In spectrum #3, which was obtained on the soot region, a prominent carbon peak is present. The presence of a minor carbon peak in spectrum 1 and 2 indicates the relative extent of carbon contamination.

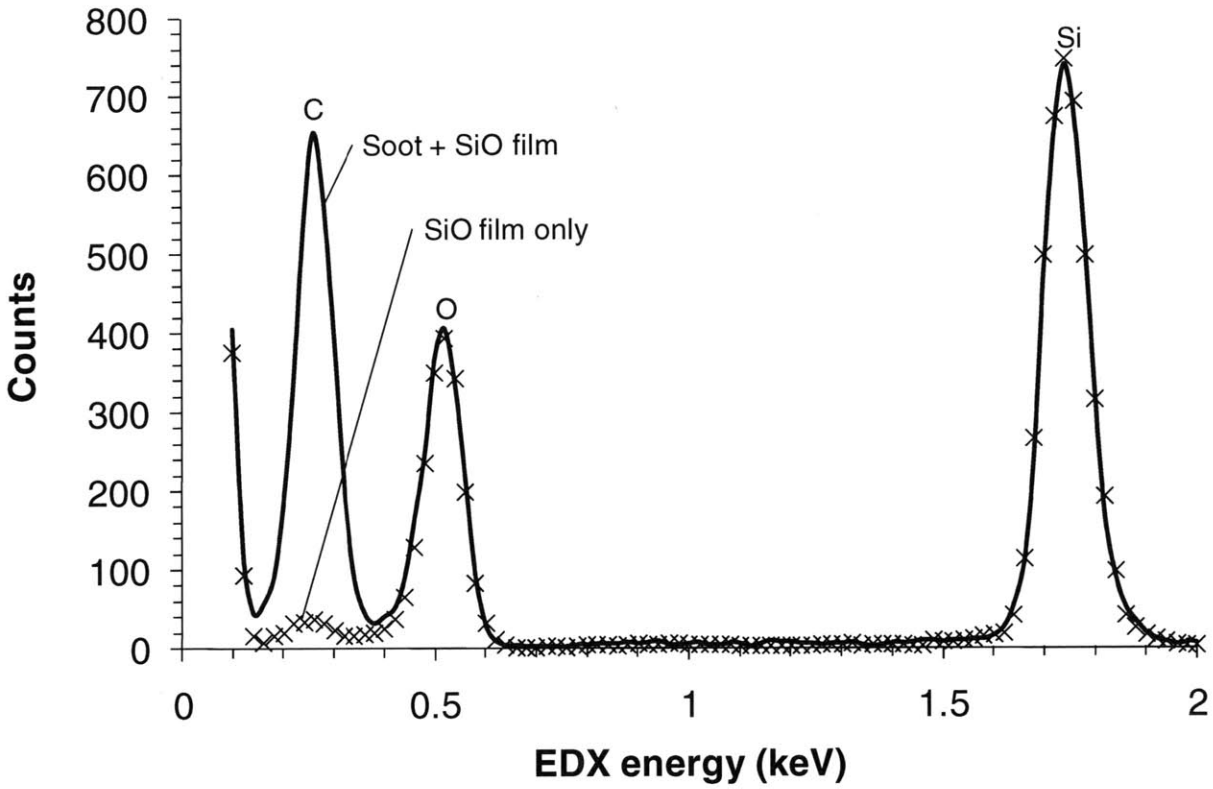

Figure 10 - 12. (c) EDX spectra of a soot region and a soot-free background.

EDX spectra from a soot region (spectra #2 and #3 as in Figure 10-12b). The soot-region (solid line) gave a purely carbon signal after the background due to SiO film (crosses) is removed.

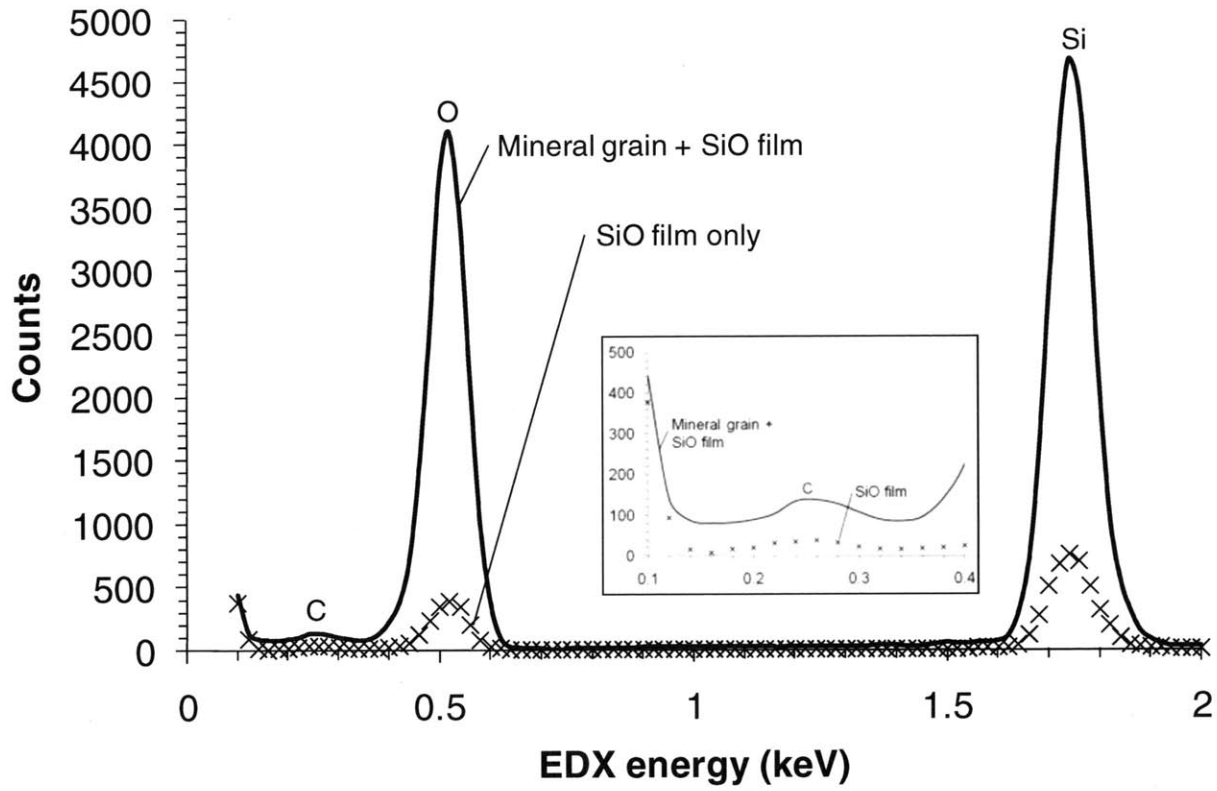

Figure 10 - 12. (d) EDX spectra of a mineral region and a soot-free background.

EDX spectra from an isolated mineral particle (solid line) on a lacey-SiO film (crosses) (spectra #1 and #2 as in Figure 10-12b). The C x-ray region is expanded in the inset.

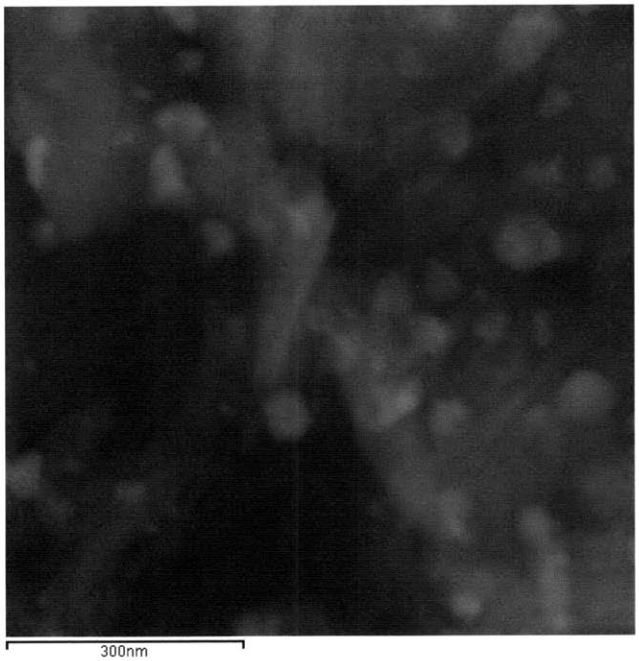

Figure 10 - 13. TEM image and EDX spectra of a mineral-dominant zone (a-f).

Figure 10 - 13. (a) TEM dark-field image of a visually mineral-dominant zone from a NIST-soot (NIST SRM #1650 Diesel Particulate Matter) amended sediment (20061010-Site#12). Background was lacey-SiO film.

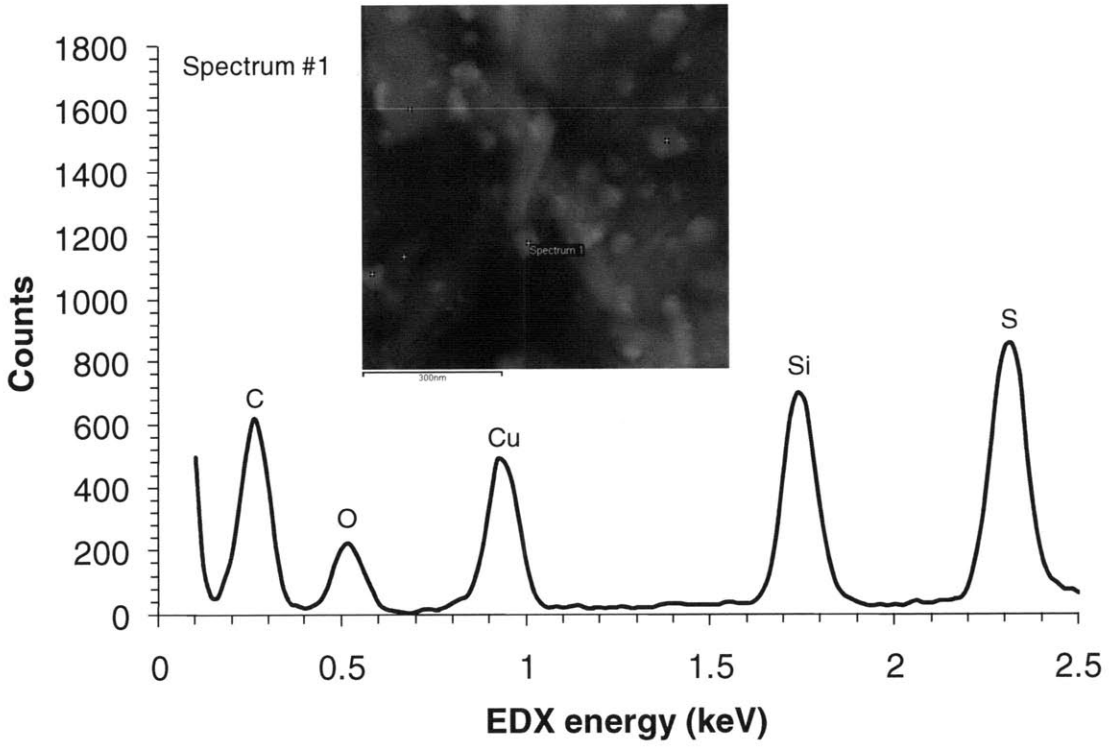

Figure 10 - 13. (b) EDX spectra from a carbon-rich mineral region (20061010-Site#12).

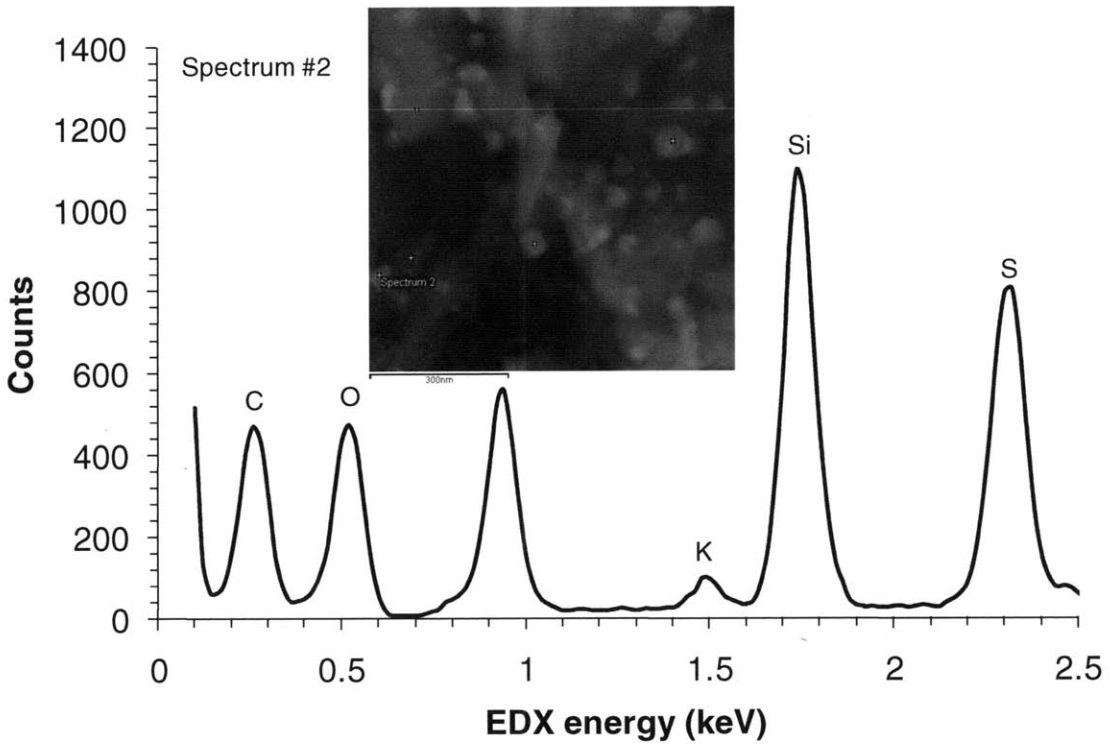

Figure 10 - 13. (c) EDX spectra from a carbon-rich mineral region (20061010-Site#12).

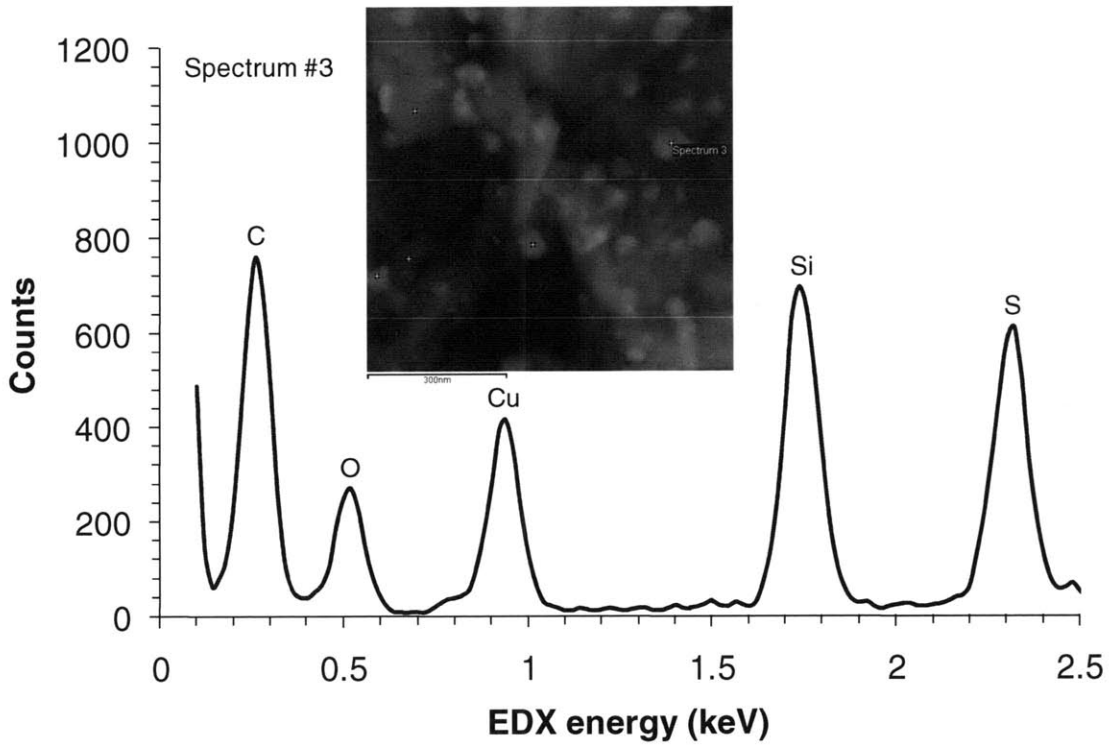

Figure 10 - 13. (d) EDX spectra from a carbon-rich mineral region (20061010-Site#12).

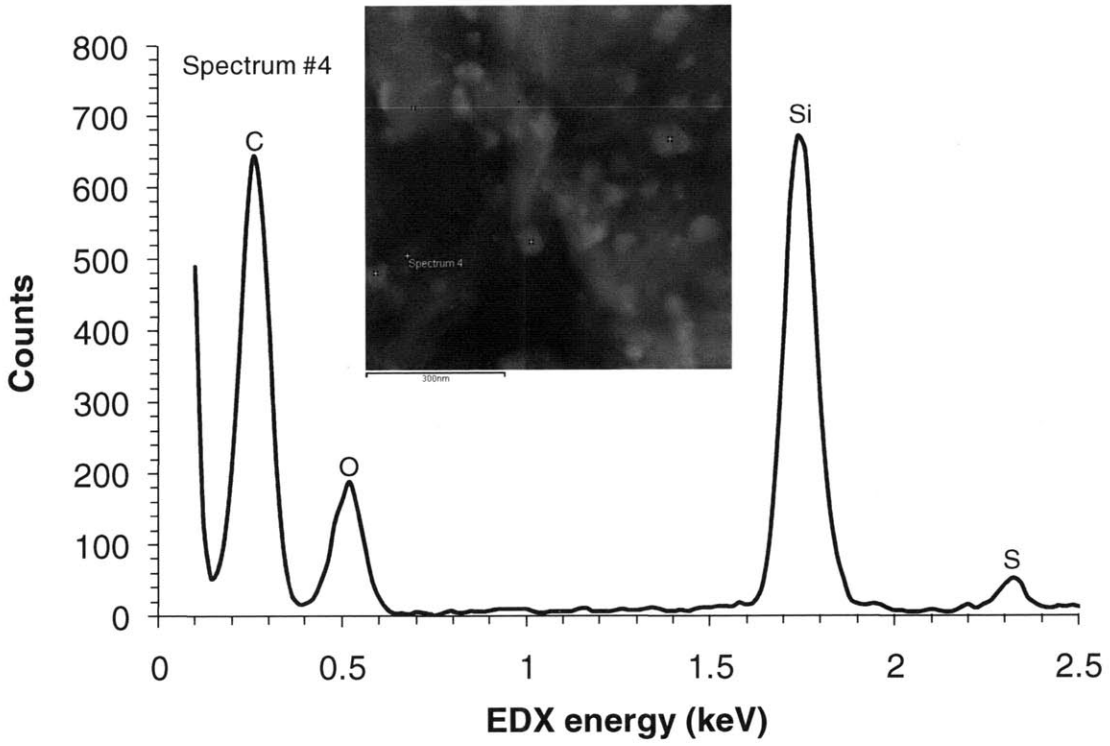

Figure 10 - 13. (e) EDX spectra from a carbon-rich mineral region (20061010-Site#12).

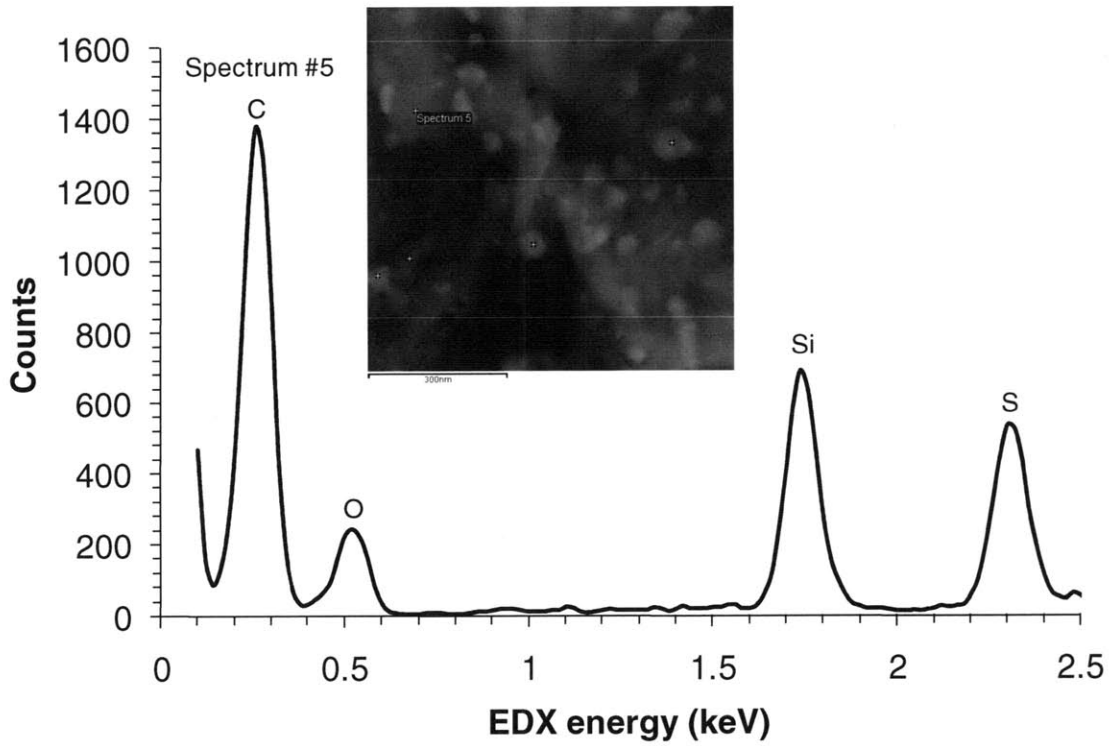

Figure 10 - 13. (f) EDX spectra from a carbon-rich mineral region (20061010-Site#12).

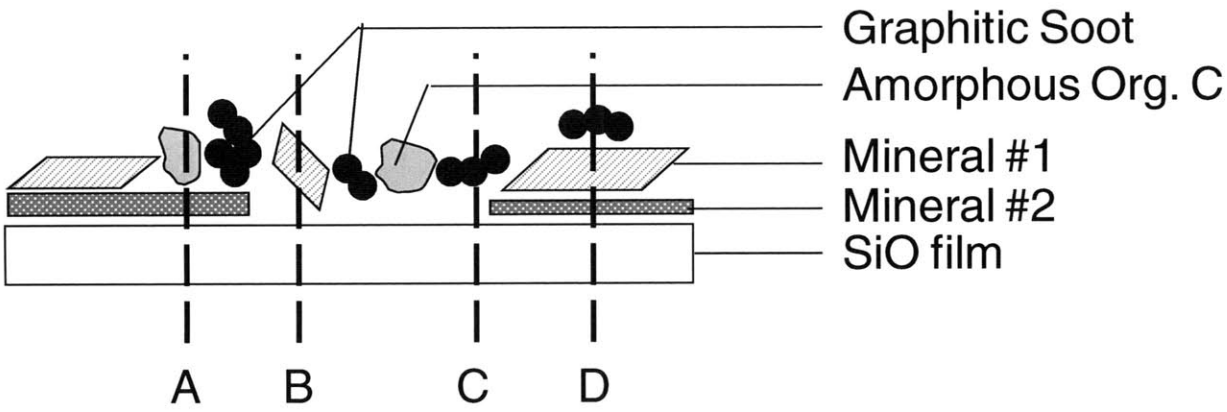

Figure 10 - 14. Correction of O signal in the presence of multiple oxygenated phases.

At locations B and C , oxygen signal can be easily corrected because there is only a single unknown phase. The fraction of oxygen signal from SiO can be estimated as in Figure 10-12a-d. At locations A and D, where there are two or more unknown phases present, correcting for inorganic-O signal can be difficult, as in the case portrayed in Figure 10-13a-f.

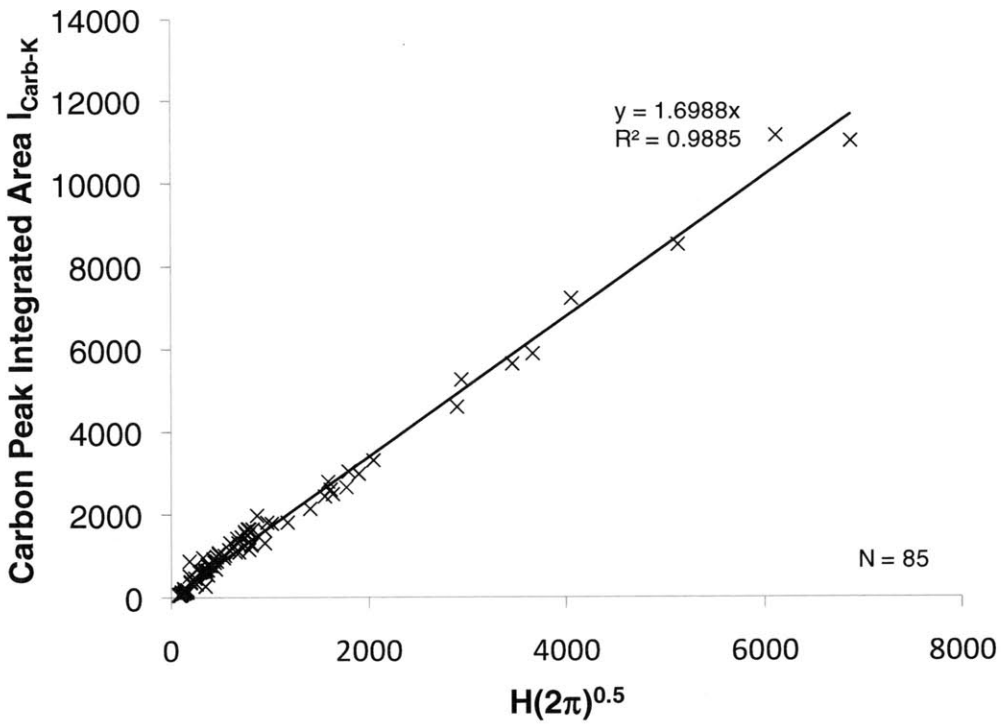

Figure 10 - 15. EDX elemental analysis: integrated area against peak height (a-d).

Figure 10 - 15. (a) Carbon σ_K regression from integrated area and peak height.

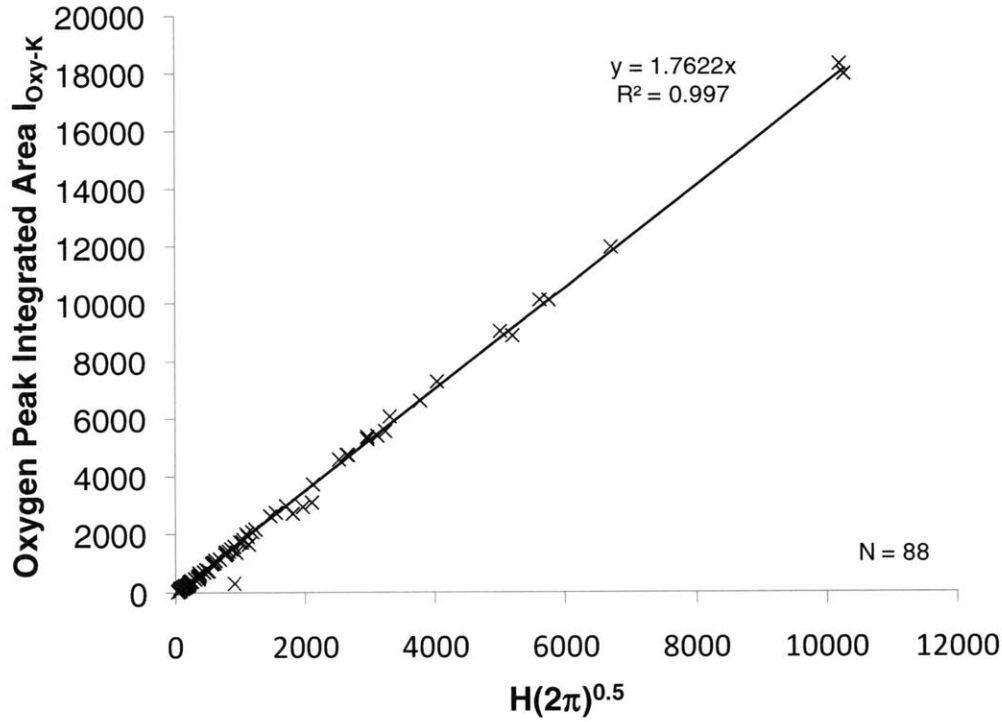

Figure 10 - 15. (b) Oxygen σ_K regression from integrated area and peak height.

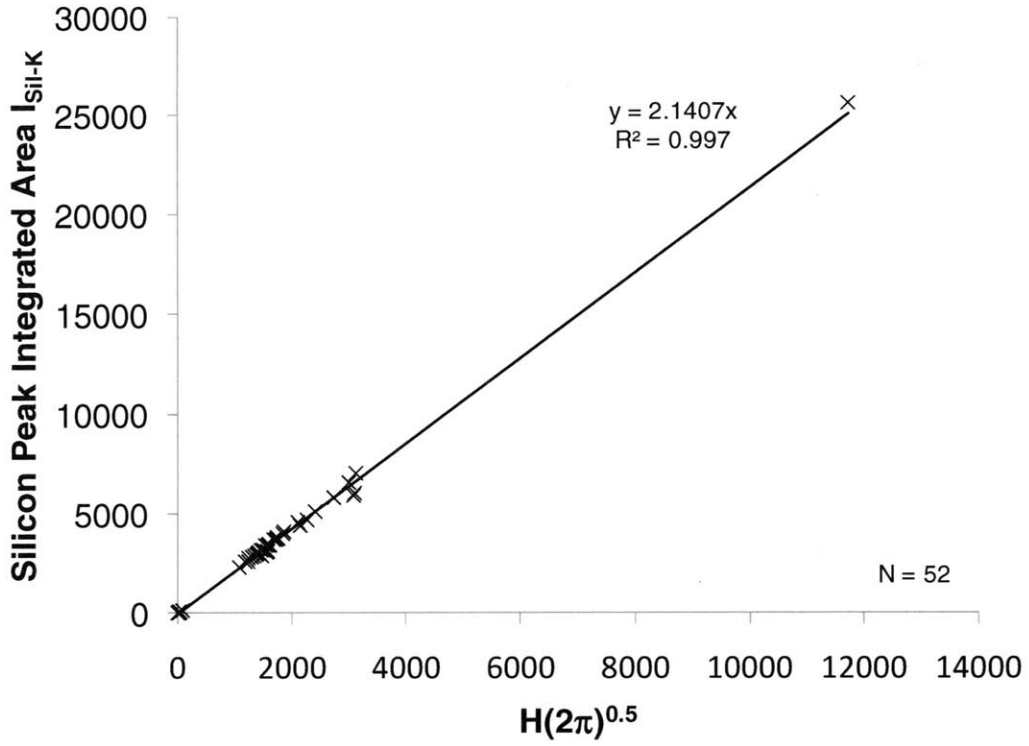

Figure 10 - 15. (c) Silicon σ_K regression from integrated area and peak height.

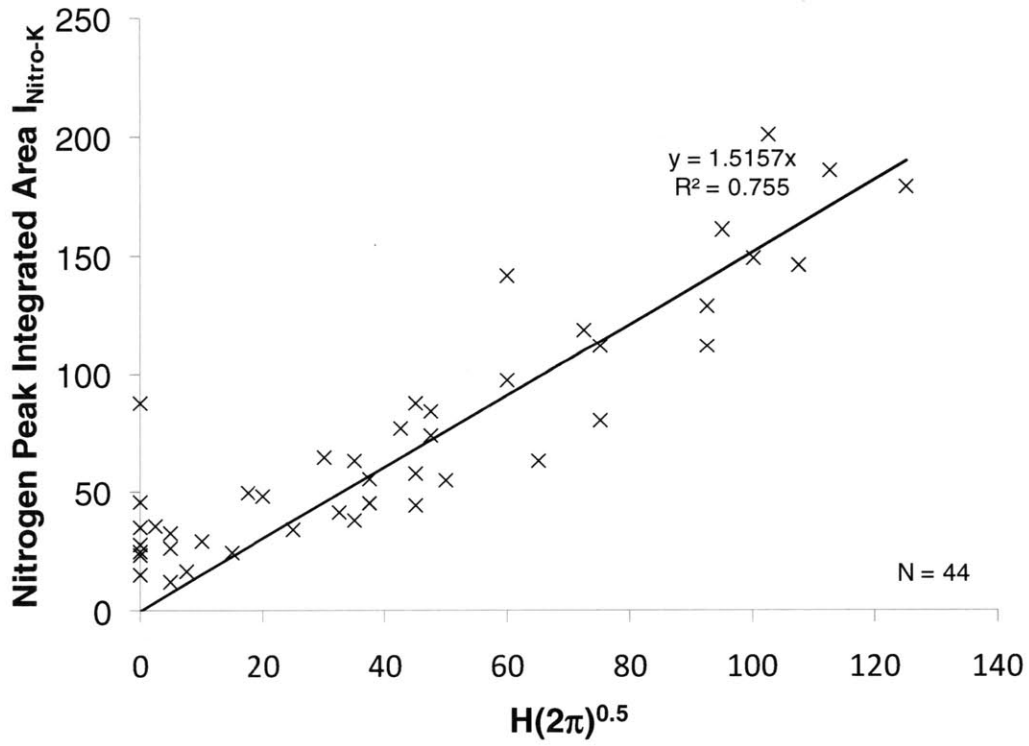

Figure 10 - 15. (d) Nitrogen σ_K regression from integrated area and peak height.

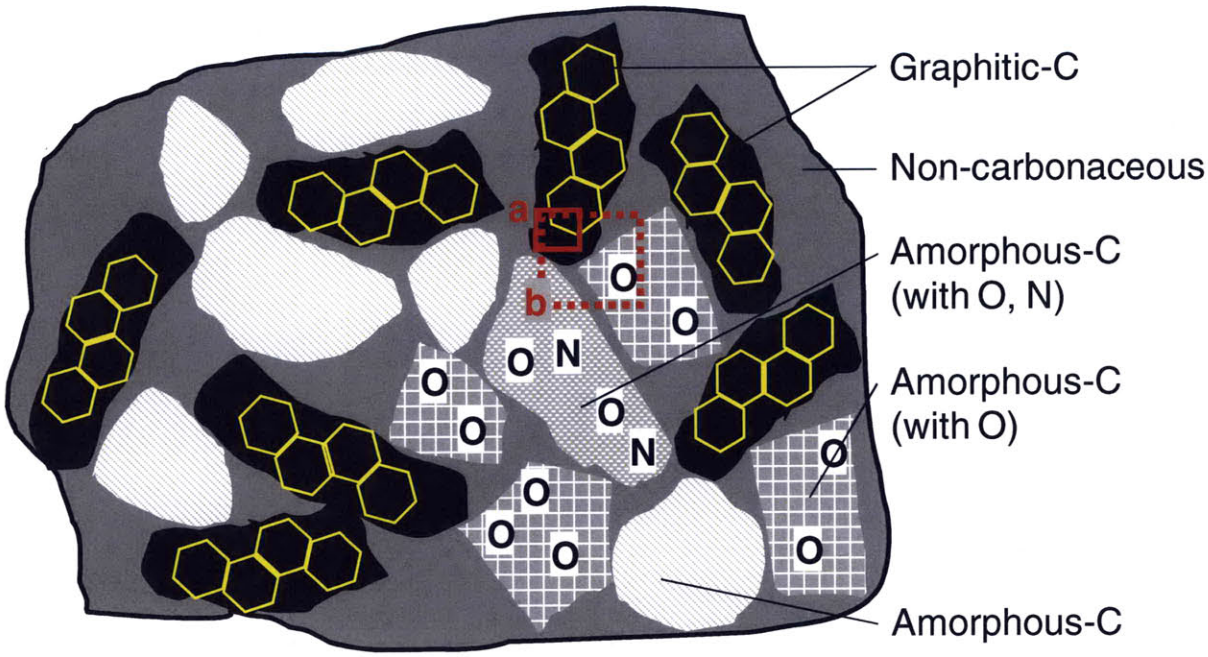

Figure 10 - 16. Heterogeneity of natural geosorbents and the limitation of bulk analyses.

This cartoon is meant to explain how compositional heterogeneity on a fine scale becomes 'distorted' when observed/quantified using bulk chemical analyses. The label 'a' denotes a region which consists of only graphitic-C. However, if the chemical analysis used can only probe with the resolution defined by 'b', then one's observation of graphitic-C would necessarily include O and amorphous-C as well.

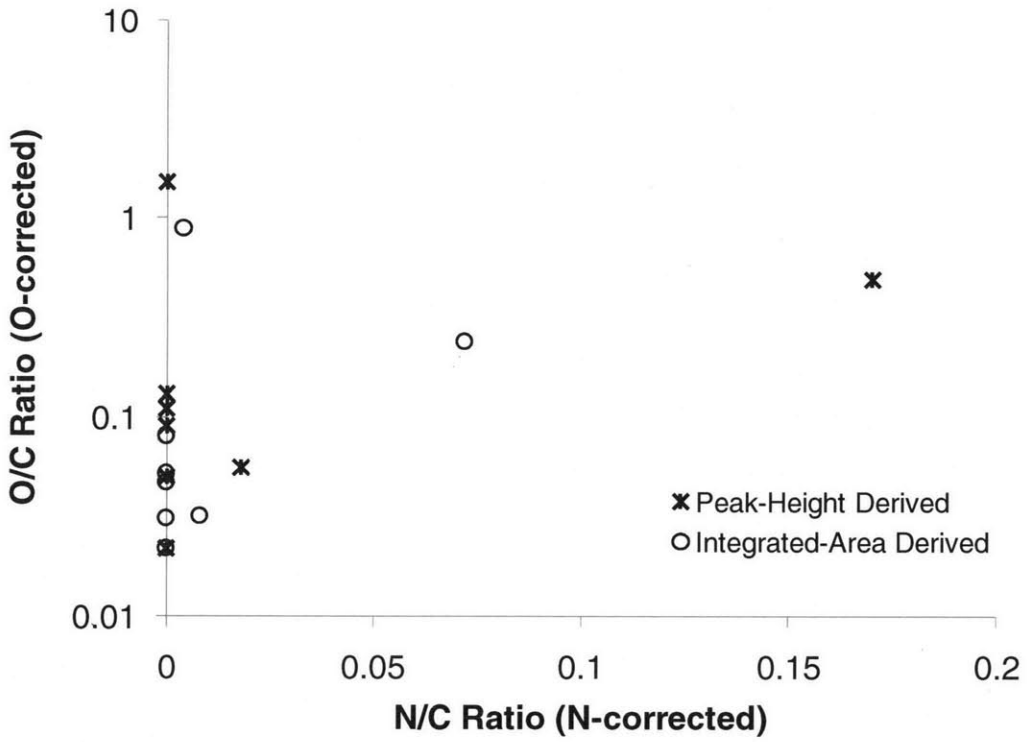

Figure 10 - 17. O/C vs N/C ratio of carbonaceous matters by point-EDX analysis.

The elemental ratios were determined using both the peak-height approach (crosses) and the integrated-area approach (circles). Error bars are omitted for visual clarity. For the list of carbon samples and the exact elemental ratio values, please refer to Table 10-4.

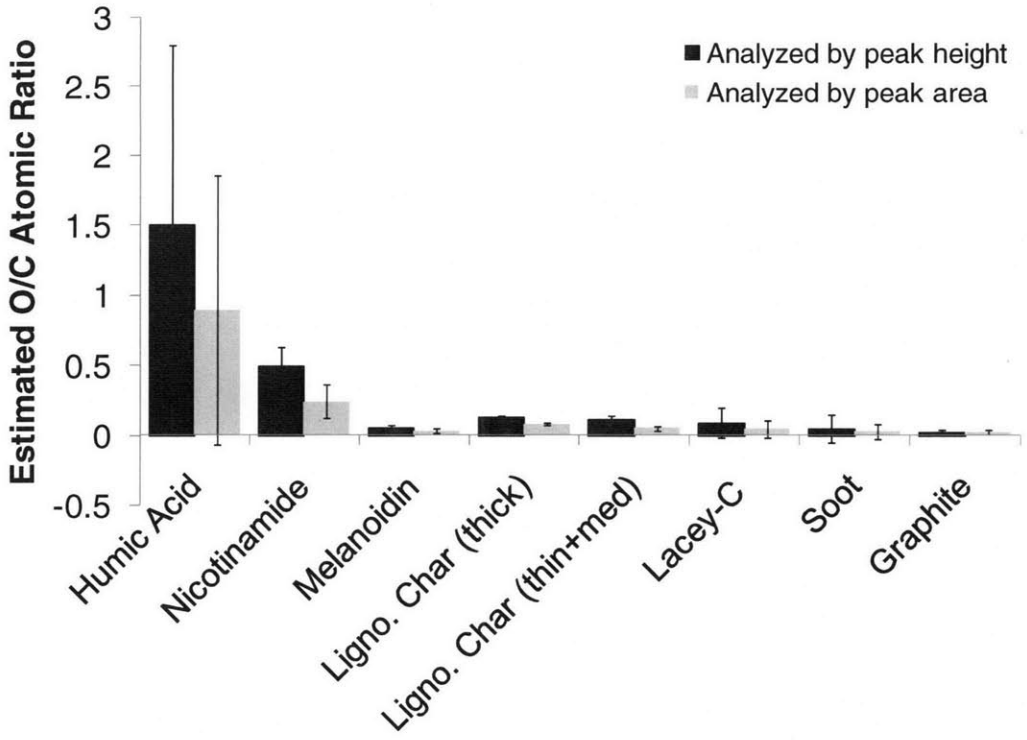

Figure 10 - 18. O/C atomic ratios of selected carbonaceous matters by point-EDX analysis.

Error bars give one standard deviation from mean. For exact values refer to Table 10-4.

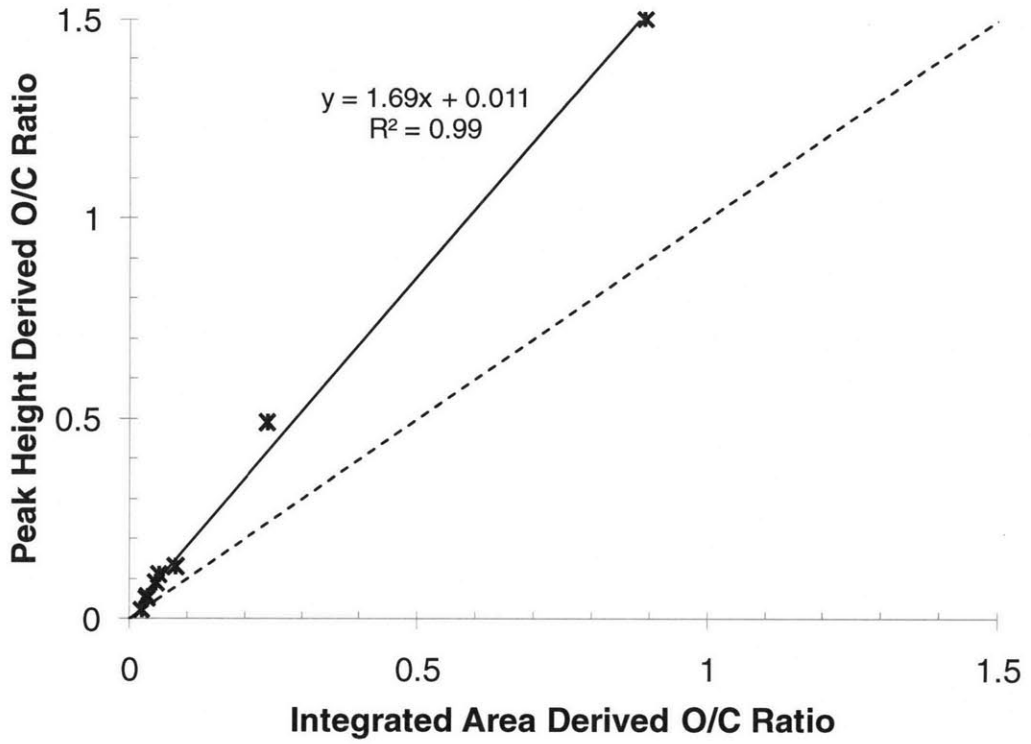

Figure 10 - 19. Discrepancy between peak-height and integrated-area derived O/C ratios.

Dashed line represents the 1-to-1 line when both methods match each other. Error bars are omitted for visual clarity.

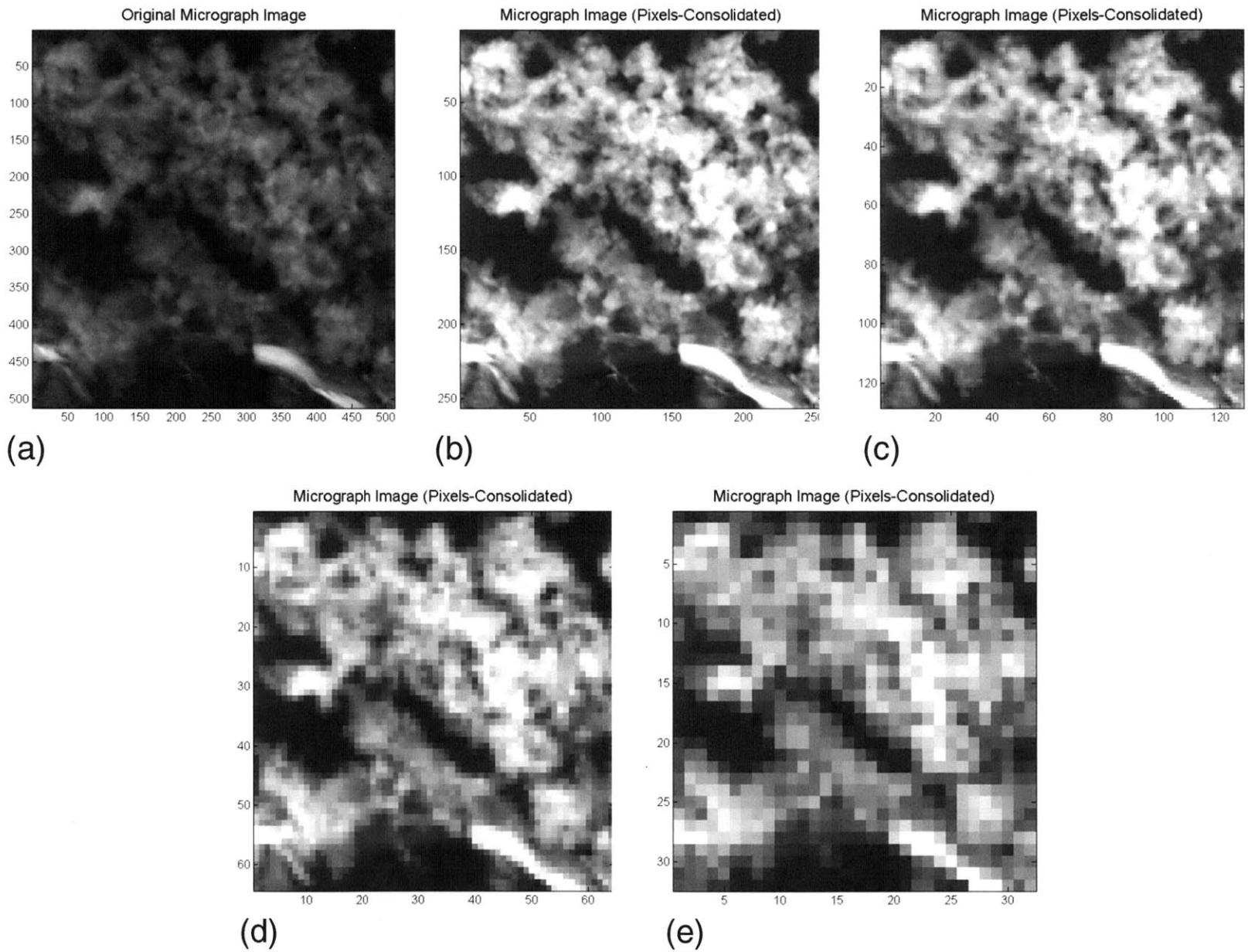
Original Micrograph Image
Micrograph Image (Pixels-Consolidated)
Micrograph Image (Pixels-Consolidated)
Micrograph Image (Pixels-Consolidated)
Micrograph Image (Pixels-Consolidated)
(a)
(b)
(c)
(d)
(e)

Figure 10 - 20. Original TEM and pixel-consolidated images of a soot-rich region.

Original TEM image of a soot-abundant region (sample 20061013-Site#3) and its pixel consolidation at 4 different resolutions: (a) original image, (b) without consolidation (256 x 256 cells), (c) 4 pixels consolidated into 1 (128 x 128 cells), (d) 16 pixels consolidated into 1 (64 x 64 cells), and (e) 64 pixels consolidated into 1 (32 x 32 cells).

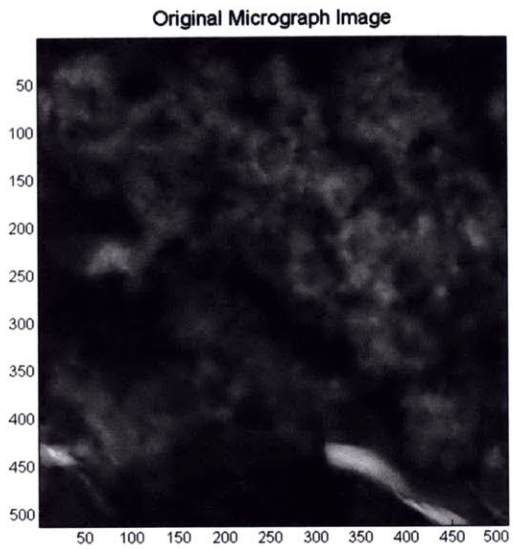
Original Micrograph Image
50
100
150
200
250
300
350
400
450
500
50 100 150 200 250 300 350 400 450 500

(a)

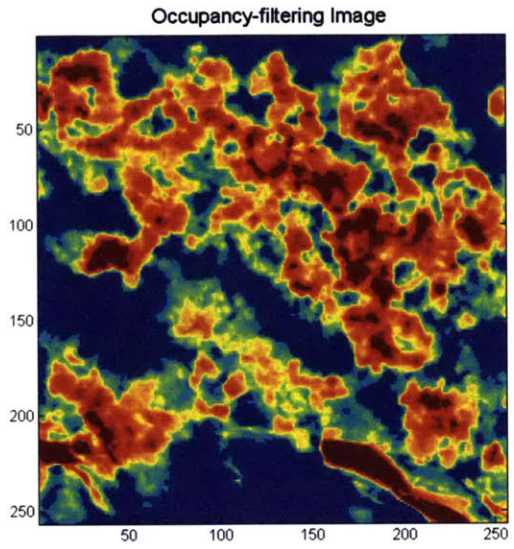
Occupancy-filtering Image
50
100
150
200
250
50 100 150 200 250

(b)

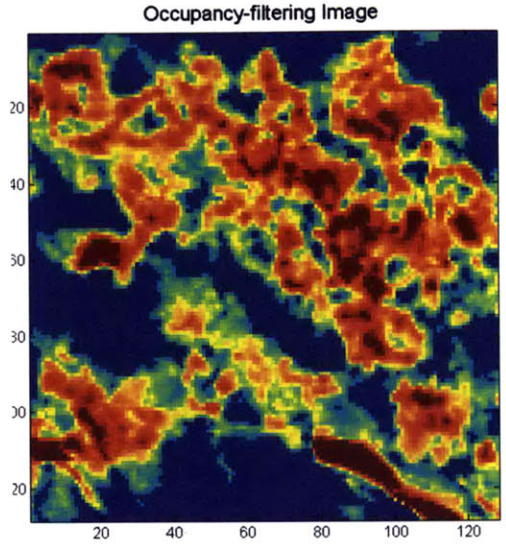
Occupancy-filtering Image
20
40
60
80
100
120

(c)

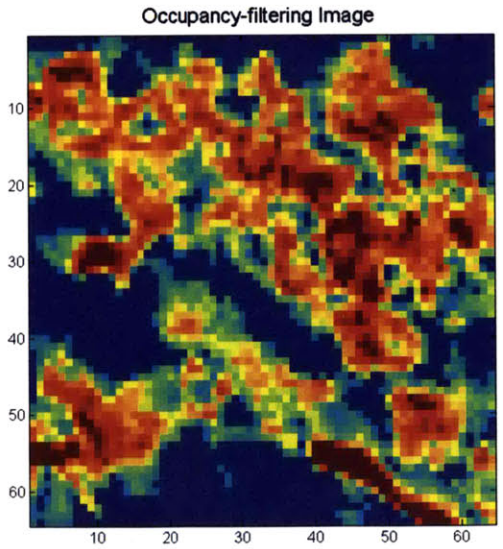
Occupancy-filtering Image
10
20
30
40
50
60
10 20 30 40 50 60

(d)

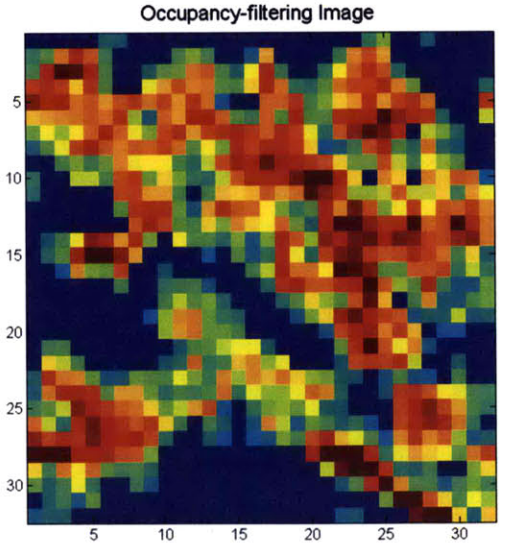
Occupancy-filtering Image
5
10
15
20
25
30
5 10 15 20 25 30

(e)

Figure 10 - 21. Occupancy filtered images of a soot-rich region.

Occupancy filtered image of a soot-abundant region (sample 20061013-Site#3) at 4 different resolutions: (a) original image, (b) without consolidation (256 x 256 cells), (c) 4 pixels consolidated into 1 (128 x 128 cells), (d) 16 pixels consolidated into 1 (64 x 64 cells), and (e) 64 pixels consolidated into 1 (32 x 32 cells). Dark blue represents non-sample background pixels and hotter colors indicate higher mass thickness and/or density.

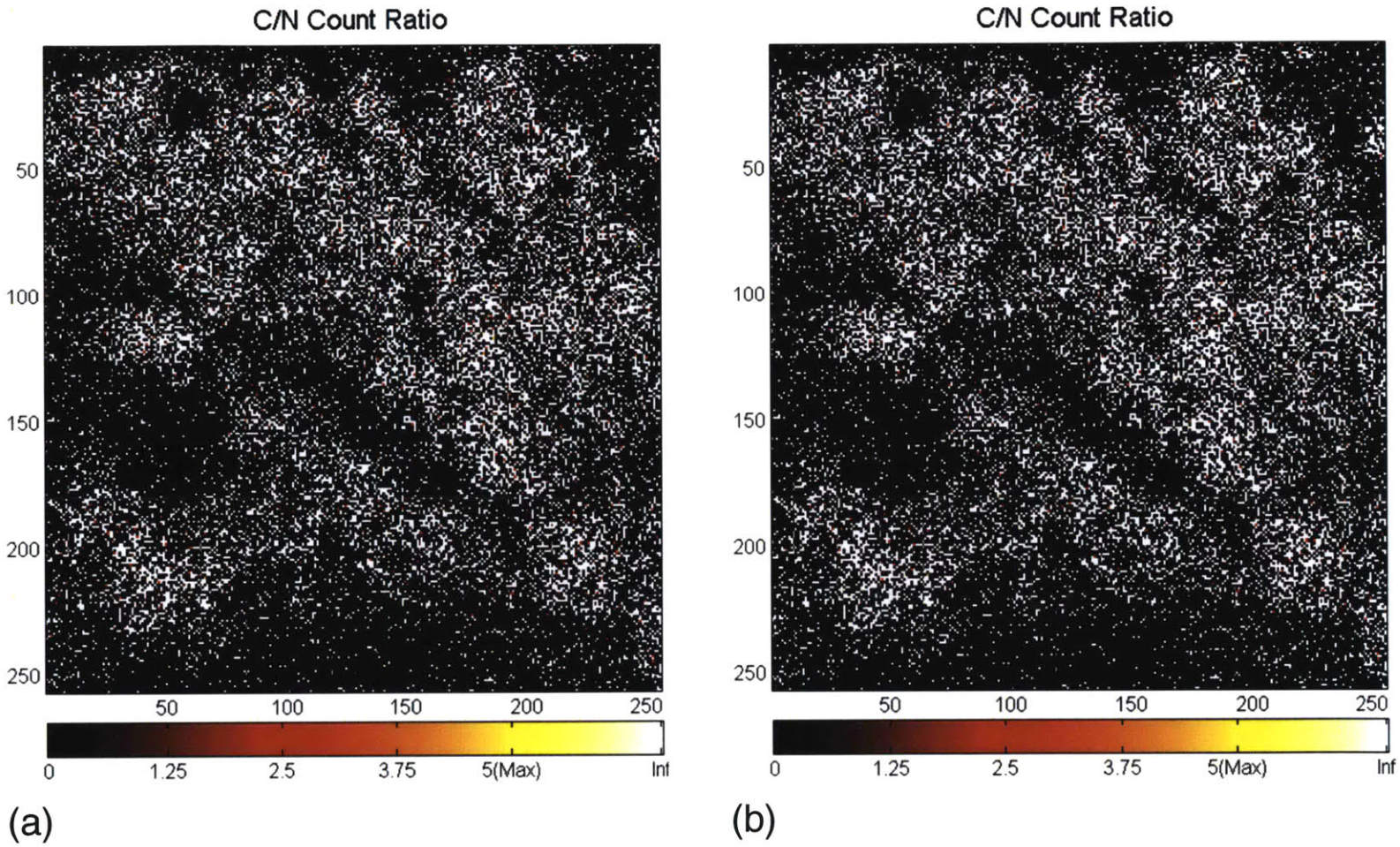

Figure 10 - 22. C/N atomic ratio of a soot-rich region (without occupancy filtering).

C/N atomic ratio of a soot-abundant region (sample 20061013-Site#3) without occupancy filtering: (a) without N 'noise' pixel correction, (b) with N 'noise' pixel correction consolidation. Both images were obtained without pixel consolidation (i.e., 256 x 256 cells). White spots indicate C/N ratio of approaching infinity (i.e., 'graphitic spots'). Dark spots indicate the absence of C X-rays.

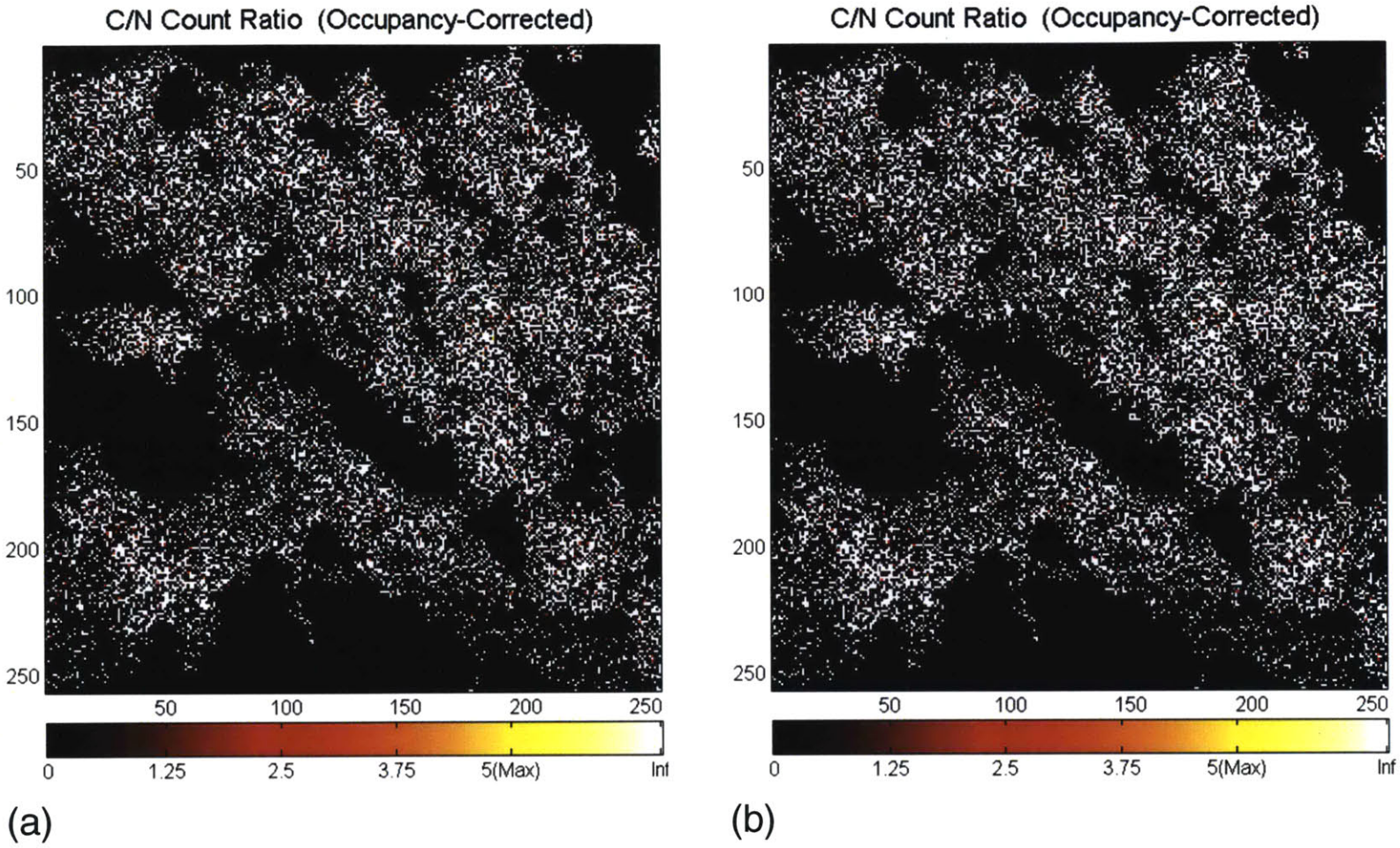

Figure 10 - 23. C/N atomic ratio of a soot-rich region (occupancy filtered).

C/N atomic ratio of a soot-abundant region (sample 20061013-Site#3) with occupancy filtering: (a) without N 'noise' pixel correction, (b) with N 'noise' pixel correction consolidation. Both images were obtained without pixel consolidation (i.e., 256 x 256 cells). White spots indicate C/N ratio of approaching infinity (i.e., 'graphitic spots'). Dark spots indicate the absence of C X-rays.

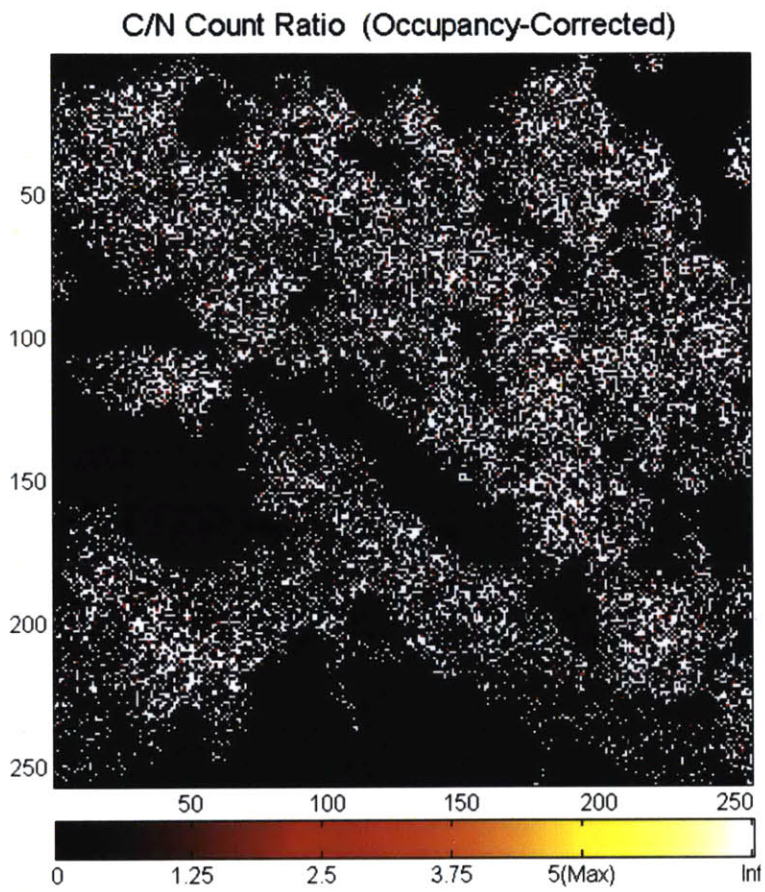
C/N Count Ratio (Occupancy-Corrected)
50
100
150
200
250
50
100
150
200
250
0
1.25
2.5
3.75
5(Max)
Inf

(a)

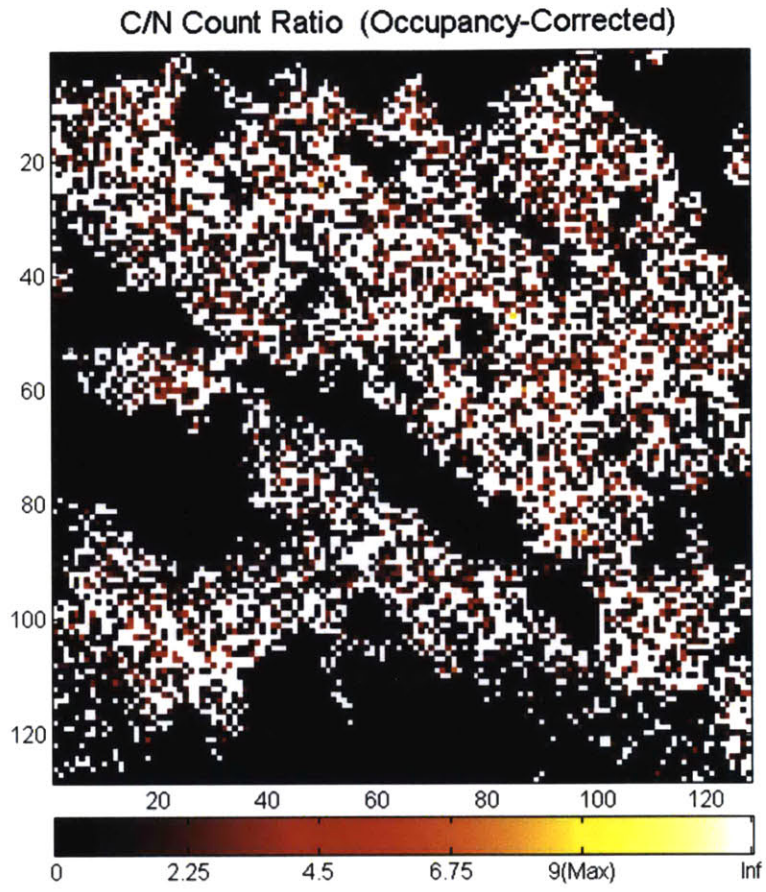
C/N Count Ratio (Occupancy-Corrected)
20
40
60
80
100
120
20
40
60
80
100
120
0
2.25
4.5
6.75
9(Max)
Inf

(b)

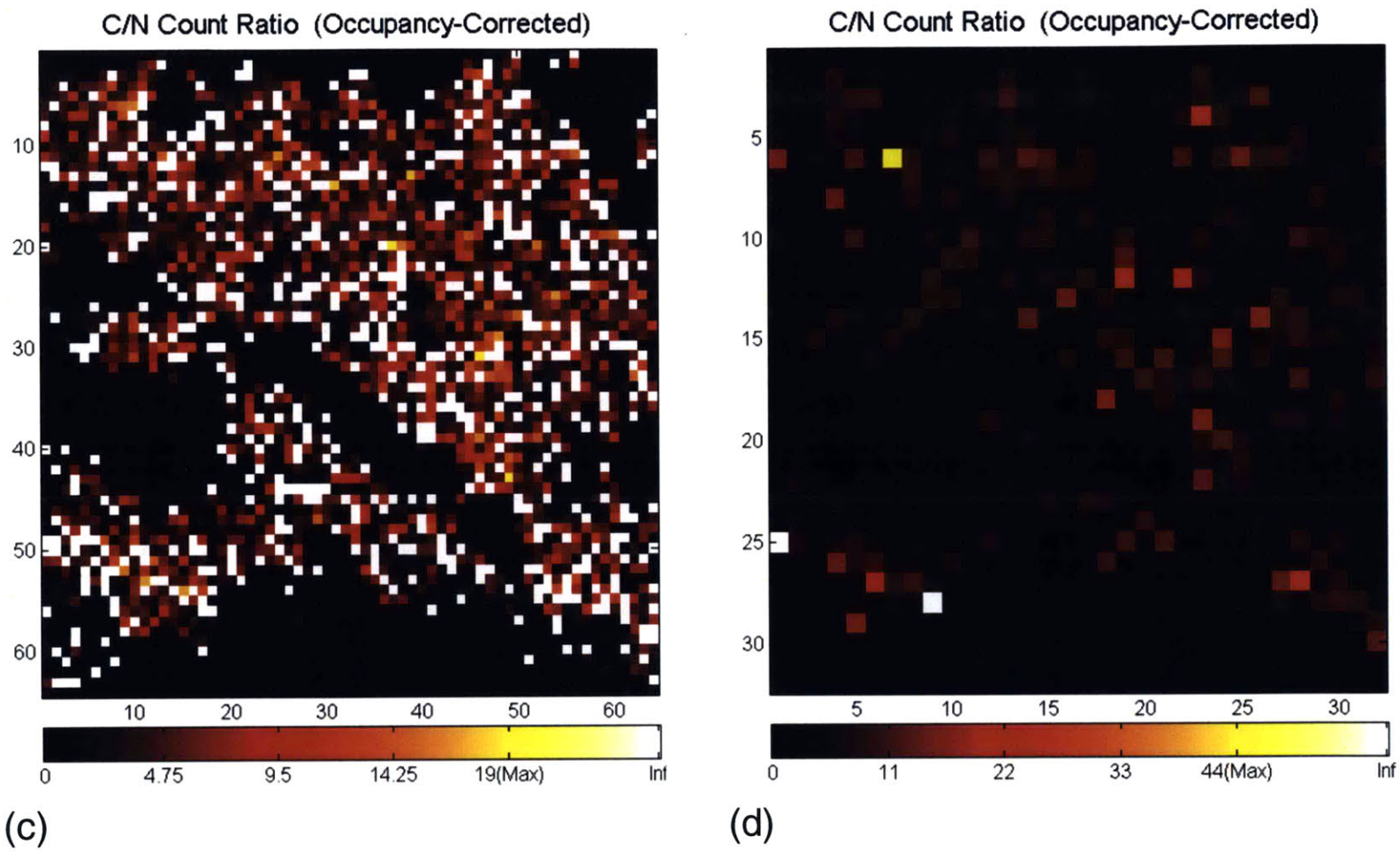

Figure 10 - 24. C/N atomic ratio of a soot-rich region at 4 different resolutions (occupancy-filtered).

C/N atomic ratio of a soot-abundant region (sample 20061013-Site#3) with occupancy filtering at 4 different resolutions: (a) without pixel consolidation (256 x 256 cells), (b) 4 pixels consolidated into 1 (128 x 128 cells), (c) 16 pixels consolidated into 1 (64 x 64 cells), and (d) 64 pixels consolidated into 1 (32 x 32 cells). White spots indicate C/N ratio of approaching infinity (i.e., 'graphitic spots'). Dark spots indicate the absence of C X-rays.

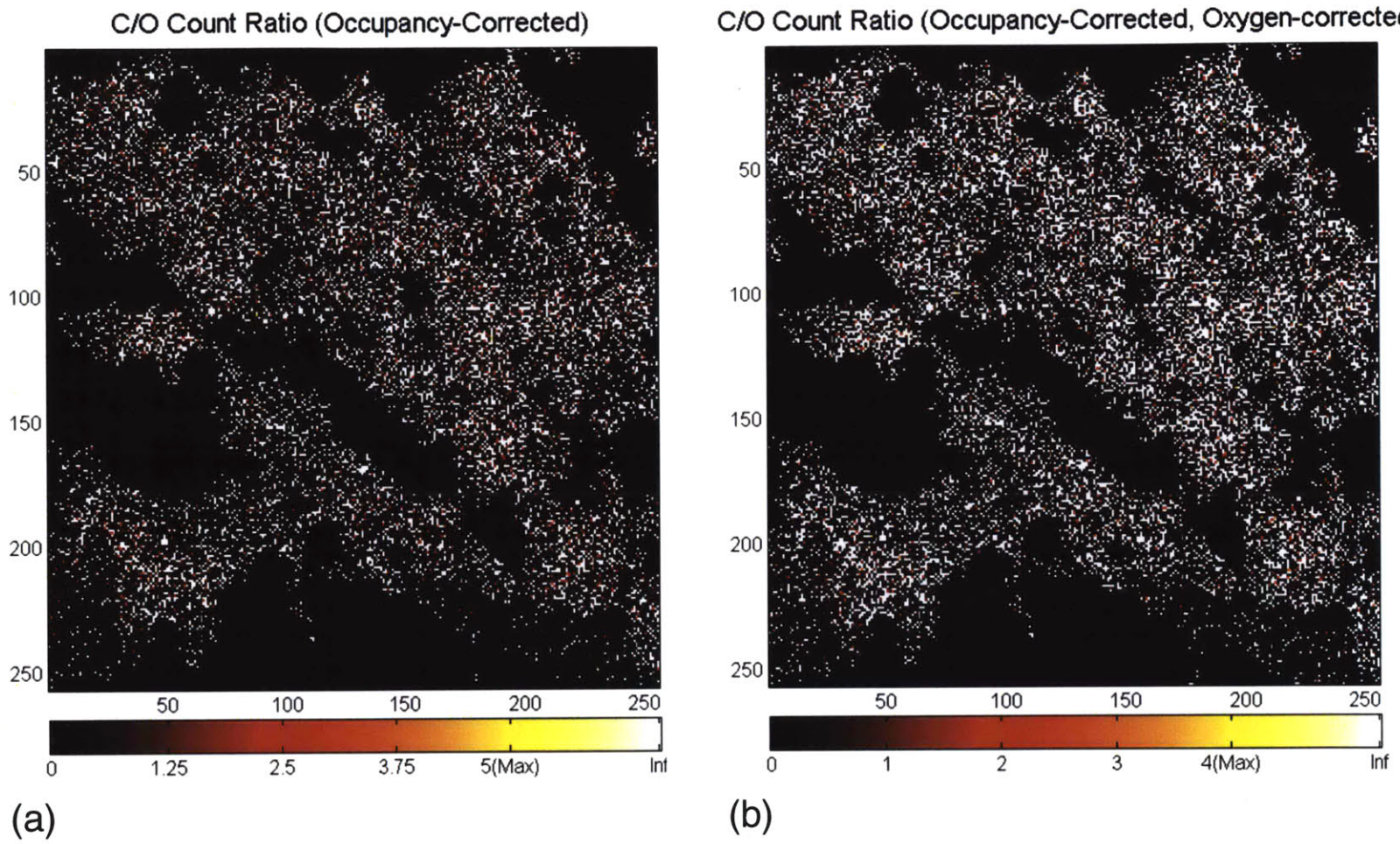

Figure 10 - 25. C/O atomic ratio of a soot-rich region with and without O-correction (occupancy-filtered).

C/O atomic ratio of a soot-abundant region (sample 20061013-Site#3) with occupancy filtering: (a) without correction for background O, (b) with background O correction. Both images were obtained without pixel consolidation (i.e., 256 x 256 cells). White spots indicate C/O ratio of approaching infinity (i.e., 'graphitic spots'). Dark spots indicate the absence of C X-rays.

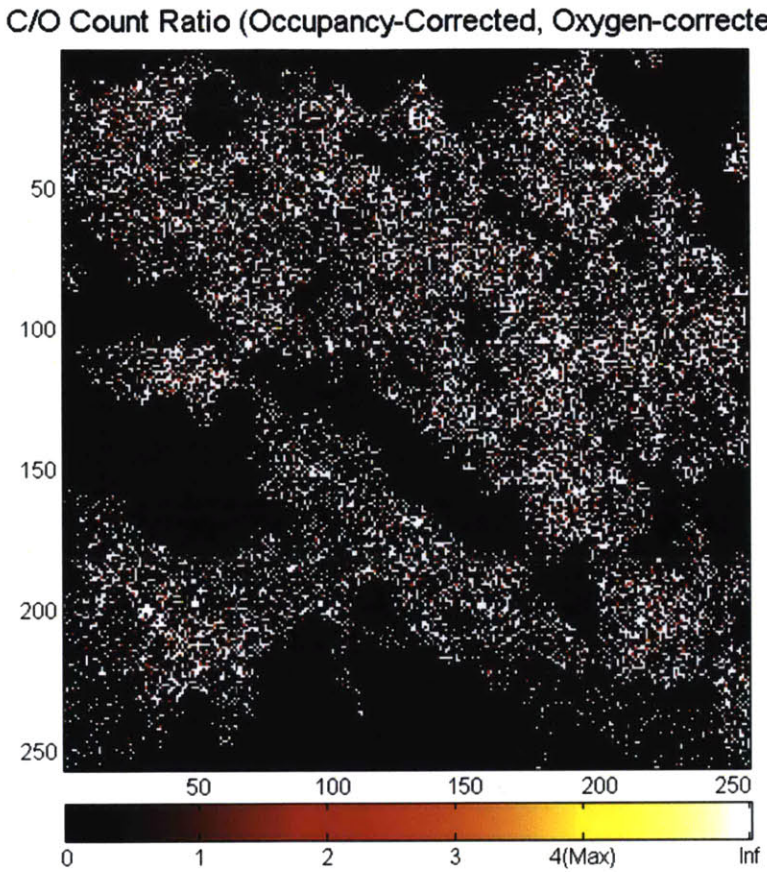
C/O Count Ratio (Occupancy-Corrected, Oxygen-corrected)
50
100
150
200
250
50
100
150
200
250
0
1
2
3
4(Max)
Inf

(a)

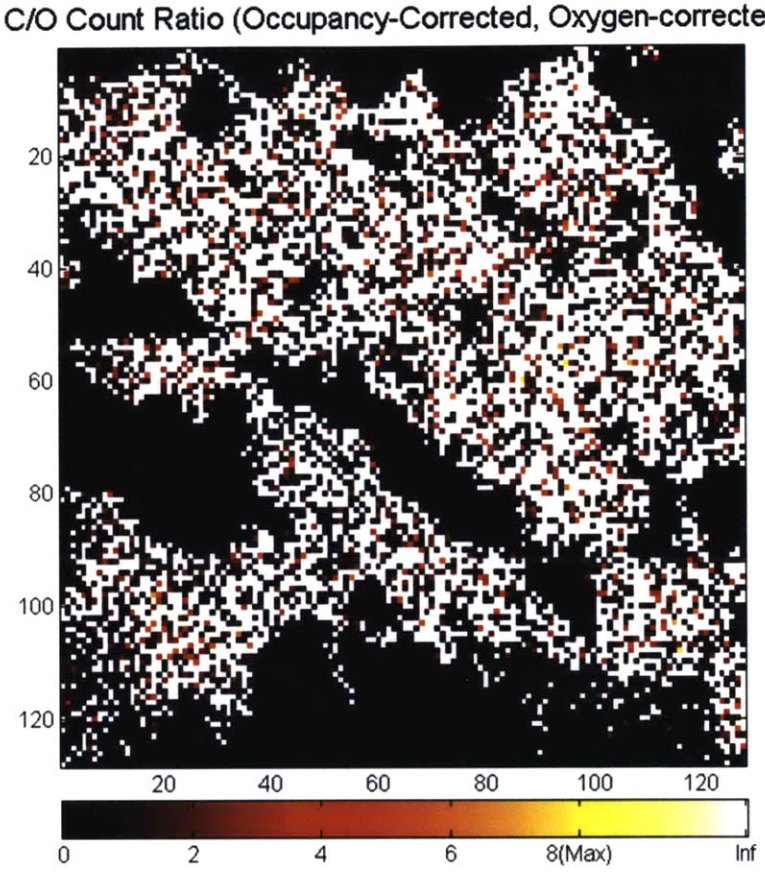
C/O Count Ratio (Occupancy-Corrected, Oxygen-corrected)
20
40
60
80
100
120
20
40
60
80
100
120
0
2
4
6
8(Max)
Inf

(b)

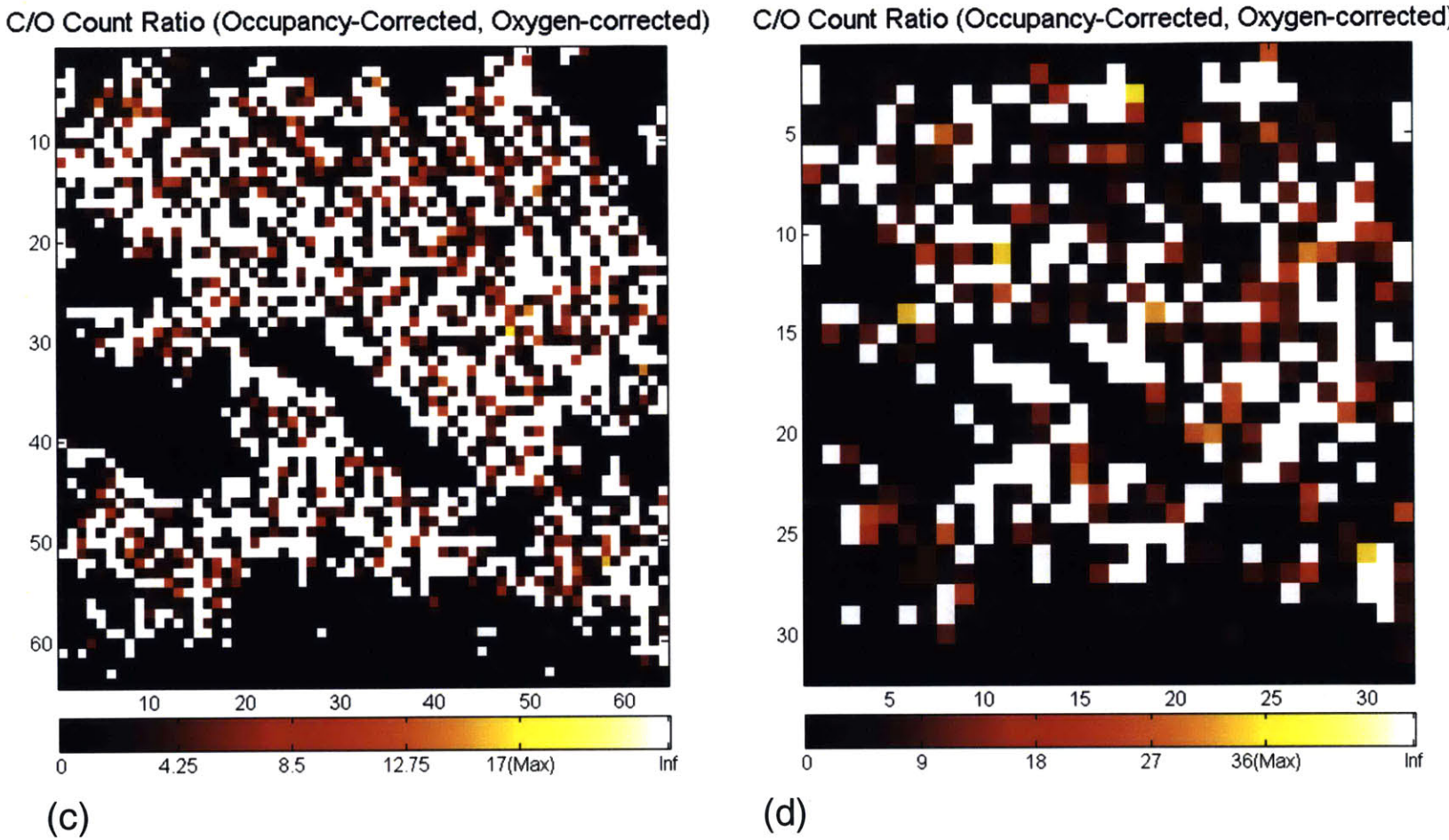

Figure 10 - 26. C/O atomic ratio of a soot-rich region at 4 different resolutions (occupancy-filtered, O-corrected).

C/O atomic ratio of a soot-abundant region (sample 20061013-Site#3) with occupancy filtering at 4 different resolutions: (a) without pixel consolidation (256 x 256 cells), (b) 4 pixels consolidated into 1 (128 x 128 cells), (c) 16 pixels consolidated into 1 (64 x 64 cells), and (d) 64 pixels consolidated into 1 (32 x 32 cells). White spots indicate C/O ratio of approaching infinity (i.e., 'graphitic spots'). Dark spots indicate the absence of C X-rays.

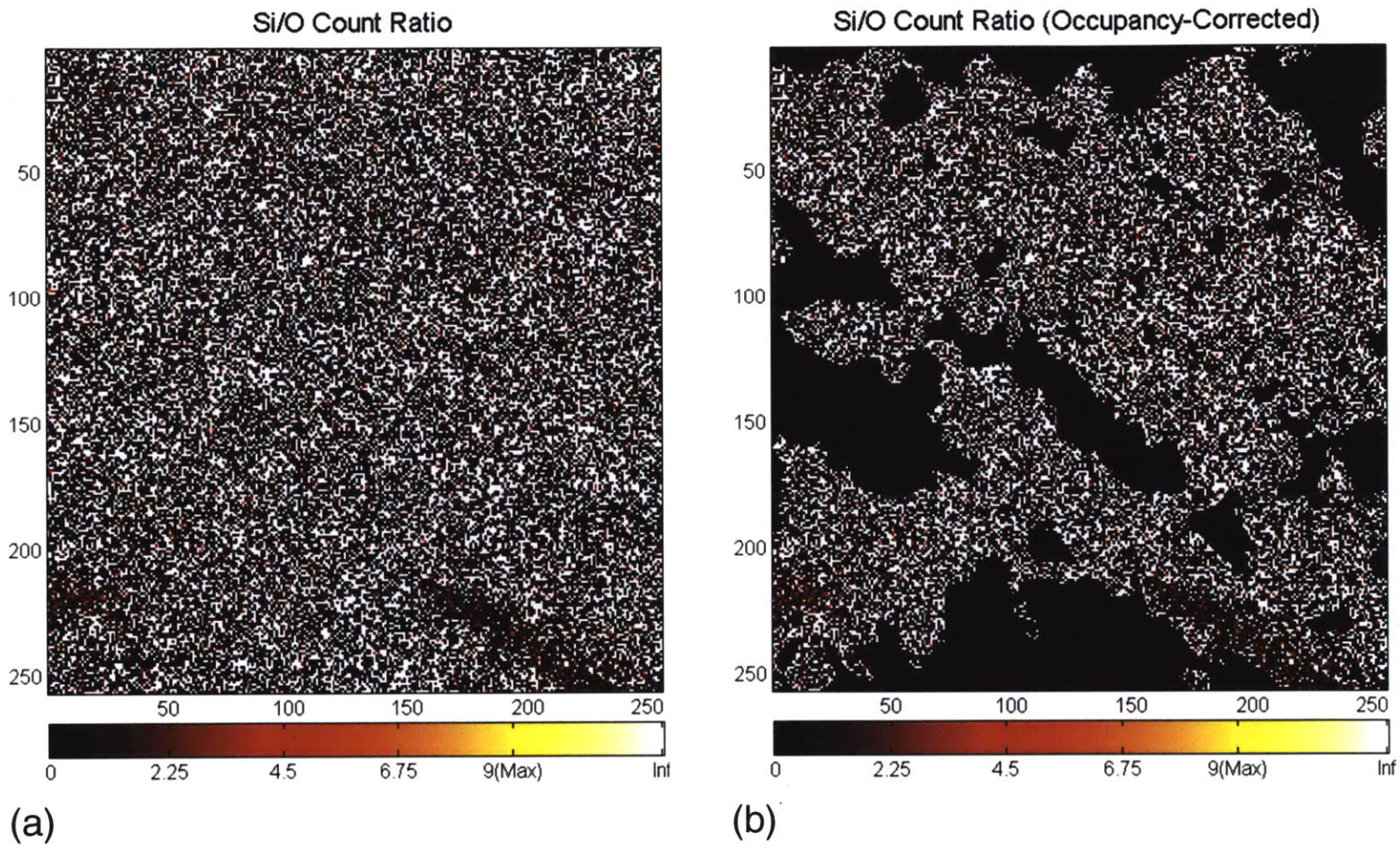

Figure 10 - 27. Si/O atomic ratio of a soot-rich region with and without occupancy filtering.

Si/O atomic ratio of a soot-abundant region (sample 20061013-Site#3): (a) without correction for occupancy, (b) with correction for occupancy. Both images were obtained without pixel consolidation (i.e., 256 x 256 cells). White spots indicate Si/O ratio of approaching infinity. Dark spots indicate the absence of Si X-rays.

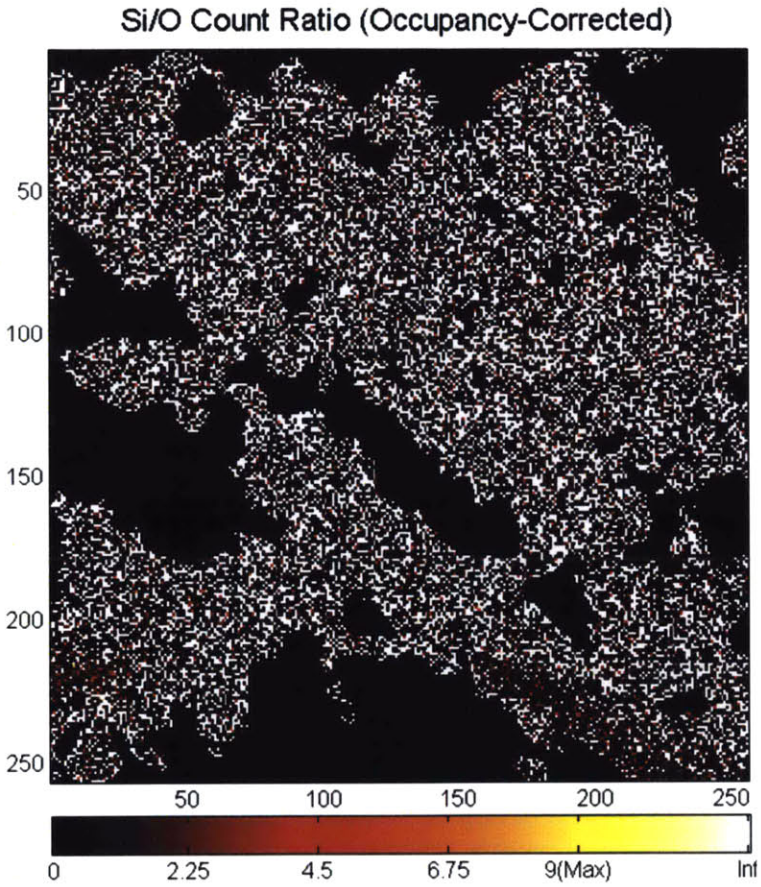
Si/O Count Ratio (Occupancy-Corrected)
50
100
150
200
250
50
100
150
200
250
0
2.25
4.5
6.75
9(Max)
Inf

(a)

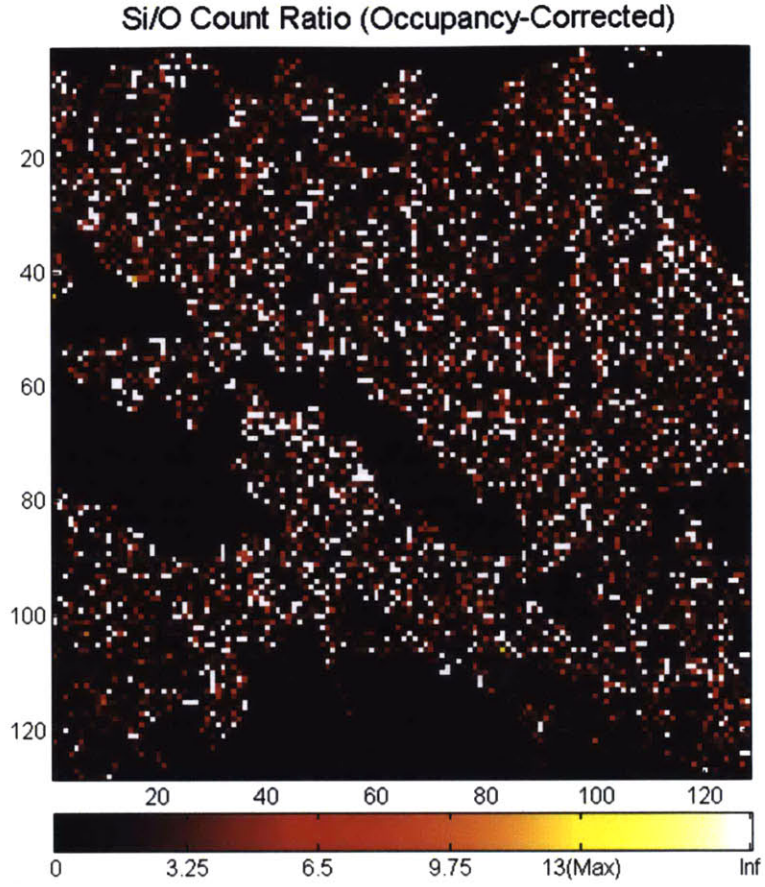
Si/O Count Ratio (Occupancy-Corrected)
20
40
60
80
100
120
20
40
60
80
100
120
0
3.25
6.5
9.75
13(Max)
Inf

(b)

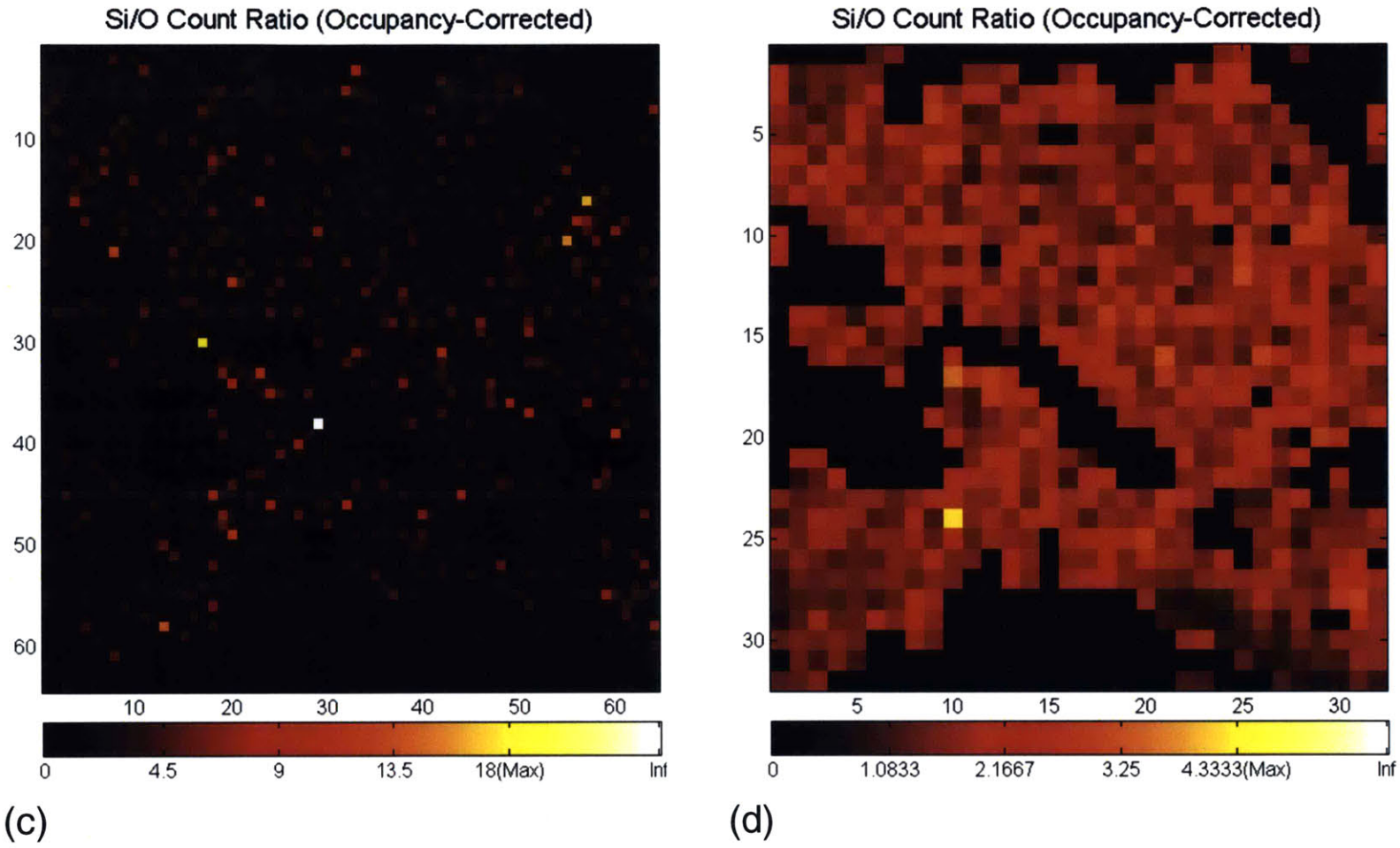

Figure 10 - 28. Si/O atomic ratio of a soot-rich region at 4 different resolutions (occupancy-filtered).

Si/O atomic ratio of a soot-abundant region (sample 20061013-Site#3) with occupancy filtering at 4 different resolutions: (a) without pixel consolidation (256 x 256 cells), (b) 4 pixels consolidated into 1 (128 x 128 cells), (c) 16 pixels consolidated into 1 (64 x 64 cells), and (d) 64 pixels consolidated into 1 (32 x 32 cells). White spots indicate Si/O ratio of approaching infinity. Dark spots indicate the absence of Si X-rays.

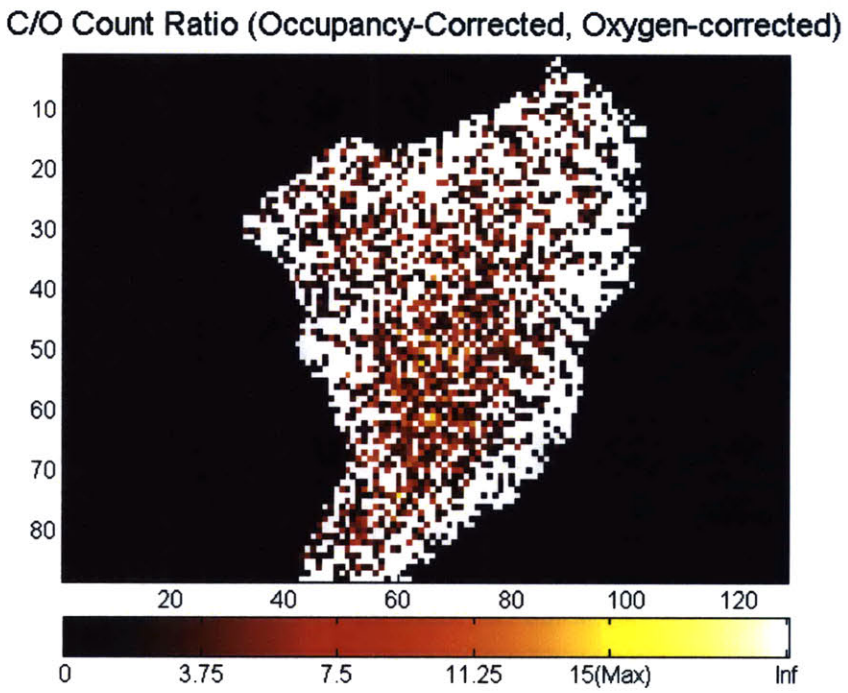
C/O Count Ratio (Occupancy-Corrected, Oxygen-corrected)
10
20
30
40
50
60
70
80
20
40
60
80
100
120
0
3.75
7.5
11.25
15(Max)
Inf

(a)

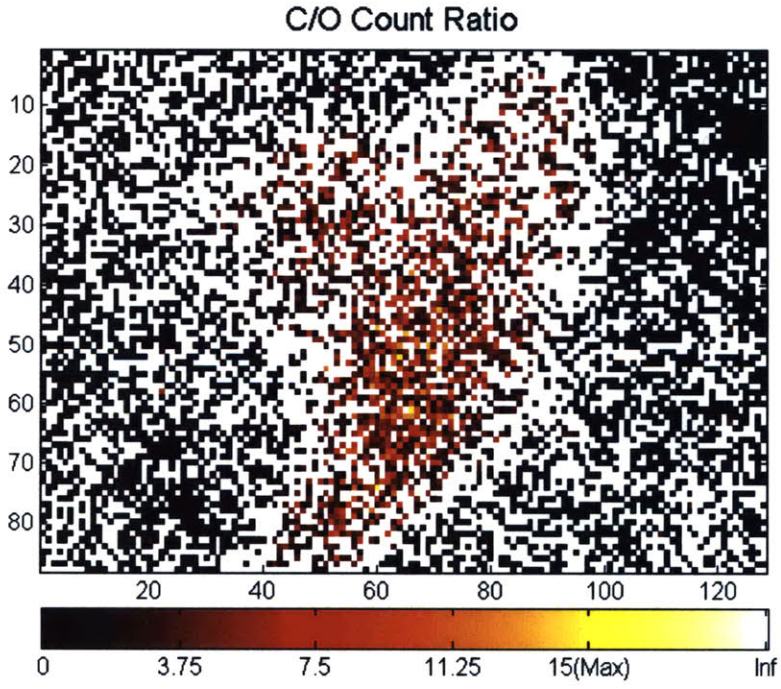
C/O Count Ratio
10
20
30
40
50
60
70
80
20
40
60
80
100
120
0
3.75
7.5
11.25
15(Max)
Inf

(b)

Figure 10 - 29. C/O map of a char particle (a-b)

Figure (a) shows the C/O map of a char particle (Lignocellulosic char site #1) with correction on background-O signals and removal of non-sample region (i.e. occupancy filtering). Figure (b) is the C/O map of the same char particle before any signal filtering or correction, showing the exclusive presence of O signals on char particle.

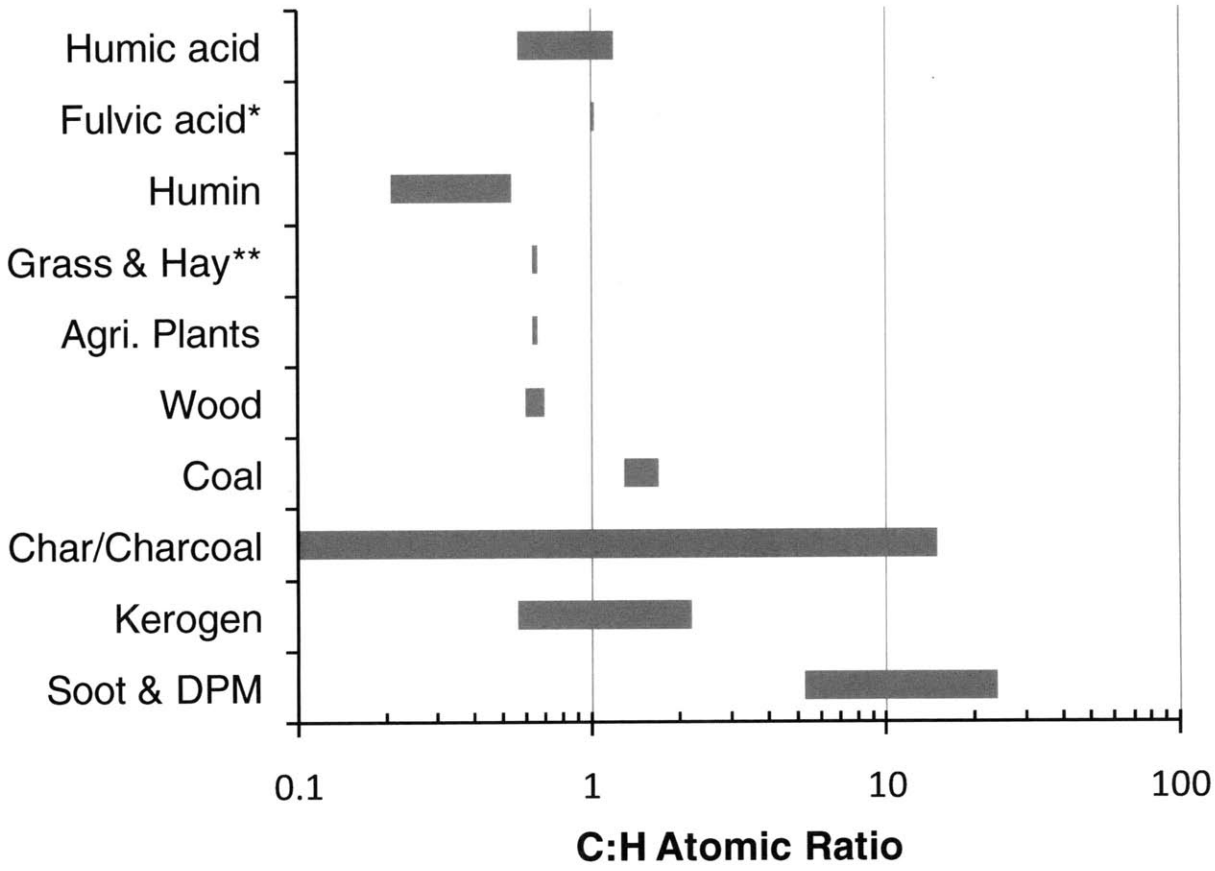

Figure 10 - 30. Elemental atomic ratios (C-H-N-O) of various carbonaceous matters.

Figure 10 - 30a. C:H atomic ratios of various carbonaceous matters.

Range values for the different categories are summarized in Table 10-9.

*, **: Note that the ratios for Fulvic acid and Grass & Hay were found to be 1 and 0.63, respectively.

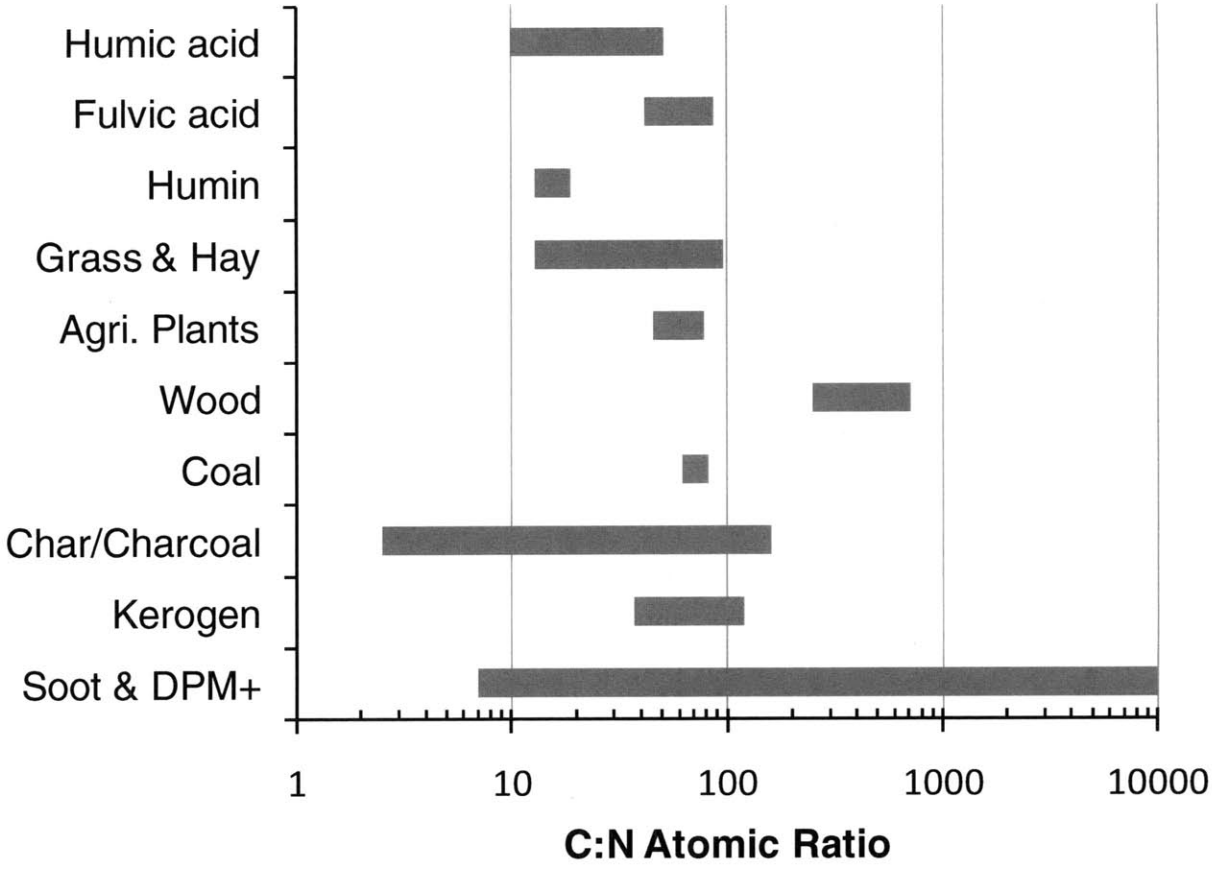

Figure 10 - 30b. C:N atomic ratios of various carbonaceous matters.

Range values for the different categories are summarized in Table 10-9.

+: Note that for one sample in the soot & DPM (diesel particulate matter) category, a C:N ratio of approaching infinity was reported, so the bar should extend beyond 10^4.

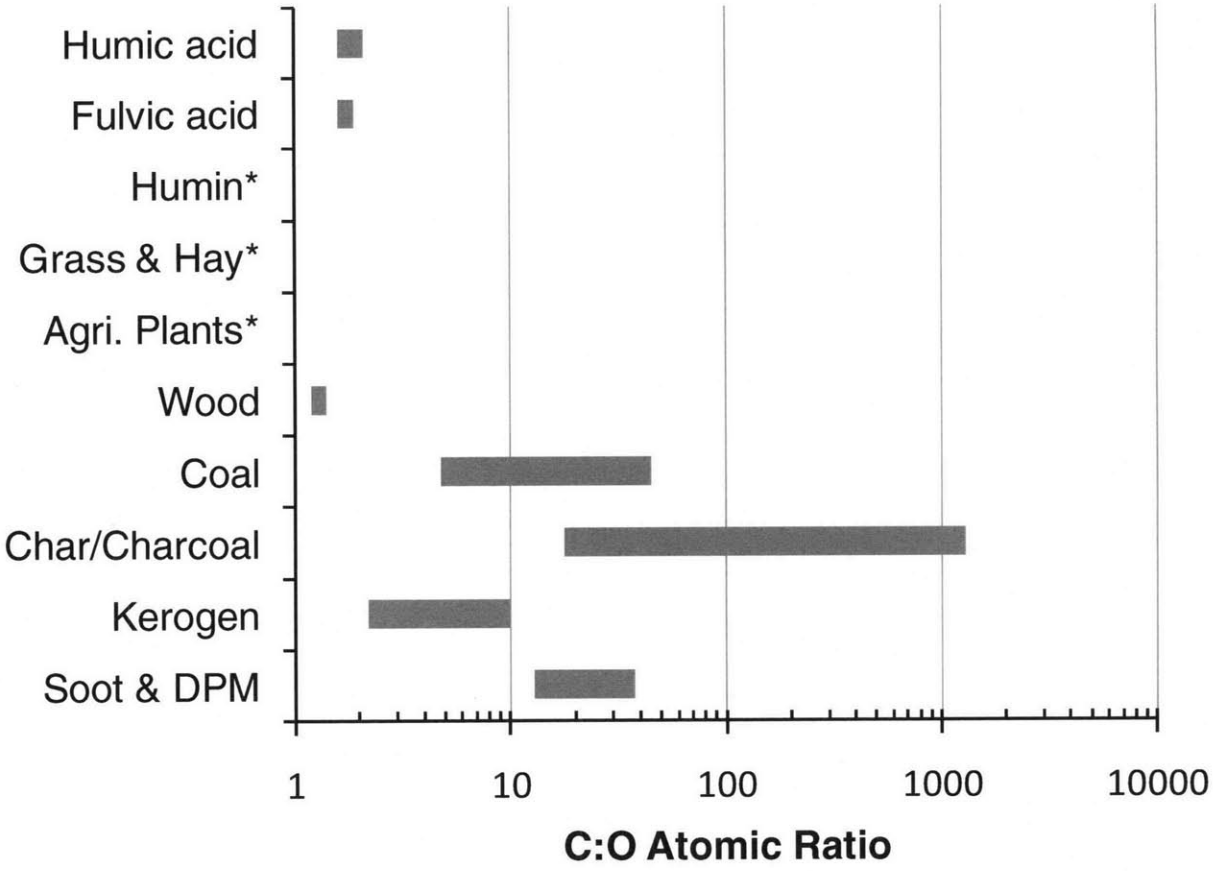

Figure 10 - 30c. C:O atomic ratios of various carbonaceous matters.

Range values for the different categories are summarized in Table 10-9.

*: Not available.

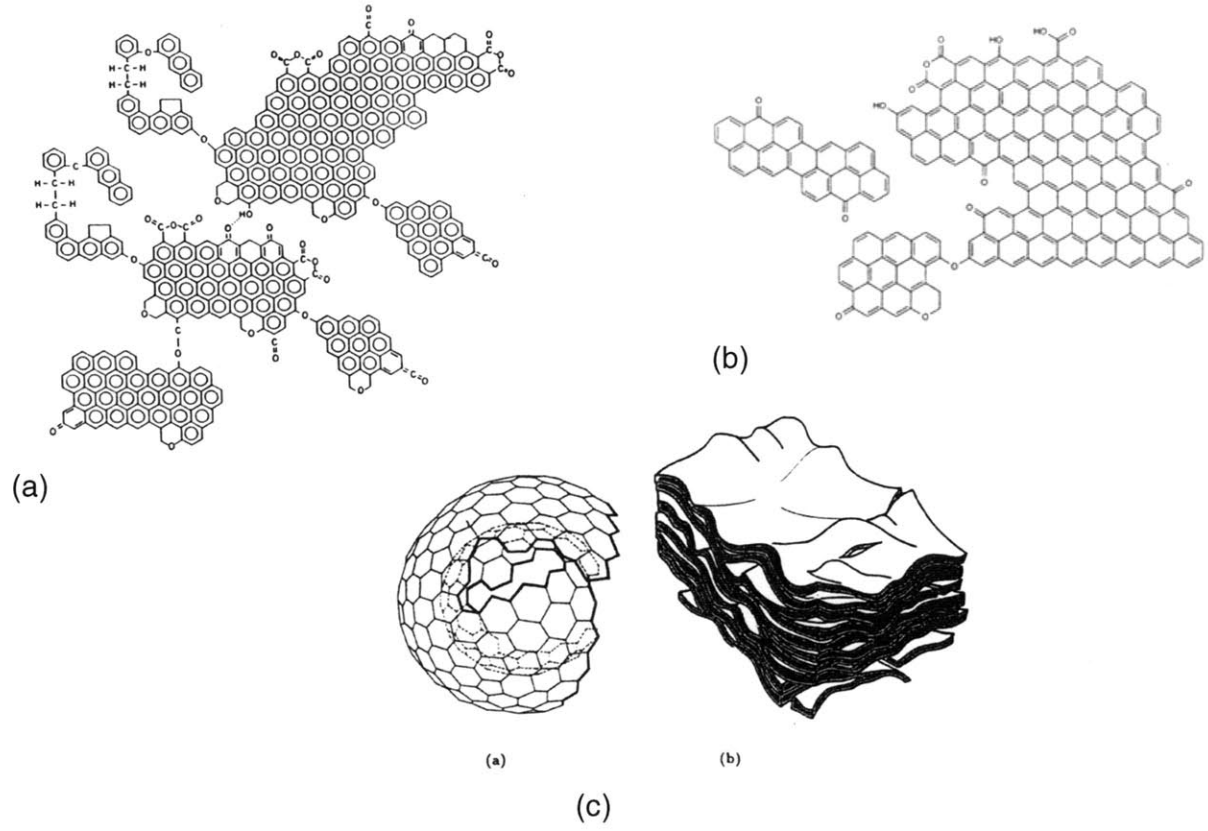

Figure 10 - 31. Structure of hexane soot.

The structural unit of a soot particle is a single sheet of predominantly aromatic structure, with minor presence of non-carbon elements such as O, N, and H at the edge, as shown in (a) (Akhter et al., 1985) and (b) (Sergides et al., 1987). The condensed sheets are consolidated in layers to form a concentric onion-like structure as in (c) (Dunne et al., 1997), which is a single soot particle. All figures are from the original publications.

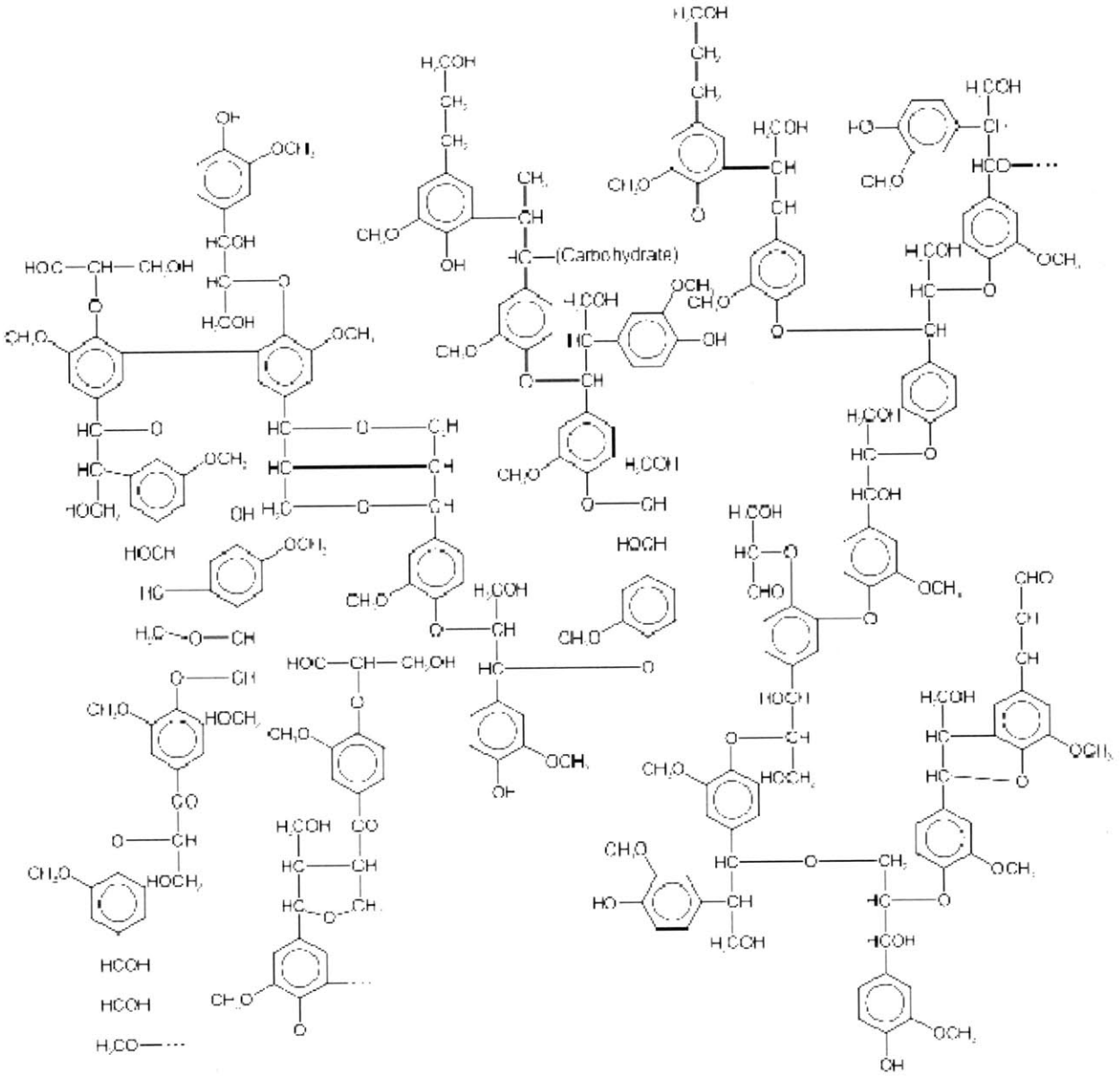

Figure 10 - 32. Structure of lignin.

From Glazer et al. 1995.

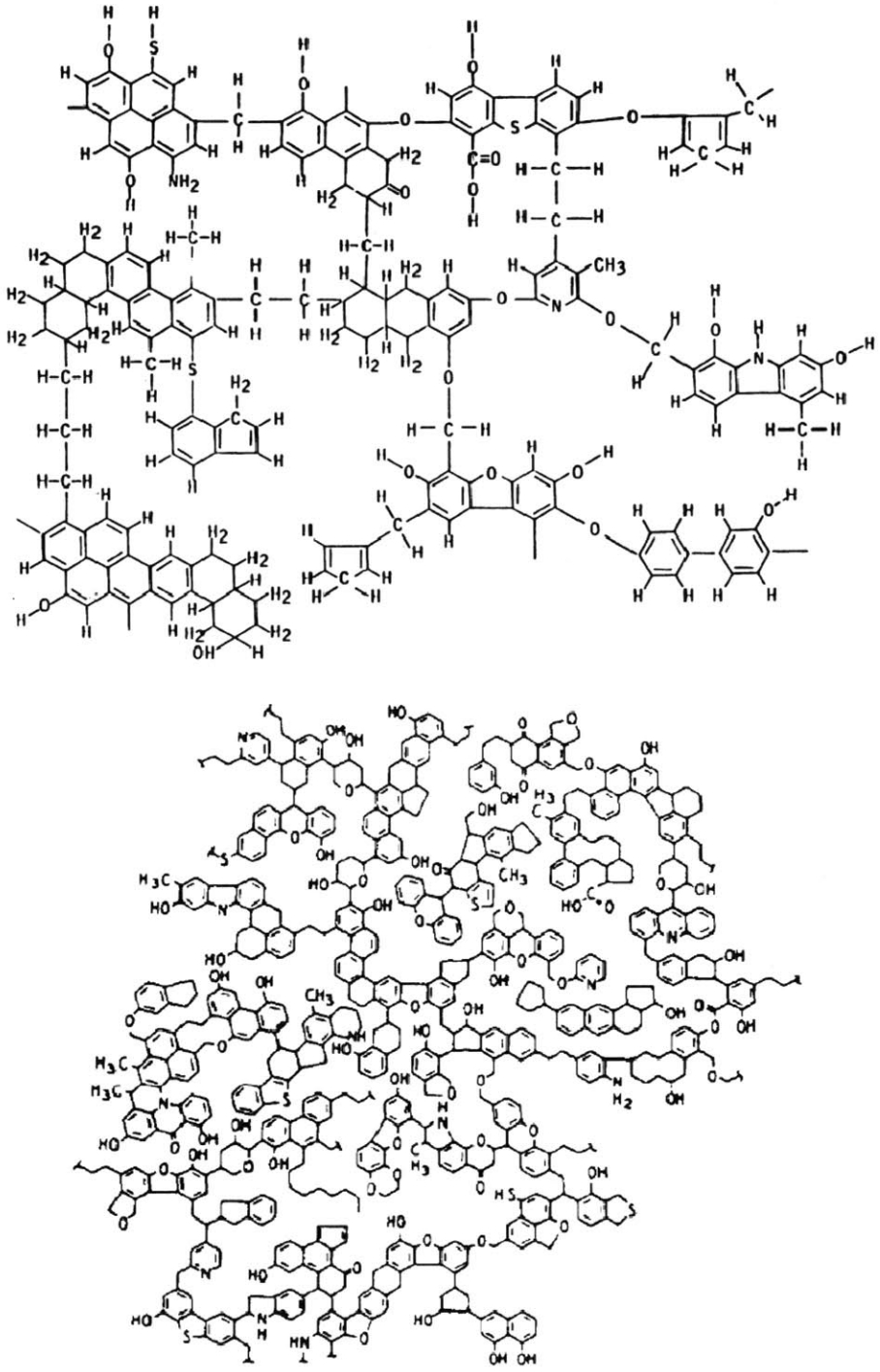

Figure 10 - 33. Conceptual structure of bituminous coal.

Upper from Levine et al. 1982 and reference within; lower from Haenel 1992 and reference within.

Chapter 11: Figures

Figure 11 - 1. Future Work: estimating total suspended solids from tidal-induced shearing of sediment bed.....534

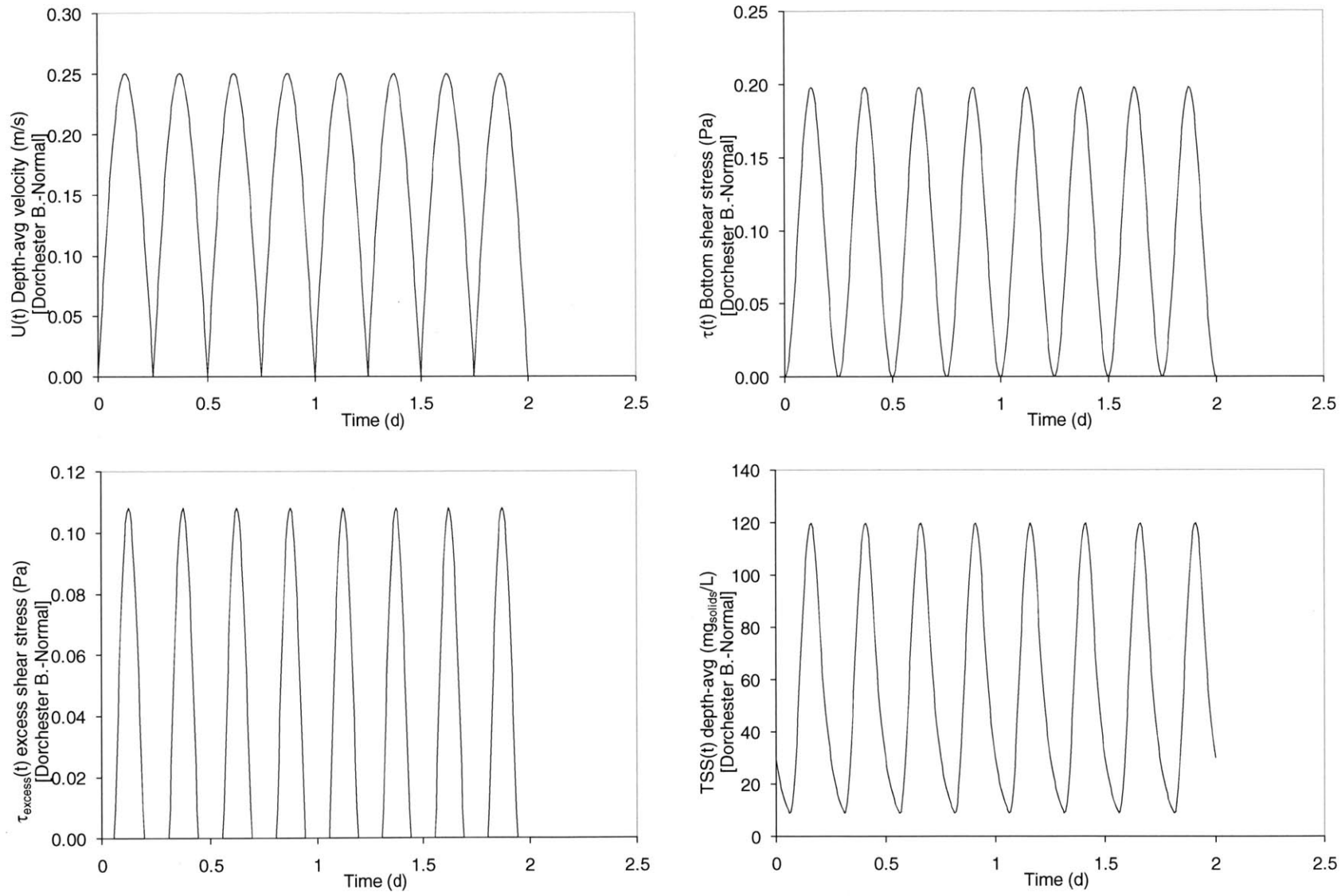

Figure 11 - 1. Future Work: estimating total suspended solids from tidal-induced shearing of sediment bed.

Chapter 1: Tables

Table 1 - 1. Sedimentary PAHs in Harbors/Estuaries near Urbanized Regions. **537**
Table 1 - 2. Sediment PAHs Quality Guidelines. **539**
Table 1 - 3. Some Recent Lawsuits related to Pollution by Xenobiotics. **540**
Table 1 - 4. Adverse effects of PAHs on Aquatic Organisms. **541**
Table 1 - 5. 'Criteria' for Constructing HOC Kinetic and Equilibrium Models. **541**
Table 1 - 6. Qualitative Contrasts between 'Soft' and 'Hard' Carbon. **542**

Table 1 - 1. Sedimentary PAHs in Harbors/Estuaries near Urbanized Regions.

Water Body	ΣPAHs ($\mu g/kg_{solids}$)	pyrene ($\mu g_{pyr}/kg_{solids}$)	Reference
North America			
Estuary, Lake			
Baltimore Harbor (MD)	(90)–46000		Ashley et al. 1999
Casco Bay (ME)	(20)–21000	1600	Kennicutt et al. 1994
Kitimat fjord, BC, Canada	(300)–10000000		Simpson et al. 1996
Naragansett Bay (RI)	(570)–220000		Hartmann et al. 2004
Lake Michigan	50-400	<5-30	Kannan et al. 2001
River			
Lower Rouge River	7500–44000	600–3500	Kannan et al. 2001
Newtown/Piles Creek	50000–100000	4000–6000	Rockne et al. 2002
Upper Detroit River	500–36000	40–2900	Kannan et al. 2001
South America			
Salina Cruz Harbor, Mexico	(30)–3200	(<10)–400	Botello et al. 1998
Santos, SP, Brazil	(80)–42000		Nishigima et al. 2001
Europe			
Estuary, Lake			
N. Irish	80–23000	3–2400	Guinan et al. 2001
Tamar (Eng.)	4900–7400	710–1100	Woodhead et al. 1999
Tyne + Wear River (Eng.)	210–43000	30–5900	Woodhead et al. 1999
Severn River/Port Talbot (Eng.)	5400–7100	600–940	Woodhead et al. 1999
Gironde (France)	20–4900	2–390	Budzinski et al. 1997
Petrol Harbor, Netherlands	1000000	200000	Cornelissen et al. 1998
Wemeldinge, Netherlands	40000		Cornelissen et al. 1998
Port of Bilbao, Spain	10000–70000		Casado-Martinez et al. 2006
Port of Coruna, Spain	2000–7000		Casado-Martinez et al. 2006
Santander Bay, Spain	(20)–340000	(<10)–45000	Viguri et al. 2002
Venice (lagoon), Italy	16000–21000		Giordano et al. 2005
Asia			
Bangkok, Thailand	500–8500		Boonyatumanond et al. 2006
Dongjiang, Xijing, Zhujiang, Canton, China	1000–6800		Luo et al. 2008
Hsin-ta Harbor, Taiwan	1200–3400		Fang et al. 2003
Hangzhou	(130)–7300	10–1500	Chen et al. 2004
Osaka Port, Japan	1000–2500**		Obana et al. 1981
Victoria Harbor, Hong	3000–450000	170–6000	Hong et al. 1995

Kong			
Shanghai, China	100–2000		Ying et al. 2008
Singapore	13000–94000	(480)-23000	Basheer et al. 2003b
Sunderban, India	(100) – 2600		Binelli et al. 2008
Xiamen Harbor, China	3000–61000	10–30	Hong et al. 1995
Yamuna River, Dehli India	9000–23000	200-5000	Agarwal et al. 2006
Africa			
Estuary, Lake			
Gulf of Suez	1000000–1600000	60000–140000	Ibrahim 2004
Dar es Salaam, Tanzania	(80)–25000		Gaspare et al. 2009
Niger Delta, Nigeria	(0.1–30)		Anyakora et al. 2005
	(20–70)		Olajire et al. 2005
Oceania			
Sydney Harbor, Australia	(<100)–380000		McCready et al. 2000
Open Sea			
Baltic Sea	(10)–2000	(<1)–110	Witt 1995
Black Sea	(30)–640	(<1)–160	Readman et al. 2002
Central Indian Basin, India	50000–150000*		Chernova et al. 1999
Pearl River Estuary (offshore)	700–1100		Luo et al. 2008
South China Sea	140–500		Luo et al. 2008
Gulf of Trieste, Adriatic Sea	30–680		Notar et al. 2001
	20–500		Magi et al. 2002

*: Total aromatic carbons instead of total PAHs.
**: PAHs with ≥4 rings.

Table 1 - 2. Sediment PAHs Quality Guidelines.

Guideline*	SLC (µg/kg)	ISQG (µg/kg)	TEC/TEL (µg/kg)	PEC/PEL (µg/kg)	ERL (µg/kg)	ERM (µg/kg)
Governmental Agencies						
Canadian	2000[3]	500–800[1]		7000[1]		
NOAA[2]			1000		2500	
Academic Publications						
Long et al. 1995					3500	23000
MacDonald et al. 1996			900	7000		
Swartz 1999	4000[2]		2900	18000		

*: ERL=Effect range-low ERM=Effect range-median ISQG=Interim sediment quality guideline
PEC/PEL=Probable effect concentation/level SLC=Screening level concentration
TEC/TEL=Threshold effect concentation/level.
1: Canadian Council of Ministers of the Environment 1999.
2: According to Burton 2002.
3: Ontario minimum environmental screening level-low. According to Burton 2002.

Table 1 - 3. Some Recent Lawsuits related to Pollution by Xenobiotics.

Chemicals	Harm claimed	Legal Parties	Penality Status
Dibromochloropropoane (DBCP; pesticide)[1]	Human Sterility	banana plantation workers vs Dow Chemicals and Dole vs (2009)	$ 97 mil.
Atrazine, Endosulfan (herbicides)[2]	Bioaccumulation in polar bears	Center for Biological Diversity vs U.S. EPA (2009)	on-going
Perfluorooctanoate (PFOA)[3]	Drinking well contamination	NJ county people vs Dupont (2009)	on-going
Vinyl chloride[4]	Cancer & neurological disorder	U.S.A. vs Colorite Specialty Resins (2008)	$ 2.3 mil.
Ozone depleting substances (ODS)[5]	Ozone depletion	U.S.A. vs Equistar Chemicals (2007)	$ 125 mil.
Chlorpyrifos (insecticide)[6]	Health Hazard	Farm workers vs US EPA	on-going
Diacetyl (food flavor)[7]	Respiratory diseases (bronchiolitis oblisterans)	Workers vs companies 2002-2007	$ 100 mil.

1: United States District Court, Southern District of Florida, Case No.: 07-22693-CIV-HUCK.
2: *U.S. lawsuit targets pesticide impact on polar bears*, Reuter, Dec 3, 2009.
3: United States District Court, District of New Jersey, Civil No.: 06-1810 (RMB).
4: United States District Court, District of New Jersey, Civil No.: 08-cv-4132 (RBK).
5: United States District Court, Northern District of Illinois.
6: United States District Court, Northern District of California.
7: www.kerrysteigerwalt.com/public/chemical-exposure/diacetyl.html

Table 1 - 4. Adverse effects of PAHs on Aquatic Organisms.

Adverse Effect	Reference
PAHs	
Affect benthic communities at multiple trophic levels	Catallo et al. 1987
Cell membrane disruption (narcosis)	Di Toro et al. 2000
Disturb drift dynamics of benthic invertebrates	Fairchild et al. 1987
DNA modification (formation of DNA-PAH adducts)	Kleinjans et al. 2002
Formation of reactive metabolic intermediates	
aryl hydrocarbon receptor (AHR)	Incardona et al. 2006
photo-modified intermediates (e.g. $^1O_2$)	Lampi et al. 2006
Reproductive/developmental disruption	
developmental failures	Incardona et al. 2006
reduced egg output	Hoffmann et al. 2006
Generic HOCs	
Disrupt aggregate behavior and survival of phytoplankton, zooplankton, algae, diatoms, weeds	Acey et al. 1987; Crompton 1997
Induce tumor development	Baumann et al. 1987
Interfere metabolic activities in fish	Tana 1988

Table 1 - 5. 'Criteria' for Constructing HOC Kinetic and Equilibrium Models.

'Criteria'	Example/Explanation
For HOC Sorption Equilibrium (isotherm)	
(i) continuum of sorbent organic compartment/matter	e.g. OC, BC
(ii) an adequately wide concentration range	
(iii) covers realistic concentration levels	
(iv) adequate equilibration time	t_{eqm}=f(temperature, OC/BC, R_{sw}, sorbate, etc)
For HOC Desorption Kinetics	
(i) native or spiked HOCs	
(ii) particle/aggregate size distribution	
(iii) solids-to-water ratio	
(iv) sorbent organic component/matter	
(v) sorption isotherm	
[*(vi) kinetic correction – if secondary uptake medium has been used for sampling*]	e.g. SPME, Tenax

Table 1 - 6. Qualitative Contrasts between 'Soft' and 'Hard' Carbon.

Descriptors	'Soft' Carbon	'Hard' Carbon
FORMATION		
Origin	Bio-derived ('living')	Geo-derived ('dead')
Formation conditions	Mild T & P	Harsh T & P
STRUCTURE		
Density	Low	High
O, N, S content	High	Low
Intra-structural mobility	Somewhat mobile	Restricted
Intra-structural order	Disordered (Amorphous)	Ordered (Crystalline)
Structural rigidity	Flexible	Rigid
OPTICAL PROPERTIES		
Color	Light	Dark
Heat absorption	Poor	Good
Light reflection	Good	Poor
PERSISTENCE		
Biodegradability	High	Low
Oxidation resistance	Low	High
Reactivity	Homogeneous (volume)	Heterogeneous (surface area)
Thermal resistance	Low	High
Turnover time	Short	Long
SORPTION OF ORGANIC COMPOUNDS		
Sorption capacity	Low	High
Sorption mode	Absorption	Adsorption

Chapter 2: Tables

Table 2 - 1. Relative intensities at characteristic pyrene fluorescence emission wavelengths by time-gated LIF[a] **544**
Table 2 - 2. Probe distance in LIF. **544**
Table 2 - 3. Test for monotonic increase in LIF signal over time[a] **545**
Table 2 - 4. % Reduction in pyrene fluorescence due to inner-filter effects. **545**
Table 2 - 5. Supernatants analyses by GC-MS and LIF[a] **546**
Table 2 - 6. Solid-associated and dissolved pyrene concentrations before and after desorption (110-240d)[a]. **547**
Table 2 - 7. Typical suspended-solids concentrations observed in estuaries, harbors, and tributaries. **548**

Table 2 - 1. Relative intensities at characteristic pyrene fluorescence emission wavelengths by time-gated LIF[a].

Characteristic $\lambda_{ems,Pyr}$ (nm)[b]	50 ng Pyr/L standard	20 ng Pyr/L standard
366	53%	73%
378	67%	69%
387	100%	100%
400	68%	67%
405-410[c]	61%	74%

a: Relative intensities are calculated by normalizing individual peak height, determined from filtered signals, to that at λ_{ems}=387 nm.
b: Characteristic emission wavelengths of pyrene.
c: Peak location ambiguous. See Figure 2-2.

Table 2 - 2. Probe distance in LIF.

Probe distance (tip of LIF probe to surface of mud layer made of 38<<75 um fraction).

Probe distance (cm)	Pyrene LIF (counts)	Std. Dev. (counts)
1	7240	2150
2	4440	250
4	4190	180
8	4160	380
10	4180	220

T-test statistics for LIF responses at different probing distance[a].

Probing distance (cm)	2	4	8	10
1[b]	-3.44	-3.75	-3.75	-3.76
2		2.14	1.63	2.09
4			0.22	0.13
8				-0.13

a: The $t_{critical}$ (2-end test, degree of freedom = 12) at significance levels of 10%, 5%, and 1% are 1.78, 2.18, and 3.06, respectively.
b: Since all t statistics between 1-cm and other distances are greater than $t_{critical}$=3.06, the LIF response at a probing distance of 1 cm is significantly different from those at greater distances. The LIF responses at 2, 4, 8, and 10 cm are statistically identical at a significance level of 5%.

Table 2 - 3. Test for monotonic increase in LIF signal over time[a].

Sediment suspensions			Pyrene standards		
[Pyrene][b] (ng/L)	Kendall τ[c]	H_o: τ=0 (α=20%)[d]	[Pyrene] (ng/L)	Kendall τ	H_o: τ=0 (α=20%)
1.2±1.2 (1^{st} min)	0.81	reject	1.0±0.3	–0.33	accept
3.1±0.5 (10^{th} min)	0.52	reject	3.5±0.3	–0.048	accept
5.9±0.7 (117^{th} min)	0.33	accept	6.2±0.3	–0.14	accept
10.2±0.6 (313^{th} hr)	–0.47	accept	10.6±0.8	–0.33	accept

a: For size fraction 38-75 um, at R_{sw}=290 mg solids/L. Data points in sediment suspensions were selected such that the mean values were close to those of the pyrene standards.

b: ± 1 standard deviation.

c: Kendall Ranking test evaluates if there is a trend between two sets of observations (here, observations are i^{th} min and dissolved pyrene levels). The Kendall Ranking τ computed according to Sheskin, D. J. *Handbook of parametric and nonparametric statistical procedures*. 2004, Chapman & Hall/CRC, Boca Raton, pp 1-1193.

d: Null hypothesis claiming no trend in LIF measurement over time. τ was tested against critical τ for a two-tailed test, with the hypothesis accepted as true when $\tau<\tau_{crit}$.

Table 2 - 4. % Reduction in pyrene fluorescence due to inner-filter effects.

R_{sw} (mg_{solids}/L)[a]	% $Reduced_{Settled}$[b]	% $Reduced_{Resuspended}$[c]
0	0%	0%
20	<1%	1%
70	1%	2%
280	3%	8%

a: For the finest sediment fraction (38-75um), with L=4cm, $(\varepsilon_{exc}+\varepsilon_{ems})C_{pyr}=3.4\times10^{-6}$abs.$cm^{-1}$.

b: Measured after suspensions were settled for 5-10min. $\alpha_{exc}/R_{sw}=2.0\times10^{-4}$, $\alpha_{ems}/R_{sw}=1.7\times10^{-4}$ (abs.L.$mg_{solids}^{-1}cm^{-1}$).

c: Measured immediately after resuspension. $\alpha_{exc}/R_{sw}=5.3\times10^{-4}$, $\alpha_{ems}/R_{sw}=4.8\times10^{-4}$ (abs.L.$mg_{solids}^{-1}cm^{-1}$).

Table 2 - 5. Supernatants analyses by GC-MS and LIF[a].

$[Pyrene]_{GC-MS}$ (ng/L)[b]	$[Pyrene]_{LIF}$ (ng/L)[b]	$[Pyrene]_{GC-MS}/[Pyrene]_{LIF}$[c]
5.7±2.0	3.3±0.9	1.7±0.8
6.1±1.3	6.1±0.8	1.0±0.3
6.3±1.5	6.6±1.1	1.0±0.3
7.3±1.5	6.5±1.2	1.1±0.3
8.5±1.5	8.8±1.0	1.0±0.2
9.3±1.8	6.6±1.0	1.4±0.4
9.6±2.4	11.0±1.3	0.9±0.2
11.1±2.0	9.7±1.2	1.2±0.3
11.9±2.2	12.8±0.9	0.9±0.2
13.9±2.5	16.2±1.6	0.9±0.2
14.8±2.8	15.6±1.2	1.0±0.2
16.5±3.0	13.9±1.2	1.2±0.2

a: Null hypothesis: sample mean $[Pyrene]_{GC-MS}/[Pyrene]_{LIF}$ = 1.095 not different from expected mean = 1. Statistic $t = 1.29 < t_{crit}$ (two-tailed t-test, with t_{crit} = 3.11, 2.72, and 1.80 for α = 1%, 5%, and 10%, respectively). Thus null hypothesis was accepted at α=1-10%.

b: ± 1 standard deviation.

c: Propagated uncertainty shown.

Table 2 - 6. Solid-associated and dissolved pyrene concentrations before and after desorption (110-240d)[a].

Size Fraction[b]	R_{sw} (mg_{solids}/L_w)	S_o[c] (ng_{pyr}/g_{solids})	f_{oc} (g_{oc}/g_{solids})	f_{bc} (g_{bc}/g_{solids})	C_{end} (ng_{pyr}/L_w)[d]	S_{end} (ng_{pyr}/g_{solids})[e]
38-75um (r_m=27um)	~20 ~70 ~280	1350 (±19%)	0.037 (±10%)	0.0035 (±9%)	3.3 (±28%), 6.6 (±21%) 6.5 (±17%), 8.8 (±16%) 9.7 (±12%), 13.9 (±18%)	1240, 720 1230, 1180 1320, 1260
75-106um (r_m=45um)	~20 ~70 ~280	3060 (±19%)	0.033 (±10%)	0.0083 (±7%)	6.6 (±16%) 11.0 (±12%) 16.2 (±10%)	2250 2790 3310
180-250um (r_m=106um)	~20 ~70 ~280	5420 (±15%)	0.031 (±9%)	0.012 (±7%)	6.1 (±13%) 12.8 (±7%) 15.6 (±8%)	4160 5150 5290

a: Desorption durations were 120d, 110d for the 38-75um runs, 180d for the 75-106um runs, and 240d for the 180-250um runs.
b: r_m = geometric mean radius.
c: Determined from best fitted mass balance using C_{end}, S_{end}, and R_{sw}.
d: Measured with time-gated LIF.
e: Single measurement, with uncertainty expected to be ±18%, as determined from repeated measurements on one sediment sample (n=7).

Table 2 - 7. Typical suspended-solids concentrations observed in estuaries, harbors, and tributaries.

Estuary/Harbor	[TSS] (mg_{solids}/L)[a]	d_{mean} (um)[b]
Boston Harbor (USA)	0.5-20 (near surface)[c] 1-50 (near bottom)[c]	30-60[i]
Chesapeake Bay[d] (USA)	<10-500	
Ems Estuary[e] (Germany-Netherlands)	10-150 (near surface) 30-300 (near bottom)	
Lower Hudson Estuary (USA)	100-400[f] 30-500[g]	 40-90[g]
San Francisco Bay[h]	20-200	

a: [TSS] = total suspended-solids concentration.

b: d_{mean} = mean diameter of suspended sediment, or that of the most abundant fraction in sediment suspension.

c: *Boston Harbor 1999 Water Quality Assessment Report*. Report #70-A C-1. Massachusetts Department of Environmental Protection, Division of Watershed Management, Worchester, **2002**.

d: *Nutrient and Sediment Concentrations, Loads, and Trends for Four Nontidal Tributaries in the Chesapeake Bay Watershed, 1997-2001*. Report 2004-5125, U.S. Geological Survey, Reston, **2005**.

e: Postma, H. Einige Bemerkungen über den Sinkstofftransport im Ems-Dollard-Gebiet. *Verh Kd Ned Geol Mijnb Genoot Geol Ser* **1960**, 19, 103-110.

f: *Final Report: Particle Trapping in the Lower Hudson Estuary*. Hudson River Foundation, **1995**.

g: Adams, R. G. Polyethylene devices and the effects of sediment resuspension on the cycling of PAHs and PCBs in the Lower Hudson Estuary. Ph.D. Thesis, Massachusetts Institute of Technology, Cambridge, **2003**, pp 1-184.

h: *Summary of Suspended-Solids Concentration Data, San Francisco Bay, California, Water Year 1997*. U.S. Geological Survey, Report 99-189, Sacramento, **1999**.

i: Ravens, T. M. Sediment resuspension in Boston Harbor. Ph.D. Thesis, Massachusetts Institute of Technology, Cambridge, **1997**, pp 1-187.

Chapter 3: Tables

Table 3 - 1. Experimental Conditions and Sorbent Properties. **550**
Table 3 - 2. Sorption Equilibration Time in Literature for PAHs in Geosorbent-Water Systems. **551**
Table 3 - 3. System Variables and Physicochemical Factors Determining Equilibration Time-Length. **553**
Table 3 - 4. Equilibration Time for Sorbents Rich in Condensed Carbons^{+}. **554**

Table 3 - 1. Experimental Conditions and Sorbent Properties.

Sorbent (size range)	f_{OC}* (g_{OC}/g_{solids})	$f_{BC\text{-}375C\text{-}24h}$* ($g_{BC}/g_{solids}$)	$S_{pyr,native}$* ($\mu g_{pyr}/kg_{solids}$)	Experiment (duration)	Condition	Grinding	Ref.
North Quincy Bay-6 (38-75 μm)-a	0.0370 (±0.0037)	0.0035 (±0.0003)	1350 (±19%)			No	Chapter 2
North Quincy Bay-6 (75-106 μm)	0.0330 (±0.0033)	0.0083 (±0.0006)	3060 (±19%)	Short-Term Desorption (4-8 months)	22°C R_{sw}:20-300 mg_{solids}/L	No	Chapter 2
North Quincy Bay-6 (180-250 μm)	0.0310 (±0.0028)	0.0120 (±0.0008)	5420 (±15%)			No	Chapter 2
North Quincy Bay-6 (38-75 μm)-b	0.0305[a] (±0.0009)	0.0033[a] (±0.0005)	2100[a] (±8%)	Long-Term Desorption Equilibrium (12-14 months)	22°C R_{sw}:1000-4000 mg_{solids}/L	Yes	Here
						No	Here
North Quincy Bay-6 (<425 μm)	0.0296[a] (±0.0034)	0.0049[a] (±0.0005)	5200[a] (±20%)	Extended Range Adsorption Equilibrium (12-months)	6, 15, 22, 37°C R_{sw}:20-600 mg_{solids}/L $C_{pyr,o}$:0.05-25 μg/L	No	Here
North Quincy Bay-5 (<425 μm)	0.0310 (±0.0002)	0.0060 (±0.0004)	n/a	(Adsorption Equilibrium <1 month)	24°C R_{sw}:100-600 mg_{solids}/L $C_{pyr,o}$:10 μg/L	No	Accardi-Dey 2002
South Dorchester Bay (<425 μm)	0.0120 (±0.0000)	0.0026 (±0.0002)	n/a		24°C R_{sw}:100-2500 mg_{solids}/L $C_{pyr,o}$:2-20 μg/L	No	Accardi-Dey 2002

*: Bracketed values were measurement uncertainties in 1 σ.
a: Averaged from triplicates of sediment samples.

Table 3 - 2. Sorption Equilibration Time in Literature for PAHs in Geosorbent-Water Systems.

Incubation Duration (d)*	Sorbate	Sorbent	R_{sw} (mg_{solids}/L_{water})	Remarks	Reference
<1	phenanthrene	sediment	80000	cont. mix.+; desorption	Kan et al. 1994
1	pyrene, dibenzanthracene	sediment, soil	100000	cont. mix.	Means et al. 1980
1-2.5	pyrene, phenanthrene	activated carbon	N/A	cont. mix.	Walters et al. 1984
<2	pyrene	sediment, soil	10 to 20000	cont. mix.	Karickhoff 1979
2-3	phenanthrene, pyrene	sediment, soil	6000 to 150000	cont. mix.	Chiou et al. 1998
<7	phenanthrene, pyrene	sediment	300000-450000	cont. mix.; T=4, 26°C	Piatt et al. 1996
<7	phenanthrene	sediment	80000	cont. mix.; adsorption	Kan et al. 1994
7	pyrene	sediment, soil	1000	cont. mix.	Wang et al. 2005
7	phenanthrene	coal, coke, activated carbon, peat	50 to 500000	manual mixing	Kleineidam et al. 2002
7-14	phenanthrene	peat, lignite, coal	100	N/A[a]; T=4 to 77°C	Wang et al. 2007
7-14	phenanthrene	soil	8000	N/A; T=4 to 77°C	Wang et al. 2007
14	phenanthrene	sediment	N/A	N/A	Ran et al. 2007
21	phenanthrene	sediment	N/A	cont. mix.	Xiao et al. 2004
7-70	phenanthrene, pyrene	soil	200-50000	cont. mix.	Xia et al. 199
14-28	phenanthrene	soil	1700-250000	cont. mix.	Huang et al. 1997b
14-28	phenanthrene	peat, sediment, BC	N/A	cont. mix.	Ran et al. 2002
20	phenanthrene, pyrene	sawdust char	125	cont. mix.	Sun et al. 2008
28	PAHs (3-5+ rings)	soot	30-300	cont. mix.; +3 g/L polyoxymethylene	Jonker et al. 2002
28	pyrene	sediment	100-2500	cont. mix.	Accardi-Dey and Gschwend 2002
28	pyrene	sediment, filter+OM	200-600	cont. mix.	Flores-Cervantes et al. 2009
28-84	phenanthrene	wood char	50-200	cont. mix.	Nguyen et al. 2007
35	phenanthrene	char	60-400	cont. mix.	Pignatello et al. 2006
35	phenanthrene	char+humic/fulvic	150-850	cont. mix.	Pignatello et al. 2006
35-50	phenanthrene	sediment, sedimentary BC	N/A	cont. mix.; +3 g/L polyoxymethylene	Cornelissen et al. 2004b

42	phenanthrene	sediment/soil	N/A	cont. mix.	Ran et al. 2003b
14/21-60	phenanthrene	sediment, soil	N/A	cont. mix.	Huang et al. 1998b; Xiao et al. 2004
21-90	phenanthrene	peat, soil, coal, shale	N/A	semi-continuous[b]	Johnson et al. 2001a
60-120	phenanthrene	soot	10	semi-continuous	Nguyen et al. 2004b
140-230	phenanthrene, pyrene	soot	2-20	cont. mix.; 4-25°C	Bucheli et al. 2000
270	phenanthrene	soil	N/A	cont. mix.	Abu et al. 2006
180-370	phenanthrene	sediment, soil, shale	N/A	semi-continuous	Huang et al. 1998a
180-370	pyrene	sediment	20-600	semi-continuous	***THIS STUDY***

*: All studies were conducted at room temperatures (20-25°C) unless noted otherwise
+: Continuous mixing (or tumbling).
a: N/A: Not available.
b: Semi-continuous: suspensions/slurries were continuously mixed for the first 30d, then manually mixed periodically with decreasing frequency (once every day, or every several days, etc).

Table 3 - 3. System Variables and Physicochemical Factors Determining Equilibration Time-Length.

Categories	Factors	
System Variables		
	solids concentration (R_{sw})	
	temperature	
	mixing/circulation	
Sorbent Morphology & Structure		
	size distribution of sorbent particles/aggregates	
	porosity in individual particles/aggregates	
	surface area to volume ratio	
Organic Sorptive Phases Properties		
	TOC quantity	
	OC type	'soft' carbon, 'hard' condensed carbons
	OC properties & structure	surface area, porosity, organic coating
	distribution of OC	uniformity
Sorbate Properties		
	molecular size	weight, molar volume
	molecular geometry	dimensions, planarity
	concentration (if nonlinear isotherm)	
	hydrophobicity	

Table 3 - 4. Equilibration Time for Sorbents Rich in Condensed Carbons[+].

Sorbent	Sorbate	f_{TOC} (g_{OC}/g_{solids})	Equilibration Time (d)*	Reference**
Soil/Sediment				
EPA-23 (lake)	phenanthrene	0.026[c]	90-180	a
EPA-22 (river)	phenanthrene	0.026[c]	30-90	a
Soil (silt-loam)	phenanthrene	0.017[§]	>270[‡]	d
Soil (sand)	phenanthrene	0.032[§]	>270[‡]	d
Soil (podzol)	phenanthrene	0.23[§]	>270[‡]	d
Shale/Kerogen				
Lachine shale	phenanthrene	0.083	>370[‡]	a
Lachine kerogen	phenanthrene	0.53	>370[‡]	a
Norwood shale	phenanthrene	0.19	>370[‡]	a
Norwood kerogen	phenanthrene	0.65	>370[‡]	a
Paxton shale	phenanthrene	0.041	30-90	a
Paxton kerogen	phenanthrene	0.35	30-90	a
Soot				
NIST SRM 1650	phenanthrene,	0.77	130	b
NIST SRM 1650	pyrene	0.77	130	b

+: All cited systems were at room temperature (20-25°C).
‡: Still increasing at the longest equilibration time, which were 370 d for reference a, and 270 d for reference d.
§: TOC of these samples were dominated by $BC_{CTO\text{-}375}$ (i.e. >90% TOC was BC).
*: Systems were judged to be at equilibrium when subsequent measurement of $\log K_d$ increased no more by 0.10 (equivalent to a 25% increase). This criterion is by no means stringent compared to the 3% defined by Wang et al. 2005.
**: a – Huang et al. 1998a; b – Bucheli et al. 2000.; c – Accardi-Dey and Gschwend 2003; d – Abu et al. 2006.

Chapter 4: Tables

Table 4 - 1. Dissolved PAH concentrations in natural waters. **556**
Table 4 - 2. Experimental Conditions and Sorbent Properties. **558**
Table 4 - 3. Surface Area of Various BC or Condensed Carbonaceous Matters. **559**
Table 4 - 4. Pore Distribution of Soot and Char/Charcoal (Industrial & Natural). **560**
Table 4 - 5. Estimates of equilibration time for desorption of pyrene in the PE-sediment experiment. **561**

Table 4 - 1. Dissolved PAH concentrations in natural waters.

(a) Dissolved Pyrene Concentrations in the Environment

Water/Water Body	C_{pyr} (ng_{pyr}/L_w)	Reference
River, Lake & Harbors		
Alexandria, Egypt (coastal)	≤ 50	Nemr et al. 2003
Boston Harbor	≤ 120	Rudnick 1998
Chesapeake Bay	≤ 5	Ko et al. 2004
	≤ 20	Gustafson et al. 1997
L. Maggiore (Italy)	≤ 5	Olivella et al. 2006
New York-New Jersey Harbor Estuary	≤ 20	Gigliotti et al. 2002
R. Blyth (England)	≤ 70	Law et al. 1997
R. Mersey (England)	≤ 160	Law et al. 1997
R. Daliao (N.E. China)	≤ 1700	Guo et al. 2007
R. Hun (N.E. China)	≤ 1000	Guo et al. 2007
R. Sampit (S. Carolina, US)	≤ 1	Bidleman et al. 1990
R. Taizi (N.E. China)	≤ 2500	Guo et al. 2007
R. Tees (England)	≤ 300	Law et al. 1997
R. Tynes (England)	≤ 100	Law et al. 1997
R. Wear (England)	≤ 50	Law et al. 1997
Winyah Bay (S. Carolina, US)	≤ 10	Bidleman et al. 1990
Rain		
Chesapeake Bay	≤ 20[a]	Leister et al. 1994

a: Volume-weighted mean.

(b) Dissolved Total PAH Concentrations in the Environment.

Water/Water Body	$C_{\Sigma PAHs}$ ($ng_{\Sigma PAHs}/L_w$)	Reference
River, Lake & Harbors		
Alexandria, Egypt (coastal)	≤ 500	Nemr et al. 2003
Chesapeake Bay	≤ 50	Ko et al. 2004
	≤ 70	Gustafson et al. 1997
L. Maggiore (Italy)	≤ 10	Olivella et al. 2006
New York-New Jersey Harbor	≤ 70	Gigliotti et al. 2002
R. Blyth (England)	≤ 650	Law et al. 1997
R. Daliao (N.E. China)	≤ 10000	Guo et al. 2007
R. Hun (N.E. China)	≤ 13000	Guo et al. 2007
R. Mersey (England)	≤ 1400	Law et al. 1997
R. Sampit (S. Carolina, US)	≤ 7	Bidleman et al. 1990
R. Taizi (N.E. China)	≤ 13500	Guo et al. 2007
R. Tees (England)	≤ 11000	Law et al. 1997
R. Tynes (England)	≤ 1000	Law et al. 1997

R. Wear (England)	≤ 400	Law et al. 1997
San Francisco Bay	≤ 120	Ross et al. 2004
Winyah Bay (S. Carolina, US)	≤ 70	Bidleman et al. 1990
Rain		
Chesapeake Bay	≤ 60[a]	Leister et al. 1994
Lake Maggiore (Italy)	≤ 75	Olivella et al. 2006
Pristine/Remote Mountain Lakes		
L. Gossenkolle (Alps)	≤ 0.4	Vilanova et al. 2001
L. Redo (Pyrenees)	≤ 0.3	Vilanova et al. 2001
Ovre Neadalsvatn (Caledonian)	≤ 0.6	Vilanova et al. 2001

a: Volume-weighted mean.

Table 4 - 2. Experimental Conditions and Sorbent Properties.

Sorbent (size range)	f_{OC}* (g_{OC}/g_{solids})	$f_{BC\text{-}375C\text{-}24h}$* ($g_{BC}/g_{solids}$)	$S_{pyr,native}$* ($\mu g_{pyr}/kg_{solids}$)	Experiment (duration)	Condition	Grinding	Ref.
North Quincy Bay-6 (38-75 μm)-a	0.0370 (±0.0037)	0.0035 (±0.0003)	1350 (±19%)			No	Chapter 2
North Quincy Bay-6 (75-106 μm)	0.0330 (±0.0033)	0.0083 (±0.0006)	3060 (±19%)	Short-Term Desorption (4-8 months)	22°C R_{sw}:20-300 mg_{solids}/L	No	Chapter 2
North Quincy Bay-6 (180-250 μm)	0.0310 (±0.0028)	0.0120 (±0.0008)	5420 (±15%)			No	Chapter 2
North Quincy Bay-6 (38-75 μm)-b	0.0305[a] (±0.0009)	0.0033[a] (±0.0005)	2100[a] (±8%)	Long-Term Desorption Equilibrium (12-14 months)	22°C R_{sw}:1000-4000 mg_{solids}/L	Yes	Here
						No	Here
North Quincy Bay-6 (<425 μm)	0.0296[a] (±0.0034)	0.0049[a] (±0.0005)	5200[a] (±20%)	Extended Range Adsorption Equilibrium (12-months)	6, 15, 22, 37°C R_{sw}:20-600 mg_{solids}/L $C_{pyr,o}$:0.05-25 μg/L	No	Here
North Quincy Bay-5 (<425 μm)	0.0310 (±0.0002)	0.0060 (±0.0004)	n/a	(Adsorption Equilibrium <1 month)	24°C R_{sw}:100-600 mg_{solids}/L $C_{pyr,o}$:10 μg/L	No	Accardi-Dey 2002
South Dorchester Bay (<425 μm)	0.0120 (±0.0000)	0.0026 (±0.0002)	n/a		24°C R_{sw}:100-2500 mg_{solids}/L $C_{pyr,o}$:2-20 μg/L	No	Accardi-Dey 2002

*: Bracketed values were measurement uncertainties in 1 σ. a: Averaged from triplicates of sediment samples.

Table 4 - 3. Surface Area of Various BC or Condensed Carbonaceous Matters.

BC or Condensed, 'Hard' Carbon	Surface Area (m^2/g_{solids})	References
'Activated' Carbon/Char/Charcoal		
charcoal	210	Kleineidam et al. 2002
lignite coke	306	Kleineidam et al. 2002
charcoal	400	Braida et al. 2003
activated carbon	790	Kleineidam et al. 2002
coconut activated carbon	1260-1530	Qiao et al. 2002
activated carbon (commercialx4)	800-1960	Jung et al. 2001
Biomass-Char/Charcoal		
wood char	2.0	Elmquist et al. 2006
straw charcoal	2.5	Fernandes et al. 2003
grass char	5.9	Elmquist et al. 2006
wood charcoal	7.0	Fernandes et al. 2003
wood char	46	Nguyen et al. 2007
Coal (‡)		
Beulah-Zap (lignite coal)	1.6	Vorres 1990
Pocahontas (bituminous coal)	1.9	Vorres 1990
6 coal samples	11-34[a], 80-246[b]	Walker et al. 1965
Loy Yang (brown coal)	7[a], 166[b]	Amarasekera et al. 1995
Morwell (brown coal)	178[b]	Amarasekera et al. 1995
Coolungoolun (brown coal)	13[a], 174[b]	Amarasekera et al. 1995
Stradbroke (brown coal)	195[b]	Amarasekera et al. 1995
Wadge 60 (hi-volat. sub-bitum.)	207[b]	Amarasekera et al. 1995
Collie (med-volat. sub-bitum.)	170[b]	Amarasekera et al. 1995
Appin (lo-volat. sub-bitum.)	196[b]	Amarasekera et al. 1995
Kerogen		
shale-containing (Wagner-II, Michigan)	1.4	Huang et. al. 1997
Lachine shale	11.1	Johnson et al. 2001
Soot		
NIST diesel soot (SRM-1650)	48	Bucheli et al. 2000
toluene soot	51	Daly et al. 2009
kerosene soot	64	Daly et al. 2009
propane-soot	65	Chan et al. 1987
n-hexane soot	74	Akhter et al. 1985
NIST diesel soot (SRM-2975)	80	Nguyen et al. 2006
hexane soot	81	Nguyen et al. 2006

diesel soot	97	Daly et al. 2009
methane-soot	87	Chan et al. 1987

‡: Surface area probed by CO_2 adsorption should be considered with caution. Interpretational difficulties on CO_2 adsorption isotherm on coal have been reported (Mahajan 1991; Larsen et al. 2004) due to (i) CO_2-induced swelling in coal matrix, (ii) dissolution of CO2 in coal matrix, (iii) arbitrary CO_2-exposure/equilibration duration, and (iv) variable adsorbate depositional area in pore surface. Mahajan (1981) even argued that CO_2-surface area for coal should not be reported due to its ambiguity.

a: Micropore area from N_2-BET adsorption isotherm. See also footnote ‡.

b: Micropore area from CO_2-BET adsorption isotherm. See also footnote ‡.

Table 4 - 4. Pore Distribution of Soot and Char/Charcoal (Industrial & Natural).

Type	Micropores (dia.<2 nm)		Mesopores (dia.:2-50 nm)	
	Pore Volume (mL/g)	Surface Area (m^2/g)	Pore Volume (mL/g)	Surface Area (m^2/g)
Activated Carbon				
Coconut BS[a]	0.427	1097	0.018	10
Agro[a]	0.435	1024	0.096	54
F-200[a]	0.248	602	0.064	30
F-400[a]	0.303	763	0.082	36
Natural Char/Charcoal				
Pine char[b]	0.015	Not Available	0.008	Not Available
Soot				
Hexane soot[c]	0.011	Not Available	0.056	Not Available
SRM 1650[c]	0.001	Not Available	0.068	Not Available
SRM 2975[c]	0.011	Not Available	0.106	Not Available

a: Paulsen et al. 1999.
b: Nguyen et al. 2007.
c: Nguyen et al. 2006.

Table 4 - 5. Estimates of equilibration time for desorption of pyrene in the PE-sediment experiment.

				1st Order Model[a]				Radial Desorption Model (Constant D_{eff})[b]			
				$K_d = Q_d$		$K_d = Q_d/5$		$K_d = Q_d$		$K_d = Q_d/5$	
No.	g_{PE}:g_{BC}	R_{sw} (mg/L)	$Q_{d,50}$ (L/kg)	$t_{95\%\text{-Eqm}}$ (d) (high est.)	$t_{95\%\text{-Eqm}}$ (d) (low est.)	$t_{95\%\text{-Eqm}}$ (d) (high est.)	$t_{95\%\text{-Eqm}}$ (d) (low est.)	$t_{95\%\text{-Eqm}}$ (d) (r=100 μm)	$t_{95\%\text{-Eqm}}$ (d) (r=10 μm)	$t_{95\%\text{-Eqm}}$ (d) (r=100 μm)	$t_{95\%\text{-Eqm}}$ (d) (r=10 μm)
1-3	60-70	50-55	$1.5\text{-}2.1\times10^6$	400-1050	< 10	1900-5000	10-40	~ 40-50	< 1	~ 70-90	<~ 1
4-6	190-200	20	$3.9\text{-}4.2\times10^6$	500-950	< 10	2400-4600	10-35	~ 100	< 1	~ 180	<~ 1
7-9	650-660	6	$13\text{-}15\times10^6$	500-900	< 10	2200-4400	10-35	~ 300	~ 1	~ 600	~ 10
10-12	1800-1900	2	$22\text{-}38\times10^6$	500-1500	<~ 10	2400-7100	10-55	~ 1000	~ 10	~ 2000	~ 20
17-19	70	110-120	$2.1\text{-}2.4\times10^6$	150-300	~ 1	800-1400	<~ 10	<~ 10	< 1	~ 20	< 1
20-22	550-600	20-40	$6.1\text{-}12\times10^6$	150-300	~ 1	800-1500	<~ 10	~ 20-40	< 1	~ 60-100	< 1

a: Where $t_{95\%-Eqm} = \frac{\ln 20}{k(K_d R_{sw}+1)}$, with k determined from the data from the desorption kinetic experiments on three size fractions of BH#6 sediment. See Appendix 4-5, part A for more details.

b: Where $t_{95\%-Eqm} = \frac{M_o - M_{t95\%-Eqm}}{M_o - M_\infty} = 1 - \sum_{n=1}^{\infty} \frac{6\beta(\beta+1)\exp\{-D_{eff} q_n^2 t_{95\%-Eqm}/r^2\}}{9+9\beta+q_n^2\beta^2}$. See Appendix 4-5, part B for more details.

Chapter 5: Tables

Table 5 - 1. Composite Isotherm Forms for regression of pyrene sorption equilibration data. **563**
Table 5 - 2. Regressed Parameters for Pyrene Sorption Isotherms at 22°C. **564**
Table 5 - 3. Regressed isotherm parameters for pyrene sorption at 6, 15, 22 and 37°C. **566**
Table 5 - 4. Fraction occluded native pyrene estimated by different methods. **569**
Table 5 - 5. Partitioning coefficients for pyrene in various solid(carbon phase)-water systems (Linear-Isotherm). **570**
Table 5 - 6. $\log K_{OC}$'s, $\log K_{BC}$'s and & n_{BC}'s (22°C) from this study. **572**
Table 5 - 7. Observed/estimated $\log K_{BC}$ & n_{BC} (or n_{Fr}) from pyrene isotherm studies. **573**
Table 5 - 8. Freundlich exponent, n_{Fr}, reported in HOC sorption studies. **574**
Table 5 - 9. $\log K_{OC}$'s & $\log K_{BC}$'s (22°C) at a glance. **574**
Table 5 - 10. Partitioning coefficients (non-linear) for pyrene and phenanthrene in various 'soft' organic materials **575**

Table 5 - 1. Composite Isotherm Forms for regression of pyrene sorption equilibration data.

Abbreviation	Composite Isotherm Form	Regressed Parameters	Number of Parameters
Lnr-Fr	$S = K_{Lnr}C + K_{Fr}C^{n}$	K_{Lnr}, K_{Fr}, n	3
Two-Fr	$S = K_{Fr,H}C^{n_H} + K_{Fr,L}C^{n_L}$	$K_{Fr,H}$, $K_{Fr,L}$, n_H, n_L	4
Lgmr-Fr	$S = K_{Fr}C^{n} + \frac{S_{Max}C}{C_{½} + C}$	K_{Fr}, n, S_{Max}, $C_{½}$	4
Lnr-Fr-Fr	$S = K_{Lnr}C + K_{Fr,1}C^{n_1} + K_{Fr,2}C^{n_2}$	K_{Lnr}, $K_{Fr,1}$, $K_{Fr,2}$, n_1, n_2	5
Lnr-Lgmr-Fr	$S = K_{Lnr}C + K_{Fr}C^{n} + \frac{S_{Max}C}{C_{½} + C}$	K_{Lnr}, K_{Fr}, n, S_{Max}, $C_{½}$	5
Three-Fr	$S = K_{Fr1}C^{n_1} + K_{Fr2}C^{n_2} + K_{Fr3}C^{n_3}$	K_{Fr1}, K_{Fr2}, K_{Fr3}, n_1, n_2, n_3	6
Occlusion-Lnr-Fr	$S = S_{occlu} + K_{Lnr}C + K_{Fr}C^{n}$	S_{occlu}, K_{Lnr}, K_{Fr}, n	4
Occlusion-Fix*	$S = S_{occlu} + K_{Lnr}C + K_{Fr}C^{n}$	S_{occlu}, n*	2
Lnr-Fr(soot)-Fr(char) **	$S = (f_{OC} - f_{char})K_{OC}C + f_{soot}K_{soot}C^{n_{soot}} + f_{char}K_{char}C^{n_{char}}$	K_{char}, f_{char}, n_{char}, (n_{soot})**	3 to 4

*: $K_{Lnr} = f_{OC}K_{OC} = f_{OC}10^{4.7}$, and $K_{Fr} = f_{BC}K_{BC} = f_{BC}10^{6.25}$.
**: $K_{soot} = 10^{6.3}$, $f_{char} + f_{OC} = f_{TOC}$, $K_{OC} = 10^{4.7}$, ($n_{soot} = 0.62$).

Table 5 - 2. Regressed Parameters for Pyrene Sorption Isotherms at 22°C.

Isotherm Form*	Parameters*	χ_υ^2	Regression Method
Lnr-Fr $S = K_{Lnr}C + K_{Fr}C^n$	K_{Lnr} = 5000 (±380) K_{Fr} = 8800 (±1200) n = 0.21 (±0.09)	0.965	Matlab, non-linear fitting Appendix 5-3
Two-Fr $S = K_{Fr,H}C^{n_H} + K_{Fr,L}C^{n_L}$	$\log_{10}K_{Fr,H}$ = 3.73–3.89 (±0.03) $n_{Fr,H}$ = 0.15–0.19 (±0.03) $\log_{10}K_{Fr,L}$ = 3.82–4.03 (±0.03) $n_{Fr,L}$ = 0.64–0.85 (±0.04)	1.15–1.89	Excel, non-linear fitting Appendix 5-6 (Matlab: Appendix 5-3)
Lgmr-Fr $S = K_{Fr}C^n + \frac{S_{Max}C}{C_{½} + C}$	$\log_{10}K_{Fr}$ = 3.97–3.98 (±0.04) n = 0.74–0.78 (±0.04) S_{Max} = 4.4–5.2×10³ (±600) $C_{½}$ = 4–15×10⁻³ (±0.008)	1.28–1.36	Excel, non-linear fitting Appendix 5-6 (Matlab: Appendix 5-3)
(!) Lnr-Fr-Fr (rejected) $S = K_{Lnr}C + K_{Fr,1}C^{n_1} + K_{Fr,2}C^{n_2}$	(!) K_{Lnr} = –3.3×10⁶ (±4.6×10⁹) (!) $K_{Fr,1}$ = 3.3×10⁶ (±4.6×10⁹) n_1 = 1.00 (±0.89) $K_{Fr,2}$ = 4000 (±8300) (!) n_2 = –0.06 (±0.59)		Matlab, non-linear fitting Appendix 5-3
(!) Lnr-Lgmr-Fr (rejected) $S = K_{Lnr}C + K_{Fr}C^n + \frac{S_{Max}C}{C_{½} + C}$	(!) K_{Lnr} = –2.6×10⁶ (±3.0×10⁹) (!) S_{Max} = 43×10⁹ (±94×10¹²) (!) $C_{½}$ = 16×10³ (±17×10⁶) K_{Fr} = 7500 (±4200) (!) n = 0.11 (±0.21)		Matlab, non-linear fitting Appendix 5-3
(!) Three-Fr (rejected)			

$\mathbf{S = K_{Fr1}C^{n_1} + K_{Fr2}C^{n_2} + K_{Fr3}C^{n_3}}$	$K_{Fr,1}$ = 13×10³ (±7.5×10³) n_1 = 0.84 (±0.15) (!) $K_{Fr,2}$ = 5.3×10³ (±9.1×10³) (!) n_2 = 0.04 (±0.71) (!) $K_{Fr,3}$ = 0 (±0) (!) n_3 = −6.78 (±1.3×10³)		Matlab, non-linear fitting Appendix 5-3
Occlusion-Lnr-Fr $\mathbf{S = S_{occlu} + K_{Lnr}C + K_{Fr}C^n}$	S_{occlu} ~1500 (1000-2000) K_{Lnr} = 3800 (±700) K_{Fr} = 9800 (±1100) n = 0.42 (±0.12)	1.17	Matlab non-linear fitting + Manual (S_{occlu}) Appendix 5-6
Occlusion-Fix* $\mathbf{S = S_{occlu} + K_{Lnr}C + K_{Fr}C^n}$	S_{occlu} = 3000–4300 (±500–800) n = 0.62–0.79 (±0.01)	0.955	Matlab, non-linear fitting Appendix 5-5
(!) Lnr-Fr(soot)-Fr(char) (rejected) $\mathbf{S = (f_{OC} - f_{char})K_{OC}C + f_{soot}K_{soot}C^{n_{soot}} + f_{char}K_{char}C^{n_{char}}}$	(!) K_{char} = 157×10³ (±1.2×10⁶) (!) f_{char} = 0.025 (±0.29) (!) n_{char} = 0.01 (±0.92) (!) n_{soot} = 0.73 (±1.0)		Matlab, non-linear fitting Appendix 5-4

*: (!) refers to regressions that were unsatisfactory (e.g. over-parameterized). It also refers to isotherm parameters that were highly uncertain or even unnecessary (e.g., n or K_{Fr} = ~0).

Table 5 - 3. Regressed isotherm parameters for pyrene sorption at 6, 15, 22 and 37°C.

**Note that only the Linear-Freundlich, the Two-Freundlich, and the Langmuir-Freundlich models were applied to sorption data at other temperatures.

(a) Linear-Freundlich Model (Parameters: K_{Lnr}, K_{Fr}, n_{Fr})*

T (°C)	5-month Data $S = K_{Lnr}C + K_{Fr}C^{n_{Fr}}$			10-month Data $S = K_{Lnr}C + K_{Fr}C^{n_{Fr}}$		
	K_{Lnr}	K_{Fr}	n_{Fr}	K_{Lnr}	K_{Fr}	n_{Fr}
6	2800 (±920)	16000 (±1400)	0.42 (±0.08)	6200 (±1300)	15000 (±2100)	0.38 (±0.11)
15	4500 (±240)	11000 (±710)	0.25 (±0.04)	4000 (±440)	7400 (±2200)	0.12 (±0.15)
22	5900 (±510)	10000 (±1300)	0.28 (±0.09)	5000 (±380)	8800 (±1200)	0.21 (±0.09)
37	2700 (±550)	7800 (±1800)	0.21 (±0.18)	1800 (±390)	5400 (±1100)	0.23 (±0.17)

* K_{Lnr} in (L_w/kg_{solids}); K_{Fr} in $(\mu g_{pyr}/kg_{solids})(L_w/\mu g_{pyr})^{nFr}$; n_{Fr} is dimensionless. Non-linear regression by Matlab (for details see Appendix 5-3).

(b) Two-Freundlich Model (Parameters: $K_{Fr,H}$, n_H, $K_{Fr,L}$, n_L)*

	5-month Data $S = K_{Fr,H}C^{n_H} + K_{Fr,L}C^{n_L}$				10-month Data $S = K_{Fr,H}C^{n_H} + K_{Fr,L}C^{n_L}$			
	High-Affinity Domain		Low-Affinity Domain		High-Affinity Domain		Low-Affinity Domain	
T (°C)	n_H	$LogK_{Fr,H}$	n_L	$LogK_{Fr,L}$	n_H	$LogK_{Fr,H}$	n_L	$LogK_{Fr,L}$
6	0.14-0.17 (±0.02)	3.94-3.97 (±0.02)	0.92-0.95 (±0.03-0.04)	3.84-3.87 (±0.02-0.03)	0.14-0.17 (±0.03-0.06)	3.92-3.98 (±0.04-0.06)	1.00-1.08 (±0.05-0.07)	3.93-4.00 (±0.04)
15	0.01-0.05 (±0.01-0.02)	3.70-3.78 (±0.01-0.02)	0.81-0.89 (±0.01-0.02)	3.90-3.99 (±0.01-0.02)	0.07-0.13 (±0.01-0.04)	3.78-3.88 (±0.01-0.05)	0.78-0.90 (±0.07-0.08)	3.65-3.80 (±0.05-0.06)
22	0.11-0.20 (±0.02-0.03)	3.84-3.90 (±0.02-0.03)	0.75-0.97 (±0.03-0.04)	3.84-4.00 (±0.03)	0.15-0.19 (±0.03-0.03)	3.73-3.89 (±0.03)	0.64-0.85 (±0.02-0.05)	3.82-4.03 (±0.02-0.04)
37	0.28-0.37 (±0.07-0.19)	3.48-3.86 (±0.05-0.13)	0.53-0.70 (±0.04-0.07)	3.73-4.01 (±0.03-0.06)	0.17-0.33 (±0.04-0.07)	3.68-3.76 (±0.03-0.05)	0.59-1.11 (±0.07-0.11)	3.15-3.59 (±0.06-0.09)

* K_{Fr} in $(\mu g_{pyr}/kg_{solids})(L_w/\mu g_{pyr})^{nFr}$; n_{Fr} is dimensionless. Regression performed manually in excel (for details see Appendix 5-8).

(c) Langmuir-Freundlich Model (Parameters: $S_{Lgmr,Max}$, $C_{½}$, K_{Fr}, n)*

T (°C)	5-month Data $S = K_{Fr}C^{n_{Fr}} + \frac{S_{Max}C}{C_{½} + C}$				10-month Data $S = K_{Fr}C^{n_{Fr}} + \frac{S_{Max}C}{C_{½} + C}$			
	High-Affinity Domain		Low-Affinity Domain		High-Affinity Domain		Low-Affinity Domain	
	S_{Max}	$C_{½}$	n_{Fr}	$LogK_{Fr}$	S_{Max}	$C_{½}$	n_{Fr}	$LogK_{Fr}$
6	$5.0\text{-}5.4\times10^{3}$ (±240-450)	$1\text{-}2\times10^{-3}$ (±0.002-0.004)	0.73-0.81 (±0.02)	4.03-4.08 (±0.02-0.02)	$5.0\text{-}5.8\times10^{3}$ (±680-920)	$2\text{-}5\times10^{-3}$ (±0.003-0.006)	0.74-0.89 (±0.06-0.07)	4.10-4.22 (±0.03-0.07)
15	$5.4\text{-}7.0\times10^{3}$ (±150-380)	$2\text{-}11\times10^{-3}$ (±0.001-0.003)	0.77-0.87 (±0.02-0.04)	3.88-4.00 (±0.02-0.04)	$4.5\text{-}5.0\times10^{3}$ (±340-4700)	$4\text{-}10\times10^{-3}$ (±0.003-0.050)	0.62-0.74 (±0.05-0.09)	3.87-3.97 (±0.04-0.07)
22	$4.9\text{-}5.6\times10^{3}$ (±330-760)	$4\text{-}7\times10^{-3}$ (±0.004-0.011)	0.81-0.91 (±0.02-0.04)	3.97-4.02 (±0.02-0.03)	$4.4\text{-}5.2\times10^{3}$ (±530-640)	$4\text{-}15\times10^{-3}$ (±0.007-0.008)	0.74-0.78 (±0.03-0.05)	3.97-3.98 (±0.03-0.04)
37	$3.7\text{-}5.9\times10^{3}$ (±1300-2400)	$14\text{-}89\times10^{-3}$ (±0.045-0.110)	0.59-0.85 (±0.05-0.09)	3.68-3.94 (±0.04-0.08)	$4.0\text{-}4.2\times10^{3}$ (±320-570)	$19\text{-}25\times10^{-3}$ (±0.013-0.025)	0.87-0.91 (±0.05-0.14)	3.48-3.52 (±0.04-0.12)

* S_{Max} in ($\mu g_{pyr}/kg_{solids}$); $C_{½}$ in ($\mu g_{pyr}/L_w$); K_{Fr} in $(\mu g_{pyr}/kg_{solids})(L_w/\mu g_{pyr})^{nFr}$; n_{Fr} is dimensionless. Regression performed manually in excel (for details see Appendix 5-8).

Table 5 - 4. Fraction occluded native pyrene estimated by different methods.

Method	fraction occluded (or $S_{occlu}/S_{pyr,o}$)	Remark & Reference
Grinding Experiment	20–30 %	assumed no occlusion in ground sediment *Chapter 4, section 3.2.1*
Visual Inspection	80–90 %	assumed singular Freundlich; *Chapter 4, section 3.4.2.5*
Isotherm Regression ('Occlusion-Fix')	60–80 %	assumed $K_{OC}=10^{4.7}$, $K_{BC}=10^{6.25}$; *Appendix 5-5*
Isotherm Regression ('Occlusion-Lnr-Fr')	20–40 %	assumed constant fraction occluded at all four temperatures; *Appendix 5-6*

Table 5 - 5. Partitioning coefficients for pyrene in various solid(carbon phase)-water systems (Linear-Isotherm).

Carbon Phase (CP)*	$\log K_{CPW}$ (L_w/kg_{solids})	$\log K_{OC}$† (L_w/kg_{OC})	Remarks	Reference
Solvent Organic Carbons				
Octanol	5.13-5.18 (in L_w/L_o)	5.35-5.40[i]		see Appendix 3-24
Synthetic Organic Carbons				
Cellulose	2.39±0.04	2.74		Jonker et al. 2008
N.I. surfactant[b]	4.40-5.23[c]	4.61-5.40		Edwards et al.1991
PA	4.84	5.13	85μm; 100hr	Doong et al. 2000
PDMS	4.14[d]	4.63		Booij et al. 2000b
	4.22[a]	4.71		Mayer et al. 2000b
	4.22-4.41			
	4.27±0.02	4.76		Jonker et al. 2008
	4.32±0.01	4.81		ter Laak et al. 2006b
PE	4.66[f]	4.73		Smedes et al. 2009
	4.7±0.1	4.77		Fernandez et al. 2009
	4.92[e]	4.99		Vinturella et al. 2004
POM	4.69±0.09	5.09		Jonker et al. 2001
TECAM	4.75[g]	4.86[h]		Tao et al. 2008
Natural Organic Carbons (Separated Phase)				
Aquatic HS		4.60-5.08	(n=3)	Peminova et al. 1999
Cuticle (tomato)		5.70		Chefetz et al. 2000
Fulvic Acid				
Coal wastewater		3.87-4.35	(n=3)	Kopinke et al. 1995, 2001
IHSS peat FA		3.78-3.93		Laor et al. 1997
Lake water FA		4.01		Kopinke et al. 2001
River FA		3.78-4.19		Schlautman et al. 1993
		3.96-4.15	(n=3)	Chin et al. 1997
		4.01-4.44		Danielsen et al. 1995
Soil FA		<4.0-4.11	(n=4)	Peminova et al. 1999
Humic acid				
Aldrich		5.02-5.08	Comp.Floc.	Laor et al. 1997
		5.18	Solub.Enh.	Chin et al. 1997
		5.36	Fluo.Quench.	Peminova et al. 1999
		5.55	PDMS	ter Laak et al. 2005
Coal wastewater		4.38-5.02	(n=4)	Kopinke et al. 1995, 2001
IHSS peat HA		5.16-5.25		Laor et al. 1997
IHSS soil HA		5.56-5.69		Laor et al. 1997

Peat HA	4.69		Chefetz et al. 2000
	5.01-5.16	(n=2)	Terashima et al. 2003
Roth	4.70		Poerschmann et al. 2001
Soil HA	4.85-5.38	(n=8)	Perminova et al. 1999
	4.62-4.94	(n=2)	Raber et al. 1998
	4.47-4.70	(n=2)	Kopinke et al. 2001
Suwannee River	4.33		Chin et al. 1997
Peat	4.94		Chefetz et al. 2000
Peat HS	4.85-5.23	(n=7)	Peminova et al. 1999
Soil HS	5.00		Peminova et al. 1999
	4.74		Gauthier et al. 1986
Suwannee River HS	5.00		Gauthier et al. 1986
Natural Organic Carbons (Deduced)			
Marine colloid OM	4.5-5.0	(n=3)	Chin et al. 1992
Sediment/Soil OM	4.80-4.83	(n=14-17)	Means et al. 1980; Karickhoff 1981
Wastewater DOM	4.53		Poerschmann et al. 1997

*: **N.I. surfactant** = non-ionic surfactants; **FA** = fulvic acids; **HA** = humic acids; **HS** = humic substances; **PA** = polyacrylate; **PDMS** = poly(dimethylsiloxane); **PE** = polyethylene; **POM** = poly(oxymethylene); **TECAM** = triolein embedded cellulose acetate membrane.

†: $f_{OC}K_{OC} = K_{CPW}$.

a: Calculated according to $\log K_{i,PDMS\text{-}W} = 1.00\log K_{IOW} - 0.91$, where $4.5 \leq \log K_{IOW} \leq 7.5$ (Mayer et al. 2000b).

b: For 4 non-ionic surfactants with average M.W. ranging from ~360 to 740 g/mol.

c: Estimated from K_M by $K_{CPW} = K_M/(MW_M * \forall_w)$, where MW_M = molar mass in kg/mol, and $\forall_w$ is mol water molecules/L_{water}.

d: Calculated according to the $\log K_{LW}$-$\log K_{OW}$ and the $\log K_{ML}$-$\log K_{OW}$ relationships and with the assumption that all K's in unit L_w/kg_{solids} (Booij et al. 1998)

e: Converted from the listed values with density of PE (0.92 kg_{PE}/L_{PE}) (Vinturella et al. 2004).

f: Calculated according to $\log K_{i,PE\text{-}W} = 0.98\log K_{IOW} - 0.37$, where $3.3 \leq \log K_{IOW} \leq 6.9$ (Smedes et al. 2009).

g: Calculated according to $\log K_{i,TECAM\text{-}W} = 0.98\log K_{IOW} - 0.28$, where $3.3 \leq \log K_{IOW} \leq 6.3$ (Tao et al. 2008).

h: Converted based on OC content of triolein ($C_{57}H_{104}O_6$).

i: Calculated as: $K_{OC} = K_{OW}/(\rho_{octanol} * f_{OC,octanol})$, where $\rho_{octanol}$=0.824 kg_{OCT}/L_{OCT}, $f_{OC,octanol}$=96/130.

Table 5 - 6. $\log K_{OC}$'s, $\log K_{BC}$'s and & n_{BC}'s (22°C) from this study.

Isotherm Model**	$\log K_{OC}$*	$\log K_{BC}$*	n_{BC}*	S_{occlu}*
This Study				
Lnr-Fr (New-OC-BC)	5.25 (±0.04)	6.25 (±0.06)	0.25 (±0.09)	---
Occlusion-Fix	4.7[a]	6.25[b] (±0.14)	0.62–0.79 (±0.01)	3000–4300 (±500–800)
Occlusion-Lnr-Fr (Occlusion-OC-BC)	5.10 (±0.10)	6.30 (±0.06)	0.42 (±0.12)	1500 (±500)
Two-Fr	5.3–5.6 (±0.03)	6.0–6.2 (±0.03)	0.15–0.19 (±0.03)	---
Lgmr-Fr	5.5 (±0.04)	---	---	---
Literature				
Accardi-Dey and Gschwend 2002	4.7	6.25 (±0.14)	0.62 (±0.12)	---
Bucheli et al. 2000	4.7	6.5 (±0.05)	1[c]	---

*: K_{OC} in L_w/kg_{OC}; K_{BC} in $(\mu g_{pyr}/kg_{BC})(L_w/\mu g_{pyr})^{nBC}$; n_{BC} (dimensionless); S_{occlu} in mg_{pyr}/kg_{solids}.
**: See Table 5-1 or 5-2 for the isotherm expressions.
a: From Karickhoff 1981; Schwarzenbach et al. 2003; b: From Accardi-Dey and Gschwend 2002;
c: The study assumed a linear BC term.

Table 5 - 7. Observed/estimated $\log K_{BC}$ & n_{BC} (or n_{Fr}) from pyrene isotherm studies.

Sorbent	C_{Eqm} ($\mu g_{pyr}/L_w$)	f_{BC}<f_{TOC}>* (g_C/g_{solids})	K_{Fr} $(\mu g/kg)(L/\mu g)^{nFr}$	$\log(K_{BC}=K_{Fr}/f_{BC})^{\dagger}$	n_{Fr}	Reference
Marine Particulate Org. Matter						
MWRA station	1-3	0.00028	700	6.39	0.57	Flores-Cervantes et al. 2009
Inner Penobscot Bay	0.7-3	0.00039	1000	6.41	0.79	Flores-Cervantes et al. 2009
Jordan Basin	0.3-3	0.00018	500	6.44	0.66	Flores-Cervantes et al. 2009
Great South Channel	0.5-2	0.00013	700	6.73	0.89	Flores-Cervantes et al. 2009
East Platts Bank	0.5-2	0.00009	400	6.62	0.58	Flores-Cervantes et al. 2009
Sediments (Freshwater)						
Doe Run Pond	10-70	<0.0234-0.0329>	2100-3800	5.58-6.11	~1	Karickhoff et al. 1979
Hickory Hill Pond	10-70	<0.0134-0.0327>	1500-3000	5.66-6.10	~1	Karickhoff et al. 1979
Oconee River	10-70	<0.0199-0.0292>	2300-3200	5.74-6.06	~1	Karickhoff et al. 1979
Sediments (Marine)						
Fort Point Channel	10-60	<0.0523>	6800	5.81-6.11	0.94	Chin et al. 1992
Lake Michigan	10-105	<0.0402>	5600	5.84-6.15	0.97	Chiou et al. 1998
Massachusetts Bay	20-110	<0.0163>	2200	5.84-6.14	0.97	Chiou et al. 1998
North Quincy Bay	1-7.5	0.0060	11500	6.28	0.42	Accardi-Dey and Gschwend 2002
	0.01-20	0.0049	8800-10000	6.25-6.31(±0.08)	0.25-0.42	**This Study**
South Dorchester Bay	0.4-10	0.0026	4500	6.24	0.68	Accardi-Dey and Gschwend 2002
Soils						
Borris Soil	0.4-100	<0.0167>	3000	5.96-6.26	0.90	ter Laak et al. 2006a
Marlett Soil	10-80	<0.0180>	3400	5.97-6.27	0.84	Chiou et al. 1998
Synthetic Carbons						
Activated Carbon	0.3-70	<0.90>	27×10^6	$7.5^{\ddagger\#}$	0.39	Walters et al. 1984
Pine sawdust charcoal#1	1-110	<0.65>	5.1×10^6	$6.9^{\ddagger}$	0.63	Sun et al. 2008
Pine sawdust charcoal#2	1-110	<0.73>	2.3×10^6	$6.5^{\ddagger}$	0.48	Sun et al. 2008
Pine sawdust charcoal#3	1-110	<0.69>	5.1×10^6	$6.9^{\ddagger}$	0.56	Sun et al. 2008

*: In cases where only f_{TOC} have been reported, f_{BC} was estimated to be 10 to 20% of f_{TOC}.

†: In cases where the isotherm was almost linear, K_{Fr} was simply taken as K_d, where $S_{Eqm}\approx K_d C_{Eqm}$. This approximate assumes that BC was present (but not quantified) in the sorbent in a typical f_{BC}:f_{OC} ratio such that the contribution to sorption capacity by OC was insignificant. This assumption should be quite valid for Fort Point Channel and Lake Michigan sediments, and the synthetic carbons.

‡: For synthetic carbons which were all pyrogenic originated, f_{BC} was assumed to be identical as f_{TOC}.

#: This was a 7-d adsorption experiment. Shih et al. (2009) showed that pyrene adsorption onto AC proceeded very slowingly. Strong partitioning would also greatly reduce the adsorption rate. There are good reasons to believe that the true $\log K_{BC,pyr} < 7.5$.

Table 5 - 8. Freundlich exponent, n_{Fr}, reported in HOC sorption studies.

n_{Fr}	Sorbate	Sorbent†	Remarks	Reference
0.1-0.2	toluene	act. carbon		Cotoruelo et al. 2007
0.15-0.25	phenol	act. carbon		Chang et al. 2000
0.2-0.3	phenol	act. carbon		Peel et al. 1980
0.2-0.3	benzene, toluene, nitrobenzene	act. carbon		Shih et al. 2009
0.3-0.5	benzene	act. carbon		Cotoruelo et al. 2007
0.3-0.6	≤3-rings PAHs	act. carbon	<3 d equilibration (!!)	Walters et al. 1984
0.3-0.7	≥4-rings PAHs	act. carbon	<3 d equilibration (!!)	Walters et al. 1984
0.4-0.6	PAHs	char		Sun et al. 2008
0.5-0.6	phenanthrene	shale/kerogen		Huang et al. 1997a; Johnson et al. 2001a
0.5-0.7	PAHs,PCB	BC	planar molecules	Cornelissen et al. 2004a

*: Where $S_{HOC} = K_{Fr}C_{HOC}^{nFr}$.
†: In all cases, the partitioning of sorbate was examined in a solid-water system.

Table 5 - 9. $\log K_{OC}$'s & $\log K_{BC}$'s (22°C) at a glance.

Source/Case	$\log K_{OC}^{*}$ $(\mu g/kg_{OC})(L_w/\mu g)^{nOC}$	$\log K_{BC}$ $(\mu g/kg_{BC})(L_w/\mu g)^{nBC}$
Literature (see Table 3-9, 3-10)		
Sediment		
freshwater	} 4.5-5.0†	5.6-6.1
marine		5.8-6.3
Soil/Soil Fractions	4.5-5.7†	6.0-6.3
Max–Min	*1.2*	*0.7*
Regression (this study; sediment-water system) (Table 5-2, 5-6)		
Linear-Freundlich	5.2-5.3† (±0.04)	6.2-6.3 (±0.08)
Occlusion (2-param.)§	4.7§	6.25§
Occlusion (4-param.)	5.1 (±0.10)	6.3 (±0.06)
Two-Freundlich	5.3-5.6 (±0.06)	6.0-6.2 (±0.06)
Langmuir-Freundlich	5.5 (±0.04)	---
Max–Min	*0.5*	*0.3*

*: For linear isotherm, n_{OC}=1, unit becomes L_w/kg_{OC}.
†: Where n_{OC} or n_{BC} = 1.
§: Not from regression. Values were taken from Accardi-Dey and Gschwend 2002.

Table 5 - 10. Partitioning coefficients (non-linear) for pyrene and phenanthrene in various 'soft' organic materials

(a) Pyrene $logK_{OC}$ and $n_{Fr,OC}$

Carbon Phase	$logK_{OC}$†	n	Remarks	Reference
Sorbate = Pyrene ($logK_{OC,pyr,LFER}$ = 4.71)*				
Biopolymer				
Cellulose	2.85	0.86		Wang et al. 2007
Chitin	2.97	0.91		Wang et al. 2007
Lignin	4.85	0.94		Wang et al. 2007
	5.65	0.62		Chefetz et al. 2000
Humic acids				
Aldrich (pH 4-11)	4.95-5.38	0.87-0.89		Pan et al. 2007
peat-derived (pH 4-11)	4.37-5.14	0.76-0.86		Pan et al. 2007
Humin	6.06	0.64		Chefetz et al. 2000

†: 'Soft' organic carbon normalized partitioning coefficient; unit = $(\mu g/kg_{OC})(L_w/\mu g)^{nFr,OC}$.
*: LFER: $logK_{OC} = 0.98logK_{OW} - 0.32$ (Schwarzenbach et al. 2003).

(b) Phenanthrene $logK_{OC}$ and $n_{Fr,OC}$

Carbon Phase	$logK_{OC}$†	n	Remarks	Reference
Sorbate = Phenanthrene ($logK_{OC,phen,LFER}$ = 4.16)				
Humic acids				
Aldrich (pH 4-11)	4.21-4.42	0.91-0.95		Pan et al. 2007
Chelsea soil (pH 2-7)	4.13-4.55	0.85-0.92		Huang et al. 1997a
peat-derived	4.32	0.91		Wen et al. 2007
Peat				
Canadian peat	4.45	0.89		Huang et al. 1997a
	4.70	0.81		Weber et al. 2002
Houghton peat	4.71	0.75		Huang et al. 1997a
Michigan peat	4.34	0.87		Huang et al. 1997a
Peat-derived fractions				
Bound humic acid	4.38	0.87		Wen et al. 2007
Lipid	4.74	0.99		Wen et al. 2007
Insoluble residue	5.03	0.72		Wen et al. 2007

†: 'Soft' organic carbon normalized partitioning coefficient; unit = $(\mu g/kg_{OC})(L_w/\mu g)^{nFr,OC}$.
*: LFER: $logK_{OC} = 0.98logK_{OW} - 0.32$ (Schwarzenbach et al. 2003).

Chapter 6: Tables

Table 6 - 1. ΔG^x and K^x expressions for Adsorption, Adsorption, and Overall Sorption. **577**
Table 6 - 2. Apparent/Overall Enthalpy of Pyrene Sorption $(\Delta H_{d,app})^{\dagger}$ **578**
Table 6 - 3. Apparent Enthalpies of Sorption $(\Delta H_{d,app})$ for PAHs in Literature.† **579**
Table 6 - 4. Apparent/Overall Entropy of Pyrene Sorption $(\Delta S_{d,app})^{\dagger}$ **580**
Table 6 - 5. Enthalpies & Entropies of Phase Changes of PAHs (at 1 Bar)‡ **581**
Table 6 - 6. Summary of Enthalpies & Entropies of Pyrene Sorption from this Study. **583**

Table 6 - 1. ΔG^x and K^x expressions for Adsorption, Adsorption, and Overall Sorption.

Case	Key Assumptions	*ΔG^x = -RTln K^x	**K (L_w/kg_{solids}) → K^x
Absorption $i_{(w)} \leftrightarrow i_{(org)}$	Homogeneous absorption into "average" organic macromolecules	$\Delta G^x_{abs} = -RTln\left(\frac{x_{iorg}}{x_{iw}}\right)$	$K_{d,abs}\frac{MW_{org}/f_{org}}{\bar{V}_w} = K^x_{abs}$
Adsorption *simple, single-i* $i_{(w)} \leftrightarrow i_{(\exists)}$	Homogeneous binding sites with single adsorbate	$\Delta G^x_{ads-ss} = -RTln\left(\frac{\Theta_i}{x_{iw}}\right)$	$\frac{K_{d,ads}}{\kappa_{i,ads}\bar{V}_w/MW_i} = K^x_{ads-ss}$
simple, H_2O-i $i_{(w)} + H_2O_{(\exists)} \leftrightarrow i_{(\exists)} + H_2O_{(w)}$	Homogeneous binding sites with H_2O and i as adsorbates	$\Delta G^x_{ads-sH2O} = -RTln\left(\frac{\Theta_i}{x_{iw}(1-\Theta_i)}\right)$	$\frac{K_{d,ads}}{\kappa_{i,ads}\bar{V}_w/MW_i} \times \frac{1}{(1-\frac{S_{i,ads}}{\kappa_{i,ads}})} = K^x_{ads-sH2O}$
simple, org-i $i_{(w)} + org_{(\exists)} \leftrightarrow i_{(\exists)} + org_{(w)}$	Homogeneous binding sites with "average" organic macromolecules and i as adsorbates	$\Delta G^x_{ads-sorg} = -RTln\left(\frac{x_{orgw}\Theta_i}{x_{iw}(1-\Theta_i)}\right)$	$\frac{K_{d,ads}}{\kappa_{i,ads}\bar{V}_w/MW_i} \times \frac{C_{orgw}\bar{V}_w/MW_{org}}{(1-\frac{S_{i,ads}}{\kappa_{i,ads}})} = K^x_{ads-sorg}$
complex *(N of a-M of ∃-i)* $i_{(w)} + a_{n(\exists m)} \leftrightarrow i_{(\exists m)} + a_{n(w)}$	Heterogeneous binding sites (M's of ∃) with multiple competing co-adsorbates (N's of a) and i as adsorbates	$\Delta G^x_{ads-cplx} = -RTln\left(\frac{\prod_1^M x^N_{i\exists m}\prod_1^N x^M_{anw}}{x^{NxM}_{iw}\prod_{1,1}^{N,M} x_{an\exists m}}\right)$	**Not Available**
Sorption (Overall) $i_{(w)} \leftrightarrow i_{("d")}$	Disregard difference between adsorption and absorption (!)	$\Delta G^x_{d,app} = -RTln\left(\frac{x_{i"d"}}{x_{iw}}\right)$	$\frac{K_d}{\kappa_{id}\bar{V}_w/MW_i} = K^x_{d,app}$

*: ΔG^x's are excess molar free energies (J/mol) defined as $\Delta G^x = RTln(\Pi\gamma_{prod}/\Pi\gamma_{rxt})$.
**: K's are all concentration-based $(\mu g_i/kg_{solids})(L_w/\mu g_i)$ with $K=S/C_{iw}$.

Table 6 - 2. Apparent/Overall Enthalpy of Pyrene Sorption ($\Delta H_{d,app}$)†

	$C_{pyr,Eqm}$ ($\mu g_{pyr}/L_w$) = 0.01-0.05	0.1-0.5	1-5	10-20
Raw Sorption Data (No Regression)				
$\Delta H_{d,app}$ (J/mol)	-28000[a] (±4200)	-14000[b] (±7000)	-30000[b] (±6800)	-24000[b] (±14000)
r^2	1.0	0.68	0.91	0.60
Purely Descriptive Fitting of Sorption Data (Quadratic Regression)*				
$\Delta H_{d,app}$ (J/mol)	-7000 (±1000)	-16500 (±3300)	-23500 (±6300)	-25000 (±13000)
r^2	0.93-1.0	0.92-0.93	0.82-0.93	0.60-0.72
Linear+Freundlich (3-Parameter) Regression*				
$\Delta H_{d,app}$ (J/mol)	-13000 (±7000)	-19000 (±5100)	-24000 (±7800)	-27000 (±8700)
r^2	0.48-0.75	0.87-0.90	0.82-0.83	0.83
Two-Freundlich (4-Parameter) Regression*				
$\Delta H_{d,app}$ (J/mol)	-20000 (±4600)	-17000 (±5100)	-21000 (±7700)	-31000 (±10000)
r^2	0.90-0.91	0.79-0.88	0.77-0.80	0.81-0.82
Langmuir-Freundlich (4-Parameter) Regression*				
$\Delta H_{d,app}$ (J/mol)	-19000 (±3100)	-17000 (±3600)	-24000 (±6600)	-25000 (±10000)
r^2	0.94-0.96	0.91-0.93	0.84-0.90	0.72-0.79

†: $\Delta H_{d,app}$'s derived from sorption data after 10-month of equilibration. For 5-month $\Delta H_{d,app}$'s, please refer to Appendix 6-7.

*: $\Delta H_{d,app}$'s were averaged values estimated at the lower and upper bound of the range.

a: No equilibrium observations were made in the 0.01-0.05 $\mu g_{pyr}/L_w$ range. Only sorption observations at 6, 15, and 22°C were regressed.

b: Data from all four temperatures were used (i.e. 6, 15, 22, and 37°C)

Table 6 - 3. Apparent Enthalpies of Sorption ($\Delta H_{d,app}$) for PAHs in Literature.[†]

PAH	logK_{OW} (L/L)	$\Delta H_{d,app}$ (kJ/mol)	T(°C)	Sorbent	Reference
Naphthalene	3.33	–1.1 to –11	4–26	sediment	Piatt et al. 1996
Fluorene	4.32	–6.4 to –10.1	10–40	soil (whole)	Chilom et al. 2005
		–20.7	10–40	peat	Chilom et al. 2005
Phenanthrene	4.57	–3.3 to –5.6	4–26	sediment	Piatt et al. 1996
		–8.3 to –17.7	7–25	soot	Bucheli et al. 2000
		–9.3	10–40	sediment (whole)	Chilom et al. 2005
		–10.3 to –14.4	10–40	soil (whole)	Chilom et al. 2005
Pyrene	5.13	–6.8 to –16	10–40	soil (whole)	Chilom et al. 2005
		–10 to –18	4–26	sediment	Piatt et al. 1996
		–20.2	10–40	peat	Chilom et al. 2005
		–21.7	10–40	sediment	Chilom et al. 2005

Table 6 - 4. Apparent/Overall Entropy of Pyrene Sorption ($\Delta S_{d,app}$)†

	$C_{pyr,Eqm}$ ($\mu g_{pyr}/L_w$) = 0.01-0.05	0.1-0.5	1-5	10-20
Raw Sorption Data (No Regression)				
$\Delta S_{d,app}$ (J/mol.K)	81[a] (±15)	114[b] (±24)	50[b] (±23)	65[b] (±48)
Purely Descriptive Fitting of Sorption Data (Quadratic Regression)*				
$\Delta S_{d,app}$ (J/mol.K)	135 (±3)	88 (±11)	54 (±22)	43 (±44)
Linear+Freundlich (3-Parameter) Regression*				
$\Delta S_{d,app}$ (J/mol.K)	130 (±25)	101 (±17)	71 (±27)	57 (±30)
Two-Freundlich (4-Parameter) Regression*				
$\Delta S_{d,app}$ (J/mol.K)	107 (±16)	107 (±18)	82 (±26)	43 (±36)
Langmuir-Freundlich (4-Parameter) Regression*				
$\Delta S_{d,app}$ (J/mol.K)	112 (±11)	105 (±12)	72 (±23)	62 (±35)

†: $\Delta S_{d,app}$'s derived from sorption data after 10-month of equilibration. The overall capacity of sorption, κ_{id}, was assumed to be the sum of $\kappa_{i,ads}$ (estimated to be about 100000 $\mu g_{pyr}/kg_{solids}$) and $\kappa_{i,abs}$ (estimated from f_{OC} = 0.0296, a $\log K_{OC}$ of 5.3 (Table 5-9), and $C_{pyr,w} = C^{sat}_{pyr,w}$ = 140 $\mu g_{pyr}/L_w$; $\kappa_{i,abs}$ ~ 827000 $\mu g_{pyr}/kg_{solids}$).
*: $\Delta S_{d,app}$'s were averaged values estimated at the lower and upper bound of the range.
a: No equilibrium observations were made in the 0.01-0.05 $\mu g_{pyr}/L_w$ range. Only sorption observations at 6, 15, and 22°C were regressed.
b: Data from all four temperatures were used (i.e. 6, 15, 22, and 37°C)

Table 6 - 5. Enthalpies & Entropies of Phase Changes of PAHs (at 1 Bar)‡

‡: *** All thermochemical data were mole-fraction based ***.

(a) Dissolution of PAHs into Water at T=25°C (PAH$_{(S)}$ → PAH$_{(W)}$)

	ΔG^x_{diss} (kJ/mol)†	ΔH^x_{diss} (kJ/mol)*	ΔS^x_{diss} (J/mol.K)*
Naphthalene	30.6 (±1.0)	26.4 (±0.5)[a]	−13.9 (±1.7)[a]
Fluorene	38.4 (±1.2)	33.3 (±0.6)[a]	−18.2 (±2.1)[a]
Phenanthrene	40.0 (±1.7)	34.3 (±0.8)[a]	−19.2 (±2.9)[a]
	39.8 (±1.6)	38.0 (±0.8)[b]	−6.0 (±2.8)[b]
Anthracene	47.7 (±1.6)	44.1 (±0.8)[a]	−11.9 (±2.6)[a]
	47.8 (±1.4)	50.9 (±0.7)[b]	+10.5 (±2.5)[b]
Pyrene	45.3 (±3.0)	35.4 (±1.5)[a]	−33.3 (±5.2)[a]
Chrysene	56.2 (±3.8)	37.3 (±1.9)[a]	−63.3 (±6.5)[a]
Benzo(a)anthracene	52.2 (±2.8)	44.6 (±1.4)[a]	−25.4 (±4.8)[a]
Benzo(a)pyrene	56.7 (±0.8)	50.3 (±0.4)[a]	−21.6 (±1.4)[a]
	57.0 (±6.1)	34.3 (±3.0)[b]	−76.0 (±10.4)[b]

*: Derived from the mole-fraction solubility data at environmental temperature ranges from (a) May et al. 1983, (b) Whitehouse 1984.

†: Computed as $\Delta G^x_{diss} = \Delta H^x_{diss} - T\Delta S^x_{diss}$.

(b) Fusion/Melting of PAHs at $T_{melting}$ (PAH$_{(S)}$ → PAH$_{(L)}$)

	$T_{melting}$ (K)	ΔH^x_{fus} (kJ/mol)*	ΔS^x_{fus} (J/mol.K)*
Naphthalene	353.4	19.1 (±0.1)[a]	54.1 (±0.7)
		19.1 (------)	54.5 (------)[b]
Fluorene	389.2	19.6 (±0.1)[a]	50.4 (±1.4)
		19.6 (------)	50.5 (------)[b]
Phenanthrene	374.2	16.5 (±0.1)[a]	44.1 (±1.3)
		16.5 (------)	44.2 (------)[b]
Anthracene	490.7	29.4 (±0.1)[a]	59.9 (±3.2)
		28.9 (------)	58.6 (------)[b]
Pyrene	424.2	17.4 (±0.1)[a]	41.0 (±2.3)
		17.1 (------)	40.3 (------)[b]
Chrysene	528.2	26.2 (±0.2)[a]	49.6 (±4.8)
		26.2 (------)	49.3 (------)[b]
Benzo(a)anthracene	433.8	21.4 (±0.3)[a]	49.3 (±2.8)
		21.4 (------)	49.2 (------)[b]
Benzo(a)pyrene	449.7	17.3 (±0.6)[a]	38.5 (±3.5)
		17.3 (------)	38.2 (------)[b]

*: Calculated from $\Delta H^x_{fus} = T_m\Delta S^x_{fus}$, or from publications (referenced by letters).

a: Roux et al. 2008. b: Paasivirta et al. 1999.

(c) Sublimation of PAHs into Gas-Phase at T=25°C ($PAH_{(S)} \rightarrow PAH_{(G)}$)

	ΔG^{x}_{sub} (kJ/mol)[b]	ΔH^{x}_{sub} (kJ/mol)[a]	ΔS^{x}_{sub} (J/mol.K)[c]
Naphthalene	22.5	72.6 (±0.3)	168
Fluorene	34.4	86.5 (±1.3)	175
Phenanthrene	38.0	92.1 (±0.6)	181
Anthracene	45.7	101.9 (±1.3)	188
Pyrene	46.2	100.3 (±1.0)	181
Chrysene	64.0	123.4 (±4.2)	199
Benzo(a)anthracene	54.8	119.5 (±5.0)	217
Benzo(a)pyrene	63.6	120.5 (±2.7)	191

a: Recommended values at 25°C from Roux et al. 2008.
b: Calculated from vapor pressure of pure solids at 25°C as $\Delta G^{x}_{sub} = -RT\ln(P^{*}_{is})$.
c: $\Delta S^{x}_{sub} = (\Delta H^{x}_{sub} - \Delta G^{x}_{sub})/T$.

(d) Fusion/Melting of PAHs into Liquid at T=25°C ($PAH_{(S)} \rightarrow PAH_{(L)}$)†

	ΔG^{x}_{fus} (kJ/mol)	ΔH^{x}_{fus} (kJ/mol)	ΔS^{x}_{fus} (J/mol.K)
Naphthalene	2 (±0.5)	20.2 (±1.0)	60.9 (±12.6)
Fluorene	4.2 (±0.4)	14.9 (±2.3)	35.7 (±2.2)
Phenanthrene	2.4 (±1.5)	13.4 (±1.9)	36.7 (±6.5)
Anthracene	9.2 (±0.5)	20.9 (±4.3)	39.2 (±4.6)
Pyrene	2.6 (±3.2)	10.6 (±3.2)	26.8 (±11.7)
Chrysene	12.8 (±1.1)	16.0 (±8.8)	10.9 (±5.2)
Benzo(a)anthracene	5.7 (±1.2)	13.3 (±5.8)	25.5 (±5.4)
Benzo(a)pyrene	6.4 (±1.3)	9.6 (±4.3)	10.5 (±20.7)

†: See **Appendix 6-5** for data derivation and assumptions.

(e) Vaporization of Sub-cooled PAHs into Gas at T=25°C ($PAH_{(L)} \rightarrow PAH_{(G)}$)†

	ΔG^{x}_{vap} (kJ/mol)	ΔH^{x}_{vap} (kJ/mol)	ΔS^{x}_{vap} (J/mol.K)
Naphthalene	20.5 (±0.5)	52.5 (±1.0)	107.2 (±12.6)
Fluorene	30.2 (±0.4)	71.7 (±2.3)	139.0 (±2.2)
Phenanthrene	35.6 (±1.5)	78.8 (±1.9)	144.7 (±6.5)
Anthracene	36.5 (±0.5)	81.1 (±4.3)	149.3 (±4.6)
Pyrene	43.7 (±3.2)	89.8 (±3.2)	154.6 (±11.7)
Chrysene	51.3 (±1.1)	107.4 (±8.8)	188.3 (±5.2)
Benzo(a)anthracene	49.1 (±1.2)	106.2 (±5.8)	191.5 (±5.4)
Benzo(a)pyrene	57.2 (±1.3)	111.0 (±4.3)	180.4 (±20.7)

†: See **Appendix 6-5** for data derivation and assumptions.

Table 6 - 6. Summary of Enthalpies & Entropies of Pyrene Sorption from this Study.

	Enthalpy (kJ/mol)	**Entropy (J/mol.K)****
Apparent/Overall	–10 to –30 (±10)	$C_{pyr} << 1\mu g_{pyr}/L_w$: 140 $C_{pyr} >> 1\mu g_{pyr}/L_w$: 40 (±10 to 30)
Absorption	–26 to –35 (±9 to 13)	40 to 60 (±30)
Adsoption		
single-solute model (*ads-ss*)	–10 to –20 (±2 to 4)	135 to 140 (±20)
solute-H_2O model (*ads-sH_2O*)		
solute-Org model (*ads-sOrg*)		10 (±10)

**: Discussed in Appendix 6-6.

Chapter 7: Tables

Table 7 - 1. Summary of Sediment Suspensions for Pyrene Desorption Kinetic Experiment at 20-22°C. **585**
Table 7 - 2. Pyrene Sorption Isotherms for *a priori* Modeling of Pyrene Desorption Kinetics (BH#6 sedimentary fractions) **586**
Table 7 - 3. Modeling conditions – a summary. **587**
Table 7 - 4. Sensitivity of predicted $C_{pyr,w,Eqm}$ to model parameters ($logK_{OC}$=5.25, $logK_{BC}$=6.25, n_{BC}=0.25) **588**
Table 7 - 5. Sensitivity of predicted equilibration half-time ($t_{½,Eqm}$) to model parameters. **589**
Table 7 - 6. Effective diffusivity ($D_{eff,pw}$, $D_{eff,surf}$, $D_{eff,OM}$) expressions in literature. **590**
Table 7 - 7. Diffusivity of PAHs in organic media and water ($D_{iorg.phase}$, $D_{iw,}$). **591**
Table 7 - 8. Effective surface diffusion coefficient ($D_{eff,surf}$) of HOCs from literature. **592**
Table 7 - 9. End-point half-time ($t_{1/2,EndPoint}$), estimated from Intraparticle Porewater Diffusion Model + Occlusion-OC-BC isotherm. **593**
Table 7 - 10. Comparison of analytical solution & modeled profiles with literature. **594**
Table 7 - 11. Empirical expressions for desorption kinetics. **595**
Table 7 - 12. BH#6/NQB desorption kinetics by empirical regression (two- and three-compartment)* **596**
Table 7 - 13. Empirical desorption rates for soil/sedimentary pyrene (literature). **597**
Table 7 - 14. Survey of previous HOC desorption studies with data modeling. **598**

Table 7 - 1. Summary of Sediment Suspensions for Pyrene Desorption Kinetic Experiment at 20-22°C.

BH#6/NQB (nominal size)	R_{sw} (mg_{solids}/L_w)	f_{oc}* (g_{oc}/g_{solids})	f_{BC}*† (g_{BC}/g_{solids})	$S_{pyr,native}$* ($\mu g_{pyr}/kg_{solids}$)	$C_{pyr,end}$ (ng_{pyr}/L_w)	t_{end} (hr)
A-Set (dia.:38-75 μm)	23 72 277	0.0375 (±10%)	0.0035 (±9%)	1420 (±9%)	3.3±0.5 6.6±0.4 8.4±0.9	2890 2880 2860
C-Set (dia.:38-75 μm)	23 71 268	0.0375 (±10%)	0.0035 (±9%)	1350 (±19%)	2.8±0.2 11.3±0.3 14.2±0.3	750 750 720
L-Set (dia.:38-75 μm)	22 70 289	0.0375 (±10%)	0.0035 (±9%)	1350 (±19%)	5.0±0.6 8.3±0.4 11.5±1.3	2670 2670 2640
K-Set (dia.:75-106 μm)	21 83 253	0.0331 (±10%)	0.0083 (±7%)	3060 (±19%)	7.1±0.7 11.9±0.8 15.1±1.5	4420 4420 4420
IHG-Set (dia.:180-250 μm)	19 68 245	0.0306 (±9%)	0.0115 (±7%)	5420 (±15%)	6.6±0.5 13.4±0.6 15.0±1.7	5840 5840 5840

*: Parenthesized values were measurement uncertainties in 1 σ.
†: Measured by chemical thermal oxidation (375°C-24hr).

Table 7 - 2. Pyrene Sorption Isotherms for *a priori* Modeling of Pyrene Desorption Kinetics (BH#6 sedimentary fractions)

Isotherm Form*	Parameters	Reference
Classical OC *(absorption into OC)* $S_{pyr} = f_{OC}K_{OC}C_{pyr,w}$	$\log K_{OC} = 4.7$*	Karickhoff 1981; Schwarzenbach et al. 2003
Old OC-BC *(absorption into OC,adsorption onto BC)* $S_{pyr} = f_{OC}K_{OC} + f_{OC}K_{BC}C_{pyr,w}^{n_{BC}}$	$\log K_{OC} = 4.7$ $\log K_{BC} = 6.25\pm0.14$ $n_{BC} = 0.62\pm0.12$	Accardi-Dey and Gschwend (2002)
New OC-BC *(absorption into OC,adsorption onto BC)* $S_{pyr} = f_{OC}K_{OC}C_{pyr,w} + f_{OC}K_{BC}C_{pyr,w}^{n_{BC}}$	$\log K_{OC} = 5.25\pm0.04$ $\log K_{BC} = 6.25\pm0.06$ $n_{BC} = 0.25\pm0.09$	Table 5-6 (this study)
Occlusion-OC-BC *(occlusion; absorption into OC, adsorption onto BC)* $\mathcal{S}_{pyr} = S_{pyr,Occlu} + f_{OC}K_{OC}C_{pyr,w} + f_{OC}K_{BC}C_{pyr,w}^{n_{BC}}$	$S_{pyr,Occlu}/S_{pyr,tot} \approx 30\ \%$ occluded $\log K_{OC} = 5.10\pm0.1$ $\log K_{BC} = 6.30\pm0.06$ $n_{BC} = 0.42\pm0.12$	Table 5-6 (this study)

*: S or $\mathcal{S}$ in unit $\mu g_{pyr}/kg_{solids}$, Cpyr,w in unit $\mu g_{pyr}/L_w$; $K_{d,pyr} = S_{pyr}/C_{pyr,w}$; For Occlusion-OC-BC form, $K_{d,pyr} = (\mathcal{S}_{pyr} - S_{pyr,Occlu})/C_{pyr,w}$.

**: K_{OC} in unit L_w/kg_{OC}; K_{BC} in unit $(\mu g_{pyr}/kg_{BC})(L_w/\mu g_{pyr})^{nBC}$; n_{BC} is dimensionless.

Table 7 - 3. Modeling conditions – a summary.

Basic Set of Conditions

Numerical Conditions

No. of Grids	41	Shape Factor	3 (spherical aggregate)
$\Delta\tau(D_{iw})$	4–80[a]	Timesteps	50–200 $\times 10^3$ $\Delta\tau(D_{iw})$'s

Physicochemical Conditions

R_{sw}	19–289 mg_{solids}/L_w	$S_{pyr,init}$	1350–5420 $\mu g_{pyr}/kg_{solids}$
radius, R	27, 45, 105 μm	$C_{pyr,init}$	0 $\mu g_{pyr}/L_w$
ρ_s	2.5 kg_{solids}/L_{solids}	f_{OC}	0.0306 – 0.0375 kg_{OC}/kg_{solids}
ϕ	0.13[b]	f_{BC}	0.0035 – 0.0115 kg_{BC}/kg_{solids}
		D_{iw}(pyrene)	7.64×10^{-10} m^2/s (T=25°C)

A priori Modeling

$logK_{OC}$, $logK_{BC}$, n_{BC}: see Table 7-2.

Best-Fit Modeling

New-OC-BC	**"Universal" OC-BC (sediment)[c]**
$logK_{OC}$ = 5.25	$logK_{OC}$ = 4.75
$logK_{BC}$ = 6.25	$logK_{BC}$ = 5.95
n_{BC}: **Fitted**	n_{BC}: **Fitted**

a: Where $\Delta\tau(D_{iw})$ is the dimensionless time and is defined as $\Delta\tau(D_{iw}) = D_{iw}\Delta t/R^2$.
b: According to Wu et al. (1988). Also refer to the discussion on intra-aggregate porosity in section 4.3.1.1 in Chapter 7.
c: See **Appendix 7-16**.

Table 7 - 4. Sensitivity of predicted $C_{pyr,w,Eqm}$ to model parameters ($logK_{OC}$=5.25, $logK_{BC}$=6.25, n_{BC}=0.25).

Parameter*	Range	Effect on $C_{pyr,w,Eqm}$	Intensity†	$C_{pyr,end,obs}$ within Variation‡	Appendix
$S_{pyr,o}$	{1420–5420}±25%[a]	$S_{pyr,o}$ ↑, $C_{pyr,Eqm}$ ↑	Strong (0.3 to 2.4 ×)	~ 50%	7-2
f_{OC}	0.0306–0.0375±10%[b]	f_{OC} ↑, $C_{pyr,Eqm}$ ↓	Negligible (near unity)	cannot explain observation	7-3
f_{BC}	0.0035–0.0115±10%[b]	f_{BC} ↑, $C_{pyr,Eqm}$ ↓	Weak (0.7 to 1.5 ×)	~ 10%	7-4
n_{BC}	0.25±0.09[a]	n_{BC} ↑, $C_{pyr,Eqm}$ ↑	Very Strong (0.03 to 5 ×)	~ 80%	7-5
$logK_{OC}$	5.25±0.15[c]	K_{OC} ↑, $C_{pyr,Eqm}$ ↓	Negligible (near unity)	cannot explain observation	7-6
$logK_{BC}$	6.25±0.15[c]	K_{BC} ↑, $C_{pyr,Eqm}$ ↓	Strong (0.3 to 3.7 ×)	~ 50%	7-7

*: **UNITS**: $S_{pyr,o}$ in ($\mu g_{pyr}/kg_{solids}$), f_{OC} in (kg_{OC}/kg_{solids}), f_{BC} in (kg_{BC}/kg_{solids}), n_{BC} is dimensionless, K_{OC} in (L_w/kg_{OC}), K_{BC} in $(\mu g_{pyr}/kg_{BC})(L_w/\mu g_{pyr})^{nBC}$,

†: Values in parentheses indicates the variation in predicted $C_{pyr,w,Eqm}$ in factors/times of the basecase prediction.

‡: Approximate percentage of observed $C_{pyr,end}$'s that falls within (can be explained by) the uncertainty/variability of a particular parameter.

a: Actual or propagated uncertainties.

b: Supposed uncertainties (greater than those measured). This allowed a more 'conservative estimate on how fOC or fBC may affect predicted $C_{pyr,Eqm}$.

c: Supposed uncertainties (greater than propagated uncertainties). The ±0.15 range was chosen to restrict variability in logK's within a factor of two (0.3 log unit).

Table 7 - 5. Sensitivity of predicted equilibration half-time ($t_{½,Eqm}$) to model parameters.

Parameter*	Range	Effect on $t_{½,Eqm}$	Intensity†	Effect on $C_{pyr,w,Eqm}$	Appendix
$S_{pyr,o}$	{1420–5420}±25%[a]	$S_{pyr,o}$ ↑, $t_{½,Eqm}$ ↑	Strong (0.01 to 2.2 ×)	$S_{pyr,o}$ ↑, $C_{pyr,Eqm}$ ↑	7-2
f_{OC}	0.0306–0.0375±10%[b]	f_{OC} ↑, $t_{½,Eqm}$ ↓	Negligible (near unity)	f_{OC} ↑, $C_{pyr,Eqm}$ ↓	7-3
f_{BC}	0.0035–0.0115±10%[b]	f_{BC} ↑, $t_{½,Eqm}$ ↓	Weak (0.11 to 1.82 ×)	f_{BC} ↑, $C_{pyr,Eqm}$ ↓	7-4
n_{BC}	0.25±0.09[a]	n_{BC} ↑, $t_{½,Eqm}$ ↑	Very Strong (0.001 to 3 ×)	n_{BC} ↑, $C_{pyr,Eqm}$ ↑	7-5
$\log K_{OC}$	5.25±0.15[c]	K_{OC} ↑, $t_{½,Eqm}$ ↓	Negligible (near unity)	K_{OC} ↑, $C_{pyr,Eqm}$ ↓	7-6
$\log K_{BC}$	6.25±0.15[c]	K_{BC} ↑, $t_{½,Eqm}$ ↓	Strong (0.005 to 3.4 ×)	K_{BC} ↑, $C_{pyr,Eqm}$ ↓	7-7
particle radius	{27–105}±50%	r ↑, $t_{½,Eqm}$ ↑	Strong (0.25 to 3 ×)	No Effect	7-8
porosity	0.13±50%	ϕ ↑, $t_{½,Eqm}$ ↓	Strong (0.4 to 5.8 ×)	No Effect	7-9
shape factor	2 (cylindrical) to 3 (spherical)	S.F. ↑, $t_{½,Eqm}$ ↓	Strong (2 to 2.9 ×)	No Effect	7-9

*: **UNITS**: $S_{pyr,o}$ in ($\mu g_{pyr}/kg_{solids}$), f_{OC} in (kg_{OC}/kg_{solids}), f_{BC} in (kg_{BC}/kg_{solids}), n_{BC} is dimensionless, K_{OC} in (L_w/kg_{OC}), K_{BC} in $(\mu g_{pyr}/kg_{BC})(L_w/\mu g_{pyr})^{nBC}$,

†: Values in parentheses indicates the variation in predicted $t_{½,Eqm}$ in factors/times of the basecase prediction.

a: Actual or propagated uncertainties.

b: Supposed uncertainties (greater than those measured). This allowed a more 'conservative estimate on how f_{OC} or f_{BC} may affect predicted $C_{pyr,Eqm}$.

c: Supposed uncertainties (greater than propagated uncertainties). The ±0.15 range was chosen to restrict variability in logK's within a factor of two (0.3 log unit).

Table 7 - 6. Effective diffusivity ($D_{eff,pw}$, $D_{eff,surf}$, $D_{eff,OM}$) expressions in literature.

Expression for $D_{eff,x}$	Reference
$D_{eff,pw}$ (pore water diffusion)	
$= \frac{(D_{iw}/T_p)\emptyset_{pw}}{K_d\rho_s + \emptyset_{pw}}$	Crittenden et al. 1986; Ball et al. 1991; Stapleton et al. 1994; Ahn et al. 2005
$= \frac{\emptyset^2{}_{pw} D_{iw}}{K'_d\rho_s(1-\emptyset_{pw}) + \emptyset_{pw}}$	Wu and Gschwend 1988; Appendix 7-12
$= \frac{\emptyset_{pw} D_{iw}/\tau}{K_d\rho_s q_m(1-\emptyset_{pw}) + \emptyset_{pw}}$	Valderrama et al. 2008
$= \frac{\emptyset_{pw} F_{pw} D_{iw}}{K'_d\rho_s\emptyset_s + \emptyset_{pw} + K'_{OM}\emptyset_{OM}}$	**(3-path case)** Appendix 7-12
$D_{eff,surf}$ (surface diffusion)	
$= \frac{K_d\rho_s D_{is}}{K_d\rho_s + \emptyset_{pw}}$	Crittenden et al. 1986; Ball et al; 1991; Stapleton et al. 1994; Ahn et al. 2005;
$= \frac{K_d\rho_s q_m(1-\emptyset_{pw}) D_{is}}{K_d\rho_s q_m(1-\emptyset_{pw}) + \emptyset_{pw}}$	Valderrama et al. 2008
$= \frac{K'_d\rho_s(1-\emptyset_{pw}) F_s D_{is}}{K'_d\rho_s(1-\emptyset_{pw}) + \emptyset_{pw}}$	Appendix 7-12
$= \frac{\rho_s\emptyset_s F_s D_{is}}{\rho_s\emptyset_s + \frac{1}{K'_d}\emptyset_{pw} + \frac{1}{K'_{d-OM}}\emptyset_{OM}}$	**(3-path case)** Appendix 7-12
$D_{eff,OM}$ (organic-matter diffusion)	
$= \frac{\emptyset_{OM} F_{OM} D_{iOM}}{K'_{d-OM}\rho_s\emptyset_s + \frac{1}{K'_{OM}}\emptyset_{pw} + \emptyset_{OM}}$	**(3-path case)** Appendix 7-12

Table 7 - 7. Diffusivity of PAHs in organic media and water ($D_{iorg.phase}$, D_{iw},).

(a) $D_{iorg.phase}$

PAHs	Organic Phase*	$D_{iorg.phase}$ (m^2/s)	Condition	Reference
napathalene	paraffin	1.8×10^{-13}	20°C-solid	Ortiz et al. 1999
(2-ring)	petrolatum	1.5×10^{-12}	20°C-gel	Ortiz et al. 1999
	transmission oil	3.4×10^{-13}	20°C-liquid	Ortiz et al. 1999
phenanthrene	biofilm ('pure')	3.5×10^{-14}	25°C-gel	Wicke et al. 2008
(3-ring)	biofilm (25% soil HA)	2.8×10^{-14}	25°C-gel	Wicke et al. 2008
	creosote NAPL	4.4×10^{-18}	23°C-liquid	Lotfabad et al. 2003
	paraffin	3.0×10^{-14}	20°C-solid	Ortiz et al. 1999
	petrolatum	6.2×10^{-14}	20°C-gel	Ortiz et al. 1999
	transmission oil	3.8×10^{-15}	20°C-liquid	Ortiz et al. 1999
	PBA-PVP	3.0×10^{-20}	25°C-micelles	Teng et al. 1998
	PVP-PEO	2.2×10^{-20}	25°C-micelles	Teng et al. 1998
	POM	1.5×10^{-14}	25°C-solid	Ahn et al. 2005
	PS-PMA	1.0×10^{-21}	25°C-micelles	Teng et al. 1998
	PS-Latex	1.2×10^{-21}	25°C-micelles	Teng et al. 1998
anthracene	creosote NAPL	2.0×10^{-18}	23°C-liquid	Lotfabad et al. 2003
(3-ring)				
fluoranthene	biofilm ('pure')	2.5×10^{-14}	25°C-gel	Wicke et al. 2008
(4-ring)	biofilm (25% soil HA)	2.0×10^{-14}	25°C-gel	Wicke et al. 2008
	creosote NAPL	4.8×10^{-18}	23°C-liquid	Lotfabad et al. 2003
pyrene	biofilm ('pure')	2.5×10^{-14}	25°C-gel	Wicke et al. 2008
(4-ring)	biofilm (25% soil HA)	2.0×10^{-14}	25°C-gel	Wicke et al. 2008
	creosote NAPL	4.4×10^{-18}	23°C-liquid	Lotfabad et al. 2003
	paraffin	7.2×10^{-16}	20°C-solid	Ortiz et al. 1999
	petrolatum	4.5×10^{-15}	20°C-gel	Ortiz et al. 1999
	transmission oil	5.3×10^{-16}	20°C-liquid	Ortiz et al. 1999
	PBA-PVP	7.0×10^{-21}	25°C-micelles	Teng et al. 1998
	PVP-PEO	6.4×10^{-21}	25°C-micelles	Teng et al. 1998
	POM	6.3×10^{-15}	25°C-solid	Ahn et al. 2005
	PS-PMA	9.4×10^{-23}	25°C-micelles	Teng et al. 1998
	PS-Latex	1.3×10^{-22}	25°C-micelles	Teng et al. 1998
chrysene	creosote NAPL	2.3×10^{-18}	23°C-liquid	Lotfabad et al. 2003
(5-ring)				

*: PBA=poly(*tert*-butylacrylate); PVP=poly(vinylpyridine); PS=polystyrene; PEO=poly(ethylene oxide); POM=polyoxymethylene.

(b) D_{iw} (T=25°C)

PAHs	D_{iw} (m^2/s)**	$D_{iw,measured}$ (m^2/s)	Reference
benezene	1.08×10^{-9}	1.09×10^{-9}	Gustafson et al. 1994
naphthalene	9.48×10^{-10}	7.49×10^{-10}	Gustafson et al. 1994
acenaphthene	8.02×10^{-10}		
fluorene	8.30×10^{-10}		
phenanthrene	7.07×10^{-10}	4.37×10^{-10}	Gustafson et al. 1994
anthracene	8.16×10^{-10}	4.18×10^{-10}	Gustafson et al. 1994
fluoranthene	7.57×10^{-10}		
pyrene	7.64×10^{-10}	7.64×10^{-10}	Gustafson et al. 1994
chrysene	7.15×10^{-10}	7.15×10^{-10}	Gustafson et al. 1994

**: Estimated according to the correlation by Hayduk et al. (1974) (also in Schwarzenbach et al. 2003).

Table 7 - 8. Effective surface diffusion coefficient ($D_{eff,surf}$) of HOCs from literature.

PAHs	Sorbent	$D_{eff,surf}$ (m^2/s)*	Reference
naphthalene	Act. Carbon	2.6×10^{-14}	Valderrama et al. 2008
acenaphthene	Act. Carbon	6.7×10^{-14}	Valderrama et al. 2008
fluorine	Act. Carbon	2.6×10^{-14}	Valderrama et al. 2008
fluoranthene	Act. Carbon	2.8×10^{-14}	Valderrama et al. 2008
anthracene	Act. Carbon	1.7×10^{-14}	Valderrama et al. 2008
phenanthrene	Act. Carbon	2.0×10^{-16}	Ahn et al. 2005
pyrene	Act. Carbon	2.4×10^{-14}	Valderrama et al. 2008
pyrene	Act. Carbon	3.0×10^{-17}	Ahn et al. 2005
pyrene	Lake sediment	$7.5.6\times10^{-14}$	Stapleton et al. 1994

*: All reported $D_{eff,surf}$ values were derived as a fitted parameter from the particular kinetic model adopted by the researchers. Kinetic experiment in Valderrama et al. was conducted at 20°C; though unclear, it is believed that the Ahn et al. and Stapleton et al. also carried out their experiments at room temperature.

Table 7 - 9. End-point half-time ($t_{1/2,EndPoint}$), estimated from Intraparticle Porewater Diffusion Model + Occlusion-OC-BC isotherm.

	$t_{1/2,EndPoint}$ (h)*		
	from model + 30% occlusion**	from obs (readoff)†	from empirical fitted equation‡
Dia.38–75 μm			
A-set			
23 ppm	10–14	10–80	1.7–3.1
72	1.4–4.8	10–50	1.6–2.1
277	<0.1–0.7	<1	0.10–0.12
C-set			
23 ppm	9–14	10–40	400–675
71	1.3–4.8	50–200	471–542
268	<0.1–0.7	50–200	400–500
L-set			
22 ppm	10–14	100–400	135–390
70	1.4–4.8	50–200	182–440
289	<0.1–0.7	2–100	1.7–2.4
Dia.75–106 μm			
K-set			
23 ppm	15–47	80–200	107–124
72	<0.1–8.2	60–100	73–82
277	<0.1–1.3	50–150	85–90
Dia.180–250 μm			
IHG-set			
21 ppm	114–253	80–100	45–48
83	0.3–56	200–400	122–134
253	<0.1–16	60–100	81–82

*: $t_{1/2,EndPoint}$ = time at which $C_{pyr,w}=C_{pyr,w,EndPoint}$. Note that $C_{pyr,w,EndPoint}$ may or may not be the same as $C_{pyr,w,Eqm}$.

**: From Intraparticle Porewater Diffusion model with 30% occlusion of native pyrene with logKoc=5.1, $logK_{BC}$=6.3, and n_{BC}=0.42.

†: Visually read off from the raw data

‡: Determined from the empirically fitted equation for the kinetic data such that the empirical fit describes $C_{pyr,w}(t) = g(t)$, then $C_{pyr,w}(t_{1/2,EndPoint}) = 0.5C_{pyr,w}(t_{EndPoint})=0.5g(t_{EndPoint})$, where $t_{EndPoint}$ was taken to be 2160–2880 h (or 3–4 mo.). The empirical equation was a constrained 2-compartment model (see **Appendix 7-19**).

Table 7 - 10. Comparison of analytical solution & modeled profiles with literature.

(a) Analytical solutions for retarded spherical radial diffusion.*

M_τ/M_∞	τ @ $f_{iw}=0.5$**		
	from Crank†	from Wu et al.†	from this study‡
0.2	0.0018	0.0011	0.0012
0.3	0.0028	0.0027	0.0027
0.5	0.0110	0.0104	0.0110
0.7	0.0324	0.0298	0.0301
0.8	0.0529	0.0495	0.0547
0.95	0.148	N/A	0.147

*: With reference to Crank (1979) [limited volume case] and Wu et al. (1988).
**: $\tau = D_{eff}t/R^2$.
†: Read off from figures.
‡: Analytical solution as presented in section 4.1.2. ($\lambda=\beta$).

(b) Cylindrical Aggregate (or Shape Factor $\upsilon = 2$).*

M_τ/M_∞	τ @ $f_{iw}=0.5$**		τ @ $f_{iw}=0.1$**	
	from Crank†	from this study‡	from Crank†	from this study‡
0.2	0.0029	0.0024	0.0001	0.0001
0.3	0.0062	0.0062	0.0003	0.0003
0.5	0.0240	0.0225	0.0013	0.0013
0.7	0.0635	0.0631	0.0053	0.0051
0.8	0.106	0.104	0.0110	0.0113
0.95	0.260	0.261	0.0676	0.0662

*: With reference to Crank (1979); limited volume case. **: $\tau = D_{eff}t/R^2$.
†: Read off from figures. ‡: From modeled profile with concentration-independent K_d. For $f_{iw}=0.5$, $K_d=50000$ L_w/kg_{solids}, $R_{sw}=20$ mg_{solids}/L_w; for $f_{iw}=0.1$, $K_d=50000$ L_w/kg_{solids}, $R_{sw}=180$ mg_{solids}/L_w.

(c) Planar Aggregate (or Shape Factor $\upsilon = 1$).*

M_τ/M_∞	τ @ $f_{iw}=0.5$**		τ @ $f_{iw}=0.1$**	
	from Crank†	from this study‡	from Crank†	from this study‡
0.2	0.0090	0.0093	0.0004	0.0004
0.3	0.0225	0.0227	0.0011	0.0012
0.5	0.0767	0.0772	0.0052	0.0051
0.7	0.188	0.190	0.0188	0.0191
0.8	0.286	0.288	0.0388	0.0395
0.95	0.640	0.625	0.176	0.176

*: With reference to Crank (1979); limited volume case. **: $\tau = D_{eff}t/R^2$.
†: Read off from figures. ‡: From modeled profile with concentration-independent K_d. For $f_{iw}=0.5$, $K_d=50000$ L_w/kg_{solids}, $R_{sw}=20$ mg_{solids}/L_w; for $f_{iw}=0.1$, $K_d=50000$ L_w/kg_{solids}, $R_{sw}=180$ mg_{solids}/L_w.

Table 7 - 11. Empirical expressions for desorption kinetics.

Type	Expression*	Parameters	Ref.
Discrete-Compartmental			
1st order (simple)	$C(t) = (S_o - S_{Eqm\|End})R_{sw}(1 - e^{-kt})$	1–2	e
1st order + instantaneous desorbing fraction	$C(t) = S_{inst,o}R_{sw} + (S_o - S_{inst,o} - S_{Eqm\|End})R_{sw}(1 - e^{-kt})$	2–3	+
Two-compartmental (simple)	$C(t) = S_{s,o}R_{sw}(1 - e^{-k_s t}) + S_{r,o}R_{sw}(e^{-k_s t} - e^{-k_r t})$	3	d, b
Two-compartmental (constrained)	$C(t) = R_{sw}[(S_{s,o} - S_{Eqm\|End})(1 - e^{-k_s t}) + S_{r,o}(e^{-k_s t} - e^{-k_r t})]$	3–4	+
Three-compartmental (simple)	$C(t) = R_{sw}\begin{bmatrix} S_{vs,o}(1 - e^{-k_{vs} t}) + \\ S_{s,o}(e^{-k_{vs} t} - e^{-k_s t}) + S_{r,o}(e^{-k_{vs} t} - e^{-k_r t}) \end{bmatrix}$	5	c
Three-compartmental (constrained)	$C(t) = R_{sw}\begin{bmatrix} (S_{vs,o} - S_{Eqm\|End})(1 - e^{-k_{vs} t}) + \\ S_{s,o}(e^{-k_{vs} t} - e^{-k_s t}) + S_{r,o}(e^{-k_{vs} t} - e^{-k_r t}) \end{bmatrix}$	5–6	+
Polynomial			
Orthogonal Polynomial Fit	$C(t) = R_{sw}S_o(a_o + a_1 t^{0.5} + a_2 t)$	3	a
Elovich Model	$C(t) = R_{sw}S_o[a_{Elo} + b_{Elo}\ln(t)]$	2	a
Half-power Model	$C(t) = R_{sw}S_o[kt^{0.5}]$	1	d
Statistical/Distributive			
Gamma-Distributive Rates Model	$C(t) = R_{sw}S_o\left\{1 - \left(\frac{b}{(b + t)}\right)^a\right\}$	2	a, f

One-compartment Weibull Model (constrained)	$C(t) = (S_o - S_{Eqm\|End})R_{sw}[1 - \exp(-kt^b)]$	2–3	+
Two-compartment Weibull Model (constrained)	$C(t) = R_{sw}\{(S_{s,o} - S_{Eqm\|End})[1 - \exp(-k_s t^{bs})] + S_{r,o}[\exp(-k_s t^{bs}) - \exp(-k_r t^{br})]\}$	5–6	+

+: Modified by the author. *: In the case where equilibrium expectation cannot be made, $S_{Eqm|End}=S_{EndPoint}$; otherwise it is S_{Eqm}.
a: Wells et al. 2004. **b**: van den Heuvel et al. 2003. **c**: Cornelissen et al. 1997b. **d**: Karickhoff et al. 1985. **e**: Wu et al. 1988
f: Culver et al. 1997; Deitsch et al. 2000.

Table 7 - 12. BH#6/NQB desorption kinetics by empirical regression (two- and three-compartment)*

Sorbent	k_{rapid} (h^{-1}) [F_{rapid}]	k_{slow} (h^{-1}) [F_{slow}]	$k_{v.slow}$ (h^{-1}) [$F_{v.slow}$]	Remark
This Study (BH#6/NQB)				
dia.: 38–75 μm				
Two-Compartment (**Constrained**)	0.44–15.6 [1–8%]	------	60–820 $\times 10^{-6}$ [92–99%]	r^2=0.58–0.96
Three-Compartment (**Constrained**)	3.8–28.4 [1–5%]	1.3–290$\times 10^{-3}$ [0.5–6%]	3.9–790000000$\times 10^{-12}$ [90–98%]	r^2=0.76–0.97
dia.: 75–106 μm				
Two-Compartment (**Constrained**)	9.6–14$\times 10^{-3}$ [2–7%]	------	59–73 $\times 10^{-6}$ [93–98%]	r^2=0.78–0.85
Three-Compartment (**Constrained**)	1.5–3.3 [1–3%]	2.3–3.4$\times 10^{-3}$ [1–8%]	0.04–110000$\times 10^{-12}$ [89–98%]	r^2=0.95–0.96
dia.: 180–250 μm				
Two-Compartment (**Constrained**)	7.5–19$\times 10^{-3}$ [1–5%]	------	7.8–34 $\times 10^{-6}$ [95–99%]	r^2=0.79–0.91
Three-Compartment (**Constrained**)	0.36–0.39 [0.4–2%]	2.8–4.8$\times 10^{-3}$ [1–4%]	0.3–240000$\times 10^{-12}$ [94–99%]	r^2=0.88–0.94

Table 7 - 13. Empirical desorption rates for soil/sedimentary pyrene (literature).

Sorbent	k_{rapid} (h^{-1}) [F_{rapid}][a]	k_{slow} (h^{-1}) [F_{slow}][b]	$k_{v.slow}$ (h^{-1}) [$F_{v.slow}$][c]	Remark	Reference
Milwaukee Har. (sed.) (dia. 63-250 μm)	0.0756 [9%]	------	13×10^{-6} [91%]	native/field-aged; coal/wood fraction	Ghosh et al. 2001
Wemeldinge (sed.)	1.64 [30.5%]	0.0545 [6.6%]	157×10^{-6} [62.9%]	native/field-aged	van Noort et al. 2003
Milwaukee Har. (sed.) (dia.<63 μm)	0.0333 [94%]	------	209×10^{-6} [6%]	native/field-aged; clay-silt fraction	Ghosh et al. 2001
Hollands Diep (sed.)	1.26 [28.9%]	0.0642 [8.4%]	219×10^{-6} [62.7%]	native/field-aged	van Noort et al. 2003
W. Bearskin (sed.)	0.22 [24%]	0.0166 [24%]	450×10^{-6} [52%]	spiked (110d)	Kukkonen et al.2003
Lake Huron 9 (sed.)	0.15 [20%]	0.0122 [25%]	490×10^{-6} [55%]	spiked (110d)	Kukkonen et al.2003
Lake Michigan (sed.)	0.32 [37%]	0.0174 [25%]	630×10^{-6} [38%]	spiked (110d)	Kukkonen et al.2003
Lake Erie (sed.)	0.30 [44%]	0.0222 [26%]	710×10^{-6} [30%]	spiked (110d)	Kukkonen et al.2003
Wemeldinge	2.8 [20%]	------	800×10^{-6} [80%]	native/field-aged	Cornelissen et al. 1998b
Lake Huron 54 (sed.)	0.15 [38%]	0.0238 [26%]	990×10^{-6} [36%]	spiked (110d)	Kukkonen et al.2003
Terwill Pond	0.23 [47%]	0.0246 [31%]	1190×10^{-6} [22%]	spiked (110d)	Kukkonen et al.2003

Ketelmeer (sed.)	0.29 [57.9%]	0.0163 [30.6%]	1310×10^{-6} [11.5%]	spiked (7d)	Gomez-Lahoz et al. 2005
Varparanta (sed.)	1.3 [52.1%]	0.033 [34.3%]	1500×10^{-6} [13.6%]	spiked (7d)	Gomez-Lahoz et al. 2005
Pond 5 (sed.)	0.32 [53%]	0.041 [29%]	1830×10^{-6} [18%]	spiked (110d)	Kukkonen et al.2003
Petrol Harbor (sed.)	0.8 [75%]	------	1900×10^{-6} [25%]	native/field-aged	Cornelissen et al. 1998b

a: Fraction of rapidly desorbing pyrene. b: Fraction of slowly desorbing pyrene. c: Fraction of very slowly desorbing pyrene.

Table 7 - 14. Survey of previous HOC desorption studies with data modeling.

(a) Mechanistic Kinetic Models

Reference	System	HOC Aging	Model & Approach	Set-up	Nonlinear Isotherm	Remarks
Carroll et al. 1994	sediment	field-aged	Polymer diffusion (best fit)	batch	No	PCBs (mixed); drying-rehydration
Stapleton et al. 1994	sediment	spiked	Intraparticle pore diffusion + boundary layer mass transfer	batch	No	pyrene
Gong et al. 1998b	sediment	spiked	Intraparticle pore diffusion (best fit)	gas purging	No	PCBs
Rugner et al. 1999	aquifer	(Adsorption)	Intraparticle pore diffusion (best fit)	batch	Yes	phenanthrene
Karapanagioti et al. 2000, 2001	aquifer/ groundwater	(Adsorption)	Intraparticle pore diffusion (best fit)	batch	Yes	phenanthrene; adsorption+biodegradation

Ghosh et al. 2001	sediment	field-aged	Diffusion (varying temperature) (best fit)	batch	No	PAHs (MW=178–252) sampling by secondary sorptive medium
Shor et al. 2003b	sediment	field-aged	Two-compartment, intraparticle pore diffusion (best fit)	batch	Yes	PAHs; sampling by secondary sorptive medium

(b) Empirical Kinetic Models

Reference	System	HOC Aging	Empirical Form§	Parameters	Set-up	Remarks
Karickhoff et al. 1985	sediment/soil	spiked	Two compartment model	2	gas purging	hexachlorobenzene, trifluralin pentachlorobenzene, pyrene
Connaughton et al. 1993	soil	spiked	Distributed rate model	2	gas purging	naphthalene
Cornelissen et al. 1997b	sediment	field-aged/ spiked	Three compartment exponential form (unconstrained)	5	batch	PCBs, PAHs; sampling by secondary sorptive medium
Culver et al. 1997	aquifer/ groundwater	field-aged	Distributed rate model (best fit)	2	CSTR, column, & batch	TCE
Schlebaum et al. 1999	soil	spiked	Composite rate form*	6	gas purging	pentachlorobenzene
Deitsch et al. 2000	soil	spiked	Distributed rate model (best fit)	2	batch	1,2-Dichlorobenzene; adsorption-desorption experiment
Ghosh et al. 2001	sediment	field-aged	Two compartment exponential form (unconstrained)	3	batch	PAHs (MW=178–252) sampling by secondary sorptive medium

Braida et al. 2002	soil	spiked	Logarithmic form**	3	batch	phenanthrene; sampling by secondary sorptive medium
van den Heuvel et al. 2003	sediment	field-aged	Three compartment exponential form (unconstrained)	5	batch	PAHs; sampling by secondary sorptive medium
Kukkonen et al. 2003	sediment	spiked	Three compartment exponential form (unconstrained)	5	batch	PCBs, PAHs; sampling by secondary sorptive medium
van Noort et al. 2003	sediment	field-aged	Three compartment exponential form (unconstrained)	5	batch	CBs, PCBs, PAHs; sampling by secondary sorptive medium
Sharer et al. 2003	soil	spiked	Compartmental model	3	batch	CBs; liquid scintillation counting
Sabbah et al. 2004	soil	spiked	Two compartment model	2	column	phenanthrene, fluoranthene
Gomez-Lahoz et al. 2005	sediment	spiked	Three compartment exponential form (unconstrained)	5	batch	PAHs; sampling by secondary sorptive medium

§: See Table 7-11 for mathematical expressions.

*: Composite rate form: $\frac{dC}{dt} = R_{sw}\left(\sum k_{s,j} S_j\right) - k_{Fr} C^n - k_{Lnr} C - k_{gp} C$. Please refer to the original publication for details.

**: Logarithmic form: $\frac{S_t}{S_o} = a + b\ln(t) + c[\ln(t)]^2$.

Chapter 8: Tables

Table 8 - 1. Validation of Diffusion Model (Infinite Bath, No Boundary Layer Case)...**602**
Table 8 - 2. $\log K_{OC}$, $\log K_{BC}$, and D_{iw} of selected PAHs used for modeling.....**603**
Table 8 - 3. Modeling conditions.....**604**

Table 8 - 1. Validation of Diffusion Model (Infinite Bath, No Boundary Layer Case).

(a) Spherical Aggregate diffusion (Shape Factor $\upsilon = 3$).*

M_τ/M_∞	$\tau = D_{eff}t/R^2$; Infinite Bath ($K_dR_{sw}=0$); $\delta=0$	
	from Crank†	Model (this study)
0.2	0.0038	0.0039
0.5	0.0306	0.0300
0.87	0.1600	0.1570
0.98	0.3600	0.3460

*: With reference to Crank (1979) [uptake fraction = 0 in the limited volume case].
†: Read off from figures.

(b) Cylindrical Aggregate (Shape Factor $\upsilon = 2$).*

M_τ/M_∞	$\tau = D_{eff}t/R^2$; Infinite Bath ($K_dR_{sw}=0$); $\delta=0$	
	from Crank†	Model (this study)
0.2	0.0088	0.0084
0.3	0.0207	0.0203
0.5	0.0645	0.0634
0.7	0.1475	0.1460
0.9	0.3364	0.3340

*: With reference to Crank (1979) [uptake fraction = 0 in the limited volume case].
†: Read off from figures.

(c) Planar Aggregate (or Shape Factor $\upsilon = 1$).*

M_τ/M_∞	$\tau = D_{eff}t/R^2$; Infinite Bath ($K_dR_{sw}=0$); $\delta=0$	
	from Crank†	Model (this study)
0.2	0.0306	0.0313
0.3	0.0708	0.0710
0.5	0.1936	0.1980
0.7	0.4058	0.4020
0.9	0.8556	0.8470

*: With reference to Crank (1979) [uptake fraction = 0 in the limited volume case].
†: Read off from figures.

Table 8 - 2. $logK_{OC}$, $logK_{BC}$, and D_{iw} of selected PAHs used for modeling.

PAH†	$logK_{BC}$* <range>	$logK_{OC}$* (L_w/kg_{OC})	D_{iw}** (m^2/s)
naphthalene (*2-ring*)	3.9[a] <N/A>	2.9	9.5×10^{-10}
phenanthrene (*3-ring*)	5.8 <5.3 – 7.1>	4.2	7.1×10^{-10}
pyrene (*4-ring*)	6.3[b] <5.6 – 6.8>	4.7	7.6×10^{-10}
benzo(a)pyrene (*5-ring*)	7.8 <6.4 – 9.1>	5.4	6.7×10^{-10}

†: Please see **Appendix 8-1** for the reported $logK_{BC}$'s and the LFER-derived $logK_{BC}$'s (References used were: Bucheli et al. 2000; Jonker et al. 2002; Accardi-Dey and Gschwend 2003; Adams 2003; Schwarzenbach et al. 2003; Lohmann et al. 2005),

*: Unit: K_{BC} in $(\mu g_{PAH}/kg_{BC})(L_w/\mu g_{PAH})^{nBC}$.

**: Estimated according to the correlation by Hayduk et al. (1974) as in Schwarzenbach et al. (2003).

a: The author could not find any reported literature value for naphthalene. This value was estimated from LFER proposed in Schwarzenbach et al. (2003).

b: The author used 6.3 instead of the range averaged value of 6.2 on the reason that 6.3 has been observed several times (the Old-OC-BC, the New-OC-BC, and the Occlusion-OC-BC isotherms).

Table 8 - 3. Modeling conditions.

(A) Silt-only Single-Domain (Homogeneous)

Basic Set of Conditions			
Numerical Conditions			
No. of Grids	41	Shape Factor	3 (spherical aggregate)
Physicochemical Conditions			
ϕ	0.15[a]	ρ_s	2.5 kg_{solids}/L_{solids}
Infinite-Bath (pyrene only) [Section 3.3]			
$S_{PAH,o}$	1000, 5000 $\mu g_{pyr}/kg_{solids}$	f_{OC}	0.02 kg_{OC}/kg_{solids}
$C_{PAH,bulk}$	constant at 0 or 0.01 $\mu g_{pyr}/L_w$	f_{BC}	0.002 kg_{BC}/kg_{solids}
δ/R	0, 0.25, 0.5, 1	Classical-OC ($logK_{OC}$=4.7)	
R_{sw}	*not applicable*	Old-OC-BC ($logK_{OC}$=4.7; $logK_{BC}$=6.3; n_{BC}=0.62)	
radius, R	100 μm	New-OC-BC ($logK_{OC}$=5.25; $logK_{BC}$=6.25; n_{BC}=0.25)	
		Occlusion ($logK_{OC}$=5.1; $logK_{BC}$=6.3; n_{BC}=0.42; 30% occlusion; see Table 5-)	
Infinite-Bath (Four PAHs) [Section 3.4]			
$S_{PAH,o}$	200, 1000, 5000 $\mu g_{pyr}/kg_{solids}$	f_{OC}	0.02 kg_{OC}/kg_{solids}
$C_{PAH,bulk}$	constant at 0 $\mu g_{pyr}/L_w$	f_{BC}	0.002 kg_{BC}/kg_{solids}
δ/R	0, 0.25, 0.5, 1	$logK_{OC}$	see Table 8-2
D_{iw}(PAH)	see Table 8-2	$logK_{BC}$	see Table 8-2
R_{sw}	*not applicable*	n_{BC}:	0.2, 0.4, 0.6, 0.8, 1
radius, R	100 μm		
Closed System (naphthalene & pyrene)			
$S_{PAH,o}$	200, 1000, 5000 $\mu g_{pyr}/kg_{solids}$	f_{OC}	0.02 kg_{OC}/kg_{solids}
$C_{PAH,bulk,o}$	0 $\mu g_{pyr}/L_w$	f_{BC}	0.002 kg_{BC}/kg_{solids}
δ/R	*not applicable*	$logK_{OC}$	see Table 8-2
D_{iw}(PAH)	see Table 8-2	$logK_{BC}$	see Table 8-2
R_{sw}	20, 200, 2000 mg_{solids}/L_w	n_{BC}:	0.4, 0.6, 0.8, 1
radius, R	10, 100 μm		

a: Rounded up to the nearest 0.05 from the value of 0.13 reported by Wu and Gschwend(1988).

(B) Char-in-Silt Dual-Domain (Heterogeneous)

Basic Set of Conditions

Numerical Conditions

No. of Grids	41 (both silt & char)	Shape Factor	3 (spherical aggregate)

Physicochemical Conditions

R_{sw}	variable	ρ_{silt}	2.5 kg_{solids}/L_{solids}
char radius, R_c	10 μm	ϕ_{silt}	0.15[b]
aggregate R_{agg}	25, 50, 100 μm	ρ_{char}	2 kg_{solids}/L_{solids}
		ϕ_{char}	0.15, 0.5, 0.9

Infinite-Bath (pyrene only) [Section 3.7]

$S_{PAH,o}$	200, 1000, 5000 $\mu g_{pyr}/kg_{solids}$	f_{OC}	0.02 kg_{OC}/kg_{solids}
$C_{PAH,bulk}$	constant at 0 $\mu g_{pyr}/L_w$	f_{BC}	0.002 kg_{BC}/kg_{solids}
δ/R	0, 0.25, 0.5, 1	$\log K_{OC}$	see Table 8-2
D_{iw}(PAH)	see Table 8-2	$\log K_{BC}$	see Table 8-2
R_{sw}	*not applicable*	n_{BC}:	0.2, 0.4, 0.6, 0.8, 1
radius, R	100 μm		

Closed System (pyrene only) [Section 3.6]

Initial Condition

$C_{agg,pw,o}$	0.050 $\mu g_{pyr}/L_w$
$C_{bulk,o}$	0 $\mu g_{pyr}/L_w$

Others

δ/R	*not applicable*
D_{iw}(PAH)	see Table 8-2
R_{sw}	20, 200, 2000 mg_{solids}/L_w

Silt Domain

f_{OC}	0.02 kg_{OC}/kg_{solids}
f_{BC}	0.002 kg_{BC}/kg_{solids}

Char Domain

f_{OC}	0 kg_{OC}/kg_{solids}
f_{BC}	1 kg_{BC}/kg_{solids}

Isotherm

$\log K_{OC}$	see Table 8-2
$\log K_{BC}$	see Table 8-2
n_{BC}:	0.4, 0.6, 0.8, 1

a: Rounded up to the nearest 0.05 from the value of 0.13 reported by Wu and Gschwend(1988).

Chapter 9: Tables

Table 9 - 1. Characteristic timescales of processes in Boston Harbor. **607**
Table 9 - 2. Summary of basecase condition/parameters for modeling.....**608**
Table 9 - 3. Sorption Isotherms Used for Regional Modeling. **610**
Table 9 - 4. Sensitivity of bed-WC EqP model at $S_{pyr,bed}$ = 10000 $\mu g_{pyr}/kg_{solids}$. **611**
Table 9 - 5. Sensitivity of TSS-WC EqP model at $S_{pyr,bed}$ = 10000 $\mu g_{pyr}/kg_{solids}$. **612**

Table 9 - 1. Characteristic timescales of processes in Boston Harbor.

Process	$t_{1/2,process}$ or $t_{process}$ (d)	Reference
Physical Process		
Resuspension of sediment	0.25	Ravens 1997
Surficial bed porewater flushing	5–20	McGroddy et al. 1995
Water column/harbor flushing	3–10	Stolzenbach et al. 1998
Transformation Process (on pyrene)		
Biodegradation	14–55	Shiaris 1989; Appendix 9-3
Direct photolysis	0.7–20 (summer) 3–90 (winter)	Appendix 9-1
Indirect photolysis	40–4000 (summer) 150–14000 (winter)	Appendix 9-2
Phase-Transfer Process		
Desorption of pyrene from suspended solids	~<0.1–7	Appendix 9-6 (table B)

Table 9 - 2. Summary of basecase condition/parameters for modeling.

(A) EqP Models

EqP Model: Surficial Bed Layer vs Water Column (Closed System)

Surficial Bed Layer Properties

Thickness (L_B)	10 cm
$\phi_{surf.bed}$	0.8 L_{pw}/L_{bed}
ρ_s	2.5 kg_{solids}/L_{solids}

Water Column Properties

Column Depth	10 m
ρ_w	1.0 kg_w/L_w

Water Column Chemical Properties

$C_{pyr,o}$	0 $\mu g_{pyr}/L_w$

Bed Chemical Properties (generic)

f_{OC}	0.02 kg_{OC}/kg_{solids}
f_{BC}	0.002 kg_{BC}/kg_{solids}
$S_{pyr,o}$	100–100000 $\mu g_{pyr}/kg_{solids}$

Bed Chemical Properties (BH6/NQB)

f_{OC}	0.0308 kg_{OC}/kg_{solids}
f_{BC}	0.006 kg_{BC}/kg_{solids}
$S_{pyr,o}$	100–100000 $\mu g_{pyr}/kg_{solids}$

Isotherm for Pyrene Sorption (see Table 9-3)

Old-OC-BC (n_{BC}=0.62)
Occlusion-OC-BC (n_{BC}=0.42)

EqP Model: Suspended Solids vs Water Column (Closed System)

Surficial Bed Layer Properties

Thickness (L_B)	10 cm
$\phi_{surf.bed}$	0.8 L_{pw}/L_{bed}
ρ_s	2.5 kg_{solids}/L_{solids}

Water Column Properties

Column Depth	10 m
ρ_w	1.0 kg_w/L_w

Water Column Chemical Properties

$C_{pyr,o}$	0 $\mu g_{pyr}/L_w$
R_{sw}	20 mg_{solids}/L_w

Bed Chemical Properties (generic)

f_{OC}	0.02 kg_{OC}/kg_{solids}
f_{BC}	0.002 kg_{BC}/kg_{solids}
$S_{pyr,o}$	100–100000 $\mu g_{pyr}/kg_{solids}$

Bed Chemical Properties (BH6/NQB)

f_{OC}	0.0308 kg_{OC}/kg_{solids}
f_{BC}	0.006 kg_{BC}/kg_{solids}
$S_{pyr,o}$	100–100000 $\mu g_{pyr}/kg_{solids}$

Isotherm for Pyrene Sorption (see Table 9-3)

Old-OC-BC (n_{BC}=0.62)
Occlusion-OC-BC (n_{BC}=0.42)

(B) Pseudo Steady State Models

Steady-State Model: $r_{TSS,des} + r_{pw,f} = r_{wc,f}$

Surficial Bed Layer Properties

Thickness (L_B)	f_{OC}
$\phi_{surf.bed}$	f_{BC}
ρ_s	$S_{pyr,o}$

Water Column Properties

Column Depth	5 m
ρ_w	1.0 kg_w/L_w

Water Column Chemical Properties

$C_{pyr,o}$	0 $\mu g_{pyr}/L_w$
$R_{sw,TSS-WC}$	10 mg_{solids}/L_w
$t_{resuspension}$	6 h per resuspension

TSS Desorption Rate

$t_{1/2,des}$	0.9–3.9 d (20–25°C)

Bed Chemical Properties (BH6/NQB)

f_{OC}	0.0308 kg_{OC}/kg_{solids}
f_{BC}	0.006 kg_{BC}/kg_{solids}
$S_{pyr,o}$	100–100000 $\mu g_{pyr}/kg_{solids}$
$S(z=0)/S(z=L_B)$	0.6
at z=0	S-Cpw Not at Eqm
at $z=L_B$	S-Cpw at Eqm

Isotherm for Pyrene Sorption (see Table 9-3)

***Old-OC-BC (n_{BC}=0.62)

Water Column Flushing Rate

$t_{WC,f}$ (low–high)	3–10 d
$t_{WC,f,geom.-mean}$	5.5 d

Porewater Flushing Rate

$t_{pw,f}$ (low–high)	5–20 d
$t_{pw,f,geom.-mean}$	10 d

Steady-State Model: $r_{TSS,des} + r_{pw,f} + r_{fresh} + r_{atm,dep} = r_{h_D} + r_{biodeg.} + r_{wc,f}$

All parameters same as above;

Freshwater Input Rate

$r_{freshwater}$	2.8 $\mu g_{pyr}/d$ (per m^2 harbor)

Direct Photolysis Rate

Halftime slope	1.28 $d/m_{WC.depth}$ (Sum.)
	4.97 $d/m_{WC.depth}$ (Win.)
$t_{1/2,dir.photolysis}$	Halftime slope*0.5*$Depth_{WC}$

Biodegradation Rate

$t_{1/2,biodeg}$ (Sum.)	14–55 d (mean = 28 d)
$t_{1/2,biodeg}$ (Win.)	55–220 d (mean = 111 d)

Atmospheric Depositional Rate

r_{atm} (Sum.)	0.02 – 0.13 $\mu g_{pyr}/m^2.d$
r_{atm} (Sum.)	0.051 (geom.-mean)
r_{atm} (Win.)	0.07 – 0.44 $\mu g_{pyr}/m^2.d$
r_{atm} (Win.)	0.175 (geom.-mean)

***: Note that the isotherm was applied only to the determination of $S_{bed,pyr}(z=L_B)$.

Table 9 - 3. Sorption Isotherms Used for Regional Modeling.

Isotherm Form*	Parameters	Reference
OC-BC Partitioning (Old OC-BC) $S_{pyr} = f_{OC}K_{OC} + f_{OC}K_{BC}C_{pyr,w}^{n_{BC}}$	$\log K_{OC} = 4.7$ $\log K_{BC} = 6.25 \pm 0.14$ $n_{BC} = 0.62 \pm 0.12$	Accardi-Dey et al. (2002)
Occlusion-OC-BC Form $\mathcal{S}_{pyr} = S_{pyr,Occlu} + f_{OC}K_{OC}C_{pyr,w} + f_{OC}K_{BC}C_{pyr,w}^{n_{BC}}$	$S_{pyr,Occlu}/S_{pyr,tot} \approx 30\ \%$ occluded $\log K_{OC} = 5.10 \pm 0.1$ $\log K_{BC} = 6.30 \pm 0.06$ $n_{BC} = 0.42 \pm 0.12$	See Table 5-4, 5-6; see also Chapter 5 section 3.1.2.6 for justification.

*: S or $\mathcal{S}$ in unit $\mu g_{pyr}/kg_{solids}$, Cpyr,w in unit $\mu g_{pyr}/L_w$; $K_{d,pyr} = S_{pyr}/C_{pyr,w}$; For Occlusion-OC-BC form, $K_{d,pyr} = (\mathcal{S}_{pyr} - S_{pyr,Occlu})/C_{pyr,w}$.

**: K_{OC} in unit L_w/kg_{OC}; K_{BC} in unit $(\mu g_{pyr}/kg_{BC})(L_w/\mu g_{pyr})^{nBC}$; n_{BC} is dimensionless.

Table 9 - 4. Sensitivity of bed-WC EqP model at $S_{pyr,bed}$ = 10000 $\mu g_{pyr}/kg_{solids}$.

For BH#6/NQB Condition with Occlusion-OC-BC Isotherm (30% occluded)

At $S_{pyr,bed}$ = 10000 $\mu g_{pyr}/kg_{solids}$	**$C_{pyr,WC}$ (ng_{pyr}/L_w)**
Observed	5–140
Parameter/Variable	
L_B = 10 cm (basecase)	206
1	186
5	203
20	207
L_{WC} = 10 m (basecase)	206
1	208
5	207
20	203
f_{OC} = 0.0308 g_{OC}/g_{solids} (basecase)	206
0.0154	234
0.0616	168
f_{BC} = 0.006 g_{BC}/g_{solids} (basecase)	206
0.003	563
0.012	50
$\log K_{BC}$ = 6.3 (basecase)	206
6.0	563
6.6	50
n_{BC} = 0.42 (basecase)	206
0.30	129
0.54	270

Table 9 - 5. Sensitivity of TSS-WC EqP model at $S_{pyr,bed}$ = 10000 $\mu g_{pyr}/kg_{solids}$.

For BH#6/NQB Condition with Occlusion-OC-BC Isotherm (30% occluded)

$S_{pyr,bed}$ set at:	**10000 $\mu g_{pyr}/kg_{solids}$ $C_{pyr,WC}$ (ng_{pyr}/L_w)**	**50000 $\mu g_{pyr}/kg_{solids}$ $C_{pyr,WC}$ (ng_{pyr}/L_w)**
Observed	5–140	5–140
Parameter/Variable		
$R_{sw,TSS-WC}$ = 20 mg_{solids}/L_w(basecase)	61	486
2	10	62
100	134	1500
500	186	2800
f_{OC} = 0.0308 g_{OC}/g_{solids} (basecase)	61	486
0.0154	63	502
0.0616	58	457
f_{BC} = 0.006 g_{BC}/g_{solids} (basecase)	61	486
0.003	90	563
0.012	29	360
$\log K_{BC}$ = 6.3 (basecase)	61	486
6.0	90	562
6.6	29	361
n_{BC} = 0.42 (basecase)	61	486
0.30	43	472
0.54	75	498

Chapter 10: Tables

Table 10 - 1. Estimated maximum thickness of various specimens within the thin-film constraints considering only C, N, and O X-ray absorption*. **614**
Table 10 - 2. Relative ratios of $Q_K\omega_K$ between carbon and nitrogen/oxygen*. **614**
Table 10 - 3. EDX peak spread, σ_K, for C, N, O, and Si. **614**
Table 10 - 4. Characteristic O/C and N/C atomic ratios determined from spot EDX analysis for various carbon matters*. **615**
Table 10 - 5. Effect of Pixel Consolidation on Coverage Fraction of Graphitic Pixels (Pure C, no N or O)*. **616**
Table 10 - 6. Quantification of BC by STEM-EDX Elemental Mapping on Selected Samples/Sites on the Basis of Sample-Occupancy*. **617**
Table 10 - 7. Fraction of Graphitic Carbon to Total Carbon in Selected Samples by STEM-EDX Elemental Mapping. **618**
Table 10 - 8. STEM-EDX derived Graphitic Fraction and Literature Values. **618**
Table 10 - 9. Elemental atomic ratios of C, N, and H in various carbonaceous matters. **619**

Table 10 - 1. Estimated maximum thickness of various specimens within the thin-film constraints considering only C, N, and O X-ray absorption*.

Specimen / Criterion	ε_{Crit}	Maximum Specimen Thickness t (nm)				
		Carbon†	SiO	SiO_2	$C_6H_{12}O_6$	$C_{12}H_{26}$
Tixier & Philibert	0.1	6	7	9	18	21
	0.25	15	17	22	45	53
	0.5	30	35	44	89	106
Goldstein et al.	0.1	22	22	32	177	77
	0.25	54	56	80	442	193
	0.5	109	112	159	884	385

* Maximum thickness of is solved by setting $\varepsilon=\varepsilon_{Crit}$ for C, N, and O X-rays. The reported thickness is the thinnest specimen out of the C, N and O-based thickness estimates. The mass absorption coefficients of the specimen were extrapolated from values obtained via the NIST online search module (Chantler et al. 2005). Coefficient estimate at K-edges was difficult due to the discontinuity. The thickness values reported here correspond to absorption coefficients obtained by simple averaging of the lowest and highest coefficients at the K-edges. For details and other thickness estimating cases, see Appendix 10-1.
† Graphite.

Table 10 - 2. Relative ratios of $Q_K\omega_K$ between carbon and nitrogen/oxygen*.

	$\Phi_{CN}=(Q\omega)_C/(Q\omega)_N$		$\Phi_{CO}=(Q\omega)_C/(Q\omega)_O$	
	a	b	a	b
Theory	0.70 – 0.89	1.23 – 1.52	0.52 – 0.79	0.92 – 1.35
Obs.	0.85 – 1.10	1.49 – 1.89	0.80 – 1.11	1.41 – 1.89

* ω_K models by Wentzel (1927), Laberrigue-Frolow & Radvanyi (1956), Byrne & Howarth (1970), and McGuire (1970) were used. For Q_K models references, see *a* and *b*.
[a] Computed from ionization cross-section models by Mott & Massey (1949), Worthington & Tomlin (1956), Green & Cosslett (1961), Gryzinski (1965), and Lotz (1970). For Q_K model details and calculation, refer to Appendix 10-2.
[b] Computed from ionization cross-section models by Drawin (1963). For Q_K model details and calculation, refer to Appendix 10-2.

Table 10 - 3. EDX peak spread, σ_K, for C, N, O, and Si.

Element*	E_{peak} (keV)	$\sigma_{K\text{-line}}$†	r^2	n
Carbon	0.28	1.70	0.99	85
Nitrogen‡	0.40	1.52	0.76	44
Corr. visual insp.		[1.51]	[0.61]	
Corr. C-bkgd		[1.21]	[0.81]	
Corr. O-bkgd		[0.69]	[0.73]	
No correction		[0.61]	[0.71]	
Oxygen	0.54	1.76	1.00	88
Silicon	1.76	2.14	1.00	52

* All peaks were associated with the K-line of the elements.
† Unit in area/count.keV = keV^{-1}.
‡ Corrected for signal-tailing from both C and O X-ray peaks by subtracting the sum of the C and O signal background, which were chosen at 180 eV and 680 eV, respectively. This correction scheme assumed that EDX peaks were symmetric and that the background at the N X-ray peak (~400 eV on EDX spectrum) was contributed only by the C and O signals.

Table 10 - 4. Characteristic O/C and N/C atomic ratios determined from spot EDX analysis for various carbon matters*.

	Integrated Area Method†			Peak Height Method‡				
	N/C	$O/C_{uncor.}$ [a]	$O/C_{corr.}$ [b]	$N/C_{uncor.}$ [c]	$O/C_{uncor.}$ [a]	$N/C_{corr.}$ [d]	$O/C_{corr.}$ [e]	n[f]
Samples								
Humic Acid[g]	0.004±0.012	1.3±1.2	0.89±0.96	0.11±0.07	2.2±1.8	0	1.5±1.3	27
Nicotinamide[g]	0.072±0.046	0.6±1.3	0.24±0.12	0.27±0.08	0.9±1.2	0.17±0.13	0.49±0.14	61
Melanoidin[h]	0.008±0.014	0.032±0.014	*No corr. req.*[k]	0.036±0.015	0.056±0.021	0.018±0.016	0.056±0.021	5
Lignocellulosic Char, thick[i]	0	0.081±0.009	n/a	0.015±0.003	0.13±0.01	0	0.13±0.01	6
Lignocellulosic Char, thin-med[j]	0	0.052±0.016	n/a	0.013±0.003	0.11±0.03	0	0.11±0.03	6
Soot[g]	0	1.0±0.5	0.031±0.055	0.079±0.026	1.4±0.7	0	0.05±0.10	10
Graphite[h]	0	0.022±0.016	*No corr. req.*[k]	0.011±0.006	0.030±0.027	0	0.022±0.022	12
Background								
Lacey-C	0	0.047±0.066	n/a	0.013±0.009	0.09±0.12	0	0.09±0.11	9
SiO	0	11±12	n/a	0.55±0.37	11±9	0	n/a	6

* Please refer to Appendix 10-5 for details on the computations.

† Determined by taking the ratio of atomic weight normalized integrated area of EDX peaks. The integrated area approach is more vigorous and accurate than the peak height method, and the readers should treat the ratios here as the "truly" observed ones.

‡ Determined by taking the ratio of elemental peak heights.

(a) Ratio of atomic-weight normalized integrated area without film-O correction.

(b) Corrected for O potentially contributed from the background SiO film. See Appendix 10-5 for more details.

(c) Without considering the tailing contribution from the neighboring C and O peaks.

(d) Tailing effects of C and O peaks are corrected. See Appendix 10-5 for more details.

(e) Corrected for O potentially contributed from the background SiO film. See Appendix 10-5 for more details.

(g) On SiO film.

(h) Over the hole (i.e. vacuum) on a lacey-C film.

(i) Determined from EDX spectra obtained from spots appeared as white in the darkfield mode (i.e., impenetrable to electrons) were considered as "thick". This is important because the sample was placed on a region with lacey-C film. Thus the elemental ratios from the thick char spots should have minimum interference from the background carbon.

(j) Determined from EDX spectra of spots appeared as grey in the darkfield mode (i.e., somewhat penetrable to electrons). Elemental ratios obtained from this category may be slightly distorted by the presence of background carbon (lacey-C film).

(k) Same as $O/C_{uncor.}$ Values Correction was not required because of probing carbon samples against vacuum which gave no background C or O signals.

Table 10 - 5. Effect of Pixel Consolidation on Coverage Fraction of Graphitic Pixels (Pure C, no N or O)*.

Deg. Consolidation	1×1 into 1 cell		2×2 into 1 cell		4×4 into 1 cell		8×8 into 1 cell		
Samples	Simple†	Occp+O_{corr}‡	Simple†	Occp+O_{corr}‡	Simple†	Occp+O_{corr}‡	Simple†	Occp+O_{corr}‡	Site Ref. #
Soot+Mineral	0.135	0.229	0.0535	0.338	0	0.0873	0	0	20061013-Si#3
Apparently Mineral+ Organic	0.0234	0.0611	0.0106	0.0527	0.0007	0.0127	0	0	20061013-Si#10
Aggregate-like	0.0151	0.0381	0.0092	0.0343	0	0.0066	0	0	20061013-Si#12

* Coverage fraction is defined as the pixels of interest over the total pixels considered as relevant. Graphitic pixels are here defined as pixels with only C X-ray but not N or O signals (or, both C/N and C/O ~ ∞).

† Simple coverage: all pixels in the image were considered as relevant for coverage calculation of graphitic pixels. No corrections were made on N or O.

‡ Occp+O_{corr}: only pixels labeled as occupied by sample were considered as relevant for coverage calculation. Furthermore, O-signal from the background SiO was corrected.

Table 10 - 6. Quantification of BC by STEM-EDX Elemental Mapping on Selected Samples/Sites on the Basis of Sample-Occupancy*.

		No correction for O or N			Bkgd-O Corrected†		O Corrected &N Reduced‡			
Sample	$f_{C>0}$[(a)]	$f_{C/N=\infty}$[(b)]	$f_{C/O=\infty}$[(c)]	$f_{C/N,C/O=\infty}$[(d)]	$f_{C/O=\infty}$[(c)]	$f_{C/N,C/O=\infty}$[(d)]	$f_{C/N,C/O=\infty}$[(d)]	Bkgd $r_{Si:O}$[(e)]	Areal Cvr[(f)]	Site Ref. #[(g)]
Soot & Mineral										
A1	0.0802	0.0690	0.0309	***0.0273***	0.0549	***0.0477***	***0.0510***	2.37	0.308	20061010-Si#5
A2	0.327	0.290	0.190	***0.168***	0.259	***0.229***	***0.236***	1.98	0.694	20061013-Si#3
Lignocellulosic Char										
B1	0.950	0.862	0.544	***0.498***	0.557	***0.510***	***0.512***	0.161	0.333	Lignochar-Si#1
B2	0.960	0.825	0.434	***0.391***	---	---	---	---	0.381	Lignochar-Si#6
Melanoidin										
C1	0.722	0.646	0.621	***0.561***	0.629	***0.567***	***0.569***	0.56	0.390	Melanoidin-Si#1
C2	0.809	0.700	0.647	***0.561***	0.651	***0.564***	***0.565***	0.098	0.265	Melanoidin-Si#3
Humic Acids										
D1	0.273	0.231	0.0851	***0.0736***	0.140	***0.120***	***0.128***	2[(h)]	1.00	20061019-Si#11
D2	0.358	0.271	0.0840	***0.0671***	0.154	***0.118***	***0.130***	2[(h)]	1.00	20061019-Si#13
Apparently Mineral										
E1	0.0192	0.0175	0.0103	***0.0093***	0.0139	***0.0126***	***0.0129***	2.11	0.955	20061010-Si#9
E2	0.238	0.225	0.187	***0.178***	0.206	***0.195***	***0.197***	3.78	0.924	20061010-Si#14
E3	0.145	0.106	0.0240	***0.0194***	0.0617	***0.0660***	***0.0812***	1.85	0.804	20061013-Si#6
E4	0.246	0.182	0.0608	***0.0517***	0.177	***0.131***	***0.158***	1.71	0.646	20061013-Si#8
Apparently Mineral + Organic										
F1	0.144	0.103	0.0288	***0.0223***	0.0834	***0.0611***	***0.0737***	1.75	0.386	20061013-Si#10
Aggregate										
G1	0.0895	0.0672	0.0178	***0.0142***	0.0505	***0.0381***	***0.0453***	2.13	0.443	20061013-Si#12

* So that, the intensity field of the original image was used to determine which pixels were occupied with non-background film mass. For details, see Appendix 10-6.

† Correct for O contribution from background SiO film. See Appendix 10-6 for further details.

‡ Correct for O contribution from background SiO film and reduce N-'noise' pixels by arbitrarily setting all pixels with 1 counts only as 'noise'. See Appendix 10-6 for further details.

(a) Fraction of sample-occupied pixels that had observed C X-ray.

(b) Fraction of sample-occupied pixels with C X-ray but no N X-ray.

(c) Fraction of sample-occupied pixels with C X-ray but no O X-ray.

(d) Fraction of sample-occupied pixels with C X-ray but no N and O X-ray.

(e) Background Si:O X-ray counts ratio as determined from area where sample was absent.

(f) Areal coverage of sample occupied pixels out of all pixels in the image.

(g) Reference site number for detail C/N, C/O, Si/O images in Appendix A and B.

(h) Background SiO not available; arbitrarily set to 2.

Table 10 - 7. Fraction of Graphitic Carbon to Total Carbon in Selected Samples by STEM-EDX Elemental Mapping.

Sample	$f_{C>0}$[(a)]	$f_{graphitic,mean}$[(b)]	$f_{graphitic/Total\ C}$[(c)]	Site Ref. #
Soot & Mineral				
A1	0.0802	0.037 (0.027-0.051)	0.47	20061010-Si#5
A2	0.327	0.20 (0.17-0.24)	0.61	20061013-Si#3
Lignocellulosic Char				
B1	0.950	0.51 (0.50-0.51)	0.53	Lignochar-Si#1
B2	0.960	0.39 (0.39)	0.41	Lignochar-Si#6
Melanoidin				
C1	0.722	0.565 (0.56-0.57)	0.78	Melanoidin-Si#1
C2	0.809	0.563 (0.56-0.57)	0.70	Melanoidin-Si#3
Humic Acids				
D1	0.273	0.097 (0.074-0.13)	0.36	20061019-Si#11
D2	0.358	0.093 (0.067-0.13)	0.26	20061019-Si#13
Apparently Mineral				
E1	0.0192	0.011 (0.009-0.013)	0.57	20061010-Si#9
E2	0.238	0.19 (0.18-0.20)	0.79	20061010-Si#14
E3	0.145	0.040 (0.019-0.081)	0.27	20061013-Si#6
E4	0.246	0.090 (0.052-0.16)	0.37	20061013-Si#8
Apparently Mineral + Organic				
F1	0.144	0.041 (0.022-0.073)	0.28	20061013-Si#10
Aggregate				
G1	0.0895	0.025 (0.014-0.045)	0.28	20061013-Si#12

(a) Areal fraction of sample-occupied pixels that had observed C X-ray.
(b) Areal fraction of graphitic pixels out of total sample-occupied pixels. Geometric mean of the minimum and maximum graphitic fractions (bracketed values) as determined from (i) no correction, (ii) O-corrected, and (iii) N&O-corrected schemes (Table 10-6).
(c) Areal fraction of graphitic pixels out of all total C-pixels. $f_{graphitic/Total\ C} = f_{graphitic,mean}/f_{C>0}$.

Table 10 - 8. STEM-EDX derived Graphitic Fraction and Literature Values.

Sample	$f_{aromatic\text{-}C}$[*]	$f_{sp^2\text{-}C}$[†]	$f_{graphitic/Total\ C}$[‡]	Reference
Soot	Appr. same as right[#]	0.54-0.76	0.47-0.61	Muller et al. 2007
Carbon Black	Appr. same as right[#]	0.77		Muller et al. 2007
Wood & Straw Char	~0.70		0.41-0.53	Hammes et al. 2006
Melanoidin	0.14-0.40		0.70-0.78	Ikan et al. 1986a,b
Coal				
Lignite	0.57-0.72			van Krevelen 1993[&]
Low Volative Bituminous	~0.90			van Krevelen 1993[&]
Humic Acids	0.13-0.40	~0.60	0.26-0.36	Appendix 10-7

[*] Atomic fraction on the basis of all C functionalities.
[†] Atomic fraction on the basis of sp^2-C and sp^3-C.
[‡] From this study as in Table 10-7.
[#] Approximately the same as $f_{sp2\text{-}C}$ because of the predominance of C and relative absence of O. See Appendix 10-7.
[&] See also references within at p. 308 of van Krevelen.

Table 10 - 9. Elemental atomic ratios of C, N, and H in various carbonaceous matters.

Carbonaceous Matter	C:H	C:N	C:O	Reference
Humic acid	0.57-1.2	10-51	1.6-2.1	Huang et al. 1997; Santos et al. 1998; Duarte et al. 2007; Trickovic et al. 2007
Humic acid (Other reviews)				
MacCarthy (2001)	0.92	18	2.1	MacCarthy 2001
Schnitzer (1977)	1.00	20	2.1	Choudhry 1984
Fulvic acid	1.0	42-87	1.6-1.9	Santos et al. 1998; Duarte et al. 2007
Fulvic acid (Other reviews)				
MacCarthy (2001)	0.79	22	1.3	MacCarthy 2001
Schnitzer (1977)	0.71	25	1.4	Choudhry 1984
Humin	0.21-0.54	13-19	n/a	Trickovic et al. 2007
Humin (n=26)	0.86	18	2.2	MacCarthy 2001
Wood	0.60-0.70	250-720	1.2-1.4	Hedges et al. 1985; Lobert 1989; Kuhlbusch et al. 1991; Baldock et al. 2002
Grass & Hay	0.63	13-97	n/a	Kuhlbusch et al. 1991, 1996
Agricultural Plants	0.63-0.66	46-79	n/a	Jenkins et al. 1991; Kuhlbusch et al. 1996
Coal	1.3-1.7	62-82	4.8-45	Matsuoka et al. 2008
Char/Charcoal	0.1-15	2.5-160	18-1300	Lacaux et al. 1994; Fernandes et al. 2003; Matsuoka et al. 2008
Kerogen	0.56-2.2	37-120	2.2-10	Long et al. 1968; Damste et al. 1993; Huang et al. 1997; Zeng et al. 2007
Soot & Diesel Particulate	5.3-24	7-Inf.	13-38	Accardi-Dey 2003; Fernandes et al. 2003; Im et al. 2008

Thermodynamics and Kinetics of Hydrophobic Organic Compound Sorption in Natural Sorbents and Quantification of Black Carbon by Electron Microscopy

Volume III

Appendices and Reference

TABLE OF CONTENT

VOLUME I (TEXT)

Chapter 1: General Introduction 15

Chapter 2: Desorption of Native Pyrene at Minute- to Month-Timescales by Time-Gated Fluorescence Spectroscopy 33

Chapter 3: Equilibration of HOC Partitioning in Sediment-Water System 51

Chapter 4: Enhanced Pyrene Sorption at Environmentally Relevant Concentrations 73

Chapter 5: Pyrene Sorption Isotherm 101

Chapter 6: Thermodynamics of Absorption and Adsorption 125

Chapter 7: Desorption Kinetics of Native Sedimentary Pyrene – Mechanistic Modeling & Prediction 147

Chapter 8: Intraparticle Porewater Diffusion Model: General Application and Particular Scenarios 193

Chapter 9: Regional Modeling of Pyrene in Harbors & Estuaries 219

Chapter 10: Quantification of Organic Carbons & Black Carbons by EDX and STEM-EDX 245

Chapter 11: Conclusion 287

VOLUME II (FIGURES AND TABLES)

FIGURES

Chapter 1 301

Chapter 2 313

Chapter 3 325

Chapter 4 341

Chapter 5 368

Chapter 6 388

Chapter 7 393

Chapter 8 427

Chapter 9 454

Chapter 10 475

Chapter 11 533

TABLES

Chapter 1 536
Chapter 2 543
Chapter 3 549
Chapter 4 555
Chapter 5 562
Chapter 6 576
Chapter 7 584
Chapter 8 601
Chapter 9 606
Chapter 10 613

VOLUME III (APPENDICES AND REFERENCE)

APPENDICES

Chapter 2 624
Chapter 3 628
Chapter 4 650
Chapter 5 668
Chapter 6 766
Chapter 7 790
Chapter 8 902
Chapter 9 928
Chapter 10 966
Appendix A: EDX (Spot) Spectra 1000
Appendix B: STEM-EDX Elemental Maps 1036
Appendix C: STEM-EDX Mapping Scripts 1094
Appendix D: Isotherm Regression Scripts 1106
Appendix E: Desorption Kinetics Scripts 1112
Appendix F: Quantification of Black Carbons by EELS and STEM-EELS 1168
Appendix G: EELS Mapping Scripts 1192
Reference 1198

Chapter 2: Appendices

Appendix 2 - 1. Detail description of Laser-Induced Fluorescence (LIF) system. 625
Appendix 2 - 2. LIF Fluorescence signal processing..... 625

Appendix 2 - 1. Detail description of Laser-Induced Fluorescence (LIF) system.

A photon pulse is generated in a N_2-laser chamber at 337 nm (optimal excitation wavelength for pyrene). A small fraction of the laser pulse is intercepted and acts as an optical trigger for the digital delay generator. The time-gated intensified charge coupled device (ICCD) camera is controlled electronically with reference to this initial optical pulse. The total delay between laser pulse and the detection of the emission photons is based on the sum of the travel time of excitation pulse from the laser to the probe, the travel time of emission signal from the probe to the camera, and the electronic delay imposed upon the ICCD by the digital delay generator. Pyrene in water has a fluorescence lifetime of 120-130 ns (Inman et al. 1990; Lakowicz 2006; Kotzick 1996). The excitation pulse travels through the probe, which is immersed in the test solution, and excites the chromophores in the solution. The time-gating mechanism ensures fluorescence signals emitted only 128 to 228 ns after the 600-psec-long laser pulse are collected. These emission signals are spectrally reorganized, captured by the camera, and stored digitally.

Appendix 2 - 2. LIF Fluorescence signal processing.

Dissolved pyrene concentrations were determined from the peak height of fluorescences at characteristic emission wavelengths. High frequency noise (see Figure 2-2) were eliminated by re-expressing via Fourier series (Matlab) using frequency truncation suited for maintaining the linearity of the calibration curve (0-60 ng_{pyr}/L, $r^2>0.99$) as well as pyrene's characteristic emission peaks. Peak height was determined from a baseline established by the averaged intensity over the 340-360 nm range (see Figure 2-2). Because the relative intensities of the other characteristic peaks changed somewhat with the dissolved concentration (see Table 2-1), pyrene's 387 nm peak was used to infer dissolved pyrene concentrations.

The Matlab scripts for LIF raw signal processing are included below:

Readlif.m

```
% preliminary read-data from *.lif file after removing pre-dkxxxx junk for
% each spectrum


fname = 'P070803b';
%fname = 'P060224a';
%fname = 'P051229a';
fext = '.lif';
fdate = '8/3/2007';
%fdate = '12/30/2005';
fpath = ['/', fname, fext];
fnonsense1 = '';
fnonsense2 = '_____';
fid = fopen(fpath, 'r');
%fid = fopen('/test2.txt', 'r');
dum = fscanf(fid, '%s', inf);
fclose(fid);
ssize = size(dum, 2);
j=1;

% remove non-sense character ''
wherenonsense1 = findstr(dum,fnonsense1);
dum(wherenonsense1)=' ';
wherenonsense2 = findstr(dum,fnonsense2);
dum(wherenonsense2)=' ';
```

```
% remove pre-date '0', date, and time
dateindx = findstr(dum, fdate);
if size(dateindx,2)>0
    s_dateindx = dateindx - 2;                  % i.e., "0",9/22/2005,09:16
    e_dateindx = dateindx + size(fdate,2) + 5;  % i.e., 0,9/22/2005,09:1"6"
    dateindxdiff = e_dateindx(1)-s_dateindx(1);
    for i = 0:dateindxdiff
        dum((s_dateindx+i))=' ';
    end
end

dumbk = dum;
schar = findstr(dum, 'dk');
echar = findstr(dum, 'e');
nrecs = size(schar, 2);
kcomma = findstr(dum, ',');
dum(1, kcomma) = ' ';
for i = 1:nrecs,
    irec = [' -999', dum(schar(i)+2:schar(i)+5)]; % irec a str of 9 chars
    dum(schar(i):echar(i)) = ' ';
    dum(schar(i):schar(i)+8) = irec;
end

rnum = str2num(dum);
rsize = size(rnum,2);
ttl = [];
% records = fix(rsize/1020);
for g = 1:rsize,
    % if seeing a new emission spectrum record
    if rnum(g)<-9990000
        %recname = ['dk', num2str(abs(g+9990000))];
        iname = abs(rnum(g)+9990000);
        onerec = [];
        onerec = [onerec; iname; rnum(g+1:g+1023)'];
        if (g+1020<rsize)
            g=g+1020;
        end
        ttl = [ttl, onerec];
        fprintf('Record #%i completed.\n', size(ttl,2));
    end
end

fnew = [fname, 'list', fext];
messagetxt=['\nWriting realigned LIF-Data to ',fnew,' ...\n'];
fprintf(messagetxt);
save(fnew, 'ttl', '-ascii', '-tabs');
fprintf('Completed.\n');
```

Lifanalysis.m

```
%
% LifAnalysis.m
% By: D. Kuo, 06 May 2005
%

ttl = load('P070803blist.lif');
fil_fname = 'P07aug03b';
%ttl = load('P060224alist.lif');
%fil_fname = 'P06feb24';
%ttl = load('P051229alist.lif');
%fil_fname = 'P05dec29';
datalength = 800;
lor = 1:150;
%hir = 651:800; till 22 Sept 2005
hir = 1:150;    % changed on 22 Sept 2005, beginning for all A-SET solutions
                % rational: x=1:150 range, signal more stable (only when
                % camera cooled at -30C such that background signal is
                % around/less than zero); also, later x (i.e. 651-800)
                % could carry tailing emission signals from chromophores,
                % therefore reducing the peak height. Now with lor and hir
                % being same, bl_slope = 0
midr = 300:325;
xlo = 75;
xhi = 725;
xmid20 = [];
xmid100 = [];
xmid120 = [];

nrecs = size(ttl, 2);
```

```
deltax = xhi-xlo;

x = (1:datalength);
[am, bm, ao, an] = LifFourierFit(ttl);
b = LifFilter(ttl, am, bm, ao, an, 1, 10, fil_fname, 800);
%s20 = LifFilter(ttl, am, bm, ao, an, 1, 20, fil_fname, 800);
s100 = LifFilter(ttl, am, bm, ao, an, 1, 100, fil_fname, 800);
%s120 = LifFilter(ttl, am, bm, ao, an, 1, 120, fil_fname, 800);


findex = b(1, :);   % file indices; 1 x nrecs
bwk = b(2:datalength+1, :);
%s20wk = s20(2:datalength+1, :);
s100wk = s100(2:datalength+1, :);
%s120wk = s120(2:datalength+1, :);

cLo_mean = mean(bwk(lor, :), 1);
cHi_mean = mean(bwk(hir, :), 1);
deltac = cHi_mean - cLo_mean;
bl_slope = deltac/deltax;

%[pk20, ipk20] = max(s20wk(midr, :), [], 1);
[pk100, ipk100] = max(s100wk(midr, :), [], 1);
%[pk120, ipk120] = max(s120wk(midr, :), [], 1);
ipk100 = ipk100 + midr(1) - 1;
%ipk120 = ipk120 + midr(1) - 1;

dx_LoPk100 = ipk100 - ones(1, nrecs)*xlo;
cUnknown100 = dx_LoPk100.*bl_slope + cLo_mean;
%dx_LoPk120 = ipk120 - ones(1, nrecs)*xlo;
%cUnknown120 = dx_LoPk120.*bl_slope + cLo_mean;

cPkHeight100 = pk100 - cUnknown100; % 1 x nrecs
%cPkHeight120 = pk120 - cUnknown120; % 1 x nrecs
optm = [findex; cLo_mean; cHi_mean; bl_slope; pk100; ipk100];
save lifdump.txt optm -ascii -tabs;
%figure, plot(x,ttl([x+1],56),'b-',  x,a([x+1],56),'r-',  x,b([x+1],56),'g-',
x,c([x+1],56),'y-',  x,d([x+1],56),'c-');

%%% matlab prompt commands:
%%% i=1; [cPkHeight100(i), b(1,i)]            % for soln w/ pyrene
%%% i=1; max(bwk(290:310,i))-cUnknown100(i)   % for water
%%% plot(x,ttl([x+1],i),'b-', x,bwk(x,i),'k-', x,s100wk(x,i),'r-');
% for plotting raw, bkgd, and s100-filtered signals

%%% HANDY PROMPT COMMANDS...
%%% j=20; x=1:350; plot(x,ttl([x+1],j),'b-', x,bwk(x,j),'k-', x,s100wk(x,j),'r-');
%%% i=21:30'; [b(1,i); cPkHeight100(i)]'
%%% j=19; max(s100wk(300:315, j))-cUnknown100(j)
```

Chapter 3: Appendices

Appendix 3 - 1. Uncertainty analyses for pyrene sorption equilibrium experiments.. **629**
Appendix 3 - 2. Mass Balance Outliers & Correction of Pyrene Loss. **634**
Appendix 3 - 3. Equilibration Plots (C vs Time) for Extended-Range Sorption Experiments. **638**
Appendix 3 - 4. Correction for Sorption Observations after 10-month Equilibration.. **640**
Appendix 3 - 5. Time Plots of Dissolved Pyrene in Grinding Sorption Experiments.. **644**
Appendix 3 - 6. Examples of Slow PAHs Adsorption in Equilibrium Studies (from Literature)..... **648**

Appendix 3 - 1. Uncertainty analyses for pyrene sorption equilibrium experiments.

(a) Uncertainties in GC-MS measurements.

Three types of uncertainties in GC-MS measurements may be distinguished and quantified: (i) uncertain arises from PAH-concentration variability in sample replicates, (ii) instrumental drifting (over time), and (iii) variability in successive measurements of a single sample.

Uncertainty (i) accounts for both the variability in instrument performance and any 'error' or variability incurred during the sample preparation process (e.g., extraction, pre-concentration, etc.). Instrumental drifting (ii), and variability in successive measurements (iii) have also been checked because of the long analysis time required for a single sample. A single GC-MS measurement requires ~35 min, and for a set of 3 samples with 2 calibration runs (before and after), this would require ~3 hours.

Tests show that the sediment extract replicates give the highest uncertainty (~20% from average, 1 stdev.) while both instrumental drifting and variability in successive runs are relatively insignificant (<5 %) (see table below). This implies that instrumental performance is relatively stable and that the dominant uncertainty for sediment extracts is inherited in the pre-processing/handling steps.

GC-MS measurement uncertainties within:

(i) Sediment Extract Replicates					
	Rep.-1[a] (ng_{pyr}/g)	Rep.-2 (ng_{pyr}/g)	Rep.-3 (ng_{pyr}/g)	Rep.-Avg. (ng_{pyr}/g)	**Stdev. (%)**
Run #1	4861	4128	6341	5110	**22%**
Run #2	5241	4161	5807	5069	**16%**
Run #3	5381	4231	6103	5238	**18%**
(ii) Instrumental Drifting					
	0^{th} Hour	~4^{th} Hour	~8^{th} Hour	Avg.	**Stdev (%)**
Rep.-1	4861	5241	5381	5161	**5%**
Rep.-2	4128	4161	4231	4173	**1%**
Rep.-3	6341	5807	6103	6084	**4%**
(iii) Successive Measurements					
	#1	#2	#3	Avg.	**Stdev (%)**
Rep.-1	5170	4916	5316	5134	**4%**

a. Three extract replicates (in hexane) of Boston Harbor site #6 sediment (dia. < 425 μm).

(b) Uncertainties in $S_{pyr,t}$ and $Q_d(t)$.

Uncertainties in $S_{pyr,t}$, and consequently $Q_d(t)$, were higher than those of $C_{pyr,t}$ and $S_{pyr,o}$. This was because $S_{pyr,t}$ (and hence $Q_d(t)$) was estimated from mass balance, thus its uncertainty included all measurement/analytical uncertainties in $C_{pyr,t}$ (≤15%) and $S_{pyr,o}$ (≤20%).

Expressing mass balance of total pyrene in any given suspension with a degradation/loss factor (f_{Loss}):

$$S_{pyr,t}M_{solids} + C_{pyr,t}V_{water} = (1 - f_{Loss})(S_{pyr,o}M_{solids} + C_{pyr,o}V_{water})$$

$$S_{pyr,t} = \frac{(1 - f_{Loss})(S_{pyr,o}M_{solids} + C_{pyr,o}V_{water}) - C_{pyr,t}V_{water}}{M_{solids}}$$

Assuming (i) negligible uncertainties in sediment mass (M_{solids}) and pyrene solution volume (V_{water}), (ii) an error of ±5% (1σ) in $C_{pyr,o}$, and (iii) an error of ±0.05 for f_{Loss}, the error (1σ) in $S_{pyr,t}$ can be estimated from the following expressions:

$$\Delta E_1 = \Delta(S_{pyr,o}M_{solids} + C_{pyr,o}V_{water}) = \sqrt{(\Delta S_{pyr,o}M_{solids})^2 + (\Delta C_{pyr,o}V_{water})^2}$$

$$\Delta E_2 = \Delta[(1 - f_{Loss})(S_{pyr,o}M_{solids} + C_{pyr,o}V_{water})] = E_2\sqrt{\left(\frac{\Delta E_1}{E_1}\right)^2 + \left(\frac{\Delta f_{Loss}}{1 - f_{Loss}}\right)^2}$$

$$\Delta E_3 = \Delta[(1 - f_{Loss})(S_{pyr,o}M_{solids} + C_{pyr,o}V_{water}) - C_{pyr,t}V_{water}] = \sqrt{(\Delta E_2)^2 + (\Delta C_{pyr,o}V_{water})^2}$$

$$\Delta S_{pyr,t} = \frac{\Delta E_3}{M_{solids}}$$

$$\Delta Q_d(t) = Q_d\sqrt{\left(\frac{\Delta S_{pyr,t}}{S_{pyr,t}}\right)^2 + \left(\frac{\Delta C_{pyr,t}}{C_{pyr,t}}\right)^2}$$

Error analyses of Q_d at different time (5-month vs 10-month) and/or mass-correction (no correction, 10%, or 18%) were summarized in the following table and frequency diagram.

Uncertainties in $Q_d(t)$ at different times and mass-correction schemes.

Uncertainty in $Q_d(t)$[a]	5-Month	10-Month No Correction	10-Month 18% Pyr. Loss[b]	10-Month 10% Pyr. Loss
Average	**17%**	**15%**	**27%**	**20%**
Std. Dev.	8%	6%	32%	10%
Min-Max	6-61%	6-29%	9-223%	9-62%

a. Uncertainty reported here is ±1σ, expressed as % of average $Q_d(t)$ value. For example, for average error of ±25% at Q_d of 10000 L/kg, the error in actual unit is 1σ±2500 L/kg.
b. Further analysis suggested that this scheme over-corrected the data by assuming too much pyrene was lost. See Appendix 3 - 4.

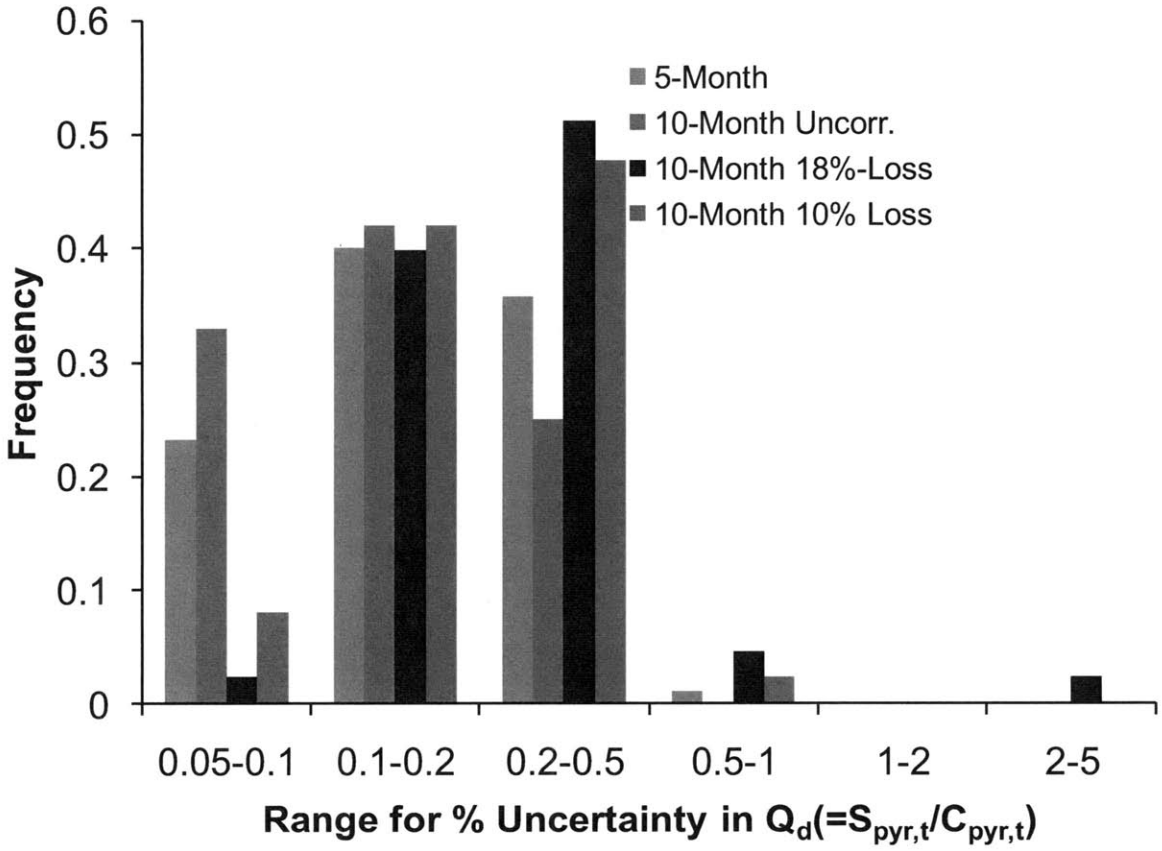

Frequency distribution of error (1σ) in $Q_{d,pyr}(t)$ at different times and mass-correction schemes.

(c) Uncertainties in Enthalpy of Sorption ΔH_d.

The dependence of ΔH on temperature can be derived from thermodynamic relationship as:

$$K = A\exp\left(\frac{-\Delta H}{RT}\right)$$

Where K is the equilibrium constant for the reaction of interest,

DH is the enthalpy of the reaction of concern [in J/mol),

T is the temperature [K],

R is the gas constant 8.314 [J/mol.K],

A is the pre-exponential coefficient [in unit consistent with K].

In the domain of natural logarithm, the enthalpy of reaction can be obtained from the slope of a lnK vs 1/T plot:

$$\ln K = \frac{-\Delta H}{RT} + \ln A$$

To estimate the error in ΔH is the same as to estimate the uncertainty in the regressed slope, which is an estimator of the real, true slope. This can be done with the following expressions (Devore 1995):

$$s^2 = \frac{\Sigma(y_i - \hat{y}_i)^2}{n-2} = \frac{\Sigma(\ln K_{i,obs} - \ln K_{i,reg})^2}{n-2}$$

$$s_{slope}{}^2 = \frac{s^2}{\Sigma(x_i - \bar{x})^2} = \frac{s^2}{\Sigma(1/T_{i,obs} - \overline{1/T})^2}$$

Where $\hat{y}$ denotes the predicted dependent variable,

1/T-bar denotes the mean 1/T for the regressed data points,

s_{slope} is the standard deviation of the slope-estimator, which is $-\Delta H/R$.

The following table summarized the relatively uncertainty in ΔH_d as a function of dissolved pyrene concentration, time of observation, and regression expression for $K_d(Q_d)$-$C_{pyr,t}$:

Relative Uncertainty (% of ΔH_d)	$C_{pyr,eqm} \sim C_{pyr,t}$ (ug/L) 0.02	0.05	0.2	2	10
5-Month					
Linear (Ln-Ln)	20%	23%	26%	40%	57%
Quadratic (Ln-Ln)	35%	23%	16%	32%	54%
10-Month (10% Pyr. Loss)					
Linear (Ln-Ln)	22%	20%	18%	27%	45%
Quadratic (Ln-Ln)	12%	23%	26%	25%	46%

Appendix 3 - 2. Mass Balance Outliers & Correction of Pyrene Loss.

(a) Mass Balance Outliers (final vs initial pyrene mass)

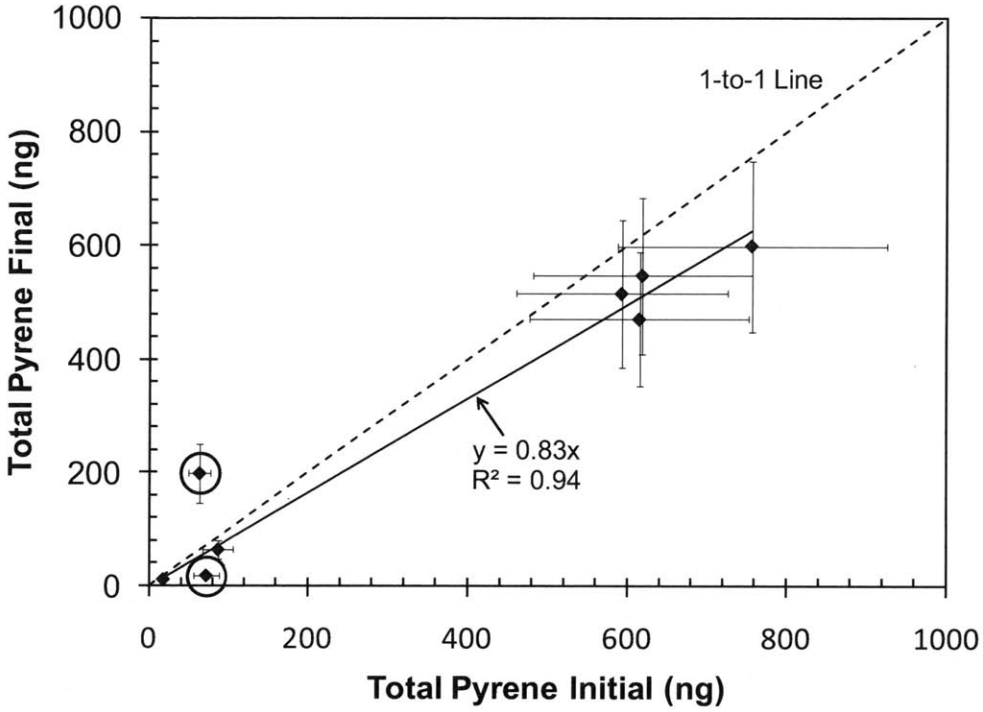

(Same as Figure 3-2)

Are the two outliers (circled) in the figure indicative of possible systematic errors? The author would like to claim that the two outliers were random in nature.

The two 'outliers' may result from (i) concentration heterogeneity in sediment solids and (ii) degradation/loss process(es) sensitive to temperature. The first scenario refers to additional variability in sorbent pyrene concentration as a function of amount of solids weighted. The idea is that we may be measuring the heterogeneity associated with relatively small sediment loading (i.e. low R_{sw}). The total initial pyrene mass was determined by analyzing grams of sediment, but the final pyrene mass measurement required extracting micrograms of sediment – that we may be approaching the elementary volume/mass for homogeneity of sorbent pyrene concentration. Thus, one would anticipate greater discrepancies in the final/initial pyrene ratio at lower solids-to-water ratios.

In the second scenario, if degradation/loss was responsible for the outlier, then it were to be the case, one would anticipate the final/initial pyrene ratio to decrease more with higher sorption temperature (e.g., greater biodegradation or volatilization).

However, the ratio of final to initial total pyrene mass revealed no dependency on solids-to-water ratio (Figure (i)), sorption temperature (Figure (ii)), or total initial pyrene (Figure (iii)), suggesting that the two anomalies were random in nature.

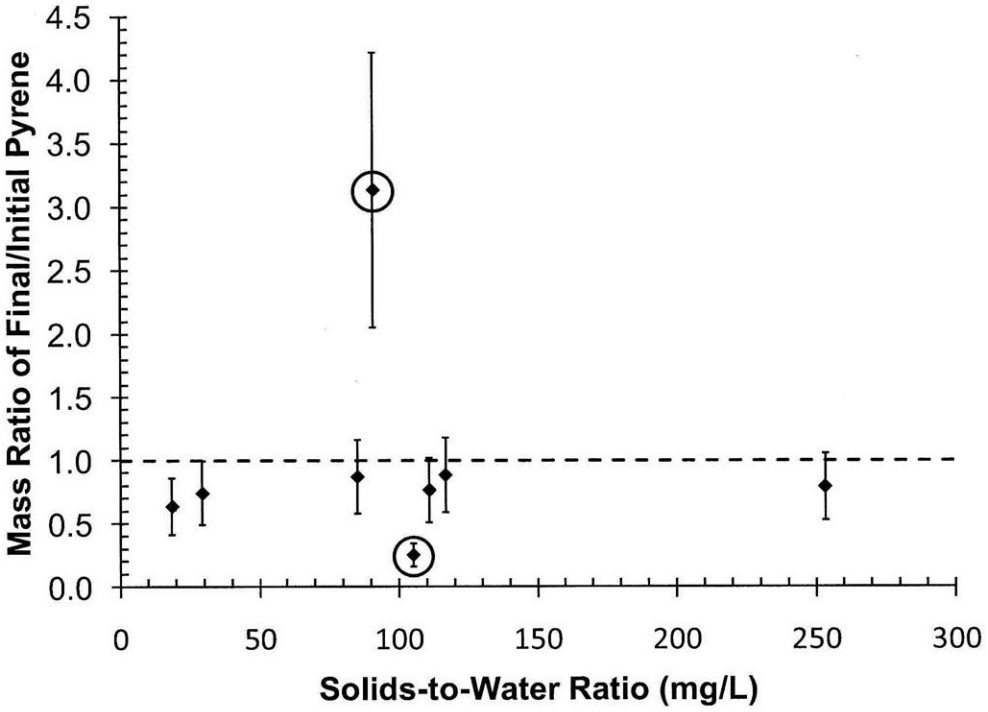

Figure (i). Dependence of final/initial total pyrene ratio on R_{sw}'s.

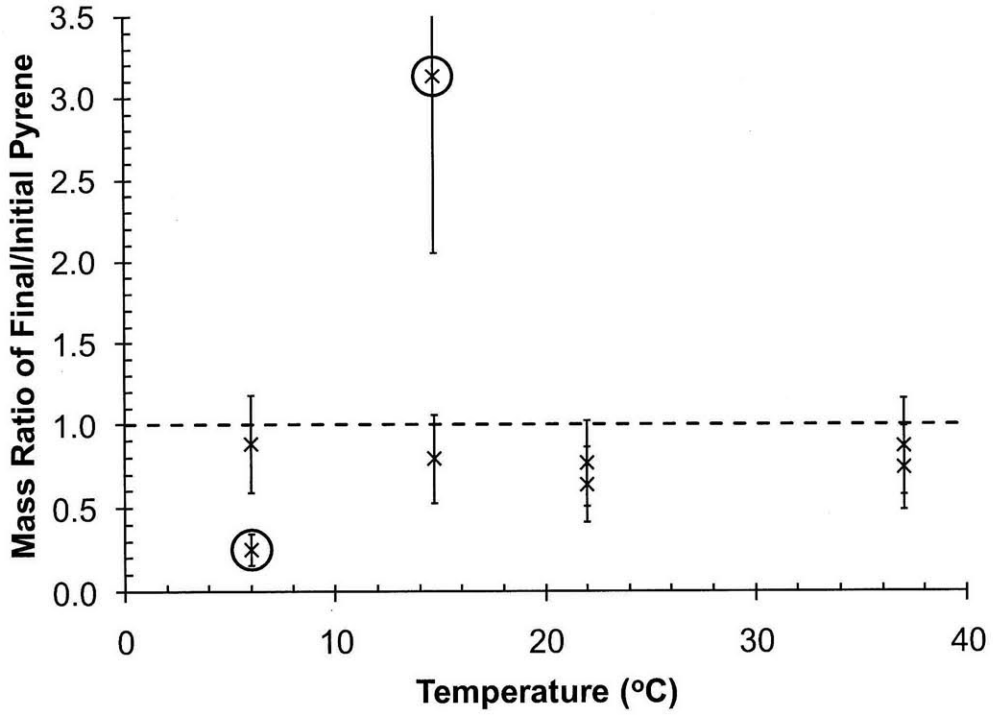

Figure (ii). Dependence of final/initial total pyrene ratio on sorption temperature.

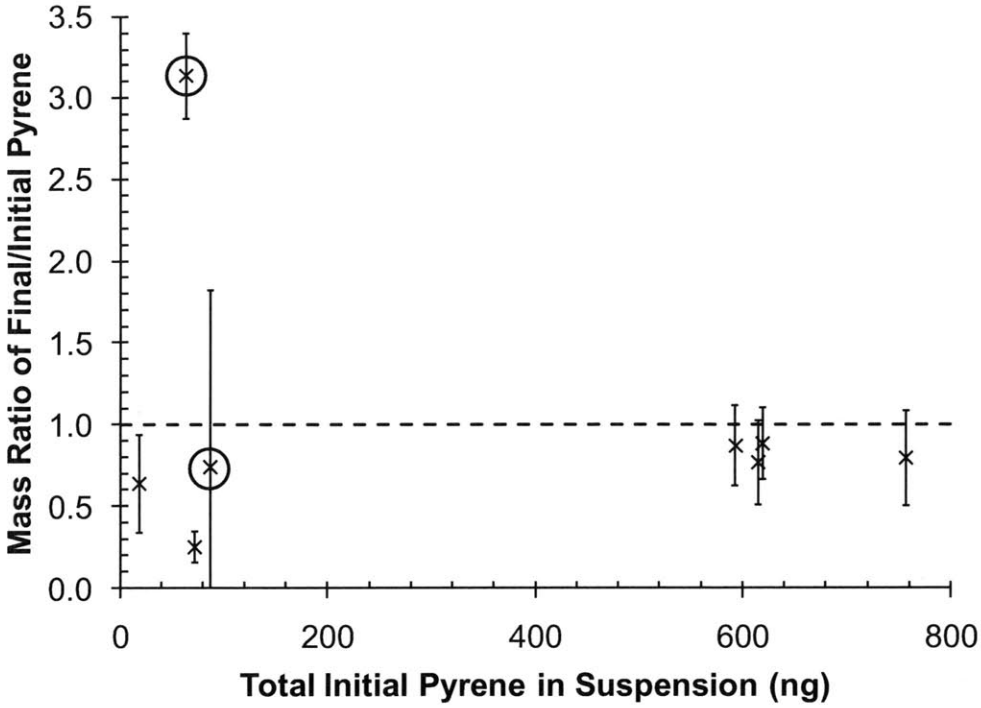

Figure (iii). Dependence of final/initial total pyrene ratio on total initial pyrene.

The figures showed the ratio of total pyrene mass of selected suspensions after 10 months to that at the beginning of the experiment as a function of (i) R_{sw}, (ii) sorption temperature, and (iii) total initial pyrene mass. The dashed-line shows where the ratio should be when pyrene is totally conserved. The error bars give uncertainty in ±1 standard deviation. The circled observations had substantial discrepancies (± factor of 2 or more) between initial and final total pyrene.

(b) Correction of Pyrene Loss

The next two questions are then whether it is necessary to correct for pyrene loss and how should the correction be applied. Most observations consistently showed less pyrene at the end than in the beginning (e.g. Figure 3-2; Figures (i) to (iii)). Even though the average loss of pyrene (~20%) was comparable to the uncertainty in the analysis of the original sediment pyrene concentration (~20%), given the evidence that dissolved pyrene did degrade over long period of time even in the presence of biocide and in the absence of light, correction should be applied. Furthermore, since the end-time dissolved pyrene levels were directly observed, only the end-time solid-phase pyrene concentrations needed to be corrected for loss of pyrene.

Correction for pyrene loss was applied on the end-time solid-phase concentrations with the following assumptions: (i) that each suspension was close to sorption equilibrium before the onset of substantial pyrene loss, (ii) that pyrene loss did not exceed a maximum of 20% of over the 10-month period, as suggested by Figure 3-2, (iii) that a common loss percentage was applied to all suspensions since the extent of loss appeared independent of sorption conditions and system factors such as temperature, R_{sw}, and total initial pyrene (Figures (i) to (iii)), and (iv) that the proper extent of correction could be better constrained by noting signs/symptoms of over-correction. The first assumption allowed the correction to be applied to the total pyrene content rather than the dissolved phase only. The assumption was supported by the observation that the dissolved pyrene level generally achieved/approached a concentration plateau after 5 months of equilibrium (Figure 3-5; Appendix 3-3). Further analyses and anomaly-plots seemed to support that the belief that about 10% of the initial total pyrene was loss over 10 months' time (Appendix 3-4).

Appendix 3 - 3. Equilibration Plots (C vs Time) for Extended-Range Sorption Experiments.

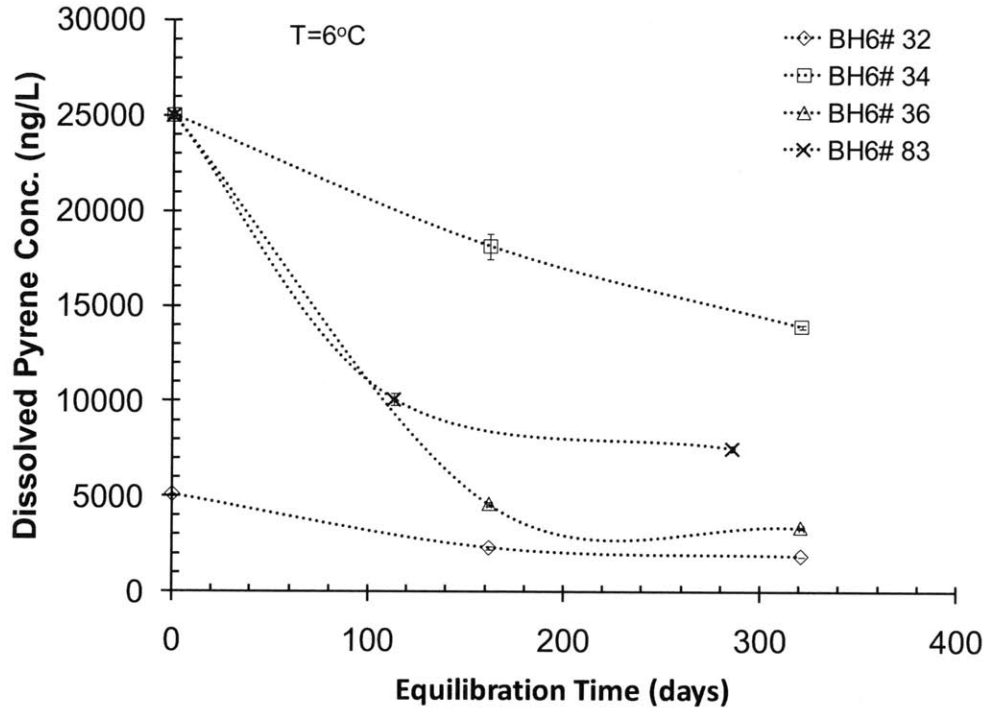

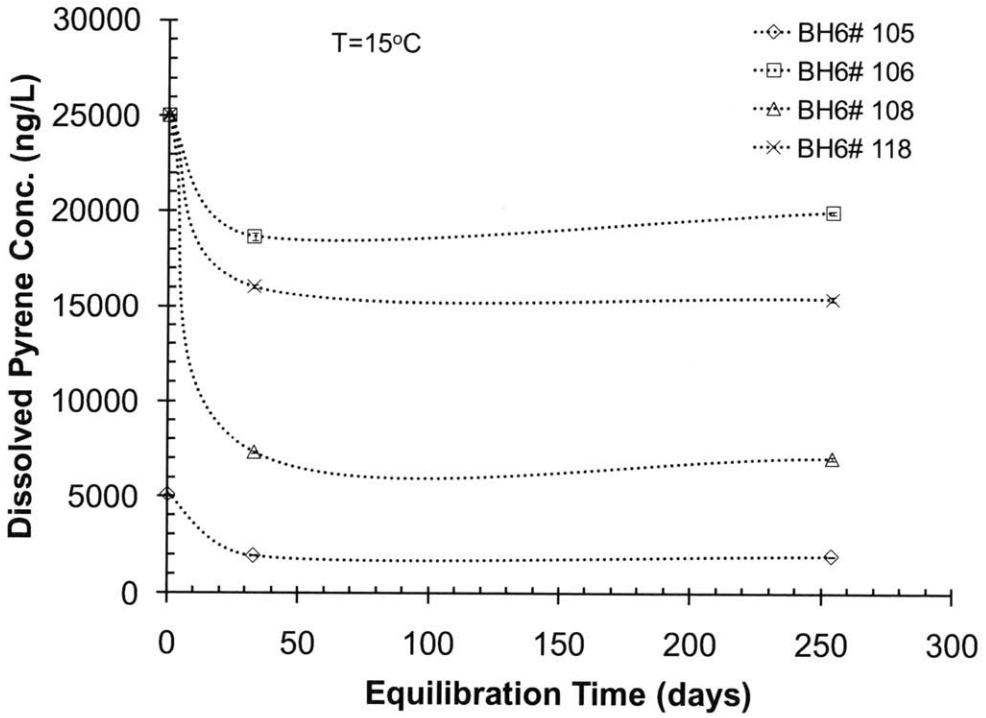

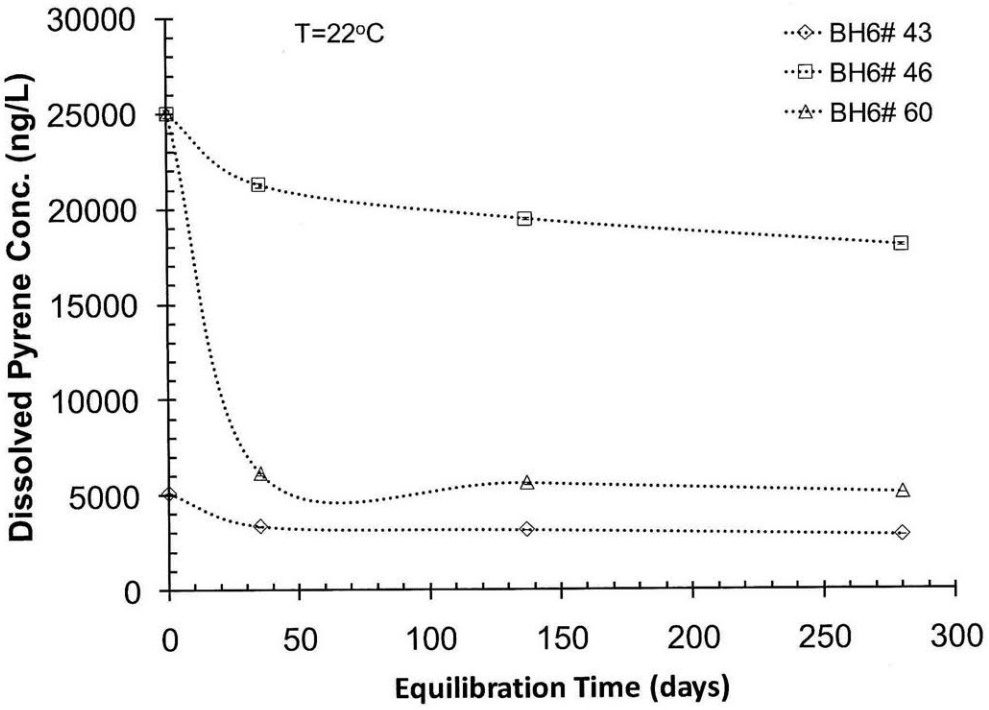
T=22°C
BH6# 43
BH6# 46
BH6# 60
Dissolved Pyrene Conc. (ng/L)
30000
25000
20000
15000
10000
5000
0
0
50
100
150
200
250
300
Equilibration Time (days)

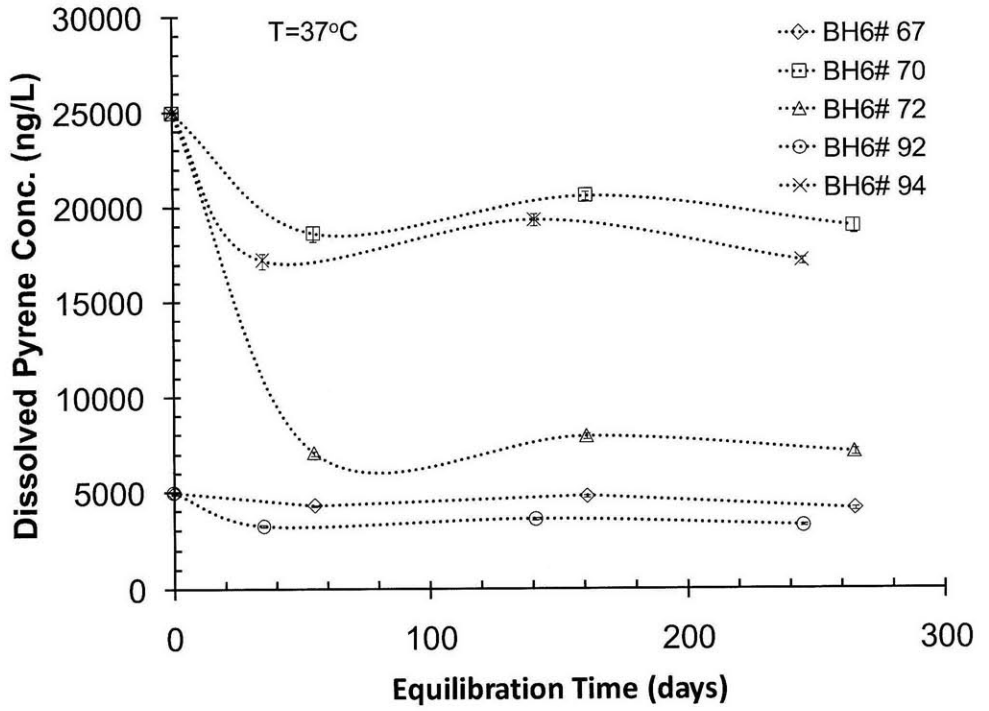
T=37°C
BH6# 67
BH6# 70
BH6# 72
BH6# 92
BH6# 94
Dissolved Pyrene Conc. (ng/L)
30000
25000
20000
15000
10000
5000
0
0
100
200
300
Equilibration Time (days)

Appendix 3 - 4. Correction for Sorption Observations after 10-month Equilibration.

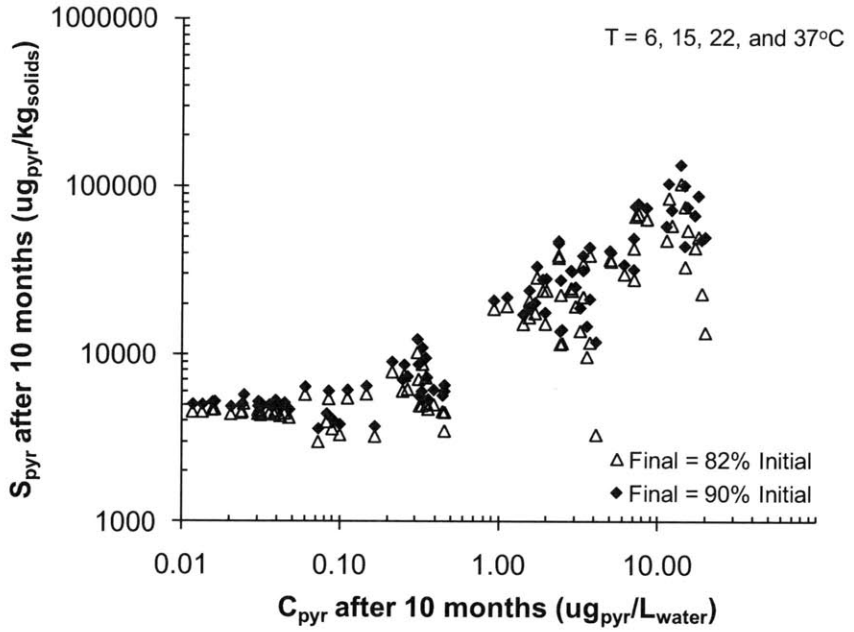

(i) Dissolved (C_{pyr}) and solid-bound (S_{pyr}) pyrene concentrations after 10-month equilibration at two correction schemes (final total pyrene = 82-90% of initial total pyrene). Uncertainties in measurements are omitted for clarity. Noted that C_{pyr}'s were observed values, and S_{pyr}'s were derived from the final total pyrene mass.

The solid-phase pyrene concentration after 10 months, S_{pyr}, was corrected using the following equation:

$$S_{pyr,t}M_{solids} + C_{pyr,t}V_{water} = (1 - f_{Loss})(S_{pyr,o}M_{solids} + C_{pyr,o}V_{water})$$

Where: M_{solids} and V_{water} are mass of solids [kg] and volume of water [L], respectively,

C_{pyr} denotes the dissolved pyrene concentration [ug_{pyr}/L_{water}],

S_{pyr} denotes the solid-phase pyrene concentration [ug_{pyr}/L_{solids}],

subscripts 'o' and 't' denote initial time and at time t (here being 10 months),

f_{Loss} denotes the fraction of pyrene loss over the 10-month period.

Since the initial total pyrene was known, and that the end-time dissolved pyrene, $C_{pyr,t}$, was directly measured, the only terms uncertain were f_{Loss} and $S_{pyr,t}$. However, from Figure 3-1 we know that the average pyrene loss should not be more than 20% of that at the beginning, so we may constrain f_{Loss} further by declaring fLoss<0.2.

Figure (i) compared the S vs C plot after applying correction scheme at f_{Loss} = 0.10 and 0.18. The plot showed considerable scattering, especially at higher C_{pyr} range. Such scattering is symptomatic of over-correction – a decrease in S_{pyr} so dramatic that $S_{pyr,over\text{-}corrected}$ is substantially lower than $S_{pyr,\ before\text{-}correction}$.

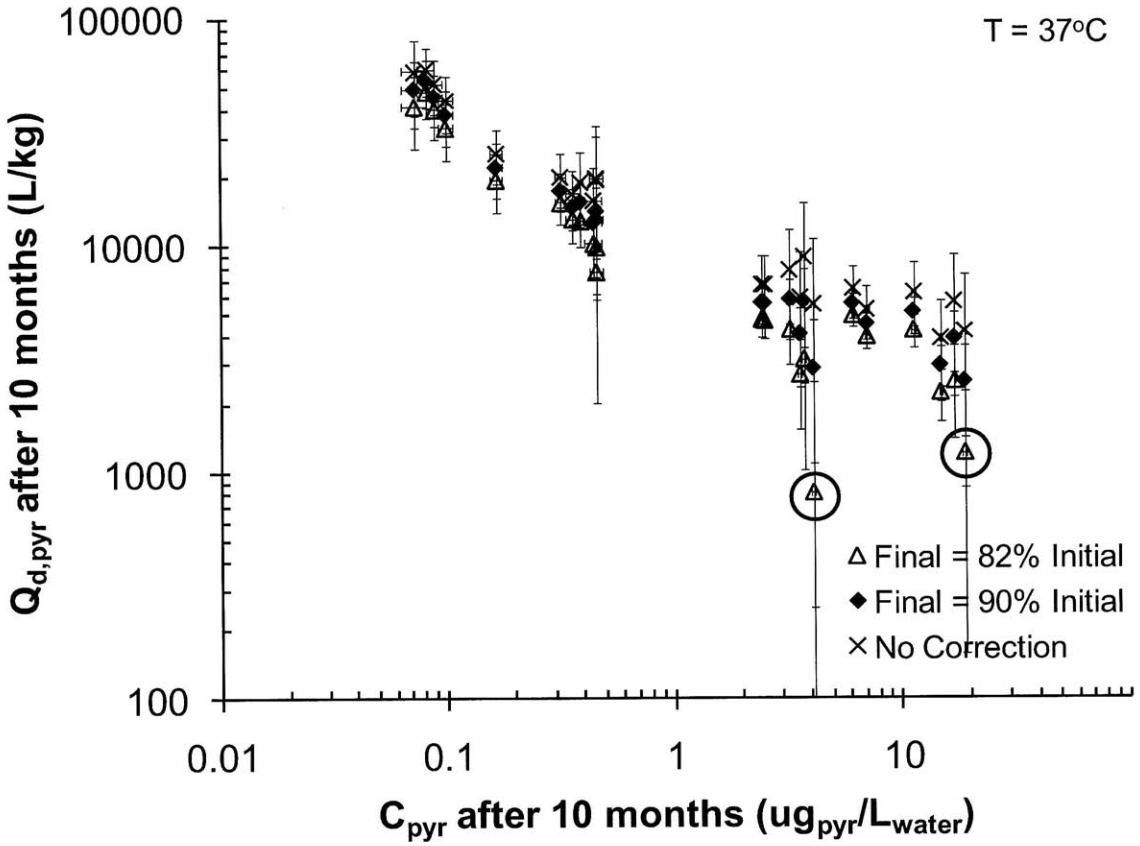

(ii) Solid-to-water distribution coefficient of pyrene (Q_d) as a function of dissolved pyrene level (C_{pyr}) at T=37°C. Q_d was computed from $S_{pyr,corrected}$ (assuming 10 or 18% of pyrene loss) and $C_{pyr,obs}$ after 10 months' time. The circled data points were instances of over-correction. Error bars represented 1 standard deviation around means.

The symptom of over-correcting pyrene loss in the case of f_{Loss} = 18% (or 'Final = 82% Initial) is demonstrated in Figure (ii). Most corrected data points were within a factor of 2 from the uncorrected points (assuming pyrene is fully conserved) with the shape of the general trend preserved. The case of f_{Loss} = 18%, however, gave rise to the two 'anomalies' (circled points), which were about half-an-order lower than before correction.

The 10% correction was a better choice became clear when one examine the instances of ratio of final/initial Q_d exceeding a factor of 2 (here taken to be the conventional uncertainty acceptable for partitioning coefficient) (Figure (iii), (iv)).

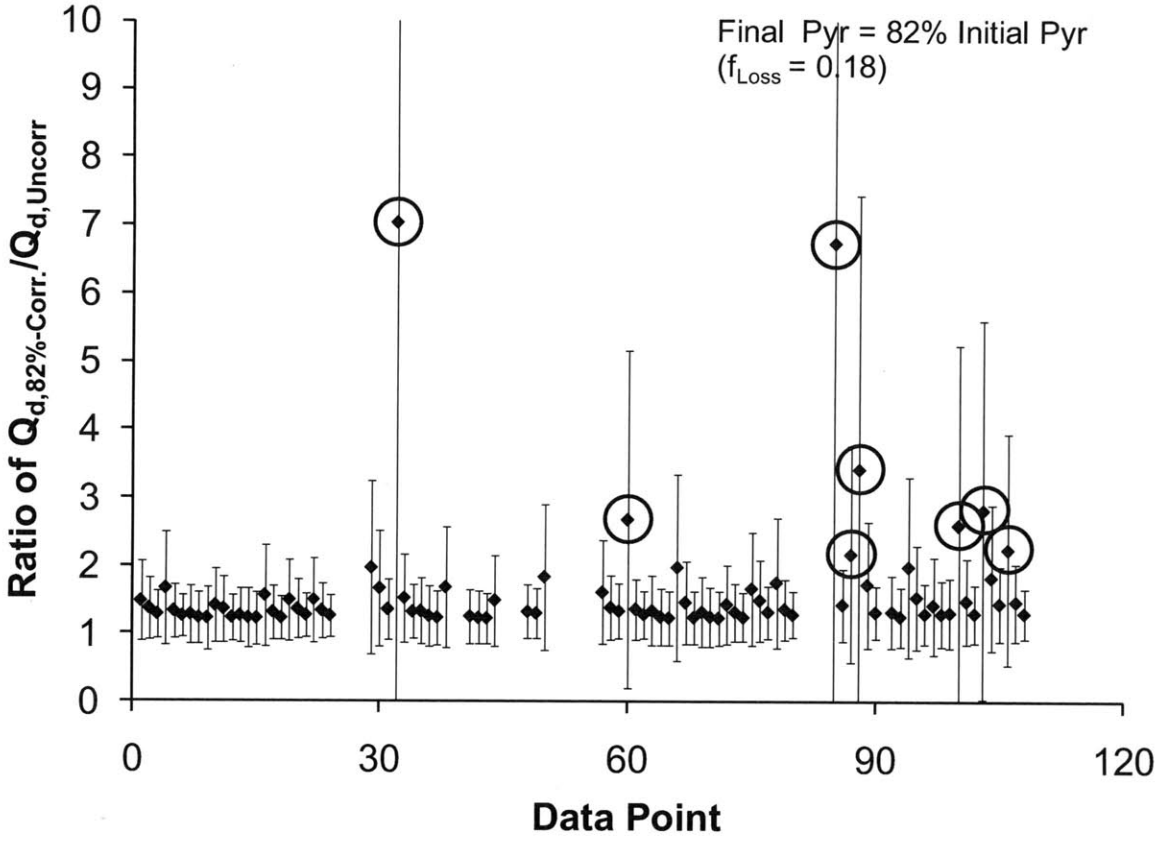

(iii) Ratio of Q_d's at all sorption temperatures assuming 18% of total initial pyrene was lost over the 10-month equilibration period. The circled data points were instances of the ratio exceeding 2, here assumed as acceptable error for partitioning constants. Error bars represented 1 standard deviation around means.

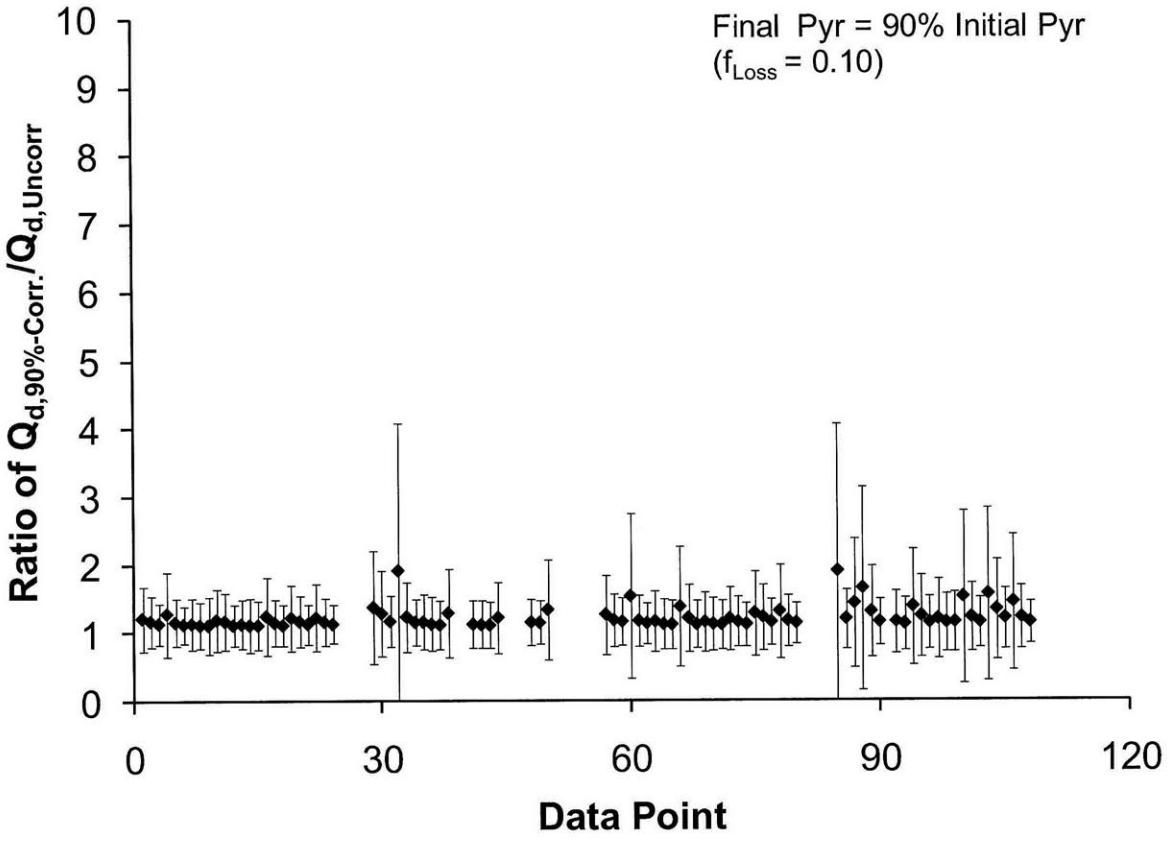

(iv) Ratio of Q_d's at all sorption temperatures assuming 10% of total initial pyrene was lost over the 10-month equilibration period. No instances of ratio exceeding 2, here assumed as acceptable error for partitioning constants, were observed. Error bars represented 1 standard deviation around means.

Appendix 3 - 5. Time Plots of Dissolved Pyrene in Grinding Sorption Experiments.

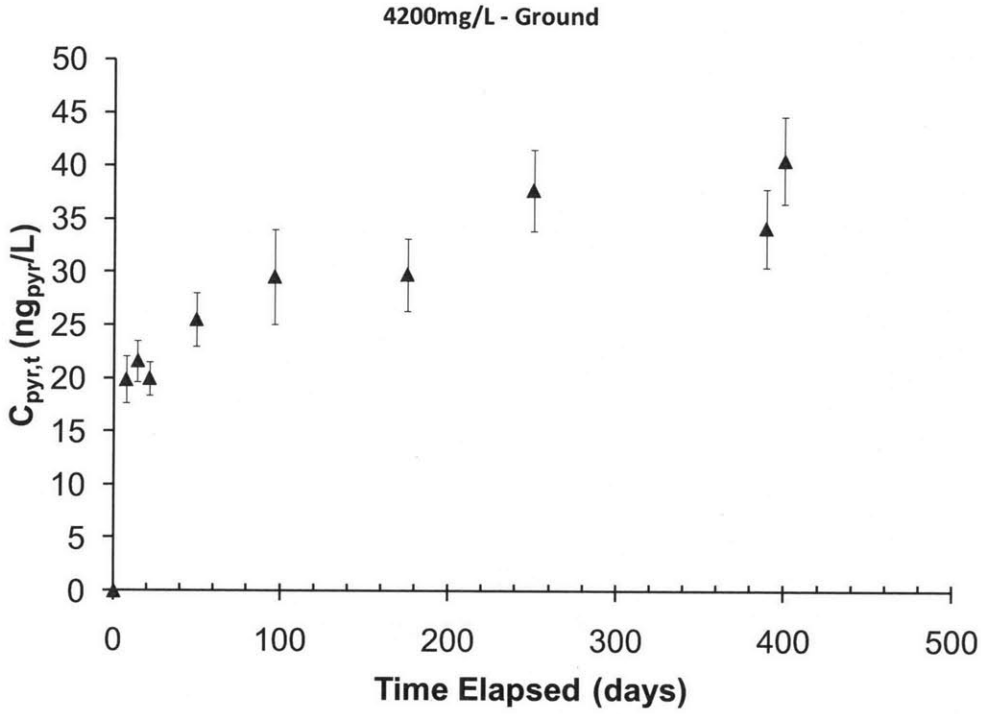

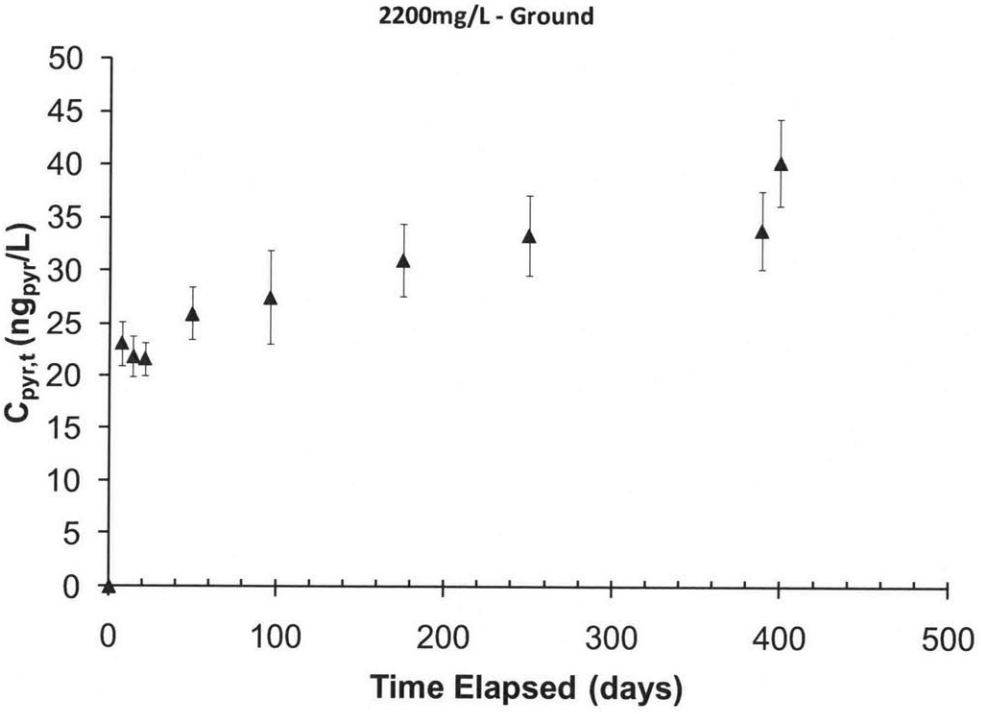

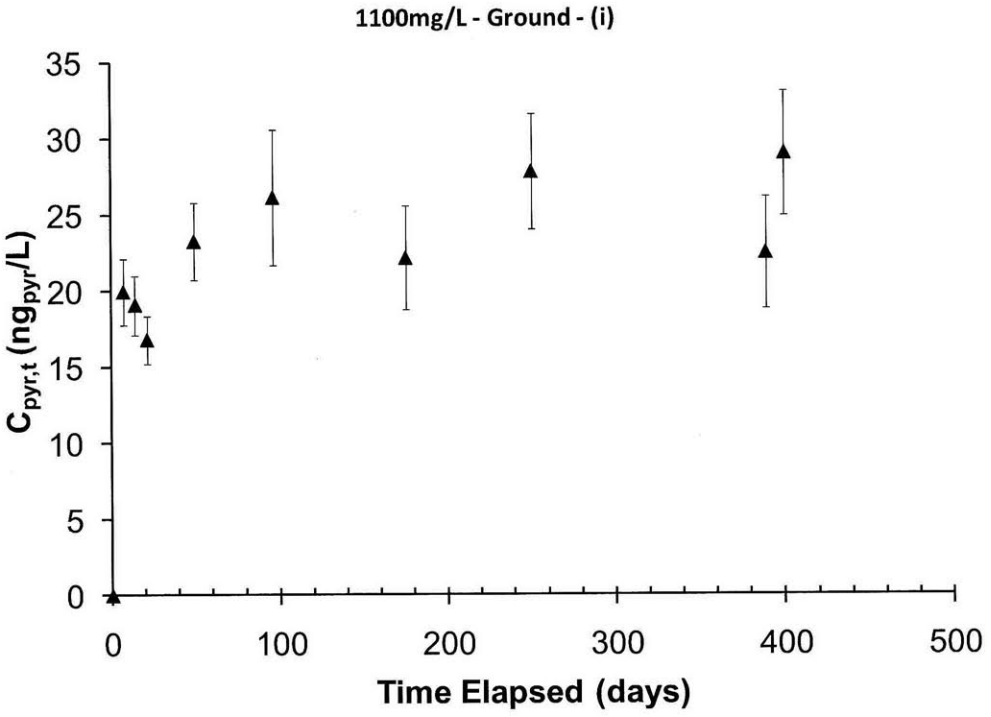
1100mg/L - Ground - (i)
35
30
25
20
15
10
5
0
$C_{pyr,t}$ (ng_{pyr}/L)
0
100
200
300
400
500
Time Elapsed (days)

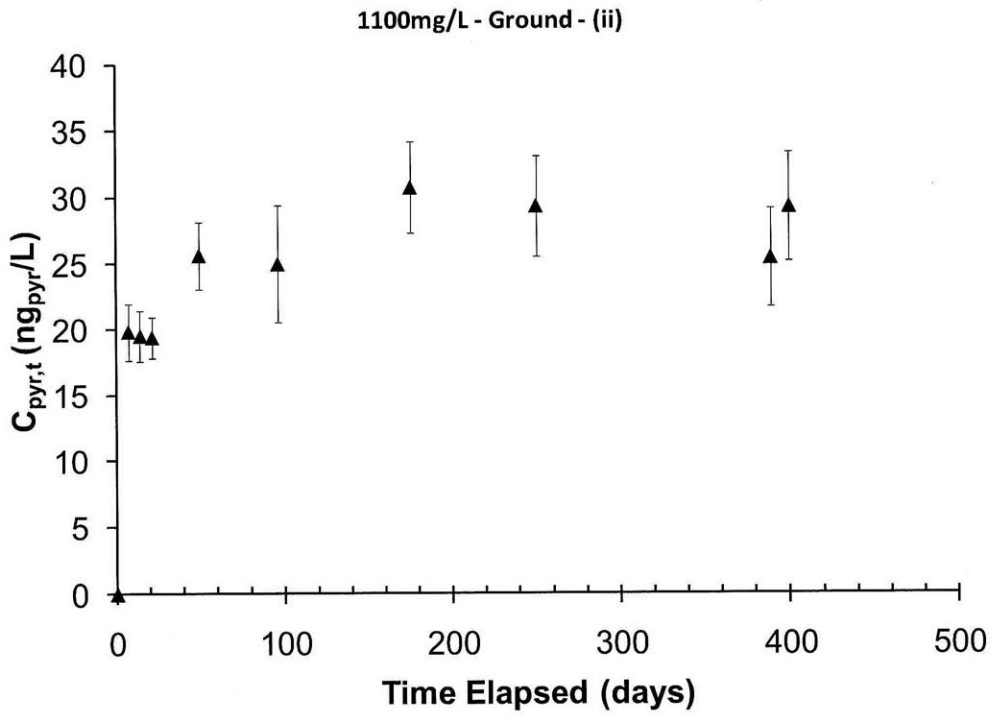
1100mg/L - Ground - (ii)
40
35
30
25
20
15
10
5
0
$C_{pyr,t}$ (ng_{pyr}/L)
0
100
200
300
400
500
Time Elapsed (days)

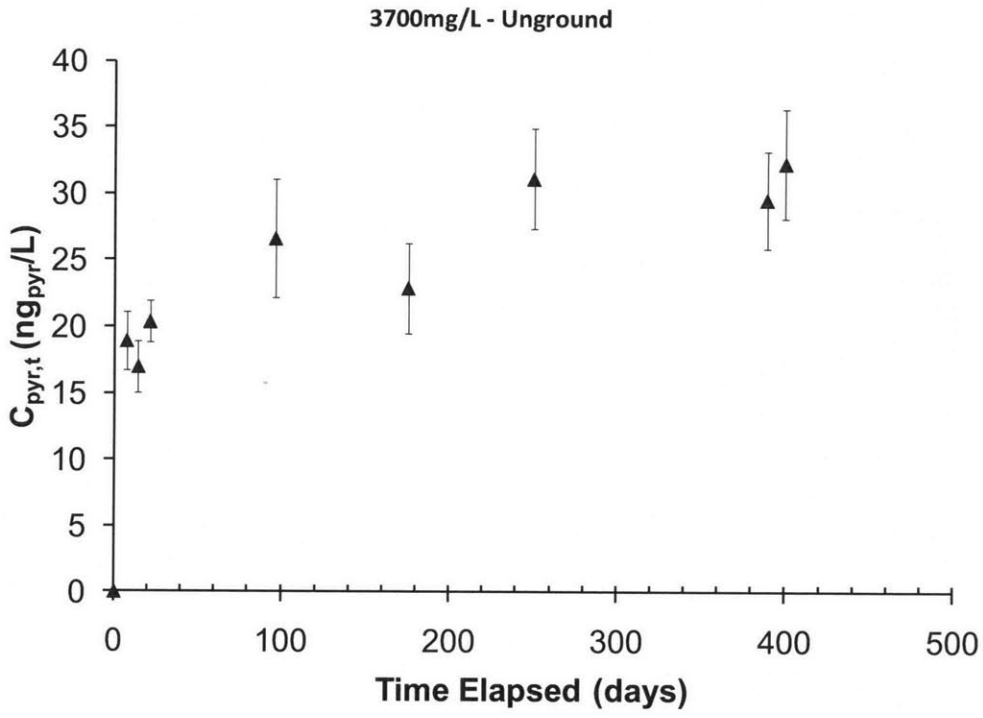
3700mg/L - Unground
$C_{pyr,t}$ (ng_{pyr}/L)
0
5
10
15
20
25
30
35
40
0
100
200
300
400
500
Time Elapsed (days)

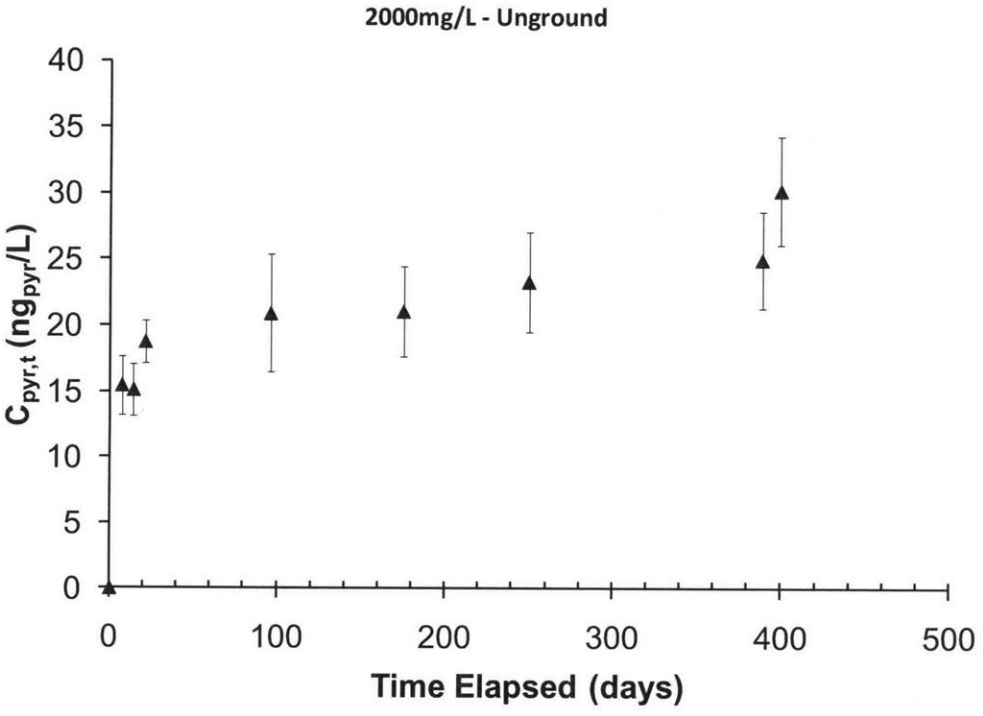
2000mg/L - Unground
$C_{pyr,t}$ (ng_{pyr}/L)
0
5
10
15
20
25
30
35
40
0
100
200
300
400
500
Time Elapsed (days)

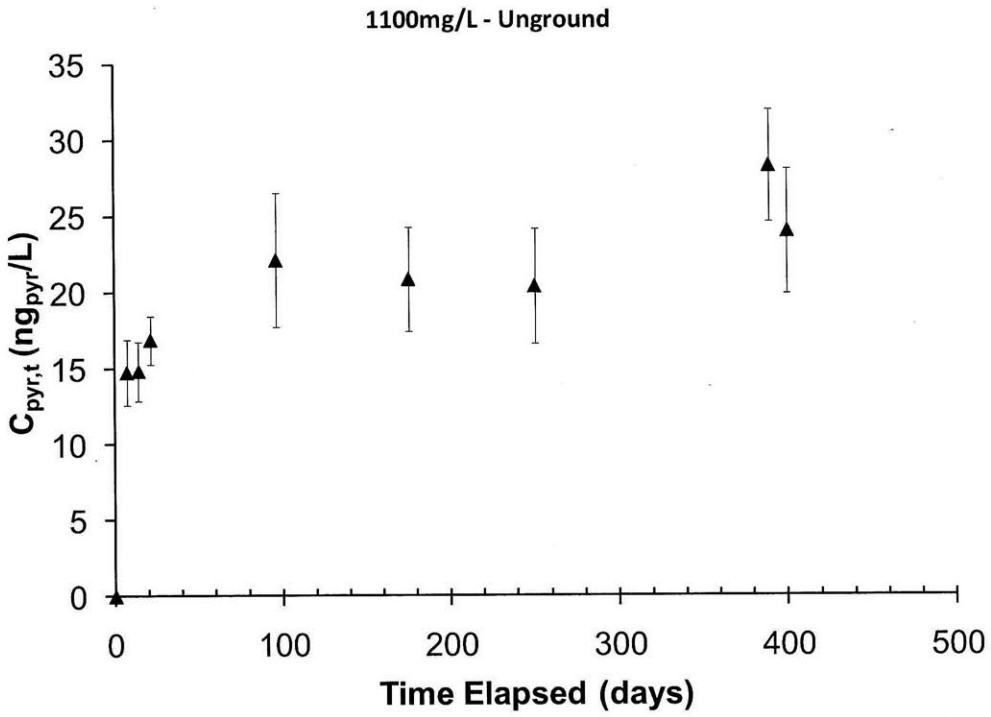
1100mg/L - Unground
35
30
25
20
15
10
5
0
$C_{pyr,t}$ (ng_{pyr}/L)
0
100
200
300
400
500
Time Elapsed (days)

Appendix 3 - 6. Examples of Slow PAHs Adsorption in Equilibrium Studies (from Literature)

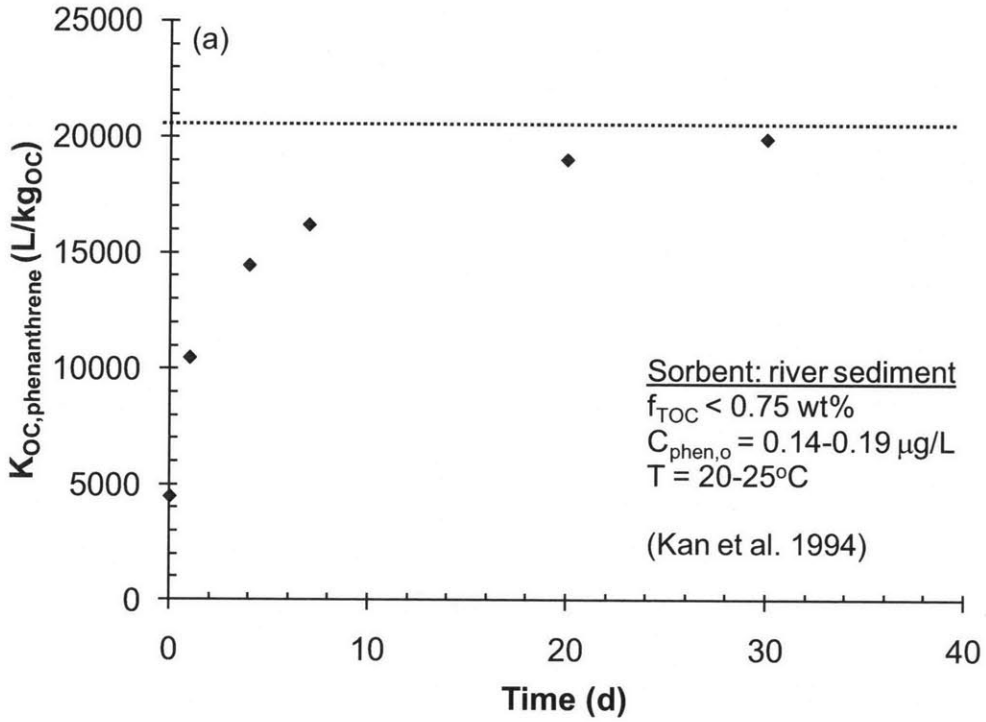

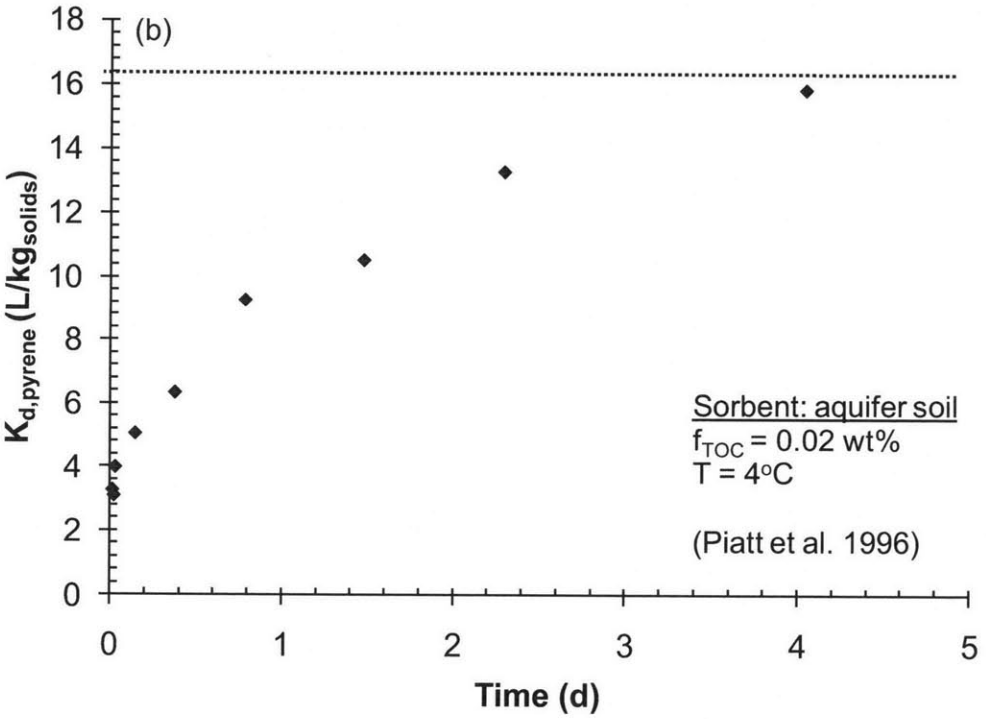

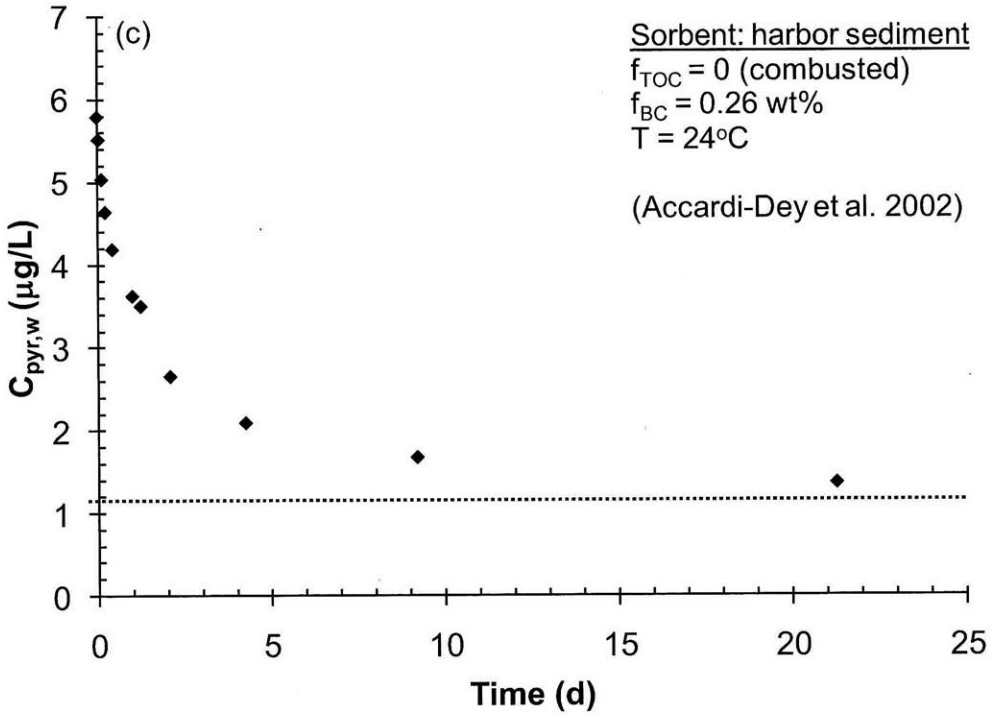

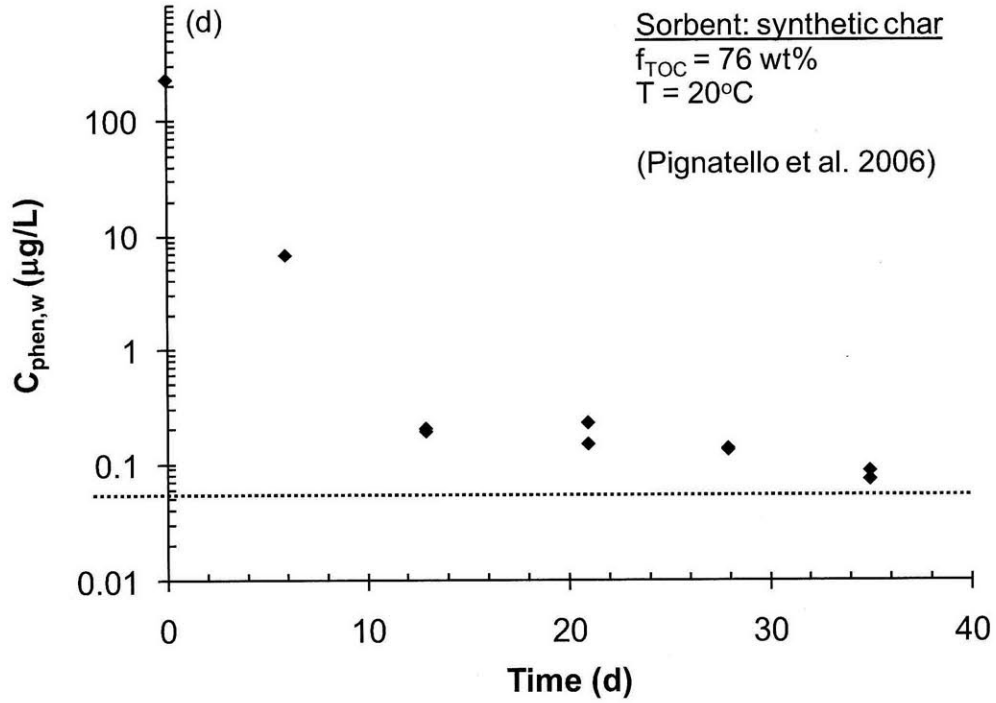

Four selected cases (reference on the figure) of non-equilibrium phenanthrene or pyrene sorption studies are presented. Phase partition equilibrium of the sorbate was claimed despite its time course showed that adsorption to be still proceeding at very slow rate. Dotted line was added to aid viewing the slow uptake behavior at later time.

Chapter 4: Appendices

Appendix 4 - 1. Long-Term Desorption Experiment: Observations after 400 d. **651**
Appendix 4 - 2. Estimates of Pyrene 'Locked-Up' (Grinding Experiment). **652**
Appendix 4 - 3. Planar Dimensions of Pyrene. **654**
Appendix 4 - 4. Estimating Pyrene Adsorption Capacity in Char/Charcoal Micropores. **655**
Appendix 4 - 5. Estimation of Equilibration Time ($t_{95\%\text{-}Eqm}$) for Pyrene Desorption in the PE-Sediment Suspension Experiment (50 d). **659**

Appendix 4 - 1. Long-Term Desorption Experiment: Observations after 400 d.

Unground NQB/BH6 (dia.:38-75 μm)				**Ground NQB/BH6** (15 min-wet grinding; dia.: <38-75 μm)			
R_{sw} (mg/L)	C_{pyr}[a] (ug/L)	S_{pyr}[b] (ug/kg)	$K_{d,pyr}$[a] (L/kg)	R_{sw} (mg/L)	C_{pyr}[a] (ug/L)	S_{pyr}[b] (ug/kg)	$K_{d,pyr}$[a] (L/kg)
(I) $K_{d,pyr}$ by LIF-Mass Balance[c]							
1059	0.0231 [0.0039]	1868	81000 [21000]	1125	0.0287 [0.0022]	1864	74000 [17000]
1059	0.0262 [0.0036]	1868	81000 [21000]	1117	0.0251 [0.0035]	1867	65000 [13000]
1963	0.0262 [0.0036]	1877	72000 [17000]	2217	0.0346 [0.0039]	1877	54000 [12000]
3660	0.0310 [0.0014]	1882	61000 [12000]	4159	0.0375 [0.0032]	1881	50000 [10000]
(II) $K_{d,pyr}$ by LIF-GCMS[d]							
1059	0.0231 [0.0039]	1693	73000 [19000]	1125	0.0287 [0.0022]	2039	71000 [15000]
1059	0.0262 [0.0036]	1693	73000 [19000]	1117	0.0251 [0.0035]	3825	152000 [37000]
1963	0.0262 [0.0036]	1478	56000 [14000]	2217	0.0346 [0.0039]	1758	51000 [12000]
3660	0.0310 [0.0014]	1565	50000 [10000]	4159	0.0375 [0.0032]	1589	42000 [9000]

a: Values in brackets are uncertainties or propagated uncertainties of 1 σ.
b: Uncertainties (1 σ) in S is estimated to be 20%.
c: Where C_{pyr} was measured by TG-LIF, and S_{pyr} determined assuming conservation of total pyrene in suspension.
d: Where both C_{pyr} and S_{pyr} were measured by TG-LIF and solvent extraction-GCMS, respectively.

Appendix 4 - 2. Estimates of Pyrene 'Locked-Up' (Grinding Experiment).

Assumptions:

(i) Equilibrium was established in suspensions containing both ground and unground sediment samples.
(ii) All solid-bound pyrene in the ground samples was available to partitioning reaction (**!!**).
(iii) In the unground samples, the solid-phase pyrene consisted of exchangeable and 'locked-up' fractions.
(iv) Total mass was conserved over the desorption time course, and the end-point solid-bound pyrene concentrations were determined via mass balance.
(v) K_d of pyrene may be treated as constant within the observed C_{pyr} range (~20 – 40 ng_{pyr}/L_w).

It should be noted that assumption (ii) may not be true as there was no evidence that the sediment particles/aggregates had been broken down to the extent that all solid-bound pyrene was exposed to water.

Following the assumptions, we can express:

$$\textbf{Unground:} \quad \mathcal{K}_{d,UnG} = \frac{S_{Locked} + S'_{Exch}}{C'_{obs}} = \frac{S_{Locked}}{C'_{obs}} + K_d$$

$$\textbf{Ground:} \quad K_d \approx K_{d,Grd} = \frac{S_{Exch}}{C_{obs}}$$

where: C'_{obs} and S'_{Exch} are the dissolved phase and exchangeable solid phase pyrene concentrations in the Unground suspensions, in units of $\mu g_{pyr}/L_w$ and $\mu g_{pyr}/kg_{solids}$, respectively,

C_{obs} and S_{Exch} are the dissolved phase and exchangeable solid phase pyrene concentrations in the Ground suspensions, in units of $\mu g_{pyr}/L_w$ and $\mu g_{pyr}/kg_{solids}$, respectively,

K_d and $K_{d,Grd}$ are the equilibrium sorption coefficients of pyrene (L_w/kg_{solids}),

$\mathcal{K}_{d,UnG}$ is the solid-phase to dissolved phase pyrene concentration ratio (L_w/kg_{solids}).

From assumptions (ii), (iii) & (v), the bound pyrene unavailable to partitioning (S_{Locked}) can be estimated by:

$$S_{Locked} = C'_{obs}(\mathcal{K}_{d,UnG} - K_d) \approx C'_{obs}(\mathcal{K}_{d,UnG} - K_{d,Grd})$$

The following tables summarize the estimated pyrene 'locked-up' in the unground samples.

Unground ($S_{pyr,o}$ = 2100 $\mu g_{pyr}/kg_{solids}$)				
R_{sw} (mg_{solids}/L_w)	Pyr Tot. ($\mu g_{pyr}/L_w$)	C'_{obs} ($\mu g_{pyr}/L_w$)	$S'_{Tot,End-pt}$ ($\mu g_{pyr}/kg_{solids}$)	$\mathcal{K}_{d,UnG}$ (L_w/kg_{solids})
1000	2.1	0.0221	2077.9	94000
2000	4.2	0.0230	2088.5	90800
4000	8.4	0.0327	2091.8	64000

Ground ($S_{pyr,o}$ = 2100 $\mu g_{pyr}/kg_{solids}$)				
R_{sw} (mg_{solids}/L_w)	Pyr Tot. ($\mu g_{pyr}/L_w$)	C_{obs} ($\mu g_{pyr}/L_w$)	S_{Exch} ($\mu g_{pyr}/kg_{solids}$)	$K_{d,Grd}$ (L_w/kg_{solids})
1000	2.1	0.0305	2069.5	67900
2000	4.2	0.0320	2084.0	65100
4000	8.4	0.0405	2089.9	51600

R_{sw} (mg_{solids}/L_w)	$\mathcal{K}_{d,UnG}$ - $K_{d,Grd}$ (L_w/kg_{solids})	C'_{obs} ($\mu g_{pyr}/L_w$)	S_{Locked} ($\mu g_{pyr}/kg$)	% Locked Up
1000	26100	0.0221	***580***	***28%***
2000	25700	0.0230	***590***	***28%***
4000	12400	0.0327	***400***	***19%***

Appendix 4 - 3. Planar Dimensions of Pyrene.

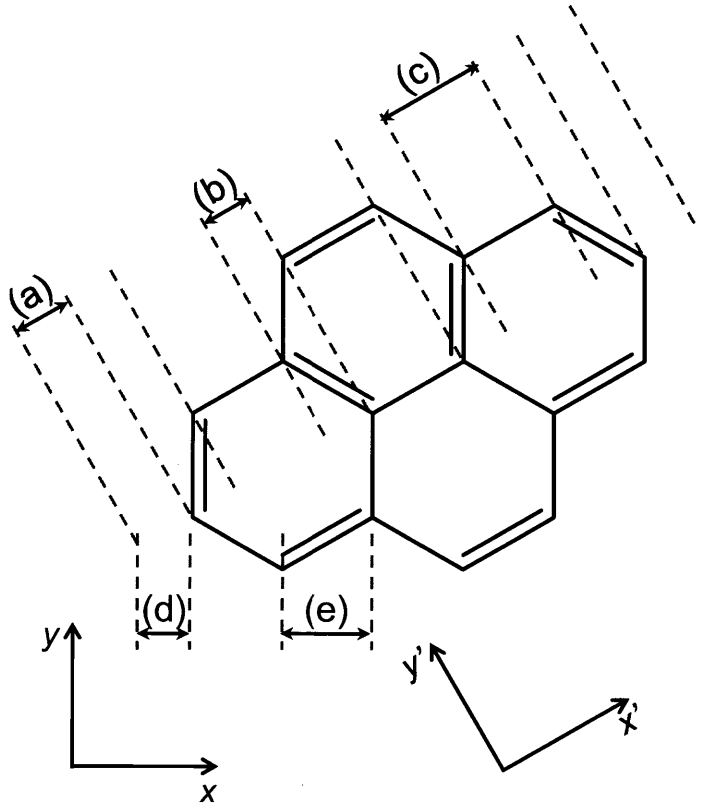

Bond Length

(a) C_{ar}-H ≈ 1.1 Å
(b) C_{ar}-C_{ar} ≈ (sin30°)1.4 Å
(c) C_{ar}-C_{ar} ≈ 1.4 Å
(d) C_{ar}-H ≈ (cos30°)1.1 Å
(e) C_{ar}-C_{ar} ≈ (cos30°)1.4 Å

Planar Dimensions

L_x = 2d+5e = 7.9 Å
L_y = 2a+3b+2c = 7.1 Å
$L_{x'}$ = 2a+4b+3c = 9.2 Å
$L_{y'}$ = 2d+4e = 6.7 Å

Bond lengths from CRC Handbook of Chemistry and Physics (Lide 1998).

Appendix 4 - 4. Estimating Pyrene Adsorption Capacity in Char/Charcoal Micropores.

In order to estimate the adsorption capacity of pyrene in the char/charcoal phase of the sediment, we need to know how much adsorbed pyrene, on a $\mu g_{pyr}/kg_{solids}$ basis, may be attributed to the char/charcoal phase. Two approaches were taken for estimating the char-bound pyrene: (a) by deducting the adsorption uptake contributed by OC and soot –BC using the OC-BC sorption prediction model, and (b) by regressing the isotherm data with function that yield a capacity term for char-bound pyrene adsorption.

In approach (a), we used the OC-BC sorption model ($K_{d,PAH} = f_{OC}K_{OC} + f_{BC}K_{BC}C_{iPAH}^{n}$) developed previously (Accardi-Dey and Gschwend 2002) for estimates of non-char bound pyrene. However, since the parameters of the said OC-BC model was derived from a higher pyrene concentration range (~0.5-20 ug_{pyr}/L_w), extrapolating the model to the ng_{pyr}/L_w range implied the following assumptions:

(i) that the distribution of adsorption site energies of the soot-BC was constant such that the exponent of n remained constant (Adamson et al. 1997),
(ii) that BC 'normalized' coefficient, K_{BC}, remained constant,
(iii) that natural non-condensed organic carbon, OC, behaved as an absorbing media rather than a surface, and that it's affinity for pyrene was invariant with the concentration of pyrene.
(iv) that a portion of char/charcoal may take up pyrene on its mesopore surface and that this portion can be treated the same as soot-BC
(v) that the mass fraction of char/charcoal, $f_{char\text{-}BC}$, is about the same as that of soot-BC, $f_{soot\text{-}BC}$, (CTO-375°C-24hr) or about 10% of the total organic carbon, f_{TOC},
(vi) that the char/charcoal mesopore surface area is about 30% that of the sum of micropore+mesopore surface area.

The char/charcoal-bound pyrene concentrations in NQB#6 were thus estimated to be around 3600-4000 $\mu g_{pyr}/kg_{solids}$ (Table below).

Case	Assumption	Char/Charcoal-bound pyrene ($\mu g_{pyr}/kg_{solids}$)
Simple OC-BC	• Char exhibits insignificant mesopore sorption	4000±200
OC-BC + char-mesopore sorption (i)	• Char mesopore surface area ~30% of meso+micropore surface area • $f_{char\text{-}BC} \sim f_{TOC} = 0.003$	3800±300
OC-BC + char-mesopore sorption (ii)	• Char mesopore surface area ~30% of meso+micropore surface area • $f_{char\text{-}BC} \sim f_{soot\text{-}BC} = 0.005$	3600±400

In approach (b), the char/charcoal-bound pyrene loading was estimated from a capacity term after regressing partitioning data with a composite Langmuir-Freundlich model:

$$S_{pyr,Eqm,T} = K_{Fr} C_{pyr,Eqm}^{\ n} + \frac{S_{Lgmr,Max} C_{pyr,Eqm}}{C_{Lgmr,½} + C_{pyr,Eqm}}$$

Where $S_{Lgmr,Max}$ was taken as the sorption capacity of pyrene in the char/charcoal micropores. The Langmuir model was applied for convenience rather than as an endorsement for the mechanistic view of monolayer adsorption of pyrene on the char/charcoal micropores surface. Alternative composite model, such as a Freundlich-Freundlich form, could fit the equilibrium distribution of pyrene equally well (Figure below).

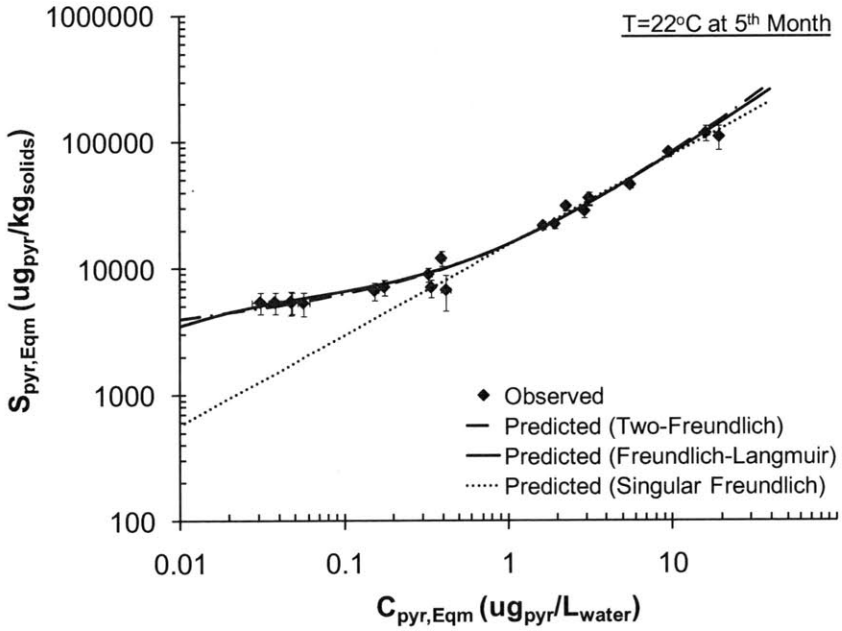

The regression approach estimated the char/charcoal-bound pyrene to be around 4500-5500 $\mu g_{pyr}/kg_{solids}$.

The surface-area based pyrene sorption capacity in char/charcoal was estimated with further assumptions:

(i) the mass fraction of char/charcoal, $f_{char\text{-}BC}$, is about the same as that of soot-BC, $f_{soot\text{-}BC}$, (CTO-375°C-24hr) or about 10% of the total organic carbon, f_{TOC},

(ii) that the char/charcoal micro+mesopore surface area was about 10 m^2/g_{char} (geometric mean of the reported extremes of 2 m^2/g_{char} and 49 m^2/g_{char}),

(iii) that char/charcoal micropores contribute to about 70% of pyrene accessible micro+mesopore surface area.

The resulting estimates of char/charcoal-pyrene sorption capacity in NQB#6 are summarized in below, together with a sensitivity analysis on the uncertainty of char/charcoal micropore area.

$S_{pyr,char-BC}$ ($\mu g_{pyr}/kg_{solids}$)	$f_{char-BC}$ (kg_{char}/kg_{solids})	$S'_{pyr,char-BC}$ ($\mu g_{pyr}/kg_{char}$)	Micropore SA ($m^2_{micropore}/g_{char}$)	$S^A_{pyr,char,micropore}$ ($\mu g_{pyr}/m^2_{micropore}$)
BASECASE				
(a) OC/BC Deduction				
3600	0.003	1.2×10^6	7	**171**
	0.005	0.72×10^6	7	**103**
4000	0.003	1.3×10^6	7	**190**
	0.005	0.80×10^6	7	**114**
(b) Regression				
4500	0.003	1.5×10^6	7	**214**
	0.005	0.90×10^6	7	**129**
5500	0.003	1.8×10^6	7	**262**
	0.005	1.1×10^6	7	**157**
SENSITIVITY ANALYSIS				
3600	0.003	1.2×10^6	5	240
	0.005	0.72×10^6	5	144
5500	0.003	1.8×10^6	5	367
	0.005	1.1×10^6	5	220
3600	0.003	1.2×10^6	9	133
	0.005	0.72×10^6	9	80
5500	0.003	1.8×10^6	9	204
	0.005	1.1×10^6	9	122

We thus estimated that if char/charcoal was present in NQB#6, from the adsorption equilibrium observations, the char/charcoal-BC should have an area-normalized pyrene sorption capacity of ~100-260 $\mu g_{pyr}/m^2_{micropore}$. Sensitivity analysis showed that the sorption capacity estimate may vary by ~50% due to uncertainty in micropore surface area and/or fraction of char-carbon.

Walters et al. (1984) reported Langmuir fitting parameters for pyrene partitioning in activated carbon (Filtrasorb 400)-water system. Assuming the said activated carbon retains similar properties throughout the years, its carbon content would be ~0.88 by weight (Rivera-Utrilla et al. 2002), with micropores contributing to ~95% of total micro+mesopore surface area (Paulsen et al. 1999). The area-normalized pyrene sorption capacity in activated carbon (Filtrasorb 400) micropores can be likewise estimated.

$S_{pyr,GAC}$ ($\mu g_{pyr}/kg_{solids}$)	$f_{GAC\text{-}char}$ ($kg_{char\text{-}C}/kg_{solids}$)	$S_{pyr,char\text{-}C}$ ($\mu g_{pyr}/kg_{char\text{-}C}$)	**Micropore SA** ($m^2_{micropore}/g_{char}$)	$S^A_{pyr,char,micropore}$ ($\mu g_{pyr}/m^2_{micropore}$)
*64×10^6	0.88[a]	73×10^6	**950**[b]	77
*83×10^6	0.88	94×10^6	**950**	99
64×10^6	0.88	73×10^6	**760**[c]	96
83×10^6	0.88	94×10^6	**760**	124

*: The lower and upper estimates of $S_{Lgmr,Max}$ ($\mu g_{pyr}/kg_{solids}$) as reported by Walters et al. (1984).
a: Assuming all total carbons in GAC were char-carbon, thus $f_{GAC\text{-}char} = f_{GAC,TOC} = 0.88$, according to the elemental analysis by Rivera-Utrilla et al. (2002).
b: Walters et al. (1984) reported a total surface area of ~1000 m^2/g_{solids} without specifying whether macropores surface area and/or geometric surface area (i.e. spherical area) were included. Here, it was assumed the value referred to the sum of micropore and mesopore surface area, and that 95% of it was in micropores.
c: According to pore distribution and surface area analysis on the identical brand of GAC (Filtrasorb 400).

The micropore area-normalized pyrene sorption capacity derived from GAC sorption experiment ($S^A_{pyr,char,micropore}$=80-120 $\mu g_{pyr}/m^2_{micropore}$) was thus comparable to that estimated for NQB#6 ($S^A_{pyr,char,micropore}$=100-260 $\mu g_{pyr}/m^2_{micropore}$).

Appendix 4 - 5. Estimation of Equilibration Time ($t_{95\%\text{-}Eqm}$) for Pyrene Desorption in the PE-Sediment Suspension Experiment (50 d).

Since it remains unclear whether equilibrium was achieved in the PE-sediment experiment after 50 d, two possible cases were considered in the estimation of equilibration time: (i) equilibrium was established after 50 d, and (ii) that all suspensions remained remotely away from equilibrium after 50 d (here, assumed that $5K_{d,pyr} = Q_{d,pyr,50d}$). These two cases were then examined under two transient sorption models: (A) the 1st order approximation model, and (B) the radial desorption constant diffusivity model.

A. 1st Order Approximation Model

1st Order Approximation Model

It has been shown in Chapter 3 that the transient sorption assuming the 1st order approximation takes the following expression:

$$\frac{C_t}{C_\infty} = 1 - \exp\{-k(K_d R_{sw} + 1)t\}$$

(Equation A-1)

Where: C_t and C_∞ are the dissolved phase sorbate (i.e. pyrene) concentrations at time t and infinite time (equilibrium),

k is the 'intrinsic' rate constant in unit d^{-1} or s^{-1},

K_d is the solid-water equilibrium partitioning/distribution coefficient of the sorbate in unit L_w/kg_{solids} (*or $L_{eqvl\text{-}w}/kg_{solids}$ when converting mass of PE present to equivalent volume of water*),

R_{sw} is the solid-to-water ratio for the entire system in unit kg_{solids}/L_w (*or $kg_{solids}/L_{eqvl\text{-}w}$ when converting mass of PE present to equivalent volume of water*),

t is time elapsed in unit d or s.

Time for equilibration, here arbitrarily defined as time required for C_t/C_∞ to reach 0.95, can be determined as follows:

$$t_{95\%-Eqm} = \frac{\ln 20}{k(K_d R_{sw} + 1)} = \frac{\ln 20}{k_{eff}}$$

(Equation A-2)

Estimation of the 'intrinsic' k

Since the masses of sediment and PE in the vessels are known, the only unknown is the 'intrinsic' rate constant k. This k was estimated by fitting the kinetic data from the short-term desorption kinetic experiment (Chapter 2) with Equation A-1. Two scenarios were considered for estimating k: (i) $K_{d,pyr}$ (*in the desorption experiment*) was

determined *a priori* with a linear-OC, non-linear-BC model (with $\log K_{BC}$=6.5 and n_{BC}=0.62), and (ii) $K_{d,pyr}$ (*in the desorption experiment*) was taken as the final ratio of S_{pyr}/C_{pyr} (i.e. $S_{pyr,end}/C_{pyr,end}$) with the final S_{pyr} determined from mass balance. The fitted k_{eff} (or k') and the 'intrinsic' k are shown in the table below (A-1). The goodness of fit varied greatly, with r^2 ranging from 0.5 to 0.9 (not shown). It turned out that the two scenarios gave fairly close estimates of k (low estimates: 3.9-7.2×10^{-5} d^{-1}; high estimates: 5.1-6.3×10^{-3} d^{-1}).

Estimation of k_{eff} & $t_{95\%\text{-}Eqm}$

The time of reaching 95% of equilibrium ($t_{95\%\text{-}Eqm}$) was then computed for both the equilibrium (table A-2) and the disequilibrium cases according to Equation A-2 (table A-3). The equivalent $K_{d,pyr}$'s and the equivalent R_{sw}'s (i.e. converting mass PE into equivalent volume of water) of the PE-sediment suspensions and the k's estimated in table A-1 were used to compute k_{eff} and hence $t_{95\%\text{-}Eqm}$.

A-1. Fitting of 'intrinsic' k (i.e. k_{fit}) of kinetic data from the Short-Term Desorption Experiment

			$K_{d,pyr}$ at $logK_{BC}$=6.5, n_{BC}=0.62				$K_{d,pyr} = S_{pyr,end}/C_{pyr,end}$			
Label	**Size (μm)**	**R_{sw} (mg/L)**	**K_d (L/kg)**	**$1+R_{sw}K_d$**	**k' $(d^{-1})^a$**	**k_{fit} $(d^{-1})^b$**	**K_d (L/kg)**	**$1+R_{sw}K_d$**	**k' $(d^{-1})^a$**	**k_{fit} $(d^{-1})^b$**
A-Set	38-75	23	42000	2.0	0.0018	***9.1E-04***	392000	10.0	0.014	***1.4E-03***
		72		4.0	0.0023	***5.6E-04***	200000	15.4	0.015	***9.5E-04***
		277		12.6	0.0015	***1.2E-04***	166000	47.0	0.013	***2.7E-04***
C-Set	38-75	23	42000	2.0	0.0037	***1.9E-03***	445000	11.2	0.035	***3.2E-03***
		71		4.0	0.0204	***5.1E-03***	105000	8.5	0.051	***6.1E-03***
		268		12.3	0.0165	***1.3E-03***	92000	25.6	0.046	***1.8E-03***
L-Series	38-75	22	42000	1.9	0.0048	***2.5E-03***	225000	5.9	0.024	***4.0E-03***
		70		3.9	0.0044	***1.1E-03***	148000	11.4	0.018	***1.6E-03***
		289		13.1	0.0043	***3.3E-04***	114000	33.8	0.020	***5.8E-04***
K-Series	75-106	21	101000	3.1	0.0021	***6.7E-04***	385000	9.1	0.0093	***1.0E-03***
		83		9.4	0.0025	***2.7E-04***	244000	21.3	0.0090	***4.2E-04***
		253		26.6	0.0028	***1.1E-04***	199000	51.3	0.0091	***1.8E-04***
I-H-G	180-250	19	118000	3.2	0.0007	***2.2E-04***	766000	15.6	0.0061	***3.9E-04***
		68		9.0	0.0015	***1.7E-04***	391000	27.6	0.0074	***2.7E-04***
		245		29.9	0.0012	***3.9E-05***	356000	88.3	0.0063	***7.2E-05***
Max k						***5.1E-03***				***6.1E-03***
Min k						***3.9E-05***				***7.2E-05***

a: k' is the estimated value of k_{eff} (i.e. in Equation A-2, $k' = [k(K_dR_{sw}+1)]_{fitted}$).
b: k_{fit} is the estimated value for the 'intrinsic' k in Equation A-1, A-2. Or $k_{fit}(K_dR_{sw}+1) = k'$.

A-2. Estimation of $t_{95\%\text{-Eqm}}$ by 1st Order Model assuming equilibrium after 50 d (i.e. $K_{d,pyr}=Q_{d,pyr,50d}$).

1st Order Model $C_t/C_\infty=1-\exp(-k_{eff}t)$					**** Assumption: Equilibrium after 50 d ($K_{d,pyr} = Q_{d,pyr,50d}$)**							
					† (I) $K_{d,pyr}$ at $\log K_{BC}=6.5$, $n_{BC}=0.62$				‡ (II) $K_{d,pyr} = S_{pyr,end}/C_{pyr,end}$			
					low $k_{fit}=3.9\times10^{-5}$ d^{-1}		high $k_{fit}=5.1\times10^{-3}$ d^{-1}		low $k_{fit}=7.2\times10^{-5}$ d^{-1}		high $k_{fit}=6.1\times10^{-3}$ d^{-1}	
PE#	gPE:gBC	R_{sw} (mg/L)	$Q_{d,pyr,50d}$ (L/kg)	$\Delta Q_{d,pyr}$ (L/kg)	k_{eff} (d^{-1})[a]	$t_{95\%\text{-Eqm}}$ (d)[b]	k_{eff} (d^{-1})[a]	$t_{95\%\text{-Eqm}}$ (d)[b]	k_{eff} (d^{-1})[a]	$t_{95\%\text{-Eqm}}$ (d)[b]	k_{eff} (d^{-1})[a]	$t_{95\%\text{-Eqm}}$ (d)[b]
1	66	51	2076533	719332	4.2E-03	***710***	5.5E-01	***5***	7.7E-03	***390***	6.5E-01	***5***
2	70	49	1463892	507107	2.8E-03	***1060***	3.7E-01	***8***	5.2E-03	***580***	4.4E-01	***7***
3	61	55	1860269	644416	4.0E-03	***740***	5.3E-01	***6***	7.4E-03	***410***	6.2E-01	***5***
4	187	20	3873686	1341884	3.1E-03	***960***	4.1E-01	***7***	5.7E-03	***520***	4.8E-01	***6***
5	190	20	4091350	1417285	3.3E-03	***920***	4.2E-01	***7***	5.9E-03	***500***	5.0E-01	***6***
6	198	19	4192142	1452200	3.2E-03	***930***	4.2E-01	***7***	5.9E-03	***510***	4.9E-01	***6***
7	652	6.1	13697442	4744933	3.3E-03	***900***	4.3E-01	***7***	6.1E-03	***490***	5.1E-01	***6***
8	658	6.1	14775635	5118430	3.6E-03	***840***	4.6E-01	***6***	6.5E-03	***460***	5.5E-01	***5***
9	655	6.1	13252493	4590798	3.2E-03	***930***	4.2E-01	***7***	5.9E-03	***510***	4.9E-01	***6***
10	1937	2.1	24371257	8442451	2.0E-03	***1470***	2.7E-01	***11***	3.7E-03	***800***	3.1E-01	***10***
11	1828	2.2	21995265	7619383	2.0E-03	***1530***	2.5E-01	***12***	3.6E-03	***840***	3.0E-01	***10***
12	1882	2.1	37835069	13106452	3.2E-03	***930***	4.2E-01	***7***	5.9E-03	***510***	5.0E-01	***6***
17	66	116	2227707	771700	1.0E-02	***290***	1.3E+00	***2***	1.9E-02	***160***	1.6E+00	***2***
18	68	123	2097334	726538	1.0E-02	***290***	1.3E+00	***2***	1.9E-02	***160***	1.6E+00	***2***
19	64	109	2385370	826317	1.0E-02	***290***	1.3E+00	***2***	1.9E-02	***160***	1.6E+00	***2***
20	580	42	6049943	2095762	1.0E-02	***300***	1.3E+00	***2***	1.8E-02	***160***	1.5E+00	***2***
21	555	22	11659155	4038850	1.0E-02	***290***	1.3E+00	***2***	1.9E-02	***160***	1.6E+00	***2***
22	578	25	10134165	3510578	1.0E-02	***300***	1.3E+00	***2***	1.9E-02	***160***	1.6E+00	***2***

**: This refers to the equivalent $K_{d,pyr}$ of the PE-sediment experiment, which was used to compute k_{eff}'s for the PE-sediment suspensions.
†: This $K_{d,pyr}$ refers to that for the data from the Short-Term Desorption Kinetic experiment; here, it was estimated *a priori* with the BC-OC sorption model. This $K_{d,pyr}$ allows the 'intrinsic' rate constant, k_{fit}, to be calculated. See table A-1.
‡: This $K_{d,pyr}$ refers to that for the data from the Short-Term Desorption Kinetic experiment; here, it was estimated using the final S_{pyr} and C_{pyr} observed in the desorption kinetic experiment. This $K_{d,pyr}$ allows the 'intrinsic' rate constant, k_{fit}, to be calculated. See table A-1.
a: $k_{eff} = k_{fit}(R_{sw}K_{d,pyr}+1)$.
b: $t_{95\%\text{-Eqm}}$ is the time elapsed such that $C_{t95\%\text{-Eqm}}/C_\infty = 0.95$.

A-3. Estimation of $t_{95\%\text{-}Eqm}$ by 1st Order Model assuming disequilibrium after 50 d (i.e. $K_{d,pyr}=Q_{d,pyr,50d}/5$).

1st Order Model $C_t/C_\infty=1-\exp(-k_{eff}t)$					**** Assumption: Disequilibrium ($K_{d,pyr} = Q_{d,pyr,50d}/5$) after 50 d**							
					† (I) $K_{d,pyr}$ at $\log K_{BC}=6.5$, $n_{BC}=0.62$				‡ (II) $K_{d,pyr} = S_{pyr,end}/C_{pyr,end}$			
					low $k_{fit}=3.9\times10^{-5}$ d^{-1}		high $k_{fit}=5.1\times10^{-3}$ d^{-1}		low $k_{fit}=7.2\times10^{-5}$ d^{-1}		high $k_{fit}=6.1\times10^{-3}$ d^{-1}	
PE#	gPE:gBC	R_{sw} (mg/L)	$Q_{d,pyr,50d}$ (L/kg)	$\Delta Q_{d,pyr}$ (L/kg)	k_{eff} $(d^{-1})^a$	$t_{95\%\text{-}Eqm}$ $(d)^b$	k_{eff} $(d^{-1})^a$	$t_{95\%\text{-}Eqm}$ $(d)^b$	k_{eff} $(d^{-1})^a$	$t_{95\%\text{-}Eqm}$ $(d)^b$	k_{eff} $(d^{-1})^a$	$t_{95\%\text{-}Eqm}$ $(d)^b$
1	66	51	2076533	719332	8.8E-04	***3420***	1.1E-01	***26***	1.6E-03	***1870***	1.3E-01	***22***
2	70	49	1463892	507107	6.0E-04	***5000***	7.8E-02	***39***	1.1E-03	***2740***	9.2E-02	***33***
3	61	55	1860269	644416	8.4E-04	***3560***	1.1E-01	***27***	1.5E-03	***1950***	1.3E-01	***23***
4	187	20	3873686	1341884	6.6E-04	***4550***	8.5E-02	***35***	1.2E-03	***2490***	1.0E-01	***30***
5	190	20	4091350	1417285	6.8E-04	***4390***	8.9E-02	***34***	1.2E-03	***2400***	1.1E-01	***29***
6	198	19	4192142	1452200	6.7E-04	***4440***	8.8E-02	***34***	1.2E-03	***2440***	1.0E-01	***29***
7	652	6.1	13697442	4744933	7.0E-04	***4290***	9.1E-02	***33***	1.3E-03	***2350***	1.1E-01	***28***
8	658	6.1	14775635	5118430	7.4E-04	***4030***	9.7E-02	***31***	1.4E-03	***2210***	1.1E-01	***26***
9	655	6.1	13252493	4590798	6.7E-04	***4440***	8.8E-02	***34***	1.2E-03	***2440***	1.0E-01	***29***
10	1937	2.1	24371257	8442451	4.4E-04	***6810***	5.7E-02	***52***	8.0E-04	***3730***	6.8E-02	***44***
11	1828	2.2	21995265	7619383	4.2E-04	***7100***	5.5E-02	***55***	7.7E-04	***3890***	6.5E-02	***46***
12	1882	2.1	37835069	13106452	6.8E-04	***4410***	8.8E-02	***34***	1.2E-03	***2420***	1.0E-01	***29***
17	66	116	2227707	771700	2.1E-03	***1440***	2.7E-01	***11***	3.8E-03	***790***	3.2E-01	***9***
18	68	123	2097334	726538	2.1E-03	***1440***	2.7E-01	***11***	3.8E-03	***790***	3.2E-01	***9***
19	64	109	2385370	826317	2.1E-03	***1440***	2.7E-01	***11***	3.8E-03	***790***	3.2E-01	***9***
20	580	42	6049943	2095762	2.0E-03	***1470***	2.7E-01	***11***	3.7E-03	***800***	3.1E-01	***10***
21	555	22	11659155	4038850	2.1E-03	***1450***	2.7E-01	***11***	3.8E-03	***790***	3.2E-01	***9***
22	578	25	10134165	3510578	2.1E-03	***1450***	2.7E-01	***11***	3.8E-03	***800***	3.2E-01	***9***

**: This refers to the equivalent $K_{d,pyr}$ of the PE-sediment experiment, which was used to compute k_{eff}'s for the PE-sediment suspensions.

†: This $K_{d,pyr}$ refers to that for the data from the Short-Term Desorption Kinetic experiment; here, it was estimated *a priori* with the BC-OC sorption model. This $K_{d,pyr}$ allows the 'intrinsic' rate constant, k_{fit}, to be calculated. See table A-1.

‡: This $K_{d,pyr}$ refers to that for the data from the Short-Term Desorption Kinetic experiment; here, it was estimated using the final S_{pyr} and C_{pyr} observed in the desorption kinetic experiment. This $K_{d,pyr}$ allows the 'intrinsic' rate constant, k_{fit}, to be calculated. See table A-1.

a: $k_{eff} = k_{fit}(R_{sw}K_{d,pyr}+1)$.

b: $t_{95\%\text{-}Eqm}$ is the time elapsed such that $C_{t95\%\text{-}Eqm}/C_\infty = 0.95$.

B. Radial Desorption Model (with constant effective diffusivity, D_{eff})

Radial Desorption Model

It has been suggested in Chapter 7 section 4.1 that the simple, 1-D, radial desorption model with the retardation of diffusion *independent of* the distribution of sorption energy (i.e. $D_{eff} \neq f\{C_{pyr}(r,t)\}$ = constant) should have the following solution (Equation B-1 to B-4):

$$\frac{M_o - M_t}{M_o - M_\infty} = 1 - \sum_{n=1}^{\infty} \frac{6\beta(\beta+1)\exp\{-D_{eff} q_n^2 t/r^2\}}{9 + 9\beta + q_n^2\beta^2}$$

(Equation B-1)

$$\tan q_n = \frac{3q_n}{3 + \beta q_n^2}; \{\text{for } q_n > 0\}$$

(Equation B-2, for q_n)

$$f_{is,Eqm} = \frac{M_\infty}{M_o} = \frac{S_\infty m_s}{S_\infty m_s + C_\infty V_w} = \frac{1}{1 + {}^1/_{K_d R_{sw}}} = \frac{1}{1+\beta}$$

(Equation B-3, for β)

$$D_{eff} = \frac{D_{iw}\theta^2}{(1-\theta)\rho_s K_d + \theta}$$

(Equation B-4, for D_{eff})

Where: β is the reciprocal of $K_d R_{sw}$ (dimensionless),

C_∞ is the dissolved pyrene concentration (or equivalent dissolved concentration) at equilibrium ($\mu g_{pyr}/L_w$ or $\mu g_{pyr}/L_{eqvl\text{-}w}$),

D_{iw} and D_{eff} are the aqueous and effective diffusivities for pyrene (m^2/s),

$f_{is,Eqm}$ is the fraction of pyrene sorbed to the sedimentary phase at equilibrium,

K_d is the solid-water equilibrium partitioning/distribution coefficient of the sorbate in unit L_w/kg_{solids} (*or $L_{eqvl\text{-}w}/kg_{solids}$ when converting mass of PE present to equivalent volume of water*),

M_o, M_t, and M_∞ are the sedimentary pyrene mass at the beginning, time t, and equilibrium, respectively (arbitrary mass unit),

q_n is the n^{th} non-zero root satisfying Equation B-2,

r is the particle/aggregate radius (m),

R_{sw} is the solid-to-water ratio for the entire system in unit kg_{solids}/L_w (*or $kg_{solids}/L_{eqvl\text{-}w}$ when converting mass of PE present to equivalent volume of water*),

ρ_s is the solid matrix dry density (kg_{solids}/L_{solids}),

S_∞ is the sedimentary pyrene concentration at equilibrium ($\mu g_{pyr}/L_w$ or $\mu g_{pyr}/kg_{solids}$),

t is time elapsed (s),

θ is the intra-aggregate porosity (dimensionless). Here assumed to be 0.15.

Here, time for equilibration is approximated by time required to reach 95% of equilibrium. That is:

$$t_{95\%-Eqm} = \frac{M_o - M_{t95\%-Eqm}}{M_o - M_\infty} = 1 - \sum_{n=1}^{\infty} \frac{6\beta(\beta+1)\exp\{-D_{eff} q_n^2 t_{95\%-Eqm}/r^2\}}{9 + 9\beta + q_n^2\beta^2}$$

(Equation B-5)

Solving q_n's

The most difficult part of this solution is exhaustively solving all q_n's via the non-linear Equation B-2. This is due to the limitation of typical root-solving functions/routines. In order to devise a root-solving strategy/algorithm, the asymptotic behavior of Equation B-2 was examined.

For small, non-zero but positive values of q_n's,

$$\tan q_n \approx q_n \approx \frac{3q_n}{3 + \beta q_n^2}$$

(Equation B-2a)

For large q_n's (i.e., $\beta q^2{}_n >> 3$), q_n may be expressed in terms of π such that:

$$q_n = m\pi + \delta; \text{where } \tan\delta \approx \delta, \text{and } m \in Int^+$$

(Equation B-2b)

This allows Equation B-2 to be re-expressed as follows for large q_n:

$$\tan q_n = \tan(m\pi + \delta) = \tan\delta \approx \frac{3}{\beta q_n} = \frac{1}{\text{large}} = \delta$$

(Equation B-2c)

This implies that a periodicity of approximately 1 π separates the large q_n's. In other words, $q_{n+1} \approx q_n + \pi$. q_n's were determined in Matlab script incorporating the asymptotic consequences shown in Equation B-2a to 2c (Appendix E, Script E-1, function F_RadDesorbConstRetard).

Estimation of $t_{95\%\text{-}Eqm}$

A dimensionless desorption-time plot was generated (figure B-1) from which the time of reaching 95% of equilibrium ($t_{95\%\text{-}Eqm}$) was read off. For comparison, $t_{95\%\text{-}Eqm}$ assuming particle/aggregate radii of 10 and 100 μm were tabulated (table B-2). In general, for a fixed K_d, a reduction in radius by x-times will reduce $t_{95\%\text{-}Eqm}$ by a factor of x^2.

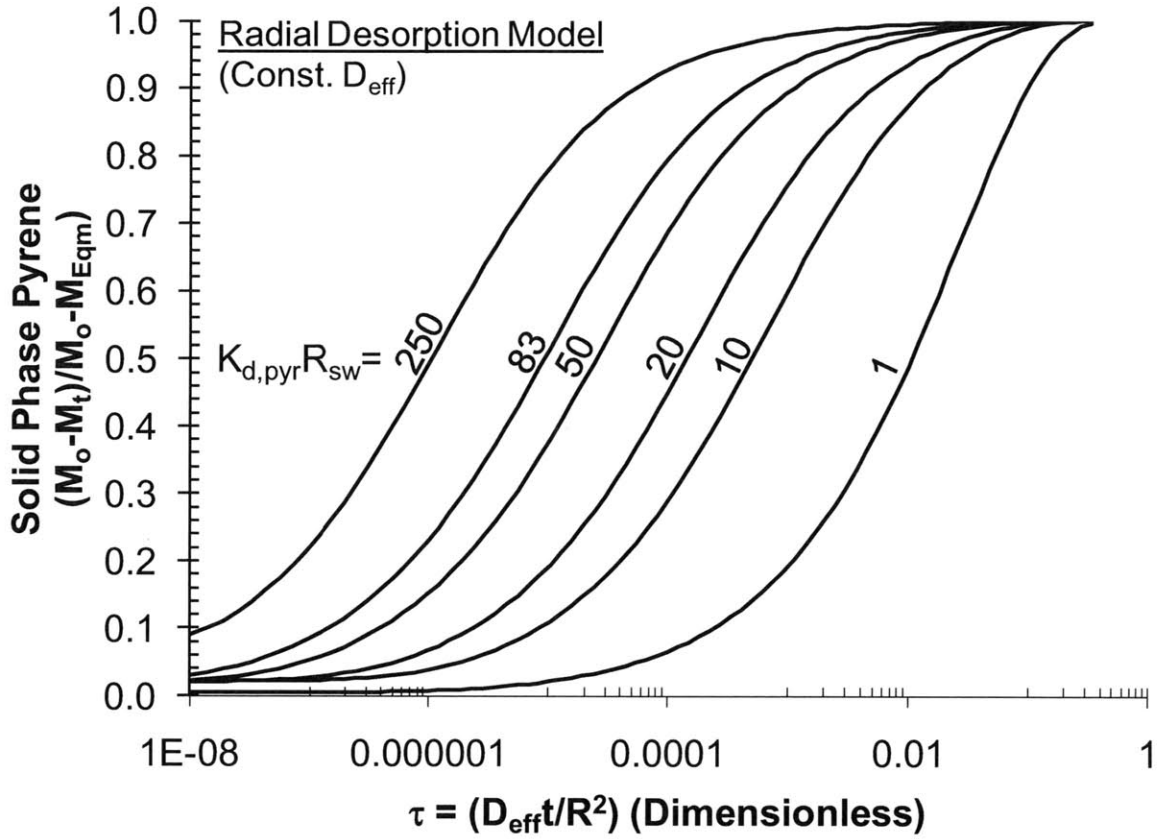

B-1. Dimensionless transient Radial Desorption plot.

B-2. Estimation of $t_{95\%\text{-}Eqm}$ by Radial Desorption Model (Constant D_{eff}) assuming equilibrium or disequilibrium after 50 d.

*Radial Desorption Model (Constant D_{eff})					Equilibrium after 50 d $^{\dagger}K_{d,pyr} = Q_{d,pyr,50d}$				Disequilibrium after 50 d $^{\dagger}K_{d,pyr} = Q_{d,pyr,50d}/5$			
PE#	gPE:gBC	R_{sw}† (mg/L)	$Q_{d,pyr,50d}$† (L/kg)	$\Delta Q_{d,pyr}$ (L/kg)	β† =1/($R_{sw}K_d$)	K_d† (L/kg)	$t_{95\%\text{-}Eqm}$ (d) (r=100 μm)	$t_{95\%\text{-}Eqm}$ (d) (r=10 μm)	β† =1/($R_{sw}K_d$)	K_d† (L/kg)	$t_{95\%\text{-}Eqm}$ (d) (r=100 μm)	$t_{95\%\text{-}Eqm}$ (d) (r=10 μm)
1	66	51	2076533	719332	9.4E-03	2076533	***40-50***	***<1***	0.047	415307	***70-90***	***~1***
2	70	49	1463892	507107	1.4E-02	1463892	***40-50***	***<1***	0.070	292778	***70-90***	***~1***
3	61	55	1860269	644416	9.8E-03	1860269	***40-50***	***<1***	0.049	372054	***70-90***	***~1***
4	187	20	3873686	1341884	1.3E-02	3873686	***~100***	***~1***	0.064	774737	***~180***	***~2***
5	190	20	4091350	1417285	1.2E-02	4091350	***~100***	***~1***	0.061	818270	***~180***	***~2***
6	198	19	4192142	1452200	1.2E-02	4192142	***~100***	***~1***	0.062	838428	***~180***	***~2***
7	652	6.1	13697442	4744933	1.2E-02	13697442	***~300***	***~3***	0.060	2739488	***~600***	***~6***
8	658	6.1	14775635	5118430	1.1E-02	14775635	***~300***	***~3***	0.056	2955127	***~600***	***~6***
9	655	6.1	13252493	4590798	1.2E-02	13252493	***~300***	***~3***	0.062	2650499	***~600***	***~6***
10	1937	2.1	24371257	8442451	2.0E-02	24371257	***~1000***	***~10***	0.098	4874251	***~2000***	***~20***
11	1828	2.2	21995265	7619383	2.1E-02	21995265	***~1000***	***~10***	0.103	4399053	***~1800***	***~20***
12	1882	2.1	37835069	13106452	1.2E-02	37835069	***~900***	***~9***	0.062	7567014	***~1600***	***~20***
17	66	116	2227707	771700	3.9E-03	2227707	***~6***	***<1***	0.019	445541	***~20***	***<1***
18	68	123	2097334	726538	3.9E-03	2097334	***~6***	***<1***	0.019	419467	***~20***	***<1***
19	64	109	2385370	826317	3.9E-03	2385370	***~6***	***<1***	0.019	477074	***~20***	***<1***
20	580	42	6049943	2095762	3.9E-03	6049943	***~20***	***<1***	0.020	1209989	***~60***	***<1***
21	555	22	11659155	4038850	3.9E-03	11659155	***~40***	***<1***	0.019	2331831	***~100***	***~1***
22	578	25	10134165	3510578	3.9E-03	10134165	***~40***	***<1***	0.019	2026833	***~100***	***~1***

*: The intra-particle/aggregate porosity, θ, was assumed to be 0.15 for all cases. Wu et al. (1988) used a value of 0.1-0.2 for θ.
†: Note that all 'R_{sw}', 'Q_d', and 'K_d' listed are in equivalent water unit (i.e. $kg_{solids}/L_{eqvl\text{-}w}$ or $L_{eqvl\text{-}w}/kg_{solids}$) by converting mass PE present to equivalent volume of water assuming $\log K_{PEW,pyr}$=4.7.

Chapter 5: Appendices

Appendix 5 - 1. Native/Equilibrium Sorbed Ratio and Solid-Phase and Sorption Isotherm. **669**
Appendix 5 - 2. Native/Equilibrium Sorbed Pyrene Ratio and $K_{d,pyr}$. **671**
Appendix 5 - 3. Regression of Sorption Data with Matlab (Figure 5-4a). **680**
Appendix 5 - 4. Regression of Sorption Data with Matlab (Figure 5-4b). **701**
Appendix 5 - 5. Regression of Sorption Data with Matlab (Figure 5-4c). **704**
Appendix 5 - 6. Regression of Sorption Data with Matlab (Figure 5-4d). **706**
Appendix 5 - 7. Parameter Ambiguity Issue in Non-linear Regression (Matlab). **719**
Appendix 5 - 8. Regression (Manual) of Sorption Data by the Two-Freundlich and .the Langmuir-Freundlich forms. **721**
Appendix 5 - 9. Regressed vs observed S_{pyr}-C_{pyr} by Two-Freundlich and Langmuir-Freundlich models. **755**
Appendix 5 - 10. Variation in $\log K_{OW,PAHs}$. **757**
Appendix 5 - 11. Pyrene Sorption Raw Data from Literature. **758**
Appendix 5 - 12. Regionalized Freundlich Descriptions of Pyrene Sorption Isotherms. **759**
Appendix 5 - 13. Unresolved 'Conflicts' on n_{BC}'s **761**

Appendix 5 - 1. Native/Equilibrium Sorbed Ratio and Solid-Phase and Sorption Isotherm.

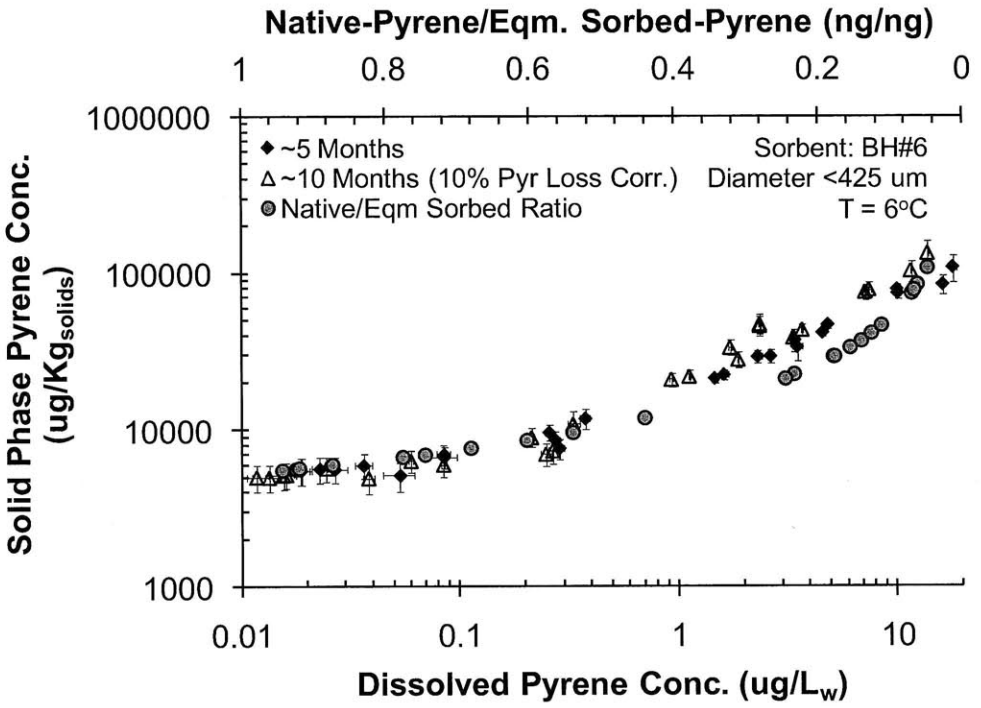

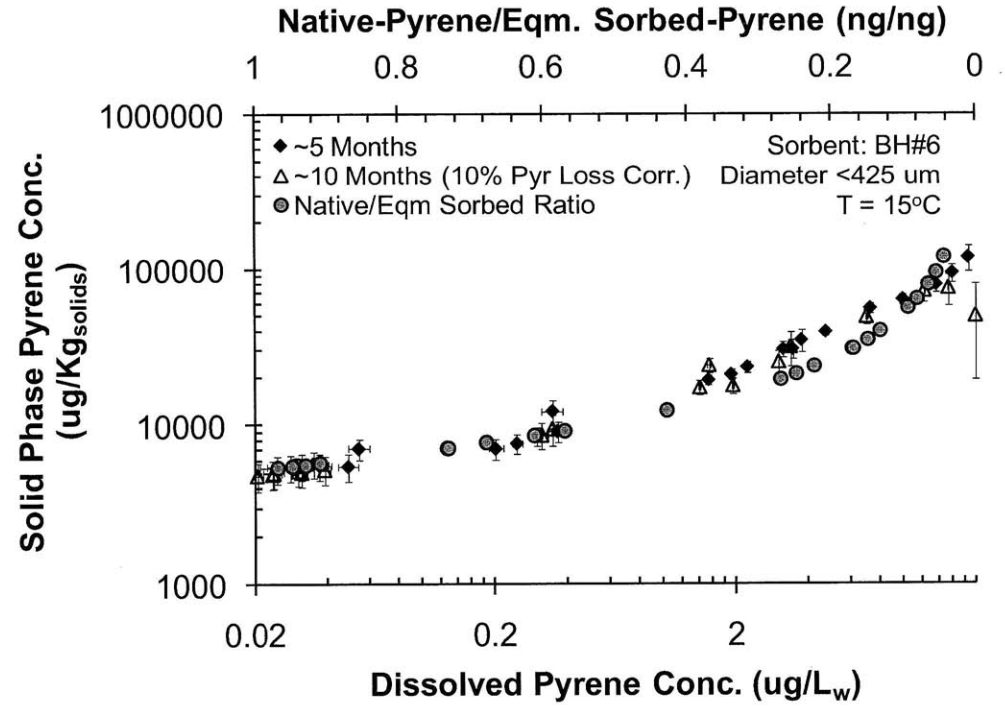

4

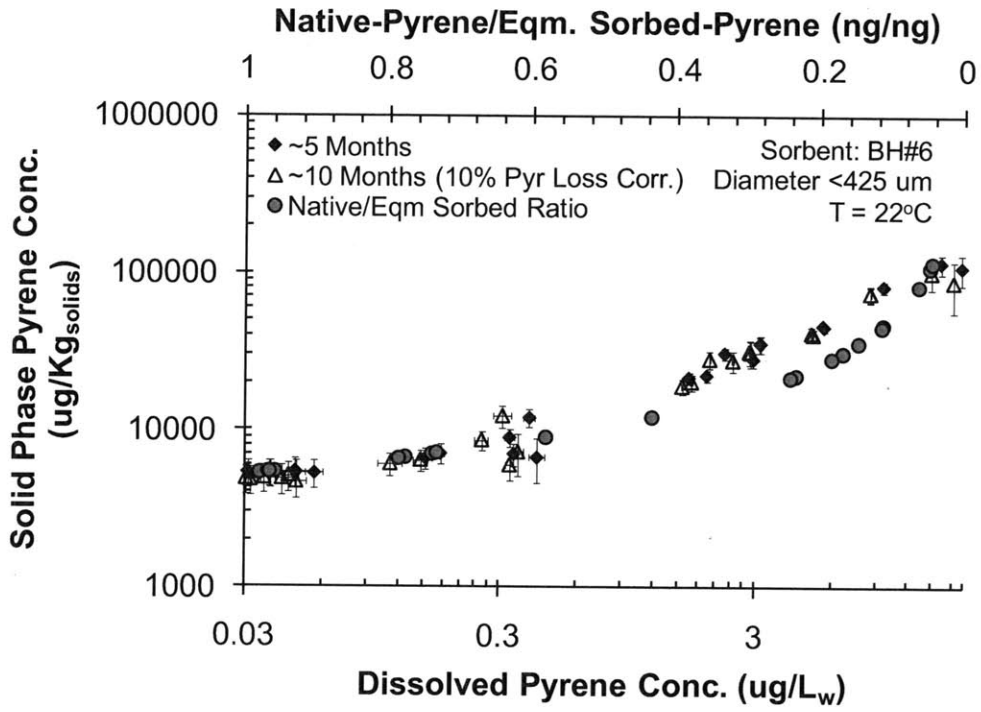
Native-Pyrene/Eqm. Sorbed-Pyrene (ng/ng)
1
0.8
0.6
0.4
0.2
0
1000000
100000
10000
1000
~5 Months
~10 Months (10% Pyr Loss Corr.)
Native/Eqm Sorbed Ratio
Sorbent: BH#6
Diameter <425 um
T = 22°C
Solid Phase Pyrene Conc. (ug/Kg solids)
0.03
0.3
3
Dissolved Pyrene Conc. (ug/Lw)

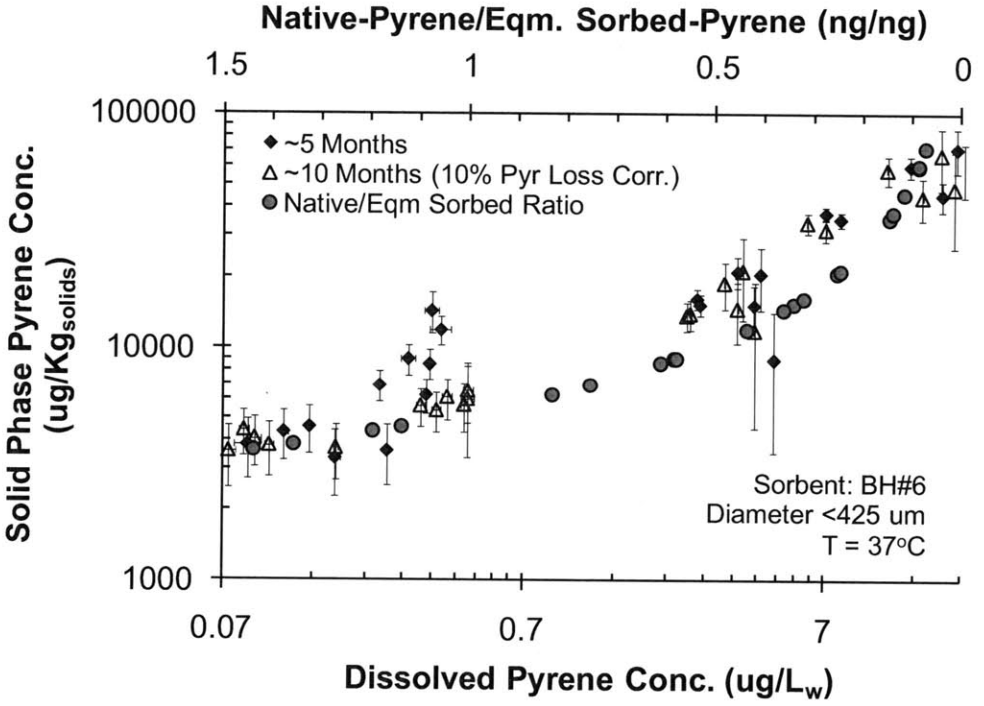
Native-Pyrene/Eqm. Sorbed-Pyrene (ng/ng)
1.5
1
0.5
0
100000
10000
1000
~5 Months
~10 Months (10% Pyr Loss Corr.)
Native/Eqm Sorbed Ratio
Sorbent: BH#6
Diameter <425 um
T = 37°C
Solid Phase Pyrene Conc. (ug/Kg solids)
0.07
0.7
7
Dissolved Pyrene Conc. (ug/Lw)

Appendix 5 - 2. Native/Equilibrium Sorbed Pyrene Ratio and $K_{d,pyr}$.

(a) Observed and Hypothetical (Singular Freundlich model) after 5-month

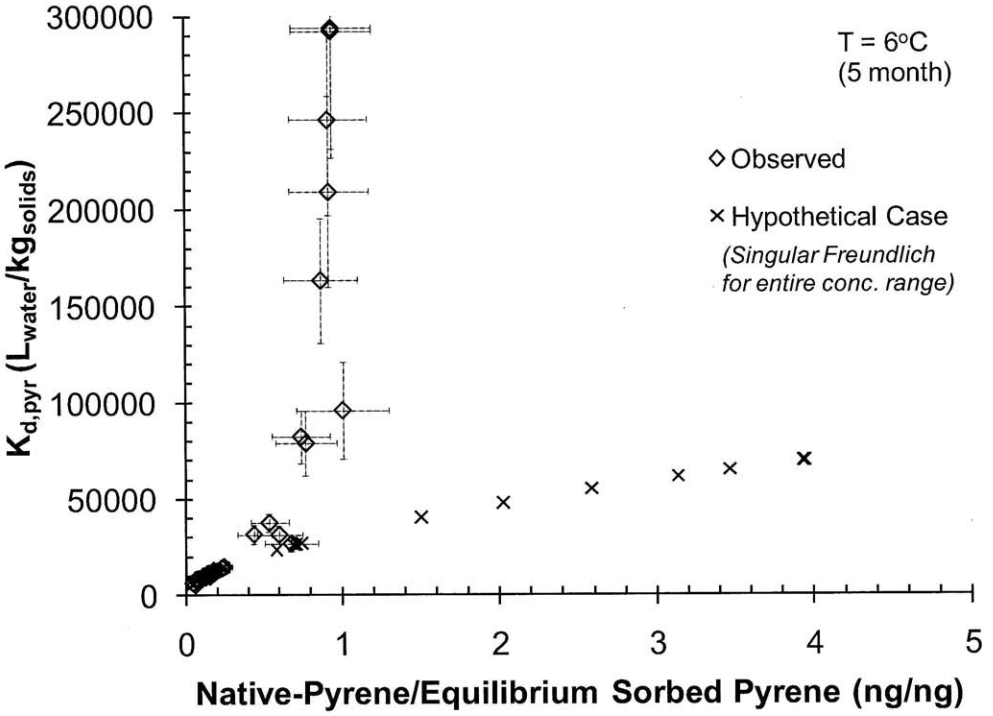

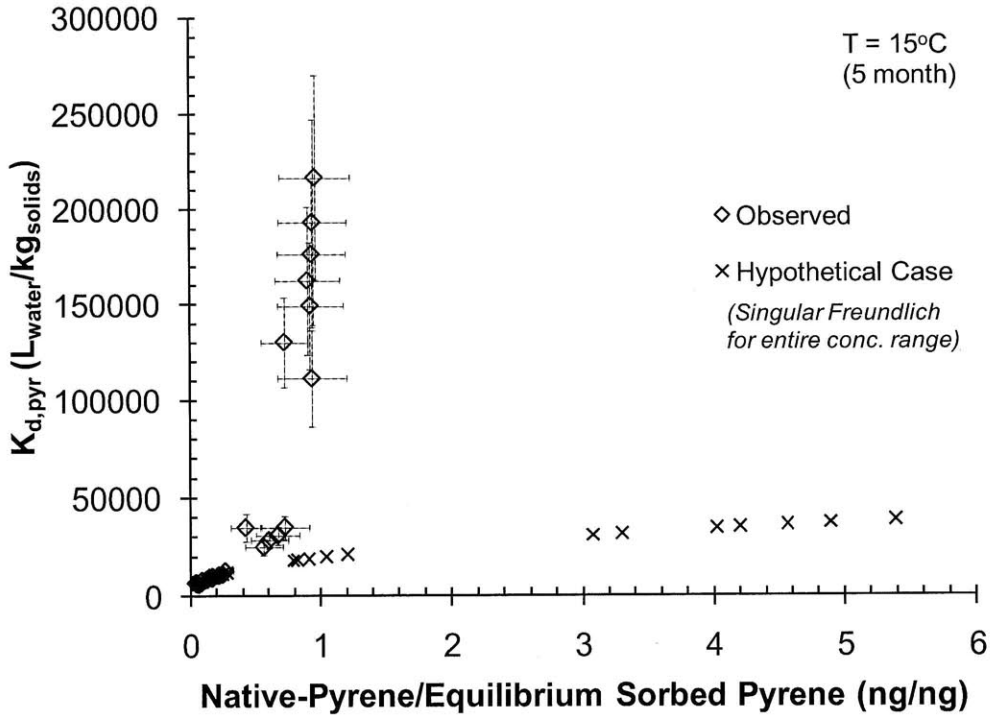

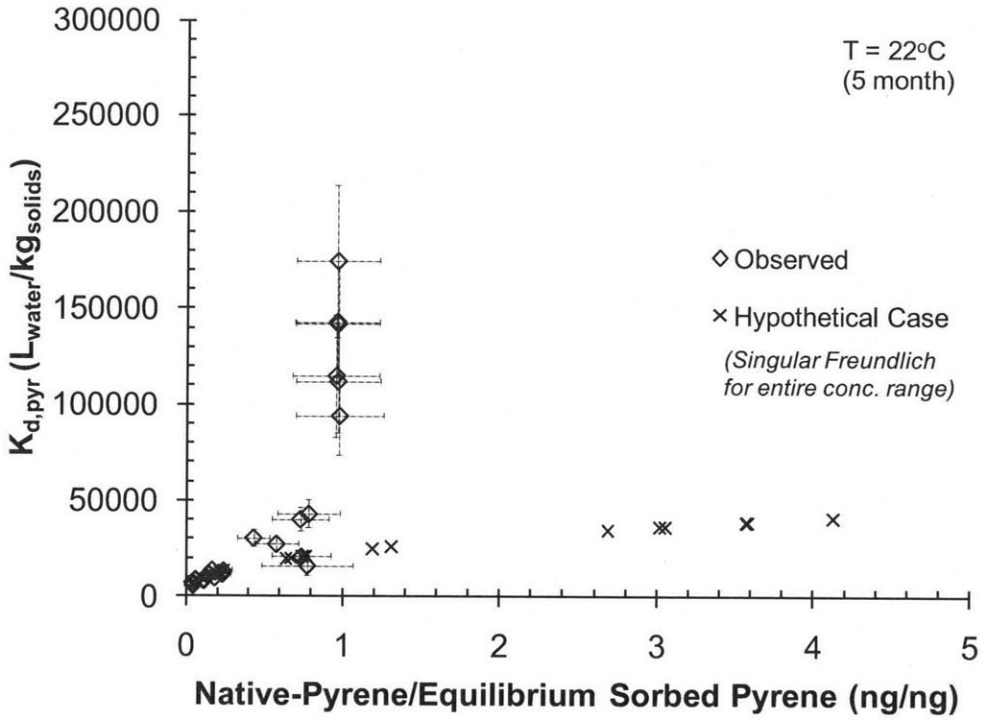
300000
250000
200000
150000
100000
50000
0
$K_{d,pyr}$ (L_{water}/kg_{solids})
T = 22°C
(5 month)
◇ Observed
× Hypothetical Case
(Singular Freundlich
for entire conc. range)
0
1
2
3
4
5
Native-Pyrene/Equilibrium Sorbed Pyrene (ng/ng)

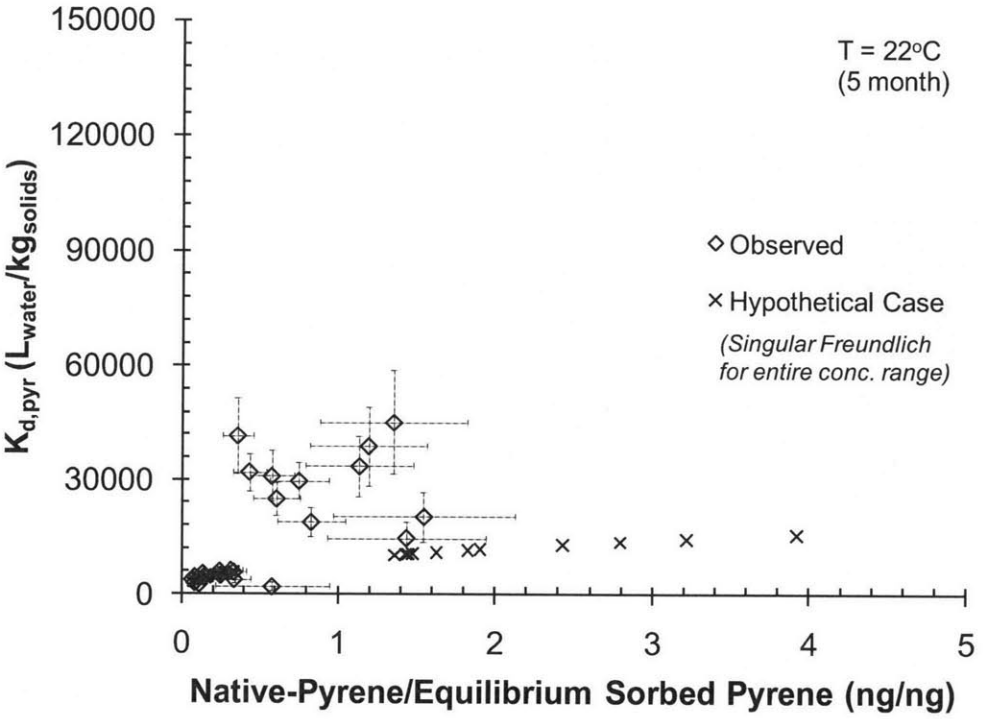
150000
120000
90000
60000
30000
0
$K_{d,pyr}$ (L_{water}/kg_{solids})
T = 22°C
(5 month)
◇ Observed
× Hypothetical Case
(Singular Freundlich
for entire conc. range)
0
1
2
3
4
5
Native-Pyrene/Equilibrium Sorbed Pyrene (ng/ng)

(b) Observed and Hypothetical (Singular Freundlich model) after 10-month (with 10% pyrene loss)

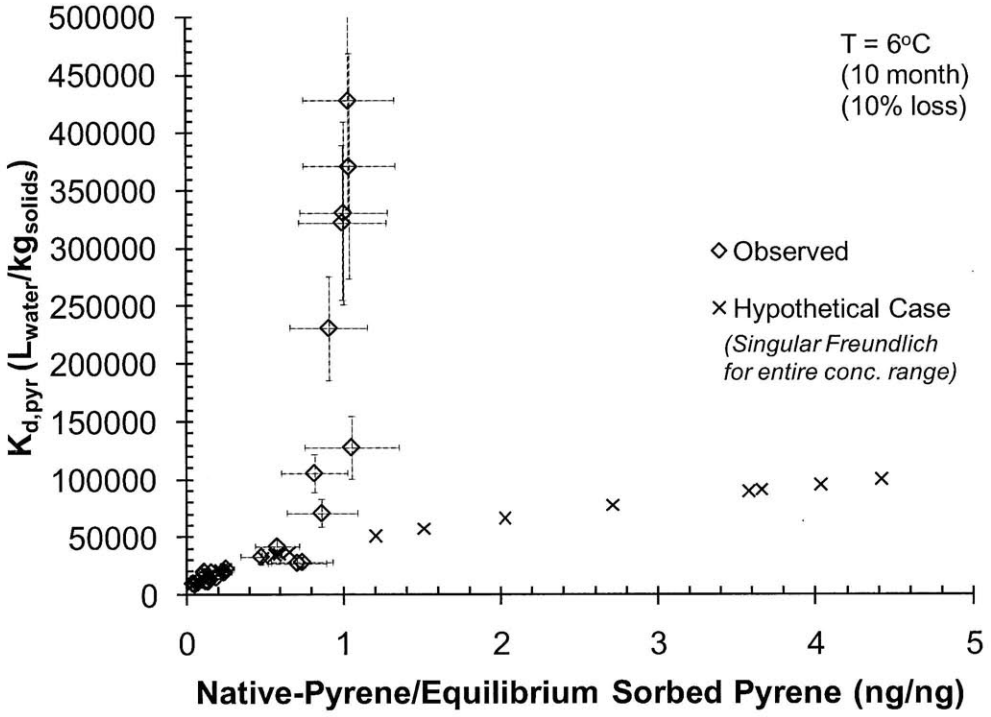

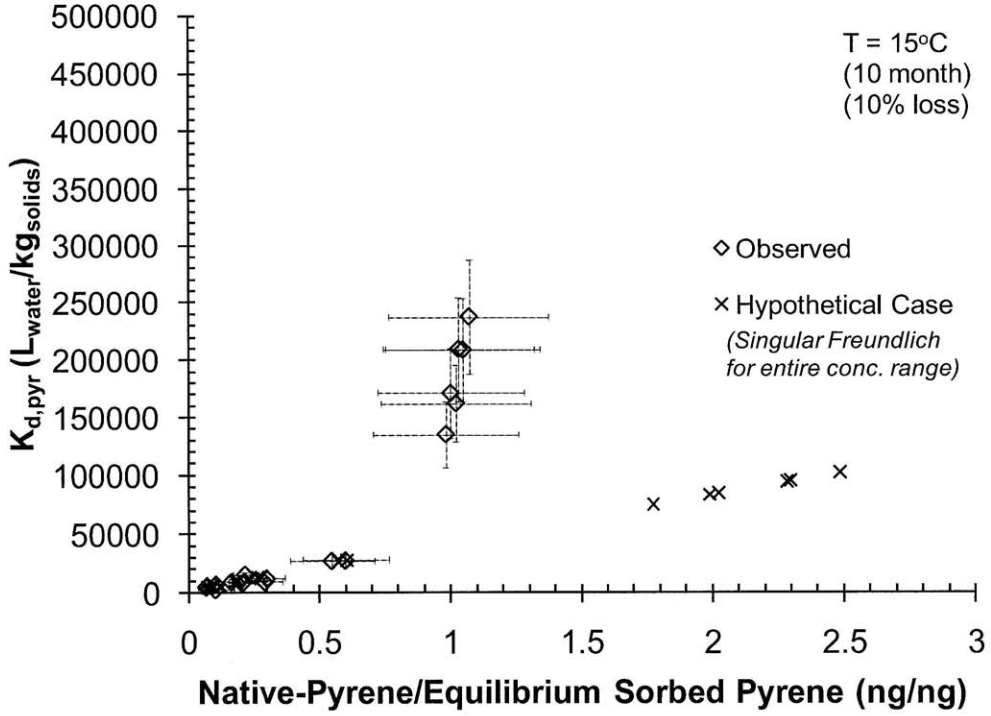

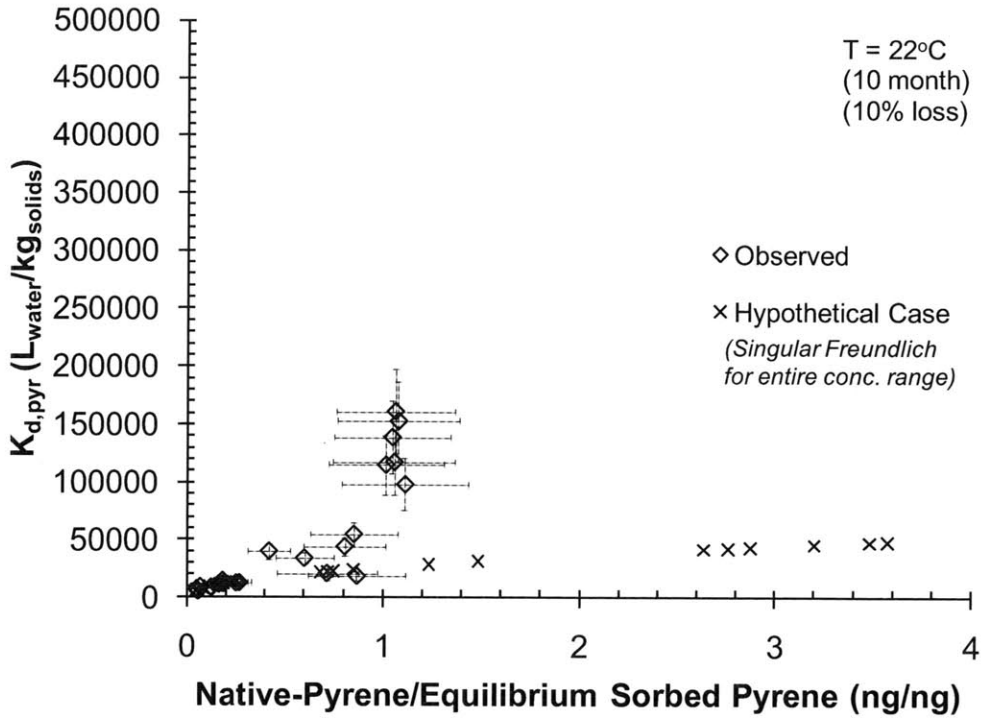
500000
450000
400000
350000
300000
250000
200000
150000
100000
50000
0
$K_{d,pyr}$ (L_{water}/kg_{solids})
T = 22°C
(10 month)
(10% loss)
◇ Observed
× Hypothetical Case
(Singular Freundlich
for entire conc. range)
0
1
2
3
4
Native-Pyrene/Equilibrium Sorbed Pyrene (ng/ng)

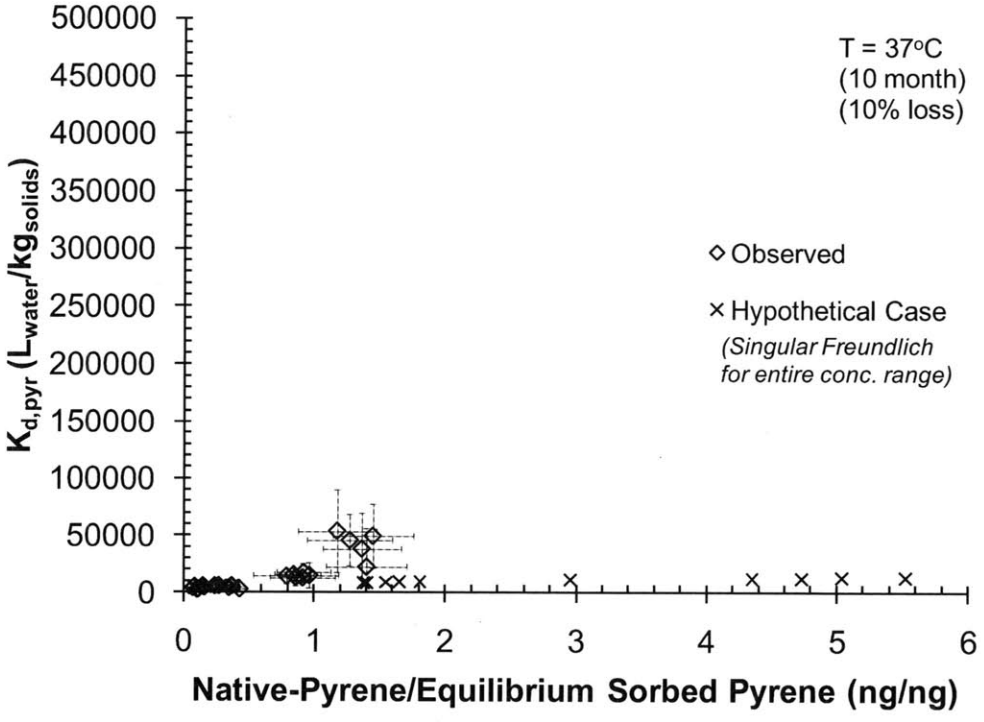
500000
450000
400000
350000
300000
250000
200000
150000
100000
50000
0
$K_{d,pyr}$ (L_{water}/kg_{solids})
T = 37°C
(10 month)
(10% loss)
◇ Observed
× Hypothetical Case
(Singular Freundlich
for entire conc. range)
0
1
2
3
4
5
6
Native-Pyrene/Equilibrium Sorbed Pyrene (ng/ng)

(c) Regressions of Sorption Observations after 5 months

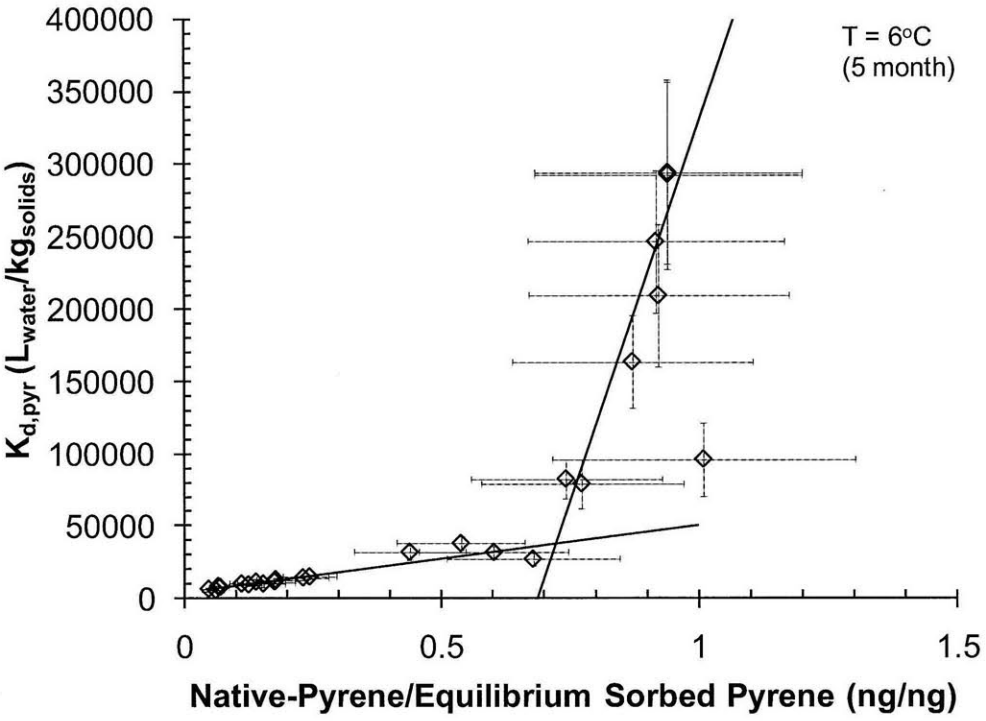

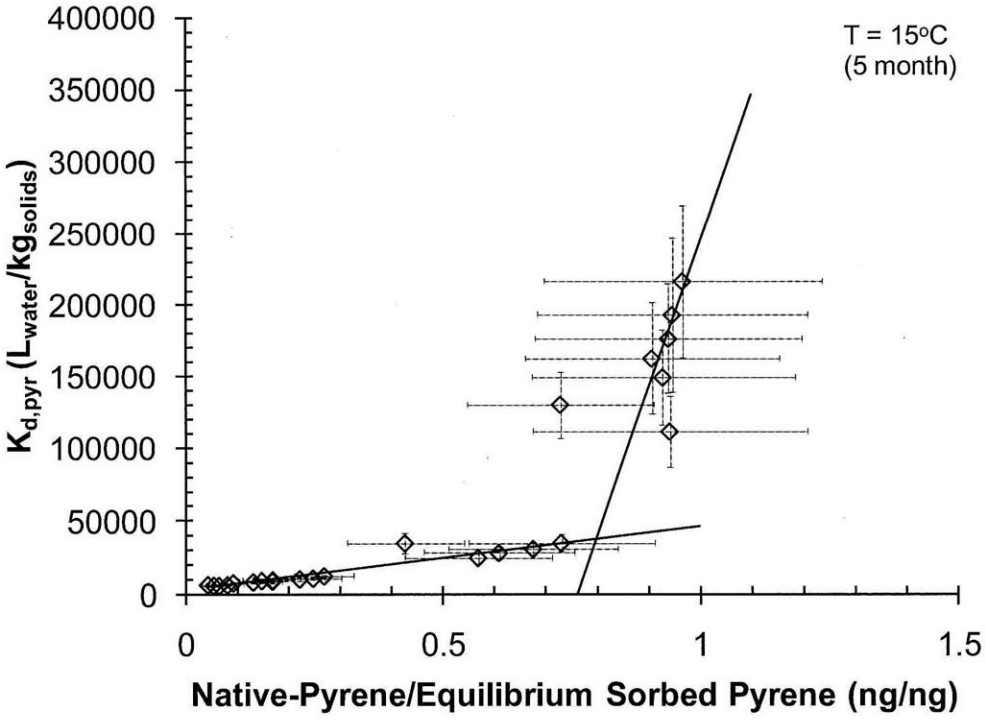

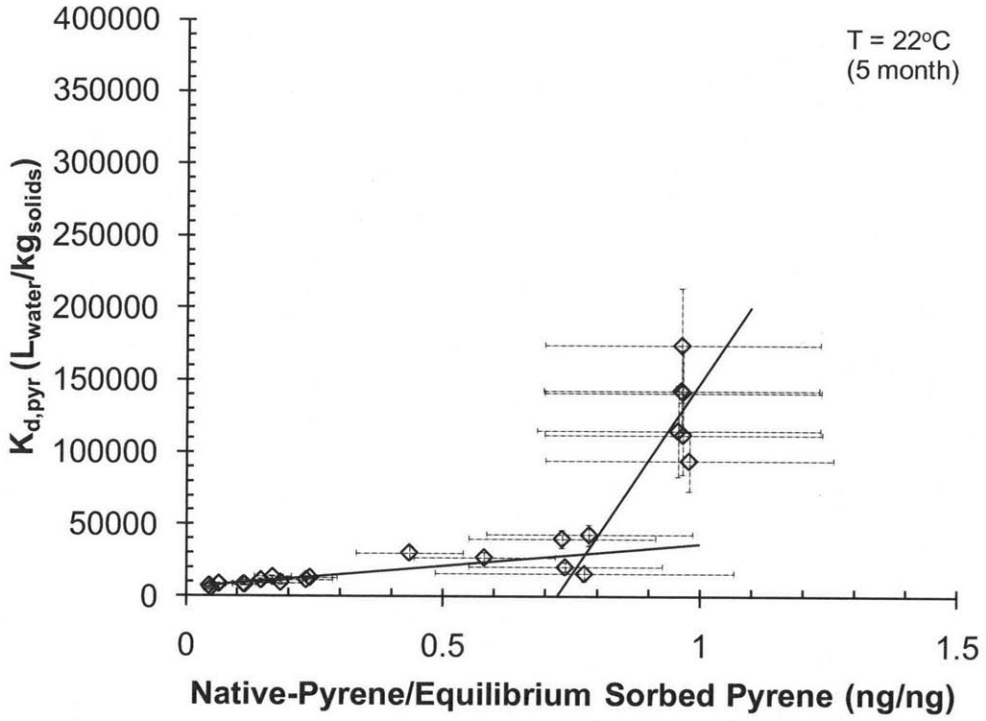
T = 22°C
(5 month)
400000
350000
300000
250000
200000
150000
100000
50000
0
$K_{d,pyr}$ (L_{water}/kg_{solids})
0
0.5
1
1.5
Native-Pyrene/Equilibrium Sorbed Pyrene (ng/ng)

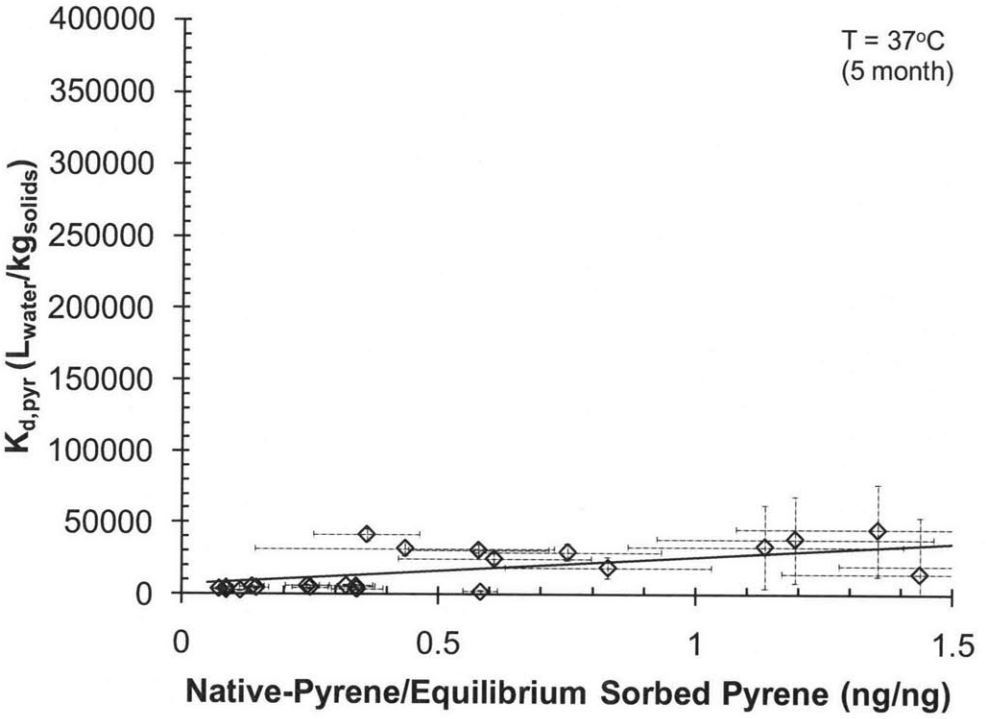
T = 37°C
(5 month)
400000
350000
300000
250000
200000
150000
100000
50000
0
$K_{d,pyr}$ (L_{water}/kg_{solids})
0
0.5
1
1.5
Native-Pyrene/Equilibrium Sorbed Pyrene (ng/ng)

(d) Regressions of Sorption Observations after 10 months (10% pyrene loss)

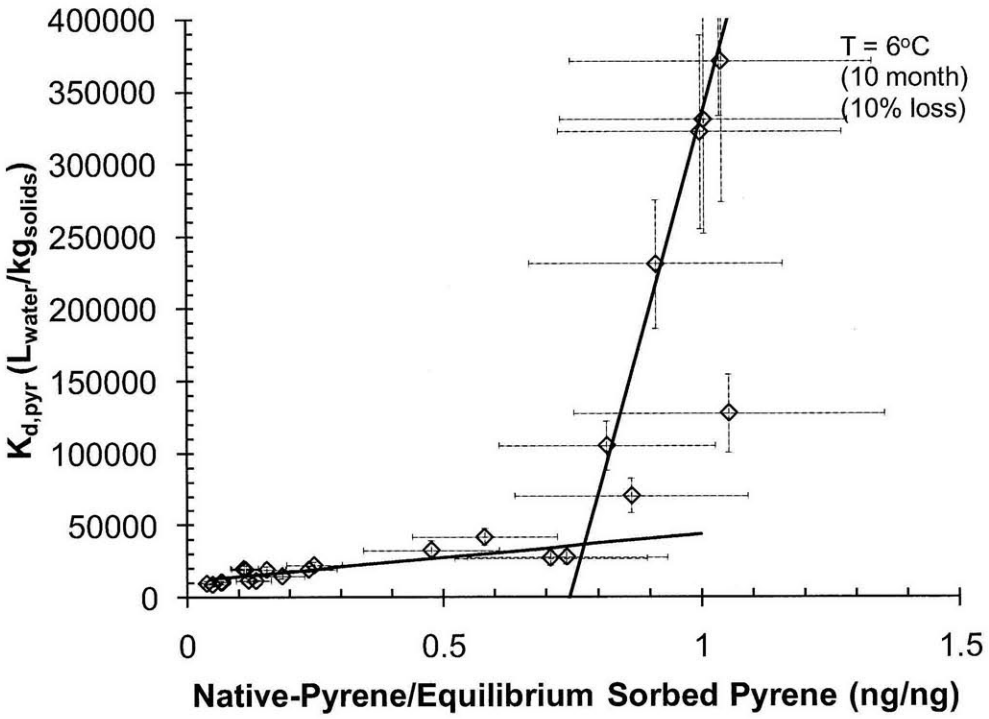

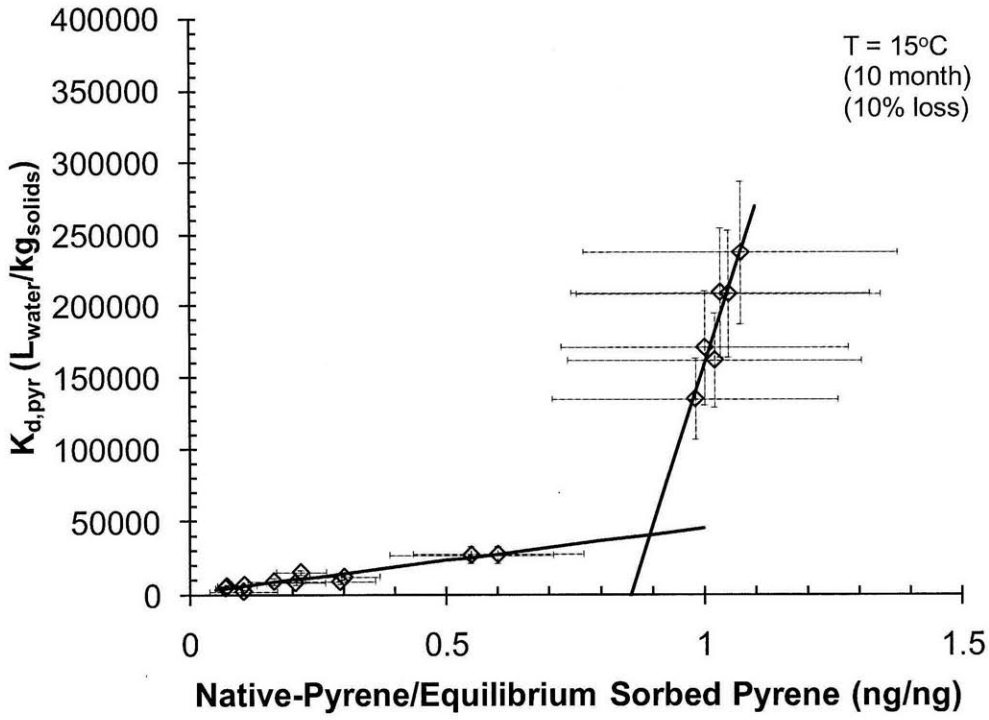

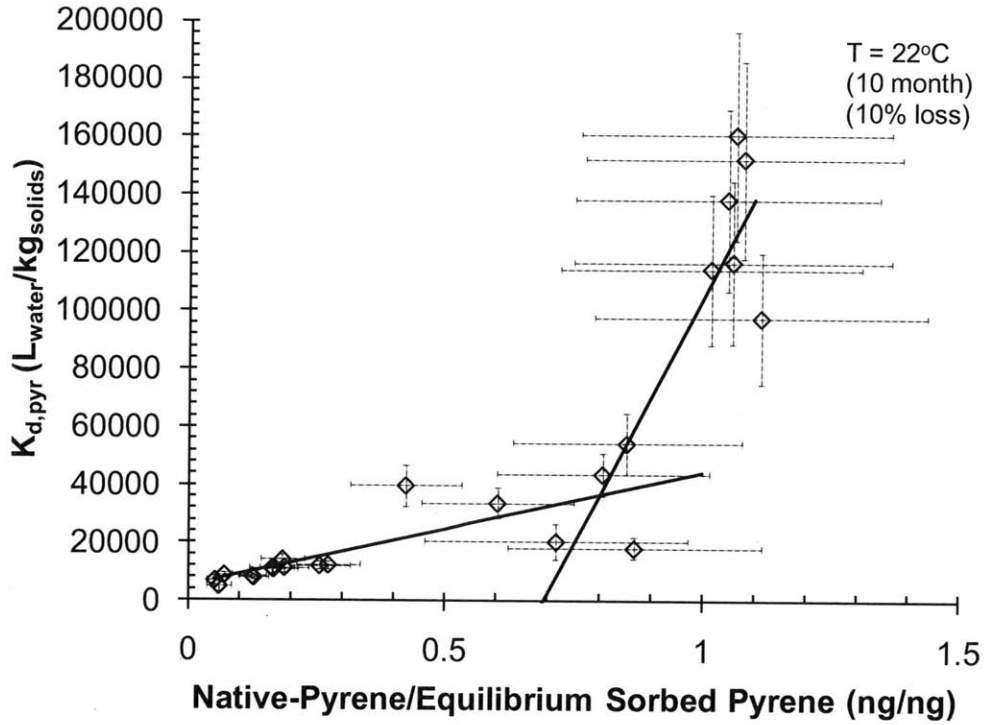
T = 22°C
(10 month)
(10% loss)
$K_{d,pyr}$ (L_{water}/kg_{solids})
200000
180000
160000
140000
120000
100000
80000
60000
40000
20000
0
0
0.5
1
1.5
Native-Pyrene/Equilibrium Sorbed Pyrene (ng/ng)

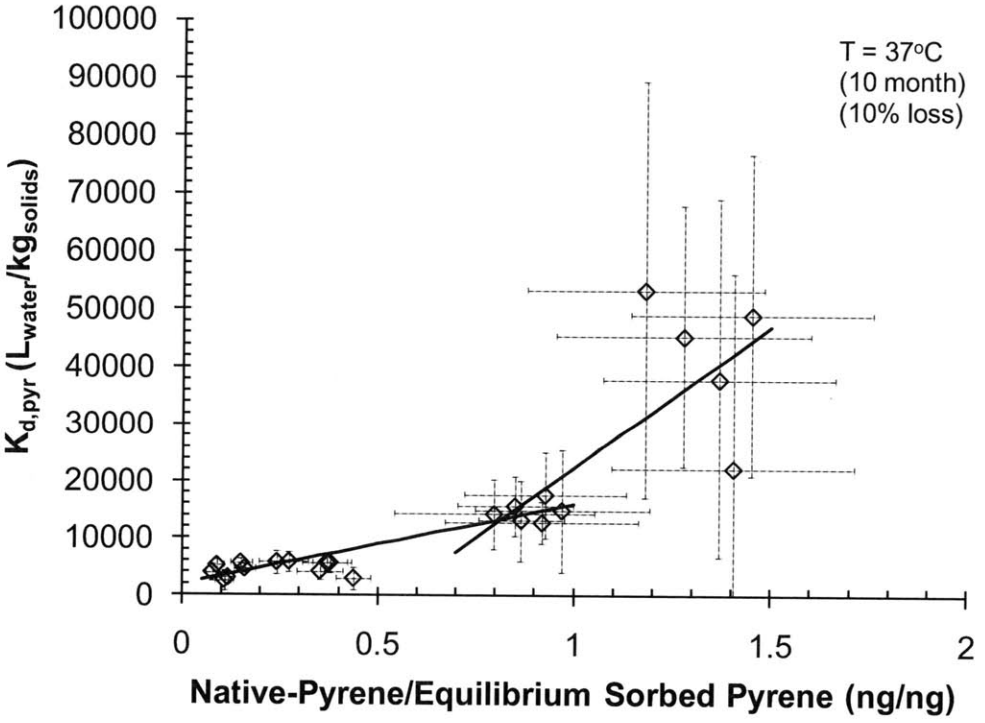
T = 37°C
(10 month)
(10% loss)
$K_{d,pyr}$ (L_{water}/kg_{solids})
100000
90000
80000
70000
60000
50000
40000
30000
20000
10000
0
0
0.5
1
1.5
2
Native-Pyrene/Equilibrium Sorbed Pyrene (ng/ng)

(e) Summary of Regression Analysis for $K_{d,pyr}$ vs Native/Equilibrium Sorbed Pyrene Ratio ($R_{pyr,s,native/eqm}$)

	Shallow Line* (low $R_{pyr,s,native/eqm}$) ($C_{pyr,Eqm}$ ~> 1 μg/L)	Steep Line* (high $R_{pyr,s,native/eqm}$) ($C_{pyr,Eqm}$ ~< 1 μg/L)	Lines Intersect at $R_{pyr,s,native/eqm}$
5-month			
6°C			0.70-0.75
Slope	46500±4900	1050000±150000	
Intercept	4000±1500	-724000±131000	
R^2	0.87	0.91	
15°C			~0.8
Slope	43700±4000	1030000±356000	
Intercept	2900±1400	-783000±334000	
R^2	0.89	0.74	
22°C			0.75-0.80
Slope	29800±5800	531000±125000	
Intercept	6300±2200	-384000±116000	
R^2	0.64	0.75	
37°C			N/A
Slope	19400±5300	-1100±24200	
Intercept	6300±3900	29900±30800	
R^2	0.41	0.00	
10-month (10% pyr. loss)			
6°C			0.75-0.80
Slope	33100±5900	1300000±149000	
Intercept	10900±2000	-972000±139000	
R^2	0.69	0.93	
15°C			~0.9
Slope	43700±5000	1120000±198000	
Intercept	1100±1500	-960000±204000	
R^2	0.89	0.89	
22°C			~0.8
Slope	39100±7300	342000±66200	
Intercept	5100±3200	-238000±64400	
R^2	0.64	0.77	
37°C			0.75-0.80
Slope	14200±900	49400±14000	
Intercept	1800±600	-27100±15700	
R^2	0.94	0.58	

*: All uncertainties are 1s of the regression coefficients. Data were regressed linearly supposing $K_{d,pyr}$ = *slope**$R_{pyr,s,native/eqm}$ + *intercept*.

Appendix 5 - 3. Regression of Sorption Data with Matlab (Figure 5-4a).

'Automated' regression of sorption data was performed in Matlab using the build-in non-linear fitting function with the Cauchy weight function. The fitting forms include:

Linear+Freundlich form (3 parameters):

$$S = K_{Lnr}\,C + K_{Fr}\,C^{n}$$

Two Freundlich form (4 parameters):

$$S = K_{Fr,1}\,C^{n1} + K_{Fr,2}\,C^{n2}$$

Langmuir-Freundlich form (4 parameters):

$$S = K_{Fr}\,C^{n} + \frac{S_{Max}\,C}{C_{½} + C}$$

Linear+Two Freundlich form (5 parameters):

$$S = K_{Lnr}\,C + K_{Fr,1}\,C^{n1} + K_{Fr,2}\,C^{n2}$$

Linear+Langmuir-Freundlich form (5 parameters):

$$S = K_{Lnr}\,C + K_{Fr}\,C^{n} + \frac{S_{Max}\,C}{C_{½} + C}$$

Three Freundlich form (5 parameters):

$$S = K_{Fr,1}\,C^{n1} + K_{Fr,2}\,C^{n2} + K_{Fr,3}\,C^{n3}$$

Where C is the dissolved phase pyrene concentration ($\mu g_{pyr}/L_w$),

$C_{½}$ is the half-concentration point in the Langmuir form ($\mu g_{pyr}/L_w$),

n is the Freundlich exponential,

K_{Lnr} is the linear form partitioning coefficient (L_w/kg_{solids}),

K_{Fr} is the Freundlich form partitioning coefficient $(\mu g_{pyr}/kg_{solids})(L_w/\mu g_{pyr})^{n}$,

S is the solid-phase pyrene concentration ($\mu g_{pyr}/kg_{solids}$),

S_{Max} is the monolayer maximum sorption capacity in the Langmuir form ($\mu g_{pyr}/kg_{solids}$).

The regressed coefficients are enlisted in the following tables, with the uncertainty (1 σ) shown in the parentheses. These coefficients may not represent a globally minimized set of parameters, for in many cases a different set of parameters would be obtained from a different set of initial parameters guess.

The figures show the raw data (x), the optimized fit (blue line), and the uncertainty in the fit estimate (red, dashed-lines, $\pm 1\ \sigma$). Residual plots of fitted vs observed solid-phase pyrene concentration were also shown.

Regression of 5-month Data (6, 15°C)*

T (°C)	Lnr+Freundlich (3 param.)		Two Freundlich (4 param.)		Langmuir-Freundlich (4 param.)		Lnr+Two Freundlich (5 param.)		Lnr-Langmuir-Frd. (5 param.)		Three Freundlich (6 param.)	
6	K_{Lnr}	2.8×10^3 (0.9×10^3)	$K_{Fr,1}$	15×10^3 (3.7×10^3)	S_{Max}	260×10^3 (75×10^3)	K_{Lnr}	-3.1×10^6 (3.9×10^9)	K_{Lnr}	-650 (11×10³)	$K_{Fr,1}$	11×10^3 (13×10^3)
			$n_{Fr,1}$	0.691 (0.077)	$C_{1/2}$	31.7 (17.7)					$n_{Fr,1}$	0.864 (2.030)
	K_{Fr}	16×10^3 (1.4×10^3)	$K_{Fr,2}$	2.5×10^3 (4.4×10^3)	K_{Fr}	8.5×10^3 (3.8×10^3)	$K_{Fr,1}$	3.1×10^6 (3.9×10^9)	S_{Max}	260×10^3 (900×10^3)	$K_{Fr,2}$	5.9×10^3 (23×10^3)
	n_{Fr}	0.417 (0.083)	$n_{Fr,2}$	-0.156 (0.477)	n_{Fr}	0.133 (0.167)	$n_{Fr,1}$	0.999 (0.877)	$C_{1/2}$	26.8 (70.9)	$n_{Fr,2}$	0.038 (0.890)
							$K_{Fr,2}$	5.0×10^3 (8.6×10^3)	K_{Fr}	7.9×10^3 (4.6×10^3)	$K_{Fr,3}$	-260 (13×10³)
							$n_{Fr,2}$	-0.010 (0.457)	n_{Fr}	0.108 (0.199)	$n_{Fr,3}$	1.70 (10.2)
	Mean Sq. Error	16×10^6		6.5×10^6		6.4×10^6		8.2×10^6		8.4×10^6		11×10^6
15	K_{Lnr}	4.5×10^3 (0.2×10^3)	$K_{Fr,1}$	11×10^3 (1.9×10^3)	S_{Max}	300×10^3 (56×10^3)	K_{Lnr}	-3.7×10^6 (5.7×10^9)	K_{Lnr}	4.5×10^3 (0.5×10^3)	$K_{Fr,1}$	4.3×10^3 (1.8×10^{12})
			$n_{Fr,1}$	0.772 (0.052)	$C_{1/2}$	41.4 (12.7)					$n_{Fr,1}$	0.704 (500×10^3)
	K_{Fr}	11×10^3 (0.7×10^3)	$K_{Fr,2}$	4.1×10^3 (2.4×10^3)	K_{Fr}	7.4×10^3 (1.6×10^3)	$K_{Fr,1}$	3.7×10^6 (5.7×10^9)	S_{Max}	20×10^3 (11×10^3)	$K_{Fr,2}$	8.1×10^3 (1.8×10^{12})
	n_{Fr}	0.248 (0.041)	$n_{Fr,2}$	-0.047 (0.173)	n_{Fr}	0.096 (0.082)	$n_{Fr,1}$	1.000 (0.652)	$C_{1/2}$	3.2 (4.1)	$n_{Fr,2}$	0.704 (260×10^3)
							$K_{Fr,2}$	4.4×10^3 (4.5×10^3)	K_{Fr}	5.7×10^3 (3.7×10^3)	$K_{Fr,3}$	2.6×10^3 (5.5×10^3)
							$n_{Fr,2}$	-0.045 (0.281)	n_{Fr}	0.024 (0.199)	$n_{Fr,3}$	-0.16 (0.483)
	Mean Sq. Error	4.2×10^6		3.4×10^6		3.7×10^6		4.5×10^6		4.2×10^6		1.5×10^6

*: Units: K_{Fr} in $(L_w/\mu g_{pyr})^{nFr}(\mu g_{pyr}/kg_{solids})$, n_{Fr} (dimensionless), S_{Max} in $(\mu g_{pyr}/kg_{solids})$, $C_{½}$ in $(\mu g_{pyr}/L_w)$.

Regression of 5-month Data (22, 37°C)*

T (°C)	Lnr+Freundlich (3 param.)		Two Freundlich (4 param.)		Langmuir-Freundlich (4 param.)		Lnr+Two Freundlich (5 param.)		Lnr-Langmuir-Frd. (5 param.)		Three Freundlich (6 param.)	
22	K_{Lnr}	5.9×10^3 (0.5×10^3)	$K_{Fr,1}$	13×10^3 (2.4×10^3)	S_{Max}	370×10^3 (73×10^3)	K_{Lnr}	-660×10^3 (0.4×10^9)	K_{Lnr}	-3.6×10^6 (3.0×10^9)	$K_{Fr,1}$	-15×10^6 (0.3×10^{12})
			$n_{Fr,1}$	0.783 (0.058)	$C_{1/2}$	38.0 (12.4)					$n_{Fr,1}$	0.417 (16×10^3)
	K_{Fr}	10×10^3 (1.3×10^3)	$K_{Fr,2}$	2.1×10^3 (3.1×10^3)	K_{Fr}	5.3×10^3 (2.4×10^3)	$K_{Fr,1}$	670×10^3 (0.4×10^9)	S_{Max}	73×10^9 (120×10^{12})	$K_{Fr,2}$	7.6×10^6 (12×10^{12})
	n_{Fr}	0.284 (0.094)	$n_{Fr,2}$	-0.223 (0.477)	n_{Fr}	0.018 (0.180)	$n_{Fr,1}$	0.998 (1.290)	$C_{1/2}$	20×10^3 (17×10^6)	$n_{Fr,2}$	0.432 (7600)
							$K_{Fr,2}$	4.0×10^3 (8.7×10^3)	K_{Fr}	5.0×10^3 (2.9×10^3)	$K_{Fr,3}$	7.4×10^6 (12×10^{12})
							$n_{Fr,2}$	-0.055 (0.633)	n_{Fr}	-0.001 (0.218)	$n_{Fr,3}$	0.403 (7900)
	Mean Sq. Error	15×10^6		15×10^6		11×10^6		16×10^6		12×10^6		20×10^6
37	K_{Lnr}	2.7×10^3 (0.6×10^3)	$K_{Fr,1}$	4.9×10^3 (15×10^3)	S_{Max}	160×10^3 (130×10^3)	K_{Lnr}	2.6×10^3 (1.4×10^3)	K_{Lnr}	2.7×10^3 (1.0×10^3)	$K_{Fr,1}$	1.7×10^3 (29×10^6)
			$n_{Fr,1}$	0.812 (0.705)	$C_{1/2}$	37.4 (61.8)					$n_{Fr,1}$	2.628 (350)
	K_{Fr}	7.8×10^3 (1.8×10^3)	$K_{Fr,2}$	5.5×10^3 (17×10^3)	K_{Fr}	5.6×10^3 (6.3×10^3)	$K_{Fr,1}$	9.1×10^3 (14×10^3)	S_{Max}	21×10^3 (350×10^3)	$K_{Fr,2}$	10×10^3 (7.5×10^3)
	n_{Fr}	0.208 (0.177)	$n_{Fr,2}$	0.089 (1.263)	n_{Fr}	0.040 (0.632)	$n_{Fr,1}$	0.073 (1.234)	$C_{1/2}$	0.035 (1.1)	$n_{Fr,2}$	0.282 (0.487)
							$K_{Fr,2}$	-340 (11×10^3)	K_{Fr}	-11×10^3 (360×10^3)	$K_{Fr,3}$	-1.5×10^3 (29×10^6)
							$n_{Fr,2}$	-1.089 (10.6)	n_{Fr}	-0.025 (0.455)	$n_{Fr,3}$	2.667 (360)
	Mean Sq. Error	31×10^6		39×10^6		37×10^6		50×10^6		45×10^6		25×10^6

*: Units: K_{Fr} in $(L_w/\mu g_{pyr})^{nFr}(\mu g_{pyr}/kg_{solids})$, n_{Fr} (dimensionless), S_{Max} in $(\mu g_{pyr}/kg_{solids})$, $C_{½}$ in $(\mu g_{pyr}/L_w)$.

Regression of 10-month Data (6, 15°C)*

T (°C)	Lnr+Freundlich (3 param.)		Two Freundlich (4 param.)		Langmuir-Freundlich (4 param.)		Lnr+Two Freundlich (5 param.)		Lnr-Langmuir-Frd. (5 param.)		Three Freundlich (6 param.)	
6	K_{Lnr}	6.2×10^3 (1.3×10^3)	$K_{Fr,1}$	17×10^3 (6.2×10^3)	S_{Max}	270×10^3 (82×10^3)	K_{Lnr}	2.1×10^3 (10×10^3)	K_{Lnr}	5.6×10^3 (1.8×10^3)	$K_{Fr,1}$	0 (0)
			$n_{Fr,1}$	0.754 (0.114)	$C_{1/2}$	20.0 (11.4)					$n_{Fr,1}$	8.889 (8.866)
	K_{Fr}	15×10^3 (2.1×10^3)	$K_{Fr,2}$	3.5×10^3 (6.9×10^3)	K_{Fr}	5.1×10^3 (4.9×10^3)	$K_{Fr,1}$	18×10^3 (6.6×10^3)	S_{Max}	46×10^3 (31×10^3)	$K_{Fr,2}$	22×10^3 (1.8×10^3)
	n_{Fr}	0.379 (0.113)	$n_{Fr,2}$	-0.017 (0.496)	n_{Fr}	0.015 (0.306)	$n_{Fr,1}$	0.623 (0.443)	$C_{1/2}$	2.5 (3.0)	$n_{Fr,2}$	0.630 (0..054)
							$K_{Fr,2}$	460 (3.2×10^3)	K_{Fr}	1.8×10^3 (4.2×10^3)	$K_{Fr,3}$	150 (750)
							$n_{Fr,2}$	-0.496 (1.544)	n_{Fr}	-0.233 (0.595)	$n_{Fr,3}$	-0.741 (1.181)
	Mean Sq. Error	24×10^6		10×10^6		25×10^6		18×10^6		16×10^6		19×10^6
15	K_{Lnr}	4.0×10^3 (440)	$K_{Fr,1}$	8.5×10^3 (16×10^3)	S_{Max}	100×10^3 (29×10^3)	K_{Lnr}	4.0×10^3 (1.1×10^3)	K_{Lnr}	-6.6×10^6 (4.8×10^9)	$K_{Fr,1}$	-1 (6)
			$n_{Fr,1}$	0.673 (0.504)	$C_{1/2}$	11.9 (12.5)					$n_{Fr,1}$	3.71 (1.13)
	K_{Fr}	7.4×10^3 (2.2×10^3)	$K_{Fr,2}$	3.5×10^3 (19×10^3)	K_{Fr}	4.2×10^3 (9.7×10^3)	$K_{Fr,1}$	7.3×10^3 (3.6×10^3)	S_{Max}	170×10^9 (250×10^{12})	$K_{Fr,2}$	2.5×10^3 (2.8×10^3)
	n_{Fr}	0.121 (0.147)	$n_{Fr,2}$	-0.048 (1.429)	n_{Fr}	-0.039 (0.714)	$n_{Fr,1}$	0.128 (0.630)	$C_{1/2}$	26×10^3 (19×10^6)	$n_{Fr,2}$	1.309 (0.507)
							$K_{Fr,2}$	1 (340)	K_{Fr}	3.8×10^3 (4.3×10^3)	$K_{Fr,3}$	8.5×10^3 (3.6×10^3)
							$n_{Fr,2}$	-1.623 125	n_{Fr}	-0.070 (0.348)	$n_{Fr,3}$	0.1548 (0.1384)
	Mean Sq. Error	31×10^6		84×10^6		80×10^6		63×10^6		22×10^6		3.9×10^6

*: Units: K_{Fr} in $(L_w/\mu g_{pyr})^{nFr}(\mu g_{pyr}/kg_{solids})$, n_{Fr} (dimensionless), S_{Max} in $(\mu g_{pyr}/kg_{solids})$, $C_{½}$ in $(\mu g_{pyr}/L_w)$.

Regression of 10-month Data (22, 37°C)*

T (°C)	Lnr+Freundlich (3 param.)		Two Freundlich (4 param.)		Langmuir-Freundlich (4 param.)		Lnr+Two Freundlich (5 param.)		Lnr-Langmuir-Frd. (5 param.)		Three Freundlich (6 param.)	
22	K_{Lnr}	5.0×10^3 (0.6×10^3)	$K_{Fr,1}$	16×10^3 (2.9×10^3)	S_{Max}	530×10^3 (140×10^3)	K_{Lnr}	-3.3×10^6 (4.6×10^9)	K_{Lnr}	-2.6×10^6 (3.0×10^9)	$K_{Fr,1}$	13×10^3 (7.5×10^3)
			$n_{Fr,1}$	0.790 (0.057)	$C_{1/2}$	49.9 (20.4)					$n_{Fr,1}$	0.838 (0.151)
	K_{Fr}	8.8×10^3 (1.2×10^3)	$K_{Fr,2}$	3.0×10^3 (3.7×10^3)	K_{Fr}	7.8×10^3 (2.6×10^3)	$K_{Fr,1}$	3.3×10^6 (4.6×10^9)	S_{Max}	43×10^9 (94×10^{12})	$K_{Fr,2}$	5.3×10^3 (9.1×10^3)
	n_{Fr}	0.215 (0.090)	$n_{Fr,2}$	-0.120 (0.387)	n_{Fr}	0.131 (0.141)	$n_{Fr,1}$	0.999 (0.886)	$C_{1/2}$	16×10^3 (17×10^6)	$n_{Fr,2}$	0.037 (0.710)
							$K_{Fr,2}$	4.0×10^3 (8.3×10^3)	K_{Fr}	7.5×10^3 (4.2×10^3)	$K_{Fr,3}$	0 (0)
							$n_{Fr,2}$	-0.056 (0.593)	n_{Fr}	0.113 (0.213)	$n_{Fr,3}$	-6.78 (1.3×10^3)
	Mean Sq. Error	13×10^6		12×10^6		10×10^6		14×10^6		15×10^6		20×10^6
37	K_{Lnr}	1.8×10^3 (0.4×10^3)	$K_{Fr,1}$	4.7×10^3 (3.7×10^3)	S_{Max}	120×10^3 (71×10^3)	K_{Lnr}	320 (3.3×10^3)	K_{Lnr}	1.4×10^3 (2.4×10^9)	$K_{Fr,1}$	5.8×10^3 (4.8×10^3)
			$n_{Fr,1}$	0.765 (0.227)	$C_{1/2}$	34.4 (35.8)					$n_{Fr,1}$	0.192 (0.531)
	K_{Fr}	5.4×10^3 (1.1×10^3)	$K_{Fr,2}$	2.0×10^3 (4.8×10^3)	K_{Fr}	3.0×10^3 (3.1×10^3)	$K_{Fr,1}$	0 (4)	S_{Max}	-76×10^6 (110×10^{15})	$K_{Fr,2}$	-8.3×10^3 (0.5×10^9)
	n_{Fr}	0.227 (0.174)	$n_{Fr,2}$	-0.182 (1.036)	n_{Fr}	-0.068 (0.540)	$n_{Fr,1}$	3.84 (4.60)	$C_{1/2}$	-61×10^6 (89×10^{15})	$n_{Fr,2}$	2.55 (410)
							$K_{Fr,2}$	7.2×10^3 (4.7×10^3)	K_{Fr}	6.2×10^3 (3.3×10^3)	$K_{Fr,3}$	8.7×10^3 (0.5×10^9)
							$n_{Fr,2}$	0.351 (0.385)	n_{Fr}	0.355 (0.326)	$n_{Fr,3}$	2.54 (400)
	Mean Sq. Error	13×10^6		18×10^6		17×10^6		18×10^6		14×10^6		25×10^6

*: Units: K_{Fr} in $(L_w/\mu g_{pyr})^{nFr}(\mu g_{pyr}/kg_{solids})$, n_{Fr} (dimensionless), S_{Max} in $(\mu g_{pyr}/kg_{solids})$, $C_{½}$ in $(\mu g_{pyr}/L_w)$.

6°C (5-month) (Non-linear Regression by Matlab)

Linear+Freundlich Fit (3 Param.)

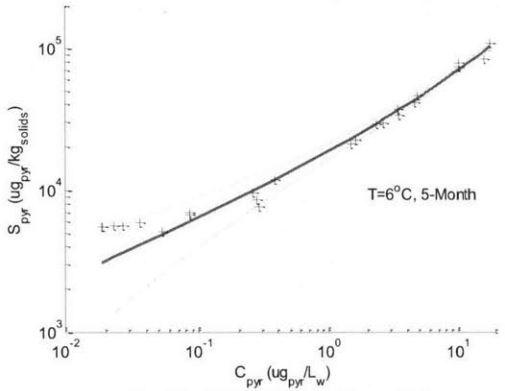

Two Freundlich Fit (4 Param.)

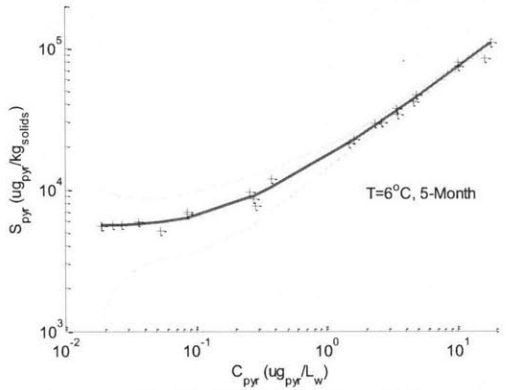

Langmuir-Freundlich Fit (4 Param.)

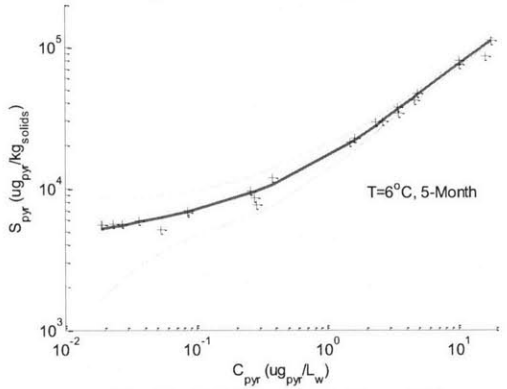

Residual Plot: Linear+Freundlich

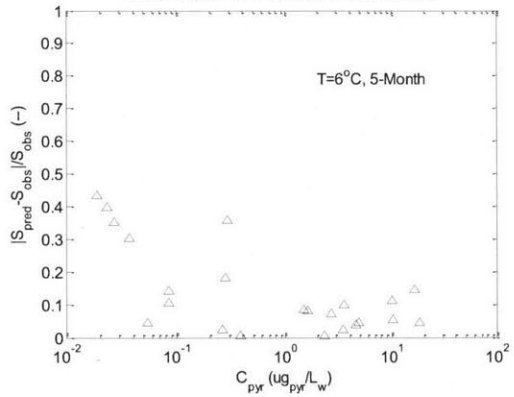

Residual Plot: Two Freundlich

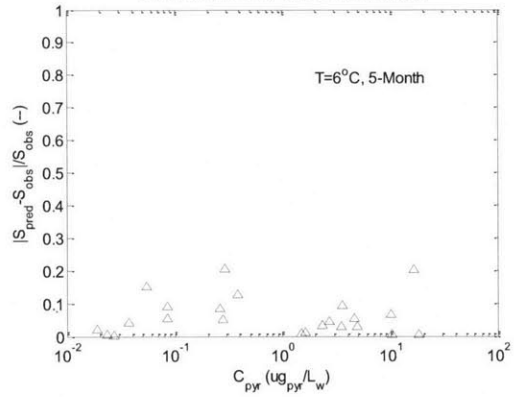

Residual Plot: Langmuir-Freundlich

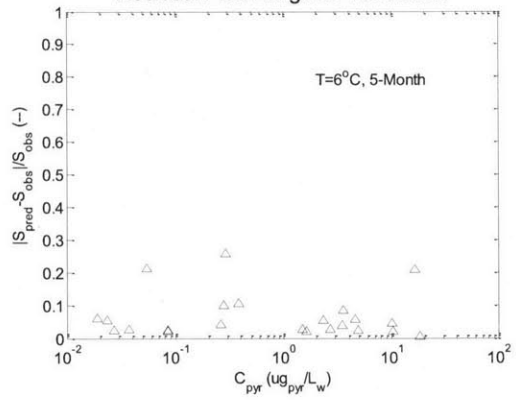

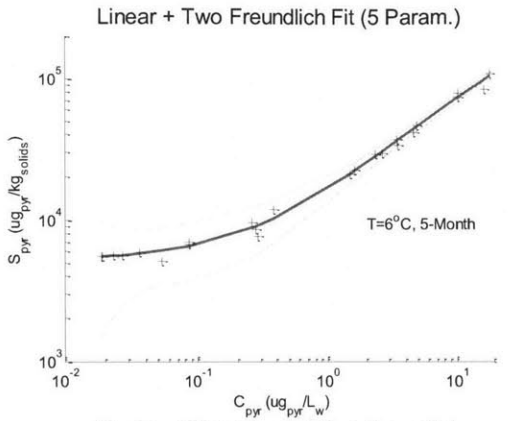
Linear + Two Freundlich Fit (5 Param.)
T=6°C, 5-Month
S_{pyr} (ug_{pyr}/kg_{solids})
C_{pyr} (ug_{pyr}/L_w)

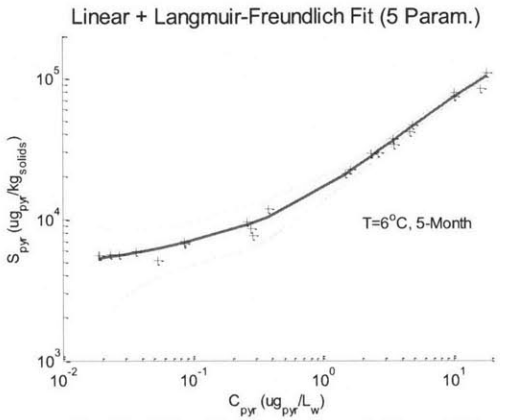
Linear + Langmuir-Freundlich Fit (5 Param.)
T=6°C, 5-Month
S_{pyr} (ug_{pyr}/kg_{solids})
C_{pyr} (ug_{pyr}/L_w)

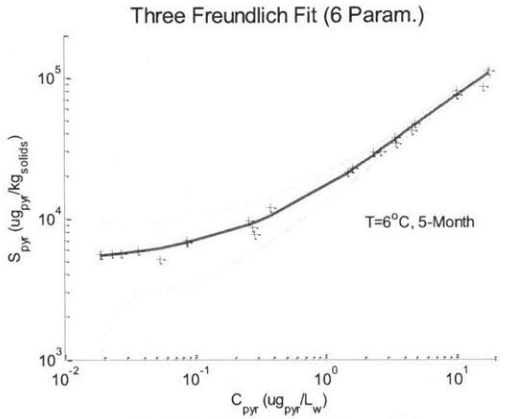
Three Freundlich Fit (6 Param.)
T=6°C, 5-Month
S_{pyr} (ug_{pyr}/kg_{solids})
C_{pyr} (ug_{pyr}/L_w)

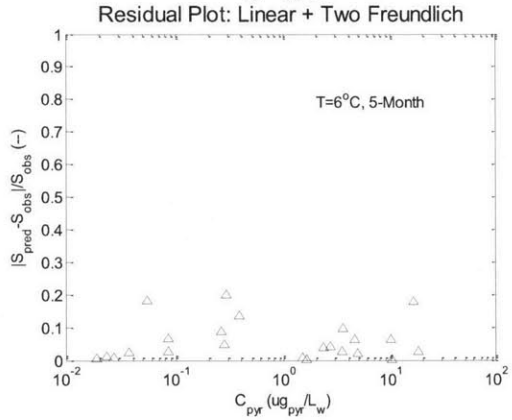
Residual Plot: Linear + Two Freundlich
T=6°C, 5-Month
$|S_{pred}-S_{obs}|/S_{obs}$ (–)
C_{pyr} (ug_{pyr}/L_w)

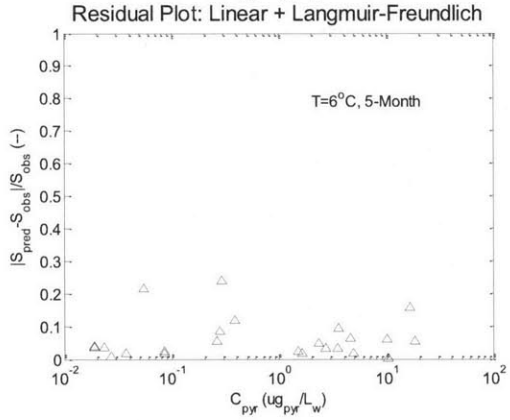
Residual Plot: Linear + Langmuir-Freundlich
T=6°C, 5-Month
$|S_{pred}-S_{obs}|/S_{obs}$ (–)
C_{pyr} (ug_{pyr}/L_w)

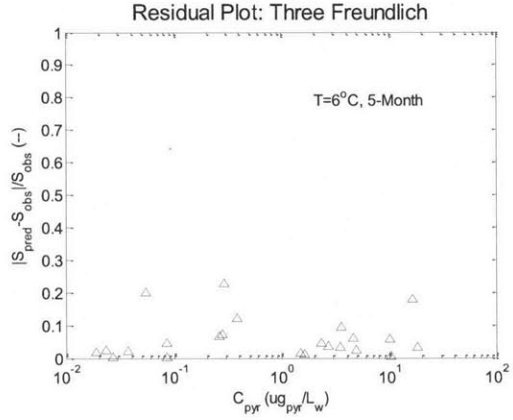
Residual Plot: Three Freundlich
T=6°C, 5-Month
$|S_{pred}-S_{obs}|/S_{obs}$ (–)
C_{pyr} (ug_{pyr}/L_w)

6°C (10-month) (Non-linear Regression by Matlab)

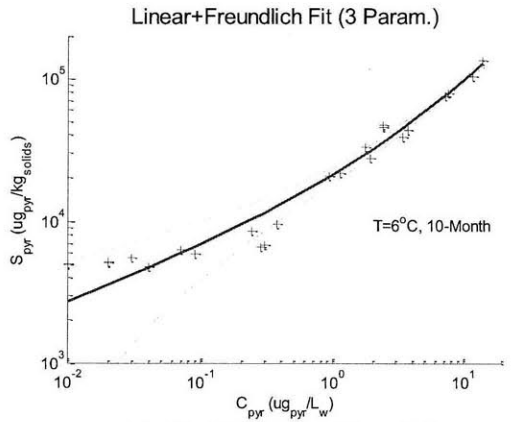

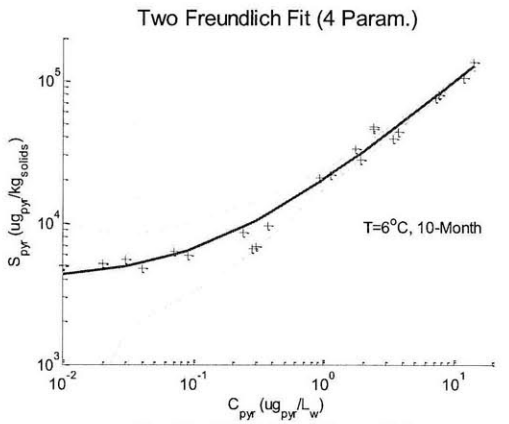

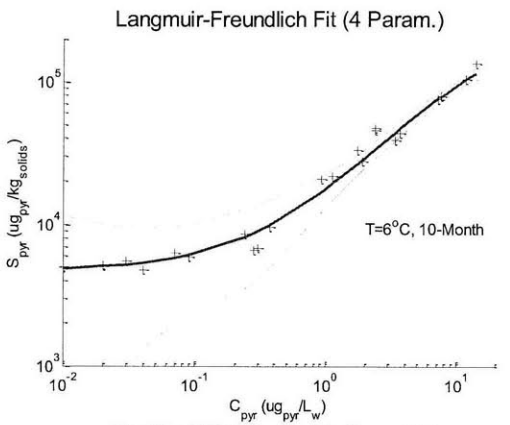

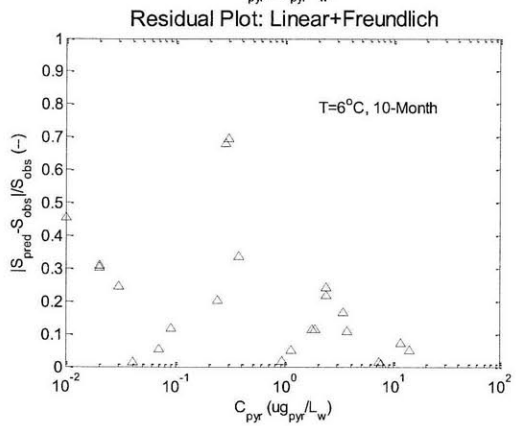

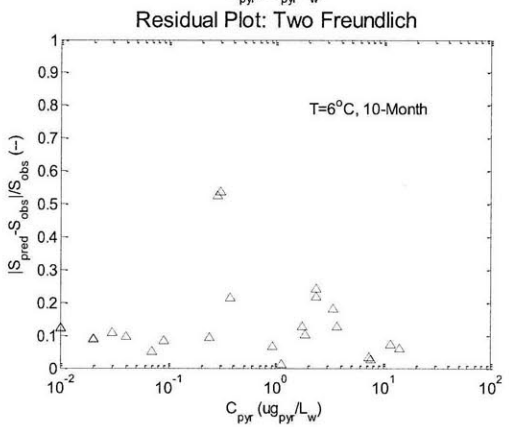

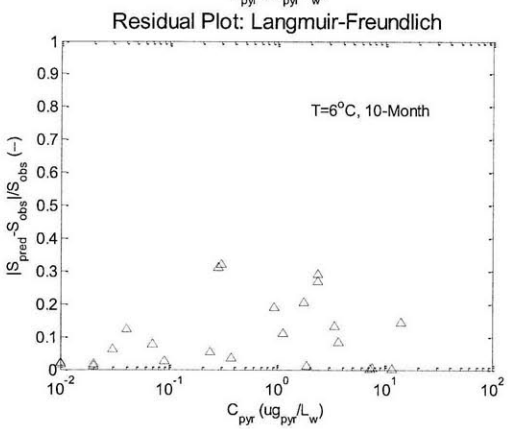

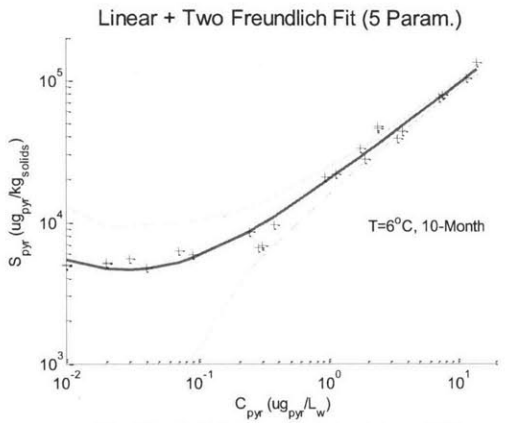
Linear + Two Freundlich Fit (5 Param.)
T=6°C, 10-Month
S_{pyr} (ug_{pyr}/kg_{solids})
C_{pyr} (ug_{pyr}/L_w)

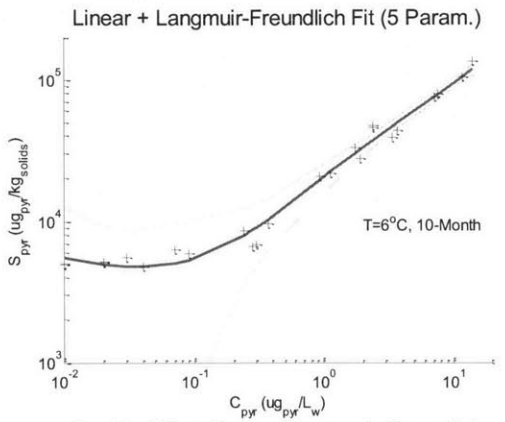
Linear + Langmuir-Freundlich Fit (5 Param.)
T=6°C, 10-Month
S_{pyr} (ug_{pyr}/kg_{solids})
C_{pyr} (ug_{pyr}/L_w)

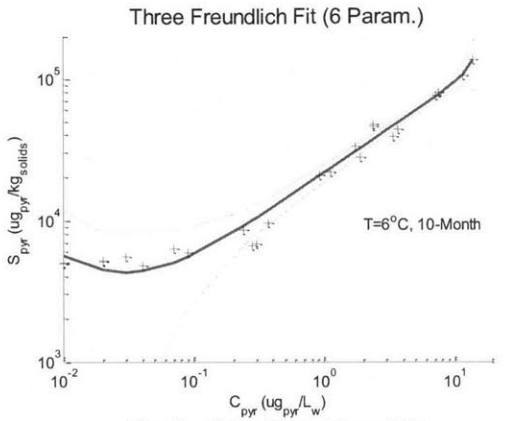
Three Freundlich Fit (6 Param.)
T=6°C, 10-Month
S_{pyr} (ug_{pyr}/kg_{solids})
C_{pyr} (ug_{pyr}/L_w)

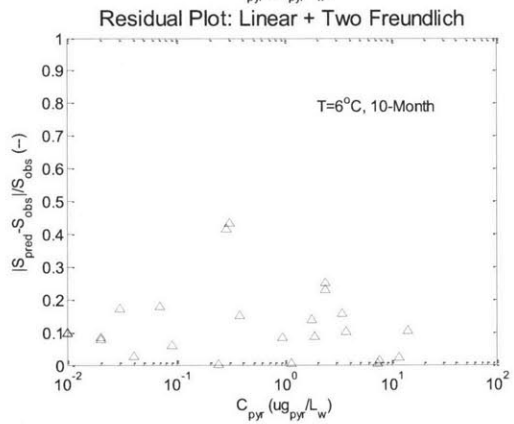
Residual Plot: Linear + Two Freundlich
T=6°C, 10-Month
$|S_{pred}-S_{obs}|/S_{obs}$ (–)
C_{pyr} (ug_{pyr}/L_w)

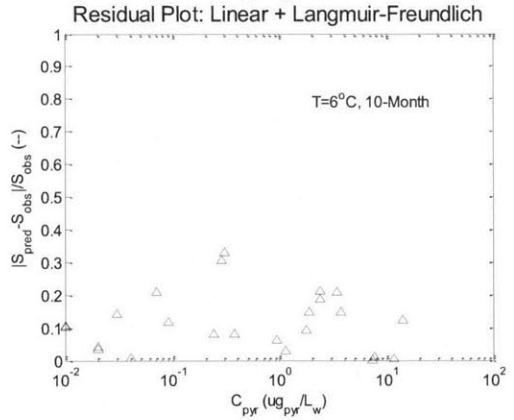
Residual Plot: Linear + Langmuir-Freundlich
T=6°C, 10-Month
$|S_{pred}-S_{obs}|/S_{obs}$ (–)
C_{pyr} (ug_{pyr}/L_w)

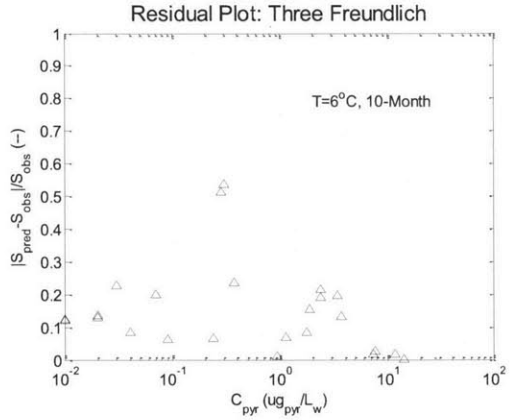
Residual Plot: Three Freundlich
T=6°C, 10-Month
$|S_{pred}-S_{obs}|/S_{obs}$ (–)
C_{pyr} (ug_{pyr}/L_w)

15°C (5-month) (Non-linear Regression by Matlab)

Linear+Freundlich Fit (3 Param.)

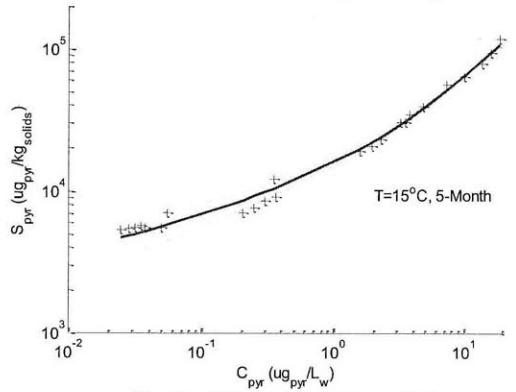

Two Freundlich Fit (4 Param.)

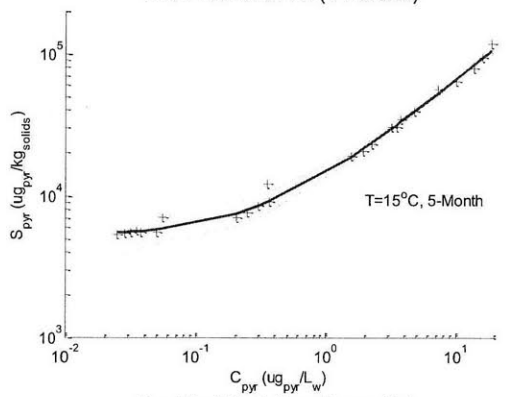

Langmuir-Freundlich Fit (4 Param.)

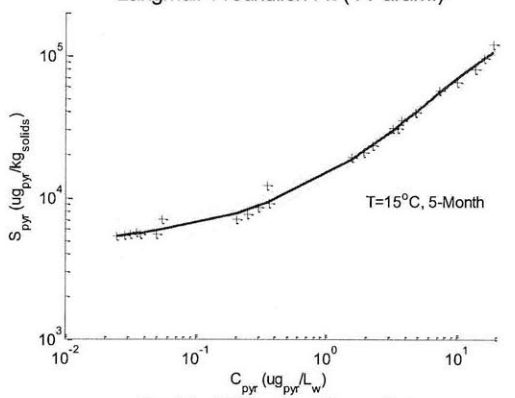

Residual Plot: Linear+Freundlich

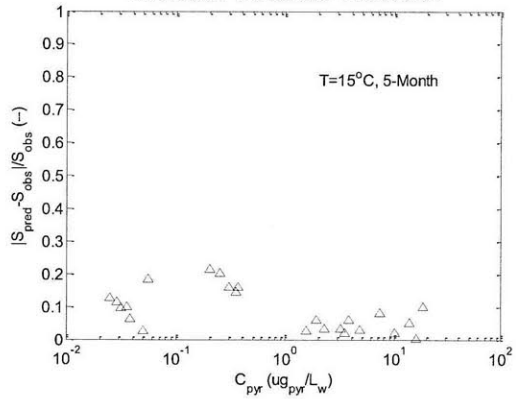

Residual Plot: Two Freundlich

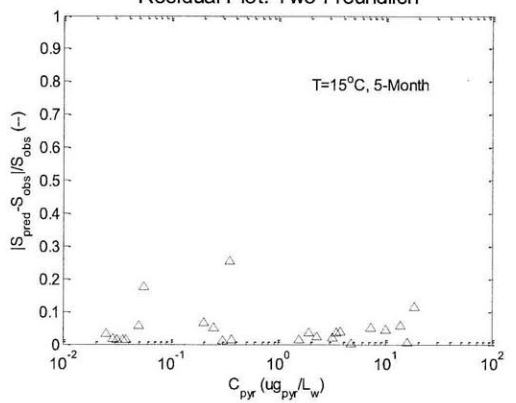

Residual Plot: Two Freundlich

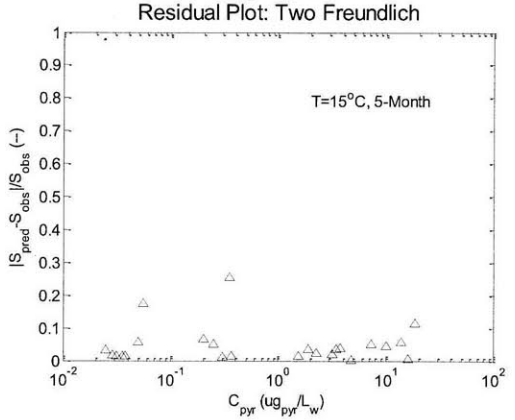

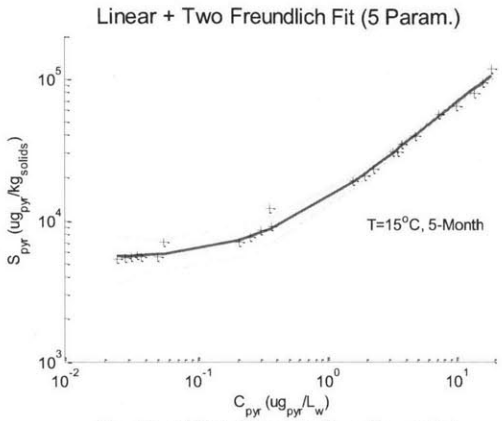
Linear + Two Freundlich Fit (5 Param.)
T=15°C, 5-Month
S_{pyr} (ug_{pyr}/kg_{solids})
C_{pyr} (ug_{pyr}/L_w)

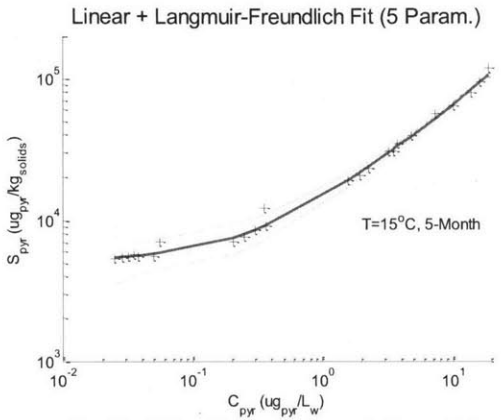
Linear + Langmuir-Freundlich Fit (5 Param.)
T=15°C, 5-Month
S_{pyr} (ug_{pyr}/kg_{solids})
C_{pyr} (ug_{pyr}/L_w)

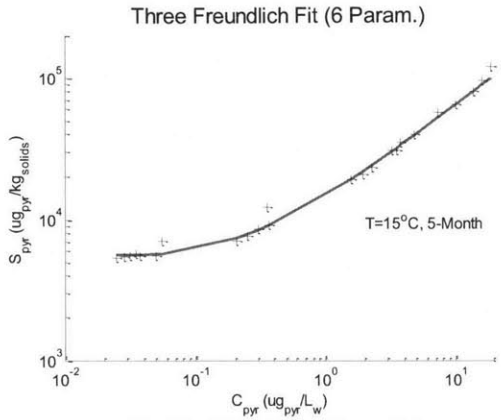
Three Freundlich Fit (6 Param.)
T=15°C, 5-Month
S_{pyr} (ug_{pyr}/kg_{solids})
C_{pyr} (ug_{pyr}/L_w)

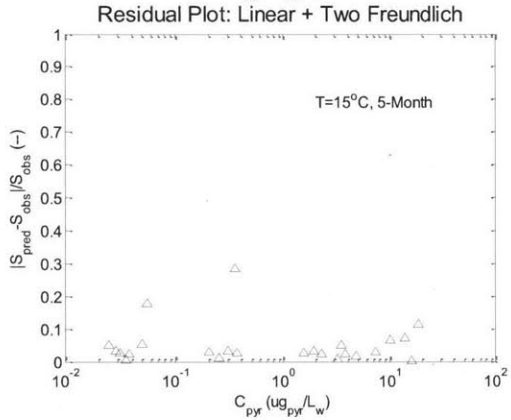
Residual Plot: Linear + Two Freundlich
T=15°C, 5-Month
$|S_{pred}-S_{obs}|/S_{obs}$ (–)
C_{pyr} (ug_{pyr}/L_w)

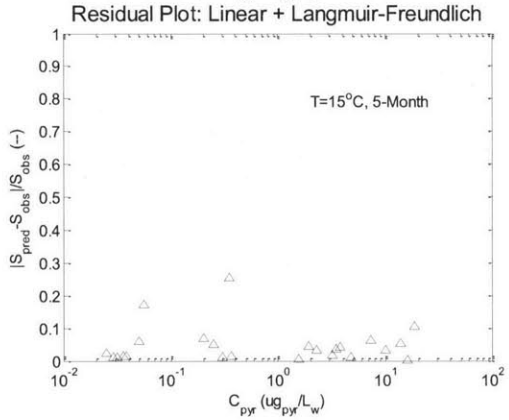
Residual Plot: Linear + Langmuir-Freundlich
T=15°C, 5-Month
$|S_{pred}-S_{obs}|/S_{obs}$ (–)
C_{pyr} (ug_{pyr}/L_w)

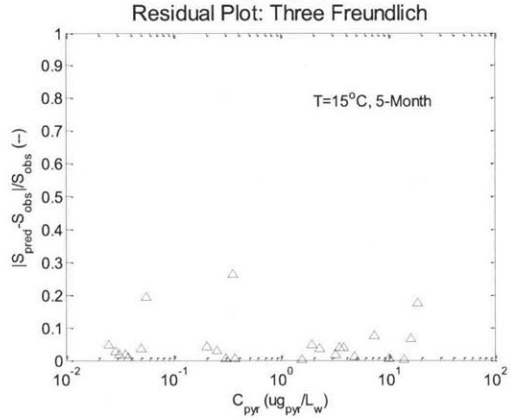
Residual Plot: Three Freundlich
T=15°C, 5-Month
$|S_{pred}-S_{obs}|/S_{obs}$ (–)
C_{pyr} (ug_{pyr}/L_w)

15°C (10-month) (Non-linear Regression by Matlab)

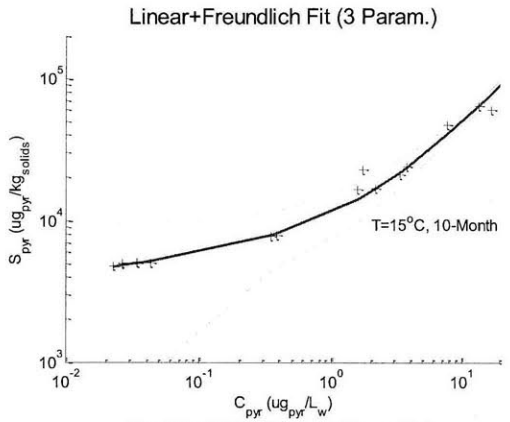

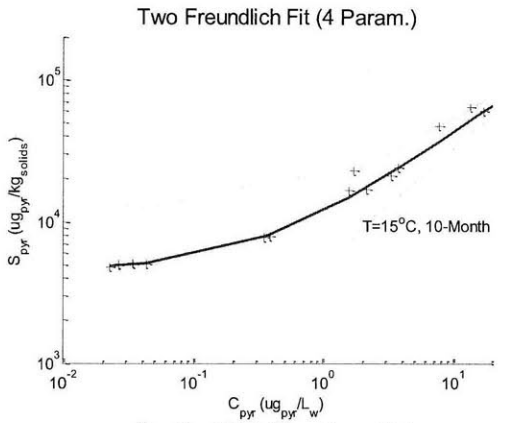

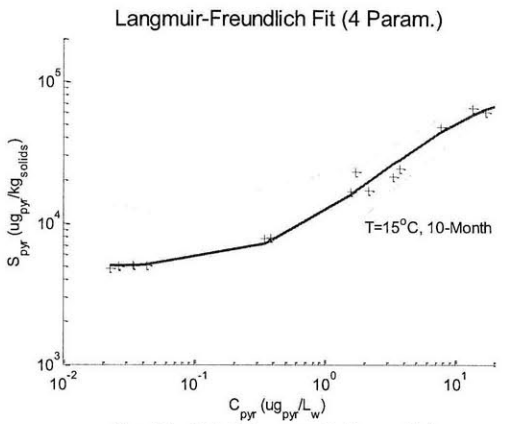

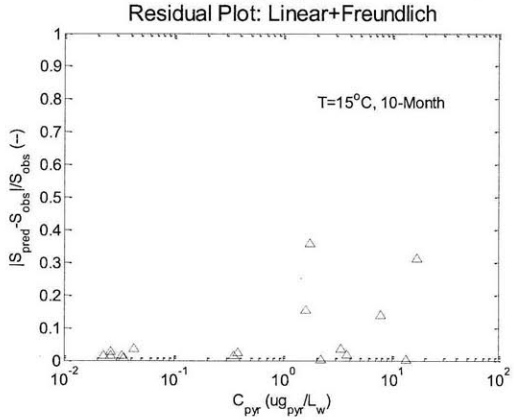

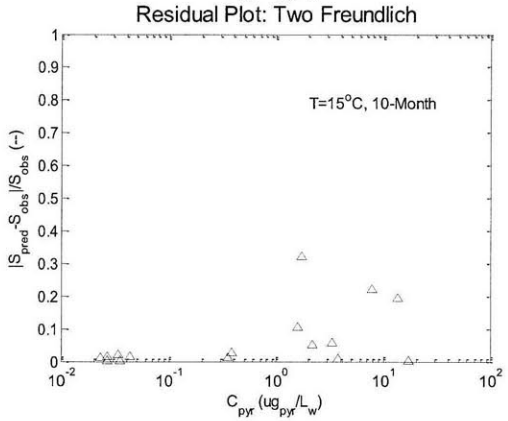

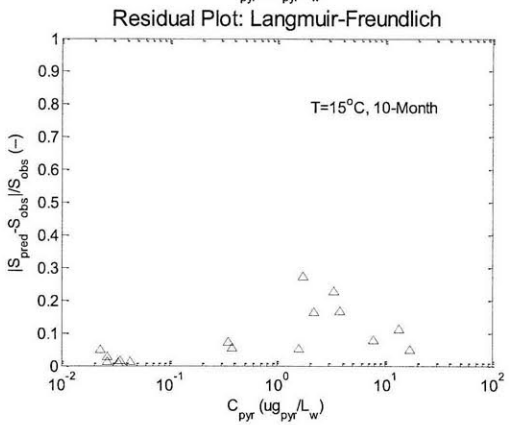

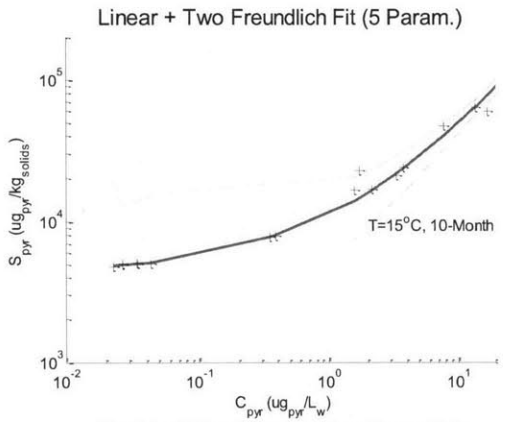
Linear + Two Freundlich Fit (5 Param.)
T=15°C, 10-Month
S_{pyr} (ug_{pyr}/kg_{solids})
C_{pyr} (ug_{pyr}/L_w)

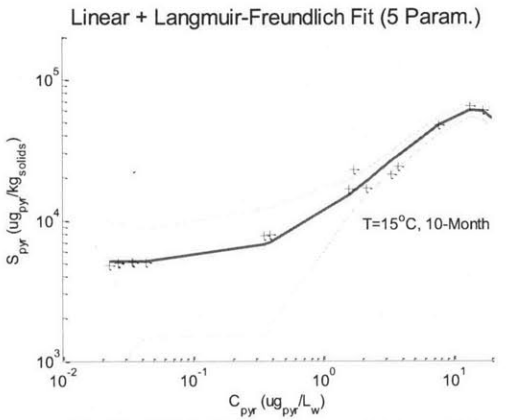
Linear + Langmuir-Freundlich Fit (5 Param.)
T=15°C, 10-Month
S_{pyr} (ug_{pyr}/kg_{solids})
C_{pyr} (ug_{pyr}/L_w)

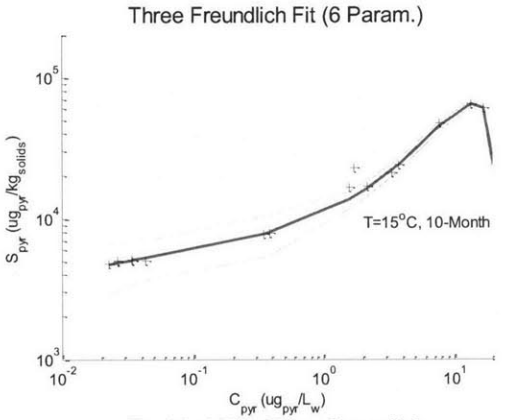
Three Freundlich Fit (6 Param.)
T=15°C, 10-Month
S_{pyr} (ug_{pyr}/kg_{solids})
C_{pyr} (ug_{pyr}/L_w)

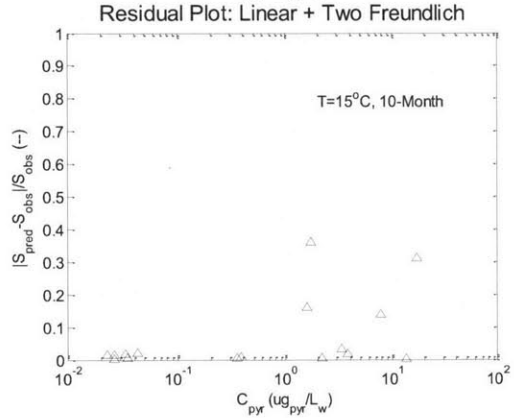
Residual Plot: Linear + Two Freundlich
T=15°C, 10-Month
$|S_{pred}-S_{obs}|/S_{obs}$ (-)
C_{pyr} (ug_{pyr}/L_w)

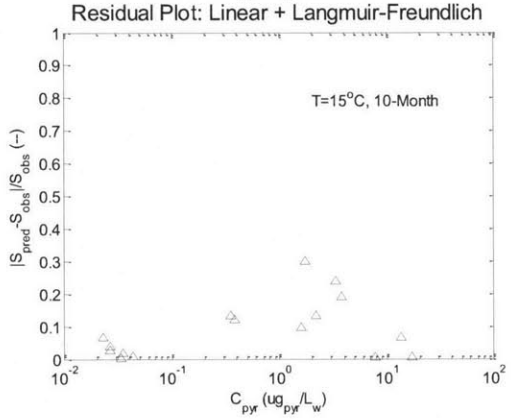
Residual Plot: Linear + Langmuir-Freundlich
T=15°C, 10-Month
$|S_{pred}-S_{obs}|/S_{obs}$ (-)
C_{pyr} (ug_{pyr}/L_w)

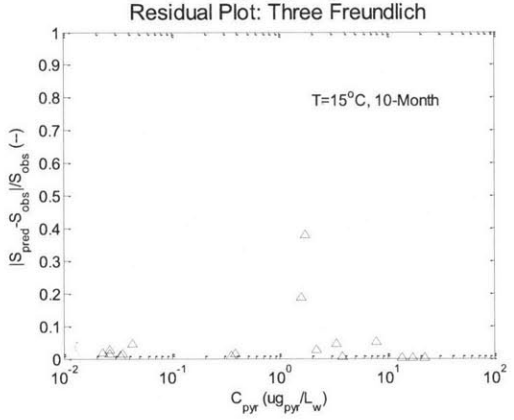
Residual Plot: Three Freundlich
T=15°C, 10-Month
$|S_{pred}-S_{obs}|/S_{obs}$ (-)
C_{pyr} (ug_{pyr}/L_w)

22°C (5-month) (Non-linear Regression by Matlab)

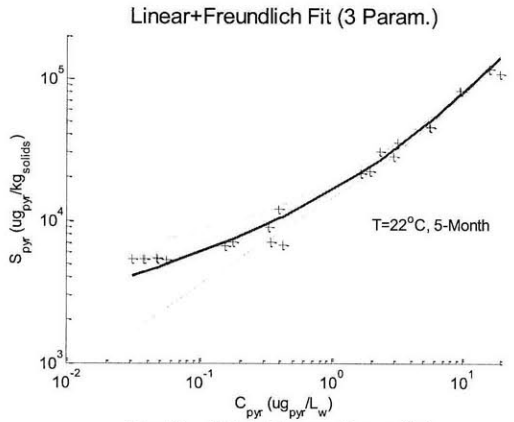

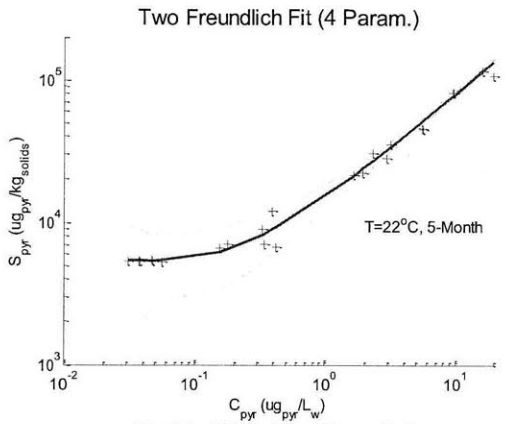

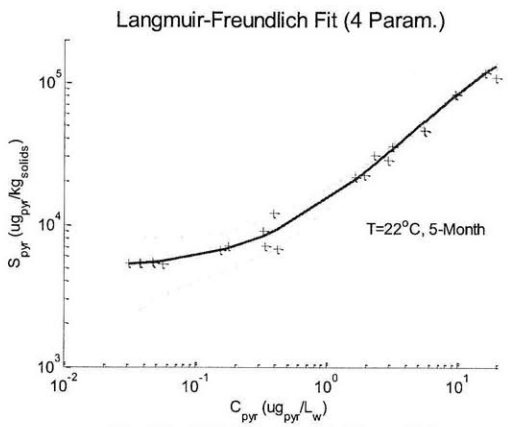

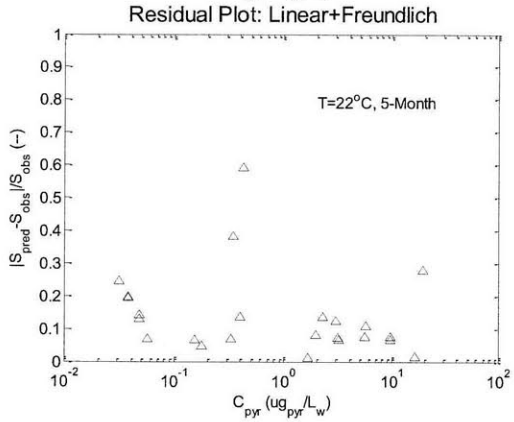

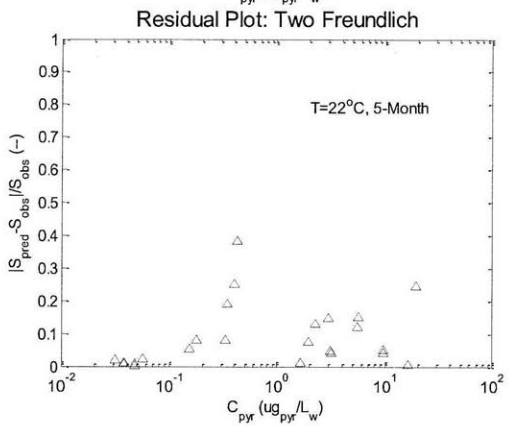

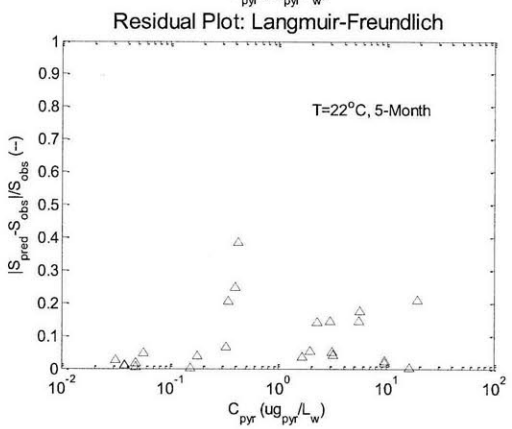

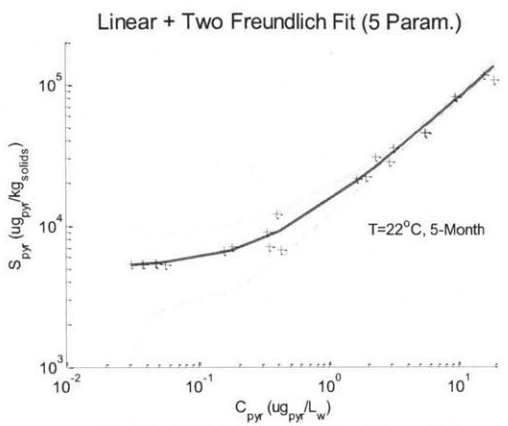
Linear + Two Freundlich Fit (5 Param.)
T=22°C, 5-Month
S_{pyr} (ug_{pyr}/kg_{solids})
C_{pyr} (ug_{pyr}/L_w)

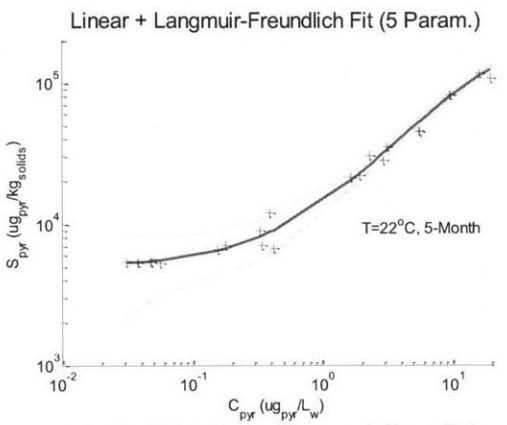
Linear + Langmuir-Freundlich Fit (5 Param.)
T=22°C, 5-Month
S_{pyr} (ug_{pyr}/kg_{solids})
C_{pyr} (ug_{pyr}/L_w)

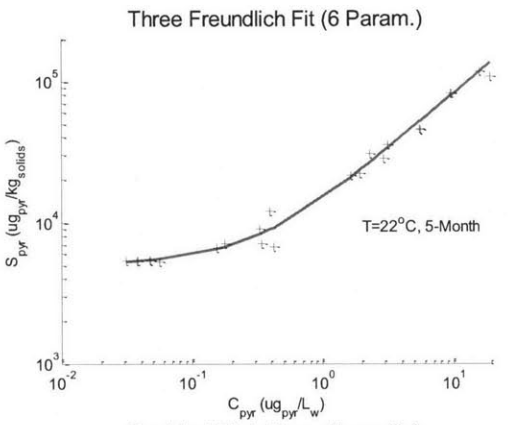
Three Freundlich Fit (6 Param.)
T=22°C, 5-Month
S_{pyr} (ug_{pyr}/kg_{solids})
C_{pyr} (ug_{pyr}/L_w)

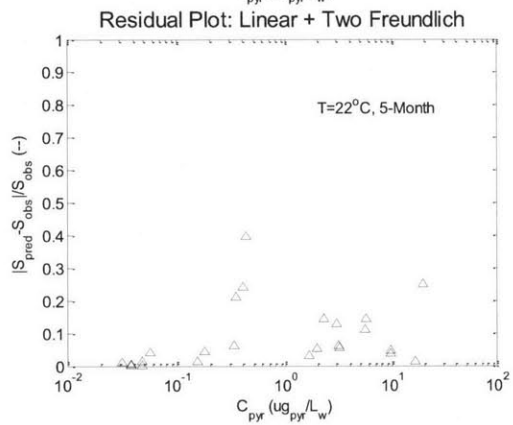
Residual Plot: Linear + Two Freundlich
T=22°C, 5-Month
$|S_{pred}-S_{obs}|/S_{obs}$ (--)
C_{pyr} (ug_{pyr}/L_w)

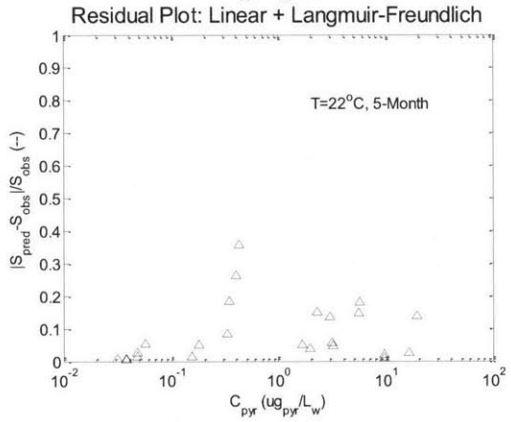
Residual Plot: Linear + Langmuir-Freundlich
T=22°C, 5-Month
$|S_{pred}-S_{obs}|/S_{obs}$ (--)
C_{pyr} (ug_{pyr}/L_w)

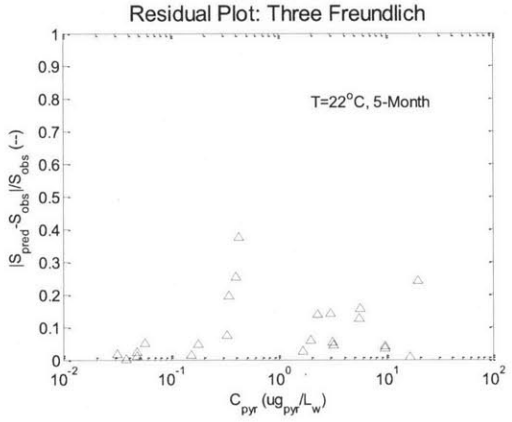
Residual Plot: Three Freundlich
T=22°C, 5-Month
$|S_{pred}-S_{obs}|/S_{obs}$ (--)
C_{pyr} (ug_{pyr}/L_w)

22°C (10-month) (Non-linear Regression by Matlab)

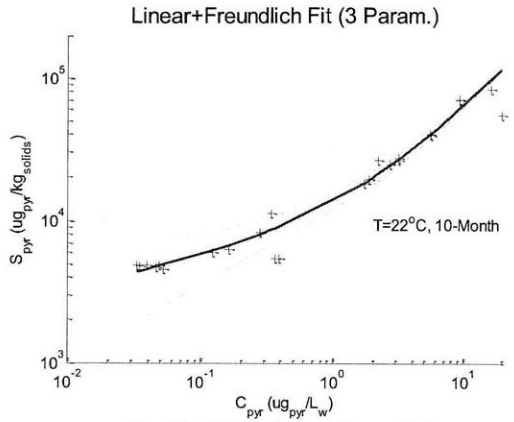

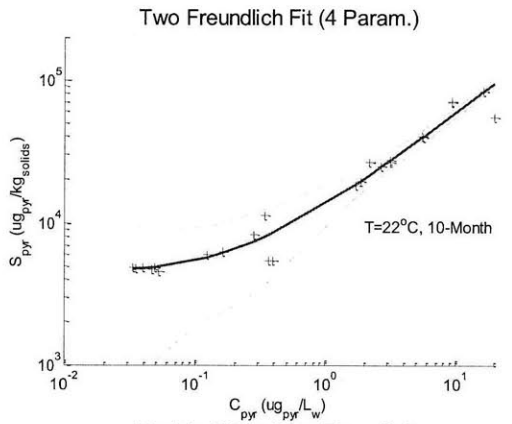

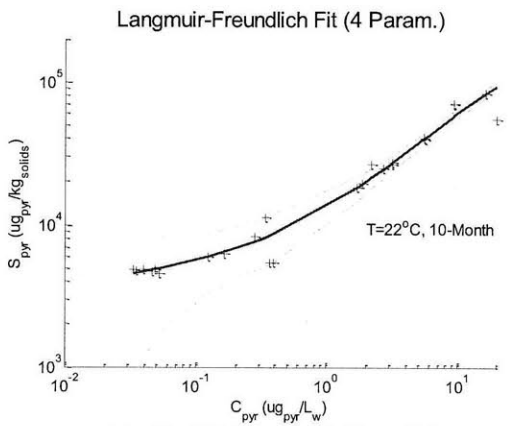

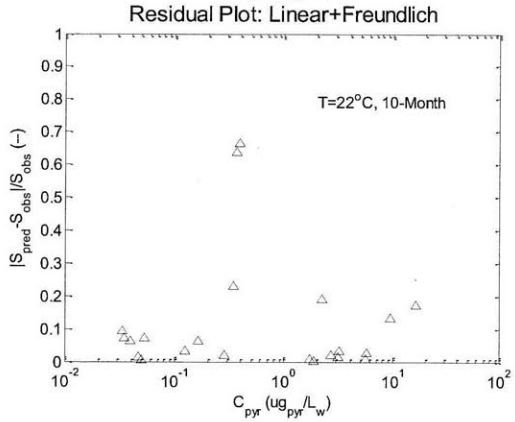

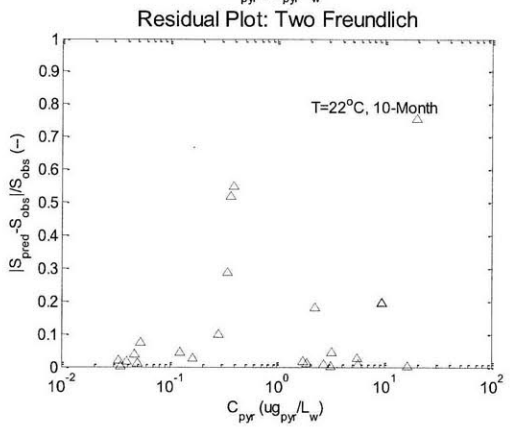

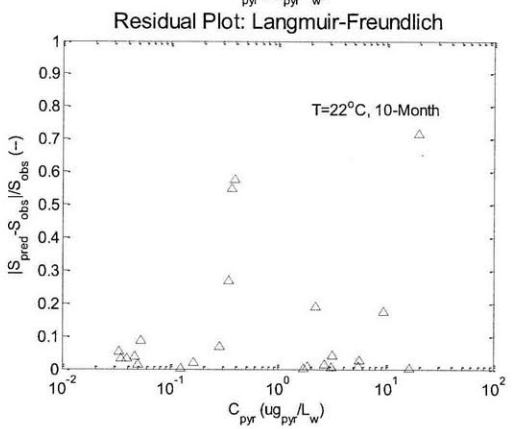

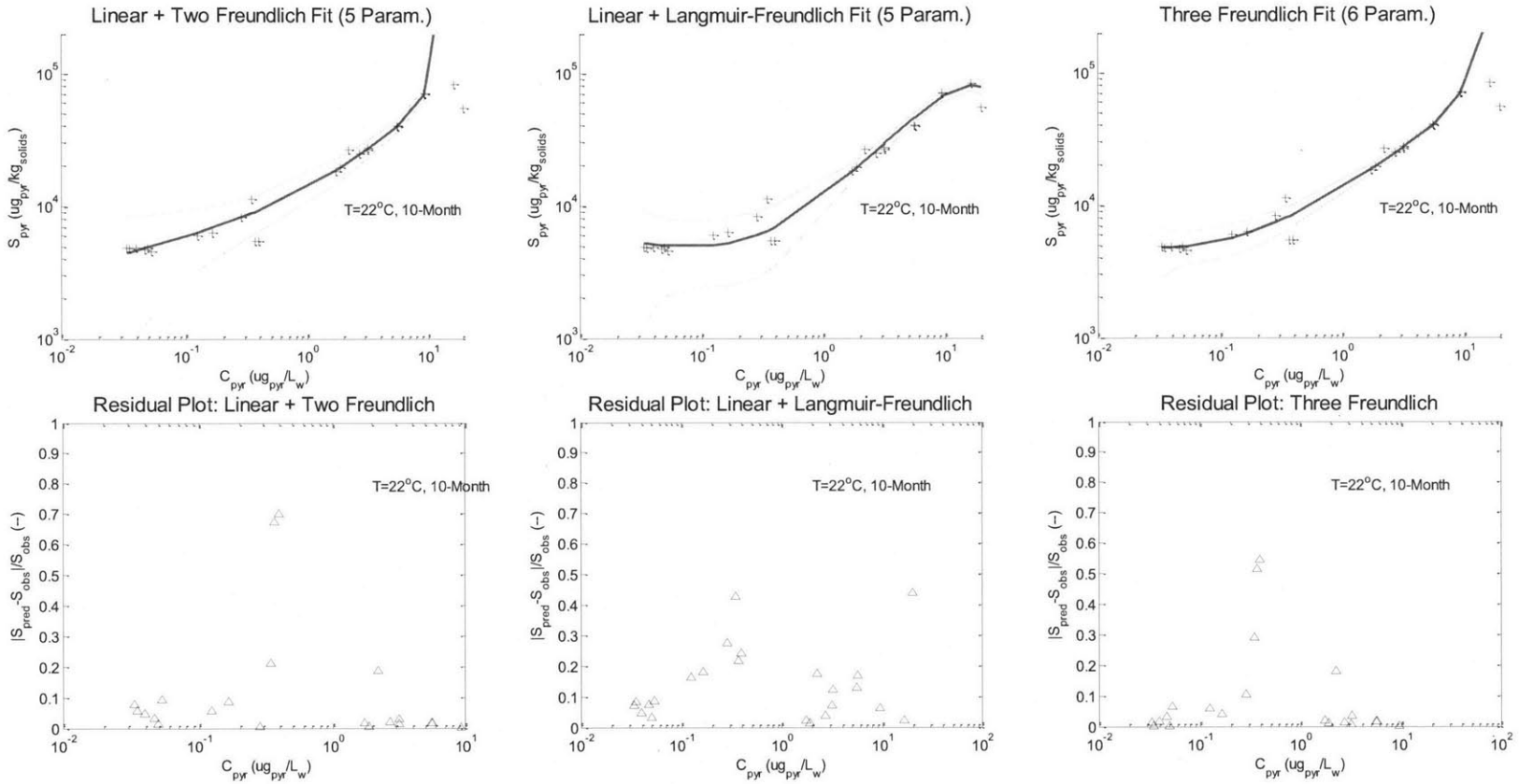
Linear + Two Freundlich Fit (5 Param.)
Linear + Langmuir-Freundlich Fit (5 Param.)
Three Freundlich Fit (6 Param.)
T=22°C, 10-Month
S_{pyr} (ug_{pyr}/kg_{solids})
C_{pyr} (ug_{pyr}/L_w)
Residual Plot: Linear + Two Freundlich
Residual Plot: Linear + Langmuir-Freundlich
Residual Plot: Three Freundlich
$|S_{pred}-S_{obs}|/S_{obs}$ (-)

37°C (5-month) (Non-linear Regression by Matlab)

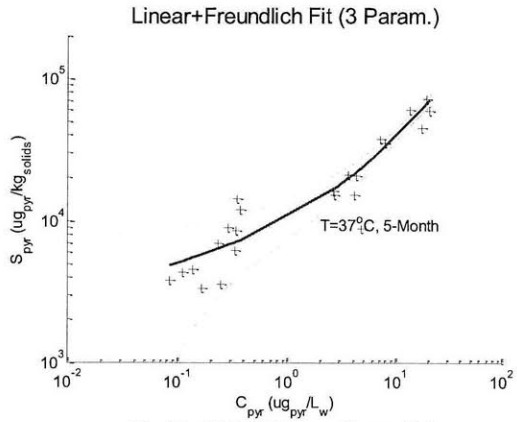

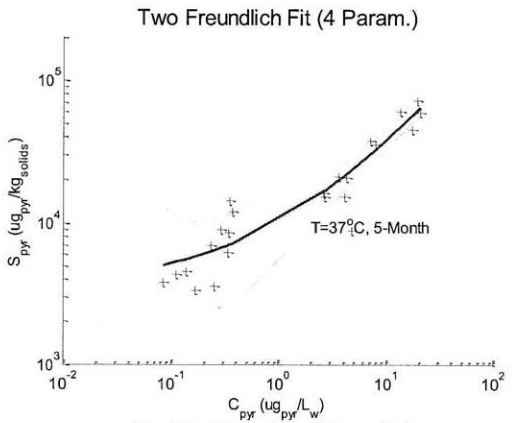

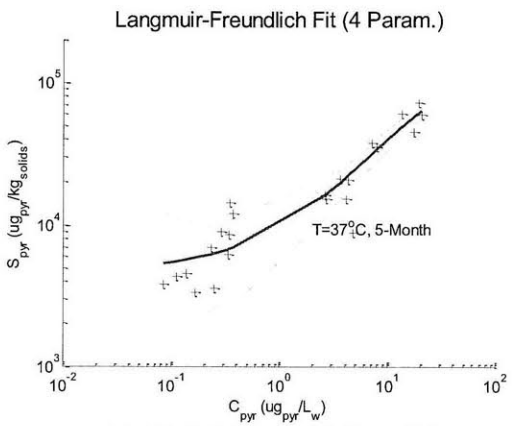

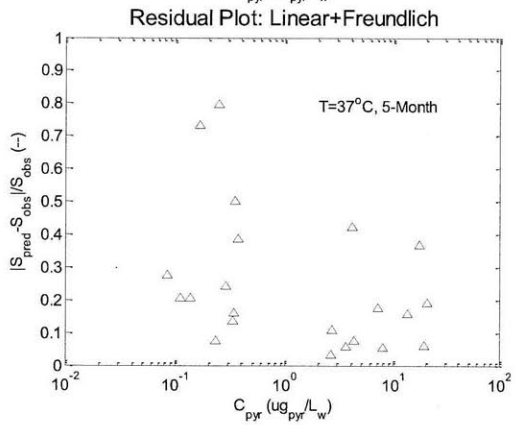

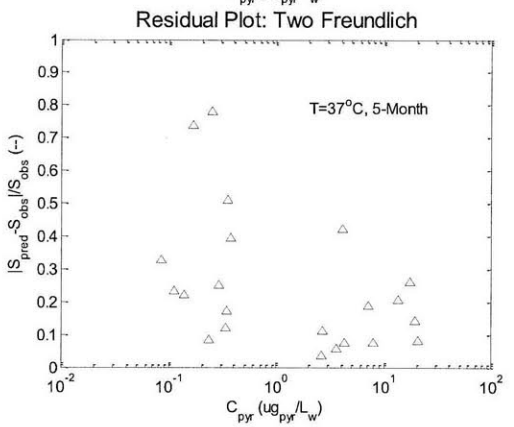

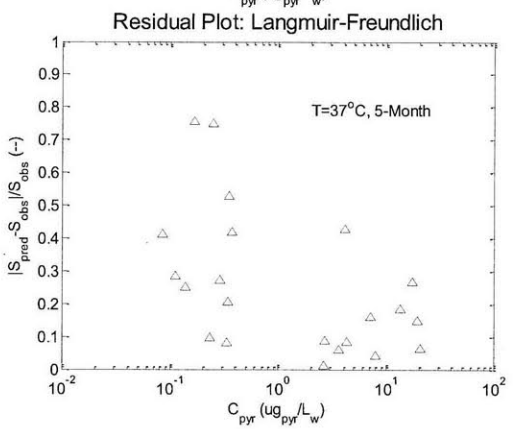

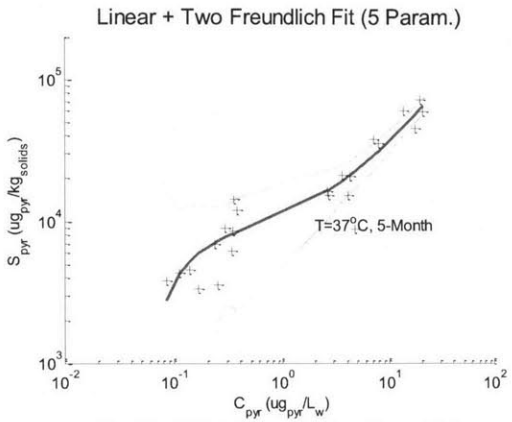
Linear + Two Freundlich Fit (5 Param.)
T=37°C, 5-Month
S_{pyr} (ug_{pyr}/kg_{solids})
C_{pyr} (ug_{pyr}/L_w)

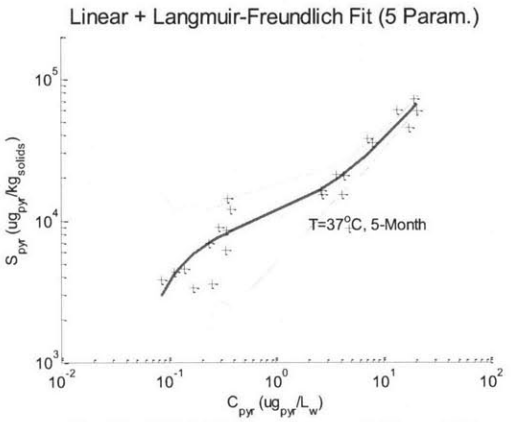
Linear + Langmuir-Freundlich Fit (5 Param.)
T=37°C, 5-Month
S_{pyr} (ug_{pyr}/kg_{solids})
C_{pyr} (ug_{pyr}/L_w)

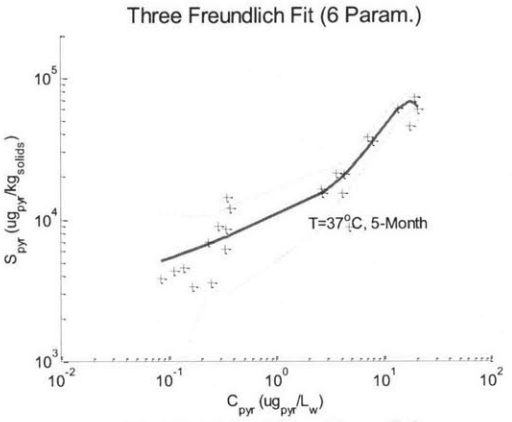
Three Freundlich Fit (6 Param.)
T=37°C, 5-Month
S_{pyr} (ug_{pyr}/kg_{solids})
C_{pyr} (ug_{pyr}/L_w)

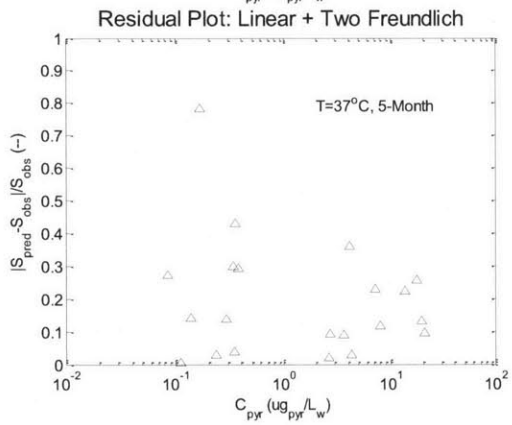
Residual Plot: Linear + Two Freundlich
T=37°C, 5-Month
$|S_{pred}-S_{obs}|/S_{obs}$ (–)
C_{pyr} (ug_{pyr}/L_w)

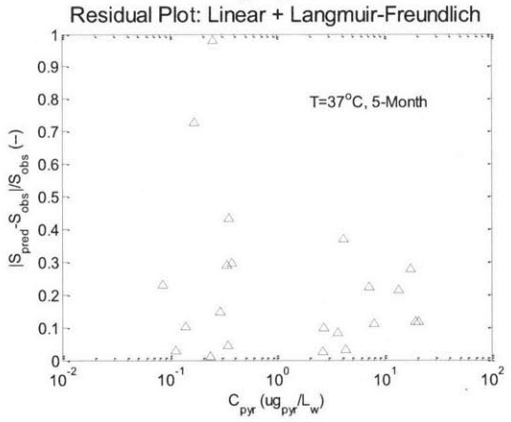
Residual Plot: Linear + Langmuir-Freundlich
T=37°C, 5-Month
$|S_{pred}-S_{obs}|/S_{obs}$ (–)
C_{pyr} (ug_{pyr}/L_w)

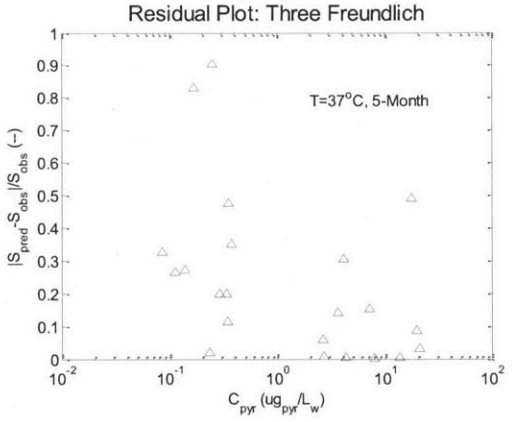
Residual Plot: Three Freundlich
T=37°C, 5-Month
$|S_{pred}-S_{obs}|/S_{obs}$ (–)
C_{pyr} (ug_{pyr}/L_w)

37°C (10-month) (Non-linear Regression by Matlab)

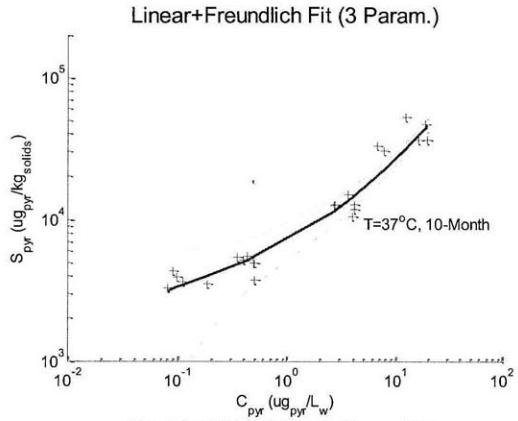

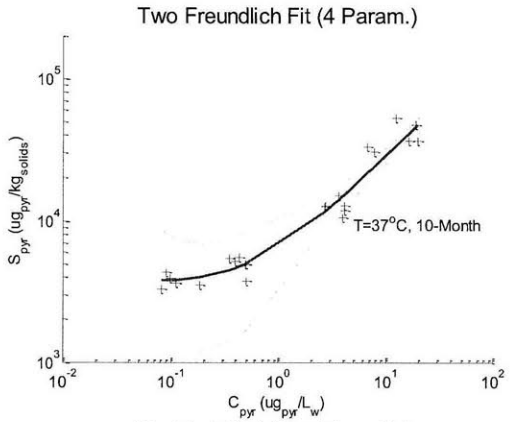

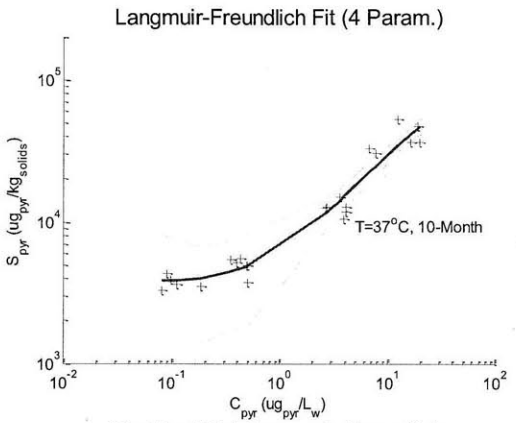

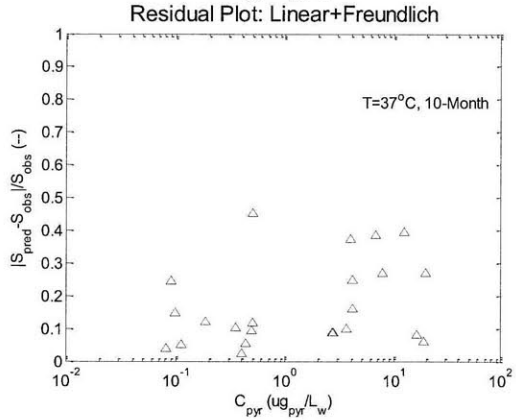

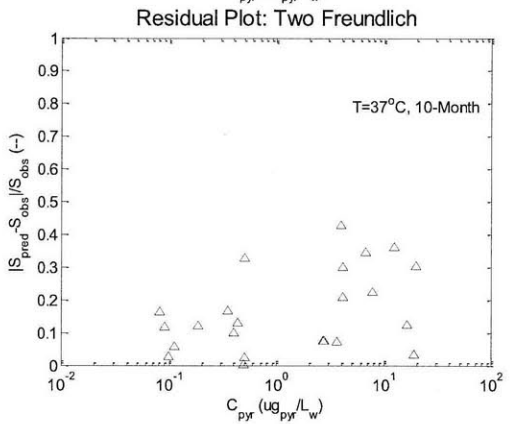

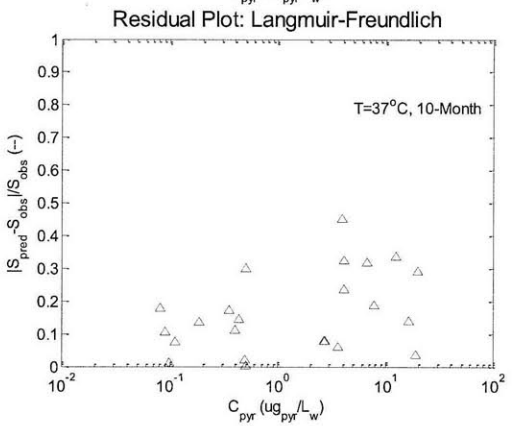

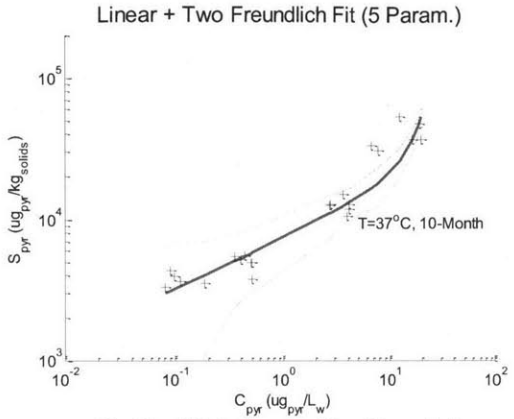
Linear + Two Freundlich Fit (5 Param.)
T=37°C, 10-Month
S_{pyr} (ug_{pyr}/kg_{solids})
C_{pyr} (ug_{pyr}/L_w)

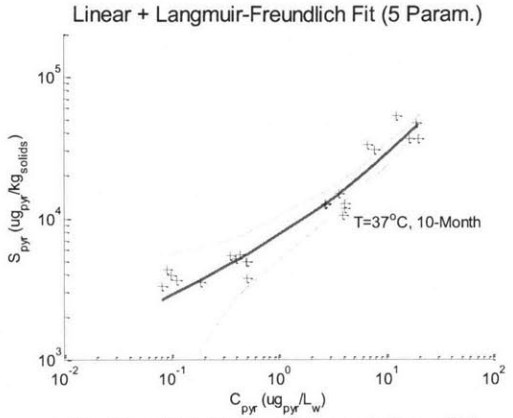
Linear + Langmuir-Freundlich Fit (5 Param.)
T=37°C, 10-Month
S_{pyr} (ug_{pyr}/kg_{solids})
C_{pyr} (ug_{pyr}/L_w)

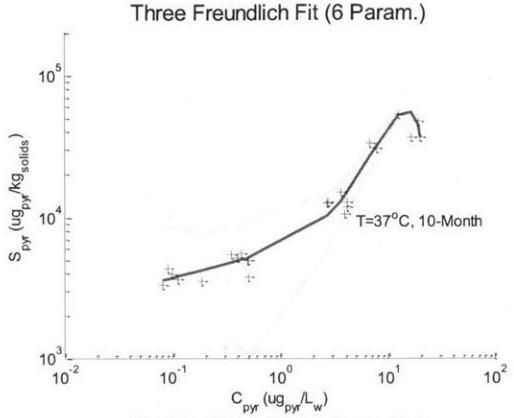
Three Freundlich Fit (6 Param.)
T=37°C, 10-Month
S_{pyr} (ug_{pyr}/kg_{solids})
C_{pyr} (ug_{pyr}/L_w)

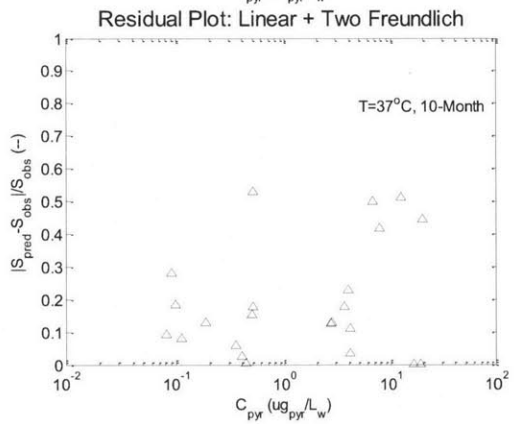
Residual Plot: Linear + Two Freundlich
T=37°C, 10-Month
$|S_{pred}-S_{obs}|/S_{obs}$ (–)
C_{pyr} (ug_{pyr}/L_w)

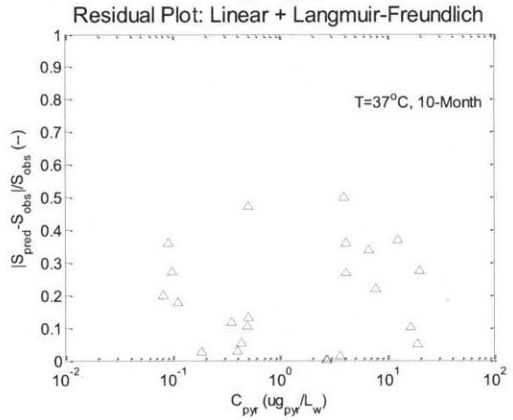
Residual Plot: Linear + Langmuir-Freundlich
T=37°C, 10-Month
$|S_{pred}-S_{obs}|/S_{obs}$ (–)
C_{pyr} (ug_{pyr}/L_w)

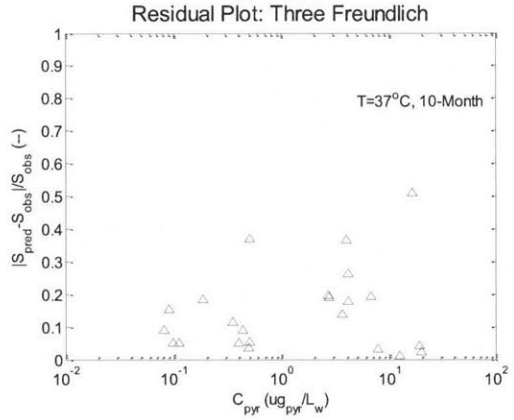
Residual Plot: Three Freundlich
T=37°C, 10-Month
$|S_{pred}-S_{obs}|/S_{obs}$ (–)
C_{pyr} (ug_{pyr}/L_w)

Appendix 5 - 4. Regression of Sorption Data with Matlab (Figure 5-4b).

Lnr-Fr(soot)-Fr(char)*	K_{char}**	f_{char}	n_{char}	n_{soot}	Mean Sq. Errors
3 parameters (fix n_{soot} to 0.62)					
5–month data	-39×10^3 ($\pm29\times10^3$)	−0.047 (±0.003)	−0.24 (±0.26)	fixed	14×10^6
10–month data	-1.8×10^6 ($\pm3.7\times10^6$)	−0.001 (±0.003)	−0.08 (±0.13)	fixed	5.3×10^6
4 parameters					
5–month data	-120×10^3 ($\pm1.6\times10^6$)	−0.024 (±0.23)	−0.11 (±1.1)	0.72 (±0.85)	17×10^6
10–month data	160×10^3 ($\pm1.2\times10^6$)	0.025 (±0.29)	0.01 (±0.92)	0.73 (±1.02)	7.5×10^6

*: $S = (f_{OC} - f_{char})K_{OC}C + f_{soot}K_{soot}C^{n_{soot}} + f_{char}K_{char}C^{n_{char}}$.

**: K_{char} in $(\mu g_{pyr}/kg_{char})(L_w/\mu g_{pyr})^{nchar}$.

Linear-Freundlich(soot)-Freundlich(char) (3 Param.) at 22°C

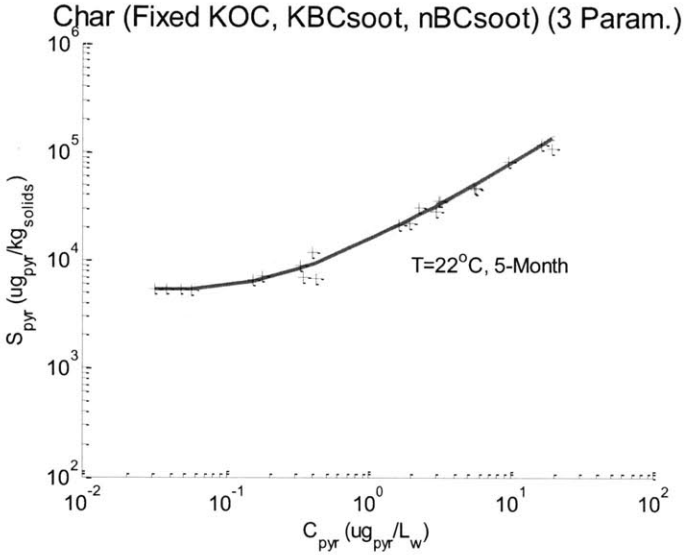

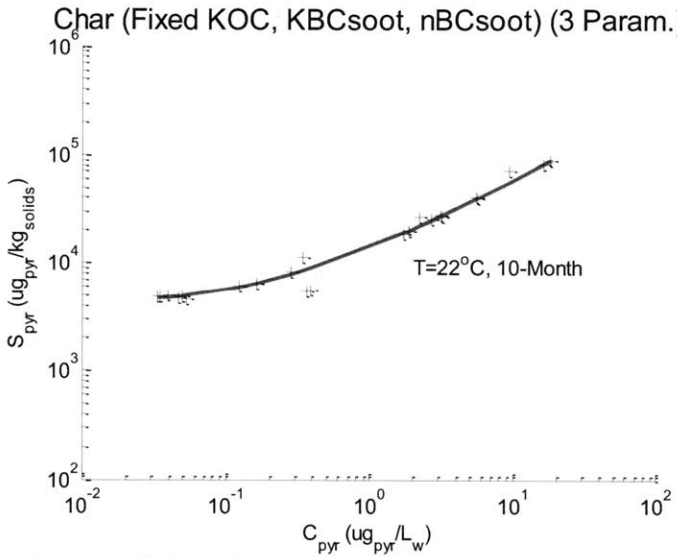

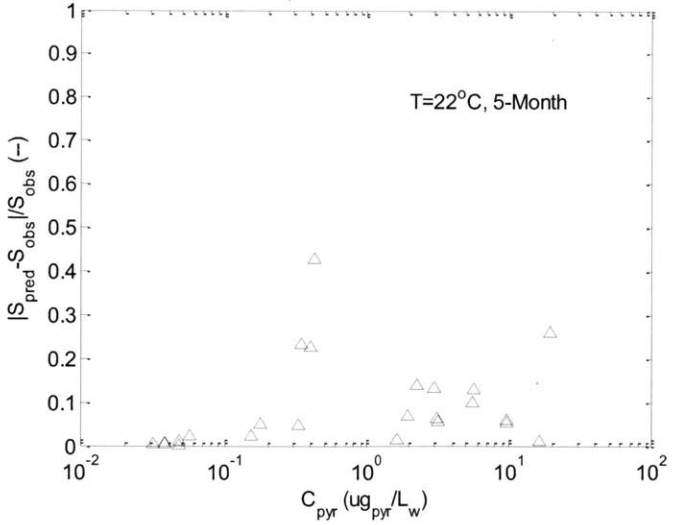

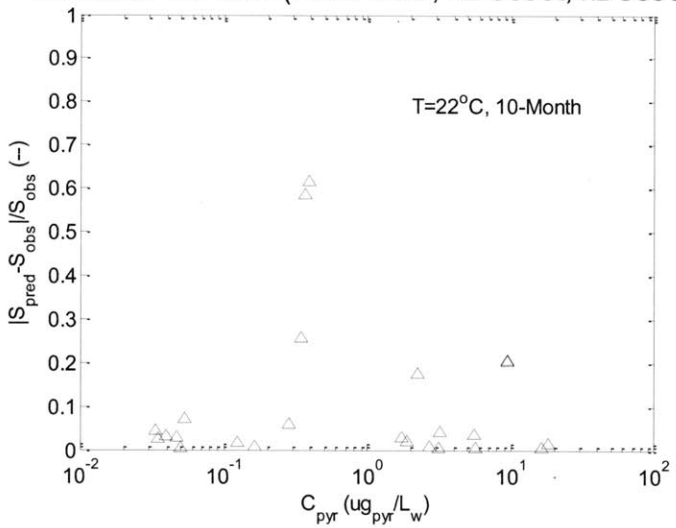

Linear-Freundlich(soot)-Freundlich(char) (<u>4 Param.</u>) at 22°C

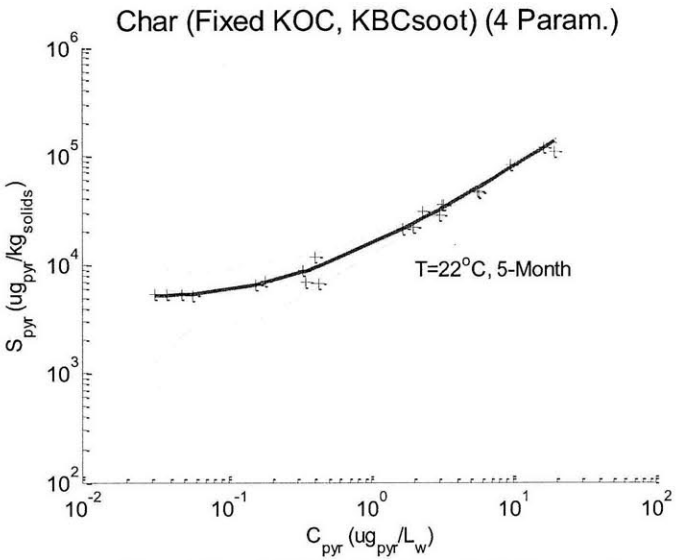

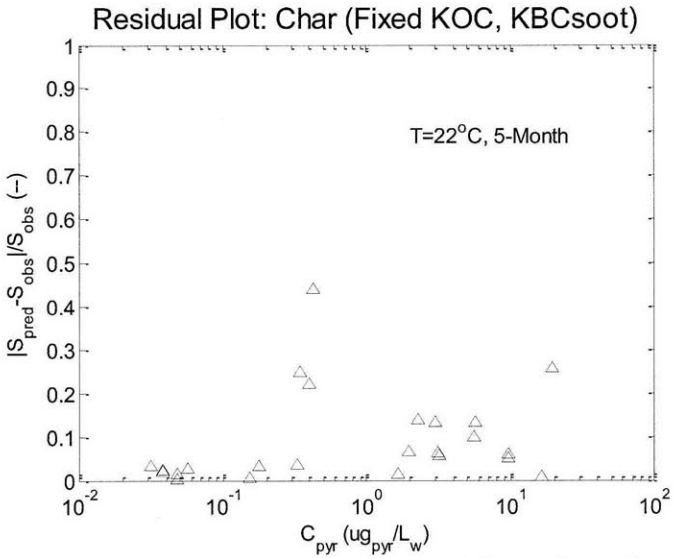

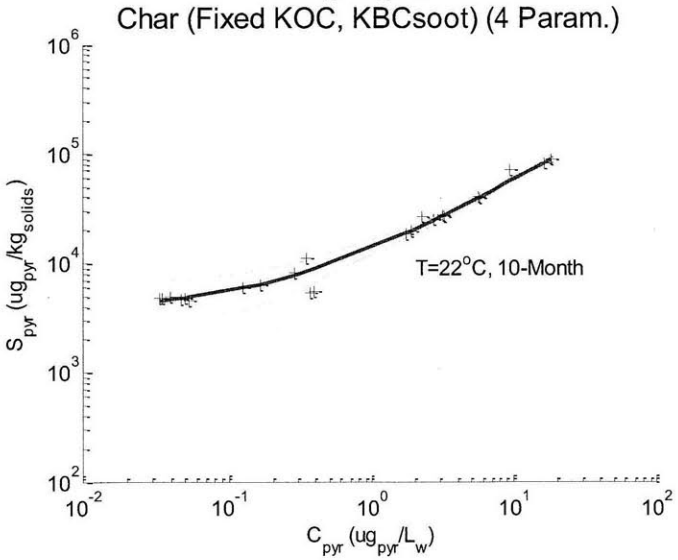

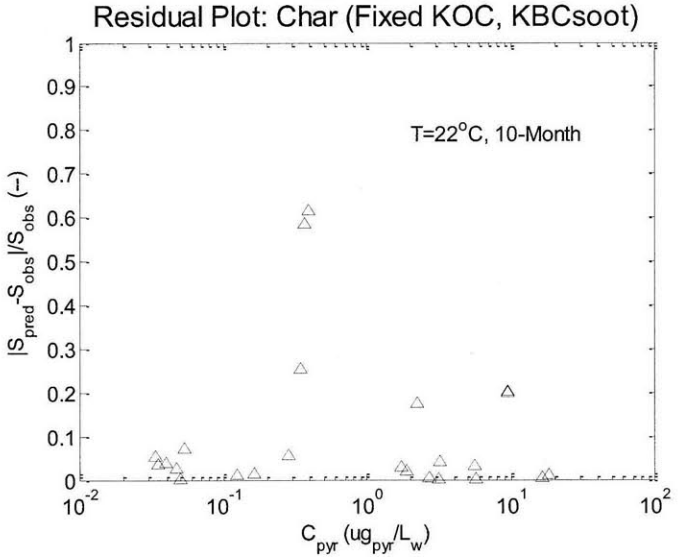

Appendix 5 - 5. Regression of Sorption Data with Matlab (Figure 5-4c).

Occlusion-Fix*	S_{occlu} ($\mu g_{pyr}/kg_{solids}$)	n	Mean Sq. Errors
5–month data	4300 (±800)	0.79 (±0.01)	11×10^6
10–month data	3000 (±500)	0.62 (±0.01)	3.6×10^6

*: 2-Parameter model: $S = S_{occlu} + f_{OC} K_{OC} C + f_{BC} K_{BC} C^n$. See also Table 5-1.

Occlusion-Fix(K_{OC},K_{BC}) model (2 Param.) at 22°C

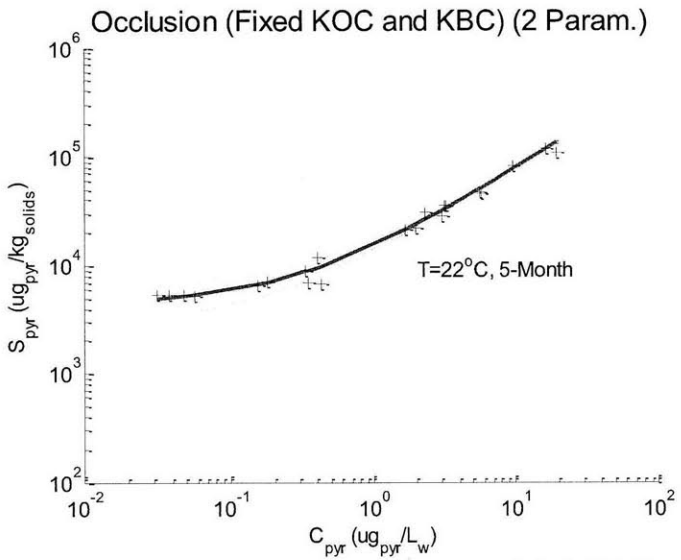

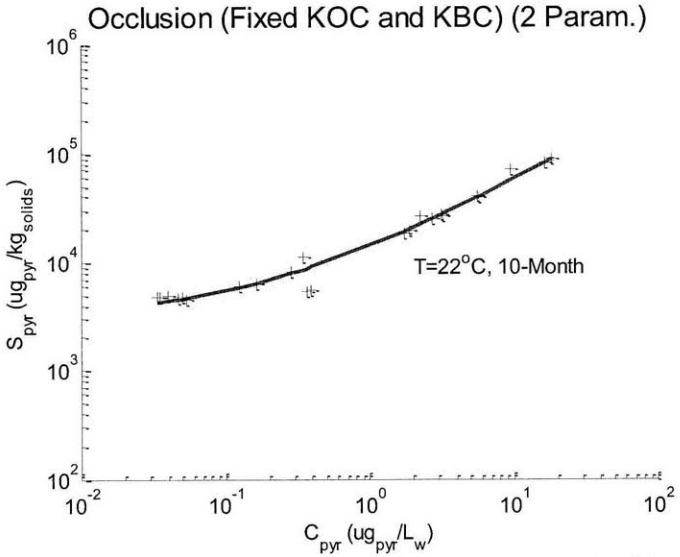

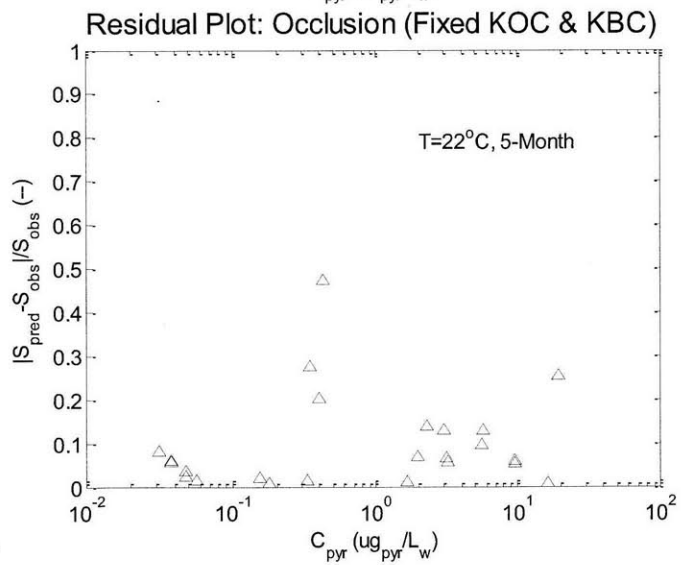

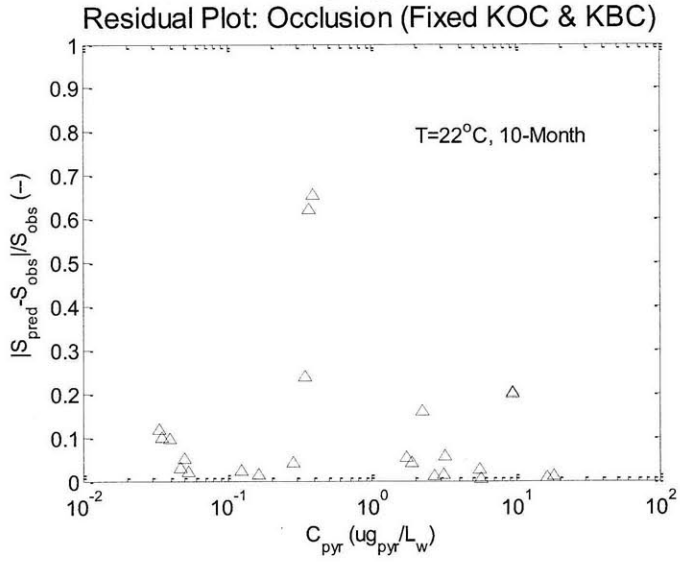

Appendix 5 - 6. Regression of Sorption Data with Matlab (Figure 5-4d).

Method

The parameters for the "Occlusion-Lnr-Fr" model (equation below) were determined by Matlab with a trial-and-error approach. This combined approach was taken because the regressed end-points varied with the initial guess values.

$$\textbf{Occlusion} - \textbf{Lnr} - \textbf{Fr}: \quad S = S_{occlu} + K_{Lnr}\,C + K_{Fr}\,C^{n}$$

In the combined approach, a value was first assumed for the occluded pyrene concentration (S_{occlu}). The accessible solid pyrene concentrations (i.e. S-S_{occlu}) were then regressed against C using Matlab routine. This was repeated for different assumed S_{occlu}'s (0, 1000, 2000, 3000, 4000 $\mu g_{pyr}/kg_{solids}$) at all four temperatures (6, 15, 22, 37°C) and two time-points (5 and 10 months). The 'best fit' S_{occlu} was determined by examining the errors of the regression (mean square errors) and the relative uncertainties of the regressed parameters.

A1. Regressed Occlusion-Lnr-Fr (4-Param) Parameters for 5 month data.

5-month	S_{occlu} = 0*	*1000**	*2000**	*3000**	*4000**
K_{Lnr} (T=6°C)	2800	3600	3100	2100	–480
	(±900)	(±600)	(±800)	(±1400)	(±3900)
K_{Fr}	16000	14000	13000	13000	14000
	(±1400)	(±1000)	(±1000)	(±1300)	(±3300)
n	0.42	0.40	0.48	0.58	0.73
	(±0.08)	(±0.06)	(±0.08)	(±0.10)	(±0.13)
Mean Sq. Err.	16×10^6	7.2×10^6	6.6×10^6	5.8×10^6	5.0×10^6
K_{Lnr} (T=15°C)	4500	4400	4200	3900	3200
	(±200)	(±300)	(±300)	(±460)	(±900)
K_{Fr}	11000	11000	9600	8700	8100
	(±700)	(±700)	(±700)	(±700)	(±860)
n	0.25	0.29	0.34	0.42	0.56
	(±0.04)	(±0.05)	(±0.06)	(±0.08)	(±0.11)
Mean Sq. Err.	4.2×10^6	4.1×10^6	3.9×10^6	3.7×10^6	3.4×10^6
K_{Lnr} (T=22°C)	5900	5700	5400	4400	-7.9×10^6
	(±500)	(±600)	(±800)	(±1900)	$(\pm14\times10^9)$
K_{Fr}	10000	9500	8700	8400	7.9×10^6
	(±1300)	(±1300)	(±1300)	(±1700)	$(\pm14\times10^9)$
n	0.28	0.34	0.42	0.58	1.0
	(±0.09)	(±0.11)	(±0.14)	(±0.20)	(±0.35)
Mean Sq. Err.	15×10^6	14×10^6	14×10^6	13×10^6	11×10^6
K_{Lnr} (T=37°C)	2700	2200	2100	1800	N/A
	(±550)	(±780)	(±980)	(±1600)	
K_{Fr}	7800	7600	6600	5800	N/A
	(±1800)	(±1900)	(±1900)	(±2000)	
n	0.21	0.30	0.37	0.48	N/A
	(±0.18)	(±0.22)	(±0.27)	(±0.37)	
Mean Sq. Err.	31×10^6	36×10^6	36×10^6	35×10^6	N/A

*: S_{occlu} in $\mu g_{pyr}/kg_{solids}$.

A2. Regressed Occlusion-Lnr-Fr (4-Param) Parameters for 10 month data.

10-month	S_{occlu} = 0*	*1000**	*2000**	*3000**	*4000**
K_{Lnr} (T=6°C)	6200	7700	5300	800	–50000
	(±1300)	(±700)	(±1900)	(±7200)	(±340×10^3)
K_{Fr}	15000	11000	13000	16000	65000
	(±2100)	(±1500)	(±2200)	(±6600)	(±340×10^3)
n	0.38	0.31	0.51	0.71	0.96
	(±0.11)	(±0.10)	(±0.15)	(±0.20)	(±0.25)
Mean Sq. Err.	24×10^6	13×10^6	15×10^6	14×10^6	11×10^6
K_{Lnr} (T=15°C)	4000	2100	1900	–2.7×10^6	–1.6×10^6
	(±400)	(±540)	(±640)	(±1.4×10^9)	(±590×10^6)
K_{Fr}	7400	10000	9200	2.7×10^6	1.6×10^6
	(±2200)	(±1400)	(±1300)	(±1.4×10^9)	(±590×10^6)
n	0.12	0.31	0.37	1.0	1.0
	(±0.15)	(±0.10)	(±0.12)	(±0.39)	(±0.38)
Mean Sq. Err.	31×10^6	11×10^6	9.8×10^6	17×10^6	11×10^6
K_{Lnr} (T=22°C)	5000	2800	2300	1200	–2.9×10^6
	(±380)	(±600)	(±880)	(±1900)	(±1.2×10^9)
K_{Fr}	8800	11000	10000	9900	2.9×10^6
	(±1200)	(±900)	(±1000)	(±1600)	(±1.2×10^9)
n	0.21	0.42	0.51	0.65	1.0
	(±0.09)	(±0.08)	(±0.10)	(±0.13)	(±0.22)
Mean Sq. Err.	13×10^6	6.7×10^6	5.8×10^6	4.7×10^6	4.2×10^6
K_{Lnr} (T=37°C)	1800	2000	2000	900	N/A
	(±400)	(±340)	(±500)	(±6200)	
K_{Fr}	5400	3900	3000	2800	N/A
	(±1100)	(±1000)	(±1000)	(±5500)	
n	0.22	0.22	0.34	0.76	N/A
	(±0.17)	(±0.21)	(±0.32)	(±0.85)	
Mean Sq. Err.	13×10^6	9.9×10^6	9.8×10^6	9.7×10^6	N/A

*: S_{occlu} in $\mu g_{pyr}/kg_{solids}$.

B. Finalizing average isotherm parameters at 22°C

The final S_{occlu} value was selected by elimination. The author concluded that S_{occlu} = 1000 and 2000 $\mu g_{pyr}/kg_{solids}$ both fit the sorption data well. S_{occlu} = 3000 or 4000 $\mu g_{pyr}/kg_{solids}$ were rejected because negative K_{Lnr} and K_{Fr} were obtained. This gave an average of S_{occlu} = 1500±500 $\mu g_{pyr}/kg_{solids}$. The final isotherm parameters were obtained as geometric means of four regression cases (2 time frames and two accepted S_{occlu}'s; see table below).

Case at 22°C	K_{Lnr}*	K_{Fr}^*	n
5-month, S_{occlu}=1000	5740 (±600)	9490 (±1270)	0.34 (±0.11)
5-month, S_{occlu}=2000	5420 (±830)	8690 (±1280)	0.42 (±0.14)
10-month, S_{occlu}=1000	2840 (±600)	10960 (±930)	0.42 (±0.08)
10-month, S_{occlu}=2000	2350 (±890)	10160 (±970)	0.51 (±0.10)
Geometric mean	***3800 (±700)***	***9800 (±1100)***	***0.42 (±0.12)***

*: K_{Lnr} in L_w/kg_{solids}, K_{Fr} in $(\mu g_{pyr}/kg_{solids})(L_w/\mu g_{pyr})^n$.

C. Regressed parameters and mean square errors of regression as a function of S_{occlu}.

C1, C2. K_{Lnr} for 5-month data and 10-month data.

C3, C4. K_{Fr} for 5-month data and 10-month data.

C5, C6. n for 5-month data and 10-month data.

C7, C8. Mean square error for 5-month data and 10-month data.

D. Confidence intervals of regression and residual plots for the "Occlusion-Lnr-Fr" model.

C1. Regressed $\underline{K_{Lnr}}$ as a function of assumed S_{occlu} at different temperatures for <u>5-month</u> data

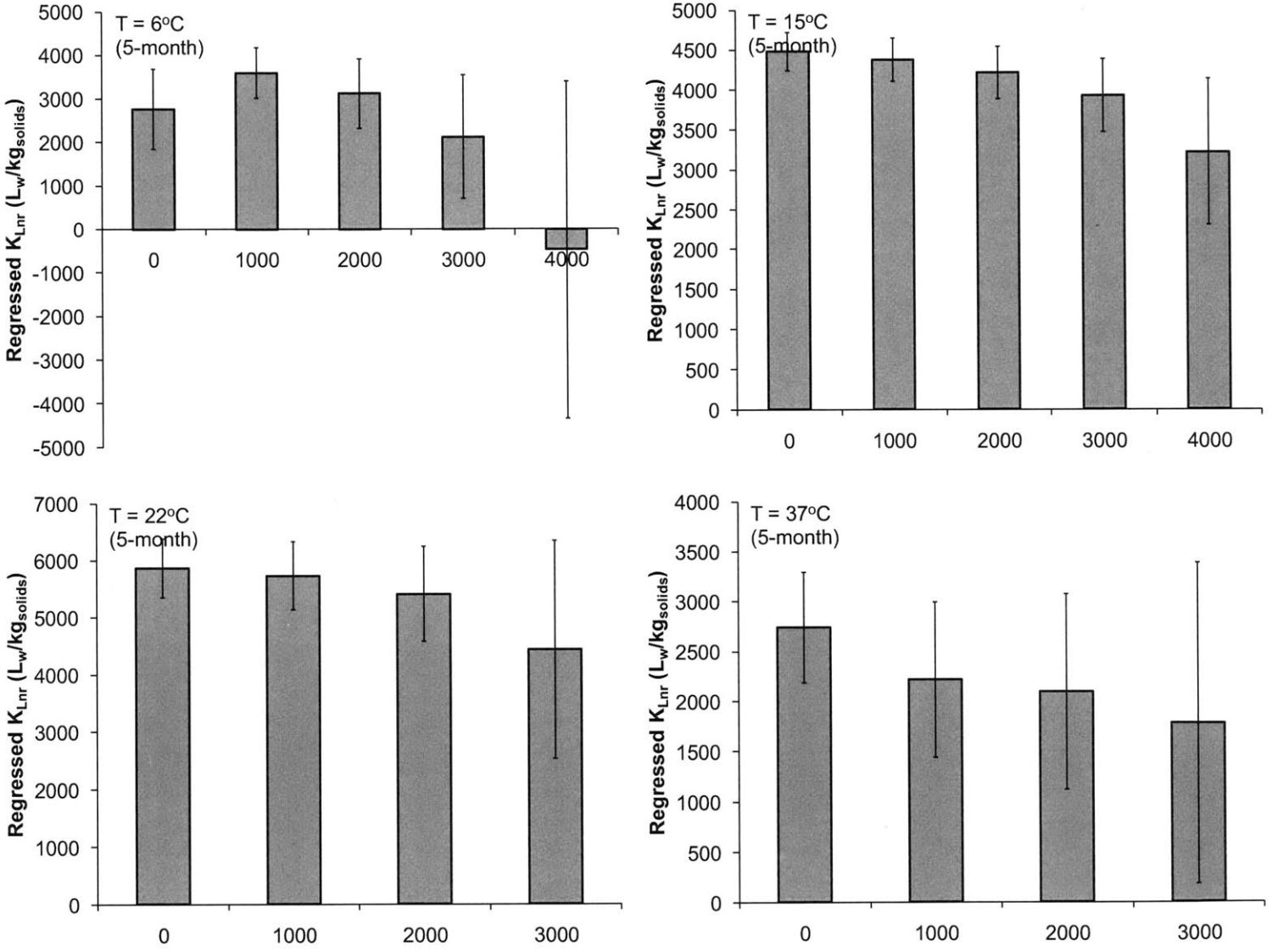

C2. Regressed $\underline{K_{Lnr}}$ as a function of assumed S_{occlu} at different temperatures for <u>10-month</u> data

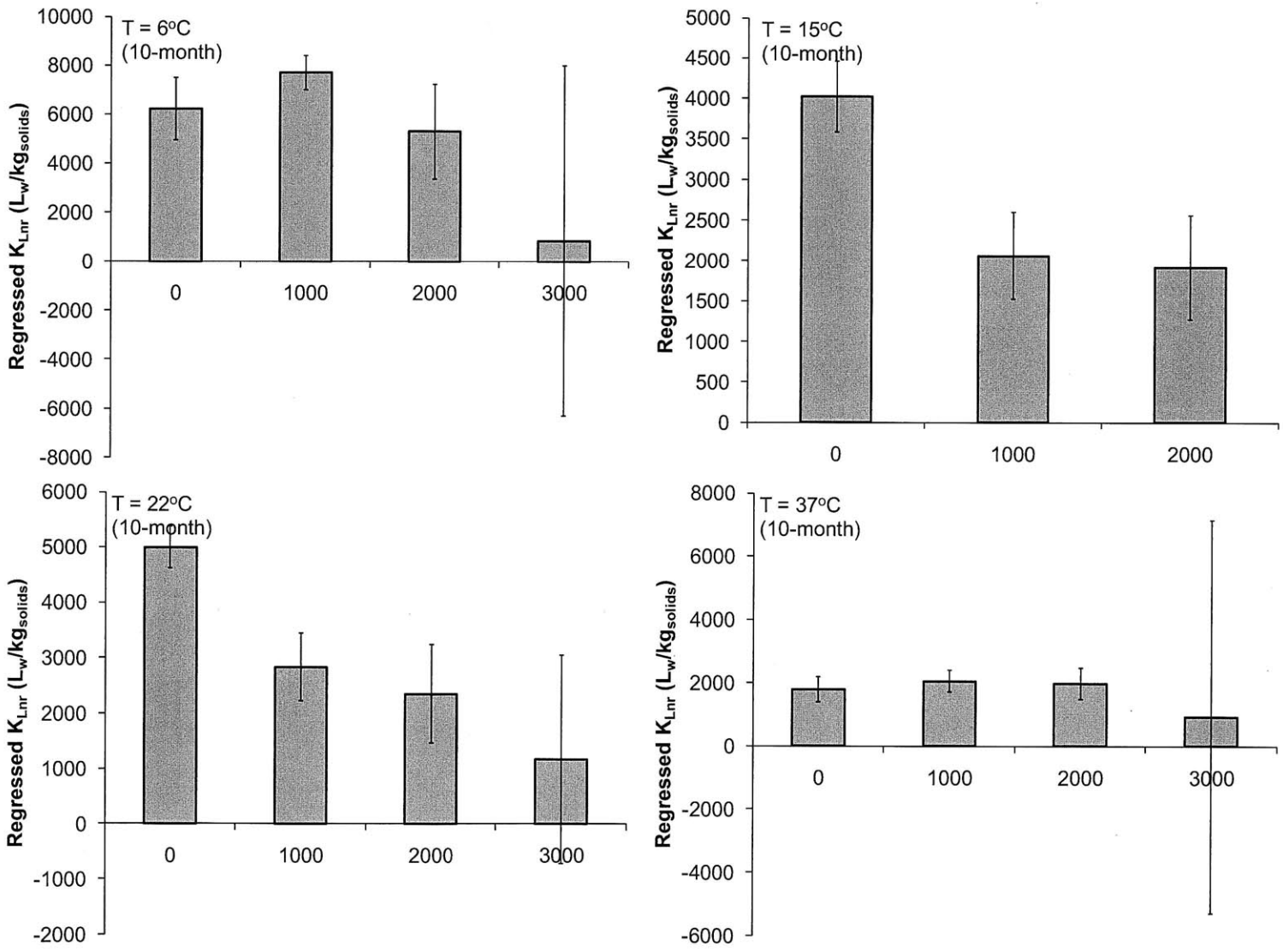

C3. Regressed $\underline{K_{Fr}}$ as a function of assumed S_{occlu} at different temperatures for <u>5-month</u> data

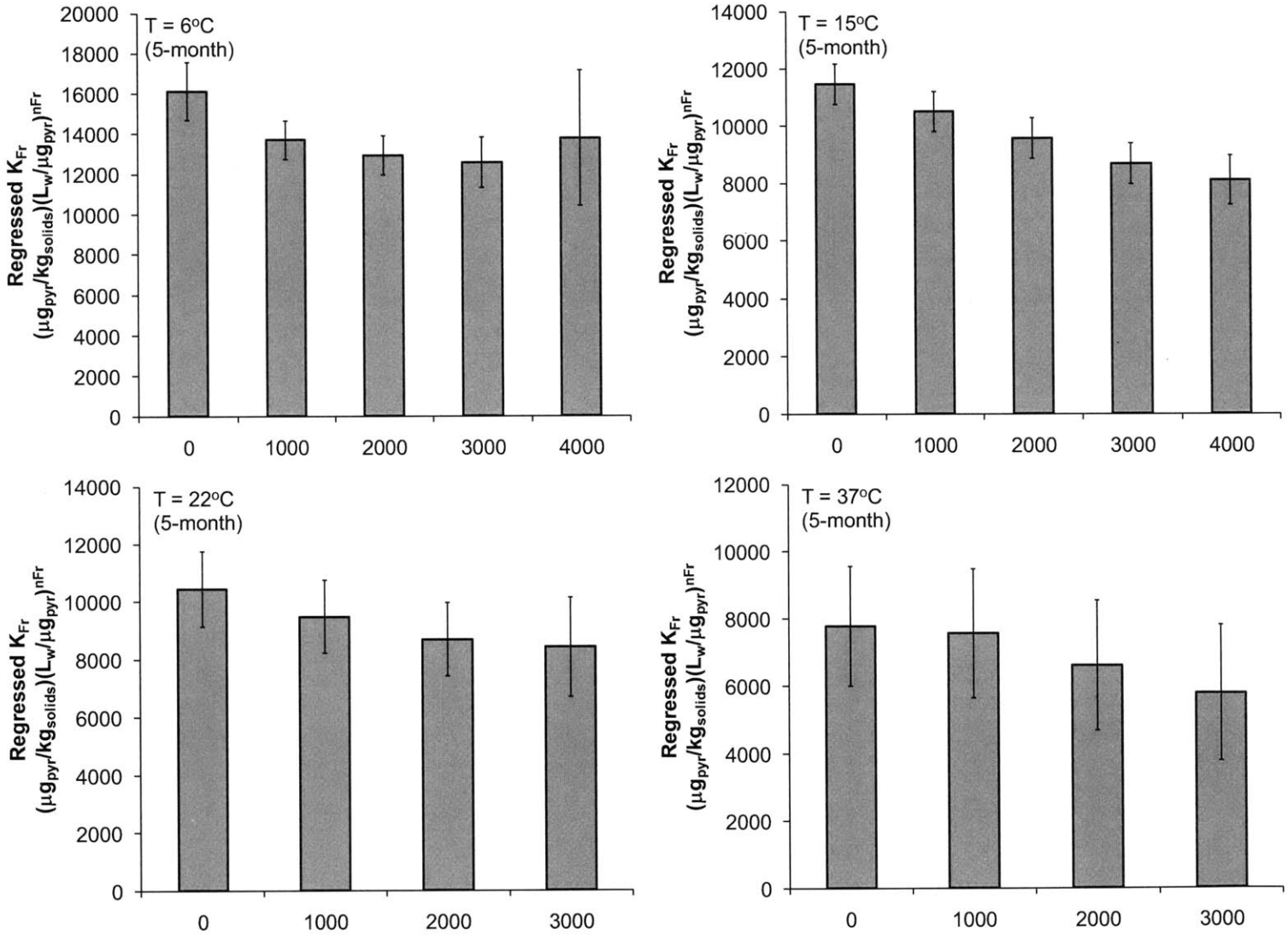

C4. Regressed $\underline{K_{Fr}}$ as a function of assumed S_{occlu} at different temperatures for <u>10-month</u> data

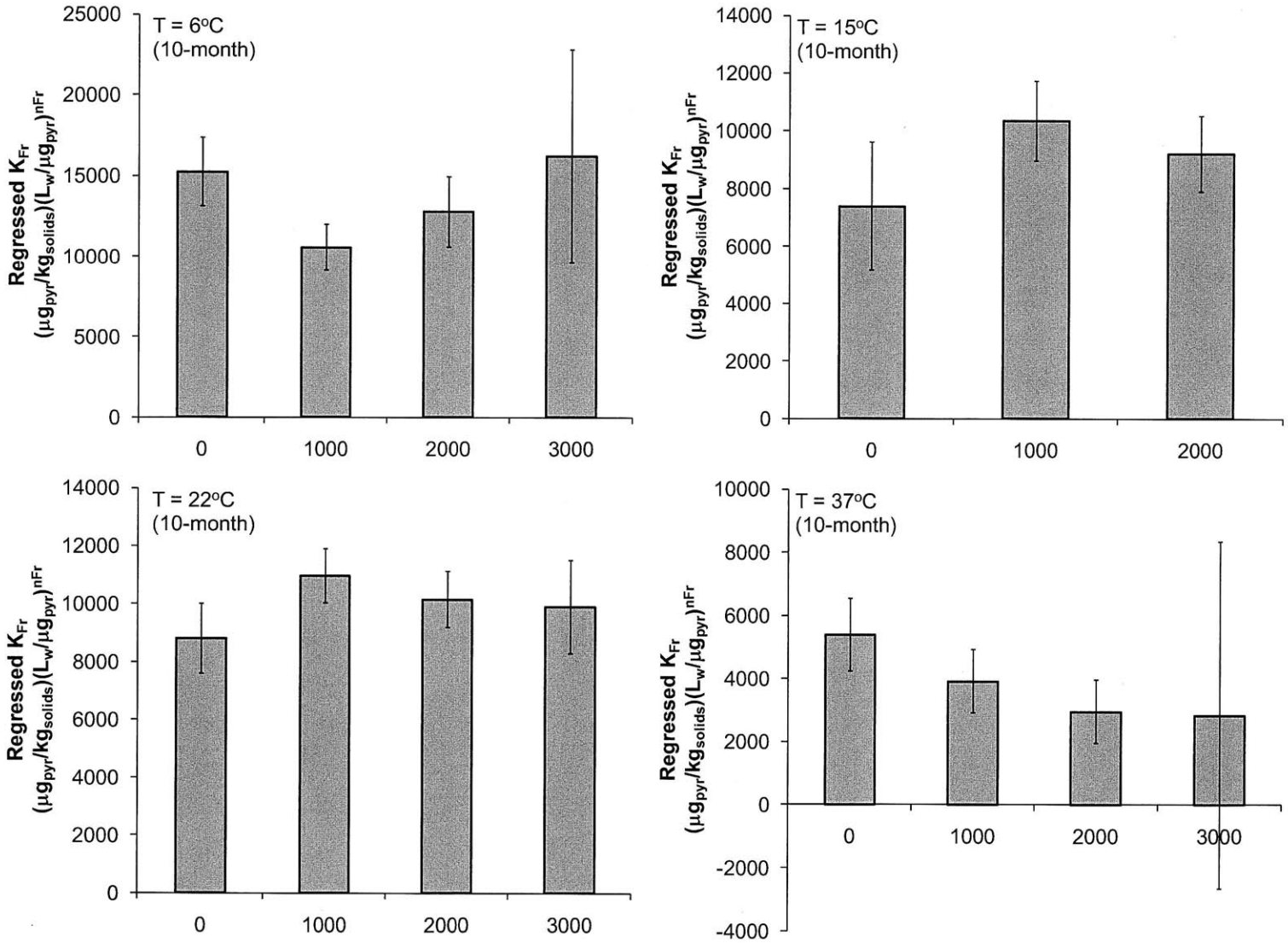

C5. Regressed n_{Fr} as a function of assumed S_{occlu} at different temperatures for 5-month data

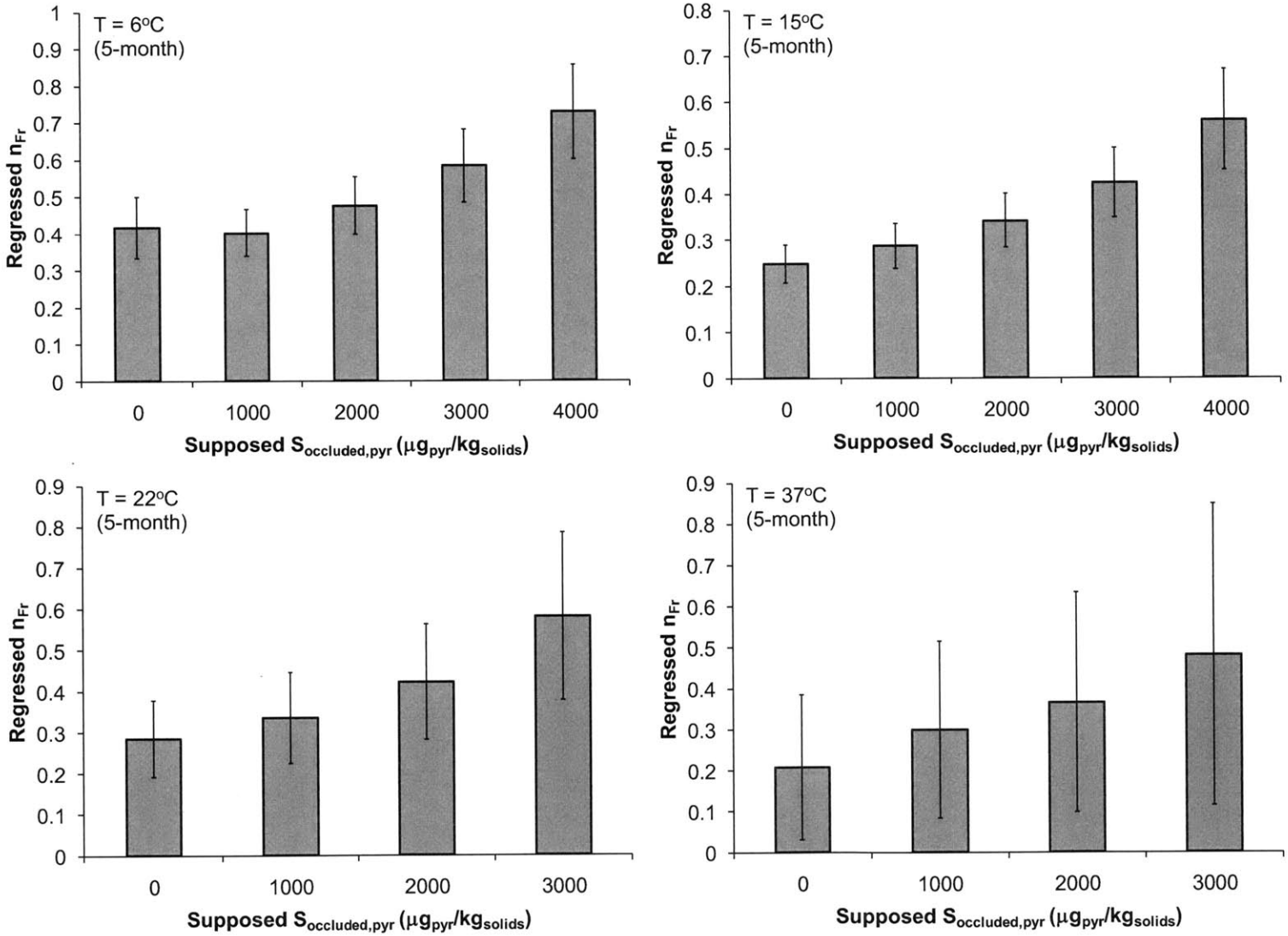

C6. Regressed $\underline{n_{Fr}}$ as a function of assumed S_{occlu} at different temperatures for <u>10-month</u> data

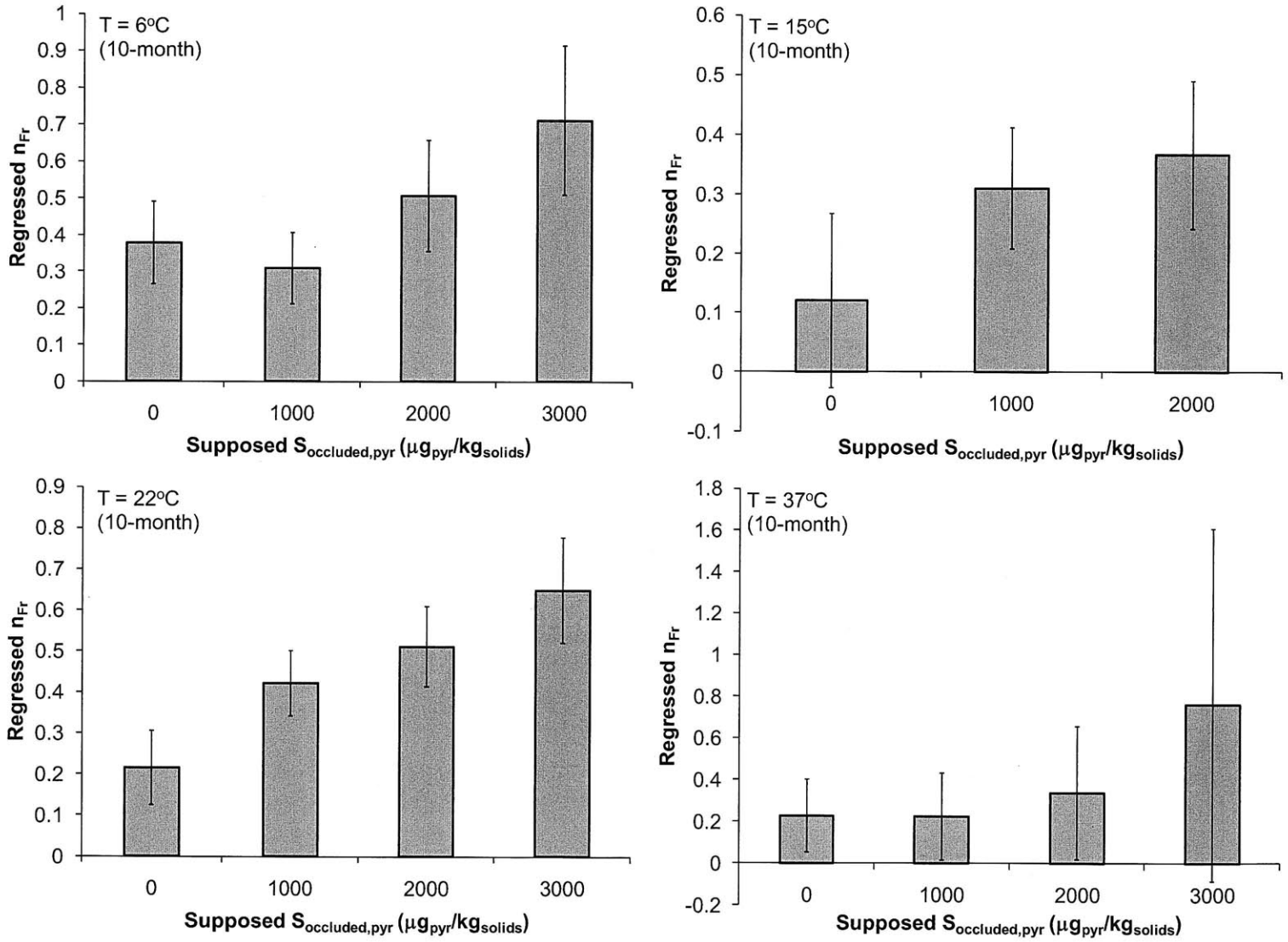

C7. Mean Square Errors of regression as a function of assumed S_{occlu} at different temperatures for 5-month data

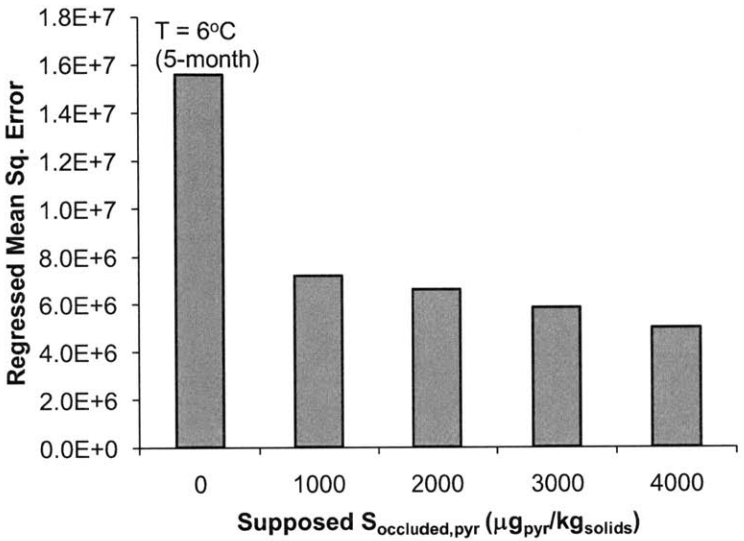

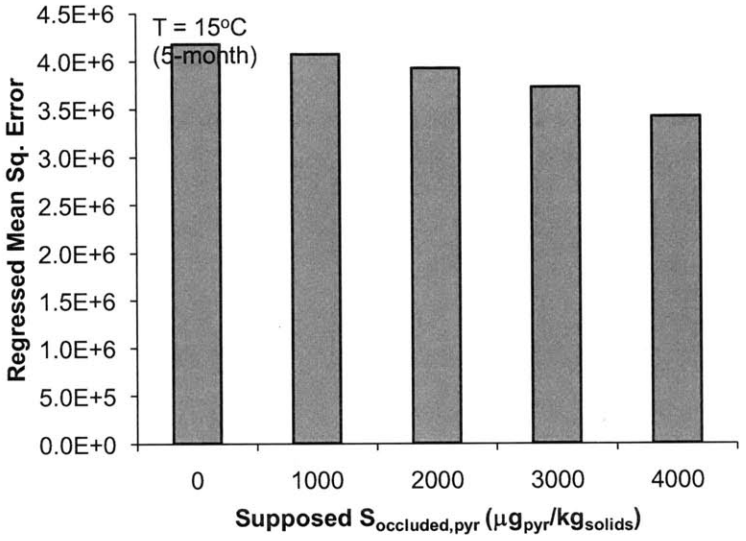

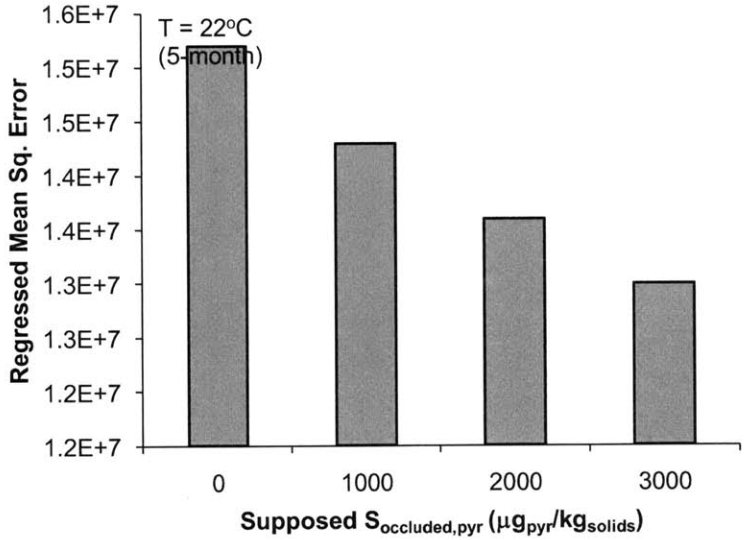

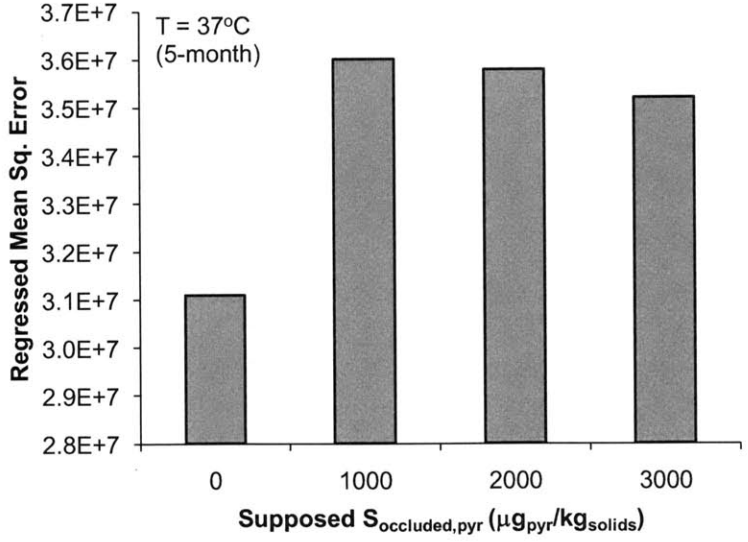

C8. Mean Square Errors of regression as a function of assumed S_{occlu} at different temperatures for 10-month data

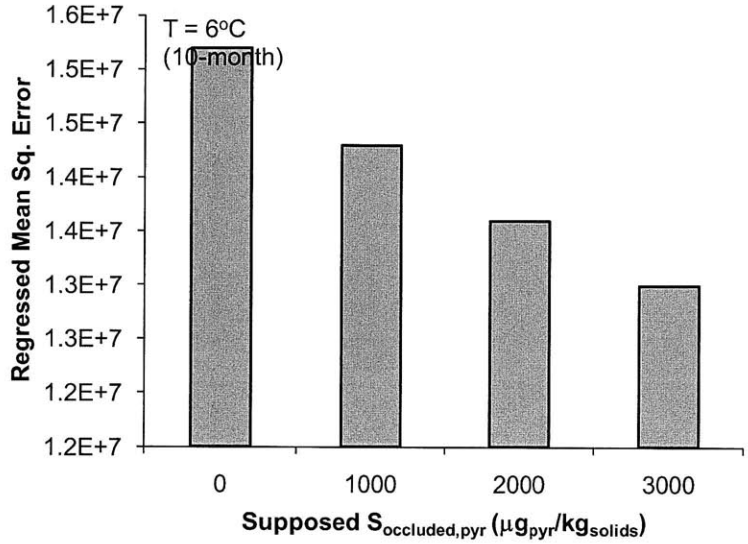

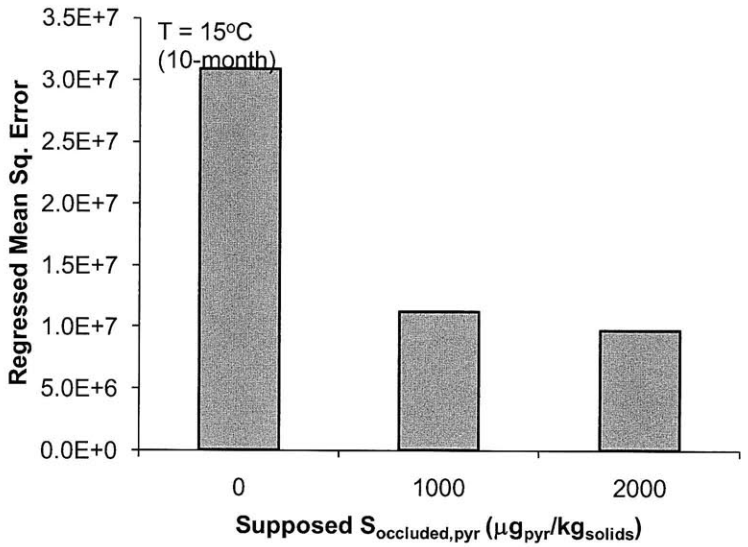

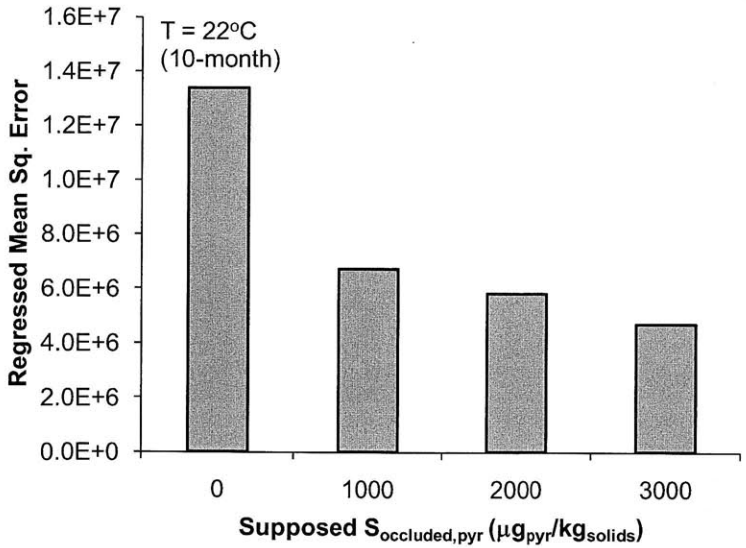

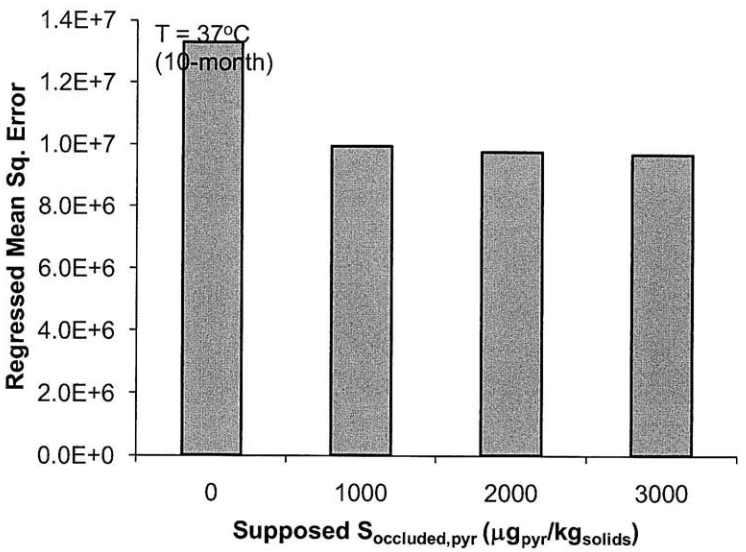

D. Occlusion-Lnr-Fr model (4 Param.) at 22°C

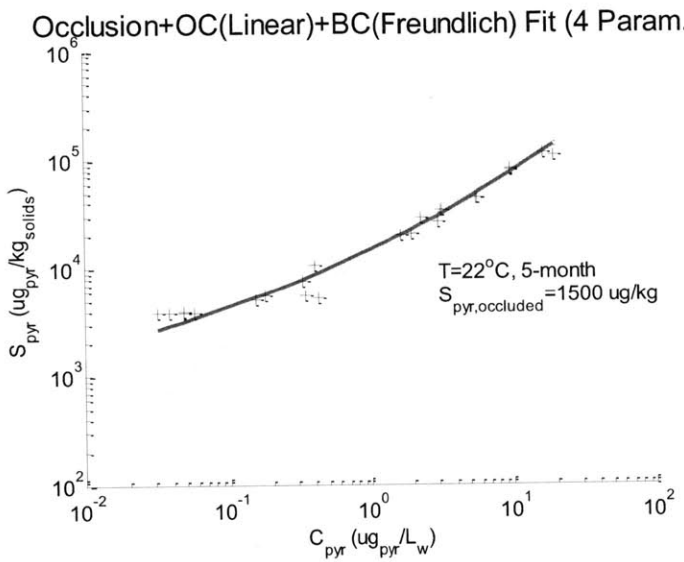

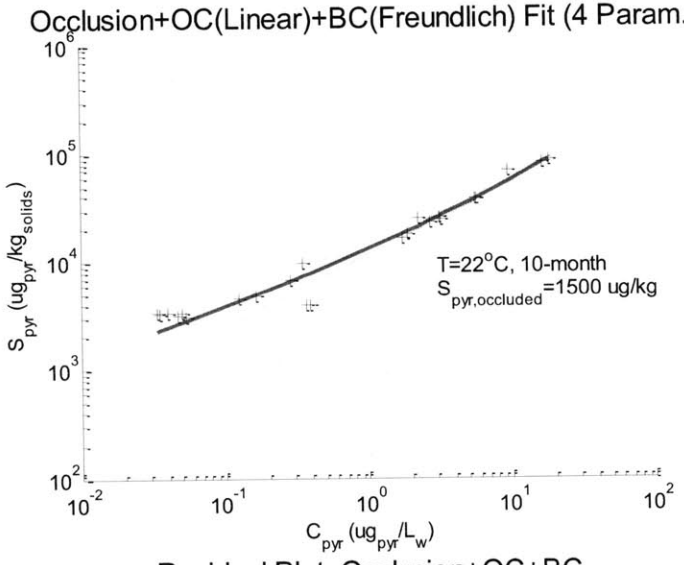

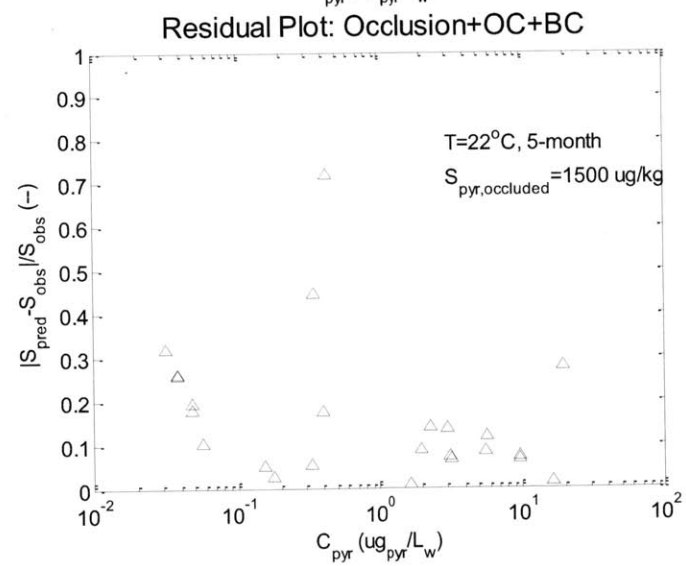

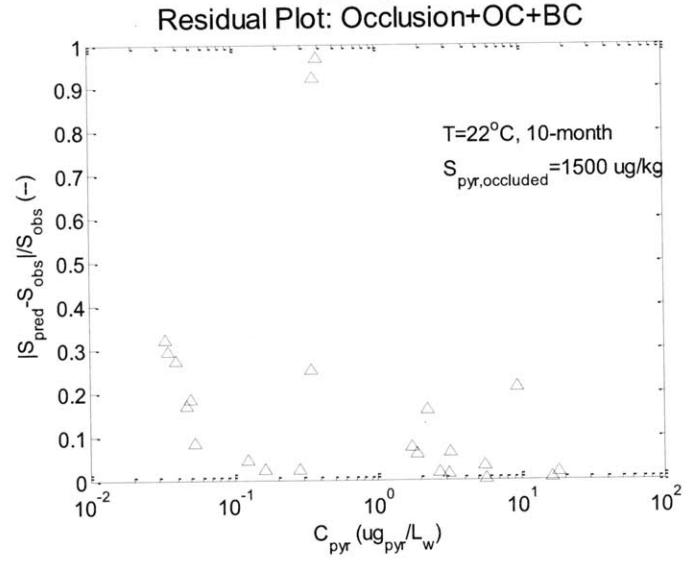

Appendix 5 - 7. Parameter Ambiguity Issue in Non-linear Regression (Matlab).

For 22°C (10-month) data*:

	Two Freundlich $S = K_{Fr,1}C^{n1} + K_{Fr,2}C^{n2}$				**Langmuir-Freundlich** $S = K_{Fr}C^{n} + \frac{S_{Max}C}{C_{½} + C}$			
		Initial Guess	Fitted	σ_{Fitted}		Initial Guess	Fitted	σ_{Fitted}
Trial 1	$K_{Fr,1}$	16000	10900	5606	S_{Max}	100000	183000	37000
	$n_{Fr,1}$	0.65	0.7187	0.1467	$C_{1/2}$	30	20.7	9.2
	$K_{Fr,2}$	13000	2695	6841	K_{Fr}	26000	4245	3751
	$n_{Fr,2}$	0.15	-0.1023	0.7887	n_{Fr}	0.8	-0.0253	0.3373
Trial 2	$K_{Fr,1}$	3000	11738	4111	S_{Max}	200000	223000	78000
	$n_{Fr,1}$	0.5	0.698	0.1091	$C_{1/2}$	30	33.5	23.3
	$K_{Fr,2}$	10000	1714	5072	K_{Fr}	5000	6910	3933
	$n_{Fr,2}$	0.5	-0.2317	0.927	n_{Fr}	0.8	0.1343	0.242
Trial 3	$K_{Fr,1}$	1500	11690	4210	S_{Max}	80000	186000	43956
	$n_{Fr,1}$	1.2	0.6992	0.1115	$C_{1/2}$	50	20.8	10.6
	$K_{Fr,2}$	1000	1775	5194	K_{Fr}	50000	4089	4340
	$n_{Fr,2}$	0.5	-0.2215	0.9165	n_{Fr}	0.2	-0.0379	0.4031

*: Units: K_{Fr} in $(L_w/\mu g_{pyr})^{nFr}(\mu g_{pyr}/kg_{solids})$, n_{Fr} (dimensionless), S_{Max} in $(\mu g_{pyr}/kg_{solids})$, $C_{½}$ in $(\mu g_{pyr}/L_w)$.

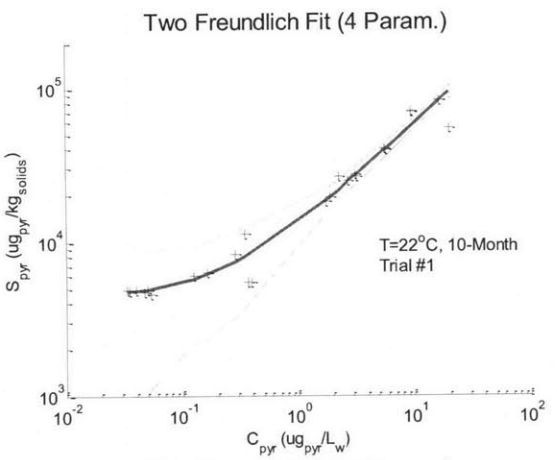
Two Freundlich Fit (4 Param.)
T=22°C, 10-Month
Trial #1
S_{pyr} (ug_{pyr}/kg_{solids})
C_{pyr} (ug_{pyr}/L_w)

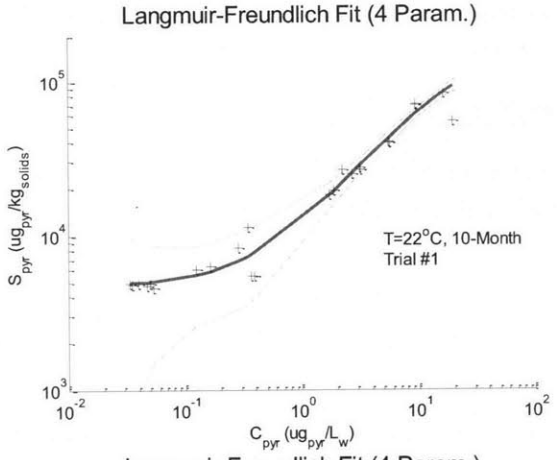
Langmuir-Freundlich Fit (4 Param.)
T=22°C, 10-Month
Trial #1
S_{pyr} (ug_{pyr}/kg_{solids})
C_{pyr} (ug_{pyr}/L_w)

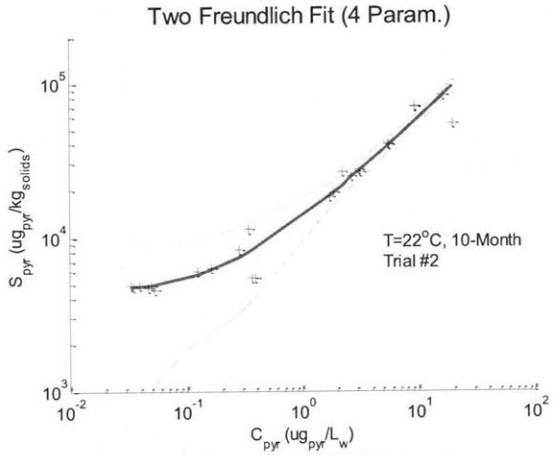
Two Freundlich Fit (4 Param.)
T=22°C, 10-Month
Trial #2
S_{pyr} (ug_{pyr}/kg_{solids})
C_{pyr} (ug_{pyr}/L_w)

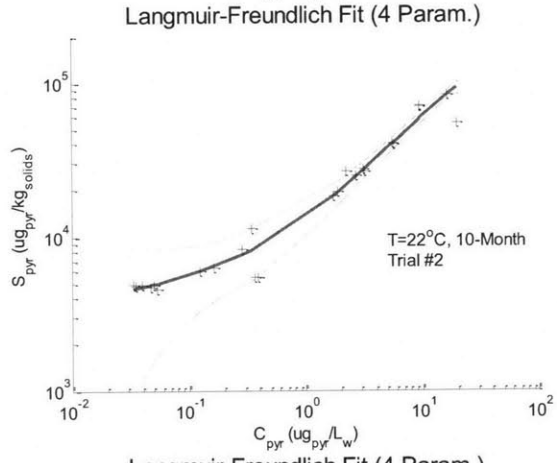
Langmuir-Freundlich Fit (4 Param.)
T=22°C, 10-Month
Trial #2
S_{pyr} (ug_{pyr}/kg_{solids})
C_{pyr} (ug_{pyr}/L_w)

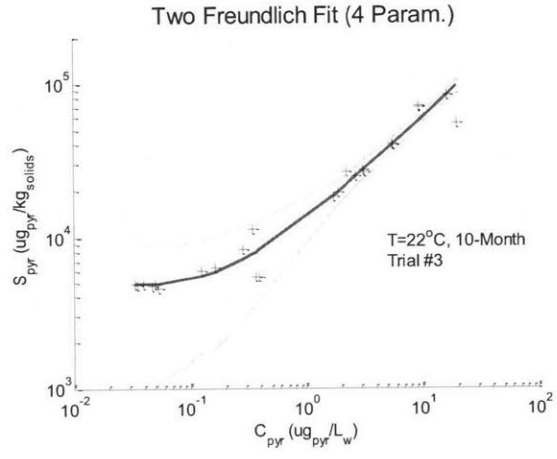
Two Freundlich Fit (4 Param.)
T=22°C, 10-Month
Trial #3
S_{pyr} (ug_{pyr}/kg_{solids})
C_{pyr} (ug_{pyr}/L_w)

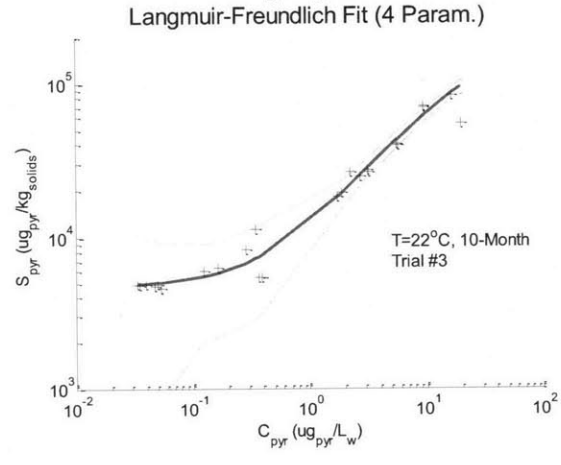
Langmuir-Freundlich Fit (4 Param.)
T=22°C, 10-Month
Trial #3
S_{pyr} (ug_{pyr}/kg_{solids})
C_{pyr} (ug_{pyr}/L_w)

Appendix 5 - 8. Regression (Manual) of Sorption Data by the Two-Freundlich and .the Langmuir-Freundlich forms.

Method of Regression

Regression of sorption data by the Two-Freundlich and the Langmuir-Freundlich forms (equations below) was conducted in Excel.

$$\textbf{Two} - \textbf{Fr}: \quad S = K_{Fr,H} C^{n_H} + K_{Fr,L} C^{n_L}$$

$$\textbf{Lgmr} - \textbf{Fr}: \quad S = K_{Fr} C^{n} + \frac{S_{Max}\, C}{C_{½} + C}$$

The regression procedure was as follows. The sorption data were divided into two groups, corresponding to the high-concentration range (or 'amended' domain; C_{pyr} ~> 1 $\mu g_{pyr}/L_w$) and the low-concentration range (or 'native' domain; C_{pyr} ~< 0.1 $\mu g_{pyr}/L_w$). The parameters for 'amended' domain, which was always described by the Freundlich form, were initially guessed. With an initial Freundlich term, the sorption contributions of the 'amended' domain were from the 'native' domain (Eqn. A-1):

$$S = S_{'native'} + S_{'amended'} = S_{'native'} + K_{Fr} C^{n}$$

$$S_{'nati\ ve'} = S - S_{'amended'} = S - (K_{Fr} C^{n})_{guess}$$

(Eqn. A-1)

The resulting $S_{'native'}$'s were then regressed against C by either the Langmuir (Eqn. A-2) or the Freundlich (Eqn. A-3) form:

$$\textbf{Langmuir 'native' domain}: \quad S_{'native'} = \frac{S_{Max}\, C}{C_{½} + C}$$

$$\frac{1}{S_{'native'}} = \frac{C_{½}}{S_{Max}}\left(\frac{1}{C}\right) + \frac{1}{S_{Max}}$$

(Eqn. A-2)

$$\textbf{Freundlich 'native' domain}: \quad S_{'native'} = K_{Fr,H} C^{n_H}$$

$$\ln S_{'native'} = n_H \ln C + \ln K_{Fr,H}$$

(Eqn. A-3)

In the linear forms (Eqn. A-2 & A-3), the 'native' domain data could be regressed with standard built-in regression function. The regressed parameters for the 'native' domain were then used to estimate the pyrene sorbed to the 'amended' domain in manner similar to Eqn. A-1:

$$S_{'amended'} = S - S_{'native',regressed}$$

(Eqn. A-4)

The $S_{'amended'}$'s were then regressed by the Freundlich form (Eqn. A-5):

$$\ln S_{'amended'} = n_L \ln C + \ln K_{Fr,L}$$

(Eqn. A-5)

Now, the regressed n and K_{Fr} could be compared with the initially guessed n and K_{Fr}. The guess parameters were updated accordingly. The procedure was repeated until (i) the guessed and the regressed n and K_{Fr} converged, and (ii) data in the two domains exhibited a good linear shape in either the lnS-lnC or the 1/S-1/C space.

Results of Regression

For each set of sorption data (i.e. at 6, 15, 22, or 37°C and at 5- or 10-month), three trial regressions were performed. The initial division of the data into the 'native' and the 'amended' domains was slightly different for each of these trial regressions. In some cases, data points were at the extremes of the domains may be removed to test the sensitivity of the regression.

The regression results are tabulated in the following tables. The domain-specific curves (i.e. linear lnS-lnC and linear 1/S-1/C plots) and the regression residual plots were also shown.

Both models fit the sorption data quite well (see modeled isotherm vs data point in Appendix 5-9).

6°C (5-month) Fitted by Two Freundlich Form*

Fit #1				Fit #2				Fit #3			
'Native' Domain (high-affinity, low C_{pyr} range)		*Amended Domain* (high-affinity, low C_{pyr} range)		*'Native' Domain* (high-affinity, low C_{pyr} range)		*Amended Domain* (high-affinity, low C_{pyr} range)		*'Native' Domain* (high-affinity, low C_{pyr} range)		*Amended Domain* (high-affinity, low C_{pyr} range)	
$log_{10}C$	$log_{10}S_{Hi}$	$log_{10}C$	$log_{10}S_{Hi}$	$log_{10}C$	$log_{10}S_{Hi}$	$log_{10}C$	$log_{10}S_{Hi}$	$log_{10}C$	$log_{10}S_{Hi}$	$log_{10}C$	$log_{10}S_{Hi}$
0.54	4.12	0.54	4.43	0.54	4.13	0.54	4.43	0.54	4.15	0.54	4.41
0.37	4.09	0.37	4.28	0.37	4.10	0.37	4.29	0.37	4.11	0.37	4.26
0.21	4.01	0.21	4.11	0.21	4.03	0.21	4.12	0.21	4.03	0.21	4.09
		1.26	4.98			1.26	4.98			1.26	4.97
1.01	3.95	1.01	4.79	1.01	3.87	1.01	4.79	1.01	4.07	1.01	4.78
0.66	4.00	0.66	4.48	0.66	4.00	0.66	4.49	0.66	4.05	0.66	4.47
-1.27	3.66			-1.27	3.67			-1.27	3.66		
-1.57	3.73			-1.57	3.73			-1.57	3.73		
-1.73	3.73			-1.73	3.73			-1.73	3.73		
-0.56	3.80	-0.56	3.12	-0.56	3.81	-0.56	3.11	-0.56	3.80	-0.56	3.03
-0.54	3.71			-0.54	3.73			-0.54	3.72		
-1.07	3.77	-1.07	2.76	-1.07	3.78	-1.07	2.67	-1.07	3.77	-1.07	2.74
-1.44	3.75			-1.44	3.75			-1.44	3.75		
-1.64	3.73			-1.64	3.74			-1.64	3.73		
-1.72	3.73			-1.72	3.73			-1.72	3.73		
-0.42	3.94	-0.42	3.62	-0.42	3.95	-0.42	3.62	-0.42	3.94	-0.42	3.59
-0.59	3.87	-0.59	3.38	-0.59	3.88	-0.59	3.38	-0.59	3.87	-0.59	3.34
-1.07	3.79	-1.07	2.93	-1.07	3.80	-1.07	2.87	-1.07	3.79	-1.07	2.92
0.55	3.95	0.55	4.36	0.55	3.96	0.55	4.37	0.55	3.99	0.55	4.34
0.42	4.02	0.42	4.28	0.42	4.03	0.42	4.29	0.42	4.04	0.42	4.26
0.17	4.01	0.17	4.08	0.17	4.02	0.17	4.08	0.17	4.02	0.17	4.05
		1.21	4.85			1.21	4.86			1.21	4.84
1.00	4.14	1.00	4.82	1.00	4.09	1.00	4.83	1.00	4.22	1.00	4.81
0.69	4.13	0.69	4.55	0.69	4.13	0.69	4.55	0.69	4.17	0.69	4.54
Slp=n_{Fr}	***0.1475***		***0.9245***		***0.1383***		***0.9502***		***0.1728***		***0.9382***
	(0.0162)		*(0.0316)*		*(0.0183)*		*(0.0346)*		*(0.0151)*		*(0.0347)*
I=logK_{Fr}	***3.9457***		***3.8711***		***3.9434***		***3.8561***		***3.9748***		***3.8425***
	(0.0162)		*(0.0243)*		*(0.0184)*		*(0.0267)*		*(0.0152)*		*(0.0268)*
R^2	***0.8054***		***0.9828***		***0.7404***		***0.9805***		***0.8672***		***0.9798***
n_{Fr} guessed			***0.92***	***n_{Fr} guessed***			***0.95***	***n_{Fr} guessed***			***0.91***
logK_{Fr} guessed			***3.89***	***logK_{Fr} guessed***			***3.87***	***logK_{Fr} guessed***			***3.88***

*** C ($\mu g_{pyr}/L_w$), S ($\mu g_{pyr}/kg_{solids}$), nFr (dimensionless), K_{Fr} $(\mu g_{pyr}/kg_{solids})(L_w/\mu g_{pyr})^{nFr}$.**

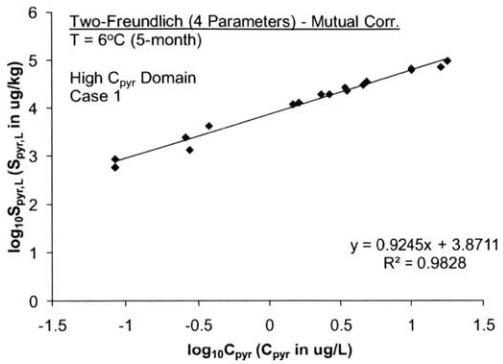
Two-Freundlich (4 Parameters) - Mutual Corr.
T = 6°C (5-month)
High C_{pyr} Domain
Case 1
y = 0.9245x + 3.8711
R² = 0.9828
$\log_{10}S_{pyr,L}$ ($S_{pyr,L}$ in ug/kg)
$\log_{10}C_{pyr}$ (C_{pyr} in ug/L)

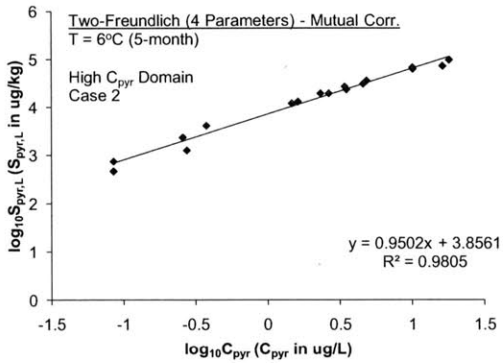
Two-Freundlich (4 Parameters) - Mutual Corr.
T = 6°C (5-month)
High C_{pyr} Domain
Case 2
y = 0.9502x + 3.8561
R² = 0.9805
$\log_{10}S_{pyr,L}$ ($S_{pyr,L}$ in ug/kg)
$\log_{10}C_{pyr}$ (C_{pyr} in ug/L)

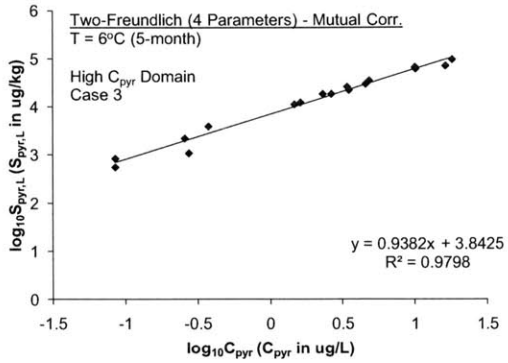
Two-Freundlich (4 Parameters) - Mutual Corr.
T = 6°C (5-month)
High C_{pyr} Domain
Case 3
y = 0.9382x + 3.8425
R² = 0.9798
$\log_{10}S_{pyr,L}$ ($S_{pyr,L}$ in ug/kg)
$\log_{10}C_{pyr}$ (C_{pyr} in ug/L)

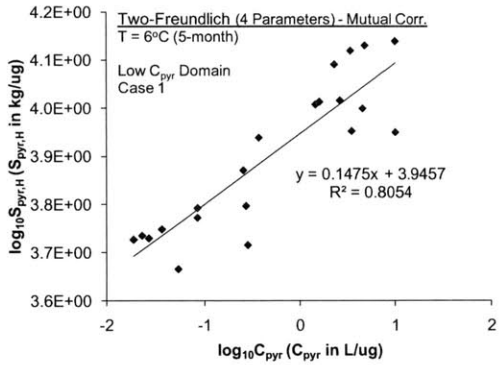
Two-Freundlich (4 Parameters) - Mutual Corr.
T = 6°C (5-month)
Low C_{pyr} Domain
Case 1
y = 0.1475x + 3.9457
R² = 0.8054
$\log_{10}S_{pyr,H}$ ($S_{pyr,H}$ in kg/ug)
$\log_{10}C_{pyr}$ (C_{pyr} in L/ug)

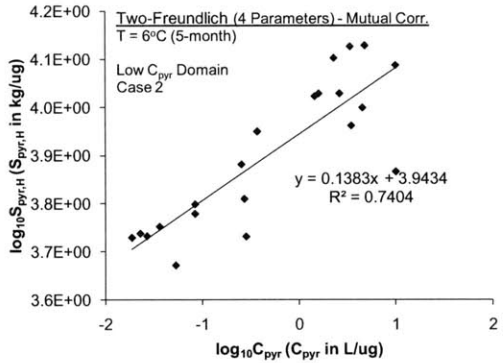
Two-Freundlich (4 Parameters) - Mutual Corr.
T = 6°C (5-month)
Low C_{pyr} Domain
Case 2
y = 0.1383x + 3.9434
R² = 0.7404
$\log_{10}S_{pyr,H}$ ($S_{pyr,H}$ in kg/ug)
$\log_{10}C_{pyr}$ (C_{pyr} in L/ug)

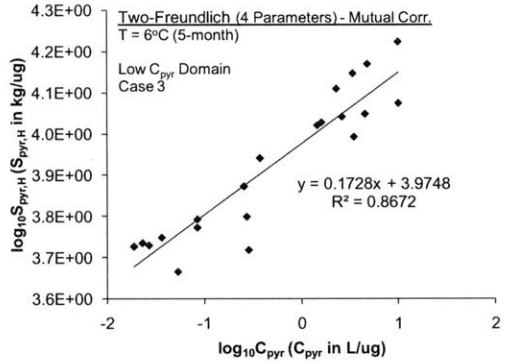
Two-Freundlich (4 Parameters) - Mutual Corr.
T = 6°C (5-month)
Low C_{pyr} Domain
Case 3
y = 0.1728x + 3.9748
R² = 0.8672
$\log_{10}S_{pyr,H}$ ($S_{pyr,H}$ in kg/ug)
$\log_{10}C_{pyr}$ (C_{pyr} in L/ug)

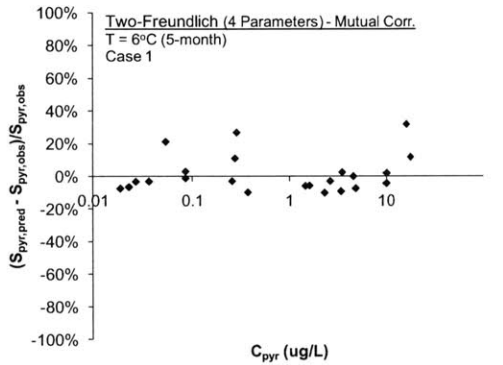
Two-Freundlich (4 Parameters) - Mutual Corr.
T = 6°C (5-month)
Case 1
$(S_{pyr,pred} - S_{pyr,obs})/S_{pyr,obs}$
C_{pyr} (ug/L)

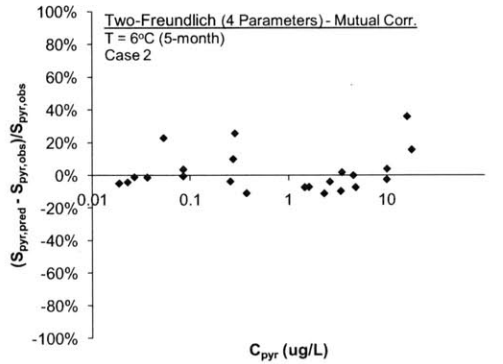
Two-Freundlich (4 Parameters) - Mutual Corr.
T = 6°C (5-month)
Case 2
$(S_{pyr,pred} - S_{pyr,obs})/S_{pyr,obs}$
C_{pyr} (ug/L)

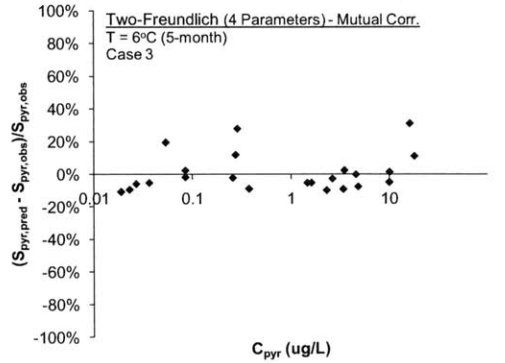
Two-Freundlich (4 Parameters) - Mutual Corr.
T = 6°C (5-month)
Case 3
$(S_{pyr,pred} - S_{pyr,obs})/S_{pyr,obs}$
C_{pyr} (ug/L)

6°C (10-month) Fitted by Two Freundlich Form*

Fit #1				Fit #2				Fit #3			
'Native' Domain (high-affinity, low C_{pyr} range)		*Amended Domain* (high-affinity, low C_{pyr} range)		*'Native' Domain* (high-affinity, low C_{pyr} range)		*Amended Domain* (high-affinity, low C_{pyr} range)		*'Native' Domain* (high-affinity, low C_{pyr} range)		*Amended Domain* (high-affinity, low C_{pyr} range)	
$log_{10}C$	$log_{10}S_{Hi}$	$log_{10}C$	$log_{10}S_{Hi}$	$log_{10}C$	$log_{10}S_{Hi}$	$log_{10}C$	$log_{10}S_{Hi}$	$log_{10}C$	$log_{10}S_{Hi}$	$log_{10}C$	$log_{10}S_{Hi}$
0.38	4.36	0.38	4.58			0.38	4.56			0.38	4.58
0.28	3.93	0.28	4.27	0.28	3.91	0.28	4.24			0.28	4.27
0.05	4.02	0.05	4.12	0.05	4.02	0.05	4.08			0.05	4.12
		1.14	5.09			1.14	5.08			1.14	5.09
		0.86	4.81			0.86	4.80			0.86	4.81
0.53	3.51	0.53	4.46			0.53	4.43			0.53	4.46
-1.37	3.65			-1.37	3.65			-1.37	3.64		
-1.75	3.70			-1.75	3.70			-1.75	3.70		
-1.83	3.69			-1.83	3.69			-1.83	3.68		
-1.03	3.71			-1.03	3.72			-1.03	3.70		
-1.57	3.73			-1.57	3.73			-1.57	3.73		
-1.76	3.70			-1.76	3.70			-1.76	3.70		
-1.89	3.69			-1.89	3.69			-1.89	3.69		
-0.44	3.78	-0.44	3.33	-0.44	3.79	-0.44	3.20	-0.44	3.77	-0.44	3.36
-0.63	3.81	-0.63	3.21	-0.63	3.81	-0.63	3.10	-0.63	3.80	-0.63	3.26
-1.18	3.76			-1.18	3.76	-1.18	2.63	-1.18	3.75	-1.18	2.81
0.38	4.33	0.38	4.56			0.38	4.54			0.38	4.56
0.24	4.19	0.24	4.38	0.24	4.18	0.24	4.36			0.24	4.39
-0.03	4.07	-0.03	4.10	-0.03	4.07	-0.03	4.06	-0.03	4.06	-0.03	4.10
		1.07	4.96			1.07	4.95			1.07	4.96
		0.88	4.83			0.88	4.81			0.88	4.83
0.57	3.63	0.57	4.52			0.57	4.50			0.57	4.52
Slp=n_{Fr}	***0.1386***		***1.0224***		***0.1748***		***1.0876***		***0.1440***		***1.0033***
	(0.0586)		*(0.0720)*		*(0.0287)*		*(0.0620)*		*(0.0365)*		*(0.0514)*
I=logK_{Fr}	***3.9318***		***3.9868***		***3.9773***		***3.9259***		***3.9240***		***4.0010***
	(0.0620)		*(0.0454)*		*(0.0349)*		*(0.0422)*		*(0.0497)*		*(0.0350)*
R^2	***0.2714***		***0.9439***		***0.7551***		***0.9595***		***0.6341***		***0.9670***
n_{Fr} guessed			***1.04***	***n_{Fr} guessed***			***1.08***	***n_{Fr} guessed***			***1.00***
logK_{Fr} guessed			***4.00***	***logK_{Fr} guessed***			***4.00***	***logK_{Fr} guessed***			***4.00***

* C ($\mu g_{pyr}/L_w$), S ($\mu g_{pyr}/kg_{solids}$), nFr (dimensionless), K_{Fr} $(\mu g_{pyr}/kg_{solids})(L_w/\mu g_{pyr})^{nFr}$.

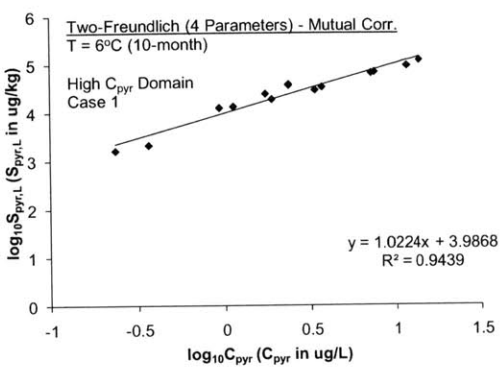
Two-Freundlich (4 Parameters) - Mutual Corr.
T = 6°C (10-month)
High C_{pyr} Domain
Case 1
y = 1.0224x + 3.9868
R² = 0.9439
$\log_{10}S_{pyr,L}$ ($S_{pyr,L}$ in ug/kg)
$\log_{10}C_{pyr}$ (C_{pyr} in ug/L)

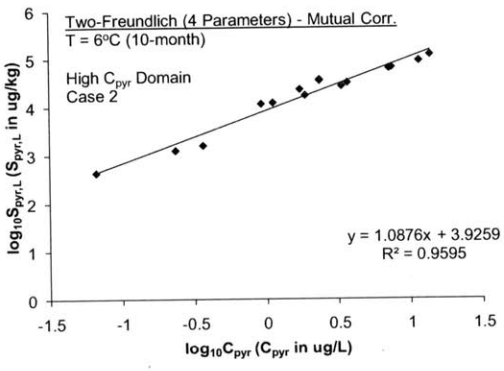
Two-Freundlich (4 Parameters) - Mutual Corr.
T = 6°C (10-month)
High C_{pyr} Domain
Case 2
y = 1.0876x + 3.9259
R² = 0.9595
$\log_{10}S_{pyr,L}$ ($S_{pyr,L}$ in ug/kg)
$\log_{10}C_{pyr}$ (C_{pyr} in ug/L)

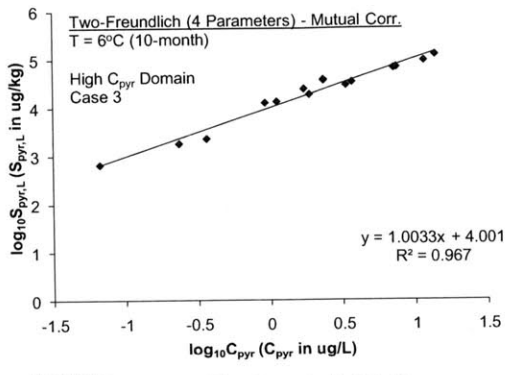
Two-Freundlich (4 Parameters) - Mutual Corr.
T = 6°C (10-month)
High C_{pyr} Domain
Case 3
y = 1.0033x + 4.001
R² = 0.967
$\log_{10}S_{pyr,L}$ ($S_{pyr,L}$ in ug/kg)
$\log_{10}C_{pyr}$ (C_{pyr} in ug/L)

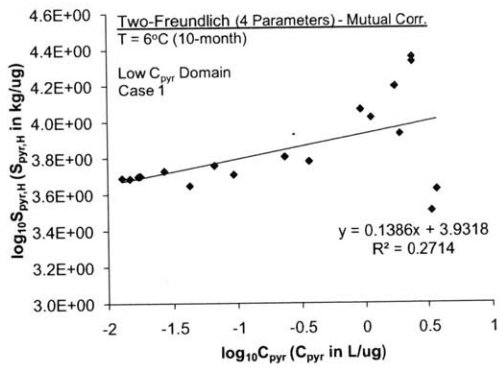
Two-Freundlich (4 Parameters) - Mutual Corr.
T = 6°C (10-month)
Low C_{pyr} Domain
Case 1
y = 0.1386x + 3.9318
R² = 0.2714
$\log_{10}S_{pyr,H}$ ($S_{pyr,H}$ in kg/ug)
$\log_{10}C_{pyr}$ (C_{pyr} in L/ug)

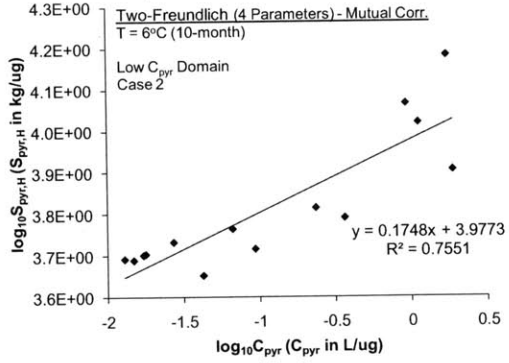
Two-Freundlich (4 Parameters) - Mutual Corr.
T = 6°C (10-month)
Low C_{pyr} Domain
Case 2
y = 0.1748x + 3.9773
R² = 0.7551
$\log_{10}S_{pyr,H}$ ($S_{pyr,H}$ in kg/ug)
$\log_{10}C_{pyr}$ (C_{pyr} in L/ug)

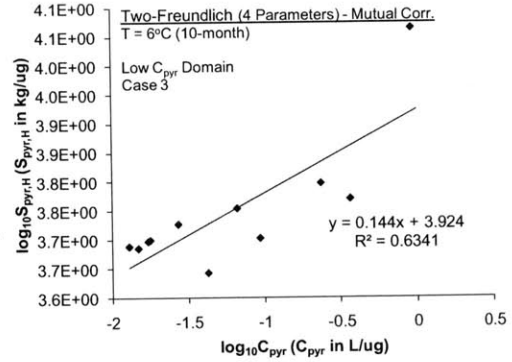
Two-Freundlich (4 Parameters) - Mutual Corr.
T = 6°C (10-month)
Low C_{pyr} Domain
Case 3
y = 0.144x + 3.924
R² = 0.6341
$\log_{10}S_{pyr,H}$ ($S_{pyr,H}$ in kg/ug)
$\log_{10}C_{pyr}$ (C_{pyr} in L/ug)

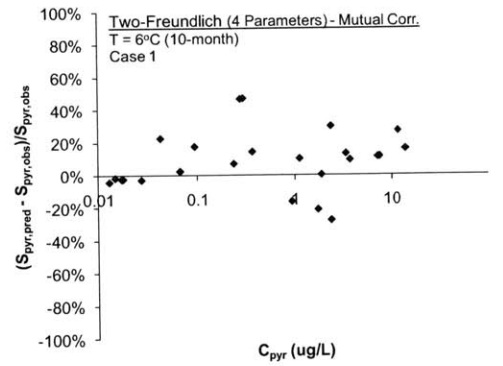
Two-Freundlich (4 Parameters) - Mutual Corr.
T = 6°C (10-month)
Case 1
$(S_{pyr,pred} - S_{pyr,obs})/S_{pyr,obs}$
C_{pyr} (ug/L)

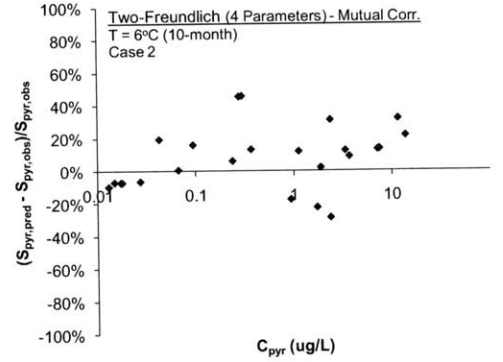
Two-Freundlich (4 Parameters) - Mutual Corr.
T = 6°C (10-month)
Case 2
$(S_{pyr,pred} - S_{pyr,obs})/S_{pyr,obs}$
C_{pyr} (ug/L)

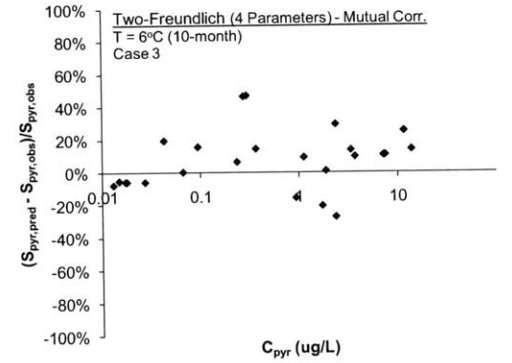
Two-Freundlich (4 Parameters) - Mutual Corr.
T = 6°C (10-month)
Case 3
$(S_{pyr,pred} - S_{pyr,obs})/S_{pyr,obs}$
C_{pyr} (ug/L)

15°C (5-month) Fitted by Two Freundlich Form*

Fit #1				Fit #2				Fit #3			
'Native' Domain (high-affinity, low C_{pyr} range)		*Amended Domain* (high-affinity, low C_{pyr} range)		*'Native' Domain* (high-affinity, low C_{pyr} range)		*Amended Domain* (high-affinity, low C_{pyr} range)		*'Native' Domain* (high-affinity, low C_{pyr} range)		*Amended Domain* (high-affinity, low C_{pyr} range)	
$log_{10}C$	$log_{10}S_{Hi}$	$log_{10}C$	$log_{10}S_{Hi}$	$log_{10}C$	$log_{10}S_{Hi}$	$log_{10}C$	$log_{10}S_{Hi}$	$log_{10}C$	$log_{10}S_{Hi}$	$log_{10}C$	$log_{10}S_{Hi}$
0.58	3.86	0.58	4.46	0.58	3.77	0.58	4.47	0.58	3.78	0.58	4.47
0.50	3.82	0.50	4.38	0.50	3.72	0.50	4.40	0.50	3.74	0.50	4.40
0.29	3.73	0.29	4.17	0.29	3.60	0.29	4.20	0.29	3.66	0.29	4.20
		1.27	5.05			1.27	5.06			1.27	5.06
		1.14	4.86			1.14	4.87			1.14	4.87
0.86	3.89	0.86	4.69	0.86	3.84	0.86	4.71			0.86	4.71
-1.30	3.68			-1.30	3.66			-1.30	3.68		
-1.45	3.72			-1.45	3.70			-1.45	3.71		
-1.50	3.70			-1.50	3.69			-1.50	3.70		
-0.52	3.72	-0.52	3.47	-0.52	3.67			-0.52	3.71	-0.52	3.53
-0.69	3.68	-0.69	3.21	-0.69	3.63			-0.69	3.67	-0.69	3.29
-1.43	3.70			-1.43	3.69			-1.43	3.70		
-1.55	3.70			-1.55	3.69			-1.55	3.70		
-1.60	3.70			-1.60	3.69			-1.60	3.70		
-0.43	3.73	-0.43	3.54	-0.43	3.67			-0.43	3.71	-0.43	3.60
-0.60	3.69	-0.60	3.33	-0.60	3.64			-0.60	3.68	-0.60	3.40
-1.26	3.80			-1.26	3.79			-1.26	3.80		
		0.54	4.38			0.54	4.41			0.54	4.40
0.35	3.75	0.35	4.23	0.35	3.62	0.35	4.26	0.35	3.67	0.35	4.26
0.19	3.80	0.19	4.12	0.19	3.70	0.19	4.15	0.19	3.76	0.19	4.15
		1.20	4.94			1.20	4.95			1.20	4.95
		1.00	4.76			1.00	4.77			1.00	4.77
		0.68	4.52			0.68	4.54			0.68	4.53
Slp=n_{Fr}	***0.0532***		***0.8926***		***0.0135***		***0.8098***		***0.0075***		***0.8564***
	(0.0131)		*(0.0148)*		*(0.0177)*		*(0.0193)*		*(0.0127)*		*(0.0126)*
I=logK_{Fr}	***3.7764***		***3.9021***		***3.7011***		***3.9850***		***3.7171***		***3.9460***
	(0.0134)		*(0.0111)*		*(0.0180)*		*(0.0155)*		*(0.0130)*		*(0.0094)*
R^2	***0.5216***		***0.9962***		***0.0373***		***0.9943***		***0.0245***		***0.9970***
n_{Fr} guessed			***0.85***	***n_{Fr} guessed***			***0.80***	***n_{Fr} guessed***			***0.85***
logK_{Fr} guessed			***3.95***	***logK_{Fr} guessed***			***4.00***	***logK_{Fr} guessed***			***3.97***

* C ($\mu g_{pyr}/L_w$), S ($\mu g_{pyr}/kg_{solids}$), nFr (dimensionless), K_{Fr} $(\mu g_{pyr}/kg_{solids})(L_w/\mu g_{pyr})^{nFr}$.

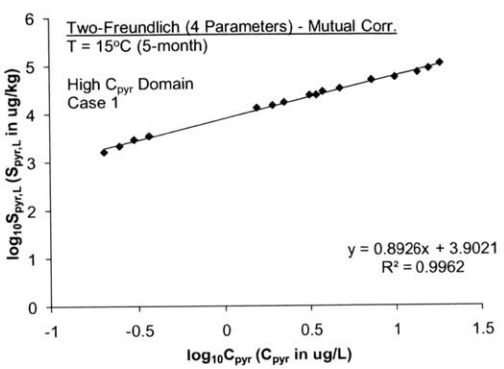
Two-Freundlich (4 Parameters) - Mutual Corr.
T = 15°C (5-month)
High C_{pyr} Domain
Case 1
y = 0.8926x + 3.9021
R² = 0.9962
$\log_{10}S_{pyr,L}$ ($S_{pyr,L}$ in ug/kg)
$\log_{10}C_{pyr}$ (C_{pyr} in ug/L)

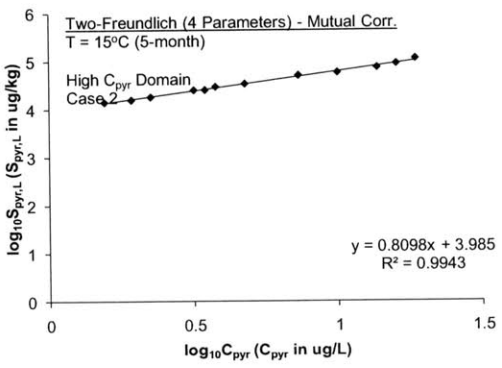
Two-Freundlich (4 Parameters) - Mutual Corr.
T = 15°C (5-month)
High C_{pyr} Domain
Case 2
y = 0.8098x + 3.985
R² = 0.9943
$\log_{10}S_{pyr,L}$ ($S_{pyr,L}$ in ug/kg)
$\log_{10}C_{pyr}$ (C_{pyr} in ug/L)

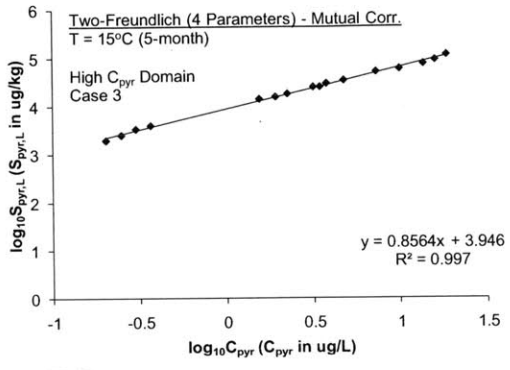
Two-Freundlich (4 Parameters) - Mutual Corr.
T = 15°C (5-month)
High C_{pyr} Domain
Case 3
y = 0.8564x + 3.946
R² = 0.997
$\log_{10}S_{pyr,L}$ ($S_{pyr,L}$ in ug/kg)
$\log_{10}C_{pyr}$ (C_{pyr} in ug/L)

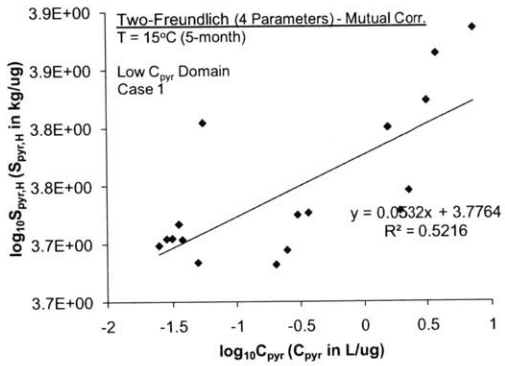
Two-Freundlich (4 Parameters) - Mutual Corr.
T = 15°C (5-month)
Low C_{pyr} Domain
Case 1
y = 0.0532x + 3.7764
R² = 0.5216
$\log_{10}S_{pyr,H}$ ($S_{pyr,H}$ in kg/ug)
$\log_{10}C_{pyr}$ (C_{pyr} in L/ug)

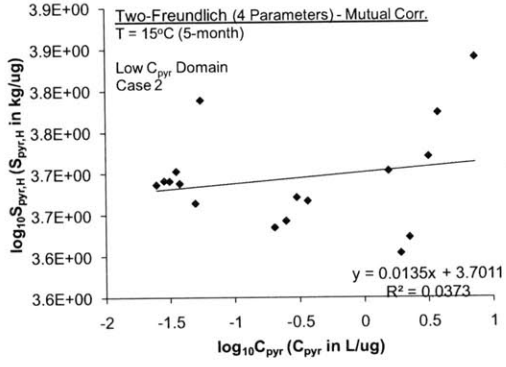
Two-Freundlich (4 Parameters) - Mutual Corr.
T = 15°C (5-month)
Low C_{pyr} Domain
Case 2
y = 0.0135x + 3.7011
R² = 0.0373
$\log_{10}S_{pyr,H}$ ($S_{pyr,H}$ in kg/ug)
$\log_{10}C_{pyr}$ (C_{pyr} in L/ug)

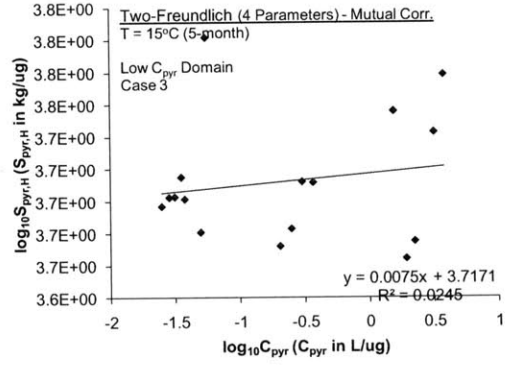
Two-Freundlich (4 Parameters) - Mutual Corr.
T = 15°C (5-month)
Low C_{pyr} Domain
Case 3
y = 0.0075x + 3.7171
R² = 0.0245
$\log_{10}S_{pyr,H}$ ($S_{pyr,H}$ in kg/ug)
$\log_{10}C_{pyr}$ (C_{pyr} in L/ug)

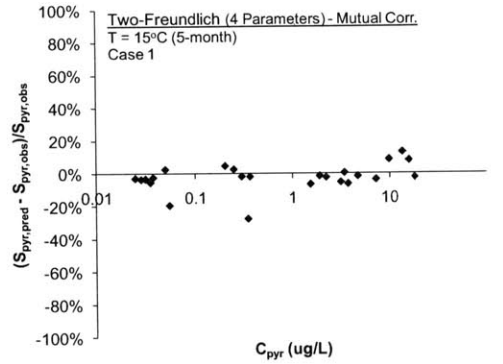
Two-Freundlich (4 Parameters) - Mutual Corr.
T = 15°C (5-month)
Case 1
$(S_{pyr,pred} - S_{pyr,obs})/S_{pyr,obs}$
C_{pyr} (ug/L)

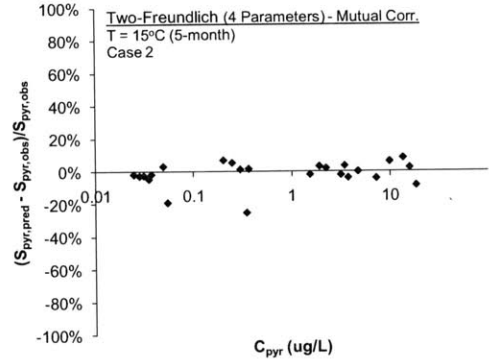
Two-Freundlich (4 Parameters) - Mutual Corr.
T = 15°C (5-month)
Case 2
$(S_{pyr,pred} - S_{pyr,obs})/S_{pyr,obs}$
C_{pyr} (ug/L)

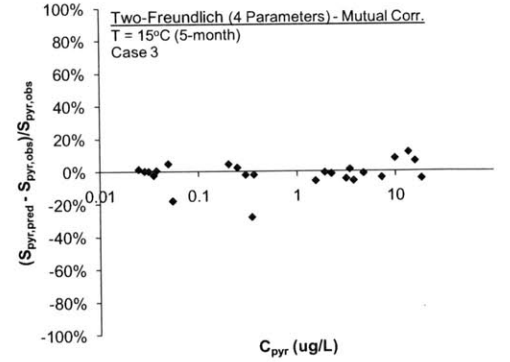
Two-Freundlich (4 Parameters) - Mutual Corr.
T = 15°C (5-month)
Case 3
$(S_{pyr,pred} - S_{pyr,obs})/S_{pyr,obs}$
C_{pyr} (ug/L)

15°C (10-month) Fitted by Two Freundlich Form*

Fit #1				Fit #2				Fit #3			
'Native' Domain (high-affinity, low C_{pyr} range)		*Amended Domain* (high-affinity, low C_{pyr} range)		*'Native' Domain* (high-affinity, low C_{pyr} range)		*Amended Domain* (high-affinity, low C_{pyr} range)		*'Native' Domain* (high-affinity, low C_{pyr} range)		*Amended Domain* (high-affinity, low C_{pyr} range)	
$\log_{10}C$	$\log_{10}S_{Hi}$	$\log_{10}C$	$\log_{10}S_{Hi}$	$\log_{10}C$	$\log_{10}S_{Hi}$	$\log_{10}C$	$\log_{10}S_{Hi}$	$\log_{10}C$	$\log_{10}S_{Hi}$	$\log_{10}C$	$\log_{10}S_{Hi}$
0.57	3.90	0.57	4.18			0.57	4.24			0.57	4.17
0.52	3.82	0.52	4.10			0.52	4.17			0.52	4.09
0.33	3.84	0.33	3.93			0.33	4.02			0.33	3.92
		1.30	4.59			1.30	4.63			1.30	4.58
		1.13	4.73			1.13	4.76			1.13	4.73
		0.89	4.57			0.89	4.60			0.89	4.57
-1.36	3.68			-1.36	3.66			-1.36	3.67		
-1.47	3.69			-1.47	3.68			-1.47	3.68		
-1.58	3.68			-1.58	3.67			-1.58	3.68		
-0.42	3.76	-0.42	3.14	-0.42	3.75	-0.42	3.37	-0.42	3.72	-0.42	3.13
-1.46	3.68			-1.46	3.67			-1.46	3.67		
-1.58	3.68			-1.58	3.67			-1.58	3.67		
-1.65	3.67			-1.65	3.66			-1.65	3.67		
-0.46	3.77	-0.46	3.11	-0.46	3.75	-0.46	3.35	-0.46	3.72	-0.46	3.10
0.23	4.17	0.23	4.18			0.23	4.23	0.23	4.10	0.23	4.17
0.20	3.96	0.20	3.95			0.20	4.02	0.20	3.85	0.20	3.93
		1.23	4.69			1.23	4.72			1.23	4.69
Slp=n_{Fr}	***0.1266***		***0.8967***		***0.0704***		***0.7841***		***0.1442***		***0.8987***
	(0.0313)		*(0.0827)*		*(0.0058)*		*(0.0649)*		*(0.0373)*		*(0.0831)*
I=logK_{Fr}	***3.8702***		***3.6568***		***3.7758***		***3.7981***		***3.8800***		***3.6458***
	(0.0337)		*(0.0634)*		*(0.0077)*		*(0.0498)*		*(0.0447)*		*(0.0637)*
R^2	***0.5978***		***0.9289***		***0.9608***		***0.9418***		***0.6507***		***0.9285***
n_{Fr} guessed			***0.89***	***n_{Fr} guessed***			***0.78***	***n_{Fr} guessed***			***0.90***
logK_{Fr} guessed			***3.70***	***logK_{Fr} guessed***			***3.70***	***logK_{Fr} guessed***			***3.81***

*** C ($\mu g_{pyr}/L_w$), S ($\mu g_{pyr}/kg_{solids}$), nFr (dimensionless), K_{Fr} $(\mu g_{pyr}/kg_{solids})(L_w/\mu g_{pyr})^{nFr}$.**

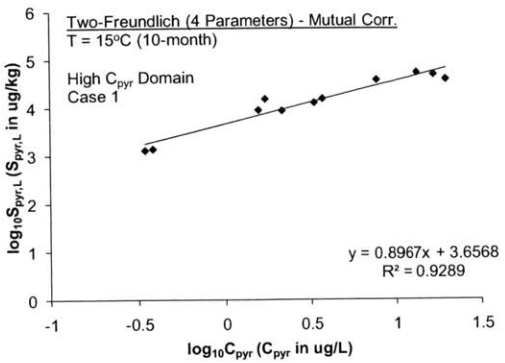
Two-Freundlich (4 Parameters) - Mutual Corr.
T = 15°C (10-month)
High C_{pyr} Domain
Case 1
y = 0.8967x + 3.6568
R² = 0.9289
$\log_{10}S_{pyr,L}$ ($S_{pyr,L}$ in ug/kg)
$\log_{10}C_{pyr}$ (C_{pyr} in ug/L)

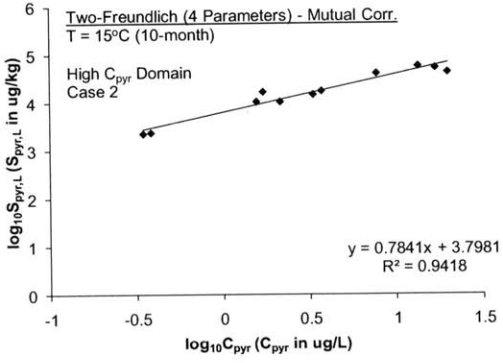
Two-Freundlich (4 Parameters) - Mutual Corr.
T = 15°C (10-month)
High C_{pyr} Domain
Case 2
y = 0.7841x + 3.7981
R² = 0.9418
$\log_{10}S_{pyr,L}$ ($S_{pyr,L}$ in ug/kg)
$\log_{10}C_{pyr}$ (C_{pyr} in ug/L)

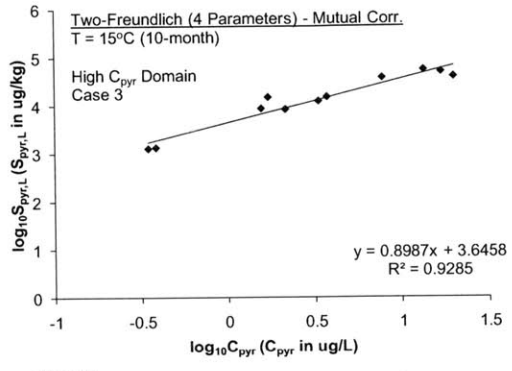
Two-Freundlich (4 Parameters) - Mutual Corr.
T = 15°C (10-month)
High C_{pyr} Domain
Case 3
y = 0.8987x + 3.6458
R² = 0.9285
$\log_{10}S_{pyr,L}$ ($S_{pyr,L}$ in ug/kg)
$\log_{10}C_{pyr}$ (C_{pyr} in ug/L)

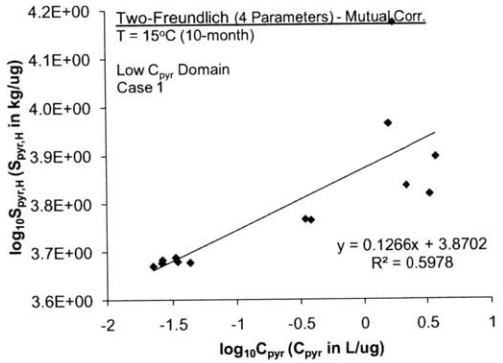
Two-Freundlich (4 Parameters) - Mutual Corr.
T = 15°C (10-month)
Low C_{pyr} Domain
Case 1
y = 0.1266x + 3.8702
R² = 0.5978
$\log_{10}S_{pyr,H}$ ($S_{pyr,H}$ in kg/ug)
$\log_{10}C_{pyr}$ (C_{pyr} in L/ug)

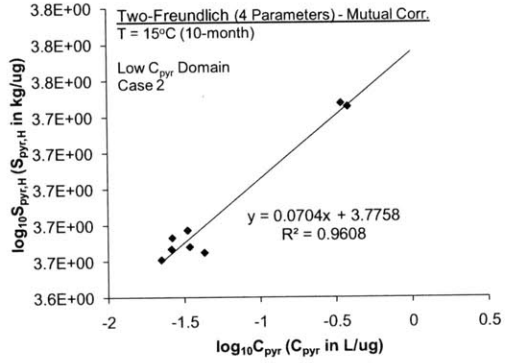
Two-Freundlich (4 Parameters) - Mutual Corr.
T = 15°C (10-month)
Low C_{pyr} Domain
Case 2
y = 0.0704x + 3.7758
R² = 0.9608
$\log_{10}S_{pyr,H}$ ($S_{pyr,H}$ in kg/ug)
$\log_{10}C_{pyr}$ (C_{pyr} in L/ug)

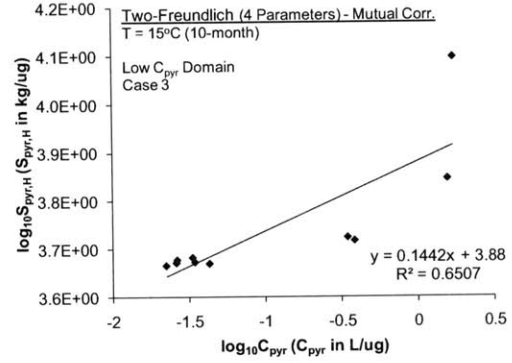
Two-Freundlich (4 Parameters) - Mutual Corr.
T = 15°C (10-month)
Low C_{pyr} Domain
Case 3
y = 0.1442x + 3.88
R² = 0.6507
$\log_{10}S_{pyr,H}$ ($S_{pyr,H}$ in kg/ug)
$\log_{10}C_{pyr}$ (C_{pyr} in L/ug)

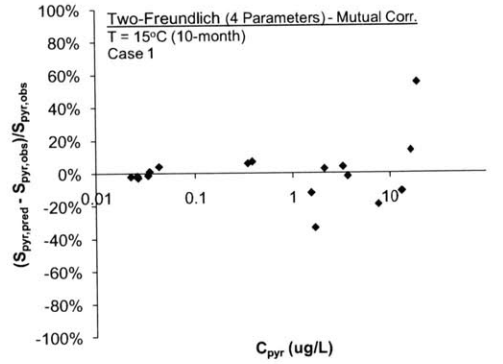
Two-Freundlich (4 Parameters) - Mutual Corr.
T = 15°C (10-month)
Case 1
$(S_{pyr,pred} - S_{pyr,obs})/S_{pyr,obs}$
C_{pyr} (ug/L)

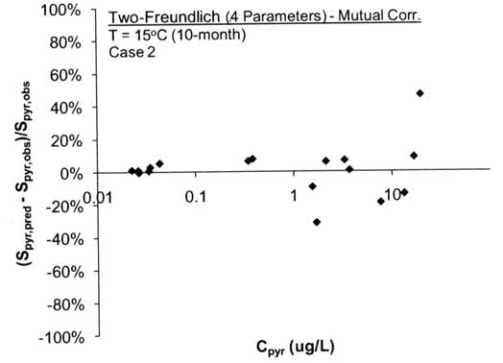
Two-Freundlich (4 Parameters) - Mutual Corr.
T = 15°C (10-month)
Case 2
$(S_{pyr,pred} - S_{pyr,obs})/S_{pyr,obs}$
C_{pyr} (ug/L)

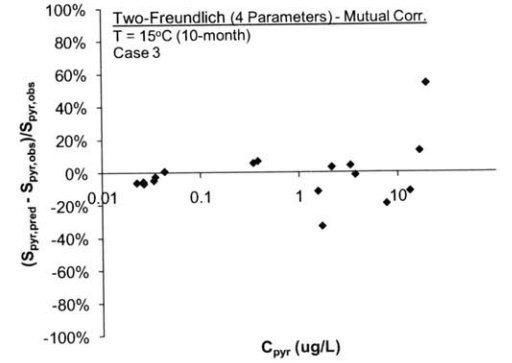
Two-Freundlich (4 Parameters) - Mutual Corr.
T = 15°C (10-month)
Case 3
$(S_{pyr,pred} - S_{pyr,obs})/S_{pyr,obs}$
C_{pyr} (ug/L)

22°C (5-month) Fitted by Two Freundlich Form*

Fit #1				Fit #2				Fit #3			
'Native' Domain (high-affinity, low C_{pyr} range)		*Amended Domain* (high-affinity, low C_{pyr} range)		*'Native' Domain* (high-affinity, low C_{pyr} range)		*Amended Domain* (high-affinity, low C_{pyr} range)		*'Native' Domain* (high-affinity, low C_{pyr} range)		*Amended Domain* (high-affinity, low C_{pyr} range)	
$log_{10}C$	$log_{10}S_{Hi}$	$log_{10}C$	$log_{10}S_{Hi}$	$log_{10}C$	$log_{10}S_{Hi}$	$log_{10}C$	$log_{10}S_{Hi}$	$log_{10}C$	$log_{10}S_{Hi}$	$log_{10}C$	$log_{10}S_{Hi}$
0.50	4.13	0.50	4.40	0.50	3.92	0.50	4.44	0.50	4.01	0.50	4.42
0.36	4.13	0.36	4.33	0.36	4.03	0.36	4.36	0.36	4.08	0.36	4.34
0.29	3.84	0.29	4.11	0.29	3.70	0.29	4.17	0.29	3.78	0.29	4.13
		1.29	4.97			1.29	4.99			1.29	4.98
		0.98	4.84			0.98	4.86			0.98	4.85
0.74	4.09	0.74	4.54			0.74	4.57			0.74	4.55
-1.25	3.63	-1.25	2.93	-1.25	3.67			-1.25	3.67		
-1.32	3.65	-1.32	3.03	-1.32	3.69			-1.32	3.69		
-1.42	3.66	-1.42	3.11	-1.42	3.70			-1.42	3.70		
-0.81	3.64	-0.81	3.06	-0.81	3.71	-0.81	2.99	-0.81	3.71	-0.81	2.89
-1.33	3.65	-1.33	3.06	-1.33	3.69			-1.33	3.69		
-1.42	3.66	-1.42	3.10	-1.42	3.70			-1.42	3.70		
-1.51	3.67	-1.51	3.16	-1.51	3.70			-1.51	3.70		
-0.40	3.86	-0.40	3.73	-0.40	3.91	-0.40	3.75	-0.40	3.92	-0.40	3.72
-0.48	3.69	-0.48	3.41	-0.48	3.76	-0.48	3.45	-0.48	3.77	-0.48	3.38
-0.75	3.66	-0.75	3.17	-0.75	3.73	-0.75	3.13	-0.75	3.73	-0.75	3.05
0.50	4.12	0.50	4.40	0.50	3.91	0.50	4.44	0.50	4.00	0.50	4.42
0.47	3.85	0.47	4.26			0.47	4.31			0.47	4.28
0.22	3.90	0.22	4.10	0.22	3.84	0.22	4.15	0.22	3.88	0.22	4.12
		1.21	5.01			1.21	5.03			1.21	5.02
		0.98	4.84			0.98	4.86			0.98	4.85
0.75	4.05	0.75	4.53			0.75	4.56			0.75	4.54
Slp=n_{Fr}	***0.2044***		***0.7476***		***0.1139***		***0.9377***		***0.1539***		***0.9741***
	(0.0264)		*(0.0341)*		*(0.0255)*		*(0.0370)*		*(0.0242)*		*(0.0409)*
I=logK_{Fr}	***3.9038***		***3.9952***		***3.8445***		***3.9119***		***3.8917***		***3.8655***
	(0.0242)		*(0.0327)*		*(0.0245)*		*(0.0274)*		*(0.0232)*		*(0.0302)*
R^2	***0.7890***		***0.9600***		***0.6047***		***0.9786***		***0.7562***		***0.9760***
n_{Fr} guessed			***0.75***	***n_{Fr} guessed***			***0.95***	***n_{Fr} guessed***			***0.93***
logK_{Fr} guessed			***3.97***	***logK_{Fr} guessed***			***3.96***	***logK_{Fr} guessed***			***3.94***

*** C ($\mu g_{pyr}/L_w$), S ($\mu g_{pyr}/kg_{solids}$), nFr (dimensionless), K_{Fr} $(\mu g_{pyr}/kg_{solids})(L_w/\mu g_{pyr})^{nFr}$.**

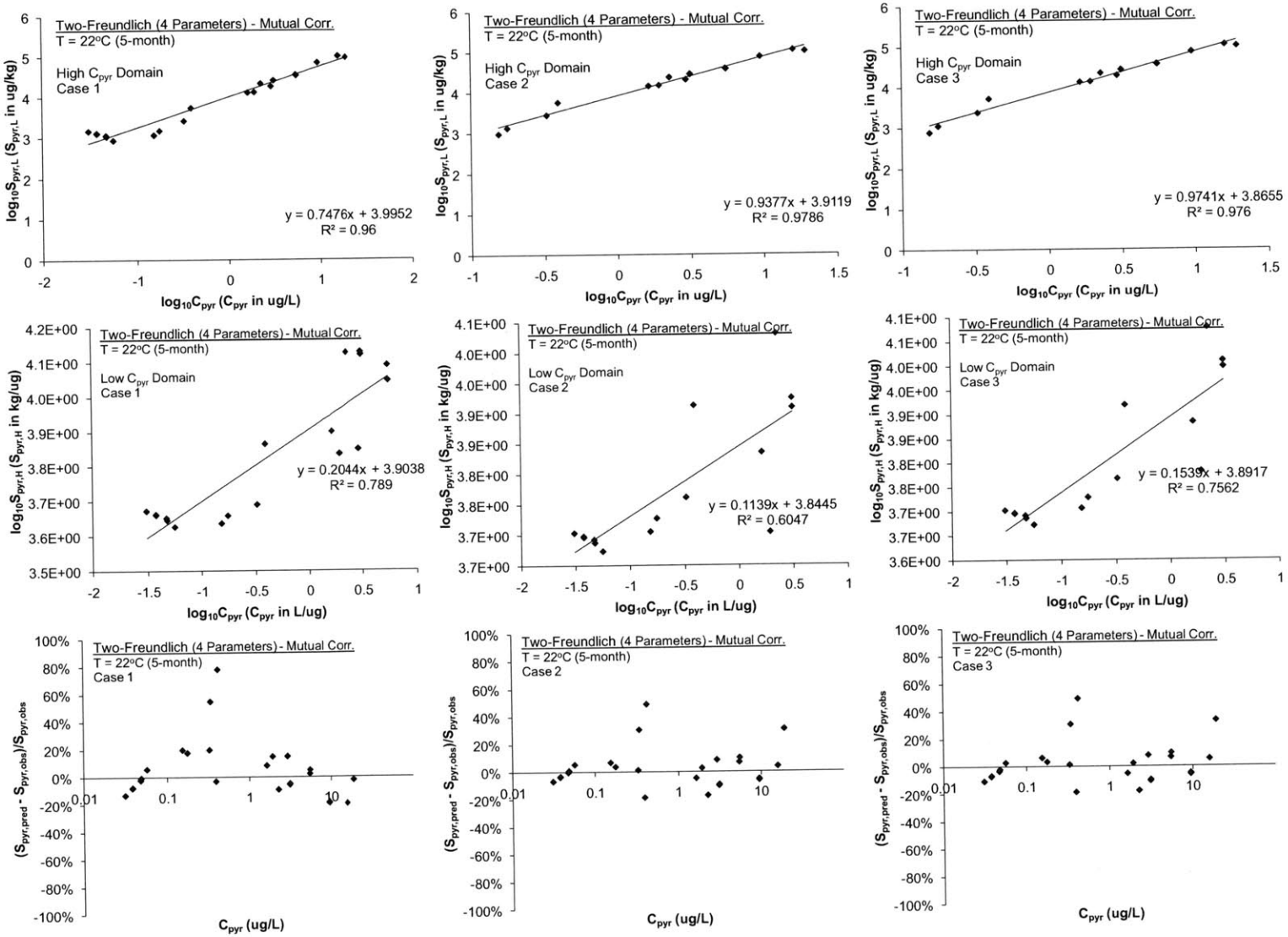
Two-Freundlich (4 Parameters) - Mutual Corr.
T = 22°C (5-month)
High C_{pyr} Domain
Case 1
y = 0.7476x + 3.9952
R² = 0.96
$\log_{10}S_{pyr,L}$ ($S_{pyr,L}$ in ug/kg)
$\log_{10}C_{pyr}$ (C_{pyr} in ug/L)
Two-Freundlich (4 Parameters) - Mutual Corr.
T = 22°C (5-month)
High C_{pyr} Domain
Case 2
y = 0.9377x + 3.9119
R² = 0.9786
$\log_{10}S_{pyr,L}$ ($S_{pyr,L}$ in ug/kg)
$\log_{10}C_{pyr}$ (C_{pyr} in ug/L)
Two-Freundlich (4 Parameters) - Mutual Corr.
T = 22°C (5-month)
High C_{pyr} Domain
Case 3
y = 0.9741x + 3.8655
R² = 0.976
$\log_{10}S_{pyr,L}$ ($S_{pyr,L}$ in ug/kg)
$\log_{10}C_{pyr}$ (C_{pyr} in ug/L)
Two-Freundlich (4 Parameters) - Mutual Corr.
T = 22°C (5-month)
Low C_{pyr} Domain
Case 1
y = 0.2044x + 3.9038
R² = 0.789
$\log_{10}S_{pyr,H}$ ($S_{pyr,H}$ in kg/ug)
$\log_{10}C_{pyr}$ (C_{pyr} in L/ug)
Two-Freundlich (4 Parameters) - Mutual Corr.
T = 22°C (5-month)
Low C_{pyr} Domain
Case 2
y = 0.1139x + 3.8445
R² = 0.6047
$\log_{10}S_{pyr,H}$ ($S_{pyr,H}$ in kg/ug)
$\log_{10}C_{pyr}$ (C_{pyr} in L/ug)
Two-Freundlich (4 Parameters) - Mutual Corr.
T = 22°C (5-month)
Low C_{pyr} Domain
Case 3
y = 0.1539x + 3.8917
R² = 0.7562
$\log_{10}S_{pyr,H}$ ($S_{pyr,H}$ in kg/ug)
$\log_{10}C_{pyr}$ (C_{pyr} in L/ug)
Two-Freundlich (4 Parameters) - Mutual Corr.
T = 22°C (5-month)
Case 1
$(S_{pyr,pred} - S_{pyr,obs})/S_{pyr,obs}$
C_{pyr} (ug/L)
Two-Freundlich (4 Parameters) - Mutual Corr.
T = 22°C (5-month)
Case 2
$(S_{pyr,pred} - S_{pyr,obs})/S_{pyr,obs}$
C_{pyr} (ug/L)
Two-Freundlich (4 Parameters) - Mutual Corr.
T = 22°C (5-month)
Case 3
$(S_{pyr,pred} - S_{pyr,obs})/S_{pyr,obs}$
C_{pyr} (ug/L)

22°C (10-month) Fitted by Two Freundlich Form*

Fit #1				Fit #2				Fit #3			
'Native' Domain (high-affinity, low C_{pyr} range)		*Amended Domain* (high-affinity, low C_{pyr} range)		*'Native' Domain* (high-affinity, low C_{pyr} range)		*Amended Domain* (high-affinity, low C_{pyr} range)		*'Native' Domain* (high-affinity, low C_{pyr} range)		*Amended Domain* (high-affinity, low C_{pyr} range)	
$log_{10}C$	$log_{10}S_{Hi}$	$log_{10}C$	$log_{10}S_{Hi}$	$log_{10}C$	$log_{10}S_{Hi}$	$log_{10}C$	$log_{10}S_{Hi}$	$log_{10}C$	$log_{10}S_{Hi}$	$log_{10}C$	$log_{10}S_{Hi}$
0.50	3.84	0.50	4.32			0.50	4.41			0.50	4.24
0.34	4.01	0.34	4.31			0.34	4.40	0.34	4.11	0.34	4.24
0.27	3.67	0.27	4.13	0.27	3.21	0.27	4.25	0.27	3.88	0.27	4.03
		1.30	4.66			1.30	4.73			1.30	4.61
		0.97	4.80			0.97	4.84			0.97	4.76
		0.74	4.52			0.74	4.59			0.74	4.47
-1.31	3.52	-1.31	3.19	-1.31	3.45	-1.31	3.31	-1.31	3.64		
-1.40	3.55	-1.40	3.22	-1.40	3.49	-1.40	3.29	-1.40	3.65		
-1.48	3.56	-1.48	3.24	-1.48	3.51	-1.48	3.27	-1.48	3.65		
-0.91	3.52	-0.91	3.34	-0.91	3.39	-0.91	3.56	-0.91	3.69	-0.91	2.93
-1.34	3.51	-1.34	3.15	-1.34	3.43	-1.34	3.27	-1.34	3.62		
-1.28	3.48	-1.28	3.09	-1.28	3.39	-1.28	3.26	-1.28	3.61		
-1.46	3.55	-1.46	3.21	-1.46	3.49	-1.46	3.25	-1.46	3.64		
-0.47	3.79	-0.47	3.83			-0.47	3.97			-0.47	3.70
-0.55	3.57	-0.55	3.59	-0.55	3.39	-0.55	3.79	-0.55	3.77	-0.55	3.34
-0.79	3.50	-0.79	3.37	-0.79	3.33	-0.79	3.61	-0.79	3.69	-0.79	2.96
0.50	3.76	0.50	4.30			0.50	4.40			0.50	4.22
0.43	3.80	0.43	4.27			0.43	4.37			0.43	4.19
0.23	3.63	0.23	4.10	0.23	3.14	0.23	4.22	0.23	3.87	0.23	3.99
		1.21	4.87			1.21	4.91			1.21	4.84
		0.97	4.80			0.97	4.84			0.97	4.77
		0.75	4.51			0.75	4.58			0.75	4.46
Slp=n_{Fr}	***0.1545***		***0.6370***		***-0.1713***		***0.6140***		***0.1917***		***0.8522***
	(0.0312)		*(0.0233)*		*(0.0191)*		*(0.0162)*		*(0.0270)*		*(0.0523)*
I=logK_{Fr}	***3.7250***		***4.0269***		***3.2266***		***4.1280***		***3.8892***		***3.8160***
	(0.0295)		*(0.0225)*		*(0.0210)*		*(0.0157)*		*(0.0286)*		*(0.0393)*
R^2	***0.6365***		***0.9740***		***0.8993***		***0.9862***		***0.8343***		***0.9499***
n_{Fr} guessed			***0.62***	***n_{Fr} guessed***			***0.59***	***n_{Fr} guessed***			***0.85***
logK_{Fr} guessed			***4.00***	***logK_{Fr} guessed***			***4.09***	***logK_{Fr} guessed***			***3.84***

* C ($\mu g_{pyr}/L_w$), S ($\mu g_{pyr}/kg_{solids}$), nFr (dimensionless), K_{Fr} $(\mu g_{pyr}/kg_{solids})(L_w/\mu g_{pyr})^{nFr}$.

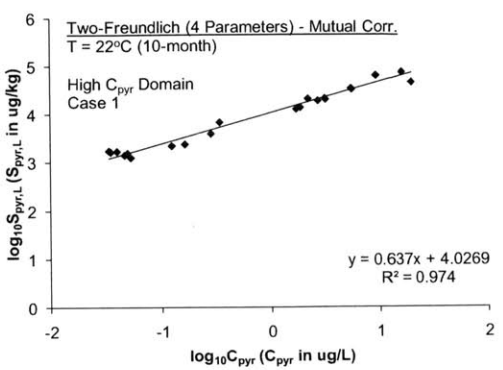
Two-Freundlich (4 Parameters) - Mutual Corr.
T = 22°C (10-month)
High C_{pyr} Domain
Case 1
y = 0.637x + 4.0269
R² = 0.974
$\log_{10}S_{pyr,L}$ ($S_{pyr,L}$ in ug/kg)
$\log_{10}C_{pyr}$ (C_{pyr} in ug/L)

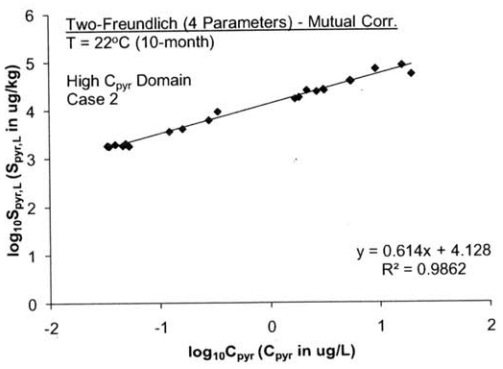
Two-Freundlich (4 Parameters) - Mutual Corr.
T = 22°C (10-month)
High C_{pyr} Domain
Case 2
y = 0.614x + 4.128
R² = 0.9862
$\log_{10}S_{pyr,L}$ ($S_{pyr,L}$ in ug/kg)
$\log_{10}C_{pyr}$ (C_{pyr} in ug/L)

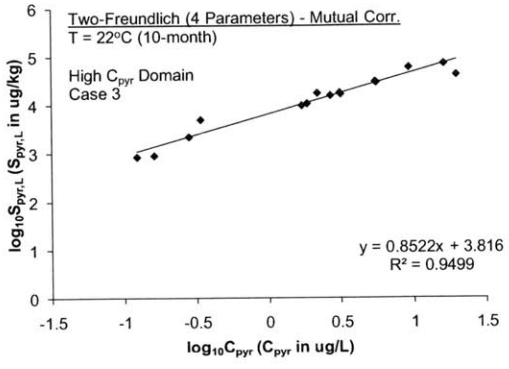
Two-Freundlich (4 Parameters) - Mutual Corr.
T = 22°C (10-month)
High C_{pyr} Domain
Case 3
y = 0.8522x + 3.816
R² = 0.9499
$\log_{10}S_{pyr,L}$ ($S_{pyr,L}$ in ug/kg)
$\log_{10}C_{pyr}$ (C_{pyr} in ug/L)

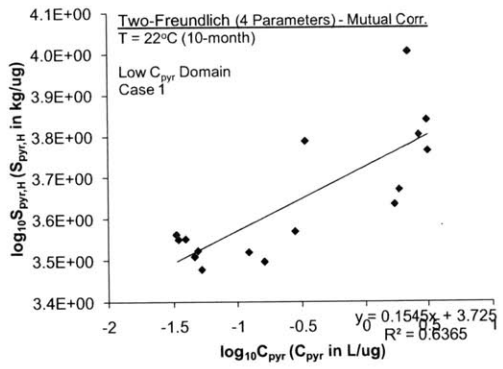
Two-Freundlich (4 Parameters) - Mutual Corr.
T = 22°C (10-month)
Low C_{pyr} Domain
Case 1
y = 0.1545x + 3.725
R² = 0.6365
$\log_{10}S_{pyr,H}$ ($S_{pyr,H}$ in kg/ug)
$\log_{10}C_{pyr}$ (C_{pyr} in L/ug)

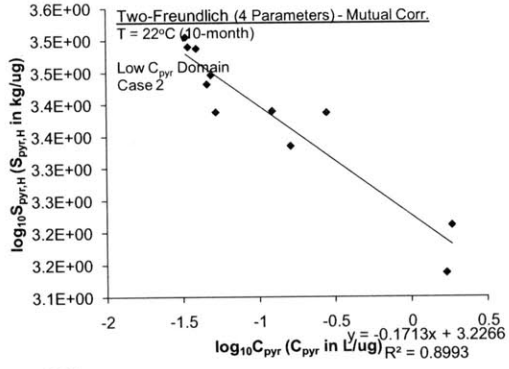
Two-Freundlich (4 Parameters) - Mutual Corr.
T = 22°C (10-month)
Low C_{pyr} Domain
Case 2
y = -0.1713x + 3.2266
R² = 0.8993
$\log_{10}S_{pyr,H}$ ($S_{pyr,H}$ in kg/ug)
$\log_{10}C_{pyr}$ (C_{pyr} in L/ug)

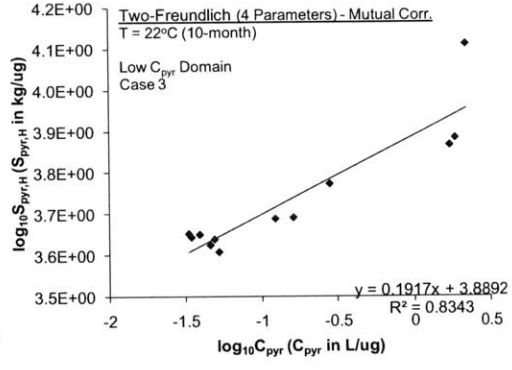
Two-Freundlich (4 Parameters) - Mutual Corr.
T = 22°C (10-month)
Low C_{pyr} Domain
Case 3
y = 0.1917x + 3.8892
R² = 0.8343
$\log_{10}S_{pyr,H}$ ($S_{pyr,H}$ in kg/ug)
$\log_{10}C_{pyr}$ (C_{pyr} in L/ug)

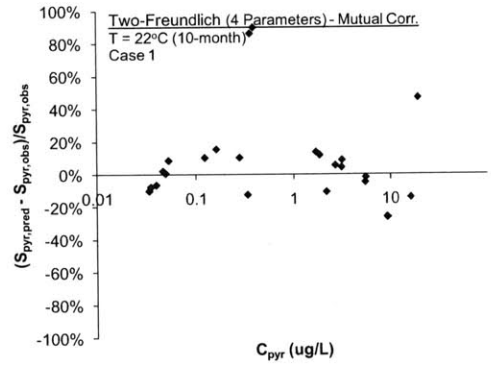
Two-Freundlich (4 Parameters) - Mutual Corr.
T = 22°C (10-month)
Case 1
$(S_{pyr,pred} - S_{pyr,obs})/S_{pyr,obs}$
C_{pyr} (ug/L)

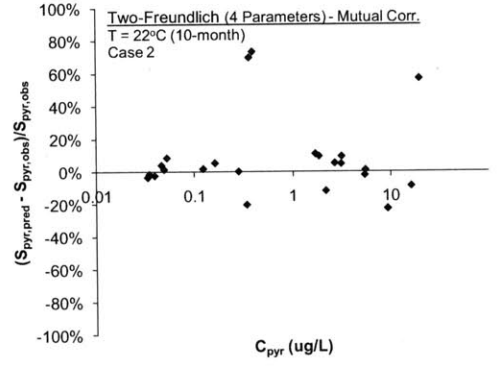
Two-Freundlich (4 Parameters) - Mutual Corr.
T = 22°C (10-month)
Case 2
$(S_{pyr,pred} - S_{pyr,obs})/S_{pyr,obs}$
C_{pyr} (ug/L)

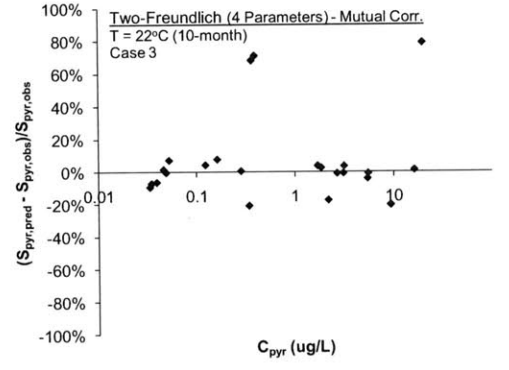
Two-Freundlich (4 Parameters) - Mutual Corr.
T = 22°C (10-month)
Case 3
$(S_{pyr,pred} - S_{pyr,obs})/S_{pyr,obs}$
C_{pyr} (ug/L)

37°C (5-month) Fitted by Two Freundlich Form*

Fit #1				Fit #2				Fit #3			
'Native' Domain (high-affinity, low C_{pyr} range)		*Amended Domain* (high-affinity, low C_{pyr} range)		*'Native' Domain* (high-affinity, low C_{pyr} range)		*Amended Domain* (high-affinity, low C_{pyr} range)		*'Native' Domain* (high-affinity, low C_{pyr} range)		*Amended Domain* (high-affinity, low C_{pyr} range)	
$log_{10}C$	$log_{10}S_{Hi}$	$log_{10}C$	$log_{10}S_{Hi}$	$log_{10}C$	$log_{10}S_{Hi}$	$log_{10}C$	$log_{10}S_{Hi}$	$log_{10}C$	$log_{10}S_{Hi}$	$log_{10}C$	$log_{10}S_{Hi}$
0.43	3.07	0.43	4.05	0.43	3.81	0.43	3.68	0.43	3.74	0.43	3.79
		1.31	4.72			1.31	4.57			1.31	4.63
		1.24	4.58			1.24	4.38			1.24	4.47
0.90	3.96	0.90	4.48	0.90	4.28	0.90	4.30	0.90	4.18	0.90	4.36
-0.78	2.74			-0.78	3.20			-0.78	3.27		
-0.86	3.32	-0.86	3.46	-0.86	3.48	-0.86	3.05	-0.86	3.52	-0.86	2.87
-0.43	3.87	-0.43	3.99	-0.43	3.96	-0.43	3.84	-0.43	3.97	-0.43	3.83
-0.46	3.63	-0.46	3.80	-0.46	3.77	-0.46	3.56	-0.46	3.79	-0.46	3.55
-0.48	3.31	-0.48	3.61	-0.48	3.56	-0.48	3.16	-0.48	3.59	-0.48	3.11
-1.07	3.29	-1.07	3.37	-1.07	3.42	-1.07	2.97	-1.07	3.46	-1.07	2.69
-0.95	3.33	-0.95	3.43	-0.95	3.47	-0.95	3.06	-0.95	3.51	-0.95	2.86
-0.61	1.91										
-0.46	4.01	-0.46	4.09	-0.46	4.07	-0.46	3.98	-0.46	4.08	-0.46	3.97
-0.54	3.71	-0.54	3.84	-0.54	3.82	-0.54	3.64	-0.54	3.83	-0.54	3.62
-0.63	3.54	-0.63	3.69	-0.63	3.68	-0.63	3.43	-0.63	3.70	-0.63	3.38
0.63	3.35	0.63	4.21	0.63	3.96	0.63	3.92	0.63	3.86	0.63	4.01
0.56	3.66	0.56	4.23	0.56	4.03	0.56	3.98	0.56	3.97	0.56	4.05
0.42	3.36	0.42	4.09	0.42	3.87	0.42	3.77	0.42	3.82	0.42	3.85
		1.29	4.81			1.29	4.70			1.29	4.74
		1.13	4.73			1.13	4.61			1.13	4.66
0.85	4.11	0.85	4.51	0.85	4.34	0.85	4.35	0.85	4.27	0.85	4.41
Slp=n_{Fr}	***0.2797***		***0.5273***		***0.3714***		***0.5995***		***0.2918***		***0.7026***
	(0.1896)		*(0.0383)*		*(0.0732)*		*(0.0645)*		*(0.0726)*		*(0.0691)*
I=logK_{Fr}	***3.4779***		***4.0085***		***3.8598***		***3.7492***		***3.8365***		***3.7277***
	(0.1292)		*(0.0318)*		*(0.0502)*		*(0.0536)*		*(0.0498)*		*(0.0574)*
R^2	***0.1267***		***0.9178***		***0.6479***		***0.8355***		***0.5354***		***0.8587***
n_{Fr} guessed			***0.58***	***n_{Fr} guessed***			***0.58***	***n_{Fr} guessed***			***0.68***
logK_{Fr} guessed			***3.90***	***logK_{Fr} guessed***			***3.70***	***logK_{Fr} guessed***			***3.70***

*** C ($\mu g_{pyr}/L_w$), S ($\mu g_{pyr}/kg_{solids}$), nFr (dimensionless), K_{Fr} $(\mu g_{pyr}/kg_{solids})(L_w/\mu g_{pyr})^{nFr}$.**

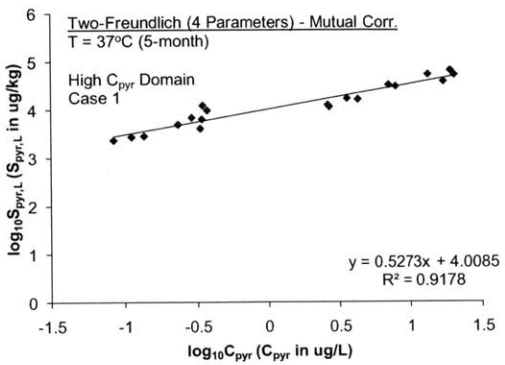
Two-Freundlich (4 Parameters) - Mutual Corr.
T = 37°C (5-month)
High C_{pyr} Domain
Case 1
y = 0.5273x + 4.0085
R² = 0.9178
$\log_{10}S_{pyr,L}$ ($S_{pyr,L}$ in ug/kg)
$\log_{10}C_{pyr}$ (C_{pyr} in ug/L)

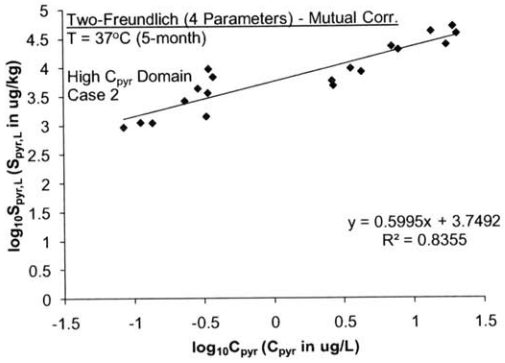
Two-Freundlich (4 Parameters) - Mutual Corr.
T = 37°C (5-month)
High C_{pyr} Domain
Case 2
y = 0.5995x + 3.7492
R² = 0.8355
$\log_{10}S_{pyr,L}$ ($S_{pyr,L}$ in ug/kg)
$\log_{10}C_{pyr}$ (C_{pyr} in ug/L)

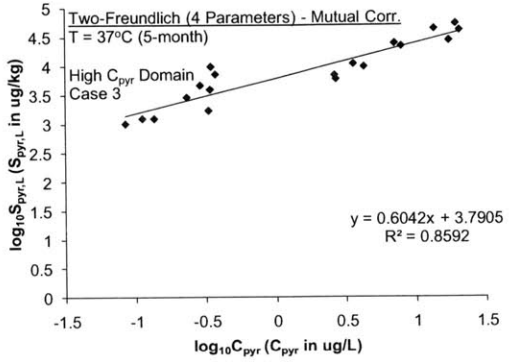
Two-Freundlich (4 Parameters) - Mutual Corr.
T = 37°C (5-month)
High C_{pyr} Domain
Case 3
y = 0.6042x + 3.7905
R² = 0.8592
$\log_{10}S_{pyr,L}$ ($S_{pyr,L}$ in ug/kg)
$\log_{10}C_{pyr}$ (C_{pyr} in ug/L)

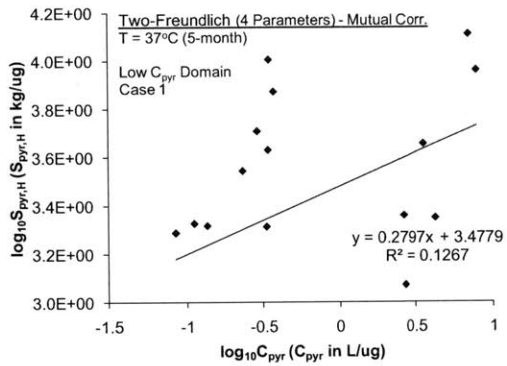
Two-Freundlich (4 Parameters) - Mutual Corr.
T = 37°C (5-month)
Low C_{pyr} Domain
Case 1
y = 0.2797x + 3.4779
R² = 0.1267
$\log_{10}S_{pyr,H}$ ($S_{pyr,H}$ in kg/ug)
$\log_{10}C_{pyr}$ (C_{pyr} in L/ug)

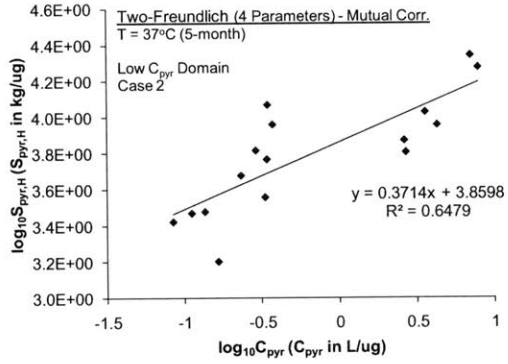
Two-Freundlich (4 Parameters) - Mutual Corr.
T = 37°C (5-month)
Low C_{pyr} Domain
Case 2
y = 0.3714x + 3.8598
R² = 0.6479
$\log_{10}S_{pyr,H}$ ($S_{pyr,H}$ in kg/ug)
$\log_{10}C_{pyr}$ (C_{pyr} in L/ug)

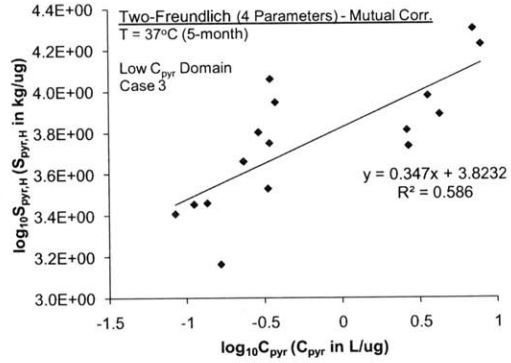
Two-Freundlich (4 Parameters) - Mutual Corr.
T = 37°C (5-month)
Low C_{pyr} Domain
Case 3
y = 0.347x + 3.8232
R² = 0.586
$\log_{10}S_{pyr,H}$ ($S_{pyr,H}$ in kg/ug)
$\log_{10}C_{pyr}$ (C_{pyr} in L/ug)

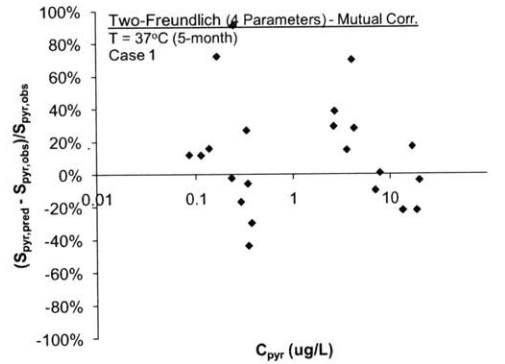
Two-Freundlich (4 Parameters) - Mutual Corr.
T = 37°C (5-month)
Case 1
$(S_{pyr,pred} - S_{pyr,obs})/S_{pyr,obs}$
C_{pyr} (ug/L)

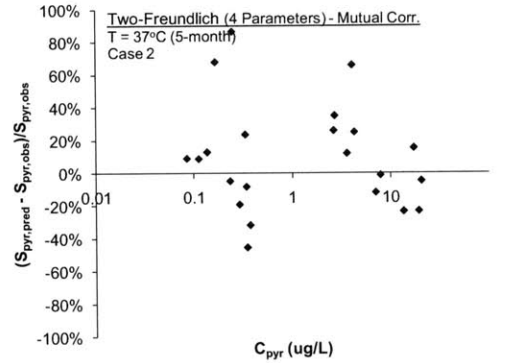
Two-Freundlich (4 Parameters) - Mutual Corr.
T = 37°C (5-month)
Case 2
$(S_{pyr,pred} - S_{pyr,obs})/S_{pyr,obs}$
C_{pyr} (ug/L)

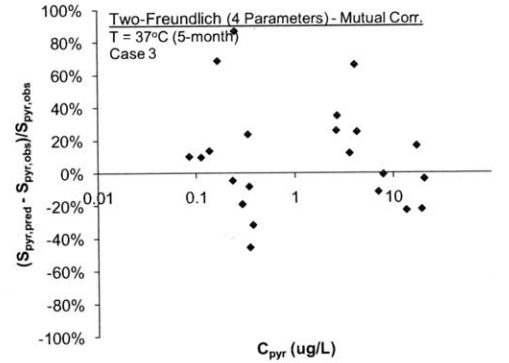
Two-Freundlich (4 Parameters) - Mutual Corr.
T = 37°C (5-month)
Case 3
$(S_{pyr,pred} - S_{pyr,obs})/S_{pyr,obs}$
C_{pyr} (ug/L)

37°C (10-month) Fitted by Two Freundlich Form*

Fit #1				Fit #2				Fit #3			
'Native' Domain (high-affinity, low C_{pyr} range)		*Amended Domain* (high-affinity, low C_{pyr} range)		*'Native' Domain* (high-affinity, low C_{pyr} range)		*Amended Domain* (high-affinity, low C_{pyr} range)		*'Native' Domain* (high-affinity, low C_{pyr} range)		*Amended Domain* (high-affinity, low C_{pyr} range)	
$log_{10}C$	$log_{10}S_{Hi}$	$log_{10}C$	$log_{10}S_{Hi}$	$log_{10}C$	$log_{10}S_{Hi}$	$log_{10}C$	$log_{10}S_{Hi}$	$log_{10}C$	$log_{10}S_{Hi}$	$log_{10}C$	$log_{10}S_{Hi}$
0.61	3.67	0.61	3.62	0.61	3.72	0.61	3.72			0.61	3.60
0.43	3.85	0.43	3.78	0.43	3.92	0.43	3.82	0.43	3.90	0.43	3.74
0.60	3.55	0.60	3.47	0.60	3.62	0.60	3.60			0.60	3.43
		1.30	4.37			1.30	4.45			1.30	4.40
		1.21	4.39			1.21	4.45			1.21	4.41
0.89	4.31	0.89	4.33			0.89	4.37			0.89	4.34
-0.96	3.44	-0.96	3.11	-0.96	3.54			-0.96	3.54		
-1.04	3.55	-1.04	3.33	-1.04	3.62			-1.04	3.63		
-0.30	3.45			-0.30	3.62			-0.30	3.62		
-0.31	3.46	-0.31	3.07	-0.31	3.63	-0.31	2.65	-0.31	3.63	-0.31	2.21
-0.40	3.52	-0.40	3.21	-0.40	3.66	-0.40	2.90	-0.40	3.66	-0.40	2.77
-1.09	3.41			-1.09	3.50			-1.09	3.51		
-1.01	3.49	-1.01	3.23	-1.01	3.58			-1.01	3.58		
-0.74	3.38			-0.74	3.52			-0.74	3.52		
-0.30	3.22			-0.30	3.48			-0.30	3.48		
-0.37	3.55	-0.37	3.27	-0.37	3.68	-0.37	3.02	-0.37	3.69	-0.37	2.91
-0.45	3.57	-0.45	3.30	-0.45	3.69	-0.45	3.05	-0.45	3.69	-0.45	2.98
0.61	3.75	0.61	3.71	0.61	3.79	0.61	3.79			0.61	3.69
0.55	3.93	0.55	3.89	0.55	3.97	0.55	3.94	0.55	3.94	0.55	3.87
0.44	3.85	0.44	3.79	0.44	3.92	0.44	3.83	0.44	3.90	0.44	3.75
		1.28	4.54			1.28	4.59			1.28	4.55
		1.10	4.62			1.10	4.65			1.10	4.63
0.83	4.37	0.83	4.38			0.83	4.42			0.83	4.39
Slp=n_{Fr}	***0.3271***		***0.5929***		***0.1710***		***1.0159***		***0.2308***		***1.1069***
	(0.0700)		*(0.0740)*		*(0.0415)*		*(0.0829)*		*(0.0400)*		*(0.1140)*
I=logK_{Fr}	***3.6830***		***3.5927***		***3.7115***		***3.2991***		***3.7558***		***3.1527***
	(0.0476)		*(0.0609)*		*(0.0272)*		*(0.0651)*		*(0.0266)*		*(0.0895)*
R^2	***0.5626***		***0.7907***		***0.5310***		***0.9147***		***0.7351***		***0.8707***
n_{Fr} guessed			***0.58***	***n_{Fr} guessed***			***1.01***	***n_{Fr} guessed***			***1.10***
logK_{Fr} guessed			***3.50***	***logK_{Fr} guessed***			***3.20***	***logK_{Fr} guessed***			***3.20***

* C ($\mu g_{pyr}/L_w$), S ($\mu g_{pyr}/kg_{solids}$), nFr (dimensionless), K_{Fr} $(\mu g_{pyr}/kg_{solids})(L_w/\mu g_{pyr})^{nFr}$.

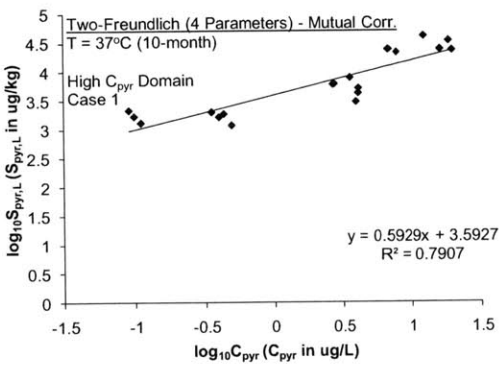
Two-Freundlich (4 Parameters) - Mutual Corr.
T = 37°C (10-month)
High C_{pyr} Domain
Case 1
y = 0.5929x + 3.5927
R² = 0.7907
$\log_{10}S_{pyr,L}$ ($S_{pyr,L}$ in ug/kg)
$\log_{10}C_{pyr}$ (C_{pyr} in ug/L)

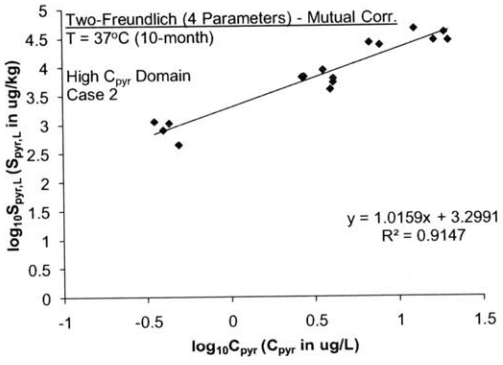
Two-Freundlich (4 Parameters) - Mutual Corr.
T = 37°C (10-month)
High C_{pyr} Domain
Case 2
y = 1.0159x + 3.2991
R² = 0.9147
$\log_{10}S_{pyr,L}$ ($S_{pyr,L}$ in ug/kg)
$\log_{10}C_{pyr}$ (C_{pyr} in ug/L)

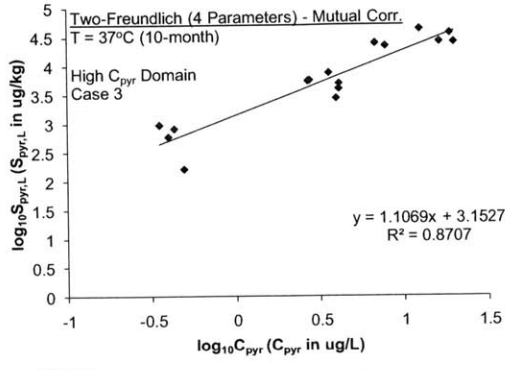
Two-Freundlich (4 Parameters) - Mutual Corr.
T = 37°C (10-month)
High C_{pyr} Domain
Case 3
y = 1.1069x + 3.1527
R² = 0.8707
$\log_{10}S_{pyr,L}$ ($S_{pyr,L}$ in ug/kg)
$\log_{10}C_{pyr}$ (C_{pyr} in ug/L)

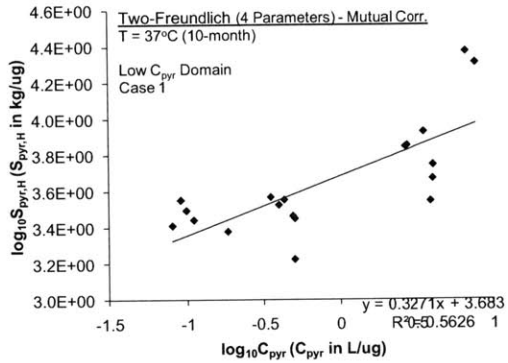
Two-Freundlich (4 Parameters) - Mutual Corr.
T = 37°C (10-month)
Low C_{pyr} Domain
Case 1
y = 0.3271x + 3.683
R² = 0.5626
$\log_{10}S_{pyr,H}$ ($S_{pyr,H}$ in kg/ug)
$\log_{10}C_{pyr}$ (C_{pyr} in L/ug)

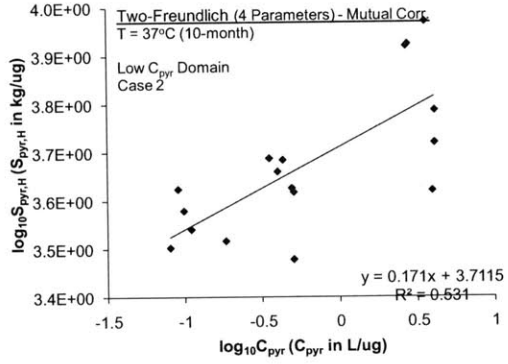
Two-Freundlich (4 Parameters) - Mutual Corr.
T = 37°C (10-month)
Low C_{pyr} Domain
Case 2
y = 0.171x + 3.7115
R² = 0.531
$\log_{10}S_{pyr,H}$ ($S_{pyr,H}$ in kg/ug)
$\log_{10}C_{pyr}$ (C_{pyr} in L/ug)

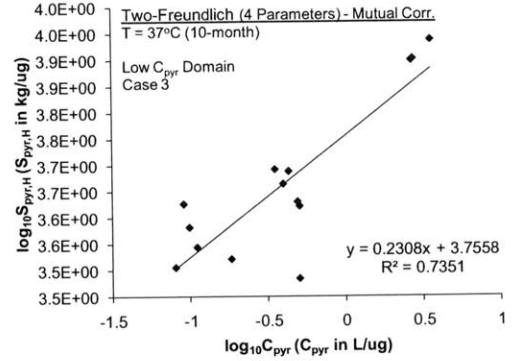
Two-Freundlich (4 Parameters) - Mutual Corr.
T = 37°C (10-month)
Low C_{pyr} Domain
Case 3
y = 0.2308x + 3.7558
R² = 0.7351
$\log_{10}S_{pyr,H}$ ($S_{pyr,H}$ in kg/ug)
$\log_{10}C_{pyr}$ (C_{pyr} in L/ug)

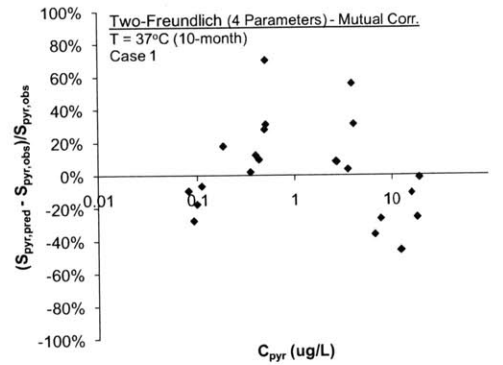
Two-Freundlich (4 Parameters) - Mutual Corr.
T = 37°C (10-month)
Case 1
$(S_{pyr,pred} - S_{pyr,obs})/S_{pyr,obs}$
C_{pyr} (ug/L)

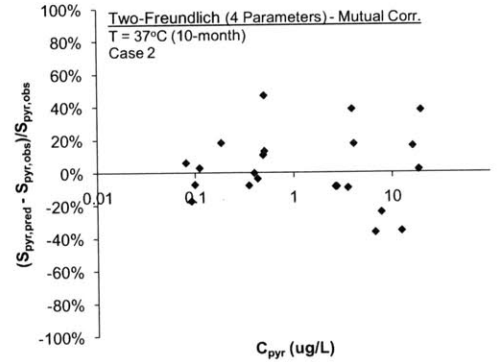
Two-Freundlich (4 Parameters) - Mutual Corr.
T = 37°C (10-month)
Case 2
$(S_{pyr,pred} - S_{pyr,obs})/S_{pyr,obs}$
C_{pyr} (ug/L)

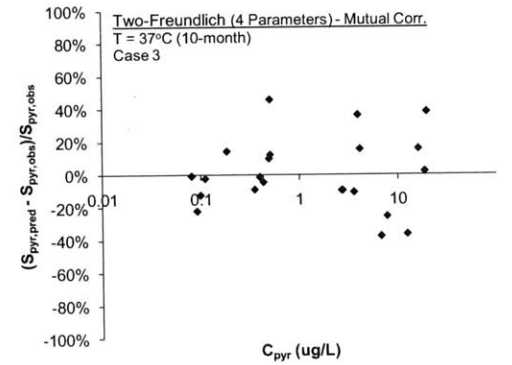
Two-Freundlich (4 Parameters) - Mutual Corr.
T = 37°C (10-month)
Case 3
$(S_{pyr,pred} - S_{pyr,obs})/S_{pyr,obs}$
C_{pyr} (ug/L)

6°C (5-month) Fitted by Langmuir-Freundlich Form*

Fit #1				Fit #2				Fit #3			
'Native' Domain (high-affinity, low C_{pyr} range)		*Amended Domain* (high-affinity, low C_{pyr} range)		*'Native' Domain* (high-affinity, low C_{pyr} range)		*Amended Domain* (high-affinity, low C_{pyr} range)		*'Native' Domain* (high-affinity, low C_{pyr} range)		*Amended Domain* (high-affinity, low C_{pyr} range)	
1/C	$1/S_{Hi}$	$\log_{10}C$	$\log_{10}S_{Hi}$	1/C	$1/S_{Hi}$	$\log_{10}C$	$\log_{10}S_{Hi}$	1/C	$1/S_{Hi}$	$\log_{10}C$	$\log_{10}S_{Hi}$
0.29	1.2E-04	0.54	4.51			0.54	4.51			0.54	4.50
0.43	1.4E-04	0.37	4.38	0.43	1.5E-04	0.37	4.38	0.43	1.4E-04	0.37	4.38
0.62	1.9E-04	0.21	4.24	0.62	1.9E-04	0.21	4.24	0.62	1.7E-04	0.21	4.23
		1.26	5.02			1.26	5.02			1.26	5.02
		1.01	4.84			1.01	4.84			1.01	4.84
0.22	1.8E-04	0.66	4.56	0.22	2.3E-04	0.66	4.56	0.22	2.8E-04	0.66	4.56
18.62	2.7E-04			18.62	2.7E-04						
37.13	2.1E-04	-1.57	2.97	37.13	2.1E-04	-1.57	2.92	37.13	2.0E-04	-1.57	2.69
53.24	2.1E-04			53.24	2.0E-04			53.24	2.0E-04		
3.63	2.6E-04	-0.56	3.56	3.63	2.5E-04	-0.56	3.57			-0.56	3.51
3.47	3.6E-04	-0.54	3.43			-0.54	3.43			-0.54	3.35
11.74	2.1E-04	-1.07	3.26	11.74	2.1E-04	-1.07	3.26	11.74	1.9E-04	-1.07	3.14
27.39	2.1E-04	-1.44	3.07	27.39	2.0E-04	-1.44	3.05	27.39	1.9E-04	-1.44	2.87
43.48	2.1E-04	-1.64	3.01	43.48	2.0E-04	-1.64	2.95	43.48	2.0E-04	-1.64	2.75
52.97	2.1E-04			52.97	2.0E-04			52.97	2.0E-04		
2.65	1.7E-04	-0.42	3.84	2.65	1.7E-04	-0.42	3.84	2.65	1.5E-04	-0.42	3.81
3.87	2.0E-04	-0.59	3.67	3.87	1.9E-04	-0.59	3.67	3.87	1.7E-04	-0.59	3.63
11.74	2.0E-04	-1.07	3.32	11.74	2.0E-04	-1.07	3.32	11.74	1.8E-04	-1.07	3.22
0.28	2.6E-04	0.55	4.46			0.55	4.46			0.55	4.45
0.38	1.9E-04	0.42	4.39	0.38	2.1E-04	0.42	4.39			0.42	4.38
0.68	1.9E-04	0.17	4.21	0.68	1.9E-04	0.17	4.21			0.17	4.20
		1.21	4.90			1.21	4.90			1.21	4.90
		1.00	4.87			1.00	4.87			1.00	4.87
0.21	1.1E-04	0.69	4.62			0.69	4.62			0.69	4.62
S_{Max}	5.0×10^3	$Slp=n_{Fr}$	0.7264	S_{Max}	5.0×10^3	$Slp=n_{Fr}$	0.7376	S_{Max}	5.4×10^3	$Slp=n_{Fr}$	0.8079
	(400)		(0.0189)		(240)		(0.0173)		(450)		(0.0187)
$C_{½}$	0.020	$I=\log K_{Fr}$	4.0818	$C_{½}$	0.0009	$I=\log K_{Fr}$	4.0774	$C_{½}$	0.0016	$I=\log K_{Fr}$	4.0257
	(0.035)		(0.0173)		(0.0019)		(0.0158)		(0.0028)		(0.0171)
R^2	0.0160	R^2	0.9874	R^2	0.0168	R^2	0.9897	R^2	0.0303	R^2	0.9899
n_{Fr} guessed			0.72	n_{Fr} guessed			0.74	n_{Fr} guessed			0.80
$\log K_{Fr}$ guessed			4.08	$\log K_{Fr}$ guessed			4.08	$\log K_{Fr}$ guessed			4.05

* C ($\mu g_{pyr}/L_w$), S ($\mu g_{pyr}/kg_{solids}$), nFr (dimensionless), K_{Fr} ($\mu g_{pyr}/kg_{solids}$)($L_w/\mu g_{pyr}$)^{nFr}, S_{Max} ($\mu g_{pyr}/kg_{solids}$), $C_{½}$ ($\mu g_{pyr}/L_w$).

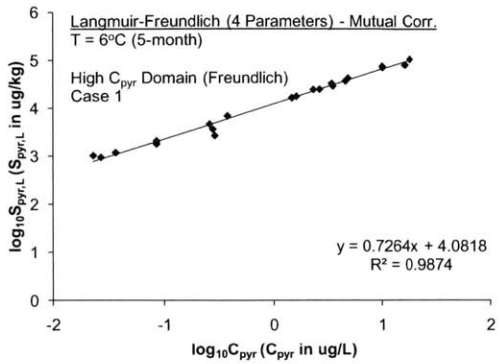
Langmuir-Freundlich (4 Parameters) - Mutual Corr.
T = 6°C (5-month)
High C_{pyr} Domain (Freundlich)
Case 1
y = 0.7264x + 4.0818
R² = 0.9874
$\log_{10}S_{pyr,L}$ ($S_{pyr,L}$ in ug/kg)
$\log_{10}C_{pyr}$ (C_{pyr} in ug/L)

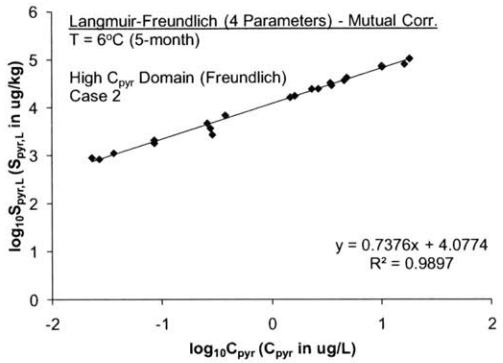
Langmuir-Freundlich (4 Parameters) - Mutual Corr.
T = 6°C (5-month)
High C_{pyr} Domain (Freundlich)
Case 2
y = 0.7376x + 4.0774
R² = 0.9897
$\log_{10}S_{pyr,L}$ ($S_{pyr,L}$ in ug/kg)
$\log_{10}C_{pyr}$ (C_{pyr} in ug/L)

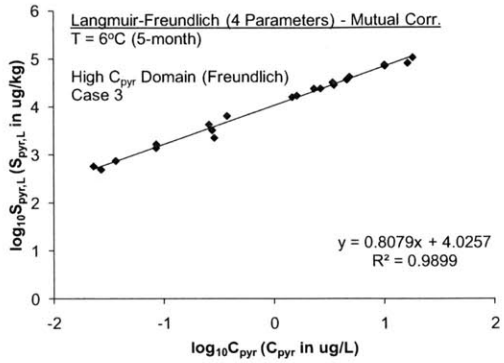
Langmuir-Freundlich (4 Parameters) - Mutual Corr.
T = 6°C (5-month)
High C_{pyr} Domain (Freundlich)
Case 3
y = 0.8079x + 4.0257
R² = 0.9899
$\log_{10}S_{pyr,L}$ ($S_{pyr,L}$ in ug/kg)
$\log_{10}C_{pyr}$ (C_{pyr} in ug/L)

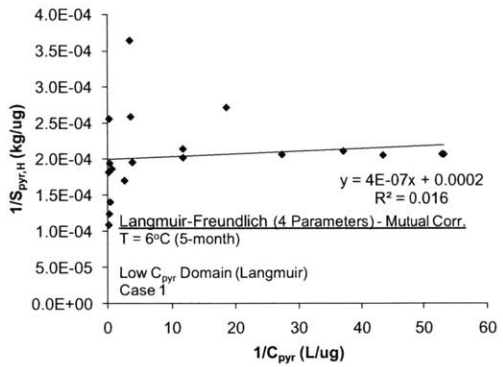
y = 4E-07x + 0.0002
R² = 0.016
Langmuir-Freundlich (4 Parameters) - Mutual Corr.
T = 6°C (5-month)
Low C_{pyr} Domain (Langmuir)
Case 1
$1/S_{pyr,H}$ (kg/ug)
$1/C_{pyr}$ (L/ug)

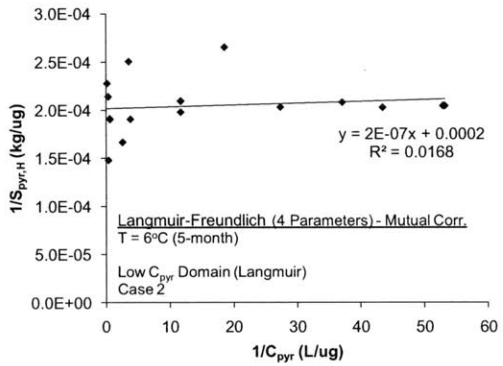
y = 2E-07x + 0.0002
R² = 0.0168
Langmuir-Freundlich (4 Parameters) - Mutual Corr.
T = 6°C (5-month)
Low C_{pyr} Domain (Langmuir)
Case 2
$1/S_{pyr,H}$ (kg/ug)
$1/C_{pyr}$ (L/ug)

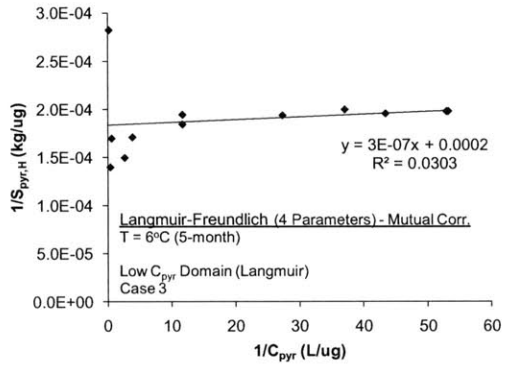
y = 3E-07x + 0.0002
R² = 0.0303
Langmuir-Freundlich (4 Parameters) - Mutual Corr.
T = 6°C (5-month)
Low C_{pyr} Domain (Langmuir)
Case 3
$1/S_{pyr,H}$ (kg/ug)
$1/C_{pyr}$ (L/ug)

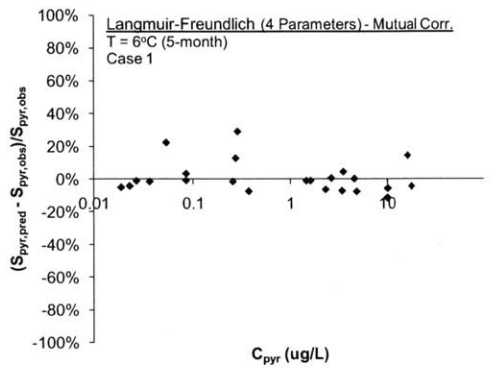
Langmuir-Freundlich (4 Parameters) - Mutual Corr.
T = 6°C (5-month)
Case 1
$(S_{pyr,pred} - S_{pyr,obs})/S_{pyr,obs}$
C_{pyr} (ug/L)

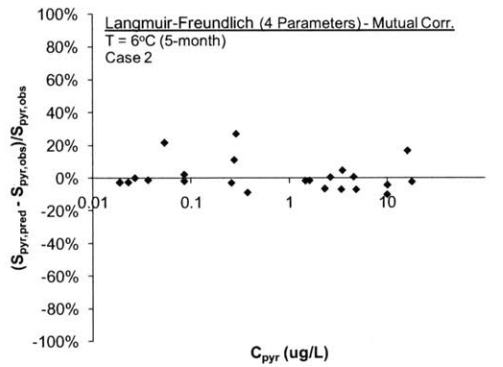
Langmuir-Freundlich (4 Parameters) - Mutual Corr.
T = 6°C (5-month)
Case 2
$(S_{pyr,pred} - S_{pyr,obs})/S_{pyr,obs}$
C_{pyr} (ug/L)

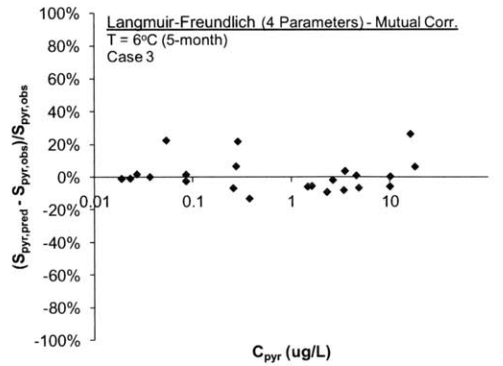
Langmuir-Freundlich (4 Parameters) - Mutual Corr.
T = 6°C (5-month)
Case 3
$(S_{pyr,pred} - S_{pyr,obs})/S_{pyr,obs}$
C_{pyr} (ug/L)

6°C (10-month) Fitted by Langmuir-Freundlich Form*

Fit #1				Fit #2				Fit #3			
'Native' Domain (high-affinity, low C_{pyr} range)		*Amended Domain* (high-affinity, low C_{pyr} range)		*'Native' Domain* (high-affinity, low C_{pyr} range)		*Amended Domain* (high-affinity, low C_{pyr} range)		*'Native' Domain* (high-affinity, low C_{pyr} range)		*Amended Domain* (high-affinity, low C_{pyr} range)	
1/C	$1/S_{Hi}$	$\log_{10}C$	$\log_{10}S_{Hi}$	1/C	$1/S_{Hi}$	$\log_{10}C$	$\log_{10}S_{Hi}$	1/C	$1/S_{Hi}$	$\log_{10}C$	$\log_{10}S_{Hi}$
0.42	4.5E-05	0.38	4.63	0.42	7.5E-05	0.38	4.62	0.42	5.9E-05	0.38	4.62
0.53	1.4E-04	0.28	4.36			0.28	4.35			0.28	4.35
0.89	1.3E-04	0.05	4.23	0.89	2.4E-04	0.05	4.21	0.89	2.2E-04	0.05	4.22
		1.14	5.11			1.14	5.11			1.14	5.11
		0.86	4.85			0.86	4.85			0.86	4.85
		0.53	4.53			0.53	4.52			0.53	4.52
23.54	2.6E-04	-1.37	1.65	23.54	2.6E-04			23.54	3.0E-04		
56.23	2.1E-04	-1.75	2.85	56.23	2.1E-04			56.23	2.3E-04		
67.43	2.2E-04	-1.83	2.79	67.43	2.2E-04			67.43	2.3E-04		
3.38	4.9E-04	-0.53	3.26								
3.63	4.6E-04	-0.56	3.22								
10.68	2.5E-04	-1.03	3.03	10.68	2.5E-04			10.68	3.0E-04		
36.81	2.0E-04	-1.57	2.98	36.81	2.0E-04			36.81	2.2E-04		
58.13	2.1E-04	-1.76	2.84	58.13	2.1E-04			58.13	2.3E-04		
77.54	2.2E-04	-1.89	2.85	77.54	2.1E-04			77.54	2.3E-04		
2.73	2.6E-04	-0.44	3.66			-0.44	3.59				
4.23	2.1E-04	-0.63	3.56	4.23	2.4E-04	-0.63	3.47	4.23	3.1E-04		
15.05	2.0E-04	-1.18	3.17	15.05	2.1E-04			15.05	2.3E-04		
0.42	4.8E-05	0.38	4.61	0.42	8.3E-05	0.38	4.60	0.42	6.4E-05	0.38	4.61
0.58	7.2E-05	0.24	4.45	0.58	1.3E-04	0.24	4.44	0.58	1.1E-04	0.24	4.45
1.07	1.1E-04	-0.03	4.20	1.07	1.7E-04	-0.03	4.18	1.07	1.7E-04	-0.03	4.19
		1.07	4.99			1.07	4.99			1.07	4.99
		0.88	4.87			0.88	4.86			0.88	4.87
		0.57	4.58			0.57	4.58			0.57	4.58
S_{Max}	5.0×10^3	$Slp=n_{Fr}$	0.8610	S_{Max}	5.8×10^3	$Slp=n_{Fr}$	0.8933	S_{Max}	5.4×10^3	$Slp=n_{Fr}$	0.7426
	(920)		(0.0697)		(680)		(0.0524)		(860)		(0.0557)
$C_{½}$	0.0021	$I=\log K_{Fr}$	4.0974	$C_{½}$	0.0045	$I=\log K_{Fr}$	4.1180	$C_{½}$	0.0051	$I=\log K_{Fr}$	4.2206
	(0.0056)		(0.0725)		(0.0032)		(0.0330)		(0.0043)		(0.0359)
R^2	0.0091	R^2	0.8741	R^2	0.1459	R^2	0.9604	R^2	0.1089	R^2	0.9467
n_{Fr} guessed			0.80	n_{Fr} guessed			0.88	n_{Fr} guessed			0.75
$\log K_{Fr}$ guessed			4.10	$\log K_{Fr}$ guessed			4.20	$\log K_{Fr}$ guessed			4.20

* C ($\mu g_{pyr}/L_w$), S ($\mu g_{pyr}/kg_{solids}$), nFr (dimensionless), K_{Fr} ($\mu g_{pyr}/kg_{solids}$)($L_w/\mu g_{pyr}$)^{nFr}, S_{Max} ($\mu g_{pyr}/kg_{solids}$), $C_{½}$ ($\mu g_{pyr}/L_w$).

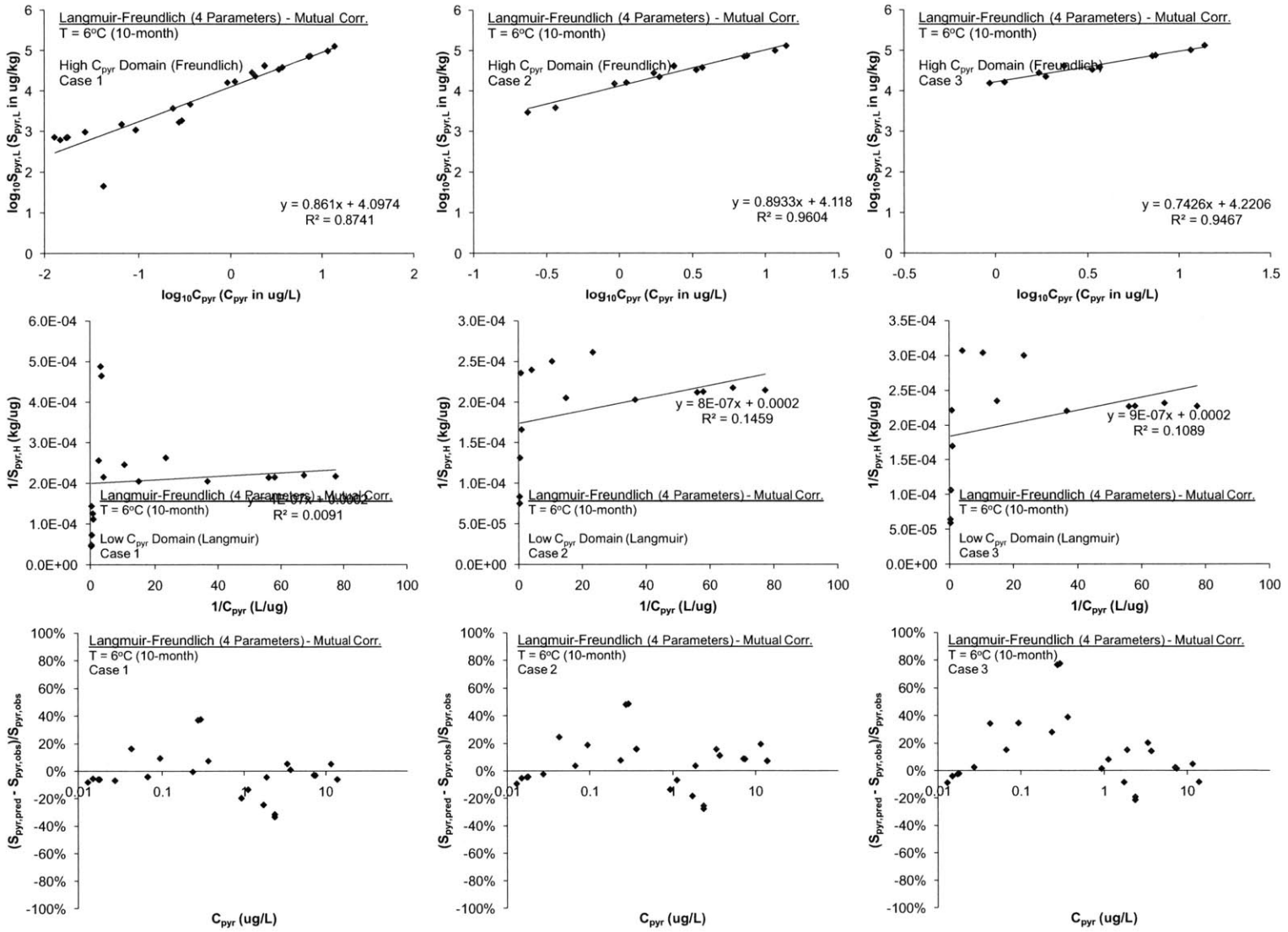
Langmuir-Freundlich (4 Parameters) - Mutual Corr.
T = 6°C (10-month)
High C_{pyr} Domain (Freundlich)
Case 1
y = 0.861x + 4.0974
R² = 0.8741
$\log_{10}S_{pyr,L}$ ($S_{pyr,L}$ in ug/kg)
$\log_{10}C_{pyr}$ (C_{pyr} in ug/L)
Langmuir-Freundlich (4 Parameters) - Mutual Corr.
T = 6°C (10-month)
High C_{pyr} Domain (Freundlich)
Case 2
y = 0.8933x + 4.118
R² = 0.9604
$\log_{10}S_{pyr,L}$ ($S_{pyr,L}$ in ug/kg)
$\log_{10}C_{pyr}$ (C_{pyr} in ug/L)
Langmuir-Freundlich (4 Parameters) - Mutual Corr.
T = 6°C (10-month)
High C_{pyr} Domain (Freundlich)
Case 3
y = 0.7426x + 4.2206
R² = 0.9467
$\log_{10}S_{pyr,L}$ ($S_{pyr,L}$ in ug/kg)
$\log_{10}C_{pyr}$ (C_{pyr} in ug/L)
Langmuir-Freundlich (4 Parameters) - Mutual Corr.
T = 6°C (10-month)
Low C_{pyr} Domain (Langmuir)
Case 1
y = 4E-07x + 0.0002
R² = 0.0091
$1/S_{pyr,H}$ (kg/ug)
$1/C_{pyr}$ (L/ug)
Langmuir-Freundlich (4 Parameters) - Mutual Corr.
T = 6°C (10-month)
Low C_{pyr} Domain (Langmuir)
Case 2
y = 8E-07x + 0.0002
R² = 0.1459
$1/S_{pyr,H}$ (kg/ug)
$1/C_{pyr}$ (L/ug)
Langmuir-Freundlich (4 Parameters) - Mutual Corr.
T = 6°C (10-month)
Low C_{pyr} Domain (Langmuir)
Case 3
y = 9E-07x + 0.0002
R² = 0.1089
$1/S_{pyr,H}$ (kg/ug)
$1/C_{pyr}$ (L/ug)
Langmuir-Freundlich (4 Parameters) - Mutual Corr.
T = 6°C (10-month)
Case 1
$(S_{pyr,pred} - S_{pyr,obs})/S_{pyr,obs}$
C_{pyr} (ug/L)
Langmuir-Freundlich (4 Parameters) - Mutual Corr.
T = 6°C (10-month)
Case 2
$(S_{pyr,pred} - S_{pyr,obs})/S_{pyr,obs}$
C_{pyr} (ug/L)
Langmuir-Freundlich (4 Parameters) - Mutual Corr.
T = 6°C (10-month)
Case 3
$(S_{pyr,pred} - S_{pyr,obs})/S_{pyr,obs}$
C_{pyr} (ug/L)

15°C (5-month) Fitted by Langmuir-Freundlich Form*

Fit #1				Fit #2				Fit #3			
'Native' Domain (high-affinity, low C_{pyr} range)		*Amended Domain* (high-affinity, low C_{pyr} range)		*'Native' Domain* (high-affinity, low C_{pyr} range)		*Amended Domain* (high-affinity, low C_{pyr} range)		*'Native' Domain* (high-affinity, low C_{pyr} range)		*Amended Domain* (high-affinity, low C_{pyr} range)	
1/C	$1/S_{Hi}$	$\log_{10}C$	$\log_{10}S_{Hi}$	1/C	$1/S_{Hi}$	$\log_{10}C$	$\log_{10}S_{Hi}$	1/C	$1/S_{Hi}$	$\log_{10}C$	$\log_{10}S_{Hi}$
0.26	1.0E-04	0.58	4.45			0.58	4.47			0.58	4.47
0.31	1.1E-04	0.50	4.37			0.50	4.40			0.50	4.40
0.52	1.5E-04	0.29	4.15	0.52	1.6E-04	0.29	4.19	0.52	1.8E-04	0.29	4.19
		1.27	5.05			1.27	5.06			1.27	5.06
		1.14	4.86			1.14	4.87			1.14	4.87
		0.86	4.69			0.86	4.70			0.86	4.71
20.16	2.0E-04			20.16	2.2E-04			20.16	2.1E-04		
28.35	1.9E-04	-1.45	2.67	28.35	2.0E-04	-1.45	2.91	28.35	1.9E-04		
31.86	1.9E-04	-1.50	2.63	31.86	2.1E-04	-1.50	2.83	31.86	2.0E-04		
2.85	1.1E-04	-0.46	3.73			-0.46	3.83			-0.46	3.83
3.31	1.7E-04	-0.52	3.26	3.31	2.0E-04	-0.52	3.49	3.31	1.9E-04	-0.52	3.50
4.91	2.0E-04	-0.69	2.70	4.91	2.3E-04	-0.69	3.23	4.91	2.1E-04	-0.69	3.25
26.64	1.9E-04	-1.43	2.40	26.64	2.1E-04	-1.43	2.81	26.64	2.0E-04		
35.15	1.9E-04	-1.55	2.71	35.15	2.1E-04	-1.55	2.84	35.15	2.0E-04		
40.24	2.0E-04	-1.60	2.78	40.24	2.1E-04	-1.60	2.82	40.24	2.0E-04		
2.72	1.7E-04	-0.43	3.37	2.72	2.0E-04	-0.43	3.57	2.72	1.9E-04	-0.43	3.58
4.01	1.9E-04	-0.60	3.00	4.01	2.2E-04	-0.60	3.36	4.01	2.0E-04	-0.60	3.37
18.25	1.5E-04	-1.26	3.13	18.25	1.6E-04	-1.26	3.30				
0.29	1.4E-04	0.54	4.37			0.54	4.40			0.54	4.40
0.44	1.4E-04	0.35	4.22	0.44	1.4E-04	0.35	4.25	0.44	1.8E-04	0.35	4.25
0.64	1.3E-04	0.19	4.09	0.64	1.5E-04	0.19	4.14	0.64	1.6E-04	0.19	4.14
		1.20	4.94			1.20	4.95			1.20	4.95
		1.00	4.75			1.00	4.77			1.00	4.77
		0.68	4.51			0.68	4.53			0.68	4.53
S_{Max}	***7.0×10^3***	***$Slp=n_{Fr}$***	***0.8664***	***S_{Max}***	***5.5×10^3***	***$Slp=n_{Fr}$***	***0.7730***	***S_{Max}***	***5.4×10^3***	***$Slp=n_{Fr}$***	***0.8393***
	(380)		*(0.0441)*		*(320)*		*(0.0228)*		*(150)*		*(0.0299)*
$C_{½}$	***0.011***	***$I=\log K_{Fr}$***	***3.8848***	***$C_{½}$***	***0.0041***	***$I=\log K_{Fr}$***	***3.9972***	***$C_{½}$***	***0.0024***	***$I=\log K_{Fr}$***	***3.9606***
	(0.003)		*(0.0433)*		*(0.0028)*		*(0.0224)*		*(0.0014)*		*(0.0220)*
R^2	***0.4845***	***R^2***	***0.9484***	***R^2***	***0.1539***	***R^2***	***0.9820***	***R^2***	***0.2201***	***R^2***	***0.9814***
n_{Fr} guessed			***0.87***	***n_{Fr} guessed***			***0.75***	***n_{Fr} guessed***			***0.84***
$\log K_{Fr}$ guessed			***3.90***	***$\log K_{Fr}$ guessed***			***3.95***	***$\log K_{Fr}$ guessed***			***3.95***

*** C ($\mu g_{pyr}/L_w$), S ($\mu g_{pyr}/kg_{solids}$), nFr (dimensionless), K_{Fr} ($\mu g_{pyr}/kg_{solids}$)($L_w/\mu g_{pyr}$)^{nFr}, S_{Max} ($\mu g_{pyr}/kg_{solids}$), $C_{½}$ ($\mu g_{pyr}/L_w$).**

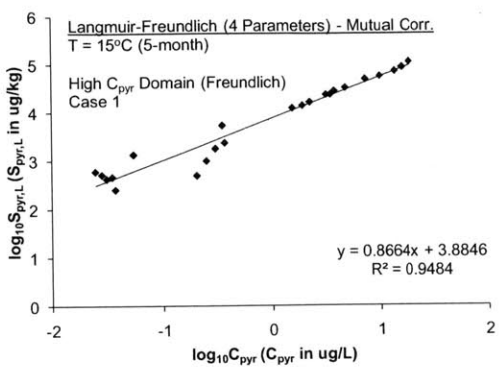
Langmuir-Freundlich (4 Parameters) - Mutual Corr.
T = 15°C (5-month)
High C_{pyr} Domain (Freundlich)
Case 1
y = 0.8664x + 3.8846
R² = 0.9484
$\log_{10}S_{pyr,L}$ ($S_{pyr,L}$ in ug/kg)
$\log_{10}C_{pyr}$ (C_{pyr} in ug/L)

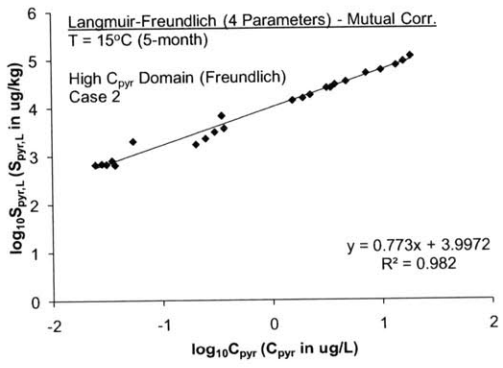
Langmuir-Freundlich (4 Parameters) - Mutual Corr.
T = 15°C (5-month)
High C_{pyr} Domain (Freundlich)
Case 2
y = 0.773x + 3.9972
R² = 0.982
$\log_{10}S_{pyr,L}$ ($S_{pyr,L}$ in ug/kg)
$\log_{10}C_{pyr}$ (C_{pyr} in ug/L)

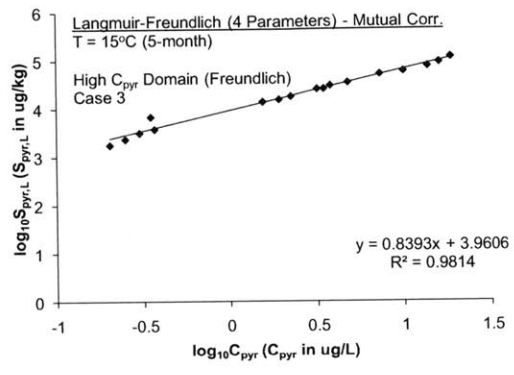
Langmuir-Freundlich (4 Parameters) - Mutual Corr.
T = 15°C (5-month)
High C_{pyr} Domain (Freundlich)
Case 3
y = 0.8393x + 3.9606
R² = 0.9814
$\log_{10}S_{pyr,L}$ ($S_{pyr,L}$ in ug/kg)
$\log_{10}C_{pyr}$ (C_{pyr} in ug/L)

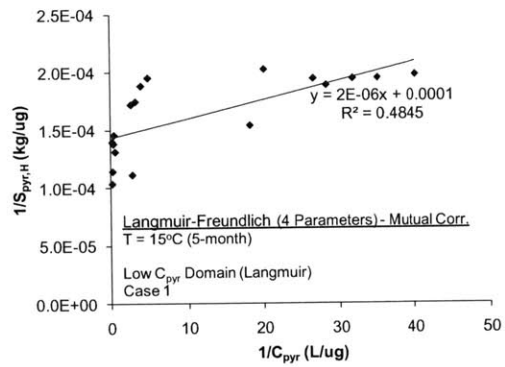
y = 2E-06x + 0.0001
R² = 0.4845
Langmuir-Freundlich (4 Parameters) - Mutual Corr.
T = 15°C (5-month)
Low C_{pyr} Domain (Langmuir)
Case 1
$1/S_{pyr,H}$ (kg/ug)
$1/C_{pyr}$ (L/ug)

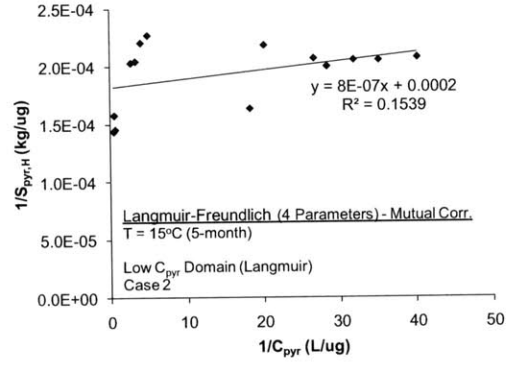
y = 8E-07x + 0.0002
R² = 0.1539
Langmuir-Freundlich (4 Parameters) - Mutual Corr.
T = 15°C (5-month)
Low C_{pyr} Domain (Langmuir)
Case 2
$1/S_{pyr,H}$ (kg/ug)
$1/C_{pyr}$ (L/ug)

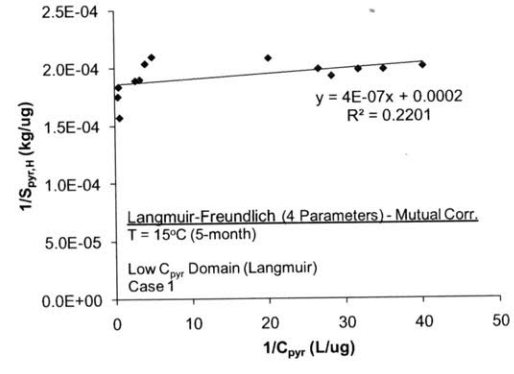
y = 4E-07x + 0.0002
R² = 0.2201
Langmuir-Freundlich (4 Parameters) - Mutual Corr.
T = 15°C (5-month)
Low C_{pyr} Domain (Langmuir)
Case 1
$1/S_{pyr,H}$ (kg/ug)
$1/C_{pyr}$ (L/ug)

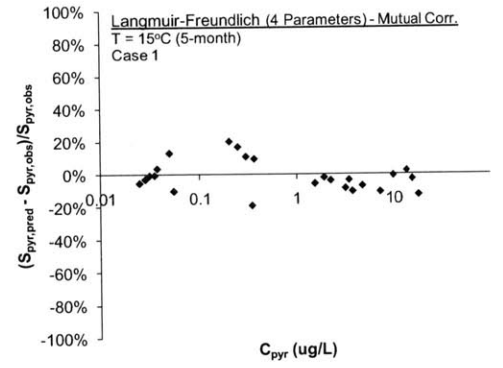
Langmuir-Freundlich (4 Parameters) - Mutual Corr.
T = 15°C (5-month)
Case 1
$(S_{pyr,pred} - S_{pyr,obs})/S_{pyr,obs}$
C_{pyr} (ug/L)

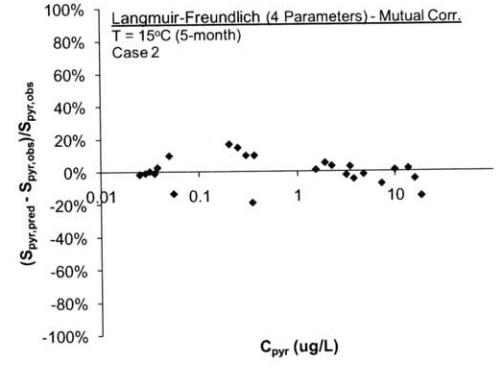
Langmuir-Freundlich (4 Parameters) - Mutual Corr.
T = 15°C (5-month)
Case 2
$(S_{pyr,pred} - S_{pyr,obs})/S_{pyr,obs}$
C_{pyr} (ug/L)

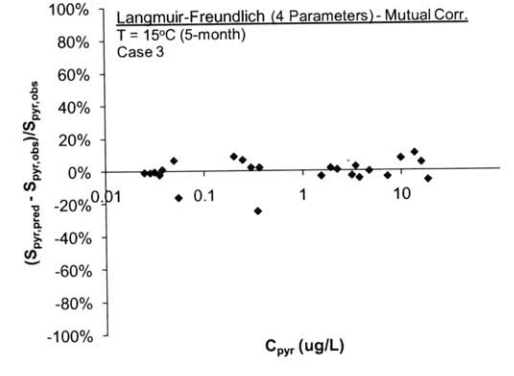
Langmuir-Freundlich (4 Parameters) - Mutual Corr.
T = 15°C (5-month)
Case 3
$(S_{pyr,pred} - S_{pyr,obs})/S_{pyr,obs}$
C_{pyr} (ug/L)

15°C (10-month) Fitted by Langmuir-Freundlich Form*

Fit #1				Fit #2				Fit #3			
'Native' Domain (high-affinity, low C_{pyr} range)		*Amended Domain* (high-affinity, low C_{pyr} range)		*'Native' Domain* (high-affinity, low C_{pyr} range)		*Amended Domain* (high-affinity, low C_{pyr} range)		*'Native' Domain* (high-affinity, low C_{pyr} range)		*Amended Domain* (high-affinity, low C_{pyr} range)	
1/C	$1/S_{Hi}$	$\log_{10}C$	$\log_{10}S_{Hi}$	1/C	$1/S_{Hi}$	$\log_{10}C$	$\log_{10}S_{Hi}$	1/C	$1/S_{Hi}$	$\log_{10}C$	$\log_{10}S_{Hi}$
0.27	-7.3E-05	0.57	4.29	0.27	1.8E-04	0.57	4.28	0.27	1.6E-04	0.57	4.28
0.30	-7.2E-05	0.52	4.22	0.30	2.4E-04	0.52	4.21	0.30	2.1E-04	0.52	4.21
0.46	-1.0E-04	0.33	4.09	0.46	2.3E-04	0.33	4.07	0.46	2.4E-04	0.33	4.07
0.05	-1.6E-05	1.30	4.66			1.30	4.65			1.30	4.65
0.07	-4.2E-05	1.13	4.78			1.13	4.77			1.13	4.77
0.13	-7.1E-05	0.89	4.63			0.89	4.63			0.89	4.62
23.15	3.3E-04			23.15	2.3E-04			23.15	2.6E-04		
29.85	2.9E-04			29.85	2.2E-04			29.85	2.4E-04		
37.69	2.8E-04			37.69	2.2E-04			37.69	2.4E-04		
		-0.42	3.55			-0.42	3.48				
28.87	3.0E-04			28.87	2.3E-04			28.87	2.5E-04		
38.13	2.9E-04			38.13	2.3E-04			38.13	2.5E-04		
44.39	2.8E-04			44.39	2.3E-04			44.39	2.5E-04		
		-0.46	3.53			-0.46	3.45				
0.58	2.6E-03	0.23	4.27			0.23	4.26			0.23	4.26
0.64	-2.2E-04	0.20	4.09	0.64	1.5E-04	0.20	4.07	0.64	1.6E-04	0.20	4.07
0.06	-2.3E-05	1.23	4.74			1.23	4.74			1.23	4.74
S_{Max}	4.5×10^3	$Slp=n_{Fr}$	0.6998	S_{Max}	5.0×10^3	$Slp=n_{Fr}$	0.7371	S_{Max}	5.0×10^3	$Slp=n_{Fr}$	0.6202
	(4700)		(0.0539)		(340)		(0.0584)		(360)		(0.0855)
$C_{½}$	0.0095	$I=\log K_{Fr}$	3.9064	$C_{½}$	0.0035	$I=\log K_{Fr}$	3.8666	$C_{½}$	0.0070	$I=\log K_{Fr}$	3.9661
	(0.003)		(0.0413)		(0.0025)		(0.0448)		(0.0027)		(0.0702)
R^2	0.0490	R^2	0.9493	R^2	0.1934	R^2	0.9465	R^2	0.4575	R^2	0.8827
n_{Fr} guessed			0.66	n_{Fr} guessed			0.73	n_{Fr} guessed			0.61
$\log K_{Fr}$ guessed			4.2	$\log K_{Fr}$ guessed			3.85	$\log K_{Fr}$ guessed			3.90

* C ($\mu g_{pyr}/L_w$), S ($\mu g_{pyr}/kg_{solids}$), nFr (dimensionless), K_{Fr} ($\mu g_{pyr}/kg_{solids}$)($L_w/\mu g_{pyr}$)^{nFr}, S_{Max} ($\mu g_{pyr}/kg_{solids}$), $C_{½}$ ($\mu g_{pyr}/L_w$).

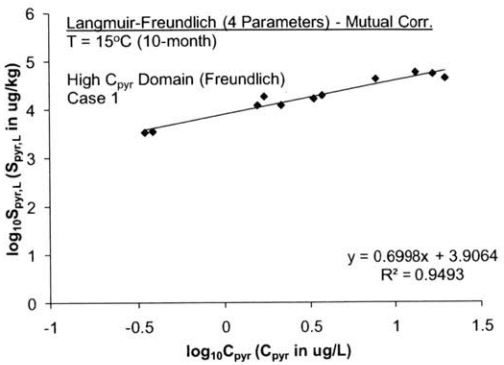
Langmuir-Freundlich (4 Parameters) - Mutual Corr.
T = 15°C (10-month)
High C_{pyr} Domain (Freundlich)
Case 1
y = 0.6998x + 3.9064
R² = 0.9493
$\log_{10}S_{pyr,L}$ ($S_{pyr,L}$ in ug/kg)
$\log_{10}C_{pyr}$ (C_{pyr} in ug/L)

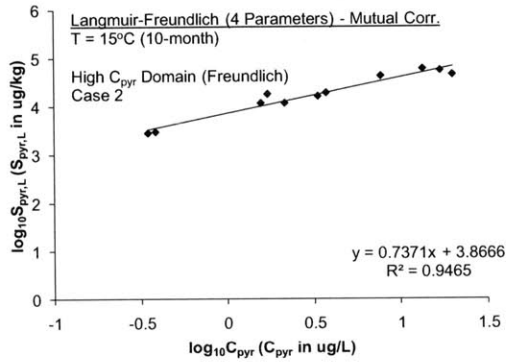
Langmuir-Freundlich (4 Parameters) - Mutual Corr.
T = 15°C (10-month)
High C_{pyr} Domain (Freundlich)
Case 2
y = 0.7371x + 3.8666
R² = 0.9465
$\log_{10}S_{pyr,L}$ ($S_{pyr,L}$ in ug/kg)
$\log_{10}C_{pyr}$ (C_{pyr} in ug/L)

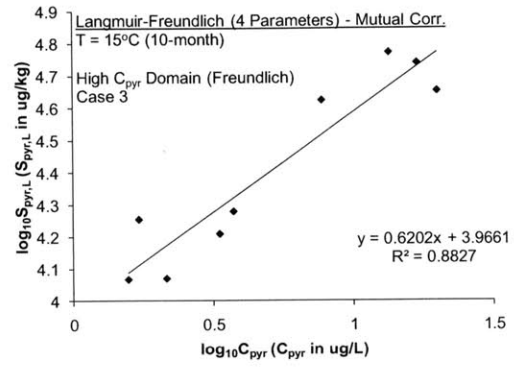
Langmuir-Freundlich (4 Parameters) - Mutual Corr.
T = 15°C (10-month)
High C_{pyr} Domain (Freundlich)
Case 3
y = 0.6202x + 3.9661
R² = 0.8827
$\log_{10}S_{pyr,L}$ ($S_{pyr,L}$ in ug/kg)
$\log_{10}C_{pyr}$ (C_{pyr} in ug/L)

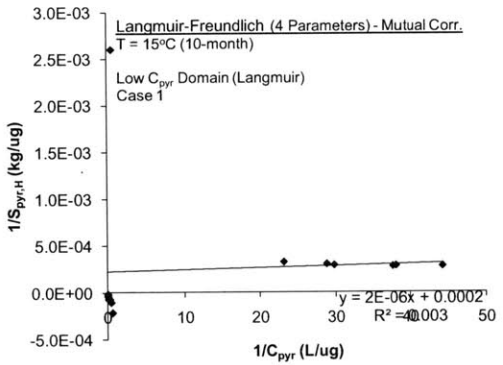
Langmuir-Freundlich (4 Parameters) - Mutual Corr.
T = 15°C (10-month)
Low C_{pyr} Domain (Langmuir)
Case 1
y = 2E-06x + 0.0002
$1/S_{pyr,H}$ (kg/ug)
$1/C_{pyr}$ (L/ug)

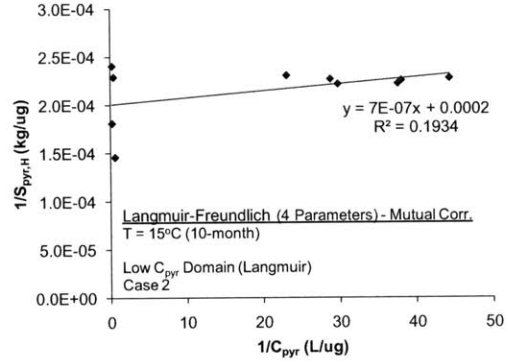
Langmuir-Freundlich (4 Parameters) - Mutual Corr.
T = 15°C (10-month)
Low C_{pyr} Domain (Langmuir)
Case 2
y = 7E-07x + 0.0002
R² = 0.1934
$1/S_{pyr,H}$ (kg/ug)
$1/C_{pyr}$ (L/ug)

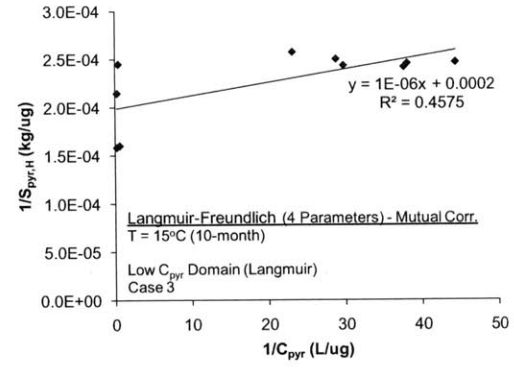
Langmuir-Freundlich (4 Parameters) - Mutual Corr.
T = 15°C (10-month)
Low C_{pyr} Domain (Langmuir)
Case 3
y = 1E-06x + 0.0002
R² = 0.4575
$1/S_{pyr,H}$ (kg/ug)
$1/C_{pyr}$ (L/ug)

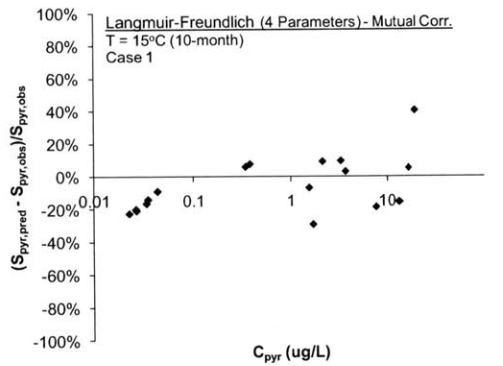
Langmuir-Freundlich (4 Parameters) - Mutual Corr.
T = 15°C (10-month)
Case 1
$(S_{pyr,pred} - S_{pyr,obs})/S_{pyr,obs}$
C_{pyr} (ug/L)

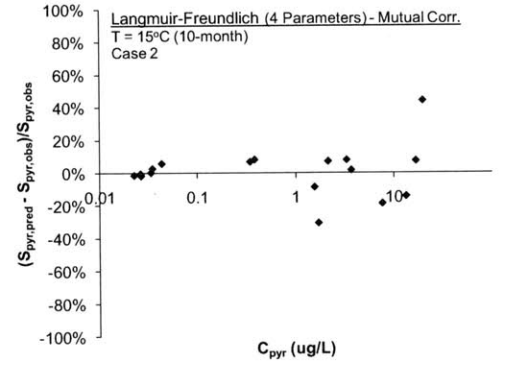
Langmuir-Freundlich (4 Parameters) - Mutual Corr.
T = 15°C (10-month)
Case 2
$(S_{pyr,pred} - S_{pyr,obs})/S_{pyr,obs}$
C_{pyr} (ug/L)

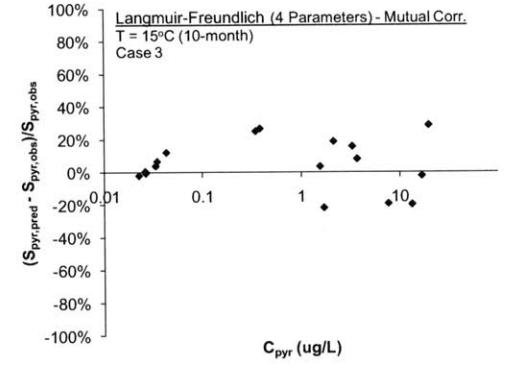
Langmuir-Freundlich (4 Parameters) - Mutual Corr.
T = 15°C (10-month)
Case 3
$(S_{pyr,pred} - S_{pyr,obs})/S_{pyr,obs}$
C_{pyr} (ug/L)

22°C (5-month) Fitted by Langmuir-Freundlich Form*

Fit #1				Fit #2				Fit #3			
'Native' Domain (high-affinity, low C_{pyr} range)		*Amended Domain* (high-affinity, low C_{pyr} range)		*'Native' Domain* (high-affinity, low C_{pyr} range)		*Amended Domain* (high-affinity, low C_{pyr} range)		*'Native' Domain* (high-affinity, low C_{pyr} range)		*Amended Domain* (high-affinity, low C_{pyr} range)	
1/C	$1/S_{Hi}$	$\log_{10}C$	$\log_{10}S_{Hi}$	1/C	$1/S_{Hi}$	$\log_{10}C$	$\log_{10}S_{Hi}$	1/C	$1/S_{Hi}$	$\log_{10}C$	$\log_{10}S_{Hi}$
0.32	9.5E-05	0.50	4.49			0.50	4.48			0.50	4.48
0.44	8.8E-05	0.36	4.41			0.36	4.40			0.36	4.40
0.51	1.9E-04	0.29	4.24	0.51	2.1E-04	0.29	4.22			0.29	4.22
		1.29	5.02			1.29	5.01			1.29	5.01
		0.98	4.89			0.98	4.88			0.98	4.88
0.18	1.5E-04	0.74	4.61			0.74	4.61			0.74	4.61
17.69	2.3E-04	-1.25	2.88	17.69	2.2E-04			17.69	2.2E-04		
20.83	2.2E-04	-1.32	2.94	20.83	2.1E-04	-1.32	2.69	20.83	2.1E-04		
26.49	2.1E-04	-1.42	2.99	26.49	2.1E-04			26.49	2.1E-04		
2.37	6.0E-04	-0.37	3.27								
2.92	3.6E-04	-0.47	3.35								
6.48	2.3E-04	-0.81	3.27	6.48	2.1E-04	-0.81	3.13	6.48	2.1E-04	-0.81	3.09
21.16	2.2E-04	-1.33	2.97	21.16	2.1E-04	-1.33	2.75	21.16	2.1E-04		
26.37	2.2E-04	-1.42	2.98	26.37	2.1E-04			26.37	2.1E-04		
32.36	2.1E-04	-1.51	3.03	32.36	2.0E-04			32.36	2.0E-04		
2.53	1.4E-04	-0.40	3.85	2.53	1.3E-04	-0.40	3.82	2.53	1.3E-04	-0.40	3.81
3.03	2.1E-04	-0.48	3.62	3.03	1.9E-04	-0.48	3.55	3.03	1.9E-04	-0.48	3.54
5.65	2.2E-04	-0.75	3.37	5.65	2.0E-04	-0.75	3.25	5.65	2.0E-04		
0.32	9.8E-05	0.50	4.48			0.50	4.48			0.50	4.47
0.34	2.3E-04	0.47	4.37			0.47	4.35			0.47	4.35
0.61	1.5E-04	0.22	4.22	0.61	1.6E-04	0.22	4.21			0.22	4.20
		1.21	5.05			1.21	5.04			1.21	5.04
		0.98	4.89			0.98	4.88			0.98	4.88
0.18	1.8E-04	0.75	4.60			0.75	4.60			0.75	4.60
S_{Max}	***4.9×10^3***	***$Slp=n_{Fr}$***	***0.8095***	***S_{Max}***	***5.5×10^3***	***$Slp=n_{Fr}$***	***0.9089***	***S_{Max}***	***5.6×10^3***	***$Slp=n_{Fr}$***	***0.8809***
	(760)		*(0.0321)*		*(330)*		*(0.0240)*		*(430)*		*(0.0380)*
$C_{½}$	***0.0039***	***$I=\log K_{Fr}$***	***4.0179***	***$C_{½}$***	***0.0060***	***$I=\log K_{Fr}$***	***3.9696***	***$C_{½}$***	***0.0071***	***$I=\log K_{Fr}$***	***3.9854***
	(0.0110)		*(0.0296)*		*(0.0035)*		*(0.0198)*		*(0.0040)*		*(0.0281)*
R^2	***0.0064***	***R^2***	***0.9667***	***R^2***	***0.2304***	***R^2***	***0.9890***	***R^2***	***0.2851***	***R^2***	***0.9764***
n_{Fr} guessed			***0.80***	***n_{Fr} guessed***			***0.88***	***n_{Fr} guessed***			***0.88***
$\log K_{Fr}$ guessed			***4.00***	***$\log K_{Fr}$ guessed***			***3.99***	***$\log K_{Fr}$ guessed***			***3.98***

* C ($\mu g_{pyr}/L_w$), S ($\mu g_{pyr}/kg_{solids}$), nFr (dimensionless), K_{Fr} ($\mu g_{pyr}/kg_{solids}$)($L_w/\mu g_{pyr}$)^{nFr}, S_{Max} ($\mu g_{pyr}/kg_{solids}$), $C_{½}$ ($\mu g_{pyr}/L_w$).

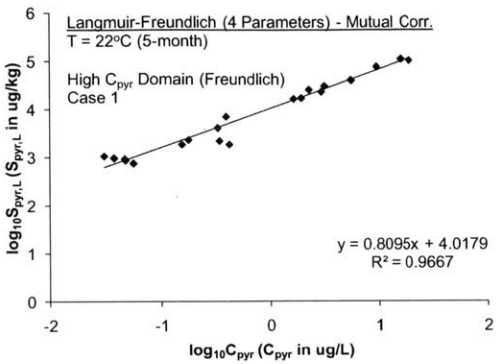
Langmuir-Freundlich (4 Parameters) - Mutual Corr.
T = 22°C (5-month)
High C_{pyr} Domain (Freundlich)
Case 1
y = 0.8095x + 4.0179
R² = 0.9667
$\log_{10}S_{pyr,L}$ ($S_{pyr,L}$ in ug/kg)
$\log_{10}C_{pyr}$ (C_{pyr} in ug/L)

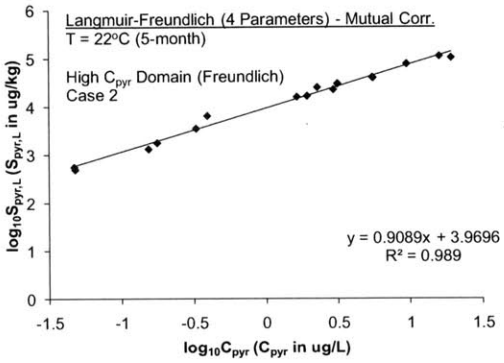
Langmuir-Freundlich (4 Parameters) - Mutual Corr.
T = 22°C (5-month)
High C_{pyr} Domain (Freundlich)
Case 2
y = 0.9089x + 3.9696
R² = 0.989
$\log_{10}S_{pyr,L}$ ($S_{pyr,L}$ in ug/kg)
$\log_{10}C_{pyr}$ (C_{pyr} in ug/L)

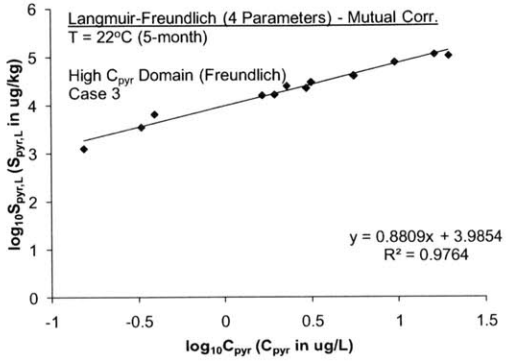
Langmuir-Freundlich (4 Parameters) - Mutual Corr.
T = 22°C (5-month)
High C_{pyr} Domain (Freundlich)
Case 3
y = 0.8809x + 3.9854
R² = 0.9764
$\log_{10}S_{pyr,L}$ ($S_{pyr,L}$ in ug/kg)
$\log_{10}C_{pyr}$ (C_{pyr} in ug/L)

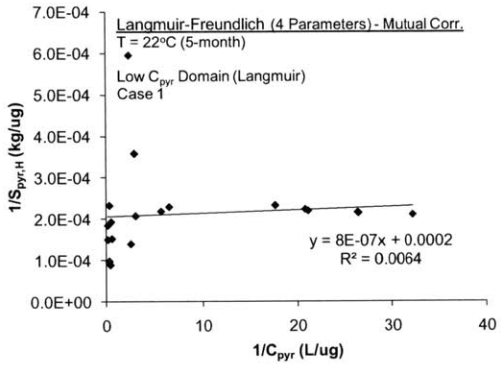
Langmuir-Freundlich (4 Parameters) - Mutual Corr.
T = 22°C (5-month)
Low C_{pyr} Domain (Langmuir)
Case 1
y = 8E-07x + 0.0002
R² = 0.0064
$1/S_{pyr,H}$ (kg/ug)
$1/C_{pyr}$ (L/ug)

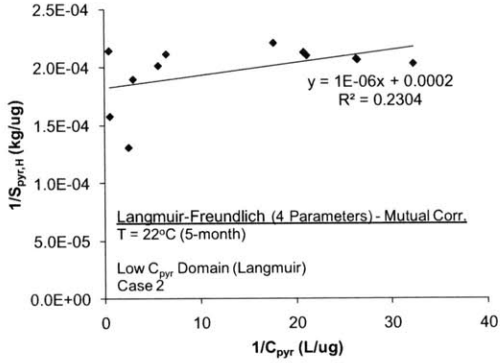
y = 1E-06x + 0.0002
R² = 0.2304
Langmuir-Freundlich (4 Parameters) - Mutual Corr.
T = 22°C (5-month)
Low C_{pyr} Domain (Langmuir)
Case 2
$1/S_{pyr,H}$ (kg/ug)
$1/C_{pyr}$ (L/ug)

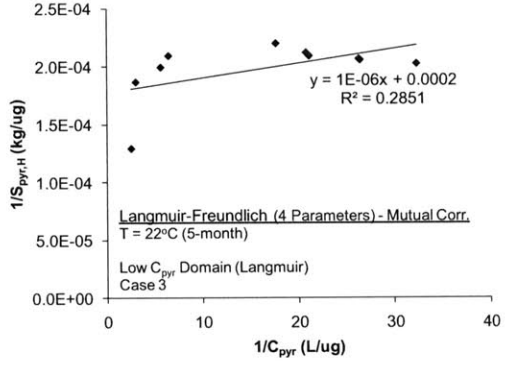
y = 1E-06x + 0.0002
R² = 0.2851
Langmuir-Freundlich (4 Parameters) - Mutual Corr.
T = 22°C (5-month)
Low C_{pyr} Domain (Langmuir)
Case 3
$1/S_{pyr,H}$ (kg/ug)
$1/C_{pyr}$ (L/ug)

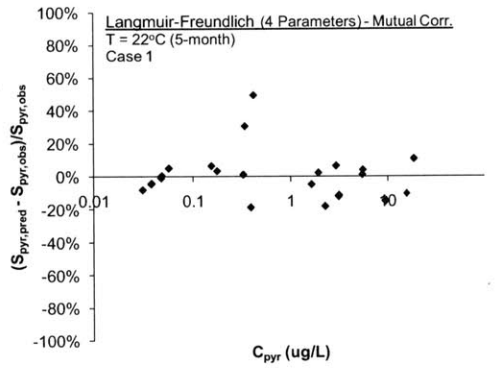
Langmuir-Freundlich (4 Parameters) - Mutual Corr.
T = 22°C (5-month)
Case 1
$(S_{pyr,pred} - S_{pyr,obs})/S_{pyr,obs}$
C_{pyr} (ug/L)

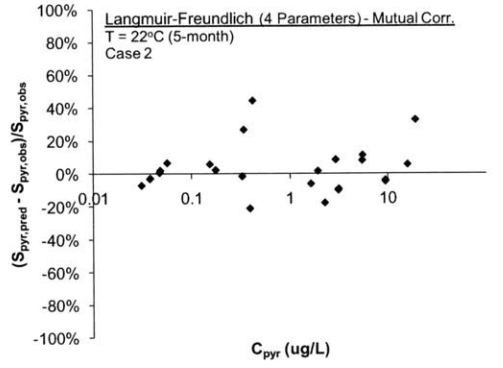
Langmuir-Freundlich (4 Parameters) - Mutual Corr.
T = 22°C (5-month)
Case 2
$(S_{pyr,pred} - S_{pyr,obs})/S_{pyr,obs}$
C_{pyr} (ug/L)

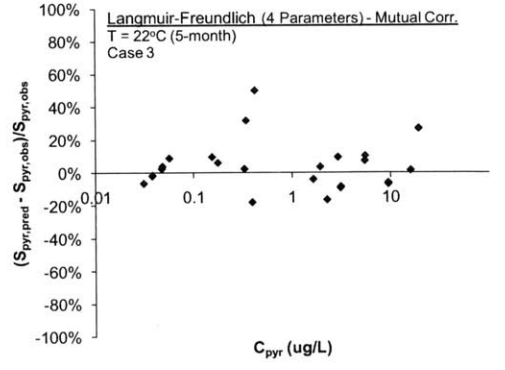
Langmuir-Freundlich (4 Parameters) - Mutual Corr.
T = 22°C (5-month)
Case 3
$(S_{pyr,pred} - S_{pyr,obs})/S_{pyr,obs}$
C_{pyr} (ug/L)

22°C (10-month) Fitted by Langmuir-Freundlich Form*

Fit #1				Fit #2				Fit #3			
'Native' Domain (high-affinity, low C_{pyr} range)		*Amended Domain* (high-affinity, low C_{pyr} range)		*'Native' Domain* (high-affinity, low C_{pyr} range)		*Amended Domain* (high-affinity, low C_{pyr} range)		*'Native' Domain* (high-affinity, low C_{pyr} range)		*Amended Domain* (high-affinity, low C_{pyr} range)	
1/C	$1/S_{Hi}$	$\log_{10}C$	$\log_{10}S_{Hi}$	1/C	$1/S_{Hi}$	$\log_{10}C$	$\log_{10}S_{Hi}$	1/C	$1/S_{Hi}$	$\log_{10}C$	$\log_{10}S_{Hi}$
		0.50	4.34	0.32	3.5E-04	0.50	4.36	0.32	2.5E-04	0.50	4.35
0.46	1.2E-04	0.34	4.33	0.46	1.3E-04	0.34	4.34	0.46	1.2E-04	0.34	4.33
		0.27	4.15	0.54	3.2E-04	0.27	4.18	0.54	2.8E-04	0.27	4.16
		1.30	4.69			1.30	4.70			1.30	4.69
		0.97	4.81			0.97	4.82			0.97	4.81
		0.74	4.55			0.74	4.56			0.74	4.55
20.36	2.6E-04	-1.31	2.95	20.36	2.6E-04	-1.31	2.92	20.36	2.6E-04		
25.38	2.5E-04	-1.40	3.06	25.38	2.4E-04			25.38	2.5E-04		
29.90	2.5E-04	-1.48	3.11	29.90	2.4E-04			29.90	2.5E-04		
8.11	2.6E-04	-0.91	3.14	8.11	2.5E-04	-0.91	3.25	8.11	2.6E-04		
21.63	2.7E-04	-1.34	2.89	21.63	2.6E-04			21.63	2.7E-04		
19.01	2.9E-04	-1.28	2.75	19.01	2.8E-04	-1.28	2.74	19.01	2.9E-04		
28.76	2.5E-04	-1.46	3.06	28.76	2.5E-04			28.76	2.5E-04		
2.94	1.5E-04	-0.47	3.80	2.94	1.4E-04	-0.47	3.84	2.94	1.5E-04	-0.47	3.81
3.55	2.3E-04	-0.55	3.52	3.55	2.2E-04	-0.55	3.59	3.55	2.3E-04	-0.55	3.54
6.16	2.7E-04	-0.79	3.20	6.16	2.5E-04	-0.79	3.32	6.16	2.7E-04	-0.79	3.24
		0.50	4.32			0.50	4.34			0.50	4.33
		0.43	4.29	0.37	3.2E-04	0.43	4.31	0.37	2.5E-04	0.43	4.30
		0.23	4.12			0.23	4.14			0.23	4.12
		1.21	4.89			1.21	4.89			1.21	4.89
		0.97	4.81	0.11	7.7E-05	0.97	4.82	0.11	5.6E-05	0.97	4.81
		0.75	4.53			0.75	4.55			0.75	4.54
S_{Max}	***5.2×10^3***	***Slp=n_{Fr}***	***0.7411***	***S_{Max}***	***4.4×10^3***	***Slp=n_{Fr}***	***0.7836***	***S_{Max}***	***5.0×10^3***	***Slp=n_{Fr}***	***0.7379***
	(640)		*(0.0306)*		*(530)*		*(0.0342)*		*(570)*		*(0.0467)*
$C_{½}$	***0.0150***	***I=logK_{Fr}***	***3.9709***	***$C_{½}$***	***0.0044***	***I=logK_{Fr}***	***3.9664***	***$C_{½}$***	***0.0130***	***I=logK_{Fr}***	***3.9839***
	(0.0069)		*(0.0295)*		*(0.0077)*		*(0.0283)*		*(0.0074)*		*(0.0346)*
R^2	***0.3728***	***R^2***	***0.9670***	***R^2***	***0.0248***	***R^2***	***0.9705***	***R^2***	***0.1910***	***R^2***	***0.9505***
n_{Fr} guessed			***0.74***	***n_{Fr} guessed***			***0.78***	***n_{Fr} guessed***			***0.74***
logK_{Fr} guessed			***4.00***	***logK_{Fr} guessed***			***4.00***	***logK_{Fr} guessed***			***4.00***

* C ($\mu g_{pyr}/L_w$), S ($\mu g_{pyr}/kg_{solids}$), nFr (dimensionless), K_{Fr} ($\mu g_{pyr}/kg_{solids}$)($L_w/\mu g_{pyr}$)^{nFr}, S_{Max} ($\mu g_{pyr}/kg_{solids}$), $C_{½}$ ($\mu g_{pyr}/L_w$).

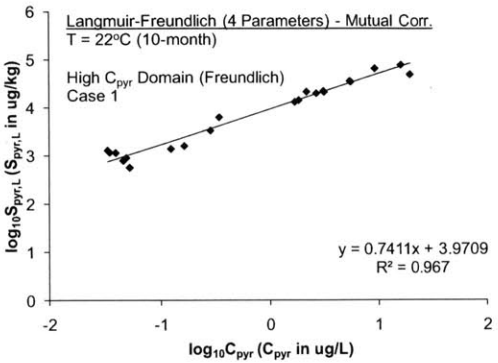
Langmuir-Freundlich (4 Parameters) - Mutual Corr.
T = 22°C (10-month)
High C_{pyr} Domain (Freundlich)
Case 1
y = 0.7411x + 3.9709
R² = 0.967
$\log_{10}S_{pyr,L}$ ($S_{pyr,L}$ in ug/kg)
$\log_{10}C_{pyr}$ (C_{pyr} in ug/L)

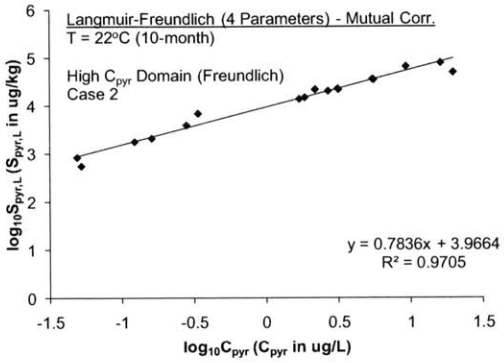
Langmuir-Freundlich (4 Parameters) - Mutual Corr.
T = 22°C (10-month)
High C_{pyr} Domain (Freundlich)
Case 2
y = 0.7836x + 3.9664
R² = 0.9705
$\log_{10}S_{pyr,L}$ ($S_{pyr,L}$ in ug/kg)
$\log_{10}C_{pyr}$ (C_{pyr} in ug/L)

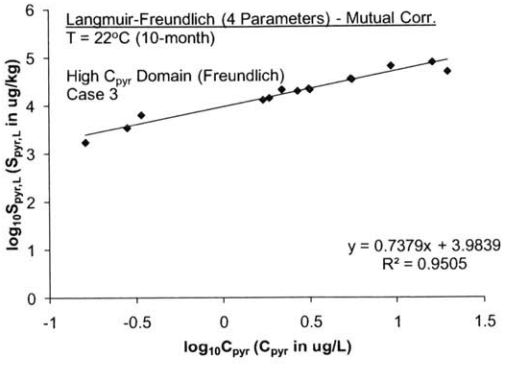
Langmuir-Freundlich (4 Parameters) - Mutual Corr.
T = 22°C (10-month)
High C_{pyr} Domain (Freundlich)
Case 3
y = 0.7379x + 3.9839
R² = 0.9505
$\log_{10}S_{pyr,L}$ ($S_{pyr,L}$ in ug/kg)
$\log_{10}C_{pyr}$ (C_{pyr} in ug/L)

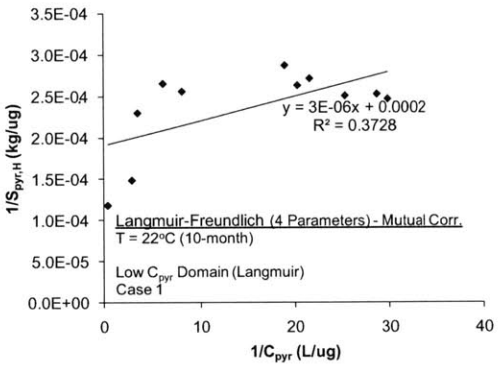
y = 3E-06x + 0.0002
R² = 0.3728
Langmuir-Freundlich (4 Parameters) - Mutual Corr.
T = 22°C (10-month)
Low C_{pyr} Domain (Langmuir)
Case 1
$1/S_{pyr,H}$ (kg/ug)
$1/C_{pyr}$ (L/ug)

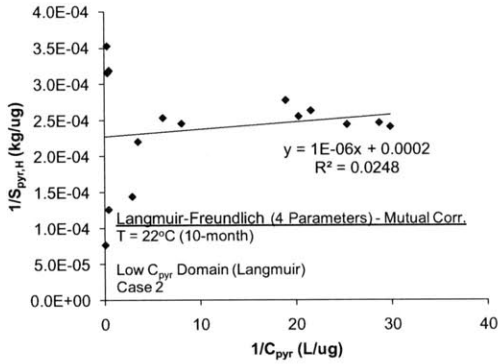
y = 1E-06x + 0.0002
R² = 0.0248
Langmuir-Freundlich (4 Parameters) - Mutual Corr.
T = 22°C (10-month)
Low C_{pyr} Domain (Langmuir)
Case 2
$1/S_{pyr,H}$ (kg/ug)
$1/C_{pyr}$ (L/ug)

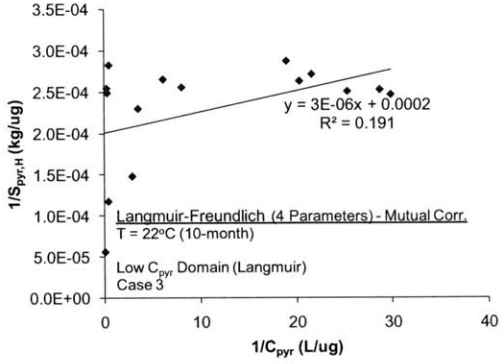
y = 3E-06x + 0.0002
R² = 0.191
Langmuir-Freundlich (4 Parameters) - Mutual Corr.
T = 22°C (10-month)
Low C_{pyr} Domain (Langmuir)
Case 3
$1/S_{pyr,H}$ (kg/ug)
$1/C_{pyr}$ (L/ug)

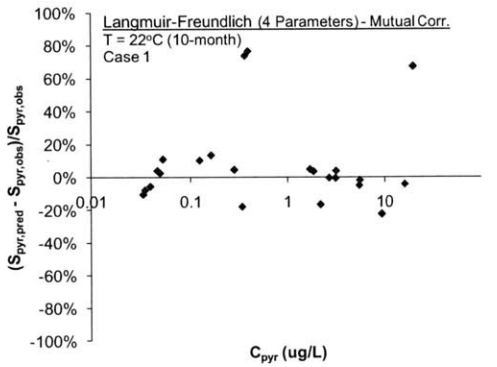
Langmuir-Freundlich (4 Parameters) - Mutual Corr.
T = 22°C (10-month)
Case 1
$(S_{pyr,pred} - S_{pyr,obs})/S_{pyr,obs}$
C_{pyr} (ug/L)

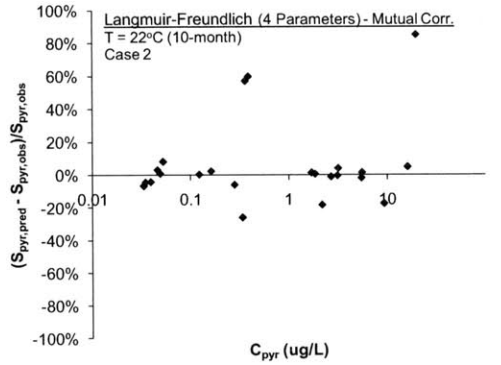
Langmuir-Freundlich (4 Parameters) - Mutual Corr.
T = 22°C (10-month)
Case 2
$(S_{pyr,pred} - S_{pyr,obs})/S_{pyr,obs}$
C_{pyr} (ug/L)

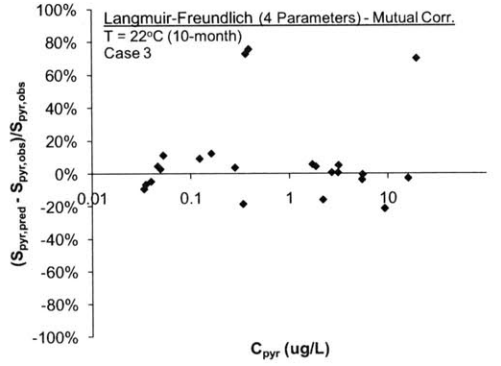
Langmuir-Freundlich (4 Parameters) - Mutual Corr.
T = 22°C (10-month)
Case 3
$(S_{pyr,pred} - S_{pyr,obs})/S_{pyr,obs}$
C_{pyr} (ug/L)

37°C (5-month) Fitted by Langmuir-Freundlich Form*

Fit #1				Fit #2				Fit #3			
'Native' Domain (high-affinity, low C_{pyr} range)		*Amended Domain* (high-affinity, low C_{pyr} range)		*'Native' Domain* (high-affinity, low C_{pyr} range)		*Amended Domain* (high-affinity, low C_{pyr} range)		*'Native' Domain* (high-affinity, low C_{pyr} range)		*Amended Domain* (high-affinity, low C_{pyr} range)	
1/C	$1/S_{Hi}$	$\log_{10}C$	$\log_{10}S_{Hi}$	1/C	$1/S_{Hi}$	$\log_{10}C$	$\log_{10}S_{Hi}$	1/C	$1/S_{Hi}$	$\log_{10}C$	$\log_{10}S_{Hi}$
0.37	9.7E-04	0.43	4.07			0.43	3.98			0.43	4.02
		0.61	4.07			0.61	3.98			0.61	4.02
0.05	8.1E-05	1.31	4.75			1.31	4.73			1.31	4.74
0.06	4.3E-04	1.24	4.62			1.24	4.59			1.24	4.60
0.13	1.2E-04	0.90	4.50			0.90	4.47			0.90	4.49
6.01	1.7E-03	-0.78	3.13								
7.32	4.7E-04	-0.86	3.44	7.32	3.3E-04	-0.86	3.00	7.32	6.0E-04		
2.67	1.3E-04	-0.43	3.97	2.67	1.1E-04	-0.43	3.86	2.67	2.0E-04		
2.92	2.3E-04	-0.46	3.77	2.92	1.8E-04	-0.46	3.58	2.92	4.6E-04		
2.99	4.8E-04	-0.48	3.56			-0.48	3.20				
11.77	5.0E-04	-1.07	3.39	11.77	3.7E-04	-1.07	2.98	11.77	5.3E-04		
8.91	4.6E-04	-0.95	3.43	8.91	3.3E-04	-0.95	3.02	8.91	5.3E-04		
		-0.61	3.10								
2.88	9.8E-05	-0.46	4.07	2.88	8.8E-05	-0.46	3.99	2.88	1.3E-04		
3.43	1.9E-04	-0.54	3.81	3.43	1.6E-04	-0.54	3.65	3.43	2.9E-04		
4.28	2.8E-04	-0.63	3.66	4.28	2.2E-04	-0.63	3.42	4.28	4.3E-04		
0.23	5.1E-04	0.63	4.23	0.23	3.1E-04	0.63	4.17			0.63	4.20
0.28	2.3E-04	0.56	4.25	0.28	1.7E-04	0.56	4.19			0.56	4.22
0.38	4.7E-04	0.42	4.10	0.38	2.6E-04	0.42	4.02			0.42	4.06
0.05	3.9E-05	1.29	4.83			1.29	4.82			1.29	4.82
0.07	4.3E-05	1.13	4.75			1.13	4.73			1.13	4.74
0.14	8.1E-05	0.85	4.53			0.85	4.50			0.85	4.51
S_{Max}	***3.7×10^3***	***$Slp=n_{Fr}$***	***0.5946***	***S_{Max}***	***5.9×10^3***	***$Slp=n_{Fr}$***	***0.6916***	***S_{Max}***	***5.1×10^3***	***$Slp=n_{Fr}$***	***0.8521***
	(1500)		*(0.0531)*		*(1300)*		*(0.0553)*		*(2400)*		*(0.0895)*
$C_{½}$	***0.140***	***$I=\log K_{Fr}$***	***3.9449***	***$C_{½}$***	***0.089***	***$I=\log K_{Fr}$***	***3.8235***	***$C_{½}$***	***0.180***	***$I=\log K_{Fr}$***	***3.6758***
	(0.110)		*(0.0431)*		*(0.045)*		*(0.0454)*		*(0.110)*		*(0.0818)*
R^2	***0.1138***	***R^2***	***0.8625***	***R^2***	***0.3423***	***R^2***	***0.8969***	***R^2***	***0.5083***	***R^2***	***0.9096***
n_{Fr} guessed			***0.59***	***n_{Fr} guessed***			***0.70***	***n_{Fr} guessed***			***0.85***
$\log K_{Fr}$ guessed			***3.90***	***$\log K_{Fr}$ guessed***			***3.80***	***$\log K_{Fr}$ guessed***			***4.20***

* C ($\mu g_{pyr}/L_w$), S ($\mu g_{pyr}/kg_{solids}$), nFr (dimensionless), K_{Fr} ($\mu g_{pyr}/kg_{solids}$)($L_w/\mu g_{pyr}$)^{nFr}, S_{Max} ($\mu g_{pyr}/kg_{solids}$), $C_{½}$ ($\mu g_{pyr}/L_w$).

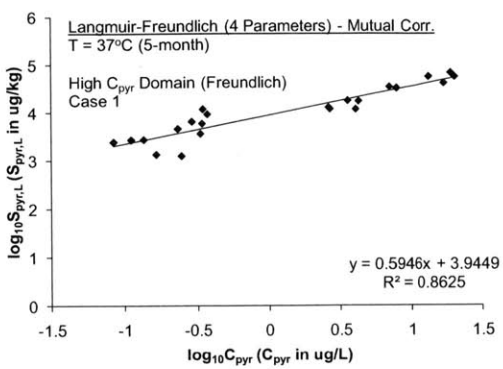
Langmuir-Freundlich (4 Parameters) - Mutual Corr.
T = 37°C (5-month)
High C_{pyr} Domain (Freundlich)
Case 1
y = 0.5946x + 3.9449
R² = 0.8625
$\log_{10}S_{pyr,L}$ ($S_{pyr,L}$ in ug/kg)
$\log_{10}C_{pyr}$ (C_{pyr} in ug/L)

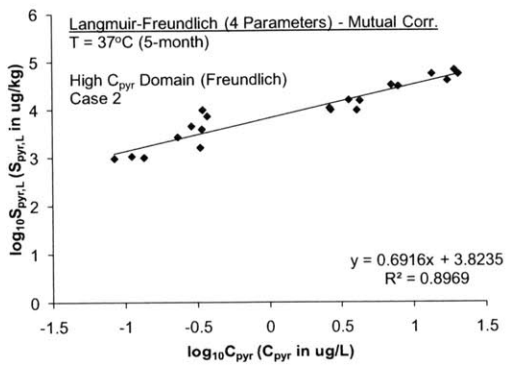
Langmuir-Freundlich (4 Parameters) - Mutual Corr.
T = 37°C (5-month)
High C_{pyr} Domain (Freundlich)
Case 2
y = 0.6916x + 3.8235
R² = 0.8969
$\log_{10}S_{pyr,L}$ ($S_{pyr,L}$ in ug/kg)
$\log_{10}C_{pyr}$ (C_{pyr} in ug/L)

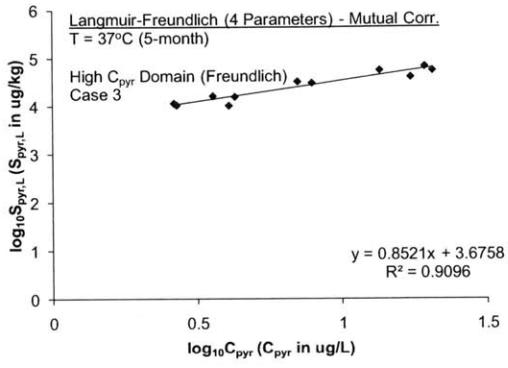
Langmuir-Freundlich (4 Parameters) - Mutual Corr.
T = 37°C (5-month)
High C_{pyr} Domain (Freundlich)
Case 3
y = 0.8521x + 3.6758
R² = 0.9096
$\log_{10}S_{pyr,L}$ ($S_{pyr,L}$ in ug/kg)
$\log_{10}C_{pyr}$ (C_{pyr} in ug/L)

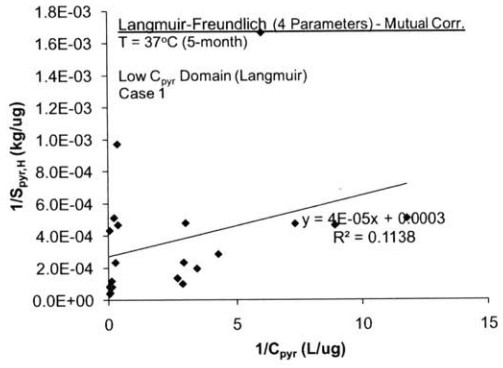
Langmuir-Freundlich (4 Parameters) - Mutual Corr.
T = 37°C (5-month)
Low C_{pyr} Domain (Langmuir)
Case 1
y = 4E-05x + 0.0003
R² = 0.1138
$1/S_{pyr,H}$ (kg/ug)
$1/C_{pyr}$ (L/ug)

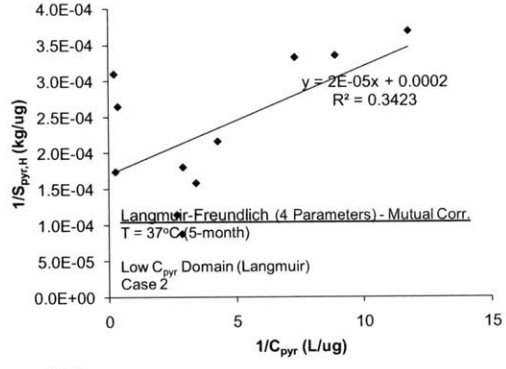
Langmuir-Freundlich (4 Parameters) - Mutual Corr.
T = 37°C (5-month)
Low C_{pyr} Domain (Langmuir)
Case 2
y = 2E-05x + 0.0002
R² = 0.3423
$1/S_{pyr,H}$ (kg/ug)
$1/C_{pyr}$ (L/ug)

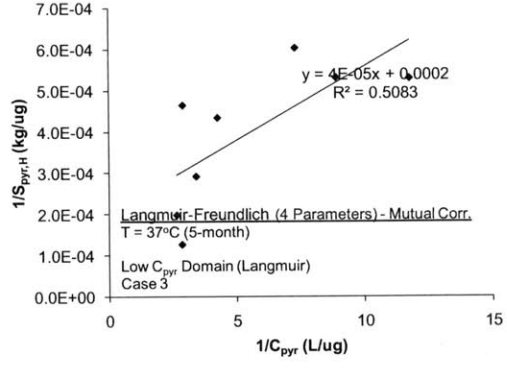
Langmuir-Freundlich (4 Parameters) - Mutual Corr.
T = 37°C (5-month)
Low C_{pyr} Domain (Langmuir)
Case 3
y = 4E-05x + 0.0002
R² = 0.5083
$1/S_{pyr,H}$ (kg/ug)
$1/C_{pyr}$ (L/ug)

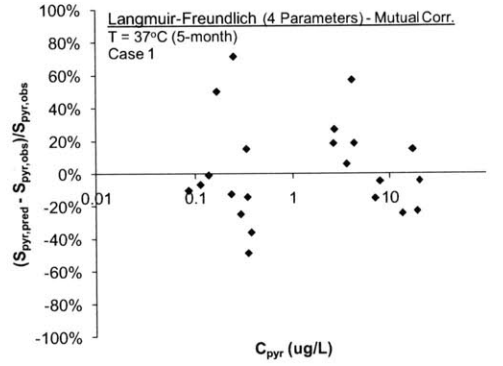
Langmuir-Freundlich (4 Parameters) - Mutual Corr.
T = 37°C (5-month)
Case 1
$(S_{pyr,pred} - S_{pyr,obs})/S_{pyr,obs}$
C_{pyr} (ug/L)

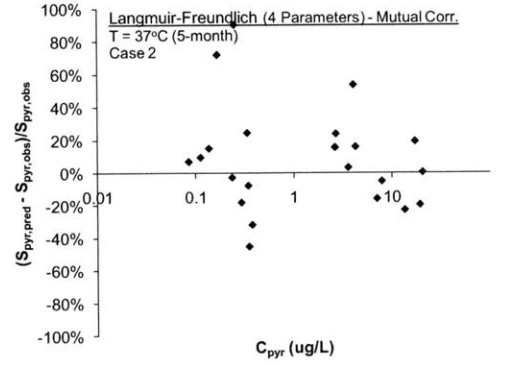
Langmuir-Freundlich (4 Parameters) - Mutual Corr.
T = 37°C (5-month)
Case 2
$(S_{pyr,pred} - S_{pyr,obs})/S_{pyr,obs}$
C_{pyr} (ug/L)

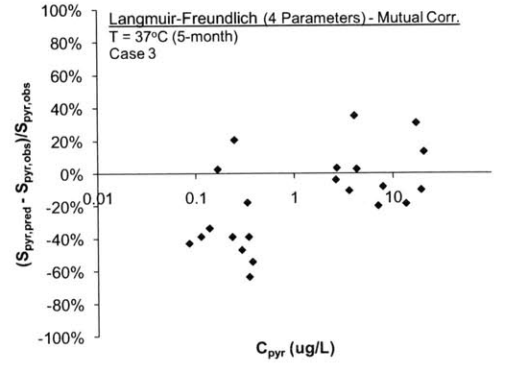
Langmuir-Freundlich (4 Parameters) - Mutual Corr.
T = 37°C (5-month)
Case 3
$(S_{pyr,pred} - S_{pyr,obs})/S_{pyr,obs}$
C_{pyr} (ug/L)

37°C (10-month) Fitted by Langmuir-Freundlich Form*

Fit #1				Fit #2				Fit #3			
'Native' Domain (high-affinity, low C_{pyr} range)		*Amended Domain* (high-affinity, low C_{pyr} range)		*'Native' Domain* (high-affinity, low C_{pyr} range)		*Amended Domain* (high-affinity, low C_{pyr} range)		*'Native' Domain* (high-affinity, low C_{pyr} range)		*Amended Domain* (high-affinity, low C_{pyr} range)	
1/C	$1/S_{Hi}$	$\log_{10}C$	$\log_{10}S_{Hi}$	1/C	$1/S_{Hi}$	$\log_{10}C$	$\log_{10}S_{Hi}$	1/C	$1/S_{Hi}$	$\log_{10}C$	$\log_{10}S_{Hi}$
		0.61	3.89			0.61	3.89			0.61	3.90
0.37	1.5E-04	0.43	3.93	0.37	2.1E-04	0.43	3.93	0.37	1.9E-04	0.43	3.94
0.25	5.0E-04	0.60	3.81			0.60	3.80			0.60	3.82
		1.30	4.51			1.30	4.51			1.30	4.51
		1.21	4.51			1.21	4.51	0.06	4.0E-04	1.21	4.51
		0.89	4.43			0.89	4.43	0.13	7.9E-05	0.89	4.43
11.01	2.5E-04			11.01	2.5E-04			11.01	2.5E-04		
1.98	2.8E-04			1.98	3.1E-04			1.98	3.2E-04	-0.30	3.05
2.04	2.7E-04			2.04	3.0E-04			2.04	3.1E-04	-0.31	3.07
2.51	2.4E-04	-0.40	3.10	2.51	2.6E-04			2.51	2.7E-04	-0.40	3.15
12.44	3.3E-04			12.44	3.4E-04			12.44	3.4E-04		
10.13	2.8E-04			10.13	2.8E-04			10.13	2.9E-04	-1.01	2.82
5.45	3.3E-04			5.45	3.5E-04			5.45	3.5E-04		
2.32	2.3E-04	-0.37	3.20	2.32	2.5E-04			2.32	2.5E-04	-0.37	3.23
2.84	2.3E-04	-0.45	3.18	2.84	2.4E-04			2.84	2.4E-04	-0.45	3.22
0.24	2.6E-04	0.61	3.94			0.61	3.93			0.61	3.94
0.28	1.4E-04	0.55	4.04	0.28	2.0E-04	0.55	4.04			0.55	4.05
0.36	1.5E-04	0.44	3.94	0.36	2.1E-04	0.44	3.94			0.44	3.95
		1.28	4.63			1.28	4.63			1.28	4.63
		1.10	4.69			1.10	4.68			1.10	4.69
		0.83	4.46			0.83	4.46			0.83	4.47
S_{Max}	4.1×10^3	$Slp=n_{Fr}$	0.8818	S_{Max}	4.2×10^3	$Slp=n_{Fr}$	0.9143	S_{Max}	4.0×10^3	$Slp=n_{Fr}$	0.8687
	(570)		(0.0622)		(320)		(0.1411)		(540)		(0.0514)
$C_{½}$	0.019	$I=\log K_{Fr}$	3.5095	$C_{½}$	0.025	$I=\log K_{Fr}$	3.4785	$C_{½}$	0.021	$I=\log K_{Fr}$	3.5152
	(0.025)		(0.0502)		(0.013)		(0.1240)		(0.023)		(0.0401)
R^2	0.0442	R^2	0.9393	R^2	0.2857	R^2	0.8076	R^2	0.0772	R^2	0.9470
n_{Fr} guessed			0.89	n_{Fr} guessed			0.91	n_{Fr} guessed			0.85
$\log K_{Fr}$ guessed			3.40	$\log K_{Fr}$ guessed			3.50	$\log K_{Fr}$ guessed			3.50

* C ($\mu g_{pyr}/L_w$), S ($\mu g_{pyr}/kg_{solids}$), nFr (dimensionless), K_{Fr} ($\mu g_{pyr}/kg_{solids}$)($L_w/\mu g_{pyr}$)^{nFr}, S_{Max} ($\mu g_{pyr}/kg_{solids}$), $C_{½}$ ($\mu g_{pyr}/L_w$).

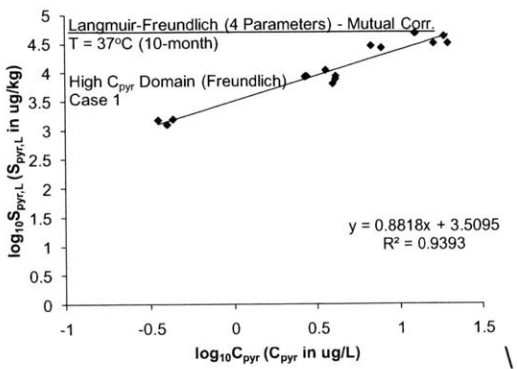
Langmuir-Freundlich (4 Parameters) - Mutual Corr.
T = 37°C (10-month)
High C_{pyr} Domain (Freundlich)
Case 1
y = 0.8818x + 3.5095
R² = 0.9393
$\log_{10}S_{pyr,L}$ ($S_{pyr,L}$ in ug/kg)
$\log_{10}C_{pyr}$ (C_{pyr} in ug/L)

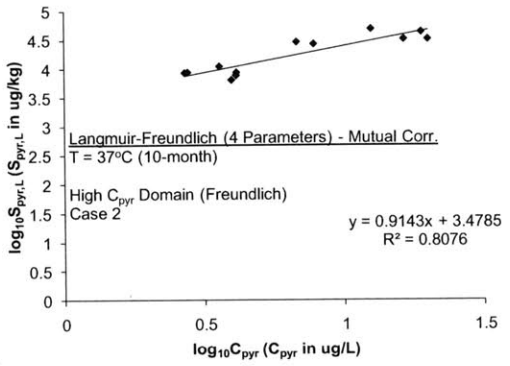
Langmuir-Freundlich (4 Parameters) - Mutual Corr.
T = 37°C (10-month)
High C_{pyr} Domain (Freundlich)
Case 2
y = 0.9143x + 3.4785
R² = 0.8076
$\log_{10}S_{pyr,L}$ ($S_{pyr,L}$ in ug/kg)
$\log_{10}C_{pyr}$ (C_{pyr} in ug/L)

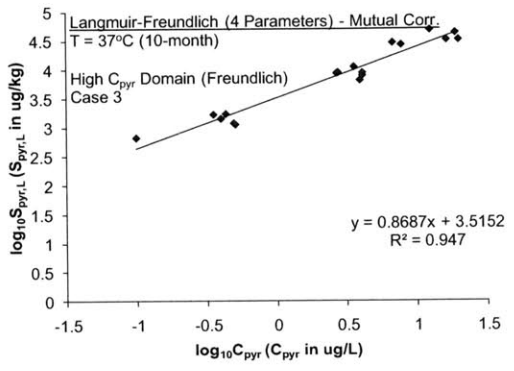
Langmuir-Freundlich (4 Parameters) - Mutual Corr.
T = 37°C (10-month)
High C_{pyr} Domain (Freundlich)
Case 3
y = 0.8687x + 3.5152
R² = 0.947
$\log_{10}S_{pyr,L}$ ($S_{pyr,L}$ in ug/kg)
$\log_{10}C_{pyr}$ (C_{pyr} in ug/L)

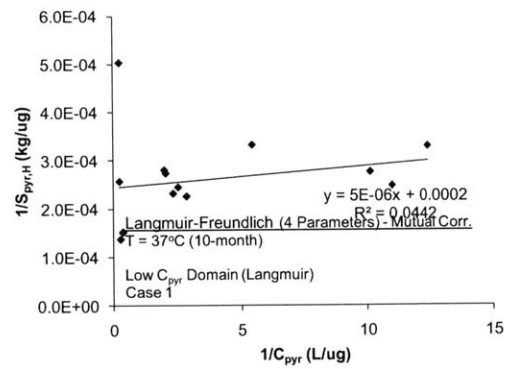
y = 5E-06x + 0.0002
R² = 0.0442
Langmuir-Freundlich (4 Parameters) - Mutual Corr.
T = 37°C (10-month)
Low C_{pyr} Domain (Langmuir)
Case 1
$1/S_{pyr,H}$ (kg/ug)
$1/C_{pyr}$ (L/ug)

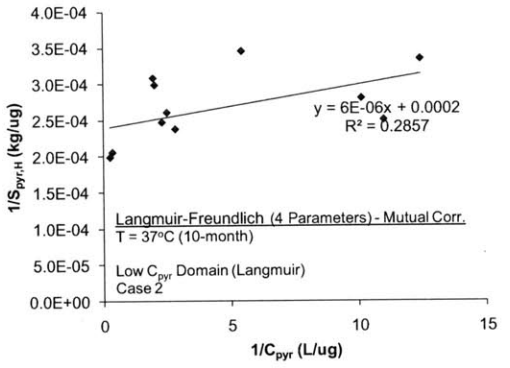
y = 6E-06x + 0.0002
R² = 0.2857
Langmuir-Freundlich (4 Parameters) - Mutual Corr.
T = 37°C (10-month)
Low C_{pyr} Domain (Langmuir)
Case 2
$1/S_{pyr,H}$ (kg/ug)
$1/C_{pyr}$ (L/ug)

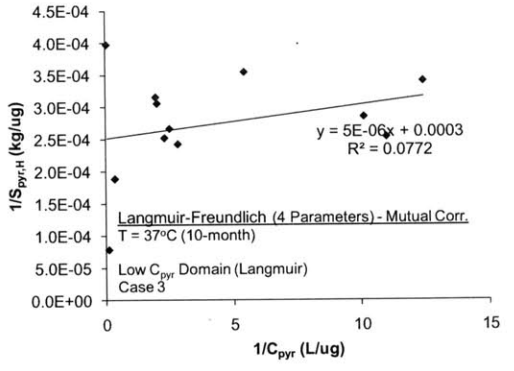
y = 5E-06x + 0.0003
R² = 0.0772
Langmuir-Freundlich (4 Parameters) - Mutual Corr.
T = 37°C (10-month)
Low C_{pyr} Domain (Langmuir)
Case 3
$1/S_{pyr,H}$ (kg/ug)
$1/C_{pyr}$ (L/ug)

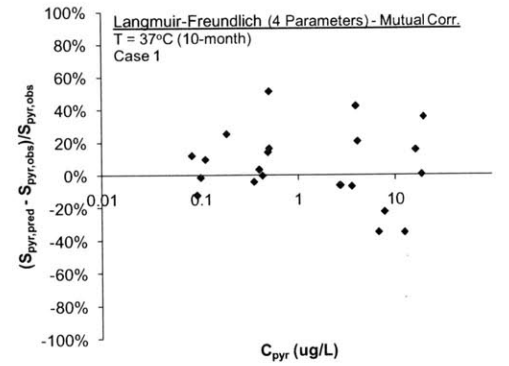
Langmuir-Freundlich (4 Parameters) - Mutual Corr.
T = 37°C (10-month)
Case 1
$(S_{pyr,pred} - S_{pyr,obs})/S_{pyr,obs}$
C_{pyr} (ug/L)

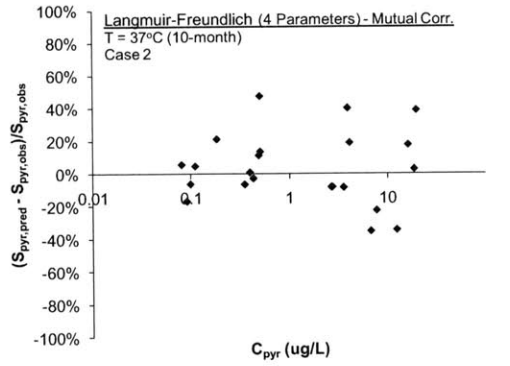
Langmuir-Freundlich (4 Parameters) - Mutual Corr.
T = 37°C (10-month)
Case 2
$(S_{pyr,pred} - S_{pyr,obs})/S_{pyr,obs}$
C_{pyr} (ug/L)

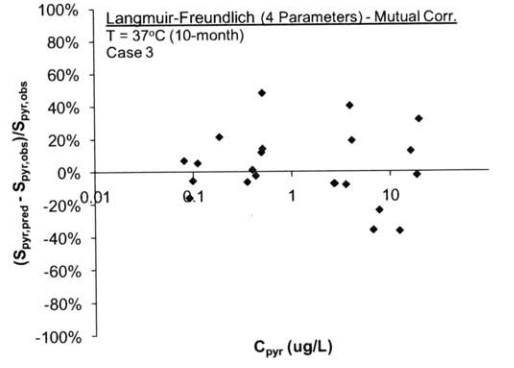
Langmuir-Freundlich (4 Parameters) - Mutual Corr.
T = 37°C (10-month)
Case 3
$(S_{pyr,pred} - S_{pyr,obs})/S_{pyr,obs}$
C_{pyr} (ug/L)

Appendix 5 - 9. Regressed vs observed S_{pyr}-C_{pyr} by Two-Freundlich and Langmuir-Freundlich models.

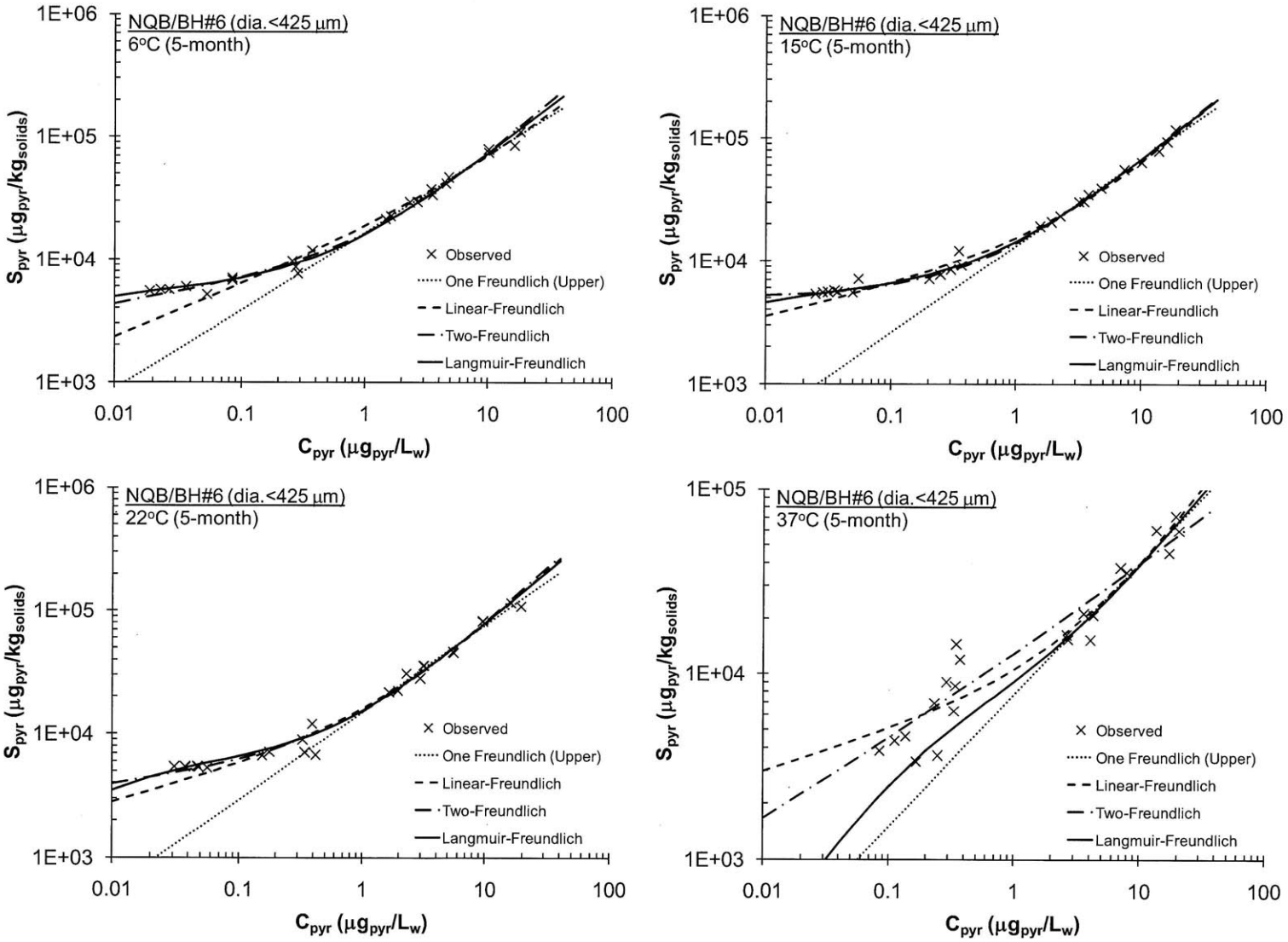

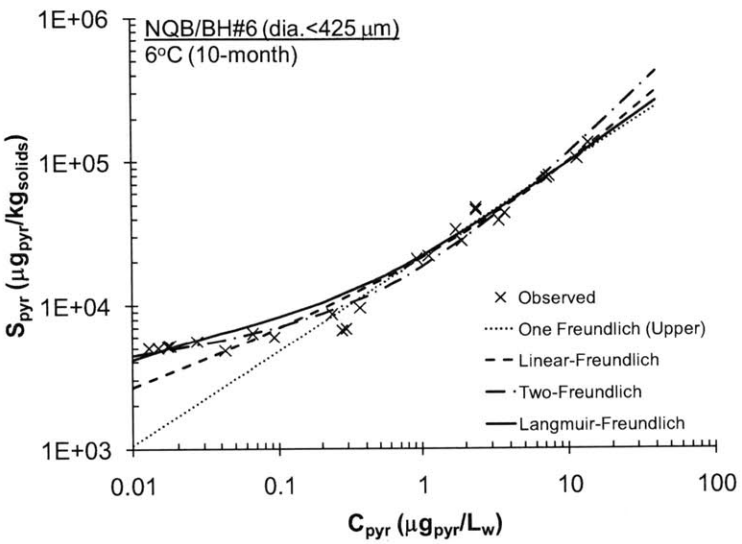
NQB/BH#6 (dia.<425 μm)
6°C (10-month)
1E+06
1E+05
1E+04
1E+03
0.01
0.1
1
10
100
S_{pyr} ($\mu g_{pyr}/kg_{solids}$)
C_{pyr} ($\mu g_{pyr}/L_w$)
Observed
One Freundlich (Upper)
Linear-Freundlich
Two-Freundlich
Langmuir-Freundlich

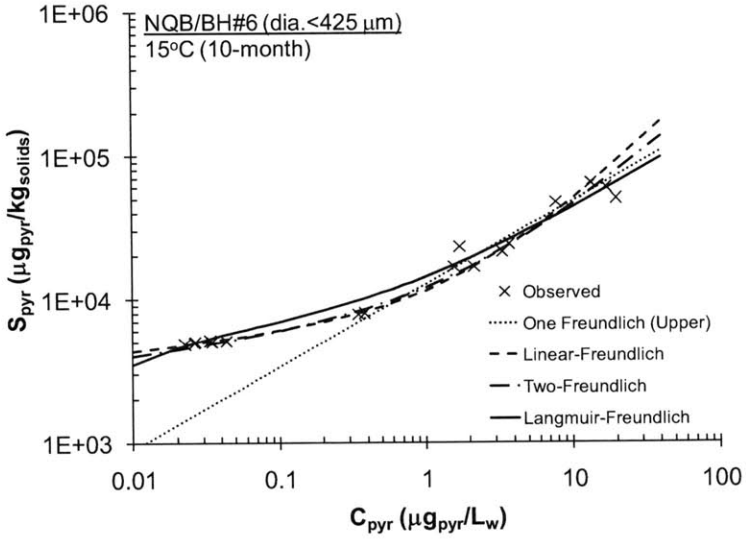
NQB/BH#6 (dia.<425 μm)
15°C (10-month)
1E+06
1E+05
1E+04
1E+03
0.01
0.1
1
10
100
S_{pyr} ($\mu g_{pyr}/kg_{solids}$)
C_{pyr} ($\mu g_{pyr}/L_w$)
Observed
One Freundlich (Upper)
Linear-Freundlich
Two-Freundlich
Langmuir-Freundlich

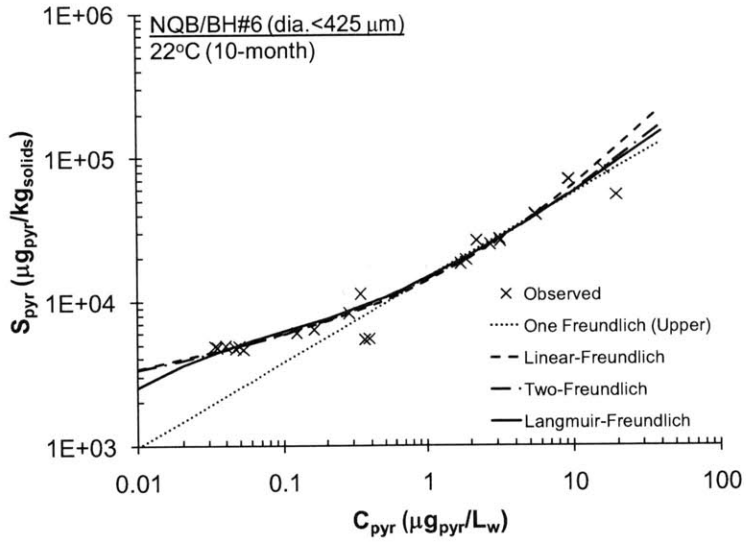
NQB/BH#6 (dia.<425 μm)
22°C (10-month)
1E+06
1E+05
1E+04
1E+03
0.01
0.1
1
10
100
S_{pyr} ($\mu g_{pyr}/kg_{solids}$)
C_{pyr} ($\mu g_{pyr}/L_w$)
Observed
One Freundlich (Upper)
Linear-Freundlich
Two-Freundlich
Langmuir-Freundlich

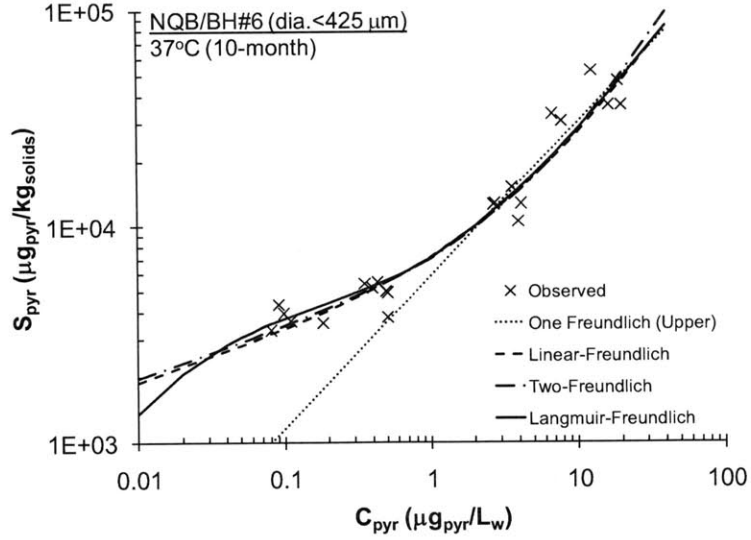
NQB/BH#6 (dia.<425 μm)
37°C (10-month)
1E+05
1E+04
1E+03
0.01
0.1
1
10
100
S_{pyr} ($\mu g_{pyr}/kg_{solids}$)
C_{pyr} ($\mu g_{pyr}/L_w$)
Observed
One Freundlich (Upper)
Linear-Freundlich
Two-Freundlich
Langmuir-Freundlich

Appendix 5 - 10. Variation in $logK_{OW,PAHs}$.

PAHs	$logK_{OW}$ ($L_w/L_{octanol}$)	References
Benzene		
	2.11	Karickhoff 1981
	2.17	Schwarzenbach et al. 2003
Naphthalene		
	3.33	Schwarzenbach et al. 2003
	3.35	Kopinke et al. 1995 (ref.w/in)
	3.36	Karickhoff 1981
	3.37	Mackay et al. 1999
Phenanthrene		
	4.46	Mackay et al. 1999
	4.57	Karickhoff 1981; Schwarzenbach et al. 2003
Pyrene	4.88	Hansch et al. 1995
	5.13	Schwarzenbach et al. 2003
	5.18	Karickhoff 1981; Mackay et al. 1999
Chrysene	5.61	Mackay et al. 1999
	5.81	Schwarzenbach et al. 2003
Benz(a)pyrene	6.04	Mackay et al. 1999
	6.13	Schwarzenbach et al. 2003
Perylene	6.25	Schwarzenbach et al. 2003
	6.50	Mackay et al. 1999

Appendix 5 - 11. Pyrene Sorption Raw Data from Literature.

The following data were obtained from tabulated data or figures.

From **Accardi-Dey and Gschwend 2002**.

South Dorchester Bay (dia. <425 μm)

$C_{pyr,Eqm}$ (μg/L)	$S_{pyr,Eqm}$ (μg/kg)
7.35	17366
6.09	19711
5.21	20237
0.91	4092
1.56	4608
1.42	4694
0.50	2756
3.01	10894
4.47	14785
10.28	29609
5.75	21772
8.49	23777
1.36	4795
1.75	2904
11.08	19829
1.05	6803
0.37	3149
5.20	13732
5.68	14191
6.45	9081
4.22	5850
1.56	8806

North Quincy Bay (dia. <425 μm)

$C_{pyr,Eqm}$ (μg/L)	$S_{pyr,Eqm}$ (μg/kg)
10.28	29609
5.75	21772
8.49	23777
1.36	4795
1.75	2904
11.08	19829
1.05	6803
0.37	3149
5.20	13732
5.68	14191
6.45	9081
4.22	5850
1.56	8806
10.28	29609

From **Chiou et al. 1998**.

Lake Michigan Sediment

$C_{pyr,Eqm}$ (μg/L)	$S_{pyr,Eqm}$ (μg/kg)
7	40000
15	60000
18	112500
23	130000
81	362500
105	580000

Massachusetts Bay Sediment

$C_{pyr,Eqm}$ (μg/L)	$S_{pyr,Eqm}$ (μg/kg)
21	40000
26	55000
58	120000
72	140000
95	220000
108	175000

Marlette Soil

$C_{pyr,Eqm}$ (μg/L)	$S_{pyr,Eqm}$ (μg/kg)
11	25000
18	41667
27	50000
38	66667
52	95833
79	133333

From **Chin et al. 1992**.

Fort Point Channel Sediment

$C_{pyr,Eqm}$ (μg/L)	$S_{pyr,Eqm}$ (μg/kg)
9	48837
15	93023
24	137209
34	193023
55	279070

From **ter Laak et al. 2006a**.

Borris Soil

$C_{pyr,Eqm}$ (μg/L)	$S_{pyr,Eqm}$ (μg/kg)
0.41	116413
1.38	316228
2.71	410393
9.07	1446772
17.17	2835959
31.43	5684601

Appendix 5 - 12. Regionalized Freundlich Descriptions of Pyrene Sorption Isotherms.

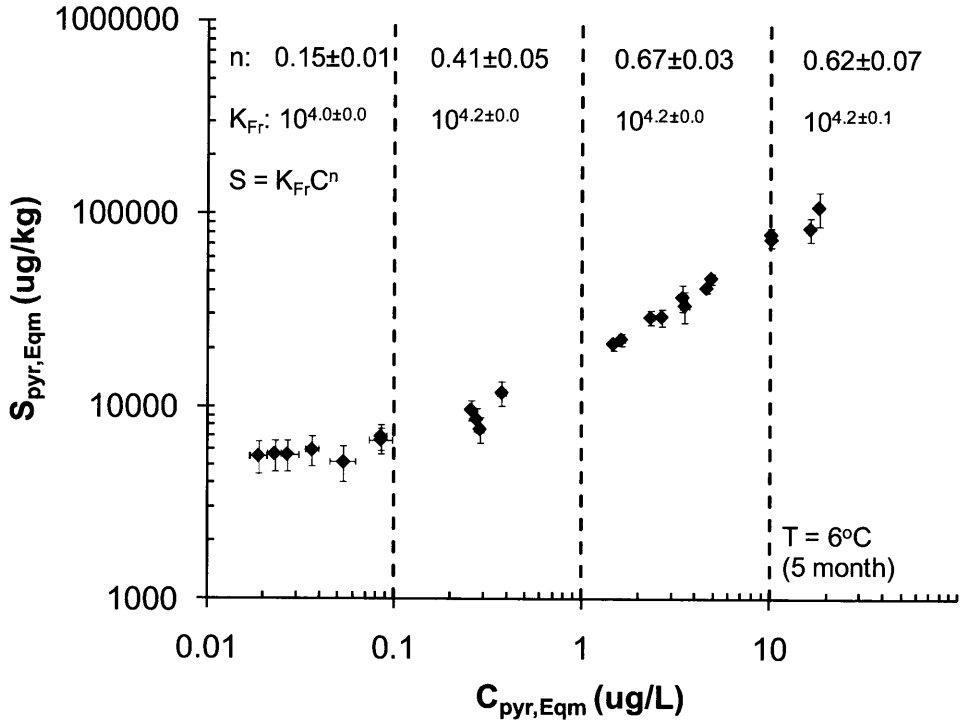

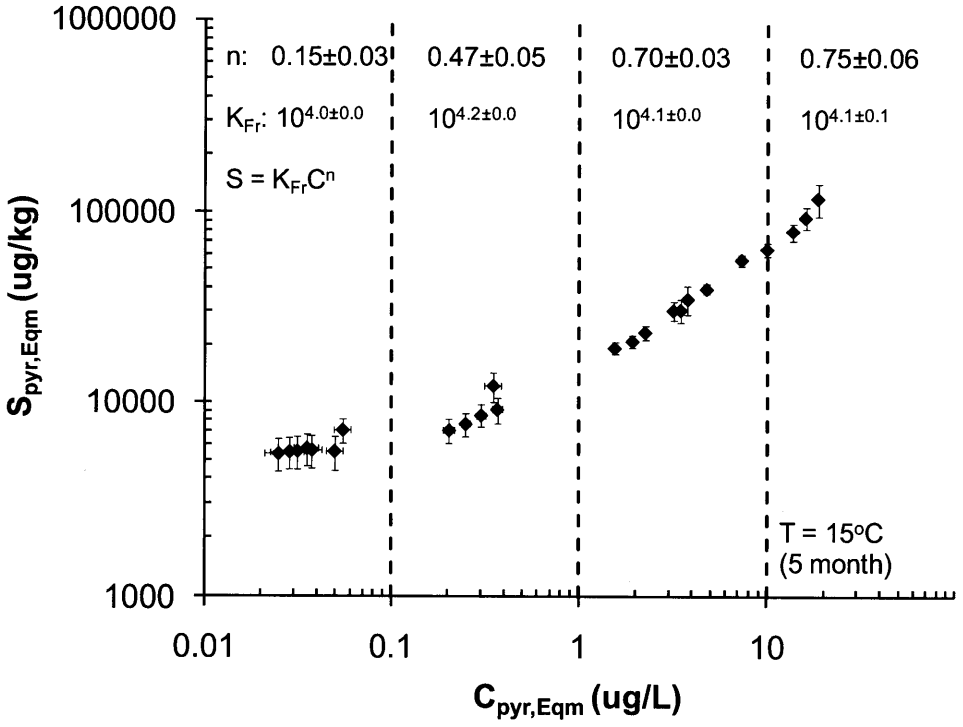

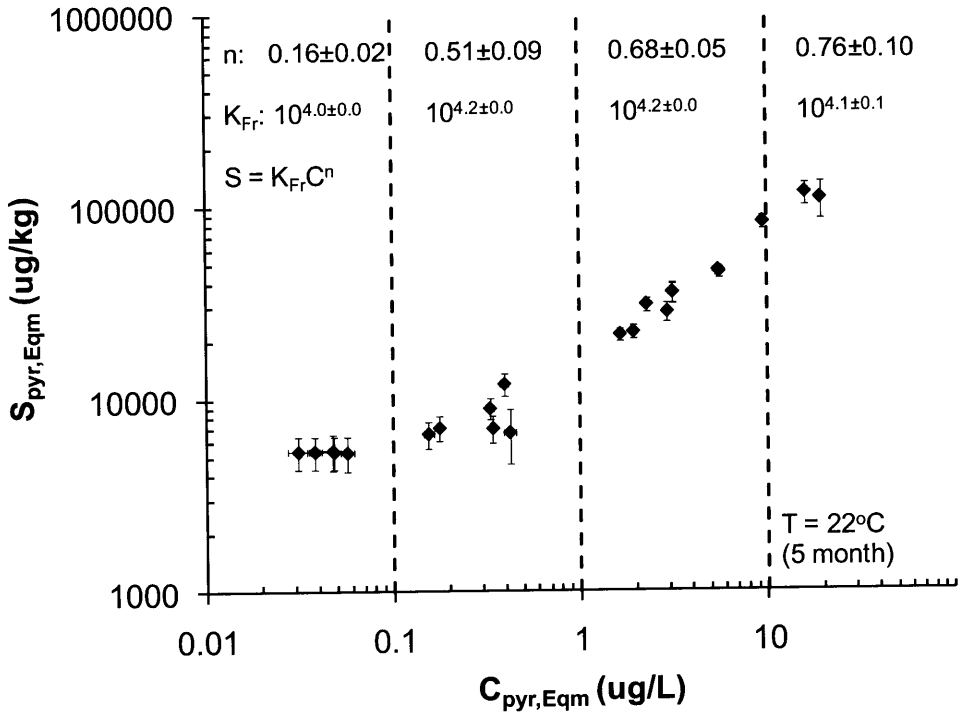
1000000
100000
10000
1000
n: 0.16±0.02
0.51±0.09
0.68±0.05
0.76±0.10
K_{Fr}: $10^{4.0\pm0.0}$
$10^{4.2\pm0.0}$
$10^{4.2\pm0.0}$
$10^{4.1\pm0.1}$
$S = K_{Fr}C^n$
T = 22°C
(5 month)
0.01
0.1
1
10
$S_{pyr,Eqm}$ (ug/kg)
$C_{pyr,Eqm}$ (ug/L)

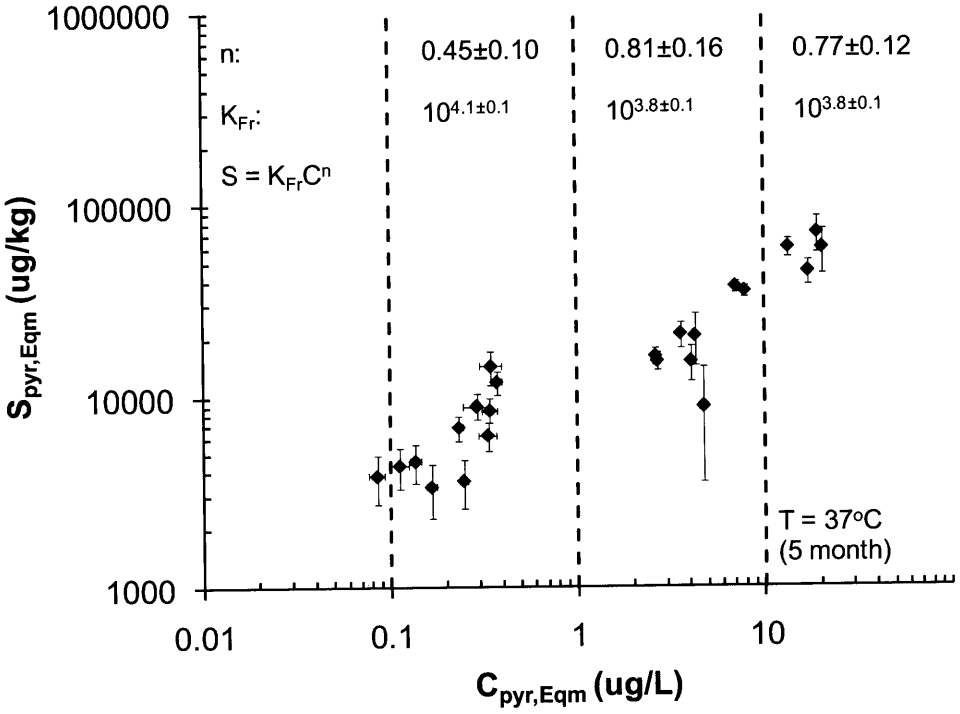
1000000
100000
10000
1000
n:
0.45±0.10
0.81±0.16
0.77±0.12
K_{Fr}:
$10^{4.1\pm0.1}$
$10^{3.8\pm0.1}$
$10^{3.8\pm0.1}$
$S = K_{Fr}C^n$
T = 37°C
(5 month)
0.01
0.1
1
10
$S_{pyr,Eqm}$ (ug/kg)
$C_{pyr,Eqm}$ (ug/L)

Appendix 5 - 13. Unresolved 'Conflicts' on n_{BC}'s.

Two independent studies (Cornelissen et al. 2004; Ran et al. 2007b) have reported, on the sorption of phenanthrene to natural geosorbents, that n_{Fr} for heat-treated geosorbents (i.e., rid of 'soft' organic materials/sorbates) to be about 0.55 whereas sorption with the original, untreated geosorbents were much closer to linearity (n_{Fr} ~0.8-0.9).

Conflicting Implications of n_{BC}

How is it possible that the sorption isotherm in this study, where the sediment was not heat-treated, should exhibit an even greater degree of non-linearity ($n_{Fr,BC}$ ~ 0.25, Table 5-3a; $n_{Fr,BC}$ ~ 0.2, Table 5-3b)? For the study by Ran et al., one may argue that the studied concentration range has not been sufficiently low (minimum $C_{phen,w}$ ~ 1 μg/L), and so they were not able to expose the energetically heterogeneous regime very significantly. For the study by Cornelissen et al., however, the concentration argument failed as ng/L level observations had been made. The sediment used by Cornelissen et al. also contained comparable amount of native sorbate (native phenanthrene ~2000 $\mu g_{phen}/kg_{solids}$ in Cornelissen et al.; native pyrene ~2000-5000 $\mu g_{pyr}/kg_{solids}$ in this study), and so it is difficult to attribute the greater non-linearity to the significant presence of native sorbates. Let us further suppose that physical occlusion of native sorbate was actually significant – that the low $n_{Fr,BC}$ derived from this study ($n_{BC,pyr}$ ~ 0.2) and that from the North Quincy Bay sediment data from Accardi-Dey and Gschwend ($n_{BC,pyr}$ ~ 0.42; raw data listed in Appendix 5-11) have been 'erroneous' for not properly excluding the physically occluded fraction. This supposition, however, prompts one to question *why* physical occlusion has not been significant for the native phenanthrene in Cornelissen et al.'s field-aged sediment? One may, at last, simply dismiss the $n_{BC,pyr}$ of 0.25-0.42 as a result of some laboratory/group-specific analytical errors/artifacts (e.g. systematic error in fluorescence spectroscopy), but how may one dismiss the even more non-linear partitioning of pyrene shown in various deep-core bulk sediments (Figure 4-8)?

The author was unable to resolve the mentioned 'conflicts'. However, the following factors may provide some partial explanation(s): the apparent 'conflicts' may be due to (i) the uptake of different sorbates, (ii) the presence of competing sorbates and organic fragments, and (iii) the use of combusted geosorbents.

Partial Explanations (I): Sorbate Difference

Sorption linearity (i.e. Freundlich n) generally varies with different sorbates for the same sorbent (Walters et al. 1984; Xing et al. 1996b; Bucheli et al. 2000). The inter-sorbate difference in sorption linearity is a function of both the sorbate properties (hydrophobicity, size, and planarity) and the sorbent properties (surface chemical structure and pore-surface distributions). For instance, n_{BC} was 1.0 and 0.67 for the sorption of phenanthrene and pyrene, respectively, onto NIST diesel soot (Bucheli et al. 2000); but the both sorbates had very similar n_{BC} (~0.4) when adsorbing onto high-surface area activated carbon (Walters et al .1984).

Partial Explanations (II): Competitive Sorption & OC-Binding

Second, competing sorbates or organic fragments also affect the energy distribution of surface sites. Sorption affinity for a sorbate generally decreases in the presence of other competing sorbates (Xing et al. 1996b; Bucheli et al. 2000; Xia et al. 2000; Weber et al. 2002; Pan et al. 2007). Such trend is understandable with a picture of limited sorption sites for multiple sorbates.

The case becomes more complex with large organic fragments such as NOM. For highly porous char, the presence of organic fragments tends to reduce the adsorption capacity of the char by blocking/filling the surfaces located in the pores (Pignatello et al. 2006). However, it is less clear if the same is applicable to less porous condensed carbons such as soot or graphite.

Earlier, the author has argued that NOM may enhance adsorption affinity of the condensed carbon surface (Chapter 4, section 3.4.3; Figure 4-14). In addition, the association of NOM with condensed graphitic phase may also enhance the absorption affinity of the 'soft', flexible NOM phase, by virtue of the long-range interaction exerted by the graphitic surface – the graphitic surface may offer additional attraction for sorbates bound in the volume of OC within the vicinity of the condensed carbon surface (Figure 5-10). Enhancement in sorption affinity due to NOM-condensed carbon association will be translated into a higher non-linearity in the isotherm.

Partial Explanations (III): Thermally Isolated BC

Third, the application of thermal-treatment to isolate BC may have the disadvantage of altering the nature of the native OC+BC phase structurally. Thermal treatment (375°C) may burn away most of the 'soft' organic matter but char some of it into BC/BC-like (i.e. partially graphitic). At the same time, a portion of the originally present BC is lost with the burning. Such loss of BC is not unlikely, as the works of Accardi-Dey (2003) (Figure 7 & 9, Chapter 3) and Nguyen et al. (2004a) have demonstrated. As a result, the thermally isolated BC-phase is more heterogeneous and less graphitic. This is somewhat supported by the diminished $\log K_{BC,phen}$ from the 375C-combusted sediment. Re-analysis of Cornelissen et al.'s phenanthrene sorption data (see below) revealed that the original and/or sorbate-stripped sediment had $\log K_{BC,phen}$ = 6 – 6.2 (n_{BC} = 0.9) while the 375°C-combusted sediment (i.e. no 'soft' organic carbon) had $\log K_{BC,phen}$ = 5.6 (n_{BC} = 0.5)[1].

[1] Sensitivity analysis showed that $\log K_{BC,phen}$ and $n_{BC,phen}$ both remained fairly independent of the uncertainties in f_{BC} or $\log K_{OC,phen}$.

Re-analysis of Sorption Data in Cornelissen et al. (2004)

KET sediment (original, untreated)

logC* (C in μg/L)	**$logS_{OC}$*** (S in $\mu g/kg_{OC}$)	**S** (S in $\mu g/kg_{solids}$)	**$logS_{BC}$†** (S_{BC} in $\mu g/kg_{BC}$)
-3.08	2.08	7	2.92
-2.68	2.56	20	3.41
-2.37	3.08	66	3.94
-2.15	3.29	107	4.15
-1.52	3.72	289	4.57
-1.28	4.02	580	4.88
-0.53	4.73	2939	5.58
-0.08	5.02	5771	5.86
0.72	5.66	25255	6.47
$n_{BC} = 0.91^{‡}$ $logK_{BC} = 5.96^{‡}$			

*: logC and log S_{OC} from figure in Cornelissen et al. (2004).
†: Calculated as $S_{BC} = (S - f_{OC}K_{OC}C)/f_{BC}$, with $logK_{OC} = 4.2$, $f_{OC} = 0.0493$, $f_{BC} = 0.0072$.
‡: From regressing $logS_{BC}$ against logC.

KET sediment (110°C-treated)

logC* (C in μg/L)	**$logS_{OC}$*** (S in $\mu g/kg_{OC}$)	**S** (S in $\mu g/kg_{solids}$)	**$logS_{BC}$†** (S_{BC} in $\mu g/kg_{BC}$)
-2.77	2.08	42	3.75
-2.43	2.56	67	3.95
-2.11	3.08	212	4.46
-1.55	3.29	453	4.78
-0.74	3.72	5231	5.85
0.02	4.02	10712	6.14
0.25	4.73	21036	6.44
0.46	5.02	37964	6.70
$n_{BC} = 0.91^{‡}$ $logK_{BC} = 6.26^{‡}$			

*: logC and log S_{OC} from figure in Cornelissen et al. (2004).
†: Calculated as $S_{BC} = (S - f_{OC}K_{OC}C)/f_{BC}$, with $logK_{OC} = 4.2$, $f_{OC} = 0.0452$, $f_{BC} = 0.0072$.
‡: From regressing $logS_{BC}$ against logC.

KET sediment (375°C-treated)

logC* (C in µg/L)	$\log S_{OC}$* (S in µg/kg$_{OC}$)	S (S in µg/kg$_{solids}$)	$\log S_{BC}$† (S_{BC} in µg/kg$_{BC}$)
-3.27	3.64	35	3.64
-3.14	3.96	73	3.96
-3.11	4.00	81	4.00
-2.37	4.43	217	4.43
-2.31	4.25	143	4.25
-2.15	4.56	292	4.56
-1.53	4.64	346	4.64
-1.55	4.89	624	4.89
-1.07	4.95	708	4.95
-0.91	4.95	708	4.95
-0.44	5.44	2210	5.44
0.10	5.81	5138	5.81
0.15	5.85	5709	5.85
0.57	5.81	5138	5.81
0.69	5.95	7050	5.95
0.77	5.96	7353	5.96

$n_{BC} = 0.54$‡
$\log K_{BC} = 5.61$‡

*: logC and log S_{OC} from figure in Cornelissen et al. (2004).
†: Calculated as $S_{BC} = (S - f_{OC}K_{OC}C)/f_{BC}$, with $\log K_{OC} = 4.2$, $f_{OC} = 0$, $f_{BC} = 0.0080$.
‡: From regressing $\log S_{BC}$ against logC.

Chapter 6: Appendices

Appendix 6 - 1. *A priori* Predictions of $\log K_{Soot\text{-}W}$'s for PAHs by Gustafsson et al. (1997b) **767**
Appendix 6 - 2. Monolayer Adsorption of Pyrene (Estimation). **768**
Appendix 6 - 3. $\Delta H_{d,ads\text{-}ss}$–, $\Delta H_{d,ads\text{-}sH2O}$–, and $\Delta H_{d,ads\text{-}sOrg}$–$C_{pyr}$ Plots. **769**
Appendix 6 - 4. $\Delta S_{d,abs}$–C_{pyr} Plots derived from the three Two-Domain Isotherms. **770**
Appendix 6 - 5. Derivation of Thermochemical Data for Phase-Transitions Reactions of Selected PAHs at 25°C. **771**
Appendix 6 - 6. Estimating Entropies of Pyrene Sorption. **776**
Appendix 6 - 7. Estimating Apparent/Overall Enthalpy ($\Delta H_{d,app}$) of Pyrene Sorption. **787**

Appendix 6 - 1. *A priori* Predictions of $logK_{Soot-W}$'s for PAHs by Gustafsson et al. (1997b)

PAH	$logK_{Soot-W}$ (L_w/kg_{soot})† (Gustafsson et al. 1997b)	$logK_{AC-W}$ (L_w/kg_{AC}) (Walters et al. 1984)*	$logK_{AC-W}$ (L_w/kg_{AC}) (Dobbs et al. 1980)*
Acenaphthene	5.8	7.2	6.2
Fluorene	6.2	7.1	6.3
Anthracene	6.7	6.8	6.5
Phenanthrene	6.4	7.0	6.5
Pyrene	7.0	7.7	
Fluoranthene	6.9	7.8	6.9
Chrysene	8.2	8.5	
Benzo(a)anthracene	7.8	7.4	
Benzo(a)pyrene	8.4		7.8
Dibenzo(a,h)-anthracene	9.3		8.2

†: Assuming an adsorption entropy of about 33 J/mol.K, and an average soot surface area of 10^5 m^2/kg_{Soot}.
*: As reported in Gustafsson et al. (1997b).

Appendix 6 - 2. Monolayer Adsorption of Pyrene (Estimation).

The objective here is to see if the adsorption of pyrene onto the sedimentary phase would exceed the sorbent's monolayer adsorption capacity. The strategy is therefore to first estimate the monolayer adsorption capacity of the NQB/BH#6 sediment, and then the maximum amount of pyrene adsorbed in the Long-Term Adsorption Equilibrium Experiment (Chapter 3 & 4).

Estimating Monolayer Adsorption Capacity

A number of assumptions were taken for estimating the monolayer adsorption capacity for pyrene: (i) that the principal adsorbing phase of the sediment was sooty BC, assumed measured by the f_{BC} value, (ii) that sedimentary soot had an average radius of 25 nm and a density of 2.2 kg/L, (iii) that all surface area of soot may be accessible and available to pyrene and/or other adsorbates, (iv) that one single pyrene would occupy about 1 nm^2 of soot surface area (see Appendix 4-3). From these assumptions, surface area of sedimentary-BC was estimated to be about 60000 m^2_{BC}/kg_{BC}, and could take up about 2×10^7 $\mu g_{pyr}/kg_{BC}$. With f_{BC} = 0.0049, the monolayer capacity was estimated to be about 1×10^5 (rounding up of 98500) $\mu g_{pyr}/kg_{solids}$. An estimate on $\kappa_{i,ads}$ would allow us to compute $K^x_{ads\text{-}ss}$ and $K^x_{ads\text{-}sH2O}$.

Estimating Amount of Pyrene Adsorbed

This estimation requires separating the contribution of adsorption from absorption, and thus we have to work with the Two-Domain isotherms. The maximum amount of pyrene adsorbed in the experiment may be calculated as the adsorbed amount corresponding to the highest, observable dissolved pyrene concentration (~ 20 $\mu g_{pyr}/L_w$). Or, more concretely:

$$\textbf{Linear + Freundlich:} \quad S_{pyr,ads} = K_{Fr}(20)^n$$

$$\textbf{Two - Freundlich:} \quad S_{pyr,ads} = K_{Fr,H}(20)^{n_H}$$

$$\textbf{Langmuir - Freundlich:} \quad S_{pyr,ads} = \frac{S_{Lgmr,Max}(20)}{C_{Lgmr,½} + (20)}$$

The estimated maximum pyrene adsorbed at all four temperatures according to the three isotherm forms (see table below) were generally much less than the estimated monolayer capacity. With only one exception, the maximum adsorbed pyrene was only about 10% of the monolayer capacity. This was, however, no conclusive evidence for saying all adsorbed pyrene molecules form monolayer on the sedimentary BC surface.

	Maximum $S_{pyr,ads}$ ($\mu g_{pyr}/kg_{solids}$)		
T (°C)	Linear+Freundlich	Two-Freundlich	Langmuir-Freundlich
6	46800	12900	5800
15	10600	11500	5000
22	10500	13700	5200
37	10800	11500	4200

Appendix 6 - 3. $\Delta H_{d,ads-ss}$–, $\Delta H_{d,ads-sH2O}$–, and $\Delta H_{d,ads-sOrg}$–C_{pyr} Plots.

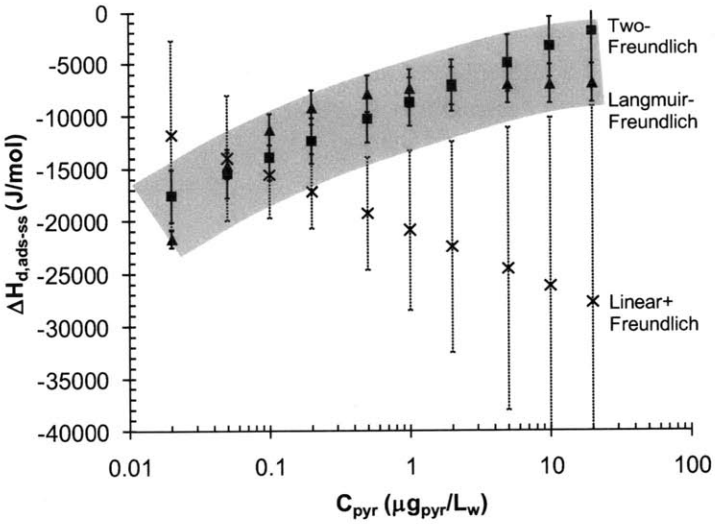

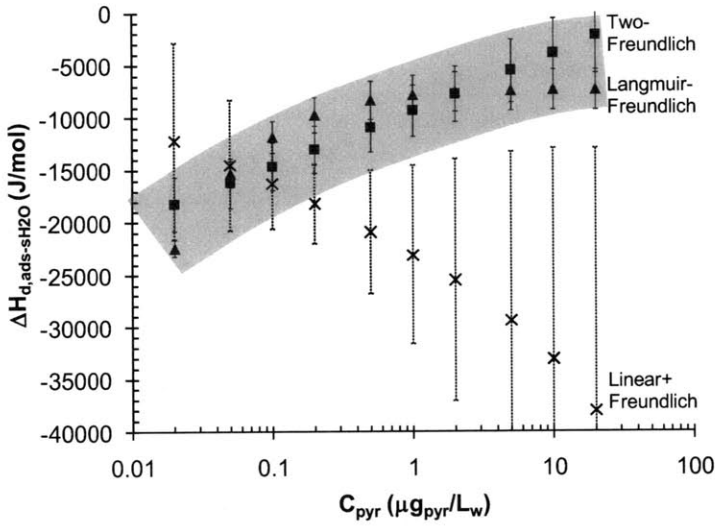

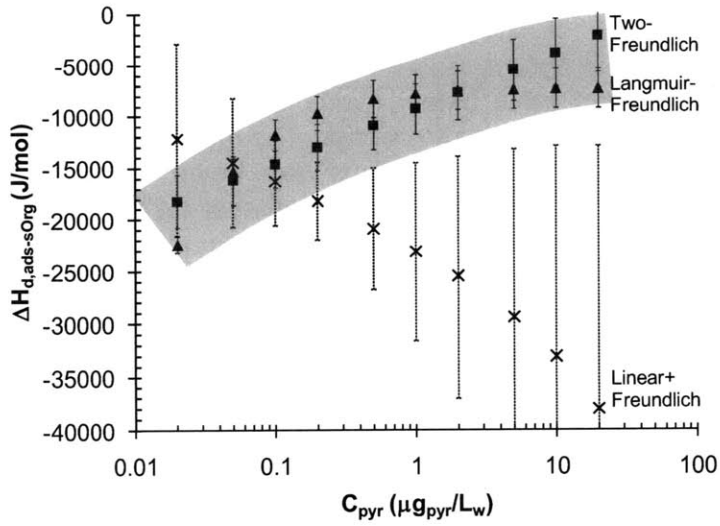

Appendix 6 - 4. $\Delta S_{d,abs}$–C_{pyr} Plots derived from the three Two-Domain Isotherms.

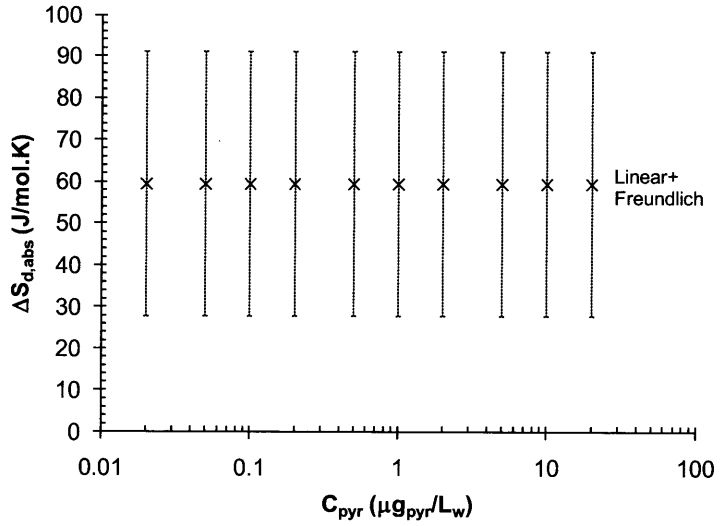

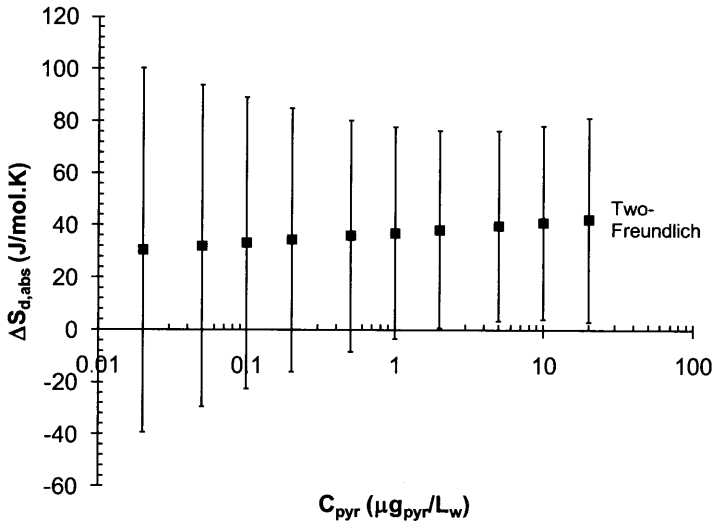

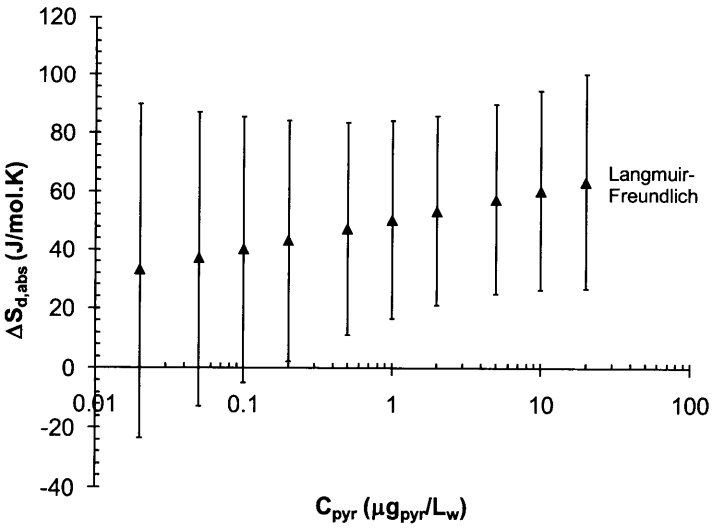

Appendix 6 - 5. Derivation of Thermochemical Data for Phase-Transitions Reactions of Selected PAHs at 25°C.

The critical review by Roux et al. (2008) provided recommended values of room temperature ΔH_{fus}, ΔH_{vap}, and ΔH_{sub} for a number of PAHs. In many cases, perhaps due to the temperature correction (i.e. via heat capacity function), the recommended values have been slightly State-Inconsistent (i.e. $\Delta X_{sub} = \Delta X_{fus} + \Delta X_{vap}$; where X is a thermodynamic state variable such as G, H, or S). This is shown as the 'error', $\varepsilon(\Delta H)$, in Table (I) below. While $\varepsilon(\Delta H)$'s of most PAHs were within <3 kJ/mol, this uncertainty, could propagate into a greater uncertainty in ΔS's (as will be shown).

Table (I): Enthalpies of Phase Transition at 25°C Recommended in Roux et al. (2008)

PAH	ΔH_{fus} (kJ/mol)	ΔH_{vap} (kJ/mol)	ΔH_{sub} (kJ/mol)	$\varepsilon(\Delta H)$* (kJ/mol)
Naphthalene	16.9 (±0.7)	49.2 (±1.0)	72.6 (±0.3)	6.5
Fluorene	15.3 (±1.4)	72.1 (±1.9)	86.5 (±1.3)	0.9
Phenanthrene	12.9 (±1.3)	78.3 (±1.8)	92.1 (±0.6)	0.9
Anthracene	19.7 (±3.2)	79.9 (±4.0)	101.9 (±1.3)	2.3
Pyrene	10.2 (±2.3)	89.4 (±3.1)	100.3 (±1.0)	0.7
Chrysene	14.8 (±4.8)	106.2 (±8.6)	123.4 (±4.2)	2.4
Benzo(a)anthracene	12.9 (±2.8)	105.8 (±3.8)	119.5 (±5.0)	0.8
Benzo(a)pyrene	15.3 (±3.5)	116.7 (±2.3)	120.5 (±2.7)	11.5

*: Calculated as $\varepsilon(\Delta H) = abs(\Delta H_{fus} + \Delta H_{vap} - \Delta H_{sub})$.

The thermochemical properties of sublimation for the selected PAHs should be most reliable as they can be inferred from direct vapor pressure measurements. Since the selected PAHs are solids at 25°C and atmospheric condition, the enthalpy of sublimation (ΔH_{sub}) should be most accurate – it can be determined from the slope of $\ln P^*_{iS}(T)$ vs 1/T and $P^*_{iS}(T)$ can be measured. ΔG_{sub}'s and ΔS_{sub}'s are also very well known as $\Delta G_{sub,i}(25°C) = -RT\ln P^*_{iS}(25°C)$ (P^*_{iS} in bar) and $(\Delta G_{sub} = \Delta H_{sub} - T\Delta S_{sub})_{25C}$.

We may choose either vaporization or fusion as 'known' using Roux et al.'s recommended enthalpy values, then estimate the ΔG for that chosen process (i.e. estimating sub-cooled liquid vapor pressure P^*_{iL}) and calculate ΔS for that process by difference. This 'choice' is 'equal' in the sense that ΔG for either process would require using thermodynamic correlations to estimate P^*_{iL}. Furthermore, if we choose fusion as the 'known' process, ΔG_{fus} may be estimated via two different correlations (estimating P^*_{iL} or evaluate ΔG_{fus} directly, both according to correlations by Myrdal et al. 1997).

Hence we may derive/estimate ΔH's, ΔG's, and ΔS's in the following way:

Table (II): The Derivation of ΔH's, ΔG's, and ΔS's for Pure Phase Transitions of PAHs at 25°C.

<table>
<tr><th>Sublimation
(Step 1)</th><th>Chosen 'Known' Process
(Step 2)</th><th>Remaining Transition
(Step 3)</th></tr>
<tr><td rowspan="3">$\Delta H_{sub}(25°C)$'s
(from Roux et al. 2008)

$\Delta G_{sub}(25°C)$'s
(from $P^*_{iS}(25°C)$)</td><td>**A**
$\Delta H_{vap}(25°C)$'s
(from Roux et al. 2008)

$\Delta G_{vap}(25°C)$'s
(estimated $P^*_{iL}(25°C)$)</td><td>$\Delta H_{fus} = \Delta H_{sub} - \Delta H_{vap}$

$\Delta G_{fus} = \Delta G_{sub} - \Delta G_{vap}$</td></tr>
<tr><td>**B**
$\Delta H_{fus}(25°C)$'s
(from Roux et al. 2008)

$\Delta G_{fus}(25°C)$'s
(estimated ΔG_{fus})</td><td rowspan="2">$\Delta H_{vap} = \Delta H_{sub} - \Delta H_{fus}$

$\Delta G_{vap} = \Delta G_{sub} - \Delta G_{fus}$</td></tr>
<tr><td>**C**
$\Delta H_{fus}(25°C)$'s
(from Roux et al. 2008)

$\Delta G_{fus}(25°C)$'s
(estimated P^*_{iL} and measured P^*_{iS})</td></tr>
<tr><td colspan="2">$\Delta S_{process}(25°C)$'s
(from $\Delta G=\Delta H-T\Delta S$)</td><td>$\Delta S_{sub} = \Delta S_{fus} + \Delta S_{vap}$
$\Delta G_X=\Delta H_X-T\Delta S_X$</td></tr>
</table>

Where P^*_{iL} (unit in bar) at temperature T (unit in K) is estimated according to (Myrdal et al. 1997, as quoted in Schwarzenbach et al. 2003):

$$\ln P^*_{iL,T} = -(21.2 + 0.3\tau + 177HBN)\left(\frac{T_b}{T} - 1\right) + (10.8 + 0.25\tau)\ln\left(\frac{T_b}{T}\right)$$

And ΔG_{fus} (unit J/mol) at temperature T (unit in K) is estimated according to (Myrdal et al. 1997, as quoted in Schwarzenbach et al. 2003):

$$\Delta G_{fus} = +(56.5 + 9.2\tau - 19.2\log\sigma)(T_m - T)$$

The final estimates for ΔX's (X=G, H or S) for vaporization and fusion at 25°C are calculated as the mean of the fusion-based and vaporization-based (i.e. Step 2) estimates of ΔX. The estimates are shown in the tables below:

Table (III): Thermochemical Properties of PAHs Sublimation at 25°C

PAH	ΔH_{sub} (kJ/mol)	ΔG^*_{sub} (kJ/mol)	ΔS_{sub} (J/mol.K)
Naphthalene	72.6 (±0.3)	22.5	168
Fluorene	86.5 (±1.3)	34.4	175
Phenanthrene	92.1 (±0.6)	38.8	181
Anthracene	101.9 (±1.3)	45.7	188
Pyrene	100.3 (±1.0)	46.2	181
Chrysene	123.4 (±4.2)	64.0	199
Benzo(a)anthracene	119.5 (±5.0)	54.8	217
Benzo(a)pyrene	120.5 (±2.7)	63.6	191

*: $\Delta G_{fus} = -RT\ln P^*_{iS}$.

Table (IVa): Thermochemical Properties of PAHs Vaporization (**Step 2, **A****) at 25°C

PAH	ΔH_{vap} (kJ/mol)	ΔG^*_{vap} (kJ/mol)	ΔS_{vap} (J/mol.K)
Naphthalene	49.2 (±1.0)	20.7	96
Fluorene	72.1 (±1.9)	30.3	140
Phenanthrene	78.3 (±1.8)	36.1	142
Anthracene	79.9 (±4.0)	36.4	146
Pyrene	89.4 (±3.1)	44.7	150
Chrysene	106.2 (±8.6)	50.9	185
Benzo(a)anthracene	105.8 (±3.8)	49.5	189
Benzo(a)pyrene	116.7 (±2.3)	57.6	198

*: $\Delta G_{vap} = -RT\ln P^*_{iL}$, where P^*_{iL} is the estimated sub-cooled liquid vapor pressure.

Table (IVb): Thermochemical Properties of PAHs Fusion (**Step 2, **A****) at 25°C

PAH	ΔH_{fus} (kJ/mol)	ΔG_{fus} (kJ/mol)	ΔS_{fus} (J/mol.K)
Naphthalene	23.4 (±1.3)	1.8	+72.4
Fluorene	14.4 (±3.2)	4.1	+34.5
Phenanthrene	13.8 (±2.4)	1.9	+39.9
Anthracene	22.0 (±5.3)	9.3	+42.6
Pyrene	10.9 (±4.1)	1.5	+31.5
Chrysene	17.2 (±12.8)	13.1	+13.8
Benzo(a)anthracene	13.7 (±8.8)	5.3	+28.2
Benzo(a)pyrene	3.8 (±5.0)	6.0	–7.4

Table (Va): Thermochemical Properties of PAHs Fusion (**Step 2, **B****) at 25°C

PAH	ΔH_{fus} (kJ/mol)	ΔG_{fus}^{*} (kJ/mol)	ΔS_{fus} (J/mol.K)
Naphthalene	16.9 (±0.7)	2.5	48.3
Fluorene	15.3 (±1.4)	4.6	35.9
Phenanthrene	12.9 (±1.3)	3.9	30.2
Anthracene	19.7 (±3.2)	8.7	36.9
Pyrene	10.2 (±2.3)	5.7	15.1
Chrysene	14.8 (±4.8)	11.7	10.4
Benzo(a)anthracene	12.9 (±2.8)	6.9	20.1
Benzo(a)pyrene	15.3 (±3.5)	7.7	25.5

*: ΔG_{fus} estimated from correlation.

Table (Vb): Thermochemical Properties of PAHs Vaporization (**Step 2, **B****) at 25°C

PAH	ΔH_{vap} (kJ/mol)	ΔG_{vap}^{*} (kJ/mol)	ΔS_{vap} (J/mol.K)
Naphthalene	55.7 (±1.0)	20.0	120
Fluorene	71.2 (±2.7)	29.8	139
Phenanthrene	79.2 (±1.8)	34.1	151
Anthracene	82.2 (±4.5)	37.0	152
Pyrene	90.1 (±3.3)	40.5	166
Chrysene	108.6 (±9.0)	52.3	189
Benzo(a)anthracene	106.6 (±7.8)	47.9	197
Benzo(a)pyrene	105.2 (±6.2)	55.9	165

Table (VIa): Thermochemical Properties of PAHs Fusion (**Step 2, **C****) at 25°C

PAH	ΔH_{fus} (kJ/mol)	ΔG_{fus}^{*} (kJ/mol)	ΔS_{fus} (J/mol.K)
Naphthalene	16.9 (±0.7)	1.9	48.3
Fluorene	15.3 (±1.4)	4.0	35.9
Phenanthrene	12.9 (±1.3)	1.9	30.2
Anthracene	19.7 (±3.2)	9.4	36.9
Pyrene	10.2 (±2.3)	1.5	15.1
Chrysene	14.8 (±4.8)	13.1	10.4
Benzo(a)anthracene	12.9 (±2.8)	5.3	20.1
Benzo(a)pyrene	15.3 (±3.5)	6.0	25.5

*: $\Delta G_{fus} = +RT\ln(P^{*}_{iL}/P^{*}_{iS})$, with P^{*}_{iS} from measurement and P^{*}_{iL} estimated from correlation.

Table (VIb): Thermochemical Properties of PAHs Vaporization (**Step 2, **C****) at 25°C

PAH	ΔH_{vap} (kJ/mol)	ΔG_{vap}^{*} (kJ/mol)	ΔS_{vap} (J/mol.K)
Naphthalene	55.7 (±1.0)	20.6	118
Fluorene	71.2 (±2.7)	30.4	137
Phenanthrene	79.2 (±1.8)	36.1	145
Anthracene	82.2 (±4.5)	36.3	154
Pyrene	90.1 (±3.3)	44.7	152
Chrysene	108.6 (±9.0)	50.9	194
Benzo(a)anthracene	106.6 (±7.8)	49.5	192
Benzo(a)pyrene	105.2 (±6.2)	57.6	160

Appendix 6 - 6. Estimating Entropies of Pyrene Sorption.

(*Note: Figure 1 to 6 are located at the end of this appendix.*)

The system generally experienced a gain in entropy (freedom in molecular motion and/or arrangement) in sorption. The entropy of absorption was similar to those for the dissolution of pure solid or sub-cooled liquid pyrene in water (Table 6-6). The entropy of adsorption was very sensitive to the mechanistic approximations made, and significantly different estimates of adsorption entropy were obtained (Table 6-6). A modified adsorption model allowing a fraction of organic co-adsorbate displaced by the adsorbing pyrene to stay associated with the sorbent phase was proposed (Eqn. 6-6a, Eqn. 6-6b; Figure 6). The true entropy of adsorption should be bound within the estimates of the simpler models, but more in the direction of greater entropies gain. It seemed that entropic change was the dominating term in determining the energetics of HOCs adsorption.

1.1.1.1. Apparent/Overall Entropy of Sorption ($\Delta S_{d,app}$)

The apparent/overall entropy of sorption ($\Delta S_{d,app}$) for pyrene was estimated in similar approaches as the apparent enthalpy. To estimate $\Delta S_{d,app}$, K_d needs to be converted to the mole-fraction based $K^x_{d,app}$, which in turns require the overall sorption capacity, κ_{id}. κ_{id} consists of contributions from (i) adsorption, which is attributed to adsorption onto condensed carbon surface (e.g. sedimentary-BC), and (ii) absorption, which is attributed to absorption into the sedimentary-OC. The adsorption capacity was estimated to be around 100000 $\mu g_{pyr}/kg_{solids}$. The absorption contribution was estimated as the maximum amount of pyrene that can be absorbed into the sedimentary-OC. At the aqueous solubility of pyrene (C^{sat}_{pyr} ~ 140 $\mu g_{pyr}/L_w$) assuming a linear partitioning into OC (f_{OC} = 0.0296 kg_{OC}/kg_{solids}; $\log K_{OC}$ of 5.3 as determined from this study and from literature values, see Table 5-9), this was estimated to be about 830000 $\mu g_{pyr}/kg_{solids}$. κ_{id} was, therefore, estimated to be around 930000 $\mu g_{pyr}/kg_{solids}$.

$\Delta S_{d,app}$ was estimated to range from 40 to 140 (±10 to 30) J/mol.K. The estimates from the different methods were summarized in Table 6-4. A plot of $\Delta S_{d,app}$–C_{pyr} showed that $\Delta S_{d,app}$ generally decreases with increasing C_{pyr} (Figure 1) Here, the overall trend with respect to C_{pyr} was more consistent among the different isotherm forms than that for the apparent enthalpy of sorption. Consider that the relative uncertainties in $\Delta S_{d,app}$'s were small, the trend may be considered as real.

Since $K^x_{d,app}$ (from which $\Delta S_{d,app}$'s were derived) is only an approximation where contributions from adsorption and absorption are lumped together (section 2.1.5), the resulting $\Delta S_{d,app}$'s should be viewed with caution. A qualitative interpretation of how $\Delta S_{d,app}$ varies with C_{pyr} would be more proper. The positive $\Delta S_{d,app}$ indicated that a greater 'freedom' (greater entropy) was gained as pyrene became sorbed to the sedimentary OC/BC phase. Pyrene, like other PAHs, does not contain any rotatable structure. Thus this gain in 'freedom' may be understood as an overall increase in the flexibility of how all molecules (especially non-pyrene species) can be arranged – for instance, the solvating H_2O molecules can assume more different arrangements when

the hydrophobic pyrene leaves the aqueous phase (Schwarzenbach et al. 2003). Positive entropy (more freedom) for sorption is consistent with the fact dissolution of solid pyrene in water makes the overall system less free ($\Delta S_{pyr,dissolution}$ at saturation $\cong$ -33.3 J/mol.K; Table 6-5a). The greater positive values of $\Delta S_{d,app}$ in the lower C_{pyr} range implied that an even greater arrangement freedom was gained when adsorption was dominant. A possible molecular picture for this would be the following: that the adsorbing pyrene is removing the less hydrophobic co-adsorbates (e.g. H_2O), which have to conform rigidly to the surface, thus allowing both the pyrene-solvating H_2O's and the less-hydrophobic co-adsorbates to be more free.

1.1.1.2. Entropy of Absorption ($\Delta S_{d,abs}$)

The entropy of absorption ($\Delta S_{d,abs}$) for pyrene was estimated in the same fashion as the enthalpy of absorption (section 3.1.1.2) by converting $K_{d,abs}$ (partitioning coefficient due to absorption only) to the mole-fraction based K^x_{abs} (Table 6-1). The $\Delta S_{d,abs}$'s estimated from the three isotherm forms over C_{pyr} are plotted in Figure 2.

Although the estimated $\Delta S_{d,abs}$'s were greatly uncertain (Figure 2), all three isotherms suggested that $\Delta S_{d,abs}$ probably ranged from about 40–60 J/mol.K. Absorption may be most comparable to the opposite of dissolution reaction. For pyrene, the entropies of dissolution at saturation of dissolved pyrene (ΔS^{sat}_{diss}) are about –33 and –62.5 J/mol.K for dissolving solid pyrene and sub-cooled liquid pyrene, respectively (Table 6-5a, b). With $\Delta S_{d,abs}$ being comparable with ($-\Delta S^{sat}_{diss}$), this means that gain in arrangement freedom when aqueous pyrene is absorbed into sedimentary-OC is about the same as the freedom gained when dissolved pyrene is 'absorbed' to its pure sub-cooled liquid or solid states. Certainly, we should be cautious not to over-interpret absorption entropies with very larger uncertainties. The errors associated with the $\Delta S_{d,abs}$ can be better observed from the individual $\Delta S_{d,abs}$–C_{pyr} plots (Appendix 6-4).

1.1.1.3. Estimating $\kappa_{i,ads}$, C_{orgw}, and MW_{org} for Adsorption Entropy

The estimation of entropy of adsorption ($\Delta S_{d,ads}$) requires assessing parameters such as adsorption capacity, $\kappa_{i,ads}$, or the concentration of 'average' organic co-adsorbate, C_{orgw}, and its molar mass MW_{org} (e.g. Table 6-1).

To estimate $\kappa_{i,ads}$, it was assumed: (i) that the principal adsorbing phase of the sediment was sooty BC, (ii) that sedimentary soot had an average radius of 25 nm and a density of 2.2 kg/L, (iii) that all surface area of soot may be accessible and available to pyrene and/or other adsorbates, (iv) that one single pyrene would occupy about 1 nm^2 of soot surface area (see Appendix 4-3). From these assumptions, surface area of sedimentary-BC was estimated to be about 60000 m^2_{BC}/kg_{BC}, and could take up about 2×10^7 $\mu g_{pyr}/kg_{BC}$. With $f_{BC} = 0.0049$, $\kappa_{i,ads}$ was estimated to be about 1×10^5 (rounding up 98500) $\mu g_{pyr}/kg_{solids}$. An estimate on $\kappa_{i,ads}$ would allow us to compute $K^x_{ads\text{-}ss}$ and $K^x_{ads\text{-}sH2O}$.

To compute $K^x_{ads\text{-}sOrg}$, we also need to evaluate C_{orgw} and MW_{org} of the 'average' organic co-adsorbates which compete with pyrene for surface sites. Here, the organic co-adsorbates were approximated with dissolved organic matter/carbon (DOC/DOM). The solids-to-water ratios in the suspensions studied here (R_{sw} ~ 20-600 mg_{solids}/L_w)

were comparable to those in the surface water system (Table 2-7). Typical DOC concentration in harbor/estuary waters is around 1–10 mg_{DOC}/L_w (Whitehouse 1985; Tremblay et al. 2005), with the variation depending on depth and closeness to DOC sources; for high solid-concentration porewater phase, DOC could increase to around 5–20 mg_{DOC}/L_w (McGroddy et al. 1995) in surficial sediment, and as high as ~50 mg_{DOC}/L_w in deeper layer (Chin et al. 1991). From these information, C_{orgw} was assumed to be around 1–20 mg_{org}/L_w.

The study by Chin et al. (1991) and the review by Gustafsson et al. (1997a) suggested that DOC may be viewed as organic species with molecular weight in the order of ~≤1000 g/mol. Considering (i) that the molecular weight of DOC is distributed and (ii) that some organic matter may be small-sized HOCs similar to pyrene, it was assumed that the MW_{org} ~ 300 g_{org}/mol_{org}.

Since the estimates of $\kappa_{i,ads}$, C_{orgw}, and MW_{org} may contain high uncertainties, sensitivity analysis was also performed for the $\Delta S_{d,ads}$'s derived from $K^x_{ads\text{-}ss}$ and $K^x_{ads\text{-}sH2O}$, and $K^x_{ads\text{-}sOrg}$.

1.1.1.4. Entropy of Adsorption ($\Delta S_{d,ads\text{-}ss}$, $\Delta S_{d,ads\text{-}sH2O}$, $\Delta S_{d,ads\text{-}sOrg}$)

As discussed earlier (section 2.1.4), it is much more difficult to evaluate the entropy of adsorption ($\Delta S_{d,ads}$). A realistic description of adsorption which allows distributions on both the surface energies and the competing co-adsorbates affinity quickly lead to unmanageable thermodynamic expressions (section 2.1.4.5). To make the entropic analysis manageable, the mechanistic picture has to be greatly simplified. It is, therefore, important to note that the $\Delta S_{d,ads}$'s presented here are a thermodynamic interpretation of the experimental K_d in the context of these simplified models.

The single-solute ($\Delta S_{d,ads\text{-}ss}$) and the solute-$H_2O$ ($\Delta S_{d,ads\text{-}sH2O}$) models both gave an estimate of the pyrene adsorption entropy to be about 135–140 (±20) J/mol.K (Figure 3). The values estimated from the Linear+Freundlich form at high C_{pyr} range (i.e. $\Delta S_{d,ads}$ decreases with C_{pyr}) were rejected on the basis that absorption was the dominating mode of sorption in the $\mu g_{pyr}/L_w$ range (section 3.1.1.3). Sensitivity analysis showed that $\Delta S_{d,ads\text{-}ss}$, for instance, was insensitive to the surface adsorption capacity, $\kappa_{i,ads}$: $\Delta S_{d,ads\text{-}ss}$ remained in the 100+ J/mol.K range despite a 25× difference in $\kappa_{i,ads}$ (Figure 4). This seemed very high when compared with the entropy of pyrene dissolution in water ($(-\Delta S^{sat}_{diss})$ = 33 and 62.5 J/mol.K, for solid pyrene and sub-cooled liquid pyrene, respectively; Table 6-5a, b). It was comparable to the entropy of vaporization of organic compounds at their boiling points ($\Delta S_{vap,i}(T_b)$ ~ 85–120 J/mol.K). However, $\Delta S_{d,ads\text{-}ss}$ or $\Delta S_{d,ads\text{-}sH2O}$ were close to the entropies of pyrene vaporization or sublimation at room temperature ($\Delta S_{vap,pyr}(25°C)$ = 155 J/mol.K; $\Delta S_{sub,pyr}(25°C)$ = 181 J/mol.K; Table 6-5c, e). Is it possible for the gain in the system's freedom to exceed that limited by 'precipitation' (i.e. $pyr_{(w)} \rightarrow pyr_{(s)}$ or $pyr_{(L)}$)? Even if this is possible, as discussed in section 3.1.2.1, could the excess gain in entropy be 60 J/mol.K?

The solute-organic-adsorbate ($\Delta S_{d,ads\text{-}sOrg}$) model gave a very different picture for adsorption entropy. $\Delta S_{d,ads\text{-}sOrg}$ was estimated to be only around 10 (±10) J/mol.K) (Figure 5). Sensitivity analysis showed that $\Delta S_{d,ads\text{-}sOrg}$ remained in the range of –10 to

40 J/mol.K, despite a 400× difference in the highly uncertain C_{orgw}/MW_{org} factor (Figure 5). This suggested that entropic contribution to pyrene adsorption was relatively insignificant, and that energetics of adsorption was primarily dominated the enthalpy term. A small $\Delta S_{d,ads\text{-}sOrg}$ is qualitatively reasonable: if the organic adsorbate and the pyrene simply 'switch place' as the adsorbed and the solvated species, the system would experience little change in the arrangement freedom.

It is unclear what the actual adsorption entropy should be, although the greatly different $\Delta S_{d,ads}$'s from the different mechanistic pictures may be resolved. At the first glance, the single-solute and the solute-H_2O models seem to be over-simplifying, for environmental geosorbents are often coated with organic matter (Mayer 1994; Holmen et al. 1997; Zimmerman et al. 2004a, b; Curry et al. 2007) due to the surface-active nature of organic matter (Hayase et al. 1983; Shinozuka et al. 1991). However, the limitation of the solute-organic model should be noted: it assumes the displaced organic to enter the aqueous phase and this may not be true (section 2.1.4.5; Eqn. 6-22). In reality, a fraction of the displaced organic may become dissolved. If this is the case, then the thermodynamic expression for the adsorption of pyrene (as '*i*') would be as follows (see Figure 6 for derivation):

$$\textbf{Adsorption (mixed):} \quad i_{(w)} + \mathrm{org}_{(\exists)} \leftrightarrow (\mathrm{A})\mathrm{org}_{(\exists+i)} + (\mathrm{A})i_{(\exists+\mathrm{org})} + (1-\mathrm{A})\mathrm{org}_{(w)} + (1-\mathrm{A})i_{(\exists)}$$

$$K^{x}{}_{ads-mix} = \frac{\left(x_{i\exists+org}\right)^{A}\left(x_{i\exists}\right)^{(1-A)}\left(x_{org\exists+i}\right)^{A}\left(x_{orgw}\right)^{(1-A)}}{x_{iw}x_{org\exists}} = \frac{\left(\Theta_i{}^{\exists+org}\right)^{A}\left(\Theta_i{}^{\exists}\right)^{(1-A)}\left(\Theta_{org}{}^{\exists+i}\right)^{A}\left(x_{orgw}\right)^{(1-A)}}{x_{iw}\Theta_{org}{}^{\exists}} = \frac{\left(\Theta_i{}^{\exists}\right)^{(1-A)}\left(x_{orgw}\right)^{(1-A)}}{x_{iw}(1-\Theta_i{}^{\exists})}$$

Eqn. 6-6a

where $\Theta_x{}^y$ is the fraction coverage of sites with energy y by adsorbate x,

A is the fraction of displaced organic co-adsorbate which *resists* solvation by water; $0 \le A \le 1$.

Supposing most of the displaced organic co-adsorbate does not become dissolved (i.e. $A \rightarrow 1$), then $(\Theta_i{}^{\exists})^{(1-A)}$ and $(x_{orgw})^{(1-A)}$ both approaches unity, and we would have:

$$K^{x}{}_{ads-mix} = \frac{\left(\Theta_i{}^{\exists}\right)^{(1-A)}\left(x_{orgw}\right)^{(1-A)}}{x_{iw}(1-\Theta_i{}^{\exists})} \approx \frac{1}{x_{iw}(1-\Theta_i{}^{\exists})}$$

Eqn. 6-6b

This means that the more realistic $K^{x}_{ads\text{-}mix}$ should have values of similar order as $K^{x}_{ads\text{-}ss}$ or $K^{x}_{ads\text{-}sH2O}$ (Table 6-1), and hence $\Delta S_{d,ads\text{-}mix}$, derived from $K^{x}_{ads\text{-}mix}$, would be approaching $\Delta S_{d,ads\text{-}ss}$ or $\Delta S_{d,ads\text{-}sH2O}$. If we know A, a better estimate for adsorption

entropy can be made. The fraction A can be estimated if the amount of DOC desorbing from sediment particle is known.

1.1.2. Concluding Enthalpies and Entropies of Sorption

The substantial uncertainties in both the enthalpies and entropies made it meaningless to characterize both ΔH_d and ΔS_d as a function of dissolve phase sorbate concentration. Instead, we tried to characterize the enthalpies and entropies of absorption and adsorption. A summary of all derived enthalpies and entropies of sorption is provided in Table 6-6. As reference for comparison, the enthalpies and entropies of phase change reactions for pyrene and other PAHs are provided in Table 6-5. The derivation (method, assumptions, and references) of enthalpy and entropy data can be found in Appendix 6-5.

The absorption/adsorption enthalpies and entropies derived from this study contained substantial uncertainties ($\sigma_{\Delta H} \leq 10$ kJ/mol; $\sigma_{\Delta S} \leq 30$ J/mol.K). Such levels of error were partly due to the fact natural sediments were highly complex and heterogeneous systems. It should also be noted that the derivation of enthalpy and entropy data can also be very 'sensitive' in simple, lab-bench systems. For instance, May et al. (1983) and Whitehouse (1984) both studied the solubility of PAHs in water at environmental range of temperatures (~0–30°C). They reported very consistent mole-fraction PAHs solubilities (and hence ΔG^x_{diss}'s) (Table 6-5a). However, the enthalpies and entropies were less consistent, with as high as 15 kJ/mol of difference in ΔH^x_{diss}, and as high as 20 to 50 J/mol.K difference in ΔS^x_{diss} (i.e. anthracene and benzo(a)pyrene; Table 6-5a). In view of the intrinsic sensitivity of enthalpy/entropy measurement, the uncertainties reported here are, perhaps, somewhat acceptable.

Despite the errors in sorption enthalpies and entropies, some qualitatively meaningful thermochemical differences between absorption and adsorption could be made. Analysis as such, to the author's knowledge, has not been performed on the sorption of HOCs to natural geosorbents. This may also be the first study to examine the thermodynamic relationships of absorption and adsorption, progressing from the most simple system to increasingly realistic case (e.g. Table 6-1). In the case of adsorption, although ΔS^x_{ads} adsorption remained unknown, the limiting values of ΔS^x_{ads} were estimated, along with a new model from which a more realistic ΔS^x_{ads} may be derived (Eqn. 6-6a, Eqn. 6-6b; Figure 6).

Enthalpy or entropy of sorption should be interpreted in the context of the mechanistic picture and any assumptions from which they are derived. For instance, the experimental data from this study may have satisfied the monolayer adsorption assumption (Appendix 6-2), but this may not be true for all cases of sorption. It has been shown that the enthalpy of adsorption can change drastically from the first-layer to the later layers for the sorption of surfactants in graphite-water system (Kiraly et al. 2005). It is possible that the enthalpies or entropies observed in many cases are only apparent or averaged values.

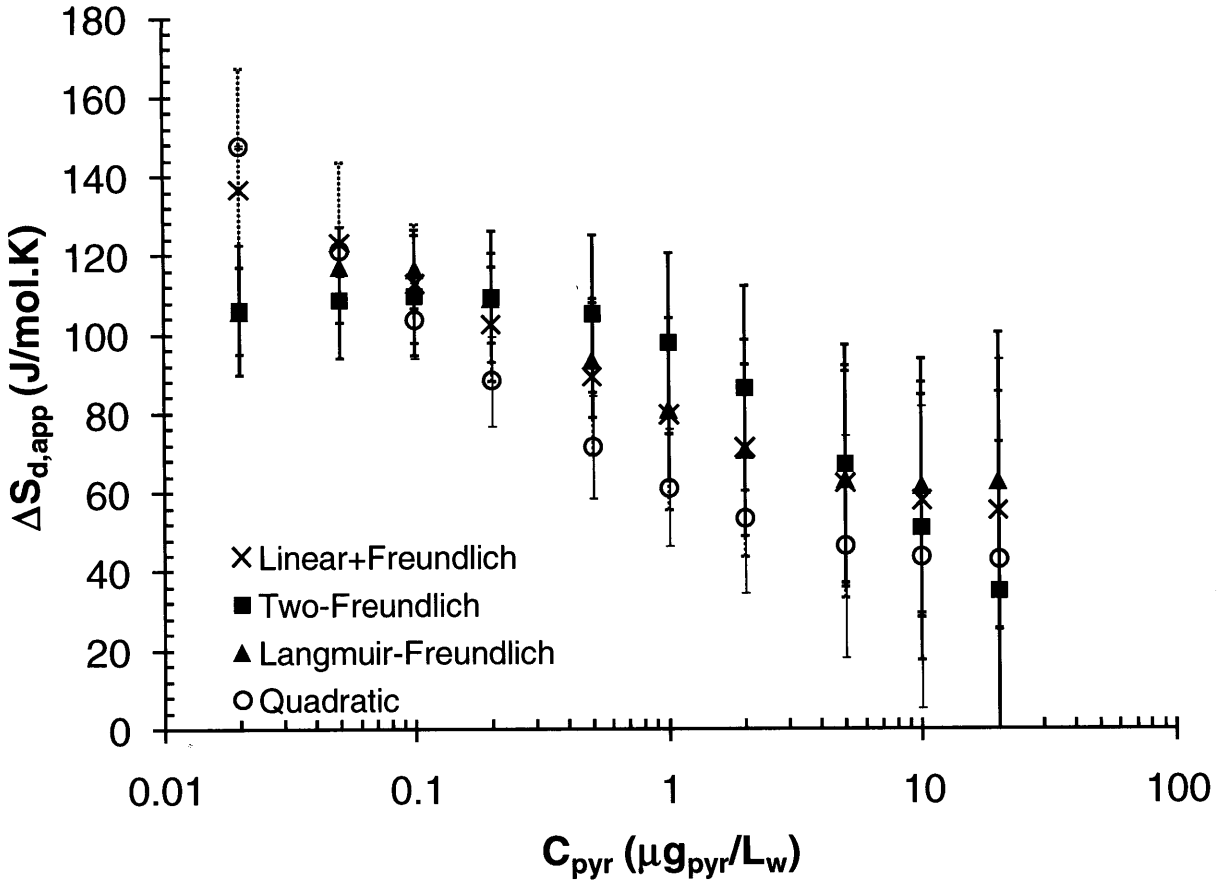

Figure 1. Apparent/Overall entropy ($\Delta S_{d,app}$) of pyrene sorption vs C_{pyr}.

The individual points are $\Delta S_{d,app}$'s at particular C_{pyr}'s evaluated by regression the $\ln K^{x}_{d,app,X}$(at C_{pyr}) vs 1/T, where the $K^{x}_{d,app,X}$'s were estimated from the listed isotherms regressed at 6, 15, 22, and 37°C. Consequently, the error bars represent the uncertainty ($\pm 1\sigma$) from the linear regressions of $\ln K^{x}_{d,app,X}$'s at particular C_{pyr}'s.

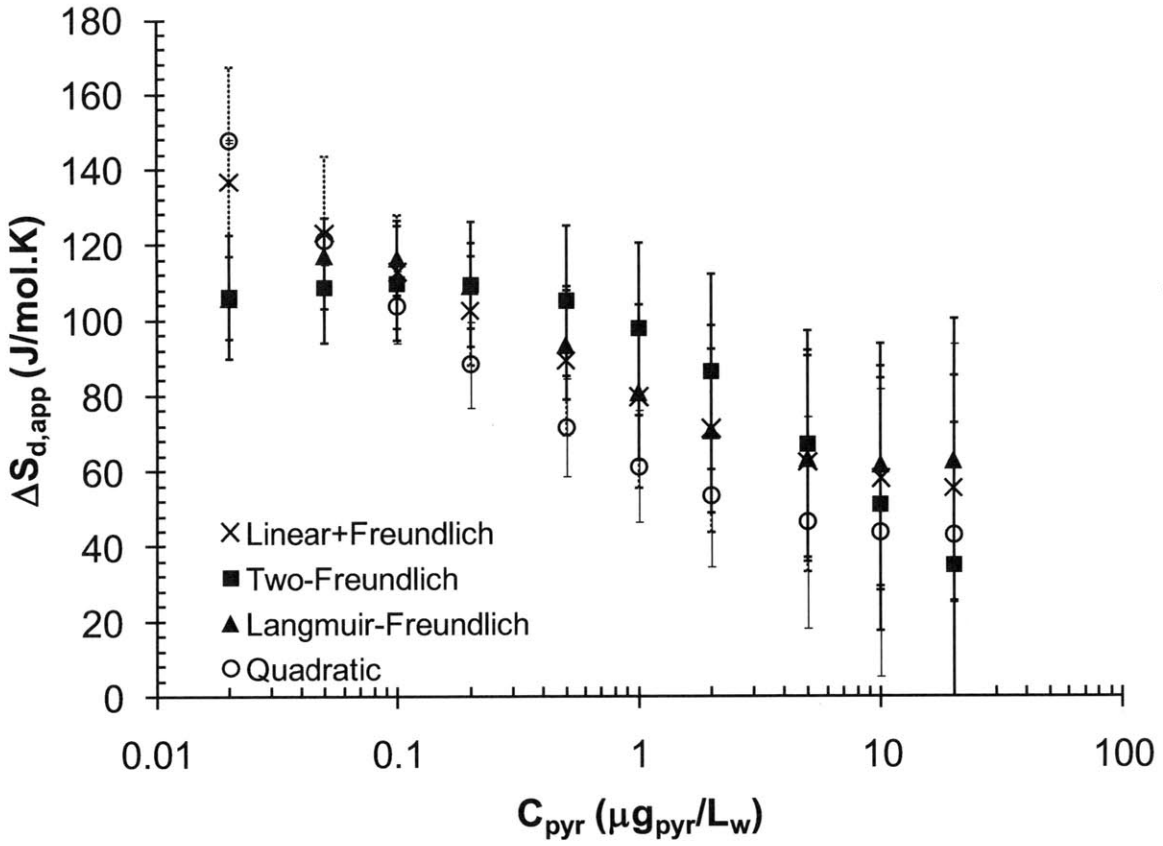

Figure 1. Apparent/Overall entropy ($\Delta S_{d,app}$) of pyrene sorption vs C_{pyr}.

The individual points are $\Delta S_{d,app}$'s at particular C_{pyr}'s evaluated by regression the $\ln K^{x}_{d,app,X}$(at C_{pyr}) vs 1/T, where the $K^{x}_{d,app,X}$'s were estimated from the listed isotherms regressed at 6, 15, 22, and 37°C. Consequently, the error bars represent the uncertainty ($\pm 1\sigma$) from the linear regressions of $\ln K^{x}_{d,app,X}$'s at particular C_{pyr}'s.

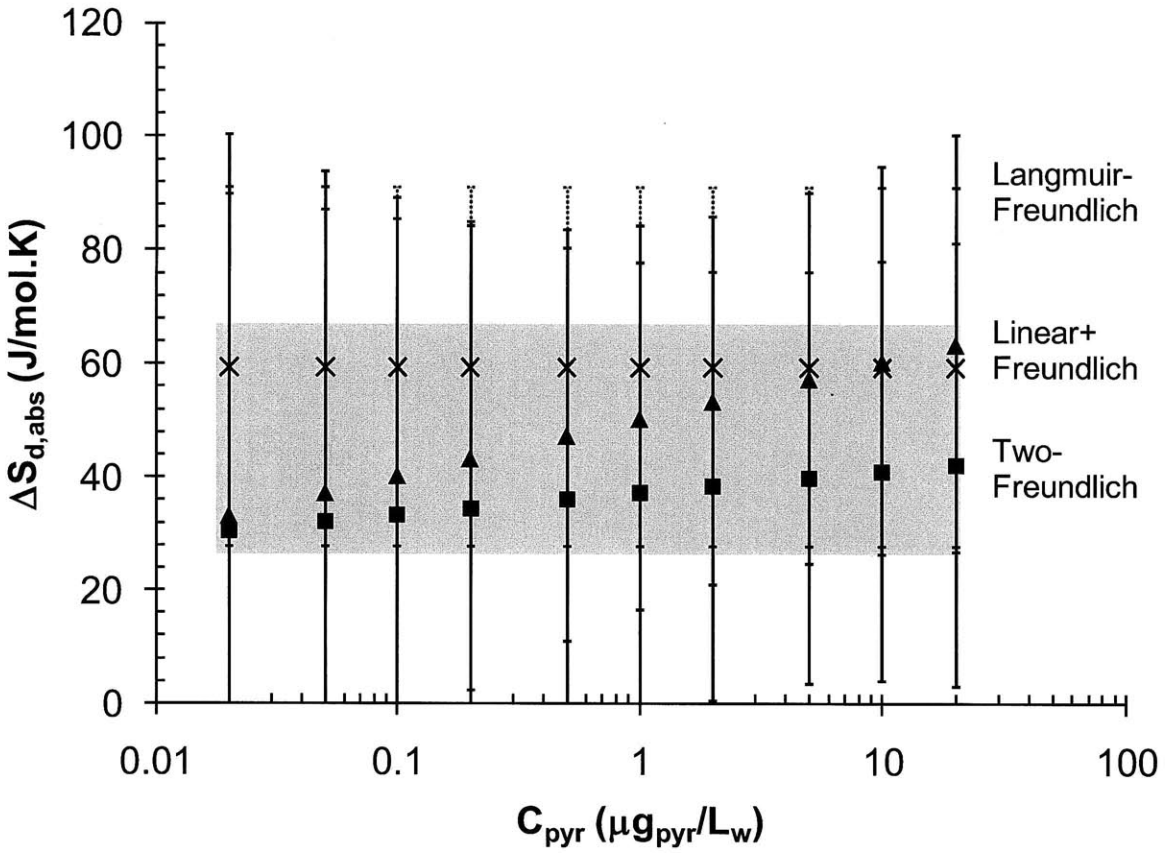

Figure 2. Absorption entropy ($\Delta S_{d,abs}$) of pyrene into sedimentary OC vs C_{pyr}.

The individual points are $\Delta S_{d,abs}$'s at particular C_{pyr}'s evaluated by regression the $\ln K^{x}_{abs,X}$(at C_{pyr}) vs 1/T, where the $K_{d,absX}$'s were estimated from the lower-affinity domain parameters regressed at 6, 15, 22, and 37°C. Consequently, the error bars represent the uncertainty ($\pm$ 1σ) from the linear regressions of $\ln K^{x}_{abs,X}$'s at particular C_{pyr}'s. The shaded region serves as visual aid for the range of $\Delta S_{d,abs}$.

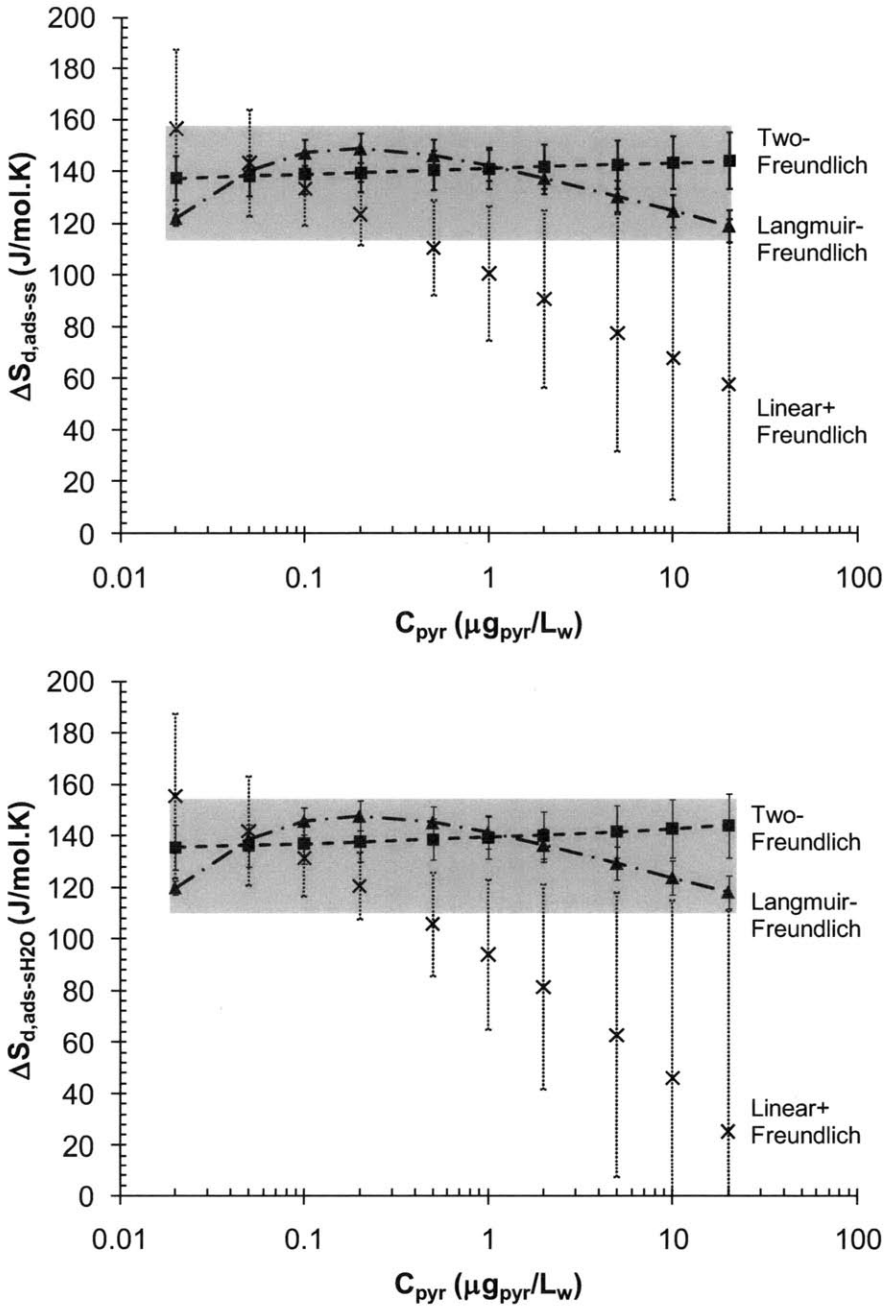

Figure 3. Absorption entropy ($\Delta S_{d,abs-ss}$, $\Delta S_{d,abs-sH2O}$) of pyrene onto sedimentary BC vs C_{pyr}.

Absorption entropy of pyrene according to the simple, single-solute picture (**Upper**: $\Delta S_{d,abs-ss}$) and the simple, solute-H_2O picture (**Lower**: $\Delta S_{d,abs-sH2O}$). The individual points are $\Delta S_{d,ads-ss/sH2O}$'s at particular C_{pyr}'s evaluated by regression the $\ln K^x_{ads-ss/sH2O}$ (at C_{pyr}) vs 1/T. Error bars represent the uncertainty ($\pm$ 1σ) from the linear regressions of $\ln K^x_{ads-ss/sH2O}$'s at particular C_{pyr}'s. The shaded region serves as visual aid for the range of values which $\Delta S_{d,ads}$ was most likely to take.

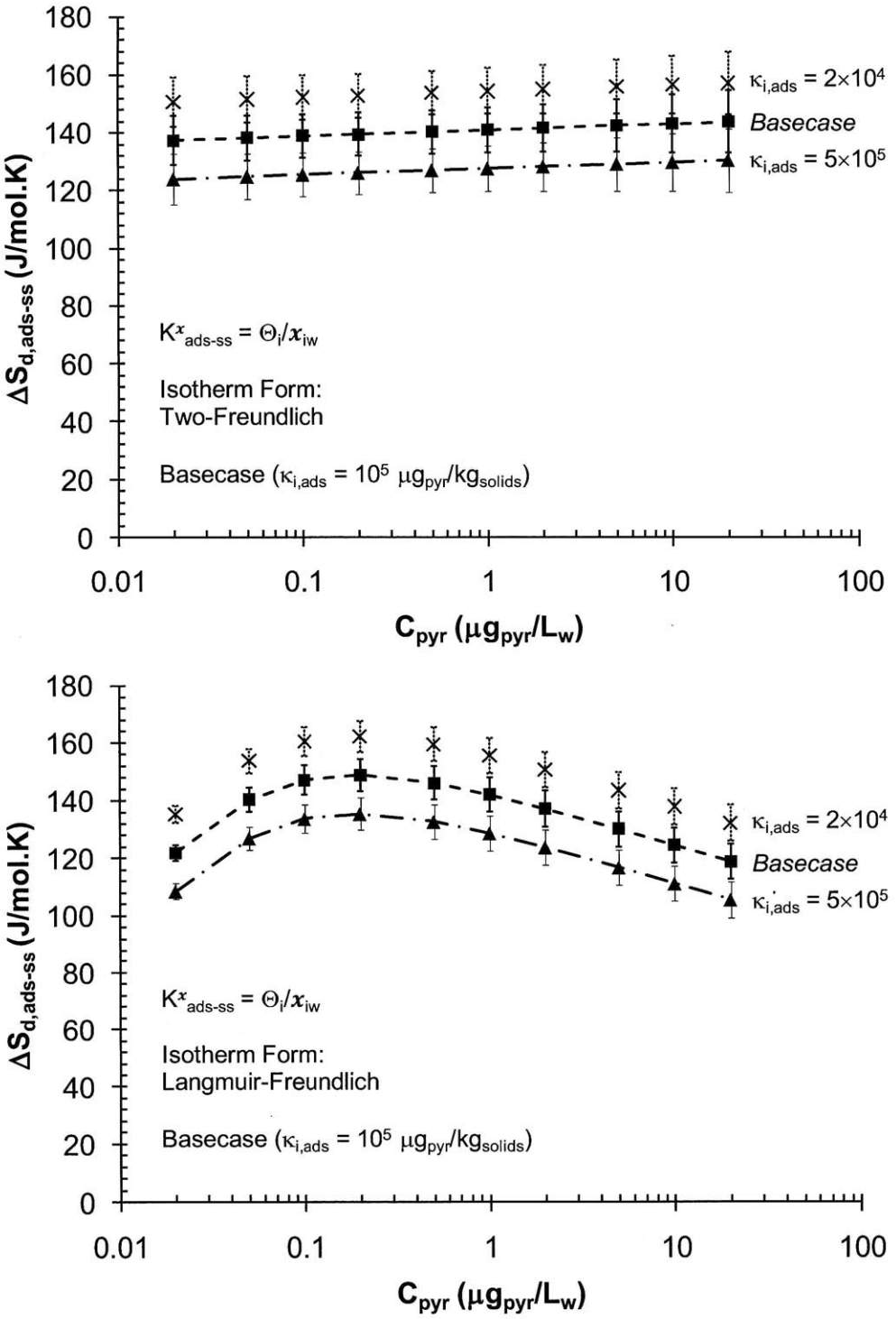

Figure 4. Sensitivity of $\Delta S_{d,abs-ss}$ to Adsorption Capacity $\kappa_{i,ads}$.

Error bars represent the uncertainty (± 1σ) from the linear regressions of $\ln K^x_{ads-ss/sH2O}$'s at particular C_{pyr}'s.

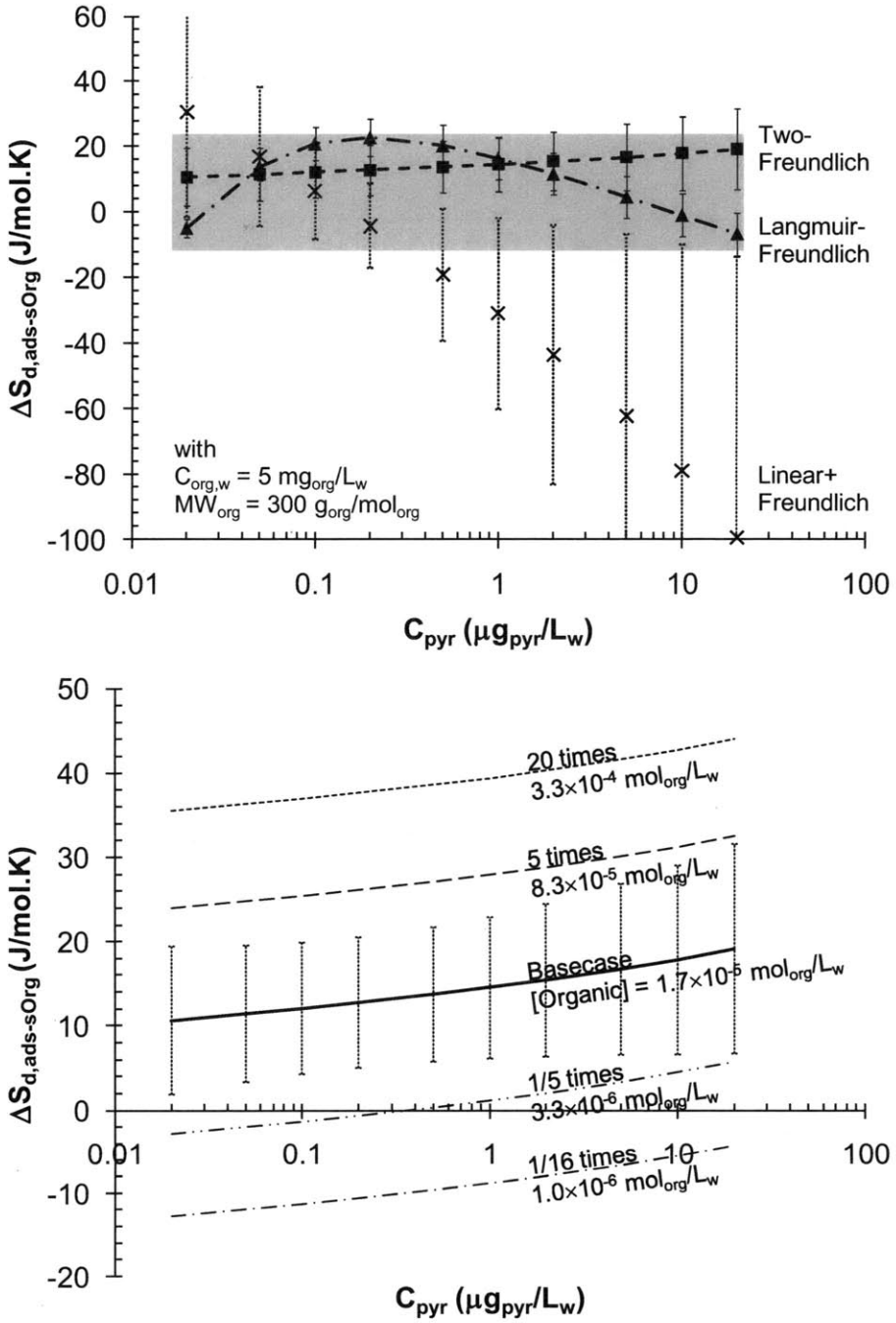

Figure 5. Absorption entropy ($\Delta S_{d,abs-sOrg}$) of pyrene onto sedimentary BC vs C_{pyr}.

Absorption entropy of pyrene according to the simple, solute-organic co-adsorbate picture at basecase (**Upper**) and the sensitivity of $\Delta S_{d,abs-sOrg}$ on uncertainty in [Organic]=C_{orgw}/MW_{org} (**Lower**). Error bars represent the uncertainty ($\pm$ 1σ) from the linear regressions of $\ln K^{x}_{ads-ss/sH2O}$'s at particular C_{pyr}'s. The shaded region serves as visual aid for the range of values which $\Delta S_{d,ads}$ was most likely to take.

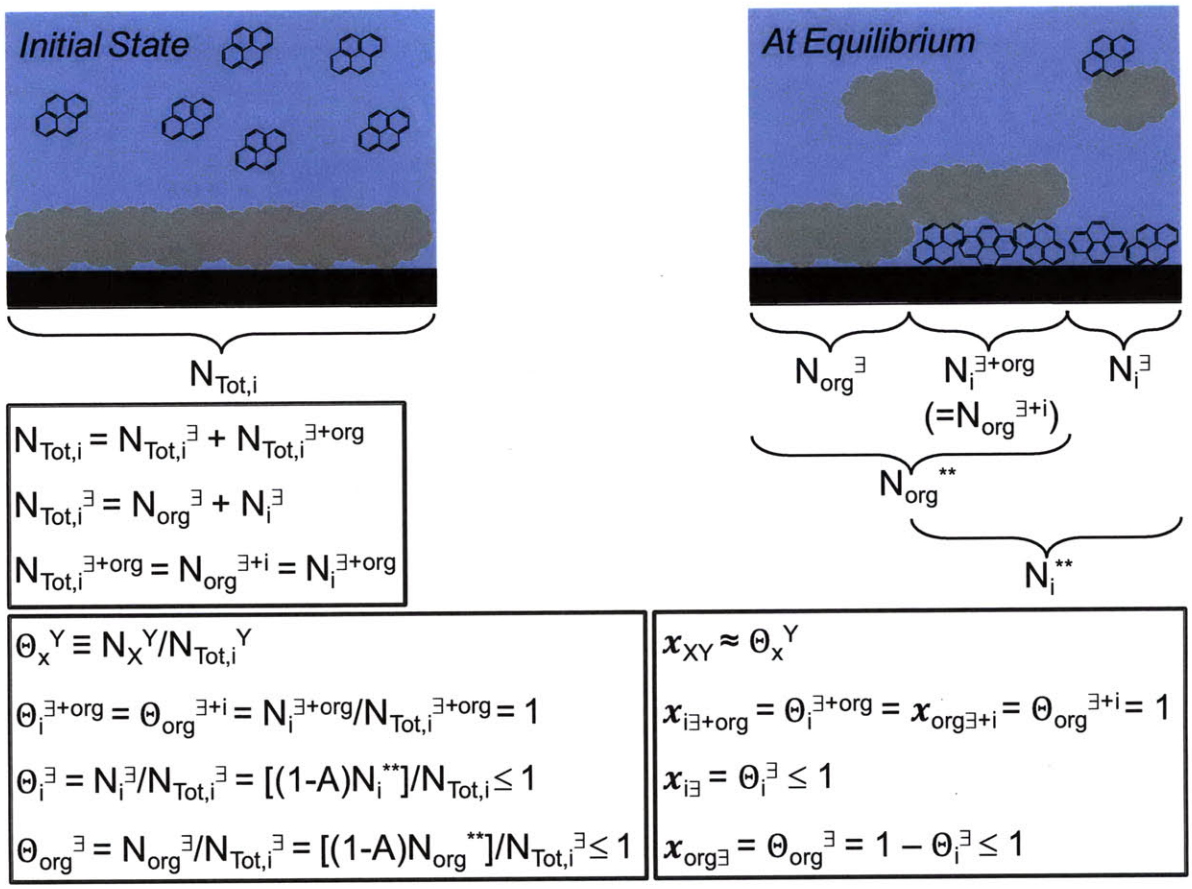

Figure 6. Derivation of the '*mixed*' adsorption model with *i* and organic co-adsorbate.

Where: N_x^Y is the number of surface sites with energy Y capable of binding *i* but occupied by X,

$N_{Tot,i}$ is the total number of sites (of all energies) capable of binding *i*,

$N_{Tot,i}^Y$ is the total number of sites of energy Y capable of binding *i*,

N_X^{**} is the total number of sites (of all energies; capable of binding *i*) occupied by X,

Θ_X^Y is the fraction coverage of sites with energy Y (capable of binding *i*) occupied by adsorbate X,

A is the fraction of displaced organic co-adsorbate which *resists* solvation by water; $0 \leq A \leq 1$,

$\boldsymbol{x}_{XY}$ is the 'mole-fraction' of adsorbate X on sites (capable of binding *i*) with energy Y.

Appendix 6 - 7. Estimating Apparent/Overall Enthalpy ($\Delta H_{d,app}$) of Pyrene Sorption.

(a) From Raw Sorption Data (*No Regression*)

	$C_{pyr,Eqm}$ ($\mu g_{pyr}/L_w$) =			
	0.01-0.05[a]	0.1-0.5[b]	1-5[b]	10-20[b]
(5-month)				
$\Delta H_{d,app}$ (J/mol)	-17000 (±400)	-10000 (±4300)	-17000 (±8300)	-15000 (±8000)
r^2	1.0	0.73	0.68	0.64
(10-month)				
$\Delta H_{d,app}$ (J/mol)	-28000 (±4200)	-14000 (±7000)	-30000 (±6800)	-24000 (±14000)
r^2	1.0	0.68	0.91	0.60

a: No equilibrium observations were made in the 0.01-0.05 $\mu g_{pyr}/L_w$ range. Only sorption observations at 6, 15, and 22°C were regressed.
b: Data from all four temperatures were used (i.e. 6, 15, 22, and 37°C)

(b) From Purely Descriptive Fitting of Sorption Data (*Regressed to Quadratic Form*)*

	$C_{pyr,Eqm}$ ($\mu g_{pyr}/L_w$) =			
	0.02-0.05[a]	0.1-0.5[b]	1-5[b]	10-20[b]
(5-month)				
$\Delta H_{d,app}$ (J/mol)	-12000 (±3400)	-10000 (±1900)	-12000 (±4400)	-16000 (±9400)
r^2	0.80-0.90	0.93-0.95	0.71-0.89	0.57-0.64
(10-month)				
$\Delta H_{d,app}$ (J/mol)	-7000 (±1000)	-16500 (±3300)	-23500 (±6300)	-25000 (±13000)
r^2	0.93-1.0	0.92-0.93	0.82-0.93	0.60-0.72

*: $\Delta H_{d,app}$'s were averaged values estimated at the lower and upper bound of the range.
a: $C_{pyr,Eqm}$ is restricted to the 0.02-0.05 $\mu g_{pyr}/L_w$ range as the extrapolation of the quadratic form is prone to give non-sensible trend.
b: Data from all four temperatures were used (i.e. 6, 15, 22, and 37°C)

(c) From Linear+Freundlich Regression of Sorption Data

	$C_{pyr,Eqm}$ ($\mu g_{pyr}/L_w$) =			
	0.02-0.05[a]	0.1-0.5[b]	1-5[b]	10-20[b]
(5-month)				
$\Delta H_{d,app}$ (J/mol)	-3100[c] (±3100)	-8600 (±1900)	-13000 (±4600)	-12000 (±8400)
r^2	0.33[c]	0.82-0.96	0.70-0.90	0.41-0.57

(10-month)				
$\Delta H_{d,app}$ (J/mol)	-13000 (±7000)	-19000 (±5100)	-24000 (±7800)	-27000 (±8700)
r^2	0.48-0.75	0.87-0.90	0.82-0.83	0.83

*: $\Delta H_{d,app}$'s were averaged values estimated at the lower and upper bound of the range.
a: $C_{pyr,Eqm}$ is restricted to the 0.02-0.05 $\mu g_{pyr}/L_w$ range as within the regression range.
b: Data from all four temperatures were used (i.e. 6, 15, 22, and 37°C)
c: Data at $C_{pyr,Eqm}$ = 0.05 $\mu g_{pyr}/L_w$.

(d) From Two-Freundlich Regression of Sorption Data

	$C_{pyr,Eqm}$ ($\mu g_{pyr}/L_w$) = 0.02-0.05[a]	0.1-0.5[b]	1-5[b]	10-20[b]
(5-month)				
$\Delta H_{d,app}$ (J/mol)	-18000 (±5400)	-8300 (±2700)	-6600 (±3100)	-15000 (±5400)
r^2	0.83-0.87	0.69-0.89	0.63-0.73	0.77-0.80
(10-month)				
$\Delta H_{d,app}$ (J/mol)	-20000 (±4600)	-17000 (±5100)	-21000 (±7700)	-31000 (±10000)
r^2	0.90-0.91	0.79-0.88	0.77-0.80	0.81-0.82

*: $\Delta H_{d,app}$'s were averaged values estimated at the lower and upper bound of the range.
a: $C_{pyr,Eqm}$ is restricted to the 0.02-0.05 $\mu g_{pyr}/L_w$ range as within the regression range.
b: Data from all four temperatures were used (i.e. 6, 15, 22, and 37°C)

(e) From Langmuir-Freundlich Regression of Sorption Data

	$C_{pyr,Eqm}$ ($\mu g_{pyr}/L_w$) = 0.02-0.05[a]	0.1-0.5[b]	1-5[b]	10-20[b]
(5-month)				
$\Delta H_{d,app}$ (J/mol)	-21000 (±6700)	-9500 (±2400)	-10000 (±3800)	-13000 (±7900)
r^2	0.83-0.84	0.85-0.94	0.68-0.89	0.56-0.61
(10-month)				
$\Delta H_{d,app}$ (J/mol)	-19000 (±3100)	-17000 (±3600)	-24000 (±6600)	-25000 (±10000)
r^2	0.94-0.96	0.91-0.93	0.84-0.90	0.72-0.79

*: $\Delta H_{d,app}$'s were averaged values estimated at the lower and upper bound of the range.
a: $C_{pyr,Eqm}$ is restricted to the 0.02-0.05 $\mu g_{pyr}/L_w$ range as within the regression range.
b: Data from all four temperatures were used (i.e. 6, 15, 22, and 37°C).

Chapter 7: Appendices

Appendix 7 - 1. *A priori* Modeling of the Observed Desorption Kinetic Profiles of Pyrene ($C_{pyr,w}$) by Four Isotherm Forms 791
Appendix 7 - 2. Sensitivity of Pyrene Desorption Kinetics (I): $S_{pyr,o}$ 806
Appendix 7 - 3. Sensitivity of Pyrene Desorption Kinetics (II): f_{OC} 811
Appendix 7 - 4. Sensitivity of Pyrene Desorption Kinetics (III): f_{BC} 816
Appendix 7 - 5. Sensitivity of Pyrene Desorption Kinetics (IV): n_{BC} 821
Appendix 7 - 6. Sensitivity of Pyrene Desorption Kinetics (V): $logK_{OC}$ 826
Appendix 7 - 7. Sensitivity of Pyrene Desorption Kinetics (VI): $logK_{BC}$ 831
Appendix 7 - 8. Sensitivity of Pyrene Desorption Kinetics (VII): particle radius R. 836
Appendix 7 - 9. Sensitivity of Pyrene Desorption Kinetics (VIII) & (IX): Porosity (ϕ) and Shape Factor (SF) 842
Appendix 7 - 10. Estimation of Numbers of BC Particles in Typical Natural Aggregates. 848
Appendix 7 - 11. Local Partitioning Equilibrium Assumption: Timescale Analysis. 851
Appendix 7 - 12. Derivation of Effective Diffusivities ($D_{eff,pw}$, $D_{eff,OM}$, $D_{eff,surf}$). 856
Appendix 7 - 13. Volume Analysis of OM-phase in Typical Soil and Sediment 860
Appendix 7 - 14. Derivation of Equations for Intra-aggregate Porewater Diffusion Model. 862
Appendix 7 - 15. Derivation of the C_{bulk} (or C_m)finite difference equation at the $(n+1)^{th}$ time step 866
Appendix 7 - 16. "Universal" Isotherm ($logK_{OC}$, $logK_{BC}$) for Pyrene 870
Appendix 7 - 17. n_{BC} Best-Fit Modeling of the Observed Desorption Kinetic Profiles of Pyrene ($C_{pyr,w}$) by the New-OC-BC isotherm and the sedimentary Universal-OC-BC isotherm. 871
Appendix 7 - 18. SEM Images of BH#6 Sediment Aggregates/Particles 877
Appendix 7 - 19. Two-Compartmental (Constrained) Regression of the BH#6/NQB Desorption Kinetic Data 878
Appendix 7 - 20. *A priori* Modeling of Desorption with the Occlusion-OC-BC Isotherm (30% occlusion) 879
Appendix 7 - 21. Regression of Desorption Kinetic Data by Empirical Models. 884
Appendix 7 - 22. OC Contents in Some Soils and Sediments 894
Appendix 7 - 23. Non-linear Isotherm and the Diffusion Equation. 896
Appendix 7 - 24. Best Fit Linear Isotherms for Pyrene Desorption Experiments 897
Appendix 7 - 25. Estimation of Pyrene Desorption Activation Energy ($E_{A,des,app}$). 899

Appendix 7 - 1. *A priori* Modeling of the Observed Desorption Kinetic Profiles of Pyrene ($C_{pyr,w}$) by Four Isotherm Forms

A-set (dia. 38–75 μm)

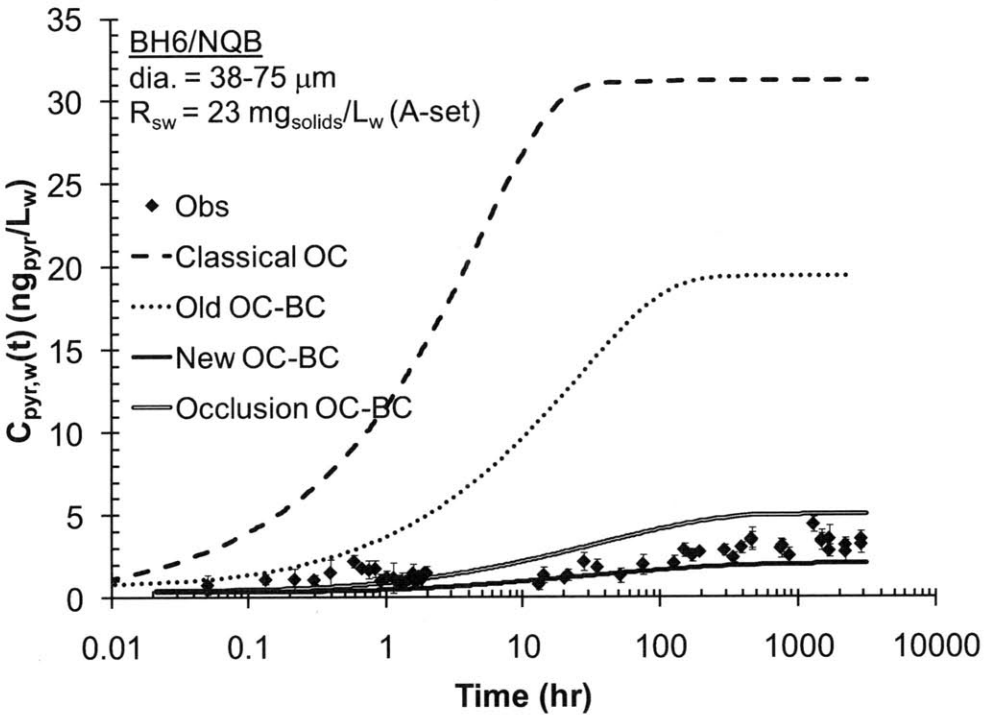

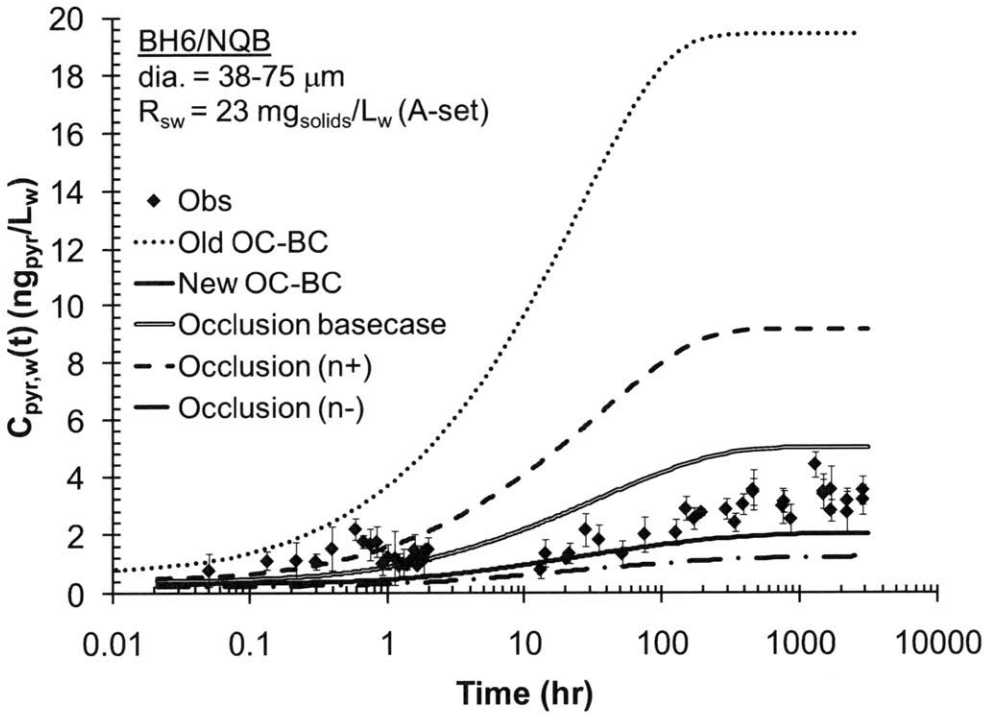

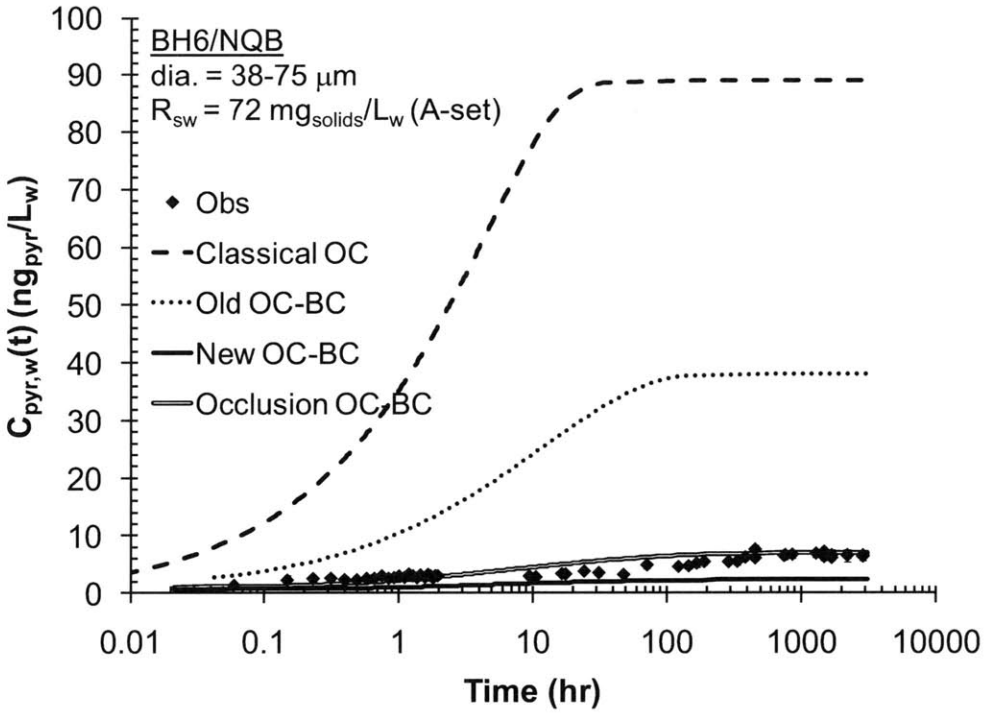
BH6/NQB
dia. = 38-75 μm
R_{sw} = 72 mg_{solids}/L_w (A-set)
Obs
Classical OC
Old OC-BC
New OC-BC
Occlusion OC-BC
$C_{pyr,w}(t)$ (ng_{pyr}/L_w)
Time (hr)
100
90
80
70
60
50
40
30
20
10
0
0.01
0.1
1
10
100
1000
10000

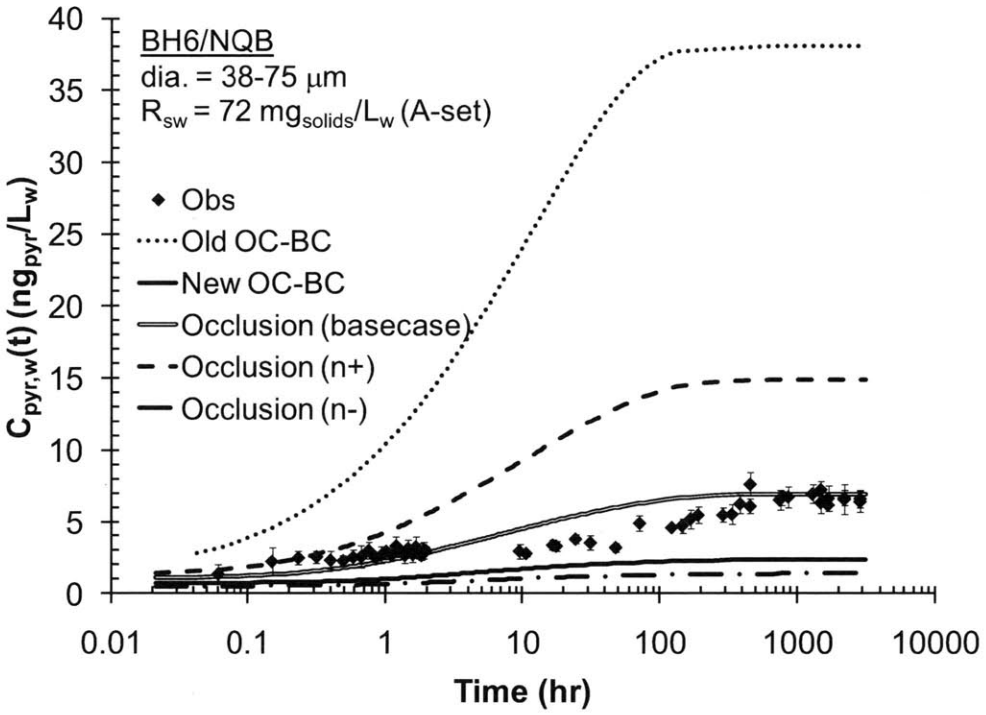
BH6/NQB
dia. = 38-75 μm
R_{sw} = 72 mg_{solids}/L_w (A-set)
Obs
Old OC-BC
New OC-BC
Occlusion (basecase)
Occlusion (n+)
Occlusion (n-)
$C_{pyr,w}(t)$ (ng_{pyr}/L_w)
Time (hr)
40
35
30
25
20
15
10
5
0
0.01
0.1
1
10
100
1000
10000

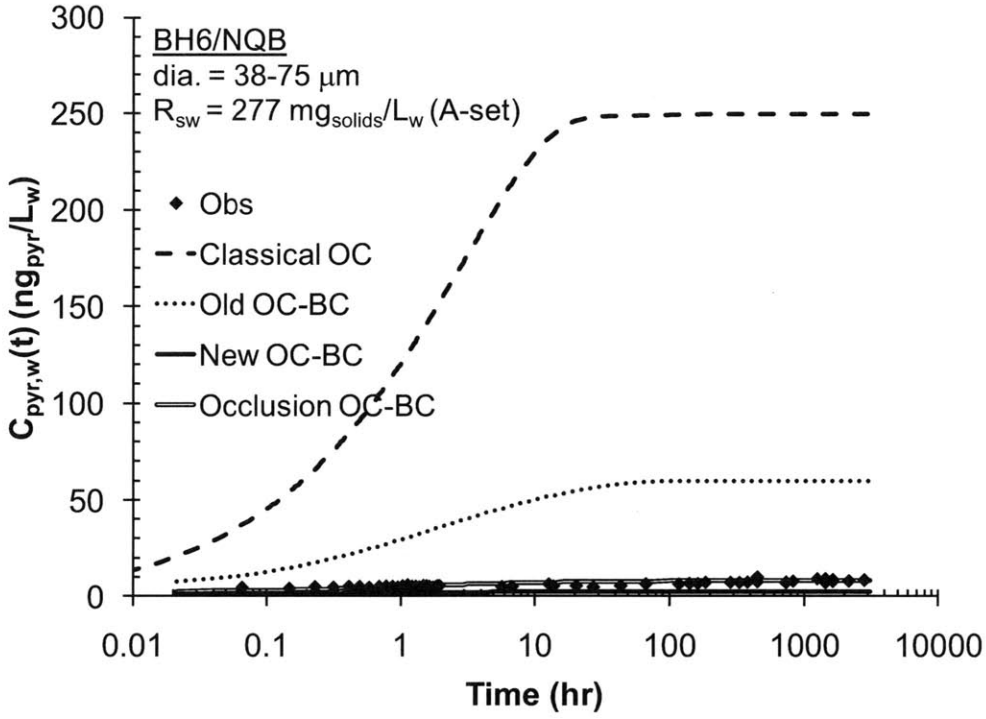
BH6/NQB
dia. = 38-75 μm
R_{sw} = 277 mg_{solids}/L_w (A-set)
Obs
Classical OC
Old OC-BC
New OC-BC
Occlusion OC-BC
$C_{pyr,w}(t)$ (ng_{pyr}/L_w)
Time (hr)
300
250
200
150
100
50
0
0.01
0.1
1
10
100
1000
10000

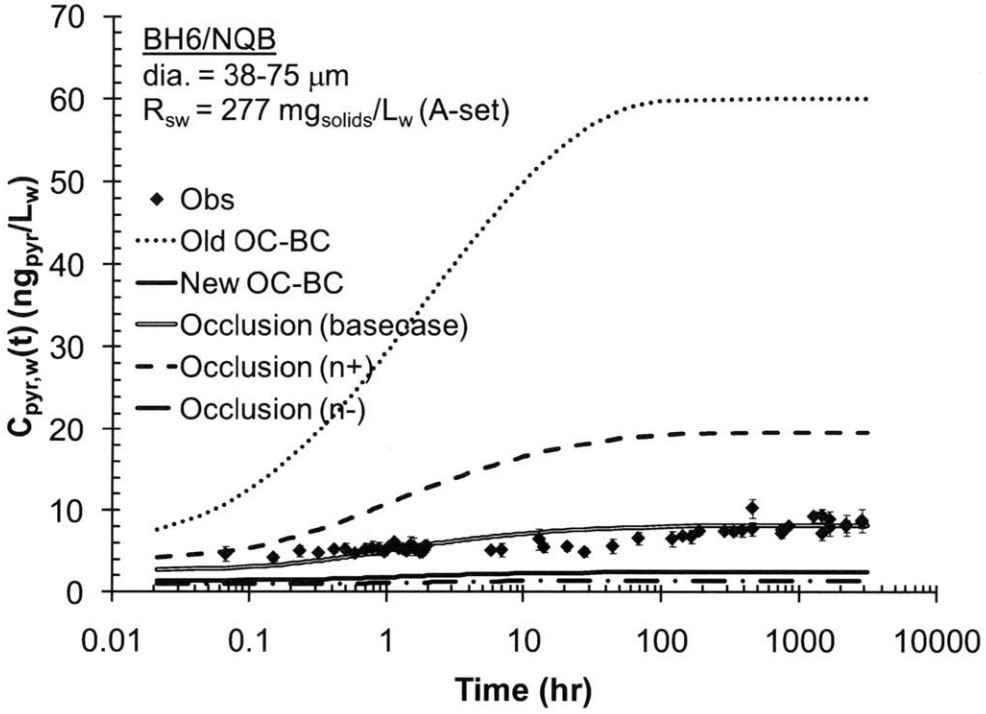
BH6/NQB
dia. = 38-75 μm
R_{sw} = 277 mg_{solids}/L_w (A-set)
Obs
Old OC-BC
New OC-BC
Occlusion (basecase)
Occlusion (n+)
Occlusion (n-)
$C_{pyr,w}(t)$ (ng_{pyr}/L_w)
Time (hr)
70
60
50
40
30
20
10
0
0.01
0.1
1
10
100
1000
10000

C-set (dia. 38–75 μm)

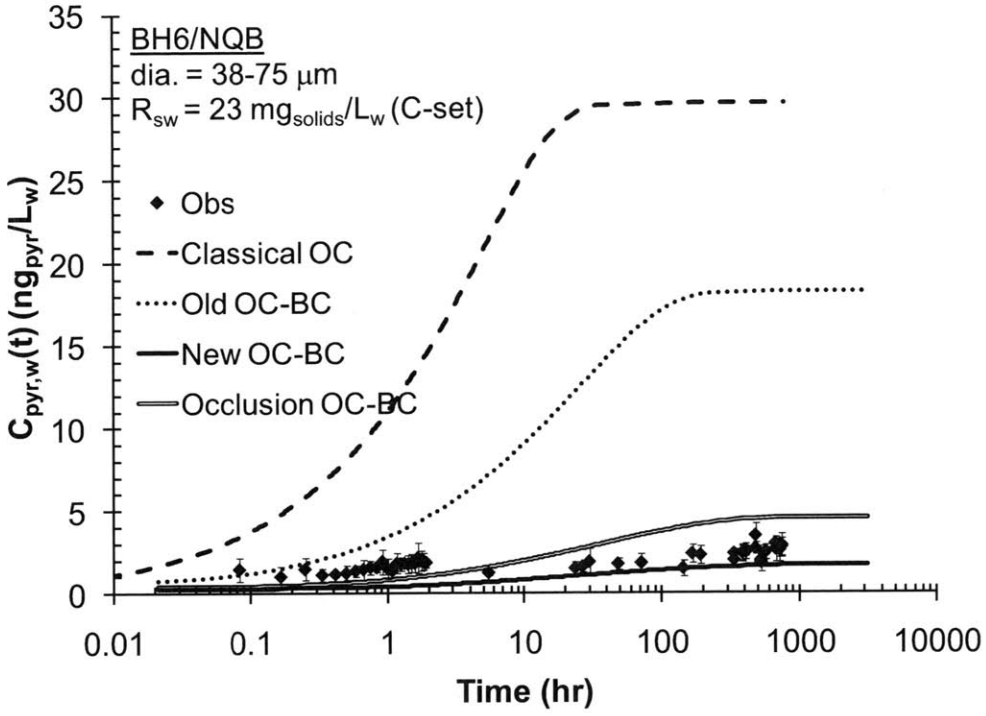

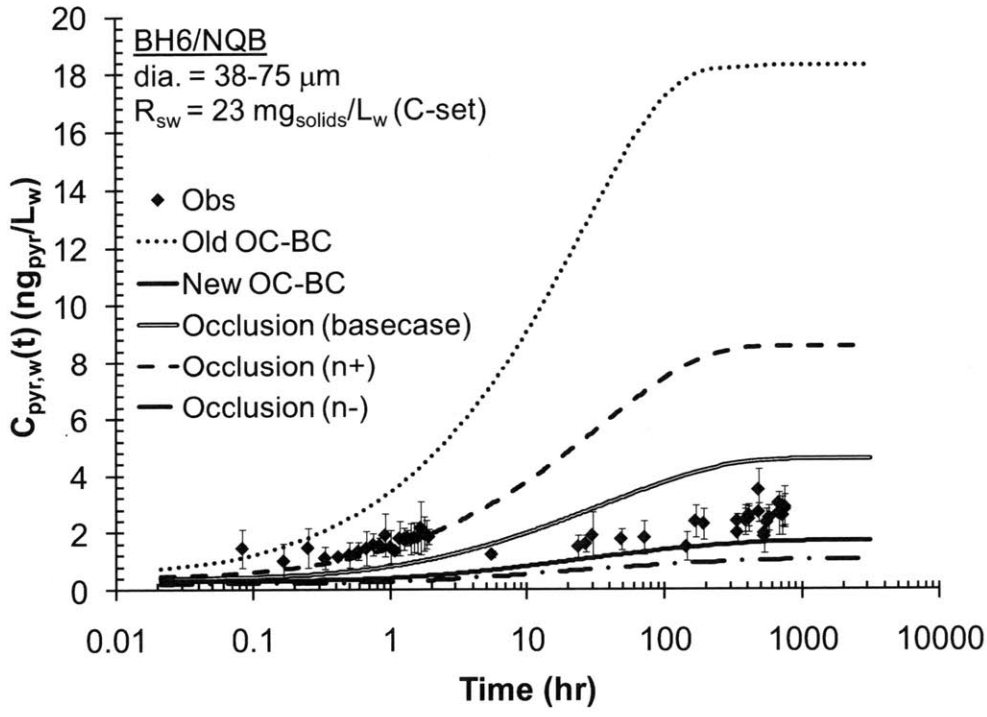

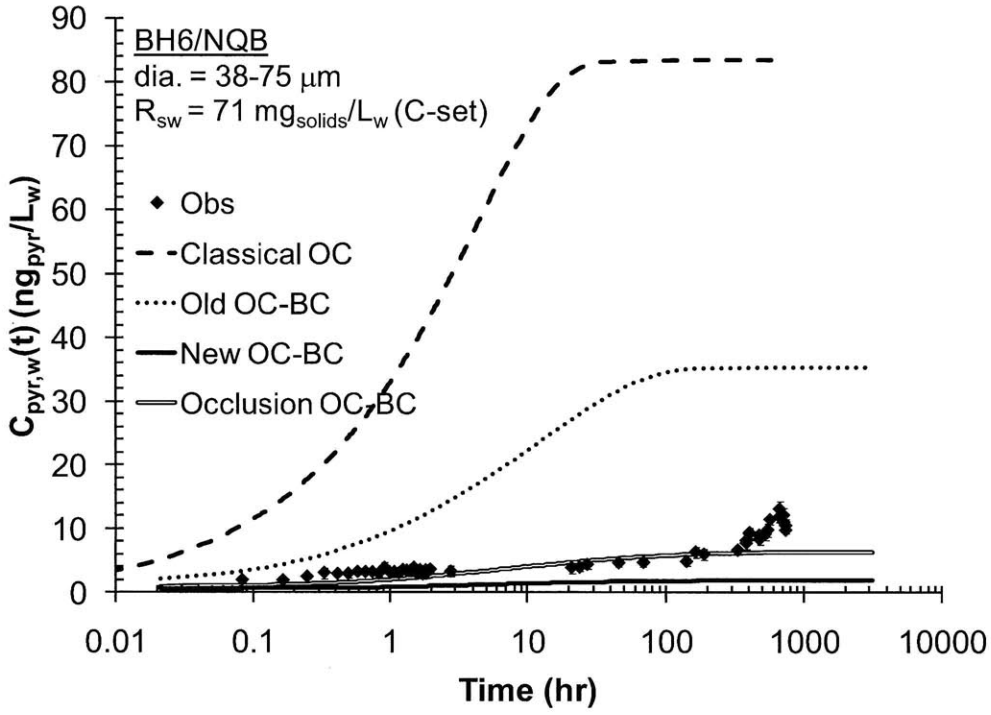
BH6/NQB
dia. = 38-75 μm
R_{sw} = 71 mg_{solids}/L_w (C-set)
Obs
Classical OC
Old OC-BC
New OC-BC
Occlusion OC-BC
$C_{pyr,w}(t)$ (ng_{pyr}/L_w)
Time (hr)
0
10
20
30
40
50
60
70
80
90
0.01
0.1
1
10
100
1000
10000

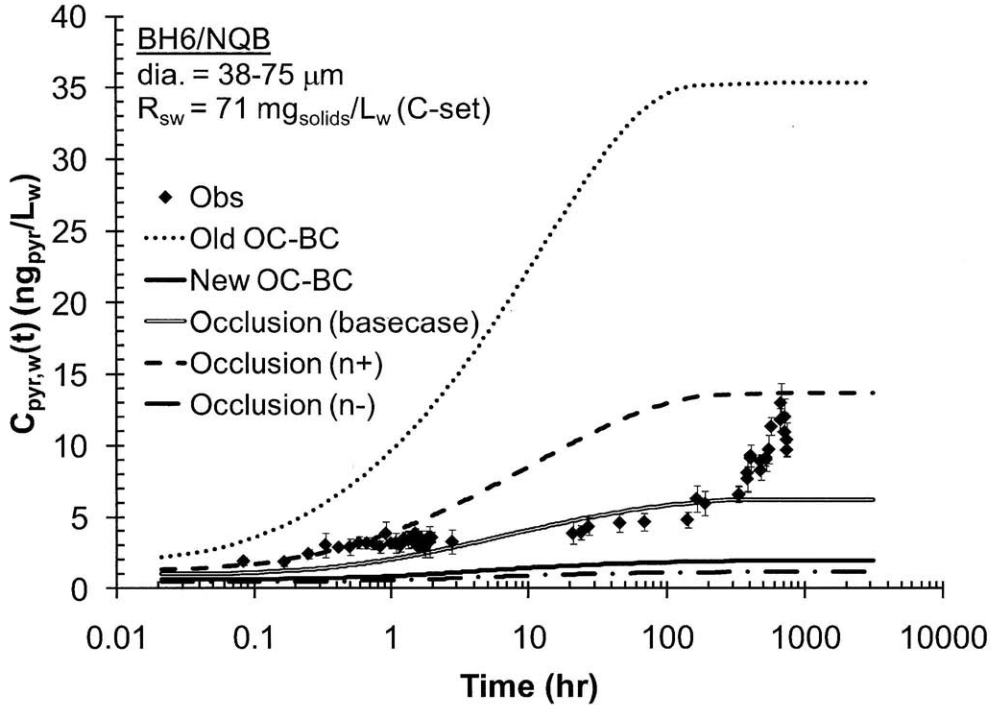
BH6/NQB
dia. = 38-75 μm
R_{sw} = 71 mg_{solids}/L_w (C-set)
Obs
Old OC-BC
New OC-BC
Occlusion (basecase)
Occlusion (n+)
Occlusion (n-)
$C_{pyr,w}(t)$ (ng_{pyr}/L_w)
Time (hr)
0
5
10
15
20
25
30
35
40
0.01
0.1
1
10
100
1000
10000

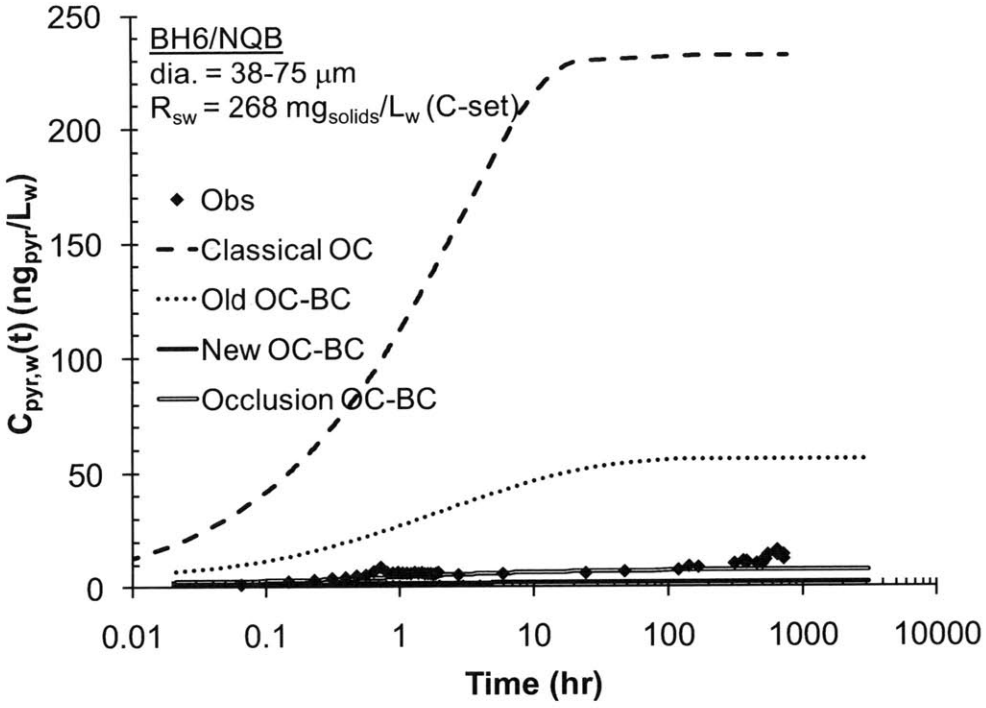
BH6/NQB
dia. = 38-75 μm
R_{sw} = 268 mg_{solids}/L_w (C-set)
Obs
Classical OC
Old OC-BC
New OC-BC
Occlusion OC-BC
$C_{pyr,w}(t)$ (ng_{pyr}/L_w)
Time (hr)
250
200
150
100
50
0
0.01
0.1
1
10
100
1000
10000

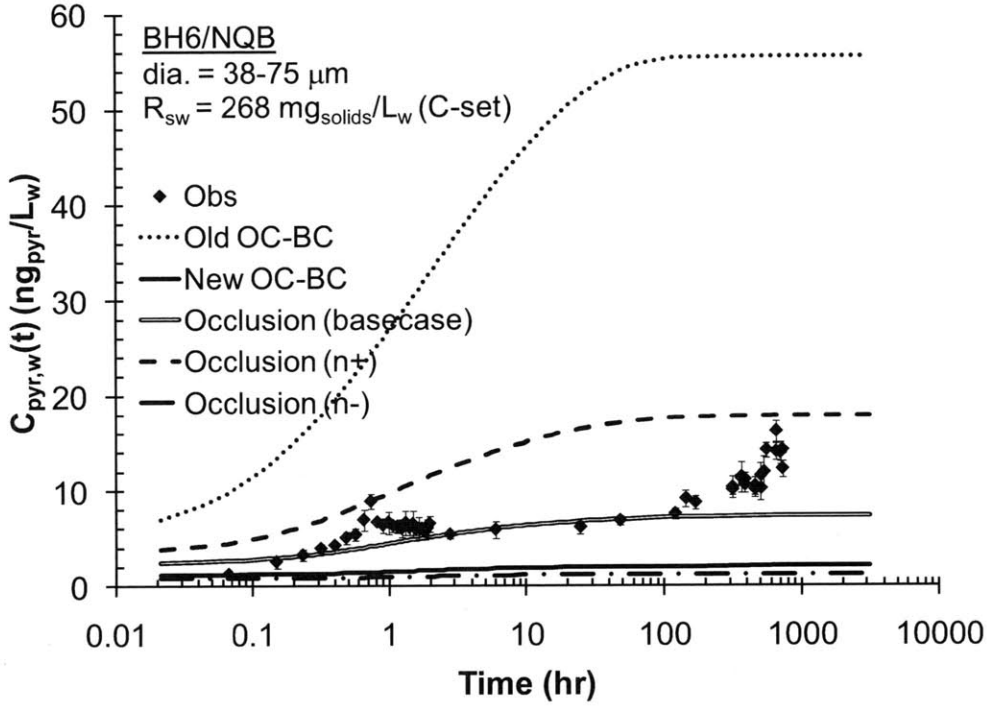
BH6/NQB
dia. = 38-75 μm
R_{sw} = 268 mg_{solids}/L_w (C-set)
Obs
Old OC-BC
New OC-BC
Occlusion (basecase)
Occlusion (n+)
Occlusion (n-)
$C_{pyr,w}(t)$ (ng_{pyr}/L_w)
Time (hr)
60
50
40
30
20
10
0
0.01
0.1
1
10
100
1000
10000

L-set (dia. 38–75 μm)

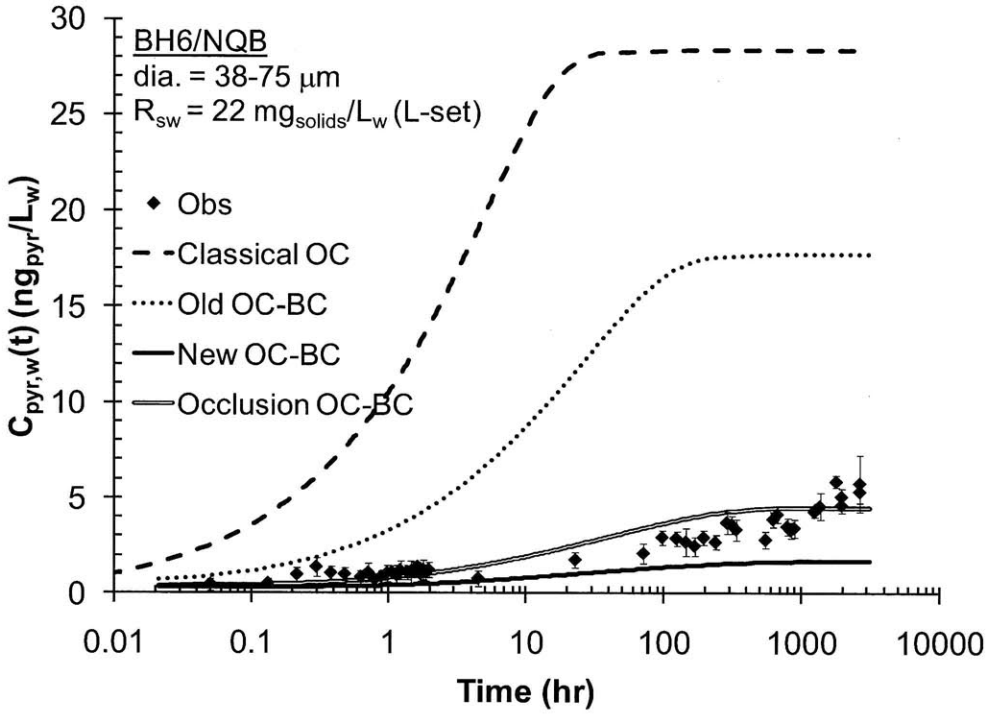

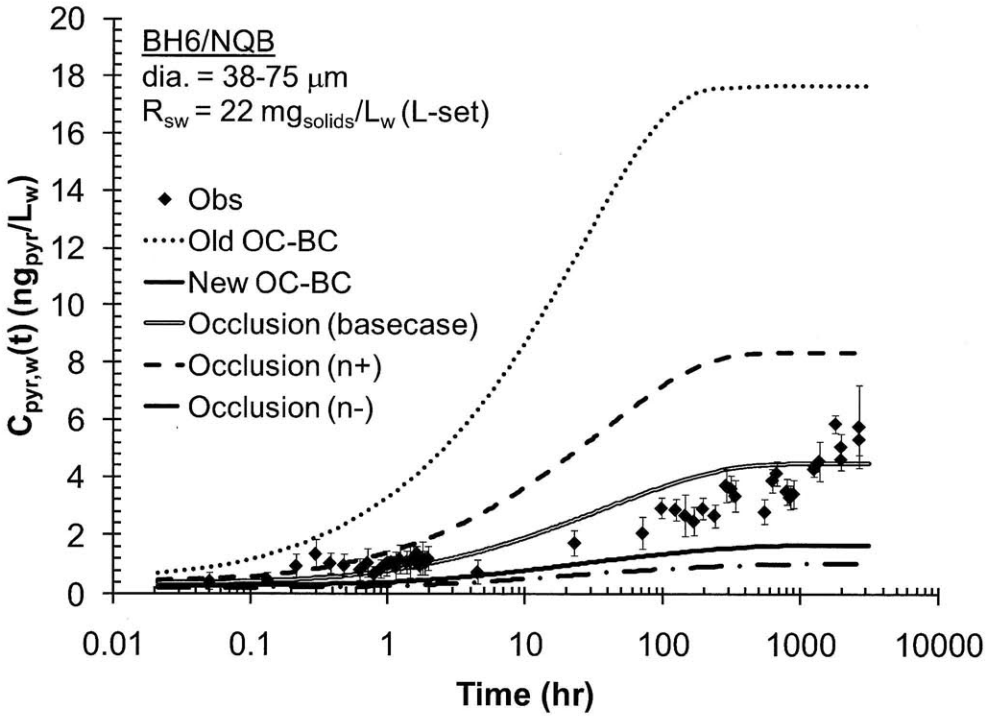

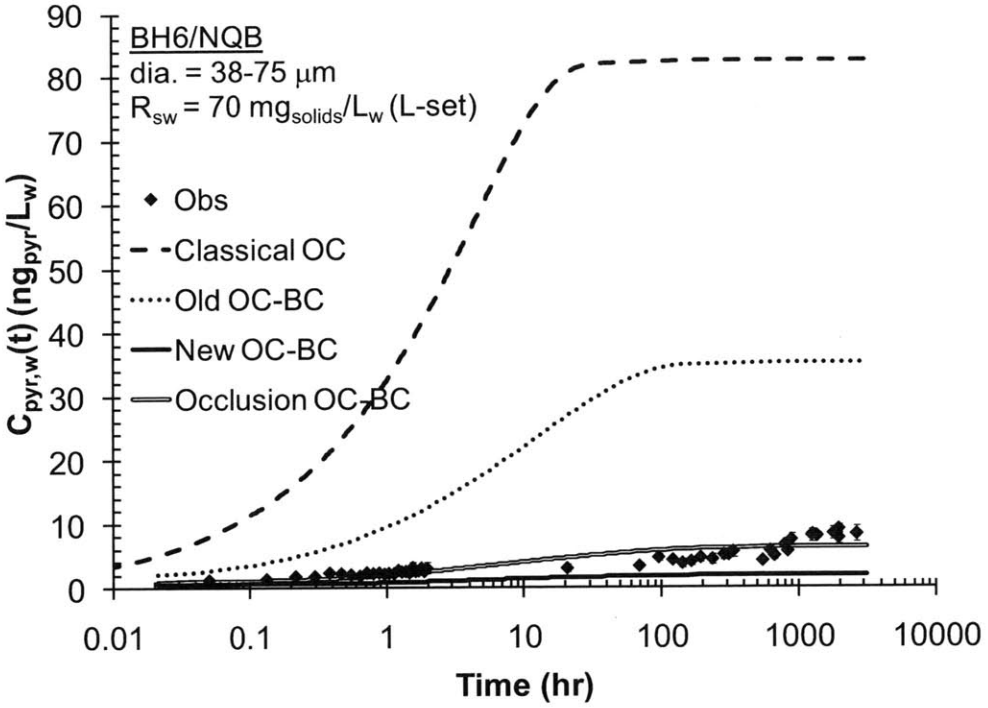
BH6/NQB
dia. = 38-75 μm
R_{sw} = 70 mg_{solids}/L_w (L-set)
Obs
Classical OC
Old OC-BC
New OC-BC
Occlusion OC-BC
$C_{pyr,w}(t)$ (ng_{pyr}/L_w)
Time (hr)

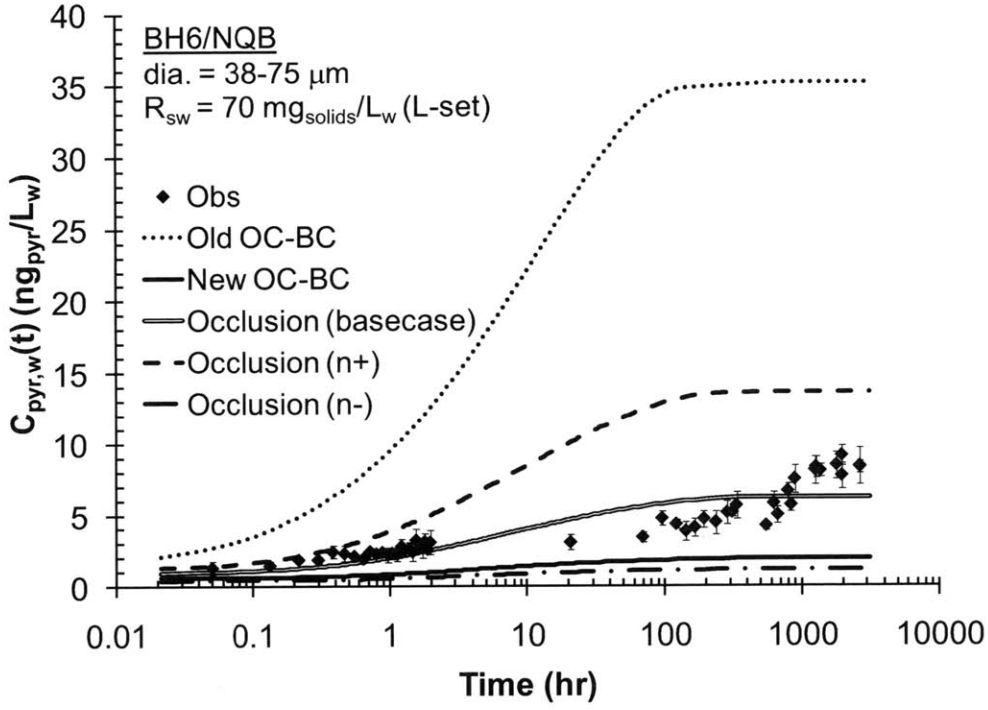
BH6/NQB
dia. = 38-75 μm
R_{sw} = 70 mg_{solids}/L_w (L-set)
Obs
Old OC-BC
New OC-BC
Occlusion (basecase)
Occlusion (n+)
Occlusion (n-)
$C_{pyr,w}(t)$ (ng_{pyr}/L_w)
Time (hr)

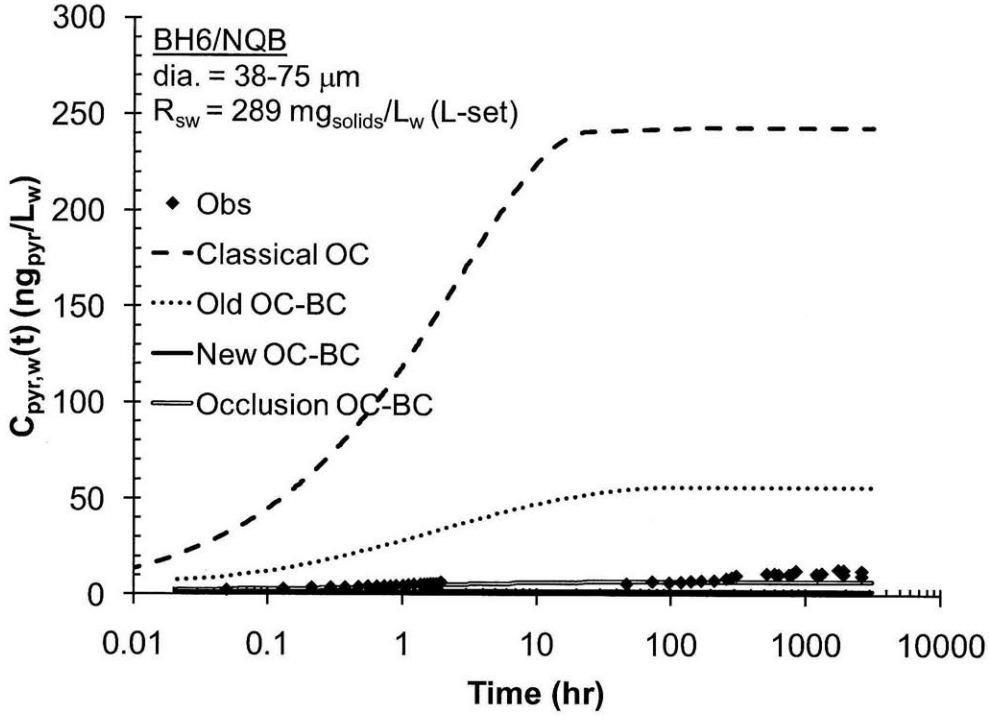
BH6/NQB
dia. = 38-75 μm
R_{sw} = 289 mg_{solids}/L_w (L-set)
Obs
Classical OC
Old OC-BC
New OC-BC
Occlusion OC-BC
$C_{pyr,w}(t)$ (ng_{pyr}/L_w)
Time (hr)
0.01
0.1
1
10
100
1000
10000
0
50
100
150
200
250
300

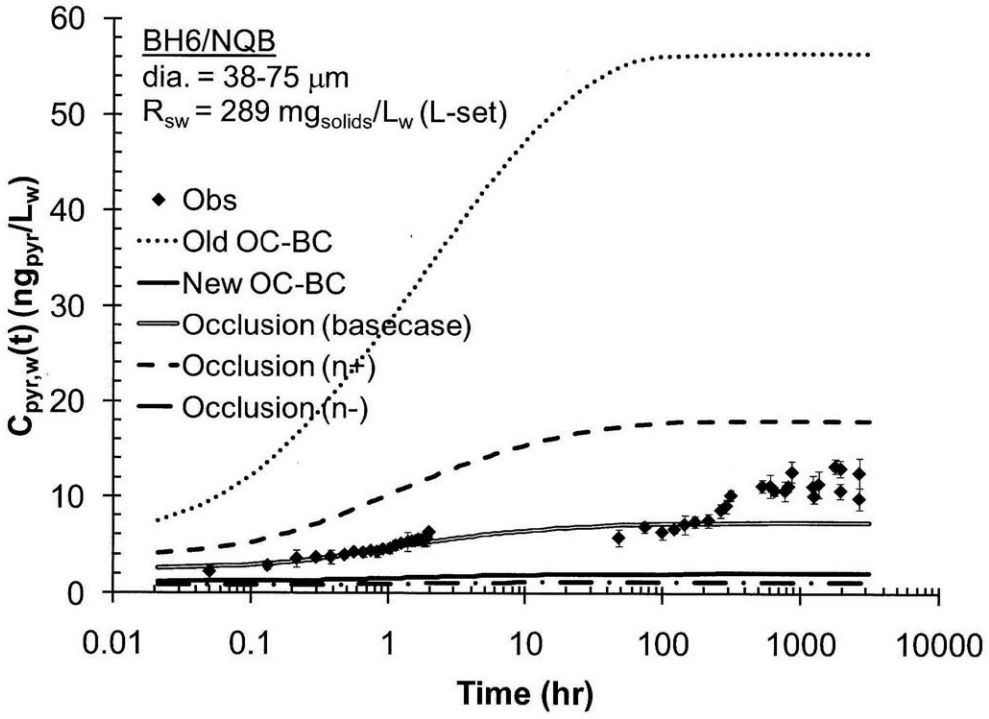
BH6/NQB
dia. = 38-75 μm
R_{sw} = 289 mg_{solids}/L_w (L-set)
Obs
Old OC-BC
New OC-BC
Occlusion (basecase)
Occlusion (n+)
Occlusion (n-)
$C_{pyr,w}(t)$ (ng_{pyr}/L_w)
Time (hr)
0.01
0.1
1
10
100
1000
10000
0
10
20
30
40
50
60

K-set (dia. 75–106 μm)

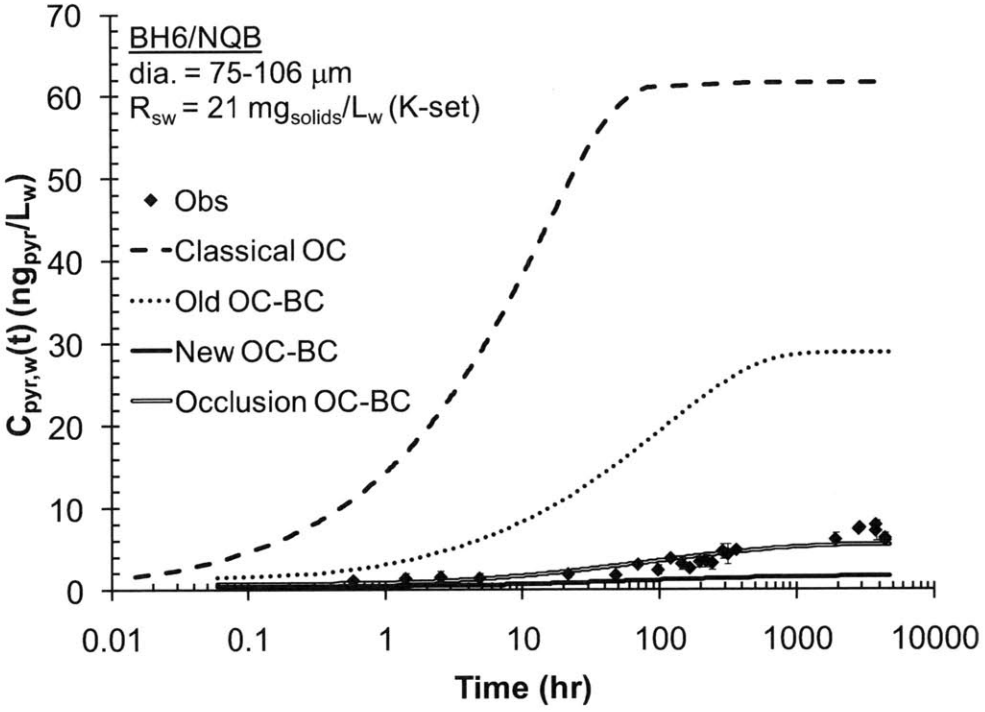

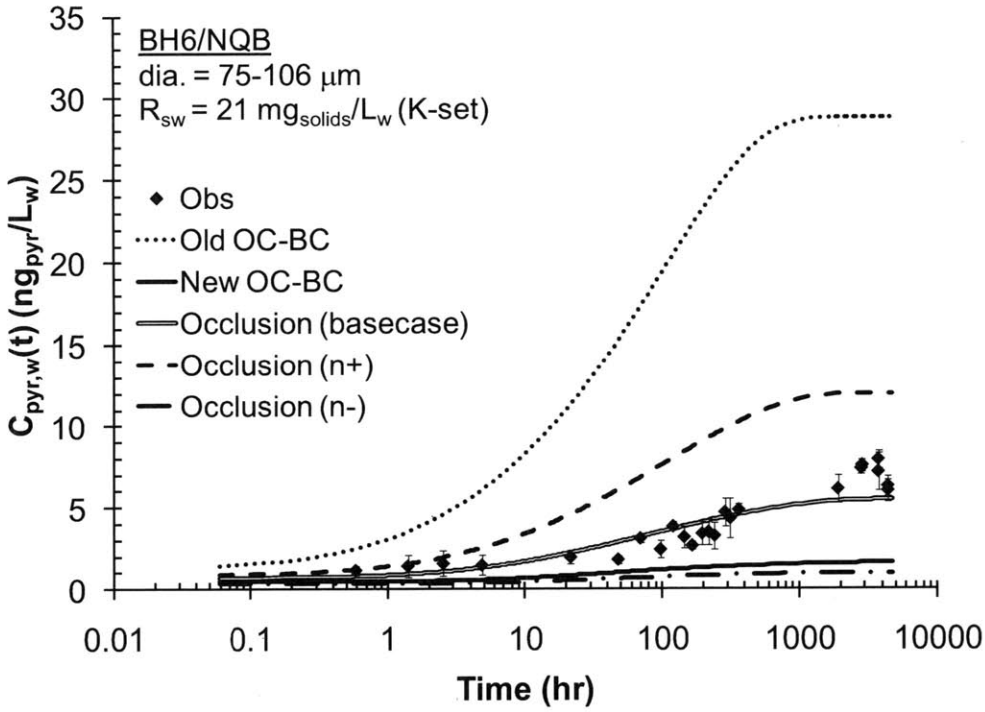

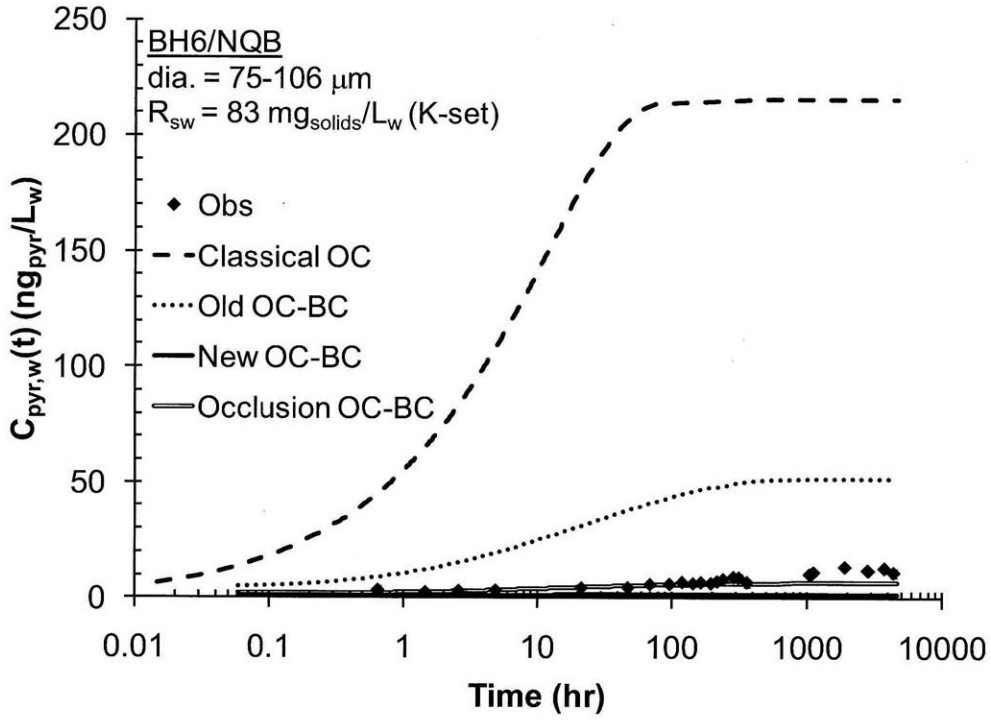
BH6/NQB
dia. = 75-106 μm
R_{sw} = 83 mg_{solids}/L_w (K-set)
Obs
Classical OC
Old OC-BC
New OC-BC
Occlusion OC-BC
$C_{pyr,w}(t)$ (ng_{pyr}/L_w)
Time (hr)
250
200
150
100
50
0
0.01
0.1
1
10
100
1000
10000

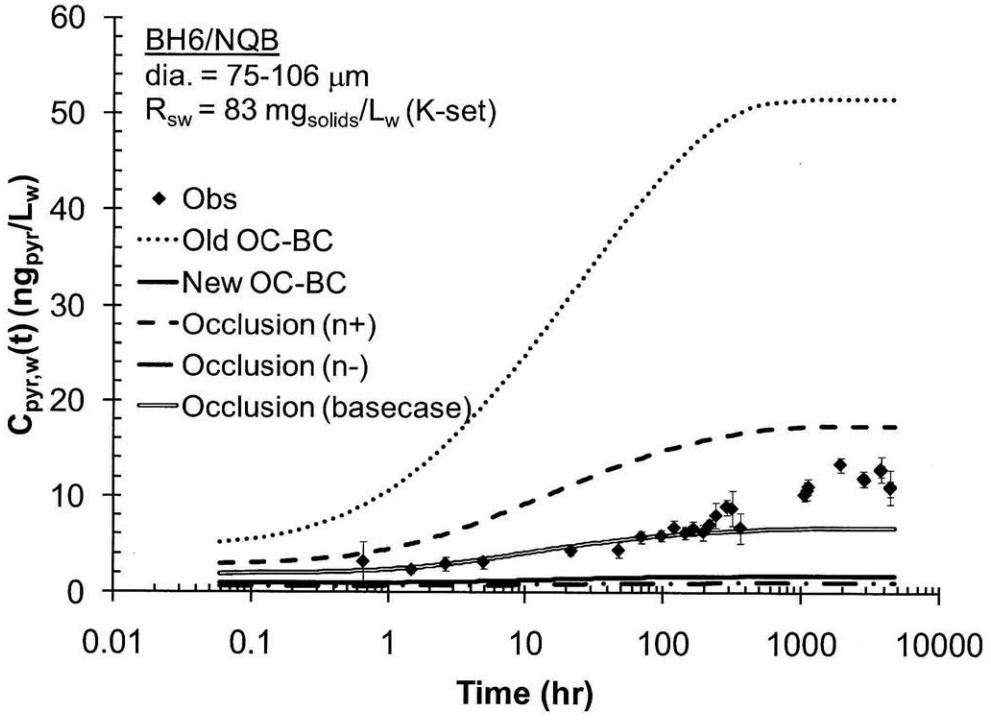
BH6/NQB
dia. = 75-106 μm
R_{sw} = 83 mg_{solids}/L_w (K-set)
Obs
Old OC-BC
New OC-BC
Occlusion (n+)
Occlusion (n-)
Occlusion (basecase)
$C_{pyr,w}(t)$ (ng_{pyr}/L_w)
Time (hr)
60
50
40
30
20
10
0
0.01
0.1
1
10
100
1000
10000

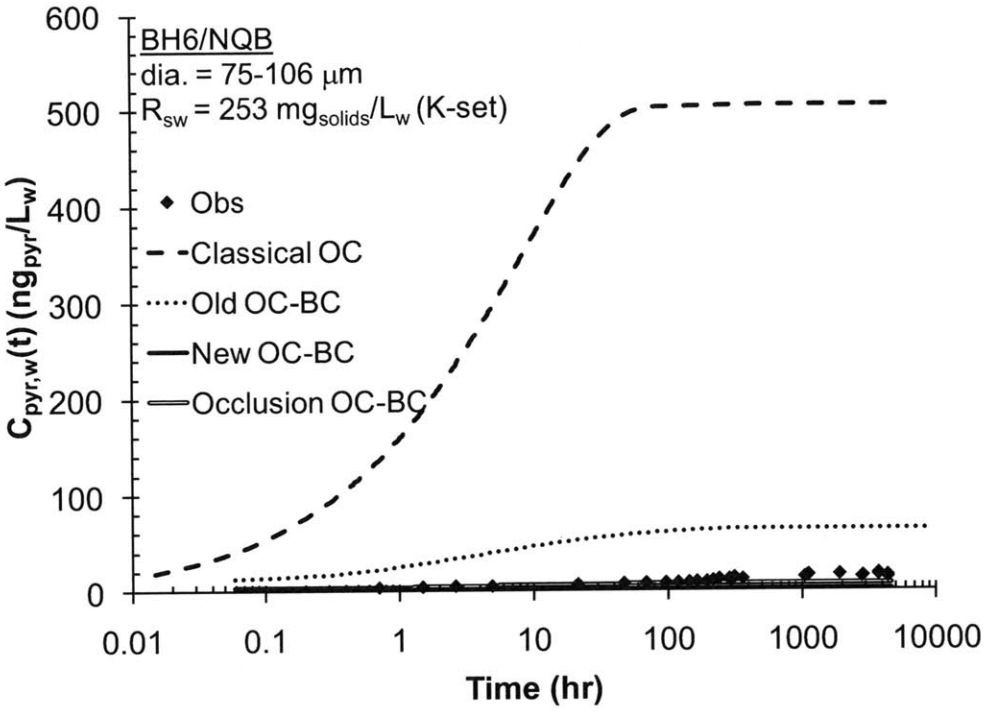
BH6/NQB
dia. = 75-106 μm
R_{sw} = 253 mg_{solids}/L_w (K-set)
Obs
Classical OC
Old OC-BC
New OC-BC
Occlusion OC-BC
$C_{pyr,w}(t)$ (ng_{pyr}/L_w)
Time (hr)
600
500
400
300
200
100
0
0.01
0.1
1
10
100
1000
10000

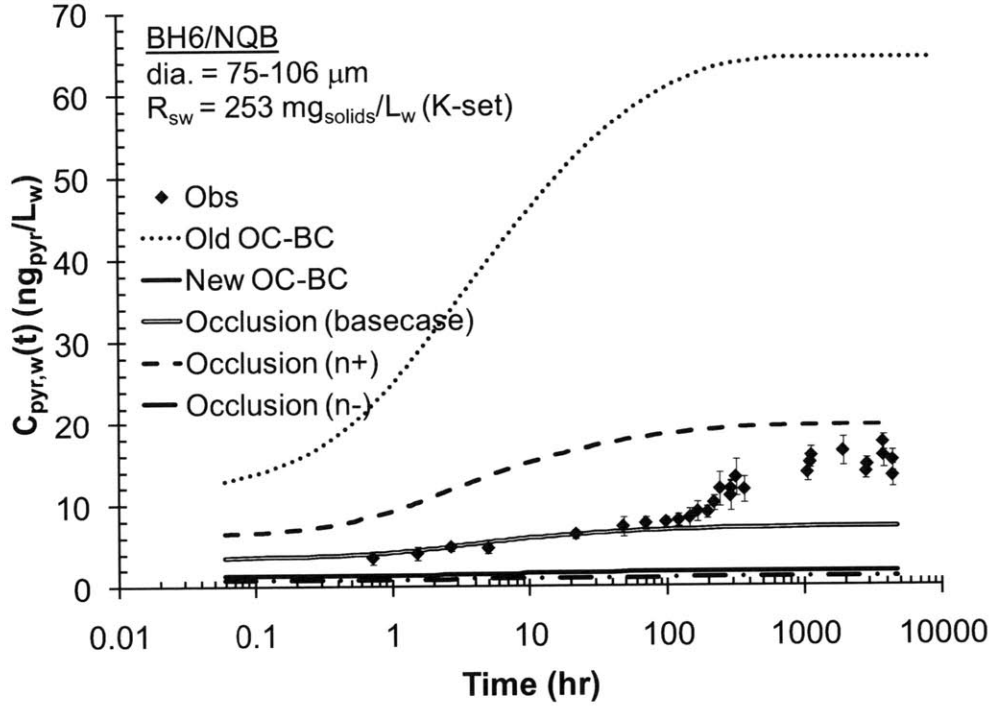
BH6/NQB
dia. = 75-106 μm
R_{sw} = 253 mg_{solids}/L_w (K-set)
Obs
Old OC-BC
New OC-BC
Occlusion (basecase)
Occlusion (n+)
Occlusion (n-)
$C_{pyr,w}(t)$ (ng_{pyr}/L_w)
Time (hr)
70
60
50
40
30
20
10
0
0.01
0.1
1
10
100
1000
10000

IHG-set (dia. 180–250 μm)

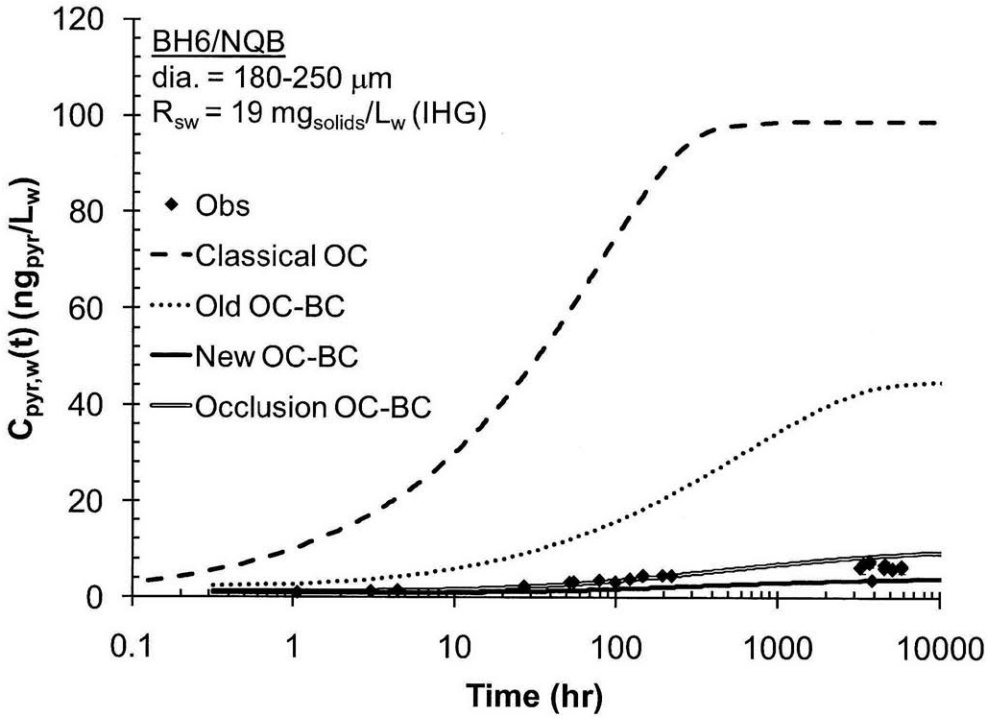

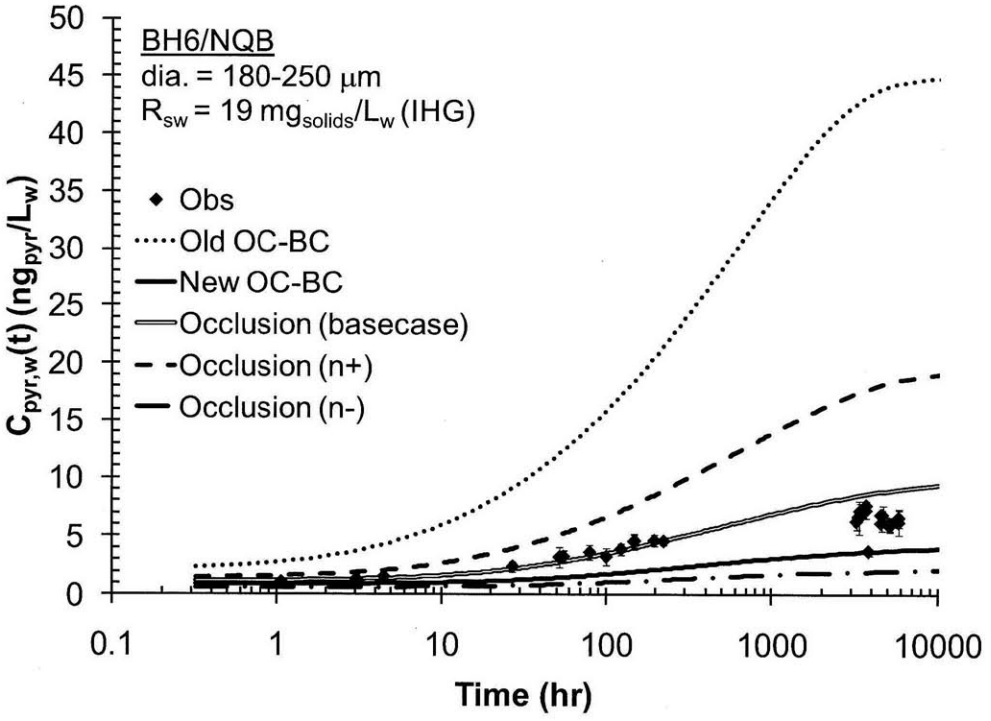

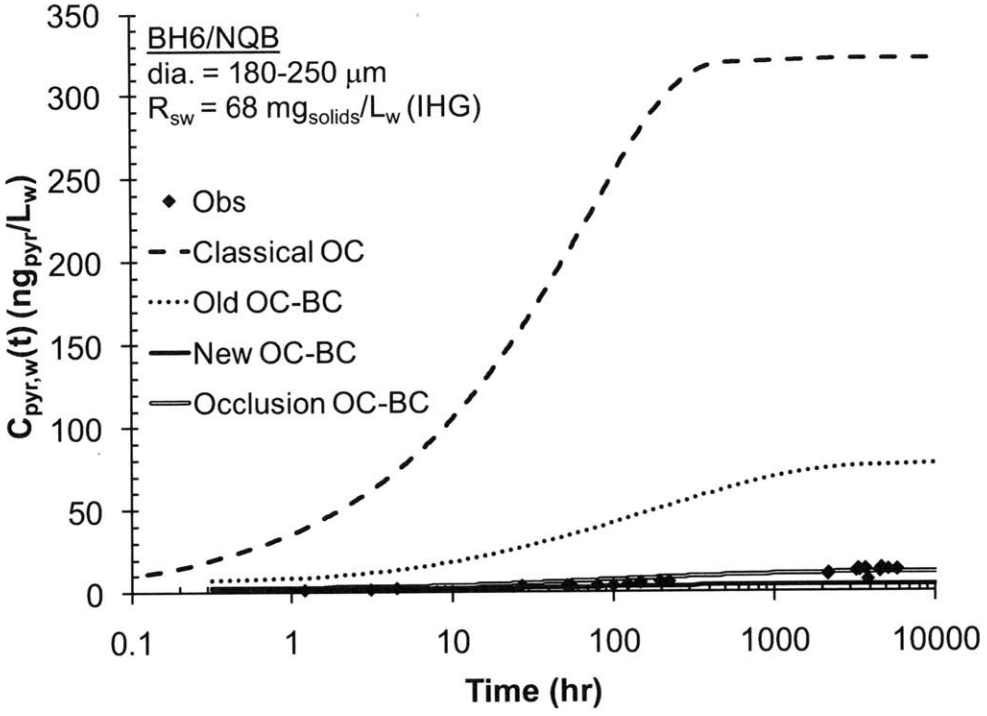
BH6/NQB
dia. = 180-250 μm
R_{sw} = 68 mg_{solids}/L_w (IHG)
Obs
Classical OC
Old OC-BC
New OC-BC
Occlusion OC-BC
$C_{pyr,w}(t)$ (ng_{pyr}/L_w)
Time (hr)

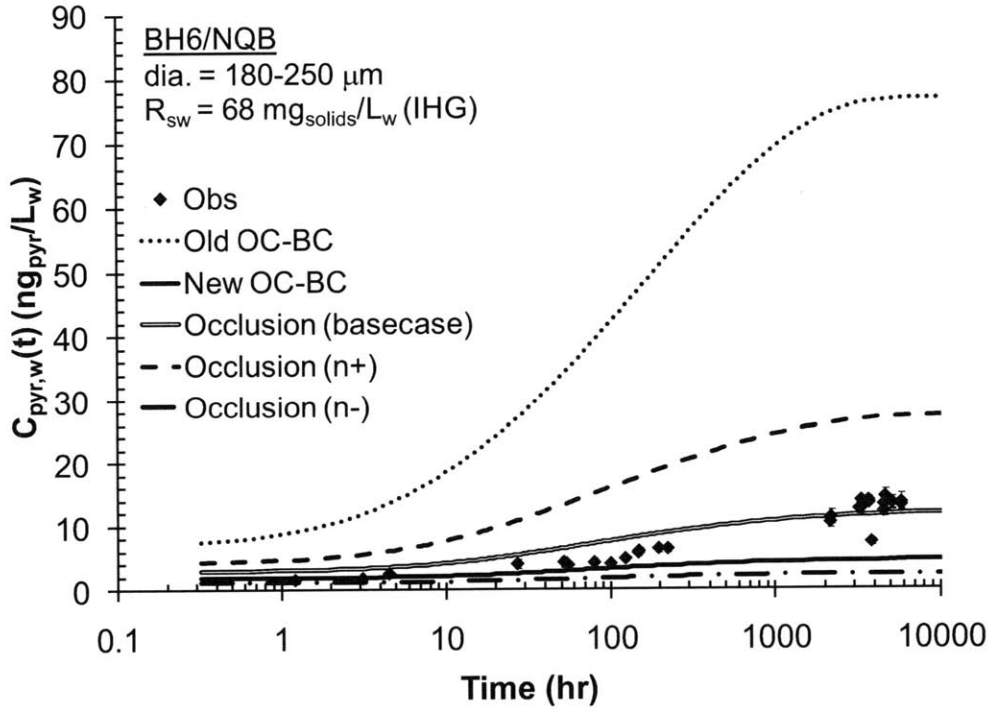
BH6/NQB
dia. = 180-250 μm
R_{sw} = 68 mg_{solids}/L_w (IHG)
Obs
Old OC-BC
New OC-BC
Occlusion (basecase)
Occlusion (n+)
Occlusion (n-)
$C_{pyr,w}(t)$ (ng_{pyr}/L_w)
Time (hr)

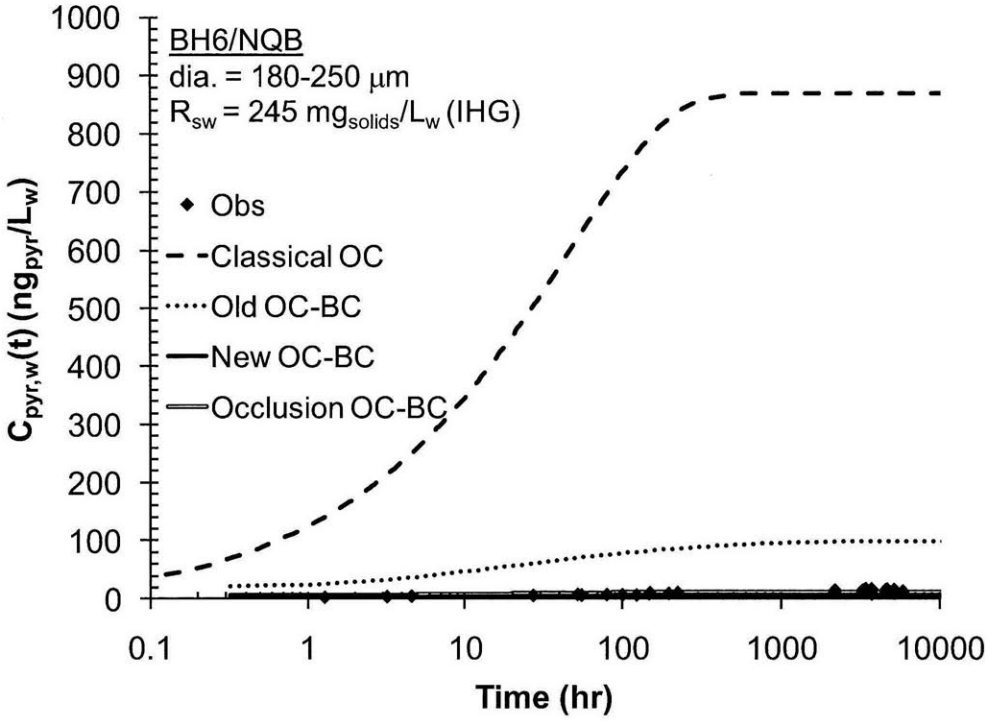
BH6/NQB
dia. = 180-250 μm
R_{sw} = 245 mg_{solids}/L_w (IHG)
Obs
Classical OC
Old OC-BC
New OC-BC
Occlusion OC-BC
$C_{pyr,w}(t)$ (ng_{pyr}/L_w)
Time (hr)
1000
900
800
700
600
500
400
300
200
100
0
0.1
1
10
100
1000
10000

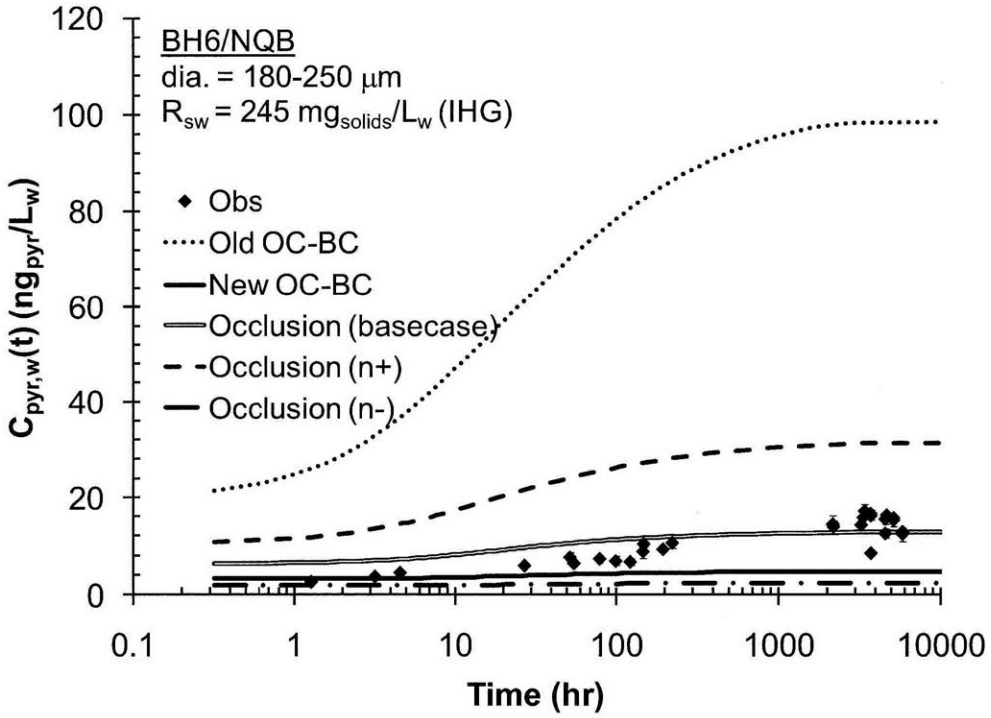
BH6/NQB
dia. = 180-250 μm
R_{sw} = 245 mg_{solids}/L_w (IHG)
Obs
Old OC-BC
New OC-BC
Occlusion (basecase)
Occlusion (n+)
Occlusion (n-)
$C_{pyr,w}(t)$ (ng_{pyr}/L_w)
Time (hr)
120
100
80
60
40
20
0
0.1
1
10
100
1000
10000

Appendix 7 - 2. Sensitivity of Pyrene Desorption Kinetics (I): $S_{pyr,o}$.

Sensitivity analysis of pyrene desorption kinetics to $S_{pyr,o}$ was conducted with the *a priori* New OC-BC model prediction as the basecase. The New OC-BC model assumed that (a) $\log K_{OC} = 5.25 \pm 0.04$, (b) $\log K_{BC} = 6.25 \pm 0.06$, (c) $n_{BC} = 0.25 \pm 0.09$, (d) no occlusion of native pyrene.

All kinetic observations (except those for the C-set) were analyzed.

A-set (dia. 38–75 μm) – Sensitivity to $S_{pyr,o}$

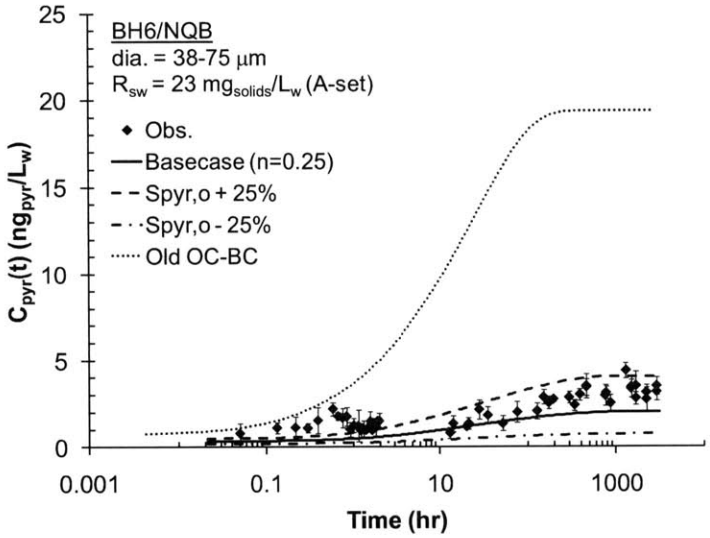

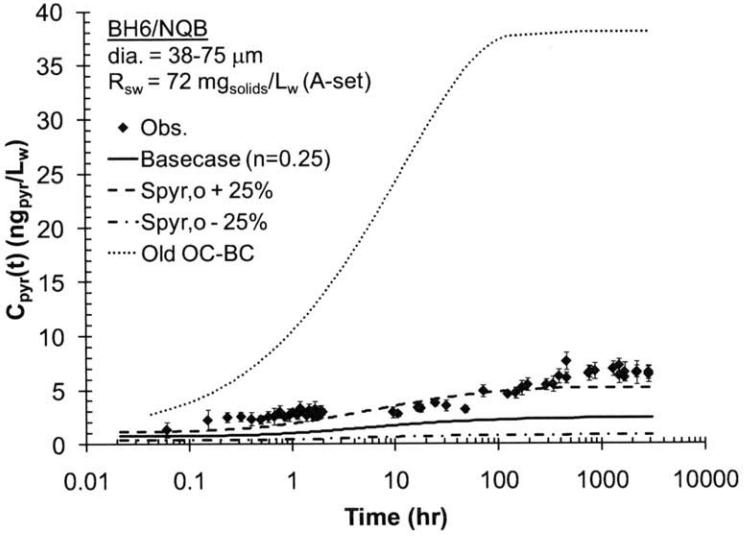

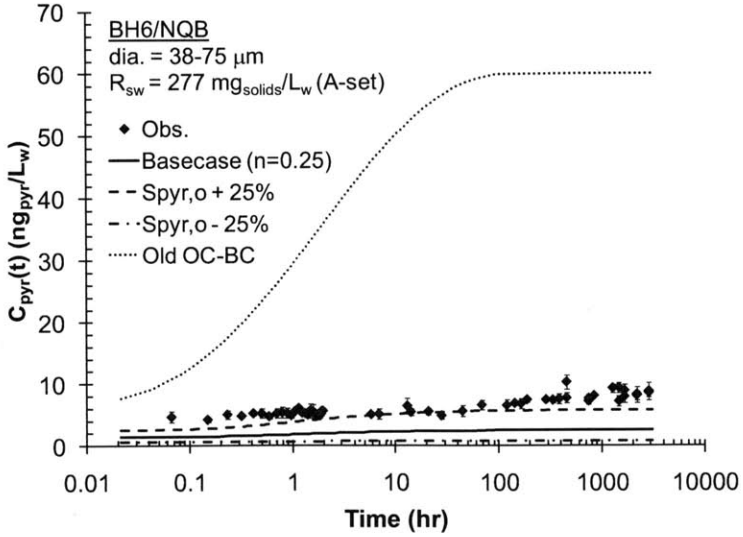

L-set (dia. 38–75 μm) – Sensitivity to $S_{pyr,o}$

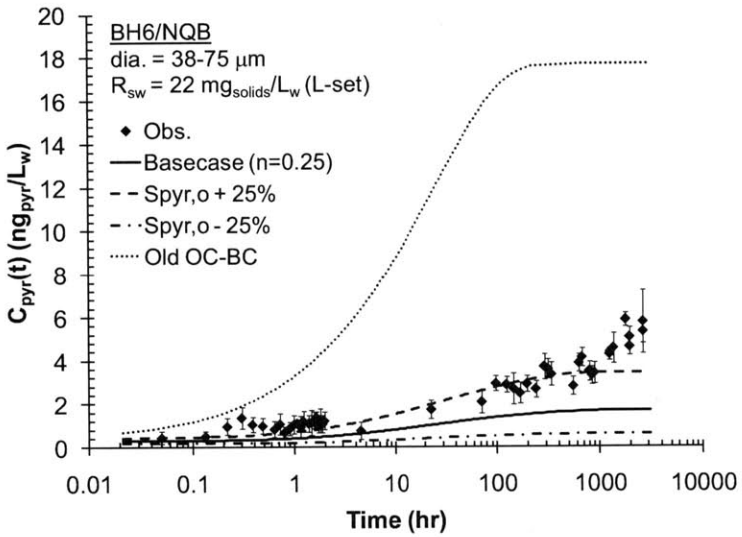

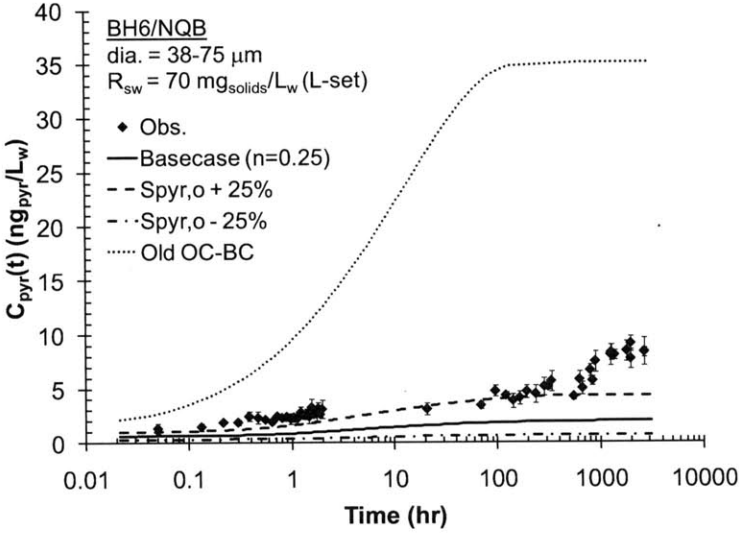

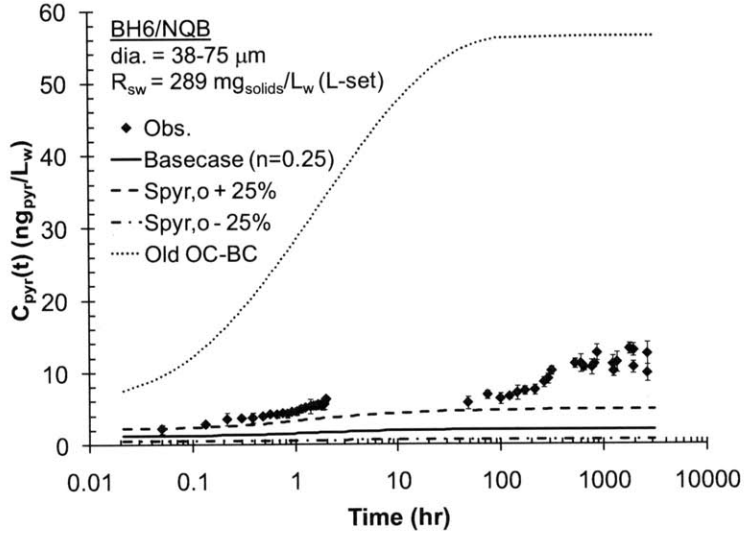

K-set (dia. 75–106 μm) – Sensitivity to $S_{pyr,o}$

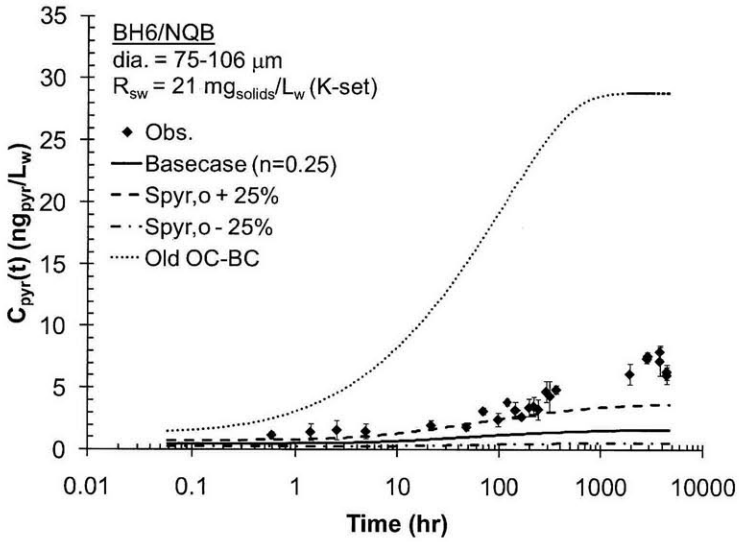

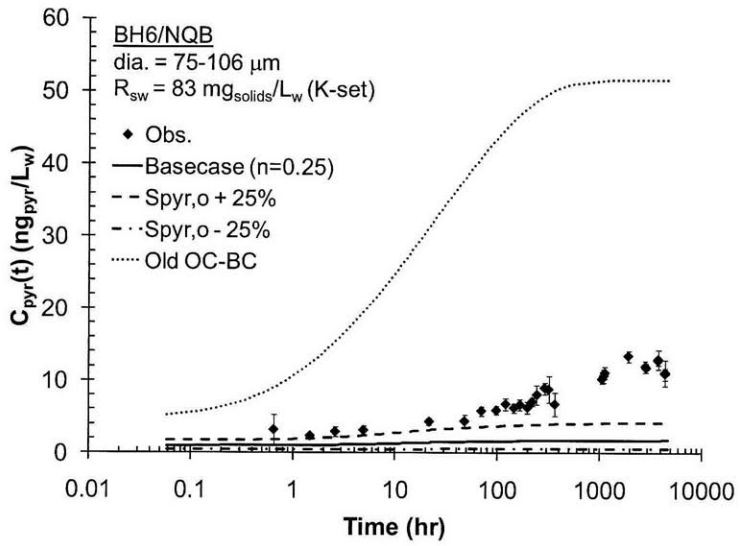

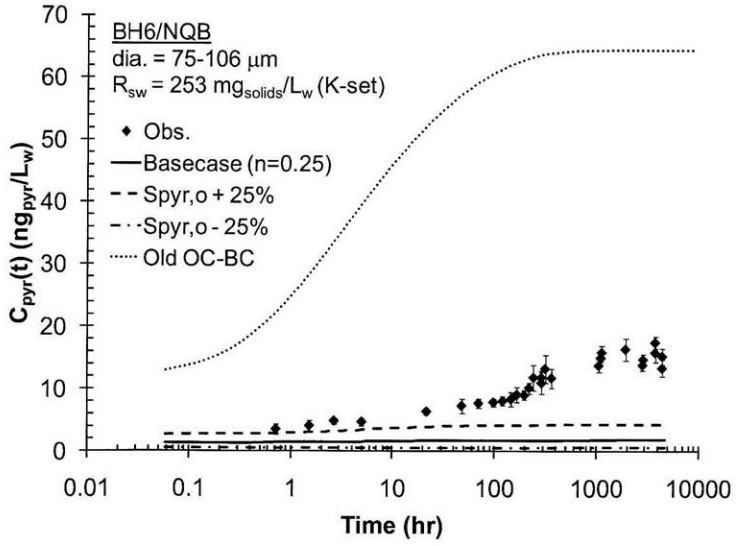

IHG-set (dia. 180–250 μm) – Sensitivity to $S_{pyr,o}$

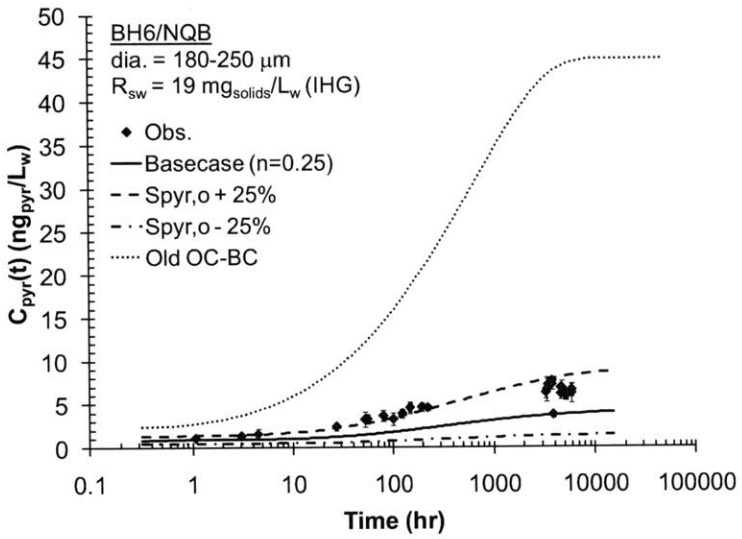

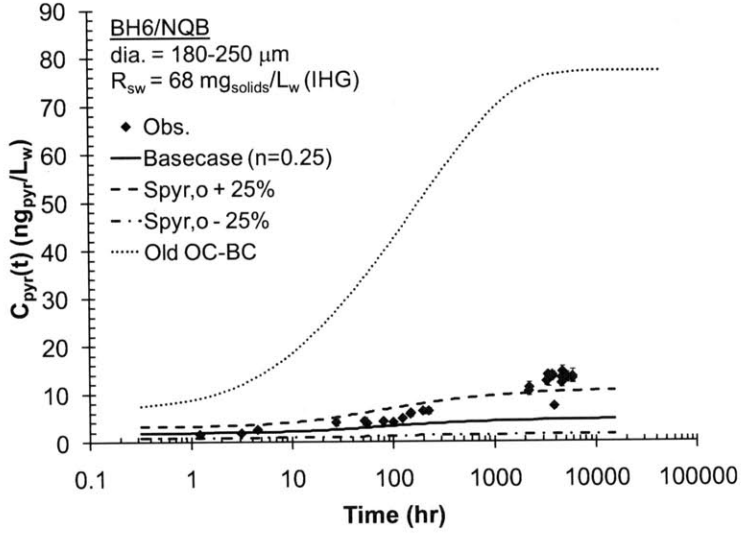

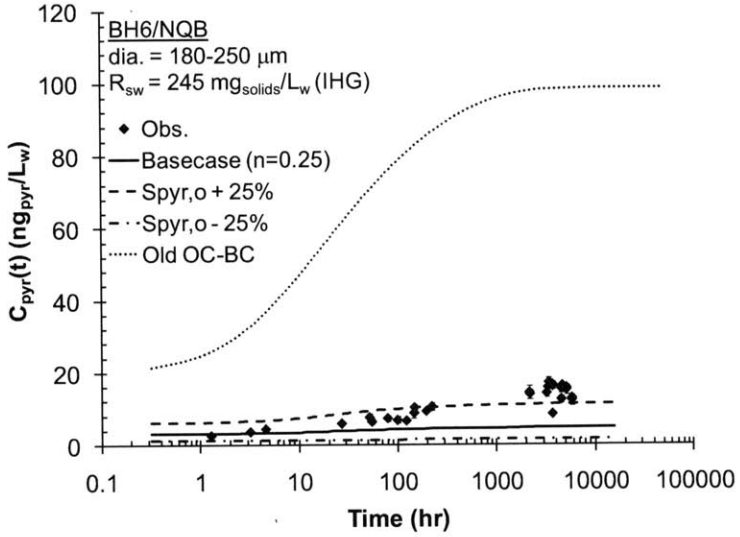

Appendix 7 - 3. Sensitivity of Pyrene Desorption Kinetics (II): f_{OC}.

Sensitivity analysis of pyrene desorption kinetics to f_{OC} was conducted with the *a priori* New OC-BC model prediction as the basecase. The New OC-BC model assumed that (a) $\log K_{OC} = 5.25 \pm 0.04$, (b) $\log K_{BC} = 6.25 \pm 0.06$, (c) $n_{BC} = 0.25 \pm 0.09$, (d) no occlusion of native pyrene.

All kinetic observations (except those for the C-set) were analyzed.

A-set (dia. 38–75 μm) – Sensitivity to f_{OC}

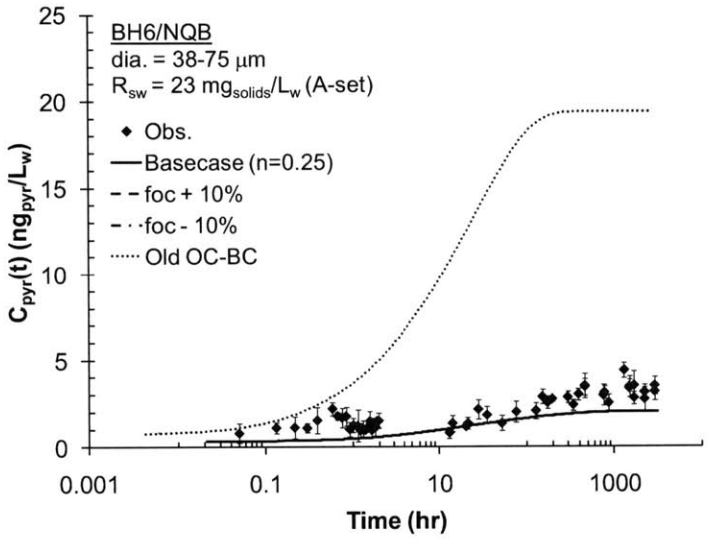

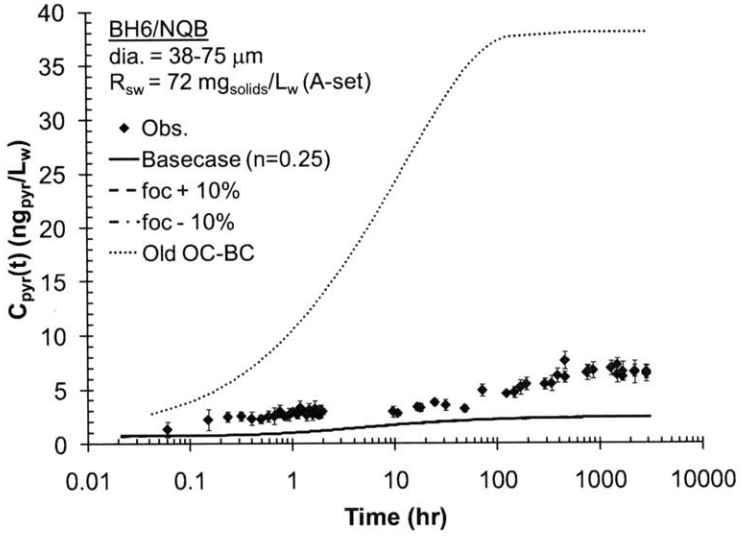

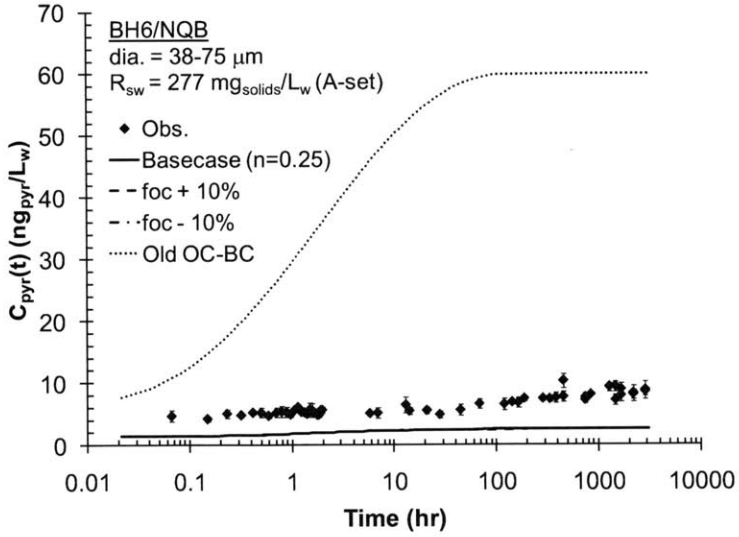

L-set (dia. 38–75 μm) – Sensitivity to f_{OC}

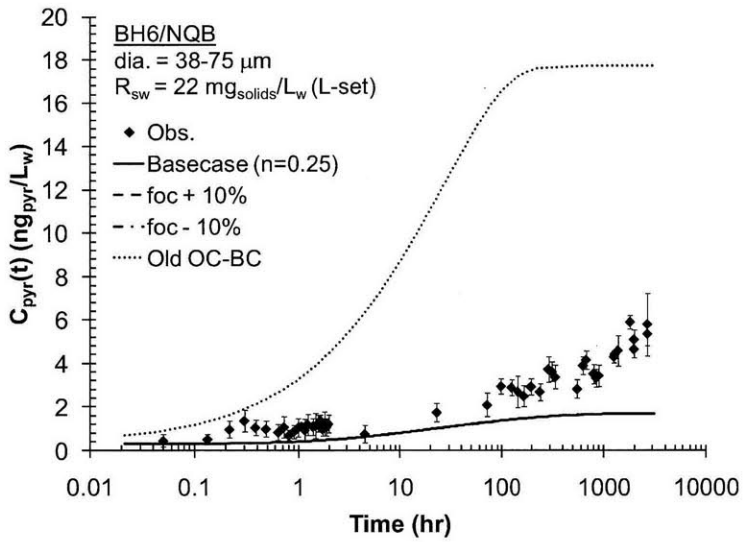

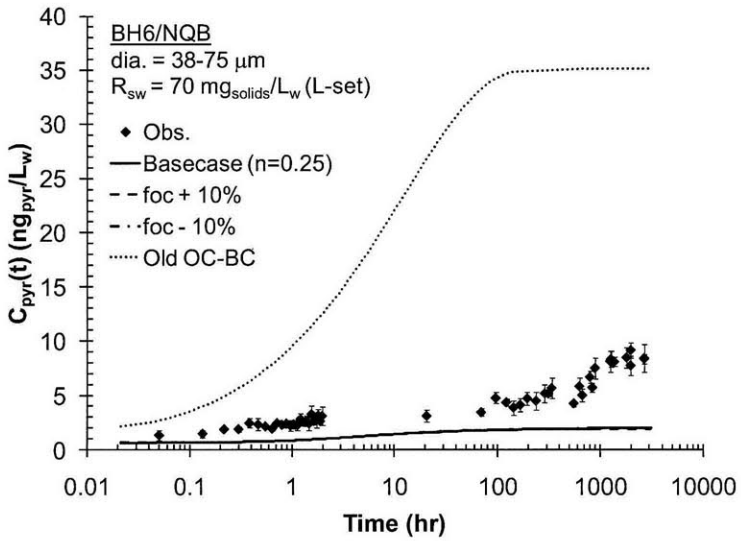

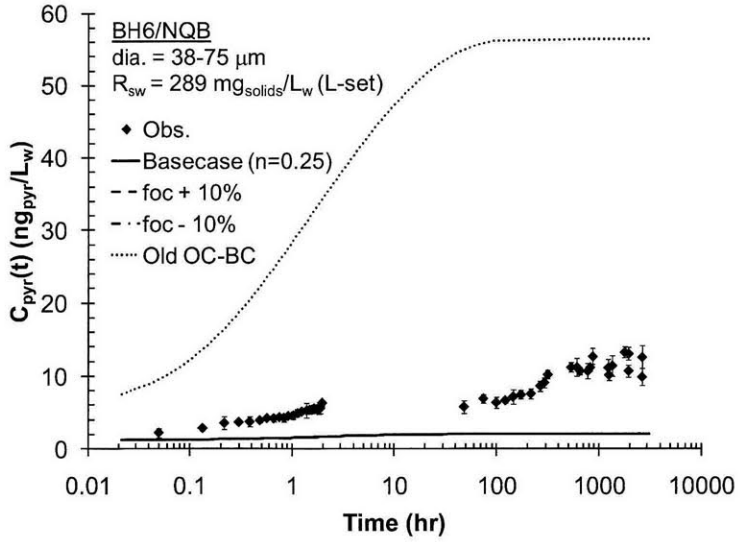

K-set (dia. 75–106 μm) – Sensitivity to f_{OC}

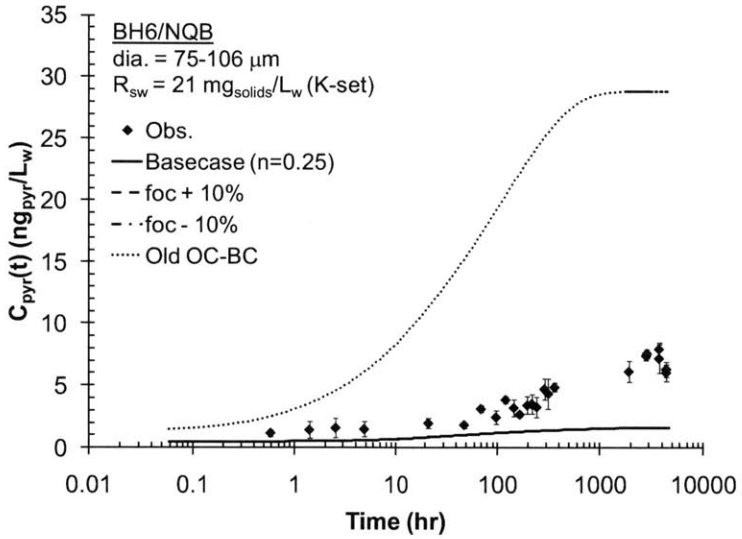

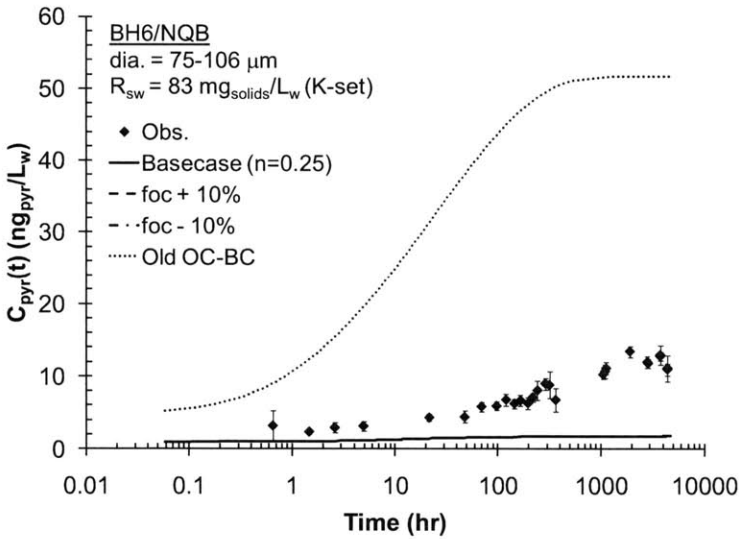

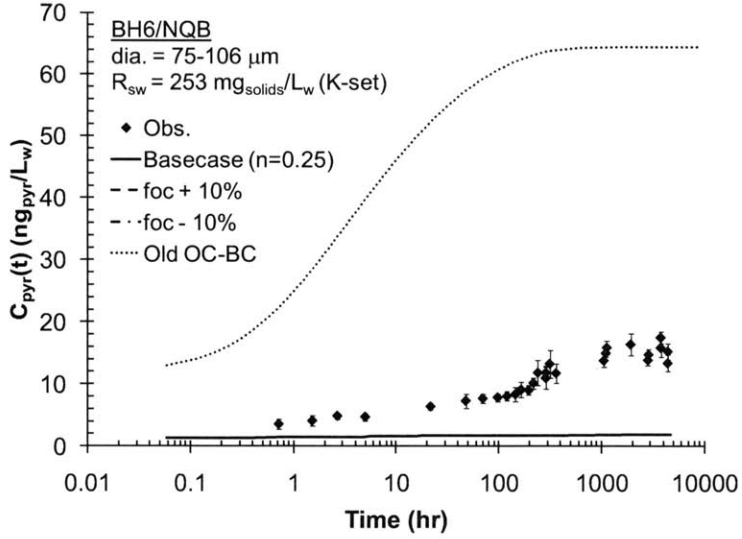

IHG-set (dia. 180–250 μm) – Sensitivity to f_{OC}

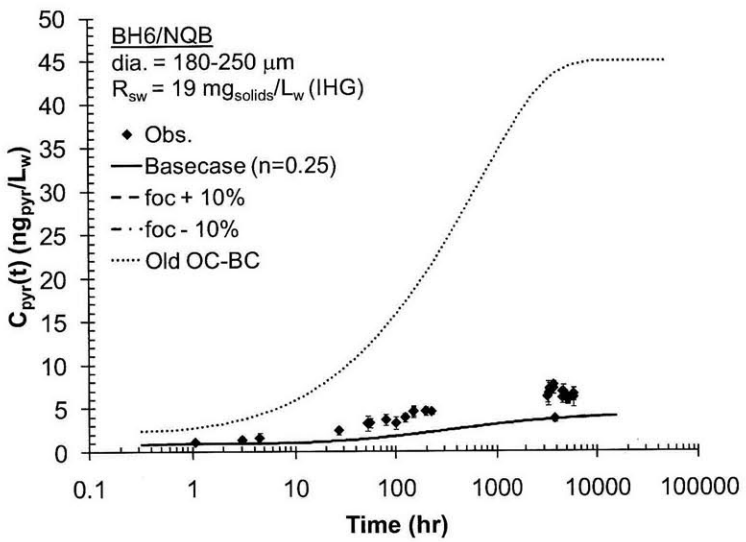

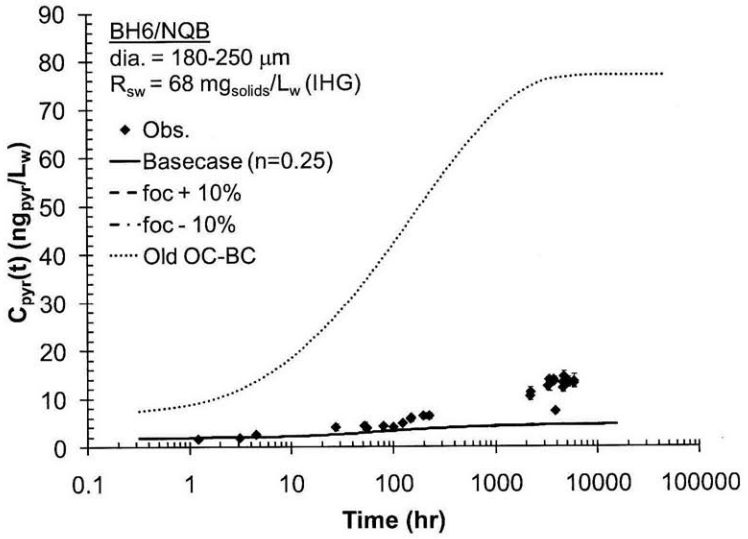

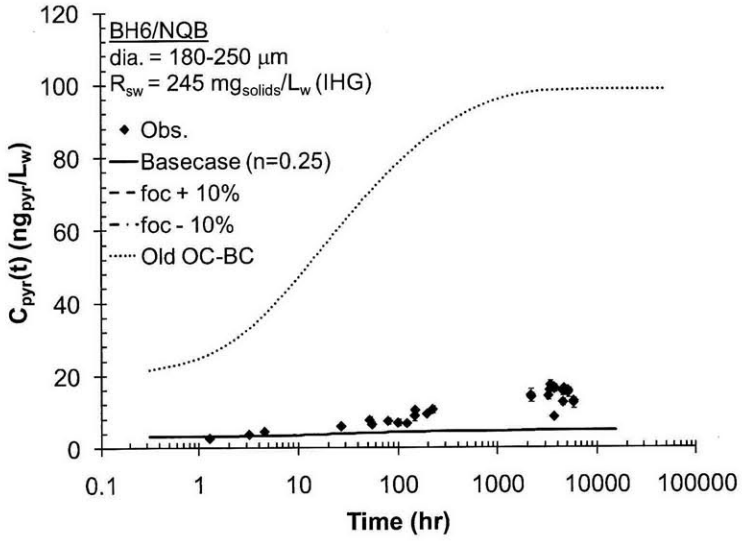

Appendix 7 - 4. Sensitivity of Pyrene Desorption Kinetics (III): f_{BC}.

Sensitivity analysis of pyrene desorption kinetics to f_{BC} was conducted with the *a priori* New OC-BC model prediction as the basecase. The New OC-BC model assumed that (a) $\log K_{OC} = 5.25 \pm 0.04$, (b) $\log K_{BC} = 6.25 \pm 0.06$, (c) $n_{BC} = 0.25 \pm 0.09$, (d) no occlusion of native pyrene.

All kinetic observations (except those for the C-set) were analyzed.

A-set (dia. 38–75 μm) – Sensitivity to f_{BC}

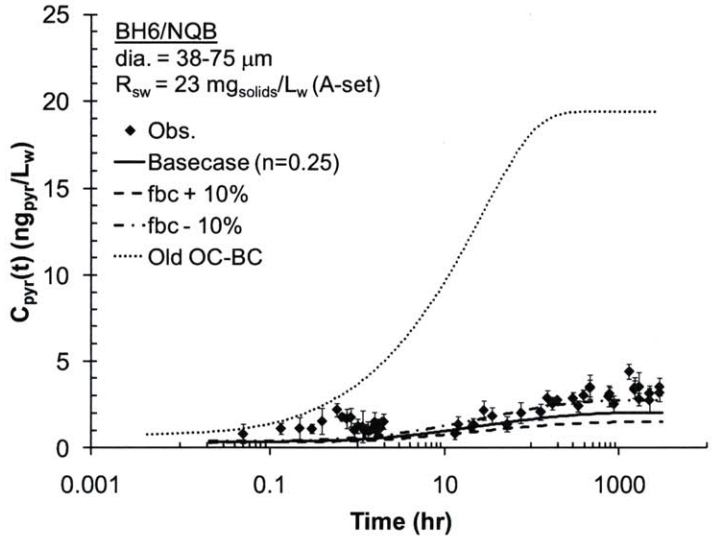

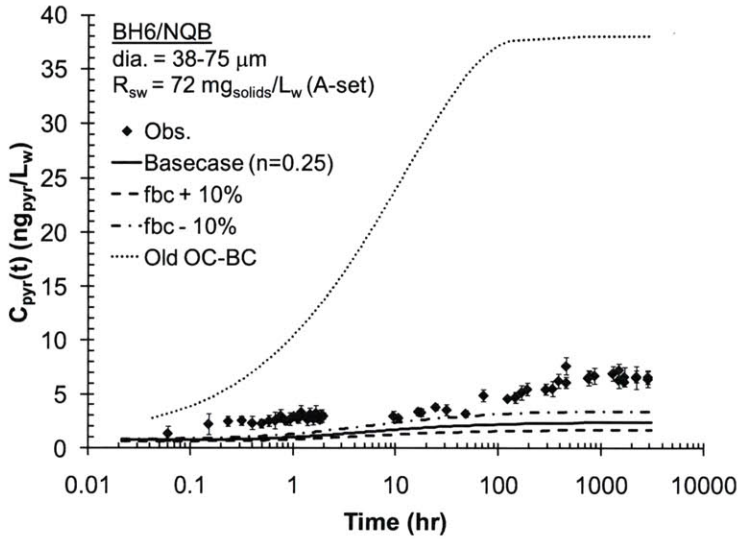

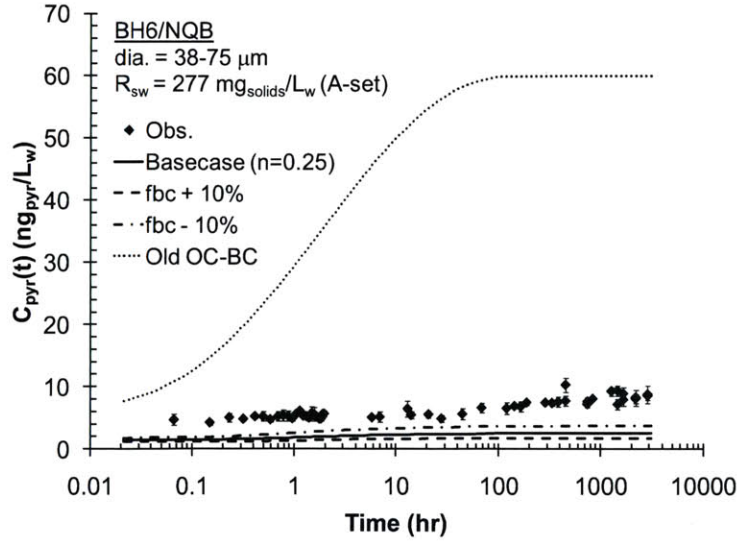

L-set (dia. 38–75 μm) – Sensitivity to f_{BC}

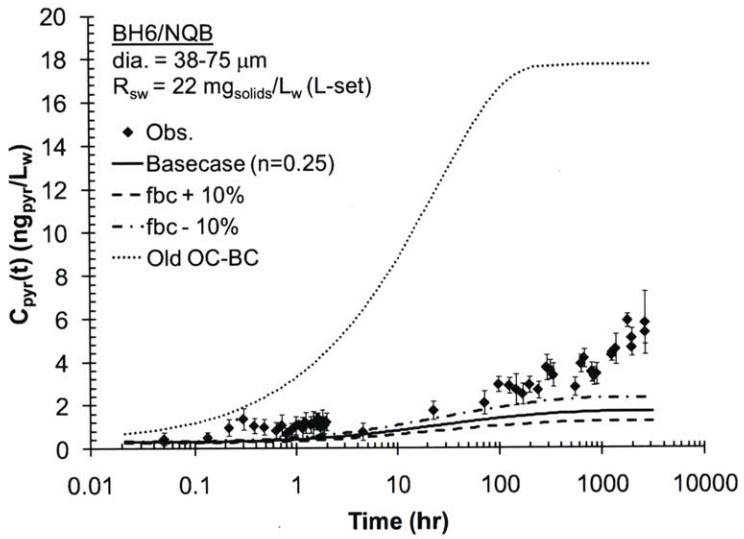

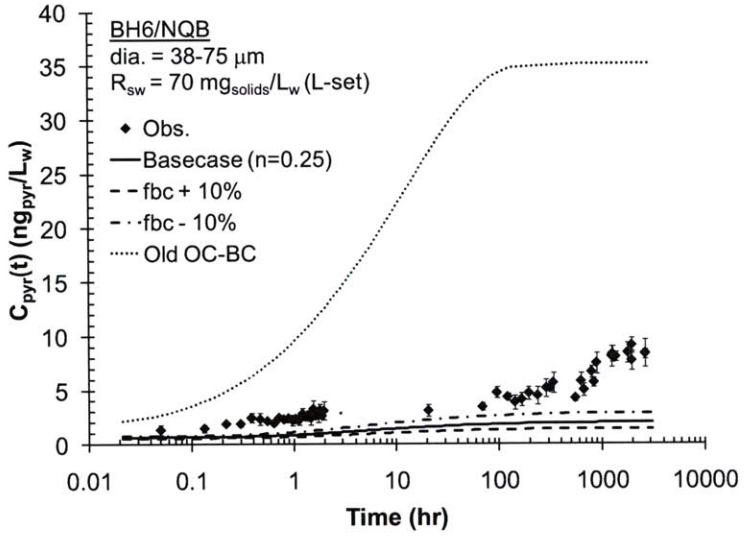

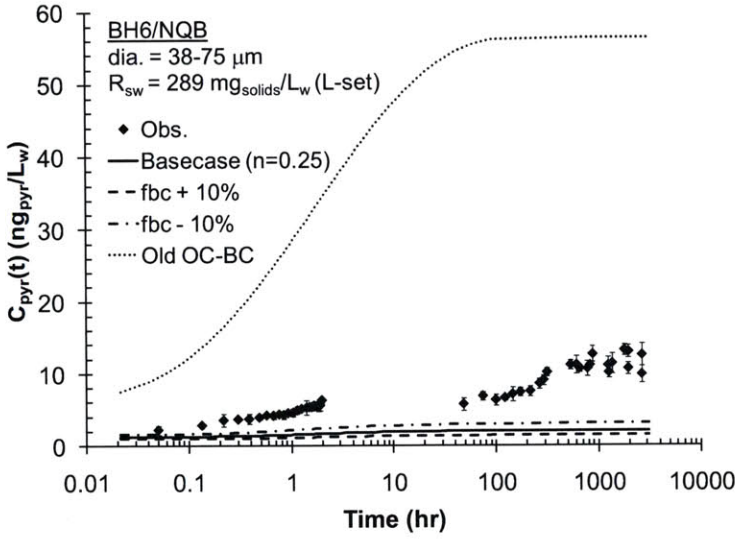

K-set (dia. 75–106 μm) – Sensitivity to f_{BC}

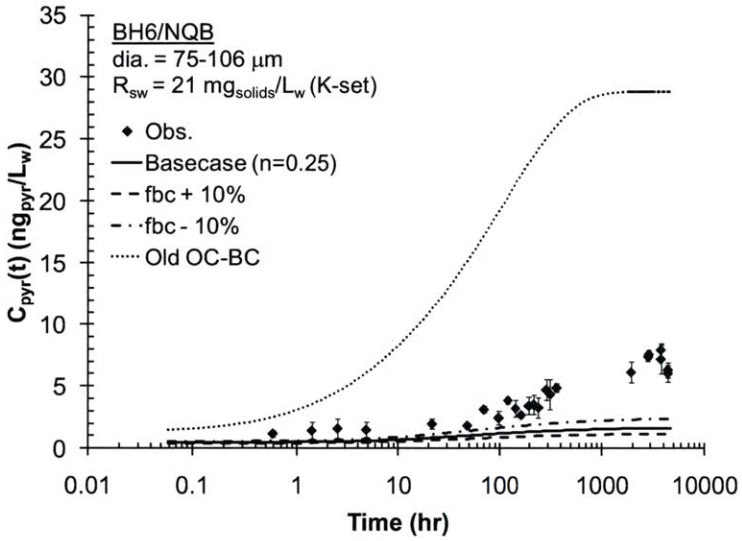

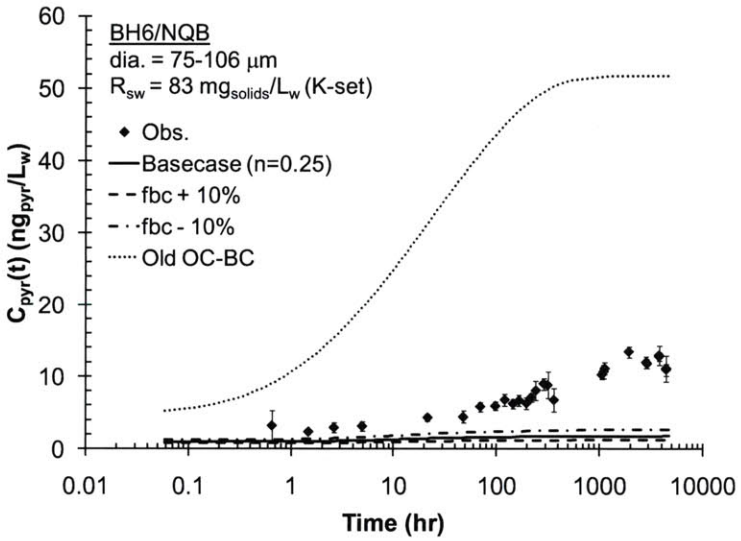

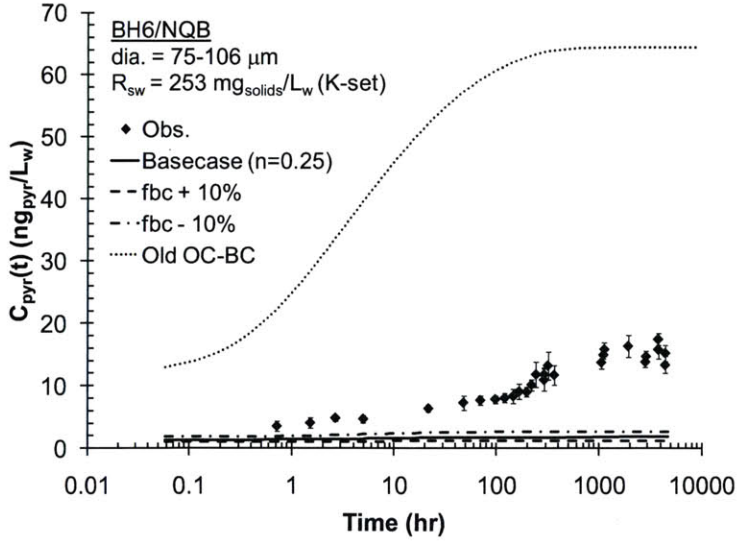

IHG-set (dia. 180–250 μm) – Sensitivity to f_{BC}

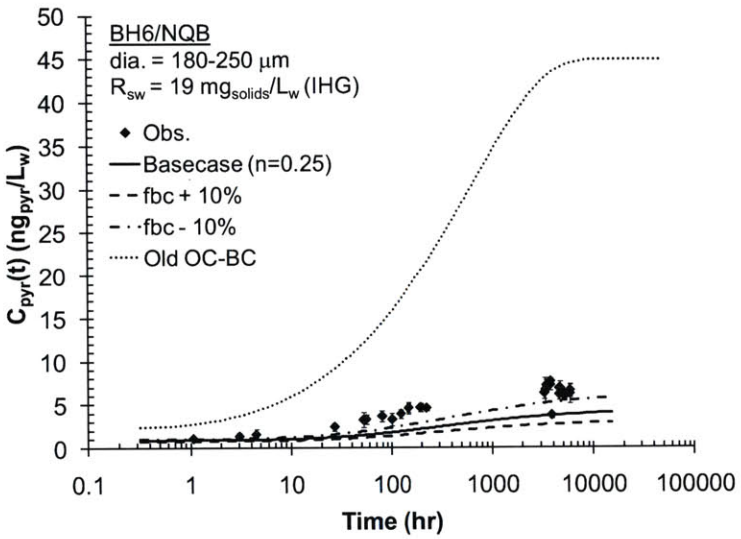

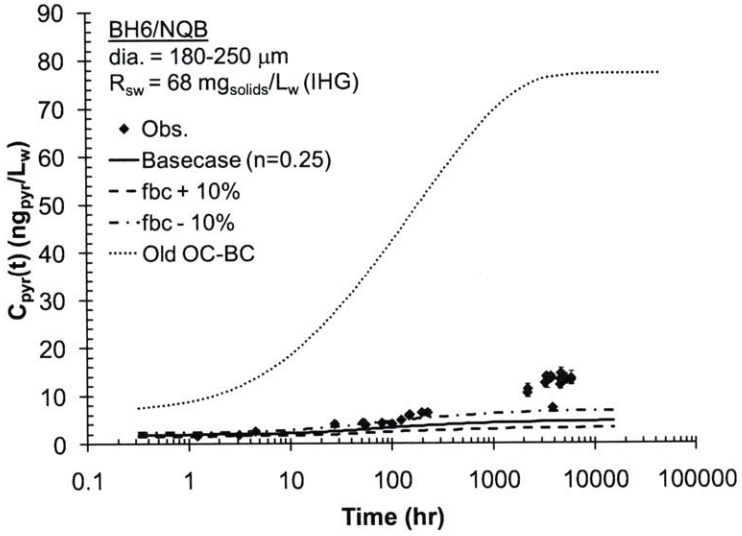

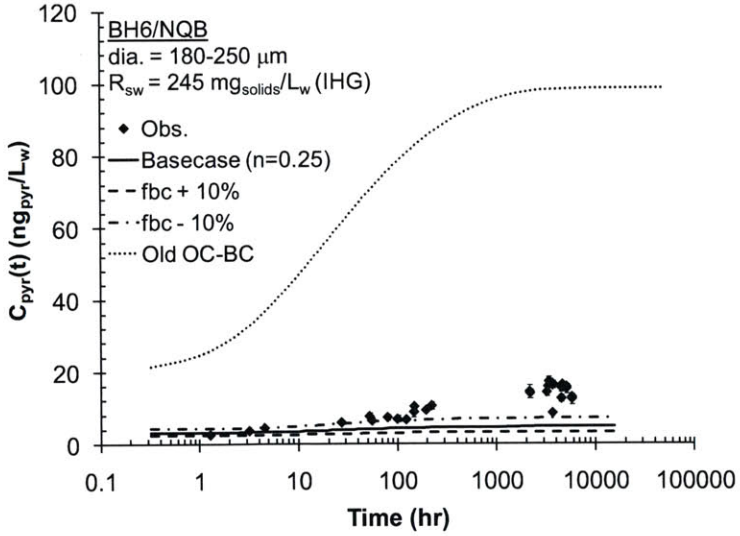

Appendix 7 - 5. Sensitivity of Pyrene Desorption Kinetics (IV): n_{BC}.

Sensitivity analysis of pyrene desorption kinetics to n_{BC} was conducted with the *a priori* New OC-BC model prediction as the basecase. The New OC-BC model assumed that (a) $\log K_{OC} = 5.25 \pm 0.04$, (b) $\log K_{BC} = 6.25 \pm 0.06$, (c) $n_{BC} = 0.25 \pm 0.09$, (d) no occlusion of native pyrene.

All kinetic observations (except those for the C-set) were analyzed.

A-set (dia. 38–75 μm) – Sensitivity to n_{BC}

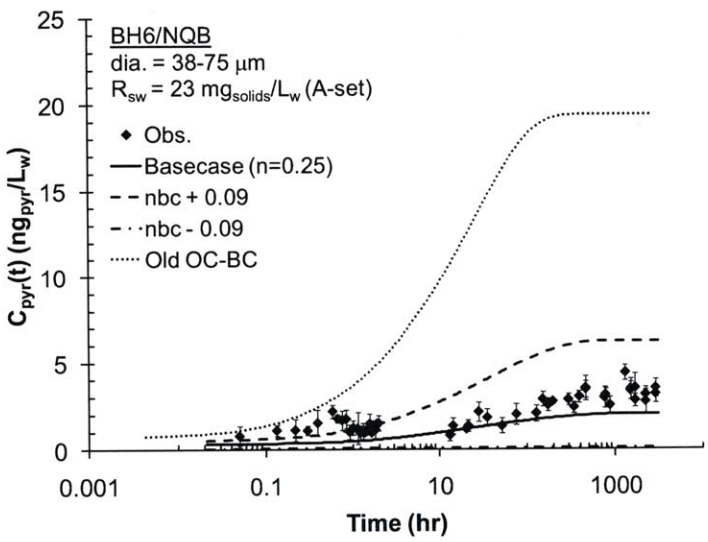

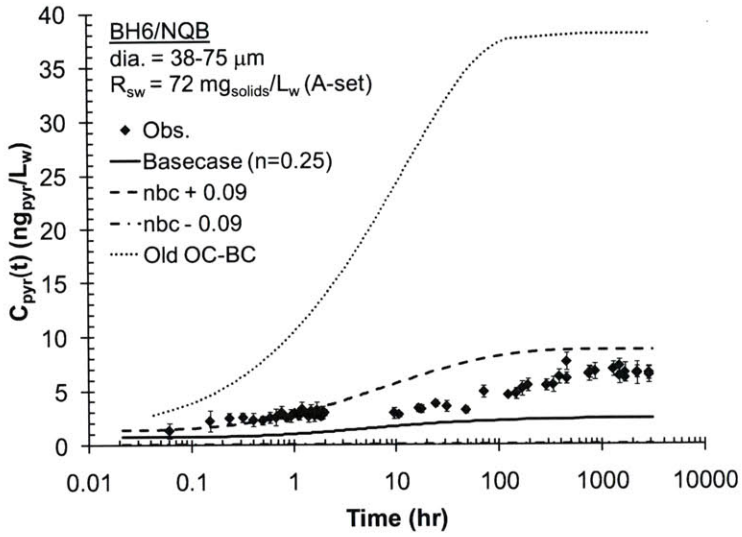

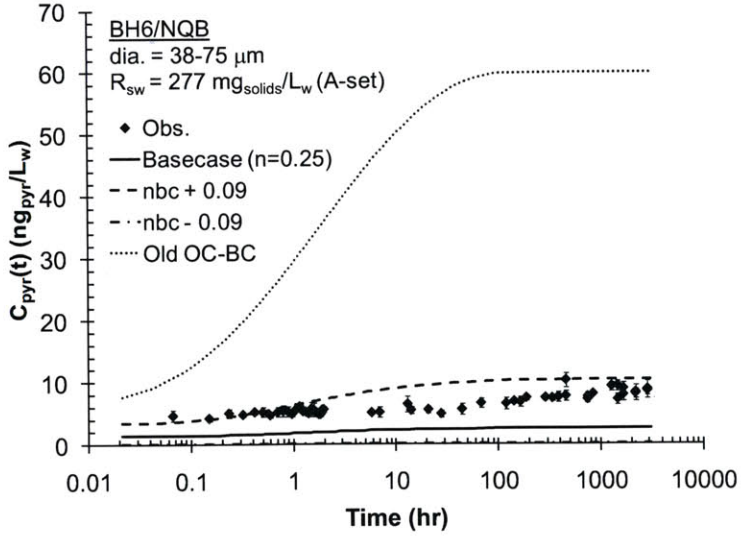

L-set (dia. 38–75 μm) – Sensitivity to n_{BC}

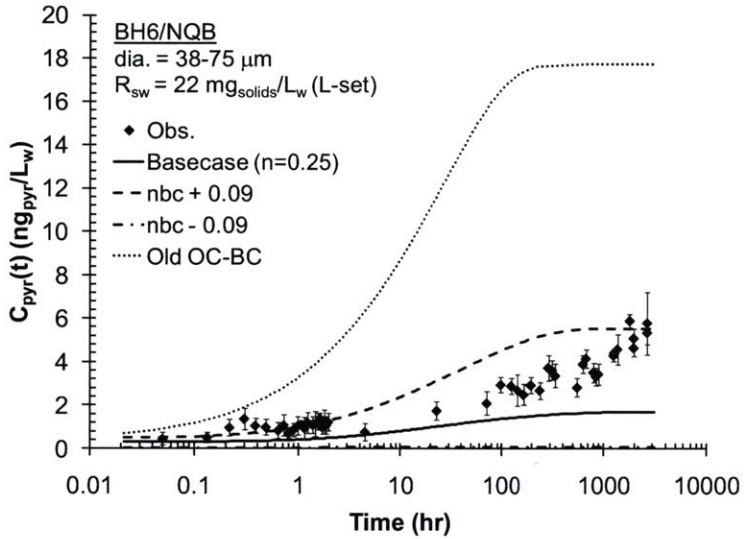

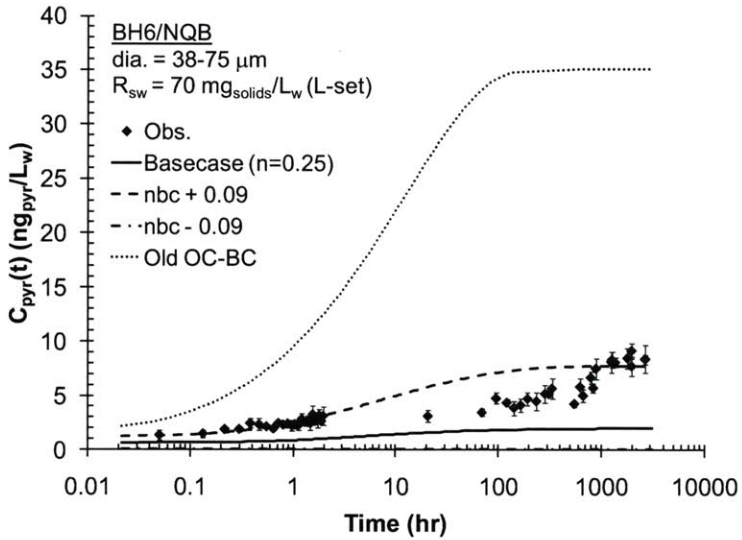

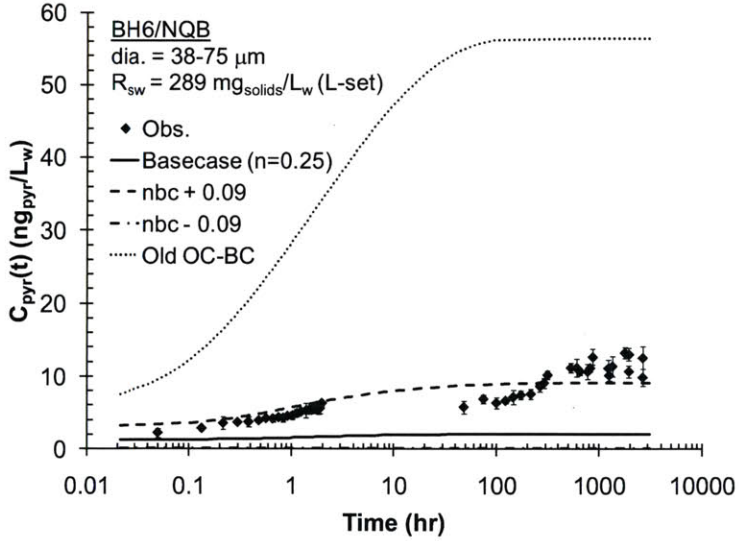

K-set (dia. 75–106 μm) – Sensitivity to n_{BC}

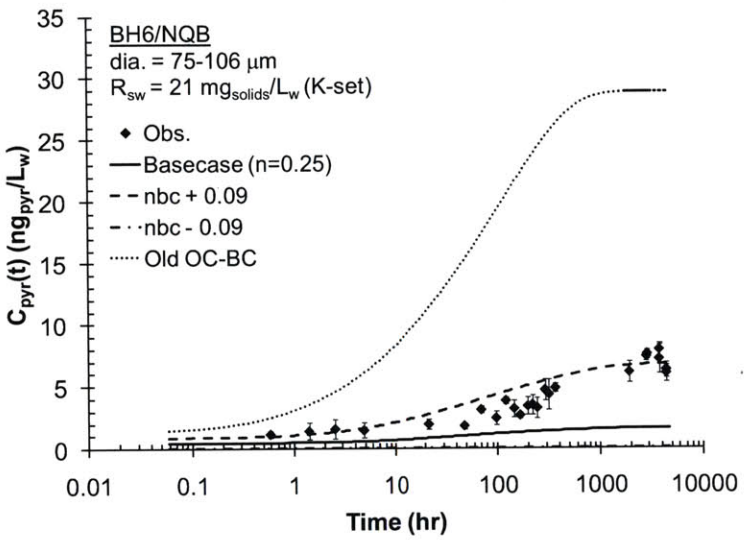

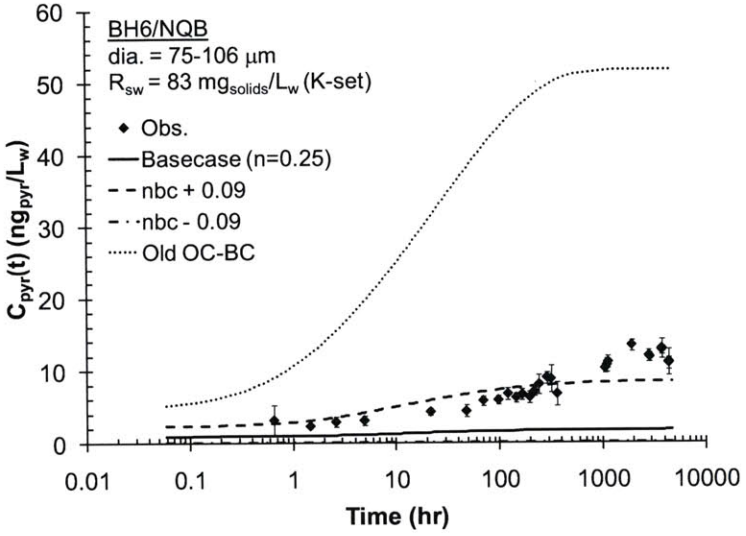

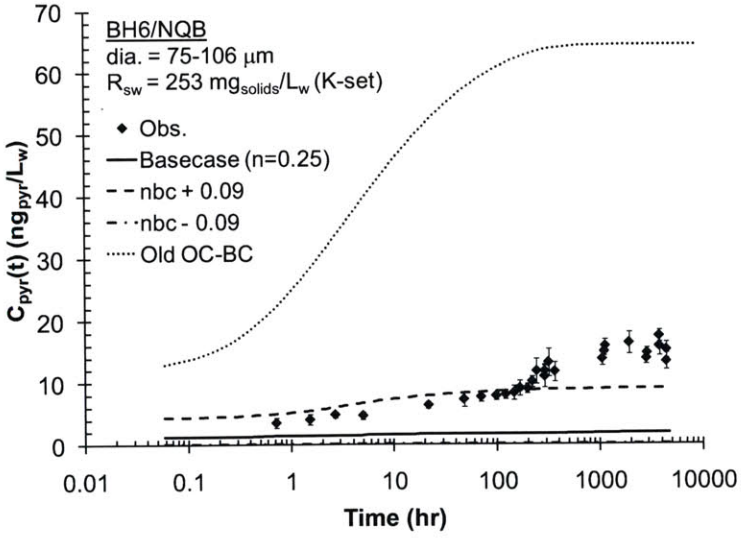

IHG-set (dia. 180–250 μm) – Sensitivity to n_{BC}

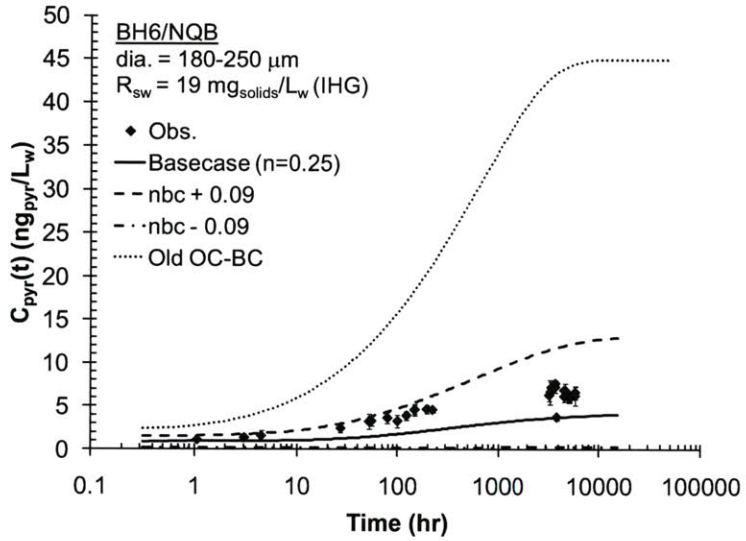

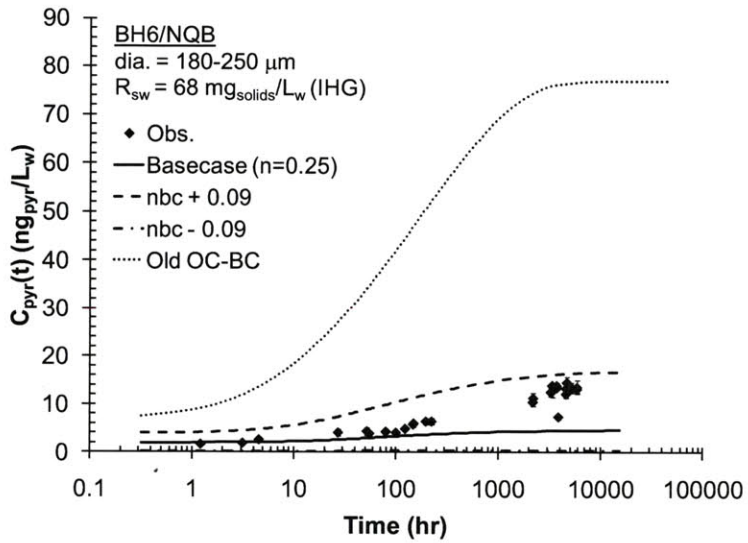

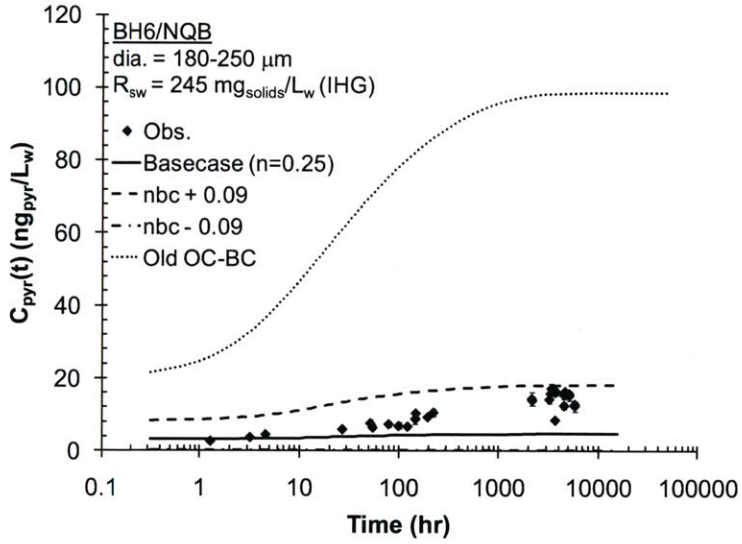

Appendix 7 - 6. Sensitivity of Pyrene Desorption Kinetics (V): $\log K_{OC}$.

Sensitivity analysis of pyrene desorption kinetics to $\log K_{OC}$ was conducted with the *a priori* New OC-BC model prediction as the basecase. The New OC-BC model assumed that (a) $\log K_{OC} = 5.25 \pm 0.04$, (b) $\log K_{BC} = 6.25 \pm 0.06$, (c) $n_{BC} = 0.25 \pm 0.09$, (d) no occlusion of native pyrene.

All kinetic observations (except those for the C-set) were analyzed.

A-set (dia. 38–75 μm) – Sensitivity to $logK_{OC}$

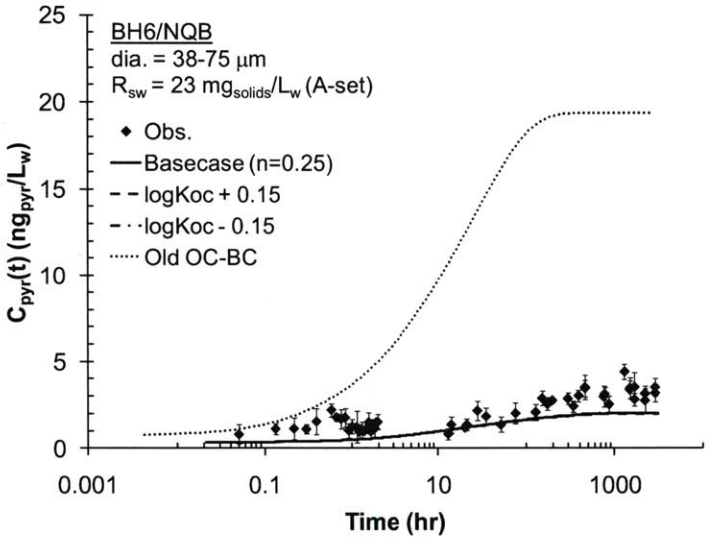

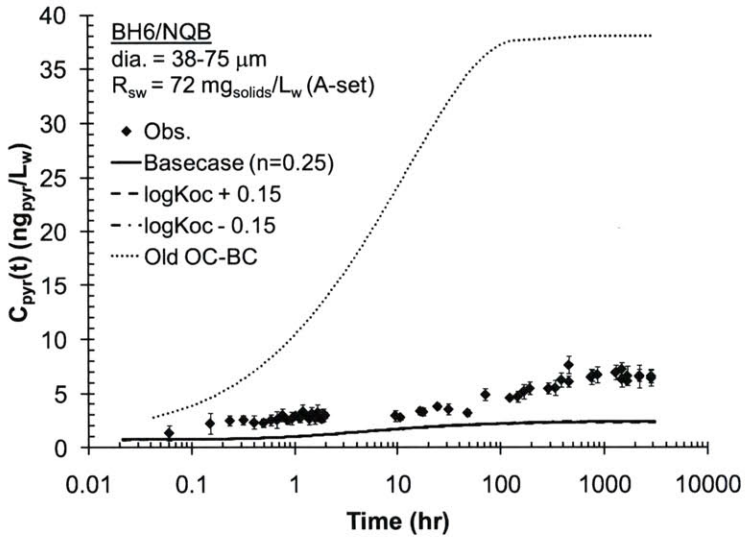

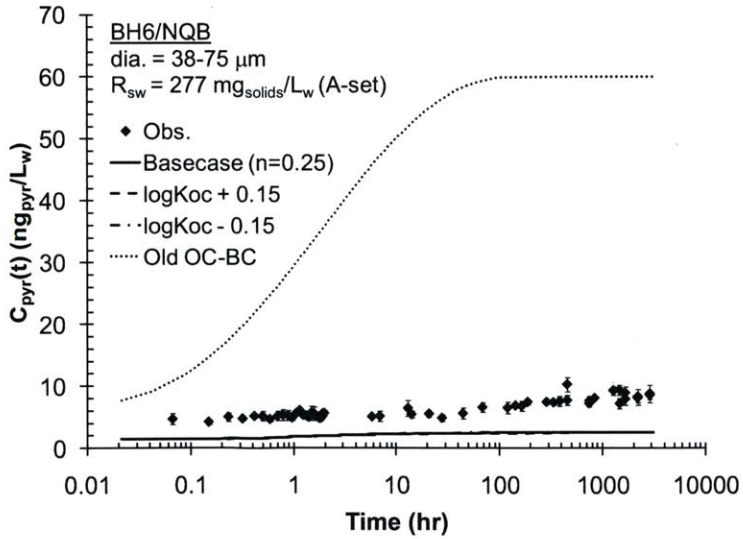

L-set (dia. 38–75 μm) – Sensitivity to $logK_{OC}$

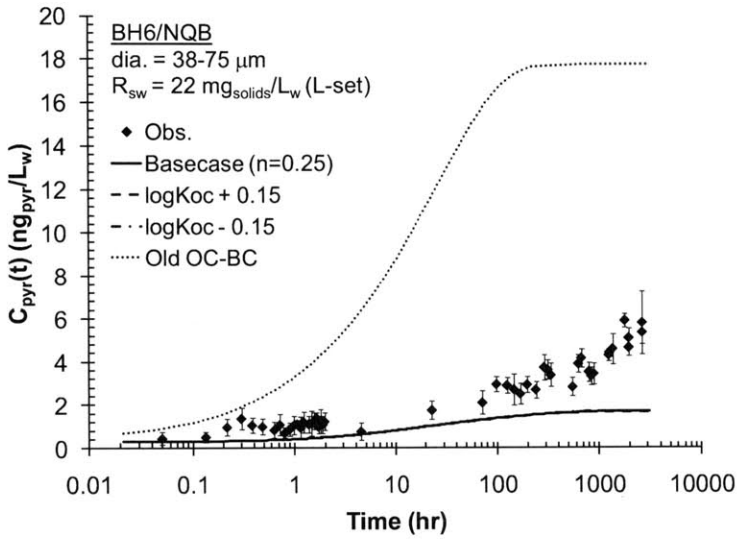

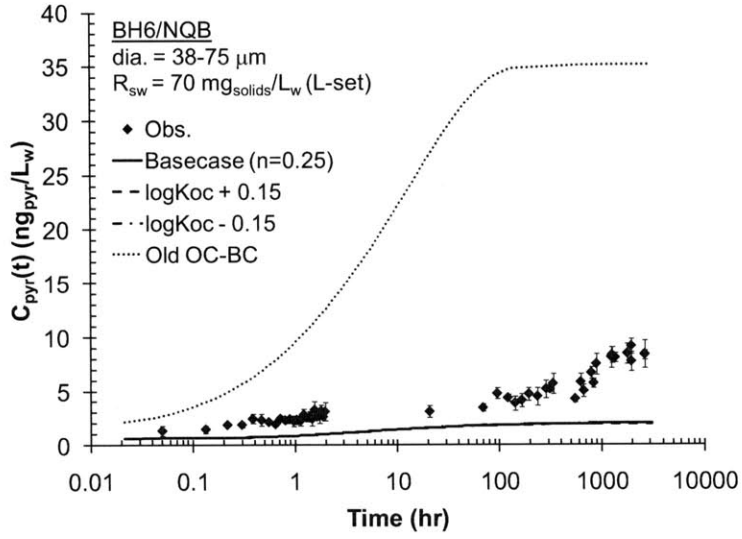

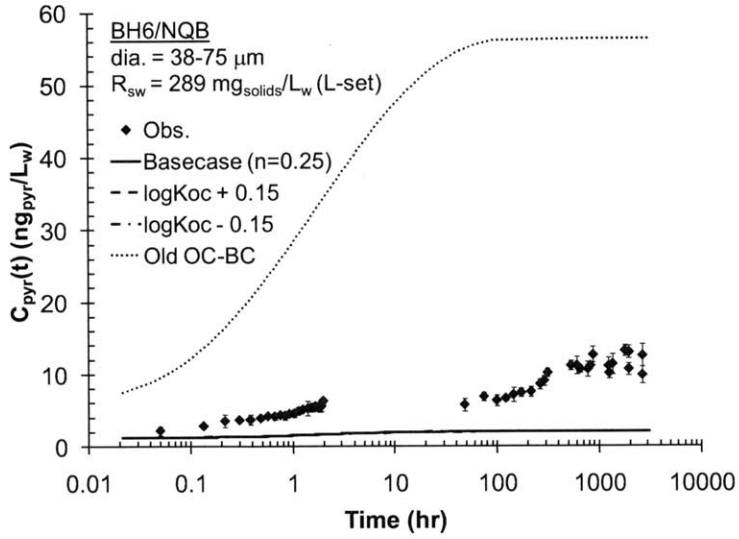

K-set (dia. 75–106 μm) – Sensitivity to $logK_{OC}$

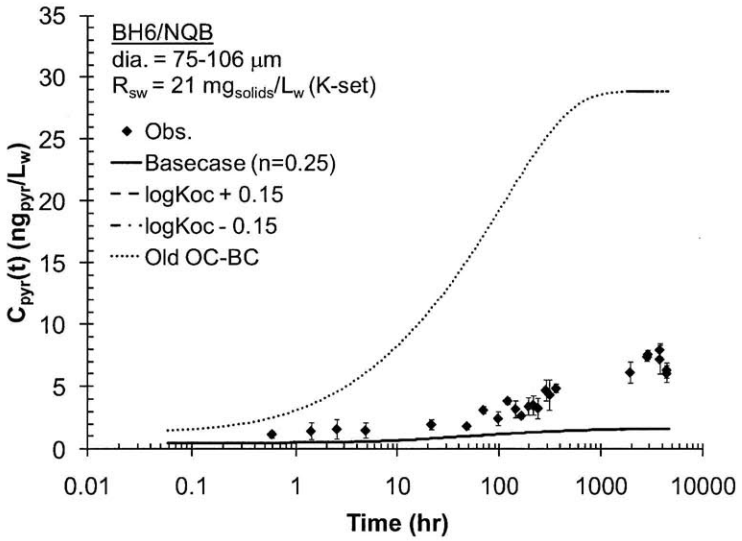

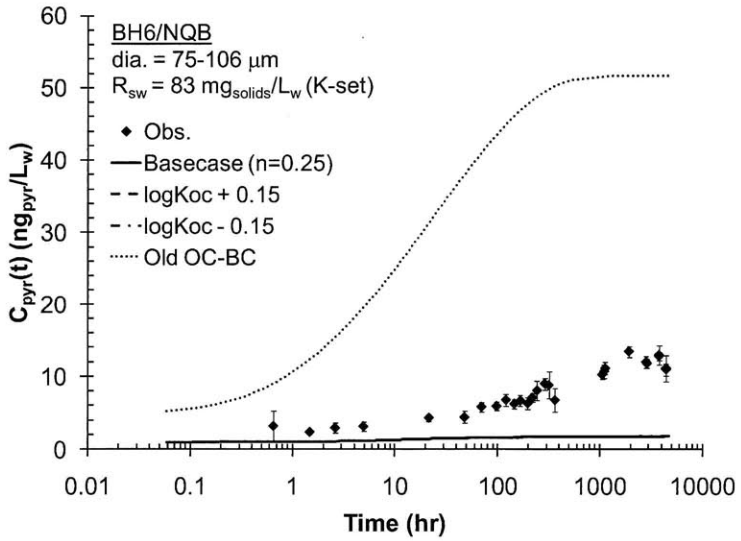

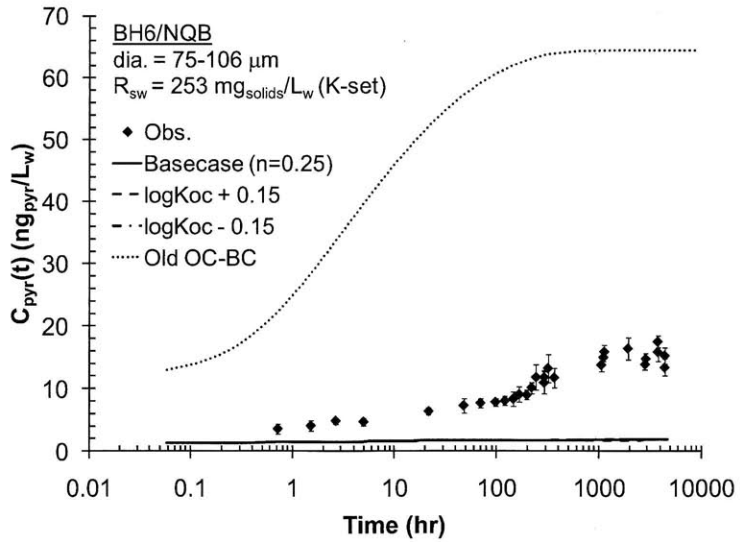

IHG-set (dia. 180–250 μm) – Sensitivity to $logK_{OC}$

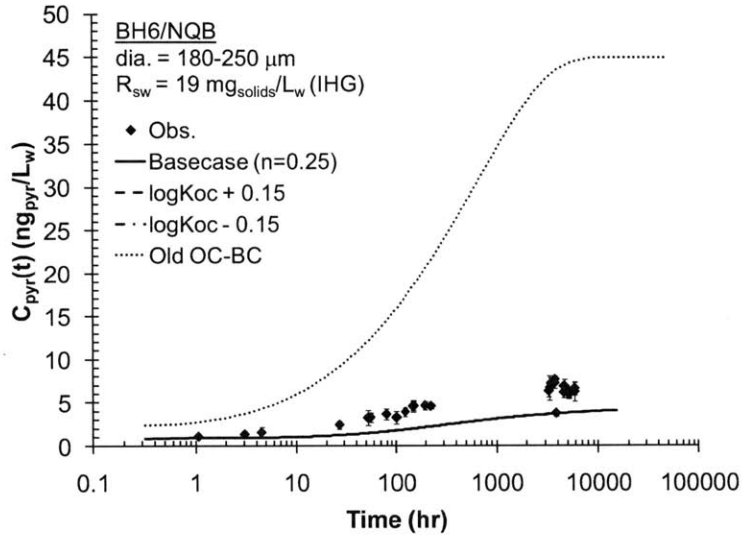

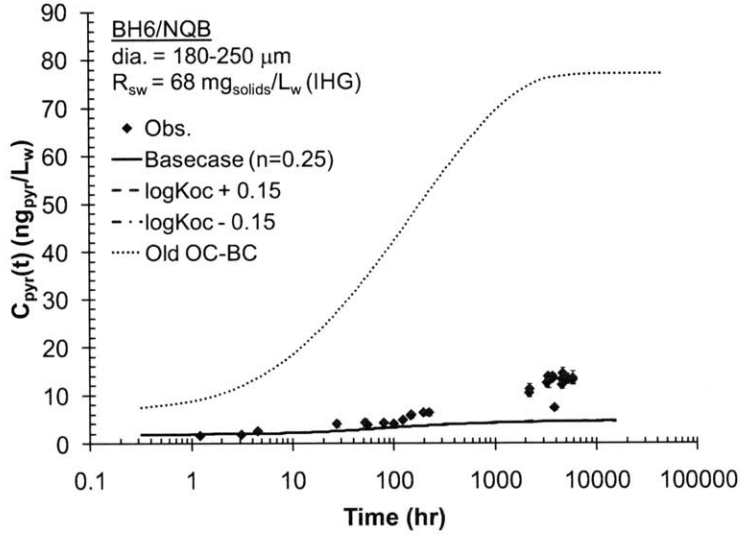

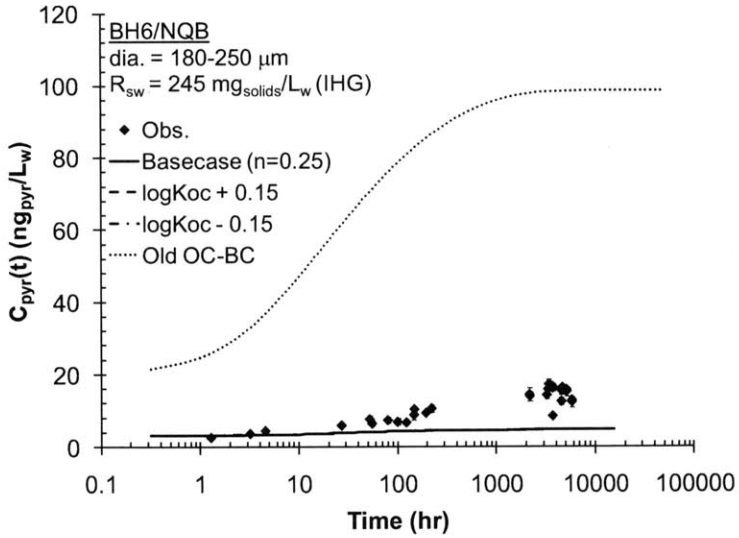

Appendix 7 - 7. Sensitivity of Pyrene Desorption Kinetics (VI): $\log K_{BC}$.

Sensitivity analysis of pyrene desorption kinetics to $\log K_{BC}$ was conducted with the *a priori* New OC-BC model prediction as the basecase. The New OC-BC model assumed that (a) $\log K_{OC} = 5.25 \pm 0.04$, (b) $\log K_{BC} = 6.25 \pm 0.06$, (c) $n_{BC} = 0.25 \pm 0.09$, (d) no occlusion of native pyrene.

All kinetic observations (except those for the C-set) were analyzed.

A-set (dia. 38–75 μm) – Sensitivity to $logK_{BC}$

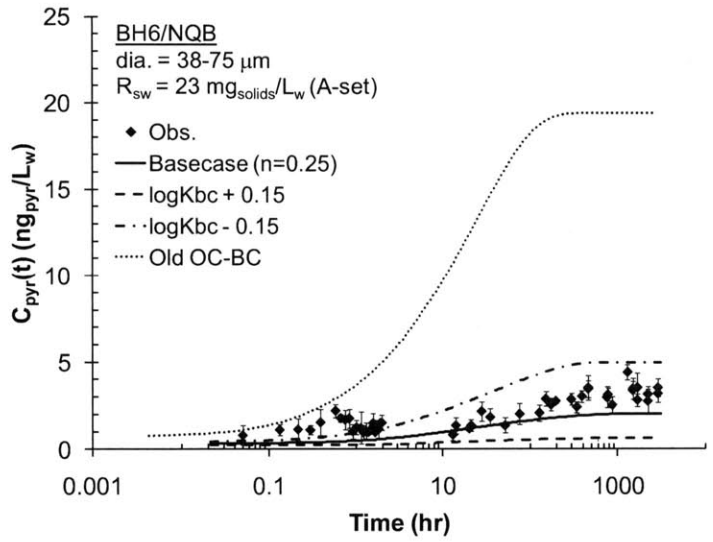

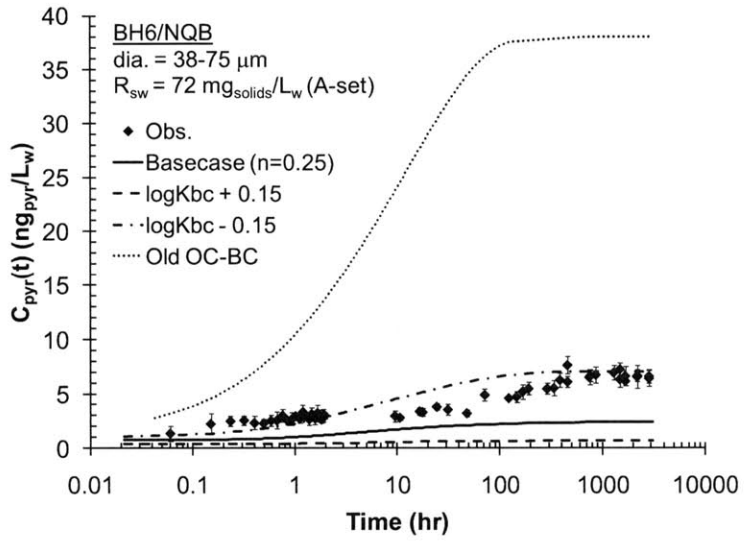

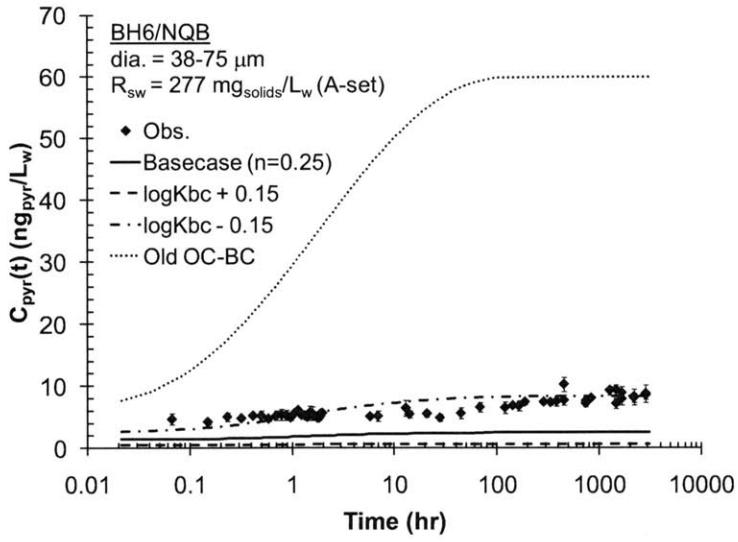

L-set (dia. 38–75 μm) – Sensitivity to $logK_{BC}$

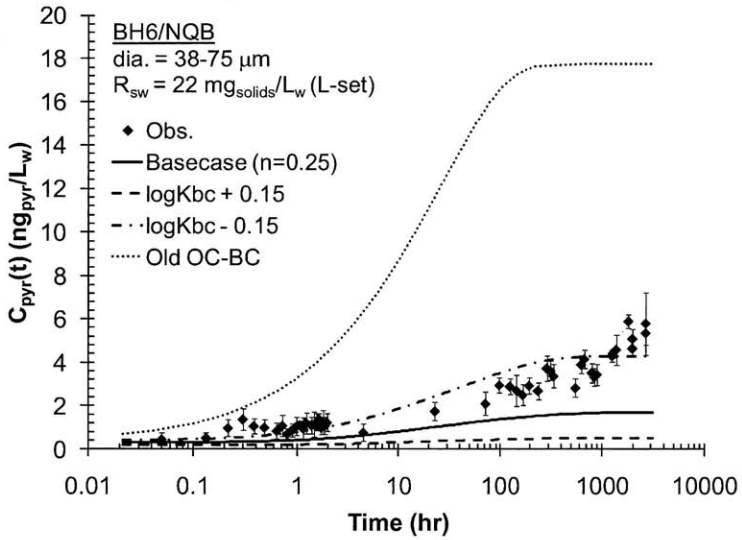

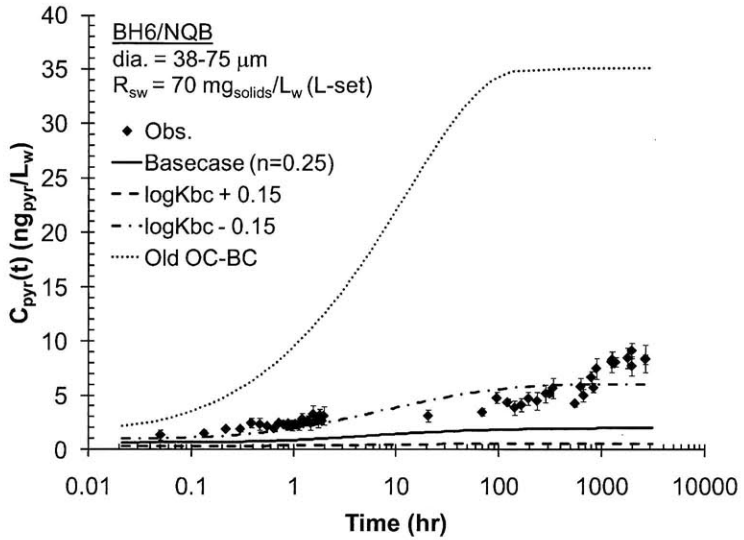

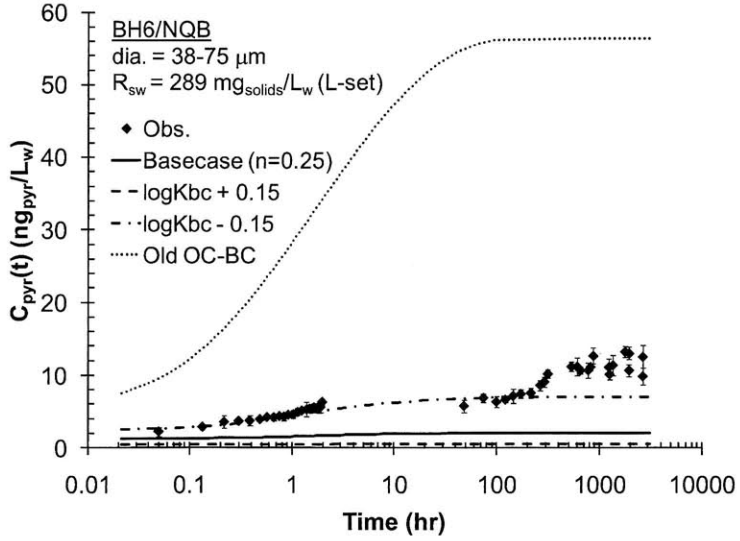

K-set (dia. 75–106 μm) – Sensitivity to $logK_{BC}$

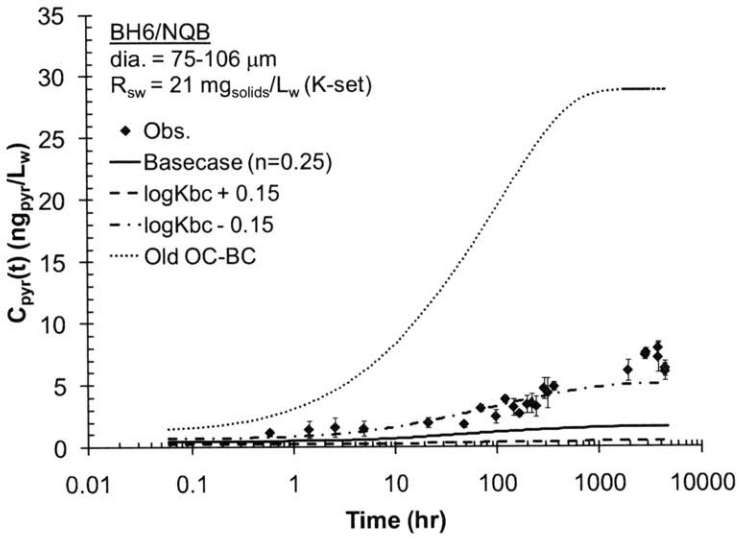

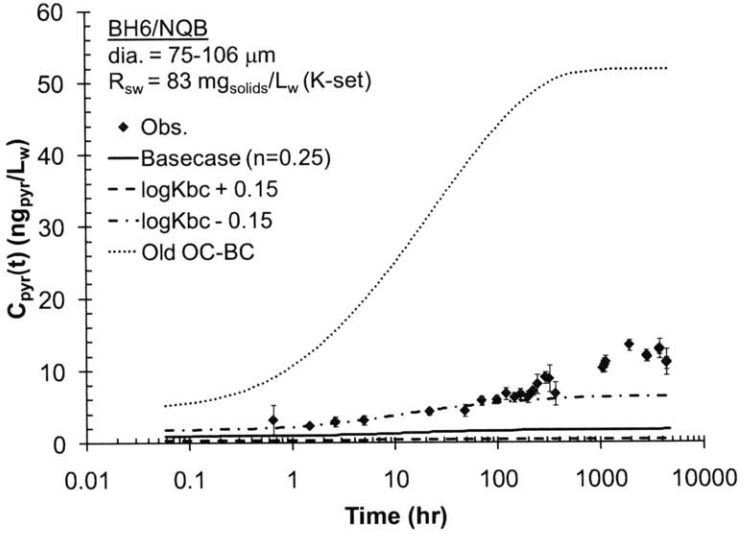

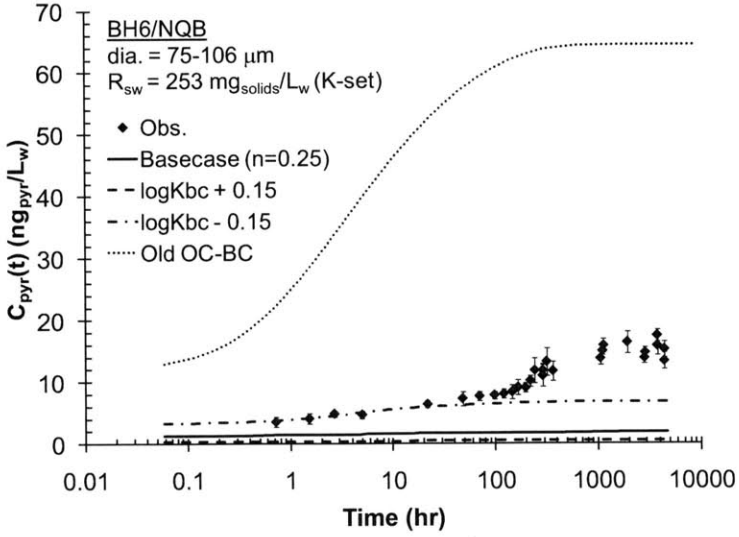

IHG-set (dia. 180–250 μm) – Sensitivity to $logK_{BC}$

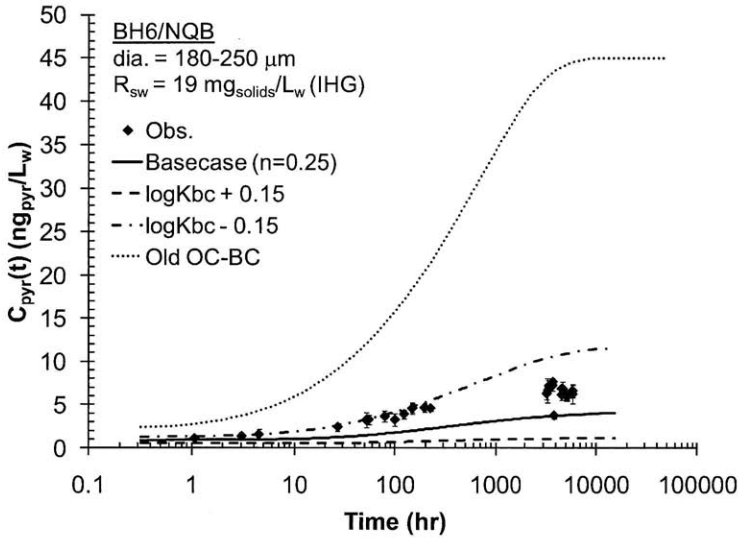

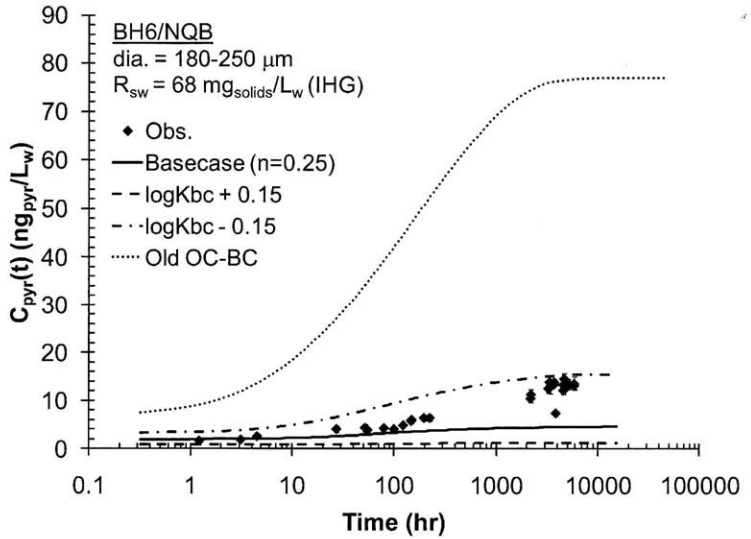

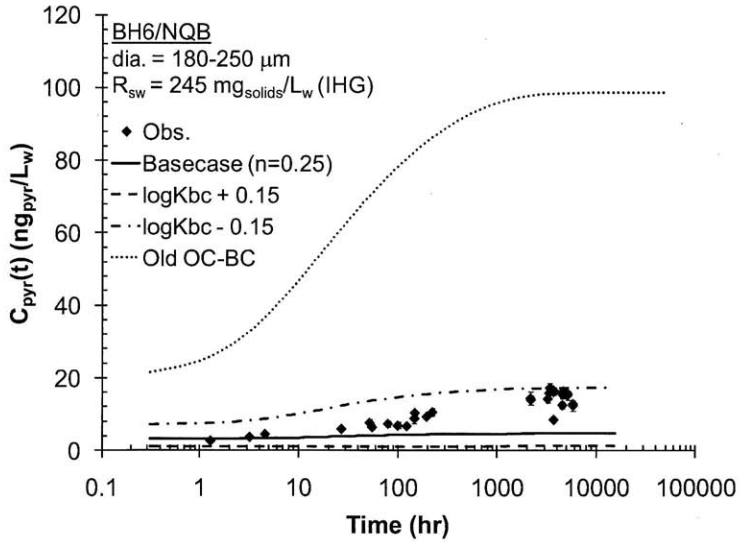

Appendix 7 - 8. Sensitivity of Pyrene Desorption Kinetics (VII): particle radius R.

Sensitivity analysis of pyrene desorption kinetics to particle radius, R, was conducted with the Generic OC-BC Best Fit as the basecase. The Generic OC-BC Best Fit assumed that (a) $\log K_{OC} = 4.75$, (b) $\log K_{BC} = 5.95$, (c) n_{BC} = manipulated fitting variable, (d) no occlusion of native pyrene. The best-fit (i.e. $C_{pyr,fitted} \sim C_{pyr,obs,end}$) n_{BC}'s for the observed data are tabulated below.

All kinetic observations were analyzed.

Set	Nominal Particle/Aggregate Size	R_{sw} (mg_{solids}/L_w)	Best Fit n_{BC}
A	38–75 μm	23	0.16
A		72	0.17
A		277	0.17
C		23	0.17
C		71	0.22
C		268	0.21
L		22	0.20
L		70	0.20
L		289	0.20
K	75–106 μm	21	0.20
K		83	0.21
K		253	0.22
IHG	180–250 μm	19	0.14
IHG		68	0.16
IHG		245	0.16

A-set (dia. 38–75 μm) – Sensitivity to Particle Radius R

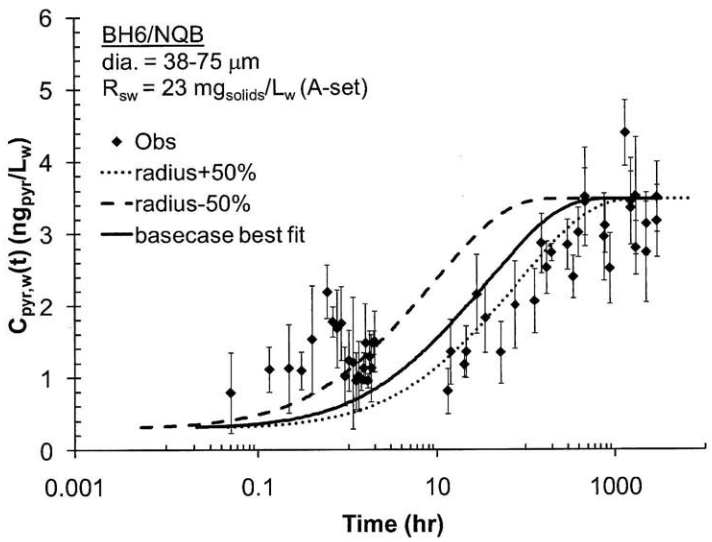

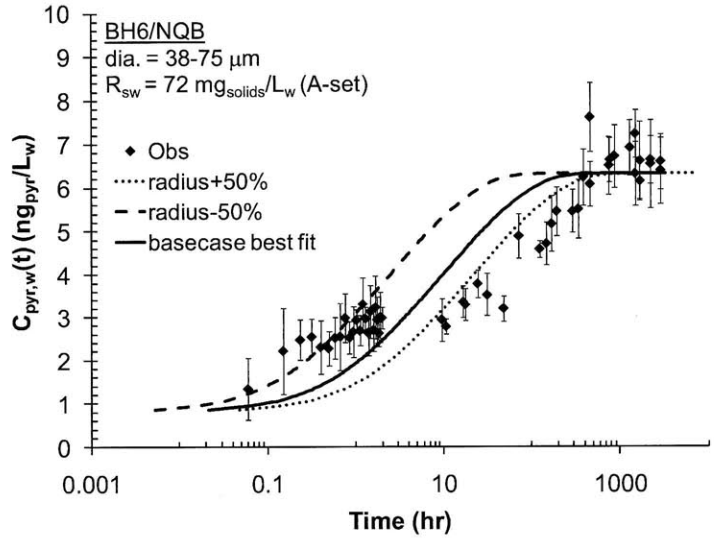

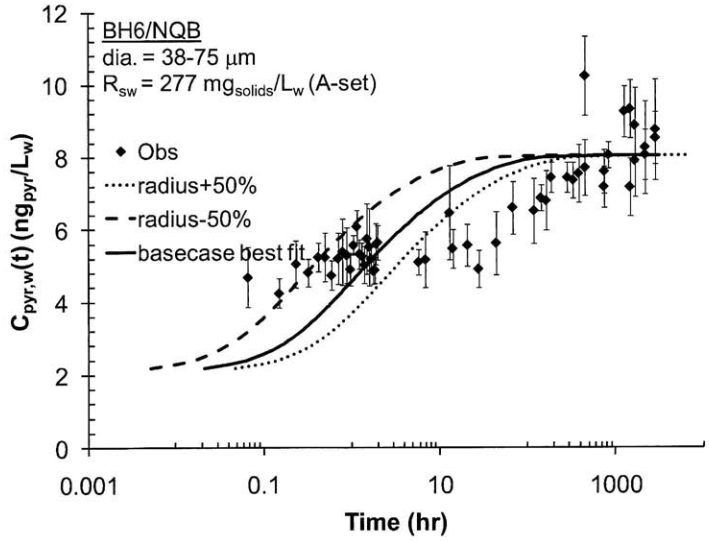

C-set (dia. 38–75 μm) – Sensitivity to Particle Radius R

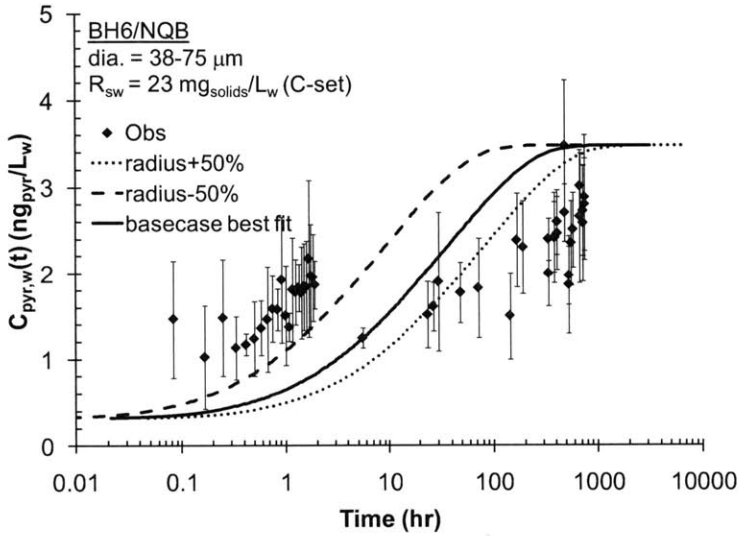

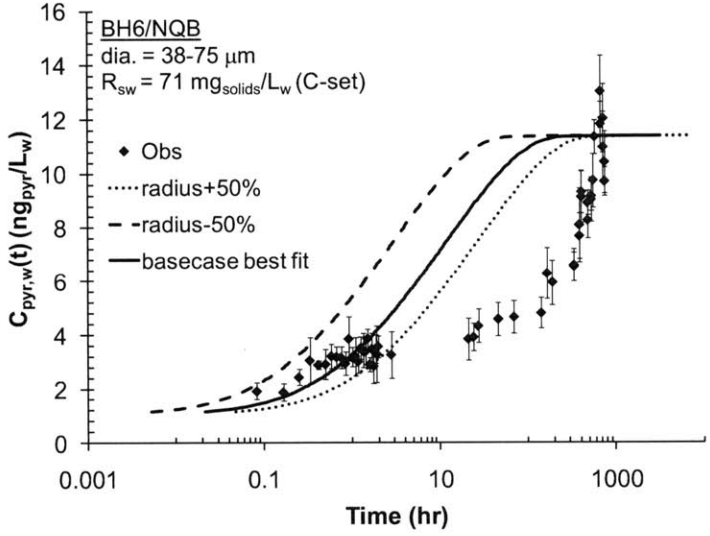

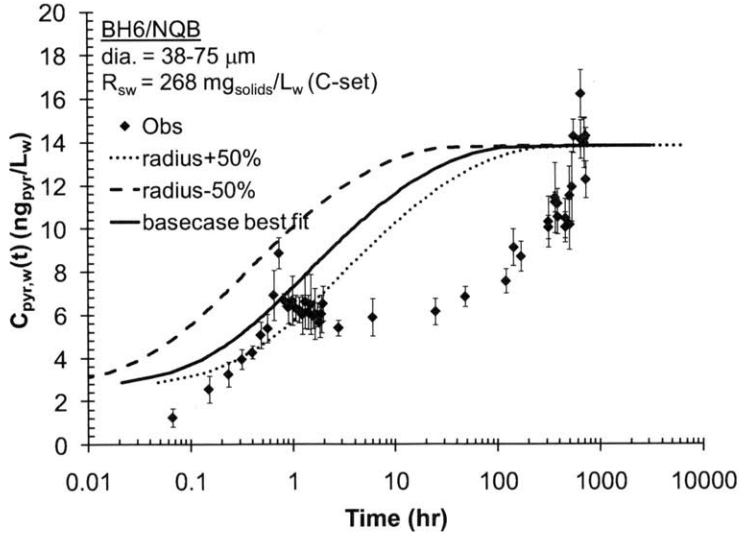

L-set (dia. 38–75 μm) – Sensitivity to Particle Radius R

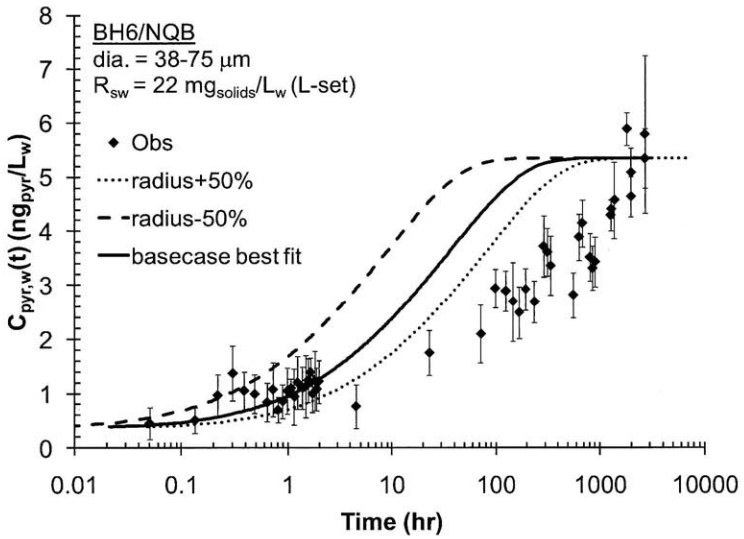

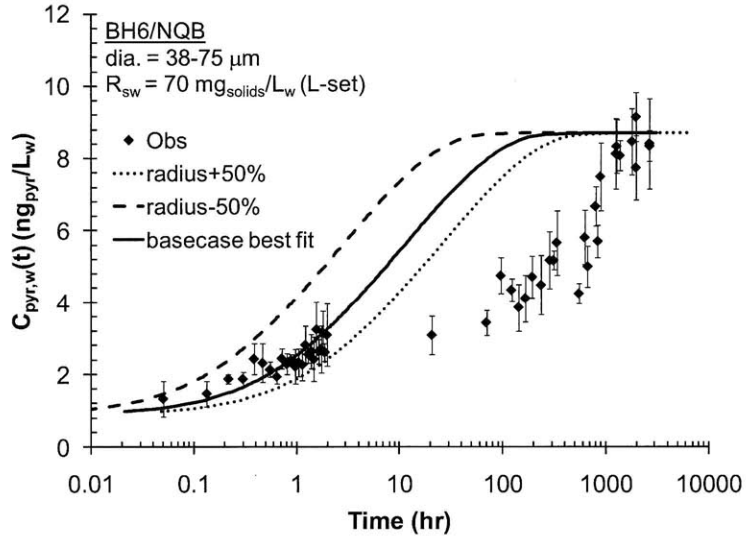

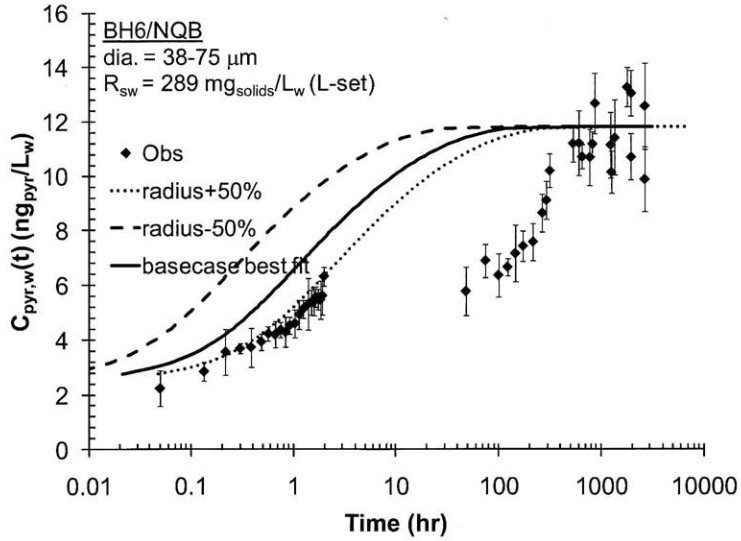

K-set (dia. 75–106 μm) – Sensitivity to Particle Radius R

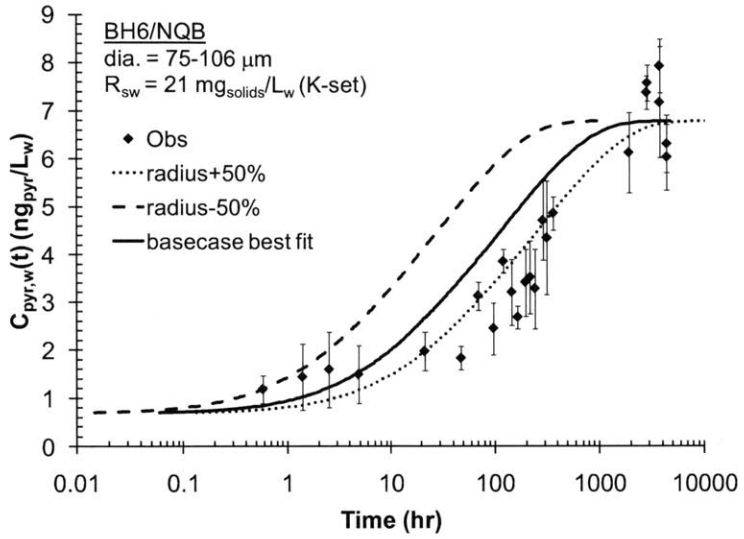

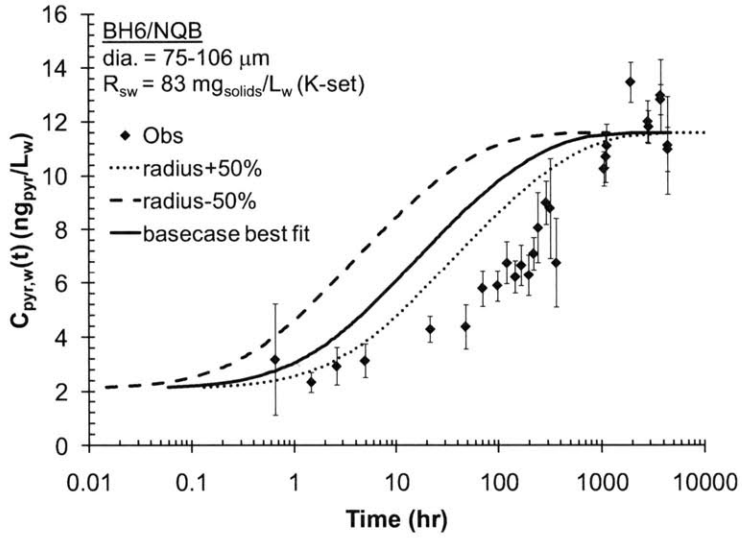

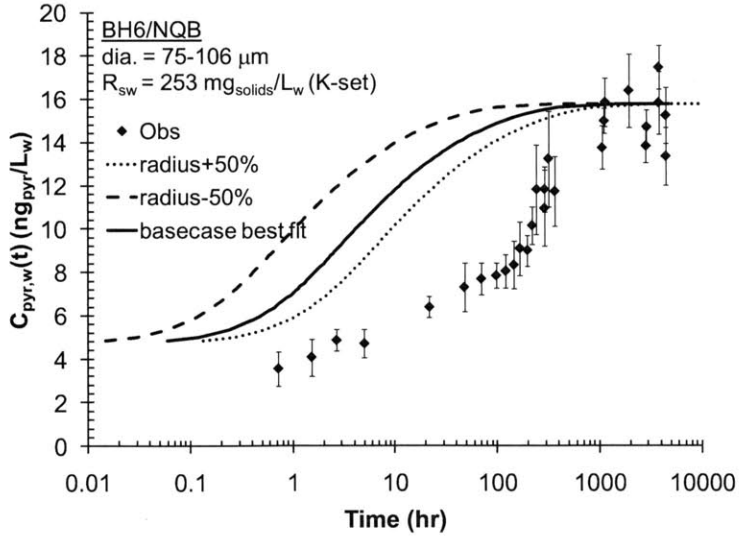

IHG-set (dia. 180–250 μm) – Sensitivity to Particle Radius R

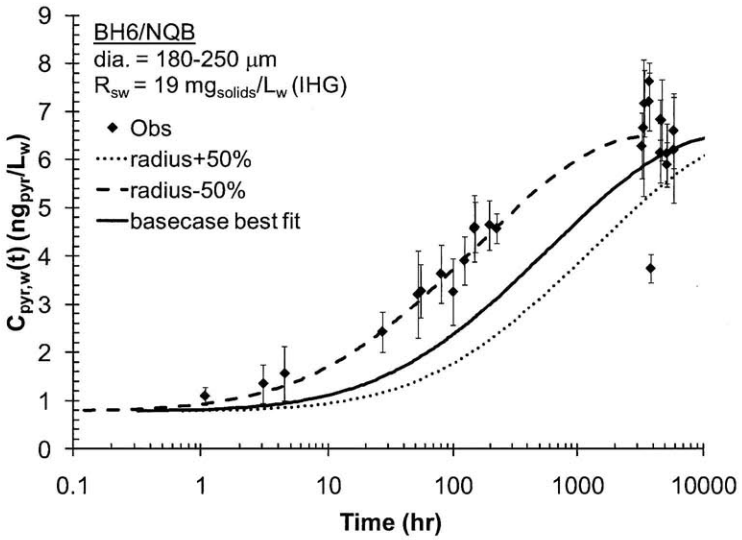

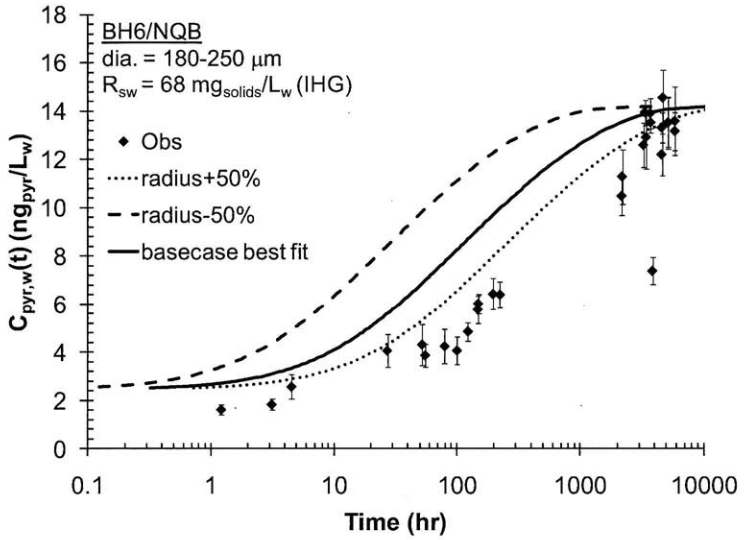

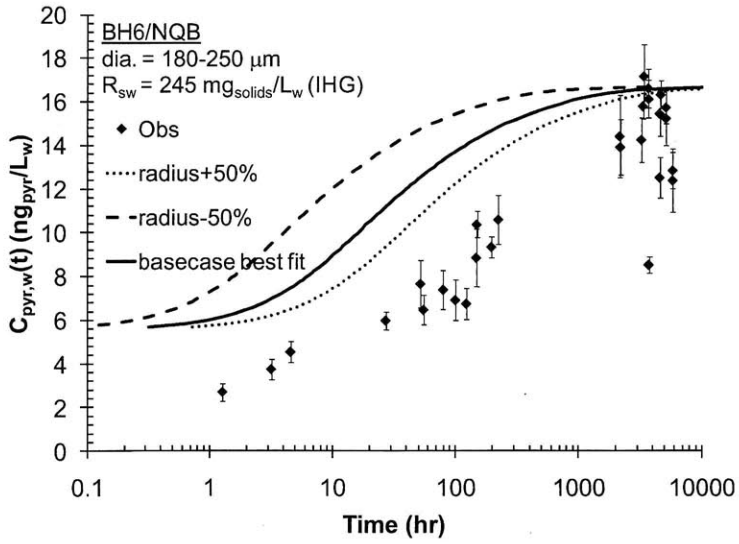

Appendix 7 - 9. Sensitivity of Pyrene Desorption Kinetics (VIII) & (IX): Porosity (ϕ) and Shape Factor (SF).

Sensitivity analysis of pyrene desorption kinetics to particle radius, R, was conducted with the Generic OC-BC Best Fit as the basecase. The Generic OC-BC Best Fit assumed that (a) $\log K_{OC} = 4.75$, (b) $\log K_{BC} = 5.95$, (c) n_{BC} = manipulated fitting variable, (d) no occlusion of native pyrene. The best-fit (i.e. $C_{pyr,fitted} \sim C_{pyr,obs,end}$) n_{BC}'s for the observed data are tabulated below. Please refer to the table in Appendix 7-9 for the best-fit n_{BC}'s.

All kinetic observations were analyzed.

A-set (dia. 38–75 μm) – Sensitivity to Porosity (ϕ) and Shape Factor (SF)

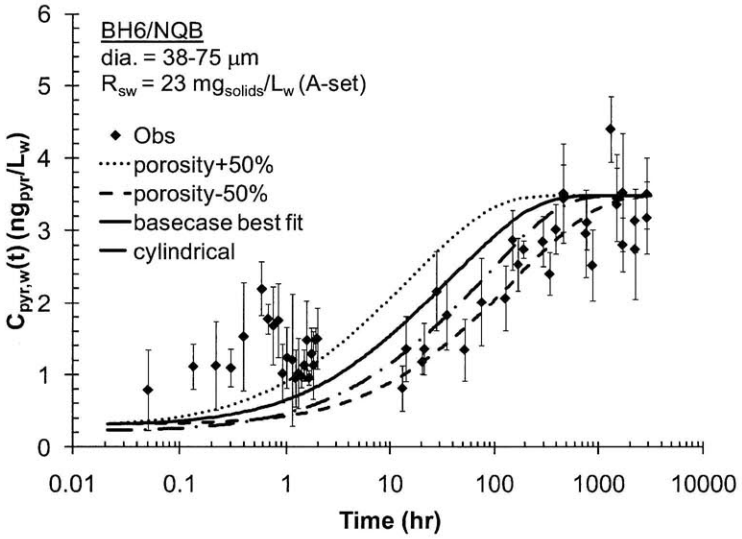

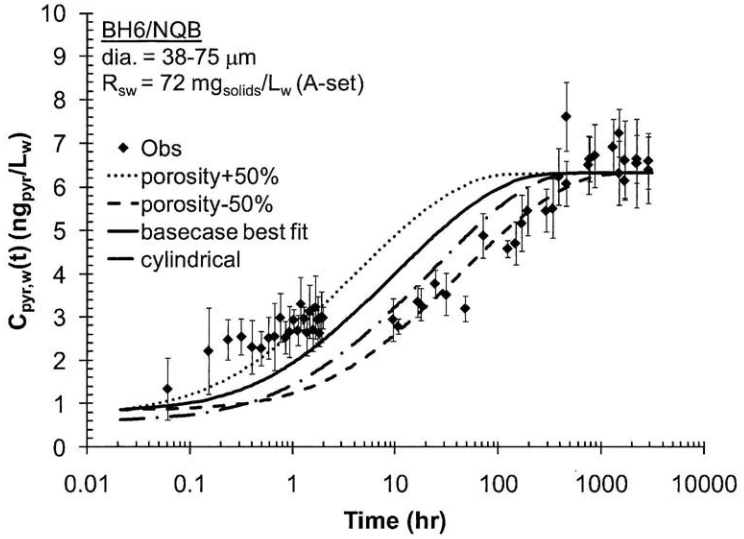

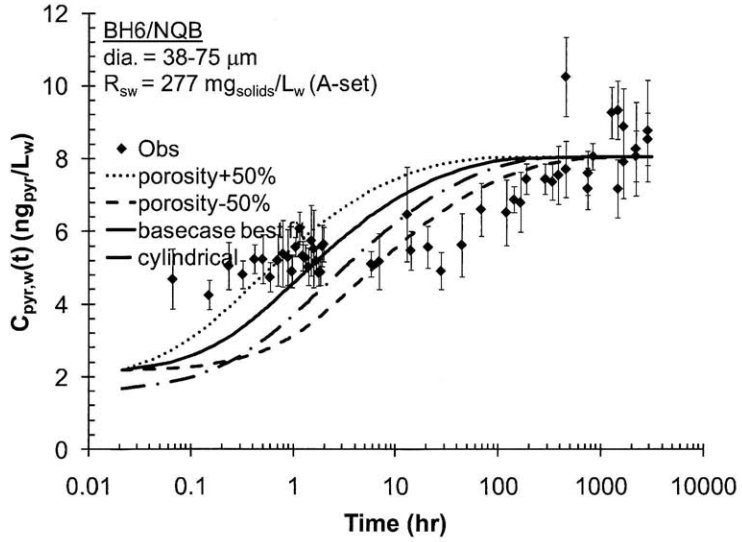

C-set (dia. 38–75 μm) – Sensitivity to Porosity (ϕ) and Shape Factor (SF)

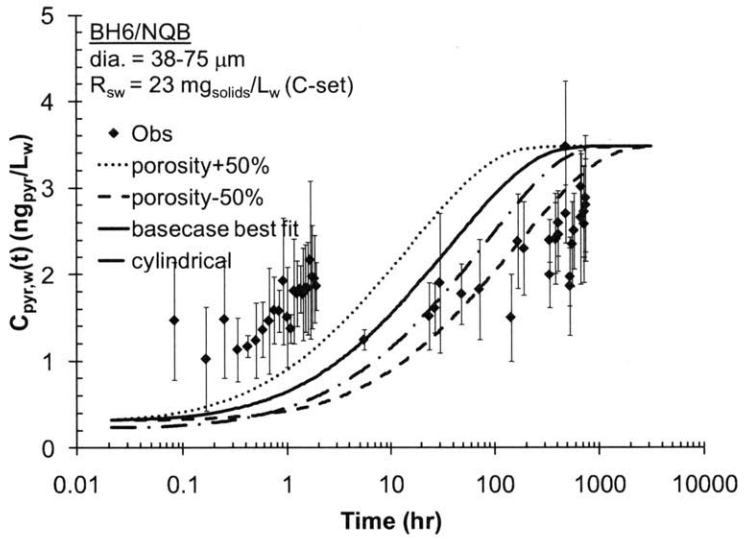

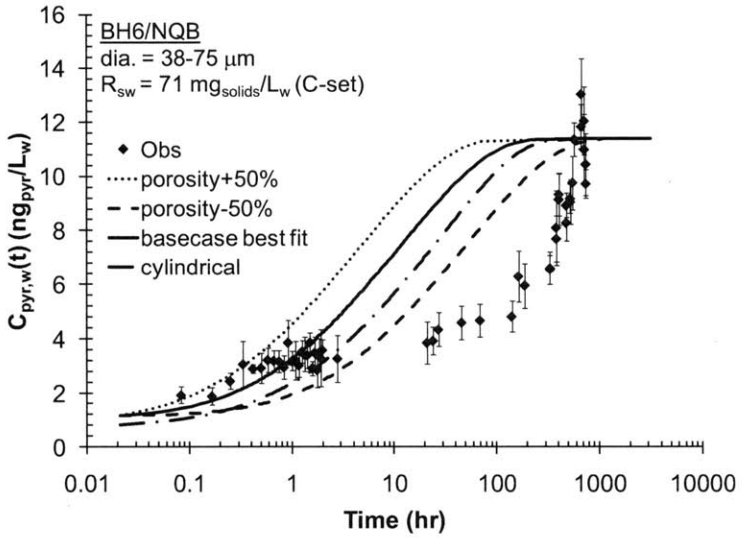

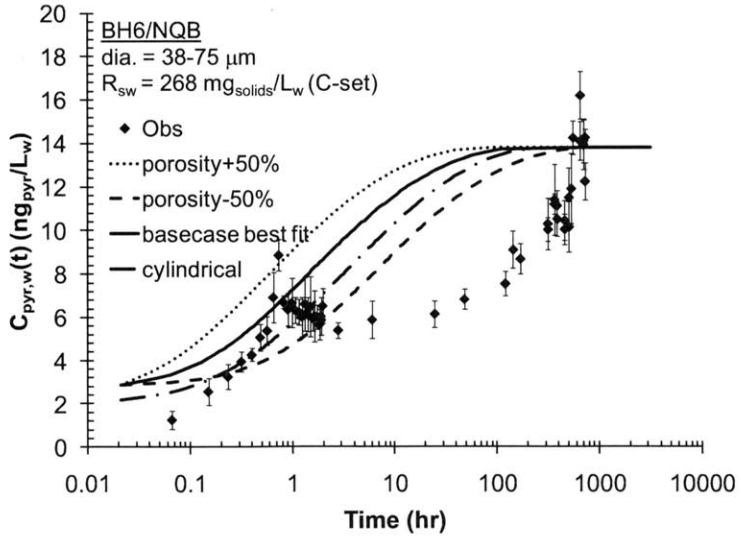

L-set (dia. 38–75 μm) – Sensitivity to Porosity (ϕ) and Shape Factor (SF)

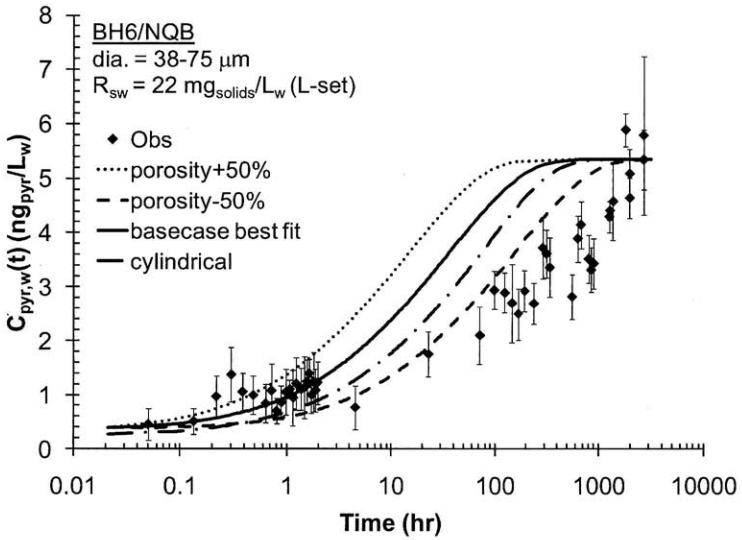

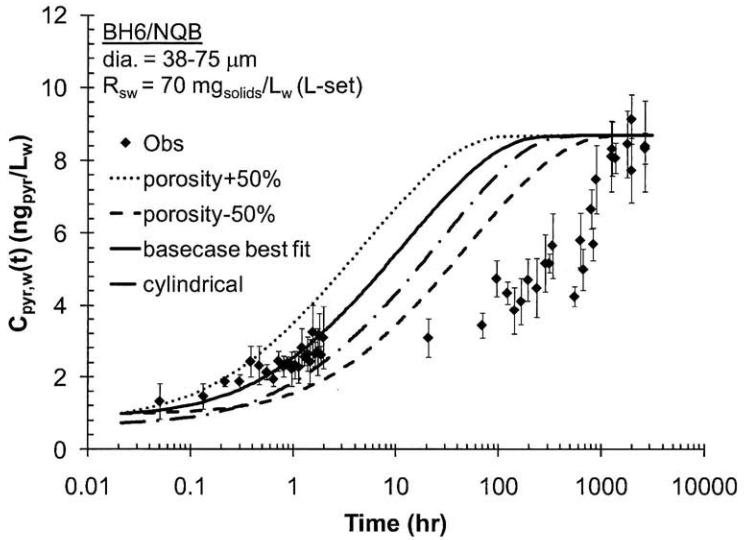

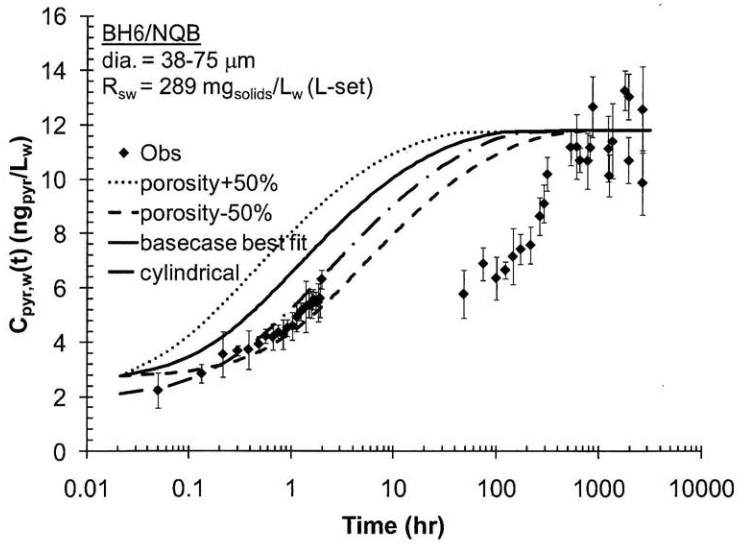

K-set (dia. 75–106 μm) – Sensitivity to Porosity (ϕ) and Shape Factor (SF)

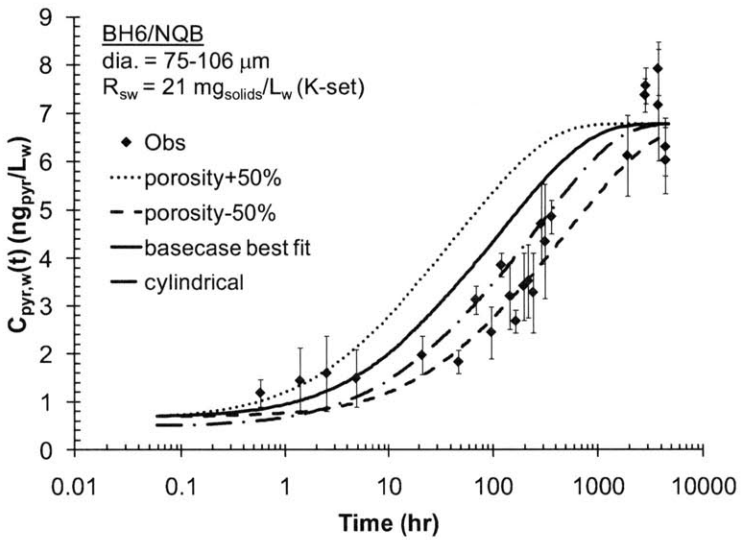

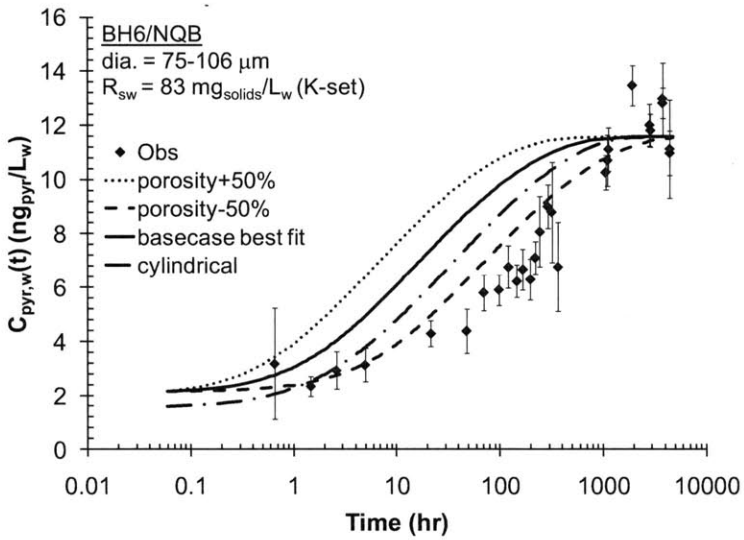

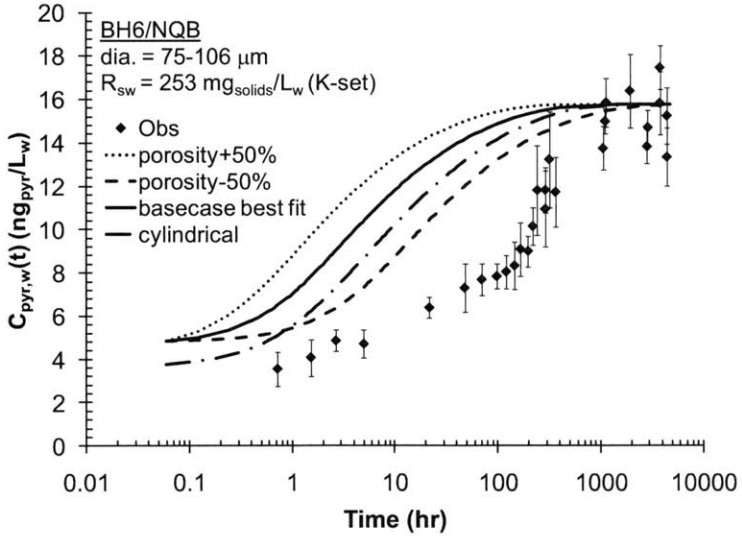

IHG-set (dia. 180–250 μm) – Sensitivity to Porosity (ϕ) and Shape Factor (SF)

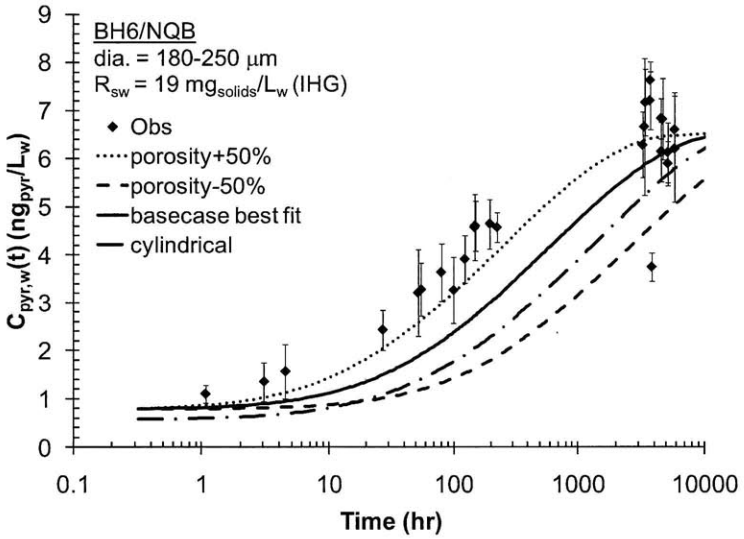

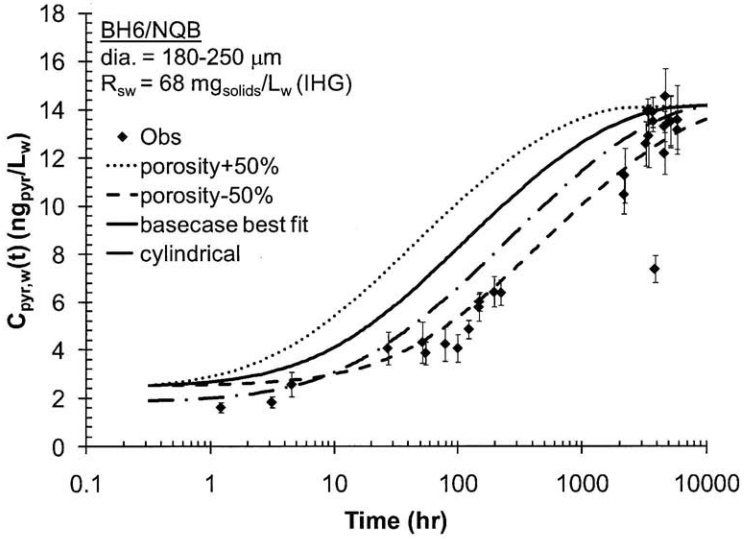

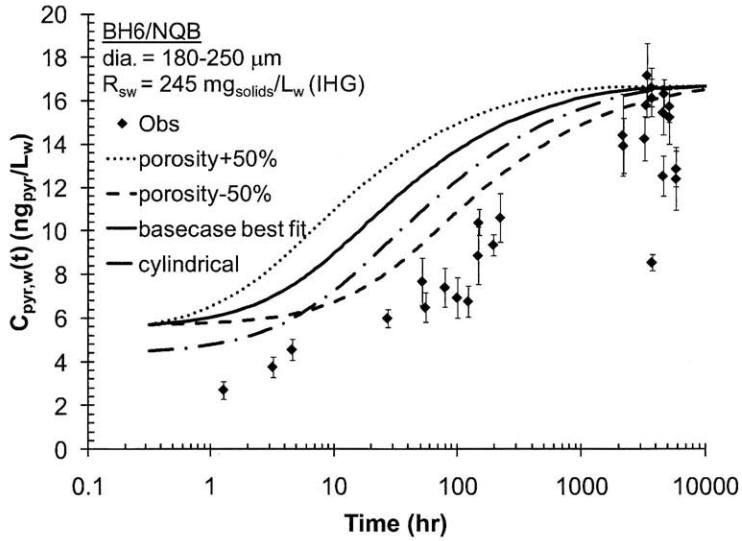

Appendix 7 - 10. Estimation of Numbers of BC Particles in Typical Natural Aggregates.

(i) nm-scale BC (e.g. soot)

Aggregate¤	$Vol._{Agg}$ (m^3)	$Mass_{Agg}$ (kg)	$Mass_{BC}$ (kg_{BC})	Soot radius (nm)	ρ_s (kg/L)	$Mass_{One.Soot}$ (kg)	Soot/Agg.†	Clusters/Agg*
r=100 μm ϕ=0.50	4.2×10^{-12}	5.2×10^{-9}	1.0×10^{-11}	10 25 50	2.2	9.2×10^{-21} 1.4×10^{-19} 1.2×10^{-18}	1.1×10^{9} 7.3×10^{7} 9.1×10^{6}	2.3×10^{7} 1.5×10^{6} 1.8×10^{5}
r=100 μm ϕ=0.25	4.2×10^{-12}	7.9×10^{-9}	1.6×10^{-11}	10 25 50	2.2	9.2×10^{-21} 1.4×10^{-19} 1.2×10^{-18}	1.7×10^{9} 1.1×10^{8} 1.4×10^{7}	3.4×10^{7} 2.2×10^{6} 2.7×10^{5}
r=50 μm ϕ=0.5	5.2×10^{-13}	6.5×10^{-10}	1.3×10^{-12}	10–50	2.2	1.2×10^{-18}– 9.2×10^{-21}	1.1×10^{6}– 1.4×10^{8}	2.3×10^{4}– 2.8×10^{6}
ϕ=0.25		9.8×10^{-10}	2.0×10^{-12}				1.7×10^{6}– 2.1×10^{8}	3.4×10^{4}– 4.3×10^{6}
r=20 μm ϕ=0.5	3.4×10^{-14}	4.2×10^{-11}	8.4×10^{-14}	10–50	2.2	1.2×10^{-18}– 9.2×10^{-21}	7.3×10^{4}– 9.1×10^{6}	1.5×10^{3}– 1.8×10^{5}
ϕ=0.25		6.3×10^{-11}	1.3×10^{-13}				1.1×10^{5}– 1.4×10^{7}	2.2×10^{3}– 2.7×10^{5}

¤: Density of average aggregate solid: $\rho_s = 2.5\ kg_{solids}/L_{agg_solid}$.
†: Estimated number of soot per aggregate.
*: Based on an estimate of 50 spheres per cluster

(ii) primary intra-aggregate grain

Aggregate¤			Grain			
	$Vol._{Agg}$ (m^3)	$Mass_{Agg}$ (kg)	radius (μm)	ρ_s (kg/L)	$Mass_{One.Grain}$ (kg)	Grain/Agg.†
r=100 μm	4.2×10^{-12}	5.2×10^{-9}	0.5	2.5	1.3×10^{-15}	4.0×10^{6}
ϕ=0.50			1		1.0×10^{-14}	5.0×10^{5}
ρ_s=2.5 kg/L			2		8.4×10^{-14}	6.3×10^{4}
			5		1.3×10^{-12}	4.0×10^{3}
r=100 μm	4.2×10^{-12}	7.9×10^{-9}	0.5	2.5	1.3×10^{-15}	6.0×10^{6}
ϕ=0.25			1		1.0×10^{-14}	7.5×10^{5}
ρ_s=2.5 kg/L			2		8.4×10^{-14}	9.4×10^{4}
			5		1.3×10^{-12}	6.0×10^{3}
r=50 μm						
ϕ=0.5	5.2×10^{-13}	6.5×10^{-10}	0.5–5	2.5	1.3×10^{-12}–1.3×10^{-15}	5.0×10^{2}–5.0×10^{5}
ϕ=0.25		9.8×10^{-10}				7.5×10^{2}–7.5×10^{5}
r=20 μm						
ϕ=0.5	3.4×10^{-14}	4.2×10^{-11}	0.5–5	2.5	1.3×10^{-12}–1.3×10^{-15}	3.2×10^{1}–3.2×10^{4}
ϕ=0.25		6.3×10^{-11}				4.8×10^{1}–4.8×10^{4}

¤: Density of average aggregate solid: $\rho_s = 2.5\ kg_{solids}/L_{agg_solid}$.
†: Estimated number of primary grains per aggregate.

(iii) μm-scale BC (e.g. char)

Aggregate¤				Char radius (μm)		Mass$_{One.Char}$ (kg)	Char/Agg.†
	Vol.$_{Agg}$ (m^3)	Mass$_{Agg}$ (kg)	Mass$_{BC}$ (kg_{BC})				
r=100 μm ϕ=0.50	4.2×10^{-12}	5.2×10^{-9}	1.0×10^{-11}	10 20	ρ_s=2 kg/L ϕ=0.25	6.3×10^{-12} 5.0×10^{-11}	1.7 0.2
				10 20	ρ_s=2 kg/L ϕ=0.75	2.1×10^{-12} 1.7×10^{-11}	5.0 0.6
r=100 μm ϕ=0.25	4.2×10^{-12}	7.9×10^{-9}	1.6×10^{-11}	10 20	ρ_s=2 kg/L ϕ=0.25	6.3×10^{-12} 5.0×10^{-11}	2.5 0.3
				10 20	ρ_s=2 kg/L ϕ=0.75	2.1×10^{-12} 1.7×10^{-11}	7.5 0.9
r=50 μm ϕ=0.5	5.2×10^{-13}	6.5×10^{-10}	1.3×10^{-12}	10 20	ρ_s=2 kg/L ϕ=0.25, 0.75	2.1×10^{-12}– 5.0×10^{-11}	0.03–0.6
ϕ=0.25		9.8×10^{-10}	2.0×10^{-12}				0.04–0.9
r=20 μm ϕ=0.5	3.4×10^{-14}	4.2×10^{-11}	8.4×10^{-14}	10 20	ρ_s=2 kg/L ϕ=0.25, 0.75	2.1×10^{-12}– 5.0×10^{-11}	0.002–0.04
ϕ=0.25		6.3×10^{-11}	1.3×10^{-13}				0.003–0.06

¤: Density of average aggregate solid: ρ_s = 2.5 $kg_{solids}/L_{agg_solid}$.
†: Estimated number of soot per aggregate.

Appendix 7 - 11. Local Partitioning Equilibrium Assumption: Timescale Analysis.

(I) Pore-diffusion timescale ($t_{local\ pore\text{-}diffusion}$)

Local pore-diffusion timescale. Pore-diffusion timescale at both the initial desorption period and the end-point can be estimated from the effective pore-water diffusion coefficient, D_{eff} (Wu et al. 1988)

$$D_{eff} = \frac{D_{iw}\,\theta^2}{(1-\theta)\rho_s K_d + \theta}$$

Where D_{iw} is the free aqueous phase diffusion coefficient (m^2/s),

D_{eff} is the effective pore-water diffusion coefficient (m^2/s)

K_d is the solid-water partitioning coefficient of the sorbate (L_w/kg_{solids})

θ is porosity (or pore-water volume fraction) (L_w/L_{agg}),

ρ_s is the solid density (kg_{solids}/L_{solids}).

Since the porosity was often used as a 'fitting' parameter for modeling kinetics (Wu et al. 1988), we may choose θ=0.5 as a more general (or 'neutral') case. K_d is relatively well known for the sediment suspensions at both the initial time and the end-point. With D_{eff} estimated and x_{local}=1μm, the initial $t_{local\ pore\text{-}diffusion}$ is simply:

$$t_{local\ pore-diffusion} = \frac{(x_{local})^2}{D_{eff}}$$

The approximate initial and end-time K_d's, the corresponding D_{eff}'s and $t_{local\ pore\text{-}diffusion}$'s are summarized below:

Suspension	Initial K_d (L/kg)	Initial D_{eff} (m^2/s)	Initial $t_{local\ p\text{-}diff}$ (h)	End-time K_d (L/kg)	End-time D_{eff} (m^2/s)	End-time $t_{local\ p\text{-}diff}$ (h)
A-set						
R_{sw} = 23 mg/L				3.8×10^{5}	4.0×10^{-16}	0.7
= 72 " "	7.4×10^{4}	2.0×10^{-15}	0.14	2.0×10^{5}	7.6×10^{-16}	0.4
= 277 " "				1.6×10^{5}	9.5×10^{-16}	0.3
C-set						
R_{sw} = 23 mg/L				3.4×10^{5}	4.5×10^{-16}	0.6
= 71 " "	7.8×10^{4}	2.0×10^{-15}	0.14	1.0×10^{5}	1.5×10^{-15}	0.2
= 268 " "				1.0×10^{5}	1.5×10^{-15}	0.2
L-set						
R_{sw} = 22 mg/L				2.2×10^{5}	6.9×10^{-16}	0.4
= 70 " "	7.8×10^{4}	2.0×10^{-15}	0.14	1.4×10^{5}	1.1×10^{-15}	0.3
= 289 " "				1.1×10^{5}	1.4×10^{-15}	0.2
K-set						
R_{sw} = 23 mg/L				3.9×10^{5}	3.9×10^{-16}	0.7
= 71 " "	7.8×10^{4}	2.0×10^{-15}	0.14	2.4×10^{5}	6.3×10^{-16}	0.4
= 268 " "				1.9×10^{5}	8.0×10^{-16}	0.3
IHG-set						
R_{sw} = 22 mg/L				7.2×10^{5}	2.1×10^{-16}	1.3
= 70 " "	1.9×10^{4}	8.0×10^{-15}	0.03	3.8×10^{5}	4.0×10^{-16}	0.7
= 289 " "				3.3×10^{5}	4.6×10^{-16}	0.6

Note that ρ_s=2.5 kg_{solids}/L_{solids}, D_{iw}(pyr,25°C) = $7.6\times10^{-10}m^2/s$. The initial K_d'sfor a given set were identical because they referred to the K_d of the native sedimentary pyrene prior to desorption.

(II) Observed desorption timescale ($t_{des,obs}$)

Initial desorption timescale. To assess the experimental desorption timescale, we need to estimate the desorption rate constant. Desorption rate at early time was estimated by the *initial rate* approach. This approach assumes (i) that the initial reaction rate can be expressed by a 1st-order kinetic, (ii) that only insignificant amount of sorbate has desorbed in the initial time such that the solid-phase concentration of the sorbate remains approximately constant. From the above assumptions, we can expression the rate of change in dissolved pyrene concentration as:

$$\left(\frac{dC_{pyr,w}}{dt}\right)_{\text{"early times"}} = k_{obs}\left(C^{s}_{eq} - C_{pyr,w}\right) = k_{obs}\left(S_{pyr,init}K_{d,pyr} - C_{pyr,w}\right)$$

Where $C_{pyr,w}$ is the dissolved phase (i.e. bulk aqueous phase) concentration of pyrene ($\mu g_{pyr}/L_w$),

C^s_{eq} is the *equivalent* dissolved pyrene concentration of the native, sedimentary-bound pyrene ($\mu g_{pyr}/L_w$),

k_{obs} is the 1st order desorption rate constant for pyrene (hr),

$K_{d,pyr}$ is the solid-water partitioning coefficient <u>at the initial condition</u> (L_w/kg_{solids}),

$S_{pyr,init}$ is the initial sedimentary pyrene concentration ($\mu g_{pyr}/kg_{solids}$).

The following equation is obtained upon integration:

$$C_{pyr,w}(t)_{\text{"early times"}} = C^s_{eq}\left(1 - e^{k_{obs}\,t}\right)$$

Or:

$$k_{obs} = \frac{1}{t}\ln\left(\frac{C^s_{eq}}{C^s_{eq} - C_{pyr,w}(t)}\right)$$

Since it is unclear where the 'early times' end, k_{obs} was estimated using two time-frame: one using the first pyrene measurement (dissolved phase) point and the time-zero point (Δt~5 min), and the other using observations within the first hour. Only the 38–75 μm suspensions were measured on minute-scale time-resolution in the first hour. Since desorption should proceed with the smallest size particles/aggregates, the estimated k_{obs}'s would provide the shortest desorption time-scale observable. Hence these k_{obs}'s should give the most stringent case of failing the consistency of local partitioning equilibrium assumption. The k_{obs}'s estimated from the suspensions and the corresponding desorption time-scale, $t_{des,obs}$, are listed in the following table:

Suspension	$k_{5\text{-min}}$ (h^{-1})	$t_{des,obs}$ (h)	$k_{1\text{-hr-lo}}$ (h^{-1})	$t_{des,obs}$ (h)	$k_{1\text{-hr-hi}}$ (h^{-1})	$t_{des,obs}$ (h)
A-set						
R_{sw} = 23 mg/L	0.83	1.2	0.074	14	0.15	6.6
= 72 " "	1.2	0.83	0.058	17	0.22	4.6
= 277 " "	4.2	0.24	0.064	16	0.51	2.0
C-set						
R_{sw} = 23 mg/L	1.07	0.93	0.039	26	0.14	7.1
= 71 " "	1.41	0.71	0.13	7.9	0.31	3.2
= 268 " "	1.13	0.88	0.59	1.7	0.70	1.4
L-set						
R_{sw} = 22 mg/L	0.53	1.9	0.012	83	0.087	12
= 70 " "	1.6	0.63	0.072	14	0.22	4.5
= 289 " "	2.8	0.36	0.159	6.3	0.43	2.3

End-time desorption timescale. The end-time observed desorption timescale was estimated by taking the reciprocal of the end-time desorption rate constant. Empirical multi-compartmental models dividing the ads/desorption kinetics into various regimes have been used to fit HOCs desorption kinetic data (Cornelissen et al. 1997b; van den Heuvel et al. 2003). Here, a modified version of the two-compartment (rapidly and slowly desorbing domains) was used to fit the experimental kinetic data. This end-time desorption rate constant was approximated as the rate constant for the slowly desorbing domain, k_{slow}, in the following two-compartment model:

$$C_{pyr,w} = (S_{slow} - S_{*end})R_{sw}\left(1 - e^{-k_{slow}\,t}\right) + S_{rapid}\,R_{sw}\left(e^{-k_{rapid}\,t} - e^{-k_{slow}\,t}\right)$$

Where $C_{pyr,w}$ is the bulk dissolved phase pyrene concentration ($\mu g_{pyr}/L_w$),

k_{slow} and k_{rapid} are the slowly desorbing domain and the rapidly desorbing domain rate constants, respectively (h^{-1})

R_{sw} is the solid-to-water ratio (kg_{solids}/L_w),

S_{slow} and S_{rapid} are the solid-phase pyrene concentrations in the slowly desorbing and the rapidly desorbing domains, respectively ($\mu g_{pyr}/kg_{solids}$),

S_{*end} is the 'end' point constrain on desorption ($\mu g_{pyr}/kg_{solids}$); here, S_{*end} was taken to be the final equilibrium concentration assuming $\log K_{BC}$=6.5, n_{BC}=0.62, and $\log K_{OC}$=4.7,

t is the desorption time elapsed (h).

The following table summarize end-time k_{slow}'s and $t_{des,obs}$:

Suspension	S_{rapid}	S_{slow}	S_{*end}	k_{rapid}	k_{slow}	$t_{des,obs}$ (h)
A-set						
R_{sw} = 23 mg/L	87	1333	811	1.2	6.0×10^{-5}	1.7×10^{4}
= 72 " "	61	1359	1105	1.0	7.1×10^{-5}	1.4×10^{4}
= 277 " "	21	1399	1315	1.6	6.7×10^{-5}	1.5×10^{4}
C-set						
R_{sw} = 23 mg/L	75	1275	778	4.7	1.4×10^{-4}	7.2×10^{3}
= 71 " "	48	1303	1052	5.3	8.2×10^{-4}	1.2×10^{3}
= 268 " "	24	1326	1247	3.8	6.3×10^{-4}	1.6×10^{3}
L-set						
R_{sw} = 22 mg/L	112	1238	766	0.44	1.5×10^{-4}	6.7×10^{3}
= 70 " "	56	1294	1048	1.0	1.6×10^{-4}	6.4×10^{3}
= 289 " "	27	1324	1253	1.0	1.3×10^{-4}	7.7×10^{3}
K-set						
R_{sw} = 23 mg/L	206	2855	2204	0.010	5.9×10^{-5}	1.7×10^{4}
= 71 " "	99	2961	2754	0.014	7.3×10^{-5}	1.4×10^{4}

= 268 " "	51	3009	2945	0.0096	4.8×10^{-5}	2.1×10^{4}
IHG-set						
R_{sw} = 22 mg/L	252	5168	3969	0.019	1.6×10^{-5}	6.3×10^{4}
= 70 " "	130	5290	4862	0.0075	3.4×10^{-5}	3.0×10^{4}
= 289 " "			5243	0.0090	7.8×10^{-6}	1.3×10^{5}(!)

Note that all S's in unit ug_{pyr}/kg_{solids} and k's in h^{-1}.

Appendix 7 - 12. Derivation of Effective Diffusivities ($D_{eff,pw}$, $D_{eff,OM}$, $D_{eff,surf}$).

Consider a three-compartment division of the intra-aggregate volume, as occupied by pore-water, organic matter, and solids (mineral+BC).

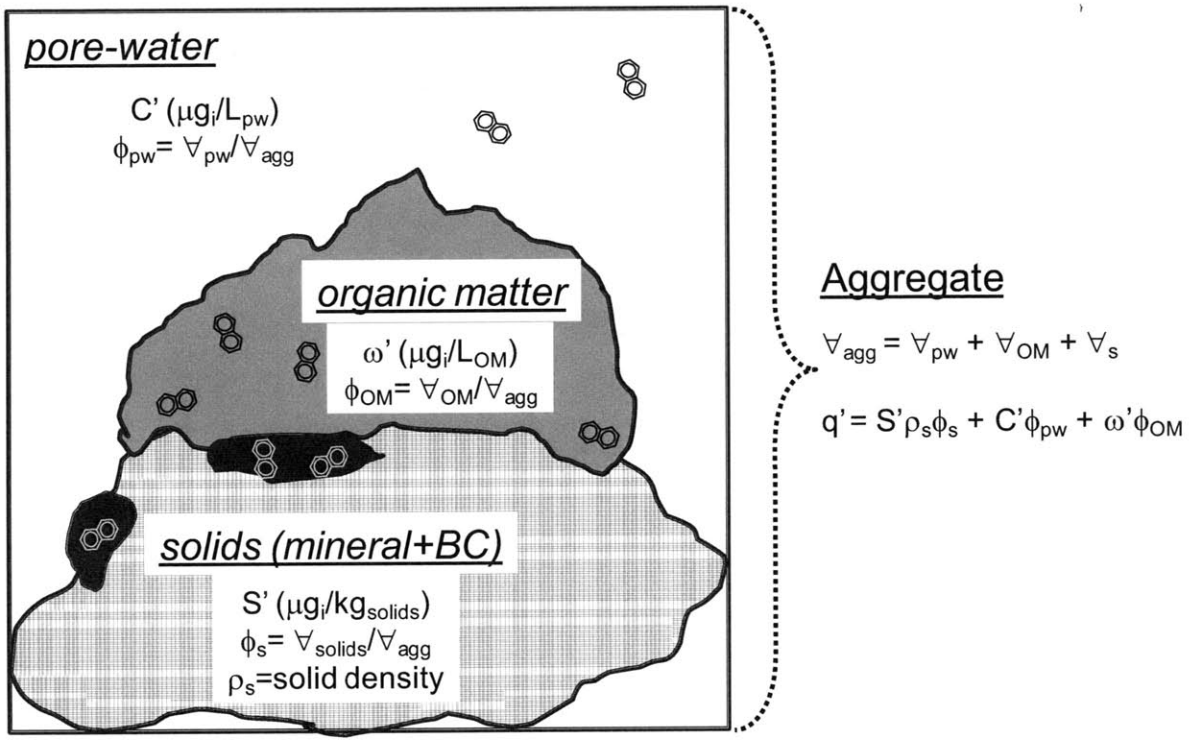

For simplicity, consider 1-D diffusion in planar coordinate. Diffusion of sorbate i in intra-aggregate pore-water, organic matter (OM), and solid surface can be expressed as the following:

$$\frac{\partial C'}{\partial t} = F_{pw}\frac{\partial}{\partial x}\left(D_{iw}\frac{\partial C'}{\partial x}\right);\quad C' \equiv \frac{\text{mass or mol } i}{\text{volume of (pore)water}}$$

$$\frac{\partial S'}{\partial t} = F_{s}\frac{\partial}{\partial x}\left(D_{is}\frac{\partial S'}{\partial x}\right);\quad S' \equiv \frac{\text{mass or mol } i}{\text{mass of solids}}$$

$$\frac{\partial \omega'}{\partial t} = F_{OM}\frac{\partial}{\partial x}\left(D_{iOM}\frac{\partial \omega'}{\partial x}\right);\quad \omega' \equiv \frac{\text{mass or mol } i}{\text{volume of OM}}$$

Eqn. App 7 - 12 - 1

Where C' is the local pore-water sorbate i concentration ($\mu g_i/L_{pw}$),

D_{iw}, D_{is}, and D_{iOM} are the diffusion coefficients of i in pure water, on 'pure' intra-aggregate solid-phase surface, and in 'pure' organic matter (m^2/s)

$D_{eff,pw}$, $D_{eff,OM}$, $D_{eff,surf}$ are the diffusion coefficients in the dimension of aggregate length (irrespective of porewater, OM/OC, BC, or mineral phase) (m^2_{agg}/s).

F_{pw}, F_s, and F_{OM} (tor,cstri) are the diffusive path modifying factors (F's≥1) for porewater, solid-phase, and OM, respectively; they account for tortuosity and constrictivity effects in the particular phase,

S' is the local solid-phase sorbate *i* concentration ($\mu g_i/kg_{solids}$),

t is time (s),

x is distance (m),

ω' is the local OM-phase sorbate *i* concentration ($\mu g_i/L_{OM}$).

We can also evaluate the concentration of the sorbate on the basis of aggregate-volume:

$$q' \equiv \frac{\text{mass or mol } i}{\text{volume of aggregate}} = S'\rho_s\emptyset_s + C'\emptyset_{pw} + \omega'\emptyset_{OM}$$

$$\emptyset_s + \emptyset_{pw} + \emptyset_{OM} = \frac{\forall_s + \forall_{pw} + \forall_{OM}}{\forall_{agg}} = 1$$

Eqn. App 7 - 12 - 2

Where ϕ_s, ϕ_{pw}, and ϕ_{OM} are the volume fractions of solids, porewater, and OM, respectively (L_s/L_{agg}, L_{pw}/L_{agg}, :L_{OM}/L_{agg}),

ρ_s is the average or effective solid-phase density for all solids (mineral, BC impenetrable to sorbate *i*) (kg_{solids}/L_s),

q' is the aggregate-volume based concentration of *i* ($\mu g_i/L_{agg}$),

$\forall_s$, $\forall_{pw}$, $\forall_{OM}$, and $\forall_{agg}$ are the volumes of solid-phase, porewater phase, OM-phase, and aggregate, respectively.

The total diffusive transport of sorbate *i* within the aggregate can be expressed in terms of q' as:

$$\frac{\partial q'}{\partial t} = \frac{\partial}{\partial x}\left(D_{tot,app}\frac{\partial q'}{\partial x}\right)$$

Eqn. App 7 - 12 - 3

From Eqn. App 7 - 12 - 2 it can be shown that:

$$\frac{\partial q'}{\partial t} = \rho_s \emptyset_s \frac{\partial S'}{\partial t} + \emptyset_{pw} \frac{\partial C'}{\partial t} + \emptyset_{OM} \frac{\partial \omega'}{\partial t}$$

$$S' = \frac{q'}{\rho_s \emptyset_s + \frac{C'}{S'} \emptyset_{pw} + \frac{\omega'}{S'} \emptyset_{OM}} = \frac{q'}{\rho_s \emptyset_s + \frac{1}{K'_d} \emptyset_{pw} + \frac{1}{K'_{d-OM}} \emptyset_{OM}}$$

$$C' = \frac{q'}{\frac{S'}{C'} \rho_s \emptyset_s + \emptyset_{pw} + \frac{\omega'}{C'} \emptyset_{OM}} = \frac{q'}{K'_d \rho_s \emptyset_s + \emptyset_{pw} + K'_{OM} \emptyset_{OM}}$$

$$\omega' = \frac{q'}{\frac{S'}{\omega'} \rho_s \emptyset_s + \frac{C'}{\omega'} \emptyset_{pw} + \emptyset_{OM}} = \frac{q'}{K'_{d-OM} \rho_s \emptyset_s + \frac{1}{K'_{OM}} \emptyset_{pw} + \emptyset_{OM}}$$

Eqn. App 7 - 12 - 4

Where $K'_d \equiv S'/C'$ (L_{pw}/kg_{solids}),

$K'_{d\text{-}OM} \equiv S'/\omega'$ (L_{OM}/kg_{solids}),

$K'_{OM} \equiv \omega'/C'$ (L_{pw}/L_{OM}).

Note the assumption of local partitioning equilibrium in the expressions for S', C', and ω' in Eqn. App 7 - 12 - 4. Combining with Eqn. App 7 - 12 - 1, and assuming the D's are independent of position (!!) we get:

$$\frac{\partial q'}{\partial t} = \rho_s \emptyset_s F_s D_{is} \frac{\partial^2 S'}{\partial x^2} + \emptyset_{pw} F_{pw} D_{iw} \frac{\partial^2 C'}{\partial x^2} + \emptyset_{OM} F_{OM} D_{iOM} \frac{\partial^2 \omega'}{\partial x^2}$$

Eqn. App 7 - 12 - 5

Re-expressing S', C', and ω' in terms of q' and other parameters, and with the assumption of {K'_d, $K'_{d\text{-}OM}$, K'_{OM}} all independent of position and concentrations (!!), we get:

$$\frac{\partial q'}{\partial t} = \left\{ \left(\frac{\rho_s \emptyset_s F_s D_{is}}{\rho_s \emptyset_s + \frac{1}{K'_d} \emptyset_{pw} + \frac{1}{K'_{d-OM}} \emptyset_{OM}} \right) + \left(\frac{\emptyset_{pw} F_{pw} D_{iw}}{K'_d \rho_s \emptyset_s + \emptyset_{pw} + K'_{OM} \emptyset_{OM}} \right) + \left(\frac{\emptyset_{OM} F_{OM} D_{iOM}}{K'_{d-OM} \rho_s \emptyset_s + \frac{1}{K'_{OM}} \emptyset_{pw} + \emptyset_{OM}} \right) \right\} \frac{\partial^2 q'}{\partial x^2} = D_{tot,app} \frac{\partial^2 q'}{\partial x^2}$$

Eqn. App 7 - 12 - 6

Hence,

$$\frac{\partial q'}{\partial t} = D_{tot,app}\frac{\partial^2 q'}{\partial x^2}$$

$$D_{tot,app} = D_{eff,pw} + D_{eff,OM} + D_{eff,surf}$$

$$D_{eff,pw} = \frac{\emptyset_{pw} F_{pw} D_{iw}}{K'_d \rho_s \emptyset_s + \emptyset_{pw} + K'_{OM} \emptyset_{OM}}$$

$$D_{eff,OM} = \frac{\emptyset_{OM} F_{OM} D_{iOM}}{K'_{d-OM} \rho_s \emptyset_s + \frac{1}{K'_{OM}} \emptyset_{pw} + \emptyset_{OM}}$$

$$D_{eff,surf} = \frac{\rho_s \emptyset_s F_s D_{is}}{\rho_s \emptyset_s + \frac{1}{K'_d} \emptyset_{pw} + \frac{1}{K'_{d-OM}} \emptyset_{OM}}$$

Eqn. App 7 - 12 - 7

The above diffusivity expressions can be simplified into the more conventional forms encountered in literature. For instance, in the absence of a separate OM phase, we can have the effective pore-water diffusivity expression as in Wu et al. (1988):

$$\emptyset_s = 1 - \emptyset_{pw}$$

$$D_{eff,pw} = \frac{\emptyset_{pw} F_{pw} D_{iw}}{K'_d \rho_s (1 - \emptyset_{pw}) + \emptyset_{pw}} = \frac{\emptyset^2{}_{pw} D_{iw}}{K'_d \rho_s (1 - \emptyset_{pw}) + \emptyset_{pw}} \{\text{assuming } F_{pw} = \emptyset_{pw}\}$$

Eqn. App 7 - 12 - 8

Similarly, the surface diffusivity (without OM diffusion) is:

$$D_{eff,surf} = \frac{\rho_s \emptyset_s F_s D_{is}}{\rho_s \emptyset_s + \frac{1}{K'_d} \emptyset_{pw}} = \frac{K'_d \rho_s (1 - \emptyset_{pw}) F_s D_{is}}{K'_d \rho_s (1 - \emptyset_{pw}) + \emptyset_{pw}}$$

Eqn. App 7 - 12 - 9

Appendix 7 - 13. Volume Analysis of OM-phase in Typical Soil and Sediment.

The porosity in a two-phase system (solids & water) is related to the bulk density (ρ_b; kg_{mass}/L_{bulk}) and the pure phase densities as:

$$\emptyset_w \equiv \frac{\forall_w}{\forall_b} = \frac{\rho_s - \rho_b}{\rho_s - \rho_w}$$

Where ϕ_w is the porosity or water-volume fraction (L_w/L_{bulk} or L_w/L_{agg}),

ρ_s, ρ_w, are the pure solid and pure water densities (kg_{solids}/L_{solids} or kg_w/L_w),

$\forall_s$, $\forall_w$ are the volumes of solid-phase, water phase, respectively.

To estimate void volume fraction in typical soil and sediment, we first construct an effective solid density ($\rho_{eff,s}$; kg_{mass}/L_{mass}) which include both the mineral phase (ρ_s = 2.65 kg_s/L_s) and the OM phase (ρ_{OM} = 0.9–1.3 kg_{OM}/L_{OM}):

$$\rho_{eff,s} = f_s \rho_s + f_{OM}\, \rho_{OM}$$

Where f_s, f_{OM} are the mass fractions of mineral solids and OM, respectively.

Hence the effective solid density (mineral+OM) $\rho_{eff,s}$ ranges from about 2.45 – 2.55 kg_{mass}/L_{mass}.

Void Fraction and OM-volume Fraction (Typical Unconsolidated Soil)

Supposing (i) typical unconsolidated soil/sediment f_{OC} ranges from 2–5 %, (ii) $f_{OM} \approx 2f_{OC}$, $f_{OM} \approx$ 5–10%, (iii) typical soil bulk density to be around 1.2–1.4 kg_{mass}/L_{bulk} (e.g. Saini 1966) and (iv) soil water content contributes insignificantly to bulk density (!!), the soil void and OM volumes can be estimated:

ρ_s (kg_s/L_s)		2.65		
ρ_{OM} (kg_{OM}/L_{OM})	0.9	0.9	1.3	1.3
f_s (kg_s/kg_{mass})	0.95	0.9	0.95	0.9
$\rho_{eff,s}$ (kg_{mass}/L_{mass})	2.5625	2.475	2.5825	2.515
ρ_{air} (kg_{air}/L_{air})		0.0012		
ρ_b (kg_{mass}/L_{bulk})		$\phi_{void,soil}=\forall_{void}/\forall_{bulk}$		
1.2	0.53	0.52	0.54	0.52
1.3	0.49	0.47	0.50	0.48
1.4	0.45	0.43	0.46	0.44
ρ_b (kg_{mass}/L_{bulk})		$\phi_{OM,soil}=\forall_{OM}/\forall_{bulk}$		
1.2	0.067	0.133	0.046	0.092
1.3	0.072	0.144	0.050	0.100
1.4	0.078	0.156	0.054	0.108

Void Fraction and OM-volume Fraction (Typical Unconsolidated Sediment)

Supposing (i) typical unconsolidated soil/sediment f_{OC} ranges from 2–5 %, (ii) $f_{OM} \approx 2f_{OC}$, $f_{OM} \approx 5$–10%, (iii) typical sediment bulk density to be around 1.05–1.25 kg_{mass}/L_{bulk} (marine; Migniot 1968; Nichols et al. 1985; Li et al. 1991) and 1.2–1.4 kg_{mass}/L_{bulk} (riverine; Li et al. 1991), and (iv) intra-aggregate void space filled with pore-water ($\rho_w \approx 1$ kg_w/L_w), the sediment void and OM volumes can be estimated:

ρ_s (kg_s/L_s)	2.65			
ρ_{OM} (kg_{OM}/L_{OM})	0.9	0.9	1.3	1.3
f_s (kg_s/kg_{mass})	0.95	0.9	0.95	0.9
$\rho_{eff,s}$ (kg_{mass}/L_{mass})	2.5625	2.475	2.5825	2.515
ρ_w (kg_w/L_w)	1			
ρ_b (kg_{mass}/L_{bulk})	$\phi_{void,sed}=\forall_{void}/\forall_{bulk}$			
1.05	0.97	0.97	0.97	0.97
1.25	0.84	0.83	0.84	0.83
1.2	0.87	0.86	0.87	0.87
1.4	0.74	0.73	0.75	0.74
ρ_b (kg_{mass}/L_{bulk})	$\phi_{OM,sed}=\forall_{OM}/\forall_{bulk}$			
1.05	0.058	0.117	0.040	0.081
1.25	0.069	0.139	0.048	0.096
1.2	0.067	0.133	0.046	0.092
1.4	0.078	0.156	0.054	0.108

Ratio of OM-volume to Total (Void-OM)-volume in Typical Soil/Sediment

Soil (Unconsolidated; f_{OM} ~ 5–10%)				
ρ_b (kg_{mass}/L_{bulk})	$\phi_{OM,soil}/(\phi_{OM,soil}+\phi_{void,soil})$			
1.2	***0.11***	***0.21***	***0.08***	***0.15***
1.3	***0.13***	***0.23***	***0.09***	***0.17***
1.4	***0.15***	***0.26***	***0.11***	***0.20***
Sediment (Unconsolidated; f_{OM} ~ 5–10%)				
ρ_b (kg_{mass}/L_{bulk})	$\phi_{OM,sed}/(\phi_{OM,sed}+\phi_{void,sed})$			
1.05	***0.06***	***0.11***	***0.04***	***0.08***
1.25	***0.08***	***0.14***	***0.05***	***0.10***
1.2	***0.07***	***0.13***	***0.05***	***0.10***
1.4	***0.09***	***0.18***	***0.07***	***0.13***

Appendix 7 - 14. Derivation of Equations for Intra-aggregate Porewater Diffusion Model.

Basic Relationships/Equations

$$\textbf{Dimensionless Length:} \quad x = \frac{r}{R}; \qquad dx = \frac{dr}{R}$$

$$\textbf{Dimensionless Time:} \quad \tau = \frac{tD_{iw}}{R^2}; \qquad d\tau = \frac{D_{iw}\,dt}{R^2}$$

$$\textbf{Flux:} \quad N = -D_{iw}\frac{\partial C}{\partial r}$$

In this appendix, note that:

$\mathbf{A_{in}}$ and $\mathbf{A_{out}}$ are surface area for the fluxes of the sorbate into and out of the shell (m^2),

$\mathbf{N_{in}}$ and $\mathbf{N_{out}}$ are the diffusive fluxes of the sorbate into and out of the shell ($\mu g_i/m^2.s$),

$\forall$ is the shell volume.

For volumes, areas, and **Shape Factor** γ:

$$\textbf{Spherical:} \quad \forall = \frac{4}{3}\pi r^3; \qquad A = 4\pi r^2; \qquad \gamma = 3$$

$$\textbf{Cylindrical:} \quad \forall = \pi r^2 h; \qquad A = 2\pi r h; \qquad \gamma = 2$$

$$\textbf{Planar:} \quad \forall = rhw; \qquad A = hw; \qquad \gamma = 1$$

Finally, the local sorbate concentration, C', and the local aggregate-volume based sorbate concentration, q', are related in the following ways:

$$q' = S'\rho_s(1-\emptyset) + C'\emptyset = [K_d\rho_s(1-\emptyset) + \emptyset]C'$$

$$\frac{\partial q'}{\partial t} = \emptyset\frac{\partial C'}{\partial t} = \emptyset F_{Tor}\frac{\partial C}{\partial t}$$

Where ϕ is the intra-aggregate porosity (or volume fraction of porewater phase) (L_{pw}/L_{agg}),

C' is the local pore-water sorbate concentration ($\mu g_i/L_{pw}$),

C is the free water (i.e., diffusion in the absence of all solids) sorbate concentration ($\mu g_i/L_w$),

q' is the local aggregate-volume based concentration of the sorbate ($\mu g_i/L_{agg}$).

Intermediate-Shell

Assuming diffusion occurs only in one spatial dimension:

$$\frac{\partial C}{\partial t}\forall = N_{in}A_{in} - N_{out}A_{out} = \left(-D_{iw}\frac{\partial C}{\partial r}\Big|_{r} A_r\right) - \left(-D_{iw}\frac{\partial C}{\partial r}\Big|_{r+\Delta r} A_{r+\Delta r}\right)$$

Upon expansion and re-arrangement, it can be shown that:

Spherical: $$\frac{\partial C}{\partial t} = \frac{1}{r^2}\frac{\partial}{\partial r}\left(D_{iw}r^2\frac{\partial C}{\partial r}\right)$$

Cylindrical: $$\frac{\partial C}{\partial t} = \frac{1}{r}\frac{\partial}{\partial r}\left(D_{iw}r\frac{\partial C}{\partial r}\right)$$

Planar: $$\frac{\partial C}{\partial t} = D_{iw}\frac{\partial^2 C}{\partial r^2}$$

The governing equation in the dimensionless form is hence:

$$\boxed{\frac{\partial q'}{\partial \tau} = \emptyset F_{Tor}\frac{1}{x^{\gamma-1}}\left[\frac{\partial}{\partial x}\left(x^{\gamma-1}\frac{\partial C'}{\partial x}\right)\right]}$$

Core-Shell

Assuming diffusion occurs only in one spatial dimension:

$$\left(\frac{\partial C}{\partial t}\forall\right)_{core} = N_{in}A_{in} - N_{out}A_{out}$$

Because there is no in-flux into the core shell (i.e. symmetrical profile at core, so gradient=0), thus $N_{in}A_{in} = 0$. Therefore we get:

Spherical: $$\left(\frac{\partial C}{\partial t}\right)_{core} = \frac{3D_{iw}}{r}\frac{\partial C}{\partial r}$$

Cylindrical: $$\left(\frac{\partial C}{\partial t}\right)_{core} = \frac{2D_{iw}}{r}\frac{\partial C}{\partial r}$$

Planar: $$\left(\frac{\partial C}{\partial t}\right)_{core} = \frac{D_{iw}}{r}\frac{\partial C}{\partial r}$$

Or in dimensionless form (with $\partial q'/\partial t = \phi \partial C'/\partial t$):

$$\boxed{\left(\frac{\partial q'}{\partial \tau}\right)_{core} = \emptyset F_{Tor}\frac{\gamma}{x}\frac{\partial C'}{\partial x}}$$

Aggregate-Averaged Properties

The aggregate-volume averaged property, J, are calculated as:

$$J = \frac{\int_{\forall} j d\forall}{\forall_{agg}}$$

Spherical: $$J = \frac{\int_0^{R_{agg}} j 4\pi r^2 dr}{4\pi {R_{agg}}^3/3} = \frac{3\int_0^{R_{agg}} j r^2 dr}{{R_{agg}}^3}$$

Cylindrical: $$J = \frac{\int_0^{R_{agg}} j 2\pi r h dr}{h\pi {R_{agg}}^2} = \frac{2\int_0^{R_{agg}} j r dr}{{R_{agg}}^2}$$

Planar: $$J = \frac{\int_0^{R_{agg}} j h w dr}{h w R_{agg}} = \frac{\int_0^{R_{agg}} j dr}{R_{agg}}$$

Where R_{agg} is the aggregate radius (m),

$\forall_{agg}$ is the aggregate volume (m^3).

Hence in dimensionless form:

$$\boxed{J = \gamma \int_0^1 j x^{\gamma-1} dx}$$

Edge Shell

(i) Boundary Layer Diffusion

The edge shell is influenced by the influx from the inner shells and the outflux through the boundary layer film:

$$\frac{\partial C}{\partial t}\forall = (N_{in}A_{in})_{R-} - (N_{out}A_{out})_{\delta} = \left(-D_{iw}\left.\frac{\partial C}{\partial r}\right|_{R-} A_{R-}\right) - \left(-D_{iw}\left.\frac{\partial C}{\partial r}\right|_{R+} A_{R+}\right)$$

Where:

$$\left.\frac{\partial C}{\partial r}\right|_{R+} = \frac{(C_{bulk} - C)}{\delta}$$

Supposing the influx and the outflux areas are approximately equal ($A_{R+} \approx A_{R-}$), then:

Spherical: $$\left(\frac{\partial C}{\partial t}\right)_{edge} = \frac{3}{R}\left\{-D_{iw}\left.\frac{\partial C}{\partial r}\right|_{R-} + D_{iw}\frac{(C_{bulk} - C)}{\delta}\right\}$$

Cylindrical: $$\left(\frac{\partial C}{\partial t}\right)_{edge} = \frac{2}{R}\left\{-D_{iw}\left.\frac{\partial C}{\partial r}\right|_{R-} + D_{iw}\frac{(C_{bulk} - C)}{\delta}\right\}$$

Planar:
$$\left(\frac{\partial C}{\partial t}\right)_{edge} = \frac{1}{R}\left\{-D_{iw}\left.\frac{\partial C}{\partial r}\right|_{R-} + D_{iw}\frac{(C_{bulk} - C)}{\delta}\right\}$$

In dimensionless form,

$$\boxed{\left(\frac{\partial q'}{\partial \tau}\right)_{edge} = \gamma\left\{-\emptyset F_{Tor}\left.\frac{\partial C'}{\partial x}\right|_{R-} + \frac{(C_{bulk} - C')}{\delta/R}\right\}}$$

Note that the porosity penalty and the tortuosity/constrictivity factor do not apply to diffusion through the boundary layer film.

(ii) Mass Balance Approach

Conservation of sorbate mass in an closed system gives:

$$\forall_{one\ agg.}\frac{dQ}{dt} + \forall_{bulk\ aq.\ one\ agg.}\frac{dC_{bulk}}{dt} = 0$$

Where C_{bulk} is the bulk aqueous phase sorbate concentration ($\mu g_i/L_w$),

$\forall_{one\ agg.}$ is the volume for one aggregate (m^3),

$\forall_{bulk\ aq.\ one\ agg.}$ is the volume of bulk aqueous phase for one aggregate (m^3),

Q is the overall averaged aggregate-volume sorbate concentration ($\mu g_i/L_{agg}$).

Since:

$$Q = \frac{\int_{\forall_{agg}} q'd\forall}{\forall_{agg}} = \frac{\int_{\forall_{core}+\forall_{intrm.}} q'd\forall}{\forall_{core} + \forall_{intrm.}} + \frac{\int_{\forall_{edge}} q'_{edge}\, d\forall}{\forall_{edge}}$$

Therefore:

$$\boxed{\frac{d}{dt}\left(\frac{\int_{\forall_{core}+\forall_{intrm.}} q'd\forall}{\forall_{core} + \forall_{intrm.}}\right) = -R_{bulk\ aq./agg}\frac{dC_{bulk}}{dt} - \frac{d}{dt}\left(\frac{\int_{\forall_{edge}} q'_{edge}\, d\forall}{\forall_{edge}}\right)}$$

Where $\forall_{core}$, $\forall_{intrm.}$, and $\forall_{edge}$ are the aggregate volumes of core, intermediate, and the edge shells, respectively (m^3),

$R_{bulk\ aq./agg}$ is the ratio of bulk aqueous phase volume to aggregate volume.

Appendix 7 - 15. Derivation of the C_{bulk} (or C_m)finite difference equation at the $(n+1)^{th}$ time step.

The non-linear finite difference equation was re-arranged to increase computational efficiency (i.e. to minimize repetitive computation involved in each timestep). More specifically, the author would like to show that:

$$\mathcal{A}_{1st}\,C'_m{}^{n+1} + \mathcal{A}_{nBC}\left(C'_m{}^{n+1}\right)^{nBC} = \left(C^n{}_{bulk} + \frac{\forall_{total\ agg.}\,Q^n}{\forall_{bulk\ aq.}} - \mathcal{B}\right)$$

where the three constants are:

$$\mathcal{A}_{1st} = \left\{1 + \frac{\forall_{total\ agg.}}{\forall_{bulk\ aq.}}\left(\frac{\gamma\Delta x}{3}\mathcal{S}_m x_m{}^{\gamma-1}\right)\left[f_{OC,m}K_{OC}\rho_s(1-\emptyset_m) + \emptyset_m\right]\right\}$$

$$\mathcal{A}_{nBC} = \left\{\frac{\forall_{total\ agg.}}{\forall_{bulk\ aq.}}\left(\frac{\gamma\Delta x}{3}\mathcal{S}_m x_m{}^{\gamma-1}\right)\left[f_{BC,m}K_{BC}\rho_s(1-\emptyset_m)\right]\right\}$$

$$\mathcal{B} = \left\{\frac{\forall_{total\ agg.}}{\forall_{bulk\ aq.}}\frac{\gamma\Delta x}{3}\left(\sum_{i=1}^{m-1}\mathcal{S}_i q'_i{}^{n+1} x_i{}^{\gamma-1}\right)\right\}$$

From pyrene mass balance between the n^{th} and the $(n+1)^{th}$ steps:

$$\forall_{bulk\ aq.}\frac{\partial C_{bulk}}{\partial t} + \forall_{total\ agg.}\frac{\partial Q}{\partial t} = 0$$

$$\frac{\forall_{bulk\ aq.}}{\forall_{total\ agg.}}\left(C^{n+1}{}_{bulk} - C^n{}_{bulk}\right) = -\left(Q^{n+1} - Q^n\right)$$

(Eqn. 7-15a)

where: n denotes the variable at n^{th} dimensionless timestep (i.e. 'current' state),

n+1 denotes the variable at the $n+1^{th}$ timestep (i.e. 'next' state),

$\forall_{total\ agg.}$ is the volume of aggregate (m^3),

$\forall_{bulk\ aq.}$ is the volume of bulk aqueous phase (m^3),

C_{bulk} is the bulk aqueous phase pyrene concentration ($\mu g/L_w$),

Q is the aggregate-averaged pyrene concentration ($\mu g/L_{agg}$).

Both C^{n}_{bulk} and Q^{n} are known quantities at n^{th} time step; the only unknown in the above equation is C^{n+1}_{bulk} and Q^{n+1}. Furthermore, Q^{n+1} can be re-expressed in terms of C^{n+1}_{bulk}, and so the mass balance equation at the $(n+1)^{th}$ time step can be solved. Q^{n+1} is simply:

$$Q^{n+1} \cong \frac{\gamma \Delta x}{3}\left[\left(\sum_{i=1}^{m-1} \mathcal{S}_i q'_i{}^{n+1} x_i{}^{\gamma-1}\right) + \mathcal{S}_m q'_m{}^{n+1} x_m{}^{\gamma-1}\right]$$

(Eqn. 7-15b)

where: $\mathcal{S}_i$ is the i^{th} coefficient (i.e. 1, 4, 2, 4, ..., 4, 1) following Simpson's 1/3 integration rule,

$\mathcal{S}_m$ is the m^{th} coefficient = 1,

q_i' is the *local* aggregate-volume based pyrene concentration in the inner grids ($\mu g/L_{agg}$),

x_i is the dimensionless spatial variable (dimensionless),

Δx is the spatial distance between two adjacent grids (dimensionless),

γ is the shape factor (dimensionless),

m is the number of grids.

The known in (Eqn. 7-15b) is $q'_m{}^{n+1}$, which can be related to the local solid-phase and local porewater pyrene concentrations in the following way:

$$q'_m{}^{n+1} = S'_m{}^{n+1}\rho_s(1-\phi_m) + \phi_m C'_m{}^{n+1}$$

(Eqn. 7-15c)

where ϕ_m is the intra-aggregate porosity (or volume fraction of porewater phase) at the m^{th} grid (L_{pw}/L_{agg}),

ρ_s is the solid density (kg_{solids}/L_{solids}),

C'_m is the local pore-water pyrene concentration ($\mu g/L_{pw}$),

S'_m is the local solid-phase pyrene concentration ($\mu g/kg_{solids}$),

Supposing the equilibrium partitioning of pyrene is valid at the local level and that the isotherm assumes an linear-OC-Freundlich-BC form (Eqn. 7-15d), $q'_m{}^{n+1}$ can be re-expressed in terms of fOC, f_{BC}, K_{OC}, and K_{BC}:

$$S' = f_{OC} K_{OC} C' + f_{BC} K_{BC} C'^{nBC}$$

(Eqn. 7-15d)

$$q'_m{}^{n+1} = \left[f_{OC} K_{OC} C'_m{}^{n+1} + f_{BC} K_{BC} \left(C'_m{}^{n+1}\right)^{nBC}\right] \rho_b + \phi_m C'_m{}^{n+1}$$

(Eqn. 7-15e)

where: ρ_b is the bulk, local aggregate density $\rho_b=\rho_s(1-\phi)$ (kg_{solids}/L_{agg}).

Let $\alpha=f_{OC}K_{OC}$ and $\beta=f_{BC}K_{BC}$, and re-arranging Eqn. 7-15e further, one gets:

$$q'_m{}^{n+1} = (\alpha\rho_b + \phi_m) C'_m{}^{n+1} + \beta\rho_b \left(C'_m{}^{n+1}\right)^{nBC}$$

(Eqn. 7-15f)

Note that $C'_m{}^{n+1}$ is simply $C^{n+1}{}_{bulk}$ since the edge shell is in contact with the bulk phase.

Substituting Eqn. 7-15f and 7-15b into Eqn. 7-15a, one gets:

$$C^{n+1}{}_{bulk} = C^n{}_{bulk} + Q^n \frac{\forall_{total\ agg.}}{\forall_{bulk\ aq.}} - Q^{n+1} \frac{\forall_{total\ agg.}}{\forall_{bulk\ aq.}}$$

$$C^{n+1}{}_{bulk} = C^n{}_{bulk} + Q^n \frac{\forall_{total\ agg.}}{\forall_{bulk\ aq.}} - \frac{\forall_{total\ agg.}}{\forall_{bulk\ aq.}} \frac{\gamma\Delta x}{3} \left[\left(\sum_{i=1}^{m-1} \mathcal{S}_i q'_i{}^{n+1} x_i{}^{\gamma-1}\right) + \mathcal{S}_m q'_m{}^{n+1} x_m{}^{\gamma-1}\right]$$

$$C^{n+1}{}_{bulk} = C^n{}_{bulk} + Q^n \frac{\forall_{total\ agg.}}{\forall_{bulk\ aq.}} - \frac{\forall_{total\ agg.}}{\forall_{bulk\ aq.}} \frac{\gamma\Delta x}{3} \left(\sum_{i=1}^{m-1} \mathcal{S}_i q'_i{}^{n+1} x_i{}^{\gamma-1}\right) - \frac{\forall_{total\ agg.}}{\forall_{bulk\ aq.}} \frac{\gamma\Delta x}{3} \mathcal{S}_m x_m{}^{\gamma-1} q'_m{}^{n+1}$$

$$C^{n+1}{}_{bulk} = C^n{}_{bulk} + Q^n \frac{\forall_{total\ agg.}}{\forall_{bulk\ aq.}} - \frac{\forall_{total\ agg.}}{\forall_{bulk\ aq.}} \frac{\gamma\Delta x}{3} \left(\sum_{i=1}^{m-1} \mathcal{S}_i q'_i{}^{n+1} x_i{}^{\gamma-1}\right) - \frac{\forall_{total\ agg.}}{\forall_{bulk\ aq.}} \frac{\gamma\Delta x}{3} \mathcal{S}_m x_m{}^{\gamma-1} [(\alpha\rho_b + \phi_m) C'_m{}^{n+1} + \beta\rho_b \left(C'_m{}^{n+1}\right)^{nBC}]$$

(Eqn. 7-15g)

If we let:

$$\mathcal{B} = \left\{\frac{\forall_{total\ agg.}}{\forall_{bulk\ aq.}} \frac{\gamma\Delta x}{3} \left(\sum_{i=1}^{m-1} \mathcal{S}_i q'_i{}^{n+1} x_i{}^{\gamma-1}\right)\right\}$$

Then Eqn. 7-15g can be simplified into:

$$C'_m{}^{n+1} = \left(C^n{}_{bulk} + \frac{\forall_{total\ agg.} Q^n}{\forall_{bulk\ aq.}} - \mathcal{B} \right) - \frac{\forall_{total\ agg.}}{\forall_{bulk\ aq.}} \frac{\gamma \Delta x}{3} \mathcal{S}_m x_m{}^{\gamma-1} [(\alpha \rho_b + \phi_m) C'_m{}^{n+1} + \beta \rho_b (C'_m{}^{n+1})^{nBC}]$$

Re-arranging coefficients in terms of $C'_m{}^{n+1}$, one gets:

$$\mathcal{A}_{1st} C'_m{}^{n+1} + \mathcal{A}_{nBC} (C'_m{}^{n+1})^{nBC} = \left(C^n{}_{bulk} + \frac{\forall_{total\ agg.} Q^n}{\forall_{bulk\ aq.}} - \mathcal{B} \right)$$

(Eqn. 7-15h)

where the three constants are:

$$\mathcal{A}_{1st} = \left\{ 1 + \frac{\forall_{total\ agg.}}{\forall_{bulk\ aq.}} \left(\frac{\gamma \Delta x}{3} \mathcal{S}_m x_m{}^{\gamma-1} \right) [f_{OC,m} K_{OC} \rho_s (1 - \emptyset_m) + \emptyset_m] \right\}$$

$$\mathcal{A}_{nBC} = \left\{ \frac{\forall_{total\ agg.}}{\forall_{bulk\ aq.}} \left(\frac{\gamma \Delta x}{3} \mathcal{S}_m x_m{}^{\gamma-1} \right) [f_{BC,m} K_{BC} \rho_s (1 - \emptyset_m)] \right\}$$

$$\mathcal{B} = \left\{ \frac{\forall_{total\ agg.}}{\forall_{bulk\ aq.}} \frac{\gamma \Delta x}{3} \left(\sum_{i=1}^{m-1} \mathcal{S}_i q'_i{}^{n+1} x_i{}^{\gamma-1} \right) \right\}$$

Appendix 7 - 16. "Universal" Isotherm ($logK_{OC}$, $logK_{BC}$) for Pyrene.

From Table 5-9 in Chapter 5:

	$logK_{OC}$ (L_w/kg_{OC})			$logK_{BC}$ ($\mu g_{pyr}/kg_{BC}$)($L_w/\mu g_{pyr}$)^{nBC}		
	low	high	mean	low	high	mean
Sediment	4.5	5	***4.75***	5.6	6.3	***5.95***
Freshwater				5.6	6.1	*5.85*
Marine				5.8	6.3	*6.05*
Soil/soil fractions	4.5	5.7	***5.1***	4.5	5.7	***5.1***
Sed/soil/soil frac.	4.5	5.7	***5.1***	5.6	6.3	***5.95***

Appendix 7 - 17. n_{BC} Best-Fit Modeling of the Observed Desorption Kinetic Profiles of Pyrene ($C_{pyr,w}$) by the New-OC-BC isotherm and the sedimentary Universal-OC-BC isotherm.

For visual clarity, the baseline New-OC-BC (n_{BC}=0.25±0.09) profiles, as well as the upper & lower-bound of the Occlusion-OC-BC profiles (i.e. n_{BC}=0.42±0.12) were omitted.

	Best-fitted n_{BC}	
	New-OC-BC ($logK_{OC}$ = 5.25 $logK_{BC}$ = 6.25)	Universal-OC-BC ($logK_{OC}$ = 4.75 $logK_{BC}$ = 5.95)
Dia.38–75 μm		
A-set		
23 ppm	0.28	0.16
72	0.31	0.17
277	0.32	0.17
C-set		
23 ppm	0.30	0.17
71	0.38	0.22
268	0.39	0.21
L-set		
22 ppm	0.33	0.20
70	0.35	0.20
289	0.36	0.20
Dia.75–106 μm		
K-set		
23 ppm	0.34	0.20
72	0.37	0.21
277	0.39	0.22
Dia.180–250 μm		
IHG-set		
21 ppm	0.28	0.14
83	0.32	0.16
253	0.33	0.16

A-set (dia. 38–75 μm) : Best Fit (tuning n_{BC}) by New-OC-BC & Universal-OC-BC Isotherms

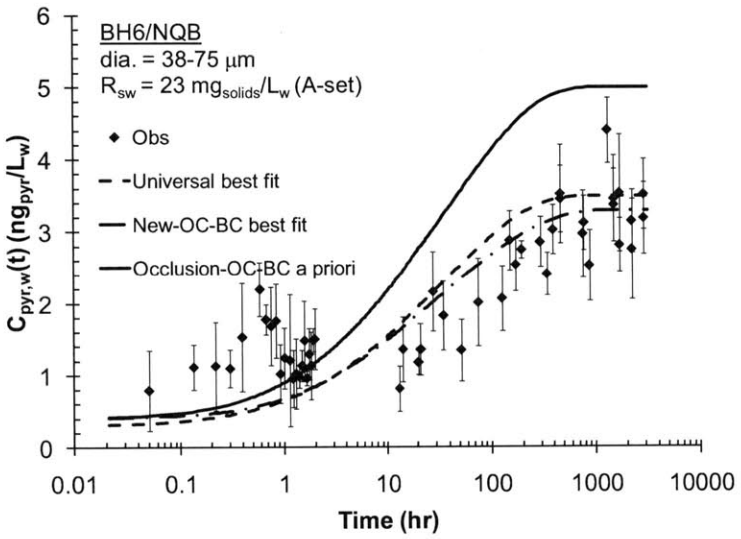

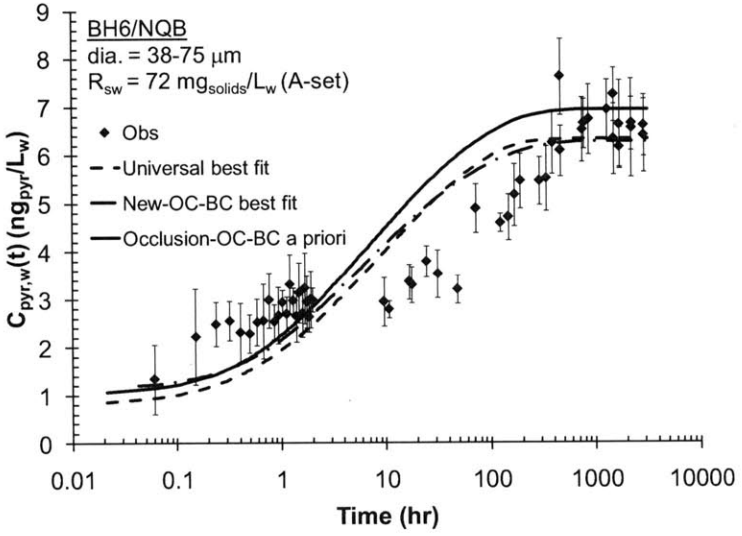

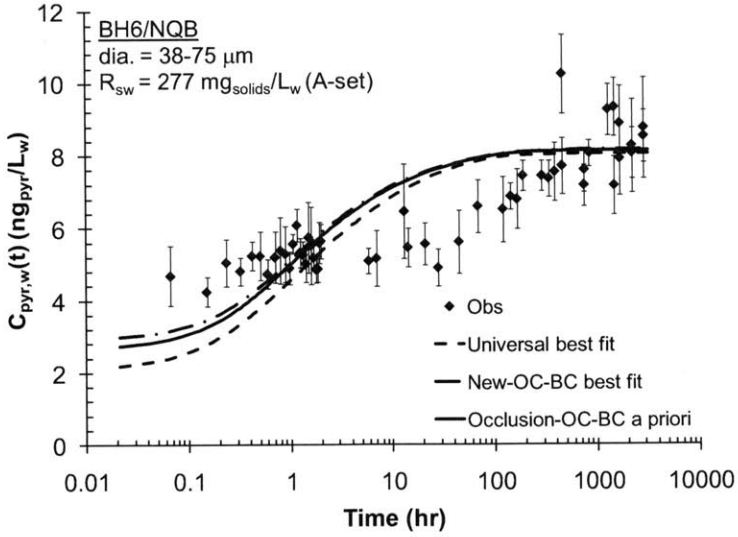

C-set (dia. 38–75 μm) : Best Fit (tuning n_{BC}) by New-OC-BC & Universal-OC-BC Isotherms

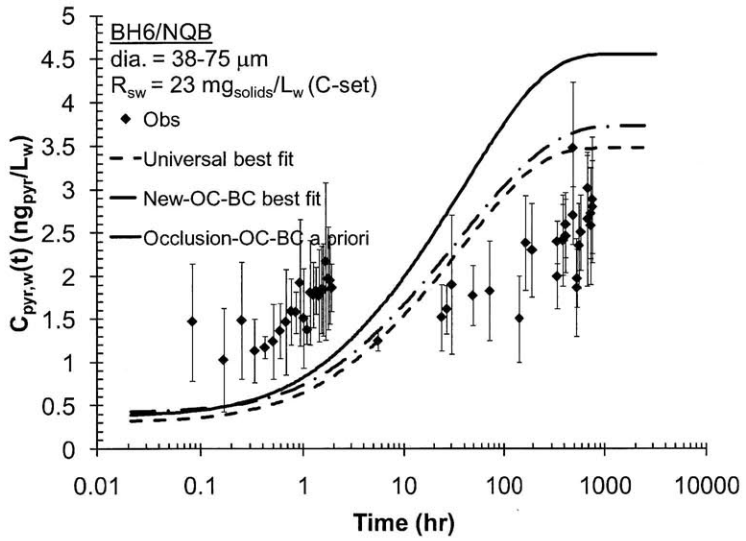

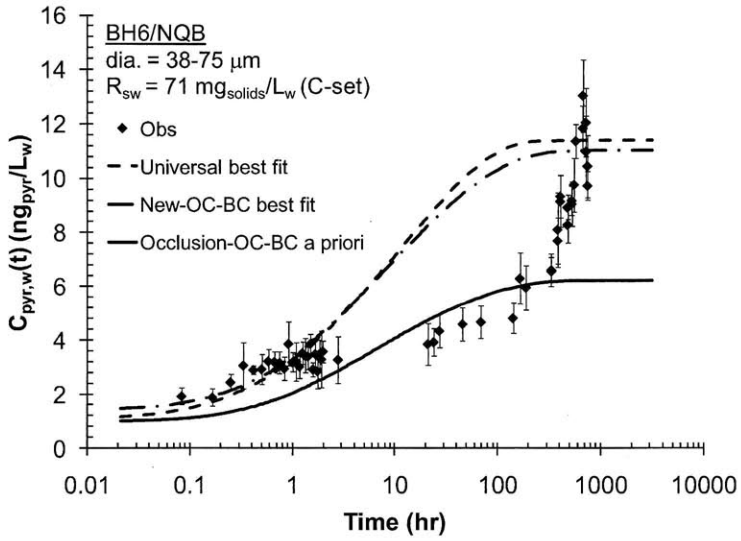

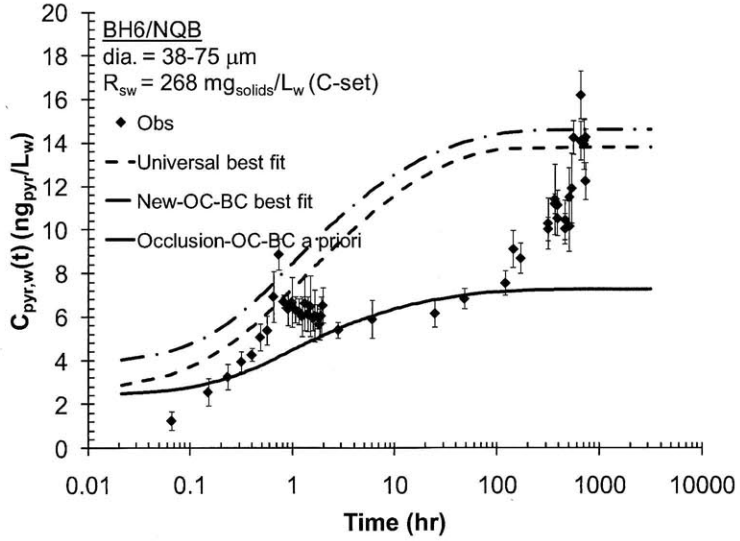

L-set (dia. 38–75 μm) : Best Fit (tuning n_{BC}) by New-OC-BC & Universal-OC-BC Isotherms

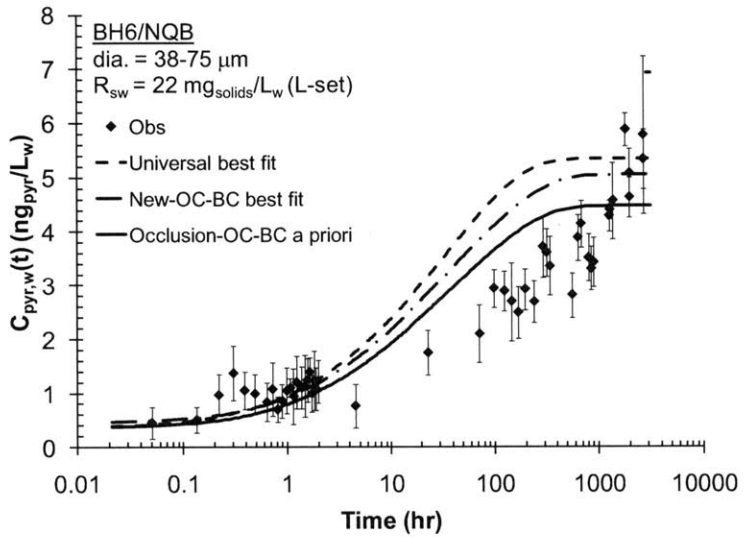

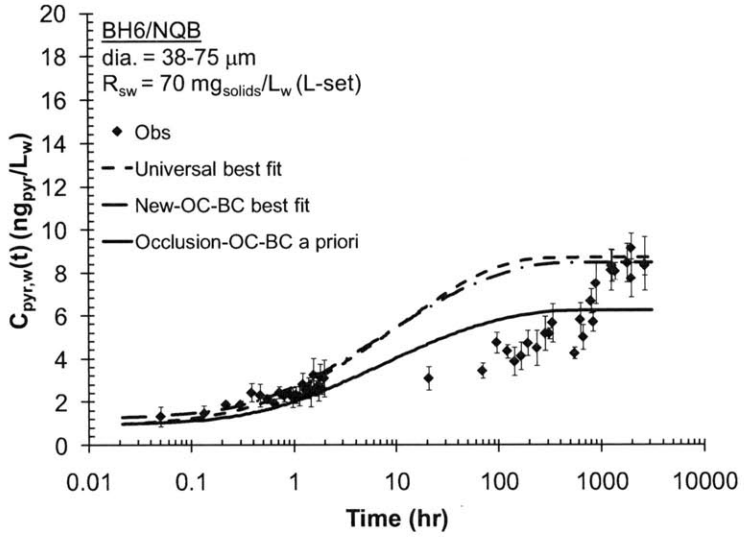

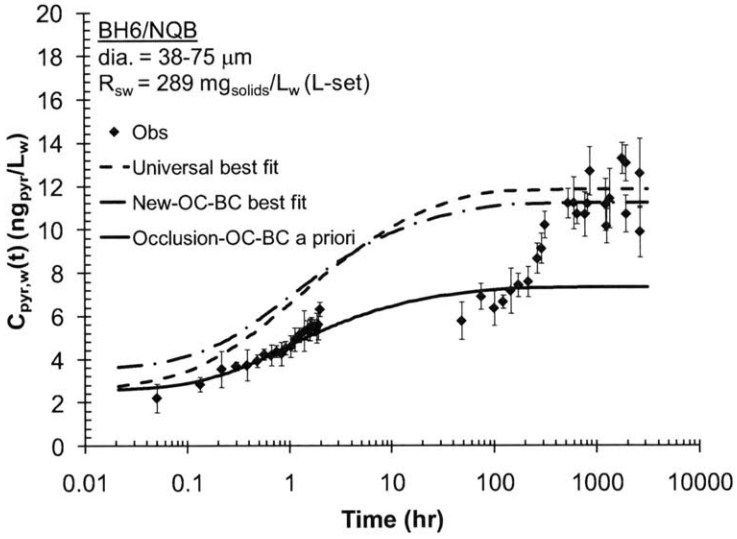

K-set (dia. 75–106 μm): Best Fit (tuning n_{BC}) by New-OC-BC & Universal-OC-BC Isotherms

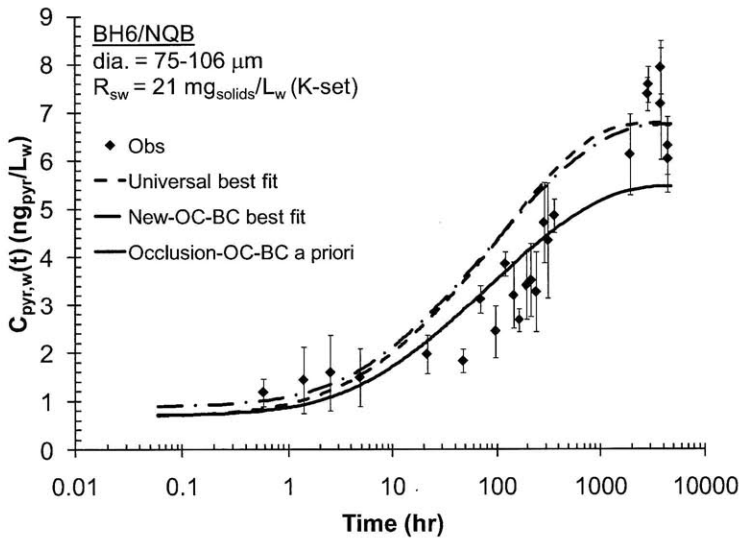

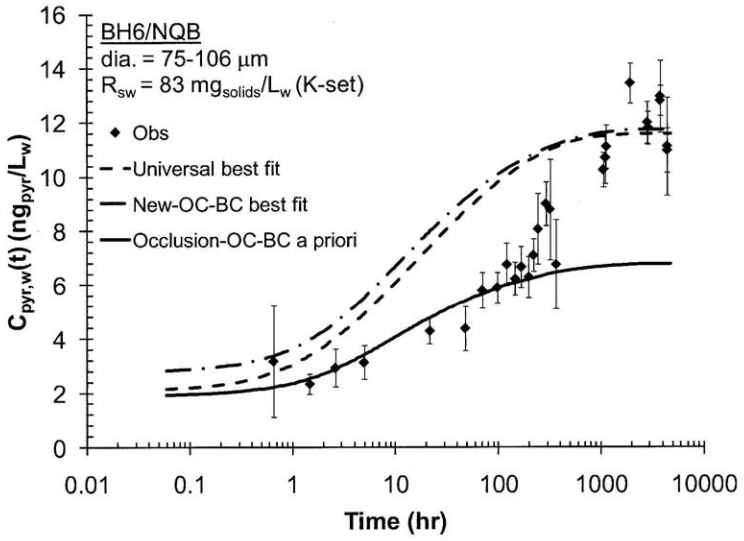

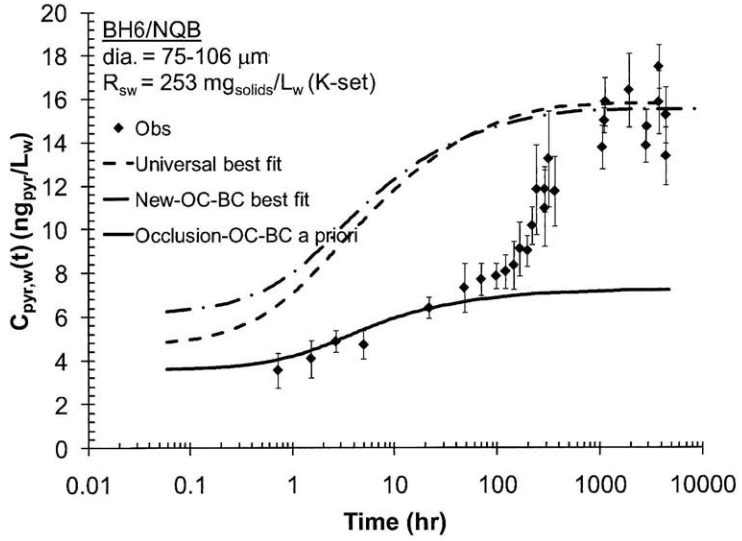

IHG-set (dia. 180–250 μm): Best Fit (tuning n_{BC}) by New-OC-BC & Universal-OC-BC Isotherms

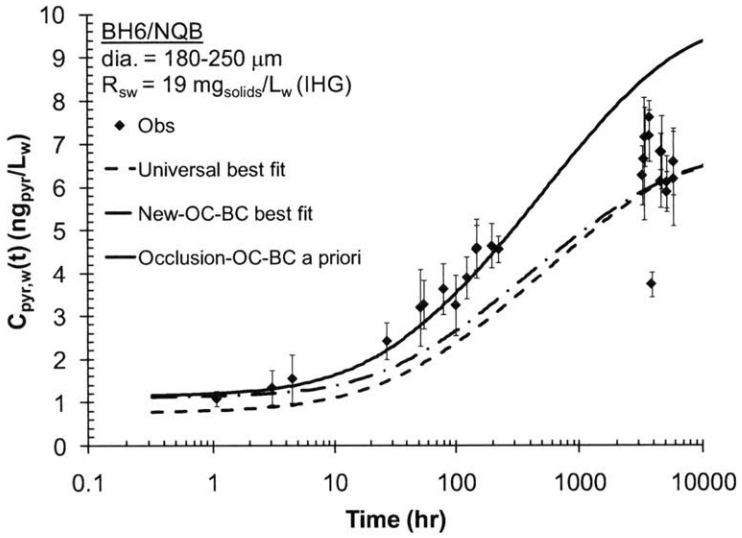

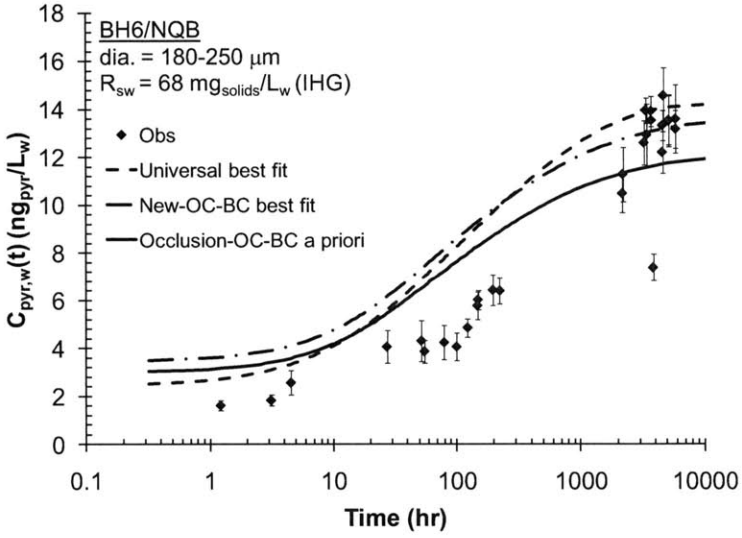

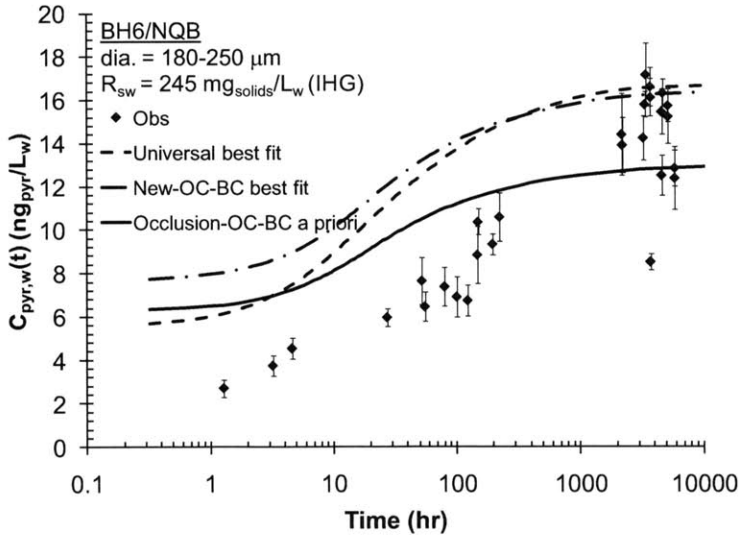

Appendix 7 - 18. SEM Images of BH#6 Sediment Aggregates/Particles

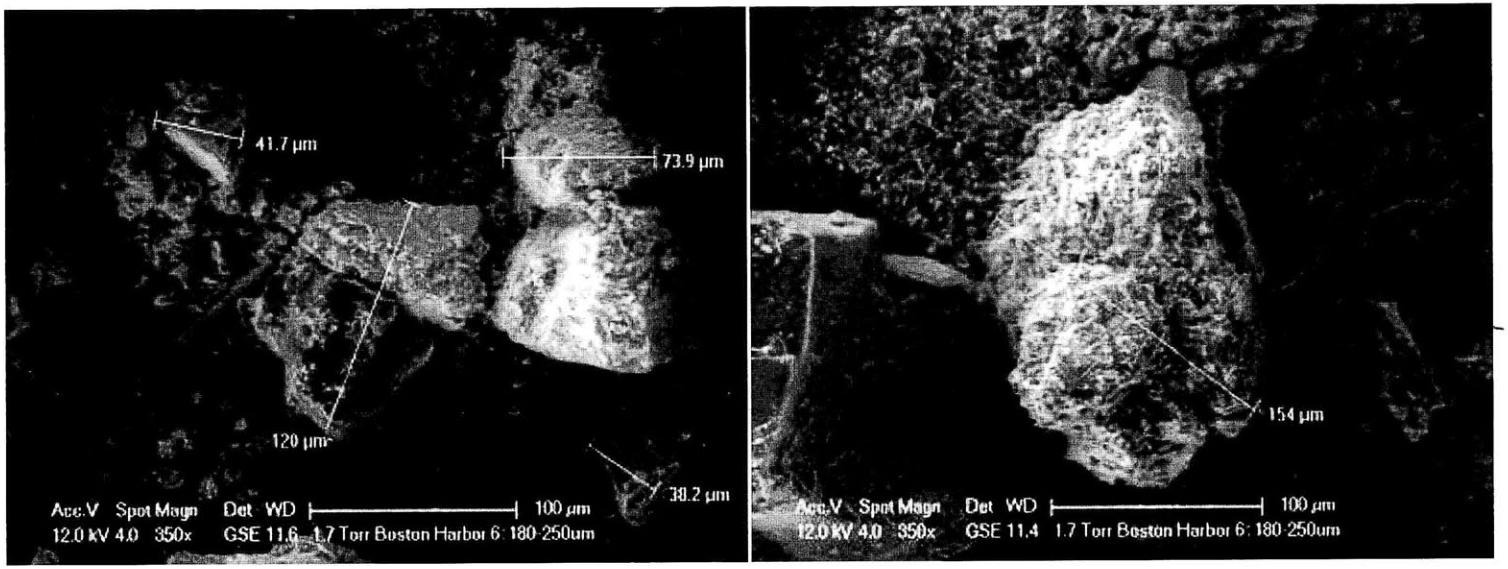

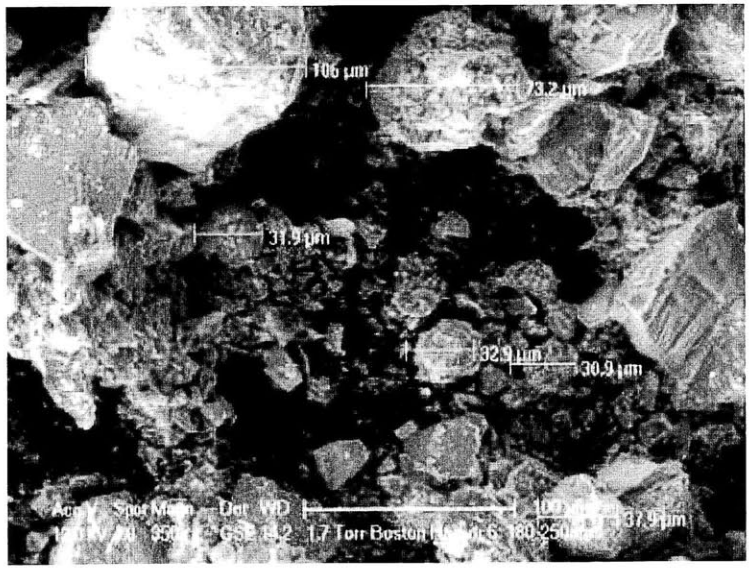

Appendix 7 - 19. Two-Compartmental (Constrained) Regression of the BH#6/NQB Desorption Kinetic Data.

$$C(t) = \mathbf{S_{slow,o}} R_{sw} [1 - \exp(-\mathbf{k_{slow}} t)] + \mathbf{S_{rapid,o}} R_{sw} [\exp(-k_{slow}\, t) - \exp(-\mathbf{k_{rapid}} t)]$$

	$S_{Eqm\|End}$	$S_{rapid,o}$	$S_{slow,o}$	k_{rapid} (h^{-1})	k_{slow} (h^{-1})	f_{rapid} (%)	r^2
38–75 μm							
A–set							
23 mg/L	811	87	522	0.33×10^{-3}	17×10^{-9}	6	0.58
72	1105	61	254	0.28×10^{-3}	20×10^{-9}	4	0.74
277	1315	21	84	4.3×10^{-3}	19×10^{-9}	1	0.70
C–set							
23 mg/L	778	75	497	1.3×10^{-3}	39×10^{-9}	6	0.75
71	1052	48	251	1.5×10^{-3}	230×10^{-9}	4	0.96
268	1247	24	79	1.0×10^{-3}	180×10^{-9}	2	0.94
L–set							
22 mg/L	766	112	472	0.12×10^{-3}	42×10^{-9}	8	0.91
70	1048	56	246	0.28×10^{-3}	43×10^{-9}	4	0.91
289	1253	27	71	0.28×10^{-3}	36×10^{-9}	2	0.85
75–106 μm							
K–set							
21 mg/L	2204	206	650	2.9×10^{-6}	16×10^{-9}	7	0.85
83	2754	99	206	3.9×10^{-6}	20×10^{-9}	3	0.83
253	2945	51	64	2.7×10^{-6}	13×10^{-9}	2	0.78
180–250 μm							
IHG–set							
19 mg/L	3969	252	1199	5.4×10^{-6}	4.4×10^{-9}	5	0.85
68	4862	130	427	2.1×10^{-6}	9.3×10^{-9}	2	0.91
245	5243	55	122	2.5×10^{-6}	2.2×10^{-9}	1	0.79

Appendix 7 - 20. *A priori* Modeling of Desorption with the Occlusion-OC-BC Isotherm (30% occlusion).

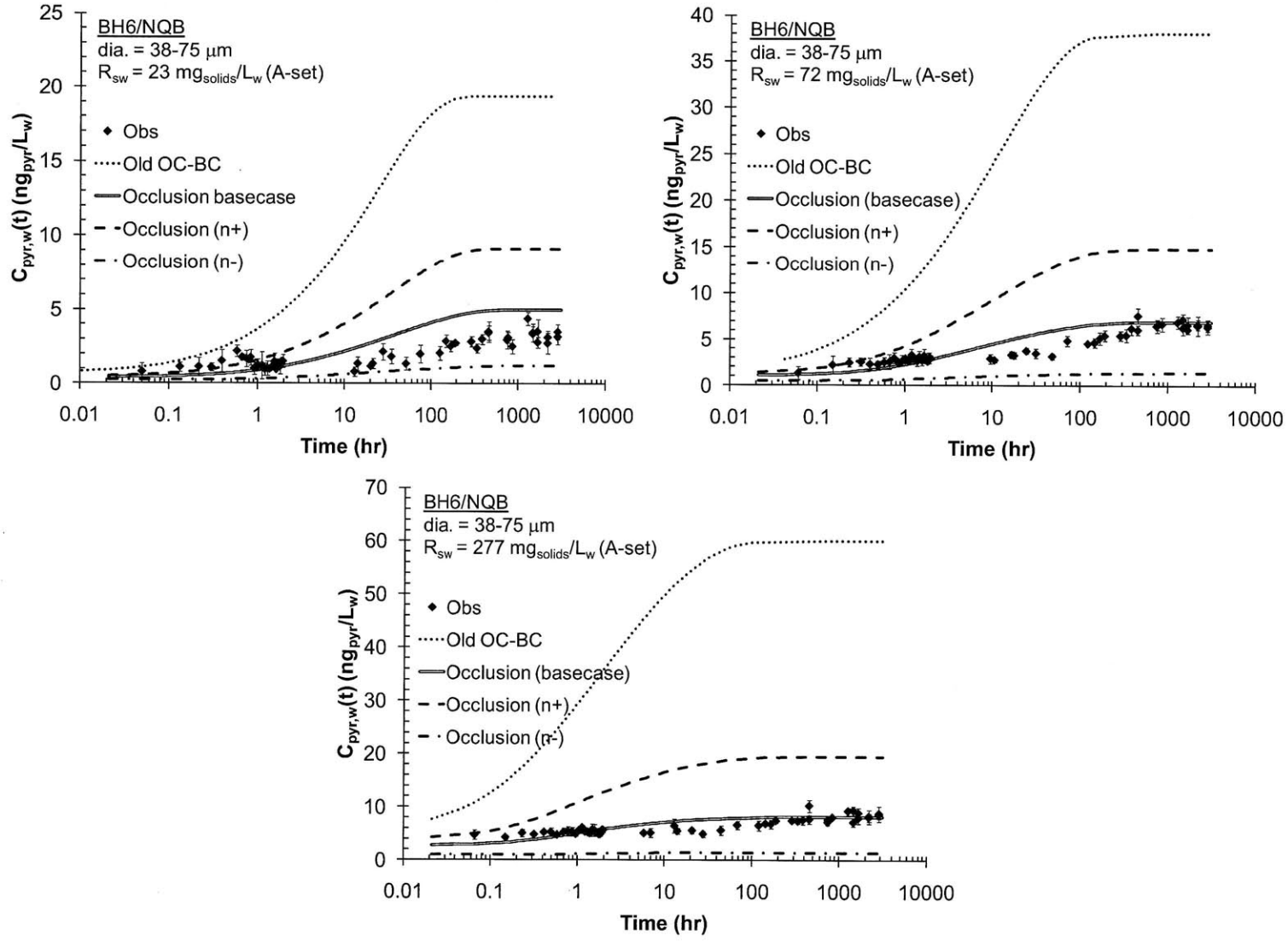

C-set (dia. 38–75 μm): *A priori* Modeling with the Occlusion-OC-BC (30% occlusion) Isotherm

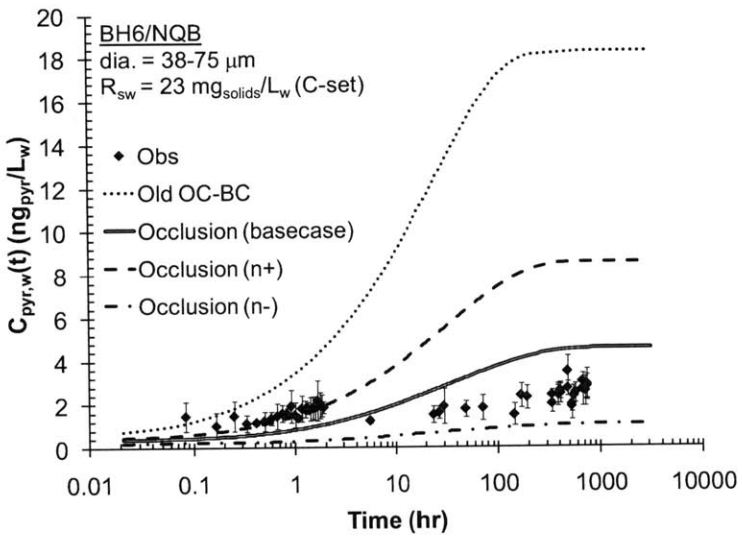

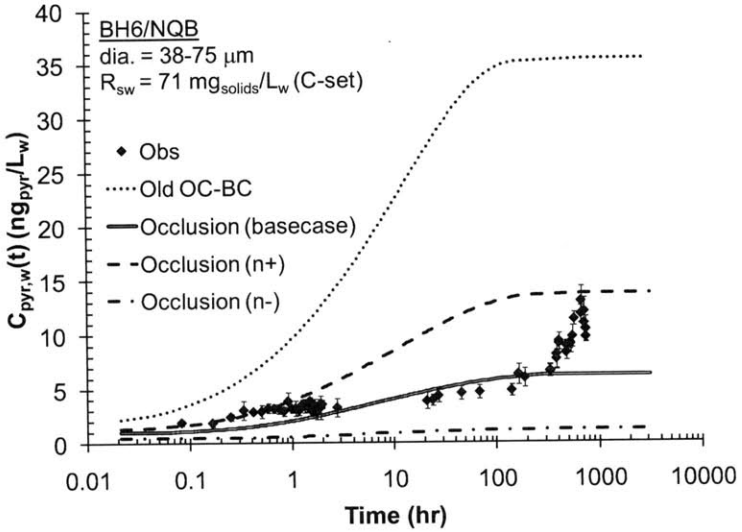

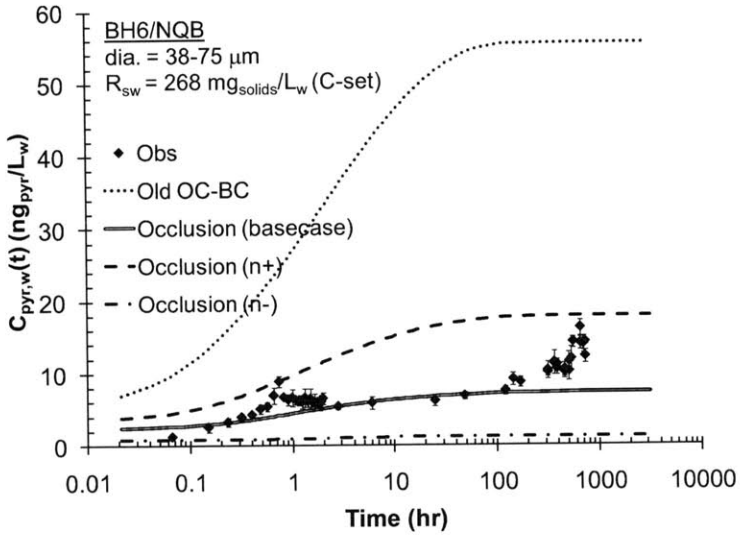

L-set (dia. 38–75 μm): *A priori* Modeling with the Occlusion-OC-BC (30% occlusion) Isotherm

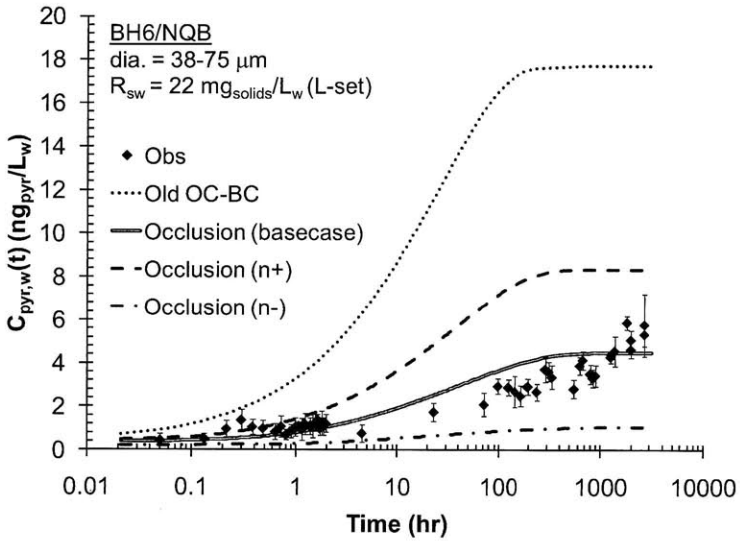

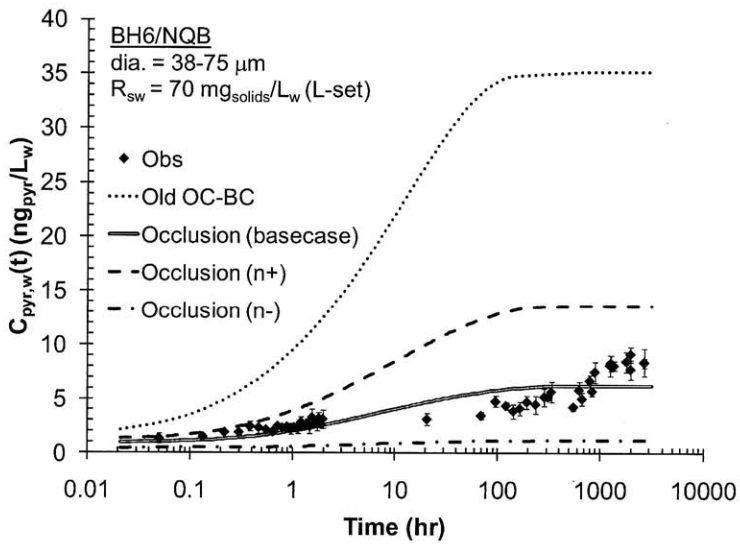

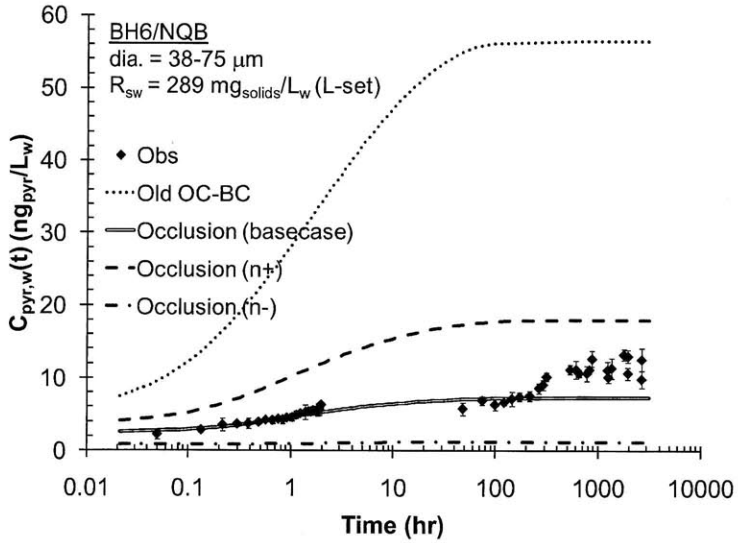

K-set (dia. 75–106 μm): *A priori* Modeling with the Occlusion-OC-BC (30% occlusion) Isotherm

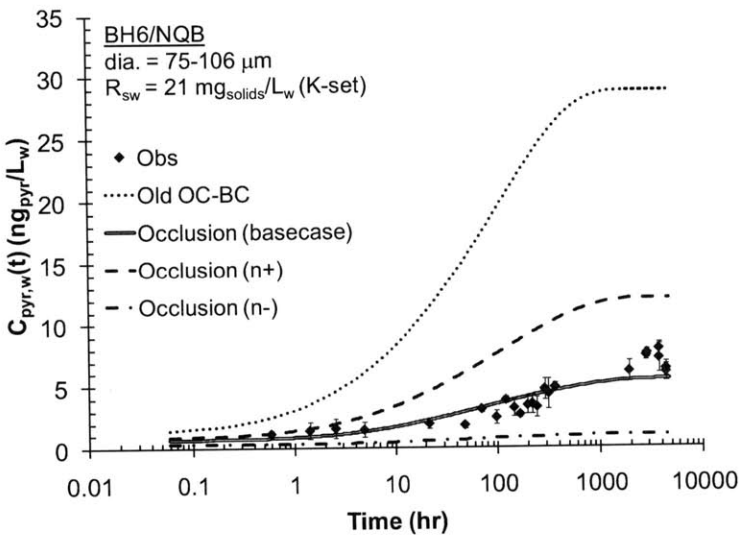

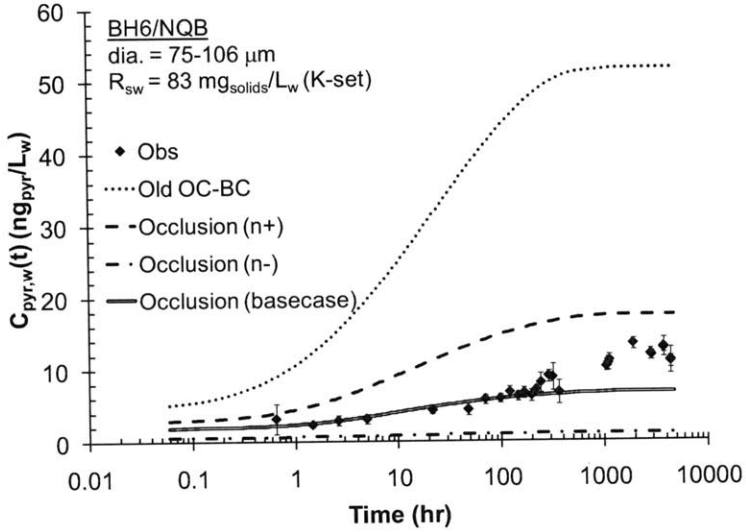

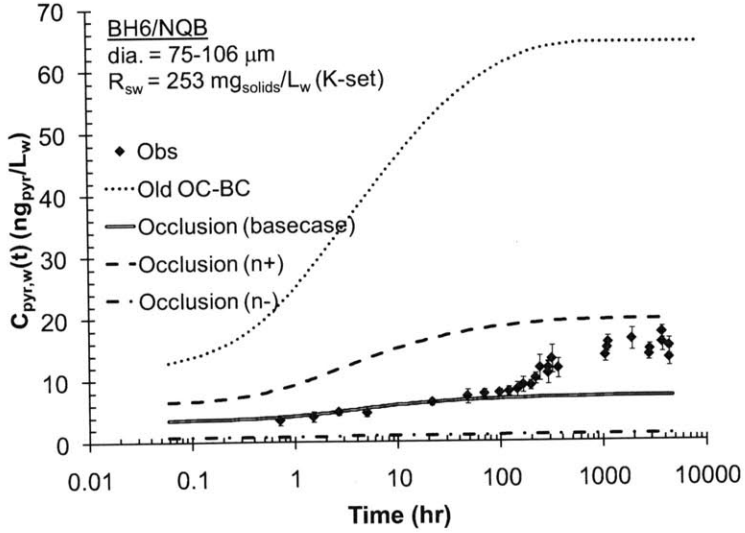

IHG-set (dia. 180–250 μm): *A priori* Modeling with the Occlusion-OC-BC (30% occlusion) Isotherm

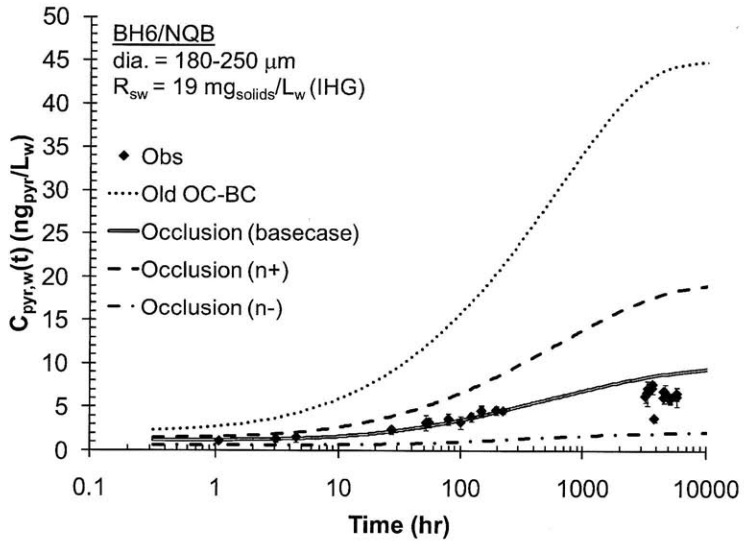

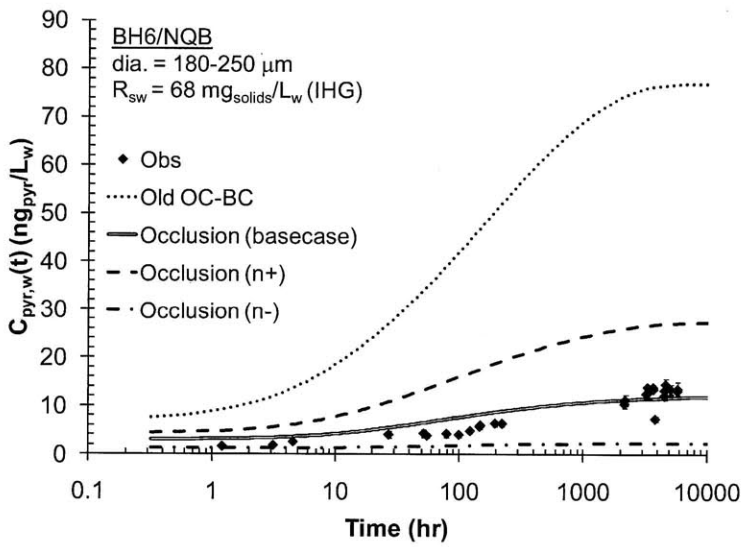

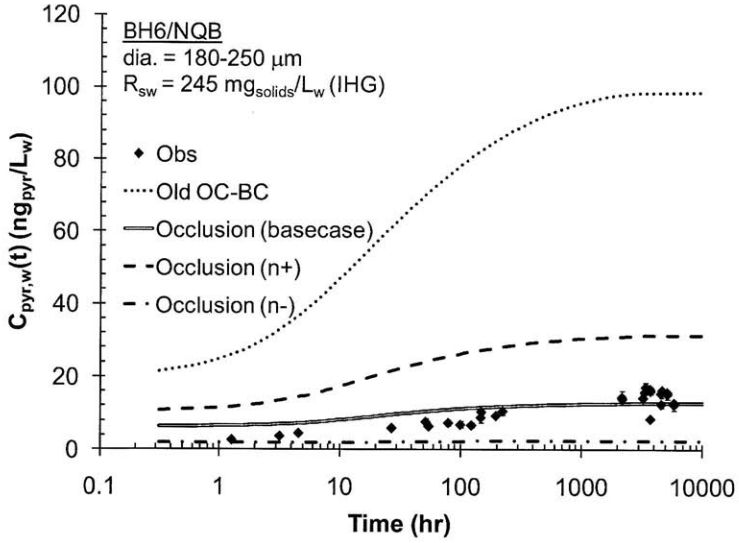

Appendix 7 - 21. Regression of Desorption Kinetic Data by Empirical Models.

Non-linear regression of kinetic data by the empirical models was performed using scripts in Matlab (Appendix E, Script E-6).

Note that 'constrained' model means that the regression/optimization was performed with the following equilibrium constraint:

$$S_o = S_{Eqm\,|End} + \sum_{\text{all compartments}} S_i$$

where: $S_{Eqm|End}$ is the end point solid-phase pyrene concentration ($\mu g_{pyr}/kg_{solids}$),

S_i is the solid-phase pyrene concentration associated with the i^{th} compartment ($\mu g_{pyr}/kg_{solids}$).

The regressed model parameters are summarized in the tables below.

(I). Exponential Model (Constrained One-Compartment + Instantaneous Desorbed Fraction; 2 parameters)

(II). Exponential Model (Unconstrained Two-Compartment; 4 parameters)

(III). Exponential Model (Constrained Two-Compartment; 4 parameters)

(IV). Exponential Model (Constrained Three-Compartment; 6 parameters)

(V). Orthogonal Polynomial Model (3 parameters)

(VI). Elovich Model (2 parameters)

(VII). Gamma-Distributed Rate Model (2 parameters)

(VIII). Weibull Model (Constrained One-Compartment; 2 parameters)

(IX). Weibull Model (Constrained Two-Compartment; 6 parameters)

(I). Exponential Model (Constrained One-Compartment + Instantaneous Desorbed Fraction; 2 parameters)

$$C(t) = \mathbf{S_{inst}} R_{sw} + (S_o - S_{Eqm\,|End} - S_{inst}) R_{sw} [1 - \exp(-\mathbf{k}t)]$$

	S_o (µg/kg)	S_{inst} (µg/kg)	$S_{Eqm\|End}$ (µg/kg)	k (h^{-1})	$f_{inst.}$ (%)	r^2
38–75 µm						
A–set						
23 mg/L	1420	69	811	81×10^{-6}	5	0.50
72	1420	46	1105	110×10^{-6}	3	0.55
277	1420	20	1315	73×10^{-6}	1	0.47
C–set						
23 mg/L	1350	69	778	160×10^{-6}	5	0.59
71	1350	44	1052	850×10^{-6}	3	0.94
268	1350	21	1247	710×10^{-6}	2	0.82
L–set						
22 mg/L	1350	65	766	220×10^{-6}	5	0.80
70	1350	40	1048	200×10^{-6}	3	0.82
289	1350	19	1253	210×10^{-6}	1	0.65
75–106 µm						
K–set						
21 mg/L	3060	122	2204	97×10^{-6}	4	0.72
83	3060	65	2754	130×10^{-6}	2	0.63
253	3060	31	2945	150×10^{-6}	1	0.54
180–250 µm						
IHG–set						
19 mg/L	5420	160	3969	33×10^{-6}	3	0.62
68	5420	60	4862	70×10^{-6}	1	0.84
245	5420	28	5243	55×10^{-6}	1	0.62

(II). Exponential Model (Unconstrained Two-Compartment; 4 parameters)

$$C(t) = \mathbf{S_{slow,o}} R_{sw} [1 - \exp(-\mathbf{k_{slow}} t)] + \mathbf{S_{rapid,o}} R_{sw} [\exp(-k_{slow}\, t) - \exp(-\mathbf{k_{rapid}} t)]$$

	S_o (µg/kg)	$S_{rapid,o}$ (µg/kg)	$S_{slow,o}$ (µg/kg)	k_{rapid} (h^{-1})	k_{slow} (h^{-1})	f_{rapid} (%)	r^2
38–75 µm							
A–set							
23 mg/L	1420	88	1332	1.1	22×10^{-6}	6	0.58
72	1420	62	1358	0.97	12×10^{-6}	4	0.74
277	1420	21	1399	15	3.7×10^{-6}	1	0.69
C–set							
23 mg/L	1350	75	1275	4.6	52×10^{-6}	6	0.75
71	1350	49	1301	4.8	130×10^{-6}	4	0.96
268	1350	24	1326	3.7	32×10^{-6}	2	0.94
L–set							
22 mg/L	1350	115	1235	0.42	50×10^{-6}	9	0.91
70	1350	59	1291	0.92	24×10^{-6}	4	0.90
289	1350	27	1323	0.95	5.5×10^{-6}	2	0.84
75–106 µm							
K–set							
21 mg/L	3060	258	2802	5.9×10^{-3}	7.0×10^{-6}	8	0.85
83	3060	107	2953	11×10^{-3}	3.6×10^{-6}	3	0.82
253	3060	52	3008	9.0×10^{-3}	0.81×10^{-6}	2	0.78
180–250 µm							
IHG–set							
19 mg/L	5420	255	5165	19×10^{-3}	3.4×10^{-6}	5	0.85
68	5420	136	5284	7.0×10^{-3}	2.3×10^{-6}	3	0.91
245	5420	55	5365	8.8×10^{-3}	1.5×10^{-6}	1	0.79

(III). Exponential Model (Constrained Two-Compartment; 4 parameters)

$$C(t) = \mathbf{S_{slow,o}} R_{sw} [1 - \exp(-\mathbf{k_{slow}} t)] + \mathbf{S_{rapid,o}} R_{sw} [\exp(-k_{slow}\, t) - \exp(-\mathbf{k_{rapid}} t)]$$

	$S_{Eqm\|End}$	$S_{rapid,o}$	$S_{slow,o}$	k_{rapid} (h^{-1})	k_{slow} (h^{-1})	f_{rapid} (%)	r^2
38–75 μm							
A–set							
23 mg/L	811	87	522	1.1	60×10^{-6}	6	0.58
72	1105	61	254	1.0	71×10^{-6}	4	0.74
277	1315	21	84	16	67×10^{-6}	1	0.70
C–set							
23 mg/L	778	75	497	4.7	140×10^{-6}	6	0.75
71	1052	48	251	5.3	820×10^{-6}	4	0.96
268	1247	24	79	3.8	630×10^{-6}	2	0.94
L–set							
22 mg/L	766	112	472	0.44	150×10^{-6}	8	0.91
70	1048	56	246	1.0	160×10^{-6}	4	0.91
289	1253	27	71	1.0	130×10^{-6}	2	0.85
75–106 μm							
K–set							
21 mg/L	2204	206	650	0.010	59×10^{-6}	7	0.85
83	2754	99	206	0.014	73×10^{-6}	3	0.83
253	2945	51	64	0.0096	48×10^{-6}	2	0.78
180–250 μm							
IHG–set							
19 mg/L	3969	252	1199	0.019	16×10^{-6}	5	0.85
68	4862	130	427	0.0075	34×10^{-6}	2	0.91
245	5243	55	122	0.0090	7.8×10^{-6}	1	0.79

(IV). Exponential Model (Constrained Three-Compartment; 6 parameters)

$$C(t) = \mathbf{S_{v.slow}} R_{sw}\left[1 - e^{-\mathbf{k_{v.slow}}t}\right] + \mathbf{S_{slow}} R_{sw}\left[e^{-k_{v.slow}\,t} - e^{-\mathbf{k_{slow}}t}\right] + \mathbf{S_{rapid}} R_{sw}\left[e^{-k_{v.slow}\,t} - e^{-\mathbf{k_{rapid}}t}\right]$$

	S_{rapid}	S_{slow}	$S_{v.slow}$	k_{rapid} (h^{-1})	k_{slow} (h^{-1})	$k_{v.slow}$ (h^{-1})	r^2
38–75 μm							
A–set							
23 mg/L	57	85	468	12	5.6×10^{-3}	25×10^{-12}	0.86
72	39	53	223	6.9	5.6×10^{-3}	3.9×10^{-12}	0.97
277	19	10	76	28	5.9×10^{-3}	7.5×10^{-6}	0.90
C–set							
23 mg/L	74	39	460	5.2	2.3×10^{-3}	45×10^{-6}	0.76
71	44	7	247	6.3	290×10^{-3}	790×10^{-6}	0.96
268	24	0	79	3.8	14×10^{-3}	630×10^{-6}	0.94
L–set							
22 mg/L	47	81	456	9.6	16×10^{-3}	130×10^{-6}	0.96
70	40	85	177	4.0	1.3×10^{-3}	46×10^{-12}	0.95
289	18	23	56	4.3	3.0×10^{-3}	9.2×10^{-12}	0.95
75–106 μm							
K–set							
21 mg/L	78	254	524	1.9	2.3×10^{-3}	2.9×10^{-12}	0.95
83	40	97	169	3.3	3.0×10^{-3}	11×10^{-6}	0.95
253	20	41	55	1.5	3.4×10^{-3}	0.04×10^{-12}	0.96
180–250 μm							
IHG–set							
19 mg/L	110	227	1114	0.36	4.8×10^{-3}	4.3×10^{-12}	0.90
68	45	102	410	0.38	2.8×10^{-3}	24×10^{-6}	0.94
245	22	37	118	0.39	3.1×10^{-3}	0.34×10^{-12}	0.88

(V). Orthogonal Polynomial Model (3 parameters)

$$C(t) = S_o R_{sw} [\mathbf{a_0} + \mathbf{a_1} t^{0.5} + \mathbf{a_2} t]$$

	a_0 (---)	a_1 ($h^{-0.5}$)	a_2 (h^{-1})	r^2
38–75 μm				
A–set				
23 mg/L	0.041	0.0015	---	0.69
72	0.028	0.00096	---	0.76
277	0.013	0.00021	---	0.64
C–set				
23 mg/L	0.048	0.0015	---	0.62
71	0.030	0.0017	0.000058	0.94
268	0.014	0.00063	0.000010	0.83
L–set				
22 mg/L	0.035	0.0032	---	0.92
70	0.024	0.0015	---	0.92
289	0.012	0.00048	---	0.81
75–106 μm				
K–set				
21 mg/L	0.029	0.0014	---	0.85
83	0.016	0.00058	---	0.79
253	0.0081	0.00022	---	0.71
180–250 μm				
IHG–set				
19 mg/L	0.024	0.00058	---	0.72
68	0.0077	0.00042	---	0.90
245	0.0042	0.00011	---	0.73

(VI). Elovich Model (2 parameters)

$C(t) = S_o R_{sw} [\mathbf{a} + \mathbf{b}\ln(t)]$

	a (---)	b (---)	r^2
38–75 μm			
A–set			
23 mg/L	0.039	0.0077	0.75
72	0.026	0.0051	0.91
277	0.013	0.0010	0.81
C–set			
23 mg/L	0.051	0.0046	0.63
71	0.032	0.0098	0.82
268	0.015	0.0028	0.81
L–set			
22 mg/L	0.035	0.0150	0.88
70	0.025	0.0065	0.85
289	0.012	0.0022	0.89
75–106 μm			
K–set			
21 mg/L	0.0029	0.0120	0.83
83	0.0043	0.0050	0.88
253	0.0031	0.0020	0.88
180–250 μm			
IHG–set			
19 mg/L	0.0066	0.0066	0.86
68	---	0.0040	0.87
245	0.0010	0.0012	0.83

(VII). Gamma-Distributed Rate Model (2 parameters)

$C(t) = S_o R_{sw}\{1 - [\mathbf{b}/(b + t)]^{\mathbf{a}}\}$

	a (---)	b (---)	r^2
38–75 μm			
A–set			
23 mg/L	0.0082	0.0082	0.77
72	0.0053	0.0073	0.92
277	0.0011	3.6×10^{-6}	0.86
C–set			
23 mg/L	0.0049	26×10^{-6}	0.71
71	0.0110	0.0580	0.83
268	0.0028	0.0042	0.83
L–set			
22 mg/L	0.0170	0.20	0.89
70	0.0069	0.0280	0.86
289	0.0023	0.0055	0.90
75–106 μm			
K–set			
21 mg/L	0.0180	6.6	0.90
83	0.0060	1.2	0.92
253	0.0022	0.34	0.91
180–250 μm			
IHG–set			
19 mg/L	0.0071	0.49	0.89
68	0.0058	9.3	0.93
245	0.0012	0.53	0.86

(VIII). Weibull Model (Constrained One-Compartment; 2 parameters)

$$C(t) = (S_o - S_{Eqm\,|End})R_{sw}\{1 - \exp(-kt^b)\}$$

	S_o (µg/kg)	k (h^{-b})	b (---)	r^2
38–75 µm				
A–set				
23 mg/L	1420	0.093	0.14	0.80
72	1420	0.12	0.14	0.93
277	1420	0.19	0.074	0.87
C–set				
23 mg/L	1350	0.13	0.081	0.72
71	1350	0.14	0.23	0.88
268	1350	0.22	0.15	0.84
L–set				
22 mg/L	1350	0.076	0.24	0.94
70	1350	0.11	0.19	0.91
289	1350	0.18	0.15	0.92
75–106 µm				
K–set				
21 mg/L	3060	0.18	0.27	0.93
83	3060	0.096	0.24	0.94
253	3060	0.14	0.22	0.92
180–250 µm				
IHG–set				
19 mg/L	5420	0.064	0.17	0.87
68	5420	0.039	0.28	0.94
245	5420	0.086	0.19	0.86

(IX). Weibull Model (Constrained Two-Compartment; 6 parameters)

$$C(t) = S_1 R_{sw}\left[1 - \exp\left(-k_1 t^{b_1}\right)\right] + S_2 R_{sw}\left[1 - \exp\left(-k_2 t^{b_2}\right)\right]$$

	S_1 (µg/kg)	S_2 (µg/kg)	k_1 (h^{-b1})	b_1 (---)	k_2 (h^{-b2})	b_2 (---)	r^2
38–75 µm							
A–set							
23 mg/L	119	490	0.33	0.24×10^{-6}	0.047	0.23	0.81
72	89	227	0.28	0.32	0.036	1.1×10^{-6}	0.90
277	24	81	0.97	0.086×10^{-6}	0.050	0.20	0.88
C–set							
23 mg/L	76	496	2.8	0.51	0.00031	0.87	0.78
71	53	245	1.9	0.41	0.00040	1.1	0.96
268	24	79	6.5	1.5	0.00056	1.0	0.94
L–set							
22 mg/L	258	325	0.20	0.23	0.000014	1.3	0.96
70	38	264	2.2	0.49	0.0070	0.52	0.95
289	17	81	2.6	0.61	0.035	0.33	0.93
75–106 µm							
K–set							
21 mg/L	458	398	0.070	0.34	0.040	0.15×10^{-6}	0.93
83	180	125	0.13	0.31	0.015	0.76×10^{-6}	0.95
253	88	27	0.22	0.097	0.00030	1.4	0.96
180–250 µm							
IHG–set							
19 mg/L	292	1159	0.049	0.60	0.040	1.4×10^{-6}	0.90
68	104	454	0.016	0.58	0.050	0.19	0.94
245	47	130	0.029	0.64	0.10	2.4×10^{-6}	0.88

Appendix 7 - 22. OC Contents in Some Soils and Sediments

(I) Soil Samples

Sorbent	f_{OC} (g/g)	Ref.	Sorbent	f_{OC} (g/g)	Ref.	Sorbent	f_{OC} (g/g)	Ref.
Picatinny sand	0.0053	[1]	P2, Spain	0.0056	[9]	NE. Bavaria 1	0.056	[14]
Woodburn silty sand	0.0123	[1]	Askov, Denmark	0.0139	[9]	NE. Bavaria 2	0.021	[14]
ACE silty-clay	0.0126	[1]	Borris, Denmark	0.0167	[9]	Turin Loess, IA	0.0011	[15]
ACE sand	0.0018	[1]	Kettering, UK	0.0209	[9]	Ceredi, WV	0.0048	[15]
Tavares, Florida	0.0086	[2]	Woodburn	0.0126	[10]	Fren Clyffe, IL	0.0130	[15]
Nahal-Oz loess	0.016	[3]	Elliot	0.0290	[10]	EPA-9	0.0011	[16]
Morasha hamra	0.005	[3]	Marlette	0.0180	[10]	EPA-14	0.0048	[16]
Borden, Ontario	0.0029	[4]	Piketon	0.0149	[10]	EPA-20	0.0130	[16]
Mt. Lemmon, Arizona	0.126	[4]	Anoka	0.0108	[10]	Bangkok M1	0.0231	[17]
Rogen, Denmark	0.017	[5]	Mata, Brazil	0.0288	[11]	Bangkok M3	0.0124	[17]
Foulum	0.015	[5]	Cerrado, Brazil	0.0295	[11]	Bangkok M7	0.0264	[17]
LHS silt-loam	0.0150	[6]	Jaiba, Brazil	0.0095	[11]	Bangkok M9	0.0406	[17]
SBS sand	0.0024	[6]	Silsoe, UK	0.0409	[11]	Bangkok M13	0.0246	[17]
CNS podzol	0.0240	[6]	Fosters, UK	0.0286	[11]	Bangkok C5	0.0099	[17]
Ny-Alesund, Norway	0.1–0.2	[7]	Woburn, UK	0.0150	[11]	Breton, Alberta	0.0528–0.0947	[18]
Tsukuba, Japan	0.07–0.08	[7]	Barnes loam	0.0139–0.0209	[12]	Akron, CO	0.0160–0.0311	[18]
Pasoh, Malaysia	0.01–0.04	[7]	Brandt silty clay loam	0.0174–0.0221	[12]	Watkinsville, GA	0.0497–0.0672	[18]
Kaldenkirchen, Germany	0.0086	[8]	Michalovce, Slovakia	0.0121	[13]	Lexington, KY	0.0229–0.0273	[18]
Merzenhausen, Germany	0.0098	[8]	N. Belgium	0.017	[14]	Hoytville, OH	0.0569–0.0756	[18]
			S. Netherlands	0.040	[14]	Swift Current, Saskatchewan	0.0318–0.0404	[18]

[1] Deitsch et al. 2000. [2] Paramasivam et al. 2000. [3] Rapp et al. 2000. [4] Hu et al. 1995. [5] de Jonge et al. 2000. [6] Abu et al. 2006. [7] Bekku et al. 2003. [8] Berns et al. 2008. [9] Celis et al. 2006. [10] Chiou et al. 1998. [11] Dell'Abate et al. 2003. [12] DeSutter et al. 2003. [13] Hiller et al. 2008. [14] Kaiser et al. 2000. [15] Karickhoff 1981. [16] Means et al. 1980. [17] Muller et al. 2000. [18] Plante et al. 2006.

(II) Sediment Samples

Sorbent	f_{OC} (g/g)	Ref.	Sorbent	f_{OC} (g/g)	Ref.	Sorbent	f_{OC} (g/g)	Ref.
Hudson River 1	0.0096	[1]	Oconee R. GA	0.0090	[6]	Punta Rossa	0.0030	[8]
Hudson River 2	0.0343	[1]	Doe Run Pond, GA	0.0130	[6]	Toro Island	0.0160	[8]
Hudson River 3	0.0459	[1]	Hickory Hill Pond, GA	0.0140	[6]	Vecchio Harbor	0.0540	[8]
Auckland, NZ	0.020	[2]	EPA-B2	0.0121	[7]	Bonifacio	0.0070	[8]
L. Michigan	0.0402	[3]	EPA-4	0.0207	[7]	Cap de Feno	0.0020	[8]
Mississippi R. LA	0.0040	[3]	EPA-5	0.0228	[7]	Castel Sardo	0.0010	[8]
Mississippi R. AK	0.0160	[3]	EPA-6	0.0072	[7]	Torres Harbor/Bay	0.0130–0.0330	[8]
Massachusetts Bay	0.0163	[3]	EPA-8	0.0015	[7]	Anse Mejan	0.0050	[8]
Spectacle Island	0.0334	[3]	EPA-15	0.0095	[7]	Saguenay Fjord, Canada	0.0189	[9]
Peddocks Island	0.0312	[3]	EPA-18	0.0066	[7]	St. Louis R., Canada	0.0710	[9]
Fort Point Channel	0.0519	[3]	EPA-21	0.0188	[7]	W. Irish Sea	0.0010–0.0290	[10]
Kyjov, Slovakia	0.0027	[4]	EPA-22	0.0167	[7]	Hangzhou	0.0030–0.0637	[11]
Lula, OK	0.0017–0.0075	[5]	EPA-23	0.0238	[7]	Mackenzie R.	0.0146–0.0184	[12]
Missouri R. #1	0.0207	[6]	EPA-26	0.0148	[7]	Beaufort Shelf	0.0113–0.0197	[12]
Missouri R. #2	0.0228	[6]	Cortiou	0.0060	[8]	Daliao R. China	0.0041–0.0260	[13]
Missouri R. #3	0.0072	[6]	St Louis Harbor	0.0130	[8]	Victoria Harbor, HK	0.0080–0.0282	[14]
Missouri R. #4	0.0015	[6]	Cap Couronne	0.0140	[8]	Detroit R.	0.0022–0.0448	[15]
Ohio R. Leavenworth	0.0095	[6]	La Planier	0.0030–0.0040	[8]	Rouge R.	0.0205–0.0808	[15]
Mississippi R. KY	0.0066	[6]	Toulon	0.0580	[8]	L. Michigan	0.0061–0.0072	[15]
Mississippi R. IL	0.0148	[6]	Lazaret Bay	0.0450	[8]	Zhujiang R. China	0.0081–0.0566	[16]
Illinois R. Lorenzo	0.0188	[6]	Porto Gulf	0.0170	[8]	Dongjiang R. China	0.0057–0.0338	[16]
Illinois R. Lacon	0.0167	[6]	Sanguinaires Is.	0.0130–0.0200	[8]	Xijiang R. China	0.0038–0.0167	[16]
Illinois-Sangamon R.	0.0238	[6]	Ajaccio Harbor	0.0190	[8]	Pearl R. Est.	0.0079–0.0102	[16]
Small stream, GA	0.0121	[6]	Eccica Island	0.0030	[8]	S. China Sea	0.0029–0.0070	[16]

[1] Carroll et al. 1994. [2] Ahrens et al. 2004. [3] Chiou et al. 1998. [4] Hiller et al. 2008. [5] Kan et al. 1994. [6] Karickhoff 1981. [7] Means et al. 1980. [8] Baumard et al. 1998. [9] Brion et al. 2005. [10] Chen et al. 2004. [11] Chen et al. 2004. [12] Goni et al. 2000. [13] Guo et al. 2007. [14] Hong et al. 1995. [15] Kannan et al. 2001. [16] Luo et al. 2008.

Appendix 7 - 23. Non-linear Isotherm and the Diffusion Equation.

The local sorbate concentration, C', and the local aggregate-volume based sorbate concentration, q', are related in the following ways (spherical system):

$$q' = S'\rho_s(1-\emptyset) + C'\emptyset = [K_d\rho_s(1-\emptyset) + \emptyset]C'$$

(7-23a)

$$\frac{\partial q'}{\partial t} = \emptyset\frac{\partial C'}{\partial t}$$

(7-23b)

$$\frac{\partial C'}{\partial t} = F_{Tor}\frac{1}{r^2}\left[\frac{\partial}{\partial r}\left(r^2 D_{iw}\frac{\partial C'}{\partial r}\right)\right]$$

(7-23c)

where ϕ is the intra-aggregate porosity (or volume fraction of porewater phase) (L_{pw}/L_{agg}),

C' is the local pore-water sorbate concentration ($\mu g_i/L_{pw}$),

D_{iw} is the free aqueous diffusivity of i (m^2/s),

F_{Tor} is the tortuosity factor accounting for longer diffusive path ($F_{Tor} \leq 1$; dimensionless),

K_d is the local solid-to-water partition coefficient of the sorbate (L_{pw}/kg_{solids}),

q' is the local aggregate-volume based concentration of the sorbate ($\mu g_i/L_{agg}$),

ρ_s is the solid phase density (kg_{solids}/L_{solids}),

S' is the local solid-phase sorbate concentration ($\mu g_i/kg_{solids}$),

r is the radial dimension (i.e. with respect to the aggregate) (m),

t is time (s).

Substituting (7-23a) and (7-23c) into (7-23b) we get:

$$\frac{\partial q'}{\partial t} = \frac{\partial\{[K_d\rho_s(1-\emptyset) + \emptyset]C'\}}{\partial t} = \emptyset F_{Tor}\frac{1}{r^2}\left[\frac{\partial}{\partial r}\left(r^2 D_{iw}\frac{\partial C'}{\partial r}\right)\right]$$

(7-23d)

For a <u>non-linear isotherm</u> (e.g. $K_d = f_{OC}K_{OC} + f_{BC}K_{BC}C'^{n-1}$), K_d is a function of C'(r,t), and hence the left hand side becomes:

$$\frac{\partial q'}{\partial t} = \frac{\partial\{[\mathbf{K_d}\rho_s(1-\emptyset)+\emptyset]C'\}}{\partial t} = \frac{\partial}{\partial t}\{[(\mathbf{f_{OC}K_{OC}} + \mathbf{f_{BC}K_{BC}C'^{n-1}})\rho_s(1-\emptyset)+\emptyset]C'\}$$

$$= \frac{\partial}{\partial t}\{[\mathbf{f_{OC}K_{OC}}\rho_s(1-\emptyset)+\emptyset]C'\} + \frac{\partial}{\partial t}\{\mathbf{f_{BC}K_{BC}C'^{n}}\rho_s(1-\emptyset)\}$$

$$= [\mathbf{f_{OC}K_{OC}}\rho_s(1-\emptyset)+\emptyset]\frac{\partial C'}{\partial t} + [\mathbf{nf_{BC}K_{BC}C'^{n-1}}\rho_s(1-\emptyset)]\frac{\partial C'}{\partial t}$$

$$= \{[\mathbf{f_{OC}K_{OC}}\rho_s(1-\emptyset)+\emptyset] + [\mathbf{nf_{BC}K_{BC}C'^{n-1}}\rho_s(1-\emptyset)]\}\frac{\partial C'}{\partial t}$$

Moving the two terms in the large brackets to the right hand side of the diffusion equation, one may define D_{eff} as:

$$\frac{\partial C'}{\partial t} = D_{eff}\frac{1}{r^2}\left[\frac{\partial}{\partial r}\left(r^2\frac{\partial C'}{\partial r}\right)\right]$$

$$D_{eff} = \frac{\emptyset F_{Tor} D_{iw}}{[\mathbf{f_{OC}K_{OC}}\rho_s(1-\emptyset)+\emptyset] + [\mathbf{nf_{BC}K_{BC}C'^{n-1}}\rho_s(1-\emptyset)]}$$

The D_{eff}'s reported in Shor et al. (2003b) and Karapanagioti et al. (2001) did not fully capture the effect of non-linearity. Only Rugner et al. (1999) reported a D_{eff} consistent with the isotherm non-linearity.

Appendix 7 - 24. Best Fit Linear Isotherms for Pyrene Desorption Experiments

The best fit linear isotherm assumes:

$$S_{pyr} = f_{TOC} K_{TOC} C_{pyr,w}$$

$$K_d = f_{TOC} K_{TOC} = (f_{OC} + f_{BC})K_{TOC}$$

(Eqn. 7-24a)

where: $C_{pyr,w}$ is the dissolved pyrene concentration ($\mu g_{pyr}/L_w$),

K_d is the solid-to-water partition coefficient for pyrene (L_w/kg_{solids}),

K_{TOC} is the TOC-normalized partition coefficient for pyrene (L_w/kg_{TOC}),

f_{OC} is the OC content of the sorbent (kg_{OC}/kg_{solids}),

f_{BC} is the BC content of the sorbent (kg_{BC}/kg_{solids}),

S_{pyr} is the sorbent-phase pyrene concentration ($\mu g_{pyr}/kg_{solids}$).

Assuming the end-point dissolved pyrene levels in all experiments to be at equilibrium, the K_d's for the individual experiments can be computed via mass balance. K_{TOC}'s can then be computed as:

$$K_{TOC} = \frac{K_d}{(f_{OC} + f_{BC})}$$

(Eqn. 7-24b)

The best-fit $\log K_{TOC}$'s of the individual desorption experiments are summarized below:

	$\log K_{TOC}$ (in unit L_w/kg_{TOC})
Dia.38–75 μm	
A-set	
23 ppm	**6.98**
72	**6.69**
277	**6.61**
C-set	
23 ppm	**7.04**
71	**6.41**
268	**6.35**
L-set	
22 ppm	**6.74**
70	**6.56**
289	**6.44**
Dia.75–106 μm	
K-set	
23 ppm	**6.97**
72	**6.77**
277	**6.68**
Dia.180–250 μm	
IHG-set	
21 ppm	**7.26**
83	**6.97**
253	**6.93**

Appendix 7 - 25. Estimation of Pyrene Desorption Activation Energy ($E_{A,des,app}$).

The apparent activation energy for desorption of native pyrene, $E_{A,des,app}$, was estimated following Arrhenius equation:

$$k_{des} = A\exp(-\frac{E_{A,des,app}}{RT})$$

(Eqn. 7-25a)

where: A is the pre-exponential constant (s^{-1}),

k_{des} is the rate constant of pyrene desorption (s^{-1}),

R is the gas constant (=8.314 J/mol.K),

T is the temperature (K).

The slowest desorption rates will be observed in suspensions with the lowest R_{sw} at the later desorption period. In this exercise, the rate constants at 8 mo and 5 yr were considered. Furthermore, a first order rate expression was also assumed such that kdes can be computed from dC/dt at 8 mo or 5 yr:

$$\frac{dC}{dt} = k_{des}\,C$$

$$k_{des} = \left(\frac{1}{C}\frac{dC}{dt}\right)_{some\ t}$$

(Eqn. 7-25b)

Using the fitted parameters for a Constrained Two-Compartment Model (Appendix 7-21(III)), both C(t) and $dC/dt|_t$ can be computed:

$$C(t) = S_{slow,o}R_{sw}[1-\exp(-k_{slow}\,t)] + S_{rapid,o}R_{sw}[\exp(-k_{slow}\,t) - \exp(-k_{rapid}\,t)]$$

$$\frac{dC}{dt} = S_{slow,o}R_{sw}k_{slow}\exp(-k_{slow}\,t) + S_{rapid,o}R_{sw}[-k_{slow}\exp(-k_{slow}\,t) + k_{rapid}\exp(-k_{rapid}\,t)]$$

(Eqn. 7-25c)

Considering the low R_{sw} suspensions in A-set, K-set, and IHG-set:

R_{sw} (mg/L)	S_{rapid} (ug/kg)	S_{slow} (ug/kg)	k_{rapid} (h^{-1})	k_{slow} (h^{-1})
(A-set) 20	90	520	1.2	60×10^{6}
(K-set) 20	210	650	0.010	59×10^{6}
(IHG-set) 20	250	1200	0.019	16×10^{6}

At t = 5760 h (8 months)

R_{sw} (mg/L)	C(t) (ug/L)	$k_{des}C(t)$ (ug/L.h)	k_{des} (s^{-1})	$E_{A,des,app}$ (kJ/mol)
(A-set) 20	0.00431	365×10^{-9}	0.24×10^{-9}	***26.2***
(K-set) 20	0.00672	368×10^{-9}	0.15×10^{-9}	***27.2***
(IHG-set) 20	0.00666	276×10^{-9}	0.12×10^{-9}	***27.9***

At t = 43200 h (5 years)

R_{sw} (mg/L)	C(t) (ug/L)	$k_{des}C(t)$ (ug/L.h)	k_{des} (s^{-1})	$E_{A,des,app}$ (kJ/mol)
(A-set) 20	0.00976	38.6×10^{-9}	1.1×10^{-9}	***33.7***
(K-set) 20	0.0123	41.1×10^{-9}	0.9×10^{-9}	***34.1***
(IHG-set) 20	0.0144	150×10^{-9}	2.9×10^{-9}	***31.3***

Chapter 8: Appendices

Appendix 8 - 1. Literature logK_{BC} for Selected PAHs. 903
Appendix 8 - 2. Infinite-Bath Desorption Profiles/Solutions for Selected PAHs (naphthalene, phenanthrene, pyrene, benzo(a)pyrene). 904
Appendix 8 - 3. Closed-System Desorption Profiles/Solutions for Selected PAHs (naphthalene & pyrene). 917

Appendix 8 - 1. Literature $logK_{BC}$ for Selected PAHs.

Experimentally Observed $logK_{BC}$.

$logK_{BC}$*	N	Remarks	Reference
naphthalene			
not found			
phenanthrene			
6.1	12	soil/sediment; isotherm study	Huang et al. 1997b; Accardi-Dey and Gschwend 2003;
5.3–7.1	4	sediment; single-point measurement	Lohmann et al. 2005
5.7	1	NIST-soot; isotherm study	Bucheli et al. 2000
5.3–6.2	6	soot, charcoal; single-point measurement	Jonker et al. 2002
benzo(a)pyrene			
6.4–7.4	4	sediment; single-point measurement	Lohmann et al. 2005
7.4–9.1	6	soot, charcoal; single-point measurement	Jonker et al. 2002

*: Unit in $(\mu g_{PAH}/kg_{BC})(L_w/\mu g_{PAH})^{nBC}$.

$logK_{BC}$ from Linear Free Energy Relationships.

	$logK_{BC}$ $(\mu g_{PAH}/kg_{BC})(L_w/\mu g_{PAH})^{nBC}$	
	Lohmann et al. 2005	Schwarzenbach et al. 2003
naphthalene		3.93
phenanthrene	6.13	5.91
benzo(a)pyrene	8.00	8.06

Appendix 8 - 2. Infinite-Bath Desorption Profiles/Solutions for Selected PAHs (naphthalene, phenanthrene, pyrene, benzo(a)pyrene).

Naphthalene ($\log K_{OC}$ = 2.9, $\log K_{BC}$ = 3.9); $S_{naph,o}$ = 200µg/kg

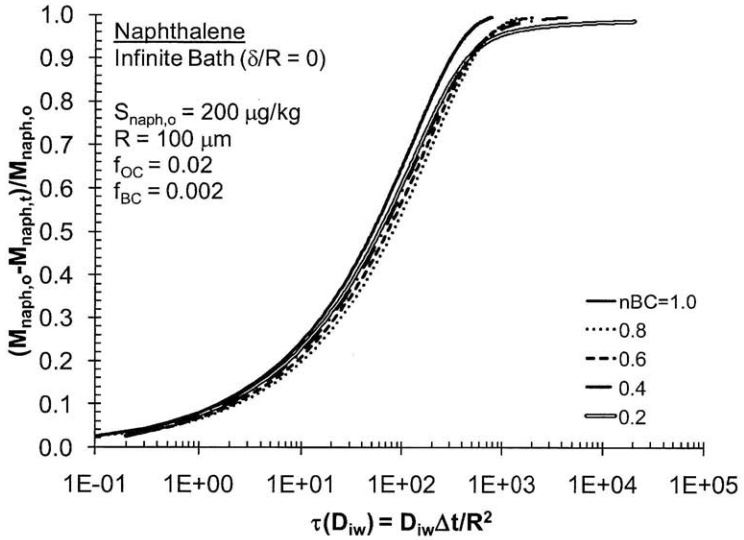

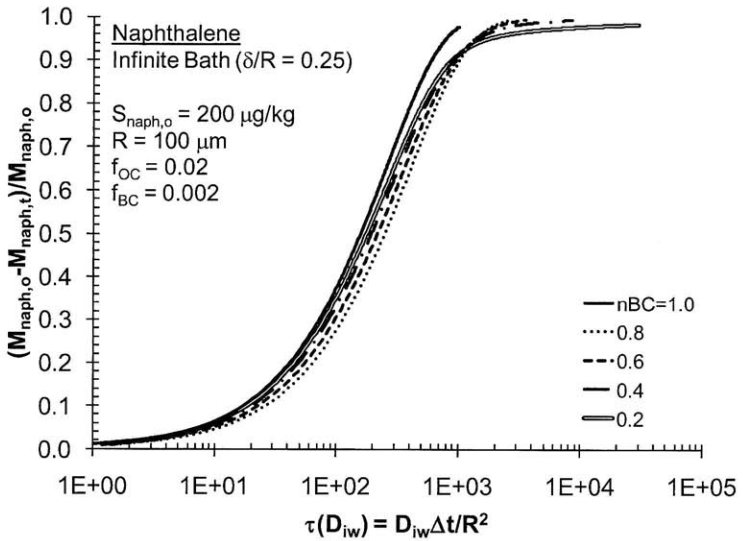

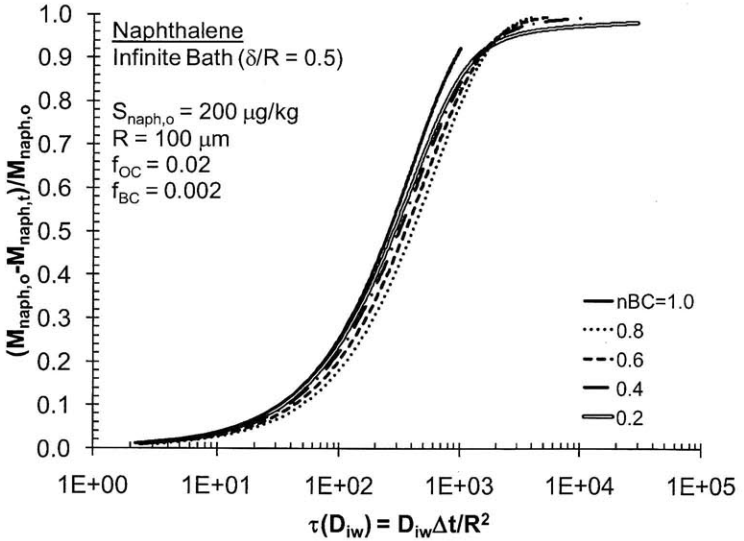

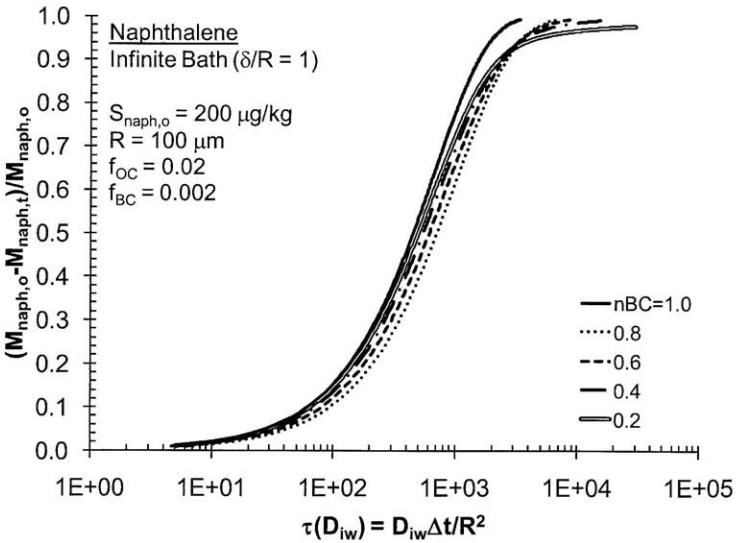

Naphthalene ($\log K_{OC}$ = 2.9, $\log K_{BC}$ = 3.9); $S_{naph,o}$ = 1000µg/kg

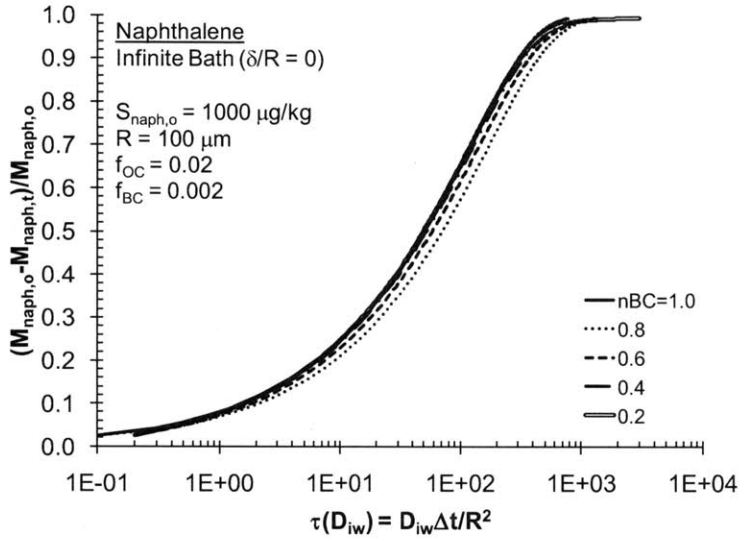

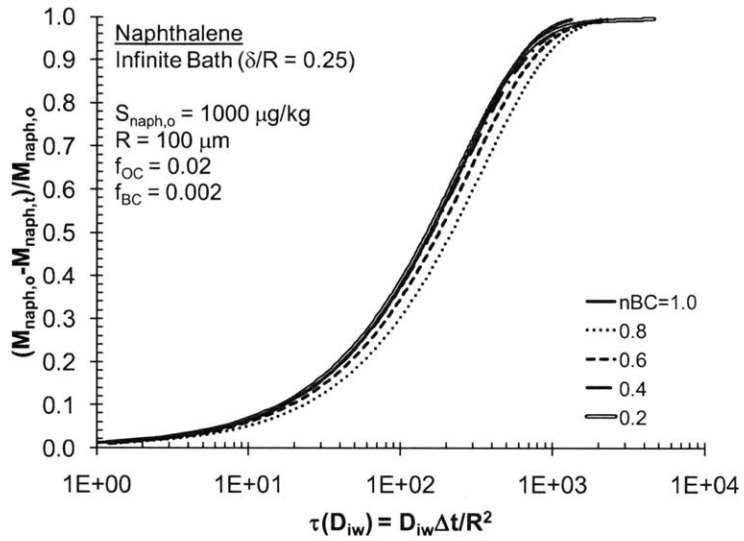

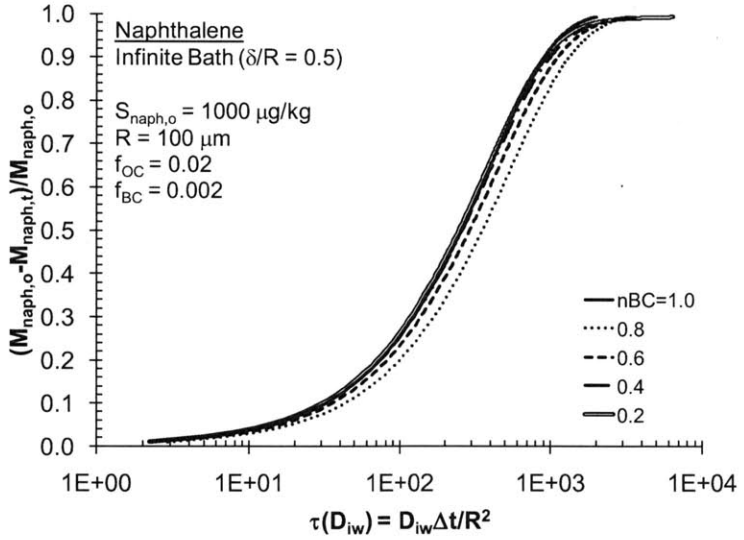

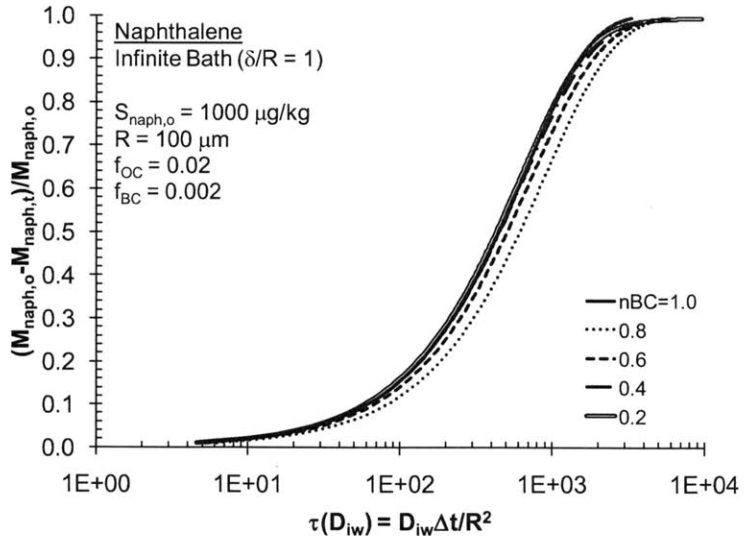

Naphthalene ($\log K_{OC}$ = 2.9, $\log K_{BC}$ = 3.9); $S_{naph,o}$ = 5000µg/kg

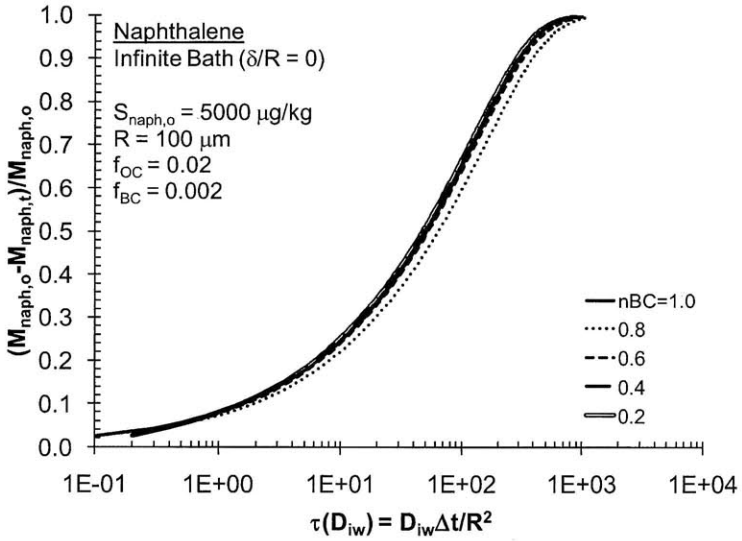

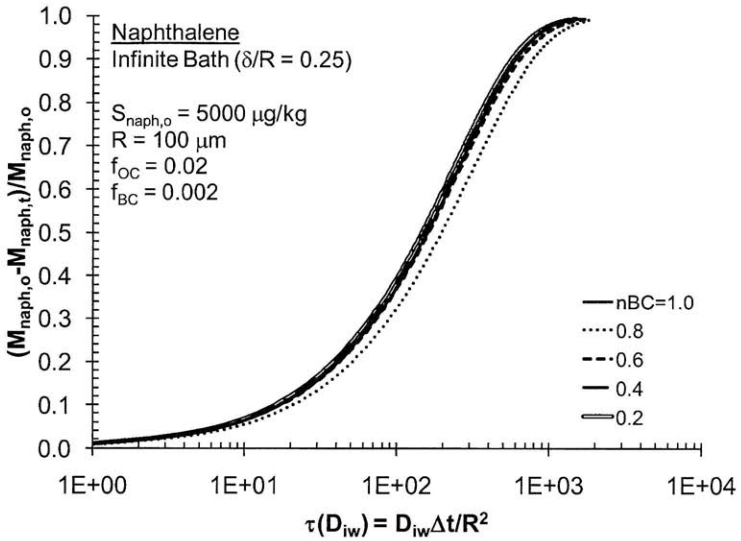

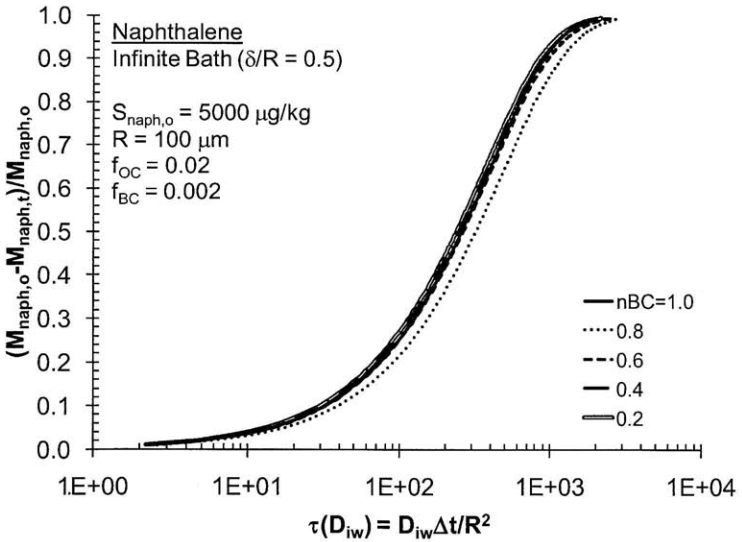

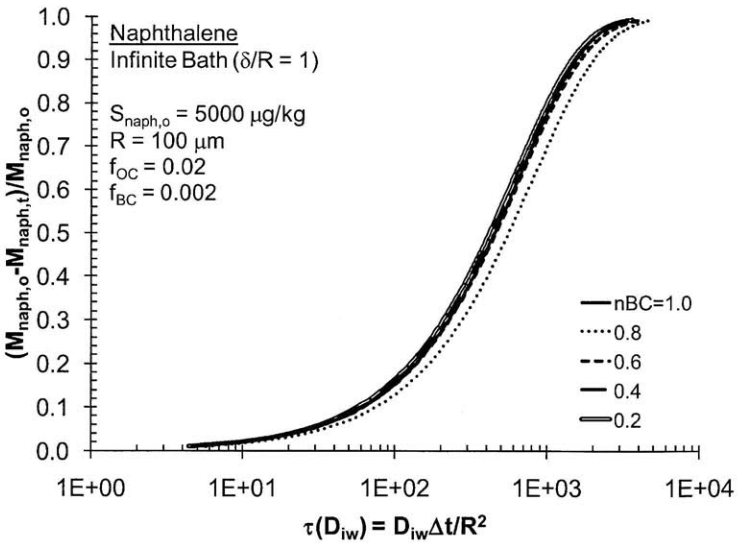

Phenanthrene ($\log K_{OC}$ = 4.2, $\log K_{BC}$ = 5.8); $S_{phe,o}$ = 200µg/kg

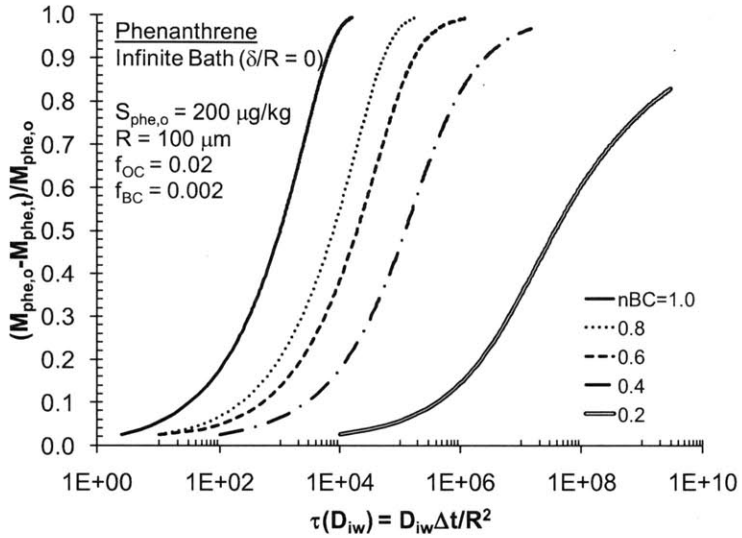

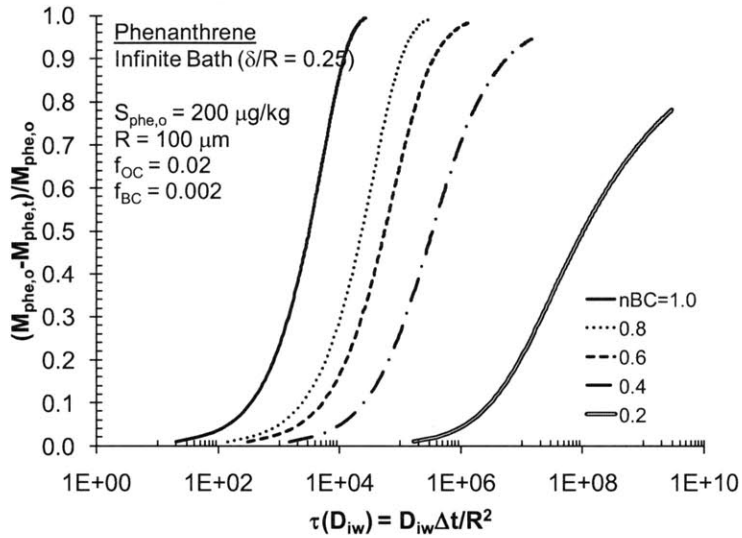

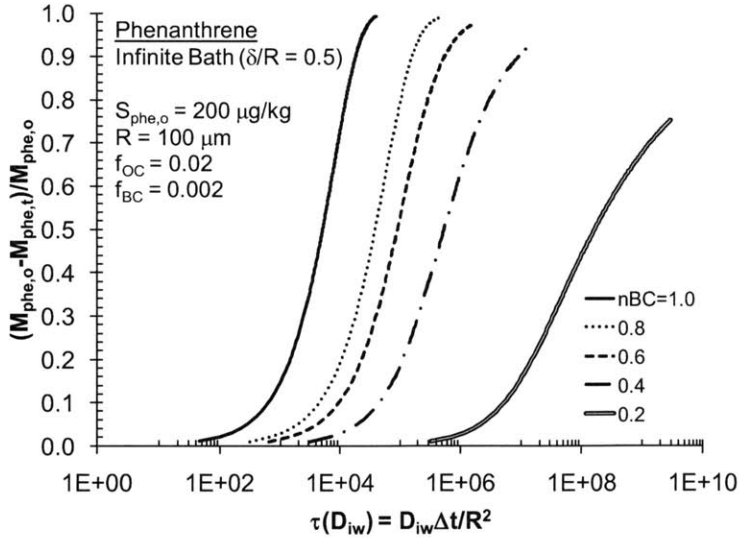

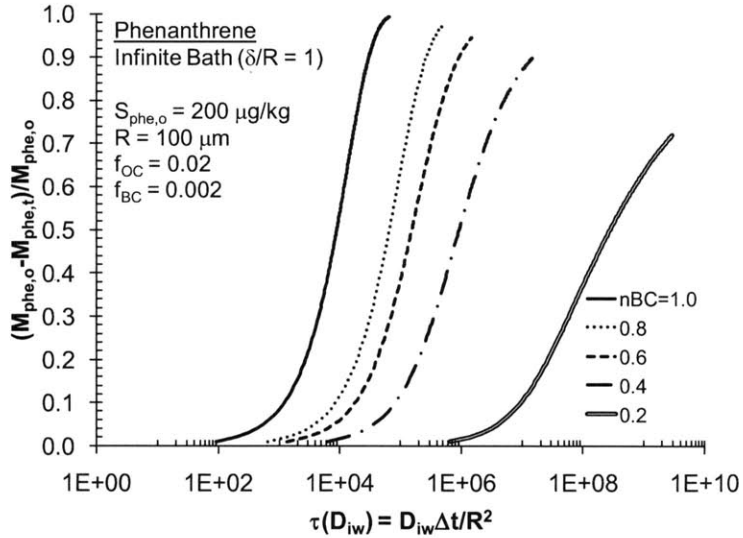

Phenanthrene ($logK_{OC}$ = 4.2, $logK_{BC}$ = 5.8); $S_{phe,o}$ = 1000µg/kg

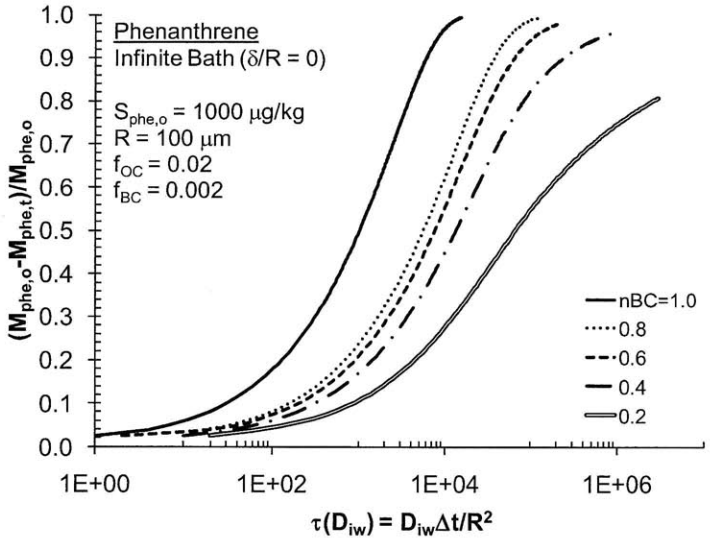

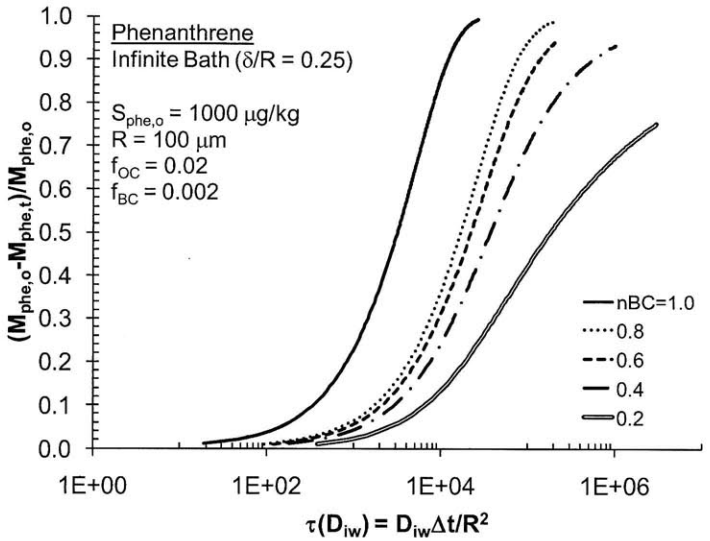

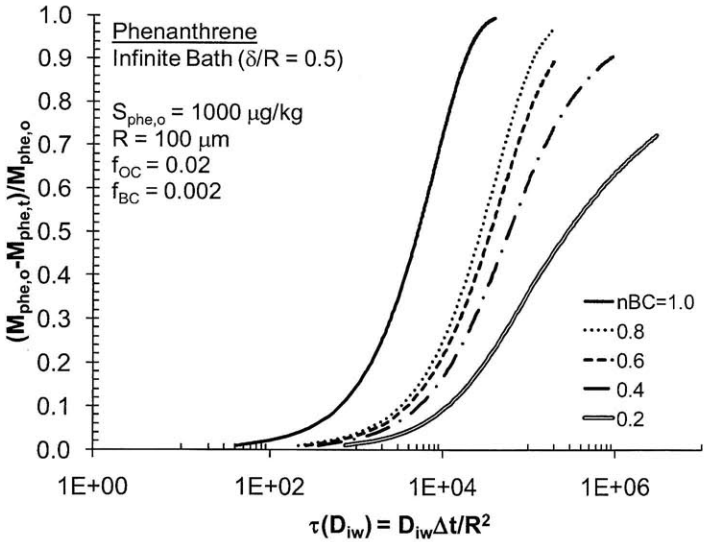

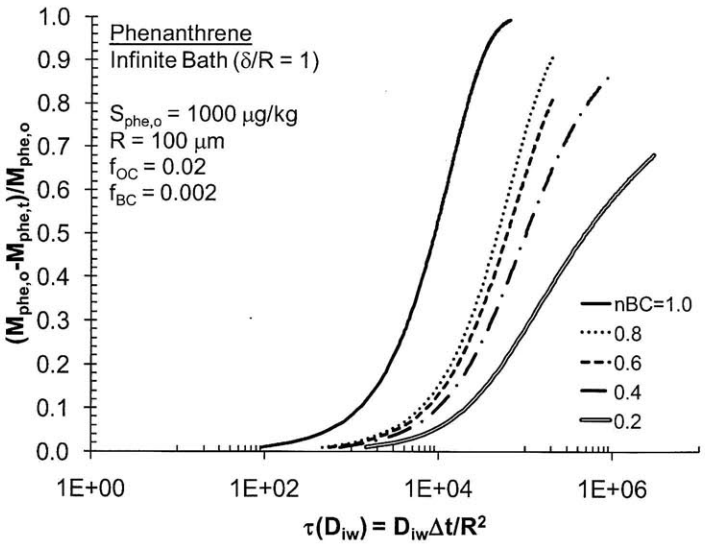

Phenanthrene ($\log K_{OC}$ = 4.2, $\log K_{BC}$ = 5.8); $S_{phe,o}$ = 5000µg/kg

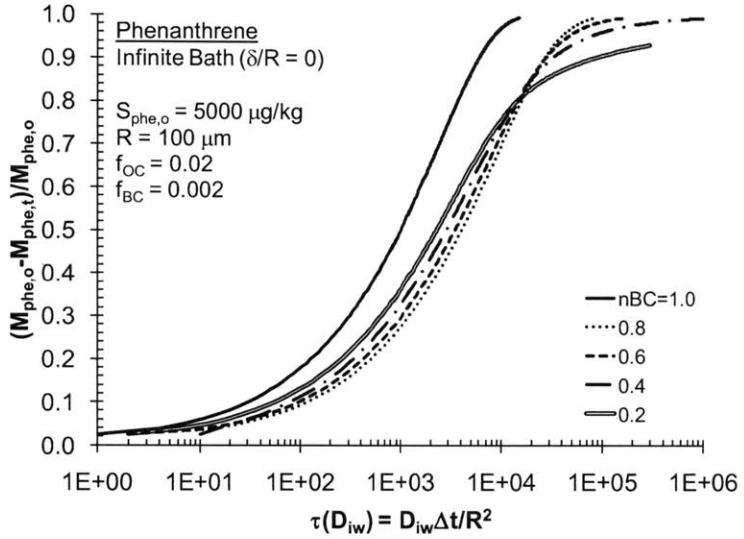

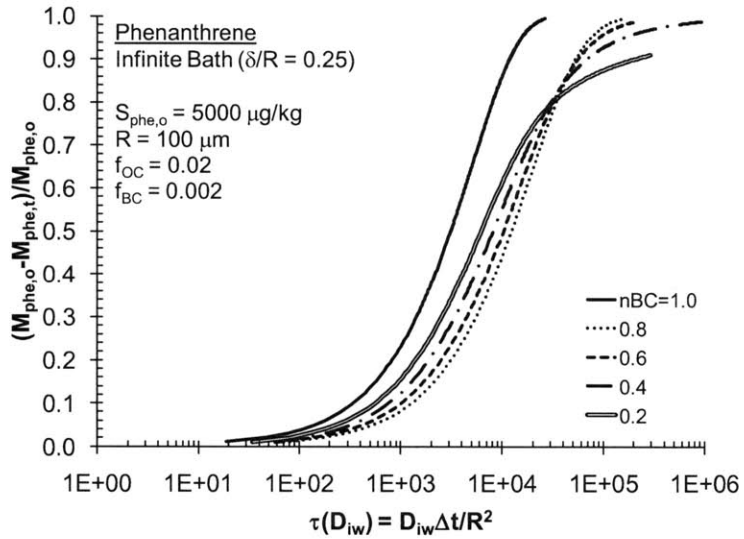

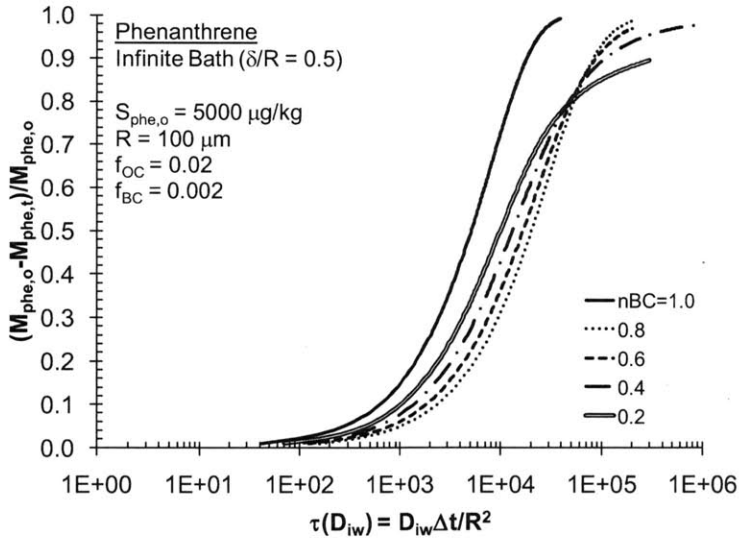

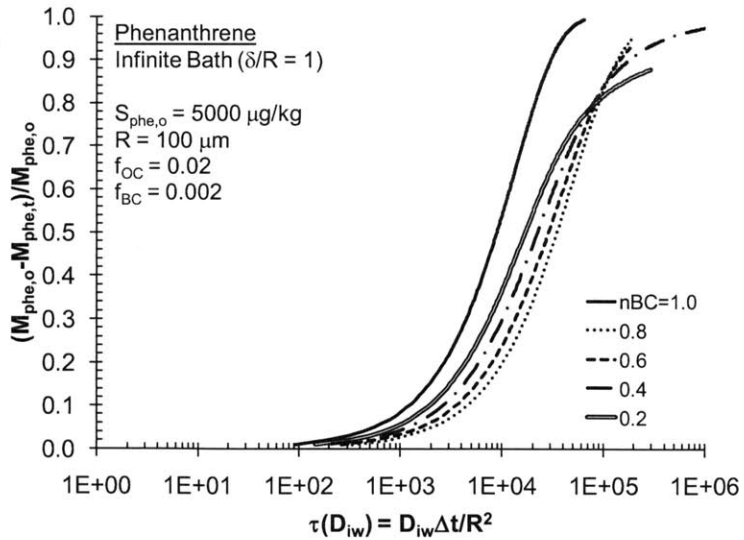

Pyrene ($\log K_{OC}$ = 4.7, $\log K_{BC}$ = 6.3); $S_{pyr,o}$ = 200µg/kg

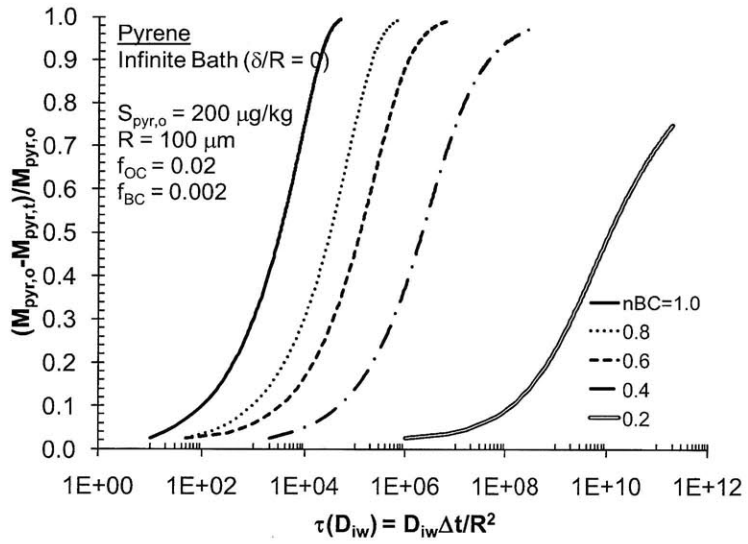

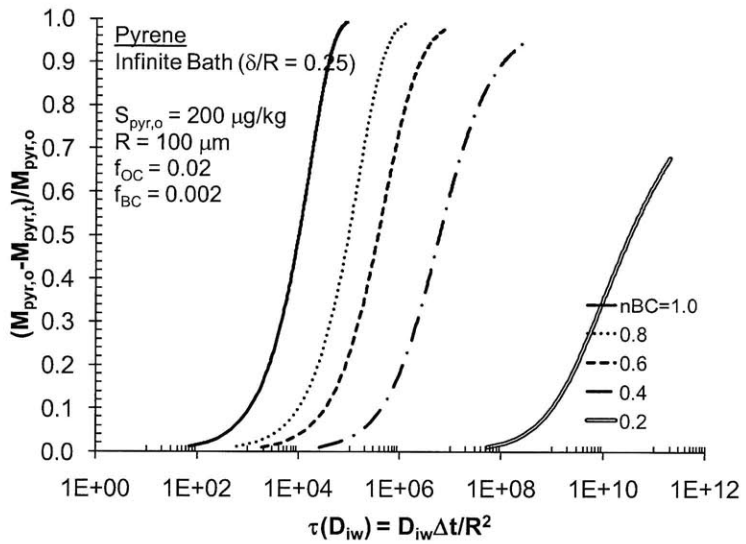

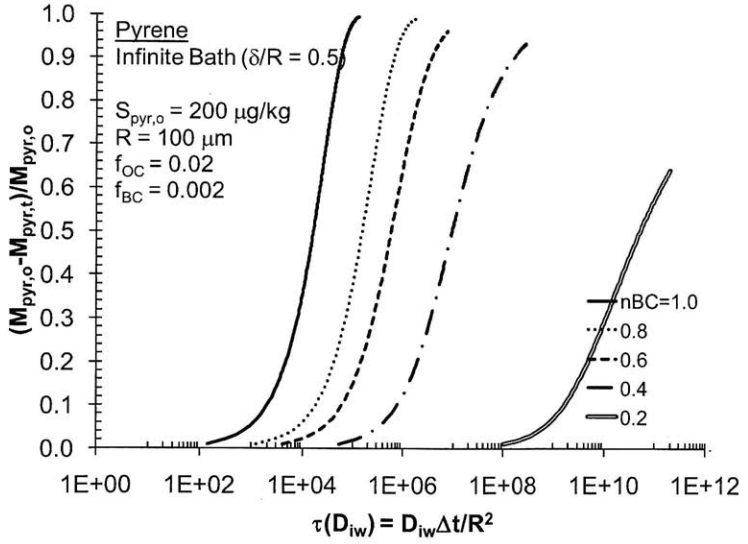

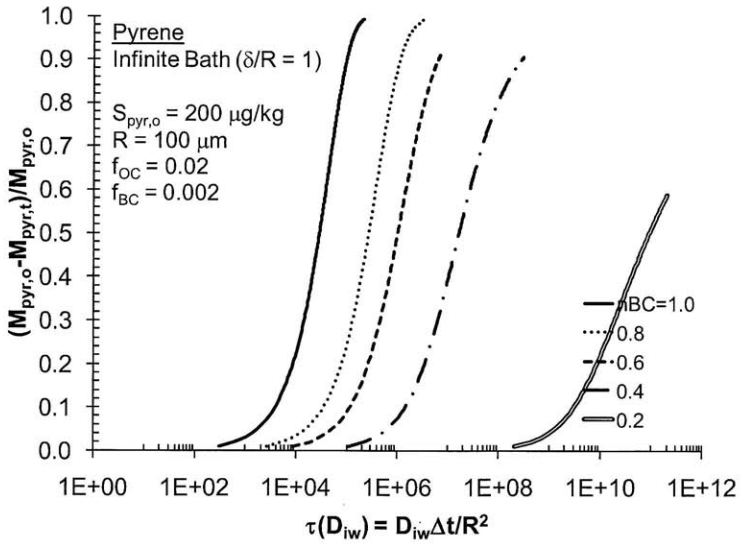

Pyrene ($\log K_{OC}$ = 4.7, $\log K_{BC}$ = 6.3); $S_{pyr,o}$ = 1000µg/kg

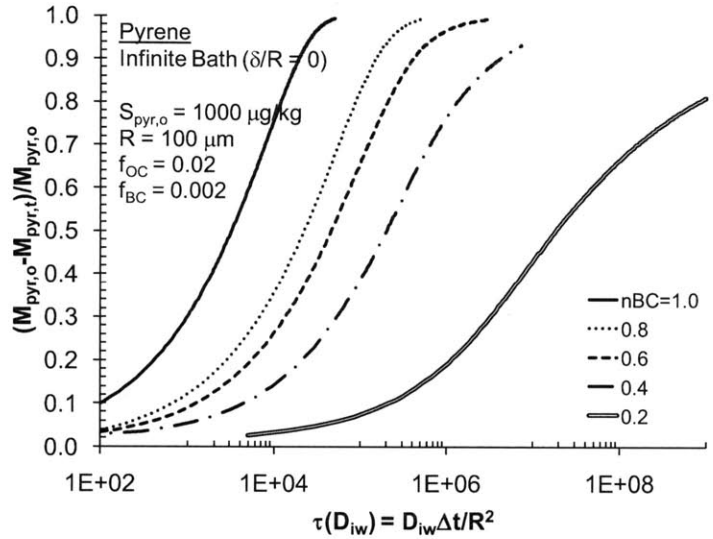

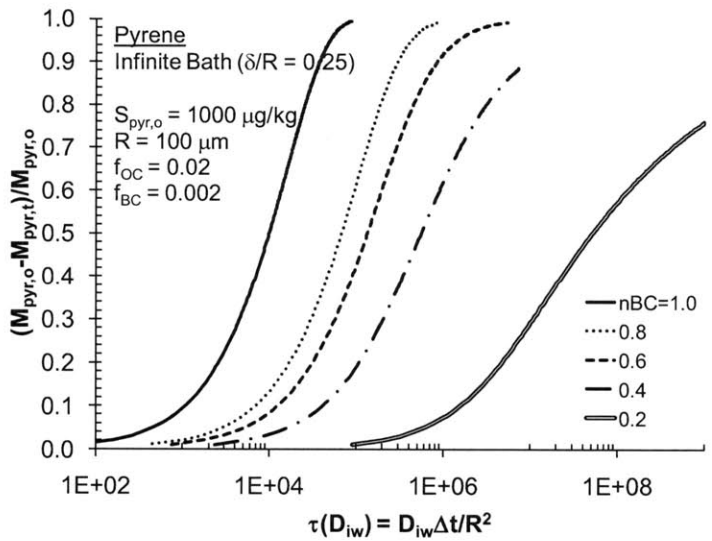

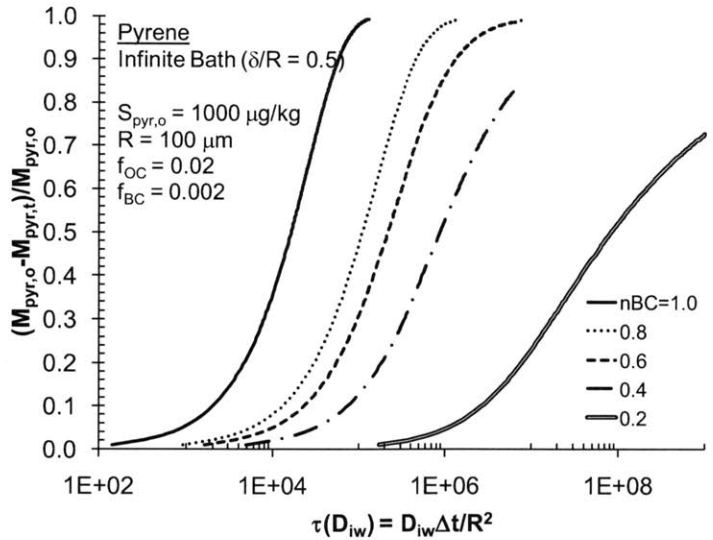

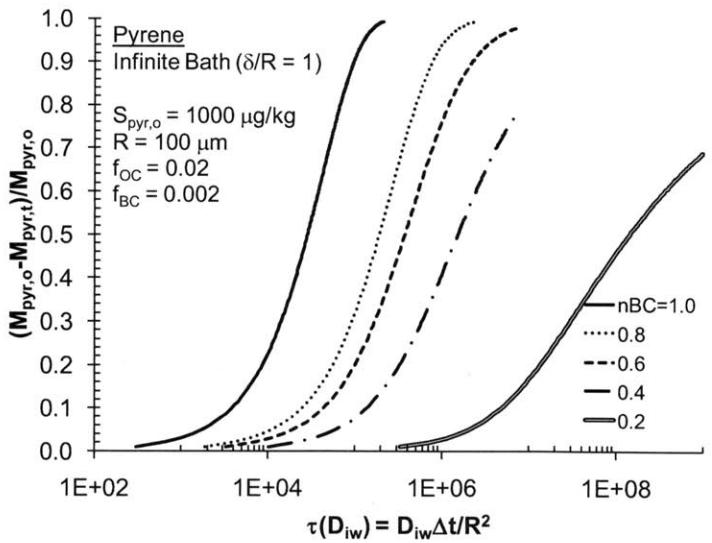

Pyrene ($\log K_{OC}$ = 4.7, $\log K_{BC}$ = 6.3); $S_{pyr,o}$ = 5000µg/kg

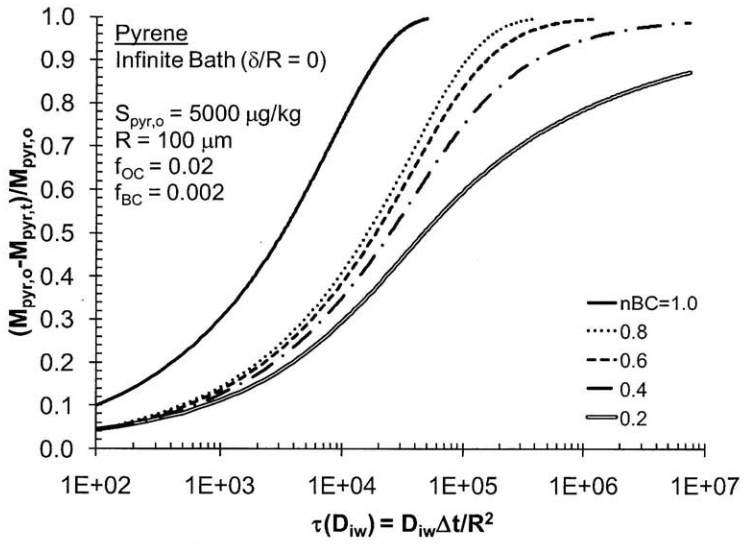

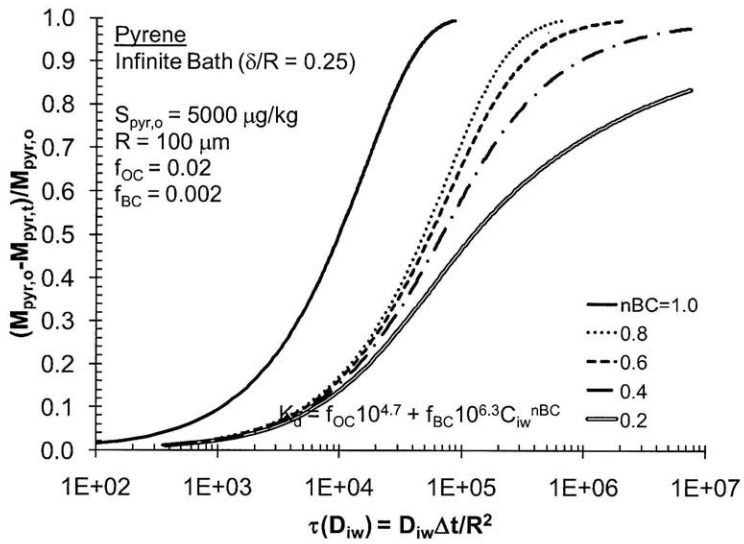

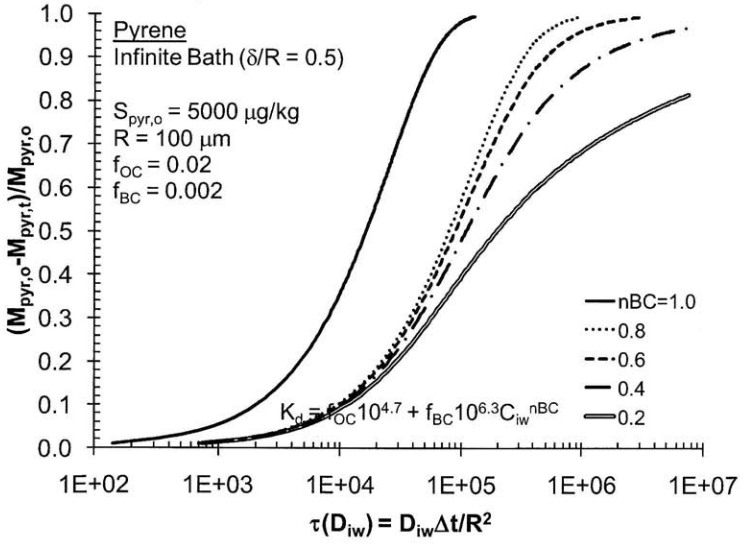

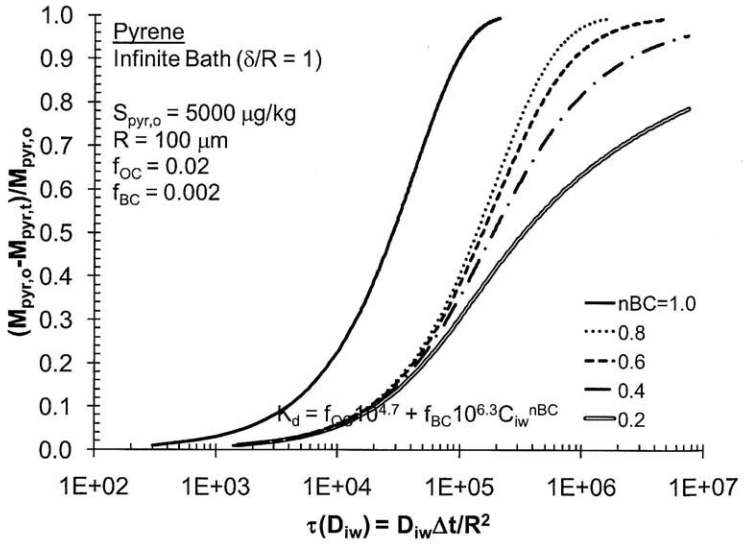

Benzo(a)pyrene ($\log K_{OC}$ = 5.4, $\log K_{BC}$ = 7.8); $S_{bap,o}$ = 200µg/kg

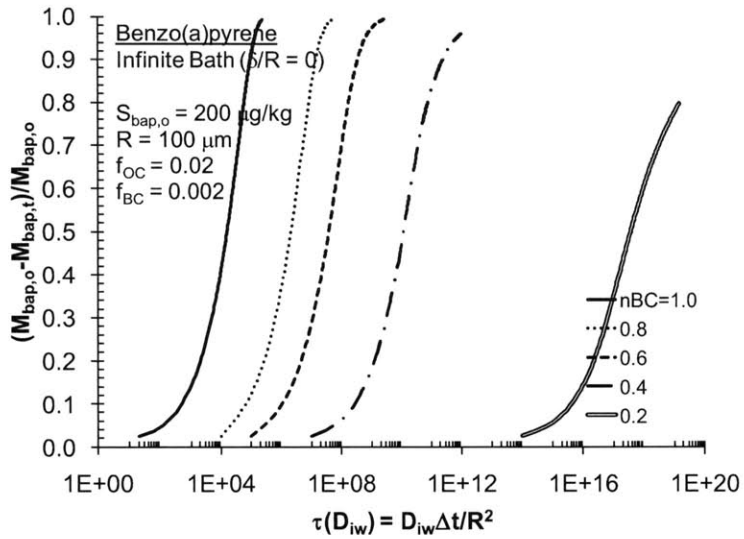

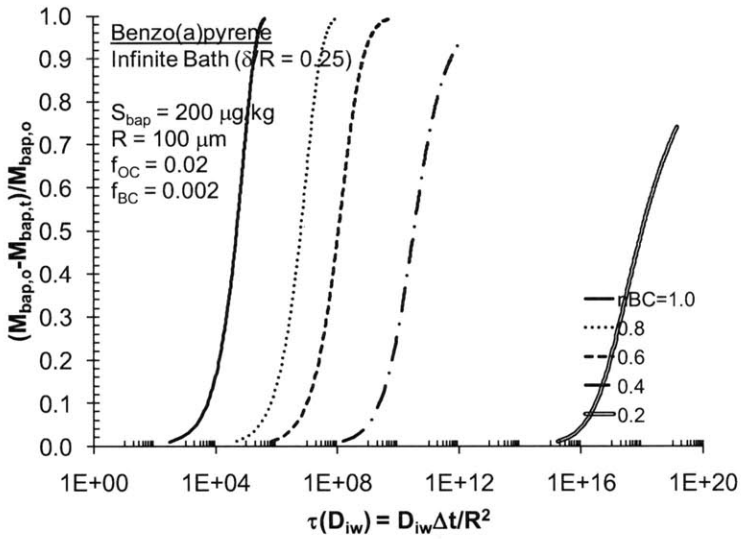

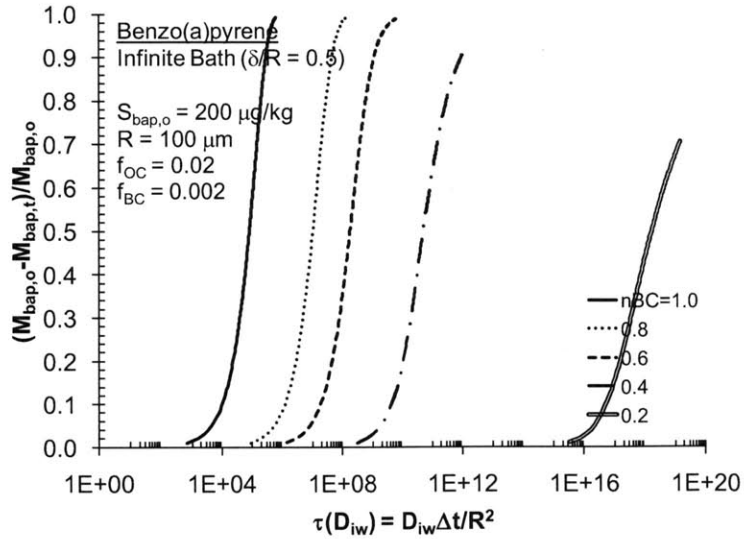

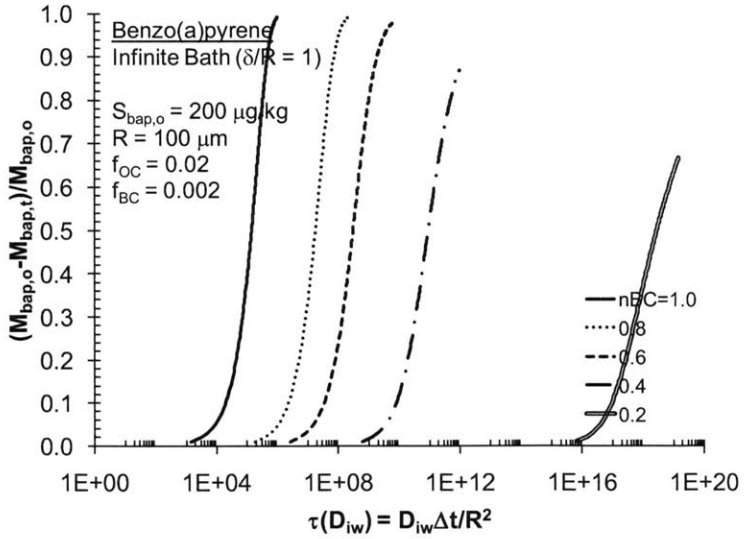

Benzo(a)pyrene ($\log K_{OC}$ = 5.4, $\log K_{BC}$ = 7.8); $S_{bap,o}$ = 1000µg/kg

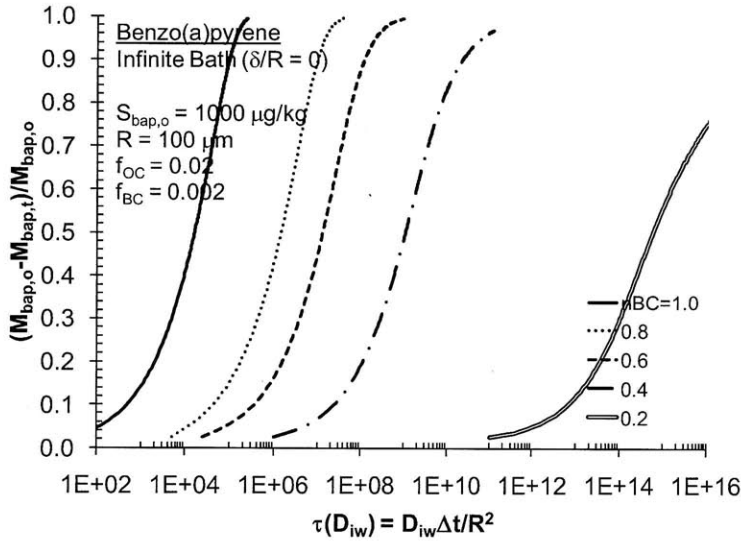

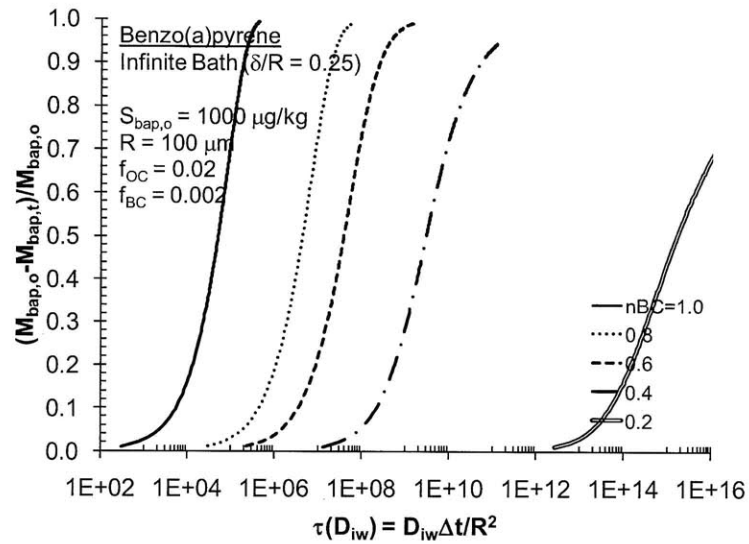

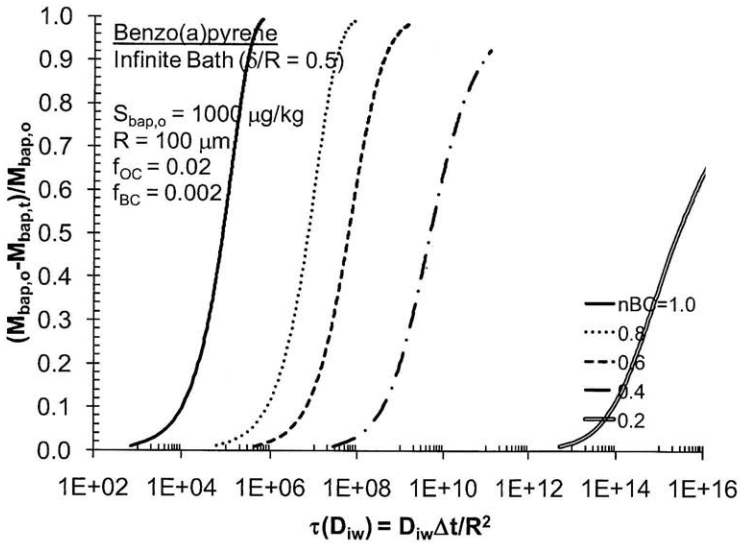

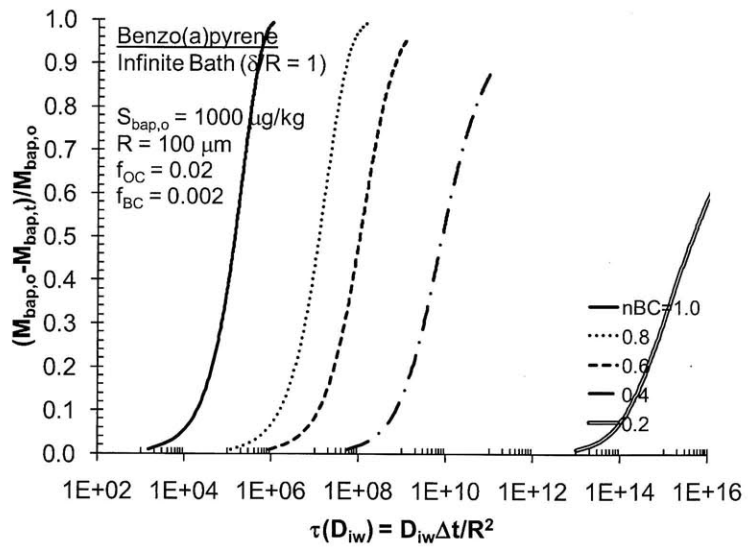

Benzo(a)pyrene ($\log K_{OC}$ = 5.4, $\log K_{BC}$ = 7.8); $S_{bap,o}$ = 5000µg/kg

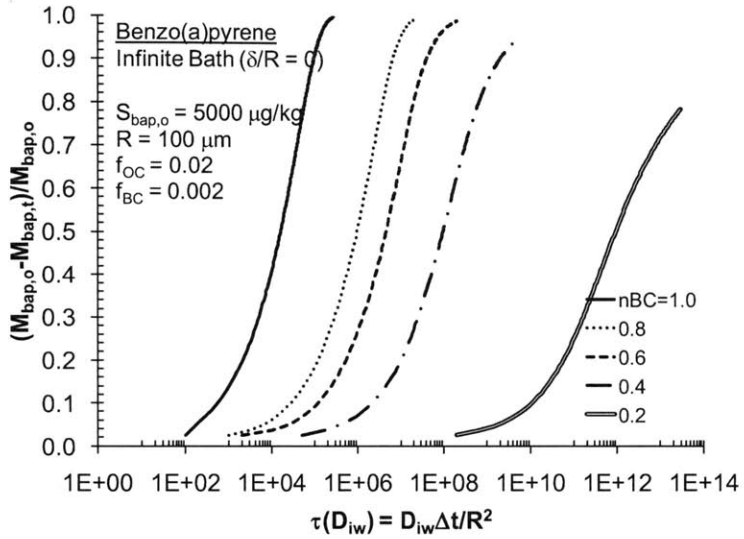

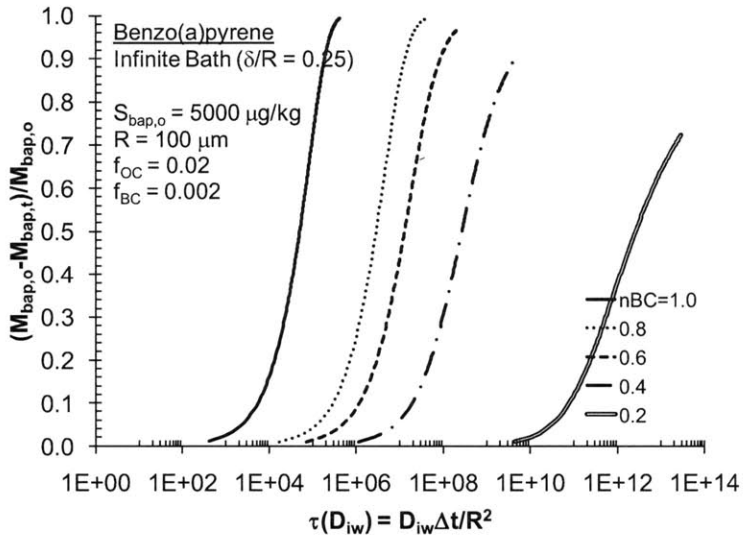

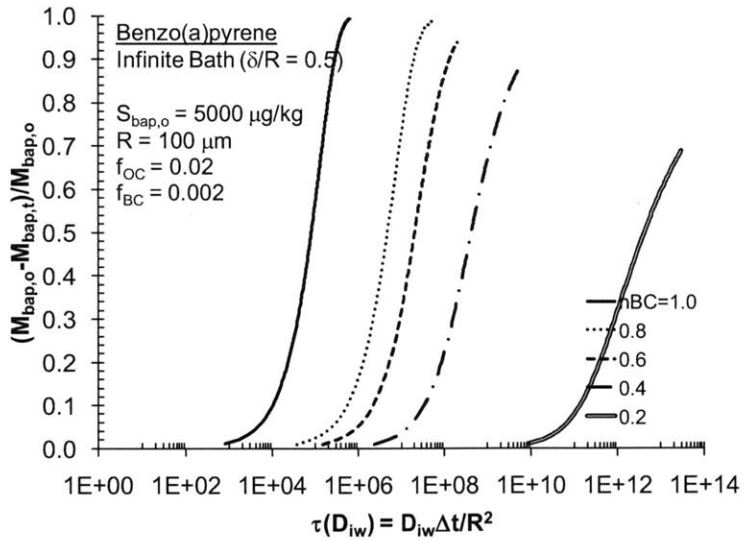

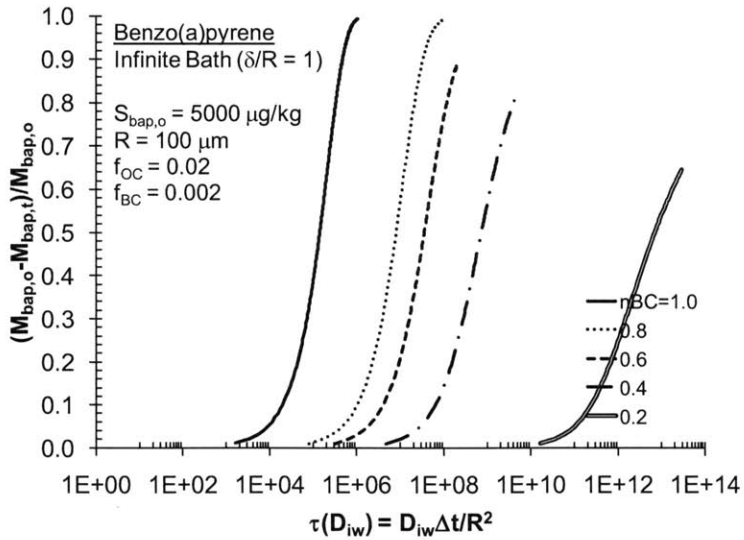

Appendix 8 - 3. Closed-System Desorption Profiles/Solutions for Selected PAHs (naphthalene & pyrene).

naphthalene, radius = 100 μm; S_o = 200, 1000, 5000 μg/kg.

pyrene, radius = 10, 100 μm; S_o = 200, 1000, 5000 μg/kg.

Naphthalene ($\log K_{OC}$ = 2.9, $\log K_{BC}$ = 3.9); $S_{naph,o}$ = 200µg/kg (Closed-System)

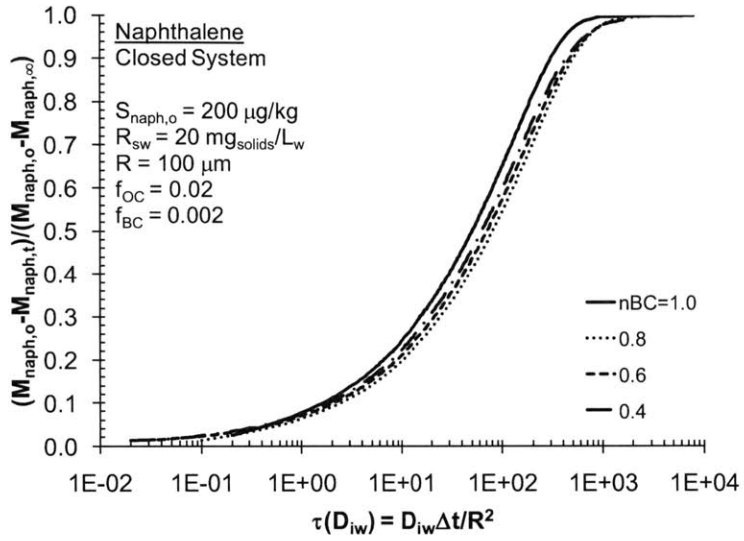

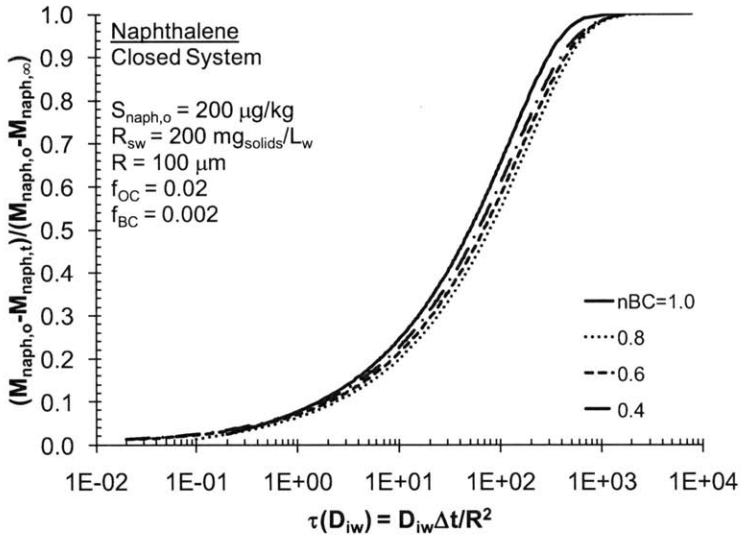

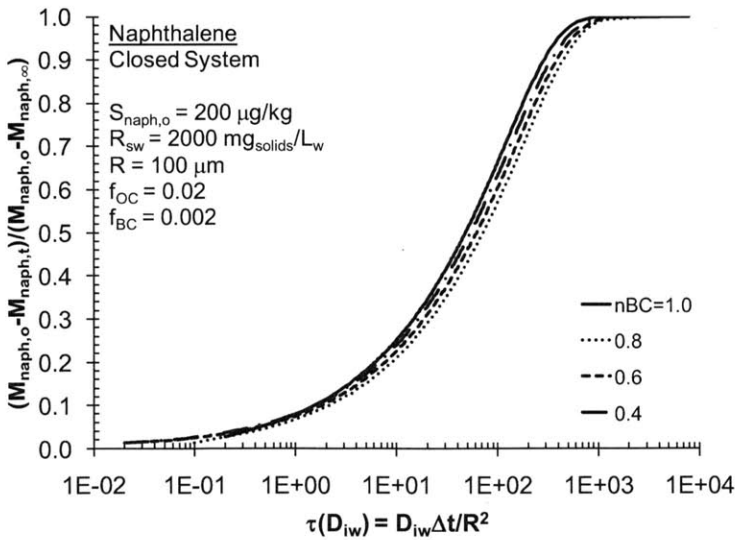

Naphthalene ($logK_{OC}$ = 2.9, $logK_{BC}$ = 3.9); $S_{naph,o}$ = 1000µg/kg (Closed-System)

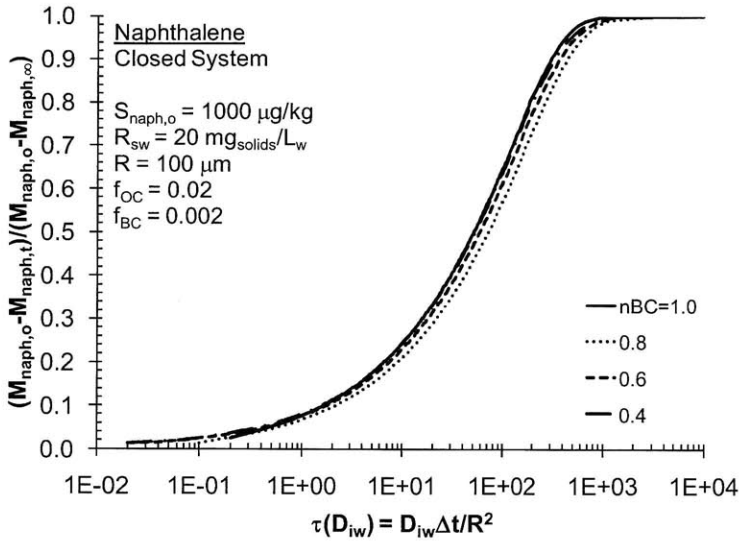

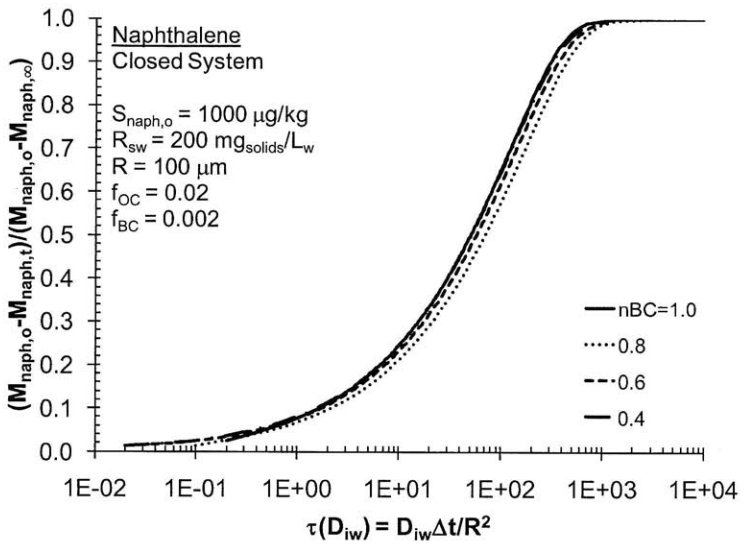

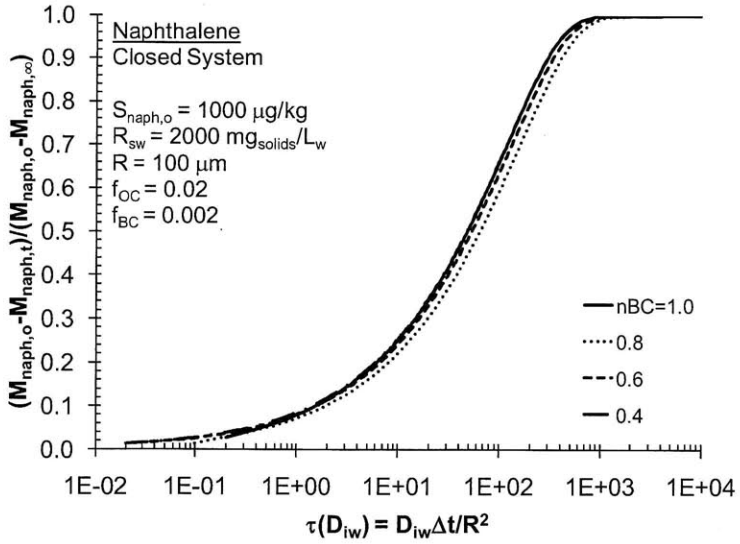

Naphthalene ($\log K_{OC}$ = 2.9, $\log K_{BC}$ = 3.9); $S_{naph,o}$ = 5000µg/kg (Closed-System)

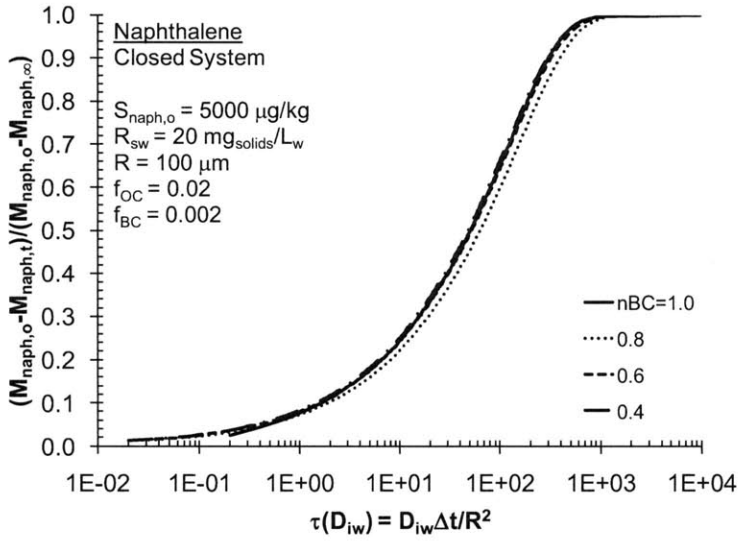

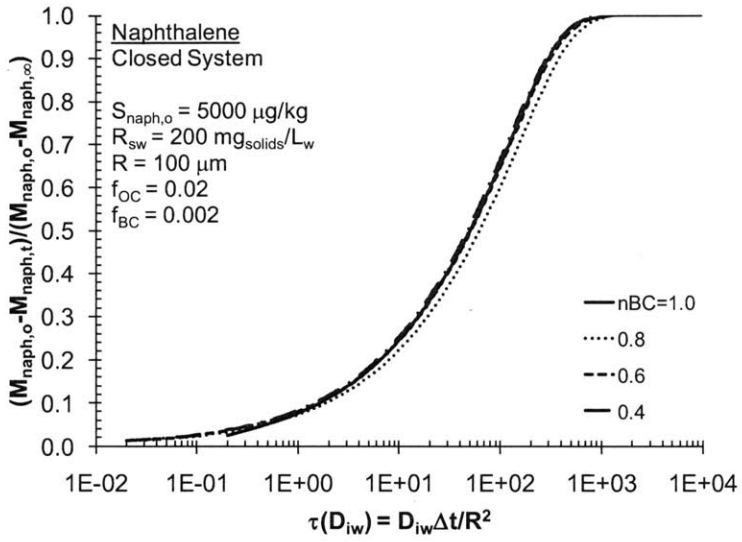

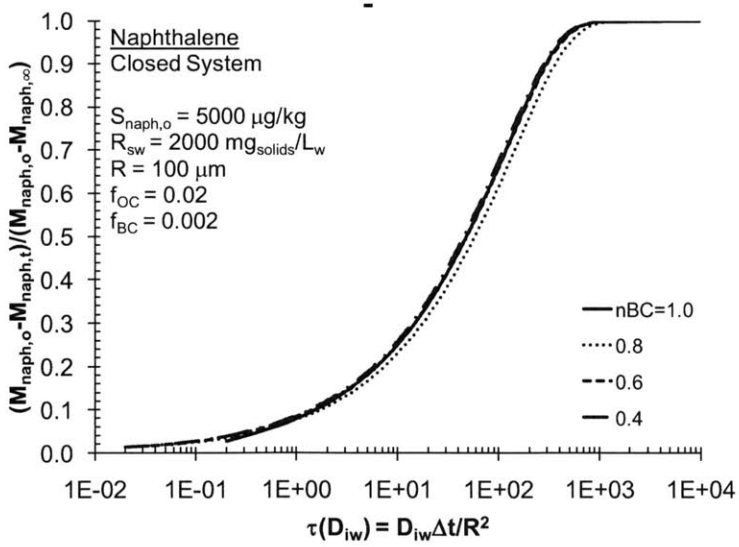

Pyrene ($\log K_{OC}$ = 4.7, $\log K_{BC}$ = 6.3); $S_{pyr,o}$ = 200µg/kg (Closed-System); Radius = 10 µm

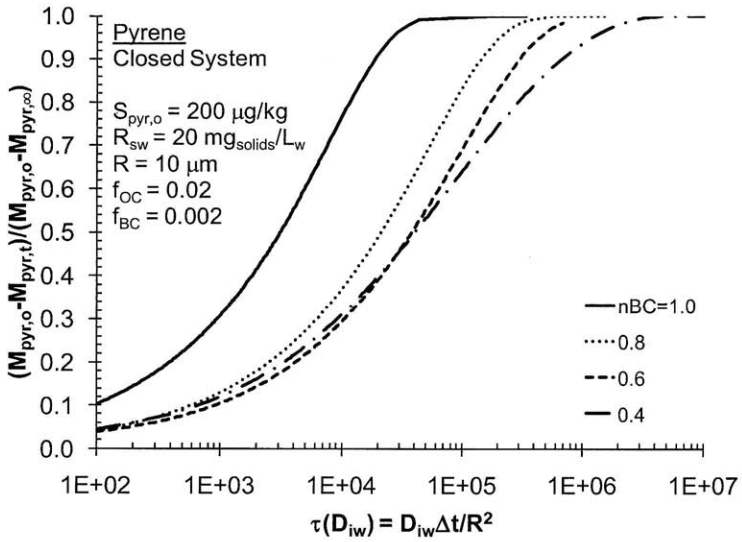

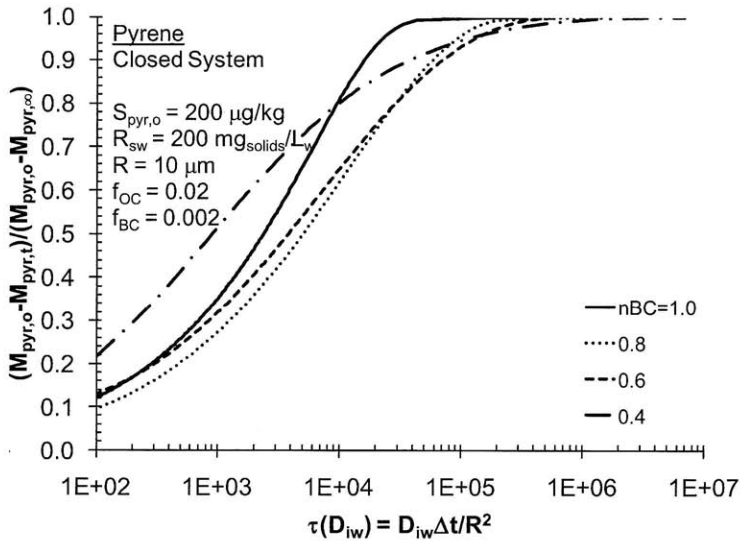

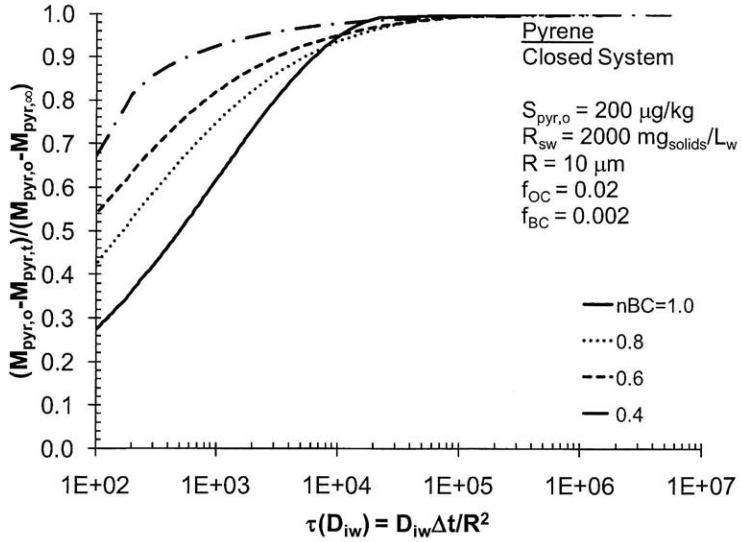

Pyrene ($\log K_{OC}$ = 4.7, $\log K_{BC}$ = 6.3); $S_{pyr,o}$ = 1000µg/kg (Closed-System); Radius = 10 µm

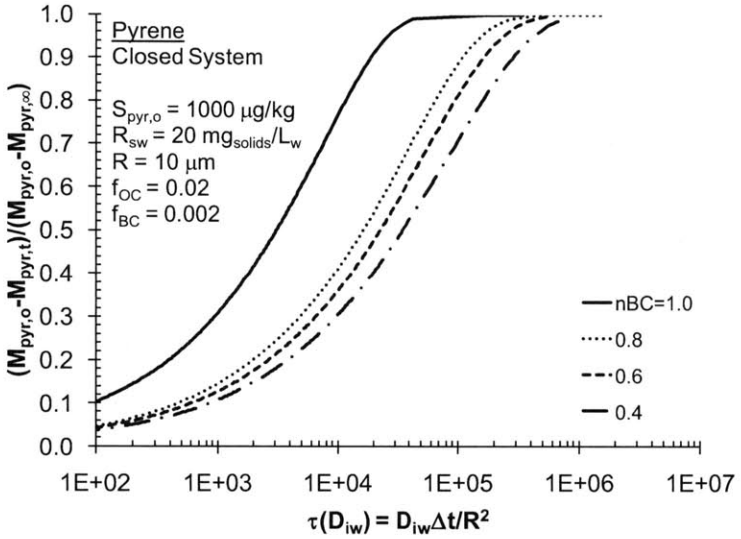

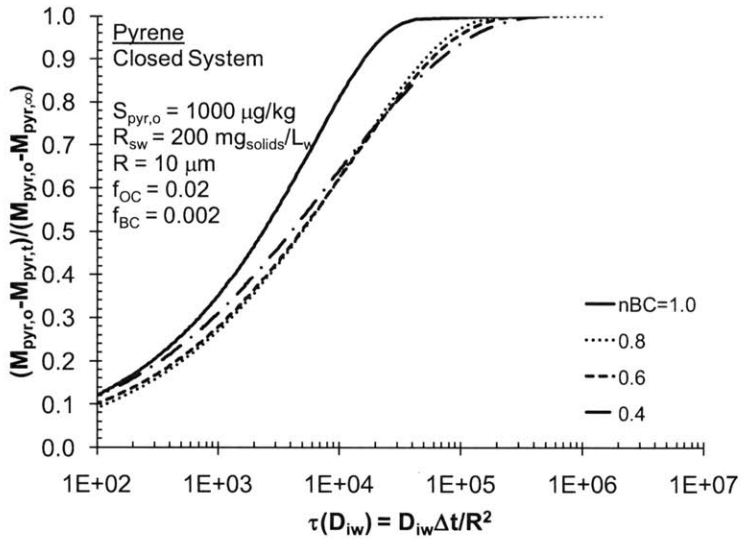

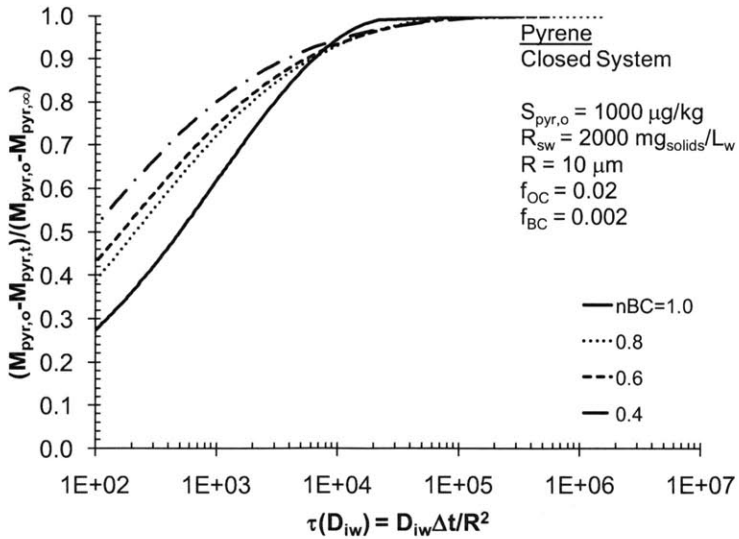

Pyrene ($\log K_{OC}$ = 4.7, $\log K_{BC}$ = 6.3); $S_{pyr,o}$ = 5000µg/kg (Closed-System); Radius = 10 µm

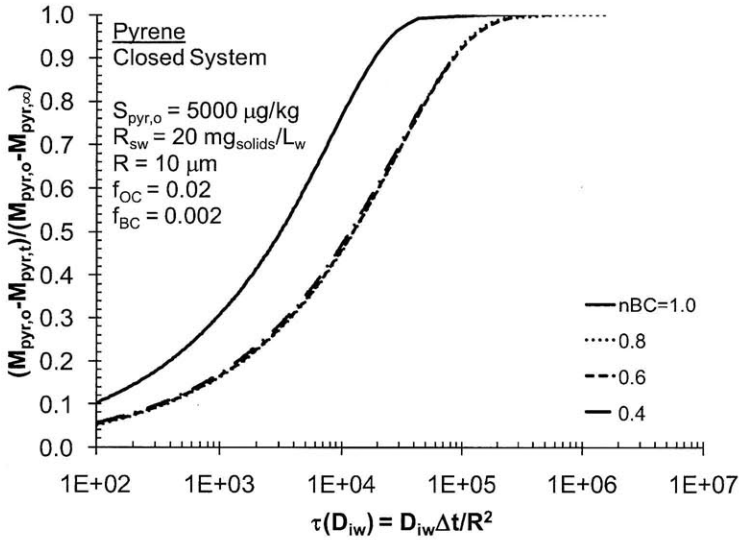

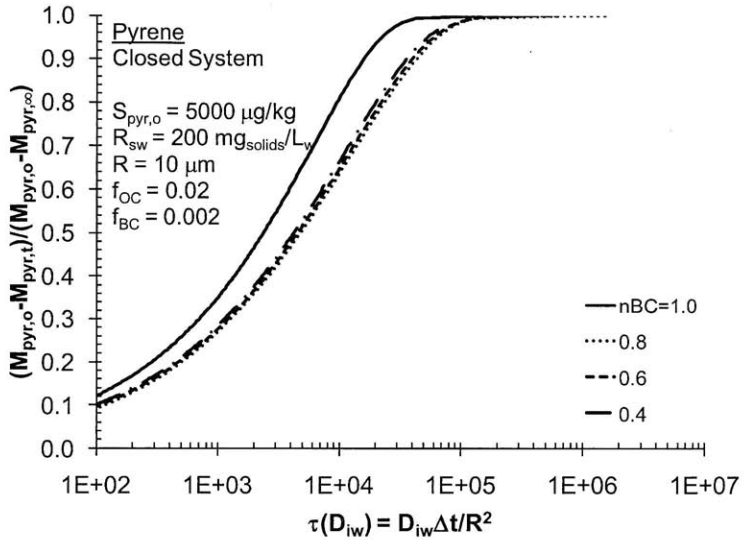

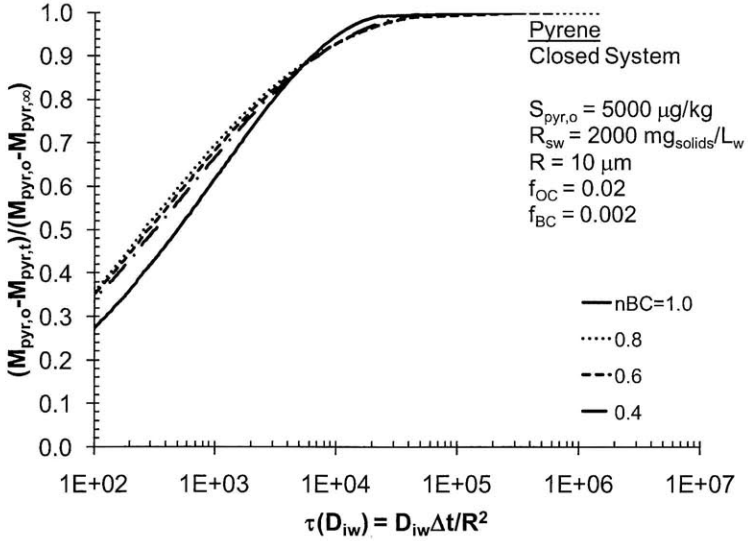

Pyrene ($logK_{OC}$ = 4.7, $logK_{BC}$ = 6.3); $S_{pyr,o}$ = 200µg/kg (Closed-System); Radius = 100 µm

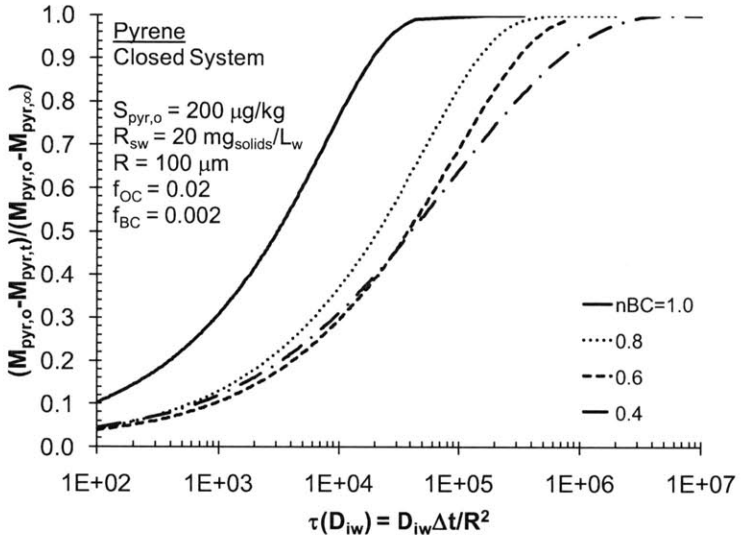

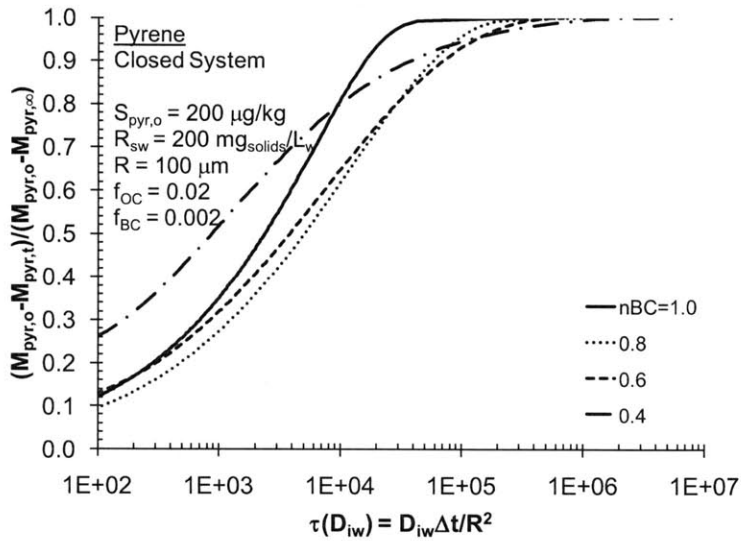

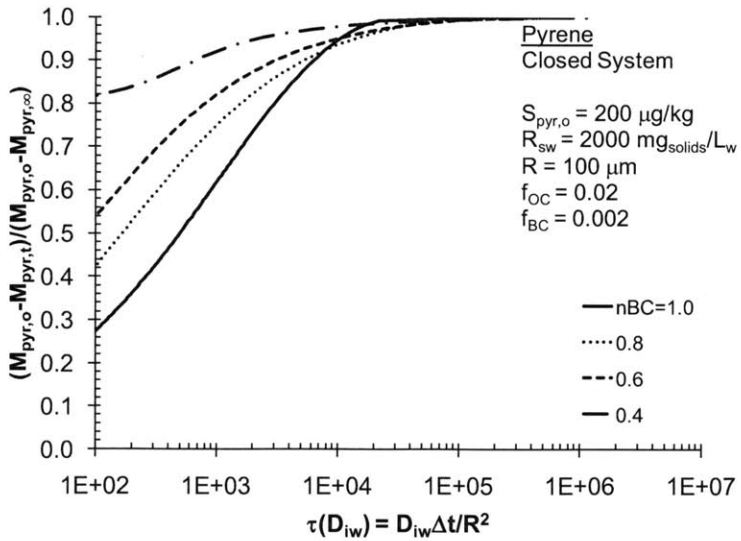

Pyrene ($\log K_{OC}$ = 4.7, $\log K_{BC}$ = 6.3); $S_{pyr,o}$ = 1000µg/kg (Closed-System); Radius = 100 µm

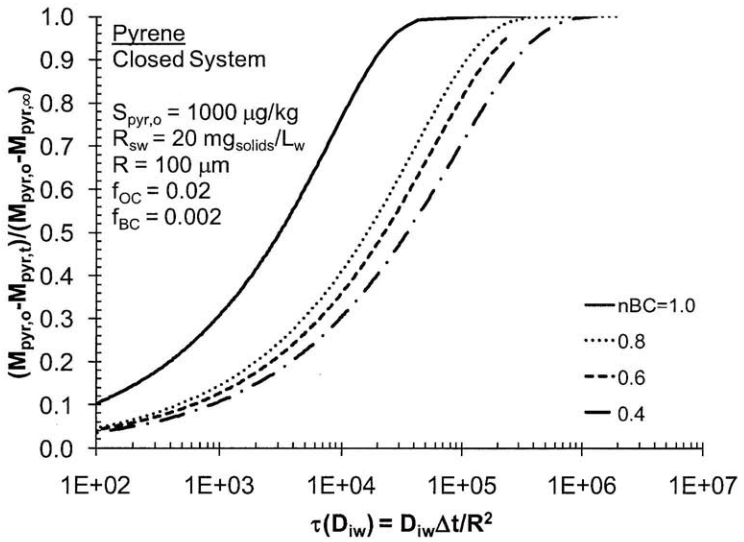

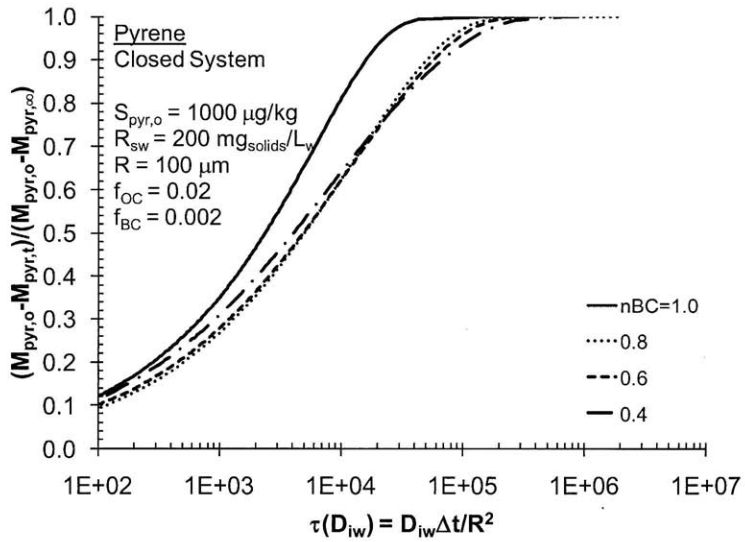

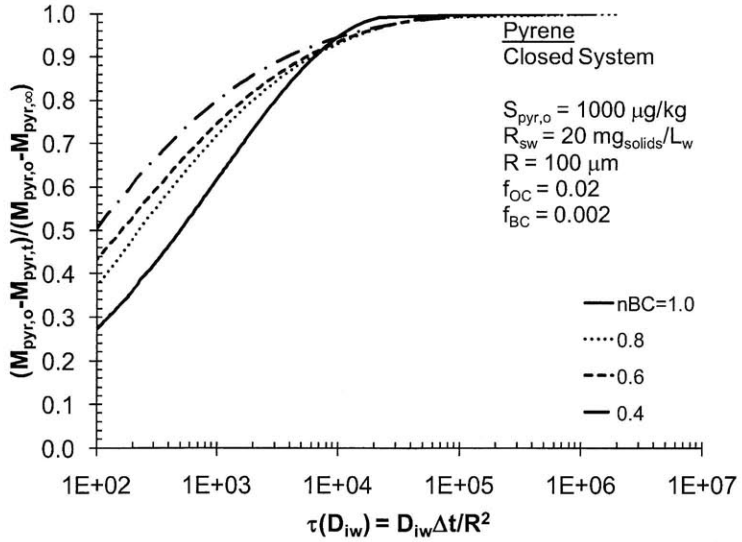

Pyrene ($\log K_{OC}$ = 4.7, $\log K_{BC}$ = 6.3); $S_{pyr,o}$ = 5000µg/kg (Closed-System); Radius = 100 µm

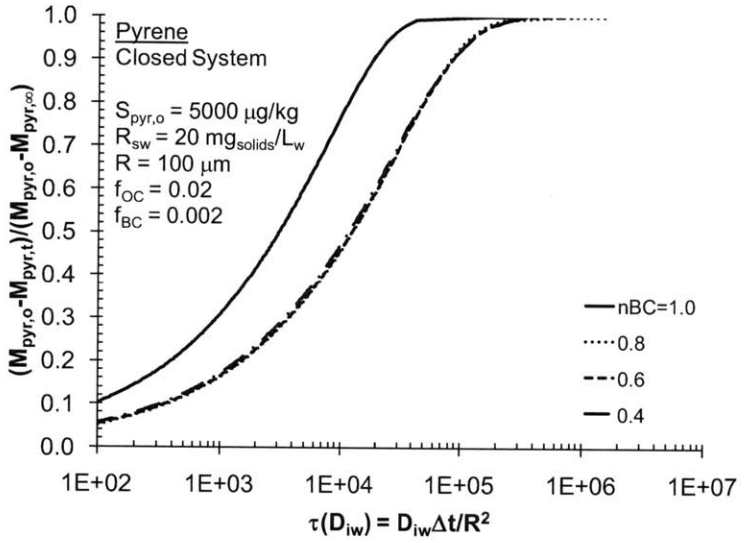

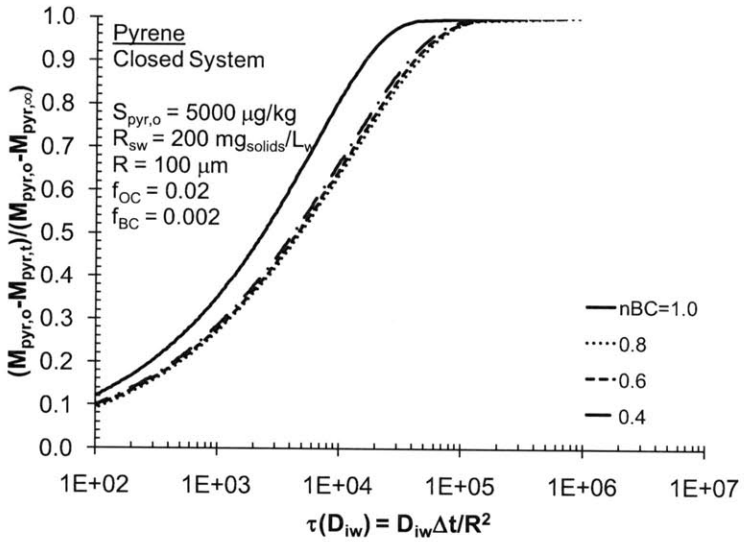

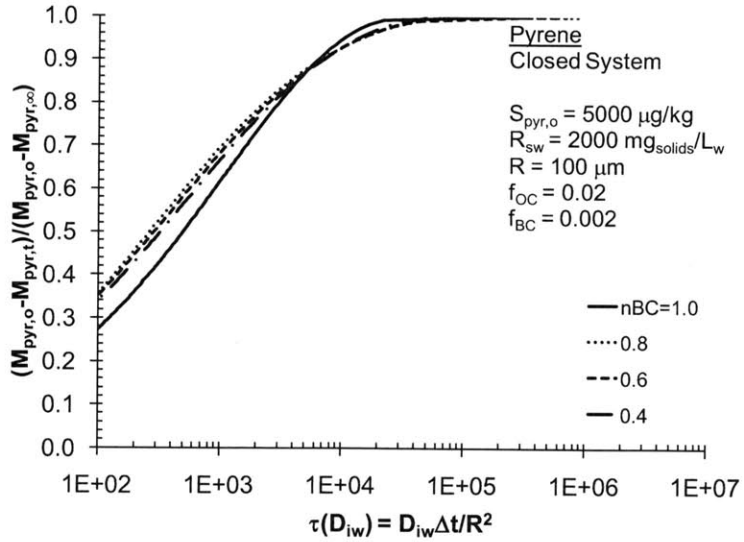

Chapter 9: Appendices

Appendix 9 - 1. Estimating Rate of Direct Photolysis of Pyrene 929
Appendix 9 - 2. Estimating Rate of Indirect Photolysis of Pyrene 937
Appendix 9 - 3. Estimating Biodegradation Rate of Pyrene. 950
Appendix 9 - 4. Seasonal atmospheric deposition rates of pyrene in Boston Harbor. 952
Appendix 9 - 5. Mean Photolysis Half-time ($t_{1/2,pyr,photolysis}$) and Water Depth. 953
Appendix 9 - 6. Derivation of Desorption Half-life ($t_{1/2,des}$). 953
Appendix 9 - 7. Sensitivity Analyses for Porewater Flushing Only Steady State Model. 957
Appendix 9 - 8. Sensitivity Analyses for the Three-Rate Steady State Model. 959
Appendix 9 - 9. Constancy of f_{retain} for Estimation of Sedimentary-Pyrene Depletion Time (EqP Models) 962
Appendix 9 - 10. Sedimentary PAHs and OC/BC contents of Boston Harbor samples analyzed by Ewald G. (~2000). 963

Appendix 9 - 1. Estimating Rate of Direct Photolysis of Pyrene

Overview

Assumptions

(i) That 'Summer' is about 20°C higher than 'Winter' case so that the intrinsic rate constants are reduced by a factor of 4.
(ii) That the concentrations of inorganic compounds in the harbor resemble that from lake studies (see notes in individual tables).
(iii) That the direct photolysis halftime is estimated assuming a first order reaction, so that $t_{1/2,pyrene,dir\text{-}photolysis}=\ln(2)/\{\Phi_{pyr}\, k^{z}_{a,tot}\}$

Parameters

-) Light absorption spectrum of pyrene was determined from aqueous pyrene standards, and was consistent with that obtained from a 95% ethanol solution (as in Friedel et al. 1951).

-) Solar irradiation intensities Table 15.3 and 15.4 in Schwarzenbach et al. 2003 were used for summer and winter scenarios.

-) $\alpha(\lambda)$ profile of Kleine Emme (Figure 15.11 in Schwarzenbach et al. 2003) was assumed for that of the Boston Harbor.

-) Dissolved organic carbon was assumed to be 3 mg_{OC}/L (taken as harbor water column DOC; Rudnick et al. 1998) for the low $t_{1/2,dir\text{-}photolysis}$ estimates, and 10 mg_{OC}/L (taken as geometric mean of bed porewater DOC's; McGroddy 1995) for the high estimates.

Decadic absorption coefficient for DOC (for estimating $\alpha(\lambda)$**)†

λ (nm)	$\alpha"_{observed}$ ($L/mg_{oc}.m$)	$\ln(\lambda)$	$\ln(\alpha")$	$\alpha"_{prediction}$* ($L/mg_{oc}.m$)
300	2.2	5.70	0.788	2.20
350	1.15	5.86	0.140	1.15
400	0.65	5.99	-0.431	0.65
		slope (m)*	*-4.24*	
		intercept (b)*	*24.96*	
		r^2	1.00	

†: From Kleine Emme, by Haag et al. 1986, according to Schwarzenbach et al. 2003, p.637.
*: So that $\ln(\alpha"_{predicted}) = m\ln(\lambda) + b$. Note that regressing the full range of reported observation (λ=300–600 nm) one would get a slope of ***–4.75*** and an intercept of ***27.9***.
**: So that $\alpha(\lambda)=\alpha"(\lambda)[DOC]$ (m^{-1}).

Summary of Results

[DOC] (mg_{OC}/L)	3	10	3	10	3	10
Z_{mix} (m)	1	1	3	3	10	10
Summer Case						
$k^z_{a,tot}=\Sigma k$	470	141	157	47	47	14
Φ_{pyr}			0.0021			
$\Phi_{pyr} k^z_{a,tot}$ (d^{-1})	9.87E-01	2.96E-01	3.29E-01	9.87E-02	9.87E-02	2.96E-02
$t_{1/2,pyrene,dir\text{-}photolysis}$ (d)	***0.7***	***2.3***	***2.1***	***7.0***	***7.0***	***23.4***
Winter Case						
$k^z_{a,tot}=\Sigma k$	121	36.4	40.4	12.1	12.1	3.6
Φ_{pyr}			0.0021			
$\Phi_{pyr} k^z_{a,tot}$ (d^{-1})	2.54E-01	7.63E-02	8.48E-02	2.54E-02	2.54E-02	7.63E-03
$t_{1/2,pyrene,dir\text{-}photolysis}$ (d)	***2.7***	***9.1***	***8.2***	***27.2***	***27.2***	***90.8***

Part A: Direct Photolysis of Pyrene (Summer 40°N)

Solar Irradiance at λ's and Molar Extinction Coefficients for $Pyrene_{(aq)}$.

λ_{cntr} (nm)	$\Delta\lambda$ (nm)	Z_{sum}(24hr) (40°N)	ε_{pyr} ($M^{-1}cm^{-1}$)	$k^{o}_{a,24h,pyr}$
297.5	2.5	2.68E-05	8575	0.53
300	2.5	1.17E-04	10832	2.91
302.5	2.5	3.60E-04	19847	16.43
305	2.5	8.47E-04	17291	33.69
307.5	2.5	1.62E-03	11513	42.90
310	2.5	2.68E-03	14424	88.91
312.5	2.5	3.94E-03	16681	151.16
315	2.5	5.30E-03	24404	297.48
317.5	2.5	6.73E-03	29557	457.51
320	2.5	8.12E-03	18597	347.33
323.1	3.75	1.45E-02	15332	511.33
330	10	5.03E-02	24084	2786.32
340	10	6.34E-02	7716	1125.12
350	10	7.03E-02	0	0.00
360	10	7.77E-02	0	0.00
370	10	8.29E-02	0	0.00
380	10	8.86E-02	0	0.00
390	10	8.32E-02	0	0.00
400	10	1.20E-01	0	0.00

Z_{mix}= 1 m (Summer 40°N)						
[DOC] (mg_{OC}/L)	3	10	3	10	3	10
λ_{cntr} (nm)	$\alpha(\lambda)(m^{-1})$	$\alpha(\lambda)(m^{-1})$	S(λ)	S(λ)	$k^{z}_{a,24h,pyr}$	$k^{z}_{a,24h,pyr}$
297.5	6.8	22.8	0.053	0.016	0.03	0.01
300	6.6	22.0	0.055	0.016	0.16	0.05
302.5	6.4	21.3	0.057	0.017	0.93	0.28
305	6.2	20.5	0.059	0.018	1.98	0.59
307.5	6.0	19.8	0.061	0.018	2.61	0.78
310	5.8	19.2	0.063	0.019	5.60	1.68
312.5	5.6	18.5	0.065	0.020	9.85	2.96
315	5.4	17.9	0.067	0.020	20.05	6.02
317.5	5.2	17.3	0.070	0.021	31.89	9.57
320	5.0	16.8	0.072	0.022	25.03	7.51
323.1	4.8	16.1	0.075	0.023	38.38	11.51
330	4.4	14.7	0.082	0.025	228.75	68.62
340	3.9	13.0	0.093	0.028	104.82	31.45
350	3.4	11.5	0.105	0.032	0.00	0.00
360	3.1	10.2	0.119	0.036	0.00	0.00
370	2.7	9.1	0.133	0.040	0.00	0.00
380	2.4	8.1	0.149	0.045	0.00	0.00
390	2.2	7.2	0.166	0.050	0.00	0.00
400	2.0	6.5	0.185	0.056	0.00	0.00
			$k^{z}_{a,tot}=\Sigma k$		*470.09*	*141.03*
	Φ_i=0.0021		$k^{z}_{a,tot}=\Phi_i k^{z}_{a,tot}$		*9.87E-01*	*2.96E-01*
			$t_{1/2,dir.photolysis}$ (d)		*0.7*	*2.3*

Z_{mix}= 3 m (Summer 40°N)

[DOC] (mg_{OC}/L)	3	10	3	10	3	10
λ_{cntr} (nm)	$\alpha(\lambda)(m^{-1})$	$\alpha(\lambda)(m^{-1})$	$S(\lambda)$	$S(\lambda)$	$k^z_{a,24h,pyr}$	$k^z_{a,24h,pyr}$
297.5	6.8	22.8	0.018	0.005	0.01	0.00
300	6.6	22.0	0.018	0.005	0.05	0.02
302.5	6.4	21.3	0.019	0.006	0.31	0.09
305	6.2	20.5	0.020	0.006	0.66	0.20
307.5	6.0	19.8	0.020	0.006	0.87	0.26
310	5.8	19.2	0.021	0.006	1.87	0.56
312.5	5.6	18.5	0.022	0.007	3.28	0.99
315	5.4	17.9	0.022	0.007	6.68	2.01
317.5	5.2	17.3	0.023	0.007	10.63	3.19
320	5.0	16.8	0.024	0.007	8.34	2.50
323.1	4.8	16.1	0.025	0.008	12.79	3.84
330	4.4	14.7	0.027	0.008	76.25	22.87
340	3.9	13.0	0.031	0.009	34.94	10.48
350	3.4	11.5	0.035	0.011	0.00	0.00
360	3.1	10.2	0.040	0.012	0.00	0.00
370	2.7	9.1	0.044	0.013	0.00	0.00
380	2.4	8.1	0.050	0.015	0.00	0.00
390	2.2	7.2	0.056	0.017	0.00	0.00
400	2.0	6.5	0.062	0.019	0.00	0.00
			$k^z_{a,tot}=\Sigma k$		***156.70***	***47.01***
	Φ_i=0.0021		$k^z_{a,tot}=\Phi_i k^z_{a,tot}$		***3.29E-01***	***9.87E-02***
			$t_{1/2,dir.photolysis}$ (d)		***2.1***	***7.0***

Z_{mix}= 5 m (Summer 40°N)

[DOC] (mg_{OC}/L)	3	10	3	10	3	10
λ_{cntr} (nm)	$\alpha(\lambda)(m^{-1})$	$\alpha(\lambda)(m^{-1})$	$S(\lambda)$	$S(\lambda)$	$k^z_{a,24h,pyr}$	$k^z_{a,24h,pyr}$
297.5	6.8	22.8	0.011	0.003	0.01	0.00
300	6.6	22.0	0.011	0.003	0.03	0.01
302.5	6.4	21.3	0.011	0.003	0.19	0.06
305	6.2	20.5	0.012	0.004	0.40	0.12
307.5	6.0	19.8	0.012	0.004	0.52	0.16
310	5.8	19.2	0.013	0.004	1.12	0.34
312.5	5.6	18.5	0.013	0.004	1.97	0.59
315	5.4	17.9	0.013	0.004	4.01	1.20
317.5	5.2	17.3	0.014	0.004	6.38	1.91
320	5.0	16.8	0.014	0.004	5.01	1.50
323.1	4.8	16.1	0.015	0.005	7.68	2.30
330	4.4	14.7	0.016	0.005	45.75	13.72
340	3.9	13.0	0.019	0.006	20.96	6.29
350	3.4	11.5	0.021	0.006	0.00	0.00
360	3.1	10.2	0.024	0.007	0.00	0.00
370	2.7	9.1	0.027	0.008	0.00	0.00
380	2.4	8.1	0.030	0.009	0.00	0.00
390	2.2	7.2	0.033	0.010	0.00	0.00
400	2.0	6.5	0.037	0.011	0.00	0.00
			$k^z_{a,tot}=\Sigma k$		***94.02***	***28.21***
	Φ_i=0.0021		$k^z_{a,tot}=\Phi_i k^z_{a,tot}$		***1.97E-01***	***5.92E-02***
			$t_{1/2,dir.photolysis}$ (d)		***3.5***	***11.7***

Z_{mix}= 10 m (Summer 40°N)						
[DOC] (mgoc/L)	3	10	3	10	3	10
λ_{cntr} (nm)	$\alpha(\lambda)(m^{-1})$	$\alpha(\lambda)(m^{-1})$	$S(\lambda)$	$S(\lambda)$	$k^z_{a,24h,pyr}$	$k^z_{a,24h,pyr}$
297.5	6.8	22.8	0.005	0.002	0.00	0.00
300	6.6	22.0	0.005	0.002	0.02	0.00
302.5	6.4	21.3	0.006	0.002	0.09	0.03
305	6.2	20.5	0.006	0.002	0.20	0.06
307.5	6.0	19.8	0.006	0.002	0.26	0.08
310	5.8	19.2	0.006	0.002	0.56	0.17
312.5	5.6	18.5	0.007	0.002	0.99	0.30
315	5.4	17.9	0.007	0.002	2.01	0.60
317.5	5.2	17.3	0.007	0.002	3.19	0.96
320	5.0	16.8	0.007	0.002	2.50	0.75
323.1	4.8	16.1	0.008	0.002	3.84	1.15
330	4.4	14.7	0.008	0.002	22.87	6.86
340	3.9	13.0	0.009	0.003	10.48	3.14
350	3.4	11.5	0.011	0.003	0.00	0.00
360	3.1	10.2	0.012	0.004	0.00	0.00
370	2.7	9.1	0.013	0.004	0.00	0.00
380	2.4	8.1	0.015	0.004	0.00	0.00
390	2.2	7.2	0.017	0.005	0.00	0.00
400	2.0	6.5	0.019	0.006	0.00	0.00
			$k^z_{a,tot}=\Sigma k$		***47.01***	***14.10***
	Φ_i=0.0021		$k^z_{a,tot}=\Phi_i k^z_{a,tot}$		***9.87E-01***	***2.96E-02***
			$t_{1/2,dir.photolysis}$ (d)		***7.0***	***23.4***

Part B: Direct Photolysis of Pyrene (Winter 40°N)

λ_{cntr} (nm)	$\Delta\lambda$ (nm)	Z_{sum}(24hr) (40°N)	ε_{pyr} ($M^{-1}cm^{-1}$)	$k^{o}_{a,24h,pyr}$
297.5	2.5	0	8575	0.00
300	2.5	2.22E-06	10832	0.06
302.5	2.5	1.31E-05	19847	0.60
305	2.5	5.17E-05	17291	2.06
307.5	2.5	1.47E-04	11513	3.89
310	2.5	3.26E-04	14424	10.81
312.5	2.5	6.04E-04	16681	23.17
315	2.5	9.64E-04	24404	54.11
317.5	2.5	1.39E-03	29557	94.49
320	2.5	1.84E-03	18597	78.70
323.1	3.75	3.58E-03	15332	126.25
330	10	1.37E-02	24084	758.90
340	10	1.87E-02	7716	331.86
350	10	2.16E-02	0	0.00
360	10	2.47E-02	0	0.00
370	10	2.70E-02	0	0.00
380	10	2.94E-02	0	0.00
390	10	2.75E-02	0	0.00
400	10	3.95E-02	0	0.00

Z_{mix}= 1 m (Winter 40°N)

[DOC] (mg_{OC}/L)	3	10	3	10	3	10
λ_{cntr} (nm)	$\alpha(\lambda)(m^{-1})$	$\alpha(\lambda)(m^{-1})$	$S(\lambda)$	$S(\lambda)$	$k^{z}_{a,24h,pyr}$	$k^{z}_{a,24h,pyr}$
297.5	6.8	22.8	0.053	0.016	0.00	0.00
300	6.6	22.0	0.055	0.016	0.00	0.00
302.5	6.4	21.3	0.057	0.017	0.03	0.01
305	6.2	20.5	0.059	0.018	0.12	0.04
307.5	6.0	19.8	0.061	0.018	0.24	0.07
310	5.8	19.2	0.063	0.019	0.68	0.20
312.5	5.6	18.5	0.065	0.020	1.51	0.45
315	5.4	17.9	0.067	0.020	3.65	1.09
317.5	5.2	17.3	0.070	0.021	6.59	1.98
320	5.0	16.8	0.072	0.022	5.67	1.70
323.1	4.8	16.1	0.075	0.023	9.48	2.84
330	4.4	14.7	0.082	0.025	62.30	18.69
340	3.9	13.0	0.093	0.028	30.92	9.28
350	3.4	11.5	0.105	0.032	0.00	0.00
360	3.1	10.2	0.119	0.036	0.00	0.00
370	2.7	9.1	0.133	0.040	0.00	0.00
380	2.4	8.1	0.149	0.045	0.00	0.00
390	2.2	7.2	0.166	0.050	0.00	0.00
400	2.0	6.5	0.185	0.056	0.00	0.00
			$k^{z}_{a,tot}=\Sigma k$		***121.19***	***36.36***
	Φ_i=0.0021		$k^{z}_{a,tot}=\Phi_i k^{z}_{a,tot}$		***2.54E-01***	***7.63E-02***
			$t_{1/2,dir.photolysis}$ (d)		***2.7***	***9.1***

Z_{mix}= 3 m (Winter 40°N)

[DOC] (mg_{OC}/L)	3	10	3	10	3	10
λ_{cntr} (nm)	$\alpha(\lambda)(m^{-1})$	$\alpha(\lambda)(m^{-1})$	$S(\lambda)$	$S(\lambda)$	$k^z_{a,24h,pyr}$	$k^z_{a,24h,pyr}$
297.5	6.8	22.8	0.018	0.005	0.00	0.00
300	6.6	22.0	0.018	0.005	0.00	0.00
302.5	6.4	21.3	0.019	0.006	0.01	0.00
305	6.2	20.5	0.020	0.006	0.04	0.01
307.5	6.0	19.8	0.020	0.006	0.08	0.02
310	5.8	19.2	0.021	0.006	0.23	0.07
312.5	5.6	18.5	0.022	0.007	0.50	0.15
315	5.4	17.9	0.022	0.007	1.22	0.36
317.5	5.2	17.3	0.023	0.007	2.20	0.66
320	5.0	16.8	0.024	0.007	1.89	0.57
323.1	4.8	16.1	0.025	0.008	3.16	0.95
330	4.4	14.7	0.027	0.008	20.77	6.23
340	3.9	13.0	0.031	0.009	10.31	3.09
350	3.4	11.5	0.035	0.011	0.00	0.00
360	3.1	10.2	0.040	0.012	0.00	0.00
370	2.7	9.1	0.044	0.013	0.00	0.00
380	2.4	8.1	0.050	0.015	0.00	0.00
390	2.2	7.2	0.056	0.017	0.00	0.00
400	2.0	6.5	0.062	0.019	0.00	0.00
			$k^z_{a,tot}=\Sigma k$		*40.40*	*12.12*
	Φ_i=0.0021		$k^z_{a,tot}=\Phi_i k^z_{a,tot}$		*8.48E-02*	*2.54E-02*
			$t_{1/2,dir.photolysis}$ (d)		*8.2*	*27.2*

Z_{mix}= 5 m (Winter 40°N)

[DOC] (mg_{OC}/L)	3	10	3	10	3	10
λ_{cntr} (nm)	$\alpha(\lambda)(m^{-1})$	$\alpha(\lambda)(m^{-1})$	$S(\lambda)$	$S(\lambda)$	$k^z_{a,24h,pyr}$	$k^z_{a,24h,pyr}$
297.5	6.8	22.8	0.011	0.003	0.00	0.00
300	6.6	22.0	0.011	0.003	0.00	0.00
302.5	6.4	21.3	0.011	0.003	0.01	0.00
305	6.2	20.5	0.012	0.004	0.02	0.01
307.5	6.0	19.8	0.012	0.004	0.05	0.01
310	5.8	19.2	0.013	0.004	0.14	0.04
312.5	5.6	18.5	0.013	0.004	0.30	0.09
315	5.4	17.9	0.013	0.004	0.73	0.22
317.5	5.2	17.3	0.014	0.004	1.32	0.40
320	5.0	16.8	0.014	0.004	1.13	0.34
323.1	4.8	16.1	0.015	0.005	1.90	0.57
330	4.4	14.7	0.016	0.005	12.46	3.74
340	3.9	13.0	0.019	0.006	6.18	1.86
350	3.4	11.5	0.021	0.006	0.00	0.00
360	3.1	10.2	0.024	0.007	0.00	0.00
370	2.7	9.1	0.027	0.008	0.00	0.00
380	2.4	8.1	0.030	0.009	0.00	0.00
390	2.2	7.2	0.033	0.010	0.00	0.00
400	2.0	6.5	0.037	0.011	0.00	0.00
			$k^z_{a,tot}=\Sigma k$		*24.24*	*7.27*
	Φ_i=0.0021		$k^z_{a,tot}=\Phi_i k^z_{a,tot}$		*5.09E-02*	*1.53E-02*
			$t_{1/2,dir.photolysis}$ (d)		*13.6*	*45.4*

Z_{mix}= 10 m (Winter 40°N)						
[DOC] (mg$_{OC}$/L)	3	10	3	10	3	10
λ_{cntr} (nm)	$\alpha(\lambda)(m^{-1})$	$\alpha(\lambda)(m^{-1})$	$S(\lambda)$	$S(\lambda)$	$k^z_{a,24h,pyr}$	$k^z_{a,24h,pyr}$
297.5	6.8	22.8	0.005	0.002	0.00	0.00
300	6.6	22.0	0.005	0.002	0.00	0.00
302.5	6.4	21.3	0.006	0.002	0.00	0.00
305	6.2	20.5	0.006	0.002	0.01	0.00
307.5	6.0	19.8	0.006	0.002	0.02	0.01
310	5.8	19.2	0.006	0.002	0.07	0.02
312.5	5.6	18.5	0.007	0.002	0.15	0.05
315	5.4	17.9	0.007	0.002	0.36	0.11
317.5	5.2	17.3	0.007	0.002	0.66	0.20
320	5.0	16.8	0.007	0.002	0.57	0.17
323.1	4.8	16.1	0.008	0.002	0.95	0.28
330	4.4	14.7	0.008	0.002	6.23	1.87
340	3.9	13.0	0.009	0.003	3.09	0.93
350	3.4	11.5	0.011	0.003	0.00	0.00
360	3.1	10.2	0.012	0.004	0.00	0.00
370	2.7	9.1	0.013	0.004	0.00	0.00
380	2.4	8.1	0.015	0.004	0.00	0.00
390	2.2	7.2	0.017	0.005	0.00	0.00
400	2.0	6.5	0.019	0.006	0.00	0.00
			$k^z_{a,tot}=\Sigma k$		***12.12***	***3.64***
	Φ_i=0.0021		$k^z_{a,tot}=\Phi_i k^z_{a,tot}$		***2.54E-02***	***7.63E-03***
			$t_{1/2,dir.photolysis}$ (d)		***27.2***	***90.8***

Appendix 9 - 2. Estimating Rate of Indirect Photolysis of Pyrene

Overview

Assumptions (Values)

(i) That 'Summer' is about 20°C higher than 'Winter' case so that the intrinsic rate constants are reduced by a factor of 4.

(ii) That the concentrations of inorganic compounds in the harbor resemble that from lake studies (see notes in individual tables).

(iii) That the pyrene indirect photolysis halftime, $t_{1/2,OH\bullet,pyrene}$, is estimated assuming a first order reaction, so that $t_{1/2,OH\bullet,pyrene}=\ln(2)/\{k_{p,pyrene}[OH^{\bullet}]\}$.

(iv) $\alpha(\lambda)$ is calculated with the $\alpha''(\lambda)$ regressed in Appendix 9-1.

Results

[DOC] (mg_{OC}/L)	3	10	3	10	3	10
Z_{mix} (m)	1	1	3	3	10	10
Summer Case						
$[OH^{\bullet}]_{24h\text{-}ss}$ (M)	2.0E-17	2.0E-18	6.5E-18	6.8E-19	2.0E-18	2.0E-19
$k_{p,pyrene}$ ($M^{-1}s^{-1}$) (**)			1.0×10^{10}			
$k_{p,pyrene}[OH^{\bullet}]$ (d^{-1})	1.7E-02	1.8E-03	5.6E-03	5.9E-04	1.7E-03	1.8E-04
$t_{1/2,OH^{\bullet},pyrene}$ (d)	***41***	***395***	***123***	***1184***	***410***	***3946***
Winter Case						
$[OH^{\bullet}]_{24h\text{-}ss}$ (M)	2.2E-17	2.3E-18	7.4E-18	7.6E-19	2.2E-18	2.3E-19
$k_{p,pyrene}$ ($M^{-1}s^{-1}$) (**)			2.5×10^{9}			
$k_{p,pyrene}[OH^{\bullet}]$ (d^{-1})	4.8E-03	5.0E-04	1.6E-03	1.7E-04	4.8E-04	5.0E-05
$t_{1/2,OH^{\bullet},pyrene}$ (d)	***145***	***1400***	***436***	***4199***	***1453***	***13997***

Part A: Indirect Photolysis of Pyrene (Summer 40°N)

Solar Irradiance at λ's and Molar Extinction Coefficients for NO_3^-(aq) and NO_2^-(aq).

λ_{cntr} (nm)	$\Delta\lambda$ (nm)	Z_{sum}(24hr) (40°N)	$\varepsilon(NO_3^-)$** ($M^{-1}cm^{-1}$)	$\varepsilon(NO_2^-)$** ($M^{-1}cm^{-1}$)	$k^{\circ}_{a,24h}(NO_3^-)$	$k^{\circ}_{a,24h}(NO_2^-)$
297.5	2.5	2.68E-05	6.8	9.0	4.2E-04	5.5E-04
300	2.5	1.17E-04	7.0	9.0	1.9E-03	2.4E-03
302.5	2.5	3.60E-04	7.2	9.0	5.9E-03	7.5E-03
305	2.5	8.47E-04	7.0	9.0	1.4E-02	1.8E-02
307.5	2.5	1.62E-03	6.8	9.2	2.5E-02	3.4E-02
310	2.5	2.68E-03	6.3	9.4	3.9E-02	5.8E-02
312.5	2.5	3.94E-03	5.6	9.6	5.1E-02	8.7E-02
315	2.5	5.30E-03	5.0	10.1	6.1E-02	1.2E-01
317.5	2.5	6.73E-03	4.0	10.5	6.2E-02	1.6E-01
320	2.5	8.12E-03	3.4	11.0	6.4E-02	2.1E-01
323.1	3.75	1.45E-02	2.3	11.5	7.8E-02	3.8E-01
330	10	5.03E-02	1.9	14.0	2.2E-01	1.6E+00
340	10	6.34E-02	1.2	18.8	1.7E-01	2.7E+00
350	10	7.03E-02	0	22.0	0.00	3.6E+00
360	10	7.77E-02	0	22.3	0.00	4.0E+00
370	10	8.29E-02	0	16.5	0.00	3.1E+00
380	10	8.86E-02	0	9.7	0.00	2.0E+00
390	10	8.32E-02	0	3.6	0.00	6.9E-01
400	10	1.20E-01	0	1.0	0.00	2.8E-01
420	30	4.77E-01	0	0	0.00	0.00
450	30	6.04E-01	0	0	0.00	0.00
480	30	6.52E-01	0	0	0.00	0.00
510	30	6.82E-01	0	0	0.00	0.00
540	30	7.09E-01	0	0	0.00	0.00
570	30	7.14E-01	0	0	0.00	0.00
600	30	7.19E-01	0	0	0.00	0.00
640	50	1.22	0	0	0.00	0.00

**: Molar extinction coefficients for NO_3^- and NO_2^- from Jankowski et al. 1999.

Z_{mix}= 1 m (Summer 40°N)

[DOC] (mg_{OC}/L)	3	10	3	10	3	10	3	10
λ_{cntr} (nm)	$\alpha(\lambda)$ (m^{-1})	$\alpha(\lambda)$ (m^{-1})	$S(\lambda)$	$S(\lambda)$	$k^z_{a,24h}(NO_3^-)$	$k^z_{a,24h}(NO_3^-)$	$k^z_{a,24h}(NO_2^-)$	$k^z_{a,24h}(NO_2^-)$
297.5	6.8	22.8	0.053	0.016	2.2E-05	6.7E-06	2.9E-05	8.8E-06
300	6.6	22.0	0.055	0.016	1.0E-04	3.1E-05	1.3E-04	4.0E-05
302.5	6.4	21.3	0.057	0.017	3.4E-04	1.0E-04	4.2E-04	1.3E-04
305	6.2	20.5	0.059	0.018	8.0E-04	2.4E-04	1.0E-03	3.1E-04
307.5	6.0	19.8	0.061	0.018	1.5E-03	4.6E-04	2.1E-03	6.3E-04
310	5.8	19.2	0.063	0.019	2.4E-03	7.3E-04	3.6E-03	1.1E-03
312.5	5.6	18.5	0.065	0.020	3.3E-03	9.9E-04	5.7E-03	1.7E-03
315	5.4	17.9	0.067	0.020	4.1E-03	1.2E-03	8.3E-03	2.5E-03
317.5	5.2	17.3	0.070	0.021	4.3E-03	1.3E-03	1.1E-02	3.4E-03
320	5.0	16.8	0.072	0.022	4.6E-03	1.4E-03	1.5E-02	4.4E-03
323.1	4.8	16.1	0.075	0.023	5.8E-03	1.7E-03	2.9E-02	8.6E-03
330	4.4	14.7	0.082	0.025	1.8E-02	5.5E-03	1.3E-01	4.0E-02
340	3.9	13.0	0.093	0.028	1.6E-02	4.8E-03	2.6E-01	7.7E-02
350	3.4	11.5	0.105	0.032	0.00	0.00	3.7E-01	1.1E-01
360	3.1	10.2	0.119	0.036	0.00	0.00	4.7E-01	1.4E-01
370	2.7	9.1	0.133	0.040	0.00	0.00	4.2E-01	1.3E-01
380	2.4	8.1	0.149	0.045	0.00	0.00	2.9E-01	8.9E-02
390	2.2	7.2	0.166	0.050	0.00	0.00	1.1E-01	3.4E-02
400	2.0	6.5	0.185	0.056	0.00	0.00	5.1E-02	1.5E-02
420	1.6	5.3	0.225	0.068	0.00	0.00	0.00	0.00
450	1.2	4.0	0.294	0.092	0.00	0.00	0.00	0.00
480	0.9	3.0	0.368	0.120	0.00	0.00	0.00	0.00
510	0.7	2.3	0.444	0.156	0.00	0.00	0.00	0.00
540	0.5	1.8	0.516	0.197	0.00	0.00	0.00	0.00
570	0.4	1.5	0.582	0.245	0.00	0.00	0.00	0.00
600	0.4	1.2	0.641	0.298	0.00	0.00	0.00	0.00
640	0.3	0.9	0.708	0.373	0.00	0.00	0.00	0.00
			$k^z_{a,tot}=\Sigma k$		***6.15E-02***	***1.85E-02***	***2.19***	***0.658***

Z_{mix}= 3 m (Summer 40°N)

[DOC] (mg_{OC}/L)	3	10	3	10	3	10	3	10
λ_{cntr} (nm)	$\alpha(\lambda)$ (m^{-1})	$\alpha(\lambda)$ (m^{-1})	$S(\lambda)$	$S(\lambda)$	$k^z_{a,24h}(NO_3^-)$	$k^z_{a,24h}(NO_3^-)$	$k^z_{a,24h}(NO_2^-)$	$k^z_{a,24h}(NO_2^-)$
297.5	6.8	22.8	0.018	0.005	7.4E-06	2.2E-06	9.8E-06	2.9E-06
300	6.6	22.0	0.018	0.005	3.4E-05	1.0E-05	4.4E-05	1.3E-05
302.5	6.4	21.3	0.019	0.006	1.1E-04	3.4E-05	1.4E-04	4.2E-05
305	6.2	20.5	0.020	0.006	2.7E-04	8.0E-05	3.4E-04	1.0E-04
307.5	6.0	19.8	0.020	0.006	5.1E-04	1.5E-04	7.0E-04	2.1E-04
310	5.8	19.2	0.021	0.006	8.1E-04	2.4E-04	1.2E-03	3.6E-04
312.5	5.6	18.5	0.022	0.007	1.1E-03	3.3E-04	1.9E-03	5.7E-04
315	5.4	17.9	0.022	0.007	1.4E-03	4.1E-04	2.8E-03	8.3E-04
317.5	5.2	17.3	0.023	0.007	1.4E-03	4.3E-04	3.8E-03	1.1E-03
320	5.0	16.8	0.024	0.007	1.5E-03	4.6E-04	4.9E-03	1.5E-03
323.1	4.8	16.1	0.025	0.008	1.9E-03	5.8E-04	9.6E-03	2.9E-03
330	4.4	14.7	0.027	0.008	6.1E-03	1.8E-03	4.4E-02	1.3E-02
340	3.9	13.0	0.031	0.009	5.3E-03	1.6E-03	8.5E-02	2.6E-02
350	3.4	11.5	0.035	0.011	0.00	0.00	1.2E-01	3.7E-02
360	3.1	10.2	0.040	0.012	0.00	0.00	1.6E-01	4.7E-02
370	2.7	9.1	0.044	0.013	0.00	0.00	1.4E-01	4.2E-02
380	2.4	8.1	0.050	0.015	0.00	0.00	9.8E-02	3.0E-02
390	2.2	7.2	0.056	0.017	0.00	0.00	3.8E-02	1.1E-02
400	2.0	6.5	0.062	0.019	0.00	0.00	1.7E-02	5.1E-03
420	1.6	5.3	0.076	0.023	0.00	0.00	0.00	0.00
450	1.2	4.0	0.102	0.031	0.00	0.00	0.00	0.00
480	0.9	3.0	0.134	0.040	0.00	0.00	0.00	0.00
510	0.7	2.3	0.173	0.052	0.00	0.00	0.00	0.00
540	0.5	1.8	0.218	0.066	0.00	0.00	0.00	0.00
570	0.4	1.5	0.270	0.083	0.00	0.00	0.00	0.00
600	0.4	1.2	0.326	0.103	0.00	0.00	0.00	0.00
640	0.3	0.9	0.403	0.136	0.00	0.00	0.00	0.00
			$k^z_{a,tot}=\Sigma k$		***2.05E-02***	***6.15E-03***	***7.31E-01***	***2.19E-01***

Z_{mix}= 10 m (Summer 40°N)

[DOC] (mg_{OC}/L)	3	10	3	10	3	10	3	10
λ_{cntr} (nm)	$\alpha(\lambda)$ (m^{-1})	$\alpha(\lambda)$ (m^{-1})	$S(\lambda)$	$S(\lambda)$	$k^z_{a,24h}(NO_3^-)$	$k^z_{a,24h}(NO_3^-)$	$k^z_{a,24h}(NO_2^-)$	$k^z_{a,24h}(NO_2^-)$
297.5	6.8	22.8	0.005	0.002	2.2E-06	6.7E-07	2.9E-06	8.8E-07
300	6.6	22.0	0.005	0.002	1.0E-05	3.1E-06	1.3E-05	4.0E-06
302.5	6.4	21.3	0.006	0.002	3.4E-05	1.0E-05	4.2E-05	1.3E-05
305	6.2	20.5	0.006	0.002	8.0E-05	2.4E-05	1.0E-04	3.1E-05
307.5	6.0	19.8	0.006	0.002	1.5E-04	4.6E-05	2.1E-04	6.3E-05
310	5.8	19.2	0.006	0.002	2.4E-04	7.3E-05	3.6E-04	1.1E-04
312.5	5.6	18.5	0.007	0.002	3.3E-04	9.9E-05	5.7E-04	1.7E-04
315	5.4	17.9	0.007	0.002	4.1E-04	1.2E-04	8.3E-04	2.5E-04
317.5	5.2	17.3	0.007	0.002	4.3E-04	1.3E-04	1.1E-03	3.4E-04
320	5.0	16.8	0.007	0.002	4.6E-04	1.4E-04	1.5E-03	4.4E-04
323.1	4.8	16.1	0.008	0.002	5.8E-04	1.7E-04	2.9E-03	8.6E-04
330	4.4	14.7	0.008	0.002	1.8E-03	5.5E-04	1.3E-02	4.0E-03
340	3.9	13.0	0.009	0.003	1.6E-03	4.8E-04	2.6E-02	7.7E-03
350	3.4	11.5	0.011	0.003	0.00	0.00	3.7E-02	1.1E-02
360	3.1	10.2	0.012	0.004	0.00	0.00	4.7E-02	1.4E-02
370	2.7	9.1	0.013	0.004	0.00	0.00	4.2E-02	1.3E-02
380	2.4	8.1	0.015	0.004	0.00	0.00	3.0E-02	8.9E-03
390	2.2	7.2	0.017	0.005	0.00	0.00	1.1E-02	3.4E-03
400	2.0	6.5	0.019	0.006	0.00	0.00	5.1E-03	1.5E-03
420	1.6	5.3	0.023	0.007	0.00	0.00	0.00	0.00
450	1.2	4.0	0.031	0.009	0.00	0.00	0.00	0.00
480	0.9	3.0	0.040	0.012	0.00	0.00	0.00	0.00
510	0.7	2.3	0.052	0.016	0.00	0.00	0.00	0.00
540	0.5	1.8	0.066	0.020	0.00	0.00	0.00	0.00
570	0.4	1.5	0.083	0.025	0.00	0.00	0.00	0.00
600	0.4	1.2	0.103	0.031	0.00	0.00	0.00	0.00
640	0.3	0.9	0.136	0.041	0.00	0.00	0.00	0.00
			$k^z_{a,tot}=\Sigma k$		***6.15E-03***	***1.85E-03***	***2.19E-01***	***6.58E-02***

Rate of $OH^{\bullet}$ Formation

[DOC] (mg_{OC}/L)	3	10	3	10	3	10
Z_{mix} (m)	1	1	3	3	10	10
With NO_3^-						
$k^z_{a,tot}=\Sigma k$	6.15E-02	1.85E-02	2.05E-02	6.15E-03	6.15E-03	1.85E-03
Φ_i=0.007*						
$[NO_3^-]=1.5\times10^{-4}$ M**						
$r_{OH^{\bullet},f}=[NO_3^-]\Phi_i k^z_{a,tot}$	6.5E-08	1.9E-08	2.2E-08	6.5E-09	6.5E-09	1.9E-09
With NO_2^-						
$k^z_{a,tot}=\Sigma k$	6.15E-02	1.85E-02	2.05E-02	6.15E-03	6.15E-03	1.85E-03
Φ_i=0.028*						
$[NO_2^-]=1.5\times10^{-6}$ M**						
$r_{OH^{\bullet},f}=[NO_2^-]\Phi_i k^z_{a,tot}$	9.2E-08	2.8E-08	3.1E-08	9.2E-09	9.2E-09	2.8E-09
from NO_3^-	6.5E-08	1.9E-08	2.2E-08	6.5E-09	6.5E-09	1.9E-09
from NO_2^-	9.2E-08	2.8E-08	3.1E-08	9.2E-09	9.2E-09	2.8E-09
$\Sigma r_{OH^{\bullet},24ss,formation}$ (Md^{-1})	***1.6E-07***	***4.7E-08***	***5.2E-08***	***1.6E-08***	***1.6E-08***	***4.7E-09***

Rate of $OH^{\bullet}$ Removal by DOC, carbonate and bicarbonate

[DOC] (mg_{OC}/L)	3	10	3	10	3	10
Z_{mix} (m)	1	1	3	3	10	10
With DOC						
$k_{OH^{\bullet}\text{-}DOC}$ ($mg_{OC}/L)^{-1}s^{-1}$ (a)				2.5×10^4		
[DOC] (mg_{OC}/L)				3 or 10		
$k_{OH^{\bullet}}[DOC]$ (d^{-1})	***6.5E+09***	***2.2E+10***	***6.5E+09***	***2.2E+10***	***6.5E+09***	***2.2E+10***
With HCO_3^-						
$k_{OH^{\bullet}\text{-}HCO3^-}$ $M^{-1}s^{-1}$ (a)				1.0×10^7		
$[HCO_3^-]$ (M) (**)				1.2×10^{-3}		
$k_{OH^{\bullet}}[HCO_3^-]$ (d^{-1})				***1.0×10^9***		
With $CO_3^=$						
$k_{OH^{\bullet}\text{-}CO3^=}$ $M^{-1}s^{-1}$ (a)				4.0×10^8		
$[CO_3^=]$ (M) (**)				1.4×10^{-5}		
$k_{OH^{\bullet}}[CO_3^=]$ (d^{-1})				***4.8×10^8***		
$\Sigma k_{OH^{\bullet},24ss,removal}$ (d^{-1})	***8.0E+09***	***2.3E+10***	***8.0E+09***	***2.3E+10***	***8.0E+09***	***2.3E+10***

*: From Jankowski et al. 1999.
**: From the Greifensee example, p.662-3, Schwarzenbach et al. 2003.
(a): Larson et al. 1988; Brezonik et al. 1998.

$[OH^{\bullet}]_{24h\text{-}ss}$ and Half-time for Pyrene Indirect Photolysis (Summer Case)

[DOC] (mg_{OC}/L)	3	10	3	10	3	10
Z_{mix} (m)	1	1	3	3	10	10
$[OH^{\bullet}]_{24h\text{-}ss}$						
$\Sigma r_{OH^{\bullet},24ss,formation}$ (Md^{-1})	1.6E-07	4.7E-08	5.2E-08	1.6E-08	1.6E-08	4.7E-09
$\Sigma k_{OH^{\bullet},24ss,removal}$ (d^{-1})	8.0E+09	2.3E+10	8.0E+09	2.3E+10	8.0E+09	2.3E+10
$[OH^{\bullet}]_{24h\text{-}ss}$ (M)	***2.0E-17***	***2.0E-18***	***6.5E-18***	***6.8E-19***	***2.0E-18***	***2.0E-19***
Pyr Indirect Photolysis						
$k_{p,pyrene}$ ($M^{-1}s^{-1}$) (**)			1.0×10^{10}			
$k_{p,pyrene}[OH^{\bullet}]$ (d^{-1})	1.7E-02	1.8E-03	5.6E-03	5.9E-04	1.7E-03	1.8E-04
$t_{1/2,OH^{\bullet},pyrene}$ (d)	***41***	***395***	***123***	***1184***	***410***	***3946***

**: From Figure 16.3 in Schwarzenbach et al. 2003.

Part B: Indirect Photolysis of Pyrene (Winter 40°N)

Solar Irradiance at λ's and Molar Extinction Coefficients for $NO_3^-_{(aq)}$ and $NO_2^-_{(aq)}$.

λ_{cntr} (nm)	$\Delta\lambda$ (nm)	Z_{sum}(24hr) (40°N)	$\varepsilon(NO_3^-)$** ($M^{-1}cm^{-1}$)	$\varepsilon(NO_2^-)$** ($M^{-1}cm^{-1}$)	$k^o_{a,24h}(NO_3^-)$	$k^o_{a,24h}(NO_2^-)$
297.5	2.5	0	6.8	9.0	0.0E+00	0.0E+00
300	2.5	2.22E-06	7.0	9.0	3.6E-05	4.6E-05
302.5	2.5	1.31E-05	7.2	9.0	2.2E-04	2.7E-04
305	2.5	5.17E-05	7.0	9.0	8.3E-04	1.1E-03
307.5	2.5	1.47E-04	6.8	9.2	2.3E-03	3.1E-03
310	2.5	3.26E-04	6.3	9.4	4.7E-03	7.0E-03
312.5	2.5	6.04E-04	5.6	9.6	7.8E-03	1.3E-02
315	2.5	9.64E-04	5.0	10.1	1.1E-02	2.2E-02
317.5	2.5	1.39E-03	4.0	10.5	1.3E-02	3.4E-02
320	2.5	1.84E-03	3.4	11.0	1.4E-02	4.7E-02
323.1	3.75	3.58E-03	2.3	11.5	1.9E-02	9.5E-02
330	10	1.37E-02	1.9	14.0	6.0E-02	4.4E-01
340	10	1.87E-02	1.2	18.8	5.0E-02	8.1E-01
350	10	2.16E-02	0	22.0	0.00	1.1E+00
360	10	2.47E-02	0	22.3	0.00	1.3E+00
370	10	2.70E-02	0	16.5	0.00	1.0E+00
380	10	2.94E-02	0	9.7	0.00	6.6E-01
390	10	2.75E-02	0	3.6	0.00	2.3E-01
400	10	3.95E-02	0	1.0	0.00	9.1E-02
420	30	1.58E-01	0	0	0.00	0.00
450	30	2.03E-01	0	0	0.00	0.00
480	30	2.21E-01	0	0	0.00	0.00
510	30	2.31E-01	0	0	0.00	0.00
540	30	2.40E-01	0	0	0.00	0.00
570	30	2.40E-01	0	0	0.00	0.00
600	30	2.44E-01	0	0	0.00	0.00
640	50	4.25E-01	0	0	0.00	0.00

**: Molar extinction coefficients for NO_3^- and NO_2^- from Jankowski et al. 1999.

Z_{mix}= 1 m (Winter 40°N)

[DOC] (mg_{OC}/L)	3	10	3	10	3	10	3	10
λ_{cntr} (nm)	$\alpha(\lambda)$ (m^{-1})	$\alpha(\lambda)$ (m^{-1})	$S(\lambda)$	$S(\lambda)$	$k^z_{a,24h}(NO_3^-)$	$k^z_{a,24h}(NO_3^-)$	$k^z_{a,24h}(NO_2^-)$	$k^z_{a,24h}(NO_2^-)$
297.5	6.8	22.8	0.053	0.016	0.00	0.0E+00	0.0E+00	0.0E+00
300	6.6	22.0	0.055	0.016	0.00	5.9E-07	2.5E-06	7.6E-07
302.5	6.4	21.3	0.057	0.017	0.00	3.7E-06	1.5E-05	4.6E-06
305	6.2	20.5	0.059	0.018	0.00	1.5E-05	6.3E-05	1.9E-05
307.5	6.0	19.8	0.061	0.018	0.00	4.2E-05	1.9E-04	5.7E-05
310	5.8	19.2	0.063	0.019	0.00	8.9E-05	4.4E-04	1.3E-04
312.5	5.6	18.5	0.065	0.020	0.00	1.5E-04	8.7E-04	2.6E-04
315	5.4	17.9	0.067	0.020	0.00	2.2E-04	1.5E-03	4.5E-04
317.5	5.2	17.3	0.070	0.021	0.00	2.7E-04	2.3E-03	7.0E-04
320	5.0	16.8	0.072	0.022	0.00	3.1E-04	3.4E-03	1.0E-03
323.1	4.8	16.1	0.075	0.023	0.00	4.3E-04	7.1E-03	2.1E-03
330	4.4	14.7	0.082	0.025	0.00	1.5E-03	3.6E-02	1.1E-02
340	3.9	13.0	0.093	0.028	0.00	1.4E-03	7.5E-02	2.3E-02
350	3.4	11.5	0.105	0.032	0.00	0.00	1.2E-01	3.5E-02
360	3.1	10.2	0.119	0.036	0.00	0.00	1.5E-01	4.5E-02
370	2.7	9.1	0.133	0.040	0.00	0.00	1.4E-01	4.1E-02
380	2.4	8.1	0.149	0.045	0.00	0.00	9.8E-02	2.9E-02
390	2.2	7.2	0.166	0.050	0.00	0.00	3.8E-02	1.1E-02
400	2.0	6.5	0.185	0.056	0.00	0.00	1.7E-02	5.1E-03
420	1.6	5.3	0.225	0.068	0.00	0.00	0.00	0.00
450	1.2	4.0	0.294	0.092	0.00	0.00	0.00	0.00
480	0.9	3.0	0.368	0.120	0.00	0.00	0.00	0.00
510	0.7	2.3	0.444	0.156	0.00	0.00	0.00	0.00
540	0.5	1.8	0.516	0.197	0.00	0.00	0.00	0.00
570	0.4	1.5	0.582	0.245	0.00	0.00	0.00	0.00
600	0.4	1.2	0.641	0.298	0.00	0.00	0.00	0.00
640	0.3	0.9	0.708	0.373	0.00	0.00	0.00	0.00
			$k^z_{a,tot}=\Sigma k$		***1.48E-02***	***4.43E-03***	***6.82E-01***	***2.05E-01***

Z_{mix}= 3 m (Winter 40°N)

[DOC] (mg_{OC}/L)	3	10	3	10	3	10	3	10
λ_{cntr} (nm)	$\alpha(\lambda)$ (m^{-1})	$\alpha(\lambda)$ (m^{-1})	$S(\lambda)$	$S(\lambda)$	$k^z_{a,24h}(NO_3^-)$	$k^z_{a,24h}(NO_3^-)$	$k^z_{a,24h}(NO_2^-)$	$k^z_{a,24h}(NO_2^-)$
297.5	6.8	22.8	0.018	0.005	0.0E+00	0.0E+00	0.0E+00	0.0E+00
300	6.6	22.0	0.018	0.005	6.5E-07	2.0E-07	8.4E-07	2.5E-07
302.5	6.4	21.3	0.019	0.006	4.1E-06	1.2E-06	5.1E-06	1.5E-06
305	6.2	20.5	0.020	0.006	1.6E-05	4.9E-06	2.1E-05	6.3E-06
307.5	6.0	19.8	0.020	0.006	4.6E-05	1.4E-05	6.3E-05	1.9E-05
310	5.8	19.2	0.021	0.006	9.8E-05	3.0E-05	1.5E-04	4.4E-05
312.5	5.6	18.5	0.022	0.007	1.7E-04	5.1E-05	2.9E-04	8.7E-05
315	5.4	17.9	0.022	0.007	2.5E-04	7.5E-05	5.0E-04	1.5E-04
317.5	5.2	17.3	0.023	0.007	3.0E-04	8.9E-05	7.8E-04	2.3E-04
320	5.0	16.8	0.024	0.007	3.5E-04	1.0E-04	1.1E-03	3.4E-04
323.1	4.8	16.1	0.025	0.008	4.8E-04	1.4E-04	2.4E-03	7.1E-04
330	4.4	14.7	0.027	0.008	1.7E-03	5.0E-04	1.2E-02	3.6E-03
340	3.9	13.0	0.031	0.009	1.6E-03	4.7E-04	2.5E-02	7.5E-03
350	3.4	11.5	0.035	0.011	0.00	0.00	3.8E-02	1.2E-02
360	3.1	10.2	0.040	0.012	0.00	0.00	5.0E-02	1.5E-02
370	2.7	9.1	0.044	0.013	0.00	0.00	4.6E-02	1.4E-02
380	2.4	8.1	0.050	0.015	0.00	0.00	3.3E-02	9.8E-03
390	2.2	7.2	0.056	0.017	0.00	0.00	1.3E-02	3.8E-03
400	2.0	6.5	0.062	0.019	0.00	0.00	5.6E-03	1.7E-03
420	1.6	5.3	0.076	0.023	0.00	0.00	0.00	0.00
450	1.2	4.0	0.102	0.031	0.00	0.00	0.00	0.00
480	0.9	3.0	0.134	0.040	0.00	0.00	0.00	0.00
510	0.7	2.3	0.173	0.052	0.00	0.00	0.00	0.00
540	0.5	1.8	0.218	0.066	0.00	0.00	0.00	0.00
570	0.4	1.5	0.270	0.083	0.00	0.00	0.00	0.00
600	0.4	1.2	0.326	0.103	0.00	0.00	0.00	0.00
640	0.3	0.9	0.403	0.136	0.00	0.00	0.00	0.00
			$k^z_{a,tot}=\Sigma k$		***4.93E-03***	***1.48E-03***	***2.27E-01***	***6.82E-02***

Z_{mix}= 10 m (Winter 40°N)

[DOC] (mg_{OC}/L)	3	10	3	10	3	10	3	10
λ_{cntr} (nm)	$\alpha(\lambda)$ (m^{-1})	$\alpha(\lambda)$ (m^{-1})	$S(\lambda)$	$S(\lambda)$	$k^z_{a,24h}(NO_3^-)$	$k^z_{a,24h}(NO_3^-)$	$k^z_{a,24h}(NO_2^-)$	$k^z_{a,24h}(NO_2^-)$
297.5	6.8	22.8	0.005	0.002	0.0E+00	0.0E+00	0.0E+00	0.0E+00
300	6.6	22.0	0.005	0.002	2.0E-07	5.9E-08	2.5E-07	7.6E-08
302.5	6.4	21.3	0.006	0.002	1.2E-06	3.7E-07	1.5E-06	4.6E-07
305	6.2	20.5	0.006	0.002	4.9E-06	1.5E-06	6.3E-06	1.9E-06
307.5	6.0	19.8	0.006	0.002	1.4E-05	4.2E-06	1.9E-05	5.7E-06
310	5.8	19.2	0.006	0.002	3.0E-05	8.9E-06	4.4E-05	1.3E-05
312.5	5.6	18.5	0.007	0.002	5.1E-05	1.5E-05	8.7E-05	2.6E-05
315	5.4	17.9	0.007	0.002	7.5E-05	2.2E-05	1.5E-04	4.5E-05
317.5	5.2	17.3	0.007	0.002	8.9E-05	2.7E-05	2.3E-04	7.0E-05
320	5.0	16.8	0.007	0.002	1.0E-04	3.1E-05	3.4E-04	1.0E-04
323.1	4.8	16.1	0.008	0.002	1.4E-04	4.3E-05	7.1E-04	2.1E-04
330	4.4	14.7	0.008	0.002	5.0E-04	1.5E-04	3.6E-03	1.1E-03
340	3.9	13.0	0.009	0.003	4.7E-04	1.4E-04	7.5E-03	2.3E-03
350	3.4	11.5	0.011	0.003	0.00	0.00	1.2E-02	3.5E-03
360	3.1	10.2	0.012	0.004	0.00	0.00	1.5E-02	4.5E-03
370	2.7	9.1	0.013	0.004	0.00	0.00	1.4E-02	4.1E-03
380	2.4	8.1	0.015	0.004	0.00	0.00	9.8E-03	2.9E-03
390	2.2	7.2	0.017	0.005	0.00	0.00	3.8E-03	1.1E-03
400	2.0	6.5	0.019	0.006	0.00	0.00	1.7E-03	5.1E-04
420	1.6	5.3	0.023	0.007	0.00	0.00	0.00	0.00
450	1.2	4.0	0.031	0.009	0.00	0.00	0.00	0.00
480	0.9	3.0	0.040	0.012	0.00	0.00	0.00	0.00
510	0.7	2.3	0.052	0.016	0.00	0.00	0.00	0.00
540	0.5	1.8	0.066	0.020	0.00	0.00	0.00	0.00
570	0.4	1.5	0.083	0.025	0.00	0.00	0.00	0.00
600	0.4	1.2	0.103	0.031	0.00	0.00	0.00	0.00
640	0.3	0.9	0.136	0.041	0.00	0.00	0.00	0.00
			$k^z_{a,tot}=\Sigma k$		***1.48E-03***	***4.43E-04***	***6.82E-02***	***2.05E-02***

Rate of $OH^{\bullet}$ Formation

[DOC] (mg_{OC}/L)	3	10	3	10	3	10
Z_{mix} (m)	1	1	3	3	10	10
With NO_3^-						
$k^z_{a,tot}=\Sigma k$	1.48E-02	4.43E-03	4.93E-03	1.48E-03	1.48E-03	4.43E-04
Φ_i=0.007*						
$[NO_3^-]=1.5\times10^{-4}$ M**						
$r_{OH^{\bullet},f}=[NO_3^-]\Phi_i k^z_{a,tot}$	1.6E-08	4.7E-09	5.2E-09	1.6E-09	1.6E-09	4.7E-10
With NO_2^-						
$k^z_{a,tot}=\Sigma k$	6.82E-01	2.05E-01	2.27E-01	6.82E-02	6.82E-02	2.05E-02
Φ_i=0.028*						
$[NO_2^-]=1.5\times10^{-6}$ M**						
$r_{OH^{\bullet},f}=[NO_2^-]\Phi_i k^z_{a,tot}$	2.9E-08	8.6E-09	9.6E-09	2.9E-09	2.9E-09	8.6E-10
from NO_3^-	1.6E-08	4.7E-09	5.2E-09	1.6E-09	1.6E-09	4.7E-10
from NO_2^-	2.9E-08	8.6E-09	9.6E-09	2.9E-09	2.9E-09	8.6E-10
$\Sigma r_{OH^{\bullet},24ss,formation}$ (Md^{-1})	***4.4E-08***	***1.3E-08***	***1.5E-08***	***4.4E-09***	***4.4E-09***	***1.3E-09***

Rate of $OH^{\bullet}$ Removal by DOC, carbonate and bicarbonate

[DOC] (mg_{OC}/L)	3	10	3	10	3	10
Z_{mix} (m)	1	1	3	3	10	10
With DOC						
$k_{OH^{\bullet}\text{-}DOC}$ $(mg_{OC}/L)^{-1}s^{-1}$ (b)			6.3×10^3			
[DOC] (mg_{OC}/L)			3 or 10			
$k_{OH^{\bullet}}[DOC]$ (d^{-1})	***1.6E+09***	***5.4E+09***	***1.6E+09***	***5.4E+09***	***1.6E+09***	***5.4E+09***
With HCO_3^-						
$k_{OH^{\bullet}\text{-}HCO3^-}$ $M^{-1}s^{-1}$ (b)			2.5×10^6			
$[HCO_3^-]$ (M) (**)			1.2×10^{-3}			
$k_{OH^{\bullet}}[HCO_3^-]$ (d^{-1})			***2.6×10^8***			
With $CO_3^=$						
$k_{OH^{\bullet}\text{-}CO3^=}$ $M^{-1}s^{-1}$ (b)			1.0×10^8			
$[CO_3^=]$ (M) (**)			1.4×10^{-5}			
$k_{OH^{\bullet}}[CO_3^=]$ (d^{-1})			***1.2×10^8***			
$\Sigma k_{OH^{\bullet},24ss,removal}$ (d^{-1})	***2.0E+09***	***5.8E+09***	***2.0E+09***	***5.8E+09***	***2.0E+09***	***5.8E+09***

*: From Jankowski et al. 1999.

**: From the Greifensee example, p.662-3, Schwarzenbach et al. 2003.

(b): Reduced by a factor of 4 from their summer values. This is based on the assumption that rate reduces by a factor of two for every decrease in temperature of 10°K, and that Summer and Winter case differs by 20°K.

$[OH^{\bullet}]_{24h\text{-}ss}$ and Half-time for Pyrene Indirect Photolysis (Winter Case)

[DOC] (mg_{OC}/L)	3	10	3	10	3	10
Z_{mix} (m)	1	1	3	3	10	10
$[OH^{\bullet}]_{24h\text{-}ss}$						
$\Sigma r_{OH^{\bullet},24ss,formation}$ (Md^{-1})	4.4E-08	1.3E-08	1.5E-08	4.4E-09	4.4E-09	1.3E-09
$\Sigma k_{OH^{\bullet},24ss,removal}$ (d^{-1})	2.0E+09	5.8E+09	2.0E+09	5.8E+09	2.0E+09	5.8E+09
$[OH^{\bullet}]_{24h\text{-}ss}$ (M)	***2.2E-17***	***2.3E-18***	***7.4E-18***	***7.6E-19***	***2.2E-18***	***2.3E-19***
Pyr Indirect Photolysis						
$k_{p,pyrene}$ ($M^{-1}s^{-1}$) (**)			2.5×10^{9}			
$k_{p,pyrene}[OH^{\bullet}]$ (d^{-1}) (b)	4.8E-03	5.0E-04	1.6E-03	1.7E-04	4.8E-04	5.0E-05
$t_{1/2,OH^{\bullet},pyrene}$ (d)	***145***	***1400***	***436***	***4199***	***1453***	***13997***

**: From Figure 16.3 in Schwarzenbach et al. 2003.
(b): Reduced by a factor of 4 from their summer values. This is based on the assumption that rate reduces by a factor of two for every decrease in temperature of 10°K, and that Summer and Winter case differs by 20°K.

Appendix 9 - 3. Estimating Biodegradation Rate of Pyrene.

Assumptions

-) That 'Summer' is about 20°C higher than 'Winter' case so that the intrinsic rate constants are reduced by a factor of 4.

-) That the biodegradation rate observed for sediment-bound pyrene is the same as that of dissolved, free pyrene (!!).

-) That the concentration of pyrene degrading microbes is kept constant and the influence microbial abundance on the rate has been incorporated into the rate constant, k_{biodeg}.

-) That the biodegradation may be considered as a first order reaction so that the halftime can be estimated as $t_{1/2,biodeg.}=\ln(2)/k_{biodeg}$.

Estimating Biodegradation Rate of Pyrene

The biodegradation rate of pyrene was estimated from the study by Shiaris (1989) where field Boston Harbor sediments (at three sites, of varying initial PAH loadings) were used.

The rate for specific PAH was estimated by regressing the observed biodegradation rate, $r_{biodeg.}$, against the initial solid-phase PAH loading, S_{PAH} (see table below). Since pyrene (4-ring) was not studied by Shiaris, the rate was assumed to be that between phenanthrene (3-ring) and benzo(a)pyrene (5-ring). This should be a reasonable assumption, as it has been shown that the rate of degradation increases with the hydrophobicity of HOCs (van Hoof et al. 2001). With this assumption, the lower and upper limits for $t_{1/2,biodeg.}$ of pyrene were 14 and 55 d, respectively.

The experiment of Shiaris was conducted at room temperature. Assuming that the same temperature applies for the Summer condition, with our first assumption, the Winter case biodegradation rates were thus 56 and 220 d, for the lower and the upper limits, respectively.

The estimated biodegradation rates of pyrene appear to be quite reasonable, as they match the degradation/uptake halftimes of PAHs (including pyrene) reported by other research groups (see second table below).

Biodegradation Halftime ($t_{1/2,biodeg.}$) for PAHs (Data from Shiaris 1989)

PAHs	$r_{biodeg.}$ (ng/g.h)	S_{PAH} (ng/g)	$k_{biodeg.}$ (h^{-1})	$t_{1/2,biodeg.}$ (d)
naphthalene				
WBR	1.16	367	0.0032	
LN	0.3	144	0.0021	
FPC	94.9	43628	0.0022	
		Regression	***0.0022***	***13.3***
		r^2	*1.0*	
phenanthrene				
WBR	1.2	228	0.0053	
LN	3.29	665	0.0049	
FPC	134	63683	0.0021	
		Regression	***0.00208***	***13.9***
		r^2	*1.0*	
benzo(a)pyr.				
WBR	0.15	198	0.00076	
LN	1.72	3382	0.00051	
FPC	49.5	94984	0.00052	
		Regression	***0.00052***	***55.4***
		r^2	*1.0*	

Biodegradation or Biouptake Halftimes Reported in Literature

PAHs	Process/Phase	$k_{process}$ (h^{-1})	$t_{1/2,process}$ (d^{-1})	Reference
fluoranthene	sediment-biodeg.	0.00047	62	Horng et al. 2001
pyrene	worm uptake	0.00113[a]	***25.7***	van Hoof et al. 2001
pyrene	worm uptake	0.00069[a]	***41.9***	ref 19 in van Hoof
pyrene	worm uptake	0.00059[a]	***48.7***	ref 39 in van Hoof
pyrene	worm uptake	0.00043[a]	***68***	ref 22 in van Hoof
pyrene	sediment-biodeg.	0.00053	***55***	Horng et al. 2001
pyrene	fecal pellets-biodeg.	0.00063	***46***	Horng et al. 2001
chrysene	sediment-biodeg.	0.00040	71	Horng et al. 2001
b(a)pyr	sediment-biodeg.	0.000075	385	Horng et al. 2001

a: Assuming f_{OC}=0.02 g_{OC}/g_{sed} and a worm-density of 0.05 g_{worm}/g_{sed}. The original rate constants reported in unit of $mg_{OC}/g_{worm}.h$.

Appendix 9 - 4. Seasonal atmospheric deposition rates of pyrene in Boston Harbor.

(a) Seasonal ΣPAHs deposition rates according to Figure 4 of Golomb et al. 1997.

	Nahant			Truro		
	Dry (ug/m^2.season)	Wet (ug/m^2.season)	Total (ug/m^2.season)	Dry (ug/m^2.season)	Wet (ug/m^2.season)	Total (ug/m^2.season)
Fall	150	70	***220***	30	90	***120***
Winter	270	130	***400***	70	60	***130***
Spring	190	50	***240***	50	30	***80***
Summer	90	30	***120***	10	30	***40***
Annual Total	700	280	***980***	160	210	***370***

(b) Annual PAH deposition rates according to Table 1 of Golomb et al. 1997.

PAH	Nahant			Truro		
	Dry (ng/m^2.yr)	Wet (ng/m^2.yr)	Total (ng/m^2.yr)	Dry (ng/m^2.yr)	Wet (ng/m^2.yr)	Total (ng/m^2.yr)
Phenanthrene	7.8×10^4	2.7×10^4	1.1×10^5	1.6×10^4	7.1×10^3	2.3×10^4
Pyrene	***7.8×10^4***	***1.9×10^4***	***9.8×10^4***	***1.1×10^4***	***5.8×10^3***	***1.7×10^4***
Benzo(a)pyrene	2.6×10^4	4.8×10^3	3.0×10^4	2.3×10^3	2.1×10^3	4.4×10^3

(c) Derived seasonal PAH depositional flux according to (a) and (b)[a].

	Nahant			Truro		
	Dry (ng/m^2.d)	Wet (ng/m^2.d)	Total (ng/m^2.d)	Dry (ng/m^2.d)	Wet (ng/m^2.d)	Total (ng/m^2.d)
Phenanthrene						
Fall	186	75	274	33	34	83
Winter	334	139	499	78	23	90
Spring	235	54	299	56	11	55
Summer	111	32	150	11	11	28
Pyrene						
Fall	186	53	***244***	23	28	***61***
Winter	334	98	***444***	53	18	***66***
Spring	235	38	***267***	38	9	***41***
Summer	111	23	***133***	8	9	***20***
Benzo(a)pyrene						
Fall	62	13	75	5	10	16
Winter	111	25	136	11	7	17
Spring	78	10	82	8	3	11
Summer	37	6	41	2	3	5

a: For example, fall total pyrene depositional flux = $(9.8\times10^4)(220/980)/90$, where 90d is assumed per season.

Appendix 9 - 5. Mean Photolysis Half-time ($t_{1/2,pyr,photolysis}$) and Water Depth.

Photolysis (direct) half-time, $t_{1/2,pyr,photolysis}$, as a function of Water Depth[a].

	Summer			Winter		
Depth (m)	Low (d)	High (d)	$Mean_{geo}$ (d)	Low (d)	High (d)	$Mean_{geo}$ (d)
1	0.7	2.3	***1.3***	2.7	9.1	***5.0***
3	2.1	7	***3.8***	8.2	27.2	***14.9***
5	3.5	11.7	***6.4***	13.6	45.4	***24.8***
10	7	23.4	***12.8***	27.2	90.8	***49.7***

a: The estimation of lower and upper half-times are documented in Appendix 9-1.

Appendix 9 - 6. Derivation of Desorption Half-life ($t_{1/2,des}$).

(A) Fitting parameters for pyrene desorption kinetics using Constrained Two-Compartment Exponential model[a].

	dia.=38-75um (L-set)	dia.=75-106um (K-set)	dia.=180-250um (IHG-set)
20 mg_{solids}/L			
S_o-S_{Eqm} ($\mu g_{pyr}/kg_{solids}$)	584	856	1451
$S_{rapid,o}$ ($\mu g_{pyr}/kg_{solids}$)	112	206	252
k_{rapid} (h^{-1})	4.4×10^{-1}	1.0×10^{-2}	1.9×10^{-2}
k_{slow} (h^{-1})	1.5×10^{-4}	5.9×10^{-5}	1.6×10^{-5}
r^2	0.91	0.85	0.85
70 mg_{solids}/L			
S_o-S_{Eqm} ($\mu g_{pyr}/kg_{solids}$)	302	306	558
$S_{rapid,o}$ ($\mu g_{pyr}/kg_{solids}$)	56	99	130
k_{rapid} (h^{-1})	1.0	1.4×10^{-2}	7.5×10^{-3}
k_{slow} (h^{-1})	1.6×10^{-4}	7.3×10^{-5}	3.4×10^{-5}
r^2	0.91	0.83	0.91
280 mg_{solids}/L			
S_o-S_{Eqm} ($\mu g_{pyr}/kg_{solids}$)	97	115	177
$S_{rapid,o}$ ($\mu g_{pyr}/kg_{solids}$)	27	51	55
k_{rapid} (h^{-1})	1.0	9.6×10^{-3}	9.0×10^{-3}
k_{slow} (h^{-1})	1.3×10^{-4}	4.8×10^{-5}	7.8×10^{-6}
r^2	0.85	0.78	0.79

a: $C_{pyr}(t) = (S_o\text{-}S_{End}|S_{Eqm})R_{sw}[1\text{-}exp(\text{-}k_{slow}t)] + S_{rapid,o}R_{sw}[exp(\text{-}k_{slow}t)\text{-}exp(\text{-}k_{fast}t)]$; $C_{pyr}(t)$, R_{sw} in units of $\mu g_{pyr}/L$ and kg_{solids}/L, respectively.

(B) Pyrene Desorption halftimes at different timeframes (7.5, 15, 30, and 90 d)[a].

R_{sw}	$t_{1/2,des}$ (d) dia.=38-75um curve fit[b]	$t_{1/2,des}$ (d) dia.=38-75um read-off[c]	$t_{1/2,des}$ (d) dia.=75-106um curve fit	$t_{1/2,des}$ (d) dia.=75-106um read-off	$t_{1/2,des}$ (d) dia.=180-250um curve fit	$t_{1/2,des}$ (d) dia.=180-250um read-off
20 mg_{solids}/L						
t_{des} =90d	5.6	5.4	4.5	7.2	1.9	4.8
30d	0.1	2.5	3.2	4.3	1.6	2.1
15d	0.1	1.3	2.9	2.3	1.5	1.5
7.5d	0.1	0.5	2.3	0.6	1.5	0.9
70 mg_{solids}/L						
t_{des} =90d	7.6	4.5	3.0	4.4	5.1	3.8
30d	0.1	2.1	2.3	2.1	4.1	3.1
15d	<0.1	0.6	2.2	1.5	3.6	1.1
7.5d	<0.1	0.2	1.9	0.6	2.6	0.6
280 mg_{solids}/L						
t_{des} =90d	0.1	1.5	3.6	2.3	3.4	2.6
30d	<0.1	1.7	3.2	1.7	3.3	1.7
15d	<0.1	0.6	2.9	1.5	3.0	1.1
7.5d	<0.1	0.1	2.3	0.2	2.4	0.4

a: These values were derived from the desorption experiment in this study using Boston Harbor sediments. Mean $t_{1/2,des}$'s were 0.9, 1.5, 2.2, and 3.9 d for the desorption timeframes of 7.5, 15, 30, and 90 d (or 180, 360, 720, and 2160h), respectively. $t_{1/2,des}$'s were estimated by averaging all 18 values (disregarding particle size and R_{sw} differences) at a given t_{frame}. The presented t1/2,des corresponded to the desorption data sets (L-set, K-set, IHG-set) as in table A in this appendix.

b: Determined by setting $C_{pyr}(t_{1/2,des})=0.5C_{pyr}(t_{frame})$, with $C_{pyr}(t) = (S_o-S_{Eqm})R_{sw}[1-\exp(-k_{slow}t)] + S_{rapid,o}R_{sw}[\exp(-k_{slow}t)-\exp(-k_{fast}t)]$.

c: Determined by visual inspection on the kinetic data so that $C_{pyr}(t_{1/2,des})=0.5C_{pyr}(t_{frame})$.

Desorption halftimes ($t_{1/2,des}$) of naphthalene[a], phenanthrene, pyrene, and benzo(a)pyrene at timeframes of 90, 30, and 15 d.

	Phenanthrene t_{frame} (d)			Pyrene t_{frame} (d)			Benzo(a)pyrene t_{frame} (d)			
Sediment/Soil	**90**	**30**	**15**	**90**	**30**	**15**	**90**	**30**	**15d**	**Ref.**
Petrol Hbr. A	0.08	0.06	0.05	0.06	0.05	0.05	2.9	1.1	0.8	[1]
Petrol Hbr. B	0.02	0.02	0.02	0.02	0.01	0.01	0.2	0.1	0.08	[1]
Wemeldinge-1	18	5.1	0.08	5.8	0.03	0.02	23	2.3	0.6	[1]
L. Michigan[b]				0.9	0.3	0.3	2.7 (5)	1.6 (2.0)	1.3 (1.3)	[2]
L. Huron 9[b]				4.3	1.7	1.0	11 (19)	5.1 (6.7)	3.3 (3.8)	[2]
L. Huron 54[b]				0.8	0.4	0.3	4.2 (8.3)	2.6 (3.8)	2.0 (2.6)	[2]
West Bearskin L.[b]				2.4	0.9	0.6	7.5 (18)	3.7 (6.3)	2.3 (3.3)	[2]
Terw. Pond[b]				0.4	0.3	0.3	3.3 (6.3)	2.1 (3.2)	1.7 (2.2)	[2]
L. Erie[b]				0.4	0.3	0.2	3.8 (3.8)	2.5 (2.3)	2.0 (1.7)	[2]
Pond 5[b]				0.15	0.21	0.19	2.9 (5)	1.8 (2.5)	1.4 (1.8)	[2]
Newtown Creek[c]	8.0	<2	<1.5	0.3	0.2	0.15	7.0	5.0	2.0	[3]
Piles Creek[c]	0.3	0.2	<0.15	0.08	0.07	0.06	1.0	0.8	<0.8	[3]
L. Ketelmeer	0.1	0.1	0.1	0.2	0.2	0.2				[4]
Varparanta	0.04	0.04	0.04	0.08	0.07	0.06				[4]
Milwaukee Hbr. (<63um)				0.9	0.9	0.9				[5]
Milwaukee Hbr. (63-250um)	0.2	0.2	0.1	0.6	0.4	0.4	1.0	0.8	0.8	[5]
Hollands Diep	4.6	1.0	0.5	0.2	0.1	0.04	3.8	0.6	0.4	[6]
Wemeldinge-2	14	1.1	0.2	0.06	0.03	0.03	9.2	0.8	0.5	[6]
Lachine Shale-1	21	11	6.5							[7]
Lachine Shale-2	26	12	7.0							[7]
Lachine Shale-3	12	7.8	5.3							[7]
Lachine Shale-4	15	9.0	5.7							[7]
Lachine Shale-5	7.5	5.5	4.4							[7]
Lachine Shale-6	6.2	4.4	3.7							[7]
Wagner Soil-1	7.5	5.6	4.4							[7]
Wagner Soil-2	7.0	5.2	4.2							[7]
Wagner Soil-3	3.5	2.5	2.2							[7]
Chelsea Soil-1	4.0	2.7	2.4							[7]
Chelsea Soil-2	9.0	2.4	1.7							[7]
Chelsea Soil-3	1.8	1.3	1.2							[7]
Chelsea Soil-4	1.0	0.7	0.6							[7]
Chelsea Soil-5	1.0	0.8	0.6							[7]

Chelsea Soil-6	1.4	1.4	1.0					[7]
Mount Pleasant silt loam-3d[c]	—	1	<1					[8]
Mount Pleasant silt loam-49d[c]	—	7	<7					[8]
Pahokee peat-3d[c]	3	12	<7					[8]
Pahokee peat-100d[c]	20	3	<1					[8]
Ohio River				4.6	4.6	4.6		[9]
Mississippi R.				0.9	0.9	0.9		[9]
Boston Hbr #6-20ppm[d]				**1.9-7.2**	**1.6-4.3**	**1.3-2.9**		**[10]**
Boston Hbr #6-70ppm[d]				**3.0-7.6**	**2.1-4.1**	**0.6-3.6**		**[10]**
Boston Hbr #6-280ppm[d]				**1.5-3.6**	**1.7-3.3**	**0.6-3.0**		**[10]**

a: Naphthalene desorption halftimes: for Petrol Hbr. A, $t_{1/2,des}$~0.04d for all three t_{des}'s; for Wemeldinge-1, $t_{1/2,des}$~20d, 7.3d, and 2.0d, for t_{des}=90d, 30d, and 15d, respectively.
b: Incubation times were 110d for pyrene, 7d (60d) for benzo(a)pyrene.
c: Determined from reading off desorption curves.
d: Determined from read-off and fitted curve in table B in the same appendix.

Ref.: [1] Cornelissen et al. 1998. [2] Kukkonen et al. 2003. [3] Rockne et al. 2002. [4] Gomez-Lahoz etal. [5] Ghosh et al. 2001. [6] van Noort et al. 2003. [7] Johnson et al. 2001. [8] White et al. 1999. [9] Karickhoff et al. 1985. **[10] From the desorption experiment in this study.**

Appendix 9 - 7. Sensitivity Analyses for Porewater Flushing Only Steady State Model.

The model assumed that pyrene released from surficial bed porewater was balanced by the removal via harbor flushing (i.e. $r_{pw,f} = r_{WC,f}$).

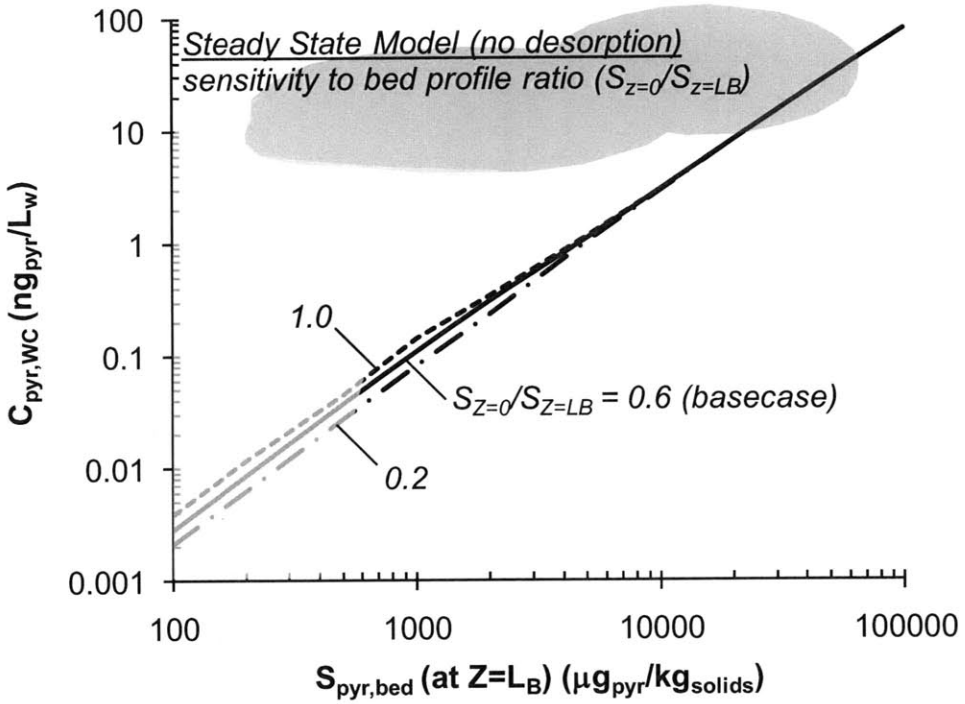

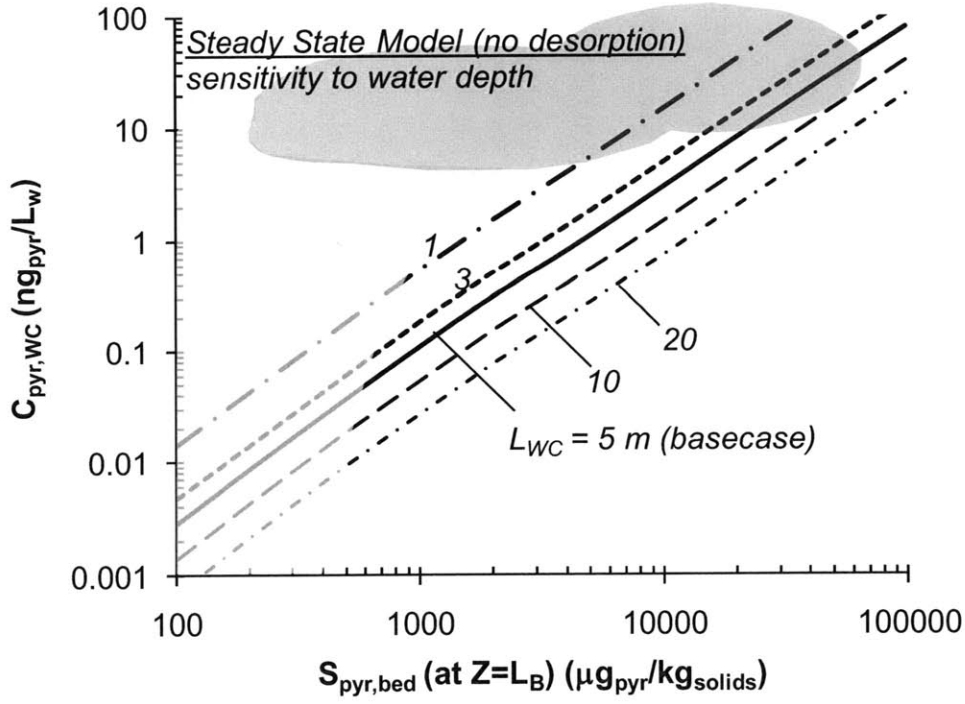

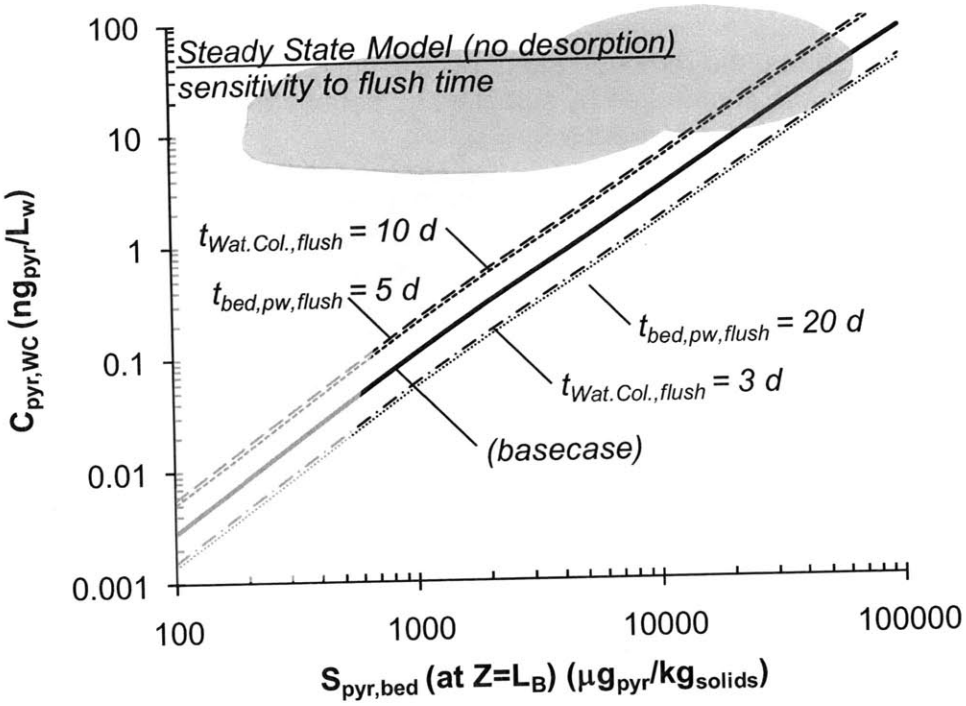

Note that the dark lenses represented field observed ranges of $C_{pyr,WC}$ and $S_{pyr,bed}$. The slightly shaded area signified where realistic $C_{pyr,WC}$ may exist but unobservable by LIF. A prediction that falls on either area may be considered as 'good' or 'satisfactory'.

Appendix 9 - 8. Sensitivity Analyses for the Three-Rate Steady State Model.

The model assumed that the removal rate of pyrene via harbor flushing ($r_{WC,f}$) was balanced by the release contributed by surficial bed porewater flushing ($r_{pw,f}$) and desorption from suspended sediment ($r_{TSS,des}$).

Note that the dark lenses represented field observed ranges of $C_{pyr,WC}$ and $S_{pyr,bed}$. The slightly shaded area signified where realistic $C_{pyr,WC}$ may exist but unobservable by LIF. A prediction that falls on either area may be considered as 'good' or 'satisfactory'.

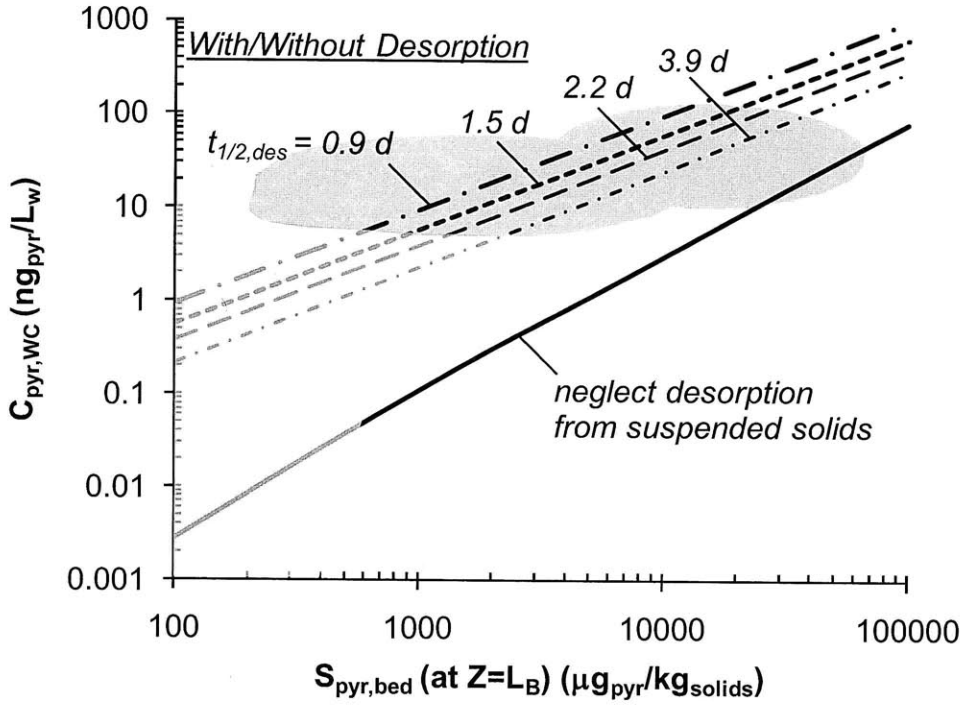

Water Column Flushing and R_{sw}

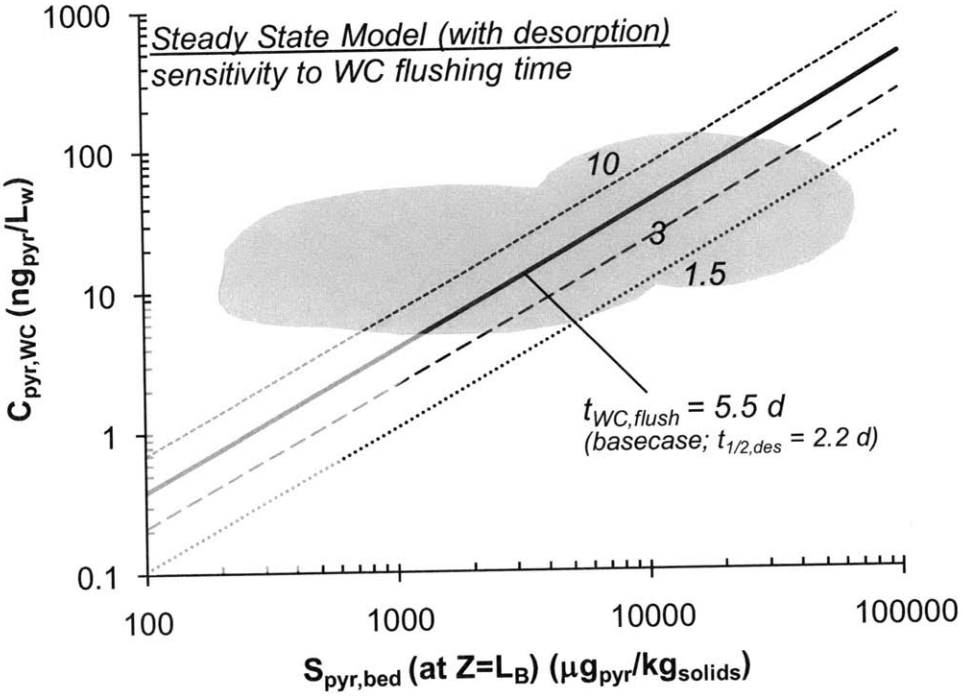

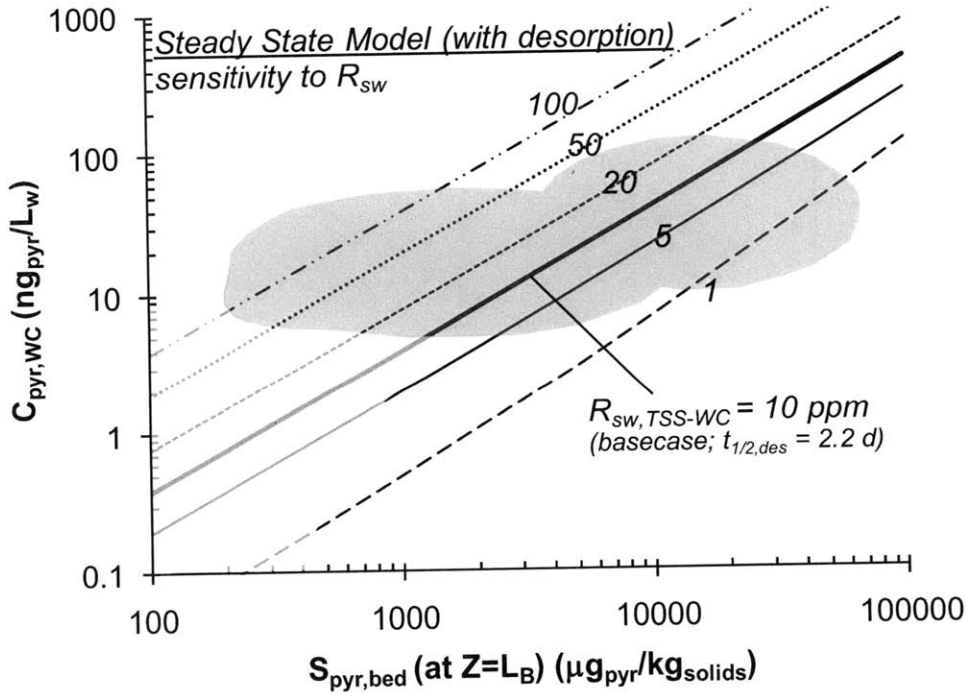

Water Depth and Bed Profile Ratio

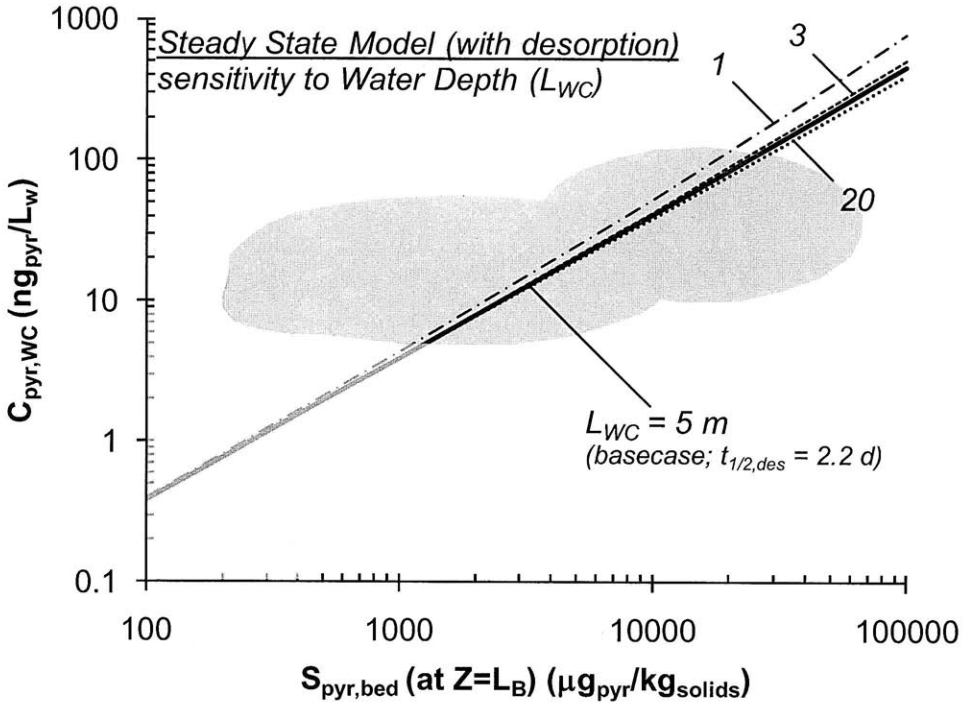

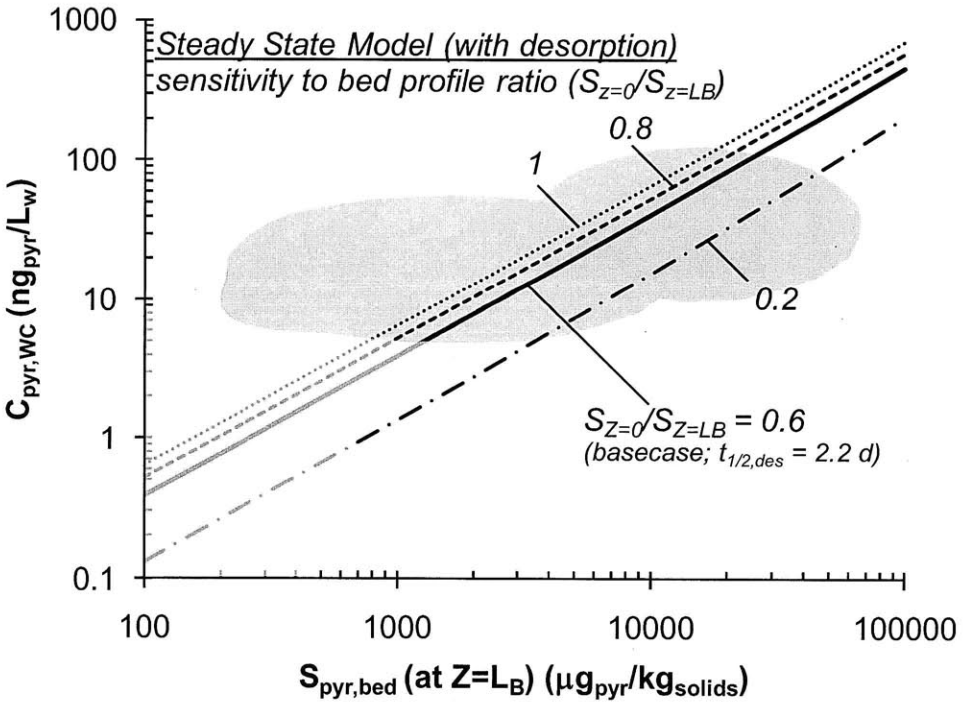

Appendix 9 - 9. Constancy of f_{retain} for Estimation of Sedimentary-Pyrene Depletion Time (EqP Models).

TSS-WC EqP ($f_{retain}=S_{Eqm}/S_o$) (for $f_{OC}=0.0308$, $f_{BC}=0.006$, Occlusion isotherm with $f_{occlu}=0$; $L_B=10$ cm, $L_{WC}=10$ m)

R_{sw} (mg/L)	$S_{pyr,o}$ ($\mu g_{pyr}/kg_{solids}$)	$C_{pyr,Eqm}$ (ng_{pyr}/L_{WC})	$S_{pyr,Eqm}$ ($\mu g_{pyr}/kg_{solids}$)	$K_{d,pyr}$ (L_{WC}/kg_{solids})	S_{Eqm}/S_o	M_B/M_{TSS}	Avg S_{Eqm}/S_o	12 h/resusp. $t_{bed,1/2}$ (d)	6 h/resusp. $t_{bed,1/2}$ (d)
10	10000	60	4000	66000	0.4	500	0.46	231	116
	5000	24	2600	108000	0.52	" "	0.59	305	152
	2500	8.5	1650	194000	0.66	" "	0.73	456	228
	1250	2.6	990	381000	0.79	" "	0.84	794	397
	625	0.7	560	835000	0.89	" "	0.92	1614	807
	312.5	0.2	300	1981000	0.95	" "	0.97	3685	1843
	156.3	0.0+	150	4940000	0.99	" "	n/a		
20	10000	100	5000	49000	0.5	250	0.56	231	116
	5000	37	3100	84500	0.63	" "	0.70	305	152
	2500	12	1900	160000	0.76	" "	0.82	456	228
	1250	3.2	1100	338000	0.87	" "	0.91	794	397
	625	0.8	5900	781000	0.94	" "	0.96	1614	807
	312.5	0.2	300	1920000	0.97	" "	0.98	3685	1843
	156.3	0.0+	150	4850000	0.99	" "	n/a		
50	10000	176	6500	36600	0.65	100	0.71	231	116
	5000	58	3840	66200	0.77	" "	0.82	305	152
	2500	16	2200	135000	0.87	" "	0.90	456	228
	1250	3.9	1170	305000	0.94	" "	0.96	794	397
	625	0.8	610	742000	0.97	" "	0.98	1614	807
	312.5	0.2	310	1870000	0.99	" "	0.99	3685	1843
	156.3	0.0+	155	4850000	1.0	" "	n/a		
100	10000	244	7560	49000	0.76	50	0.81	231	116
	5000	73	4270	84500	0.85	" "	0.89	305	152
	2500	18.5	2320	160000	0.93	" "	0.95	456	228
	1250	4.1	1210	338000	0.97	" "	0.98	794	397
	625	0.9	620	726000	0.99	" "	0.99	1614	807
	312.5	0.2	310	1860000	0.99	" "	1.0	3685	1843
	156.3	0.0+	156	4850000	1.0	" "	n/a		

Appendix 9 - 10. Sedimentary PAHs and OC/BC contents of Boston Harbor samples analyzed by Ewald G. (~2000).

Method & Material (Ewald, G.)

Sediments and soft-shelled clams, Mya arenaria, were collected in mid-December 1999. The main sampling area was located south of Moon Head, Quincy Bay, centred around 42°18.10'N, 71°00.00'W (samples 1-16). Samples 18-22 were taken from east of Squantum marina in Dorchester Bay, centered at 42°17.90'N, 71°0102'W. The clams were collected during low tide from all sections of the exposed tidal-zone. The M.arenaria siphon wholes were located and the clams were dug up with a pitch spade. The sediments immediately surrounding the clam in a ca 5-cm radius were also collected. At most locations, if clams of different sizes were found, several individuals were collected. The clams were rinsed in tap water and were frozen at –20°C within hours after collection as were the sediments.

The sediment and individual clams were extracted using chloroform and methanol (chloroform:methanol:water 1:2:0.8) where the clam water content was included in the ratios. The clams were shucked out of their shell, the gut content was removed as far as possible, and homogenised whole in the organic solvents with an Omni 5100 homogeniser equipped with a 20mm generator probe. After phase separation (addition of one portion of chloroform and one of water) and the transfer of the chloroform phase to a new test-tube the methanol:water phase was re-extracted by addition of a new portion of chloroform. The sediments ca 10-20g wet weight were extracted by shaking followed by untrasonication for 30 min and left for 24 h prior phase separation. Twice the procedure was repeated, after removal of the chloroform phase, by adding a new portion of chloroform.

Subsamples were taken from all extracts for weight determination of lipids and other extracted organics. The subsamples withdrawn for clean-up corresponded ca 25 mg of lipids concerning the clams, and 5g dry weight for the sediments. Cleanup was performed with wet-packed activated silica (6g, Silica Gel 100-200 Mesh, EM Science, Germany) columns and two fractions were obtained. Fraction 1 (FI) eluted with 50 ml hexane containing non polar compounds such as PCBs, and fraction 2 (FII) eluted with 50 ml of hexane:methylene chloride (9:1) containing PAHs. The fractions were concentrated by evaporating the solvents with N2-gas down to ca 1ml prior GC/MS analysis. All solvents were "Ultra resi-analysed" (J.T. Baker, U.S.A.).

Location of Sediment Samples (MacFarlane, J.)

PAHs and OC/BC Contents (Ewald, G.)

Sediment characteristics and concentration of PAHs normalised to sediment dry weight of fine particles (ng/g DW). The different measures of sediment organic content; organig matter, total organic carbon content and soot-like organic carbon, are also normalised to the fraction of fine sediment particles DW.

Site	%FINE	%OM	%LIPID	%totOC	%SOOT	PH	AN	FL	PY	BAP	PCB52	PCB105	PCB128
1	20	5.68	0.36	2.17	0.34	6793	1146	4712	3488	2338	1.8	2.2	1.9
2	29	4.88	0.67	1.7	0.96	8382	1391	10005	6954	2330	6.2	7.0	3.4
3	37	5.73	0.91	2.68	0.62	21591	6812	29047	26028	5117	7.7	9.7	3.6
4	48	1.23	0.39	1.34	0.19	14513	2480	17236	12133	16484	5.3	3.5	1.3
5	71	5.51	1.11	3	1.07	23711	3976	18115	16950	3334	13.2	9.0	4.2
6	84	8.74	1.93	5.02	0.93	15995	2883	20225	18773	16440	17.0	14.3	4.6
7	45	0.89	0.07	0.2	0.17	80	13	57	49	20	0.4	0.8	0.3
8	50	1.24	0.10	1.13	0.14	98	23	84	34	54	0.6	1.5	0.7
9	53	1.53	0.09	0.41	0.12	29	7	86	38	71	0.6	1.1	0.5
10	53	1.70	0.08	0.86	0.13	191	37	139	98	90	0.3	0.2	0.1
11	16	0.93	0.16	0.38	0.1	858	159		571	1667	1.6	2.0	1.4
12	38	3.50	0.55	2.47	1.2	25037	4535	4071	3619	12454	25.9	37.9	18.5
13	43	3.36	0.45	3.26	1.03	4201	779	6008	1179	7249	15.2	15.0	4.7
14	37	4.46	0.55	3.69	0.6	1693	258				4.9	9.5	3.7
15	30	3.40	0.37	2.31	0.32	1202	225	1311	1046	438	3.2	5.6	2.6
16	42	2.21	0.26	2.06	0.26	339	63		216	637	2.9	3.4	1.6
18	71	2.43	0.24	1.73	0.55	1049	288	1252	1003	320	4.9	4.8	1.6
19	88	3.72	0.28	1.96	0.49	190	53	532	646	153	10.0	7.7	2.8
20	97	4.12	0.28	2.02	0.35	27	7	92	74	91	4.6	8.4	3.5
21	98	2.86	0.25	2.02	0.4	62	24	276	113	197	2.6	3.6	1.2
22	40	2.47	0.09	1.35	0.57	208	37	59	39	16	0.3	0.2	0.1

Chapter 10: Appendices

Appendix 10 - 1. Estimation of maximum specimen thickness acceptable to the thin-film approximation. **967**
Appendix 10 - 2. Estimation of inner-shell ionization cross-section area, Q_K, and X-ray fluorescence yield, ω_K, and $(Q_K\omega_K)_y/(Q_K\omega_K)_z$ ratios for C, N, and O. **972**
Appendix 10 - 3. Maximum dimensions of representative coal or lignin structure at sub-micron scale according to proposed conceptual cartoons. **975**
Appendix 10 - 4. Number of pixels per soot or char particle in a STEM mode **975**
Appendix 10 - 5. EDX Single Spot Elemental Ratio Analysis **976**
Appendix 10 - 6. EDX Elemental Mapping Quantitative Analysis **992**
Appendix 10 - 7. sp^2-C and Aromatic-C Fractions in Various Carbonaceous Matters **993**
Appendix 10 - 8. Detail elemental ratios of carbonaceous matters. **995**
Appendix 10 - 9. Estimates of electron beam broadening in a 100 nm-thick specimen at 200-250 kV **998**
Appendix 10 - 10. Densities of selected carbonaceous matters and mineral phases **999**

Appendix 10 - 1. Estimation of maximum specimen thickness acceptable to the thin-film approximation.

(a) Plots of mass absorption (attenuation) coefficients μ/ρ of representative carbon and mineral specimens.

Energy-dependence of mass absorption coefficients, μ/ρ, of carbon (representing BC), glucose (representing non-condensed organic carbons), and SiO_2 (representing inorganic mineral phases) are plotted. The sharp discontinuities present in the plots mark the various energy transition edges. For example, for the carbon plot, the discontinuity occurs at ~284 eV, corresponding to the carbon K-edge. Data were generated from the NIST online module for mass attenuation coefficients (Chantler et al. 2005).

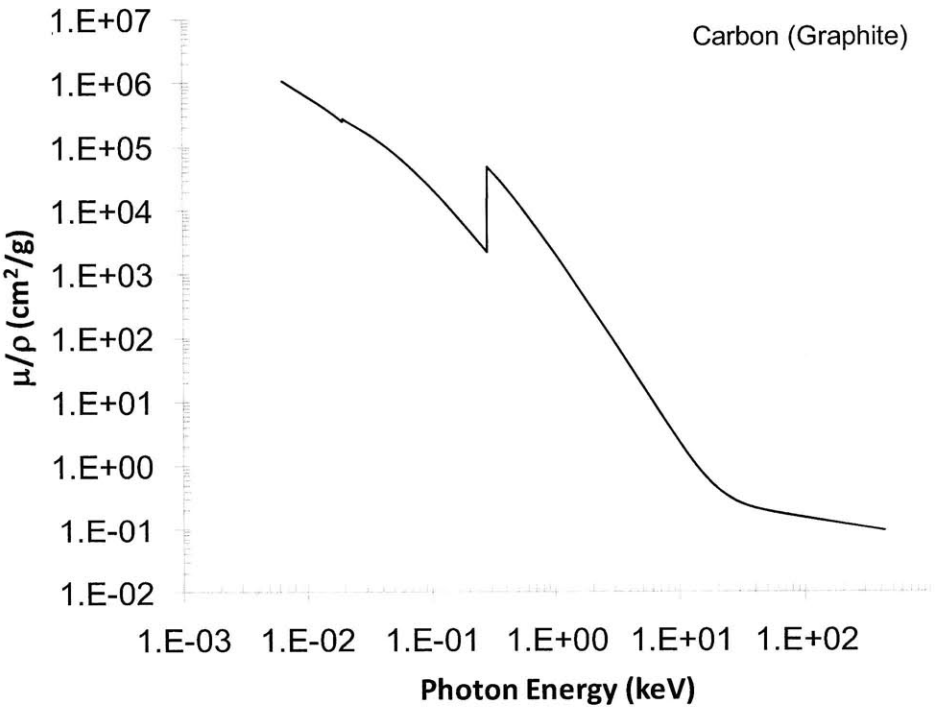

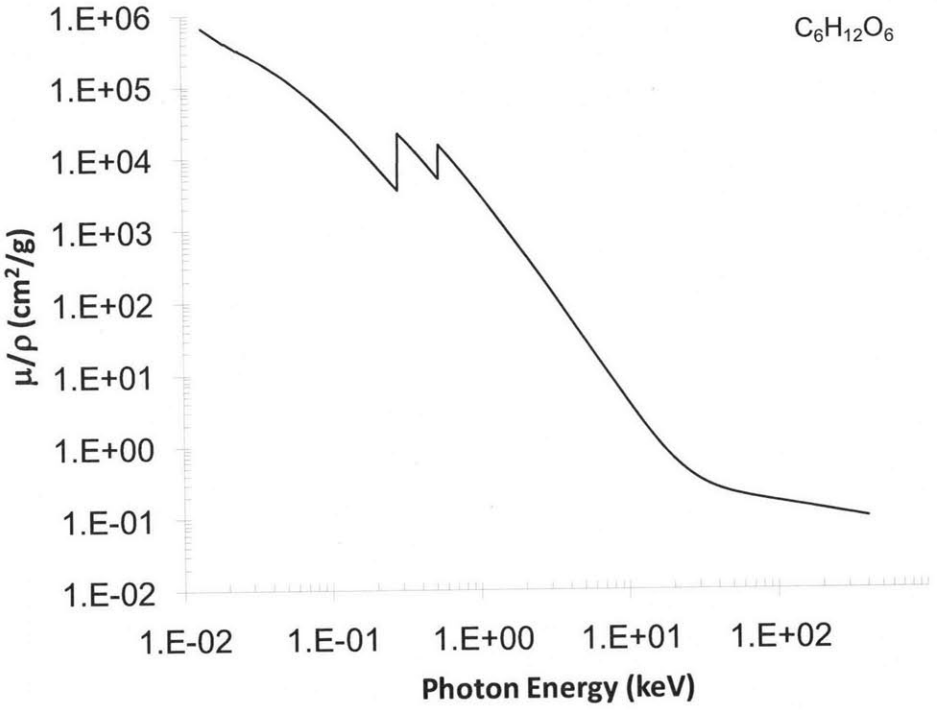
$C_6H_{12}O_6$
1.E+06
1.E+05
1.E+04
1.E+03
1.E+02
1.E+01
1.E+00
1.E-01
1.E-02
μ/ρ (cm²/g)
1.E-02
1.E-01
1.E+00
1.E+01
1.E+02
Photon Energy (keV)

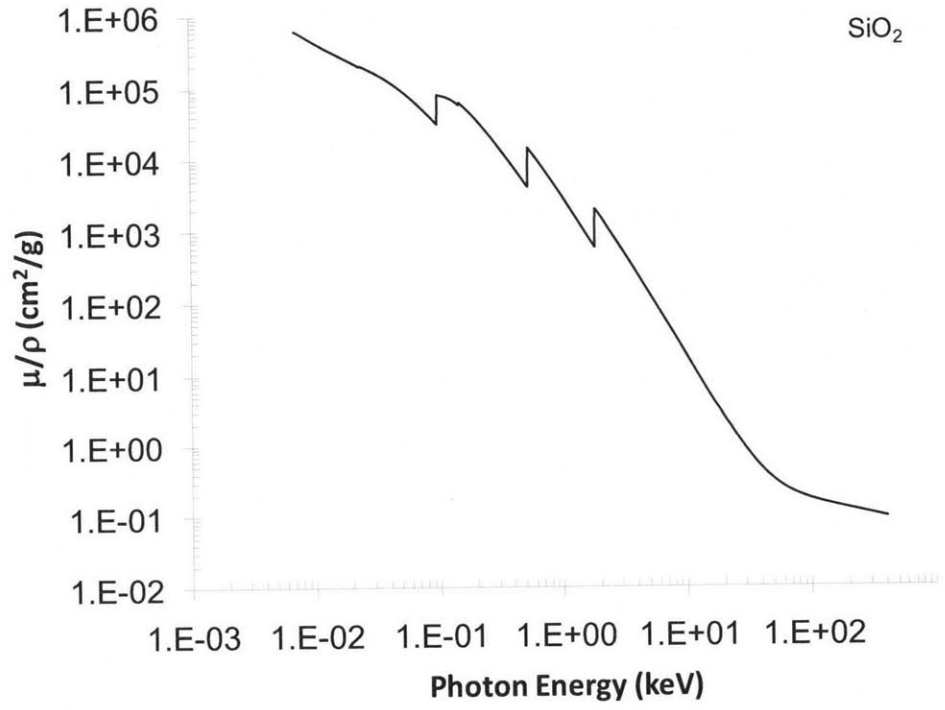
SiO_2
1.E+06
1.E+05
1.E+04
1.E+03
1.E+02
1.E+01
1.E+00
1.E-01
1.E-02
μ/ρ (cm²/g)
1.E-03
1.E-02
1.E-01
1.E+00
1.E+01
1.E+02
Photon Energy (keV)

(b) Mass absorption (or attenuation) coefficients for C, N, and O X-rays in selected specimens according to Chantler et al. 2005.

Specimen / Scheme	Mass Absorption Coefficient μ/ρ (cm^2/g)				
	Carbon	SiO	SiO_2	$C_6H_{12}O_6$	$C_{12}H_{26}$
	ρ=2.26 g/cm^3	~2.2 g/cm^3	~2.2 g/cm^3	~1.5 g/cm^3	0.75 g/cm^3
Fixed X-ray energies*					
C (284 eV)	2190	22440	17784	3556	1920
N (400 eV)	23136	10156	8036	10433	19598
O (532 eV)	11365	6223	5704	6827	9625
Fixed & Edge-Averaging†					
C	25286	22440	17784	12777	21462
N	23136	10156	8036	10433	19598
O	11365	8512	9080	10199	9625
Fixed & Edge-Range‡					
C	2190-48382	22440	17784	3556-21998	1920-41004
N	23136	10156	8036	10433	19598
O	11365	5078-11946	4015-14145	5141-15256	9625

* Absorption coefficients for C, N, and O X-rays were determined at 284, 400, and 532 eV, respectively by linear interpolating between the two closest points. This is a rigid scheme that disregards the slight shifting of the edges when C, N, and O are bonded differently.

Uncertainties in μ/ρ were estimated to be approximately 50-100% for C and N, and <50% for O, according to Henke et al. 1993.

† Determined in the same way as in *, except at the edges, average values of the minimum and the maximum absorption coefficients were used. This allows uncertainties associated with slight energy shifts.

‡ Minimum and maximum absorption coefficients at the edges are reported.

Bastin et al. (Scott et al. 1995) gave an independent estimates on self-absorption coefficients of C, N, and O as 2373, 1810, and 983 cm^2/g, respectively. Their estimates were in fair agreement with those obtained from the NIST online module: 2190, 1497, and 1087 cm^2/g for self-absorption of C, N, and O X-rays, respectively. Both sets correspond to the lower-end absorption coefficients at the K-edges.

(c) Estimated maximum allowed specimen thickness in accordance with the thin-film approximation.

Maximum specimen thickness was calculated using two independent criteria (Goldstein 1979):

Tixier & Philibert thin-film criterion:

$$\varepsilon \equiv \left(\frac{\mu}{\rho}\right)_{Comp} \delta \csc\alpha < \varepsilon_{Crit}$$

Goldstein et al. thin-film criterion for X-rays of elements y and z:

$$\varepsilon \equiv \left[\left(\frac{\mu}{\rho}\right)^{y}_{Comp} - \left(\frac{\mu}{\rho}\right)^{z}_{Comp}\right]\frac{\delta}{2}\csc\alpha < \varepsilon_{Crit}$$

Where μ/ρ [cm^2/g] is the mass absorption (Goldstein 1979; Scott et al. 1995) or mass attenuation coefficient (Hubbell et al. 1996; Chantler et al. 2005) which describes how strongly the specimen is absorbing the X-ray of element y (or z),

δ, known as the mass thickness [g/cm^2], is defined as the product of the specimen density and the thickness t (i.e., $\delta \equiv \rho t$),

$\csc\alpha$ correcting for the extended pathlength due to the placement of X-ray detector at an angle of α (i.e., X-ray take off angle),

ε is the error estimated for no X-ray absorption in the sample,

ε_{Crit} is the allowed/acceptable level of error or uncertainty resulting from no X-ray absorption correction.

Criterion \ Specimen		Maximum Specimen Thickness t (nm)				
		Carbon†	SiO	SiO_2	$C_6H_{12}O_6$	$C_{12}H_{26}$
Tixier & Philibert Fixed energies	ε_{Crit}=0.1					
	C	69	7	9	64	238
	N	7	15	19	22	23
	O	13	25	27	33	47
	ε_{Crit}=0.25					
	C	173	17	22	160	594
	N	16	38	48	55	58
	O	33	62	68	83	118
	ε_{Crit}=0.5					
	C	346	35	44	321	1188
	N	33	77	97	109	116
	O	67	125	136	167	237
Fixed energies & edge-avg.*	ε_{Crit}=0.1					
	C	6	7	9	18	21
	N	7	15	19	22	23
	O	13	18	17	22	47
	ε_{Crit}=0.25					
	C	15	17	22	45	53
	N	16	38	48	55	58
	O	33	46	43	56	118
	ε_{Crit}=0.5					
	C	30	35	44	89	106
	N	33	77	97	109	116
	O	67	91	86	112	237
Goldstein et al. Fixed energies	ε_{Crit}=0.1					
	C-N	14	25	32	66	52
	C-O	33	19	26	139	118
	ε_{Crit}=0.25					
	C-N	36	63	80	166	129
	C-O	82	48	64	348	296
	ε_{Crit}=0.5					
	C-N	72	127	159	332	258
	C-O	165	96	129	697	592
Fixed energies & edge-avg.*	ε_{Crit}=0.1					
	C-N	141	25	32	195	489
	C-O	22	22	36	177	77
	ε_{Crit}=0.25					
	C-N	352	63	80	486	1224
	C-O	54	56	89	442	193
	ε_{Crit}=0.5					
	C-N	704	127	159	973	2447
	C-O	109	112	179	884	385

* The final scheme used for evaluating the validity of thin-film approximation and the maximum thickness values reported in Table 10-**1**.

Appendix 10 - 2. Estimation of inner-shell ionization cross-section area, Q_K, and X-ray fluorescence yield, ω_K, and $(Q_K\omega_K)_y/(Q_K\omega_K)_z$ ratios for C, N, and O.

(a) Models of Ionization Cross-section Area, Q_K

	Q_KE_c ($cm^2.eV^2$)*,†	Parameters	Notes	Reference
Mott & Massey (1949)	$aN_K b\frac{\ln(cU)}{U}$	a = 6.51×10^{-14} b = 0.35 c = 2.42		Powell 1976
Worthington & Tomlin (1956)	$aN_K b\frac{\ln(\frac{4U}{c+de^{1-U}})}{U}$	a = 6.51×10^{-14} b = 0.35 c = 1.65 d = 2.35		Powell 1976
Green & Cosslett (1961)	$a\frac{\ln(U)}{U}$	a = 7.92×10^{-14}		Green et al 1961; Loretto 1994
Gryzinski (1965)	$aN_K b\frac{1}{U}\left(\frac{U-1}{U+1}\right)^{1.5}\times$ $(1+\frac{2}{3}\left(\frac{1}{2U}\right)\ln(2.7+(U-1)^{0.5}))$	a = 6.51×10^{-14} b = 0.35		Gryzinski 1965; Powell 1976
Drawin (1963)	$aN_K b\frac{\ln(cU)}{U}$	a = 6.51×10^{-14} b = 0.66 c = 1.25		Powell 1976
Lotz (1970)	$aN_K\frac{(\ln U)}{U}[1-be^{-C(U-1)}]$	a = 4×10^{-14} b = 0.75 c = 0.5		Powell 1976

* Where N_K is the number of electrons in the K-shell (i.e., 2), U us the overvoltage ratio defined as the energy ratio of $E_{electron}/E_C$, with E_C as the inner-shell ionization energy.
† E_C for C, N, and O are ~284, 400, and 532 eV, respectively (Isaacson 1972; Egerton 1996).

(b) Models of X-ray Fluorescence Yield, ω_K.

	ω_K*	Parameters	Notes	Reference
Wentzel (1927)	$\frac{Z^4}{(a+Z^4)}$	a = 9×10^5	Z ≤ 10	Tawara et al. 1973; Loretto 1994
Laberrigue-Frolow & Radvanyi 1956	$\frac{(a+bZ+CZ^3)^4}{1+(a+bZ+CZ^3)^4}$	a = -0.0217 b = 0.03318 c = -1.14×10^{-6}	Z ≤ 16	Green et al. 1961
McGuire 1970	$\frac{(Z-1)^4}{[a+(Z-1)^4]}$	a = 8×10^5	Z ≤ 16	Hink et al. 1971
Byrne & Howarth 1970	$\frac{1}{[1+\frac{a}{Z^b}^4]}$	a = 1.16×10^5 b = 3.36	Z ~ 15 to 60	Hink et al. 1971
Hanke et al. 1985	$a+bZ+cZ^2+dZ^3$	a = 0.337 b = -0.060 c = 3.31×10^{-3} d = 3.93×10^{-5}	12 ≤ Z ≤ 42	Hanke et al. 1985

* Where Z is the atomic number of the element of interest.

(c) Observed Fluorescence Yield (ω_K)*.

	Lowest ω_K	Highest ω_K
Carbon	0.00088	0.0035
Nitrogen	0.0015	0.0047
Oxygen	0.0022	0.0065

* From Tawara et al. 1973 and references within.

(d) $(Q_K\omega_K)_{carbon}/(Q_K\omega_K)_{nitrogen}$ estimated from models and observations in (a) and (b).

ω_K \ Q_K	Mott & Massey	Worthington & Tomlin	Green & Cosslett	Gryzinski	Drawin	Lotz
Wentzel	0.80	0.80	0.80	0.79	1.37	0.80
Laberrigue-Frolow & Radvanyi	0.74	0.74	0.75	0.74	1.28	0.75
McGuire	0.71	0.71	0.72	0.70	1.23	0.72
Byrne & Howarth	0.88	0.88	0.89	0.87	1.52	0.89
Hanke et al.*	1.97	1.97	1.98	1.94	3.39	1.98
Observed (Low)	0.86	0.87	0.87	0.85	1.49	0.87
Observed (High)	1.10	1.10	1.10	1.08	1.89	1.10

* Hanke et al.'s model gives a trend such that ω_K decreases with increasing atomic number. This is contrary to qualitative expectation from theory as well as inconsistent with what other ω_K models predict. The incorrect trend produced for C, N, and O was most likely mathematical in nature, resulting from the cubic polynomial function employed by Hanke et al.

(e) $(Q_K\omega_K)_{carbon}/(Q_K\omega_K)_{oxygen}$ estimated from models and observations in (a) and (b).

ω_K \ Q_K	Mott & Massey	Worthington & Tomlin	Green & Cosslett	Gryzinski	Drawin	Lotz
Wentzel	0.65	0.65	0.66	0.63	1.12	0.66
Laberrigue-Frolow & Radvanyi	0.58	0.58	0.58	0.63	0.99	0.58
McGuire	0.53	0.53	0.54	0.52	0.92	0.54
Byrne & Howarth	0.78	0.78	0.79	0.76	1.35	0.79
Hanke et al.*	3.67	3.67	3.71	3.59	6.33	3.71
Observed (Low)	0.82	0.82	0.83	0.80	1.41	0.83
Observed (High)	1.10	1.10	1.11	1.07	1.89	1.11

* See footnote in (d).

(f) Sample calculation of Q_KW_K.

Consider the estimate of $(Q_K\omega_K)_{carbon}/(Q_K\omega_K)_{oxygen}$ by Mott & Massey's Q_K model and Wentzel's ω_K model. The electron microscope used for EDX spot analysis was VG HB603, and it was operating with an accelerated voltage of 250 kV.

E_o (J) = Accelerated voltage (V) × e^- charge (C)

= 250000 V × 1.602×10^{-19} C

= 4.0×10^{-14} J

= $\underline{2.5\times10^{5}\ eV}$

U = E_o/E_c

$U_{carb.}$ = 2.5×10^{5} eV / 284 eV

= $\underline{8.8\times10^{2}}$

$U_{oxyg.}$ = 2.5×10^{5} eV / 532 eV

= $\underline{4.7\times10^{2}}$

$Q_K E_C^2 = 6.51\times10^{-14} N_K 0.35[\ln(2.42U)]/U$

where N_K = 2 for carbon and oxygen K-shell ionization.

$\omega_K = Z^4/(900000+Z^4)$

where Z = 6 for carbon and 8 for oxygen

For carbon:

$Q_K E_C^2 = 4.0\times10^{-16}$ cm^2eV^2

$Q_{carb.,K} = 4.9\times10^{-21}$ cm^2

For oxygen:

$Q_K E_C^2 = 6.8\times10^{-16}$ cm^2eV^2

$Q_{carb.,K} = 2.4\times10^{-21}$ cm^2

Therefore, $(Q_K\omega_K)_{carbon}/(Q_K\omega_K)_{oxygen}$:

= $(4.9\times10^{-21}\ cm^2 \times 0.0014)/(2.4\times10^{-21}\ cm^2 \times 0.0045)$

= $\underline{0.65}$

Appendix 10 - 3. Maximum dimensions of representative coal or lignin structure at sub-micron scale according to proposed conceptual cartoons.

The calculation here assumes that:

1) the proposed structures of coal and lignin in Figure 8-3 and 8-4 are realistic and are statistically representative of 'coal' and 'lignin' at sub-micron levels,

2) the functional groups and fragments in the structures are, in reality, interacting with each other to form a three-dimensional shape instead of the flat, stretched-out structure as depicted in the cartoon, and so actual dimension of the realistic representative 'coal' or 'lignin' cannot be larger than those determined from the cartoon, and

3) consider the bond lengths between C, H, O, and N all to be about 1.6Å (corresponds to C_{sp3}-C_{sp3} bond) which should be the longest bond length possible in typical environmental organic geosorbents.

For the lignin cartoon, the flat layout has a dimension of about 30 bonds, or about 4.8 nm. For the coal cartoon, the dimension of any one side is no more than 40 bonds at an angle of 30° to the dimensional direction, and so each side is no more than $40 \times 1.6 \times \cos 30^\circ$ and amounts to about 5.5 nm. Thus, the real lignin and the coal representative structure should assume dimension less ~5 nm.

Appendix 10 - 4. Number of pixels per soot or char particle in a STEM mode

	Particle Radius (nm)	Max. Projected Area (nm^2)*	# Pixels (4 nm/pix)†	# Pixels (5 nm/pix)†
Soot	10	310	20	10
	15	710	40	30
	20	1300	80	50
	25	2000	130	80
Char	5×10^3	79×10^6	4.9×10^6	3.2×10^6
	10×10^3	310×10^6	19×10^6	12×10^6
	20×10^3	1300×10^6	81×10^6	52×10^6

* Max. projected area = πr^2.

† # pixels per particle = max. projected area/area per pixel. Area per pixel = x^2, where x = 4 or 5 nm/pix.

Appendix 10 - 5. EDX Single Spot Elemental Ratio Analysis

(a) Ratio Determination by the Integrated-Area Method

The software for STEM-EDX, INCA, provided compositional summary (in weight % of element x) by analyzing the integrated area under individual EDX peaks. If a particular element has a very small contribution (e.g., N peak is often very small), the user need to force the analytical module to 'perceive' the presence of the peak, and then perform a compositional analysis.

Elemental Atomic Ratio (Uncorrected). The elemental ratio between two elements, y and z, as approximated by the ratio of the integrated area under the two elemental EDX peak is then:

$$\frac{n_y}{n_z} \approx \frac{I_{y,K}}{I_{z,K_{uncor}}} = \frac{W_{y,K}/MW_y}{W_{z,K}/MW_z}$$

Where n_y/n_z is the atomic ratio between elements y and z,

$I_{y,K}/I_{z,K}$ is the intensity ratio of K-line X-rays emitted by elements y and z,

$W_{y\ or\ z,K}$ is the weight percent of element y or z as determined by INCA,

$MW_{y\ or\ z}$ is the molecular weight in g/mol

C/O Ratio (Background-O corrected). In the case of C and O, O X-ray contributed from the background SiO film can be corrected if a background ratio between Si and O can be established:

$$\frac{n_C}{n_O} \approx \frac{I_{C,K}}{I_{O,K_{corr}}} = \frac{W_{C,K}/MW_C}{(W_{O,K} - W_{Si,K} \times R_{Bkgd\ -O:Si})/MW_O}$$

Where n_C/n_O is the carbon to oxygen atomic ratio,

W is the weight percent of carbon, oxygen, or silicon as reported by INCA,

MW is the molecular weight of carbon or oxygen in g/mol,

$R_{Bkgd\text{-}O:Si}$ is the mean background (non-occupied area) oxygen to silicon weight % ratio, or

$$R_{Bkgd\ -O:Si} = \frac{1}{M} \sum_{All\ Bkgd\ Spots}^{i=1\ to\ M} \left(\frac{W_{O,K}}{W_{Si,K}}\right)_i$$

(b) Ratio Determination by the Peak-Height Method

Elemental Atomic Ratio (Uncorrected). The EDX spectrum of an examined spot was used to estimate the atomic ratio between two elements as well as any other necessary correction.

$$\frac{n_y}{n_z} \approx \frac{I_{y,K}}{I_{z,K_{uncor}}} \approx \frac{H_{y,K}}{H_{z,K}}$$

Where n_y/n_z is the atomic ratio between elements y and z,

$I_{y,K}/I_{z,K}$ is the intensity ratio of K-line X-rays emitted by elements y and z,

H is the peak height (X-ray counts) of y or z as reported in the raw EDX spectrum

C/O Ratio (Background-O corrected). The expression is in exact form as that in the integrated-area method:

$$\frac{n_C}{n_O} \approx \frac{I_{C,K}}{I_{O,K_{corr}}} \approx \frac{H_{C,K}}{H_{O,K} - H_{Si,K} \times R_{Bkgd-O:Si}}$$

Where n_C/n_O is the carbon to oxygen atomic ratio,

H is the peak height of carbon, oxygen, or silicon,

$R_{Bkgd-O:Si}$ is the mean background (non-occupied area) oxygen to silicon peak height ratio, or

$$R_{Bkgd-O:Si} = \frac{1}{M} \sum_{\text{All Bkgd Spots}}^{\text{i=1 to M}} \left(\frac{H_{O,K}}{H_{Si,K}}\right)_i$$

C/N Ratio (C, O-tailings corrected). The N EDX peak is often interfered by the shoulders of the neighboring C and O peaks. The correction used here assumes that (i) all individual peaks are symmetrical around the peak maximum, and (ii) background contribution from elements other than C and O is insignificant. These two assumptions are not necessarily valid especially when X-ray of other elements are detected and the C and O peaks are being relatively small.

With the assumptions, the X-ray count registered at the N peak-maximum (400 eV) is then a sum of truly N X-ray count and the X-ray counts of C and O tailings, which can be assessed by the counts registered at the other shoulder with an equal distance (see figure below). The contribution by C on the N peak maximum is therefore the same as

the C count at 160 eV (Δa = distance between C and N peak maxima = 120 eV; the mirror energy position = 280 – 120 eV = 160 eV.). Similarly, the tailing imposed by the O peak can be quantified at 680 eV (Δb = distance between N and O peak maxima = 140 eV; the mirror energy position = 540 + 140 eV = 680 eV.)

The tailings-corrected C/N atomic ratio based on peak-height is then:

$$\frac{n_C}{n_N} \approx \frac{I_{C,K}}{I_{N,K_{corr}}} \approx \frac{H_{C,K}}{H_{400eV} - H_{O,K,680eV} \times H_{C,K,160eV}}$$

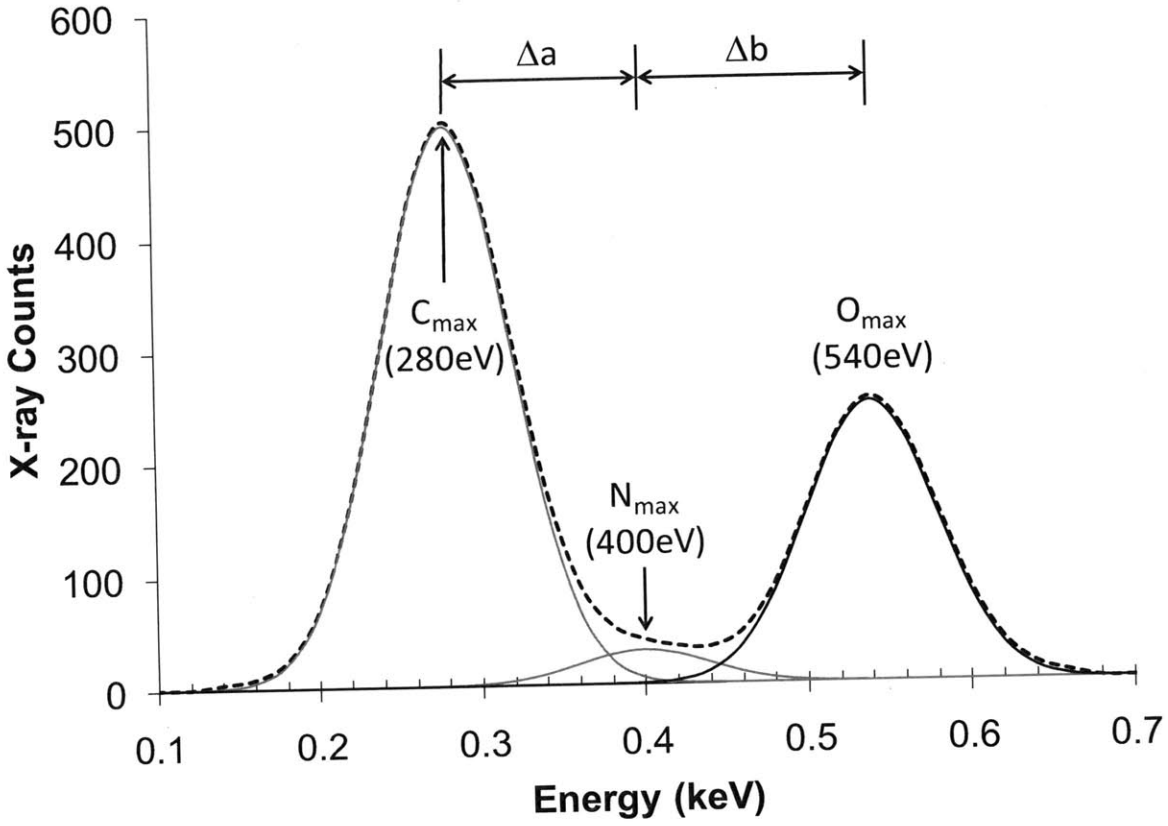

Figure: Correcting tailing effects in N EDX peak height.

(c) Data and Calculation by Peak-Height Method

Date	Site #	Spec#	Type	Peak Height C	N	N"[a]	O	Si	C/N	C/N"	C/O	O/Si[b]	O"[c]	C/O"
20061010	Si #2	1	Miner+SiO	138	142	0	4104	4674	1.0	*Inf*	0.0			
		2	SiO	38	20	0	393	747	1.9	*Inf*	0.1	*0.53*		
		3	Soot+SiO	654	33	0	407	740	19.8	*Inf*	1.6		*18*	*37.0*
20061010	Si #6	1	App. Miner.	621	31	0	224	699	20.0	*Inf*	2.8			
		2	App. Miner.	470	43	0	474	1095	10.9	*Inf*	1.0			
		3	App. Miner.	760	40	0	270	696	19.0	*Inf*	2.8			
		4	App. Miner.	644	18	0	189	671	35.8	*Inf*	3.4			
		5	App. Miner.	1379	33	0	244	689	41.8	*Inf*	5.7			
20061010	Si #12	1	App. Miner.	621	31	0	224	699	20.0	*Inf*	2.8			
		2	App. Miner.	470	43	0	474	1095	10.9	*Inf*	1.0			
		3	App. Miner.	760	40	0	270	696	19.0	*Inf*	2.8			
		4	App. Miner.	644	18	0	189	671	35.8	*Inf*	3.4			
		5	App. Miner.	1379	33	0	244	689	41.8	*Inf*	5.7			
20061013	Si #1	2	SiO	32	12	0	201	375	2.7	*Inf*	0.2	*0.54*		
		3	SiO	57	24	0	302	588	2.4	*Inf*	0.2	*0.51*		
		4	Soot+SiO	325	23	0	337	598	14.1	*Inf*	1.0		*23*	*14.0*
		5	Soot+SiO	275	20	0	311	615	13.8	*Inf*	0.9		*0*	*Inf*
		6	Soot+SiO	709	32	0	359	647	22.2	*Inf*	2.0		*19*	*36.4*
20061019	Si #2	1	HA	829	37	0	729	66	22.4	*Inf*	1.1		*696*	*1.2*
		2	HA	1432	67	0	1532	67	21.4	*Inf*	0.9		*1499*	*1.0*
		3	HA	104	6	0	92	8	17.3	*Inf*	1.1		*88*	*1.2*
	Si #5	1	HA	261	12	0	231		21.8	*Inf*	1.1		*231*	*1.1*
		3	HA	2046	131	0	2291		15.6	*Inf*	0.9		*2291*	*0.9*
		4	HA	282	21	0	308		13.4	*Inf*	0.9		*308*	*0.9*
		5	HA	1173	62	0	1059		18.9	*Inf*	1.1		*1059*	*1.1*
	Si #7	2	HA	819	40	0	847	565	20.5	*Inf*	1.0		*565*	*1.5*
		3	HA	2741	220	0	4078	860	12.5	*Inf*	0.7		*3648*	*0.8*
		4	HA	702	59	0	1292	962	11.9	*Inf*	0.5		*811*	*0.9*
		5	HA	636	26	0	614	500	24.5	*Inf*	1.0		*364*	*1.7*
		6	HA	1619	77	0	1504	575	21.0	*Inf*	1.1		*1217*	*1.3*
Date	Site #	Spec#	Type	Peak Height C	N	N"[a]	O	Si	C/N	C/N"	C/O	O/Si[b]	O"[c]	C/O"

20061019	Si #11	1	HA	93	30	0	437	500	3.1	*Inf*	0.2			***187***	***0.5***
		2	HA	1193	102	0	2074	518	11.7	*Inf*	0.6			***1815***	***0.7***
		3	HA	65	13	0	238	435	5.0	*Inf*	0.3			***21***	***3.2***
		4	HA	717	80	0	1999	1252	9.0	*Inf*	0.4			***1373***	***0.5***
		5	HA	239	55	0	1611	909	4.3	*Inf*	0.1			***1157***	***0.2***
		6	HA	561	62	0	1175	535	9.0	*Inf*	0.5			***908***	***0.6***
		7	HA	379	86	0	2673	590	4.4	*Inf*	0.1			***2378***	***0.2***
		8	HA	408	51	0	1051	534	8.0	*Inf*	0.4			***784***	***0.5***
		9	HA	314	61	0	1320	622	5.1	*Inf*	0.2			***1009***	***0.3***
	Si #13	3	HA	147	23	0	443	568	6.4	*Inf*	0.3			***159***	***0.9***
		4	HA	130	15	0	302	476	8.7	*Inf*	0.4			***64***	***2.0***
		5	HA	1155	60	0	1176	702	19.3	*Inf*	1.0			***825***	***1.4***
		6	HA	1461	64	0	1007	632	22.8	*Inf*	1.5			***691***	***2.1***
		7	HA	2438	118	0	2241	626	20.7	*Inf*	1.1			***1928***	***1.3***
		8	HA	179	24	0	580	550	7.5	*Inf*	0.3			***305***	***0.6***
20061103	Si #2	1	App. Miner.	9	12	0	258	536	0.8	*Inf*	0.0			***0***	*Inf*
		2	App. Miner.	14	17	1	357	557	0.8	***14.0***	0.0			***79***	***0.2***
		3	App. Miner.	12	15	0	483	626	0.8	*Inf*	0.0			***170***	***0.1***
		4	App. Miner.	8	13	0	333	557	0.6	*Inf*	0.0			***55***	***0.1***
		5	App. Miner.	18	15	0	639	698	1.2	*Inf*	0.0			***290***	***0.1***
	Si #3	1	Soot+SiO	95	9	0	162	468	10.6	*Inf*	0.6			***0***	*Inf*
		2	Soot+SiO	65	9	0	149	477	7.2	*Inf*	0.4			***0***	*Inf*
	Si #5	1	Soot+SiO	61	5	0	157	451	12.2	*Inf*	0.4			***0***	*Inf*
		2	SiO	7	9	0	200	485	0.8	*Inf*	0.0	***0.41***			
		3	Soot+SiO	107	9	0	235	492	11.9	*Inf*	0.5			***35***	***3.0***
		4	Soot+SiO	168	12	0	176	470	14.0	*Inf*	1.0			***0***	*Inf*
		5	SiO	19	8	0	196	470	2.4	*Inf*	0.1	***0.42***			
		6	Soot+SiO	168	13	0	200	470	12.9	*Inf*	0.8			***9***	***18.1***
		7	SiO	25	7	0	182	469	3.6	*Inf*	0.1	***0.39***			

Date	Site #	Spec#	Type	Peak Height C	N	N"[a]	O	Si	C/N	C/N"	C/O	O/Si[b]	O"[c]	C/O"
20061108	Si #9	1	Nicot.	119	36	19	218	281	3.3	6.3	0.5		78	1.5
		2	Nicot.	112	28	16	50	5	4.0	7.0	2.2		48	2.4
		3	Nicot.	106	32	17	65	3	3.3	6.2	1.6		64	1.7
		4	Nicot.	60	12	4	22	5	5.0	15.0	2.7		20	3.1
		5	Nicot.	91	21	15	37	2	4.3	6.1	2.5		36	2.5
		6	Nicot.	57	9	2	21	1	6.3	28.5	2.7		21	2.8
	Si #11	3	Nicot.	40	10	5	25	1	4.0	8.0	1.6		25	1.6
		4	Nicot.	39	8	3	14	2	4.9	13.0	2.8		13	3.0
		5	Nicot.	32	10	6	19	2	3.2	5.3	1.7		18	1.8
		6	Nicot.	48	9	1	23	1	5.3	48.0	2.1		23	2.1
		7	Nicot.	32	5	2	13	2	6.4	16.0	2.5		12	2.7
		8	Nicot.	31	10	6	22	2	3.1	5.2	1.4		21	1.5
		9	Nicot.	35	9	4	28	1	3.9	8.8	1.3		28	1.3
	Si #12	1	Nicot.	48	25	17	197	312	1.9	2.8	0.2		41	1.2
		2	Nicot.	115	23	13	53	5	5.0	8.8	2.2		51	2.3
		3	Nicot.	79	21	12	40	8	3.8	6.6	2.0		36	2.2
		4	Nicot.	75	19	10	30	4	3.9	7.5	2.5		28	2.7
		5	Nicot.	79	14	12	25	3	5.6	6.6	3.2		24	3.4
		6	Nicot.	99	30	8	57	5	3.3	12.4	1.7		55	1.8
	Si #13	1	Nicot.	157	61	26	449	683	2.6	6.0	0.3		108	1.5
		2	Nicot.	78	27	4	372	612	2.9	19.5	0.2		66	1.2
		3	Nicot.	75	37	6	357	611	2.0	12.5	0.2		52	1.5
		4	Nicot.	181	43	22	81	4	4.2	8.2	2.2		79	2.3
		5	Nicot.	146	34	15	75	10	4.3	9.7	1.9		70	2.1
		6	Nicot.	208	50	21	99	10	4.2	9.9	2.1		94	2.2
		7	Nicot.	217	43	16	74	7	5.0	13.6	2.9		71	3.1
		8	Nicot.	169	52	31	89	11	3.3	5.5	1.9		84	2.0
		9	Nicot.	182	41	23	85	3	4.4	7.9	2.1		84	2.2

Date	Site #	Spec#	Type	Peak Height C	N	N"[a]	O	Si	C/N	C/N"	C/O	O/Si[b]	O"[c]	C/O"
20061108	Si #14	1	Nicot.	299	129	61	835	1241	2.3	4.9	0.4		215	1.4
		2	Nicot.	193	92	37	782	1242	2.1	5.2	0.2		161	1.2
		3	Nicot.	148	64	3	722	1231	2.3	49.3	0.2		107	1.4
		4	Nicot.	231	64	35	114	13	3.6	6.6	2.0		108	2.1
		5	Nicot.	388	108	60	191	21	3.6	6.5	2.0		181	2.1
		6	Nicot.	311	92	51	136	15	3.4	6.1	2.3		129	2.4
		7	Nicot.	310	88	50	147	6	3.5	6.2	2.1		144	2.2
		8	Nicot.	295	80	48	147	11	3.7	6.1	2.0		142	2.1
		9	Nicot.	347	86	44	147	15	4.0	7.9	2.4		140	2.5
	Si #16	1	Nicot.	175	45	24	83	33	3.9	7.3	2.1		67	2.6
		2	Nicot.	331	71	34	136	15	4.7	9.7	2.4		129	2.6
		3	Nicot.	265	62	36	136	7	4.3	7.4	1.9		133	2.0
		4	Nicot.	314	66	30	138	7	4.8	10.5	2.3		135	2.3
		5	Nicot.	269	66	35	115	17	4.1	7.7	2.3		107	2.5
		6	Nicot.	380	91	45	174	14	4.2	8.4	2.2		167	2.3
		7	Nicot.	324	80	50	140	12	4.1	6.5	2.3		134	2.4
	Si #17	1	Nicot.	136	34	17	53	4	4.0	8.0	2.6		51	2.7
		2	Nicot.	122	31	6	67	6	3.9	20.3	1.8		64	1.9
		3	Nicot.	121	30	6	55	4	4.0	20.2	2.2		53	2.3
		4	Nicot.	95	25	15	40	9	3.8	6.3	2.4		36	2.7
		5	Nicot.	105	27	12	49	3	3.9	8.8	2.1		48	2.2
		6	Nicot.	194	51	26	81	8	3.8	7.5	2.4		77	2.5
		7	Nicot.	138	34	11	85	10	4.1	12.5	1.6		80	1.7
		8	Nicot.	145	35	19	61	3	4.1	7.6	2.4		60	2.4
		9	Nicot.	160	34	18	75	5	4.7	8.9	2.1		73	2.2

Date	Site #	Spec#	Type	Peak Height C	N	N"[a]	O	Si	C/N	C/N"	C/O	O/Si[b]	O"[c]	C/O"
20061108	Si #18	1	Nicot.	34	5	16	16	2	6.8	***2.1***	2.1		***15***	***2.3***
		2	Nicot.	51	15	31	31	2	3.4	***1.6***	1.6		***30***	***1.7***
		3	Nicot.	61	14	28	28	3	4.4	***2.2***	2.2		***27***	***2.3***
		4	Nicot.	69	19	39	39	7	3.6	***1.8***	1.8		***36***	***1.9***
		5	Nicot.	49	9	20	20	2	5.4	***2.5***	2.5		***19***	***2.6***
		6	Nicot.	78	21	33	33	4	3.7	***2.4***	2.4		***31***	***2.5***
		7	Nicot.	83	21	39	39	2	4.0	***2.1***	2.1		***38***	***2.2***
		8	Nicot.	54	14	20	20	3	3.9	***2.7***	2.7		***19***	***2.9***
20081117	Si #3	2	Lacey-C	164	3	0	11	5	54.7	***Inf***	14.9		***9***	***19.3***
		4	Lacey-C	234	5	0	21	4	46.8	***Inf***	11.1		***19***	***12.3***
		6	Graphite	592	5	0	5	5	118.4	***Inf***	118.4		***3***	***236.8***
		7	Graphite	2556	19	0	33	23	134.5	***Inf***	77.5		***22***	***118.9***
		8	Graphite	525	5	0	5	5	105.0	***Inf***	105.0		***3***	***210.0***
		9	Graphite	81	2	0	5	5	40.5	***Inf***	16.2		***3***	***32.4***
	Si #5	2	Graphite	184	3	0	12	3	61.3	***Inf***	15.3		***11***	***17.5***
		4	Graphite	100	2	0	9	3	50.0	***Inf***	11.1		***8***	***13.3***
		5	Graphite	617	3	0	4	4	205.7	***Inf***	154.3		***2***	***308.5***
		8	Graphite	424	4	0	9	3	106.0	***Inf***	47.1		***8***	***56.5***
	Si #8	2	Lacey-C	210	5	0	54	3	42.0	***Inf***	3.9		***53***	***4.0***
		4	Lacey-C	193	4	0	64	5	48.3	***Inf***	3.0		***62***	***3.1***
		5	Graphite	2069	12	0	28	12	172.4	***Inf***	73.9		***22***	***94.0***
		6	Graphite	403	4	0	15	10	100.8	***Inf***	26.9		***10***	***40.3***
		8	Graphite	557	6	0	10	8	92.8	***Inf***	55.7		***6***	***92.8***
		9	Graphite	685	5	0	11	4	137.0	***Inf***	62.3		***9***	***76.1***
LignoChar	Si #1	2	Thick-Char	1850.0	19.0	0	272.0	0	97.4	***Inf***	6.8		***272***	***6.8***
on Lacey-C		3	Thick-Char	665.0	11	0	78.0	0	60.5	***60.5***	Inf			***78***

Date	Site #	Spec#	Type	Peak Height C	N	N"[a]	O	Si	C/N	C/N"	C/O	O/Si[b]	O"[c]	C/O"
LignoChar on Lacey-C	Si #3	3	Thick-Char	1416	21	0	200	0	67.4	*Inf*	7.1		*200*	*7.1*
		4	Thick-Char	661	11	0	76	0	60.1	*Inf*	8.7		*76*	*8.7*
		5	Med-Char	700	6	0	61	0	116.7	*Inf*	11.5		*61*	*11.5*
		6	Lacey-C	203	0	0	5	0	Inf	*Inf*	40.6		*5*	*40.6*
		7	Med-Char	887	12	0	106	0	73.9	*Inf*	8.4		*106*	*8.4*
		8	Med-Char	554	7	0	54	0	79.1	*Inf*	10.3		*54*	*10.3*
		9	Thin-Char	459	5	0	36	0	91.8	*Inf*	12.8		*36*	*12.8*
		10	Lacey-C	231	1	0	5	0	231.0	*Inf*	46.2		*5*	*46.2*
	Si #4	1	Thick-Char	1484	24	0	179	0	61.8	*Inf*	8.3		*179*	*8.3*
		2	Thick-Char	1239	16	0	145	0	77.4	*Inf*	8.5		*145*	*8.5*
		3	Lacey-C	225	1	0	2	0	225.0	*Inf*	112.5		*2*	*112.5*
		4	Thin-Char	370	3	0	19	0	123.3	*Inf*	19.5		*19*	*19.5*
		5	Thin-Char	420	4	0	33	0	105.0	*Inf*	12.7		*33*	*12.7*
		6	Lacey-C	241	4	0	5	0	60.3	*Inf*	48.2		*5*	*48.2*
Melanoidin on Lacey-C	Si #5	1	Lacey-C	691	5	0	9	0	138.2	*Inf*	76.8		*9*	*76.8*
		2	Mela/ Vac	951	22	0	33	0	43.2	*43.2*	Inf			*33*
		3	Mela/ Vac	1604	81	53	130	0	19.8	*30.3*	12.3		*130*	*12.3*
		4	Mela/ Vac	1733	66	35	97	0	26.3	*49.5*	17.9		*97*	*17.9*
		5	Mela/ Vac	1993	103	70	146	0	19.3	*28.5*	13.7		*146*	*13.7*
		6	Mela/ Vac	1415	27	5	50	0	52.4	*283.0*	28.3		*50*	*28.3*
Urban Dust Lacey-C	Si #5	3	um-part-vac	21	5	16	29	608	4.2	*1.3*	0.7		*0*	*Inf*
		6	sub-um-part-vac	19	4	0	11	61	4.8	*Inf*	1.7		*0*	*Inf*
		9	um-part-vac	30	10	20	111	782	3.0	*1.5*	0.3		*0*	*Inf*
		10	um-part-vac	22	3	19	38	401	7.3	*1.2*	0.6		*0*	*Inf*
		11	nm-part-vac	7	0	0	0	1	Inf	*Inf*	Inf		*0*	*Inf*
		13	nm-part-vac	18	1	0	7	15	18.0	*Inf*	2.6		*0*	*Inf*
		15	nm-part-vac	13	0	13	2	2	Inf	*1.0*	6.5		*1*	*13.0*
		16	nm-part-vac	13	0	0	1	1	Inf	*Inf*	13.0		*1*	*26.0*
		17	nm-part-vac	15	1	0	11	30	15.0	*Inf*	1.4		*0*	*Inf*
		18	nm-part-vac	12	1	11	4	6	12.0	*1.1*	3.0		*1*	*12.0*

(a) N peak counts with C and O tailings corrected. **(b)** Background Si/O ratio. **(c)** Background corrected O. O" = O – Si×$(Si/O)_{bkgd}$. For shaded values, the view contained no sample-freed background area, thus a $(Si/O)_{bkgd}$ of 0.5 was assumed.

(d) Data and Calculation by Integrated Area Method

				Wt %[(a)]	Wt %[(a)]	Wt %[(a)]	Wt %[(a)]	Wt Ratio[(b)]	Wt %[(a)]	Atomic Ratio		
Date	Site #	Spec#	Type	C	N	O	Si	O/Si	O"	C/N	C/O	C/O"
20061010	Si #2	1	Miner+SiO	0.8	0.0	43.8	51.7	*0.52*	17.1	***Inf***	***0.0***	***0.1***
		2	SiO	2.1	0.6	26.4	51.1	***0.52***		***4.1***	***0.1***	
		3	Soot+SiO	33.0	0.0	17.8	34.3	*0.52*	0.1	***Inf***	***2.5***	***794.1***
20061010	Si #6	1	App. Miner.	2.1	0.0	24.9	50.7	*0.50*	0.0	***Inf***	***0.1***	***Inf***
		2	App. Miner.	4.4	0.1	28.6	44.6	*0.50*	6.3	***78.0***	***0.2***	***0.9***
		3	App. Miner.	1.2	0.0	30.4	38.6	*0.50*	11.1	***Inf***	***0.1***	***0.1***
		4	App. Miner.	1.0	0.1	33.9	33.9	*0.50*	16.9	***9.2***	***0.0***	***0.1***
		5	App. Miner.	3.5	0.0	30.8	44.9	*0.50*	8.4	***Inf***	***0.2***	***0.6***
20061010	Si #12	1	App. Miner.	10.2	0.0	3.2	10.7	*0.50*	0.0	***Inf***	***4.3***	***Inf***
		2	App. Miner.	8.3	0.2	7.3	16.6	*0.50*	0.0	***46.1***	***1.5***	***Inf***
		3	App. Miner.	16.6	0.0	4.9	14.0	*0.50*	0.0	***Inf***	***4.5***	***Inf***
		4	App. Miner.	37.9	0.0	9.1	36.2	*0.50*	0.0	***Inf***	***5.5***	***Inf***
		5	App. Miner.	46.3	0.0	6.9	19.5	*0.50*	0.0	***Inf***	***8.9***	***Inf***
20061013	Si #1	2	SiO	4.1	0.0	24.6	46.0	***0.54***		***Inf***	***0.2***	
		3	SiO	3.9	0.0	23.9	48.2	***0.50***		***Inf***	***0.2***	
		4	Soot+SiO	22.3	0.0	20.1	35.8	*0.52*	1.6	***Inf***	***1.5***	***18.0***
		5	Soot+SiO	19.9	0.0	18.9	40.6	*0.52*	0.0	***Inf***	***1.4***	***Inf***
		6	Soot+SiO	33.7	0.0	15.6	27.8	*0.52*	1.2	***Inf***	***2.9***	***36.7***
20061019	Si #2	1	HA	26.5	0.0	16.9	0.8	*0.50*	16.5	***Inf***	***2.1***	***2.1***
		2	HA	29.5	0.0	24.3	0.2	*0.50*	24.2	***Inf***	***1.6***	***1.6***
		3	HA	20.3	0.0	9.9	0.0	*0.50*	9.9	***Inf***	***2.7***	***2.7***
	Si #5	1	HA	17.5	0.0	11.1	0.1	*0.50*	11.0	***Inf***	***2.1***	***2.1***
		3	HA	27.2	0.0	23.8	0.1	*0.50*	23.7	***Inf***	***1.5***	***1.5***
		4	HA	15.6	0.0	10.4	0.2	*0.50*	10.3	***Inf***	***2.0***	***2.0***
		5	HA	39.3	0.0	25.3	0.0	*0.50*	25.3	***Inf***	***2.1***	***2.1***

Date	Site #	Spec#	Type	Wt %[a] C	Wt %[a] N	Wt %[a] O	Wt %[a] Si	Wt Ratio[b] O/Si	Wt %[a] O"	Atomic Ratio C/N	Atomic Ratio C/O	Atomic Ratio C/O"
20061019	Si #7	2	HA	31.6	0.0	28.0	19.0	*0.50*	18.6	***Inf***	***1.5***	***2.3***
		3	HA	27.0	0.0	35.7	7.2	*0.50*	32.1	***Inf***	***1.0***	***1.1***
		4	HA	22.3	0.0	26.3	19.3	*0.50*	16.6	***Inf***	***1.1***	***1.8***
		5	HA	23.8	0.0	18.0	14.0	*0.50*	10.9	***Inf***	***1.8***	***2.9***
		6	HA	37.2	0.0	24.6	9.1	*0.50*	20.1	***Inf***	***2.0***	***2.5***
	Si #11	1	HA	9.3	0.0	27.6	31.3	*0.50*	12.0	***Inf***	***0.4***	***1.0***
		2	HA	34.5	0.0	38.5	9.5	*0.50*	33.7	***Inf***	***1.2***	***1.4***
		3	HA	8.5	0.0	17.2	31.1	*0.50*	1.7	***Inf***	***0.7***	***6.7***
		4	HA	16.0	0.1	40.6	26.0	*0.50*	27.5	***144.5***	***0.5***	***0.8***
		5	HA	6.3	0.0	37.7	20.4	*0.50*	27.5	***Inf***	***0.2***	***0.3***
		6	HA	25.2	0.0	31.7	13.8	*0.50*	24.8	***Inf***	***1.1***	***1.4***
		7	HA	7.8	0.4	51.3	10.5	*0.50*	46.1	***24.2***	***0.2***	***0.2***
		8	HA	20.4	0.0	32.4	16.2	*0.50*	24.3	***Inf***	***0.8***	***1.1***
		9	HA	10.0	0.6	37.1	16.2	*0.50*	29.0	***20.4***	***0.4***	***0.5***
	Si #13	3	HA	12.5	0.0	26.2	34.1	*0.50*	9.1	***Inf***	***0.6***	***1.8***
		4	HA	16.1	0.0	18.3	28.1	*0.50*	4.3	***Inf***	***1.2***	***5.1***
		5	HA	33.5	0.0	30.3	18.0	*0.50*	21.3	***Inf***	***1.5***	***2.1***
		6	HA	30.9	0.0	19.0	10.9	*0.50*	13.5	***Inf***	***2.2***	***3.0***
		7	HA	42.0	0.0	24.7	6.1	*0.50*	21.7	***Inf***	***2.3***	***2.6***
		8	HA	9.9	0.0	31.5	29.6	*0.50*	16.6	***Inf***	***0.4***	***0.8***
20061103	Si #2	1	App. Miner.	0.3	0.0	20.6	45.5	*0.50*	0.0	***Inf***	***0.0***	***Inf***
		2	App. Miner.	2.4	0.5	23.7	38.3	*0.50*	4.5	***5.7***	***0.1***	***0.7***
		3	App. Miner.	0.1	0.0	29.7	39.0	*0.50*	10.2	***Inf***	***0.0***	***0.0***
		4	App. Miner.	1.8	0.0	22.6	37.6	*0.50*	3.8	***Inf***	***0.1***	***0.6***
		5	App. Miner.	1.6	0.0	27.8	32.2	*0.50*	11.7	***Inf***	***0.1***	***0.2***
	Si #3	1	Soot+SiO	10.3	0.0	16.6	49.4	*0.40*	0.0	***Inf***	***0.8***	***Inf***
		2	Soot+SiO	6.9	0.2	16.5	49.8	*0.40*	0.0	***Inf***	***0.6***	***Inf***

Date	Site #	Spec#	Type	Wt %[a] C	Wt %[a] N	Wt %[a] O	Wt %[a] Si	Wt Ratio[b] O/Si	Wt %[a] O"	Atomic Ratio C/N	Atomic Ratio C/O	Atomic Ratio C/O"
20061103	Si #5	1	Soot+SiO	7.1	0.0	17.4	51.7	*0.40*	0.0	***Inf***	***0.5***	***Inf***
		2	SiO	0.5	0.0	23.2	56.1	***0.41***		***Inf***	***0.0***	
		3	Soot+SiO	10.0	0.0	19.9	44.1	*0.40*	2.4	***Inf***	***0.7***	***5.7***
		4	Soot+SiO	15.9	0.0	15.0	42.6	*0.40*	0.0	***Inf***	***1.4***	***Inf***
		5	SiO	1.7	0.0	21.9	55.1	***0.40***		***Inf***	***0.1***	
		6	Soot+SiO	16.2	0.0	17.6	41.7	*0.40*	1.0	***Inf***	***1.2***	***21.9***
		7	SiO	10.6	0.0	18.1	47.3	***0.38***		***Inf***	***0.8***	
20061108	Si #9	1	Nicot.	16.9	3.3	27.1	40.8	*0.50*	6.7	***5.9***	***0.8***	***3.4***
		2	Nicot.	47.5	3.8	13.4	0.6	*0.50*	13.1	***14.8***	***4.7***	***4.8***
		3	Nicot.	43.0	3.4	15.7	0.3	*0.50*	15.6	***14.7***	***3.6***	***3.7***
		4	Nicot.	48.0	2.6	9.1	1.1	*0.50*	8.5	***21.8***	***7.0***	***7.5***
		5	Nicot.	50.0	2.9	11.8	0.0	*0.50*	11.8	***20.3***	***5.6***	***5.6***
		6	Nicot.	44.3	6.3	13.9	0.0	*0.50*	13.9	***8.3***	***4.3***	***4.3***
	Si #11	3	Nicot.	8.4	0.8	25.2	45.9	*0.50*	2.3	***12.5***	***0.4***	***5.0***
		4	Nicot.	2.2	0.0	28.5	50.7	*0.50*	3.2	***Inf***	***0.1***	***0.9***
		5	Nicot.	40.4	6.3	20.6	0.0	*0.50*	20.6	***7.4***	***2.6***	***2.6***
		6	Nicot.	47.0	5.5	18.8	0.0	*0.50*	18.8	***10.0***	***3.3***	***3.3***
		7	Nicot.	34.8	9.5	18.2	0.2	*0.50*	18.1	***4.3***	***2.6***	***2.6***
		8	Nicot.	42.5	3.8	19.4	0.6	*0.50*	19.1	***13.2***	***2.9***	***3.0***
		9	Nicot.	39.1	5.0	16.6	1.3	*0.50*	15.9	***9.1***	***3.1***	***3.3***
	Si #12	1	Nicot.	10.1	1.3	23.7	41.4	*0.50*	3.0	***9.5***	***0.6***	***4.5***
		2	Nicot.	40.8	1.6	11.5	0.6	*0.50*	11.2	***30.5***	***4.7***	***4.9***
		3	Nicot.	33.5	3.5	10.9	1.6	*0.50*	10.1	***11.3***	***4.1***	***4.4***
		4	Nicot.	51.9	2.0	11.1	0.4	*0.50*	10.8	***30.5***	***6.3***	***6.4***
		5	Nicot.	33.3	1.8	6.8	0.7	*0.50*	6.5	***21.4***	***6.5***	***6.9***
		6	Nicot.	40.7	8.6	18.4	1.1	*0.50*	17.8	***5.5***	***3.0***	***3.0***

Date	Site #	Spec#	Type	Wt %[a] C	Wt %[a] N	Wt %[a] O	Wt %[a] Si	Wt Ratio[b] O/Si	Wt %[a] O"	Atomic Ratio C/N	Atomic Ratio C/O	Atomic Ratio C/O"
20061108	Si #13	1	Nicot.	13.9	0.7	22.4	36.5	*0.50*	4.1	***23.6***	***0.8***	***4.5***
		2	Nicot.	9.1	0.1	23.6	43.4	*0.50*	1.9	***110.0***	***0.5***	***6.4***
		3	Nicot.	5.8	1.2	21.5	40.7	*0.50*	1.2	***5.6***	***0.4***	***6.5***
		4	Nicot.	40.9	3.5	11.1	0.2	*0.50*	11.0	***13.8***	***4.9***	***5.0***
		5	Nicot.	30.6	1.6	11.2	0.9	*0.50*	10.8	***23.0***	***3.6***	***3.8***
		6	Nicot.	39.0	2.0	11.9	0.5	*0.50*	11.7	***22.6***	***4.4***	***4.5***
		7	Nicot.	40.0	2.1	8.3	0.4	*0.50*	8.1	***22.0***	***6.4***	***6.6***
		8	Nicot.	35.9	3.2	11.3	1.2	*0.50*	10.8	***13.0***	***4.2***	***4.4***
		9	Nicot.	40.7	2.7	11.5	0.0	*0.50*	11.4	***17.7***	***4.7***	***4.7***
	Si #14	1	Nicot.	14.2	1.2	21.5	34.6	*0.50*	4.2	***13.3***	***0.9***	***4.5***
		2	Nicot.	11.3	0.6	24.1	40.7	*0.50*	3.8	***22.6***	***0.6***	***4.0***
		3	Nicot.	8.9	0.1	23.0	41.7	*0.50*	2.2	***105.6***	***0.5***	***5.5***
		4	Nicot.	31.4	2.8	9.7	0.5	*0.50*	9.4	***13.3***	***4.3***	***4.5***
		5	Nicot.	35.6	3.0	11.2	1.1	*0.50*	10.6	***13.7***	***4.2***	***4.5***
		6	Nicot.	37.4	3.1	9.3	0.4	*0.50*	9.1	***14.1***	***5.4***	***5.5***
		7	Nicot.	39.5	3.9	11.3	0.1	*0.50*	11.3	***11.9***	***4.6***	***4.7***
		8	Nicot.	36.0	3.0	10.5	0.2	*0.50*	10.3	***14.2***	***4.6***	***4.6***
		9	Nicot.	41.6	2.0	10.8	0.4	*0.50*	10.5	***24.0***	***5.2***	***5.3***
	Si #16	1	Nicot.	30.3	2.2	8.8	3.0	*0.50*	7.3	***15.8***	***4.6***	***5.5***
		2	Nicot.	39.6	2.9	10.2	0.4	*0.50*	10.0	***15.7***	***5.2***	***5.3***
		3	Nicot.	44.1	3.0	12.9	0.6	*0.50*	12.6	***17.4***	***4.6***	***4.7***
		4	Nicot.	41.2	1.2	10.6	0.1	*0.50*	10.5	***40.4***	***5.2***	***5.2***
		5	Nicot.	39.2	2.1	10.8	0.8	*0.50*	10.4	***22.3***	***4.9***	***5.0***
		6	Nicot.	35.4	2.4	11.9	0.6	*0.50*	11.6	***17.1***	***4.0***	***4.1***
		7	Nicot.	33.1	4.5	10.5	0.4	*0.50*	10.3	***8.5***	***4.2***	***4.3***

Date	Site #	Spec#	Type	Wt %[a] C	Wt %[a] N	Wt %[a] O	Wt %[a] Si	Wt Ratio[b] O/Si	Wt %[a] O"	*Atomic Ratio* C/N	*Atomic Ratio* C/O	*Atomic Ratio* C/O"
20061108	Si #17	1	Nicot.	39.2	2.1	8.5	0.9	*0.50*	8.0	***22.2***	***6.2***	***6.5***
		2	Nicot.	32.1	0.7	9.7	0.2	*0.50*	9.6	***54.0***	***4.4***	***4.4***
		3	Nicot.	34.2	1.5	8.7	0.0	*0.50*	8.7	***27.2***	***5.3***	***5.3***
		4	Nicot.	33.4	2.3	9.5	1.1	*0.50*	8.9	***17.1***	***4.7***	***5.0***
		5	Nicot.	43.9	2.1	10.5	0.0	*0.50*	10.5	***24.4***	***5.6***	***5.6***
		6	Nicot.	40.8	1.4	9.3	0.5	*0.50*	9.1	***33.2***	***5.8***	***6.0***
		7	Nicot.	32.5	2.2	12.8	0.8	*0.50*	12.4	***17.6***	***3.4***	***3.5***
		8	Nicot.	42.2	2.6	10.5	0.3	*0.50*	10.3	***19.0***	***5.4***	***5.5***
		9	Nicot.	39.9	2.8	10.9	0.4	*0.50*	10.7	***16.6***	***4.9***	***5.0***
	Si #18	1	Nicot.	37.1	5.1	13.4	0.6	*0.50*	13.1	***8.5***	***3.7***	***3.8***
		2	Nicot.	42.9	4.8	13.8	0.2	*0.50*	13.8	***10.5***	***4.1***	***4.2***
		3	Nicot.	41.9	2.9	13.0	1.1	*0.50*	12.5	***16.8***	***4.3***	***4.5***
		4	Nicot.	24.6	5.7	14.0	3.5	*0.50*	12.3	***5.1***	***2.3***	***2.7***
		5	Nicot.	36.7	1.9	10.0	0.0	*0.50*	10.0	***22.5***	***4.9***	***4.9***
		6	Nicot.	44.7	4.4	11.8	1.0	*0.50*	11.3	***11.9***	***5.1***	***5.3***
		7	Nicot.	45.3	4.0	13.2	0.0	*0.50*	13.2	***13.3***	***4.6***	***4.6***
		8	Nicot.	47.8	0.7	10.5	1.2	*0.50*	9.9	***75.6***	***6.1***	***6.4***
20081117	Si #3	2	Lacey-C	53.4	0.0	2.3				***Inf***	***31.2***	
		4	Lacey-C	58.9	0.0	4.7				***Inf***	***16.8***	
		6	Graphite	87.2	0.0	0.6				***Inf***	***179.4***	
		7	Graphite	92.3	0.0	2.5				***Inf***	***49.3***	
		8	Graphite	67.8	0.0					***Inf***	***Inf***	
		9	Graphite	34.4	0.0	1.7				***Inf***	***27.4***	
	Si #5	2	Graphite	56.5	0.0	3.1				***Inf***	***24.1***	
		4	Graphite	41.7	0.0	2.7				***Inf***	***20.7***	
		5	Graphite	84.9	0.0	0.2				***Inf***	***503.3***	
		8	Graphite	70.3	0.0	2.3				***Inf***	***41.3***	

Date	Site #	Spec#	Type	Wt %[a] C	Wt %[a] N	Wt %[a] O	Wt %[a] Si	Wt Ratio[b] O/Si	Wt %[a] O"	Atomic Ratio C/N	Atomic Ratio C/O	Atomic Ratio C/O"
20081117	Si #8	2	Lacey-C	48.6	0.0	11.2				*Inf*	*5.8*	
		4	Lacey-C	58.6	0.0	11.2				*Inf*	*7.0*	
		5	Graphite	92.5	0.0	0.6				*Inf*	*212.6*	
		6	Graphite	64.1	0.0	2.6				*Inf*	*33.4*	
		8	Graphite	80.3	0.0	2.5				*Inf*	*43.7*	
		9	Graphite	84.1	0.0	2.5				*Inf*	*45.2*	
LignoChar	Si #1	2	Thick-Char	90.6	0.0	11.4				*Inf*	*10.6*	
on Lacey-C		3	Thick-Char	93.3	0.0	9.3				*Inf*	*13.3*	
	Si #3	3	Thick-Char	88.9	0.0	10.9				*Inf*	*10.9*	
		4	Thick-Char	90.5	0.0	9.3				*Inf*	*13.0*	
		5	Med-Char	94.8	0.0	7.0				*Inf*	*18.2*	
		6	Lacey-C	96.7	0.0					*Inf*	*Inf*	
		7	Med-Char	90.1	0.0	9.0				*Inf*	*13.4*	
		8	Med-Char	91.9	0.0	7.9				*Inf*	*15.6*	
		9	Thin-Char	95.5	0.0	5.9				*Inf*	*21.8*	
		10	Lacey-C	98.3	0.0					*Inf*	*Inf*	
	Si #4	1	Thick-Char	92.8	0.0	9.2				*Inf*	*13.5*	
		2	Thick-Char	92.9	0.0	9.1				*Inf*	*13.7*	
		3	Lacey-C	102.2	0.0					*Inf*	*Inf*	
		4	Thin-Char	94.8	0.0	3.7				*Inf*	*34.3*	
		5	Thin-Char	93.2	0.0	5.3				*Inf*	*23.4*	
		6	Lacey-C	94.5	0.0	1.6				*Inf*	*78.7*	
Melanoidin	Si #5	1	Lacey-C	95.5	0.0	0.7				*Inf*	*190.1*	
on Lacey-C		2	Mela/ Vac	91.1	0.0	2.1				*Inf*	*58.1*	
		3	Mela/ Vac	86.3	0.9	5.6				*115.7*	*20.7*	
		4	Mela/ Vac	90.1	0.0	4.5				*Inf*	*26.6*	
		5	Mela/ Vac	84.3	3.2	4.6				*30.7*	*24.5*	
		6	Mela/ Vac	89.7	0.0	2.2				*Inf*	*54.1*	

Date	Site #	Spec#	Type	Wt %[(a)] C	Wt %[(a)] N	Wt %[(a)] O	Wt %[(a)] Si	Wt Ratio[(b)] O/Si	Wt %[(a)] O"	*Atomic Ratio* C/N	C/O	C/O"
Urban	Si #5	3	um-part-vac	0.9	0.0	1.3	20.6			***Inf***	***0.9***	
Dust on Lacey-C		6	sub-um-part-vac	0.9	0.2	0.4	1.3			***4.1***	***2.7***	
		9	um-part-vac	1.1	0.2	4.2	19.2			***7.3***	***0.4***	
		10	um-part-vac	1.5	0.0	2.4	19.3			***Inf***	***0.9***	
		11	nm-part-vac	23.7	0.3	0.0	3.2			***102.2***	***Inf***	
		13	nm-part-vac	5.8	0.0	2.1	2.6			***Inf***	***3.6***	
		15	nm-part-vac	23.6	0.0	1.3	0.8			***Inf***	***24.8***	
		16	nm-part-vac	44.8	5.3	1.1	0.6			***9.8***	***53.7***	
		17	nm-part-vac	3.6	0.0	2.2	4.2			***Inf***	***2.2***	
		18	nm-part-vac	16.7	0.0	4.1				***Inf***	***5.4***	

(a) N peak counts with C and O tailings corrected. (b) Background Si/O ratio. (c) Background corrected O. O" = O – Si×$(Si/O)_{bkgd}$. For shaded values, the view contained no sample-freed background area, thus a $(Si/O)_{bkgd}$ of 0.5 was assumed.

Appendix 10 - 6. EDX Elemental Mapping Quantitative Analysis

Spatial quantitative mapping of BC by STEM-EDX can be divided into three major stages. The entire operation is summarized in the flowchart below.

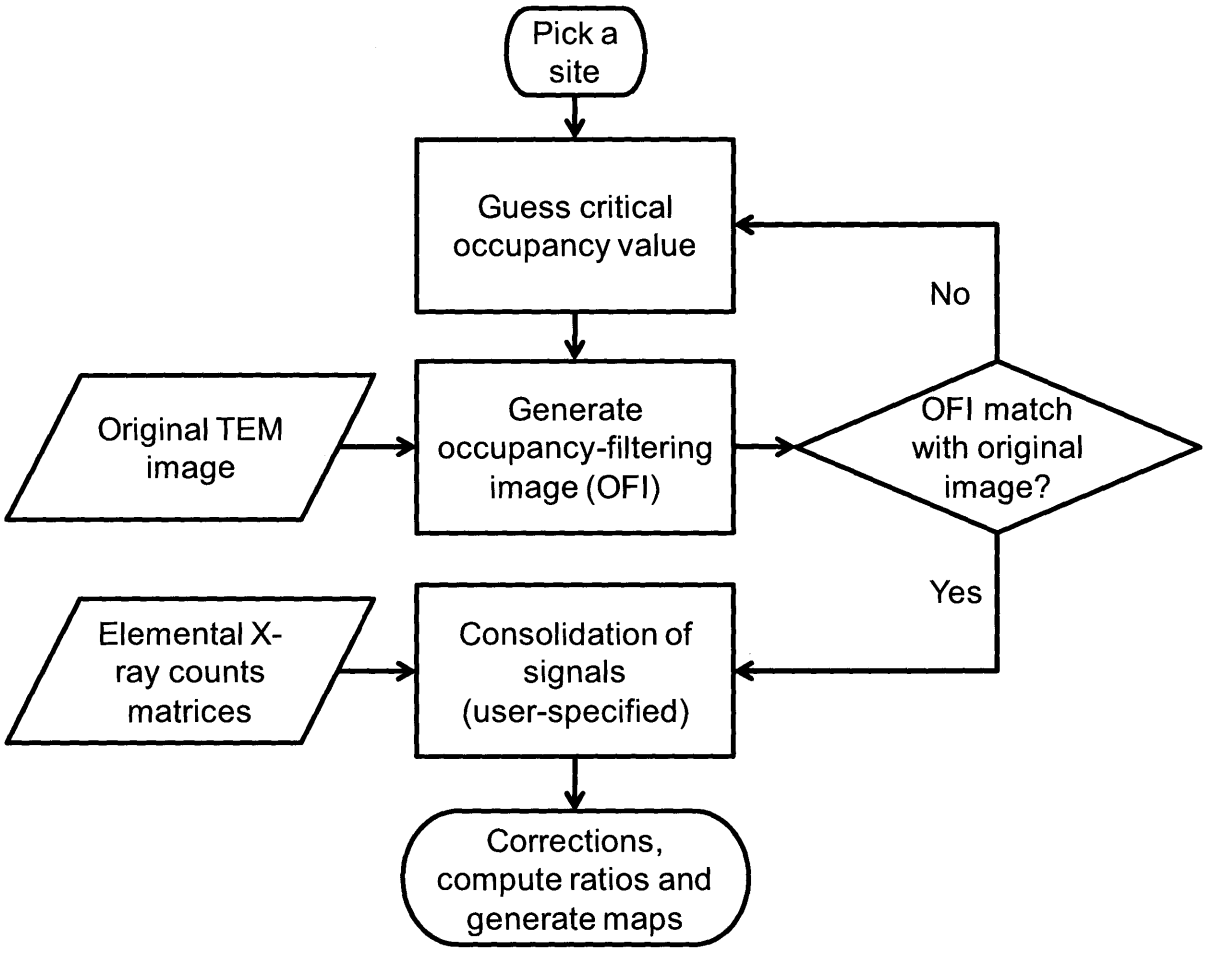

In the first stage, the user defines which area in the micrograph belongs to sample and which area is the background. Assuming the micrograph is taken in the dark-field mode, area with sample should appear brighter than area with background film, and area which has nothing at all should be the darkest. The user guesses a pixel intensity threshold for the micrograph. The Matlab routine views all pixels with intensity less than the threshold as background, and generates an trial occupancy-filtering image (OFI) using the complementary pixels. The user then compares the OFI with the original micrograph to see if the threshold is appropriate. The process is repeated (i.e., guessing the intensity threshold) until there is a satisfactory match between the OFI and the original micrograph.

In the second stage, the elemental signals in the pixels are consolidated (summed) into larger cells. The default option is no consolidation (i.e. each pixel is one cell). The available consolidation options are: 2x2 pixels into 1 cell, 4x4 pixels into 1 cell, and 8x8

pixels into 1 cell. The example below shows the 2x2-into-1 (or 4-into-1) consolidation case:

0	2	0	7
1	3	0	2
0	0	5	4
0	2	6	2

Becomes →

6	9
2	17

Consolidation should be used with caution.

In the third stage, the computer routine performs correction on background-O signals, computes various elemental ratios for all cells, and generates elemental ratio maps. In the case where 'noise' N correction is performed, all cells with non-zero N counts is reduced by 1. This reduction is arbitrary and is based on the qualitative observations that it is fairly frequent to observe singular N count pixels in the background region.

Appendix 10 - 7. sp^2-C and Aromatic-C Fractions in Various Carbonaceous Matters

(a) Theoretical and Empirical sp^3-C Abundance in Humic Acids.

	sp^3-C/sp^2-C	sp^2-C/Total-C*
Theoretical Model[†]		
Fuchs	0.5	0.67
Dragunov	0.68	0.60
Bergmann	0.65	0.61
Schulten * Schnitzer	0.76 (0.68-0.84)	0.57
Jansen et al.	0.56	0.64
Empirically Observed[‡]		
Amherst HA	0.53	0.65
New Hampshire HA	0.73	0.58
New York HA	0.61	0.62
Aldrich HA	0.81	0.55
ARC HA	0.24	0.81
IHSS HA	0.28	0.78

* Estimated from sp^3-C/sp^2-C ratio assuming Total-C to be a sum of sp^3 and sp^2-C. sp^2-C/Total-C = 1/(1+X), with X=sp^3-C/sp^2-C ratio.

† From Mao et al. 1998 and references within.

‡ Reported by Mao et al. 1998 from NMR domain area analysis and chemical analysis. sp2-C here consists of all C=O variants.

(b) Empirically Observed C Functionality in Various Humic Substances*.

% C-functionality	Alkyl-C	Carbohydrate-C	O-Alkyl-C	Aromatic-C	Phenolic-C	Carbonyl-C	Carboxyl-C	Reference
Soil Humic Substances								
Hubbard Brook Forest HA	54		21	13		12		(a)
Hubbard Brook Forest FA	35		30	20		15		(a)
Soil HA (Udic)	50			39.5	4.5			(b)
Soil FA (Spodosol)	47.7			34	3.7			(b)
Organic Ore								
(N. Dakota - 1)	68.2			21	4.6			(b)
(N. Dakota - 2)	58.3			28.9	7			(b)
(Utah)	60			23.2	8.1			(b)
(New Mexico)	53.8			33.3	7			(b)
(Wyoming)	55.5			31.2	6.3			(b)
(Alberta)	65.6			26.6	4.2			(b)
Miscellaneous								
Bog HA (Rumney)	29.6		33.3	25.8		2.2	9.2	(c)
Alga HA	40		36.3	11.3		1.7	10.8	(c)
Charred plant HA	12.2	13.7		60.2		13.9		(d)
Volcanic ash soil HA	9.5	9.5		63		17.9		(d)

* HA: humic acids; FA: fulvic acids.
(a) Ussiri et al. 2001.
(b) Schnitzer et al. 2001.
(c) Ghabbour et al. 1998.
(d) Shindo et al. 2001.

(c) sp^2-C Fractions and Oxygen Content in Soot, Carbon Black, and Graphite*

	sp^2-C/Total-C†	Surface O fraction‡
Soot		
Spark Discharge Soot	0.54	0.17
Diesel Engine Soot (Euro IV)	0.66	0.12
Diesel Engine Soot (Black Smoke)	0.76	0.074
Industrial Carbon Black		
Furnace Soot	0.77	0.03
Lamp Black	0.77	0.005
Graphite	1.0	0

* Muller et al. 2007.

† Determined from quantitative areal analysis of sp^2-C peak in electron energy loss spectra.

‡ Determined from X-ray photoelectron spectroscopy. The reported value was atomic fraction defined as $O_{surface}/(C_{surface}+O_{surface})$.

Appendix 10 - 8. Detail elemental ratios of carbonaceous matters.

Carbonaceous Matter	C:H	C:N	C:O	Reference
Humics & Humins				
Chelsea humic acid	1.1	15	1.7	Huang et al. 1997 EST 2562
Humic acid	0.61±0.04 [0.57-0.66] {10}	11±0.6 [10-12] {10}	n/a	Trickovic et al. 2007
Humic acid (R. Vouga)	1.2	27	2.1	Santos et al. 1998
Humic acid (Suwannee R.)	1.0	51	1.6	Duarte et al. 2007
Fulvic acid (R. Vouga)	1.0	42	1.9	Santos et al. 1998
Fulvic acid (Suwannee R.)	1.0	87	1.6	Duarte et al. 2007
Wat. Sol. Aerosol O.M.	0.78±0.0 [0.70-0.84] {14}	25±5.5 [16-32] {14}	2.2±0.2 [1.8-2.4] {14}	Duarte et al. 2007
Humin	[0.21-0.54] {2}	[13-19] {2}	n/a	Trickovic et al. 2007
Soil HA				
Amherst Agri.	1.01	16		Anderson et al. 2001
Hadley Agri.	1.02	15		Anderson et al. 2001
Las Reyes Agri.	1.10	17		Anderson et al. 2001
New York Agri.	0.89	16	1.9	Mao et al. 1998
Spodosol	0.86	16	2.3	Schnitzer et al. 2001
Udic	0.86	16	2.3	Schnitzer et al. 2001
Peat & Bog HA				
Amherst (P)	0.99	24	1.8	Mao et al. 1998

Bad Pyrmont (P)	0.80	35	1.6	Mao et al. 1998
Irish (P)	0.76	28	1.6	Mao et al. 1998
Rumney (B)	0.82	31	1.8	Mao et al. 1998
Humics (Commercial & Standards)				
Aldrich	1.12	70	2.3	Mao et al. 1998
ARC	1.17	50	1.9	Mao et al. 1998
IHSS	1.21	63	2.2	Mao et al. 1998
Wood				
Alder	0.65	260	1.2	Hedges et al. 1985
Beech	0.60	250	n/a	Lobert 1989
Oak	0.70	280	1.4	Hedges et al. 1985
Sapwood	0.66	700	1.4	Baldock et al. 2002
Spruce	0.68	550	1.3	Hedges et al. 1985
Unspecified	n/a	720±2.0 [716-720] {3}	n/a	Kuhlbusch et al. 1991
Grass & Hay				
Hay	n/a	39±0.0 {6}	n/a	Kuhlbusch et al. 1991
Savannah grass	n/a	89±0.1 {10}	n/a	Kuhlbusch et al. 1991
Unspecified grass 1	0.63	97	n/a	Kuhlbusch et al. 1996
Unspecified grass 2	n/a	13	n/a	Kuhlbusch et al. 1991
Agricultural Plants				
Herb	0.66	46	n/a	Kuhlbusch et al. 1996
Rice straw	0.63	79	n/a	Jenkins et al. 1991
Organic Ore				
Alberta	1.39	50	2.9	Schnitzer et al. 2001
N. Dakota – 1	1.37	69	3.2	Schnitzer et al. 2001
N. Dakota – 2	1.30	60	2.8	Schnitzer et al. 2001
New Mexico	1.37	53	2.8	Schnitzer et al. 2001
Utah	0.28	24	1.0	Schnitzer et al. 2001
Wyoming	1.29	49	2.7	Schnitzer et al. 2001
Coal				
Beular-Zap	1.3	71	4.8	Matsuoka et al. 2008
Illinois No.6	1.3	65	7.7	Matsuoka et al. 2008
Pittsburgh No.8	1.23	55	13.7	Gale et al. 1995
Pocahontas	1.7	82	44.9	Matsuoka et al. 2008
Upper Freeport	1.5	62	15.2	Matsuoka et al. 2008
Utah Blind Canyon	1.15	55	8.2	Gale et al. 1995
Char/Charcoal				
Charcoal	2.5	160	n/a	Lacaux et al. 1994
Straw char	0.1	2.5	n/a	Fernandes et al. 2003
Wood char	15.2	105	n/a	Fernandes et al. 2003
Vegetation fire residues	6.1	40	n/a	Fernandes et al. 2003
Coal-burned char	4.3±0.3 [4.0-4.7] {4}	69±8.6 [62-80] {4}	400±590 [18-1300] {4}	Matsuoka et al. 2008
Kerogen				

Campins	0.66	43	8.1	Damste et al. 1993
Cerdanya	0.77	38	4.3	Damste et al. 1993
Brown, immature	0.80	210	2.2	Zeng et al. 2007
Lachine	0.93	37	8.0	Huang et al. 1997 EST 2562
Norwood	0.70	37	7.2	Huang et al. 1997 EST 2562
Pachino	2.2±0.6	65±16	7.0±1.0	Long et al. 1968
Paxton	0.73	45	2.9	Huang et al. 1997 EST 2562
Ribesalbes	0.56	120	10	Damste et al. 1993
Seicli	1.2±0.2	53±2.3	7.2±0.9	Long et al. 1968
Soot & Diesel Particulate				
BC Ref. Mat. (AGU Steering)	5.3±0.3	Inf. (no N)	38±0.8	Im et al. 2008
Chimney soot (domestic)	8.9	17	n/a	Fernandes et al. 2003
NIST SRM 1649a (urban dust)	7.2	7	n/a	Fernandes et al. 2003
NIST SRM 1650 Diesel PM	n/a	~60	n/a	Accardi-Dey 2003
NIST SRM 1650a Diesel PM	24	54	n/a	Fernandes et al. 2003
NIST SRM 2975 Diesel PM	6.1±0.1	210±0.5	13±0.3	Im et al. 2008

Appendix 10 - 9. Estimates of electron beam broadening in a 100 nm-thick specimen at 200-250 kV

Goldstein et al. (Goldstein 1979; Jones et al. 1981; Scott et al. 1995) estimated beam broadening, b, as:

$$b \equiv k\frac{Z}{E_o}\left(\frac{\rho}{A}\right)^{0.5} t^{1.5}$$

where: b is the broadening [cm],

k is a coefficient accounting for the geometry of scattering = 7.22×10^5 (Jones et al. 1981; Scott et al. 1995),

Z is the atomic number,

E_o is the accelerated voltage of the microscope [V],

ρ is the density of the sample [g/cm^3],

A is the atomic weight of the sample,

t is the specimen thickness [cm]

Assuming (i) 100 nm-thick specimen, and (ii) 200-250 kV, then the broadening:

Specimen	Z (or Z_{avg})*	ρ (g/cm^3)	A (amu)	b (nm)
Carbon (graphite)	6.0	2.2†	12.0	2.3-2.9
Silicon	14.0	2.33	28.3	3.7-4.6
CH_2O	6.7	1.5†	30.0	1.4-1.7
SiO_2	10.8	2.2†	60.3	1.9-2.4
Iron	26.0	7.87	55.8	8.9-11.1

* In the case of a composite specimen such as CH_2O, the weight-averaged Z, Z_{avg}, is calculated as $\Sigma(ZAS)_i/\Sigma(AS)_i$, with Z_i = atomic number, A_i = atomic weight, and S_i = stoichiometry of element i in the composite.

† Approximate values.

Appendix 10 - 10. Densities of selected carbonaceous matters and mineral phases

Materials*	Formula	ρ (g/cm^3)
Carbon (Pure)	C	
Amor-C		1.8-2.1
Diamond		3.5
Graphite		2.2
Carbon-Rich		
Carbon Black (2700°C)		1.9-2.0[a]
Diesel Particulate Matter (EPA)		1.5-1.8[a]
Sugars		
Glucose	$C_6H_{12}O_6$	1.56
Sucrose	$C_{12}H_{22}O_{11}$	1.58
Mineral phases		
Albite	$NaAlSi_3O_8$	2.63
Calcite	$CaCO_3$	2.71
Dolomite	$CaMg(CO_3)_2$	2.86
Goethite	FeO(OH)	4.3
Gypsum	$CaSO_4 \cdot 2H_2O$	2.32
Halite	NaCl	2.17
Illite	$KAl_4[Si_7AlO_{20}](OH)_4$	2.8
Muscovite	$KAl_2Si_3AlO_{10}(OH,F)_2$	2.83
Quartz	SiO_2	2.65

*: Compiled from CRC Handbook of Chemistry and Physics (Lide 2008).
a: Ross et al. 1982.

Appendix A: EDX (Spot) Spectra

Figure A - 1. Mineral + NIST-soot (20061010-Site#2). **1001**
Figure A - 2. Mineral + NIST-soot (20061010-Site#6). **1003**
Figure A - 3. Sedimentary mineral phases (no apparent soot) (20061010-Site#12). **1006**
Figure A - 4. Soot-rich region in soot-amended sediment (20061013-Site#1)..... **1009**
Figure A - 5. Humic substance (20061019-Site#5). **1012**
Figure A - 6. Humic substance (20061019-Site#7). **1015**
Figure A - 7. Humic substance (20061019-Site#11). **1019**
Figure A - 8. Sedimentary mineral phases (no apparent soot) (20061103-Site#2). **1024**
Figure A - 9. Soot-rich region in soot-amended sediment (20061103-Site#3)..... **1027**
Figure A - 10. Soot-rich region in soot-amended sediment (20061103-Site#5)..... **1029**
Figure A - 11. Nicotinamide (20061108-Site#11). **1033**

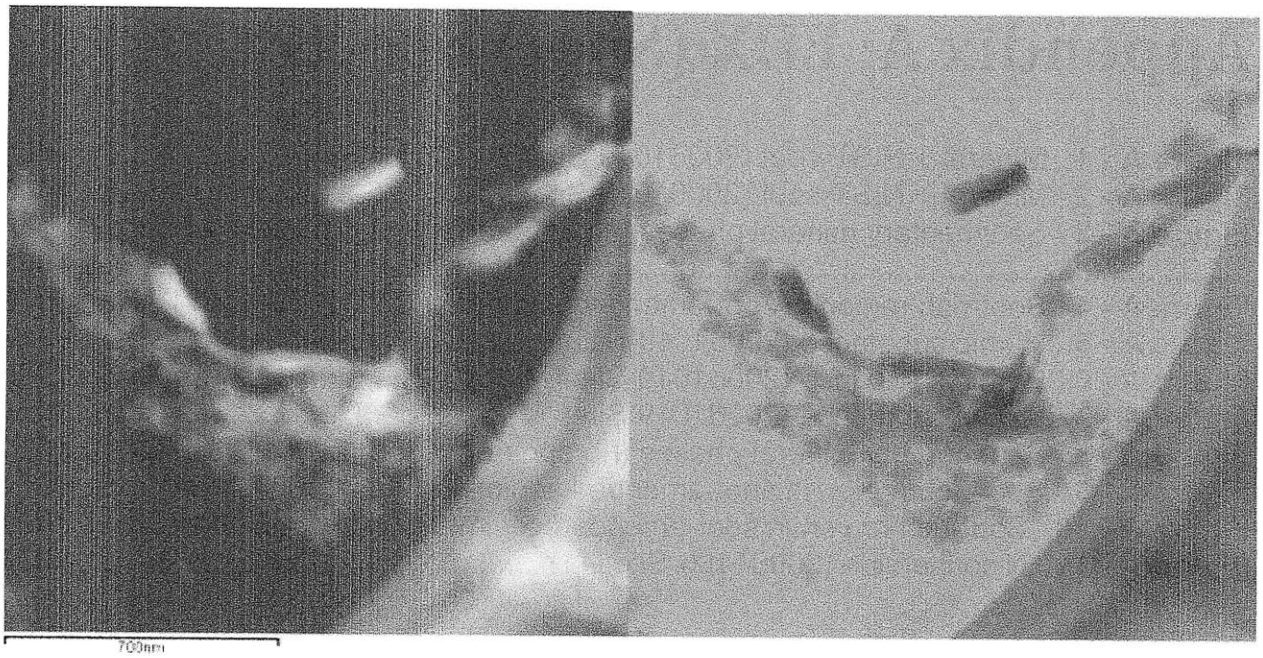

Figure A - 1. Mineral + NIST-soot (20061010-Site#2).

(a) Original TEM images. (NIST SRM #1650 Diesel Particulate Matter) amended sediments (Boston Harbor #6, 180-250 μm) on lacey-SiO film (20061010-Site#2).

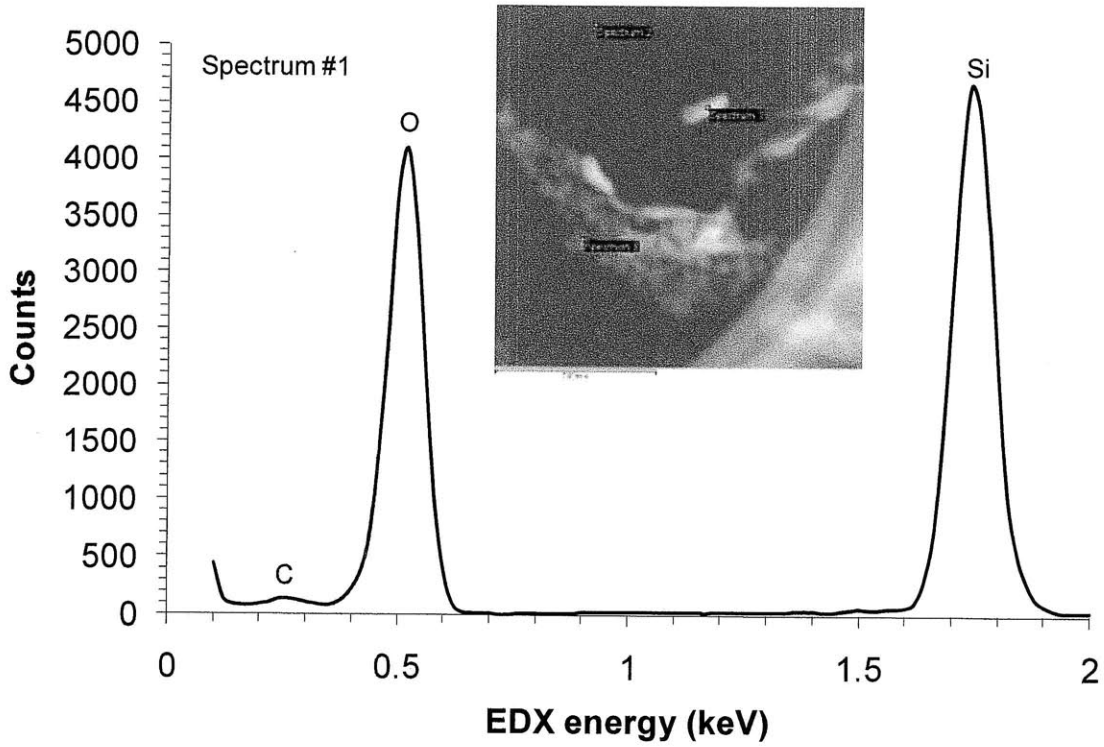

(b) Sample 20061010-Site#2: EDX spectrum at spot #1.

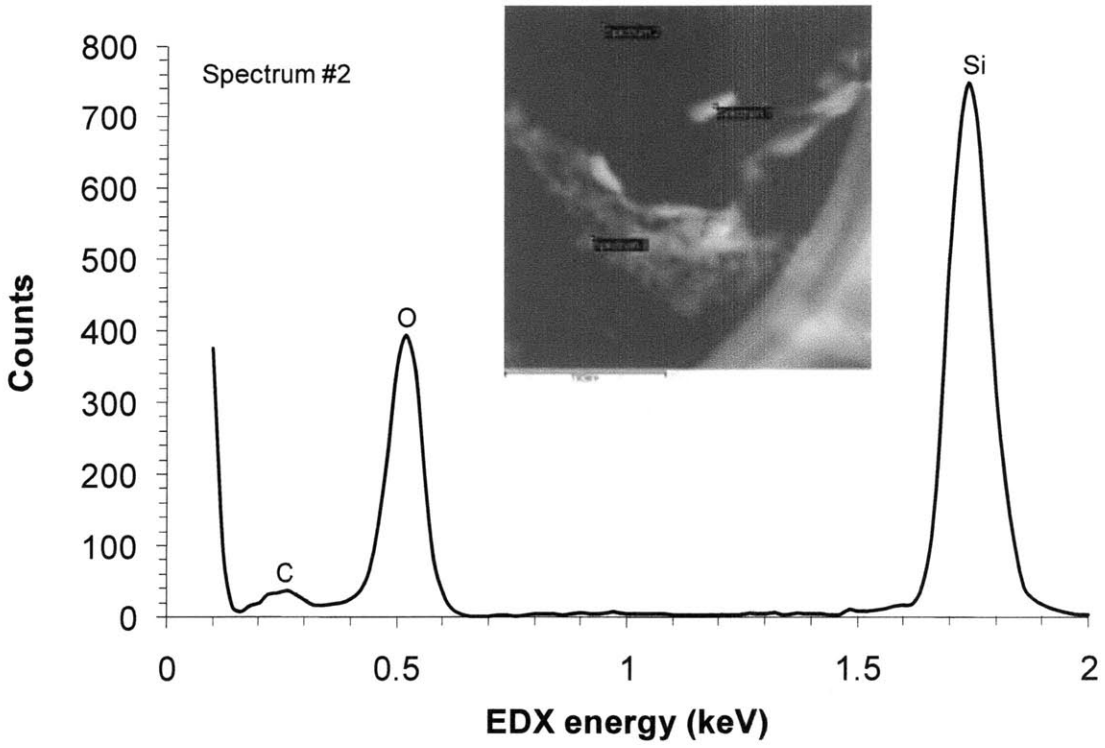

(c) Sample 20061010-Site#2: EDX spectrum at spot #2.

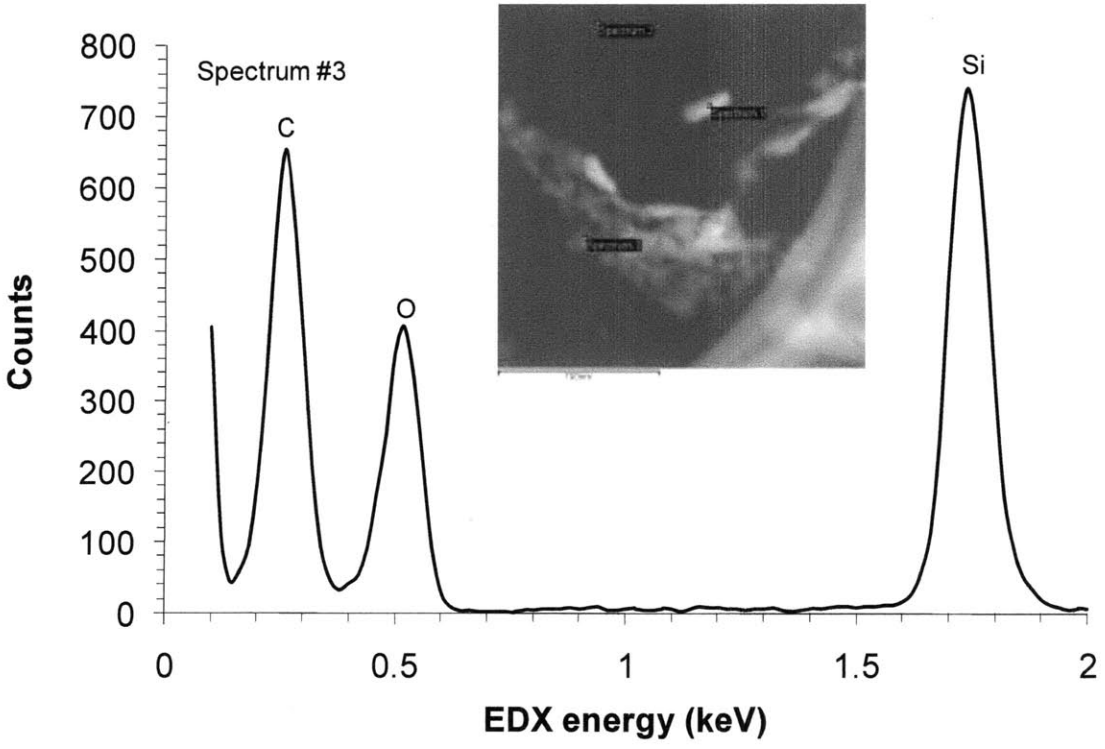

(d) Sample 20061010-Site#2: EDX spectrum at spot #3.

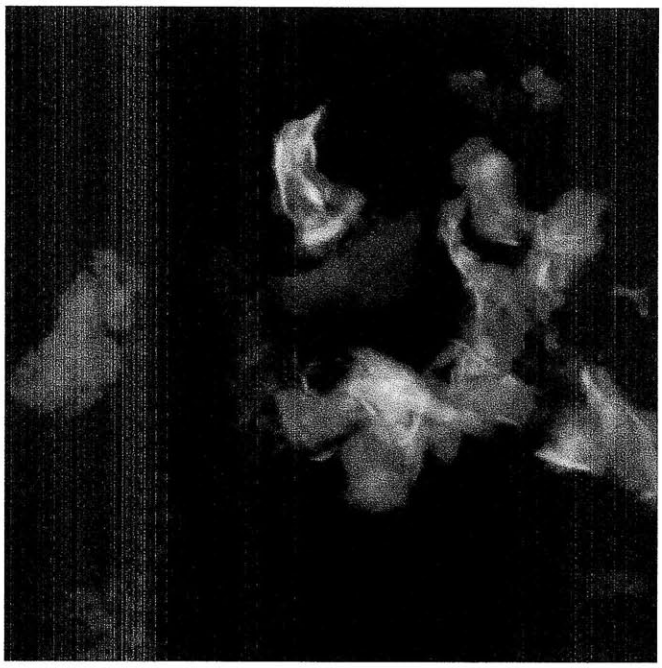

Figure A - 2. Mineral + NIST-soot (20061010-Site#6).

(a) Original TEM image. (NIST SRM #1650 Diesel Particulate Matter) amended sediments (Boston Harbor #6, 180-250 μm) on lacey-SiO film (20061010-Site#6).

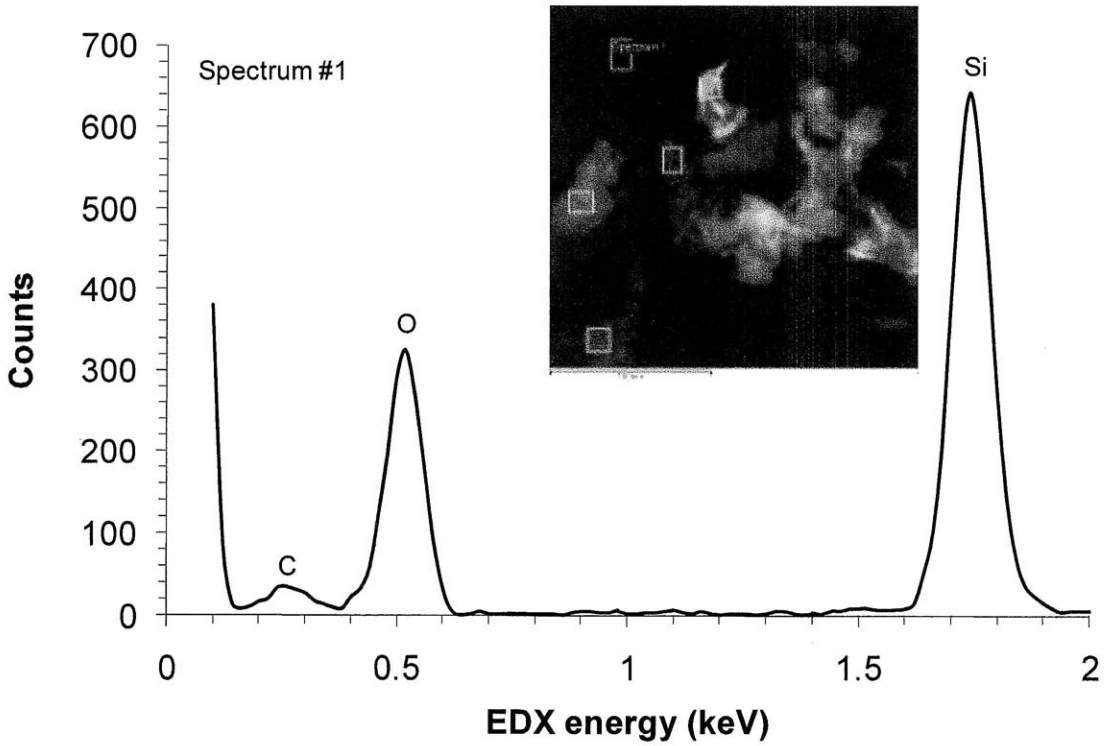

(b) Sample 20061010-Site#6: EDX spectrum at spot #1.

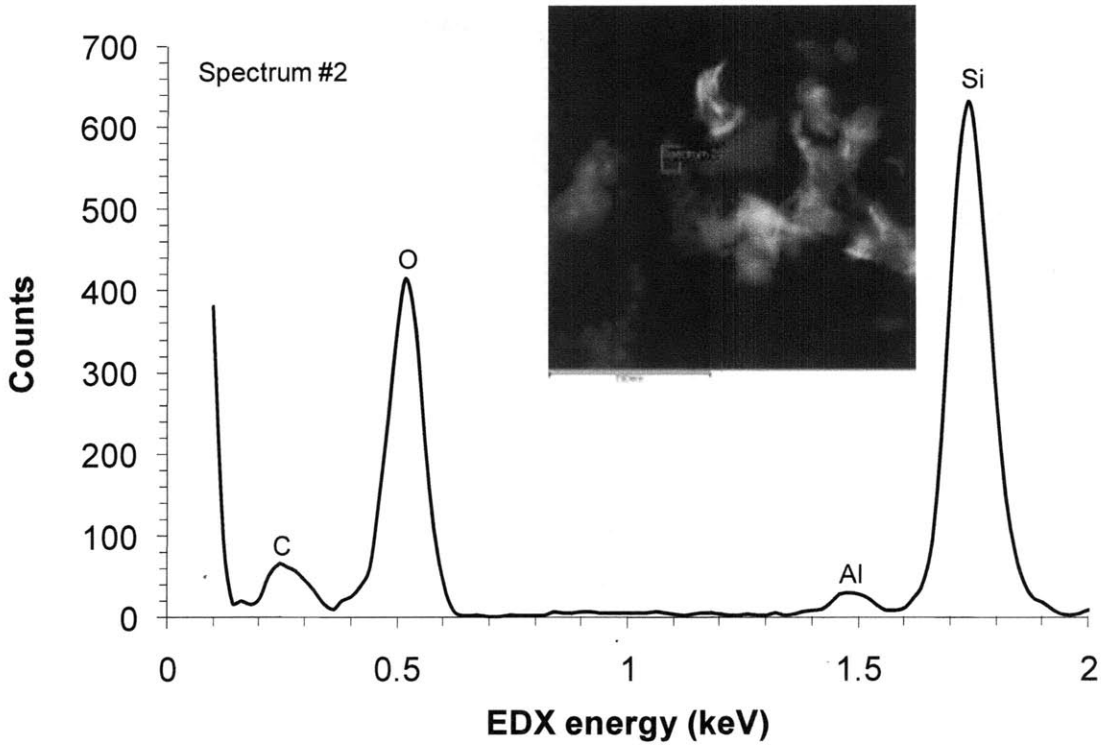

(c) Sample 20061010-Site#6: EDX spectrum at spot #2.

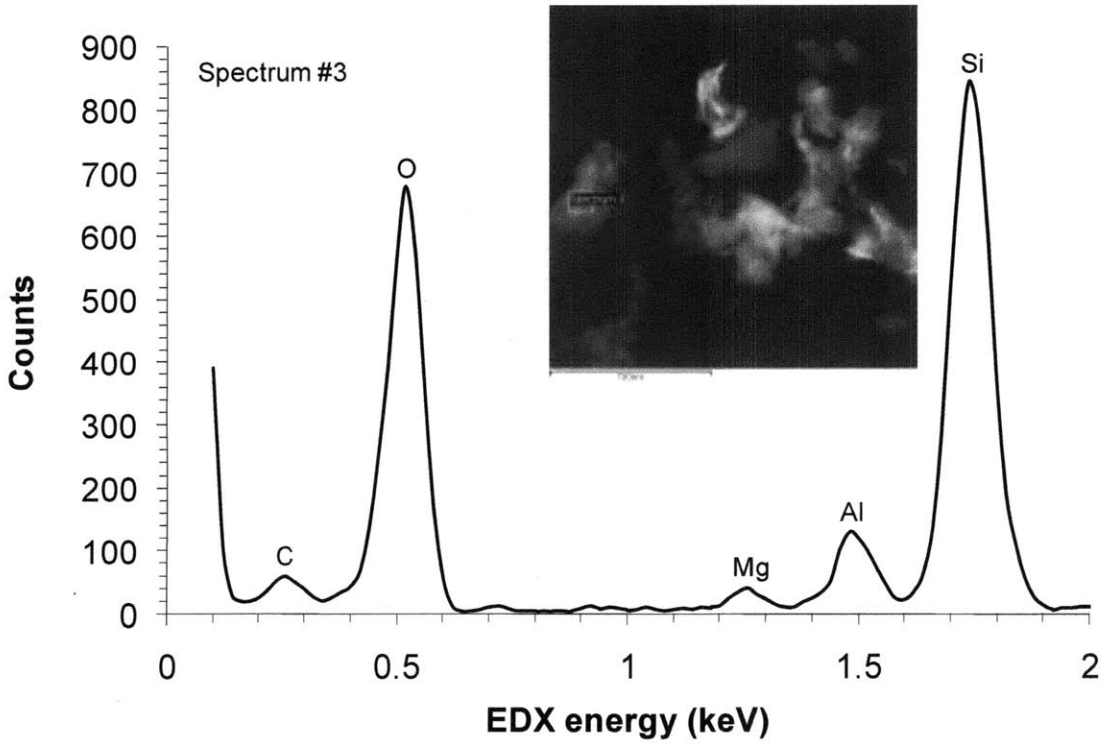

(d) Sample 20061010-Site#6: EDX spectrum at spot #3.

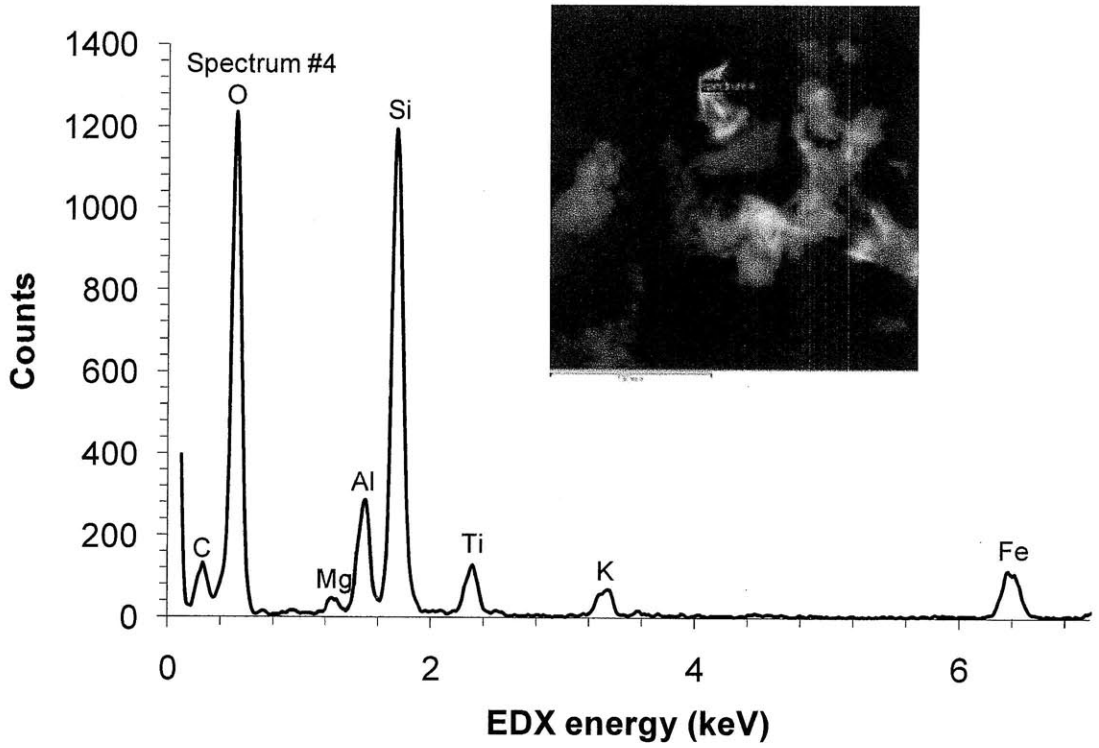

(e) Sample 20061010-Site#6: EDX spectrum at spot #4.

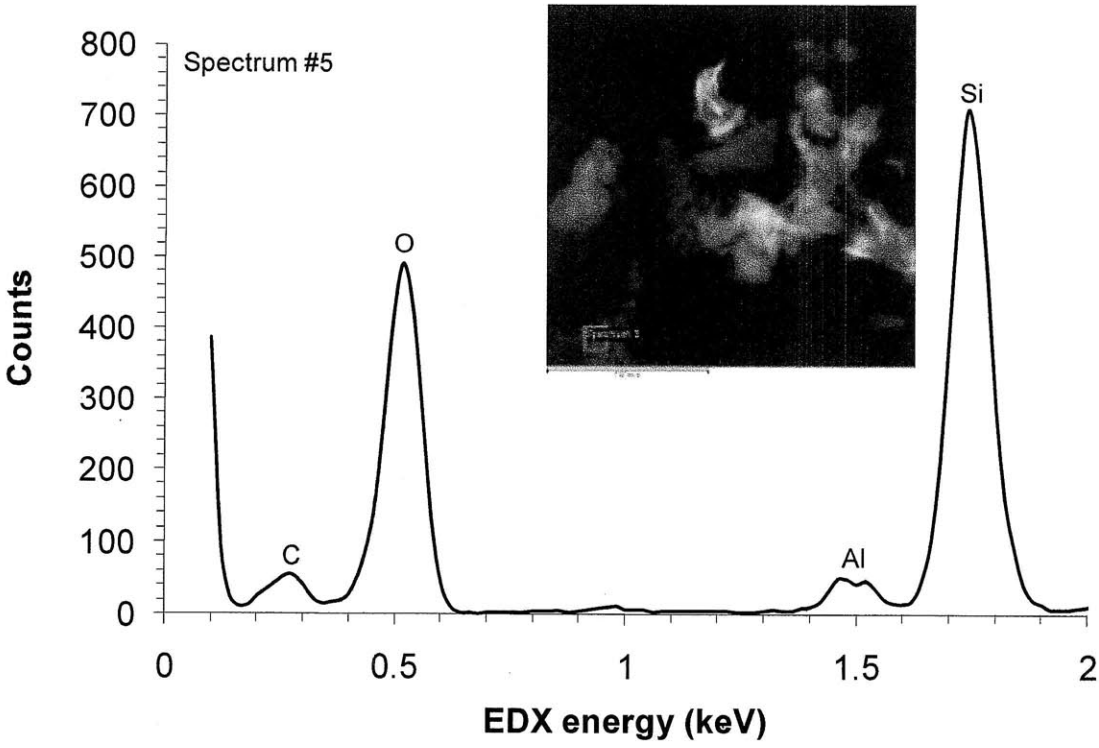

(f) Sample 20061010-Site#6: EDX spectrum at spot #5.

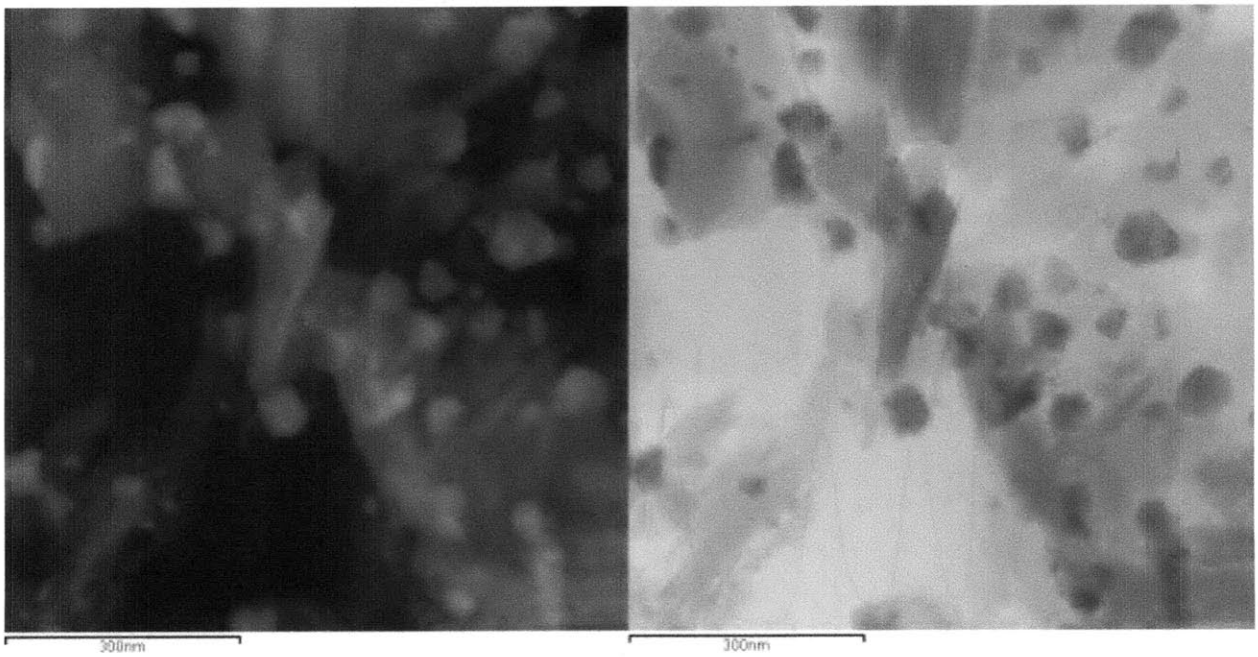

Figure A - 3. Sedimentary mineral phases (no apparent soot) (20061010-Site#12).

(a) Original TEM images. A region with no apparent presence of soot clusters in NIST-soot (NIST SRM #1650 Diesel Particulate Matter) amended sediments (Boston Harbor #6, 180-250 μm) on lacey-SiO film (20061010-Site#12).

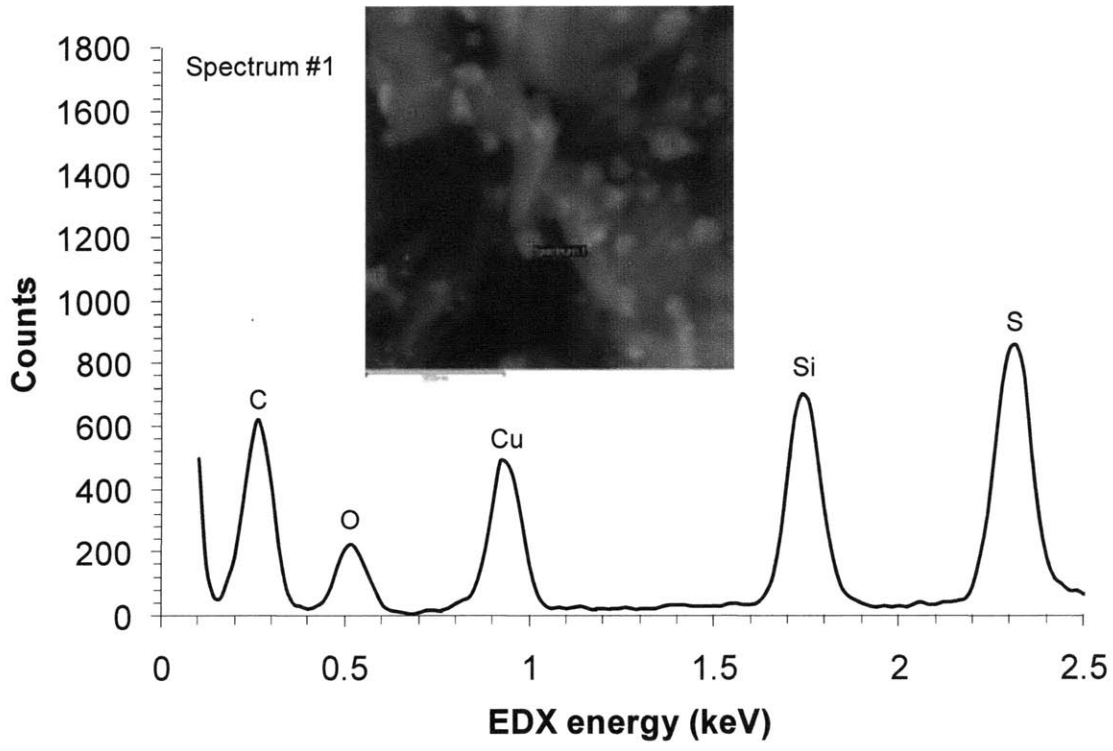

(b) Sample 20061010-Site#12: EDX spectrum at spot #1.

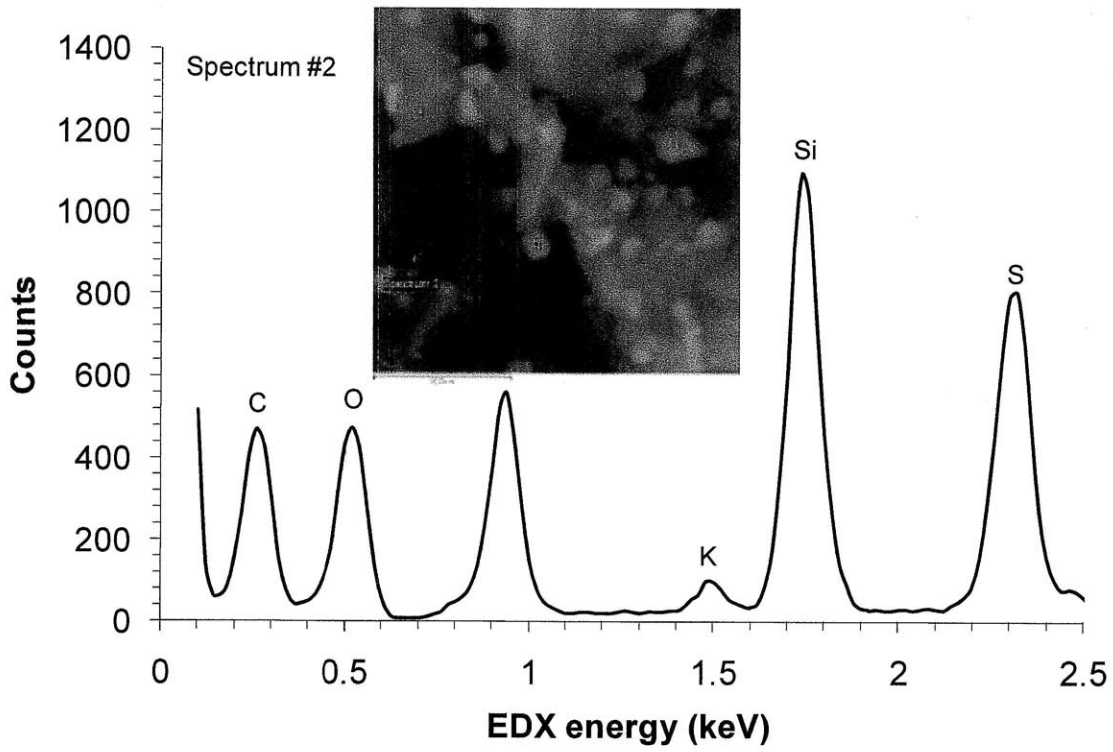

(c) Sample 20061010-Site#12: EDX spectrum at spot #2.

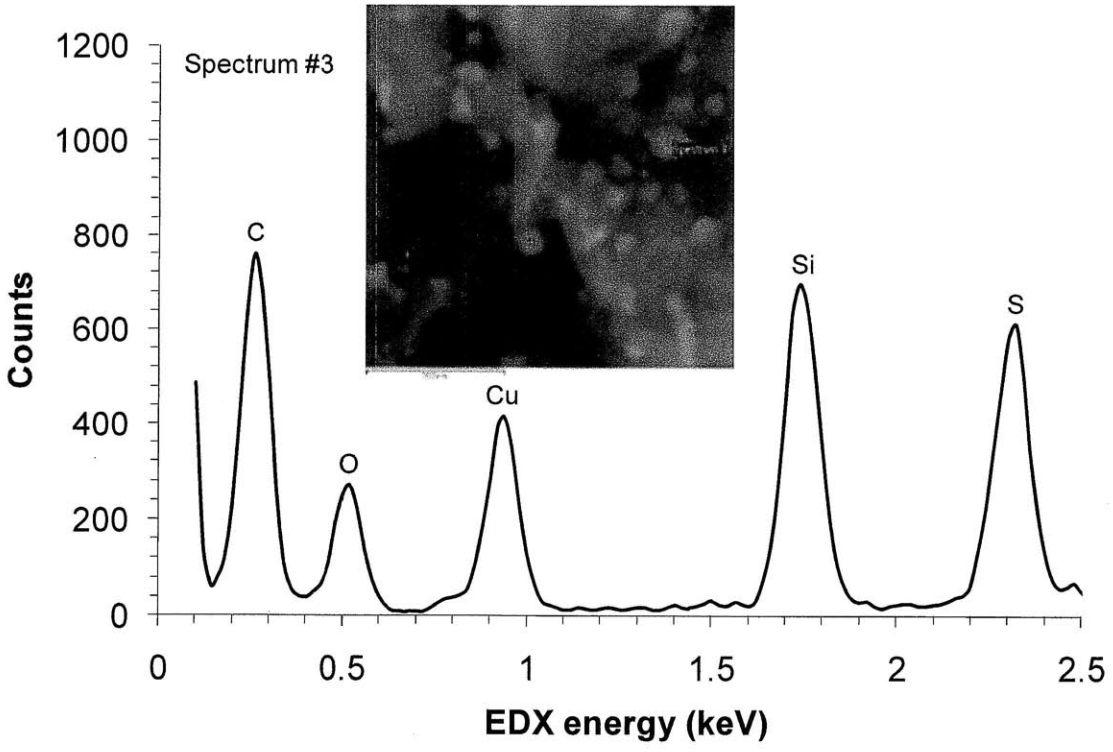

(d) Sample 20061010-Site#12: EDX spectrum at spot #3.

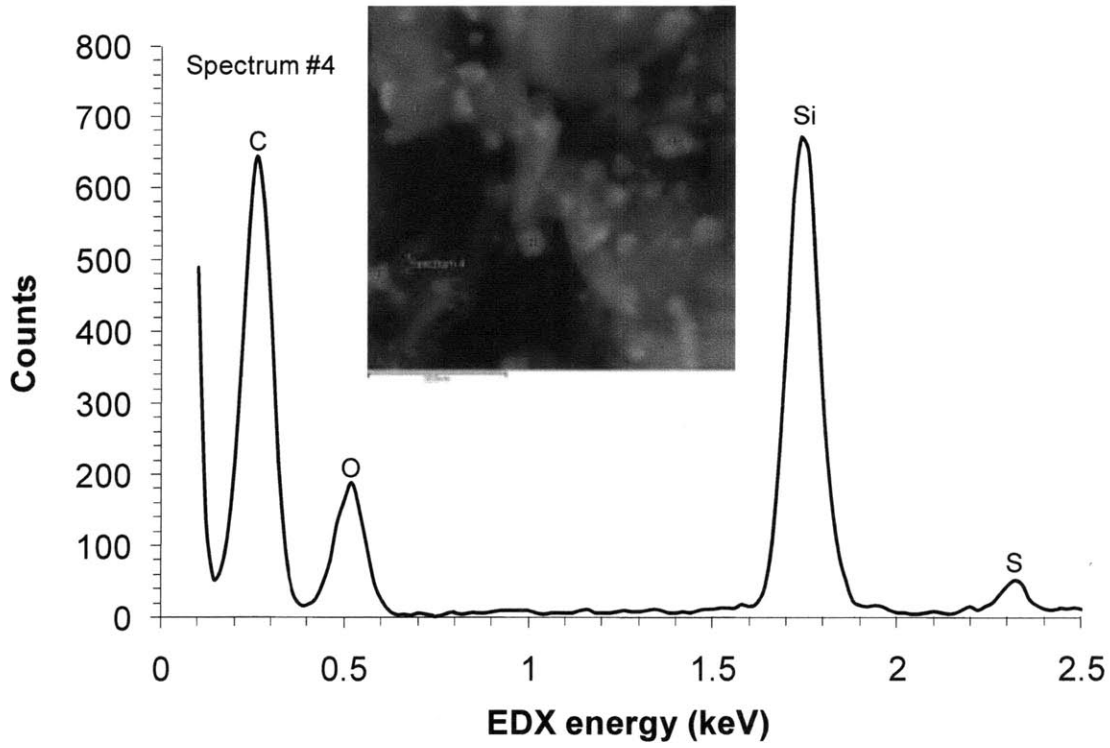

(e) Sample 20061010-Site#12: EDX spectrum at spot #4.

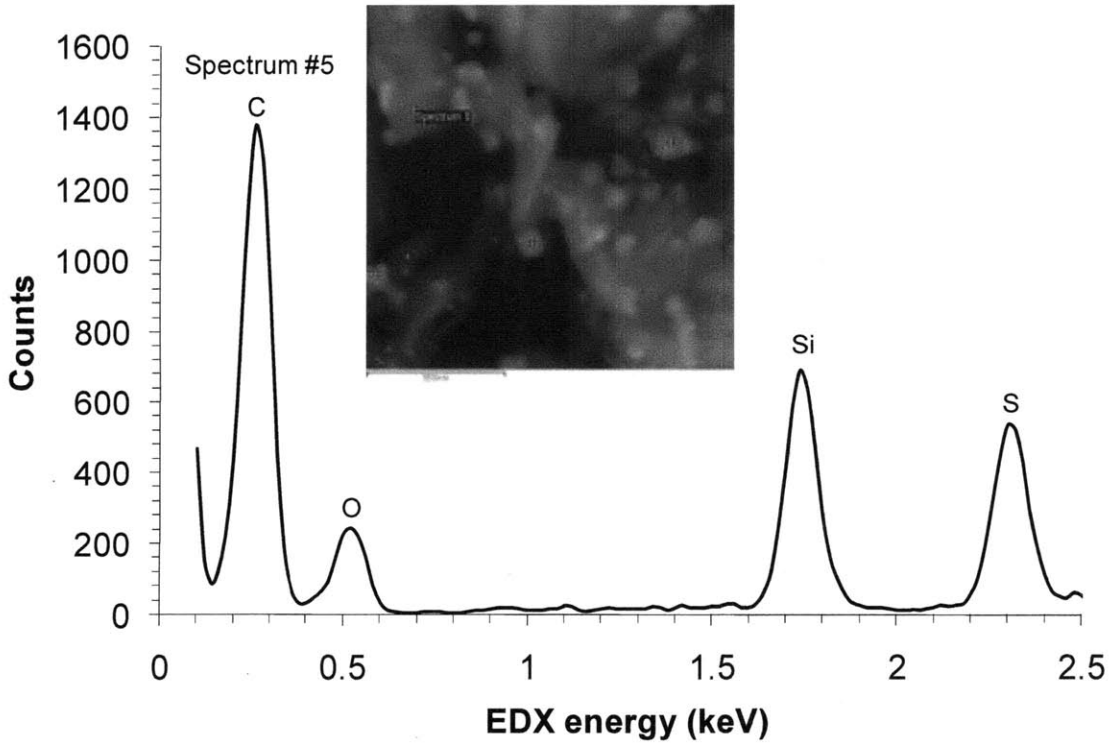

(f) Sample 20061010-Site#12: EDX spectrum at spot #5.

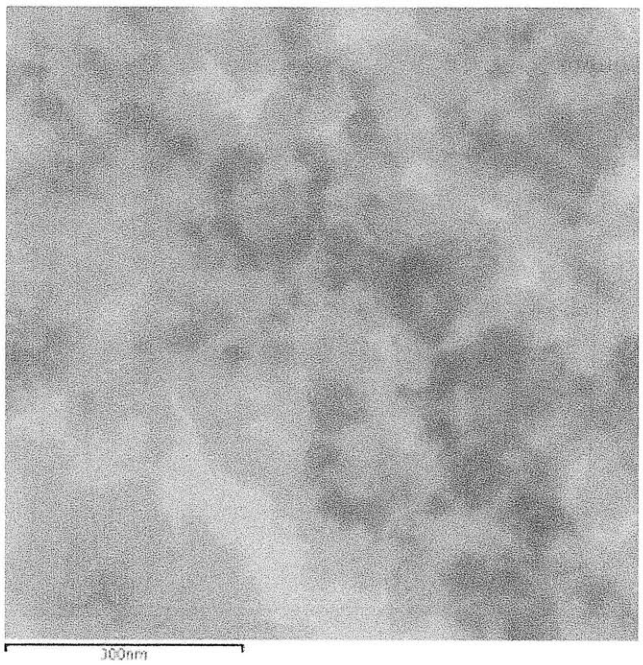

Figure A - 4. Soot-rich region in soot-amended sediment (20061013-Site#1).

(a) Original TEM image. A soot-rich region in NIST-soot (NIST SRM #1650 Diesel Particulate Matter) amended sediments (Boston Harbor #6, 180-250 μm) on lacey-SiO film (20061013-Site#1).

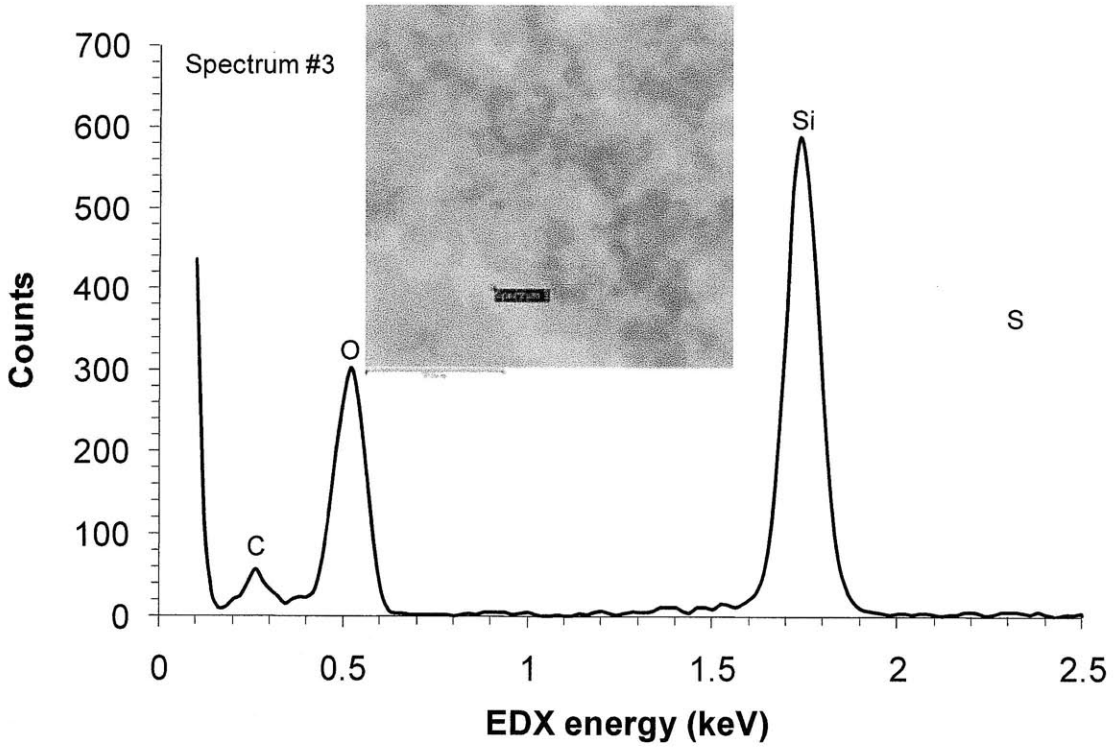

(b) Sample 20061013-Site#1: EDX spectrum at spot #3.

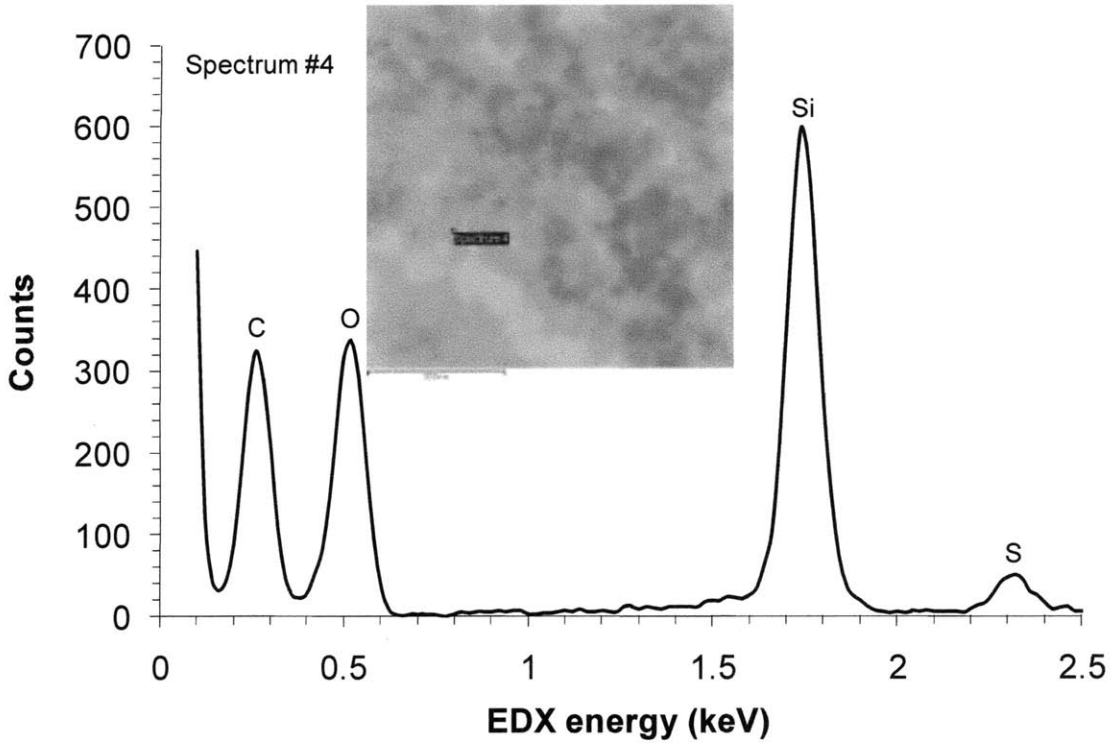

(c) Sample 20061013-Site#1: EDX spectrum at spot #4.

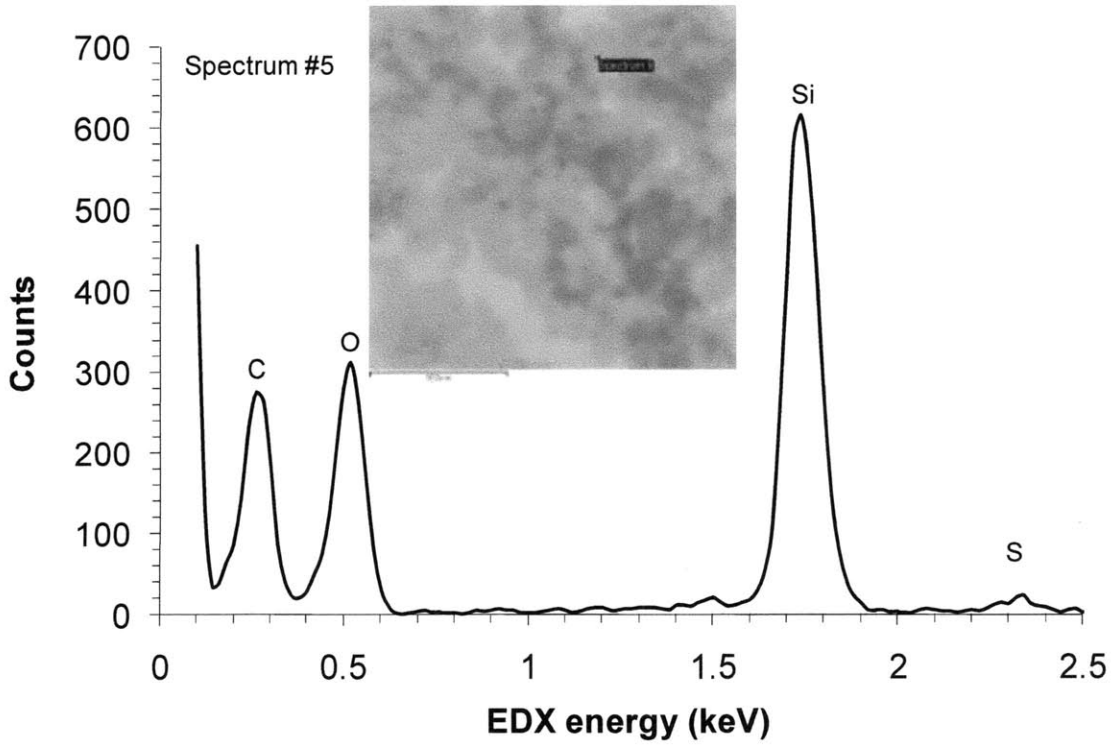

(d) Sample 20061013-Site#1: EDX spectrum at spot #5.

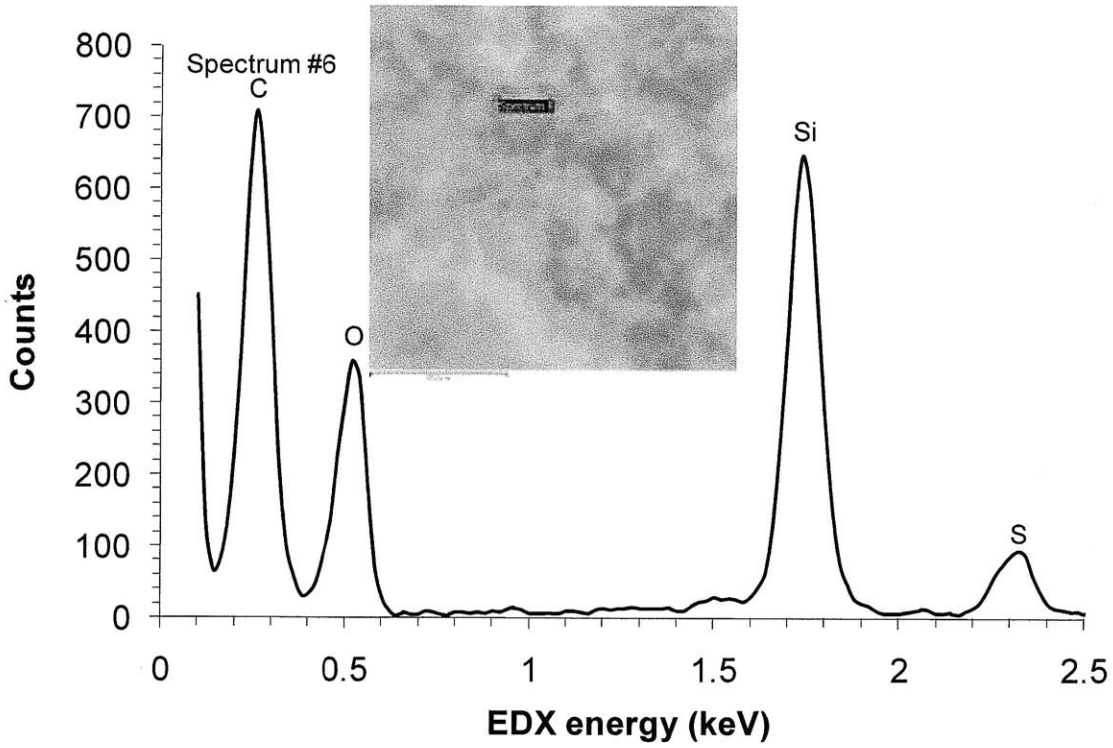

(e) Sample 20061013-Site#1: EDX spectrum at spot #6.

Figure A - 5. Humic substance (20061019-Site#5).

(a) Original TEM image. Humic substance on lacey-SiO film (20061019-Site#5).

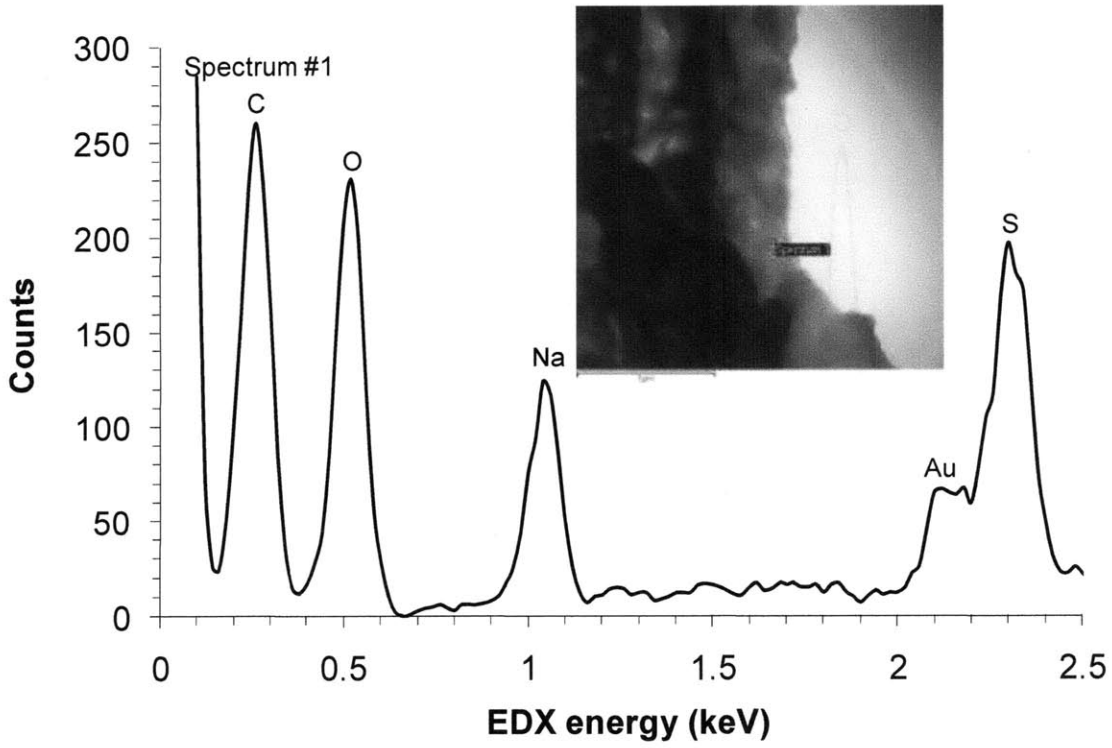

(b) Sample 20061019-Site#5: EDX spectrum at spot #1.

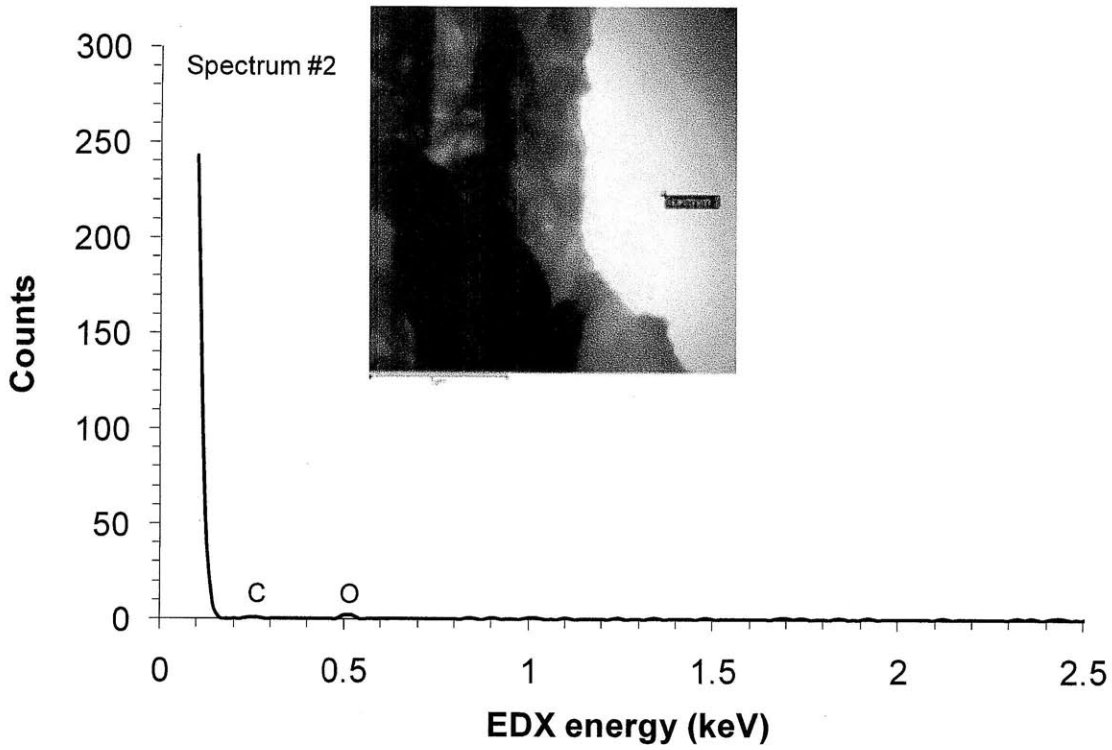

(c) Sample 20061019-Site#5: EDX spectrum at spot #2.

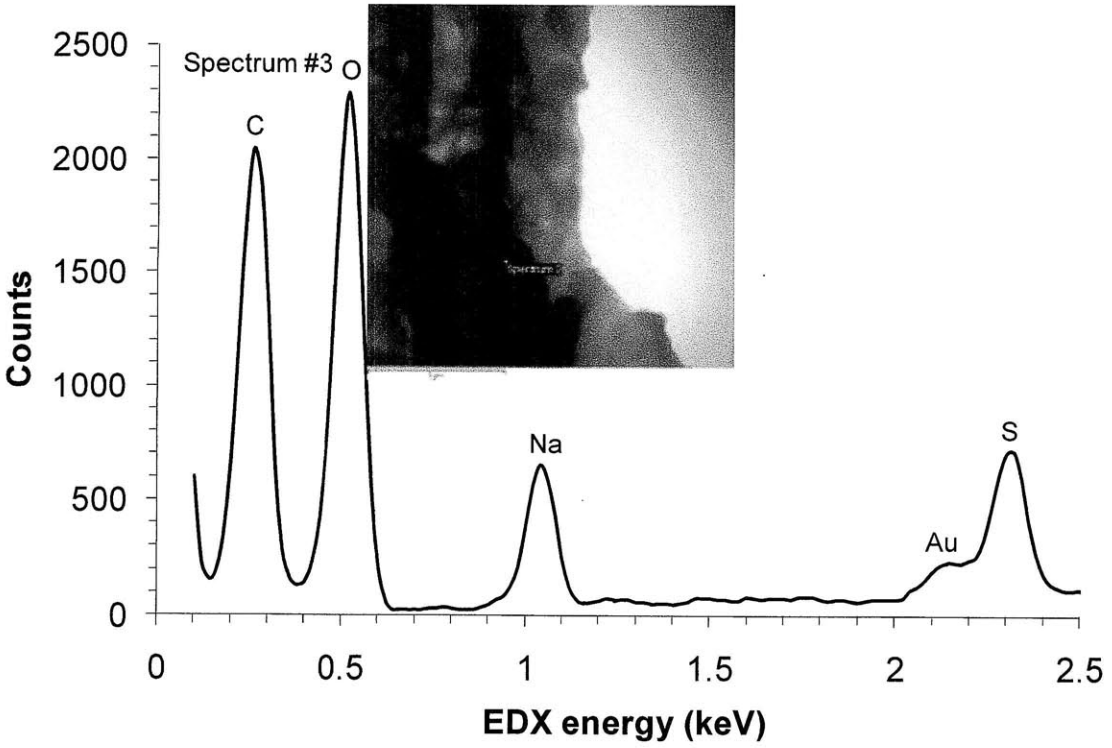

(d) Sample 20061019-Site#5: EDX spectrum at spot #3.

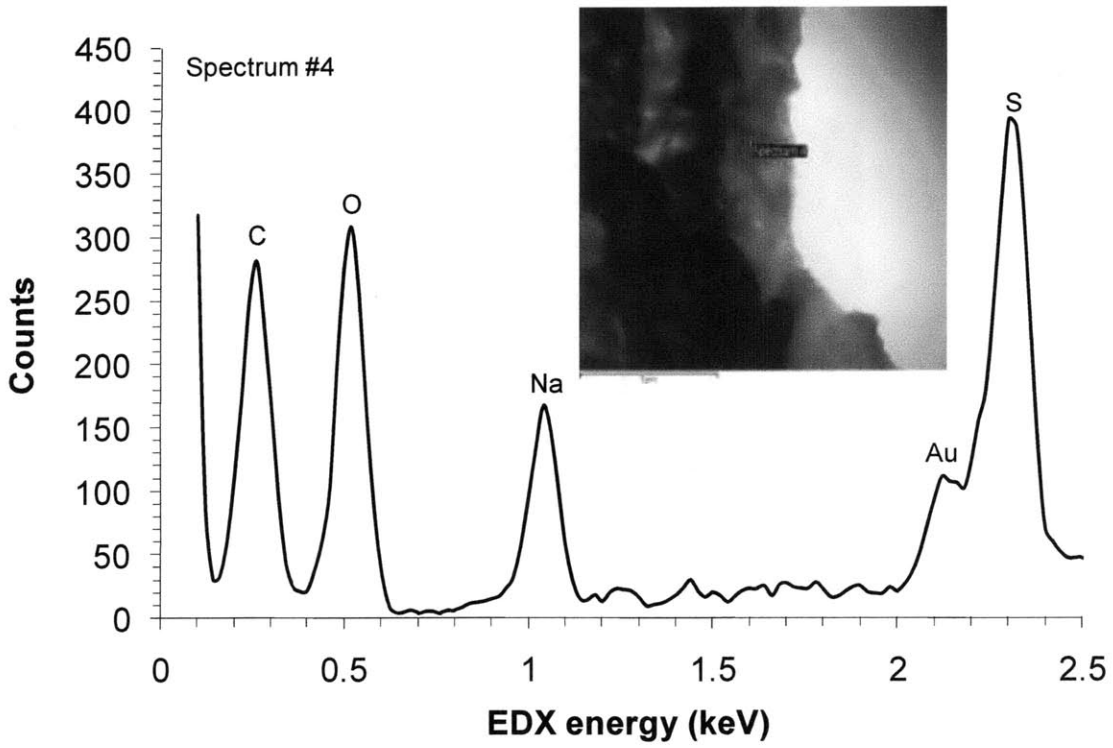

(e) Sample 20061019-Site#5: EDX spectrum at spot #4.

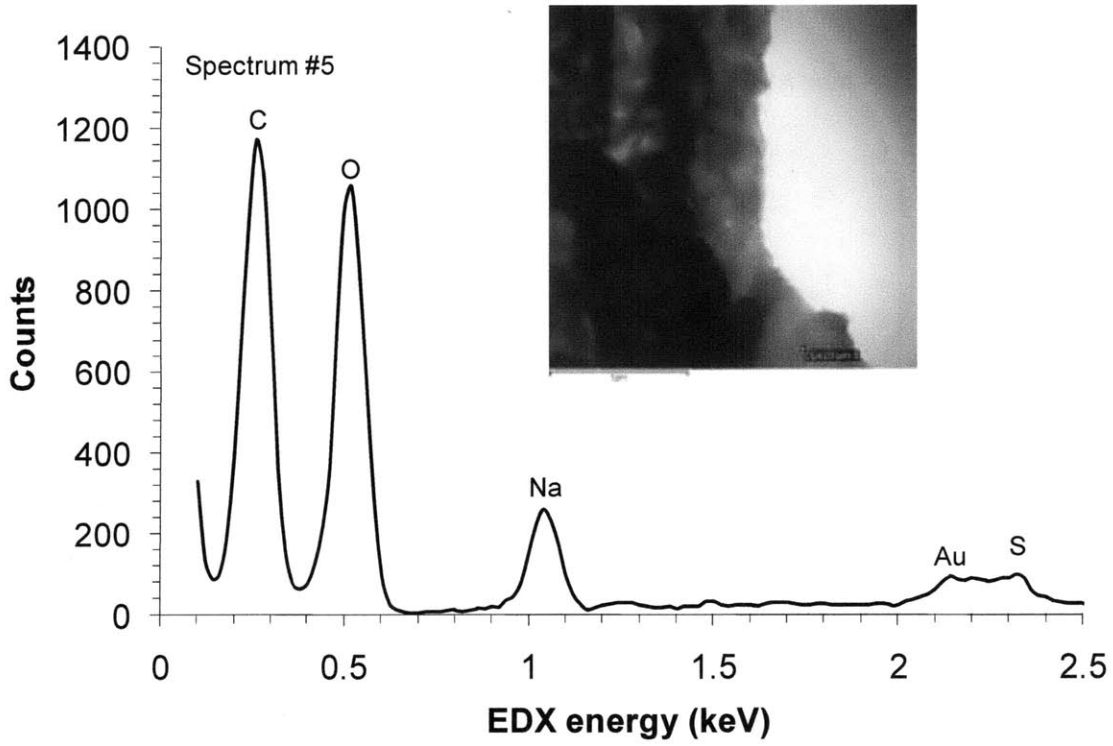

(f) Sample 20061019-Site#5: EDX spectrum at spot #5.

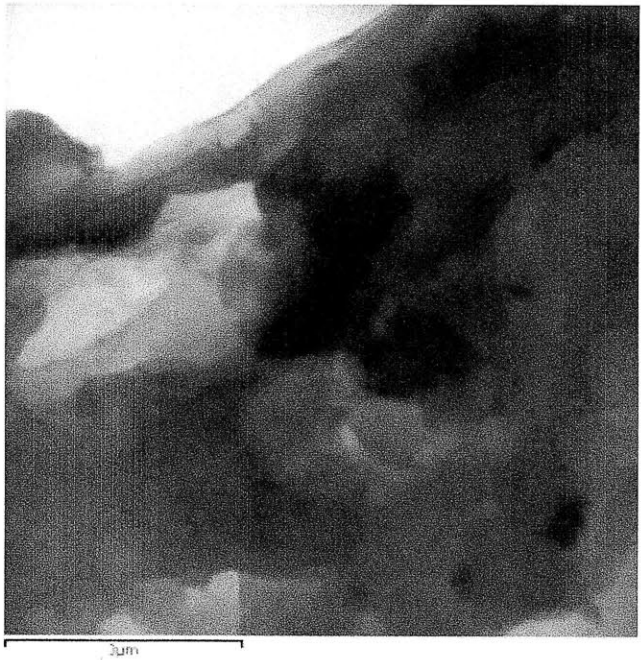

Figure A - 6. Humic substance (20061019-Site#7).

(a) Original TEM image. Humic substance on lacey-SiO film (20061019-Site#7).

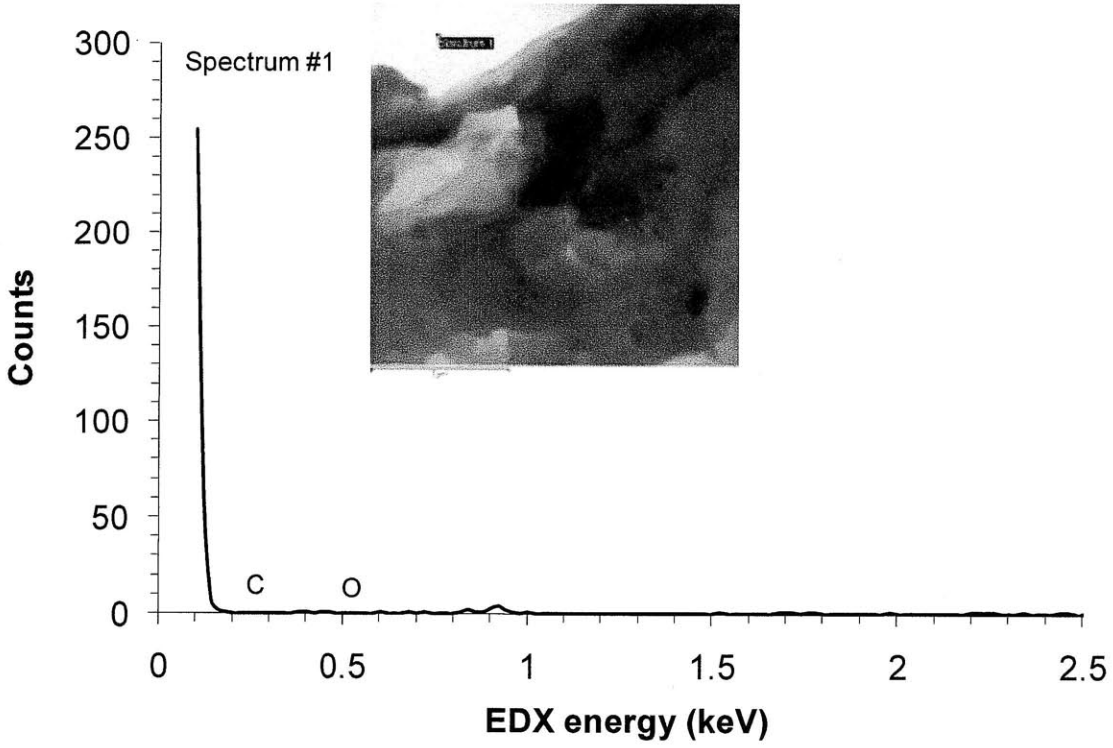

(b) Sample 20061019-Site#7: EDX spectrum at spot #1.

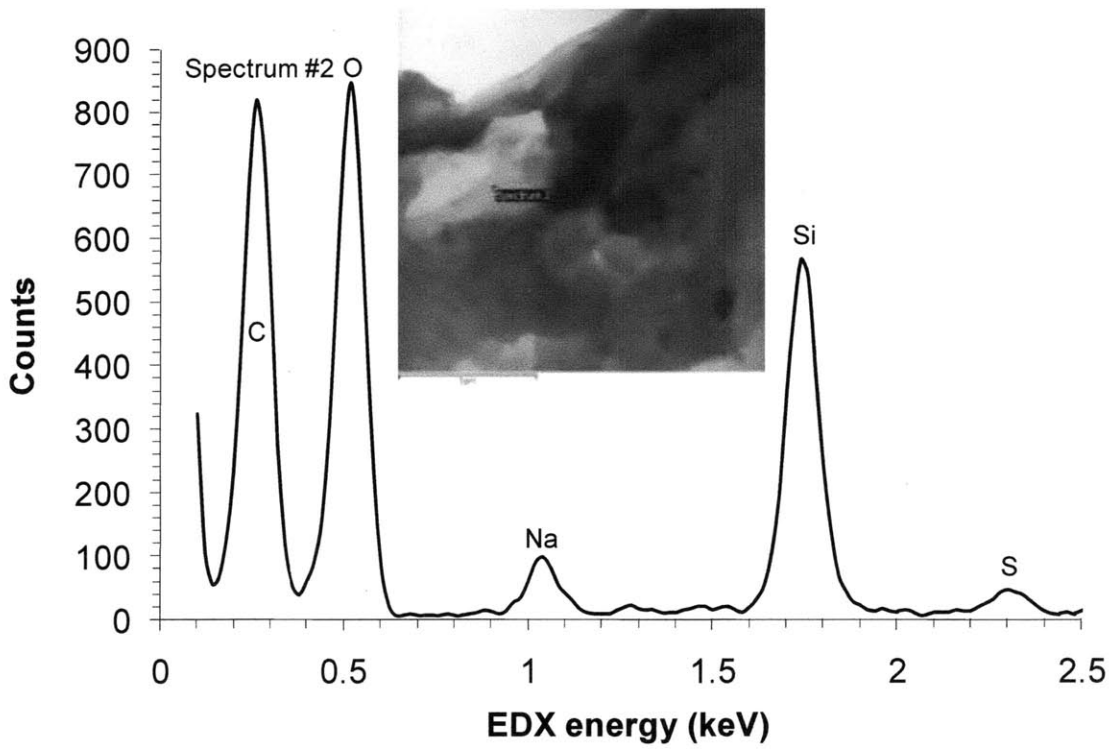

(c) Sample 20061019-Site#7: EDX spectrum at spot #2.

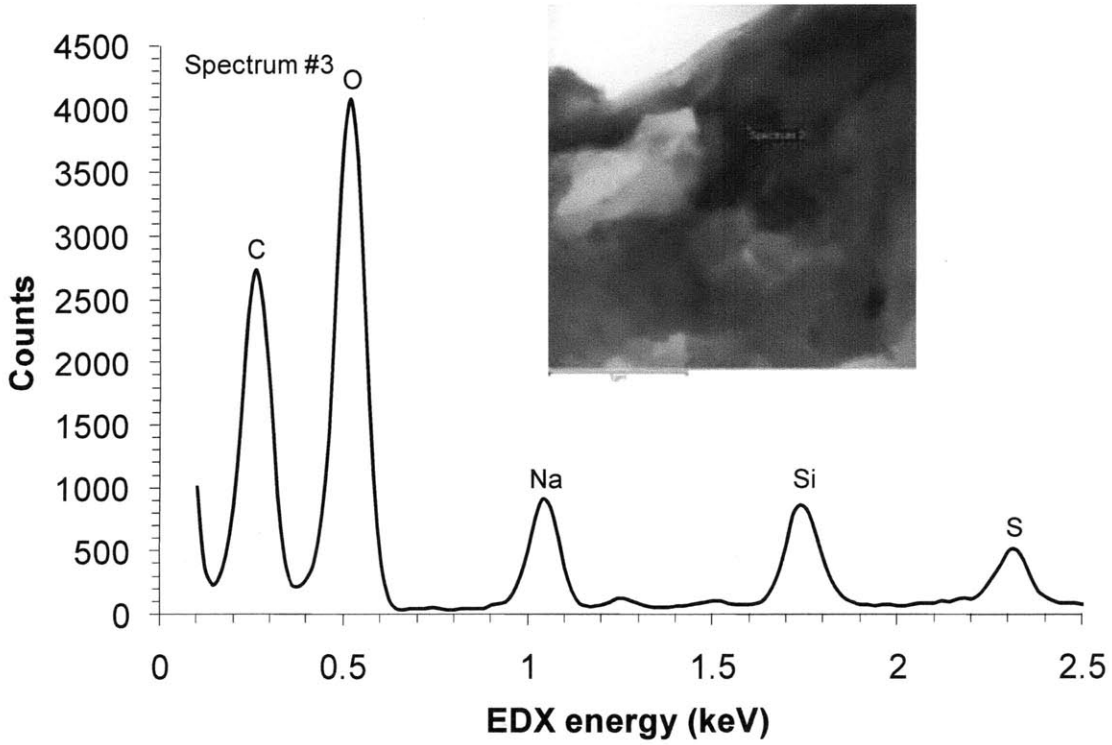

(d) Sample 20061019-Site#7: EDX spectrum at spot #3.

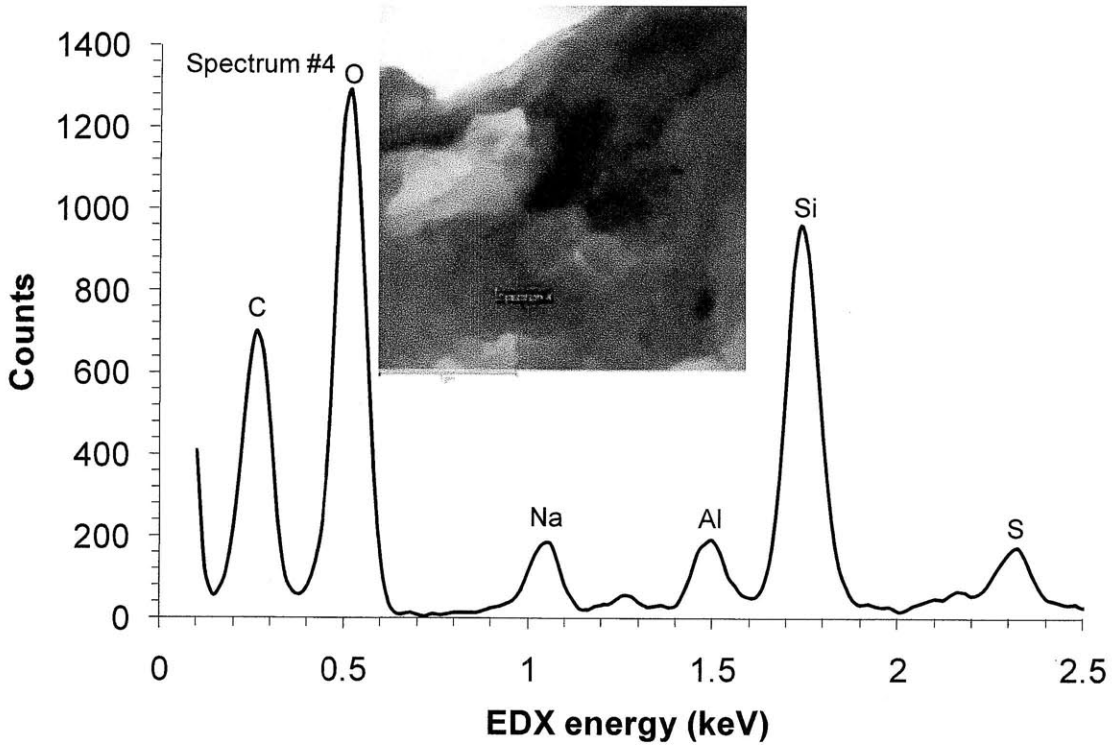

(e) Sample 20061019-Site#7: EDX spectrum at spot #4.

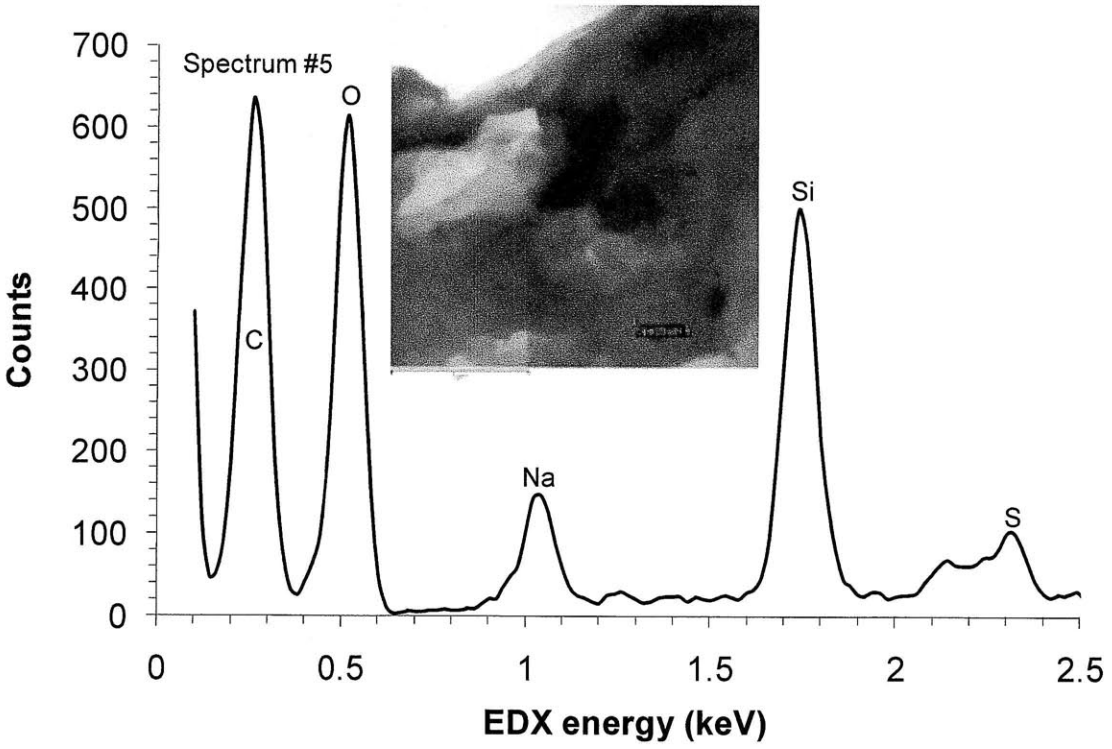

(f) Sample 20061019-Site#7: EDX spectrum at spot #5.

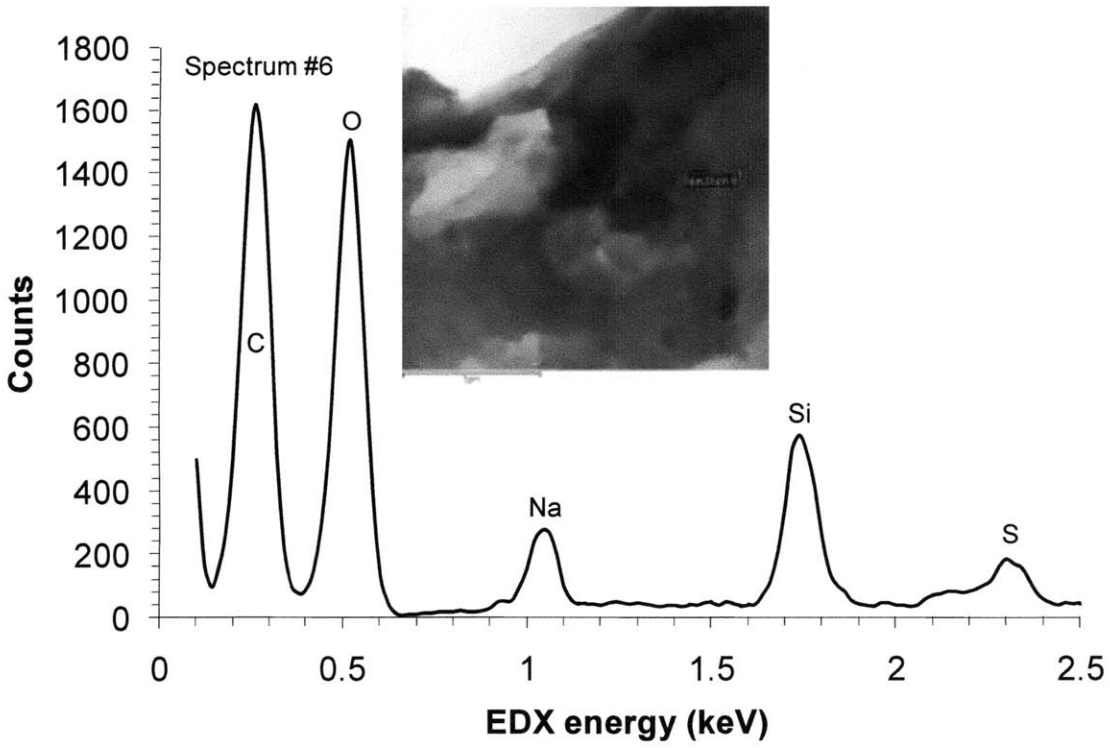

(g) Sample 20061019-Site#7: EDX spectrum at spot #6.

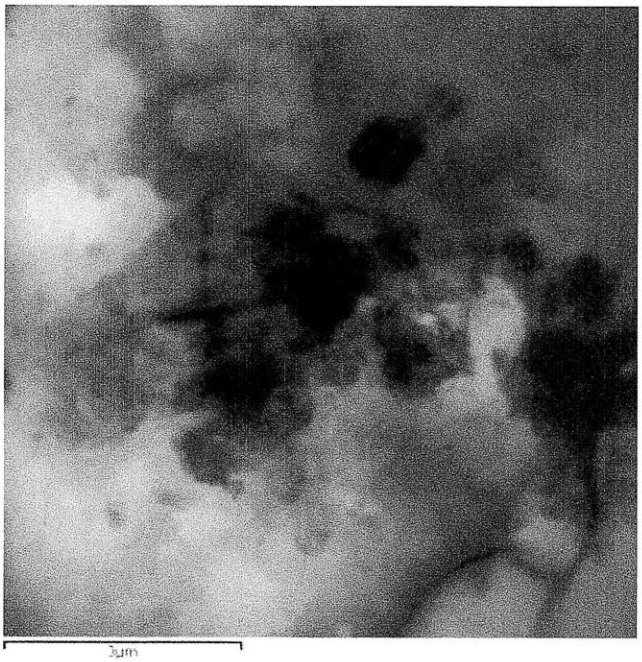

Figure A - 7. Humic substance (20061019-Site#11).

(a) Original TEM image. Humic substance on lacey-SiO film (20061019-Site#11).

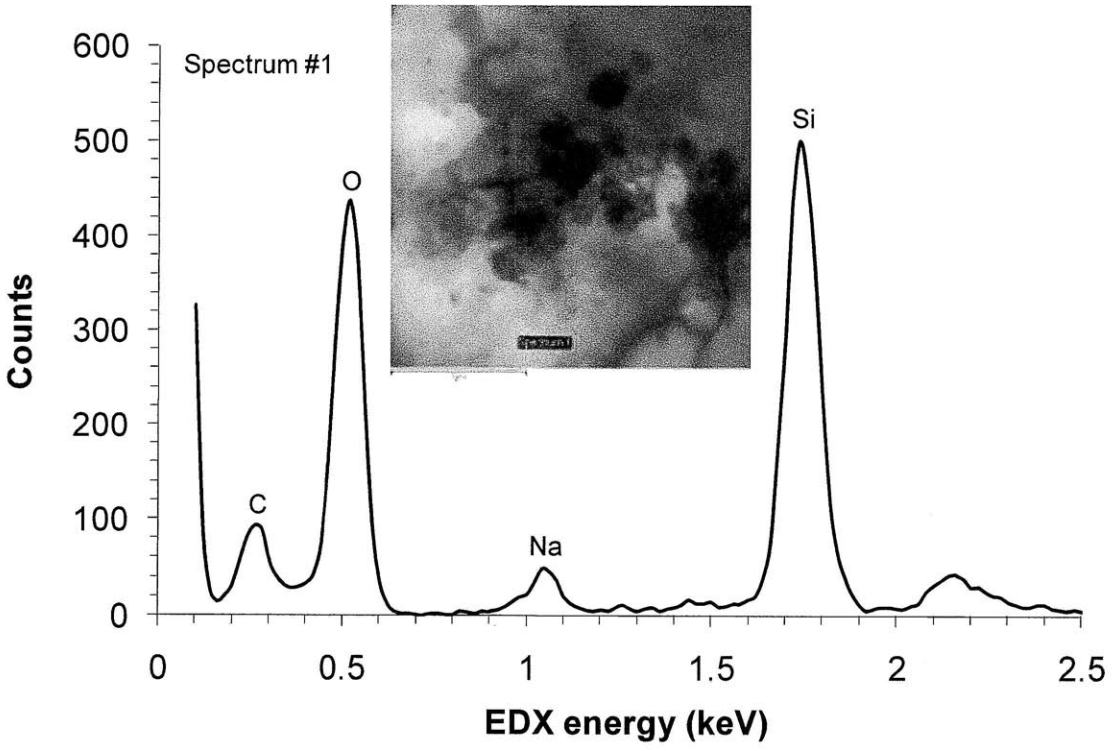

(b) Sample 20061019-Site#11: EDX spectrum at spot #1.

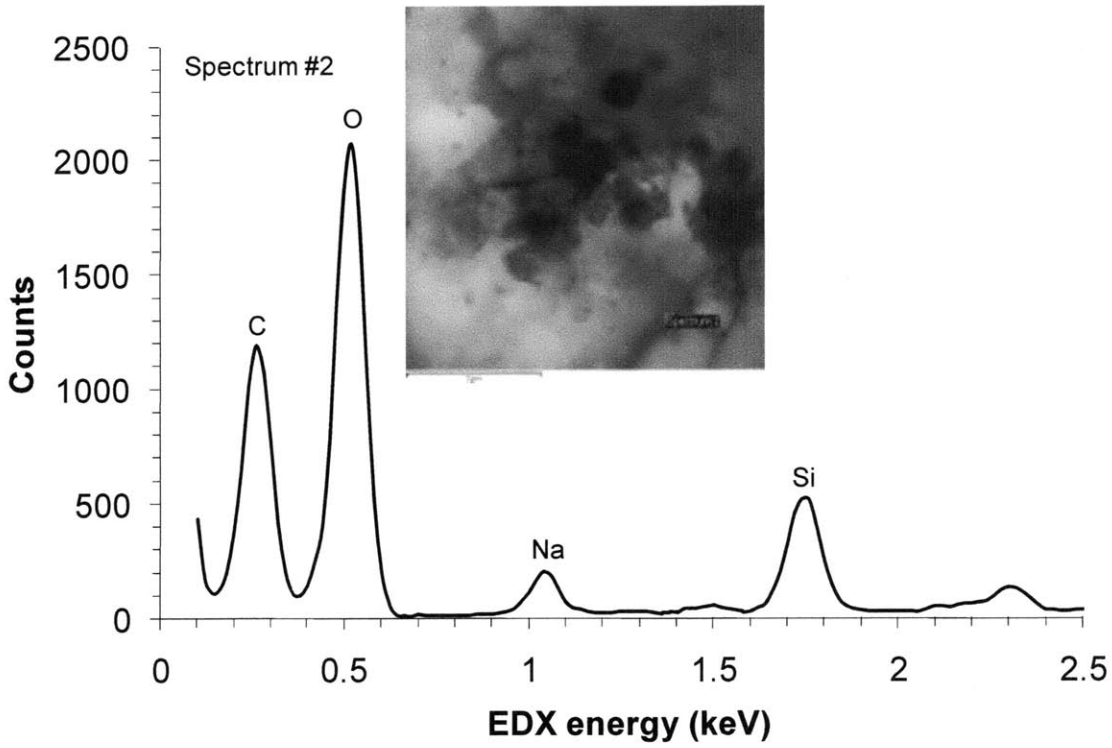

(c) Sample 20061019-Site#11: EDX spectrum at spot #2.

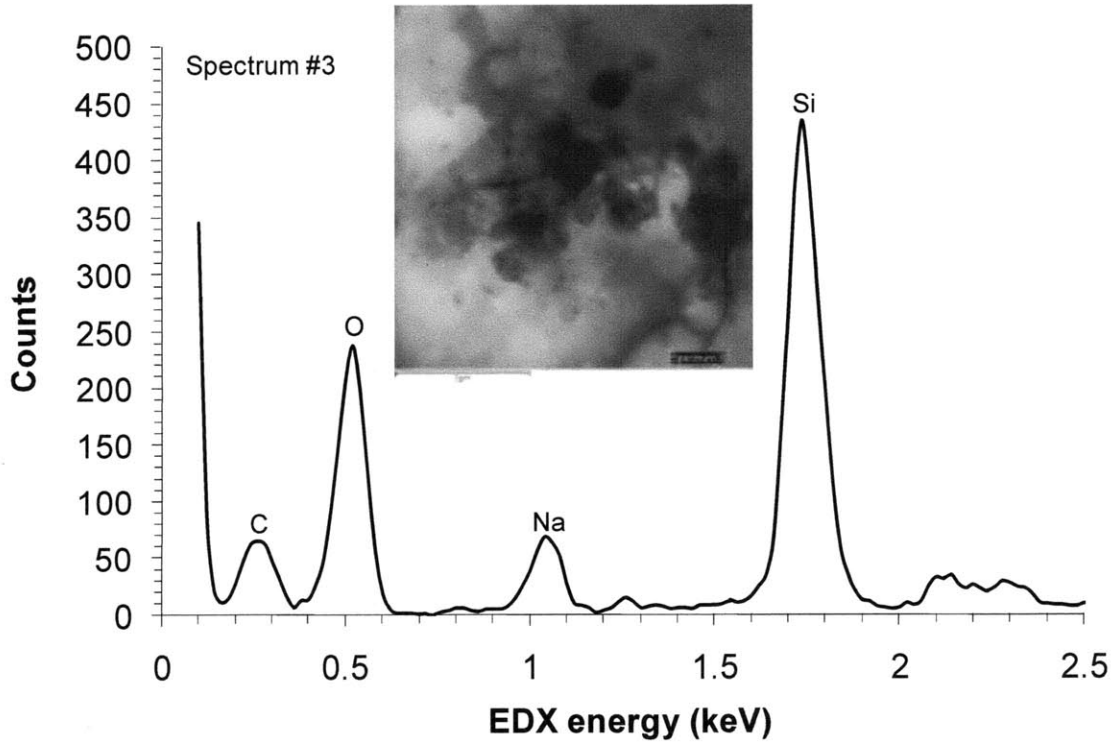

(d) Sample 20061019-Site#11: EDX spectrum at spot #3.

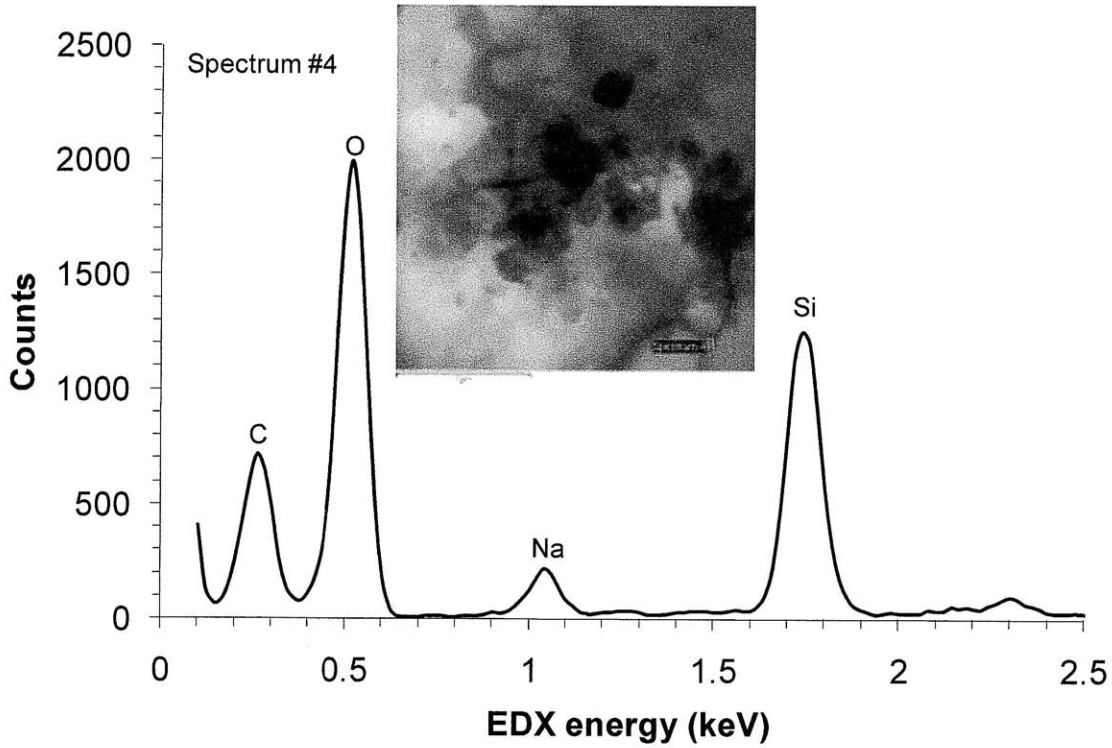

(e) Sample 20061019-Site#11: EDX spectrum at spot #4.

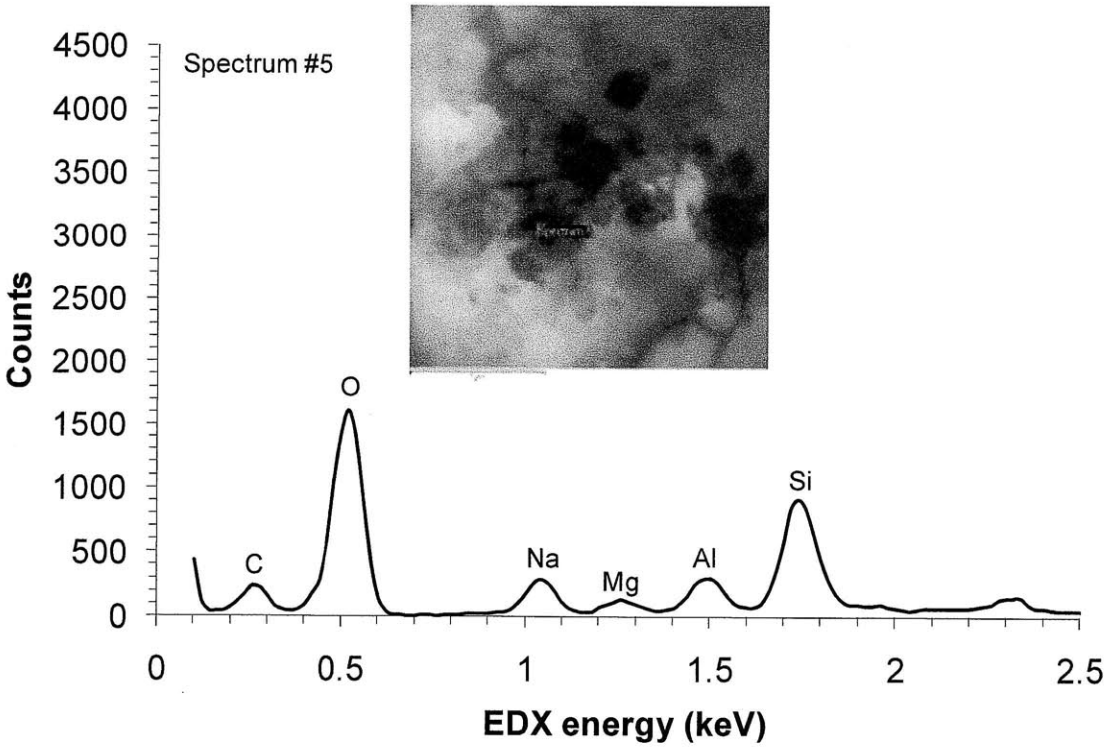

(f) Sample 20061019-Site#11: EDX spectrum at spot #5.

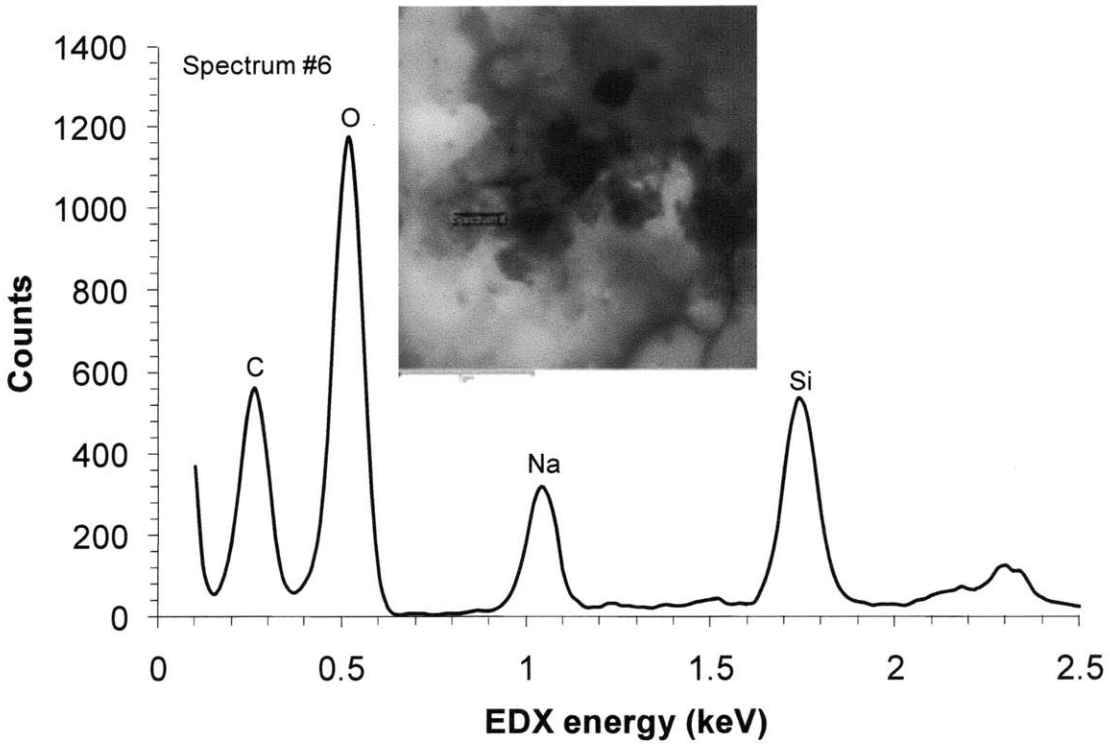

(g) Sample 20061019-Site#11: EDX spectrum at spot #6.

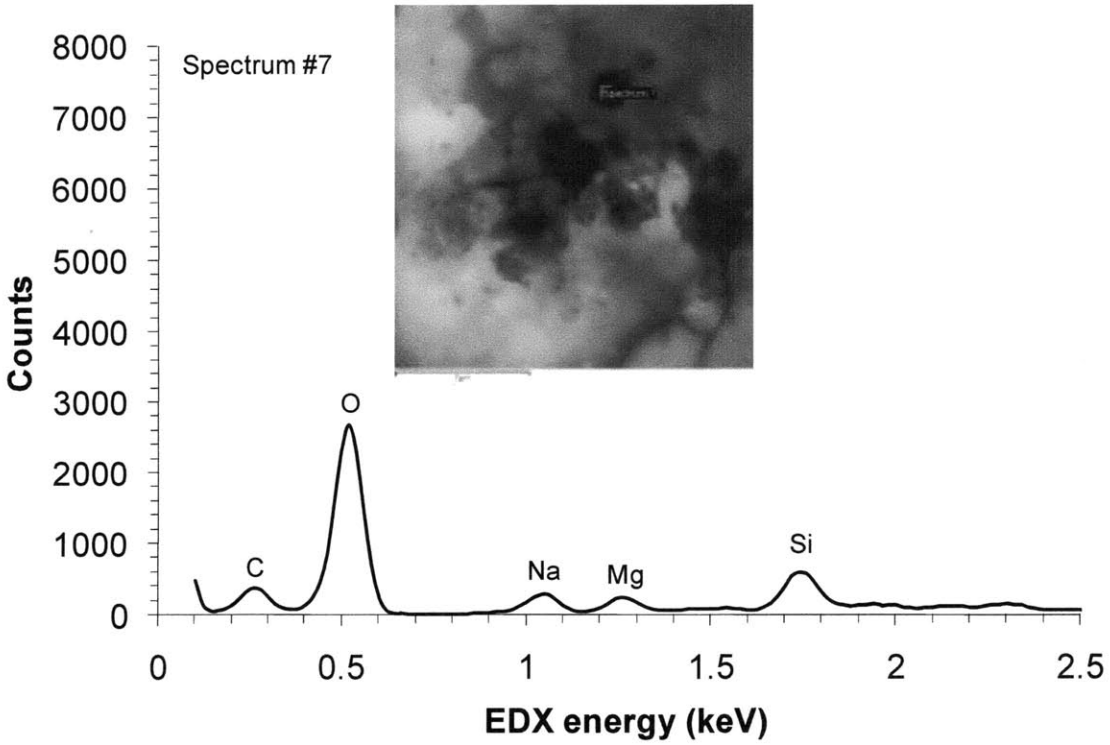

(h) Sample 20061019-Site#11: EDX spectrum at spot #7.

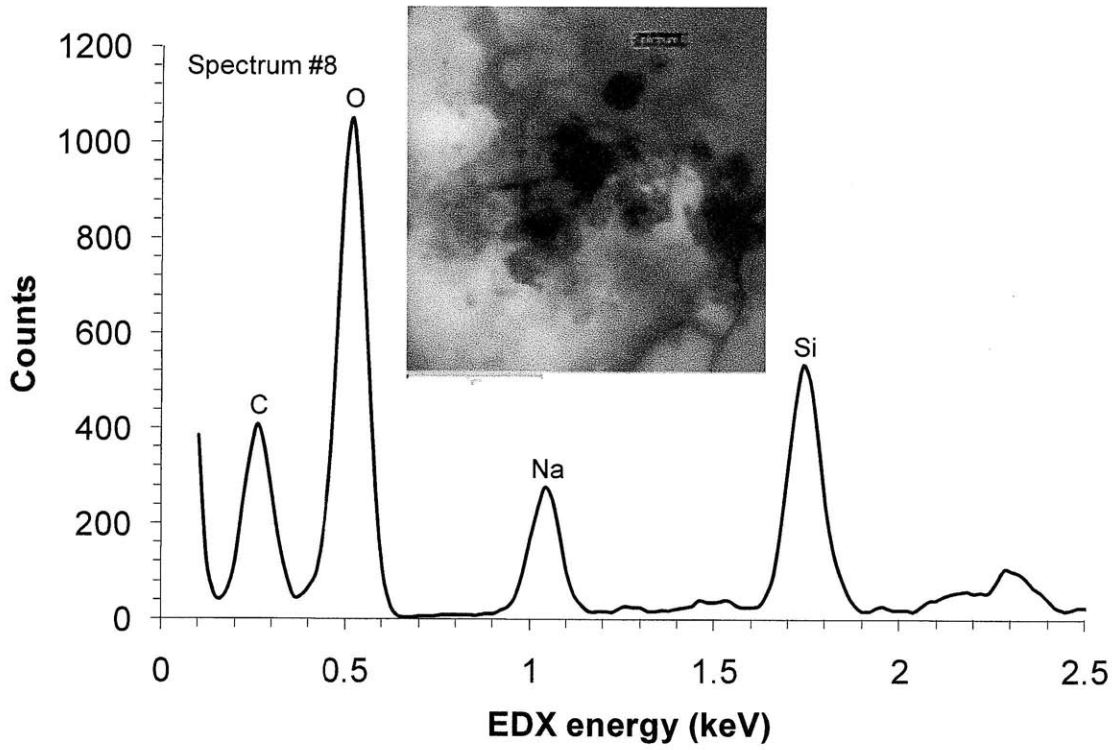

(i) Sample 20061019-Site#11: EDX spectrum at spot #8.

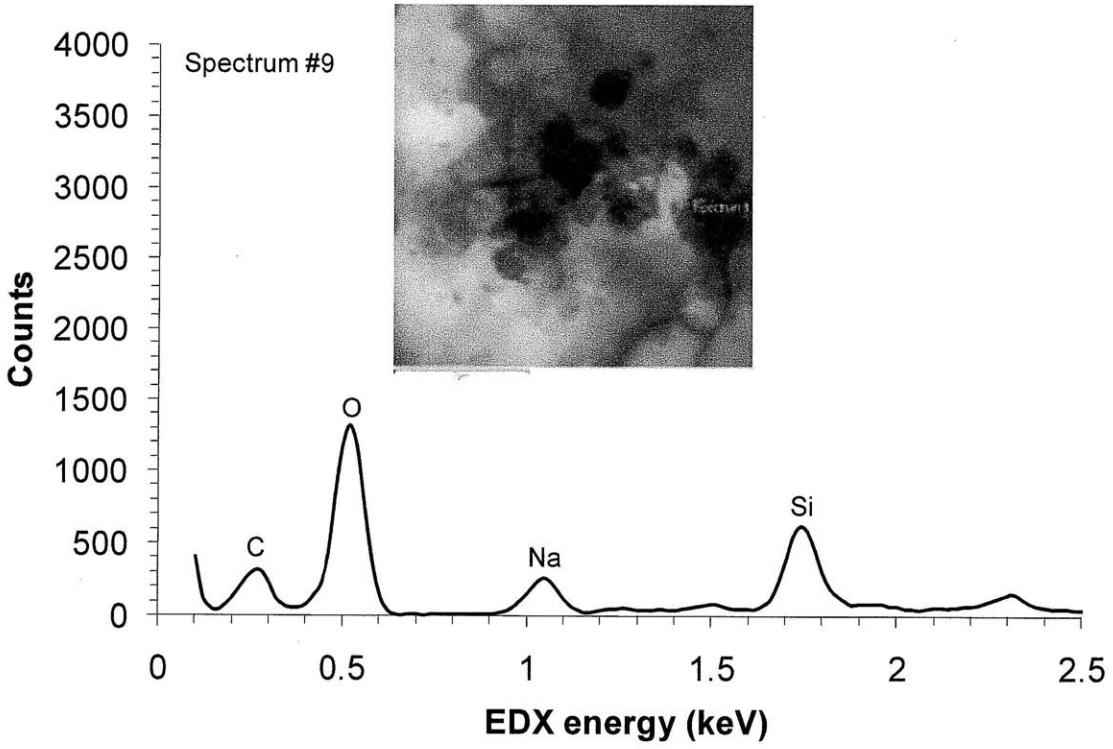

(j) Sample 20061019-Site#11: EDX spectrum at spot #9.

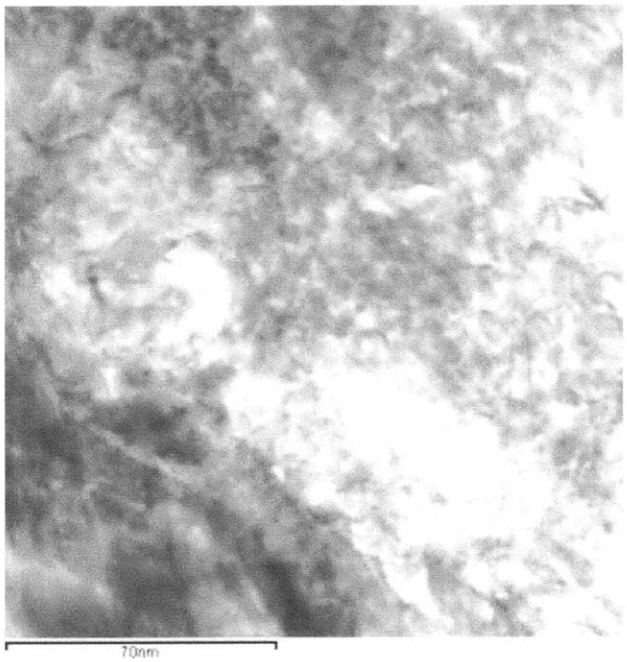

Figure A - 8. Sedimentary mineral phases (no apparent soot) (20061103-Site#2).

(a) Original TEM image. A region with no apparent presence of soot clusters in NIST-soot (NIST SRM #1650 Diesel Particulate Matter) amended sediments (Boston Harbor #6, 180-250 μm) on lacey-SiO film (20061103-Site#2).

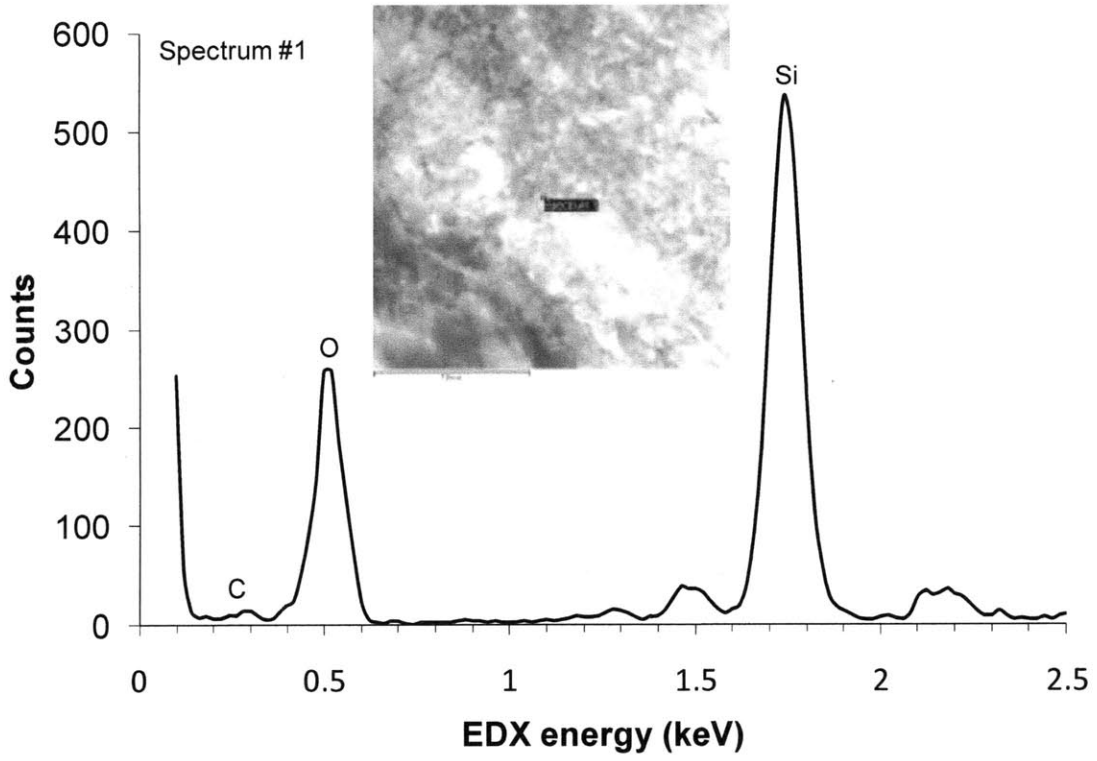

(b) Sample 20061103-Site#2: EDX spectrum at spot #1.

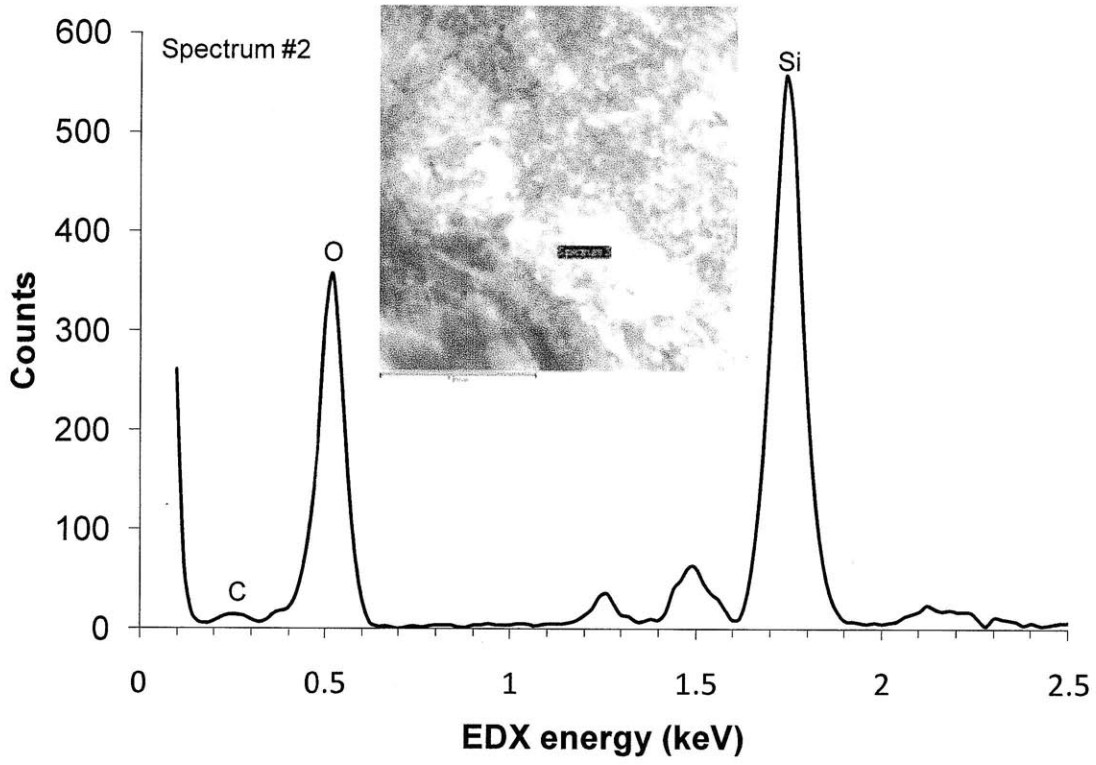

(c) Sample 20061103-Site#2: EDX spectrum at spot #2.

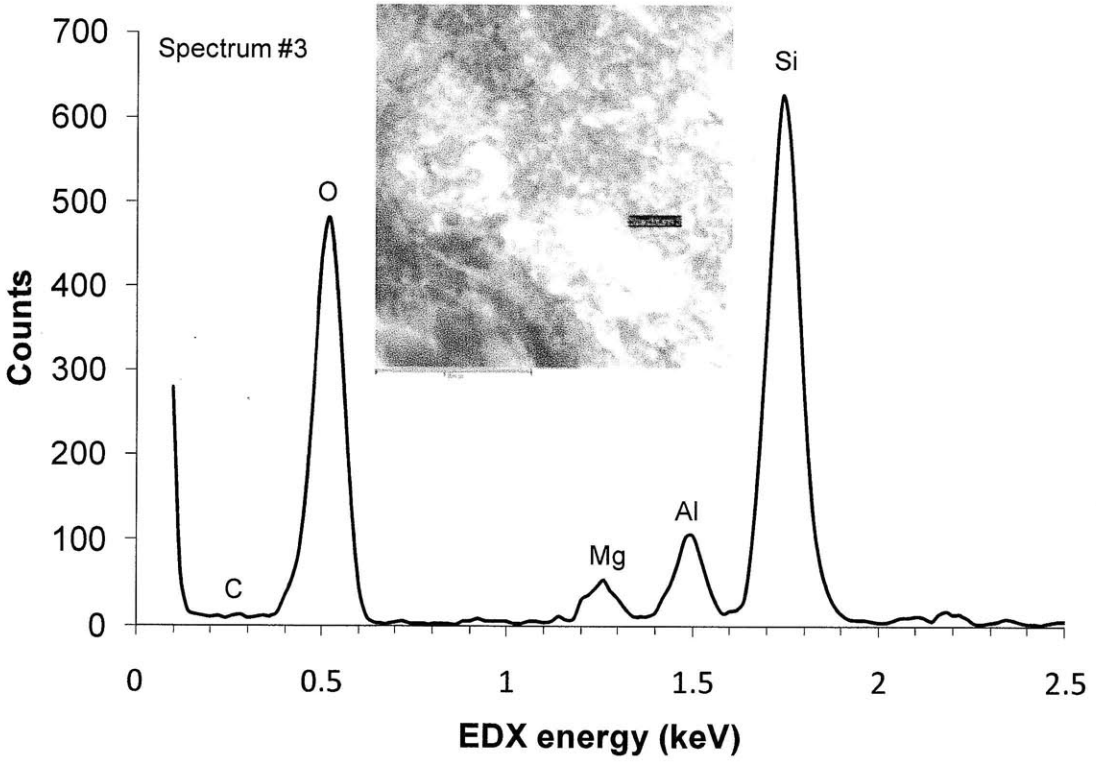

(d) Sample 20061103-Site#2: EDX spectrum at spot #3.

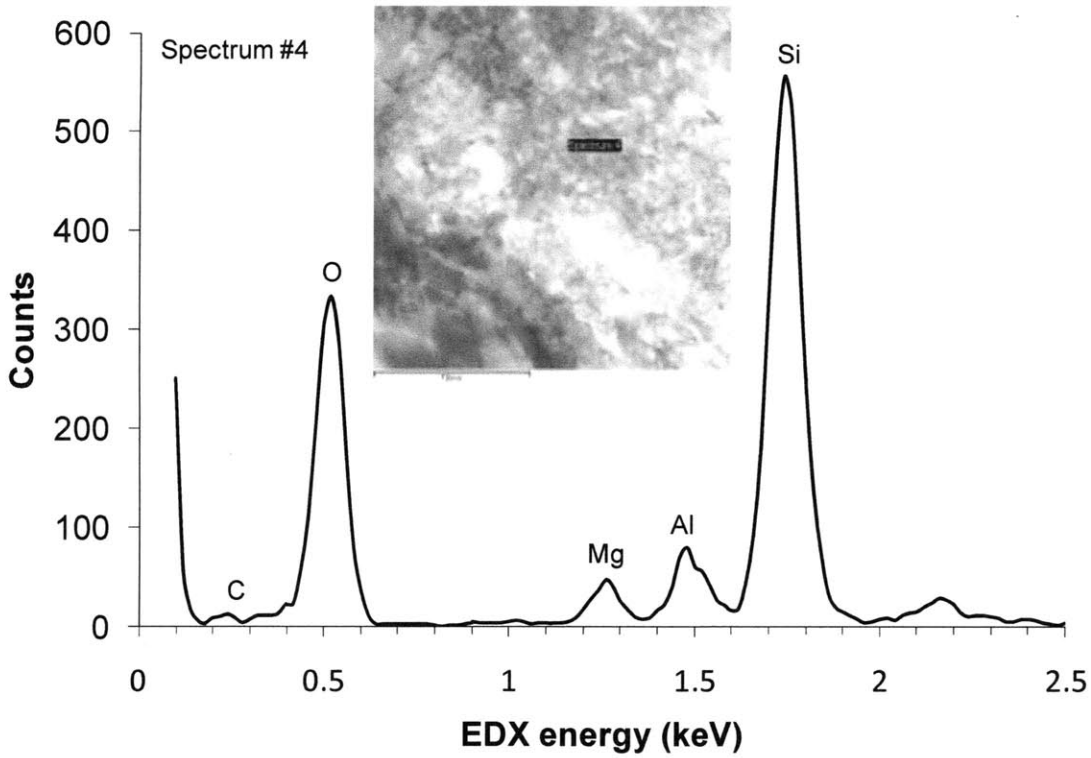

(e) Sample 20061103-Site#2: EDX spectrum at spot #4.

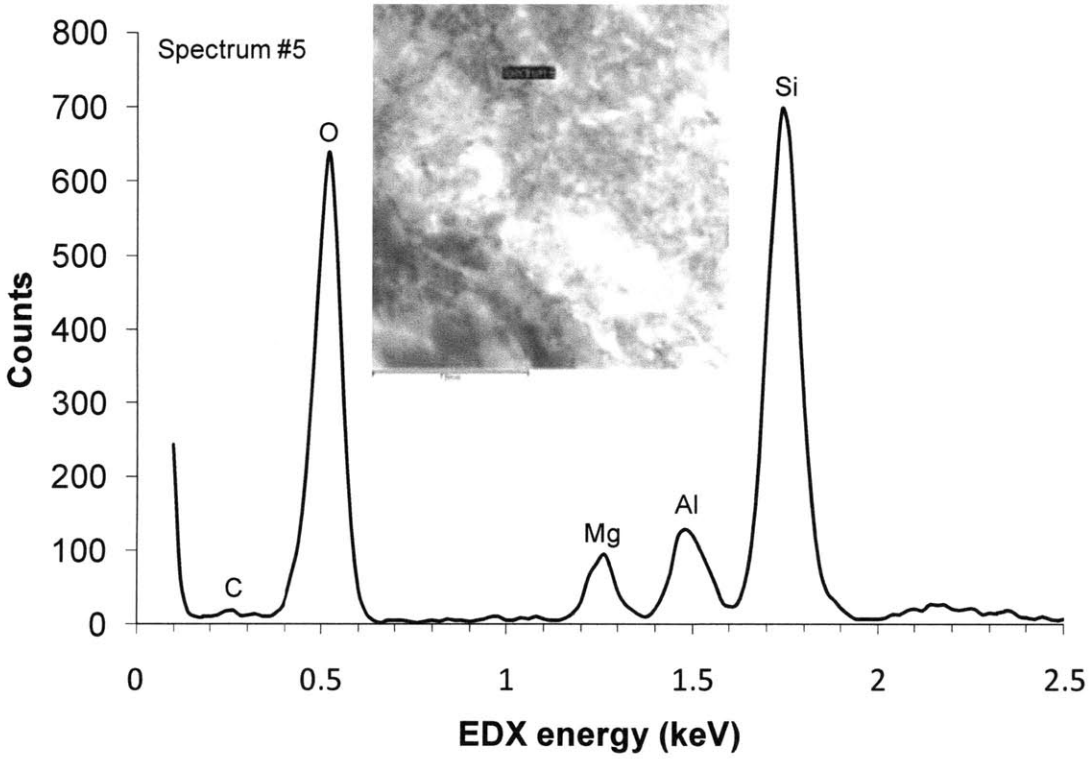

(f) Sample 20061103-Site#2: EDX spectrum at spot #5.

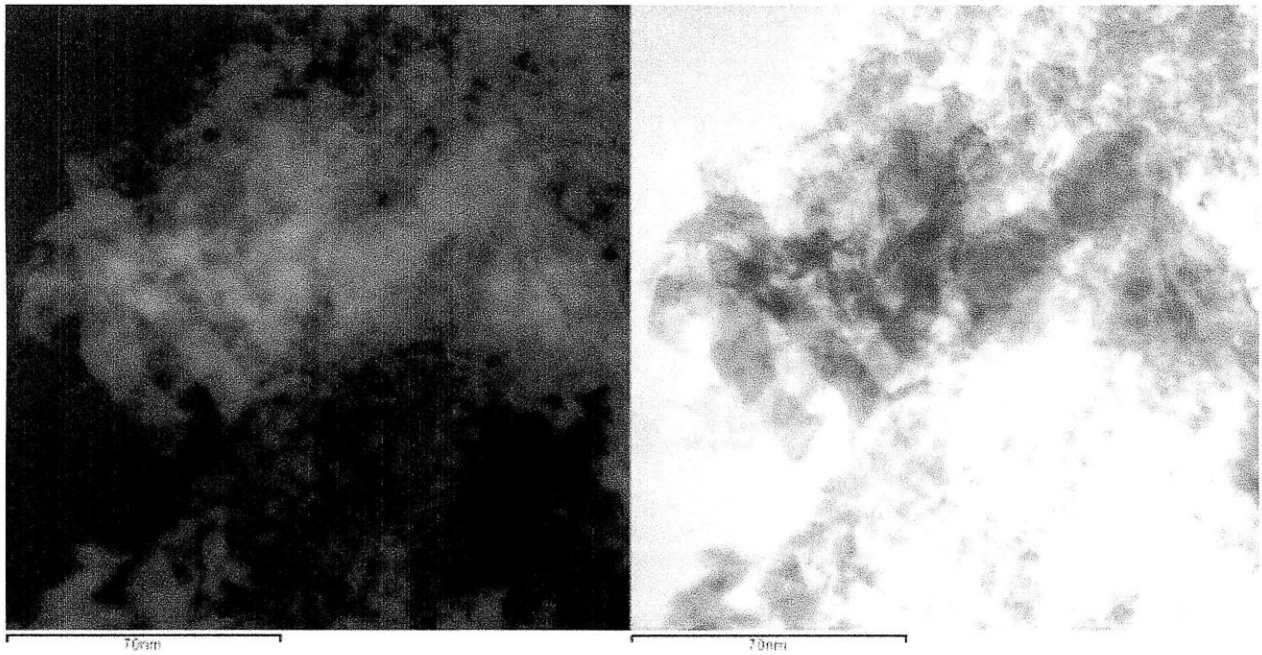

Figure A - 9. Soot-rich region in soot-amended sediment (20061103-Site#3).

(a) Original TEM image. A soot-rich region in NIST-soot (NIST SRM #1650 Diesel Particulate Matter) amended sediments (Boston Harbor #6, 180-250 μm) on lacey-SiO film (20061103-Site#3).

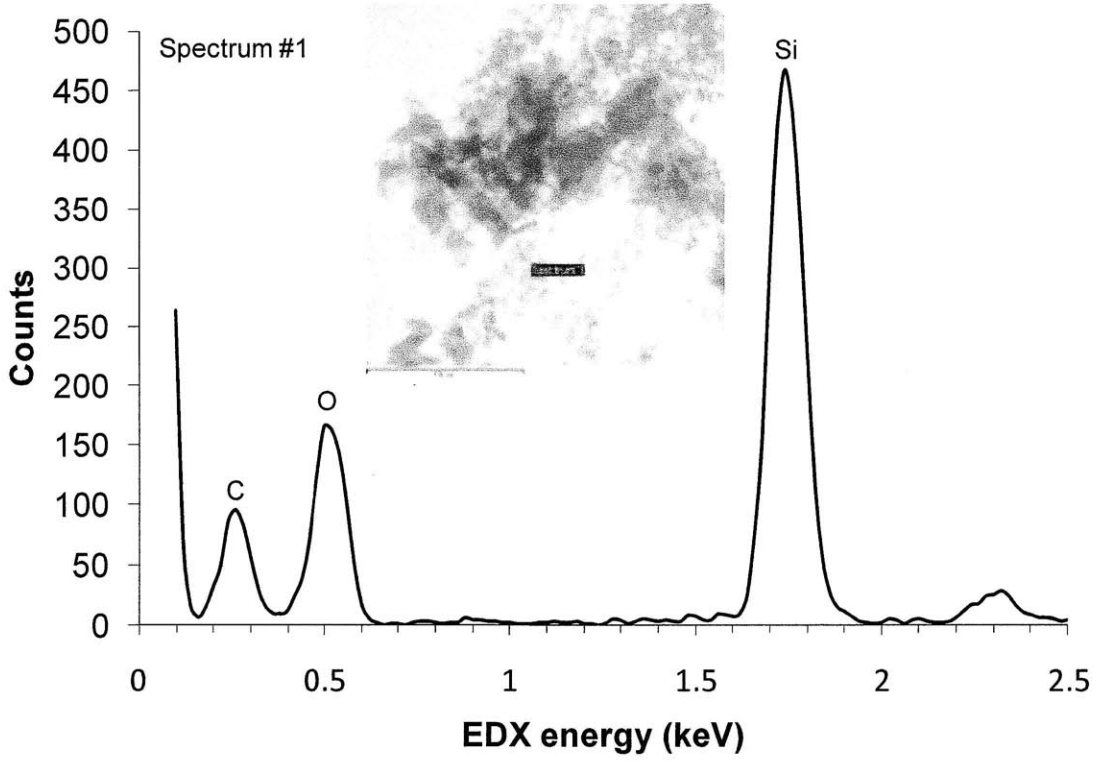

(b) Sample 20061103-Site#3: EDX spectrum at spot #1.

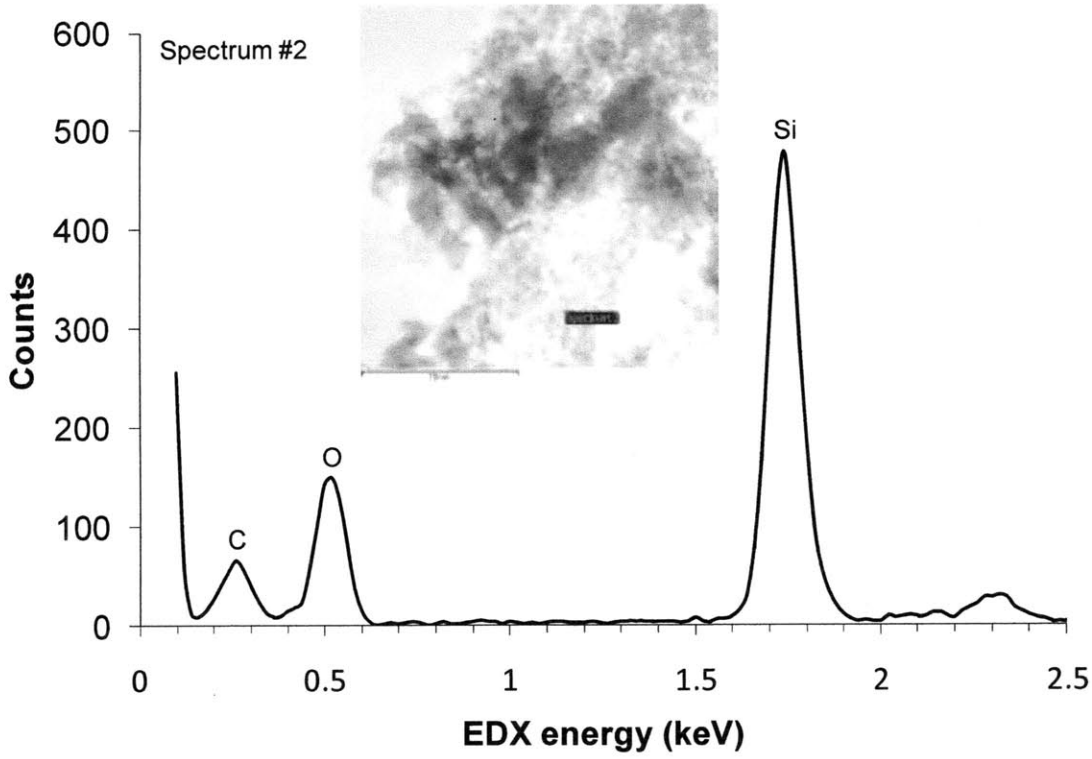

(c) Sample 20061103-Site#3: EDX spectrum at spot #2.

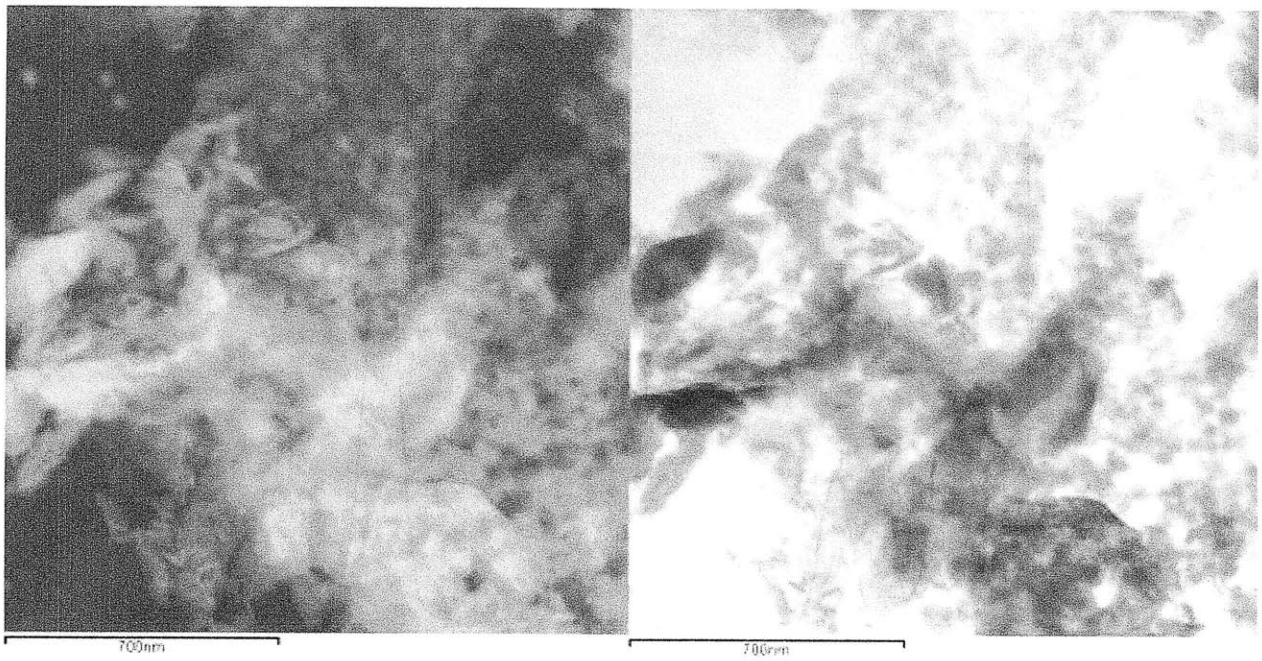

Figure A - 10. Soot-rich region in soot-amended sediment (20061103-Site#5).

(a) Original TEM image. A soot-rich region in NIST-soot (NIST SRM #1650 Diesel Particulate Matter) amended sediments (Boston Harbor #6, 180-250 μm) on lacey-SiO film (20061103-Site#5).

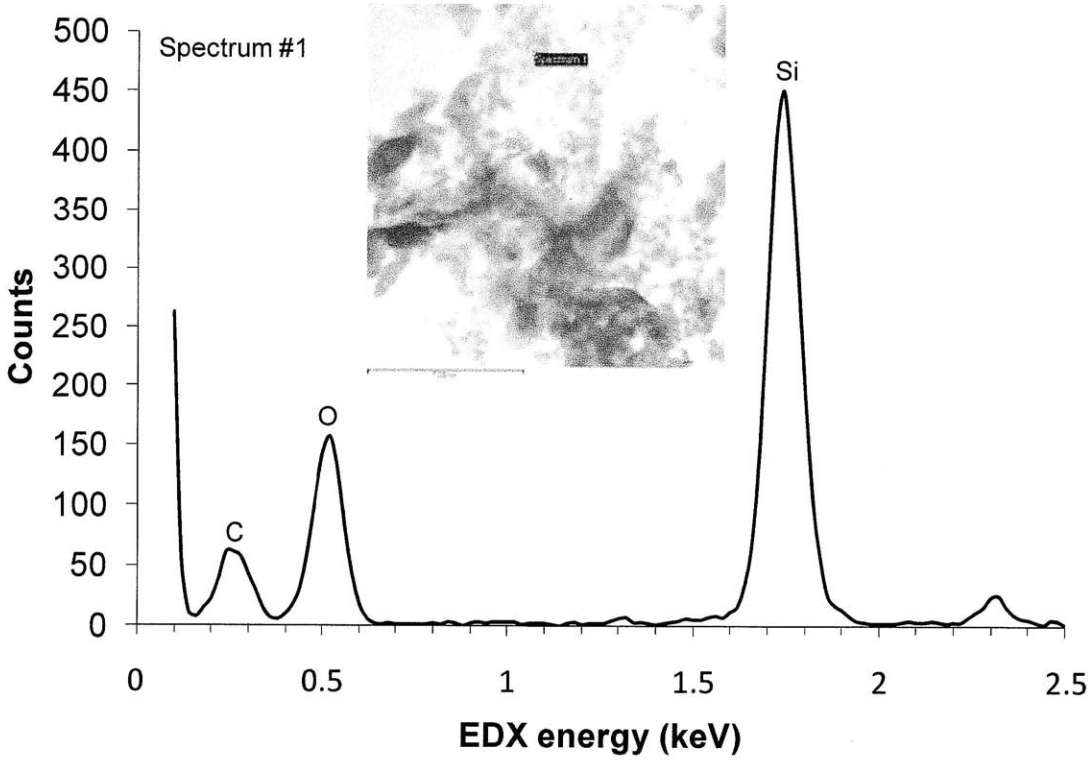

(b) Sample 20061103-Site#5: EDX spectrum at spot #1.

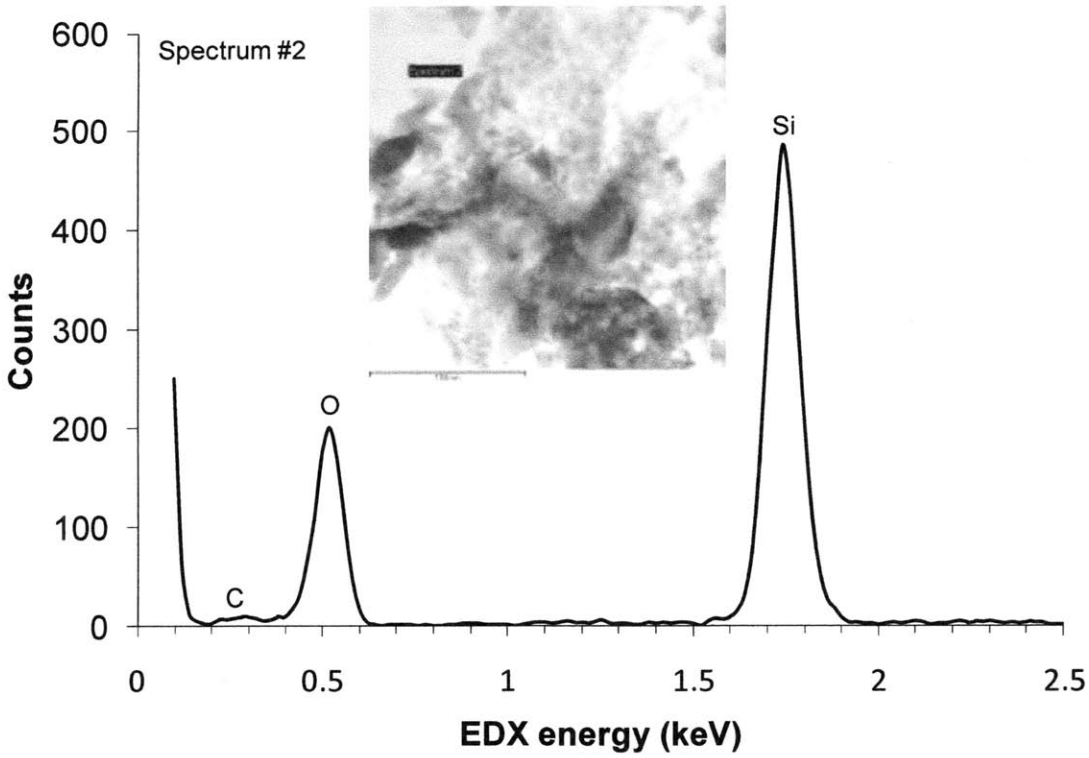

(c) Sample 20061103-Site#5: EDX spectrum at spot #2.

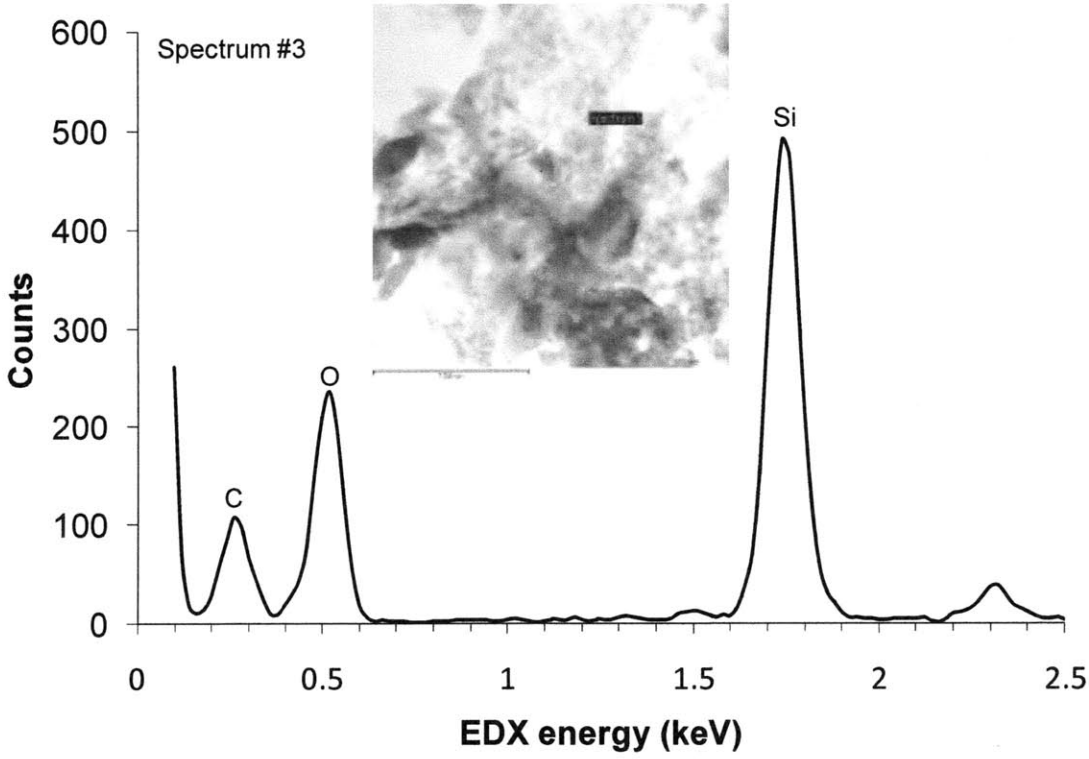

(d) Sample 20061103-Site#5: EDX spectrum at spot #3.

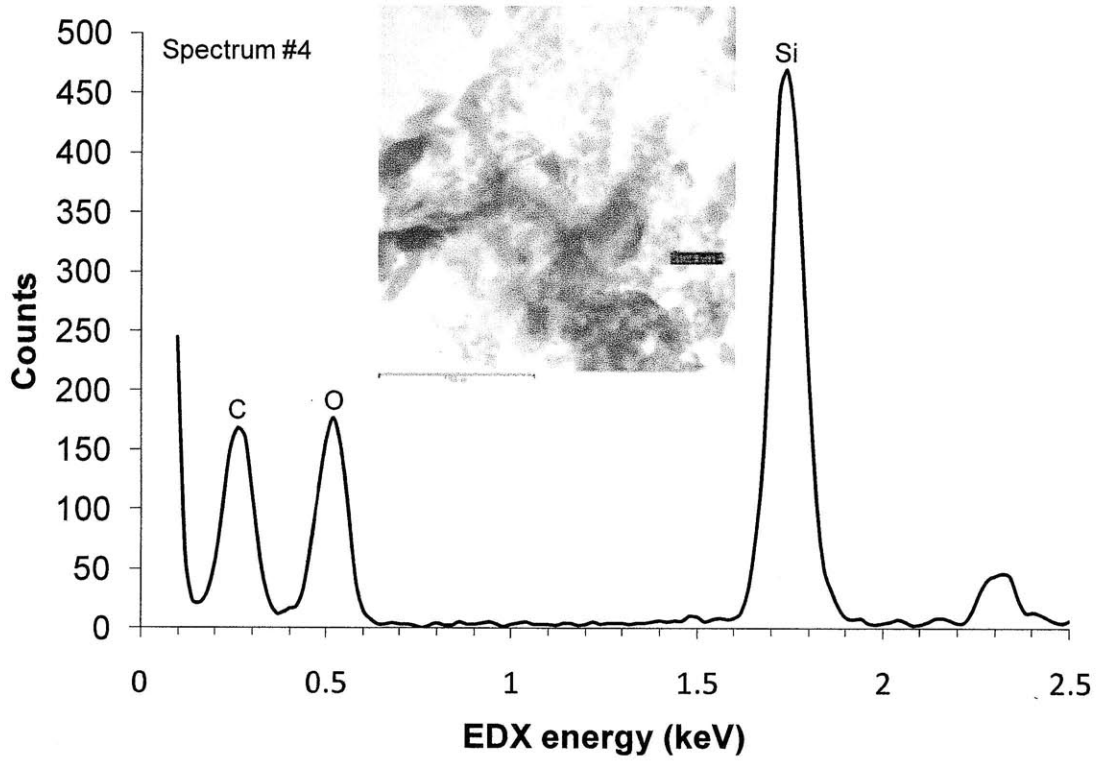

(e) Sample 20061103-Site#5: EDX spectrum at spot #4.

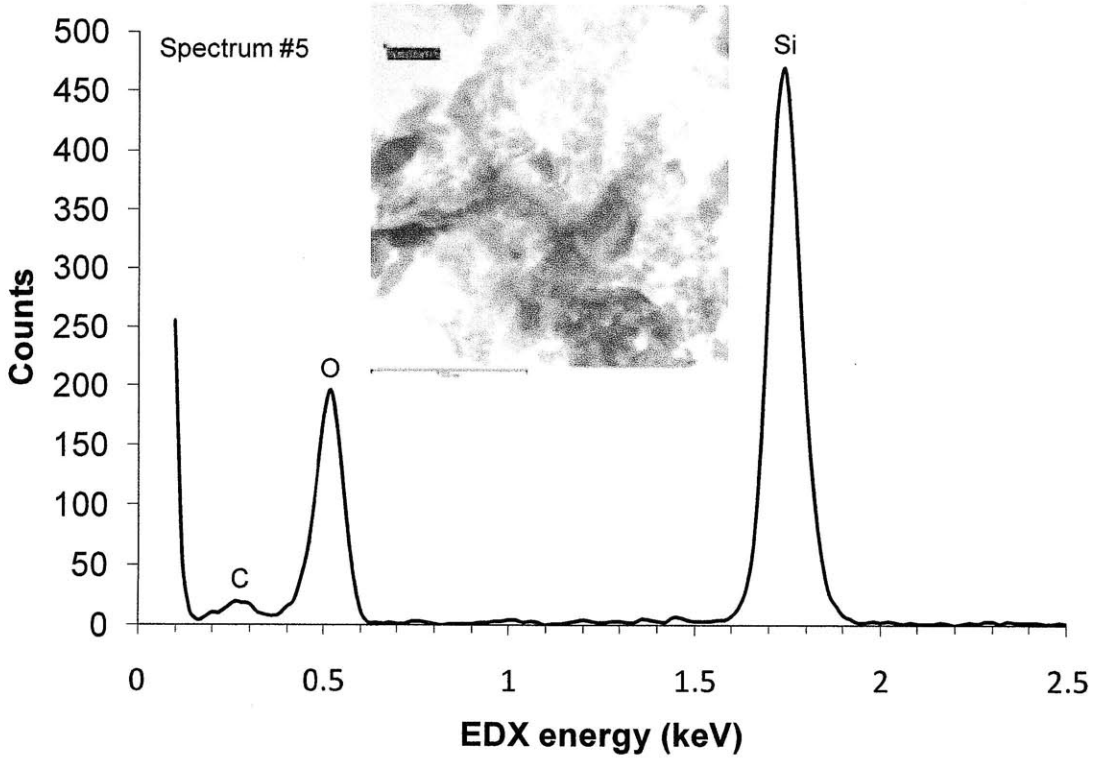

(f) Sample 20061103-Site#5: EDX spectrum at spot #5.

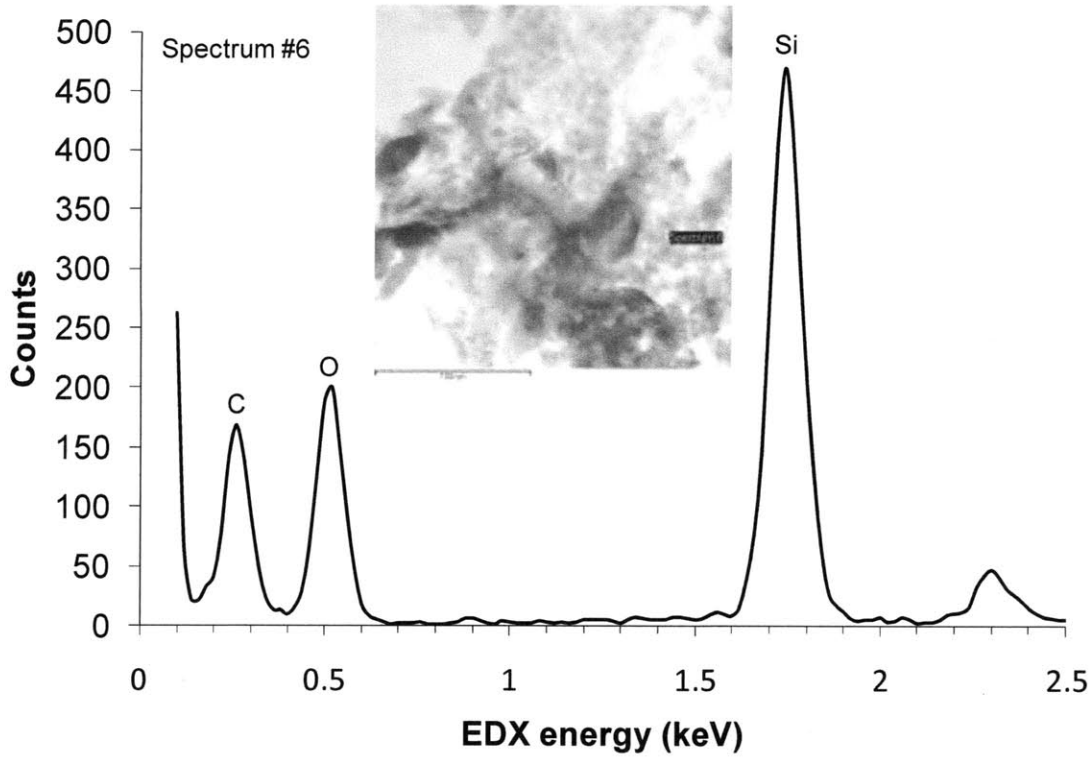

(g) Sample 20061103-Site#5: EDX spectrum at spot #6.

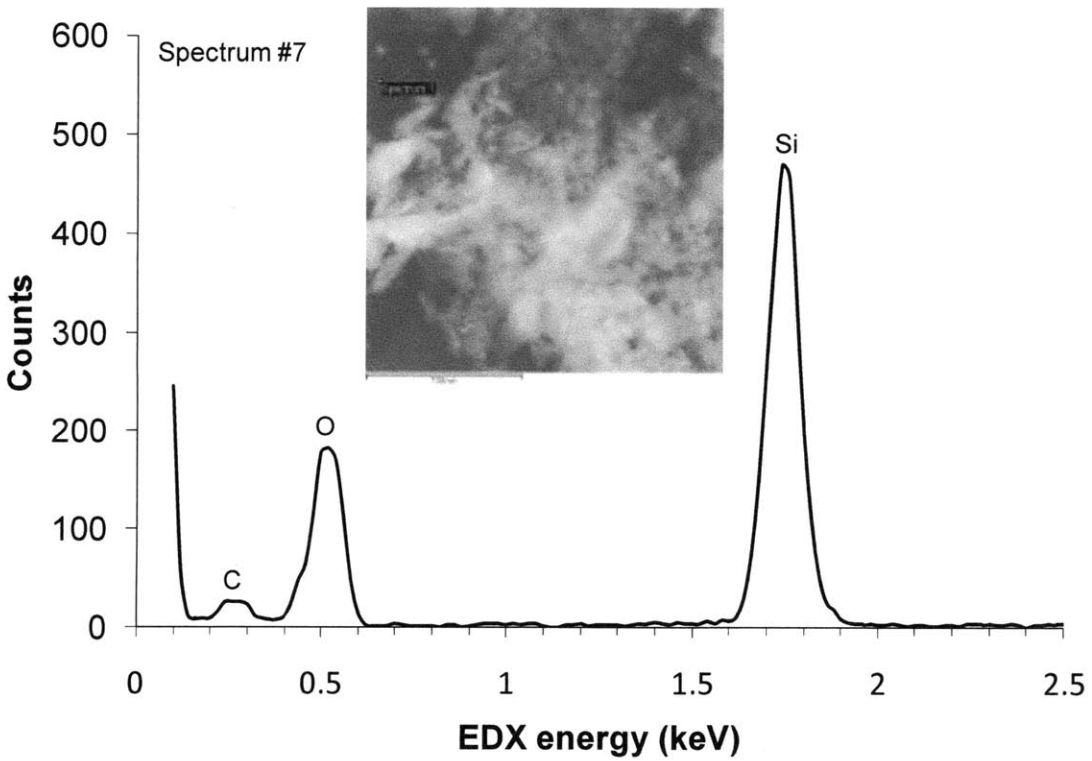

(h) Sample 20061103-Site#5: EDX spectrum at spot #7.

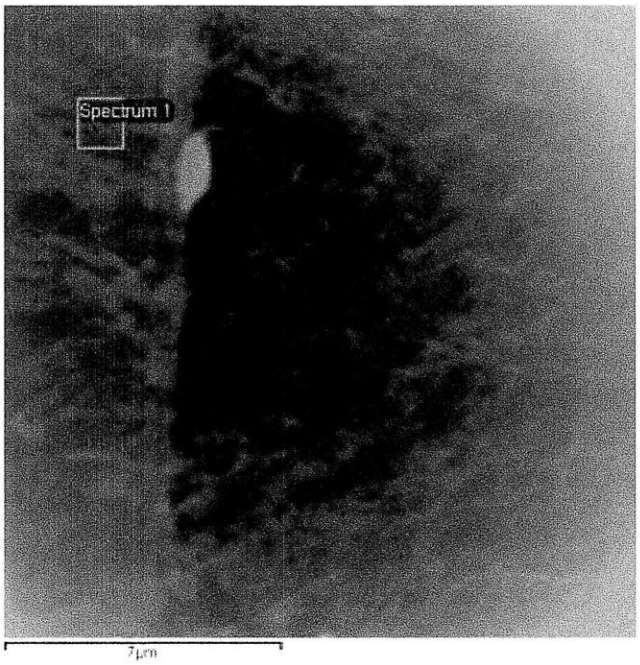

Figure A - 11. Nicotinamide (20061108-Site#11).

(a) Original TEM image. Nicotinamide ($C_6H_6N_2O$) on lacey-SiO film (20061108-Site#11).

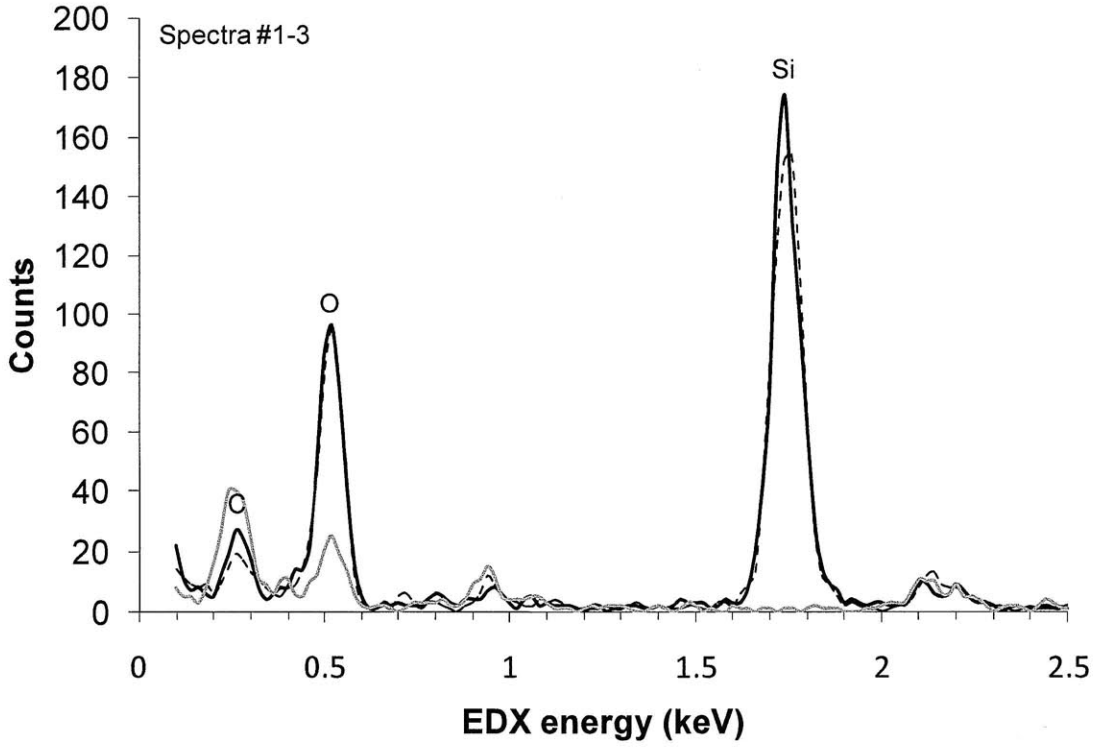

(b) Sample 20061108-Site#11: EDX spectrum at spot #3.

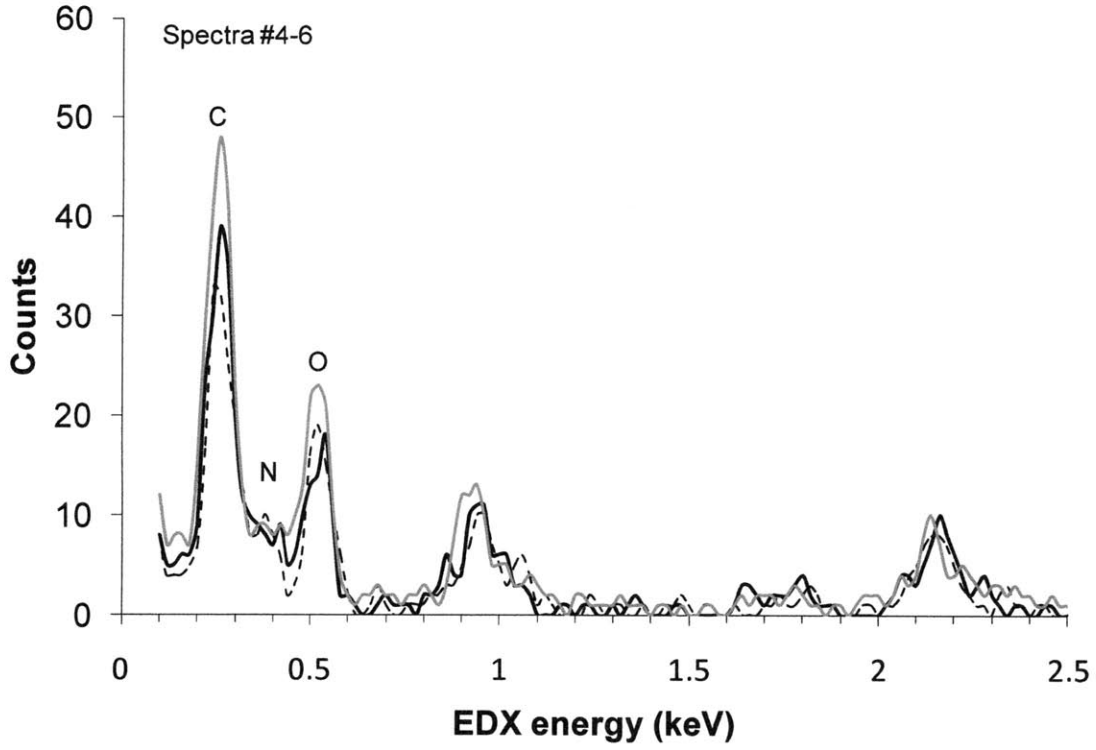

(c) Sample 20061108-Site#11: EDX spectra at spot #4 to #6.

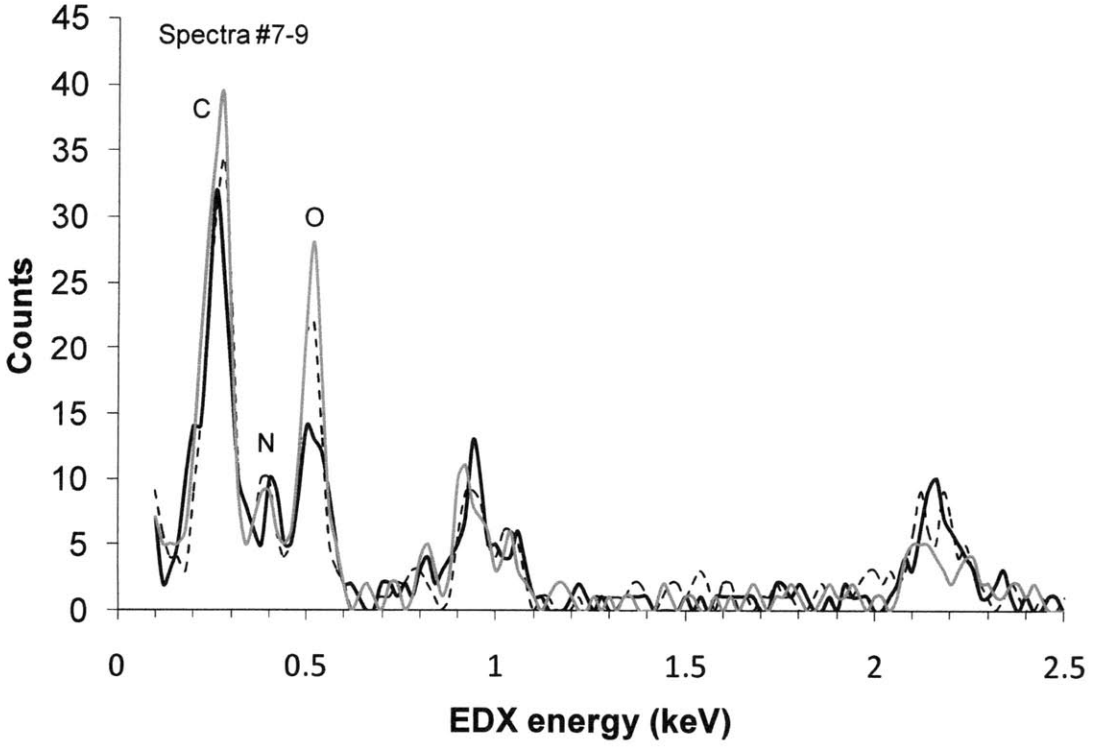

(d) Sample 20061108-Site#11: EDX spectra at spot #7 to #9.

Appendix B: STEM-EDX Elemental Maps

20061010-Site #5 1037
20061010-Site #9 1041
20061010-Site #14 1045
20061013-Site #3 1049
20061013-Site #6 1053
20061013-Site #8 1057
20061013-Site #10 1061
20061013-Site #12 1065
20061019-Site #11 1069
20061019-Site #13 1073
Lignocellulosic Char-Site #1 1077
Lignocellulosic Char-Site #6 1081
Melanoidin-Site #1 1085
Melanoidin-Site #3 1089

20061010-Site #5

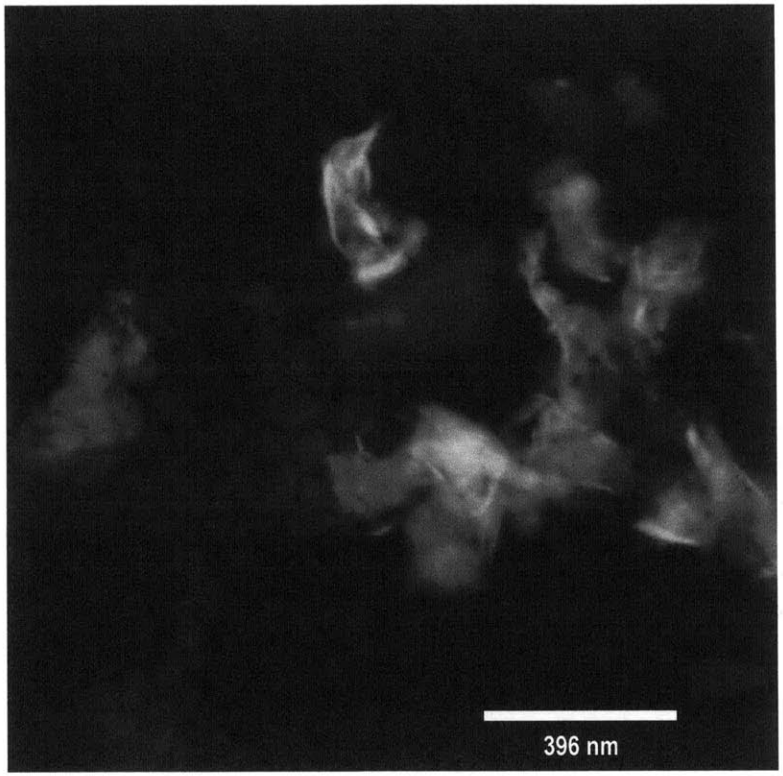

Sample: NIST soot (SRM 1650) amended Boston Harbor #6 sediment (180-250 μm)

Site Description: Apparent mineral phases with soot clusters

Dimension: 1.585×1.585 μm (256×256 pixels)

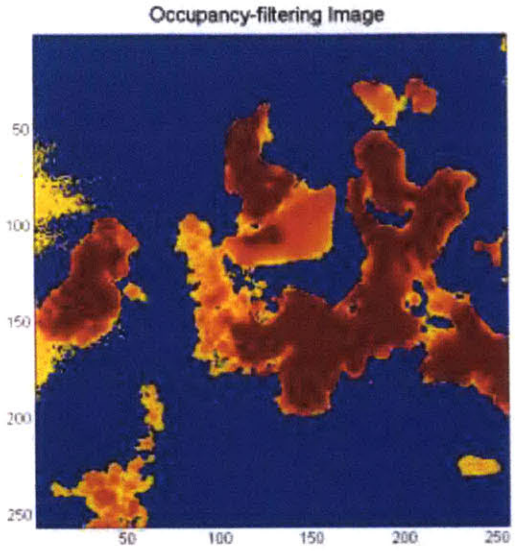
Occupancy-filtering Image
50
100
150
200
250
50
100
150
200
250

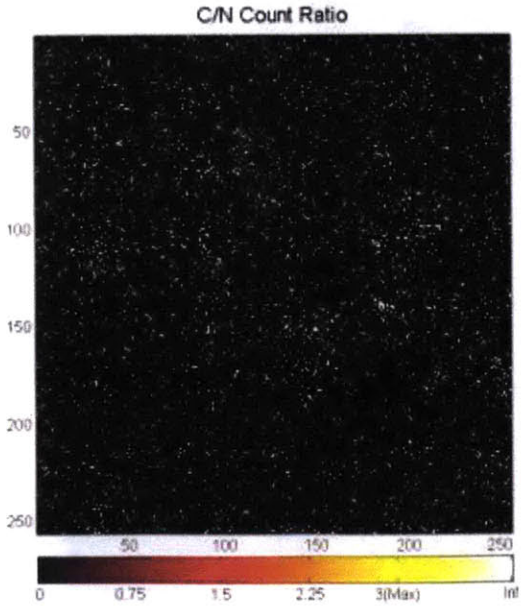
C/N Count Ratio
50
100
150
200
250
50
100
150
200
250
0
0.75
1.5
2.25
3(Max)
Inf

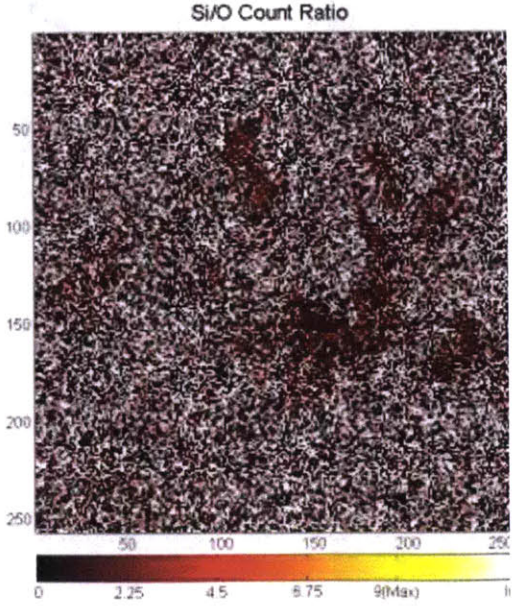
Si/O Count Ratio
50
100
150
200
250
50
100
150
200
0
2.25
4.5
6.75
9(Max)

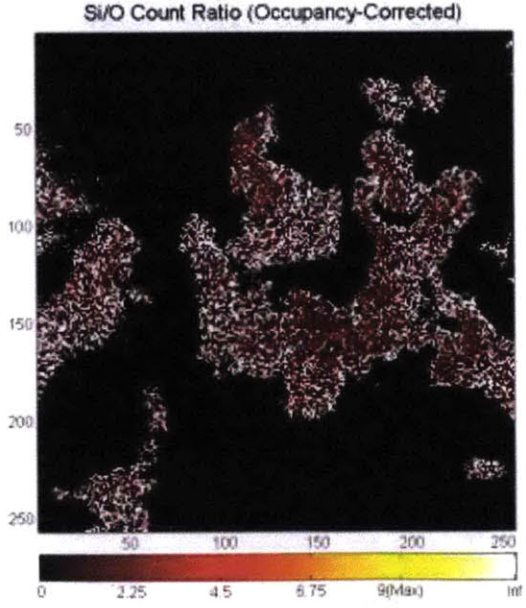
Si/O Count Ratio (Occupancy-Corrected)
50
100
150
200
250
50
100
150
200
250
0
2.25
4.5
6.75
9(Max)
Inf

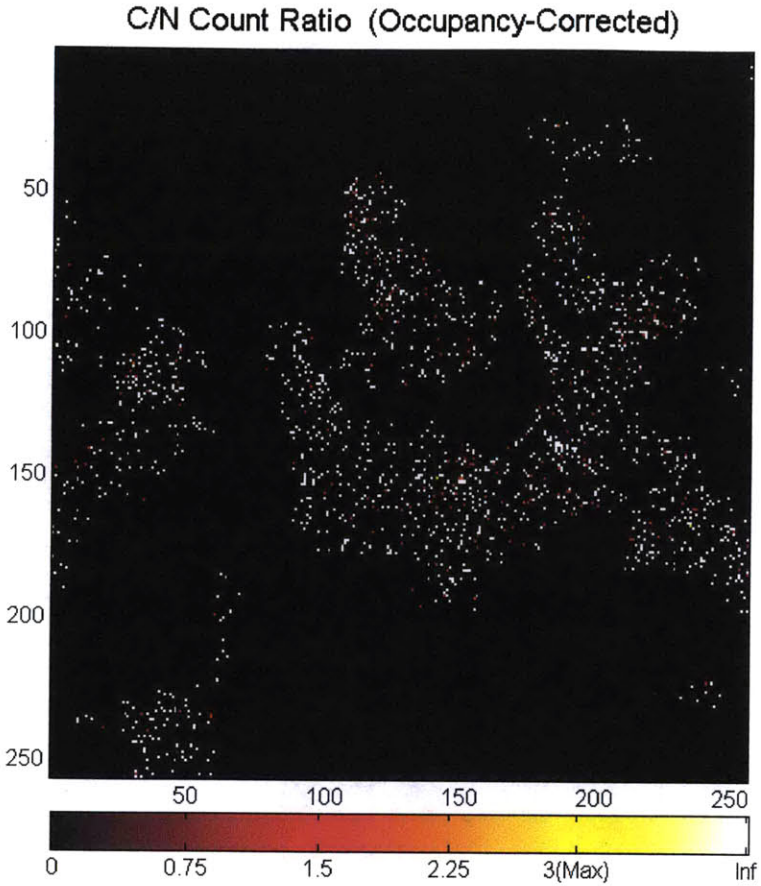

(a) No N 'noise' reduction

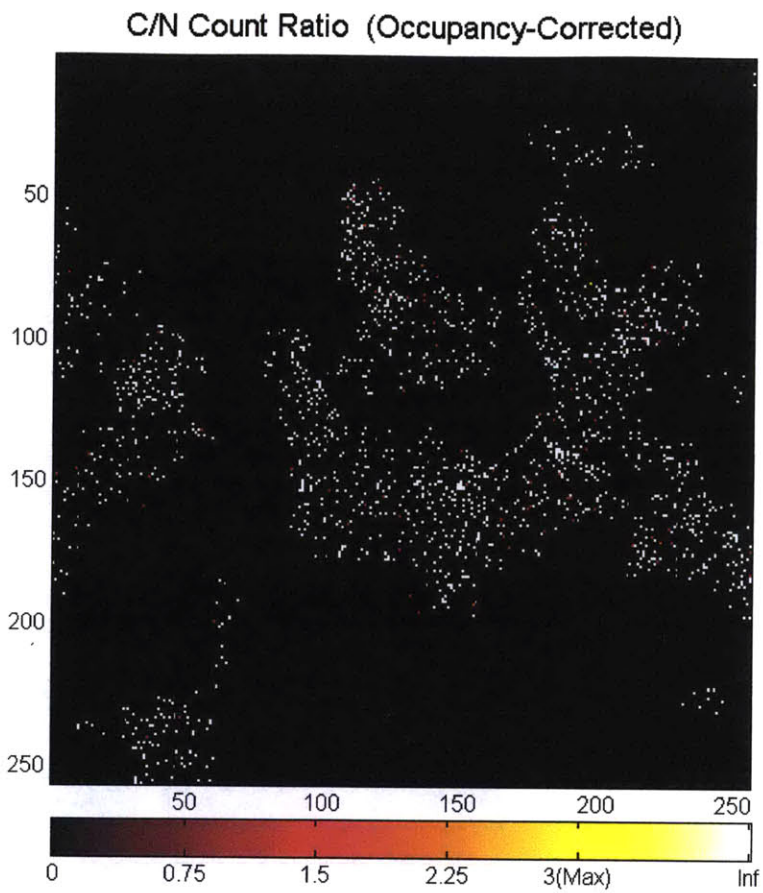

(b) N 'noise' reduction (by 1)

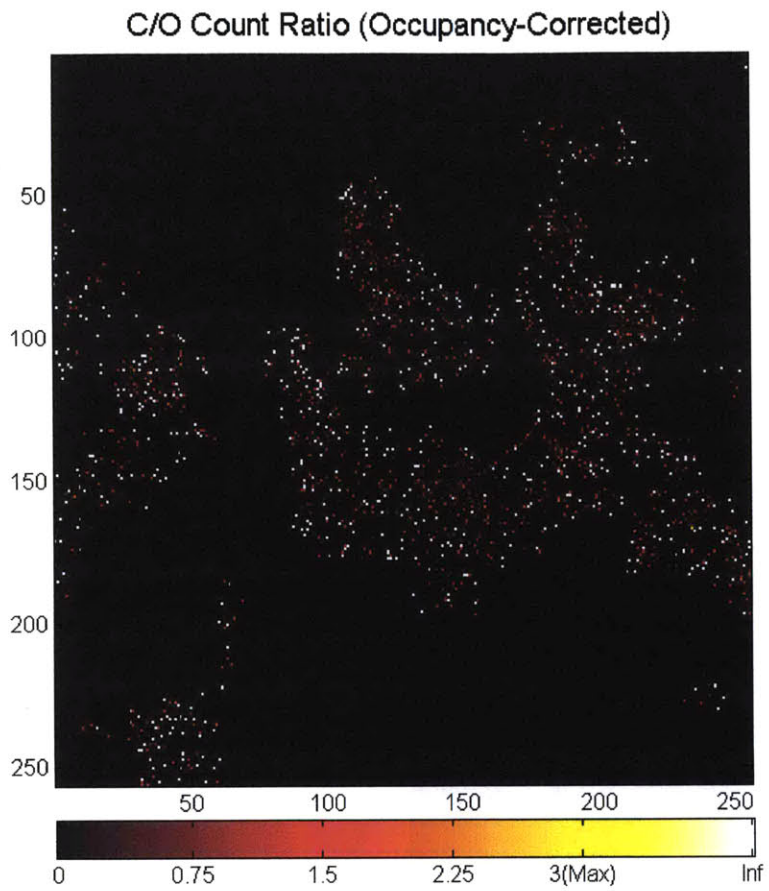

(a) No background O correction

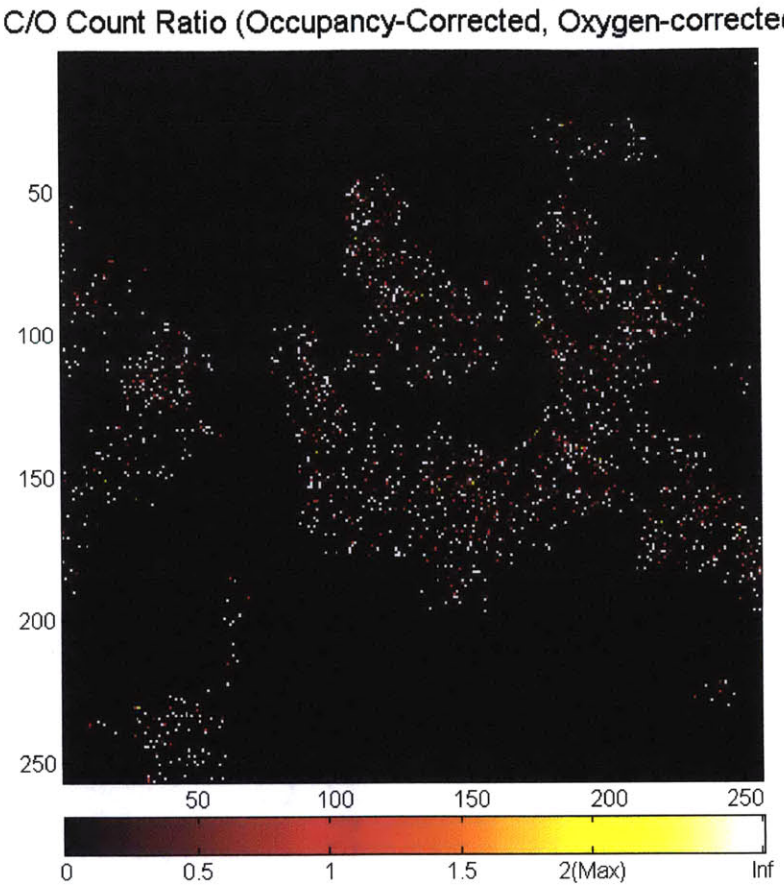

(b) Background O corrected

20061010-Site #9

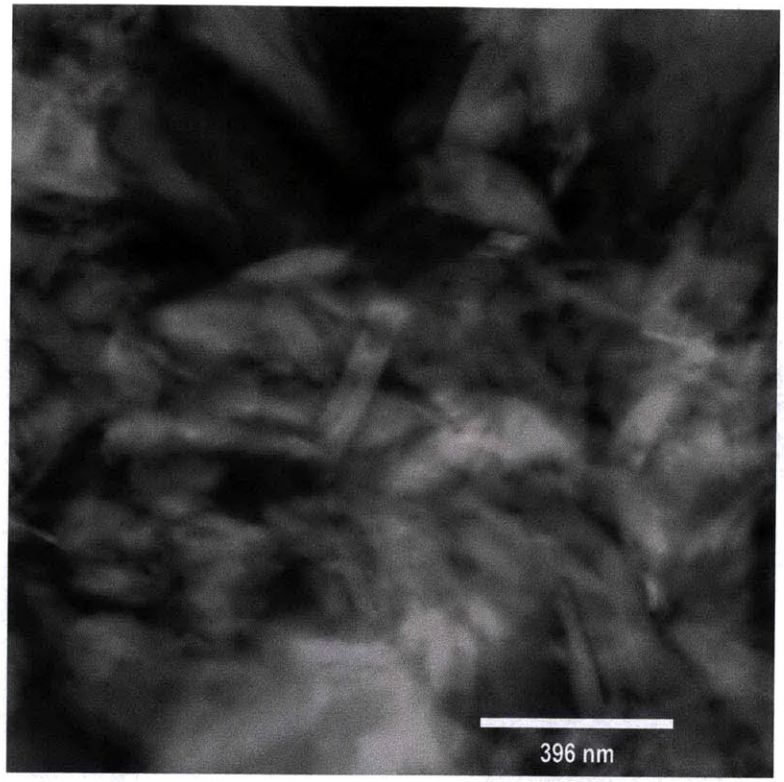

Sample: NIST soot (SRM 1650) amended Boston Harbor #6 sediment (180-250 μm)

Site Description: Apparent mineral phases

Dimension: 1.585×1.585 μm (256×256 pixels)

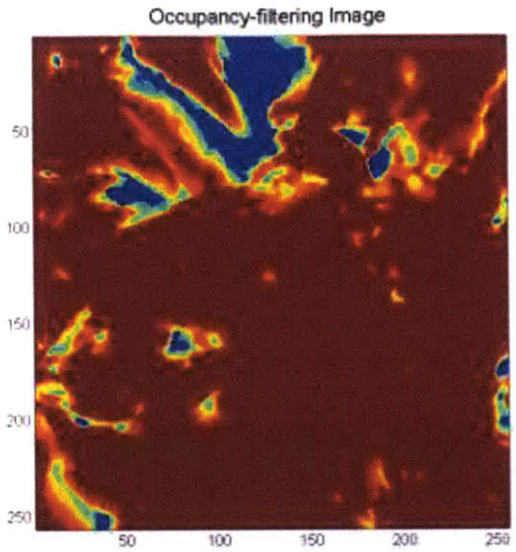
Occupancy-filtering Image
50
100
150
200
250
50
100
150
200
250

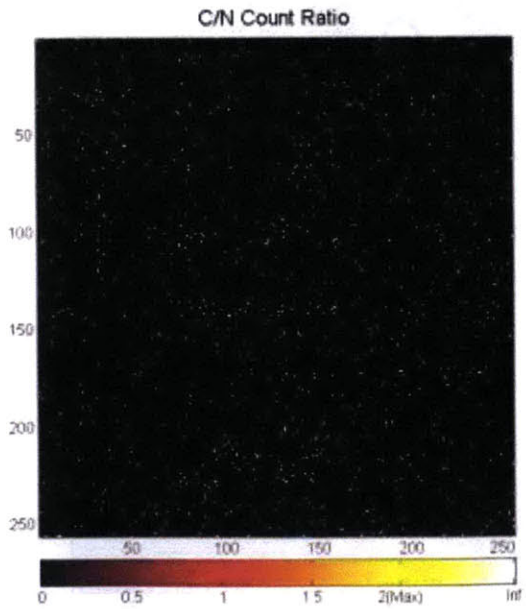
C/N Count Ratio
50
100
150
200
250
50
100
150
200
250
0
0.5
1
1.5
2(Max)
Inf

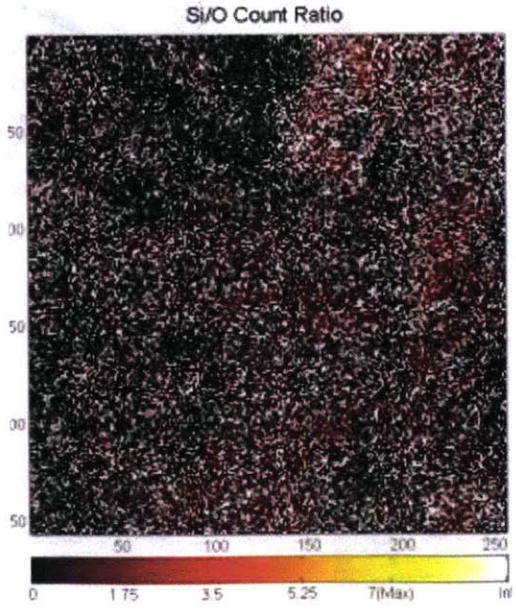
Si/O Count Ratio
50
100
150
200
250
50
100
150
200
250
0
1.75
3.5
5.25
7(Max)
Inf

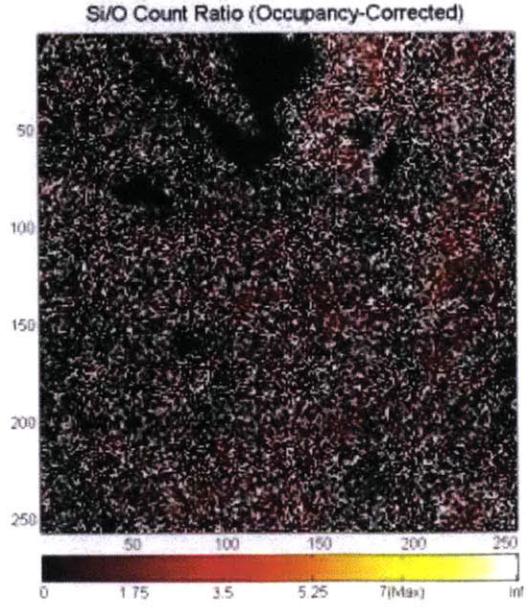
Si/O Count Ratio (Occupancy-Corrected)
50
100
150
200
250
50
100
150
200
250
0
1.75
3.5
5.25
7(Max)
Inf

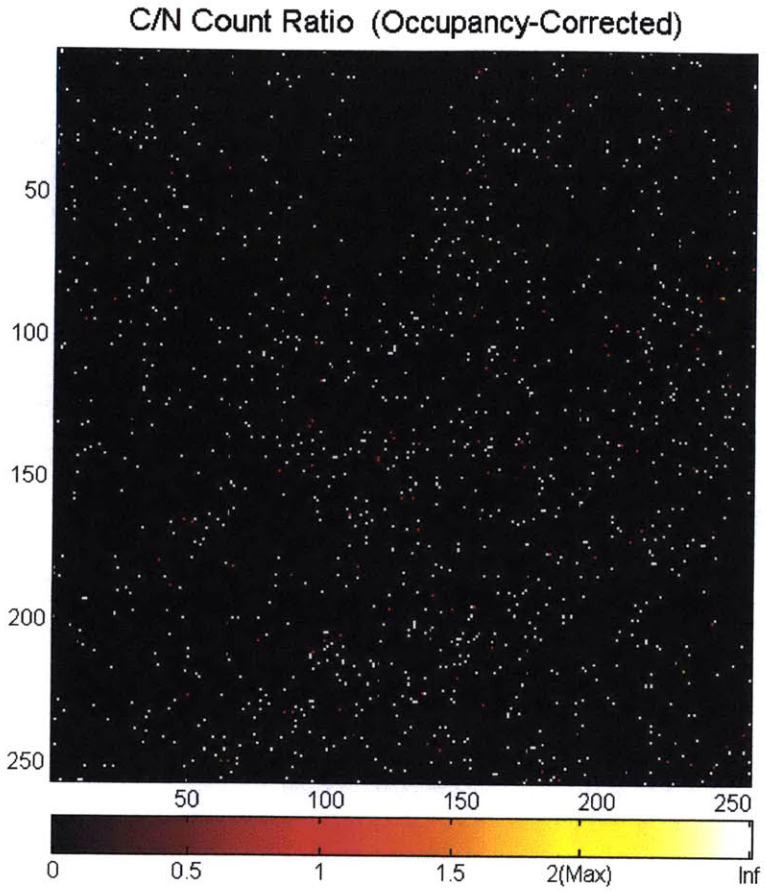

(a) No N 'noise' reduction

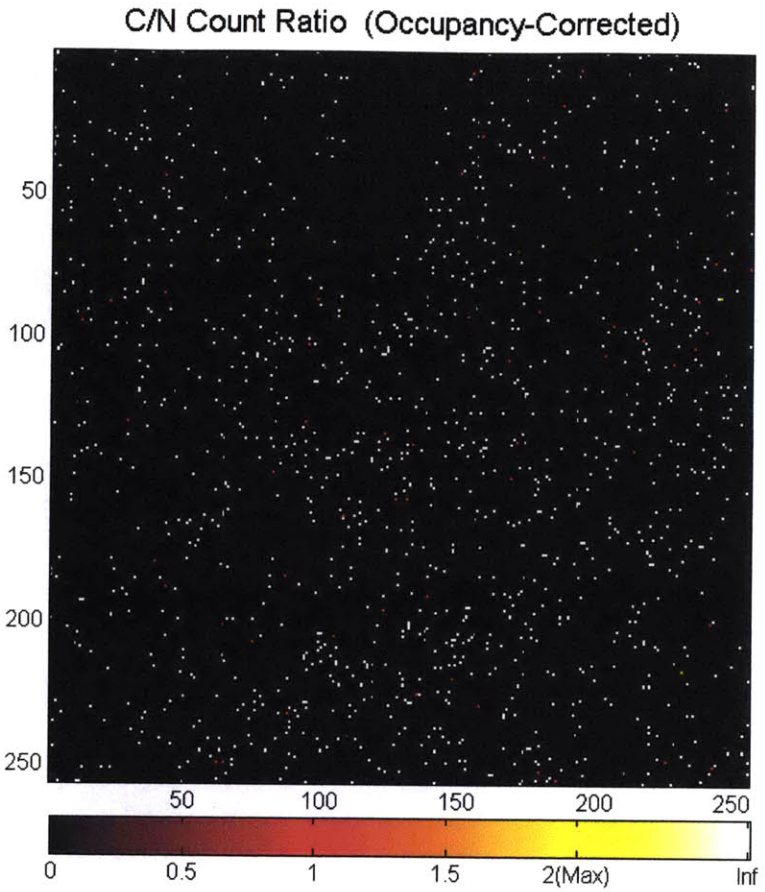

(b) N 'noise' reduction (by 1)

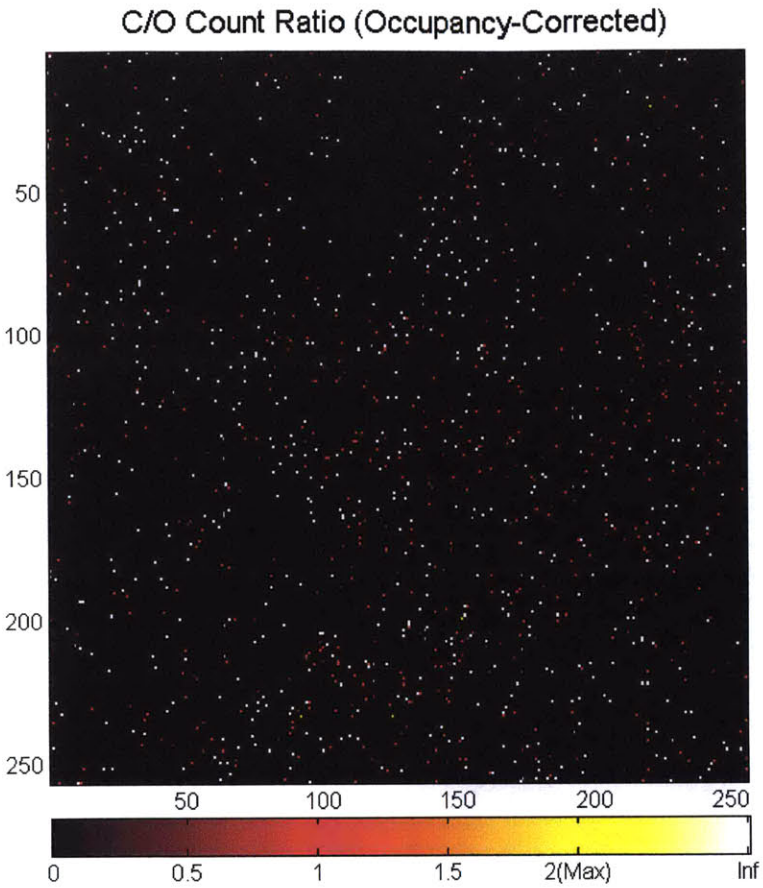

(a) No background O correction

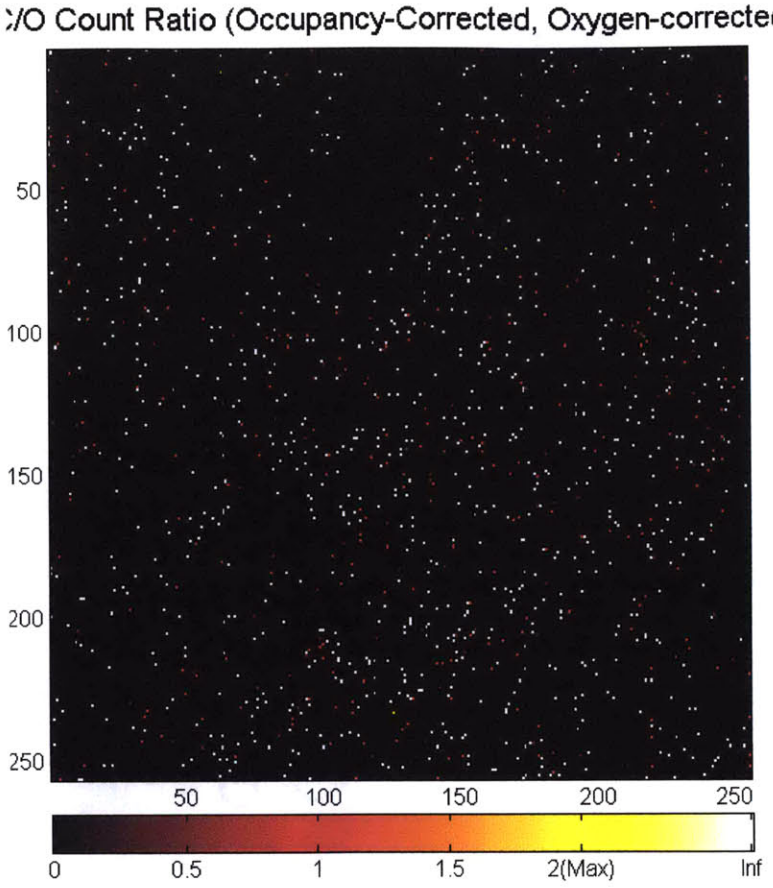

(b) Background O corrected

20061010-Site #14

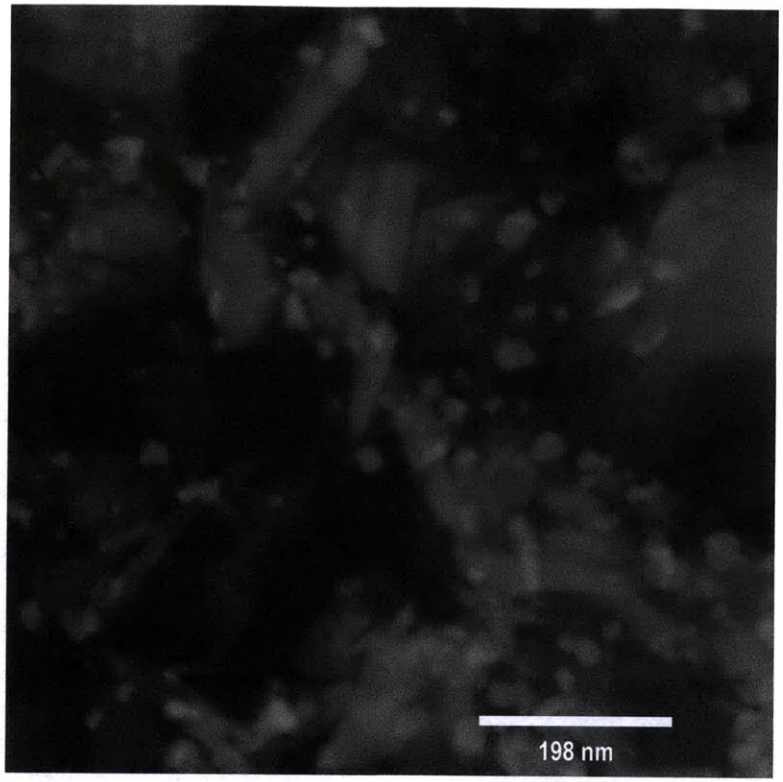

Sample: NIST soot (SRM 1650) amended Boston Harbor #6 sediment (180-250 μm)

Site Description: Apparent mineral phases

Dimension: 0.793×0.793 μm (256×256 pixels)

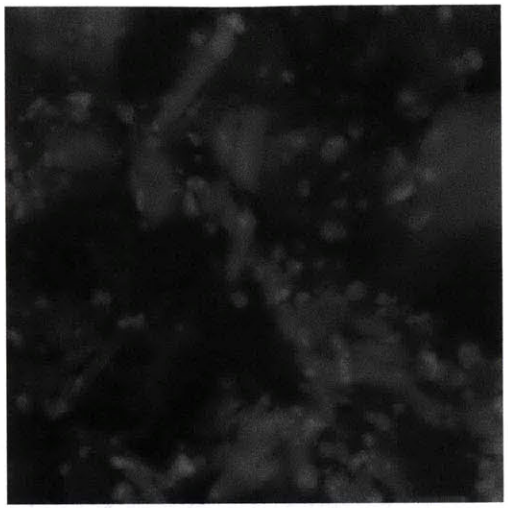

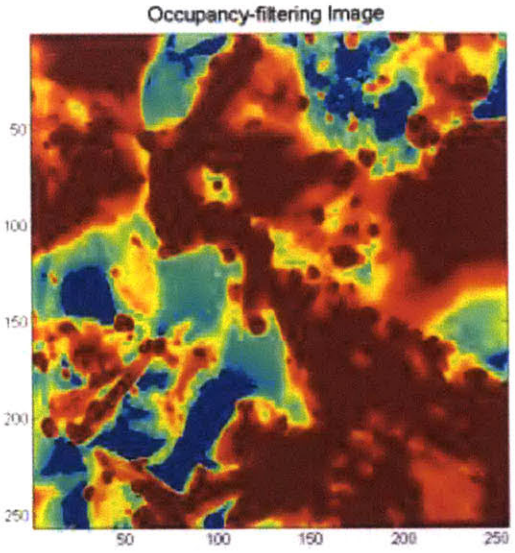
Occupancy-filtering Image
50
100
150
200
250
50
100
150
200
250

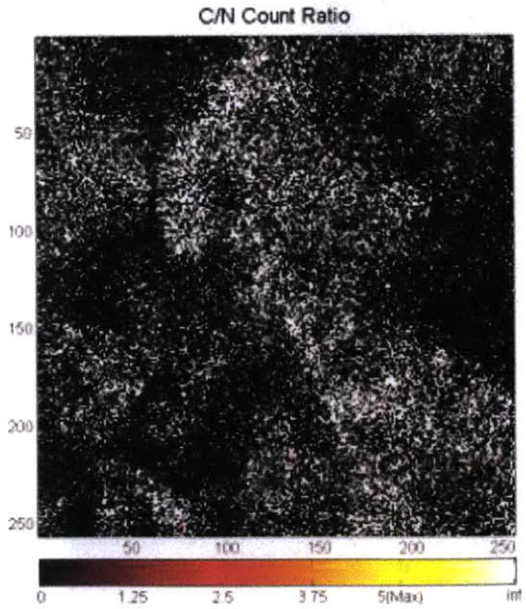
C/N Count Ratio
50
100
150
200
250
50
100
150
200
250
0
1.25
2.5
3.75
5(Max)
inf

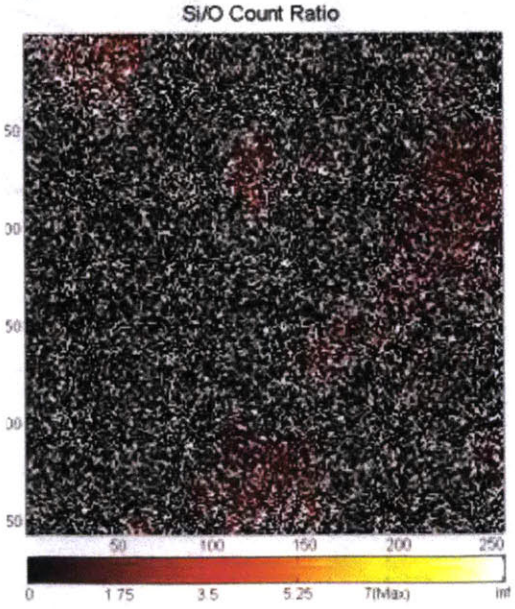
Si/O Count Ratio
50
100
150
200
250
50
100
150
200
250
0
1.75
3.5
5.25
7(Max)
inf

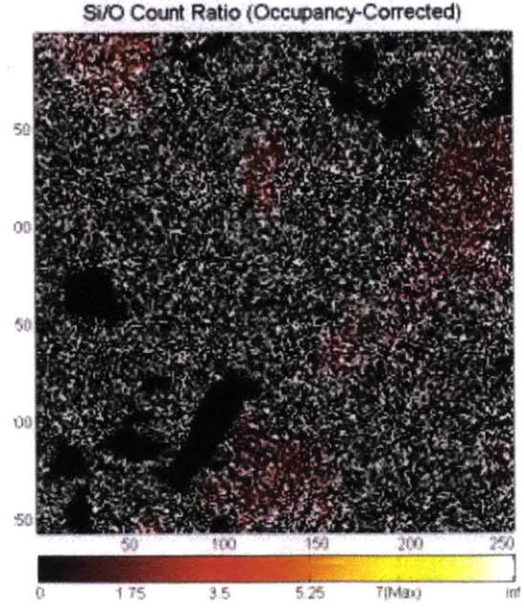
Si/O Count Ratio (Occupancy-Corrected)
50
100
150
200
250
50
100
150
200
250
0
1.75
3.5
5.25
7(Max)
inf

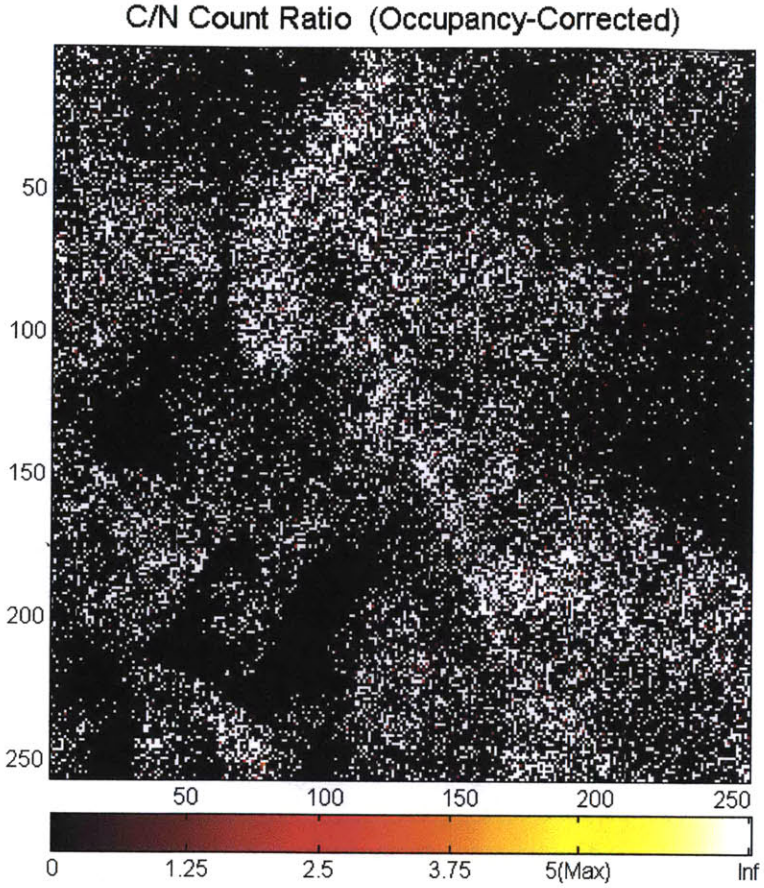

(a) No N 'noise' reduction

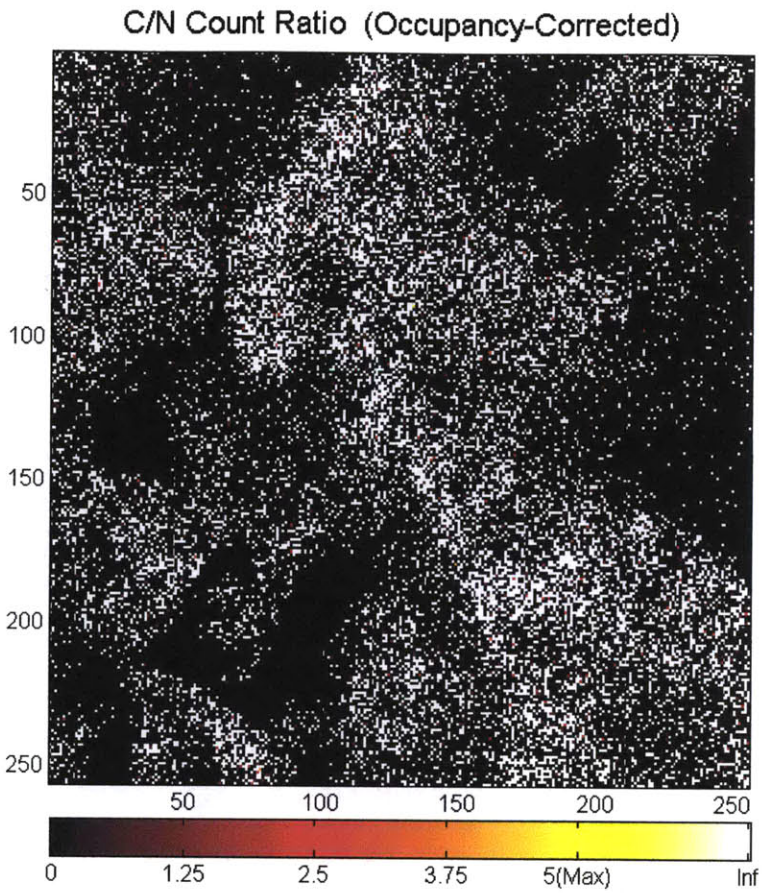

(b) N 'noise' reduction (by 1)

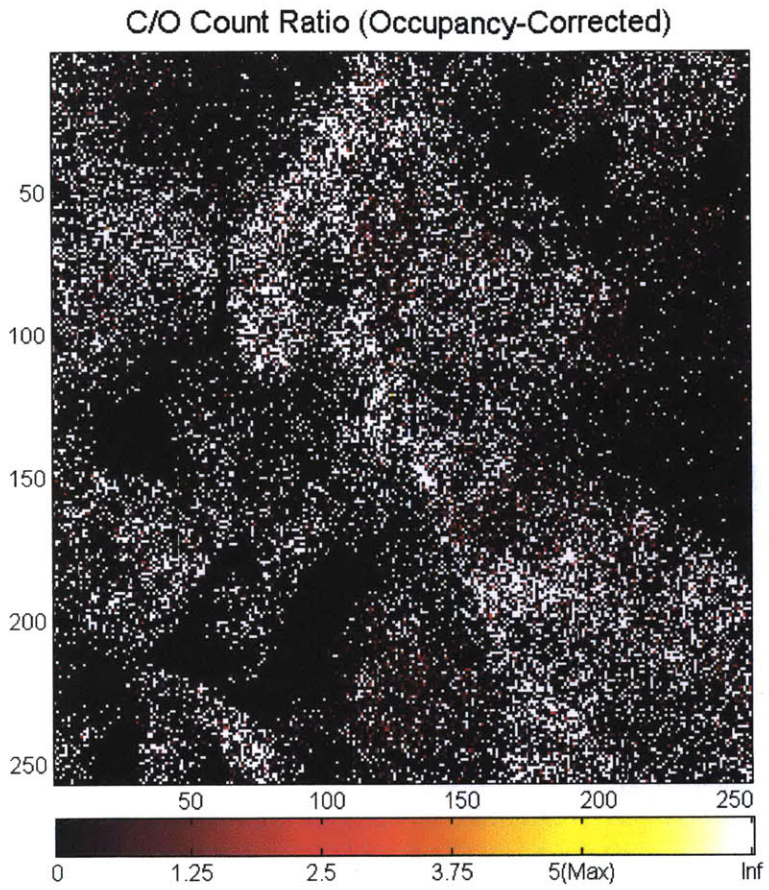

(a) No background O correction

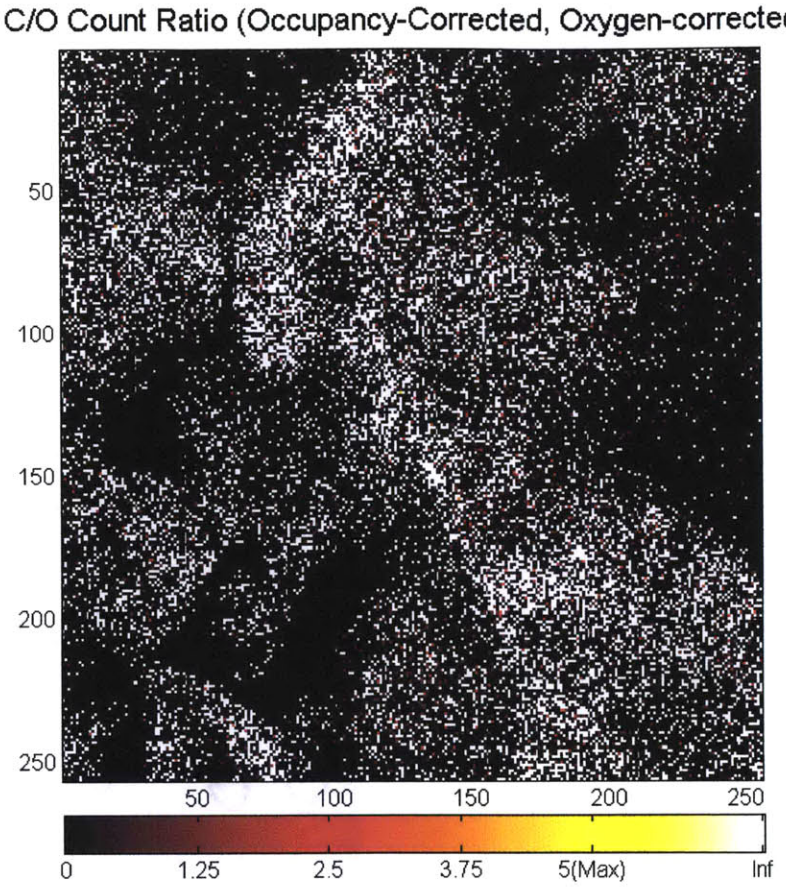

(b) Background O corrected

20061013-Site #3

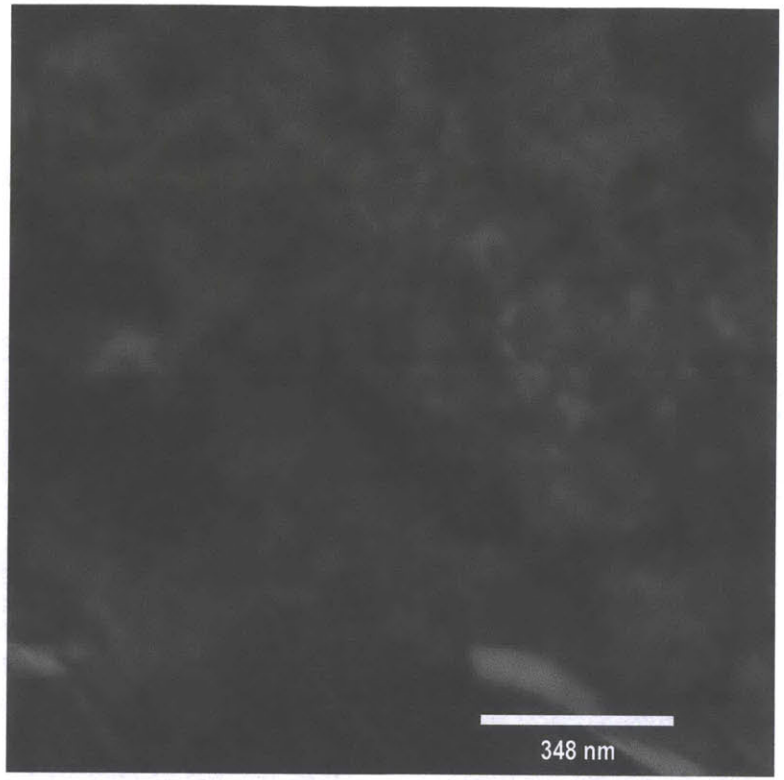

Sample: NIST soot (SRM 1650) amended Boston Harbor #6 sediment (180-250 μm)

Site Description: Soot clusters (dominant) with minor mineral phases

Dimension: 1.390×1.390 μm (256×256 pixels)

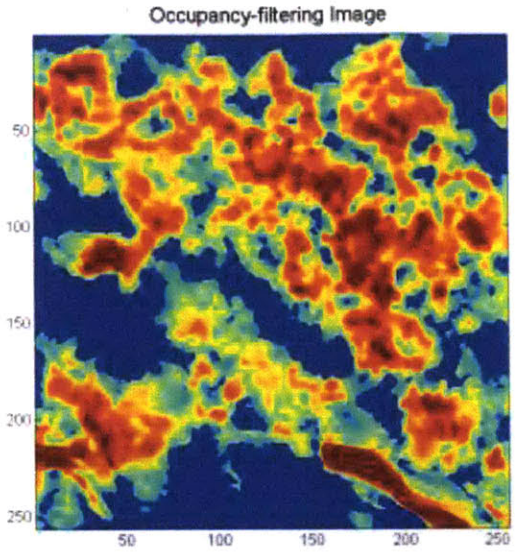
Occupancy-filtering Image
50
100
150
200
250
50
100
150
200
250

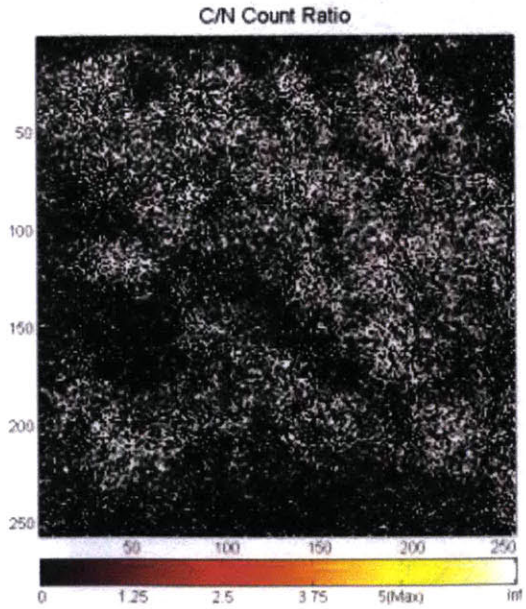
C/N Count Ratio
50
100
150
200
250
50
100
150
200
250
0
1.25
2.5
3.75
5(Max)
inf

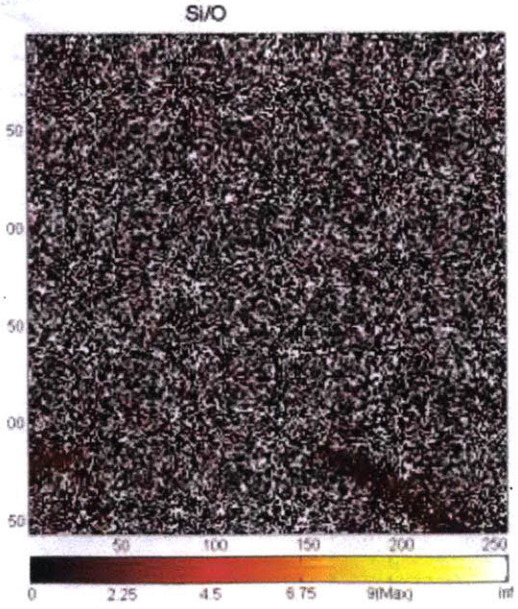
Si/O
50
00
50
00
50
50
100
150
200
250
0
2.25
4.5
6.75
9(Max)
inf

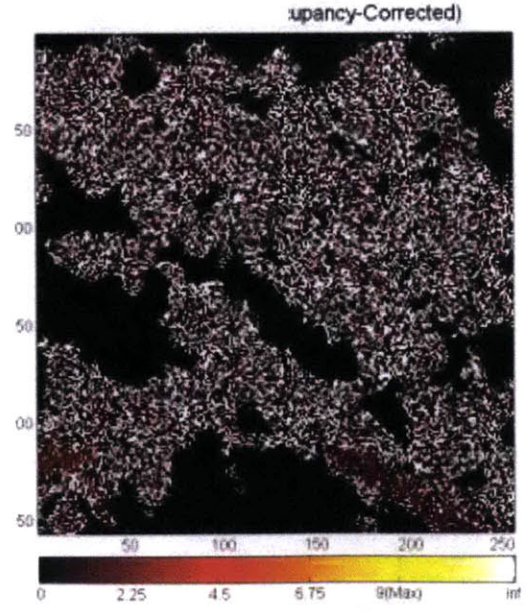
upancy-Corrected)
50
00
50
00
50
50
100
150
200
250
0
2.25
4.5
6.75
9(Max)
inf

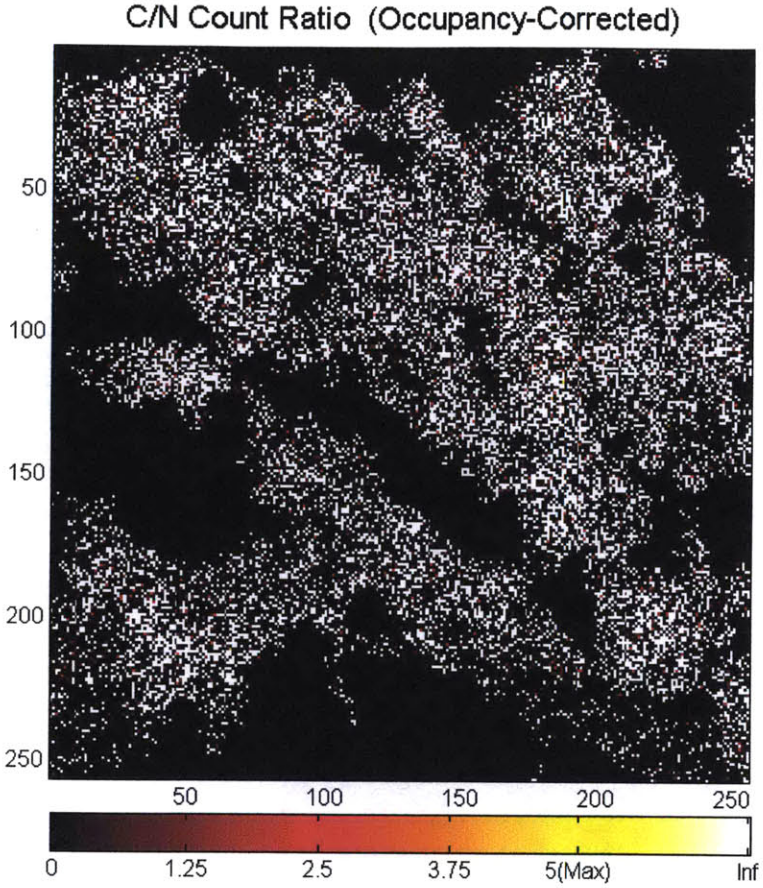

(a) No N 'noise' reduction

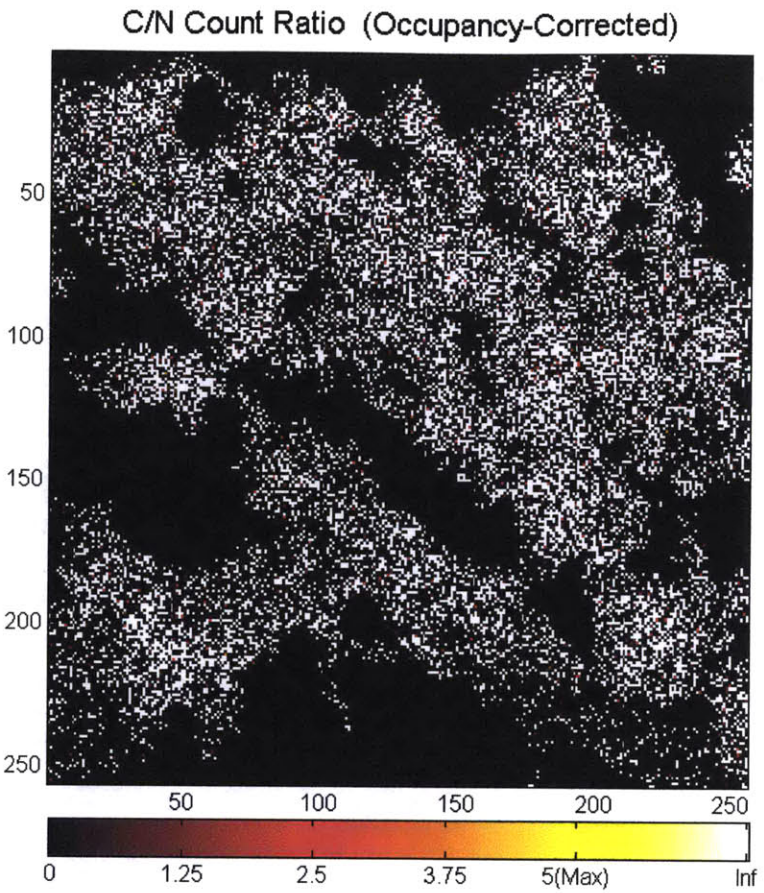

(b) N 'noise' reduction (by 1)

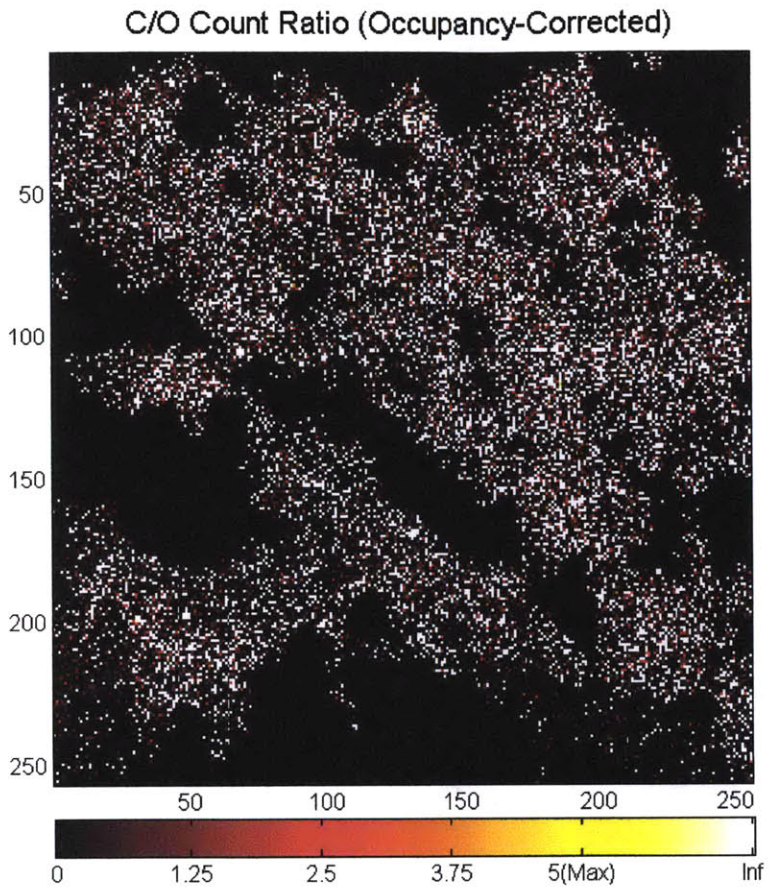

(a) No background O correction

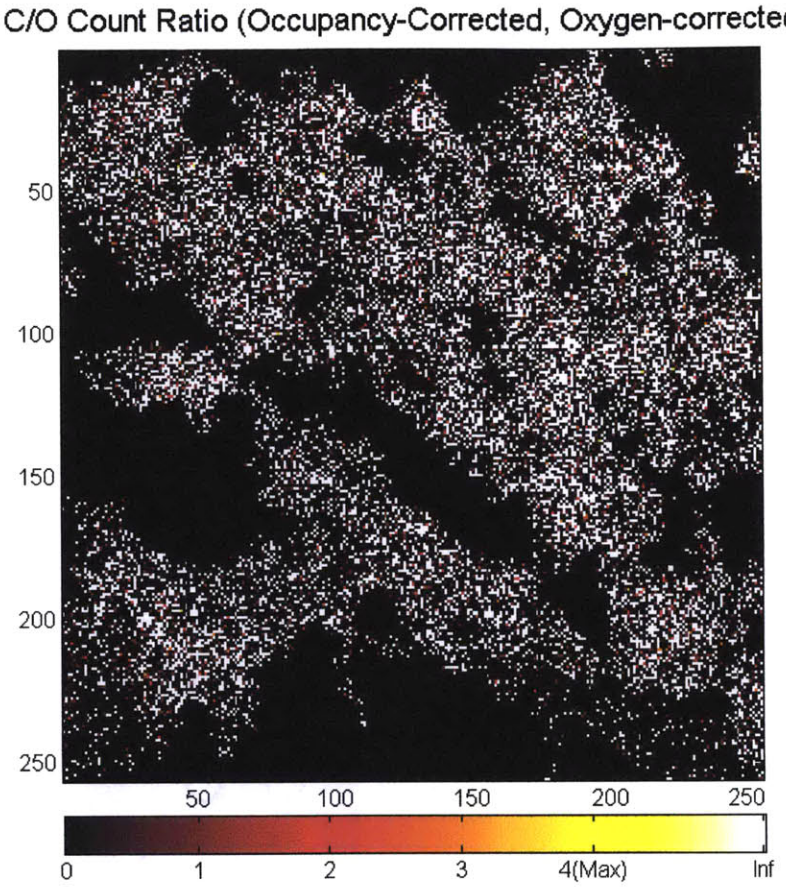

(b) Background O corrected

20061013-Site #6

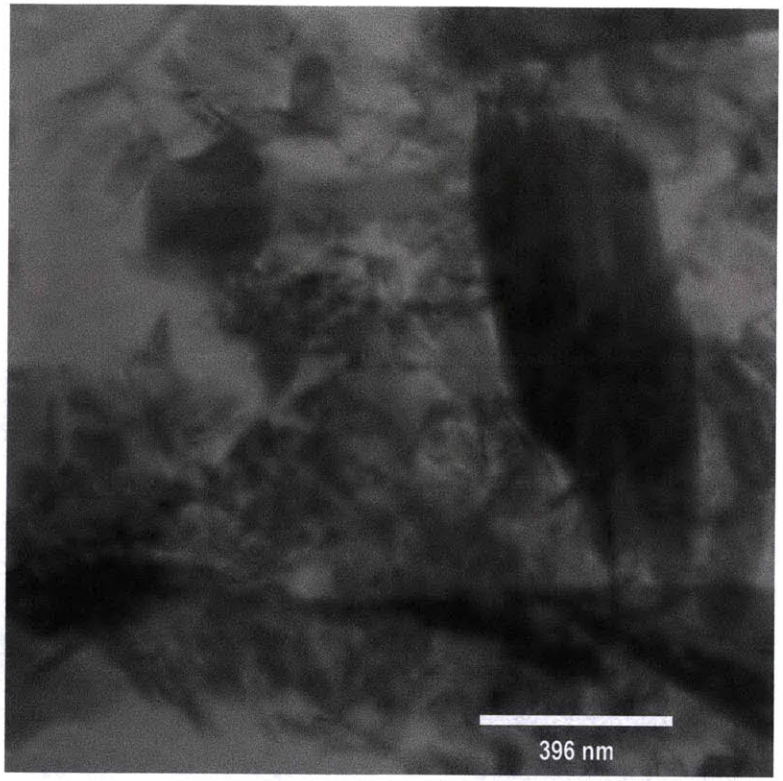

Sample: NIST soot (SRM 1650) amended Boston Harbor #6 sediment (180-250 μm)

Site Description: Apparent mineral phases

Dimension: 1.585×1.585 μm (256×256 pixels)

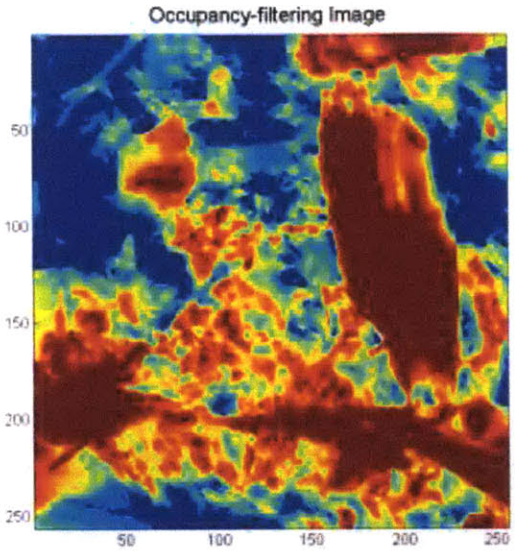
Occupancy-filtering Image
50
100
150
200
250
50
100
150
200
250

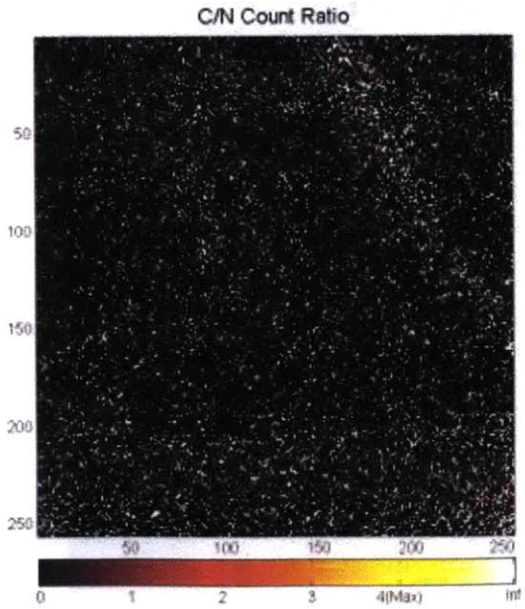
C/N Count Ratio
50
100
150
200
250
50
100
150
200
250
0
1
2
3
4(Max)
Inf

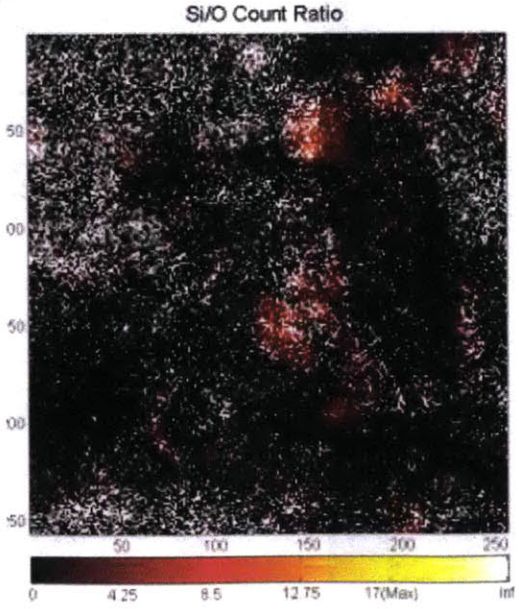
Si/O Count Ratio
50
100
150
200
250
50
100
150
200
250
0
4.25
8.5
12.75
17(Max)
Inf

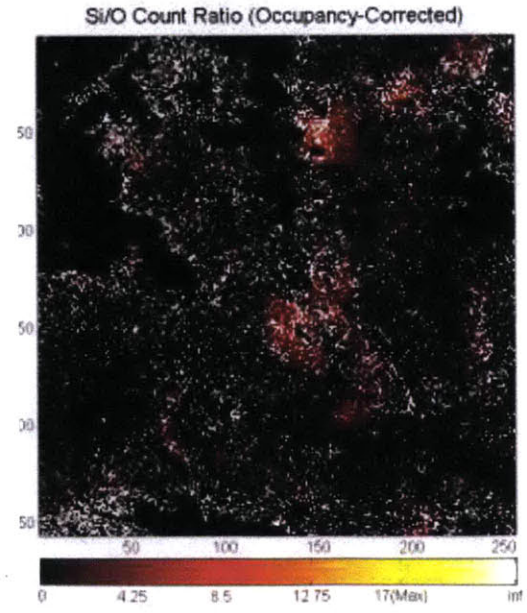
Si/O Count Ratio (Occupancy-Corrected)
50
100
150
200
250
50
100
150
200
250
0
4.25
8.5
12.75
17(Max)
Inf

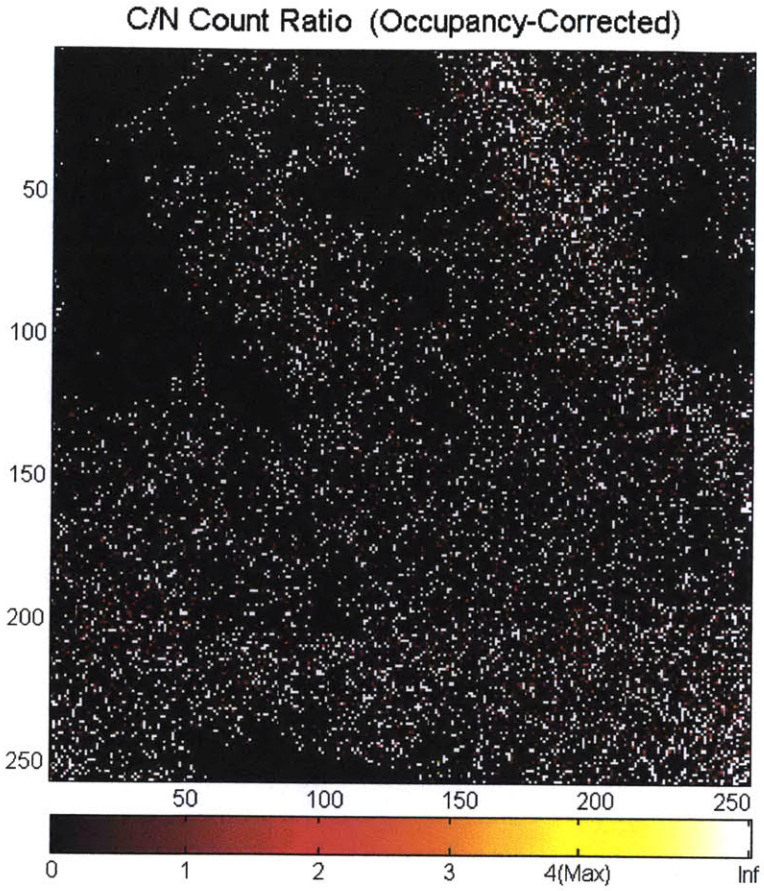

(a) No N 'noise' reduction

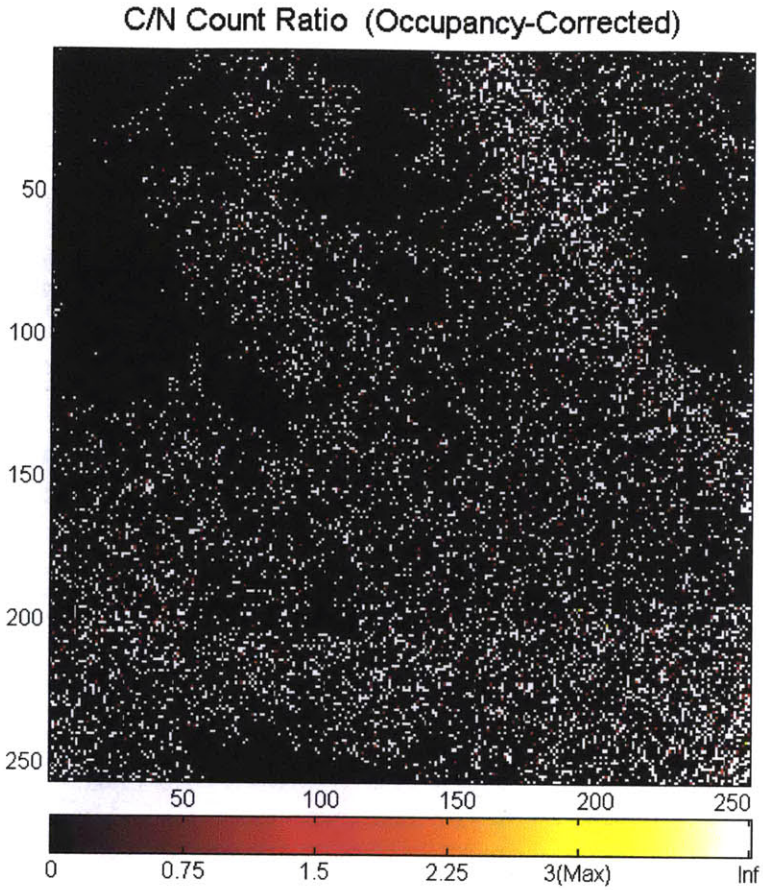

(b) N 'noise' reduction (by 1)

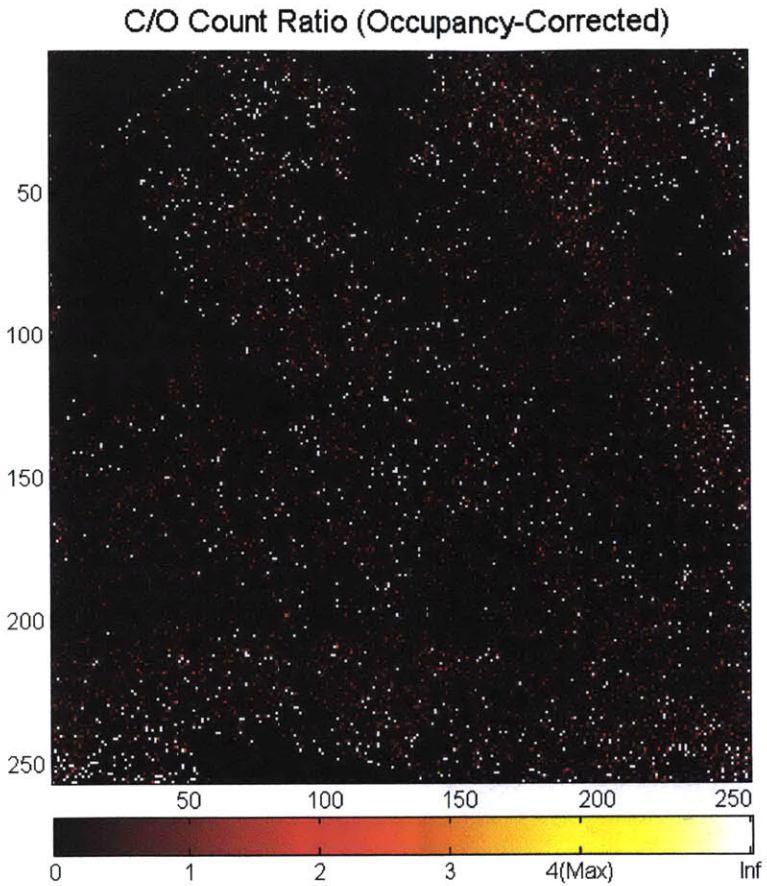

(a) No background O correction

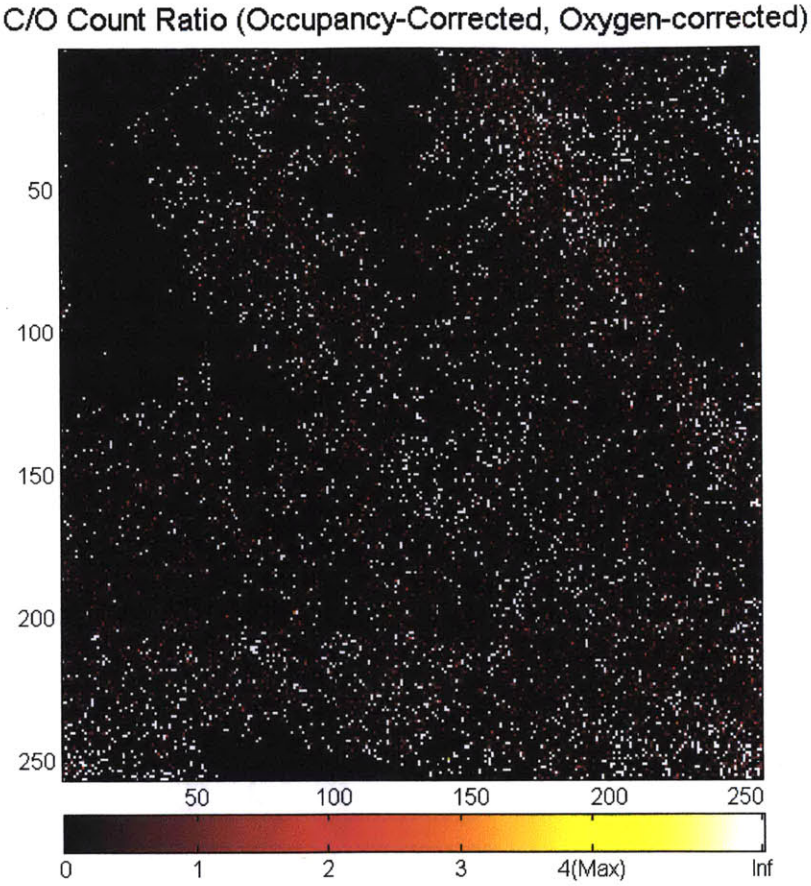

(b) Background O corrected

20061013-Site #8

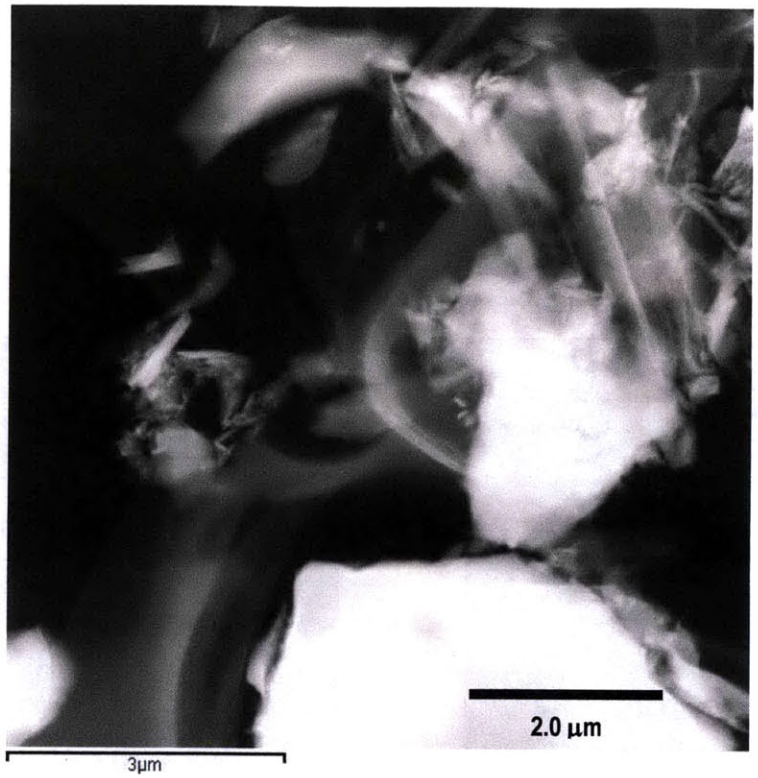

Sample: NIST soot (SRM 1650) amended Boston Harbor #6 sediment (180-250 µm)

Site Description: Apparent mineral phases

Dimension: 7.926×7.926 µm (256×256 pixels)

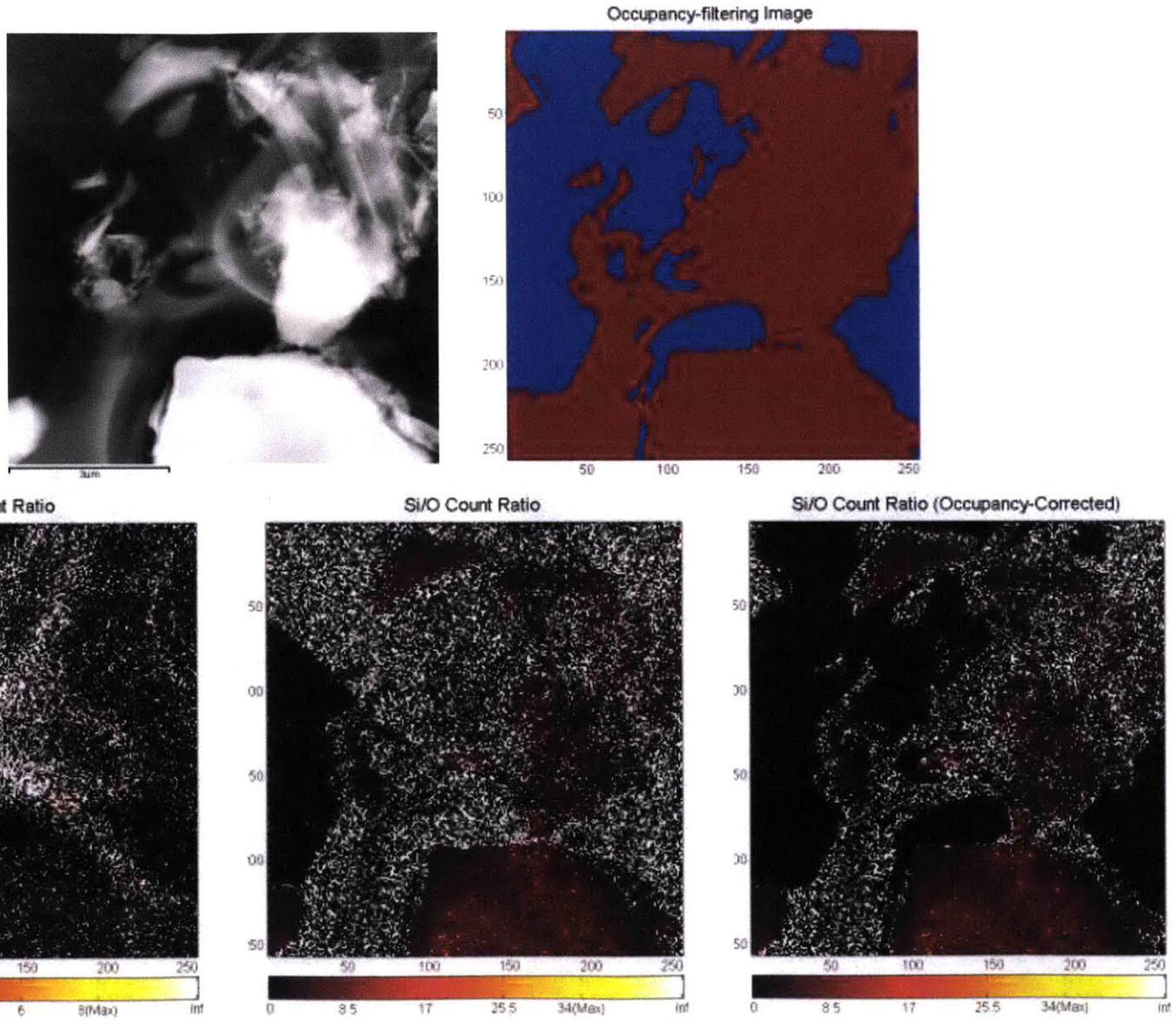
Occupancy-filtering Image
C/N Count Ratio
Si/O Count Ratio
Si/O Count Ratio (Occupancy-Corrected)
50
100
150
200
250
0
2
4
6
8(Max)
inf
8.5
17
25.5
34(Max)

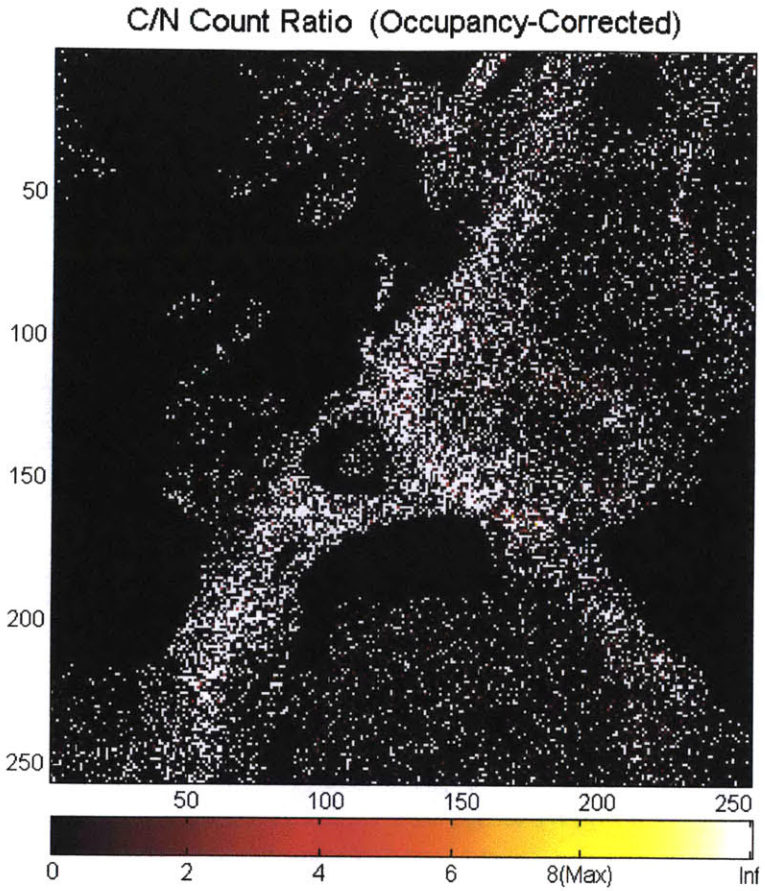

(a) No N 'noise' reduction

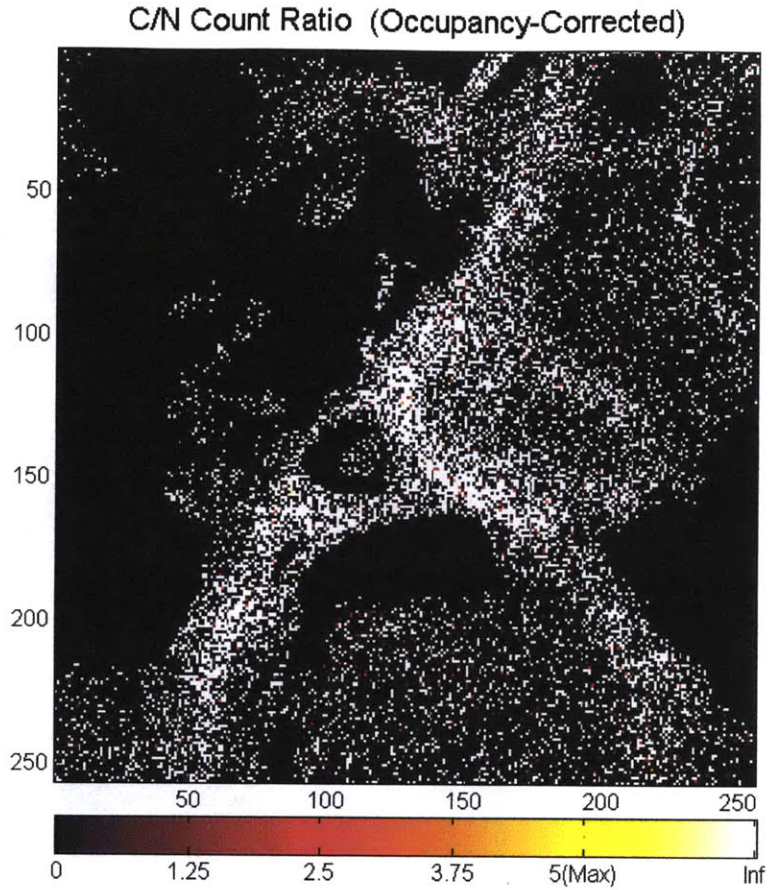

(b) N 'noise' reduction (by 1)

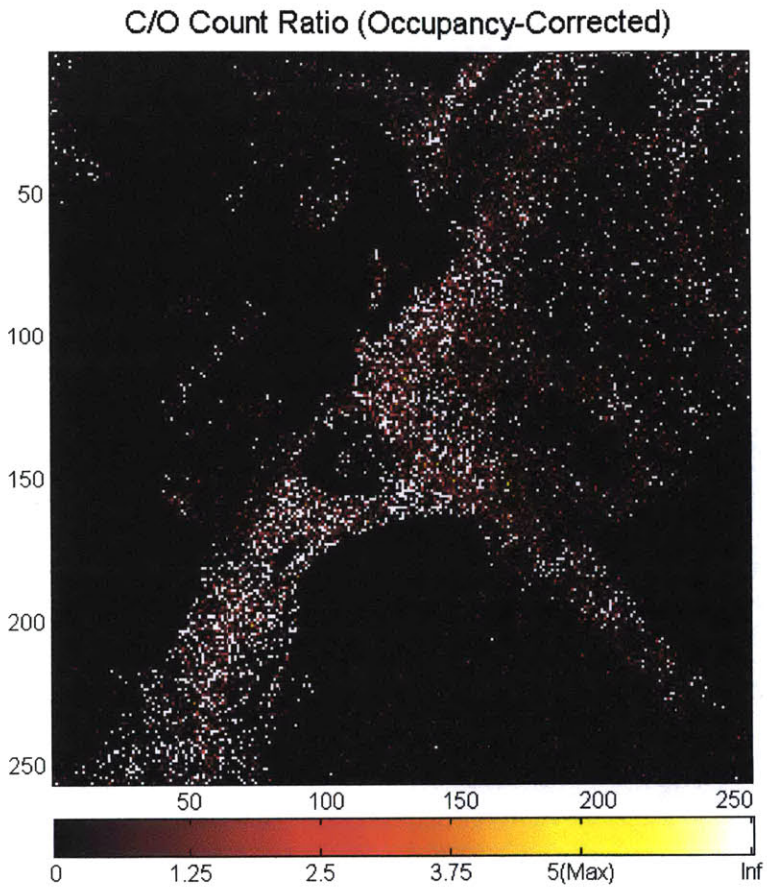

(a) No background O correction

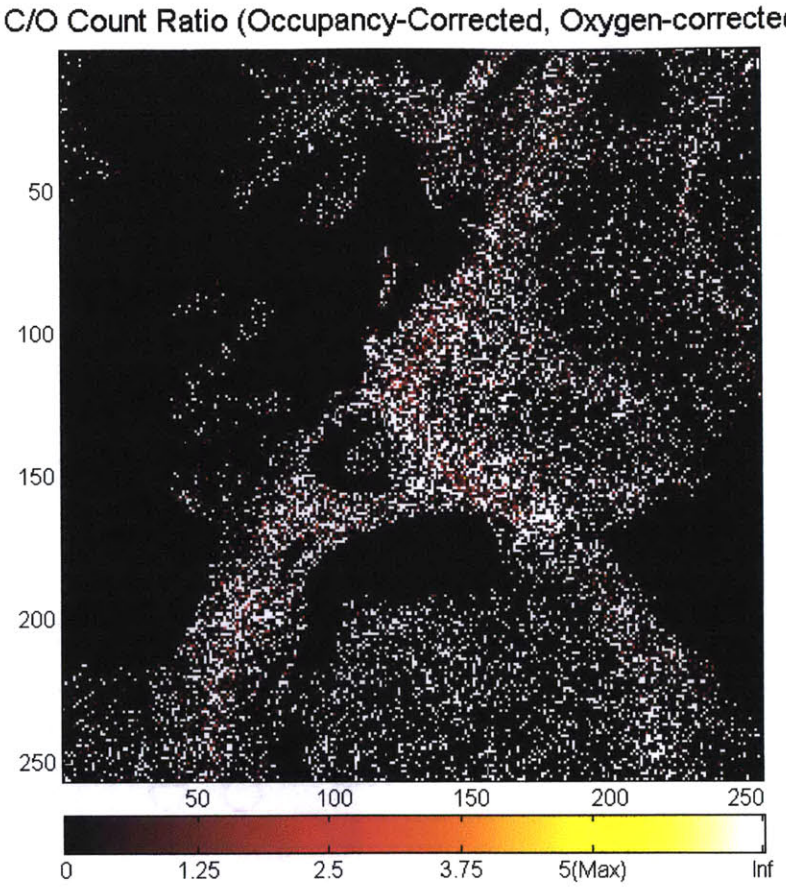

(b) Background O corrected

20061013-Site #10

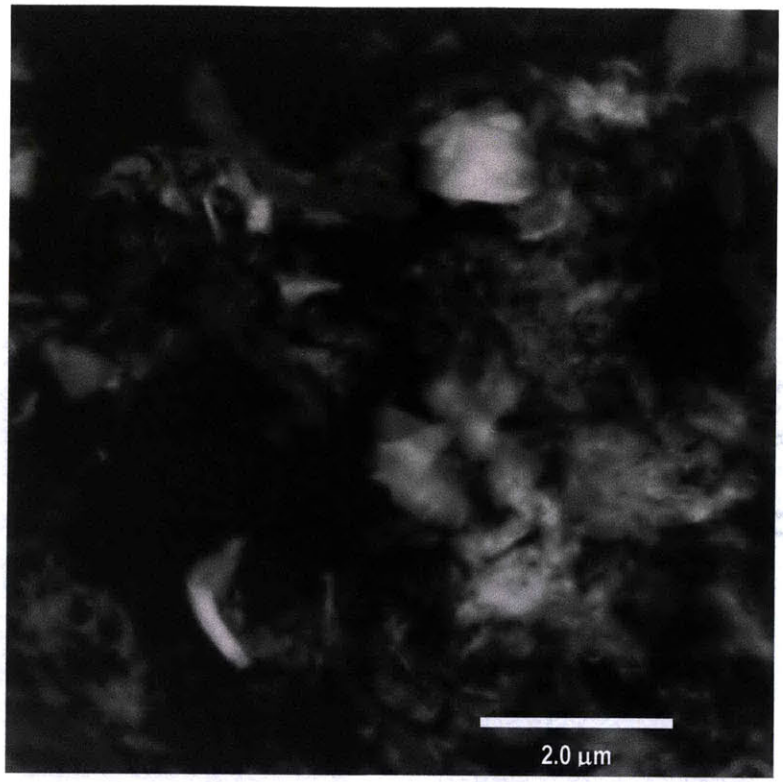

Sample: NIST soot (SRM 1650) amended Boston Harbor #6 sediment (180-250 μm)

Site Description: Apparent mineral phases & organic-looking phases

Dimension: 7.926×7.926 μm (256×256 pixels)

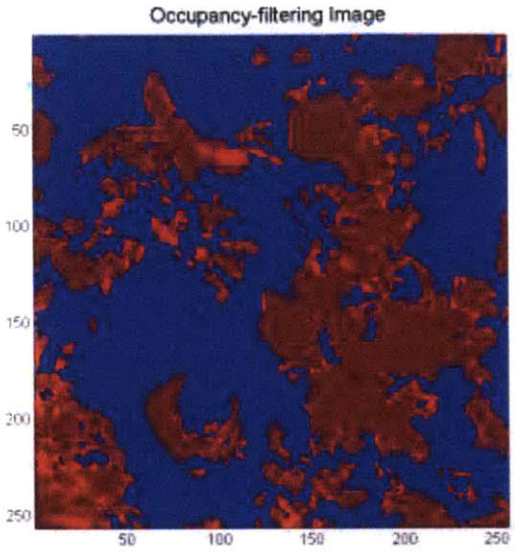
Occupancy-filtering Image
50
100
150
200
250
50
100
150
200
250

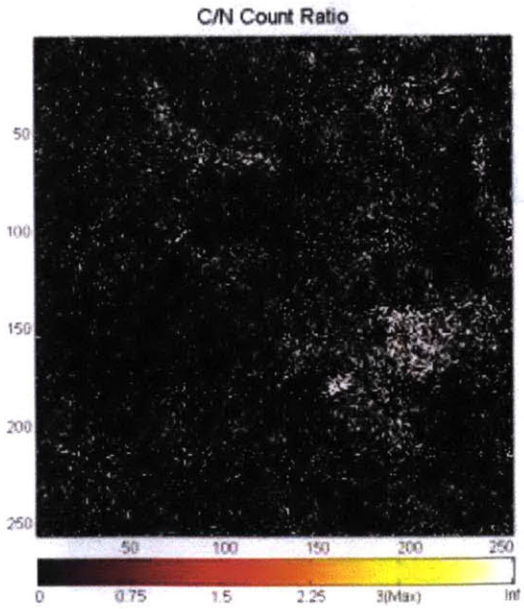
C/N Count Ratio
50
100
150
200
250
50
100
150
200
250
0
0.75
1.5
2.25
3(Max)
Inf

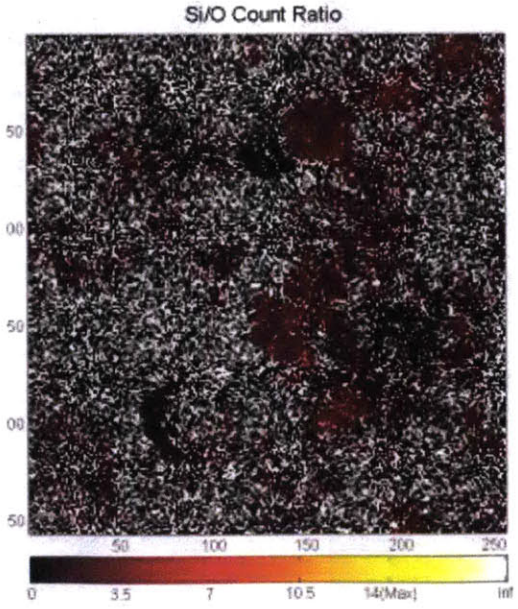
Si/O Count Ratio
50
100
150
200
250
50
100
150
200
250
0
3.5
7
10.5
14(Max)
Inf

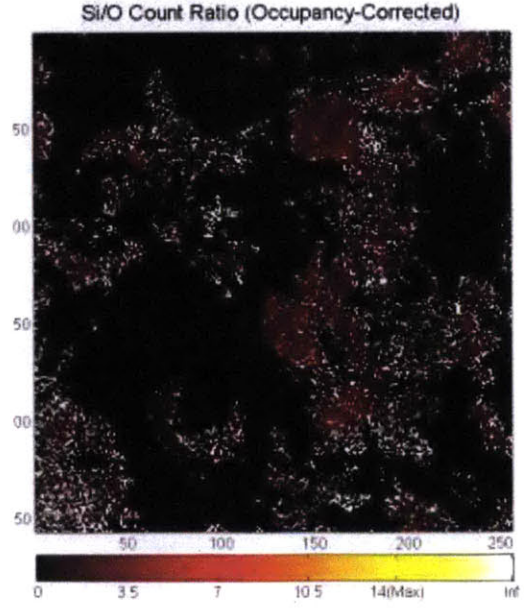
Si/O Count Ratio (Occupancy-Corrected)
50
100
150
200
250
50
100
150
200
250
0
3.5
7
10.5
14(Max)
Inf

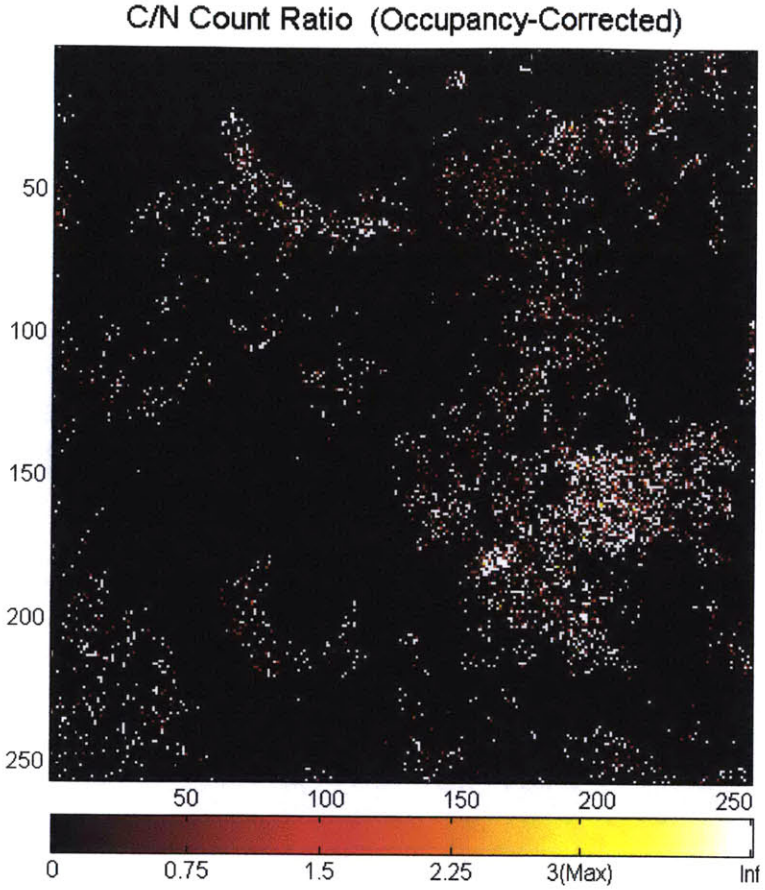

(a) No N 'noise' reduction

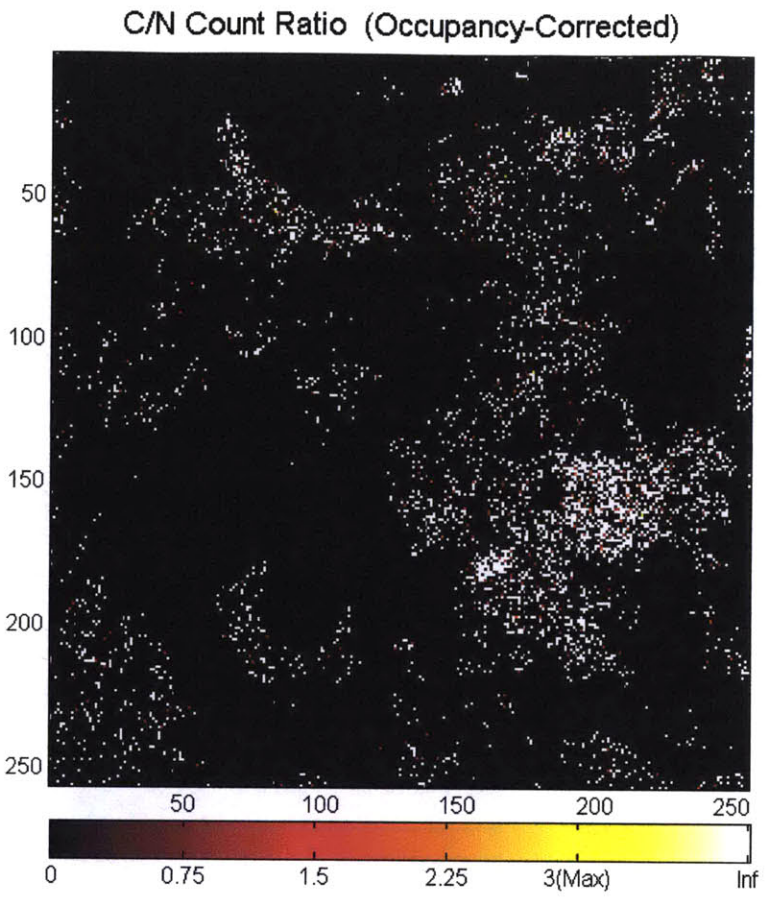

(b) N 'noise' reduction (by 1)

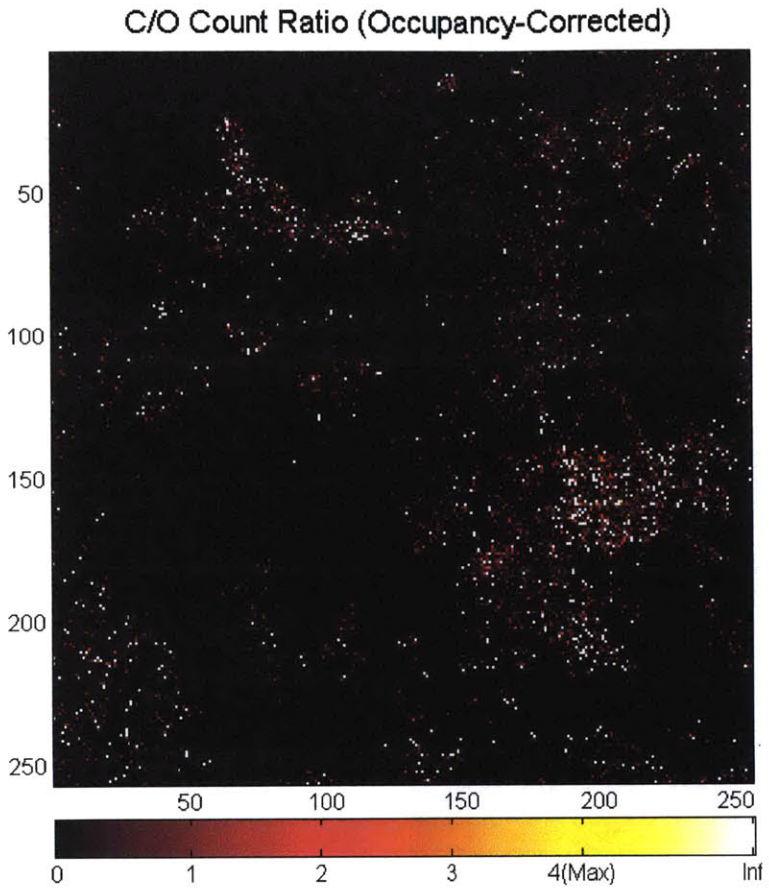

(a) No background O correction

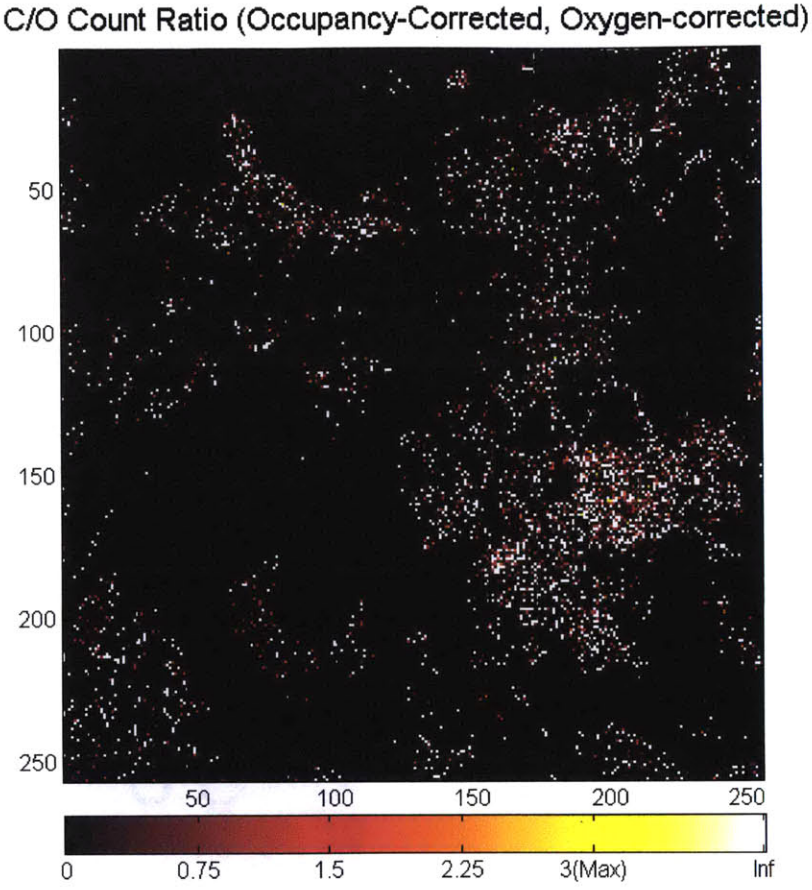

(b) Background O corrected

20061013-Site #12

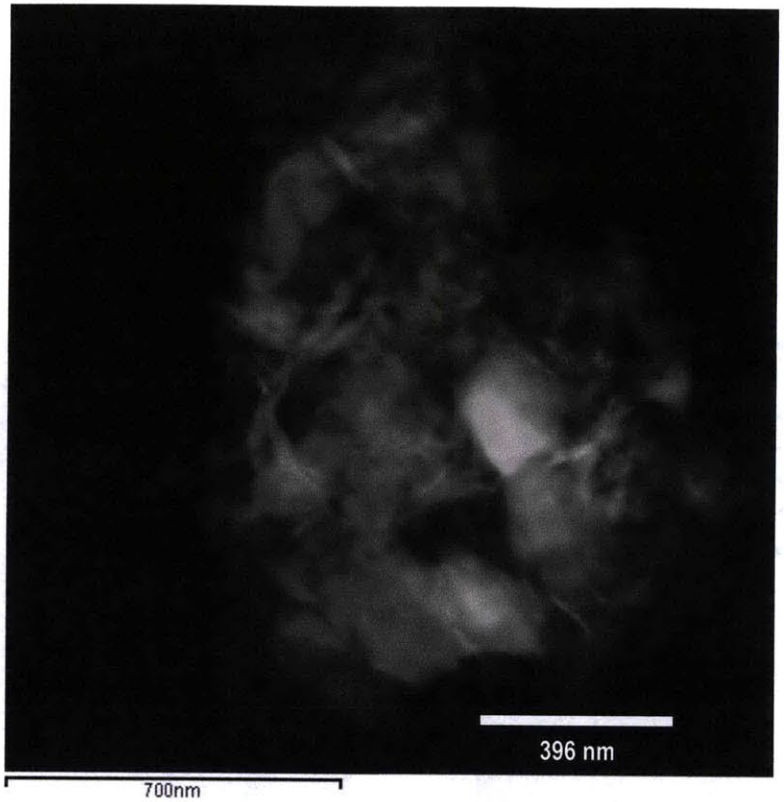

Sample: NIST soot (SRM 1650) amended Boston Harbor #6 sediment (180-250 μm)

Site Description: Aggregate-like area

Dimension: 1.585×1.585 μm (256×256 pixels)

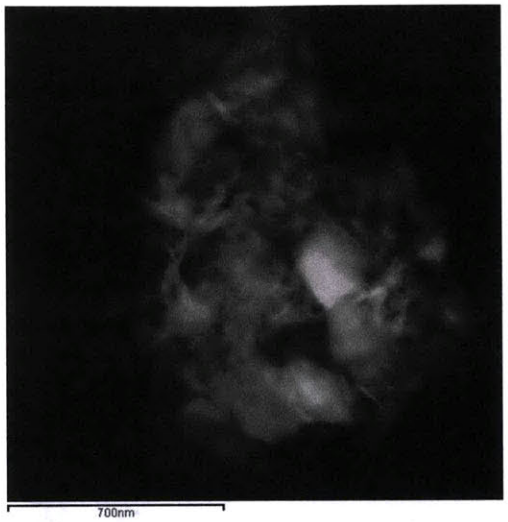
700nm

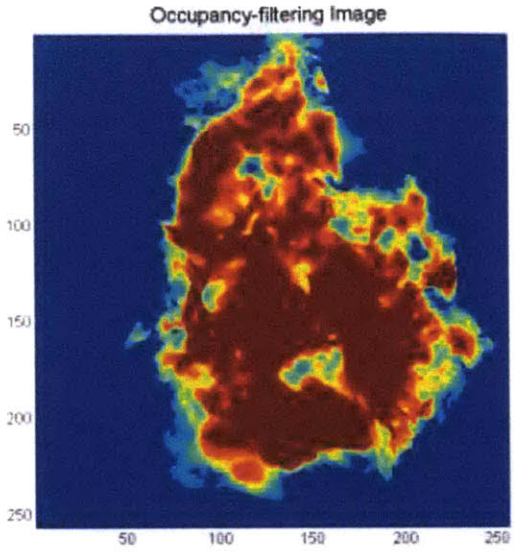
Occupancy-filtering Image
50
100
150
200
250
50
100
150
200
250

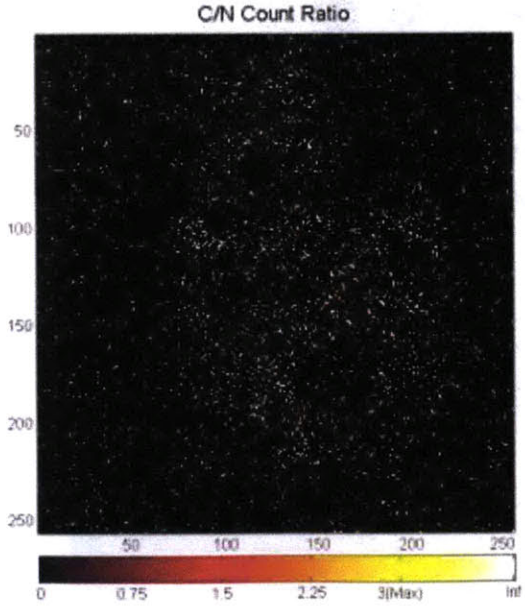
C/N Count Ratio
50
100
150
200
250
50
100
150
200
250
0
0.75
1.5
2.25
3(Max)
Inf

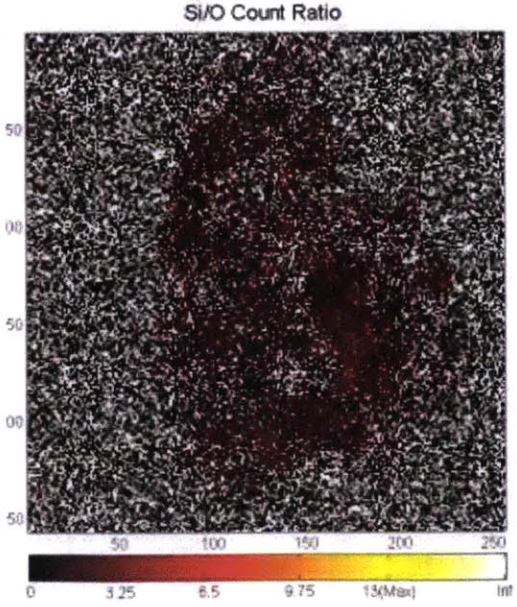
Si/O Count Ratio
50
100
150
200
250
50
100
150
200
250
0
3.25
6.5
9.75
13(Max)
Inf

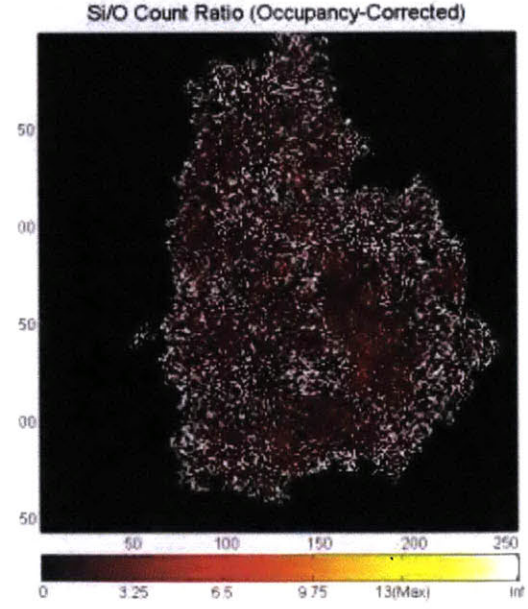
Si/O Count Ratio (Occupancy-Corrected)
50
100
150
200
250
50
100
150
200
250
0
3.25
6.5
9.75
13(Max)
Inf

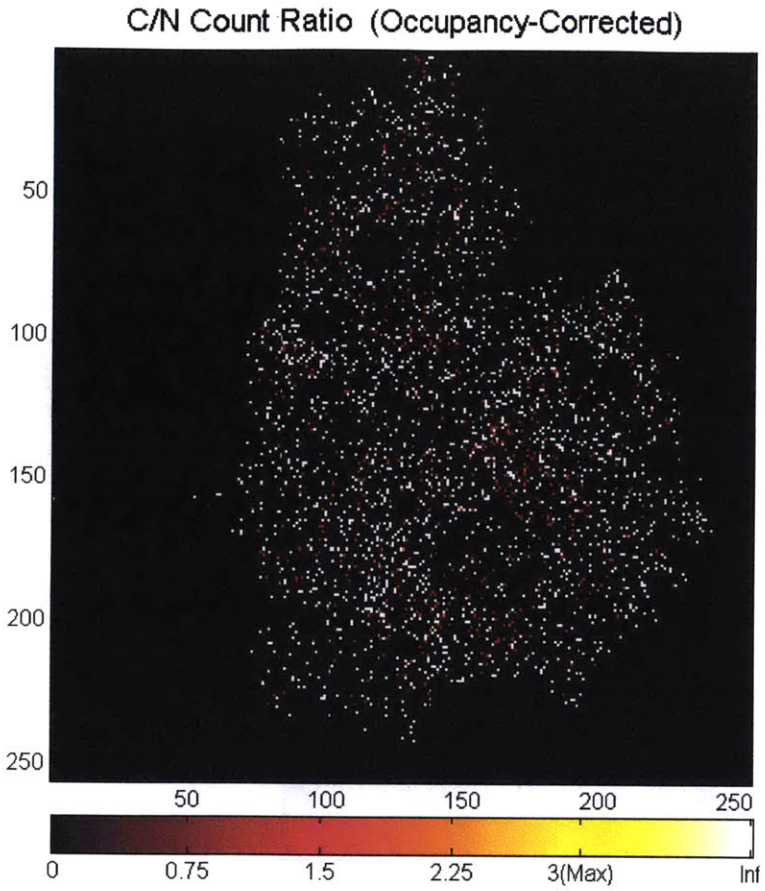

(a) No N 'noise' reduction

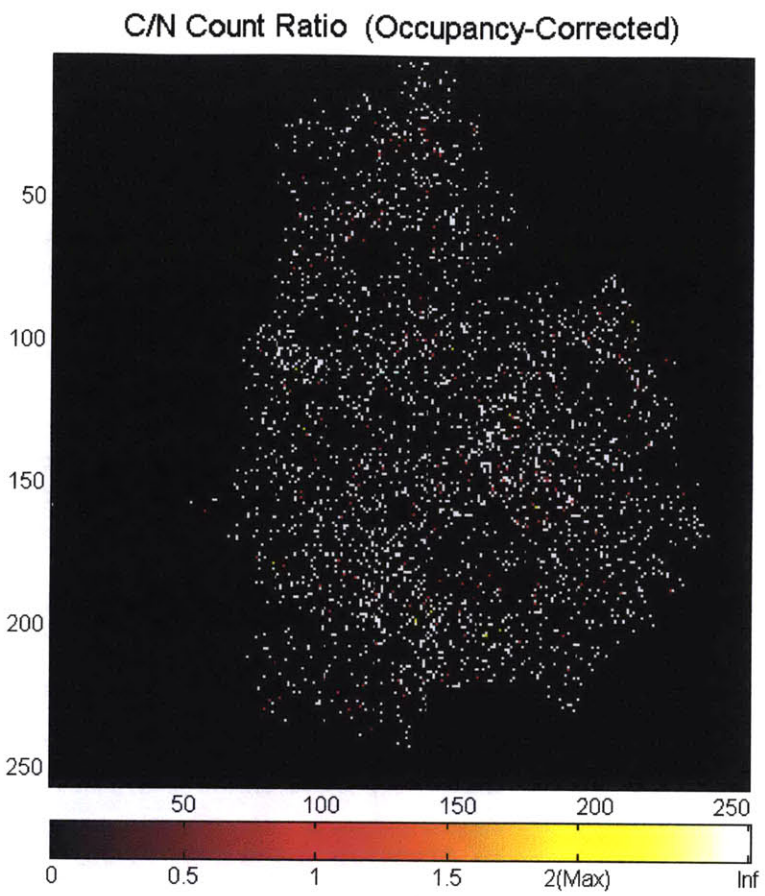

(b) N 'noise' reduction (by 1)

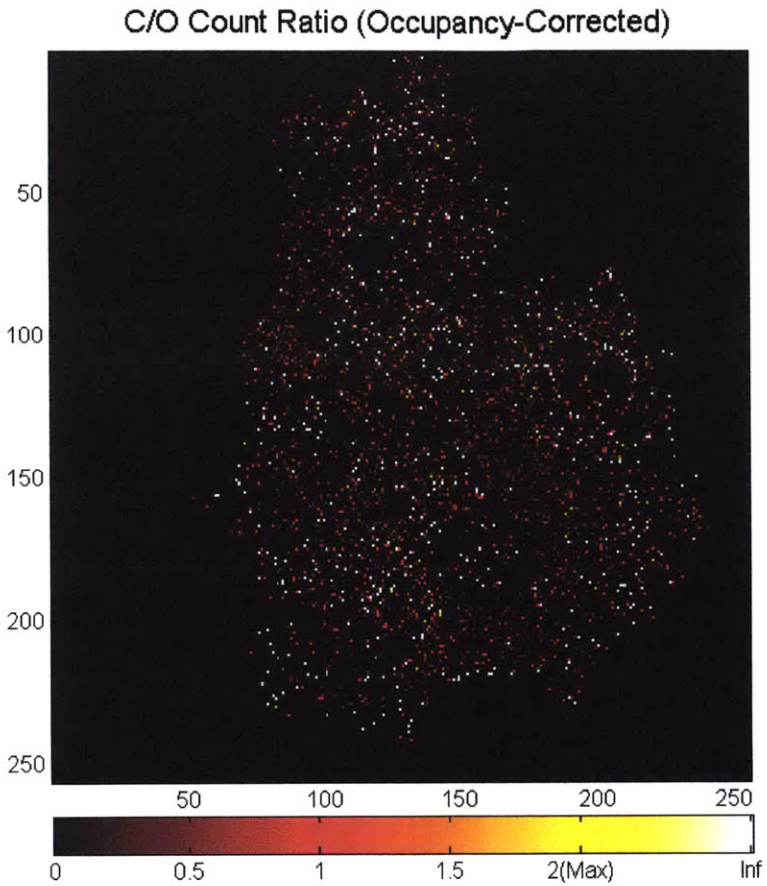

(a) No background O correction

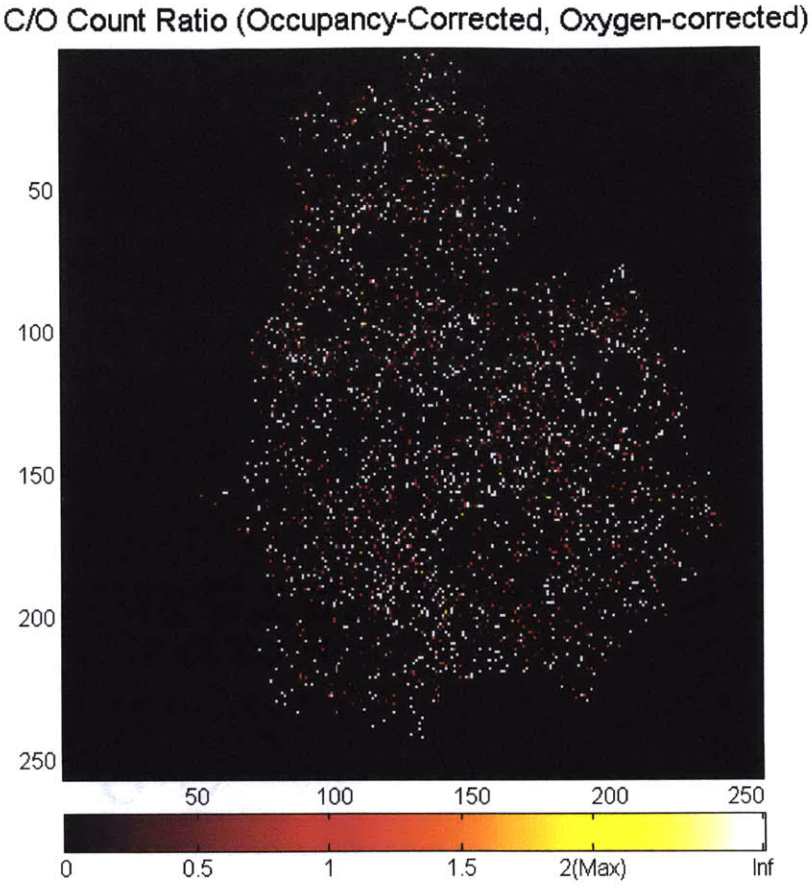

(b) Background O corrected

20061019-Site #11

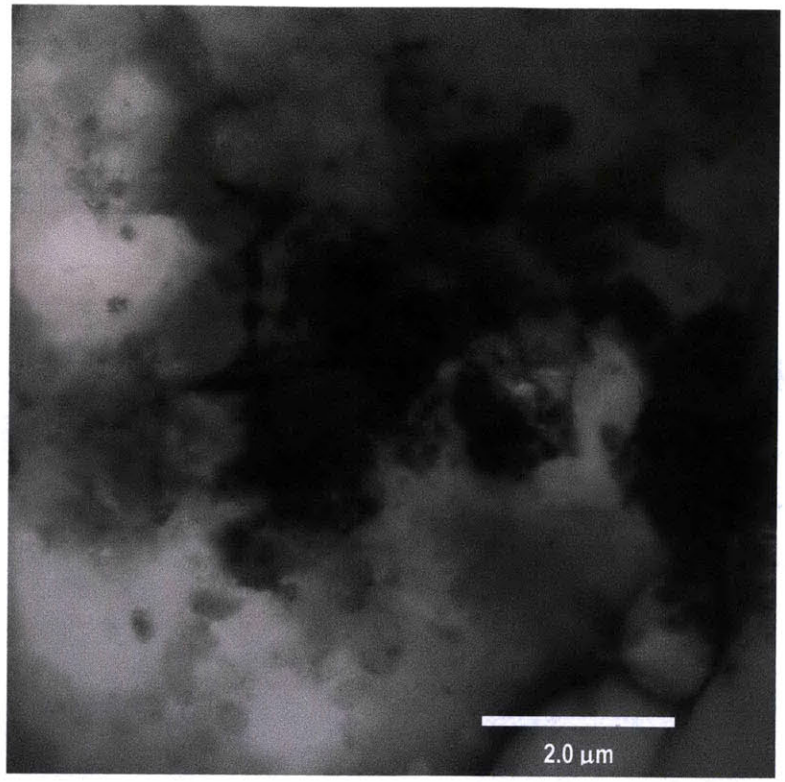

Sample: Humic acids (Aldrich)

Site Description: Humic acids

Dimension: 7.926×7.926 µm (256×256 pixels)

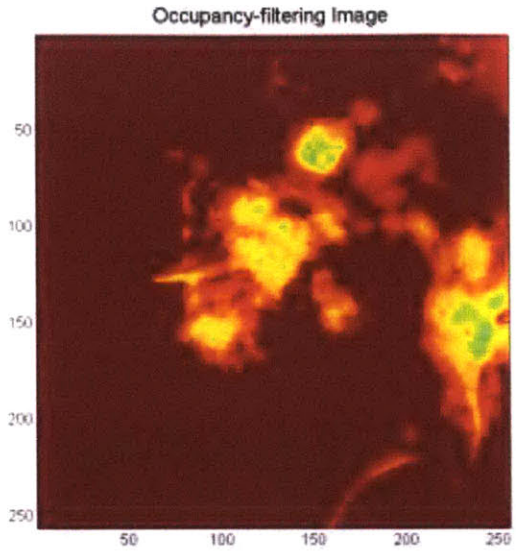
Occupancy-filtering Image
50
100
150
200
250
50
100
150
200
250

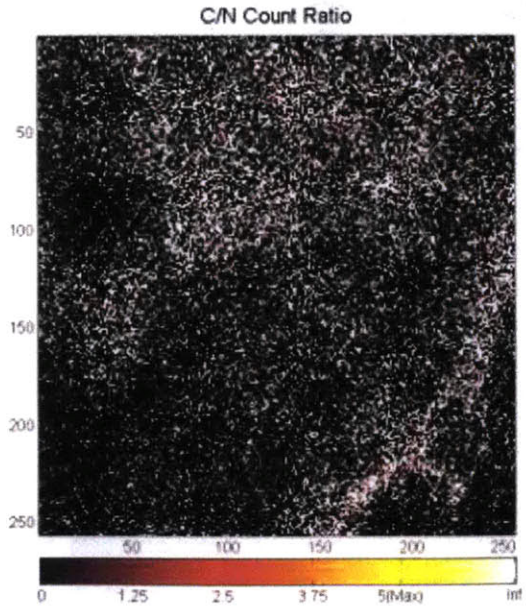
C/N Count Ratio
50
100
150
200
250
50
100
150
200
250
0
1.25
2.5
3.75
5(Max)
Inf

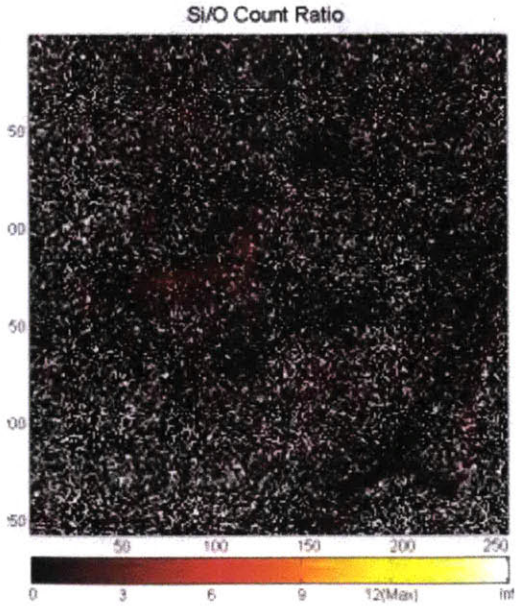
Si/O Count Ratio
50
100
150
200
250
50
100
150
200
250
0
3
6
9
12(Max)
Inf

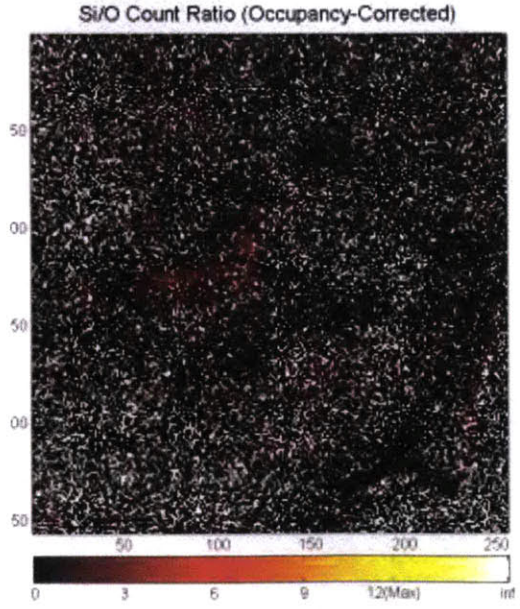
Si/O Count Ratio (Occupancy-Corrected)
50
100
150
200
250
50
100
150
200
250
0
3
6
9
12(Max)
Inf

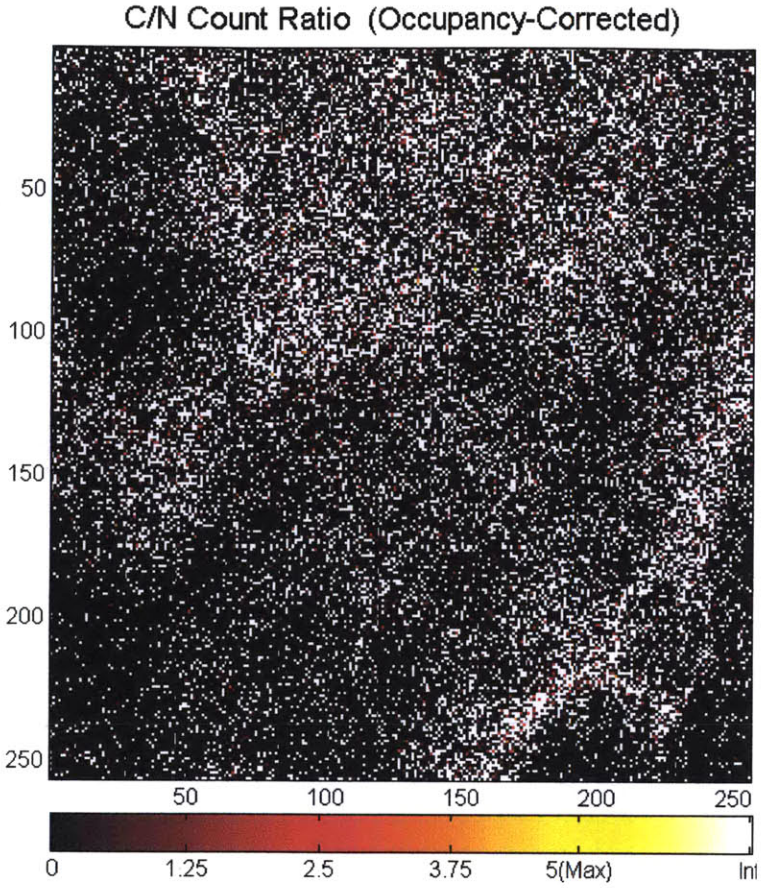

(a) No N 'noise' reduction

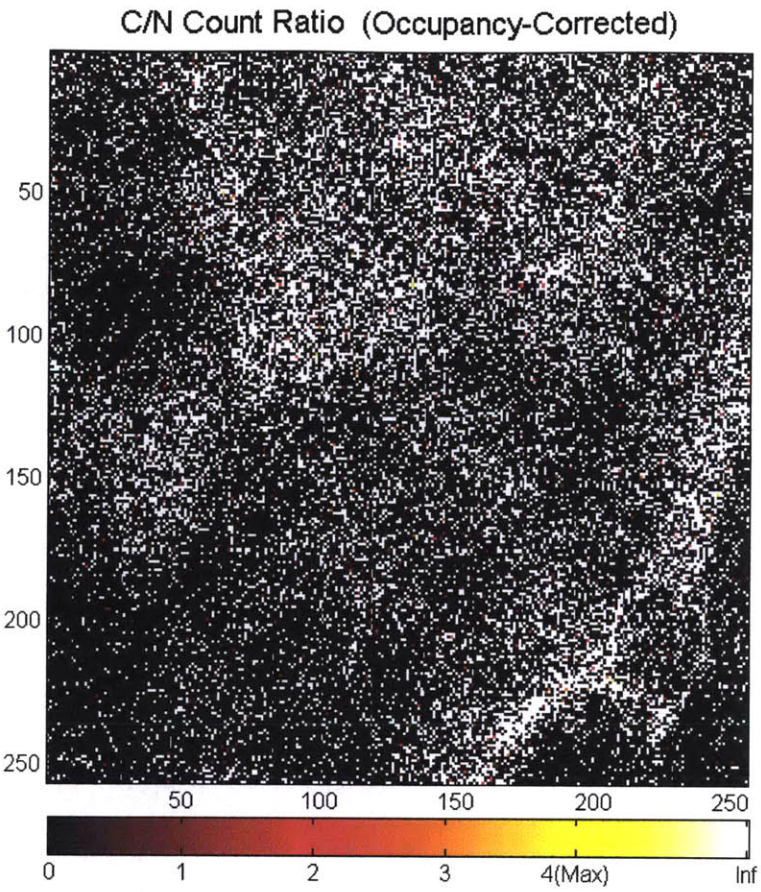

(b) N 'noise' reduction (by 1)

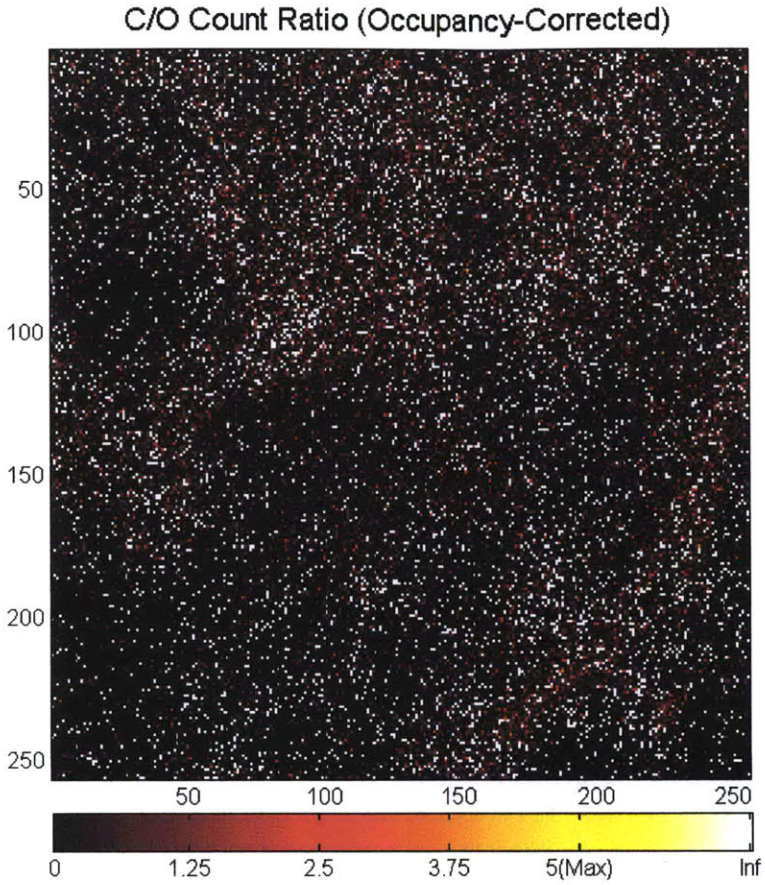

(a) No background O correction

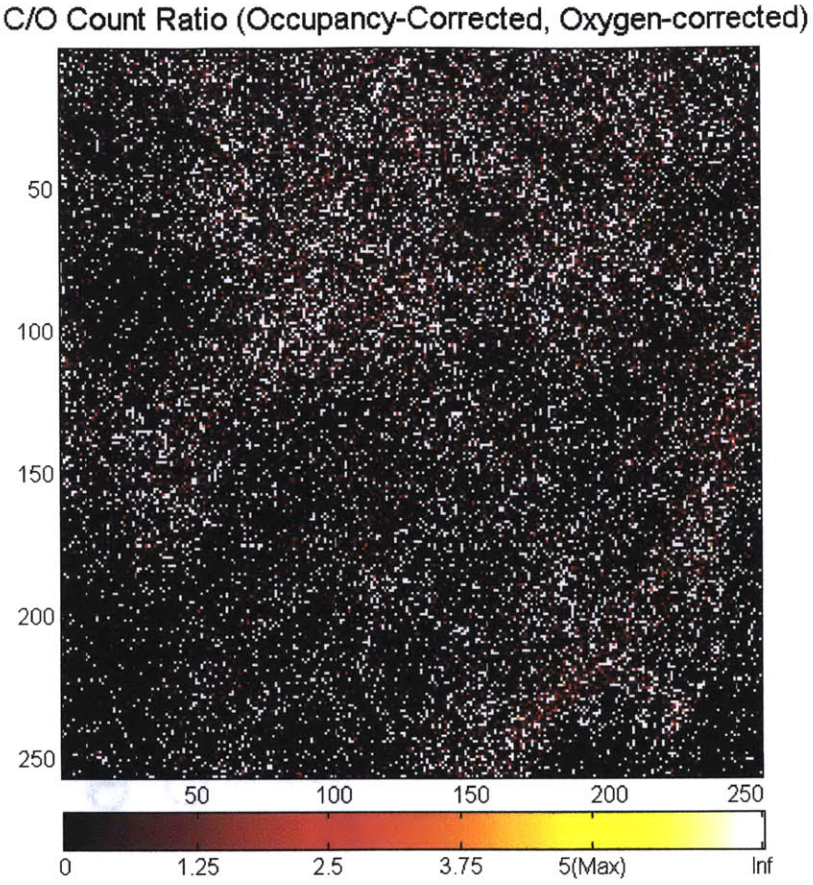

(b) Background O corrected

20061019-Site #13

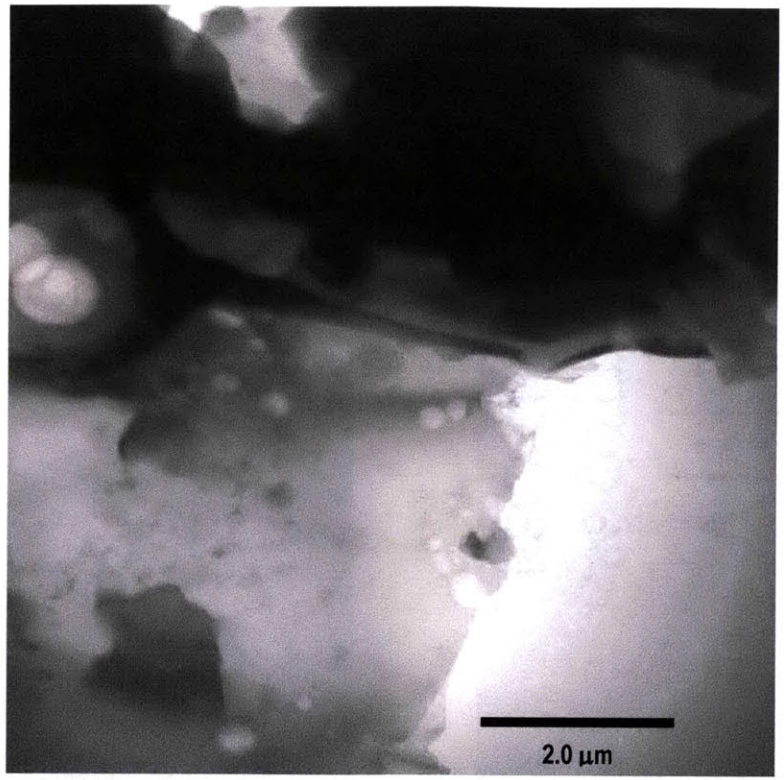

Sample: Humic acids (Aldrich)

Site Description: Humic acids

Dimension: 7.926×7.926 µm (256×256 pixels)

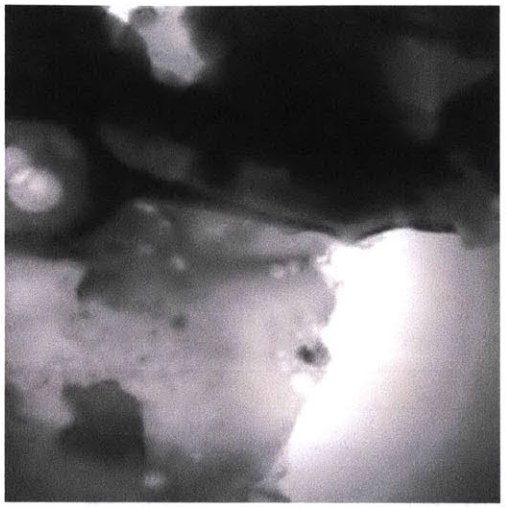

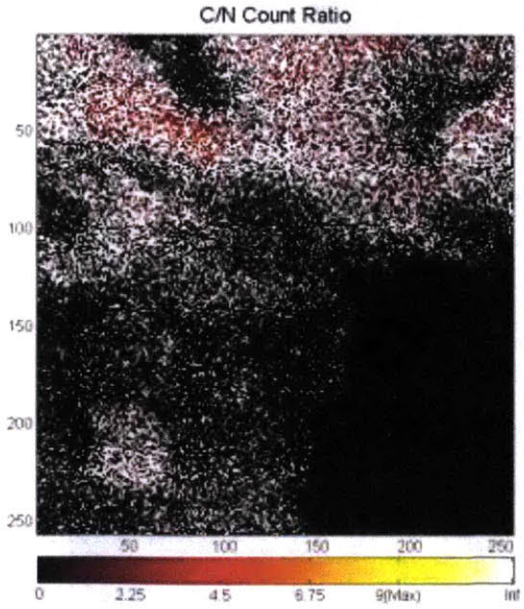
C/N Count Ratio
50
100
150
200
250
50
100
150
200
250
0
2.25
4.5
6.75
9(Max)
Int

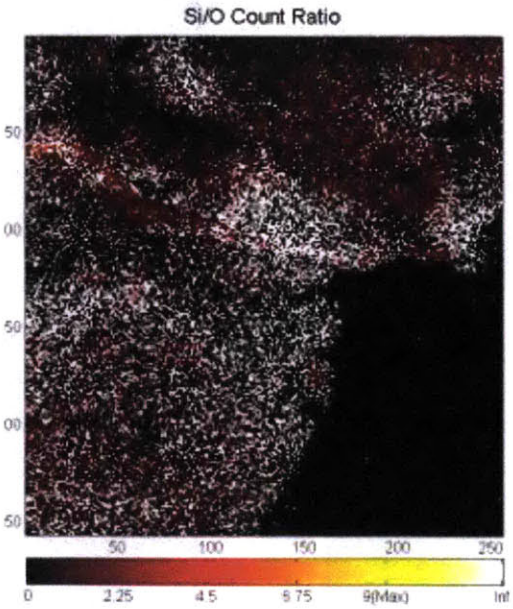
Si/O Count Ratio
50
00
50
00
50
50
100
150
200
250
0
2.25
4.5
6.75
9(Max)
Int

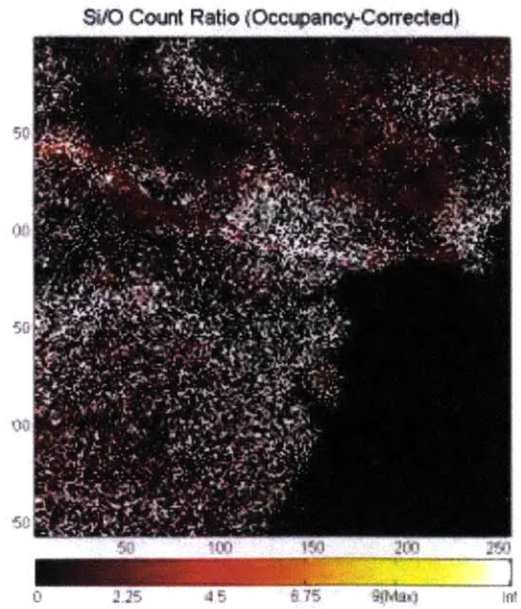
Si/O Count Ratio (Occupancy-Corrected)
50
00
50
00
50
50
100
150
200
250
0
2.25
4.5
6.75
9(Max)
Int

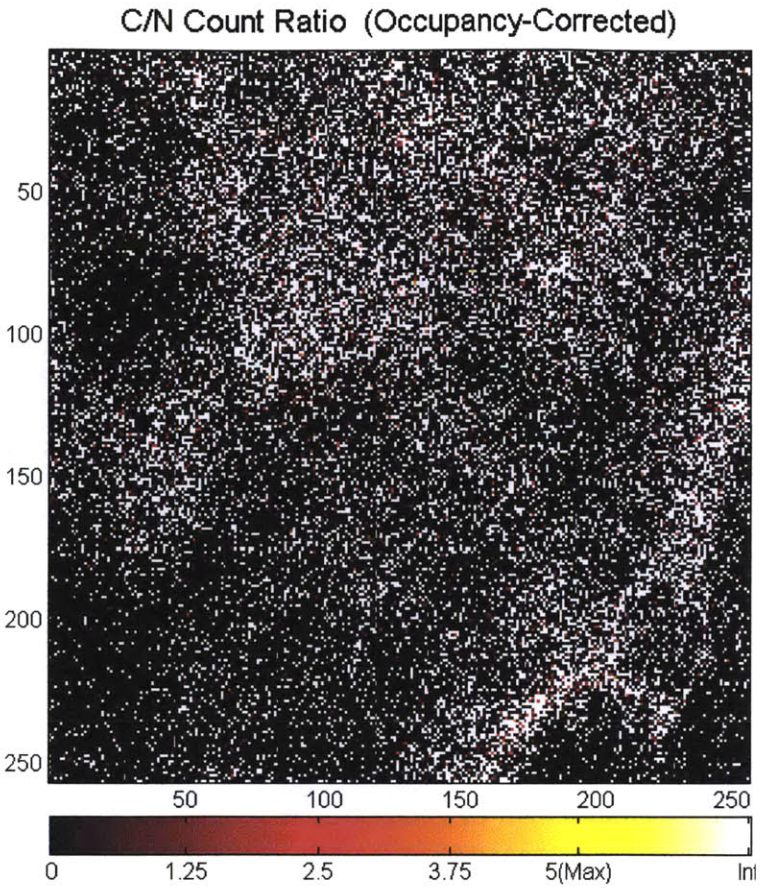

(a) No N 'noise' reduction

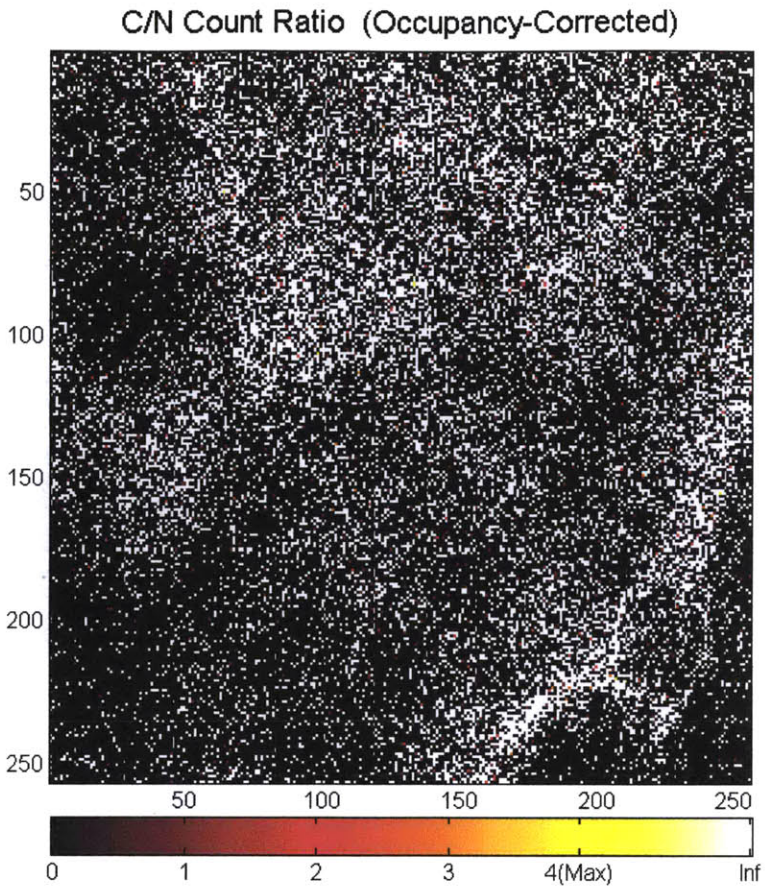

(b) N 'noise' reduction (by 1)

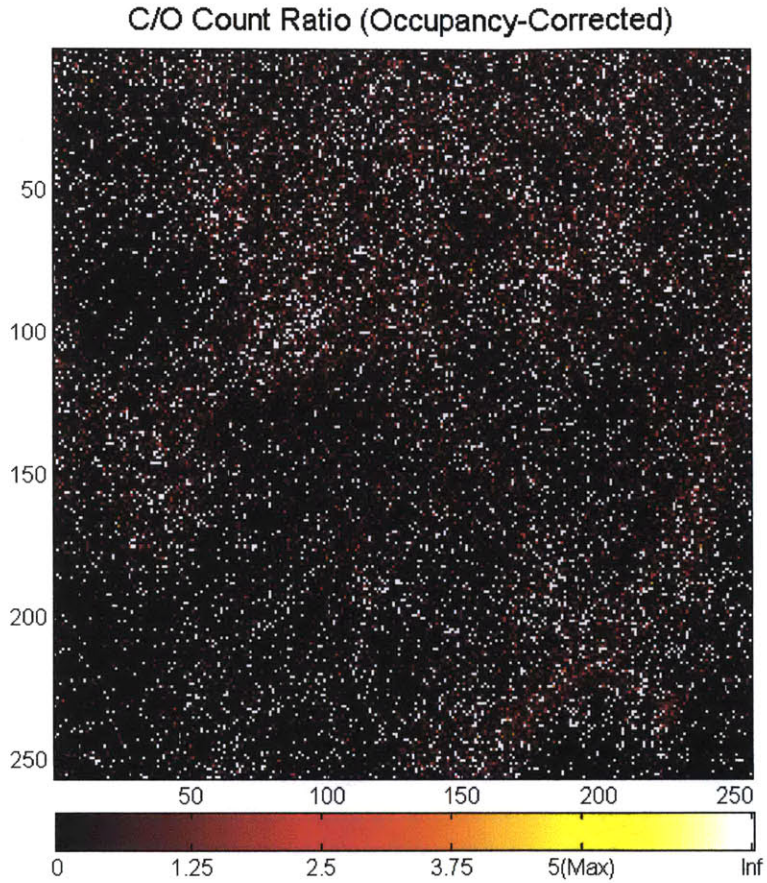

(a) No background O correction

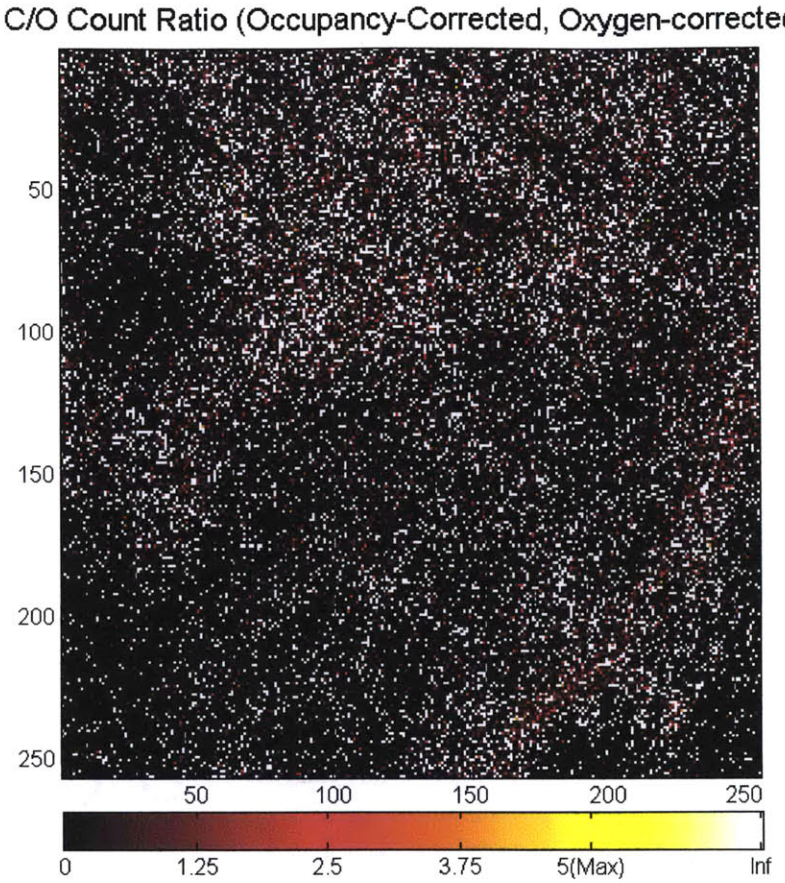

(b) Background O corrected

Lignocellulosic Char-Site #1

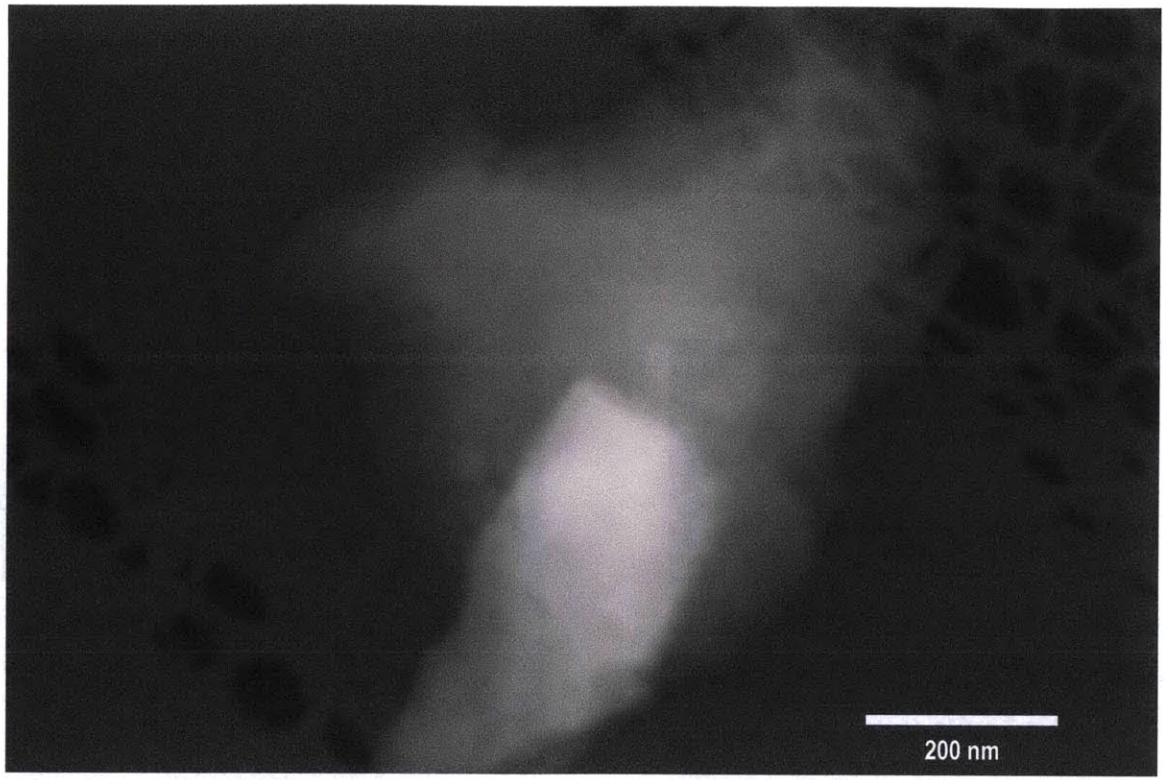

Sample: Lignocellulosic Char (Univ. of Zurich)

Site Description: Char particle

Dimension: 0.825 × 1.20 μm (88×128 pixels)

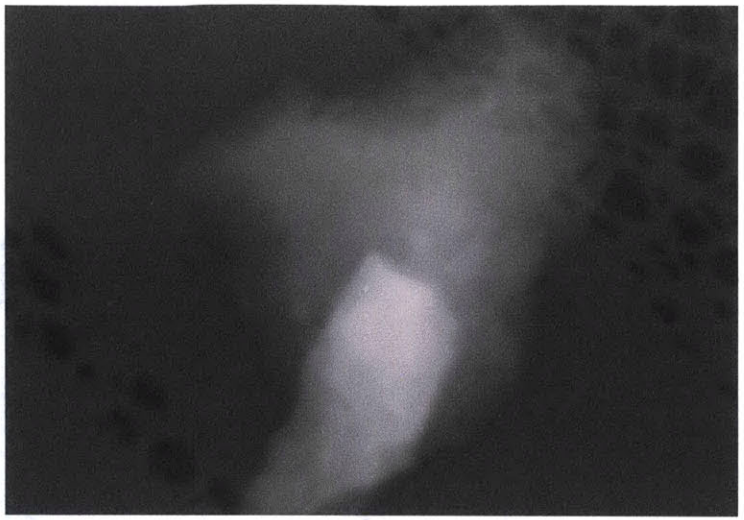

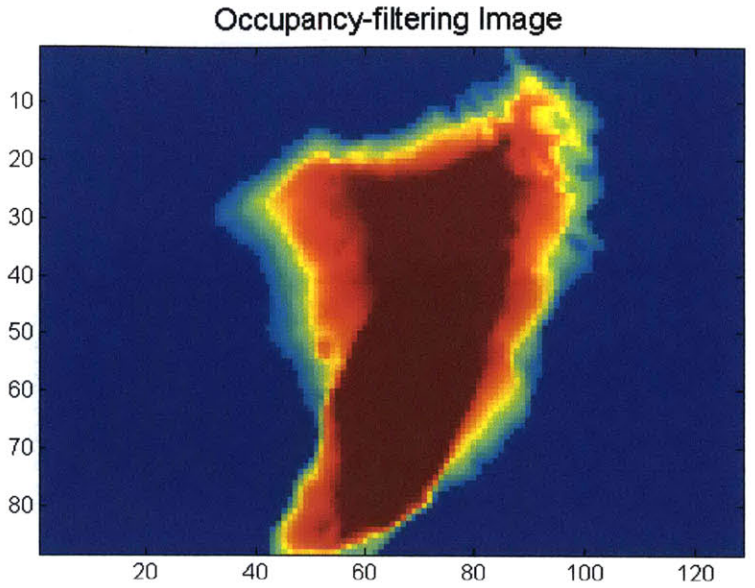
Occupancy-filtering Image
10
20
30
40
50
60
70
80
20
40
60
80
100
120

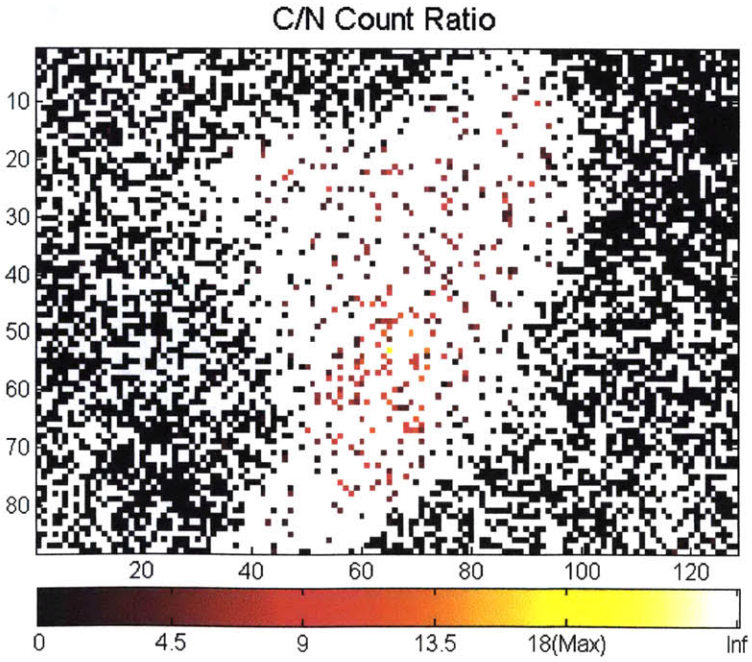
C/N Count Ratio
10
20
30
40
50
60
70
80
20
40
60
80
100
120
0
4.5
9
13.5
18(Max)
Inf

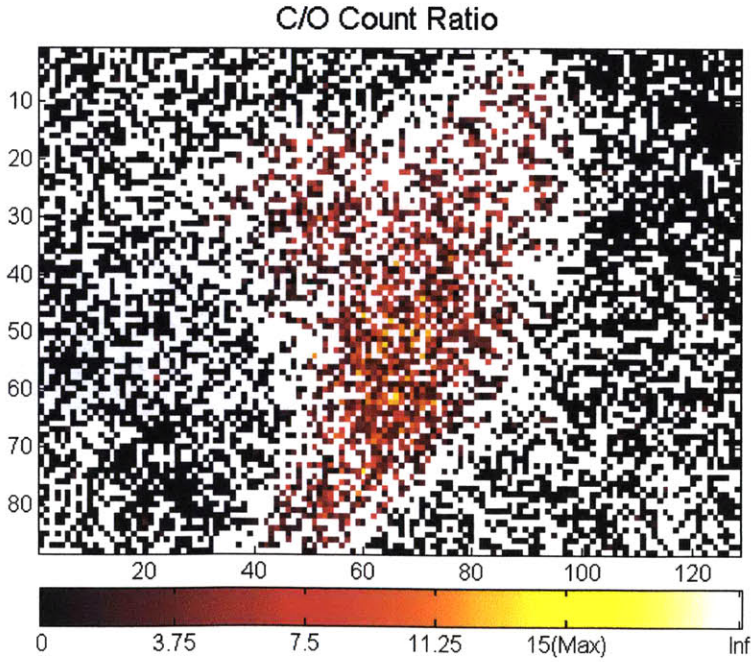
C/O Count Ratio
10
20
30
40
50
60
70
80
20
40
60
80
100
120
0
3.75
7.5
11.25
15(Max)
Inf

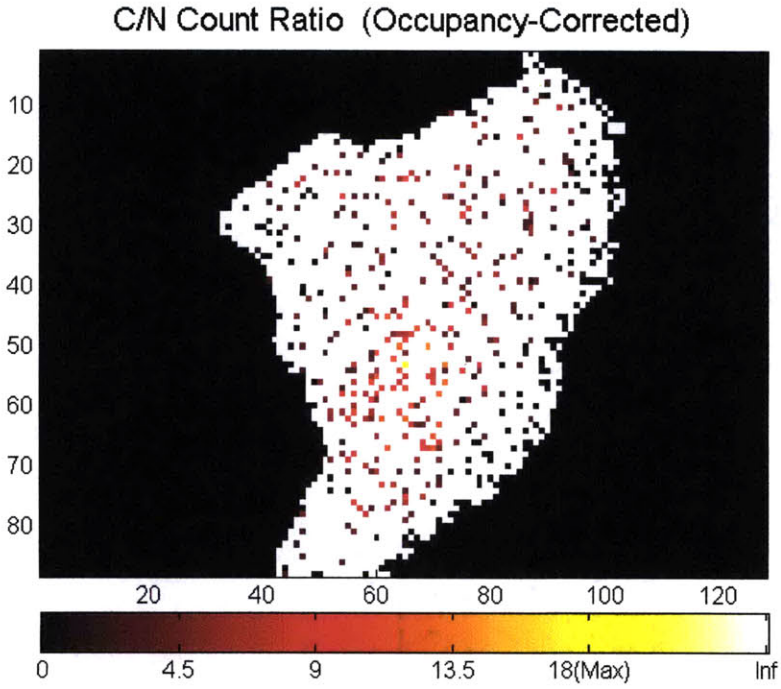

(a) No N 'noise' reduction

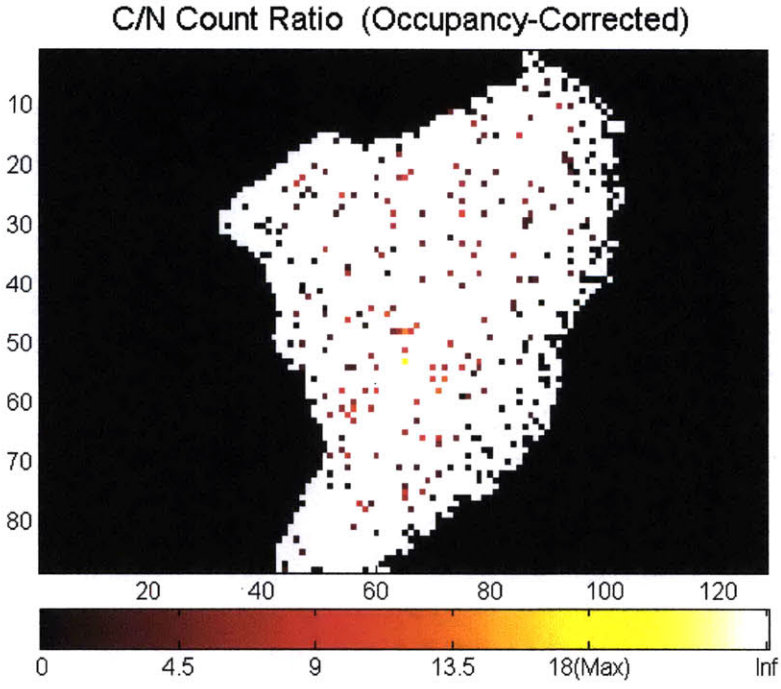

(b) N 'noise' reduction (by 1)

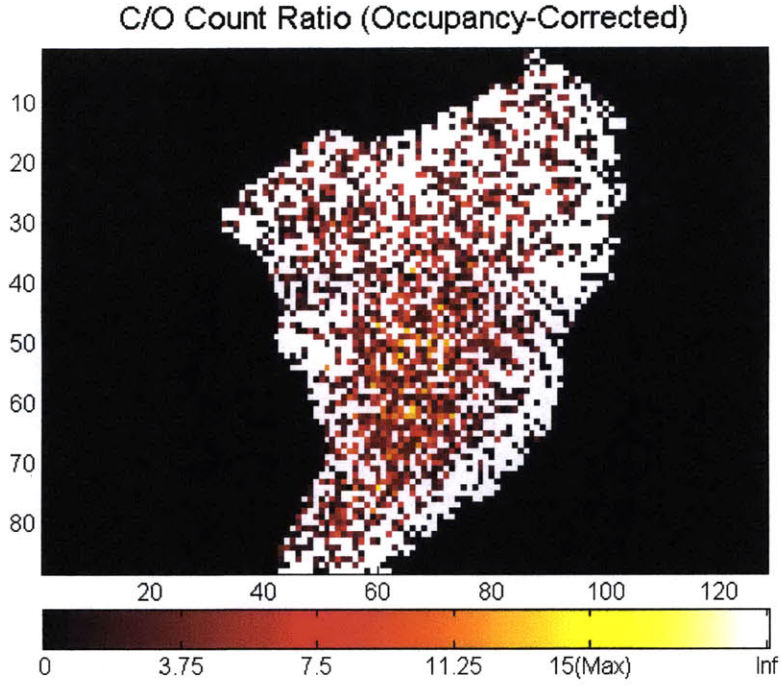

(a) No background O correction

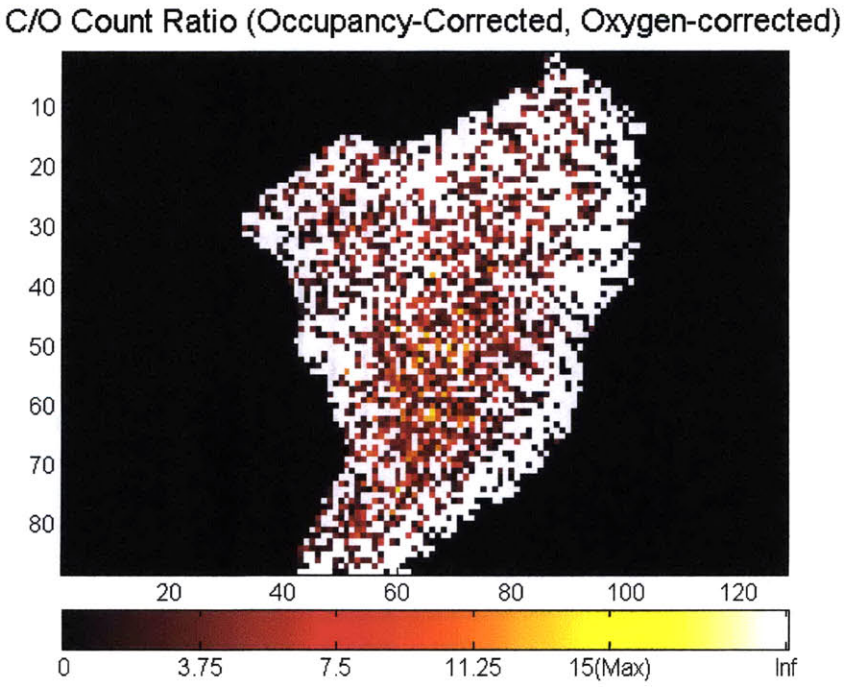

(b) Background O corrected

Lignocellulosic Char-Site #6

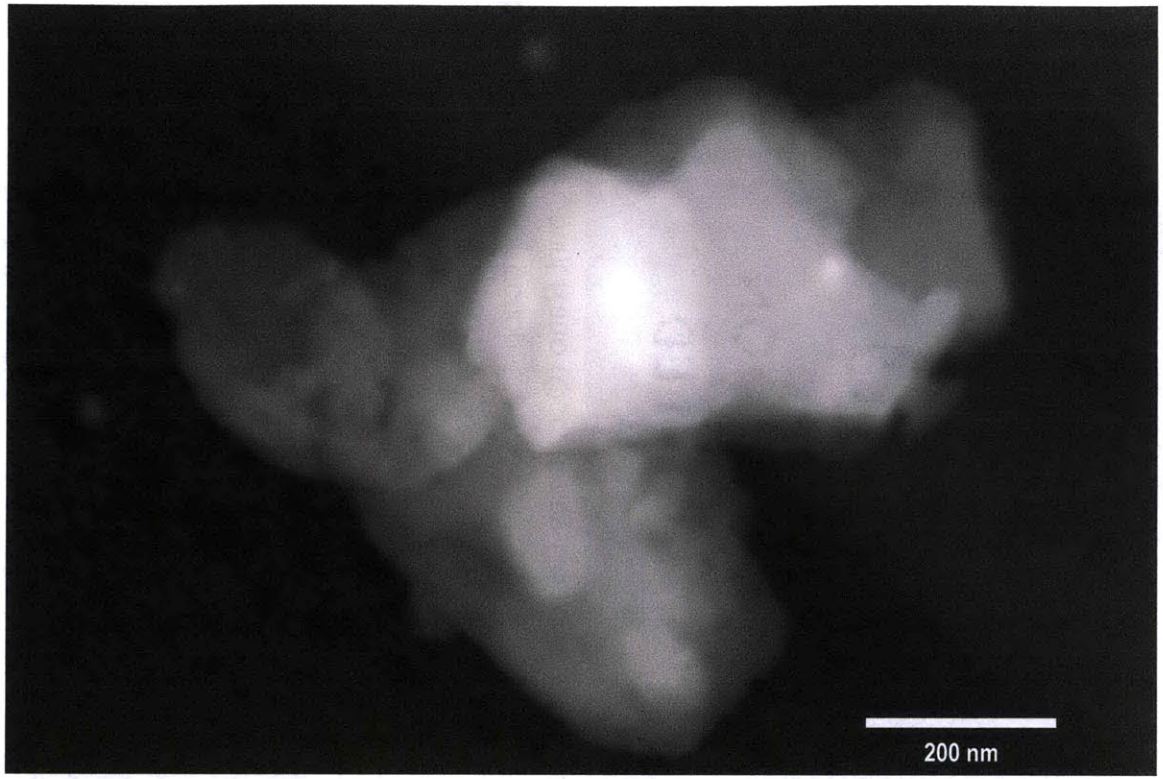

Sample: Lignocellulosic Char (Univ. of Zurich)

Site Description: Char particle

Dimension: 0.825 × 1.20 μm (88×128 pixels)

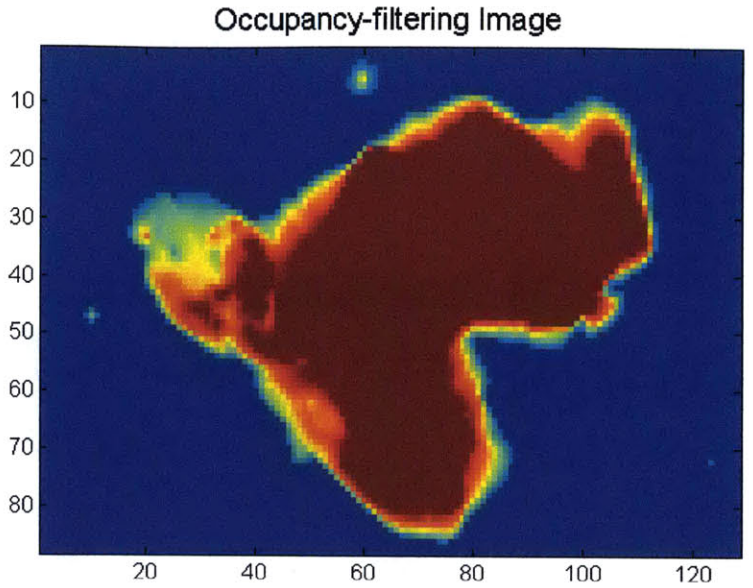
Occupancy-filtering Image
10
20
30
40
50
60
70
80
20
40
60
80
100
120

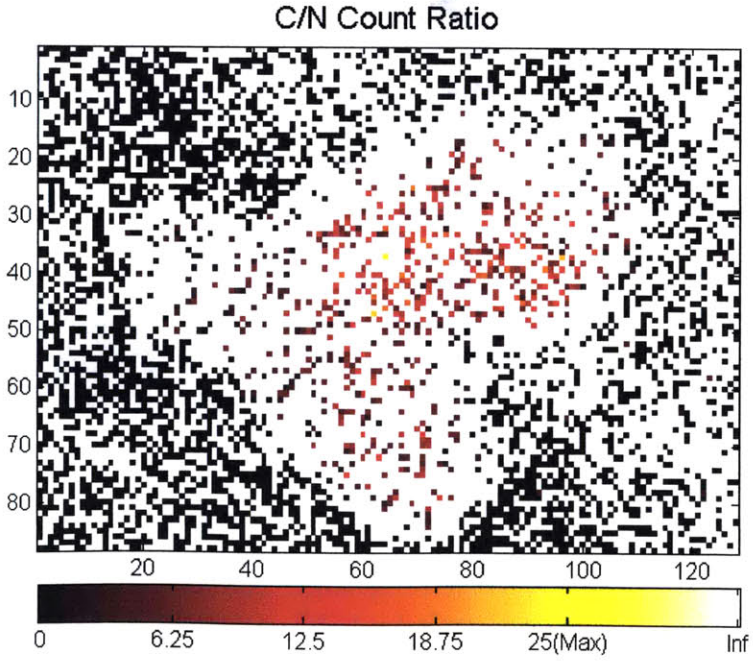
C/N Count Ratio
10
20
30
40
50
60
70
80
20
40
60
80
100
120
0
6.25
12.5
18.75
25(Max)
Inf

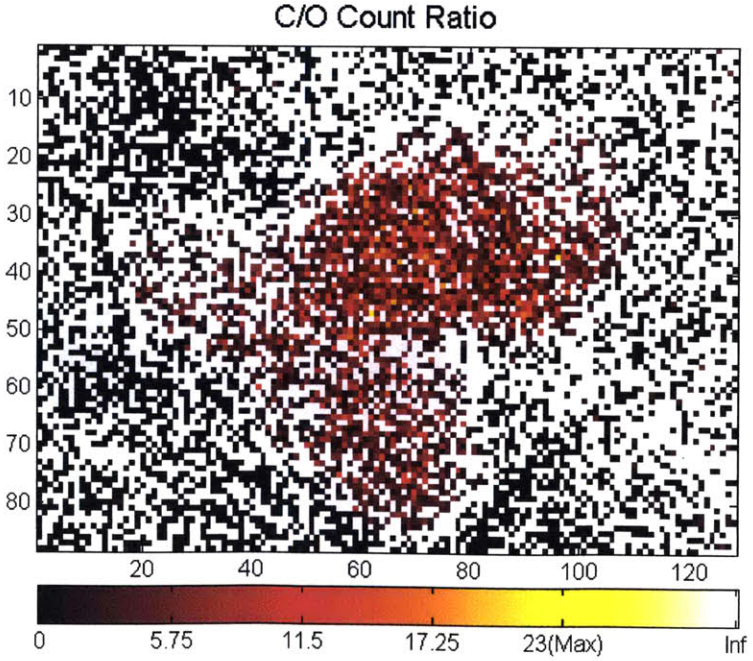
C/O Count Ratio
10
20
30
40
50
60
70
80
20
40
60
80
100
120
0
5.75
11.5
17.25
23(Max)
Inf

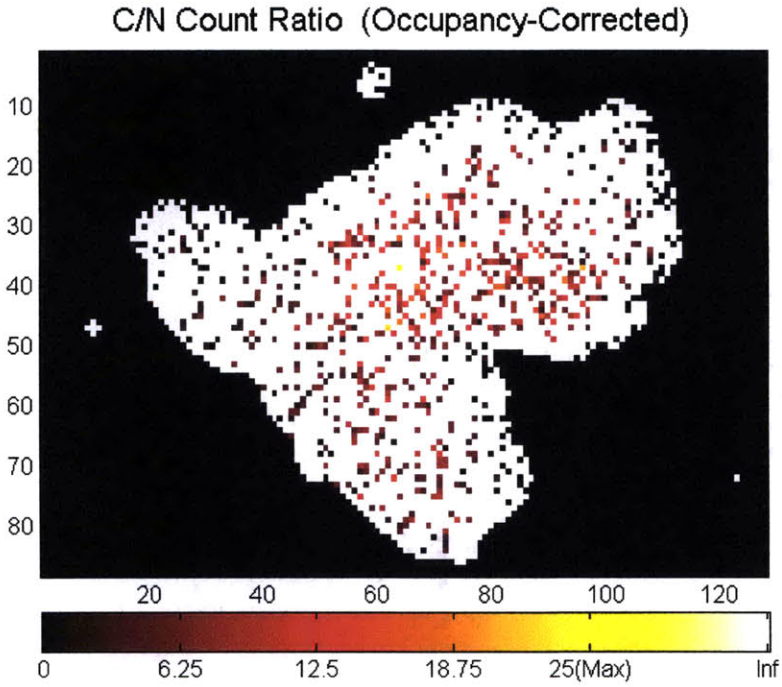

(a) No N 'noise' reduction

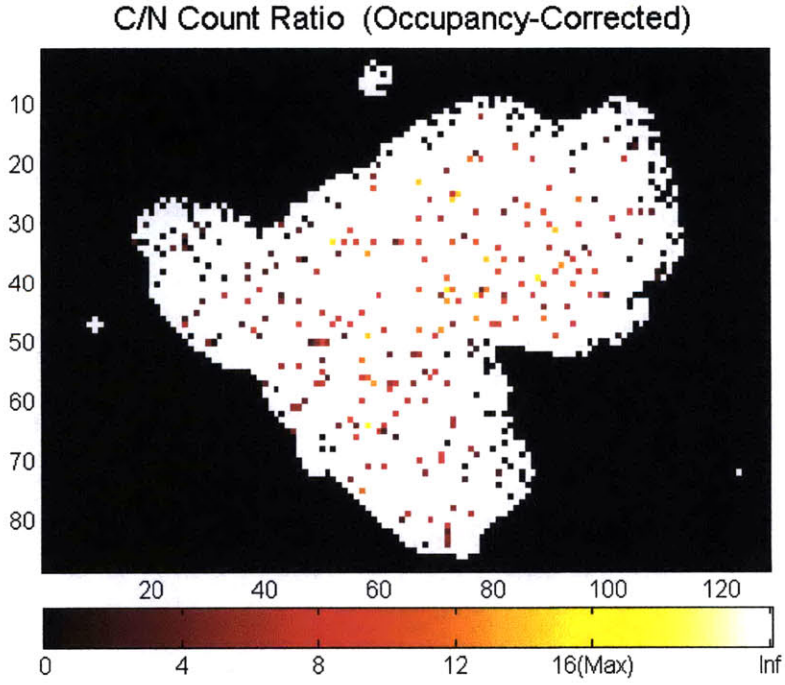

(b) N 'noise' reduction (by 1)

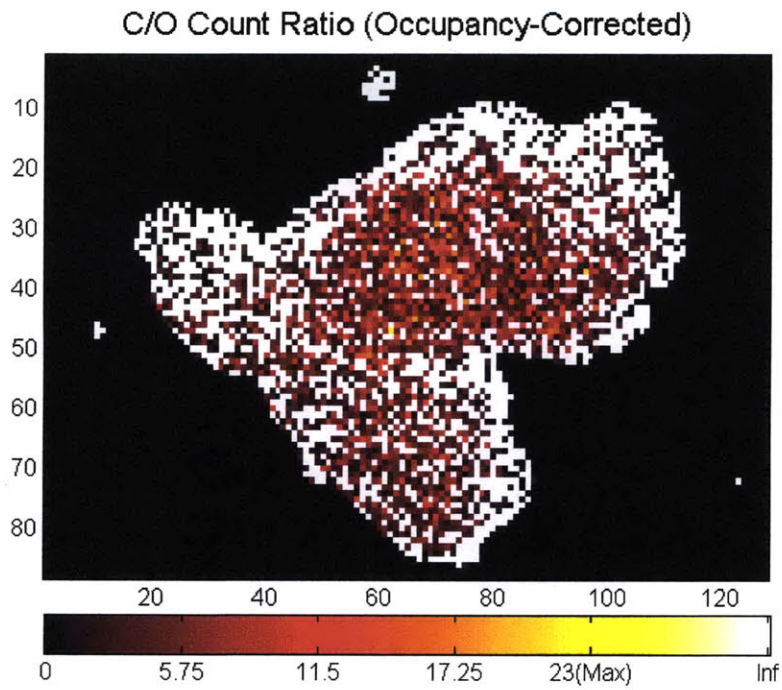

(a) No background O correction

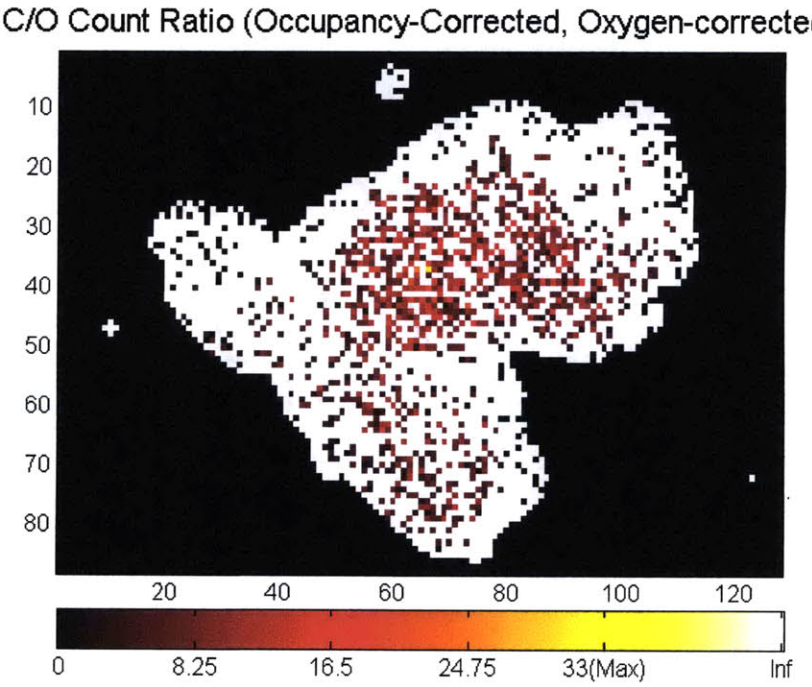

(b) Background O corrected

Melanoidin-Site #1

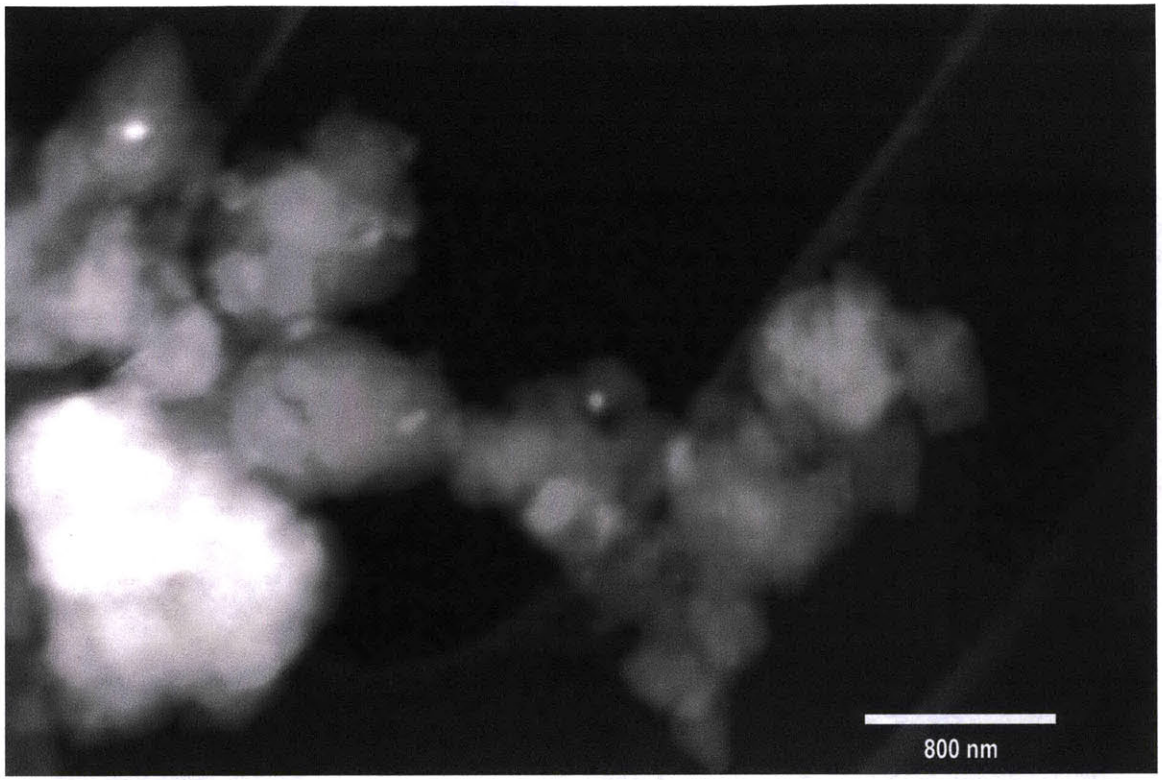

Sample: Melanoidin (Univ. of Zurich)

Site Description: Melanoidin particles

Dimension: 3.30 × 4.80 μm (88×128 pixels)

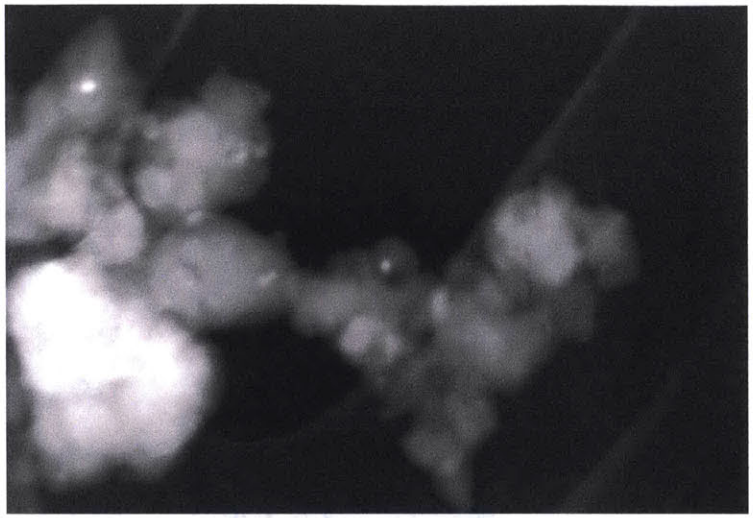

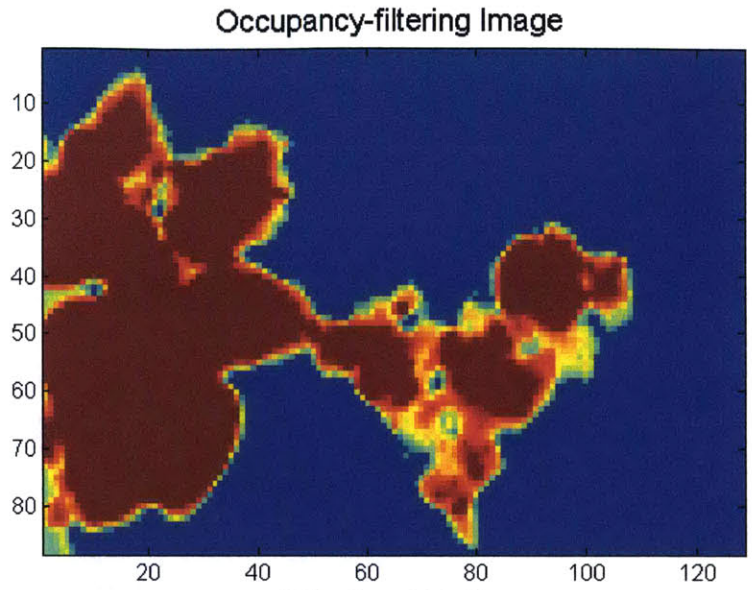
Occupancy-filtering Image
10
20
30
40
50
60
70
80
20
40
60
80
100
120

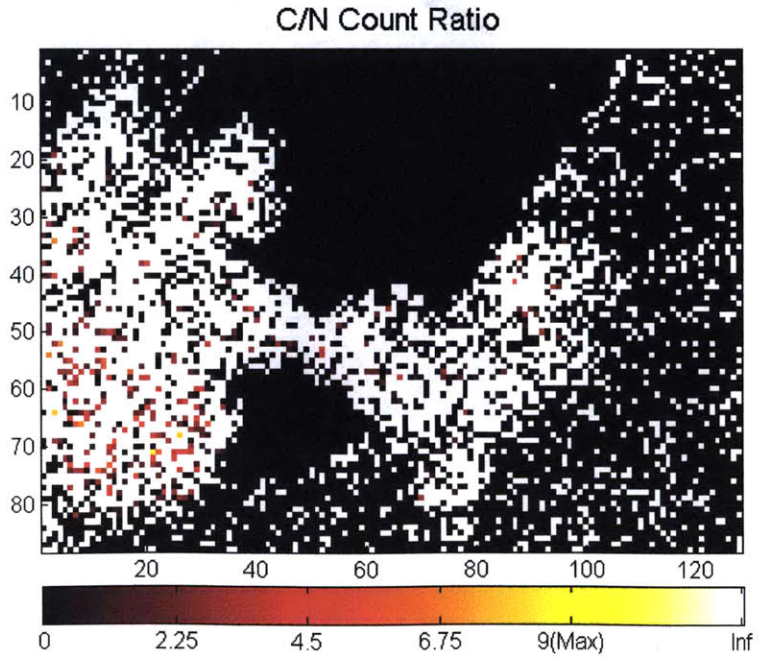
C/N Count Ratio
10
20
30
40
50
60
70
80
20
40
60
80
100
120
0
2.25
4.5
6.75
9(Max)
Inf

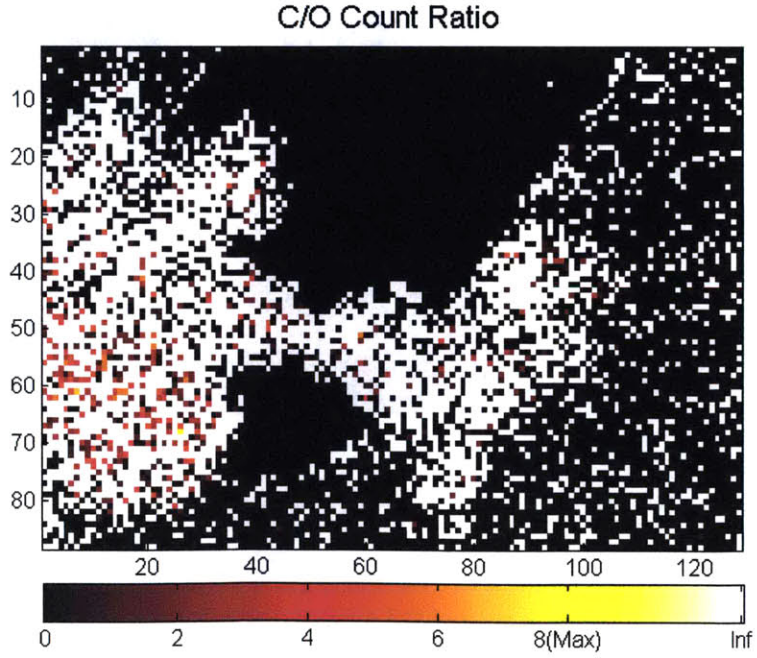
C/O Count Ratio
10
20
30
40
50
60
70
80
20
40
60
80
100
120
0
2
4
6
8(Max)
Inf

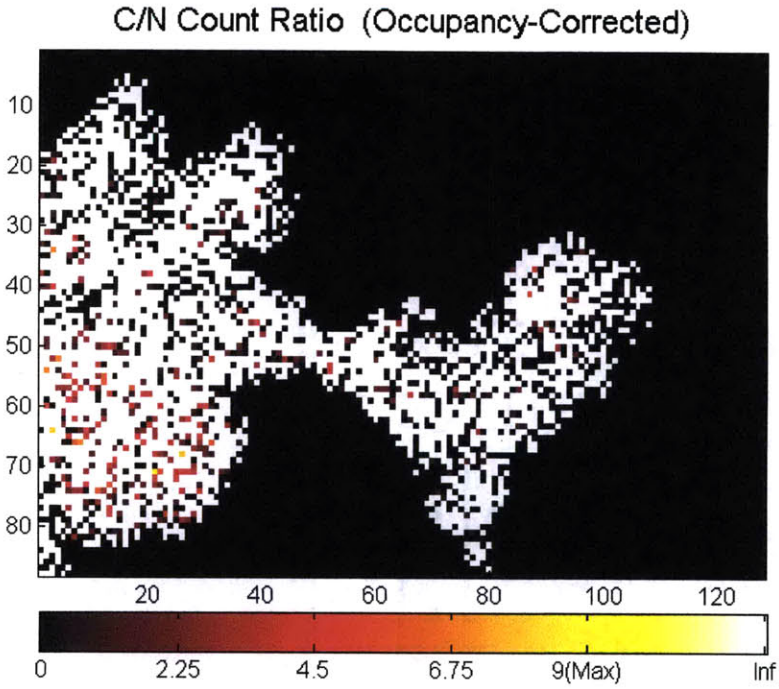

(a) No N 'noise' reduction

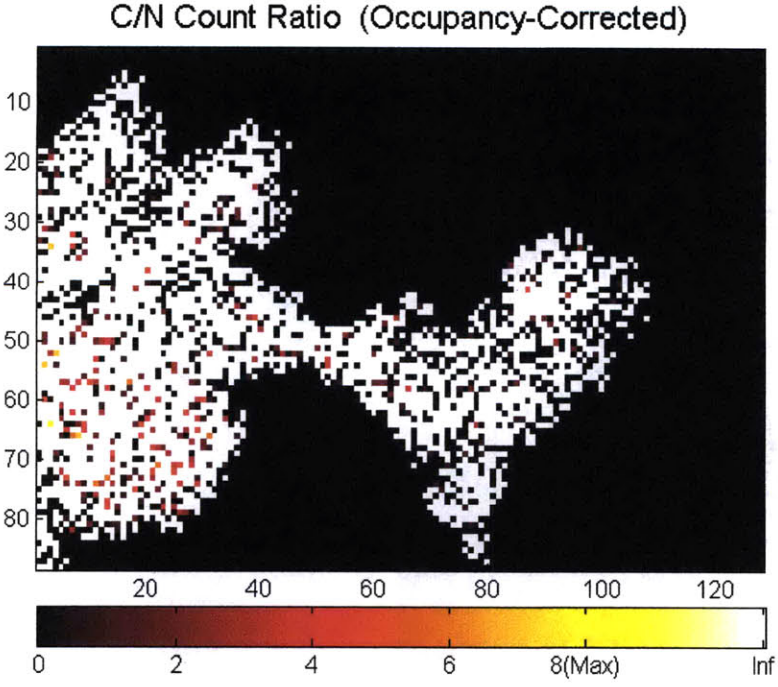

(b) N 'noise' reduction (by 1)

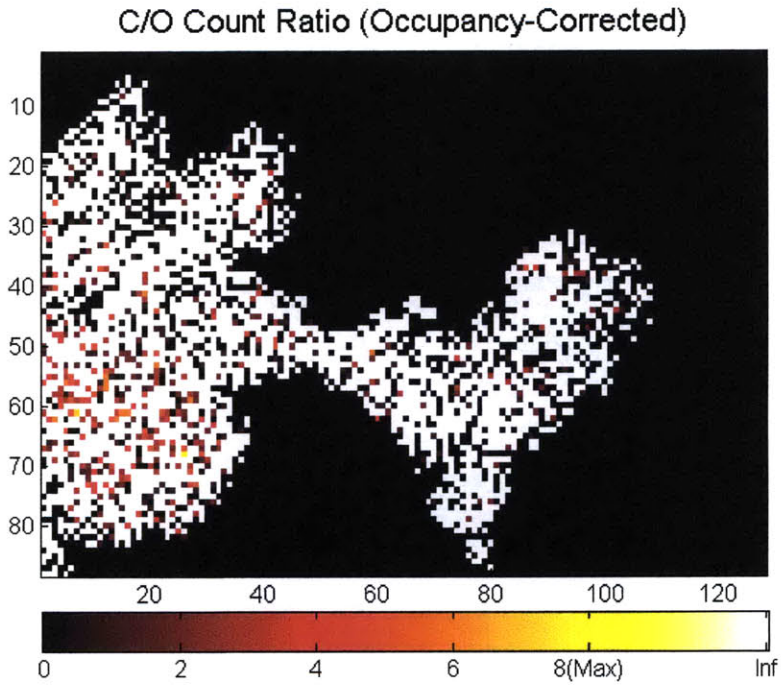

(a) No background O correction

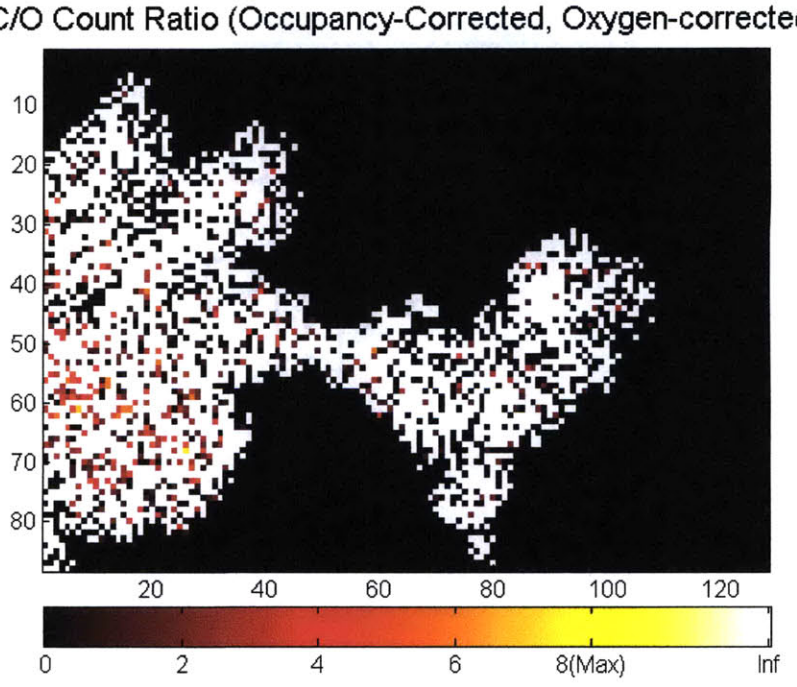

(b) Background O corrected

Melanoidin-Site #3

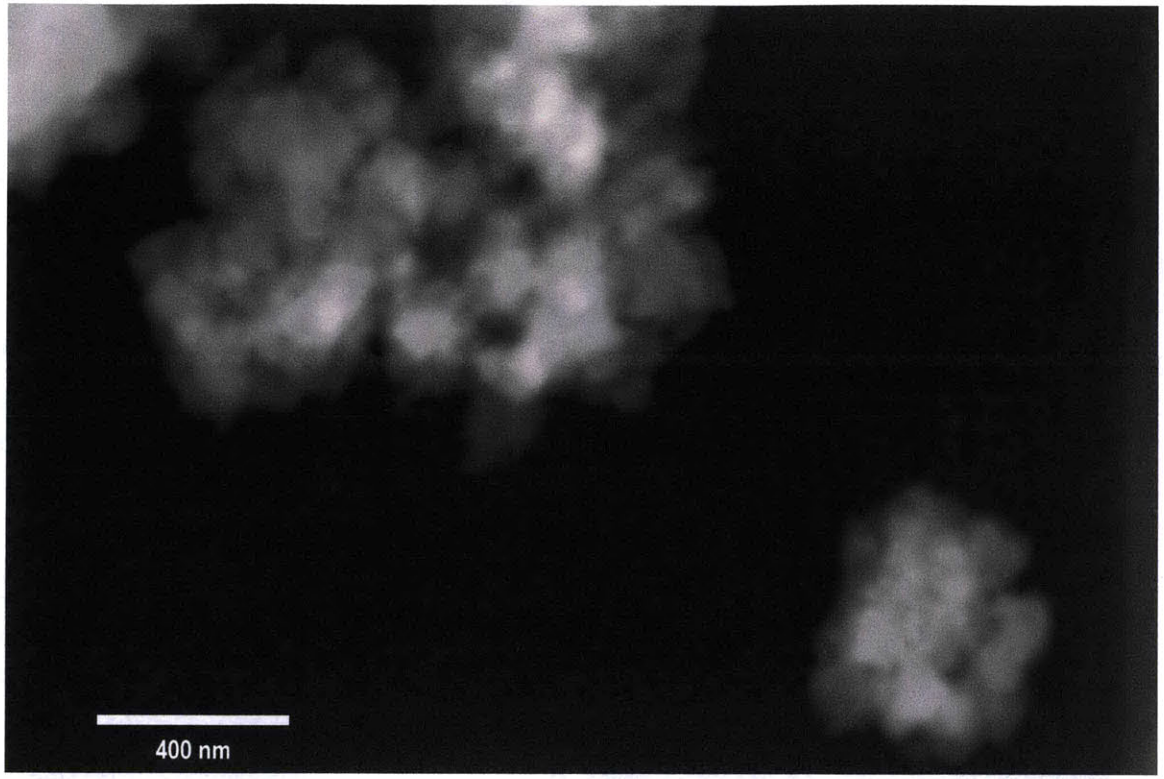

Sample: Melanoidin (Univ. of Zurich)

Site Description: Melanoidin particles

Dimension: 1.65 × 2.40 μm (88×128 pixels)

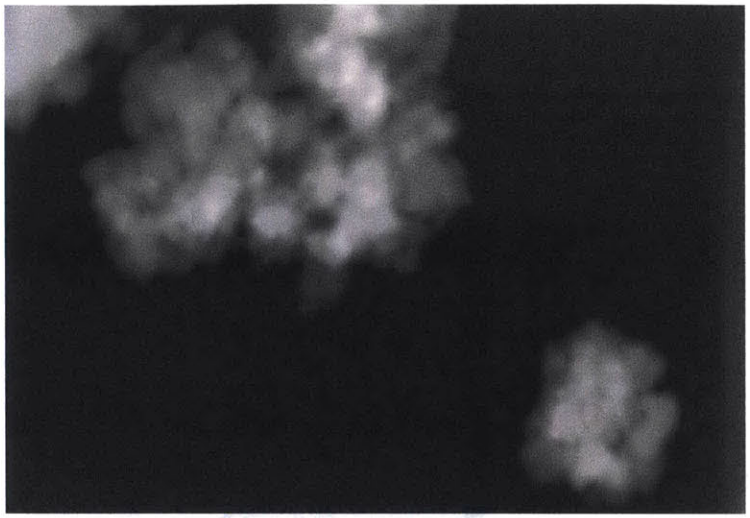

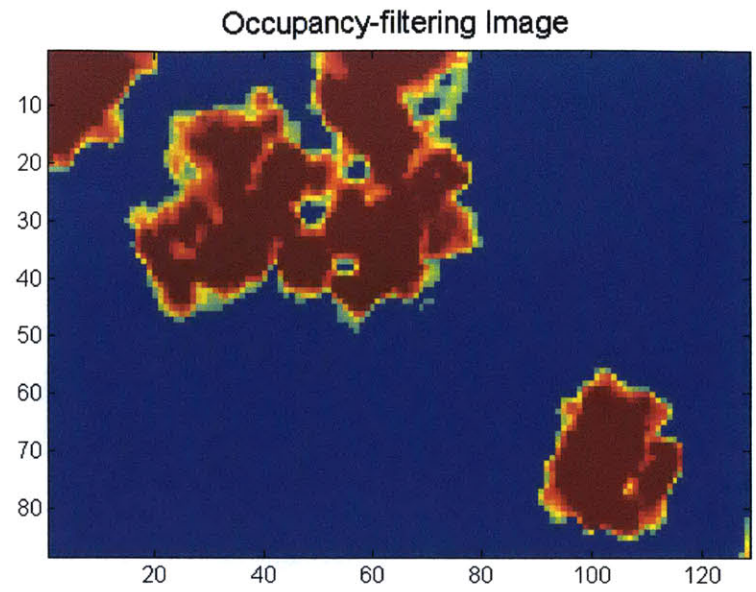
Occupancy-filtering Image
10
20
30
40
50
60
70
80
20
40
60
80
100
120

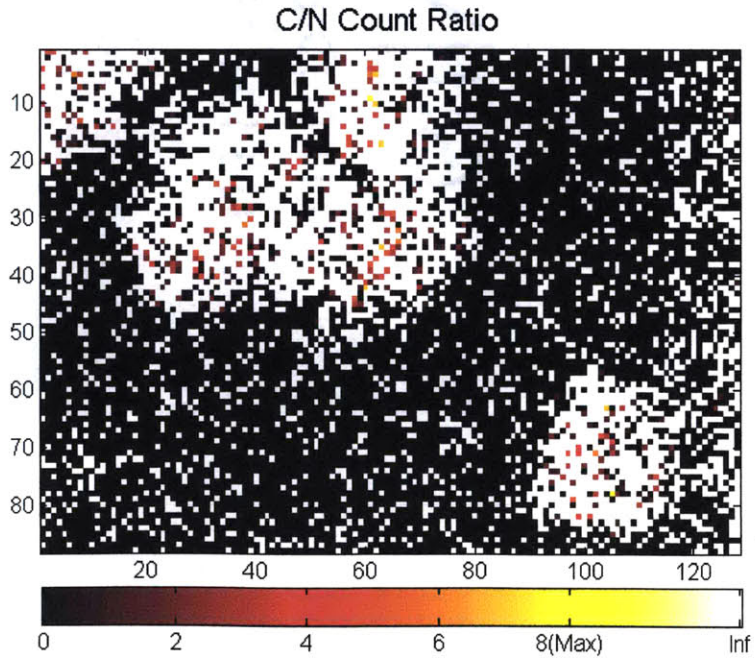
C/N Count Ratio
10
20
30
40
50
60
70
80
20
40
60
80
100
120
0
2
4
6
8(Max)
Inf

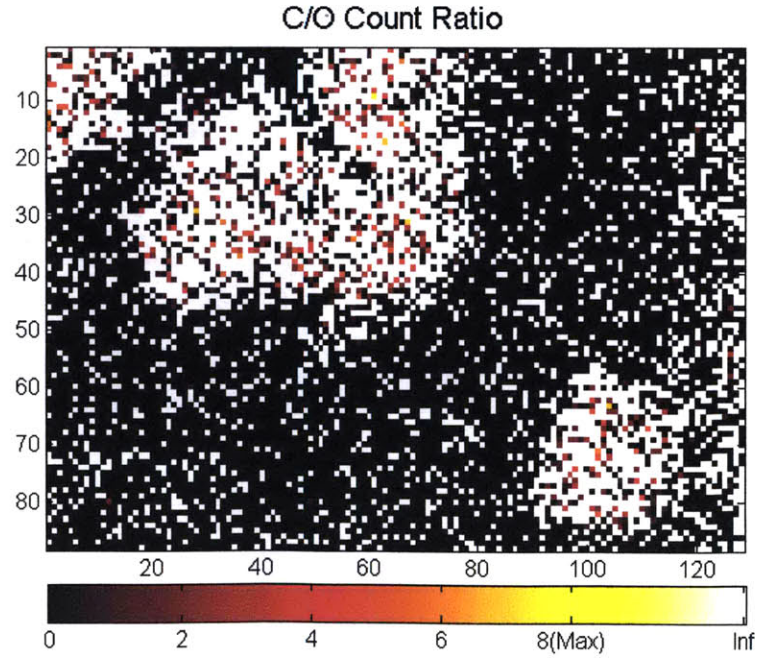
C/O Count Ratio
10
20
30
40
50
60
70
80
20
40
60
80
100
120
0
2
4
6
8(Max)
Inf

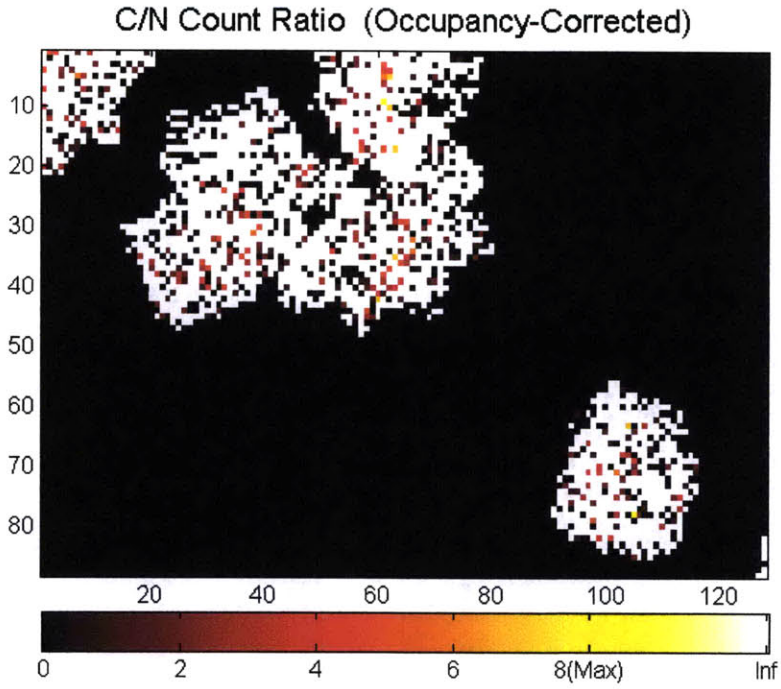

(a) No N 'noise' reduction

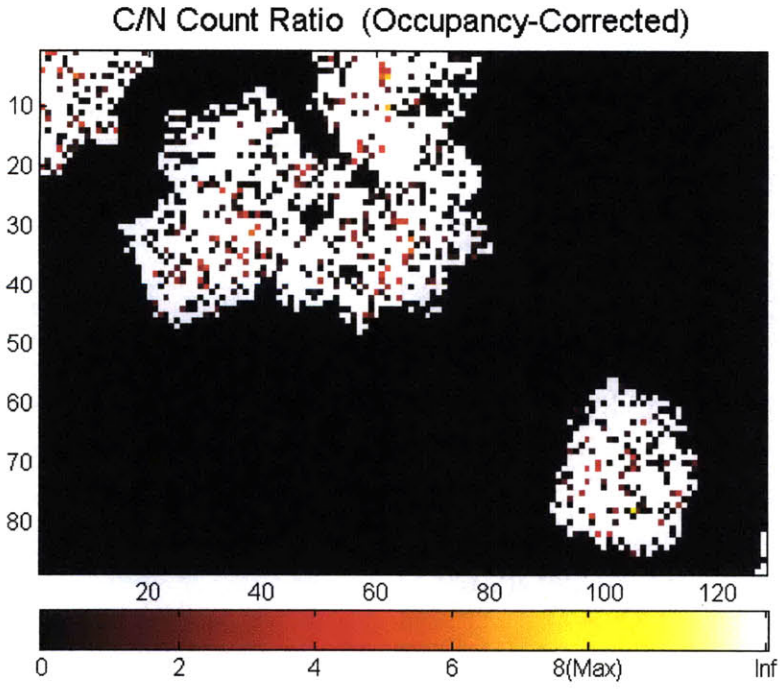

(b) N 'noise' reduction (by 1)

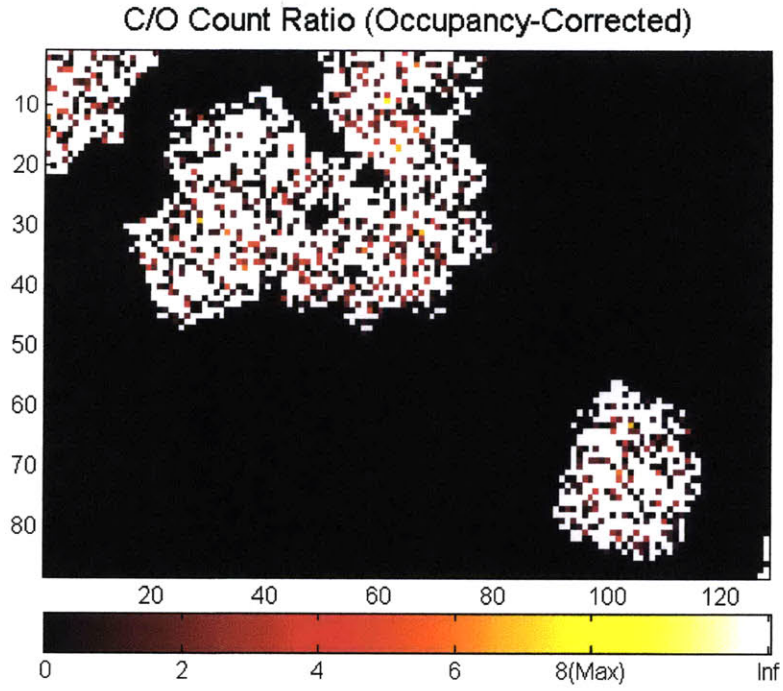

(a) No background O correction

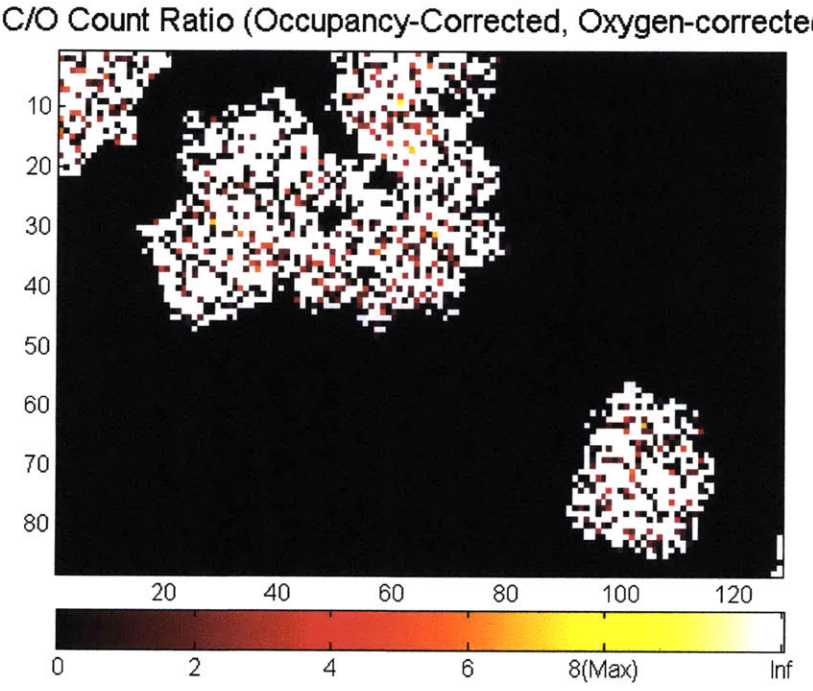

(b) Background O corrected

Appendix C: STEM-EDX Mapping Scripts

Script C - 1. STEM-EDX Mapping for Square Image..... **1094**
Script C - 2. STEM-EDX Mapping for Rectangular Image..... **1100**

Script C - 1. STEM-EDX Mapping for Square Image.

```
%%%
%%% Function EDXElemMapOldStyle.m
%%%
%%% Compute elemental map ratio of data from STEM-EDX
%%%
%%% By: Dave Kuo, 14 July 2008
%%%
%%%

function [a, b, e, f, g, h, i] = EDXElemMapOldStyle(NumRep, RemoveNSingular, FigYes);

%%% IMPORTANT: SETUP PARAMETERS
rawC        = load('c.tsv');
rawN        = load('n.tsv');
rawO        = load('o.tsv');
rawSi       = load('si.tsv');
im2crit     = 25;
im3crit     = 100;
OrigImage   = 'si3.tif';

tmp = imread(OrigImage);
%deltatmp = max(max(tmp))-min(min(tmp));
%tmp = round(64*tmp/max(max(tmp)));
if FigYes == 1
    figure, image(tmp);
end
size(rawC), size(tmp)

NumPixs     = size(rawC, 1)^2;
BasicCvr    = [sum(sum(rawC>0)), sum(sum(rawN>0)), sum(sum(rawO>0)),
sum(sum(rawSi>0))]/NumPixs;

% remove noise in N count by subtracting 1 away from rawN if C and O both
% present in the pixel
if RemoveNSingular == 1         % reduce N singal in pixel with only 1 count
    rawN        = rawN - (rawN >= 1 & rawC > 0 & rawO > 0);
    sum(sum(rawN))
    [sum(sum(rawC)), sum(sum(rawN)), sum(sum(rawO))]
end

if NumRep == 1                  % simply count ratio in each pixel
    dumCN       = rawC./rawN;
    dumCO       = rawC./rawO;
    dumSiO      = rawSi./rawO;
    cgrp        = rawC;
    ngrp        = rawN;
    ogrp        = rawO;
    sigrp       = rawSi;
    imbase      = zeros(size(cgrp,1), size(cgrp,2));
    imdummy     = imread(OrigImage);
    imdelta     = 2*NumRep - 1;
    for i = 1:size(cgrp,1)
        for j = 1:size(cgrp,2)
            imy = 2*(i-1)*NumRep+1;
            jmx  = 2*(j-1)*NumRep+1;
            imyd = imy + imdelta;
            jmxd = jmx + imdelta;
            imbase(i, j)    = sum(sum(imdummy(imy:imyd,jmx:jmxd)));
        end
    end
    imbase      = imbase/(2*NumRep)^2;      % i.e, 1px, 2x2; 4px, 8x8
```

```
end

if NumRep > 1                    % ratio in grouped pixels
    xsize       = size(rawC, 2); % number of columns
    ysize       = size(rawC, 1); % number of rows
    xgrp        = xsize/NumRep;
    ygrp        = ysize/NumRep;
    cgrp        = zeros(xgrp, ygrp);
    ngrp        = cgrp;     ogrp        = cgrp;     sigrp       = cgrp;
    imbase      = cgrp;
    imdummy     = imread(OrigImage);
    delta       = NumRep - 1;
    imdelta     = 2*NumRep - 1;
    for i = 1:ygrp
        for j = 1:xgrp
            iy  = (i-1)*NumRep+1;
            jx  = (j-1)*NumRep+1;
            imy = 2*(i-1)*NumRep+1;
            jmx  = 2*(j-1)*NumRep+1;
            iyd = iy + delta;
            jxd = jx + delta;
            imyd = imy + imdelta;
            jmxd = jmx + imdelta;
            cgrp(i, j)      = sum(sum(rawC(iy:iyd,jx:jxd)));
            ngrp(i, j)      = sum(sum(rawN(iy:iyd,jx:jxd)));
            ogrp(i, j)      = sum(sum(rawO(iy:iyd,jx:jxd)));
            sigrp(i, j)     = sum(sum(rawSi(iy:iyd,jx:jxd)));
            imbase(i, j)    = sum(sum(imdummy(imy:imyd,jmx:jmxd)));
        end
    end
    imbase      = imbase/(2*NumRep)^2;      % i.e, 1px, 2x2; 4px, 8x8
    dumCN       = cgrp./ngrp;
    dumCO       = cgrp./ogrp;
    dumSiO      = sigrp./ogrp;
end

nrow        = size(dumCN,1);     % number of rows
ncol        = size(dumCN,2);     % number of columns

dumCN(isnan(dumCN))     = 0;        % set all cell with NaN to 0
dumCO(isnan(dumCO))     = 0;        % same as above
dumSiO(isnan(dumSiO))   = 0;        % same as above

totpix                  = size(cgrp, 1)^2;

%%% simple, no occupancy-correction CN ratio
cn1                     = zeros(nrow, ncol);
NcnNZ                   = sum(sum(dumCN>0))
testcninf               = dumCN;
testcninf(dumCN>0)      = Inf;
Ncninf                  = sum(sum(isinf(dumCN)));
Ncnfin                  = NcnNZ - Ncninf;
NZcnCvr_tot             = NcnNZ/totpix;
NZcnCvr_fin             = Ncnfin/totpix;
if FigYes == 1
    cn1(isinf(dumCN))       = 128;
    cn2                     = dumCN;
    cn2(isinf(dumCN))       = 0;
    cnfmx                   = max(max(cn2));            % max, finite c:n ratio
    cn3                     = cn2./cnfmx*96;
    cnmap                   = cn1 + cn3;
    cnflb                   = cnfmx/4;
    cnbarlabel              =
{'0',num2str(cnflb),num2str(cnflb*2),num2str(cnflb*3),[num2str(cnfmx),'(Max)'],'Inf'};
    cntick                  = [1, 25, 49, 73, 97, 128]; % acc to a 128-color map
    figure, image(cnmap), colormap(hot(128));

colorbar('southoutside','xtick',cntick,'xticklabel',cnbarlabel,'Fontname','Arial','Fontsiz
e',12);
    set(gcf,'position',[1, 1, 641, 726]);
    title('C/N Count Ratio', 'Fontname', 'Arial', 'Fontsize', 16);
    set(gca,'Fontname', 'arial', 'Fontsize', 12);
end


%%% simple, no occupancy-correction CO ratio
co1                     = zeros(nrow, ncol);
NcoNZ                   = sum(sum(dumCO>0))
Ncoinf                  = sum(sum(isinf(dumCO)));
Ncofin                  = NcoNZ - Ncoinf;
NZcoCvr_tot             = NcoNZ/totpix;
```

```
NZcoCvr_fin          = Ncofin/totpix;
if FigYes == 1
    co1(isinf(dumCO))       = 128;
    co2                     = dumCO;
    co2(isinf(dumCO))       = 0;
    cofmx                   = max(max(co2));
    co3                     = co2./max(max(co2))*96;
    comap                   = co1 + co3;
    coflb                   = cofmx/4;
    cobarlabel              =
{'0',num2str(coflb),num2str(coflb*2),num2str(coflb*3),[num2str(cofmx),'(Max)'],'Inf'};
    cotick                  = [1, 25, 49, 73, 97, 128]; % acc to a 128-color map
    figure, image(comap), colormap(hot(128));

colorbar('southoutside','xtick',cotick,'xticklabel',cobarlabel,'Fontname','Arial','Fontsiz
e',12);
    set(gcf,'position',[1, 1, 641, 726]);
    title('C/O Count Ratio', 'Fontname', 'Arial', 'Fontsize', 16);
    set(gca,'Fontname', 'arial', 'Fontsize', 12);
    %colorbar('southoutside','xtick',cotick,'xticklabel',cobarlabel,'Fontname','Arial','Fo
ntsize',12);
end


%%% simple, no occupancy-correction SiO ratio
sio1                    = zeros(nrow, ncol);
NsioNZ                  = sum(sum(dumSiO>0));
Nsioinf                 = sum(sum(isinf(dumSiO)));
Nsiofin                 = NsioNZ - Nsioinf;
NZsioCvr_tot            = NsioNZ/totpix;
NZsioCvr_fin            = Nsiofin/totpix;
if FigYes == 1
    sio1(isinf(dumSiO))     = 128;
    sio2                    = dumSiO;
    sio2(isinf(dumSiO))     = 0;
    siofmx                  = max(max(sio2));           % max, finite Si:O ratio
    sio3                    = sio2./siofmx*96;
    siomap                  = sio1 + sio3;
    sioflb                  = siofmx/4;
    siobarlabel             =
{'0',num2str(sioflb),num2str(sioflb*2),num2str(sioflb*3),[num2str(siofmx),'(Max)'],'Inf'};
    siotick                 = [1, 25, 49, 73, 97, 128]; % acc to a 128-color map
    figure, image(siomap), colormap(hot(128));

colorbar('southoutside','xtick',siotick,'xticklabel',siobarlabel,'Fontname','Arial','Fonts
ize',12);
    set(gcf,'position',[1, 1, 641, 726]);
    title('Si/O Count Ratio', 'Fontname', 'Arial', 'Fontsize', 16);
    set(gca,'Fontname', 'arial', 'Fontsize', 12);
end


%%% output simple ratio results
NZcno_bothcvr           = sum(sum(dumCO>0 & dumCN>0));
NZcno_totcvr            = sum(sum(dumCO>0)+sum(dumCN>0));
NZcno_bothinfinity      = sum(sum(isinf(dumCO) & isinf(dumCN)));
fprintf('Simple Ratio Coverage\n');
fprintf('f_CNtot: %2.4f     f_CNfin: %2.4f \n',NZcnCvr_tot, NZcnCvr_fin);
fprintf('f_COtot: %2.4f     f_COfin: %2.4f \n',NZcoCvr_tot, NZcoCvr_fin);
fprintf('f_SiOtot: %2.4f     f_SiOfin: %2.4f \n',NZsioCvr_tot, NZsioCvr_fin);
fprintf('f_CN_or_CO_tot: %2.4f     \n',NZcno_totcvr/totpix);
fprintf('f_CN&COboth: %2.4f     \n',NZcno_bothcvr/totpix);
fprintf('f_CN&CO-infinity: %2.4f     \n', NZcno_bothinfinity/totpix);
fprintf('total pixels: %5.1f      \n\n\n', totpix);

sumtestcninf            = sum(sum(isinf(testcninf)));
fprintf('testcninf: %5.1f     \n', sumtestcninf);
fprintf('newCNO inf: %2.4f     \n\n\n', sum(sum(isinf(dumCO) & isinf(testcninf)))/totpix);


%%%
%%% SAMPLE OCCUPANCY FILTERED ELEMENTAL RATIO
%%%

%%% print ORIGINAL IMAGE in ORIGINAL RESOLUTION in grayscale
%figure;
aa=imread(OrigImage);
%%%%% uses the following two lines ONLY for 20061013-Site #6, 20061019-Site #13 *****
%aa=max(max(aa))-aa;
%imbase=max(max(imbase))-imbase;
```

```
im2                 = imbase;
im3                 = imbase;
im2(imbase<im2crit) = 0;        % treat pixels with values < 40 as blank/bkgd
im3(imbase<im3crit) = 0;        % treat pixels with values < 50 as blank/bkgd
%figure, image(im2), set(gcf,'position',[1, 1, 641, 641]);
%figure, image(im3), set(gcf,'position',[1, 1, 641, 641]);

if FigYes == 1
    image(aa), set(gcf,'position',[1, 1, 641, 641]), colormap(gray);
    title('Original Micrograph Image', 'Fontname', 'Arial', 'Fontsize', 16);
    set(gca,'Fontname', 'arial', 'Fontsize', 12);

    %%% print FILTERED-image in grayscale
    figure, image(imbase), set(gcf,'position',[1, 1, 641, 641]), colormap(gray);
    title('Micrograph Image (Pixels-Consolidated)', 'Fontname', 'Arial', 'Fontsize', 16);
    set(gca,'Fontname', 'arial', 'Fontsize', 12);

    %%% print omic-filter image, ***IM2*** in default colormap (blue-red scale)
    figure, image(im2), set(gcf,'position',[1, 1, 641, 641]);
    title('Occupancy-filtering Image', 'Fontname', 'Arial', 'Fontsize', 16);
    set(gca,'Fontname', 'arial', 'Fontsize', 12);
end

%%% set im2 as the sample-occupancy filtering basis matrix
imfil               = im2;
figure, image (imfil);
%%% filtering of ratios via Original Matter-Image Confirmation (OMIC)\
size(imfil);
omic_totpix         = sum(sum(imfil>0));              % count total sample-occupied pixels
%imk                 = imfil;
%imk(imfil>0)        = 1;
%figure, image(imk);
%%% OMIC for C:N
omic_dumCN          = dumCN;
%size(omic_dumCN), size(imfil), size(im2)
omic_dumCN(imfil==0)= 0;                             % filter out signals in non-occupied
pixels
omic_cntot          = sum(sum(omic_dumCN>0));        % count all pixels with +ve ratio
omic_cninf          = sum(sum(isinf(omic_dumCN)));   % count pixels with ratio=infinity
omic_cnfin          = omic_cntot - omic_cninf;       % pixels with finite counts
omic_f_cntot        = omic_cntot/omic_totpix;
omic_f_cnfin        = omic_cnfin/omic_totpix;
if FigYes == 1
    cn1                     = zeros(nrow, ncol);
    cn1(isinf(omic_dumCN))  = 128;
    cn2                     = omic_dumCN;
    cn2(isinf(omic_dumCN))  = 0;
    cnfmx                   = max(max(cn2));            % max, finite c:n ratio
    cn3                     = cn2./cnfmx*96;
    cnmap                   = cn1 + cn3;
    cnflb                   = cnfmx/4;
    cnbarlabel              =
{'0',num2str(cnflb),num2str(cnflb*2),num2str(cnflb*3),[num2str(cnfmx),'(Max)'],'Inf'};
    cntick                  = [1, 25, 49, 73, 97, 128]; % acc to a 128-color map
    figure, image(cnmap), colormap(hot(128));

colorbar('southoutside','xtick',cntick,'xticklabel',cnbarlabel,'Fontname','Arial','Fontsiz
e',12);
    set(gcf,'position',[1, 1, 641, 726]);
    title('C/N Count Ratio  (Occupancy-Corrected)', 'Fontname', 'Arial', 'Fontsize', 16);
    set(gca,'Fontname', 'arial', 'Fontsize', 12);
end

%%% OMIC for C:N
omic_dumCO          = dumCO;
omic_dumCO(imfil==0)= 0;                             % filter out signals in non-occupied
pixels
omic_cotot          = sum(sum(omic_dumCO>0));        % count all pixels with +ve ratio
omic_coinf          = sum(sum(isinf(omic_dumCO)));   % count pixels with ratio=infinity
omic_cofin          = omic_cotot - omic_coinf;       % pixels with finite counts
omic_f_cotot        = omic_cotot/omic_totpix;
omic_f_cofin        = omic_cofin/omic_totpix;
if FigYes == 1
    co1                     = zeros(nrow, ncol);
    co1(isinf(omic_dumCO))  = 128;
    co2                     = omic_dumCO;
    co2(isinf(omic_dumCO))  = 0;
    cofmx                   = max(max(co2));
    co3                     = co2./max(max(co2))*96;
    comap                   = co1 + co3;
    coflb                   = cofmx/4;
```

```
    cobarlabel              =
{'0',num2str(coflb),num2str(coflb*2),num2str(coflb*3),[num2str(cofmx),'(Max)'],'Inf'};
    cotick                  = [1, 25, 49, 73, 97, 128]; % acc to a 128-color map
    figure, image(comap), colormap(hot(128));

colorbar('southoutside','xtick',cotick,'xticklabel',cobarlabel,'Fontname','Arial','Fontsiz
e',12);
    set(gcf,'position',[1, 1, 641, 726]);
    title('C/O Count Ratio (Occupancy-Corrected)', 'Fontname', 'Arial', 'Fontsize', 16);
    set(gca,'Fontname', 'arial', 'Fontsize', 12);
end

%%% OMIC for Si:O
omic_dumSiO          = dumSiO;
omic_dumSiO(imfil==0)= 0;                                % filter out signals in non-occupied
pixels
omic_siotot          = sum(sum(omic_dumSiO>0));          % count all pixels with +ve ratio
omic_sioinf          = sum(sum(isinf(omic_dumSiO)));     % count pixels with ratio=infinity
omic_siofin          = omic_siotot - omic_sioinf;        % pixels with finite counts
omic_f_siotot        = omic_siotot/omic_totpix;
omic_f_siofin        = omic_siofin/omic_totpix;
if FigYes == 1
    sio1                     = zeros(nrow, ncol);
    sio1(isinf(omic_dumSiO)) = 128;
    sio2                     = omic_dumSiO;
    sio2(isinf(omic_dumSiO)) = 0;
    siofmx                   = max(max(sio2));
    sio3                     = sio2./max(max(sio2))*96;
    siomap                   = sio1 + sio3;
    sioflb                   = siofmx/4;
    siobarlabel              =
{'0',num2str(sioflb),num2str(sioflb*2),num2str(sioflb*3),[num2str(siofmx),'(Max)'],'Inf'};
    siotick                  = [1, 25, 49, 73, 97, 128]; % acc to a 128-color map
    figure, image(siomap), colormap(hot(128));

colorbar('southoutside','xtick',siotick,'xticklabel',siobarlabel,'Fontname','Arial','Fonts
ize',12);
    set(gcf,'position',[1, 1, 641, 726]);
    title('Si/O Count Ratio (Occupancy-Corrected)', 'Fontname', 'Arial', 'Fontsize', 16);
    set(gca,'Fontname', 'arial', 'Fontsize', 12);
end

%%% output occupany-filtering ratio results
NZcno_bothcvr           = sum(sum(omic_dumCO>0 & omic_dumCN>0));
NZcno_bothinfinity      = sum(sum(isinf(omic_dumCO) & isinf(omic_dumCN)));
fprintf('Occupancy-Based Coverage\n');
fprintf('omic_f_CNtot: %2.4f     omic_f_CNfin: %2.4f \n', omic_f_cntot, omic_f_cnfin);
fprintf('omic_f_COtot: %2.4f     omic_f_COfin: %2.4f \n', omic_f_cotot, omic_f_cofin);
fprintf('omic_f_SiOtot: %2.4f     omic_f_SiOfin: %2.4f \n', omic_f_siotot, omic_f_siofin);
fprintf('omic_f_CN&COtot: %2.4f     \n',NZcno_bothcvr/omic_totpix);
fprintf('omic_f_CN&CO-infinity: %2.4f     \n', NZcno_bothinfinity/omic_totpix);
fprintf('sample-occupied pixels: %6.0f     \n', omic_totpix);
fprintf('sample coverage: %2.4f     \n', omic_totpix/totpix);
fprintf('total pixels: %6.0f     \n\n\n', totpix);



%%% OMIC for C:N + O-reduction according to bkgdSiO ratio determined from
%%% non-occupancy region
%%%

%%% estimate bkgd SiO signal from non-occupied area
bkgdSi               = sigrp;
bkgdO                = ogrp;
%size(bkgdSi), size(imfil)

bkgdSi(imfil>0)      = 0;
totbkgdSi            = sum(sum(bkgdSi));
bkgdO(imfil>0)       = 0;
totbkgdO             = sum(sum(bkgdO));
%%%
%%% Bkgd SiO ratio
%%%
bkgdSiO              = totbkgdSi/totbkgdO;
%bkgdSiO               = 2;

%%% find pixels that require O correction (i.e., C:O>0, Si:O>0, and Si:O
%%% not infinite
%new_omic_dumCO           = omic_dumCO;
```

```
%ocorrmatrx              = omic_dumCO(omic_dumCO>0 & omic_dumSiO>0 &
~isinf(omic_dumSiO))   % mark pixels that need O-correction
newogrp                  = ogrp - ceil(sigrp/bkgdSiO);
newogrp(newogrp<0)       = 0;

newomic_dumCO            = cgrp./newogrp;
newomic_dumCO(isnan(newomic_dumCO))     = 0;            % remove 'NaN' pixels
newomic_dumCO(imfil==0)= 0;                             % filter out signals in non-
occupied pixels
newomic_cotot            = sum(sum(newomic_dumCO>0));       % count all pixels with +ve
ratio
newomic_coinf            = sum(sum(isinf(newomic_dumCO)));  % count pixels with
ratio=infinity
newomic_cofin            = newomic_cotot - newomic_coinf;      % pixels with finite counts
newomic_f_cotot          = newomic_cotot/omic_totpix;
newomic_f_cofin          = newomic_cofin/omic_totpix;
if FigYes == 1
    newco1                      = zeros(nrow, ncol);
    newco1(isinf(newomic_dumCO))  = 128;
    newco2                      = newomic_dumCO;
    newco2(isinf(newomic_dumCO))  = 0;
    newcofmx                    = max(max(newco2));
    newco3                      = newco2./max(max(newco2))*96;
    newcomap                    = newco1 + newco3;
    newcoflb                    = newcofmx/4;
    newcobarlabel               =
{'0',num2str(newcoflb),num2str(newcoflb*2),num2str(newcoflb*3),[num2str(newcofmx),'(Max)']
,'Inf'};
    newcotick                   = [1, 25, 49, 73, 97, 128]; % acc to a 128-color map
    figure, image(newcomap), colormap(hot(128));

colorbar('southoutside','xtick',newcotick,'xticklabel',newcobarlabel,'Fontname','Arial','F
ontsize',12);
    set(gcf,'position',[1, 1, 641, 726]);
    title('C/O Count Ratio (Occupancy-Corrected, Oxygen-corrected)', 'Fontname', 'Arial',
'Fontsize', 16);
    set(gca,'Fontname', 'arial', 'Fontsize', 12);
end

%%% output occupany-filtering ratio results
NZcno_bothcvr           = sum(sum(newomic_dumCO>0 & omic_dumCN>0));
NZcno_bothinfinity      = sum(sum(isinf(newomic_dumCO) & isinf(omic_dumCN)));
fprintf('Occupancy-Based Oxygen-Corrected Coverage\n');
fprintf('Background SiO: %2.4f \n', bkgdSiO);
fprintf('omic_f_COtot: %2.4f     omic_f_COfin: %2.4f \n', newomic_f_cotot,
newomic_f_cofin);
fprintf('omic_f_CN&COtot: %2.4f     \n',NZcno_bothcvr/omic_totpix);
fprintf('omic_f_CN&CO-infinity: %2.4f     \n', NZcno_bothinfinity/omic_totpix);
fprintf('sample-occupied pixels: %6.0f     \n', omic_totpix);
fprintf('sample coverage: %2.4f     \n', omic_totpix/totpix);
fprintf('total pixels: %6.0f     \n\n\n', totpix);


%%% return function output parameters
a=BasicCvr;
b=bkgdSiO;
e=cgrp;
f=ngrp;
g=ogrp;
h=a;
i=b;
```

Script C - 2. STEM-EDX Mapping for Rectangular Image.

```
%%%
%%% Function EDXElemMapOldStyle.m
%%%
%%% Compute elemental map ratio of data from STEM-EDX
%%%
%%% By: Dave Kuo, 14 July 2008
%%%
%%%

function [a, b, e, f, g, h, i] = EDXElemMapOldStyle(NumRep, RemoveNSingular, FigYes);

%%% IMPORTANT: SETUP PARAMETERS
rawC        = load('c.tsv');
rawN        = load('n.tsv');
rawO        = load('o.tsv');
rawSi       = load('si.tsv');
im2crit     = 25;
im3crit     = 100;
OrigImage   = 'si3.tif';

tmp = imread(OrigImage);
%deltatmp = max(max(tmp))-min(min(tmp));
%tmp = round(64*tmp/max(max(tmp)));
if FigYes == 1
    figure, image(tmp);
end
size(rawC), size(tmp)

NumPixs     = size(rawC, 1)^2;
BasicCvr    = [sum(sum(rawC>0)), sum(sum(rawN>0)), sum(sum(rawO>0)),
sum(sum(rawSi>0))]/NumPixs;

% remove noise in N count by subtracting 1 away from rawN if C and O both
% present in the pixel
if RemoveNSingular == 1         % reduce N singal in pixel with only 1 count
    rawN        = rawN - (rawN >= 1 & rawC > 0 & rawO > 0);
    sum(sum(rawN))
    [sum(sum(rawC)), sum(sum(rawN)), sum(sum(rawO))]
end

if NumRep == 1                  % simply count ratio in each pixel
    dumCN       = rawC./rawN;
    dumCO       = rawC./rawO;
    dumSiO      = rawSi./rawO;
    cgrp        = rawC;
    ngrp        = rawN;
    ogrp        = rawO;
    sigrp       = rawSi;
    imbase      = zeros(size(cgrp,1), size(cgrp,2));
    imdummy     = imread(OrigImage);
    imdelta     = 2*NumRep - 1;
    for i = 1:size(cgrp,1)
        for j = 1:size(cgrp,2)
            imy = 2*(i-1)*NumRep+1;
            jmx  = 2*(j-1)*NumRep+1;
            imyd = imy + imdelta;
            jmxd = jmx + imdelta;
            imbase(i, j)    = sum(sum(imdummy(imy:imyd,jmx:jmxd)));
        end
    end
    imbase      = imbase/(2*NumRep)^2;      % i.e, 1px, 2x2; 4px, 8x8
end

if NumRep > 1                   % ratio in grouped pixels
    xsize       = size(rawC, 2); % number of columns
    ysize       = size(rawC, 1); % number of rows
    xgrp        = xsize/NumRep;
    ygrp        = ysize/NumRep;
    cgrp        = zeros(xgrp, ygrp);
    ngrp        = cgrp;     ogrp        = cgrp;     sigrp       = cgrp;
    imbase      = cgrp;
    imdummy     = imread(OrigImage);
    delta       = NumRep - 1;
    imdelta     = 2*NumRep - 1;
    for i = 1:ygrp
        for j = 1:xgrp
            iy  = (i-1)*NumRep+1;
            jx  = (j-1)*NumRep+1;
```

```
            imy = 2*(i-1)*NumRep+1;
            jmx  = 2*(j-1)*NumRep+1;
            iyd = iy + delta;
            jxd = jx + delta;
            imyd = imy + imdelta;
            jmxd = jmx + imdelta;
            cgrp(i, j)      = sum(sum(rawC(iy:iyd,jx:jxd)));
            ngrp(i, j)      = sum(sum(rawN(iy:iyd,jx:jxd)));
            ogrp(i, j)      = sum(sum(rawO(iy:iyd,jx:jxd)));
            sigrp(i, j)     = sum(sum(rawSi(iy:iyd,jx:jxd)));
            imbase(i, j)    = sum(sum(imdummy(imy:imyd,jmx:jmxd)));
        end
    end
    imbase      = imbase/(2*NumRep)^2;      % i.e, 1px, 2x2; 4px, 8x8
    dumCN       = cgrp./ngrp;
    dumCO       = cgrp./ogrp;
    dumSiO      = sigrp./ogrp;
end

nrow        = size(dumCN,1);     % number of rows
ncol        = size(dumCN,2);     % number of columns

dumCN(isnan(dumCN))     = 0;        % set all cell with NaN to 0
dumCO(isnan(dumCO))     = 0;        % same as above
dumSiO(isnan(dumSiO))   = 0;        % same as above

totpix                  = size(cgrp, 1)^2;

%%% simple, no occupancy-correction CN ratio
cn1                     = zeros(nrow, ncol);
NcnNZ                   = sum(sum(dumCN>0))
testcninf               = dumCN;
testcninf(dumCN>0)      = Inf;
Ncninf                  = sum(sum(isinf(dumCN)));
Ncnfin                  = NcnNZ - Ncninf;
NZcnCvr_tot             = NcnNZ/totpix;
NZcnCvr_fin             = Ncnfin/totpix;
if FigYes == 1
    cn1(isinf(dumCN))       = 128;
    cn2                     = dumCN;
    cn2(isinf(dumCN))       = 0;
    cnfmx                   = max(max(cn2));            % max, finite c:n ratio
    cn3                     = cn2./cnfmx*96;
    cnmap                   = cn1 + cn3;
    cnflb                   = cnfmx/4;
    cnbarlabel              =
{'0',num2str(cnflb),num2str(cnflb*2),num2str(cnflb*3),[num2str(cnfmx),'(Max)'],'Inf'};
    cntick                  = [1, 25, 49, 73, 97, 128]; % acc to a 128-color map
    figure, image(cnmap), colormap(hot(128));

colorbar('southoutside','xtick',cntick,'xticklabel',cnbarlabel,'Fontname','Arial','Fontsiz
e',12);
    set(gcf,'position',[1, 1, 641, 726]);
    title('C/N Count Ratio', 'Fontname', 'Arial', 'Fontsize', 16);
    set(gca,'Fontname', 'arial', 'Fontsize', 12);
end


%%% simple, no occupancy-correction CO ratio
co1                     = zeros(nrow, ncol);
NcoNZ                   = sum(sum(dumCO>0))
Ncoinf                  = sum(sum(isinf(dumCO)));
Ncofin                  = NcoNZ - Ncoinf;
NZcoCvr_tot             = NcoNZ/totpix;
NZcoCvr_fin             = Ncofin/totpix;
if FigYes == 1
    co1(isinf(dumCO))       = 128;
    co2                     = dumCO;
    co2(isinf(dumCO))       = 0;
    cofmx                   = max(max(co2));
    co3                     = co2./max(max(co2))*96;
    comap                   = co1 + co3;
    coflb                   = cofmx/4;
    cobarlabel              =
{'0',num2str(coflb),num2str(coflb*2),num2str(coflb*3),[num2str(cofmx),'(Max)'],'Inf'};
    cotick                  = [1, 25, 49, 73, 97, 128]; % acc to a 128-color map
    figure, image(comap), colormap(hot(128));

colorbar('southoutside','xtick',cotick,'xticklabel',cobarlabel,'Fontname','Arial','Fontsiz
e',12);
    set(gcf,'position',[1, 1, 641, 726]);
```

```
    title('C/O Count Ratio', 'Fontname', 'Arial', 'Fontsize', 16);
    set(gca,'Fontname', 'arial', 'Fontsize', 12);
    %colorbar('southoutside','xtick',cotick,'xticklabel',cobarlabel,'Fontname','Arial','Fo
ntsize',12);
end


%%% simple, no occupancy-correction SiO ratio
sio1                    = zeros(nrow, ncol);
NsioNZ                  = sum(sum(dumSiO>0));
Nsioinf                 = sum(sum(isinf(dumSiO)));
Nsiofin                 = NsioNZ - Nsioinf;
NZsioCvr_tot            = NsioNZ/totpix;
NZsioCvr_fin            = Nsiofin/totpix;
if FigYes == 1
    sio1(isinf(dumSiO))     = 128;
    sio2                    = dumSiO;
    sio2(isinf(dumSiO))     = 0;
    siofmx                  = max(max(sio2));           % max, finite Si:O ratio
    sio3                    = sio2./siofmx*96;
    siomap                  = sio1 + sio3;
    sioflb                  = siofmx/4;
    siobarlabel             =
{'0',num2str(sioflb),num2str(sioflb*2),num2str(sioflb*3),[num2str(siofmx),'(Max)'],'Inf'};
    siotick                 = [1, 25, 49, 73, 97, 128]; % acc to a 128-color map
    figure, image(siomap), colormap(hot(128));

colorbar('southoutside','xtick',siotick,'xticklabel',siobarlabel,'Fontname','Arial','Fonts
ize',12);
    set(gcf,'position',[1, 1, 641, 726]);
    title('Si/O Count Ratio', 'Fontname', 'Arial', 'Fontsize', 16);
    set(gca,'Fontname', 'arial', 'Fontsize', 12);
end


%%% output simple ratio results
NZcno_bothcvr           = sum(sum(dumCO>0 & dumCN>0));
NZcno_totcvr            = sum(sum(dumCO>0)+sum(dumCN>0));
NZcno_bothinfinity      = sum(sum(isinf(dumCO) & isinf(dumCN)));
fprintf('Simple Ratio Coverage\n');
fprintf('f_CNtot: %2.4f     f_CNfin: %2.4f \n',NZcnCvr_tot, NZcnCvr_fin);
fprintf('f_COtot: %2.4f     f_COfin: %2.4f \n',NZcoCvr_tot, NZcoCvr_fin);
fprintf('f_SiOtot: %2.4f     f_SiOfin: %2.4f \n',NZsioCvr_tot, NZsioCvr_fin);
fprintf('f_CN_or_CO_tot: %2.4f     \n',NZcno_totcvr/totpix);
fprintf('f_CN&COboth: %2.4f     \n',NZcno_bothcvr/totpix);
fprintf('f_CN&CO-infinity: %2.4f     \n', NZcno_bothinfinity/totpix);
fprintf('total pixels: %5.1f      \n\n\n', totpix);

sumtestcninf            = sum(sum(isinf(testcninf)));
fprintf('testcninf: %5.1f     \n', sumtestcninf);
fprintf('newCNO inf: %2.4f     \n\n\n', sum(sum(isinf(dumCO) & isinf(testcninf)))/totpix);


%%%
%%% SAMPLE OCCUPANCY FILTERED ELEMENTAL RATIO
%%%

%%% print ORIGINAL IMAGE in ORIGINAL RESOLUTION in grayscale
%figure;
aa=imread(OrigImage);
%%%%% uses the following two lines ONLY for 20061013-Site #6, 20061019-Site #13 *****
%aa=max(max(aa))-aa;
%imbase=max(max(imbase))-imbase;

im2                 = imbase;
im3                 = imbase;
im2(imbase<im2crit) = 0;        % treat pixels with values < 40 as blank/bkgd
im3(imbase<im3crit) = 0;        % treat pixels with values < 50 as blank/bkgd
%figure, image(im2), set(gcf,'position',[1, 1, 641, 641]);
%figure, image(im3), set(gcf,'position',[1, 1, 641, 641]);

if FigYes == 1
    image(aa), set(gcf,'position',[1, 1, 641, 641]), colormap(gray);
    title('Original Micrograph Image', 'Fontname', 'Arial', 'Fontsize', 16);
    set(gca,'Fontname', 'arial', 'Fontsize', 12);

    %%% print FILTERED-image in grayscale
    figure, image(imbase), set(gcf,'position',[1, 1, 641, 641]), colormap(gray);
    title('Micrograph Image (Pixels-Consolidated)', 'Fontname', 'Arial', 'Fontsize', 16);
    set(gca,'Fontname', 'arial', 'Fontsize', 12);
```

```
    %%% print omic-filter image, ***IM2*** in default colormap (blue-red scale)
    figure, image(im2), set(gcf,'position',[1, 1, 641, 641]);
    title('Occupancy-filtering Image', 'Fontname', 'Arial', 'Fontsize', 16);
    set(gca,'Fontname', 'arial', 'Fontsize', 12);
end

%%% set im2 as the sample-occupancy filtering basis matrix
imfil               = im2;
figure, image (imfil);
%%% filtering of ratios via Original Matter-Image Confirmation (OMIC)\
size(imfil);
omic_totpix         = sum(sum(imfil>0));              % count total sample-occupied pixels
%imk                 = imfil;
%imk(imfil>0)        = 1;
%figure, image(imk);
%%% OMIC for C:N
omic_dumCN          = dumCN;
%size(omic_dumCN), size(imfil), size(im2)
omic_dumCN(imfil==0)= 0;                              % filter out signals in non-occupied
pixels
omic_cntot          = sum(sum(omic_dumCN>0));         % count all pixels with +ve ratio
omic_cninf          = sum(sum(isinf(omic_dumCN)));    % count pixels with ratio=infinity
omic_cnfin          = omic_cntot - omic_cninf;        % pixels with finite counts
omic_f_cntot        = omic_cntot/omic_totpix;
omic_f_cnfin        = omic_cnfin/omic_totpix;
if FigYes == 1
    cn1                     = zeros(nrow, ncol);
    cn1(isinf(omic_dumCN))  = 128;
    cn2                     = omic_dumCN;
    cn2(isinf(omic_dumCN))  = 0;
    cnfmx                   = max(max(cn2));            % max, finite c:n ratio
    cn3                     = cn2./cnfmx*96;
    cnmap                   = cn1 + cn3;
    cnflb                   = cnfmx/4;
    cnbarlabel              =
{'0',num2str(cnflb),num2str(cnflb*2),num2str(cnflb*3),[num2str(cnfmx),'(Max)'],'Inf'};
    cntick                  = [1, 25, 49, 73, 97, 128]; % acc to a 128-color map
    figure, image(cnmap), colormap(hot(128));

colorbar('southoutside','xtick',cntick,'xticklabel',cnbarlabel,'Fontname','Arial','Fontsiz
e',12);
    set(gcf,'position',[1, 1, 641, 726]);
    title('C/N Count Ratio  (Occupancy-Corrected)', 'Fontname', 'Arial', 'Fontsize', 16);
    set(gca,'Fontname', 'arial', 'Fontsize', 12);
end

%%% OMIC for C:N
omic_dumCO          = dumCO;
omic_dumCO(imfil==0)= 0;                              % filter out signals in non-occupied
pixels
omic_cotot          = sum(sum(omic_dumCO>0));         % count all pixels with +ve ratio
omic_coinf          = sum(sum(isinf(omic_dumCO)));    % count pixels with ratio=infinity
omic_cofin          = omic_cotot - omic_coinf;        % pixels with finite counts
omic_f_cotot        = omic_cotot/omic_totpix;
omic_f_cofin        = omic_cofin/omic_totpix;
if FigYes == 1
    co1                     = zeros(nrow, ncol);
    co1(isinf(omic_dumCO))  = 128;
    co2                     = omic_dumCO;
    co2(isinf(omic_dumCO))  = 0;
    cofmx                   = max(max(co2));
    co3                     = co2./max(max(co2))*96;
    comap                   = co1 + co3;
    coflb                   = cofmx/4;
    cobarlabel              =
{'0',num2str(coflb),num2str(coflb*2),num2str(coflb*3),[num2str(cofmx),'(Max)'],'Inf'};
    cotick                  = [1, 25, 49, 73, 97, 128]; % acc to a 128-color map
    figure, image(comap), colormap(hot(128));

colorbar('southoutside','xtick',cotick,'xticklabel',cobarlabel,'Fontname','Arial','Fontsiz
e',12);
    set(gcf,'position',[1, 1, 641, 726]);
    title('C/O Count Ratio (Occupancy-Corrected)', 'Fontname', 'Arial', 'Fontsize', 16);
    set(gca,'Fontname', 'arial', 'Fontsize', 12);
end

%%% OMIC for Si:O
omic_dumSiO         = dumSiO;
omic_dumSiO(imfil==0)= 0;                             % filter out signals in non-occupied
pixels
omic_siotot         = sum(sum(omic_dumSiO>0));        % count all pixels with +ve ratio
```

```
omic_sioinf          = sum(sum(isinf(omic_dumSiO)));  % count pixels with ratio=infinity
omic_siofin          = omic_siotot - omic_sioinf;      % pixels with finite counts
omic_f_siotot        = omic_siotot/omic_totpix;
omic_f_siofin        = omic_siofin/omic_totpix;
if FigYes == 1
    sio1                      = zeros(nrow, ncol);
    sio1(isinf(omic_dumSiO)) = 128;
    sio2                      = omic_dumSiO;
    sio2(isinf(omic_dumSiO)) = 0;
    siofmx                    = max(max(sio2));
    sio3                      = sio2./max(max(sio2))*96;
    siomap                    = sio1 + sio3;
    sioflb                    = siofmx/4;
    siobarlabel               =
{'0',num2str(sioflb),num2str(sioflb*2),num2str(sioflb*3),[num2str(siofmx),'(Max)'],'Inf'};
    siotick                   = [1, 25, 49, 73, 97, 128]; % acc to a 128-color map
    figure, image(siomap), colormap(hot(128));

colorbar('southoutside','xtick',siotick,'xticklabel',siobarlabel,'Fontname','Arial','Fonts
ize',12);
    set(gcf,'position',[1, 1, 641, 726]);
    title('Si/O Count Ratio (Occupancy-Corrected)', 'Fontname', 'Arial', 'Fontsize', 16);
    set(gca,'Fontname', 'arial', 'Fontsize', 12);
end

%%% output occupany-filtering ratio results
NZcno_bothcvr           = sum(sum(omic_dumCO>0 & omic_dumCN>0));
NZcno_bothinfinity      = sum(sum(isinf(omic_dumCO) & isinf(omic_dumCN)));
fprintf('Occupancy-Based Coverage\n');
fprintf('omic_f_CNtot: %2.4f     omic_f_CNfin: %2.4f \n', omic_f_cntot, omic_f_cnfin);
fprintf('omic_f_COtot: %2.4f     omic_f_COfin: %2.4f \n', omic_f_cotot, omic_f_cofin);
fprintf('omic_f_SiOtot: %2.4f     omic_f_SiOfin: %2.4f \n', omic_f_siotot, omic_f_siofin);
fprintf('omic_f_CN&COtot: %2.4f     \n',NZcno_bothcvr/omic_totpix);
fprintf('omic_f_CN&CO-infinity: %2.4f     \n', NZcno_bothinfinity/omic_totpix);
fprintf('sample-occupied pixels: %6.0f     \n', omic_totpix);
fprintf('sample coverage: %2.4f     \n', omic_totpix/totpix);
fprintf('total pixels: %6.0f     \n\n\n', totpix);



%%% OMIC for C:N + O-reduction according to bkgdSiO ratio determined from
%%% non-occupancy region
%%%

%%% estimate bkgd SiO signal from non-occupied area
bkgdSi               = sigrp;
bkgdO                = ogrp;
%size(bkgdSi), size(imfil)

bkgdSi(imfil>0)      = 0;
totbkgdSi            = sum(sum(bkgdSi));
bkgdO(imfil>0)       = 0;
totbkgdO             = sum(sum(bkgdO));
%%%
%%% Bkgd SiO ratio
%%%
bkgdSiO              = totbkgdSi/totbkgdO;
%bkgdSiO               = 2;

%%% find pixels that require O correction (i.e., C:O>0, Si:O>0, and Si:O
%%% not infinite
%new_omic_dumCO          = omic_dumCO;
%ocorrmatrx              = omic_dumCO(omic_dumCO>0 & omic_dumSiO>0 &
~isinf(omic_dumSiO))   % mark pixels that need O-correction
newogrp                  = ogrp - ceil(sigrp/bkgdSiO);
newogrp(newogrp<0)       = 0;

newomic_dumCO          = cgrp./newogrp;
newomic_dumCO(isnan(newomic_dumCO))     = 0;           % remove 'NaN' pixels
newomic_dumCO(imfil==0)= 0;                           % filter out signals in non-
occupied pixels
newomic_cotot          = sum(sum(newomic_dumCO>0));       % count all pixels with +ve
ratio
newomic_coinf          = sum(sum(isinf(newomic_dumCO)));  % count pixels with
ratio=infinity
newomic_cofin          = newomic_cotot - newomic_coinf;      % pixels with finite counts
newomic_f_cotot        = newomic_cotot/omic_totpix;
newomic_f_cofin        = newomic_cofin/omic_totpix;
if FigYes == 1
    newco1                    = zeros(nrow, ncol);
```

```
    newco1(isinf(newomic_dumCO))  = 128;
    newco2                        = newomic_dumCO;
    newco2(isinf(newomic_dumCO))  = 0;
    newcofmx                      = max(max(newco2));
    newco3                        = newco2./max(max(newco2))*96;
    newcomap                      = newco1 + newco3;
    newcoflb                      = newcofmx/4;
    newcobarlabel                 =
{'0',num2str(newcoflb),num2str(newcoflb*2),num2str(newcoflb*3),[num2str(newcofmx),'(Max)']
,'Inf'};
    newcotick                     = [1, 25, 49, 73, 97, 128]; % acc to a 128-color map
    figure, image(newcomap), colormap(hot(128));

colorbar('southoutside','xtick',newcotick,'xticklabel',newcobarlabel,'Fontname','Arial','F
ontsize',12);
    set(gcf,'position',[1, 1, 641, 726]);
    title('C/O Count Ratio (Occupancy-Corrected, Oxygen-corrected)', 'Fontname', 'Arial',
'Fontsize', 16);
    set(gca,'Fontname', 'arial', 'Fontsize', 12);
end

%%% output occupany-filtering ratio results
NZcno_bothcvr           = sum(sum(newomic_dumCO>0 & omic_dumCN>0));
NZcno_bothinfinity      = sum(sum(isinf(newomic_dumCO) & isinf(omic_dumCN)));
fprintf('Occupancy-Based Oxygen-Corrected Coverage\n');
fprintf('Background SiO: %2.4f \n', bkgdSiO);
fprintf('omic_f_COtot: %2.4f     omic_f_COfin: %2.4f \n', newomic_f_cotot,
newomic_f_cofin);
fprintf('omic_f_CN&COtot: %2.4f     \n',NZcno_bothcvr/omic_totpix);
fprintf('omic_f_CN&CO-infinity: %2.4f     \n', NZcno_bothinfinity/omic_totpix);
fprintf('sample-occupied pixels: %6.0f     \n', omic_totpix);
fprintf('sample coverage: %2.4f     \n', omic_totpix/totpix);
fprintf('total pixels: %6.0f     \n\n\n', totpix);


%%% return function output parameters
a=BasicCvr;
b=bkgdSiO;
e=cgrp;
f=ngrp;
g=ogrp;
h=a;
i=b;
```

Appendix D: Isotherm Regression Scripts

Script D - 1. Regression of Sorption Data to Various Models by Matlab Nonlinear-Fitting. 1106
Script D - 2. Models of Isotherm as Functions. 1110

Script D - 1. Regression of Sorption Data to Various Models by Matlab Nonlinear-Fitting.

```
%%%
%%% IsothermNlrFit.m
%%% Isotherm (S-C) Non-linear Fit
%%%
%%% By: Dave Kuo, 12 May 2009
%%%
%%% for general fitting of data to custom equation-form using nlinfit()
%%%

% Clear memory and screen
clear all; close all;

% SplData: 2 columns; 1st col as {x}, 2nd col as {y}
RawFileName = 'SplData.txt';
RawData     = load(RawFileName);
NumPoints   = size(RawData, 1);            % num of rows = num of data points
RawX        = RawData(:, 1);               % first column of RawData; Ciw (ug/L)
RawY        = RawData(:, 2);               % second column of RawData; Si (ug/kg)

% Data Information
info1       = 'T=37^oC, 10-Month';
textpos     = [5, 10000];

% Figure Axis Limits for X & Y-axes
xrange      = [0.01, 100];
yrange      = [1000, 200000];

% Setting Fitting Options
FitOptions      = statset('MaxIter', 50000, 'Robust', 'on', 'WgtFun', 'Cauchy');


% Lnr+Freundlich Fit (3 params)
GuessVector = [500, 17000, 0.75]';
% Recall: [cfit, r, j] = nlinfit(x, y, 'EqnForm, InitialGuessVector);
[cfitLnrF, r, j, sig, MSELnrF]= nlinfit(RawX, RawY, 'EqnFormLnrFrdlich', GuessVector,
FitOptions);
ci              = nlparci(cfitLnrF, r, 'covar', sig, 'alpha', 0.1587*2);   % alpha =
0.1587*2, ci = 1 sigma
NewX            = sort(RawX);
[ypred,delta]   = nlpredci('EqnFormLnrFrdlich', NewX, cfitLnrF, r, 'covar', sig);

figure, hold on;
line(NewX, ypred, 'Color', 'b', 'LineWidth', 2.5, 'LineStyle', '-');
line(NewX, ypred+delta, 'Color', 'r', 'LineWidth', 1, 'LineStyle', '--');
line(NewX, ypred-delta, 'Color', 'r', 'LineWidth', 1, 'LineStyle', '--');
plot(RawX, RawY, 'k+')
set(gca, 'XScale', 'log', 'YScale', 'log', 'YLim', yrange, 'XLim', xrange, 'Fontname',
'arial', 'Fontsize', 12);
title('Linear+Freundlich Fit (3 Param.)', 'Fontname', 'Arial', 'Fontsize', 16);
ylabel('S_p_y_r (ug_p_y_r/kg_s_o_l_i_d_s)', 'Fontname', 'arial', 'Fontsize', 12);
xlabel('C_p_y_r (ug_p_y_r/L_w)', 'Fontname', 'arial', 'Fontsize', 12);
text(textpos(1), textpos(2), info1, 'Fontname', 'arial', 'Fontsize', 12);

figure, plot(RawX, abs(r)./RawY, 'k^');
set(gca, 'XScale', 'log', 'YLim', [0, 1], 'Fontname', 'arial', 'Fontsize', 12);
title('Residual Plot: Linear+Freundlich', 'Fontname', 'Arial', 'Fontsize', 16);
ylabel('|S_p_r_e_d-S_o_b_s|/S_o_b_s (--)', 'Fontname', 'arial', 'Fontsize', 12);
xlabel('C_p_y_r (ug_p_y_r/L_w)', 'Fontname', 'arial', 'Fontsize', 12);
```

```
text(textpos(1), 0.8, info1, 'Fontname', 'arial', 'Fontsize', 12);
cfitLnrF, sLnrF=ci(:, 2)-cfitLnrF, rLnrF=r;                % Fitted Coeffs + 1 sigma for
Coeffs


% 2-Freundlich Fit (4 params)
%GuessVector = [16000, 0.65, 13000, 0.15]';
GuessVector = [5000, 0.85, 9000, 0.25]';      % 37oC possible #1
% Recall: [cfit, r, j] = nlinfit(x, y, 'EqnForm, InitialGuessVector);
[cfit2F, r, j, sig, MSE2F]  = nlinfit(RawX, RawY, 'EqnForm2Frdlich', GuessVector,
FitOptions);
ci              = nlparci(cfit2F, r, 'covar', sig, 'alpha', 0.1587*2);   % alpha =
0.1587*2, ci = 1 sigma
NewX            = sort(RawX);
[ypred,delta]   = nlpredci('EqnForm2Frdlich', NewX, cfit2F, r, 'covar', sig);

figure, hold on;
line(NewX, ypred, 'Color', 'b', 'LineWidth', 2.5, 'LineStyle', '-');
line(NewX, ypred+delta, 'Color', 'r', 'LineWidth', 1, 'LineStyle', '--');
line(NewX, ypred-delta, 'Color', 'r', 'LineWidth', 1, 'LineStyle', '--');
plot(RawX, RawY, 'k+')
set(gca, 'XScale', 'log', 'YScale', 'log', 'YLim', yrange, 'XLim', xrange, 'Fontname',
'arial', 'Fontsize', 12);
title('Two Freundlich Fit (4 Param.)', 'Fontname', 'Arial', 'Fontsize', 16);
ylabel('S_p_y_r (ug_p_y_r/kg_s_o_l_i_d_s)', 'Fontname', 'arial', 'Fontsize', 12);
xlabel('C_p_y_r (ug_p_y_r/L_w)', 'Fontname', 'arial', 'Fontsize', 12);
text(textpos(1), textpos(2), info1, 'Fontname', 'arial', 'Fontsize', 12);

figure, plot(RawX, abs(r)./RawY, 'k^');
set(gca, 'XScale', 'log', 'YLim', [0, 1], 'Fontname', 'arial', 'Fontsize', 12);
title('Residual Plot: Two Freundlich', 'Fontname', 'Arial', 'Fontsize', 16);
ylabel('|S_p_r_e_d-S_o_b_s|/S_o_b_s (--)', 'Fontname', 'arial', 'Fontsize', 12);
xlabel('C_p_y_r (ug_p_y_r/L_w)', 'Fontname', 'arial', 'Fontsize', 12);
text(textpos(1), 0.8, info1, 'Fontname', 'arial', 'Fontsize', 12);
cfit2F, s2F=ci(:, 2)-cfit2F;                               % Fitted Coeffs + 1 sigma for Coeffs


% Langmir-Freundlich Fit (4 params)
%GuessVector = [100000, 20, 26000, 0.7]';       % 37C, 5-month
GuessVector = [50000, 15, 50000, 0.95]';
[cfitLF, r, j, sig, MSELF]  = nlinfit(RawX, RawY, 'EqnFormLgmrFrdlich', GuessVector,
FitOptions);
ci              = nlparci(cfitLF, r, 'covar', sig, 'alpha', 0.1587*2);   % alpha =
0.1587*2, ci = 1 sigma
NewX            = sort(RawX);
[ypred,delta]   = nlpredci('EqnFormLgmrFrdlich', NewX, cfitLF, r, 'covar', sig);

figure, hold on;
line(NewX, ypred, 'Color', 'b', 'LineWidth', 2.5, 'LineStyle', '-');
line(NewX, ypred+delta, 'Color', 'r', 'LineWidth', 1, 'LineStyle', '--');
line(NewX, ypred-delta, 'Color', 'r', 'LineWidth', 1, 'LineStyle', '--');
plot(RawX, RawY, 'k+')
set(gca, 'XScale', 'log', 'YScale', 'log', 'YLim', yrange, 'XLim', xrange, 'Fontname',
'arial', 'Fontsize', 12);
title('Langmuir-Freundlich Fit (4 Param.)', 'Fontname', 'Arial', 'Fontsize', 16);
ylabel('S_p_y_r (ug_p_y_r/kg_s_o_l_i_d_s)', 'Fontname', 'arial', 'Fontsize', 12);
xlabel('C_p_y_r (ug_p_y_r/L_w)', 'Fontname', 'arial', 'Fontsize', 12);
text(textpos(1), textpos(2), info1, 'Fontname', 'arial', 'Fontsize', 12);

figure, plot(RawX, abs(r)./RawY, 'k^');
set(gca, 'XScale', 'log', 'YLim', [0, 1], 'Fontname', 'arial', 'Fontsize', 12);
title('Residual Plot: Langmuir-Freundlich', 'Fontname', 'Arial', 'Fontsize', 16);
ylabel('|S_p_r_e_d-S_o_b_s|/S_o_b_s (--)', 'Fontname', 'arial', 'Fontsize', 12);
xlabel('C_p_y_r (ug_p_y_r/L_w)', 'Fontname', 'arial', 'Fontsize', 12);
text(textpos(1), 0.8, info1, 'Fontname', 'arial', 'Fontsize', 12);
cfitLF, sLF=ci(:, 2)-cfitLF;                               % Fitted Coeffs + 1 sigma for Coeffs


% Lnr + 2-Freundlich Fit (5 params)
%GuessVector = [100, cfit2F(1), cfit2F(2), cfit2F(3), cfit2F(4)]';
%GuessVector = [10, 10000, 0.75, 1000, 0.1]';
%GuessVector = [50, 100000, 0.65, 10000, 0.10]';     % for 37oC 5-month
GuessVector = [20, 60000, 0.85, 20000, 0.10]';     % for 37oC 10-month
% Recall: [cfit, r, j] = nlinfit(x, y, 'EqnForm, InitialGuessVector);
FitOptions      = statset('MaxIter', 1000000, 'Robust', 'on', 'WgtFun', 'bisquare');
[cfitLnr2F, r, j, sig, MSELnr2F]  = nlinfit(RawX, RawY, 'EqnFormLnr2Frdlich', GuessVector,
FitOptions);
ci              = nlparci(cfitLnr2F, r, 'covar', sig, 'alpha', 0.1587*2);   % alpha =
0.1587*2, ci = 1 sigma
NewX            = sort(RawX);
```

```
[ypred,delta]   = nlpredci('EqnFormLnr2Frdlich', NewX, cfitLnr2F, r, 'covar', sig);

figure, hold on;
line(NewX, ypred, 'Color', 'b', 'LineWidth', 2.5, 'LineStyle', '-');
line(NewX, ypred+delta, 'Color', 'r', 'LineWidth', 1, 'LineStyle', '--');
line(NewX, ypred-delta, 'Color', 'r', 'LineWidth', 1, 'LineStyle', '--');
plot(RawX, RawY, 'k+')
set(gca, 'XScale', 'log', 'YScale', 'log', 'YLim', yrange, 'XLim', xrange, 'Fontname',
'arial', 'Fontsize', 12);
title('Linear + Two Freundlich Fit (5 Param.)', 'Fontname', 'Arial', 'Fontsize', 16);
ylabel('S_p_y_r (ug_p_y_r/kg_s_o_l_i_d_s)', 'Fontname', 'arial', 'Fontsize', 12);
xlabel('C_p_y_r (ug_p_y_r/L_w)', 'Fontname', 'arial', 'Fontsize', 12);
text(textpos(1), textpos(2), info1, 'Fontname', 'arial', 'Fontsize', 12);

figure, plot(RawX, abs(r)./RawY, 'k^');
set(gca, 'XScale', 'log', 'YLim', [0, 1], 'Fontname', 'arial', 'Fontsize', 12);
title('Residual Plot: Linear + Two Freundlich', 'Fontname', 'Arial', 'Fontsize', 16);
ylabel('|S_p_r_e_d-S_o_b_s|/S_o_b_s (--)', 'Fontname', 'arial', 'Fontsize', 12);
xlabel('C_p_y_r (ug_p_y_r/L_w)', 'Fontname', 'arial', 'Fontsize', 12);
text(textpos(1), 0.8, info1, 'Fontname', 'arial', 'Fontsize', 12);
cfitLnr2F, sLnr2F=ci(:, 2)-cfitLnr2F;                          % Fitted Coeffs + 1 sigma for
Coeffs


% Lnr+Langmuir-Freundlich Fit (5 params)
%GuessVector = [5000, cfitLF(1), cfitLF(2), cfitLF(3), cfitLF(4)]';
%GuessVector = [10, 100000, 0.5, 10000, 0.10]';     % for 37oC - possible #1
%GuessVector = [100, 100000, 0.5, 10000, 0.10]';     % for 37oC - 5-month possible #1
%GuessVector = [20, 20000, 5, 20000, 0.10]';     % for 37oC - 10-month possible #1
GuessVector = [10, 50000, 5, 50000, 0.95]';     % for 37oC - 10-month possible #2
%GuessVector = [2000, 200000, 20, 6000, 0.1]';
% Recall: [cfit, r, j] = nlinfit(x, y, 'EqnForm, InitialGuessVector);
FitOptions      = statset('MaxIter', 50000, 'Robust', 'on', 'WgtFun', 'fair');
[cfitLnrLF, r, j, sig, MSELnrLF]  = nlinfit(RawX, RawY, 'EqnFormLnrLgmrFrdlich',
GuessVector, FitOptions);
ci              = nlparci(cfitLnrLF, r, 'covar', sig, 'alpha', 0.1587*2);   % alpha =
0.1587*2, ci = 1 sigma
NewX            = sort(RawX);
[ypred,delta]   = nlpredci('EqnFormLnrLgmrFrdlich', NewX, cfitLnrLF, r, 'covar', sig);

figure, hold on;
line(NewX, ypred, 'Color', 'b', 'LineWidth', 2.5, 'LineStyle', '-');
line(NewX, ypred+delta, 'Color', 'r', 'LineWidth', 1, 'LineStyle', '--');
line(NewX, ypred-delta, 'Color', 'r', 'LineWidth', 1, 'LineStyle', '--');
plot(RawX, RawY, 'k+')
set(gca, 'XScale', 'log', 'YScale', 'log', 'YLim', yrange, 'XLim', xrange, 'Fontname',
'arial', 'Fontsize', 12);
title('Linear + Langmuir-Freundlich Fit (5 Param.)', 'Fontname', 'Arial', 'Fontsize', 16);
ylabel('S_p_y_r (ug_p_y_r/kg_s_o_l_i_d_s)', 'Fontname', 'arial', 'Fontsize', 12);
xlabel('C_p_y_r (ug_p_y_r/L_w)', 'Fontname', 'arial', 'Fontsize', 12);
text(textpos(1), textpos(2), info1, 'Fontname', 'arial', 'Fontsize', 12);

figure, plot(RawX, abs(r)./RawY, 'k^');
set(gca, 'XScale', 'log', 'YLim', [0, 1], 'Fontname', 'arial', 'Fontsize', 12);
title('Residual Plot: Linear + Langmuir-Freundlich', 'Fontname', 'Arial', 'Fontsize', 16);
ylabel('|S_p_r_e_d-S_o_b_s|/S_o_b_s (--)', 'Fontname', 'arial', 'Fontsize', 12);
xlabel('C_p_y_r (ug_p_y_r/L_w)', 'Fontname', 'arial', 'Fontsize', 12);
text(textpos(1), 0.8, info1, 'Fontname', 'arial', 'Fontsize', 12);
cfitLnrLF, sLnrLF=ci(:, 2)-cfitLnrLF;                          % Fitted Coeffs + 1 sigma for
Coeffs


% 3-Freundlich Fit (6 params)
r = []; j = []; GuessVector = [];
%GuessVector = [7000, 1, cfit2F(1), cfit2F(2), cfit2F(3), cfit2F(4)]';
%GuessVector = [1000, 2, 20000, 0.70, 3000, 0.1]';
%GuessVector = [50000, 0.9, 15000, 0.3, 10000, 0.10]';     % for 37oC - possible #1
%GuessVector = [50000, 0.9, 10000, 0.3, 20000, 0.10]';     % for 37oC - 5-month possible
#2
GuessVector = [50000, 0.8, 15000, 0.6, 3000, 0.30]';     % for 37oC - 10-month possible #1
FitOptions      = statset('MaxIter', 1000000, 'Robust', 'on', 'WgtFun', 'cauchy');
[cfit3F, r, j, sig, MSE3F]  = nlinfit(RawX, RawY, 'EqnForm3Frdlich', GuessVector,
FitOptions);
ci              = nlparci(cfit3F, r, 'covar', sig, 'alpha', 0.1587*2);   % alpha =
0.1587*2, ci = 1 sigma
NewX            = sort(RawX);
[ypred,delta]   = nlpredci('EqnForm3Frdlich', NewX, cfit3F, r, 'covar', sig);

figure, hold on;
line(NewX, ypred, 'Color', 'b', 'LineWidth', 2.5, 'LineStyle', '-');
line(NewX, ypred+delta, 'Color', 'r', 'LineWidth', 1, 'LineStyle', '--');
```

```
line(NewX, ypred-delta, 'Color', 'r', 'LineWidth', 1, 'LineStyle', '--');
plot(RawX, RawY, 'k+')
set(gca, 'XScale', 'log', 'YScale', 'log', 'YLim', yrange, 'XLim', xrange, 'Fontname',
'arial', 'Fontsize', 12);
title('Three Freundlich Fit (6 Param.)', 'Fontname', 'Arial', 'Fontsize', 16);
ylabel('S_p_y_r (ug_p_y_r/kg_s_o_l_i_d_s)', 'Fontname', 'arial', 'Fontsize', 12);
xlabel('C_p_y_r (ug_p_y_r/L_w)', 'Fontname', 'arial', 'Fontsize', 12);
text(textpos(1), textpos(2), info1, 'Fontname', 'arial', 'Fontsize', 12);
s3F = ci(:, 2)-cfit3F;

figure, plot(RawX, abs(r)./RawY, 'k^');
set(gca, 'XScale', 'log', 'YLim', [0, 1], 'Fontname', 'arial', 'Fontsize', 12);
title('Residual Plot: Three Freundlich', 'Fontname', 'Arial', 'Fontsize', 16);
ylabel('|S_p_r_e_d-S_o_b_s|/S_o_b_s (--)', 'Fontname', 'arial', 'Fontsize', 12);
xlabel('C_p_y_r (ug_p_y_r/L_w)', 'Fontname', 'arial', 'Fontsize', 12);
text(textpos(1), 0.8, info1, 'Fontname', 'arial', 'Fontsize', 12);
cfit3F, s3F;                          % Fitted Coeffs + 1 sigma for Coeffs


% Display Fitted Parameters on Screen
fprintf('Linear + Freundlich Fit:\n');
fprintf('Mean Sq. of Errors: %10.0f\n', MSELnrF);
fprintf('Klnr = %6.0f (%7.0f)\n', cfitLnrF(1), sLnrF(1));
fprintf('KFr = %6.0f (%7.0f)   nFr = %1.5f (%1.5f) \n\n\n', cfitLnrF(2), sLnrF(2),
cfitLnrF(3), sLnrF(3));

fprintf('Two Freundlich Fit:\n');
fprintf('Mean Sq. of Errors: %10.0f\n', MSE2F);
fprintf('KFr1 = %6.0f (%7.0f)   nFr1 = %1.5f (%1.5f) \n', cfit2F(1), s2F(1), cfit2F(2),
s2F(2));
fprintf('KFr2 = %6.0f (%7.0f)   nFr2 = %1.5f (%1.5f) \n\n\n', cfit2F(3), s2F(3), cfit2F(4),
s2F(4));

fprintf('Langmuir-Freundlich Fit:\n');
fprintf('Mean Sq. of Errors: %10.0f\n', MSELF);
fprintf('Smax = %6.0f (%7.0f)   Chalf = %3.3f (%3.3f) \n', cfitLF(1), sLF(1), cfitLF(2),
sLF(2));
fprintf('KFr = %6.0f (%7.0f)   nFr = %1.5f (%1.5f) \n\n\n', cfitLF(3), sLF(3), cfitLF(4),
sLF(4));

fprintf('Linear + Two Freundlich Fit:\n');
fprintf('Mean Sq. of Errors: %10.0f\n', MSELnr2F);
fprintf('Klnr = %6.0f (%7.0f)\n', cfitLnr2F(1), sLnr2F(1));
fprintf('KFr1 = %6.0f (%7.0f)   nFr1 = %1.5f (%1.5f) \n', cfitLnr2F(2), sLnr2F(2),
cfitLnr2F(3), sLnr2F(3));
fprintf('KFr2 = %6.0f (%7.0f)   nFr2 = %1.5f (%1.5f) \n\n\n', cfitLnr2F(4), sLnr2F(4),
cfitLnr2F(5), sLnr2F(5));

fprintf('Linear + Langmuir-Freundlich Fit:\n');
fprintf('Mean Sq. of Errors: %10.0f\n', MSELnrLF);
fprintf('Klnr = %6.0f (%7.0f)\n', cfitLnrLF(1), sLnrLF(1));
fprintf('Smax = %6.0f (%7.0f)   Chalf = %3.3f (%3.3f) \n', cfitLnrLF(2), sLnrLF(2),
cfitLnrLF(3), sLnrLF(3));
fprintf('KFr = %6.0f (%7.0f)   nFr = %1.5f (%1.5f) \n\n\n', cfitLnrLF(4), sLnrLF(4),
cfitLnrLF(5), sLnrLF(5));

fprintf('Three Freundlich Fit:\n');
fprintf('Mean Sq. of Errors: %10.0f\n', MSE3F);
fprintf('KFr1 = %6.0f (%7.0f)   nFr1 = %1.5f (%1.5f) \n', cfit3F(1), s3F(1), cfit3F(2),
s3F(2));
fprintf('KFr2 = %6.0f (%7.0f)   nFr2 = %1.5f (%1.5f) \n', cfit3F(3), s3F(3), cfit3F(4),
s3F(4));
fprintf('KFr3 = %6.0f (%7.0f)   nFr3 = %1.5f (%1.5f) \n\n\n', cfit3F(5), s3F(5), cfit3F(6),
s3F(6));
```

Script D - 2. Models of Isotherm as Functions.

A. Linear+Freundlich Form (3 parameters)

```
%%%
%%% EqnFormLnrFrdlich.m
%%%

function yEqnForm   = EqnFormLnrFrdlich(Param, x)

KLnr            = Param(1);
Kf              = Param(2);
n               = Param(3);
yS              = KLnr.*x + Kf.*x.^n;
yEqnForm        = yS;
```

B. Langmuir-Freundlich Form (4 parameters)

```
%%%
%%% EqnFormLgmrFrdlich.m
%%%

function yEqnForm   = EqnFormLgmrFrdlich(Param, x)

Smax            = Param(1);
Chalf           = Param(2);
Kf              = Param(3);
n               = Param(4);
yS              = Smax.*x./(x+Chalf) + Kf.*x.^n;
yEqnForm        = yS;
```

C. Two Freundlich Form (4 parameters)

```
%%%
%%% EqnForm2Frdlich.m
%%%

function yEqnForm   = EqnForm2Frdlich(Param, x)
Kf1             = Param(1);
n1              = Param(2);
Kf2             = Param(3);
n2              = Param(4);
yS              = Kf1.*x.^n1 + Kf2.*x.^n2;
yEqnForm        = yS;
```

D. Linear+Two Freundlich Form (5 parameters)

```
%%%
%%% EqnFormLnr2Frdlich.m
%%%

function yEqnForm   = EqnFormLnr2Frdlich(Param, x)

KLnr            = Param(1);
Kf1             = Param(2);
n1              = Param(3);
Kf2             = Param(4);
n2              = Param(5);
yS              = KLnr.*x + Kf1.*x.^n1 + Kf2.*x.^n2;
yEqnForm        = yS;
```

E. Linear+Langmuir-Freundlich Form (5 parameters)

```
%%%
%%% EqnFormLnrLgmrFrdlich.m
%%%
```

```
function yEqnForm   = EqnFormLnrLgmrFrdlich(Param, x)

KLnr            = Param(1);
Smax            = Param(2);
Chalf           = Param(3);
Kf              = Param(4);
n               = Param(5);
yS              = KLnr.*x + Smax.*x./(x+Chalf) + Kf.*x.^n;
yEqnForm        = yS;
```

F. Three Freundlich Form (6 parameters)

```
%%%
%%% EqnForm3Frdlich.m
%%%

function yEqnForm   = EqnForm3Frdlich(Param, x)

Kf0             = Param(1);
n0              = Param(2);
Kf1             = Param(3);
n1              = Param(4);
Kf2             = Param(5);
n2              = Param(6);
yS              = Kf0.*x.^n0 + Kf1.*x.^n1 + Kf2.*x.^n2;
yEqnForm        = yS;
```

Appendix E: Desorption Kinetics Scripts

Script E - 1. Analytical Solution of 1-D Radial Diffusion (Constant K_d or D_{eff})..... **1112**
Script E - 2. Solving Non-linear Root by Newton's Method. **1115**
Script E - 3. Desorption Modeling (Intra-particle Pore Diffusion) with Occlusion..... **1116**
Script E - 4. Desorption Modeling (Intra-particle Pore Diffusion) (No occlusion) **1121**
Script E - 5. Functions Called by the Desorption Model **1126**
Script E - 6. Scripts for Empirical Regression of Kinetic Data **1128**
Script E - 7. Char-in-Silt Heterogeneous Model (Infinite Bath) **1148**
Script E - 8. Char-in-Silt Heterogeneous Model (Closed System) **1156**
Script E - 9. Homogeneous (Silt-only) Aggregate Desorption Model (Infinite Bath) **1163**

Script E - 1. Analytical Solution of 1-D Radial Diffusion (Constant K_d or D_{eff})

RadialDesorbFigure

```
%
% RadialDesorbFigure.m
% By: Dave Kuo, 3 Dec 2009
%
% Generate desorption profiles (analytical solution) on several Kd*Rsw's
%

clear all;
Koc      = 50000;              % unit: L/kgOC
foc      = 1;                  % kgOC/kgsolids
Kd       = Koc*foc             % unit: L/kg
Rsw      = 20e-6;               % unit: kg/L
%Kd       = 2e6;                % unit: L/kg;      for Chapter 3
%Rsw      = 5e-6;               % unit: kg/L;      for Chapter 3
beta     = 1/(Kd*Rsw);           % = 1/(Kd*Rsw) (dimensionless)
%beta     = 100;                % manually specified;      for Chapter 3

%%% Effective Diffusivity (Deff)
intraagg_porosity   = 0.15;
solid_density       = 2.5;     % unit: kgsolids/Lsolids
edta                = 0.89;
MolarV              = 202.3/1.27;   % for pyrene
Diw_cm   = 13.26e-5/( (edta^1.14)*(MolarV^0.589) );    % [cm2/s]
Diw_m    = Diw_cm / 1e4;                                                    % [m2/s]
Diw      = Diw_m;
Deff     = Diw*intraagg_porosity.^2/((1-
intraagg_porosity)*solid_density*Kd+intraagg_porosity);

r        = 100 * 1e-6;        % unit: radius in m
timegrid= 101;                % No of time grids
timeseed= 1.2;                % initial time seed, in seconds

% Param    = [beta, Deff, r, timegrid, timeseed];
%Param    = [beta, Deff, r, timegrid, timeseed];
Param    = [beta, Deff, r, timegrid, timeseed];
[set1, qns]     = F_RadDesorbConstRetard(Param);
save outdata.txt set1 -ASCII
figure, semilogx(set1(:, 1), set1(:, 2), 'k-');
xupper  = 10^( ceil( log10(max(set1(:,1))) ) );
xlim([1e-5, xupper]);
save outqns.txt qns -ASCII

%set0     = F_RadDesorbConstRetard([0.001, 1e-9, 1, 101, 1.5]);
%set30     = F_RadDesorbConstRetard([2, 1e-9, 1, 101, 1.5]);
%set50     = F_RadDesorbConstRetard([1, 1e-9, 1, 101, 1.5]);
%set90     = F_RadDesorbConstRetard([0.1, 1e-9, 1, 101, 1.5]);
```

```
%setall   = [set0, set30, set50, set90];
%save outdata2.txt setall -ASCII

%ylim([0, 1]);
%set(gcf,'position',[1, 1, 721, 480]);
%title('Solid-Phase Pyrene Profile by Radial Diffusion Model with C-Independent
Retardation', 'Fontname', 'Arial', 'Fontsize', 16);
%set(gca,'Fontname', 'arial', 'Fontsize', 12);
%xlabel('Time (d)', 'Fontname', 'Arial', 'Fontsize', 12);
%ylabel('Solid-Phase [(M_o-M_t)/(M_o-M_E_q_m)]_p_y_r', 'Fontname', 'Arial', 'Fontsize',
12);

text('Fontname','arial','FontSize',12);
%text1 = ['K_d_,_p_y_r_ = ', num2str(Kd), ' L/kg'];
%text2 = ['R_s_w = ', num2str(Rsw), ' kg/L'];
%text3 = ['Beta = R_s_w*K_d_,_p_y_r = ', num2str(beta1)];
%text(0.001, 0.85, text1);
%text(0.001, 0.75, text2);
%text(0.001, 0.65, text3);
```

F_RadDesorbConstRetard

```
%
% function F_RadDesorbConstRetard
% 1-D Radial Desorption with Linear Retardation-Diffusion
% **Analytical Solution**
%
% By Dave Kuo, 3 Dec 2009
%
% simple desorption from spherical solids into clean, finite water
% Linear Retardation Factor: constant Kd (hence constant Deff)
%

% Function Parameters
% Param(1) = beta = 1/(Kd*Rsw) (i.e. system Rsw)
% Param(2) = effective diffusivity
% Param(3) = radius of sphere

% Function Returns: ReturnMat
% Column 1: td = time in days
% Column 2: MMRatio = (Mo-Mt)/(Mo-MEqm)
%

function [ReturnMat, qns]  = F_RadDesorbConstRetard(Param)
beta    = Param(1);          % unit: dimensionless
Deff    = Param(2);          % unit: m2/s
r       = Param(3);          % unit: m
tgrid   = Param(4);          % No of time grids; no unit
tseed   = Param(5);          % time seed, in unit seconds

%%% Qn function such that f(qn) = 0
f       = @(q) abs(3.*q./(3+beta.*q.^2) - tan(q));

%%% Finding qn's
ini     = pi              % for beta < 1
%ini     = 3.3             % for beta > 1
xqa     = ini:pi:ini+10*pi;
for i = 1:size(xqa,2)
    xqa(i)  = fminsearch(f, xqa(i));
end
xqa

%%% Method 2: Incr = qn(i+1)-qn(i)...
ib      = max(xqa);
%xqb     = ib:3.134:ib+3.134*10;
lim_b   = 5000;
xqb     = ones(1, lim_b);
xqb(1:5)= xqa(3:7);
for i = 6:lim_b
    dum     = xqb(i-1) + xqb(i-1) - xqb(i-2);
    xqb(i)  = fminsearch(f, dum);
end
xq      = [xqa, xqb];
size(xq)
%xq      = [xqa, xqb, xqc, xqd, xqe, xqf];
```

```
%size(xq)


%xqb      = max(xqa):3.131:3.131*1000;
%xq       = [xqa, xqb];
%xq       = 4.4755:3.1307:3.1307*5000;
%xq       = 0.01:0.01:;
n         = size(xq, 2);
qns       = [];
apprt     = [];
for i = 1:n
    apprt   = [apprt; fminsearch(f, xq(i))];
end
apprt(1:10)'
zerothreshold   = 0.001;     % upper bound for approximate roots:
                             % s.t. |left_f - right_f| < zerothreshold
dummy     = apprt(apprt>zerothreshold);
qns       = dummy(1);
for i = 2:size(dummy)
    diff    = dummy(i) - qns;
    if (sum(diff<0.01)==0)
        qns = [qns; dummy(i)];
    end
end
%rootcheck       = feval(f, qns);


%%% Compute MMRatio = (Mo-Mt)/(Mo-Meqm) as a function of t, beta, qn, radius)
dum2      = (1:tgrid)-1;
tm        = (dum2.*tseed.^(dum2))';         % unit: time in seconds; [m x 1]
Qn        = qns';                                 % [1 x n]
expon     = (-Deff/r^2)*tm*(Qn.^2);               % [m x n]
numer     = 6*beta*(beta+1)*exp(expon);
frame     = ones(size(tm, 1), size(Qn, 2));       % [m x n] of ones
denom     = 9+9*frame*beta+ ones(size(tm,1),1)*Qn.^2*beta^2;
series    = numer./denom;
MMRatio = 1-sum(series, 2);

%%% Return td and MMRatio
td          = tm/3600/24;       % unit: day
ReturnMat   = [td, MMRatio];
```

Script E - 2. Solving Non-linear Root by Newton's Method.

NewtonSolveC

```
function [ConvrgeC] = NewtonSolveC(InitGuess, alpha, beta, FrdlichN, fixed)

%%%
```

Script E - 3. Desorption Modeling (Intra-particle Pore Diffusion) with Occlusion

Desorption (IPD Model) with Occlusion (focclu)

```
%%%
%%% a priori Simulation of Sedimentary-HOCs Desorption Kinetics
%%% WITH OCCLUSION
%%% & Linear-Freundlih Isotherm
%%%
%%% By: Dave Kuo
%%% Date: 15 Jan 2010
%%%

% Compute intrinsic diffusivity Diw
Diw_m = F_Diffusivity ('pyrene', 'water');                                    % [m2/s]

%%% Set system properties
% ISOTHERM SETTING
%
% foc, fbc     : org carbon, black carbon content of aggregate [g_carbon/g_solid]
% Koc, Kbc     : partition coefficient for chemical i [L_solv/kg_carbon]
% FrdlichN     : Freundlich exponent
% CmplmFrdlichN: complimentary Freundlich exponent
%
focclu = 0.30;          % fraction OCCLUDED such that Sinit = So*(1-focclu)
foc = 0.0375;           % for method validation only
fbc = 0.0035;           % for method validation only
%Koc = 10^(0.98*5.13 - 0.32);   % actual
Koc = 10^5.1;           % Linear+Freundlich Fit (Chapter 3)
FrdlichN = 0.42;
Kbc = 10^6.3;           % Linear+Freundlich Fit (Chapter 3)
CmplmFrdlichN = 1 - FrdlichN;

% DESORPTION SCENARIO
%
% {'homogeneous 0.13 sooty-silt',  '5um char in 100um silt'}
DesorptionScenario = 'homogeneous 0.13 sooty-silt';
ShapeFactor    = 3;   % 3 for spherical; 2 for cylindrical; 1 for slab

% SEDIMENT CHARACTERISTICS
%
% rho_s        : strict solid density [Kg_solid/L_solid]
% rsw_ppm      : overall system solid-to-water ratio [mg_solid/L_solv]
% rsw          : overall system solid-to-water ratio [Kg_solid/L_solv]
% rad_um       : particle radius [um]
% rad_m        : particle radius [m]
rho_s          = 2.5;
%rsw_ppm       = 300;
rsw_ppm        = 72;
rsw            = rsw_ppm/1e6;
rad_um         = 27;
rad_m          = rad_um/1e6;

% GRID AND TIME STEP SIZES
%
% m            : number of grids
% Co_crit      : 'Courant' criterion
% Pe_crit      : 'Peclet' criterion
% Timesteps    : Number of timesteps
% dr           : differential radius [m]
% dx           : = dr/rad_m = differential radius [--]
% dtow         : = Diw*dt/(R^2) = differential timestep [--]
% Timesteps    : # timesteps, each dtow [--]
m              = 41;
dr             = 1/(m-1)*rad_m;
dx             = dr/rad_m;
Co_crit        = 0.8; % <1
Pe_crit        = 0.01;% <2
CoByPe_crit = Co_crit/Pe_crit;
dtow           = CoByPe_crit;
dt             = dtow*(rad_m^2)/Diw_m;
Timesteps      = 15.0e4;

% SPATIAL MATRICES
%
gridindex      = (1:1:m);            % 1 x m {1  2  3  ...  m}
inrgds         = (2:m-1);            % 1 x m-2 {2  3  4  ...  m-1}
x              = (gridindex-1)*dx;   % 1 x m {X1  X2  X3  ...  Xm}
x_miu_les_1    = x.^(ShapeFactor-1); % 1 x m
```

```
x_hlf          = (gridindex-0.5)*dx; % 1 x m {X1.5  X2.5  X3.5  ...  Xm-0.5  (xm+0.5!)}
x_hlf_miu_les_1= x_hlf.^(ShapeFactor-1);     % 1 x m {X1.5  X2.5  X3.5  ...  Xm-0.5  (xm+0.5!)}

% INITIAL CONDITIONS
%
% porosity     : porosity(x) {n} [L_void/L_agg]
% tortuosity   : tortuosity(x) {f(n)}
% S_init       : initial solid phase conc'n, (S') [ug_i/kg_solid = ng i/g_solid]
% C_init       : initial pore fluid conc'n, (C') [ug_i/L_por_aq]
CharPorosity   = 0.20;        % synthetic char from Braida et al.(Pignatello), 2003 EST
CharTortuosity = 0.20;        % assumed to be same as porosity
SiltPorosity   = 0.13;        % fitting value by Wu and Gschwend, 1986 EST
SiltTortuosity = 0.13;        % assumed to be same as porosity; Wu and Gschwend, 1988 Wat Res Res
S_init         = 1420; % [ug_i/kg_solid or ng_i/g_solid]
S_init         = S_init*(1-focclu);
C_init         = NewtonSolveC (1e-40, foc*Koc, fbc*Kbc, FrdlichN, S_init); % [ug_i/L_agg]
switch DesorptionScenario
  case 'homogeneous 0.13 sooty-silt'
      PorosityX       = F_SetAggProperty('homogeneous', m, SiltPorosity);
      TortuosityX     = F_SetAggProperty('homogeneous', m, SiltTortuosity);
      focX            = F_SetAggProperty('homogeneous', m, foc);
      fbcX            = F_SetAggProperty('homogeneous', m, fbc);
      S_initX         = F_SetAggProperty('homogeneous', m, S_init);
end
rho_bulkX             = rho_s*(1-PorosityX);% [kg_solid/L_agg]
AggAvgPorosity        = F_AggregateAvgProperty(ShapeFactor, x, PorosityX, dx);
TortuosityHlfX        = (TortuosityX(1:m-1)+TortuosityX(2:m)) ./ 2;       % 1 x (m-1) !!!
PorosityHlfX          = (PorosityX(1:m-1)+PorosityX(2:m)) ./ 2;    % 1 x (m-1) !!!

% VRatio              : volumetric ratio of bulk solvent phase to aggregate(solid+porous fluid)
V_one_agg             = 4/3*pi*(rad_m^3);
Mass_one_agg          = (1-AggAvgPorosity)*V_one_agg*rho_s;
V_one_nonagg          = Mass_one_agg/rsw;
VRatio                = V_one_nonagg/V_one_agg;    % Same as VRatio = ((1-f_porsity)*rho_s)/rsw;

% Q_initX             : initial aggregate(solid+porous fluid) volume-averaged concentration
[ug_i/L_agg]
% C_initX             : initial spatial C' within aggregate [ug_i/L_agg]
% C_blk_init          : initial non-agg/bulk aq. phase concentration [ug_i/L_solv]
C_initX               = NewtonSolveC (1e-40, focX*Koc, fbcX*Kbc, FrdlichN, S_initX);
Q_initX               = S_initX.*rho_bulkX + PorosityX.*C_initX;
Q_initAvg             = F_AggregateAvgProperty(ShapeFactor, x, Q_initX, dx);
C_blk_init            = 0;

% GapF        : gap factor for initial non-agg/bulk aq. phase conc'n, such that C_init =
Ceqm_init/GapF
% dfpexp      : the exponent of the fitting porosity n on the numerator
GapF = 1; %%%%% CLOSED SYSTEM, MASS CONSERVED
dfpexp = 2;


%%%
%%% Calculate expected eqm aq. conc.: C_blk_eqm
%%%
% Z_init              : Mass_init/V_agg = Q_initAvg + C_blk_init*V_nonagg/V_agg]
Z_init                = Q_initAvg + C_blk_init*VRatio;                              % [ug_i/L_agg]
Y_1stOrder            = Koc*focX.*rho_bulkX + PorosityX;
Y_FrdlichN            = Kbc*fbcX.*rho_bulkX;
Coeff_1stOrder        = F_AggregateAvgProperty(ShapeFactor, x, Y_1stOrder, dx) + VRatio;
Coeff_FrdlichN        = F_AggregateAvgProperty(ShapeFactor, x, Y_FrdlichN, dx);
C_blk_eqm             = NewtonSolveC(1e-40, Coeff_1stOrder, Coeff_FrdlichN, FrdlichN, Z_init);
S_eqmX                = C_blk_eqm*Koc*focX + (C_blk_eqm^FrdlichN)*Kbc*fbcX;
Q_eqmX                = S_eqmX.*rho_bulkX + C_blk_eqm*PorosityX;
Q_eqmAvg              = F_AggregateAvgProperty(ShapeFactor, x, Q_eqmX, dx);


%%%
%%% Date output information
%%%
Fpath          = '/BC_Model_2010/ModelOutput/';
Ffilename      = ['BH6_A_Rsw',num2str(rsw_ppm),'_Grd_',num2str(m),'_OC51_BC63_n042_OccluBest'];
ISOTH_p        = [foc, Koc, fbc, Kbc, FrdlichN];
SEDI_p         = [rho_s, rsw, rad_m, V_one_agg, V_one_nonagg, AggAvgPorosity, VRatio];
CONC_p         = [S_init, C_init, Q_initAvg, C_blk_init];
SIMU_p         = [m, dr, dx, Co_crit, Pe_crit, CoByPe_crit, dtow, dt, Timesteps];
EQM_p          = [C_blk_eqm, Q_eqmAvg];
F_OutputSystemParameters(Fpath,Ffilename,'PYRENE',Diw_m,ISOTH_p, SEDI_p, CONC_p, SIMU_p, EQM_p);


%%%
%%% SOLVING RETARDED DIFFUSIONAL EQN BY ITERATIONS
```

```
%%%
% Constants
% For innermost grid calc, grid = 1
k_innermost = dtow * ShapeFactor * TortuosityHlfX(1) * PorosityHlfX(1) / dx / x_hlf(1);   %
scalar

% For intermediate grids calc, grid = 2 to m-1
k_intermedi = dtow/((dx)^2) .* PorosityX ./ x_miu_les_1;    % 1 x m-2

% For C_blk_next OR C_nextX(m) calc, grid = m
q_next_m       = ShapeFactor*x_miu_les_1(m)*dx*1/3; % coeff for Q_next_m; 1 being Simpson's
coeff
alpha_m        = focX(m)*Koc;
beta_m         = fbcX(m)*Kbc;
CnxtlstOrder= (1 + q_next_m*(alpha_m*rho_bulkX(m)+PorosityX(m))/VRatio);
CnxtFrdlichN= q_next_m * beta_m * rho_bulkX(m) / VRatio;
AlstOrder      = Koc*focX.*rho_bulkX + PorosityX;          % 1st Order coeff for solving
C_nextX(i) from Q_nextX(i)
AFrdlichN      = Kbc*fbcX.*rho_bulkX; % Frdlich N coeff for solving C_nextX(i) from Q_nextX(i)
%x= (gridindex-1)*dx;          % 1 x m {X1  X2  X3  ...  Xm}
%x_miu_les_1   = x.^(ShapeFactor-1); % 1 x m
%x_hlf         = (gridindex-0.5)*dx; % 1 x m {X1.5  X2.5  X3.5  ...  Xm-0.5  (xm+0.5!)}
%x_hlf_miu_les_1 = x_hlf.^(ShapeFactor-1);   % 1 x m {X1.5  X2.5  X3.5  ...  Xm-0.5  (xm+0.5!)}

C_nowX         = C_initX;
S_nowX         = S_initX;
Q_nowX         = Q_initX;
Q_nowAvg       = Q_initAvg;
C_blk_now      = C_blk_init;
C_blk_mark     = C_blk_init;                 % for determining if profiles should be
recorded/saved at ith step

C_nextX        = zeros(1, m);                % initialize; 1 x m of zeroes
S_nextX        = zeros(1, m);                % 1 x m of zeroes
Q_nextX        = zeros(1, m);                % 1 x m of zeroes

DATA_OVRALL    = [];          % data matrix for overall results (C_blk, Q_Avg, S_Avg, etc)
DATA_C_tx      = [];          % data matrix for temporal-spatial, C(x,t) [ug_i/L_void]
DATA_S_tx      = [];          % data matrix for temporal-spatial, S(x,t) [ug_i/kg_solid]
DATA_Q_tx      = [];          % data matrix for temporal-spatial, Q(x,t) [ug_i/L_agg]
DATA_Kd_tx     = [];          % data matrix for temporal-spatial Kd = S(x,t) / C(x,t)
DATA_Z_tx      = [];          % data matrix for Z(t) = Q_nowAvg + C_blkAvg*VRatio [ug/L_agg]

% Save time-zero condition
DATA_C_tx                     = [DATA_C_tx; [0, 0, C_initX]];
DATA_S_tx                     = [DATA_S_tx; [0, 0, S_initX]];
DATA_Q_tx                     = [DATA_Q_tx; [0, 0, Q_initX]];
DATA_Kd_tx                    = [DATA_Kd_tx; [0, 0, S_initX./C_initX]];
DATA_Z_tx                     = [DATA_Z_tx; [0, 0, Z_init, 0]];

tic
for itime=1:Timesteps,

   %% INNERMOST GRID (grid 1) CALC
   Q_nextX(1)  = Q_nowX(1) + k_innermost*(C_nowX(2)-C_nowX(1));
   C_nextX(1)  = NewtonSolveC(1e-40, AlstOrder(1), AFrdlichN(1), FrdlichN, Q_nextX(1));
   S_nextX(1)  = focX(1)*Koc*C_nextX(1) + fbcX(1)*Kbc*(C_nextX(1)^FrdlichN);

   %% INTERMEDIATE GRIDS (grids 2 to [m-1]) CALC
   dum_iplus1 = []; dum_iminus1 = []; dum_i = [];
   dum_iplus1       = k_intermedi(inrgds).*x_hlf_miu_les_1(inrgds).*TortuosityHlfX(inrgds);
       % Coeff for C_nowX(i+1)
   dum_iminus1      = k_intermedi(inrgds).*x_hlf_miu_les_1(inrgds-1).*TortuosityHlfX(inrgds-1);%
Coeff for C_nowX(i-1)
   dum_i            = dum_iplus1 + dum_iminus1;
                                                                  % Coeff for C_nowX(i)
   Q_nextX(inrgds)  = Q_nowX(inrgds) + dum_iplus1.*C_nowX(inrgds+1) + dum_iminus1.*C_nowX(inrgds-
1) - dum_i.*C_nowX(inrgds);
   C_nextX(inrgds)  = NewtonSolveC(1e-40, AlstOrder(inrgds), AFrdlichN(inrgds), FrdlichN,
Q_nextX(inrgds));
   S_nextX(inrgds)  = Koc*focX(inrgds).*C_nextX(inrgds) +
Kbc*fbcX(inrgds).*(C_nextX(inrgds).^FrdlichN);

   %% C_blk_next CALC
   dum_Q_nextX  = [Q_nextX(1:m-1), 0];
                  % dummy for calculating q_next_cnst
   q_next_cnst  = F_AggregateAvgProperty(ShapeFactor, x, dum_Q_nextX, dx);
   CnxtConstant = (Q_nowAvg - q_next_cnst)/VRatio + C_blk_now;
   C_blk_next   = NewtonSolveC (1e-40, CnxtlstOrder, CnxtFrdlichN, FrdlichN, CnxtConstant);
   C_nextX(m)   = C_blk_next;
   S_nextX(m)   = alpha_m*C_nextX(m) + beta_m*(C_nextX(m)^FrdlichN);
```

```
   Q_nextX(m)    = S_nextX(m)*rho_bulkX(m) + PorosityX(m)*C_nextX(m);

   %% UPDATE CONCENTRATIONS
   %% all "NOW" concs represent values after itime of timesteps, thus to be recorded as occuring
at [itime*dtow]
   C_nowX              = C_nextX;
   S_nowX              = S_nextX;
   Q_nowX              = Q_nextX;
   C_blk_now           = C_blk_next;
   Q_nowAvg            = F_AggregateAvgProperty(ShapeFactor, x, Q_nextX, dx);

   %% SAVE MODELLED PROFILE
   %% ***REM: all "NOW" quantities are the LATEST quantities for itime# of steps***
   C_blk_diff = abs((C_blk_now - C_blk_mark)/C_blk_mark);
   if C_blk_diff>0.01
      AbsT_hrs  = itime*dt/3600;             % time in hrs
      AbsTow    = itime*dtow;                % dimensionless time [--]
      TimeEntry = [AbsTow, AbsT_hrs];% i.e. [tow, t_in_hrs]; 1 x 2
      Magg_Meqm = Q_nowAvg/Q_eqmAvg; % Mass of i in agg at itimeth step / Mass of i in agg at
eqm (t->inf)

      %% Storing overall desorption result at ith timestep, or [itime*dt] secs
      C_nowAvg                = F_AggregateAvgProperty(ShapeFactor, x, C_nowX, dx);
      S_nowAvg                = F_AggregateAvgProperty(ShapeFactor, x, S_nowX, dx);
      OneEntry_OVRALL = [TimeEntry, C_nowAvg, S_nowAvg, Q_nowAvg, C_blk_now, C_blk_now/C_blk_eqm,
Magg_Meqm];
      DATA_OVRALL             = [DATA_OVRALL; OneEntry_OVRALL];

      %% Storing temporal-spatial result at ith timestep
      DATA_C_tx               = [DATA_C_tx; [TimeEntry, C_nowX]];
      DATA_S_tx               = [DATA_S_tx; [TimeEntry, S_nowX]];
      DATA_Q_tx               = [DATA_Q_tx; [TimeEntry, Q_nowX]];
      DATA_Kd_tx              = [DATA_Kd_tx; [TimeEntry, S_nowX./C_nowX]];
      Z_now                   = Q_nowAvg+C_blk_now*VRatio;
      DZ_now_les_init         = Z_now - Z_init;
      DATA_Z_tx               = [DATA_Z_tx; [TimeEntry, Z_now, DZ_now_les_init]];

      %% Update C_blk_mark ***!!!***
      C_blk_mark              = C_blk_now;

   elseif (itime>30000)&(mod(itime, 4000)==0)
      AbsT_hrs = itime*dt/3600;              % time in hrs
      AbsTow   = itime*dtow;                 % dimensionless time [--]
      TimeEntry= [AbsTow, AbsT_hrs];% i.e. [tow, t_in_hrs]; 1 x 2
      Magg_Meqm= Q_nowAvg/Q_eqmAvg;   % Mass of i in agg at itimeth step / Mass of i in agg at
eqm (t->inf)

      %% Storing overall desorption result at ith timestep, or [itime*dt] secs
      C_nowAvg                = F_AggregateAvgProperty(ShapeFactor, x, C_nowX, dx);
      S_nowAvg                = F_AggregateAvgProperty(ShapeFactor, x, S_nowX, dx);
      OneEntry_OVRALL = [TimeEntry, C_nowAvg, S_nowAvg, Q_nowAvg, C_blk_now, C_blk_now/C_blk_eqm,
Magg_Meqm];
      DATA_OVRALL             = [DATA_OVRALL; OneEntry_OVRALL];

      %% Storing temporal-spatial result at ith timestep
      DATA_C_tx               = [DATA_C_tx; [TimeEntry, C_nowX]];
      DATA_S_tx               = [DATA_S_tx; [TimeEntry, S_nowX]];
      DATA_Q_tx               = [DATA_Q_tx; [TimeEntry, Q_nowX]];
      DATA_Kd_tx              = [DATA_Kd_tx; [TimeEntry, S_nowX./C_nowX]];
      Z_now                   = Q_nowAvg+C_blk_now*VRatio;
      DZ_now_les_init  = Z_now - Z_init;
      DATA_Z_tx               = [DATA_Z_tx; [TimeEntry, Z_now, DZ_now_les_init]];

      %% Update C_blk_mark ***!!!***
      C_blk_mark              = C_blk_now;

   end  % end if-elseif
   if mod(itime, 1000)==0,
      fprintf ('%i\n', itime);
   end
end


%%%
%%% Write modeling results to files
%%%
Fpath_OVRALL    = [Fpath, Ffilename, '.ovr'];
Fpath_C_tx      = [Fpath, Ffilename, '.c'];
Fpath_S_tx      = [Fpath, Ffilename, '.s'];
Fpath_Q_tx      = [Fpath, Ffilename, '.q'];
Fpath_Kd_tx     = [Fpath, Ffilename, '.kd'];
```

```
Fpath_Z_tx     = [Fpath, Ffilename, '.z'];

save ovrall DATA_OVRALL -ASCII
save c DATA_C_tx -ASCII
save s DATA_S_tx -ASCII
save q DATA_Q_tx -ASCII
save kd DATA_Kd_tx -ASCII
save z DATA_Z_tx -ASCII

dos(['ren ovrall ',Ffilename,'_Ovrall.txt']);
dos(['ren c ',Ffilename,'_C.txt']);
dos(['ren s ',Ffilename,'_S.txt']);
dos(['ren q ',Ffilename,'_Q.txt']);
dos(['ren kd ',Ffilename,'_Kd.txt']);
dos(['ren z ',Ffilename,'_Z.txt']);

toc
```

Script E - 4. Desorption Modeling (Intra-particle Pore Diffusion) (No occlusion)

Desorption (IPD Model) (No occlusion)

```
%%%
%%% a priori Simulation of Sedimentary-HOCs Desorption Kinetics
%%% Linear-Freundlih Isotherm (No Occlusion)
%%%
%%% By: Dave Kuo
%%% Date: 15 Jan 2010
%%%


%%%
%%% Compute intrinsic diffusivity Diw
%%%

Diw_m = F_Diffusivity ('pyrene', 'water');                                    % [m2/s]


%%%
%%% Set system properties
%%%

% ISOTHERM SETTING
%
% foc, fbc     : org carbon, black carbon content of aggregate [g_carbon/g_solid]
% Koc, Kbc     : partition coefficient for chemical i [L_solv/kg_carbon]
% FrdlichN     : Freundlich exponent
% CmplmFrdlichN: complimentary Freundlich exponent
%
%foc = 0.041;          % for BH6
%fbc = 0.0035;         % for BH6
foc = 0.0331;          % for method validation only
fbc = 0.0083;          % for method validation only
%Koc = 10^(0.98*5.13 - 0.32);   % actual
Koc = 10^4.75;         % Linear+Freundlich Fit (Chapter 3)
FrdlichN = 0.20;
Kbc = 10^5.95;         % Linear+Freundlich Fit (Chapter 3)

CmplmFrdlichN = 1 - FrdlichN;

% DESORPTION SCENARIO
%
% {'homogeneous 0.13 sooty-silt',  '5um char in 100um silt'}
DesorptionScenario = 'homogeneous 0.13 sooty-silt';
ShapeFactor    = 3;    % 3 for spherical; 2 for cylindrical; 1 for slab


% SEDIMENT CHARACTERISTICS
%
% rho_s        : strict solid density [Kg_solid/L_solid]
% rsw_ppm      : overall system solid-to-water ratio [mg_solid/L_solv]
% rsw          : overall system solid-to-water ratio [Kg_solid/L_solv]
% rad_um       : particle radius [um]
% rad_m        : particle radius [m]
rho_s          = 2.5;
%rsw_ppm       = 300;
rsw_ppm        = 21;
rsw            = rsw_ppm/1e6;
rad_um         = 45;
rad_m          = rad_um/1e6;

% GRID AND TIME STEP SIZES
%
% m            : number of grids
% Co_crit      : 'Courant' criterion
% Pe_crit      : 'Peclet' criterion
% Timesteps    : Number of timesteps
% dr           : differential radius [m]
% dx           : = dr/rad_m = differential radius [--]
% dtow         : = Diw*dt/(R^2) = differential timestep [--]
% Timesteps    : # timesteps, each dtow [--]
m              = 41;
dr             = 1/(m-1)*rad_m;
dx             = dr/rad_m;
Co_crit        = 0.80; % <1
Pe_crit        = 0.01; % <2
CoByPe_crit    = Co_crit/Pe_crit;
```

```
%CoByPe_crit = 20000;
dtow         = CoByPe_crit;
dt           = dtow*(rad_m^2)/Diw_m;
Timesteps    = 8.0e4;

% SPATIAL MATRICES
%
gridindex      = (1:1:m);                    % 1 x m {1  2  3  ...  m}
inrgds         = (2:m-1);                    % 1 x m-2 {2  3  4  ...  m-1}
x              = (gridindex-1)*dx;           % 1 x m {X1  X2  X3  ...  Xm}
x_miu_les_1    = x.^(ShapeFactor-1);         % 1 x m
x_hlf          = (gridindex-0.5)*dx;         % 1 x m {X1.5  X2.5  X3.5  ...  Xm-0.5  (xm+0.5!)}
x_hlf_miu_les_1= x_hlf.^(ShapeFactor-1);     % 1 x m {X1.5  X2.5  X3.5  ...  Xm-0.5  (xm+0.5!)}


% INITIAL CONDITIONS
%
% porosity     : porosity(x) {n} [L_void/L_agg]
% tortuosity   : tortuosity(x) {f(n)}
% S_init       : initial solid phase conc'n, (S') [ug_i/kg_solid = ng i/g_solid]
% C_init       : initial pore fluid conc'n, (C') [ug_i/L_por_aq]
CharPorosity   = 0.20;        % synthetic char from Braida et al.(Pignatello), 2003 EST
CharTortuosity = 0.20;        % assumed to be same as porosity
SiltPorosity   = 0.13;        % fitting value by Wu and Gschwend, 1986 EST
SiltTortuosity = 0.13;        % assumed to be same as porosity; Wu and Gschwend, 1988 Wat Res Res
S_init         = 3060; % [ug_i/kg_solid or ng_i/g_solid]
C_init         = NewtonSolveC (1e-40, foc*Koc, fbc*Kbc, FrdlichN, S_init); % [ug_i/L_agg]
switch DesorptionScenario
  case 'homogeneous 0.13 sooty-silt'
      PorosityX      = F_SetAggProperty('homogeneous', m, SiltPorosity);
      TortuosityX    = F_SetAggProperty('homogeneous', m, SiltTortuosity);
      focX           = F_SetAggProperty('homogeneous', m, foc);
      fbcX           = F_SetAggProperty('homogeneous', m, fbc);
      S_initX        = F_SetAggProperty('homogeneous', m, S_init);
end
rho_bulkX            = rho_s*(1-PorosityX);% [kg_solid/L_agg]
AggAvgPorosity       = F_AggregateAvgProperty(ShapeFactor, x, PorosityX, dx);
TortuosityHlfX       = (TortuosityX(1:m-1)+TortuosityX(2:m)) ./ 2;       % 1 x (m-1) !!!
PorosityHlfX         = (PorosityX(1:m-1)+PorosityX(2:m)) ./ 2;           % 1 x (m-1) !!!

% VRatio             : volumetric ratio of bulk solvent phase to aggregate(solid+porous fluid)
V_one_agg            = 4/3*pi*(rad_m^3);
Mass_one_agg         = (1-AggAvgPorosity)*V_one_agg*rho_s;
V_one_nonagg         = Mass_one_agg/rsw;
VRatio               = V_one_nonagg/V_one_agg;    % Same as VRatio = ((1-f_porsity)*rho_s)/rsw;

% Q_initX            : initial aggregate(solid+porous fluid) volume-averaged concentration
[ug_i/L_agg]
% C_initX            : initial spatial C' within aggregate [ug_i/L_agg]
% C_blk_init   : initial non-agg/bulk aq. phase concentration [ug_i/L_solv]
C_initX              = NewtonSolveC (1e-40, focX*Koc, fbcX*Kbc, FrdlichN, S_initX);
Q_initX              = S_initX.*rho_bulkX + PorosityX.*C_initX;
Q_initAvg            = F_AggregateAvgProperty(ShapeFactor, x, Q_initX, dx);
C_blk_init           = 0;

% GapF         : gap factor for initial non-agg/bulk aq. phase conc'n, such that C_init =
Ceqm_init/GapF
% dfpexp       : the exponent of the fitting porosity n on the numerator
GapF = 1; %%%%% CLOSED SYSTEM, MASS CONSERVED
dfpexp = 2;

%%%
%%% Calculate expected eqm aq. conc.: C_blk_eqm
%%%
% Z_init             : Mass_init/V_agg = Q_initAvg + C_blk_init*V_nonagg/V_agg]
Z_init               = Q_initAvg + C_blk_init*VRatio;              % [ug_i/L_agg]
Y_1stOrder           = Koc*focX.*rho_bulkX + PorosityX;
Y_FrdlichN           = Kbc*fbcX.*rho_bulkX;
Coeff_1stOrder       = F_AggregateAvgProperty(ShapeFactor, x, Y_1stOrder, dx) + VRatio;
Coeff_FrdlichN       = F_AggregateAvgProperty(ShapeFactor, x, Y_FrdlichN, dx);
C_blk_eqm            = NewtonSolveC(1e-40, Coeff_1stOrder, Coeff_FrdlichN, FrdlichN, Z_init);
S_eqmX               = C_blk_eqm*Koc*focX + (C_blk_eqm^FrdlichN)*Kbc*fbcX;
Q_eqmX               = S_eqmX.*rho_bulkX + C_blk_eqm*PorosityX;
Q_eqmAvg             = F_AggregateAvgProperty(ShapeFactor, x, Q_eqmX, dx);


%%%
%%% Date output information
%%%
Fpath          = '/BC_Model_2010/ModelOutput/';
Ffilename      = ['BH6_K_Rsw',num2str(rsw_ppm),'_Grd_',num2str(m),'_OC475_BC595_n020_UnivBest'];;
```

```
ISOTH_p         = [foc, Koc, fbc, Kbc, FrdlichN];
SEDI_p          = [rho_s, rsw, rad_m, V_one_agg, V_one_nonagg, AggAvgPorosity, VRatio];
CONC_p          = [S_init, C_init, Q_initAvg, C_blk_init];
SIMU_p          = [m, dr, dx, Co_crit, Pe_crit, CoByPe_crit, dtow, dt, Timesteps];
EQM_p           = [C_blk_eqm, Q_eqmAvg];
F_OutputSystemParameters(Fpath,Ffilename,'PYRENE',Diw_m,ISOTH_p, SEDI_p, CONC_p, SIMU_p, EQM_p);


%%%
%%% SOLVING RETARDED DIFFUSIONAL EQN BY ITERATIONS
%%%


% Constants


% For innermost grid calc, grid = 1
k_innermost = dtow * ShapeFactor * TortuosityHlfX(1) * PorosityHlfX(1) / dx / x_hlf(1);   %
scalar



% For intermediate grids calc, grid = 2 to m-1
k_intermedi = dtow/((dx)^2) .* PorosityX ./ x_miu_les_1;          % 1 x m-2



% For C_blk_next OR C_nextX(m) calc, grid = m
q_next_m              = ShapeFactor*x_miu_les_1(m)*dx*1/3; % coeff for Q_next_m; 1 being
Simpson's coeff
alpha_m         = focX(m)*Koc;
beta_m          = fbcX(m)*Kbc;
Cnxt1stOrder= (1 + q_next_m*(alpha_m*rho_bulkX(m)+PorosityX(m))/VRatio);
CnxtFrdlichN= q_next_m * beta_m * rho_bulkX(m) / VRatio;
A1stOrder       = Koc*focX.*rho_bulkX + PorosityX;          % 1st Order coeff for solving
C_nextX(i) from Q_nextX(i)
AFrdlichN       = Kbc*fbcX.*rho_bulkX;  % Frdlich N coeff for solving C_nextX(i) from Q_nextX(i)
%x= (gridindex-1)*dx;                                    % 1 x m {X1  X2  X3  ...  Xm}
%x_miu_les_1= x.^(ShapeFactor-1);                        % 1 x m
%x_hlf = (gridindex-0.5)*dx;         % 1 x m {X1.5  X2.5  X3.5  ...  Xm-0.5  (xm+0.5!)}
%x_hlf_miu_les_1 = x_hlf.^(ShapeFactor-1);               % 1 x m {X1.5  X2.5  X3.5  ...  Xm-0.5
(xm+0.5!)}

C_nowX          = C_initX;
S_nowX          = S_initX;
Q_nowX          = Q_initX;
Q_nowAvg        = Q_initAvg;
C_blk_now       = C_blk_init;
C_blk_mark      = C_blk_init;               % for determining if profiles should be
recorded/saved at ith step

C_nextX         = zeros(1, m);              % initialize; 1 x m of zeroes
S_nextX         = zeros(1, m);              % 1 x m of zeroes
Q_nextX         = zeros(1, m);              % 1 x m of zeroes

DATA_OVRALL     = [];           % data matrix for overall results (C_blk, Q_Avg, S_Avg, etc)
DATA_C_tx       = [];           % data matrix for temporal-spatial, C(x,t) [ug_i/L_void]
DATA_S_tx       = [];           % data matrix for temporal-spatial, S(x,t) [ug_i/kg_solid]
DATA_Q_tx       = [];           % data matrix for temporal-spatial, Q(x,t) [ug_i/L_agg]
DATA_Kd_tx      = [];           % data matrix for temporal-spatial Kd = S(x,t) / C(x,t)
DATA_Z_tx       = [];           % data matrix for Z(t) = Q_nowAvg + C_blkAvg*VRatio [ug/L_agg]

% Save time-zero condition
DATA_C_tx       = [DATA_C_tx; [0, 0, C_initX]];
DATA_S_tx       = [DATA_S_tx; [0, 0, S_initX]];
DATA_Q_tx       = [DATA_Q_tx; [0, 0, Q_initX]];
DATA_Kd_tx      = [DATA_Kd_tx; [0, 0, S_initX./C_initX]];
DATA_Z_tx       = [DATA_Z_tx; [0, 0, Z_init, 0]];

tic
for itime=1:Timesteps,

   %% INNERMOST GRID (grid 1) CALC
   Q_nextX(1)   = Q_nowX(1) + k_innermost*(C_nowX(2)-C_nowX(1));
   C_nextX(1)   = NewtonSolveC(1e-40, A1stOrder(1), AFrdlichN(1), FrdlichN, Q_nextX(1));
   S_nextX(1)   = focX(1)*Koc*C_nextX(1) + fbcX(1)*Kbc*(C_nextX(1)^FrdlichN);
```

```
   %% INTERMEDIATE GRIDS (grids 2 to [m-1]) CALC
   dum_iplus1 = []; dum_iminus1 = []; dum_i = [];
   dum_iplus1  = k_intermedi(inrgds).*x_hlf_miu_les_1(inrgds).*TortuosityHlfX(inrgds);          %
Coeff for C_nowX(i+1)
   dum_iminus1 = k_intermedi(inrgds).*x_hlf_miu_les_1(inrgds-1).*TortuosityHlfX(inrgds-1);% Coeff
for C_nowX(i-1)
   dum_i       = dum_iplus1 + dum_iminus1;
                                                          % Coeff for C_nowX(i)
   Q_nextX(inrgds) = Q_nowX(inrgds) + dum_iplus1.*C_nowX(inrgds+1) + dum_iminus1.*C_nowX(inrgds-1)
- dum_i.*C_nowX(inrgds);
   C_nextX(inrgds) = NewtonSolveC(1e-40, A1stOrder(inrgds), AFrdlichN(inrgds), FrdlichN,
Q_nextX(inrgds));
   S_nextX(inrgds) = Koc*focX(inrgds).*C_nextX(inrgds) +
Kbc*fbcX(inrgds).*(C_nextX(inrgds).^FrdlichN);

   %% C_blk_next CALC
   dum_Q_nextX = [Q_nextX(1:m-1), 0];
               % dummy for calculating q_next_cnst
   q_next_cnst = F_AggregateAvgProperty(ShapeFactor, x, dum_Q_nextX, dx);
   CnxtConstant= (Q_nowAvg - q_next_cnst)/VRatio + C_blk_now;
   C_blk_next  = NewtonSolveC (1e-40, Cnxt1stOrder, CnxtFrdlichN, FrdlichN, CnxtConstant);
   C_nextX(m)  = C_blk_next;
   S_nextX(m)  = alpha_m*C_nextX(m) + beta_m*(C_nextX(m)^FrdlichN);
   Q_nextX(m)  = S_nextX(m)*rho_bulkX(m) + PorosityX(m)*C_nextX(m);

   %% UPDATE CONCENTRATIONS
   %% all "NOW" concs represent values after itime of timesteps, thus to be recorded as occuring
at [itime*dtow]
   C_nowX      = C_nextX;
   S_nowX      = S_nextX;
   Q_nowX      = Q_nextX;
   C_blk_now   = C_blk_next;
   Q_nowAvg    = F_AggregateAvgProperty(ShapeFactor, x, Q_nextX, dx);

   %% SAVE MODELLED PROFILE
   %% ***REM: all "NOW" quantities are the LATEST quantities for itime# of steps***
   C_blk_diff = abs((C_blk_now - C_blk_mark)/C_blk_mark);
   if C_blk_diff>0.01
      AbsT_hrs = itime*dt/3600;       % time in hrs
      AbsTow   = itime*dtow;          % dimensionless time [--]
      TimeEntry= [AbsTow, AbsT_hrs]; % i.e. [tow, t_in_hrs]; 1 x 2
      Magg_Meqm= Q_nowAvg/Q_eqmAvg;  % Mass of i in agg at itimeth step / Mass of i in agg at
eqm (t->inf)

      %% Storing overall desorption result at ith timestep, or [itime*dt] secs
      C_nowAvg         = F_AggregateAvgProperty(ShapeFactor, x, C_nowX, dx);
      S_nowAvg         = F_AggregateAvgProperty(ShapeFactor, x, S_nowX, dx);
      OneEntry_OVRALL = [TimeEntry, C_nowAvg, S_nowAvg, Q_nowAvg, C_blk_now, C_blk_now/C_blk_eqm,
Magg_Meqm];
      DATA_OVRALL      = [DATA_OVRALL; OneEntry_OVRALL];

      %% Storing temporal-spatial result at ith timestep
      DATA_C_tx        = [DATA_C_tx; [TimeEntry, C_nowX]];
      DATA_S_tx        = [DATA_S_tx; [TimeEntry, S_nowX]];
      DATA_Q_tx        = [DATA_Q_tx; [TimeEntry, Q_nowX]];
      DATA_Kd_tx       = [DATA_Kd_tx; [TimeEntry, S_nowX./C_nowX]];
      Z_now            = Q_nowAvg+C_blk_now*VRatio;
      DZ_now_les_init  = Z_now - Z_init;
      DATA_Z_tx        = [DATA_Z_tx; [TimeEntry, Z_now, DZ_now_les_init]];

      %% Update C_blk_mark ***!!!***
      C_blk_mark       = C_blk_now;

   elseif (itime>30000)&(mod(itime, 4000)==0)
      AbsT_hrs = itime*dt/3600;              % time in hrs
      AbsTow   = itime*dtow;                 % dimensionless time [--]
      TimeEntry= [AbsTow, AbsT_hrs];% i.e. [tow, t_in_hrs]; 1 x 2
      Magg_Meqm= Q_nowAvg/Q_eqmAvg;  % Mass of i in agg at itimeth step / Mass of i in agg at
eqm (t->inf)

      %% Storing overall desorption result at ith timestep, or [itime*dt] secs
      C_nowAvg         = F_AggregateAvgProperty(ShapeFactor, x, C_nowX, dx);
      S_nowAvg         = F_AggregateAvgProperty(ShapeFactor, x, S_nowX, dx);
      OneEntry_OVRALL = [TimeEntry, C_nowAvg, S_nowAvg, Q_nowAvg, C_blk_now, C_blk_now/C_blk_eqm,
Magg_Meqm];
      DATA_OVRALL      = [DATA_OVRALL; OneEntry_OVRALL];

      %% Storing temporal-spatial result at ith timestep
      DATA_C_tx        = [DATA_C_tx; [TimeEntry, C_nowX]];
      DATA_S_tx        = [DATA_S_tx; [TimeEntry, S_nowX]];
      DATA_Q_tx        = [DATA_Q_tx; [TimeEntry, Q_nowX]];
```

```
      DATA_Kd_tx       = [DATA_Kd_tx; [TimeEntry, S_nowX./C_nowX]];
      Z_now            = Q_nowAvg+C_blk_now*VRatio;
      DZ_now_les_init  = Z_now - Z_init;
      DATA_Z_tx        = [DATA_Z_tx; [TimeEntry, Z_now, DZ_now_les_init]];

      %% Update C_blk_mark ***!!!***
      C_blk_mark       = C_blk_now;

   end % end if-elseif
   if mod(itime, 1000)==0,
      fprintf ('%i\n', itime);
   end
end


%%%
%%% Write modeling results to files
%%%
Fpath_OVRALL   = [Fpath, Ffilename, '.ovr'];
Fpath_C_tx     = [Fpath, Ffilename, '.c'];
Fpath_S_tx     = [Fpath, Ffilename, '.s'];
Fpath_Q_tx     = [Fpath, Ffilename, '.q'];
Fpath_Kd_tx    = [Fpath, Ffilename, '.kd'];
Fpath_Z_tx     = [Fpath, Ffilename, '.z'];

save ovrall DATA_OVRALL -ASCII
save c DATA_C_tx -ASCII
save s DATA_S_tx -ASCII
save q DATA_Q_tx -ASCII
save kd DATA_Kd_tx -ASCII
save z DATA_Z_tx -ASCII

dos(['ren ovrall ',Ffilename,'_Ovrall.txt']);
dos(['ren c ',Ffilename,'_C.txt']);
dos(['ren s ',Ffilename,'_S.txt']);
dos(['ren q ',Ffilename,'_Q.txt']);
dos(['ren kd ',Ffilename,'_Kd.txt']);
dos(['ren z ',Ffilename,'_Z.txt']);

toc
```

Script E - 5. Functions Called by the Desorption Model

F_Diffusivity (Calculate D_{iw})

```
%
% Function F_Diffusivity
% By: Dave Kuo
% Date: 15 Sept 2005
%
% Calculate diffusivity at T=25C, P=1 atm, for HOC_i in solvent Solv, return Diw_m [m2/s]

% edta_solv     : solvent viscosity [cp] at T=25C
% rho_i         : density of chemical i [g/cm3]
% MW_i          : molecular wt of chemical i [g/mol]
function [Diw_m] = F_Diffusivity(HOC_i, Solv)

if strcmp(HOC_i,'pyrene')
   rho_i = 1.27;
   MW_i  = 202.3;
elseif strcmp(HOC_i,'naphthalene')
   rho_i = 1.16;
   MW_i  = 128.2;
elseif strcmp(HOC_i,'fluoranthene')
   rho_i = 1.25;
   MW_i  = 202.3;
elseif strcmp(HOC_i,'phenanthrene')
   rho_i = 0.98;
   MW_i  = 178.2;
elseif strcmp(HOC_i,'anthracene')
   rho_i = 1.25;
   MW_i  = 178.2;
elseif strcmp(HOC_i,'bap')
   rho_i = 1.28;
   MW_i  = 252.3;
end

if strcmp(Solv,'water')
   edta = 0.89;
end

MolarV_i = MW_i/rho_i;
        % [cm3/mol]
Diw_cm = 13.26e-5/( (edta^1.14)*(MolarV_i^0.589) );         % [cm2/s]
Diw_m = Diw_cm / 1e4;
        % [m2/s]
```

F_SetAggProperty (Set distribution of property within aggregate)

```
%
% Function F_SetAggProperty
% By: Dave Kuo
% Date: 11 Oct 2005
%
% Initialize aggregate spatial property y(X) according to case; return yX
% property can be: porosity, tortuosity, foc, fbc, etc

% DesorpCase    : specify tortuosity scenarios
% m             : # grids
% yi            : y-values for ith compartments
% CharEnd_m     : last grid point for property y in char-compartment
% yX            : spatial y matrix; 1 x m
function [yX] = F_SetAggProperty(DesorpCase, m, y1, y2, CharEnd_m)

switch DesorpCase
  case 'homogeneous'                    %% porosity is homogeneous throughout
        yX = ones(1, m)*y1;
  case 'char-in-silt-central'           %% two-compartment, char in central
        yX = [ones(1, CharEnd_m)*y1, ones(1, (m-CharEnd_m))*y2];
end
```

F_AggregateAvgProperty (Calculate aggregate-averaged property)

```
% Function F_AggregateAvgProperty
% By: Dave Kuo
% Calculate aggregate-averaged property such as Q_bar, porosity_bar
% Integrate by SIMPSON's 1/3 RULE, with grids from 1 to m, m ODD-numbered

% ShapeFactor    : 3 for sphere, 2 for cylinder, 1 for slab
% X              : dimensionless spatial matrix;       1 x m
% Y              : property y=func(x);                 1 x m
% deltaX         : delta x [or =(b-a)/intervals]       scalar

function [AggAvgY] = F_AggregateAvgProperty(ShapeFactor, X, Y, deltaX)
m                       = size(Y,2);
ingr                    = 2:(m-1);              % 1 x m-2
minone(1, 1:(m-2))      = -1;                   % 1 x m-2
altminone = minone.^ingr;                       % {1 -1  1 -1  1 -1...}
threes(1, 1:(m-2))      = 3;                          % {3  3  3  3  3  3...}
CoeffSimpson            = [1, threes+altminone, 1];   % 1 x m; {1 4 2 4..2 4 1}

% summing along row, for all m columns...
AggAvgY = ShapeFactor*deltaX/3 * sum(CoeffSimpson.*Y.*(X.^(ShapeFactor-1)), 2);
```

NewtonSolveC (Solve non-linear equation in the Linear-Freundlich Form)

```
function [ConvrgeC] = NewtonSolveC(InitGuess, alpha, beta, FrdlichN, fixed)

%%%
```

Script E - 6. Scripts for Empirical Regression of Kinetic Data

Exponential Model (Constrained One-Compartment + Instantaneous Desorbed Fraction)

$$C(t) = \mathbf{S_{inst}} R_{sw} + (S_o - S_{Eqm\,|End} - S_{inst}) R_{sw} [1 - \exp(-\mathbf{k}t)]$$

Exponential Model (Constrained Two-Compartment)

$$C(t) = \mathbf{S_{slow,o}} R_{sw} [1 - \exp(-\mathbf{k_{slow}}t)] + \mathbf{S_{rapid,o}} R_{sw} [\exp(-k_{slow}\, t) - \exp(-\mathbf{k_{rapid}}t)]$$

where: $S_o = S_{slow\,,o} + S_{rapid\,,o} + S_{Eqm\,|End}$

Exponential Model (Unconstrained Two-Compartment)

$$C(t) = \mathbf{S_{slow,o}} R_{sw} [1 - \exp(-\mathbf{k_{slow}}t)] + \mathbf{S_{rapid,o}} R_{sw} [\exp(-k_{slow}\, t) - \exp(-\mathbf{k_{rapid}}t)]$$

where: $S_o = S_{slow\,,o} + S_{rapid\,,o}$

Exponential Model (Constrained Three-Compartment)

$$C(t) = \mathbf{S_{v.slow}} R_{sw} [1 - e^{-\mathbf{k_{v.slow}}t}] + \mathbf{S_{slow}} R_{sw} [e^{-k_{v.slow}\, t} - e^{-\mathbf{k_{slow}}t}] + \mathbf{S_{rapid}} R_{sw} [e^{-k_{v.slow}\, t} - e^{-\mathbf{k_{rapid}}t}]$$

where: $S_o = S_{v.slow} + +S_{slow} + S_{rapid} + S_{Eqm\,|End}$

Orthogonal Polynomial Model

$$C(t) = S_o R_{sw} [\mathbf{a_0} + \mathbf{a_1} t^{0.5} + \mathbf{a_2} t]$$

Elovich Model

$$C(t) = S_o R_{sw} [\mathbf{a} + \mathbf{b} \ln(t)]$$

Gamma-Distributed Rate Model

$$C(t) = S_o R_{sw} \{1 - [\mathbf{b}/(b + t)]^{\mathbf{a}}\}$$

Weibull Model (Constrained One-Compartment)

$$C(t) = (S_o - S_{Eqm\,|End}) R_{sw} \{1 - \exp(-kt^b)\}$$

Weibull Model (Constrained Two-Compartment)

$$C(t) = \mathbf{S_1} R_{sw} [1 - \exp(-\mathbf{k_1} t^{\mathbf{b_1}})] + \mathbf{S_2} R_{sw} [1 - \exp(-\mathbf{k_2} t^{\mathbf{b_2}})]$$

where: $S_o = S_1 + +S_2 + S_{Eqm\,|End}$

Constrained Instantaneous Desorbed Fraction + 1st Order Exponential

Function RunConstrainInstDesorb1stOrderFit

```
function FitEndStatus = RunConstrainInstDesorb1stOrderFit

% By: Dave Kuo
% Date: 12 Sept 2006
%
% Fitting of desorption kinetic data to CONSTRAINED 1st Order model
% 2-parameter fitting: k, S_inst
%
% Model used: Constrain1stOrderModel
%
% To fit desorption data with non-linear regression:
%
% 1) modify: datafile to be loaded, exp-set name, etc
% 2) modify: S_init and rsw in Simple1stOrderModel
% 3) Run RunConstrain1stOrderFit

clear;
close all;

xydata = load ('Rxtor_lowrsw_data.txt');
figtext = 'Rxtor I low rsw';
pathfilename = [cd,'\Rxtor_lowrsw_ConstrainInstDesorb1stOrderFit.txt'];
time        = xydata(:,1);          % independent var; [hr]
C_obs       = xydata(:,2)/1000;     % so that in [ug_pyr/L]; dependent var

k_guess    = 0.001;                 % [hr-1]
S_inst_guess= 20;                   % [ug_pyr/kg_solids]

GuessVector         = [k_guess, S_inst_guess];
[FittedParameters, FitResid, J] = nlinfit(time, C_obs, 'ConstrainInstDesorb1stOrderModel',
GuessVector);

% Plots prediction (from the fit) against observation, and gives other
% stats info

FittedParametersCI  = nlparci(FittedParameters, FitResid, J);
[C_pred, OneDelta]  = nlpredci('ConstrainInstDesorb1stOrderModel', time, FittedParameters,
FitResid, J);

lgt = log(time);
xydatahat = [time, lgt, C_obs, C_pred, OneDelta];
SumResidSq = sum(FitResid.^2);
text0 = ['Regressed Parameters:'];
text1 = ['k (hr^-^1): ', num2str(FittedParameters(1))];
text2 = ['S_i_n_s_t_._d_e_s (ug/kg): ', num2str(FittedParameters(2))];

figure;
pretitle = 'Plots of Constrained 1st Order, instant. desorb. (1 mobile, 1 inst. des.)
Exponential Model Fitting of ';
titletxt = [pretitle, figtext];

subplot(1,3,1), plot(time, C_obs, 'bx', time, C_pred, 'r.'), xlabel('Time Elaspsed (hr)'),
ylabel('C_p_y_r (ug/L)');
subplot(1,3,2), plot(lgt, C_obs, 'bx', lgt, C_pred, 'r.'), xlabel('Log of Time Elaspsed
(hr/hr)'), ylabel('C_p_y_r (ug/L)');
title({titletxt; ''; ''});
h = get(gcf, 'CurrentAxes'); TX = get(h, 'XLim'); TY = get(h, 'YLim'); TxtPosX =
0.4*(TX(2)-TX(1))+TX(1); TxtPosY = 0.1*(TY(2)-TY(1))+TY(1);
text(TxtPosX, TxtPosY,{text0; text1; text2});
subplot(1,3,3), plot(lgt, C_obs, 'bx', lgt, C_pred, 'r.', lgt, C_pred+OneDelta, 'k-', lgt,
C_pred-OneDelta, 'k-'),
xlabel('Log of Time Elapsed (hr/hr)'), ylabel('C_p_y_r (ug/L)');

figure; h = get(gcf, 'CurrentAxes');
plot(lgt, C_obs, 'bx', lgt, C_pred, 'r.', lgt, C_pred+OneDelta, 'k-', lgt, C_pred-OneDelta,
'k-');
title({titletxt; ''; ''});
xlabel('Log of Time Elapsed (hr/hr)'), ylabel('C_p_y_r (ug/L)');
h = get(gcf, 'CurrentAxes'); TX = get(h, 'XLim'); TY = get(h, 'YLim'); TxtPosX =
0.4*(TX(2)-TX(1))+TX(1); TxtPosY = 0.1*(TY(2)-TY(1))+TY(1);
text(TxtPosX, TxtPosY,{text0; text1; text2});

figure; h = get(gcf, 'CurrentAxes');
plot(time, C_obs, 'bx', time, C_pred, 'r.', time, C_pred+OneDelta, 'k-', time, C_pred-
OneDelta, 'k-');
```

```
title({titletxt; ''; ''});
xlabel('Time Elaspsed (hr)'), ylabel('C_p_y_r (ug/L)');
h = get(gcf, 'CurrentAxes'); TX = get(h, 'XLim'); TY = get(h, 'YLim'); TxtPosX =
0.4*(TX(2)-TX(1))+TX(1); TxtPosY = 0.1*(TY(2)-TY(1))+TY(1);
text(TxtPosX, TxtPosY,{text0; text1; text2});

OutMat = [time, lgt, 1000*C_obs, 1000*C_pred, 1000*OneDelta];
fid = fopen(pathfilename,'w');
fprintf(fid, '   Time(hr)   Log(time)   C_pyr_obs(ng/L)   C_pyr_pred(ng/L)
1_Sigma(ng/L)\n');
for i=1:size(OutMat,1)
    fprintf(fid, '   %6.1f   %3.4f   %4.2f   %4.2f   %4.4f\n', OutMat(i, 1), OutMat(i, 2),
OutMat(i, 3), OutMat(i, 4), OutMat(i, 5));
end
fprintf(fid, '   k_fit   %3.10f\n', FittedParameters(1));
fprintf(fid, '   S_inst_fit   %7.1f\n', FittedParameters(2));
fprintf(fid, '   SumOfResid^2   %3.10f\n', SumResidSq);
fclose(fid);

FitEndStatus = [FittedParameters, SumResidSq];
```

Function ConstrainInstDesorb1stOrderModel

```
function yhat = ConstrainInstDesorb1stOrderModel(param_guess, x_time)

% By: Dave Kuo
% Date: 12 Sept 2006
%
% Constrained 1st order model, with 1 mobile compartment and 1 instantaneous desorbed
compartment
%
% x_time        : independent variable
% param_guess   : initial guess for all fitted parameters
% S_init        : initial solid pyr loading [ug_pyr/kg_solids]
% rsw           : solid-to-water ratio [kg_solids/L_wat]
%
% yhat          : predicted dissolved pyrene, C(t)_hat [ug/L]
% k             : fitted desorption rate for compartment #1 [hr-1]
% S_inst        : fitted instantaneous desorbed compartment [ug_pyr/kg_solids]
%

%%%
%%% CAUTION!!! --> MUST CHECK   S_init   AND   rsw !!!
%%%

S_init      = 5420;         % [ug_pyr/kg_solids]
S_eqm       = 3969;           % [ug_pyr/kg_solids]
rsw         = 19/1e6;       % [kg_solids/L_wat]

k           = param_guess(1);
S_instant   = param_guess(2);

yhat        = S_instant*rsw + (S_init-S_eqm-S_instant)*rsw*(1-exp(-k.*x_time));
```

Constrained Two-Compartment Exponential Model

Function RunConstrainTwoCompartmentNoInstFit

```
function FitEndStatus = RunConstrainTwoCompartmentNoInstFit

% By: Dave Kuo
% Date: 12 Sept 2006
%
% Non-linear fitting of desorption kinetic data to constrained 2-compartment no instant
desorbing fraction model
% 3-parameter fitting: S_1_0, k1, k2
% see van den Heuvel et al., Chemosphere, v53, 1097, yr 2003
%
% Model used: TwoCompartmentModel
%
% To fit desorption data with non-linear regression:
```

```
%
% Edit RunTwoCompartmentFit
% 1) modify: datafile to be loaded, exp-set name, etc
% 2) modify: S_init and rsw in TwoCompartmentModel
% 3) Run RunTwoCompartmentFit

clear;
close all;

xydata = load ('K_lowrsw_data.txt');
figtext = 'K-set low rsw';
pathfilename = [cd,'\K_lowrsw_2CmprtNoInstfit.txt'];
time        = xydata(:,1);          % independent var; [hr]
C_obs       = xydata(:,2)/1000;     % so that in [ug_pyr/L]; dependent var

S_1_0_guess = 300;                 % [ug_pyr/kg_solids]
k1_guess    = 0.001;                 % [hr-1]
k2_guess    = 0.0001;                  % [hr-1]

GuessVector         = [S_1_0_guess, k1_guess, k2_guess];
[FittedParameters, FitResid, J] = nlinfit(time, C_obs,
'ConstrainTwoCompartmentNoInstModel', GuessVector);

% Plots prediction (from the fit) against observation, and gives other
% stats info

FittedParametersCI  = nlparci(FittedParameters, FitResid, J);
[C_pred, OneDelta]  = nlpredci('ConstrainTwoCompartmentNoInstModel', time,
FittedParameters, FitResid, J);

lgt = log(time);
xydatahat = [time, lgt, C_obs, C_pred, OneDelta];
SumResidSq = sum(FitResid.^2);
text0 = ['Regressed Parameters:'];
text1 = ['S_1_,_o (ug/L): ', num2str(round(FittedParameters(1)))];
text2 = ['k_1 (hr^-^1): ', num2str(FittedParameters(2))];
text3 = ['k_2 (hr^-^1): ', num2str(FittedParameters(3))];

figure;
pretitle = 'Plots of Constrained 2-Compartment (no inst. des.) Exponential Model Fitting
of ';
titletxt = [pretitle, figtext];

subplot(1,3,1), plot(time, C_obs, 'bx', time, C_pred, 'r.'), xlabel('Time Elaspsed (hr)'),
ylabel('C_p_y_r (ug/L)');
subplot(1,3,2), plot(lgt, C_obs, 'bx', lgt, C_pred, 'r.'), xlabel('Log of Time Elaspsed
(hr/hr)'), ylabel('C_p_y_r (ug/L)');
title({titletxt; ''; ''});
h = get(gcf, 'CurrentAxes'); TX = get(h, 'XLim'); TY = get(h, 'YLim'); TxtPosX =
0.4*(TX(2)-TX(1))+TX(1); TxtPosY = 0.1*(TY(2)-TY(1))+TY(1);
text(TxtPosX, TxtPosY,{text0; text1; text2; text3});
subplot(1,3,3), plot(lgt, C_obs, 'bx', lgt, C_pred, 'r.', lgt, C_pred+OneDelta, 'k-', lgt,
C_pred-OneDelta, 'k-'),
xlabel('Log of Time Elapsed (hr/hr)'), ylabel('C_p_y_r (ug/L)');

figure; h = get(gcf, 'CurrentAxes');
plot(lgt, C_obs, 'bx', lgt, C_pred, 'r.', lgt, C_pred+OneDelta, 'k-', lgt, C_pred-OneDelta,
'k-');
title({titletxt; ''; ''});
xlabel('Log of Time Elapsed (hr/hr)'), ylabel('C_p_y_r (ug/L)');
h = get(gcf, 'CurrentAxes'); TX = get(h, 'XLim'); TY = get(h, 'YLim'); TxtPosX =
0.4*(TX(2)-TX(1))+TX(1); TxtPosY = 0.1*(TY(2)-TY(1))+TY(1);
text(TxtPosX, TxtPosY,{text0; text1; text2; text3});

figure; h = get(gcf, 'CurrentAxes');
plot(time, C_obs, 'bx', time, C_pred, 'r.', time, C_pred+OneDelta, 'k-', time, C_pred-
OneDelta, 'k-');
title({titletxt; ''; ''});
xlabel('Time Elaspsed (hr)'), ylabel('C_p_y_r (ug/L)');
h = get(gcf, 'CurrentAxes'); TX = get(h, 'XLim'); TY = get(h, 'YLim'); TxtPosX =
0.4*(TX(2)-TX(1))+TX(1); TxtPosY = 0.1*(TY(2)-TY(1))+TY(1);
text(TxtPosX, TxtPosY,{text0; text1; text2; text3});

OutMat = [time, lgt, 1000*C_obs, 1000*C_pred, 1000*OneDelta];
fid = fopen(pathfilename,'w');
fprintf(fid, '   Time(hr)   Log(time)   C_pyr_obs(ng/L)   C_pyr_pred(ng/L)
1_Sigma(ng/L)\n');
for i=1:size(OutMat,1)
    fprintf(fid, '   %6.1f   %3.4f   %4.2f   %4.2f   %4.4f\n', OutMat(i, 1), OutMat(i, 2),
OutMat(i, 3), OutMat(i, 4), OutMat(i, 5));
end
```

```
fprintf(fid, '   S_1_0_fit   %7.1f\n', FittedParameters(1));
fprintf(fid, '   k1_fit   %3.10f\n', FittedParameters(2));
fprintf(fid, '   k2_fit   %3.10f\n', FittedParameters(3));
fprintf(fid, '   SumOfResid^2   %3.10f\n', SumResidSq);
fclose(fid);

FitEndStatus = [FittedParameters, SumResidSq];
```

Function ConstrainTwoCompartmentNoInstModel

```
function yhat = ConstrainTwoCompartmentNoInstModel(param_guess, x_time)

% By: Dave Kuo
% Date: 12 Sept 2006
%
% Constrained 2-compartment, no instantaneous desorbing fraction model for desorption
kinetic data fit (non-linear)
% see van den Heuvel et al., Chemosphere, v53, 1097, yr 2003
%
% x_time        : independent variable
% param_guess   : initial guess for all fitted parameters
% S_init        : initial solid pyr loading [ug_pyr/kg_solids]
% rsw           : solid-to-water ratio [kg_solids/L_wat]
%
% MODEL FORM:
% yhat = S_init*rsw*[1-exp(-k2*t)] + S_1_0*rsw*[exp(-k2*t)-exp(-k1*t)]
% where:
%
% yhat          : predicted dissolved pyrene, C(t)_hat [ug/L]
% S_1_0         : fitted solid compartment #1 loading [ug_pyr/kg_solids]
% k1            : fitted desorption rate for compartment #1 [hr-1]
% k2            : fitted desorption rate for compartment #2 [hr-1]
%
% NOTES:
%
% 1) S(t) = S1(t) + S2(t), at all t
% 2) S(t)M + C(t)V = S(0)M, at all t
% 3) dS_i/dt = -k_i*S_i
% 4) C(t)V = S(0)M - S1(t)M - S2(t)M
%
% To fit desorption data with non-linear regression:
% Edit RunTwoCompartmentFit
% modify: datafile to be loaded, exp-set name, etc
% Run RunTwoCompartmentFit

%%%
%%% CAUTION!!! --> MUST CHECK   S_init   AND   rsw !!!
%%%

S_init      = 3060;          % [ug_pyr/kg_solids]
S_eqm       = 2204;             % [ug_pyr/kg_solids]
S_mobile    = S_init - S_eqm;   % [ug_pyr/kg_solids]
rsw         = 21/1e6;        % [kg_solids/L_wat]

S_1_0       = param_guess(1);
k1          = param_guess(2);
k2          = param_guess(3);

SR_mob      = S_mobile*rsw;   % [ug_pyr/L_wat]
SR_1_0      = S_1_0*rsw;    % [ug_pyr/L_wat]

yhat        = SR_mob*(1-exp(-k2.*x_time)) + SR_1_0*(exp(-k2.*x_time)-exp(-k1.*x_time));
```

Unconstrained Two-Compartment Exponential Model

Function RunTwoCompartmentFit

```
function FitEndStatus = RunTwoCompartmentFit

% By: Dave Kuo
% Date: 12 Sept 2006
```

```
%
% Non-linear fitting of desorption kinetic data to 2-compartment model
% 3-parameter fitting: S_1_0, k1, k2
% see van den Heuvel et al., Chemosphere, v53, 1097, yr 2003
%
% Model used: TwoCompartmentModel
%
% To fit desorption data with non-linear regression:
%
% Edit RunTwoCompartmentFit
% 1) modify: datafile to be loaded, exp-set name, etc
% 2) modify: S_init and rsw in TwoCompartmentModel
% 3) Run RunTwoCompartmentFit

clear;
close all;

xydata = load ('Rxtor_hirsw_data.txt');
figtext = 'Rxtor G hi rsw';
pathfilename = [cd,'\Rxtor_hirsw_fit.txt'];
time        = xydata(:,1);          % independent var; [hr]
C_obs       = xydata(:,2)/1000;     % so that in [ug_pyr/L]; dependent var

S_1_0_guess = 300;                 % [ug_pyr/kg_solids]
k1_guess    = 0.02;                 % [hr-1]
k2_guess    = 0.0001;                  % [hr-1]

GuessVector         = [S_1_0_guess, k1_guess, k2_guess];
[FittedParameters, FitResid, J] = nlinfit(time, C_obs, 'TwoCompartmentModel', GuessVector);

% Plots prediction (from the fit) against observation, and gives other
% stats info

FittedParametersCI  = nlparci(FittedParameters, FitResid, J);
[C_pred, OneDelta]  = nlpredci('TwoCompartmentModel', time, FittedParameters, FitResid, J);

lgt = log(time);
xydatahat = [time, lgt, C_obs, C_pred, OneDelta];
SumResidSq = sum(FitResid.^2);
text0 = ['Regressed Parameters:'];
text1 = ['S_1_,_o (ug/L): ', num2str(round(FittedParameters(1)))];
text2 = ['k_1 (hr^-^1): ', num2str(FittedParameters(2))];
text3 = ['k_2 (hr^-^1): ', num2str(FittedParameters(3))];

fprintf('Fitted parameters\n');
fprintf('S_1_0_fit(ug_pyr/kg_solids)   k1_fit(hr-1)   k2_fit(hr-1)\n');
FittedParameters(1), FittedParameters(2), FittedParameters(3),
fprintf('\n\n\n');

figure;
pretitle = 'Plots of Constrained 2-Compartment (no inst. des.) Exponential Model Fitting
of ';
titletxt = [pretitle, figtext];

subplot(1,3,1), plot(time, C_obs, 'bx', time, C_pred, 'r.'), xlabel('Time Elaspsed (hr)'),
ylabel('C_p_y_r (ug/L)');
subplot(1,3,2), plot(lgt, C_obs, 'bx', lgt, C_pred, 'r.'), xlabel('Log of Time Elaspsed
(hr/hr)'), ylabel('C_p_y_r (ug/L)');
title({titletxt; ''; ''});
h = get(gcf, 'CurrentAxes'); TX = get(h, 'XLim'); TY = get(h, 'YLim'); TxtPosX =
0.4*(TX(2)-TX(1))+TX(1); TxtPosY = 0.1*(TY(2)-TY(1))+TY(1);
text(TxtPosX, TxtPosY,{text0; text1; text2; text3});
subplot(1,3,3), plot(lgt, C_obs, 'bx', lgt, C_pred, 'r.', lgt, C_pred+OneDelta, 'k-', lgt,
C_pred-OneDelta, 'k-'),
xlabel('Log of Time Elapsed (hr/hr)'), ylabel('C_p_y_r (ug/L)');

figure; h = get(gcf, 'CurrentAxes');
plot(lgt, C_obs, 'bx', lgt, C_pred, 'r.', lgt, C_pred+OneDelta, 'k-', lgt, C_pred-OneDelta,
'k-');
title({titletxt; ''; ''});
xlabel('Log of Time Elapsed (hr/hr)'), ylabel('C_p_y_r (ug/L)');
h = get(gcf, 'CurrentAxes'); TX = get(h, 'XLim'); TY = get(h, 'YLim'); TxtPosX =
0.4*(TX(2)-TX(1))+TX(1); TxtPosY = 0.1*(TY(2)-TY(1))+TY(1);
text(TxtPosX, TxtPosY,{text0; text1; text2; text3});

figure; h = get(gcf, 'CurrentAxes');
plot(time, C_obs, 'bx', time, C_pred, 'r.', time, C_pred+OneDelta, 'k-', time, C_pred-
OneDelta, 'k-');
title({titletxt; ''; ''});
xlabel('Time Elaspsed (hr)'), ylabel('C_p_y_r (ug/L)');
```

```
h = get(gcf, 'CurrentAxes'); TX = get(h, 'XLim'); TY = get(h, 'YLim'); TxtPosX =
0.4*(TX(2)-TX(1))+TX(1); TxtPosY = 0.1*(TY(2)-TY(1))+TY(1);
text(TxtPosX, TxtPosY,{text0; text1; text2; text3});

OutMat = [time, lgt, 1000*C_obs, 1000*C_pred, 1000*OneDelta];
fid = fopen(pathfilename,'w');
fprintf(fid, '   Time(hr)   Log(time)   C_pyr_obs(ng/L)   C_pyr_pred(ng/L)
1_Sigma(ng/L)\n');
for i=1:size(OutMat,1)
    fprintf(fid, '   %6.1f   %3.4f   %4.2f   %4.2f   %4.4f\n', OutMat(i, 1), OutMat(i, 2),
OutMat(i, 3), OutMat(i, 4), OutMat(i, 5));
end
fprintf(fid, '   S_1_0_fit   %7.1f\n', FittedParameters(1));
fprintf(fid, '   k1_fit   %3.10f\n', FittedParameters(2));
fprintf(fid, '   k2_fit   %3.10f\n', FittedParameters(3));
fclose(fid);

FitEndStatus = [FittedParameters, SumResidSq];
```

Function TwoCompartmentModel

```
function yhat = TwoCompartmentModel(param_guess, x_time)

% By: Dave Kuo
% Date: 12 Sept 2006
%
% 2-compartment model for desorption kinetic data fit (non-linear)
% see van den Heuvel et al., Chemosphere, v53, 1097, yr 2003
%
% x_time        : independent variable
% param_guess   : initial guess for all fitted parameters
% S_init        : initial solid pyr loading [ug_pyr/kg_solids]
% rsw           : solid-to-water ratio [kg_solids/L_wat]
%
% MODEL FORM:
% yhat = S_init*rsw*[1-exp(-k2*t)] + S_1_0*rsw*[exp(-k2*t)-exp(-k1*t)]
% where:
%
% yhat          : predicted dissolved pyrene, C(t)_hat [ug/L]
% S_1_0         : fitted solid compartment #1 loading [ug_pyr/kg_solids]
% k1            : fitted desorption rate for compartment #1 [hr-1]
% k2            : fitted desorption rate for compartment #2 [hr-1]
%
% NOTES:
%
% 1) S(t) = S1(t) + S2(t), at all t
% 2) S(t)M + C(t)V = S(0)M, at all t
% 3) dS_i/dt = -k_i*S_i
% 4) C(t)V = S(0)M - S1(t)M - S2(t)M
%
% To fit desorption data with non-linear regression:
% Edit RunTwoCompartmentFit
% modify: datafile to be loaded, exp-set name, etc
% Run RunTwoCompartmentFit

%%%
%%% CAUTION!!! --> MUST CHECK   S_init   AND   rsw !!!
%%%

S_init      = 5420;          % [ug_pyr/kg_solids]
rsw         = 245/1e6;        % [kg_solids/L_wat]

S_1_0       = param_guess(1);
k1          = param_guess(2);
k2          = param_guess(3);

SR_init     = S_init*rsw;   % [ug_pyr/L_wat]
SR_1_0      = S_1_0*rsw;    % [ug_pyr/L_wat]

yhat        = SR_init*(1-exp(-k2.*x_time)) + SR_1_0*(exp(-k2.*x_time)-exp(-k1.*x_time));
```

Constrained Three-Compartment Exponential Model

Function RunConstrainThreeCompartmentFit

```
function FitEndStatus = RunConstrainThreeCompartmentFit

% By: Dave Kuo
% Date: 13 Sept 2006
%
% Non-linear fitting of desorption kinetic data to constrained 3-compartment model
% 5-parameter fitting: S_1_0, S_2_0, k1, k2, k3
% CONSTRAINING S_end = S_eqm, which is predicted from nonlinearKocKbc
% isotherm
%
% Model used: ConstrainThreeCompartmentModel
%
% To fit desorption data with non-linear regression:
%
% Edit RunConstrainThreeCompartmentFit
% 1) modify: datafile to be loaded, exp-set name, etc
% 2) modify: S_init and rsw in ConstrainThreeCompartmentModel
% 3) Run RunConstrainThreeCompartmentFit

clear;
close all;

xydata = load ('L_hirsw_data.txt');
figtext = 'L-set hi rsw';
pathfilename = [cd,'\L_hirsw_fit.txt'];

time        = xydata(:,1);          % independent var; [hr]
C_obs       = xydata(:,2)/1000;     % so that in [ug_pyr/L]; dependent var

S_1_0_guess = 17;
S_2_0_guess = 20;
k1_guess = 2;
%S_1_0_guess = 2;                  % [ug_pyr/kg_solids]
%S_2_0_guess = 200;                  % [ug_pyr/kg_solids]
%k1_guess    = 0.1;                 % [hr-1]
k2_guess    = 0.003;                % [hr-1]
k3_guess    = 5e-14;%0.00004;             % [hr-1]


GuessVector         = [S_1_0_guess, S_2_0_guess, k1_guess, k2_guess, k3_guess];
[FittedParameters, FitResid, J] = nlinfit(time, C_obs, 'ConstrainThreeCompartmentModel',
GuessVector);

%save FitResid -ASCII -DOUBLE -TABS;
%size(FitResid)

S_init      = 1350;             % [ug_pyr/kg_solids]
S_eqm       = 1253;             % [ug_pyr/kg_solids]
S_mobile    = S_init - S_eqm;   % [ug_pyr/kg_solids]
rsw         = 289/1e6;          % [kg_solids/L_wat]

syms S10 S20 k1 k2 k3;
modelform = S_mobile*rsw*(1-exp(-k3.*time)) + S10*rsw*(exp(-k3.*time)-exp(-k1.*time)) +
S20*rsw*(exp(-k3.*time)-exp(-k2.*time)); % symbolic form with 5 fit para as variables
%size(modelform)
%varmatrix = [S10 S20 k1 k2 k3];
%varmatrix = [k3 S10 k1 S20 k2];
varmatrix = [k1 k2 k3 S10 S20];
JacobVar = jacobian(modelform, varmatrix);
JacobMat = subs(JacobVar, varmatrix, FittedParameters);

JDiff = J(:,1:4)-JacobMat(:,1:4);
%[J JacobMat]
if JDiff==0
    fprintf('JDifference is zero.\n');
end

%yhat = ConstrainThreeCompartmentModel(FittedParameters, time);
%if ((C_obs-yhat-FitResid)==0)
%    fprintf('Residual difference is zero.\n');
%end

%size(J)
%size(yhat)
%size(FittedParameters);
```

```
%jacobian(yhat, FittedParameters);

% Plots prediction (from the fit) against observation, and gives other
% stats info

FittedParametersCI  = nlparci(FittedParameters, FitResid, J);
[C_pred, OneDelta]  = nlpredci('ConstrainThreeCompartmentModel', time, FittedParameters,
FitResid, J);

lgt = log(time);
xydatahat = [time, lgt, C_obs, C_pred, OneDelta];
AbsFit = abs(FittedParameters);
text0 = ['Regressed Parameters:'];
text1 = ['S_1_,_o (ug/L): ', num2str(round(AbsFit(1)))];
text2 = ['S_2_,_o (ug/L): ', num2str(round(AbsFit(2)))];
text3 = ['k_1 (hr^-^1): ', num2str(AbsFit(3))];
text4 = ['k_2 (hr^-^1): ', num2str(AbsFit(4))];
text5 = ['k_3 (hr^-^1): ', num2str(AbsFit(5))];

figure;
pretitle = 'Plots of Constrained 3-Compartment Exponential Model Fitting of ';
titletxt = [pretitle, figtext];

subplot(1,3,1), plot(time, C_obs, 'bx', time, C_pred, 'r.'), xlabel('Time Elaspsed (hr)'),
ylabel('C_p_y_r (ug/L)');
subplot(1,3,2), plot(lgt, C_obs, 'bx', lgt, C_pred, 'r.'), xlabel('Log of Time Elaspsed
(hr/hr)'), ylabel('C_p_y_r (ug/L)');
title({titletxt; ''; ''});
h = get(gcf, 'CurrentAxes'); TX = get(h, 'XLim'); TY = get(h, 'YLim'); TxtPosX =
0.4*(TX(2)-TX(1))+TX(1); TxtPosY = 0.1*(TY(2)-TY(1))+TY(1);
text(TxtPosX, TxtPosY,{text0; text1; text2; text3; text4; text5});
subplot(1,3,3), plot(lgt, C_obs, 'bx', lgt, C_pred, 'r.', lgt, C_pred+OneDelta, 'k-', lgt,
C_pred-OneDelta, 'k-'),
xlabel('Log of Time Elapsed (hr/hr)'), ylabel('C_p_y_r (ug/L)');


figure; h = get(gcf, 'CurrentAxes');
plot(lgt, C_obs, 'bx', lgt, C_pred, 'r.', lgt, C_pred+OneDelta, 'k-', lgt, C_pred-OneDelta,
'k-');
title({titletxt; ''; ''});
xlabel('Log of Time Elapsed (hr/hr)'), ylabel('C_p_y_r (ug/L)');
h = get(gcf, 'CurrentAxes'); TX = get(h, 'XLim'); TY = get(h, 'YLim'); TxtPosX =
0.4*(TX(2)-TX(1))+TX(1); TxtPosY = 0.1*(TY(2)-TY(1))+TY(1);
text(TxtPosX, TxtPosY,{text0; text1; text2; text3; text4; text5});

figure; h = get(gcf, 'CurrentAxes');
plot(time, C_obs, 'bx', time, C_pred, 'r.', time, C_pred+OneDelta, 'k-', time, C_pred-
OneDelta, 'k-');
title({titletxt; ''; ''});
xlabel('Time Elaspsed (hr)'), ylabel('C_p_y_r (ug/L)');
h = get(gcf, 'CurrentAxes'); TX = get(h, 'XLim'); TY = get(h, 'YLim'); TxtPosX =
0.4*(TX(2)-TX(1))+TX(1); TxtPosY = 0.1*(TY(2)-TY(1))+TY(1);
text(TxtPosX, TxtPosY,{text0; text1; text2; text3; text4; text5});

OutMat = [time, lgt, 1000*C_obs, 1000*C_pred, 1000*OneDelta];
fid = fopen(pathfilename,'w');
fprintf(fid, '   Time(hr)   Log(time)   C_pyr_obs(ng/L)   C_pyr_pred(ng/L)
1_Sigma(ng/L)\n');
for i=1:size(OutMat,1)
    fprintf(fid, '   %6.1f   %3.4f   %4.2f   %4.2f   %4.4f\n', OutMat(i, 1), OutMat(i, 2),
OutMat(i, 3), OutMat(i, 4), OutMat(i, 5));
end
fprintf(fid, '   S_1_0_fit   %7.1f\n', FittedParameters(1));
fprintf(fid, '   S_2_0_fit   %7.1f\n', FittedParameters(2));
fprintf(fid, '   k1_fit   %3.16f\n', FittedParameters(3));
fprintf(fid, '   k2_fit   %3.16f\n', FittedParameters(4));
fprintf(fid, '   k3_fit   %3.16f\n', FittedParameters(5));
fclose(fid);

ResidSq = sum(FitResid.^2);
FitEndStatus = [FittedParameters ResidSq];
```

Function ConstrainThreeCompartmentModel

```
function yhat = ConstrainThreeCompartmentModel(param_guess, x_time)

% By: Dave Kuo
% Date: 13 Sept 2006
%
```

```
% Constrained 3-compartment model for desorption kinetic data fit (non-linear)
% modified based upon TwoCompartmentModel
%
% Here, desorption beyound S_eqm is prohibited
%
% x_time        : independent variable
% param_guess   : initial guess for all fitted parameters
% S_init        : initial solid pyr loading [ug_pyr/kg_solids]
% rsw           : solid-to-water ratio [kg_solids/L_wat]
%
% MODEL FORM:
% yhat = (S_init-S_eqm)*rsw*[1-exp(-k3*t)] + S_1_0*rsw*[exp(-k3*t)-exp(-k1*t)] +
% S_2_0*rsw*[exp(-k3*t)-exp(-k2*t)]
%
% where:
%
% yhat          : predicted dissolved pyrene, C(t)_hat [ug/L]
% S_1_0         : fitted solid compartment #1 loading [ug_pyr/kg_solids]
% S_2_0         : fitted solid compartment #2 loading [ug_pyr/kg_solids]
% k1            : fitted desorption rate for compartment #1 [hr-1]
% k2            : fitted desorption rate for compartment #2 [hr-1]
% k3            : fitted desorption rate for compartment #3 [hr-1]
%
% NOTES:
%
% 1) S(t) = S1(t) + S2(t), at all t
% 2) S(t)M + C(t)V = S(0)M, at all t
% 3) dS_i/dt = -k_i*S_i
% 4) C(t)V = S(0)M - S1(t)M - S2(t)M
%
% To fit desorption data with non-linear regression:
% Edit RunTwoCompartmentFit
% modify: datafile to be loaded, exp-set name, etc
% Run RunTwoCompartmentFit

%%%
%%% CAUTION!!! --> MUST CHECK   S_init   AND   rsw !!!
%%%

S_init      = 1350;             % [ug_pyr/kg_solids]
S_eqm       = 1253;             % [ug_pyr/kg_solids]
S_mobile    = S_init - S_eqm;   % [ug_pyr/kg_solids]
rsw         = 289/1e6;          % [kg_solids/L_wat]

% the following allow regressed coefficients to be negative...
%S_1_0       = param_guess(1);
%S_2_0       = param_guess(2);
%k1          = param_guess(3);
%k2          = param_guess(4);
%k3          = param_guess(5);

% the following force all regressed coefficients to be positive...
% i.e., even if reporting negative k1, k2, k3, in the computation of least
% error yhat, they will take on positive values only

% ENSURE 1) ALL S's POSITIVE, AND 2) CONVERSATION OF MASS
if (param_guess(2)<0) & (param_guess(1)>0)
    S_1_0   = param_guess(1) + param_guess(2);
    S_2_0   = abs(param_guess(2));
elseif (param_guess(1)<0) & (param_guess(2)>0)
    S_2_0   = param_guess(2) + param_guess(1);
    S_1_0   = abs(param_guess(1));
elseif (param_guess(1)<0) & (param_guess(2)<0)
    S_1_0   = rand(1)*S_mobile;
    S_2_0   = (S_mobile-S_1_0)*0.5;
elseif ((S_mobile-param_guess(1)-param_guess(2))<0)
    S_1_0   = rand(1)*S_mobile;
    S_2_0   = (S_mobile-S_1_0)*0.5;
else
    S_1_0   = param_guess(1);
    S_2_0   = param_guess(2);
end

if (S_1_0<0) | (S_2_0<0) | ((S_mobile-S_1_0-S_2_0)<0)
    fprintf('Bad!!!');
end

% ENSURE ALL k's POSITIVE
k1          = abs(param_guess(3));
k2          = abs(param_guess(4));
k3          = abs(param_guess(5));
```

```
SR_mob      = S_mobile*rsw;   % [ug_pyr/L_wat]
SR_1_0      = S_1_0*rsw;    % [ug_pyr/L_wat]
SR_2_0      = S_2_0*rsw;    % [ug_pyr/L_wat]
%S_mobile-S_1_0-S_2_0
%if (S_1_0<0) | (S_2_0<0) | (k1<0) | (k2<0) | (k3<0)
%    fprintf('BAD!!');
%end

yhat        = SR_mob*(1-exp(-k3.*x_time)) + SR_1_0*(exp(-k3.*x_time)-exp(-k1.*x_time)) +
SR_2_0*(exp(-k3.*x_time)-exp(-k2.*x_time));
```

Orthogonal Polynomial Model

Function RunOrthoPolyFit

```
function FitEndStatus = RunOrthoPolyFit

% By: Dave Kuo
% Date: 12 Sept 2006
%
% Fitting of desorption kinetic data to Orthogonal Polynomial Model
%
% Model used: OrthoPolyModel
%
% To fit desorption data with non-linear regression:
%

clear;
close all;

xydata = load ('A_hirsw_data.txt');
figtext = 'A-set hi rsw';
pathfilename = [cd,'\A_hirsw_OrthoPolyFit.txt'];
time        = xydata(:,1);          % independent var; [hr]
C_obs       = xydata(:,2)/1000;     % so that in [ug_pyr/L]; dependent var

A0_guess    = 0.1;                  % [--]
A1_guess    = 0.001;                % [hr-0.5]
A2_guess    = 0.0;              % [hr-1]

GuessVector         = [A0_guess A1_guess A2_guess];
[FittedParameters, FitResid, J] = nlinfit(time, C_obs, 'OrthoPolyModel', GuessVector);

% Plots prediction (from the fit) against observation, and gives other
% stats info

FittedParametersCI  = nlparci(FittedParameters, FitResid, J);
[C_pred, OneDelta]  = nlpredci('OrthoPolyModel', time, FittedParameters, FitResid, J);

lgt = log(time);
xydatahat   = [time, lgt, C_obs, C_pred, OneDelta];
SumResidSq  = sum(FitResid.^2);
R2          = rsq(C_obs, C_pred);
text0 = ['Regressed Parameters:'];
text1 = ['A0 (--): ', num2str(FittedParameters(1))];
text2 = ['A1 (hr^-^0^.^5): ', num2str(FittedParameters(2))];
text3 = ['A2 (hr^-^1): ', num2str(FittedParameters(3))];

figure;
pretitle = 'Plots of Orthogonal Polynomial Fitting of ';
titletxt = [pretitle, figtext];

subplot(1,3,1), plot(time, C_obs, 'bx', time, C_pred, 'r.'), xlabel('Time Elaspsed (hr)'),
ylabel('C_p_y_r (ug/L)');
subplot(1,3,2), plot(lgt, C_obs, 'bx', lgt, C_pred, 'r.'), xlabel('Log of Time Elaspsed
(hr/hr)'), ylabel('C_p_y_r (ug/L)');
title({titletxt; ''; ''});
h = get(gcf, 'CurrentAxes'); TX = get(h, 'XLim'); TY = get(h, 'YLim'); TxtPosX =
0.4*(TX(2)-TX(1))+TX(1); TxtPosY = 0.1*(TY(2)-TY(1))+TY(1);
text(TxtPosX, TxtPosY,{text0; text1; text2; text3});
subplot(1,3,3), plot(lgt, C_obs, 'bx', lgt, C_pred, 'r.', lgt, C_pred+OneDelta, 'k-', lgt,
C_pred-OneDelta, 'k-'),
```

```
xlabel('Log of Time Elapsed (hr/hr)'), ylabel('C_p_y_r (ug/L)');

figure; h = get(gcf, 'CurrentAxes');
plot(lgt, C_obs, 'bx', lgt, C_pred, 'r.', lgt, C_pred+OneDelta, 'k-', lgt, C_pred-OneDelta,
'k-');
title({titletxt; ''; ''});
xlabel('Log of Time Elapsed (hr/hr)'), ylabel('C_p_y_r (ug/L)');
h = get(gcf, 'CurrentAxes'); TX = get(h, 'XLim'); TY = get(h, 'YLim'); TxtPosX =
0.4*(TX(2)-TX(1))+TX(1); TxtPosY = 0.1*(TY(2)-TY(1))+TY(1);
text(TxtPosX, TxtPosY,{text0; text1; text2; text3});

figure; h = get(gcf, 'CurrentAxes');
plot(time, C_obs, 'bx', time, C_pred, 'r.', time, C_pred+OneDelta, 'k-', time, C_pred-
OneDelta, 'k-');
title({titletxt; ''; ''});
xlabel('Time Elaspsed (hr)'), ylabel('C_p_y_r (ug/L)');
h = get(gcf, 'CurrentAxes'); TX = get(h, 'XLim'); TY = get(h, 'YLim'); TxtPosX =
0.4*(TX(2)-TX(1))+TX(1); TxtPosY = 0.1*(TY(2)-TY(1))+TY(1);
text(TxtPosX, TxtPosY,{text0; text1; text2; text3});

OutMat = [time, lgt, 1000*C_obs, 1000*C_pred, 1000*OneDelta];
fid = fopen(pathfilename,'w');
fprintf(fid, '   Time(hr)   Log(time)   C_pyr_obs(ng/L)   C_pyr_pred(ng/L)
1_Sigma(ng/L)\n');
for i=1:size(OutMat,1)
    fprintf(fid, '   %6.1f   %3.4f   %4.2f   %4.2f   %4.4f\n', OutMat(i, 1), OutMat(i, 2),
OutMat(i, 3), OutMat(i, 4), OutMat(i, 5));
end
fprintf(fid, '   a0   %3.10f\n', FittedParameters(1));
fprintf(fid, '   a1   %3.10f\n', FittedParameters(2));
fprintf(fid, '   a2   %3.10f\n', FittedParameters(3));
fprintf(fid, '   SumOfResid^2   %3.10f\n', SumResidSq);
fprintf(fid, '   R^2   %3.4f\n', R2);
fclose(fid);

FitEndStatus = [FittedParameters, SumResidSq, R2];
```

Function OrthoPolyModel

```
function yhat = OrthoPolyModel(param_guess, x_time)

% By: Dave Kuo
% Date: 21 Sept 2006
%
% Orthogonal Polynomial model
% ref: Wells et al., J Mater Chem, v14, 2461 yr 2004
%
% x_time        : independent variable
% param_guess   : initial guess for all fitted parameters
% S_init        : initial solid pyr loading [ug_pyr/kg_solids]
% rsw           : solid-to-water ratio [kg_solids/L_wat]
%
% Model:
% S(t)/S(t=0) = 1 - [Ao + A1*t^0.5 + A2*t]
% Since:
% C(t)V + S(t)V = SoM
% C(t) = rsw*(So-S(t)) = So*rsw*[
%
% yhat          : predicted dissolved pyrene, C(t)_hat [ug/L]
% Ao, A1, A2    : fitted parameters [--, hr-0.5, hr-1]
%

%%%
%%% CAUTION!!! --> MUST CHECK   S_init   AND   rsw !!!
%%%

S_init      = 1420;         % [ug_pyr/kg_solids]
rsw         = 277/1e6;       % [kg_solids/L_wat]

A0          = param_guess(1);
A1          = param_guess(2);
A2          = param_guess(3);

%yhat        = S_init*rsw*(A0 + A1.*(x_time.^0.5) + A2.*x_time);
yhat        = S_init*rsw*(A0 + A1.*(x_time.^0.5));
```

Elovich Model

Function RunElovichFit

```
function FitEndStatus = RunElovichFit

% By: Dave Kuo
% Date: 21 Sept 2006
%
% Fitting of desorption kinetic data to Elovich model
% 2-parameter fitting: k
%
% Model used: ElovichModel
%

clear;
close all;

xydata = load ('L_lowrsw_data.txt');
xydata = xydata(2:size(xydata,1), :);
figtext = 'L-set low rsw';
pathfilename = [cd,'\L_lowrsw_ElovichFit.txt'];
time        = xydata(:,1);          % independent var; [hr]
C_obs       = xydata(:,2)/1000;     % so that in [ug_pyr/L]; dependent var

Ae_guess    = 0.0;                  % [--]
Be_guess    =1e-3;                % [--]


GuessVector         = [Ae_guess  Be_guess];
[FittedParameters, FitResid, J] = nlinfit(time, C_obs, 'ElovichModel', GuessVector);

% Plots prediction (from the fit) against observation, and gives other
% stats info

FittedParametersCI  = nlparci(FittedParameters, FitResid, J);
[C_pred, OneDelta]  = nlpredci('ElovichModel', time, FittedParameters, FitResid, J);

lgt = log(time);
xydatahat   = [time, lgt, C_obs, C_pred, OneDelta];
SumResidSq  = sum(FitResid.^2);
R2          = rsq(C_obs, C_pred);
text0 = ['Regressed Parameters:'];
text1 = ['A_E_l_o (--): ', num2str(FittedParameters(1))];
text2 = ['B_E_l_o (--): ', num2str(FittedParameters(2))];

figure;
pretitle = 'Plots of Elovich Fitting of ';
titletxt = [pretitle, figtext];

subplot(1,3,1), plot(time, C_obs, 'bx', time, C_pred, 'r.'), xlabel('Time Elaspsed (hr)'),
ylabel('C_p_y_r (ug/L)');
subplot(1,3,2), plot(lgt, C_obs, 'bx', lgt, C_pred, 'r.'), xlabel('Log of Time Elaspsed
(hr/hr)'), ylabel('C_p_y_r (ug/L)');
title({titletxt; ''; ''});
h = get(gcf, 'CurrentAxes'); TX = get(h, 'XLim'); TY = get(h, 'YLim'); TxtPosX =
0.4*(TX(2)-TX(1))+TX(1); TxtPosY = 0.1*(TY(2)-TY(1))+TY(1);
text(TxtPosX, TxtPosY,{text0; text1; text2});
subplot(1,3,3), plot(lgt, C_obs, 'bx', lgt, C_pred, 'r.', lgt, C_pred+OneDelta, 'k-', lgt,
C_pred-OneDelta, 'k-'),
xlabel('Log of Time Elapsed (hr/hr)'), ylabel('C_p_y_r (ug/L)');

figure; h = get(gcf, 'CurrentAxes');
plot(lgt, C_obs, 'bx', lgt, C_pred, 'r.', lgt, C_pred+OneDelta, 'k-', lgt, C_pred-OneDelta,
'k-');
title({titletxt; ''; ''});
xlabel('Log of Time Elapsed (hr/hr)'), ylabel('C_p_y_r (ug/L)');
h = get(gcf, 'CurrentAxes'); TX = get(h, 'XLim'); TY = get(h, 'YLim'); TxtPosX =
0.4*(TX(2)-TX(1))+TX(1); TxtPosY = 0.1*(TY(2)-TY(1))+TY(1);
text(TxtPosX, TxtPosY,{text0; text1; text2});

figure; h = get(gcf, 'CurrentAxes');
plot(time, C_obs, 'bx', time, C_pred, 'r.', time, C_pred+OneDelta, 'k-', time, C_pred-
OneDelta, 'k-');
title({titletxt; ''; ''});
xlabel('Time Elaspsed (hr)'), ylabel('C_p_y_r (ug/L)');
h = get(gcf, 'CurrentAxes'); TX = get(h, 'XLim'); TY = get(h, 'YLim'); TxtPosX =
0.4*(TX(2)-TX(1))+TX(1); TxtPosY = 0.1*(TY(2)-TY(1))+TY(1);
text(TxtPosX, TxtPosY,{text0; text1; text2});
```

```
OutMat = [time, lgt, 1000*C_obs, 1000*C_pred, 1000*OneDelta];
fid = fopen(pathfilename,'w');
fprintf(fid, '   Time(hr)   Log(time)   C_pyr_obs(ng/L)   C_pyr_pred(ng/L)
1_Sigma(ng/L)\n');
for i=1:size(OutMat,1)
    fprintf(fid, '   %6.1f   %3.4f   %4.2f   %4.2f   %4.4f\n', OutMat(i, 1), OutMat(i, 2),
OutMat(i, 3), OutMat(i, 4), OutMat(i, 5));
end
fprintf(fid, '   A_e   %3.10f\n', FittedParameters(1));
fprintf(fid, '   B_e   %3.10f\n', FittedParameters(2));
fprintf(fid, '   SumOfResid^2   %3.10f\n', SumResidSq);
fprintf(fid, '   R^2   %3.4f\n', R2);
fclose(fid);

FitEndStatus = [FittedParameters, SumResidSq, R2];
```

Function ElovichModel

```
function yhat = ElovichModel(param_guess, x_time)

% By: Dave Kuo
% Date: 21 Sept 2006
%
% Elovich model
% ref: Wells et al., J Mater Chem, v14, 2461 yr 2004
%
% x_time        : independent variable
% param_guess   : initial guess for all fitted parameters
% S_init        : initial solid pyr loading [ug_pyr/kg_solids]
% rsw           : solid-to-water ratio [kg_solids/L_wat]
%
% Model:
% S(t)/S(t=0) = 1 - [Ae + Be*ln(t)]
% Since:
% C(t)V + S(t)V = SoM
% C(t) = rsw*(So-S(t)) = So*rsw*[Ae + Be*ln(t)]
%
% yhat          : predicted dissolved pyrene, C(t)_hat [ug/L]
% Ae, Be        : fitted parameters [--]
%

%%%
%%% CAUTION!!! --> MUST CHECK   S_init   AND   rsw !!!
%%%

S_init      = 1350;         % [ug_pyr/kg_solids]
rsw         = 22/1e6;       % [kg_solids/L_wat]

Ae          = param_guess(1);
Be          = param_guess(2);
yhat        = S_init*rsw*(Ae + Be.*log(x_time));
%yhat        = S_init*rsw*(Be.*log(x_time));
```

Gamma Distributed Rate Model

Function RunGammaRateFit

```
function FitEndStatus = RunGammaRateFit

% By: Dave Kuo
% Date: 21 Sept 2006
%
% Fitting of desorption kinetic data to Gamma-distributed rates model
% 2-parameter fitting: alpha, beta
%
% Model used: GammaRateModel
%

clear;
close all;

xydata = load ('Rxtor_hirsw_data.txt');
```

```
figtext = 'Rxtor G hi rsw';
pathfilename = [cd,'\Rxtor_hirsw_GammaRateFit.txt'];
time        = xydata(:,1);          % independent var; [hr]
C_obs       = xydata(:,2)/1000;     % so that in [ug_pyr/L]; dependent var

alpha_guess   = 0.0;                  % [--]
beta_guess    =1e-3;                  % [--]


GuessVector         = [alpha_guess beta_guess];
[FittedParameters, FitResid, J] = nlinfit(time, C_obs, 'GammaRateModel', GuessVector);

% Plots prediction (from the fit) against observation, and gives other
% stats info

FittedParametersCI  = nlparci(FittedParameters, FitResid, J);
[C_pred, OneDelta]  = nlpredci('GammaRateModel', time, FittedParameters, FitResid, J);

lgt = log(time);
xydatahat   = [time, lgt, C_obs, C_pred, OneDelta];
SumResidSq  = sum(FitResid.^2);
R2          = rsq(C_obs, C_pred);
text0 = ['Regressed Parameters:'];
text1 = ['alpha (--): ', num2str(FittedParameters(1))];
text2 = ['beta (--): ', num2str(FittedParameters(2))];

figure;
pretitle = 'Plots of Gamma-distributed Rates Fitting of ';
titletxt = [pretitle, figtext];

subplot(1,3,1), plot(time, C_obs, 'bx', time, C_pred, 'r.'), xlabel('Time Elaspsed (hr)'),
ylabel('C_p_y_r (ug/L)');
subplot(1,3,2), plot(lgt, C_obs, 'bx', lgt, C_pred, 'r.'), xlabel('Log of Time Elaspsed
(hr/hr)'), ylabel('C_p_y_r (ug/L)');
title({titletxt; ''; ''});
h = get(gcf, 'CurrentAxes'); TX = get(h, 'XLim'); TY = get(h, 'YLim'); TxtPosX =
0.4*(TX(2)-TX(1))+TX(1); TxtPosY = 0.1*(TY(2)-TY(1))+TY(1);
text(TxtPosX, TxtPosY,{text0; text1; text2});
subplot(1,3,3), plot(lgt, C_obs, 'bx', lgt, C_pred, 'r.', lgt, C_pred+OneDelta, 'k-', lgt,
C_pred-OneDelta, 'k-'),
xlabel('Log of Time Elapsed (hr/hr)'), ylabel('C_p_y_r (ug/L)');

figure; h = get(gcf, 'CurrentAxes');
plot(lgt, C_obs, 'bx', lgt, C_pred, 'r.', lgt, C_pred+OneDelta, 'k-', lgt, C_pred-OneDelta,
'k-');
title({titletxt; ''; ''});
xlabel('Log of Time Elapsed (hr/hr)'), ylabel('C_p_y_r (ug/L)');
h = get(gcf, 'CurrentAxes'); TX = get(h, 'XLim'); TY = get(h, 'YLim'); TxtPosX =
0.4*(TX(2)-TX(1))+TX(1); TxtPosY = 0.1*(TY(2)-TY(1))+TY(1);
text(TxtPosX, TxtPosY,{text0; text1; text2});

figure; h = get(gcf, 'CurrentAxes');
plot(time, C_obs, 'bx', time, C_pred, 'r.', time, C_pred+OneDelta, 'k-', time, C_pred-
OneDelta, 'k-');
title({titletxt; ''; ''});
xlabel('Time Elaspsed (hr)'), ylabel('C_p_y_r (ug/L)');
h = get(gcf, 'CurrentAxes'); TX = get(h, 'XLim'); TY = get(h, 'YLim'); TxtPosX =
0.4*(TX(2)-TX(1))+TX(1); TxtPosY = 0.1*(TY(2)-TY(1))+TY(1);
text(TxtPosX, TxtPosY,{text0; text1; text2});

OutMat = [time, lgt, 1000*C_obs, 1000*C_pred, 1000*OneDelta];
fid = fopen(pathfilename,'w');
fprintf(fid, '   Time(hr)   Log(time)   C_pyr_obs(ng/L)   C_pyr_pred(ng/L)
1_Sigma(ng/L)\n');
for i=1:size(OutMat,1)
    fprintf(fid, '   %6.1f   %3.4f   %4.2f   %4.2f   %4.4f\n', OutMat(i, 1), OutMat(i, 2),
OutMat(i, 3), OutMat(i, 4), OutMat(i, 5));
end
fprintf(fid, '   alpha   %3.10f\n', FittedParameters(1));
fprintf(fid, '   beta   %3.10f\n', FittedParameters(2));
fprintf(fid, '   SumOfResid^2   %3.10f\n', SumResidSq);
fprintf(fid, '   R^2   %3.4f\n', R2);
fclose(fid);

FitEndStatus = [FittedParameters, SumResidSq, R2];
```

Function GammaRateModel

```
function yhat = GammaRateModel(param_guess, x_time)

% By: Dave Kuo
% Date: 21 Sept 2006
%
% Gamma-distributed Rates model
% ref: Wells et al., J Mater Chem, v14, 2461 yr 2004
%
% x_time        : independent variable
% param_guess   : initial guess for all fitted parameters
% S_init        : initial solid pyr loading [ug_pyr/kg_solids]
% rsw           : solid-to-water ratio [kg_solids/L_wat]
%
% Model:
% S(t)/S(t=0) = [beta/(beta + t)]^alpha
% Since:
% C(t)V + S(t)V = SoM
% C(t) = rsw*(So-S(t)) = So*rsw*{1 - [beta/(beta + t)]^alpha}
%
% yhat          : predicted dissolved pyrene, C(t)_hat [ug/L]
% Ae, Be        : fitted parameters [--]
%

%%%
%%% CAUTION!!! --> MUST CHECK   S_init   AND   rsw !!!
%%%

S_init      = 5420;         % [ug_pyr/kg_solids]
rsw         = 245/1e6;       % [kg_solids/L_wat]

a           = param_guess(1);
b           = param_guess(2);

yhat        = S_init*rsw*(1 - (b./(b+x_time)).^a);
```

Weibull Distributed Rate (Constrained Single-Compartment) Model

Function RunConstrain1CompartWeibullFit

```
function FitEndStatus = RunConstrain1CompartWeibullFit

% By: Dave Kuo
% Date: 21 Sept 2006
%
% Fitting of desorption kinetic data to S_eqm constrained, SINGLE
% compartment, Weibull-distributed Fit
% 2-parameter fitting: k(=1/a), beta
%
% ref: Wells et al., J Mater Chem, v14, 2461 yr 2004
%

clear;
close all;

xydata = load ('L_medrsw_data.txt');
figtext = 'L-set med rsw';
pathfilename = [cd,'\L_medrsw_Constrain1CompartWeibullFit.txt'];
time        = xydata(:,1);          % independent var; [hr]
C_obs       = xydata(:,2)/1000;     % so that in [ug_pyr/L]; dependent var

k_guess     = 0.0;                  % [hr-1]
beta_guess  = 1e-3;                 % [--]


GuessVector         = [k_guess beta_guess];
[FittedParameters, FitResid, J] = nlinfit(time, C_obs, 'Constrain1CompartWeibullModel',
GuessVector);

% Plots prediction (from the fit) against observation, and gives other
% stats info
```

```
FittedParametersCI  = nlparci(FittedParameters, FitResid, J);
[C_pred, OneDelta]  = nlpredci('Constrain1CompartWeibullModel', time, FittedParameters,
FitResid, J);

lgt = log(time);
xydatahat   = [time, lgt, C_obs, C_pred, OneDelta];
SumResidSq  = sum(FitResid.^2);
R2          = rsq(C_obs, C_pred);
text0 = ['Regressed Parameters:'];
text1 = ['alpha (--): ', num2str(FittedParameters(1))];
text2 = ['beta (--): ', num2str(FittedParameters(2))];

figure;
pretitle = 'Plots of S_e_q_m-constrained, One compartment Weibull Fitting of ';
titletxt = [pretitle, figtext];

subplot(1,3,1), plot(time, C_obs, 'bx', time, C_pred, 'r.'), xlabel('Time Elaspsed (hr)'),
ylabel('C_p_y_r (ug/L)');
subplot(1,3,2), plot(lgt, C_obs, 'bx', lgt, C_pred, 'r.'), xlabel('Log of Time Elaspsed
(hr/hr)'), ylabel('C_p_y_r (ug/L)');
title({titletxt; ''; ''});
h = get(gcf, 'CurrentAxes'); TX = get(h, 'XLim'); TY = get(h, 'YLim'); TxtPosX =
0.4*(TX(2)-TX(1))+TX(1); TxtPosY = 0.1*(TY(2)-TY(1))+TY(1);
text(TxtPosX, TxtPosY,{text0; text1; text2});
subplot(1,3,3), plot(lgt, C_obs, 'bx', lgt, C_pred, 'r.', lgt, C_pred+OneDelta, 'k-', lgt,
C_pred-OneDelta, 'k-'),
xlabel('Log of Time Elapsed (hr/hr)'), ylabel('C_p_y_r (ug/L)');

figure; h = get(gcf, 'CurrentAxes');
plot(lgt, C_obs, 'bx', lgt, C_pred, 'r.', lgt, C_pred+OneDelta, 'k-', lgt, C_pred-OneDelta,
'k-');
title({titletxt; ''; ''});
xlabel('Log of Time Elapsed (hr/hr)'), ylabel('C_p_y_r (ug/L)');
h = get(gcf, 'CurrentAxes'); TX = get(h, 'XLim'); TY = get(h, 'YLim'); TxtPosX =
0.4*(TX(2)-TX(1))+TX(1); TxtPosY = 0.1*(TY(2)-TY(1))+TY(1);
text(TxtPosX, TxtPosY,{text0; text1; text2});

figure; h = get(gcf, 'CurrentAxes');
plot(time, C_obs, 'bx', time, C_pred, 'r.', time, C_pred+OneDelta, 'k-', time, C_pred-
OneDelta, 'k-');
title({titletxt; ''; ''});
xlabel('Time Elaspsed (hr)'), ylabel('C_p_y_r (ug/L)');
h = get(gcf, 'CurrentAxes'); TX = get(h, 'XLim'); TY = get(h, 'YLim'); TxtPosX =
0.4*(TX(2)-TX(1))+TX(1); TxtPosY = 0.1*(TY(2)-TY(1))+TY(1);
text(TxtPosX, TxtPosY,{text0; text1; text2});

OutMat = [time, lgt, 1000*C_obs, 1000*C_pred, 1000*OneDelta];
fid = fopen(pathfilename,'w');
fprintf(fid, '   Time(hr)   Log(time)   C_pyr_obs(ng/L)   C_pyr_pred(ng/L)
1_Sigma(ng/L)\n');
for i=1:size(OutMat,1)
    fprintf(fid, '   %6.1f   %3.4f   %4.2f   %4.2f   %4.4f\n', OutMat(i, 1), OutMat(i, 2),
OutMat(i, 3), OutMat(i, 4), OutMat(i, 5));
end
fprintf(fid, '   k[hr^-1]   %3.10f\n', FittedParameters(1));
fprintf(fid, '   beta[--]   %3.10f\n', FittedParameters(2));
fprintf(fid, '   SumOfResid^2   %3.10f\n', SumResidSq);
fprintf(fid, '   R^2   %3.4f\n', R2);
fclose(fid);

FitEndStatus = [FittedParameters, SumResidSq, R2];
```

Function Constrain1CompartWeibullModel

```
function yhat = Constrain1CompartWeibullModel(param_guess, x_time)

% By: Dave Kuo
% Date: 21 Sept 2006
%
% S_eqm constrained, SINGLE compartment, Weibull-distributed Model
% ref: Wells et al., J Mater Chem, v14, 2461 yr 2004
%
% x_time        : independent variable
% param_guess   : initial guess for all fitted parameters
% S_init        : initial solid pyr loading [ug_pyr/kg_solids]
% S_eqm         : equilibrium solid phase loading [ug_pyr/kg_solids]
% S_mob_init    : initial (at t=0) mobile/desorbable loading [ug_pyr/kg_solids]
% rsw           : solid-to-water ratio [kg_solids/L_wat]
%
```

```
% yhat          : predicted dissolved pyrene, C(t)_hat [ug/L]
% k             : Weibull rate constant [hr-1]
% beta          : Weibull form factor [--]
%

%%%
%%% CAUTION!!! --> MUST CHECK   S_init   AND   rsw !!!
%%%

S_init      = 1350;         % [ug_pyr/kg_solids]
S_eqm       = 1048;         % [ug_pyr/kg_solids]
S_mob_init  = S_init-S_eqm; % [ug_pyr/kg_solids]
rsw         = 70/1e6;      % [kg_solids/L_wat]

k           = param_guess(1);
b           = param_guess(2);

yhat        = S_mob_init*rsw*(1 - exp(-k.*(x_time.^b)));
```

Weibull Distributed Rate (Constrained Two-Compartment) Model

Function RunConstrain2CompartWeibullFit

```
function FitEndStatus = RunConstrain2CompartWeibullFit

% By: Dave Kuo
% Date: 21 Sept 2006
%
% Fitting of desorption kinetic data to S_eqm constrained, TWO
% compartment, Weibull-distributed Fit
% 5-parameter fitting: S_1_0, k1(=1/a1), k2(=1/a2), b1, b2
%
% ref: Wells et al., J Mater Chem, v14, 2461 yr 2004
%

clear;
close all;

xydata = load ('Rxtor_lowrsw_data.txt');
%xydata = xydata(2:size(xydata, 1), :);
figtext = 'Rxtor I low rsw';
pathfilename = [cd,'\Rxtor_lowrsw_Constrain2CompartWeibullFit.txt'];
time        = xydata(:,1);          % independent var; [hr]
C_obs       = xydata(:,2)/1000;     % so that in [ug_pyr/L]; dependent var

S10_guess   = 5;                   % [ug_pyr/kg_solids]
k1_guess    = 0.1;                 % [hr-1]
k2_guess    = 0.02;                % [hr-1]
b1_guess    = 0;                  % [-]
b2_guess    = 0;                  % [-]


GuessVector         = [S10_guess k1_guess k2_guess b1_guess b2_guess];
[FittedParameters, FitResid, J] = nlinfit(time, C_obs, 'Constrain2CompartWeibullModel',
GuessVector);

% Plots prediction (from the fit) against observation, and gives other
% stats info

FittedParametersCI  = nlparci(FittedParameters, FitResid, J);
[C_pred, OneDelta]  = nlpredci('Constrain2CompartWeibullModel', time, FittedParameters,
FitResid, J);

lgt = log(time);
xydatahat   = [time, lgt, C_obs, C_pred, OneDelta];
SumResidSq  = sum(FitResid.^2);
%sumy        = sum(C_obs*1000)
%sumy_sq     = sumy.^2
%diffy       = 1000*(C_obs-C_pred);
%sumdiffy_sq    = sum(diffy.^2)
%sumofsqs    = sum((1000*C_obs).^2)
%SST      = sumofsqs - sumy_sq/53
%rr          = 1 - sumdiffy_sq/SST
R2          = rsq(C_obs*1000, C_pred*1000);
```

```
text0 = ['Regressed Parameters:'];
text1 = ['S_1_,_0 (ug/kg): ', num2str(FittedParameters(1))];
text2 = ['k_1 (hr^-^1): ', num2str(FittedParameters(2))];
text3 = ['k_2 (hr^-^1): ', num2str(FittedParameters(3))];
text4 = ['b_1 (-): ', num2str(FittedParameters(4))];
text5 = ['b_2 (-): ', num2str(FittedParameters(5))];

figure;
pretitle = 'Plots of S_e_q_m-constrained, Two-compartment Weibull Fitting of ';
titletxt = [pretitle, figtext];

subplot(1,3,1), plot(time, C_obs, 'bx', time, C_pred, 'r.'), xlabel('Time Elaspsed (hr)'),
ylabel('C_p_y_r (ug/L)');
subplot(1,3,2), plot(lgt, C_obs, 'bx', lgt, C_pred, 'r.'), xlabel('Log of Time Elaspsed
(hr/hr)'), ylabel('C_p_y_r (ug/L)');
title({titletxt; ''; ''});
h = get(gcf, 'CurrentAxes'); TX = get(h, 'XLim'); TY = get(h, 'YLim'); TxtPosX =
0.4*(TX(2)-TX(1))+TX(1); TxtPosY = 0.1*(TY(2)-TY(1))+TY(1);
text(TxtPosX, TxtPosY,{text0; text1; text2; text3; text4; text5});
subplot(1,3,3), plot(lgt, C_obs, 'bx', lgt, C_pred, 'r.', lgt, C_pred+OneDelta, 'k-', lgt,
C_pred-OneDelta, 'k-'),
xlabel('Log of Time Elapsed (hr/hr)'), ylabel('C_p_y_r (ug/L)');

figure; h = get(gcf, 'CurrentAxes');
plot(lgt, C_obs, 'bx', lgt, C_pred, 'r.', lgt, C_pred+OneDelta, 'k-', lgt, C_pred-OneDelta,
'k-');
title({titletxt; ''; ''});
xlabel('Log of Time Elapsed (hr/hr)'), ylabel('C_p_y_r (ug/L)');
h = get(gcf, 'CurrentAxes'); TX = get(h, 'XLim'); TY = get(h, 'YLim'); TxtPosX =
0.4*(TX(2)-TX(1))+TX(1); TxtPosY = 0.1*(TY(2)-TY(1))+TY(1);
text(TxtPosX, TxtPosY,{text0; text1; text2; text3; text4; text5});

figure; h = get(gcf, 'CurrentAxes');
plot(time, C_obs, 'bx', time, C_pred, 'r.', time, C_pred+OneDelta, 'k-', time, C_pred-
OneDelta, 'k-');
title({titletxt; ''; ''});
xlabel('Time Elaspsed (hr)'), ylabel('C_p_y_r (ug/L)');
h = get(gcf, 'CurrentAxes'); TX = get(h, 'XLim'); TY = get(h, 'YLim'); TxtPosX =
0.4*(TX(2)-TX(1))+TX(1); TxtPosY = 0.1*(TY(2)-TY(1))+TY(1);
text(TxtPosX, TxtPosY,{text0; text1; text2; text3; text4; text5});

OutMat = [time, lgt, 1000*C_obs, 1000*C_pred, 1000*OneDelta];
fid = fopen(pathfilename,'w');
fprintf(fid, '   Time(hr)   Log(time)   C_pyr_obs(ng/L)   C_pyr_pred(ng/L)
1_Sigma(ng/L)\n');
for i=1:size(OutMat,1)
    fprintf(fid, '   %6.1f   %3.4f   %4.2f   %4.2f   %4.4f\n', OutMat(i, 1), OutMat(i, 2),
OutMat(i, 3), OutMat(i, 4), OutMat(i, 5));
end
fprintf(fid, '   S_1_0[ug/kg]   %7.1f\n', FittedParameters(1));
fprintf(fid, '   k1[hr^-1]   %3.10f\n', FittedParameters(2));
fprintf(fid, '   k2[hr^-1]   %3.10f\n', FittedParameters(3));
fprintf(fid, '   b1[--]   %3.10f\n', FittedParameters(4));
fprintf(fid, '   b2[--]   %3.10f\n', FittedParameters(5));
fprintf(fid, '   SumOfResid^2   %3.10f\n', SumResidSq);
fprintf(fid, '   R^2   %3.4f\n', R2);
fclose(fid);

FitEndStatus = [FittedParameters, SumResidSq, R2];
```

Function Constrain2CompartWeibullModel

```
function yhat = Constrain2CompartWeibullModel(param_guess, x_time)

% By: Dave Kuo
% Date: 21 Sept 2006
%
% S_eqm constrained, TWO-compartment, Weibull-distributed Model
% ref: Wells et al., J Mater Chem, v14, 2461 yr 2004
%
% x_time        : independent variable
% param_guess   : initial guess for all fitted parameters
% S_init        : initial solid pyr loading [ug_pyr/kg_solids]
% S_eqm         : equilibrium solid phase loading [ug_pyr/kg_solids]
% S_mob_init    : initial (at t=0) mobile/desorbable loading [ug_pyr/kg_solids]
% rsw           : solid-to-water ratio [kg_solids/L_wat]
%
% yhat          : predicted dissolved pyrene, C(t)_hat [ug/L]
% S_1_0         : fitted compartment 1 HOC loading [ug_pyr/kg_solids]
```

```
% k1, k2         : Weibull rate constants [hr-1]
% b1, b2         : Weibull form factors [--]
%

%%%
%%% CAUTION!!! --> MUST CHECK   S_init   AND   rsw !!!
%%%

S_init      = 5420;         % [ug_pyr/kg_solids]
S_eqm       = 3969;         % [ug_pyr/kg_solids]
S_mob_init  = S_init-S_eqm; % [ug_pyr/kg_solids]
rsw         = 19/1e6;       % [kg_solids/L_wat]

S_1_init    = param_guess(1);
k1          = param_guess(2);
k2          = param_guess(3);
b1          = param_guess(4);
b2          = param_guess(5);

yhat        = S_mob_init*rsw*(1 - exp(-k2.*(x_time.^b2))) + S_1_init*rsw*(exp(-
k2.*(x_time.^b2)) - exp(-k1.*(x_time.^b1))) ;
```

Script E - 7. Char-in-Silt Heterogeneous Model (Infinite Bath)

*Please see **Script E – 5** for other functions called by the main program.*

Char-in-Silt-Infinite-Bath (Main Program)

```
%%%
%%% a priori simulation of sedimental-HOCs desorption kinetics for
%%%
%%% CHAR CENTRALLY EMBEDDED IN SILT AGGREGATE CASE IN INFINITE BATH
%%%
%%% By: Dave Kuo
%%% Date: Jan-Feb 2010
%%%

%%%
%%% Compute intrinsic diffusivity Diw
%%%
HOCName = 'pyrene';
Diw_m = F_Diffusivity (HOCName, 'water');                                    % [m2/s]

%%%
%%% Set system properties
%%%

% ISOTHERM SETTING
%
% foc, fbc              : org carbon, black carbon content of aggregate [g_carbon/g_solid]
% Koc, Kbc      : partition coefficient for chemical i [L_solv/kg_carbon]
% FrdlichN              : Freundlich exponent
% CmplmFrdlichN: complimentary Freundlich exponent
%
foc_c           = 0;            % org. carbon mass fraction in CHAR compartment
fbc_c                   = 1;            % blk. carbon mass fraction in CHAR compartment
foc_s                   = 0.02;         % org. carbon mass fraction in SILT compartment
fbc_s                   = 0.002;        % blk. carbon mass fraction in SILT compartment
Koc                     = 10^4.7;
Kbc_char        = 10^6.3;       % Kbc for char-BC
Kbc_soot        = 10^6.3;       % Kbc for soot-BC
FrdlichN_c      = 0.6;          % Frdlich exponent for char-BC
FrdlichN_s      = 0.6;          % Frdlich exponent for soot-BC

% DESORPTION SCENARIO
% {'homogeneous 0.13 sooty-silt',  '5um char in 100um silt'}
DesorptionScenario = '5um char in 100um silt';
ShapeFactor     = 3;                                                         % 3 for
spherical; 2 for cylindrical; 1 for slab


% SEDIMENT CHARACTERISTICS
%
% rho_s                 : strict solid density [Kg_solid/L_solid]
% rsw_ppm               : overall system solid-to-water ratio [mg_solid/L_solv]
% rsw                   : overall system solid-to-water ratio [Kg_solid/L_solv]
% rad_um        : particle radius [um]
% rad_m                 : particle radius [m]
rho_s_silt      = 2.5;
rho_s_char      = 2;
rsw_ppm  = 200;
rsw             = rsw_ppm/1e6;
rad_um          = 100;
rad_m           = rad_um/1e6;
rad_char_um     = 10;
rad_char_m      = rad_char_um/1e6;
%blt_m       = rad_m/4;      % boundary layer thickness; here set as half of aggregate
radius
blt_m       = rad_m/2;      % boundary layer thickness; here set as half of aggregate
radius
%blt_m      = 0;            % Crank-analogous
blt_x       = blt_m/rad_m;  % NOTE: use boundary layer in dimensionless form


% GRID AND TIME STEP SIZES
%
% m                     : number of grids
% Co_crit               : 'Courant' criterion
% Pe_crit               : 'Peclet' criterion
% Timesteps     : Number of timesteps
```

```
% dr                    : differential radius [m]
% dx                    : = dr/rad_m = differential radius [--]
% dtow                  : = Diw*dt/(R^2) = differential timestep [--]
% Timesteps             : # timesteps, each dtow [--]
mc                      = 41;                   % # grids in CHAR compartment
ms                      = 41;                   % # grids in SILT compartment
drc                     = 1/(mc-1) * rad_char_m;
drs                     = 1/(ms-1) * (rad_m - rad_char_m);
dxc                     = drc/rad_char_m;               % rad_char_m   = "R_c"
dxs     = drs/rad_m;            % rad_m = "R_agg"
SFitLimit= 5;                   % Limiting silt_grid in polynomial fitting of CS_nowX for
estimating CC_nowX_mc_plus_1
Co_crit  = 5;           % <1
Pe_crit  = 0.05;        % <2
CoByPe_crit     = Co_crit/Pe_crit;
dtow            = CoByPe_crit;
dt              = dtow*(rad_m^2)/Diw_m;
Timesteps       = 250e4; %5.0e3;
%Timesteps      = 4e6; %5.0e3;

% SPATIAL MATRICES
%
gridc           = (1:1:mc);             % 1 x mc; CHAR domain grid-index
grids           = (1:1:ms);             % 1 x ms; SILT domain grid-index
ingrc           = (2:mc-1);             % 1 x mc-2 {2  3  4  ...  mc-2}; CHAR innergrids
ingrs           = (2:ms-1);             % 1 x ms-2 {2  3  4  ...  ms-2}; SILT innergrids
xc              = (gridc-1)*dxc;        % 1 x mc; CHAR domain x
xsB             = rad_char_m/rad_m;     % "X_sub(s,b)"
xs              = xsB + (grids-1)*dxs;% 1 x ms; SILT domain x
Silt_Divider    = (1-xsB^ShapeFactor);% scalar; used when computing SILT-avg quantity
xc_mulz1        = xc.^(ShapeFactor-1);% 1 x mc; "xc^(miu-1)"
xs_mulz1        = xs.^(ShapeFactor-1);% 1 x ms; "xs^(miu-1)"
xc_hlf          = xc+0.5*dxc;           % 1 x mc; {X1.5  X2.5  X3.5  ...  Xmc-0.5
(Xmc+0.5!)}
xs_hlf          = xs+0.5*dxs;           % 1 x ms; {X1.5  X2.5  X3.5  ...  Xms-0.5
(Xms+0.5!)}
xc_hlf_mulz1    = xc_hlf.^(ShapeFactor-1);    % 1 x mc; {X1.5  X2.5  X3.5  ...  Xmc-0.5
(xmc+0.5!)}
xs_hlf_mulz1    = xs_hlf.^(ShapeFactor-1);    % 1 x ms; {X1.5  X2.5  X3.5  ...  Xms-0.5
(xms+0.5!)}


% INITIAL CONDITIONS
%
% porosity      : porosity(x) {n} [L_void/L_agg]
% tortuosity    : tortuosity(x) {f(n)}
% S_init        : initial solid phase conc'n, (S') [ug_i/kg_solid = ng i/g_solid]
% C_init        : initial pore fluid conc'n, (C') [ug_i/L_por_aq]
CharPorosity    = 0.50;         % synthetic char from Braida et al.(Pignatello), 2003 EST
CharTortuosity  = 0.50;         % assumed to be same as porosity
SiltPorosity    = 0.15;         % fitting value by Wu and Gschwend, 1986 EST
SiltTortuosity  = 0.15;         % assumed to be same as porosity; Wu and Gschwend, 1988 Wat
Res Res
CC_init         = 0.02;    % ug/L
SC_init         = foc_c*Koc*CC_init + fbc_c*Kbc_soot*(CC_init^FrdlichN_c);
CS_init         = CC_init;      % i.e. same pore-fluid phase activity of i in both CHAR and
SILT compartments
%[CC_init, CS_init]
SS_init         = foc_s*Koc*CS_init + fbc_s*Kbc_soot*(CS_init^FrdlichN_s);
C_blk_set       = 0;        % SET-POINT for bulk dissolved phase concentration

switch DesorptionScenario
   case '5um char in 100um silt'
      % Set CHAR domain properties
      PorcX     = F_SetAggProperty('homogeneous', mc, CharPorosity);        % CHAR domain
porosity(x)
      TorcX     = F_SetAggProperty('homogeneous', mc, CharTortuosity);      % CHAR domain
tortuosity(x)
      foc_cX    = F_SetAggProperty('homogeneous', mc, foc_c);                           %
CHAR domain foc(x)
      fbc_cX    = F_SetAggProperty('homogeneous', mc, fbc_c);                           %
CHAR domain fbc(x)
      SC_initX  = F_SetAggProperty('homogeneous', mc, SC_init);                         %
CHAR domain S_init(x)
      % Set SILT domain properties
      PorsX     = F_SetAggProperty('homogeneous', ms, SiltPorosity);        % SILT domain
porosity(x)
      TorsX     = F_SetAggProperty('homogeneous', ms, SiltTortuosity);      % SILT domain
tortuosity(x)
      foc_sX    = F_SetAggProperty('homogeneous', ms, foc_s);                           %
SILT domain foc(x)
```

```
      fbc_sX    = F_SetAggProperty('homogeneous', ms, fbc_s);                                %
SILT domain fbc(x)
      SS_initX  = F_SetAggProperty('homogeneous', ms, SS_init);                              %
SILT domain S_init(x)
end

rho_bcX          = rho_s_char*(1-PorcX);       % [kg_CHAR/L_agg]
rho_bsX          = rho_s_silt*(1-PorsX);       % [kg_SILT/L_agg]

% ***AggAvgPorosity            = F_AggregateAvgProperty(ShapeFactor, x, PorosityX, dx);
PorcHlfX         = (PorcX(1:mc-1)+PorcX(2:mc)) ./ 2;
 % 1 x (mc-1) !!!
PorsHlfX         = (PorsX(1:ms-1)+PorsX(2:ms)) ./ 2;
 % 1 x (ms-1) !!!
TorcHlfX         = (TorcX(1:mc-1)+TorcX(2:mc)) ./ 2;
 % 1 x (mc-1) !!!
TorsHlfX         = (TorsX(1:ms-1)+TorsX(2:ms)) ./ 2;
 % 1 x (ms-1) !!!
CharAvgPor       = F_AggregateAvgProperty(ShapeFactor, xc, PorcX, dxc);
SiltAvgPor       = F_AggregateAvgProperty(ShapeFactor, xs, PorsX, dxs) / Silt_Divider;

% VRatio         : volumetric ratio of bulk solvent phase to aggregate(solid+porous fluid)
V_one_char       = 4/3*pi*(rad_char_m^3);
V_one_agg        = 4/3*pi*(rad_m^3);
V_one_silt       = V_one_agg - V_one_char;
Mass_one_char    = (1-CharAvgPor) * V_one_char * rho_s_char;
Mass_one_silt    = (1-SiltAvgPor) * V_one_silt * rho_s_silt;
Mass_one_agg     = Mass_one_char + Mass_one_silt;
V_one_nonagg     = Mass_one_agg/rsw;
VRatio           = V_one_nonagg/V_one_agg;    % Same as VRatio = ((1-f_porsity)*rho_s)/rsw;

% Q_initX        : initial aggregate(solid+porous fluid) volume-averaged concentration
[ug_i/L_agg]
% C_initX        : initial spatial C' within aggregate [ug_i/L_agg]
% C_blk_init     : initial non-agg/bulk aq. phase concentration [ug_i/L_solv]
CC_initX         = NewtonSolveC (1e-40, foc_cX*Koc, fbc_cX*Kbc_char, FrdlichN_c, SC_initX);
if SS_initX == 0
    CS_initX     = F_SetAggProperty('homogeneous', ms, 0);
else
    CS_initX     = NewtonSolveC (1e-40, foc_sX*Koc, fbc_sX*Kbc_soot, FrdlichN_s, SS_initX);
end
CS_initX;
QC_initX         = SC_initX.*rho_bcX + PorcX.*CC_initX;
QS_initX         = SS_initX.*rho_bsX + PorsX.*CS_initX;
QC_initAvg       = F_AggregateAvgProperty(ShapeFactor, xc, QC_initX, dxc);
QS_initAvg       = F_AggregateAvgProperty(ShapeFactor, xs, QS_initX, dxs) / Silt_Divider;
Q_initAvg        = (QC_initAvg*V_one_char + QS_initAvg*V_one_silt) / V_one_agg;
C_blk_init       = C_blk_set;

% GapF           : gap factor for initial non-agg/bulk aq. phase conc'n, such that C_init =
Ceqm_init/GapF
% dfpexp         : the exponent of the fitting porosity n on the numerator
GapF = 1; %%%%% CLOSED SYSTEM, MASS CONSERVED
dfpexp = 2;


%%%
%%% Calculate expected eqm aq. conc.: C_blk_eqm
%%%
W_init                           = Q_initAvg*V_one_agg + C_blk_init*V_one_nonagg;           %
[ug_i]
YC_1stOrder              = Koc*foc_cX.*rho_bcX + PorcX;
YS_1stOrder              = Koc*foc_sX.*rho_bsX + PorsX;
YC_FrdlichN              = Kbc_char*fbc_cX.*rho_bcX;
YS_FrdlichN              = Kbc_soot*fbc_sX.*rho_bsX;
dum_C_1stOrder           = F_AggregateAvgProperty(ShapeFactor, xc, YC_1stOrder, dxc) *
V_one_char;
dum_S_1stOrder           = F_AggregateAvgProperty(ShapeFactor, xs, YS_1stOrder, dxs) /
Silt_Divider * V_one_silt;
Coeff_1stOrder           = dum_C_1stOrder + dum_S_1stOrder + V_one_nonagg;
dum_C_FrdlichN           = F_AggregateAvgProperty(ShapeFactor, xc, YC_FrdlichN, dxc) *
V_one_char;
dum_S_FrdlichN           = F_AggregateAvgProperty(ShapeFactor, xs, YS_FrdlichN, dxs) /
Silt_Divider * V_one_silt;
Coeff_FrdlichN           = dum_C_FrdlichN + dum_S_FrdlichN;
%%%%%%%  !!! ASSUMING SAME FrdlichN for both compartments when solving for C_blk_eqm !!!
%C_blk_eqm                = NewtonSolveC(1e-40, Coeff_1stOrder, Coeff_FrdlichN, FrdlichN_s,
W_init);
C_blk_eqm                = C_blk_set;
SC_eqmX                  = C_blk_eqm*Koc*foc_cX + (C_blk_eqm^FrdlichN_c)*Kbc_char*fbc_cX;
SS_eqmX                  = C_blk_eqm*Koc*foc_sX + (C_blk_eqm^FrdlichN_s)*Kbc_soot*fbc_sX;
```

```
QC_eqmX                 = SC_eqmX.*rho_bcX + C_blk_eqm*PorcX;
QS_eqmX                 = SS_eqmX.*rho_bsX + C_blk_eqm*PorsX;
QC_eqmAvg               = F_AggregateAvgProperty(ShapeFactor, xc, QC_eqmX, dxc);
QS_eqmAvg               = F_AggregateAvgProperty(ShapeFactor, xs, QS_eqmX, dxs) /
Silt_Divider;
Q_eqmAvg                = (QC_eqmAvg*V_one_char + QS_eqmAvg*V_one_silt) / V_one_agg;
Q_lossAvg               = Q_initAvg - Q_eqmAvg;


%%%
%%% Date output information
%%%
Fpath    = '/BC/ModelOutput/';
Ffile1   =
['MTCharSilt_',HOCName,'_Rad',num2str(rad_um),'_RadC',num2str(rad_char_um),'_Rsw',num2str(
rsw_ppm),'_Cinit',num2str(CC_init),'_Cblkinit',num2str(C_blk_init),'_SF',
num2str(ShapeFactor)];
Ffile2   =
['_OC',num2str(round(log10(Koc)*100)),'_BC',num2str(round(log10(Kbc_soot)*100)),'_nBC',num
2str(FrdlichN_s*100),'_BLTx',num2str(blt_x)];
Ffile3   =
['_focC',num2str(foc_c*100),'_fbcC',num2str(fbc_c*100),'_focS',num2str(foc_s*100),'_fbcS',
num2str(fbc_s*100),'_PoroChar',num2str(CharPorosity),'_PoroSilt',num2str(SiltPorosity)];
%Ffilename       = 'CharValidationPureOC_20ppmKd5000Poly3_80Char';
Ffilename       = [Ffile1, Ffile2, Ffile3];

%%%
%%% SOLVING RETARDED DIFFUSIONAL EQN BY ITERATIONS
%%%
% Constants
% For CHAR innermost grid calc, grid = 1
kc_inrmost      = dtow * ShapeFactor * TorcHlfX(1) * PorcHlfX(1) / dxc / xc_hlf(1);
        % scalar
%k_innermost = dtow * ShapeFactor * TortuosityHlfX(1) * PorosityHlfX(1) / dx / x_hlf(1);  %
scalar

% For CHAR intermediate grids calc, grid = 2 to mc-1
kc_intermd      = dtow/(dxc^2) .* PorcX ./ xc_mulz1;
 % 1 x (mc-2)
%k_intermedi = dtow/((dx)^2) .* PorosityX ./ x_miu_les_1;                                %
1 x m

% For CHAR-SILT interface, grid = Xc,mc, or Xs,1
kcs                     = dtow/(dxc^2)*0.5*(PorcX(mc)+PorsX(1))/xc_mulz1(mc);           %
scalar

% For SILT intermediate grids calc, grid = 2 to ms-1
ks_intermd      = dtow/(dxs^2) .* PorsX ./ xs_mulz1;
 % 1 x (ms-2)

% For C_blk_next OR C_nextX(m) calc, grid = ms
q_csnext_ms = ShapeFactor*xs_mulz1(ms)*dxs*1/3/Silt_Divider; % coeff for QS_next_ms;
scalar
alpha_ms        = foc_sX(ms)*Koc;
                                % "alpha_ms"
beta_ms         = fbc_sX(ms)*Kbc_soot;
                % "beta_ms"
CnxtcsFirstOrder  = V_one_nonagg + V_one_silt*q_csnext_ms*(alpha_ms*rho_bsX(ms)+PorsX(ms));
CnxtcsFrdlichN          = V_one_silt*q_csnext_ms*beta_ms*rho_bsX(ms);

AC1stOrder      = Koc*foc_cX.*rho_bcX + PorcX;                  % 1st Order coeff for
solving CC_nextX(i) from QC_nextX(i)
ACFrdlichN      = Kbc_char*fbc_cX.*rho_bcX;                     % Frdlich N coeff for
solving CC_nextX(i) from QC_nextX(i)
AS1stOrder      = Koc*foc_sX.*rho_bsX + PorsX;                  % 1st Order coeff for
solving CS_nextX(i) from QS_nextX(i)
ASFrdlichN      = Kbc_soot*fbc_sX.*rho_bsX;                     % Frdlich N coeff for
solving CS_nextX(i) from QS_nextX(i)

%x                                       = (gridindex-1)*dx;
 % 1 x m {X1  X2  X3  ...  Xm}
%x_miu_les_1                    = x.^(ShapeFactor-1);                   % 1 x m
%x_hlf                          = (gridindex-0.5)*dx;                   % 1 x m
{X1.5  X2.5  X3.5  ...  Xm-0.5  (xm+0.5!)}
%x_hlf_miu_les_1        = x_hlf.^(ShapeFactor-1);               % 1 x m {X1.5  X2.5
X3.5  ...  Xm-0.5  (xm+0.5!)}

CC_nowX         = CC_initX;                     CS_nowX         = CS_initX;
SC_nowX         = SC_initX;                     SS_nowX         = SS_initX;
QC_nowX         = QC_initX;                     QS_nowX         = QS_initX;
QC_nowAvg       = QC_initAvg;           QS_nowAvg       = QS_initAvg;
```

```
Q_nowAvg = Q_initAvg;
C_blk_now       = C_blk_init;
%C_blk_mark     = C_blk_init;                % for determining if profiles should be
recorded/saved at ith step
Q_Avg_mark  = Q_nowAvg;

CC_nextX        = zeros(1, mc);              % initialize; 1 x m of zeroes
SC_nextX        = zeros(1, mc);              % 1 x m of zeroes
QC_nextX        = zeros(1, mc);              % 1 x m of zeroes
CS_nextX        = zeros(1, ms);              % initialize; 1 x m of zeroes
SS_nextX        = zeros(1, ms);              % 1 x m of zeroes
QS_nextX        = zeros(1, ms);              % 1 x m of zeroes

DATA_OVRALL     = [];                                   % data matrix for overall
results (C_blk, Q_Avg, S_Avg, etc)
DATA_CC_tx      = [];                                   % data matrix for temporal-
spatial, CC(x,t) [ug_i/L_void]
DATA_SC_tx      = [];                                   % data matrix for temporal-
spatial, SC(x,t) [ug_i/kg_solid]
DATA_QC_tx      = [];                                   % data matrix for temporal-
spatial, QC(x,t) [ug_i/L_agg]
DATA_KdC_tx     = [];                                   % data matrix for temporal-
spatial KdC = SC(x,t) / CC(x,t)

DATA_CS_tx      = [];                                   % data matrix for temporal-
spatial, CS(x,t) [ug_i/L_void]
DATA_SS_tx      = [];                                   % data matrix for temporal-
spatial, SS(x,t) [ug_i/kg_solid]
DATA_QS_tx      = [];                                   % data matrix for temporal-
spatial, QS(x,t) [ug_i/L_agg]
DATA_KdS_tx     = [];                                   % data matrix for temporal-
spatial KdS = SS(x,t) / CS(x,t)

DATA_W_tx       = [];                                   % data matrix for W(t) =
Q_nowAvg*V_one_agg + C_blkAvg*V_one_nonagg [ug i]

% Save time-zero condition
DATA_CC_tx                      = [DATA_CC_tx; [0, 0, CC_initX]];
DATA_SC_tx                      = [DATA_SC_tx; [0, 0, SC_initX]];
DATA_QC_tx                      = [DATA_QC_tx; [0, 0, QC_initX]];
DATA_KdC_tx                     = [DATA_KdC_tx; [0, 0, SC_initX./CC_initX]];

DATA_CS_tx                      = [DATA_CS_tx; [0, 0, CS_initX]];
DATA_SS_tx                      = [DATA_SS_tx; [0, 0, SS_initX]];
DATA_QS_tx                      = [DATA_QS_tx; [0, 0, QS_initX]];
DATA_KdS_tx                     = [DATA_KdS_tx; [0, 0, SS_initX./CS_initX]];

DATA_W_tx                       = [DATA_W_tx; [0, 0, W_init, 0]];

tic
for itime=1:Timesteps,

   %% INNERMOST GRID X[char,1] CALC
   QC_nextX(1)  = QC_nowX(1) + kc_inrmost*(CC_nowX(2)-CC_nowX(1));
   CC_nextX(1)  = NewtonSolveC(1e-40, AC1stOrder(1), ACFrdlichN(1), FrdlichN_c,
QC_nextX(1));
   if sum(CC_nextX(1)<0)
      disp ('CC_nextX(1) negative.');
   end
   SC_nextX(1)  = foc_cX(1)*Koc*CC_nextX(1) + fbc_cX(1)*Kbc_char*(CC_nextX(1)^FrdlichN_c);

   %% INTERMEDIATE GRIDS X[char, 2 to mc-1) CALC
   dumc_ip1 = []; dumc_im1 = []; dumc_i = [];
   dumc_ip1                     =
kc_intermd(ingrc).*xc_hlf_mulz1(ingrc).*TorcHlfX(ingrc);                        %
Coeff for CC_nowX(i+1)
   dumc_im1                     = kc_intermd(ingrc).*xc_hlf_mulz1(ingrc-
1).*TorcHlfX(ingrc-1);
                                  % Coeff for CC_nowX(i-1)
   dumc_i                       = dumc_ip1 + dumc_im1;
                                                                                % Coeff
for CC_nowX(i)
   QC_nextX(ingrc)      = QC_nowX(ingrc) + dumc_ip1.*CC_nowX(ingrc+1) +
dumc_im1.*CC_nowX(ingrc-1) - dumc_i.*CC_nowX(ingrc);
   CC_nextX(ingrc)      = NewtonSolveC(1e-40, AC1stOrder(ingrc), ACFrdlichN(ingrc),
FrdlichN_c, QC_nextX(ingrc));
   if sum(CC_nextX(ingrc)<0)
      disp ('CC_nextX(innergrids) negative.');
   end
   SC_nextX(ingrc)      = Koc*foc_cX(ingrc).*CC_nextX(ingrc) +
Kbc_char*fbc_cX(ingrc).*(CC_nextX(ingrc).^FrdlichN_c);
```

```
%   dum_iplus1  = k_intermedi(inrgds).*x_hlf_miu_les_1(inrgds).*TortuosityHlfX(inrgds);
 % Coeff for C_nowX(i+1)
%   dum_iminus1 = k_intermedi(inrgds).*x_hlf_miu_les_1(inrgds-1).*TortuosityHlfX(inrgds-
1);% Coeff for C_nowX(i-1)
%   dum_i                       = dum_iplus1 + dum_iminus1;
                                                                                % Coeff for
C_nowX(i)
%   Q_nextX(inrgds) = Q_nowX(inrgds) + dum_iplus1.*C_nowX(inrgds+1) +
dum_iminus1.*C_nowX(inrgds-1) - dum_i.*C_nowX(inrgds);
%   C_nextX(inrgds) = NewtonSolveC(1e-40, A1stOrder(inrgds), AFrdlichN(inrgds), FrdlichN,
Q_nextX(inrgds));
%   S_nextX(inrgds) = Koc*focX(inrgds).*C_nextX(inrgds) +
Kbc*fbcX(inrgds).*(C_nextX(inrgds).^FrdlichN);

   %% DETERMINE CC_nowX(mc+1) FROM FITTING OF CS_nowX(1..ms) WITH 3rd Order Polynomial
   PSiltC       = polyfit(xs(1:SFitLimit), CS_nowX(1:SFitLimit), 3);
   C_mcplus1= polyval(PSiltC, xsB+dxc);       % Interpolated CC_now_mc_plus_1, the grid is
located in SILT domain

   %% CHAR-SILT INTERFACE GRID X[char, mc] OR X[silt, 1] CALC
   dumI_ip1 = []; dumI_im1 = []; dumI_i = [];
   dumI_ip1 = kcs.*xc_hlf_mulz1(mc).*TorsHlfX(1);
              % Coeff for CC_nowX(mc+1)


        % using SILT-domain Tortuosity
   dumI_im1                        = kcs.*xc_hlf_mulz1(mc-1).*TorcHlfX(mc-1);
                                % Coeff for CC_nowX(mc-1)
   dumI_i                             = dumI_ip1 + dumI_im1;
                                                          % Coeff for CC_nowX(mc)
   %[QC_nowX(mc), CC_nowX(mc-1), CC_nowX(mc), dumI_ip1, C_mcplus1, dumI_im1, dumI_i]
   QC_nextX(mc)         = QC_nowX(mc) + dumI_ip1.*C_mcplus1 + dumI_im1.*CC_nowX(mc-1) -
dumI_i.*CC_nowX(mc);
   CC_nextX(mc)         = NewtonSolveC(1e-40, AC1stOrder(mc), ACFrdlichN(mc), FrdlichN_c,
QC_nextX(mc));
   %[QC_nextX(mc), CC_nextX(mc)]
   if sum(CC_nextX(mc)<0)
      disp ('CC_nextX(mc) negative.');
   end
   SC_nextX(mc)         = Koc*foc_cX(mc)*CC_nextX(mc) +
Kbc_char*fbc_cX(mc)*(CC_nextX(mc)^FrdlichN_c);

   CS_nextX(1)                  = CC_nextX(mc);                                  % By
continuity of pore-fluid (i.e. V_void) phase concentration
   SS_nextX(1)                  = Koc*foc_sX(1)*CS_nextX(1) +
Kbc_soot*fbc_sX(1)*(CS_nextX(1)^FrdlichN_s);
   QS_nextX(1)                  = SS_nextX(1)*rho_bsX(1) + PorsX(1)*CS_nextX(1);
   if sum(CS_nextX(1)<0)
      disp ('CS_nextX(1) negative.');
   end

   QC_nextAvg                   = F_AggregateAvgProperty(ShapeFactor, xc, QC_nextX, dxc);

   %% INTERMEDIATE GRIDS X[silt, 2 to ms-1) CALC
   dums_ip1 = []; dums_im1 = []; dums_i = [];
   dums_ip1                     = ks_intermd(ingrs).*xs_hlf_mulz1(ingrs).*TorsHlfX(ingrs);
                         % Coeff for CS_nowX(i+1)
   dums_im1                     = ks_intermd(ingrs).*xs_hlf_mulz1(ingrs-1).*TorsHlfX(ingrs-
1);                             % Coeff for CS_nowX(i-1)
   dums_i                       = dums_ip1 + dums_im1;
                                                       % Coeff for CS_nowX(i)
   QS_nextX(ingrs)      = QS_nowX(ingrs) + dums_ip1.*CS_nowX(ingrs+1) +
dums_im1.*CS_nowX(ingrs-1) - dums_i.*CS_nowX(ingrs);
   CS_nextX(ingrs)      = NewtonSolveC(1e-40, AS1stOrder(ingrs), ASFrdlichN(ingrs),
FrdlichN_s, QS_nextX(ingrs));
   if sum(CS_nextX(ingrs)<0)
      disp ('CS_nextX(innergrids) negative.');
   end
   SS_nextX(ingrs)      = Koc*foc_sX(ingrs).*CS_nextX(ingrs) +
Kbc_soot*fbc_sX(ingrs).*(CS_nextX(ingrs).^FrdlichN_s);

   % Calc CS_nextX(m) by linear interpolation
   C_blk_next    = C_blk_set;
   Slopebltms    = (C_blk_next - CS_nextX(ms-1))/(dxs+blt_x);
   CS_nextX(ms)  = dxs*Slopebltms + CS_nextX(ms-1);
   SS_nextX(ms) = alpha_ms*CS_nextX(ms) + beta_ms*(CS_nextX(ms)^FrdlichN_s);
   QS_nextX(ms) = SS_nextX(ms)*rho_bsX(ms) + PorsX(ms)*CS_nextX(ms);

   % UPDATE CONCENTRATIONS
   % all "NOW" concs represent values after itime of timesteps, thus to be recorded as
occuring at [itime*dtow]
```

```
   CC_nowX              = CC_nextX;                                CS_nowX         = CS_nextX;
   SC_nowX              = SC_nextX;                                SS_nowX         = SS_nextX;
   QC_nowX              = QC_nextX;                                QS_nowX         = QS_nextX;
   C_blk_now     = C_blk_next;
   QC_nowAvg     = QC_nextAvg;
   QS_nowAvg     = F_AggregateAvgProperty(ShapeFactor, xs, QS_nextX, dxs) / Silt_Divider;
   Q_nowAvg             = (QC_nowAvg*V_one_char + QS_nowAvg*V_one_silt) / V_one_agg;


   % SAVE MODELLED PROFILE
   % ***REM: all "NOW" quantities are the LATEST quantities for itime# of steps***
   % C_blk_diff = abs((C_blk_now - C_blk_mark)/C_blk_mark);
   Q_Avg_diff = abs((Q_nowAvg - Q_Avg_mark)/Q_Avg_mark);
   if Q_Avg_diff>0.01
      AbsT_hrs  = itime*dt/3600;              % time in hrs
      AbsTow    = itime*dtow;                 % dimensionless time [--]
      TimeEntry= [AbsTow, AbsT_hrs];% i.e. [tow, t_in_hrs]; 1 x 2
      Magg_Meqm = (Q_initAvg - Q_nowAvg)/(Q_lossAvg);

      % Storing overall desorption result at ith timestep, or [itime*dt] secs
      CC_nowAvg                = F_AggregateAvgProperty(ShapeFactor, xc, CC_nowX, dxc);
      CS_nowAvg                = F_AggregateAvgProperty(ShapeFactor, xs, CS_nowX, dxs) /
Silt_Divider;
      C_nowAvg                = (CC_nowAvg*V_one_char + CS_nowAvg*V_one_silt) / V_one_agg;
      SC_nowAvg                = F_AggregateAvgProperty(ShapeFactor, xc, SC_nowX, dxc);
      SS_nowAvg                = F_AggregateAvgProperty(ShapeFactor, xs, SS_nowX, dxs) /
Silt_Divider;
      S_nowAvg                = (SC_nowAvg*V_one_char + SS_nowAvg*V_one_silt) / V_one_agg;
      OneEntry_OVRALL   = [TimeEntry, C_nowAvg, S_nowAvg, Q_nowAvg, C_blk_now, Magg_Meqm];
      DATA_OVRALL              = [DATA_OVRALL; OneEntry_OVRALL];

      %% Storing temporal-spatial result at ith timestep
      DATA_CC_tx                      = [DATA_CC_tx; [TimeEntry, CC_nowX]];
      DATA_SC_tx                      = [DATA_SC_tx; [TimeEntry, SC_nowX]];
      DATA_QC_tx                      = [DATA_QC_tx; [TimeEntry, QC_nowX]];
      DATA_KdC_tx                     = [DATA_KdC_tx; [TimeEntry, SC_nowX./CC_nowX]];

      DATA_CS_tx                      = [DATA_CS_tx; [TimeEntry, CS_nowX]];
      DATA_SS_tx                      = [DATA_SS_tx; [TimeEntry, SS_nowX]];
      DATA_QS_tx                      = [DATA_QS_tx; [TimeEntry, QS_nowX]];
      DATA_KdS_tx                     = [DATA_KdS_tx; [TimeEntry, SS_nowX./CS_nowX]];

      W_now                           = QC_nowAvg*V_one_char + QS_nowAvg*V_one_silt +
C_blk_now*V_one_nonagg;
      DW_now_les_init   = W_now - W_init;
      DATA_W_tx                = [DATA_W_tx; [TimeEntry, W_now, DW_now_les_init]];

      %% Update C_blk_mark ***!!!***
      Q_Avg_mark         = Q_nowAvg;

   elseif (itime>30000)&(mod(itime, 4000)==0)
      AbsT_hrs  = itime*dt/3600;              % time in hrs
      AbsTow    = itime*dtow;                 % dimensionless time [--]
      TimeEntry= [AbsTow, AbsT_hrs];% i.e. [tow, t_in_hrs]; 1 x 2
      %Magg_Meqm= Q_nowAvg/Q_eqmAvg;   % Mass of i in agg at itimeth step / Mass of i in
agg at eqm (t->inf)
      Magg_Meqm = (Q_initAvg - Q_nowAvg)/(Q_lossAvg);

      %% Storing overall desorption result at ith timestep, or [itime*dt] secs
      CC_nowAvg                = F_AggregateAvgProperty(ShapeFactor, xc, CC_nowX, dxc);
      CS_nowAvg                = F_AggregateAvgProperty(ShapeFactor, xs, CS_nowX, dxs) /
Silt_Divider;
      C_nowAvg                = (CC_nowAvg*V_one_char + CS_nowAvg*V_one_silt) / V_one_agg;
      SC_nowAvg                = F_AggregateAvgProperty(ShapeFactor, xc, SC_nowX, dxc);
      SS_nowAvg                = F_AggregateAvgProperty(ShapeFactor, xs, SS_nowX, dxs) /
Silt_Divider;
      S_nowAvg                = (SC_nowAvg*V_one_char + SS_nowAvg*V_one_silt) / V_one_agg;
      OneEntry_OVRALL   = [TimeEntry, C_nowAvg, S_nowAvg, Q_nowAvg, C_blk_now, Magg_Meqm];
      DATA_OVRALL              = [DATA_OVRALL; OneEntry_OVRALL];

      %% Storing temporal-spatial result at ith timestep
      DATA_CC_tx                      = [DATA_CC_tx; [TimeEntry, CC_nowX]];
      DATA_SC_tx                      = [DATA_SC_tx; [TimeEntry, SC_nowX]];
   DATA_QC_tx                 = [DATA_QC_tx; [TimeEntry, QC_nowX]];
      DATA_KdC_tx                     = [DATA_KdC_tx; [TimeEntry, SC_nowX./CC_nowX]];

      DATA_CS_tx                      = [DATA_CS_tx; [TimeEntry, CS_nowX]];
      DATA_SS_tx                      = [DATA_SS_tx; [TimeEntry, SS_nowX]];
   DATA_QS_tx                 = [DATA_QS_tx; [TimeEntry, QS_nowX]];
      DATA_KdS_tx                     = [DATA_KdS_tx; [TimeEntry, SS_nowX./CS_nowX]];
```

```
      W_now                                    = QC_nowAvg*V_one_char +
QS_nowAvg*V_one_silt + C_blk_now*V_one_nonagg;
      DW_now_les_init   = W_now - W_init;
      DATA_W_tx                = [DATA_W_tx; [TimeEntry, W_now, DW_now_les_init]];

      % Update C_blk_mark ***!!!***
      %C_blk_mark              = C_blk_now;
      Q_Avg_mark        = Q_nowAvg;

   end   % end if-elseif
   if mod(itime, 2500)==0,
      fprintf ('%i\n', itime);
   end
end


%%%
%%% Write modeling results to files
%%%

Fpath_OVRALL= [Fpath, Ffilename, '.ovr'];
Fpath_C_tx      = [Fpath, Ffilename, '.c'];
Fpath_S_tx      = [Fpath, Ffilename, '.s'];
Fpath_Q_tx      = [Fpath, Ffilename, '.q'];
Fpath_Kd_tx     = [Fpath, Ffilename, '.kd'];
Fpath_Z_tx      = [Fpath, Ffilename, '.z'];


% Overall modelign results
save ovrall DATA_OVRALL -ASCII
dos(['ren ovrall ',Ffilename,'_Ovrall.txt']);

% Char-phase modeling results
save cc DATA_CC_tx -ASCII
save sc DATA_SC_tx -ASCII
save qc DATA_QC_tx -ASCII
save kdc DATA_KdC_tx -ASCII
dos(['ren cc ',Ffilename,'_Cchar.txt']);
dos(['ren sc ',Ffilename,'_Schar.txt']);
dos(['ren qc ',Ffilename,'_Qchar.txt']);
dos(['ren kdc ',Ffilename,'_Kdchar.txt']);

% Silt-phase modeling results
save cs DATA_CS_tx -ASCII
save ss DATA_SS_tx -ASCII
save qs DATA_QS_tx -ASCII
save kds DATA_KdS_tx -ASCII
dos(['ren cs ',Ffilename,'_Csilt.txt']);
dos(['ren ss ',Ffilename,'_Ssilt.txt']);
dos(['ren qs ',Ffilename,'_Qsilt.txt']);
dos(['ren kds ',Ffilename,'_Kdsilt.txt']);

% Mass balance check, "W"
save www DATA_W_tx -ASCII
dos(['ren www ',Ffilename,'_www.txt']);

toc
```

Script E - 8. Char-in-Silt Heterogeneous Model (Closed System)

*Please see **Script E – 5** for other functions called by the main program.*

Char-in-Silt-Closed-System (Main Program)

```
%%%
%%% a priori simulation of sedimental-HOCs desorption kinetics for
%%%
%%% CHAR CENTRALLY EMBEDDED IN SILT AGGREGATE CASE (Closed System)
%%%
%%% By: Dave Kuo
%%% Date: 13 October 2005
%%%


%%%
%%% Compute intrinsic diffusivity Diw
%%%
HOCName = 'pyrene';
Diw_m = F_Diffusivity (HOCName, 'water');            % [m2/s]


%%%
%%% Set system properties
%%%

% ISOTHERM SETTING
%
% foc, fbc      : org carbon, black carbon content of aggregate [g_carbon/g_solid]
% Koc, Kbc      : partition coefficient for chemical i [L_solv/kg_carbon]
% FrdlichN      : Freundlich exponent
% CmplmFrdlichN: complimentary Freundlich exponent
%
foc_c           = 0;          % org. carbon mass fraction in CHAR compartment
fbc_c           = 1;          % blk. carbon mass fraction in CHAR compartment
foc_s           = 0.02;       % org. carbon mass fraction in SILT compartment
fbc_s           = 0.002;      % blk. carbon mass fraction in SILT compartment
Koc             = 10^4.7;
%Kbc = 10^6.4; %Ball's correlation Kbc = 10^(1.6*5.13 - 1.4);
Kbc_char        = 10^6.3;     % Kbc for char-BC
Kbc_soot        = 10^6.3;     % Kbc for soot-BC
FrdlichN_c      = 0.6;        % Frdlich exponent for char-BC
FrdlichN_s      = 0.6;        % Frdlich exponent for soot-BC

% DESORPTION SCENARIO
%
% {'homogeneous 0.13 sooty-silt',  '5um char in 100um silt'}
%DesorptionScenario = 'homogeneous 0.13 sooty-silt';
DesorptionScenario = '5um char in 100um silt';
ShapeFactor     = 3;                                          % 3 for
spherical; 2 for cylindrical; 1 for slab


% SEDIMENT CHARACTERISTICS
%
% rho_s         : strict solid density [Kg_solid/L_solid]
% rsw_ppm       : overall system solid-to-water ratio [mg_solid/L_solv]
% rsw           : overall system solid-to-water ratio [Kg_solid/L_solv]
% rad_um        : particle radius [um]
% rad_m         : particle radius [m]
rho_s_silt      = 2.5;
rho_s_char      = 2.0;
rsw_ppm         = 20;
rsw             = rsw_ppm/1e6;
rad_um          = 25;
rad_m           = rad_um/1e6;
rad_char_um     = 10;
rad_char_m      = rad_char_um/1e6;

% GRID AND TIME STEP SIZES
%
% m             : number of grids
% Co_crit       : 'Courant' criterion
% Pe_crit       : 'Peclet' criterion
% Timesteps     : Number of timesteps
% dr            : differential radius [m]
% dx            : = dr/rad_m = differential radius [--]
```

```
% dtow          : = Diw*dt/(R^2) = differential timestep [--]
% Timesteps     : # timesteps, each dtow [--]
mc               = 41;                  % # grids in CHAR compartment
ms               = 41;                  % # grids in SILT compartment
drc              = 1/(mc-1) * rad_char_m;
drs              = 1/(ms-1) * (rad_m - rad_char_m);
dxc              = drc/rad_char_m;              % rad_char_m   = "R_c"
dxs              = drs/rad_m;                   % rad_m                  = "R_agg"
SFitLimit        = 5;                   % Limiting silt_grid in polynomial fitting of
CS_nowX for estimating CC_nowX_mc_plus_1
Co_crit          = 2;           % <1
Pe_crit          = 0.05;        % <2
CoByPe_crit = Co_crit/Pe_crit;
dtow             = CoByPe_crit;
dt               = dtow*(rad_m^2)/Diw_m;
Timesteps        = 40e4; %5.0e3;
%Timesteps       = 4e6; %5.0e3;

% SPATIAL MATRICES
%
gridc            = (1:1:mc);                                                    % 1 x
mc; CHAR domain grid-index
grids            = (1:1:ms);                                                    % 1 x
ms; SILT domain grid-index
ingrc            = (2:mc-1);                                                    % 1 x
mc-2 {2  3  4  ...  mc-2}; CHAR innergrids
ingrs            = (2:ms-1);                                                    % 1 x
ms-2 {2  3  4  ...  ms-2}; SILT innergrids
xc               = (gridc-1)*dxc;                                    % 1 x mc; CHAR
domain x
xsB              = rad_char_m/rad_m;                          % "X_sub(s,b)"
xs               = xsB + (grids-1)*dxs;                % 1 x ms; SILT domain x
Silt_Divider     = (1-xsB^ShapeFactor);                % scalar; used when computing
SILT-avg quantity
xc_mulz1         = xc.^(ShapeFactor-1);                % 1 x mc; "xc^(miu-1)"
xs_mulz1         = xs.^(ShapeFactor-1);                % 1 x ms; "xs^(miu-1)"
xc_hlf           = xc+0.5*dxc;                                          % 1 x mc;
{X1.5  X2.5  X3.5  ...  Xmc-0.5  (Xmc+0.5!)}
xs_hlf           = xs+0.5*dxs;                                          % 1 x ms;
{X1.5  X2.5  X3.5  ...  Xms-0.5  (Xms+0.5!)}
xc_hlf_mulz1     = xc_hlf.^(ShapeFactor-1);            % 1 x mc; {X1.5  X2.5
X3.5  ...  Xmc-0.5  (xmc+0.5!)}
xs_hlf_mulz1     = xs_hlf.^(ShapeFactor-1);            % 1 x ms; {X1.5  X2.5
X3.5  ...  Xms-0.5  (xms+0.5!)}


% INITIAL CONDITIONS
%
% porosity       : porosity(x) {n} [L_void/L_agg]
% tortuosity     : tortuosity(x) {f(n)}
% S_init         : initial solid phase conc'n, (S') [ug_i/kg_solid = ng i/g_solid]
% C_init         : initial pore fluid conc'n, (C') [ug_i/L_por_aq]
CharPorosity     = 0.90;        % synthetic char from Braida et al.(Pignatello), 2003 EST
CharTortuosity   = 0.90;        % assumed to be same as porosity
SiltPorosity     = 0.15;        % fitting value by Wu and Gschwend, 1986 EST
SiltTortuosity   = 0.15;        % assumed to be same as porosity; Wu and Gschwend, 1988 Wat
Res Res
CC_init          = 0.050;    % ug/L
SC_init          = foc_c*Koc*CC_init + fbc_c*Kbc_soot*(CC_init^FrdlichN_c);
%SC_init         = 2100;                % [ug_i/kg_CHAR or ng_i/g_CHAR]
%CC_init         = NewtonSolveC (1e-40, foc_c*Koc, fbc_c*Kbc_char, FrdlichN_c, SC_init); %
[ug_i/L_agg]
CS_init          = CC_init;     % i.e. same pore-fluid phase activity of i in both CHAR and
SILT compartments
%[CC_init, CS_init]
SS_init          = foc_s*Koc*CS_init + fbc_s*Kbc_soot*(CS_init^FrdlichN_s);
%SS_init         = 2100;                % [ug_i/kg_SILT or ng_i/g_SILT]
%CS_init         = NewtonSolveC (1e-40, foc_s*Koc, fbc_s*Kbc_soot, FrdlichN_s, SS_init); %
[ug_i/L_agg]


switch DesorptionScenario
   case '5um char in 100um silt'
      %% Set CHAR domain properties
      PorCX      = F_SetAggProperty('homogeneous', mc, CharPorosity);       % CHAR domain
porosity(x)
      TorCX      = F_SetAggProperty('homogeneous', mc, CharTortuosity);     % CHAR domain
tortuosity(x)
      foc_CX     = F_SetAggProperty('homogeneous', mc, foc_c);                          %
CHAR domain foc(x)
```

```
      fbc_cX    = F_SetAggProperty('homogeneous', mc, fbc_c);                          %
CHAR domain fbc(x)
      SC_initX  = F_SetAggProperty('homogeneous', mc, SC_init);                        %
CHAR domain S_init(x)
      %% Set SILT domain properties
      PorsX     = F_SetAggProperty('homogeneous', ms, SiltPorosity);       % SILT domain
porosity(x)
      TorsX     = F_SetAggProperty('homogeneous', ms, SiltTortuosity);     % SILT domain
tortuosity(x)
      foc_sX    = F_SetAggProperty('homogeneous', ms, foc_s);                          %
SILT domain foc(x)
      fbc_sX    = F_SetAggProperty('homogeneous', ms, fbc_s);                          %
SILT domain fbc(x)
      SS_initX  = F_SetAggProperty('homogeneous', ms, SS_init);                        %
SILT domain S_init(x)
end

rho_bcX         = rho_s_char*(1-PorcX);       % [kg_CHAR/L_agg]
rho_bsX         = rho_s_silt*(1-PorsX);       % [kg_SILT/L_agg]

% *****AggAvgPorosity          = F_AggregateAvgProperty(ShapeFactor, x, PorosityX, dx);
PorcHlfX        = (PorcX(1:mc-1)+PorcX(2:mc)) ./ 2;          % 1 x (mc-1) !!!
PorsHlfX        = (PorsX(1:ms-1)+PorsX(2:ms)) ./ 2;          % 1 x (ms-1) !!!
TorcHlfX        = (TorcX(1:mc-1)+TorcX(2:mc)) ./ 2;          % 1 x (mc-1) !!!
TorsHlfX        = (TorsX(1:ms-1)+TorsX(2:ms)) ./ 2;          % 1 x (ms-1) !!!
CharAvgPor      = F_AggregateAvgProperty(ShapeFactor, xc, PorcX, dxc);
SiltAvgPor      = F_AggregateAvgProperty(ShapeFactor, xs, PorsX, dxs) / Silt_Divider;

% VRatio        : volumetric ratio of bulk solvent phase to aggregate(solid+porous fluid)
V_one_char      = 4/3*pi*(rad_char_m^3);
V_one_agg       = 4/3*pi*(rad_m^3);
V_one_silt      = V_one_agg - V_one_char;
Mass_one_char   = (1-CharAvgPor) * V_one_char * rho_s_char;
Mass_one_silt   = (1-SiltAvgPor) * V_one_silt * rho_s_silt;
Mass_one_agg    = Mass_one_char + Mass_one_silt;
V_one_nonagg    = Mass_one_agg/rsw;
VRatio          = V_one_nonagg/V_one_agg;    % Same as VRatio = ((1-f_porsity)*rho_s)/rsw;

% Q_initX       : initial aggregate(solid+porous fluid) volume-averaged concentration
[ug_i/L_agg]
% C_initX       : initial spatial C' within aggregate [ug_i/L_agg]
% C_blk_init    : initial non-agg/bulk aq. phase concentration [ug_i/L_solv]
CC_initX        = NewtonSolveC (1e-40, foc_cX*Koc, fbc_cX*Kbc_char, FrdlichN_c, SC_initX);
if SS_initX == 0
    CS_initX    = F_SetAggProperty('homogeneous', ms, 0);
else
    CS_initX    = NewtonSolveC (1e-40, foc_sX*Koc, fbc_sX*Kbc_soot, FrdlichN_s, SS_initX);
end
CS_initX;
QC_initX        = SC_initX.*rho_bcX + PorcX.*CC_initX;
QS_initX        = SS_initX.*rho_bsX + PorsX.*CS_initX;
QC_initAvg      = F_AggregateAvgProperty(ShapeFactor, xc, QC_initX, dxc);
QS_initAvg      = F_AggregateAvgProperty(ShapeFactor, xs, QS_initX, dxs) / Silt_Divider;
Q_initAvg       = (QC_initAvg*V_one_char + QS_initAvg*V_one_silt) / V_one_agg;
C_blk_init      = 0;

% GapF          : gap factor for initial non-agg/bulk aq. phase conc'n, such that C_init =
Ceqm_init/GapF
% dfpexp        : the exponent of the fitting porosity n on the numerator
GapF = 1; %%%%% CLOSED SYSTEM, MASS CONSERVED
dfpexp = 2;


%%%
%%% Calculate expected eqm aq. conc.: C_blk_eqm
%%%
W_init          = Q_initAvg*V_one_agg + C_blk_init*V_one_nonagg;           % [ug_i]
YC_1stOrder     = Koc*foc_cX.*rho_bcX + PorcX;
YS_1stOrder     = Koc*foc_sX.*rho_bsX + PorsX;
YC_FrdlichN     = Kbc_char*fbc_cX.*rho_bcX;
YS_FrdlichN     = Kbc_soot*fbc_sX.*rho_bsX;
dum_C_1stOrder  = F_AggregateAvgProperty(ShapeFactor, xc, YC_1stOrder, dxc) * V_one_char;
dum_S_1stOrder  = F_AggregateAvgProperty(ShapeFactor, xs, YS_1stOrder, dxs) / Silt_Divider
* V_one_silt;
Coeff_1stOrder  = dum_C_1stOrder + dum_S_1stOrder + V_one_nonagg;
dum_C_FrdlichN  = F_AggregateAvgProperty(ShapeFactor, xc, YC_FrdlichN, dxc) * V_one_char;
dum_S_FrdlichN  = F_AggregateAvgProperty(ShapeFactor, xs, YS_FrdlichN, dxs) / Silt_Divider
* V_one_silt;
Coeff_FrdlichN  = dum_C_FrdlichN + dum_S_FrdlichN;
%  !!! ASSUMING SAME FrdlichN for both compartments when solving for C_blk_eqm !!!
C_blk_eqm       = NewtonSolveC(1e-40, Coeff_1stOrder, Coeff_FrdlichN, FrdlichN_s, W_init);
```

```
SC_eqmX          = C_blk_eqm*Koc*foc_cX + (C_blk_eqm^FrdlichN_c)*Kbc_char*fbc_cX;
SS_eqmX          = C_blk_eqm*Koc*foc_sX + (C_blk_eqm^FrdlichN_s)*Kbc_soot*fbc_sX;
QC_eqmX          = SC_eqmX.*rho_bcX + C_blk_eqm*PorcX;
QS_eqmX          = SS_eqmX.*rho_bsX + C_blk_eqm*PorsX;
QC_eqmAvg        = F_AggregateAvgProperty(ShapeFactor, xc, QC_eqmX, dxc);
QS_eqmAvg        = F_AggregateAvgProperty(ShapeFactor, xs, QS_eqmX, dxs) / Silt_Divider;
Q_eqmAvg         = (QC_eqmAvg*V_one_char + QS_eqmAvg*V_one_silt) / V_one_agg;


%%%
%%% Date output information
%%%
Fpath    = '/BC/ModelOutput/';
Ffile1   =
['CharSilt_',HOCName,'_Rad',num2str(rad_um),'_RadC',num2str(rad_char_um),'_Rsw',num2str(rs
w_ppm),'_Cinit',num2str(CC_init),'_Cblkinit',num2str(C_blk_init),'_SF',
num2str(ShapeFactor)];
Ffile2   =
['_OC',num2str(round(log10(Koc)*100)),'_BC',num2str(round(log10(Kbc_soot)*100)),'_nBC',num
2str(FrdlichN_s*100)];
Ffile3   =
['_focC',num2str(foc_c*100),'_fbcC',num2str(fbc_c*100),'_focS',num2str(foc_s*100),'_fbcS',
num2str(fbc_s*100),'_PoroChar',num2str(CharPorosity),'_PoroSilt',num2str(SiltPorosity)];
%Ffilename       = 'CharValidationPureOC_20ppmKd5000Poly3_80Char';
Ffilename        = [Ffile1, Ffile2, Ffile3];
%%%%%%%%% TO BE CHANGED .....! ! !  ! ! ! !
%ISOTH_p         = [foc, Koc, fbc, Kbc, FrdlichN];
%SEDI_p          = [rho_s, rsw, rad_m, V_one_agg, V_one_nonagg, AggAvgPorosity, VRatio];
%CONC_p          = [S_init, C_init, Q_initAvg, C_blk_init];
%SIMU_p          = [m, dr, dx, Co_crit, Pe_crit, CoByPe_crit, dtow, dt, Timesteps];
%EQM_p           = [C_blk_eqm, Q_eqmAvg];
%F_OutputSystemParameters(Fpath,Ffilename,'PYRENE',Diw_m,ISOTH_p, SEDI_p, CONC_p, SIMU_p,
EQM_p);


%%%
%%% SOLVING RETARDED DIFFUSIONAL EQN BY ITERATIONS
%%%
% Constants
% For CHAR innermost grid calc, grid = 1
kc_inrmost       = dtow * ShapeFactor * TorcHlfX(1) * PorcHlfX(1) / dxc / xc_hlf(1);
        % scalar
%k_innermost = dtow * ShapeFactor * TortuosityHlfX(1) * PorosityHlfX(1) / dx / x_hlf(1);  %
scalar

% For CHAR intermediate grids calc, grid = 2 to mc-1
kc_intermd       = dtow/(dxc^2) .* PorcX ./ xc_mulz1;
 % 1 x (mc-2)
%k_intermedi = dtow/((dx)^2) .* PorosityX ./ x_miu_les_1;                                  %
1 x m

% For CHAR-SILT interface, grid = Xc,mc, or Xs,1
kcs                      = dtow/(dxc^2)*0.5*(PorcX(mc)+PorsX(1))/xc_mulz1(mc);             %
scalar

% For SILT intermediate grids calc, grid = 2 to ms-1
ks_intermd       = dtow/(dxs^2) .* PorsX ./ xs_mulz1;
 % 1 x (ms-2)

% For C_blk_next OR C_nextX(m) calc, grid = ms
q_csnext_ms = ShapeFactor*xs_mulz1(ms)*dxs*1/3/Silt_Divider; % coeff for QS_next_ms;
scalar
alpha_ms         = foc_sX(ms)*Koc;              % "alpha_ms"
beta_ms          = fbc_sX(ms)*Kbc_soot;         % "beta_ms"
CnxtcsFirstOrder = V_one_nonagg + V_one_silt*q_csnext_ms*(alpha_ms*rho_bsX(ms)+PorsX(ms));
CnxtcsFrdlichN   = V_one_silt*q_csnext_ms*beta_ms*rho_bsX(ms);

AC1stOrder       = Koc*foc_cX.*rho_bcX + PorcX;       % 1st Order coeff for solving
CC_nextX(i) from QC_nextX(i)
ACFrdlichN       = Kbc_char*fbc_cX.*rho_bcX;          % Frdlich N coeff for solving
CC_nextX(i) from QC_nextX(i)
AS1stOrder       = Koc*foc_sX.*rho_bsX + PorsX;       % 1st Order coeff for solving
CS_nextX(i) from QS_nextX(i)
ASFrdlichN       = Kbc_soot*fbc_sX.*rho_bsX;          % Frdlich N coeff for solving
CS_nextX(i) from QS_nextX(i)

%x                = (gridindex-1)*dx;   % 1 x m {X1  X2  X3  ...  Xm}
%x_miu_les_1      = x.^(ShapeFactor-1); % 1 x m
%x_hlf            = (gridindex-0.5)*dx; % 1 x m {X1.5  X2.5  X3.5  ...  Xm-0.5  (xm+0.5!)}
%x_hlf_miu_les_1= x_hlf.^(ShapeFactor-1);% 1 x m {X1.5  X2.5  X3.5  ...  Xm-0.5  (xm+0.5!)}
```

```
CC_nowX          = CC_initX;                    CS_nowX          = CS_initX;
SC_nowX          = SC_initX;                    SS_nowX          = SS_initX;
QC_nowX          = QC_initX;                    QS_nowX          = QS_initX;
QC_nowAvg        = QC_initAvg;                  QS_nowAvg        = QS_initAvg;
Q_nowAvg         = Q_initAvg;
C_blk_now        = C_blk_init;
C_blk_mark       = C_blk_init;                  % for determining if profiles should be
recorded/saved at ith step

CC_nextX         = zeros(1, mc);                % initialize; 1 x m of zeroes
SC_nextX         = zeros(1, mc);                % 1 x m of zeroes
QC_nextX         = zeros(1, mc);                % 1 x m of zeroes
CS_nextX         = zeros(1, ms);                % initialize; 1 x m of zeroes
SS_nextX         = zeros(1, ms);                % 1 x m of zeroes
QS_nextX         = zeros(1, ms);                % 1 x m of zeroes

DATA_OVRALL      = [];  % data matrix for overall results (C_blk, Q_Avg, S_Avg, etc)
DATA_CC_tx       = [];  % data matrix for temporal-spatial, CC(x,t) [ug_i/L_void]
DATA_SC_tx       = [];  % data matrix for temporal-spatial, SC(x,t) [ug_i/kg_solid]
DATA_QC_tx       = [];  % data matrix for temporal-spatial, QC(x,t) [ug_i/L_agg]
DATA_KdC_tx      = [];  % data matrix for temporal-spatial KdC = SC(x,t) / CC(x,t)

DATA_CS_tx       = [];  % data matrix for temporal-spatial, CS(x,t) [ug_i/L_void]
DATA_SS_tx       = [];  % data matrix for temporal-spatial, SS(x,t) [ug_i/kg_solid]
DATA_QS_tx       = [];  % data matrix for temporal-spatial, QS(x,t) [ug_i/L_agg]
DATA_KdS_tx      = [];  % data matrix for temporal-spatial KdS = SS(x,t) / CS(x,t)

DATA_W_tx        = [];  % data matrix for W(t) = Q_nowAvg*V_one_agg + C_blkAvg*V_one_nonagg
[ug i]

% Save time-zero condition
DATA_CC_tx       = [DATA_CC_tx; [0, 0, CC_initX]];
DATA_SC_tx       = [DATA_SC_tx; [0, 0, SC_initX]];
DATA_QC_tx       = [DATA_QC_tx; [0, 0, QC_initX]];
DATA_KdC_tx      = [DATA_KdC_tx; [0, 0, SC_initX./CC_initX]];

DATA_CS_tx       = [DATA_CS_tx; [0, 0, CS_initX]];
DATA_SS_tx       = [DATA_SS_tx; [0, 0, SS_initX]];
DATA_QS_tx       = [DATA_QS_tx; [0, 0, QS_initX]];
DATA_KdS_tx      = [DATA_KdS_tx; [0, 0, SS_initX./CS_initX]];

DATA_W_tx        = [DATA_W_tx; [0, 0, W_init, 0]];

tic
for itime=1:Timesteps,

   %% INNERMOST GRID X[char,1] CALC
   QC_nextX(1)   = QC_nowX(1) + kc_inrmost*(CC_nowX(2)-CC_nowX(1));
   CC_nextX(1)   = NewtonSolveC(1e-40, AC1stOrder(1), ACFrdlichN(1), FrdlichN_c,
QC_nextX(1));
   if sum(CC_nextX(1)<0)
      disp ('CC_nextX(1) negative.');
   end
   SC_nextX(1)   = foc_cX(1)*Koc*CC_nextX(1) + fbc_cX(1)*Kbc_char*(CC_nextX(1)^FrdlichN_c);

   %% INTERMEDIATE GRIDS X[char, 2 to mc-1] CALC
   dumc_ip1 = []; dumc_im1 = []; dumc_i = [];
   dumc_ip1      = kc_intermd(ingrc).*xc_hlf_mulz1(ingrc).*TorcHlfX(ingrc);
         % Coeff for CC_nowX(i+1)
   dumc_im1      = kc_intermd(ingrc).*xc_hlf_mulz1(ingrc-1).*TorcHlfX(ingrc-1);
         % Coeff for CC_nowX(i-1)
   dumc_i        = dumc_ip1 + dumc_im1;
                                                  % Coeff for CC_nowX(i)
   QC_nextX(ingrc)       = QC_nowX(ingrc) + dumc_ip1.*CC_nowX(ingrc+1) +
dumc_im1.*CC_nowX(ingrc-1) - dumc_i.*CC_nowX(ingrc);
   CC_nextX(ingrc)       = NewtonSolveC(1e-40, AC1stOrder(ingrc), ACFrdlichN(ingrc),
FrdlichN_c, QC_nextX(ingrc));
   if sum(CC_nextX(ingrc)<0)
      disp ('CC_nextX(innergrids) negative.');
   end
   SC_nextX(ingrc)       = Koc*foc_cX(ingrc).*CC_nextX(ingrc) +
Kbc_char*fbc_cX(ingrc).*(CC_nextX(ingrc).^FrdlichN_c);

   %% DETERMINE CC_nowX(mc+1) FROM FITTING OF CS_nowX(1..ms) WITH 3rd Order Polynomial
   PSiltC        = polyfit(xs(1:SFitLimit), CS_nowX(1:SFitLimit), 3);
   C_mcplus1= polyval(PSiltC, xsB+dxc);       % Interpolated CC_now_mc_plus_1, the grid is
located in SILT domain

   %% CHAR-SILT INTERFACE GRID X[char, mc] OR X[silt, 1] CALC
   dumI_ip1 = []; dumI_im1 = []; dumI_i = [];
```

```
   dumI_ip1      = kcs.*xc_hlf_mulz1(mc).*TorsHlfX(1);
                   % Coeff for CC_nowX(mc+1)


         % using SILT-domain Tortuosity
   dumI_im1      = kcs.*xc_hlf_mulz1(mc-1).*TorcHlfX(mc-1);
         % Coeff for CC_nowX(mc-1)
   dumI_i        = dumI_ip1 + dumI_im1;
                                        % Coeff for CC_nowX(mc)
   %[QC_nowX(mc), CC_nowX(mc-1), CC_nowX(mc), dumI_ip1, C_mcplus1, dumI_im1, dumI_i]
   QC_nextX(mc)          = QC_nowX(mc) + dumI_ip1.*C_mcplus1 + dumI_im1.*CC_nowX(mc-1) -
dumI_i.*CC_nowX(mc);
   CC_nextX(mc)          = NewtonSolveC(1e-40, AC1stOrder(mc), ACFrdlichN(mc), FrdlichN_c,
QC_nextX(mc));
   %[QC_nextX(mc), CC_nextX(mc)]
   if sum(CC_nextX(mc)<0)
      disp ('CC_nextX(mc) negative.');
   end
   SC_nextX(mc)          = Koc*foc_cX(mc)*CC_nextX(mc) +
Kbc_char*fbc_cX(mc)*(CC_nextX(mc)^FrdlichN_c);

   CS_nextX(1)                  = CC_nextX(mc);                                  % By
continuity of pore-fluid (i.e. V_void) phase concentration
   SS_nextX(1)                  = Koc*foc_sX(1)*CS_nextX(1) +
Kbc_soot*fbc_sX(1)*(CS_nextX(1)^FrdlichN_s);
   QS_nextX(1)                  = SS_nextX(1)*rho_bsX(1) + PorsX(1)*CS_nextX(1);
   if sum(CS_nextX(1)<0)
      disp ('CS_nextX(1) negative.');
   end

   QC_nextAvg    = F_AggregateAvgProperty(ShapeFactor, xc, QC_nextX, dxc);

   %% INTERMEDIATE GRIDS X[silt, 2 to ms-1) CALC
   dums_ip1 = []; dums_im1 = []; dums_i = [];
   dums_ip1      = ks_intermd(ingrs).*xs_hlf_mulz1(ingrs).*TorsHlfX(ingrs);
         % Coeff for CS_nowX(i+1)
   dums_im1      = ks_intermd(ingrs).*xs_hlf_mulz1(ingrs-1).*TorsHlfX(ingrs-1);
         % Coeff for CS_nowX(i-1)
   dums_i        = dums_ip1 + dums_im1;
                                        % Coeff for CS_nowX(i)
   QS_nextX(ingrs)       = QS_nowX(ingrs) + dums_ip1.*CS_nowX(ingrs+1) +
dums_im1.*CS_nowX(ingrs-1) - dums_i.*CS_nowX(ingrs);
   CS_nextX(ingrs)       = NewtonSolveC(1e-40, AS1stOrder(ingrs), ASFrdlichN(ingrs),
FrdlichN_s, QS_nextX(ingrs));
   if sum(CS_nextX(ingrs)<0)
      disp ('CS_nextX(innergrids) negative.');
   end
   SS_nextX(ingrs)       = Koc*foc_sX(ingrs).*CS_nextX(ingrs) +
Kbc_soot*fbc_sX(ingrs).*(CS_nextX(ingrs).^FrdlichN_s);

   % C_blk_next AND CS_nextX(ms) CALC
   dum_QS_nextX = [QS_nextX(1:ms-1), 0];
 % dummy for calculating q_csnext_cnst
   q_csnext_cnst= F_AggregateAvgProperty(ShapeFactor, xs, dum_QS_nextX, dxs) /
Silt_Divider;
   Const_nowterms    = QC_nowAvg*V_one_char + QS_nowAvg*V_one_silt + C_blk_now*V_one_nonagg;
   Const_nxtterms    = QC_nextAvg*V_one_char + V_one_silt*q_csnext_cnst;
   CnxtcsConstant        = Const_nowterms - Const_nxtterms;
 %%%%%%%% ASSUMING SOLVING WITH SOOT-Frdlich-N !!!!!! %%%%%%
   C_blk_next            = NewtonSolveC (1e-40, Cnxtcs1stOrder, CnxtcsFrdlichN, FrdlichN_s,
CnxtcsConstant);
   CS_nextX(ms) = C_blk_next;
   if sum(CS_nextX(ms)<0)
      disp ('CS_nextX(ms) negative.');
      itime
      exitp = input('Press ctrl-c...');
   end
   SS_nextX(ms) = alpha_ms*CS_nextX(ms) + beta_ms*(CS_nextX(ms)^FrdlichN_s);
   QS_nextX(ms) = SS_nextX(ms)*rho_bsX(ms) + PorsX(ms)*CS_nextX(ms);

   % UPDATE CONCENTRATIONS
   % all "NOW" concs represent values after itime of timesteps, thus to be recorded as
occuring at [itime*dtow]
   CC_nowX       = CC_nextX;                              CS_nowX       = CS_nextX;
   SC_nowX       = SC_nextX;                              SS_nowX       = SS_nextX;
   QC_nowX       = QC_nextX;                              QS_nowX       = QS_nextX;
   C_blk_now     = C_blk_next;
   QC_nowAvg     = QC_nextAvg;
   QS_nowAvg     = F_AggregateAvgProperty(ShapeFactor, xs, QS_nextX, dxs) / Silt_Divider;
   Q_nowAvg              = (QC_nowAvg*V_one_char + QS_nowAvg*V_one_silt) / V_one_agg;
```

```
   % SAVE MODELLED PROFILE
   % ***REM: all "NOW" quantities are the LATEST quantities for itime# of steps***
   C_blk_diff = abs((C_blk_now - C_blk_mark)/C_blk_mark);
   if C_blk_diff>0.01
      AbsT_hrs  = itime*dt/3600;              % time in hrs
      AbsTow    = itime*dtow;                 % dimensionless time [--]
      TimeEntry= [AbsTow, AbsT_hrs];% i.e. [tow, t_in_hrs]; 1 x 2
      Magg_Meqm= Q_nowAvg/Q_eqmAvg;    % Mass of i in agg at itimeth step / Mass of i in
agg at eqm (t->inf)

      % Storing overall desorption result at ith timestep, or [itime*dt] secs
      CC_nowAvg = F_AggregateAvgProperty(ShapeFactor, xc, CC_nowX, dxc);
      CS_nowAvg = F_AggregateAvgProperty(ShapeFactor, xs, CS_nowX, dxs) / Silt_Divider;
      C_nowAvg  = (CC_nowAvg*V_one_char + CS_nowAvg*V_one_silt) / V_one_agg;
      SC_nowAvg = F_AggregateAvgProperty(ShapeFactor, xc, SC_nowX, dxc);
      SS_nowAvg = F_AggregateAvgProperty(ShapeFactor, xs, SS_nowX, dxs) / Silt_Divider;
      S_nowAvg  = (SC_nowAvg*V_one_char + SS_nowAvg*V_one_silt) / V_one_agg;
      OneEntry_OVRALL   = [TimeEntry, C_nowAvg, S_nowAvg, Q_nowAvg, C_blk_now,
C_blk_now/C_blk_eqm, Magg_Meqm];
      DATA_OVRALL              = [DATA_OVRALL; OneEntry_OVRALL];

      % Storing temporal-spatial result at ith timestep
      DATA_CC_tx        = [DATA_CC_tx; [TimeEntry, CC_nowX]];
      DATA_SC_tx        = [DATA_SC_tx; [TimeEntry, SC_nowX]];
      DATA_QC_tx        = [DATA_QC_tx; [TimeEntry, QC_nowX]];
      DATA_KdC_tx       = [DATA_KdC_tx; [TimeEntry, SC_nowX./CC_nowX]];

      DATA_CS_tx        = [DATA_CS_tx; [TimeEntry, CS_nowX]];
      DATA_SS_tx        = [DATA_SS_tx; [TimeEntry, SS_nowX]];
      DATA_QS_tx        = [DATA_QS_tx; [TimeEntry, QS_nowX]];
      DATA_KdS_tx       = [DATA_KdS_tx; [TimeEntry, SS_nowX./CS_nowX]];

      W_now     = QC_nowAvg*V_one_char + QS_nowAvg*V_one_silt + C_blk_now*V_one_nonagg;
      DW_now_les_init   = W_now - W_init;
      DATA_W_tx         = [DATA_W_tx; [TimeEntry, W_now, DW_now_les_init]];

      % Update C_blk_mark ***!!!***
      C_blk_mark        = C_blk_now;

   elseif (itime>30000)&(mod(itime, 4000)==0)
      AbsT_hrs  = itime*dt/3600;              % time in hrs
      AbsTow    = itime*dtow;                 % dimensionless time [--]
      TimeEntry= [AbsTow, AbsT_hrs];% i.e. [tow, t_in_hrs]; 1 x 2
      Magg_Meqm= Q_nowAvg/Q_eqmAvg;    % Mass of i in agg at itimeth step / Mass of i in
agg at eqm (t->inf)

      %% Storing overall desorption result at ith timestep, or [itime*dt] secs
      CC_nowAvg = F_AggregateAvgProperty(ShapeFactor, xc, CC_nowX, dxc);
      CS_nowAvg = F_AggregateAvgProperty(ShapeFactor, xs, CS_nowX, dxs) / Silt_Divider;
      C_nowAvg  = (CC_nowAvg*V_one_char + CS_nowAvg*V_one_silt) / V_one_agg;
      SC_nowAvg = F_AggregateAvgProperty(ShapeFactor, xc, SC_nowX, dxc);
      SS_nowAvg = F_AggregateAvgProperty(ShapeFactor, xs, SS_nowX, dxs) / Silt_Divider;
      S_nowAvg  = (SC_nowAvg*V_one_char + SS_nowAvg*V_one_silt) / V_one_agg;
      OneEntry_OVRALL   = [TimeEntry, C_nowAvg, S_nowAvg, Q_nowAvg, C_blk_now,
C_blk_now/C_blk_eqm, Magg_Meqm];
      DATA_OVRALL              = [DATA_OVRALL; OneEntry_OVRALL];

      %% Storing temporal-spatial result at ith timestep
      DATA_CC_tx        = [DATA_CC_tx; [TimeEntry, CC_nowX]];
      DATA_SC_tx        = [DATA_SC_tx; [TimeEntry, SC_nowX]];
    DATA_QC_tx          = [DATA_QC_tx; [TimeEntry, QC_nowX]];
      DATA_KdC_tx       = [DATA_KdC_tx; [TimeEntry, SC_nowX./CC_nowX]];

      DATA_CS_tx        = [DATA_CS_tx; [TimeEntry, CS_nowX]];
      DATA_SS_tx        = [DATA_SS_tx; [TimeEntry, SS_nowX]];
    DATA_QS_tx          = [DATA_QS_tx; [TimeEntry, QS_nowX]];
      DATA_KdS_tx       = [DATA_KdS_tx; [TimeEntry, SS_nowX./CS_nowX]];

      W_now     = QC_nowAvg*V_one_char + QS_nowAvg*V_one_silt + C_blk_now*V_one_nonagg;
      DW_now_les_init   = W_now - W_init;
      DATA_W_tx         = [DATA_W_tx; [TimeEntry, W_now, DW_now_les_init]];

      %% Update C_blk_mark ***!!!***
      C_blk_mark        = C_blk_now;

   end   % end if-elseif
   if mod(itime, 2500)==0,
      fprintf ('%i\n', itime);
   end
end
```

```
%%%
%%% Write modeling results to files
%%%

Fpath_OVRALL= [Fpath, Ffilename, '.ovr'];
Fpath_C_tx      = [Fpath, Ffilename, '.c'];
Fpath_S_tx      = [Fpath, Ffilename, '.s'];
Fpath_Q_tx      = [Fpath, Ffilename, '.q'];
Fpath_Kd_tx     = [Fpath, Ffilename, '.kd'];
Fpath_Z_tx      = [Fpath, Ffilename, '.z'];


% Overall modelign results
save ovrall DATA_OVRALL -ASCII
dos(['ren ovrall ',Ffilename,'_Ovrall.txt']);

% Char-phase modeling results
save cc DATA_CC_tx -ASCII
save sc DATA_SC_tx -ASCII
save qc DATA_QC_tx -ASCII
save kdc DATA_KdC_tx -ASCII
dos(['ren cc ',Ffilename,'_Cchar.txt']);
dos(['ren sc ',Ffilename,'_Schar.txt']);
dos(['ren qc ',Ffilename,'_Qchar.txt']);
dos(['ren kdc ',Ffilename,'_Kdchar.txt']);

% Silt-phase modeling results
save cs DATA_CS_tx -ASCII
save ss DATA_SS_tx -ASCII
save qs DATA_QS_tx -ASCII
save kds DATA_KdS_tx -ASCII
dos(['ren cs ',Ffilename,'_Csilt.txt']);
dos(['ren ss ',Ffilename,'_Ssilt.txt']);
dos(['ren qs ',Ffilename,'_Qsilt.txt']);
dos(['ren kds ',Ffilename,'_Kdsilt.txt']);

% Mass balance check, "W"
save www DATA_W_tx -ASCII
dos(['ren www ',Ffilename,'_www.txt']);

toc
```

Script E - 9. Homogeneous (Silt-only) Aggregate Desorption Model (Infinite Bath)

*Please see **Script E – 5** for other functions called by the main program.*

Silt-Desorption-Infinite-Bath (Main Program)

```
%%%
%%% a priori simulation of sedimental-HOCs desorption kinetics with
%%% Diffusion across boundary layer film delta, to a constant Cbulk
%%% By: Dave Kuo
%%% Date: 7 Mar 2010
%%%


%%%
%%% Compute intrinsic diffusivity Diw
%%%

Diw_m = F_Diffusivity ('pyrene', 'water');                                    % [m2/s]


%%%
%%% Set system properties
%%%

% ISOTHERM SETTING
%
% foc, fbc      : org carbon, black carbon content of aggregate [g_carbon/g_solid]
% Koc, Kbc      : partition coefficient for chemical i [L_solv/kg_carbon]
% FrdlichN      : Freundlich exponent
% CmplmFrdlichN: complimentary Freundlich exponent
```

```
%
foc = 0.02;     % for method validation only
fbc = 0.002;    % for method validation only
Koc = 10^5.25;  % Linear+Freundlich Fit (Chapter 3)
FrdlichN = 0.25;
Kbc = 10^6.25;  % Linear+Freundlich Fit (Chapter 3)

CmplmFrdlichN = 1 - FrdlichN;

% DESORPTION SCENARIO
%
% {'homogeneous 0.13 sooty-silt',  '5um char in 100um silt'}
DesorptionScenario = 'homogeneous 0.13 sooty-silt';
ShapeFactor     = 3;                                                    % 3 for
spherical; 2 for cylindrical; 1 for slab


% SEDIMENT CHARACTERISTICS
%
% rho_s         : strict solid density [Kg_solid/L_solid]
% rsw_ppm       : overall system solid-to-water ratio [mg_solid/L_solv]
% rsw           : overall system solid-to-water ratio [Kg_solid/L_solv]
% rad_um        : particle radius [um]
% rad_m         : particle radius [m]
rho_s           = 2.5;
%rsw_ppm        = 300;
rsw_ppm         = 200;
rsw             = rsw_ppm/1e6;
rad_um          = 100;
rad_m           = rad_um/1e6;
blt_m           = rad_m;      % boundary layer thickness; here set as half of aggregate
radius
%blt_m          = 0;            % Crank-analogous
blt_x           = blt_m/rad_m;  % NOTE: use boundary layer in dimensionless form

% GRID AND TIME STEP SIZES
%
% m             : number of grids
% Co_crit       : 'Courant' criterion
% Pe_crit       : 'Peclet' criterion
% Timesteps     : Number of timesteps
% dr            : differential radius [m]
% dx            : = dr/rad_m = differential radius [--]
% dtow          : = Diw*dt/(R^2) = differential timestep [--]
% Timesteps     : # timesteps, each dtow [--]
m               = 41;
dr              = 1/(m-1)*rad_m;
dx              = dr/rad_m;
Co_crit         = 0.8; % <1
Pe_crit         = 0.01;% <2
CoByPe_crit     = Co_crit/Pe_crit;
dtow            = 100; % small dtow as limited by the Boundary Layer diffusion (fastest
step...)
dt              = dtow*(rad_m^2)/Diw_m;
Timesteps       = 30.0e4;

% SPATIAL MATRICES
%
gridindex       = (1:1:m);            % 1 x m {1  2  3  ...  m}
inrgds          = (2:m-1);            % 1 x m-2 {2  3  4  ...  m-1}
x               = (gridindex-1)*dx;   % 1 x m {X1  X2  X3  ...  Xm}
x_miu_les_1     = x.^(ShapeFactor-1); % 1 x m
x_hlf           = (gridindex-0.5)*dx; % 1 x m {X1.5  X2.5  X3.5  ...  Xm-0.5  (xm+0.5!)}
x_hlf_miu_les_1 = x_hlf.^(ShapeFactor-1);     % 1 x m {X1.5  X2.5  X3.5  ...  Xm-0.5
(xm+0.5!)}

% INITIAL CONDITIONS
%
% porosity      : porosity(x) {n} [L_void/L_agg]
% tortuosity    : tortuosity(x) {f(n)}
% S_init        : initial solid phase conc'n, (S') [ug_i/kg_solid = ng i/g_solid]
% C_init        : initial pore fluid conc'n, (C') [ug_i/L_por_aq]
CharPorosity    = 0.15;       % synthetic char from Braida et al.(Pignatello), 2003 EST
CharTortuosity  = 0.15;       % assumed to be same as porosity
SiltPorosity    = 0.15;       % fitting value by Wu and Gschwend, 1986 EST
SiltTortuosity  = 0.15;       % assumed to be same as porosity; Wu and Gschwend, 1988 Wat
Res Res
S_init          = 5000; % [ug_i/kg_solid or ng_i/g_solid]
C_init          = NewtonSolveC (1e-40, foc*Koc, fbc*Kbc, FrdlichN, S_init); % [ug_i/L_agg]
C_blk_set       = 0;        % SET-POINT for bulk dissolved phase concentration
switch DesorptionScenario
```

```
  case 'homogeneous 0.13 sooty-silt'
     PorosityX   = F_SetAggProperty('homogeneous', m, SiltPorosity);
     TortuosityX = F_SetAggProperty('homogeneous', m, SiltTortuosity);
     focX        = F_SetAggProperty('homogeneous', m, foc);
     fbcX        = F_SetAggProperty('homogeneous', m, fbc);
     S_initX     = F_SetAggProperty('homogeneous', m, S_init);
end
rho_bulkX        = rho_s*(1-PorosityX);% [kg_solid/L_agg]
AggAvgPorosity   = F_AggregateAvgProperty(ShapeFactor, x, PorosityX, dx);
TortuosityHlfX   = (TortuosityX(1:m-1)+TortuosityX(2:m)) ./ 2;       % 1 x (m-1) !!!
PorosityHlfX     = (PorosityX(1:m-1)+PorosityX(2:m)) ./ 2;           % 1 x (m-1) !!!

% VRatio         : volumetric ratio of bulk solvent phase to aggregate(solid+porous fluid)
V_one_agg        = 4/3*pi*(rad_m^3);
Mass_one_agg     = (1-AggAvgPorosity)*V_one_agg*rho_s;
V_one_nonagg     = Mass_one_agg/rsw;
VRatio           = V_one_nonagg/V_one_agg;    % Same as VRatio = ((1-f_porsity)*rho_s)/rsw;

C_initX          = NewtonSolveC (1e-40, focX*Koc, fbcX*Kbc, FrdlichN, S_initX);
Q_initX          = S_initX.*rho_bulkX + PorosityX.*C_initX;
Q_initAvg        = F_AggregateAvgProperty(ShapeFactor, x, Q_initX, dx);
C_blk_init       = C_blk_set;

%%%
%%% Calculate expected eqm aq. conc.: C_blk_eqm
%%%
% Z_init         : Mass_init/V_agg = Q_initAvg + C_blk_init*V_nonagg/V_agg]
Z_init           = Q_initAvg + C_blk_init*VRatio;                          % [ug_i/L_agg]
Y_1stOrder       = Koc*focX.*rho_bulkX + PorosityX;
Y_FrdlichN       = Kbc*fbcX.*rho_bulkX;
Coeff_1stOrder   = F_AggregateAvgProperty(ShapeFactor, x, Y_1stOrder, dx) + VRatio;
Coeff_FrdlichN   = F_AggregateAvgProperty(ShapeFactor, x, Y_FrdlichN, dx);
C_blk_eqm        = C_blk_set;
S_eqmX           = C_blk_eqm*Koc*focX + (C_blk_eqm^FrdlichN)*Kbc*fbcX;
Q_eqmX           = S_eqmX.*rho_bulkX + C_blk_eqm*PorosityX;
Q_eqmAvg         = F_AggregateAvgProperty(ShapeFactor, x, Q_eqmX, dx);
Q_lossAvg        = Q_initAvg - Q_eqmAvg;

%%%
%%% Date output information
%%%
Fpath            = '/BC_Model_2010/ModelOutput/';
Ffile1           =
['MT_Rad',num2str(rad_um),'_Rsw',num2str(rsw_ppm),'_Sinit',num2str(S_init),'_Cblkset',num2
str(C_blk_set),'_Grd',num2str(m), '_SF', num2str(ShapeFactor)];
Ffile2           =
['_OC',num2str(round(log10(Koc)*100)),'_BC',num2str(round(log10(Kbc)*100)),'_nBC',num2str(
FrdlichN*100),'_BLT',num2str(blt_x)];
Ffile3           = ['_foc',num2str(foc*100),'_fbc',num2str(fbc*100)];
Ffilename        = [Ffile1, Ffile2, Ffile3];
ISOTH_p          = [foc, Koc, fbc, Kbc, FrdlichN];
SEDI_p           = [rho_s, rsw, rad_m, V_one_agg, V_one_nonagg, AggAvgPorosity, VRatio];
CONC_p           = [S_init, C_init, Q_initAvg, C_blk_init];
SIMU_p           = [m, dr, dx, Co_crit, Pe_crit, CoByPe_crit, dtow, dt, Timesteps];
EQM_p            = [C_blk_eqm, Q_eqmAvg];
F_OutputSystemParameters(Fpath,Ffilename,'PYRENE',Diw_m,ISOTH_p, SEDI_p, CONC_p, SIMU_p,
EQM_p);

%%%
%%% SOLVING RETARDED DIFFUSIONAL EQN BY ITERATIONS
%%%
% Constants
% For innermost grid calc, grid = 1
k_innermost = dtow * ShapeFactor * TortuosityHlfX(1) * PorosityHlfX(1) / dx / x_hlf(1);   %
scalar

% For intermediate grids calc, grid = 2 to m-1
k_intermedi = dtow/((dx)^2) .* PorosityX ./ x_miu_les_1;                                  %
1 x m-2

% For C_blk_next OR C_nextX(m) calc, grid = m
q_next_m         = ShapeFactor*x_miu_les_1(m)*dx*1/3; % coeff for Q_next_m; 1 being
Simpson's coeff
alpha_m          = focX(m)*Koc;
beta_m           = fbcX(m)*Kbc;
CnxtlstOrder= (1 + q_next_m*(alpha_m*rho_bulkX(m)+PorosityX(m))/VRatio);
CnxtFrdlichN= q_next_m * beta_m * rho_bulkX(m) / VRatio;
A1stOrder        = Koc*focX.*rho_bulkX + PorosityX;          % 1st Order coeff for solving
C_nextX(i) from Q_nextX(i)
AFrdlichN        = Kbc*fbcX.*rho_bulkX;                      % Frdlich N coeff for solving
C_nextX(i) from Q_nextX(i)
```

```
C_nowX          = C_initX;
S_nowX          = S_initX;
Q_nowX          = Q_initX;
Q_nowAvg        = Q_initAvg;
C_blk_now       = C_blk_init;
Q_Avg_mark      = Q_nowAvg;

C_nextX         = zeros(1, m);              % initialize; 1 x m of zeroes
S_nextX         = zeros(1, m);              % 1 x m of zeroes
Q_nextX         = zeros(1, m);              % 1 x m of zeroes

DATA_OVRALL     = [];  % data matrix for overall results (C_blk, Q_Avg, S_Avg, etc)
DATA_C_tx       = [];  % data matrix for temporal-spatial, C(x,t) [ug_i/L_void]
DATA_S_tx       = [];  % data matrix for temporal-spatial, S(x,t) [ug_i/kg_solid]
DATA_Q_tx       = [];  % data matrix for temporal-spatial, Q(x,t) [ug_i/L_agg]
DATA_Kd_tx      = [];  % data matrix for temporal-spatial Kd = S(x,t) / C(x,t)
DATA_Z_tx       = [];  % data matrix for Z(t) = Q_nowAvg + C_blkAvg*VRatio [ug/L_agg]

% Save time-zero condition
DATA_C_tx       = [DATA_C_tx; [0, 0, C_initX]];
DATA_S_tx       = [DATA_S_tx; [0, 0, S_initX]];
DATA_Q_tx       = [DATA_Q_tx; [0, 0, Q_initX]];
DATA_Kd_tx      = [DATA_Kd_tx; [0, 0, S_initX./C_initX]];
DATA_Z_tx       = [DATA_Z_tx; [0, 0, Z_init, 0]];

tic
for itime=1:Timesteps,

   %% INNERMOST GRID (grid 1) CALC
   Q_nextX(1)    = Q_nowX(1) + k_innermost*(C_nowX(2)-C_nowX(1));
   C_nextX(1)    = NewtonSolveC(1e-40, A1stOrder(1), AFrdlichN(1), FrdlichN, Q_nextX(1));
   S_nextX(1)    = focX(1)*Koc*C_nextX(1) + fbcX(1)*Kbc*(C_nextX(1)^FrdlichN);

   %% INTERMEDIATE GRIDS (grids 2 to [m-1]) CALC
   dum_iplus1 = []; dum_iminus1 = []; dum_i = [];
   dum_iplus1    = k_intermedi(inrgds).*x_hlf_miu_les_1(inrgds).*TortuosityHlfX(inrgds);
 % Coeff for C_nowX(i+1)
   dum_iminus1 =  k_intermedi(inrgds).*x_hlf_miu_les_1(inrgds-1).*TortuosityHlfX(inrgds-1);%
Coeff for C_nowX(i-1)
   dum_i         = dum_iplus1 + dum_iminus1;   % Coeff for C_nowX(i)
   Q_nextX(inrgds) = Q_nowX(inrgds) + dum_iplus1.*C_nowX(inrgds+1) +
dum_iminus1.*C_nowX(inrgds-1) - dum_i.*C_nowX(inrgds);
   C_nextX(inrgds) = NewtonSolveC(1e-40, A1stOrder(inrgds), AFrdlichN(inrgds), FrdlichN,
Q_nextX(inrgds));
   S_nextX(inrgds) = Koc*focX(inrgds).*C_nextX(inrgds) +
Kbc*fbcX(inrgds).*(C_nextX(inrgds).^FrdlichN);

   % Calc C_nextX(m) by linear interpolation
   C_blk_next    = C_blk_set;
   Slopebltm     = (C_blk_next - C_nextX(m-1))/(dx+blt_x);
   C_nextX(m)    = dx*Slopebltm + C_nextX(m-1);
   S_nextX(m)    = alpha_m*C_nextX(m) + beta_m*(C_nextX(m)^FrdlichN);
   Q_nextX(m)    = S_nextX(m)*rho_bulkX(m) + PorosityX(m)*C_nextX(m);

   %% UPDATE CONCENTRATIONS
   %% all "NOW" concs represent values after itime of timesteps, thus to be
   %% recorded as occuring at [itime*dtow]
   C_nowX               = C_nextX;
   S_nowX               = S_nextX;
   Q_nowX               = Q_nextX;
   C_blk_now            = C_blk_next;
   Q_nowAvg             = F_AggregateAvgProperty(ShapeFactor, x, Q_nextX, dx);

   %% SAVE MODELLED PROFILE
   %% ***REM: all "NOW" quantities are the LATEST quantities for itime# of steps***
   %% C_blk_diff = abs((C_blk_now - C_blk_mark)/C_blk_mark);
   Q_Avg_diff = abs((Q_nowAvg - Q_Avg_mark)/Q_Avg_mark);
   if Q_Avg_diff>0.01
      AbsT_hrs   = itime*dt/3600;              % time in hrs
      AbsTow     = itime*dtow;                 % dimensionless time [--]
      TimeEntry = [AbsTow, AbsT_hrs];% i.e. [tow, t_in_hrs]; 1 x 2
      Magg_Meqm = (Q_initAvg - Q_nowAvg)/(Q_lossAvg);

      % Storing overall desorption result at ith timestep, or [itime*dt] secs
      C_nowAvg   = F_AggregateAvgProperty(ShapeFactor, x, C_nowX, dx);
      S_nowAvg   = F_AggregateAvgProperty(ShapeFactor, x, S_nowX, dx);
      OneEntry_OVRALL   = [TimeEntry, C_nowAvg, S_nowAvg, Q_nowAvg, C_blk_now, Magg_Meqm];
      DATA_OVRALL              = [DATA_OVRALL; OneEntry_OVRALL];

      % Storing temporal-spatial result at ith timestep
```

```
      DATA_C_tx         = [DATA_C_tx; [TimeEntry, C_nowX]];
      DATA_S_tx         = [DATA_S_tx; [TimeEntry, S_nowX]];
   DATA_Q_tx            = [DATA_Q_tx; [TimeEntry, Q_nowX]];
      DATA_Kd_tx        = [DATA_Kd_tx; [TimeEntry, S_nowX./C_nowX]];
      Z_now             = Q_nowAvg+C_blk_now*VRatio;
      DZ_now_les_init   = Z_now - Z_init;
      DATA_Z_tx         = [DATA_Z_tx; [TimeEntry, Z_now, DZ_now_les_init]];

      %% Update C_blk_mark ***!!!***
      %%C_blk_mark      = C_blk_now;
      Q_Avg_mark        = Q_nowAvg;

   elseif (itime>30000)&(mod(itime, 4000)==0)
      AbsT_hrs  = itime*dt/3600;              % time in hrs
      AbsTow    = itime*dtow;                 % dimensionless time [--]
      TimeEntry= [AbsTow, AbsT_hrs];% i.e. [tow, t_in_hrs]; 1 x 2
      Magg_Meqm = (Q_initAvg - Q_nowAvg)/(Q_lossAvg);

      % Storing overall desorption result at ith timestep, or [itime*dt] secs
      C_nowAvg              = F_AggregateAvgProperty(ShapeFactor, x, C_nowX, dx);
      S_nowAvg                    = F_AggregateAvgProperty(ShapeFactor, x, S_nowX, dx);
      OneEntry_OVRALL       = [TimeEntry, C_nowAvg, S_nowAvg, Q_nowAvg, C_blk_now,
Magg_Meqm];
      DATA_OVRALL           = [DATA_OVRALL; OneEntry_OVRALL];

      % Storing temporal-spatial result at ith timestep
      DATA_C_tx               = [DATA_C_tx; [TimeEntry, C_nowX]];
      DATA_S_tx               = [DATA_S_tx; [TimeEntry, S_nowX]];
   DATA_Q_tx                  = [DATA_Q_tx; [TimeEntry, Q_nowX]];
   DATA_Kd_tx                 = [DATA_Kd_tx; [TimeEntry, S_nowX./C_nowX]];
      Z_now                   = Q_nowAvg+C_blk_now*VRatio;
      DZ_now_les_init       = Z_now - Z_init;
      DATA_Z_tx             = [DATA_Z_tx; [TimeEntry, Z_now, DZ_now_les_init]];

      %% Update C_blk_mark ***!!!***
      %%C_blk_mark      = C_blk_now;
      Q_Avg_mark        = Q_nowAvg;

   end   % end if-elseif
   if mod(itime, 2000)==0,
      fprintf ('%i\n', itime);
   end
end


%%%
%%% Write modeling results to files
%%%
Fpath_OVRALL= [Fpath, Ffilename, '.ovr'];
Fpath_C_tx      = [Fpath, Ffilename, '.c'];
Fpath_S_tx      = [Fpath, Ffilename, '.s'];
Fpath_Q_tx      = [Fpath, Ffilename, '.q'];
Fpath_Kd_tx     = [Fpath, Ffilename, '.kd'];
Fpath_Z_tx      = [Fpath, Ffilename, '.z'];

save ovrall DATA_OVRALL -ASCII
save c DATA_C_tx -ASCII
save s DATA_S_tx -ASCII
save q DATA_Q_tx -ASCII
save kd DATA_Kd_tx -ASCII
save z DATA_Z_tx -ASCII

dos(['ren ovrall ',Ffilename,'_Ovrall.txt']);
dos(['ren c ',Ffilename,'_C.txt']);
dos(['ren s ',Ffilename,'_S.txt']);
dos(['ren q ',Ffilename,'_Q.txt']);
dos(['ren kd ',Ffilename,'_Kd.txt']);
dos(['ren z ',Ffilename,'_Z.txt']);

toc
```

Appendix F: Quantification of Black Carbons by EELS and STEM-EELS

Table of Content for Appendix F

1. Introduction and Objectives 1169

1.1. Introduction 1169

1.1.1. Electron Energy Loss Spectroscopy (EELS) 1169

1.1.2. Quantitative EELS 1170

1.1.2.1. Spot- or Point-Analysis 1170

1.1.2.2. Areal Analysis 1170

1.2. Chapter Objectives 1170

2. Methodology & Experimental 1170

2.1. Materials and Samples 1170

2.1.1. Samples 1170

2.1.2. Materials for Microscopy Specimen Preparation 1171

2.2. EM Specimen Preparation 1171

2.2.1. Standard Materials Specimen 1171

2.3. Electron Microscope 1171

2.3.1. Electron Microscope Specifications 1171

2.4. EELS Mapping Procedure 1171

2.4.1. (I) Spectrum Acquisition 1172

2.4.2. (II) Extraction of C-peak Information 1172

2.4.3. (III) Quantification of C_{sp2}=C_{sp2} Content 1172

2.4.4. (IV) C_{sp2}=C_{sp2} Maps 1172

2.5. Data Processing 1173

3. Results & Discussion 1173

3.1. EELS Signature of BC: Spot/Point Analysis 1173

3.1.1. Peak Ratios of π^*/σ^* and $\Delta\pi^*/\sigma^*$ 1173

3.1.2. EEL Spectra of Sediment Sample 1174

3.2. Quantification of BC by EELS Mapping 1174

3.2.1. Mapping of C_{sp2}=C_{sp2} Content in Sediment Sample 1174

3.2.2. Challenges in EELS Mapping 1175
3.2.3. Recommended Direction for Future Work 1175

1. Introduction and Objectives

1.1. Introduction

The needs for developing an alternative, electron microscopy (EM) based method to quantify black carbon (BC) in natural sorbents have been discussed in Chapter 10 (section 1.1.1). The application of energy-dispersive X-ray (EDX) spectroscopy for BC quantification was also demonstrated (Chapter 10). In this chapter, the author will show and demonstrate how electron energy loss spectroscopy (EELS) – an alternative analytical EM method – may be used to quantify environmental BC. Although the author has not completed the EELS-BC method development, the preliminary materials presented here will be helpful for further work on the method.

1.1.1. Electron Energy Loss Spectroscopy (EELS)

The main reason to explore EELS for BC quantification is that it can differentiate the bonding types of elements in a composite structure (Edgerton 1996; Ahn 2004). The main difficulty of the EDX-based BC method is that the identity of BC has to be based on elemental ratio(s) of carbon, oxygen, and nitrogen. However, the setting of cut-off criteria of C:N (or C:O) may be somewhat arbitrary. Furthermore, in the EDX method, there are occasions where carbonaceous materials will be incorrectly identified as BC (e.g. polyethylene or diamond, which contains no oxygen or nitrogen).

One can, however, identify the different types of atomic interactions using EELS (Table F-1). The table summarizes the amount of energy that an electron loses when it interacts with electrons of the carbon atoms involved in different types of bonding (e.g. sp^2 vs sp^3; bonded to O, H or with another C). The amount of energy lost by the incoming electron causes the excitation of inner shell electron (e.g. 1s $\rightarrow$ $1\pi^*$). In general, more energy is required for exciting inner shell e^- when the bonding has less e^- density (e.g. harder to excite C-C than C=C; Table F-1) or when other atom is more electronegative (e.g. harder to excite C-O than C-C; Table F-1).

If pure graphite may be regarded as 'pure' or idealized BC, then the C_{sp2}=C_{sp2} bond (or the 1s $\rightarrow$ $1\pi^*$ (C=C) in Table F-1) can be used to identify environmental BC. The C_{sp2}=C_{sp2} or 'graphitic' peak often appears as the first sharp tiny spike around 284 eV, as demonstrated by EEL spectra in Figure F-1 (Jeanne-Rose et al. 2003; Bentley et al. 2004; Hata et al. 2004; Chen et al. 2005). A number of studies have used the C_{sp2}=C_{sp2} EELS peak as a signature for BC in aerosol (Katrinak et al. 1992;), soot (Posfai et al. 2003) or soil samples (Lehmann et al. 2005; Liang et al. 2006).

1.1.2. Quantitative EELS

1.1.2.1. Spot- or Point-Analysis

Quantitative EELS analysis has been applied in the past for compositional and/or structural analysis. Leapman et al. (1988) used EELS to analyze the N:P elemental ratio of DNA. They reported a good match between expected and EELS-derived ratios. Seepujak et al. (2006) studied the crystallinity of carbon nanotubes and how it may be affected by the presence of N atoms in the nanotubes. They found that the nanotube structural became increasingly amorphous with higher N content. Jeanne-Rose et al. (2003) also used EELS to understand how pyrolysis temperature affected the sp^2-hybridized C content in activated charcoal. Katrinak et al. (1992) attempted to characterize the carbon π^*/σ^* ratio in aerosols and inferred the presence of elemental carbon (or BC) with the ratio.

1.1.2.2. Areal Analysis

The application of EELS in conjunction with TEM/STEM is necessary for quantifying environmental BC, and a number of past studies have shown that quantification via 2-D mapping may be possible. TEM-EELS has been used to understand the effect of inhaled smoke particles on pulmonary tissue (Mitchelson 1992), the aggregation of OM in sediment samples (Furukawa 2000), and the degradation of root structure in soil (Watteau et al. 1996). In these studies, carbon signals from EEL spectra were used to identify the relevant carbonaceous entities (i.e. BC or OM) among other structures (e.g. epithelial tissues, clay grains).

The true application of EELS 2-D mapping was found in the studies by Wroblewski (1991) and Leapman et al. (1999). Wroblewski et al. studied mitochondrial granules and had showed maps (pixels) of Ca and C as determined by EELS with nm-scale resolution. Leapman et al. (1999) studied the structure of DNA by mapping how P was distributed in the cell. However, it should be noted these two studies used EELS to obtain elemental maps without differentiating the types of bonding involved.

1.2. Chapter Objectives

The main objective of this chapter is to document the preliminary effort in applying EELS to quantification of environmental BC.

2. Methodology & Experimental

2.1. Materials and Samples

2.1.1. Samples

Samples used in spot/point-EELS analysis included diesel particulate matters (or soot) (NIST SRM 1650a), sodium dodecyl sulfate (Na-C_{12}-SO_4; $CH_3(CH_2)_{11}OSO_3Na$) (Mallinckrodt 99.85%), poly(ethylene glycol) (PEG; $H(OCH_2CH_2)_nOH$; MW~3400 g/mol)

(Aldrich), wood (commercial plywood). Sediment samples were obtained from Boston Harbor and Hudson River estuary.

2.1.2. Materials for Microscopy Specimen Preparation

Sediment samples were fixed in elemental sulfur (J.T.Baker, sublimed) prior to microtomy; the wood sample was microtomed without fixation. Suspension of diesel soot was prepared in ethyl acetate (BDH) and was directly dispensed onto the microscopy grids. Na-C_{12}-SO_4 and PEG were dispensed as solution (prepared in clean water) onto the microscopy grids. A number of microscopy grids were used/tested for holding specimens: (i) lacey SiO film on 200 mesh Cu-grid, (ii) lacey-C film on 200 mesh Cu-grid (Lacey formvar substrate, carbon coated, Cat #10975; Ladd Research, USA), (iii) pure SiO film on 200 mesh Cu-grid, and (iv) silicon nitride (Si_3N_4) membrane (1.0×1.0 mm window, Prod #21502, Ted Pella Inc., USA). All specimens were held on lacey SiO with the exception of graphite, lignocellulosic char, melanoidin which were placed on lacey-C.

2.2. EM Specimen Preparation

Sample fixation and microtomy procedures were similar to those described previously (Chapter 10 section 2.2.1.2 and section 2.2.5).

2.2.1. Standard Materials Specimen

Suspensions of char, melanoidin, and urban dust were prepared in ethyl acetate with approximately <0.1-0.2 g of mass into 3-5 ml of ethyl acetate. Char and urban dust looked very fine and were used without grinding. Melanoidin required grinding because of the presence of light-brownish mm-scale particles amidst the finer, white powder. Small amount (~uL) of the suspensions was dispensed onto Cu grid with lacey-C or SiO film. The specimens were stored away for later view after being dried under a study lamp (60 W).

2.3. Electron Microscope

2.3.1. Electron Microscope Specifications

EELS analysis (both spot and mapping modes) was performed with a JEOL-EELS analytical system, which consisted of a JEOL 2010FEG analytical TEM/STEM and a Gatan imaging filter for EELS. JEOL 2010FEG was operated at 200 kV and had an image resolution of 0.195 nm point-to-point. The acquisition of EEL spectra/maps and the subsequent processing (e.g. background removal) were all performed using DigitalMicrograph (Gatan, Inc).

2.4. EELS Mapping Procedure

The quantitative mapping procedure consisted of four major steps: (i) spectrum acquisition, (ii) extraction of C-peak information, (iii) quantification of C_{sp2}=C_{sp2} content, and (iv) map generation.

2.4.1. (I) Spectrum Acquisition

The acquisition began by navigating to an area of interest. This area typically contained (a) materials of interest (e.g. sediment aggregates, soot), (b) background film (i.e. as "control" for carbon signals), and (c) vacuum/hole (for microscopic control; optional).

A dark-field image was usually taken before the acquisition of EELS map. This initial image served several purposes. First, it showed the morphological features of the sampled area. Second, it served as a reference picture for the extent of carbon contamination during spectral mapping. Third, it may be used to indicate and/or correct 'drifting' or distortion of the sampled area.

After taking an initial TEM image, a map of zero-loss peak (ZLP) was taken. The zero-loss peak information was useful for evaluating specimen thickness and correcting plural scattering effect (e.g. Figure F-2; also see Egerton 1996). The zero-loss peak height was also indicative of the overall sensitivity of EEL signals from the specimen (i.e. if the ZLP heights are often low, the area is probably too thick for EEL analysis. Thus ZLP information can be used to locate a "good" area for EEL mapping).

Next, the EEL map of the C k-edge peaks was acquired. The procedure was the same as that for the ZLP except using a different energy loss range.

2.4.2. (II) Extraction of C-peak Information

Background signal and plural scattering event were removed with the built-in functions in the data-analysis software (DigitalMicrograph, Gatan). The pre-C edge background was removed using a power-law procedure (Egerton 1996). Plural scattering effect (see Figure F-2) was removed with the ZLP map. These two steps removed the signal interference due to pre-edge background and plural scattering in every single C k-edge spectrum in the map. The raw spectra (with background and plural scattering removed) were smoothed using the Savitzky-Golay method (with window/span=10; done in Matlab). The resulting spectral map was then ready for quantitative analysis.

2.4.3. (III) Quantification of C_{sp2}=C_{sp2} Content

C_{sp2}=C_{sp2} content was quantified by integrating the peak area associated with the $1s \rightarrow 1\pi^*$ transition. Several assumptions were made in this method. First, it was assumed that the typical C-EEL spectra to be similar to those in Figure F-4 – that the spectra always had a broad, 'main' peak around in the vicinity of 290–300 eV. For each spectrum (i.e. for a particular pixel in the EEL map), the maximum of this main, broad C-peak was located. A baseline (a 2^{nd} order polynomial fitting function) was constructed using the points in the pre-edge region and the points immediately preceding the location of the broad peak maximum (Figure F-8). The C_{sp2}=C_{sp2} peak was integrated from the smoothed spectrum after the subtraction of the polynomial baseline (Figure F-8).

2.4.4. (IV) C_{sp2}=C_{sp2} Maps

After the C_{sp2}=C_{sp2} transition peaks in all pixels were integrated, two maps can be generated: (i) a C_{sp2}=C_{sp2} peak area map normalized to the global maximum C_{sp2}=C_{sp2} peak area observed in a given map, and (ii) a C_{sp2}=C_{sp2} peak area map normalized to

the broad main C-peak area of the local pixel. The resulting matrices were then scaled to a blue-red color spectrum for visual convenience.

2.5. Data Processing

Data processing on EEL spectral maps was performed by a custom Matlab script. The script can be found in Appendix G. Other simple data processing was performed in Excel and/or Matlab.

3. Results & Discussion

3.1. EELS Signature of BC: Spot/Point Analysis

3.1.1. Peak Ratios of π^*/σ^* and $\Delta\pi^*/\sigma^*$

One way to quantify the BC content at a given spot in a sample is by considering the peak intensity associated with the $1s \rightarrow 1\pi^*$ (C=C) transition. This can be done by considering: (i) the absolute amount of $C_{sp2}=C_{sp2}$ bonds, (ii) the relative abundance of $C_{sp2}=C_{sp2}$ bonds.

The first approach requires calibration and the sample thickness (at the examined spot) with which the $1s \rightarrow 1\pi^*$ peak can be normalized. Although sample thickness can be estimated, it requires operational parameters of the EM, a zero-loss peak profile (Figure F-3), and the elemental composition at the spot. However, elemental composition may need to be estimated for real environmental samples (e.g. approximated from bulk chemical properties such as f_{OC} and mineral contents). The error of such approximation will be propagated into the estimated abundance of the $C_{sp2}=C_{sp2}$ bond.

The second approach is simpler for one only needs another peak for normalization. The abundance of a particular bond is proportional to the integrated peak area of its corresponding EELS peak (Stohr 1992; Egerton 1996). As an approximation, one may consider the bond abundance with the peak height (π^*), as in the EDX-analysis (Chapter 10 section 3.3.1.3). The peak height ratio approach has also been applied before for C_{sp2} bond in aerosol (Katrinak et al. 1992).

However, the peak-height approximation is less appropriate for $C_{sp2}=C_{sp2}$ peak than in the previous chapter because the C_{sp2} peak is closely convoluted with EEL signals from other C peaks. As is shown in Figure F-4 (also in Figure F-1), the C_{sp2} transition peak often appears as a tiny spike on the slope of the main C-signal. A crude approximation is to take the tip of the spike ($\Delta\pi^*$) as the C_{sp2} transition peak height. Using the main peak around 300 eV (Figure F-4) for normalization (i.e. σ^*=peak height), the two peak height ratios, π^*/σ^* and $\Delta\pi^*/\sigma^*$, were computed (Figure F-5). The results are summarized in Table F-2.

Different carbonaceous materials certainly have different EELS signatures, as is shown in Table F-2. Both π^*/σ^* and $\Delta\pi^*/\sigma^*$ reflected the structural differences among the

tested materials. Diesel soot had the highest C_{sp2}=C_{sp2} content, with π^*/σ^* at around 0.54–0.59 (±0.06), and this agreed well with the values reported by Katrinak et al. (1992) (π^*/σ^* for aerosol ~0.5 to 0.6). Lacey-C film also contained fairly high C_{sp2}=C_{sp2} content (π^*/σ^*=0.48±0.02). The positive π^*/σ^* observed for Na-C_{12}-SO_4 and PEG were probably due to the background signal from the lacey-C film, for neither chemicals possessed any C=C bond. In the case of wood, the overall π^*/σ^* ratio was similar to those of Na-C_{12}-SO_4 and PEG; however, the EEL spectra for wood could be divided into two categories, with one poor in C=C content (π^*/σ^* ~ 0.21±0.26) and the other similar to soot (π^*/σ^* = 0.54±0.06). The C=C enriched spectra may represent the aromatic structures in the wood lignin.

The $\Delta\pi^*/\sigma^*$ ratio also exhibited a trend similar to that in π^*/σ^* for the tested samples (Table F-2). A plot of $\Delta\pi^*$ vs σ^* (Figure F-6) revealed that spectra with a strong C_{sp2}=C_{sp2} spike appeared to have similar slopes (~0.08–0.09). This "identity" may be used to identify aromatic/graphitic components in a given sample (for instance, the aromatic content in wood).

The point-EEL spectra also demonstrated the reduction of signal sensitivity by the background film (Table F-3). The highest signal sensitivity was obtained without any background film (i.e. "Soot over vacuum"), followed by lacey-C film and SiO film. While the SiO film has the advantage of being C-free, it generally allows fewer electrons to penetrate through the specimen than lacey-C film. SiO films are around 200 nm in thickness while lacey-C film can be as thin as 100 nm or less (communication with the grid manufacturer). EELS is generally more sensitive to light elements (e.g. C, N, O) than the heavier ones (e.g. Si, Na) because fewer electrons can penetrate through specimen/thin-film containing higher content of heavy atoms (Budd et al. 1998; Egerton 1996). For diesel soot, the sensitivity difference between the lacey-C film and the SiO film was not substantial, but for sediment samples – where the mineral grains constitute the dominant phase – the use of lacey-C film may be advantageous.

3.1.2. EEL Spectra of Sediment Sample

EELS can distinguish between organic and inorganic carbonaceous matter in real sediment samples. Three sample EEL spectra of Hudson River sediment are shown in Figure F-7. Spectrum (a) showed a spot dominated by inorganic calcium carbonate with insignificant amount of C=C bond. Spectrum (b) showed a spot where the carbonate content was relatively low. The main feature of spectrum (b) – a large and broad hill extending from 290 to 300 eV – resembled those shown in Figure F-4. This means that with EELS, the presence of inorganic carbonates can be corrected (for instance, as a first approximation, one can use the Ca peaks to correct for carbonate).

3.2. Quantification of BC by EELS Mapping

3.2.1. Mapping of C_{sp2}=C_{sp2} Content in Sediment Sample

The quantitative EELS mapping procedure for C_{sp2}=C_{sp2} content was tested in several sediment specimens. However, the method has not been extensively tested with

different samples. Here, the author will only discuss its potential for areal BC quantification with some sample C_{sp2}=C_{sp2} maps.

The potential of the quantitative EELS mapping for BC was tested on a sediment sample (BH#6 sediment) and is illustrated in Figure F-9 to F-11. Figure F-9 shows the original STEM image and an discretized image of the specimen. The morphological features from the STEM image were not sufficient to indicate whether BC was present. The global-maximum normalized C_{sp2}=C_{sp2} map of the area is shown in Figure F-10. If one assumes the relatively C_{sp2}-enriched pixel as BC-like, then about 4–10 of the pixels of the map may be considered as BC-like. This means that about 0.4–1 % of the viewd area may be BC-like, and this estimated is consistent with the typical BC content in sediments. A similar estimate and conclusion can be reached using the local C-peak normalized C_{sp2}=C_{sp2} map (Figure F-11).

3.2.2. Challenges in EELS Mapping

The first challenge is electron beam induced hydrocarbon contamination (Figure F-12). Carbon contamination may be hard to predict, as demonstrated by the evolution of the C-edge peaks over 10s of seconds (Figure F-13). There is also the challenge of specimen drift during the acquisition (Figure F-14).

A bigger challenge is the trade-off between enhanced sensitivity (with the thinner lacey-C film) and reduced carbon background (with the thicker but 'C-free' SiO film). The author has considered using Si_3N_4 as an alternative to SiO film, but Si_3N_4 grid seemed to be even harder to use than SiO film (Si_3N_4 film seems to be more brittle and thicker; it is also much more expensive than grids with SiO film).

3.2.3. Recommended Direction for Future Work

It may be more efficient to use lacey-C film to hold sample, and use the sample-free region to correct for the background C signal contributed by the film. It should also be noted that the documented quantitative method is still an approximation. The correct way to extract the C_{sp2}=C_{sp2} peak from a large broad background signal is by deconvoluting the constituent peaks. This was where the author stopped in the exploration of an EELS-based BC quantification method.

Table F - 1. Carbon atomic interactions indicated by electron energy loss.

Transition**	e^- Energy Loss (eV)	Observed in:
$1s \rightarrow 1\pi^*$ (C=C)	284–286	graphite, amorphous carbon, Pb-isooctanoate
$1s \rightarrow 1\pi^*$ ($C_{phenolic}$-OH=C, $C_{ketonic}$=O)	286–287	
$1s \rightarrow 1\sigma^*$ ($C_{aliphatic}$-H)	287–288	Pb-isooctanoate
$1s \rightarrow 1\pi^*$ (C_{amidic}=O)	288	
$1s \rightarrow 1\pi^*$ ($C_{carboxylic}$=O)	288–290	$PbCO_3^{2-}$, Pb-isooctanoate
$1s \rightarrow 1\sigma^*$ (C-C)	291	graphite, amorphous carbon, Pb-isooctanoate
$1s \rightarrow 1\sigma^*$ ($C_{carboxylic}$-O)	299–300	$PbCO_3^{2-}$, Pb-isooctanoate

** Information compiled from Wery et al. 1993 and Wan et al. 2007.

Table F - 2. Spot-EELS analysis: π^*/σ^* signatures of various carbonaceous materials.

Sample	**π^*/σ^* Ratio†**	**$\Delta\pi^*/\sigma^*$ Ratio‡**	**No. of obs.**
Diesel soot (NIST SRM 1650a)			
over vacuum	0.588±0.034	0.057±0.010	12
on SiO film	0.556±0.036	0.055±0.012	18
on lacey-C film	0.538±0.061	0.038±0.011	8
Lacey-C film	0.480±0.024	0.039±0.005	9
Sodium dodecyl sulfate	0.360±0.279	0.027±0.024	6
Poly(ethylene glycol)	0.429±0.244	0.017±0.017	9
Wood	0.335±0.264	0.017±0.020	14
soot-like spectra	0.540±0.062	0.037±0.013	7
other spectra	0.208±0.262	0.003±0.004	7

†: Peak height ratio of $1s \rightarrow 1\pi^*$ (C=C) to $1s \rightarrow 1\sigma^*$ (C-C). See also Figure

Table F - 3. Intensity of C-signal as a function of grid holder film.

Grid Holder Film	**Intensity at ~300 eV**	**No. of obs.**
Soot over vacuum (i.e. no film)	150000±27000	12
Soot on Lacey-C film	100000±63000	8
Soot on SiO	75000±21000	18
Lacey-C film only	41000±12000	9

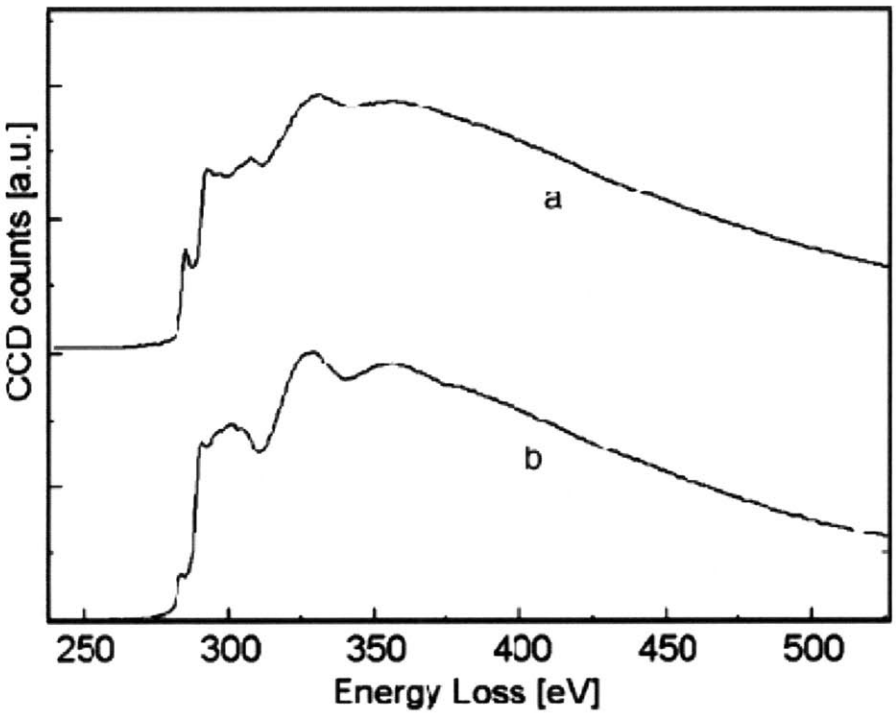

(I) (a) non-catalytic graphitization of wood charcoal; (b) catalytic graphitization of wood charcoal (Hata et al. 2004).

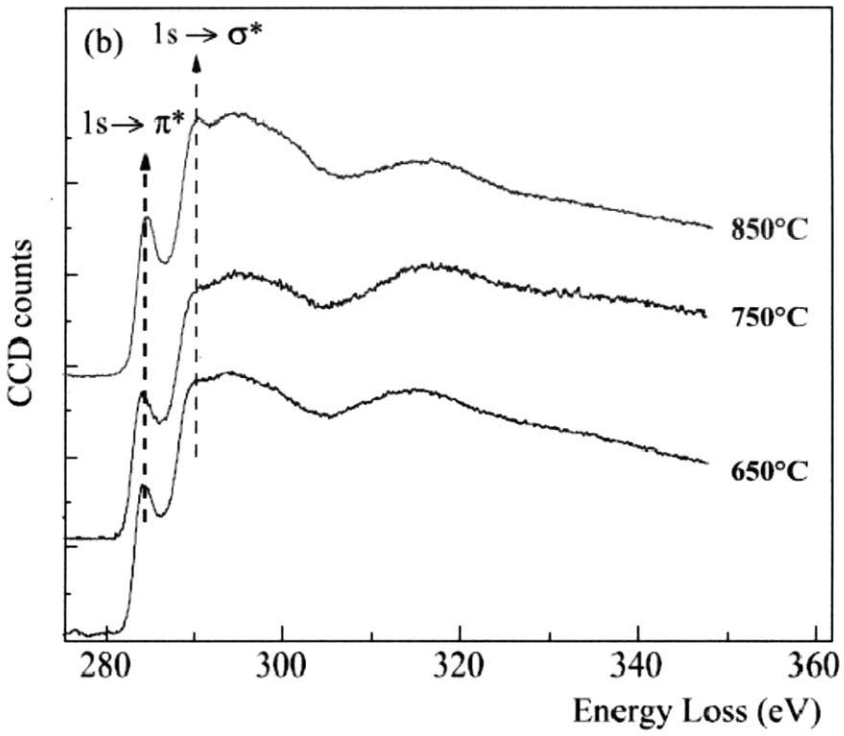

(II) charcoal prepared from pyrolysis of almond shells (Jeanne-Rose et al. 2003).

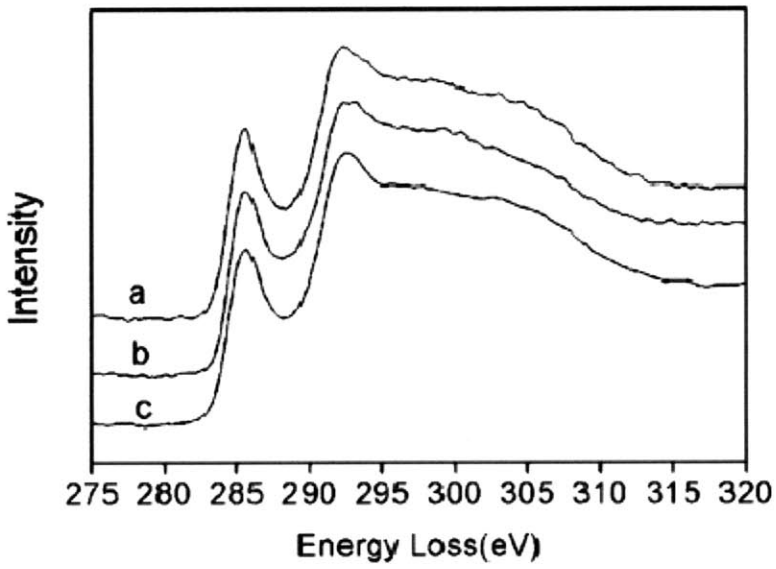

(III) soot derived from (a) coal, (b) residual oil, and (c) diesel (Chen et al. 2005).

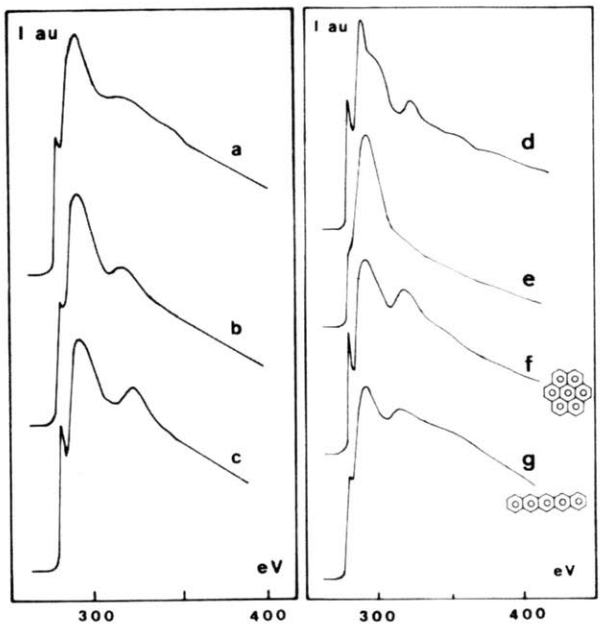

Fig. 8.24 Carbon K-ELNES from coke deposits on (a) USHY, (b) H-OFF, and (c) H-ZSM-5 zeolites compared with (d) graphite, (e) amorphous carbon, (f) coronene, and (g) pentacene reference materials [8.80].

(IV) various carbonaceous materials (Bentley et al. 2004).

Figure F - 1. EEL spectra of carbonaceous materials with high C_{sp2}=C_{sp2} content.

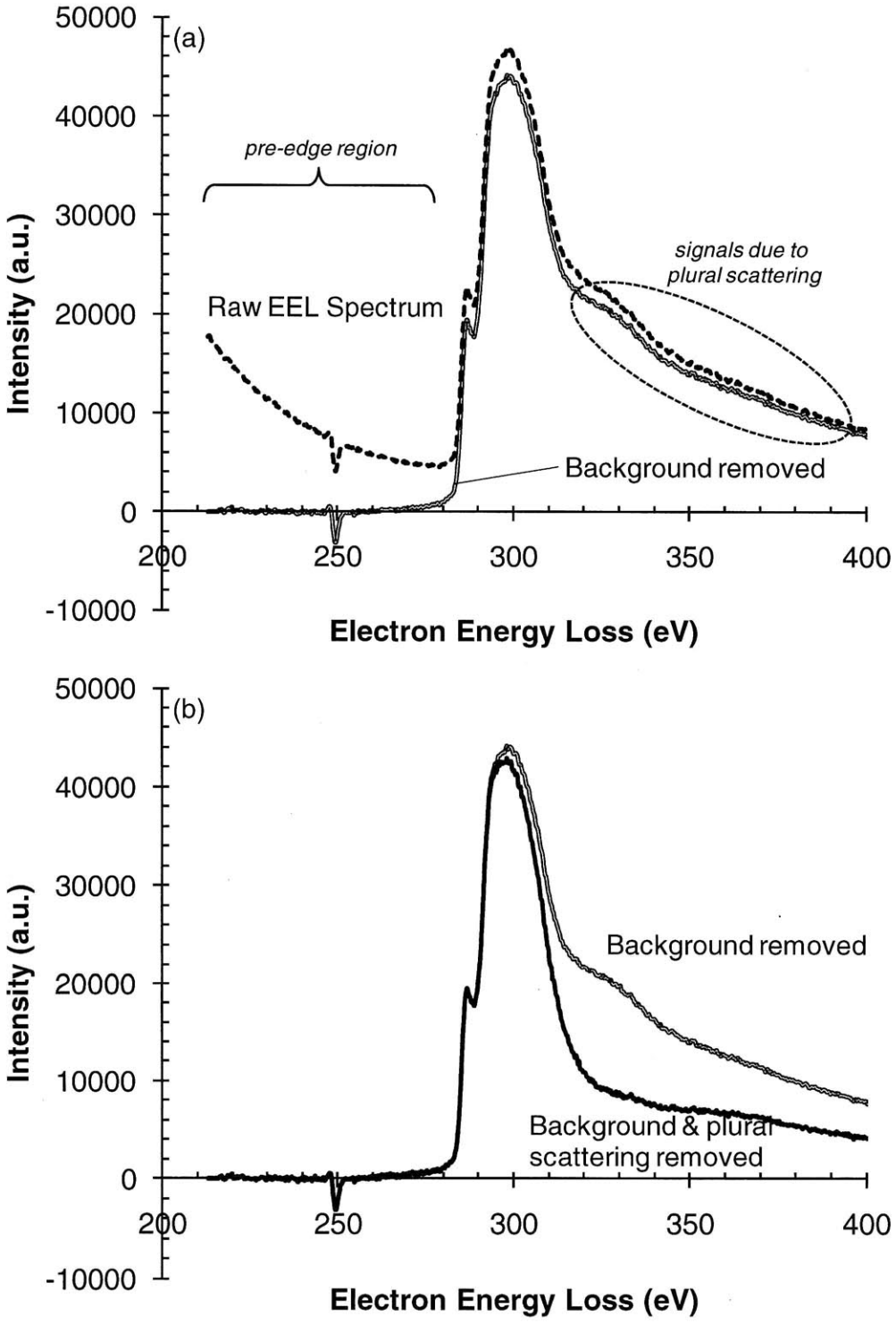

Figure F - 2. Removal of background signal and plural scattering in EELS.

Background signal and plural scattering effect were removed using built-in functions in DigitalMicrograph.

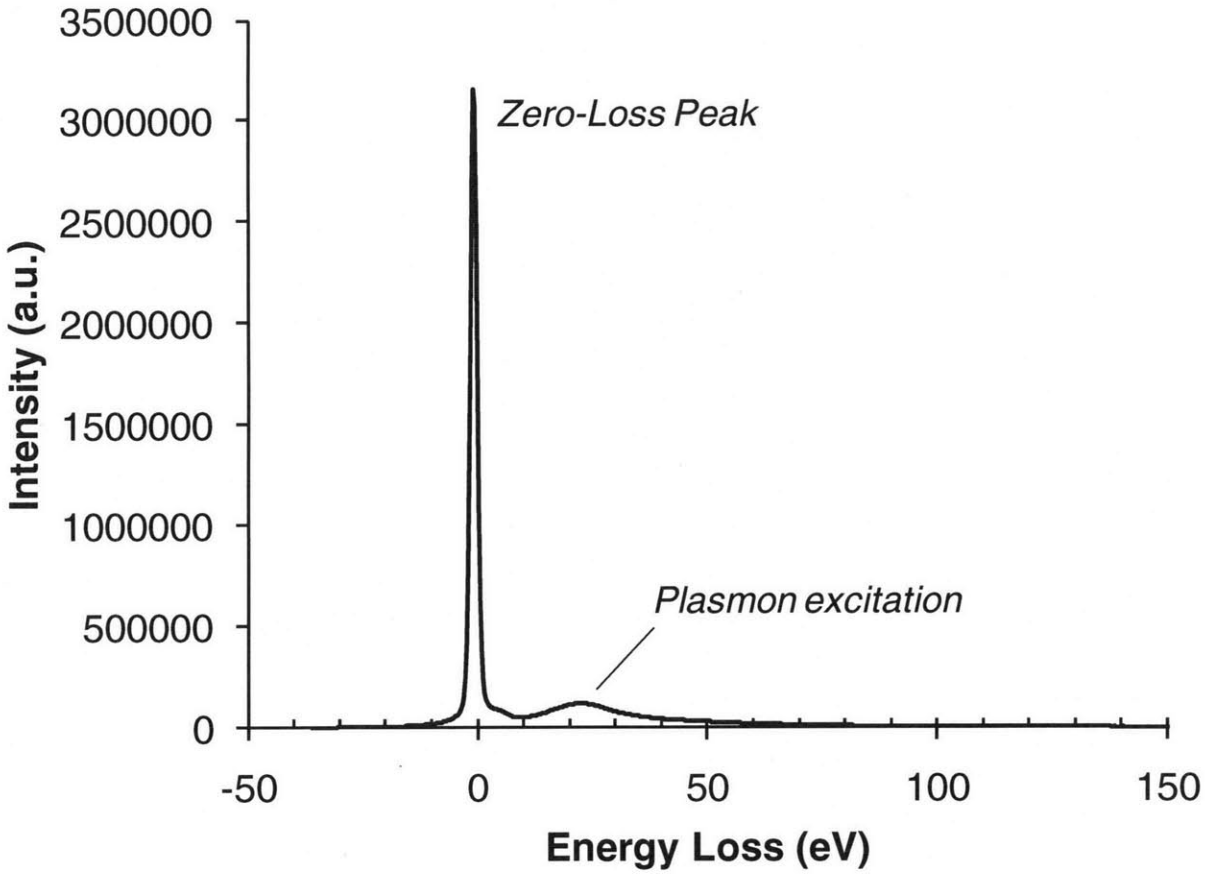

Figure F - 3. Zero-loss peak and energy loss due to plasmon excitation.

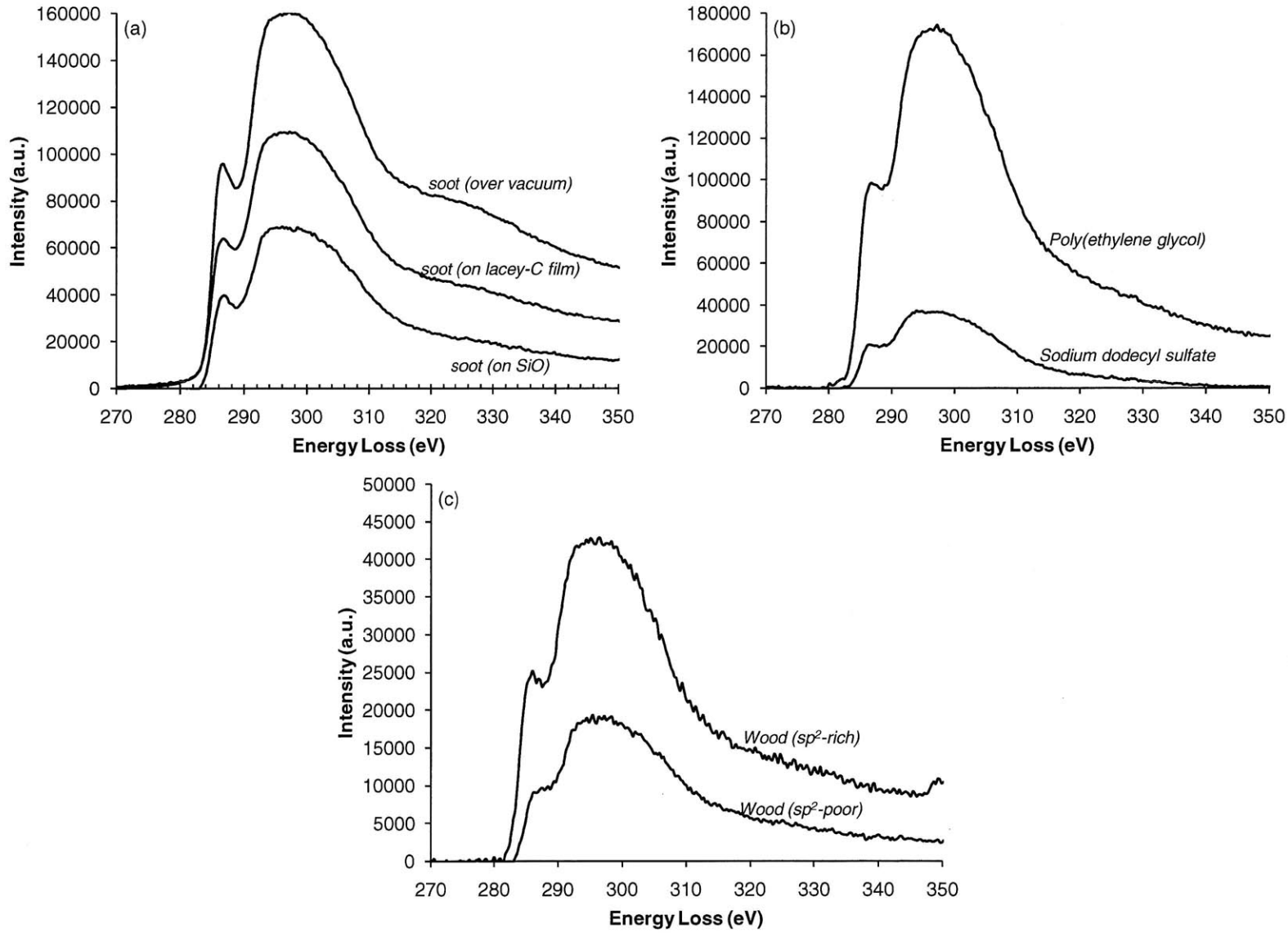

Figure F - 4. EEL spectra of soot, PEG, Na-C_{12}-SO_4, and wood (this study).

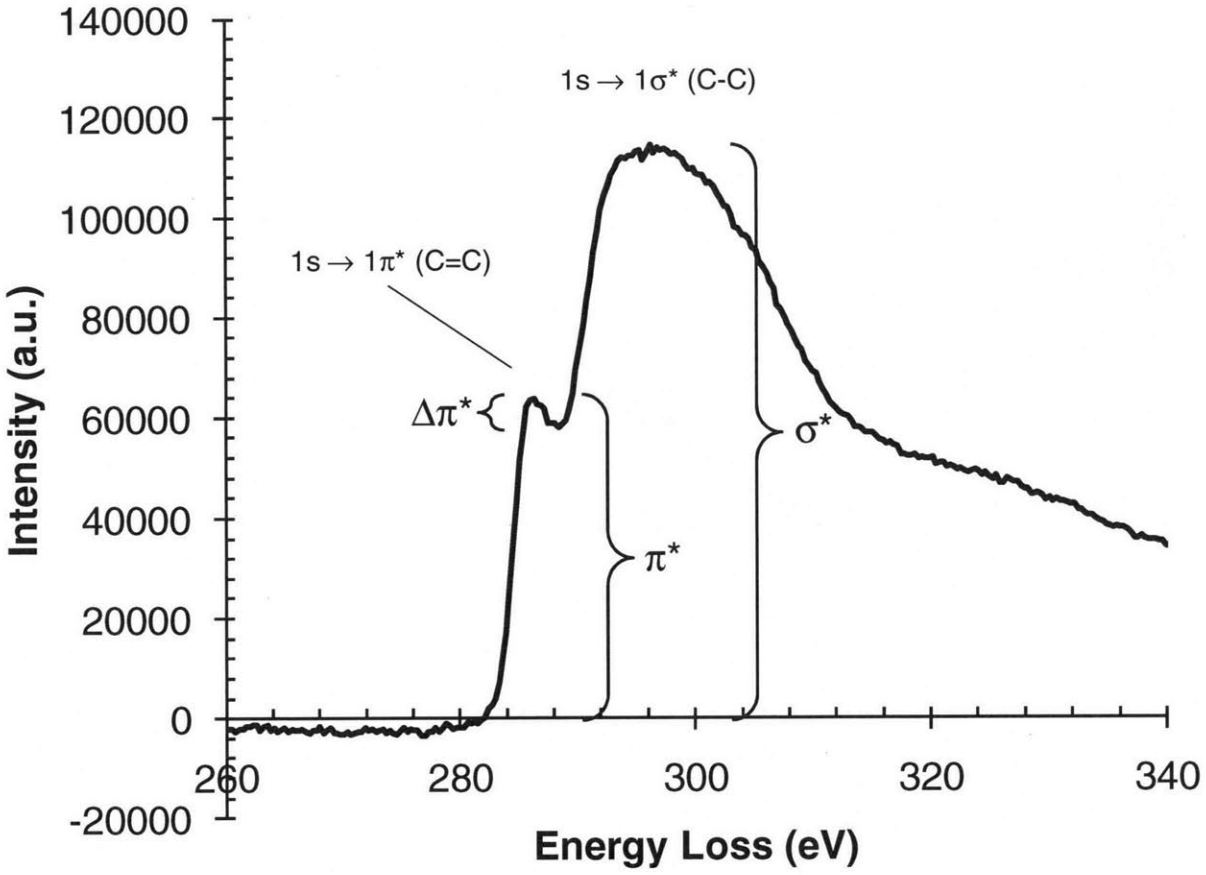

Figure F - 5. Estimating C_{sp2}=C_{sp2} content via peak height ratios.

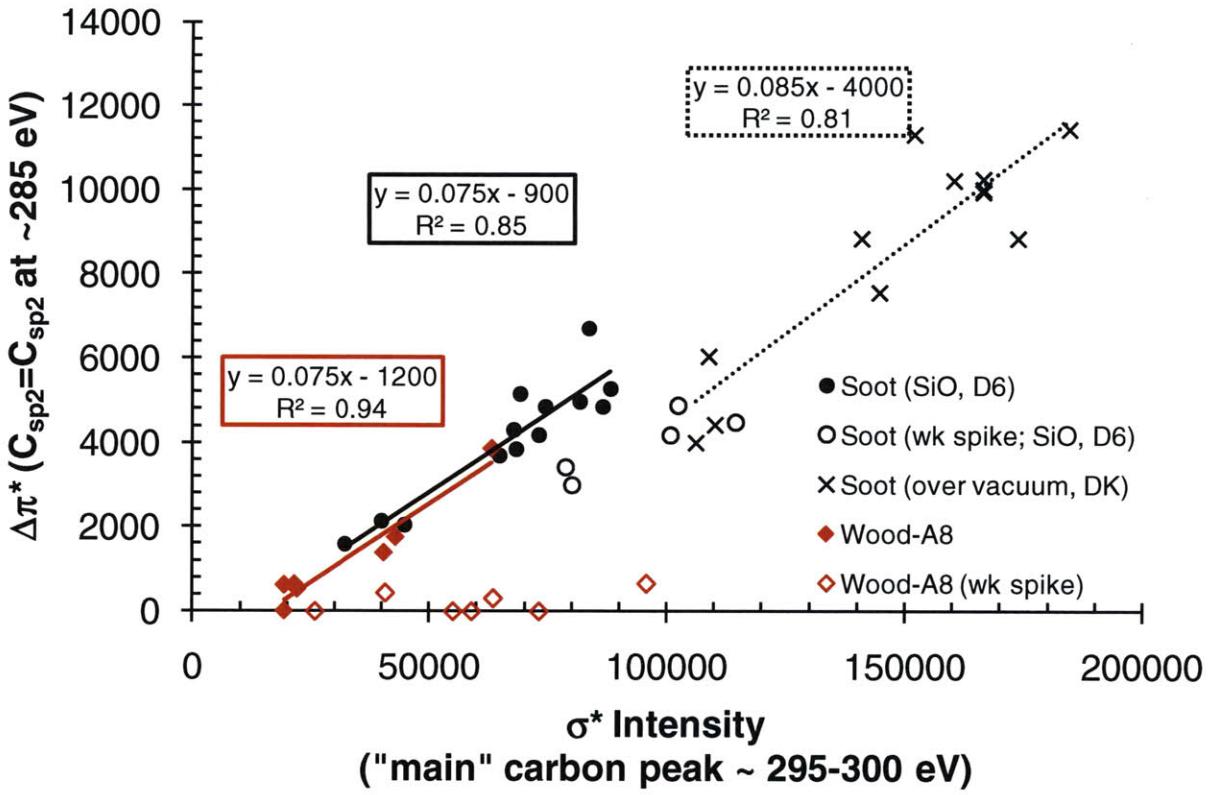

Figure F - 6. $\Delta\pi^*$-vs-σ^* for wood and soot samples.

The figure shows the relationship between $\Delta\pi^*$ and σ^* (see Figure F-5 for definitions) in wood and soot samples. The EEL spectra for soot included data from soot-over-vacuum and soot-on-SiO. EEL spectra were divided into two categories (except that for soot-over-vacuum), where the spectra in one group had a strong C_{sp2}=C_{sp2} spike, and those in the other group had a visually diminished spike ("wk spike").

The slope of $\Delta\pi^*$-vs-σ^* appeared to be fairly constant for both soot and wood (slope ~ 0.08–0.09).

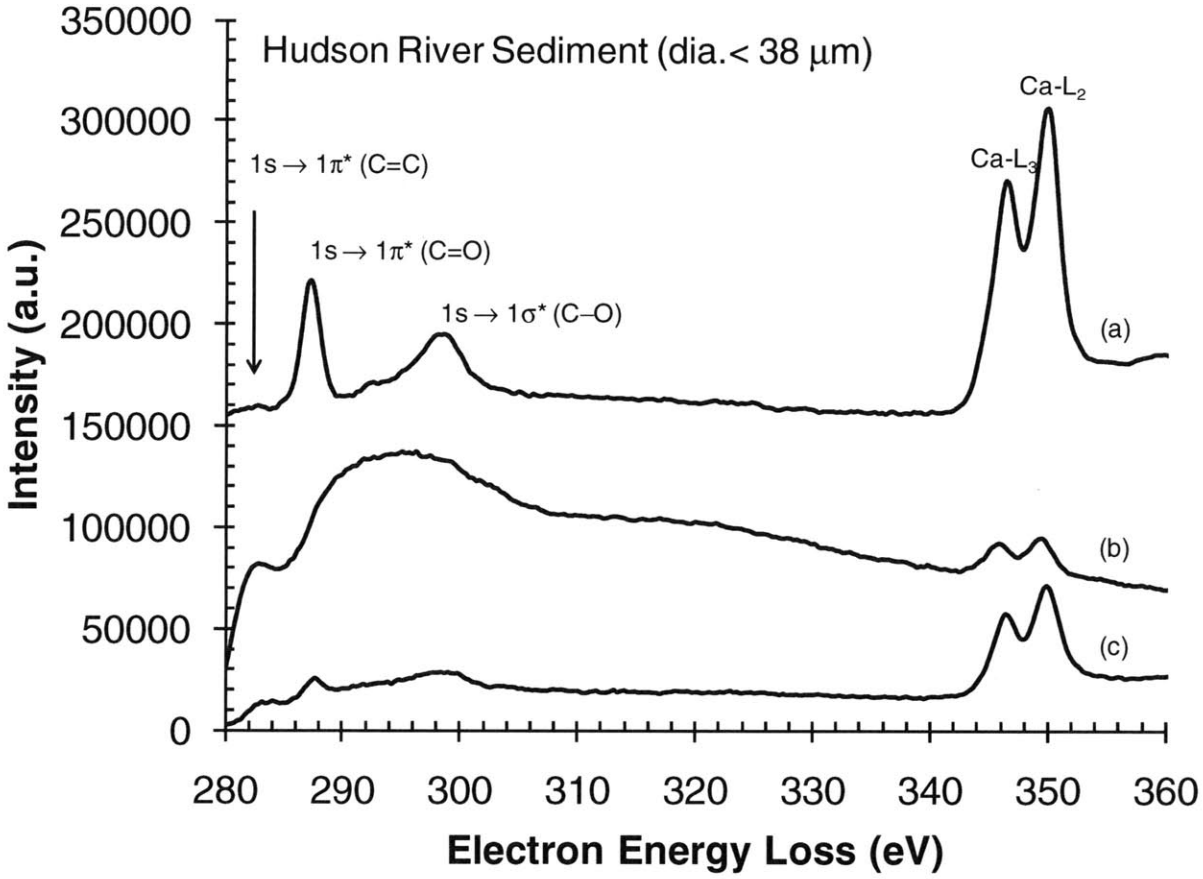

Figure F - 7. EEL spectra of Hudson River Sediment.

In (a), the spectrum showed no C_{sp2}=C_{sp2} bond but the presence of C=O and $C_{carboxylic}$-O bonds. These peaks, together with the strong Ca signals (at 347, 350 eV), suggested that the examined spot was dominated by calcium carbonate.

In (b), the spectrum showed a visible C_{sp2}=C_{sp2} transition peak and a large structure (~290 to 300 eV) with relatively small Ca peaks. The examined spot probably contain mostly amorphous carbon (which gave rise to the large structure) with some C=C and carbonate bonds.

In (c), the spectrum can be viewed as a combination of (a) and (c).

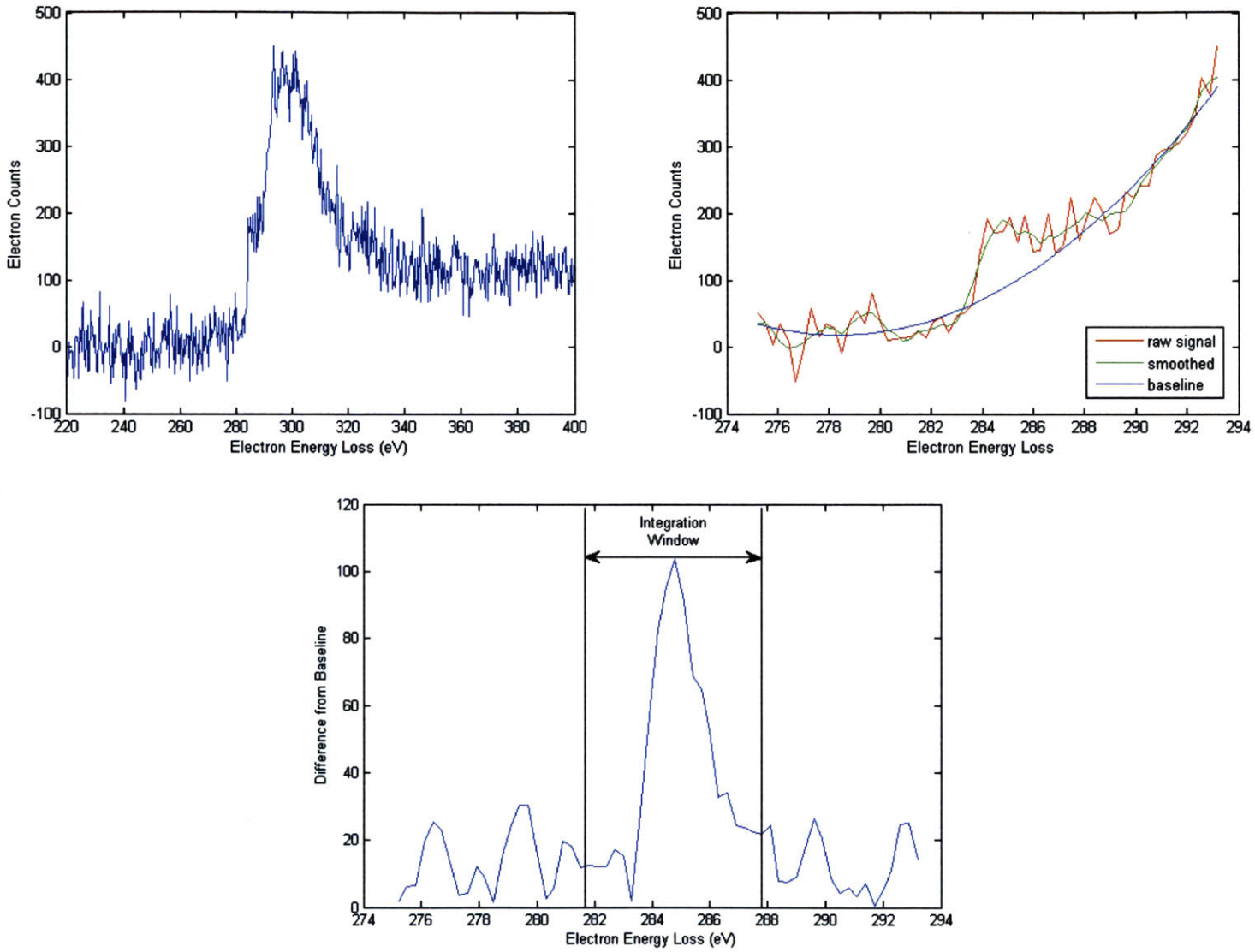

Figure F - 8. Quantification of C_{sp2}=C_{sp2} peak via integration assuming a polynomial baseline.

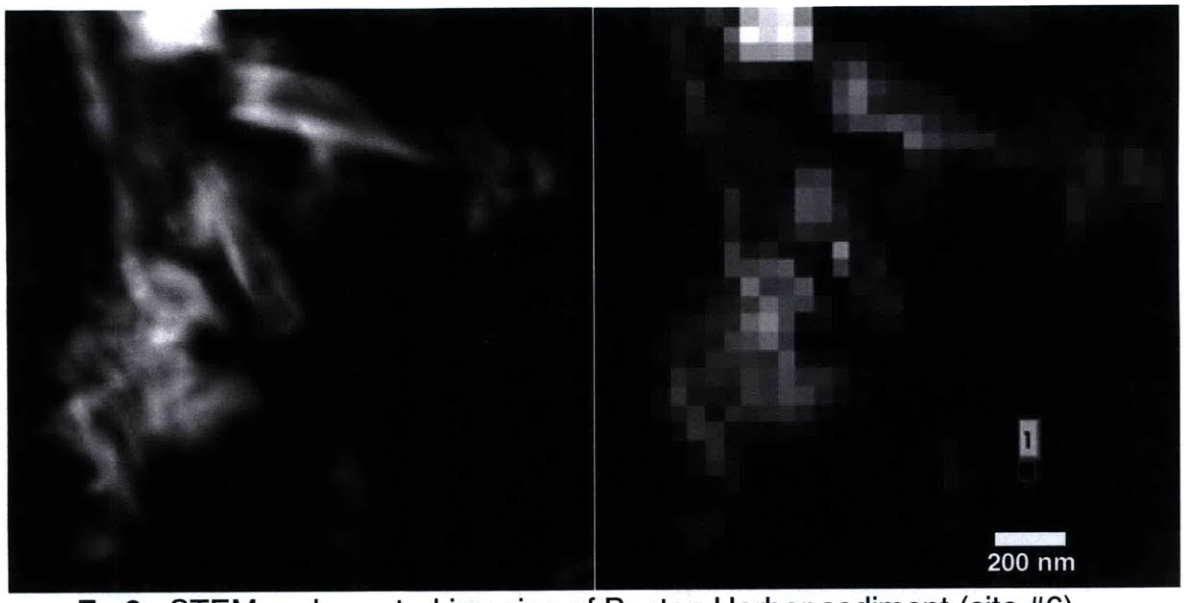

Figure F - 9. STEM and spectral imaging of Boston Harbor sediment (site #6).

STEM micrograph (left) revealed no indication to the chemical nature of the materials in view.

The spectrum imaging of the same area (right) contained 32 x 32 pixels (each pixel was about 43 to 50 nm in size). The map contained a matrix of EEL spectra for all 32 x 32 pixels.

Sample information: BH#6, radius ~ 100 μm; 50 kx.

[Signal-BH6rad100_D9_50kx_Cluster_01_MapCP_32x32_2_0sPix-Corr (RMPS).txt]

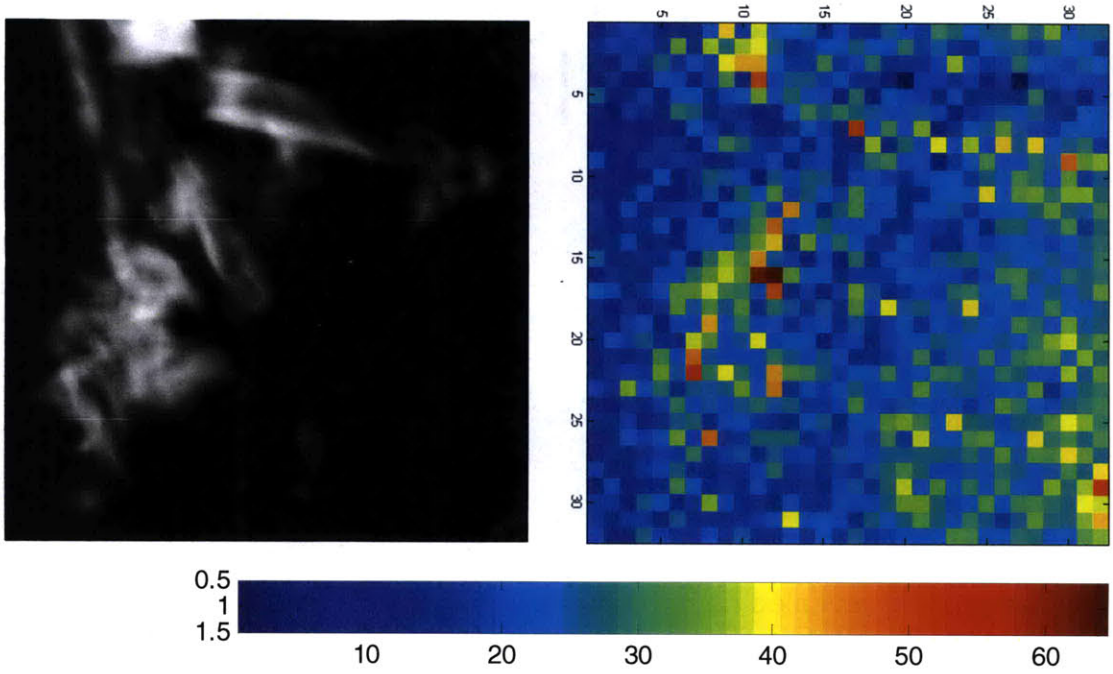

Figure F - 10. Map of C_{sp2}=C_{sp2} peak normalized to global C-peak maximum.

The map corresponds to the image in Figure F-9.

A note on the colorscale: 64(dark red) = 2900 area unit. C_{sp2} area in a given pixel = colorscale/64*2900 area unit.

[Signal-BH6rad100_D9_50kx_Cluster_01_MapCP_32x32_2_0sPix-Corr (RMPS).txt]

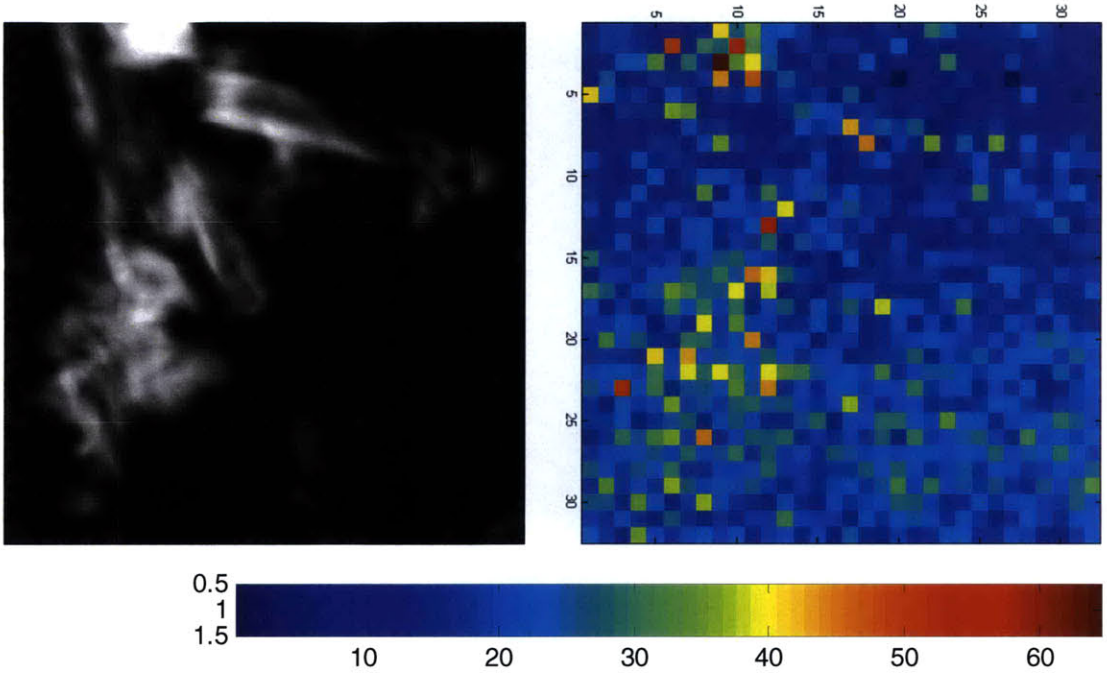

Figure F - 11. Map of C_{sp2}=C_{sp2} peak normalized to local main C-peak.

The map corresponds to the image in Figure F-9.

A note on the colorscale: 64(dark red) = 1.

C_{sp2} area/major-C-area = colorscale/64

[Signal-BH6rad100_D9_50kx_Cluster_01_MapCP_32x32_2_0sPix-Corr (RMPS).txt]

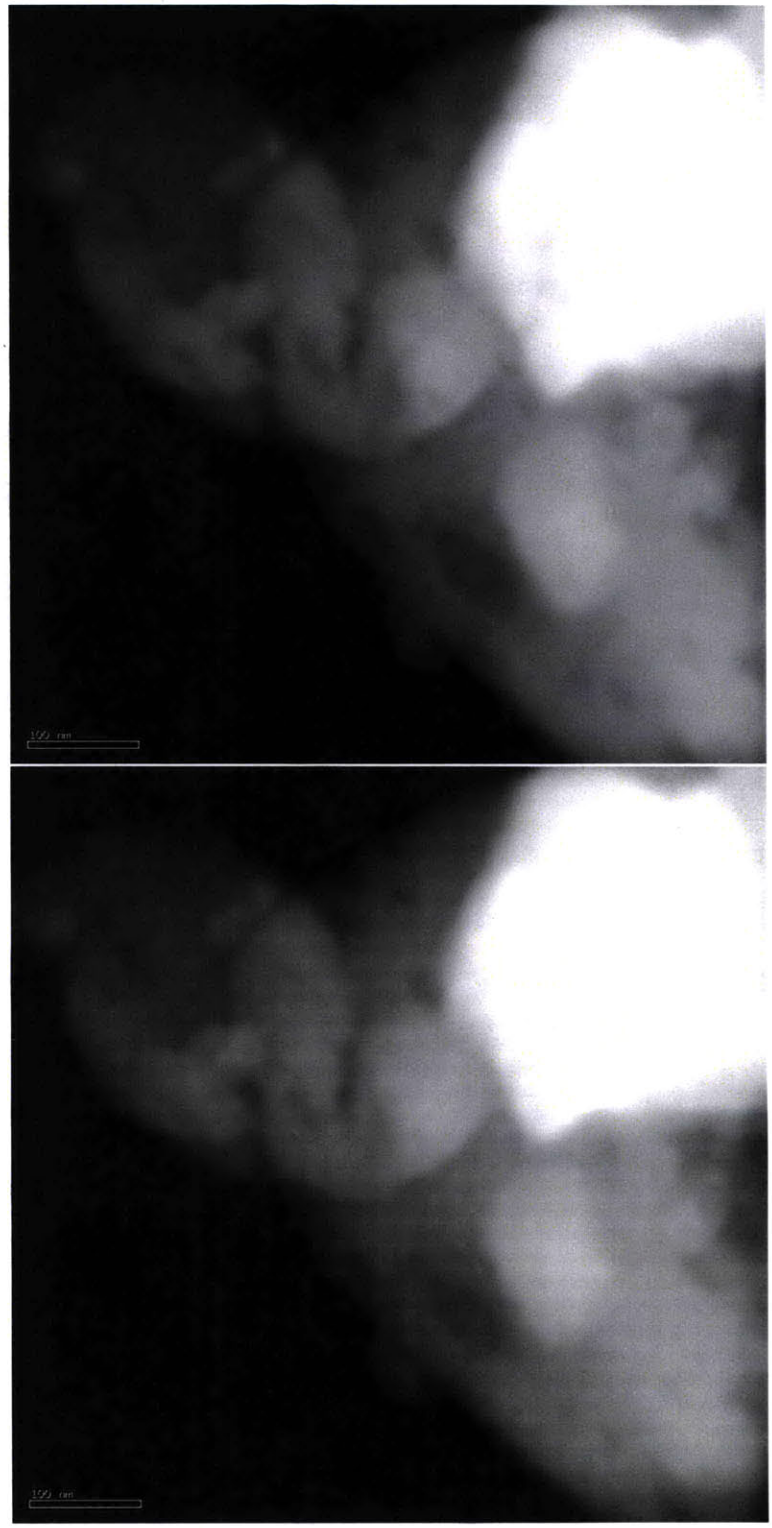

Figure F - 12. Beam-induced hydrocarbon contamination in EELS mapping.

Lignocellulosic char before (top) and after (bottom) EELS mapping. Tiny dots are indicative of hydrocarbon contamination induced by electron beam. Scale-bar = 100 nm.

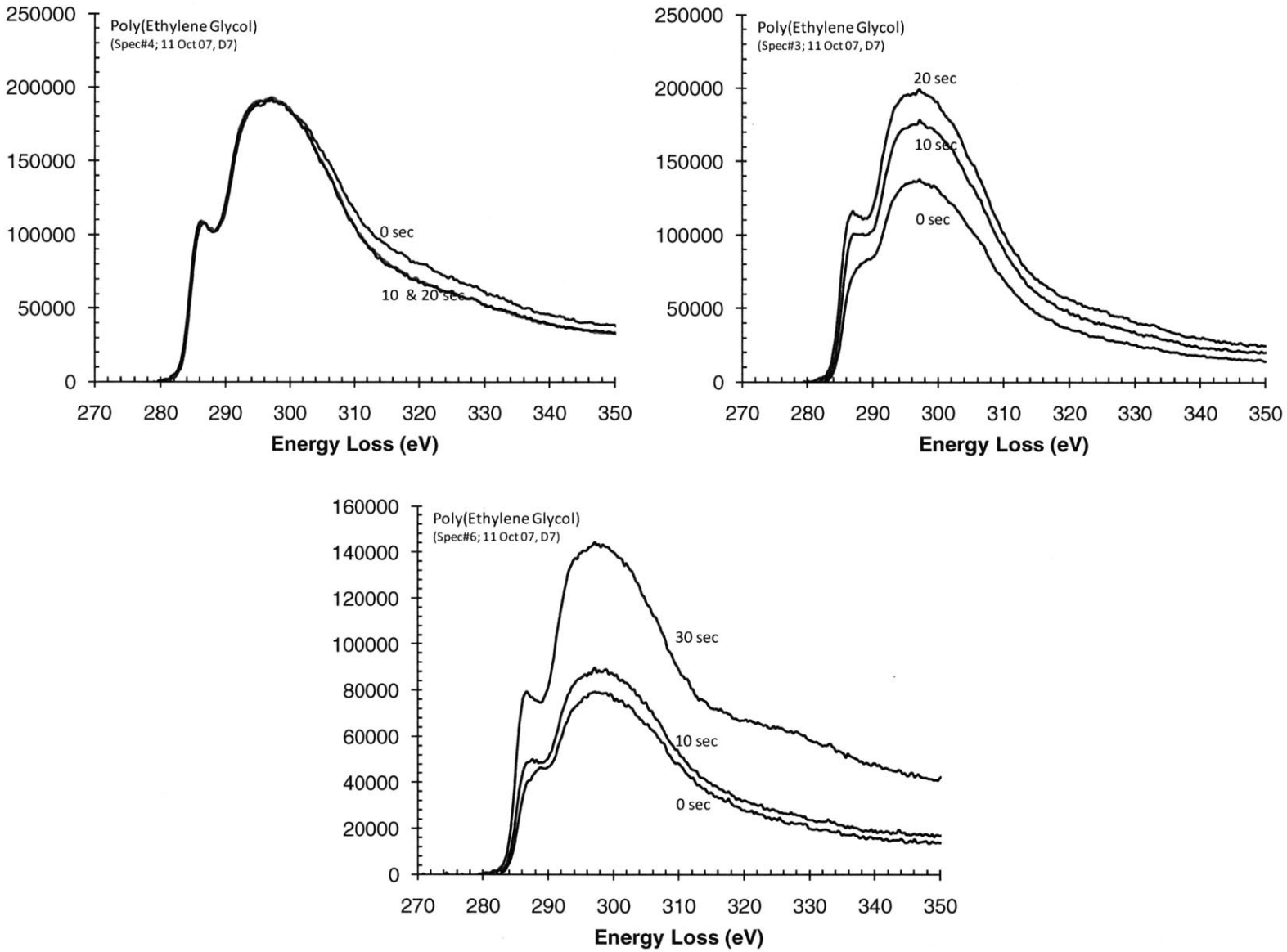

Figure F - 13. Evolution of hydrocarbon contamination in the C K-edge region.

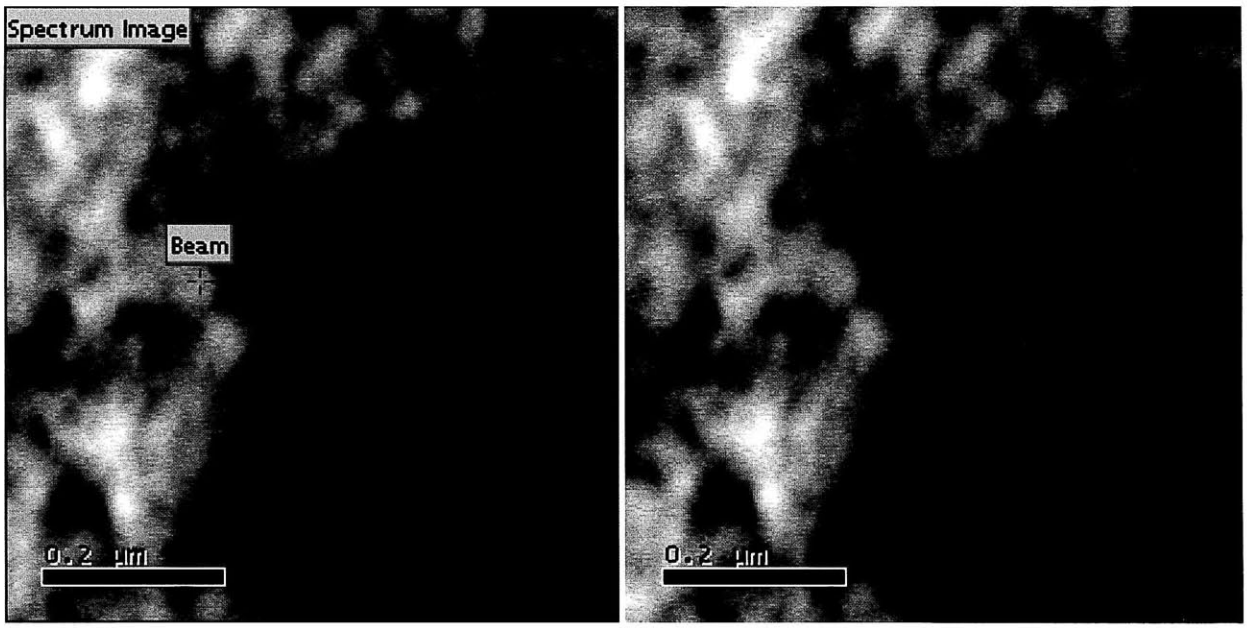

Figure F - 14. Drift of specimen during EELS map acquisition.

Micrograph of soot before (left) and after (right) the acquisition of EELS map.

Appendix G: EELS Mapping Scripts

Spectral EELS processing and generation C_{sp2}=C_{sp2} maps.

EELSMapSP2Presence

```
%%%
%%% EELSMapSP2Presence
%%%
%%% Map the presence of SP2 carbon in a raw EELS spectral map
%%%

%echo off all;

%RawFileName = 'LignoCharS15-100kx-CharB-EELS-CP-32x32-0_5spix.txt';
%RawFileName = 'S18-80kx-Graphite-Cfilm-H-EELSmap-01-32x32-0_2spix.txt';
%RawFileName = 'C-film-100kx-EELS-CP-32x32-0_5spix.txt';
RawFileName = 'Signal-BH6rad100_D9_50kx_Cluster_01_MapCP_32x32_2_0sPix-Corr (RMPS).txt';
%RawFileName = 'Signal-SootSiO-D8_150kx_SonSiO_02_MapCP32x32_1_0sPix (RMPS).txt';
%RawFileName = 'Signal-SootSDS_150kx_SDSOnSiO_01_MapCP32x32_0_5sPix (RMPS).txt';
%RawFileName =  'Signal-SootSDS_150kx_SootOnSiO(SDSmaybe)_02_MapCP32x32_0_5sPix (RMPS).txt';
%OneRawSpec = load('S18-50kx-Graphite-E-spec-01.txt');
%OneRawSpec = load('S18-50kx-Cfilm-spec-05.txt');


Raw3DSpec   = EELSMapExtract(RawFileName);
%figure, plot(squeeze(Raw3DSpec(10,10,:)));

%a=SpecWork(20,20, Raw3DSpec, 'plot', [1]);

%%%%% MODULE A %%%%%
%c = SpecWork(1, 1, Raw3DSpec, 'countc', [100, 400, 600]);
%c = Raw3DSpec(:,:,450);
%netmaxc = max(max(c));
%normalizedc = c/netmaxc;
%figure, image(normalizedc*64);
%mscale=(1:64);
%figure, image(mscale);


%%%%% MODULE B %%%%%
%fullw   = (1:1024)';
%OneEELS = reshape(Raw3DSpec(20, 20, :), 1, 1024);
%smOneEELS   = SpecWork(20, 20, Raw3DSpec, 's', [1, 5]);
%figure, plot(fullw, OneEELS, 'r'); hold on, plot(fullw, smOneEELS, 'b');


%%%%% MODULE C %%%%%
sp2area=SpecWork(20, 20, Raw3DSpec, 'sp2ex', [100, 390, 405, 430, 445, 10, 1]);
%sp2vsC=SpecWork(20, 20, Raw3DSpec, 'sp2ex', [500, 390, 405, 430, 445, 10, 0]);%
%figure, image(sp2area/max(max(sp2area))*64);
%figure, image(sp2vsC/max(max(sp2vsC))*64);
%figure, image(1:64);
%slice=Raw3DSpec(:,:,450);
%figure, image(slice/max(max(slice))*64);

%GuessVector     = [area_guess   gamma_guess   wr_guess];
%%%%% !!! need to estimate GuessVector from individual spectrum...!!!
%GuessVector     = [area_guess   gamma_guess   wr_guess];
%%% REM: FitEndStatus = [FittedParameters, SumResidSq, R2]
%FitEndStatus    = RunLorentzianFitW5(w_work, y_obs_work, GuessVector);

%ssd1_3DSpec = SpecWork(1, 1, Raw3DSpec, 'ssd1', [100, 1, 50, 50]);

%ssd1OneSpec = SpecWork(1, 1, OneRawSpec, 'ssd1', [2, 1, 50, 50]);
%[a, b] = EELSPeakFinder(1, 1, ssd1OneSpec,'pkfinder',[2, 280, 480, 500, 900]);
%figure, plot(OneRawSpec,'b'); hold on, plot(ssd1_3DSpec,'r');

%[a, b] = EELSPeakFinder(20,20,ssd1_3DSpec,'pkfinder',[1,1,50,50]);
%figure, plot(a);

echo off all;
```

```
%[Cln_ssd1, AmorYN, Amor1st, GraphYN, Graph1st] = SpecWork(1, 1, ssd1_3DSpec, 'ynm', [100,
150, 350, 400, 900, 10, 150, 230, 240, 350]);
%[Cln_ssd1, AmorYN, Amor1st, GraphYN, Graph1st] = SpecWork(1,1,ssd1_3DSpec,'ynm', [100,
150, 350, 400, 900, 10, 280, 350, 360, 450]);
%[Cln_ssd1, AmorYN, Amor1st, GraphYN, Graph1st] = SpecWork(1, 1,ssd1_3DSpec, 'ynm', [100,
190, 390, 400, 900, 10, 190, 290, 290, 390]);

%figure, image(AmorYN); figure, image(GraphYN); figure, image(Amor1st*2.5); figure,
image(Graph1st*2.5);

%save(Amor1st, 'S18-CFilmCtrl-Amor1st-32x32-0_5spix');

%SpecWork(10, 5, ssd1_3DSpec, 'p', 1);
```

Function Specwork

```
%
% Function SpecWork
% For doing various tasks on a given EELS map
% By Dave Kuo, 13 Sept 2007
%
% TaskName = 'plot', plot spectrum at pixel defined by x & y
%

function [ResultMtrx, SecondResultMtrx, TertResultMtrx, QuarResultMtrx, QuintResultMtrx] =
SpecWork(x, y, Mtrx_3DSpec, TaskName, TaskOption)

echo off all;

ResultMtrx = [];
switch lower(TaskName)
    case {'plot', 'p'}
        if TaskOption==1                % pop-up as new figure
            figure
        end
        hold on; OneTmpSpec = reshape(Mtrx_3DSpec(x, y, :), 1, 1024);
        plot(OneTmpSpec);
        ResultMtrx = OneTmpSpec;
    case {'smooth', 's'}
        if TaskOption(1)==1         % smooth single spectrum on map
            ResultMtrx = smooth(reshape(Mtrx_3DSpec(x, y, :), 1, 1024), TaskOption(2),
'sgolay');
            %figure, plot(ResultMtrx);
        elseif TaskOption(1)==100     % smooth all spectra on map
            n = size(Mtrx_3DSpec, 1);   % # pixels per dimension
            ResultMtrx = zeros(n, n, 1024);
            for i = 1:n
                for j = 1:n
                    ResultMtrx(i,j,:) = smooth(reshape(Mtrx_3DSpec(i,j,:),1,1024),
TaskOption(2), 'sgolay');
                end
            end
        end
    case {'countc', 'cc'}               % counting carbon-edge peak within user-defined
energy-loss range
        RangeS = TaskOption(2);         % start index of the peak-range
        RangeE = TaskOption(3);         % end index of peak-range
        if TaskOption(1)==1             % single spectrum
            OneTmpSpec = reshape(Mtrx_3DSpec(x, y, :), 1, 1024);
            ResultMtrx = max(OneTmpSpec(RangeS:RangeE));
        elseif TaskOption(1)==100       % whole map
            n = size(Mtrx_3DSpec, 1);   % # pixels per dimension
            PeakCountMap = zeros(n, n);
            for i = 1:n
                for j = 1:n
                    OneTmpSpec = []; OneTmpSpec = reshape(Mtrx_3DSpec(i,j,:),1,1024);
                    PeakCountMap(i,j) = max(OneTmpSpec(RangeS:RangeE));
                end
            end
            ResultMtrx = PeakCountMap;
        end
    case {'drv1st', 'd1'}               % 1st derivative only
        if TaskOption(1)==1             % single spectrum case
            ResultMtrx = gradient(reshape(Mtrx_3DSpec(x, y, :), 1, 1024), TaskOption(2));
        elseif TaskOption(1)==100       % entire map case
            n = size(Mtrx_3DSpec, 1);   % # pixels per dimension
            ResultMtrx = zeros(n, n, 1024);
```

```
            for i = 1:n
                for j = 1:n
                    ResultMtrx(i,j,:) = gradient(reshape(Mtrx_3DSpec(i,j,:),1,1024),
TaskOption(2));
                end
            end
        end
    case {'drv2nd', 'd2'}                % 2nd derivative only
        if TaskOption(1)==1              % single spectrum case
            ResultMtrx = gradient(gradient(reshape(Mtrx_3DSpec(x, y, :), 1, 1024),
TaskOption(2)));
        elseif TaskOption(1)==100        % entire map case
            n = size(Mtrx_3DSpec, 1);    % # pixels per dimension
            ResultMtrx = zeros(n, n, 1024);
            for i = 1:n
                for j = 1:n
                    ResultMtrx(i,j,:) =
gradient(gradient(reshape(Mtrx_3DSpec(i,j,:),1,1024), TaskOption(2)));
                end
            end
        end
    case {'sdrv1st','sd1'}               % 1st derivative, then smoothed
        if TaskOption(1)==1              % single spectrum case
            dum = gradient(reshape(Mtrx_3DSpec(x, y, :), 1, 1024), TaskOption(2));
            ResultMtrx = smooth(dum, TaskOption(3), 'sgolay');
        elseif TaskOption(1)==100        % entire map case
            n = size(Mtrx_3DSpec, 1);    % # pixels per dimension
            ResultMtrx = zeros(n, n, 1024);
            for i = 1:n
                for j = 1:n
                    dum = [];
                    dum = gradient(reshape(Mtrx_3DSpec(i,j,:),1,1024), TaskOption(2));
                    ResultMtrx(i,j,:) = smooth(dum, TaskOption(3), 'sgolay');
                end
            end
        end
    case {'dbl_sdrv1st','ssd1'}          % double smoothing upon 1st derivative
        if TaskOption(1)==1              % single spectrum given entire map case
            dum = gradient(reshape(Mtrx_3DSpec(x, y, :), 1, 1024), TaskOption(2));
            ResultMtrx = smooth(smooth(dum, TaskOption(3), 'sgolay'), TaskOption(4),
'sgolay');
        elseif TaskOption(1)==2          % single spectrum input only
            dum = gradient(Mtrx_3DSpec, TaskOption(2));
            ResultMtrx = smooth(smooth(dum, TaskOption(3), 'sgolay'), TaskOption(4),
'sgolay');
        elseif TaskOption(1)==100        % entire map case
            n = size(Mtrx_3DSpec, 1);    % # pixels per dimension
            ResultMtrx = zeros(n, n, 1024);
            for i = 1:n
                for j = 1:n
                    dum = [];
                    dum = gradient(reshape(Mtrx_3DSpec(i,j,:),1,1024), TaskOption(2));
                    ResultMtrx(i,j,:) = smooth(smooth(dum, TaskOption(3), 'sgolay'),
TaskOption(4), 'sgolay');
                end
            end
        end
    case {'reg_baseline','b'}            % establish baseline via regression
        if TaskOption(1)==1              % single spectrum case
            %%% TaskOption Matrix
            %%% [1 or 100, CarbonStart, CarbonEnd, xstart, xend, pkwidth]
            [ResultMtrx, SecondResultMtrx] = EELSPeakFinder(x, y, Mtrx_3DSpec, TaskName,
TaskOption);
        elseif TaskOption(1)==100        % entire map case
            %%% TaskOption Matrix
            %%% [1 or 100, CarbonStart, CarbonEnd, xstart, xend, pkwidth, AmorStart,
AmorEnd, GraphStart, GraphEnd]
            n = size(Mtrx_3DSpec, 1);    % # pixels per dimension
            ResultMtrx = zeros(n, n, 1024);
            AmorYesNoMap = zeros(n, n); Amor1stDerivMagMap = zeros(n, n);
            GraphYesNoMap = zeros(n, n); Graph1stDerivMagMap = zeros(n, n);
            for i = 1:n
                for j = 1:n
                    OneR = []; OneCPks = []; PkPos = []; Pk1stDerivHt = [];
                    [OneR, OneCPks] = EELSPeakFinder(i, j, Mtrx_3DSpec, TaskName,
TaskOption);
                    if size(OneCPks, 1)==0          % observed no carbon peaks at all
                        AmorYesNoMap(i, j) = 0; Amor1stDerivMagMap(i, j) = 0;
                        GraphYesNoMap(i, j) = 0; Graph1stDerivMagMap(i, j) = 0;
                    else
                        PkPos = OneCPks(:, 1);
```

```
                        Pk1stDerivHt = OneCPks(:, 2);
                        TestAmorPk = sum(PkPos>AmorStart & PkPos<AmorEnd);
                        TestGraphPk = sum(PkPos>GraphStart & PkPos<GraphEnd);
                        if TestAmorPk==0                % observe no Amorphous-SP3 peak
                            AmorYesNoMap(i, j) = 0; Amor1stDerivMagMap(i, j) = 0;
                        elseif TestAmorPk>1             % multiple Amorphous-SP3 peaks?
                            AmorYesNoMap(i, j) = TestAmorPk;
                            Amor1stDerivMagMap(i, j) =
max(Pk1stDerivHt(find(PkPos>AmorStart & PkPos<AmorEnd)));
                        else                            % only see 1 Amorphous-SP3 peak,
normal case
                            AmorYesNoMap(i, j) = 1;
                            Amor1stDerivMagMap(i, j) = Pk1stDerivHt(find(PkPos>AmorStart &
PkPos<AmorEnd))
                        end
                        if TestGraphPk==0               % observe no Graphitic-SP2 peak
                            GraphYesNoMap(i, j) = 0; Graph1stDerivMagMap(i, j) = 0;
                        elseif TestGraphPk>1            % multiple Graphitic-SP2 peaks?
                            GraphYesNoMap(i, j) = TestGraphPk;
                            Graph1stDerivMagMap(i, j) =
max(Pk1stDerivHt(find(PkPos>GraphStart & PkPos<GraphEnd)));
                        else                            % only see 1 Graphitic-SP2 peak,
normal case
                            GraphYesNoMap(i, j) = 1;
                            Graph1stDerivMagMap(i, j) = Pk1stDerivHt(find(PkPos>GraphStart
& PkPos<GraphEnd))
                        end
                    end     % end if
                    ResultMtrx(i, j, :) = OneR;
                end         % end j loop
            end             % end i loop
            SecondResultMtrx = AmorYesNoMap; TertResultMtrx = Amor1stDerivMagMap;
            QuarResultMtrx = GraphYesNoMap; QuintResultMtrx = Graph1stDerivMagMap;
        end
    case {'maxpk','mp'}                 % find max peak size within a given range and its
location
    % TaskOption = [SingleOrMap  RangeStart  RangeEnd  PeakCountOrPkLoc]
        if TaskOption(1)==1             % single spectrum case
            OneTmpSpec = reshape(Mtrx_3DSpec(x, y, :), 1, 1024);
            [pkcount pkloc] = max(OneTmpSpec(TaskOption(2):TaskOption(3)));
            ResultMtrx      = [pkcount pkloc];
        elseif TaskOption(1)==100       % entire map case
            rs = TaskOption(2); re = TaskOption(3);
            [pkcount pkloc] = max(Mtrx_3DSpec(:, :, rs:re), [], 3);          % two 32x32x1
matrices
            if TaskOption(4)==1         % return peak count
                ResultMtrx  = pkcount;
            elseif TaskOption(4)==2     % return peak location
                ResultMtrx  = pkloc;
            end
        end
    case {'sp2spikeextract','sp2ex'}    % extract peak area of sp2 C=C
    % TaskOption = [SingOrMap preRS preRE pkRS pkRE SmoothWind plotfit?]
        swin    = TaskOption(6);
        if TaskOption(1)==1             % single spectrum case
            preRS   = TaskOption(2);    preRE   = TaskOption(3);
            pkRS    = TaskOption(4);    pkRE    = TaskOption(5);
            preSP2  = (preRS:preRE)';
            pkSP2   = (pkRS:pkRE)';

            OneSpec     = reshape(Mtrx_3DSpec(x, y, :), 1, 1024);
            smOneSpec   = smooth(OneSpec, swin, 'sgolay');

            qw          = [preSP2;pkSP2];                           % column matrix
            qy          = [smOneSpec(preSP2); smOneSpec(pkSP2)];    % column matrix
            p           = polyfit(qw, qy, 2);                       % polynomial fit, 2nd
order

            subw        = (preRS:pkRE)';
            qysubw      = smOneSpec(subw);                          % smoothed data points
            qyhatsubw   = p(1)*subw.^2 + p(2)*subw + p(3);          % prediction from
polyfit
            diff        = qysubw - qyhatsubw;
            absdiff     = abs(diff);

            IntRange    = ((preRE-preRS+1):(pkRS-preRS))';
            sp2Area     = sum(absdiff(IntRange));
            if TaskOption(7)==1         % plot raw, smoo, and fitted curve
                figure, plot(subw, OneSpec(subw), 'r', subw, smOneSpec(subw), 'g', subw,
qyhatsubw, 'b');
                figure, plot(subw, absdiff);
```

```
            end
            ResultMtrx  = sp2Area;
        elseif TaskOption(1)==100       % entire map case
            n = size(Mtrx_3DSpec, 1);   % # pixels per dimension
            sm3DSpec = zeros(n, n, 1024);
            ResultMtrx  = zeros(32,32);
            for i = 1:n
                for j = 1:n
                    % smoothing
                    sm3DSpec(i,j,:) = smooth(reshape(Mtrx_3DSpec(i,j,:),1,1024), swin,
'sgolay');
                    smOneSpec       = reshape(sm3DSpec(i,j,:),1,1024)';

                    % search max C-peak
                    [pkc pkloc]     = max(smOneSpec(TaskOption(2):TaskOption(5)));
                    pkloc           = pkloc + TaskOption(2) - 1;            %
****IMPORTANT****

                    % define fitting energy-loss window
                    pkRE            = pkloc;
                    pkRS            = pkloc - 15;
                    preRS           = pkloc - 60;
                    preRE           = preRS + 15;
                    preSP2  = (preRS:preRE)';
                    pkSP2   = (pkRS:pkRE)';

                    qw          = [preSP2;pkSP2];
                    subw        = (preRS:pkRE)';
                    IntRange    = ((preRE-preRS+1):(pkRS-preRS))';

                    qy          = [smOneSpec(preSP2); smOneSpec(pkSP2)];    % column
matrix
                    p           = polyfit(qw, qy, 2);                       % polynomial
fit, 2nd order
                    qyhatsubw   = p(1)*subw.^2 + p(2)*subw + p(3);          % prediction
from polyfit
                    absdiff     = abs(smOneSpec(subw) - qyhatsubw);
                    ResultMtrx(i,j) = sum(absdiff(IntRange));
                    if (TaskOption(7)==1)&(i==x)&(j==y)                     % plot raw,
smoo, and fitted curve
                        OneSpec     = reshape(Mtrx_3DSpec(x, y, :), 1, 1024);
                        figure, plot(subw*0.3+160, OneSpec(subw), 'r', subw*0.3+160,
smOneSpec(subw), 'g', subw*0.3+160, qyhatsubw, 'b');
                        figure, plot(subw*0.3+160, absdiff);
                    end
                end
            end
        elseif TaskOption(1)==500       % entire map case, sp2 relative to major c peak
            n = size(Mtrx_3DSpec, 1);   % # pixels per dimension
            sm3DSpec = zeros(n, n, 1024);
            ResultMtrx  = zeros(32,32);
            for i = 1:n
                for j = 1:n
                    % smoothing
                    sm3DSpec(i,j,:) = smooth(reshape(Mtrx_3DSpec(i,j,:),1,1024), swin,
'sgolay');
                    smOneSpec       = reshape(sm3DSpec(i,j,:),1,1024)';

                    % search max C-peak
                    [pkc pkloc]     = max(smOneSpec(TaskOption(2):TaskOption(5)));
                    pkloc           = pkloc + TaskOption(2) - 1;            %
****IMPORTANT****

                    % define fitting energy-loss window
                    pkRE            = pkloc;
                    pkRS            = pkloc - 15;
                    preRS           = pkloc - 60;
                    preRE           = preRS + 15;
                    preSP2  = (preRS:preRE)';
                    pkSP2   = (pkRS:pkRE)';

                    qw          = [preSP2;pkSP2];
                    subw        = (preRS:pkRE)';
                    IntRange    = ((preRE-preRS+1):(pkRS-preRS))';

                    qy          = [smOneSpec(preSP2); smOneSpec(pkSP2)];    % column
matrix
                    p           = polyfit(qw, qy, 2);                       % polynomial
fit, 2nd order
                    qyhatsubw   = p(1)*subw.^2 + p(2)*subw + p(3);          % prediction
from polyfit
```

```
                    absdiff     = abs(smOneSpec(subw) - qyhatsubw);

                    dum         = smOneSpec;
                    dum(1:350)  = 0;
                    mainCpkArea = 2*sum(abs(dum(1:pkloc)-0));              % i.e., only
summing half of the peak
                    %figure, plot(1:600,abs(dum(1:600-0)));
                    ResultMtrx(i,j) = sum(absdiff(IntRange))/mainCpkArea;
                    if (TaskOption(7)==1)&(i==x)&(j==y)                    % plot raw,
smoo, and fitted curve
                        OneSpec     = reshape(Mtrx_3DSpec(x, y, :), 1, 1024);
                        figure, plot(subw, OneSpec(subw), 'r', subw, smOneSpec(subw), 'g',
subw, qyhatsubw, 'b');
                        figure, plot(subw, absdiff);
                    end
                end
            end
        end

    case {'yesnomap','ynm'}             % establish Yes-No map via regression
        if TaskOption(1)==1             % single spectrum case
            %%% TaskOption Matrix
            %%% [1 or 100, CarbonStart, CarbonEnd, xstart, xend, pkwidth]
            [ResultMtrx, SecondResultMtrx] = EELSPeakFinder(x, y, Mtrx_3DSpec, TaskName,
TaskOption);
        elseif TaskOption(1)==100       % entire map case
            %%% TaskOption Matrix
            %%% [1 or 100, CarbonStart, CarbonEnd, xstart, xend, pkwidth, AmorStart,
AmorEnd, GraphStart, GraphEnd]
            n = size(Mtrx_3DSpec, 1);   % # pixels per dimension
            ResultMtrx = zeros(n, n, 1024);
            AmorStart = TaskOption(7); AmorEnd = TaskOption(8); GraphStart = TaskOption(9);
GraphEnd = TaskOption(10);
            AmorYesNoMap = zeros(n, n); Amor1stDerivMagMap = zeros(n, n);
            GraphYesNoMap = zeros(n, n); Graph1stDerivMagMap = zeros(n, n);
            for i = 1:n
                for j = 1:n
                    OneR = []; OneCPks = []; PkPos = []; Pk1stDerivHt = [];
                    [OneR, OneCPks] = EELSPeakFinder(i, j, Mtrx_3DSpec, TaskName,
TaskOption);
                    if size(OneCPks, 1)==0          % observed no carbon peaks at all
                        AmorYesNoMap(i, j) = 0; Amor1stDerivMagMap(i, j) = 0;
                        GraphYesNoMap(i, j) = 0; Graph1stDerivMagMap(i, j) = 0;
                    else
                        PkPos = OneCPks(:, 1);
                        Pk1stDerivHt = OneCPks(:, 2);
                        TestAmorPk = sum(PkPos>AmorStart & PkPos<AmorEnd);
                        TestGraphPk = sum(PkPos>GraphStart & PkPos<GraphEnd);
                        if TestAmorPk==0            % observe no Amorphous-SP3 peak
                            AmorYesNoMap(i, j) = 0; Amor1stDerivMagMap(i, j) = 0;
                        elseif TestAmorPk>1         % multiple Amorphous-SP3 peaks?
                            AmorYesNoMap(i, j) = TestAmorPk;
                            Amor1stDerivMagMap(i, j) =
max(Pk1stDerivHt(find(PkPos>AmorStart & PkPos<AmorEnd)));
                        else                        % only see 1 Amorphous-SP3 peak,
normal case
                            AmorYesNoMap(i, j) = 1;
                            Amor1stDerivMagMap(i, j) = Pk1stDerivHt(find(PkPos>AmorStart &
PkPos<AmorEnd))
                        end
                        if TestGraphPk==0           % observe no Graphitic-SP2 peak
                            GraphYesNoMap(i, j) = 0; Graph1stDerivMagMap(i, j) = 0;
                        elseif TestGraphPk>1        % multiple Graphitic-SP2 peaks?
                            GraphYesNoMap(i, j) = TestGraphPk;
                            Graph1stDerivMagMap(i, j) =
max(Pk1stDerivHt(find(PkPos>GraphStart & PkPos<GraphEnd)));
                        else                        % only see 1 Graphitic-SP2 peak,
normal case
                            GraphYesNoMap(i, j) = 1;
                            Graph1stDerivMagMap(i, j) = Pk1stDerivHt(find(PkPos>GraphStart
& PkPos<GraphEnd))
                        end
                    end     % end if
                    ResultMtrx(i, j, :) = OneR;
                end         % end j loop
            end             % end i loop
            SecondResultMtrx = AmorYesNoMap; TertResultMtrx = Amor1stDerivMagMap;
            QuarResultMtrx = GraphYesNoMap; QuintResultMtrx = Graph1stDerivMagMap;
        end
end
end
```

Reference

A

Abu, A.; Smith, S. Adsorption and slow desorption of phenanthrene aged in soils. *Environ. Sci. Technol.* ***2006***, 40, 5409-5414.

Accardi-Dey, A.; Gschwend, P.M. Assessing the combined roles of natural organic matter and black carbon as sorbents in sediments. *Environ. Sci. Technol.* ***2002***, 36, 21-29.

Accardi-Dey, A. Black carbon in marine sediments: quantification and implications for the sorption of polycyclic aromatic hydrocarbons. Ph.D. Theses, Massachusetts Institute of Technology-Woods Hole Oceanographic Institution, ***2003***, pp 1-278.

Accardi-Dey, A.; Gschwend, P.M. Reinterpreting literature sorption data considering both absorption into organic carbon and adsorption onto black carbon. *Environ. Sci. Technol.* ***2003***, 37, 99-106.

Acey, R.; Healy, P.; Unger, T.F.; Ford, C.E.; Hudson, R.A. Growth and aggregation behavior of representative phytoplankton as affected by the environmental contaminant di-n-butyl phthalate. *Environ. Contam. Toxicol.* ***1987***, 39, 1-6.

Achman, D.R.; Brownawell, B.J.; Zhang, L. Exchange of polychlorinated biphenyls between sediment and water in the Hudson River Estuary. *Estuaries* ***1996***, 19, 950-965.

Ackerman, T.P.; Toon, O.B. Absorption of visible radiation in atmosphere containing mixtures of absorbing and nonabsorbing particles. *Appl. Optics* ***1981***, 20, 3661-3668.

Adachi, K.; Buseck, P.R. Internally mixed soot, sulfates, and organic matter in aerosol particles from Mexico City. *Atmos. Chem. Phys.* ***2008***, 8, 6469-6481.

Adams, R.G. Polyethylene devices and the effects of sediment resuspension on the cycling of PAHs and PCBs in the Lower Hudson Estuary. Ph.D. Thesis, Massachusetts Institute of Technology, Cambridge, ***2003***, pp 1-184.

Adams, R.G.; Lohmann, R.; Fernandez, L.A.; MacFarlane, J.K.; Gschwend, P.M. Polyethylene devices: passive samplers for measuring dissolved hydrophobic organic compounds in aquatic environments. *Environ. Sci. Technol.* ***2007***, 41, 1317-1323.

Adamson, A.W.; Gast, A.P. *Physical Chemistry of Surfaces.* ***1997***, pp. 1-784, Wiley.

Adriaens, P.; Fu, Q.; Grbic-Galic, D. Bioavailability and transformation of highly chlorinated dibenzo-*p*-dioxins and dibenzofurans in anaerobic soils and sediments. *Environ. Sci. Technol.* ***1995***, 29, 2252-2260.

Agarwal, T.; Khillare, P.S.; Shridhar, V. PAHs contamination in bank sediment of the Yamuna River, Delhi, India. *Environ. Monit. Assess.* ***2006***, 123, 151-166.

Ahn, C.C. (ed.). *Transmission Electron Energy Loss Spectrometry in Materials Science and the EELS Atlas.* ***2004***, pp. 1-457, Wiley-VCH.

Ahn, S.; Werner, D.; Karapanagioti, H.K.; McGlothlin, D.R.; Zare, R.N.; Luthy, R.G. Phenanthrene and pyrene sorption and intraparticle diffusion in polyoxymethylene, coke, and activated carbon. *Environ. Sci. Technol.* ***2005***, 39, 6516-6526.

Ahn, S.; Werner, D.; Luthy, R. G. Physicochemical characterization of coke-plant soil for the assessment of polycyclic aromatic hydrocarbon availability and the feasibility of phytoremediation. *Environ. Toxicol. Chem.* ***2005b***, 24, 2185-2195.

Ahrens, M.J.; Depree, C.V. Inhomogeneous distribution of polycyclic aromatic hydrocarbons in different size and density fractions of contaminated sediment from Auckland Harbour, New Zealand: an opportunity for mitigation. *Mar. Pollut. Bull.* ***2004***, 48, 341-350.

Akhter, M.S.; Chughtai, A.R.; Smith, D.M. The structure of hexane soot I: spectroscopic studies. *Appl. Spectroscopy,* ***1985***, 39, 143-153, 1985.

Alber, M.; Chan, A.; *Sources of contaminants to Boston Harbor: revised loading estimates. Report ENQUAD 1994-01*, ***1994***, pp. 1-93, Massachusetts Water Resources Authority.

Albers, P.W.; Klein, H.; Lox, E.S.; Seibold, K.; Prescher, G.; Parker, S.F. INS-, SIMS- and XPS-investigation of diesel engine exhaust particles. *Phys. Chem. Chem. Phys.* ***2000***, 2, 1051-1058.

Alexander, D.T.L.; Crozier, P.A.; Anderson, J.R. Brown carbon spheres in East Asian outflow and their optical properties. *Science* ***2008***, 321, 833-836.

Alexander, M. Aging, bioavailability, and overestimation of risk from environmental pollutants. *Environ. Sci. Technol.* ***2000***, 34, 4259-4265.

Alexis, M.A.; Rasse, D.P.; Rumpel, C.; Bardoux, G.; Pechot, N.; Schmalzer, P.; Drake, B.; Mariotti, A. Fire impact on C and N losses and charcoal production in a scrub oak ecosystem. *Biogeochem.* ***2007***, 82, 201-216.

Alldredge, A.L.; Silver, M.W. Characteristics, dynamics and significance of marine snow. *Prog. Oceanog.* ***1988***, 20, 41-82.

Allen-King, R.M.; Grathwohl, P.; Ball, W.P. New modeling paradigms for the sorption of hydrophobic organic chemicals to heterogeneous carbonaceous matter in soils, sediments, and rocks. *Adv. Water Resources* ***2002***, 25, 985-1016.

Amarasekera, G.; Scarlett, M.J.; Mainwaring, D.E. Micropore size distribution and specific interactions in coals. *Fuel* ***1995***, 74, 115-118.

Anderson, T.; Shifley, L.; Amarasiriwardena, D.; Siripinyanond, A.; Xing, B.; Barnes, R.M. Characterization of trace metals complexed to humic acids derived from agricultural soils, annelid composts, and sediment by flow field-flow fractionation-inductively coupled plasma-mass spectrometry (Flow FFF-ICP-MS). In *Humic Substances – Structures, Models and Functions*, (eds. Ghabbour, E.A.; Davies, G.), pp 165-177, Royal Society of Chemistry, Cambridge, ***2001***.

Andreae, M.O.; Gelencser, A. Black carbon or brown carbon? The nature of light-absorbing carbonaceous aerosols. *Atmos. Chem. Phys.* ***2006***, 6, 3131-3148.

Andreae, M.O.; Schmid, O.; Yang, H.; Chand, D.; Yu, J.Z.; Zeng, L.M.; Zhang, Y.H. Optical properties and chemical composition of the atmospheric aerosol in urban Guangzhou, China. *Atmos. Environ.* ***2008***, 42, 6335-6350.

Anyakora, C.; Ogbeche, A.; Palmer, P.; Coker, H.; Ukpo, G.; Ogah, C. GC/MS analysis of polynuclear aromatic hydrocarbons in sediment samples from the Niger Delta region. *Chemosphere* ***2005***, 60, 990-997.

Arnott, W.P.; Moosmuller, H.; Rogers, C.F.; Jin, T.F.; Bruch, R. Photoacoustic spectrometer for measuring light absorption by aerosol: instrument description. *Atmos. Environ.* ***1999***, 33, 2845-2852.

Arp, H.P.H.; Breedveld, G.D.; Cornelissen, G. Estimating the in situ sediment-porewater distribution of PAHs and chlorinated aromatic hydrocarbons in anthropogenic impacted sediments. *Environ. Sci. Technol.* ***2009***, 43, 5576-5585.

Ashley, J.T.F.; Baker, J.E. Hydrophobic organic contaminants in surficial sediments of Baltimore Harbor: inventories and sources. *Environ. Toxicol. Chem.* ***1999***, 18, 838-849.

Ault, A.P.; Moore, M.J.; Furutani, H.; Prather, K.A. Impact of emissions from the Los Angeles Port Region on San Diego air quality during regional transport events. *Environ. Sci. Technol.* ***2009***, 43, 3500-3506.

B

Backhus, D.A.; Gschwend, P.M. Fluorescent polycyclic aromatic hydrocarbons as probes for studying the impact of colloids on pollutant transport in groundwater. *Environ. Sci. Technol.* ***1990***, 24, 1214-1223.

Bailey, A.W.; Anderdon, M.L. Fire temperatures in glass, shrub and Aspen forest communities of central Alberta. *J. Range Manage.* ***1980***, 33, 37-40.

Baldock, J.A.; Smernik, R.J. Chemical composition and bioavailability of thermally altered Pinus resinosa (Red pine) wood. *Org. Geochem.* ***2002***, 33, 1093-1109.

Ball, W.P.; Roberts, P.V. Long-term sorption of halogenated organic-chemicals by aquifer material. 2. Intraparticle diffusion. *Environ. Sci. Technol.* ***1991***, 25, 1237-1249.

Baker, J.E.; Eisenreich, S.J. Concentrations and fluxes of polycyclic aromatic hydrocarbons and polychlorinated biphenyls across the air-water interface of Lake Superior. *Environ. Sci. Technol.* ***1990***, 24, 342-352.

Baker, J.E.; Eisenreich, S.J.; Eadie, B.J. Sediment trap fluxes and benthic recycling of organic carbon, polycyclic aromatic hydrocarbons, and polychlorobiphenyl congeners in Lake Superior. *Environ. Sci. Technol.* ***1991***, 25, 500-509.

Barring, H.; Bucheli, T.D.; Broman, D.; Gustafsson, O. Soot-water distribution coefficients for polychlorinated dibenzo-p-dioxins, polychlorinated dibenzofurans and polybrominated diphenylethers determined with the soot cosolvency-column method. *Chemosphere* ***2002***, 49, 515-523.

Barriuso, E.; Houot, S.; Serrawittling, C. Influence of compost addition to soil on the behaviour of herbicides. *Pesticide Sci.* ***1997***, 49, 65-75.

Basheer, C.; Obbard, J.P.; Lee, H.K. Persistent organic pollutants in Singapore's coastal marine environment: Part II, seawater. *Wat. Air Soil Pollut.* ***2003a***, 149, 295-313.

Basheer, C.; Obbard, J.P.; Lee, H.K. Persistent organic pollutants in Singapore's coastal marine environment: Part II, sediments. *Wat. Air Soil Pollut.* ***2003b***, 149, 315-325.

Baumann, P.C.; Smith, W.D.; Parland, W.K. Tumor frequencies and contaminant concentrations in brown bullheads from an industrialized river and a recreational lake. *Trans. Amer. Fish. Soc.* ***1987***, 116, 79-86.

Baumann, T.; Haaszio, S.; Niessner, R. Applications of a laser-induced fluorescence spectroscopy sensor in aquatic systems. *Water Res.* ***2000***, 34, 1318-1326.

Baumard, P.; Budzinskia, H.; Garriguesa, P.; Sorbeb, J.C.; Burgeotc, T.; Bellocqa, J. Concentrations of PAHs (polycyclic aromatic hydrocarbons) in various marine organisms in relation to those in sediments and to trophic level. *Mar. Pollut. Bull.* ***1998***, 36, 951-960.

Bekku, Y.S.; Nakatsubo, T.; Kume, A.; Adachi, M.; Koizumi, H. Effect of warming on the temperature dependence of soil respiration rate in arctic, temperate and tropical soils. *Appl. Soil Ecol.* ***2003***, 22, 205-210.

Berner, R.A. *Early Diagenesis – A Theoretical Approach.* ***1980***, pp. 1-241, Princeton Series in Geochemistry.

Bennett, R.H.; Bryant, W.R.; Keller, G.H. Clay fabric of selected submarine sediments: fundamental properties and models. *J. Sediment. Petrol.* ***1981***, 51, 217-231.

Bennett, R.H.; Fischer, K.M.; Lavoie, D.L.; Bryant, W.R.; Rezak, R. Porometry and fabric of marine clay and carbonate sediments: determinants of permeability. *Mar. Geol.* ***1989***, 89, 127-152.

Bennett, R.H.; O'Brien, N.R.; Hulbert, M.H. Determinants of clay and shale microfabric signatures: processes and mechanisms. In *Microstructures of Fine-Grained Sediments: From Mud to Shale*, (eds. Bennett, R.H.; Bryant, W.R.; Hulbert, M.H.), pp. 5-32, Springer-Verlag, Berlin, ***1991***.

Bentley, J.; Graetz, J. Application to ceramics, catalysts and transition metal oxides. In *Transmission Electron Energy Loss Spectrometry in Materials Science and the EELS Atlas.* (Ahn, C.C., (ed)). ***2004***, pp. 271-316, Wiley-VCH.

Berns, A.E.; Philipp, H.; Narres, H.D.; Burauel, P.; Vereecken, H.; Tappe, W. Effect of gamma-sterilization and autoclaving on soil organic matter structure as studied by solid state NMR, UV and fluorescence spectroscopy. *Euro. J. Soil Sci.* ***2008***, 59, 540-550.

Bevington, P.R.; Robinson, D.K. *Data Reduction and Error Analysis for the Physical Sciences.* ***1992***, pp. 1-328, McGraw-Hill.

Biagini, E.; Narducci, P.; Tognotti, L. Size and structural characterization of lignin-cellulosic fuels after the rapid devolatilization. *Fuel* ***2008***, 87, 177-186.

Bidlack, J.; Malone, M.; Benson, R. Molecular structure and component integration of secondary cell walls in plants. *Proc. Okla. Acad. Sci.* ***1992***, 72, 51-56.

Binelli, A.; Sarkar, S.K.; Chatterjee, M.; Riva, C.; Parolini, M.; Bhattacharya, B.D.; Bhattacharya, A.K.; Satpathy, K.K. A comparison of sediment quality guidelines for toxicity assessment in the Sunderban wetlands (Bay of Bengal, India). *Chemosphere* ***2008***, 73, 1129-1137.

Birch, M.E. Analysis of carbonaceous aerosols: interlaboratory comparison. *Analyst* ***1998***, 123, 851-857.

Birch, M.E.; Cary, R.A. Elemental carbon-based method for monitoring occupational exposures to particulate diesel exhaust. *Aerosol Sci. Technol.* ***1996***, 25, 221-241.

Bird, M.I.; Cali, J.A. A million-year record of fire in sub-Saharan Africa. *Nature* ***1998***, 394, 767-769.

Bird, M.I.; Grocke, D.R. Determination of the abundance and carbon isotope composition of elemental carbon in sediments. *Geochim. Comsochim. Acta* ***1997***, 61, 3413-3423.

Bird, M.I.; Moyo, C.; Veenendaal, E.M.; Lloyd, J.; Frost, P. Stability of elemental carbon in a savanna soil. *Global Biogeochem. Cycles* ***1999***, 13, 923-932.

Birdwell, J.; Cook, R.L.; Thibodeaux, L.J. Desorption kinetics of hydrophobic organic chemicals from sediment to water: A review of data and models. *Environ. Toxicol. Chem.* ***2007a***, 26, 424-434.

Birdwell, J.E.; Thibodeaux, L.J. A kinetic model of short-term dissolved contaminant release during dredge-generated bed sediment resuspension. *Environ. Eng. Sci.* ***2007b***, 24, 1431-1442.

Blake, W.H.; Droppo, I.G.; Humphreys, G.S.; Doerr, S.H.; Shakesby, R.A.; Wallbrink, P.J. *J. Geosphys. Res.* ***2007***, 112, F02020.

Bloom, P.R.; Bleam, W.F.; Xia, K. X-ray spectroscopy applications for the study of humic substances. In *Humic Substances and Chemical Contaminants*. (eds. Clapp, C.E.; Hayes, M.H.B.; Senesi, N.; Bloom, P.R.; Jardine, P.M.), pp 317-350, Soil Science Society of America, Madison, ***2001***.

Boerjan, W.; Ralph, J.; Baucher, M. Lignin biosynthesis. *Annu. Rev. Plant Biol.* ***2003***, 54, 519-546.

Bond, T.C.; Bergstrom, R.W. Light absorption by carbonaceous particles: an investigative review. *Aerosol Sci. Technol.* ***2006a***, 40, 27-67.

Bond, T.C.; Habib, G.; Bergstrom, R.W. Limitations in the enhancement of visible light absorption due to mixing state. *J. Geophys. Res.* ***2006b***, 111, D20211.

Bond, T.C.; Streets, D.G.; Yarber, K.F.; Nelson, S.M.; Woo, J.-H.; Klimont, Z. A technology-based global inventory of black and organic carbon emissions from combustion, *J. Geophys. Res.* ***2004***, 109, D14203, doi:10.1029/2003JD003697.

Bond, T.C.; Sun, H.L. Can reducing black carbon emissions counteract global warming? *Environ. Sci. Technol.* ***2005***, 39, 5921-5926.

Booij, K.; Sleiderink, H.M.; Smedes, F. Calibrating the uptake kinetics of semipermeable membrane devices using exposure standards. *Environ. Toxicol. Chem.* ***1998***, 17, 1236-1245.

Boonyatumanond, R.; Wattayakorn, G.; Togo, A.; Takada, H. Distribution and origins of polycyclic aromatic hydrocarbons (PAHs) in riverine, estuarine, and marine sediments in Thailand. *Mar. Pollut. Bull.* ***2006***, 52, 942-956.

Botello, A.V.; Villanueva, S.F.; Diaz, G.G.; Escobar-Briones, E. Polycyclic aromatic hydrocarbons in sediments from Salina Cruz Harbour and coastal areas, Oaxaca, Mexico. *Mar. Pollut. Bull.* ***1998***, 36, 554-558.

Boudreau, B.P. *Diagenetic Models and their Implementation.* ***1997***, pp. 1-414, Springer-Verlag.

Bouloubassi, I.; Saliot, A. Composition and sources of dissolved and particulate PAH in surface waters from the Rhone Delta (NW Mediterranean). *Mar. Pollut. Bull.* ***1991***, 22, 588-594.

Braida, W.J.; Pignatello, J.J.; Lu, Y.; Ravikovitch, P.I.; Neimark, A.V.; Xing, B. Sorption hysteresis of benzene in charcoal particles. Environ. Sci. Technol. 2003, 37, 409-417.

Braun, A. Carbon speciation in airborne particulate matter with C (1s) NEXAFS spectroscopy. *J. Environ. Monit.* ***2005***, 7, 1059-1065.

Breedveld, G.D.; Pelletier, E.; St. Louis, R.; Cornelissen, G. Sorption characteristics of polycyclic aromatic hydrocarbons in aluminum smelter residues. *Environ. Sci. Technol.* ***2007***, 41, 2542-2547.

Brezonik, P.L.; Fulkerson-Brekken, J. Nitrate-induced photolysis in natural waters: controls on concentrations of hydroxyl radical photo-intermediates by natural scavenging agents. *Environ. Sci. Technol.* ***1998***, 32, 3004-3010.

Bridges, T.S.; Ells, S.; Hayes, D.; Mount, D.; Nadeau, S.C.; Palermo, M.R.; Patmont, C.; Schroeder, P. *The four Rs of environmental dredging: resuspension, release, residual, and risk. Report ERDC/EL TR-08-04, Feb.* ***2008***, pp. 1-56, US Army Corps of Engineers.

Brion, D.; Pelletier, E. Modelling PAHs adsorption and sequestration in freshwater and marine sediments. *Chemosphere* ***2005***, 61, 867-876.

Brodowski, S.; Amelung, W.; Haumaier, L.; Abetz, C.; Zech, W. Morphological and chemical properties of black carbon in physical soil fractions as revealed by scanning electron microscopy and energy-dispersive X-ray spectroscopy. *Geoderma* ***2005***, 128, 116-129.

Brodowski, S.; John, B.; Flessa, H.; Amelung, W. Aggregate-occluded black carbon in soil. *Euro. J. Soil Sci.* ***2006***, 57, 539-546.

Brodowski, S.; Rodionov, A.; Haumaier, L.; Glaser, B.; Amelung, W. Revised black carbon assessment using benzene polycarboxylic acids. *Org. Geochem.* ***2005***, 36, 1299-1310.

Brookes, P.; Newbold, R.F.; Osborne, M.R. Mechanism of the carcinogenicty of polycyclic aromatic hydrocarbons. In *Environmental carcinogenesis occurrence, risk, evaluation and mechanics*, Emmelot, P. and Krick, E. (Eds.), 123-142, Elsevier, New York, ***1979***.

Brown, J.R.; Kronberg, B.I.; Fife, W.S. Semi-quantitative ESCA examination of coal and coal ash surfaces. *Fuel* ***1981***, 60, 439-446.

Brownawell, B.J. The role of colloidal organic matter in the marine geochemistry of PCBs. Ph.D. Theses, Massachusetts Institute of Technology-Woods Hole Oceanographic Institution, ***1986***, pp 1-318.

Brunauer, S.; Deming, L.S.; Deming, W.E.; Teller, E. On a theory of the van der Waals adsorption of gases. *J. Am. Chem. Soc.* ***1940***, 62, 1723-1732.

Brunauer, S.; Emmett, P.H.; Teller, E. Adsorption of gases in multimolecular layers. *J. Am. Chem. Soc.* ***1938***, 60, 309-319.

Brusseau, M.L.; Jessup, R.E.; Rao, P.S.C. Nonequilibrium sorption of organic-chemicals – elucidation of rate-limiting processes. *Environ. Sci. Technol.* ***1991***, 25, 134-142.

Brusseau, M.L. and Rao, P.S.C. The influence of sorbate-organic matter interactions on sorption nonequilibrium. *Chemosphere* ***1989***, 18, 1691-1706.

Bruun, S.; Jensen, E.S.; Jensen, L.S. Microbial mineralization and assimilation of black carbon: Dependency on degree of thermal alteration. *Org. Geochem.* ***2008a***, 39, 839-845.

Bruun, S.; Thomsen, I.K.; Christensen, B.T.; Jensen, L.S. In search of stable soil organic carbon fractions: a comparison of methods applied to soils labelled with ^{14}C for 40 days or 40 years. *Euro. J. Soil Sci.* ***2008b***, 59, 247-256.

Bucheli, T.D.; Gustafsson, O. Quantification of the soot-water distribution coefficient of PAHs provides mechanistic basis for enhanced sorption observations. *Environ. Sci. Technol.* ***2000***, 34, 5144-5151.

Budd, P.M.; Goodhew, P.J. *Light-Element Analysis in the Transmission Electron Microscope: WEDX and EELS.* ***1988***, pp. 1-73, Oxford University Press/Royal Microscopical Society.

Budzinski, H.; Jones, I.; Bellocq, J.; Pierard, C.; Garrigues, P. Evaluation of sediment contamination by polycyclic aromatic hydrocarbons in the Gironde estuary. *Mar. Chem.* ***1997***, 58, 85-97.

Burchiel, S.W.; Luster, M.I. Signaling by environmental polycyclic aromatic hydrocarbons in Human Lymphocytes. *Clinical Immunol.* ***2001***, 98, 2-10.

Burgess, C.E.; Redlich, P.J.; Sakurovs, R.J.; Jackson, W.R.; Marshall, M. Structural characterization of some North American Coals. *Energy Fuels* ***1998***, 12, 570-573.

Burgess, R.M.; Scott, K.J. The significance of inplace contaminated marine sediments on the water column: processes and effects. In *Sediment Toxicity Assessment*, Burton G.A. Jr. (ed.), 129-154, Lewis Publishing, ***1992***.

Burkhard, L.P.; Cook, P.M.; Lukasewycz, M.T. Organic carbon-water concentration quotients (Π_{SOC}s and π_{POC}s): measuring apparent chemical disequilibria and exploring the impact of black carbon in Lake Michigan. *Environ. Sci. Technol.* ***2008***, 42, 3615-3621.

Burton, G.A. Sediment quality criteria in use around the world. *Limnol.* ***2002***, 3, 65-75.

Buseck, P.R.; Jun, H.B. Conversion of carbonaceous material to graphite during metamorphism. *Geochim. Comsochim. Acta* ***1985***, 49, 2003-2016.

Buseck, P.R.; Tsipursky, S.J.; Hettich, R. Fullerenes from the geological environment. *Science* ***1992***, 257, 215-217.

C

Cachier, H.; Bremond, M.P.; Buat-Menard, P. Carbonaceous aerosols from different tropical biomass burning sources. *Nature* ***1989a***, 340, 371-373.

Cachier, H.; Bremond, M.P.; Buat-Menard, P. Determination of atmospheric soot carbon with a simple thermal method. *Tellus B* ***1989b***, 41, 379-390.

Cachier, H.; Bremond, M.P.; Buat-Menard, P. Thermal separation of soot carbon. *Aerosol Sci. Technol.* ***1989c***, 10, 358-364.

Canadian Council of Ministers of the Environment. Canadian sediment quality guidelines for the protection of aquatif life: polycyclic aromatic hydrocarbons (PAHs). ***1999***, pp. 1-15, In *Canadian environmental quality guidelines*, Canadian Council of Ministers of the Environment.

Carroll, K.M.; Harkness, M.R.; Bracco, A.A.; Balcarcel, R.R. Application of a permeant/polymer diffusional model to the desorption of polychlorinated biphenyls from Hudson River sediments. *Environ. Sci. Technol.* ***1994***, 28, 253-258.

Carton, A.; Isla, T.; AlvarezBenedi, J. Sorption-desorption of imazamethabenz on three Spanish soils. *J. Agric. Food Chem.* ***1997***, 45, 1454-1458.

Casado-Martinez, M.C.; Buceta, J.L.; Belzunce, M.J.; Delvalls, T.A. Using sediment quality guidelines for dredged material management in commercial ports from Spain. *Environ. Intern.* ***2006***, 32, 388-396.

Catallo, W.J. and Gambrell, R.P. The effects of high-levels of polycyclic aromatic-hydrocarbons on sediment physicochemical properties and benthic organisms in a polluted stream. *Chemosphere* ***1987***, 16, 1053-1063.

Celis, R.; Real, M.; Hermosin, M.C.; Cornejo, J. Desorption, persistence, and leaching of dibenzofuran in European soils. *Soil Sci. Soc. Am. J.* ***2006***, 70, 1310-1317.

Certini, G. Effects of fire on properties of forest soils: a review. *Oecologia* ***2005***, 143, 1-10.

Chan, M.-L.; Jones, J.M.; Pourkashanian, M.; Williams, A. The oxidative reactivity of coal chars in relation to their structure. *Fuel* ***1999***, 78, 1539-1552.

Chan, M.-L.; Moody, K.N.; Mullins, J.R.; Williams, A. Low-temperature oxidation of soot. *Fuel* ***1987***, 66, 1694-1698.

Chang, H.T.; Furuya, E.G.; Miura, Y.; Noll, K.E. Effect of surface functional group on Freundlich adsorption isotherm. *Wat. Sci. Technol.* ***2000***, 42, 161-166.

Chantler, C.T. Theoretical form factor, attenuation and scattering tabulation for Z=1-92 from E=1-10eV to E=0.4-1.0 MeV. *J. Phys. Chem. Ref. Data* ***1995***, 24, 71-643.

Chantler, C.T. Detailed Tabulation of Atomic Form Factors, Photoelectric Absorption and Scattering Cross Section, and Mass Attenuation Coefficients in the Vicinity of Absorption Edges in the Soft X-Ray (Z = 30-36, Z = 60-89, E = 0.1 keV-10 keV), Addressing Convergence Issues of Earlier Work 597-1048.

Chantler, C.T.; Olsen, K.; Dragoset, R.A.; Chang, J.; Kishore, A.R.; Kotochigova, S.A.; Zucker, D.S. X-Ray Form Factor, Attenuation and Scattering Tables (version 2.1). National Institute of Standards and Technology ***2005***: http://physics.nist.gov/ffast.

Charlesworth, M.; Service, M.; Gibson, C.E. PAH contamination of western Irish Sea sediments. *Mar. Pollut. Bull.* ***2002***, 44, 1421-1434.

Chefetz, B.; Deshmukh, A.P.; Hatcher, P.G.; Guthrie, E.A. Pyrene sorption by natural organic matter. *Environ. Sci. Technol.* ***2000***, 34, 2925-2930.

Chefetz, B.; Salloum, M.J.; Deshmukh, A.P.; Hatcher, P.G. Structural components of humic acids as determined by chemical modifications and carbon-13 NMR, pyrolysis-, and thermochemolysis-gas chromatography/mass spectrometry. *Soil Sci. Soc. Am. J.* ***2002***, 66, 1159-1171.

Chen, H.X.; Dobbins, R.A. Crystallogenesis of particles formed in hydrocarbon combustion. *Combust. Sci. Technol.* ***2000***, 159, 108-128.

Chen, B.; Xuan, X.; Zhu, L.; Wang, L.; Gao, Y.; Yang, K.; Shen, X.; Lou, B. Distributions of polycyclic aromatic hydrocarbons in surface waters, sediments and soils of Hangzhou City, China. *Wat. Res.* ***2004***, 38, 3558-3568.

Chen, R.F.; Chadwick, D.B.; Lieberman, S.H. The application of time-resolved spectrofluorometry to measuring benthic fluxes of organic compounds. *Org. Geochem.* ***1997***, 26, 67-77.

Chen, Y.; Shah, N.; Braun, A.; Huggins, F.E.; Huffman, G.P. Electron microscopy investigation of carbonaceous particulate matter generated by combustion of fossil fuels. *Energy & Fuels* ***2005***, 19, 1644-1651.

Cheng, C.H.; Lehmann, J.; Engelhard, M.H. Natural oxidation of black carbon in soils: changes in molecular form and surface charge along a climosequence. *Geochim. Cosmochim. Acta* ***2008***, 72, 1598-1610.

Cheng, C.H.; Lehmann, J.; Thies, J.E.; Burton, S.D.; Engelhard, M.H. Oxidation of black carbon by biotic and abiotic processes. *Org. Geochem.* ***2006***, 37, 1477-1488.

Cheng, C.Y.; Atkinson, J.F.; Depinto, J.V. Desorption during resuspension events – kinetic V equilibrium-model. *Mar. Freshwat. Res.* ***1995***, 46, 251-256.

Cheng, Y.F.; Eichler, H.; Wiedensohler, A.; Heintzenberg, J.; Zhang, Y.H.; Hu, M.; Herrmann, H.; Zeng, L.M.; Liu, S.; Gnauk, T.; Bruggemann, E.; He, L.Y. Mixing state of elemental carbon and non-light-absorbing aerosol components derived from in situ particle optical properties at Xinken in Pearl River Delta of China. *J. Geophys. Res.* ***2006***, 111, D20204.

Chernova, T.G.; Paropkari, A.L.; Pikovskii, Y.I.; Alekseeva, T.A. Hydrocarbons in the Bay of Bengal and Central Indian Basin bottom sediments: indicates of geochemical processes in the lithosphere. *Mar. Chem.* ***1999***, 66, 231-243.

Chilom, G.; Kohl, S.D.; Rice, J.A. The influence of lipids on the energetics of uptake of polycyclic aromatic hydrocarbons by natural organic matter. *J. Environ. Qual.* ***2005***, 34, 1055-1062.

Chin, W.C.; Orellana, M.V.; Verdugo, P. Spontaneous assembly of marine dissolved organic matter into polymer gels. *Nature* ***1998***, 391, 568-572.

Chin, Y.P.; Aiken, G.R.; Danielsen, K.M. Binding of pyrene to aquatic and commercial humic substances: the role of molecular weight and aromaticity. *Environ. Sci. Technol.* ***1997***, 31, 1630-1635.

Chin, Y.P.; Gschwend, P.M. The abundance, distribution, and configuration of porewater organic colloids in recent sediments. *Geochim. Cosmochim. Acta* ***1991***, 55, 1309-1317.

Chin, Y.P.; Weber, W.J. Estimating the effects of dispersed organic polymers on the sorption of contaminants by natural solids. 1. A predictive thermodynamic humic substance organic solute interaction-model. *Environ. Sci. Technol.* ***1989***, 23, 978-984.

Chin, Y.P.; Gschwend, P.M. Partitioning of polycyclic aromatic hydrocarbons to marine porewater organic colloids. *Environ. Sci .Technol.* ***1992***, 26, 1621-1626.

Chiou, C.T.; Peters, L.J.; Freed, V.H. Physical concept of soil-water equilibria for non-ionic organic-compounds. *Science* ***1979***, 206, 831-832.

Chiou, C.T.; Porter, P.E.; Schmedding, D.W. Partition equilibria of nonionic organic compounds between soil organic matter and water. *Environ. Sci. Technol.* ***1983***, 17, 227-231.

Chiou, C.T.; Malcolm, R.L.; Brinton, T.I.; Kile, D.E. Water solubility enhancement of some organic pollutants and pesticides by dissolved humic and fulvic acids. *Environ. Sci. Technol.* ***1986***, 20, 502-508.

Chiou, C.T.; Lee, J.F.; Boyd, S.A. The surface area of soil organic matter. *Environ. Sci. Technol.* ***1990***, 24, 1164-1166.

Chiou, C.T.; McGroddy, S.E.; Kile, D.E. Partition characteristics of polycyclic aromatic hydrocarbons on soils and sediments. *Environ. Sci. Technol.* ***1998***, 32, 264-269.

Chiou, W.A.; Bryant, W.R.; Bennett, R.H. Clay fabric of gassy submarine sediments. In *Microstructures of Fine-Grained Sediments: From Mud to Shale*, (eds. Bennett, R.H.; Bryant, W.R.; Hulbert, M.H.), pp. 333-352, Springer-Verlag, Berlin, ***1991***.

Choudhry, G.G. *Humic Substances: structural, photophysical, photochemical and free radical aspects and interactions with environmental chemicals.* ***1984***, pp. 1-185, Gordon and Breach Science Publishers.

Chow, J.C.; Watson, J.G.; Crow, D.; Lowenthal, D.H.; Merrifield, T. Comparison of IMPROVE and NIOSH carbon measurements. *Aerosol Sci. Technol.* ***2001***, 34, 23-34.

Chow, J.C.; Watson, J.G.; Pritchett, L.C.; Pierson, W.R.; Frazier, C.A.; Purcell, R.G. The DRI Thermal/Optimal Reflectance carbon analysis system: description, evaluation and applications in U.S. air quality studies. *Atmos. Environ. A,* ***1993***, 27, 1185-1201.

Chylek, P.; Johnson, B.; Wu, H. Black carbon concentration in a Greenland Dye-3 ice core. *Geophys. Res. Lett.* ***1992***, 19, 1951-1953.

Chylek, P.; Wong, J. Effect of absorbing aerosols on global radiation budget. *Geophys. Res. Lett.* ***1995***, 22, 929-931.

Clark, J.S. Particle motion and the theory of charcoal analysis: Source area, transport, deposition, and sampling. *Quaternary Res.* ***1988a***, 30, 67-80.

Clark, J.S. Stratigraphic charcoal analysis on petrographic thin sections: Application to fire history in northwestern Minnesota. *Quaternary Res.* ***1988b***, 30, 81-91.

Clark, J.S.; Royall, P.D. Local and regional sediment charcoal evidence for fire regimes in presettlement north-eastern North America. *J. Ecol.* ***1996***, 84, 365-382.

Clark, J.S.; Royall, P.D. Pre-Industrial particulate emissions and carbon sequestration from biomass burning in North America. *Biogeochemistry* ***1994***, 24, 35-51.

Clark, J.S.; Royall, P.D. Particle-size evidence for source areas of charcoal accumulation in late Holocene sediments of eastern North American lakes. *Quaternary Res.* ***1995***, 43, 80-89

Clark, T.L.; Radke, L.; Coen, J.; Middleton, D. Analysis of small-scale convective dynamics in a crown fire using infrared video camera imagery. *J. Appl. Meteor.* ***1999***, 38, 1401-1420.

Clarke, A.D.; Noone, K.J.; Heintzenberg, J.; Warren, S.G.; Covert, D.S. *Atmos. Environ.* ***1987***, 21, 1455-1465.

Coates, J.D.; Anderson, R.T.; Lovley, D.R. Oxidation of polycyclic aromatic hydrocarbons under sulfate-reducing conditions. *Appl. Environ. Microbiol.* ***1996***, 62, 1099-1101.

Conder, J.M.; La Point, T.W.; Lotufo, G.R.; Steevens. J.A. Nondestructive, minimal-disturbance, direct-burial solid-phase microextraction fiber technique for measuring TNT in sediment. *Environ. Sci. Technol.* ***2003***, 37, 1625-1632.

Conrad, A.U.; Comber, S.D.; Simkiss, K. Pyrene bioavailability; effect of sediment-chemical contact time on routes of uptake in an oligochaete worm. *Chemosphere* ***2002***, 49, 447-454.

Cope, M.J.; Chaloner, W.G. Fossil charcoal as evidence of past atmospheric composition. *Nature* ***1980***, 283, 647-649.

Corn, M.; Montgomery, T.L.; Reitz, R.J. Atmospheric particulates: specific surface areas and densities. *Science* ***1968***, 159, 1350-1351.

Cornelissen, G.; Breedveld, G.D.; Naes, K.; Oen, A.M.P.; Ruus, A. Bioaccumulation of native polycyclic aromatic hydrocarbons from sediment by a polychaete and a gastropod: Freely dissolved concentrations and activated carbon amendment. *Environ. Toxicol. Chem.* ***2006***, 25, 2349-2355.

Cornelissen, G.; Elmquist, M.; Groth, I.; Gustafsson, O. Effect of sorbate planarity on environmental black carbon sorption. *Environ. Sci. Technol.* ***2004a***, 38, 3574-3580.

Cornelissen, G.; Gustafsson, O. Sorption of phenanthrene to environmental black carbon in sediment with and without organic matter and native sorbates. *Environ. Sci. Technol.* ***2004b***, 38, 148-155.

Cornelissen, G.; Gustafsson, O. Importance of unburned coal carbon, black carbon, and amorphous organic carbon to phenanthrene sorption in sediment. *Environ. Sci. Technol.* ***2005a***, 39, 764-769.

Cornelissen, G.; Gustafsson, O.; Bucheli, T.D.; Jonker, M.T.O.; Koelmans, A.A.; van Noort, P.C.M. Extensive sorption of organic compounds to black carbon, coal and kerogen in sediments and soils: mechanisms and consequences for distribution, bioaccumulation, and biodegradation. *Environ. Sci. Technol.* ***2005b***, 39, 6881-6895.

Cornelissen, G.; van Noort, P.C.M.; Govers, H.A.J. Mechanism of slow desorption of organic compounds from sediments: A study using model sorbents. *Environ. Sci. Technol.* ***1998a***, 32, 3124-3131.

Cornelissen, G.; van Noort, P.C.M.; Govers, H.A. Desorption kinetics of chlorobenzenes, polycyclic aromatic hydrocarbons, and polychlorinated biphenyls: sediment extraction with Tenax and effects of contact time and solute hydrophobicity. *Environ. Toxicol. Chem.* ***1997a***, 16, 1351-1357.

Cornelissen, G.; van Noort, P.C.M.; Parsons, J.R.; Govers, H.A. Temperature dependence of a slow adsorption and desorption kinetics of organic compounds in sediments. *Environ. Sci. Technol.* ***1997b***, 31, 454-460.

Cornelissen, G.; van der Pal, M.; van Noort, P.C.M.; Govers, H.A.J. Competitive effects on the slow desorption of organic compounds from sediments. *Chemosphere* ***1999a***, 39, 1971-1981.

Cornelissen, G.; Rigterink, H.; Ferdinandy, M.M.A.; van Noort, P.C.M. Rapidly desorbing fractions of PAHs in contaminated sediments as a predictor of the extent of bioremediation. *Environ. Sci. Technol.* ***1998b***, 32, 966-970.

Cornelissen, G.; van Zuilen, H.; van Noort, P.C.M. Particle size dependence of slow desorption of *in situ* PAHs from sediments. *Chemosphere* ***1999b***, 38, 2369-2380.

Cosovic, B.; Vojvodic, V. Adsorption behavior of the hydrophobic fraction of organic matter in natural waters. *Mar. Chem.* ***1989***, 28, 183-198.

Cotoruelo, L.M.; Marques, M.D.; Rodriguez-Mirasol, J.; Cordero, T.; Rodriguez, J.J. Adsorption of aromatic compounds on activated carbons from lignin: equilibrium and thermodynamic study. *Ind. Eng. Chem. Res.* ***2007***, 46, 4982-4990.

Cousins, I.T.; McLachlan, M.S.; Jones, K.C. Lack of an aging effect on the soil-air partitioning of polychlorinated biphenyls. *Environ. Sci. Technol.* ***1998***, 32, 2734-2740.

Covert, D.S.; Heintzenberg, J. Measurement of the degree of internal/external mixing of hygroscopic compounds and soot in atmospheric aerosols. *Sci. Total Environ.* ***1984***, 36, 347-352.

Crank, J. *The Mathematics of Diffusion.* ***1979***, pp. 1-414, Oxford Clarendon Press.

Crittenden, J.C.; Hutzler, N.J.; Geyer, D.G.; Oravitz, J.L.; Friedman, G. Transport of organic compounds with saturated groundwater flow: model development and parameter sensitivity. *Wat. Resour. Res.* ***1986***, 22, 271-284.

Crompton, T.R. *Toxicants in the aqueous ecosystem.* ***1997***, pp. 1-382, Wiley.

Crusius, J.; Anderson, R.F. Core compression and surficial sediment loss of lake sediments of high porosity caused by gravity coring. *Limnol. Oceanogr.* ***1991***, 36, 1021-1031.

Crusius, J.; Bothner, M.H.; Sommerfield, C.K. Bioturbation depths, rates and processes in Massachusetts Bay sediments inferred from modeling of ^{210}Pb and $^{239+240}$Pu profiles. *Estuar. Coastal Shelf Sci.* ***2004***, 61, 643-655.

Crutzen, P.J. and Andreae, M.O. Biomass burning in the Tropics: impact on atmospheric chemistry and biogeochemical cycles. *Science* ***1990***, 250, 1669-1678.

Culver, T.B.; Hallisey, S.P.; Sahoo, D.; Deitsch, J.J.; Smith, J.A. Modeling the desorption of organic contaminants from long-term contaminated soil using distributed mass transfer rates. *Environ. Sci. Technol.* ***1997***, 31, 1581-1588.

Currie, L.A.; Benner, B.A.; Kessler, J.D.; Klinedinst, D.B.; Klouda, G.A.; Marolf, J.V.; Slater, J.F.; Wise, S.A.; Cachier, H.; Cary, R.; Chow, J.C.; Watson, J.; Druffel, E.R.M.; Masiello, C.A.; Eglinton, T.I.; Pearson, A.; Reddy, C.M.; Gustafsson, O.; Quinn, J.G.; Hartmann, P.C.; Hedges, J.I.; Prentice, K.M.; Kirchstetter, T.W.; Novakov, T.; Puxbaum, H.; Schmidt H. A critical evaluation of interlaboratory data on total, elemental, and isotopic carbon in the carbonaceous particle reference material, NIST SRM 1649a. *J. Res. Natl. Inst. Stand.* ***2002***, 107, 279-298.

Curry, K.J.; Bennett, R.H.; Mayer, L.M.; Curry, A.; Abril, M.; Biesiot, P.M.; Hulbert, M.H. Direct visualization of clay microfabric signatures driving organic matter preservation in fine-grained sediment. *Geochim. Cosmochim. Acta* ***2007***, 71, 1709-1720.

Cuypers, C.; Grotenhuis, T.; Nierop, K.G.J.; Franco, E.M.; de Jager, A.; Rulkens, W. Amorphous and condensed organic matter domains: the effect of persulfate oxidation on the composition of soil/sediment organic matter. *Chemosphere* ***2002***, 48, 919-931.

Czimczik, C.I.; Preston, C.M.; Schmidt, M.W.I.; Werner, R.A.; Schulze, E.D. Effects of charring on mass, organic carbon, and stable carbon isotope composition of wood. *Org. Geochem.* ***2002***, 33, 1207-1223.

Czimczik, C.I.; Masiello, C.A. Controls on black carbon storage in soils. *Global Biogeochem. Cycles* ***2007***, 21, GB3005, doi:10.1029/2006GB002798.

D

Dai, X.; Boutton, T.W.; Glaser, B.; Ansley, R.J.; Zech, W. Black carbon in a temperate mixed-grass savanna. *Soil Biol. Biochem.* ***2005***, 37, 1879-1881.

Daly, H.M.; Horn, A.B. Heterogeneous chemistry of toluene, kerosene and diesel soots. *Phys. Chem. Chem. Phys.* ***2009***, 11, 1069-1076.

Damste, J.S.S.; de las Heras, F.X.C.; van Bergen, P.F.; de Leeuw, J.W. Characterization of Tertiary Catalan lacustrine oil shales: discovery of extremely organic sulphur-rich type I kerogens. *Geochim. Cosmochim. Acta* ***1993***, 57, 389-415.

Danielsen, K.M.; Chin, Y.P.; Buterbaugh, J.S.; Gustafson, T.L.; Traina, S.J. Solubility enhancement and fluorescence quenching of pyrene by humic substances: the effect of dissolved oxygen on quenching processes. *Environ. Sci. Technol.* ***1995***, 29, 2162-2165.

Daulan, C.; Lyubchik, S.B.; Rouzaud, J.-N.; Beguin, F. Influence of anthracite pretreatment in the preparation of activated carbons. *Fuel* ***1998***, 77, 495-502.

Deen, W.M. *Analysis of Transport Phenomena.* ***1998***, pp.1-597, Oxford.

Deitsch, J.J.; Smith, J.A.; Culver, T.B.; Brown, R.A.; Riddle, S.A. Distributed-rate model analysis of 1,2-dichlorobenzene batch sorption and desorption rates for five natural sorbents.

Dell'Abate, M.T.; Benedetti, A.; Brookes, P.C. Hyphenated techniques of thermal analysis for characterization of soil humic substances. *J. Sep. Sci.* ***2003***, 26, 433-440.

DeSutter, T.M.; Clay, S.A.; Clay, D.E. Atrazine sorption and desorption as affected by aggregate size, particle size, and soil type. *Weed Sci.* ***2003***, 51, 456-462.

Devore, J.L. *Probability and Statistics for Engineering and the Sciences.* ***1995***, pp. 1-743, ITP.

Diercks, A.R.; Asper, V.L. In situ settling speeds of marine snow aggregates below the mixed layer: Black Sea and Gulf of Mexico. *Deep-Sea Res. I* ***1997***, 44, 385-398.

Dickens, A.F.; Gelinas, Y.; Masiello, C.A.; Wakeham, S.; Hedges, J.I. Reburial of fossil organic carbon in marine sediments. *Nature* ***2004***, 427, 336-339.

Di Toro, D.M.; Horzempa, L.M. Reversible and resistant components of PCB adsorption-desorption: Isotherms. *Environ. Sci. Technol.* ***1982***, 16, 594-602.

Di Toro, D.M.; McGrath, J.A.; Hansen, D.J. Technical basis for narcotic chemicals and polycyclic aromatic hydrocarbon criteria. I. Water and tissue. *Environ. Toxicol. Chem.* ***2000***, 19, 1951-1970.

Doerr, S.H.; Shakesby, R.A.; Blake, W.H.; Chafer, C.J.; Humphreys, G.S.; Wallbrink, P.J. Effects of differing wildfire severities on soil wettability and implications for hydrological response. *J. Hydrol.* ***2006***, 319, 295-311.

Donahue, W.F.; Allen, E.W.; Schindler, D.W. Impacts of coal-fired power plants on trace metals and polycyclic aromatic hydrocarbons (PAHs) in lake sediments in central Alberta, Canada. *J. Paleolimnol.* ***2006***, 35, 111-128.

Doong, R.A.; Chang, S.M. Determination of distribution coefficients of priority polycyclic aromatic hydrocarbons using solid-phase microextraction. *Anal. Chem.* ***2000***, 72, 3647-3652.

Doong, R.A.; Lin, Y.T. Characterization and distribution of polycyclic aromatic hydrocarbon contaminations in surface sediment and water from Gao-ping River, Taiwan. *Wat. Res.* ***2004***, 38, 1733-1744.

Drake, D.E.; Eganhouse, R.; McArthur, W. Physical and chemical effects of grain aggregates on the Palos Verdes margin, southern California. *Cont. Shelf Res.* ***2002***, 22, 967-986.

Droppo, I.G.; Ross, N.; Skafel, M.; Liss, S.N. Biostabilization of cohesive sediment beds in a freshwater wave-dominated environment. *Limnol. Oceanogr.* ***2007***, 52, 577-589.

Duarte, R.B.M.O.; Santos, E.B.H.; Pio, C.A.; Duarte, A.C. Comparison of structural features of water-soluble organic matter from atmospheric aerosols with those of aquatic humic substances. *Atmos. Environ.* ***2007***, 41, 8100-8113.

Dunne, L.J.; Nolan, P.F.; Munn, J.; Terrones, M.; Jones, T.; Kathirgamanathan, P.; Fernandez, J.; Hudson, A.D. Experimental verification of the dominant influence of extended carbon networks on the structural, electrical and magnetic properties of a common soot. *J. Phys.: Condens. Matter,* ***1997***, 9, 10661-10673.

Dyer, K.R. *Coastal and Estuarine Sediment Dynamics.* ***1986***, pp. 1-342, Wiley.

E

Ebbesen, T.W.; Hiura, H.; Hedenquist, J.W.; de Ronde, C.E.J.; Andersen, A.; Often, O.; Melezhik, V.A. Origins of fullerenes in rocks. *Science* ***1995***, 268, 1634-1635.

Edelvang, K.; Austen, I. The temporal variation of flocs and fecal pellets in a tidal channel. *Estuarine Coastal Shelf Sci.* ***1997***, 44, 361-367.

Edzwald, J.K.; Upchurch, J.B.; O'Melia, C.R. Coagulation in estuaries. *Environ. Sci. Technol.* ***1974***, 8, 58-63.

Egerton, R.F. *Electron Energy-Loss Spectroscopy in the Electron Microscope.* ***1996***, pp. 1-485, Springer.

Egerton, R.F.; Li, P.; Malac, M. Radiation damage in the TEM and SEM. *Micron* ***2004***, 35, 399-409.

Egerton, R.F.; Rossouw, C.J. Direct measurement of contamination and etching rates in an electron beam. *J. Phys. D: Appl. Phys.* ***1976***, 9, 659-663.

Eggleton, J.; Thomas, K.V. A review of factors affecting the release and bioavailability of contaminants during sediment disturbance events. *Environ. Intern.* ***2004***, 30, 973-980.

Ehlers, L.J.; Luthy, R.G. Contaminant bioavailability in soil and sediment. *Environ. Sci. Technol.* ***2003***, 37, 295A-302A.

Eisma, D. Flocculation and de-flocculation of suspended matter in estuaries. *Neth. J. Sea. Res.* ***1986***, 20, 183-199.

Eisma, D. *Suspended Matter in the Aquatic Environment.* ***1993***, pp.1-315, Springer-Verlag.

Elmquist, M.; Cornelissen, G.; Kukulska, Z.; Gustafsson, O. Distinct oxidative stabilities of char versus soot black carbon: implications for quantification and environmental recalcitrance. *Global Biogeochem. Cycles* ***2006***, 20, GB2009.

Elmquist, M.; Zencak, Z.; Gustafsson, O. A 700 year sediment record of black carbon and polycyclic aromatic hydrocarbons near the EMEP air monitoring station in Aspvreten, Sweden. *Environ. Sci. Technol.* ***2007***, 41, 6926-6932.

Enell, A.; Reichenberg, F.; Ewald, G.; Warfvinge, P. Desorption kinetics studies on PAH-contaminated soil under varying temperatures. *Chemosphere* ***2005***, 61, 1529-1538.

Engle, D.M.; Bidwell, T.G.; Ewing, A.L.; Williams, J.R. A technique for quantifying fire behavior in grassland fire ecology studies. *Southwestern Naturalist* ***1989***, 34, 79-84.

Erickson, M.J.; Turner, C.L.; Thibodeaux, L.J. Field observation and modeling of dissolved fraction sediment-water exchange coefficients for PCBs in the Hudson River. *Environ. Sci. Technol.* ***2005***, 39, 549-556.

Erm, A.; Alari, V.; Kouts, T. Transport of sediments resuspended by ferries. *IEEE Xplore* (digital library at ieeexplore.ieee.org) ***2008***, No. 978-1-4244-2268-5/08.

Ewald, G. Unpublished sedimentary PAHs and OC/BC data on Boston Harbor sediments. ***~2000*** (see Appendix 9-9).

F

Fairchild, J.F.; Boyle, T.; English, W.R.; Rabeni, C. Effects of sediment and contaminated sediment on structural and functional components of experimental stream ecosystems. *Water Air Soil Poll.* ***1987***, 36, 271-293.

Fang, C.; Smith, P.; Moncrieff, J.B.; Smith, J.U. Similar response of labile and resistant soil organic matter pools to changes in temperature. *Nature* ***2005***, 433, 57-59.

Fang, M.-D.; Lee, C.-L.; Yu, C.-S. Distribution and source recognition of polycyclic aromatic hydrocarbons in the sediments of Hsin-ta Harbour and adjacent costal areas, Taiwan. *Mar. Pollut. Bull.* ***2003***, 46, 941-953.

Farley, K.J.; Morel, F.M.M. Role of coagulation in the kinetics of sedimentation. *Environ. Sci. Technol.* ***1986***, 20, 187-195.

Farrell, J.; Reinhard, M. Desorption of halogenated organics from model solids, sediments, and soil under unsaturated conditions. 1. Isotherms. *Environ. Sci. Technol.,* ***1994***, 28, 53-62.

Faulon, J.L. Calculating the Number-Averaged Molecular Weight (M0) of Aromatic and Hydroaromatic Clusters in Coal using Rubber Elasticity Theory. *Energy Fuels* ***1994***, 8, 1020-1023.

Fearnside, P.M.; Graca P.M.L.A.; Filho, N.L.; Rodrigues, F.J.A.; Robinson, J.M. Tropical forest burning in Brazilian Amazonia: measurement of biomass loading, burning efficiency and charcoal formation at Altamira, Para. *For. Ecol. Manage.* ***1999***, 123, 65-79.

Fearnside, P.M.; Graca P.M.L.A.; Rodrigues, F.J.A. Burning of Amazonian rainforests: burning efficiency and charcoal formation in forest cleared for cattle pasture near Manaus, Brazil. *For. Ecol. Manage.* ***2001***, 146, 115-128.

Fearnside, P.M.; Niwton, L.; Fernandes, F.M. Rainforest Burning and the Global Carbon Budget: Biomass, Combustion Efficiency, and Charcoal Formation in the Brazilian Amazon. *J. Geophys. Res.* ***1993***, 98, 16733-16743.

Feitelberg, A.S.; Longwell, J.P.; Sarofim, A.F. Metal enhanced soot and PAH formation. *Combust. Flame* ***1993***, 92, 241-253.

Ferge, T.; Karg, E.; Schroppel, A.; Coffee, K.R.; Tobias, H.J.; Frank, M.; Gard, E.E.; Zimmermann, R. Fast determination of the relative elemental and organic carbon content of aerosol samples by on-line single-particle aerosol time-of-flight mass spectrometry. *Environ. Sci. Technol.* ***2006***, 40, 3327-3335.

Fernandes, M.B.; Skjemstad, J.O.; Johnson, B.B.; Wells, J.D.; Brooks, P. Characterization of carbonaceous combustion residues. I. Morphological, elemental and spectroscopic features. *Chemosphere* ***2003***, 51, 785-795.

Fernandez, I.; Cabaneiro, A.; Carballas, T. Carbon mineralization dynamics in soils after wildfires in two Galician forests. *Soil Biol. Biochem.* ***1999***, 31, 1853-1865.

Fernandez, L.A.; MacFarlane, J.K.; Tcaciuc, A.P.; Gschwend, P.M. Measurement of freely dissolved PAH concentrations in sediment beds using passive sampling with low-density polyethylene strips. *Environ. Sci. Technol.* ***2009***, 43, 1430-1436.

Ferris, F.G.; Tazaki, K.; Fyfe, W.S. Iron oxides in acid mine drainage environments and their association with bacteria. *Chem. Geol.* ***1989***, 74, 321-330.

Filipe, O.M.S.; Vidal, M.M.; Duarte, A.C.; Santos, E.B.H. Adsorption-desorption behavior of Thiram onto humic acid. *J. Agric. Food Chem.* ***2009***, 57, 4906-4912.

Flores-Cervantes, D.X. Black carbon in the Gulf of Maine: new insights into inputs and cycling of combustion-derived organic carbon. Ph.D. Theses, Massachusetts Institute of Technology, ***2008***, pp 1-295.

Flores-Cervantes, D.X.; Reddy, C.M.; Gschwend, P.M. Inferring black carbon concentrations in particulate organic matter by observing pyrene fluorescence losses. *Environ. Sci. Technol.* ***2009***, 43, 4864-4870.

Forster, G.D.; Wright, D.A. Unsubstitute polycyclic aromatic hydrocarbons in sediments, clams, and clam worms from Chesapeake Bay. *Mar. Pollut. Bull.* ***1988***, 19, 459-465.

Forster, P.; Ramaswamy, V.; Artaxo, P.; Berntsen, T.; Betts, R.; Fahey, D.W.; Haywood, J.; Lean, J.; Lowe, D.C.; Myhre, G.; Nganga, J.; Prinn, R.; Raga, G.; Schulz, M.; van Dorland, R. Chanes in atmospheric constituents and in radiative forcing. In *Climate Change 2007: The Physical Science Basis. Contribution of Working Group I to the Fourth Assessment Report of the Intergovernmental Panel on Climate Change*, (eds. Solomon, S.; Qin, D.; Manning, M.; Chen, Z.; Marquis, M.; Averyt, K.B.; Tignor, M.; Miller, H.L.), pp 129-234, Cambridge University Press, Cambridge, ***2007***.

Fredlund, M.D.; Fredlund, D.G.; Wilson, G.W. An equation to represent grain-size distribution. *Can. Geotech. J.* ***2000***, 37, 817-827.

Friedel, R.A.; Orchin, M. *Ultraviolet spectra of aromatic compounds.* ***1951***, pp.1-52, Wiley.

Frosch, D.; Westphal, C. Melamine resins and their application in electron microscopy. *Elec. Micr. Rev.* ***1989***, 2, 231-255.

Frost, D.C.; Leeder, W.R.; Tapping, R.L. X-ray photoelectron spectroscopic investigation of coal. *Fuel* ***1974***, 53, 206-211.

Fu, G.; Kan, A.T.; Tomson, M. Adsorption and desorption hysteresis of PAHs in surface sediment. *Environ. Toxicol. Chem.* ***1994***, 13, 1559-1567.

Furukawa, Y. Energy-filtering transmission electron microscopy (EFTEM) and electron energy-loss spectroscopy (EELS) investigation of clay-organic matter aggregates in aquatic sediments. *Org. Geochem.* ***2000***, 31, 735-744.

Furukawa, Y.; Watkins, J.L.; Kim, J.; Curry, K.J.; Bennett, R.H. Aggregation of montmorillonite and organic matter in aqueous media containing artificial seawater. *Geochem. Trans.* ***2009***, 10, Art. No.2.

G

Gagosian, R.B.; Peltzer, E.T. The importance of atmospheric input of terrestrial organic material to deep sea sediments. *Org. Geochem.* ***1986***, 10, 661-669.

Gagosian, R.B.; Peltzer, E.T.; Merrill, J.T. Long-range transport of terrestrially derived lipids in aerosols from the South-Pacific. *Nature* ***1987***, 325, 800-804.

Gale, T.K.; Bartholomew, C.H.; Fletcher, T.H. Decreases in the swelling and porosity of bituminous coals during devolatilization at high heating rates. *Combust. Flame* ***1995***, 100, 94-100.

Gallup, J.L.; Sachs, J.D.; Mellinger, A.D. Geography and economic development. *Intern. Regional Sci. Rev.* ***1999***, 22, 179-224.

Garcette-Lepecq, A.; Derenne, S.; Largeau, C.; Bouloubassi, I.; Saliot, A. Origin and formation pathways of kerogen-like organic matter in recent sediments off the Danube delta (northwestern Black Sea). *Org. Geochem.* ***2000***, 31, 1663-1683.

Gardner, B.; Hewitt, C.N.; Jones, K.C. PAHs in air adjacent to two inland water bodies. *Environ. Sci. Technol.* ***1995***, 29, 2405-2413.

Gaspare, L.; Machiwa, J.F.; Mdachi, S.J.M.; Streck, G.; Brack, W. Polycyclic aromatic hydrocarbon (PAH) contamination of surface sediments and oysters from the inter-tidal areas of Dar es Salaam, Tanzania. *Environ. Pollut.* ***2009***, 157, 24-34.

Gauthier, A.; Derenne, S.; Largeau, C.; Dupont, L.; Guillon, E.; Dumonceau, J.; Aplincourt, M. Comparative study of lingo-cellulosic material from wheat straw of pure and mixed standard compounds via solid state 13C NMR spectroscopy, conventional pyrolysis and TMAH thermochemolysis. *J. Anal. Appl. Pyrolysis* ***2003***, 67, 277-293.

van Geen, A. and Luoma, S.N. The impact of human activities on sediments of San Francisco Bay, California: an overview. *Mar. Chem.* ***1999***, 64, 1-6.

Gelinas, Y.; Prentice, K.M.; Baldock, J.A.; Hedges, J.I. An Improved Thermal Oxidation Method for the Quantification of Soot/Graphitic Black Carbon in Sediments and Soils. *Environ. Sci. Technol.* ***2001***, 35, 3519-3525.

Georgi, A.; Kopinke, F.D. Validation of a modified Flory-Huggins concept for description of hydrophobic organic compound sorption on dissolved humic substances. *Environ. Toxicol. Chem.* ***2002***, 21, 1766-1774.

Gergova, K.; Eser, S. Effects of activation method on the pore structure of activated carbons from apricot stones. *Carbon* ***1996***, 34, 879-888.

Gevao, B.; Hamilton-Taylor, J.; Jones, K.C. Towards a complete mass balance and model for PCBs and PAHs in a small rural lake, Cumbria, U.K. *Limnol. Oceanogr.* ***2000***, 45, 881-894.

Ghabbour, E.A.; Davies, G.; O'Donaughy, K.; Smith, T.L.; Goodwillie, M.E. Adsorption of a plant- and a soil-derived humic acid on the common clay kaolinite. In *Humic Substances – Structures, Properties and Uses*, (eds. Davies, G.; Ghabbour, E.A.), pp 185-194, Royal Society of Chemistry, Cambridge, ***1998***.

Ghosh, U.; Gillette, J.S.; Luthy, R.G.; Zare, R.N. Microscale location, characterization, and association of polycyclic aromatic hydrocarbons on harbor sediment particles. *Environ. Sci. Technol.* ***2000***, 34, 1729-1736.

Ghosh, U.; Talley, J.W.; Luthy, R.G. Particle-scale investigation of PAH desorption kinetics and thermodynamics from sediment. *Environ. Sci. Technol.* ***2001***, 35, 3468-3475.

Ghosh, U.; Zimmerman, J.R.; Luthy, R.G. PCB and PAH speciation among particle types in contaminated harbor sediments and effects on PAH bioavailability. *Environ. Sci. Technol.* ***2003***, 37, 2209-2217.

Gigliotti, C.L.; Brunciak, P.A.; Dachs, J.; Glenn, T.R.; Nelson, E.D.; Totten, L.A.; Eisenreich, S.J. Air-water exchange of polycyclic aromatic hydrocarbons in the New York-New Jersey, USA, Harbor Estuary. *Environ. Toxicol. Chem.* ***2002***, 21, 235-244.

Gilchrist, G.F.R.; Gamble, D.S.; Kodama, H.; Khan, S.U. Atrazine interactions with clay minerals: kinetics and equilibria of sorption. *J. Agric. Food Chem.* ***1993***, 41, 1748-1755.

Giordano, A.; Stante, L.; Pirozzi, F.; Cesaro, R.; Bortone, G. *J. Hazard. Mater. B* ***2005***, 119, 159-166.

Glaser, B.; Balashov, E.; Haumaier, L.; Guggenberger, G.; Zech, W. Black carbon in density fractions of anthropogenic soils of the Brazilian Amazon region. *Org. Geochem.* ***2000***, 31, 669-678.

Glaser, B.; Haumaier, L.; Guggenberger, G.; Zech, W. Black carbon in soils: the use of benzenecarboxylic acids as specific markers. *Org. Geochem.* ***1998***, 29, 811-819.

Glaser, B.; Knorr, K.-H. Isotopic evidence for condensed aromatics from non-pyrogenic sources in soils – implications for current methods for quantifying soil black carbon. *Rapid Commun. Mass Spectrom.* ***2008***, 22, 935-942.

Glazer, A.W.; Nikaido, H. *Microbial Biotechnology.* ***1995***, pp. 1-340, W.H. Freeman.

Goldberg, E.D. *Black Carbon in the Environment.* ***1985***, pp. 1-198, Wiley.

Goldberg, E.D.; Gamble, E.; Griffin, J.J.; Koide, M. Pollution history of Narragansett Bay as recorded in its sediments. *Estuar. Coastal Mar. Sci.* ***1977***, 5, 549-561.

Goldberg, E.D.; Hodge, V.G.; Griffin, J.J.; Koide, M.; Edgington, D.N. Impact of fossil-fuel combustion on the sediments of Lake-Michigan. *Environ. Sci. Technol.* ***1981***, 15, 466-471.

Goldstein, H.L.; Siegmunce, C.W. Influence of heavy oil composition and boiler combustion conditions on particulate emissions. *Environ. Sci. Technol.* ***1976***, 10, 1109-1114.

Goldstein, J.I. Principles of thin film X-ray microanalysis. In *Introduction to Analytical Electron Microscopy*, (eds. Hren, J.J.; Goldstein, J.I.; Joy, D.C.), pp 83-120., Plenum, New York, ***1979***.

Golomb, D.; Ryan, D.; Underhill, J.; Wade, T.; Zemba, S. Atmospheric deposition of toxics onto Massachusetts Bay — II. Polycyclic aromatic hydrocarbons. *Atmos. Environ.* ***1997***, 31, 1361-1368.

Gomez-Lahoz, C.; Ortega-Calvo, J.J. Effect of slow desorption on the kinetics of biodegradation of polycyclic aromatic hydrocarbons. *Environ. Sci. Technol.* ***2005***, 39, 8776-8783.

Gong, Y.; Depinto, J.V.; Rhee, G.-Y.; Liu, X. Desorption rates of two PCB congeners from suspended sediments — I. experimental results. *Wat. Res.* ***1998a***, 32, 2507-2517.

Gong, Y.; Depinto, J.V. Desorption rates of two PCB congeners from suspended sediments — II. model simulation. *Wat. Res.* ***1998b***, 32, 2518-2532.

Goni, M.A.; Yunker, M.B.; Macdonald, R.W.; Eglinton, T.I. Distribution and sources of organic biomarkers in arctic sediments from the Mackenzie River and Beaufort Shelf. *Mar. Chem.* ***2000***, 71, 23-51.

Graham, J.S.; Conn, J.S. Sorption of Metribuzin and Metolachlor in Alaskan subarctic agricultural soils. *Weed Sci.* ***1992***, 40, 155-160.

de Grave, S.; Whitaker, A. Benthic community re-adjustment following dredging of a muddy-maerl matrix. *Mar. Pollut. Bull.* ***1999***, 38, 102-108.

Green, M.; Cosslett, V.E. The efficiency of production of characteristic X-radiation in thick targets of a pure element. *Proc. Phys. Soc.* ***1961***, 78, 1206-1214.

Greenfield, B.K.; Davis, J.A. A PAH fate model for San Francisco Bay. *Chemosphere* ***2005***, 515-530.

Gregory, J. Rates of flocculation of latex particles by cationic polymers. *J. Colloid Interface Sci.* ***1973***, 42, 448-456.

Gregory, J. Polymer adsorption and flocculation in sheared suspensions. *Colloids Surf.* ***1988***, 31, 231-253.

Gregory, J. Fundamentals of flocculation. *Crit. Rev. Environ. Control* ***1989***, 19, 185-230.

Griffin, J.J.; Goldberg, E.D. The fluxes of elemental carbon in coastal marine sediments. *Limnol. Oceanogr.* ***1975***, 20, 456-463.

Griffin, J.J.; Goldberg, E.D. Morphologies and origin of elemental carbon in the environment. *Science* ***1979***, 206, 563-565.

Griffin, J.J.; Goldberg, E.D. Sphericity as a characteristic of solids from fossil fuel burning in a Lake Michigan sediment. *Geochim. Cosmochim. Acta* ***1981***, 45, 763-769.

Grimmer, G. *Environmental carcinogens: polycyclic aromatic hydrocarbons.* ***1983***, pp. 1-261, CRC press.

Grisi, B.; Grace, C.; Brookes, P.C.; Benedetti, A.; Dell'Abate, M.T. Temperature effects on organic matter and microbial biomass dynamics in temperate and tropical soils. *Soil Biol. Biochem.* ***1998***, 30, 1309-1315.

Grundl, T.J.; Aldstadt, J.H.; Harb, J.G.; St. Germain, R.W.; Schweitzer, R.C. Demonstration of a method for the direct determination of polycyclic aromatic hydrocarbons in submerged sediments. *Environ. Sci. Technol.* ***2003***, 37, 1189–1197.

Gryzinski, M. Classical theory of atomic collisions. I. Theory of inelastic collisions. *Phys. Rev.* ***1965***, 138, A336-A358.

Gu, B.; Schmitt, J.; Chen, Z.; Liang, L.; McCarthy, J.F. Adsorption and desorption of natural organic matter on iron oxide: mechanisms and models. *Environ. Sci. Technol.* ***1994***, 28, 38-46.

Gu, B.; Schmitt, J.; Chen, Z.; Liang, L.; McCarthy, J.F. Adsorption and desorption of different organic matter fractions on iron oxide. *Geochim. Cosmochim. Acta* ***1995***, 59, 219-229.

Guerin, W.F.; Boyd, S.A. Bioavailability of naphthalene associated with natural and synthetic sorbents. *Wat. Res.* ***1997***, 31, 1504-1512.

Guinan, J.; Charlesworth, M.; Service, M.; Oliver, T. Sources and geochemical constraints of polycyclic aromatic hydrocarbons (PAHs) in sediments and mussels of two Northern Irish sea-loughs. *Mar. Pollut. Bull.* ***2001***, 42, 1073-1081.

Guo, J.; Lua, A.C. Characterization of chars pyrolyzed from oil palm stones for the preparation of activated carbons. *J. Anal. Appl. Pyrolysis* ***1998***, 46, 113-125.

Guo, J.; Lua, A.C. Characterization of adsorbent prepared from oil-palm shell by CO_2 activation for removal of gaseous pollutants. *Mater. Lett.* ***2002***, 55, 334-339.

Guo, W.; He, M.; Yang, Z.; Lin, C.; Quan, X.; Wang, H. Distribution of polycyclic aromatic hydrocarbons in water, suspended particulate matter and sediment from Daliao River watershed, China. *Chemosphere* ***2007***, 68, 93-104.

Gustafson, K.E.; Dickhut, R.M. Molecular diffusivity of polycyclic aromatic hydrocarbons in aqueous solution. *J. Chem. Eng. Data* ***1994***, 39, 281-285.

Gustafson, K.E.; Dickhut, R.M. Distribution of polycyclic aromatic hydrocarbons in southern Chesapeake Bay surface water: evaluation of three methods for determining freely dissolved water concentrations. *Environ. Toxicol. Chem.* ***1997***, 16, 452-461.

Gustafsson, O.; Bucheli, T. D.; Kukulska, Z.; Andersson, M.; Largeau, C.; Rouzad, J.; Reddy, C. M.; Eglinton, T. I. Evaluation of a protocol for the quantification of black carbon in sediments. *Global Biogeochem. Cycles* ***2001***, 15, 881-890.

Gustafsson, O.; Gschwend, P.M. Aquatic colloids: concepts, definitions, and current challenges. *Limnol. Oceanogr.* ***1997a***, 42, 519-528.

Gustafsson, O.; Gschwend, P.M. Soot as a strong partition medium for polycyclic aromatic hydrocarbons in aquatic systems. In *Molecular Markers in Environmental Geochemistry* (ed. Eganhouse, R.P.), pp. 365-381, ACS Symposium Series, Washington, ***1997b***.

Gustafsson, O.; Haghseta, F.; Chan, C.; Macfarlane, J.K.; Gschwend, P.M. Quantification of the dilute sedimentary soot phase: implications for PAH speciation and bioavailability. *Environ. Sci. Technol.* ***1997***, 31, 203-209.

Guthrie-Nichols, E.; Grasham, A.; Kazunga, C.; Sangaiah, R.; Gold, A.; Bortiatynski, J.; Salloum, M.; Hatcher, P. The effect of aging on pyrene transformation in sediments. *Environ. Sci. Technol.* ***2003***, 22, 40-49.

Gwaze, P.; Schmid, O.; Annegarn, H.J.; Andreae, M.O.; Huth, J.; Helas, G. *J. Aerosol Sci.* ***2006***, 37, 820-838.

H

Haenel, M.W. Recent Progress in coal structure research. *Fuel* ***1992***, 71, 1211-1223.

Haggerty, R.; Gorelick, M. Multiple-rate mass transfer for modeling diffusion and surface rections in media with pore-scale heterogeneity. *Wat. Resour. Res.* ***1995***, 31, 2383-2400.

Hahn, H.H.; Stumm, W. Kinetics of coagulation with hydrolyzed Al(III): The rate-determining step. *J. Colloid Interface Sci.* ***1968***, 28, 134-144.

Hammes, K.; Schmidt, M.W.I.; Smernik, R.J; Currie, L.A.; Ball, W.P.; Nguyen, T.H.; Louchouarn, P.; Houel, S.; Gustafsson, O.; Elmquist, M.; Cornelissen, G.; Skjemstad, J.O.; Masiello, C.A.; Song, J.; Peng, P.; Mitra, S.; Dunn, J.C.; Hatcher, P.G.; Hockaday, W.C.; Smith, D.M.; Hartkopf-Froeder, C.; Boehmer, A.; Luer, B.; Huebert, B.J.; Amelung, W.; Brodowski, S.; Huang, L.; Zhang, W.; Gschwend, P.M.; Flores-Cervantes, D.X.; Largeau, C.; Rouzaud, J.N.; Rumpel, C.; Guggenberger, G.; Kaiser, K.; Rodionov, A.; Gonzalez-Vila, F.J.; Gonzalez-Perez, J.A.; de la Rosa, J.M.; Manning, D.A.C.; Lopez-Capel, E.; Ding, L. Comparison of quantification methods to measure fire-derived (black/elemental) carbon in soils and sediments using reference materials from soil, water, sediment and the atmosphere. *Glob. Biogeochem. Cyc.* ***2007***, 21, Art. No. GB3016.

Hammes, K.; Smernik, R.J.; Skjemstad, J.O.; Herzog, A.; Vogt, U.F.; Schmidt, M.W.I. Synthesis and characterisation of laboratory-charred grass straw (Oryza sativa) and chestnut wood (Castanea sativa) as reference materials for black carbon quantification. *Org. Geochem.* ***2006***, 37, 1629-1633.

Hammes, K.; Smernik, R.J.; Skjemstad, J.O.; Schmidt, M.W.I. Characterisation and evaluation of reference materials for black carbon analysis using elemental composition, colour, BET surface area and C-13 NMR spectroscopy. *Appl. Geochem.* ***2008a***, 23, 2113-2122.

Hammes, K.; Torn, M.S.; Lapenas, A.G.; Schmidt, M.W.I. Centennial black carbon turnover observed in a Russian steppe soil. *Biogeosci.* ***2008b***, 5, 1339-1350.

Hanke, W.; Wernisch, J.; Pohn, C. Fluorescence yields, ω_K ($12 \leq Z \leq 42$) and ω_L ($38 \leq Z \leq 79$) , from a comparison of literature and experiments (SEM). *X-ray Spectrom.* ***1985***, 14, 43-47.

Hansch, C.; Leo, A.; Hoekman, D. *Exploring QSAR.* ***1995***, American Chemical Society.

Hansen, A.M.; Leckie, J.O. Time-dependent adsorption in near coastal marine sediments: a two-step model. *Adv. Wat. Resour.* ***1998***, 21, 523-531.

Hartmann, P.C.; Quinn, J.G.; Cairns, R.W.; King, J.W. The distribution and sources of polycyclic aromatic hydrocarbons in Narragansett Bay surface sediments. *Mar. Pollut. Bull.* ***2004***, 48, 351-358.

Hata, T.; Vystavel, T.; Bronsveld, P.; DeHosson, J.; Kikuchi, H.; Nishimiya, K.; Imamura, Y. Catalytic carbonization of wood charcoal: graphite or diamond? *Carbon* ***2004***, 42, 961-964.

Hatzinger, P.B.; Alexander, M. Effect of aging of chemicals in soil on their biodegradability and extractability. *Environ. Sci. Technol.* ***1995***, 29, 537-545.

Hatzinger, P.B.; Fuller, M.E.; Rungmakol, D.; Schuster, R.L.; Steffan, R.J. Enhancing the attenuation of explosives in surface soils at military facilities: sorption-desorption isotherms. *Environ. Toxicol. Chem.* ***2004***, 23, 306-312.

Hayduk, W.; Laudie, H. Prediction of diffusion coefficients for non-electrolytes in dilute aqueous solutions. *AIChE J.* ***1974***, 20, 611-615.

Haven, D.S.; Morales-Alamo, R. Biodeposition by oysters and other invertebrate filter feeders. *Limnol. Oceanogr.* ***1966***, 11, 487-498.

Hawley, N. Settling velocity distribution of natural aggregates. *J. Geophys. Res.* ***1982***, 87, C12, 9489-9498.

Hawthorne, S.B.; Grabanski, C.B.; Miller, D.J. Measured partitioning coefficients for parent and alkyl polycyclic aromatic hydrocarbons in 114 historically contaminated sediments: Part 1. K_{OC} values. *Environ. Toxicol. Chem.* ***2006***, 25, 2901-2911.

Hawthorne, S.B.; Grabanski, C.B.; Miller, D.J. Measured partition coefficients for parent and alkyl polycyclic aromatic hydrocarbons in 114 historically contaminated sediments: part 2. Testing the k(oc)k(bc) two carbon-type model. *Environ. Toxicol. Chem.* ***2007***, 26, 2505-2516.

Hawthorne, S.B.; St. Germain, R.W.; Azzolina, N.A. Laser-induced fluorescence coupled with solid-phase microextraction for in situ determination of PAHs in sediment pore water. *Environ. Sci. Technol.* ***2008***, 42, 8021-8026.

Hayase, K.; Tsubota, H. Sedimentary humic acid and fulvic acid as surface active substances. *Geochim. Cosmochim. Acta* ***1983***, 47, 947-952.

Haynes, B.S.; Wagner, H.G. Soot formation. *Prog. Energy Combust. Sci.* ***1981***, 7, 229-273.

Haywood, J.; Boucher, O. Estimates of the direct and indirect radiative forcing due to tropospheric aerosols: a review. *Rev. Geophysics* ***2000***, 38, 513-543.

Haywood, J.M.; Roberts, D.L.; Slingo, A.; Edwards, J.M.; Shine, K.P. General circulation model calculations of the direct radiative forcing by anthropogenic sulfate and fossil-fuel soot aerosol. *J. Climate* ***1997***, 10, 1562-1577.

Hedges, J.I.; Cowie, G.L.; Ertel, J.R. Degradation of carbohydrates and lignins in buried woods. *Geochim. Cosmochim. Acta* ***1985***, 49, 701-711.

Hellou, J.; Steller, S.; Zitko, V.; Leonard, J.; King, T.; Milligan, T.G.; Yeats, P. Distribution of PACs in surficial sediments and bioavailability to mussels, Mytilus edulis of Halifax Harbour. *Mar. Environ. Res.* ***2002***, 53, 357-379.

Hemsley, A.R.; Barrie, P.J.; Scott, A.C. C-13 Solid-state NMR-spectroscopy of fossil sporopollenins – variation in composition independent of diagenesis. *Fuel* ***1995***, 74, 1009-1012.

Hemsley, A.R.; Scott, A.C.; Barrie, P.J.; Chaloner, W.G. Studies of fossil and modern spore wall biomacromolecules using C-13 solid state NMR. *Annals Botany* ***1996***, 78, 83-94.

Henke, B.L.; Gullikson, E.C.; Davis, J.C. X-ray interactions: photoabsorption, scattering, transmission and reflection at E=50-30 000 eV, Z-1-92. *At. Data Nucl. Data Tables* ***1993***, 54, 181-342.

Henson, J.M. Melanin. In *Biopolymers – Lignin, Humic Substances and Coal*, (eds. Hofrichter, M.; Steinbuchel, A.), pp 229-246, Wiley-VCH, Weinheim, ***2001***.

van den Heuvel, H.; Le Couriaut, T.; McMullen, B.M.; Lozac'h, F.; van Noort, P. Maximum capacities for adsorption of phenanthrene in the slowly and very slowly desorbing domains in nineteen soils and sediments. *Environ. Toxicol. Chem.* ***2005***, 24, 830-835.

van den Heuvel, H.; van Noort, P.C.M. Competition for adsorption between added phenanthrene and in situ PAHs in two sediments. *Chemosphere* ***2003***, 53, 1097-1103.

van den Heuvel, H.; van Noort, P.C.M. Quantification of total native compounds on phenanthrene-specific adsorption sites in the very slow desorption domain of 16 sediments and soils. *Chemosphere* ***2006***, 65, 245-249.

Hildemann, L.M.; Markowski, G.R.; Cass, G.R. Chemical-composition of emissions from urban sources of fine organic aerosol. *Environ. Sci. Technol.* ***1991***, 25, 744-759.

Hiller, E.; Jurkovic, L.; Bartal, M. Effect of temperature on the distribution of polycyclic aromatic hydrocarbons in soil and sediment. *Soil Wat. Res.* ***2008***, 3, 231-240.

Hink, W.; Paschke, H. K-shell-fluorescence yield for carbon and other light elements. *Phys. Rev. A.* ***1971***, 4, 507-511.

Hinz, C. Description of sorption data with isotherm equations. *Geoderma* ***2001***, 99, 225-243.

Hitzenberger, R.; Jennings, S.G.; Larson, S.M.; Dillner, A.; Cachier, H.; Galambos, Z.; Rouc, A.; Spain, T.G. Intercomparison of measurement methods for black carbon aerosols. *Atmos. Environ.* ***1999***, 33, 2823-2833.

van Hoof, P.L.; Kukkonen, J.V.K.; Landrum, P.F. Impact of sediment manipulation of the bioaccumulation of polycyclic aromatic hydrocarbons from field-contaminated and laboratory-dosed sediments by an oligochaete. *Environ. Toxicol. Chem.* ***2001***, 20, 1752-1761.

Hoffmann, J.L.; Oris, J.T. Altered gene expression: a mechanism for reproductive toxicity in zebrafish exposed to benzo(a)pyrene. *Aquatic Toxicol.* ***2006***, 78, 332-340.

van Hoof, P.L.; Kukkonen, J.V.K.; Landrum, P.F. Impact of sediment manipulation of the bioaccumulation of polycyclic aromatic hydrocarbons from field-contaminated and laboratory-dosed sediments by an oligochaete. *Environ. Toxicol. Chem.* ***2001***, 20, 1752-1761.

Holmen, B.A.; Gschwend, P.M. Estimating sorption rates of hydrophobic organic compounds in iron oxide- and aluminosilicate clay-coated aquifer sands. *Environ. Sci. Technol.* ***1997***, 31, 105-113.

Hong, H.; Xu, L.; Zhang, L.; Chen, J.C.; Wong, Y.S.; Wan, T.S.M. Environmental fate and chemistry of organic pollutants in the sediment of Xiamen and Victoria Harbours. *Mar. Pollut. Bull.* ***1995***, 31, 229-236.

Hong, L.; Ghosh, U.; Mahajan, T.; Zare, R.N.; Luthy, R.G. PAH sorption mechanism and partitioning behavior in lampblack-impacted soils from former oil-gas plant sites. *Environ. Sci. Technol.* ***2003***, 37, 3625-3634.

Hong, L.; Luthy, R.G. Availability of polycyclic aromatic hydrocarbons from lampblack-impacted soils at former oil-gas plant sites in California, USA. *Environ. Toxicol. Chem.* ***2007***, 26, 394-405.

Horng, C Y.; Taghon, G.L. Loss rates of polycyclic aromatic hydrocarbons from sediment and deposit-feeder fecal pellets. *Environ. Toxicol. Chem.* ***2001***, 20, 1465-1473.

Horvath, H. Atmospheric light absorption – A review. *Atmos. Environ.* ***1993***, 27A, 293-317.

Hossain, S.; Eyre, B.D.; McKee, L.J. Impacts of dredging on dry season suspended sediment concentration in the Brisbane River estuary, Queensland, Australia. *Estuar. Coastal Shelf Sci.* ***2004***, 61, 539-545.

Houghton, R.A. Balancing the global carbon budget. *Ann. Rev. Earth Planet. Sci.* ***2007***, 35, 313-347.

Howdeshell, M.J.; Hites, R.A. Transport of Detroit River pollutants from Lake Erie by episodic resuspension events. *Environ. Sci. Technol.* ***1994***, 28, 1691-1697.

Hren, J.J. Barriers to AEM: contamination and etching. In *Introduction to Analytical Electron Microscopy*, (eds. Hren, J.J.; Goldstein, J.I.; Joy, D.C.), pp 481-505, Plenum, New York, ***1979***.

Hsieh, Y.M.; Tsai, M.S. Physical and chemical analyses of unburned carbon from oil-fired fly ash. *Carbon* ***2003***, 41, 2317-2324.

Hu, Q.; Wang, X.; Brusseau, M.L. Quantitative structure-activity relationships for evaluating the influence of sorbate structure on sorption of organic compounds by soil. *Environ. Toxicol. Chem.* ***1995***, 14, 1133-1140.

Huang, L.; Brook, J.R.; Zhang, W.; Li, S.M.; Graham, L.; Ernst, D.; Chiculescu, A.; Lu, G. Stable isotope measurements of carbon fractions (OC/EC) in airborne particulate: a new dimension for source characterization and apportionment. *Atmos. Environ.* ***2006***, 40, 2690-2705.

Huang, W.L.; Weber, W.J. A distributed reactivity model for sorption by soils and sediments. 10. Relationships between desorption, hysteresis, and the chemical characteristics of organic domains. *Environ. Sci. Technol.* ***1997a***, 31, 2562-2569.

Huang, W.L.; Weber, W.J. A distributed reactivity model for sorption by soils and sediments. 11. Slow concentration-dependent sorption rates. *Environ. Sci. Technol.* ***1998a***, 32, 3549-3555.

Huang, W.L.; Yu, H.; Weber, W.J. Hysteresis in the sorption and desorption of hydrophobic organic contaminants by soils and sediments. 1. A comparative analysis of experimental protocols. *J. Contam. Hydrol.* ***1998b***, 31, 129-148.

Huang, W.L.; Young, T.M.; Schlautman, M.A.; Yu, H.; Weber, W.L. A distributed reactivity model for sorption by soils and sediments. 9. General isotherm nonlinearity and applicability of the dual reactive domain model. *Environ. Sci. Technol.* ***1997b***, 31, 1703-1710.

Hubbell, J.H.; Seltzer, S.M. Tables of X-ray mass attenuation coefficients and mass energy-absorption coefficients. *NIST Physical Reference Data* ***1996***, National Institute of Standards and Technology (NISTIR 5632): http://physics.nist.gov/PhysRefData/XrayMassCoef/cover.html.

Huesemann, M.H.; Hausmann, T.S.; Fortman, T.J. Assessment of bioavailability limitations during slurry biodegradation of petroleum hydrocarbons in aged soils. *Environ. Toxicol. Chem.* ***2003***, 22, 2853-2860.

ten Hulscher, T.E.M.; Postma, J.; den Besten, P.J.; Stroomberg, G.J.; Belfroid, A.; Wegener, J.W.; Faber, J.H.; van der Pol, J.J.C.; Hendriks, A.J.; van Noort, P.C.M. Tenax extraction mimics benthic and terrestrial bioavailability of organic compounds. *Environ. Toxciol. Chem.* ***2003***, 22, 2258-2265.

ten Hulscher, T.E.M.; Vrind, B.A.; van den Heuvel, H.; van der Velde, L.E.; van Noort, P.C.M.; Beurskens, J.E.M.; Govers, H.A.J. Triphasic desorption of highly resistant chlorobenzenes, polychlorinated biphenyls, and polycyclic aromatic hydrocarbons in field contaminated sediment. *Environ. Sci. Technol.* ***1993***, 33, 126-132.

Hundal, L.S.; Shea, P.J.; Comfort, S.D.; Powers, W.L.; Singh, J. Long-term TNT sorption and bound residue formation in soil. *J. Environ. Qual.* ***1997***, 26, 896-904.

Hundsdorfer, W.; Verwer, J.G. *Numerical Solution of Time-Dependent Advection-Diffusion-Reaction Equations.* ***2003***, pp. 1-471, Springer.

Hunt J.R. Particle dynamic in seawater: implications for predicting the fate of discharged particles. *Environ. Sci. Technol.* ***1982***, 16, 303-309.

Hunter, M.A.; Kan, A.T.; Tomson, M.B. Development of a surrogate sediment to study the mechanisms responsible for adsorption/desorption hysteresis. *Environ. Sci. Technol.* ***1996***, 30, 2278-2285.

I

IARC (International Agency for Research on Cancer). Carbon black - IARC Summary & Evaluation, Vol. 65, ***1996***. http://www.inchem.org/documents/iarc/vol65/carbon.html.

Ibrahim, M.B.M. Levels and sources of polycyclic aromatic hydrocarbons in sediments from the Gulf of Suez. *Mar. Pollut. Bull.* ***2004***, 49, 356-367.

Iinuma, Y.; Bruggemann, E.; Gnauk, T.; Muller, K.; Andreae, M.O.; Helas, G.; Parmar, R.; Herrmann, H. Source characterization of biomass burning particles: The combustion of selected European conifers, African hardwood, savanna grass, and German and Indonesian peat. *J. Geophys. Res.* ***2007***, 112, D08209.

Ikan, R.; Ioselis, P.; Rubinsztain, Y.; Aizenshtat, Z.; Pugmire, R.; Anderson, L.L.; Ishiwatari, R. Carbohydrate origin of humic substances. *Naturwissenschaften* ***1986a***, 73, 150-151.

Ikan, R.; Rubinsztain, Y.; Ioselis, P.; Aizenshtat, Z.; Pugmire, R.; Anderson, L.L.; Woolfenden, W.R. Carbon-13 cross polarized magic-angle samples spinning nuclear magnetic resonance of melanoidins. *Org. Geochem,* ***1986b***, 9, 199-212.

Ikenaka, Y.; Eun, H.; Watanabe, E.; Kumon, F.; Miyabara, Y. Estimation of sources and inflow of dioxins and polycyclic aromatic hydrocarbons from the sediment core of Lake Suwa, Japan. *Environ. Pollut.* ***2005***, 138, 529-537.

Im, J.; Lee, C.M.; Coates, J.T. Comparison of two reference black carbons using a planar PCB as a model sorbate. *Chemosphere* ***2008***, 71, 621-628.

Imboden, D.M.; Emerson, S. Natural radon and phosphorus as limnological tracers: horizontal and vertical eddy diffusion in Greifensee. *Limnol. Oceanogr.* ***1978***, 23, 77-90.

Incardona, J.P.; Day, H.L.; Collier, T.K.; Scholz, N.L. Developmental toxicity of 4-ring polycyclic aromatic hydrocarbons in zebrafish is differentially dependent on AH receptor isotorms and hepatic cytochrome P4501A metabolism. *Toxicol. Appl. Pharmacol.* ***2006***, 217, 308-321.

Inman, S.M.; Thibado, P.; Theriault, G.A.; Lieberman, S.H. Development of a pulsed-laser, fiber-optic-based fluorimeter: determination of fluorescence decay times of polycyclic aromatic hydrocarbons in sea water. *Anal. Chim. Acta* ***1990***, 239, 45-51.

Isaacson, M. Interaction of 25 keV electrons with the nucleic acid bases, adenine, thymine, and uracil. II. Inner shell excitation and inelastic scattering cross sections. *J. Chem. Phys.* ***1972***, 56, 1813-1818.

Itaya, A.; Fujita, Y.; Kato, N.; Okamoto, K. Surface diffusion coefficient in aqueous phases adsorption on macroreticular adsorbents. *J. Chem. Engrg. Jpn* ***1987***, 20, 638-640.

J

Jacobson, M.Z. A physically-based treatment of elemental carbon optics: implications for global direct forcing of aerosols. *Geophys. Res. Lett.* ***2000***, 27, 217-220.

Jacobson, M.Z. Strong radiative heating due to the mixing state of black carbon in atmospheric aerosols. *Nature* ***2001***, 409, 695-697.

Jacobson, M.Z. Control of fossil-fuel particulate black carbon and organic matter, possibly the most effective method of slowing global warming, *J. Geophys. Res.* ***2002***, 107, 4410, doi:10.1029/2001JD001376.

Jager, T.; Baerselman, R.; Dijkman, E.; De Groot, A.C.; Hogendoorn, E.A.; De Jong, A.; Kruitbosch, J.A.W.; Peijnenburg, W.J.G.M. Availability of polycyclic aromatic hydrocarbons to earthworms (Eisenia andrei, Oligochaeta) in field-polluted soils and soil-sediment mixtures. *Environ. Toxicol. Chem.* ***2003***, 22, 767-775.

Jankowski, J.J.; Kieber, D.J.; Mopper, K. Nitrate and nitrite ultraviolet actinometers. *Photochem. Phototbiol.* ***1999***, 70, 319-328.

Jeanne-Rose, V.; Golabkan, V.; Mansot, J.L.; Largitte, L.; Cesaire, T.; Ouensanga, A. An EELS-based study of the effects of pyrolysis on natural carbonaceous materials used for activated charcoal preparation. *J. Microsc.* ***2003***, 210, 53-59.

Jenkins, B.M.; Turn, S.Q.; Williams, R.B.; Chang, D.P.Y.; Raabe, O.G.; Paskind, J.; Teague, S. Quantitative assessment of gaseous and condensed phase emissions from open burning of biomass in a combustion wind tunnel. In *Global Biomass Burning* (eds. Levine, J.S.), pp. 305-317, MIT Press, ***1991***.

Jeong, S.; Wander, M.M.; Kleineidam, S.; Grathwohl, P.; Ligouis, B.; Werth, C.J. The role of condensed carbonaceous materials on the sorption of hydrophobic organic contaminants in subsurface sediments. *Environ. Sci. Technol.* ***2008***, 42, 1458-1464.

Jing, L.; Ridd, P.V. Wave-current bottom shear stresses and sediment resuspension in Cleveland Bay, Australia. *Coastal Eng.* ***1996***, 29, 169-186.

Johnson, D.W.; Curtis, P.S. Effects of forest management on soil C and N storage: meta analysis. *For. Ecol. Manage.* ***2001***, 140, 227-238.

Johnson, M.D.; Huang, W.; Weber, W.J.Jr. A distributed reactivity model for sorption by soils and sediments. 13. Simulated diagenesis of natural sediment organic matter and its impact on sorption/desorption equilibria. *Environ. Sci. Technol.* ***2001a***, 35, 1680-1687.

Johnson, M.D.; Keinath, T.M.; Weber, W.J. A distributed reactivity model for sorption by soils and sediments. 14. Characterization and modeling of phenanthrene desorption rates. *Environ. Sci. Technol.* ***2001b***, 35, 1688-1695.

Johnson, S.E.; Herman, J.S.; Mills, A.L.; Hornberger, G.M. Bioavailability and desorption characteristics of aged, nonextractable atrazine in soil. *Environ. Toxicol. Chem.* ***1999***, 18, 1747-1754.

Jones, G.S.; Jones, A.; Roberts, D.L.; Stott, P.A.; Williams, K.D. Sensitivity of global-scale climate change attribution results to inclusion of fossil fuel black carbon aerosol. *Geophys. Res. Lett.* ***2005***, 32, L14701.

Jones, I.P.; Loretto, M.H. Some aspects of quantitative STEM X-ray-microanalysis. *J. Microsc.,* ***1981***, 124, 3-13.

Jones, T.P.; Chaloner, W.G. Fossil charcoal, its recognition and palaeoatmospheric significance. *Paleogeo. Palaeoclimatol. Palaeoecol.* ***1991***, 97, 39-50.

de Jonge, H.; de Jonge, L.W.; Mittelmeijer-Hazeleger, M.C. The microporous structure of organic and mineral soil materials. *Soil Sci.* ***2000***, 165, 99-108.

Jonker, M.T.O. Absorption of polycyclic aromatic hydrocarbons to cellulose. *Chemosphere* ***2008***, 70, 778-782.

Jonker, M.T.O.; Koelmans, A.A. Sorption of Polycyclic Aromatic Hydrocarbons and Polychlorinated Biphenyls to Soot and Soot-like Materials in the Aqueous Environment: Mechanistic Considerations. *Environ. Sci. Technol.* ***2002***, 36, 3725-3734.

Jonker, M.T.O.; Hoenderboom, A.M.; Koelmans, A.A. Effects of sedimentary sootlike materials on bioaccumulation and sorption of polychlorinated biphenyls. *Environ. Toxicol. Chem.* ***2004***, 23, 2563-2570.

Jung, M.-W.; Ahn, K.-H.; Lee, Y.; Kim, K.-P.; Rhee, J.-S.; Park, J.T.; Paeng, K.-J. Adsorption characteristics of phenol and chlorophenols on granular activated carbons (GAC). *Microchem. J.* ***2001***, 70, 123-131.

K

Kach, D.J.; Ward, J.E. The role of marine aggregates in the ingestion of picoplankton-size particles by suspension-feeding molluscs. *Mar. Biol.* ***2008***, 153, 797-805.

Kalnejais, L. H.; Martin, W. R.; Signell, R. P.; Bothner, M. H. Role of sediment resuspension in the remobilization of particulate-phase metals from coastal sediments. *Environ. Sci. Technol.* ***2007***, 41, 2282-2288.

Kan, A.T.; Fu, G.; Hunter, M.; Chen, W.; Ward, C.H.; Tomson, M.B. Irreversible sorption of neutral hydrocarbons to sediments: experimental observations and model predictions. *Environ. Sci. Technol.* ***1998***, 32, 892-902.

Kan, A.T.; Fu, G.; Tomson, M.B. Adsorption/desorption hysteresis in organic pollutant and soil/sediment interaction. *Environ. Sci. Technol.* ***1994***, 28, 859-867.

Kang, S.; Xing, B. Phenanthrene sorption to sequentially extracted soil humic acids and humins. *Environ. Sci. Technol.* ***2005***, 39, 134-140.

Kannan, K.; Kober, J.L.; Kang, Y.-S.; Masunaga, S.; Nakanishi, J.; Ostaszewski, A.; Giesy, J.P. Polychlorinated naphthalenes, biphenyls, dibenzo-p-dioxins, and dibenzofurans as well as polycyclic aromatic hydrocarbons and alkylphenols in sediment from the Detroit and rouge rivers, Michigan, USA. *Env. Toxicol. Chem.* ***2001***, 20, 1878-1889.

Karapanagioti, H.K.; Gossard, C.M.; Strevett, K.A.; Kolar, R.L.; Sabatini, D.A. Model coupling intraparticle diffusion/sorption, nonlinear sorption, and biodegradation processes. *J. Contam. Hydrol.* ***2001***, 48, 1-21.

Karapanagioti, H.K.; Kleineidam, S.; Sabatini, D.A.; Grathwohl, P.; Ligouis, B. Impacts of heterogeneous organic matter on phenanthrene sorption: equilibrium and kinetics studies with aquifer material. *Environ. Sci. Technol.* ***2000***, 34, 406-414.

Karickhoff, S.W. Semi-empirical estimation of sorption of hydrophobic pollutants on natural sediments and soils. *Chemosphere* ***1981***, 10, 833-846.

Karickhoff, S.W.; Brown, D.S.; Scott, T.A. Sorption of hydrophobic pollutants on natural sediments. *Wat. Res.* ***1979***, 13, 241-248.

Karickhoff, S.W.; Morris, K.R. Sorption dynamics of hydrophobic pollutants in sediment suspensions. *Environ. Toxicol. Chem.* ***1985***, 4, 469-479.

Karls, J.F.; Christensen, E.R. Carbon particles in dated sediments from Lake Michigan, Green Bay, and Tributaries. *Environ. Sci. Technol.* ***1998***, 32, 225-231.

Katrinak, K.A.; Rez, P.; Buseck, P.R. Structural variations in individual carbonaceous particles from an urban aerosol. *Environ. Sci. Technol.* ***1992***, 26, 1967-1976.

Keil, R.G.; Hu, F.S.; Tsamakis, E.C.; Hedges, J.I. Pollen in marine-sediments as an indicator of oxidation of organic-matter. *Nature* ***1994***, 369, 639-641.

Kelleher, B.P.; Simpson, A.J. Humic substances in soils: are they really chemically distinct. *Environ. Sci. Technol.* ***2006***, 40, 4605-4611.

Kelsey, J.W.; Kottler, B.D.; Alexander, M. Selective chemical extractants to predict bioavailability of soil-aged organic chemicals. *Environ. Sci. Technol.* ***1997***, 31, 214-217.

Kennicutt, M.C.; Wade, T.L.; Presley, B.J.; Requejo, A.G.; Brooks, J.M. Sediment contaminants in Casco Bay, Maine: inventories, sources, and potential for biological impact. *Environ. Sci. Technol.* ***1994***, 28, 1-15.

Ketterings, Q.M.; Bigham, J.M.; Laperche, V. Changes in soil mineralogy and texture caused by slash-and-burn fires in Sumatra, Indonesia. *Soil Sci. Soc. Am. J.* ***2000***, 64, 1108-1117.

Kiem, R.; Kogel-Knabner, I. Contribution of lignin and polysaccharides to the refractory carbon pool in C-depleted arable soils. *Soil Biol. Biochem.* ***2003***, 35, 101-118.

Kile, D.E.; Chiou, C.T. Water-solubility enhancement of non-ionic organic contaminants. In *Aquatic Humic Substances: Influence of Fate and Treatment of Pollutants* (Eds. Suffet, I.H.; MacCarthy, P.), pp. 131-157, American Chemical Society, Washington, ***1989***.

Kim, G.B.; Maruya, K.A.; Lee, R.F.; Lee, J.-H.; Koh, C.-H.; Tanabe, S. Distribution and sources of polycyclic aromatic hydrocarbons in sediments from Kyeonggi Bay, Korea. *Mar. Pollut. Bull.* ***1999***, 38 1, pp. 7–15.

Kim, H.; Ralph, J.; Yahiaoui, N.; Pean, M.; Boudet, A.-M. Cross-coupling of hydroxycinnamyl aldehydes into lignins. *Org. Lett.* ***2000***, 2, 2197-2200.

Kim, J.-W.; Sohn, M.-H.; Kim, D.-S.; Sohn, S.-M.; Kwon, Y.-S. Production of granular activated carbon from waste walnut shell and its adsorption characteristics for Cu^{2+} ion. *J. Hazard. Mater. B* ***2001***, 85, 301-315.

Kim, E.J.; Oh, J.E.; Chang, Y.S. Effects of forest fire on the level and distribution of PCDD/Fs and PAHs in soil. *Sci. Tot. Environ.* ***2003***, 311, 177-189.

Kim, S.; Kim, Y.K. Apparent desorption kinetics of phenol in organic solvents from spent activated carbon saturated with phenol. *Chem. Engrg. J.* ***2004***, 98, 237-243.

Kim, Y.J.; Osako, M. Effect of adsorption capacity of dissolved humic matter on leachability of dioxins from raw and treated fly ashes of municipal solid waste incinerators. *Arch. Environ. Contam. Toxicol.* ***2004***, 46, 8-16.

King, A.J.; Readman, J.W.; Zhou, J.L. Behaviour of polycyclic aromatic hydrocarbons in dissolved colloidal, and particulate phases in sedimentary cores. *Intern. J. Environ. Anal. Chem.* ***2007***, 87, 211-225.

Kiraly, Z.; Findenegg, G.H. Pulsed-flow microcalorimetric study of the template-monolayer region of nonionic surfactants adsorbed at the graphite/water interface. *Langmuir* ***2005***, 21, 5047-5054.

Kleineidam, S.; Rugner, H.; Ligouis, B.; Grathwohl, P. Organic matter facies and equilibrium sorption of phenanthrene. *Environ. Sci. Technol.* ***1999***, 33, 1637-1644.

Kleineidam, S.; Schuth, C.; Grathwohl, P. Solubility-normalized combined adsorption-partitioning sorption isotherms for organic pollutants. *Environ. Sci. Technol.* ***2002***, 36, 4689-4697.

Kleinjans, J.C.S.; van Schooten, F.J. Ecogenotoxicology: the evolving field. *Environ. Toxicol. Pharmacol.* ***2002***, 11, 173-179.

Knaapen, A.; Borm, P.J.A.; Albrecht, C.; Schins, R.P.F. Inhaled particles and lung cancer. Part A: mechanisms. *Int. J. Cancer* ***2004***, 109, 799-809.

Knicker, H.; How does fire affect the nature and stability of soil organic nitrogen and carbon? A review. *Biogeochem.* ***2007***, 85, 91-118.

Ko, F.C. and Baker, J.E. Partitioning of hydrophobic organic contaminants to resuspended sediments and plankton in the mesohaline Chesapeake Bay. *Mar. Chem.* ***1995***, 49, 171-188.

Komiyama, H.; Smith, J.M. Intraparticle mass transport in liquid-filled pores. *AIChE J.* ***1974a***, 20, 728-734.

Komiyama, H.; Smith, J.M. Surface diffusion in liquid-filled pores. *AIChE J.* ***1974b***, 20, 1110-1117.

Kopinke, F.D.; Georgi, A.; MacKenzie, K. Sorption of pyrene to dissolved humic substances and related model polymers. 1. Structure-property correlation. *Environ. Sci. Technol.* ***2001***, 35, 2536-2542.

Kopinke, F.D.; Porschmann, J.; Stottmeister, U. Sorption of organic pollutants on anthropogenic humic matter. *Environ. Sci. Technol.* ***1995***, 29, 941-950.

Kotzick, R.; Niessner, R. Application of time-resolved, laser-induced and fiber-optically guided fluorescence for monitoring of a PAH-contaminated remediation site. *Fresenius J. Anal. Chem.* ***1996***, 354, 72-76.

Kraaij, R.H.; Ciarelli, S.; Tolls, J.; Kater, B.J.; Belfroid, A. Bioavailability of lab-contaminated and native polycyclic aromatic hydrocarbons to the amphipod *Corophium volutator* relates to chemical desorption. *Environ. Toxicol. Chem.,* ***2001***, 20, 1716-1724.

Kraaij, R.; Seinen, W.; Tolls, J.; Cornelissen, G.; Belfroid, A.C. Direct evidence of sequestration in sediments affecting the bioavailability of hydrophobic organic chemicals to benthic deposit-feeders. *Environ. Sci. Technol.* ***2002a***, 36, 3525-3529.

Kraaij, R.H.; Tolls, J.; Sijm, D.; Cornelissen, G.; Heikens, A.; Belfroid, A. Effects of contact time on the sequestration and bioavailability of different classes of hydrophobic organic chemicals to benthic oligochaetes (*tubificidae*). *Environ. Toxicol. Chem.* ***2002b***, 21, 752-759.

Kranck, K. Flocculation of suspended sediment in the sea. *Nature* ***1973***, 246, 348-350.

Kranck, K. Experiments on the significance of flocculation of fine-grained sediment in still water. *Can. J. Earth Sci.* ***1980***, 17, 1515-1526.

Kranck, K. Interparticle grain size relationships resulting from flocculation. In *Microstructures of Fine-Grained Sediments: From Mud to Shale*, (eds. Bennett, R.H.; Bryant, W.R.; Hulbert, M.H.), pp. 125-130, Springer-Verlag, Berlin, ***1991***.

Krauss, M.; Wilcke, W.; Zech, W. Availability of polycyclic aromatic hydrocarbons (PAHs) and polychlorinated biphenyls (PCBs) to earthworms in urban soils. *Environ. Sci. Technol.* ***2000***, 34, 4335-4340.

Kralovec, A.C.; Christensen, E.R.; van Camp, R.P. Fossil fuel and wood combustion as recorded by carbon particles in Lake Erie sediments 1850-1998. *Environ. Sci. Technol.* ***2002***, 36, 1405-1413.

Krestinin, A.V. Detailed modeling of soot formation in hydrocarbon pyrolysis. *Combust. Flame* ***2000***, 12, 513-524.

van Krevelen, D.W. Coal: *Typology, Physics, Chemistry, Constitution.* ***1993***, pp. 1-979, Elsevier.

Krivacsy, Z.; Hoffer, A.; Sarvari, Z.; Temesi, D.; Baltensperger, U.; Nyeki, S.; Weingartner, E.; Kleefeld, S.; Jennings, S.G. Role of organic and black carbon in the chemical composition of atmospheric aerosol at European background sites. *Atmos. Environ.* ***2001***, 35, 6231-6244.

Krivacsy, Z.; Kiss, G.; Ceburnis, D.; Jennings, G.; Maenhaut, W.; Salma, I.; Shooter, D. Study of water-soluble atmospheric humic matter in urban and marine environments. *Atmos. Res.* ***2008***, 87, 1-12.

Krull, E.S.; Swanston, C.W.; Skjemstad, J.O.; McGowan, J.A. Importance of charcoal in determining the age and chemistry of organic carbon in surface soils. *J. Geophys. Res.* ***2006***, G04001.

Krutz, L.J.; Senseman, S.A.; McInnes, K.J.; Zuberer, D.A.; Tierney, D.P. Adsorption and desorption of atrazine, desethylatrazine, deisopropylatrazine, and hydroxyatrazine in vegetated filter strip and cultivated soil. *J. Agric. Food Chem.* ***2003***, 51, 7379-7384.

Kuhlbusch, T.A.J. Black carbon and carbon cycle. *Science* ***1998***, 280, 1903-1904.

Kuhlbusch, T.A.J.; Lobert, J.M.; Crutzen, P.J.; Warneck, P. Molecular nitrogen emissions from denitrification during biomass burning. *Nature* ***1991***, 351, 135-137.

Kuhlbusch, T.A.J.; Crutzen, P.J. Toward a global estimate of black carbon in residues of vegetation fires representing a sink of atmospheric CO_2 and a source of O_2. *Global Biochem. Cycles* ***1995***, 9, 491-501.

Kuhlbusch, T.A.J.; Andreae, M.O.; Cachier, H.; Goldammer, J.G.; Lacaux, J.-P.; Shea, R.; Crutzen, P.J. Black carbon formation by savanna fires: measurements and implications for the global carbon cycle. *J. Geophys. Res.* ***1996***, 101, D19, 23651-23665.

Kukkonen, J.V.K.; Landrum, P.F.; Mitra, S.; Gossiaux, D.C.; Gunnarsson, J.; Weston, D. Sediment characteristics affecting desorption kinetics of select PAH and PCB congeners for seven laboratory spiked sediments. *Environ. Sci. Technol.* ***2003***, 37, 4656-4663.

Kumada, K. *Chemistry of Soil Organic Matter.* ***1987***, pp. 1-241, Japan Scientific Societies Press & Elsevier.

Kuo, D.T.F.; Adams, R.G.; Rudnick, S.M.; Chen, R.F.; Gschwend, P.M. Investigating desorption of native pyrene from sediment on minute- to month-timescales by time-gated fluorescence spectroscopy. *Environ. Sci. Technol.* ***2007***, 41, 7752-7758.

L

ter Laak, T.L.; Agbo, S.O.; Barendregt, A.; Hermens, J.L.M. Freely dissolved concentrations of PAHs in soil pore water: Measurements via solid-phase extraction and consequences for soil tests. *Environ. Sci. Technol.* ***2006a***, 40, 1307-1313.

ter Laak, T.L.; Barendregt, A.; Hermens, J.L.M. Freely dissolved pore water concentrations and sorption coefficients of PAHs in spiked, aged, and field-contaminated soils. *Environ. Sci. Technol.* ***2006b***, 40, 2184-2190.

ter Laak, T.L.; Barendregt, A.; Hermens, J.L.M. Grinding and sieving soil affects the availability of organic contaminants: a kinetic analysis. *Chemosphere* ***2007***, 69, 613-620.

ter Laak, T.L.; Durjava, M.; Struijs, J.; Hermens, J.L.M. Solid phase dosing and sampling technique to determine partition coefficients of hydrophobic chemicals in complex matrixes. *Environ. Sci. Technol.* ***2005***, 39, 3736-3742.

Lacaux, J.-P.; Brocard, D.; Lacaux, C.; Delmas, R.; Brou, A; Yoboue V.; Koffi, M. Traditional charcoal making: an important source of atmospheric pollution in the African tropics. *Atmos. Res.* ***1994***, 35, 71-76.

Lack, D.A.; Cappa, C.D.; Covert, D.S.; Baynard, T.; Massoli, P.; Sierau, B.; Bates, T.S.; Quinn, P.K.; Lovejoy, E.R.; Ravishankara, A.R. Bias in filter-based aerosol light absorption measurements due to organic aerosol loading: Evidence from ambient measurements. *Aerosol Sci. Technol.* ***2008***, 42, 1033-1041.

Laird, D.A.; Yen, P.Y.; Koskinen, W.C. Steinheimer, T.R.; Dowdy, R.H. Sorption of atrazine on soil clay components. *Environ. Sci. Technol.* ***1994***, 28, 1054-1061.

Lakowicz, J.R. *Principles of Fluorescence Spectroscopy.* ***2006***, pp. 1-954, Springer.

Lam, B.; Baer, A.; Alaee, M.; Lefebvre, B.; Moser, A.; Williamds, A.; Simpson, A.J. Major structural components in freshwater dissolved organic matter. *Environ. Sci. Technol.* ***2007***, 41, 8240-8247.

Lamoureux, E.M.; Brownawell, B.J. Chemical and biological availability of sediment-sorbed hydrophobic organic contaminants. *Environ. Toxicol. Chem.* ***1999***, 18, 1733-1741.

Lampi, M.A.; Gurska, J.; McDonald, K.I.C.; Xie, F.; Huang, X.D.; Dixon, D.G.; Greenberg, B.M. Photoinduced toxicity of polycyclic aromatic hydrocarbons to *daphnia magna*: ultraviolet-mediated effects and the toxicity of polycyclic aromatic hydrocarbon photoproducts. *Environ. Toxicol. Chem.* ***2005***, 25, 1079-1087.

Lapuerta, M.; Martos, F.J.; Herreros, J.M. Effect of engine operating conditions on the size of primary particles composing diesel soot agglomerates. *J. Aerosol Sci.* ***2007***, 38, 455-466.

Laor, Y.; Rebhun, M. Complexation-Flocculation: A new method to determine binding coefficients of organic contaminants to dissolved humic substances. *Environ. Sci. Technol.* ***1997***, 31, 3558-3564.

Laquerriere, P.; Michel, J.; Balossier, G.; Chenais, B. Light elements quantification in stimulated cells cryosections studied by electron probe microanalysis. *Micron* ***2002***, 33, 597-603.

Larsen, J.W. The effects of dissolved CO_2 on coal structure and properties. *Int. J. Coal Geol.* ***2004***, 57, 63-70.

Larson, R.A.; Zepp, R. Reactivity of the carbonate radical with aniline derivatives. *Environ. Toxciol. Chem.* ***1988***, 7, 265-274.

Larsson, P. Contaminated sediments of lakes and oceans act as sources of chlorinated hydrocarbons for release to water and atmosphere. *Nature* ***1985***, 317, 347-349.

Latimer, J.S.; Davis, W.R.; Keith, D.J. Mobilization of PAHS and PCBs from in-place contaminated marine resuspension events. *Estuar. Coast. Shelf Sci.* ***1999***, 49, 577-595.

Lavanchy, V.M.H.; Gaggeler, H.W.; Nyeki, S.; Baltensperger, U. Elemental carbon (EC) and black carbon measurement with a thermal method and an aethalometer at the high-alpine research station Jungfraujoch. *Atmos. Environ.* ***1999a***, 33, 2759-2769.

Lavanchy, V.M.H.; Gaggeler, H.W.; Schotterer, U.; Schwikowski, M.; Baltensperger, U. Historical record of carbonaceous particle concentrations from a European high-alpine glacier (Colle Gnifetti, Switzerland). *J. Geophys. Res.* ***1999b***, 104, 21227-21236.

Lavoie, D.M.; Lavoie, D.L.; Pittenger, H.A.; Bennett, R.H. Bulk sediment properties interpreted in light of qualitative and quantitative microfabric analysis. *Geo-Mar. Lett.* ***1996***, 16, 226-231.

Law, R.J.; Dawes, V.J.; Woodhead, R.J.; Matthiessen, P. Polycyclic aromatic hydrocarbons (PAH) in seawater around England and Wales. *Mar. Pollut. Bull.* ***1997***, 34, 306-322.

Leapman, R.D.; Ornberg, R.L. Quantitative electron energy loss spectroscopy in biology. *Ultramicrosc.* ***1988***, 24, 251-268.

Leapman, R.D.; Rizzo, N.W. Towards single atom analysis of biological structures. *Ultramicrosc.* ***1999***, 78, 251-268.

Lee, M.L.; Hites, R.A. Characterization of sulfur-containing polycyclic aromatic-compounds in carbon-blacks. *Anal. Chem.* ***1976***, 48, 1890-1893.

Lehmann, J.; Liang, B.Q.; Solomon, D.; Lerotic, M.; Luizao, F.; Kinyangi, J.; Schafer, T.; Wirick, S.; Jacobsen, C. Near-edge X-ray absorption fine structure (NEXAFS) spectroscopy for mapping nano-scale distribution of organic carbon forms in soil: Application to black carbon particles. *Global Biogeochem. Cycles,* ***2005***, 19, GB1013.

Leifeld, J. Thermal stability of black carbon characterised by oxidative differential scanning calorimetry. *Org. Geochem.* ***2007***, 38, 112-127.

Leifeld, J.; Fenner, S.; Muller, M. Mobility of black carbon in drained peatland soils. *Biogeosci.* ***2007***, 4, 425-432.

Leifeld, J.; Franko, U.; Schulz, E. Thermal stability responses of soil organic matter to long-term fertilization practices. *Biogeosci.* ***2006***, 3, 371-374.

Leister, D.L.; Baker, J.E. Atmospheric deposition of organic contaminants to the Chesapeake Bay. *Atmos. Environ.* ***1994***, 28, 1499-1520.

Leppard, G.G. Evaluation of electron microscope techniques for the description of aquatic colloids. In *Environmental Particles* (eds. Buffle, J. and van Leeuwan H.P.), ***1993***, pp. 233-289, Intl. Union Pure Appl. Chem.

van Leussen, W. Aggregation of particles, settling velocity of mud flocs: A review. In *Environmental Particles* (eds. Buffle, J. and van Leeuwan H.P.), ***1993***, pp. 347-403, Intl. Union Pure Appl. Chem.

Levich, V.G. *Physicochemical Hydrodynamics.* ***1962***, pp. 1-700, Prentice-Hall.

Levine, D.G.; Schlosberg, R.H.; Silbernagel, B.G. Understanding the chemistry and physics of coal structure. *Proc. Natl. Acad. Sci. USA,* ***1982***, 79, 3365-3370.

Levinton, J.S. *Marine Biology – Function, Biodiversity, Ecology.* ***2001***, pp. 1-515, Oxford.

Lewis, K.; Arnott, W.P.; Moosmuller, H.; Wold, C.E. Strong spectral variation of biomass smoke light absorption and single scattering albedo observed with a novel dual-wavelength photoacoustic instrument. *J. Geophys. Res. – Atmos.* ***2008***, 113, D16203.

Li, H.; Bennett, R.H. The significance of sediment-flow dynamics on clay microstructure development: riverine and continental shelf environments. In *Microstructures of Fine-Grained Sediments: From Mud to Shale*, (eds. Bennett, R.H.; Bryant, W.R.; Hulbert, M.H.), pp. 193-202, Springer-Verlag, Berlin, ***1991***.

Li, L.; Quinlivan, P.A.; Knappe, D.R.U. Effects of activated carbon surface chemistry and pore structure on the adsorption of organic contaminants from aqueous solution. *Carbon* ***2002***, 40, 2085-2100.

Liang, B.; Lehmann, J.; Solomon, D.; Kinyangi, J.; Grossman, J.; O'Neill, B.; Skjemstad, J.O.; Thies, J.; Luizao, F.J.; Petersen, J.; Neves, E.G. Black Carbon increases cation exchange capacity in soils. *Soil Sci. Soc. Am. J.* ***2006***, 70, 1719-1730.

Lick, W. The sediment-water flux of HOCs due to "diffusion" or is there a well-mixed layer? If there is, does it matter? *Environ. Sci. Technol.* ***2006***, 40, 5610-5617.

Lide, D.R. (ed.). *CRC Handbook of Chemistry and Physics (88th Edition, Internet online version)*, **2008**, CRC Press/Taylor and Francis, Boca Raton.

Litton, C.M.; Santelices, R. Effect of wildfire on soil physical and chemical properties in a *Nothofagus glauca* forest, Chile. *Revista Chile. Historia Natural* ***2003***, 76, 529-542.

Liu, J.Y. Scanning transmission electron microscopy and its application to the study of nanoparticles and nanoparticle systems. *J. Electron Microsc.* ***2005***, 54, 251-278.

Liu, X.; Zhang, G.; Li, J.; Cheng, H.R.; Qi, S.H.; Li, X.D.; Jones, K.C. Polycyclic aromatic hydrocarbons (PAHs) in the air of Chinese cities. *J.Environ. Monit.* ***2007***, 9, 1092-1098.

Lobinski, R.; Moulin, C.; Ortega, R. Imaging and speciation of trace elements in biological environment. *Biochimie* ***2006***, 88, 1591-1604.

Lobert, J.M. Verbrennung pflanzlicher Biomasse als Quelle atmosphärischer Spurengase: Cyanoverbindungen, CO , CO_2, und NOx. Ph.D. Thesis, Johannes Gutenberg-Univ. Mainz, ***1989***.

Lohmann, R.; Harner, T.; Thomas, G.O.; Jones, K.C. A comparative study of the gas-particle partitioning of PCDD/Fs, PCBs, and PAHs. *Environ. Sci. Technol.* ***2000***, 34, 4943-4951.

Lohmann, R.; MacFarlane, J.K.; Gschwend, P.M. Importance of black carbon to sorption of native PAHs, PCBs, and PCDDs in Boston and New York Harbor sediments. *Environ. Sci. Technol.* ***2005***, 39, 141-148.

Long, G.; Neglia, S.; Favretto, L. The metamorphism of the kerogen from triassic Black Shales, southeast Sicily. *Geochim. Cosmochim. Acta* ***1968***, 32, 647-656.

Long, E.R.; MacDonald, D.D.; Smith, S.L.; Calder, F.D. Incidence of adverse biological effects within ranges of chemical concentrations in marine and estuarine sediments. *Environ. Manage.* ***1995***, 19, 81-97.

Lopez-Capel, E.; Sohi, S.P.; Gaunt, J.L.; Manning, D.A.C. Use of thermogravimetry-differential scanning calorimetry to characterize modelable soil organic matter fractions. *Soil Sci. Soc. Am. J.* ***2005***, 69, 136-140.

Loretto, M.H. *Electron Beam Analysis of Materials*. ***1994***, pp. 1-272, Chapman & Hall.

Lotfabad, S.K.; Gray, M.R. Transport and reaction processes in bioremediation of organic contaminants. 2. roles of aggregate size in soil remediation in a slurry bioreactor. *Inter. J. Chemical React. Engrg.* ***2003***, 1, No. A19.

Lu, X. Reible, D.D.; Fleeger, J.W. Bioavailability of polycyclic aromatic hydrocarbons in field-contaminated Anacostia River (Washington, DC) sediment. *Environ. Toxicol. Chem.* ***2006***, 25, 2869-2874.

Lu, Y. F.; Pignatello, J.J. Demonstration of the "Conditioning effect" in soil organic matter in support of a pore deformation mechanism for sorption hysteresis. *Environ. Sci. Technol.* ***2002***, 36, 4553-4561.

Luo, X.J.; Chen, S.J.; Mai, B.X.; Sheng, G.Y.; Fu, J.M.; Zeng, E.Y. Distribution, source apportionment, and transport of PAHs in sediments from the Pearl River Delta and the Northern South China Sea. *Arch. Environ. Contam. Toxicol.* ***2008***, 55, 11-20.

Luthy, R.G.; Aiken, G.R.; Brusseau, M.L.; Cunningham, S.D.; Gschwend, P.M.; Pignatello, J.J.; Reinhard, M.; Traina, S.J.; Weber, Jr. W.J.; Westall, J.C. Sequestration of hydrophobic organic contaminants by geosorbents. *Environ. Sci. Technol.* ***1997***, 31, 3341-3347.

M

Ma, K.C.; Shiu, W.Y.; Mackay, D. *A critically reviewd compilation of physical and chemical and persistence data for 110 selected EMPPL substances*; A report prepared for the Ontario Ministry of Environment, Water Resources Branch, 1990.

Ma, W.C.; van Kleunen, A.; Immerzeel, J.; de Maagd, P.G.J. Bioaccumulation of polycyclic aromatic hydrocarbons by earthworms: assessment of equilibrium partitioning theory in in situ studies and water experiments. *Environ. Toxicol. Chem.* ***1998***, 17, 1730-1737.

de Maagd, P.G.J.; Sinnige, T.L.; Schrap, S.M.; Opperhuizen, A.; Sijm, D.T.H.M. Sorption coefficients of polycyclic aromatic hydrocarbons for two lake sediments: Influence of the bactericide sodium azide. *Environ. Toxicol. Chem.* ***1998***, 17, 1899-1907.

MacDonald, D.D.; Carr, R.S.; Calder, F.D.; Long, E.R.; Ingersoll, C.G. Development and evaluation of sediment quality guidelines for Florida coastal waters. *Ecotoxciol.* ***1996***, 56, 253-278.

Mackay, D.; Shiu, W.Y.; Ma, K.C. *Physical-Chemical Properties and Environmental Fate Handbook*. **1999**, CRC.

Mackay, D. *Multimedia Environmental Models: The Fugacity Approach.* ***2001***, pp. 1-272. CRC.

Macleod, C.J.A.; Semple, K.T. Influence of contact time on extractability and degradation of pyrene in soils. *Environ. Sci. Technol.* ***2000***, 34, 4952-4957.

Mader, B.T.; Flagan, R.C.; Seinfeld, J.H. Sampling Atmospheric Carbonaceous Aerosols Using a Particle Trap Impactor/Denuder Sampler. *Environ. Sci. Technol.* ***2001a***, 35, 4857-4867.

Mader, B.T.; Pankow, J.F. Gas/solid partitioning of semivolatile organic compounds (SOCs) to air filters. 3. An analysis of gas adsorption artifacts in measurements of atmospheric SOCs and organic carbon (OC) when using Teflon membrane filters and quartz fiber filters. *Environ. Sci. Technol.* ***2001b***, 35, 3422-3432.

Mader, B.T.; Schauer, J.J.; Seinfeld, J.H.; Flagan, R.C.; Yu, J.Z.; Yang, H.; Lim, H.-J.; Turpin, B.J.; Deminter, J.T.; Heidemann, G.; Bae, M.S.; Quinn, P.; Bates, T.; Eatough, D.J.; Huebert, B.J.; Bertram, T.; Howell, S. Sampling methods used for the collection of particle-phase organic and elemental carbon during ACE-Asia. *Atmos. Environ.* ***2003***, 37, 1435-1449.

Magi, E.; Bianco, R.; Ianni, C.; Di Carro, M. Distribution of polycyclic aromatic hydrocarbons in the sediments of the Adriatic Sea. *Environ. Pollut.* ***2002***, 119, 91-98.

Mahajan, O.P. CO_2 surface area of coals: the 25-year paradox. *Carbon* ***1991***, 29, 735-742.

Manes, M. Activated carbon adsorption fundamentals. In *Encyclopedia of Environmental Analysis and Remediation*, (ed. Meyers, R.A.), pp 26-68, John Wiley, New York, ***1998***.

Mao, J.; Hu, W.; Schmidt-Rohr, K.; Davies, G.; Ghabbour, E.A.; Xing, B. Structure and elemental composition of humic acids: comparison of solid-state 13C NMR calculations and

chemical analyses. In *Humic Substances – Structures, Properties and Uses*, (eds. Davies, G.; Ghabbour, E.A.), pp 79-90, Royal Society of Chemistry, Cambridge, ***1998***.

Marcelo C.B.; Martinelli, L.A.; Krusche, A.V.; Gudeman, J.; Moreira, M.; Victoria, R.L.; Ometto, J.P.H.B.; Ballester, M.V.R.; Aufdenkampe, A.K.; Richey, J.E.; Hedges, J.I. Riverine organic matter composition as a function of land use changes, southwest Amazon. *Ecol. Appl.* ***2004***, 14, S263-S279.

Marschner, B.; Brodowski, S.; Dreves, A.; Gleixner, G.; Gude, A.; Grootes, P.M.; Hamer, U.; Heim, A.; Jandl, G.; Ji, R.; Kaiser, K.; Kalbitz, K.; Kramer, C.; Leinweber, P.; Rethemeyer, J.; Schaffer, A.; Schmidt, M.W.I.; Schwark, L.; Wiesenberg, G.L.B. How relevant is recalcitrance for the stabilization of organic matter in soils? *J. Plant Nutr. Soil Sci.* ***2008***, 171, 91-110.

Martins, J.V.; Artaxo, P.; Liousse, C.; Reid, J.S.; Hobbs, P.V.; Kaufman, Y.J. Effects of black carbon content, particle size, and mixing on light absorption by aerosols from biomass burning in Brazil. *J. Geophys. Res.* ***1998***, 103, 32041-32050.

Maruya, K.A.; Risebrough, R.W.; Horne, A.J. Partitioning of polynuclear aromatic hydrocarbons between sediments from San Francisco Bay and their porewaters. *Environ. Sci. Technol.* ***1996***, 30, 2942-2947.

Maruya, K.A.; Zeng, E.Y.; Tsukada, D.; Bay, S.M. A passive sampler based on solid-phase microextraction for quantifying hydrophobic organic contaminants in sediment pore water. *Environ. Toxicol. Chem.* ***2009***, 28, 733-740.

Masiello, C.A. New directions in black carbon organic geochemistry. *Mar. Chem.* ***2004***, 92, 201-213.

Masiello, C.A.; Druffel, E.R.M. Black carbon in deep-sea sediments. *Science* ***1998***, 280, 1911-1913.

Masiello, C.A.; Druffel, E.R.M.; Currie, L.A. Radiocarbon measurements of black carbon in aerosols and ocean sediments. *Geochim. Cosmochim. Acta* ***2002***, 66, 1025-1036.

Masiello, C.A.; Druffel, E.R.M. Carbon isotope geochemistry of the Santa Clara River. *Global Biogeochem. Cycles* ***2001***, 15, 407-416.

Mastral, A.M.; Mayoral, M.C.; Rivera, J.; Maldonado, F. New approach to coal structure through its evolution during dry catalytic hydrogenation. *Energy Fuels* ***1997***, 11, 483-490.

Mataix-Solera, J.; Doerr, S.H. Hydrophobicity and aggregate stability in calcareous topsoils from fire-affected pine forests in southeastern Spain. *Geoderma* ***2004***, 118, 77-88.

Mathis, U.; Mohr, M.; Kaegi, R.; Bertola, A.; Boulouchos, K. Influence of diesel engine combustion parametes on primary soot particle diameter. *Environ. Sci. Technol.* ***2005***, 39, 1887-1892.

Matscheko, N.; Lundstedt, S.; Svensson, L.; Harju, M.; Tysklind, M. Accumulation and elimination of 16 polycyclic aromatic compounds in the earthworm (*Eisenia fetida*). *Environ. Toxicol. Chem.* ***2002***, 21, 1724-1729.

Matsuoka, K.; Akahane, T.; Aso, H.; Sharma, A.; Tomita, A. The size of polyaromatic layer of coal char estimated from elemental analysis data. *Fuel* ***2008***, 87, 539-545.

Mattheij, R.M.M; Rienstra, S.W.; tenThije Boonkkamp, J.H.M. *Partial Differential Equations – Modeling, Analysis, Computation.* ***2005***, pp. 1-665, Society for Industrial and Applied Mathematics.

May, W.E.; Wasik, S.P.; Miller, M.M.; Tewari, Y.B.; Brown-Thomas, J.M.; Goldberg, R.N. Solution thermodynamics of some slightly soluble hydrocarbons in water. *J. Chem. Eng. Data* ***1983***, 28, 197-200.

Mayer, J.; Eigenthaler, U.; Plitzko, J.M.; Dettenwanger, F. Quantitative analysis of electron spectroscopic imaging series. *Micron* ***1997***, 28, 361-370.

Mayer, L.M. Surface area control of organic carbon accumulation in continental shelf sediments. *Geochim. Cosmochim. Acta* ***1994***, 58, 1271-1284.

Mayer, P.; Vaes, W.H.J.; Hermens, J.L.M. Absorption of hydrophobic compounds into the poly(dimethylsiloxane) coating of solid-phase microextraction fibers: High partition coefficients and fluorescence microscopy images. *Anal. Chem.* ***2000a***, 72, 459-464.

Mayer, P.; Vaes, W.H.J.; Wijnker, F.; Legierse, K.C.H.M.; Kraaij, R.H.; Tolls, J.; Hermens, J.L.M. Sensing dissolved sediment porewater concentrations of persistent and bioaccumulative pollutants using disposable solid-phase microextraction fibers. *Environ. Sci. Technol.* ***2000b***, 34, 5177-5183.

McAnally, W.H.; Mehta, A.J. Collisional aggregation of fine estuarial sediment. In *Coastal and Estuarine Fine Sediment Processes*, (eds. McAnally, W.H.; Mehta, A.J.), pp 19-39, Elsevier, ***2001***.

McLachlan, M.S.; Czub, G.; Wania, F. The influence of vertical sorbed phase transport on the fate of organic chemicals in surface soils. *Environ. Sci. Technol.* ***2002***, 36, 4860-4867.

McCready, S.; Slee, D.J.; Birch, F.G.; Taylor, S.E. The distribution of polycyclic aromatic hydrocarbons in surficial sediments of Sydney Harbour, Australia. *Mar. Pollut. Bull.* ***2000***, 40, 999-1006.

McDowell, D.M.; O'Connor, B.A. *Hydraulic Behavior of Estuaries.* ***1977***, pp. 1-292, Wiley and Sons.

McGinley, P.M.; Katz, L.E.; Weber, W.J. A distributed reactivity model for sorption by soils and sediments. 2. Multicomponent systems and competitive effects. *Environ. Sci. Technol.* ***1993***, 27, 1524-1531.

McGroddy, S.E. Sediment-porewater partitioning of PAHs and PCBs in Boston Harbor, Mass. Ph.D. Thesis, University of Massachusetts at Boston, ***1993***, pp 1-255.

McGroddy, S.E.; Farrington, J.W.; Gschwend, P.M. Comparison of the *in situ* and desorption sediment–water partitioning of polycyclic aromatic hydrocarbons and polychlorinated biphenyls. *Environ. Sci. Technol.* ***1996***, 30, 172-177.

McGroddy, S.E.; Farrington, J.W. Sediment porewater partitioning of polycyclic aromatic hydrocarbons in three cores from Boston Harbor, Massachusetts. *Environ. Sci. Technol.* ***1995***, 29, 1542-1550.

McKnight, D.M.; Aiken, G.R. Sources and age of aquatic humus. In *Aquatic Humic Substances: Ecology and Biogeochemistry*, (Eds. Hessen, D.O.; Tranvik, L.J.) pp 9-39, Springer, Berlin, **1998**.

Means, J.C.; Wood, S.G.; Hassett, J.J.; Banwart, W.L. Sorption of polynuclear aromatic-hydrocarbons by sediments and soils. *Environ. Sci. Technol.* ***1980***, 14, 1524-1528, 1980.

Medalia, A.I.; Rivin, D. Particulate carbon and other components of soot and carbon-black. *Carbon* ***1982***, 20, 481-492.

Middelburg, J.J.; Nieuwenhuize, J.; van Breugel, P. Black carbon in marine sediments. *Mar. Chem.* ***1999***, 65, 245-252.

Migniot, C. A study of the physical properties of various forms of very fine sediments and their behavior under hydrodynamic action. *La Houille Blanche* ***1968***, 7, 591-620.

Miller, A.; Ahlstrand, G.; Kittelson, D.; Zachariah, M. The fate of metal (Fe) during diesel combustion: Morphology, chemistry, and formation pathways of nanoparticles. *Combust. Flame* ***2007***, 149, 129-143.

Miller, C.T. and Weber, W.J. Jr. Sorption of hydrophobic organic pollutants in saturated soil systems. *J. Contam. Hydrol.* ***1986***, 1, 243-261.

Miller, K.P.; Borgeest, C.; Greenfeld, C.; Tomic, D.; Flaws, J.A. In utero effects of chemicals on reproductive tissues in females. *Toxicol. Appl. Pharmacol.* ***2004***, 198, 111–131.

Milligan, J.B.; Thomas, K.M.; Crelling, J.C. Solvent swelling of maceral concentrates. *Energy Fuels* ***1997***, 11, 364-371.

Mills, K.L.; Cheng, P.J. Carbon black production. U.S. Patent No. 4368182, ***1983***. U.S. Patent and Trademark Office.

Minoura, K.; Osaka, Y. Sediments and sedimentary processes in Mutsu Bay, Japan: pelletization as the most important mode in depositing argillaceous sediments. *Mar. Geol.* ***1992***, 103, 487-502.

Mitchelson, B.P. The electron energy-loss spectroscopic analysis of inhaled smoke particles. *J. Microsc.* ***1992***, 166, 381-387.

Mitra, S.; Dellapenna, T.M.; Dickhut, R.M. Polycyclic aromatic hydrocarbon distribution within lower Hudson River estuarine sediments: physical mixing vs. sediment geochemistry. *Estuar. Coast. Shelf Sci.* ***1999***, 49, 311-326.

Mitra, S.; Bianchi, T.S.; Guo, L.; Santschi, P.H. Terrestrially derived dissolved organic matter in the Chesapeake Bay and the Middle Atlantic Bight. *Geochim. Comsochim. Acta* ***2000a***, 64, 3547-3557.

Mitra, S.; Klerks, P.L.; Bianchi, T.S.; Means, J.; Carman, K.R. Effects of estuarine organic matter biogeochemistry on the bioaccumulation of PAHs by two epibenthic species. *Estuaries* ***2000b***, 23, 864-876.

Miyabe, K.; Takeuchi, S. Analysis of surface diffusion phenomena in liquid phase adsorption. *J. Phys. Chem. B* ***1997***, 101, 7773-7779.

Miyabe, K.; Guiochon, G. Correlation between surface diffusion and molecular diffusion in reversed-phase liquid chromatography. *J. Phys. Chem. B* ***2001***, 105, 9202-9209.

Moermond, C.T.A.; Roessink, I.; Jonker, M.T.O.; Meijer, T.; Koelmans, A.A. Impact of polychlorinated biphenyl and polycyclic aromatic hydrocarbon sequestration in sediment on bioaccumulation in aquatic food webs. *Environ. Toxicol. Chem.* ***2007***, 26, 607-615.

Moldanova, J.; Fridell, E.; Popovicheva, O.; Demirdjian, B.; Tishkova, V.; Faccinetto, A.; Focsa, C. *Atmos. Environ.* ***2009***, 43, 2632-2641.

Moon, C.F. The microstructure of clay sediments. *Earth Sci. Rev.* ***1972***, 8, 303-321.

Moore, H.B. The specific identification of fecal pellets. *J. Mar. Biol. Ass.* ***1931***, 17, 359-365.

Moosmuller, H.; Arnott, W.P.; Rogers, C.F.; Chow, J.C.; Frazier, C.A.; Sherman, L.E.; Dietrich, D.L. Photoacoustic and filter measurements related to aerosol light absorption during the Northern Front Range Air Quality Study (Colorado 1996/1997). *J. Geophys. Res – Atmos.* ***1998***, 103, 28149-28157.

Morgan, J.W. Defining grassland fire events and the response of perennial plants to annual fire in temperate grasslands of south-eastern Australia. *Plant Ecol.* ***1999***, 144, 127-144.

Morrica, P.; Barbato, F.; Giordano, A.; Seccia, S.; Ungaro, F. Adsorption and desorption of imazosulfuron by soil. *J. Agric. Food Chem.* ***2000***, 48, 6132-6137.

Moteki, N.; Kondo, Y. Effects of mixing state on black carbon measuremens by laser-induced incandescence. *Aerosol Sci. Technol.* ***2007***, 41, 398-417.

Muller, J.-O.; Su, D.S.; Wild, U.; Schlogl, R. Bulk and surface structural investigations of diesel engine soot and carbon black. *Phys. Chem. Chem. Phys.* ***2007***, 9, 4018-4025.

Muller, S.; Wilcke, W.; Kanchanakool, N.; Zech, W. Polycyclic aromatic hydrocarbons (PAHs) and polychlorinated biphenyls (PCBs) in particle-size separates of urban soils in Bangkok, Thailand. *Soil Sci.* ***2000***, 165, 412-419.

Murr, L.E.; Bang, J.J. Electron microscope comparisons of fine and ultra-fine carbonaceous and non-carbonaceous, airborne particulates. *Atmos. Environ.* ***2003***, 37, 4795-4806.

Myhre, G.; Stordal, F.; Restad, K.; Isaksen, I.S.A. Estimation of the direct radiative forcing due to sulfate and soot aerosols. *Tellus* ***1998***, 50B, 463-477.

Myrdal, P.B.; Yalkowski, S.H. Estimating pure component vapor pressures of complex organic molecules. *Ind. Eng. Chem. Res.* ***1997***, 36, 2494-2499.

N

Nam, K.; Kim, J.Y.; Oh, D.I. Effect of soil aggregation on the biodegradation of phenanthrene aged in soil. *Environ. Pollut.* ***2003***, 121, 147-151.

National Academy of Science. *Bioavailability of contaminants in soils and sediments: processes, tools and applications.* ***2003***, pp. 1-438, National Academies Press.

National Research Council – Division on Earth and Life Studies. *Sediment Dredging at Superfund Megasites: Assessing the Effectiveness.* ***2007***, pp. 1-316, National Academies Press.

Neff, J.M. *Polycyclic aromatic hydrocarbons in the aquatic environment, sources, fates, and biological effects. 1979*, pp. 1-262, Applied Science Publisher.

El Nemr, A.; Abd-Allah, A.M.A. Contamination of polycyclic aromatic hydrocarbons (PAHs) in microlayer and subsurface waters along Alexandria coast, Egypt. *Chemosphere* ***2003***, 52, 1711-1716.

Nguyen, B.T.; Lehmann, J.; Kinyangi, J.; Smernik, R.; Riha, S.J.; Engelhard, M.H. Long-term black carbon dynamics in cultivated soil. *Biogeochem.* ***2008***, 89, 295-308.

Nguyen, T.H.; Ball, W.P. Absorption and adsorption of hydrophobic organic contaminants to diesel and hexane soot. *Environ. Sci. Technol.* ***2006***, 40, 2958-2964.

Nguyen, T.H.; Brown, R.A.; Ball, W.P. An evaluation of thermal resistance as a measure of black carbon content in diesel soot, wood char, and sediment. *Org. Geochem.* ***2004a***, 35, 217-234.

Nguyen, T.H.; Cho, H.H.; Poster, D.L.; Ball, W.P. Evidence for a pore-filling mechanism in th adsorption of aromatic hydrocarbons to a natural wood char. *Environ. Sci. Technol.* ***2007***, 41, 1212-1217.

Nguyen, T.H.; Goss, K.U.; Ball, W.P. Polyparameter linear free energy relationships for estimating the equilibrium partition of organic compounds between water and the natural organi matter in soils and sediments. *Environ. Sci. Technol.* ***2005***, 39, 913-924.

Nguyen, T.H.; Sabbah, I.; Ball, W.P. Immobilization of soot particles in a silica matrix: a sorbent-carrier system for studying organic chemical sorption. *Environ. Sci. Technol.* ***2005***, 39, 6527-6534.

Nguyen, T.H.; Sabbah, I.; Ball, W.P. Sorption nonlinearity for organic contaminants with diesel soot: method development and isotherm interpretation. *Environ. Sci. Technol.* ***2004b***, 38, 3595-3603.

Nichols, M.M.; Biggs, R.B. Estuaries, In *Coastal Sedimentary Environments*, (ed. Davis Jr., R.A.), pp 77-186, Springer-Verlag, Berlin, ***1985***.

Niederer, C.; Schwarzenbach, R.P.; Goss, K.U. Elucidating differences in the sorption properties of 10 humic and fulvic acids for polar and nonpolar organic chemicals. *Environ. Sci. Technol.* ***2007***, 41, 6711-6717.

Nienow, A.M.; Roberts, J.T. Heterogeneous chemistry of carbon aerosols. *Annu. Rev. Phys. Chem.* ***2006***, 57, 105-128.

Niessner, R.; Panne, U.; Schroder, H. Fiberoptic sensor for the determination of polynuclear aromatic-hydrocarbons with time-resolved, laser-induced fluorescence. *Anal. Chim. Acta* ***1991***, 255, 231-243.

Nishigima, F.N.; Weber, R.R.; Bicego, M.C. Aliphatic and aromatic hydrocarbons in sediments of Santos and Cananeia, SP, Brazil. *Mar. Pollut. Bull.* ***2001***, 42, 1064-1072.

N.O.A.A. *Sediment toxicity in U.S. coastal waters.* National Oceanic and Atmospheric Administration, Coastal Monitoring and Bioeffects Division, Office of Ocean Resources Conservation and Assessment, Coastal Ocean Program, ***1998***.

Noel, M.; Santhanam, R. Electrochemistry of graphite intercalation compounds. *J. Power Sources* ***1998***, 72, 53-65.

van Noort, P.C.M. A thermodynamics-based estimation model for adsorption of organic compounds by carbonaceous materials in environmental sorbents. *Environ. Toxicol. Chem.* ***2003***, 22, 1179-1188.

van Noort, P.C.M.; Cornelissen, G.; ten Hulscher, T.E.M.; Vrind, B.A.; Rigterink, H.; Belfroid, A. Slow and very slow desorption of organic compounds from sediment: influence of sorbate planarity. *Water Research* ***2003***, 37, 2317-2322.

Northcott, G.L.; Jones, K.C. Partitioning, extractability, and formation of nonextractable PAH residues in soil. 1. Compound differences in aging and sequestration. *Environ. Sci. Technol.* ***2001a***, 35, 1103-1110.

Northcott, G.L.; Jones, K.C. Partitioning, extractability, and formation of nonextractable PAH residues in soil. 2. Effects on compound dissolution behavior. *Environ. Sci. Technol.* ***2001b***, 35, 1111-1117.

Notar, M.; Leskovsek, H.; Faganeli, J. Composition, distribution and sources of polycyclic aromatic hydrocarbons in sediments of the Gulf of Trieste, northern Adriatic Sea. *Mar. Pollut. Bull.* ***2001***, 42, 36-44.

Novakov, T.; Corrigan, C.E. Thermal characterization of biomass smoke particles. *Mikrochim. Acta* ***1995***, 119, 157-166.

Novakov, T.; Hegg, D.A.; Hobbs, P.V. Airborne measurements of carbonaceous aerosols on the East Coast of the United States. *J. Geophys. Res.,* ***1997***, 102, 30023-30030.

Nowell, A.R.M.; Jumars, P.A.; Eckman, J.E. Effects of biological activity on the entrainment of marine sediments. *Mar. Geol.* ***1981***, 42, 133-153.

O

Obana, H.; Hori, S.; Kashimoto, T. Determination of polycyclic aromatic hydrocarbons in marine samples by high-performance liquid chromatography. *Bull. Environ. Contam. Toxicol.* ***1981***, 26, 613-620.

Ogren, J.A.; Charlson, R.J.; Groblicki, P.J. Determination of elemental carbon in rainwater. *Anal. Chem.* ***1983***, 55, 1569-1572.

Ogren J.A. Groblicki, P.J.; Charlson, R.J. Measurement of the removal rate of elemental carbon from the atmosphere. *Sci. Total Environ.* ***1984***, 36, 329-338.

Ohta, K.; Handa, N. Trends and factors governing polycyclic aromatic hydrocarbon levels in Tokyo Bay sediments. *Geochim. Cosmochim. Acta* ***1983***, 47, 1651-1654.

Okada, K.; Ikegami, M.; Uchino, O.; Nikaidou, Y.; Zaizen, Y.; Tsutsumi, Y.; Makino, Y. Extremely high proportions of soot particles in the upper troposphere over Japan. *Geophys. Res. Lett.* ***1992***, 19, 921-924.

Olajire, A.A.; Altenburger, R.; Kuster, E.; Brack, W. Chemical and ecotoxicological assessment of polycyclic aromatic hydrocarbon-contaminated sediments of the Niger Delta, Southern Nigeria. *Sci. Tot. Environ.* ***2005***, 340, 123-136.

Olivella, M.A. Polycyclic aromatic hydrocarbons in rainwater and surface waters of Lake Maggiore, a subalpine lake in Northern Italy. *Chemosphere* ***2006***, 63, 116-131.

Ortiz, E.; Kraatz, M.; Luthy, R.G. Organic phase resistance to dissolution of polycyclic aromatic hydrocarbon compounds. *Environ. Sci. Technol.* ***1999***, 33, 235-242.

OSPAR Commission. Assessment of the environmental impact of dredging for navigational purposes. *Publication No. 366/2008,* ***2008***, pp. 1-17.

P

Paasivirta, J.; Sinkkonen, S.; Mikkelson, P.; Rantio, T.; Wania, F. Estimation of vapor pressures, solubilities and Henry's Law constants of selected persistent organic pollutants as functions of temperature. *Chemosphere* ***1999***, 39, 811-832.

Pagliai, A.M.B.; Varriale, A.M.C.; Crema, R.; Galletti, M.C.; Zunarelli, R.V. Environmental impact of extensive dredging in a coastal marine area. *Mar. Pollut. Bull.* ***1985***, 16, 483-488.

Palotas, A.B.; Rainey, L.C.; Feldermann, C.J.; Sarofim, A.F.; Vander Sande, J.B. Soot morphology: an application of image analysis in high-resolution transmission electron microscopy. *Microsc. Res. Technique* ***1996***, 33, 266-278.

Pamukcu, S.; Tuncan, M. Influence of some physicochemical activities on mechanical behavior of clays. In *Microstructures of Fine-Grained Sediments: From Mud to Shale*, (eds. Bennett, R.H.; Bryant, W.R.; Hulbert, M.H.), pp. 241-254, Springer-Verlag, Berlin, ***1991***.

Pan, B.; Ghosh, S.; Xing, B. Nonideal binding between dissolved humic acids and polyaromatic hydrocarbons. *Environ. Sci. Technol.* ***2007***, 41, 6472-6478.

Pantea, D.; Brochu, S.; Thiboutot, S.; Ampleman, G.; Scholz, G. A morphological investigation of soot produced by the detonation of munitions. *Chemosphere* ***2006***, 65, 821-831.

Paramasivam, S.; Alva, A.K.; Fares, A. An evaluation of soil water status using tensiometers in a sandy soil profile under citrus production. *Soil Sci.* ***2000***, 165, 343-353.

Park, S.-K.; Jung, W.-Y. Preparation and structural characterization of activated carbons based on polymeric resin. *J. Colloid Interface Sci.* ***2002***, 250, 196-200.

Parker, C.A. *Photoluminescence of solutions.* ***1968***, pp. 1-544, Elsevier.

Paul, E.A.; Morris, S.J.; Conant, R.T.; Plante, A.F. Does the acid hydrolysis-incubation method measure meaningful soil organi carbon pools? *Soil Sci. Soc. Am. J.* ***2006***, 70, 1023-1035.

Paulsen, P.D.; Moore, B.C.; Cannon, F.S. Applicability of adsorption equations to argon, nitrogen and volatile organic compound adsorption onto activated carbon. *Carbon* ***1999***, 37, 1843-1853.

Peel, R.G.; Benedek, A. Attainment of equilibrium in activated carbon isotherm studies. *Environ. Sci. Technol.* ***1980*** 14, 66-71.

Peel, R.G.; Benedek, A.; Crowe, C.M. A branched pore kinetic model for activated carbon adsorption. *AIChE J.* ***1981***, 27, 26-32.

Penn, A.; Murphy, G.; Barker, S.; Henk, W.; Penn, L. Combustion-derived ultrafine particles transport organic toxicants to target respiratory cells. *Environ. Health Perspect.* ***2005***, 113, 956-963.

Penner, J.E.; Eddleman, H.; Novakov, T. Towards the development of a global inventory for black carbon emissions. *Atmos. Environ. A* ***1993***, 27, 1277-1295.

Penner, J.E.; Novakov, T. Carbonaceous particles in the atmosphere: a historical perspective to the Fifth International Conference on Carbonaceous Particles in the Atmosphere. *J. Geophys. Res.* ***1996***, 101, 19373-19378.

Penner, J.E.; Zhang, S.Y.; Chuang, C.C. Soot and smoke aerosol may not warm climate. *J. Geophys. Res.* ***2003***, 108, Art. No. 4657.

Perera, F.P.; Li, Z.G.; Whyatt, R.; Hoepner, L.; Wang, S.A.; Camann, D.; Rauh, V. Prenatal airborne polycyclic aromatic hydrocarbon exposure and child IQ at age 5 years. *Pediatrics* ***2009***, 124, E195-E202.

Perminova, I.V.; Grechishcheva, N.Y.; Petrosyan, V.S. Relationships between structure and binding affinity of humic substances for polycyclic aromatic hydrocarbons: relevance of molecular descriptors. *Environ. Sci. Technol.* ***1999***, 33, 3781-3787.

Perry, D.L.; Grint, A. Application of XPS to coal characterization. *Fuel* ***1983***, 62, 1024-1033.

Petsch, S.T.; Smernik, R.J.; Eglinton, T.I.; Oades, J.M. A solid state ^{13}C-NMR study of kerogen degradation during black shale weathering. *Geochim. Cosmochim. Acta* ***2001***, 65, 1867-1882.

Petzold, A.; Kopp, C.; Niessner, R. The dependence of the specific attenuation cross-section on black carbon mass fraction and particle size. *Atmos. Environ.* ***1997***, 31, 661-672.

Petzold, A.; Niessner, R. Photoacoustic soot sensor for in-situ black carbon monitoring. *Appl. Phys. B* ***1996***, 63, 191-197.

Piatt, J.J.; Backhus, D.A.; Capel, P.D.; Eisenreich, S.J. Temperature-dependent sorption of naphthalene, phenanthrene and pyrone to low organic carbon aquifer sediments. *Environ. Sci. Technol.* ***1996***, 30, 751-760.

Pignatello, J.J. Slowly reversible sorption of aliphatic halocarbons in soils. I. Formation of residual fractions. *Environ. Toxicol. Chem.* ***1990***, 9, 1107-1115.

Pignatello, J.J.; Ferrandino, F.J.; Huang, L.Q. Elution of aged and freshly added herbicides from a soil. *Environ. Sci. Technol.* ***1993***, 27, 1563-1571.

Pignatello, J.J.; Kwon, S.; Lu, Y. Effect of natural organic substances on the surface and adsorptive properties of environmental black carbon (char): attenuation of surface activity by humic and fulvic acids. *Environ. Sci. Technol.* ***2006***, 40, 7757-7763.

Pignatello, J.J.; Xing, B. Mechanisms of slow sorption or organic chemicals to natural particles. *Environ. Sci. Technol.* ***1996***, 30, 1-11.

Pike, J.; Kemp, A.E.S. Silt aggregates in laminated marine sediment produced by agglutinated foraminifera. *J. Sed. Res.* ***1996***, 66, 625-631.

Plante, A.F.; Conant, R.T.; Paul, E.A.; Paustian, K.; Six, J. Acid hydrolysis of easily dispersed and microaggregate-derived silt- and clay-sized fractions to isolate resistant soil organic matter. *Euro. J. Soil Sci.* ***2006***, 57, 456-467.

Poerschmann, J.; Zhang, Z.; Kopinke, F.D.; Pawliszyn, J. Solid phase microextraction for determining the distribution of chemicals in aqueous matrices. *Anal. Chem.* ***1997***, 69, 597-600.

Poirier, N.; Derenne, S.; Rouzaud, J.N.; Largeau, C.; Mariotti, A.; Balesdent, J.; Maquet, J. *Org. Geochem.* ***2000***, 31, 813-827.

Polanyi, M. Adsorption aus Losungen beschrankt loslicher stoffe. *Z. Phys.* ***1920***, 2, 111-116.

Poschl, U. Aerosol particle analysis: challenges and progress. *Anal. Bioanal. Chem.* ***2003***, 375, 30-32.

Posfai, M.; Anderson, J.R.; Buseck, P.R.; Sievering, H. Soot and sulfate aerosol particles in the remote marine troposphere. *J. Geophys. Res.* ***1999***, 104, 21685-21693.

Posfai, M.; Simonics, R.; Li, J.; Hobbs, P.V.; Buseck, P.R. Individual aerosol particles from biomass burning in southern Africa: 1. Compositions and size distribution of carbonaceous particles. *J. Geophys. Res.* ***2003***, 108(D13), 8483.

Powell, C.J. Cross sections for ionization fo inner-shell electrons by electrons. *Rev. Mod. Phys.* ***1976***, 48, 33-47.

Powell, T.G.; Boreham, C.J.; Smyth, M.; Russell, N.; Cook, A.C. Petroleum source rock assessment in nonmarine sequences – pyrolysis and petrographic analysis of Australian coals and carbonaceous shales. *Org. Geochem.* ***1991***, 17, 375-394.

Prado, G.; Lahaye, J. Physical aspects of nucleation and growth of soot particles. In *Particulate Carbon Formation During Combustion*, (eds. Siegla, D.C.; Smith, G.W.), pp 143-175, Plenum, New York, ***1981***.

Pranovi, F.; Giovanardi, O. The impact of hydraulic dredging for short-necked clams, *Tapes* spp. on an infaunal community in the lagoon of Venice. *Sci. Mar.* ***1994***, 58, 345-353.

Preston, C.M.; Schmidt, M.W.I. Black (pyrogenic) carbon: a synthesis of current knowledge and uncertainties with special consideration of boreal regions. *Biogeosci.* ***2006***, 3, 397-420.

Pritchard, D.W.; Okubo, A.; Carter, H.H. Observations and theory of eddy movement and diffusion of an introduced tracer material in the surface layers of the sea. In *Disposal of Radioactive Wastes into Sea, Oceans and Surface Waters*, International Atomic Energy Agency, ***1966***.

Probstein, R.F. *Physicochemical Hydrodynamics.* ***2003***, pp. 1-400, Wiley-Interscience.

Q

Qiao, W.; Korai, Y.; Mochida, I.; Hori, Y.; Maeda, T. Preparation of an activated carbon artifact: oxidative modification of coconut shell-based carbon to improve the strength. *Cabon* ***2002***, 40, 351-358.

R

Raber, B.; Kogel-Knabner, I.; Stein, C.; Klem, D. Partitioning of polycyclic aromatic hydrocarbons to dissolved organic matter from different soils. *Chemosphere* ***1998***, 36, 79-97.

Rainey, L.; Palotas, A.; Bolsaitis, P.; Vander Sande, J.B.; Sarofim, A.F. Application of high resolution electron microscopy for the characterization and source assignment of diesel particulates. *Appl. Occup. Environ. Hyg.* ***1996***, 11, 777-781.

Ramanathan, V.; Carmichael, G. Global and regional climate changes due to black carbon. *Nature Geosci.* ***2008***, 1, 221-227.

Ramesh, A.; Walker, S.A.; Hood, D.B.; Guillen, M.D.; Schneider, K.; Weyand, E.H. Bioavailability and risk assessment of orally ingested polycyclic aromatic hydrocarbons. *Int. J. Toxicol.* ***2004***, 23, 301–333.

Ran, Y.; Huang W.; Rao, P.S.C.; Liu, D.; Sheng, G.; Fu, J. The role of condensed organic matter in the nonlinear sorption of hydrophobic organic contaminants by a peat and sediments. *J. Environ. Qual.* ***2002***, 31, 1953-1962.

Ran, Y.; Xiao, B.; Fu, J.; Sheng, G. Sorption and desorption hysteresis of organic contaminants by kerogen in a sandy aquifer material. *Chemosphere* ***2003a***, 50, 1365-1376.

Ran, Y.; Xiao, B.; Huang, W.; Peng, P.; Liu, D.; Fu, J.; Sheng, G. Kerogen in aquifer material and its strong sorption for nonionic organic pollutants. *J. Environ. Qual.* ***2003b***, 32, 1701-1709.

Ran, Y.; Sun, K.; Ma, X.X.; Wang, G.H.; Grathwohl, P.; Zeng, E.Y. Effect of condensed organic matter on solvent extraction and aqueous leaching of polycyclic aromatic hydrocarbons in soils and sediments. *Environ. Poll.* ***2007a***, 148, 529-538.

Ran, Y.; Sun, K.; Yang, Y.; Xing, B.; Zeng, E. Strong sorption of phenanthrene by condensed organic matter in soils and sediments. *Environ. Sci. Technol.* ***2007b***, 41, 3952-3958.

Ravens, T.M. Sediment resuspension in Boston Harbor. Ph.D. Thesis, Massachusetts Institute of Technology, Cambridge, ***1997***, pp 1-187.

Ravens, T.M.; Madsen, O.S.; Signell, R.P.; Adams, E.E.; Gschwend, P.M. Hydrodynamic forcing and sediment character in Boston Harbor. *J. Waterway, Port, Coastal, and Ocean Eng.* ***1998***, 124, 40-42.

Readman, J.W.; Fillmann, G.; Tolosa, I.; Bartocci, J.; Villeneuve, J.-P.; Catinni, C.; Mee, L.D. Petroleum and PAH contamination of the Black Sea. *Mar. Pollut. Bull.* ***2002***, 44, 48-62.

Reddy, C.M.; Pearson, A.; Xu, L.; McNichol, A.P.; Benner, B.A.; Wise, S.A.; Klouda, G.A.; Currie, L.A.; Eglinton, T.I. Radiocarbon as a tool to apportion the sources of polycyclic aromatic hydrocarbons and black carbon in environmental samples. *Environ. Sci. Technol.* ***2002***, 36, 1774-1782.

Redlich, Ph.; Carroll, D.L.; Ajayan, P.M. High spatial resolution imaging and spectroscopy in nanostructures. *Curr. Opin. Solid State Mater. Sci.* ***1999***, 4, 325–336.

Reisinger, P.; Wonaschutz, A.; Hitzenberger, R.; Petzold, A.; Bauer, H.; Jankowski, N.; Puxbaum, H.; Chi, X.; Maenhaut, W. Intercomparison of measurement techniques for black or

elemental carbon under urban background conditions in wintertime: influence of biomass combustion. *Environ. Sci. Technol.* ***2008***, 42, 884-889.

Riemer, N.; Vogel, H.; Vogel, B. Soot aging time scales in polluted regions during day and night. *Atmos. Chem. Phys.* ***2004***, 4, 1885-1893.

Rivera-Utrilla, J.; Sanchez-Polo, M. Ozonation of 1,3,6-naphthalenetrisulphonic acid catalysed by activated carbon in aqueous phase. *Appl. Catal. B Environ.* ***2002***, 39, 319-329.

Robert, S.; Blanc, G.; Schafer, J.; Lavaux, G.; Abril, G. Metal mobilization in the Gironde Estuary (France): the role of the soft mud layer in the maximum turbidity zone. *Mar. Chem.* ***2004***, 87, 1-13.

Robertson, B.K.; Jjemba, P.K. Enhanced bioavailability of sorbed 2,4,6-trinitrotoluene (TNT) by a bacterial consortium. *Chemosphere* ***2005***, 58, 263-270.

Rockne, K.J.; Shor, L.M.; Young, L.Y.; Taghon, G.L.; Kosson, D.S. Distributed sequestration and release of PAHs in weathered sediment: the role of sediment structure and organic carbon properties. *Environ. Sci. Technol.* ***2002***, 36, 2636-2644.

Rockne, K.J.; Taghon, G.L.; Kosson, D.S. Pore structure of soot deposits from several combustion sources. *Chemosphere* ***2000***, 41, 1125-1135.

de la Rosa, J.M.; Knicker, H.; Lopez-Capel, E.; Manning, D.A.C.; Gonzalez-Perez, J.A.; Gonzalez-Vila, F.J. Direct detection of black carbon in soils by Py-GC/MS, carbon-13 NMR spectroscopy and thermogravimetric techniques. *Soil Sci. Soc. Am. J.* ***2008***, 72, 258-267.

Rosen, H.; Hansen, A.D.A.; Gundel, L.; Novakov, T. Identification of the optically absorbing component in urban aerosols. *Appl. Opt.* ***1978***, 17, 3859-3861.

Ross, M.M.; Risby, T.H. Physicochemical properties of diesel particulate matter. *Colloids Surf.* ***1982***, 5, 17-31.

Ross, R.M.; Oros, D.R. Polycyclic aromatic hydrocarbons in the San Francisco Bay water column: sources, spatial distribution, and temporal trends (1993-2001). *Chemosphere* ***2004***, 57, 909-920.

Roux, M.V.; Temprado, M.; Chickos, J.S.; Nagano, Y. Critically evaluated thermochemical properties of polycyclic aromatic hydrocarbons. *J. Phys. Chem. Ref. Data* ***2008***, 37, 1855-1996.

Rudnick, S.M. In situ fluorescence detection of polycyclic aromatic hydrocarbons (PAH) in the marine environment. Ph.D. Thesis, University of Massachusetts at Boston, ***1998***, pp 1-206.

Rudnick, S.M.; Chen, R.F. Laser-induced fluorescence of pyrene and other polycyclic aromatic hydrocarbons (PAH) in seawater. *Talanta* ***1998***, 47, 907-919.

S

Sabbah, I.; Rebhun, M.; Gerstl, Z. An independent prediction of the effect of dissolved organic matter on the transport of polycyclic aromatic hydrocarbons. *J. Contam. Hydrol.* ***2004***, 75, 55-70.

Sadler, M.; Charlson, R.J.; Rosen, H.; Novakov, T. An intercomparison of the integrating plate and the laser transmission methods for determination of aerosol absorption coefficients. *Atmos. Environ.* ***1981***, 15, 1265-1268.

Saini, G.R. Organic matter as a measure of bulk density of soil. *Nature* ***1966***, 210, 1295-1296.

Sakurovs, R. Interactions between a bituminous coal and aromatic hydrocarbons at elevated temperatures. *Energy Fuels* ***1998***, 12, 631-636.

Salma, I.; Ocskay, R.; Lang, G.G. Properties of atmospheric humic-like substances – water system. *Atmos. Chem. Phys.* ***2008***, 8, 2243-2254.

Salomons, W.; de Rooij, N.M.; Kerdijk, H.; Bril, J. Sediments as sources of contaminants? *Hydrobiol.* ***1987***, 149, 13-30.

Sanchez-Moyano, J.E.; Estacio, F.J.; Garcia-Adiego, E.M.; Garcia-Gomez, J.C. Dredging impact on the benthic community of an unaltered inlet in southern Spain. *Helgol. Mar. Res.* ***2004***, 58, 32-39.

Sander, M.; Lu, Y.; Pignatello, J.J. Conditioning-annealing studies of natural organic matter solids linking irreversible sorption to irreversible structural expansion. *Environ. Sci. Technol.* ***2006***, 40, 170-178.

Sander, M.; Pignatello, J.J. On the reversibility of sorption to black carbon: distinguishing true hysteresis from artificial hysteresis caused by dilution of a competing adsorbate. *Environ. Sci. Technol.* ***2007***, 41, 843-849.

San Miguel, G.; Fowler, G.D.; Dall'Orso, M.; Sollars, C.J. Porosity and surface characteristics of activated carbons produced from waste tyre rubber. *J. Chem. Technol. Biotechnol.* ***2001***, 77, 1-8.

Santos, E.B.H.; Duarte, A.C. The influence of pulp and paper mill effluents on the composition of the humic fraction of aquatic organic matter. *Wat. Res.* ***1998***, 32, 597–608.

Schamm, S.; Zanchi, G. Contamination and the quantitative exploitation of EELS low-loss experiments. *Ultramicroscopy* ***2001***, 88, 211-217.

Scheffer, M. Ecology of Shallow Lakes. ***2004***, pp. 1-357, Kluwer Academic Publishers.

Schlautman, M.A.; Morgan, J.J. Effects of aqueous chemistry on the binding of polycyclic aromatic hydrocarbons by dissolved humic materials. *Environ. Sci. Technol.* ***1993***, 27, 961-969.

Schlebaum, W.; Schraa, G.; van Riemsdijk, W.H. Influence of nonlinear sorption kinetics on the slow-desorbing organic contaminant fraction in soil. *Environ. Sci. Technol.* ***1999***, 33, 1413-1417.

Schmid, E.M.; Skjemstad, J.O.; Glaser, B.; Knicker, H.; Kogel-Knabner, I. Detection of charred organic matter in soils from a Neolithic settlement in Southern Bavaria, Germany. *Geoderma* ***2002***, 107, 71-91.

Schmidt, M.W.I.; Noack, A.G. Black carbon in soils and sediments: analysis, distribution, implications, and current challenges. *Glob. Biogeochem. Cycles* ***2000***, 14, 777-793.

Schmidt, M.W.I.; Skjemstad, J.O.; Czimczik, C.I.; Glaser, B.; Prentice, K.M.; Gelinas, Y.; Kulbusch, T.A.J. Comparative analysis of black carbon in soils. *Glob. Biogeochem. Cycles* ***2001***, 15, 163-167.

Schmidt, M.W.I.; Skjemstad, J.O.; Gehrt, E.; Kogel-Knabner, I. Charred organic carbon in German chernozemic soils. *Euro. J. Soil Sci.* ***1999***, 50, 351-365.

Schmidt, M.W.I.; Skjemstad, J.O.; Jager, C. Carbon isotope geochemistry and nanomorphology of soil black carbon: black chernozemic soils in central Europe originate from ancient biomass burning. *Glob. Biogeochem. Cyc.* ***2002***, 16, Art No. 1123.

Schneider, A.R.; Eadie, B.J.; Baker, J.E. Episodic particle transport events controlling PAH and PCB cycling in Grand Traverse Bay, Lake Michigan. *Environ. Sci. Technol.* ***2002***, 36, 1181-1190.

Schnitzer, M.; Dinel, M.; Pare, T.; Schulten, H.-R.; Ozdoba, D. Some chemical and spectroscopic characterization of six organic ores. In *Humic Substances – Structures, Models and Functions*, (eds. Ghabbour, E.A.; Davies, G.), pp 315-328, Royal Society of Chemistry, Cambridge, ***2001***.

Schnitzler, F.; Lavorenti, A.; Berns, A.E.; Drewes, N.; Vereecken, H.; Burauel, P. The influence of maize residues on the mobility and binding of benazolin: Investigating physically extracted soil fractions. *Environ. Pollut.* ***2007***, 147, 4-13.

Schubel, J.R. Turbidity maximum of the Northern Chesapeake Bay. *Science* ***1968***, 161, 1013-1015.

Schultz, E. Size-fractionated measurement of coarse black carbon particles in deposition samples. *Atmos. Environ. A* ***1993***, 27, 1241-1249.

Schwartz, E.; Scow, K.M. Using biodegradation kinetics to measure availability of aged phenanthrene to bacteria inoculated into soil. *Environ. Toxicol. Chem.* ***1999***, 18, 1742-1746.

Schwarz, J.P.; Spackman, J.R.; Fahey, D.W.; Gao, R.S.; Lohmann, U.; Stier, P.; Watts, L.A.; Thomson, D.S.; Lack, D.A.; Pfister, L.; Mahoney, M.J.; Baumgardner, D.; Wilson, J.C.; Reeves, J.M. Coatings and their enhancement of black carbon light absorption in the tropical atmosphere. *J. Geophys, Res.* ***2008***, 113, D03203.

Schwarzenbach, R.P.; Gschwend, P.M.; Imboden, D.M. *Environmental organic chemistry.* ***2003***, pp. 1-1313, Wiley-Interscience.

Scott, V.D.; Love, G.; Reed, S.J.B. *Quantitative Electron-Probe Microanalysis.* ***1995***, pp. 1-311, Ellis Horwood.

Seepujak, A.; Bangert, U.; Harvey, A.J.; Blank, V.D.; Kulnitskiy, B.A.; Batov, D.V. EEL calculations and measurements of graphite and graphitic-CN_x core-losses. *J. Phys. Conf. Series* ***2006***, 26, 161-164.

Selley, R.C. *Applied Sedimentology.* ***2000***, pp. 1-521, Academic Press.

Semeniuk, T.A.; Wise, M.E.; Martin, S.T.; Russell, L.M.; Buseck, P.R. Hygroscopic behavior of aerosol particles from biomass fires using environmental transmission electron microscopy. *J. Atmos. Chem.* ***2007***, 56, 259-273.

Senesi, N.; Loffredo, E.; D'Orazio, V.; Brunetti, G.; Miano, T.M. Adsorption of pesticides by humic acids from organic amendments and soils. In *Humic Substances and Chemical Contaminants*. (eds. Clapp, C.E.; Hayes, M.H.B.; Senesi, N.; Bloom, P.R.; Jardine, P.M.), pp 129-153, Soil Science Society of America, Madison, ***2001***.

Senus, M.P.; Langland, M.J.; Moyer, D.L. Nutrient and sediment concentrations, loads, and trends for four nontidal tributaries in the Chesapeake Bay Watershed, 1997–2001. *Scientific Investigations Report 2004-5125*, ***2004***, pp. 1-60, U.S. Geological Survey.

Sergides, C.A.; Jassim, J.A.; Chughtai, A.R.; Smith, D.M. The structure of hexane soot. 3. Ozonation studies. *Appl. Spectrosc.* ***1987***, 41, 482-492.

Sharer, M.; Park, J.H.; Voice, T.C.; Boyd, S.A. Time dependence of chlorobenzene sorption/desorption by soils. *Soil Sci. Soc. Am. J.* ***2003***, 67, 1740-1745.

Sheldon, R.W.; Sutcliffe, W.H.; Prakash, A. The production of particles in the surface waters of the ocean with particular reference to the Sargasso Sea. *Limnol. Oceanogr.* ***1973***, 19, 719-733.

Sheremata, T.W.; Thiboutot, S.; Ampleman, G.; Paquet, L.; Halasz, A.; Hawari, J. Fate of 2,4,6-trinitrotoluene and its metabolites in natural and model soil systems. *Environ. Sci. Technol.* ***1999***, 33, 4002-4008.

Shiaris, M.P. Seasonal biotransformation of naphthalene, phenanthrene, and benzo[a]pyrene in surficial estuarine sediments. *Appl. Environ. Microbiol.* ***1989***, 55, 1391-1399.

Shiaris, M.P.; Jambard-Sweet, D. Polycyclic aromatic hydrocarbons in surficial sediments of Boston Harbor, Massachusetts, USA. *Mar. Pollut. Bull.* ***1986***, 17, 469-472.

Shih, Y.S.; Gschwend, P.M. Evaluating activated carbon-water sorption coefficients or organic compounds using a linear solvation energy relationship approach and sorbate chemical activities. *Environ. Sci. Technol.* ***2009***, 43, 851-857.

Shim, H.-S.; Hajaligol, M.R.; Baliga, V.L. Oxidation behavior of biomass chars: pectin and *Populus deltoides*. *Fuel* ***2004***, 83, 1495-1503.

Shindo, H.; Honma, H. Significance of burning vegetation in the formation of black humic acids in Japanese volcanic ash soils. In *Humic Substances – Structures, Models and Functions*, (eds. Ghabbour, E.A.; Davies, G.), pp 297-306, Royal Society of Chemistry, Cambridge, ***2001***.

Shinozuka, N.; Lee, C. Aggregate formation of humic acids from marine sediments. *Mar. Chem.* ***1991***, 33, 229-241.

Shiraiwa, M.; Kondo, Y.; Moteki, N.; Takegawa, N.; Miyazaki, Y.; Blake, D.R. Evolution of mixing state of black carbon in polluted air from Tokyo. *Geophys. Res. Lett.* ***2007***, 34, L16803.

Shor, L.M.; Liang, W.; Rockne, K.J.; Young, L.Y.; Taghon, G.L.; Kosson, D.S. Intra-aggregate mass transport-limited bioavailability of polycyclic aromatic hydrocarbons to mycobacterium strain PC01. *Environ. Sci. Technol.* ***2003a***, 37, 1545-1552.

Shor, L.M.; Rockne, K.J.; Taghon, G.L.; Young, L.Y.; Kosson, D.S. Desorption kinetics for field-aged polycyclic aromatic hydrocarbons from sediments. *Environ. Sci. Technol.* ***2003b***, 37, 1535-1544.

Sigle, W. Analytical transmission electron microscopy. *Annu. Rev. Mater. Res.* ***2005***, 35, 239-314.

Simo, R.; Grimalt, J.O.; Albaiges, J. Loss of unburned-fuel hydrocarbons from combustion aerosols during atmospheric transport. *Environ. Sci. Technol.* ***1997***, 31, 2697-2700.

Simpson, C.D.; Mosi, A.A.; Cullen, W.R.; Reimer, K.J. Composition and distribution of polycyclic aromatic hydrocarbon contamination in surficial marine sediments from Kitimat Harbor, Canada. *Sci. Tot. Environ.* ***1996***, 181, 265-278.

Simpson, M.J.; Hatcher, P.G. Determination of black carbon in natural organic matter by chemical oxidation and solid-state ^{13}C nuclear magnetic resonance spectroscopy. *Org. Geochem.* ***2004a***, 35, 923-935.

Simpson, M.J.; Hatcher, P.G. Overestimates of black carbon in soils and sediments. *Naturwissenschaften* ***2004b***, 91, 436-440.

Simpson, M.J.; Otto, A.; Feng, X. Comparison of solid-state carbon-13 nuclear magnetic resonance and organic matter biomarkers for assessing soil organic matter degradation. *Soil Sci. Soc. Am. J.* ***2008***, 72, 268-276.

Singh, J.; Comfort, S.D.; Hundal, L.S.; Shea, P.J. Long-term RDX sorption and fate in soil. *J. Environ. Qual.* ***1998***, 27, 572-577.

Singh, D.K.; Agarwal, H.C. Persistence of DDT and nature of bound residues in soil at higher altitude. *Environ. Sci. Technol.* ***1995***, 29, 2301-2304.

Skjemstad, J.O.; Clarke, P.; Taylor, J.A.; Oades, J.M.; McClure, S.G. The chemistry and nature of protected carbon in soil. *Aust. J. Soil Res.* ***1996***, 34, 251-271.

Skjemstad, J.O.; Taylor, J.A.; Smernik, R.J. Estimation of charcoal (char) in soils. *Comm. Soil Sci. Plant Analysis* ***1999***, 30, 2283-2298.

Skjemstad, J.O.; Reicosky, D.C.; Wilts, A.R.; McGowan, J.A. Charcoal carbon in U.S. agricultural soils. *Soil Sci. Soc. Am. J.* ***2002***, 66, 1249-1255.

Smart, M.M.; Rada, R.G.; Nielsen, D.N.; Claflin, T.O. The effect of commercial and recreational traffic on the resuspension of sediment in Navigation Pool 9 of the Upper Mississippi River. *Hydrobiologia* ***1985***, 126, 263-274.

Smayda, T.J. Measurements of the sinking rate of fecal pellets. *Limnol. Oceanogr.* ***1969***, 14, 621-625.

Smedes, F.; Geertsma, R.W.; van der Zande, T.; Booij, K. Polymer-water partition coefficients of hydrophobic compounds for passive sampling: application of cosolvent models for validation. *Environ. Sci. Technol.* ***2009***, 43, 7047-7054.

Smekens, A; Godoi, R.H.M.; Vervoort, M.; van Espen, P.; Potgieter-Vermaak, S.S.; van Grieken, R. Characterization of individual soot aggregates from different sources using image analysis. *J. Atmos. Chem.* ***2007***, 56, 211-223.

Smernik, R.J.; Baldock, J.A.; Oades, J.M. Impact of remote protonation on ^{13}C CPMAS NMR quantitation of charred and uncharred wood. *Solid State Nucl. Magn. Resonance* ***2002a***, 22, 71-82.

Smernik, R.J.; Baldock, J.A.; Oades, J.M. Whittaker, A.K. Determination of $T_{1\rho}H$ relaxation rates in charred and uncharred wood and consequences for NMR quantitation. *Solid State Nucl. Magn. Resonance* ***2002b***, 22, 50-70.

Smith, D.M.; Griffin, J.J.; Goldberg, E.D. Elemental carbon in marine sediments: a baseline for burning. *Nature* ***1973***, 241, 268-270.

Smith, D.M.; Griffin, J.J.; Goldberg, E.D. Spectrometric method for the quantitative determination of elemental carbon. *Anal. Chem.* ***1975***, 47, 233-238.

Smith, G.D. *Numerical Solution of Partial Differential Equations – Finite Difference Methods.* ***1985***, pp. 1-337, Oxford University Press.

Smith, I. M. (1988). *U.S. Patent No. 123,445.* Washington, DC: U.S. Patent and Trademark Office.

Solomon, D.; Lehmann, J.; Kinyangi, J.; Liang, B.; Schafer, T. Carbon K-edge NEXAFS and FTIR-ATR spectroscopic investigation of organic carbon speciation in soils. *Soil Sci. Soc. Am. J.* ***2005***, 69, 107-119.

Song, J.; Alam, M.; Boehman, A.K.; Kim, U. Examination of the oxidation behavior of biodiesel soot. *Combust. Flame* ***2006***, 146, 589-604.

Song, J.; Peng, P.; Huang, W. Black carbon and kerogen in soils and sediments. 1. Quantification and characterization. *Environ. Sci. Technol.* ***2002***, 36, 3960-3967.

Sorensen, H.S.; Rosenberg, P.; Petersen, H.I.; Sorensen, L.H. Char porosity characterization by scanning electron microscopy and image analysis. *Fuel* ***2000***, 79, 1379-1388.

Sormunen, A.J.; Koistinen, J.; Leppanen, M.T.; Kukkonen, J.V.K. Desorption of sediment-associated polychlorinated dibenzo-*p*-dioxins, dibenzofurans, diphenyl ethers and hydroxyldiphenyl ethers from contaminated sediment. *Chemosphere* ***2008***, 72, 1-7.

Spence, J.C.H. Absorption spectroscopy with sub-angstrom beams: ELS in STEM. *Rep. Prog. Phys.* ***2006***, 69, 725-758.

Spencer, M.T.; Holecek, J.C.; Corrigan, C.E.; Ramanathan, V.; Prather, K.A. Size-resolved chemical composition of aerosol particles during a monsoonal transition period over the Indian Ocean. *J. Geophys. Res.* ***2008***, 113, D16305.

Spurlock, F.C.; Biggar, J.W. Thermodynamics of organic chemical partition in soils. 1. Development of a general partition model and application to linear isotherms. *Environ. Sci. Technol.* ***1994***, 28, 989-995.

Srinivas, S.P.; Mutharasan, R. Inner filter effects and their interferences in the interpretation of culture fluorescence. *Biotechnol. Bioeng.* ***1987***, 30, 769-774.

Stanmore, B.R.; Brilhac, J.F.; Gilot, P. The oxidation of soot: a review of experiments, mechanisms and models. *Carbon* ***2001***, 39, 2247-2268.

Stapleton, J.M.; Mihelcic, J.R.; Lueking, D.R. Adsorption and desorption kinetics of pyrene onto a Great Lakes sediment. *J. Great Lakes Res.* ***1994***, 20, 561-568.

Stevenson, F.J. *Humus Chemistry – Genesis, Composition, Reactions.* ***1982***, pp. 1-443, Wiley-Interscience.

Stewart, C.E.; Plante, A.F.; Paustian, K.; Conant, R.T. Six, J. Soil carbon saturation: linking concept and measurable carbon pools. *Soil Sci. Soc. Am. J.* ***2008***, 72, 379-392.

Stoffyn-Egli, P.; Potter, T.M.; Leonard, J.D.; Pocklington, R. The identification of black carbon particles with the analytical scanning electron microscope: methods and initial results. *Sci. Total Environ.* ***1997***, 198, 211-223.

Stohr, J. *NEXAFS Spectroscopy.* ***1992***, pp. 1-403, Springer-Verlag.

Stokes, J.D.; Paton, G.I.; Semple, K.T. Behaviour and assessment of bioavailability of organic contaminants in soil: relevance for risk assessment and remediation. *Soil Use Manage.* ***2006***, 21, 475-486.

Stolzenbach, K.D.; Adams, E.E. (Eds.). *Contaminated Sediments in Boston Harbor.* ***1998***, pp. 1-170, MIT Sea Grant College Program: Cambridge.

Stone, M.; Krishnappan, B.G. Floc morphology and size distribution of cohesive sediment in steady-state flow. *Wat. Res.* ***2003***, 37, 2739-2747.

Stone, M.; Krishnappan, B.G.; Emelko, M.B. The effect of bed age and shear stress on the particle morphology of eroded cohesive river sediment in an annular flume. *Wat. Res.* ***2008***, 42, 4179-4187.

Storey, J.M.E.; Pankow, J.F. Gas-particle partitioning of semi-volatile organic compounds to model atmospheric particulate materials – I. Sorption to graphite, sodium chloride, alumina, and silica particles under low humidity conditions. *Atmos. Environ.* ***1992***, 26A, 435-443.

Strikwerda, J.C. *Finite Difference Schemes and Partial Differential Equations.* ***1989***, pp. 1-386, Wadsworth & Brooks/Cole Mathematics Series.

Stumm, W.; Morgan, J.J. *Aquatic Chemistry: Chemical Equilibria and Rates in Natural Waters.* ***1996***, pp. 1-1022, Wiley.

Sun, H.; Zhou, Z. Impacts of charcoal characteristics on sorption of polycyclic aromatic hydrocarbons. *Chemosphere* ***2008***, 71, 2113-2120.

Suzuki, M.; Fujii, T. Concentration dependence of surface diffusion coefficient of propionic acid in activated carbon particles. *AIChE J.* ***1982***, 28, 380-385.

Swartz, C.H.; Ulery, A.L.; Gschwend, P.M. An AEM-TEM study of nanometer-scale mineral associations in an aquifer sand: Implications for colloid mobilization. *Geochim. Cosmo. Acta* ***1997***, 61, 707-718.

Swartz, R.C. Consensus sediment quality guidelines for PAH mixtures. *Environ. Toxicol. Chem.* ***1999***, 18, 780-787.

T

Tabak, H.H.; Lazorchak, J.M.; Lei, L.; Khodadoust, A.P.; Antia, J.E.; Bagchi, R.; Suidan, M.T. Studies on bioremediation of polycyclic aromatic hydrocarbon-contaminated sediments: bioavailability, biodegradability, and toxicity issues. *Environ. Toxicol. Chem.* ***2003***, 22, 473-482.

Taghon, G.L.; Nowell, A.R.M.; Jumars, P.A. Transport and breakdown of fecal pellets – biological and sedimentological consequences. *Limnol. Oceanogr.* ***1984***, 29, 64-72.

Talley, J.W.; Ghosh, U.; Tucker, S.G.; Furey, J.S.; Luthy, R.G. Particle-scale understanding of the bioavailability of PAHs in sediment. *Environ. Sci. Technol.* ***2002***, 36, 477-483.

Tana, J.J. Sublethal effects of chlorinated phenols and resin acids on rainbow-trout (salmo-gairdneri). *Wat. Sci. Technol.* ***1988***, 20, 77-85.

Tao, S.; Xu, F.; Liu, W.; Cui, Y.; Coveney, R.M. A chemical extraction method for mimicking bioavailability of polycyclic aromatic hydrocarbons to wheat grown in soils containing various amounts of organic matter. *Environ. Sci. Technol.* ***2006***, 40, 2219-2224.

Tao, Y.Q.; Zhang, S.Z.; Wang, Z.J.; Ke, R.H.; Shan, X.Q.; Christie, P. Biomimetic accumulation of PAHs from soils by triolein-embedded cellulose acetate membranes (TECAMs) to estimate their bioavailability. *Wat. Res.* ***2008***, 42, 754-762.

Tawara, H.; Harrison, K.G.; de Heer, F.J. X-ray emission cross sections and fluorescence yields for light atoms and molecules by electron impact. *Physica* ***1973***, 63, 351-367.

Teng, H.; Ho, J.-A.; Hsu, Y.-F.; Hsieh, C.-T. Preparation of activated carbons from bituminous coals with CO_2 activation. 1. Effects of oxygen content in raw coals. *Ind. Eng. Chem. Res.* ***1996***, 35, 4043-4049.

Teng, Y.; Morrison, M.E.; Munk, P.; Webber, S.E. Release kinetics studies of aromatic molecules into water from block polymer micelles. *Macromolecules* ***1998***, 31, 3578-3587.

Terashima, M.; Tanaka, S.; Fukushima, M. Distribution behavior of pyrene to adsorbed humic acids on Kaolin. *J. Environ. Qual.* ***2003***, 32, 591-598.

Thibodeaux, L.J.; Bierman, V.J. The bioturbation driven chemical release process. *Environ. Sci. Technol.* ***2003***, 37, 252A-258A.

Thibodeaux, L.J.; Valsaraj, K.T.; Reible, D.D. Bioturbation-driven transport of hydrophobic organic contaminants from bed sediment. *Environ. Eng. Sci.* ***2001***, 18, 215-223.

Tipping, E. The adsorption of aquatic humic substances by iron oxides. *Geochim. Cosmochim. Acta,* ***1981***, 45, 191-199.

Tracey, G.A. and Hansen D.J. Use of biota-sediment accumulation factors to assess similarity of nonionic organic chemical exposure to benthically-coupled organisms of differing trophic mode. *Arch. Env. Contam. Toxicol.* ***1996***, 30, 467-475.

Travis, E.R.; Bruce, N.C.; Rosser, S.J. Microbial and plant ecology of a long-term TNT-contaminated site. *Environ. Pollut.* ***2008***, 153, 119-126.

Tremblay, L.; Kohl, S.D.; Rice, J.A.; Gagne, J.P. Effects of temperature, salinity, and dissolved humic substances on the sorption of polycyclic aromatic hydrocarbons to estuarine particles. *Mar. Chem.* ***2005***, 96, 21-34.

Trickovic, J.; Ivancev-Tumbas, I.; Dalmacija, B.; Nikolic, A.; Trifunovic, S. Pentachlorobenzene sorption onto sediment organic matter. *Org. Geochem.* ***2007***, 38, 1757-1769.

Turner, R.; Roberts, N.; Jones, M.D. Climatic pacing of Mediterranean fire histories from lake sedimentary microcharcoal. *Global Planet. Change* ***2008***, 63, 317-324.

U

United Nations, Department of Economic and Social Affairs, *Population Division: World Urbanization Prospects, the 2009 Revision.* ***2010***, New York.

U.S. Department of Agriculture, Natural Resources Conservation Service. *National Soil Survey Handbook.* ***2007***, Title 430-VI, http://soils.usda.gov/technical/handbook/

U.S. EPA. *Charles River Sediment/Water Quality Analysis Project Report.* U.S. EPA Region I, New England, Jan ***1997***, pp 1-45.

U.S. EPA. *EPA's contaminated sediment management strategy.* U.S. EPA Office of Water, ***1998***.

U.S. EPA. *Procedures for the derivation of equilibrium partitioning sediment benchmarks (ESBs) for the protection of benthic organisms: PAH mixtures.* U.S. EPA Office of Water, ***2003***.

Ussiri, D.A.; Johnson, C.E. Effects of clear-cutting on structure and chemistry of soil humic substances of the Hubbard Brook Experimental Forest, New Hamshire, USA. In *Humic Substances – Structures, Models and Functions*, (eds. Ghabbour, E.A.; Davies, G.), pp 281-296, Royal Society of Chemistry, Cambridge, ***2001***.

V

Valderrama, C.; Gamisans, X.; de las Heras, X.; Farran, A.; Cortina, J.L. Sorption kinetics of polycyclic aromatic hydrocarbons removal using granular activated carbon: intraparticle diffusion coefficients. *J. Hazard. Mater.* ***2008***, 157, 386-396.

Varlot, K.; Martin, J.M. Optimization of ELNES processing using a four-parameter function: application to SiC fibers. *Surf. Interface Anal.* ***1999***, 27, 29-34.

Vassallo, A.M.; Wilson, M.A.; Collin, P.J.; Oades, J.M.; Waters, A.G.; Malcolm, R.L. Structural analysis of geochemical samples by solid-state nuclear magnetic resonance spectrometry. Role of paramagnetic materials. *Anal. Chem.* ***1987***, 59, 558-562.

Vandenbroucke, M.; Largeau, C. Kerogen origin, evolution and structure. *Org. Geochem.* ***2007***, 38, 719-833.

Verdin, A.; Sahraoui, A.L.H.; Newsam, R.; Robinson, G.; Durand, R. Polycyclic aromatic hydrocarbons storage by *Fusarium solani* in intracellular lipid vesicles. *Environ. Pollut.* ***2005***, 133, 283-291.

Viguri, J.; Verde, J.; Irabien, A. Environmental assessment of polycyclic aromatic hydrocarbons (PAHs) in surface sediments of the Santander Bay, northern Spain. *Chemosphere* ***2002***, 48, 157-165.

Vilanova, R.M.; Fernandez, P.; Martinez, C.; Grimalt, J.O. Polycyclic aromatic hydrocarbons in remote mountain lake waters. *Wat. Res.* ***2001***, 35, 3916-3926.

Vinturella, A.E.; Burgess, R.M.; Coull, B.A.; Thompson, K.M.; Shine, J.P. Use of passive samples to mimic uptake of polycyclic aromatic hydrocarbons by benthic polychaetes. *Environ. Sci. Technol.* ***2004***, 38, 1154-1160.

Vorres, K. The Argonne Premium Coal Sample Program. *Energy Fuels,* ***1990***, 4, 420-426.

W

Wakeham, S.G. Aliphatic and polycyclic aromatic hydrocarbons in Black Sea sediments. *Mar. Chem.* ***1996***, 53, 187-205.

Walaszek, W.; Ay, P. Porosity and interior structure analysis of pellet-flocs. *Colloids Surf. A* ***2006***, 280, 155-162.

Walker, J.D.; Stocks, B.J. Thermocouple errors in forest fire research. *Fire Technol.* ***1968***, 4, 59-62.

Walker, P.L.; Kini, K.A. Measurement of ultrafine surface area of coals. *Fuel* ***1965***, 44, 453-459.

Walters, R.W.; Luthy, R.G. Equilibrium adsorption of polycyclic aromatic hydrocarbons from water onto activated carbon. *Environ. Sci. Technol.* ***1984***, 18, 395-403.

Wan, J.; Tyliszczak, T.; Tokunaga, T.K. Organic carbon distribution, speciation, and elemental correlations within soil microaggregates: Applications of STXM and NEXAFS spectroscopy. *Geochim. Cosmochim. Acta* ***2007***, 71, 5439-5449.

Wang, B.; Lee, S.C.; Ho, K.F.; Kang, Y.M. Characteristics of emissions of air pollutants from burning of incense in temples, Hong Kong. *Sci. Tot. Environ.* ***2007***, 377, 52-60.

Wang, G.; Kleineidam, S.; Grathwohl, P. Sorption/desorption reversibility of phenanthrene in soils and carbonaceous materials. *Environ. Sci. Technol.* ***2007***, 41, 1186-1193.

Wang, X.; Sato, T.; Xing, B. Sorption and displacement of pyrene in soils and sediments. *Environ. Sci .Technol.* ***2005***, 39, 8712-8718.

Wang, X.; Xing, B. Importance of structural makeup of biopolymers for organic contaminant sorption. *Environ. Sci. Technol.* ***2007***, 41, 3559-3565.

Wang, X.C.; Zhang, Y.X.; Chen, R.F. Distribution and partitioning of polycyclic aromatic hydrocarbons (PAHs) in different size fractions in sediments from Boston Harbor, United States. *Mar. Pollut. Bull.* ***2001***, 11, 1139-1149.

Watson, J.G.; Chow, J.C.; Chen, L.W.A. Summary of organic and elemental carbon/black carbon analysis methods and intercomparisons. *Aerosol Air Qual. Res.* ***2005***, 5, 65-102.

Watteau, F.; Villemin, G.; Mansot, J.L.; Ghanbaja, J.; Toutain, F. Localization and characterization by electron energy loss spectroscopy (EELS) of the brown cellular substances of beech roots. *Soil. Biol. Biochem.* ***1996***, 28, 1327-1332.

Watteau, F.; Villemin, G. Ultrastructural study of the biogeochemical cycle of silicon in the soil and litter of a temperate forest. *Euro. J. Soil Sci.* ***2001***, 52, 385-396.

Weakly, H.E.; McCalla, T.M.; Haskins, F.A. Size distribution of soil aggregates as influenced by microorganisms. *Agronomy Faculty Publications*, University of Nebraska, ***1967***, 75-77

Weber, W.J.; Miller, C.T. Modeling the sorption of hydrophobic contaminants by aquifer materials – I. rates and equilibria. *Wat. Res.* ***1988***, 22, 457-464.

Weber, W.J.; Kim, S.H.; Johnson, M.D. Distributed reactivity model for sorption by soils and sediments. 15. High-concentration co-contaminant effects on phenanthrene sorption and desorption. *Environ. Sci. Technol.* ***2002***, 36, 3625-3634.

Wells, M.; Wick, L. Y.; Harms, H. Model polymer release system study of PAH bioaccessibility: the relationship between "rapid" release and bioaccessibility. *Environ. Sci. Technol.* ***2005***, 39, 1055-1063.

Wells, M.; Wick, L.Y.; Harms, H. Perspectives on modeling the release of hydrophobic organic contaminants drawn from model polymer release systems. *J. Mater. Chem.* ***2004***, 14, 2461-2472.

Welp, T.; Hayes, D.; Tubman, M.; McDowell, S.; Fredette, T.; Clausner, J.; Albro, C. *Dredge Bucket Comparison Demonstration at Boston Harbor. Report ERDC/CHL CHETN-VI-35, Mar.* ***2001***, pp. 1-13 , US Amry Corps of Engineers.

Wen, B.; Zhang, J.J.; Zhang, S.Z.; Shan, X.Q.; Khan, S.U.; Xing, B. Phenanthrene sorption to soil humic acid and different humin fractions. *Environ. Sci. Technol.* ***2007***, 41, 3165-3171.

Werth, C.J.; Reinhard, M. Effects of temperature on trichloroethylene desorption from silica gel and natural sediments. 2. Kinetics. *Environ. Sci. Technol.* ***1997***, 31, 697-703.

Wery, J.; Mansot, J.L. Quantitative study of irradiation damage in organo-metallic colloidal particles. *Microsc. Microanal. Microstruct.* ***1993***, 4, 87-100.

Wetzel, R.G. *Limnology — lake and river ecosystems.* ***2001***, pp. 1-1006, Academic press.

Wheat, P.E.; Tumeo, M.A. Ultrasound induced aqueous polycyclic aromatic hydrocarbon reactivity. *Ultrason. Sonochem.* ***1997***, 4, 55-59.

Whelan, R.J. *The Ecology of Fire.* ***1995***, pp. 1-343, Cambridge University Press.

White, J.C.; Alexander, M. Reduced biodegradability of desorption-resistant fractions of polycyclic aromatic hydrocarbons in soil and aquifer solids. *Environ. Toxicol. Chem.* ***1996***, 15, 1973-1978.

White, J.C.; Hunter, M.; Nam, K.P.; Pignatello, J.J.; Alexander, M. Correlation between biological and physical availabilities of phenanthrene in soils and soil humin in aging experiments. *Environ. Toxicol. Chem.* ***1999***, 18, 1720-1727.

White, J.C.; Hunter, M.; Pignatello, J.J.; Alexander, M. Increase in bioavailability of aged phenanthrene in soils by competitive displacement with pyrene. *Environ. Toxicol. Chem.* ***1999***, 18, 1728-1732.

White, K.L. An overview of immunotoxicology and carcinogenic polycyclic aromatic hydrocarbons. *J. Env. Sci. Health – Part C, Env. Carcin. Rev.* ***1986***, 4, 163-202.

Whitehouse, B.G. The effects of temperature and salinity on the aqueous solubility of polynuclear aromatic hydrocarbons. *Mar. Chem.* ***1984***, 14, 319-332.

Whitehouse, B. The effects of dissolved organic matter on the aqueous partitioning of polynuclear aromatic hydrocarbons. *Estuarine Coastal Shelf Sci.* ***1985***, 20, 393-402.

Wiberg, P.L.; Drake, D.E.; Harris, C.K. Noble, M. Sediment transport on the Palos Verdes shelf over seasonal to decadal time scales. *Cont. Shelf. Res.* ***2002a***, 22, 987-1004.

Wiberg, P.L.; Harris, C.K. Desorption of p,p'-DDE from sediment during resuspension events on the Palos Verdes shelf, California: a modeling approach. *Cont. Shelf Res.* ***2002b***, 22, 1005-1023.

Wicke, D.; Bockelmann, U.; Reemtsma, T. Environmental influences on the partitioning and diffusion of hydrophobic organic contaminants in microbial biofilms. *Environ. Sci. Technol.* ***2008***, 42, 1990-1996.

Wilson, M.A.; Vassallo, A.M.; Perdue, E.M.; Reuter, J.H. Compositional and solid-state nuclear magnetic resonance study of humic and fulvic acid fractions of soil organic matter. *Anal. Chem.* ***1987***, 59, 551-558.

Witt, G. Polycyclic aromatic hydrocarbons in water and sediment of the Baltic Sea. *Mar. Pollut. Bull.* ***1995***, 31, 237-248.

Wolbach, W.S.; Anders, E. Elemental carbon in sediments – determination and isotopic analysis in the presence of kerogen. *Geochim. Cosmochim. Acta* ***1989***, 53, 1637-1647.

Wolbach, W.S.; Gilmour, I.; Anders, E>; Orth, C.J.; Brooks, R.R. Global fire at the Cretaceous tertiary boundary. *Nature* ***1988***, 334, 665-669

Wolff, G.T.; Countess, R.J.; Groblicki, P.J.; Ferman, M.A.; Cadle, S.H.; Muhlbaier, J. Visibility-reducing species in the Denver 'Brown Cloud'—II. Sources and temporal patterns. *Atmos. Environ.* ***1981***, 15, 2485-2502.

Woodhead, R.J.; Law, R.J.; Matthiessen, P. Polycyclic aromatic hydrocarbons in surface sediments around England and Wales, and their possible biological significance. *Mar. Pollut. Bull.* ***1999***, 38, 773-790.

Worringen, A.; Ebert, M.; Trautmann, T.; Weinbruch, S.; Helas, G. Optical properties of internally mixed ammonium sulfate and soot particles-a study of individual aerosol particles and ambient aerosol populations. *Appl. Optics* ***2008***, 47, 3835-3845.

Wotton, R.S.; Malmqvist, B.; Muotka, T.; Larsson, K. Fecal pellets from a dense aggregation of suspension-feeders in a stream: an example of ecosystem engineering. *Limnol. Oceanogr.* ***1998***, 43, 719-725.

Wotton, R.S.; Warren, L.L. Impacts of suspension feeders on the modification and transport of stream seston. *Arch. Hydrobiol.* ***2007***, 169, 231-236.

Wroblewski, J.; Wroblewski, R.; Mory, C.; Colliex, C. Elemental analysis and fine structure of mitochondrial granules in growth plate chondrocytes studied by electron energy loss spectroscopy and energy dispersive x-ray microanalysis. *Scanning Microsc.* ***1991***, 5, 885-894.

Wu, S.C.; Gschwend, P.M. Sorption kinetics of hydrophobic organic-compounds to natural sediments and soils. *Environ. Sci. Technol.* ***1986***, 20, 717-725.

Wu, S.C.; Gschwend, P.M. Numerical modeling of sorption kinetics of organic compounds to soil and sediment particles. *Wat. Resour. Res.* ***1988***, 24, 1373-1383.

X

Xia, G; Ball, W.P. Adsorption-partitioning uptake of nine low-polarity organic chemicals on a natural sorbent. *Environ. Sci. Technol.* ***1999***, 33, 262-269.

Xia, G.; Ball, W.P. Polanyi-based models for the competitive sorption of low-polarity organic contaminants on a natural sorbent. *Environ. Sci. Technol.* ***2000***, 34, 1246-1253.

Xia, G.; Pignatello, J.J. Detailed sorption isotherms of polar and apolar compounds in a high-organic soil. *Environ. Sci. Technol.* ***2001***, 35, 84-94.

Xia, X.H.; Yu, H.; Yang, Z.F.; Huang, G.H. Biodegradation of polycyclic aromatic hydrocarbons in the natural waters of the Yellow River: Effects of high sediment content on biodegradation. *Chemosphere* ***2006***, 65, 457-466.

Xiao, B.; Yu, Z.; Huang, W. Song, J.; Peng, P. Black carbon and kerogen in soils and sediments. 2. Their roles in equilibrium sorption of less-polar organic pollutants. *Environ. Sci. Technol.* ***2004***, 38, 5842-5852.

Xing, B.; Pignatello, J.J. Time-dependent isotherm shape of organic compounds in soil organic matter: implications for sorption mechanism. *Environ. Toxicol. Chem.* ***1996a***, 15, 1282-1288.

Xing, B.; Pignatello, J.J.; Gigliotti, B. Competitive sorption between atrazine and other organic compounds in soils and model sorbents. *Environ. Sci. Technol.* ***1996b***, 30, 2432-2440.

Xing, B.; Pignatello, J.J. Dual-model sorption of low-polarity compounds in glassy poly(vinyl chloride) and soil organic matter. *Environ. Sci. Technol.* ***1997***, 31, 792-799.

Y

Yamashita, N.; Kannan, K.; Imagawa, T.; Villeneuve, D.L.; Hashimoto, S.; Miyazaki, A.; Giesy, J.P. Vertical profile of polychlorinated dibenzo-p-dioxins, dibenzofurans, naphthalenes, biphenyles, polycyclic aromatic hydrocarbons, and alkylphenols in a sediment core from Tokyo Bay, Japan. *Environ. Sci. Technol.* ***2000***, 34, 3560-3567.

Yang, W.C.; Duan, L.; Zhang, N.; Zhang, C.D.; Shipley, H.J.; Kan, A.T.; Tomson, M.B.; Chen, W. Resistant desorption of hydrophobic organic contaminants in typical Chinese soils: Implications for long-term fate and soil quality standards. *Environ. Toxicol. Chem.* ***2008***, 27, 235-242.

Yang, Y.; Sheng, G. Enhanced pesticide sorption by soils containing particulate matter from crop residue burns. *Environ. Sci. Technol.* ***2003***, 37, 3635-3639.

Yapp, C.J.; Poths, H. Carbon in natural goethites. *Geochim. Cosmochim. Acta* ***1986***, 50, 1213-1220.

Ying, L.; Ling, C.; Zhao, J.; Huang, Q.; Zhu, Z.; Gao, H. Distribution and sources of polycyclic aromatic hydrocarbons in surface sediments of rivers and an estuary in Shanghai, China. *Environ. Pollut.* ***2008***, 154, 298-305.

Yoon, T.H.; Benzerara, K.; Ahn, S.; Luthy, R.G.; Tyliszczak, T.; Brown, G.E. Nanometer-scale chemical heterogeneities of black carbon materials and their impacts on PCB sorption properties: soft X-ray spectromicroscopy study. *Environ. Sci. Technol.* ***2006***, 40, 5923-5929.

Young, T.M.; Weber, W.J. A distributed reactivity model for sorption by soils and sediments. 3. Effects of diagenetic processes on sorption energetics. *Environ. Sci. Technol.* ***1995***, 29, 92-97.

Young, D.F. and Ball, W.P. Two-region linear/nonlinear sorption modeling: batch and column experiments. *Environ. Toxicol. Chem.* ***1999***, 18, 1686-1693.

Yu, B.; Dong, H.; Jiang, H.; Guo, L.V.; Eberl, D.; Li, S.; Kim, J. The role of clay minerals in the preservation of organic matter in sediments of Qinghai Lake, NW China. *Clays Clay Minerals* ***2009***, 57, 213-226.

Yu, Z.Q.; Sharma, S.; Huang, W.L. Differential roles of humic acid and particulate organic matter in the equilibrium sorption of atrazine by soils. *Environ. Toxicol. Chem.* ***2006***, 25, 1975-1983.

Yuan, Y.; Wei, H.; Zhao, L.; Jiang, W. Observatios of sediment resuspension and settling off the mouth of Jiaozhou Bay, Yellow Sea. *Continental Shelf Res.* ***2008***, 28, 2630-2643.

Yue, Z.; Economy, J. Synthesis of highly mesoporous carbon pellets from carbon black and polymer binder by chemical activation. *Microporous Mesoporous Mater.* ***2006***, 96, 314-320.

Z

Zabawa, C.F. Microstructure of agglomerated suspended sediments in northern Chesapeake Bay Estuary. *Science* ***1978***, 202, 49-51.

Zajac, G.W.; Gallas, J.M.;Cheng, J.; Eisner, M.; Moss, S.C.; Alvarado-Swaisgood, A.E. The fundamental unit of synthetic melanin: a verification by tunneling microscopy X-ray scattering results. *Biochim. Biophys. Acta* ***1994***, 1199, 271-278.

Zaluzec, N.J. Quantitative x-ray microanalysis: instrumental considerations and applications to material science. In *Introduction to Analytical Electron Microscopy*, (eds. Hren, J.J.; Goldstein, J.I.; Joy, D.C.), pp 121-167., Plenum, New York, ***1979***.

Zeledon-Toruno, Z.C.; Lao-Luque, C.; de las Heras, F.X.C.; Sole-Sardans, M. Removal of PAHs from water using an immature coal (leonardite). *Chemosphere* ***2007***, 67, 505-512.

Zeng, Y.; Wu, C. Raman and infrared spectroscopic study of kerogen treated at elevated temperatures and pressures. *Fuel* ***2007***, 86, 1192-1200.

Zern, A.; Mayer, J.; Janakiraman, N.; Weinmann, M.; Bill, J.; Ruhle, M. Quantitative EFTEM study of precursor-derived Si-B-C-N ceramics. *J. Euro. Ceram. Soc.* ***2002***, 22, 1621-1629.

Zhao, D.; Pignatello, J.J.; White, J.C.; Braida, W. Dual-mode modeling of competitive and concentration-dependent sorption and desorption kinetics of polycyclic aromatic hydrocarbons in soils. *Wat. Resour. Res.* ***2001***, 37, 2205-2212.

Zhou, J.L.; Fileman, T.W.; Evans, S.; Donkin, P.; Fauzi, R.; Mantoura, C.; Rowland, S.J. Seasonal distribution of dissolved pesticides and polynuclear aromatic hydrocarbons in the Humber Estuary and Humber Coastal Zone. *Mar. Pollut. Bull.* ***1996***, 32, 599-608.

Zhu, L.; Chen, B.; Wang, J.; Shen, H. Pollution survey of polycyclic aromatic hydrocarbons in surface water of Hangzhou, China. *Chemosphere,* ***2004***, 56, 1085-1095.

Zielinska, B.; Sagebiel, J.; Arnott, W.P.; Rogers, C.F.; Kelly, K.E.; Wagner, D.A.; Lighty, J.S.; Sarofim, A.F.; Palmer, G. Phase and Size Distribution of Polycyclic Aromatic Hydrocarbons in Diesel and Gasoline Vehicle Emissions. *Environ. Sci. Technol.* ***2004***, 38, 2557-2567.

Zierold, K.; Michel, J.; Terryn, C.; Balossier, G. The distribution of light elements in biological cells measured by electron probe X-ray microanalysis of cryosections. *Microsc. Microanal.* ***2005***, 11, 138-145.

Zimmerman, A.R.; Chorover, J.; Goyne, K.W.; Brantley, S.L. Protection of mesopore-adsorbed organic matter from enzymatic degradation. *Environ. Sci. Technol.* ***2004a***, 38, 4542-4548.

Zimmerman, A.R.; Goyne, K.W.; Chorover, J.; Komarneni, S.; Brantley, S.L. Mineral mesopore effects on nitrogenous organic matter adsorption. *Org. Geochem.* ***2004b***, 35, 355-375.

Zoller, W.H.; Gordon, G.E.; Gladney, E.S.; Jones, A.G. In 'Traces elements in the environment.', pp.31-47, Advances in Chemistry Ser. No. 123, ACS, Washington, D.C., 1973.